

Dekker Encyclopedia of Nanoscience and Nanotechnology

Volume 3

Met-Nano

Pages 1797–2676

edited by

James A. Schwarz

Syracuse University, Syracuse, New York, U.S.A.

Cristian I. Contescu

Material Methods LLC, Newport Beach, California, U.S.A.

Karol Putyera

Shiva Technologies, Syracuse, New York, U.S.A.



MARCEL DEKKER, INC.

NEW YORK • BASEL

Volume 1:

Main image: Courtesy of Tommaso Baldacchini and John T. Fourkas.

Detail: Courtesy of Kay Severin.

Volume 2:

Main image: Courtesy of Hamidou Haidara.

Detail: Courtesy of Jean-Yves Raty.

Volume 3:

Main image: Courtesy of Tony Van Buuren and Jürgen M. Plitzko.

Detail: Courtesy of Kay Severin.

Volume 4:

Main image: Courtesy of A. I. Gusev and colleagues.

Detail: Courtesy of Jean-Yves Raty.

Volume 5:

Main image: Courtesy of Ioan Balint.

Detail: Courtesy of Lars-Oliver Essen.

ISBN: Print: 0-8247-5055-1

ISBN: Online: 0-8247-5046-2

ISBN: Combo: 0-8247-4797-6

ISBN: Volume 1: 0-8247-5047-0

ISBN: Volume 2: 0-8247-5048-9

ISBN: Volume 3: 0-8247-5049-7

ISBN: Volume 4: 0-8247-5050-0

ISBN: Volume 5: 0-8247-5051-9

Library of Congress Cataloging-in-Publication Data

A catalog record of this book is available from the Library of Congress.

This book is printed on acid-free paper.

Headquarters

Marcel Dekker, Inc.

270 Madison Avenue, New York, NY 10016

tel: 212-696-9000; fax: 212-685-4540

Eastern Hemisphere Distribution

Marcel Dekker AG

Hutgasse 4, Postfach 812, CH-4001 Basel, Switzerland

tel: 41-61-260-6300; fax: 41-61-260-6333

World Wide Web

<http://www.dekker.com>

The publisher offers discounts on this book when ordered in bulk quantities. For more information, write to Special Sales/ Professional Marketing at the headquarters address above.

Copyright © 2004 by Marcel Dekker, Inc. (except as noted on the opening page of each article.) All Rights Reserved.

Neither this book nor any part may be reproduced or transmitted in any form or by any means, electronic or mechanical, including photocopying, microfilming, and recording, or by any information storage and retrieval system, without permission in writing from the publisher.

Current printing (last digit):

10 9 8 7 6 5 4 3 2 1

PRINTED IN THE UNITED STATES OF AMERICA

James A. Schwarz

Syracuse University, Syracuse, New York, U.S.A.

Cristian I. Contescu

Material Methods LLC, Newport Beach, California, U.S.A.

Karol Putyera

Shiva Technologies, Syracuse, New York, U.S.A.

Editorial Advisory Board

Frank Armatís

*Advanced Materials Technology Center,
3M Corporation, St. Paul, Minnesota, U.S.A.*

R. Terry K. Baker

*Catalytic Materials Ltd., Holliston, Massachusetts,
U.S.A.*

Robert Birge

*Department of Chemistry, University of Connecticut,
Storrs, Connecticut, U.S.A.*

Vijoleta Braach-Maksvytis

*CSIRO Executive Management Council, Australian
Government, Lindfield, New South Wales, Australia*

Gianfranco Cerofolini

ST Microelectronics, Milan, Italy

Stephen Y. Chou

*Department of Electrical Engineering, Princeton
University, Princeton, New Jersey, U.S.A.*

Morinobu Endo

*Department of Engineering, Shinshu University,
Nagano, Japan*

Toshiaki Enoki

*Department of Chemistry, Tokyo Institute of
Technology, Tokyo, Japan*

Gerhard Ertl

*Department of Physical Chemistry, Fritz Haber
Institute of the Max Planck Society, Berlin, Germany*

Robert Glass

*Lawrence Livermore National Laboratory,
Livermore, California, U.S.A.*

D. Wayne Goodman

*Department of Chemistry, Texas A&M University,
College Station, Texas, U.S.A.*

Elias Greenbaum

*Chemical Sciences Division, Oak Ridge National
Laboratory, Oak Ridge, Tennessee, U.S.A.*

Hans-Joachim Güntherodt

*Institut für Physik der Universität Basel,
Basel, Switzerland*

Norbert Hampp

*Department of Chemistry, Philipps University,
Marburg, Germany*

Tim Harper

CMP-Cientifica S.L., Madrid, Spain

Arthur Hubbard

*Santa Barbara Science Project, Santa Barbara,
California, U.S.A.*

Enrique Iglesia

*Department of Chemical Engineering, University of
California, Berkeley, California, U.S.A.*

Mietek Jaroniec

*Department of Chemistry, Kent State University,
Kent, Ohio, U.S.A.*

Andy Kaldor

*ExxonMobil Research and Engineering, Annandale,
New Jersey, U.S.A.*

Jürgen Kirschner

*Max-Planck-Institut für Mikrostrukturphysik,
Halle, Germany*

Laszlo B. Kish

*Department of Electrical Engineering,
Texas A&M University, College Station, Texas,
U.S.A.*

Kenneth Klabunde

*Department of Chemistry, Kansas State University,
Manhattan, Kansas, U.S.A.*

James Leckie

*Department of Civil and Environmental
Engineering, School of Engineering,
Stanford University, Stanford, California,
U.S.A.*

Charles M. Lieber

*Department of Chemistry and Chemical Biology,
Harvard University, Cambridge, Massachusetts,
U.S.A.*

Chad Mirkin

*Department of Chemistry, Northwestern University,
Evanston, Illinois, U.S.A.*

Shuming Nie

*Department of Chemistry, Indiana University,
Bloomington, Indiana, U.S.A.*

Jens K. Norskov

*Department of Physics, Technical University of
Denmark, Lyngby, Denmark*

Mark Reed

*Department of Electrical Engineering and Applied
Physics, Yale University, New Haven, Connecticut,
U.S.A.*

David C. Rees

Astex Technology Ltd., Cambridge, U.K.

Stacey L. Ristinmaa-Sörensen

*Department of Physics, University of Lund,
Lund, Sweden*

John A. Rogers

*Bell Laboratories, Lucent Technologies,
Murray Hill, New Jersey, U.S.A.*

Debra R. Rolinson

*Advanced Electrochemical Materials,
Naval Research Laboratory, Washington,
District of Columbia, U.S.A.*

Jurgen Ruhe

*Institute for Microsystem Technology, Albert-Ludwig
University, Frieberg, Germany*

Purnesh Seegopaul,

Umicore USA Inc., Hillsborough, New Jersey, U.S.A.

Stu Soled

*ExxonMobil Research and Engineering, Annandale,
New Jersey, U.S.A.*

Stephan J. Stranick

*National Institute of Standards and Technology
(NIST), Gaithersburg, Maryland, U.S.A.*

Arthur ten Wolde

*Confederation of Netherlands Industry and
Employers VNO-NCW, The Hague, The Netherlands*

Frederick Tepper

Argonide Corp., Sanford, Florida, U.S.A.

Gary Tompa

*Structured Materials Industries, Inc., Piscataway,
New Jersey, U.S.A.*

Robert Trew

*Bradley Department of Electrical and Computer
Engineering, Virginia Technical Institute,
Blacksburg, Virginia, U.S.A.*

Etienne F. Vansant

*Department of Chemistry, University of Antwerp
(UIA), Wilrijk, Belgium*

Younan Xia

*Department of Chemistry, University of Washington,
Seattle, Washington, U.S.A.*

Peidong Yang

*Department of Chemistry, University of California,
Berkeley, California, U.S.A.*

List of Contributors

- Nehal I. Abu-Lail** / *Worcester Polytechnic Institute, Worcester, Massachusetts, U.S.A.*
- R. Shane Addleman** / *Pacific Northwest National Laboratory, Richland, Washington, U.S.A.*
- Rigoberto C. Advincula** / *University of Alabama at Birmingham, Birmingham, Alabama, U.S.A.* / *University of Houston, Houston, Texas, U.S.A.*
- Sean R. Agnew** / *University of Virginia, Charlottesville, Virginia, U.S.A.*
- Brahim Akdim** / *AFRL/ML, Wright-Patterson Air Force Base, Ohio, U.S.A.*
- Joseph Akkara** / *National Science Foundation, Arlington, Virginia, U.S.A.*
- Tomoyuki Akutagawa** / *Hokkaido University, Sapporo, Japan*
- Markus Albrecht** / *Institut für Organische Chemie, Aachen, Germany*
- A. Paul Alivisatos** / *University of California, Berkeley, California, U.S.A.*
- Charles W. Allen** / *Argonne National Laboratory, Argonne, Illinois, U.S.A.*
- Tsuneya Ando** / *Tokyo Institute of Technology, Tokyo, Japan*
- Ronald P. Andres** / *Purdue University, West Lafayette, Indiana, U.S.A.*
- Mikhail A. Anisimov** / *University of Maryland, College Park, Maryland, U.S.A.*
- Masakazu Aono** / *National Institute for Materials Science, Ibaraki, Japan*
- Hajime Asahi** / *Osaka University, Osaka, Japan*
- K. Asakawa** / *The Femtosecond Technology Research Association (FESTA), Ibaraki, Japan*
- B. J. Ash** / *Sandia National Laboratories, Albuquerque, New Mexico, U.S.A.*
- Masafumi Ata** / *SONY Corporation, Yokohama, Japan*
- Plamen B. Atanasov** / *The University of New Mexico, Albuquerque, New Mexico, U.S.A.*
- Elizabeth K. Auty** / *University of Bristol, Bristol, United Kingdom*
- Eric Ayars** / *California State University—Chico, Chico, California, U.S.A.*
- George Bachand** / *Sandia National Laboratories, Albuquerque, New Mexico, U.S.A.*
- Kannan Balasubramanian** / *Max-Planck-Institut für Festkörperforschung, Stuttgart, Germany*
- Ganesh Balasubramanian** / *University of Cincinnati, Cincinnati, Ohio, U.S.A.*
- Anna C. Balazs** / *University of Pittsburgh, Pittsburgh, Pennsylvania, U.S.A.*
- Tommaso Baldacchini** / *Boston College, Chestnut Hill, Massachusetts, U.S.A.*
- Ioan Balint** / *Romanian Academy, Bucharest, Romania*
- S. Bandyopadhyay** / *Virginia Commonwealth University, Richmond, Virginia, U.S.A.*
- Rajarshi Banerjee** / *The Ohio State University, Columbus, Ohio, U.S.A.*
- Sarbajit Banerjee** / *State University of New York at Stony Brook, Stony Brook, New York, U.S.A.*
- Maria C. Bartelt** / *Lawrence Livermore National Laboratory, Livermore, California, U.S.A.*
- James D. Batteas** / *National Institute of Standards and Technology, Gaithersburg, Maryland, U.S.A.*
- Jan Becher** / *University of Southern Denmark, Odense, Denmark*
- Paul D. Beer** / *University of Oxford, Oxford, United Kingdom*
- Silke Behrens** / *Institute of Technical Chemistry, Karlsruhe, Germany*
- Elena Bekyarova** / *University of California, Riverside, California, U.S.A.*

- G. Benedek** / *Università di Milano Bicocca, Milan, Italy*
- Yaakov Benenson** / *Weizmann Institute of Science, Rehovot, Israel*
- M. Bernasconi** / *Università di Milano Bicocca, Milan, Italy*
- Steven L. Bernasek** / *Princeton University, Princeton, New Jersey, U.S.A.*
- Alexey Bezryadin** / *University of Illinois at Urbana-Champaign, Champaign, Illinois, U.S.A.*
- Ajay Kumar Bhagi** / *University of Delhi, Delhi, India*
- Dhruba Jyoti Bharali** / *State University of New York, Buffalo, New York, U.S.A.*
- T. A. Birks** / *University of Bath, Bath, United Kingdom*
- Jerome C. Birnbaum** / *Pacific Northwest National Laboratory, Richland, Washington, U.S.A.*
- Harvey W. Blanch** / *University of California, Berkeley, California, U.S.A.*
- Alexandre Blumstein** / *University of Massachusetts, Lowell, Massachusetts, U.S.A.*
- Andrew B. Bocarsly** / *Princeton University, Princeton, New Jersey, U.S.A.*
- Michael R. Bockstaller** / *Massachusetts Institute of Technology, Cambridge, Massachusetts, U.S.A.*
- A. Bogicevic** / *Ford Motor Company, Dearborn, Michigan, U.S.A.*
- Anthony Bollinger** / *University of Illinois at Urbana-Champaign, Urbana, Illinois, U.S.A.*
- Olga V. Boltalina** / *M. V. Lomonosov Moscow State University, Moscow, Russia*
- Mila Boncheva** / *Harvard University, Cambridge, Massachusetts, U.S.A.*
- Helmut Bönnemann** / *Max Planck Institut für Kohlenforschung, Mülheim an der Ruhr, Germany*
- Arijit Bose** / *University of Rhode Island, Kingston, Rhode Island, U.S.A.*
- Eduardo J. Bottani** / *Instituto de Investigaciones Fisicoquímicas Teóricas y Aplicadas, (UNLP, CIC, CONICET), La Plata, Argentina*
- Laurent Bouteiller** / *Université Pierre et Marie Curie, Paris, France*
- Charles Brands** / *Virginia Polytechnic Institute and State University, Blacksburg, Virginia, U.S.A.*
- Paul S. Braterman** / *University of North Texas, Denton, Texas, U.S.A.*
- Roberto J. Brea** / *Universidad de Santiago de Compostela, Santiago de Compostela, Spain*
- Lyudmila M. Bronstein** / *Indiana University, Bloomington, Indiana, U.S.A.*
- E. A. Martijn Brouwer** / *University of Twente, Enschede, The Netherlands*
- Ronald C. Brown** / *Mercyhurst College, Erie, Pennsylvania, U.S.A.*
- Nigel D. Browning** / *University of California, Davis, California, U.S.A.*
- Marko Burghard** / *Max-Planck-Institut für Festkörperforschung, Stuttgart, Germany*
- Daryle H. Busch** / *University of Kansas, Lawrence, Kansas, U.S.A.*
- Harshala Butala** / *University of Mississippi, University, Mississippi, U.S.A.*
- Gavin A. Buxton** / *University of Pittsburgh, Pittsburgh, Pennsylvania, U.S.A.*
- Mark E. Byrne** / *Auburn University, Auburn, Alabama, U.S.A.*
- Valérie Cabuil** / *Université Pierre et Marie Curie, Paris, France*
- Tahir Cader** / *Isothermal Systems Research, Clarkston, Washington, U.S.A.*
- Yuguang Cai** / *Princeton University, Princeton, New Jersey, U.S.A.*
- Terri A. Camesano** / *Worcester Polytechnic Institute, Worcester, Massachusetts, U.S.A.*
- Autumn T. Carlsen** / *University at Albany—State University of New York, Albany, New York, U.S.A.*
- Andrew D. W. Carswell** / *University of Oklahoma, Norman, Oklahoma, U.S.A.*
- Alessandro Casnati** / *Università di Parma, Parma, Italy*
- Mehmet S. Celik** / *Istanbul Technical University, Istanbul, Turkey*
- Gianfranco Cerofolini** / *STMicroelectronics, Catania, Italy*
- Neil R. Champness** / *The University of Nottingham, Nottingham, United Kingdom*
- Selena Chan** / *University of Rochester, Rochester, New York, U.S.A.*
- Christophe Chassenieux** / *Université Pierre et Marie Curie, Paris, France*

- James R. Chelikowsky** / *University of Minnesota, Minneapolis, Minnesota, U.S.A.*
- Bin Chen** / *National Aeronautics and Space Administration (NASA), Moffett Field, California, U.S.A.*
- Chenggang Chen** / *University of Dayton Research Institute, Dayton, Ohio, U.S.A.* / *Air Force Research Laboratory, Wright-Patterson Air Force Base, Ohio, U.S.A.*
- Zhan Chen** / *University of Michigan, Ann Arbor, Michigan, U.S.A.*
- Lifeng Chi** / *Westfälische Wilhelms-Universität Münster, Münster, Germany*
- Russell R. Chianelli** / *The University of Texas, El Paso, Texas, U.S.A.*
- Jeong-Min Cho** / *University of Florida, Gainesville, Florida, U.S.A.*
- Kwang-Min Choi** / *Osaka University, Osaka, Japan*
- Thomas Clifford** / *University of Kansas, Lawrence, Kansas, U.S.A.*
- Luise S. Couchman** / *Naval Research Laboratory, Washington, District of Columbia, U.S.A.*
- Christophe Coudret** / *Centre d'Elaboration de Matériaux et d'Etudes Structurales (CEMES), Centre National de la Recherche Scientifique (CNRS), Toulouse, France*
- Alexander Couzis** / *City College of City University of New York, New York, New York, U.S.A.*
- Mercedes Crego-Calama** / *University of Twente, Enschede, The Netherlands*
- B. Roldan Cuenya** / *University of California, Santa Barbara, California, U.S.A.*
- Brian M. Cullum** / *University of Maryland, Baltimore County, Baltimore, Maryland, U.S.A.*
- Peter T. Cummings** / *Vanderbilt University, Nashville, Tennessee, U.S.A.* / *Oak Ridge National Laboratory, Oak Ridge, Tennessee, U.S.A.*
- Joan E. Curry** / *University of Arizona, Tucson, Arizona, U.S.A.*
- Lars Dähne** / *Capsulation Nanoscience AG, Berlin, Germany*
- Sheng Dai** / *Oak Ridge National Laboratory, Oak Ridge, Tennessee, U.S.A.*
- Enrico Dalcanale** / *Università di Parma, Parma, Italy*
- Anthony P. Davis** / *University of Bristol, Bristol, United Kingdom*
- Jason J. Davis** / *University of Oxford, Oxford, United Kingdom*
- Richey M. Davis** / *Virginia Polytechnic Institute and State University, Blacksburg, Virginia, U.S.A.*
- Robert J. Davis** / *University of Virginia, Charlottesville, Virginia, U.S.A.*
- Thomas F. Degnan, Jr.** / *ExxonMobil Research and Engineering Company, Annandale, New Jersey, U.S.A.*
- Thierry Delair** / *École Normale Supérieure de Lyon, Lyon, France*
- Aránzazu del Campo** / *Max Planck Institute for Polymer Research, Mainz, Germany*
- Pedro A. Derosa** / *University of South Carolina, Columbia, South Carolina, U.S.A.*
- Roland Dersch** / *Philipps-Universität Marburg, Marburg, Germany*
- A. Prasanna de Silva** / *School of Chemistry at Queen's University, Belfast, Northern Ireland*
- James J. De Yoreo** / *Lawrence Livermore National Laboratory, Livermore, California, U.S.A.*
- Stephan Diekmann** / *Institut für Molekulare Biotechnologie, Jena, Germany*
- João C. Diniz da Costa** / *The University of Queensland, Brisbane, Queensland, Australia*
- Dionysios D. Dionysiou** / *University of Cincinnati, Cincinnati, Ohio, U.S.A.*
- Mark M. Disko** / *ExxonMobil Research and Engineering, Annandale, New Jersey, U.S.A.*
- Stephen K. Doorn** / *Los Alamos National Laboratory, Los Alamos, New Mexico, U.S.A.*
- Bogdan Dragnea** / *Indiana University, Bloomington, Indiana, U.S.A.*
- Charles Michael Drain** / *Hunter College of the City University of New York, New York, New York, U.S.A.* / *The Rockefeller University, New York, New York, U.S.A.*
- Jaroslav Drelich** / *Michigan Technological University, Houghton, Michigan, U.S.A.*
- G. Dresselhaus** / *Massachusetts Institute of Technology, Cambridge, Massachusetts, U.S.A.*
- Mildred S. Dresselhaus** / *Massachusetts Institute of Technology, Cambridge, Massachusetts, U.S.A.*
- Xiaofeng Duan** / *AFRL/ML, Wright-Patterson Air Force Base, Ohio, U.S.A.*
- Yves F. Dufrêne** / *Université catholique de Louvain, Louvain-la-Neuve, Belgium*

- Etienne Duguet** / *Institut de Chimie de la Matière Condensée de Bordeaux, CNRS, Pessac, France*
- Kathleen A. Dunn** / *University at Albany—State University of New York, Albany, New York, U.S.A.*
- R. D. Dupuis** / *The University of Texas at Austin, Austin, Texas, U.S.A.*
- Anne-Sophie Duwez** / *Université catholique de Louvain, Louvain-la-Neuve, Belgium*
- Kohki Ebitani** / *Osaka University, Osaka, Japan*
- A. Eitan** / *Rensselaer Polytechnic Institute, Troy, New York, U.S.A.*
- Jeremiah Ejiolor** / *Purdue University, West Lafayette, Indiana, U.S.A.*
- Vladimir I. Elokhin** / *Boraskov Institute of Catalysis, Novosibirsk, Russia*
- Todd Emrick** / *University of Massachusetts, Amherst, Massachusetts, U.S.A.*
- Morinobu Endo** / *Shinshu University, Nagano, Japan*
- Jonah Erlebacher** / *Johns Hopkins University, Baltimore, Maryland, U.S.A.*
- Bahri Ersoy** / *Afyon Kocatepe University, Afyon, Turkey*
- Lars-Oliver Essen** / *Philipps University, Marburg, Germany*
- Louise S. Evans** / *University of Southampton, Southampton, United Kingdom*
- Jeffrey D. Evanseck** / *Duquesne University, Pittsburgh, Pennsylvania, U.S.A.*
- Rodney C. Ewing** / *University of Michigan, Ann Arbor, Michigan, U.S.A.*
- D. Howard Fairbrother** / *The Johns Hopkins University, Baltimore, Maryland, U.S.A.*
- Xiaowu Fan** / *University of Alabama at Birmingham, Birmingham, Alabama, U.S.A.*
- Zhigang Fang** / *University of Utah, Salt Lake City, Utah, U.S.A.*
- Philippe M. Fauchet** / *University of Rochester, Rochester, New York, U.S.A.*
- H.-J. Fecht** / *University of Ulm, Ulm, Germany*
- X. Feng** / *Ferro Corporation, Independence, Ohio, U.S.A.*
- Ben L. Feringa** / *University of Groningen, Groningen, The Netherlands*
- Shaun F. Filocamo** / *Boston University, Boston, Massachusetts, U.S.A.*
- Paul D. I. Fletcher** / *University of Hull, Hull, United Kingdom*
- Robert E. Fontana, Jr.** / *IBM Almaden Research Center, San Jose, California, U.S.A.*
- Christy Ford** / *Tulane University, New Orleans, Louisiana, U.S.A.*
- John T. Fourkas** / *Boston College, Chestnut Hill, Massachusetts, U.S.A.*
- Elzbieta Frackowiak** / *Poznan University of Technology, Poznan, Poland*
- Thomas Franklin** / *Massachusetts Institute of Technology, Cambridge, Massachusetts, U.S.A.*
- Hamish L. Fraser** / *The Ohio State University, Columbus, Ohio, U.S.A.*
- Wolfgang Fritzsche** / *Institute for Physical High Technology (IPHT), Jena, Germany*
- Glen E. Fryxell** / *Pacific Northwest National Laboratory, Richland, Washington, U.S.A.*
- Jürgen-Hinrich Fuhrhop** / *Freie Universität Berlin, Berlin, Germany*
- T. A. Fulton** / *Lucent Technologies, Murray Hill, New Jersey, U.S.A.*
- Kunio Furusawa** / *University of Tsukuba, Ibaraki, Japan*
- Charles-André Fustin** / *Max Planck Institute for Polymer Research, Mainz, Germany*
- Aurelian C. Gâlcă** / *University of Twente, Enschede, The Netherlands*
- Philip A. Gale** / *University of Southampton, Southampton, United Kingdom*
- Giulia Galli** / *Lawrence Livermore National Laboratory, Livermore, California, U.S.A.*
- Ignacio L. Garzón** / *Universidad Nacional Autónoma de México, Mexico City, Mexico*
- J. Gaudioso** / *Sandia National Laboratories, Albuquerque, New Mexico, U.S.A.*
- Andrew J. Gellman** / *Carnegie Mellon University, Pittsburgh, Pennsylvania, U.S.A.*
- Bruce C. Gibb** / *University of New Orleans, New Orleans, Louisiana, U.S.A.*
- Jeffrey C. Gibeling** / *University of California, Davis, California, U.S.A.*
- Harry W. Gibson** / *Virginia Polytechnic Institute and State University, Blacksburg, Virginia, U.S.A.*

- David S. Ginley** / *National Renewable Energy Laboratory (NREL), Golden, Colorado, U.S.A.*
- Anit Giri** / *Nanomat, Inc., North Huntingdon, Pennsylvania, U.S.A.*
- Michael Gleiche** / *Westfälische Wilhelms-Universität Münster, Münster, Germany*
- William A. Goddard** / *California Institute of Technology, Pasadena, California, U.S.A.*
- George W. Gokel** / *Washington University School of Medicine, St. Louis, Missouri, U.S.A.*
- Shun-ichi Gonda** / *Fukui University of Technology, Fukui, Japan*
- D. Wayne Goodman** / *Texas A&M University, College Station, Texas, U.S.A.*
- Lionel Goodman** / *Rutgers, The State University of New Jersey, New Brunswick, New Jersey, U.S.A.*
- Brian P. Grady** / *University of Oklahoma, Norman, Oklahoma, U.S.A.*
- Juan R. Granja** / *Universidade de Santiago de Compostela, Santiago de Compostela, Spain*
- Christine S. Grant** / *North Carolina State University, Raleigh, North Carolina, U.S.A.*
- Vicki H. Grassian** / *University of Iowa, Iowa City, Iowa, U.S.A.*
- Jay W. Grate** / *Pacific Northwest National Laboratory, Richland, Washington, U.S.A.*
- Elias Greenbaum** / *Oak Ridge National Laboratory, Oak Ridge, Tennessee, U.S.A.* / *The University of Tennessee, Knoxville, Tennessee, U.S.A.*
- Andreas Greiner** / *Philipps-Universität Marburg, Marburg, Germany*
- Mark W. Grinstaff** / *Boston University, Boston, Massachusetts, U.S.A.*
- Edward Grochowski** / *IBM Almaden Research Center, San Jose, California, U.S.A.*
- Gwen M. Gross** / *University of Washington, Seattle, Washington, U.S.A.*
- Joanna R. Groza** / *University of California, Davis, California, U.S.A.*
- Dirk M. Guldi** / *University of Notre Dame, Notre Dame, Indiana, U.S.A.*
- Jianchang Guo** / *Emory University, Atlanta, Georgia, U.S.A.*
- Vinay K. Gupta** / *University of Illinois at Urbana-Champaign, Urbana, Illinois, U.S.A.*
- Alexandr I. Gusev** / *Russian Academy of Sciences, Yekaterinburg, Russia*
- Matthew Guzy** / *Virginia Polytechnic Institute and State University, Blacksburg, Virginia, U.S.A.*
- Kwon-Soo Ha** / *Kangwon National University School of Medicine, Chunchon, South Korea*
- Robert C. Haddon** / *University of California, Riverside, California, U.S.A.*
- Hamidou Haidara** / *Institut de Chimie des Surfaces et Interfaces-ICSI-CNRS, Mulhouse, France*
- Wolfgang Haiss** / *University of Liverpool, Liverpool, United Kingdom*
- Kimberly Hamad-Schifferli** / *Massachusetts Institute of Technology, Cambridge, Massachusetts, U.S.A.*
- Jingmin Han** / *University of Alberta, Edmonton, Alberta, Canada*
- Encai Hao** / *Northwestern University, Evanston, Illinois, U.S.A.*
- J. W. Harrell** / *The University of Alabama, Tuscaloosa, Alabama, U.S.A.*
- Stephen J. Haswell** / *University of Hull, Hull, United Kingdom*
- Bryan C. Hathorn** / *Oak Ridge National Laboratory, Oak Ridge, Tennessee, U.S.A.*
- Takuya Hayashi** / *Shinshu University, Nagano, Japan*
- Jibao He** / *Tulane University, New Orleans, Louisiana, U.S.A.*
- J. R. Heflin** / *Virginia Polytechnic Institute and State University, Blacksburg, Virginia, U.S.A.*
- James M. Helt** / *College of Staten Island and Graduate Center of the City University of New York, New York, New York, U.S.A.*
- Hans-Peter Hentze** / *University of Delaware, Newark, Delaware, U.S.A.*
- Henry Hess** / *University of Washington, Seattle, Washington, U.S.A.*
- Daniel A. Higgins** / *Kansas State University, Manhattan, Kansas, U.S.A.*
- Alexander Hillisch** / *EnTec GmbH, Jena, Germany*
- J. Zachary Hilt** / *The University of Texas, Austin, Texas, U.S.A.*
- Satoshi Hirosawa** / *Sumitomo Special Metals Company, Ltd., Osaka, Japan*

- Andreas Hirsch** / *Friedrich Alexander Universität Erlangen-Nürnberg, Erlangen, Germany*
- Eric M. V. Hoek** / *University of California, Riverside, California, U.S.A.*
- Peter M. Hoffmann** / *Wayne State University, Detroit, Michigan, U.S.A.*
- J. Hone** / *Columbia University, New York, New York, U.S.A.*
- Louisa J. Hope-Weeks** / *Lawrence Livermore National Laboratory, Livermore, California, U.S.A.*
- David Hopkins** / *University of Illinois at Urbana-Champaign, Urbana, Illinois, U.S.A.*
- Scott R. Horner** / *University of Rochester, Rochester, New York, U.S.A.*
- Yanwen Hou** / *Kansas State University, Manhattan, Kansas, U.S.A.*
- Hui Hu** / *University of California, Riverside, California, U.S.A.*
- Zhibing Hu** / *University of North Texas, Denton, Texas, U.S.A.*
- Yu-Wen Huang** / *University of Illinois at Urbana-Champaign, Urbana, Illinois, U.S.A.*
- Mark Hughes** / *University of Cambridge, Cambridge, United Kingdom*
- Deborah E. Hunka** / *Sandia National Laboratories, Albuquerque, New Mexico, U.S.A.*
- Ho Jung Hwang** / *Chung-Ang University, Seoul, South Korea*
- Akihisa Inoue** / *Tohoku University, Sendai, Japan*
- Yasushi Inouye** / *Osaka University, Osaka, Japan*
- Stephan Irle** / *Emory University, Atlanta, Georgia, U.S.A.*
- Kelvin Isaacson** / *University of Alberta, Edmonton, Alberta, Canada*
- Toshihiro Ishikawa** / *Ube Industries Ltd., Ube Research Laboratory, Yamaguchi, Japan*
- Hiroyuki Isobe** / *The University of Tokyo, Tokyo, Japan*
- Mikhail E. Itkis** / *University of California, Riverside, California, U.S.A.*
- Takashi Ito** / *Fujitsu Ltd., Tokyo, Japan*
- Heinrich M. Jaeger** / *University of Chicago, Chicago, Illinois, U.S.A.*
- Dustin K. James** / *Rice University, Houston, Texas, U.S.A.*
- David B. Janes** / *Purdue University, West Lafayette, Indiana, U.S.A.*
- Andrés Jaramillo-Botero** / *Pontificia Universidad Javeriana, Cali, Colombia*
- Anna Jawor** / *University of California, Riverside, California, U.S.A.*
- Andreas Jentys** / *Technische Universität München, Garching, Germany*
- Christian Joachim** / *Centre d'Elaboration de Matériaux et d'Etudes Structurales (CEMES), Centre National de la Recherche Scientifique (CNRS), Toulouse, France*
- Vijay John** / *Tulane University, New Orleans, Louisiana, U.S.A.*
- Katrina A. Jolliffe** / *University of Sydney, Sydney, New South Wales, Australia*
- Ulrich Jonas** / *Max Planck Institute for Polymer Research, Mainz, Germany*
- Clinton D. Jones** / *Georgia Institute of Technology, Atlanta, Georgia, U.S.A.*
- A. Jorio** / *Universidade Federal de Minas Gerais, Belo Horizonte, Brazil*
- Leonid Kaledin** / *Argonide Corporation, Sanford, Florida, U.S.A.*
- Alain E. Kaloyeros** / *University at Albany—State University of New York, Albany, New York, U.S.A.*
- Toshiya Kamikado** / *Communications Research Laboratory, Kobe, Japan*
- Kiyotomi Kaneda** / *Osaka University, Osaka, Japan*
- Jeong Won Kang** / *Chung-Ang University, Seoul, South Korea*
- David Kaplan** / *Tufts University, Medford, Massachusetts, U.S.A.*
- Pramesh N. Kapoor** / *University of Delhi, Delhi, India*
- Hiromichi Kataura** / *Tokyo Metropolitan University, Tokyo, Japan*
- Satoshi Kawata** / *Osaka University, Osaka, Japan*
- Christine D. Keating** / *Pennsylvania State University, University Park, Pennsylvania, U.S.A.*
- Klaus Kern** / *Max-Planck-Institut für Festkörperforschung, Stuttgart, Germany*

- Miklos Kertesz** / *Georgetown University, Washington, District of Columbia, U.S.A.*
- Abbas Khaleel** / *United Arab Emirates University, Al-Ain, United Arab Emirates*
- Aleksandr Khitun** / *University of California, Los Angeles, California, U.S.A.*
- David T. Kim** / *University of California, Berkeley, California, U.S.A.*
- Dong Wook Kim** / *Korea Research Institute of Chemical Technology, Daejeon, South Korea*
- Jungbae Kim** / *Pacific Northwest National Laboratory, Richland, Washington, U.S.A.*
- Kwang S. Kim** / *Pohang University of Science and Technology, Pohang, South Korea*
- Sungsoo Kim** / *University of Illinois at Urbana-Champaign, Champaign, Illinois, U.S.A.*
- Yoong Ahm Kim** / *Shinshu University, Nagano, Japan*
- R. Allen Kimel** / *Pennsylvania State University, University Park, Pennsylvania, U.S.A.*
- Laszlo B. Kish** / *Texas A&M University, College Station, Texas, U.S.A.*
- Kenneth J. Klabunde** / *Kansas State University, Manhattan, Kansas, U.S.A.*
- Jennifer E. Klare** / *Lawrence Livermore National Laboratory, Livermore, California, U.S.A.*
- Paul G. Klemens** / *University of Connecticut, Storrs, Connecticut, U.S.A.*
- Robert F. Klie** / *Brookhaven National Laboratory, Upton, New York, U.S.A.*
- J. C. Knight** / *University of Bath, Bath, United Kingdom*
- Carl C. Koch** / *North Carolina State University, Raleigh, North Carolina, U.S.A.*
- Kenichiro Koga** / *Okayama University, Okayama, Japan*
- Punit Kohli** / *University of Florida, Gainesville, Florida, U.S.A.*
- S. Kohmoto** / *The Femtosecond Technology Research Association (FESTA), Ibaraki, Japan*
- Toshihiro Kondo** / *Hokkaido University, Sapporo, Japan*
- E. Stefan Kooij** / *University of Twente, Enschede, The Netherlands*
- Nicholas A. Kotov** / *Oklahoma State University, Stillwater, Oklahoma, U.S.A.*
- Vladimír Král** / *Institute of Chemical Technology, Prague, Czech Republic*
- Ilona Kretschmar** / *Yale University, New Haven, Connecticut, U.S.A.*
- Xiomara C. Kretschmer** / *The University of Texas, El Paso, Texas, U.S.A.*
- A. J. Kropf** / *Argonne National Laboratory, Argonne, Illinois, U.S.A.*
- Bon-Cheol Ku** / *University of Massachusetts, Lowell, Massachusetts, U.S.A.*
- Clifford P. Kubiak** / *University of California—San Diego, La Jolla, California, U.S.A.*
- Debasish Kuila** / *Louisiana Tech University, Ruston, Louisiana, U.S.A.*
- Jayant Kumar** / *University of Massachusetts, Lowell, Massachusetts, U.S.A.*
- Nitin Kumar** / *Massachusetts Institute of Technology, Cambridge, Massachusetts, U.S.A.*
- Daniel Y. Kwok** / *University of Alberta, Edmonton, Alberta, Canada*
- Soon-Bark Kwon** / *Kwangju Institute of Science and Technology, Gwangju, South Korea*
- Dominique Larcher** / *Université de Picardie—Jules Verne, Amiens, France*
- Sarah C. Larsen** / *University of Iowa, Iowa City, Iowa, U.S.A.*
- Jean-Pierre Launay** / *Centre d'Elaboration de Matériaux et d'Etudes Structurales (CEMES), Centre National de la Recherche Scientifique (CNRS), Toulouse, France*
- Valentina Lazarescu** / *Institute of Physical Chemistry "I. G. Murgulescu," Bucharest, Romania*
- Nikolai N. Ledentsov** / *Technische Universität Berlin, Berlin, Germany*
- Haiwon Lee** / *Hanyang University, Seoul, South Korea*
- Han Myoung Lee** / *Pohang University of Science and Technology, Pohang, South Korea*
- Ken Won Lee** / *Kwangju Institute of Science and Technology, Gwangju, South Korea*
- Seunghyun Lee** / *Hanyang University, Seoul, South Korea*
- Steven Lenhert** / *Westfälische Wilhelms-Universität Münster, Münster, Germany*
- Kam W. Leong** / *The Johns Hopkins University School of Medicine, Baltimore, Maryland, U.S.A.*

- Johannes A. Lercher** / *Technische Universität München, Garching, Germany*
- Marat I. Lerner** / *Russian Academy of Sciences, Tomsk, Russia*
- Rastislav Levicky** / *Columbia University, New York, New York, U.S.A.*
- Guangtao Li** / *Freie Universität Berlin, Berlin, Germany*
- Liang-shi Li** / *University of California, Berkeley, California, U.S.A.*
- Tianquan Lian** / *Emory University, Atlanta, Georgia, U.S.A.*
- Chengdu Liang** / *Oak Ridge National Laboratory, Oak Ridge, Tennessee, U.S.A.*
- Xuemei Liang** / *Wayne State University, Detroit, Michigan, U.S.A.*
- Yeshayahu Lifshitz** / *City University of Hong Kong, Hong Kong, China* / *Soreq Nuclear Research Center, Yavne, Israel*
- Peter T. Lillehei** / *NASA-Langley Research Center, Hampton, Virginia, U.S.A.*
- Xiao Min Lin** / *Argonne National Laboratory, Argonne, Illinois, U.S.A.*
- Yuehe Lin** / *Pacific Northwest National Laboratory, Richland, Washington, U.S.A.*
- Leonard F. Lindoy** / *University of Sydney, Sydney, New South Wales, Australia*
- J. Liu** / *Sandia National Laboratory, Albuquerque, New Mexico, U.S.A.*
- Jian Liu** / *Michigan Technological University, Houghton, Michigan, U.S.A.*
- Jianlin Liu** / *University of California, Riverside, California, U.S.A.*
- Jingyue Liu** / *Monsanto Company, St. Louis, Missouri, U.S.A.*
- Zhen Liu** / *Columbia University, New York, New York, U.S.A.*
- Jason Locklin** / *University of Houston, Houston, Texas, U.S.A.*
- Yueh-Lin Loo** / *The University of Texas, Austin, Texas, U.S.A.*
- Gabriel P. López** / *The University of New Mexico, Albuquerque, New Mexico, U.S.A.*
- Dmitri Valentinovich Louzguine** / *Tohoku University, Sendai, Japan*
- J. Christopher Love** / *Harvard University, Cambridge, Massachusetts, U.S.A.*
- Fang Lu** / *Pacific Northwest National Laboratory, Richland, Washington, U.S.A.*
- G. Q. (Max) Lu** / *The University of Queensland, Brisbane, Queensland, Australia*
- Nan Lu** / *Westfälische Wilhelms-Universität Münster, Münster, Germany*
- Yan-Yeung Luk** / *University of Wisconsin—Madison, Madison, Wisconsin, U.S.A.*
- Simon O. Lumsdon** / *DuPont Central Research and Development, Wilmington, Delaware, U.S.A.*
- L. Andrew Lyon** / *Georgia Institute of Technology, Atlanta, Georgia, U.S.A.*
- Alexander P. Lyubartsev** / *Stockholm University, Stockholm, Sweden*
- Jeffrey D. Madura** / *Duquesne University, Pittsburgh, Pennsylvania, U.S.A.*
- Kenzo Maehashi** / *Osaka University, Osaka, Japan*
- Thomas F. Magnera** / *University of Colorado, Boulder, Colorado, U.S.A.*
- Amitesh Maiti** / *Accelrys Inc., San Diego, California, U.S.A.*
- Amarnath Maitra** / *University of Delhi, Delhi, India*
- Tatiana L. Makarova** / *Umea University, Umea, Sweden*
- Sergey A. Maksimenko** / *Belarus State University, Minsk, Belarus*
- Arif A. Mamedov** / *Oklahoma State University and Nomadics, Inc., Stillwater, Oklahoma, U.S.A.*
- Nataliya N. Mamedova** / *Oklahoma State University, Stillwater, Oklahoma, U.S.A.*
- Guangzhao Mao** / *Wayne State University, Detroit, Michigan, U.S.A.*
- Gabriela Marinescu** / *"I. G. Murgulescu" Institute of the Romanian Academy, Bucharest, Romania*
- C. L. Marshall** / *Argonne National Laboratory, Argonne, Illinois, U.S.A.*
- Charles R. Martin** / *University of Florida, Gainesville, Florida, U.S.A.*
- Shinro Mashiko** / *Communications Research Laboratory, Kobe, Japan*
- Hiroshi Matsui** / *The City University of New York, Hunter College, New York, New York, U.S.A.*

- Hideo Matsumura** / *National Institute of Advanced Industrial Science and Technology, Tsukuba, Japan*
- Hideki Matsuoka** / *Kyoto University, Kyoto, Japan*
- S. V. Mattigod** / *Pacific Northwest National Laboratory, Richland, Washington, U.S.A.*
- F. Maurigh** / *DIEGM University of Udine, Udine, Italy*
- Mikhail V. Maximov** / *Ioffe Physico-Technical Institute, St. Petersburg, Russia*
- Clare McCabe** / *Colorado School of Mines, Golden, Colorado, U.S.A.*
- Nathan D. McClenaghan** / *School of Chemistry at Queen's University, Belfast, Northern Ireland*
- E. W. McFarland** / *University of California, Santa Barbara, California, U.S.A.*
- Duncan J. McGillivray** / *Oxford University, Oxford, United Kingdom*
- Gary McPherson** / *Tulane University, New Orleans, Louisiana, U.S.A.*
- Claude F. Meares** / *University of California, Davis, California, U.S.A.*
- Mark S. Meier** / *University of Kentucky, Lexington, Kentucky, U.S.A.*
- Latika Menon** / *Texas Tech University, Lubbock, Texas, U.S.A.*
- Curtis W. Meuse** / *National Institute of Standards and Technology, Gaithersburg, Maryland, U.S.A.*
- Agnes A. Mewe** / *University of Twente, Enschede, The Netherlands*
- F. Miani** / *DIEGM University of Udine, Udine, Italy*
- Weifang Miao** / *Nanomat, Inc., North Huntingdon, Pennsylvania, U.S.A.*
- Josef Michl** / *University of Colorado, Boulder, Colorado, U.S.A.*
- Laszlo Mihaly** / *The State University of New York at Stony Brook, Stony Brook, New York, U.S.A.*
- Abigail E. Miller** / *Lawrence Livermore National Laboratory, Livermore, California, U.S.A.*
- Benjamin L. Miller** / *University of Rochester, Rochester, New York, U.S.A.*
- J. T. Miller** / *British Petroleum (BP), Naperville, Illinois, U.S.A.*
- Scott A. Miller** / *University of Florida, Gainesville, Florida, U.S.A.*
- Ioana Mindru** / *"I. G. Murgulescu" Institute of the Romanian Academy, Bucharest, Romania*
- Christophe Mingotaud** / *Laboratoire des IMRCP, Université Paul Sabatier, Toulouse, France*
- John W. Mintmire** / *Oklahoma State University, Stillwater, Oklahoma, U.S.A.*
- Francis M. Mirabella, Jr.** / *Equistar Chemicals, LP, Cincinnati, Ohio, U.S.A.*
- Susmita Mitra** / *University of Delhi, Delhi, India*
- Akane Miyazaki** / *Tokyo Institute of Technology, Yokohama, Japan*
- Tomoo Mizugaki** / *Osaka University, Osaka, Japan*
- Peter Moeck** / *Portland State University, Portland, Oregon, U.S.A.*
- Carlo D. Montemagno** / *University of California, Los Angeles, California, U.S.A.*
- Keiji Morokuma** / *Emory University, Atlanta, Georgia, U.S.A.*
- Karine Mougín** / *Institut de Chimie des Surfaces et Interfaces-ICSI-CNRS, Mulhouse, France*
- Emiko Mouri** / *Kyoto University, Kyoto, Japan*
- Douglas Mulhall** / *Marsh Harbour, Bahamas*
- Ravichandra S. Mulukutla** / *Nanoscale Materials, Inc., Manhattan, Kansas, U.S.A.*
- Kei Murakoshi** / *Osaka University, Osaka, Japan*
- Makoto Murata** / *Osaka University, Osaka, Japan*
- Michael Murphey** / *University of Illinois at Urbana-Champaign, Urbana, Illinois, U.S.A.*
- Mustafa Musameh** / *New Mexico State University, Las Cruces, New Mexico, U.S.A.*
- Aleksandr V. Myshlyavtsev** / *Omsk State Technical University, Omsk, Russia*
- Edward M. Nadgorny** / *Michigan Technological University, Houghton, Michigan, U.S.A.*
- K. S. Nagabhushana** / *Max Planck Institut für Kohlenforschung, Mülheim an der Ruhr, Germany*
- Eiichi Nakamura** / *The University of Tokyo, Tokyo, Japan*
- H. Nakamura** / *The Femtosecond Technology Research Association (FESTA), Ibaraki, Japan*

- Takayoshi Nakamura** / *Hokkaido University, Sapporo, Japan*
- Hisao Nakashima** / *Osaka University, Osaka, Japan*
- Yoshihiro Nakato** / *Osaka University, Osaka, Japan*
- Richard M. Narske** / *Augustana College, Rock Island, Illinois, U.S.A.*
- Alexandra Navrotsky** / *University of California, Davis, California, U.S.A.*
- David A. Nelson** / *Pacific Northwest National Laboratory, Richland, Washington, U.S.A.*
- Sarah A. Nespolo** / *University of Melbourne, Melbourne, Victoria, Australia*
- M. K. Neylon** / *Argonne National Laboratory, Argonne, Illinois, U.S.A.*
- Patrick J. Neyman** / *Virginia Polytechnic Institute and State University, Blacksburg, Virginia, U.S.A.*
- K. Y. Simon Ng** / *Wayne State University, Detroit, Michigan, U.S.A.*
- Richard J. Nichols** / *University of Liverpool, Liverpool, United Kingdom*
- Marc Nicklaus** / *National Cancer Institute, Frederick, Maryland, U.S.A.*
- David E. Nikles** / *The University of Alabama, Tuscaloosa, Alabama, U.S.A.*
- S. Nishikawa** / *The Femtosecond Technology Research Association (FESTA), Ibaraki, Japan*
- Sandip Niyogi** / *University of California, Riverside, California, U.S.A.*
- Ijeoma M. Nnebe** / *Carnegie Mellon University, Pittsburgh, Pennsylvania, U.S.A.*
- Donald W. Noid** / *Oak Ridge National Laboratory, Oak Ridge, Tennessee, U.S.A.*
- Tyler B. Norsten** / *University of Massachusetts, Amherst, Massachusetts, U.S.A.*
- Aleksandr Noy** / *Lawrence Livermore National Laboratory, Livermore, California, U.S.A.*
- Stacie Nunes** / *State University of New York at New Paltz, New Paltz, New York, U.S.A.*
- Masayuki Okamura** / *Hokkaido University, Sapporo, Japan*
- Yuji Okawa** / *National Institute for Materials Science, Ibaraki, Japan*
- Masahiko Ooe** / *Osaka University, Osaka, Japan*
- Neil S. Oxtoby** / *The University of Nottingham, Nottingham, United Kingdom*
- Ruth Pachter** / *AFRL/ML, Wright-Patterson Air Force Base, Ohio, U.S.A.*
- Christopher S. Palenik** / *University of Michigan, Ann Arbor, Michigan, U.S.A.*
- Chandra Sekhar Palla** / *University of Delaware, Newark, Delaware, U.S.A.*
- Raghuveer Parthasarathy** / *University of Chicago, Chicago, Illinois, U.S.A.* / *University of California, Berkeley, California, U.S.A.*
- Sandeep Patel** / *Hunter College of the City University of New York, New York, New York, U.S.A.*
- Luminita Patron** / *"I. G. Murgulescu" Institute of the Romanian Academy, Bucharest, Romania*
- Derek Patton** / *University of Houston, Houston, Texas, U.S.A.*
- Sandrine Pensac** / *Université Pierre et Marie Curie, Paris, France*
- John H. Perepezko** / *University of Wisconsin, Madison, Wisconsin, U.S.A.*
- Myriam Perez De la Rosa** / *The University of Texas, El Paso, Texas, U.S.A.*
- Christopher C. Perry** / *The Johns Hopkins University, Baltimore, Maryland, U.S.A.*
- Claire S. Peyratout** / *Max Planck Institute of Colloids and Interfaces, Potsdam, Germany*
- M. P. Pileni** / *Université Pierre et Marie Curie (Paris VI), Paris, France*
- M. A. Pimenta** / *Universidade Federal de Minas Gerais, Belo Horizonte, Brazil*
- Frédéric Pincet** / *Laboratoire de Physique Statistique de l'Ecole Normale Supérieure, Paris, France*
- Laura Pirondini** / *Università di Parma, Parma, Italy*
- Bene Poelsema** / *University of Twente, Enschede, The Netherlands*
- Karsten Pohl** / *University of New Hampshire, Durham, New Hampshire, U.S.A.*
- Vojislava Pophristic** / *University of Pennsylvania, Philadelphia, Pennsylvania, U.S.A.*
- Daniel Portinha** / *Université Pierre et Marie Curie, Paris, France*
- B. L. V. Prasad** / *Kansas State University, Manhattan, Kansas, U.S.A.*

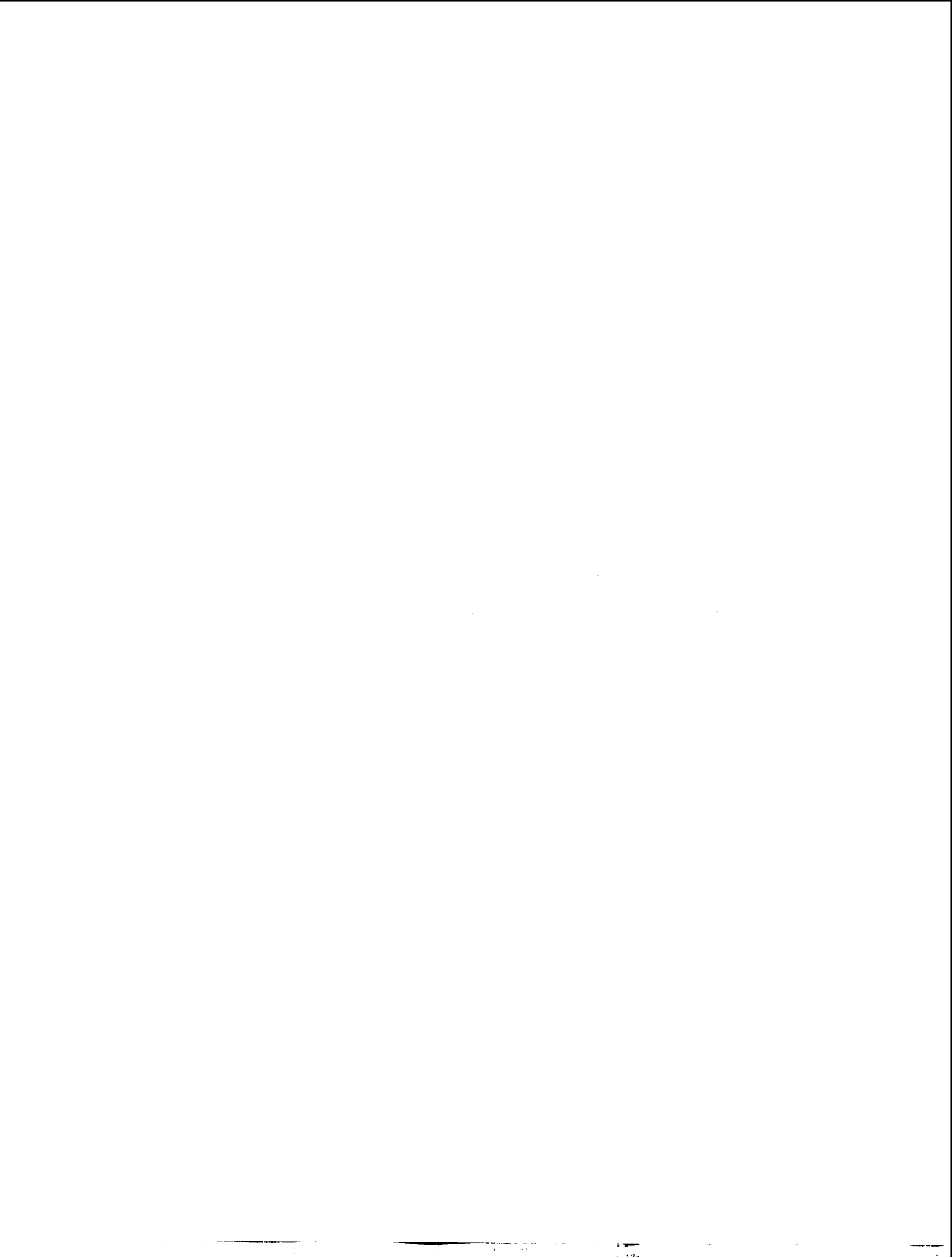
- Maurizio Prato** / *Università di Trieste, Trieste, Italy*
- Aaron Puzder** / *Lawrence Livermore National Laboratory, Livermore, California, U.S.A.*
- Georgios Pyrgiotakis** / *University of Florida, Gainesville, Florida, U.S.A.*
- Clayton J. Radke** / *University of California, Berkeley, California, U.S.A.*
- Srikanth Raghunathan** / *Nanomat, Inc., North Huntingdon, Pennsylvania, U.S.A.*
- Krishnaswami S. Raja** / *The Scripps Research Institute, La Jolla, California, U.S.A.*
- S. Ramakrishnan** / *University of Illinois at Urbana-Champaign, Urbana, Illinois, U.S.A.*
- G. V. Rama Rao** / *The University of New Mexico, Albuquerque, New Mexico, U.S.A.*
- David M. Rampulla** / *Carnegie Mellon University, Pittsburgh, Pennsylvania, U.S.A.*
- Lev Rapoport** / *Holon Academic Institute of Technology, Holon, Israel*
- Jean-Yves Raty** / *University of Liège, Sart-Tilman, Belgium*
- Serge Ravaine** / *Centre de Recherche Paul Pascal, CNRS, Pessac, France*
- Stéphane Reculosa** / *Centre de Recherche Paul Pascal, CNRS, Pessac, France*
- Mark A. Reed** / *Yale University, New Haven, Connecticut, U.S.A.*
- David N. Reinhoudt** / *University of Twente, Enschede, The Netherlands*
- Mikas Remeika** / *University of Illinois at Urbana-Champaign, Urbana, Illinois, U.S.A.*
- Maja Remskar** / *Jozef Stefan Institute, Ljubljana, Slovenia*
- Zhifeng Ren** / *Boston College, Chestnut Hill, Massachusetts, U.S.A.*
- Ryan M. Richards** / *International University of Bremen, Bremen, Germany*
- Carlos Rinaldi** / *University of Puerto Rico, Mayagüez, Puerto Rico*
- P. J. Roberts** / *BlazePhotonics Ltd., Bath, United Kingdom*
- Jose A. Rodriguez** / *Brookhaven National Laboratory, Upton, New York, U.S.A.*
- Miguel Rodriguez** / *Oak Ridge National Laboratory, Oak Ridge, Tennessee, U.S.A.*
- Andrey Rogachev** / *University of Illinois at Urbana-Champaign, Urbana, Illinois, U.S.A.*
- John A. Rogers** / *University of Illinois at Urbana-Champaign, Urbana, Illinois, U.S.A.*
- Harry W. Rollins** / *Idaho National Engineering and Environmental Laboratory, Idaho Falls, Idaho, U.S.A.*
- Björn T. Rosner** / *University of Wisconsin, Madison, Wisconsin, U.S.A.*
- Vincent M. Rotello** / *University of Massachusetts, Amherst, Massachusetts, U.S.A.*
- Wielsaw J. Roth** / *ExxonMobil Research and Engineering Company, Annandale, New Jersey, U.S.A.*
- Jason H. Rouse** / *NASA-Langley Research Center, Hampton, Virginia, U.S.A.*
- James F. Rusling** / *University of Connecticut, Storrs, Connecticut, U.S.A.*
- P. St.J. Russell** / *University of Bath, Bath, United Kingdom*
- Ajit Sadana** / *University of Mississippi, University, Mississippi, U.S.A.*
- R. Saito** / *University of Electro-Communications, Tokyo, Japan*
- Mark R. Sambrook** / *University of Oxford, Oxford, United Kingdom*
- Lynne A. Samuelson** / *University of Massachusetts, Lowell, Massachusetts, U.S.A.*
- Charlene A. Sanders** / *Oak Ridge National Laboratory, Oak Ridge, Tennessee, U.S.A.*
- Francesco Sansone** / *Università di Parma, Parma, Italy*
- Venugopal Santhanam** / *Universität Duisburg-Essen, Essen, Germany*
- Amitav Sanyal** / *University of Massachusetts, Amherst, Massachusetts, U.S.A.*
- D. Y. Sasaki** / *Sandia National Laboratories, Albuquerque, New Mexico, U.S.A.*
- Daniel M. Schaadt** / *University of California—San Diego, La Jolla, California, U.S.A.*
- L. S. Schadler** / *Rensselaer Polytechnic Institute, Troy, New York, U.S.A.*
- David J. Schiffrin** / *University of Liverpool, Liverpool, United Kingdom*
- Jacob J. Schmidt** / *University of California, Los Angeles, California, U.S.A.*
- James W. Schneider** / *Carnegie Mellon University, Pittsburgh, Pennsylvania, U.S.A.*

- Holger Schönherr** / *University of Twente, Enschede, The Netherlands*
- Christian Schüller** / *Universität Hamburg, Hamburg, Germany*
- Purnesh Seegopaul** / *Umicore USA Inc., Hillsborough, New Jersey, U.S.A.*
- Jorge M. Seminario** / *University of South Carolina, Columbia, South Carolina, U.S.A.*
- Mamoru Senna** / *Keio University, Yokohama, Japan*
- Jonathan L. Sessler** / *The University of Texas at Austin, Austin, Texas, U.S.A.*
- Kay Severin** / *École Polytechnique Fédérale de Lausanne, Lausanne, Switzerland*
- Sean E. Shaheen** / *National Renewable Energy Laboratory (NREL), Golden, Colorado, U.S.A.*
- Ehud Shapiro** / *Weizmann Institute of Science, Rehovot, Israel*
- Yury E. Shapiro** / *Bar-Ilan University, Ramat-Gan, Israel*
- P. C. Sharma** / *University of California, Los Angeles, California, U.S.A.*
- Pramod K. Sharma** / *Nanomaterials, Inc., North Huntingdon, Pennsylvania, U.S.A.*
- Roy Shenhar** / *University of Massachusetts, Amherst, Massachusetts, U.S.A.*
- Peter M. A. Sherwood** / *Kansas State University, Manhattan, Kansas, U.S.A.*
- Masashi Shiraishi** / *SONY Corporation, Yokohama, Japan*
- Tatiana V. Shishkanova** / *Institute of Chemical Technology, Czech Republic*
- Ulrich Siggel** / *Technischen Universität Berlin, Berlin, Germany*
- Wolfgang M. Sigmund** / *University of Florida, Gainesville, Florida, U.S.A.*
- Richard Silberglitt** / *RAND Corporation, Arlington, Virginia, U.S.A.*
- Kevin Sill** / *University of Massachusetts, Amherst, Massachusetts, U.S.A.*
- Amit Singh** / *NEI Corporation, Piscataway, New Jersey, U.S.A.*
- Rhonda Skaggs** / *Pacific Northwest National Laboratory, Richland, Washington, U.S.A.*
- Ganesh Skandan** / *NEI Corporation, Piscataway, New Jersey, U.S.A.*
- Gregory Ya. Slepian** / *Belarus State University, Minsk, Belarus*
- Gabriela Smeureanu** / *Hunter College of the City University of New York, New York, New York, U.S.A.*
- James N. Smith** / *National Center for Atmospheric Research, Boulder, Colorado, U.S.A.*
- Karl Sohlberg** / *Drexel University, Philadelphia, Pennsylvania, U.S.A.*
- G. S. Solomon** / *Stanford University, Stanford, California, U.S.A.*
- Michael J. Solomon** / *University of Michigan, Ann Arbor, Michigan, U.S.A.*
- Anongnat Somwangthanoj** / *University of Michigan, Ann Arbor, Michigan, U.S.A.*
- Wenbo Song** / *Hokkaido University, Sapporo, Japan*
- A. G. Souza Filho** / *Universidade Federal do Ceará, Fortaleza, Brazil*
- Patrick T. Spicer** / *The Procter & Gamble Company, West Chester, Ohio, U.S.A.*
- Ivan Stensgaard** / *University of Aarhus, Aarhus, Denmark*
- Geoffrey W. Stevens** / *University of Melbourne, Melbourne, Victoria, Australia*
- Rebecca L. Stoermer** / *Pennsylvania State University, University Park, Pennsylvania, U.S.A.*
- Savka I. Stoeva** / *Kansas State University, Manhattan, Kansas, U.S.A.*
- Peter K. Stoimenov** / *Kansas State University, Manhattan, Kansas, U.S.A.*
- Steven H. Strauss** / *Colorado State University, Fort Collins, Colorado, U.S.A.*
- Pieter Stroeve** / *University of California, Davis, California, U.S.A.*
- Makram T. Suidan** / *University of Cincinnati, Cincinnati, Ohio, U.S.A.*
- Gleb B. Sukhorukov** / *Max-Planck-Institute of Colloids and Interfaces, Potsdam/Golm, Germany*
- Bobby G. Sumpter** / *Oak Ridge National Laboratory, Oak Ridge, Tennessee, U.S.A.*
- Kai Sun** / *University of Illinois at Chicago, Chicago, Illinois, U.S.A.*
- Guangyu Sun** / *National Cancer Institute, Frederick, Maryland, U.S.A.*
- Xiangcheng Sun** / *The University of Alabama, Tuscaloosa, Alabama, U.S.A.*

- Aydin K. Sunol** / *University of South Florida, Tampa, Florida, U.S.A.*
- Sermin G. Sunol** / *University of South Florida, Tampa, Florida, U.S.A.*
- Robert E. Synovec** / *University of Washington, Seattle, Washington, U.S.A.*
- Makoto Tadokoro** / *Osaka City University, Osaka, Japan*
- Atsushi Takahara** / *Kyushu University, Fukuoka, Japan*
- Taishi Takenobu** / *SONY Corporation, Yokohama, Japan*
- Hideki Tanaka** / *Okayama University, Okayama, Japan*
- Zhiyong Tang** / *University of Michigan, Ann Arbor, Michigan, U.S.A.*
- P. Tarakeshwar** / *Pohang University of Science and Technology, Pohang, South Korea*
- Jean-Marie Tarascon** / *Université de Picardie—Jules Verne, Amiens, France*
- Vandana R. Tarigopula** / *University of South Carolina, Columbia, South Carolina, U.S.A.*
- Juan M. D. Tascón** / *Instituto Nacional del Carbón, CSIC, Oviedo, Spain*
- Boyd R. Taylor** / *Lawrence Livermore National Laboratory, Livermore, California, U.S.A.*
- Reshef Tenne** / *Weizmann Institute, Rehovot, Israel*
- Frederick Tepper** / *Argonide Corporation, Sanford, Florida, U.S.A.*
- Roger Terrill** / *San Jose State University, San Jose, California, U.S.A.*
- Mauricio Terrones** / *Institute Potosino of Scientific and Technological Research (IPICYT), San Luis Potosí, Mexico*
- V. A. Tertykh** / *National Academy of Sciences of Ukraine, Kyiv, Ukraine*
- Edwin L. Thomas** / *Massachusetts Institute of Technology, Cambridge, Massachusetts, U.S.A.*
- Gregory B. Thompson** / *The Ohio State University, Columbus, Ohio, U.S.A.*
- Steven M. Thornberg** / *Sandia National Laboratories, Albuquerque, New Mexico, U.S.A.*
- Bernd Tieke** / *Universität zu Köln, Köln, Germany*
- Tia Benson Tolle** / *Air Force Research Laboratory, Wright-Patterson Air Force Base, Ohio, U.S.A.*
- Anna W. Topol** / *IBM T. J. Watson Research Center, Yorktown Heights, New York, U.S.A.*
- Jessica Torres** / *The Johns Hopkins University, Baltimore, Maryland, U.S.A.*
- Naoki Toshima** / *Tokyo University of Science, Yamaguchi, Japan*
- James M. Tour** / *Rice University, Houston, Texas, U.S.A.*
- Ali Toutianoush** / *Universität zu Köln, Köln, Germany*
- Günter E. M. Tovar** / *University of Stuttgart, Stuttgart, Germany*
- Costas Tsouris** / *Oak Ridge National Laboratory, Oak Ridge, Tennessee, U.S.A.*
- Yi Tu** / *Boston College, Chestnut Hill, Massachusetts, U.S.A.*
- Royale S. Underhill** / *Defence Research and Development Canada—Atlantic, Dartmouth, Nova Scotia, Canada*
- Rocco Ungaro** / *Università di Parma, Parma, Italy*
- Eberhard Unger** / *Institute of Molecular Biotechnology, Jena, Germany*
- Kohei Uosaki** / *Hokkaido University, Sapporo, Japan*
- Satoshi Utsunomiya** / *University of Michigan, Ann Arbor, Michigan, U.S.A.*
- Martin Valík** / *Institute of Chemical Technology, Prague, Czech Republic*
- Kevin E. Van Cott** / *Virginia Polytechnic Institute and State University, Blacksburg, Virginia, U.S.A.*
- G. Julius Vancso** / *University of Twente, Enschede, The Netherlands*
- Richard A. van Delden** / *University of Groningen, Groningen, The Netherlands*
- Daniel W. van der Weide** / *University of Wisconsin, Madison, Wisconsin, U.S.A.*
- Paul R. Van Tassel** / *Yale University, New Haven, Connecticut, U.S.A.*
- Natalia Varaksa** / *University of Colorado, Boulder, Colorado, U.S.A.*
- James C. Vartuli** / *ExxonMobil Research and Engineering Company, Annandale, New Jersey, U.S.A.*
- Stephanie Butler Velegol** / *Pennsylvania State University, State College, Pennsylvania, U.S.A.*
- Orlin D. Velev** / *North Carolina State University, Raleigh, North Carolina, U.S.A.*

- Alexei Yu. Vinogradov** / *Osaka City University, Osaka, Japan*
- Viriya Vithayaveroj** / *Georgia Institute of Technology, Atlanta, Georgia, U.S.A.*
- Viola Vogel** / *University of Washington, Seattle, Washington, U.S.A.*
- Pete Vukusic** / *Exeter University, Exeter, United Kingdom*
- Anthony J. Wagner** / *The Johns Hopkins University, Baltimore, Maryland, U.S.A.*
- Chien M. Wai** / *University of Idaho, Moscow, Idaho, U.S.A.*
- Joseph Wang** / *New Mexico State University, Las Cruces, New Mexico, U.S.A.*
- Kang L. Wang** / *University of California, Los Angeles, California, U.S.A.*
- Qian Wang** / *University of South Carolina, Columbia, South Carolina, U.S.A.*
- Shaopeng Wang** / *Nomadics Inc., Stillwater, Oklahoma, U.S.A.*
- Zhong Lin Wang** / *Georgia Institute of Technology, Atlanta, Georgia, U.S.A.*
- Paul Watts** / *University of Hull, Hull, United Kingdom*
- Achim Weber** / *University of Stuttgart, Stuttgart, Germany*
- Thomas J. Webster** / *Purdue University, West Lafayette, Indiana, U.S.A.*
- Brandon L. Weeks** / *Lawrence Livermore National Laboratory, Livermore, California, U.S.A.*
- Alexander Wei** / *Purdue University, West Lafayette, Indiana, U.S.A.*
- Jie Wen** / *The Johns Hopkins University School of Medicine, Baltimore, Maryland, U.S.A.*
- Joachim H. Wendorff** / *Philipps-Universität Marburg, Marburg, Germany*
- Carter T. White** / *Naval Research Laboratory, Washington, District of Columbia, U.S.A.*
- George M. Whitesides** / *Harvard University, Cambridge, Massachusetts, U.S.A.*
- James Wicksted** / *Oklahoma State University, Stillwater, Oklahoma, U.S.A.*
- J. P. Wilcoxon** / *Sandia National Laboratories, Albuquerque, New Mexico, U.S.A.*
- Andrew Williamson** / *Lawrence Livermore National Laboratory, Livermore, California, U.S.A.*
- Marc Wirtz** / *PPG Industries, Inc., Monroeville, Pennsylvania, U.S.A.*
- Daniel B. Wolfe** / *Harvard University, Cambridge, Massachusetts, U.S.A.*
- Glenn M. Wolfe** / *The Johns Hopkins University, Baltimore, Maryland, U.S.A.*
- Stanislaus S. Wong** / *State University of New York at Stony Brook, Stony Brook, New York, U.S.A.* / *Brookhaven National Laboratory, Upton, New York, U.S.A.*
- Bruce W. Woods** / *Lawrence Livermore National Laboratory, Livermore, California, U.S.A.*
- Herbert Wormeester** / *University of Twente, Enschede, The Netherlands*
- Fanxin Wu** / *University of California, Santa Cruz, California, U.S.A.*
- H. Wu** / *Pacific Northwest National Laboratory, Richland, Washington, U.S.A.*
- Jianzhong Wu** / *University of California, Riverside, California, U.S.A.*
- You-Ting Wu** / *North Carolina State University, Raleigh, North Carolina, U.S.A.*
- Chuanjun Xia** / *University of Alabama at Birmingham, Birmingham, Alabama, U.S.A.*
- Wei Xing** / *The University of Queensland, Brisbane, Queensland, Australia*
- Zhi Ping Xu** / *University of North Texas, Denton, Texas, U.S.A.*
- Dalia G. Yablon** / *ExxonMobil Research and Engineering, Annandale, New Jersey, U.S.A.*
- Boris I. Yakobson** / *Rice University, Houston, Texas, U.S.A.*
- Juchao Yan** / *Eastern New Mexico University, Portales, New Mexico, U.S.A.*
- Z. F. Yan** / *University of Petroleum, Dongying, China*
- Bai Yang** / *Jilin University, Changchun, People's Republic of China*
- Chao Yang** / *Lawrence Berkeley National Laboratory, Berkeley, California, U.S.A.*
- Jun Yang** / *University of Alberta, Edmonton, Alberta, Canada*
- Kun-Lin Yang** / *Georgia Institute of Technology, Atlanta, Georgia, U.S.A.*
- T. Yang** / *The Femtosecond Technology Research Association (FESTA), Ibaraki, Japan*

- Wassana Yantasee** / *Pacific Northwest National Laboratory, Richland, Washington, U.S.A.*
- Xiang-Rong Ye** / *Pacific Northwest National Laboratory, Richland, Washington, U.S.A.* / *University of Idaho, Moscow, Idaho, U.S.A.*
- Sotira Yiacoumi** / *Georgia Institute of Technology, Atlanta, Georgia, U.S.A.*
- Shiyoshi Yokoyama** / *Communications Research Laboratory, Kobe, Japan*
- Takashi Yokoyama** / *Yokohama City University, Yokohama, Japan* / *National Institute for Materials Science, Tsukuba, Japan*
- Seunghoo Yoo** / *University of Massachusetts, Amherst, Massachusetts, U.S.A.*
- Yi Yu** / *Chinese Academy of Sciences, Changchun, People's Republic of China*
- Markus Zahn** / *Massachusetts Institute of Technology, Cambridge, Massachusetts, U.S.A.*
- Mondona Zangeneh** / *San Jose State University, San Jose, California, U.S.A.*
- Stefan Zauscher** / *Duke University, Durham, North Carolina, U.S.A.*
- T. S. Zemanian** / *Pacific Northwest National Laboratory, Richland, Washington, U.S.A.*
- Hua Chun Zeng** / *National University of Singapore, Singapore*
- Dajie Zhang** / *The Johns Hopkins University, Baltimore, Maryland, U.S.A.*
- Gang Zhang** / *Jilin University, Changchun, People's Republic of China*
- Jin Z. Zhang** / *University of California, Santa Cruz, California, U.S.A.*
- Junhu Zhang** / *Jilin University, Changchun, People's Republic of China*
- Kai Zhang** / *Jilin University, Changchun, People's Republic of China*
- X. B. Zhang** / *The University of Texas at Austin, Austin, Texas, U.S.A.*
- Xunli Zhang** / *University of Hull, Hull, United Kingdom*
- Zongtao Zhang** / *Oak Ridge National Laboratory, Oak Ridge, Tennessee, U.S.A.*
- Bin Zhao** / *University of California, Riverside, California, U.S.A.*
- Genady Zhavnerko** / *The National Academy of Sciences of Belarus, Minsk, Belarus*
- Xiange Zheng** / *Drexel University, Philadelphia, Pennsylvania, U.S.A.*
- N. B. Zhitenev** / *Lucent Technologies, Murray Hill, New Jersey, U.S.A.*
- Zhigang Zhou** / *Duquesne University, Pittsburgh, Pennsylvania, U.S.A.*
- Shu Zhu** / *Princeton University, Princeton, New Jersey, U.S.A.*
- C. F. Zukoski** / *University of Illinois at Urbana-Champaign, Urbana, Illinois, U.S.A.*



Preface

Nanoscience encompasses all scientific phenomena that transpire in dimensions spanning the range of multiple atom clusters, molecular aggregates, supermolecular structures, polymers and biomolecules. In other words, nanoscience is the science of the nanoscale—or the very, very minute. Nanotechnology, the technological use of these properties and phenomena, has the potential to revolutionize a breathtaking range of fields, across practically all domains of human activity. The intense interest in using nanostructures stems from the promise that they boast superior electrical, optical, mechanical, chemical, or biochemical properties. There is little doubt that the use of these new materials and systems will lay the ground for the new technological revolution of the 21st century. Research in nanoscience is exploding as scientists from chemistry, physics, and biology, including colloid and polymer chemistry, materials and surface science, and biochemistry, biophysics and molecular biology have begun to examine the superior properties that characterize materials and phenomena at the nanoscale.

The *Dekker Encyclopedia of Nanoscience and Nanotechnology* is a vehicle by which scientists and the interested public can explore the most recent developments in today's nanomaterials, and preview several of their foreseen applications of tomorrow. The subject areas of this five-volume collective work include, but are not limited to, chemistry, physics, molecular and quantum biology, materials science and engineering, and computer science. The topics include fullerenes and carbon nanotubes, quantum dots and inorganic nanowires, interfacial chemistry, nanostructures, analytical and characterization methods, design and fabrication techniques of nanocomposites, properties of functional nanomaterials, nanostructured catalysts, molecular electronics, optical devices, bionanotechnology, colloidal phenomena—even future and environmental considerations about nanotechnology. In short, the reference strives to encompass, document, and organize the enormous proliferation of information that has emerged from the revolution at the nanoscale.

It is the editors' hopes that the *Dekker Encyclopedia of Nanoscience and Nanotechnology* will help researchers, graduate students, undergraduate students, and nonprofessionals all better understand and participate in this remarkable emerging field. To keep the reference accessible, the *Encyclopedia* is published in both online and print formats. The print version consists of multiple traditional hardbound volumes with articles arranged alphabetically. The front matter to each volume provides an alphabetical Table of Contents and a Topical Table of Contents. An index at the back of each volume is intended as a further guide.

The online version of the *Encyclopedia* has been created by coupling the content of the print edition with a powerful search engine and user-friendly interface. The online database is dynamic, with additional articles added each quarter. As with the print edition, users will be able to browse the alphabetical and topical Table of Contents, but they will also be able to search for entries by keywords.

The editors of the *Dekker Encyclopedia of Nanoscience and Nanotechnology* could not have accomplished their feat without the help of many. We first thank the authors of more than 300 articles which, as recognized experts in their fields, lend their credibility and prestige to the *Encyclopedia*. In addition, the editors were joined by an esteemed International Editorial Advisory Board whose input was crucial to shaping the reference. Success in the coordination of the activities that has resulted in this final product is due to the remarkable staff at Marcel

Dekker, Inc. We are indebted to the direction provided to us by Ellen Lichtenstein, Carolyn Hall, Oona Schmid, Susan Lee, Joanne Jay, and Jeeran Ok. In particular, the creative ideas and boundless energy that Oona Schmid has demonstrated is greatly acknowledged by the three of us. We also thank Anita Lekhwani for her confidence in us as editors and Russell Dekker for his support and encouragement.

James A. Schwarz
Syracuse University, Syracuse, New York

Cristian I. Contescu
Material Methods LLC, Newport Beach, California

Karol Putyera
Shiva Technologies, Syracuse, New York

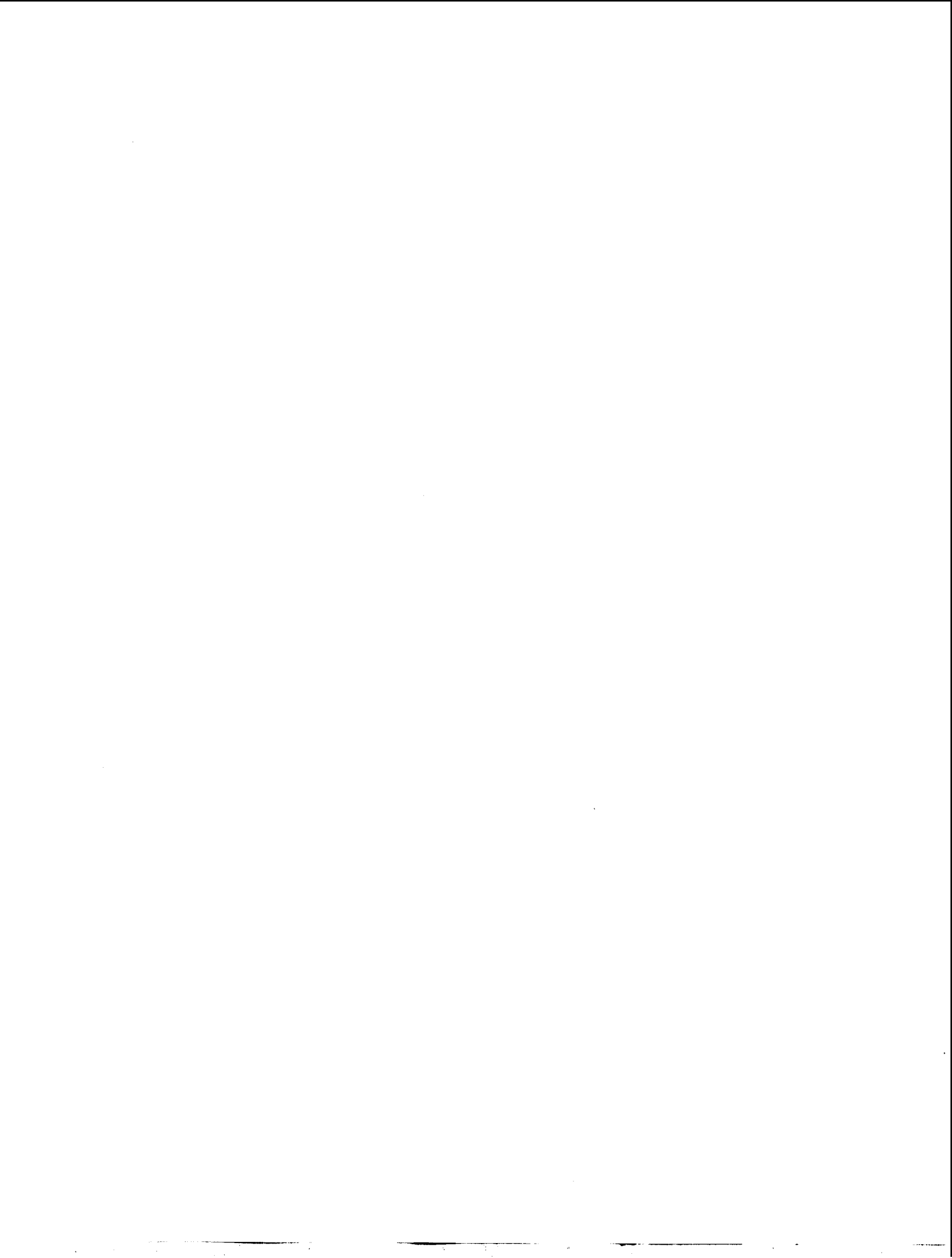
A Note on Terminology

New terms, based on the prefix *nano*, have gained broad circulation, unified the older terminology, and defined the topics of newly found disciplines. Just as the research community has struggled to restrict when and where the prefix *nano* can be appropriately used, we too struggled with the *Dekker Encyclopedia of Nanoscience and Nanotechnology* to avoid puncturing every sentence with the prefix *nano*. As this terminology develops, the online edition of the *Encyclopedia* will be able to incorporate these new conventions.

But at the time of publication of the first edition of the *Encyclopedia* these questions are still unresolved. One definition that has been proposed in order to remove the ambiguity would limit the use of the *nano* prefix to research and development of objects having the key property that they have at least one dimension in the range of 1 to 100 nanometers. New advances in synthetic methods for making such structures, combined with new analytical and manipulation tools, made it possible to refine methods to the point where *de novo* designed objects with nanoscopic dimension can, in many cases, be assembled in molecule-pure form or spatially organized structures. These systems, designed through processes that exhibit fundamental control over the physical and chemical attributes of molecular-scale structures, can be combined to form larger structures.

However, the *Dekker Encyclopedia of Nanoscience and Nanotechnology* has numerous entries that include the words micro and meso. Thus the use of the term *nano*, which, according to one broadly circulated definition, only limits research and technology to development in the length scale of approximately 1–100 nanometer range, is not simply a metric of length. Science at the nanoscale does not accept rigid limits on dimensionality. Indeed the very utility of nanoscience may be compromised by arbitrarily circumscribing its reach. After all, for ancient Greeks, the term "nanos" meant a dwarf. Keeping this in mind, we attempted in this reference to use the term *nano* to refer to objects and their subsequent processing into newly created structures, devices, or systems that have novel properties and functions because of their small and/or intermediate size. In other words, **size and performance** are the critical parameters that provide the requisite conditions to justify the use of the term *nano*.

By adopting a more elastic definition, which on one hand spans sizes from a few nanometer(s) to one (or a few) hundred(s) nanometers, but at the same time recognizes that the properties and performance of nanoobjects are rooted in their nanoscopic size, we believe that we made justice to all views that currently shape this field of continuous development and hope that other investigators—at universities, state laboratories, and in industries—will follow our lead.



Contents

<i>Preface</i>	xxiii
<i>A Note on Terminology</i>	xxv
Volume 1	
Adhesion Between Surfaces Coated with Self-Assembled Monolayers: Effect of Humidity / <i>Joan E. Curry, Sungsoo Kim</i>	1
Adhesion of a Cell on a Substrate / <i>Frédéric Pincet</i>	11
Adsorption of Polymers and Proteins on Heterogeneous Surfaces / <i>Vinay K. Gupta,</i> <i>Yu-Wen Huang</i>	23
Aerosol Nanoparticles: Theory of Coagulation / <i>Ken Won Lee, Soon-Bark Kwon</i>	35
Aerospace Applications for Epoxy Layered-Silicate Nanocomposites / <i>Chenggang Chen,</i> <i>Tia Benson Tolle</i>	45
Anion-Templated Self-Assembly: Inorganic Compounds / <i>Louise S. Evans,</i> <i>Philip A. Gale</i>	55
Anion-Templated Self-Assembly: Organic Compounds / <i>Paul D. Beer,</i> <i>Mark R. Sambrook</i>	69
Anodization Patterned on Aluminum Surfaces / <i>Juchao Yan, G.V. Rama Rao,</i> <i>Plamen B. Atanassov, Gabriel P. López</i>	83
Antibodies and Other Ligand-Receptor Systems with Infinite Binding Affinity / <i>Claude F. Meares</i>	89
Atmospheric Nanoparticles: Formation and Physicochemical Properties / <i>James N. Smith</i>	95
Atomic Force Microscope Nanolithography on Organized Molecular Films / <i>Seunghyun Lee, Haiwon Lee</i>	109
Atomic Force Microscopy and Single-Molecule Force Microscopy Studies of Biopolymers / <i>Nehal I. Abu-Lail, Terri A. Camesano</i>	119
Atomic Force Microscopy Imaging and Force Spectroscopy of Microbial Cell Surfaces / <i>Yves F. Dufrêne</i>	133
Atomic Force Microscopy Imaging Artifacts / <i>Stephanie Butler Velegol</i>	143
Atomic Force Microscopy Studies of Hydrogen-Bonded Nanostructures on Surfaces / <i>Holger Schönherr, Mercedes Crego-Calama, G. Julius Vancso, David N. Reinhoudt</i>	155
Atomic Force Microscopy Studies of Metal Ion Sorption / <i>Viriya Vithayaveroj, Sotira Yiacoumi,</i> <i>Costas Tsouris</i>	169
Atomic Scale Studies of Heterogeneous Catalysts / <i>Robert F. Klie, Kai Sun,</i> <i>Mark M. Disko, Jingyue Liu, Nigel D. Browning</i>	179
Axle Molecules Threaded Through Macrocycles / <i>Daryle H. Busch,</i> <i>Thomas Clifford</i>	195
Barcoded Nanowires / <i>Rebecca L. Stoermer, Christine D. Keating</i>	205
Barrier Properties of Ordered Multilayer Polymer Nanocomposites / <i>Bon-Cheol Ku,</i> <i>Alexandre Blumstein, Jayant Kumar, Lynne A. Samuelson, Dong Wook Kim</i>	213
Basic Nanostructured Catalysts / <i>Robert J. Davis</i>	225

Biocatalytic Single Enzyme Nanoparticles / Jay W. Grate, Jungbae Kim	235
Biological and Chemical Weapon Decontamination by Nanoparticles / Peter K. Stoimenov, Kenneth J. Klabunde	241
Biomedical Applications: Tissue Engineering, Therapeutic Devices, and Diagnostic Systems / J. Zachary Hilt, Mark E. Byrne	247
Biomedical Implants from Nanostructured Materials / Jeremiah Ejiolor, Thomas J. Webster	263
Bio-Microarrays Based on Functional Nanoparticles / Günter E. M. Tovar, Achim Weber	277
Biomimetic Approaches to the Design of Functional, Self-Assembling Systems / Mila Boncheva, George M. Whitesides	287
Biomimetic Macrocyclic Receptors for Carboxylate Anion Recognition / Rocco Ungaro, Alessandro Casnati, Francesco Sansone	295
Biomolecular Structure at Interfaces Measured by Infrared Spectroscopy / Curtis W. Meuse	311
Bionanoparticles / Krishnaswami S. Raja, Qian Wang	321
Bioremediation of Environmental Contaminants in Soil, Water, and Air / Xiomara C. Kretschmer, Russell R. Chianelli	331
Biosensor Applications: Porous Silicon Microcavities / Benjamin L. Miller, Philippe M. Fauchet, Scott R. Horner, Selena Chan	343
Biosensor Applications: Surface Engineering / Genady Zhavnerko, Kwon-Soo Ha	351
Biosensors Based on Carbon Nanotubes / Yuehe Lin, Wassana Yantasee, Fang Lu, Joseph Wang, Mustafa Musameh, Yi Tu, Zhifeng Ren	361
Biosensors for Detection of Chemical Warfare Agents / Elias Greenbaum, Miguel Rodriguez, Charlene A. Sanders	375
Biosurfaces: Water Structure at Interfaces / Yan-Yeung Luk	389
Block Copolymers Nanoparticles / Sandrine Pensec, Daniel Portinha, Laurent Bouteiller, Christophe Chassenieux	405
Carbon Forms Structured by Energetic Species: Amorphous, Nanotubes, and Crystalline / Yeshayahu Lifshitz	415
Carbon Nanotube Electrodes / Valentina Lazarescu	425
Carbon Nanotube Interconnects / Alain E. Kaloyeros, Kathleen A. Dunn, Autumn T. Carlsen, Anna W. Topol	435
Carbon Nanotube-Conducting Polymer Composites in Supercapacitors / Mark Hughes	447
Carbon Nanotubes and Metal Oxide Nanoribbons: Molecular Modeling / Amitesh Maiti	461
Carbon Nanotubes and Other Carbon Materials / Morinobu Endo, Yoong Ahm Kim, Takuya Hayashi, Mauricio Terrones, Mildred S. Dresselhaus	475
Carbon Nanotubes: Chemistry / Bin Zhao, Hui Hu, Elena Bekyarova, Mikhail E. Itkis, Sandip Niyogi, Robert C. Haddon	493
Carbon Nanotubes: Electrochemical Modification / Kannan Balasubramanian, Marko Burghard, Klaus Kern	507
Carbon Nanotubes: Electro-osmotic Flow Control in Membranes / Scott A. Miller, Charles R. Martin	519
Carbon Nanotubes: Energetics of Hydrogen Chemisorption / Ronald C. Brown	529
Carbon Nanotubes for Storage of Energy: Super Capacitors / Elzbieta Frackowiak	537
Carbon Nanotubes, Gas Adsorption on / Juan M. D. Tascón, Eduardo J. Bottani	547
Carbon Nanotubes: Hydrogen Storage and Its Mechanisms / Masashi Shiraiishi, Taishi Takenobu, Hiromichi Kataura, Masafumi Ata	557
Carbon Nanotubes: Incorporation Within Multilayered Polyelectrolyte Films / Jason H. Rouse, Peter T. Lillehei	567

Carbon Nanotubes: Optical Properties / <i>R. Saito, M. S. Dresselhaus, G. Dresselhaus, A. Jorio, A. G. Souza Filho, M. A. Pimenta</i>	575
Carbon Nanotubes: Supramolecular Mechanics / <i>Boris I. Yakobson, Luise S. Couchman</i>	587
Carbon Nanotubes: Thermal Properties / <i>J. Hone</i>	603
Catalysis by Supported Gold Nanoclusters / <i>D. Wayne Goodman</i>	611
Catalytic Processes over Supported Nanoparticles: Simulations / <i>Vladimir I. Elokhin, Aleksandr V. Myshlyavtsev</i>	621
Catalytic Properties of Micro- and Mesoporous Nanomaterials / <i>Johannes A. Lercher, Andreas Jentys</i>	633
Chaotic Transport in Antidot Lattices / <i>Tsuneya Ando</i>	649
Charge Carrier Dynamics of Nanoparticles / <i>Fanxin Wu, Jin Z. Zhang</i>	667
Charge Transfer in Metal–Molecule Heterostructures / <i>Debasish Kuila, David B. Janes, Clifford P. Kubiak</i>	683
Charge Transport Properties of Multilayer Nanostructures / <i>Daniel M. Schaadt</i>	699
Colloid Systems: Micelles, Nanocrystals, and Nanocrystal Superlattices / <i>B. L. V. Prasad, Savka I. Stoeva</i>	709
Colloidal Germanium Nanoparticles / <i>Boyd R. Taylor, Louisa J. Hope-Weeks</i>	717
Colloidal Micro- and Nanostructures Assembled on Patterned Surfaces / <i>Aránzazu del Campo, Anne-Sophie Duwez, Charles-André Fustin, Ulrich Jonas</i>	725
Colloidal Nanometals as Fuel Cell Catalyst Precursors / <i>Helmut Bönnemann, K. S. Nagabhushana</i>	739
Colloidal Nanoparticles: Aggregation Patterns at Model Molecular Surfaces / <i>Hamidou Haidara, Karine Mougin</i>	761
Colloidal Nanoparticles: Electrokinetic Characterization / <i>Kunio Furusawa, Hideo Matsumura</i>	773
Computational Analysis of Cadmium Sulfide (CdS) Nanocrystals / <i>Stacie Nunes, Zhigang Zhou, Jeffrey D. Evanseck, Jeffrey D. Madura</i>	787
Computational Analysis of Switchable Catenanes / <i>Xiang Zheng, Karl Sohlberg</i>	797
Computational Analysis of Switchable Rotaxanes / <i>Xiang Zheng, Karl Sohlberg</i>	807
Computational Analysis Using Normal and Multibody Modes / <i>Bryan C. Hathorn, Donald W. Noid, Bobby G. Sumpter, Chao Yang, William A. Goddard</i>	823
Computer-Aided Design of DNA-Based Nanoinstruments / <i>Alexander Hillisch, Stephan Diekmann</i>	833
Coordination Framework Topology: Influence of Using Multimodal Ligands / <i>Neil R. Champness, Neil S. Oxtoby</i>	845
Core/Shell Hydrogel Nanoparticles / <i>Clinton D. Jones, L. Andrew Lyon</i>	855
Core/Shell Nanospheres, Hollow Capsules, and Bottles / <i>Gang Zhang, Kai Zhang, Yi Yu, Bai Yang</i>	865
Cubosomes: Bicontinuous Liquid Crystalline Nanoparticles / <i>Patrick T. Spicer</i>	881
Volume 2	
Dealloying of Binary Alloys: Evolution of Nanoporosity / <i>Jonah Erlebacher</i>	893
Dendritic Nanocatalysts / <i>Kiyotomi Kaneda, Masahiko Ooe, Makoto Murata, Tomoo Mizugaki, Kohki Ebitani</i>	903
Dimensionally Graded Semiconductor Nanoparticle Films / <i>Arif A. Mamedov, Nicholas A. Kotov, Nataliya N. Mamedova</i>	913
Dip-Pen Nanolithography Using MHA and Optical Inks / <i>Brandon L. Weeks, Aleksandr Noy, Abigail E. Miller, Jennifer E. Klare, Bruce W. Woods, James J. De Yoreo</i>	923
Direct Force Measurement of Liposomes by Atomic Force Microscopy / <i>Guangzhao Mao, Xuemei Liang, K. Y. Simon Ng</i>	933

Dissymmetrical Nanoparticles / Stéphane Reculusa, Christophe Mingotaud, Etienne Duguet, Serge Ravaine	943
DNA-Conjugated Metal Nanoparticles: Applications in Chip-Detection / Wolfgang Fritzsche	955
Deoxyribonucleic Acid (DNA) Hybridization: Electronic Control / Kimberly Hamad-Schifferli	963
DNA Interactions with Functionalized Emulsions / Thierry Delair	977
Dynamic Atomic Force Microscopy Studies to Characterize Heterogeneous Surfaces / Ijeoma M. Nnebe, James W. Schneider	987
Electrical Double Layer Formation / Kun-Lin Yang, Sotira Yiacoumi, Costas Tsouris	1001
Electrically Conducting Polymeric Nanostructures: Techniques for One-Dimensional Synthesis / Andrew D. W. Carswell, Brian P. Grady	1015
Electrically Functional Nanostructures / Orlin D. Velev, Simon O. Lumsdon	1025
Electrochemical Langmuir Trough / Natalia Varaksa, Thomas F. Magnera, Josef Michl	1043
Electrochemical Sensors Based on Functionalized Nanoporous Silica / Yuehe Lin, Wassana Yantasee, Glen E. Fryxell	1051
Electrochemical Toxicity Sensors / James F. Rusling	1063
Electrochemically Self-Assembled Nanoarrays / S. Bandyopadhyay	1073
Electron Microscopy Imaging Techniques in Environmental and Geological Science / Satoshi Utsunomiya, Christopher S. Palenik, Rodney C. Ewing	1087
Electronic Switches / Richard J. Nichols, David J. Schiffrin, Wolfgang Haiss	1099
Enantioselectivity on Surfaces with Chiral Nanostructures / David M. Rampulla, Andrew J. Gellman	1113
Environmental and Sensing Applications of Molecular Self-Assembly / G. E. Fryxell, R. Shane Addleman, S. V. Mattigod, Y. Lin, T. S. Zemanian, H. Wu, Jerome C. Birnbaum, J. Liu, X. Feng	1125
Environmental Catalysts Based on Nanocrystalline Zeolites / Vicki H. Grassian, Sarah C. Larsen	1137
Environmental Nanoparticles / Alexandra Navrotsky	1147
Environmental Separation and Reactions: Zeolite Membranes / Wei Xing, João C. Diniz da Costa, G. Q. (Max) Lu, Z. F. Yan	1157
Ethane Preferred Conformation / Lionel Goodman, Vojislava Pophristic	1167
Fluorofullerenes / Olga V. Boltalina, Steven H. Strauss	1175
Fractal Analysis of Binding Kinetics on Biosensor Surfaces / Harshala Butala, Ajit Sadana	1191
Fullerenes and Carbon Nanotubes / Laszlo Mihaly	1203
Fullerenes: Chemistry / Mark S. Meier	1213
Fullerenes: Identification of Isomers Based on Nuclear Magnetic Resonance Spectra / Guangyu Sun	1223
Fullerenes: Topology and Structure / G. Benedek, M. Bernasconi	1235
Functionalization of Nanotube Surfaces / Stanislaus S. Wong, Sarbajit Banerjee	1251
Functionalization of Silica Surfaces / V. A. Tertykh	1269
Functionalization of Surface Layers on Ceramics / Toshihiro Ishikawa	1277
Gold Nanoclusters: Structural Disorder and Chirality at the Nanoscale / Ignacio L. Garzón	1287
Gold Nanoparticles on Titania: Activation and Behavior / Jose A. Rodriguez	1297
Guests Within Large Synthetic Hydrophobic Pockets Synthesized Using Polymer and Conventional Techniques / Bruce C. Gibb	1305

Guests Within Large Synthetic Hydrophobic Pockets Synthesized via Self-Assembly / Bruce C. Gibb	1329
Heterogeneous Surfaces with Nanosized Channel Lattices / Lifeng Chi, Michael Gleiche, Steven Lenhart, Nan Lu	1357
Hierarchically Imprinted Nanostructures for Separation of Metal Ions / Sheng Dai, Zongtao Zhang, Chengdu Liang	1369
High-Resolution Mass Spectrometry Studies of Heterogeneous Catalytic Reactions / Steven M. Thornberg, Deborah E. Hunka	1381
High Strength Alloys Containing Nanogranular Phases / Dmitri Valentinovich Louzguine, Akihisa Inoue	1393
Hydrogel Nanoparticles Synthesized by Cross-Linked Polyvinylpyrrolidone / Susmita Mitra, Dhruva Jyoti Bharali, Amarnath Maitra	1403
Ice Nanotubes Inside Carbon Nanotubes / Kenichiro Koga, Hideki Tanaka	1415
In Situ Electron Microscopy Techniques / Charles W. Allen	1425
Indium Arsenide (InAs) Islands on Silicon / P. C. Sharma, Kang L. Wang	1439
Inorganic Nanotubes: Structure, Synthesis, and Properties / Reshef Tenne	1447
Inorganic Nanotubes Synthesized by Chemical Transport Reactions / Maja Remskar	1457
Integrated Methods: Applications in Quantum Chemistry / Stephan Irle, Keiji Morokuma	1467
Intercalated Polypropylene Nanocomposites / Michael J. Solomon, Anongnat Somwangthanaroj	1483
Interfacial Forces Between a Solid Colloidal Particle and a Liquid / Sarah A. Nespolo, Geoffrey W. Stevens	1491
Interfacial Phenomena and Chemical Selectivity / Vinay K. Gupta	1505
Ionic Strength Effects: Tunable Nanocrystal Distribution in Colloidal Gold Films / E. Stefan Kooij, E. A. Martijn Brouwer, Herbert Wormeester, Bene Poelsema	1515
Iron Oxide Nanoparticles / Mamoru Senna	1525
Island Nucleation, Predictions of / Maria C. Bartelt (Deceased)	1533
Lab-on-a-Chip Micro Reactors for Chemical Synthesis / Paul D. I. Fletcher, Stephen J. Haswell, Paul Watts, Xunli Zhang	1547
Laser-Based Deposition Technique: Patterning Nanoparticles into Microstructures / Edward M. Nadgorny, Jaroslaw Drelich	1565
Layer-by-Layer Assembly of Gold Nanoclusters Modified with Self-Assembled Monolayers / Kohei Uosaki, Wenbo Song, Masayuki Okamura, Toshihiro Kondo	1581
Layer-by-Layer Assembly of Polyelectrolyte Films: Membrane and Catalyst Applications / Bernd Tieke, Ali Toutianoush	1591
Layer-by-Layer Assembly of Semiconducting and Photoreactive Bolaform Amphiphiles / Jason Locklin, Derek Patton, Chuanjun Xia, Xiaowu Fan, Rigoberto C. Advincula	1607
Layer-by-Layer Assembly of Thin Films of Mixed Nanoparticles / Jianchang Guo, Tianquan Lian, Encai Hao	1623
Liquid Crystals and Nanostructured Surfaces: A Novel System for Detecting Protein Binding Events / Yan-Yeung Luk	1635
Luminescence of Nanoparticle-Labeled Antibodies and Antigens / Shaopeng Wang, Nicholas A. Kotov	1647
Magnetic Behavior of Polymerized Fullerenes / Tatiana L. Makarova	1655
Magnetic Nanomaterials: Conventional Synthesis and Properties / Dajie Zhang	1665

Magnetic Nanomaterials: Nonconventional Synthesis and Chemical Design / <i>Luminita Patron, Ioana Mindru, Gabriela Marinescu</i>	1683
Magnetic Nanoparticles: Applications for Granular Recording Media / <i>David E. Nikles, J. W. Harrell</i>	1701
Magnetic Nanoparticles: Preparation and Properties / <i>Valérie Cabuil</i>	1715
Magnetic Nanoparticles in Fluid Suspension: Ferrofluid Applications / <i>Carlos Rinaldi, Thomas Franklin, Markus Zahn, Tahir Cader</i>	1731
Magnetic Properties of Nanocomposite Permanent Magnets / <i>Satoshi Hirosawa</i>	1749
Magnetic Properties of Nanoparticle Assemblies / <i>Xiangcheng Sun</i>	1761
Mechanical Properties of Nanowires and Nanobelts / <i>Zhong Lin Wang</i>	1773
Mechanosynthesis of Nanophase Powders / <i>F. Miani, F. Maurigh</i>	1787
Volume 3	
Mesoporous Materials (M41S): From Discovery to Application / <i>James C. Vartuli, Wielsaw J. Roth, Thomas F. Degnan, Jr.</i>	1797
Metal Clusters on Oxides / <i>Ivan Stensgaard</i>	1813
Metal Nanoparticle Ensembles: Collective Optical Properties / <i>Alexander Wei</i>	1821
Metal Nanoparticles and Their Self-Assembly into Electronic Nanostructures / <i>Venugopal Santhanam, Ronald P. Andres</i>	1829
Metal Nanoparticles Modified with Molecular Receptors / <i>Jian Liu</i>	1841
Metal Nanoparticles Prepared in Supercritical Carbon Dioxide Solutions / <i>Harry W. Rollins</i>	1851
Metal Nanoparticles Protected with Monolayers: Applications for Chemical Vapor Sensing and Gas Chromatography / <i>Jay W. Grate, David A. Nelson, Rhonda Skaggs, Robert E. Synovec, Gwen M. Gross</i>	1859
Metal Nanoparticles Used as Catalysts / <i>Naoki Toshima</i>	1869
Metal Nanostructures Synthesized by Photoexcitation / <i>Kei Murakoshi, Yoshihiro Nakato</i>	1881
Metal-Oxide Interfaces: Toward Design via Control of Defect Density / <i>A. Bogicevic</i>	1895
Metal Oxide Nanoparticles / <i>Ryan M. Richards</i>	1905
Metallic Nanopowders: An Overview / <i>Frederick Tepper, Marat I. Lerner, David S. Ginley</i>	1921
Metallic Nanopowders: Rocket Propulsion Applications / <i>Leonid Kaledin, Fred Tepper</i>	1935
Mica Surfaces: Charge Nucleation and Wear / <i>James M. Helt, James D. Batteas</i>	1947
Microgel Dispersions: Colloidal Forces and Phase Behavior / <i>Jianzhong Wu, Zhibing Hu</i>	1967
Microweighing in Supercritical Carbon Dioxide / <i>You-Ting Wu, Christine S. Grant</i>	1977
Mineral Nanoparticles: Electrokinetics / <i>Mehmet S. Celik, Bahri Ersoy</i>	1991
Mixed Metal Oxide Nanoparticles / <i>Pramesh N. Kapoor, Ajay Kumar Bhagi, Ravichandra S. Mulukutla, Kenneth J. Klabunde</i>	2007
Molecular Assembly of Nanowires / <i>Tomoyuki Akutagawa, Takayoshi Nakamura, Jan Becher</i>	2019
Molecular Assembly Organosilanes / <i>Atsushi Takahara</i>	2031
Molecular Computing Machines / <i>Yaakov Benenson, Ehud Shapiro</i>	2043
Molecular Designs for Self-Organized Superstructures / <i>Makoto Tadokoro</i>	2057
Molecular Electronic Logic and Memory / <i>Dustin K. James, James M. Tour</i>	2067
Molecular Electronics: Analysis and Design of Switchable and Programmable Devices Using Ab Initio Methods / <i>Pedro A. Derosa, Vandana R. Tarigopula, Jorge M. Seminario</i>	2081

Molecular Manipulator Dynamic Design Criteria / <i>Andrés Jaramillo-Botero</i>	2101
Molecular Motor-Powered Nanodevices: Mechanisms for Control / <i>Jacob J. Schmidt, Carlo D. Montemagno</i>	2113
Molecular Probes of Cation–Arene Interactions / <i>George W. Gokel</i>	2123
Molecular Simulations of DNA Counterion Distributions / <i>Alexander P. Lyubartsev</i>	2131
Molecular Switches / <i>Jean-Pierre Launay, Christophe Coudret, Christian Joachim</i>	2145
Molecular Switches and Unidirectional Molecular Motors: Light-Induced Switching and Motion / <i>Richard A. van Delden, Ben L. Feringa</i>	2159
Molecular Wires / <i>Dustin K. James, James M. Tour</i>	2177
Moore’s Law, Performance and Power Dissipation / <i>Laszlo B. Kish</i>	2197
Motor Proteins in Synthetic Materials and Devices / <i>Henry Hess, George Bachand, Viola Vogel</i>	2201
Nano-Mesoscopic Interface: Hybrid Devices / <i>Gianfranco Cerofolini</i>	2211
Nanoarrays Synthesized from Porous Alumina / <i>Latika Menon</i>	2221
Nanoceramics / <i>Abbas Khaleel</i>	2237
Nanocrystal Arrays: Self-Assembly and Physical Properties / <i>Xiao Min Lin, Raghuvveer Parthasarathy, Heinrich M. Jaeger</i>	2245
Nanocrystal Dispersed Platinum Particles: Preparation and Catalytic Properties / <i>Ioan Balint, Akane Miyazaki</i>	2259
Nanocrystalline Materials: Fatigue / <i>Alexei Yu. Vinogradov, Sean R. Agnew</i>	2269
Nanocrystalline Materials: Synthesis and Properties / <i>Alexandr I. Gusev</i>	2289
Nanocrystallization / <i>John H. Perepezko</i>	2305
Nanocrystals Synthesized in Colloidal Self-Assemblies / <i>M. P. Pileni</i>	2317
Nanodiamonds / <i>Jean-Yves Raty, Giulia Galli</i>	2329
Nanoencapsulation of Bioactive Substances / <i>Yury E. Shapiro</i>	2339
Nanoengineered Capsules with Specific Layer Structures / <i>Lars Dähne, Claire S. Peyratout</i>	2355
Nanoengineered Polymer Microcapsules / <i>Gleb B. Sukhorukov</i>	2369
Nanofilms in Giant Magnetoresistance Heads / <i>Edward Grochowski, Robert E. Fontana, Jr.</i>	2383
Nanofiltration Separations / <i>Eric M. V. Hoek, Anna Jawor</i>	2399
Nanolithography: Length-Scale Limitations / <i>Takashi Ito</i>	2413
Nanomaterials and Molecular Devices: De Novo Design Theory / <i>Kwang S. Kim, P. Tarakeshwar, Han Myoung Lee</i>	2423
Nanomaterials: Manufacturing, Processing, and Applications / <i>Pramod K. Sharma, Weifang Miao, Anit Giri, Srikanth Raghunathan</i>	2435
Nanomaterials: New Trends / <i>Richard Silberglitt</i>	2451
Nanomaterials: Recent Advances in Technology and Industry / <i>Ganesh Skandan, Amit Singhal</i>	2465
Nanoparticles: Generation, Surface Functionalization, and Ion Sensing / <i>Jason J. Davis, Paul D. Beer</i>	2477
Nanoparticles: Synthesis in Polymer Substrates / <i>Bai Yang, Junhu Zhang</i>	2493
Nanostructure and Dynamic Organization of Lipid Membranes / <i>J. Gaudioso, D. Y. Sasaki</i>	2507
Nanostructure of Ionic Amphiphilic Block Copolymer Monolayer at Air / Water Interface / <i>Emiko Mouri, Hideki Matsuoka</i>	2519
Nanostructured Catalysts / <i>Ravichandra S. Mulukutla</i>	2531
Nanostructured Catalytic Materials: Design and Synthesis / <i>Hua Chun Zeng</i>	2539

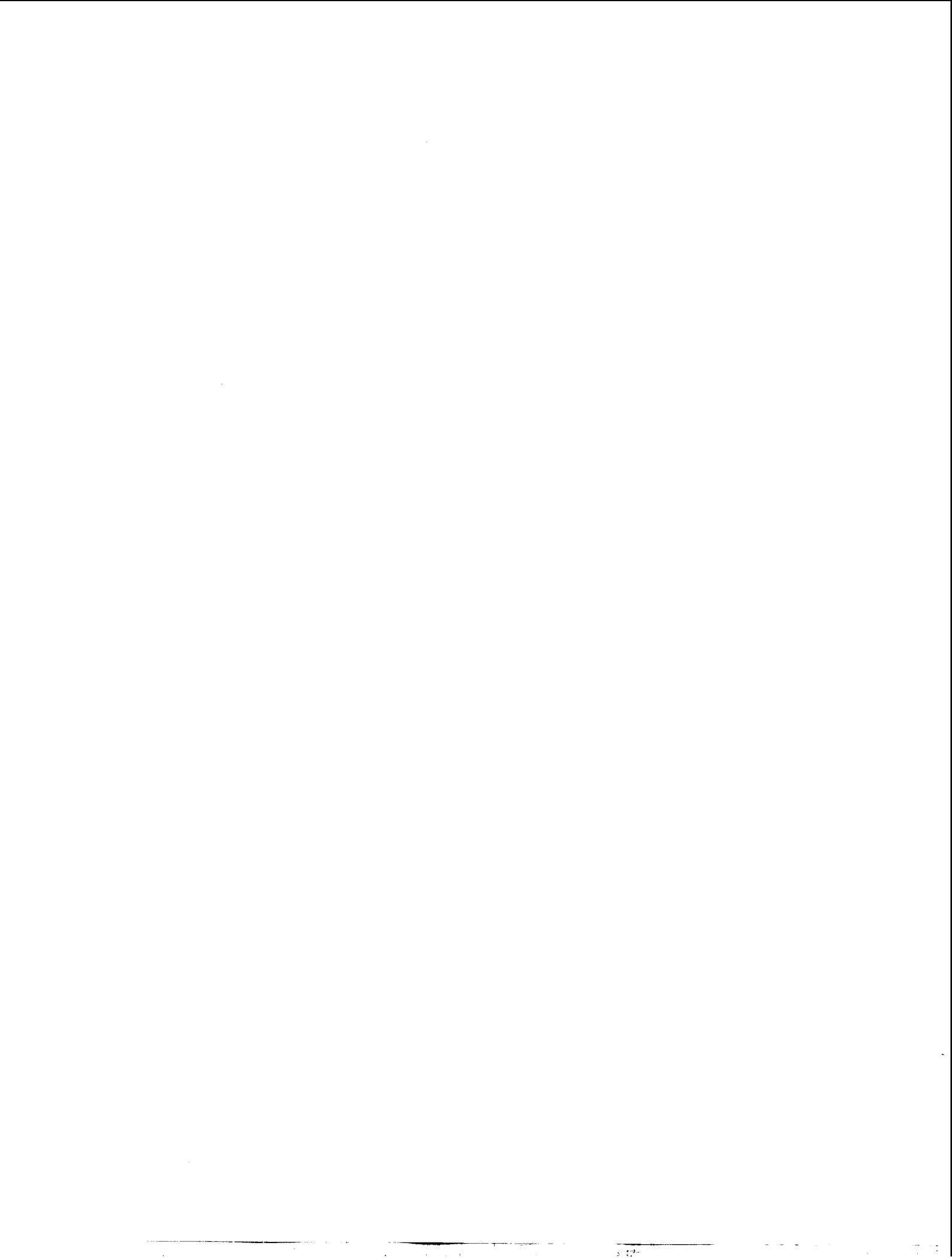
Nanostructured Composites Using Carbon-Derived Fibers / <i>Peter M. A. Sherwood</i>	2551
Nanostructures Synthesized by Deposition of Metals on Microtubule Supports / <i>Silke Behrens, Eberhard Unger</i>	2563
Nanostructured Materials Synthesized by Mechanical Attrition / <i>Carl C. Koch</i>	2571
Nanostructured Materials Synthesized by Mechanical Means / <i>H.-J. Fecht</i>	2583
Nanostructured Materials Synthesized in Supercritical Fluid / <i>Yuehe Lin,</i> <i>Xiang-Rong Ye, Chien M. Wai</i>	2595
Nanostructured Ultrastrong Materials / <i>Nicholas A. Kotov, Arif A. Mamedov,</i> <i>Dirk M. Guldi, Zhiyong Tang, Maurizio Prato, James Wicksted, Andreas Hirsch</i>	2607
Nanostructures Based on Conducting Polymers / <i>Shaun F. Filocamo,</i> <i>Mark W. Grinstaff</i>	2615
Nanostructures Based on Layered Transition Metal Chalcogenides / <i>Russell R. Chianelli, Myriam Perez De la Rosa</i>	2627
Nanostructures Derived from Phase Separated Polymers / <i>Michael R. Bockstaller,</i> <i>Edwin L. Thomas</i>	2641
Nanostructures Replicated by Polymer Molding / <i>Daniel B. Wolfe,</i> <i>J. Christopher Love, George M. Whitesides</i>	2657
Nanotube Sensors / <i>Marc Wirtz, Charles R. Martin</i>	2667
Volume 4	
Near-Field Microscopy Techniques / <i>Björn T. Rosner, Daniel W. van der Weide</i>	2677
Near-Field Raman Spectroscopy / <i>Eric Ayars</i>	2687
Near-Field Raman Spectroscopy: Enhancing Spatial Resolution Using Metallic Tips / <i>Satoshi Kawata, Yasushi Inouye</i>	2695
Near-Field Scanning Optical Microscopy: Chemical Imaging / <i>Bogdan Dragnea</i>	2703
Nucleation of Nanoparticles in Ultrathin Polymer Films / <i>Pieter Stroeve</i>	2713
Nucleoside- and Nucleobase-Substituted Oligopyrrolic Macrocycles / <i>Vladimír Král, Martin Valík, Tatiana V. Shishkanova, Jonathan L. Sessler</i>	2721
Oil-Filled Nanocapsules / <i>Royale S. Underhill</i>	2739
Optical Molecular Devices / <i>A. Prasanna de Silva, Nathan D. McClenaghan</i>	2749
Optical Nanosensors and Nanobiosensors / <i>Brian M. Cullum</i>	2757
Ordered Vesicles at the Silicon–Water Interface / <i>Duncan J. McGillivray</i>	2769
Organofullerenes in Water / <i>Eiichi Nakamura, Hiroyuki Isobe</i>	2779
Oxide Nanoparticles: Electrochemical Performance / <i>Dominique Larcher,</i> <i>Jean-Marie Tarascon</i>	2791
Palladium Nanoclusters: Preparation and Synthesis / <i>Kiyotomi Kaneda,</i> <i>Kwang-Min Choi, Tomoo Mizugaki, Kohki Ebitani</i>	2803
Phase Behavior of Nanoparticle Suspensions / <i>S. Ramakrishnan, C. F. Zukoski</i>	2813
Phase Transfer of Monosaccharides Through Noncovalent Interactions / <i>Elizabeth K. Auty, Anthony P. Davis</i>	2825
Photochemistry of Membrane-Coated Nanoparticles / <i>Ulrich Siggel,</i> <i>Guangtao Li, Jürgen-Hinrich Fuhrhop</i>	2835
Photonic Crystal Fibers / <i>P. St.J. Russell, J. C. Knight, T. A. Birks, P. J. Roberts</i>	2853
Photonic Applications of Printed and Molded Nanostructures / <i>John A. Rogers</i>	2869
Photovoltaics for the Next Generation: Organic-Based Solar Cells / <i>Sean E. Shaheen, David S. Ginley</i>	2879
Polyelectrolyte–Surfactant Complex Nanoparticles / <i>Hans-Peter Hentze</i>	2897
Polymer Colloids and Their Metallation / <i>Lyudmila M. Bronstein</i>	2903
Polymer Nanocomposites with Particle and Carbon Nanotube Fillers / <i>B. J. Ash, A. Eitan, L. S. Schadler</i>	2917

Polymer Nanofibers Prepared by Electrospinning / Roland Dersch, Andreas Greiner, Joachim H. Wendorff	2931
Polymer Nanoparticles for Gene Delivery: Synthesis and Processing / Jie Wen, Kam W. Leong	2939
Polymer Nanowires by Controlled Chain Polymerization / Yuji Okawa, Masakazu Aono	2951
Polymer-Clay Nanocomposites and Polymer Brushes from Clay Surfaces / Xiaowu Fan, Chuanjun Xia, Rigoberto C. Advincula	2959
Polymeric and Biomolecular Nanostructures: Fabrication by Scanning Probe Lithography / Stefan Zauscher	2973
Polymer-Mediated Self-Assembly of Nanoparticles / Tyler B. Norsten, Amitav Sanyal, Roy Shenhar, Vincent M. Rotello	2985
Polymer-Nanoparticle Composites / Kevin Sill, Seunghoo Yoo, Todd Emrick	2999
Polypropylene and Thermoplastic Olefins Nanocomposites / Francis M. Mirabella, Jr.	3015
Protein Adsorption Kinetics Under an Applied Electric Field / Paul R. Van Tassel	3031
Protein Adsorption Studied by Atomic Force Microscopy / David T. Kim, Harvey W. Blanch, Clayton J. Radke	3041
Protein Nanotubes as Building Blocks / Hiroshi Matsui	3065
Proteins: Structure and Interaction Patterns to Solid Surfaces / Thomas J. Webster	3079
Quantum Dot Arrays: Electromagnetic Properties / Sergey A. Maksimenko, Gregory Ya. Slepyan	3097
Quantum Dot Lasers / Mikhail V. Maximov, Nikolai N. Ledentsov	3109
Quantum Dots: Electronic Coupling and Structural Ordering / G. S. Solomon	3127
Quantum Dots: Inelastic Light Scattering from Electronic Excitations / Christian Schüller	3155
Quantum Dots Made of Cadmium Selenide (CdSe): Formation and Characterization / Kenzo Maehashi, Hisao Nakashima	3167
Quantum Dots Made of Metals: Preparation and Characterization / J. P. Wilcoxon	3177
Quantum Dots: Phonons in Self-Assembled Multiple Germanium Structures / Jianlin Liu, Aleksandr Khitun, Kang L. Wang	3203
Quantum Dots, Self-Assembled: Calculation of Electronic Structures and Optical Properties / Andrew Williamson	3213
Quantum Dots, Self-Formed: Structural and Optical Characterization / Shun-ichi Gonda, Hajime Asahi	3227
Quantum Dots, Semiconductor: Atomic Ordering over Time / Peter Moeck	3237
Quantum Dots, Semiconductor: Site-Controlled Self-Organization / S. Kohmoto, H. Nakamura, S. Nishikawa, T. Yang, K. Asakawa	3247
Quantum Rods Made of Cadmium Selenide (CdSe): Anisotropy / Liang-shi Li, A. Paul Alivisatos	3255
Raman Spectroscopy Studies of Carbon Nanotube-Polymer Composites / Bin Chen	3267
Ring Structures from Nanoparticles and Other Nanoscale Building Blocks / Zhen Liu, Rastislav Levicky	3281
Risk Assessment and Benefits / Douglas Mulhall	3289
Volume 5	
Scanning Single-Electron Transistor Microscopy / N. B. Zhitenev, T. A. Fulton	3297
Scanning Tunneling Microscopy of Chiral Pair Self-Assembled Monolayers / Yuguang Cai, Steven L. Bernasek	3305

Self-Assembled Monolayers: Chemical and Physical Modification Under Vacuum Conditions / Jessica Torres, Anthony J. Wagner, Christopher C. Perry, Glenn M. Wolfe, D. Howard Fairbrother	3315
Self-Assembled Monolayers: Effects of Surface Nanostructure on Wetting / Jun Yang, Jingmin Han, Kelvin Isaacson, Daniel Y. Kwok	3331
Self-Assembled Silane Monolayers: Conversion of Cyano to Carboxylic Termination / Chandra Sekhar Palla, Alexander Couzis	3345
Self-Assembled Thin Films: Optical Characterization / Herbert Wormeester, E. Stefan Kooij, Bene Poelsema	3361
Self-Assembly and Biocatalysis of Polymers and Polymer-Ceramic Composites / Christy Ford, Vijay John, Gary McPherson, Jibao He, Joseph Akkara, David Kaplan, Arijit Bose	3373
Self-Assembly and Multiple Phases of Layered Double Hydroxides / Zhi Ping Xu, Paul S. Braterman	3387
Self-Assembly Directed by NH-O Hydrogen Bonding / Katrina A. Jolliffe, Leonard F. Lindoy	3399
Self-Assembly of Cavitand-Based Coordination Cages / Laura Pirondini, Enrico Dalcanale	3415
Self-Assembly of Chiral and Pseudochiral Molecules at Interfaces / Dalia G. Yablon	3431
Self-Assembly of Cyclic Peptides in Hydrogen-Bonded Nanotubes / Roberto J. Brea, Juan R. Granja	3439
Self-Assembly of Nanocolloidal Gold Films / E. Stefan Kooij, E. A. Martijn Brouwer, Agnes A. Mewe, Herbert Wormeester, Bene Poelsema	3459
Self-Assembly of Organic Films for Nonlinear Optical Materials / Matthew Guzy, Richey M. Davis, Patrick J. Neyman, Charles Brands, J. R. Heflin, Harry W. Gibson, Kevin E. Van Cott	3471
Self-Assembly of Porphyrinic Materials on Surfaces / Charles Michael Drain, James D. Batteas, Gabriela Smeureanu, Sandeep Patel	3481
Self-Assembly of Redox-Responsive Receptors / Kay Severin	3503
Self-Assembly of Two- and Three-Dimensional Nanostructures for Electronic Applications / Ilona Kretzschmar, Mark A. Reed	3513
Sensors Based on Chemicurrents / B. Roldan Cuenya, E. W. McFarland	3527
Silane Self-Assembled Monolayers: Nanoscale Domains by Sequential Adsorption / Nitin Kumar	3539
Silicon Nanoclusters: Simulations / Aaron Puzder	3551
Silicon Nanocrystals: Quantum Confinement / James R. Chelikowsky	3563
Single Molecule Spectroscopy Studies to Characterize Nanomaterials / Daniel A. Higgins, Yanwen Hou	3575
Single-Walled Carbon Nanotubes: Density Functional Theory Study on Field Emission Properties / Xiaofeng Duan, Brahim Akdim, Ruth Pachter	3597
Single-Walled Carbon Nanotubes: Geometries, Electronic Properties, and Actuation / Guangyu Sun, Marc Nicklaus, Miklos Kertesz	3605
Single-Walled Carbon Nanotubes: Separation Using Capillary Electrophoresis / Stephen K. Doorn	3617
Single-Walled Carbon Nanotubes: Structures and Symmetries / Carter T. White, John W. Mintmire	3629
Small Amplitude Atomic Force Microscopy / Peter M. Hoffmann	3641
Smart Nanotubes for Biotechnology and Biocatalysis / Charles R. Martin, Punit Kohli	3655
Spin-Coated Cyanogels / Shu Zhu, Andrew B. Bocarsly	3667
Stability of Nanostructures on Surfaces / Karsten Pohl	3675

Structural and Optical Anisotropy in Nanoporous Anodic Aluminum Oxide / <i>E. Stefan Kooij, Aurelian C. Gálcă, Herbert Wormeester, Bene Poelsema</i>	3685
Structural Base of Halide Transport Through Biological Membranes / <i>Lars-Oliver Essen</i>	3697
Structural Color / <i>Pete Vukusic</i>	3713
Structural Nanomaterials / <i>Joanna R. Groza, Jeffrey C. Gibeling</i>	3723
Structural Transitions in Thin Films / <i>Rajarshi Banerjee, Gregory B. Thompson,</i> <i>Hamish L. Fraser</i>	3737
Sum Frequency Generation Vibrational Spectroscopy Studies of Molecular Orientation at Interfaces / <i>Zhan Chen</i>	3749
Superconducting Nanowires Templated by Single Molecules / <i>Alexey Bezryadin,</i> <i>Anthony Bollinger, David Hopkins, Michael Murphey,</i> <i>Mikas Remeika, Andrey Rogachev</i>	3761
Supramolecular Aggregates with Controlled Size and Shape on Solid Surfaces / <i>Takashi Yokoyama, Toshiya Kamikado, Shiyoshi Yokoyama, Shinro Mashiko</i>	3775
Supramolecular Networks Synthesized in Nanoparticle-Polymer Mixtures / <i>Anna C. Balazs, Gavin A. Buxton</i>	3785
Surface Chemistry of Nanocrystalline Oxides of Magnesium and Aluminum / <i>Richard M. Narske</i>	3795
Surface Forces on Nanoparticles Determined by Direct Measurement / <i>Jeong-Min Cho, Georgios Pyrgiotakis, Wolfgang M. Sigmund</i>	3805
Surface Plasmon Spectra of Silver and Gold Nanoparticle Assemblies / <i>Mondona Zangeneh, Roger Terrill</i>	3819
Template-Directed Assembly of Dinuclear Triple-Stranded Helicates / <i>Markus Albrecht</i>	3831
Templating Aerogels for Tunable Nanoporosity / <i>Aydin K. Sunol,</i> <i>Sermin G. Sunol</i>	3843
Templating Polymer Crystal Growth Using Block Copolymers / <i>Yueh-Lin Loo</i>	3853
Thermal Conductivity of Nanoceramics / <i>Paul G. Klemens</i>	3867
Thermal Effect on the Luminescence Properties of Quantum Dots / <i>X. B. Zhang, R. D. Dupuis</i>	3873
Thermal Properties of Nanobridges / <i>Jeong Won Kang, Ho Jung Hwang</i>	3883
Thermodynamics at the Meso- and Nanoscale / <i>Mikhail A. Anisimov</i>	3893
Three-Dimensional Nanofabrication Using Multiphoton Absorption / <i>John T. Fourkas, Tommaso Baldacchini</i>	3905
Titanium Dioxide Coatings on Stainless Steel / <i>Ganesh Balasubramanian,</i> <i>Dionysios D. Dionysiou, Makram T. Suidan</i>	3917
Tribology at the Nanoscale / <i>Peter T. Cummings, Clare McCabe</i>	3927
Tribology of Inorganic Nanoparticles / <i>Lev Rapoport</i>	3933
Tungsten Carbide-Cobalt Nanocomposites: Production and Mechanical Properties / <i>Purnesh Seegopaul, Zhigang Fang</i>	3943
X-Ray Absorption Studies of Catalyst Nanostructures / <i>J. T. Miller,</i> <i>M. K. Neylon, C. L. Marshall, A. J. Kropf</i>	3953
Yttria-Tetragonally Stabilized Zirconia: Aqueous Synthesis and Processing / <i>R. Allen Kimel</i>	3973

Index



Topical Contents

Analytical and Characterization Methods

Atomic Force Microscopy and Single-Molecule Force Microscopy Studies of Biopolymers
Atomic Force Microscopy Imaging Artifacts
Atomic Force Microscopy Studies of Metal Ion Sorption
Direct Force Measurement of Liposomes by Atomic Force Microscopy
Dynamic Atomic Force Microscopy Studies to Characterize Heterogeneous Surfaces
Electron Microscopy Imaging Techniques in Environmental and Geological Science
Fullerenes: Identification of Isomers Based on Nuclear Magnetic Resonance Spectra
High-Resolution Mass Spectrometry Studies of Heterogeneous Catalytic Reactions
In Situ Electron Microscopy Techniques
Near-Field Microscopy Techniques
Near-Field Raman Spectroscopy
Near-Field Scanning Optical Microscopy: Enhancing Spatial Resolution Using Metallic Tips
Near-Field Scanning Optical Microscopy: Chemical Imaging
Protein Adsorption Studied by Atomic Force Microscopy
Scanning Single-Electron Transistor Microscopy
Scanning Tunneling Microscopy of Chiral Pair Self-Assembled Monolayers
Self-Assembled Thin Films: Optical Characterization
Single Molecule Spectroscopy Studies to Characterize Nanomaterials
Small-Amplitude Atomic Force Microscopy
Structural Color
Sum Frequency Generation Vibrational Spectroscopy Studies of Molecular Orientation at Interfaces
Surface Forces on Nanoparticles Determined by Direct Measurement
Surface Plasmon Spectra of Silver and Gold Nanoparticle Assemblies
X-Ray Absorption Studies of Catalyst Nanostructures

Bionanotechnology

Atomic Force Microscopy Imaging and Force Spectroscopy of Microbial Cell Surfaces
Biocatalytic Single-Enzyme Nanoparticles
Biomedical Applications: Tissue Engineering, Therapeutic Devices, and Diagnostic Systems
Biomedical Implants from Nanostructured Materials
Bio-Microarrays Based on Functional Nanoparticles
Biomolecular Structure at Interfaces Measured by Infrared Spectroscopy
Bionanoparticles
Biosensor Applications: Surface Engineering
Biosensors Based on Carbon Nanotubes
Computer-Aided Design of DNA-Based Nanoinstruments
DNA Hybridization: Electronic Control
DNA Interactions with Functionalized Emulsions
DNA-Conjugated Metal Nanoparticles: Applications in Chip Detection
Electrochemical Sensors Based on Functionalized Nanoporous Silica
Fractal Analysis of Binding Kinetics on Biosensor Surfaces
Hierarchically Imprinted Nanostructures for Separation of Metal Ions
Liquid Crystals and Nanostructured Surfaces: A Novel System for Detecting Protein-Binding Events
Motor Proteins in Synthetic Materials and Devices
Nanoencapsulation of Bioactive Substances

Nucleoside- and Nucleobase-Substituted Olygopyrrolic Macrocycles
 Optical Nanosensors and Nanobiosensors
 Protein Adsorption Kinetics Under an Applied Electric Field
 Protein Adsorption Studied by Atomic Force Microscopy
 Protein Nanotubes as Building Blocks
 Proteins: Structure and Interaction Patterns to Solid Surfaces
 Smart Nanotubes for Biotechnology and Biocatalysis
 Structural Base of Halide Transport Through Biological Membranes

Carbon Nanotubes

Biosensors Based on Carbon Nanotubes
 Carbon Forms Structured by Energetic Species: Amorphous, Nanotubes, and Crystalline
 Carbon Nanotube Electrodes
 Carbon Nanotube Interconnects
 Carbon Nanotubes and Other Carbon Materials
 Carbon Nanotubes for Storage of Energy: Super Capacitors
 Carbon Nanotubes: Chemistry
 Carbon Nanotubes: Electrochemical Modification
 Carbon Nanotubes: Electroosmotic Flow Control in Membranes
 Carbon Nanotubes: Energetics of Hydrogen Chemisorption
 Carbon Nanotubes, Gas Adsorption on
 Carbon Nanotubes: Hydrogen Storage and Its Mechanisms
 Carbon Nanotubes: Optical Properties
 Carbon Nanotubes: Supramolecular Mechanics
 Carbon Nanotubes: Thermal Properties
 Fullerenes and Carbon Nanotubes
 Ice Nanotubes Inside Carbon Nanotubes
 Nanodiamonds
 Nanostructured Ultrastrong Materials
 Raman Spectroscopy Studies of Carbon Nanotube-Polymer Composites
 Single-Walled Carbon Nanotubes: Density Functional Theory Study on Field Emission Properties
 Single-Walled Carbon Nanotubes: Geometries, Electronic Properties, and Actuation
 Single-Walled Carbon Nanotubes: Separation Using Capillary Electrophoresis
 Single-Walled Carbon Nanotubes: Structures and Symmetries
 Thermal Conductivity of Nanoceramics

Catalysts and Catalysis at the Nanoscale

Atomic Scale Studies of Heterogeneous Catalysts
 Basic Nanostructured Catalysts
 Biocatalytic Single-Enzyme Nanoparticles
 Catalysis by Supported Gold Nanoclusters
 Catalytic Properties of Micro- and Mesoporous Nanomaterials
 Colloidal Nanometals as Fuel Cell Catalyst Precursors
 Dendritic Nanocatalysts
 Environmental Catalysts Based on Nanocrystalline Zeolites
 High-Resolution Mass Spectrometry Studies of Heterogeneous Catalytic Reactions
 Layer-by-Layer Assembly of Polyelectrolyte Films: Membrane and Catalyst Applications
 Layer-by-Layer Assembly of Semiconducting and Photoreactive Bolaform Amphiphiles
 Metal Clusters on Oxides
 Metal Nanoparticles Used as Catalysts
 Nanocrystal Dispersed Platinum Particles: Preparation and Catalytic Properties
 Nanostructured Catalysts
 Nanostructured Catalytic Materials: Design and Synthesis
 Palladium Nanoclusters: Preparation and Synthesis
 Self-Assembly and Biocatalysis of Polymers and Polymer-Ceramic Composites
 Smart Nanotubes for Biotechnology and Biocatalysis
 Stability of Nanostructures on Surfaces
 X-Ray Absorption Studies of Catalyst Nanostructures

Colloidal Phenomena

Aerosol Nanoparticles: Theory of Coagulation
 Colloid Systems: Micelles, Nanocrystals, and Nanocrystal Superlattices
 Colloidal Germanium Nanoparticles
 Colloidal Nanoparticles: Aggregation Patterns at Model Molecular Surfaces
 Colloidal Nanoparticles: Electrokinetic Characterization
 Hydrogel Nanoparticles Made of Cross-Linked Polyvinylpyrrolidone
 Interfacial Forces Between a Solid Colloidal Particle and a Liquid
 Ionic Strength Effects: Tunable Nanocrystal Distribution in Colloidal Gold Films
 Microgel Dispersions: Colloidal Forces and Phase Behavior
 Mineral Nanoparticles: Electrokinetics
 Nanocrystals Synthesized in Colloidal Self-Assemblies
 Nanoengineered Polymer Microcapsules
 Polymer Colloids and Their Metallation
 Self-Assembly of Nanocolloidal Gold Films

Computational and Theoretical Modeling

Carbon Nanotubes and Metal Oxide Nanoribbons: Molecular Modeling
 Carbon Nanotubes: Electroosmotic Flow Control in Membranes
 Catalytic Processes over Supported Nanoparticles: Simulations
 Chaotic Transport in Antidot Lattices
 Colloidal Nanoparticles: Aggregation Patterns at Model Molecular Surfaces
 Computational Analysis of Cadmium Sulfide (CdS) Nanocrystals
 Computational Analysis of Switchable Catenanes
 Computational Analysis of Switchable Rotaxanes
 Computational Analysis Using Normal and Multibody Modes
 Ethane-Preferred Conformation
 Integrated Methods; Applications in Quantum Chemistry
 Island Nucleation, Predictions of
 Molecular Computing Machines
 Molecular Probes of Cation-Arene Interactions
 Molecular Simulations of DNA Counterion Distributions
 Molecular Wires
 Moore's Law: Performance and Power Dissipation
 Nanomaterials and Molecular Devices: De Novo Design Theory
 Quantum Dots, Self-Assembled: Calculation of Electronic Structures and Optical Properties
 Silicon Nanoclusters: Simulations
 Single-Walled Carbon Nanotubes: Geometries, Electronic Properties, and Actuation
 Thermodynamics at the Meso- and Nanoscale
 Tribology at the Nanoscale

Design and Fabrication of Nanocomposites

Aerospace Applications for Epoxy Layered-Silicate Nanocomposites
 Atomic Force Microscope Nanolithography on Organized Molecular Films
 Barrier Properties of Ordered Multilayer Polymer Nanocomposites
 Carbon Nanotube-Conducting Polymer Composites in Supercapacitors
 Carbon Nanotubes: Incorporation Within Multilayered Polyelectrolyte Films
 Colloidal Micro- and Nanostructures Assembled on Patterned Surfaces
 Dimensionally Graded Semiconductor Nanoparticle Films
 Dip-Pen Nanolithography Using MHA and Optical Inks
 Functionalization of Nanotube Surfaces
 High-Strength Alloys Containing Nanogranular Phases
 Lab-on-a-Chip Micro Reactors for Chemical Synthesis
 Laser-Based Deposition Technique: Patterning Nanoparticles into Microstructures
 Layer-by-Layer Assembly of Semiconducting and Photoreactive Bolaform Amphiphiles
 Layer-by-Layer Assembly of Thin Films of Mixed Nanoparticles
 Magnetic Properties of Nanocomposite Permanent Magnets

Mechanosynthesis of Nanophase Powders
 Metal Nanostructures Synthesized by Photoexcitation
 Microweighing in Supercritical Carbon Dioxide
 Nanolithography: Length-Scale Limitations
 Nanomaterials: New Trends
 Nanostructured Composites Using Carbon-Derived Fibers
 Nanostructured Materials Synthesized by Deposition of Metals on Microtubule Supports
 Nanostructures Replicated by Polymer Molding
 Nucleation of Nanoparticles in Ultrathin Polymer Films
 Polymer Nanocomposites with Particle and Carbon Nanotube Fillers
 Polymer Nanofibers Prepared by Electrospinning
 Polymer Nanowires Conjugated by Controlled Chain Polymerization
 Polymer-Clay Nanocomposites and Polymer Brushes from Clay Surfaces
 Polymer-Nanoparticle Composites
 Polypropylene and Thermoplastic Olefin Nanocomposites
 Self-Assembly and Biocatalysis of Polymers and Polymer-Ceramic Composites
 Spin-Coated Cyanogels
 Structural Nanomaterials
 Structural Transitions in Thin Films
 Superconducting Nanowires Templated by Single Molecules
 Template-Directed Assembly of Dinuclear Triple-Stranded Helicates
 Templating Polymer Crystal Growth Using Block Copolymers
 Three-Dimensional Nanofabrication Using Multiphoton Absorption
 Tungsten Carbide-Cobalt Nanocomposites: Production and Mechanical Properties

Environmental Applications and Societal Implications

Atmospheric Nanoparticles: Formation and Physicochemical Properties
 Biological and Chemical Weapon Decontamination by Nanoparticles
 Bioremediation of Environmental Contaminants in Soil, Water, and Air
 Biosensors for Detection of Chemical Warfare Agents
 Environmental Catalysts Based on Nanocrystalline Zeolites
 Environmental Nanoparticles
 Environmental Separation and Reactions: Zeolite Membranes
 Gold Nanoparticles on Titania: Activation and Behavior
 Nanofiltration Separations
 Nanomaterials: New Trends
 Photovoltaics for the Next Generation: Organic-Based Solar Cells
 Risk Assessment and Benefits

Fullerenes

Fluorofullerenes
 Fullerenes and Carbon Nanotubes
 Fullerenes: Chemistry
 Fullerenes: Identification of Isomers Based on Nuclear Magnetic Resonance Spectra
 Fullerenes: Topology and Structure
 Magnetic Behavior of Polymerized Fullerenes
 Organofullerenes in Water

Functional Nanomaterials

Catalysis by Supported Gold Nanoclusters
 Charge Carrier Dynamics of Nanoparticles
 Electrically Conducting Polymeric Nanostructures: Techniques for One-Dimensional Synthesis
 Intercalated Polypropylene Nanocomposites
 Iron Oxide Nanoparticles
 Layer-by-Layer Assembly of Polyelectrolyte Films: Membrane and Catalyst Applications
 Magnetic Nanomaterials: Conventional Synthesis and Properties
 Magnetic Nanoparticles in Fluid Suspension: Ferrofluid Applications
 Magnetic Nanoparticles: Applications for Granular Recording Media

Magnetic Nanoparticles: Preparation and Properties
Magnetic Properties of Nanoparticle Assemblies
Mesoporous Materials (M41S): From Discovery to Application
Metal Nanoparticles Modified with Molecular Receptors
Metal Nanoparticles Protected with Monolayers: Applications for Chemical Vapor Sensing and Gas Chromatography
Metal Oxide Nanoparticles
Metallic Nanopowders: An Overview
Metallic Nanopowders: Rocket Propulsion Applications
Metal-Oxide Interfaces: Toward Design via Control of Defect Density
Mixed Metal Oxide Nanoparticles
Nanoarrays Synthesized from Porous Alumina
Nanoengineered Capsules with Specific Layer Structures
Nanofilms in Giant Magnetoresistance Heads
Oxide Nanoparticles: Electrochemical Performance
Photochemistry of Membrane-Coated Nanoparticles
Photonic Crystal Fibers
Photovoltaics for the Next Generation: Organic-Based Solar Cells
Polymer Colloids and Their Metallation
Quantum Dots Made of Metals: Preparation and Characterization
Structural and Optical Anisotropy in Nanoporous Anodic Aluminum Oxide
Titanium Dioxide Coatings on Stainless Steel

Inorganic Nanowires

Barcoded Nanowires
Electrically Functional Nanostructures
Inorganic Nanotubes Synthesized by Chemical Transport Reactions
Inorganic Nanotubes: Structure, Synthesis, and Properties
Mechanical Properties of Nanowires and Nanobelts
Molecular Assembly of Nanowires
Molecular Wires
Superconducting Nanowires Templated by Single Molecules
Thermal Properties of Nanobridges

Molecular Electronics and Devices

Biomedical Applications: Tissue Engineering, Therapeutic Devices, and Diagnostic Systems
Charge Transfer in Metal-Molecule Heterostructures
Colloidal Germanium Nanoparticles
DNA Hybridization: Electronic Control
Metal Nanoparticles and Self-Assembly into Electronic Nanostructures
Molecular Assembly of Nanowires
Molecular Electronic Logic and Memory
Molecular Electronics: Analysis and Design of Switchable and Programmable Devices Using Ab Initio Methods
Molecular Manipulator Dynamic Design Criteria
Molecular Motor-Powered Nanodevices: Mechanisms for Control
Molecular Switches
Molecular Switches and Unidirectional Molecular Motors: Light-Induced Switching and Motion
Molecular Wires
Nanomaterials and Molecular Devices: De Novo Design Theory
Nano-Mesosopic Interface: Hybrid Devices
Optical Molecular Devices

Nanostructures and Nanophase Structures

Biological and Chemical Weapon Decontamination by Nanoparticles
Block Copolymer Nanoparticles
Charge Transport Properties of Multilayer Nanostructures
Colloidal Nanometals as Fuel Cell Catalyst Precursors
Colloidal Nanoparticles: Aggregation Patterns at Model Molecular Surfaces
Coordination Framework Topology: Influence of Using Multimodal Ligands

Core/Shell Hydrogel Nanoparticles
 Core/Shell Nanospheres, Hollow Capsules, and Bottles
 Cubosomes: Bicontinuous Liquid Crystalline Nanoparticles
 Dealloying of Binary Alloys: Evolution of Nanoporosity
 Dissymmetrical Nanoparticles
 Gold Nanoclusters: Structural Disorder and Chirality
 Magnetic Nanomaterials: Nonconventional Synthesis and Chemical Design
 Metal Nanoparticle Ensembles: Collective Optical Properties
 Metal Nanoparticles Prepared in Supercritical Carbon Dioxide Solutions
 Nanoceramics
 Nanocrystal Arrays: Self-Assembly and Physical Properties
 Nanocrystalline Materials: Fatigue
 Nanocrystalline Materials: Synthesis and Properties
 Nanocrystallization
 Nanocrystals Synthesized in Colloid Self-Assemblies
 Nanoengineered Polymer Microcapsules
 Nanomaterials: Manufacturing, Processing, and Applications
 Nanomaterials: Recent Advances in Technology and Industry
 Nanoparticles: Generation, Surface Functionalization, and Ion Sensing
 Nanoparticles: Synthesis in Polymer Substrates
 Nanostructured Materials Synthesized by Mechanical Attrition
 Nanostructured Materials Synthesized by Mechanical Means
 Nanostructured Materials Synthesized in Supercritical Fluid
 Nanostructures Based on Conducting Polymers
 Nanostructures Based on Layered Transition Metal Chalcogenides
 Photonic Applications of Printed and Molded Nanostructures
 Polymer Nanoparticles for Gene Delivery: Synthesis and Processing
 Polymeric and Biomolecular Nanostructures: Fabrication by Scanning Probe Lithography
 Self-Assembly of Two- and Three-Dimensional Nanostructures for Electronic Applications

Optical Devices

Optical Molecular Devices
 Optical Nanosensors and Nanobiosensors
 Photonic Applications of Printed and Molded Nanostructures
 Quantum Dot Lasers
 Quantum Dots Made of Cadmium Selenide (CdSe): Formation and Characterization
 Quantum Dots, Self-Assembled: Calculation of Electronic Structures and Optical Properties
 Quantum Dots: Inelastic Light Scattering from Electronic Excitations
 Self-Assembly of Organic Films for Nonlinear Optical Materials
 Structural and Optical Anisotropy in Nanoporous Anodic Aluminum Oxide

Quantum Dots

Colloidal Germanium Nanoparticles
 Indium Arsenide (InAs) Islands on Silicon
 Integrated Methods: Applications in Quantum Chemistry
 Luminescence of Nanoparticle-Labeled Antibodies and Antigens
 Quantum Dot Arrays: Electromagnetic Properties
 Quantum Dot Lasers
 Quantum Dots Made of Cadmium Selenide (CdSe): Formation and Characterization
 Quantum Dots, Self-Formed: Structural and Optical Characterization
 Quantum Dots, Semiconductor: Atomic Ordering over Time
 Quantum Dots, Semiconductor: Site-Controlled Self-Organization
 Quantum Dots: Electronic Coupling and Structural Ordering
 Quantum Dots: Inelastic Light Scattering from Electronic Excitations
 Quantum Dots: Phonons in Self-Assembled Multiple Germanium Structures
 Quantum Rods Made of Cadmium Selenide (CdSe): Anisotropy
 Silicon Nanocrystals: Quantum Confinement
 Thermal Effect on the Luminescence Properties of Quantum Dots

Self Assembly and Self Organization

Adhesion Between Surfaces Coated with Self-Assembled Monolayers: Effect of Humidity
 Adsorption of Polymers and Proteins on Heterogeneous Surfaces
 Biomimetic Approaches to the Design of Functional, Self-Assembling Systems
 Biosurfaces: Water Structure at Interfaces
 Electrochemically Self-Assembled Nanoarrays
 Environmental and Sensing Applications of Molecular Self-Assembly
 Guests Within Large Synthetic Hydrophobic Pockets Synthesized via Self-Assembly
 Layer-by-Layer Assembly of Gold Nanoclusters Modified with Self-Assembled Monolayers
 Molecular Assembly of Organosilanes
 Nanostructures Derived from Phase-Separated Polymers
 Oil-Filled Nanocapsules
 Phase Behavior of Nanoparticle Suspensions
 Polyelectrolyte-Surfactant Complex Nanoparticles
 Polymer-Mediated Self-Assembly of Nanoparticles
 Ring Structures from Nanoparticles and Other Nanoscale Building Blocks
 Self-Assembled Monolayers: Chemical and Physical Modification Under Vacuum Conditions
 Self-Assembled Monolayers: Effects of Surface Nanostructure on Wetting
 Self-Assembled Silane Monolayers: Conversion of Cyano to Carboxylic Termination
 Self-Assembly and Multiple Phases of Layered Double Hydroxides
 Self-Assembly Directed by NH–O Hydrogen Bonding
 Self-Assembly of Cavitand-Based Coordination Cages
 Self-Assembly of Chiral and Pseudochiral Molecules at Interfaces
 Self-Assembly of Cyclic Peptides in Hydrogen-Bonded Nanotubes
 Self-Assembly of Nanocolloidal Gold Films
 Self-Assembly of Organic Films for Nonlinear Optical Materials
 Self-Assembly of Porphyrinic Materials on Surfaces
 Silane Self-Assembled Monolayers: Nanoscale Domains by Sequential Adsorption
 Templating Aerogels for Tunable Nanoporosity

Sensors and Actuators

Antibodies and Other Ligand–Receptor Systems with Infinite Binding Affinity
 Biomimetic Macrocyclic Receptors for Carboxylate Anion Recognition
 Biosensor Applications: Porous Silicon Microcavities
 Biosensor Applications: Surface Engineering
 Biosensors Based on Carbon Nanotubes
 Biosensors for Detection of Chemical Warfare Agents
 Electrochemical Sensors Based on Functionalized Nanoporous Silica
 Electrochemical Toxicity Sensors
 Electronic Switches
 Fractal Analysis of Binding Kinetics on Biosensor Surfaces
 Nanostructure and Dynamic Organization in Lipid Membranes
 Nanotube Sensors
 Optical Nanosensors and Nanobiosensors
 Self-Assembly of Redox-Responsive Receptors
 Sensors Based on Chemically Currents

Supramolecular Chemistry

Anion-Templated Self-Assembly: Inorganic Compounds
 Anion-Templated Self-Assembly: Organic Compounds
 Atomic Force Microscopy Studies of Hydrogen-Bonded Nanostructures on Surfaces
 Axle Molecules Threaded Through Macrocycles
 Carbon Nanotubes: Supramolecular Mechanics
 Guests Within Large Synthetic Hydrophobic Pockets Synthesized Using Polymer and Conventional Techniques
 Molecular Assembly of Nanowires
 Molecular Designs for Self-Organized Superstructures
 Molecular Designs for Self-Organized Superstructures

Nanocrystallization
Phase Transfer of Monosaccharides Through Noncovalent Interactions
Supramolecular Aggregates with Controlled Size and Shape on Solid Surfaces
Supramolecular Networks Synthesized in Nanoparticle-Polymer Mixtures

Surface and Interfacial Chemistry

Adhesion of a Cell on a Substrate
Anodization Patterned on Aluminum Surfaces
Biomolecular Structure at Interfaces Measured by Infrared Spectroscopy
Biosensor Applications: Surface Engineering
Biosurfaces: Water Structure at Interfaces
DNA Hybridization: Electronic Control
Electrical Double Layer Formation
Electrochemical Langmuir Trough
Enantioselectivity on Surfaces with Chiral Nanostructures
Functionalization of Nanotube Surfaces
Functionalization of Silica Surfaces
Functionalization of Surface Layers on Ceramics
Heterogeneous Surfaces with Nanosized Channel Lattices
Interfacial Forces Between a Solid Colloidal Particle and a Liquid
Interfacial Phenomena and Chemical Selectivity
Metal-Oxide Interfaces: Toward Design via Control of Defect Density
Mica Surfaces: Charge Nucleation and Wear
Nanoarrays Synthesized from Porous Alumina
Nanostructure of Ionic Amphiphilic Block Copolymers Monolayer at Air/Water Interface
Nanostructures Derived from Phase-Separated Polymers
Ordered Vesicles at the Silicon-Water Interface
Self-Assembled Monolayers: Effects of Surface Nanostructure on Wetting
Stability of Nanostructures on Surfaces
Sum Frequency Generation Vibrational Spectroscopy Studies of Molecular Orientation at Interfaces
Surface Chemistry of Nanocrystalline Oxides of Magnesium and Aluminum
Tribology of Inorganic Nanoparticles
Yttria-Tetragonally Stabilized Zirconia: Aqueous Synthesis and Processing

Mesoporous Materials (M41S): From Discovery to Application

James C. Vartuli
Wielsaw J. Roth
Thomas F. Degnan, Jr.

ExxonMobil Research and Engineering Company, Annandale, New Jersey, U.S.A.

INTRODUCTION

The quest for new molecular sieves in the late 1980s led Mobil researchers to the discovery of a family of nanostructured mesoporous materials known as M41S.^[1-3] MCM-41 is undoubtedly the best known and most widely studied of this family of materials, each synthesized via a self-assembled liquid crystal mechanism involving sol-gel precursors which form a hexagonally packed rod-shaped micelle structure.^[4] The other members of the M41S family are the cubic (MCM-48) and lamellar (MCM-50) forms. This article describes the progression of M41S materials from discovery through characterization and development. ExxonMobil has very recently commercialized MCM-41 for an undisclosed application. Its decade-long journey from initial identification to commercial application is similar in duration to that of many novel materials. Yet there were many unique challenges posed by the synthesis and development of such a novel material. This is its story.

THE DISCOVERY OF THE M41S MATERIALS FAMILY

Like most discoveries of novel materials, the discovery of Mobil's M41S mesoporous molecular sieves was an unanticipated outcome of the application of observational skills, knowledge, and techniques developed over many years of effort in synthesizing large pore catalytically active frameworks. Like many major petroleum companies, Mobil had a material synthesis effort attempting to identify new zeolites that could selectively convert high molecular weight petroleum-based molecules. In the mid-1980s, Mobil Technology Company had a significant effort in developing pillared layered materials. This class of materials, theoretically, offered the ability to tune pore size, active site density, and composition; variables that the traditional aluminosilicate zeolites did not possess. By varying the pillar size and pillar density, the Mobil researchers learned that pore systems could be tuned for the desired application. The pillar composition also ap-

peared to be adjustable so various chemistries could be effected. Unfortunately, although significant progress was made in designing these pillared layered materials,^[5] realistically these materials did not have sufficient thermal and hydrothermal stability or catalytic activity to be used in most petroleum processes. Furthermore, the pillar composition could not be as varied as initially conceived. Toward the end of the decade, a small group of researchers at Mobil's Paulsboro Laboratory approached this effort of discovering large pore frameworks by attempting to combine both the concepts of the pillared layered materials and the formation of zeolites. The approach was to consider that some zeolites were formed via layered intermediates. Thus if this intermediate could be isolated and used as a layered composition to form pillared porous materials; the resultant product would be composed of crystalline walls that would be thermally stable and catalytically active. This concept had credibility because of a new layered framework that was discovered during that time.^[6] It was designated by Mobil as MCM-22 (MWW).

We noted that upon thermal treatment of the as-synthesized MCM-22, the X-ray diffraction pattern of the material shifted to higher 2θ values, similar to that of swollen layered materials when the intercalate is removed. In layered materials the low-angle lines associated with the interlayer distance shifted to lower d -spacings consistent with the removal of the organic template intercalate and the collapse of the layers. However, in the as-synthesized MCM-22 sample, this shift of the d -spacings, upon thermal treatment, was subtle, $\sim 2\text{--}3\text{\AA}$, and the base crystalline framework remained relatively unaffected. This suggested that the MCM-22 zeolite was composed of crystalline layers that were linked together by weak chemical bonds during the synthesis. Upon thermal treatment, these chemical linkages became much stronger, as the layers condensed onto each other.

Using the as-synthesized zeolite material, with the template intact and prior to any thermal exposure, we attempted to delaminate or separate these crystalline layers of the MCM-22 "precursor." A pillared layered material resulting from this delamination and subsequent

pillaring was obtained and identified as MCM-36.^[7,8] The process involved the initial intercalation of the layers using an alkyltrimethylammonium compound followed by the insertion of stable inorganic pillars using a reactive silica source such as tetraethylorthosilicate.

The layered zeolite precursors, exemplified by the MCM-22 case, differed from their layered predecessors such as clays and layered silicates in possessing layers with high zeolite activity and porosity. Obviously, these were very attractive from the catalyst standpoint. Another feature distinguishing the layered zeolite precursors from the other layered materials was their resistance to swelling by ion exchange with neutral or mildly basic media, such as quaternary ammonium salts or amines. It was only with the introduction of a quaternary ammonium surfactant in a hydroxide form, specifically cetyltrimethylammonium hydroxide solution obtained by anion exchange of the halide solution with hydroxide, that successful swelling of the layered zeolite precursor was demonstrated. The use of an apparently equivalent medium, a mixture of surfactant halide and another hydroxide, instead of the anion exchanged surfactant hydroxide, was ineffective.^[9]

This general approach of interrupting zeolite syntheses, isolating the layered zeolite precursors, and using these potential crystalline layered materials as reagents to form large pore active catalysts was investigated for other zeolite families such as ZSM-35, or synthetic ferrierite. In this system, the ferrierite sheet, pre-Fer, may be the principal building unit of the resultant zeolite material. To optimize the formation of these layered precursors, several reaction conditions were identified and imposed on the traditional zeolite synthesis. The zeolite synthesis was interrupted prior to any X-ray diffraction evidence of crystallinity. The interruption could be initiated at any point within ~25% to 75% of the total expected synthesis time. High concentrations of the intercalate, an alkyltrimethylammonium salt, at high pH were added to this interrupted zeolite precursor media. In other syntheses, a reactive silica source, tetramethylammonium silicate, was also added as a potential pillaring agent. These new synthesis mixtures were then subjected to additional hydrothermal treatment in an attempt to form the zeolite-layered hybrid. In many instances, the resulting product exhibited some very unusual properties.

The X-ray diffraction pattern was essentially featureless except for one broad low-angle peak at about $2^\circ 2\theta$. This X-ray diffraction pattern was intriguing because the original zeolite templating agent still existed in the synthesis composition. Apparently, the reaction conditions and time and temperature sequence were changed during the addition of the quaternary salt. This inhibited the formation of the originally intended zeolite. Normally, even this low-angle line might not have been observed,

except that we were using a chromium X-ray source instead of the typical copper tube. The chromium source, which is very useful for low-angle peak detection, was a remnant from our pillared layered material research effort. The other unusual properties on this unknown material were the extremely high BET surface areas and hydrocarbon sorption capacities. These BET surface area values, typically $>600 \text{ m}^2/\text{g}$, were many times those normally observed for zeolite samples. The hydrocarbon (*n*-hexane and cyclohexane) sorption capacities were in excess of 50 wt.%, also abnormally high compared to our typical microporous samples. In fact, our analytical laboratories initially incorrectly believed that their test equipment was broken or out of standard because of the results obtained from these initial mesoporous materials.

In a separate and concurrent synthesis study, the cetyltrimethylammonium hydroxide was used directly as a structure-directing agent in zeolite-like hydrothermal syntheses. The product properties were similar to those generated in the layered zeolite precursor systems, i.e., characterized by a low-angle line in an X-ray diffraction pattern corresponding to large *d*-spacing and unusually high BET surface area and adsorption capacities. Thus both interrupted zeolite precursor systems and direct introduction of cetyltrimethylammonium hydroxide as a template resulted in the mesoporous molecular sieve products. As described below, subsequent detailed characterization studies allowed elucidation of the nature of these remarkable materials.

Obviously, these abovementioned unusual physical properties are characteristics of the mesoporous molecular sieves. However, with only one broad low-angle X-ray diffraction peak and the uniquely high values for both surface area and hydrocarbon sorption as data, this was insufficient to fully identify the nature of these materials. We initially concluded from this one broad X-ray diffraction peak material that we had completely disrupted the interlayer connectivity of layered zeolite hybrids, and the resulting X-ray diffraction was simply a repeat of the thickness of the layered precursor of about 4.0 nm. A key in the identification of this new class of porous materials was the observation, by TEM analyses, of a trace amount of MCM-41 in one of our samples. At this time, our small research group had the luxury of having as one of the members, a microscopist, Mike Leonowicz, who typically would conduct analyses on some of our more unusual samples. The observation of trace quantities of MCM-41, the uniform hexagonal pore structure, in one of the interrupted synthesis preparations provided us with hard evidence of this new class of materials (Fig. 1).

In a relatively short time, we were able to produce sufficient excellent quality samples of MCM-41 to characterize these materials by X-ray diffraction, pore

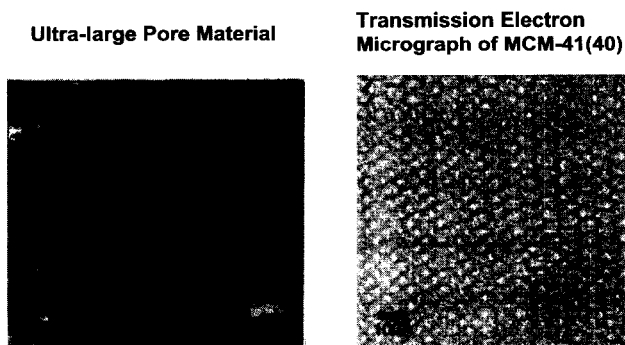


Fig. 1 The initial discovery by TEM analysis of MCM-41. (From Ref. [1].) (View this art in color at www.dekker.com.)

size distribution, sorption capacities, and NMR and to evaluate them for catalytic applications. Many researchers at both the Paulsboro and Princeton Laboratories were involved in this effort. In all cases, we were analyzing a new class of materials that presented unique data. For example, the pore size distribution was remarkable; the narrow pore size appeared to be like that of microporous materials but within the mesopore range. As mentioned previously, the hydrocarbon sorption capacity was unique. Benzene sorption isotherms clearly indicated pore condensation inflections at benzene partial pressures indicative of mesopore size channels. These inflections were typically not observed with microporous materials because of the low partial pressures needed. We were also able to synthesize various pore size materials using both different alkyl chain lengths of the cationic surfactant as

well as taking advantage of micellar swelling.^[10] These techniques improved our knowledge of micelles and liquid crystal chemistry improved. Both this knowledge base and the resultant samples helped to establish the basis for the mechanism of formation of these materials.

In retrospect, the synthesis conditions that we were using to try and obtain our layered zeolite hybrids, high pH, high surfactant concentration, and a reactive silica source, were synthesis conditions conducive to the formation of the mesoporous molecular sieves. The discovery and identification of other members of this new class of porous materials, MCM-48 and MCM-50, came several months later as a result of a detailed study relating the effect of surfactant concentration on the silica reagent (Fig. 2). The discovery of these additional two members of the mesoporous molecular sieve family was another key factor in developing the proposed mechanism of formation.

The discovery of this new class of materials, mesoporous molecular sieves, posed several challenges for our understanding of the formation of porous materials. Our first conclusion, based on both the hexagonal ordering of the pores, as seen in TEM analyses, and the XRD pattern, was that we had discovered one of the crystalline phases predicted by Smith and Dydrich,^[11] known as the 81(n) family of frameworks. The theoretical XRD pattern of this family almost matched that of some of our best samples of MCM-41. It was not until we obtained the silica NMR data that we determined that our material was not typical of crystalline frameworks that we had expected. The realization that XRD patterns could be generated by the order of the pores and not the crystalline structure was another key feature of this new class of porous materials.

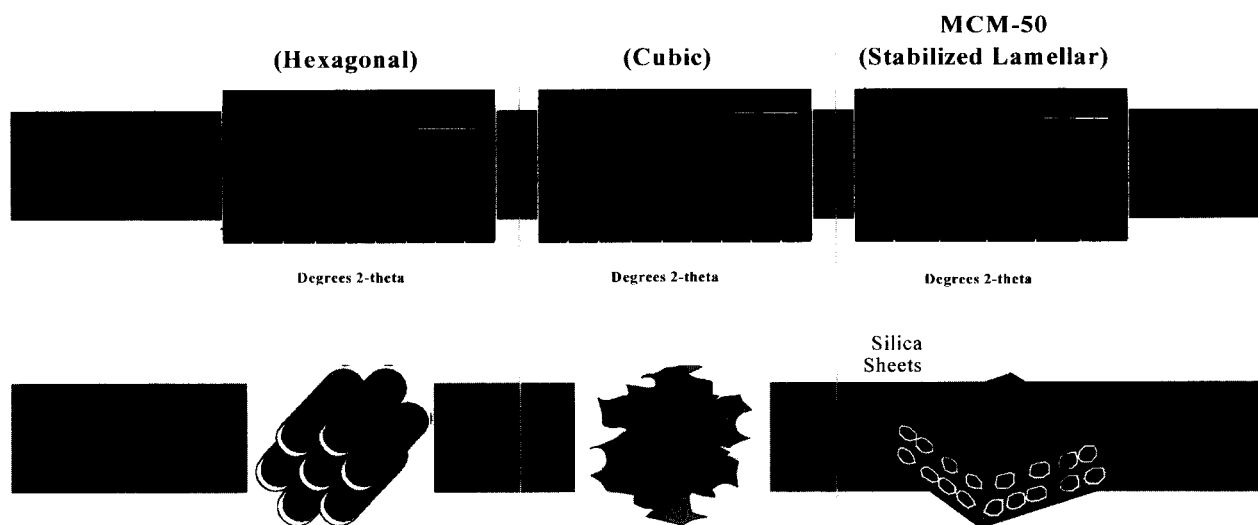


Fig. 2 The M41S family of materials including MCM-41, MCM-48, and MCM-50. (View this art in color at www.dekker.com.)

M

The mechanism of formation was also a challenge, which led to many long debates within our research group. We initially approached the concept of formation of these materials like traditional zeolite chemists. Our first premise was that the materials were formed by some sort of templating structure or pore filling agent. This meant, in the case of the mesoporous molecular sieves, that the templating agent was an aggregation of molecules and not the discrete molecules that normally template microporous structures (Fig. 3). Based on our limited knowledge of liquid crystal structures and micelles, we initially concluded that the liquid crystal structure existed prior to the formation of the molecular sieve. In the case of the MCM-41, this would be the hexagonal liquid crystal phase.

However, this simple mechanistic pathway was not universally accepted within our group of researchers. Alternatively, it was proposed that the silicate reagent also affected the formation of these materials. And it was this proposed route that gathered more popularity as more data were obtained. A significant set of data appeared to help establish the preferred mechanistic route. This was a group of experiments that studied the effect of various levels of surfactant (SUR) as a function of silica. By changing the SUR/Si molar ratio we were able to synthesize MCM-41, -48, and -50 while keeping all of the other synthesis conditions the same.^[12,13] These conditions would then exclude the possibility of any preformed liquid crystalline phase prior to the formation of the silicon phase, as we used the same surfactant solution and concentration for all experiments, only changing the amount of silica added. These data supported the concept that the anion, in this case, the silicate species, significantly affected the formation of the resultant

template of the mesoporous molecular sieves (Fig. 4). These data were some of the evidence that led us to propose the possible mechanisms of formation that we published in our initial articles.^[1,4]

In retrospect, both proposed pathways proved to be valid. The predominate pathway appears to be the anionic species initiated one (using cationic surfactants). This concept was explained and expanded upon by many researchers, specifically by the group at the University of Santa Barbara headed by Galen Stucky.^[14,15] A Michigan State University group, headed by Tom Pinnavaia, expanded this mechanistic pathway further to include neutrally charged directing agents such as polymers.^[16,17] Later, researchers at the University of South Hampton demonstrated the other proposed pathway, originally labeled the liquid crystal phase initiated pathway.^[18,19] Attard and his co-researchers used a preformed liquid crystal phase to synthesize both a silica and a metal (platinum alloy) mesoporous molecular sieve.

M41S SYNTHESIS DEVELOPMENT

When contrasted with the development of many high silica zeolites, MCM-41 posed several synthetic challenges that were immediately evident after its discovery. The first of these was the need to remove an inordinately large amount of surfactant that remained occluded in the pores of this mesoporous molecular sieve. Compared to a typical 5 to 8 wt.% organic component in most high silica zeolites, MCM-41 contained as much as 50 wt.% organic. Organic structure directing agents (SDA) are typically removed from zeolites by careful calcination or ion exchange. Calcination is normally preferred because of

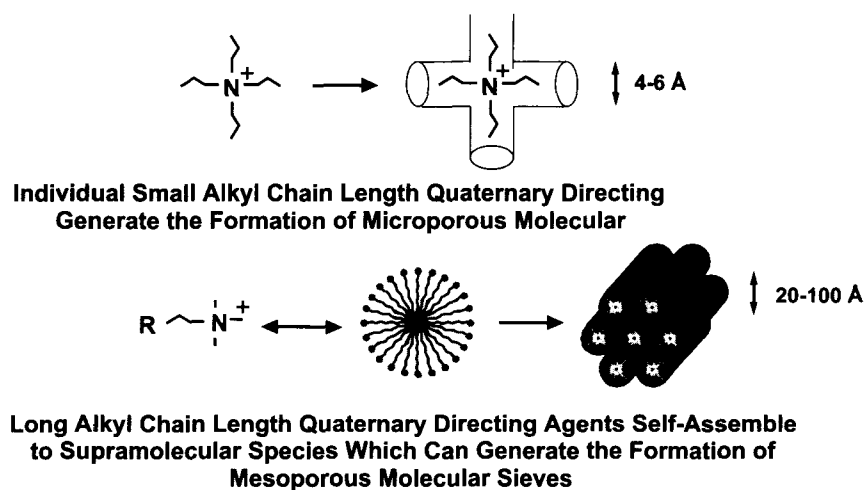


Fig. 3 The role of quaternary directing agents. (From Refs. [1] and [4].) (View this art in color at www.dekker.com.)

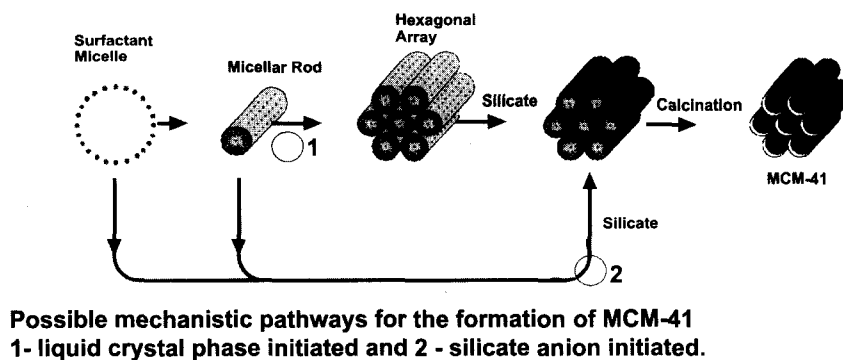


Fig. 4 The proposed mechanism of formation pathways. (From Ref. [1].) (View this art in color at www.dekker.com.)

the ease with which the gaseous effluent can be handled. Ion exchange is normally more difficult either because of the ionic selectivity of the zeolite for the SDA or because the SDA may literally be locked inside of the zeolite by virtue of being situated at pore intersections or in the super cages. While the bulky hexadecyltrimethylammonium cation in MCM-41 was more amenable to ion exchange than the SDA in most unidimensional pore zeolites, the pH of the exchange step had to be carefully monitored. In the absence of CTMA the material was extremely sensitive to alkaline conditions. The ion exchange route was also attractive because it allowed us to recover the majority of the expensive surfactant. The surfactant recovered from the ion exchange step could be easily combined with that recovered from the residual mother liquor. In the initial synthesis preparations, a significant amount of the surfactant remained in the mother liquor. It was clear that organic recovery and subsequent recycle use would substantially reduce the manufacturing cost. Several routes for recovering the surfactant from the as-synthesized MCM-41 were evaluated.

A second challenge was the need to develop an agreed upon protocol for determining MCM-41 product quality both during the synthesis and immediately following drying and post-processing. While MCM-41 is a highly ordered structure, its walls are amorphous. We found that the surface area, hydroxyl content, wall thickness, and even the pore diameter were highly dependent on synthesis conditions. Whereas X-ray powder diffraction can be used to very quickly quantify the crystallinity of zeolites, this was not the case in MCM-41 or any of the M41S materials. The pH of the synthesis liquor for zeolites can also be followed as a rough indicator of the crystallinity of these structured materials. However, this protocol was not useful for determining the precise degree to which a fully formed MCM-41 material is obtained. It remained for the final product to be treated to remove the surfactant before a good assessment of MCM-41 product quality

could be made through adsorption capacity and low-angle X-ray peak location.

A third challenge was to change the silica reagents from expensive tetramethylammonium silicate (TMA-Si) and tetraethylorthosilicate (TEOS) to more reasonably priced sources. While cost was an important consideration, the availability, handling, and disposal issues associated with TEOS were most compelling. Identification of alternate reagents brought about a whole new series of problems associated with material and phase purity and the impacts on subsequent catalytic performance.

Fundamental studies of the mechanism of MCM-41S formation provided insight into a convenient laboratory synthesis route.¹²⁰ Our studies showed that high quality MCM-41 with consistently uniform 4.0-nm pores could be produced in the laboratory under very reasonable conditions. X-ray analyses showed that the preferred synthesis conditions produced materials exhibiting four peaks with positions corresponding to hexagonal symmetry. Subsequent analysis confirmed that the MCM-41 had high BET surface area, a large pore capacity, and very narrow pore size distribution as discerned by its nitrogen adsorption/desorption isotherm.

While much of the development was based upon our previous experience with the commercialization of high silica zeolites, one major difference was the apparent ease with which MCM-41 could be formed. Our initial studies showed that the M41S family of materials could be formed at much milder conditions than zeolites. In fact, it was quickly found that pure material could be formed even at ambient conditions and in relatively short duration (i.e., 6 to 12 hr) syntheses. However, the ease of making this material was deceptive, because the stability of MCM-41 varied significantly with synthesis conditions. Usually, the stability increased with synthesis time and temperature.

Surprisingly, our analysis of fully dried "retained" samples that were placed in storage for several weeks with the occluded surfactant still present showed that the

material became amorphous with time. This reversion produced a series of concerns regarding the stability of the material to storage even under mild conditions. Later studies showed that the synthesis conditions and the prompt removal of the surfactant were critical to improving the stability of mesoporous M41S. The studies also suggested that calcination was preferred to ion exchange for applications where hydrothermal stability was important.

Synthesis efforts within Mobil in the early and mid-1990s focused in two objectives: 1) identify and develop to a modest scale commercially attractive routes for producing MCM-41 materials with a range of pore diameters and acidity; and 2) broaden the compositional range and synthesis approaches to produce additional exploratory materials. The progress was closely linked to parallel catalytic evaluation studies looking at a range of applications (vide infra). Exploratory materials syntheses first focused on the production of both aluminosilicate and metalloaluminophosphate M41S materials including silicoaluminophosphate. Almost simultaneously, studies were initiated around the incorporation of metals either during the synthesis or post-synthesis. Later, in recognizing that these mesoporous materials were slightly less acidic than zeolites, we carried out studies aimed at incorporating acidity by post-treatment techniques such as impregnating MCM-41 with heteropoly acids.

We recognized very early on that these materials had uncharacteristically large surface silanol concentrations. NMR studies showed that nearly 40% of the silicon atoms located on the surface of the walls could be associated with hydroxyls. The silanols can be functionalized to modify M41S pore size and the hydrophobicity as well as serve as anchoring sites for attachment of selective groups for separation applications. The availability of large quantities of silanol groups led to a series of functionalization studies. The work provided the foundation for the synthesis of phase transfer catalysts built around M41S as well as the underlying concepts needed for anchoring the aforementioned heteropoly acid catalysts.

FUNCTIONAL PRODUCT DEVELOPMENT CHALLENGES

The functional form of molecular-sieve-based catalysts and adsorbents is a tablet, pellet, or extrudate where the active material is incorporated as a component with materials such as binders, weighting agents, or other active materials. Among the challenges addressed during development was the potential for collapse of the mesoporous structure under the pressures implicit in the forming steps. As crystalline structures, zeolites have the rigidity needed to withstand inordinately high point pressures. However, M41S materials with amorphous walls sur-

rounding large amounts of occluded surfactant had to be viewed differently.

Binding of M41S materials where the surfactant had been removed prior to forming proved to be even more challenging. Not only was the collapse of the pores a more significant concern, but intrusion and pore blockage from some of the gel-type binder systems became an important consideration. Solubilization of the binder system and loss of physical integrity during ion exchange of uncalcined particles also had to be addressed. While calcination remained an attractive process option for removing the hexadecyltrimethylammonium structure directing agent post-forming, the burden on the gaseous effluent abatement systems proved a considerable obstacle.

Most commercial applications of molecular sieves are developed around volumetric constraints, where the challenge is to load as much of the active material as possible into a given volume. This drives product development programs toward formed products with higher levels of the active component and lower levels of binder or weighting components with the limits being set by physical (e.g., crush) strength. The framework density of M41S is approximately 70% of typical zeolites. This translates directly into a lower particle density. Thus, balancing the fraction of M41S in the formed particle with the fraction and type of binder and weighting agent in the finished particle became a key consideration in maximizing the amount of M41S in the process vessel.

APPLICATIONS OF MCM-41

Because evaluations of larger pore exfoliated pillared layered materials were already under way at the time of its discovery, MCM-41 was able to be quickly screened for a number of applications of interest to Mobil. Not surprisingly, most of these focused on petroleum refining, polymer, and petrochemical manufacture applications. Later, applications outside of the core petroleum and petrochemical businesses were identified. Much of this story can be traced through the ExxonMobil patent literature.

Because the initial commercial application of MCM-41 remains undisclosed by ExxonMobil, and very few results from the applications directed research have been published, we will focus on information provided in issued US patents as well as on similar studies published in the open literature. That the first commercial application of such a scientifically exciting new material required nearly a decade is an interesting story in itself. The protracted development resulted not nearly as much from the technical hurdles implicit in the identification of a commercially attractive route for synthesis, forming, and activation of MCM-41, as it did from the difficulty in identifying a commercial application with the technical incentives,

inherent risk profile, and economics required to justify the introduction of such a unique new material.

In the following, MCM-41 is discussed in terms of its attributes as: 1) a refining catalyst or catalyst component; 2) a petrochemical catalyst or catalyst component; and 3) an adsorbent or material otherwise used for separation. Additional applications such as sensors, optical guides, and fuel cell electrodes are also highlighted. Unless otherwise indicated, the MCM-41 materials used in these studies had diameters of approximately 4.0 nm. However, this does not connote that the same material was used throughout. Composition (e.g., aluminum content) varied considerably depending upon targeted application and synthesis conditions. This review of applications examined by ExxonMobil is not intended to be exhaustive. Comprehensive surveys of potential applications of mesoporous materials, including MCM-41, have been published by On et al.^[21] and Zhao et al.^[22]

CATALYTIC APPLICATIONS OF MCM-41

Refining and Polymerization Catalysis

Kresge et al.^[23–25] describe a broad range of hydrocarbon conversion processes over MCM-41 including aromatic dealkylation, cracking, and hydrocracking. Their work established the catalytic activity of MCM-41 and its

ability to perform both as a solid acid catalyst and as a catalyst support for hydrocarbon conversions in general. No performance comparisons were made with other solid acid catalysts.

Catalytic Cracking

Catalytic cracking is the most widely deployed catalytic petroleum refining process. Nearly 35 wt.% of all gasoline is produced by cracking of gas oils and atmospheric resid over large pore ultrastable Y (USY) zeolite catalysts. The products include both fuel and petrochemical feedstocks. For many years, researchers have looked for larger pore alternatives to USY or to large pore materials to supplement the effectiveness of USY in fluidized catalytic cracking (FCC) particularly for processing heavy hydrocarbons. Aufdembrink et al.^[26] examined MCM-41 alone and in combination with USY for catalytic cracking vacuum gas oils and atmospheric resids. The catalysts were mildly steamed to simulate equilibrated FCC regeneration conditions. Their performance comparisons showed that equilibrated MCM-41 was superior to amorphous silica–alumina both in its cracking activity and in its propensity for producing larger amounts of gasoline at equivalent coke yield. Comparisons at equivalent conversions to gasoline, distillate, and light gases, showed that MCM-41 was more selective for heavy oil conversion, again

Table 1 Comparison of MCM-41 and silica–alumina catalysts in catalytic cracking of Joliet sour heavy gas oil (516°C, fixed-fluidized bed reactor; 1 min on stream, catalyst/oil=2 to 6)

	Yields, wt. %		
	Silica–alumina ^a	MCM-41 ^a	Difference
<i>Comparison at equivalent coke yields (=4 wt. %)</i>			
Coke, wt. %	4.0	4.0	–
Conversion, wt. %	48.5	56.8	8.3
C4's, vol. %	9.7	13.3	3.6
C5's, vol. %	3.7	4.7	1.0
C ₅ ⁺ gasoline, wt. %	32.6	37.2	4.6
Gasoline, RON	92	92	–
Light fuel oil, wt. %	36.7	32.2	(4.5)
Heavy fuel oil, wt. %	14.7	11.0	(3.7)
<i>Comparison at equivalent conversion (=55 wt. %)</i>			
Conversion, wt. %	55.0	55.0	–
Coke, wt. %	4.7	3.3	(1.4)
C5's, vol. %	3.8	4.6	0.8
C ₅ ⁺ gasoline, wt. %	34.9	36.0	1.1
Gasoline, RON	92	92	–
Light fuel oil, wt. %	35.0	33.6	(1.4)
Heavy fuel oil, wt. %	13.1	11.3	(1.8)

Source: From Ref. [26].

^aBoth catalysts steamed for 4 hr, 45% steam, 650°C.

producing more gasoline than the amorphous silica-alumina. This is shown in Table 1.

However, in a similar gas oil cracking comparison, MCM-41 was not nearly as active or as gasoline selective as USY, although it was more selective in converting the heavier fractions in fully formulated catalysts. This comparison is shown in Table 2.

Similar investigations by Corma et al.^[27] suggested that fresh MCM-41 had unique cracking selectivities, producing significantly higher amounts of gasoline and less coke than USY, but that the selectivity disappeared once the material was steamed under simulated FCC regeneration conditions. Corma et al.^[28] concluded that MCM-41 partially collapsed when steamed to produce a material resembling silica-alumina. The corollary was that MCM-41 lacked the hydrothermal stability needed for it to be useful as an FCC catalyst component.

Nickel and vanadium are present in small concentrations especially in heavier hydrocarbon feedstocks where they tend to degrade typical FCC catalyst performance as they accumulate on the catalyst. In a recent study, Balko et al.^[29] found that MCM-41 could be used as an FCC catalyst component to very effectively trap and concentrate the metals so that they are much less deleterious to FCC catalyst performance. MCM-41, when used at low levels (5 to 30 wt.%) in conjunction with the USY zeolite, acted as a metals "getter" and protected the cracking function by effectively passivating the metals. MCM-41 could be added as a component in the cracking catalyst particle or could be added as a separate particle.

Oligomerization Catalysts

Pelrine et al.^[30,31] evaluated a chromium-impregnated MCM-41 as an oligomerization catalyst for the production

of high viscosity synthetic lubricants. Evaluations were carried out in a fixed bed reactor using 1-decene and reaction temperatures ranging from 120°C to 182°C at LHSV=1.9 to 2.0 hr⁻¹. The analysis showed that MCM-41 could produce a significantly higher viscosity product than, for example, a commercial Cr/SiO₂ polymerization catalyst under the same reaction conditions. The same reaction catalyzed by chromium acetate-impregnated and calcined MCM-41 was used to demonstrate the concept and utility of functionalized MCM-41.^[32] Bhole et al.^[33] extended the oligomerization concept to Ni/MCM-41 catalysts for dimerization of lower molecular weight olefins. The principal application was for C₃ to C₁₀ olefin dimerization primarily to produce gasoline. In their study the performance of Ni/MCM-41 catalysts compared favorably to Ni-based Dimersol[®] catalysts.

Le et al.^[34] used MCM-41 to selectively react the C₃-C₅ olefins in a mixed stream of lower molecular weight (MW) olefins and paraffins with the intent of producing a heavier oligomer stream that could be readily separated from the lower MW paraffin-enriched stream. Reaction conditions used in the study were 120°C, 10.3 MPa, and LHSV=1.8 hr⁻¹. The resulting oligomers were highly branched and could be converted to tertiary olefins suitable for a number of applications via subsequent selective disproportionation or cracking over, for example, a zeolitic catalyst. Specific applications are for the production of tertiary C₄ and C₅ olefins for subsequent paraffin-olefin alkylation or oxygenate production.^[35]

Bhole et al.^[36] investigated metals-free MCM-41 for the oligomerization of olefins for the production of higher molecular weight products as, for example, fuels, lubricants, fuel additives, and detergents. For acid-catalyzed propylene oligomerization, they found MCM-41 particularly selective for trimer and tetramer synthesis, materials

Table 2 Comparison of 35% MCM-41 and 35% USY catalysts^a in catalytic cracking of Joliet sour heavy gas oil (516°C, fixed-fluidized bed reactor; 1 min on stream, catalyst/oil=2 to 6)

	Yields, wt. %		
	USY ^b	MCM-41 ^c	Difference
<i>Equivalent conversion</i>			
Conversion, vol. %	65.0	65.0	-
Coke, wt. %	2.4	6.0	3.6
C ₄ 's, vol. %	14.2	16.1	1.9
C ₅ 's, vol. %	10.2	9.7	(0.5)
C ₅ ⁺ gasoline, wt. %	43.2	37.4	(5.8)
Gasoline, RON	92.1	91.6	(0.5)
Light fuel oil, wt. %	28.1	28.9	0.8
Heavy fuel oil, wt. %	9.8	8.3	(1.5)

Source: From Ref. [26].

^a35 wt. % active component (MCM-41 or USY)/65 wt. % binder; spray dried catalysts.

^bSteamed for 10 hr, 45% steam, 788°C.

^cSteamed for 4 hr, 45% steam, 650°C.

that are well suited for clean gasoline. Reaction temperatures ranged from 40°C to 250°C and pressures ranged from 0.1 to 13 MPa.

Hydrocracking

MCM-41 alone, or in combination with zeolites such as USY, has been examined as the active component in vacuum gas oil and lube hydrocracking catalysts. Degnan et al.^[37–39] examined the performance of NiW-impregnated USY/MCM-41/Al₂O₃ catalysts and found them to be superior in activity and comparable in selectivity to several commercial distillate selective hydrocracking catalysts. The work was further extended to hydrocracking heavier feedstocks to produce lubricants.^[40–42] Fig. 5 compares the hydrocracking activity of NiW/MCM-41 and a conventional NiW/fluorided alumina lube hydrocracking catalyst for conversion of heavy slack wax at 13.7 MPa, 1 LHSV. The comparison, at equivalent conditions of 13.8 MPa, LHSV=1 hr⁻¹, shows that MCM-41 is more active for conversion of this heavy hydrocarbon feed.

Work by Apelian et al.^[40] and Marler and Mazzone^[41–42] also showed that MCM-41 could be combined with a strong hydrogenation function to subsequently hydroisomerize the heavy hydrocrackate to produce high-quality, low pour point lubricants. In a similar study, Corma et al.^[43] compared the mild hydrocracking performance of NiMo (12 wt.% MoO₃, 3 wt.% NiO) supported on MCM-41 with that of amorphous silica–alumina and USY zeolite catalysts with the same Ni and Mo loadings. The feedstock was vacuum gas oil. The MCM-41 catalyst was superior to the other catalysts

in hydrodesulfurization, hydrodenitrogenation, and hydrocracking activities in single-stage hydrocracking. When a hydrotreating stage was used in front of the hydrocracking stage, the USY catalyst became more active than the MCM-41 catalyst, but MCM-41 was still significantly more active than the amorphous silica–alumina catalyst. Most importantly, the MCM-41 catalyst distillate selectivity was better than that of USY and was very similar to the silica–alumina catalyst. A number of other studies have also pointed to MCM-41 as a superior distillate selective hydrocracking catalyst.^[44–45]

Hydrodemetallation

Vanadium, nickel, iron, and other trace metals pose problems in processing heavy oils because they foul catalysts and cause undesirable side reactions. Kresge et al.^[46] showed that MCM-41 (*d*-spacing >1.8 nm) was very active for removing trace metals from petroleum residua and shale oils. Nickel- or molybdenum-impregnated MCM-41 extrudates (MCM-41/Al₂O₃) were found to be particularly selective for the removal of iron, vanadium, nickel, and even arsenic. Shih also found that staging MCM-41 materials of different pore sizes, with the largest pore size material positioned first to see the oil, was a particularly effective strategy for hydrodemetallation.^[47] Fig. 6, taken from Shih's patent, shows the effect of MCM-41 pore diameter on metals uptake effectiveness using hydrodesulfurization (HDS) activity as a basis for comparison. As metals accumulate on the catalyst they tend to poison HDS activity. The comparison shows that MCM-41 with 8.0-nm pores has a greater metals capacity than smaller pore MCM-41.

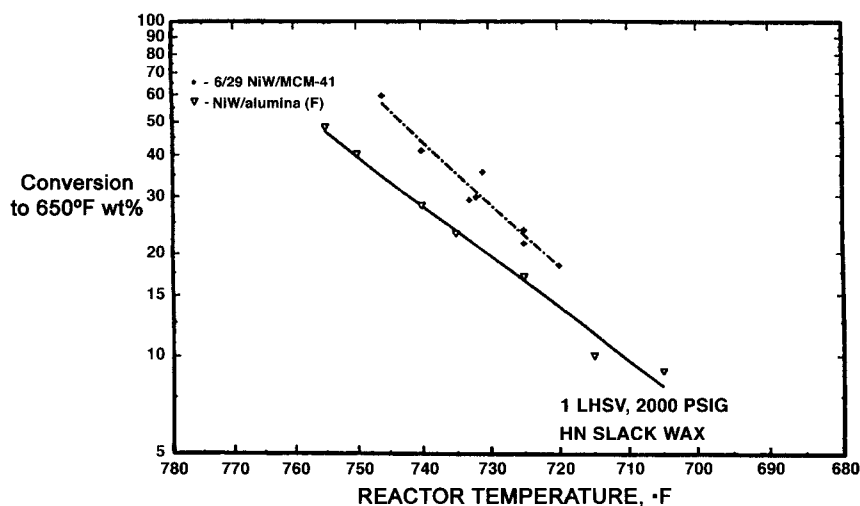


Fig. 5 Comparison of the hydrocracking activities of NiW/MCM-41 and NiW/fluorided alumina demonstrating the superior cracking activity of the MCM-41 catalyst. (From Ref. [40].)

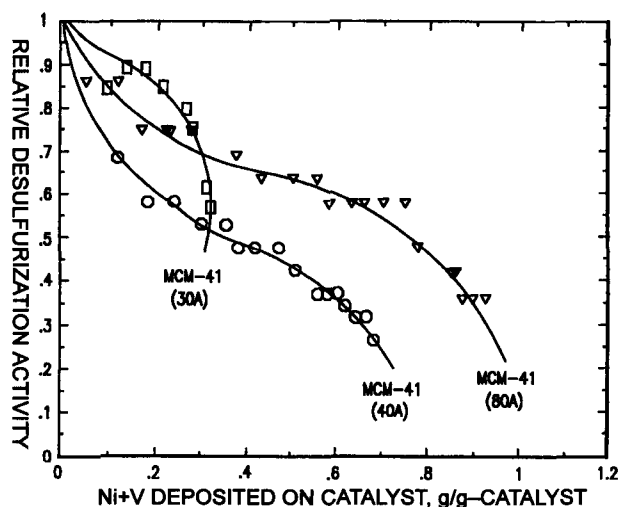


Fig. 6 Hydrodemetallation activity comparison—effect of MCM-41 pore diameter. (From Ref. [47].)

Hydrogenation

Given its large surface area ($>600 \text{ m}^2/\text{g}$) and its large concentration of silanol groups that are easily functionalized or ion exchanged, MCM-41 is an obvious choice as a support material for metals in both precious and base metal hydrogenation catalysts. Evaluations by Baker et al.^[48] and Degnan et al.^[49] showed that MCM-41 was more active than other conventional supports for long-chain olefin and heavy aromatic hydrogenation. The specific applications cited are for polyalphaolefin (PAO) saturation for synthetic lube hydrofinishing and for alkylaromatics hydrogenation for color and viscosity index (VI) improvement. Similarly, Borghard et al.^[50] demonstrated that metal impregnated MCM-41 is a very active catalyst for the saturation of highly aromatic feedstocks under relatively mild hydrogenation conditions. Hydro-treating highly aromatic cracked distillate stocks with NiMo- or CoMo/MCM-41 or other strong hydrogenation metals supported on MCM-41 to produce low aromatic distillates, e.g., for high-quality diesel fuels, is described by Apelian et al.^[51]

Similarly, Corma et al.^[52] found that MCM-41 provided an excellent medium for dispersion of Pt particles, and that the Pt/MCM-41 catalysts were superior in overall hydrogenation activity for naphthalene saturation when compared to Pt supported on amorphous silica-alumina, zeolite USY, γ -alumina, and silica. These investigators demonstrated that sulfur tolerance was a strong function of molecular sieve aluminum content. Pt supported on USY and Al-rich MCM-41 was superior in sulfur tolerance to Pt located on the other supports. They were able to confirm the sulfur tolerance in the hydro-

genation of a mildly hydrotreated light cycle oil (LCO) containing approximately 70 wt.% aromatics and 400 ppm sulfur.

Hydroisomerization

When combined with a strong hydrogenation function (e.g., Pt or Pd) MCM-41 is an effective long-chain paraffin isomerization catalyst once trace nitrogen and sulfur compounds are removed. This is shown in the aforementioned hydroprocessing patents^[42,48] where Marler and Mazone demonstrated that MCM-41 could be used to improve the viscometric properties of hydro-processed or synthetic lubricating oils. DelRossi et al.^[53] extended the hydroisomerization studies to lower molecular weight hydrocarbon feeds and found that noble metal MCM-41 catalysts are both active and selective for isomerization of C_4 to C_8 paraffins. Similar results were obtained by Chaudhari et al.^[54] in their analysis of noble-metal-impregnated MCM-41 for *n*-hexane isomerization.

Olefin Disproportionation

Higher molecular weight olefins can be converted to lower, more highly branched and often more valuable lower molecular weight olefins through disproportionation. The process is not used widely but has the potential for providing incremental lower molecular olefins as a feedstock for paraffin-olefin alkylation for fuels or for petrochemical applications. Le and Thompson^[55,56] determined that MCM-41 was an attractive cracking catalyst for the conversion of light olefinic gasoline to propylene and isobutylene.

Light Olefin-Paraffin Alkylation

MCM-41 is an attractive support for either Lewis or Bronsted acids used in the alkylation of C_4 to C_{12} isoparaffins with $<\text{C}_{10}$ olefins.^[57,58] The principal application of low molecular weight isoparaffin-olefin alkylation is for the production of high-octane C_5 to C_{12} isoparaffins for gasoline. These studies highlighted the ability of MCM-41 to concentrate the acid and increase its effectiveness by nearly an order of magnitude over the free acid as measured by the amount of alkylate produced at the same volumetric acid to oil ratio. Typical reaction conditions for both Bronsted (H_2SO_4) and Lewis (BF_3) acid/MCM-41 catalyzed paraffin-olefin alkylation were -20°C to 200°C , 0.7 to 1.4 MPa, and an isobutane/2-butene molar ratio of 10:1. The reactions were carried out in batch reactors for a preset duration.

Kresge et al.^[59] and DelRossi et al.^[60] found that the performance of MCM-41 for this application could be improved if the activity of MCM-41 could be increased

Table 3 Comparison of isoparaffin-olefin alkylation selectivities and activities of high surface area heteropoly acid catalysts effect of supports

Conditions: Isobutane/2-butene ratio=50:1; 3.4 MPa; 121°C; batch autoclave			
Support	MCM-41	SiO ₂ (Cab-O-Sil)	Alumina
Support surface area, m ² /g	738	159	207
H ₃ PW ₁₂ O ₄₀ , wt. %	75	75	75
Olefin conversion, wt. %	87	60	66
Yield, gram C ₅ +/gram 2-C ₄ =	1.1	1.0	1.2
Total product distribution, wt. %			
C ₅ -C ₇	9.1	2.8	5.5
C ₈	57.2	69.7	58.8
C ₉	34.0	27.5	35.7
C ₈ product distribution, wt. %			
TMP (trimethylpentane)	23.9	13.8	13.2
DMH (dimethylhexane)	35.8	25.3	28.0
Unknown	40.3	60.9	58.9
TMP/DMH	0.7	0.5	0.5
TMP/ (C ₈ -TMP)	0.3	0.2	0.2

Source: From Ref. [60].

through the addition of heteropoly acids via, for example, impregnation with phosphotungstic acid, H₃PW₁₂O₄₀. In batch experiments with 50:1 isobutane/2-butene molar ratio, 121°C, 3.4 MPa, incorporation of 50 to 75 wt. % of the heteropoly anion, via impregnation, significantly improved both the catalyst activity and the yield of desirable trimethylpentane (TMP) and dimethylhexane (DMH) isomers. Comparison catalysts prepared by impregnation of equivalent loadings of H₃PW₁₂O₄₀ onto high surface silica and high surface alumina did not produce nearly equivalent activities or TMP and DMH yields. This comparison is shown in Table 3.

PETROCHEMICAL CATALYSIS

Aromatics Alkylation

MCM-41 is an effective catalyst for olefin alkylation of single-ring aromatics under milder conditions than are used in, for example, ZSM-5. Le^[61] evaluated MCM-41 combined with an alumina binder for the production of ethylbenzene via benzene alkylation and found that the same ethylene conversion could be achieved at a reaction temperature that was 40°C lower than with ZSM-5. Polyalkylated benzene yields were higher, but MCM-41 produced no undesirable xylenes. Conditions were 2.1–3.4 MPa and a benzene/ethylene (molar) ratio=10:1.

Le^[62] also identified MCM-41 as an attractive catalyst for single- and multiring aromatic alkylation with higher molecular weight olefins. Higher molecular weight olefins

are used to alkylate aromatics to produce linear alkyl benzenes (LABs). Linear alkyl benzenes are the basis for linear alkyl benzene sulfonate (LAS). Linear alkyl benzene sulfonate is used widely as a large component in liquid detergents. Le's work is focused on the alkylation of mono- and polycyclic aromatics for lube additive and detergent applications.

PHASE TRANSFER CATALYSTS

Hellring and Beck^[63] found that MCM-41 containing a stabilized onium ion, such as cetyltrimethylammonium (CTMA) cation, could effectively catalyze dual-phase reactions within the MCM-41 pores. To demonstrate the concept, Hellring and Beck reacted water insoluble bromopentane with potassium iodide in an agitated aqueous medium to produce iodopentane. Addition of CTMA-MCM-41 to the stirred dual-phase mixture greatly increased the reaction rate. The results implied that CTMA, which is amphiphilic, is able to concentrate bromopentane and increase its interaction with iodide, which is closely associated with the CTMA cation.

CATALYTIC DECOMPOSITION OF NITROGEN OXIDES

Vanadium- and titanium-impregnated high surface area alumina or silica is a commercially attractive selective catalytic reduction (SCR) catalyst for NO_x reduction. Beck et al.^[64] compared several TiV/MCM-41 samples

with conventional metal-oxide-based SCR catalysts and found the MCM-41 materials were comparable in both NO_x removal selectivity and activity. The ability of the high surface area of MCM-41 to support large amounts of highly dispersed titanium and vanadium was believed to account for the high activity of the MCM-41 catalyst.

APPLICATION OF MCM-41 TO SEPARATIONS

MCM-41 can be used to separate at least one component from a mixture of gaseous or liquid components as described in the patent of Beck et al.^[65] The examples provided in this reference relate mainly to separation of higher and lower viscosity components of a mixture. The concept of using MCM-41 alone or as a composite in a membrane or as an active component in chromatographic separation media is described by Herbst et al.^[66] Among the contemplated uses are size exclusion applications such as the bioseparation of endotoxins or pyrogens. In another study, Kuehl^[67] examined MCM-41 as a selective sorbate for the removal of large molecules such as polynuclear aromatics (PNAs) from fluids and gases. The applications range from wastewater and catalyst regeneration gas cleanup to the reduction of PNAs in hydrocarbon fuels.

OTHER APPLICATIONS

A wide array of other MCM-41 applications have been investigated, each based on the unique composition, uniform pore size, and extraordinarily high surface area of the M41S family of materials. While the reviews by On et al.^[21] and Zhao et al.^[22] have described many of these, we want to highlight three applications outside the realm of catalysts and adsorbents. The first relates to the use of MCM-41 and M41S materials as key components in microoptical and microelectronic applications. Beck et al.^[68] determined that M41S materials, when processed to include quantum clusters of semiconducting inorganic or organic compounds, have unique nonlinear optical properties useful as frequency mixers, frequency doublers, and parametric amplifiers. Extended uses are for beam steering, optical switching, and image processing.

In the second application, MCM-41 is used as a central component in a sensor device.^[69] Electrical, optical, or gravimetric systems designed around MCM-41 detect, for example, the presence of specific gases, changes in pH, or the presence of metal ions. The examples describe a range of biological, chemical, and physical sensor applications including the selective detection of benzene, ammonia, nickel, formaldehyde, and carbon monoxide.

Finally, Ozin et al.^[70] describe the use of M41S (nickel/platinum)-yttria-zirconia M41S materials as thermally stable electrode materials in solid oxide fuel cells. The mesoporous materials, which are synthesized in aqueous media using glycometallates and metal complexes, have the highest known surface area of any form of (metal)-yttria-stabilized zirconia and thus improve the efficiency of solid oxide fuel cells.

CONCLUSION

For many new materials, traversing the path from discovery to commercial application can take as long as a decade. This was certainly true for MCM-41, the most widely studied representative of a new class of materials known as the M41S family. Commercialization of MCM-41 required approximately 10 years as issues surrounding scale-up of the synthesis, raw materials selection, and post-processing had to be addressed. However, the major challenge was associated with identification of an application where the performance advantages justified the risks and costs associated with the targeted commercialization. Initial commercializations of truly new materials are, by their very nature, expensive and associated with a large degree of uncertainty. The initial application bears all of the developmental costs which normally represents a significant hurdle in the development of any truly "step out" material.

Now that MCM-41 is commercial, we anticipate that several new applications will be pursued. Work on mesoporous materials such as M41S continues in many laboratories around the world as witnessed by the consistent increase in both M41S-related patents and publications since the discovery of MCM-41, the first member of this family, in 1989.

ACKNOWLEDGMENT

The authors would like to thank ExxonMobil Corporation for permission to publish this review.

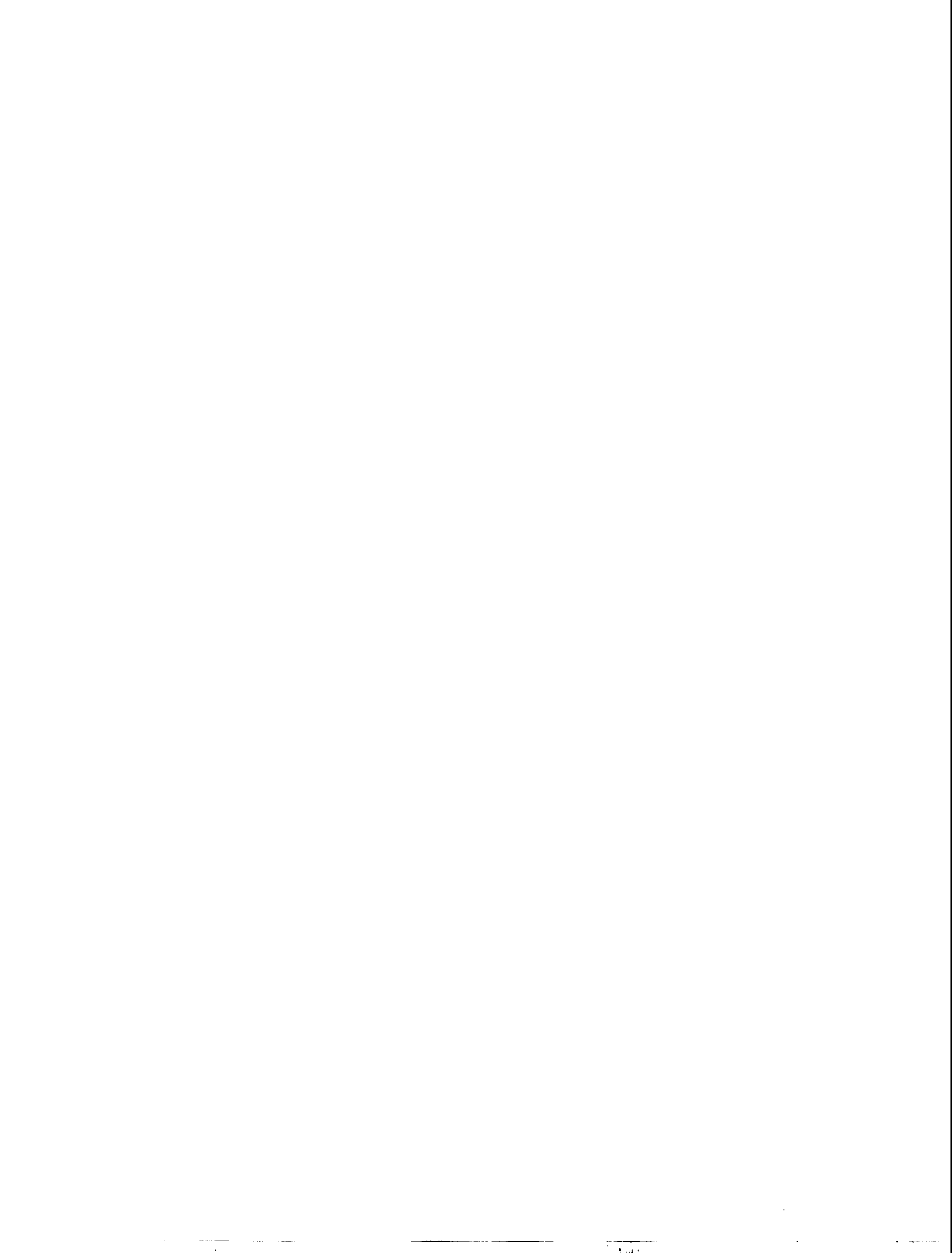
REFERENCES

1. Kresge, C.T.; Leonowicz, M.E.; Roth, W.J.; Vartuli, J.C.; Beck, J.S. Ordered mesoporous molecular sieves synthesized by a liquid-crystal template mechanism. *Nature* **1992**, *359*, 710-712.
2. Kresge, C.T.; Leonowicz, M.E.; Roth, W.J.; Vartuli, J.C. Synthetic Mesoporous Crystalline Material. US

- Patent 5,098,684, March 24, 1992. Mobil Oil Corporation.
3. Kresge, C.T.; Leonowicz, M.E.; Roth, W.J.; Vartuli, J.C. Of Synthetic Porous Crystalline Material, Its Synthesis. US Patent 5,102,643, April 7, 1992. Mobil Oil Corporation.
 4. Beck, J.S.; Vartuli, J.C.; Roth, W.J.; Leonowicz, M.E.; Kresge, C.T.; Schmitt, K.D.; Chu, C.T.-W.; Olson, D.H.; Sheppard, E.W.; McCullen, S.B.; Higgins, J.B.; Schlenker, J.L. A new family of mesoporous molecular sieves prepared with liquid crystal templates. *J. Am. Chem. Soc.* **1992**, *114*, 10834–10843.
 5. Landis, M.E.; Aufdembrink, B.A.; Chu, P.; Johnson, I.D.; Kirker, G.W.; Rubin, M.K. Preparation of molecular sieves from dense layered metal oxides. *J. Am. Chem. Soc.* **1991**, *113*, 3189–3192.
 6. Leonowicz, M.E.; Lawton, J.A.; Lawton, S.L.; Rubin, M.K. MCM-22: A molecular sieve with two independent multidimensional channel systems. *Science* **1994**, *264*, 1910–1915.
 7. Kresge, C.T.; Roth, W.J.; Simmons, K.G.; Vartuli, J.C.; Crystalline Oxide Material. US Patent 5,229,341, July 20, 1993. Mobil Oil Corporation.
 8. Roth, W.J.; Kresge, C.T.; Vartuli, J.C.; Leonowicz, M.E.; Fung, A.S.; McCullen, S.B. MCM-36: The First Pillared Molecular Sieve with Zeolite Properties. In *Catalysis by Microporous Materials*; Beyer, H.K., Karge, H.G., Kiricsi, I., Nagy, J.B., Eds.; Studies in Surface Science and Catalysis; Elsevier Science, 1995; Vol. 94, 301.
 9. Roth, W.J.; Vartuli, J.C. Preparation of exfoliated zeolites from layered precursors: The role of pH and the nature of intercalating media. *Stud. Surf. Sci. Catal.* **2002**, *141*, 273.
 10. Beck, J.S. Method for Synthesizing Mesoporous Crystalline Material. US Patent 5,057,296, October 15, 1991. Mobil Oil Corporation.
 11. Smith, J.V.; Dydrich, W.J. Nets with channels of unlimited diameter. *Nature* **1984**, *309*, 607–608.
 12. Vartuli, J.C.; Schmitt, K.D.; Kresge, C.T.; Roth, W.J.; Leonowicz, M.E.; McCullen, S.B.; Hellring, S.D.; Beck, J.S.; Schlenker, J.L.; Olsen, D.H.; Sheppard, E.W. Effects of surfactant/silica molar ratios on the formation of mesoporous molecular sieves: Inorganic mimicry of surfactant liquid-crystal phases and mechanistic implications. *Chem. Mater.* **1994**, *6*, 2317–2326.
 13. Beck, J.S.; Vartuli, J.C.; Kennedy, G.J.; Kresge, C.T.; Roth, W.J.; Schramm, S.E. Molecular or supramolecular templating: Defining the role of surfactant chemistry in the formation of microporous and mesoporous molecular sieves. *Chem. Mater.* **1994**, *6* (10), 1816–1821.
 14. Stucky, G.D.; Monnier, A.; Schueth, F.; Huo, Q.; Firouzi, D.I.; Janicke, M.; Chmelka, B.F. Molecular and atomic arrays in nano- and mesoporous materials synthesis. *Mol. Crystals Liq. Crystals* **1994**, *240*, 187–196.
 15. Firouzi, A.; Kumar, D.; Bull, L.M.; Besier, T.; Siegar, P.; Huo, Q.; Walker, S.A.; Zasadzinski, J.; Glinka, A.G.; Nicol, J.; Marogloese, D.; Stucky, G.D.; Chmelka, B.F. Cooperative organization of inorganic surfactant and biomimetic assemblies. *Science* **1995**, *267*, 1138–1143.
 16. Tanev, P.T.; Chibwe, M.; Pinnavaia, T.J. Titanium-containing mesoporous molecular sieves for catalytic oxidation of aromatic compounds. *Nature* **1994**, *368*, 321–324.
 17. Pinnavaia, T.J.; Zhang, W. Catalytic properties of mesoporous molecular sieves prepared by neutral surfactant assembly. *Stud. Surf. Sci. Catal.* **1998**, *117*, 23–36.
 18. Attard, G.S.; Glyde, J.C.; Goltner, C.G. Liquid-crystalline phases as templates for the synthesis of mesoporous silica. *Nature* **1995**, *378*, 366.
 19. Attard, G.S.; Leclerc, S.A.A.; Maniquet, S.; Russell, A.E.; Nandakumer, I.; Gollas, B.R.; Bartlett, P.N. Ordered mesoporous silicas prepared from both micellar solutions and liquid crystal phases. *Micro. Meso. Mater.* **2001**, *44–45*, 159–163.
 20. Roth, W.J.; Vartuli, J.C. The effect of stoichiometry and synthesis conditions on the properties of the mesoporous M41S family of silicates. *Stud. Surf. Sci. Catal.* **2001**, *135*, 134–139.
 21. On, D.T.; Desplandier-Giscard, D.; Danumah, C.; Kaliaguine, S. Perspectives in catalytic applications of mesostructured materials. *Appl. Catal., A Gen.* **2001**, *222*, 299–357.
 22. Zhao, X.S.; Lu, G.Q.; Millar, G.J. Advances in mesoporous molecular sieve MCM-41. *Ind. Eng. Chem. Res.* **1996**, *35*, 2075–2090.
 23. Kresge, C.T.; Leonowicz, M.E.; Roth, W.J.; Vartuli, J.C.; Catalytic Conversion. US Patent 5,174,888, December 29, 1992. Mobil Oil Corporation.
 24. Kresge, C.T.; Leonowicz, M.E.; Roth, W.J.; Vartuli, J.C.; Catalytic Conversion. US Patent 5,196,633, March 23, 1993. Mobil Oil Corporation.
 25. Beck, J.S.; Kresge, C.T.; McCullen, S.B.; Roth, W.J.; Vartuli, J.C.; Hydrocarbon Conversion Process Employing a Porous Material. US Patent 5,370,785. Mobil Oil Corporation.
 26. Aufdembrink, B.A.; Chester, A.W.; Herbst, J.A.; Kresge, C.T. Ultra Large Pore Cracking Catalyst and Process for Catalytic Cracking. US Patent 5,258,114, November 2, 1993. Mobil Oil Corporation.
 27. Corma, A.; Grande, M.S.; Gonzalez-Alfaro, V.;

- Orchilles, A.V. Cracking activity and hydrothermal stability of MCM-41 and its comparison with amorphous silica-alumina and a USY zeolite. *J. Catal.* **1996**, *159* (2), 375–382.
28. Corma, A.; Fornes, M.T.; Navarro, M.T.; Perezpariente, J. Acidity and stability of MCM-41 crystalline aluminosilicates. *J. Catal.* **1994**, *148* (2), 569–574.
 29. Balko, J.W.; Chester, A.W.; Quinones, A.R. FCC Metal Traps Based on Ultra Large Pore Crystalline Material. US Patent 5,965,474, October 12, 1999. Mobil Oil Corporation.
 30. Pelrine, B.P.; Schmitt, K.D.; Vartuli, J.C. Production of Olefin Oligomer Lubricants. US Patent 5,105,051, April 14, 1992. Mobil Oil Corporation.
 31. Pelrine, B.P.; Schmitt, K.D.; Vartuli, J.C. Olefin Oligomerization Catalyst. US Patent 5,270,273, December 14, 1993. Mobil Oil Corporation.
 32. Beck, J.S.; Calabro, D.C.; McCullen, S.B.; Pelrine, B.P.; Schmitt, K.D.; Vartuli, J.C. Catalytic Conversion over Modified Synthetic Mesoporous Material. US 5,200,058, April 6, 1993. Mobil Oil Corporation.
 33. Bhore, N.A.; Johnson, I.D.; Keville, K.M.; Le, Q.N.; Yokomizo, G. Catalytic Oligomerization Process Using Modified Crystalline Material. US Patent 5,260,501, November 9, 1993.
 34. Le, Q.N.; Thompson, R.T.; Yokomizo, G.H. Catalytic Olefin Upgrading Process Using Synthetic Mesoporous Crystalline Material. US Patent 5,134,242, July 28, 1992. Mobil Oil Corporation.
 35. Le, Q.N.; Thompson, R.T.; Yokomizo, G.H. Multistage Olefin Upgrading Process Using Synthetic Mesoporous Crystalline Material. US Patent 5,134,241, July 28, 1992. Mobil Oil Corporation.
 36. Bhore, N.A.; Le, Q.N.; Yokomizo, G.H. Catalytic Oligomerization Process Using Synthetic Mesoporous Crystalline Material. US Patent 5,134,243, July 28, 1993. Mobil Oil Corporation.
 37. Degnan, T.F.; Keville, K.M.; Landis, M.E.; Marler, D.O.; Mazzone, D.N. Hydrocracking Process Using Ultra-Large Pore Size Catalysts. US Patent 5,183,557, February 2, 1993. Mobil Oil Corporation.
 38. Degnan, T.F.; Keville, K.M.; Marler, D.O.; Mazzone, D.N. Hydrocracking with Ultra Large Pore Size Catalysts. US Patent 5,281,328, January 25, 1994. Mobil Oil Corporation.
 39. Degnan, T.F.; Keville, K.M.; Landis, M.E.; Marler, D.O.; Mazzone, D.N. Hydrocracking Process Using Ultra-Large Pore Size Catalysts. US Patent 5,290,744, March 1, 1994. Mobil Oil Corporation.
 40. Apelian, M.R.; Degnan, T.F.; Marler, D.O.; Mazzone, D.N. Production of Lubricants by Hydrocracking and Hydroisomerization. US Patent 5,264,116, November 23, 1993.
 41. Marler, D.O.; Mazzone, D.N. Production of Hydrocracked Lubricants. US Patent 5,277,792, January 11, 1994. Mobil Oil Corporation.
 42. Marler, D.O.; Mazzone, D.N. Production of High Viscosity Lubricants. US 5,288,395, February 22, 1994. Mobil Oil Corporation.
 43. Corma, A.; Martinez, A.; Martinezsoria, V.; Monton, J.B. Hydrocracking of vacuum gas oil on the novel mesoporous MCM-41 aluminosilicate catalyst. *J. Catal.* **1995**, *153* (1), 25–31.
 44. Klemt, A.; Taouli, A.; Koch, H.; Reschetilowski, W. The preparation of hydrocracking catalysts using mesoporous aluminosilicates MCM-41—Influence of the preparation conditions on the catalytic behavior. *Stud. Surf. Sci. Catal.* **1999**, *127*, 405–408.
 45. Klemt, A.; Reschetilowski, W. New hydrocracking catalysts based on mesoporous Al-MCM-41 materials. *Chem. Eng. Technol.* **2002**, *25* (2), 137–139.
 46. Kresge, C.T.; Leonowicz, M.E.; Roth, W.J.; Vartuli, J.C.; Keville, K.M.; Shih, S.S.; Degnan, T.F.; Dwyer, F.G.; Landis, M.E. Demetallation of Hydrocarbon Feedstocks With a Synthetic Mesoporous Crystalline Material. US Patent 5,183,561, February 2, 1993. Mobil Oil Corporation.
 47. Shih, S.S. Upgrading of a Hydrocarbon Feedstock Utilizing a Graded Mesoporous Catalyst System. US Patent 5,344,553, September 6, 1994. Mobil Oil Corporation.
 48. Baker, C.L.; Chu, C.T.-W.; Mazzone, D.N.; Page, N.M. Lubricant Hydrocracking Process. US Patent 5,468,368, November 21, 1995. Mobil Oil Corporation.
 49. Degnan, T.F.; Dougherty, R.C.; Hatzikos, G.H.; Shih, S.S.; Yan, T.Y. Hydrogenation Process. US Patent 5,573,657, November 12, 1996. Mobil Oil Corporation.
 50. Borghard, W.S.; Chu, C.T.-W.; Degnan, T.F.; Shih, S.S. Aromatics Saturation with Catalysts Comprising Crystalline Ultra-Large Pore Oxide Materials. US Patent 5,264,641, November 23, 1993. Mobil Oil Corporation.
 51. Apelian, M.R.; Degnan, T.F.; Shih, S.S. Catalyst and Process for Producing Low-Aromatics Distillates. US Patent 5,451,312, September 19, 1995. Mobil Oil Corporation.
 52. Corma, A.; Martinez, A.; Martinez-Soria, V. Hydrogenation of aromatics in diesel fuels on Pt/MCM-41 catalysts. *J. Catal.* **1997**, *169* (2), 480–489.
 53. DelRossi, K.J.; Hatzikos, G.H.; Huss, A. Paraffin Isomerization Process Utilizing a Catalyst Comprising a Mesoporous Crystalline Material. US Patent 5,256,277, October 26, 1993. Mobil Oil Corporation.
 54. Chaudhari, K.; Das, T.K.; Chandwadkar, A.J.; Sivasanker, S. Mesoporous aluminosilicate of the

- MCM-41 type: Its activity in *n*-hexane isomerization. *J. Catal.* **1999**, *186* (1), 81–90.
55. Le, Q.N.; Thompson, R.L. Olefin Upgrading by Selective Conversion with Synthetic Mesoporous Crystalline Material. US Patent 5,191,144, March 2, 1993. Mobil Oil Corporation.
 56. Le, Q.N.; Thompson, R.T. Catalytic Process for Hydrocarbon Cracking Using Synthetic Mesoporous Crystalline Material. US Patent 5,232,580, August 3, 1993.
 57. Degnan, T.F.; Del Rossi, K.J.; Huss, A. Isoparaffin/Olefin Alkylation. US Patent 5,191,148, March 2, 1994. Mobil Oil Corporation.
 58. DelRossi, K.J. Isoparaffin/Olefin Alkylation. US Patent 5,191,147, March 2, 1994. Mobil Oil Corporation.
 59. Kresge, C.T.; Marler, D.O.; Rav, G.S.; Rose, B.H. Supported Heteropoly Acid Catalysts for Isoparaffin–Olefin Alkylation Reactions. US Patent 5,324,881, June 28, 1994. Mobil Oil Corporation.
 60. DelRossi, K.J.; Jablonski, G.A.; Kresge, C.T.; Kuehl, G.H.; Marler, D.O.; Rav, G.S.; Rose, B.H. Supported Heteropoly Acid Catalysts. US Patent 5,475,178, December 12, 1995. Mobil Oil Corporation.
 61. Le, Q.N. Production of Ethylbenzene. US Patent 5,118, 894, June 2, 1992. Mobil Oil Corporation.
 62. Le, Q.N. Aromatics Alkylation Process. US Patent 5,191,134, March 2, 1993. Mobil Oil Corporation.
 63. Hellring, S.D.; Beck, J.S. Phase-Transfer Catalysis with Onium-Containing Synthetic Mesoporous Crystalline Material. US Patent 5,347,060, September 13, 1994. Mobil Oil Corporation.
 64. Beck, J.S.; Socha, R.F.; Shihabi, D.S.; Vartuli, J.C. Selective Catalytic Reduction of Nitrogen Oxides. US Patent 5,143,707, September 1, 1992. Mobil Oil Corporation.
 65. Beck, J.S.; Calabro, D.C.; McCullen, S.B.; Pelrine, B.P.; Schmitt, K.D.; Vartuli, J.C. Sorption Separation over Modified Synthetic Mesoporous Material. US 5,220,101, June 15, 1993. Mobil Oil Corporation.
 66. Herbst, J.A.; Kresge, C.T.; Olson, D.H.; Schmitt, K.D.; Vartuli, J.C.; Wang, D.I.C. Method of Separation of Substances. US Patent 5,378,440, January 3, 1995. Mobil Oil Corporation.
 67. Kuehl, G.H. Removal of Large Molecules from a Fluid. US Patent 5,583,277, December 10, 1996. Mobil Oil Corporation.
 68. Beck, J.S.; Kuehl, G.H.; Olson, D.H.; Schlenker, J.L.; Stucky, G.D.; Vartuli, J.C. M41S Materials Having Nonlinear Optical Properties. US Patent 5,348,687, September 20, 1994. Mobil Oil Corporation.
 69. Olson, D.H.; Stucky, G.D.; Vartuli, J.C. Sensor Device Containing Mesoporous Crystalline Material. US Patent 5,364,797, November 15, 1994. Mobil Oil Corporation.
 70. Ozin, G.A.; Mamak, M.; Coombs, N.A. Mesoporous Oxide Compositions and Solid Oxide Fuel Cells. US Patent 6,420,063, July 16, 2002. Mobil Oil Corporation.



Metal Clusters on Oxides

Ivan Stensgaard

University of Aarhus, Aarhus, Denmark

M

INTRODUCTION

Metal clusters on oxides play a profound role in modern-day society because such systems are the basic ingredients in catalysts used for environmental protection, refining of fossil fuels, and production of chemicals. In the automotive three-way catalytic converter, for example, chemical reactions take place on nanometer-scale metal particles of Rh, Pt, and/or Pd distributed on an oxide of a high surface area, typically alumina.

Catalysis has thus been the main motivation for research on metal clusters on oxides. The improved ability to control the size and distribution of metal clusters coupled with the development of techniques for better characterization of the structural, electronic and chemical properties of metal clusters on oxides (primarily scanning probe techniques) has spurred an increased research activity in the field. Consequently, a series of interesting new results have been obtained, which have demonstrated how, e.g., the properties of the metal clusters may change in the nanometer-scale regime due to quantum size effects.

Atomic-scale investigations of industrial catalysts are hampered by the complexity of the systems. In this article emphasis will therefore be on metal clusters on oxides prepared and investigated in laboratory research environments, i.e., under ultrahigh vacuum (UHV) conditions. The advantage of such model systems is that they lend themselves much more readily to investigations based on a large variety of surface science tools. The article is intended to give the reader an overview of the techniques for synthesis and characterization of model systems, as well as to address important issues that are relevant for metal clusters on oxides in general. For further reading, reference is given to a number of reviews on metals on oxides.^[1-5]

SUBSTRATE PREPARATION, GROWTH, AND CLUSTER MORPHOLOGY

Fig. 1 shows an image of a ruthenium catalyst for ammonia synthesis recorded with high-resolution transmission electron microscopy (HRTEM).^[6] The Ru metal clusters appear as dark, almost circular regions on a lighter

background of MgAl₂O₄. The experimental challenge of investigating (at the atomic level) systems of a structural complexity such as that in Fig. 1 is still so formidable that strong efforts are made to derive information from structurally simpler systems. In the following, focus will be on techniques for creating model systems of metal clusters on oxides.

Substrate Preparation

Typically, the metal clusters are supported on low-index surfaces of crystalline metal or semiconductor oxides, such as MgO, Al₂O₃, TiO₂, Fe₂O₃, ZnO, and SiO₂. The surface science of metal oxides has been treated in an excellent monograph.^[7] Unfortunately, the preparation of clean and well-ordered oxide surfaces on a bulk specimen still remains an experimental challenge.^[1] The standard procedures for creating clean, well-ordered *metal* surfaces include polishing and etching, followed by ion sputtering to remove impurities and annealing to reestablish the crystal order. Such procedures, when applied to oxides, will, in many cases, lead to poor order or loss of stoichiometry due to preferential sputtering and/or thermally induced segregation.

As an alternative, in situ cleavage of bulk oxide specimens under UHV may be considered. However, materials such as SiO₂, Al₂O₃, and TiO₂ are difficult to cleave successfully in the sense that the cleavage plane will not coincide with an extended low-index plane, and that the surface may locally be very rough. Successfully cleaved surfaces can be used for one-shot experiments. To remove deposited metal, sputtering/annealing cycles are necessary.

Being large band gap materials the oxides are strongly insulating, adding to the difficulty and a severe drawback because when working with oxide surfaces most experimental techniques involve electron transfer, leading to charging effects. The charging problem has spurred the development of alternative schemes, where the oxide is made conductive by the introduction of point defects, or the oxide is grown in the form of an ultrathin film on a metallic substrate^[1-4,8,9] that allows for electric transport through the film, e.g., in the form of a tunneling current.

Examples of the two types of alternative schemes are shown in Fig. 2 in the form of scanning tunneling microscopy (STM) images of a TiO₂ bulk crystal surface and

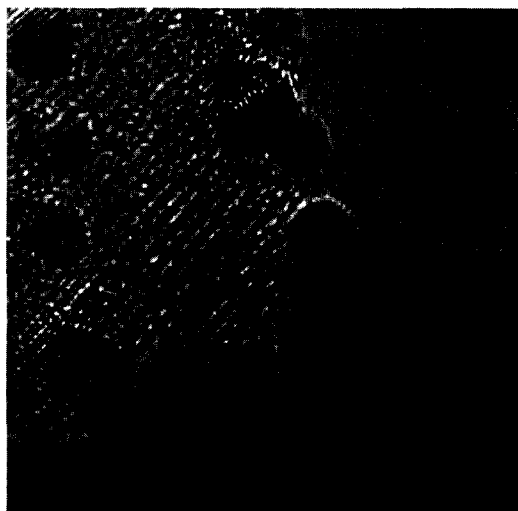


Fig. 1 High-resolution TEM micrograph of a ruthenium catalyst for ammonia synthesis. The almost circular dark regions are Ru metal clusters. The oxide is MgAl_2O_4 . (From Fig. 3 of Ref. [6], with permission of Kluwer Academic Publishers.)

an Al_2O_3 thin film surface. Titanium dioxide is used extensively, not only for heterogeneous catalysts, but in several other technologically important areas such as photocatalysis and sensor technology. Bulk TiO_2 in its rutile form has a band gap of 3 eV, but thermal reduction under vacuum leads to oxygen deficiencies which create a shallow donor level in the gap, giving rise to a sufficiently increased conductivity for performing experiments such as STM on the surface.^[7,8] The (110) surface of TiO_2 in its rutile form shown in Fig. 2a is the most intensively studied TiO_2 surface and it has become a prototype of a metal oxide.^[10] Aluminum oxide (alumina), Al_2O_3 , is extremely important in both ceramics and catalysis. A band gap of 8–9 eV makes Al_2O_3 an excellent insulator, and Al_2O_3 surfaces are not easily accessible for surface science experiments. Fortunately, thin alumina films can easily be prepared.^[8,9] Oxidation at elevated temperatures, for example, of a (110) NiAl alloy single crystal surface results in the formation of an alumina film.^[3,11] The ensuing film depicted in Fig. 2b has a thickness of only ≈ 0.5 nm, less than the thickness of a unit cell of $\gamma\text{-Al}_2\text{O}_3$ or $\alpha\text{-Al}_2\text{O}_3$, but nevertheless sufficiently thick to have most of the properties of $\gamma\text{-Al}_2\text{O}_3$.^[3] And importantly, electron transport through the film is easily achieved, facilitating, e.g., STM investigations.

Metal Deposition

The standard technique for metal deposition on extended oxide surfaces is vapor deposition, where a metal in close

proximity to the oxide is heated to a temperature at which the metal has a suitable vapor pressure. Metal atoms will then impinge on the oxide surface at thermal energy. At room temperature (RT), the reevaporation probability for metal atoms is generally very low, i.e., the sticking probability is close to unity.

After landing, the metal adatoms may diffuse on the surface with a diffusion constant D determined by

$$D = (va^2/4) \exp(-E_d/kT) \quad (1)$$

for 2-D diffusion. Here v is a frequency factor of the order of 10^{13} Hz, a is the distance between neighboring adsorption sites, E_d is the energy barrier for diffusion, k is the Boltzmann constant, and T the absolute temperature. Diffusion can therefore be enhanced by an increase in temperature.

In a time interval τ the diffusing adatoms will travel a root-mean-square (rms) distance l given by

$$l = (4D\tau)^{1/2} \quad (2)$$

For sufficient metal coverage the diffusion process leads to nucleation. If the diffusing metal atom attaches itself to a surface defect (such as a step edge), the nucleation is heterogeneous. If, on the other hand, diffusing adatoms meet and form stable nuclei, the nucleation is termed homogeneous. In general, only a few atoms need to agglomerate to form stable nuclei. The minimum number of other adatoms that a diffusing metal adatom must meet to form a stable nucleus is called the critical cluster (or island) size. Thus if a metal dimer is stable, the critical cluster size is one.

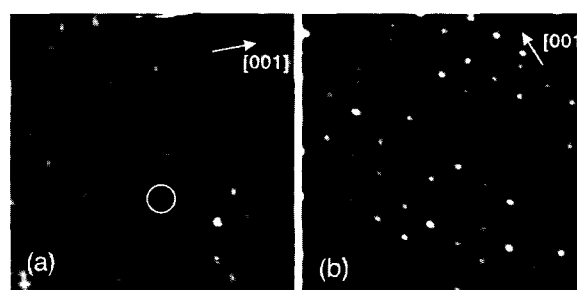


Fig. 2 STM images of oxides. (a) A clean TiO_2 (110) surface (13×13 nm²). The bright lines are rows of Ti atoms. The bright dots imaged between the Ti rows (see circle) are vacancies in rows of oxygen atoms which are in bridge positions relative to underlying Ti atoms. (Courtesy: Renald Schaub, CAMP, University of Aarhus.) (b) A thin Al_2O_3 film grown on NiAl(110) by oxidation. The two dark lines are antiphase domain boundaries relieving strain due to a mismatch between the film and the substrate (20×20 nm²).

Continued metal evaporation does not lead to an ever-increasing density of clusters. The saturation density N is determined by parameters such as the rate R at which atoms impinge on the surface, the temperature T , the frequency factor ν from the diffusion constant D (Eq. 1), the diffusion barrier E_d , and the critical cluster size i .^[12] It is important to realize that for a given metal–oxide system, the saturation density of clusters can be controlled by changing the substrate temperature during nucleation and/or the evaporation rate R .

When the saturation density of clusters has been reached, the clusters will grow by attachment of further adatoms. Although exceptions exist, the growth modes can conveniently be divided into three classes: *Frank van der Merwe* growth in which the metal grows layer-by-layer across the entire surface, *Volmer–Weber* growth in which metal grows as 3-D islands separated by bare oxide, and *Stranski–Krastanow* growth which starts as layer-by-layer growth, but with 3-D islands appearing after a few monolayers. Based on a model in which the cluster is treated as a liquid droplet on the support surface it is possible to have some preconception of the growth mode of a particular metal–oxide system. If γ_{met} and γ_{ox} denote the surface energies of the metal and the oxide, respectively, and γ_{int} the interface energy, the following rule can be established:^[13]

$$\gamma_{\text{ox}} \geq \gamma_{\text{met}} + \gamma_{\text{int}} : \text{layer - by - layer growth} \quad (3a)$$

$$\gamma_{\text{ox}} < \gamma_{\text{met}} + \gamma_{\text{int}} : \text{3-D cluster growth} \quad (3b)$$

Expressions (3a) and (3b) apply to the thermodynamical equilibrium. It is important to note that film growth is a kinetic process which does not take place at thermodynamic equilibrium (growth is incompatible with equilibrium!). The expressions are therefore applicable only to growth conditions which are close to equilibrium. As the free energies of the mid-to-late transition metals and the noble metals are frequently larger than the free energies of the supporting oxides, 3-D growth rather than layer-by-layer growth is to be expected for such systems. This is, indeed, confirmed by experiments.^[1] In the following, 3-D cluster growth is assumed.

Cluster Morphology

The thermodynamic equilibrium shape of a *free* metal cluster can be found from the Wulff theorem^[14] if the surface free energies of the low-index surfaces are known. The basis of the theorem is that for a given volume, the equilibrium shape must be determined by minimizing the total surface free energy. The ensuing theorem states that the ratio between the real-space distance d_i from the

cluster center to the facet plane i and the surface energy γ_i of this facet is a constant:

$$d_i/\gamma_i = c \text{ (constant)} \quad (4)$$

Fig. 3a shows a free cluster with a shape determined by the relative values of the surface energies γ_{100} , γ_{110} , and γ_{111} . A cross section of the cluster along the (110) plane is shown in Fig. 3b. The relative area of the different facets clearly depends on the relative values of γ_{100} , γ_{110} , and γ_{111} .

If the metal cluster is formed on an oxide, a metal–oxide interface is created. The free energy of the interface is given by the Dupré equation:

$$\gamma_{\text{int}} = \gamma_{\text{met}} + \gamma_{\text{ox}} - W_{\text{adh}} \quad (5)$$

where γ_{int} is the interface energy, γ_{met} and γ_{ox} the surface free energy of the contact facet of the cluster and the substrate, respectively, and W_{adh} the adhesion energy, i.e., the work per unit area needed to separate the cluster and the substrate.

The equilibrium shape of a *supported* cluster can now be found using a modified Wulff construction scheme,^[15] by replacing the free energy of the surface in contact with the substrate with an effective surface energy γ^* , which is the difference between the interface energy and the surface energy of the oxide:

$$\gamma^* = \gamma_{\text{int}} - \gamma_{\text{ox}} \quad (6)$$

The height H of the supported cluster, relative to that of a free cluster, thus depends on γ^* . For a cluster residing on a {111} facet (Fig. 4), the cluster will adopt its free-space form on the oxide if $\gamma^* = \gamma_{111}$. For smaller values of γ^* the cluster gets truncated [Fig. 4a], and for negative values of γ^* , the height of the supported cluster becomes less than half the height of the free cluster, as illustrated in Fig. 4b. An experimental value of the γ^*

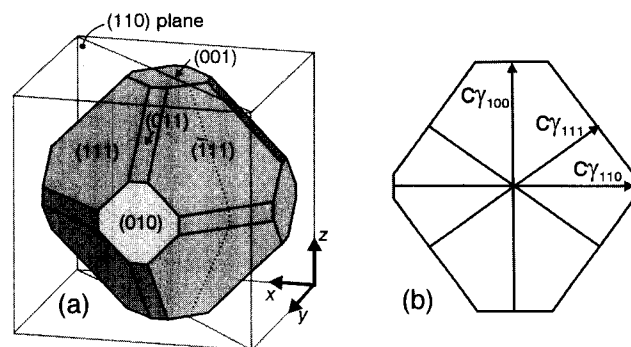


Fig. 3 The Wulff construction. (a) Cluster displaying three types of facets. (b) Cross section of the cluster along the (110) plane. (View this art in color at www.dekker.com.)

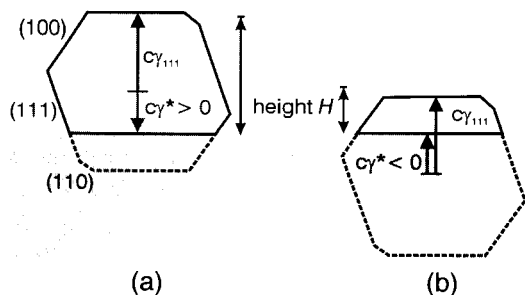


Fig. 4 Cross section of a cluster supported on a {111} facet for a positive (a) and a negative (b) value of the effective surface energy γ^* . H denotes the height of the cluster. (View this art in color at www.dekker.com.)

can be derived from the observed, detailed morphology of the clusters in terms of the cluster surface energies.^[16] From Eqs. 5 and 6

$$W_{\text{adh}} = \gamma_{\text{met}} - \gamma^* \quad (7)$$

Again, γ_{met} denotes the surface free energy of the metal cluster facet in contact with the oxide. The work of adhesion can therefore be derived from experiments, if the surface energies are known.

The Wulff construction is basically a continuum description which does not consider the discrete nature (finite number of atoms) of the clusters, and neglects the formation energy of corner and edge atoms, which play an important role in small clusters. Nevertheless, the theorem has been extremely successful in predicting or rationalizing shapes of metal clusters on oxides.

TWO CASE STUDIES

A large amount of metal/oxide combinations have been studied and an impressive amount of knowledge has been gained. In the following, focus will be on two different metal/oxide systems which have attracted special attention. The two systems will serve to illustrate fundamental properties, results, considerations, and problems related to research on metal clusters on oxides in general.

Palladium on Al_2O_3

Palladium on alumina is an important catalyst for partial or complete oxidation in many catalytic processes. The system has therefore been studied extensively, both in the form of industrial catalysts and as a model system. Most laboratory studies of Pd on alumina have been carried out on Al_2O_3 thin films because of the insulating nature of bulk Al_2O_3 . Fig. 5a is an STM image showing the result of Pd evaporation onto a thin Al_2O_3 layer formed by ox-

idation of NiAl(110) (cf. Fig. 2b). As expected from surface free energy considerations, Pd grows in the form of 3-D clusters (Volmer–Weber growth). For room temperature, low-coverage deposition of Pd on well-ordered films, the spatial distribution of the clusters is heavily influenced by the intrinsic defect structure of the film with a tendency for the clusters to nucleate at step edges and domain boundaries.

From Fig. 5a it is evident that a large fraction of the clusters are hexagonal in shape. On films with large domains up to 50% of the clusters are hexagonal in shape,^[16] reflecting the fact that these clusters are crystalline. The remaining clusters have not necessarily adopted their thermodynamical equilibrium form because of incorporated defects, insufficient temperature, etc. Because of the finite size of the STM tip the clusters are imaged as a convolution of the cluster and the tip shapes. This leads to a certain rounding of edges and corners as illustrated in Fig. 5b which displays height contours of a single Pd cluster.^[17] Based on atomic resolution STM,^[16] the facets of the cluster can be identified: The top facet is of {111} orientation while the sides are {111} and {100}

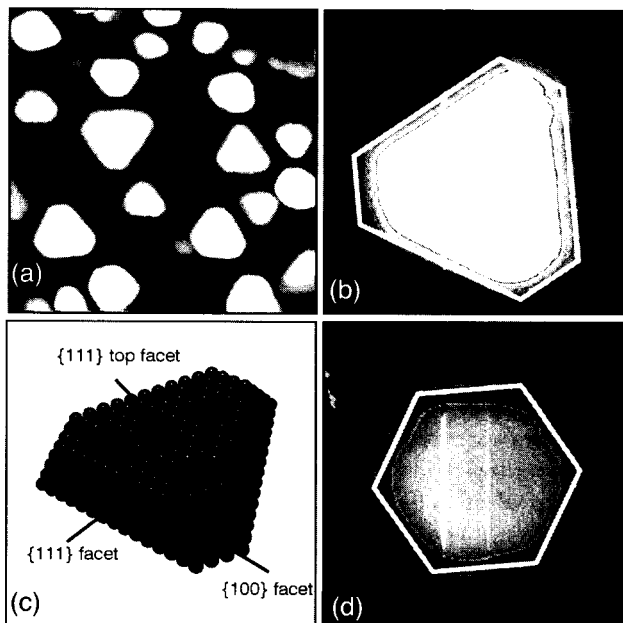


Fig. 5 (a) STM image of nanoclusters on $\text{Al}_2\text{O}_3/\text{NiAl}(110)$. Note the characteristic hexagonal shape of many clusters. ($50 \times 50 \text{ nm}^2$). (b) Height contours (thin lines) of a single Pd cluster. The thick line indicates the idealized, regular form. ($15 \times 15 \text{ nm}^2$). (c) Ball model of a cluster displaying {100} and {111} facets. (d) Height contours (thin lines) of a Cu cluster, closely resembling a regular hexagon (thick line), ($9 \times 9 \text{ nm}^2$). [(b) and (d) are reprinted from Ref. [17]. Copyright 2001, with permission from Elsevier.] (View this art in color at www.dekker.com.)

facets. For comparison, Fig. 5c shows a ball model of a cluster. As discussed earlier, the general shape of the cluster is governed by the surface and interface energies (modified Wulff construction). The clusters do not display any {110} facet, either because γ_{110} is too large compared to γ_{100} and γ_{111} (cf. Fig. 3b), or because the cluster is too small to develop a genuine {110} facet. Fig. 5d shows the height contours of a Cu cluster formed under similar conditions.^[17] In this case the shape of the top facet approaches a regular hexagon, illustrating how the surface energies influence the cluster morphology.

The principal objective for dispersing the active metal in a catalyst in the form of nanosized clusters is to increase the surface area. There are, however, several reasons why the dispersion, i.e., the formation of clusters, may influence the reactivity and make it deviate from that of corresponding, extended surfaces. First of all, the number of edge and corner sites will obviously increase dramatically. If such sites are active (see "Gold on TiO₂" section), the dispersion will promote an increase in activity which is easily explained. Secondly, exposure to gases may have different effects on extended surfaces and clusters dispersed on oxides. As an example, exposure of an extended Pd(111) surface to O₂ is known to result in the formation of a (2 × 2) structure, i.e., a structure with a unit cell four times bigger than the substrate unit cell. Exposure of a clean Pd nanocrystal [Fig. 6a] to O₂ has the same effect in the central portion of the top {111} facet, but an entirely new structure develops along the facet edge, as shown in Fig. 6b.^[18] It is beyond the scope of this article to discuss this phenomenon in detail; suffice it to state that the adsorption of gases on nanoclusters may cause reconstructions along facet edges, thereby creating new, possibly catalytically active sites. For very small clusters, the presence of gas may therefore influence the structure of the entire cluster.

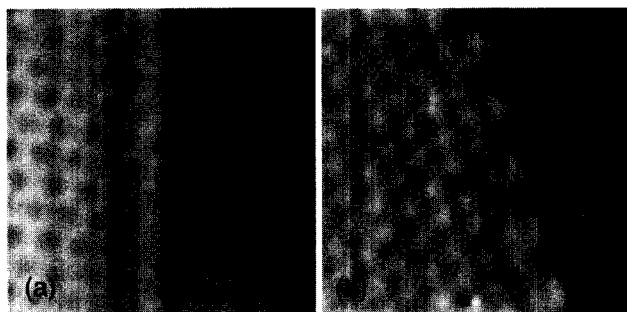


Fig. 6 Two atomically resolved STM images ($2.5 \times 2.5 \text{ nm}^2$) of a Pd cluster before (a) and after (b) exposure to O₂. The (2 × 2) oxygen adlayer in (b) is not imaged by STM, but a severe reordering of the facet edge has taken place. (View this art in color at www.dekker.com.)

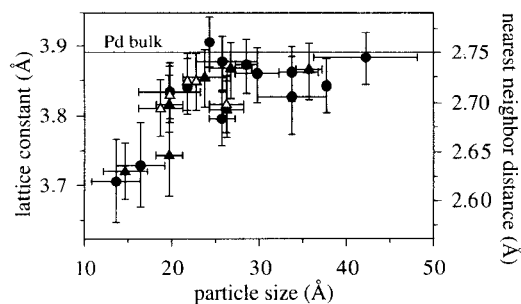


Fig. 7 Atomic spacing in Pd clusters on $\gamma\text{-Al}_2\text{O}_3/\text{NiAl}(110)$ as a function of cluster size. Horizontal bars illustrate the difference in length and width of the clusters whereas the vertical bars are estimated errors. (From Ref. [21]. Copyright 1999, American Chemical Society.)

The previous example is related to adsorption under static conditions, i.e., at a fixed temperature and in an unchanging atmosphere of (low pressure) oxygen. What happens to the cluster morphology when the cluster is exposed to gases at a higher pressure and temperature, i.e., under industrial catalytic conditions? An answer was recently found based on an in situ investigation.^[19] Model catalysts of Cu nanoparticles on ZnO (equivalent to the industrial methanol synthesis catalyst) were imaged with TEM in a high-pressure cell. The Cu nanocrystals were found to undergo dynamic, reversible shape changes in response to changes in the gaseous environment. The changes were found to be caused by adsorbate-induced changes in the surface energies and by changes in the interface energy. To describe and understand the catalytic properties of nanoscale clusters, *dynamic* effects on the nanocrystal morphology must therefore be included.

Dispersion may lead to effects of an even more subtle origin. Consider, for example, the sensitivity to changes in the lattice parameter. Because of the increased importance of the surface stress for smaller clusters, the lattice parameter is expected to decrease for decreasing cluster size.^[20] Fig. 7 shows an experimental verification obtained for Pd on Al₂O₃ on the basis of TEM measurements.^[21] The smallest clusters (size $\approx 1.5 \text{ nm}$) show a 4–5% reduction in lattice parameter. A smaller lattice parameter results in a broadening of the d-band. Compare to the effect of bringing atoms together to form a solid: The atomic levels broaden and become energy bands. The closer the atoms the stronger the broadening. For transition metals with d-bands that are more than half-filled, such as Pd, the broadening results in a downward shift of the d-band center to maintain the degree of filling. According to the d-band model, a shift in the d-band center relative to the Fermi energy will be correlated with a change in binding energy.^[22] Hence a change in the lattice parameter will influence the reactive properties of

the cluster. An indisputable experimental verification of this effect on clusters is still lacking, but changes in the reactivity of a metallic surface induced by a change in lattice parameter has been reported for a (0001)-oriented Ru sample in an area where an edge dislocation intersects the surface.^[23] On one side of the dislocation the lattice is compressed, and on the other side it is stretched. When analyzing the results of NO dissociation on the surface with STM, a much larger concentration of N atoms appeared at the stretched than at the compressed and the defect-free surface, signaling an enhanced reactivity of the stretched surface in accordance with the d-band model.^[22]

For tiny (few-atom) clusters, the electronic structure cannot be properly described in a band structure model. Instead the energy levels may be described in a picture based on molecular orbitals. The energy levels, and hence the reactivity, will therefore be very sensitive to the detailed size and shape of the cluster.

In this section a number of concepts which are central in the description of catalytically active metal clusters have been described, whereas the role of the substrate has been neglected, apart from its part in providing a passive, high surface-area matrix (structural promoter) for the dispersed metal clusters. Increasing evidence has been found that the oxide in many cases plays a much more active and decisive role than hitherto expected. References to some aspects of metal-oxide interaction will be made in the next section.

Gold on TiO₂

Gold is generally accepted to be the noblest of all the metals because of its electronic structure with a filled 5d band.^[24] Only little attention has therefore been paid to gold as a potential catalyst. Nevertheless, when gold is highly dispersed on select oxide surfaces in the form of

nanosized clusters, its chemistry changes dramatically and surprisingly a high activity and/or selectivity is exhibited in catalytic processes such as the low-temperature oxidation of CO.^[25] The observation that the chemical properties of gold depend on the support and in particular on the size of the Au clusters has spurred an intense search for the underlying physical origin.

When Au is evaporated onto a TiO₂ surface (cleaned by Ar ion sputtering and vacuum annealed to ≈ 1000 K), the Au atoms form clusters that nucleate at defects. Apart from major defects such as steps, the main nucleation sites are the bridging-oxygen vacancies shown in Fig. 2a.^[26] A single oxygen vacancy will bind up to three Au atoms and for larger Au clusters, the Au/TiO₂ interface will contain a high density of oxygen vacancies.

Fig. 8A shows an STM image of a 50 \times 50-nm area of a TiO₂ (110) surface with a large number of Au clusters (bright protrusions).^[27] As already mentioned the average cluster size can be varied by adjusting the evaporation flux, temperature, and total dose. By measuring the turnover frequency (TOF), i.e., the number of reactions taking place per Au atom per second, for CO oxidation as a function of the Au cluster size, a clear correlation between the TOF and the cluster diameter was revealed, showing a distinct maximum for a Au cluster diameter of ≈ 3 nm.^[27]

In the search for the origin of this effect, the electronic properties of the Au clusters were investigated with scanning tunneling spectroscopy (STS).^[27] In this technique, the STM tip is positioned on top of a particular cluster, and the tunnel current I is recorded as a function of the tunnel voltage V . The resulting I - V curves reflect the electronic properties of the clusters and can be correlated with cluster size and geometry, as shown in Fig. 8B. A perfectly metallic cluster on a conducting substrate should display a simple ohmic behavior, i.e., a straight line as I - V curve. From Fig. 8B it is evident that the smaller the

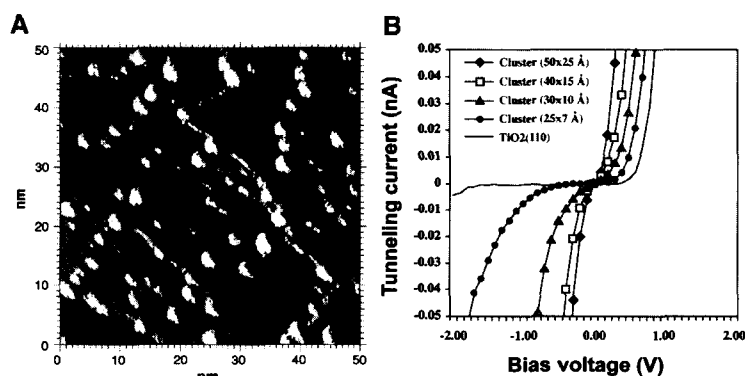


Fig. 8 (A) Constant-current STM image of Au/TiO₂(110). The total amount of Au corresponds to 0.25 monolayer. (B) Scanning tunneling spectroscopy data acquired for Au clusters of varying sizes on the TiO₂(110) surface. For reference the STS data of the TiO₂ substrate are also shown. (From Ref. [27]. Copyright 1998, American Association for the Advancement of Science.)

cluster the stronger the deviation from simple ohmic behavior is observed. When the dimension of the cluster is decreased, a plateau of zero tunnel current develops around zero bias voltage corresponding to the appearance of a band gap between the valence and the conduction band. For comparison, an STS curve for the TiO₂ substrate, having a wider band gap than the Au clusters, is also included in Fig. 8B. These measurements provide a fine illustration of how quantum size effects become important when the dimensions of metal clusters are reduced, but do not by themselves explain the peak in activity for a given cluster size.

To elucidate the mechanism behind the observed activity, the possible role of the substrate must also be considered. It is well known that the support may take part in reactions, for example via spillover effects where reactants may be formed at the metal clusters or the oxide and migrate from one to the other. The active role of an oxide support during CO oxidation over supported Au catalysts has been investigated theoretically and experimentally with conflicting results (see Ref. [28] and references therein). To illustrate the complexity of the problem, reference is made to a case study: a theory study based on density functional theory (DFT) calculations.^[29] MgO rather than TiO₂ was chosen as a substrate because of its structural simplicity and appearance in the experimental literature (Au clusters on MgO have also been shown to be reactive to CO oxidation at RT and even below.)^[30] The higher reactivity of supported nanometer-sized Au clusters was found to originate from two effects: 1) the oxide acts as a structural promoter, leading to the formation of small Au clusters with low-coordinated Au edge sites that readily bind CO; 2) the proximity of the oxide stabilizes a peroxo-like reaction intermediate CO₂.

It remains to be seen how general such mechanisms are, but the example serves to illustrate how the catalytic process may rely on an intricate interplay between the metal cluster and the oxide, and how challenging it is to sort out the relative importance of different effects.

CONCLUSION

In this article, emphasis has been on the synthesis and characterization of metal clusters on relatively flat, extended oxides which mimic real, metal-based catalysts sufficiently well to be exploited as model systems. Based on two case stories, Pd/Al₂O₃ and Au/TiO₂, a number of issues relevant for such systems have been introduced and discussed. Many other fascinating applications of metal clusters on oxides may be developed in the near future. Examples can already be found in the literature, such as the fabrication of single-electron transistors based on

contacting Au nanoclusters on SiO₂ with carbon nanotubes.^[31] While each example is of interest in its own area, the principal importance of metal clusters on oxides is unquestionably still in the field of catalysis.

ACKNOWLEDGMENTS

Fruitful collaboration with K. Højrup Hansen is gratefully acknowledged. This work was supported by the Danish National Research Foundation through the Center for Atomic-Scale Materials Physics.

REFERENCES

1. Campbell, C.T. Ultrathin metal films and articles on oxide surfaces: Structural, electronic and chemisorptive properties. *Surf. Sci. Rep.* **1997**, *27*, 1–111.
2. Henry, C.R. Surface studies of supported model catalysts. *Surf. Sci. Rep.* **1998**, *31*, 231–325.
3. Bäumer, M.; Freund, H.-J. Metal deposits on well-ordered oxide films. *Prog. Surf. Sci.* **1999**, *61*, 127–198.
4. Santra, A.K.; Goodman, D.W. Oxide-supported metal clusters: Models for heterogeneous catalysts. *J. Phys., Condens. Matter* **2002**, *14*, R31–R62.
5. Freund, H.-J. Clusters and islands on oxides: From catalysis via electronics and magnetism to optics. *Surf. Sci.* **2002**, *500*, 271–299.
6. Hansen, T.W.; Hansen, P.L.; Dahl, S.; Jacobsen, C.J.H. Support effect and active sites on promoted ruthenium catalysts for ammonia synthesis. *Catal. Letters* **2002**, *84*, 7–12.
7. Henrich, V.E.; Cox, P.A. *The Surface Science of Metal Oxides*; Cambridge University Press: Cambridge, Great Britain, 1994.
8. Chambers, S.A. Epitaxial growth and properties of thin films. *Surf. Sci. Rep.* **2000**, *39*, 105–180.
9. Franchy, R. Growth of thin, crystalline oxide, nitride and oxynitride films on metal and metal alloy surfaces. *Surf. Sci. Rep.* **2000**, *38*, 195–294.
10. Diebold, U. The surface science of titanium dioxide. *Surf. Sci. Rep.* **2003**, *48*, 53–229.
11. Libuda, J.; Winkelmann, F.; Bäumer, M.; Freund, H.-J.; Bertrams, T.; Neddermeyer, H.; Müller, K. Structure and defects of an ordered alumina film on NiAl(110). *Surf. Sci.* **1994**, *318*, 61–73.
12. Venables, J.A. Atomic processes in crystal growth. *Surf. Sci.* **1994**, *299/300*, 798–817.
13. Bauer, E. Phänomenologische Theorie der Kristallabscheidung an Oberflächen. *Z. Kristallogr.* **1958**, *110*, 372.

14. Wulff, G. Zur Frage der Geschwindigkeit des Wachstums und der Auflösung der Kristallflächen. *Z. Kristallogr.* **1901**, *34*, 449–530.
15. Winterbottom, W.L. Equilibrium shape of a small particle in contact with a foreign substrate. *Acta Metall.* **1967**, *15*, 303–310.
16. Højrup Hansen, K.; Worren, T.; Stempel, S.; Lægsgaard, E.; Bäumer, M.; Freund, H.-J.; Besenbacher, F.; Stensgaard, I. Palladium nanocrystals on Al_2O_3 : Structure and adhesion energy. *Phys. Rev. Lett.* **1999**, *83*, 4120–4123.
17. Worren, T.; Højrup Hansen, K.; Lægsgaard, E.; Besenbacher, F.; Stensgaard, I. Copper clusters on $\text{Al}_2\text{O}_3/\text{NiAl}(110)$ studied with STM. *Surf. Sci.* **2001**, *477*, 8–16.
18. Højrup Hansen, K.; Šljivančanin, Ž.; Lægsgaard, E.; Besenbacher, F.; Stensgaard, I. Adsorption of O_2 and NO on Pd nanocrystals supported on $\text{Al}_2\text{O}_3/\text{NiAl}(110)$: Overlayer and edge structures. *Surf. Sci.* **2002**, *505*, 25–38.
19. Hansen, P.L.; Wagner, J.B.; Helveg, S.; Rostrup-Nielsen, J.R.; Clausen, B.S.; Topsøe, H. Atom-resolved imaging of dynamic shape changes in supported copper nanocrystals. *Science* **2002**, *295*, 2053–2055.
20. Henry, C. Growth, structure and morphology of supported metal clusters studied by surface science techniques. *Cryst. Res. Technol.* **1998**, *33*, 1119–1140.
21. Nepijko, S.A.; Klimenkov, M.; Adelt, M.; Kuhlenbeck, H.; Schlögl, R.; Freund, H.-J. Structural investigation of palladium clusters on $\gamma\text{-Al}_2\text{O}_3(111)/\text{NiAl}(110)$ with transmission electron microscopy. *Langmuir* **1999**, *15*, 5309–5313.
22. Hammer, B.; Nørskov, J.K. Theoretical surface science and catalysis—Calculations and concepts. *Adv. Catal.* **2000**, *45*, 71.
23. Wintterlin, J.; Zambelli, T.; Trost, J.; Greely, J.; Mavrikakis, M. Atomic-scale evidence for an enhanced catalytic reactivity of stretched surfaces. *Angew. Chem., Int. Ed.* **2003**, *42*, 2850–2853.
24. Hammer, B.; Nørskov, J.K. Why gold is the noblest of all the metals. *Nature* **1995**, *376*, 238–240.
25. Haruta, M. Size- and support-dependency in the catalysis of gold. *Catal. Today* **1997**, *36*, 153–166.
26. Wahlström, E.; Lopez, N.; Schaub, R.; Thostrup, P.; Rønnau, A.; Africh, C.; Lægsgaard, E.; Nørskov, J.K.; Besenbacher, F. Bonding of gold nanoclusters to oxygen vacancies on rutile $\text{TiO}_2(110)$. *Phys. Rev. Lett.* **2003**, *90*, 026101-1-4.
27. Valden, M.; Lai, X.; Goodman, D.W. Onset of catalytic activity of gold clusters on titania with the appearance of non-metallic properties. *Science* **1998**, *281*, 1647–1650.
28. Schubert, M.M.; Hackenberg, S.; van Veen, A.C.; Muhler, M.; Plzak, V.; Behm, R.J. CO oxidation over supported gold catalysts—“Inert” and “Active” support materials and their role for the oxygen supply during reaction. *J. Catal.* **2001**, *197*, 113–122.
29. Molina, L.M.; Hammer, B. Active role of oxide support during CO oxidation at Au/MgO . *Phys. Rev. Lett.* **2003**, *90*, 206102-1-4.
30. Grisel, R.J.H.; Nieuwenhuys, B.E. Selective oxidation of CO, over supported Au catalysts. *J. Catal.* **2001**, *199*, 48–59.
31. Thelander, C.; Magnusson, M.H.; Deppert, K.; Samuelson, L.; Poulsen, P.R.; Nygård, J.; Borggren, J. Gold nanoparticles single-electron transistor with carbon nanotube leads. *Appl. Phys. Lett.* **2001**, *79*, 2108–2110.

Metal Nanoparticle Ensembles: Collective Optical Properties

Alexander Wei

Purdue University, West Lafayette, Indiana, U.S.A.

INTRODUCTION

Ensembles of gold and silver nanoparticles in the 10- to 100-nm size range exhibit collective electromagnetic properties, which can be tuned according to particle size and interparticle spacing. Self-assembly is a critical enabling mechanism for organizing nanoparticles into ensembles with well-defined lattice structures or geometries, if particle dispersion forces can be adequately controlled. Presented here are several recent theoretical and experimental studies on metal nanoparticle assemblies with novel and technologically appealing optical properties. For example, gold nanoparticles with intense plasmon resonances can be organized into planar arrays or spherical ensembles around dielectric cores, and serve as substrates for surface-enhanced Raman scattering (SERS). Recent theoretical developments indicate that the electromagnetic field factors responsible for such enhancements can be further tuned by adjusting the diameter-spacing ratio, enabling the optimization of metal nanoparticle ensembles for various applications in sensing and nanophotonics.

SURFACE PLASMONS

Gold and silver nanostructures are well known to exhibit electrodynamic phenomena commonly referred to as surface plasmons (see entry on “Surface Plasmon Spectra of Gold and Silver Nanoparticles”). These are generated by the collective excitation of free electrons in the metal particle, in response to a characteristic electromagnetic frequency. The surface plasmon modes of metal nanostructures have essentially the same function as radio antennas, except that they resonate in the optical and near-infrared (NIR) regions of the electromagnetic spectrum. Surface plasmons can be categorized into two types: localized plasmon resonances, in which incident light is absorbed or scattered by the oscillating electric dipoles within a metal nanoparticle, and surface plasmon polaritons, which propagate along metal surfaces in a waveguide-like fashion until released at some distance from their point of origin (Fig. 1). Localized plasmon resonances generate electromagnetic field factors, which en-

hance linear and nonlinear optical effects near the metal surface. The localized plasmonic responses of individual metal nanoparticles are now quite well understood and have been summarized in several recent works.^[1-3] On the other hand, metal nanoparticle ensembles can support both localized and propagating surface plasmon modes, whose physical relationships are less well defined. Regardless of the complexity of these phenomena, the plasmonic coupling of metal nanostructures with light enhances a broad range of useful optical phenomena, such as resonant light scattering (RLS), surface plasmon resonance (SPR), and SERS, all of which have tremendous potential for ultrasensitive chemical and biomolecular detection and analysis.

The plasmonic responses of coupled metal nanostructures are capable of intensifying local electromagnetic fields by many orders of magnitude. For example, many of the early SERS observations in the late 1970s and early 1980s were performed using kinetically formed aggregates of Ag and Au nanoparticles.^[4] Interest in SERS has been further stoked by reports of single-molecule SERS spectroscopy;^[5-7] however, the reproducibility of such activities has been poor. Despite strong evidence that aggregated nanoparticles can generate “hot spots” that produce enormous enhancements in Raman intensities, these vary widely from sample to sample and often disappear after a few days’ aging. The conditions that enable reproducibly high SERS enhancements have yet to be established, and constitute an important challenge in nanomaterials synthesis.

FABRICATION OF NANOPARTICLE ASSEMBLIES

In the last few years, significant progress has been made in the fabrication and optical characterization of metal nanoparticle assemblies in one, two, and three dimensions. Much of this work has been directed toward the self-assembly and materials properties of nanoparticle assemblies in which the unit particle size is below 10 nm (radius $R < 5$ nm); these have been reviewed elsewhere.^[8-10] More recently, several investigations have focused on



Fig. 1 Incident light on nanostructured metal surfaces can result in localized (standing) plasmon resonances (a), propagation of surface plasmon waves (b), or a combination of the two (c). Excitation of conduction electrons produces local electromagnetic fields (pink) near the metal surfaces. (View this art in color at www.dekker.com.)

metal nanoparticle assemblies with unit structures in the 10- to 100-nm range, the central theme of this entry. Both theoretical considerations and experimental investigations of discrete clusters and extended arrays of these mid-nanometer-sized nanoparticles will be discussed. It will become evident that in addition to particle size, structural parameters such as interparticle distance, lattice geometry, and periodic order also have important roles in the collective optical responses of these ensembles.

Discrete Clusters of Metal Nanoparticles

Plasmon-resonant nanoparticles can experience significant dipolar coupling when their interparticle separation δ is on the order of diameter $2R$ or less where R is nanoparticle radius, giving rise to additional plasmon modes. Effective-medium theories such as the Maxwell-Garnett formula, which can accurately describe the plasmon resonance of isolated metal particles below 30 nm, can provide only a limited approximation of the optical responses by coupled nanoparticles.^[11] These approximations lose their accuracy if δ is much less than one particle diameter ($\delta < 1.5R$), at which point evanescent (near-field) coupling becomes significant.

Simulations of discrete N -particle systems based on generalized Mie theory^[11,12] or numerical approaches such as discrete dipole approximation^[13,14] appear to provide more consistent models of coupled metal nanoparticles. These have been used to predict the extinction and ab-

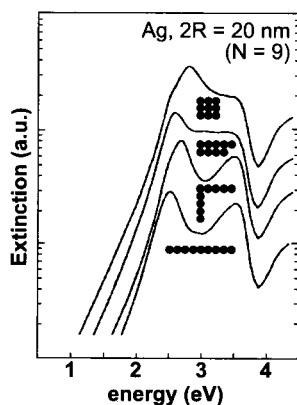


Fig. 2 Extinction spectra of 20-nm Ag particle aggregates in different geometries, as calculated by generalized Mie theory. (Adapted from Ref. [1].)

sorption cross sections of specific aggregate structures, such as chained particles in linear or bent conformations (Fig. 2). Linear chains of Ag nanoparticles produce longitudinal plasmon resonances at strongly redshifted wavelengths, whereas close-packed aggregates exhibit less pronounced shifts in their collective plasmon resonance frequencies. The optical responses of these N -particle clusters in fact correlate closely with anisotropic metal particles of similar overall shape, such as nanorods^[15,16] and nanoprisms.^[13,14,17]

More recent theoretical treatments have given emphasis to the local electromagnetic fields generated near the metal nanoparticle surfaces, with the objective of defining regions with the highest field factors (often quantified as a function of $|E/E_0|$ where E and E_0 are the plasmon-enhanced and incident electric field intensities) for a given frequency ω . This is especially important for surface-enhanced spectroscopies such as SERS, in which signals are amplified as a function of $G_{EM} = |E(\omega)/E_0(\omega)|^2 \cdot |E(\omega')/E_0(\omega')|^2$, where G_{EM} is the local Raman enhancement factor and ω and ω' are the incident and Stokes-shifted frequencies, respectively.^[18] In the simplest case of a two-sphere system, it is widely agreed that local field factors are greatest when the two particles are almost touching. Xu and coworkers have performed electrostatics calculations on pairs of Au and Ag particles (10–90 nm) separated by as little as 1 nm, and suggested G_{EM} values more than 10^{11} for the best cases.^[19] These localized enhancements are exquisitely sensitive to interparticle spacing; changes in δ by just a few nanometers can cause the local enhancements to drop by several orders of magnitude (Fig. 3). These calculations, in conjunction

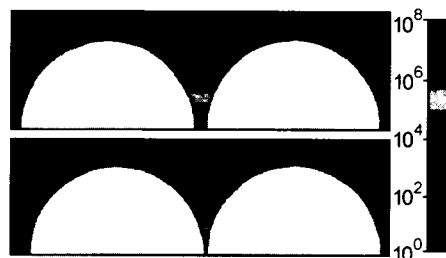


Fig. 3 Electrostatics simulation of local field enhancements (G_{EM}) between two 90-nm Ag particles at interparticle separations of $\delta = 5.5$ and 1.0 nm. (From Ref. [19].) (View this art in color at www.dekker.com.)



Fig. 4 Finite-difference time-domain simulation of electric fields (red) localized within a linear array of 50-nm Au particles (blue), with interparticle separations of $\delta=75$ nm. (From Ref. [23].) (View this art in color at www.dekker.com.)

with experimental studies by the same group,^[7,20] imply that nanoparticle dimers have potential as substrates for routine single-molecule SERS, given a reliable method for localizing analytes in regions of high field.

Linear Arrays of Metal Nanoparticles

Linear (1-D) arrays of metal nanoparticles have attracted much interest for their potential to transport energy in an antenna-like fashion and serve as near-field optical waveguides at subwavelength dimensions, with the possibility of integrating nanophotonics with far-field optical devices.^[21] Theoretical calculations of vectorial energy transport through chains of closely spaced 50-nm Au nanospheres suggest remarkably high levels of transmission at optical resonance, with optimized losses ranging between 10 and 25 dB per micron (Fig. 4).^[22,23] Several methods for producing nanoparticle 1-D arrays have been reported, including self-assembly on prepatterned surfaces^[24] and inside of nanoporous templates^[25,26] as well as by directed assembly using scanning probe microscopy tips.^[21]

Recent experimental studies on plasmonic 1-D nanoarrays have so far been promising. Proof of concept was established by Krenn and coworkers, who used photon scanning tunneling microscopy to image near-field excitations within Au nanoparticle chains.^[27] Near-field optical transport in linear arrays of Au nanoparticles and Ag nanorods was also recently demonstrated by Maier et al.^[23,28] The latter case was shown to support plasmon propagation with losses as low as 6 dB per 200 nm, which suggests their feasible integration into all-photonic device architectures.

Two-Dimensional Arrays of Metal Nanoparticles

Several methods have been employed for arranging metal nanoparticles into periodic and aperiodic two-dimensional (2-D) lattices. Periodically ordered 2-D arrays

with relatively large interparticle spacings ($D/2R=1.5$ to 5, where center-to-center distance $D=2R+\delta$) have been fabricated by electron-beam lithography^[29,30] or by self-assembly on lithographically defined surfaces^[24] (for some recent examples see Refs. [31,32]). Aperiodic 2-D arrays of the same genre have also been produced by self-assembly techniques, mostly by random sequential adsorption onto charged surfaces.^[33–37] For these cases, the collective optical properties of nanoparticles are dominated by dipolar coupling mechanisms; however, their responses are more complex than predicted by classical dipole–dipole interactions, whose strength varies with $1/D^3$. Particles larger than 30 nm can exhibit sizable retardation effects in their dipolar interactions, and this can impact both the wavelength and decay time of their coupled plasmon resonances.^[29,38] For example, Chumanov et al. observed a remarkable blueshifting and narrowing of extinction maxima in submonolayer films of 100-nm Ag particles as a function of packing density.^[33] This was later reproduced in lithographically defined Ag nanoparticle 2-D arrays, and reexamined as a function of particle diameter–spacing ratio.^[37] Recent theoretical analyses by Zhao and coworkers suggest that the blueshifting and narrowing are largely due to radiative dipolar coupling, an electrodynamic term that scales largely with $1/D$.^[39]

Aperiodic 2-D arrays may also provide a practical and straightforward method for preparing SERS substrates.^[34–36] Submonolayer ensembles of colloidal metal particles can be prepared with packing densities of up to 30% (Fig. 5, left), which is well below the close-packing limit ($\sim 90\%$) but sufficient to produce significant electromagnetic coupling and SERS.^[34–36,40] Electrostatic self-assembly of Au nanoparticles on spherical submicron particles has also been reported recently;^[41] in this case, packing densities on the order of 50% can be achieved by increasing the nanoparticles' surface potentials, with a concomitant enhancement in electromagnetic coupling (Fig. 5, right).

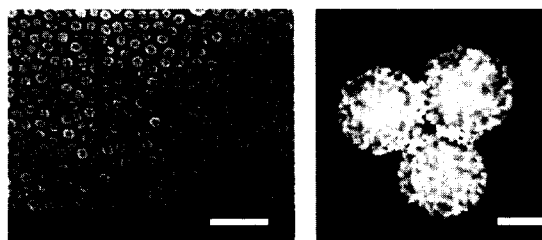


Fig. 5 Left: planar ensemble of 40-nm Au particles adsorbed onto thiol-functionalized SiO₂. (From Ref. [40]. Copyright 1995, American Chemical Society.) Right: spherical core-shell ensembles of 30-nm particles adsorbed onto amine-functionalized 390-nm SiO₂ particles. (From Ref. [41].) Scale bar=200 nm in both images.

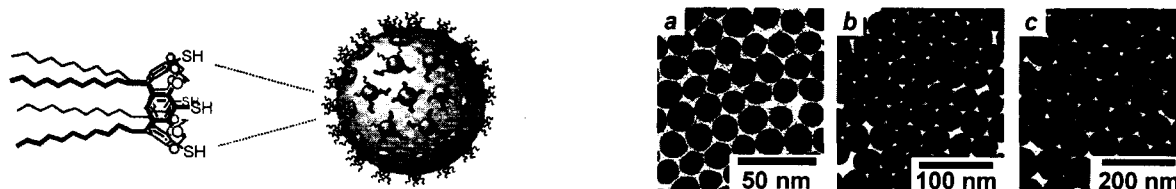


Fig. 6 Self-organized 2-D arrays of resorcinarene-encapsulated Au nanoparticles. Unit particle sizes: (a) 16 nm; (b) 34 nm; (c) 87 nm. (From Ref. [45]. Copyright 2001, American Chemical Society.) (View this art in color at www.dekker.com.)

2-D nanoparticle arrays with much smaller interparticle spacings ($D/2R < 1.1$) are likely to support strong near-field coupling as well as dipolar coupling, and should be excellent substrates for generating SERS and other surface-enhanced spectroscopies. In principle, such nanoparticle ensembles should also be accessible by thermodynamic self-assembly; however, metal particles in the midnanometer size range experience strong interaction potentials that can promote kinetic aggregation, resulting in poorly defined structures. This can be viewed as a problem in dispersion control: If repulsive interactions can offset particle self-attraction at close range, conditions for thermodynamically controlled self-organization can be achieved. Earlier demonstrations by Schmid et al.^[42] and by Giersig and Mulvaney^[43,44] have indicated that colloidal Au particles can be organized into close-packed domains with local 2-D order.

A general method for organizing metal nanoparticles into hexagonal close-packed 2-D arrays has recently been developed by Wei and coworkers, using multivalent macrocyclic surfactants known as resorcinarenes.^[45,46] These compounds are capable of extracting colloidal Au particles from aqueous suspensions and dispersing them in-

to organic solvents or at air-water interfaces.^[47] In the latter case, resorcinarene-stabilized nanoparticles as large as 170 nm have been organized into 2-D arrays with excellent local order (Fig. 6). Here the $D/2R$ ratios are well below 1.1; careful inspection of the TEM images reveals an inverse correlation between array periodicity and interparticle spacing δ , most likely due to greater van der Waals attraction with unit particle size.

The periodic 2-D nanoparticle arrays exhibit size-dependent optical properties at visible and NIR wavelengths. The gold nanoparticle films vary in hue from blue ($2R = 16$ nm) to a faint gray ($2R > 70$ nm), the latter being strongly absorptive in the NIR region (Fig. 7). The specular reflectance is also dependent on periodic structure, with maximum reflectance of white light observed for $2R$ between 40 and 70 nm.^[48] These variable reflectivities can be attributed to several effects: 1) an angular dependency in attenuated reflection as a function of surface roughness, a well-studied phenomenon in metallic thin films,^[49] 2) size-dependent optical absorption, with significant absorptivities in the visible region for nanoparticle arrays with periodicities below 40 nm; and 3) size-dependent increases in Mie scattering, a phenomenon that has been

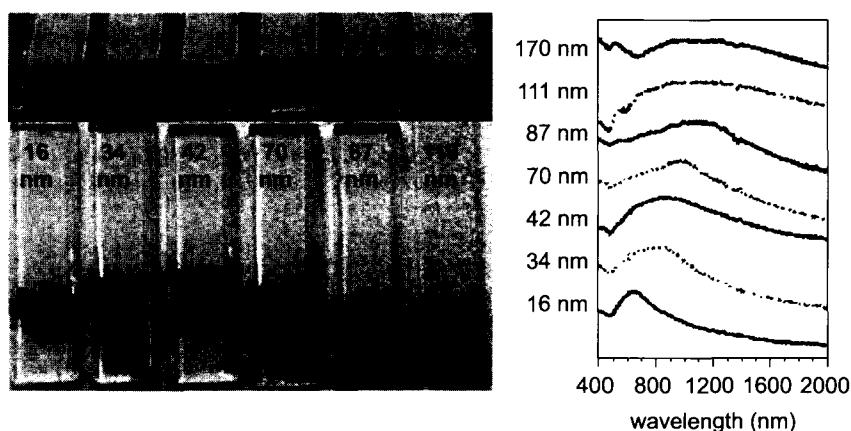


Fig. 7 Size-dependent optical properties of Au nanoparticle arrays. (From Refs. [45,48].) Left: 2-D nanoparticle arrays transferred onto annealed quartz substrates, as viewed directly (bottom) and with specular reflectance (top, $\theta_i = 60^\circ$). Substrates are approximately 1 cm wide. (Reproduced by permission of the Materials Research Society.) Right: extinction spectra of 2-D nanoparticle arrays. (Copyright 2001, American Chemical Society.) (View this art in color at www.dekker.com.)

characterized for nanoparticles and nanostructured metal surfaces with roughnesses on the order of 40 nm or more.^[1,2,49]

The 2-D nanoparticle arrays also exhibit size-dependent SERS activities, with excellent levels of signal enhancement in many cases.^[50] Surface-averaged Raman signals generated from the adsorbed resorcinarenes could be optimized as a function of periodicity and excitation wavelength, with enhancements as high as 10^7 . The observed trends are in accord with previous theoretical calculations describing electromagnetic SERS,^[51–54] and also with SERS studies on disordered metal colloid aggregates.^[55–57] However, the resorcinarene-stabilized nanoparticle arrays have considerable advantages in reproducibility and stability, and retain essentially all SERS activity more than a year after self-assembly. Additional signal enhancement could be obtained by increasing the solid angle of incidence and collection; the angle-dependent Raman intensities suggest that propagating surface plasmons in the Au nanoparticle films contribute significantly to the SERS effect.

The colloidal Au nanoparticle arrays are capable of detecting exogenous analytes by SERS and thus have potential as spectroscopic chemical sensors.^[50] Volatile organic compounds adsorbed onto the array surface produce a detectable signal within seconds; removal of the surfactant layer by plasma treatment further increases the arrays' sensitivities and enables the reproducible detection of analytes in aqueous solutions at micromolar concentrations.^[58] However, recent theoretical calculations indicate that detection limits can be further lowered by adjusting the interparticle spacing. An incremental change in δ delocalizes field intensities but at the same time increases the available sampling space for analyte detection. Recent calculations by Genov et al. indicate that the surface-averaged enhancement factor G_R (as opposed to the local factor G_{EM}) from periodic nanoparticle arrays can be maximized as a function of excitation wavelength

at a given value of $2R/\delta$, and can surpass that produced by disordered metal–dielectric films by several orders of magnitude (Fig. 8).^[59]

3-D Superlattices of Metal and Metalodielectric Nanoparticles

In addition to enhancing spontaneous emission events such as SERS, metal nanoparticle superlattices may also be capable of blocking electromagnetic radiation at select frequencies, i.e., a photonic band gap. Highly monodisperse particles on the order of an optical wavelength are well known to crystallize into 3-D superlattices, and often produce opalescent Bragg reflections. Colloidal crystals may also exhibit photonic band gaps in the visible to NIR range, and have been highly sought after as a way to manipulate the flow of light.^[60] In principle, a photonic band gap can be engineered from nearly any type of material by periodically modulating its dielectric properties. However, lattices with relatively low dielectric contrast are not optimal materials for designing photonic band gaps at optical wavelengths. Periodic metal–dielectric nanostructures are capable of much stronger optical modulation; “inverse-opal” metal-coated colloidal crystals have recently been fabricated and have some promise as photonic band-gap materials.^[61]

Theoretical studies by Moroz indicate that plasmonic colloidal crystals can support a complete photonic band gap in the visible and even the near-UV range.^[62] Close-packed, face-centered cubic (FCC) crystals of colloidal Ag particles were calculated to possess tunable band gaps, at frequencies defined by the particle radius and plasma wavelength (R/λ_p) and with relative gap widths between 5% and 10% as defined by $(\Delta\omega/\omega_c)$, the gap width to mid-gap frequency ratio. The photonic band gaps were predicted to be greatest for colloidal crystals with $R/\lambda_p > 0.9$; for Ag, 3-D arrays of large, submicron-sized

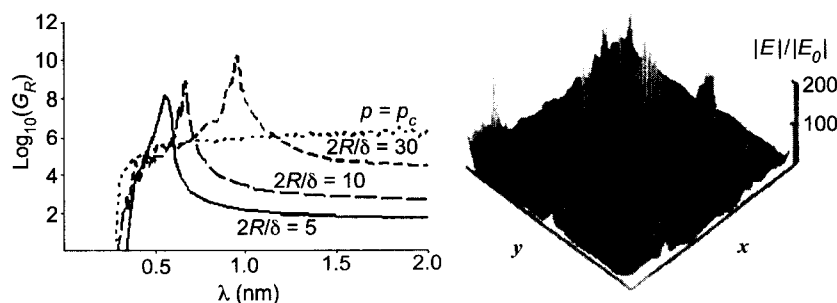


Fig. 8 Left: numerical calculations of surface-averaged field enhancements (G_R) from 2-D hexagonal superlattices, with diameter-spacing ratios of 5, 10 and 30, vs. a random metal–dielectric film at the percolation threshold ($p=p_c$). (From Ref. [59].) (Copyright 2003, American Chemical Society.) Right: local field distribution within a hexagonal lattice produced by p -polarized light ($\lambda=600$ nm, $2R/\delta=10$).

particles would be needed to produce band gaps for visible wavelengths.

A related study by Zhang et al. suggests that tunable photonic band gaps can also be made using metal-coated, core-shell nanoparticles as 3-D array elements.^[63] The band gaps of these materials are predicted to be less dependent on long-range order, a critical and challenging issue in the self-assembly of colloidal crystals. Photonic band gaps have been calculated for FCC lattices of SiO₂/Ag core-shell nanoparticles of different sizes and packing densities: 500/50-nm core-shell particles at 45% packing density are expected to have a robust band gap centered at $\lambda=1.5 \mu\text{m}$, whereas 160/50-nm core-shell particles at 42% packing density are expected to have a band gap across the visible spectrum. Graf and van Blaaderen have recently reported a closely related core-shell colloidal crystal, in which a second dielectric shell has been grown around the metal-coated nanoparticle.^[64] The outermost SiO₂ shell reduces the van der Waals interactions considerably, and permits their self-organization into colloidal crystals with fractional densities close to that proposed by Zhang et al.^[63]

CONCLUSION

In closing, the controlled assembly of metal nanoparticles into well-defined structures can yield novel collective electromagnetic behavior, with excellent potential for function and application. Chemical and bioanalytical nanosensors have already reached a remarkably advanced stage of development, with detection and analysis bordering on the single-molecule limit, and the emerging area of nanophotonics may have long-term impact on telecommunications and device integration.

ACKNOWLEDGMENTS

The author wishes to thank Beomseok Kim, Steven Tripp, and Bryce Sadtler for their valuable efforts toward the preparation and analysis of the planar and spherical Au nanoparticle arrays, and Dentcho Genov, Andrey Sarychev, and Vladimir Shalaev for related theoretical investigations. Financial support from the National Science Foundation, the National Institutes of Health, and Department of Defense are gratefully acknowledged.

REFERENCES

1. Kreibig, U.; Vollmer, M. *Optical Properties of Metal Clusters*; Springer: New York, 1995.
2. Yguerabide, J.; Yguerabide, E.E. Light-scattering submicroscopic particles as highly fluorescent

- analogues and their use as tracer labels in clinical and biological applications. I. Theory. *Anal. Biochem.* **1998**, *262*, 137–156.
3. Wei, A. Plasmonic Nanomaterials: Enhanced Optical Properties from Metal Nanoparticles and their Ensembles. In *Nanoparticles: Building Blocks for Nanotechnology*; Rotello, V.M., Ed.; Kluwer Academic: New York, 2003; 173–200.
4. Moskovits, M. Surface enhanced spectroscopy. *Rev. Mod. Phys.* **1985**, *57*, 783–826.
5. Kneipp, K.; Wang, Y.; Kneipp, H.; Perelman, L.T.; Itzkan, I.; Dasari, R.R.; Feld, M.S. Single molecule detection using surface-enhanced Raman scattering. *Phys. Rev. Lett.* **1997**, *78*, 1667–1670.
6. Nie, S.; Emory, S.R. Probing single molecules and single nanoparticles by surface-enhanced Raman scattering. *Science* **1997**, *275*, 1102–1106.
7. Xu, H.X.; Bjerneld, E.J.; Käll, M.; Borjesson, L. Spectroscopy of single hemoglobin molecules by surface enhanced Raman scattering. *Phys. Rev. Lett.* **1999**, *83*, 4357–4360.
8. Collier, C.P.; Vossmeier, T.; Heath, J.R. Nanocrystal superlattices. *Annu. Rev. Phys. Chem.* **1998**, *49*, 371–404.
9. Shipway, A.N.; Katz, E.; Willner, I. Nanoparticle arrays on surfaces for electronic, optical, and sensor applications. *ChemPhysChem* **2000**, *1*, 18–52.
10. Pileni, M.P. Nanocrystal self-assemblies: Fabrication and collective properties. *J. Phys. Chem., B* **2001**, *105*, 3358–3371.
11. Ung, T.; Liz-Marzan, L.M.; Mulvaney, P. Optical properties of thin films of Au@SiO₂ particles. *J. Phys. Chem., B* **2001**, *105*, 3441–3452.
12. Quinten, M. Optical effects associated with aggregates of clusters. *J. Clust. Sci.* **1999**, *10*, 319–358.
13. Jensen, T.; Kelly, L.; Lazarides, A.; Schatz, G.C. Electrodynamics of noble metal nanoparticles and nanoparticle clusters. *J. Clust. Sci.* **1999**, *10*, 295–317.
14. Kelly, K.L.; Coronado, E.; Zhao, L.L.; Schatz, G.C. The optical properties of metal nanoparticles: The influence of size, shape, and dielectric environment. *J. Phys. Chem., B* **2003**, *107*, 668–677.
15. van der Zande, B.; Böhmer, M.R.; Fokkink, L.G.J.; Schönenberger, C. Colloidal dispersions of gold rods: Synthesis and optical properties. *Langmuir* **2000**, *16*, 451–458.
16. Link, S.; El-Sayed, M.A. Optical properties and ultrafast dynamics of metallic nanocrystals. *Annu. Rev. Phys. Chem.* **2003**, *54*, 331–366.
17. Jensen, T.R.; Malinsky, M.D.; Haynes, C.L.; Van Duyne, R.P. Nanosphere lithography: Tunable localized surface plasmon resonance spectra of silver nanoparticles. *J. Phys. Chem., B* **2000**, *104*, 10549–10556.

18. Weitz, D.A.; Garoff, S.; Gramila, T.J. Excitation spectra of surface-enhanced Raman scattering on silver-island films. *Opt. Lett.* **1982**, *7*, 168–170.
19. Xu, H.; Aizpurua, J.; Käll, M.; Apell, P. Electromagnetic contributions to single-molecule sensitivity in surface-enhanced Raman scattering. *Phys. Rev., E* **2000**, *62*, 4318–4324.
20. Xu, H.; Käll, M. Polarization-dependent surface-enhanced Raman scattering of isolated silver nanoaggregates. *ChemPhysChem*. **2003**, *4*, 1001–1005.
21. Maier, S.A.; Brongersma, M.L.; Kik, P.G.; Meltzer, S.; Requicha, A.A.G.; Atwater, H.A. Plasmonics—A route to nanoscale optical devices. *Adv. Mater.* **2001**, *13*, 1501–1505.
22. Quinten, M.; Leitner, A.; Krenn, J.R.; Aussenegg, F.R. Electromagnetic energy transport via linear chains of silver nanoparticles. *Opt. Lett.* **1998**, *23*, 1331–1333.
23. Maier, S.A.; Kik, P.G.; Atwater, H.A. Observation of coupled plasmon–polariton modes in Au nanoparticle chain waveguides of different lengths: Estimation of waveguide loss. *Appl. Phys. Lett.* **2002**, *81*, 1714–1716.
24. Li, H.-W.; Muir, B.V.O.; Fichet, G.; Huck, W.T.S. Nanocontact printing: A route to sub-50-nm-scale chemical and biological patterning. *Langmuir* **2003**, *19*, 1963–1965.
25. Hornyak, G.; Kröll, M.; Pugin, R.; Sawitowski, T.; Schmid, G.; Bovin, J.-O.; Karsson, G.; Hofmeister, H.; Hopfe, S. Gold clusters and colloids in alumina nanotubes. *Chem. Eur. J.* **1997**, *3*, 1951–1956.
26. Nagle, L.; Fitzmaurice, D. Templated nanowire assembly on the surface of a patterned nanosphere. *Adv. Mater.* **2003**, *15*, 933–935.
27. Krenn, J.R.; Dereux, A.; Weeber, J.C.; Bourillot, E.; Lacroute, Y.; Goudonnet, J.P.; Schider, G.; Gotschy, W.; Leitner, A.; Aussenegg, F.R.; Girard, C. Squeezing the optical near-field zone by plasmon coupling of metallic nanoparticles. *Phys. Rev. Lett.* **1999**, *82*, 2590–2593.
28. Maier, S.A.; Kik, P.G.; Atwater, H.A.; Meltzer, S.; Harel, E.; Koel, B.E.; Requicha, A.A.G. Local detection of electromagnetic energy transport below the diffraction limit in metal nanoparticle plasmon waveguides. *Nat. Mater.* **2003**, *2*, 229–232.
29. Lamprecht, B.; Schider, G.; Lechner, R.T.; Ditzlacher, H.; Krenn, J.R.; Leitner, A.; Aussenegg, F.R. Metal nanoparticle gratings: Influence of dipolar particle interaction on the plasmon resonance. *Phys. Rev. Lett.* **2000**, *84*, 4721–4724.
30. Haynes, C.L.; McFarland, A.D.; Zhao, L.; Van Duyne, R.P.; Schatz, G.C.; Gunnarsson, L.; Prikulis, J.; Kasemo, B.; Käll, M. Nanoparticle optics: The importance of radiative dipole coupling in two-dimensional nanoparticle arrays. *J. Phys. Chem., B* **2003**, *107*, 7337–7342.
31. Ivanisevic, A.; Im, J.-H.; Lee, K.-B.; Park, S.-J.; Demers, L.M.; Watson, K.J.; Mirkin, C.A. Redox-controlled orthogonal assembly of charged nanostructures. *J. Am. Chem. Soc.* **2001**, *123*, 12424–12425.
32. Lu, Y.; Yin, Y.; Li, Z.-Y.; Xia, Y. Synthesis and self-assembly of Au@SiO₂ core–shell colloids. *Nano Lett.* **2002**, *2*, 785–788.
33. Chumanov, G.; Sokolov, K.; Cotton, T.M. Unusual extinction spectra of nanometer-sized silver particles arranged in two-dimensional arrays. *J. Phys. Chem.* **1996**, *100*, 5166–5168.
34. Freeman, R.G.; Grabar, K.C.; Allison, K.J.; Bright, R.M.; Davis, J.A.; Guthrie, A.P.; Hommer, M.B.; Jackson, M.A.; Smith, P.C.; Walter, D.G.; Natan, M.J. Self-assembled metal colloid monolayers: An approach to SERS substrates. *Science* **1995**, *267*, 1629–1632.
35. Grabar, K.C.; Freeman, R.G.; Hommer, M.B.; Natan, M.J. Preparation and characterization of Au colloid monolayers. *Anal. Chem.* **1995**, *67*, 735–743.
36. Grabar, K.C.; Smith, P.C.; Musick, M.D.; Davis, J.A.; Walter, D.G.; Jackson, M.A.; Guthrie, A.P.; Natan, M.J. Kinetic control of interparticle spacing in Au colloid-based surfaces: Rational nanometer-scale architecture. *J. Am. Chem. Soc.* **1996**, *118*, 1148–1153.
37. Hanarp, P.; Käll, M.; Sutherland, D.S. Optical properties of short ranged ordered arrays of nanometer gold disks prepared by colloidal lithography. *J. Phys. Chem., B* **2003**, *107*, 5768–5772.
38. Meier, M.; Wokaun, A.; Liao, P.F. Enhanced fields on rough surfaces: Dipolar interactions among particles of sizes exceeding the Rayleigh limit. *J. Opt. Soc. Am., B* **1985**, *2*, 931–949.
39. Zhao, L.; Kelly, K.L.; Schatz, G.C. The extinction spectra of silver nanoparticle arrays: Influence of array structure on plasma wavelength and width. *J. Phys. Chem., B* **2003**, *107*, 7343–7350.
40. Chumanov, G.; Sokolov, K.; Gregory, B.W.; Cotton, T.M. Colloidal metal films as a substrate for surface-enhanced spectroscopy. *J. Phys. Chem.* **1995**, *99*, 9466–9471.
41. Sadtler, B.; Wei, A. Spherical ensembles of gold nanoparticles on silica: Electrostatic and size effects. *Chem. Commun.* **2002**, 1604–1605.
42. Schmid, G.; Lehnert, A.; Kreibig, U.; Adamczyk, Z.; Belouschek, P. Synthese und elektronenmikroskopische untersuchung kontrolliert gewaschener, ligandstabilisierter Goldkolloide sowie theoretische Überlegungen zur Oberflächenbelegung durch Kolloide. *Z. Naturforsch.* **1990**, *45b*, 989–994.

43. Giersig, M.; Mulvaney, P. Formation of ordered two-dimensional gold colloid lattices by electrophoretic deposition. *J. Phys. Chem.* **1993**, *97*, 6334–6336.
44. Giersig, M.; Mulvaney, P. Preparation of ordered colloid monolayers by electrophoretic deposition. *Langmuir* **1993**, *9*, 3408–3413.
45. Kim, B.; Tripp, S.L.; Wei, A. Self-organization of large gold nanoparticle arrays. *J. Am. Chem. Soc.* **2001**, *123*, 7955–7956.
46. Wei, A.; Kim, B.; Pusztay, S.V.; Tripp, S.L.; Balasubramanian, R. Resorcinarene-encapsulated nanoparticles: Building blocks for self-assembled nanostructures. *J. Incl. Phenom. Macrocycl. Chem.* **2001**, *41*, 83–86.
47. Balasubramanian, R.; Kim, B.; Tripp, S.L.; Wang, X.; Lieberman, M.; Wei, A. Dispersion and stability studies of resorcinarene-encapsulated gold nanoparticles. *Langmuir* **2002**, *18*, 3676–3681.
48. Kim, B.; Tripp, S.L.; Wei, A. Tuning the optical properties of large gold nanoparticle arrays. *MRS Symp. Proc.* **2001**, *676*, 1–7. Y.6.1.
49. Raether, H. *Surface Plasmons on Smooth and Rough Surfaces and on Gratings*; Springer: Berlin, 1988.
50. Wei, A.; Kim, B.; Sadtler, B.; Tripp, S.L. Tunable surface-enhanced Raman scattering from large gold nanoparticle arrays. *ChemPhysChem* **2001**, *2*, 743–745.
51. Aravind, P.K.; Nitzan, A.; Metiu, H. The interaction between electromagnetic resonances and its role in spectroscopic studies of molecules adsorbed on colloidal particles or metal spheres. *Surf. Sci.* **1981**, *110*, 189–204.
52. Wang, D.-S.; Kerker, M. Enhanced Raman scattering by molecules adsorbed at the surface of colloidal spheroids. *Phys. Rev., B* **1981**, *24*, 1777–1790.
53. Liver, N.; Nitzan, A.; Gersten, J.I. Local fields in cavity sites of rough dielectric surfaces. *Chem. Phys. Lett.* **1984**, *111*, 449–454.
54. Zeman, E.J.; Schatz, G.C. An accurate electromagnetic theory study of surface enhancement factors for Ag, Au, Cu, Li, Na, Al, Ga, In, Zn, and Cd. *J. Phys. Chem.* **1987**, *91*, 634–643.
55. Blatchford, C.G.; Campbell, J.R.; Creighton, J.A. Plasma resonance-enhanced Raman scattering by adsorbates on gold colloids: The effects of aggregation. *Surf. Sci.* **1982**, *120*, 435–455.
56. Kneipp, K.; Dasari, R.R.; Wang, Y. Near-infrared surface-enhanced Raman scattering (NIR SERS) on colloidal silver and gold. *Appl. Spectrosc.* **1994**, *48*, 951–955.
57. Maxwell, D.J.; Emory, S.R.; Nie, S. Nanostructured thin-film materials with surface-enhanced optical properties. *Chem. Mater.* **2001**, *13*, 1082–1088.
58. Kim, B.; Wei, A. Unpublished results.
59. Genov, D.A.; Sarychev, A.K.; Shalaev, V.M.; Wei, A. Resonant field enhancements from metal nanoparticle arrays. *Nano Lett.* **2003**, *in press*.
60. Joannopoulos, J.D.; Meade, R.D.; Winn, J.N. *Photonic Crystals: Molding the Flow of Light*; Princeton University Press: Princeton, 1995.
61. Braun, P.B.; Wiltzius, P. Macroporous materials—Electrochemically grown photonic crystals. *Curr. Opin. Colloid Interface Sci.* **2002**, *7*, 116–123.
62. Moroz, A. Three-dimensional complete photonic band-gap structures in the visible. *Phys. Rev. Lett.* **1999**, *83*, 5274–5277.
63. Zhang, W.Y.; Lei, X.Y.; Wang, Z.L.; Zheng, D.G.; Tam, W.Y.; Chan, C.T.; Sheng, P. Robust photonic band gap from tunable scatterers. *Phys. Rev. Lett.* **2000**, *84*, 2853–2856.
64. Graf, C.; van Blaaderen, A. Metallo-dielectric colloidal core-shell particles for photonic applications. *Langmuir* **2002**, *18*, 524–534.

Metal Nanoparticles and Self-Assembly into Electronic Nanostructures

M

Venugopal Santhanam

Universität Duisburg-Essen, Essen, Germany

Ronald P. Andres

Purdue University, West Lafayette, Indiana, U.S.A.

INTRODUCTION

Nanotechnology is a catchword that evokes excitement in researchers and captures the imagination of laymen. The excitement in the research community stems from the fact that theoretically predicted variations in the physical properties of solid objects as their dimensions approach a few nanometers ($1 \text{ nm} = 10^{-9} \text{ m}$)—viz. lowering of melting point, Coulomb charging, novel magnetic, optical phenomena, etc.—have been verified experimentally.^[1–4] This experimental verification has been possible because of rapid strides made over the last two decades, both in techniques for synthesis and in tools for characterization of individual nanoscale objects. These advances have also opened up a vast array of potential technological applications and have occurred just as the limits of photolithography-based solid-state technology are being reached. Coupled with the revolutionary impact of solid-state electronic devices on our lives, advances in synthesis, manipulation, and characterization of nanomaterials have made nanotechnology—and in particular nanoelectronics—a cynosure of public interest.

There are two alternative approaches for fabricating nanoelectronic devices: the “top-down” and the “bottom-up” approaches. The top-down approach is similar to current photolithographic techniques used to produce microelectronic devices. It consists of “chiseling” nanometer-scale features in bulk materials. Using such techniques as e-beam lithography and x-ray phase shift lithography, this approach can now produce nanoscale features ($< 50 \text{ nm}$) and has the decided advantage of being compatible with current microelectronic processing methods and design concepts. However, this approach suffers from two important drawbacks: 1) processing costs rise exponentially as feature size decreases; and 2) the surfaces and interfaces produced by this approach exhibit atomic-scale imperfections, which critically degrade device performance as feature size approaches nanometer dimensions. The bottom-up approach consists of “building” the device or circuit by assembling it from preformed

nanoscale “bricks.” Bottom-up processing, involving the serial manipulation of nanoscale objects, is technologically impractical. However, it is often possible to induce nanoscale objects to assemble themselves into desired structures. It is such biologically inspired self-assembly which holds the greatest promise.

There are a number of interesting nanoelectronic building blocks, viz. metal nanocrystals and nanowires (both magnetic and nonmagnetic), semiconductor nanocrystals and nanowires, and carbon nanotubes. In this chapter, we focus solely on nonmagnetic metal nanocrystals. Two characteristics of metal nanoparticles are critical for assessing their usefulness in nanoelectronic applications: 1) the ease with which bare metal particles cold weld on contact to form hard aggregates; and 2) the tendency of metal particles to oxidize in an atmospheric environment especially in the presence of water molecules. The first characteristic means that the surface of a metal nanoparticle must be passivated by attachment of a monolayer of capping ligands or surfactant molecules before any attempt is made to assemble these particles into a uniform nanostructure. We will refer to such encapsulated particles as molecularly protected nanoparticles (MPNs). The second characteristic means that only noble metals such as Au and Ag will form nanoparticles that are not rapidly oxidized when exposed to an atmospheric environment. Linear alkanethiol molecules readily react in solution with both Au and Ag nanoparticles to form stable MPNs. These MPNs can be manipulated as stable physical species in a variety of organic solvents. The ability to manipulate Au and Ag MPNs in organic liquids, to synthesize macroscopic quantities of these particles with diameters in the 2–20 nm range, and to control the interparticle spacing in arrays of these particles by changing the length of the alkanethiol molecules coating the metal core make Au and Ag MPNs ideal building blocks for the self-assembly of nanoelectronic devices. To date, most studies of metal MPNs are of Au nanoparticles encapsulated by an alkanethiol monolayer.

ELECTRONIC APPLICATIONS OF METAL NANOPARTICLES

The simplest metal nanoparticle-based electronic material is fabricated by suspending Au MPNs in an organic solvent such as toluene, casting or spraying this suspension on a solid substrate, and allowing the solvent to evaporate. The nanoparticles agglomerate as the solvent evaporates to form a loosely aggregated solid. If the original suspension is dilute and care is taken to allow the solvent to evaporate slowly, small 3-D superlattice domains or "ordered MPN crystals" form as the suspension becomes supersaturated; however, in general, the solid phase that forms is amorphous. The closest interparticle spacing in the solid is determined by the length of the alkanethiol molecules encapsulating the Au particles. Because this spacing is on the order of a nanometer, these amorphous solids are weak electrical conductors in which electrons tunnel through the organic layers separating the Au particles and hop from particle to particle. Snow and Wohltjen^[5] have measured the electrical conductivity of amorphous films of Au MPNs as a function of the ratio of the diameter of the gold core to the length of the alkanethiol encapsulant. They measured electrical conductivities ranging from 10^{-6} to 10^{-12} $(\Omega \text{ cm})^{-1}$ and found that the conductivity at a given temperature increases as this ratio is increased. They have also shown that, when such an MPN solid is exposed to volatile organic vapors, its electrical conductivity is a function of the partial pressure of the organic molecule.^[6] This effect is most probably because of the absorption of the organic molecule into the alkanethiol layer surrounding the gold nanoparticles. Quantum tunneling varies exponentially with distance, and a small swelling of this layer results in a large variation in tunnel resistance. Thus even as simple a structure as an amorphous solid of Au MPNs constitutes an interesting electronic material, and a film of this nanostructured material can act as a chemi-resistive sensor. Unfortunately, films of alkanethiol-coated

Au nanoparticles are not strongly species-selective.^[6] However, adding different chemical functionalities to the ligand shell around the Au particles may be a way to increase the chemselectivity of the film.

Amorphous films of Au MPNs can also be used to fabricate low-resistance electrical conductors on flexible substrates. Low-resistance conductors are important components of high- Q inductors, capacitors, tuned circuits, and interconnects. An inexpensive method for fabricating such conductors on flexible substrates is critical for the development of ultralow-cost microelectronic systems such as radiofrequency identification tags. Using a dense suspension of Au MPNs in a volatile organic liquid, it is possible to print micron-thick lines via either ink jet or silk screen techniques on a substrate. If the Au particle diameter and the alkanethiol encapsulant are optimized, these low-conductivity Au MPN lines can be converted into high-conductivity Au lines. This transformation is made possible by the low melting temperature and low shear resistance of Au nanoparticles.^[2,7,8] It is accomplished either by thermally annealing the lines at a relatively low temperature ($<150^\circ\text{C}$),^[9] or by exposing them to laser radiation.^[10]

Although the electrical conduction behavior of an amorphous film of Au MPNs has technological potential, placing a single Au MPN between two electrodes provides a much richer range of electronic behavior. In this configuration (Fig. 1), the nanoparticle is able to suppress all electrical conduction at low-bias voltages. This phenomenon is called "Coulomb blockade." Coulomb blockade occurs when the electrostatic energy increase caused by adding a single electron on a capacitively coupled metal island is much larger than the thermal energy of the electrons:

$$e^2/2C \gg k_B T \quad (1)$$

where e is the charge on an electron, C is the effective capacitance of the metal island, k_B is the Boltzmann

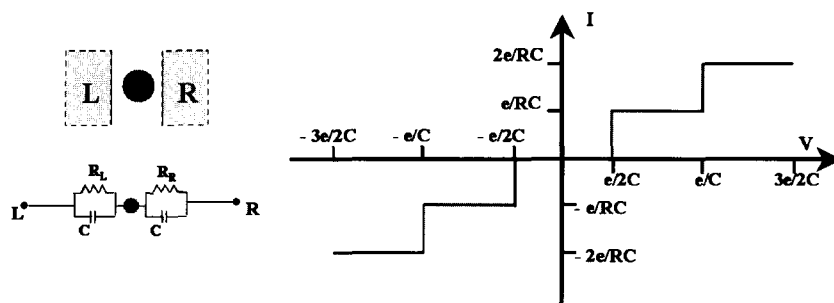


Fig. 1 (a) Schematic representation and equivalent circuit of nanostructure consisting of a single metal MPN placed between two electrodes. (b) Ideal I - V curve for this nanostructure illustrating Coulomb blockade at low bias and Coulomb staircase as bias is increased. (View this art in color at www.dekker.com.)

constant, and T is the absolute temperature of the metal island. In the case of metal MPNs, the capacitance C is directly proportional to the radius of the metal nanoparticle. For room temperature operation, Eq. 1 is satisfied when the particle diameter is less than approximately 2–3 nm. Larger particles are able to suppress all electron transport only if their temperature is lowered. For Coulomb blockade to be observed, the tunneling resistance (R) to and from the metal island must also be much greater than the resistance quantum (R_Q):

$$R \gg R_Q \quad (2)$$

where $R_Q = h/2e^2$ ($\sim 12.9 \times 10^3 \Omega$), with h being the Planck's constant.

When both Eqs. 1 and 2 are satisfied, the I - V curve for an asymmetric junction ($R_R \gg R_L$ or $R_L \gg R_R$) shows characteristic steps in the current, called "Coulomb staircase" (Fig. 1). The asymmetry in the resistance means that the flow of electrons is controlled either at the right or left tunnel junction, and so electrons tend to accumulate on the metal island. Because of the electrostatic energy associated with the charging of the island, an additional electron is not added at steady state until this excess energy is compensated for by increasing the external bias. Both Coulomb blockade and Coulomb staircase phenomena have been experimentally verified at room temperature using an Au MPN.^[3,11] In this experiment, a scanning tunneling microscope (STM) was used to measure the I - V characteristics of a vertical nanostructure, fabricated by depositing a single 2-nm-diameter gold particle on a gold substrate that had been coated with a self-assembled monolayer (SAM) of a double-ended thiol molecule.

The structure shown in Fig. 1 is the simplest example of a large class of nanoelectronic logic and data storage devices that are based on the controllable transfer of single electrons between small conducting islands sepa-

rated by tunnel barriers.^[12] For example, Tucker^[13] proposed a nanoscale field effect transistor (FET) based on modulating the voltage range of the Coulomb blockade by applying an asymmetric bias on a conducting island transverse to the direction of current propagation. Fabrication of such a single electron tunneling-field effect transistor (SET-FET), using metal nanoparticles, requires the ability to place 1-D chains of metal MPNs on an insulating substrate with variable interparticle spacing and the ability to address a nanoparticle having a diameter of ~ 2 nm from three directions. At present, there does not appear to be any way to self-assemble such a device. Although, in principle, any SET architecture can be constructed using metal MPNs, the technical difficulties involved in self-assembling complex SET circuits that can operate at room temperature seem overwhelming.

Roychowdhury et al.^[14] have suggested a logic architecture (Fig. 2) involving metal MPNs that does not require room temperature Coulomb blockade for its operation. This architecture consists of a uniform 2-D array of Au MPNs with input and output addressing along the edges of the array. The nanoparticles are coupled through electron tunneling barriers both to each other and to a semiconductor substrate that is a resonant tunneling diode (RTD) structure. The computation is performed by allowing the array to relax to its ground state, which depends on the Coulomb interactions of adjacent islands for a particular set of input voltages. This 2-D array architecture is compatible with the self-assembly and microcontact printing techniques described later in the present chapter, and recent reports on the formation of 8-nm-wide metallic lines^[15] and addressable cantilever arrays^[16] suggest that edge addressing issues and even readout of the charge state of individual nanoparticles may be tractable.

The weak interaction forces that exist between metal MPNs, although ideal for promoting self-assembly from solution, are not strong enough to produce 1-D, 2-D, or

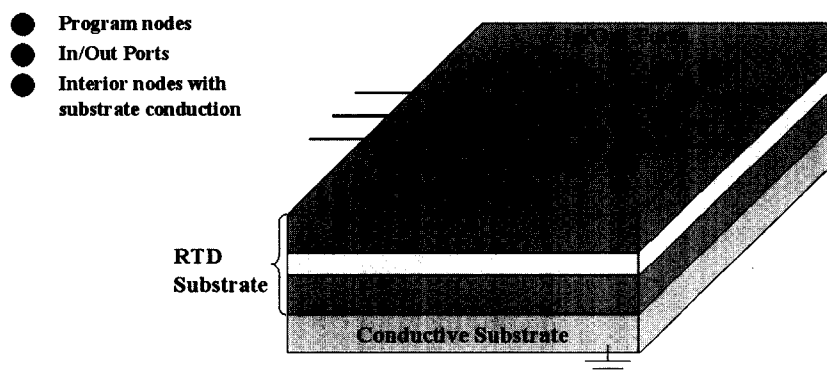


Fig. 2 Schematic of nanoelectronic architecture proposed by Roychowdhury et al. for Boolean logic. Nanostructure consists of an ordered 2-D array of Au MPNs linked to a RTD substrate. (From Ref. [14]. ©IEEE, 1997.) (View this art in color at www.dekker.com.)

3-D arrays that are structurally robust. Thus it is often necessary to strengthen the self-assembled structures formed by Au MPNs. This can be accomplished by displacing the monofunctional alkanethiol molecules coating the particles with difunctional molecules that bind the particles to each other or to the substrate. Both dithiol molecules and diisonitrile molecules are able to displace monothiol molecules from Au.^[17,18] Attaching conjugated molecules having distributed electronic states in the gap between adjacent metal nanoparticles in an array, or between a metal nanoparticle and a substrate, is also an attractive way to self-assemble another kind of electronic nanostructure. The metal–molecule–metal bridge that is established in this manner is the focus of the emerging field of molecular electronics.^[19,20] The diode structure shown in Fig. 1 can now be thought of as being replaced by one in which the conjugated linking molecule takes the place of the Au MPN. To date, experimental measurements of electron transport through such metal–molecule–metal structures have been attempted either by introducing a “nano” gap between two metal electrodes and adsorbing the desired organic molecules on the electrodes, or by STM manipulation of metal atoms and a single organic molecule on a substrate. An elegant example of this latter type of experiment is reported in the recent paper by Nazin et al.^[21] Although interesting electronic behavior has been demonstrated,^[22] the problem of how to self-assemble logic or memory circuits is still unsolved. A fruitful approach to this problem may be to self-assemble

molecular electronic devices using “linked arrays” of metal MPNs.

Au MPNs have been used to fabricate lateral structures that are linked by conjugated molecules. Andres et al.^[17] fabricated a linked monolayer of Au nanoparticles in the gap between lithographically defined electrodes by first self-assembling a uniform superlattice array of Au MPNs and then by replacing the alkanethiol molecules coating the Au particles with difunctional conjugated molecules. They measured electron transport in this monolayer film. Datta et al.^[23] have proposed the use of quasi-1-D conductive ribbons of linked metal nanoparticles, which they term “molecular ribbons,” as interconnects for semiconductor devices. It is difficult to fabricate linked monolayer films that are free of defects when the length of the linking molecule does not closely match the spacing in the original MPN array. One way to solve this problem is to fabricate a linked bilayer film, such as that shown in Fig. 3.^[24] This bilayer consists of two monolayers of Au MPNs with a molecular interconnect covalently linking the two layers. This nanostructure has been proposed as the basis of a novel chemiresistive sensor.^[24] It is hypothesized that target molecules that ligate with the linking molecules will shift the electronic energy levels of the linking molecules, thereby changing the tunnel resistance between the two layers and the electrical conductivity of the film. If this hypothesis is confirmed, this scheme would provide a generic method for fabricating chemi-selective sensing elements.

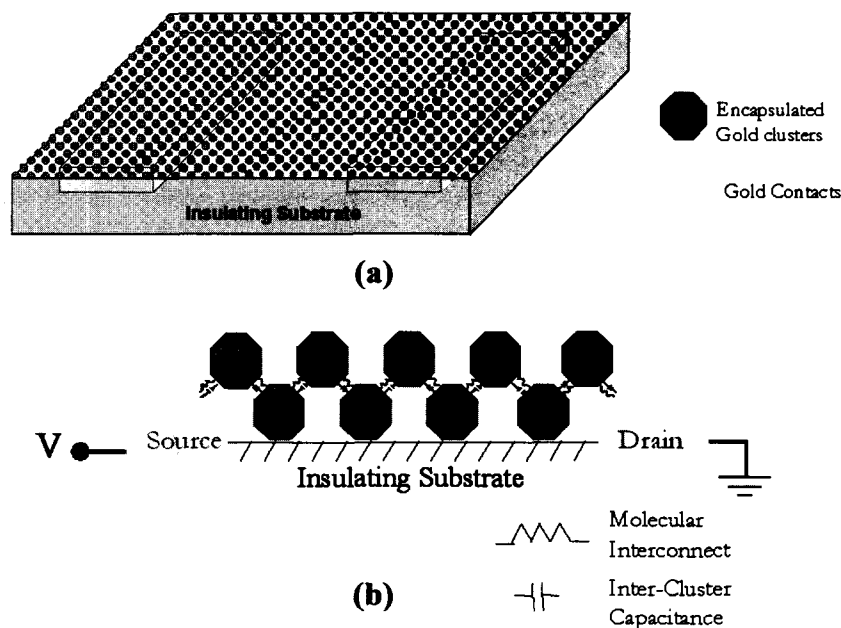


Fig. 3 Schematic representation of a chemiresistive sensor element proposed by Santhanam. (a) Plane view and (b) cross-sectional view. Nanostructure consists of a uniform bilayer of Au MPNs in which the two layers are interconnected by adsorbate-specific organic molecules. This bilayer forms the channel of an electrical diode. (From Ref. [24].) (View this art in color at www.dekker.com.)

Au MPNs have also been used to construct linked vertical structures. They have been utilized as nanoscale contacts on a semiconductor substrate^[25] and as nanoscale switches on top of redox molecules.^[26] Such linked vertical structures represent an attractive paradigm for molecular electronics-based devices.

Metal MPNs are also being studied for hybrid microelectronic applications such as floating gate memory cells and multiple tunnel junction devices.^[27,28] Metal nanoparticles provide an attractive choice for these applications because of the abundance of electrons near the Fermi level and the ability to tune their work function by changing the metal.

MPN SYNTHESIS

Metal MPNs can be synthesized either in the gas phase or in liquid solution. In either case, the essential requirement for synthesizing particles with a narrow size distribution is to initiate a temporally discrete homogeneous nucleation event followed by a slow growth regime, and to prevent particle aggregation. An apparatus for gas-phase synthesis of metal nanoparticles is shown schematically in Fig. 4.^[29,30] Metal atoms, evaporated from a single crucible or a series of crucibles located in a resistively heated oven, are entrained in helium and induced to condense by mixing the hot flow from the oven with a room temperature stream of helium. Controlling conditions in the oven and helium flows controls the mean particle size. The particles are thermally annealed in the

gas phase by passing the aerosol mixture through a tube furnace. They are scrubbed from the gas phase by contact with a mist of organic solvent containing surfactant molecules and collected as a stable colloidal suspension. The reactor shown in Fig. 4 also has provision for expanding a portion of the aerosol stream into a vacuum chamber to form a particle beam. Potential advantages of gas-phase synthesis are: 1) the ability to synthesize extremely small particles and to vary the mean particle size over a wide range; 2) the ability to produce pure metal particles, which may then be encapsulated with a wide variety of surfactants; 3) the ability to produce mixed metal particles even when the constituent metals are immiscible at room temperature; and 4) the ability to thermally anneal metal particles before encapsulating them with an organic surfactant.

Solution-based techniques for the synthesis of metal nanoparticles are based on the reduction of positively charged metal ions or ion complexes in solution usually in the presence of a capping ligand to arrest particle growth at a desired size. The major advantage of solution synthesis is the simplicity of the required equipment. The major disadvantage is the need for removal of excess reactants and for isolation of the particles as pure MPNs. In the case of Au particles, encapsulation by alkanethiols simplifies the isolation and purification steps greatly. A general technique for solution synthesis of nanoparticles with a controlled size and a narrow size distribution is to isolate small volumes of aqueous solution in which particle growth takes place by means of nonionic inverse micelles.^[31,32] However, two homogeneous solution

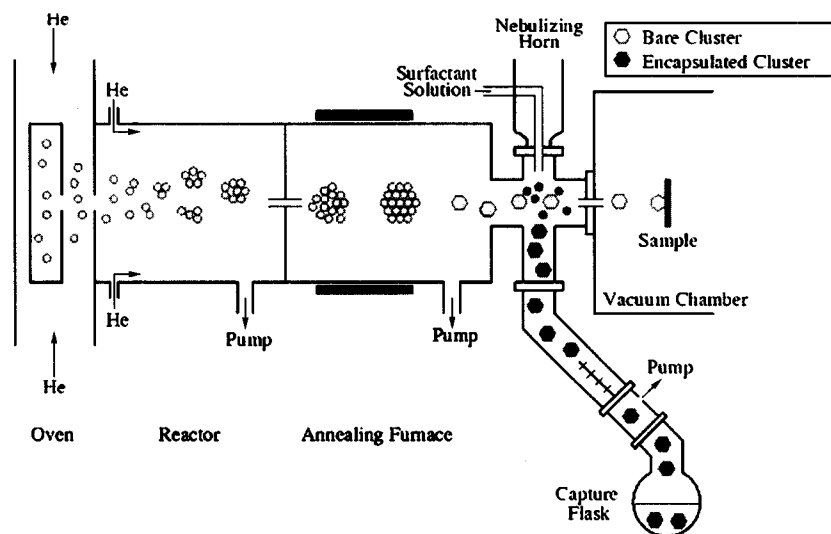


Fig. 4 Schematic representation of an aerosol reactor used to produce metal MPNs with a narrow size distribution. Metal atoms are condensed in a helium flow to form bare metal clusters (nanoparticles). The aerosol containing the nanoparticles then passes through an annealing furnace, after which the particles are encapsulated with an appropriate surfactant molecule and captured as a colloidal suspension. (View this art in color at www.dekker.com.)

methods are more commonly used for the production of Au MPNs. The first method is reported by Brust et al.^[33] This is a two-phase (water-toluene) reduction of AuCl_4^- by sodium borohydride in the presence of an alkanethiol. The Au ions are transferred to the toluene phase using tetraoctylammonium bromide, where they are simultaneously reduced by borohydride and capped by the alkanethiol. Once encapsulated Au particles have formed, they are precipitated from the toluene solution by the addition of a polar solvent, and then washed, dried, and resuspended in a nonpolar solvent such as toluene, hexane, or chloroform. The second method is reported by Giersig and Mulvaney.^[34] This method makes use of the classical method of Turkevich et al.,^[35] which produces charge-stabilized Au particles by reduction of AuCl_4^- in water using trisodium citrate as the reducing agent. An alkanethiol dissolved in tetrahydrofuran (THF) is then added to this aqueous solution, causing encapsulation of the Au particles and their gradual flocculation. The capped Au particles can be extracted into cyclohexane. They are precipitated from cyclohexane by the addition of a polar solvent, and then washed, dried, and resuspended in a nonpolar solvent. Au MPNs produced by the Giersig method retain a residual charge before they are extracted into cyclohexane and can be deposited on a conducting substrate by electrophoresis.^[34] After they have been washed, dried, and resuspended in a nonpolar solvent, there does not seem to be any difference between Au MPNs produced by the two methods; however, the Brust method appears to be more suitable for the synthesis of smaller particles (<5 nm) and the Giersig method appears to be more suitable for the synthesis of larger particles (>5 nm).

The standard deviation of the diameter distribution of particles synthesized by either the Brust method or the Giersig method is about 10%. The size distribution can be narrowed by fractional crystallization.^[36] This involves selective precipitation of the particles in a solvent mixture containing a good solvent and a poor solvent such as toluene/acetone. Whetten et al.^[37] have used selective precipitation in the presence of excess alkanethiol surfactants to refine the size distribution of Au MPNs synthesized by the Brust method. Starting with Au MPNs having a mean diameter in the 1- to 2-nm range, they were able to prepare monodispersed samples having a fixed number of gold atoms. Stoeva et al.^[38] have found that it is possible to refine both the size distribution and faceting of Au MPNs simply by heating a concentrated suspension of the particles in a process they have termed "digestive ripening."

Au MPNs produced by solution synthesis are compact, nearly spherical particles with a narrow size distribution that can be improved by size-selective precipitation;

however, the gold cores are not necessarily faceted single crystals. Whetten et al.^[37] report that in the 1.5- to 3.5-nm range, Au MPNs synthesized by the Brust method have faceted gold cores that are primarily single crystals with a face-centered cubic (FCC) lattice and a lattice constant close to the bulk gold value of 0.409 nm. High-resolution transmission electron microscopy (HRTEM) analysis of Au MPNs that were synthesized by the Giersig method with diameters in the 5- to 20-nm range reveals that these particles are primarily polycrystalline.^[39] This is also true for Au MPNs with diameters greater than a few nanometers that are synthesized by gas-phase condensation, unless they are thermally annealed by heating them above their melting temperature and then allowing them to recrystallize in the gas phase. Then they become predominantly single crystals or singly twinned crystals with an FCC lattice and a lattice constant of 0.409 nm.^[24,39]

The ultimate Au MPN as far as controlled size and crystal structure are concerned is the triphosphine ligand-protected 55-gold-atom particle synthesized by Schmid et al.^[40] almost two decades ago. These particles have an icosahedral geometry and exhibit Coulomb blockade behavior at room temperature. They played an important role in establishing the quantum size behavior of metal MPNs and in suggesting possible electronic applications of encapsulated metal nanoparticles.^[41,42] However, the complex synthesis of these particles, which requires anaerobic conditions and diborane as a reducing agent, and the difficulty of replacing the triphosphine ligands with other ligands have led to these particles being studied much less than alkanethiol-encapsulated Au particles. A more convenient synthesis technique and schemes for utilizing exchange reactions to modify the characteristics of these particles have been reported.^[43]

Because of their simplicity and flexibility, the solution-based synthesis routes of Brust et al.^[33] and Giersig and Mulvaney^[34] are currently the methods of choice for preparing Au MPNs for electronic applications. Similar solution-based methods are available for preparing semiconductor and magnetic metal MPNs.^[36,44] Methods utilizing safer solvents and biosynthetic routes are being explored to address environmental concerns.^[45,46]

FABRICATION OF ORDERED MPN ARRAYS

The ability to assemble nanometer-scale metal islands or particles into ordered arrays is a prerequisite for the successful fabrication of nanoscale electronic devices based on these building blocks. In what follows, we focus on self-assembly methods involving metal MPNs. "Top-down" approaches using resist-based lithographic patterning will not be discussed at all. However, two methods

that do not make use of metal MPNs are worth mentioning. The first technique is to self-assemble an ordered monolayer of polystyrene or silica spheres on a substrate and thermally evaporate metal atoms onto this colloidal mask. This results in nanometer-scale metal deposits forming on the areas of the substrate not masked by the colloidal spheres.¹⁴⁷¹ The second technique involves synthesis of metal nanoparticles inside structures formed using diblock polymers.^{148,491} The major drawbacks of both of these schemes are that the metal islands or particles have largely uncontrolled shapes and typically have interparticle spacings much larger than molecular dimensions. Because of the ease by which Au nanoparticles can be thermally annealed, the first of these drawbacks may not be severe in the case of Au. Nevertheless, the large interparticle spacings make it difficult to see how electronic circuits can be fabricated using these methods. Self-assembly of MPNs that have been preselected as to size, shape, and surface chemistry into ordered arrays seems to be the most promising approach for fabricating nanoscale electronic devices.

3-D Arrays

Starting with metal MPNs that have a narrow size distribution, it is relatively easy to produce ordered 3-D arrays or superlattices, in which the MPNs take the place of atoms in conventional crystals. Ordered 3-D arrays are formed by supporting a drop of the colloidal nanoparticle suspension on a flat surface and slowly evaporating the solvent. Encapsulated metal nanoparticles typically self-assemble into an FCC or HCP superlattice.^{138,501} Faceted, single-crystal Au MPNs often adopt preferred orientations in both 2-D and 3-D arrays in which the (111) atomic planes of each Au particle align parallel to the (111) atomic planes of all the other Au particles and to the surface of the supporting substrate.^{138,391}

2-D Arrays

Uniform, close-packed monolayers of MPNs are an essential component of many proposed nanoelectronic devices. There are several techniques for fabricating nanoparticle monolayers by self-assembly. These fall into three categories: 1) field-enhanced or molecular interaction-induced deposition from a colloidal solution of MPNs onto a solid substrate; 2) drop casting or spin coating of a suspension of MPNs onto a solid substrate and allowing of the solvent to evaporate; and 3) spreading of a suspension of hydrophobic MPNs in an organic solvent on a water surface, allowing of the solvent to evaporate, and transferring of the floating MPN film to a solid substrate.

Giersig and Mulvaney¹³⁴¹ employed electrophoretic deposition at field strengths of 1 V/cm to deposit a monolayer of Au MPNs on a carbon film-coated TEM grid. The monolayer was polycrystalline with small hexagonal close-packed domains. When the nanoparticles were deposited without an electric field, no ordering was observed. The adsorption of MPNs from solution onto functionalized surfaces has also been used to form nanoparticle monolayers. In this case, the substrate is coated with a “tether” molecule having a strong affinity for the particles. The substrate is immersed in a colloidal solution of MPNs, removed after a period of time, and rinsed to remove unbound particles. The MPN monolayer formed in this manner is amorphous and is seldom dense (Fig. 5a).^{151,521} This approach can also be used to form multilayers if, after the deposition of each monolayer, the monofunctional molecule encapsulating the particles is replaced by a difunctional molecule such as a dithiol. The major drawback of these methods for electronic applications is the lack of long-range order in the particle film.

The simplest method of forming a monolayer of MPNs is to spread a thin film of a colloidal suspension containing the particles either by drop casting or spin

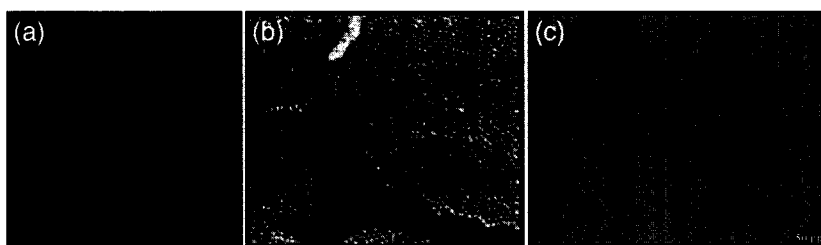


Fig. 5 Examples of nanoparticle monolayers self-assembled by three different methods. (a) Scanning electron microscopy (SEM) micrograph of a monolayer formed by adsorption of the particles onto a substrate coated with a bifunctional tether molecule. (From Ref. [51]. ©ACS, 2000.) (b) SEM micrograph of a monolayer produced by compression of nanoparticle rafts on a Langmuir trough. (From Ref. [56]. ©AIP, 2001.) (c) TEM micrograph of a monolayer formed by drop casting a colloidal suspension of nanoparticles on a carbon film-coated TEM grid.

coating on a substrate that is wet by the solvent, and to allow the solvent to evaporate.^[17] As the solvent evaporates, small monolayer islands form on the substrate. These islands result from the breakup of the liquid film because of dewetting as the film thickness approaches molecular dimensions. The monolayer islands are dense and consist of small hexagonal close-packed domains (Fig. 5c). An important parameter for optimizing the size and degree of order in these monolayer domains is the rate of evaporation of the solvent. However, the key to forming large ordered regions are the uniformity and smoothness of the substrate.^[53] Surface nonuniformities arrest the lateral mobility of the nanoparticles and result in microscopic voids and grain boundaries in the particle film.

A liquid/liquid interface, because of its inherent uniformity in the lateral direction and nonuniformity in the vertical direction, provides an ideal surface for self-assembling 2-D arrays of nanoparticles. Usually the self-assembly process is carried out by casting an organic suspension containing nanoparticles, which are encapsulated by a hydrophobic molecule, on a water surface and by allowing the solvent to evaporate. The number of nanoparticles spread on the water surface is taken to be smaller than the number needed to form a dense monolayer. When the organic solvent evaporates, discrete monolayer rafts of nanoparticles form on the water surface. These monolayer domains are often well-ordered but cover only a fraction of the surface area. A dense monolayer is obtained by decreasing the area available to the particle rafts using a Langmuir trough.^[54-56] As the area of the trough is decreased, the monolayer rafts collide with each other and coalesce. Without an organic solvent present, the monolayer domains typically exhibit solidlike behavior and resist deformation. Collier et al.^[57] were able to make use of the rigid behavior of a nanoparticle film supported on a water surface to carefully compress a film of Ag MPNs and to measure a reversible insulator-to-metal transition as the film was compressed and the tunneling distance between adjacent particles was decreased. Unfortunately, this rigid behavior often results in microscopic voids (Fig. 5b) and multilayer domains in monolayers assembled using a Langmuir trough.^[56]

Schmid and Beyer^[58] have proposed an intriguing variation on the classical technique. They introduce an amphiphilic molecule that has a strong affinity for the nanoparticles to assist in the formation of an ordered particle monolayer. They first self-assemble a layer of these molecules at an organic / water interface. When nanoparticles are introduced to the system, they adsorb on the amphiphilic layer and assemble into monolayer sheets or ribbons, depending on the experimental conditions.

Santhanam et al.^[59] have also proposed a modification of the classical technique. They are able to self-assemble uniform, ordered 2-D arrays of Au MPNs on a water surface by controlling the nucleation and growth of the particle monolayer. This is accomplished by designing a cell that establishes a "concave" lens of colloidal solution on the water surface (Fig. 6). As the solvent evaporates, the organic layer thins fastest at the center of the cell and, at some point, a monolayer array of MPNs nucleates at this spot. The periphery of this 2-D array is defined by a circular contact line. As more solvent evaporates, additional MPNs deposit at the edge of the particle monolayer, and the contact line moves steadily outward. The advantage of this technique is that new particles are added to the growing monolayer in the presence of solvent molecules. This ensures enough particle mobility to largely eliminate microscopic holes and grain boundaries, and promotes the formation of a close-packed crystalline monolayer. Fig. 7 shows a photograph of a film of 5-nm-diameter Au MPNs that was self-assembled on a water surface using this technique. The different hue seen near the edge of the cell arises from the increased curvature of the water interface at the cell wall, which leads to contact line instabilities. This results in alternating bands of multilayer regions surrounding the uniform monolayer region in the center of the cell. Fig. 7 also shows TEM micrographs of samples of this Au MPN film taken near the center and the edge of the cell. These images clearly illustrate the long-range translational ordering of the monolayer that forms in the center of the cell and the nature of the multilayer bands that form at the edge of the cell. A bilayer film can be produced on the water surface simply by increasing the concentration of the particles in the initial colloidal solution.

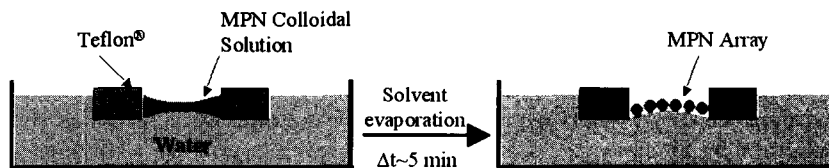


Fig. 6 Schematic illustration of the process proposed by Santhanam et al. for self-assembly of a uniform close-packed monolayer of metal MPNs by controlling the nucleation and growth of the monolayer film on a water surface. (From Ref. [59]. © ACS, 2003.) (View this art in color at www.dekker.com.)

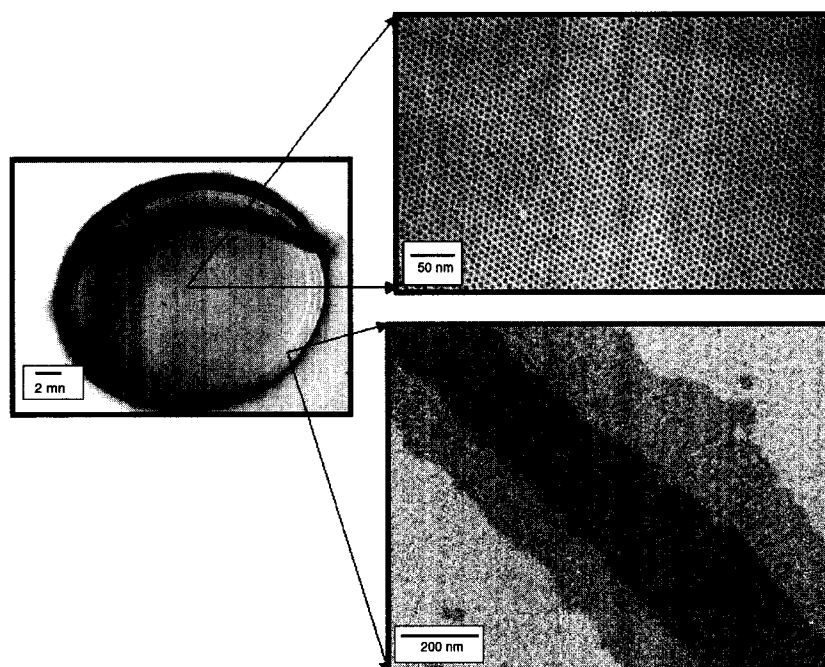


Fig. 7 Photograph of a film of 5-nm-diameter Au MPNs that were self-assembled on a water surface using the method of Santhanam et al. The two inserts are TEM micrographs of samples of this nanoparticle film that were transferred to carbon film-coated TEM grids. The upper insert is taken from the central portion of the film, which is a uniform close-packed monolayer with a diameter of approximately 1 cm. The lower insert is taken from the outer edge of the film and shows one of the multilayer bands that form near the wall of the cell. (From Ref. [59]. ©ACS, 2003.) (*View this art in color at www.dekker.com.*)

Once a high-quality monolayer of MPNs is self-assembled on the water surface, if it is to be used for constructing an electronic device, it must be transferred to a solid substrate. This transfer has been accomplished by either dipping the substrate through the water surface and slowly withdrawing it [Langmuir–Blodgett (LB) method], or by holding the substrate parallel to the water surface and touching it to the nanoparticle film [Langmuir–Schaefer (LS) method]. Although Santhanam et al.^[59] found the LS method preferable, it proved unsatisfactory when the substrate was large and/or hydrophilic. As a

result, they developed a two-step transfer process. First, using the LS method, the nanoparticle film is transferred from the water surface to a polydimethylsiloxane (PDMS) pad. After carefully wicking off any water drops that adhere to the transferred nanoparticle film, the PDMS pad is then pressed conformally onto the desired substrate. This technique is analogous to conventional microcontact printing,^[60] with the nanoparticle monolayer taking the place of the molecular ink. This two-step printing technique facilitates the formation of MPN films with a controlled number of layers. This can be achieved either

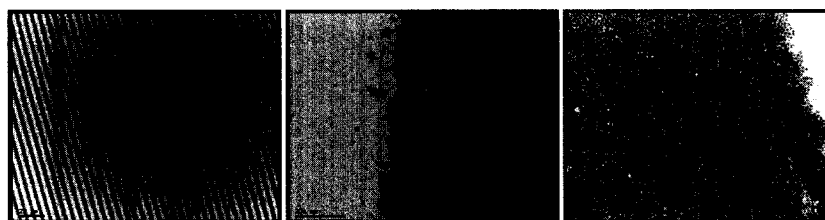


Fig. 8 TEM micrographs of a bilayer film of 5-nm-diameter Au MPNs that were deposited as a pattern of parallel lines on a silicon nitride substrate using the two-step process proposed by Santhanam et al. The low-magnification micrograph on the left shows the lines printed on the substrate. The higher-magnification micrograph in the center shows the relatively sharp edge of one of the lines. The highest-magnification micrograph on the right shows the dense close-packed nanostructure of the film at the edge of one of the lines. (From Ref. [61]. ©ACS, 2003.)

by repeating the process for a desired number of cycles and printing the monolayers one on top of the other, or by picking up the monolayers successively onto the same elastomeric pad and then using a single printing step. The use of a PDMS stamp also allows the formation of patterned monolayer and multilayer arrays of MPNs by using an appropriately structured elastomeric pad.^[24,61] Fig. 8 shows TEM images at three different magnifications of a bilayer film of 5-nm-diameter Au MPNs that has been patterned into a series of micron-scale lines and printed on a Si₃N₄ substrate.^[24,61]

1-D Arrays

The ability to form 1-D arrays or thin ribbons of metal MPNs is important in the context of using linked metal MPNs as interconnects. However, because metal MPNs are nearly spherical in shape, this is a difficult pattern to produce by self-assembly and can be accomplished only with the help of appropriate templates to direct the self-assembly process. For example, carbon nanotubes, long-chain polymers, and DNA strands can be decorated with MPNs to produce quasi-1-D chains, and MPNs can be assembled inside a nanotube or adsorbed on a thin line fabricated on a substrate. Hornyak et al.^[62] have synthesized nanoporous alumina membranes with controlled pore size and narrow pore size distribution, and used the pores as a template to form quasi-1-D chains of Au MPNs. A colloidal solution of the particles was drawn by means of a vacuum into the pores. On evaporation of the solvent, some of the pores were found to be filled with MPN chains. Gleich et al.^[63] made use of the wetting instability of a monolayer transferred onto a solid substrate to produce channels on the order of 200 nm in width and were able to form quasi-1-D chains of MPNs by drop casting a colloidal solution onto this template. Quasi-1-D arrays or ribbons of MPNs have also been prepared by patterning a 2-D monolayer of MPNs using e-beam lithography.^[64] In principle, the PDMS stamping technique described in "2-D Arrays" could be extended to produce nanometer-scale ribbons of metal MPNs using an appropriate master to mold the PDMS stamp. The technique of Melosh et al.,^[15] which makes use of selective etching of a GaAs/AlGaAs superlattice to generate thin parallel trenches, could possibly be used as the master, or a master could be generated using e-beam lithography and PMMA resist.

CONCLUSION

Au MPNs are attractive building blocks for fabricating nanoelectronic devices by self-assembly. The synthesis of

Au MPNs with a mean diameter in the 2- to 20-nm range, with a narrow size distribution, and with a monolayer coating of alkanethiol molecules is, by now, a standard procedure. The assembly of these particles to form chemiresistive films and low-resistivity printable conductors is well established. Recent results describing the self-assembly of high-quality monolayer films of Au MPNs on a water surface and the discovery that these films can be transferred as patterned close-packed arrays onto any reasonably flat substrate have opened up a wide range of potential nanoelectronic applications. What remains is the need to establish methods to reproducibly link these ordered arrays of alkanethiol-encapsulated gold particles with conjugated organic molecules to form nanometer-scale interconnects and molecular electronic circuits.

REFERENCES

1. Andres, R.P.; Averback, R.S.; Brown, W.L.; Brus, L.E.; Goddard, W.A.; Kaldor, A.; Louie, S.G.; Moscovits, M.; Peercy, P.S.; Riley, S.J.; Siegel, R.W.; Spaepen, F.; Wang, Y.J. Research opportunities on clusters and cluster-assembled materials. *J. Mater. Res.* **1989**, *4* (3), 704.
2. Castro, T.; Reifengerger, R.; Choi, E.; Andres, R.P. Size-dependent melting temperature of individual nanometer-sized metallic clusters. *Phys. Rev.*, **B** **1990**, *42* (13), 8548.
3. Andres, R.P.; Bein, T.; Dorogi, M.; Feng, S.; Henderson, J.I.; Kubiak, C.P.; Mahoney, W.; Osifchin, R.G.; Reifengerger, R. Coulomb staircase at room temperature in a self-assembled molecular nanostructure. *Science* **1996**, *272*, 1323.
4. Simon, U. Charge transport in nanoparticle arrangements. *Adv. Mater.* **1998**, *10* (17), 1487.
5. Snow, A.W.; Wohltjen, H. Size-induced metal to semiconductor transition in a stabilized gold cluster ensemble. *Chem. Mater.* **1998**, *10* (4), 947.
6. Wohltjen, H.; Snow, A.W. Colloidal metal-insulator-metal ensemble chemiresistor sensor. *Anal. Chem.* **1998**, *70* (14), 2856.
7. Buffat, Ph.; Borel, J.-P. Size-effect on the melting temperature of gold particles. *Phys. Rev.*, **A** **1976**, *13* (6), 2287.
8. Schaefer, D.M.; Patil, A.; Andres, R.P.; Reifengerger, R. Nanoindentation of a supported Au cluster. *Appl. Phys. Lett.* **1993**, *63* (12), 1492.
9. Huang, D.; Liao, F.; Moles, S.; Redinger, D.; Subramanian, V. Plastic-compatible low resistance printable gold nanoparticle conductors for flexible electronics. *J. Electrochem Soc.* **2003**, *150* (7), G412.
10. Bieri, N.R.; Chung, J.; Haferi, S.E.; Poulikakos, D.;

- Grigoropoulos, C.P. Microstructuring by printing and laser curing of nanoparticle solutions. *Appl. Phys. Lett.* **2003**, *82* (20), 3529.
11. Andres, R.P.; Datta, S.; Dorogi, M.; Gomez, J.; Henderson, J.I.; Janes, D.B.; Kolagunta, V.R.; Kubiak, C.P.; Mahoney, W.; Osifchin, R.F.; Reifenger, R.; Samanta, M.P.; Tian, W. Room temperature Coulomb blockade and Coulomb staircase from self-assembled nanostructures. *J. Vac. Sci. Technol., A* **1996**, *14* (3), 1180.
 12. Likharev, K.K. Single-electron devices and their applications. *Proc. IEEE* **1999**, *87* (4), 606.
 13. Tucker, J.R. Complementary digital logic based on the Coulomb blockade. *J. Appl. Phys.* **1992**, *72* (9), 4399.
 14. Roychowdhury, V.P.; Janes, D.B.; Bandyopadhyay, S. Nanoelectronic architecture for Boolean logic. *Proc. IEEE* **1997**, *85* (4), 574.
 15. Melosh, N.A.; Boukai, A.; Diana, F.; Gerardot, B.; Badolato, A.; Petroff, P.M.; Heath, J.R. Ultrahigh-density nanowire lattices and circuits. *Science* **2003**, *300*, 112.
 16. Vettiger, P.; Cross, G.; Despont, M.; Dreschler, U.; Dürig, U.; Gotsmann, B.; Härberle, W.; Lantz, M.A.; Rothuizen, H.E.; Stutz, R.; Binnig, G. The Millipede—Nanotechnology entering data storage. *IEEE Trans. Nanotechnol.* **2002**, *1* (1), 39.
 17. Andres, R.P.; Bielefeld, J.D.; Henderson, J.I.; Janes, D.B.; Kolagunta, V.R.; Kubiak, C.P.; Mahoney, W.J.; Osifchin, R.G. Self-assembly of a two-dimensional superlattice of molecularly linked metal clusters. *Science* **1996**, *273*, 1690.
 18. Henderson, J.I.; Ferrence, G.M.; Feng, S.; Bein, T.; Kubiak, C.P. Self-assembled monolayers of dithiols, diisocyanides, and isocyanothiols on gold: "Chemically sticky" surfaces for covalent attachment of metal clusters and studies of interfacial electron transfer. *Inorg. Chim. Acta* **1996**, *242*, 115.
 19. Aviram, A.; Ratner, M.A. Molecular rectifiers. *Chem. Phys. Lett.* **1974**, *29* (2), 277.
 20. Avouris, P. Molecular electronics with carbon nanotubes. *Acc. Chem. Res.* **2002**, *35* (12), 1026.
 21. Nazin, G.V.; Qiu, X.H.; Ho, W. Visualization and spectroscopy of a metal–molecule–metal bridge. *Science* **2003**, *302*, 77.
 22. Chen, J.; Reed, M.A.; Rawlett, A.M.; Tour, J.M. Large on–off ratios and negative differential resistance in a molecular electronic device. *Science* **1997**, *278*, 252.
 23. Datta, S.; Janes, D.B.; Andres, R.P.; Kubiak, C.P.; Reifenger, R.G. Molecular ribbons. *Semicond. Sci. Technol.* **1998**, *13* (12), 1347.
 24. Santhanam, V. Fabrication of Nanoelectronic Devices Using Self-Assembled 2D Arrays of Monolayer Protected Clusters. Ph.D. Thesis; Purdue University, 2002.
 25. Lee, T.; Liu, J.; Janes, D.B.; Kolagunta, V.R.; Dicke, J.; Andres, R.P.; Lauterbach, J.; Melloch, M.R.; McInturff, D.; Woodall, J.M.; Reifenger, R. An ohmic nanocontact to GaAs. *Appl. Phys. Lett.* **2000**, *74* (19), 2869.
 26. Gittins, D.I.; Bethell, D.; Schiffrin, D.J.; Nichols, R.J. A nanometre-scale electronic switch consisting of a metal cluster and redox-addressable groups. *Nature* **2000**, *408*, 67.
 27. Liu, Z.; Kim, M.; Narayanan, V.; Kann, E.C. Process and device characteristics of self-assembled metal nano-crystal EEPROM. *Superlattices Microstruct.* **2000**, *28* (5–6), 393.
 28. Mizuta, H.; Müller, H.-O.; Tsukagoshi, K.; Williams, D.; Durrani, Z.; Irvine, A.; Evans, G.; Amakawa, S.; Nakazato, K.; Ahmed, H. Nanoscale Coulomb blockade memory and logic devices. *Nanotechnology* **2001**, *12* (2), 155.
 29. Park, S.B. Optimal Design of a Reactor for Gas-Phase Generation of Metal Microclusters. Ph.D. Thesis; Purdue University, 1988.
 30. Patil, A.N. Synthesis and Characterization of Structured One and Two Component Clusters. Ph.D. Thesis; Purdue University, 1994.
 31. Pileni, M.P. Nanosized particles made in colloidal assemblies. *Langmuir* **1997**, *13* (13), 3266.
 32. Martin, J.E.; Wilcoxon, J.P.; Odinek, J.; Provencio, P.J. Control of the interparticle spacing in gold nanoparticle superlattices. *Phys. Chem., B* **2000**, *104* (40), 9475.
 33. Brust, M.; Walker, M.; Bethell, D.; Schiffrin, D.J.; Whyman, R. Synthesis of thiol-derivatised gold nanoparticles in a two-phase liquid–liquid system. *J. Chem. Soc., Chem. Commun.* **1994**, *7*, 801.
 34. Giersig, M.; Mulvaney, P. Preparation of ordered monolayers by electrophoretic deposition. *Langmuir* **1993**, *9* (12), 3408.
 35. Turkevich, J.; Stevenson, P.C.; Hillier, J. A study of the nucleation and growth processes in the synthesis of colloidal gold. *Discuss. Faraday Soc.* **1951**, *11*, 55.
 36. Murray, C.B.; Norris, D.J.; Bawendi, M.G. Synthesis and characterization of nearly monodisperse CdE (E=S, Se, Te) semiconductor nanocrystallites. *J. Am. Chem. Soc.* **1993**, *115* (5), 8706.
 37. Whetten, R.L.; Houry, J.T.; Alvarez, M.M.; Murthy, S.; Vezmar, I.; Wang, Z.L.; Stephens, P.W.; Cleveland, C.L.; Luedtke, W.D.; Landman, U. Nanocrystal gold molecules. *Adv. Mater.* **1996**, *8* (5), 428.
 38. Stoeva, S.; Klabunde, K.J.; Sorensen, C.; Dragieva, I. Gram-scale synthesis of monodisperse gold

- colloids by the solvated metal atom dispersions method and digestive ripening and their organization into two- and three-dimensional structures. *J. Am. Chem. Soc.* **2002**, *124* (10), 2305.
39. Du, Y. TEM Characterization of Au Nanoclusters and Two-Dimensional Au Cluster Arrays. M.S. Thesis; Purdue University, 2000.
 40. Schmid, G.; Pfeil, R.; Boese, R.; Bandermann, F.; Meyer, S.; Calis, G.H.M.; van der Velden, J. Au₅₅[P(C₆H₅)₃]₁₂C₁₆—Ein goldcluster ungewöhnlicher gröÙe. *Chem. Ber.* **1981**, *114*, 3634.
 41. Schön, G.; Simon, U. A fascinating new field in colloid science: Small ligand-stabilized metal clusters and possible application to microelectronics: Part I. State of the art. *Colloid Polym. Sci.* **1995**, *273* (2), 101.
 42. Schön, G.; Simon, U. A fascinating new field in colloid science: Small ligand-stabilized metal clusters and possible applications to microelectronics: Part II. Future directions. *Colloid Polym. Sci.* **1995**, *273* (3), 202.
 43. Weare, W.W.; Reed, S.M.; Warner, M.G.; Hutchinson, J.E. Improved synthesis of small ($d_{\text{core}} = 1.5$ nm) phosphine-stabilized gold nanoparticles. *J. Am. Chem. Soc.* **2000**, *122* (51), 12890.
 44. Murray, C.B.; Sun, S.; Gaschler, W.; Doyle, H.; Betley, T.A.; Kagan, C.R. Colloidal synthesis of nanocrystals and nanocrystal superlattices. *IBM J. Res. Develop.* **2001**, *45* (1), 47.
 45. Ghosh, A.; Patra, C.R.; Mukherjee, P.; Sastry, M.; Kumar, R. Preparation and stabilization of gold nanoparticles formed by in situ reduction of aqueous chloroaurate ions within surface-modified mesoporous silica. *Microporous Mesoporous Mater.* **2003**, *58* (3), 201.
 46. Pum, D.; Sleytr, U.B. The application of bacterial S-layers in molecular nanotechnology. *Trends Biotechnol.* **1999**, *7* (1), 8.
 47. Hulteen, J.C.; Van Duyne, R.P. Nanosphere lithography: A materials general fabrication process for periodic particle array surfaces. *J. Vac. Sci. Technol., A* **1995**, *13* (3), 1553.
 48. Spatz, J.P.; Roescher, A.; Moller, M. Gold nanoparticles in micellar poly(styrene)- β -poly(ethylene oxide) films—Size and interparticle control in monoparticulate films. *Adv. Mater.* **1996**, *8*, 337.
 49. Spatz, J.P.; Mossner, St.; Moller, M. Mineralization of gold nanoparticles in a block copolymer microemulsion. *Chem. Eur. J.* **1996**, *2*, 1552.
 50. Harfenist, S.A.; Wang, Z.L.; Whetten, R.L.; Vezmar, I.; Alvarez, M.M. Three-dimensional hexagonal close-packed superlattice of passivated Ag nanocrystals. *Adv. Mater.* **1997**, *9* (10), 817.
 51. Zheng, J.W.; Zhu, Z.H.; Chen, H.F.; Liu, Z.F. Nanopatterned assembling of colloidal gold nanoparticles on silicon. *Langmuir* **2000**, *16* (10), 4409.
 52. Sato, T.; Brown, D.; Johnson, B.F.G. Nucleation and growth of nano-gold colloidal lattices. *Chem. Commun.* **1997**, *11*, 1007.
 53. Lin, X.M.; Jaeger, H.M.; Sorensen, C.M.; Klabunde, K.J. Formation of long-range-ordered nanocrystal superlattices on silicon nitride substrates. *J. Phys. Chem., B* **2001**, *105* (17), 3353.
 54. Heath, J.R.; Knobler, C.M.; Leff, D.V. Pressure/temperature phase diagrams and superlattices of organically functionalized metal nanocrystal monolayers: The influence of particle size, size distribution, and surface passivant. *J. Phys. Chem., B* **1997**, *101* (2), 189.
 55. Bourgoïn, J.-P.; Kergueris, C.; Lefevre, E.; Palacin, S. Langmuir-Blodgett films of thiol-capped gold nanoclusters: Fabrication and electrical properties. *Thin Solid Films* **1998**, *327–329*, 515.
 56. Huang, S.; Tsutsui, G.; Sakaue, H.; Shingubara, S.; Takahagi, T. Formation of a large-scale Langmuir-Blodgett monolayer of alkanethiol-encapsulated gold particles. *J. Vac. Sci. Technol.* **2001**, *19* (1), 115.
 57. Collier, C.P.; Henrichs, S.; Shiang, J.J.; Saykally, R.J.; Heath, J.R. Reversible tuning of silver quantum dot monolayer through the metal-insulator transition. *Science* **1997**, *277*, 1978.
 58. Schmid, G.; Beyer, N. A new approach to well-ordered quantum dots. *Eur. J. Inorg. Chem.* **2000**, *2000* (5), 835.
 59. Santhanam, V.; Liu, J.; Agarwal, R.; Andres, R.P. Self-assembly of uniform monolayer arrays of nanoparticles. *Langmuir* **2003**, *19* (19), 7881.
 60. Xia, Y.; Rogers, J.A.; Paul, K.E.; Whitesides, G.M. Unconventional methods for fabricating and patterning nanostructures. *Chem. Rev.* **1999**, *99*, 1823.
 61. Santhanam, V.; Andres, R.P. Microcontact printing of uniform nanoparticle arrays. *Nano Lett.* **2004**, *in press*.
 62. Hornyak, G.L.; Kröll, M.; Pugin, R.; Sawitowski, Th.; Schmid, G.; Bovin, J.-O.; Karsson, G.; Hofmeister, H.; Hopfe, S. Gold clusters and colloids in alumina nanotubes. *Chem. Eur. J.* **1997**, *3* (12), 1951.
 63. Gleich, M.; Chi, L.F.; Fuchs, H. Nanoscopic channel lattices with controlled anisotropic wetting. *Nature* **2000**, *403* (2), 173.
 64. Werts, M.H.V.; Lambert, M.; Bourgoïn, J.P.; Brust, M. Nanometer scale patterning of Langmuir-Blodgett films of gold nanoparticles by electron beam lithography. *Nano Lett.* **2002**, *2* (1), 43.

Metal Nanoparticles Modified with Molecular Receptors

Jian Liu

Michigan Technological University, Houghton, Michigan, U.S.A.

INTRODUCTION

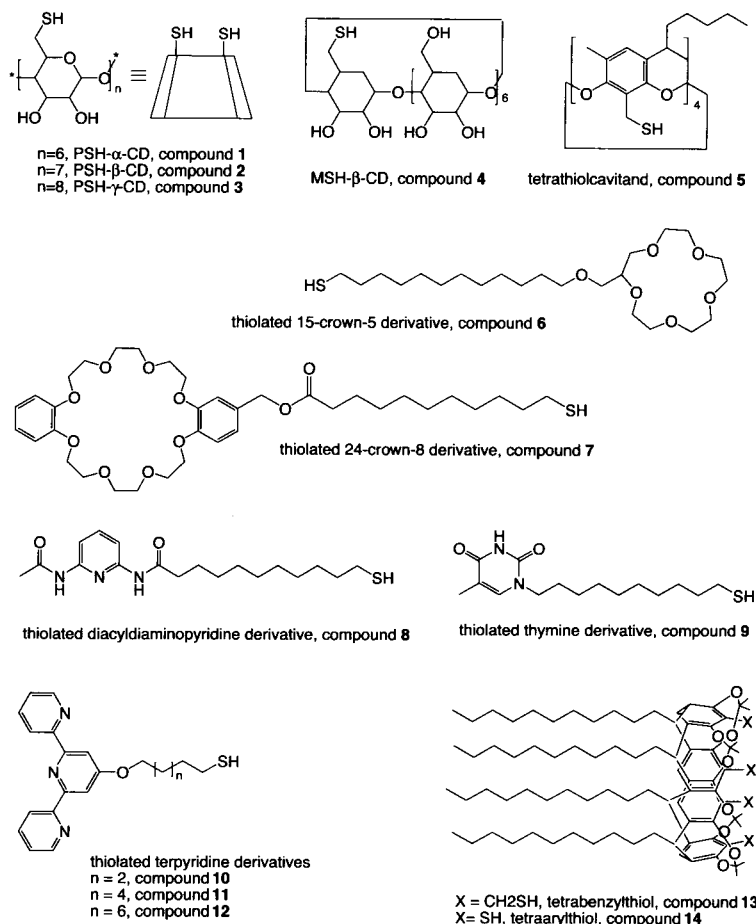
Presently, monolayer-protected metal nanoparticles (MPNPs) are the subjects of some exciting and very active interdisciplinary research because of the rapid development of preparation methods using organic thiols as stabilizers. The organic monolayer not only protects the particles from agglomeration, but also furnishes a scaffold for the construction of different functional entities on their surfaces leading to a broad range of interesting applications. Among these studies, the attachment of molecular receptors capable of engaging in well-defined host-guest interactions is receiving considerable attention.^[1] This article summarizes recent advancements in the development and applications of artificial receptor-modified metal nanoparticles. The research work on metal nanoparticles modified with biological species, such as DNA, was reviewed recently,^[2] thus this topic will not be included here.

PREPARATION OF RECEPTOR-MODIFIED METAL NANOPARTICLES

There has been a great advance^[3] in the development of synthetic methodology for the preparation of MPNPs after a seminar report from Brust et al.^[4] In their approach, metal nanoparticles were prepared by chemical reduction of corresponding salts under a mild condition using NaBH_4 as the reducing agent. The presence of thiol ligands with various stoichiometries to metal salt in the reaction resulted in metal nanoparticles ranging in size between 2 and 8 nm. Molecular receptors on metal nanoparticles can be introduced by directly using the thiolated receptor as the capping agent during the particle formation. An alternative approach uses the ligand-exchange^[3] method to further elaborate the preformed MPNPs with thiolated receptors. In the first case, a crucial consideration is the solubility of the receptor in the reaction media because metal salts are not soluble in nonpolar organic solvents. For example, Kaifer et al. developed a special method to prepare the water-soluble Au,^[5] Pt,^[6] and Pd^[6,7] nanoparticles modified with perthiolated cyclodextrins (PSH-CDs, Chart 1). In this approach, the special solvent, dimethyl sulfoxide (DMSO) or dimethylformamide (DMF), was used as the reaction media to

bring all reacting components, the PSH-CD, the corresponding metal salt, and NaBH_4 in the same phase. This one-phase, one-step (1P-1S) approach eliminates the use of phase transfer reagents in a typical two-phase, one-step (2P-1S) method.^[4] In the 1P-1S method, the final particle size is influenced not only by the concentration of thiols^[5] but also by the nature of these molecules. For instance, a "macrocylic effect" was observed during the preparation of Ag nanoparticles in DMF.^[8] Perthiolated β -CD (PSH- β -CD) was found to be more efficient as a capping ligand than monothiolated β -CD (MSH- β -CD, Chart 1). Similarly, a tetrathiol cavitand derivative (Chart 1) was also more efficient than a simple monothiol model compound. This sort of "macrocylic effect" probably results from an increased probability of surface attachment for the multidentate thiols, as they possess more functional groups capable of initiating their chemisorption process. In addition, once the surface attachment starts, their multidentate character may lead to a more robust, multi-point anchoring of the ligand. Therefore, this macrocylic effect in metal nanoparticle capping reactions may have both a kinetic and a thermodynamic origin.

PSH-CD-modified metal nanoparticles prepared by 1P-1S approach have a diameter less than 10 nm. To obtain PSH- β -CD-modified gold nanoparticles (PSH- β -CD-Au) larger than 10 nm, a 2S method was applied. Preprepared, citrate-stabilized gold nanoparticles (13 nm in diameter)^[9] were further modified with PSH- β -CDs by ligand exchange with citrate on the particle surface in the aqueous solution.^[10] A similar strategy was used by Lin et al.^[11] to prepare Au nanoparticles (18 nm in diameter) modified with thiolated crown ether derivatives (Chart 1). Interestingly, surface-modified gold nanoparticles with even larger size (16–87 nm in diameter) were prepared by extracting citrate-stabilized particles in aqueous solutions into toluene or chloroform with thiolated resorcinarene derivatives (Chart 1),^[12] the compounds relevant to some macrocylic receptors. These tetrathiolated resorcinarenes improved the dispersion and robustness of midnanometer-sized gold nanoparticles in organic solvents. However, the authors clearly demonstrated that the tetraarylthiol adsorbed on the surface is much weaker as compared to tetrabenzylthiol. This is another case that shows how the nature of the thiol compound affects the passivation on metal nanoparticles. Direct modification of Au particles



(4 nm in diameter) with another type of crown derivative (Chart 1) was also achieved^[13] by adapting Brust's 2P-1S approach.^[4] Rotello et al.^[14-16] introduced their organic receptors (Chart 1) by using ligand exchange approach to preformed, alkanethiol-modified Au particles in organic solvents. Multivalent receptors were also introduced by the same group on Au particles with similar methodology.^[17] In the sense of practical application, the ligand exchange approach provides an easier way to control the number of receptors on each particle, which is one of the key factors for molecular recognition at particle surfaces.

Particle size characterization is usually carried out by transmission electron microscopy (TEM). The solubility of MPNPs in various solvents affords a unique opportunity to characterize them by using standard solution-phase techniques such as nuclear magnetic resonance (NMR) and UV-vis spectroscopies. For example, a ¹H NMR spectrum of gold nanoparticles modified with perthiolated γ -CD (PSH- γ -CD-Au) in D₂O affords the broadened proton resonances from surface-immobilized γ -CDs (Fig. 1).^[18] Such phenomenon is consistent with the observation obtained by Templeton and coworkers.^[3] In

these systems, the resonances of those protons closer to the metal surface are more seriously broadened, whereas the effect is less pronounced for the protons that are farther away. Fast relaxation and environmental heterogeneities are thought to be responsible for these line-broadening effects. The UV-vis spectroscopic study revealed that PSH- β -CD-AuNPs with small size (3 nm in diameter) presented a relatively weak surface plasmon band (SP band) around 520 nm. In contrast, the bigger particles (13 nm in diameter) gave a strong SP band, which may serve as a signal for visibly probing chemical and biological species in the solution.

MOLECULAR RECOGNITION AT THE SURFACES OF RECEPTOR-MODIFIED METAL NANOPARTICLES

The purpose of introducing molecular receptors on metal nanoparticle surfaces is to endow these nanoscale entities with the capability of engaging molecular recognition. Electrochemistry and UV-vis spectroscopy are the two

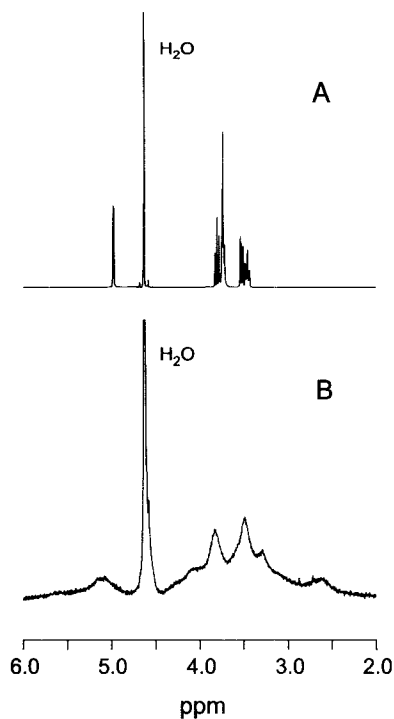
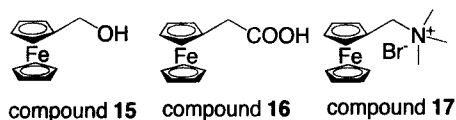


Fig. 1 ^1H NMR spectra (400 MHz, D_2O) of (A) free γ -CD and (B) PSH- γ -CD-Au. (From Ref. [29]. Copyright 2001, American Chemical Society.)

common techniques used to study the molecular recognition events on particle surfaces in various solutions. Several aspects in this scenario are addressed as follows.

Recognition of Redox-Active Species

An important feature of cyclodextrin (CD)-modified metal nanoparticles is their excellent aqueous solubility. This property is probably contributed by the polarity of the secondary hydroxyl groups on cyclodextrin (CD) receptors, which afford a polar character to the surface of nanoparticles. Surface attachment of the CD hosts through their primary faces necessarily leaves the wider, secondary faces exposed to the solution phase, a configuration that favors binding between the immobilized CDs and appropriate guests in the solution.

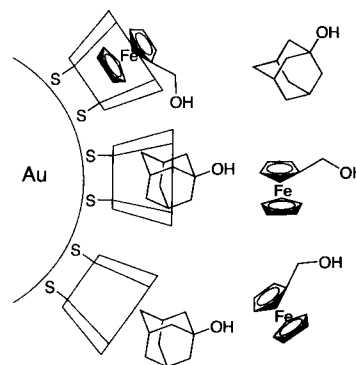


Liu et al. used some water-soluble, electroactive molecules (Chart 2) to study the complexation ability of surface-immobilized β -CDs on metal nanoparticles in aqueous solutions. For example, addition of PSH- β -CD-

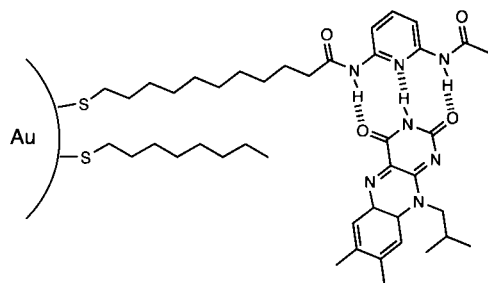
Au led to two pronounced effects on the electrochemical response of ferrocenemethanol:^[51] 1) it decreased the current of the voltammetric wave, and 2) it shifted the apparent half-wave potential to more positive values. Both effects clearly indicated that ferrocenemethanol was forming inclusion complexes with the CD receptors immobilized on the gold nanoparticles. This was further verified by addition of 1-adamantanol to the same solution. Adamantanol, being also an excellent guest for inclusion complexation by β -CD,^[19] competed effectively with ferrocenemethanol for the available CD binding sites on the surface of the gold particles (Scheme 1). As a result, most of the ferrocenemethanol molecules were displaced from their binding sites and released back to the bulk solution, giving rise to a voltammetric response very similar to that recorded in the absence of the β -CD-Au.

The host-binding ability of β -CD immobilized on gold nanoparticles was further verified using compound 17 as guest probe in a ^1H NMR study.^[18] The displacement and broadening of the ferrocene proton resonance in the presence of PSH- β -CD-Au were attributed to the formation of the inclusion complexes on the nanoparticle surfaces, as they were similar to those observed upon the addition of free β -CD to solutions of ferrocene derivatives. The substantial line broadening must have resulted also from the association of the ferrocene guest to the massive nanoparticles, and was probably related to chemical exchange (free ferrocene going to bound ferrocene and back), as well as to relaxation effects in the bound state. Note that when the ferrocene guest was bound to a CD cavity, it became a part of a rather large supramolecular assembly.

A similar redox-controlled recognition event on receptor-modified metal nanoparticles was also demonstrated by Boal and Rotello in a different nanoparticle system. Reversible complexation between flavin (Fl_{ox}) and diamidopyridine (DAP) tethered on gold nanoparticles was successfully controlled electrochemically in



Scheme 1 Competitive binding of ferrocene methanol and 1-adamantanol to the β -CD host immobilized on a gold nanoparticle.



Scheme 2 Recognition of flavin by surface-immobilized diacyldiaminopyridine.

chloroform (Scheme 2).^[14] Moreover, the same group investigated the multitopic recognition at gold nanoparticles by creating multivalent recognition sites through tethering both DAP and pyrene on the same particle surface. A stronger recognition of electron-deficient Fl_{ox} on particle surfaces was achieved through hydrogen bonding to DAP units and favorable π stacking with the electron-rich pyrene units.^[17,20]

Recognition of Cations

Lin et al.^[11] reported an efficient recognition of K⁺ by 15-crown-5-modified gold nanoparticles (18 nm in diameter) in aqueous solution containing physiologically important cations, such as Li⁺, Cs⁺, NH₄⁺, Mg²⁺, Ca²⁺, and an excess amount of Na⁺. Upon exposure to K⁺, the color of the nanoparticle solution changed from red to blue corresponding to the surface plasmon absorption of dispersed and aggregated nanoparticles. The authors postulated that one potassium ion efficiently bound to two crown moieties tethered to two different nanoparticles forming a sandwichlike 2:1 complex, which led to the aggregation of nanoparticles.

Recognition of Anions

Gold nanoparticles modified with a mixed monolayer of alkanethiols and amidoferrocenylalkanethiol were used as effective exoreceptors for electrochemically sensing H₂PO₄⁻ and HSO₄⁻.^[21] The authors found that the redox potential of amidoferrocenyl group was perturbed by the synergy among the hydrogen bonding, electrostatic interaction, and topology of mixed monolayer to recognize H₂PO₄⁻ and HSO₄⁻ on particle surfaces. However, the potential change is much smaller for HSO₄⁻ than for H₂PO₄⁻, showing certain selectivity of the recognition of these particles. The same group extended this work to gold nanoparticles modified with thiol dendrons containing three redox-active amidoferrocenyl or silylferrocenyl units.^[22] These surface-functionalized particles could

effectively recognize H₂PO₄⁻. More insights about the stereoelectronic effect of amidoferrocenyl group on the recognition of oxoanions at gold nanoparticle surfaces were reported recently from the same group.^[23] The recognition properties were weakened by permethylation of one Cp ring (electron releasing and sterically demanding) on amidoferrocenyl moiety but enhanced by acetylation of the same ring (electron withdrawing). Thus, the authors claimed, the stereoelectronic property of the amidoferrocenyl group acted as the key role for the recognition by the amidoferrocenium form through the hydrogen bonding between the -NH- amido group and the charged terminal oxygen atom of the oxoanions. The recognition properties of gold nanoparticles functionalized with metallodendrons were further discussed in a recent report.^[24] Gold nanoparticles modified with up to 360 silylferrocenyl units on each particle were achieved. These dendronized gold nanoparticles combine the advantages of dendrimers and nanoparticles as sensors for the selective recognition of H₂PO₄⁻ and adenosine-5'-triphosphate (ATP²⁻) even in the presence of other anions. A dendritic effect on the recognition properties was clearly observed; in other words, the shift of the ferrocenyl redox potential upon introduction of the anion became larger as the generation number of dendrons increased.

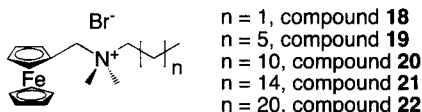
Watanabe et al. developed amide-functionalized gold nanoparticles as a prototype for optical recognition of various anions, such as H₂PO₄⁻, HSO₄⁻, AcO⁻, and NO₃⁻, in organic solvents.^[25] Interestingly, the addition of anions initially caused a decrease in the surface plasmon absorption of gold nanoparticles. However, the intensity of this SP band increased when excess anion existed in the CH₂Cl₂. The authors reasoned that initial decrease of the SP band was because of the anion-induced aggregation of gold nanoparticles. Further addition of anion caused the disaggregation of the suprananoparticles composed of particles and anions.

RECEPTOR-MODIFIED METAL NANOPARTICLES AS BUILDING BLOCKS IN THE SELF-ASSEMBLY OF ORGANIC-INORGANIC NANOCOMPOSITES

Metal nanoparticles modified with molecular receptors are excellent candidates as "building blocks" for the bottom-up construction of organic/inorganic hybrid nanocomposites in solution phase by using the noncovalent molecular interactions at particle surfaces. Such nanoscale systems may serve as the initial prototypes in the fabrication of nanoelectronic devices. Several aspects of this scenario will be summarized in this section. A detailed discussion about the research work on this topic from Shenhar and Rotello can be found in a recent review.^[26]

Receptor-Modified Metal Nanoparticles as Templates for the Construction of Micellar Structures

In a recent report, Liu et al.^[18] reasoned that the introduction of molecular species by molecular recognition at PSH-CD-Au might lead to reversible functionalization of particle surfaces. Therefore, a series of ferrocene derivatives with different lengths of aliphatic chains (Chart 3) were used to examine this idea.

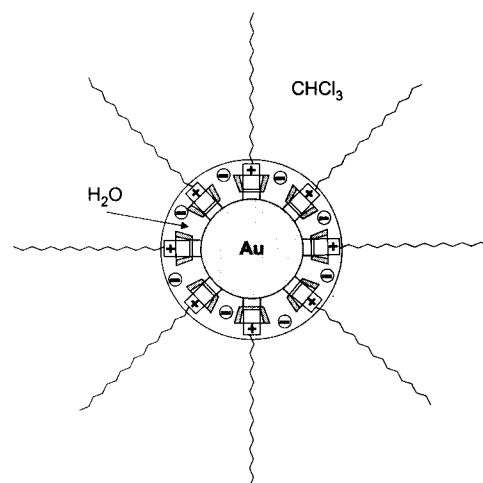


Mixing a chloroform phase containing **22** with an aqueous solution containing PSH- β -CD-Au caused a color change of the organic phase from initial yellow to brown. The visible absorption spectrum of this solution clearly revealed two distinct bands residing at 430 and 510 nm, corresponding to the absorptions by the ferrocene residues and the nanoparticles (SP band), respectively. The obvious conclusion from these results was that compound **22** acted as an efficient phase transfer agent for the water-soluble PSH- β -CD-Au and enabled their solubilization in the chloroform phase. Further study showed that only compounds **20**, **21**, and **22** (with aliphatic chains of 12, 16, and 22 carbon atoms) effectively promoted the solubilization of the PSH- β -CD-Au in the chloroform phase; compounds **18** and **19** (with shorter aliphatic chains of 3 and 7 carbon atoms) were ineffective. This finding strongly suggested that the long aliphatic chains of ferrocene derivatives could effectively cover the particle surfaces after the complexation with surface-immobilized β -CDs leading to more hydrophobic aggregates, which favored organic solvents. The effectiveness of phase transfer was enhanced when the initial concentration of either ferrocene derivatives or PSH- β -CD-Au increased, which perfectly matched the transfer mechanism that involved the formation of interfacial complexes between the CD hosts on the nanoparticles and the ferrocene residues of the amphiphilic guests. Notably, PSH- β -CD-Au were more effectively solubilized in the organic phase than PSH- α -CD-Au under identical experimental conditions. This finding was in excellent agreement with the well-established selectivity of ferrocene derivatives for β -CD hosts compared to α -CD (or γ -CD) and provided additional support to the proposed involvement of nanoparticle/CD-ferrocene complexation in the phase transfer mechanism. Photon correlation spectroscopy (PCS) measurements verified that no aggregation happened after the phase

transfer of PSH-CD-Au in chloroform. Gold nanoparticles still stayed individually in the solution with long-term stability.

Based on these findings, such phase transfer was believed to be accomplished by host-guest complexation between surface-immobilized CDs and ferrocene derivatives at gold nanoparticle surfaces. As the formation of inclusion complexes took place in the aqueous solution, water molecules were also transferred along with the nanoparticles into the chloroform solution leading to the stable complex in this organic solvent. The presence of the positively charged nitrogen atoms near the ferrocene subunits probably assisted in transferring water molecules and counterions to the organic phase. Further experiments supported this proposed mechanism. Thus, the proposed idealized structure of the nanoparticles after their transfer to the chloroform phase had some similarities with the structure of reverse micelles. Liu et al.^[18] concluded that these nanoparticle-centered assemblies were conceptually similar to *gold-filled reverse micelles* (Scheme 3).

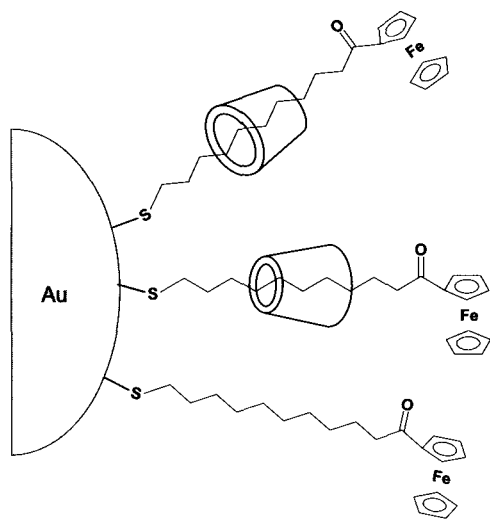
A similar micellar structure was also fabricated in Frankamp's group.^[16] The hydrogen bonding between the thymine tethered on gold nanoparticles and the complementary diaminotriazine on a copolymer yielded a polymer/nanoparticle composite in which the polymer blocks bearing the diaminotriazine closely interacted with nanoparticles resulting in a spherical core, whereas the polystyrene units acted as the hydrophobic tails projecting out into the solution. Lala et al.^[27] also reported a relevant result in which gold nanoparticles capped with inclusion complexes of α -CD and alkanethiols were transferred into the chloroform phase by using a similar strategy discussed above.



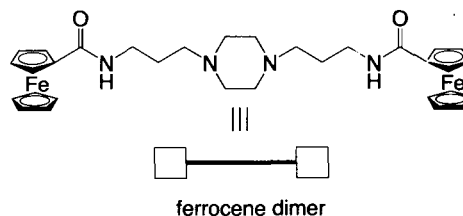
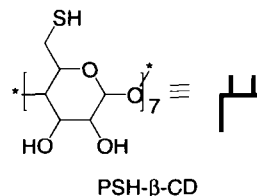
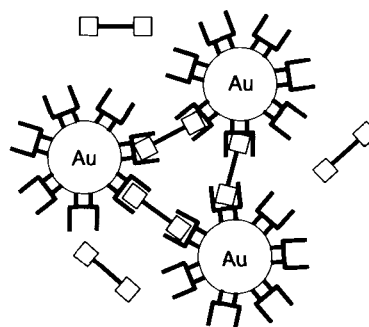
Scheme 3 Proposed structure for the assemblies formed upon transfer of the PSH- β -CD-Au into chloroform solution.

Fabrication of Rotaxanes on Metal Nanoparticles

One of the fast-growing research fields in nanochemistry is the construction of molecular architectures on nanoparticle surfaces. By employing the well-known host-guest chemistry between CDs and organic molecules, Liu et al. built, for the first time, a nanoparticle-supported rotaxane system,^[28] which provides an interesting example of molecular structure for the further development of the functional nanoscopic systems at nanoparticle scaffolds. Ligand exchange of a thiolated ferrocene derivative solubilized by α -CD with the citrate on citrate-stabilized gold nanoparticle (13 nm) in an aqueous solution led to the attachment of this compound on the particle surfaces. Further study of these materials revealed that some α -CDs were trapped on particles. On the other hand, when long-chain aliphatic thiols were used under identical conditions for the preparation of thiol-modified gold nanoparticles, no α -CD was detected after the necessary purification. These data suggested that the dynamic character of the complex between CD and alkanethiol allowed dissociation to take place after attachment to the gold surface, whereas the bulky ferrocene group at one end of the thiolated ferrocene derivative precluded α -CD dissociation from the complex after its attachment on the particle. Thus, a novel molecular structure obtained in this study was a "gold-supported rotaxane" in which one of the rotaxanes' stopper groups was the gold nanosphere itself (Scheme 4). Interestingly, Fitzmaurice and coworkers reported^[13] a pseudorotaxane system on gold nanoparticles by binding dibenzylammonium cation in a crown derivative tethered on particle surfaces.



Scheme 4 Nanoparticle-supported rotaxane.



Scheme 5 Gold nanoparticle aggregate driven by molecular recognition between surface-immobilized PSH- β -CD and ferrocene dimer.

Fabrication of Nanoparticle Networks in Aqueous Solutions

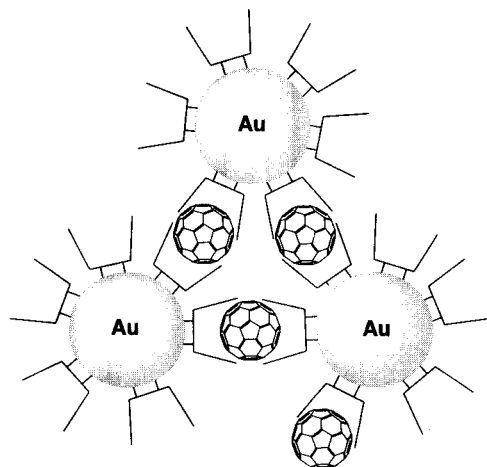
Host-guest chemistry has been used as the general strategy to self-assemble receptor-modified metal nanoparticles in aqueous solutions. Liu et al. reported their first attempt in this research direction by using PSH- β -CD-Au (12.5 nm) as building blocks and ferrocene dimers (Scheme 5) as "linkers" in aqueous solutions.^[10]

It was found that the addition of a ferrocene dimer to an aqueous PSH- β -CD-Au solution initially caused a red shift of the SP band. Almost immediately, slow precipitation of a red solid took place, accompanied by the attenuation of the intensity of the SP band. After several control experiments, the authors verified that such flocculation was driven by the host-guest interaction between β -CDs anchored on gold nanoparticle surfaces and the ferrocene dimers in the aqueous solution. In the process of complexation, two ferrocene sites in the same molecule bound with two β -CDs on different particles resulting in the network nanoparticle aggregates. Thus, the ferrocene dimer acted as the linker in self-assembly of nanoparticles in aqueous solutions. In addition, such aggregation process could be tuned by the addition of free host or

guest molecules in the solution. For instance, introduction of β -CD in the same solution slowed and even shut down the aggregation process as free CD competed with surface-attached CD hosts for the available ferrocene groups. Thus, the flocculation was hindered because the dimers could not form a significant number of linkages between nanoparticles. Temperature also played an important role. Increasing the temperature diminished the extent of flocculation, resulting from the decrease in binding constant between the ferrocene residues and the β -CD hosts.

By using similar host-guest chemistry, another type of interesting organic/inorganic nanocomposites was constructed in the aqueous solution.^[29] Direct mixing of PSH- γ -CD-Au (3 nm) and solid C_{60} in water led to large nanoparticle aggregates with average size of around 290 nm as characterized by PCS analysis and TEM measurement. In an alternative approach, mixing a toluene phase of C_{60} with a PSH- γ -CD-Au aqueous solution at 0°C also yielded similar nanoparticle aggregates in aqueous media. It is known that γ -CD can form stable 2:1 complex with C_{60} in aqueous solution.^[30] Therefore, the authors reasoned that the solubilization of C_{60} in aqueous solution was attributed to its complexation by the nanoparticle-attached γ -CD hosts. Interestingly, the 2:1 stoichiometry of this complex suggests that the fullerene molecules may behave as *noncovalent linkers* between the nanoparticles, leading to their aggregation (Scheme 6).

Boal's group developed a "brick and mortar" approach in the fabrication of three-dimensional organic/inorganic nanostructures using receptor-modified gold nanoparticles as building blocks and polymers tethered with complementary recognition units as the glue. The three-point hydrogen bonding between the thymine-functionalized gold nanoparticles and diaminotriazine-functionalized polystyrene poly-Triaz yielded micro-



Scheme 6 Fullerene-induced network of PSH- γ -CD-Au in aqueous solution.

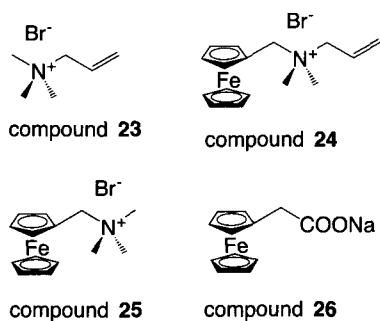
spheric structures 97 ± 17 nm in diameter.^[31] The temperature had a profound effect on the assembly process. At -20°C , the largest microscale clusters were obtained, which were 10 times larger than the aggregates formed at 23°C . Each of these clusters was composed of 0.6–5.0 million individual gold nanoparticles representing the most complex synthetic structures known. Norsten's group also reported a nanoparticle network system by using metal ions as the linkage. The chelation of various metal ions, Fe(II), Zn(II), Cu(II), and Ag(I), with two terpyridines that were tethered to separate nanoparticles resulted in the network aggregates.^[15] The stability of these structures could be controlled by changing the solvent, adding excess terpyridine, or through the choice of bridging metal.

Ryan and coworkers reported that silver nanocrystals stabilized by chemisorption of a mixture of an alkane thiol and a thiolated dibenzo-24-crown-8 could form the nanoparticle aggregates by adding a small amount of bis-dibenzylammonium through the formation of crown-ammonium pseudorotaxane assembly.^[32] It was also shown that the addition of excess dibenzylammonium cation or dibenzo-24-crown-8 inhibited further aggregation. This novel demonstration of controlled nanocrystal aggregation pointed the way toward the programmed assembly of complex nanocrystal architectures in solution. In a subsequent work, the same group reported the first example of binary nanostructures composing two different types of inorganic nanoparticles by using a similar recognition-directed templating strategy.^[33] Dibenzo-24-crown-8-modified Ag nanoparticles (7 nm in diameter) recognized and bound to dibenzylammonium cation modified silica nanosphere (180 nm in diameter) via pseudorotaxane formation. Such templating process was proved to be reversibly controlled.

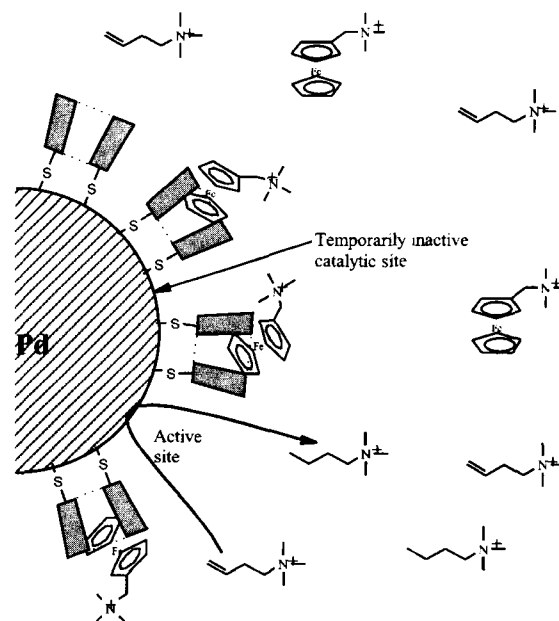
RECEPTOR-MODIFIED METAL NANOPARTICLES AS NOVEL CATALYSTS

The increasing interest in using metal nanoparticles as catalysts is due to their high surface to volume ratio. In a recent and elegant work, Crooks and coworkers have prepared catalytically active metal nanoparticles encapsulated inside dendrimers.^[34] The dendrimer effectively stabilizes the nanoparticles without passivating their surfaces, and its branched structure acts as a "molecular filter" imparting selectivity to the catalyst assembly. Recently, Kaifer et al.^[6,7] reported several research works on the development of CD-modified Pt and Pd nanoparticles for catalytic reactions in aqueous solutions. Special effort has been made in tuning the catalytic activity of these CD-modified nanoparticles through introduction of host-guest interactions on their surfaces.

In an initial attempt,^[6] water-soluble PSH- β -CD-modified Pt and Pd nanoparticles (13 to 15 nm in diameter) were prepared in DMSO-H₂O mixed solvents by reducing corresponding metal salts using borohydride as reducing agent. Both Pt and Pd nanoparticles prepared here could successfully catalyze the hydrogenation of allylamine to propylamine in aqueous solutions. The ease of recovering the metal catalysts through precipitation with ethanol from the reaction medium provided an opportunity to recycle the catalyst for the hydrogenation reactions. The authors then focused their attention on the "selectivity" in the catalytic process. In this case, smaller Pd nanoparticles (3 nm) modified with β -CD were made in DMF. These β -CD-modified Pd nanoparticles (PSH- β -CD-Pd) behaved as efficient catalysts for the selective hydrogenation of different substrates (Chart 4) in aqueous media. Interestingly, adding millimolar concentrations of **25** to the reaction mixture substantially decreased the rate of hydrogenation of **23**. However, the addition of similar concentrations of tetramethylammonium bromide or tetraethylammonium bromide had a much smaller effect on the rate of hydrogenation of **23**. Similarly, the negatively charged ferrocene derivative **26** and adamantanol (a neutral β -CD guest) were considerably less effective than **25** as catalyst inhibitors. All these data support the idea that **25** acts as an effective inhibitor of the catalytic activity of the PSH- β -CD-Pd because of (1) its ability to act as a guest with the CD cavities and (2) its positive charge.



Further evidence of the strong correlation between inhibition by **25** and its binding ability with the CDs that decorated the Pd nanoparticles was obtained by investigating the concentration dependence of the reaction rate. The data obtained showed the saturation behavior that was clearly associated with the binding isotherm of the ferrocene derivatives in the binding sites (CD cavities) on the surface of the nanoparticles. The authors also found out that the actual effect of compound **25** to inhibit the hydrogenation of substrates **23** and **24** differed. Compound **25** was a more effective inhibitor with **23** than **24**. This was probably because of the ferrocene group present in **24**, which increased its affinity to the CD-modified na-



Scheme 7 Complexation control of the accessibility of reacting sites on PSH- β -CD-Pd for hydrogenation reaction. (From Ref. [7]. Copyright 2001, American Chemical Society.)

nanoparticles. Thus, **25** competed with the substrate itself (**24**) for the available binding sites, and its overall inhibition effect was strongly curtailed. The results presented in that work clearly showed that (1) PSH- β -CD-Pds were active catalysts for the hydrogenation of water-soluble alkenes **23** and **24**, (2) catalytic activity could be substantially decreased by addition of the cationic ferrocene derivative **25**, and (3) the inhibiting character of **25** was due to its ability to create Coulombic barriers for the approach of the positively charged substrates (Scheme 7), resulting in the decrease in the surface density of catalytic active sites. These Pd nanoparticles served as heterogeneous catalysts while their small sizes and solubility properties approach those of homogeneous catalysts. These Pd nanoparticles were further used as the efficient catalysts for Suzuki reactions in aqueous media.^[35]

CONCLUSION

This article summarizes the recent advancement on the preparation and applications of molecular receptor-modified metal nanoparticles. Although, substantial progress has been achieved in these past years, this research field is still in its infancy. More work needs to be done in the future to reveal fundamental insights and explore more applications for these nanoscale materials. For example,

water solubility of these receptor-modified metal nanoparticles is the key factor for the development of chemical and biological sensors. To make three-dimensional nanocomposites self-organized by molecular recognition with long-range order and the controllable interparticle space is still a big challenge. High stereoselectivity provided by molecular receptors on metal particle surfaces is desired for the development of ecoefficient, environmentally benign heterogeneous catalysts. The author expects a great advancement in this research field in next few years.

REFERENCES

1. Liu, J.; Alvarez, J.; Kaifer, A.E. Metal nanoparticles with a knack for molecular recognition. *Adv. Mater.* **2000**, *12*, 1381–1383.
2. Storhoff, J.J.; Mirkin, C.A. Programmed materials synthesis with DNA. *Chem. Rev.* **1999**, *99*, 1849–1862.
3. Templeton, A.C.; Wuelfing, W.P.; Murray, R.W. Monolayer-protected cluster molecules. *Acc. Chem. Res.* **2000**, *33*, 27–36.
4. Brust, M.; Walker, M.; Bethell, D.; Schiffrin, D.J.; Whyman, R. Synthesis of thiol-derivatized gold nanoparticles in a two-phase liquid–liquid system. *Chem. Commun.* **1994**, 801–802.
5. Liu, J.; Ong, W.; Roman, E.; Lynn, M.J.; Kaifer, A.E. Cyclodextrin-modified gold nanospheres. *Langmuir* **2000**, *16*, 3000–3002.
6. Alvarez, J.; Liu, J.; Roman, E.; Kaifer, A.E. Water-soluble platinum and palladium nanoparticles modified with thiolated β -cyclodextrin. *Chem. Commun.* **2000**, 1151–1152.
7. Liu, J.; Alvarez, J.; Ong, W.; Roman, E.; Kaifer, A.E. Tuning the catalytic activity of cyclodextrin-modified palladium nanoparticles through host–guest binding interactions. *Langmuir* **2001**, *17*, 6762–6764.
8. Liu, J.; Ong, W.; Kaifer, A.E.; Peinador, C. A “macrocylic effect” on the formation of capped silver nanoparticles in DMF. *Langmuir* **2002**, *18*, 5981–5983.
9. Grabar, K.C.; Freeman, R.G.; Hommer, M.B.; Natan, M.J. Preparation and characterization monolayers. *Anal. Chem.* **1995**, *67*, 735–743.
10. Liu, J.; Mendoza, S.; Roman, E.; Lynn, M.J.; Xu, R.; Kaifer, A.E. Cyclodextrin-modified gold nanospheres. Host–guest interactions at work to control colloidal properties. *J. Am. Chem. Soc.* **1999**, *121*, 4304–4305.
11. Lin, S.-Y.; Liu, S.-W.; Lin, C.-M.; Chen, C.-h. Recognition of potassium ion in water by 15-crown-5 functionalized gold nanoparticles. *Anal. Chem.* **2002**, *74*, 330–335.
12. Balasubramanian, R.; Kim, B.; Tripp, S.L.; Wang, X.; Lieberman, M.; Wei, A. Dispersion and stability studies of resorcinarene-encapsulated gold nanoparticles. *Langmuir* **2002**, *18*, 3676–3681.
13. Fitzmaurice, D.; Rao, S.N.; Preece, J.A.; Stoddart, J.F.; Wenger, S.; Zaccheroni, N. Heterosupramolecular chemistry: Programmed pseudorotaxane assembly at the surface of a nanocrystal. *Angew. Chem., Int. Ed.* **1999**, *38*, 1147–1150.
14. Boal, A.K.; Rotello, V.M. Redox-modulated recognition of flavin by functionalized gold nanoparticles. *J. Am. Chem. Soc.* **1999**, *121*, 4914–4915.
15. Norsten, T.B.; Frankamp, B.L.; Rotello, V.M. Metal directed assembly of terpyridine-functionalized gold nanoparticles. *Nano Lett.* **2002**, *2*, 1345–1348.
16. Frankamp, B.L.; Uzun, O.; Ilhan, F.; Boal, A.K.; Rotello, V.M. Recognition-mediated assembly of nanoparticles into micellar structures with diblock copolymers. *J. Am. Chem. Soc.* **2002**, *124*, 892–893.
17. Boal, A.K.; Rotello, V.M. Fabrication and self-optimization of multivalent receptors on nanoparticle scaffolds. *J. Am. Chem. Soc.* **2000**, *122*, 734–735.
18. Liu, J.; Alvarez, J.; Ong, W.; Roman, E.; Kaifer, A.E. Phase transfer of hydrophilic, cyclodextrin-modified gold nanoparticles to chloroform solutions. *J. Am. Chem. Soc.* **2001**, *123*, 11148–11154.
19. Godínez, L.A.; Schwartz, L.; Criss, C.M.; Kaifer, A.E. Thermodynamic studies on the cyclodextrin complexation of aromatic and aliphatic guests in water and water–urea mixtures. Experimental evidence for the interaction of urea with arene surfaces. *J. Phys. Chem., B* **1997**, *101*, 3376–3380.
20. Boal, A.K.; Rotello, V.M. Radial control of recognition and redox processes with multivalent nanoparticle hosts. *J. Am. Chem. Soc.* **2002**, *124*, 5019–5024.
21. Labande, A.; Astruc, D. Colloids as redox sensors: Recognition of H_2PO_4^- and HSO_4^- by amidoferrocenylalkylthiol–gold nanoparticles. *Chem. Commun.* **2000**, *12*, 1007–1008.
22. Daniel, M.-C.; Ruiz, J.; Nlate, S.; Palumbo, J.; Blais, J.-C.; Astruc, D. Gold nanoparticles containing redox-active supramolecular dendrons that recognize H_2PO_4^- . *Chem. Commun.* **2001**, *19*, 2000–2001.
23. Labande, A.; Ruiz, J.; Astruc, D. Supramolecular gold nanoparticles for the redox recognition of oxoanions: Syntheses, titrations, stereoelectronic effects, and selectivity. *J. Am. Chem. Soc.* **2002**, *124*, 1782–1789.

24. Daniel, M.-C.; Ruiz, J.; Nlate, S.; Blais, J.-C.; Astruc, D. Nanoscopic assemblies between supra-molecular redox active metallodendrons and gold nanoparticles: Synthesis, characterization, and selective recognition of H_2PO_4^- , HSO_4^- , and adenosine-5'-triphosphate (ATP^{2-}) anions. *J. Am. Chem. Soc.* **2003**, *125*, 2617–2628.
25. Watanabe, S.; Sonobe, M.; Arai, M.; Tazume, Y.; Matsuo, T.; Nakamura, T.; Yoshida, K. Enhanced optical sensing of anions with amide-functionalized gold nanoparticles. *Chem. Commun.* **2002**, *23*, 2866–2867.
26. Shenhar, R.; Rotello, V.M. Nanoparticles: Scaffolds and building blocks. *Acc. Chem. Res.* **2003**, *36*, 549–561.
27. Lala, N.; Lalbegi, S.P.; Adyanthaya, S.D.; Sastry, M. Phase transfer of aqueous gold colloidal particles capped with inclusion complexes of cyclodextrin and alkanethiol molecules into chloroform. *Langmuir* **2001**, *17*, 3766–3768.
28. Liu, J.; Xu, R.; Kaifer, A.E. In situ modification of the surface of gold colloidal particles. Preparation of cyclodextrin-based rotaxanes supported on gold nanospheres. *Langmuir* **1998**, *14*, 7337–7339.
29. Liu, J.; Alvarez, J.; Ong, W.; Kaifer, A.E. Network aggregates formed by C_{60} and gold nanoparticles capped with β -cyclodextrin hosts. *Nano Lett.* **2001**, *1*, 57–60.
30. Yoshida, Z.; Takekuma, H.; Takekuma, S.; Matsubara, Y. Molecular recognition of C_{60} with γ -cyclodextrin. *Angew. Chem., Int. Ed.* **1994**, *33*, 1597–1599.
31. Boal, A.K.; Ilhan, F.; DeRouchey, J.E.; Thurn-Albrecht, T.; Russell, T.P.; Rotello, V.M. Self-assembly of nanoparticles into structured spherical and network aggregates. *Nature* **2000**, *404*, 746–748.
32. Ryan, D.; Rao, S.N.; Rensmo, H.; Fitzmaurice, D.; Preece, J.A.; Wenger, S.; Stoddart, J.F.; Zaccheroni, N. Heterosupramolecular chemistry: Recognition initiated and inhibited silver nanocrystal aggregation by pseudorotaxane assembly. *J. Am. Chem. Soc.* **2000**, *122*, 6252–6257.
33. Ryan, D.; Nagle, L.; Rensmo, H.; Fitzmaurice, D. Programmed assembly of binary nanostructures in solution. *J. Phys. Chem., B* **2002**, *106*, 5371–5377.
34. Crooks, R.M.; Zhao, M.; Sun, L.; Chechik, V.; Yeung, L.K. Dendrimer-encapsulated metal nanoparticles: Synthesis, characterization, and applications to catalysis. *Acc. Chem. Res.* **2001**, *34*, 181–190.
35. Strimbu, L.; Liu, J.; Kaifer, A.E. Cyclodextrin-capped palladium nanoparticles as catalysts for the Suzuki reaction. *Langmuir* **2003**, *19*, 483–485.

Metal Nanoparticles Prepared in Supercritical Carbon Dioxide Solutions

M

Harry W. Rollins

*Idaho National Engineering and Environmental Laboratory,
Idaho Falls, Idaho, U.S.A.*

INTRODUCTION

The novel optical, electronic, and/or magnetic properties of metal and semiconductor nanoparticles have resulted in extensive research on new methods for their preparation. An ideal preparation method would allow the particle size, size distribution, crystallinity, and particle shape to be easily controlled, and would be applicable to a wide variety of material systems. Numerous preparation methods have been reported, each with its inherent advantages and disadvantages; however, an ideal method has yet to emerge. The most widely applied methods for nanoparticle preparation include the sonochemical reduction of organometallic reagents,^[1,2] the solvothermal method of Alivisatos,^[3] reactions in microemulsions,^[4-6] the polyol method (reduction by alcohols),^[7-9] and the use of polymer and sol-gel materials as hosts.^[10-13]

In addition to these methods, there are a variety of methods that take advantage of the unique properties of a supercritical fluid.^[14,15] Through simple variations of temperature and pressure, the properties of a supercritical fluid can be continuously tuned from gas-like to liquid-like without undergoing a phase change. Nanoparticle preparation methods that utilize supercritical fluids are briefly reviewed below using the following categories: Rapid Expansion of Supercritical Solutions (RESS), Reactive Supercritical Fluid Processing, and Supercritical Fluid Microemulsions. Because of its easily accessible critical temperature and pressure and environmentally benign nature, carbon dioxide is the most widely used supercritical solvent. Supercritical CO₂ is unfortunately a poor solvent for many polar or ionic species, which has impeded its use in the preparation of metal and semiconductor nanoparticles. We have developed a reactive supercritical fluid processing method using supercritical carbon dioxide for the preparation of metal and metal sulfide particles and used it to prepare narrowly distributed nanoparticles of silver (Ag) and silver sulfide (Ag₂S). The preparation and characterization of these materials and the effects of processing conditions on particle properties is reported.

NANOPARTICLE PREPARATION METHODS USING SUPERCRITICAL FLUIDS

Rapid Expansion of Supercritical Solutions

The Rapid Expansion of Supercritical Solutions (RESS) process takes advantage of the pressure dependence of solute solubility in supercritical fluids. In this method, a supercritical solution of the solute is prepared by dissolving the solute in an appropriate solvent and then pressurizing and heating the solution to above its critical point. (Alternatively, the solute can be directly dissolved by the solvent at supercritical conditions.) The supercritical solution is rapidly expanded through a small nozzle or orifice into a region at lower pressure, where the solute is insoluble. The very rapid reduction in pressure results in the precipitation of the solute. The timescale for the precipitation has been estimated to be on the order of 10⁻⁷ sec,^[16] which results in the homogeneous nucleation and precipitation of the solute. A wide variety of organic, polymeric, and inorganic nanoparticles have been prepared by RESS.^[17-23] Organic particles prepared using this method typically have a wide particle-size distribution and are in the ~1- μ m size range. Particle size is highly dependent on solute concentration, with smaller particles being produced at lower concentrations. Ginosar et al.^[24] reported that the on-line particle-size analysis for the RESS preparation of phenanthrene nanoparticles from carbon dioxide solutions consists of a bimodal distribution of primary nanoparticles and much larger micron-sized aggregates. Processing by RESS using carbon dioxide solutions has primarily been used in the preparation of organic nanoparticles because of the limited solubility of inorganic salts and polymers in CO₂. Smith, Matson, Petersen, and coworkers^[18,20,25] have used supercritical water solutions for the RESS preparation of SiO₂ and GeO₂ nanoparticles. Processing of SiO₂ by RESS using a preexpansion temperature of 470°C at 590 bar and an expansion nozzle with an inner diameter of 60 μ m resulted in the formation of particles with diameters from less than 0.1 to 0.5 μ m. Variation of the SiO₂

concentration from 10 to 500 ppm resulted in SiO₂ particles with diameters from less than 0.01 to 0.5 μm, with larger particles being produced at higher SiO₂ concentrations. Variation of the processing conditions has been used to generate thin films of the inorganic material. Supercritical carbon dioxide has been used for the RESS preparation of triiron dodecacarbonyl, dimanganese decacarbonyl, and chromium hexacarbonyl.^[26] The triiron dodecacarbonyl particles ranged in diameter from 1 to 10 μm.

Reactive Supercritical Fluid Processing

The RESS process is a precipitation process based on the pressure dependence of solute solubility in supercritical fluids. Unfortunately, metals and metal sulfides are insoluble in most solvents, thus precluding their direct preparation by RESS. Using aqueous solutions of metal salts, the RESS process has been used to prepare metal oxide nanoparticles. Processing of Fe(NO₃)₃ solutions by RESS using water at 500°C and 100 MPa and orifices with diameters of 50–200 μm resulted in the formation of Fe₂O₃ nanoparticles with diameters of 20–40 nm.^[27] Oxidation of metal salts in pressurized water at high temperatures is typically referred to as hydrothermal processing and is a common method in the synthesis of metal oxides. Hydrothermal treatment using batch-type reactions affords little control over the solution temperature and duration of exposure and typically results in the formation of micron-scale particles. Careful control of the reaction conditions has been demonstrated using a flowing system in which the aqueous solution of the metal salt is rapidly mixed with a preheated water stream. Variation of the temperature and flow rate of each stream and the residence time at high temperature can be precisely controlled and limited to short exposure times. Using flowing systems, Poliakoff and coworkers^[28,29] were able to prepare nanoparticles of Ce_{1-x}Zr_xO₂ and MFe₂O₄ (M=Co, Ni, Zn) with particle sizes of ~10 nm. Solutions of metal salts in alcohols have also been processed using high temperatures and pressures to prepare nanoparticles of a variety of metals.^[30,31]

Sun and coworkers^[15,32–36] have developed a reactive supercritical fluid method for the preparation of metal and metal sulfide particles based on the RESS process. In this method, a metal salt is dissolved in a polar solvent, which is then pressurized and heated to supercritical conditions. The supercritical solution is then rapidly expanded through a small nozzle or orifice into a liquid solution containing a second reactant (e.g., reducing agent or sodium sulfide). The method is versatile and can be used with a variety of metal salts, supercritical fluids, and reagents. They have used this method to prepare nanoparticles of the metals, Ag, Cu, Fe, Ni, and Co, as well as

the metal sulfides, CdS, Ag₂S, and PbS. The particles produced have average diameters of ≤10 nm with particle-size distributions of ~1 nm. Solvents used include methanol, ethanol, acetone, tetrahydrofuran, and ammonia. Particle aggregation is minimized by collecting the sample in liquid solution and can be further prevented through the use of polymer surfactants such as poly(*N*-vinyl-2-pyrrolidone) (PVP).

Supercritical Fluid Microemulsions

To overcome the limited solubility of polar compounds, particularly metal salts, in carbon dioxide, several researchers have used reverse micelles. Wai and coworkers^[37,38] reported the preparation of silver and copper nanoparticles using water-in-CO₂ reverse micelles. Silver and copper salts were dissolved in the aqueous core of reverse micelles formed with sodium bis(2-ethylhexyl) sulfosuccinate (AOT) and the cosurfactant perfluoropolyether phosphate in supercritical carbon dioxide. The cosurfactant perfluoropolyether phosphate is necessary to dissolve the AOT, which is not soluble in carbon dioxide. Addition of a reducing agent to the reverse micelle solutions resulted in the formation of metallic Ag or Cu nanoparticles with 5–15 nm diameters.^[37,38] AgI, AgBr, and AgCl nanoparticles (3–15 nm) have been prepared by mixing two carbon dioxide microemulsions, one containing AgNO₃ and the other containing NaI, NaBr, or NaCl.^[39] A fluorinated analog of AOT has been synthesized and used for the preparation of CdS and ZnS nanoparticles by mixing two CO₂ reverse micelle solutions, one containing the metal salt and the other Na₂S.^[40] The average diameter was calculated from the band gap and varied from 2.7 to 4.2 nm depending on the water to surfactant ratio. Formation of water-in-CO₂ microemulsions by perfluoropolyether surfactants has been demonstrated^[41–44] and used to prepare CdS nanoparticles.^[45] Sun et al.^[46] have used perfluoropolyether ammonium carboxylate water-in-CO₂ microemulsions to dissolve AgNO₃, which was then rapidly expanded into a room temperature solution of sodium borohydride resulting in Ag nanoparticles.

RESULTS AND DISCUSSION

We have developed a reactive supercritical fluid nanoparticle preparation method based on the RESS process that uses supercritical carbon dioxide as the solvent. In this method, neutral metal salts are dissolved in carbon dioxide using tributyl phosphate (TBP). The method can be used with a variety of metal salts and can be used for the preparation of both metal and metal sulfide nanoparticles. The particles thus prepared have average diameters

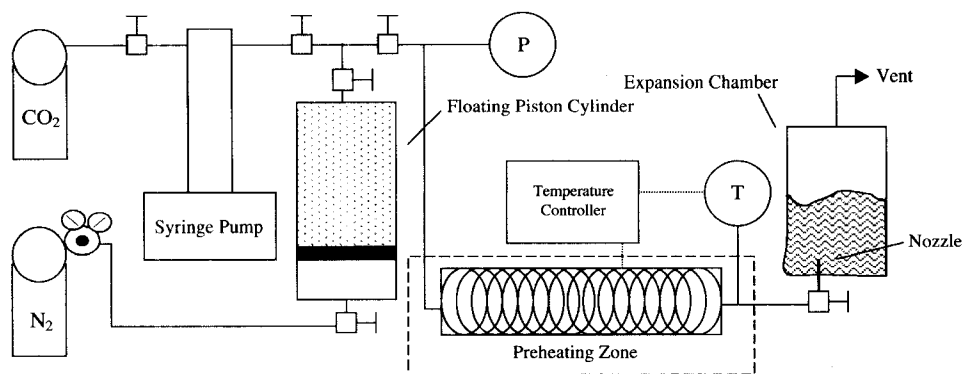


Fig. 1 Experimental apparatus for the reactive RESS preparation of nanoparticles. (View this art in color at www.dekker.com.)

of approximately 10 nm, with narrow size distributions. The preparation and characterization of silver and silver sulfide nanoparticles is presented.

Silver Nanoparticles

The experimental apparatus for the reactive RESS preparation of nanoparticles is shown in Fig. 1. The system consists of an ISCO model 260D syringe pump, a floating piston cylinder (TEMCO model CFT-50-50, 300-cm³ volume), a high-pressure nitrogen cylinder and regulator, a preheating zone with ~40 ft of 1/16-in. o.d. tubing in an aluminum clamshell, an Omega CN4800 temperature controller with k-type thermocouple in contact with the fluid, a 127- μ m i.d. by 10-cm-long

nozzle, and an expansion chamber. For the preparation of silver nanoparticles, CF₃SO₃Ag solution in tributyl phosphate (TBP) was added to the floating piston cylinder, which was filled with liquid CO₂ and pressurized to 2000 psi at room temperature. The amount of CO₂ was gravimetrically determined. The floating piston cylinder was placed on a horizontal platform rocker and allowed to equilibrate for at least 2 hr. The preheating zone was brought to temperature and allowed to equilibrate. A solution of NaBH₄ in ethanol or methanol (150 ml) was immediately prepared before use and was placed in the expansion chamber. The polymer PVP (molecular weight 360,000, ~3.5 mg/mL) was also dissolved in the NaBH₄ alcohol solution to prevent particle aggregation. An excess of sodium borohydride was used for the preparation

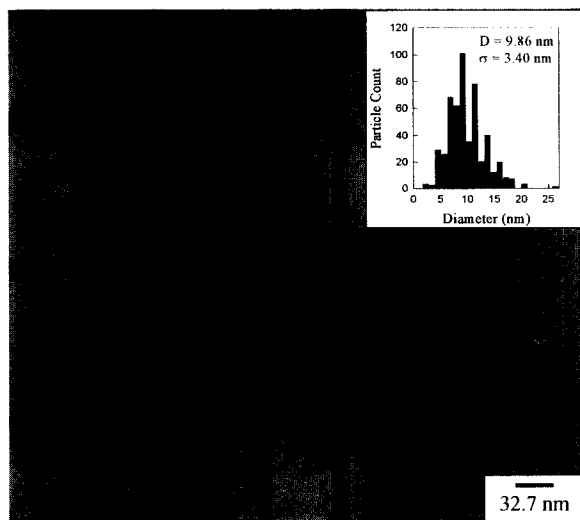


Fig. 2 Transmission electron micrograph of silver nanoparticles prepared from supercritical CO₂ solution at 70°C, 3500 psi, with 0.22 wt.% TBP. The particle-size distribution is shown in the inset. (View this art in color at www.dekker.com.)

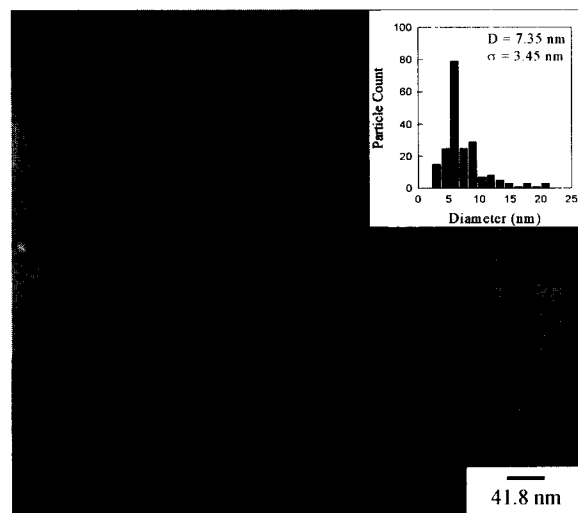


Fig. 3 Transmission electron micrograph of silver nanoparticles prepared from supercritical CO₂ solution at 110°C, 3500 psi, with 0.24 wt.% TBP. The particle-size distribution is shown in the inset. (View this art in color at www.dekker.com.)

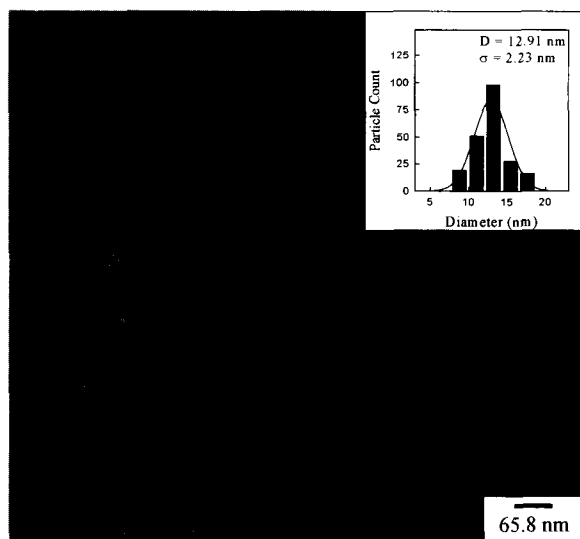


Fig. 4 Transmission electron micrograph of silver nanoparticles prepared from supercritical CO_2 solution at 104°C , 3500 psi, with 1.41 wt.% TBP. The particle-size histogram and Gaussian-distribution analysis are shown in the inset. (View this art in color at www.dekker.com.)

of all samples ($[\text{NaBH}_4]/[\text{Ag}^+] = 3\text{--}5$). The $\text{CF}_3\text{SO}_3\text{Ag}$ solution in CO_2/TBP was pressurized to 3500 psi using nitrogen on the back side of the piston. The system temperature was equilibrated by flowing CO_2 at 3500 psi for ~ 5 min. The CO_2 flow was stopped and the $\text{CF}_3\text{SO}_3\text{Ag}$ solution flow was initiated and expanded into the NaBH_4 solution.

The NaBH_4 solution immediately turned yellow upon addition of $\text{CF}_3\text{SO}_3\text{Ag}$ solution, typical of silver nanoparticle suspensions. The resulting suspension was then characterized using X-ray diffraction (XRD), transmission electron microscopy (TEM), and UV-Vis absorption spectroscopy. For TEM analysis, a drop of the suspension was placed on a carbon-coated Cu grid, allowed to dry, rinsed with hexane, and then dried in a vacuum oven at $100\text{--}120^\circ\text{C}$ overnight to remove residual TBP. For UV-Vis analysis, the samples were diluted to an optical density < 1 using 0.2-cm path length cuvettes. For XRD analysis, the sample was dried on a rotary evaporator at up to 80°C . Upon removal of the alcohol, the silver particles and PVP polymer precipitated and the remaining TBP liquid was decanted. The sample was rinsed with hexane and then dried in a vacuum oven. X-ray diffraction patterns for the samples matched the powder diffraction file reference patterns for face-centered cubic silver (04-0783).

Several silver nanoparticle samples were prepared using different expansion temperatures and concentrations of TBP. Transmission electron microscopy analysis and particle-size distributions are shown in Figs. 2–4 for

Table 1 Properties of silver and silver sulfide nanoparticles prepared by reactive RESS processing using CO_2 solutions

	Temperature ($^\circ\text{C}$)	[TBP] (wt.%)	Diameter (nm)	σ (nm)
Silver	70	0.22	9.9	3.4
Silver	110	0.24	7.4	3.5
Silver	104	1.41	12.9	2.2
Silver sulfide	50	0.23	3.1	1.2
Silver sulfide	70	0.23	3.0	1.0
Silver sulfide	110	1.38	7.2	1.8

several silver nanoparticle samples. Particle diameters and size distributions were determined from the TEM micrographs and are based on a minimum of 200 particles. The samples shown in Figs. 2 and 3 were both prepared using 0.2 wt.% TBP. The sample prepared using a temperature of 70°C has an average particle diameter of 9.9 nm, while the sample prepared at 110°C has an average diameter of 7.4 nm. The particle diameter standard deviation is ~ 3.5 nm for both samples. Analysis by TEM of a sample prepared using a temperature of 104°C and [TBP] of 1.41 wt.% has an average diameter of 12.9 nm and a standard deviation of 2.2 nm. Sample preparation conditions and results from TEM analysis are summarized in Table 1. Particle diameter shows a slight dependence on expansion temperature, with smaller particles produced at lower temperature. The particle size and distributions were highly dependent on TBP concentration, with larger, more uniform particles prepared at higher TBP concentrations. The absorption spectra of the 9.9- and 12.9-nm diameter silver nanoparticles are shown in Fig. 5, and both samples exhibit the characteristic surface plasmon absorption band. The 12.9-nm diameter

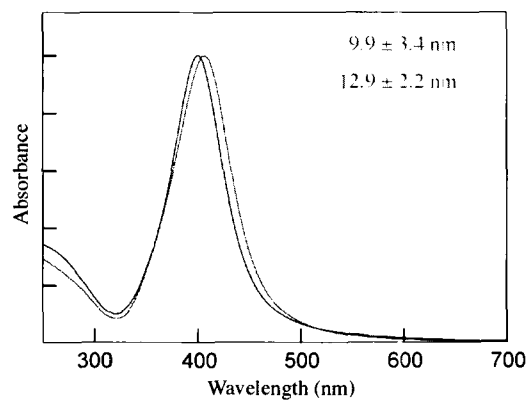


Fig. 5 Normalized absorption spectra of silver nanoparticles prepared from supercritical CO_2 solutions. (View this art in color at www.dekker.com.)

sample is red shifted and broader than the 9.9-nm diameter sample. The absorption maximums are at 406.5 nm (68 nm FWHM) and 399.5 nm (62 nm FWHM) for the 12.9- and 9.9-nm samples, respectively.

Silver Sulfide Nanoparticles

Silver sulfide nanoparticles were prepared using the reactive RESS processing method. The preparation conditions were the same as those used for the preparation of silver metal nanoparticles except that the expansion chamber contained a methanol solution of Na_2S with PVP. Excess Na_2S was used in the preparation of all the samples ($[\text{S}^{2-}]/[\text{Ag}^+] \approx 7.5$). X-ray diffraction analysis of the samples matched the reference pattern for monoclinic Ag_2S (75-1061). Transmission electron micrographs and particle-size distributions for silver sulfide nanoparticles are shown in Figs. 6–8. Preparation conditions and TEM results are summarized in Table 1. The samples prepared using temperatures of 50°C (Fig. 6) and 70°C (Fig. 7) were both prepared using 0.2 wt.% TBP. The sample prepared using an expansion temperature of 50°C had an average diameter of 3.1 ± 1.2 nm and the sample prepared using 70°C had an average diameter of 3.0 ± 1.0 nm. The expansion temperature had little, if any, effect on particle size; however, the sample prepared using 50°C had a slightly larger size distribution. Silver sulfide nanoparticles were considerably smaller than silver metal particles prepared using similar conditions. For samples prepared using an expansion temperature of

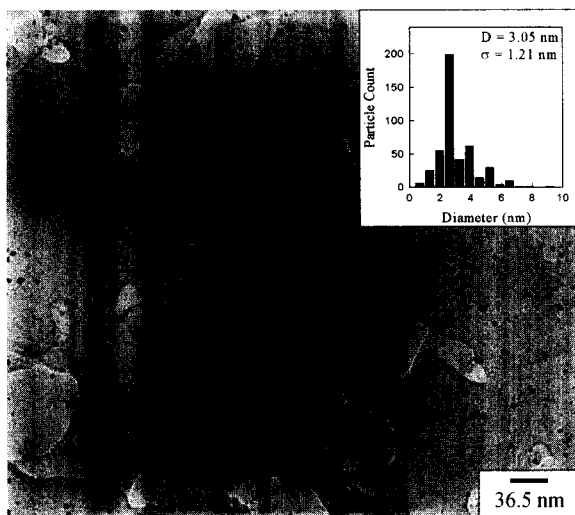


Fig. 6 Transmission electron micrograph of silver sulfide nanoparticles prepared from supercritical CO_2 solution at 50°C, 3500 psi, with 0.23 wt.% TBP. The particle-size distribution is shown in the inset. (View this art in color at www.dekker.com.)

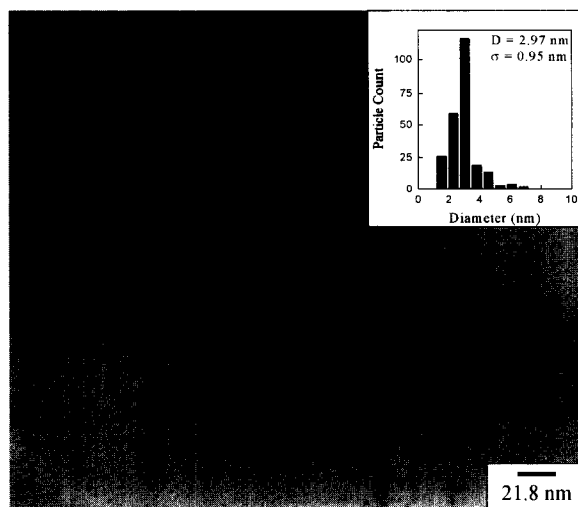


Fig. 7 Transmission electron micrograph of silver sulfide nanoparticles prepared from supercritical CO_2 solution at 70°C, 3500 psi, with 0.23 wt.% TBP. The particle-size distribution is shown in the inset. (View this art in color at www.dekker.com.)

70°C and 0.2 wt.% TBP, silver nanoparticles were 9.9 ± 3.4 nm, while silver sulfide nanoparticles were 3.0 ± 1.0 nm. Silver sulfide nanoparticles prepared using an expansion temperature of 110°C and 1.38 wt.% TBP had an average diameter of 7.2 ± 1.8 nm (Fig. 8). Particle size and size distribution are larger for the silver sulfide sample prepared using higher TBP concentration. The

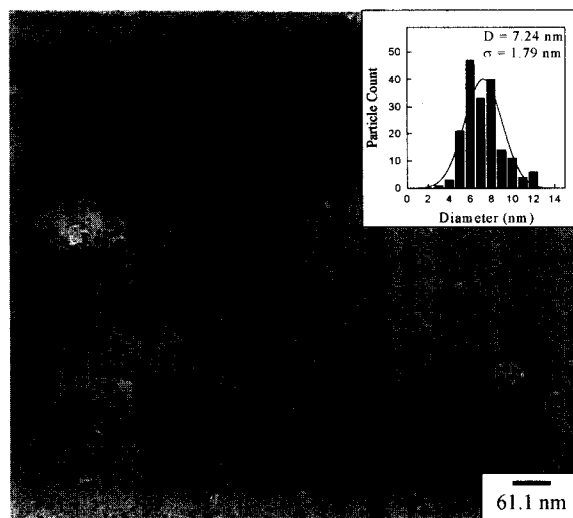


Fig. 8 Transmission electron micrograph of silver sulfide nanoparticles prepared from supercritical CO_2 solution at 110°C, 3500 psi, with 1.38 wt.% TBP. The particle-size histogram and Gaussian-distribution analysis are shown in the inset. (View this art in color at www.dekker.com.)

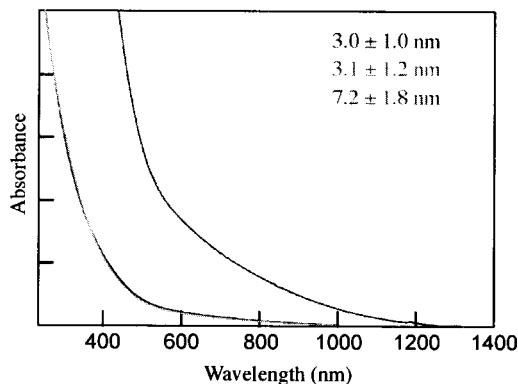


Fig. 9 Absorption spectra of silver sulfide nanoparticles prepared from supercritical CO₂ solutions. (View this art in color at www.dekker.com.)

UV-Vis-NIR absorption spectra of the silver sulfide nanoparticle suspensions are shown in Fig. 9. The samples with average diameters of ~ 3 nm have an absorption onset at ~ 950 nm, while the sample with an average diameter of 7.2 nm has an absorption onset at ~ 1250 nm. This is consistent with a shift in band gap (and absorption onset) to higher energies with decreasing particle size for semiconductor nanoparticles.

CONCLUSION

Silver and silver sulfide nanoparticles with average diameters ~ 10 nm with narrow size distributions have been prepared using a reactive supercritical fluid processing method. In this method, a neutral metal salt is dissolved in CO₂ using tributyl phosphate. The supercritical solution of the metal salt is rapidly expanded into a liquid solution containing a second reactant, resulting in the formation of metal or metal sulfide nanoparticles. The nanoparticles have been characterized by powder X-ray diffraction, transmission electron microscopy, and absorption spectroscopy. The particle size and size distribution depend on preparation conditions, most notably on TBP concentration.

ACKNOWLEDGMENTS

This work was supported by the U.S. Department of Energy through the INEEL Laboratory Directed Research and Development (LDRD) Program under DOE Idaho Operations Office Contract DE-AC07-99ID13727.

REFERENCES

- Suslick, K.S.; Fang, M.M.; Hyeon, T. Sonochemical synthesis of iron colloids. *J. Am. Chem. Soc.* **1996**, *118* (47), 11960–11961.
- Suslick, K.S.; Choe, S.B.; Cichowlas, A.A.; Grinstaff, M.W. Sonochemical synthesis of amorphous iron. *Nature* **1991**, *353* (6343), 414–416.
- Alivisatos, A.P. Semiconductor clusters, nanocrystals, and quantum dots. *Science* **1996**, *271* (5251), 933–937.
- Motte, L.; Billoudet, F.; Pileni, M.P. Synthesis in situ of nanosize silver sulphide semiconductor particles in reverse micelles. *J. Mater. Sci.* **1996**, *31* (1), 38–42.
- Petit, C.; Lixon, P.; Pileni, M.P. In-situ synthesis of silver nanocluster in AOT reverse micelles. *J. Phys. Chem.* **1993**, *97* (49), 12974–12983.
- Lisiecki, I.; Pileni, M.P. Synthesis of copper metallic clusters using reverse micelles as microreactors. *J. Am. Chem. Soc.* **1993**, *115* (10), 3887–3896.
- Chakroune, N.; Viau, G.; Ricolleau, C.; Fievet-Vincent, F.; Fievet, F. Cobalt-based anisotropic particles prepared by the polyol process. *J. Mater. Chem.* **2003**, *13* (2), 312–318.
- Feldmann, C.; Metzmacher, C. Polyol mediated synthesis of nanoscale MS particles (M=Zn, Cd, Hg). *J. Mater. Chem.* **2001**, *11* (10), 2603–2606.
- Feldmann, C. Polyol-mediated synthesis of nanoscale functional materials. *Adv. Funct. Mater.* **2003**, *13* (2), 101–107.
- Blackburn, J.M.; Long, D.P.; Cabanas, A.; Watkins, J.J. Deposition of conformal copper and nickel films from supercritical carbon dioxide. *Science* **2001**, *294* (5540), 141–145.
- Cao, Y.; Hu, J.C.; Hong, Z.S.; Deng, J.F.; Fan, K.N. Characterization of high-surface-area zirconia aerogel synthesized from combined alcohothermal and supercritical fluid drying techniques. *Catal. Letters* **2002**, *81* (1–2), 107–112.
- Casula, M.F.; Corrias, A.; Paschina, G. FeCo-SiO₂ nanocomposite aerogels by high temperature supercritical drying. *J. Mater. Chem.* **2002**, *12* (5), 1505–1510.
- Watkins, J.J.; McCarthy, T.J. Polymer/metal nanocomposite synthesis in supercritical CO₂. *Chem. Mater.* **1995**, *7* (11), 1991–1994.
- Rollins, H.W. Ph.D. Dissertation; Clemson University, 1999.
- Sun, Y.-P.; Rollins, H.W.; Jayasundera, B.; Meziari, M.J.; Bunker, C.E. *Supercritical Fluid Technology in Materials Science and Engineering: Synthesis, Properties, and Applications*; Sun,

- Y.P., Ed.; Marcel Dekker: New York, 2002; 491–576.
16. Lele, A.K.; Shine, A.D. Effect of RESS dynamics on polymer morphology. *Ind. Eng. Chem. Res.* **1994**, *33* (6), 1476–1485.
 17. Eckert, C.A.; Knutson, B.L.; Debenedetti, P.G. Supercritical fluids as solvents for chemical and materials processing. *Nature* **1996**, *383* (6598), 313–318.
 18. Matson, D.W.; Fulton, J.L.; Petersen, R.C.; Smith, R.D. Rapid expansion of supercritical fluid solutions—Solute formation of powders, thin-films, and fibers. *Ind. Eng. Chem. Res.* **1987**, *26* (11), 2298–2306.
 19. Blasig, A.; Shi, C.M.; Enick, R.M.; Thies, M.C. Effect of concentration and degree of saturation on RESS of a CO₂-soluble fluoropolymer. *Ind. Eng. Chem. Res.* **2002**, *41* (20), 4976–4983.
 20. Petersen, R.C.; Matson, D.W.; Smith, R.D. Rapid precipitation of low vapor-pressure solids from supercritical fluid solutions—The formation of thin-films and powders. *J. Am. Chem. Soc.* **1986**, *108* (8), 2100–2102.
 21. Chernyak, Y.; Henon, F.; Harris, R.B.; Gould, R.D.; Franklin, R.K.; Edwards, J.R.; Desimone, J.M.; Carbonell, R.G. Formation of perfluoropolyether coatings by the rapid expansion of supercritical solutions (RESS) process. Part 1: Experimental results. *Ind. Eng. Chem. Res.* **2001**, *40* (26), 6118–6126.
 22. Mawson, S.; Johnston, K.P.; Combes, J.R.; Desimone, J.M. Formation of poly(1,1,2,2-tetrahydroperfluorodecyl acrylate) submicron fibers and particles from supercritical carbon-dioxide solutions. *Macromolecules* **1995**, *28* (9), 3182–3191.
 23. Debenedetti, P.G.; Tom, J.W.; Kwauk, X.; Yeo, S.D. Rapid expansion of supercritical solutions (RESS)—Fundamentals and applications. *Fluid Phase Equilib.* **1993**, *82*, 311–321.
 24. Ginosar, D.M.; Swank, W.D.; McMurtrey, R.D.; Carmack, W.J. In *Flow-Field Studies of the RESS Process*, Proceedings of the 5th International Symposium on Supercritical Fluids, Atlanta, Georgia, April 8–12, 2000.
 25. Matson, D.W.; Smith, R.D. Supercritical fluid technologies for ceramic-processing applications. *J. Am. Ceram. Soc.* **1989**, *72* (6), 871–881.
 26. Williams, J.R.; Clifford, A.A.; Bartle, K.D.; Kee, T.P. The production of fine particles of metal complexes using supercritical fluids. *Powder Technol.* **1998**, *96* (2), 158–162.
 27. Burukhin, A.A.; Churagulov, B.R.; Oleynikov, N.N.; Kolen'ko, Y.V. *Nanostructured Powders and Their Industrial Applications*; Mater. Res. Soc. Symp. Proc., Materials Research Society: Warrendale, PA, 1998; Vol. 520, 171.
 28. Cabanas, A.; Poliakoff, M. The continuous hydrothermal synthesis of nano-particulate ferrites in near critical and supercritical water. *J. Mater. Chem.* **2001**, *11* (5), 1408–1416.
 29. Cabanas, A.; Darr, J.A.; Lester, E.; Poliakoff, M. Continuous hydrothermal synthesis of inorganic materials in a near-critical water flow reactor; the one-step synthesis of nano-particulate Ce_{1-x}Zr_xO₂ (x=0–1) solid solutions. *J. Mater. Chem.* **2001**, *11* (2), 561–568.
 30. Pessey, V.; Garriga, R.; Weill, F.; Chevalier, B.; Etourneau, J.; Cansell, F. Core-shell materials elaboration in supercritical mixture CO₂/ethanol. *Ind. Eng. Chem. Res.* **2000**, *39* (12), 4714–4719.
 31. Sheldrick, W.S.; Wachhold, M. Solventothermal synthesis of solid-state chalcogenidometalates. *Angew. Chem., Int. Ed. Engl.* **1997**, *36* (3), 207–224.
 32. Sun, Y.P.; Rollins, H.W. Preparation of polymer-protected semiconductor nanoparticles through the rapid expansion of supercritical fluid solution. *Chem. Phys. Lett.* **1998**, *288* (2–4), 585–588.
 33. Sun, Y.P.; Rollins, H.W.; Guduru, R. Preparations of nickel, cobalt, and iron nanoparticles through the rapid expansion of supercritical fluid solutions (RESS) and chemical reduction. *Chem. Mater.* **1999**, *11* (1), 7–9.
 34. Meziari, M.J.; Rollins, H.W.; Allard, L.F.; Sun, Y.P. Protein-protected nanoparticles from rapid expansion of supercritical solution into aqueous solution. *J. Phys. Chem., B* **2002**, *106* (43), 11178–11182.
 35. Sun, Y.P.; Guduru, R.; Lin, F.; Whiteside, T. Preparation of nanoscale semiconductors through the rapid expansion of supercritical solution (RESS) into liquid solution. *Ind. Eng. Chem. Res.* **2000**, *39* (12), 4663–4669.
 36. Sun, Y.P.; Riggs, J.E.; Rollins, H.W.; Guduru, R. Strong optical limiting of silver-containing nanocrystalline particles in stable suspensions. *J. Phys. Chem., B* **1999**, *103* (1), 77–82.
 37. Ohde, H.; Hunt, F.; Wai, C.M. Synthesis of silver and copper nanoparticles in a water-in-supercritical-carbon dioxide microemulsion. *Chem. Mater.* **2001**, *13* (11), 4130–4135.
 38. Ji, M.; Chen, X.Y.; Wai, C.M.; Fulton, J.L. Synthesizing and dispersing silver nanoparticles in a water-in-supercritical carbon dioxide microemulsion. *J. Am. Chem. Soc.* **1999**, *121* (11), 2631–2632.

39. Ohde, H.; Rodriguez, J.M.; Ye, X.R.; Wai, C.M. Synthesizing silver halide nanoparticles in supercritical carbon dioxide utilizing a water-in-CO₂ microemulsion. *Chem. Commun.* **2000**, (23), 2353–2354.
40. Ohde, H.; Ohde, M.; Bailey, F.; Kim, H.; Wai, C.M. Water-in-CO₂ microemulsions as nanoreactors for synthesizing Cds and Zns nanoparticles in supercritical CO₂. *Nano Lett.* **2002**, 2 (7), 721–724.
41. Lee, C.T.; Ryoo, W.; Smith, P.G.; Arellano, J.; Mitchell, D.R.; Lagow, R.J.; Webber, S.E.; Johnston, K.P. Carbon dioxide-in-water microemulsions. *J. Am. Chem. Soc.* **2003**, 125 (10), 3181–3189.
42. Nagashima, K.; Lee, C.T.; Xu, B.; Johnston, K.P.; Desimone, J.M.; Johnson, C.S. NMR studies of water transport and proton exchange in water-in-carbon dioxide microemulsions. *J. Phys. Chem., B* **2003**, 107 (9), 1962–1968.
43. Da Rocha, S.R.P.; Johnston, K.P.; Rossky, P.J. Surfactant-modified CO₂-water interface: A molecular view. *J. Phys. Chem., B* **2002**, 106 (51), 13250–13261.
44. Meziani, M.J.; Sun, Y.P. Spectrophotometry study of aqueous salt solution in carbon dioxide microemulsions. *Langmuir* **2002**, 18 (10), 3787–3791.
45. Holmes, J.D.; Bhargava, P.A.; Korgel, B.A.; Johnston, K.P. Synthesis of cadmium sulfide Q particles in water-in-CO₂ microemulsions. *Langmuir* **1999**, 15 (20), 6613–6615.
46. Sun, Y.P.; Atorngitjawat, P.; Meziani, M.J. Preparation of silver nanoparticles via rapid expansion of water in carbon dioxide microemulsion into reductant solution. *Langmuir* **2001**, 17 (19), 5707–5710.

Metal Nanoparticles Protected with Monolayers: Applications for Chemical Vapor Sensing and Gas Chromatography

Jay W. Grate
David A. Nelson
Rhonda Skaggs

Pacific Northwest National Laboratory, Richland, Washington, U.S.A.

Robert E. Synovec
Gwen M. Gross

University of Washington, Seattle, Washington, U.S.A.

INTRODUCTION

Nanoparticles and nanoparticle-based materials are of considerable interest for their unique properties and their potential for use in a variety of applications. Metal nanoparticles, in which each particle's surface is coated with a protective organic monolayer, are of particular interest because the surface monolayer stabilizes them relative to aggregation and they can be taken up into solutions.^[1-4] As a result, they can be processed into thin films for device applications. We will refer to these materials as monolayer-protected nanoparticles (MPNs). Typically, the metal is gold and the organic layer is a self-assembled thiol layer, and this composition will be assumed throughout the remainder of this chapter. A diversity of materials and properties is readily accessible by straightforward synthetic procedures, either by the structures of the monolayer-forming thiols used in the synthesis, or by postsynthetic modifications of the monolayers. A particularly promising application for these materials is as selective layers on chemical vapor sensors. In this role, the thin film of MPNs on the device surface serves to collect and concentrate gas molecules at the sensor's surface. Their sorptive properties also lend them to use as new nanostructured gas chromatographic stationary phases. This chapter will focus on the sorptive properties of MPNs as they relate to chemical sensors and gas chromatography (GC).

BACKGROUND

The use of a sorptive layer to collect and concentrate vapor molecules at a sensor's surface is shown schematically in Fig. 1. The presence of these sorbed vapor molecules can then be detected in a variety of ways,

depending on the transduction mechanism of the sensor device. Acoustic wave devices, such as the thickness shear mode (TSM) device or the surface acoustic wave (SAW) device, transduce the presence of the vapor as an increase in mass detected by a change in the acoustic wave velocity.^[5-8] Typically, the acoustic wave velocity change is measured as a change in oscillator frequency.

A schematic diagram of an MPN as an individual particle, its component parts, and a film is shown in Fig. 2. The film represents a cross section where gold cores are separated by the organic monolayers, with areas of lower density suggested between the MPNs. As a sorptive layer, molecules could sorb into the thiol material and/or the free volume associated with areas of lower density.

Chemiresistor devices measure a change in the resistance of the applied thin films as a function of the sorbed gas or vapor.^[9-12] Because an MPN film on such a device carries the current, it participates directly in the transduction mechanism.^[12] These films consist of metal particles separated from one another, insulating monolayers on their surfaces (Fig. 2). The current observed as electrons travel through a film from particle core to particle core can be modulated by the sorption of vapor molecules in the insulating regions. These insulating regions are of molecular dimensions, hence the sorption of molecules can represent a significant perturbation. Wohltjen and Snow^[12] described MPN-sensing films as metal-insulator-metal ensembles (MIMEs) in recognition of the nanostructure of the films.

Regardless of the transduction mechanism chosen, the sorption of a vapor into the MPN film represents a significant aspect of the sensor response. The amount of vapor uptake and the rate of vapor uptake by these film materials provide useful information for understanding and interpreting sensor response behavior. Differences in the sorption of various vapors (i.e., selectivity) provide the

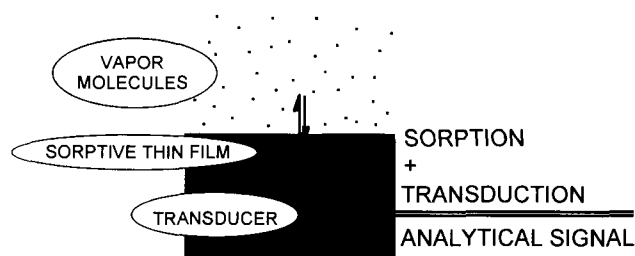


Fig. 1 Schematic diagram of the mechanism for a chemical vapor sensor where the sorption of a vapor from the gas phase into a sorptive layer on the transducer surface results in an analytical signal.

basis for discriminating among vapors using arrays of such sensors, and for separating vapors using GC.

SYNTHESIS AND PROPERTIES

The typical synthesis procedure for MPNs involves the reduction of gold salts in the presence of a monolayer-forming thiol. A two-phase water/toluene process with a phase transfer salt was first reported by Brust et al.^[2] and has been used by many others as well.^[12–15] For example, alkanethiol-protected gold nanoparticles are typically prepared starting with solutions of $\text{HAuCl}_4 \cdot \text{H}_2\text{O}$ in water, alkanethiol in toluene, sodium borohydride as the reducing agent in water, and tetraoctylammonium bromide as the phase transfer salt in toluene. The aqueous HAuCl_4 solution is added to the toluene solution containing tetraoctylammonium bromide. After thorough stirring to transfer AuCl_4^- anions into the toluene, the dodecanethiol/toluene solution is added followed by the aqueous NaBH_4 solution. The product MPNs are recovered from the toluene phase.

MPNs can also be prepared in one-phase procedures that have been used, for example, for a variety of ar-

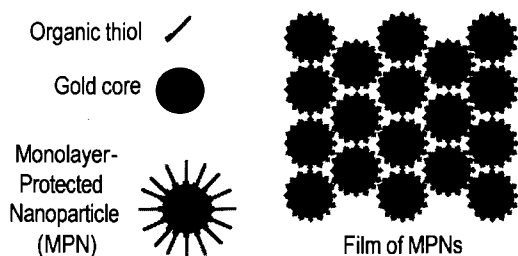


Fig. 2 Schematic diagram of a gold nanoparticle protected with organic thiol monolayer, along with a hypothetical film where the gold cores are black, the monolayer material is gray, and there are areas of potentially lower density between the particles that may facilitate vapor diffusion and sorption.

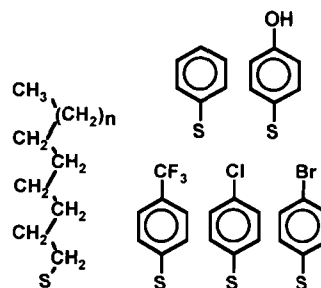


Fig. 3 A selection of thiol structures that have been used as monolayers on gold nanoparticles. The alkanethiols indicated on the left typically range from octanethiol to dodecanethiol ($n = 1-5$).

enethiol-protected gold nanoparticles. The single-phase methanol/water synthesis was developed by Brust et al.^[1] and used by others.^[15,16] A synthesis method from solvated metal atoms has also been described, where vaporized metal atoms and solvent vapors are codeposited as a frozen mixture, followed by reaction with the thiol.^[17] This method is effective at generating gram quantities of MPNs that are unambiguously free of ionic impurities from reducing agents or phase transfer reagents.

A great variety of thiol ligands have been used in the synthesis of MPNs, some of which are shown in Fig. 3. Alkanethiols have been particularly popular, whereas the substituted arene thiols provide a facile method to incorporate varying functionality in the structure. In addition, the ligand shell can be synthetically modified by organic reactions with organic ligands. Additional examples of thiols used and postsynthetic modifications can be found in Ref. [3].

Preparations are typically polydisperse in particle size. The metal cores can be observed and measured by high-resolution transmission electron microscopy (TEM). An example of a TEM of a monolayer of MPNs is shown in Fig. 4. Particle core sizes in most studies average between 1.5 and 5 nm in diameter. It is believed that the cores prefer to reach discrete sizes with closed-shell structures (i.e., completed outermost layers of gold on the particle or crystal), although nonequilibrium structures may be produced under kinetically controlled growth conditions.^[3] A number of studies have described the ripening of nanoparticle sizes after synthesis.^[17–22] Particle sizes may increase with time and heating under appropriate conditions; however, reduction in gold core size has also been described by heating in neat thiol. Ripening of nanoparticles appears to lead to a more uniform size distribution than that obtained during synthesis.

A variety of additional characterization methods are also frequently applied. Thermogravimetric analysis (TGA) provides a measure of the mass percentages of gold

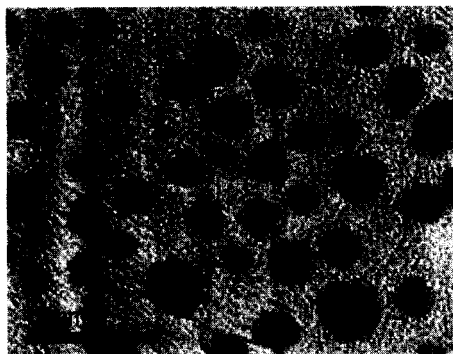


Fig. 4 TEM image of a polydisperse sample of bromobenzenethiol-protected gold nanoparticles.

and organic material in the prepared sample. Ideally, the organic material is all gold-bound thiol; however, impure samples may also contain excess free thiol, the corresponding disulfide, or phase transfer salt. Infrared spectra are sometimes used to look for the presence of phase transfer salt. Free thiol or disulfide can be observed by chromatographic methods including thin layer chromatography and liquid chromatography.

Additional techniques that have been applied to the study of MPNs include small-angle X-ray scattering (SAXS), conventional and synchrotron X-ray diffraction, mass spectrometry, scanning tunneling microscopy (STM), atomic force microscopy (AFM), differential scanning calorimetry, and nuclear magnetic resonance (NMR), to name a few. Detailed structural studies of carefully crystallized samples of alkanethiol-protected gold nanoparticles have been described.^[4]

Of particular interest with regard to sorption are the relative proportions of the organic thiol material serving as a sorptive medium and the gold cores whose volume excludes sorbed molecules. The mass ratios of gold and thiol can be determined from TGA, where the organic material burns off, leaving gold. From our own data^[15] as well as data in the literature,^[13,14,23] it is found that MPN materials are typically 75–90% metal by mass and only 10–25% organic by mass. Nevertheless, these proportions are reversed when volume fractions are considered. We have estimated that typical volume fractions are 70–90% organic material by volume and only 10–30% metal by volume, using the densities of bulk gold and condensed phase thiols to convert mass fractions to volume fractions.^[15] Thus despite the low mass percentage of sorptive organic material, these materials are actually primarily sorptive organic material by volume.

Low-volume fractions of gold—and hence high-volume fractions of thiol—are also indicated by structural studies.^[4] In studies of crystalline samples of MPNs with alkanethiol ligands, the gold cores have been assumed to

have the density of bulk gold metal, and the volume not occupied by gold has been found to have a density very close to that of the bulk thiol.^[24]

SORPTIVE PROPERTIES AS MEASURED USING ACOUSTIC WAVE SENSORS

Sorption, the Partition Coefficient, and Chemical Sensor Response

The analytical signal of a coated microsensors entails the sorption of the vapor and transduction of the presence of the vapor in the film.^[25,26] The vapor sensor's response R is empirically expressed as a function of the gas-phase concentration of the test vapor C_v as in Eq. 1, and this is the basis of the calibration curve:

$$R = f(C_v) \quad (1)$$

Nevertheless, the sensor's response is more directly a function of the concentration of the vapor in the sorptive coating C_s as indicated in Eq. 2:

$$R = f(C_s) \quad (2)$$

The ratio of the concentrations C_v and C_s is given by the thermodynamic partition coefficient K (Eq. 3):

$$K = C_s/C_v \quad (3)$$

Consequently, the response function to the vapor concentration in the film (Eq. 2) can be expressed as a function of the product of the gas-phase vapor concentration and the partition coefficient (Eq. 4):

$$R = f(KC_v) \quad (4)$$

Hence knowledge of the partitioning of vapors into sensor films (i.e., absorption) is fundamental to understanding sensor performance and mechanism.^[25,26] We are particularly interested on how this knowledge can help to elucidate the relative roles of sorption and transduction in observed sensitivities and detection limits. Partition coefficients are also fundamental to the separation of vapors by GC.

Vapor Sorption by Nanoparticle Films

Four MPN materials were selected for detailed studies on sorptive behavior.^[15] These four were satisfactorily characterized and all gave rapid and reversible sorption of the test vapors considered. They were MPNs with dodecanethiol, benzenethiol, chlorobenzenethiol, and trifluoromethylbenzenethiol ligands.

Vapor sorption measurements were made on TSM devices spray-coated with an amount of MPN material,

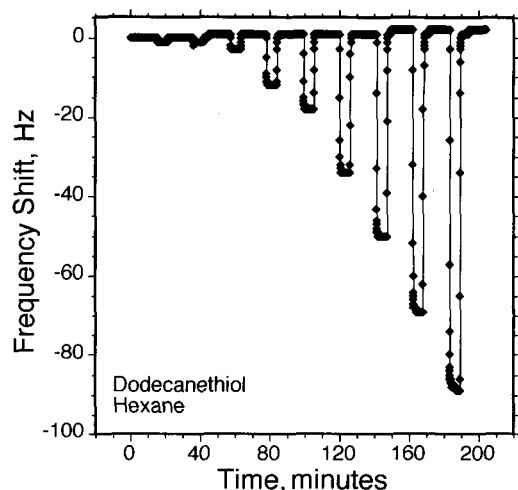


Fig. 5 Response of a dodecanethiol-protected gold nanoparticle film on a TSM device to increasing concentrations of hexane. Data points are shown 2 sec apart.

yielding approximately 10 kHz frequency shifts (an indication of film thickness).^[15] Impedance measurements were made to assure that the MPN layers on the TSM devices yield gravimetric sensors and valid vapor uptake measurements can be made. The test sensors were evaluated against four vapors: *n*-hexane, toluene, 2-butanone, and 1-butanol. These vapors represent a diverse set of properties to probe differences in behavior and chemical selectivity among the nanoparticle materials. Sensor responses to the test vapors were generally rapid and reversible, with exposures leading to steady-state or near-steady-state responses within the 6-min exposure period. Examples of such responses are shown in Fig. 5.

Calibration curves for vapor on four MPN a selected coatings are shown in Fig. 6. This figure includes calibration curves for two polymers selected for comparison. Polymers are widely used in chemical sensing and their sorptive properties have been examined in detail. The selected polymers—poly(isobutylene), PIB, and poly(epichlorohydrin), PECH—have been used in a variety of vapor-sensing studies, including sorption measurements on 10-MHz TSM devices.^[27] They represent simple prototypical sorptive polymers whose structures and sorptive properties have been described in detail elsewhere.^[26–29] The data for the polymers were normalized to 10-kHz films to match the film amounts applied to the MPN-coated sensors.

The calibration curves show two main points. First, the curves are linear or nearly linear in the vapor concentration range considered. We found that TSM sensors with dodecanethiol, chlorobenzenethiol, and trifluoromethyl-

benzenethiol yielded calibration curves with small intercepts (typically 1 Hz or less) and high correlation coefficients (typically 0.998 or higher for R^2 as evidence for linearity).^[15] For gravimetric sensors at a fixed temperature, linear calibration curves indicate linear sorption isotherms over the test concentration ranges.

Second, from the results in Fig. 6 and others we have published,^[15] it is apparent that the sorption of the test vapors by the MPN films is typically less than the sorption of vapors by the selected polymers. The most sorptive nanoparticle films for any test were less sorptive on a per-mass basis than the best sorptive polymer considered within the concentration range studies, the polymer being better by a factor of 2–2.5. This analysis compares the sorptive properties on a mass of vapor sorbed per mass of sorbent material.

Nevertheless, vapor sorption is often quantified based on the partition coefficient defined in Eq. 3, where the concentration of vapor in the sorbent phase is in grams per liter; thus quantification of sorption is measured on a mass-per-volume basis. The partition coefficient is related to gravimetric sensor responses according to Eq. 5.^[30]

$$\Delta f_v = \Delta f_s C_v K / \rho \quad (5)$$

The frequency shifts indicated by Δf_s and Δf_v refer to the shift obtained on coating the bare sensor with the sorptive coating, and the shift observed when the sorptive coating absorbs a vapor. This relationship assumes that the observed frequency shifts are caused by the bulk absorption

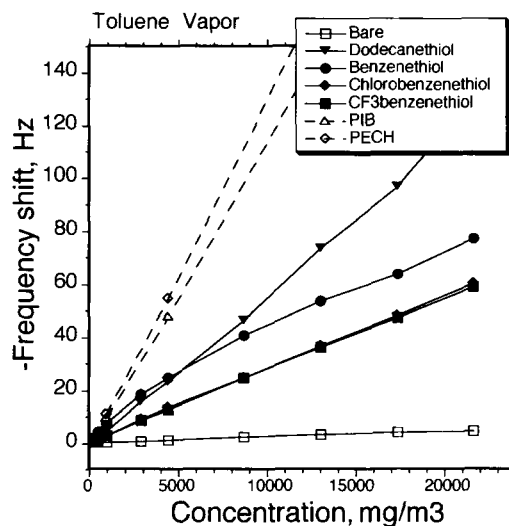


Fig. 6 Calibration curves for toluene on a series of monolayer-protected gold nanoparticles with data for two polymers, PIB and PECH, included for comparison.

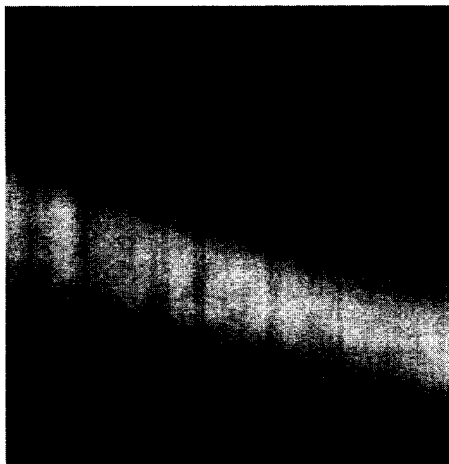


Fig. 7 Scanning electron microscope image of a cross section of the open tubular GC column coated with the dodecanethiol-protected gold nanoparticles, shown as the light band between the silica column material and the column lumen. The band is 60 nm thick.

of vapor in the film. The ρ parameter is the sorptive material density. Densities of the applied films are required to convert observed frequency shifts to partition coefficients for vapor sorption. Based on the mass fractions of gold and thiol in the film materials as determined by TGA, and the bulk densities of the condensed-phase gold and thiol materials, estimates of the required densities were determined for the calculation of partition coefficients according to Eq. 5.^[15] On a per-volume basis, the sorption of organic vapors by these MPN materials is of the same order of magnitude as the polymers at this concentration. Thus it appears unlikely that the nanoparticle-based materials considered are more sorptive than the conventional polymers. If the actual densities of the film materials were lower than the estimated values used in the calculations (i.e., because of inefficient packing and/or large free volumes), then the actual partition coefficients would be proportionately lower, and it would still be true that these nanoparticle-based materials are not more sorptive than the polymers used for comparison.

The sorptive properties of these nanoparticle films prepared by monothiols can also be compared with networked nanoparticle films containing bridging dithiols. Quantitative data on vapor uptake of the latter films as measured on TSM devices by Han et al.^[31] were compared with our quantitative data on vapor uptake by the monothiol-based MPNs.^[15] After converting the reported data to similar units, it appears that the networked films sorb organic vapors with gravimetric sensitivity of the same order of magnitude as the monothiol-based materi-

als, with the sorption by the particular alkanethiol-based film in our study being somewhat greater than the particular alkanedithiol-based film in their study.^[32]

NANOPARTICLE FILMS AS GAS CHROMATOGRAPHIC PHASES

Our interest in the sorptive behavior of these nanoparticle materials prompted us to investigate them as gas chromatographic phases. Dodecanethiol-protected gold nanoparticles were examined using an open tubular column configuration.^[33] The nanoparticles were deposited on the inner walls of a deactivated silica capillary (0.530 mm i.d.) by deposition from a dichloromethane solution passed as a plug through the length of the column. This process was repeated until a layer yielding a uniform brown color was obtained. Scanning electron microscopy was used to characterize the thickness and consistency of the nanoparticle film. A film of 60 nm thickness in a 2-m column was used for subsequent chromatographic experiments. A cross-sectional image of the MPN film in the capillary is shown in Fig. 7.

Several test mixtures were separated on the open tubular GC column using both isothermal and temperature-ramped protocols. Rapid separations with good peak shapes and resolution were obtained.^[33] Figs. 8 and 9 illustrate the separation of an eight-component mixture

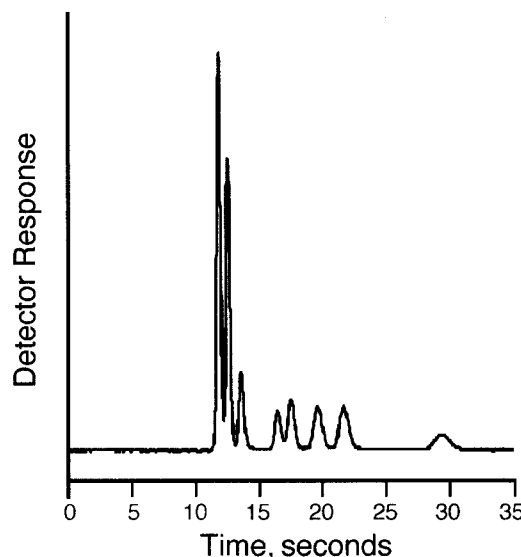


Fig. 8 Separation of an eight-component mixture on the nanoparticle-coated GC column under isothermal conditions at 50°C. The eight vapors were ethanol, benzene, 1-butanol, 3-heptanone, chlorobenzene, 3-octanone, anisole, and decane.

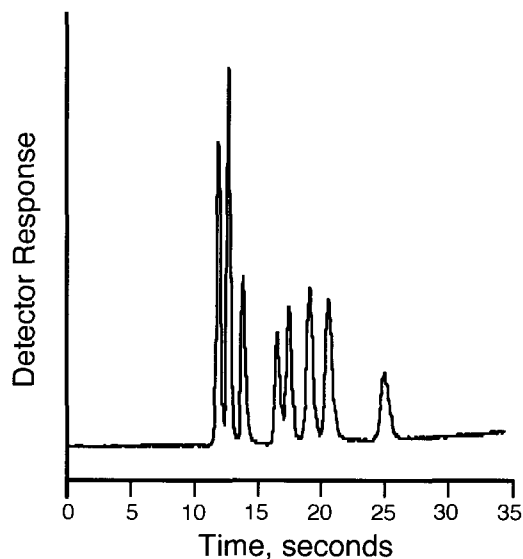


Fig. 9 Separation of the same eight-component mixture as in Fig. 8 under temperature-ramped conditions from 40°C to 80°C at 70°C/min.

under isothermal and temperature-ramped conditions. Determination of reduced plate height as function of linear flow velocity indicated an efficient open tubular system. The performance of the MPN-coated column was compared with a commercial polymer stationary phase AT-1 in the same column length and inside diameter, and comparable phase thickness (100 vs. 60 μm for the MPN phase). These two columns were found to have comparable separation efficiencies. These experiments demonstrate that MPN materials can be successfully coated as chromatographic phases for open tubular GC, yielding chromatographically efficient columns.^[33]

We have further demonstrated that MPNs can be coated in $100 \times 100 \mu\text{m}^2$ square-bore capillaries.^[34] Polymeric stationary phases present problems in the columns with noncircular channels because the material tends to be thicker in the corners than on the other sides. Using the MPN materials, this effect was greatly reduced and an efficient chromatographic system was obtained. The phase thickness on the column sidewalls was 15 nm. A seven-component mixture representing four compound classes was separated in 2 sec on a 1.3-m column. These results are shown in Fig. 10.

Columns with noncircular channels are of interest because microfabricated GC columns (i.e., microGC or GC-on-a-chip) typically have angular channels as a result of the etching and capping process. Thus the square bore capillary GC columns just described serve as a model for microGC angular channels, while focusing on the per-

formance of the stationary phase and not on the rest of a microGC system. Our result demonstrated that the MPN materials have advantageous coating properties for microGC systems.

NANOPARTICLE FILMS AS CONDUCTIVE SENSING LAYERS ON CHEMIRESTOR SENSORS

As noted in the background material, MPN films can be used as the selective layer on chemiresistor sensors, which measure changes in the electrical conductivity of the films as a function of changing vapor concentration. Initial investigations by a number of groups have demonstrated the potential of MPN-based films for chemical vapor sensing by this mechanism.

Wohltjen and Snow^[12] reported the first use of MPN-coated chemiresistors as vapor sensors, demonstrating large decreases in the conductance of an octanethiol-based MPN film in response to toluene and trichloroethene.^[35] Snow and Wohltjen have observed that MPN-coated chemiresistors can offer detention limits that are significantly better than those of polymer-coated SAW devices (A. W. Snow, Naval Research Laboratory, 2000, personal

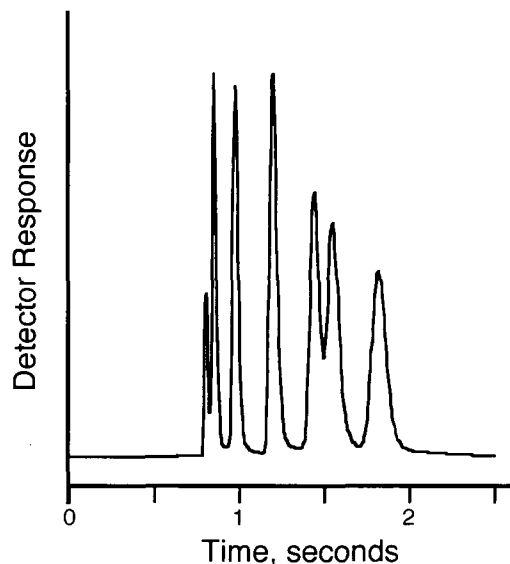


Fig. 10 High-speed separation of seven components using the dodecanethiol MPN stationary phase within the $100\text{-}\mu\text{m}^2$ square-bore capillary. The retention order is: methyl ethyl ketone, benzene, octane, chlorobenzene, anisole, 3-octanone, and decane. The separations were obtained by using a 1.3-m column at 75°C operated under constant pressure conditions at 25 psi ($\sim 200 \text{ cm/sec}$ hydrogen gas).

communication).^a Subsequently, Evans et al.^[16] demonstrated that chemiresistor devices with four different ar-enthioi-based MPN films yielded different patterns for each of the eight vapors, although it was observed that reproducibility was a concern for some vapors on some sensors. Additional work by this group attributed MPN-coated chemiresistor responses to film permittivity changes at low vapor concentrations and to film swelling that increases core-core distance at high vapor concentrations.^[38]

Han et al.^[31] investigated novel networked nanoparticle film materials containing bridging dithiols between gold cores as layers on both chemiresistor and TSM devices. Vapor uptake as measured on the TSM device was correlated with film resistance changes as measured by the chemiresistor. Zamborini et al.^[39] also described both chemiresistor and TSM sensor measurements on networked nanoparticle materials; these authors concluded that film swelling as a result of vapor uptake leads to reduced electron-hopping rates. Gold nanoparticle/dendrimer composites have also been used as layers on chemiresistor vapor sensors.^[40-43] Joseph et al.^[44] have also examined gold nanoparticle alkanedithiol films prepared by a layer-by-layer assembly process directly on sensor surfaces. These films showed linear current-voltage characteristics and reversible responses to toluene and tetrachloroethene. Responses were consistent with a film swelling mechanism. In experiments with alkylene chains of varying lengths, it was found that the normalized vapor responses increased exponentially with increasing alkanedithiol length.

Cai and Zellers^[45] described the vapor-sensing performance of MPN-coated chemiresistors with either octanethiol-protected gold nanoparticle or 2-phenylethanethiol-protected gold nanoparticles. Rapid and reversible responses to most of the 11 test vapors were observed in direct exposures. Detection limits were reported to be 10- to 90-fold (with 20 as a typical value) better than those of selected polymer-coated SAW sensors. The sensors were also used as detectors for GC.

CONCLUSION

Vapor sorption by a sensing film on a chemical micro-sensor is a fundamental influence on sensor response and performance. Our studies have examined the sorption of vapors by gold nanoparticle materials protected with or-

ganic thiols, where the organic thiol represents the largest volume fraction of the material and its structure influences vapor sorption and selectivity. The nanoparticle-based films considered here were less sorptive than the selected polymers on a per-mass basis. Partition coefficients, which measure the mass of vapor sorbed per volume of the sorptive phase, were estimated for these MPN materials and were found to be comparable with, or less than, those of the polymer layers. Strictly from the standpoint of sorption, these materials do not appear to have advantages over polymers as sensing layers.

Nevertheless, others have reported that chemiresistor sensors coated with MPN films can offer better detection limits than polymer-coated vapor sensors,^[36,37,45] such as those based on SAW devices or those based on chemiresistors coated with carbon black-containing polymers. If this is the case, and the MPN layers and polymer layers absorb similar amounts of vapor, then it follows that the lower detection limits for MPN-coated chemiresistors must be because of more signal-to-noise ratio per sorbed vapor molecule. Apparently, the electron transfer from one nanoparticle to another is very sensitive to the sorption of vapors into the spaces between the conducting gold nanoparticle cores. These spaces are of molecular dimensions. The implications are that nanostructure materials can be used in the design of new chemical sensors with superior properties.

As sorptive materials, MPN films may also be used in other microanalytical applications. We have demonstrated that these materials can be advantageously used as sorptive stationary phases in GC. In addition, they appear to offer advantages over conventional polymers with respect to angular chromatographic channels; thus they may be useful in microfabricated channels and structures.

ACKNOWLEDGMENTS

The authors thank Dr. Scott Elder for initial syntheses of some of the nanoparticle materials and Alice Dohnalkova for TEM images. J. W. G. thanks Dr. Arthur Snow for informative and motivating discussion of the work on nanoparticle-coated sensors at the Naval Research Laboratory in March 2000 as well as helpful discussions subsequently, and Dr. Laura Hughes for a review of the manuscript. This work was funded by the U.S. Department of Energy via the Laboratory Directed Research and Development funds administered by the Pacific Northwest National Laboratory. A portion of the research was performed at the W. R. Wiley Environmental Molecular Sciences Laboratory, a national scientific user facility sponsored by the U.S. Department of Energy's Office of Biological and Environmental Research and located at the

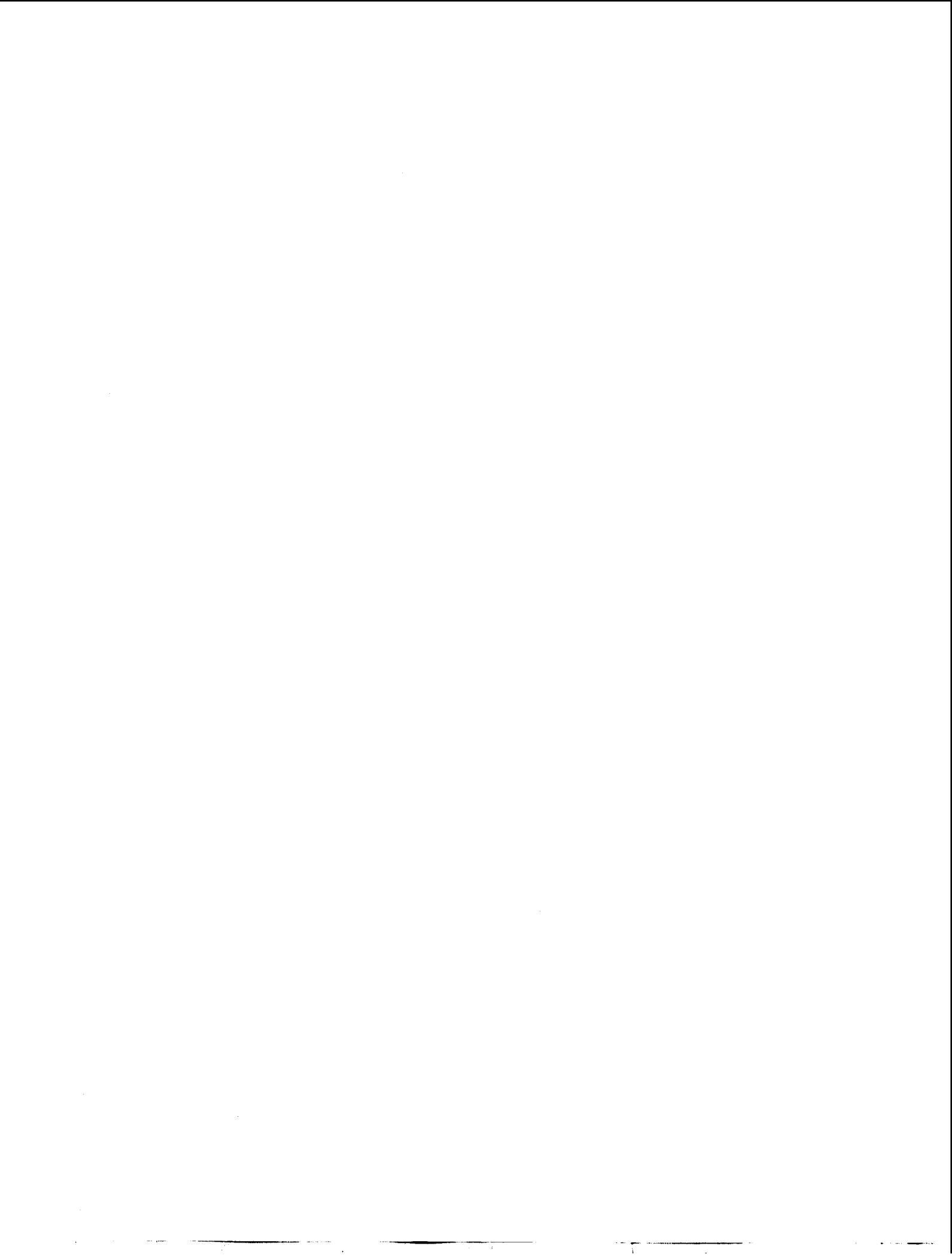
^aComparisons between chemiresistor vapor sensors coated with monolayer-protected nanoparticles and surface acoustic wave vapor sensors coated with polymers have been presented by Refs. [36] and [37].

Pacific Northwest National Laboratory. The Pacific Northwest National Laboratory is operated for the U.S. DOE by the Battelle Memorial Institute.

REFERENCES

1. Brust, M.; Fink, J.; Bethell, D.; Schiffrin, D.J.; Keily, C. Synthesis and reactions of functionalized gold nanoparticles. *J. Chem. Soc., Chem. Commun.* **1995**, 1655–1656.
2. Brust, M.; Walker, M.; Bethell, D.; Schiffrin, D.J.; Whyman, R. Synthesis of thiol-derivatized fold nanoparticles in a two-phase liquid-liquid system. *J. Chem. Soc., Chem. Commun.* **1994**, 801–802.
3. Templeton, A.C.; Wuelfing, W.P.; Murray, R.W. Monolayer-protected cluster molecules. *Acc. Chem. Res.* **2000**, *33*, 27–36.
4. Whetten, R.L.; Shafiqullin, M.N.; Khoury, J.T.; Shcaaff, T.G.; Vezmar, I.; Alvarez, M.M.; Wilkinson, A. Crystal structures of molecular gold nanocrystal arrays. *Acc. Chem. Res.* **1999**, *32*, 397–406.
5. Grate, J.W. Acoustic wave microsensor arrays for vapor sensing. *Chem. Rev.* **2000**, *100*, 2627–2647.
6. Grate, J.W.; Frye, G.C. Acoustic wave sensors. *Sens. Update* **1996**, *2*, 37–83.
7. Grate, J.W.; Martin, S.J.; White, R.M. Acoustic wave microsensors. *Anal. Chem.* **1993**, *65*, 940A.
8. Grate, J.W.; Martin, S.J.; White, R.M. Acoustic wave microsensors, Part II. *Anal. Chem.* **1993**, *65*, 987A–996A.
9. Barger, W.R.; Klusty, M.A.; Snow, A.W.; Grate, J.W.; Ballantine, D.S.; Wohltjen, H. Surface acoustic wave sensors, chemiresistor sensors and hybrids using both techniques simultaneously to detect vapors. *Proc. Electrochem. Soc.* **1987**, *87-15*, 198–217.
10. Grate, J.W.; Rose-Pehrsson, S.; Barger, W.R. Langmuir-Blodgett films of a nickel dithiolene complex on chemical microsensors for the detection of hydrazine. *Langmuir* **1988**, *4*, 1293–1301.
11. Grate, J.W.; Klusty, M.; Barger, W.R.; Snow, A.W. Role of selective sorption in chemiresistor sensors for organophosphorus detection. *Anal. Chem.* **1990**, *62*, 1927–1934.
12. Wohltjen, H.; Snow, A.W. Colloidal metal-insulator-metal ensemble chemiresistor sensor. *Anal. Chem.* **1998**, *70*, 2856–2859.
13. Hostetler, M.J.; Wingate, J.E.; Zhong, C.-J.; Harris, J.E.; Vachet, R.W.; Clark, M.R.; Londono, J.D.; Green, S.J.; Stokes, J.J.; Wignall, G.D.; Glish, G.L.; Porter, M.D.; Evans, N.D.; Murray, R.W. Alkanethiolate gold cluster molecules with core diameters from 1.4 to 5.2 nanometers: Core and monolayer properties as a function of core size. *Langmuir* **1998**, *14*, 17–30.
14. Chen, S.; Murray, R.W. Arenethiolate monolayer-protected gold clusters. *Langmuir* **1999**, *15*, 682–689.
15. Grate, J.W.; Nelson, D.A.; Skaggs, R. Sorptive behavior of monolayer-protected gold nanoparticle films: Implications for chemical vapor sensing. *Anal. Chem.* **2003**, *75*, 1868–1879.
16. Evans, S.D.; Johnson, S.R.; Cheng, Y.L.; Shen, T. Vapour sensing using hybrid organic-inorganic nanostructured materials. *J. Mater. Chem.* **2000**, *10*, 183–188.
17. Stoeva, S.; Klabunde, K.J.; Sorensen, C.M.; Dragieva, I. Gram-scale synthesis of monodisperse gold colloids by the solvated metal atom dispersion method and digestive ripening and their organization into two- and three-dimensional structures. *J. Am. Chem. Soc.* **2002**, *124*, 2305–2311.
18. Prasad, B.L.V.; Stoeva, S.I.; Sorensen, C.M.; Klabunde, K.J. Digestive-ripening agents for gold nanoparticles: Alternatives to thiols. *Chem. Mater.* **2003**, *15*, 935–942.
19. Maye, M.M.; Zheng, W.X.; Leibowitz, F.L.; Ly, N.K.; Eichelberger, H.H.; Zhong, C.J. An investigation of temperature-manipulated size and shape evolution of preformed core-shell nanoparticles. *Mater. Res. Soc. Symp. Proc.* **2000**, *580*, 201–206.
20. Prasad, B.L.V.; Stoeva, S.I.; Sorensen, C.M.; Klabunde, K.J. Digestive ripening of thiolated gold nanoparticles: The effect of alkyl chain length. *Langmuir* **2002**, *18*, 7515–7520.
21. Lin, X.M.; Sorensen, C.M.; Klabunde, K.J. Digestive ripening, nanophase segregation and superlattice formation in gold nanocrystal colloids. *J. Nanopart. Res.* **2000**, *2*, 157–164.
22. Zhong, C.J.; Zhang, W.X.; Leibowitz, F.L.; Eichelberger, H.H. Size and shape evolution of core-shell nanocrystals. *Chem. Commun. (Cambridge)* **1999**, 1211–1212.
23. Snow, A.W.; Wohltjen, H. Size-induced metal-to-semiconductor transition in a stabilized gold cluster ensemble. *Chem. Mater.* **1998**, *10*, 947–949.
24. Shaaff, T.G.; Shafiqullin, M.N.; Khoury, J.T.; Vezmar, I.; Whetten, R.L. Properties of a ubiquitous 29 kDa Au:SR cluster compound. *J. Phys. Chem., B* **2001**, *105*, 8785–8796.
25. Grate, J.W.; Abraham, M.H. Solubility interactions and the design of chemically selective sorbent coatings for chemical sensors and arrays. *Sens. Actuators, B* **1991**, *3*, 85–111.

26. Grate, J.W.; Abraham, M.H.; McGill, R.A. Sorbent polymer materials for chemical sensors and arrays. *Handb. Biosens. Electron. Noses* **1997**, 593–612.
27. Grate, J.W.; Kaganove, S.N.; Bhethanabotla, V.R. Examination of mass and modulus contributions to thickness shear mode and surface acoustic wave vapor sensor responses using partition coefficients. *Faraday Discuss.* **1997**, *107*, 259–283.
28. Abraham, M.H.; Andonian-Haftvan, J.; Du, C.M.; Diart, V.; Whiting, G.S.; Grate, J.W.; McGill, R.A. Hydrogen bonding: Part 29. Characterization of 14 sorbent coatings for chemical microsensors using a new solvation equation. *J. Chem. Soc., Perkin Trans. 2* **1995**, 369–378.
29. Grate, J.W.; Kaganove, S.N.; Bhethanabotla, V.R. Comparison of polymer/gas partition coefficients calculated from responses of thickness shear mode and surface acoustic wave vapor sensors. *Anal. Chem.* **1998**, *70*, 199–203.
30. Grate, J.W.; Snow, A.; Ballantine, D.S., Jr.; Wohltjen, H.; Abraham, M.H.; McGill, R.A.; Sasson, P. Determination of partition coefficients from surface acoustic wave vapor sensor responses and correlation with gas-liquid chromatographic partition coefficients. *Anal. Chem.* **1988**, *60*, 869–875.
31. Han, L.; Daniel, D.R.; Maye, M.M.; Zhong, C.-J. Core-shell nanostructured nanoparticle films as chemically sensitive interfaces. *Anal. Chem.* **2001**, *73*, 4441–4449.
32. Grate, J.W. Sorptive behavior of monolayer-protected gold nanoparticle films containing alkanethiols and alkanedithiols. *Anal. Chem.* **2003**, *75*, 6759–6759.
33. Gross, G.M.; Nelson, D.A.; Grate, J.W.; Synovec, R.E. Monolayer-protected gold nanoparticles as a stationary phase for open tubular gas chromatography. *Anal. Chem.* **2003**, *75*, 4558–4564.
34. Gross, G.M.; Grate, J.W.; Synovec, R.E. Monolayer-protected gold nanoparticles as an efficient stationary phase for open tubular gas chromatography using a square capillary: A model for chip-based GC in square cornered microfabricated channels. **2003**. Submitted for publication.
35. Materials, Method and Apparatus for Detecting and Monitoring Chemical Species, provisional filing date of November 24, 1997.
36. Snow; et al. Defense Applications of Nanomaterials. ACS Meeting, San Diego, April 2001.
37. Snow; et al. AVS Topical Conference on Understanding and Operating in Threat Environments, Monterey, CA, April 30–May 2, 2002.
38. Zhang, H.L.; Evans, S.D.; Henderson, J.R.; Miles, R.E.; Shen, T.H. Vapour sensing using surface functionalized gold nanoparticles. *Nanotechnology* **2002**, *13*, 439–444.
39. Zamborini, F.P.; Leopold, M.C.; Hicks, J.F.; Kulesza, P.J.; Malik, M.A.; Murray, R.W. Electron hopping conductivity and vapor sensing properties of flexible network polymer films of metal nanoparticles. *J. Am. Chem. Soc.* **2002**, *124*, 8958–8964.
40. Krasteva, N.; Guse, B.; Besnard, I.; Yasuda, A.; Vossmeier, T. Gold nanoparticle/PPI-dendrimer based chemiresistors. Vapor-sensing properties as a function of the dendrimer size. *Sens. Actuators, B, Chem.* **2003**, *92*, 137–143.
41. Krasteva, N.; Krustev, R.; Yasuda, A.; Vossmeier, T. Vapor sorption in self-assembled gold nanoparticle/dendrimer films studied by specular neutron reflectometry. *Langmuir* **2003**, *19*, 7754–7760.
42. Krasteva, N.; Besnard, I.; Guse, B.; Bauer, R.E.; Muellen, K.; Yasuda, A.; Vossmeier, T. Self-assembled gold nanoparticle/dendrimer composite films for vapor sensing applications. *Nano Lett.* **2002**, *2*, 551–555.
43. Vossmeier, T.; Guse, B.; Besnard, I.; Bauer, R.E.; Mullen, K.; Yasuda, A. Gold nanoparticle/polyphenylene dendrimer composite films. Preparation and vapor-sensing properties. *Adv. Mater.* **2002**, *14*, 238–242.
44. Joseph, Y.; Besnard, I.; Rosenberger, M.; Guse, B.; Nothofer, H.-G.; Wessels, J.M.; Wild, U.; Knop-Gericke, A.; Su, D.; Schloegl, R.; Yasuda, A.; Vossmeier, T. Self-assembled gold nanoparticle/alkanedithiol films: Preparation, electron microscopy, XPS-analysis, charge transport, and vapor-sensing properties. *J. Phys. Chem., B* **2003**, *107*, 7406–7413.
45. Cai, Q.-Y.; Zellers, E.T. Dual-chemiresistor GC detector employing monolayer-protected metal nanocluster interfaces. *Anal. Chem.* **2002**, *74*, 3533–3539.



Metal Nanoparticles Used as Catalysts

Naoki Toshima

Tokyo University of Science, Yamaguchi, Japan

INTRODUCTION

“Metal nanoparticles” receive much attention because of their uniform size and sharp size distribution in nanometers, and because they are easily prepared as a result of recent developments in nanoscience and nanotechnology. In addition, catalysts based on such metal nanoparticles are highly active and selective. They also exhibit a long lifetime for several kinds of chemical reactions. In this article, a background on the use of metal nanoparticles as catalyst is first briefly discussed. Then, preparation, characterization, structures, and catalyses of metal nanoparticles, especially of bimetallic nanoparticles, are described. The prospects on the use of metal nanoparticles as catalysts^[1–8] are summarized in the last section.

METAL NANOPARTICLES AS CATALYSTS

There is a long history since metal has been known to work as a catalyst for various kinds of reactions. The catalytic sites of metals are located on its surface. This means that metal nanoparticles of 1–10-nm size (thus, having a large surface-to-volume ratio) are expected to work as effective catalysts. The surface-to-volume ratio increases with decreasing particle size. In other words, the ratio of surface atoms with respect to all atoms in a particle increases with decreasing particle size. Fig. 1 shows the dependence of the ratio of surface atoms of Au nanoparticles on the radius of nanoparticles, assuming that Au nanoparticles have the same fcc (face-centered cubic) crystalline structure as that of the bulk gold. Fig. 1 shows that the smaller the size, the larger is the ratio. Another characteristic property of the nanoparticles is the quantum size effect. Although bulk metal has a band structure, the electronic energy levels of metal nanoparticles with size of a few nanometers are rather separated as shown in Fig. 2.^[9] This may have an advantage as a catalyst.

When metal nanoparticles are used as catalysts, it is necessary for the metal nanoparticles to be stabilized under the catalytic reaction conditions. Otherwise, metal nanoparticles can very easily coagulate in solution to form aggregates, which are less effective as catalysts than the original ones. There are two ways to stabilize metal nanoparticles: One is to immobilize the metal

nanoparticles on inorganic supports, resulting in heterogeneous catalysts. The other method is to surround metal nanoparticles with stabilizers, resulting in homogeneous catalysts, or more precisely, homogenized heterogeneous catalysts.

In practical industries, heterogeneous catalysts are often used because they are easy to handle. They can be used in tubular reaction vessels for gaseous reactions in continuous reaction processes, and thus are effective for mass production of conventional chemicals. However, metal nanoparticles often cannot keep their shapes and properties when immobilized on inorganic supports. For example, interactions between metal particles and inorganic supports are often very strong in the supported catalysts. This strong interaction can sometimes increase the stability and activity of catalysts, but in some cases can make the catalytic properties worse.

In contrast, metal nanoparticles in solution, especially those stabilized by polymers, are less affected by the stabilizers than those immobilized on inorganic supports because the interaction between metal nanoparticles and capping polymers is usually very weak in comparison with that between metal nanoparticles and inorganic supports. The structure models of a conventional heterogeneous metal catalyst and a typical metal nanoparticle catalyst are shown in Fig. 3.

In metal nanoparticles stabilized by strong coordination with organic ligand molecules, the story is quite different from those stabilized by polymers. Because the strongly coordinating organic molecules can occupy the surface of metal nanoparticles, the reaction substrates cannot attack the surface of metal nanoparticles. Thus metal nanoparticles strongly coordinated by organic ligands cannot work as effective catalysts.

The advantages of using metal nanoparticles as catalysts are the following:^[1,4]

1. The size and shape of metal nanoparticles are easily controlled by the preparation conditions.
2. Metal nanoparticles dispersed in solution can be used as catalysts in solution like homogeneous catalysts. Thus the temperature applied to the catalyst is below the boiling point of the solvent.
3. Metal nanoparticles dispersing in solution are transparent to light. Thus they can be used as photocatalysts.

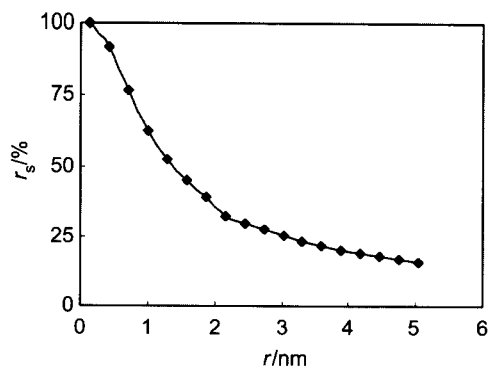


Fig. 1 Dependence of the ratio of surface atoms (r_s) on the radius (r) of gold nanoparticles. (View this art in color at www.dekker.com.)

- Metal nanoparticles capped by organic polymers can be functionalized by modifying the organic polymers.
- It is possible to prepare bimetallic and trimetallic nanoparticles with various compositions and structures. The catalytic activity and selectivity of these metal nanoparticles can be controlled by varying the composition and structure.
- Metal nanoparticles immobilized on solid supports can be used as catalysts even for the reactions in a gaseous phase.
- Metal nanoparticles dispersed in solution or immobilized on solid supports are usually more active and selective as catalysts under mild reaction conditions than the conventional industrial catalysts.

The metal nanoparticles dispersed in solution and used as catalysts can be characterized not only by their own structure but also by the structure of the organic layers surrounding them. Both structures provide various functions to the metal nanoparticles used as catalysts.

The structure of a metal nanoparticle capped by an organic layer is shown in Fig. 4. The diameter d of core

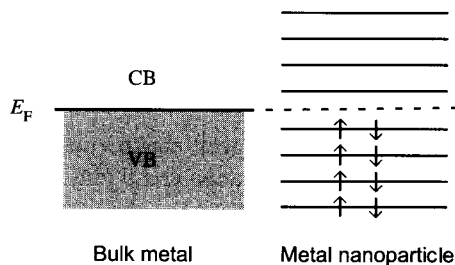


Fig. 2 Formation of separated energy-levels of metal nanoparticles by a quantum size effect.

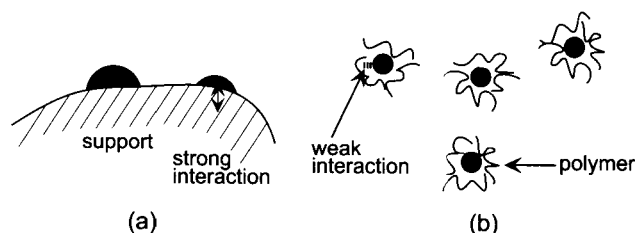


Fig. 3 Schematic illustration of the structures of (a) conventional metal catalyst and (b) metal nanoparticles capped by polymers.

metal nanoparticles can be easily measured by transmission electron microscopy (TEM). The thickness δ of the organic layer or the total diameter D including the organic layer can be measured by various methods depending on the kind of organic layer. In solution, hydrodynamic radius provides $D/2$. When the hydrodynamic radius is large enough, it can be measured by a light scattering method. However, when the hydrodynamic radius is small, it can still be measured by a Taylor dispersion method if the size is homogeneous or uniform enough.^[10] When the organic layer is composed of soluble polymers, the direct measurement of D is not so easy. The thickness δ was proposed to be measured by the amount of polymers adsorbed on the surface of metal nanoparticles.^[11] Because it is not easy to measure D in solution, measurement using scanning tunnel microscopy (STM) was performed in the dry state.^[12]

In solution, the metal nanoparticles interact with each other by weak interaction forces; they form "superstructures," the size of which can be measured by small-angle X-ray scattering (SAXS).^[13]

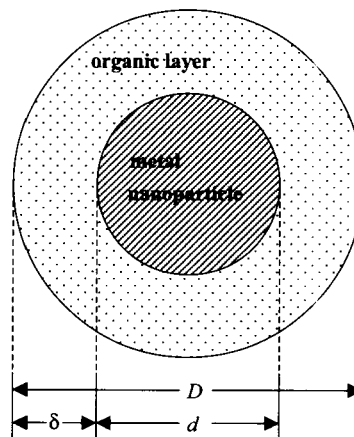


Fig. 4 Illustration of the metal nanoparticle capped by an organic layer.

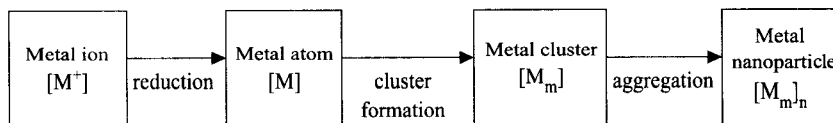


Fig. 5 Formation of metal nanoparticles by a chemical method.

PREPARATION AND CHARACTERIZATION OF METAL NANOPARTICLES

Metal nanoparticles are defined as metal particles of nanometer size, which have a rather uniform size in the range of 1–10 nm. Metal nanoparticles with rather strict structures are called metal nanoclusters. Metal nanoparticles immobilized on solid supports or dispersed in solution can be used as catalysts.

Preparation of Metal Nanoparticles Used as Catalysts

Metal nanoparticles with a rather uniform size can be prepared by both physical and chemical methods. In the physical method, sometimes called the top-down-type method, metal nanoparticles are prepared by decomposition of bulk metal with mechanical force, vaporization, laser abrasion, and so on, which can provide higher energy to bulk metal than the bond energy of metal. In the chemical method, sometimes called a bottom-up-type method, the preparation process starts from reduction of metal ions to metal atoms, which is followed by aggregation resulting in metal nanoparticles Fig. 5. Both physical and chemical methods have their own advantages. However, chemical methods are now considered to be better than physical methods from the viewpoints of reproducibility, homogeneity (e.g., uniformity in size), and mass production.

The production of metal nanoparticles by chemical methods requires some techniques by which coagulation is prevented. For example, electrostatic and steric repulsions among metal nanoparticles are used for this purpose. To prevent coagulation and to keep the dispersity of metal nanoparticles by electrostatic repulsion, electrical charges are provided. Adsorption of ions on the surface of metal nanoparticles is a simple way to acquire such charges Fig. 6a. The typical conventional colloidal dispersions of metal nanoparticles are usually stabilized by this method.

The most satisfying method for stabilization of metal nanoparticles by steric repulsion is the dispersion of metal nanoparticles in solid such as glass. However, in this case, the metal nanoparticles cannot work as catalysts because the substrate molecules cannot attack the surface of metal nanoparticles. Thus adsorption of metal nanoparticles on

the surface of inorganic supports or immobilization in porous solids is often used for stabilization of metal nanoparticles by steric repulsion on solids Fig. 6b&c.

For the stabilization of metal nanoparticles in solution by steric repulsion, attachment of organic molecules or organic macromolecules on the surface of metal nanoparticles is easily considered to be a favorite method. An organic molecule with S and/or N atom(s), for example, is used as a ligand, which strongly bonds to metal nanoparticles Fig. 6d. In the case of organic macromolecules, the molecule is strongly attached to the metal nanoparticle because the macromolecule interacts with the surface of a

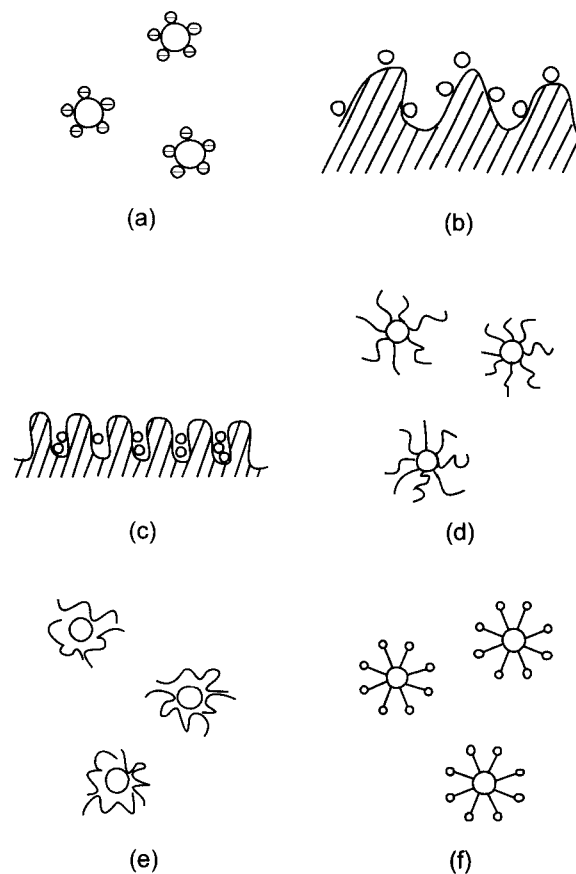


Fig. 6 Various metal nanoparticles stabilized by (a) electric charge, (b) inorganic supports, (c) porous solids, (d) organic molecules, (e) soluble macromolecules, and (f) surfactants.

metal nanoparticle at many sites although each interaction may be weak Fig. 6e. Organic molecules with low molecular weight can occasionally act as if they were a macromolecule when the interactions among the organic molecules are strong enough. In micelles and reverse micelles, surfactant molecules aggregate and protect the metal nanoparticles from coagulation Fig. 6f.

One of the simplest and most reproducible methods for preparation of metal nanoparticles is alcohol reduction of precious metal ions in alcohol-water in the presence of water-soluble polymers such as poly(*N*-vinyl-2-pyrrolidone) (PVP).^[14] This process is schematically shown in Fig. 7. Thus the precious metal ions form complexes with polymers at first. The metal ions can be reduced by alcohol to produce polymer-metal atom complexes accompanying aldehyde formation from alcohol.

Other chemical reductants, such as hydrazine, molecular hydrogen, glycol, sodium borohydride, etc., can be used instead of alcohol. Energy, such as photoenergy, X-ray, γ -ray, electron beam, microwave, ultrasonic wave, electrolysis, etc., can also be used in solution in the presence of stabilizers to break the bond or reduce the metal ions to 0-valent metal atoms resulting in metal nanoparticles.

Other stabilizers such as organic ligands can be used instead of protective polymers. In general, the presence of strong ligands requires a strong reductant if the reduction is carried out in the presence of stabilizers. Otherwise, stabilizers must be immediately added after the reduction and coagulation of metal atoms to form metal nanoparticles and before the aggregation of metal nanoparticles to form the precipitates.

Metal nanoparticles stabilized by weakly coordinating polymers are considered as the best metal nanoparticle catalyst because substrate molecules can easily attack the surface of metal nanoparticles and the reaction smoothly

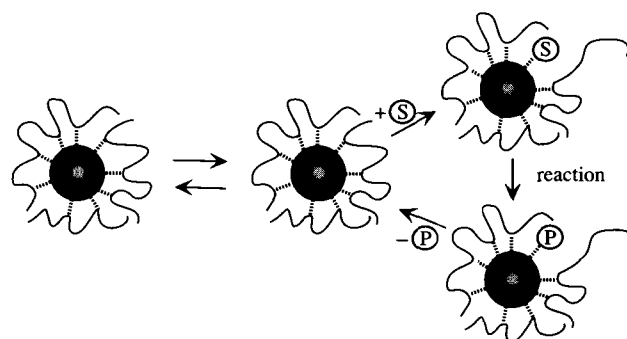


Fig. 8 Illustration of the catalytic reaction process of a metal nanoparticle catalyst stabilized by weakly coordinating polymers. \odot : reaction substrate; \ominus : reaction product. (From Ref. [7].)

occurs as shown in Fig. 8. Because the polymer molecule weakly coordinates with the metal nanoparticle, the substrate molecules can replace the polymer on the surface of metal nanoparticle. When the reaction occurs on the surface and the substrate changes to a product, then the product can easily be removed from the surface because it cannot strongly interact with the metal surface. Upon removal of the product, the parts of the polymer that were left on the metal surface can now interact with the metal surface again and cover the metal nanoparticle. This kind of reversible capping of the polymer on the metal surface cannot occur in organic ligands with low molecular weight, although organic ligands or ionic species play an important role to control the shape of metal nanoparticles.

The metal nanoparticles immobilized on solid supports can be prepared by immobilization of the separately prepared metal nanoparticles on solid supports. Immobilization can be carried out by chemisorption or chemical bond formation between metal nanoparticles and solid supports. The immobilized metal nanoparticles thus prepared work

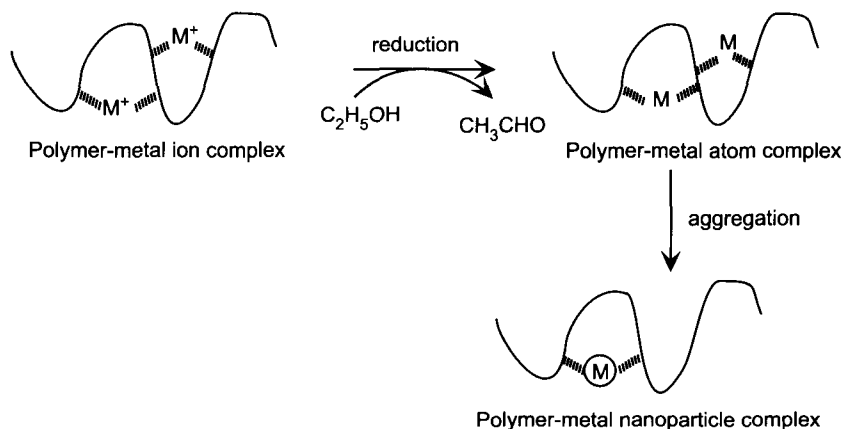


Fig. 7 Preparation of polymer-capped metal nanoparticle by alcohol reduction.

as industrial catalysts for reactions in solution as well as in gaseous phase.

Characterization of Metal Nanoparticles

Metal nanoparticles can be characterized by a combination of the following methods.^[2,3]

1. Transmission electron microscopy (TEM). This is the simplest and most reliable method to measure the size and shape of metal nanoparticles. The average size is usually calculated by counting the sizes of about 200 particles. High-resolution TEM (HR-TEM) can provide information not only on the particle size and shape but also on the crystalline structure of metal nanoparticles. When energy-dispersive X-ray microanalysis (EDX) is used in conjunction with TEM, elemental information of metal nanoparticles can be obtained. The localized elemental information is also obtained by electron energy-loss spectroscopy (EELS) in conjunction with energy-filtering TEM (EF-TEM).
2. Ultraviolet and visible absorption spectroscopy (UV/VIS). The color change is a very useful and convenient method to identify the chemical change from the solution of metal ions to the dispersion of metal nanoparticles. The colloidal dispersions of Au, Ag, and Cu (Group 11 elements) have a red to yellow color because of their plasmon absorption, the peak position of which varies depending on the particle size and the extent of coagulation. The plasmon absorption of other metal nanoparticles is located in a UV region and is often difficult to clearly detect.
3. Infrared spectroscopy (IR). The IR spectra can provide information on organic layers surrounding metal nanoparticles. For example, the coordination of poly(*N*-vinyl-2-pyrrolidone) (PVP) onto the surface of metal nanoparticles was revealed by a shift of C=O stretching vibration absorption in the IR spectra. The structure of organic layers and the interaction of organic layers with metal nanoparticles are effective in the catalysis of metal nanoparticles. Thus information given by the IR spectra is very important in some cases. The IR spectra can also be used to understand the surface structure of the metal nanoparticles. The IR spectra of carbon monoxide adsorbed on the surface metal are so often used to identify the element of the surface metal of bimetallic nanoparticles.
4. X-ray diffraction (XRD). The solid structure of metal nanoparticles can be investigated by XRD. For monometallic nanoparticles, XRD can give information on the phase changes depending on the particle size. X-ray diffraction can determine if the bimetallic system is composed of the mixtures of two kinds of monometallic nanoparticles or of single bimetallic nanoparticles in which two elements are included in one particle.
5. X-ray photoelectron spectroscopy (XPS). Photoelectron spectroscopy is used to obtain information on the state of metal, e.g., the oxidation state of metal on the surface. Metal on the surface is often oxidized by air. So the 0-valency of surface metal must be confirmed by using XPS or other methods. When polymers cover the metal nanoparticles, clear XPS spectra of the metal cannot be observed. In this case, the removal of covering polymers from the surface of metal nanoparticles is required. Etching of covering polymers could be useful for this purpose. The polymers can also be removed from the metal nanoparticles by washing the nanoparticles adsorbed on thiol-modified silica supports with a good solvent. The quantitative analysis of XPS spectra of bimetallic nanoparticles can suggest the elements present in the surface region of nanoparticles.
6. Surface enhanced Raman spectroscopy (SERS). The SERS spectra can be obtained in the case of nanoparticles containing Au, Ag, and/or Cu. Quantitative analysis of enhanced Raman spectra can provide information about the adsorbing structures of organic molecules on the metal nanoparticles. Not only monometallic nanoparticles but also bimetallic nanoparticles containing Au, Ag, or Cu can enhance Raman spectra.
7. Scanning probe microscopy (SPM). Scanning probe microscopy techniques such as scanning tunneling microscopy (STM) and atomic force microscopy (AFM) can give information on the total size of metal nanoparticles capped by organic layers and the coagulating structure (superstructure) of capped metal nanoparticles. The superstructure sometimes has an effect on catalysis of capped metal nanoparticles. Although SPM is usually used for observation of dry samples, the superstructure at dry state is often thought to be similar to that in solution.
8. Extended X-ray absorption fine structure (EXAFS). This is one of the most powerful characterization methods to determine the detailed structure of metal nanoparticles, especially bimetallic nanoparticles. Because big synchrotron radiation facilities are now available, the EXAFS technique becomes useful for structure analysis of nanoparticles of precious metals. EXAFS can provide the number of atoms surrounding the X-ray absorbing atom and their interatomic distances involved in the various coordination shells, as well as the electron density. However, to obtain exact information, the sample of

metal nanoparticles should be homogeneous, i.e., uniform in size and narrow in size distribution. Because the number of atoms surrounding the X-ray absorbing atom and even their interatomic distances can vary with the size of metal nanoparticles, we succeeded to give a core/shell structure model for Pd/Pt (4:1, mol/mol) bimetallic nanoparticles capped by poly(*N*-vinyl-2-pyrrolidone) (PVP), because they are very homogeneous (mono-dispersed) and stable.

9. Small-angle X-ray scattering (SAXS). Analysis of SAXS data can give information on rather long regularity, for example, size of superstructures.
10. Thermogravimetry (TG) and differential thermal analysis (DTA). Thermal analysis (TG and DTA) can give information not only on composition and structure of organic layers but also on the phase transition of metal.
11. Dynamic light scattering (DLS). This method gives the hydrodynamic radius; that is, the size of metal nanoparticles including organic layers.

STRUCTURE CONTROL OF BIMETALLIC NANOPARTICLES

Bimetallic nanoparticles, in which each particle contains two metal elements, are very important and interesting from the viewpoint of catalysis of metal nanoparticles because catalytic performance is very often affected by the addition of another element to the metal. In addition, the structure of bimetallic nanoparticles is strongly related with the catalytic performance.

Typical structures of bimetallic nanoparticles are illustrated in Fig. 9. These bimetallic nanoparticles have two kinds of metal-metal bonds, i.e., a homobond and a

heterobond. If the metal particles are composed of atoms A and B, the homobond is either an A-A bond or a B-B bond, while an A-B bond is a heterobond. If the binding energies of the homobonds are same with that of the heterobond, the random alloy or solid solution should be the thermodynamically most stable structure. If the homobonds are much stronger than the heterobond, no bimetallic particles may be produced but only the mixture of two kinds of monometallic particles will be favorably obtained. However, in practice, there are no such big differences between the two kinds of bonds in precious metals. When heterobonds are preferred over homobonds, a heterobondphilic structure may be obtained.^[15] The opposite case gives a homobondphilic structure. Hence a core/shell structure, a kind of homobondphilic structure, is obtained as a thermodynamically stable structure. In contrast, an inverted core/shell structure is thermodynamically metastable. Such metastable structures can be constructed by the concept of kinetic control. Thus the structure of bimetallic nanoparticles depends on the kind of a couple of elements used.

Bimetallic Nanoparticles Composed of a Couple of Platinum-Group Elements

Bimetallic nanoparticles of two kinds of platinum-group elements such as Pt, Pd, Au, etc. can be produced by coreduction of the corresponding metal ions in refluxing alcohol-water in the presence of water-soluble polymer. The coreduction usually gives colloidal dispersions of bimetallic nanoparticles with a core/shell structure, a kind of homobondphilic structure. For example, the solution of PdCl₂ and H₂PtCl₆ in refluxing ethanol-water in the presence of PVP gives colloidal dispersion of Pd/Pt bimetallic nanoparticles with a Pt-core/Pd-shell structures.^[16] From HAuCl₄ and PdCl₂, Au-core/Pd-shell structured bimetallic nanoparticles were obtained.^[17]

The easiness of core formation increases in the order of Rh < Pd < Pt < Au. Thus Rh is the most easily shell-forming element. The core/shell structure is constructed via the complexes shown in Fig. 9. Two factors control the core/shell structure: 1) redox potential of metal ions; and 2) coordination ability of metal atom to the polymer.^[18]

The PVP-protected Pd/Pt bimetallic nanoparticles work as a catalyst for partial hydrogenation of 1,3-cyclooctadiene to cyclooctene under mild conditions. The catalytic activity depends on the composition of Pd and Pt. The highest activity can be achieved by the Pd/Pt ratio (4:1, mol/mol) of bimetallic nanoparticles, in which 13 atoms of Pt form a core and 42 atoms of Pd surround the Pt core to form a shell.^[16]

The mechanism of formation of Pd/Pt bimetallic nanoparticles with a thermodynamically stable Pt-core/

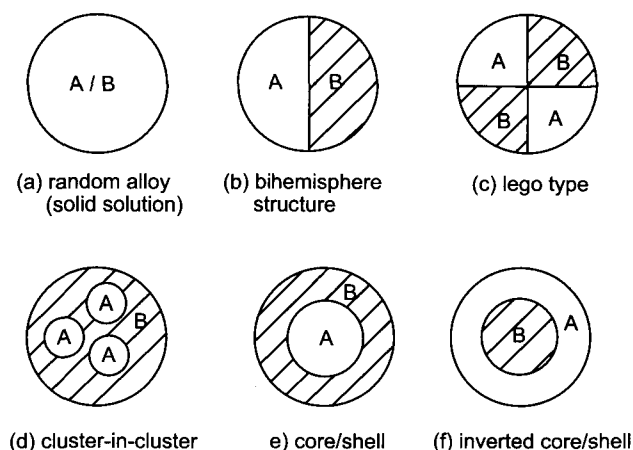


Fig. 9 Various structures of bimetallic nanoparticles.

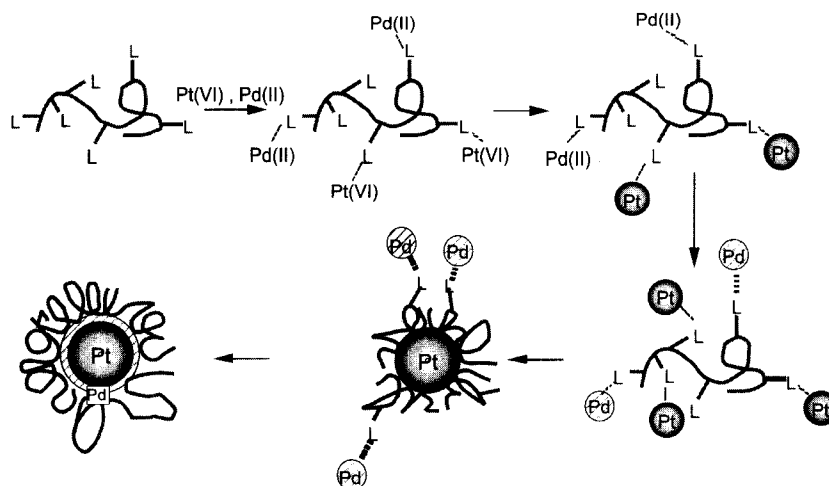


Fig. 10 Proposed formation mechanism of Pt-core/Pd-shell-structured bimetallic nanoparticles. (From Ref. [18].) (View this art in color at www.dekker.com.)

Pd-shell structure has been proposed as shown in Fig. 10. In this process, easily reduced Pt(IV) ions are first reduced to produce Pt atoms that form a Pt core. Less easily reduced Pd(II) ions later produce Pd atoms, which deposit on the Pt core to form a Pd shell.

An inverted core/shell structure can be prepared by the so-called sacrificial hydrogen reduction method.^[19] For example, Pd-core/Pt-shell bimetallic nanoparticles can successfully be prepared by this method. Successive reduction of Pd(II) and Pt(IV) ions cannot produce the inverted core/shell structured bimetallic nanoparticles, because addition of Pt(IV) ions to Pd(0) core nanoparticles results in redox reaction between them to form Pt(0) nanoparticles and Pd ions. Hence before the addition of Pt(IV) ions, the dispersion of Pd-core nanoparticles is treated with molecular hydrogen, forming hydride-covered Pd nanoparticles. Addition of Pt(IV) ions into the hydride-covered Pd nanoparticles produces Pt atoms, which immediately deposit on Pd cores to form Pd-core/Pt-shell, i.e., inverted core/shell structured bimetallic nanoparticles. This sacrificial hydrogen reduction method is useful for constructing other kinds of core/shell structured bimetallic nanoparticles.

Bimetallic Nanoparticles Composed of an Iron-Group Element and a Platinum-Group Element

Reduction of ions of an iron-group element (transition metal in the third period) is more difficult than those of a platinum-group element. Nevertheless, ions of an iron-group element can easily be reduced to the corresponding atoms in the coexistence of nanoparticles of a platinum-group element. For example, copper(I) and palladium(II)

can be reduced by ethylene glycol at ca. 200°C to produce the dispersions of Cu/Pd bimetallic nanoparticles,^[20] which are surprisingly stable even under air. The structure of Cu/Pd bimetallic nanoparticles is analyzed to be a random alloy (solid solution) on the basis of preliminary EXAFS measurements. The precise EXAFS analysis has recently concluded that the Cu/Pd bimetallic nanoparticles thus prepared have a heterobondphilic structure Fig. 11 rather than a random alloy structure.^[15] The Cu/Pd bimetallic nanoparticles work as catalysts both for hydration of nitriles and hydrogenation of olefins, suggesting that both Cu and Pd atoms are located on the surface of the nanoparticles, because the Cu and Pd are generally known as active catalysts for the former and the latter reaction, respectively. Bimetallic nanoparticles with other combinations such as Cu/Pt, Ni/Pd, Ni/Pt, Fe/Pd, and Fe/Pt can be prepared by the same method.^[21,22]

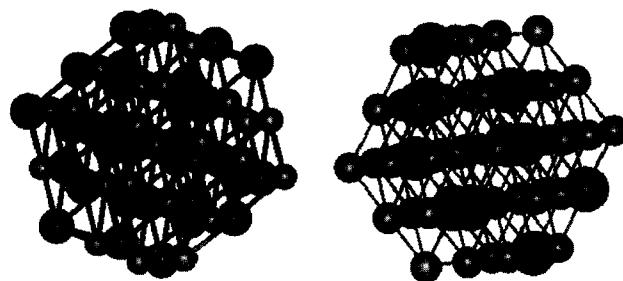


Fig. 11 Model structures for Cu/Pd 1:1 (left panel) and Cu/Pd 4:1 (right panel) bimetallic nanoparticles. Big dark balls correspond to Pd. (From Ref. [15].) (View this art in color at www.dekker.com.)

Formation of Bimetallic Nanoparticles by Mixing Two Kinds of Monometallic Nanoparticles; Self-Organization of Metal Nanoparticles

Self-organization is one of the most important concepts in supramolecular science. In the formation of bimetallic nanoparticles from two kinds of metal atoms, the bimetallic structures, such as a core/shell, random alloy, and heterobondphilic structure, are controlled by self-organization in practice.

Another type of self-organization has recently been observed to produce pseudo-core/shell structured bimetallic nanoparticles by mixing two kinds of monometallic nanoparticles in solution.^[23] Mixing of colloidal dispersions of PVP-protected Ag nanoparticles with those of PVP-protected Rh nanoparticles in solution at room temperature was found to result in a kind of "fusion" to produce colloidal dispersions of Ag/Rh bimetallic nanoparticles with a pseudo-core/shell structure in a few hours Fig. 12. Poly(*N*-vinyl-2-pyrrolidone) is suggested to play an important role for this self-organization. However, the driving force as well as the conditions for this self-organization is not well understood yet.

Nevertheless, Pd/Ag/Rh and Pt/Pd/Rh trimetallic nanoparticles with a triple core/shell structure have recently been successfully prepared by this method.

CATALYSES OF METAL NANOPARTICLES

Metal nanoparticles are used as catalysts for various kinds of reactions in dispersions or on supports, which are summarized here. Metal nanoparticles stabilized by weakly coordinating polymers are considered to be an effective catalyst, which works as shown in Fig. 8. As for polymer-protected metal nanoparticle catalysts, the catalytic performance, i.e., activity and selectivity, is affected not only by the structures of metal nanoparticles but also by those of the surrounding polymers.

Reduction

Hydrogenation of C–C multiple bonds is catalyzed by many kinds of precious metal nanoparticles. The ac-

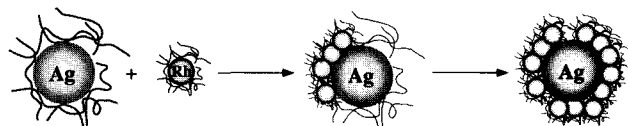


Fig. 12 Formation of pseudo-Ag-core/Rh-shell-structured bimetallic nanoparticles. (From Ref. [23].) (View this art in color at www.dekker.com.)

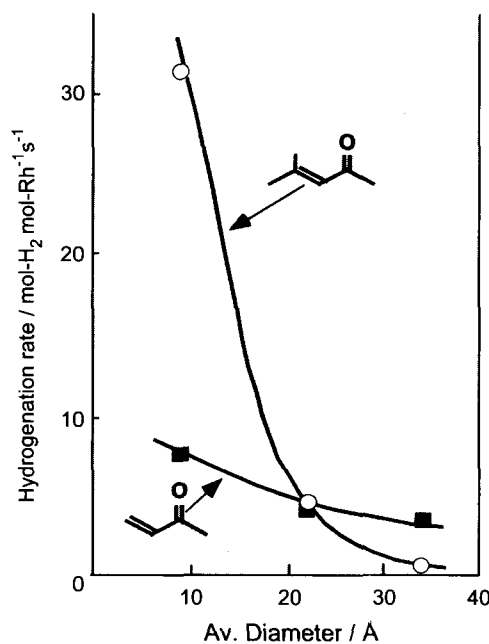


Fig. 13 Size effect of catalytic activity of PVP-protected Rh nanoparticle catalysts for hydrogenation of internal and vinyl olefins. [From *Shokubai* 1985, 27, 488.] (View this art in color at www.dekker.com.)

tivity depends not only on the kind of metal element but also on the size and shape of metal nanoparticles. One of the most significant examples of the size effect is shown for hydrogenation of internal olefins catalyzed

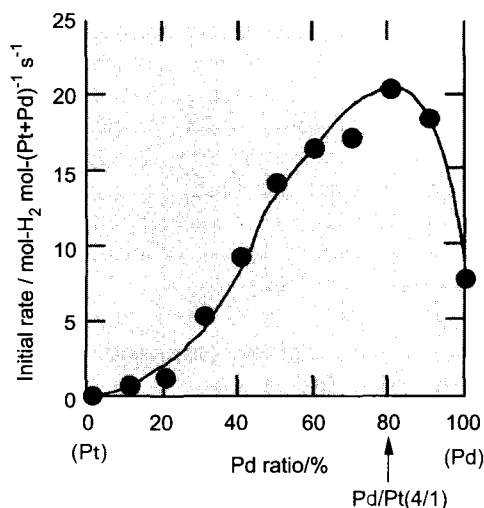
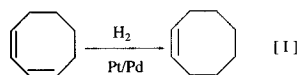


Fig. 14 Dependence of the catalytic activity of PVP-protected Pd/Pt bimetallic nanoparticles for partial hydrogenation of cyclooctadiene upon the composition of the nanoparticles. (From *J. Chem. Soc. Faraday Trans.* 1993, 89, 2537.) (View this art in color at www.dekker.com.)

by PVP-protected Rh nanoparticle catalysts prepared by an alcohol reduction method Fig. 13.^[1]

In bimetallic nanometal catalysts, the activity depends on the composition and structure of bimetallic nanoparticles.^[3] For example, PVP-protected Pd/Pt bimetallic nanoparticles with a core/shell structure show the highest catalytic activity for partial hydrogenation of 1,3-cyclooctadiene to cyclooctene Formula I at a 4:1 atomic ratio of Pd to Pt Fig. 14, in which the Pt core is covered by an atomic layer of Pd.^[16] This means that the catalytic active site of the metal nanoparticles is located on the surface Pd atoms and that the Pt core adjacent to the Pd has an electronic effect on the surface Pd atoms. In other words, the additional Pt atoms do not have an ensemble effect, but a ligand effect, on the active Pd sites.



The catalytic selectivity of metal nanoparticles can sometimes be controlled by their sizes and shapes. The selectivity of partial hydrogenation of cyclopentadiene catalyzed by PPV-protected Pd nanoparticles rapidly increases when the diameter of Pd nanoparticles is below 2 nm.^[1]

The selectivity is more often controlled by the organic layer surrounding metal nanoparticles. 10-Undecenoic acid is much more easily hydrogenated than 2-undecenoic acid when catalyzed by Pd nanoparticles stabilized by nonionic surfactant molecules.^[24] This selectivity control is shown in Fig. 15. Polyclodextrin-covered metal nanoparticles are also effective catalysts for the reaction with high substrate selectivity because the cyclodextrin cavity can recognize the substrate molecule.

Enantioselective hydrogenation can be achieved by using metal nanoparticles capped by chiral stabilizers such as cinchonidine and dihydrocinchoxidine in dispersions and on inorganic supports.^[25]

The reduction of C=O bond was reported to be catalyzed by Rh nanoparticles. The reduction of nitrobenzene

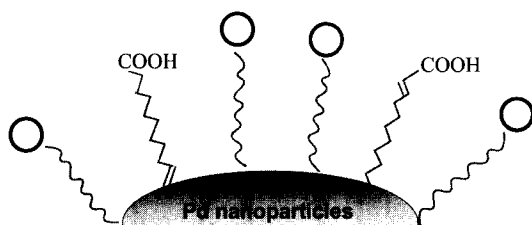


Fig. 15 Schematic illustration of selectivity control of surfactant-protected Pd nanoparticle catalysts for hydrogenation of 2- and 10-undecenoic acid. (From Ref. [24].) (View this art in color at www.dekker.com.)

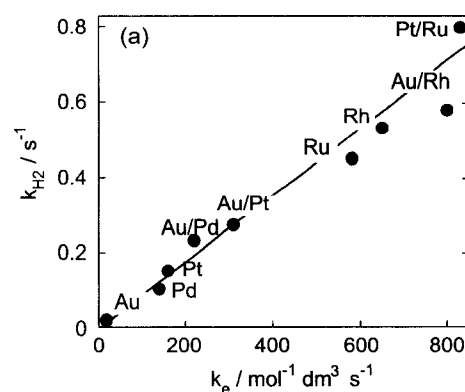
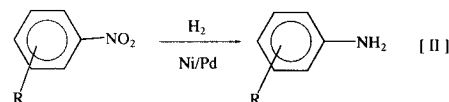


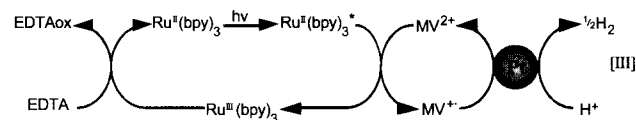
Fig. 16 Relationship between hydrogen generation rate and electron transfer rate over various kinds of metal nanoparticle catalysts. (From Ref. [26].)

to aniline by hydrogen at room temperature Formula II was catalyzed by PVP-protected Ni/Pd bimetallic nanoparticles, prepared by glycol reduction at 190°C. In nitrobenzene, the atomic ratio Ni/Pd=1:4 gave the most active catalyst, while in the other substituted nitrobenzene, the ratio was 2:3.



Visible-Light-Induced Hydrogen Generation

Because metal nanoparticles in dispersions are transparent to visible light, their application to catalyses for photochemical reactions is preferred over conventional solid catalysts. Colloidal dispersions of Pt nanoparticles in water was used for visible-light-induced hydrogen generation in the system of metal nanoparticles/methyl viologen (electron mediator)/trisbipyridineruthenium(II) dichloride (photosensitizer)/ethylenediaminetetraacetic acid disodium salt (electron donor) Formula III.

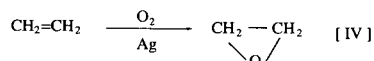


Various kinds of bimetallic nanoparticles were recently examined as catalysts of the above reaction. It was found that the hydrogen generation rate is proportional to the rate of electron transfer from methyl viologen cation radical to the metal nanoparticles as shown in Fig. 16, and that the bimetallic nanoparticles are more active as a catalyst than the corresponding monometallic nanoparticles.^[26]

Oxidation

Oxidation is one of the most general chemical reactions and is often applied to industrial processes. Nevertheless, there are few reports on the application of metal nanoparticle catalysts for oxidation reactions. This is because organic stabilizers are easily oxidized, resulting in their decomposition. Hence development of the stabilizers strong against oxidation is very important.

Oxidation of ethylene to ethylene oxide by molecular oxygen Formula IV is catalyzed by Ag nanoparticles stabilized by poly(sodium acrylate). The reaction proceeds under the pressure of ethylene and oxygen at 170°C.^[27]

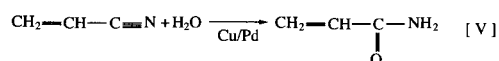


Catalytic oxidation is enhanced by the presence of Cs(I) and Re(VII) ions, which are immobilized on the stabilizer poly(acrylate). The catalytic activity of Ag nanoparticles depends on the protecting polymer. Polyacrylate-protected Ag nanoparticles have much higher activity than PVP-protected ones especially at high temperature. This is probably because of the stronger coordinations of polyacrylate to Ag nanoparticles.

Other examples include oxidation of cyclooctane to cyclooctanal and cyclooctanone by *t*-butyl hydroperoxide (*t*-BHP) catalyzed by Ru nanoparticles in a biphasic system, and oxidation of D-glucose to D-gluconate by molecular oxygen catalyzed by tetraalkylammonium-stabilized Pd/Pt bimetallic nanoparticles on charcoal.^[28]

Hydration

Selective hydration of acrylonitrile, which is catalyzed by copper catalysts, is used for industrial production of acrylamide. The same reaction can proceed by using Cu nanoparticles as catalysts. The colloidal dispersions of PVP-protected Cu nanoparticles were prepared by NaBH₄ reduction of Cu(II) ions and applied to the catalyst for this reaction.^[1] However, Cu nanoparticles are easily oxidized by the contaminant air and are not stable enough to be repeatedly used. To stabilize Cu nanoparticles, Cu/Pd bimetallic nanoparticles were prepared by coreduction of Cu and Pd ions by glycol at 190°C in the presence of PVP.^[20] The bimetallic nanoparticles are more stable, and much more active as the catalyst for hydration of acrylonitrile to acrylamide Formula V than the simple Cu monometallic nanoparticles.



C-C Bond Formation

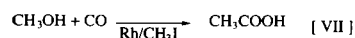
The C-C bond formation is a useful reaction in organic syntheses and is often catalyzed by homogeneous catalysts of organometallic complexes. Metal nanoparticles have recently been used instead of organometallic complexes as catalysts for C-C bond formation. Because these reactions are catalyzed by ionic species of precious metals in homogeneous catalysts, real active species of these metal nanoparticle catalysts are often considered to be the ionic species produced by oxidation of metal nanoparticles. Further research is required to understand the real reaction mechanism.

Heck reaction, the coupling between aromatic and vinyl carbons Formula VI, was found to be catalyzed by Pd nanoparticles in the presence of base at a rather high temperature.^[29,30]

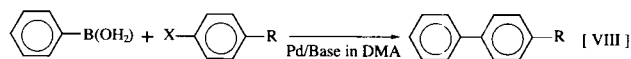


Because the reaction requires a rather high temperature, enough stable polymers are preferred as the stabilizer for the metal nanoparticles used as catalysts.

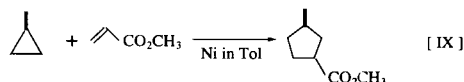
Carbonylation of methanol to directly produce acetic acid Formula VII is catalyzed by a homogeneous Rh catalyst. Poly(*N*-vinyl-2-pyrrolidone)-protected Rh nanoparticles were used as the catalyst of this reaction at 140°C under CO pressure.



Suzuki reaction, which is useful for direct coupling of two different benzene rings Formula VIII, were catalyzed by Pd and Pd/Ni nanoparticles.^[31] The stability of the PVP-protected Pd nanoparticles was investigated as well.^[32]



[3+2] Cycloaddition reaction between methylene-cyclopropane and methyl acrylate in reflux toluene Formula IX was catalyzed by Ni nanoparticles immobilized on alumina.^[33]



In these C–C coupling reactions, the catalytic activity of metal nanoparticles is less than the corresponding homogeneous organometallic catalysts. However, metal nanoparticle catalysts have an advantage for repeated usage. For the practical use of metal nanoparticles as catalysts, further investigations of stable protective polymers and of immobilization on inorganic supports as well as of the reaction mechanism will be required.

CONCLUSION

Catalysts based on metal nanoparticles have recently received much attention because investigations in the field of metal nanoparticles has rapidly developed. Now many techniques have been reported to control the structures of metal nanoparticles, not only the structures of metal parts but also the structure of organic layers surrounding them. By using these techniques, metal nanoparticles can be constructed according to the design.

Metal nanoparticles can be used as catalysts not only in dispersions but also on solid supports. In dispersions, metal nanoparticles can be used as catalysts only for reactions in a solution, while on solid supports they can be used both in solution and in gaseous phase. Thus metal nanoparticles are now applied to catalysts for various kinds of reactions. The number of the reactions for which metal nanoparticles are used as catalysts is going to rapidly increase. In the field of environmental catalysts, which are the largest in the market of catalysts, conventional catalysts may be replaced by metal nanoparticles designed for this purpose.

REFERENCES

1. Hirai, H.; Toshima, N. Polymer-Attached Catalysis. In *Tailored Metal Catalysts*; Iwasawa, Y., Ed.; D. Reidel Pub. Co.: Dordrecht, 1975; 87–140.
2. *Clusters and Colloids. From Theory to Application*; Schmid, G., Ed.; VCH: Weinheim, 1994.
3. Toshima, N.; Yonezawa, T. Bimetallic nanoparticles—Novel materials for chemical and physical application. *New J. Chem.* **1998**, *22*, 1179–1201.
4. Toshima, N.; Shiraiishi, Y. Catalysis by Metallic Colloids. In *Encyclopedia of Surface and Colloid Science*; Hubbard, A.T., Ed.; Marcel Dekker: New York, 2002; 879–886.
5. Roucoux, A.; Schulz, J.; Patin, H. Reduced transition metal colloids: A novel family of reusable catalysts? *Chem. Rev.* **2002**, *102*, 3757–3778.
6. Teranishi, T.; Toshima, N. Preparation, Characterization, and Properties of Bimetallic Nanoparticles. In *Catalysis and Electrocatalysis at Nanoparticles Surfaces*; Wieckowski, A., Sarinova, E.R., Vayenas, C.G., Eds.; Marcel Dekker: New York, 2003; 379–407.
7. Toshima, N. Metal Nanoparticles for Catalysis. In *Nanoscale Materials*; Liz-Marzán, L.M., Kamat, P.V., Eds.; Kluwer Academic Pub.: Boston, 2003; 79–96.
8. Moreno-Nañas, M.; Pleixats, R. Formation of carbon–carbon bonds under catalysis by transition-metal nanoparticles. *Acc. Chem. Res.* **2003**, *36* (8), 638–643.
9. Kobayashi, S.-I.; Goto, H.; Katsumoto, S. Kubo Effects in Small Particles of Metals. In *Mesoscopic Materials and Clusters*; Arai, T., Ed.; Springer: Berlin, 1999; 113–122.
10. Yonezawa, T.; Tominaga, T.; Toshima, N. Novel characterization of the structure of surfactants on nanoscopic metal clusters by a physico-chemical method. *Langmuir* **1995**, *11*, 4601–4606.
11. Hirai, H.; Yakura, N. Protecting polymers in suspension of metal nanoparticles. *Polym. Adv. Technol.* **2001**, *12*, 724–733.
12. Reetz, M.T.; Helbig; Quaiser, S.A.; Stimming, U.; Breuer, N.; Vogel, R. Visualization of surfactants on nanostructured palladium clusters by a combination of STM and high-resolution TEM. *Science* **1995**, *267*, 367–369.
13. Hashimoto, T.; Saijo, K.; Harada, M.; Toshima, N. Small-angle X-ray scattering analysis of polymer-protected platinum, rhodium, and platinum/rhodium colloidal dispersions. *J. Chem. Phys.* **1998**, *109* (13), 5627–5638.
14. Hirai, H.; Nakao, Y.; Toshima, N.; Adachi, K. Colloidal rhodium in polyvinyl alcohol as hydrogenation catalyst of olefins. *Chem. Lett.* **1976**, 905.
15. Bian, C.-R.; Suzuki, S.; Asakura, K.; Ping, L.; Toshima, N. EXAFS studies on the structure of the PVP-stabilized Cu/Pd nanoclusters colloiddally dispersed in solution. *J. Phys. Chem., B* **2002**, *106* (34), 8587–8598.
16. Toshima, N.; Harada, M.; Yonezawa, T.; Kushihashi, K.; Asakura, K. Structural analysis of polymer-protected Pd–Pt bimetallic clusters as dispersed catalysts by using extended X-ray absorption fine structure spectroscopy. *J. Phys. Chem.* **1991**, *95*, 7448–7453.
17. Toshima, N.; Harada, M.; Yamazaki, Y.; Asakura, K. Catalytic activity and structural analysis of polymer-protected Au–Pd bimetallic clusters prepared by the simultaneous reduction of HAuCl₄ and PdCl₂. *J. Phys. Chem.* **1992**, *96*, 9927–9933.
18. Yonezawa, T.; Toshima, N. Mechanistic consideration of formation of polymer-protected nanoscopic

- bimetallic clusters. *J. Chem. Soc., Faraday Trans.* **1995**, *91*, 4111–4119.
19. Wang, Y.; Toshima, N. Preparation of Pd–Pt bimetallic colloids with controllable core/shell structures. *J. Phys. Chem., B* **1997**, *101*, 5301–5306.
 20. Toshima, N.; Wang, Y. Preparation and catalysis of novel colloidal dispersions of copper/noble metal bimetallic clusters. *Langmuir* **1994**, *10*, 4574–4580.
 21. Lu, P.; Teranishi, T.; Asakura, K.; Miyake, M.; Toshima, N. Polymer-protected Ni/Pd bimetallic nano-clusters; preparation, characterization and catalysis for hydrogenation of nitrobenzene. *J. Phys. Chem., B* **1999**, *103* (44), 9673–9682.
 22. Sun, S.; Murray, C.B.; Weller, D.; Folks, L.; Mosen, A. Monodisperse FePt nanoparticles and ferromagnetic FePt nanocrystal superlattices. *Science* **2000**, *287*, 1989–1992.
 23. Hirakawa, K.; Toshima, N. Ag/Rh bimetallic nanoparticles formed by self-assembly from Ag and Rh monometallic nanoparticles in solution. *Chem. Lett.* **2003**, *32* (1), 78–79.
 24. Toshima, N.; Takahashi, T. Colloidal dispersion of platinum and palladium cluster embedded in micelles. Preparation and application to catalysis for hydrogenation of olefins. *Bull. Chem. Soc. Jpn.* **1992**, *65*, 400–409.
 25. Bönemann, H.; Braun, G.A. Enantioselective hydrogenations on platinum colloids. *Angew. Chem., Int. Ed. Engl.* **1996**, *35*, 1992–1995.
 26. Toshima, N.; Hirakawa, K. Polymer-protected bimetallic nanocluster catalysts having core/shell structure for accelerated electron transfer in visible-light-induced hydrogen generation. *Polym. J.* **1999**, *31* (11-2), 1127–1192.
 27. Shiraishi, Y.; Toshima, N. Oxidation of ethylene catalysed by colloidal dispersions of poly(sodium acrylate)-protected silver nanoclusters. *Colloids Surf., A* **2000**, *169* (1–3), 59–66.
 28. Bönemann, H.; Brojoux, W.; Tilling, A.S.; Siepen, K. Application of heterogeneous colloid catalysts for the preparation of fine chemicals. *Top. Catal.* **1998**, *4* (3,4), 217–227.
 29. Beller, M.; Fischer, H.; Kuehlein, K.; Reisinger, C.P.; Herrmann, W.A. First palladium-catalyzed Heck reactions with efficient colloidal catalyst systems. *J. Organomet. Chem.* **1996**, *520* (1–2), 257–259.
 30. Reetz, M.T.; Lohmer, G. Propylene carbonate stabilized nanostructured palladium clusters as catalysts in Heck reactions. *Chem. Commun.* **1996**, (16), 1921–1922.
 31. Reetz, M.T.; Breinbaner, R.; Wanninger, K. Suzuki and Heck reactions catalyzed by preformed palladium clusters and palladium/nickel bimetallic clusters. *Tetrahedron Lett.* **1996**, *37* (27), 4499–4502.
 32. Narayanan, R.; El-Sayed, M.A. Effect of catalysis on the stability of metallic nanoparticles; Suzuki reaction catalyzed by PVP–palladium nanoparticles. *J. Am. Chem. Soc.* **2003**, *125* (27), 8340–8347.
 33. Reetz, M.T.; Breinbauer, R.; Wedemann, P.; Binger, P. Nanostructured nickel-clusters as catalysts in [3+2] cycloaddition reactions. *Tetrahedron* **1998**, *34* (7), 1233–1240.

Metal Nanostructures Synthesized by Photoexcitation

Kei Murakoshi
Yoshihiro Nakato

Osaka University, Osaka, Japan

INTRODUCTION

The current interest in the structural control of metal and semiconductor materials in the nanoscale region has been rapidly promoted in terms of construction of ultrasensitive and low-energy-consumption devices.^[1] Recently developed nanodevice technologies using scanning probe microscopy have allowed us to construct ultrasmall structures on an atomic scale.^[2] However, this method is not adaptable to mass production because it is too slow, especially for sizes of more than a few nanometers. This situation, together with the limitation of the size control to about a hundred nanometers for conventional photolithographic techniques, clearly indicates that the creation of nanodevices sized between a few nanometers and tens of nanometers remains an undeveloped aspect of the present nanotechnology (Fig. 1). Thus we should develop methods of effective and high-speed construction of desirable nanostructure in this size region.

To solve the problem, we have proposed the idea of applying localized photoexcitation at metal nanostructures for the structural controls. Generally, metal nanoparticles such as Au, Ag, and Cu show characteristic surface plasmon absorption in the visible–near-infrared wavelength region (Fig. 2).^[3,4] The electric field induced by excited surface plasmons is highly localized, and the direction of its polarization can be controlled by changing the wavelength and polarization of illumination light. Thus if the localized field can be utilized to induce electrochemical reactions, such as metal dissolution and deposition, the effect can be applied to change and control the metal nanostructures (Fig. 3).

OVERVIEW

There have been numerous reports on structural changes of metal nanoparticles under photoillumination;^[5,6] unfortunately, most of them describe fragmentation and structural deformation of the particles. There are few reports concerning structural control in a nanometer region by photoillumination. Generally, it is known that the quantum efficiency of photoelectrochemical reactions at metals is extremely low because of the very short

lifetime of photoexcited electrons or holes in the system. But it should be noted that there are several interesting examples to prove the possibility of the plasmon-mediated photoinduced electron transfer phenomenon in photoemission experiments using roughened metal electrodes.^[7–11] For example, Fedurco et al.^[7] reported that increments in photocurrent reduced carbon dioxide in solution at roughened Ag electrode. The quantum yield of the photocurrent exhibited a sharp maximum at the peak wavelength of surface plasmon of Ag electrode. The results suggest that plasmon-mediated photoinduced electron transfer at metal electrode may be possible if an appropriate electron acceptor/donor exists at the interface. Metal deposition and dissolution could be involved in the reactions for the structural control.

In this review, we summarize our recent developments to control metal nanostructures via photoillumination. After brief summaries of the research, the possibilities of future applications will be discussed.

PHOTOINDUCED ANISOTROPIC AGGLOMERATION OF GOLD NANOPARTICLES IN SOLUTION AND ON Au(111) SINGLE CRYSTAL SURFACE

One of the promising ways to construct well-organized periodic nanostructures is the use of self-assembling processes of colloidal crystal agglomeration.^[12–16] When the surface charge of inorganic nanoparticles with a narrow size distribution are carefully controlled in the course of the preparations, the nanoparticles form agglomerates with a highly ordered superstructure. Examples of well-ordered colloidal particles composed of nanosized metal and semiconductor crystals have been reported. If one can control the interaction between particles, desirable periodic superstructures and anisotropies can be introduced into the nanosized colloidal crystals. To demonstrate the possibility of combining photoexcitation for this aim, we investigated anisotropic agglomeration of gold nanoparticles (diameters ca. 6 nm) modified with organic thiols by photoillumination with monochromatic light in aqueous media.^[17]

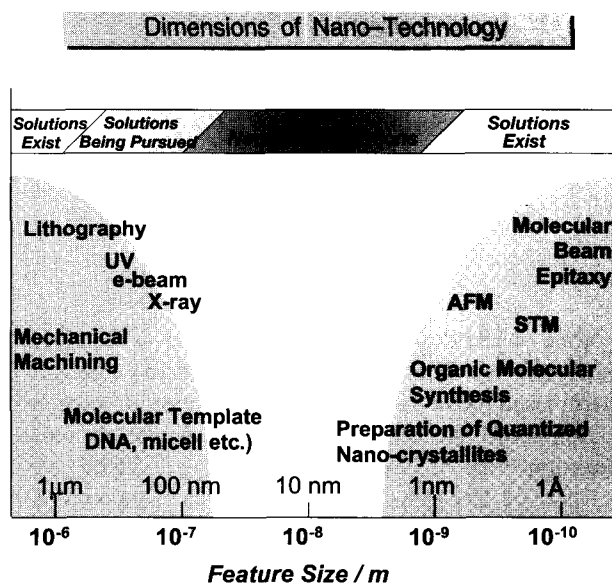


Fig. 1 Dimensions of nanotechnology. (View this art in color at www.dekker.com.)

Fig. 4 shows time-dependent spectral changes of gold nanoparticles after adding a surface-modifying reagent, thionicotinamide (TNA), in the dark and under illumination. In Fig. 4a and b, the initial spectrum with a single absorption peak at 520 nm in the dark is accompanied by evolution of an absorption band at wavelengths longer

Color of Spherical Metal Nano-particles in Solution ($d = 10\text{--}20\text{ nm}$)

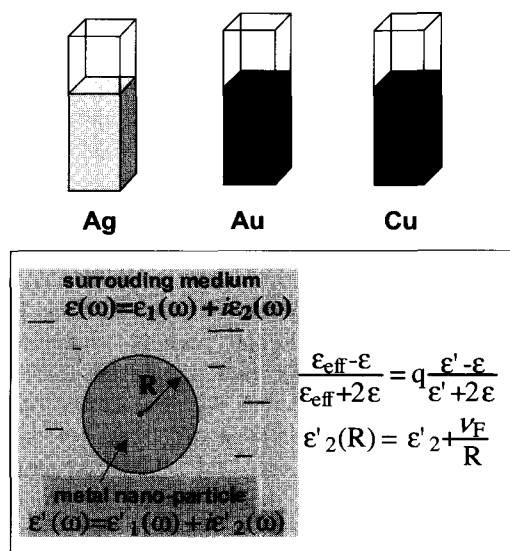


Fig. 2 Color of the plasmon absorption of metal nanoparticles. (View this art in color at www.dekker.com.)

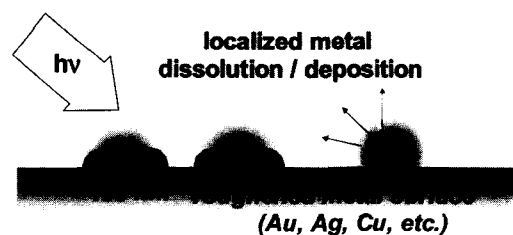


Fig. 3 Schematic presentation of electric field at roughened metal surface under illumination. (View this art in color at www.dekker.com.)

than 700 nm. After ca. 300 sec, the spectrum demonstrated double peaks at 520 and 720 nm. These changes can be attributed to agglomeration of gold nanoparticles by surface modification with the added reagent. The two absorption maxima of 520 and 720 nm can be attributed to the excitation of the transverse and longitudinal modes of surface plasmons in anisotropic agglomerates, respectively.^[3,4] The modifying reagent should be bound on the gold surface via strongly interacting groups of thiol and/or amide.^[18] The formation of such binding is expected to reduce or diminish anionic surface charges on the gold nanoparticles, leading to an increase in van der Waals attractive forces among the surface-modified gold nanoparticles, and hence resulting in agglomeration. Fig. 4c–f shows the effect of photoillumination on agglomeration of the gold nanoparticles. Under illumination at 830 nm, agglomeration was slightly accelerated. The evolution of the new absorption band above 700 nm became faster than that in the dark, showing the saturation in about 200 sec after the addition of TNA. In the case of 530-nm illumination, such acceleration of agglomeration was also observed, and further became faster than the illumination at 830 nm. The evolution of the new band above 700 nm reached saturation in about 180 sec. For the illumination at 830 and 530 nm, the absorption intensities also decreased after the saturation. The decreases reflect further aggregation and precipitation of the nanoparticles in solution. This result indicates that photoillumination accelerates the agglomeration of gold nanoparticles depending on the wavelength of the illumination light.

The above-presented photoinduced agglomeration reflects the change in the interaction between the gold nanoparticles by surface plasmon excitation. The interaction between colloidal particles was described by the total interaction potential consisting of an attractive van der Waals potential and a repulsive electrostatic potential in the DLOV theory.^[19] The former potential contains a constant term determined by material- and geometry-dependent dispersion of coupled surface plasma oscillation frequencies. It was suggested that photoexcitation of the oscillations induces additional attractive forces via

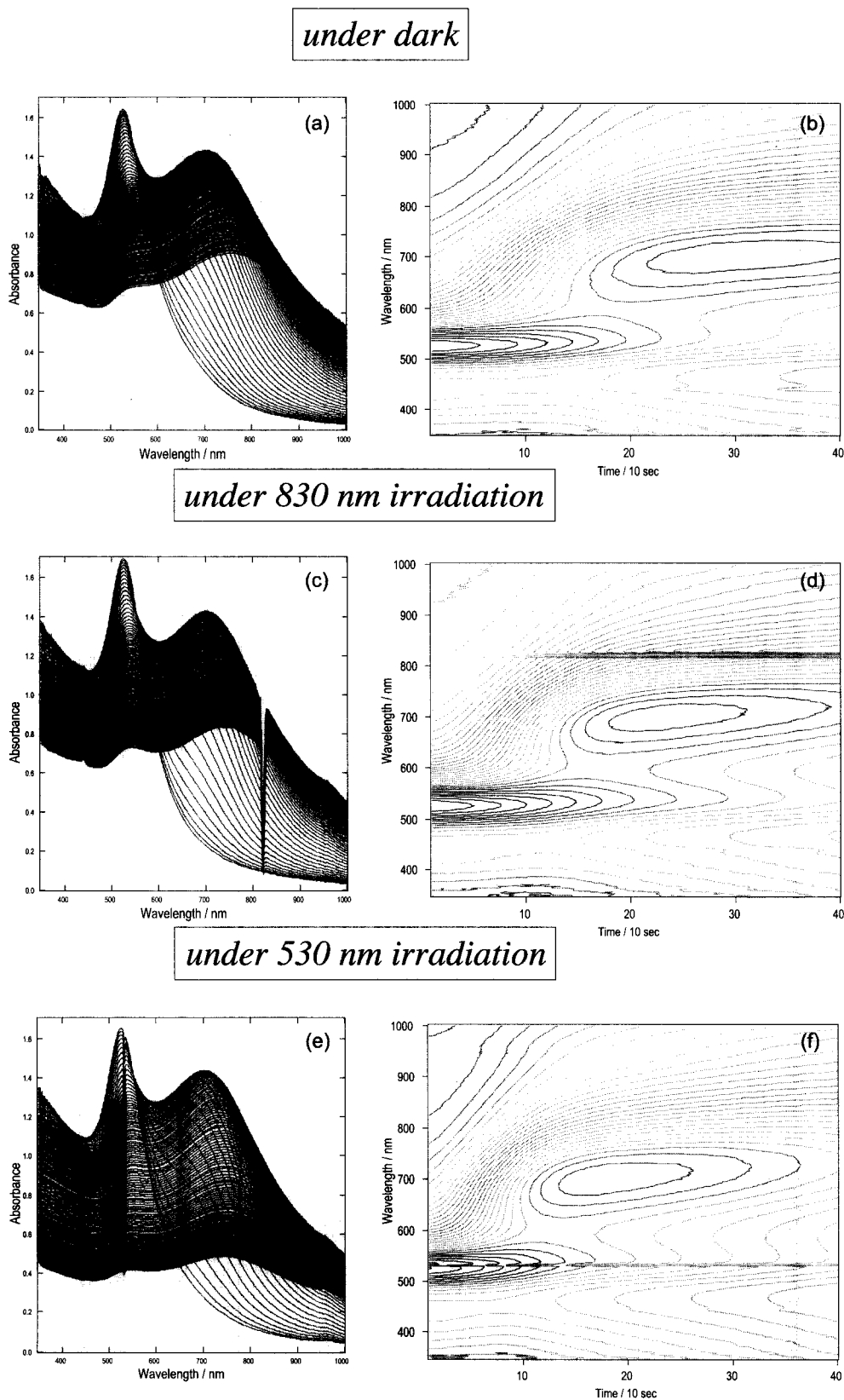


Fig. 4 Time-dependent absorption spectra of an aqueous solution containing gold nanoparticles modified with thionicotinamide. Measurements were performed 120 times at intervals of 10 sec, (a) in the dark, (c) under illumination at 830 nm, and (e) under illumination at 530 nm. Contour plots of time-dependent absorption spectra of the same systems, (b) in the dark, (d) under illumination at 830 nm, and (f) under illumination at 530 nm. (View this art in color at www.dekker.com.)

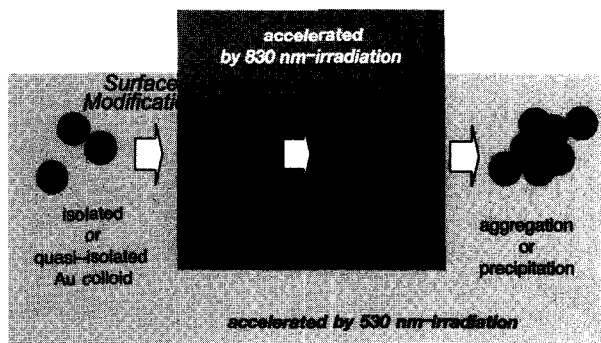


Fig. 5 Agglomeration process of the gold nano-particles in solution. (View this art in color at www.dekker.com.)

electromagnetic multipolar interactions. The results of the photoinduced agglomeration shown here should also be attributed to the photoinduced increase in the attractive force between the gold nanoparticles via surface plasmon excitation by illumination at 830 and 530 nm (Fig. 5). The wavelength dependence, i.e., slightly higher acceleration of agglomeration as well as earlier start of precipitation by 530-nm illumination than those by 830-nm illumination, may suggest another contribution of photoexcitation than the expected one. Illumination at 530 nm is known to cause not only plasmon excitation but also interband excitation of the gold nanoparticles, leading to photochemical reactions.^[6] The relatively higher-energy excitation often results in destruction of the particles via electron ejection from them, fragmentation, and fusion. On the other hand, illumination at 830 nm under the present condition does not seem to cause structural deformation of individual particles. Furthermore, the excitation of the longitudinal mode at 830 nm is expected to induce anisotropic polarization along the long axis of the anisotropic agglomeration. Although the present results on the wavelength dependence of photoinduced agglomeration suggest that the 530-nm illumination is more effective in speed, it seems that the illumination at 830 nm is a more suitable perturbation to cause aniso-

tropic agglomeration via plasmon excitation without any degradation of the gold nanoparticles.

The behavior of adsorption of the gold nanoparticles on Au(111) surfaces under photoillumination was also investigated. Surface modified gold nanoparticles are adsorbed on Au(111) surface. We reported that their agglomerates on the Au(111) surface, prepared by immersion of the surface in the solution of gold nanoparticles, formed dot-interconnected lines of gold particles with a single particle width.^[20] When the immersion conditions, such as the concentration of the gold nanoparticles and the immersion time, were changed, the coverage of the nanoparticles on the surface could be altered. Fig. 6 shows scanning tunneling microscopic (STM) images of the gold nanoparticles on the Au(111) surfaces prepared under 830-nm light illumination with different magnifications for different places. The images clearly show that each line of arrays is composed of the gold nanoparticles with the diameter of ca. 6 nm. Fig. 6b shows that the linear arrayed structure of the gold nanoparticles is formed on a typical structure of steps and terraces of the Au(111) surface with a monoatomic height at step edges crossing at 60° with each other, suggesting that the coverage of the nanoparticles should be a monolayer. It is also seen that the aligned arrays are parallel to the direction of one of the steps [Fig. 6c]. Although some vacancies or pits of the nanoparticles are observed, the alignment of the gold nanoparticles is not affected by such imperfections. It should be noted that this linearly arrayed structure was not observed at the surface prepared under dark or under illumination at 530 nm.^[17]

As shown before, the photoillumination should cause an additional attractive interaction between the gold nanoparticles. The excitation at a long wavelength of 830 nm corresponds to the excitation of the longitudinal mode of surface plasmons in the anisotropic gold agglomerates, which propagates in the long-axis direction. The selective excitation of this mode is expected to cause an anisotropic electric field, leading to agglomeration in one specific direction. Isotropic excitation at 530 nm will not be able to induce such an anisotropic field, leading to



Fig. 6 Scanning tunneling microscopic images of linear arrayed structures of gold nanoparticles adsorbed on a Au(111) surface prepared under illumination at 830nm. (View this art in color at www.dekker.com.)

random adsorption of nanoparticles. In addition, relatively strong excitation at 530 nm caused the destruction of the nanoparticles as observed in the solution experiments.

In this section, we have shown the promoting effect of photoillumination on agglomeration of surface-modified gold nanoparticles. The additional interactions between the particles were induced by photoillumination, and were controlled by changing the wavelength of illuminating light. In the case of adsorption onto the Au(111) surface, the illumination also affected the adsorption structure. The illumination at 830 nm led to the formation of a closed-packed and linearly arrayed superstructure on the surface. The results imply that photoillumination can be applied to control the superstructure of colloidal metal nanoparticles.

NANOSCALE STRUCTURAL CHARACTERISTICS OF PHOTODISSOLVED Au(111) SINGLE CRYSTALLINE SURFACE

We investigated the effect of photoillumination on electrochemical dissolution of a gold electrode in KCl electrolyte. Structural changes in the surface morphology of metal electrodes by photoillumination have been recognized, especially in the field of surface-enhanced Raman scattering (SERS) spectroscopy.^[21–23] Enhancement factors of the scattering signal are very sensitive to the surface microscopic morphology.^[24–26] There are several reports on the change in SERS enhancement factors by photoillumination during electrochemical roughening in halide solutions.^[21–23] The difference in

the scattering intensity may reflect the structural characteristics of the surface prepared under the illumination. Thus the dissolution of metal electrode under photoillumination is expected to give some characteristic features, which differ from the surfaces prepared under the dark. In this section, the structure of the photoilluminated electrode surface was characterized by STM. Comparison between the electrodes prepared under darkness and photoillumination conditions shows the effect of photoexcitation of metal on the electrochemical reaction.^[27]

Several surface structures of Au(111) surface prepared by electrochemical dissolution were shown in Fig. 7. Under the dark conditions, it was found that the change of the surface structure was observed when the potential became more positive than 0.6 V vs. an Ag/AgCl reference electrode. Fig. 7a shows STM images of the surface after the positive polarization at 1.0 V under the dark. Formation of a random-valley structure at the terrace was shown in the image. Potential cycling between oxidation and reduction potentials (–0.1 and 1.0 V) resulted in a further roughened surface, consisting of spherical particles with the diameter of 20–30 nm as shown in Fig. 7b. The surfaces prepared in the dark had neither flat parts nor residual step lines. Fig. 7c exhibits a photodissolved surface formed at a relatively negative potential of 0 V. The image shows that structural changes can be caused at much more negative potentials under the photoillumination than that in the dark. As the structural characteristics, homogeneous islands approximately 15 nm in size were found on the surface. The height of the islands was quite uniform, and the trace of the step edge was seen as a well-aligned dot-line structure of the islands.

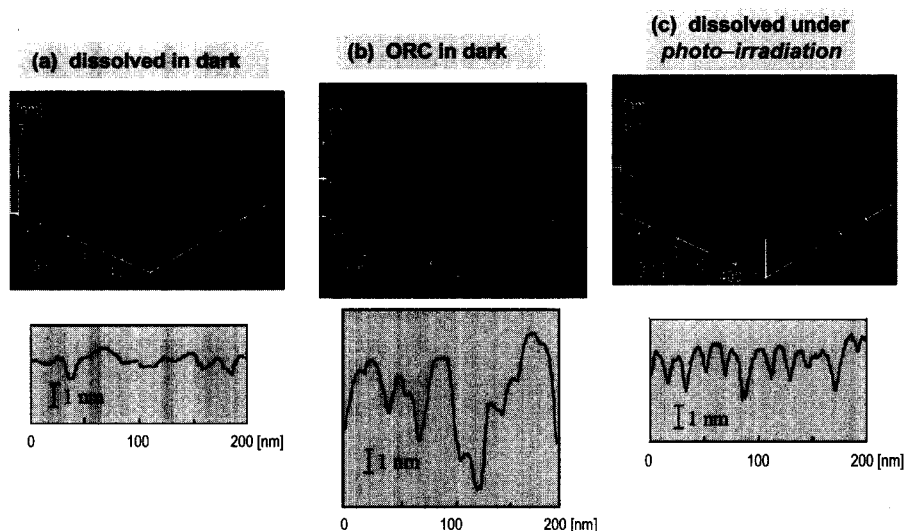


Fig. 7 Scanning tunneling microscopic images and vertical sectional views of Au(111) surface kept at (a) 1.0 V for 5 sec under darkness, (b) –0.1 V for 5 sec after positive polarization at 1.0 V for 5 sec under darkness, and (c) 0 V for 5 sec under photoillumination; observed area was 500 × 500 nm. (View this art in color at www.dekker.com.)

Comparison of the vertical sectional view of the surface to the surfaces prepared under the dark condition [Fig. 7a,b] shows that the size of the islands and the depth of the valleys are uniform.

Photoillumination of metal surfaces excites electrons and holes, and thus could induce electron transfer reactions if electron donors/acceptors exist at the interface. In the present system, a gold electrode dissolves via oxidation of gold forming AuCl_4^- when a sufficiently positive potential (>0.8 V) is applied. Photoexcitation at 830 nm can generate excited holes with energy of 1.49 eV relative to the Fermi level, leading to the oxidative dissolution of the surface at a more negative potential. In addition to this effect of the potential, there were interesting structural characteristics observed at the dissolution under the dark. As shown in Fig. 7c, the island structure had a relatively narrow size distribution. Theoretical calculation of the electric field, taking into consideration strong electromagnetic coupling on the metal surface, predicted the creation of a very localized plasmon mode at the valley of the periodic superstructure.^[28,29] Calculation results show that the strongest electric field is highly localized at the bottom of the valley between the particles. Thus, in the present case, after the formation of these randomly distributed valleys, some of them, whose separation distance is the same as the period of the photoexcited field induced by 830-nm light illumination, are selectively excited and form a localized field at the bottom of the valleys. Such a localized field could induce localized photodissolution of the metal via resonant electronic excitation. Formation of the periodic structure by photoillumination may be explained by the selective dissolution caused by a periodic electromagnetic field on the surface.

Scanning tunneling microscopic images proved that dissolution of the gold electrode was accelerated by photoillumination. At the surface prepared under the illumination, the size distribution of the islands was relatively small, and the heights of the islands were uniform. The selective dissolution caused by a periodic electromagnetic field on the surface may contribute to the formation of such uniform structure. The present results imply that the photoillumination can be applied to control the structure of metals in the size around 10 nm via photodissolution.

PHOTOINDUCED SINGLE METAL-DOT DEPOSITION ONTO METAL SURFACE

Photoinduced electron transfer reactions via plasmon excitation have been reported in several roughened metal electrode systems.^[7-11] For further developments as a novel method of nanostructural control in the size between

a few nanometers and tens of nanometers, coupling the phenomenon with an electrochemical scanning tunneling microscope (EC-STM) system could prove interesting.^[30,31] Several attempts have been reported on using photoirradiation for the tunneling gap of STM systems for nanostructure fabrication.^[32-38] Although some of these studies succeeded in the preparation of nanostructures on solid surfaces, several problems still remain. When light is irradiated in the STM gap, thermal expansion of the tip and the sample substrates is observed as the most prominent effect.^[32-34,36,39-49] This contribution is difficult to control, and often changes the distance of the gap leading to the deformation of the prepared structures. Thus it is important to identify the conditions that minimize the thermal expansion. Appropriate potential control of the electrodes in EC-STM systems is expected to improve the reaction efficiency of the photoinduced metal deposition.^[50]

In this section, the effect of the photoirradiation on the gap between the Au(111) surface and the tip of the electrochemical STM was shown. Relatively weak light (100 mW/cm^2) was irradiated in the gap in the present experiment. During the irradiation for 10 msec, the position of the tip was fixed at the central part of the observed area under the constant tunneling current mode. After the irradiation, the tip was again scanned to obtain the surface image. This relatively weak light irradiation in the gap between the tip and the surface of the Au(111) electrode, whose potential was maintained at 0.4 V vs. Ag/AgCl in aqueous solution containing 0.1 M CuSO_4 , resulted in the formation of a small island structure on the Au(111) surface in the vicinity of the tip (Fig. 8). The island structure was formed on the surface just below the tip only when the light was irradiated at the point of the gap. The island was dissolved when the potential of the electrode was maintained at 0.6 V, indicating that the island is a photodeposited Cu dot. This fact indicates that a Cu metal nanodot can be prepared by the photoirradiation of an atomically smooth surface of a metal electrode in the vicinity of the metal tip. The position of the dot can be controlled by changing the position of the metal tip of the electrochemical STM.

In this system, the contribution of the plasmon mode was successfully applied to construct a single metal-dot structure on the smooth Au(111) surface in the vicinity of the thin metal tip. Ukraintsev and Yates^[40] proposed the possibility that the tip can work as a conical antenna or a waveguide for the light under irradiation. Thus it is expected that the enhanced field was induced by photoirradiation in the gap between the smooth metal surface.^[35,51-53] The field can induce the highly localized excitation of electrons at that point, leading to position-selective metal deposition onto the electrode surface, in the vicinity of the tip. As a result, a dot 15 nm in size

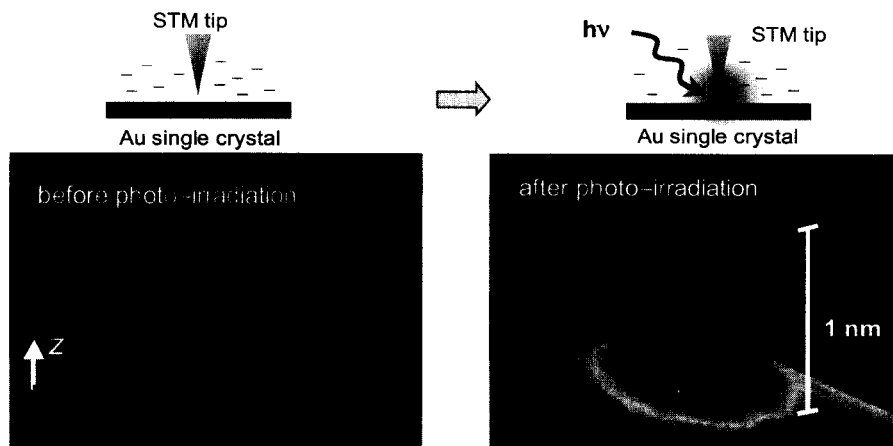


Fig. 8 Electrochemical scanning tunneling microscope image of Cu nanodot on Au(111) single crystalline electrodes prepared by photoirradiation with power of 100 mW/cm^2 for 10 msec. (View this art in color at www.dekker.com.)

and 1 nm in height was prepared on the Au(111) surface (Fig. 8). The fact that the preparation of the dot was achieved under relatively weak light irradiation proves the effective antenna effect of the tip in localizing the excitation. The method of position-selective photodeposition may be applied as a novel method to construct three-dimensional metal nanostructures on the solid surface.

PHOTOINDUCED STRUCTURAL CHANGES OF SILVER NANOPARTICLES ON GLASS SUBSTRATE IN SOLUTION UNDER AN ELECTRIC FIELD

In the field of structural control of metal nanoparticles, several important topics remain unresolved. One of these areas involves the application of an external electric field for structural control. It is desirable to achieve control of metal nanostructures on surfaces of insulating materials, as metal nanostructures constructed for use as conducting materials. In this case, structural control of metals must be conducted via electrochemical dissolution and deposition without donation of charge from the substrate electrode. Numerous reports exist, describing sophisticated techniques pertaining to construction of metal nanostructures on electrodes of conducting materials,^[54–56] as well as photoinduced structural changes of dispersed metal nanoclusters in solution. However, little documentation occurs with respect to induction of the electrochemical reaction of metal dissolution/deposition to control the metal nanostructure adsorbed on insulating materials, in the absence of an external electric circuit.^[57,58] Investigation of the combined effects of an external electric field and photoillumination is expected to give useful informa-

tion on the structural control of metal nanostructures on insulating materials. The investigation shown here clarified the effect of photoirradiation of Ag nanoparticles adsorbed on a glass substrate under an electric field in solution.^[59,60]

Application of an electric field to the Ag nanoparticles on glass immersed in solution was conducted employing a two-electrode cell (Fig. 9). Ag nanoparticles on a glass plate were prepared by the method of sputter deposition. The size of the hemispherical islands was approximately

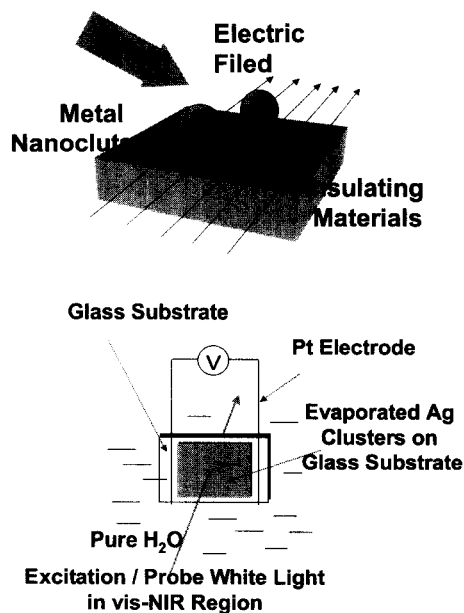


Fig. 9 Schematic presentation of experimental setup and two-electrode cell. (View this art in color at www.dekker.com.)

20 nm in diameter (Fig. 10). The absorption spectrum of the film showed a plasmon absorption peak at 480 nm in air (Fig. 10). The absorption spectra of the Ag nanoparticles changed as a result of photoirradiation under an external electric field in water. Fig. 11 shows the time-dependent changes in the absorption spectra of the Ag nanoparticles on the glass plate during photoirradiation at various intensities (0.06, 0.26, and 0.90 mW/cm²) under applying an electric field of 20 V/cm. Absorption around the spectral peak wavelength (approximately 500 nm) decreased as a result of photoirradiation. Slight changes in the absorption were observed in the wavelength region below 420 nm.

The rate of the changes linearly increased as the intensity of the irradiated light increased. Fig. 12 displays the dependence of photoirradiation intensity on the change in the absorption of the nanoparticles. The increase in the level of the changes was nearly linear with increasing intensity of irradiation. The effect of the applied electric field is also presented as the difference in the slope of the intensity dependence. The slope of an applied electric field of 20 V/cm was greater than twice that observed in the absence of an applied field. These results prove that photoirradiation induces dissolution of Ag particles even under relatively weak light irradiation in the range of mW/cm²; moreover, the findings indicate that photodissolution accelerates upon application of an external elec-

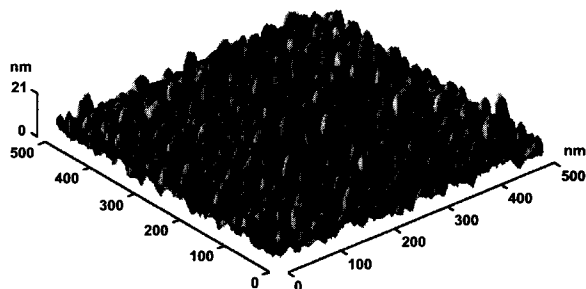
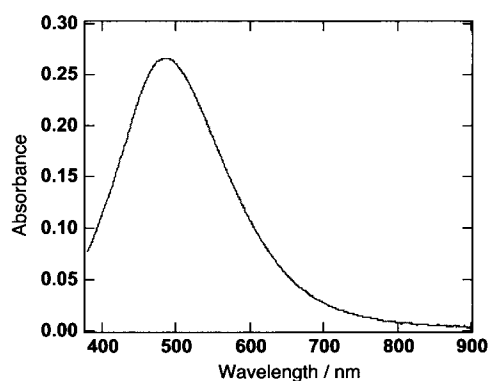


Fig. 10 Absorption spectrum (top) and an atomic force microscopic image (bottom) of evaporated Ag nanoparticles on a glass substrate. (View this art in color at www.dekker.com.)

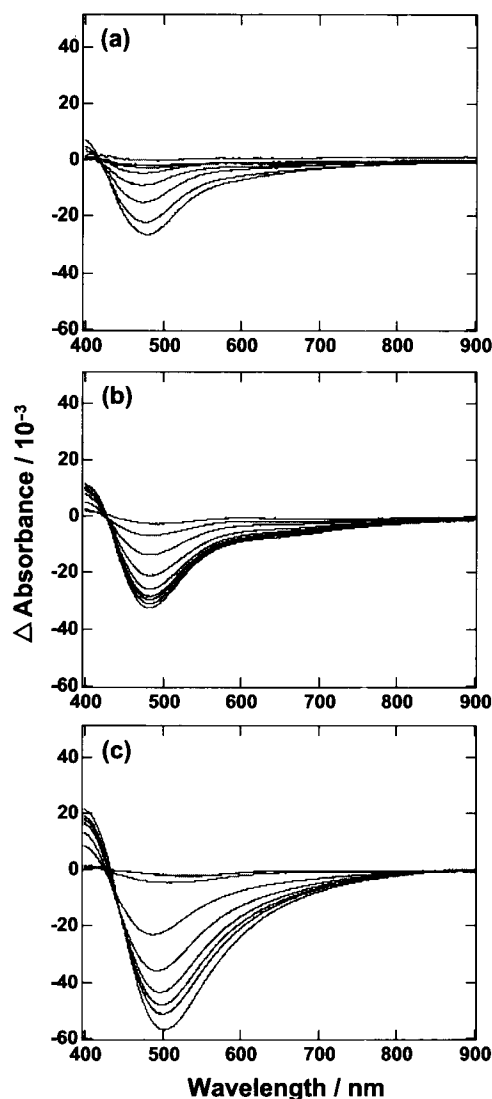


Fig. 11 Time-dependent absorption spectral change of the evaporated gold nanoparticles on a glass substrate in pure water during irradiation at 0.06 mW/cm² (a), 0.26 mW/cm² (b), and 0.90 mW/cm² (c). Applied electric field was 20 V/cm. Measurements were performed nine times at intervals of 15 sec. (View this art in color at www.dekker.com.)

tric field in solution. It should be noted that dissolution caused by application of an electric field alone without photoirradiation was minor, compared with the case involving the combination of an electric field and irradiation. Only slight incremental intrinsic dissolution of nanoparticles was evident upon application of an electric field in solution under darkness.

The synergetic effect of the weak light and the electric field was also detected in the structural changes. Fig. 13 displays AFM images of as-prepared Ag nanoparticles and those following treatment with light only, and with light and the electric field. The treatments with light only

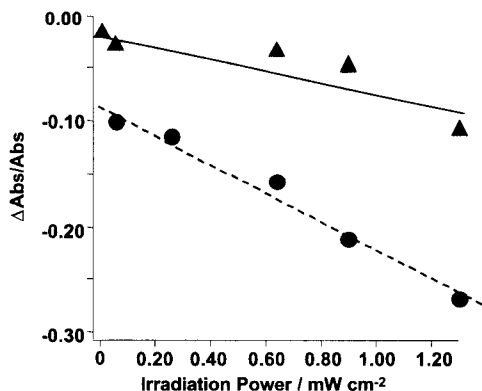


Fig. 12 Dependence of irradiation power on the absorption change at 500 nm of the gold film observed in the absence of an electric field (solid line) and upon application of an external electric field (20 V/cm) (broken line) for 120 sec.

resulted in slight decreases in the number of Ag nanoparticles without apparent size changes in the particles. On the other hand, the combined perturbations led to significant changes in particle size. The original size of approximately 20 nm in the prepared samples increased to 50–100 nm following polarization under irradiation. The particles were interconnected, forming anisotropic shapes. These changes in the size of the nanoparticles were more apparent when the irradiated light intensity became stronger (Fig. 13). This observed structural change suggests that photoirradiation under an external electric field induces deposition of Ag to specific particles as well

as dissolution. This dissolution of the particles leads to an increase of the interparticle distance. The spectral blue shift shown in Fig. 3 seems to reflect this decrease in the interaction between the particles rather than the change in the size of the nanoparticles.

The effect of photoirradiation with respect to acceleration of dissolution under an electric field may be considered as follows. In comparison to the relatively large-sized metal particles, the present electric polarization of Ag nanoparticles approximately 20 nm in size should be much smaller, and would be on the order of 10^{-5} V. Although this polarization appears to be insufficient to induce an electrochemical reaction, photoirradiation may assist the increase in polarization of the nanoparticles via photoexcitation. When resonant electronic excitation of nanoparticles is induced via plasmon excitation, the resultant polarization corresponding to several electron volts can generate electrochemical reactions such as metal dissolution and deposition (Fig. 14).

In the present system, possible electrochemical reactions in a single particle during the initial stage may include the oxidation reaction of Ag metal dissolution, the reductive reaction of hydrogen evolution, dissolved oxygen, and/or native oxide partially covering the surface of the Ag nanoparticle.^[61] As the reaction proceeds, a Ag^+ ion is likely to be generated by dissolution, and diffuse to the neighboring particles. When a Ag^+ ion arrives at a neighboring particle, Ag deposition could occur as a dominant reductive reaction at the particles, leading to changes in the size of the Ag nanoparticles. The applied electric field can assist the migration of the Ag^+

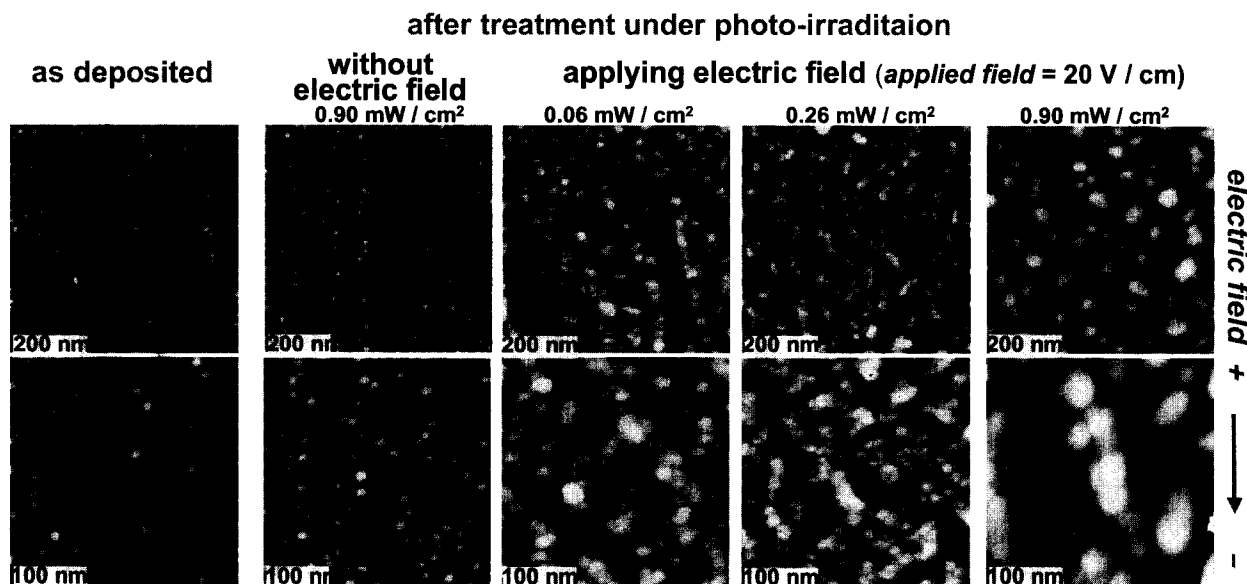


Fig. 13 Atomic microscopic images of the evaporated Ag nanoparticles on a glass substrate, as-deposited, following only irradiation, and following irradiation and an electric field. Dimensions are indicated on the images. (View this art in color at www.dekker.com.)

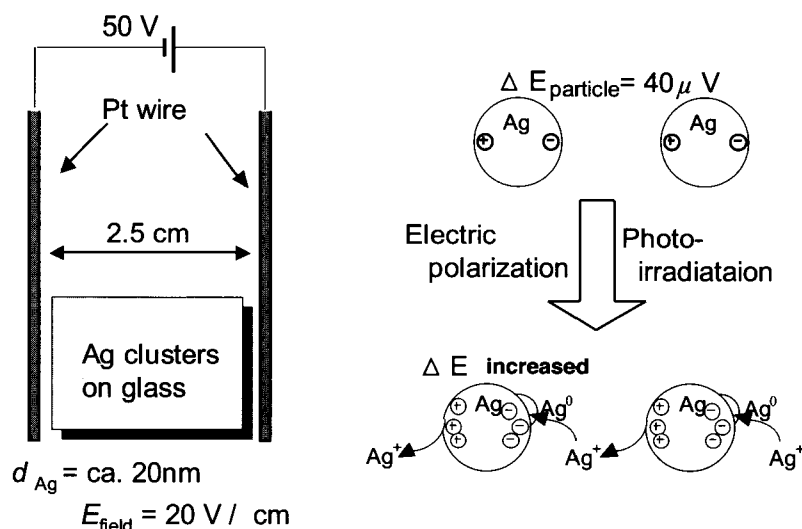


Fig. 14 Proposed mechanism of the photoinduced structural change under an external electric field in solution. (View this art in color at www.dekker.com.)

ions; consequently, the electric field accelerates the present reactions.

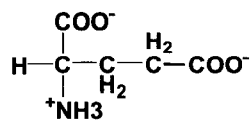
The results shown here proved that photoirradiation of metal nanoparticles under polarization by an external electric field accelerates structural changes in Ag nanoparticles. The reaction can be attributed to the highly localized electrochemical reactions of metal dissolution/deposition on the surface of the Ag nanoparticles. This phenomenon can be utilized for structural control of Ag nanoparticles adsorbed on the surface of an insulating material, circumventing the need for an external electric circuit.

CHANGES IN NEAR-INFRARED OPTICAL RESPONSE OF METAL THIN FILM ON GLASS SUBSTRATE BY ELECTRIC POLARIZATION IN SOLUTION

The technique of applying an external electric field to metal nanostructures could be used to control the optical properties of metal thin films on glass. One of the promising applications of metal nanostructures is their use as substrates for single molecular detection employing surface-enhanced Raman scattering (SERS).^[62–65] The phenomenon utilizes localized electromagnetic fields at the metal nanostructure under photoirradiation. Although the SERS enhancement has often included visible excitation because of its very sensitive resonance condition, the importance of near-infrared (NIR) excitation has also been recognized because of the advantages associated

with nonfluorescence properties and lower damage in photosensitive target molecules.^[66,67] Recently, theoretical calculations proved that the effective electromagnetic enhancement via near-infrared excitation would be possible if some appropriate metal nanostructures were constructed.^[29] Recent efforts have focused on preparation of the NIR-SERS active substrates using well-controlled structural units.^[25,68] Although several sophisticated methods were successful with respect to generation of fully reproducible NIR-SERS activity, the preparations were often complicated because of the need for specialized synthetic or preparative techniques. Furthermore, additional tuning for optimized NIR-SERS activity is rather difficult following the preparation. Thus novel facile and controllable techniques to prepare NIR-SERS active substrates should be developed.^[69]

Near-infrared SERS activity of the Ag on Au film on glass substrate under electric polarization was evaluated in aqueous solution containing 1 mM glutamic acid. Spectra were obtained in situ from the near-infrared laser Raman microscope system with excitation wavelength of 780 nm.^[70] Intensity of the SERS significantly increased upon application of an external electric field to the film (Fig. 15). The empirical signal enhancement factor, which was determined from the peak integration ratio of the SERS vibration at 1400 cm^{-1} to the unenhanced signal from the solution of a defined sample concentration, was found to be greater than 10^7 . The value is comparable to the recently reported value of the near-infrared SERS from carefully prepared gold nanoparticle superstructures possessing a precisely controlled periodic structure.^[71,72] Strong enhancement of greater than 10^7 in the present



glutamic acid

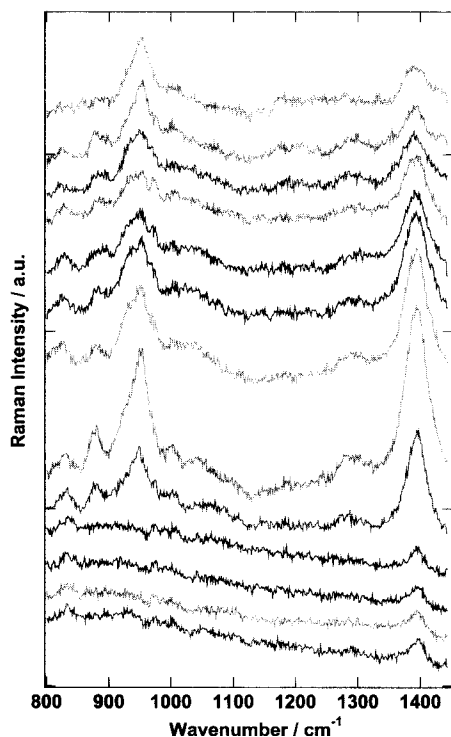


Fig. 15 Time-dependent SERS signals from the Ag on Au film during application of an external electric field. Measurements were performed at 20-sec intervals (from bottom to top). Two spectra at the top were at 420 and 480 sec after applying field. (View this art in color at www.dekker.com.)

systems could be attributable to the small particle structure characterized by diameters of approximately 10–20 nm on the Ag on Au film.

In this investigation, the NIR-SERS activity of an Ag on Au thin film was controlled via application of an external field to the metal thin films on an insulating substrate in solution. We found a novel application of an external electric field to the control of metal nanostructures on an insulating material in solution. As the result of the structural change of the Ag on Au thin film, significant enhancement of the near-infrared Raman scattering of amino acid molecules in solution was achieved (Fig. 16). The method is an extremely facile and effective technique in terms of control of NIR optical properties of such thin metal films on an insulating material in solution. Moreover, this procedure should be applied in the preparation of substrates displaying optimized NIR-SERS activity for various highly sensitive molecular sensors.

CONCLUSION AND FUTURE PERSPECTIVE

We have demonstrated that selective excitation of a specific surface plasmon mode of metal nanostructures can be employed as a perturbation for effective structural control. Useful effects on the particle interaction and highly localized electrochemical reaction were found in several nanostructured metal systems. The phenomena can be applied as a novel method to control metal nanostructures in the size region between a few nanometers and a hundred nanometers. As for the use of the method in future technologies, further optimization is required, utilizing the specificities of the wavelength and the polarization of the light for finer-size tuning at the metal nanostructures. Control in the contribution of the heat caused by photoillumination is also important for more precise structural control in the nanometer-size region. Despite these still unsolved issues, the structural control via localized

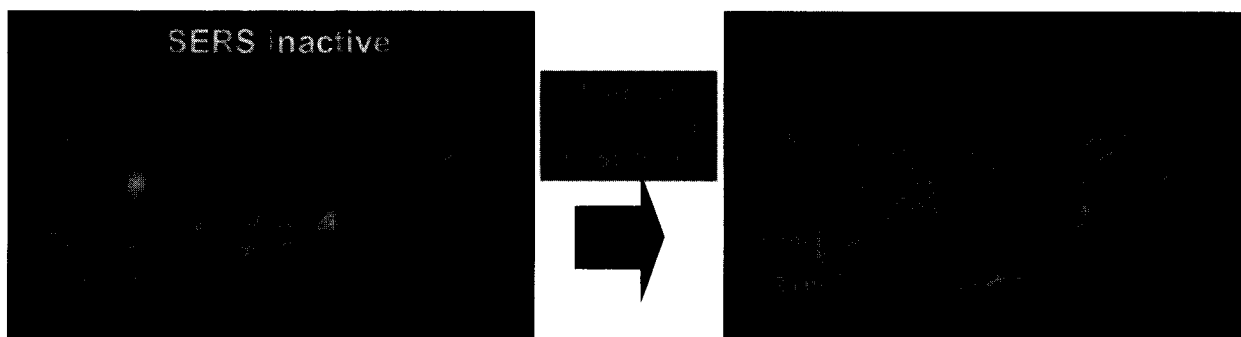


Fig. 16 Surface structures of the Ag on Au film before and after the application of an external electric field. (View this art in color at www.dekker.com.)

photoexcitation should be one of the promising approaches to construct nanostructures in a size region, which remains underdeveloped in the present nanotechnology.

ACKNOWLEDGMENTS

We would like to thank our collaborators, Messrs. T. Kitamura, H. Tanaka, Y. Sawai, and M. Suzuki, and Dr. J. Li in Osaka University, who, together with the authors, performed most of the work presented here. Grateful acknowledgment is also made to Dr. K. Ajito, NTT Basic Research Laboratories, for stimulating discussion and his contribution for in situ confocal near-infrared Raman measurements. This work was partially supported by a Grant-in-Aid for Scientific Research from the Ministry of Education, Culture, Sports, Science and Technology, Japan.

REFERENCES

1. Timp, G. *Nanotechnology*; Springer-Verlag: New York, 1999.
2. Nyffenegger, R.M.; Penner, R.M. Nanometer-scale surface modification using the scanning probe microscope: Progress since 1991. *Chem. Rev.* **1997**, *97*, 1195–1230.
3. Quinten, M.; Kreibig, U. Optical properties of aggregates of small metal particles. *Surf. Sci.* **1986**, *172*, 557–577.
4. Kreibig, U. *Handbook of Optical Properties*; Hummel, R.E., Wismann, P., Eds.; CRC Press: New York, 1997; Vol. 2. Chap. 7.
5. Henglein, A. Small-particle research: Physicochemical properties of extremely small colloidal metal and semiconductor particles. *Chem. Rev.* **1989**, *89*, 1861–1873.
6. Kamat, P.V. Photophysical, photochemical and photocatalytic aspects of metal nanoparticles. *J. Phys. Chem., B* **2002**, *106*, 7729–7744.
7. Fedurco, M.; Shklover, V.; Augustynski, J. Effect of halide ion adsorption upon plasmon-mediated photoelectron emission at the silver/solution interface. *J. Phys. Chem., B* **1997**, *101*, 5158–5165.
8. Kostecki, R.; Augustynski, J. Unusually strong cathodic photoeffect at silver in contact with aqueous solutions containing carbon dioxide. *Chem. Phys. Lett.* **1992**, *194*, 386–390.
9. Kostecki, R.; Augustynski, J. Photon-driven reduction reactions on silver. *J. Appl. Electrochem.* **1993**, *23*, 567–572.
10. Kostecki, R.; Augustynski, J. Effect of the surface roughness on the spectral distribution of photoemission current at the silver/solution contact. *J. Appl. Phys.* **1995**, *77*, 4701–4705.
11. Sass, J.K.; Laucht, H.; Kliewer, K.L. Photoemission studies of silver with low-energy (3 to 5 eV), obliquely incident light. *Phys. Rev. Lett.* **1975**, *35*, 1461–1464.
12. Fendler, J.H. Self-assembled nanostructured materials. *Chem. Mater.* **1996**, *8*, 1616–1624.
13. Motte, L.; Billoudet, F.; Lacaze, E.; Pileni, M.P. Self-organization of size-selected nanoparticles into three-dimensional superlattice. *Adv. Mater.* **1996**, *8*, 1018–1020.
14. Pileni, M.M. Nanosized particles made in colloidal assemblies. *Langmuir* **1998**, *13*, 3266–3276.
15. Murray, C.B.; Kagan, C.R.; Bawendi, M.G. Self-organization of CdSe nanocrystallites into three-dimensional quantum dot superlattices. *Science* **1995**, *270*, 1335–1338.
16. Kiely, C.J.; Fink, J.; Brust, M.; Bethell, D.; Schiffrin, D.J. Spontaneous ordering of bimodal ensembles of nanoscopic cluster. *Nature* **1998**, *396*, 444–446.
17. Murakoshi, K.; Nakato, Y. Formation of linearly arrayed structure of gold nanoparticles on gold single crystal surfaces. *Adv. Mater.* **2000**, *12*, 791–795.
18. Fujiwara, H.; Yanagida, S.; Kamat, P.V. Visible light induced fusion and fragmentation of TNA-modified gold nanoparticles. *J. Phys. Chem., B* **1999**, *103*, 2589–2591.
19. Eckstein, H.; Kreibig, U. Light induced aggregation of Au particles. *Z. Phys. D* **1993**, *26*, 239–241.
20. Murakoshi, K.; Nakato, Y. Anisotropic agglomeration of surface-modified gold nanoparticles in solution and on solid surfaces. *Jpn. J. Appl. Phys.* **2000**, *39*, 4633–4634.
21. Barz, F.; J.G.G., II; Philpott, M.R.; Weaver, M.J. Effect of laser illumination during oxidation–reduction cycles upon surface-enhanced Raman scattering from silver electrodes. *Chem. Phys. Lett.* **1982**, *91*, 291–295.
22. Chen, T.T.; Raben, K.U.V.; Owen, J.F.; Chang, R.K.; Laube, B.L. Laser illumination effects on the surface morphology, cyclic voltammetry, and surface-enhanced Raman scattering of Ag electrodes. *Chem. Phys. Lett.* **1982**, *91*, 494–500.
23. Macomber, S.H.; Furtak, T.E.; Devine, T.M. Enhanced Raman characterization of adsorbed water at the electrochemical double layer on silver. *Chem. Phys. Lett.* **1982**, *90*, 439–444.
24. Brike, R.L.; Lombardi, J.R. Surface-Enhanced

- Raman Scattering. In *Spectroelectrochemistry*; Gale, R.J., Ed.; Plenum Press: New York, 1988; 263–348.
25. Lyon, L.A.; Keating, C.D.; Fox, A.P.; Baker, B.E.; He, L.; Nicewarner, S.R.; Mulvaney, S.P.; Natan, M.J. Raman spectroscopy. *Anal. Chem.* **1998**, *70*, 341R–361R.
 26. Tian, Z.-Q.; Ren, B.; Wu, D.-Y. Surface-enhanced Raman scattering: From noble to transition metals and from rough surfaces to ordered nanostructures. *J. Phys. Chem., B* **2002**, *106*, 9463–9483.
 27. Murakoshi, K.; Kitamura, T.; Nakato, Z.Z. Nano-scale structural characteristics of photodissolved gold (111) single crystalline surface. *Jpn. J. Appl. Phys.* **2001**, *40*, 1918–1922.
 28. Garcia-Vidal, F.J.; Pendry, J.B. Collective theory for surface enhanced Raman scattering. *Phys. Rev. Lett.* **1996**, *77*, 1163–1166.
 29. Xu, H.; Aizpurua, J.; Kall, M. Electromagnetic contributions to single-molecule sensitivity in surface-enhanced Raman scattering. *Phys. Rev., E* **2000**, *62*, 4318–4324.
 30. Schindler, W.; Hugelmann, P.; Hugelmann, M.; Kartner, F.X. Localized electrochemical nucleation and growth of low-dimensional metal structures. *J. Electroanal. Chem.* **2002**, *522*, 49–57.
 31. Itaya, K. In situ scanning tunneling microscopy in electrolyte solutions. *Prog. Surf. Sci.* **1998**, *58*, 121–248.
 32. Dohnalek, Z.; Lyubinetsky, I.; Yates, J.T., Jr. Laser pulse desorption under scanning tunneling microscope tip—Cl removal from single site on Si(100). *J. Vac. Sci. Technol.* **1997**, *A15*, 1488–1492.
 33. Liu, C.-Y.; Bard, A.J. Irradiation-induced nanometer-scale surface etching of a CdSe film with a scanning tunneling microscope. *Chem. Phys. Lett.* **1990**, *174*, 162–166.
 34. Jersch, J.; Dickmann, K. Nanostructure fabrication using laser field enhancement in the near field of a scanning tunneling microscope tip. *Appl. Phys. Lett.* **1996**, *68*, 868–870.
 35. Demming, F.; Jersch, J.; Dickmann, K.; Geshev, P.I. Calculation of the field enhancement on laser-illuminated scanning probe tips by the boundary element method. *Appl. Phys., B* **1998**, *66*, 593–598.
 36. Jersch, J.; Demming, F.; Dickmann, K. Field enhancement of optical radiation in the nearfield of scanning probe microscope tips. *Appl. Phys., A* **1998**, *64*, 29–32.
 37. Yau, S.-T.; Saltz, D.; Nayfeh, M.H. Laser-assisted deposition of nanometer structures using a scanning tunneling microscope. *Appl. Phys. Lett.* **1990**, *57*, 2913–2915.
 38. Yau, S.-T.; Saltz, D.; Nayfeh, M.H. Scanning tunneling microscope-laser fabrication of nanostructures. *J. Vac. Sci. Technol., B* **1990**, *9*, 1371–1375.
 39. Hamers, R.J.; Markert, K. Atomically resolved carrier recombination at Si(111)-(7*7) surfaces. *Phys. Rev. Lett.* **1990**, *64*, 1051–1054.
 40. Ukraintsev, V.A.; Yates, J.T., Jr. Nanosecond laser induced single atom deposition with nanometer spatial resolution using a STM. *J. Appl. Phys.* **1996**, *80*, 2561–2571.
 41. Lyubinetsky, I.; Dohnalek, Z.; Ukraintsev, V.A.; Yates, J.T., Jr. Transient tunneling current in laser-assisted scanning tunneling microscopy. *J. Appl. Phys.* **1997**, *82*, 4115–4117.
 42. Jersch, J.; Demming, F.; Fedotov, I.; Dickmann, K. Time-resolved current response of a nanosecond laser pulse illuminated STM tip. *Appl. Phys., A* **1999**, *68*, 637–641.
 43. Jersch, J.; Demming, F.; Hildenhagen, L.J.; Dickmann, K. Field enhancement of optical radiation in the nearfield of scanning probe microscope tips. *Appl. Phys., A* **1998**, *66*, 29–34.
 44. Boneberg, J.; Tresp, M.; Ochmann, M.; Münzer, H.-J.; Leiderer, P. Time-resolved measurements of the response of a STM tip upon illumination with a nanosecond laser pulse. *Appl. Phys., A* **1998**, *66*, 615–619.
 45. Boneberg, J.; Münzer, H.-J.; Tresp, M.; Ochmann, M.; Leiderer, P. The mechanism of nanostructuring upon nanosecond laser irradiation of a STM tip. *Appl. Phys., A* **1998**, *67*, 381–384.
 46. Boneberg, J.; Lohrmann, M.; Böhmisch, M.; Burmeister, F.; Lux-Steiner, M.; Leiderer, P.Z. Electrical field induced growth of triangular nanometer structures on WSe₂. *Phys. B* **1996**, *99*, 567–570.
 47. Hiesgen, R.; Meissner, D. Nanoscale characterization of semiconductor surfaces by spatially resolved photocurrent measurements. *Fresenius' J. Anal. Chem.* **1997**, *358*, 54–58.
 48. Hiesgen, R.; Meissner, D. Nanoscale photocurrent variations at metal-modified semiconductor surfaces. *J. Phys. Chem.* **1998**, *102*, 6549–6557.
 49. Murakoshi, K.; Kitamura, T.; Nakato, Y. Localized photoresponses of nanostructured metal surfaces observed by a scanning tunneling microscope. *Phys. Chem., Chem. Phys.* **2001**, *3*, 4572–4577.
 50. Sawai, Y.; Suzuki, M.; Murakoshi, K.; Nakato, Y. Photo-induced single metal-dot deposition onto an Au electrode.
 51. Geshev, P.I.; Demming, F.; Jersch, J.; Dickmann, K. Calculation of the temperature distribution on laser-illuminated scanning probe tips. *Appl. Phys., B* **2000**, *70*, 91–97.

52. Kroo, N.; Thost, J.-P.; Völcker, M.; Krieger, W.; Walther, H. Decay length of surface plasmons determined with a tunnelling microscope. *Europhys. Lett.* **1991**, *15*, 289–293.
53. Moller, R.; Abrecht, U.; Boneberg, J.; Koslowski, B.; Leiderer, P.; Dransfeld. Detection of surface plasmons by scanning tunneling microscopy. *J. Vac. Sci. Technol.* **1991**, *B9*, 506–509.
54. Engelmann, G.E.; Ziegler, J.C.; Kolb, D.M. Electrochemical fabrication of large arrays of metal nanoclusters. *Surf. Sci.* **1998**, *401*, L420–L424.
55. Kolb, D.M.; Ullmann, R.; Will, T. Nanofabrication of small copper clusters on gold(111) electrodes by a scanning tunneling microscope. *Science* **1997**, *275*, 1097.
56. Schuster, R.; Kirchner, V.; Allongue, P.; Ertl, G. Electrochemical micromachining. *Science* **2000**, *289*, 98–101.
57. Bradley, J.-C.; Chen, H.-M.; Crawford, J.; Eckert, J.; Ernazarova, K.; Kurzeja, T.; Lin, M.; McGee, M.; Nadler, W.; Stephens, S.G. Creating electric contacts between Cu particles. *Nature* **1997**, *389*, 268–271.
58. Bradley, J.-C.; Crawford, J.; McGee, M.; Stephens, S.G. A contactless method for the directed formation of submicrometer copper wires. *J. Electrochem. Soc.* **1998**, *145*, L45–L47.
59. Murakoshi, K.; Tanaka, H.; Sawai, Y.; Nakato, Y. Photo-induced structural changes of silver nanoparticles on glass substrate in solution under an electric field. *J. Phys. Chem., B* **2002**, *106*, 3041–3045.
60. Murakoshi, K.; Tanaka, H.; Sawai, Y.; Nakato, Y. Effect of photo-irradiation and external electric field on structural change of metal nano-dots in solution. *Surf. Sci.* **2003**, *532–535*, 1109–1115.
61. Peyser, L.A.; Vinson, A.E.; Bartko, A.P.; Dickson, R.M. Photoactivated fluorescence from individual silver nanoclusters. *Science* **2001**, *291*, 103–106.
62. Michaels, A.M.; Nirmal, M.; Brus, L.E. Surface enhanced Raman spectroscopy of individual rhodamine 6G molecules on large Ag nanocrystals. *J. Am. Chem. Soc.* **1999**, *121*, 9932–9939.
63. Maruyama, Y.; Ishikawa, M.; Futamata, M. Surface-enhanced Raman scattering of single adenine molecules on silver colloidal particles. *Chem. Lett.* **2001**, 834–835.
64. Kneipp, K.; Kneipp, H.; Kartha, V.B.; Manoharan, R.; Deinum, G.; Itzkan, I.; Dasari, R.R.; Feld, M.S. Detection and identification of a single DNA base molecule using surface-enhanced Raman scattering (SERS). *Phys. Rev., E* **1998**, *56*, R6281–R6284.
65. Nie, S.; Emory, S.R. Probing single molecules and single nanoparticles by surface-enhanced Raman scattering. *Science* **1997**, *275*, 1102–1106.
66. Ajito, K.; Torimitsu, K. Near-infrared Raman spectroscopy of single particles. *Trends Anal. Chem.* **2001**, *20*, 255–262.
67. Manfait, M.; Nabiev, I. *Raman Microscopy: Developments and Applications*; Turrell, G., Corset, J., Eds.; Academic Press: London, 1996; 379–420.
68. Vo-Dinh, T. Surface-enhanced Raman spectroscopy using metallic nanostructures. *Trends Anal. Chem.* **1998**, *17*, 557–582.
69. Murakoshi, K.; Ajito, K.; Jingze, L.; Sawai, Y.; Torimitsu, K.; Tanaka, H.; Nakato, Y. Control of near infrared surface-enhanced Raman scattering activity of Ag on Au thin film prepared on glass substrate by external electric polarization in solution. submitted.
70. Ajito, K.; Morita, M.; Torimitsu, K. Investigation of the molecular extraction process in single subpicoliter droplets using a near-infrared laser Raman trapping system. *Anal. Chem.* **2000**, *72*, 4721–4725.
71. Kim, B.; Tripp, S.L.; Wei, A. Self-organization of large gold nanoparticle arrays. *J. Am. Chem. Soc.* **2001**, *123*, 7955–7956.
72. Wei, A.; Kim, B.; Sadtler, B.; Tripp, S.L. Tunable surface-enhanced Raman scattering from large gold nanoparticle arrays. *Chem. Phys. Chem.* **2001**, *12*, 743–745.

Metal–Oxide Interfaces: Toward Design via Control of Defect Density

M

A. Bogicevic

Ford Motor Company, Dearborn, Michigan, U.S.A.

INTRODUCTION

Ever since metals and ceramics were first joined together, mankind has striven to control this bond to enable the development of new and superior composite products. Transistors, catalytic converters, light bulbs, jet engine turbines, cutting tools, and dental implants are but a few examples of every day products that depend on the integrity of metal–ceramic interfaces. Further technology development is, in an increasing number of applications, rapidly reaching a point where precise atomic-level control of the composite interface is required. This is already a reality in the ever-shrinking world of microelectronics components, where device performance relies on metal–oxide junctions, often only a few atomic layers thick, and in emerging fields such as nano-fabricated catalysts and nano-electromechanical systems.

The ability to control the formation and stability of composite interfaces can be generally viewed as requiring two critical components: an adequate understanding of what factors determine interface formation and integrity, and the actual means to manipulate the interface using that insight. Atomic defects and impurities are well known to strongly influence interface formation and can, these days, be relatively well controlled experimentally. However, the poor understanding of *how* such defects affect individual metal–oxide systems currently represents a major obstacle for using defect control to one's advantage in tailoring interfaces. The large variations in system behavior with respect to any given defect situation indicate the complexity of the problem. This intricacy is ultimately rooted in the quantum mechanical nature of nano-sized components, which, in itself, can lead to the emergence of new properties, e.g., the onset of catalytic ignition of normally inert metals.^[1] Therefore, first-principles parameter-free atomistic calculations are a useful complement to well-controlled experiments for shedding some light on this problem. Substantial progress has been made lately on both theoretical and experimental ends, and this article highlights some of these developments with regard to simple point defects. While the focus here falls on applications involving thin metal films and dispersed metal particles on metal oxides, certain generalizations can be made

for other materials, as well as the inverse situation encompassing the growth of oxides on metals.

In the following, a brief overview of metal–oxide bonding is given from a theorist's perspective, as an introduction to the important concepts of adhesion, wetting, and nucleation and growth processes. A natural division is made into thermodynamic and kinetic aspects of interface control, and the discussion then shifts to the role of common point defects and the prospects of defect-mediated control of metal–oxide interfaces.

METAL–OXIDE INTERFACE

The nature and strength of the bond between a metal and an oxide varies, often sensitively, with the constituent materials and their preparation, e.g., surface morphology, metal coverage, gas phase atmosphere, etc. A number of different adhesion mechanisms have been reported, including weak van der Waals dispersion forces between induced surface dipoles, electrostatic polarization binding, and strong ionic and covalent bonding (the latter being more directional).^[2–5] Several reviews on the general science of metal–oxide interfaces have been recently published. Recommended background literature includes the excellent reviews on the surface science of metal oxides by Henrich and Cox,^[6] and on metal–oxide interfaces by Finnis^[2] and by Campbell.^[7]

Single metal atoms tend to form relatively strong chemical bonds to most oxide surfaces.^[2,4,5] This is mainly the result of a severe under-coordination of the metal atom (compared to its favored bulk state), which is therefore reactive with the surface. These ionic or covalent metal–oxide bonds are correspondingly quite short, normally around 1–2 Å.^[4,5,8,9] Typical bond strengths range from 1 to several eV, and are normally referred to as adsorption or desorption energies—defined as the energy required to remove a metal atom to the vacuum level. The metal–oxide bonds tend to further strengthen at various oxide surface defects, e.g., anion/cation vacancies, which can trap and immobilize diffusing metal atoms (as discussed in detail below). Fig. 1 illustrates how the adsorbate–substrate bonds shorten and strengthen on ultrathin (≈ 5 Å) alumina films as the

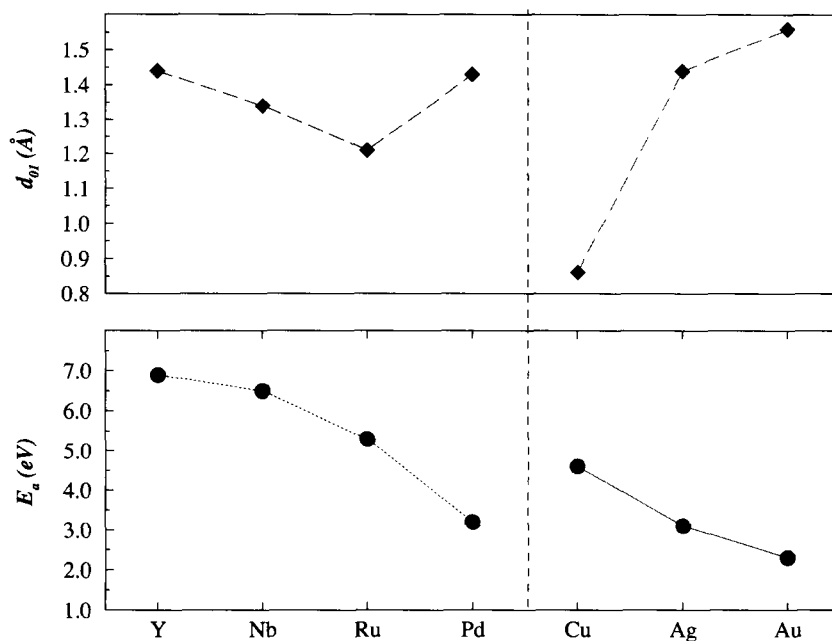


Fig. 1 Low coverage metal–oxide bond lengths (d_{01}) and metal adsorption energies (E_a) for various metal atoms deposited on thin alumina films. The dashed line separates 4d elements and the Group IB coinsage metals. Note how the metal–oxide bond lengths (d_{01}) increase down and to the left in the periodic table as the metal cation radii increase, with an attendant weakening of the adsorption energy. Note also the exception to this bond length–bond strength relation for the Ru–Nb–Y series, which is attributable to multiple ionization for Nb and Y (cf. Ru–Pd–Ag that are all singly ionized). (View this art in color at www.dekker.com.)

adsorbate radius decreases (see Ref. [5]). For ionic adsorbate–substrate bonds, the metal atoms normally occupy the electrostatically favored position at low coverages,^[3–5,9] although this rule of thumb weakens with oxide covalency. Strong chemical bonds tend to introduce new states in the band gap of the oxide, and one often finds a moderate to strong net spin polarization on the metal atom.^[9]

As the metal coverage increases, metal–metal bonds are strengthened at the expense of weakened metal–oxide bonds. At some point, the very nature of the interfacial bond can change, and several theoretical studies have suggested simple polarization binding^[10,11] as the origin of metal–oxide cohesion at coverages near and above 1 monolayer (ML).^[5] This image interaction-based binding is considerably weaker than the ionic and covalent bonds typically found at low coverages. Fig. 2 illustrates the polarization binding found in a number of metal–oxide systems at the atomic level. The transition to increased metal coverage is marked by a lengthening of the metal–oxide bonds, typically by about 1 Å or more,^[5,9] accompanied by a substantially weakened metal–oxide bond. This is illustrated in Fig. 3 for single-layer ML thick metal films atop an ultrathin alumina substrate. The exact coverage at which metallic states appear depends on several factors, but has been estimated to be about 2/3 ML in certain systems.^[5]

As the metal film or particle grows thicker, its cohesion to the oxide decreases only slightly in the case of polarization binding, and stabilizes already at about 2 ML.^[5] This is a simple consequence of the image

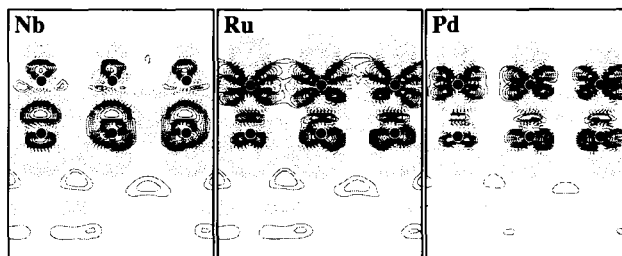


Fig. 2 Charge density difference plot that illustrates how single-layer Nb, Ru, and Pd metal films adhere to a thin alumina support by means of polarization binding atop the oxide anions (see Ref. [5] for details). Solid lines indicate charge accumulation, dashed lines charge depletion, and the position of the topmost oxygen ions and the adsorbate atoms is indicated with (six) filled dots. As one moves to the right in the periodic table (PT), d -shell filling increases, there is more charge rehybridization, and less of the ionic core exposed, resulting in weakened metal–oxide bonds. Note the counterpolarization of the oxygen ions in the top layer of the oxide, which thus actively participate to some degree in the bond formation. (View this art in color at www.dekker.com.)

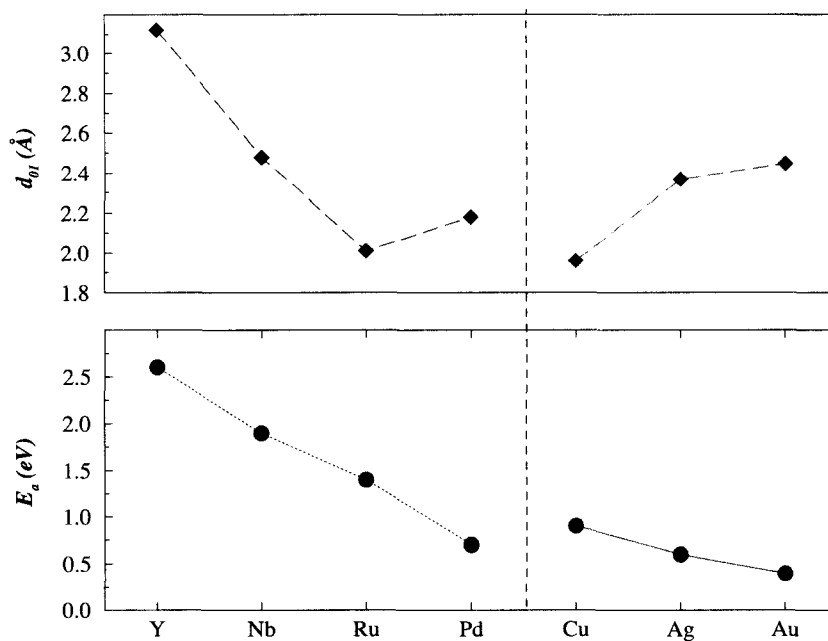


Fig. 3 High coverage adhesion energies and film–oxide separations for various metal films deposited on ultrathin alumina films. The trends are similar to those at low coverage (cf. Fig. 1), which is largely attributable to atomic size arguments here as well, although the far-left elements again behave anomalously because of the rehybridization illustrated in Fig. 2. (View this art in color at www.dekker.com.)

interaction bonding, which is to first order independent of the metal film thickness. The interface structure can change at any time during the film formation, as existing bonds are broken and new ones are formed. During initial film formation, this tends to happen because of improving metal coordination. For example, Pt clusters on MgO(100) occupy initially both anion and cation sites to maximize their coordination, but spread out to anion sites only as the cluster becomes larger and starts forming a metal film.^[9] In other circumstances, it is the variation in elastic strain energy within the growing metal film that leads to change of interface structure, as reported in a systematic study of metal film growth atop thin alumina films.^[5] Here it was found that elastically soft single-layer films preferred a buckled adsorption atop cations, while at 2 ML and above, all metal films preferred unrumpled atop anion adsorption because of the accumulated strain energy penalty.^[5] Overlayer strain is also often relieved through misfit dislocations, which can already appear at a few ML film thickness, leaving behind epitaxial interface domains.

Adhesion and Wetting (Thermodynamics)

Thermodynamic analyses constitute a good starting point for assessing interface morphology and stability [kinetics are discussed in the section “Nucleation and Growth (Kinetics)”]. The work of adhesion W_{ad} describes the

reversible free-energy change for cleaving an interface to produce surfaces in equilibrium with their environments. It is defined by the Dupré equation as

$$W_{ad} = \sigma_m + \sigma_o - \gamma_{mo} \quad (1)$$

where the three terms on the right-hand side of Eq. 1 denote the surface energies of the metal and the oxide, and their mutual interface energy.^a The work of adhesion is directly correlated to the degree to which a metal will wet an oxide, with the contact angle θ given by

$$\cos \theta = \frac{\sigma_o - \gamma_{mo}}{\sigma_m} \quad (2)$$

The smaller the contact angle θ , the greater the wettability of the oxide by the metal, as illustrated in Fig. 4.

In some applications, good wetting that results in a uniform metal film atop the oxide is desired (e.g., metal–oxide electronic junctions), while in other situations one instead strives to decrease the wetting to improve metal particle dispersion (e.g., catalysis applications). High oxide surface energies and low metal surface energies

^aThe work of adhesion is closely related to the work of separation W_{sep} , which is a fundamental interfacial quantity that establishes the minimum work needed to cleave a metal–oxide interface into two free surfaces. A detailed discussion on this topic is given in Ref. [2].

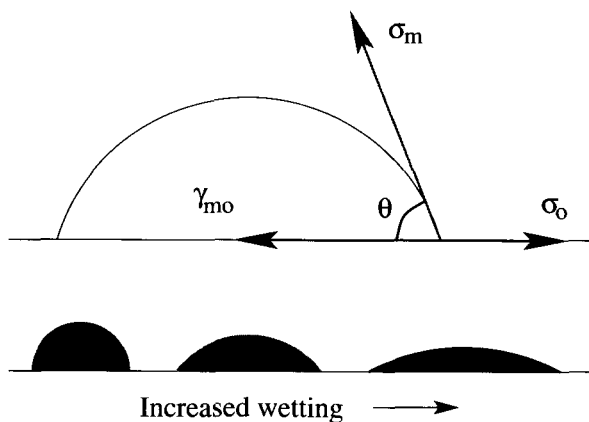


Fig. 4 Schematic illustration of how the contact angle θ is determined by surface/interface energies, and how wetting increases with a smaller contact angle. Nonwetting occurs for $\theta > 90^\circ$, wetting for $< 90^\circ$, and perfect wetting or spreading for $\theta = 0^\circ$. (View this art in color at www.dekker.com.)

thus favor wetting of an oxide by the metal, as does increasing the interface energy.^b

At this moment, it is useful to make a note about theoretical adhesion studies between metals and oxides. If one starts from unrealistic surfaces (e.g., nonstoichiometric oxides), which may not spontaneously reconstruct because of constraints, artificially strong interface energies will be computed because such surfaces are unstable and therefore very reactive. This is particularly important for oxide surfaces, and the simple recipe for avoiding such misconstructions is to ensure that the surface free energies are realistic, if not in agreement with experiment. The alternative is to include the energetic penalty of altering a realistic oxide into a reactive state by taking into account the displaced oxide material in the energetic balance.

Nucleation and Growth (Kinetics)

Metal–oxide interfaces are, in a number of applications, manufactured through controlled growth of one component atop the other. The most common growth modes in epitaxial growth are layer-by-layer Frank–Van der Merwe (FV) growth, three-dimensional Volmer–Weber (VW) growth, and the Stranski–Krastanov (SK) growth mode that transitions from FV to VW growth after a few initial layers (Fig. 5). The two-dimensional FV growth mode corresponds to complete wetting, and is expected on

thermodynamic grounds for systems in which $\sigma_o - \gamma_{mo} > \sigma_m$. Correspondingly, three-dimensional VW growth is expected for the opposite scenario where $\sigma_o - \gamma_{mo} < \sigma_m$, and the intermediate 2-D–3-D SK mode for situations in which $\sigma_o - \gamma_{mo} \simeq \sigma_m$.

These types of free-energy analyses outline the thermodynamic limits of achievable interface morphologies. In reality, it can be technically quite difficult to realize the desired interface properties within these limits. In addition, there is frequently a need to also join non-wetting materials. The fact that epitaxial growth is a highly nonequilibrium process is part of the problem with achieving thermodynamically stable interfaces, but also enables joining nominally nonwetting materials. This kind of interface manipulation is enabled by kinetic control of the microscopic pathways that the system undergoes as one material is grown atop the other.

Mean-field nucleation theory provides a suitable mathematical framework for understanding the role that different atomic diffusion and reaction processes play in determining film morphology. As atoms arrive on the surface from the gas phase, they diffuse and meet to form the smallest stable island nuclei, e.g., dimers. As more atoms are deposited, the further growth of these nuclei competes with the formation of new nuclei. At the saturation density of stable nuclei, any further deposition leads exclusively to island growth. The mean-field assumption that the monomer density in between islands is homogeneous facilitates a simple analytical solution to the time evolution of island densities.

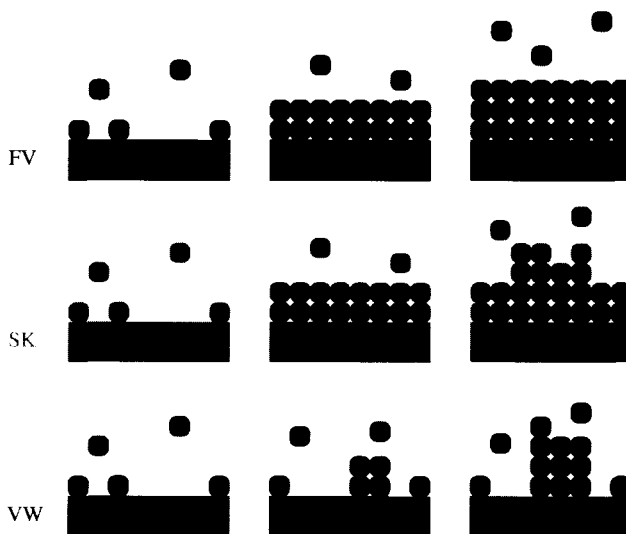


Fig. 5 Schematic illustration of three common epitaxial growth modes. The SK growth mode starts out in a layer-by-layer FV fashion, and later transitions to a 3-D VW-type growth. (View this art in color at www.dekker.com.)

^bThe sign conventions differ in the literature, so some caution must be taken when comparing the three relevant energies. While a higher surface free energy is typically associated with an energetic penalty, a higher interface energy is often taken to mean more energetically favored.

As an example illustrating the important concepts of a critical nucleus size and its relation to atomic processes that can be manipulated via defect density, the simple case of 2-D nucleation and growth with stable dimers is considered next. The rate equations for the density of single atoms n_1 and stable metal islands n_x then read,^[12]

$$\frac{dn_1}{dt} = F - 2\tau_1 D n_1^2 - \tau_x D n_1 n_x - \phi_x F (F t - n_1) - 2\phi_1 F n_1 \quad (3)$$

$$\frac{dn_x}{dt} = \tau_1 D n_1^2 + \phi F n_1 - 2n_x (F - dn_1/dt) \quad (4)$$

where the subscript x denotes the number of atoms in the island, τ represents the capture rates, D is the adatom diffusivity, F is the influx rate of atoms, t is the time, and ϕ relates to direct impingement on existing islands. Incorporating the standard Arrhenius relation for thermally activated processes within transition state theory, $v = v_0 \exp(-E/k_B T)$, where v represents the process rate, v_0 the vibrational prefactor, k_B the Boltzmann factor, and E the activation energy of the process, and using the approximate mean free path relation $l \simeq (D/F)^{1/6}$, one arrives at the general island density expression for 2-D islands in the complete condensation regime,

$$n_x = \eta(\theta, i) \left(\frac{D}{F}\right)^{-\chi} \exp\left(\frac{E_i}{(i+2)k_B T}\right) \quad (5)$$

with the scaling exponent χ given by

$$\chi = \frac{i}{i+2} \quad (6)$$

and where θ denotes the coverage and η represents a universal scaling function of the coverage θ . The *critical* island size i represents the number of atoms in the smallest stable nucleus minus one, and E_i its binding energy ($E_1=0$). From Eqs. 5 and 6, it is evident that these last two parameters, in particular, strongly affect the island density, which is the primary means to kinetic control of growth morphology. This is the primary subject of the remainder of this paper.

ROLE OF DEFECTS

There are essentially two approaches to tailoring metal-oxide interfaces: manipulation of thermodynamic energies and manipulation of growth kinetics. In the first case, one strives to adjust the interface energy or the surface energies of the constituents, while the second approach encompasses adjusting the nucleation and growth kinetics. Point defects in particular were repeatedly shown to strong-

ly influence or control both interface formation and interface stability^[13-16] as well as the chemical reactivity of thus formed overlayers.^[1,6,7,10,17-19] Even in well-controlled ultrahigh vacuum environments, relatively modest defect densities on the order of 10^{12} cm^{-2} (roughly 1 defect per 1000 surface atoms) have been known to dominate the nucleation and growth process of interface formation.^[14,16] For example, it was recently shown that even low 10^{-11} mbar pressure chambers allowed for low-level impurities to completely change the growth mode of Pt(111) from flat films (FW) to 3-D dispersed particles (VW).^[20]

The presence of point defects is often noted indirectly, e.g., via sample coloration, or by the way the metal island density varies in growth experiments (see below). Sometimes, it is discrepancies with other studies that eventually lead to the realization of defect-affected systems. In the Pt example above, new experiments prompted by variances with first-principles calculations revealed that 0.001 ML of adsorbed CO was responsible for the unexpected 3-D growth.^[20] In other examples, hydroxyl groups from dissociated water were identified as nucleation centers in several metal-oxide systems,^[21-24] as confirmed by first-principles theoretical calculations.^[8,23] The mechanism by which hydroxyls tend to nucleate metal islands on oxides is discussed in some detail in Refs. [8,23,24]. Other defects that have been commonly held responsible for affecting metal-oxide interface formation are hydrogen, carbon, sulphur, and other contaminants, as well as intrinsic oxide point defects such as oxide vacancies.

A common misconception in the literature is that the trapping ability of a defect is also a signature of its propensity to preferentially nucleate metal islands. If one ignores the interaction between the trapped atom and the sea of diffusing adatoms, there is actually *no* net effect whatsoever on the nucleation and growth process. All that would happen upon the trapping is that the population of diffusing adatoms and the availability of surface sites would decrease by the number of trapped atoms. In essence, this would be equivalent to considering a smaller portion of the growth area, resulting in no net perturbation.

Clearly then, at the very heart of nucleation and growth lies the interaction between metal adatoms, and its manipulation is grounded in the modification of these interactions. A defect will preferentially nucleate metal islands if, and only if, it stabilizes the metal-metal bond(s) of the cluster compared with the same cluster on the defect-free surface. Specifically, the defect must enhance the binding energy of the smallest stable cluster, henceforth referred to as the *core* cluster. The core cluster is what the critical cluster, introduced earlier, becomes upon the addition of a single atom. Thus, one distinguishes between unstable, critical, core, and stable clusters, which

contain $n < n_i$, n_i , $n_i + 1$, and $n > n_i + 1$ atoms, respectively, with i representing the critical cluster size.

It is evident from these arguments alone that the concept of critical and core clusters are central in any growth process, and that the trapping energy of clusters smaller than the core cluster are not (single atoms included). This is also reflected in the nucleation theory expressions for the island density, which carry an exponential dependence of the core cluster binding energy (cf. Eq. 5). Depending on the metal-oxide system and the overall growth conditions, the core cluster can consist of a dimer, trimer, tetramer, or even larger aggregates. In many instances, dimers (pairs of atoms) constitute the core cluster ($i=1$). In this case, the appropriate quantity entering Eq. 5 is the dimer binding energy E_b , which is defined with respect to two infinitely separated adatoms. A good indication of whether a defect may preferentially nucleate metal islands for $i=1$, is to thus consider whether it enhances E_b . For a discussion of how cluster mobility enters the picture, and the conditions under which larger clusters than dimers may become critical, the reader is referred to the excellent review of nucleation and aggregation by Brune.^[12]

At this point, it is important to realize that, in some cases, even significant changes in core cluster binding energies brought about by defects can be absolutely irrelevant for the nucleation and growth process. The relevance of defect-mediated changes in the binding energy of the core nucleus depends on the degree of perturbation and on the relevant growth conditions. For example, a change in E_b of, say, 1 eV on top of an already strong dimer bond of several eVs will barely perturb the nucleation process under most growth conditions—once two atoms meet, they will stick together for a sufficiently long time to nucleate an island irrespective of the actual dimer binding energy. Conversely, the same change of 1 eV in a system with relatively weak dimer bonds of an eV or less will have a tremendous effect under the same growth conditions. Clearly, the relevant measure here is to consider the relative change the defect brings about in the core cluster binding energy compared with its absolute value on the pristine surface, and to view that perturbation in light of the growth conditions (e.g., temperature and flux), cf. Eq. 5.

NUCLEATION AT OXIDE VACANCIES

The role of intrinsic oxide point defects in metal-oxide interface formation remains quite controversial. It has been suggested in several studies that surface anion vacancies serve as nucleation centers for metal islands by trapping metal adatoms, thereby strongly affecting the growth kinetics and consequent growth modes.^[16,27-29] A

number of theoretical first-principles studies have shown that both single metal atoms and metal films bind stronger, in the former case much stronger, to oxide surfaces containing intrinsic defects such as oxygen vacancies.^[8,9,27,28,30-32] Oxygen vacancies in particular were suggested as the most likely candidate for nucleating metal islands.^[16,30] However, there is, to this date, no direct experimental or theoretical evidence to support this supposition. Direct experimental verification remains elusive, not least because of the inherent difficulty in atomically resolving insulating oxide surfaces. Instead, indications of defect-controlled nucleation and growth often comes from noting that the metal island density n_x stays constant over a wide range of deposition temperatures T and/or deposition fluxes F ,^[15,16] cf. Eq. 5. Theoretical studies, while supporting the trapping model, have not adequately addressed the issue of nucleation, which involves the buildup of metal-metal bonds on the oxide surface. The first theoretical study to actually do so suggested that oxygen vacancies on MgO(100) do not preferentially nucleate Pt islands, contrary to prevailing speculations.^[18] Subsequent studies of a number of other systems lend further support to these initial findings, and provide a physical explanation to why highly reactive vacancies do not necessarily nucleate metal islands.^[9] In the following, these arguments are recounted and elaborated on to explain why the ability of oxygen vacancies (and other defects) to trap individual atoms is, in general, not a good indication of their propensity to preferentially nucleate metal islands.

Anion and cation vacancies can both exist in several charge states in most oxides. The F_s surface anion vacancy results from the removal an oxygen atom, and contains two electrons that are weakly trapped by the electrostatic Madelung potential. These electrons give rise to electronic surface states, which at a sufficient (bulk) density of vacancies can often be seen by the naked eye through coloration of the oxide. The F_s center (the F stems from the German *Farbe* for color) can be viewed as a core-less oxygen ion, although a much more reactive one at that. In the case of divalent oxides, one can construe two additional types of anion vacancies, the singly charged paramagnetic F_s^+ center and the doubly charged F_s^{2+} center, where one or both of the color center electrons are absent. The F_s center is typically the most stable of these anion vacancies,^[25,26] and also the most well studied one. The generalization to oxides of other valency, and to the corresponding cation vacancies is analogous.

Trapping of Individual Adatoms

The first thing to keep in mind when considering oxide vacancies is that they are undoubtedly more reactive than most, if not all, other sites on the otherwise pristine

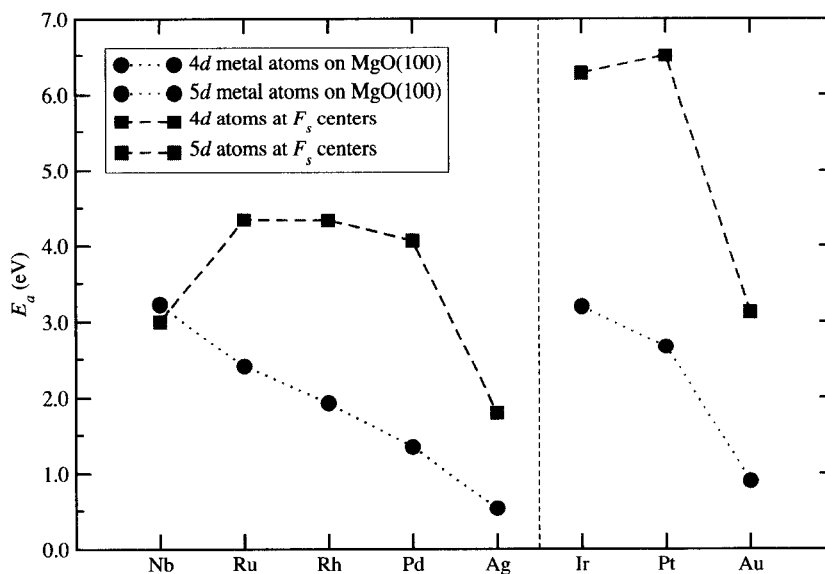


Fig. 6 Adsorption energies E_a at regular sites (atop anions) on MgO(100) and at F_s centers at 1/36 ML coverage for a string of 4d and 5d metal elements across the periodic table, as computed within generalized gradient approximation of density functional theory (DFT-GGA). (From Ref. [9].) The main point of this figure is to illustrate the considerable strengthening of the metal–oxide bond at the oxygen vacancy, with the only exception Nb being due to its large size preventing sufficient penetration of the vacancy.^c (View this art in color at www.dekker.com.)

oxide surface. Their reactivity can be appreciated by considering the energetic penalty of creating the defects. The anion vacancy formation energy (F_s center) for MgO(100) is a huge 13.5 eV, which is a rather representative value for other oxides as well (the corresponding cation formation energy is reportedly 13.1 eV).^[8] Therefore, it is not very surprising that both anion and cation vacancies are extremely reactive and will trap and immobilize nearly any metal (or nonmetal) atom that comes near. The natural abundance of surface vacancies in thermodynamic equilibrium is obviously quite low because of their large formation energy. However, intentional creation of oxide vacancies can be accomplished using a variety of experimental techniques, including ultraviolet (UV) irradiation in reducing atmospheres, ion beam sputtering, and doping with aliovalent cations.^[33,34]

The trapping ability of neutral oxygen vacancies is illustrated in Fig. 6, which shows the adsorption energy of individual metal atoms at regular sites (atop anions) and at F_s centers on MgO(100) (where they sit deeply inside the vacancy).^[9] The adsorption energies increase substantially at the F_s defect compared with the surface in all cases except Nb, which is too large to fill the vacancy.^c

^cAtoms too large to sufficiently fill the vacancy may not bind as strongly because of the exponentially decaying Madelung field away from the surface.

The color center electrons are largely transferred to the trapped metal atoms, which assume a negative charge. Similar results have been noted in several other systems,^[8,9,27,28,30–32,35] several of which have also suggested that the trapped metal atoms develop a significantly enhanced activity toward other adsorbates.

Impact on Cluster Stability

To assess whether there is a preference for metal islands to nucleate at oxide vacancies, it is thus appropriate to compare the dimer binding energies at the vacancy and on the defect-free surface. The dimer binding energy at the vacancy is defined with respect to one atom trapped in the vacancy and the other infinitely far apart on the defect-free surface. For details about adsorption geometries of dimers, the reader is referred to Ref. [9].

Fig. 7 displays the dimer binding energy for a variety of metal dimers at regular sites and at F_s centers on MgO(100).^[9] The dimer binding on the pristine surface is noted to increase to the left in the periodic table. This trend follows that of the bulk cohesive energy of these metals, and can be well understood by simple d -shell filling arguments: the strongest metal–metal bonds occur for half-filled d -shells, and so as the antibonding d -states become increasingly more occupied to the right of Nb, the bond strength decreases accordingly. Silver and gold both

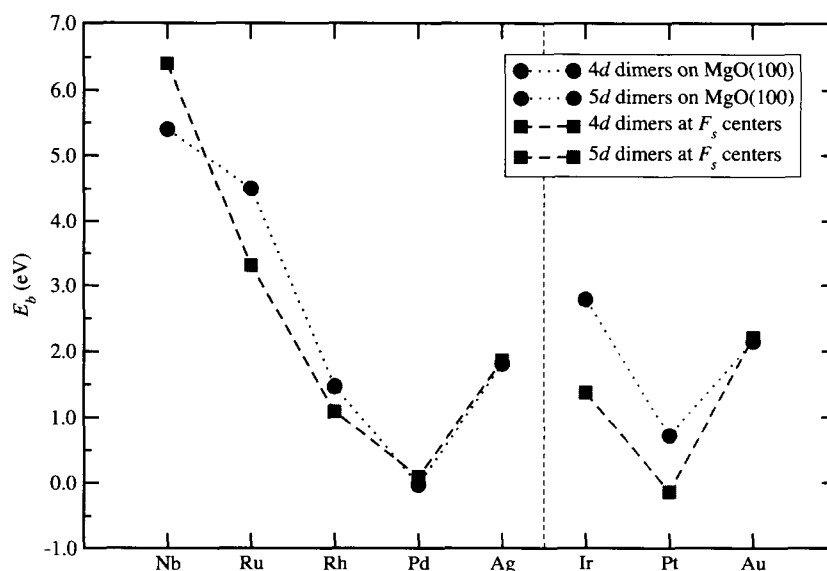


Fig. 7 Dimer binding energies E_b on the defect-free terrace of MgO(100) and at F_s centers at 1/18 ML coverage for various 4d and 5d metal elements, as computed within DFT-GGA. (From Ref. [9].) (View this art in color at www.dekker.com.)

behave somewhat anomalously in this regard, a well-known fallacy of the d -shell model in alloy theory involving these elements.

Fig. 7 further shows that the dimer binding trend at the F_s vacancy is quite similar to that on the defect-free surface, and that, in several cases, the adatom–adatom bond is actually weakened at the defect. More importantly, it is evident from a comparison between Figs. 6 and 7 that there is no apparent relation between how well vacancies stabilize atoms (universally) vs. how they affect dimer bonds (quite varied). These results lend tangible support to the main conclusion of the previous section—that it is inappropriate to deduce a defect’s ability to nucleate islands based solely on how strongly it traps individual atoms.

A good part of these observations can be understood by simple bond-order and d -shell filling arguments. Bond-order and rebonding considerations state that the stronger one of the dimer atoms interacts with a third party, the weaker its bond becomes to its partner adatom, as noted in Fig. 7. The fact that the dimer binding trend at and away from vacancies is the same originates from the d -shell filling arguments outlined above. However, depending on the amount of charge transfer to the dimer, one would expect a shift in the maximum, to the left in the periodic table for F_s vacancies. The reasoning here is as follows. As a second atom joins an already trapped atom at the F_s vacancy, electron density from the color center electrons is shared between the two atoms. This is evident from a lengthening of the adatom–adatom bond, by the dimer tilt angles being toward neighboring oxide cations, and from

charge density analyses.^[9] In Group VIII elements, this adds to antibonding levels because the d -shells are overfull, thereby weakening the adatom–adatom bonds. In contrast, the opposite happens to the far left in the periodic table (Nb and beyond), where added electron density to the underfilled d -shell strengthens the dimer bond. In the extreme case of complete transfer of the two color center electrons, one would therefore expect the maximum adatom–adatom binding to be shifted by one element to the left in the periodic table. The noble metals bind only weakly to the oxide, and their dimers are less prone to interact with the F_s defects. This results in a weak perturbation of the dimer bond due to lesser charge exchange, as attested by the dimer bond strengths being quite near gas phase values (e.g., 1.7 eV for Ag.^[36]).

As mentioned previously, changes in core cluster energies resulting from defects may or may not be relevant, depending on the magnitude of both relative and absolute energies, as well as the growth conditions, cf. Eq. 5. A closer examination of Fig. 7 suggests that F_s vacancies on MgO are unlikely to significantly affect the nucleation kinetics of, e.g., Nb, Ru, Ag, and Au, while Pd, Pt, and possibly also Ir, should be considerably more sensitive to such defects.

While d -shell filling arguments seem to provide a useful perspective on metal nucleation at defects, there are a number of other factors that likewise influence the core cluster binding energy. The size of the metal atom has already been mentioned, as it affects its trapping and amount of charge transfer to the atom and subsequent clusters. The degree of covalency is another factor which

varies depending on the type of metal bonding, e.g., s - p and s - d_{σ} bonding, and which affects the ability to form multidirectional bonds.^[37] For large enough clusters, the ability to relieve mismatch strain becomes energetically competitive and is clearly affected by adsorption geometry. In addition, the d -shell filling arguments become less indicative as the cluster becomes bigger and the charge is shared over more atoms. Studies of how larger clusters are affected by F_s vacancies are reported elsewhere.^[9]

CONCLUSION

This paper emphasizes the need of a microscopic understanding of nucleation kinetics and adhesion energetics to facilitate defect-mediated engineering of metal–oxide interfaces. For example, it is shown via straightforward nucleation theory analyses that single-atom trapping is, by default, not a good indicator of a defect's ability to preferentially nucleate metal islands as it omits the crucial aspect of metal–metal bond formation. The principal conclusions in this regard can be summarized as:

1. Defects affect metal–oxide interfaces by changing the nucleation kinetics, by modifying adhesion and thereby wetting energetics, or both.
2. To assess whether a defect serves as a preferential nucleation center, it is not sufficient to consider only single atom trapping. A better measure is how well the defect stabilizes the binding energy of the core cluster.
3. The stabilization of the core cluster must be viewed in light of both the absolute core cluster binding energy and the growth conditions to assess its impact on nucleation dynamics.

The neutral oxygen vacancy defect, whose much-debated role as potential nucleation center remains a controversial topic, is considered in some detail within the nucleation theory framework. A series of first-principles calculations very clearly shows the disconnect between single-atom trapping and core cluster stabilization at F_s centers on magnesia. These calculations further demonstrate considerable variations in cluster formation energies depending on metal species, which is interpreted by using d -shell filling arguments. The computed energies suggest that, in several cases, F_s centers on magnesia do not, in fact, stabilize island formation. While nucleation theory and chemical arguments provide a reasonably well-grounded basis for interpreting the role of defects in metal–oxide interface formation, more studies are needed for quantitative predictions and generality assessments. In particular, it would be interesting to extend these studies to other

metal–oxide systems, and to quantify the formation barriers for dimers at and away from defects where charge transfer to/from the adsorbates may play an important role. In addition, more studies are needed to assess whether defects that destabilize initial cluster formation may actually increase the monomer density between the defect sites, and thereby promote nucleation away from the defects. More studies are also needed to provide a better understanding of cluster geometries, to which the energetics underpinning all nucleation arguments are extremely sensitive.

REFERENCES

1. Valden, M.; Lai, X.; Goodman, D.W. Onset of catalytic activity of gold clusters on titania with the appearance of nonmetallic properties. *Science* **1998**, *281*, 1647–1650.
2. Finnis, M.W. The theory of metal–ceramic interfaces. *J. Phys., Condens. Matter* **1996**, *8*, 5811–5836.
3. Verdozzi, C.; Jennison, D.R.; Schultz, P.A.; Sears, M.P. Sapphire (0001) surface, clean and with d -metal overlayers. *Phys. Rev. Lett.* **1999**, *82*, 799–802.
4. Yudanov, I.; Pacchioni, G.; Neyman, K.; Rösch, N. Systematic density-functional study of the adsorption of transition metal atoms on the MgO(001) surface. *J. Phys. Chem., B* **1997**, *101*, 2786–2792.
5. Bogicevic, A.; Jennison, D.R. Variations in the nature of metal adsorption on ultrathin Al₂O₃ films. *Phys. Rev. Lett.* **1999**, *82*, 4050–4053.
6. Heinrich, V.E.; Cox, P.A. *The Surface Science of Metal Oxides*; Cambridge University Press: Cambridge, England, 1996.
7. Campbell, C.T. Ultrathin metal films; particles on oxide surfaces: Structural, electronic and chemisorptive properties. *Surf. Sci. Rep.* **1997**, *27*, 1–111.
8. Bogicevic, A.; Jennison, D.R. Role of surface vacancies and water products for metal nucleation: Pt/MgO(100). *Surf. Sci. Lett.* **1999**, *437*, L741–L747.
9. Bogicevic, A.; Jennison, D.R. Effect of oxide vacancies on metal island nucleation defect density. *Surf. Sci. Lett.* **2002**, *515*, L481–L486.
10. Zhukovskii, Y.F.; Kotomin, E.A.; Jacobs, P.W.M.; Stoneham, A.M. Ab initio modeling of metal adhesion on oxide surfaces with defects. *Phys. Rev. Lett.* **2000**, *84*, 1256–1259.
11. Finnis, M.W.; Stoneham, A.M.; Tasker, P.W. Approaches to Modelling Metal/Ceramic Interfaces. In *Metal–Ceramic Interfaces*; Rühle, M., Evans,

- A.G., Ashby, M.F., Hirth, J.P., Eds.; Pergamon: Oxford, 1990; 35–44.
12. Brune, H. Microscopic view of epitaxial metal growth: Nucleation and aggregation. *Surf. Sci. Rep.* **1998**, *31*, 121–230.
 13. Harsdorff, M. Heterogeneous nucleation and growth of thin films. *Thin Solid Films* **1982**, *90*, 1–14.
 14. Fahsold, G.; Pucci, A.; Rieder, K.H. Growth of Fe on MgO(001) studied by He-atom scattering. *Phys. Rev., B* **2000**, *61*, 8475–8483.
 15. Bäumer, M.; Frank, M.; Heemeier, M.; Rühnemuth, R.; Stemperl, S.; Freund, H.-J. Nucleation and growth of transition metals on a thin alumina film. *Surf. Sci.* **2000**, *454–456*, 957–962.
 16. Haas, G.; Menck, A.; Brune, H.; Barth, J.V.; Venables, J.A.; Kern, K. Nucleation and growth of supported clusters at defect sites: Pd/MgO(001). *Phys. Rev., B* **2000**, *61*, 11105–11108.
 17. Henry, C.R. Surface studies of supported model catalysts. *Surf. Sci. Rep.* **1998**, *31*, 235–325.
 18. Lodziana, Z.; Nørskov, J.K. Adsorption of Cu and Pd on α -Al₂O₃(0001) surfaces with different stoichiometries. *J. Chem. Phys.* **2001**, *115*, 11261–11267.
 19. Hammer, B. Adsorbate–oxide interactions during the NO+CO reaction on MgO(100) supported Pd monolayer films. *Phys. Rev. Lett.* **2002**, *89*, 016102.1–016102.4.
 20. Kalff, M.; Comsa, G.; Michely, T. How sensitive is epitaxial growth to adsorbates? *Phys. Rev. Lett.* **1998**, *81*, 1255.
 21. Ertl, G.; Freund, H.-J. Catalysis and surface science. *Phys. Today* **1999**, *52*, 32–38.
 22. Libuda, J.; Frank, M.; Sandell, A.; Andersson, S.; Brühweiler, P.A.; Bäumer, M.; Mårtensson, N.; Freund, H.-J. Interaction of rhodium with hydroxylated alumina model substrates. *Surf. Sci.* **1997**, *384*, 106–119.
 23. Kelber, J.A.; Niu, C.; Shepherd, K.; Jennison, D.R.; Bogicevic, A. Copper wetting of α -Al₂O₃(0001): Theory and experiment. *Surf. Sci.* **2000**, *446*, 76–88.
 24. Chambers, S.A.; Droubay, T.; Jennison, D.R.; Mattsson, T.R. Laminar growth of ultrathin metal films on metal oxides: Co on hydroxylated α -Al₂O₃(0001). *Science* **2002**, *297*, 827–831.
 25. Scorza, E.; Birkenheuer, U.; Pisani, C. The oxygen vacancy at the surface and in bulk MgO: An embedded-cluster study. *J. Chem. Phys.* **1997**, *107*, 9645–9658.
 26. Pacchioni, G.; Pescarmona, P. Structure; stability of oxygen vacancies on sub-surface, terraces, and low-coordinated surface sites of MgO: An ab-initio study. *Surf. Sci.* **1998**, *412–413*, 657–671.
 27. Ferrari, A.M.; Pacchioni, G. Metal deposition on oxide surfaces: A quantum-chemical study of the interaction of Rb, Pd, and Ag atoms with the surface vacancies of MgO. *J. Phys. Chem.* **1996**, *100*, 9032–9037.
 28. Matveev, A.V.; Neyman, K.M.; Yudanov, I.V.; Rösch, N. Adsorption of transition metal atoms on oxygen vacancies and regular sites of the MgO(001) surface. *Surf. Sci.* **1999**, *426*, 123–139.
 29. Kim, Y.D.; Stultz, J.; Wei, T.; Goodman, D.W. Interaction of Ag with MgO(100). *J. Phys. Chem., B* **2002**, *106*, 6827–6830.
 30. Giordano, L.; Goniakovski, J.; Pacchioni, G. Characteristics of Pd adsorption on the MgO(100) surface: Role of oxygen vacancies. *Phys. Rev., B* **2001**, *64*, 075417.1–075417.9.
 31. Zhukovskii, Y.F.; Kotomin, E.A.; Jacobs, P.W.M.; Stoneham, A.M. Ab initio modeling of metal adhesion on oxide surfaces with defects. *Phys. Rev. Lett.* **2000**, *84*, 1256–1259.
 32. Yang, Z.; Wu, R.; Zhang, Q.; Goodman, D.W. Adsorption of Au on an O-deficient MgO(001) surface. *Phys. Rev., B* **2002**, *65*, 155407.1–155407.8.
 33. Tench, A.J. Temperature effects on the hyperfine coupling of a surface centre. *Surf. Sci.* **1971**, *25*, 625–632. See, e.g.
 34. Bogicevic, A.; Wolverton, C. Nature and strength of defect interactions in cubic stabilized zirconia. *Phys. Rev., B* **2003**, *67*, 024106.1–024106.13.
 35. Becker, T.; Boas, C.; Burghaus, U.; Wöll, C. Adsorption probability of CO on a metal oxide: The case of oxygen-terminated ZnO and the influence of defects. *Phys. Rev., B* **2000**, *61*, 4538–4541.
 36. Ferrari, A.M.; Xiao, C.Y.; Neyman, K.M.; Pacchioni, G.; Rösch, N. Pd and Ag dimers and tetramers adsorbed at the MgO(001) surface: A density-functional study. *Phys. Chem., Chem. Phys.* **1999**, *1*, 4655–4661.
 37. Bogicevic, A. Metal-on-metal bonding and rebonding revisited. *Phys. Rev. Lett.* **1999**, *82*, 5301–5304.

Metal Oxide Nanoparticles

Ryan M. Richards

International University of Bremen, Bremen, Germany

M

INTRODUCTION

Metal oxides include materials with a wide range of properties and applications. When the size of these materials is brought down to the nanometer regime, a number of size-dependent properties arise primarily as a result of surface chemistry. This field of nanoscience is facilitated by the fact that many of the systems of interest have been extensively studied in the bulk form and therefore provide ready comparisons with the nanoparticle systems.

The insulating oxides are made up of the metals from the left and right sides of the periodic table. Typical examples of insulating oxides include MgO, CaO, Al₂O₃, and SiO₂. The oxides of the metals in the middle of the periodic table (Sc to Zn) make up the semiconducting or metallic oxides. Typical examples include ZnO, TiO₂, NiO, Fe₂O₃, and Cr₂O₃. Additionally, the transition metal oxides, which include the oxides of Ru, Mo, W, Pt, V, and so forth, are of particular interest for applications in catalysis, sensor materials, and other potential applications.

OVERVIEW

The surface chemistry effects result from the large number of atoms at the surface of nanoscale materials. In spherical nanoparticles, for example, at a size of 3 nm, 50% of the atoms or ions are on the surface, allowing the possibility of manipulation of bulk properties by surface effects and allowing near stoichiometric chemical reaction.^[1] When strong chemical bonding is present, delocalization can vary with size; this, in turn, can lead to different chemical and physical properties.^[2]

Because of the refractory nature of most of the metal oxides, the formation of the ultrasmall particles is facilitated.^[2] The highly ionic nature of some materials, especially MgO, Al₂O₃, ZrO₂, and TiO₂, allows the formation of many stable defect sites, including edges, corners, and anion/cation vacancies. In choosing materials for study, MgO and CaO were found to be attractive because they are highly ionic and have high melting points, and it would be expected that samples of very small particle size might be stable and isolable. Furthermore, reactive

surface sites on these oxides have been extensively studied, especially for MgO crystals and powders.

It should also be noted that materials prepared via aerogel methods have very low densities, can be translucent or transparent, have low thermal conductivities, and have unusual acoustic properties. They have found various applications, including as detectors for radiation, super-insulators, solar concentrators, coatings, glass precursors, catalysts, insecticides, and destructive adsorbents. It has been shown that nanoparticles of ceramic materials (which includes some metal oxides) can be compressed at relatively low temperatures into solids that possess better flexibility and malleability than traditional ceramics.^[2] It should also be noted that nanoparticles of crystalline substances have about 10¹⁹ interfaces/cm³ and range in surface area up to 800 m²/g. Upon compaction, but without growing the nanocrystals, solids with multitudinous grain boundaries are formed. In the case of TiO₂,^[3] solid samples are obtained that undergo plastic deformation at room temperature, presumably by diffusional creep. It has been proposed that further work in the area of consolidated nanophase materials may lead to ceramics with increased flexibility, less brittleness, and perhaps greater strength.^[2] It may also be possible to form materials with a large fraction of atoms at grain boundaries, perhaps in arrangements that are unique. Additionally, it may be possible to produce binary materials of normally immiscible compounds or elements.

The very high surface areas of nanoscale particles gives rise to a number of defect sites. There have been numerous studies of their surfaces in an attempt to clarify the type of defect sites that can exist.^[4-7] The most common defects are coordinatively unsaturated ions due to planes, edges, corners, anion/cation vacancies, and electron excess centers. Such sites are often attributed as the active sites for many useful and interesting reactions, including methane activation,^[8] D₂-CH exchange,^[9] CO oligomerization,^[10-12] oxygen exchange in CO₂,^[13] and H₂O.^[14]

STRUCTURE AND BONDING

Determining the exact nature of structure and bonding in nanomaterials is particularly difficult because, generally, these materials are made of very small crystallites or are

amorphous. Recent advances in crystallography for powders and crystals employing X-ray, electron, and neutron diffraction have provided insight into the structures of metal oxides. Metal oxides crystallize in a variety of structures, and bonding in these materials can range from ionic (MgO , Fe_{1-x}O) to metallic (TiO , ReO_3).^[15]

An understanding of not only the crystal structure and bonding, but also the local microstructures, which result from defects, is necessary to understand the structure of complex transition metal oxides. Of course, on the nanoparticulate scale, the number of defects due to edges, corners, centers, and other surface imperfections is greatly enhanced by the large surface area (Fig. 1). The pursuit of an understanding of the structure/property relationship is integral to the understanding of the unique properties observed on the nanoscale.

In bulk structures, five types of crystals can be defined based on bonding considerations: covalent, ionic, metallic, molecular (van der Waals), and hydrogen bonded. These structures are also present on the nanoscale; however, one must also consider the number of atoms at the surface when examining the structure of nanoscale materials. Ionic crystals are formed when highly electronegative and highly electropositive elements are combined in a lattice. It has been found that the ionic model is a poor approximation for crystals containing large anions and small cations (e.g., oxides and sulfides), where the

covalent contribution to bonding becomes significant.^[15] Van der Waals interactions play a crucial role in many transition metal oxides, especially those with layered structures. In many oxide hydrates or hydroxy oxides, hydrogen bonding also contributes to the cohesive energy. In most transition metal oxides, the bonding is only partly ionic; however, there are several examples that are primarily ionic such as MgO and CaO . In other words, there is a considerable overlap between the orbitals of the cations and anions. Many transition metal oxides also exhibit metallic properties.

Inorganic compounds of the formula AB can have the rock salt (B1), CsCl (B2), Zn blend (B3), Wurtzite (B4), or NiAs (B8) structure.^[16] Alkaline earth metal oxides, such as MgO and monoxides of 3d transition metals, as well as Lanthanides and Actinides, such as TiO , NiO , EuO , and NpO , exhibit the rock salt structure with the 6:6 octahedral coordination.

Defects

Because of the number of atoms at the surface and the limited number of atoms within the lattice, the chemistry and bonding of oxide nanoparticles is greatly affected by the defect sites present. Point defects in crystals, such as vacancies and interstitials described by Schottky and Frenkel, account for the transport properties of ionic solids.^[16] However, it appears that the point defect model is valid only when the defect concentration (or the deviation from stoichiometry) is extremely small. The defects that occur in the ionic solids are grouped into the following classes: point, linear, planar, and volumetric defects. Point defects are a result of the absence of one of the constituent atoms (or ions) on the lattice sites, or their presence in interstitial positions. Foreign atoms or ions present in the lattice represent another type of point defect. Point defects cause displacements on neighboring atoms or ions because of polarization in the surrounding region. A cationic vacancy in an ionic solid will have an electronegative charge, causing displacements of neighboring anions.^[15] The energy of formation of a point defect mainly depends on the atomic arrangement in the immediate neighborhood of the corresponding to rows of atoms that do not possess the right coordination. Boundaries between small crystallites (grain boundaries), stacking faults, crystallographic shear planes, twin boundaries, and antiphase boundaries are planar defects. Three-dimensional volumetric defects are a result of segregating point defects.

The common point defects in ionic solids are Schottky pairs (pairs of cation and anion vacancies) and Frenkel defects (cation or anion interstitial plus a vacancy).^[16] When there is a large concentration of Schottky pairs, the measured pycnometric density of the solid is considerably lower than the density calculated from the X-ray unit cell

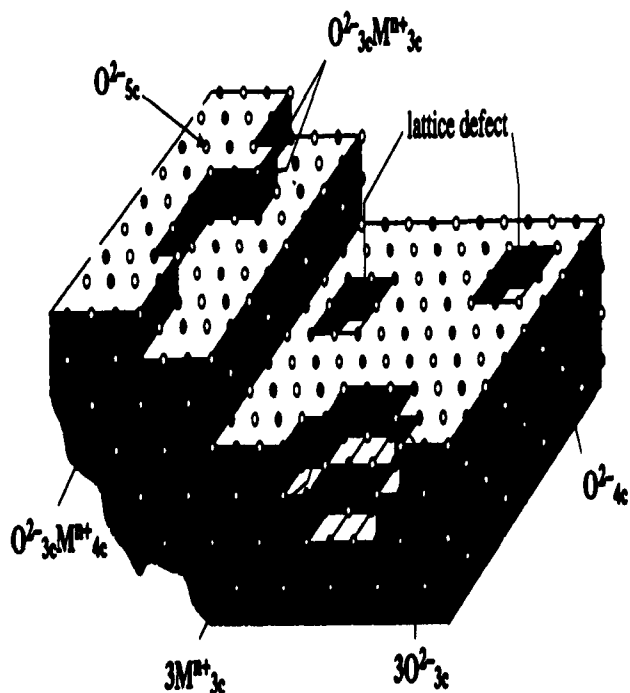


Fig. 1 A representation of the various defects present on metal oxides. (From Ref. [162].)

dimensions (e.g., VO_x).^[15] Creation of defects is generally an endothermic process. Thus the formation energies of vacancies in ionic solids are generally 2eV or more. Therefore, the intrinsic defect concentration in these solids is extremely low even at high temperatures.^[15]

The surface of a crystal constitutes a planar, 2-D defect. The environment of atoms or ions on the surface of a crystal is considerably different from that in the bulk. In polycrystalline materials, there are grain boundaries between the particles. The interface between two solid phases is an important factor in determining the course of reactions, crystal growth, and so on. An interface may be coherent, incoherent, or semicoherent. It is coherent when the interface matches perfectly between the contact planes of two solid planes. Epitaxial growth occurs when there is considerable mismatch (semicoherent interface).

In close packed solids, one also often encounters stacking faults. For example, in a solid with cubic close packing, ABC ABC ABC, there can be a fault such as ABC AB ABC. Other types of planar defects include tilt boundary (array of periodically space of edge dislocations), twist boundary (array of screw dislocations), twin boundary (a layer with mirror plane symmetry with respect to the rotation of one part of the crystal, on a specific plane, with respect to another, and antiphase boundary across which the sublattice occupation becomes interchanged).

The radius of the oxide anion (1.44 Å) given by Shannon and Prewitt is larger than most cations.^[15] However, in crystals, the ionic radii correspond to free ions and not ions. The anions in crystals are subjected to a positive Madelung potential, which gives rise to a contraction of the charge cloud, while cations are subjected to negative potential causing an opposite effect.^[15]

Generally, phase purity is hard to achieve, especially for phases containing more than one cation.^[17] Often, phase segregation occurs, and so the particles are a mixture of other possible phases derivable from the precursors.

SYNTHESIS

One of the areas of fundamental importance to the understanding and development of nanoscale materials, is the development of synthetic methods that allows the scientist control over such parameters as particle size, shape, and size distributions. While considerable progress has taken place in recent years, one of the major challenges to scientists is the development of a "synthetic toolbox," which would afford access to size and shape control of structures on the nanoscale and conversely allow scientists to study the effects these parameters impart to the chemical and physical properties of the nanoparticles.

The syntheses of nanoscale particles are generally grouped into two broad categories: "bottom up" and "top

down." Those materials prepared from atomic precursors that come together to form clusters, and subsequently nanoparticles are referred to as "bottom up" preparations. Conversely, when the nanoscale is reached by physically tearing down larger building blocks, the process is referred to as "top down."

"Bottom up" preparation methods are of primary interest to chemists and materials scientists because the fundamental building blocks are atoms. Gaining control over the way these fundamental building blocks come together and form particles are among the most sought-after goals of synthetic chemists. Therefore these methods will be the focus of this section. Interest in "bottom up" approaches to nanoscale oxides and other materials is clearly indicated by the number of reports and reviews on this subject.^[18-34] Indeed, there are numerous "bottom up" approaches to the preparation of nanoscale materials and metal oxides are no exception. Generally, the preparations can be divided into two basic categories: physical and chemical. Several physical aerosol methods were reported for the synthesis of nano-size particles of oxide materials. These include gas condensation techniques,^[35-41] spray pyrolysis,^[39,42-48] thermochemical decomposition of metal-organic precursors in flame reactors,^[41,49-51] and other aerosol processes named after the energy sources applied to provide the high temperatures during gas-particle conversion. The most common and widely used "bottom up" wet chemical method for the preparation of nanoscale oxides has been the sol-gel process. Other wet chemistry methods including novel microemulsion techniques, oxidation of metal colloids, and precipitation from solutions have also been used.

The methods of sample preparation are naturally the determining factors in producing different morphologies.^[11] For example, burning Mg in O_2 (MgO smoke) yields 40-80 nm cubes and hexagonal plates, while thermal decomposition of $\text{Mg}(\text{OH})_2$, MgCO_3 , and especially $\text{Mg}(\text{NO}_3)_2$ yields irregular shapes often exhibiting hexagonal platelets. Surface areas can range from 10 m^2/g (MgO smoke) to 250 m^2/g for $\text{Mg}(\text{OH})_2$ thermal decomposition, but surface areas of about 150 m^2/g are typical. In the case of calcium oxide, surface areas can range from 1 to 100 m^2/g when prepared by analogous methods, but typically about 50 m^2/g is typical.

Physical/Aerosol Methods

Vapor condensation methods

Gas condensation techniques to produce nanoparticles directly from a supersaturated vapor of metals are among the earliest methods for producing nanoparticles. They generally involve two steps: first, a metallic nanophase powder is condensed under inert convection gas after a

supersaturated vapor of the metal is obtained inside a chamber. A high pressure of inert gas is usually needed to achieve supersaturation, then the powder is oxidized by allowing oxygen into the chamber. This postoxidation is a critical step and very often it becomes necessary for this process is to be performed slowly. Because of the large exothermic reaction, particles heat up for short times (usually less than 1 sec) to temperatures as high as 1000°C, resulting in their agglomeration into large particles by rapid diffusion processes. A subsequent annealing process at higher temperature is often required to complete the oxidation. For further information on these processes, please see Refs. [52–57].

Supersaturated vapor has been achieved by many different vaporization methods. The most common techniques include thermal evaporation,^[57–65] sputtering,^[35,39,66,67] and laser methods.^[36,41]

Gas condensation methods to prepare nanoparticles directly from supersaturated vapor have many advantages over other techniques including: versatility, ease in performance and analysis, and high-purity products. They can also be employed to produce films and coatings. In spite of the success of these methods, the drawback lies in the high production cost because of low yields and the difficulty in scaling-up. Heating techniques have other disadvantages that include the possibility of reactions between the metal vapors and the heating source materials. Furthermore, the operating temperature is limited by the choice of the source material, and because of that, they cannot be used to make a wide variety of materials. For further discussion on supersaturation, particle nucleation and growth, and the transport and collection of the particles, see Ref. [54].

Spray pyrolysis

Spray pyrolysis is another useful method for the synthesis of high-purity homogeneous oxide powders.^[39,42–48] This technique has been known by several other names including solution aerosol thermolysis,^[45] evaporative decomposition of solutions,^[46] plasma vaporization of solutions,^[47] and aerosol decomposition.^[48] The starting materials in this process are chemical precursors, usually appropriate salts, in solution, sol, or suspension form. The process involves the generation of aerosol droplets by nebulizing or “atomization” of the starting solution, sol, or suspension. The generated droplets undergo evaporation and solute condensation within the droplet, drying, thermolysis of the precipitate particle at higher temperature to form a microporous particle, and finally, sintering to form a dense particle.

Aqueous solutions are usually used because of their low cost, safety, and the availability of a wide range of water-soluble salts. Metal chloride and nitrate salts are com-

monly used as precursors because of their high solubility. Precursors that have low solubility or those which may induce impurities, such as acetates that lead to carbon in the products, are not preferred.^[43,46] For further details on atomization techniques, refer to Refs. [39,43–46].

During the transformation of the aerosol droplets into particles, different processes are involved including solvent evaporation, precipitation of dissolved precursor, and thermolysis of precipitated particles. One advantage to this process is that all of these processes take place in one step. Other advantages include the production of high-purity nano-size particles, the homogeneity of the particles as a result of the homogeneity of the original solution, the fact that each droplet/particle undergoes the same reaction conditions, and no subsequent milling is necessary. Disadvantages of spray pyrolysis include the large amounts of necessary solvents and the difficulty in scaling up the production. The use of large amounts of nonaqueous solvents increases production expenses because of the high cost of pure solvents and the need for proper disposal.

Combustion methods

The combustion synthesis technique consists of bringing a saturated aqueous solution of the desired metals salts and suitable organic fuel to boil, until the mixture ignites a self-sustaining and rather fast combustion reaction takes off, resulting in a dry, usually crystalline, fine oxide powder. By simple calcination, the metal nitrates can, of course, be decomposed into melt oxides upon heating to or above the phase transformation temperature.

Flame processes have been widely used to synthesize nanosize powders of oxide materials. In this process, chemical precursors are vaporized and then oxidized in a combustion process using a fuel/oxidant mixture such as propane/oxygen or methane/air.^[49] It combines the rapid thermal decomposition of a precursor/carrier gas stream in a reduced pressure environment with thermophoretically driven deposition of the rapidly condensed product particles on a cold substrate.^[51] The flame usually provides a high temperature (1200–3000 K), which promotes rapid gas-phase chemical reactions.^[41] Several types of flame reactors have been used in research settings and have produced numerous types of nanoscale metal oxides.^[41,49–51,68–73]

Mechanochemical synthesis

Mechanochemical synthesis involves the mechanical activation of solid state displacement reactions. This process has been successfully used recently to make nanoparticles of a number of materials including ceramics, such as Al₂O₃ and ZrO₂.^[74–79] It involves the milling of precursor powders (usually a salt and a metal oxide) to form a

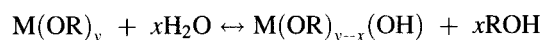
nanoscale composite structure of the starting materials, which react during milling and subsequent heating, if necessary, to form a mixture of dispersed nanocrystals of the desired oxide within a soluble salt matrix.

Chemical Methods

Sol-gel technique

Sol-gel techniques have long been known for the preparations of metal oxides and have been described in several books and reviews.^[18,19-25,27-34] The process is typically used to prepare metal oxides via the hydrolysis of metal reactive precursors, usually alkoxides in an alcoholic solution, resulting in the corresponding hydroxide. Condensation of the hydroxide molecules by giving off water leads to the formation of a network of metal hydroxide. When all hydroxide species are linked in one network-like structure, gelation is achieved and a dense porous gel is obtained. The gel is a polymer of a three-dimensional skeleton surrounding interconnected pores. Removal of the solvents and appropriate drying of the gel results in an ultrafine powder of the metal hydroxide. Further heat treatment of the hydroxide leads to the corresponding ultrafine powder of the metal oxide. Because the process starts with a nanosized unit, and undergoes reactions on the nanometer scale, it results in nanometer materials.

The chemical and physical properties of the final product are primarily determined by the hydrolysis and drying steps. Hydrolysis of metal alkoxides ($M(OR)_y$) involve nucleophilic reactions with water as follows:



The mechanism of this reaction involves the addition of a negatively charged $HO^{\delta-}$ group to the positively charged metal center ($M^{\delta+}$). The positively charged proton is then transferred to an alkoxy group followed by the removal of ROH. Condensation occurs when the hydroxide molecules bind together as they release water molecules and a gel/network of the hydroxide is obtained, as demonstrated below. The rates at which hydrolysis and condensation take place are important parameters affecting the properties of the final product. Slower and more controlled hydrolysis typically leads to smaller particle sizes and more unique properties. Hydrolysis and condensation rates depend on the electronegativity of the metal atom, the alkoxy group, solvent system, and the molecular structure of the metal

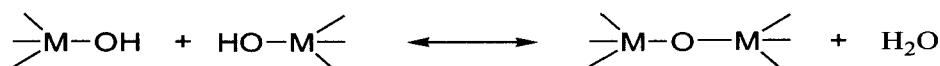
alkoxide. Those metals with higher electronegativities undergo hydrolysis more slowly than those with lower electronegativities. For example, the hydrolysis rate of $Ti(OEt)_4$ is about 5 orders of magnitude greater than that of $Si(OEt)_4$. Hence the gelation times of silicon alkoxides are much longer (on the order of days) than those of titanium alkoxides (seconds or minutes).^[43] The sensitivity of metal alkoxides toward hydrolysis decreases as the OR group size increases. Smaller OR groups lead to higher reactivity of the corresponding alkoxide toward water and, in some cases, results in uncontrolled precipitation of the hydroxide.

Because alcohol interchange reactions are possible, the choice of solvents in sol-gel processes is very important. As an example, when silica gel was prepared from $Si(OMe)_4$ and heated to $600^\circ C$, and when ethanol was used as a solvent, the surface area was $300 \text{ m}^2/\text{g}$ with mean pore diameter of 29 \AA . However, when methanol was used, the surface area dropped to $170 \text{ m}^2/\text{g}$ and the mean pore diameter increased to 36 \AA .^[20]

The rate of hydrolysis also becomes slower as the coordination number around the metal center in the alkoxide increases. Therefore alkoxides that tend to form oligomers usually show slower rates of hydrolysis, and hence, are easier to control and handle. *n*-Butoxide ($O-n\text{-Bu}$) is often preferred as a precursor to different oxides including TiO_2 and Al_2O_3 because it is the largest alkoxy group that does not prevent oligomerization.^[21]

Careful handling in dry atmospheres is required to avoid rapid hydrolysis and uncontrolled precipitation because most metal alkoxides are highly reactive toward water. For alkoxides with low rates of hydrolysis, acid or base catalysts can be used to enhance the process. The relatively negative alkoxides are protonated by acids creating a better leaving group and eliminating the need for proton transfer in the transition state. Alternatively, bases provide better nucleophiles (OH^-) for hydrolysis; however, deprotonation of metal hydroxide groups enhances their condensation rates.

Developments in the areas of solvent removal and drying facilitated the production of nanoscale metal oxides with novel properties. When drying is achieved by evaporation under normal conditions, the gel network shrinks as a result of capillary pressure that occurs and the hydroxide product obtained is referred to as xerogel. However, if supercritical drying is applied by using a high-pressure autoclave reactor at temperatures higher than the critical temperatures of solvents, less shrinkage of the gel network occurs as there is no capillary pressure and no liquid-vapor interface, which allows the pore structure to remain largely intact. The hydroxide product



obtained in this manner is referred to as an aerogel. Aerogel powders usually demonstrate higher porosities and larger surface areas compared to analogous xerogel powders. Aerogel processing has been very useful in producing highly divided powders of different metal oxides^[18,26,80] (Figs. 2 and 3).

Sol-gel processes have several advantages over other techniques for the synthesis of nanoscale metal oxides. Because the process begins with a relatively homogeneous mixture, the resulting product is a uniform ultrafine porous powder. Furthermore, sol-gel processing has the advantage in that it can also be scaled up to accommodate industrial-scale production (personal Contact with Nantek Inc., Manhattan, KS, June 1999).

Numerous metal oxide nanoparticles were produced by making some modifications to the traditional aerogel method. One modification involved the addition of large amounts of aromatic hydrocarbons to the alcohol-methoxide solutions before hydrolysis and alcogel formation. This was carried out to further reduce the surface tension of the solvent mix and to facilitate solvent removal during the alcogel-aerogel transformation.^[1,18,81] The resulting nanoparticles exhibited higher surface areas, smaller crystallite sizes, and more porosity for samples of MgO, CaO, TiO₂, and ZrO₂ [these samples are often referred to as aerogel preparation (AP) samples for aerogel or autoclave preparation].^[17,82]



Fig. 2 TEM micrograph of the nanostructure of CP MgO. Note that, here, there is no porosity and all of the nanocrystals have agglomerated together. (From Ref. [113].)



Fig. 3 TEM micrograph of the nanostructure of AP MgO (supercritical solvent removal). Here the porosity is formed by the interconnected cubic nanocrystals of MgO. (From Ref. [113].)

Reverse microemulsions/micelles method

The reverse micelle approach is one of the recent promising routes to nanocrystalline materials. Several recent studies have shown that this approach is a potential candidate to synthesize nanocrystalline metal oxide powders with well-defined and controlled properties.^[83-90] By carefully controlling reaction parameters, this technique affords a great deal of control over the particle size and shape.

Surfactants dissolved in organic solvents form spheroidal aggregates called reverse micelles. In the presence of water, the polar head groups of the surfactant molecules organize themselves around small water droplets, small water pools (~ 100 Å), leading to dispersion of the aqueous phase in the continuous oil phase as shown in Fig. 4.^[91-93]

Reverse micelles are used to prepare nanoparticles by using a water solution of reactive precursors that can be converted to insoluble nanoparticles. Nanoparticle synthesis inside the micelles can be achieved by different methods including hydrolysis of reactive precursors, such as alkoxides, and precipitation reactions of metal salts.^[84,85] Solvent removal and subsequent calcination leads to the final product. A variety of surfactants can be

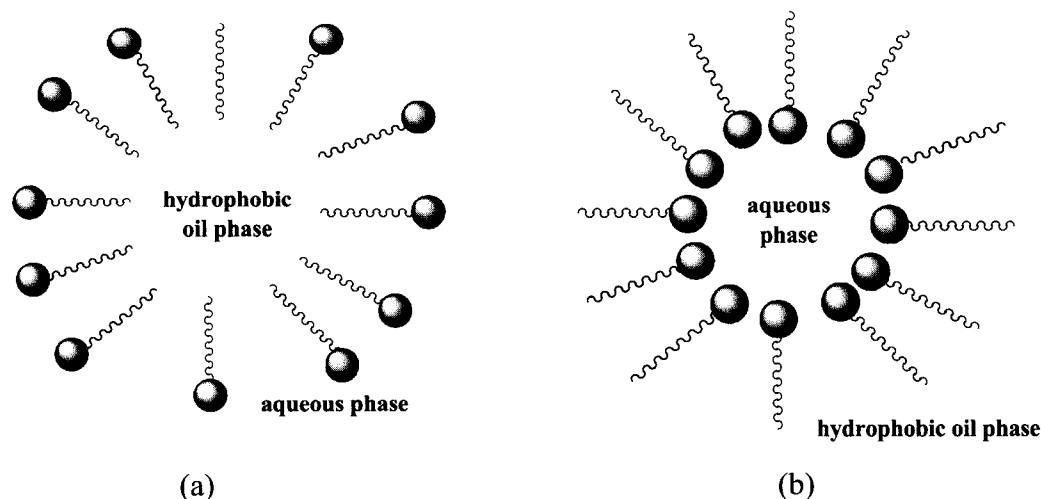


Fig. 4 Schematic representation of (a) micelle and (b) inverse micelle.

used in these processes such as, pentadecaoxyethylene nonylphenylether (TNP-35),^[85] decaoxyethylene nonylphenyl ether (TNT-10),^[85] poly(oxyethylene)₅ nonyl phenol ether (NP5),^[90] and many others that are commercially available. Several parameters, such as the concentration of the reactive precursor in the micelle and the weight percentage of the aqueous phase in the microemulsion, affect the properties, including particle size, particle size distribution, agglomerate size, and phases of the final oxide powders. There are several advantages to using this method—the preparation of very small particles and the ability to control the particle size. Disadvantages include low production yields and the need to use large amount of liquids.

Low-temperature wet-chemical synthesis; precipitation from solutions

One of the conventional methods to prepare nanoparticles of metal oxide ceramics is the precipitation method.^[94–96] This process involves dissolving a salt precursor, usually chloride, oxychloride, or nitrate, such as AlCl_3 to make Al_2O_3 , $\text{Y}(\text{NO}_3)_3$ to make Y_2O_3 , and ZrCl_2 to make ZrO_2 . The corresponding metal hydroxides usually form and precipitate in water by adding a base solution such as sodium hydroxide or ammonium hydroxide solution. The resulting chloride salts, i.e., NaCl or NH_4Cl , are then washed away and the hydroxide is calcined after filtration and washing to obtain the final oxide powder. This method is useful in preparing composites of different oxides by coprecipitation of the corresponding hydroxides in the same solution. One of the disadvantages of this method is the difficulty to control the particle size and size

distribution. Very often, fast (uncontrolled) precipitation takes place resulting in large particles.

Colloidal methods

Some nanostructured metal oxides can also be prepared through the oxidation of metal colloids. Nanosized (i.e., 3–5 nm) colloidal $\text{Fe}(0)$, $\text{Co}(0)$, and $\text{Ni}(0)$ particles are very oxophilic both in solution and in powder form, and cannot be redispersed after exposition to air. However, the precisely controlled, stoichiometric addition of argon-diluted air to an organic solution of a 3-nm $\text{Fe}(0)$ -sol stabilized by $\text{N}(\text{octyl})_4^+\text{Br}^-$ leads to a rusty-brown solution of colloidal Fe^{3+} oxide, which can be isolated and redissolved, e.g., in THF.^[97] Colloidal CoO nanoparticles have also been prepared by air oxidation of $\text{N}(\text{octyl})_4^+\text{Br}^-$ stabilized $\text{Co}(0)$ particles^[98] (Fig. 5).

Particles prepared via the colloidal approach are also easily supported to form heterogeneous catalysts. It was shown that air oxidation at room temperature leads to surface passivation. Consequently, the resulting particles show a composite structure with a metallic core surrounded by an oxide surface layer.^[99] Recently, a new process for the manufacture of a water-soluble PtO_2 colloid has been developed, which is significant because of its use as a water-soluble “Adams catalyst.”^[100,101] Colloidal PtO_2 stabilized by carbo- or sulfobetaines, respectively, were prepared by simple hydrolysis/condensation of metal salts under basic aqueous conditions in the presence of the surfactants. This method was further exploited to give bi- and trimetallic colloidal metal oxides used as precursors for fuel cell catalysts, e.g., colloidal Pt/RuO_x and Pt/Ru/WO_x .^[102]

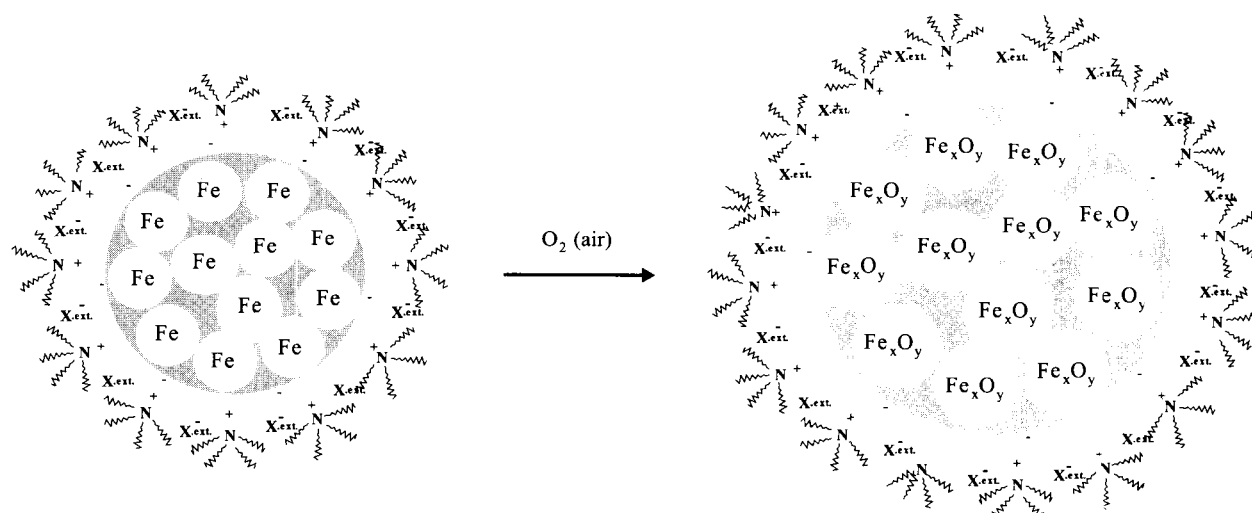


Fig. 5 Schematic representation of the oxidation of tetraalkylammonium stabilized colloids. (From Ref. [97].)

SPECIFIC PROPERTIES AND APPLICATIONS

As previously mentioned, the properties of nanoparticles are usually size-dependent. When prepared in nanometer size particles, materials exhibit unique chemical and physical properties that are remarkably different than those of the corresponding bulk materials. The study of physical and chemical properties of nanoparticles is of great interest as a way to explore the gradual transition from atomic or molecular to condensed matter systems.

As the size of a particle decreases, the percentage of atoms residing on the surface increases. As an example, a study on different samples of MgO nanoparticles has revealed that for particles ~ 4 nm in diameter, $\sim 30\%$ of the atoms are surface atoms.^[18] Naturally, surface atoms/ions are expected to be more reactive than their bulk counterparts as a result of coordinative unsaturation. Because of this and the fact that the surface-to-volume ratio is large, it is not unusual to see unique behavior and characteristics for nanoparticles. This particle size effect is a characteristic of different nanomaterials including metal oxides.

In this section, we will briefly discuss some selected properties of nanophase metal oxides showing significant size dependence.

Chemical Properties: Acid/Base Behavior of Metal Oxide Surfaces

Metal oxides are often hard acids or bases (e.g., MgO, Al₂O₃), so they possess sites capable of catalyzing acid/base chemistry. Several insulating oxides and oxide

composites were found to be potential catalysts for a variety of important reactions as a result of their surface basicity or acidity.^[103–107] Some selected reactions typical to metal oxides include dehydration of alcohols, cracking of hydrocarbons, isomerization of olefins and paraffins, dehydrohalogenations, alkylations, and esterifications.

Acidity and basicity vary from one metal oxide to another. Several metal oxides exhibit surface basic behavior, such as MgO, CaO, and SrO, while others are considered to be acidic solids that possess more and stronger acidic sites on their surfaces, such as Al₂O₃. Acid/base behavior and the presence of several types of deficiencies in the lattice and on the surface are two major driving forces for surface reactivity of metal oxides. When metal oxides are prepared in nanostructures, the percentage of coordinatively unsaturated ions, especially on edges and corners, increases significantly. Consequently, surface chemistry effects, which are barely noticeable in large particle systems, become overwhelming in nanoparticle systems. These effects are demonstrated by enhanced surface reactivities and catalytic potentials possessed by many nanoparticle systems of metal oxides.^[108–112]

Two of the most intensively studied nanoparticulate systems of the metal oxides are MgO and CaO. Two types of nanocrystalline oxides have been prepared and thoroughly studied; a "conventional preparation" (CP), and an "aerogel preparation" (AP).^[1,17,18,81] Nanocrystalline MgO prepared by a modified aerogel procedure (AP), yields a fine, white powder of 400–500 m²/g and 4 nm average crystallite size. High-resolution transmission electron microscope (TEM) imaging of a single crystallite indicated a polyhedral structure suggesting the presence of

high surface concentrations of edge/corner sites, and various exposed crystal planes (such as 002, 001, 111).^[113] Conversely, the conventional preparation (CP) yields particles with surface areas of 150–200 m²/g and 8 nm average crystallites.

If intrinsic surface chemistry differences due to size are to be uncovered, consider that in bulk MgO the effective ionic charges are close to +2, whereas the MgO molecule is much more covalent with effective charges close to +1.^[11] Lower coordination surface ions such as Mg_{3c}²⁺, Mg_{4c}²⁺, O_{3c}²⁻, and O_{4c}²⁻ are expected to have effective charges between +1 and +2. Surface sites on crystalline and powdered MgO have been probed by theoretical as well as experimental efforts. Ab Initio calculations with H₂ have been used to probe perfect crystal surfaces and various defect sites. On the perfect (100) MgO surface, H₂ has a small adsorption energy and does not dissociate. However, temperature programmed desorption methods have shown that polycrystalline samples do dissociate H₂, probably on O_{3c}–Mg_{3c} sites. These sites are apparently very active for heterolytic H₂ dissociation. The micro-faceted (111) surface of MgO is particularly reactive, and steps, kinks, and point defects (ion vacancies and substitutions) are also important. Indeed, the unique catalytic properties of defective MgO surfaces also depend on a plethora of unusual coordination sites.

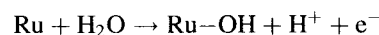
There have also been studies of the Lewis acid and base sites of metal oxide nanoparticles using a variety of techniques. For example, through the use of probe molecules, electron spin resonance (ESR) was used to quantify the Lewis acid and base site on AP–MgO.^[114] Surprisingly, AP MgO was found to possess both types of Lewis sites, which is very interesting because MgO is not typically associated with acid catalysis, and it is believed that this is the first observation of this type of Lewis acid activity on MgO.^[115]

Catalytic properties of transition metal oxides

The development of nanoscale transition metal oxides has been of importance to several applications, especially in catalysis. Transition metal oxides that are electrically conductive are of fundamental importance to catalysis and, in particular, to fuel cells. Ion and electron transfer reactions required for these applications require high surface area materials with defective or charged surfaces.^[116] Water-soluble PtO₂ (i.e., a colloidal “Adams catalyst”) has been applied in the immobilized form for the reductive amination of benzaldehyde by *n*-propylamine.^[100,101] The selectivity in favor of the desired monobenzylated product was found to be >99% and the immobilized PtO₂ was found to be 4–5 times more active than the commercial Adams catalysts. The PtO₂ colloid

was also effective in the hydrogenation of carbonyl compounds, or of olefins in solution or in immobilized form.

The most active and CO-tolerant fuel cell catalysts [direct methanol fuel cell (DMFC) and proton exchange membrane fuel cell (PEMFC)] have been shown to contain oxides and hydrous oxides of Pt and Ru. Recent studies have revealed that practical Pt–Ru blacks are not single phase materials, but are instead bulk mixtures of Pt metal, Pt hydrous oxides, and hydrous and dehydrated RuO. A proposed mechanism for the increased CO tolerance is that Pt-adsorbed CO is removed via an oxygen transfer step from electrogenerated Ru–OH because Ru(0) transfers oxygen more effectively than Pt(0). Additionally, recent studies have suggested that the presence of metal oxides (in particular, Ru, Sn, and Mo) in electrocatalysts working with a carbon containing feed show improved CO tolerance.^[117,118] It is generally accepted that this is a result of the oxide interacting with the CO-poisoned metal (usually Pt) and oxidizing the CO to CO₂. Because these metal oxides are composed of metals with high oxidation potentials, the hydrous oxides are readily regenerated by water in the feed.



Furthermore, by combining Pt/Ru alloy catalysts with transmission metal oxides (WO_x, MoO_x, VO_x) improved DMFC catalysts have been produced. Electrochemical results demonstrated that the introduction of the oxides leads to an improvement of the catalytic activity toward methanol oxidation.^[119] The addition of a transition metal oxide to the PtRu catalyst led to a decrease in the methanol oxidation and surface oxide formation with the most effective being VO_x.

Ruthenium oxide, in particular, has been the subject of numerous investigations because of the numerous chemical and electrical applications it can be used for. Ruthenium oxide also catalyzes the Fischer Tropsch methanation of CO₂, and selectively hydrogenates benzene and its derivatives to cyclohexane and relevant cycloalkenes.^[120] Solid state nuclear magnetic resonance (NMR) investigations of hydrous ruthenium oxide prepared using LiOH have demonstrated that the mobility of water molecules and their interaction with ruthenium oxides play an important role in proton charge density.^[121]

RuO₂–TiO₂ aerogels have been prepared and the redistribution of electrical properties on the nanoscale have been studied. It was found that the electrical

(electronic and protonic) transport properties of the bulk $\text{RuO}_2\text{-TiO}_2$ are redistributed when synthesized as an aerogel. Electron transport dominates the characteristics of the dense form, while protonic transport of the hydrous oxide surfaces governs the electrical properties of the aerogel.^[122] Anhydrous RuO_2 is also used as a thick film resistor but the hydrous oxide is preferred in electrocatalysis.^[123] RuO_2 electrodes are generally prepared by the thermal decomposition of $\text{RuCl}_3 \cdot y\text{H}_2\text{O}$,^[124] which produces hydrous materials that are more correctly described as $\text{RuO}_x \cdot y\text{H}_2\text{O}$ or RuO_xH_y .

Adsorptive Properties

Compared to their conventionally prepared and commercial counterparts, nanoparticles of several metal oxides exhibit a significantly enhanced ability to chemically adsorb and dissociate a variety of organic molecules on their surfaces. One of the great promises that nanoparticles of metal oxides hold in chemical applications is their remarkable ability to chemically adsorb a wide variety of molecules, especially organic molecules that are of concern as environmental hazards.

Several oxides have shown promise in this field including MgO , CaO , Al_2O_3 , SiO_2 , and ZnO . A wide range of molecules including chlorinated hydrocarbons, phosphorous compounds, alcohols, aldehydes, ketones, and amines were found to strongly adsorb and chemically decompose on the surfaces of these oxides.^[125-133] Details and examples on this subject are discussed in the literature.^[1,134]

It has been proposed that as particles become smaller in size, they may take on different morphologies, which may alter their surface chemistry and adsorption properties in addition to increasing the surface area and porosities.^[135] One of the most intriguing observations was that nanocrystals prepared by the altered aerogel approach have exhibited higher surface chemical reactivities than more conventionally prepared samples (precipitation of hydroxides followed by vacuum dehydration, herein referred to as CP samples).^[135] For example, in the reaction of $2\text{CaO} + \text{CCl}_4 \rightarrow 2\text{CaCl}_2 + \text{CO}_2$, AP (aerogel prepared) samples demonstrated reaction efficiencies twice those of CP samples and 30 times higher than commercial samples.^[1,136] For the adsorption of SO_2 , AP MgO adsorbed three times as much as CP MgO/nm^2 .^[137,138] For the destructive adsorption of $\text{CH}_3(\text{CH}_3\text{O})_2\text{PO}$, the reaction efficiency was four times higher for AP MgO than CP MgO , and 50 times higher than for CM MgO .^[139] This high reactivity observed at both room temperature and high temperatures observed for numerous reactions demonstrates that this is not an effect of higher surface area alone. Nanoparticles (especially the AP samples)

have been shown to possess a much greater number of defect sites per unit surface area, which are believed to be responsible for the observed chemistry.

Physical/Mechanical Properties

Many physical properties of nanoscale metal oxides are also size-dependent. Most of the physical properties are dominated by those of the surface, which differ from the bulk because of the different bonding geometries present in nanoscale materials. Several systems of nano-phase oxides have exhibited quite interesting and potentially useful mechanical properties, which creates the necessity for much more work on exploring their physical properties.

Improved sintering and hardness properties

Unique consolidation and compaction properties have been observed in ceramics produced from nanophase powders. Ceramic is processed from nanophase powders by first compacting a powder composed of individual ceramic particles (usually less than 50 nm in size) into a raw shape (often called a green body), then it is heated at elevated temperatures. Densification occurs as a result of diffusion of vacancies out of pores (to grain boundaries) leading to sample shrinkage, which is referred to as pressureless sintering. Fortunately, nanophase powders were found to compact as easily as their analogous submicron particles. Samples have to be sintered at the lowest temperature possible for a time sufficient to remove the residual porosity and establish coherent grain boundaries to avoid particle size growth. Successful sintering enhances the hardness of materials. However, if, hardness decreases with sintering, only grain growth is occurring.^[54]

Experimental evidence has demonstrated that nanophase powders densify at faster rates than commercial (submicron) particles. The slow densification of commercial samples is a result of their larger grain and pore sizes. It has also been found that faster densification rates allow achieving a given density at smaller grain sizes, before serious growth takes place. As a result of their small particle and pore sizes, nanocrystalline powders sinter to much greater densities than their conventional analogs at the same temperature. This also demonstrates that nanocrystalline powders, as compared to conventional powders, reach the same density at much lower temperatures, which eliminates the need for very high temperatures.^[54,133,140-142]

Nonuniform heating where the outside layers of the particles densifies into a hard impervious shell, which constrains the inside of the sample from normal shrinking leading to some cracking as a result of strain

incompatibility, is one disadvantage that can occur with fast densification. This problem can be avoided by several ways. The most efficient way is to heat the samples slowly to reduce the shrinkage in the outer shell while heat is transported to the inner regions.^[143] Additionally, high-density nanostructured oxide systems including Y_2O_3 , TiO_2 and ZrO_2 have been achieved via pressure-assisted sintering, and it has been shown that applying some pressure during sintering can increase the densification rate and suppress the particle growth.^[144,145]

Reduced brittleness and enhanced ductility and superplasticity

The ability of some polycrystalline materials to undergo extensive tensile deformation without necking or fracture is referred to as superplasticity and ductility. Theoretical and experimental results provide evidence for the possibility that, traditionally, brittle materials can be ductilized by reducing their particle and grain sizes. Brittle ceramics can be superplastically deformed at modest temperatures and then heat-treated at higher temperatures for high-temperature strengthening when made from nanocrystalline precursors. The great interest in this property stems from the fact that brittle fracture is a technical barrier in the use of ceramics in load-bearing applications. This interest in the superplasticity of oxide materials has been growing after it was experimentally demonstrated in 1986 that yttria-stabilized tetragonal zirconia polycrystals could be elongated by over 100% in tension.^[145,146] Similar behavior was later demonstrated by other nanophase ceramic systems involving Al_2O_3 , TiO_2 , and ZnO .^[147-155]

One important use of superplasticity in ceramics is diffusion bonding, where two ceramic parts are pressed together at moderate temperatures and pressures to form a seamless bond through diffusion and grain growth across the interface. Diffusion bonds form more easily in nanocrystalline ceramics than in larger-grained ceramics as a result of both the enhanced plastic flow of nanocrystalline ceramics and the larger number of grain boundaries they provide for diffusional flux across the interface.^[156,157]

Other properties of ceramics that are size-dependent include electrical and optical properties. An increase in the electrical resistance and dielectric constant was observed for nanophase ceramic materials as a result of their small particle sizes.^[158,159] An effect on optical properties of ceramic materials was also found because of their nanometer particle sizes. As an example, nanoparticles of TiO_2 were found to become a more efficient ultraviolet (UV) absorber.^[160] In conclusion, nanophase ceramic powders and metal oxides hold great promise for better materials

with unique desired properties and potential applications as compared to their large-grained counterparts.

Additional selected size dependent properties

Lead zirconate–titanate (PZT), a solution of ferroelectric $PbTiO_3$ ($T_c=490^\circ C$) and antiferroelectric $PbZrO_3$ ($T_c=230^\circ C$), belongs to the ferroelectric family of perovskite structure with a general formula of ABO_3 (where A=mono or divalent, and B=tri to hexavalent ions).^[158] Nanoscale PZT particles (25 nm) were synthesized by using an in situ method. Powder X-ray diffraction (XRD) studies of these particles found the sample X-ray amorphous and produced single phase PZT after heating at $500^\circ C$.

Nanophase powders of $Y_xZr_{1-x}O_{2-x/2}$ have been prepared from a mixture of commercially available ZrO_2 and Y_2O_3 powders.^[161] It was found that, depending on the starting powder mixture composition, the yttrium content in the nanophases can be controlled and the tetragonal or cubic phases can be obtained. Tetragonal or a mixture of tetragonal and cubic were observed for low yttria content (3.5% mol yttria), and cubic for higher yttria contents (19, 54, and 76% mol yttria). These powders were found to have a most probable grain radius of about 10–12 nm and the grains appear as isolated unstrained single crystals with polyhedral shapes. The grain shapes appeared to be polyhedral and not very anisotropic. Lattice fringes were parallel to the surfaces demonstrating that (100) and (111) faces dominate.

CONCLUSION

Nanoscale metal oxides are of considerable importance to both the fundamental understanding of size-dependent properties and numerous applications. While, in many cases, a basic understanding of the bonding and structure present in these systems has been determined, there is still a great deal of work to be carried out. Additionally, the methods for the preparation of oxide systems is a continually evolving area of science. Ultimately, developments in the areas of synthesis, instrumentation, and modeling will aid scientists as we try to gain an understanding of the relationships between physical, electronic, and chemical properties.

Developing a “tool box” of synthetic methods, which would afford scientists the possibility to put atoms together into nanomaterials with predetermined shapes and sizes, is an ongoing effort among preparative chemists. Another ongoing effort is the search for relationships between these shapes and sizes, and the chemical and electronic properties observed. As rapid

advances take place in these areas, we will begin to see the potential of nanoscience begin to realize its potential. Metal oxides should be at the forefront of these advances in nanoscience because of their stability and the amount of information that has been gathered about their bulk counterparts through the years.

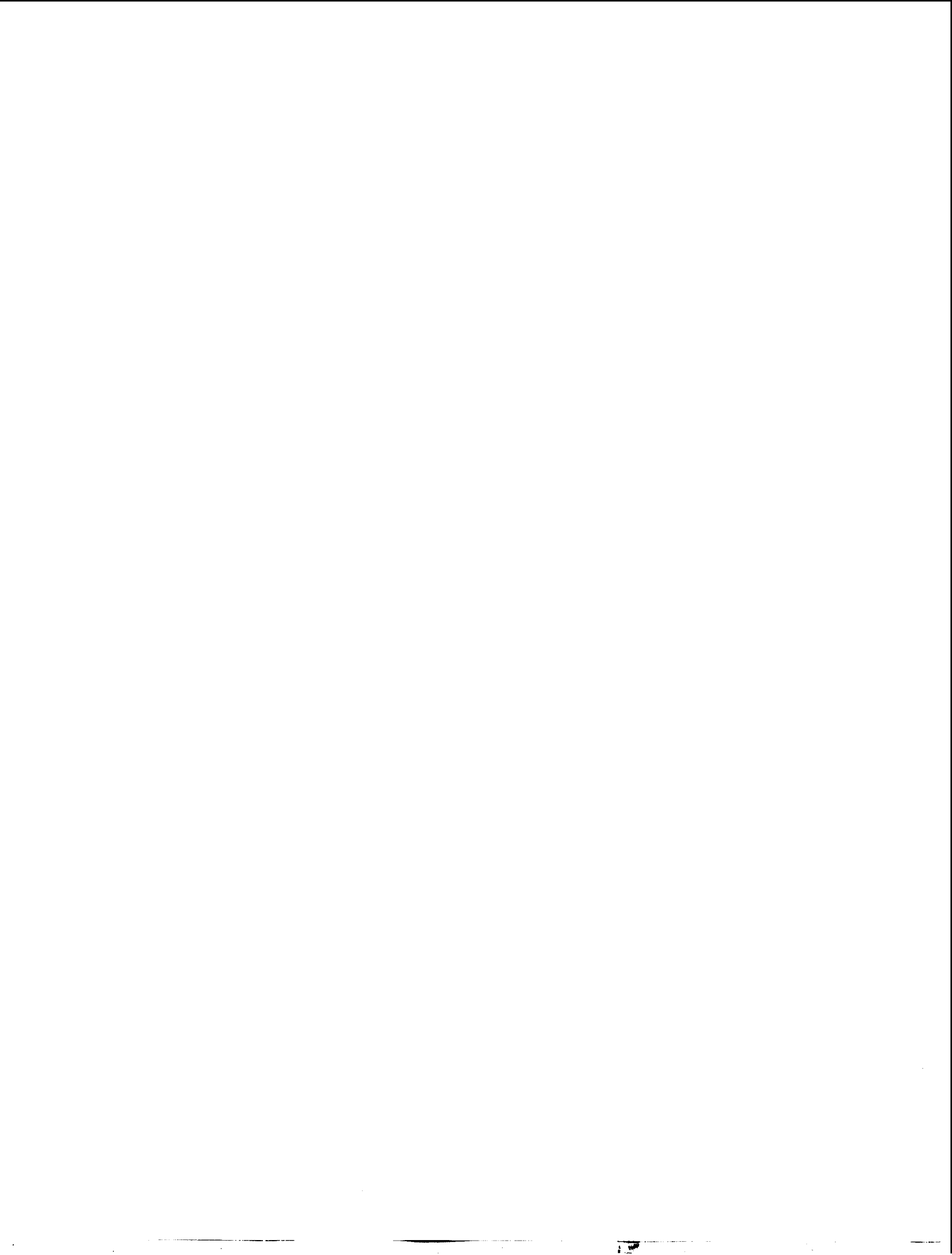
REFERENCES

1. Klabunde, K.J.; Stark, J.V.; Koper, O.; Mohs, C.; Park, D.G.; Decker, S.; Jiang, Y.; Lagadic, I.; Zhang, D. *J. Phys. Chem.* **1996**, *100*, 12142–12153.
2. Klabunde, K.J.; Mohs, C. Nanoparticles and Nanostructural Materials. In *Chemistry of Advanced Materials: An Overview*; Interrante, L.V., Hampden-Smith, M.J., Eds.; Wiley-VCH: New York, 1998; 317, Chapter 7.
3. Siegel, R.W.; Ramasamy, S.; Hahn, H.; Zonquuan, L.; Timg, L.; Gronsky, R. *J. Mater. Res.* **1988**, *3*, 1367.
4. Liu, H.; Feng, L.; Zhang, X.; Xue, O. *J. Phys. Chem.* **1995**, *99*, 332.
5. Tanabe, K. *Solid Acids and Bases*; Academic Press: San Diego, CA, 1970.
6. Utiyama, M.; Hattori, H.; Tanabe, K. *J. Catal.* **1978**, *53*, 237.
7. Morris, R.M.; Klabunde, K.J. *Inorg. Chem.* **1983**, *22*, 682.
8. Driscoll, D.J.; Martin, W.; Wang, J.X.; Lunsford, J.H. *J. Am. Chem. Soc.* **1985**, 107.
9. Hoq, M.F.; Klabunde, K.J. *J. Am. Chem. Soc.* **1986**, *108*, 2114.
10. Morris, R.M.; Klabunde, K.J. *J. Am. Chem. Soc.* **1983**, *105*, 2633.
11. Nygren, M.A.; Pettersson, L.G.M.; Barandiaran, Z.; Siejo, L. *J. Phys. Chem.* **1994**, *100*, 2010.
12. Tashiro, T.; Ito, J.; Sim, R.B.; Miyazawa, K.; Hamada, E.; Toi, K.; Kobayashi, H.; Ito, T. *J. Phys. Chem.* **1995**, *99*, 6115.
13. Tsuji, H.; Shishido, T.; Okamura, A.; Gao, Y.; Hattori, H.; Kita, H. *J. Chem. Soc., Faraday Trans.* **1994**, 803.
14. Li, Y.X.; Klabunde, K.J. *Chem. Mater.* **1992**, *4*, 611.
15. Rao, C.N.R.; Raveau, B. *Transition Metal Oxides, Structure, Properties, and Synthesis of Ceramic Oxides*, 2nd Ed.; Wiley-VCH: New York, 1998; 4.
16. Shriver, D.F.; Atkins, P.W.; Langford, C.H. *Inorganic Chemistry*; W.H. Freeman and Co.: New York, 1990.
17. Klabunde, K.J.; Stark, J.V.; Koper, O.; Mohs, C.; Khaleel, A.; Glavec, G.; Zhang, D.; Sorensen, C.M.; Hadjipanayis, G.C. *Nanophase Materials*; Hadjipanayis, G.C., Siegel, R.W., Eds.; Kluwer Academic Publishers: Dordrecht, The Netherlands, 1994.
18. Itoh, H.; Utamapanya, S.; Stark, J.V.; Klabunde, K.J.; Schlup, J.R. *Chem. Mater.* **1993**, *5*, 71.
19. Palkar, V.R. *Nanostruct. Mater.* **1999**, *11* (3), 369.
20. *Chemistry of Advanced Materials: An Overview*; Interrante, L.V., Hampden-Smith, M.J., Eds.; Wiley-VCH: New York, 1998.
21. Barringer, E.A.; Bowen, H.K. *J. Am. Ceram. Soc.* **1982**, *65*, C-199.
22. Gesser, H.D.; Gosswami, P.C. *Chem. Rev.* **1989**, *89*, 765.
23. Bourell, D.L. *J. Am. Ceram. Soc.* **1993**, *76*, 705.
24. Chatry, M.; Henry, M.; Livage, J. *Mater. Res. Bull.* **1994**, *29*, 517.
25. Kumazawa, H.; Inoue, T.; Sasa, E. *Chem. Eng. J.* **1994**, *55*, 93.
26. Hatakeyama, F.; Kanzaki, S. *J. Am. Ceram. Soc.* **1990**, *73* (7), 2107.
27. Hench, L.L.; West, J.K. *Chem. Rev.* **1990**, *90*, 33.
28. Yi, G.; Sayer, M. *Ceram. Bull.* **1991**, *70*, 1173.
29. Avnir, D. *Acc. Chem. Res.* **1995**, *28*, 328.
30. Chandler, C.D.; Roger, C.; Hampden-Smith, M.J. *Chem. Rev.* **1993**, *93*, 1205.
31. Brinker, C.J.; Scherer, C.W. *Sol-Gel Science*; Academic Press: San Diego, CA, 1990.
32. Segal, D. *Chemical Synthesis of Advanced Ceramic Materials*; Cambridge University Press: Cambridge, UK, 1989.
33. *Sol-Gel Optics: Processing and Applications*; Klein, L., Ed.; Kluwer: Boston, MA, 1993.
34. Narula, C.K. *Ceramic Precursor Technology and Its Applications*; Marcel Dekker: New York, 1995.
35. Siegel, R.W.; Ramasamy, S.; Hahn, H.; Zongquuan, L.; Ting, L.; Gronsky, R. *J. Mater. Res.* **1988**, *3*, 1367.
36. El-Shall, M.S.; Slack, W.; Vann, W.; Kane, D.; Hanely, D. *J. Phys. Chem.* **1994**, *98* (12), 3067.
37. Huibin, X.; Shusong, T.; Ngal, L.T. *Trans. NF Soc.* **1992**, *2*, 58.
38. Baraton, M.I.; El-Shall, M.S. *Nanostruct. Mater.* **1995**, *6*, 301.
39. *Nanophase Materials*; Hadjipanayis, G.C., Siegel, R.W., Eds.; Kluwer Academic Publishers: Dordrecht, The Netherlands, 1994; pp. 73, 85–88, 109–116.
40. Huh, M.Y.; Kim, S.H.; Ahn, J.P.; Park, J.K.; Kim, B.K. *Nanostruct. Mater.* **1999**, *11* (2), 211.
41. *Nanotechnology, Molecularly Designed Materials*;

- Cow, G.M., Gonsalves, K.E., Eds.; American Chemical Society: Washington, DC, 1996; pp. 64–78, 79–99.
42. Kodas, T.T. *Adv. Mater.* **1989**, *6*, 180.
43. Janackovic, D.; Jokanovic, V.; Kostic-Gvozdenovic, L.; Uskokovic, D. *Nanostruct. Mater.* **1998**, *10* (3), 341.
44. Messing, G.L.; Zhang, S.C.; Jayanthi, G.V. *J. Am. Ceram. Soc.* **1993**, *76* (11), 2707.
45. Jayanthi, G.V.; Zhang, S.C.; Messing, G.L. *J. Aerosol Sci. Technol.* **1993**, *19* (4), 478.
46. Messing, G.L.; Gardner, T. *J. Am. Ceram. Soc. Bull.* **1984**, *64*, 1498.
47. Pollinger, J.P.; Messing, G.L. *J. Aerosol Sci. Technol.* **1993**, *19* (4), 217.
48. Kodas, T.T.; Datye, A.; Lee, V.; Engler, E. *J. Appl. Phys.* **1989**, *65*, 2149.
49. Ulrich, G.D.; Riehl, J.W. *J. Colloid Interface Sci. Technol.* **1982**, *87*, 257.
50. Lindackers, D.; Janzen, C.; Rellinghaus, B.; Wassermann, E.F.; Roth, P. *Nanostruct. Mater.* **1998**, *10* (8), 1247.
51. Skanadan, G.; Chen, Y.-J.; Glumac, N.; Kear, B.H. *Nanostruct. Mater.* **1999**, *11* (2), 149.
52. Granqvist, C.G.; Buhrman, R.A. *J. Appl. Phys.* **1976**, *47*, 2200.
53. Ichinose, N.; Ozaki, Y.; Kashu, S. *Superfine Particle Technology*; Springer-Verlag: New York, 1992.
54. *Nanoparticles: Synthesis, Properties and Applications*; Edelstein, A.S., Cammarato, R.C., Eds.; Institute of Physics Publishing: Philadelphia, PA, 1996; pp. 13–54, 170.
55. Gleiter, H. *Prog. Mater. Sci.* **1989**, *33*, 223.
56. Birringer, R.; Herr, U.; Gleiter, H. *Trans. Jpn. Inst. Met. Suppl.* **1986**, *27*, 43.
57. *Mesoscopic Materials and Clusters. Their Physical and Chemical Properties*; Arai, T., Mihama, K., Yamamoto, K., Sugano, S., Eds.; Springer-Verlag: New York, 1999; 275–283.
58. Pfund, A.H. *Phys. Rev.* **1930**, *35*, 1434.
59. Burger, H.; van Cittert, P.H. *Z. Phys.* **1930**, *66*, 210.
60. Harris, L.; Feffries, D.; Siegel, B.M. *J. Appl. Phys.* **1948**, *19*, 791.
61. Uyeda, R. *J. Cryst. Growth* **1974**, *24*, 69.
62. Chaudhari, P.; Matthews, J.W. *Appl. Phys. Lett.* **1970**, *17*, 115.
63. Kaito, C.; Fujita, K.; Shibahara, H.; Shiojiri, M. *Jpn. J. Appl. Phys.* **1977**, *16*, 697.
64. Kaito, C.M. *Jpn. J. Appl. Phys.* **1978**, *17*, 601.
65. Rouanet, A.; Solmon, H.; Pichelin, G.; Rouicau, C.; Sibieude, F.; Monty, C. *Nanostruct. Mater.* **1995**, *6* (1–4), 283.
66. Hahn, H.; Averbach, R.S. *Appl. Phys. Lett.* **1990**, *67*, 1113.
67. Mayo, M.J.; Siegel, R.W.; Narayanasamy, A.; Nix, W.D. *J. Mater. Res.* **1990**, *5*, 1073.
68. Singhal, A.; Skandan, G.; Wang, A.; Glumac, N.; Kear, B.H.; Hunt, R.D. *Nanostruct. Mater.* **1999**, *11* (4), 545.
69. Wu, M.K.; Windeler, R.S.; Steiner, C.K.R.; Friedlander, S.K. *Aerosol Sci. Technol.* **1993**, *19*, 527.
70. Lindackers, D.; Strecker, M.G.D.; Roth, P.; Janzen, C.; Pratsinis, S.E. *Combust. Sci. Technol.* **1997**, *123*, 287.
71. Glumac, N.G.; Chen, Y.J.; Skandan, G.; Kear, B. *Mater. Lett.* **1998**, *34*, 148.
72. Zacharia, M.R.; Chin, D.; Semerjian, H.G.; Katz, J.L. *Combust. Flame* **1989**, *78*, 287.
73. Hung, C.H.; Katz, J.L. *J. Mater. Res.* **1992**, *7*, 1861.
74. Zeng, D.; Hampden-Smith, M.J. *Chem. Mater.* **1992**, *4*, 968.
75. Ding, J.; Tsuzuki, T.; McCormick, P.G. *Nanostruct. Mater.* **1997**, *8* (1), 75.
76. Ding, J.; Miao, W.F.; McCormick, P.G.; Street, R. *Appl. Phys. Lett.* **1995**, *67*, 3804.
77. Ding, J.; Tsuzuki, T.; McCormick, P.G.; Street, R. *J. Phys., D, Appl. Phys.* **1996**, *29*, 2365.
78. Ding, J.; Tsuzuki, T.; McCormick, P.G. *Nanostruct. Mater.* **1997**, *8* (6), 739.
79. Matteazzi, P.; Basset, D.; Miani, F. *Nanostruct. Mater.* **1993**, *2*, 70.
80. White, D.A.; Oleff, S.M.; Fox, J.R. *Adv. Ceram. Mater.* **1987**, *2* (1), 53.
81. Utampanya, S.; Klabunde, K.J.; Schlup, J.R. *Chem. Mater.* **1991**, *3*, 175.
82. Bedilo, A.; Klabunde, K.J. *Chem. Mater.* **1993**, *5*, 500.
83. Herrig, H.; Hempelmann, R. *Mater. Lett.* **1996**, *27*, 287.
84. Bruch, C.; Kruger, J.K.; Unruh, H.G. *Ber. Bunsenges. Phys. Chem.* **1997**, *101* (11), 1761.
85. Hartl, W.; Beck, C.; Roth, M.; Meyer, F.; Hempelmann, R. *Ber. Bunsenges. Phys. Chem.* **1997**, *101* (11), 1714.
86. Gan, L.M.; Chan, H.S.O.; Zhang, L.H.; Chew, C.H.; Loo, B.H. *Mater. Chem. Phys.* **1994**, *37*, 263.
87. Gan, L.M.; Zhang, L.S.; Chan, H.S.O.; Chew, C.H.; Loo, B.H. *J. Mater. Sci.* **1996**, *31*, 1071.
88. Wang, J.; Lee, S.E.; Ng, S.C.; Gan, L.M. *Mater. Lett.* **1997**, *30*, 119.
89. Lim, J.K.; Wang, J.; Ng, S.C.; Gan, L.M. *Mater. Lett.* **1996**, *28*, 431.
90. Fang, J.; Wang, J.; Ng, S.C.; Chew, C.H.; Gan, L.M. *Nanostruct. Mater.* **1997**, *8* (4), 499.
91. Rosano, H.L.; Claussen, M. *Microemulsion Systems*; Marcel Dekker Inc.: New York, 1987.

92. *Progress in Microemulsions*; Martellucci, S., Chester, A.N., Eds.; Plenum Press: New York, 1989.
93. Pileni, M.P. *J. Phys. Chem.* **1993**, *97*, 6961.
94. Gao, L.; Wang, H.Z.; Hong, J.S.; Miyamoto, H.; Miyamoto, K.; Nishikawa, Y.; Torre, S.D.D.L. *Nanostruct. Mater.* **1999**, *11* (1), 43.
95. Qian, Z.; Shi, J.L. *Nanostruct. Mater.* **1998**, *10* (2), 235.
96. Rao, R.M.; Rao, K.; Prasada, A.V.; Komameni, S. *Mater. Lett.* **1996**, *1* (28), 463.
97. Boennemann, H.; Braun, G.; Brijoux, W.; Brinkmann, R.; Schulze Tilling, A.; Seevogel, K.; Siepen, K. *J. Organomet. Chem.* **1996**, *520*, 143–162.
98. Reetz, M.T.; Quaiser, S.; Winter, M.; Becker, J.A.; Schaefer, R.; Stimming, U.; Marmann, A.; Vogel, R.; Konno, T. *Angew. Chem. Ind. Ed.* **1996**, *35*, 2092–2094.
99. Verelst, M.; Ould Ely, T.; Amiens, C.; Snoeck, E.; Lecante, P.; Mosset, A.; Respaud, M.; Broto, J.-M.; Chaudret, B. *Chem. Mater.* **1999**, *11*, 2702–2708.
100. PCT/EP 99/08594 (November 9, 1999), M.T. Reetz and M. Koch (to Studiengesellschaft Kohle m.b.H.).
101. Reetz, M.T.; Koch, M. *J. Am. Chem. Soc.* **1999**, *121*, 7933–7934.
102. Koch, M. Ph.D. Thesis; Verlag: Mainz, 1999, ISBN 3-89653-514-5.
103. Philipp, R.; Omata, K.; Aoki, A.; Fujimoto, K. *J. Catal.* **1992**, *134*, 422.
104. Ito, T.; Wang, J.-X.; Liu, C.-H.; Lunsford, J.H. *J. Am. Chem. Soc.* **1985**, *107*, 5062.
105. Driscoll, D.J.; Martir, W.; Wang, J.-X.; Lunsford, J.H. *J. Am. Chem. Soc.* **1985**, *107*, 58.
106. Peng, X.D.; Richards, D.A.; Stair, P.C. *J. Catal.* **1990**, *121*, 99.
107. Stakheev, A.Yu.; Shapiro, E.S.; Apijok, J. *J. Phys. Chem.* **1993**, *97*, 5668.
108. Mayo, M.J.; Seidensticker, J.R.; Hague, D.C.; Carim, A.H. *Nanostruct. Mater.* **1999**, *11* (2), 271.
109. Vishwanathan, B.; Tanka, B.; Toyoshima, L. *Langmuir* **1986**, *2*, 113.
110. Sun, N.; Klabunde, K.J. *J. Am. Chem. Soc.* **1999**, *121*, 5587.
111. Sun, N.; Klabunde, K.J. *J. Catal.* **1999**, *185*, 506.
112. Jiang, Y.; Decker, S.; Mohs, C.; Klabunde, K.J. *J. Catal.* **1998**, *180*, 24.
113. Richards, R.; Li, W.; Decker, S.; Davidson, C.; Koper, O.; Zaikovski, V.; Volodin, A.; Rieker, T.; Klabunde, K.J. *J. Am. Chem. Soc.* **2000**, *22* (20), 4921.
114. Richards, R.; Volodin, A.; Klabunde, K.J., in preparation.
115. Richards, R.M.; Volodin, A.M.; Bedilo, A.F.; Klabunde, K.J. *Phys. Chem. Chem. Phys.* **2002**, submitted.
116. Swider, K.E.; Merzbacher, C.I.; Hagans, P.L.; Rolison, D.R. *Chem. Mater.* **1997**, *9*, 1248–1255.
117. Rolison, D.; Hagans, P.; Swider, K.; Long, J. *Langmuir* **1999**, *15*, 774–779.
118. Long, J.; Stroud, R.; Swider-Lyons, K.; Rolison, D. *J. Phys. Chem., B* **2000**, *104*, 9772–9776.
119. Lasch, K.; Joerissen, L.; Garche, J. *J. Power Sources* **1999**, *84*, 225–230.
120. Paseka, I. *Appl. Catal., A Gen.* **2001**, *207*, 257–265.
121. Ma, Z.; Zheng, J.; Fu, R. *Chem. Phys. Lett.* **2000**, *331*, 64–70.
122. Swider, K.E.; Merzbacher, C.I.; Hagans, P.L.; Rolison, D.R. *Chem. Mater.* **1997**, *9*, 1248–1255.
123. Trasatti, S. *Electrochim. Acta* **1991**, *36*, 225.
124. Battaglin, G.; Caarnera, A.; Della Mia, G. *J. Chem. Soc., Faraday Trans.* **1985**, *81*, 2995.
125. Klabunde, K.J.; Khaleel, A.; Park, D. *High Temp. Mater. Sci.* **1995**, *33*, 99.
126. Khaleel, A.; Klabunde, K.J. *Nanophase Materials*; Hadjipanayis, G.C., Siegel, R.W., Eds.; Kluwer Academic Publishers: Dordrecht, The Netherlands, 1994; 785.
127. Klabunde, K.J.; Li, Y.; Khaleel, A. *Nanophase Materials*; Hadjipanayis, G.C., Siegel, R.W., Eds.; Kluwer Academic Publishers: Dordrecht, The Netherlands, 1994; 757.
128. Khaleel, A.; Li, W.; Klabunde, K.J. *Nanostruct. Mater.* **1999**, *12*, 463.
129. Khaleel, A.; Kapoor, P.N. *Nanostruct. Mater.* **1999**, *11* (4), 459.
130. Koper, O.B.; Wovchko, E.A.; Glass, J.A.; Yates, J.T., Jr.; Klabunde, K.J. *Langmuir* **1995**, *11*, 2054.
131. Wagner, G.W.; Bartram, P.W.; Koper, O.; Klabunde, K.J. *J. Phys. Chem., B* **1999**, *103*, 3225.
132. Masel, R.I. *Principles of Adsorption and Reaction on Solid Surfaces*; John Wiley and Sons, Inc.: New York, 1996.
133. Henrich, V.; Cox, P.A. *Metal Oxides*; Cambridge University Press: New York, 1994.
134. Klabunde, K.J.; Mulukutla, R.S. *Chemical and Catalytic Aspects of Nanocrystals. Nanoscale Materials in Chemistry*; Wiley-Interscience: New York, 2001; 223–263.
135. Koper, O.; Lagadic, I.; Volodin, A.; Klabunde, K.J. *Chem. Mater.* **1997**, *9*, 2468.
136. Li, Y.X.; Koper, O.; Atteya, M.; Klabunde, K.J. *Chem. Mater.* **1992**, *4*, 323.

137. Stark, J.V.; Park, D.G.; Lagadic, I.; Klabunde, K.J. *Chem. Mater.* **1996**, 1904.
138. Stark, J.V.; Klabunde, K.J. *Chem. Mater.* **1996**, 8, 1913.
139. Li, Y.X.; Klabunde, K.J. *Langmuir* **1991**, 7, 1388.
140. Karch, J.; Birringer, R. *Ceram. Int.* **1990**, 16, 291.
141. Apte, P.; Suits, B.H.; Siegel, R.W. *Nanostruct. Mater.* **1997**, 9 (1–8), 501.
142. Mayo, M.J. *J. Mater. Res.* **1990**, 5 (5), 1073.
143. Chen, D.-J.; Mayo, M.J. *Nanostruct. Mater.* **1993**, 2, 469.
144. Hadjipanayis, G.C.; Siegel, R.W. *Nanophase Materials, Synthesis—Properties—Applications*; Kluwer Academic Publishing: London, 1994; 263–273.
145. Hahn, H.; Averback, R.S. *Mater. Res. Soc. Symp.* **1991**, 206, 561.
146. Nieh, T.G.; Wadsworth, J. *Acta Metall. Mater.* **1990**, 38, 1121.
147. Wakai, F.; Kato, H. *Adv. Ceram. Mater.* **1988**, 3, 71.
148. Nieh, T.G.; McNally, C.M.; Wadsworth, J. *Scr. Metall.* **1989**, 23, 457.
149. Karch, J.; Birringer, R.; Gleiter, H. *Nature* **1987**, 330, 556.
150. Hahn, H.; Averback, R.S. *J. Am. Ceram. Soc.* **1991**, 74, 2918.
151. Mayo, M.J.; Siegel, R.W.; Liao, Y.X.; Nix, W.D. *J. Mater. Res.* **1992**, 7, 973.
152. Koch, C.C.; Morris, D.G.; Lu, K.L.; Inoue, A. *Mater. Res. Bull.* **1999**, 24 (2), 54.
153. Nieh, T.G.; McNally, C.M.; Wadsworth, J. *J. Met.* **1989**, 31.
154. Maehara, Y.; Langdon, T.G. *J. Mater. Sci.* **1990**, 25, 2275.
155. Nieh, T.J.; Wadsworth, J.; Wakai, F. *Int. Mat. Rev.* **1991**, 36, 146.
156. Cross, T.H.; Mayo, M.J. *Nanostruct. Mater.* **1994**, 3, 163.
157. Weertman, J.R.; Farkas, D.; Hemker, K.; Kung, H.; Mayo, M.; Mitra, R.; Swygenhoven, H.V. *Mater. Res. Bull.* **1999**, 24 (2), 44.
158. Das, R.N.; Pramanik, P. *Nanostruct. Mater.* **1998**, 10 (8), 1371–1377.
159. Saito, S. *Fine Ceramics*; Elsevier: New York, 1985; Ohmsha Ltd., Tokyo.
160. Gleiter, H. *Nanostruct. Mater.* **1995**, 6, 3.
161. Rouanet, A.; Pichelin, G.; Roucau, C.; Snoeck, E.; Monty, C. *Nanophase Materials*; Hadjipanayis, G.C., Siegel, R.W., Eds.; Kluwer Academic Publishers: Dordrecht, The Netherlands, 1994; 85–88.
162. Dyrek, K.; Che, M. *Chem. Rev.* **1997**, 97, 305–331.



Metallic Nanopowders: An Overview

M

Frederick Tepper

Argonide Corporation, Sanford, Florida, U.S.A.

Marat I. Lerner

Russian Academy of Sciences, Tomsk, Russia

David S. Ginley

National Renewable Energy Laboratory (NREL), Golden, Colorado, U.S.A.

INTRODUCTION

It is now widely recognized that the fundamental properties of materials strongly depend on the size of crystallites, especially if they are in the nanometer regime. Most of the physical, optical, and electronic properties of a bulk solid vary when the crystallites are in the nanoscale regime. If the grain size can be maintained at nanoscale dimensions, this creates major opportunities to design advanced materials with enhanced properties.

The emerging nanometals industry encompasses nanoparticles, nanolayers, thin films, nanofibers, and bulk nano-structured metals and alloys. This chapter focuses on metal nanoparticles, their properties and uses, with special emphasis on those manufactured by the electroexplosion of metal wire (EEW), a process that is the most commercialized and has produced the greatest diversity of metal nanopowders.

Nanometals are in the process of becoming one of the major feedstocks for a host of emerging technologies and industries. The body of knowledge on nanosize particles has grown throughout the latter part of the twentieth century as various processes for producing them were developed. With the exception of precious metals, most of the focus has been on ceramics and nonmetallic materials. More recently, there has been an increasing interest in other metallic nanoparticles. Handling them is problematic because they are highly reactive and difficult to produce, handle, and ship.

Nanosize precious metals have already had a long history of development and use as catalysts and in photography because of their chemical stability in water and air. Precious metal catalysts in a ceramic matrix, as in automotive catalysts, or dispersed homogeneously in media have had a profound affect on industrial processes. The increasing availability of other nanosize metals should lead to a plethora of new applications from composites to chemicals.

NANOMETAL PROCESSES

There are over a dozen companies that are currently developing processes for nano metal particles, but only a few companies routinely manufacture and supply them. Production quantities are currently limited to only grams or a few kilograms but some companies claim they are building facilities to produce tens to hundreds of kilograms per day. As a result of the small quantities, the prices range from several hundred to a few thousand dollars per kilogram. Most companies do not stock nano metal powders but will produce them on a custom basis.

The manufacturing processes for micron-scale powders, such as water atomization, are generally not adaptable to nanometer size metal powders, mostly because the powders would be oxidized in the environment in which they are produced. The methods currently being developed for nanosize particles include the following:

Ball milling—This method is capable of milling brittle materials to nanometer size, but fails for ductile metals such as copper unless milling is performed at cryogenic temperatures. Milling produces nonspherical particles with a broad particle size range. Dry milling of the more reactive metals can result in their contamination by air but wet milling under an organic fluid can protect the powder. Dry milling in an inert atmosphere is more complex and expensive.

Precipitation from aqueous solution—Such processes are limited to precious metals because most other nanosize powders will react with water, causing surface contamination and, in the case of reactive metals, rapid and sometimes violent reaction. Metals that are precipitated from aqueous solutions generally tend to be porous and highly agglomerated. For example, silver particles can be produced^[1] via the reduction of acidic silver salt solutions using aldehydes in the presence of silica sol, but the powder is highly agglomerated. The silica is

subsequently hydrolyzed in caustic, and aided by a surfactant, it is separated from the agglomerated silver powder. Bonet et al.^[2] describe a method for producing deagglomerated precious metal particles smaller than 10 nm by heating a mixture of precious metal salts with hot (~150°C) ethylene glycol using polyvinylpyrrolidone (PVP) to minimize agglomeration.

Organometallic synthesis in solution—This method employs the use of kinetically controlled reactions of organometallic precursors usually in nonaqueous solvents to product metal nanoparticles. The process can also utilize redox chemistry to reduce an inorganic precursor. The advantage of this process is that monodisperse populations of small (<50 nm) particles is possible, and the disadvantage is that Schlenk-type techniques may be necessary.

Evaporation/condensation under vacuum—Vacuum-driven thermal evaporation is limited to low-boiling-point metals such as aluminum and copper. Higher-boiling-point materials can be evaporated by e-beam or laser heating, but the capital and operating costs of such processes are high, favoring the development of processes that operate at or near ambient pressure.

Evaporation/condensation of the metal in an inert gas environment—Because most of the nanometals will react with oxygen or nitrogen to form oxides and nitrides, such processes require an inert gas cover. Generally, argon is used because of its lower cost compared to helium. Higher energy or impulse heating, such as laser bombardment or electric discharge, can attain higher temperatures and volatilize higher boiling metals compared to slower heating, e.g., via resistance heating of a crucible containing the molten metal. Ablation is well suited to refractory materials especially when employing laser-based heating. This has been performed both with excimer and CO₂ lasers for a variety of high melting materials. Once evaporated, the metal nucleates in the cold inert gas and coalesces to larger particles during transport to the collector. Eifert and Gunther^[3] describe a pilot-scale reactor using a cryogenically cooled condenser with a scraper to remove product from the condenser. Other collection approaches involve an electrostatic filter and cyclone separators.

Thermal decomposition of a salt or organometallic precursor in a flame or plasma—Axelbaum et al.^[4] produced nanosize metal particles submerged in a sodium chloride shell by flame reaction of a metal salt such as titanium tetrachloride with sodium vapor in argon. The NaCl encapsulate is removed from the particles by both washing and subsequent sublimation at 800°C. There is potential for ionic contamination of the product, as well as sintering that could occur during sublimation of the salt.

The electroexploded wire (EEW) process—The EEW process is a physical process converting wire into nano particles in the absence of any chemical reaction that could contaminate the product. It is capable of producing a wide spectrum of nanopowders including high and low boiling metals as well as complex alloys. The EEW process has a very long history. In 1773, Edward Nairne applied an electrical pulse to a wire, causing it to explode in air to form aerosols of metal oxide. The EEW phenomenon also occurs at the moment of burnout of an incandescent filament, when a thinned filament is explosively converted to aerosolized powders in the burned out bulb, producing a momentary brilliant flash. The EEW principal is also used in exploding bridge wire (EBW) explosive detonators. There was a considerable amount of research carried out on EBWs in the 1940s and 1950s, showing that the pulse duration is only a few microseconds long and temperatures higher than 15,000 K are reached at the moment of explosion.

In the 1970s and 1980s, institutes of the Russian Academy of Sciences located in Tomsk, Siberia, invested considerable effort in developing the EEW process. Their innovation included adaptation of the process within an inert gas chamber and an effective mechanism for feeding wire from an internal spool to an electrode. Prior to 1995, most of their emphasis was for producing nano aluminum for energetics and nano copper for use in lubricating oil.

In 1994, Argonide Corporation was founded to commercialize EEW nanopowders. In 1997, a cooperative research and development agreement (CRADA) between the Department of Energy (DOE) and Argonide funded these Russian groups to further develop the process. Funds were also provided to the National Renewable Energy and Los Alamos National laboratories for characterization of the nano powders. With the exception of a 2-year halt during 1998–1999, the program continues to the present. The focus of this joint effort is on process improvement and applications development.

EEW powders can be produced from any metal that is available as ductile wire. Kilogram quantities have been produced with aluminum, copper, nickel, tin, indium, zinc, titanium, tungsten, niobium, tantalum, and silver and gram quantities with gold, palladium, and platinum. The alloys that have been produced include stainless steel, Hastelloy, and nickel–titanium.

Fig. 1 shows an EEW machine, where the main reactor is seen in the upper center. The chamber and associated piping include either one or two cyclone separators (one is visible under the main chamber). A reel of wire is enclosed in the right side of the chamber and is then fed through an electrically insulated baffle.

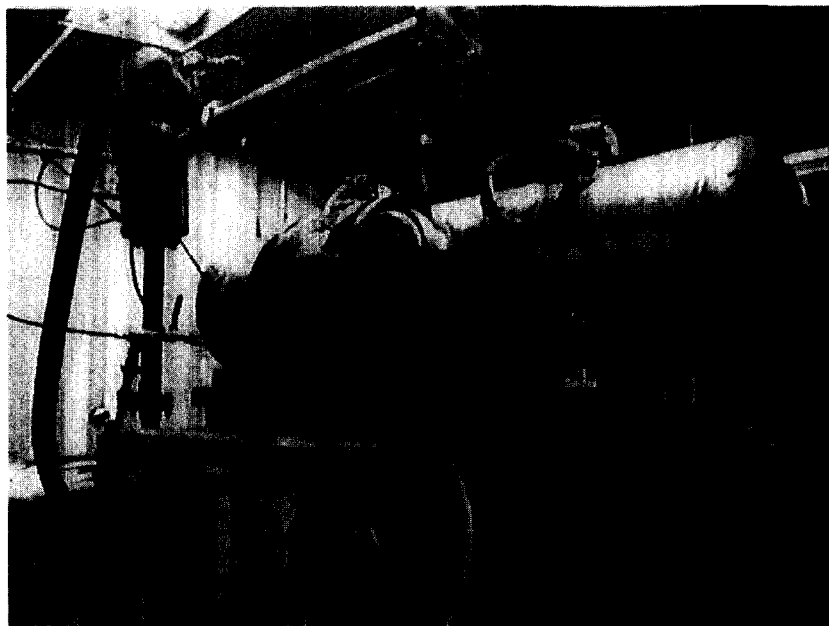


Fig. 1 Electroexplosion machine.

When the wire contacts a strike plate located in the center of the chamber, the circuit is closed causing a large pulse (10^2 – 10^3 J in 1 μ sec) to flow through the wire, creating a plasma. A very strong field is formed that contains the plasma during the microsecond pulse. When the vapor pressure of the metal exceeds the ability of the field to contain the plasma, there is an interruption in current flow, and containment by the field is lost, allowing clusters of metal atoms to be projected at supersonic speed through the argon. The metal clusters are less than about 10 nm, but coalescence occurs as flowing argon (at 2–3 atm) transports the clusters to a cyclone separator, where the now agglomerated particles are collected. At this point, further growth and coalescence is frozen, producing spherical particles with an average particle size of 40–150 nm, depending on the wire size, exploding regime, and freezing point of the metal. X-ray diffraction shows the powders to be relatively pure elemental metal.

Several hundred grams of powder per hour are produced in a single exploder with the rate proportional to the specific gravity of the metal. The energy density introduced in an exploding wire is one of the most important parameters in the process. Pulse energy is optimized by balancing the energy input with the diameter of the wire to produce electrical energy equivalent to the sublimation energy of the metal. With the current power supplies, the best trade-off between the particle size and production rate is achieved by using 0.3-mm diameter wire and results in nanopowders with an average size of

100 nm. Smaller particles (down to about 50 nm average particle size) are produced by substantial reduction in wire diameter, but at the cost of reduced throughput of metal powders. Below a critical energy density, no explosion will occur and the wire is evaporated leading to coarser particles.

Particle size can also be reduced by a higher rate of electrical explosions and by reducing the overpressure of inert gas. Low levels of active gases, such as nitrogen and oxygen, if added to the argon in the reactor, often result in reduced particle size without much contamination of the metal. The apparent mechanism is the formation of fine oxide coatings such as aluminum oxide on aluminum, inhibiting coalescence of the metal particles. Excessive oxygen will result in the production of nanosize metal oxides such as (γ) aluminum and titanium oxides, with particle size about 30–50 nm in diameter.

Powder is collected in the separators until they contain about 1 kg. The collector is frequently emptied into a collection drum. The EEW process is scalable, and a newer reactor design increases the throughput of the reactor and minimizes downtime. In the newer device, the explosion frequency has been increased from about 0.5 to 3 Hz, as recirculation of the argon gas is increased. A feed-through system was developed so that a large spool of wire can be fed into the reactor without opening the chamber and interrupting the process. Also, the arrangement and length of the piping was altered to improve sedimentation, particularly of occasional large particles that are produced by the conventional process.

The EEW process is limited to particles with average sizes less than about 300 nm. Particles as small as 20 nm have been made in experimental quantities. Virtually all the metals produced by this process are combustible, and several of them, such as aluminum, iron, titanium, and zirconium, are either pyrophoric or nearly so. The powders are collected and protected from oxidation by the argon in the reactor. The more reactive powders are transferred to liquid hydrocarbon. In the case of Alex[®] nanoaluminum, the particles are passivated by adding dry air before removing it from the chamber and are then packaged as a dry powder.

All EEW powders are handled and shipped as hazardous (combustible) metal powder. Alex[®] is the nanometal made in the greatest quantity, followed by nickel, copper, tungsten, stainless steel, silver, and zinc. While Ni, Cu, and W may oxidize when exposed to air, they are relatively well behaved compared to dry iron, stainless steel, or titanium powders. The preferred method of packaging dry metal powders is in glass ampoules, and they are offered in quantities of at least 100 g net weight of powder.

The principal advantages of the EEW process are:

1. As with gas condensation techniques, contamination by chemical reactants or by reaction with solvents is avoided.
2. Spherical particles are ordinarily produced.
3. As compared to other high-temperature processes, virtually all of the electrical energy in the EEW process is directly converted to heat. There is little

opportunity for convection or radiation heat loss during the very rapid ($\sim 1 \mu\text{sec}$) pulse.

4. Alloys can be converted to nanopowder with no measurable segregation as compared to evaporative processes, where the composition of the particles will vary.
5. The process operates with pressurized inert gas, simplifying the weight and cost of the reactor and piping.

Alloys are produced on a custom basis, so long as the fine wire is either commercially available in a continuous filament or can be produced with sufficient ductility to be fed into the wire feed mechanism without breakage.

PHYSICAL AND CHEMICAL PROPERTIES

Table 1 summarizes the surface area and crystallographic character of several EEW powders including aluminum oxide (γ phase) and aluminum nitride. As with other nanopowders, the principal difference in the physical and chemical properties of nanometals results from their greater surface area as compared to fine (micron) size particles. The surface area is inversely proportional to the square of the diameter of the particle, so a 100-nm spherical particle has a surface 1000 times greater than a 10- μm particle. This creates opportunity for creating materials with new and useful properties, but also poses difficulty in handling, shipping, and storage.

Table 1 Electroexploded nanopowders and their characteristics

Powder	Particle size distribution function	Average particle size [nm]	Metal content [%]	Surface area [m^2/g]	Particle morphology	Crystalline defects
Al	Normal-logarithmic	80–150	Passivated ≥ 92	8–18	Spherical	Numerous defects
Al	Normal Gaussian	30–50	Depends on particle size distribution	20–48	Crystallites	No information
Cu	Normal logarithmic	100–150	passivated ≥ 90 nonpassivated ≥ 96	5–8	Spherical	Numerous defects
Cu	Normal Gaussian	30–50	passivated ≥ 90 nonpassivated ≥ 96	~ 12	Crystallite faces	Small amount of defects
Ni	Normal logarithmic	80–100	passivated ≥ 95 nonpassivated ≈ 99	4.5–6	Spherical	Numerous defects
Ni	Normal Gaussian	30–50	passivated ≥ 95 nonpassivated ≈ 99	~ 7.5	Crystallite faces	Small amount of defects
Zn	Normal logarithmic	100–200	passivated ≥ 90	4.1–6	Spherical	Numerous defects
$\gamma\text{-Al}_2\text{O}_3$	Normal Gaussian	30–50	Not applicable	20–45	Spherical	Small amount of defects
AlN	Normal Gaussian	50–60	Not applicable	~ 36	Crystallite faces	Small amount of defects

A scanning electron microscopy photo of Alex[®] nanopowder is seen in Fig. 2. Surface area [Brunauer–Emmett–Teller (BET)] measurement is generally a good surrogate for determining average particle size because EEW powders are mostly spherical, fully dense, and smooth. The surface area of Alex[®] with 100 nm average particle size ranges from about 10 to 20 m²/g. Fig. 3 shows a sector of an Alex[®] particle with a passivation coating about 2.5–3 nm thick. X-ray powder diffraction shows these particles are primarily metallic aluminum, while the coating is principally aluminum oxide with minor amounts of nitride and an oxynitride. The amount of active aluminum for a 100-nm size average particle is approximately 88–90 wt.%. The oxide content rises with diminishing particle size, as the 3-nm oxide layer comprises an increasingly greater mass.

The thermal properties [differential thermal analysis (DTA)] of Alex[®] powder when heated in air, oxygen, and nitrogen was compared^[5] to that of micron size aluminum. Alex[®] powder reacts rapidly with these gases, producing very sharp exotherms that occur well below the melting point (660°C) of aluminum, while 20- μ m-size aluminum does not react until about 1000°C.

An organic coating has been developed for many of the nanometals and is being used for coating aluminum and other reactive nanometals. The coating (called L-Alex[®]) is based on the reaction of a carboxylic acid

(palmitic) acid with the aluminum powder rather than coating it with oxide. The resistance of L-Alex[®] to moisture attack during accelerated aging was compared^[6] to oxide-coated Alex[®] and to a 17- μ m-size aluminum powder (Cap45a). The test involved exposure of a thin layer of the aluminum particles in a dish within a temperature humidity chamber. Each day, a sample of each powder was removed and titrated for residual aluminum metal. The powder in the dish was mixed daily to expose fresh surface. Aging was performed at several temperatures and humidity levels from room temperature and dry conditions to a maximum of 60°C/75% relative humidity (RH). Fig. 4 shows a 20% and 70% aluminum metal loss, respectively, in the case of Cap45a and Alex[®] powders, but the L-Alex[®] showed little aluminum loss throughout the 40-day test exposure. The study also showed that bayerite (Al(OH)₃) is the major product of hydrolysis rather than Al₂O₃. Degradation of the Cap45a powder ceased after day 12 when exposed to harsher conditions as a result of the buildup of a layer of bayerite.

Melting point is one of the properties that can be altered by reducing particle size down into the nanometer range. Fig. 5 shows the melting point of gold^[7] as a function of particle size. Melting point reduction is not really significant until the particle size is less than about 10 nm.

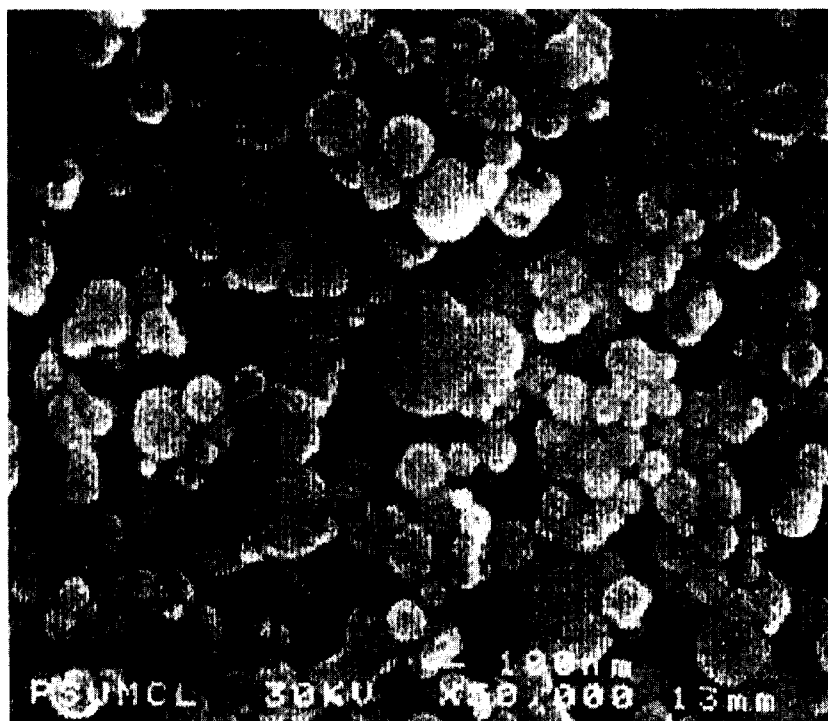


Fig. 2 Field emission electron microscopic view of Alex[®] (50,000 \times).

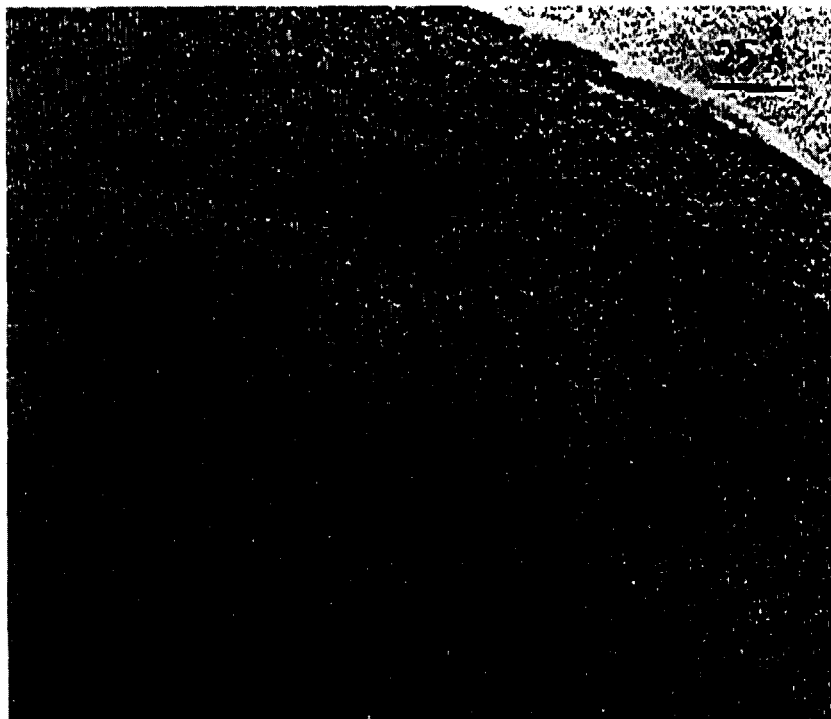


Fig. 3 High-resolution (400,000 \times) transmission electron microscope of alumina layer on the surface of spherical Alex[®] particle.

EEW powders have crystal defects, faults, and twins caused by rapid quenching during the process. Fig. 6 shows a high-resolution transmission electron microscope (TEM) view of EEW nickel showing twins and polytwins. The clusters are propelled by electroexplosion at 2 km/sec through the cold argon, which results in a quenching rate of about 10^8 °C/sec. The disorder in the EEW aluminum crystal extends into the oxide outer layer, causing the powders to be physically metastable and more chemically

reactive. Fig. 7 is a DTA of EEW silver showing an exotherm at about 220°C, far below the melting point (960°C) of silver. The internal energy is estimated to be about 40% of the heat of fusion. When alloy wire is electroexploded, the very high quench rates often produces nonequilibrium phases. For example, EEW 300-stainless steel can be heterogeneous, containing not only the expected austenite phase, but also alpha iron, nickel, and others components in the Fe-Ni-Cr phase diagram.

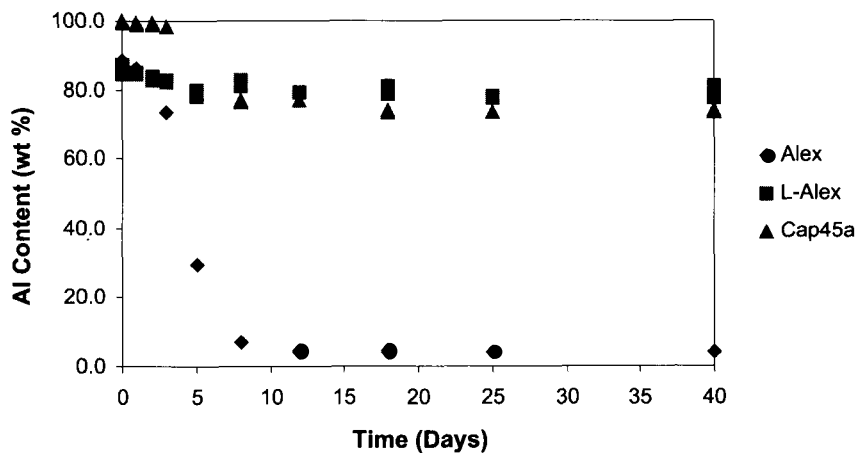


Fig. 4 Aluminum powder accelerated aging in 60°C/75% RH air. (View this art in color at www.dekker.com.)

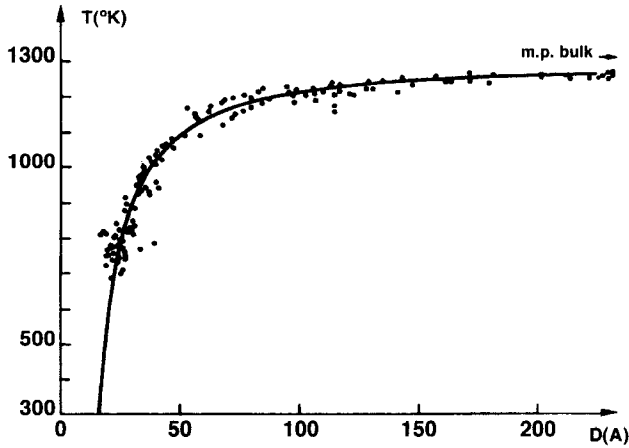


Fig. 5 Melting point of gold particles as a function of particle size.

APPLICATIONS

Nanomaterials and nanotechnology are currently receiving major attention and publicity as a future market. While certain ceramic nanopowders have reached commercial status, nano metals are still in the research stage and sales average about 1 kg per order. Prices are hundreds of dollars per kilogram, and while substantial reductions in cost are anticipated, nanopowders will always be more expensive than conventional size powders. In addition,

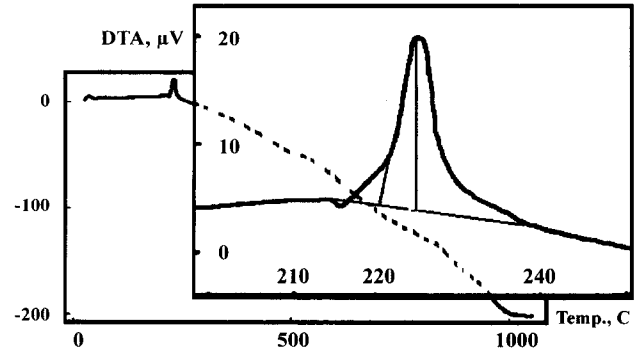


Fig. 7 DTA of EEW silver particles. (Courtesy of Los Alamos National Laboratory.)

they bear higher shipping and handling costs. Therefore the focus of nanopowder suppliers is on applications, in which there is high value added by the nanosize particles. Target markets include energetics, microelectronics, metallurgical coatings, biotechnology, and niche powder metallurgy applications.

Energetics

Aluminum is a highly energetic combustion fuel, particularly on a volumetric basis. For more than a century, it has been used as an additive in energetic compositions such as thermite, in explosives and pyrotechnics, and



Fig. 6 Crystallographic defects in EEW nickel.



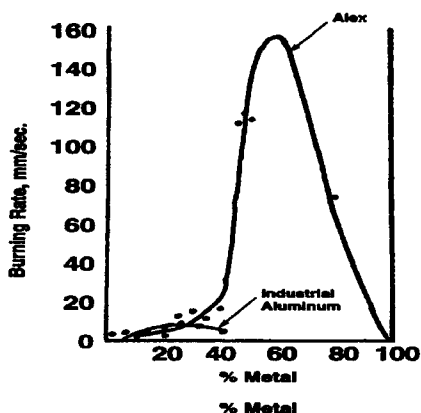


Fig. 8 Burning rate of aluminum/ammonium perchlorate powder mixes.

more recently, in rocket propellants. Because of its high surface area, nano aluminum provides a number of advantages over conventional aluminum powder, particularly with respect to burning rate. Fig. 8 shows that substituting Alex[®] for a conventional micron size ($\sim 20 \mu\text{m}$) aluminum in a mixture with ammonium perchlorate can increase the burning rate about 20 times.^[8] Nano aluminum also ignites more rapidly. When combusted in an air shock tube, Alex[®] has an ignition delay of only 3 μsec compared to 600 μsec for 3- μm diameter aluminum powder.

Rocket Propellants

Rapid burning increases the thrust and speed of a rocket engine, and higher thrust is desired in many advanced missile systems. Several researchers^[8-10] have noted a doubling of burning rate when Alex[®] is substituted for micron size aluminum in conventional solid rocket propellants such as Al/ammonium perchlorate/hydroxy-terminated isobutylene binder (Al/AP/HTPB). The rapid burning is attributed to the smaller particle size and (much) larger surface area. A model developed for aluminum particle combustion in a rocket engine predicts that nano aluminum would burn very rapidly. This model^[11] describes the life of the burning particle as proportional to the square of the particle diameter. Experimental data shows that a 5- μm aluminum particle survives for about 4 msec in a rocket engine. Extrapolation of the d^2 model down to a 100-nm diameter predicts that the particle would be consumed in about 600 nsec, about 4 orders of magnitude shorter than the micron-size particle. High-speed photography of a burning propellant surface confirms that a nano aluminum particle is completely consumed at the surface of the burning grain rather than

being propelled into the burning flow stream as in the case of the micron size aluminum. A faster burning grain is also more efficient because combustion is complete within the engine rather than in the exhaust stream of the rocket. The hybrid rocket engine would also benefit from nano aluminum as a fuel ingredient. The classic hybrid uses liquid oxygen with a rubber base binder (HTPB) grain that contains either no oxidizer, or just enough to react with the HTPB so as to be a gas generator. Pyrolysis of the rubber creates low-molecular-weight organic molecules that are forced into the engine and then react with liquid oxygen. If aluminum is added to a solid fuel such as HTPB, there is a theoretical increase in rocket performance, but unfortunately micron size aluminum does not burn effectively in such a hybrid. However, Chiavarini et al.^[12] found that adding 10 wt.% Alex[®] to an HTPB slab increased the regression rate by 70% and also resulted in smoother burning compared to the pure HTPB slab.

Aluminum, if gelled into kerosene, increases the volumetric energy density of the liquid rocket fuel. Unfortunately, micron size aluminum does not burn efficiently when immersed in kerosene; however, nano aluminum additive is completely combusted.^[13] The higher temperatures created by combustion of nano aluminum also accelerates the combustion of the kerosene.

Explosives

Reshetov et al.^[14] were the first to notice that nano aluminum influences the detonation velocity of high explosives. When less than 30 wt.%, nano aluminum is added to hexamethyl-3-nitroamine (HMX) (Fig. 9), detonation velocity (VoD) decreased from 5400 to 4700 m/sec, about equivalent to that of explosives when micron size aluminum is added to HMX. However, beyond 30 wt.%, there is a rapid rise in VoD to 7000 m/sec. Even

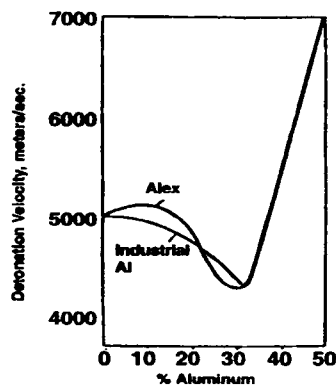


Fig. 9 Detonation velocity as a function of aluminum in HMX explosive.



where the VoD is not affected, the force of the detonation is enhanced by the rapid reaction of the nano aluminum with the gases generated behind the detonation wave.

The affect of nano aluminum on enhanced detonation was demonstrated experimentally in the United States and Europe, and several organizations are studying Alex[®]'s use in explosives. When incorporated into ammonium dinitramide, Alex[®] was shown^[15] to increase VoD from 4380 m/sec for a 97% dinitramide (balance Viton binder) to 5070 m/sec (73:24:3 ADN/Alex[®]/Viton). Identical loading of conventional aluminum had a detrimental effect on VoD. Similarly, detonation tube experiments comparing type 40XD flake aluminum and Alex[®] in N₂ gas dispersed lactose/Al/ammonium perchlorate compositions showed VoD enhancements for Alex[®] over the flake grade at four different Al concentrations.^[16] Most recently, a collaborative program between Australian (DMSO-Adelaide) and Canadian (DREV) laboratories has demonstrated a beneficial enhancement for both VoD and brisance for a number of trinitrotoluene (TNT)-based tritonal and H-6 derivatives containing Alex[®].^[17] VoD enhancements of 200–300 m/sec and improvements in brisance of up to 27% were observed in a number of tritonal charges when conventional aluminum grades were substituted for Alex[®].

Gun Propellants

When Alex[®] is added to gun propellants, the burning rate was nearly doubled as compared to high caloric conventional double-base propellants.^[18] Simultaneously, the pressure exponent of Vieille's burning law decreases from more than 0.8 for double base propellant to 0.66, resulting in more stable burning. Such aluminized gun propellants would be useful as a burning rate accelerator, as an igniter in high-pressure rocket propulsion, and as a booster.

Miscellaneous Pyrotechnics

Metal/oxide pyrotechnic heat sources (thermite) are enhanced with faster burning nanosize aluminum. Mix-

tures of nano size aluminum and nano MoO₃ powder results in a very fast burning material. The reaction rate can be altered to develop energy release rates spanning the range between conventional explosives and conventional thermites. Such mixtures have application in advanced munitions, pyrotechnics, detonators, and primers.

Self-Heating Synthesis (SHS)

Refractory compounds or alloys may be synthesized by direct reaction using the heat generated by metal/metal reaction or as in thermite, where a metal reduces an inorganic compound. Table 2^[19] shows several reactions in which EEW powders were used to form intermetallic alloys. At 200°C, a pellet of EEW copper and micron zinc powder can react within a second producing light and forming brass. Pressed pellets of Alex[®] and amorphous boron, when heated to 500°C and ignited by a hot wire, immediately forms aluminum diboride, while ordinary aluminum and boron would have to be heated above 1000°C for several hours to form the diboride. Nickel aluminide and alloys of aluminum with tungsten, iron, nickel, or molybdenum were produced at much lower temperatures and at shorter times than could be achieved by reacting micron size powders.

Electrically Conductive Inks and Pastes

The goal of shrinking circuits and increasing functionality has resulted in a continuing search for new and improved processes in electronic packaging. Metal powders such as copper, gold, nickel, tin, and solder are formed into pastes and used for electronic interconnects. Copper pastes are used in the production of hybrid multi-chip module (MCM) circuits. The pastes are printed on ceramics such as aluminum oxide and more recently aluminum nitride to produce highly dense, thick film circuits. Nanosize powders provide a flatter surface topology and more precise edge definition and line spacing that would be attainable as compared to conventionally sized powders. Precise patterning ensures lower cross-talk between

Table 2 Alloying reactions in EEW pressed pellets

Metal 1	Metal 2	Reaction method	Product/comments
EEW Cu	Coarse Zn—30%	hot wire at 25C	Brass verified by XRD
EEW Al	Amorphous B	hot wire at 500C	AlB ₂ produced
EEW Al	Coarse Ni	hot wire at 25C	Al-Ni alloy principal phase
EEW Al	Coarse Fe	hot wire at 25C	FeAl, FeAl ₃ and Fe ₂ Al ₅
EEW Al	EEW W (60 wt %)	self-ignited at 300C	WAl ₄ and WAl ₅
EEW Al	Coarse Mo	no reaction	
EEW Al	EEW Mo	self-ignited at 300C	Al ₁₂ Mo, Al ₅ Mo and Al ₄ Mo

adjacent conductor lines. While such better edge definition is not attainable in silk screening patterns because of resolution limits of the process, newer patterning methods such as photo-patterned thick film processes could benefit from the smaller features of nanosize particles.

Metal-filled polymers also play an important role in microelectronics, including electrically conductive adhesives, polymers for shielding from radiofrequency radiation, and in magnetic polymeric layers. In most cases, high aspect ratio fibers and flakes are used because of the greater opportunity for conductor/conductor contact within the composite. Nano metal powders offer an advantage in increased electronic conductivity because of an increase in the number of point-to-point contacts. The authors developed silver-filled polyurethane and epoxy adhesives having an electronic conductivity of 1×10^{-5} and $2 \times 10^{-6} \Omega \text{ m}$, respectively, which are improvements over silver flake-filled polymers. The conductivity of the composite is enhanced by agglomerated particles that are particularly prevalent in EEW silver.

Nanostructures

Over the last few years, there have been extensive studies on nanostructures, with an expectation that they will form superplastic or ultrahigh strength, tough materials. Smaller grains result in greater strength, generally following the classic Hall-Petch relation, at least for grain sizes 50 nm and larger. Extrapolations forecast 2–7 times higher hardness and 2–3 times the tensile strength as compared to parts produced from conventional powders. Furthermore, the boundaries formed in a nanocrystalline structure tend to have higher ductility. Thus in contrast to most methods of strengthening metals, nanostructures have the potential dual benefit of increasing strength while also maintaining or increasing ductility.

There is a dilemma in that smaller grain size of a nano powder based compact recrystallize and grow at lower temperature, countering efforts to form nanostructures. Consolidation methods, such as equal channel angular extrusion (ECAE), that do not rely on much heating can densify the compact to greater than 99% while minimizing grain growth.

The breadth of potential applications for nanostructured metals and alloys is considerable. The higher tensile strength and fatigue strength, and even the enhanced ductility that have been reported in nanostructured metals can impact any application in which strength or strength-to-weight ratios are critical properties. Transportation, aerospace, sports products, implantable medical components, and chemical and food processing applications appear promising.

Low-Temperature Sintering

The onset of sintering occurs substantially lower in temperature with nanosize particles. Eifert et al.^[20] achieved a decrease in the onset of sintering of tantalum from about 1800 to 900°C when the particle size is reduced from 2 μm to 50 nm. The onset of sintering of 40 nm iron powder is as low as 370 K, approximately 21% of the melting point as compared to ~ 900 K, or 50% of melting for 2- μm -size iron powder.^[21,22] The challenge of the nanoparticulate approach is that the pores are readily formed in nano sinters at low temperatures, and they tend to slow full densification unless there is some strain induced in the porous compact to prevent the stabilization of larger pores.

MISCELLANEOUS APPLICATIONS

Wear-resistant and microelectronic coatings can be formed from slurries of nanopowders. For example, the authors bonded a pattern of copper particles to glass by laser irradiation of a dried nanopowder paste deposited by silkscreen. The laser melted the individual particles to form circular disks approximately 1 μm in diameter in a line pattern with resolution of approximately 5 μm . The particles then provided a seed layer for the electroless deposition of additional copper to form a circuit pattern.

Selective laser sintering of metal powders is used for the computerized 3-D design and production of rapid tooling. Nanopowders are likely to be superior to conventional powders in that they sinter more readily and produce parts with tighter tolerance because of their smaller particle size.

Nanosize nickel-titanium alloys are being evaluated as source materials for producing memory alloy components.

Sintered metal disks are used in industrial filtration because of their capability to operate at elevated temperature and in corrosive environments. Disks produced from nanopowders would result in smaller pore size and would be more effective in filtering submicron particles.

A new class of heat transfer fluids is being developed where nanocrystalline particles are being suspended in liquids such as water or oil.^[23] Copper oxide (5 vol.%) suspended in water results in an improvement in thermal conductivity of almost 60% as compared to water without nanoparticles. Direct evaporation of copper nanoparticles into pump oil results in similar improvements in thermal conductivity compared to oxide-in-water systems, but more importantly, requires far smaller concentrations of dispersed nanocrystalline powder.

Gold and other spheres are being considered for use as carriers of pharmaceutical and therapeutic agents through

the blood stream to target organs. Colloidal gold particles have also been exploited in several bioanalytical methods, including a proposed DNA detection method.^[24]

Iron powder, if injected into underground water plumes, will destroy trace halogenated solvents. "Iron walls," which are permeable reactive barriers injected into the plumes, containing zerovalent iron, intercepts halogen-saturated solvents causing their dechlorination. For chlorinated ethenes (perchloroethylene (PCE) and trichloroethylene (TCE)), the products are mostly fully dechlorinated although some chlorinated alkanes yield partial dechlorination products that may still be a pollution problem. There have now been many feasibility studies, pilot tests, small- to medium-scale demonstration projects, and full-scale applications performed by numerous groups. The authors have found that nano-iron is far more effective in converting perchloroethylene to dichloroethylene than micron size iron. Also, nano iron has potential for the conversion of trace As [+3] to As [+5] so that it could be filtered from drinking water.

Nanosize particles interact differently with the electromagnetic energy spectrum than do micron size particles. For instance, solid particles, with sizes substantially below $< 1/20$ of the wavelength of light are transparent so that the film can be strengthened by adding inorganic particles without affecting transparency.

Nanosize metallic silver is being considered as a biocide for water purification and in medical formulations.

Nanosize copper is used as an additive in lubricating oils and sold in Russia. Tarasov et al.^[25] showed that adding 0.5% nano copper to lubricating oil reduces friction in rubbing surfaces, particularly when under high load as in heavy-duty engines, thereby extending their life. The lubricating mechanism is believed to be the deposition of nano copper particles onto the surfaces of a hot friction pair, producing a softer metal surface on the aggravated surface. Such mixtures may prove to be superior to existing lubricants such as those containing Teflon particles.

Nanosize metal particles also have potential as precursors for the synthesis of a wide variety of inorganic compounds such as oxides with complex stoichiometry and with unique sizes, shapes, and reactivities. Furthermore, they have potential as precursors in the direct synthesis of metal organic compounds.

SAFETY, HANDLING, AND SHIPPING CONSIDERATIONS

Nano-metal powders are regarded as hazardous materials, particularly with respect to shipping regulations. Depart-

ment of Transportation and International Air Transport Authority (IATA) require the user to test and categorize such powders relative to the combustion hazard prior to shipment. Should testing under the protocol show the powders to be pyrophoric in air, then shipment on passenger aircraft is disallowed. United Parcel Service and other carriers will not handle pyrophoric materials. The powders may be passivated by oxidizing their surface as in the case of nano aluminum, coating with an organic as in the case of L-Alex^(®), or immersion in a compatible liquid such as a hydrocarbon.

Working safety is also an issue with nano metal powders. Caution must be exercised to minimize the danger of untoward ignition and burning. Efforts should be directed to minimize the possibility of static ignition, *particularly when there is an oxidant mixed in with the powder*. Such oxidants include metal oxides and other oxidizing salts and halogenated organic liquids and solids. For instance, magnesium or aluminum mixed with Teflon powder is a highly reactive pyrotechnic. Users should study Material Safety Data Sheets (MSDS) before using nano metals. High efficiency particulate air (HEPA)-type respiratory filters should be used in operations where there is an opportunity for encountering nanoparticulate dust.

An issue common to most forms of nano metal powders is packaging to assure purity. Glass ampoules are superior to packaging in plastic containers, although ampoules would still not be acceptable under Department of Transportation (DOT) or IATA rules if the powder is pyrophoric. In this case, the powders have to be submerged in liquid hydrocarbon and sealed to prevent the ingress of air to minimize contamination.

CONCLUSION

The burgeoning field of nanotechnology is forecast to have an economic impact as great as biotechnology or microelectronics. Nano powders including nano metals are likely to be key source materials in this new industry. The EEW process is one of several methods being commercialized for manufacturing nano metal powders. EEW powders are readily produced from any metal or alloy that can be produced in the form of fine metal wire including elemental metals such as aluminum and copper, refractory metals such as titanium, tantalum, and tungsten, and alloys such as stainless steel and nickel-titanium.

Applications for nano metals include energetics such as rocket propellants, explosives and pyrotechnics, in self-heating synthesis of inorganic compounds and alloys, in high-strength nano structured metals, electrically conducting inks for microcircuits and in advanced capacitors, in environmental remediation, as carriers for

bioactive and medical therapeutics, and in wear-resistant coatings. Most of the sales of nano powders are for small quantities to researchers investigating new properties with potential applications not discernable at this writing, but which are likely to add to the potential growth of this subindustry.

ACKNOWLEDGMENTS

We are grateful for the support of the Department of Energy and its Incentives for Prevention of Proliferation (IPP) under the cooperative agreement. We are also grateful to the U.S. Industrial Coalition of Washington, DC, which has collaborated in the funding efforts.

We also appreciate the efforts of the team at the National Renewable Energy Laboratory including Ms. Tanya Rivkin, Mr. Alexander Miedaner, and Calvin Curtis as well as Dr. Joel Katz of Los Alamos National Laboratory who contributed their time in characterizing the powders.

Lastly, we want to thank the many Russian scientists and engineers that contributed their knowledge and effort in developing the EEW technology and in manufacturing the powders.

REFERENCES

1. Tosun, G.; Glicksman, H.D. Process for Making Finely Divided Particles of Silver Metals. US Patent 5,188,660, Feb. 1993.
2. Bonet, F.; Delmas, V.; Grugeon, S.; Herrera-Urbina, R.; Silver, P.Y.; Tekaiia-Elhsissen, K. Synthesis of monodisperse Au, Pt, Pd, Ru and Ir nanoparticles in ethylene glycol in. *Nanostruct. Mater.* **1999**, *11* (8), 1277–1284.
3. Eifert, H.; Gunther, B. Metallic nanopowders. *ASM Handb. Powder Metal Technol. Appl.* **1998**, *7*, 77–79.
4. Axelbaum, R.L.; Rosen, L.J.; DuFaux, D.P. Method and Apparatus for Producing High Purity and Unagglomerated Submicron Particles. US Patent 5,498,446, March 1996.
5. Mench, M.M.; Kuo, K.K.; Yeh, C.L.; Lu, Y.C. Comparison of thermal behavior of regular and ultra-fine aluminum powders (Alex[®]) made from plasma explosion process. *Combust. Sci. Technol.* **1998**, *135*, 269–292.
6. Cliff, M.; Tepper, F.; Lisetsky, V. In *Ageing Characteristics of Alex[®] Nanosize Aluminum*, 37th AIAA Joint Propulsion Meeting, Salt Lake City, July 8–11, 2001; AIAA–2001–3287.
7. Buffat, Ph.; Borel, J.P. Size effect of the meeting temperature of gold particles. *Phys. Rev.* **1976**, *A 13*, 2287.
8. Ivanov, G.V.; Tepper, F. In *Activated Aluminum as a Stored Energy Source for Propellants. Challenges in Propellants and Combustion*, Symposium on Chemical Propulsion, Stockholm, May 1996; Kuo, K.K., Ed.; Begell House: New York, 1997; 636–645.
9. Mench, M.M.; Yeh, C.L.; Kuo, K.K. In *Propellant Burning Rate Enhancement and Thermal Behaviour of Ultrafine Aluminium Powders (Alex[®])*, The 29th International Annual Conference of ICT, Karlsruhe, Germany, 30 June–3 July, 1998.
10. Simonenko, V.N.; Zarko, V.E. In *Comparative Studying the Combustion Behaviour of Composite Propellants Containing Ultrafine Aluminium*, The 30th International Annual Conference of ICT, Karlsruhe, Germany, 29 June–2 July, 1999.
11. Law, C.K. A simplified theoretical model for the vapor-phase combustion of metal particles. *Combust. Sci. Technol.* **1973**, *7*, 197–212.
12. Chiaverini, M.J.; Serin, N.; Johnson, D.K.; Lu, Y.C.; Kuo, K.K.; Risha, G.A. In *Combustion Behavior of HTPB-Based Solid Fuels in a Hybrid Rocket Simulator*, 1996 JANNAF Propulsion Meeting, Albuquerque, Dec., 1996.
13. Tepper, F.; Kaledin, L. In *Nano Aluminum as a Combustion Accelerant for Kerosene in Air Breathing Systems*, 39th AIAA Aerospace Science Meeting, Reno, Jan. 10, 2001; AIAA–2001–0521.
14. Reshetov, A.A.; Shneider, V.B.; Yavorovski, N.A. *Ultradispersed Aluminum's Influence on the Speed of Detonation of Hexagen*; Mendeleev All-Union Society: Chernogolovka, 1984; Vol. 1, Abstracts.
15. Bedford, C.D.; Aumann, C.E.; Thompson, D.; Miller, P.J. In *Effect of Metal Particle Size on the Detonation Properties of ADN/Aluminum*, TTCP WTP-4 Technical Workshop, Quebec, Canada, 1998.
16. Tulis, A.J.; Sumida, W.K.; Dillon, J.; Comeyne, W.; Heberlein, D.C. Submicron aluminum particle size influence on detonation of dispersed fuel-oxidiser powders. *Arch. Combust.* **1998**, *18* (1–4), 157–164.
17. Brousseau, P.; Cliff, M.D. In *The Effect of Ultrafine Aluminum Powder on the Detonation Properties of Various Explosives*, The 32th International Annual Conference of ICT, Karlsruhe, Germany, July 3–6, 2001.
18. Baschung, B.; Grune, D.; Licht, H.H.; Samirant, M. In *Combustion Phenomena of a Solid Propellant Based on Aluminum Powder*, 5th International

- Symposium on Special Topics in Chemical Propulsion (5-ISICP), Stresa, Italy, June 19–22, 2000.
19. Ivanov, G.V.; Lerner, M.I.; Tepper, F. *Intermetallic Alloy Formation from Nanophase Metal Powders Produced by Electro-Exploding Wires*; World Powder Metallurgy Congress: Washington, D.C., June, 1996.
 20. Eifert, H.; Gunther, B.; Konig, T.; Meisel, R.L.; Winter, G. In *CVR Production and Sinter Characteristics of Tantalum Nano-Powders*, Int. Conf. On Tungsten, Refractory Metals and Alloys, Orlando, FL, Nov. 16–19, 1997.
 21. Bourell, D.L.; Kaysser, W.A. Nanocrystalline iron sintering behavior and microstructured development. *Metall. Mater. Trans., A* **1994**, *25*, 677–685.
 22. Perez, R.J.; Huang, B.; Sharif, A.A.; Lavernia, E.J. Thermal Stability of Cryomilled Fe–10 wt.% Al. In *Synthesis and Processing of Nanocrystalline Powder*; Bourell, D.L., Ed.; The Minerals, Metals & Materials Society (TMS): Warrendale, PA, 1996; 273–280.
 23. Eastman, J.A.; Choi, U.S.; Li, S.; Thompson, L.J.; Lee, S. Enhanced thermal conductivity through the development of nanofluids. *Mater. Res. Soc. Symp. Proc.* **1997**, *457*, 3–11.
 24. Elghanian, R.; Storhoff, J.J.; Mucic, R.C.; Letsinger, R.L.; Mirkin, C.A. Selective colorimetric detection of polynucleotides based on the distance-dependent optical properties of gold nanoparticles. *Science* **1997**, *277*, 1078–1081.
 25. Tarasov, S.; Kolubaev, A.; Belyaev, S.; Lerner, M.; Tepper, F. Study of friction reduction by nanocopper additives to motor oil. *Wear* **2002**, *252*, 63–69.



Metallic Nanopowders: Rocket Propulsion Applications

Leonid Kaledin
Frederick Tepper

Argonide Corporation, Sanford, Florida, U.S.A.

INTRODUCTION

Active metal powders are extensively used as fuels in most solid rocket propellants because of the high energy produced during their combustion. The specific impulse (I_{sp}) of the rocket engine is proportional to $(T_c/M)^{1/2}$, where T_c is chamber temperature and M is molecular weight of combustion products. Thus the best propellants are those that produce the highest combustion temperature and the smallest possible molecular weight of the combustion products. Therefore the best oxidizers are fluorine and oxygen and the best fuels are lithium, beryllium, boron, aluminum, and magnesium. Lithium is extremely reactive and beryllium is extremely toxic so these are impractical in rocket applications. That leaves boron, aluminum, and magnesium powders as primary candidates.

Aluminum is a major ingredient in solid rocket fuels, often combined in a rubbery binder along with particles of oxidizer. When burning aluminum in solid propellants, the energy utilized can be diminished because the droplets agglomerate, producing larger droplets and slower combustion that can occur too late (after the nozzle) to be effective. The agglomerates, although partially oxidized, often slag up on the internal surfaces of the engine, reducing combustion efficiency and weighing down the vehicle.

As with solid propellants, adding aluminum to liquid fuels would also provide a theoretical advantage in higher volumetric energy density, but the metal must be uniformly dispersed and remain so in the hydrocarbon. As with solid propellants, aluminum combustion must be rapid enough so that it is consumed within the rocket engine. The most effective means of achieving complete combustion is to use powders with particle sizes at least an order of magnitude or two smaller than the metal powder ordinarily used in solid propellants. This article focuses on Alex[®] nanosize aluminum particles manufactured by the electroexplosion of metal wire ("EEW") and its use in liquid and solid rocket propellants.

BACKGROUND

Metal Powders for Solid Rocket Engines

Boron has been considered for many years as a candidate solid rocket fuel as it has a high energy content on both a gravimetric (I_{sp}) and volumetric (density I_{sp}) basis. In practice it has been difficult to realize these advantages as the combustion is severely hindered by a layer of oxide layer (B_2O_3) on the particle surface and boron's vapor pressure is too low to escape the droplet, limiting the gas-phase oxidation to a much slower heterogeneous surface reaction.^[1-3]

Aluminum has always been recognized as a highly energetic reactant for solid rocket fuels and one that can be more practically applied than boron. Because its specific gravity is high (2.7 g/cm^3) relative to organic fuels, it is particularly advantageous for increasing density specific impulse, thereby reducing the size and therefore the weight of the rocket. It is generally used with ammonium perchlorate (AP) as a solid oxidizer and the two solid phases are held together with a rubber base binder such as hydroxy-terminated polybutadiene (HTPB) resin. Aluminum and its oxides are nontoxic and nonpolluting. While AP has been the oxidizer of choice, it is a groundwater pollutant and it also produces large quantities of hydrogen chloride in rocket exhaust. Newer and more energetic oxidizers such as ammonium dinitramide (AND) are being considered, primarily because they do not produce halogens in the exhaust. Also, there are efforts to replace HTPB with more energetic binders such as glycidyl azide polymer (GAP).

Metal Powders for Liquid Rocket Engines

When burning aluminum in solid propellants, the delivered performance is affected because it agglomerates while molten. Duterque^[4] collected the ash of aluminum from a solid propellant burn and found that it contained a

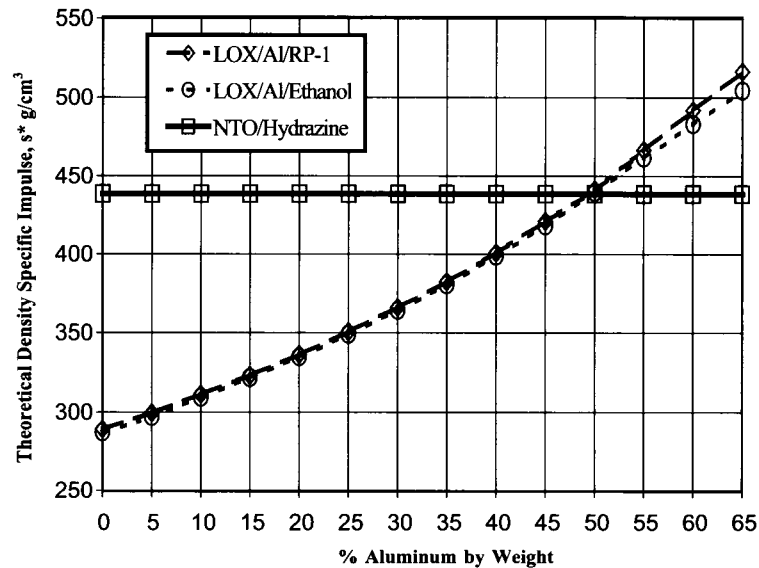


Fig. 1 Theoretical density specific impulse (vacuum, 100:1 expansion ratio) of aluminized bi-propellants.

significant amount of unburned aluminum. Despite this deficiency, aluminum is quite attractive and it is used widely in solid propellants, particularly as the aluminum oxide particle reduces or suppresses combustion instability by damping of combustion waves.^[5]

Dispersing metal particles as a gel in liquid propellants have been studied analytically and experimentally for more than 69 years^[6] because of the higher specific impulse afforded by adding active metals such as aluminum. NASA^[7-13] studied its use into gelled RP-1 (kerosene) for bi-propellant liquid propellant systems. It has also been considered as an additive to liquid hydrogen^[14] because it would thicken the hydrogen, increasing safety in the event of leakage. Palaszewski and Rapp^[11] suggest that given the suitable rheological tailoring, metallized propellants offer tremendous safety advantages. Design studies conducted for NASA missions show that aluminized gelled RP-1 with liquid oxygen can deliver rocket engine efficiencies that are comparable to that of traditional liquid propellants. Palaszewski and Rapp^[11] discuss how using O₂/RP-1/Al gel propellants as a replacement for the liquid rocket booster in the space shuttle boosters results in shorter boosters for the same payload size due to the increased propellant density. This in turn has the potential to deliver a higher payload mass over its solid counterpart. Fig. 1 shows the volumetric energy density calculated using the Propellant Evaluation Program (PEP) code^[15] for aluminized RP-1 and ethanol fluids and compares these two fuels with nitrogen tetroxide/hydrazine, a highly energetic bi-propellant but one that is toxic and environmentally unfriendly. The computed energy available increases consistently with increasing aluminum content.

Unfortunately, conventional aluminum powder, when burning in liquid hydrocarbon fuel, also agglomerates as in the case of solid propellants, reducing delivered specific impulse (I_{sp}). Wong and Turns^[16] noted significant Al agglomeration in burning JP-10 resulting in inefficient combustion. And as in the case of solid propellant engines using aluminum, this agglomeration would result in unburned combustion products deposited on engine walls.

Metal Powders in Liquid Monopropellants

In the late 1950s and early 1960s, Atlantic Research studied the combustion of Arcogel, a gel of aluminum powder, ammonium perchlorate with dioctyl adipate as a liquid carrier. They found that such mixtures had adequate (6 months) shelf life and good stability under high acceleration loading and vibration. Arcogel was extensively characterized and found to be nondetonable and insensitive to ignition. They also conducted small motor tests. However, they found the viscosity to be unacceptably high at low temperatures (-55°C). In the early 1990s, this work was continued,^[17] evaluating nitrated ester/AP/Al, hydrogen peroxide/Al, and HN/water/Al gels. All were found to have limited promise because of their sensitivity to premature ignition or detonation.

Environmental Issues

Regulatory environmental requirements are forcing new choices for rocket propellant ingredients. For instance, ammonium perchlorate (AP), the oxidizer of choice for solid propellants, is falling out of favor because hydrogen



chloride is a significant combustion product. Toxicological constraints are also affecting the choice of liquid propellants. For instance, hydrazine, which is extensively used, is very toxic, as is nitrogen tetroxide. Threshold limit value (TLV) concentrations for hydrazine are fractions of a part per million, often below the limits of detection (LOD) of continuous monitoring instruments. Those working with this fluid often have to wear completely encapsulated suits. In addition to AP, there are two other inorganic oxidizers that have potential for solid propellants—ammonium nitrate (AN) and ammonium dinitramide. Another oxidizer being developed in the Netherlands is hydrazinium nitroformate (HNF).

Fluids such as ethanol^[18,19] and methanol^[20] are being considered as nontoxic options in bi-propellant system. Boeing^[21,22] reported on the hazardous and costly operations associated with monomethyl hydrazine (MMH) and nitrogen tetroxide propellants related to the Space Shuttle Orbiter OMS/RCS system which culminated in NASA's selection of ethanol/LOX as the bi-propellant. They designed such a propellant system and projected improvements in vehicle weight, complexity, and operational cost. They believe that the design solutions are applicable to other space-based cryogenic propulsion and power generation systems. Aluminizing these nontoxic fuels could substantially enhance propellant energy density without causing any environmental or toxic concerns.

Effect utilization of aluminum's combustion energy in propellants resolves a number of problems—improved performance, particularly on a volumetric basis, and achieving that with no penalty as a pollutant or a toxin.

NANOMETAL POWDER FUELS

Many of the difficulties related to inefficient burning of aluminum powder in solid (as well as liquid) propellants could be ameliorated if the particle size of the powder were small enough. Nanosize aluminum was first prepared in the early 1970s by Russian scientists in Siberia,^[23] who formed the powder by electroexploding metal wires (EEW). The EEW method is described in a separate article of this Encyclopedia. Most of the Russian work was focused on producing nanosize aluminum for its potential use as a metal additive for rocket propellant fuel.

Electroexploding metal wire aluminum powder (Alex[®]) consists of spherical particles that are fully dense and about 100 nm in size. Because they are so active, during collection they form hard agglomerates. Because these particles are potentially pyrophoric, the final step in the manufacturing process involves controlled oxidation with dry air to form a passivating layer approximately 3 nm thick. Oxygen analysis shows the coating to be about 92–95% aluminum (between about 85% and 89% as oxide). X-ray diffraction shows the crystallites to be essen-

tially aluminum, while the coating has been found^[24] to be principally aluminum oxide, with some aluminum nitride and some aluminum oxy-nitride. The passivation step is controllable and thinner passivation layers are readily obtained, but the U.S. Department of Transportation (DOT) and International Air Transport Association (IATA) prevent air shipment of pyrophoric materials, so sufficient coverage is necessary to assure no pyrophoricity.

When ignited in air Alex[®] appears to have two separate ignition steps. The first occurs at lower temperatures (400–500°C) and a second where the powder burns white hot. Mench et al.^[25] studied the thermal behavior of Alex[®] powder and compared it to micron-size aluminum. Their data show that Alex[®] powder has very sharp exotherms when heated in air, oxygen, or nitrogen. These occur well below the melting point (660°C) of aluminum, while 20- μ m-size aluminum does not react with oxygen or air until about 1000°C.

A coated version of nano-aluminum (L-Alex[®]) is based on the replacement of the oxide coating by reaction with palmitic acid to form a monomolecular layer of palmitate. This version was tested by boiling the coated Alex[®] in water for an hour and the resulting coating appears to protect the metal, while ordinary Alex[®] would have reacted within minutes. Accelerated aging testing showed^[26] L-Alex[®] to be superior in moisture and oxidation resistance to conventional Alex[®].

Alex[®] as an Additive to Solid Propellants

Ivanov and Tepper^[23] reported a 10- to 20-fold increase in burning rate if air-passivated Alex[®] was substituted for ordinary propellant grade aluminum when mixed with ammonium perchlorate powder (no binder). Sigman and co-workers^[27] also reported that the burning rate of Alex[®] with AP (again no binder) was 10 times greater than with other micron-size aluminum powders. Chiaverini et al.^[28] reported that Alex[®] when added to HTPB binder produced a substantial increase in the burning rate in oxygen.

The agglomeration of aluminum droplets has been studied by Simonenko and Zarko^[29] who noted that there was a growth in aluminum oxide particles collected from the combustion products of a solid propellant grain as compared to that of the original particle size of the aluminum. They also noted that there was a substantial amount of aluminum left within the residual products they collected. In a separate study Glotov and co-workers^[30] noted that the replacement of commercial aluminum by Alex[®] in quantities as small as 8 wt.% increases burning rate and decreases agglomerate size as well as increases the amount of oxidation. For example, total replacement of commercial aluminum by Alex[®] increases combustion efficiency to 99.2% as compared to 94.28% for coarse aluminum.

There have been considerable studies and modeling of the combustion of aluminum in a solid rocket engine. The Brooks and Beckstead model^[31] estimates that the life of the particle is proportional to the particle size raised to the power of n with nominal values of approximately 1.5 to 1.8.^[32] The life of a 35- μm particle is about 6 msec. Extrapolating the Brooks and Beckstead equation for the burning time of a 100-nm-size particle (Alex[®]) results in a lifetime of only approximately 160 and 920 nsec, respectively, for $n=1.8$ and $n=1.5$.

Experimental observations support the very short life computed for combustion of an Alex[®] particle that had originated from a solid propellant. Wang and co-workers^[33] found that when Alex particles are flash-heated to the boiling point, 2740 K, in the presence of a nitrocellulose (NC) oxidizer, the energy release occurs in ~ 5 nsec even much faster than predicted by the Brooks and Beckstead model. Ivanov and Tepper^[23] noted from high-speed cinematographic photographs of a burning propellant that the combustion of Alex[®] is complete at the burning surface, while micron-size aluminum is known to burn throughout the throat and often past the nozzle.

Alex[®] as an Additive to Hybrid Propellants

The classic hybrid technology uses LOX with an HTPB grain that contains either no oxidizer, or just enough to react with the HTPB so as to be a gas generator. This creates low molecular weight organics that are forced into the engine and then react with the liquid oxidizer. The hybrid fuel technology offers a number of advantages including the ability to throttle the engine in real time, stop and start and shift from combustion with on-board oxidizers to air. Should the mission require rapid launching, then the hybrid with storable oxidizers offers advantages over cryogenic fuels. Also, the grain case is smaller and much lighter without the heavy inorganic oxidizer that is in conventional solid propellants. Hybrid solid propellants are much easier, safer, and less costly to manufacture because the oxidizer is not combined into the grain. Also, there are fewer corrosion problems as the fuel is solid. These advantages would be very useful in a rocket-based combined-cycle (RBCC) engine.^[34]

Hybrid problems include the fact that the distance of the flame to the burning surface is an order of magnitude larger than with solid propellant. This makes heat transfer an order of magnitude smaller and consequently the regression rate is an order of magnitude smaller. Because the main flow is rather stratified, the mixing process and therefore the combustion can be incomplete. To achieve complete mixing and combustion of oxidizer and fuel, an aft combustion chamber is added to the hybrid motor.

However, many of these problems can be ameliorated by adding Alex[®]. Chiaverini et al.^[28] added 10 wt.%

Table 1 Specific impulse of aluminized HTPB resins with liquid oxygen (LOX)

Fuel			I_{sp} (vacuum) ^a , sec	I_{sp} density, sec g/cm ³
Metal	Carrier	Oxidizer		
0% Al	100% HTPB	LOX	371	392
25% Al	75% HTPB	LOX	376	423
50% Al	50% HTPB	LOX	370	458
	Hydrazine	N ₂ O ₄	362	442

^aAt chamber pressure of 6.895 MPa (1000 psia) and expansion ratio of 100:1.

Alex[®] to an HTPB slab and found an increase of 70% in the regression rate. They also noted much smoother burning in the case of Alex[®]-loaded HTPB. Table 1 shows how using Alex[®] increases the specific impulse and density-specific impulse of a hybrid and compares it to NTO/Hydrazine.

Alex[®] as an Additive to Liquid Propellants

Palaszewski and Powell,^[35] in some theoretical computations, demonstrated that 0-, 5-, and 55-wt.% aluminum loaded into RP-1 gel propellants provide benefits over neat RP-1. The 0-wt.% loading is attractive when safety over traditional RP-1 (ungelled) is desired and the 5-wt.% loading gave the maximum theoretical specific impulse. The 55-wt.% loading was chosen based on the fact that a liquid-based booster with O₂/RP-1/Al could conform to the volume constraints of the current solid rocket booster even with potential two-phase flow losses taken into account. Palaszewski and Zakany^[7,9] did some combustion experiments with these three mixes using micron-size aluminum for the 5% and 55% loadings. While relatively good performance was obtained, the engine efficiencies were not sufficient for NASA missions.

Mechanisms of Combustion of Gelled Aluminized Propellants

The combustion of a heterogeneous two-phase gel of liquid fuel and aluminum particles is essentially a two-step process. The first step is the combustion of the liquid droplet, which involves boiling of the liquid. A vapor blanket of fuel exists around the two-phase droplet and the flame zone is at some distance beyond the liquid-gas interface, protecting the aluminum from oxidation. At the temperatures and pressures that exist in the rocket engine, the aluminum will be molten. Aluminum combustion would be delayed until the hydrocarbon is burned away,

and during that interval the micron-size aluminum droplets could coalesce. The smaller the hydrocarbon droplet the less time there is for the aluminum to agglomerate. The second step in the process involves the combustion of the now dry aluminum droplet. The mechanisms associated with this second step would be very similar to that occurring had the particles been generated from a solid propellant grain such as Al/organic binder/solid inorganic oxidizer. A nanosize aluminum particle would therefore be expected to have a life less than a microsecond, several orders of magnitude shorter than if micron-size aluminum had been dispersed into the kerosene.

Development and Formulation of Aluminized Gels

The authors were sponsored by NASA to evaluate the benefits of using Alex[®] in lieu of micron-size aluminum powder as a dispersed phase in RP-1.^[36] Wetting and gelling agents were used as additives to aid in homogenization and providing dynamic stability. Fumed silica (Cab-O-Sil[®] grade M5) was used as a gellant and the stability of the gel was determined by centrifugation for 1 hr at 1300 rpm. It was found that when Alex[®] loading was greater than about 25 wt.%, fumed silica was unnecessary as the powder acts as a pseudo-gellant. A 30 wt.% Alex[®] in RP-1 gel was found to be dynamically stable when stored for 2 years at room temperature. A nonanionic surfactant, specifically Tween-85 (polyoxyethylene sorbitan trioleate), was used because it was more effective as a

wetting and dispersing agent for the aluminum particles than anionic and cationic surfactants.

The viscosity of the gelled formulations was then measured so as to determine the practicality of pumping the mixture and spraying it into a combustion chamber. Spray characteristics of a given gas-liquid injector are a function of the liquid surface tension and the gas and liquid velocities, densities, and viscosities.^[37] Liquid propellants typically have viscosities near 1 mPa sec and have Newtonian-type flow behavior.

Green and co-workers^[37] reported absolute viscosity value of 1.89 mPa sec for RP-1. This value remains constant in a wide range of applied shear rates from 1 to 100,000 sec⁻¹. Gelled propellants typically have viscosity in the range of 20 to 50 mPa sec at the shear rates in the range of 10⁵ to 10⁶ sec⁻¹ that are typically encountered in engine injectors.^[38] This is within the range of the pumping systems currently used in rocket engines. As the viscosity of a gelled fuel is a function of variables other than temperature (e.g., shear rate and temporal rheological effects such as thixotropy and gel relaxation time), the rheology is non-Newtonian, and viscometry is reported as "apparent" viscosity at a specific shear rate.

Fig. 2 shows the viscosity of Alexgel fluids and compares them with the viscosity measurements of Rapp^[39] for micron-size aluminum/fumed silica/RP-1 gel permitting extrapolation to strains characteristic of the injector. Note the reduced viscosity when a surfactant is added to a 30% Alex[®]/RP-1. A power law rheological model ($\tau = K \cdot \dot{\gamma}^n$, where τ is a shear stress, $\dot{\gamma}$ is a shear rate, n is effective flow behavior index, and K is a constant of

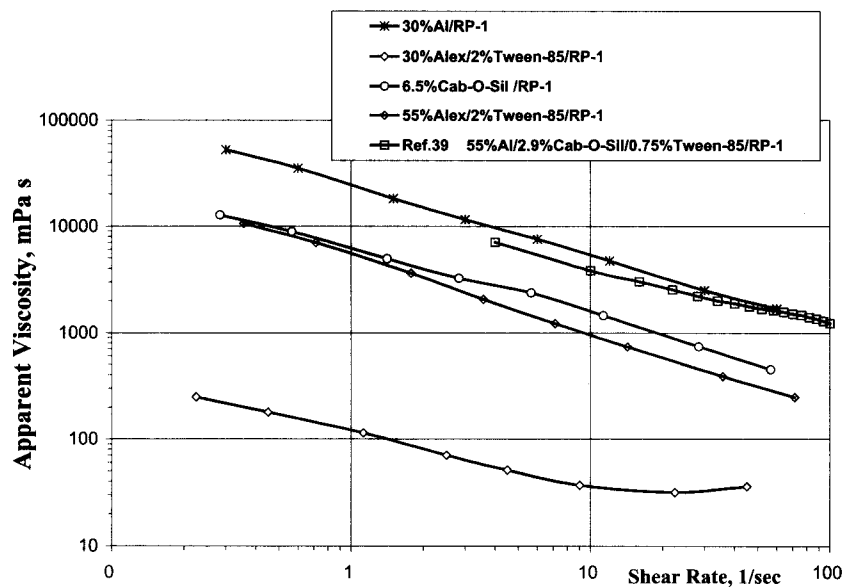


Fig. 2 Apparent viscosity of aluminized fuels.

effective consistency) can be applied to model flow behavior. In general, power law is applicable to model flow behavior of pseudo-plastic fluids with zero yield point. Gelled fuels evaluated in Refs. [7], [9], [39], and [40] have very small yield values ranging from 0.03 to 22 Pa. These yield points are greatly exceeded in injector fluid flow, so their contributions are negligible. By extrapolation of viscosity data to high shear rates using a power law rheological model to the large shear rates encountered in engine injectors, the gels have viscosity near kerosene and therefore within the capability of the pumping systems currently used in rocket engines.

Ignition Delay Measurements

Fig. 3 is a stainless steel combustion bomb^[41] used to measure ignition delay of kerosene and its aluminized versions. The injection port is water cooled to keep the gel (or neat RP-1) at ambient temperature. Fuel temperatures are monitored by a thermocouple at the nozzle close to the tip. The bomb, containing an oxidizing gas of known pressure, is preheated to a defined temperature. Using a piston powered by high-pressure argon, approximately 0.3 cm³ of fuel is injected into the bomb and it auto-ignites at temperatures above about 400°C. An internal transducer measures pressure rise due to combustion. The time is measured from the first movement of the piston

forcing the fluid into the chamber until there is a rapid rise of pressure. Generally, the pressure rise due to combustion is 2–4 times the original pressure, depending upon whether the gas is air or oxygen. The inner length of the bomb is 10 cm, which is the maximum length of the spray pattern. The transit time of the spray to the farthest end of the internal space is approximately 25 msec. At lower temperatures where reaction was slow, the spray would deposit on the inner walls, and the ignition delay extended out to hundreds of milliseconds. This appears to be characteristic of the time for auto-ignition of the gel as a film on the wall of the chamber rather than during the spray interval.

Combustion of Metallized RP-1

Fig. 4 shows chemical ignition delay times of neat RP-1, gelled RP-1, and aluminized gelled RP-1 in hot oxygen^[40] at a fixed pressure at 0.8 MPa and at four different test temperatures (410°C, 460°C, 520°C, and 580°C). Gelled RP-1 was used as a control rather than neat RP-1, to attain equivalent viscosity and permit comparison of the combustion of control vs. the aluminized fluids under similar spray patterns as predicted by the power law model. The gelled RP-1 (6.5-wt.% silica) had a viscosity at high shear rates equivalent to 30% Alex[®]/RP-1. The data in Fig. 4 indicate that the 30-wt.% Alexgel ignites

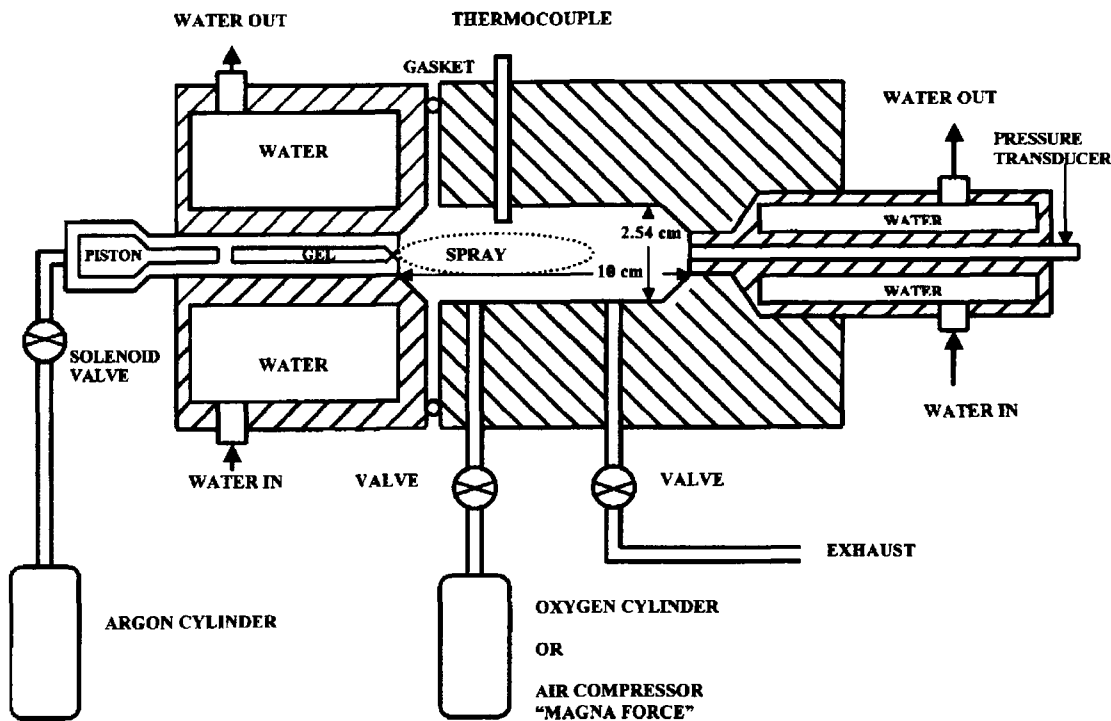


Fig. 3 Device for measuring ignition delay times of gels.

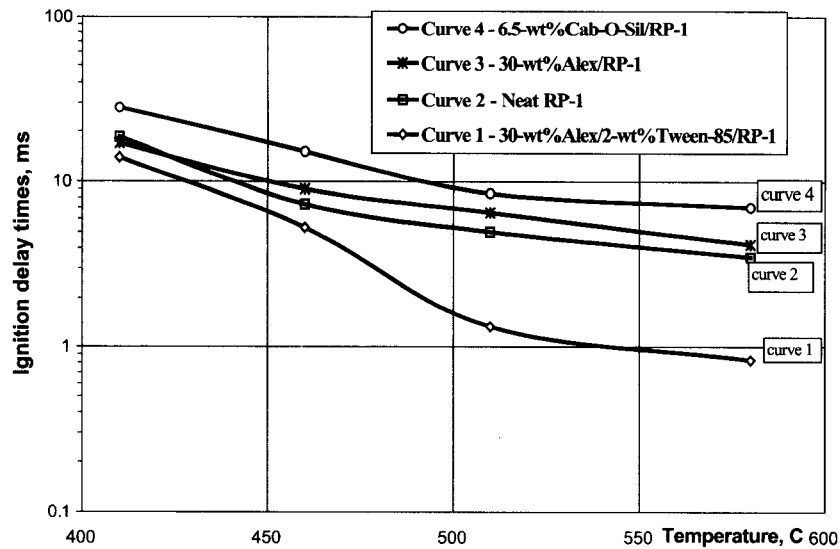


Fig. 4 Average ignition delay in hot oxygen vs. temperature.

faster than gelled RP-1, but about equivalent to that of pure kerosene. However, a surfactant when added to the 30-wt.% Alexgel reduces ignition delay below that of pure RP-1 kerosene (compare curve 1 and curve 2), demonstrating that Alex[®] acts as combustion accelerant for kerosene. Estimations based on the power law model indicate that apparent viscosity of this gel is comparable to that of RP-1 at injector shear rates ($6.3 \cdot 10^4 \text{ sec}^{-1}$). Gels produced from 5- μm aluminum did not show any reduction in ignition delay.

Similar experiments were repeated except in air^[40] rather than oxygen, and at an initial air pressure of 1.1

MPa. Four different fuels were examined: gelled RP-1, 25-wt.% Alexgel, neat RP-1, and 30-wt.% L-Alex[®]/2-wt.% Tween-85/RP-1 fuel. Tests were performed at four different temperatures (430°C, 550°C, 580°C, and 600°C). The data in Fig. 5 indicate that 25-wt.% Alexgel (curve 3) ignites faster by approximately 30% than gelled RP-1 (curve 4). Curve 1 shows that the L-Alex[®] version ignites faster by factor of 2–3 than neat RP-1 (curve 2). As it was noted earlier, these two fluids have similar fluidity at high shear rates, confirming that L-Alex[®] is even more superior as a combustion accelerant than Alex[®] in an air environment.

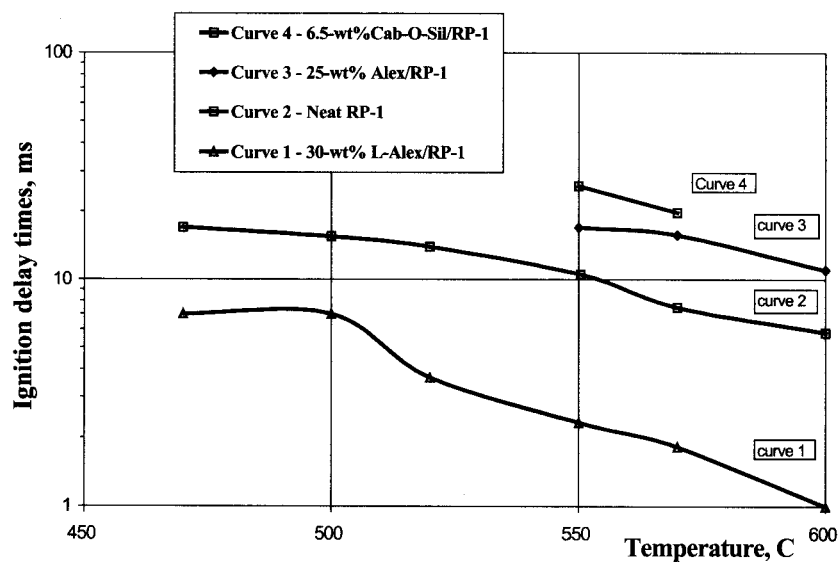


Fig. 5 Average ignition delay of different fuels in air vs. temperature.

“Combustion” in Nitrogen

Alex[®] is known to react rapidly with gaseous nitrogen and this is supported by the DTA data of Mench et al.^[25] This characteristic would be of benefit in air-breathing engines, permitting incipient combustion to occur and support these engines when they are starved for air. Alex[®]/RP-1 gels (55-wt.% Al) were sprayed into pure nitrogen at 750°C showing incipient combustion, but substantially slower than in air or oxygen. Nevertheless, the energy generated by this reaction can contribute to heat generation, while minimizing the opportunity for flame-out in air-breathing engines such as RBCC systems.

Small Rocket Engine Tests

The combustion performance of Alexgels was measured in a small rocket engine by Mordosky et al.^[42] The objective was to measure flame temperature, specific impulse, and c^* combustion efficiency (defined as $P_c A_c / dm/dt$).^[43]

In order to compare rocket test results obtained from different test engines, it is beneficial to have exactly the same fuel and oxidizer compositions as well as approximately the same operational conditions. The small rocket engine constructed by Mordosky et al.^[42] was 30.5 cm long with an internal diameter of 12.0 cm. Combustion of Alexgels was done in gaseous oxygen. The aluminum loadings (Table 2) were the same, but there were some variations in the surfactant and gellant. Table 3 shows average values of adjusted c^* efficiency of the Penn State fuels as compared to the work of Palaszewski and Zakany.^[7,9] They show that:

- (i) The 5-wt.% Alex[®]/RP-1 gel burns more efficiently as compared to 5-wt.%Al/RP-1 gel using coarse aluminum.
- (ii) The 55-wt.% Alex[®]/RP-1 gel burns more efficiently as compared to 55-wt.%Al/RP-1 gel.
- (iii) The 5-wt.% Alex[®]/RP-1 gel burns with the same efficiency as neat RP-1, although the viscosity of

the neat RP-1 is very much lower than that of gelled RP-1 or Alex[®]-loaded gels.

These data show that the combustion of the nano aluminum overcomes the deficiency of a larger droplet spray pattern associated with higher viscosity of the Alexgels. They also measured the aluminum oxide that is produced during combustion and found it to be submicron in size.

APPLICATIONS OF ALEXGELS

Hydrocarbon-Based Liquid Rocket Engines

Combustion bomb testing reinforced by small rocket engine tests shows that Alex[®] nano aluminum powder provides improvement in volumetric energy density over pure kerosene while micron-size aluminum burns inefficiently when dispersed in hydrocarbon. Another benefit is the reduction of metal slagging on the walls of the rocket engine.

Hydrocarbon-Based RBCC Systems

Cryogenic hydrogen is being considered for RBCC engines. However, maintaining this cryogenic fuel over long duration flights, such as its use for re-entry, is problematic. Should hydrocarbon fuel be considered for RBCC engines, then adding Alex[®] would provide the same potential benefits as its use in hypersonics, i.e., flame stability and increased output in the air augmented mode, while providing increases in volumetric I_{sp} in the rocket mode as well.

Pulse Detonation Engines

Another possible use for aluminizing kerosene is in pulse detonation engines (PDEs). The detonation of kerosene in air has yet to be demonstrated. The potential for reducing ignition delay into the submillisecond regime by adding

Table 2 Compositions of the RP-1/Alex[®] gel propellants tested at Penn State

Metal loading weight percentage	Liquid fuel (RP-1)	Metal powder (Alex)	Gellant (SiO ₂)	Surfactant (Tween-85)
0 wt. %	95%	0%	5%	0%
5 wt. %	90%	5%	5%	0%
10 wt. %	86%	10%	4%	0%
30 wt. %	68.2%	30%	1.3%	0.5%
55 wt. %	43.3%	55%	0.4%	1.3%

Table 3 Average values of normalized c_{avg}^* efficiency of NASA gels to the Penn State gels

Gel formulation	c_{avg}^* (Alex [®])	c_{avg}^* (coarse Al, adjusted)	c^*
			Ratio of nano/coarse aluminum [c_{avg}^* (Alex [®])/ c_{avg}^* (Al, adjusted)]
Neat RP-1	—	88.9±1.8	—
5 wt.%	88.3±1.7	78.1±2.4	1.132±0.036
55 wt.%	83.0±2.2	77.8±2.4	1.07±0.04

Alex[®] is almost certain. Further reductions of particle size, enhanced by finer sprays as well as organic layered aluminum such as the L-Alex[®], could result in overcoming the difficulty in detonating kerosene.

Liquid Hydrogen Engines

Adding aluminum to cryogenic hydrogen to form gels has been suggested by Starkovich et al.^[14] as a means to increase volumetric energy density and at the same time increase the containment of a liquid hydrogen leak. Such benefits could also be useful for a liquid hydrogen RBCC engine, where Alex[®] could also serve to increase flame stability during the air cycle.

CONCLUSION

Gels of Alex[®] in RP-1 are dynamically stable at least over the short term and matched the viscosity of coarse aluminum gelled into RP-1 (Fig. 2). Ignition delays of nano-aluminized gels were always shorter than gelled RP-1 (equivalent viscosity) as well as neat RP-1, which has lower viscosity. Alex[®] acts as a combustion accelerant for RP-1, and probably other kerosenes as well. An organic coated version of Alex[®] (L-Alex[®]) was developed and found to have ignition delays in air lower than RP-1 by a factor of 2–3. These findings are relevant to advanced rocket combined cycle engines, hypersonic (scramjet) engines, and perhaps pulse detonation engines. Coarse aluminum is *not* a combustion accelerant for RP-1 in oxygen.

Rocket engine testing at Penn State showed that the 5-wt.% and 55-wt.% Alexgels burn *substantially* more efficiently than coarse aluminum. The 5-wt.% Alex[®]/RP-1 gel burns with the same efficiency as neat RP-1, although the viscosity of the neat RP-1 is very much lower than that of gelled RP-1 or micron-size aluminized gels. Apparently, the kinetics of combustion of the nano aluminum overcomes the larger droplets of the spray caused by higher viscosity.

The overall conclusion is that loading Alex[®] into RP-1 improved its combustion kinetics and efficiency as

compared to neat RP-1, and better than published values for micron-size aluminum gels. Moreover, Alex[®] additions would result in improving the combustion of kerosene in air-breathing engines.

ACKNOWLEDGMENTS

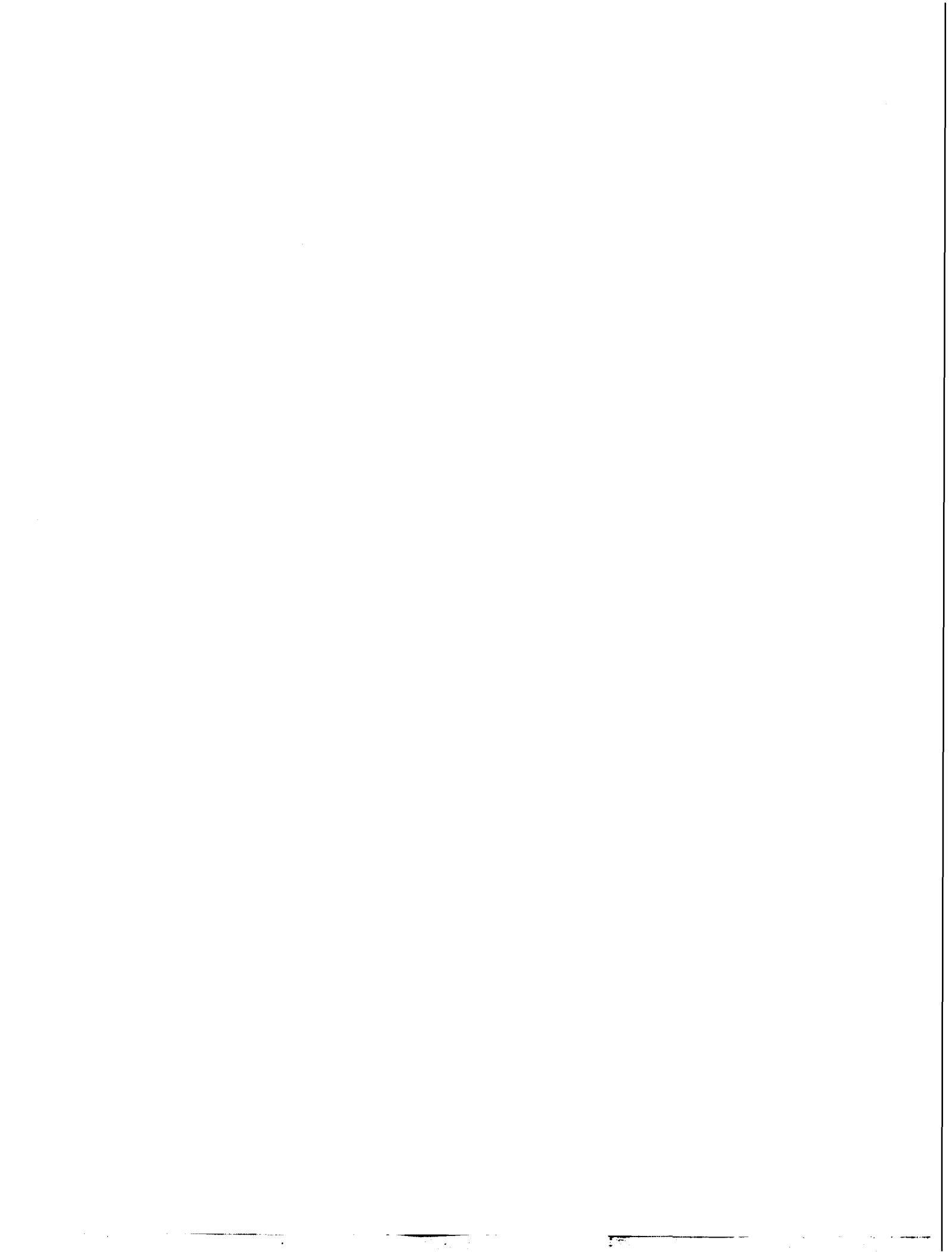
We appreciate the support of NASA Glenn Research Center under Contract No. NAS 3-99117, under the guidance of Brian Palaszewski, technical representative.

REFERENCES

- Spalding, M.J.; Krier, H.; Burton, R.L. Chemical Kinetics of Boron Combustion in High Pressure Ar/F/O₂ Mixtures. 34th AIAA/ASME/SAE/ASEE Joint Propulsion Conference & Exhibit, Cleveland, USA, July 13–15, 1998. AIAA-98-3823.
- Ulas, A.; Kuo, K.K.; Gotzmer, C. Effect of Fluorine-Containing Species on Ignition and Combustion of Boron Particles: Experiment and Theory. In *Combustion of Energetic Materials*; Kuo, K.K., DeLuca, L.T., Eds.; Begell House: New York, 2002; 453–463.
- Vigot, C.; Cochet, A.; Guin, C. Combustion Behavior of Boron-Based Solid Propellants in a Ducted Rocket. In *Combustion of Boron-Based Solid Propellants and Solid Fuels*; Kuo, K.K., Ed.; CRC: Boca Raton, 1993; 386–401.
- Duterque, J. Experimental Studies of Aluminum Agglomeration in Solid Rocket Motors. In *Challenges in Propellants and Combustion*; Kuo, K.K., Ed.; Begell House: New York, 1997; 693–705.
- Price, E.W. Solid rocket combustion instability. An American historical account. Nonsteady burning of combustion stability of solid propellants. *Prog. Astronaut.* **1992**, *143*, 1–16.
- Sanger, E. *Raketenflugtechnik*; R. Oldenburg: Berlin, Germany, 1933.
- Palaszewski, B.; Zakany, J.S. Metallized Gelled Propellants: Oxygen/RP-1/Aluminum Rocket

- Combustion Experiments. 31st AIAA/ASME/SAE/ASEE Joint Propulsion Conference and Exhibit, San Diego, CA, July 10–12, 1995. AIAA 95-2435.
8. Rapp, D.C.; Zurawski, R.L. Characterization of Aluminum/RP-1 Gel Propellant Properties. 24th AIAA/ASME/SAE/ASEE Joint Propulsion Conference, Boston, MA, July 11–13, 1988. AIAA-88-2821.
 9. Palaszewski, B.; Zakany, J.S. Metallized Gelled Propellants: Oxygen/RP-1/Aluminum Rocket Heat Transfer and Combustion Measurements. 32nd AIAA/ASME/SAE/ASEE Joint Propulsion Conference, Lake Buena Vista, FL, July 1–3, 1996. AIAA-96-2622.
 10. Galecki, D.L. Ignition and Combustion of Metallized Propellants. AIAA Propulsion Conf., Monterey, CA, July 10–12, 1989. AIAA-89-2883.
 11. Palaszewski, B.; Rapp, D. Design Issues for Propulsion Systems Using Metallized Propellants. AIAA/NASA/OAI Conference on Advanced SEI Technologies, Cleveland, Sept. 1991. AIAA-91-3484.
 12. Palaszewski, B. Metallized Gelled Propellants Experiences and Lessons Learned: Oxygen/RP-1/Aluminum Rocket Engine Testing. JANNAF/CPIA Gelled Propulsion Technology Symposium, Huntsville, AL, September 19–21, 1995.
 13. Palaszewski, B.A. *Upper Stages Using Liquid Propulsion and Metallized Propellants*, NASA Tech. Paper 3191, 1992.
 14. Starkovich, J.; Adams, S.; Palaszewski, B. Nanoparticulate Gellants for Metallized Gelled Liquid Hydrogen with Aluminum. NASA Tech. Memo 107280, 32nd AIAA/ASME/SAE/ASEE Joint Propulsion Conference, Lake Buena Vista, FL, July 1–3, 1996. AIAA-96-3234.
 15. Cruise, D.R. *Theoretical Computations of Equilibrium Composition, Thermodynamic Properties, and Performance Characteristics of Propellant System*; Naval Weapon Center: Chana Lake, CA, 1991.
 16. Wong, S.C.; Turns, S.R. Disruptive burning of aluminum/carbon slurry droplets. *Combust. Sci. Technol.* **1989**, *66*, 75–92.
 17. Nieder, E.G.; Harrod, C.E.; Rapp, D.C.; Palaszewski, B.A. *Metallized Gelled Monopropellants*, NASA Tech. Memorandum 105418, April 1995.
 18. Woodward, R.D.; Miller, K.L.; Bazarov, V.G.; Guerin, G.F.; Pal, S.; Santoro, R.J. Injector Research for Shuttle OMS Upgrade Using LOX/Ethanol Propellants. 34th AIAA Joint Propulsion Conference, Cleveland, OH, July 13–15, 1998. AIAA-98-3816.
 19. Hurlbert, E.; Applewhite, J.; Nguyen, T.; Reed, B.; Baojiong, Z.; Yue, W. Nontoxic orbital maneuvering and reaction control systems for reusable spacecraft. *J. Propuls. Power* **1998**, *14* (5), 676–687.
 20. Pellaccio, D.G.; Chew, G.; Lowther, S.E.; Zubrin, R.M. Low Cost, Methanol Fueled Rocket Propulsion Technology. AIAA/ASME/SAE/ASEE Joint Propulsion Conference, Cleveland, OH, July 12–15, 1998. AIAA-98-3209.
 21. Lak, T.; Rodriguez, H.; Chandler, F.O.; Jenkins, D. Non-Toxic Cryogenic Storage for OMS/RCS Shuttle Upgrade. 34th AIAA/ASME/SAE/ASEE Joint Propulsion Conference, Cleveland, OH, July 12–15, 1998. AIAA-98-3818.
 22. Rodriguez, H.; Cakiraga, T.; Olsen, A.; Rehagen, R. Non-Toxic System Architecture for Space Shuttle Applications. 34th AIAA/ASME/SAE/ASEE Joint Propulsion Conference, Cleveland, OH, July 12–15, 1998. AIAA-98-3821.
 23. Ivanov, G.V.; Tepper, F. Activated Aluminum as a Stored Energy Source for Propellants. In *Challenges in Propellants and Combustion*; Kuo, K.K., Ed.; Begell House: New York, 1997; 636–645.
 24. Katz, J.; Tepper, F.; Ivanov, G.V.; Lerner, M.I.; Davidovich, V.I. 34th AIAA/ASME/SAE/ASEE Joint Propulsion Conference, Cleveland, OH, July 12–15, 1998.
 25. Mench, M.M.; Kuo, K.K.; Yeh, C.L.; Lu, Y.C. Comparison of thermal behavior of regular and ultra-fine aluminum powders (Alex[®]) made from plasma explosion process. *Combust. Sci. Technol.* **1998**, *135*, 269–292.
 26. Cliff, M.; Tepper, F.; Lisetsky, V. Ageing Characteristics of Alex[®] Nanosize Aluminum. 37th AIAA Joint Propulsion Meeting, Salt Lake City, July 8–11, 2001. AIAA-2001-3287.
 27. Sigman, R.K.; Zachary, E.K.; Chakravarthy, S.R.; Freeman, J.M.; Price, E.W. Preliminary Characterization of the Combustion Behavior of Alex[®] in Solid Propellants. JANNAF Propulsion Meeting, West Palm Beach, FL, Dec. 1997.
 28. Chiaverini, M.J.; Serin, N.; Johnson, D.K.; Lu, Y.C.; Kuo, K.K. Instantaneous Regression Behavior of HTPB Solid Fuels Burning with GOX in a Simulated Hybrid Rocket Motor. In *Challenges in Propellants and Combustion*; Kuo, K.K., Ed.; Begell House: New York, 1997; 719–733.
 29. Simonenko, V.N.; Zarko, V.E. Comparative Studying the Combustion Behavior of Composite Propellants Containing Ultra Fine Aluminum. In *Energetic Materials. Production, Processing and Characterization*, 30th International Annual Conference of ICT, Karlsruhe, Germany, June 2000; 130.
 30. Glotov, O.G.; Zarko, V.E.; Beckstead, M.W. Agglomerate and Oxide Particles Generated in

- Combustion of Alex[®] Containing Solid Propellants. In *Energetic Materials. Production, Processing and Characterization*, 31th International Annual Conference of ICT, Karlsruhe, Germany, June 1999; 21.
31. Brooks, K.P.; Beckstead, M.K. The Dynamics of Aluminum Combustion. 30th JANNAF Combustion Subcommittee Meeting, Nov. 1993; 337–356.
 32. Beckstead, M.W.; Newbold, B.R.; Waroquet, C. A Summary of Aluminum Combustion. 50th JANNAF Propulsion Meeting, 2001; 201–220. Vol. 1.
 33. Wang, S.; Yang, Ya.; Sun, Zh.; Dlott, D.D. Fast spectroscopy of energy release in nanometric explosives. *Chem. Phys. Lett.* **2003**, *368* (1), 183–188.
 34. Hueter, U. Creating an airline to the stars. *Aerosp. Am.* **April 1999**, 40–44.
 35. Palaszewski, B.; Powell, R. Launch Vehicle Propulsion Using Metallized Propellants. AIAA 91-2050, 27th AIAA/ASME/SAE/ASEE Joint Propulsion Conference and Exhibit, Sacramento, CA, June 24–27, 1991.
 36. Tepper, F.; Kaledin, L.A. Combustion Characteristics of Kerosene Containing Alex[®] Nano-Aluminum. Fifth International Symposium on Special Topics in Chemical Propulsion: Combustion of Energetic Materials, Stresa, Italy, June 18–22, 2000.
 37. Green, J.M.; Rapp, D.C.; Roncace, J. Flow Visualization of a Rocket Injector Spray Using Gelled Propellant Stimulants. 27th AIAA/SAE/ASME/ASEE Joint Propulsion Conference, Sacramento, CA, June 24–27, 1991. AIAA-91-2198.
 38. Thompson, D.M. Pressure Drop Model for Gel Propellants in Cylindrical Injectors Using Viscosity as a Parameter. JANNAF Propulsion Meeting, Cleveland, OH, July 15–17, 1998.
 39. Rapp, D.C. Rheology of Aluminum/RP-1 Metallized Propellants Employing Gelling and Surface Active Agents. M.Sc. Thesis; Case Western Reserve University, 1989.
 40. Tepper, F.; Kaledin, L.A. Combustion Characteristics of Kerosene Containing Alex[®] Nano-Aluminum. In *Combustion of Energetic Materials*; Kuo, K.K., DeLuca, L.T., Eds.; Begell House: New York, 2002; 195–205.
 41. Ryan, T.W., III; Stapper, B. *Diesel Fuel Ignition Quality as Determined in a Constant Volume Combustion Bomb*, SAE Paper 870586, February 1987.
 42. Mordosky, J.W.; Zhang, B.Q.; Harting, G.C.; Kuo, K.K.; Tepper, F.; Kaledin, L.A. Combustion of Gelled RP-1 Propellant with Alex[®] Particles in Gaseous Oxygen Atomized Sprays. In *Combustion of Energetic Materials*; Kuo, K.K., DeLuca, L.T., Eds.; Begell House: New York, 2002; 206–218.
 43. Sutton, G.P. *Rocket Propulsion Elements: An Introduction to the Engineering of Rockets*, 6th Ed.; John Wiley and Sons, Inc.: New York, 1992.



Mica Surfaces: Charge Nucleation and Wear

James M. Helt

College of Staten Island and Graduate Center of the City University of New York, New York, New York, U.S.A.

James D. Batteas

National Institute of Standards and Technology, Gaithersburg, Maryland, U.S.A.

INTRODUCTION

The area of nanotribology has advanced greatly in the past 17 years with the introduction of scanned probe microscopies^[1] for the characterization of surface properties.^[2–9] The ability to probe the details of structure, friction, and adhesion on a local atomic/molecular scale affords a definitive approach for understanding the mechanisms of wear at the most fundamental level. Muscovite mica, a layered aluminosilicate in the form of $\text{KAl}_2(\text{Si}_3\text{AlO}_{10})(\text{OH})_2$, has been a suitable standard for atomic force microscopy (AFM)^[11] investigations of the atomic scale relationship between friction,^[10–26] adhesion,^[10,13,14,16,23,25,27–31] and wear^[14–16,23,32,33] due to the ability to readily generate large areas of atomically smooth surface. The rich solution chemistry of mica, attributed to the Brønsted acid sites $[\text{Si}-\text{O}(\text{H})-\text{Al}]$ within the basal (001) plane and its alternating sheet structure, combine with the vast atomically flat surface areas created when cleaved, to give a model substrate for examining a variety of phenomena. These include studies of double layer forces,^[28,30,34–40] van der Waals forces,^[38,41–43] ion binding and mobility,^[35,44–46] monitoring the recoil tracks of alpha particles,^[17,47] the characteristics of polymers at interfaces,^[38,48,49] and ordering of discrete water layers.^[38,43,50]

This review will be limited to a discussion on the wear of mica surfaces, with instructive comparisons drawn to other systems. The overall scope and outline of the chapter is detailed as follows.

As the area of nanotribology is too vast for us to cover in this review,^[5,51,52] we shall endeavor to provide a perspective on studies as related to the mica surface, with a focus on direct observations of charge nucleation and defect formation, further limited to scanned probe microscopy studies. Relevant oxide and inorganic systems that have exhibited behavior paralleling that of mica will also be discussed. We will first begin with a description of the structure and chemistry of the mica surface followed by an overview of the scanned probe methodologies employed in the investigation of nanotribological properties of mica surfaces. This includes the operating principles of the

atomic force microscope (AFM), lateral force (or friction) measurements by AFM, as well as adhesion measurements. Moreover, as one wishes often to quantify such details we will also describe methodologies used to calibrate the signals retrieved from such experiments and then provide a brief description of a standardized approach for the measurement of wear at surfaces, whereby the details of the tip contact area will be explicitly taken into consideration when evaluating the number of scans needed to induce wear at an interface. After describing these approaches, we will then focus on the wear of the mica surface, including the impact of water, and functionalization of the mica surface with alkylsilanes.

MICA SURFACES

The outermost mica surface typically exposes a hexagonally arrayed pattern of oxygen atoms, with a periodicity of 0.52 nm (Fig. 1A). Mica is comprised of a layered aluminosilicate structure with a periodicity of 1.0 nm normal to the (001) crystal basal plane (Fig. 1B), which is defined by a repeating boundary layer of K^+ .^[53,54] The K^+ ions electrostatically bind the sheets together and act to neutralize the net negative charge associated with the partial substitution of Si with Al (on average one out of every four). It is at these boundaries that cleavage is preferred and is where shearing of the layers most readily occurs. Under aqueous conditions of low electrolyte concentrations, the outermost K^+ layers are solvated into solution and exchanged with H^+ .^[19,30,34–36,44,46] This ready displacement has hindered direct imaging of the K^+ terminated mica surface. The surface of mica may also be readily functionalized by a range of chemistries. Some of the most popular involve the organization of self-assembled monolayers of triethoxy- or trichloro-derivatized alkylsilanes, which can form densely packed structures on mica.^[20,55–65] This provides a means of investigating lubricant layers as protective barriers for the minimization of friction and wear.

To date, most surface wear studies have focused on the evaluation of surface structure before and after

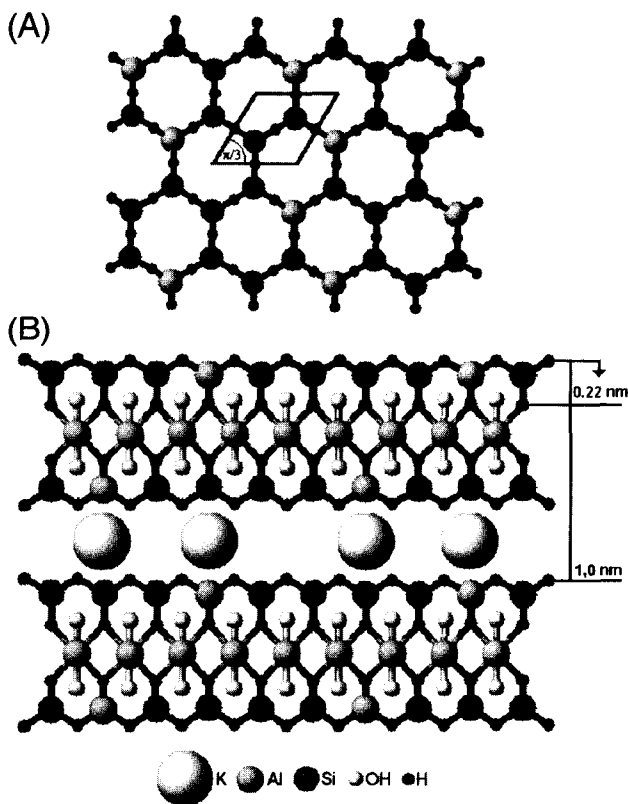


Fig. 1 (A) Pictorial representation of the mica (001) cleavage plane showing the 0.52-nm lattice periodicity. (B) Repeating layered structure of mica along the *c* axis with interlayer distances referenced to the basal plane.

wear,^[15,33,66–71] thus missing the key stage of the nucleation of defects that ultimately results in the gross structural changes observed. Although some studies have investigated the time evolution of wear using scanned probes,^[14,16,72–77] the different approaches presented can make it difficult to compare experiments from different laboratories, and a more standardized approach is required. This is in part because of the typically large contact area between the AFM tip and the surface being worn, which frequently exceeds the area density of defects nucleated. Thus, an averaging over the contact renders the low population of defects “invisible” to the probe tip until gross wear has occurred.

Investigations of the wear of oxide surfaces such as mica and silica have unique difficulties when probing wear at the atomic level, which are associated with the chemical complexity of the surfaces, especially in the presence of water^[71,78–87] where the surface charge density is highly pH dependent.^[66,79–81,88,89] A recent demonstration by Maw et al. illustrates the incongruous wear behavior that exists for ceramics in solution (pH = 7).^[32] Specifically, they found that a Si₃N₄ tip

exhibited pronounced wear after being rastered against a quartz substrate for 25 scans at ~120 nN of force. However, under similar conditions the Si₃N₄ tip exhibited little wear when the surface was mica. Here the disparity has been attributed to the relevant population of silanol (Si–OH) groups that can form bonds between the tip and substrate, which facilitates removal of tip materials. As the basal plane of mica possesses a Brønsted acid site, because of the 1 in 4 substitution of Si for Al, it is expected that the ionization potential of the surface is largely controlled by this site (at least at lower pH's), and therefore the chemically active Si–O[−] or M–OH should be in minute quantities.^[40,46,65,90] Because the isoelectric point (IEP) of quartz is between pH 2 and 3, it is apparent that at pH 7 a significant number of Si–O[−] and Si–OH groups are available for condensation at the tip–quartz contact.^[78] The influence of such tribochemically active species in initiating surface degradation is evident and illustrates the necessity to account for this when choosing material pairs for a given application, i.e., the chemistries should be complementary. This certainly applies to device applications such as microelectromechanical systems (MEMS) where interfacial chemical forces can readily dominate the moving contacts within the device.^[70,91–96]

The organization of the water molecules^[38,43,50] and counterions^[19] immediately at the oxide surface may also impact the evolution of surface defects. Studies of the influence of water on the wear of oxide surfaces show a critical dependence on the amount of water present^[14] and, in the case of solvation of the surface, the local pH of the surrounding water environment. Much of the wear processes present at oxides can be attributed to the catalytic activity of water (more appropriately the OH[−] ion) on the metal–oxygen and silicon–oxygen bonds present on such surfaces, the details of which have been investigated for many years.

SCANNED PROBE METHODOLOGIES

Atomic Force Microscopy: General Methodology

In atomic force microscopy, a sharp tip with a radius of curvature ranging between 10 and 50 nm is scanned over a surface using a piezoelectric translator to control the position of the tip relative to the sample. The forces acting between the tip and sample (these can be van der Waals, electrostatic, or magnetic in nature) act to attract or repel the tip to or from the surface, which in turn alters the bending of the lever to which the tip is attached. In most conventional AFMs, lever deflections are detected by reflecting a laser beam off the back of the cantilever onto a quadrant photodiode. The photodiode signals are split to

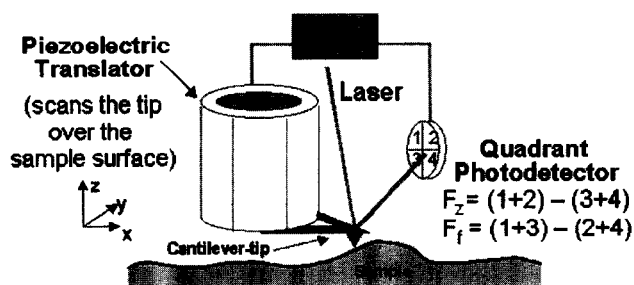


Fig. 2 Schematic of an atomic force microscope. In this configuration, the tip is scanned over a fixed sample. The cantilever–tip assembly is mounted on a piezoelectric translator, which controls the tip position over the surface. In contact mode, the tip is pressed against the surface until a fixed set point force is reached (F_0). The deflection of the lever is detected by a quadrant photodiode from which the normal force (F_z) and torsional (frictional) force (F_f) may be measured. As the tip is scanned over the surface a feedback loop raises and lowers the tip depending on whether the normal force is larger than or less than the set point force to maintain a constant force. (View this art in color at www.dekker.com.)

allow detection of the normal or torsional motions of the cantilever–tip assembly (Fig. 2). These motions can in turn (when appropriately calibrated, as discussed later) be translated into the normal and lateral forces acting between the tip and surface. The AFM can be operated in several imaging modes, including contact, noncontact/tapping, amplitude, and phase-modulated force or frictional force imaging. For nanotribological studies, contact and frictional force imaging modes are the most frequently used.

In contact mode the tip is brought in contact with the surface until the lever experiences a fixed amount of deflection. Assuming that this amount of deflection stays within a linear limit, then a Hooke's law response can be assumed. If the lever spring constant is known (see below) then the amount of deflection can be converted into the force applied between the tip and surface. During imaging, a feedback loop is then used to maintain a fixed amount of lever deflection (constant normal force) by repeatedly moving the piezoelectric translators up and/or down, hence following the topography of the surface. The lateral force signals are concomitantly acquired with the topographic images allowing for correlations to be drawn between the two. The lateral force signal is an excellent indicator of changes in local chemistry even when obvious topographic differences are not present. For example, the spatial organization of films consisting of both hydrophobic and hydrophilic end-groups, which have the same thickness and appear uniform in topography, can be easily distinguished in the frictional images [Fig. 3A (2–3)].

Lateral Force (Friction and Shear) Measurements

Eventhough qualitative lateral force, or frictional response, can be readily obtained by AFM, quantifying frictional forces can be a daunting task. This is due to the difficulties associated with calibration of the lateral spring constants for AFM cantilevers (see below). Here we briefly discuss the type of information, which may be obtained from lateral force or shear force measurements. In lateral force measurements, friction is assessed using a friction loop. The friction loop is generated from the forward and reverse scans plotting the lateral force data vs. distance (Fig. 3B). Initially, the tip sticks to the surface and the torsional force on the lever increases without the sliding motion of the tip. Once the static friction has been overcome, then the tip will begin to slide over the surface and the sliding friction may be determined (Fig. 3B). The shear modulus of the surface may also be measured using this same basic approach. To evaluate the shear modulus, the tip is oscillated in the scan direction and the slope of the friction force (F_f) vs. distance signal is measured prior to sliding. This slope value contains the combined stiffness of the tip–sample contact (Eq. 1) from which the shear modulus of the surface may be determined.

$$\frac{dF_f}{dx} = k_{\text{total}} = \left(\frac{1}{k_{\text{lever}}} + \frac{1}{k_{\text{contact}}} \right)^{-1} \quad (1)$$

A significant advantage of this measurement is that the details of the tip size ultimately fall out of the calculation, removing a potential source of error. The reader is directed to the literature for a more complete description of lateral stiffness measurements.^[97]

MAKING QUANTITATIVE MEASUREMENTS

Calibration of AFM Cantilevers

AFM cantilevers can be bought from numerous sources and most frequently come as V-shaped or rectangular springboard-shaped levers. The levers are generally made from silicon and silicon nitride. Coatings are often applied to enhance the reflectivity of the laser beam. The reflective coating, however, can add strain to the levers when used in vacuum because of heating. The average lever spring constants provided by the manufacturer are often inaccurate and quantitative measurements should not be based on these values. Therefore, each lever should be independently calibrated, preferably via an in situ methodology.

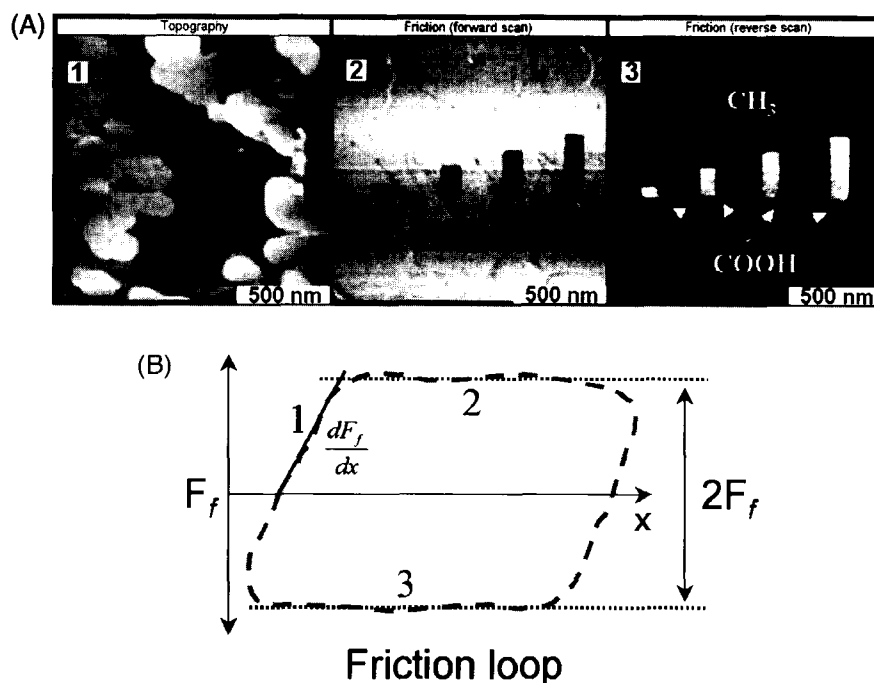


Fig. 3 (A) Topographic (1) and forward and reverse friction images (2, 3) of mercaptoundecanoic acid grafted into a dodecanethiol self-assembled monolayer on Au. Whereas the topographic image shows almost no height contrast in the image because of the near equivalent heights of the two materials, the friction images clearly show the “chemical” contrast of the $-\text{COOH}$ terminated regions vs. the $-\text{CH}_3$ terminated regions. (B) Schematic of a friction loop. Initially the tip sticks to the surface (1) until the static friction between the tip and surface is overcome. The tip then enters a sliding friction regime (2). As the scan is reversed, the signal in the photodetector becomes negative (3) and a reverse trace is produced. The “frictional” force is the average of the forward and reverse friction traces. The stiffness of the contact may be deduced from the slope of the friction loop (dF_f/dx) before sliding. (View this art in color at www.dekker.com.)

The determination of lever force constants is less demanding for a rectangular cantilever beam,^[98] but it still requires nontrivial details of the lever’s dimensions and physical constants, e.g., modulus and Poisson ratio. These details become more difficult to define for metal-coated levers, as the coating significantly modifies the lever’s elastic properties. For a rectangular beam of length L , width w , thickness t , Young’s modulus E , the stiffness k is given by:

$$k_{\text{lever}} = \frac{Ewt^3}{4L^3} \quad (2)$$

Errors inherent to the determination of the spring constant come from difficulties in accurately measuring (by SEM) the thickness of the lever. In addition, for chemical vapor deposited silicon nitride levers, variations in E can also occur. If a bulk value for E is used, the thickness can be determined by measuring the resonance frequency of the cantilever.^[99] However, this method works only for uncoated monolithic cantilevers.^[100] The formulae for the spring constants for V-shaped levers are much more

complicated.^[101] Uncoated, single-crystal silicon cantilevers are perhaps the best choice for which the force constant can be reliably determined by using Eq. 2 and the resonance frequency.^[102]

A range of methods for the calibration of the normal^[99–114] and torsional (lateral) force constants^[101,105,110,115,116] of AFM cantilevers have been described. A recent method proposed by Sader et al. appears to be reliable and simple to perform for rectangular levers.^[107] It relies on measuring the resonance frequency and the quality factor of the cantilever in air. Use of the hydrodynamic function relates the damping of the lever resonance by air to the quality factor, and the dependence of E and t are eliminated from the resulting formula for the force constant.

Probe Tip Characterization

A problem of quite a different nature is an accurate measurement of the AFM tip shape and composition. With

respect to tip geometry, continuum mechanics requires a priori knowledge of the probe shape, mechanical properties, and physical dimensions in order for the models to be properly applied.^[117,118] Carpick et al. illustrated this point rather succinctly in an instructive set of experiments with nonparabolic Pt tips on a mica substrate in ultrahigh vacuum (UHV).^[12]

There are several in situ methods to characterize the tip shape, where an AFM topographic image is used to deconvolute the tip and sample geometry.^[119–121] Separation of the tip and sample contributions by contact imaging of known, or at least sharp, sample features allows determination of the tip.^[104,105,120–131] Ex situ tip imaging by electron microscopy has also been performed.^[103] Some of these measurements have revealed that a number of microfabricated cantilevers possess double tips and other unsuitable tip structures.^[122,125,130,131] This demonstrates the importance of tip characterization in nanotribological measurements. Thin film coatings applied to the microfabricated levers can provide robust, smooth, and even conductive coatings.^[132,133] Further work in this direction would be useful in providing a wider array of dependable tip structures and materials.

Detailed control of tip chemistry is still a difficulty of scan probe studies with commonly used tips (e.g., silicon nitride) possessing a variable stoichiometry.^[89,112,134] Coating with inert metals (such as Au or Pt) or functionalization with alkylsilanes or alkanethiols is often useful; however, one must be aware of the “chemical” compatibility and how this can translate into “anomalous” wear behavior.^[32] The chemical composition of the tip is equally important, but is also challenging to determine or control. Qian and coworkers have shown that the AFM tip is readily chemically modified when scanned in contact with various materials,^[25] even tips that have been coated with self-assembled monolayers to control their chemistry. They recommend “running in” the tip with a standard sample to give reproducible results. The stresses that take place in a nanocontact can be very large, and so modification of both the chemistry and structure of the tip is an important consideration.

Adhesion Measurements

When quantifying adhesion and interfacial energies from AFM measurements, often the contact mechanics model developed by Johnson, Kendall, and Roberts (JKR)^[118,135] is used to analyze adhesion data from force–distance spectroscopy. Determination of the most appropriate continuum mechanics model to use, however, requires consideration of the range of forces and the materials operative at the contact. The JKR model is often applied

to highly adhesive, compliant contacts, whereas the Derjauin–Müller–Toporov (DMT) model relates to stiff, weakly adhering contacts.^[117,136] Attention has been given to identifying which model is most appropriate and therefore best describes the contact for a given material pair; the reader is directed to the references for the complete treatments.^[135–138] The application of such models to AFM force of adhesion measurements (F_{adh}) enables the number of interacting species (and consequently the average “unit” interaction force or energy) to be derived from the estimated contact area and the average molecular packing density. Using the JKR model, one can see that the F_{adh} (AFM pull-off force) is related to the work of adhesion, W_{adh} , and the reduced radius, R , of the tip–surface contact:

$$F_{adh} = -\frac{3}{2}\pi RW_{adh} \quad (3)$$

The work of adhesion, a formalism of Dupré from 1869, is a combination of the tip–surface (γ_{ts}), tip–solvent (γ_{tl}), and surface–solvent (γ_{sl}) interfacial energies ($W_{adh} = \gamma_{sl} + \gamma_{tl} - \gamma_{ts}$). For tip–surface combinations that have the same chemical composition, the surface energy may be estimated directly from the adhesion measurement ($W_{adh} = 2\gamma_{sl}$) because $\gamma_{sl} = \gamma_{tl}$, with $\gamma_{ts} = 0$. Furthermore, the effective contact radius at separation, r_s , from the JKR model is given as:

$$r_s = \left(\frac{3\pi W_{adh} R^2}{2K}\right)^{1/3} \quad (4)$$

where K is the reduced elastic modulus of the tip and surface. Using the contact area at separation and the assumed packing density of the molecules at the surfaces in contact, an estimate of the adhesion force or interaction energy on a per molecule basis can be made.

The accuracy of the interfacial energies and per molecule values obtained with this approach must be carefully evaluated, as several sources of error exist in the various elements of the calculation. These include imprecise knowledge of the contact, including the tip radius, packing densities of molecular monolayers on the modified surfaces, as well as unknown elastic properties of the contact. Such properties are typically assumed to be dominated by those of the underlying substrate, and the bulk values of the surface and/or tip materials (Au, Si, mica, Si_3N_4 , SiO_2) are often used in these calculations.^[159–61,139] Moreover, as mentioned earlier, if the molecular packing densities of the monolayers being evaluated are not known (as is frequently the case with a typical AFM tip), then estimations must be used.

Watching Wear with the AFM (How Many Scans Does It Take?)

Atomic force microscopy tips, acting as single asperities, have proven indispensable in actively mediating the transition of a substrate surface from its native state to the defect nucleation regime (rupture of terminating surface bonds) and finally to the molecular-fragment abstraction (gross wear) regime.^[114,73-77,140-142] Unifying empirical evidence pertaining to the intimate details of defect nucleation is essential to properly aid the current effort of wear map modeling on the micro- and macroscopic scales, situations with multiple asperity contacts, and a multitude of wear mechanisms operating in concert.^[51,143] To ease comparison of data compiled from numerous research facilities within the field, guidelines outlining the optimal experimental protocol for an SPM study are desirable. Recent developments in modeling tip-activated dissolution of calcite and brushite by Dickinson et al. has given impressive results and holds promise for evaluating other "model" systems.^[74-77] Salmeron and Kopta have recently used a model, similar to the one adopted by Dickinson et al., in their studies of tip induced mica surface degradation under low vacuum with variable humidity.^[14] In this work, the objective was to evaluate the critical defect density necessary for the onset of gross surface degradation (abstraction of the surface terminating SiO₃ molecular fragments). The progressive layer removal illustrated the fidelity of inducing defects; however, linear regression analysis obtained a collected physical constant (B_0) that

was appreciably higher than anticipated. This could be attributed to scan overlap, which can lead to significant additional history of unintentional wear on the surface.

Here we outline a strategy for conducting wear trials with AFM, based on the Hertzian theory of *elastic* contacts,^[144] to account for the degree of scan overlap in AFM wear trials, and arrive at an interesting *contact radius–line step* (CRLS) relationship.^[145] This approach is intended to 1) account for additional scan history that line-scan overlap imparts to a surface and to experimentally quantify the impact of this overlap on the propagation of defects; 2) eliminate the systematic error in reported scan history (experimental number of scans, $N_{\text{scans}}^{\text{Exp}}$) for wear trials performed with line-scan overlap; and 3) examine previous load (F_z) and frequency ($N_{\text{scans}}^{\text{Exp}}$) studies to reevaluate activation parameters for defect nucleation. Furthermore, the extent of wear can be predicted with application of CRLS analysis for *paired* overlap and nonoverlap wear trials, giving a unique perspective of the fundamental kinetics and thermodynamics of defect nucleation and growth.

Contact Radius–Line Step Analysis

A brief description of CRLS analysis follows with a focus on its application rather than on the details of its derivation. A comprehensive discussion of CRLS model and experiments is described elsewhere.^[145] First, consider the general case of obtaining an AFM micrograph or performing a wear trial. In either instance, one of many

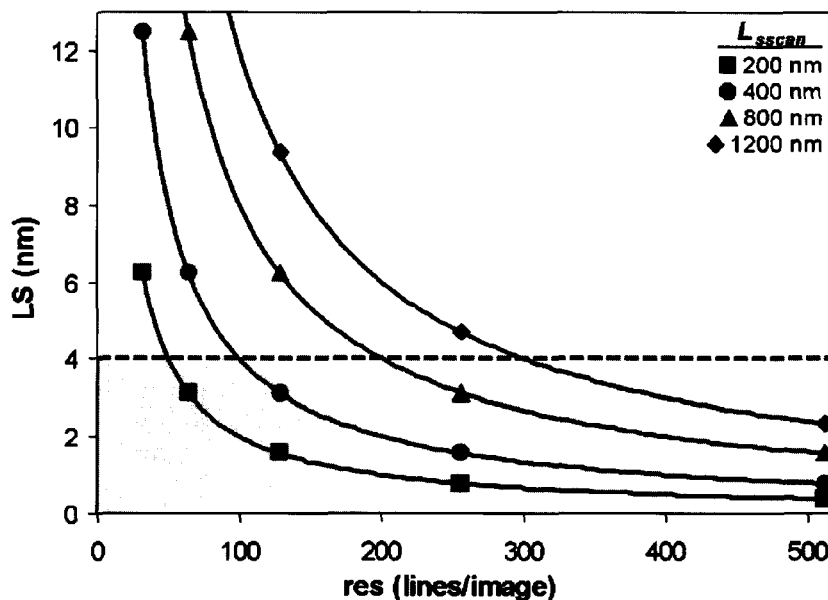


Fig. 4 Inverse relationship between image line step (LS) and image resolution (res) for several slow scan lengths L_{scan} . The dashed line and accompanying shaded region illustrate the occurrence of scan overlap during AFM imaging for contacts with a contact radius $a \geq 2$ nm. For wear trials this implies that scan overlap will systematically contribute unaccounted attempts to defect production.

parameters set during image acquisition is the image resolution (*res*), the number of lines scanned per image. Typically, it is adjustable within the range of 8–1024 lines/image, depending on the design specifications of the microscope used. Although it is not generally thought of as an adjustable parameter for use in experimentation, it is readily illustrated that *res* can play an important role when assessing the number of scans required to induce wear. Its importance arises because *res* dictates the magnitude of the line step (LS), i.e., the distance the tip moves in the slow scan (L_{sscan}) direction after each forward–reverse trace. Fig. 4 illustrates the inverse relationship between LS and *res* for the specified slow scan lengths (L_{sscan}). Before we show how LS ties into defect production, we introduce the Hertzian definition of the contact radius (*a*) as defined for an AFM tip compressed against flat elastic body without adhesion (Eqs. 5 and 6):^[118]

$$a = \left(\frac{3RF_z}{4\varepsilon} \right)^{1/3} \quad (5)$$

with

$$\varepsilon = \left(\frac{1 - \nu_1^2}{E_1} + \frac{1 - \nu_2^2}{E_2} \right)^{-1} \quad (6)$$

Here *R*, F_z , and ε are the tip radius of curvature, the applied normal force, and the combined elastic modulus given in terms of the individual tip and substrate Poisson ratios (ν_i) and Young's moduli (E_i). It is apparent that at a typical *res* of 256 lines/image, the LS is <4 nm for all L_{sscan} below $\sim 1 \mu\text{m}$ in length. Thus, unless $a \leq 2 \text{ nm}$, overlap from successive scans will occur, and shows that avoidance of scan overlap and its effects are difficult to realize when probing regions with nanoscopic dimensions.

If we make the assertion that ideal scanning conditions for assessing wear as a function of the number of scans requires imaging conditions with no scan overlap, it is recognized that the line step (LS) must be greater than or equal to the contact diameter. Using the Hertz definition of *a* and the condition that ideal AFM wear trials have $\text{LS} = 2a$, the ideal ratio of contact radius to line step (CRLS) is 0.5. Furthermore, line-scan overlap is avoided (neglecting drift) when CRLS is $\leq 1/2$. This further implies that an ideal AFM wear trial, with $\text{LS} = 2a$, will have an ideal slow scan length, $L_{\text{sscan}}^{\text{CRLS}}$, given by Eq. 7. Expression (7) reveals an important relationship between the AFM scanning parameters, $L_{\text{sscan}}^{\text{CRLS}}$ and *res*, and the applied normal load. A

$L_{\text{sscan}}^{\text{CRLS}}$ vs. F_z plot is especially useful for conducting internally consistent load (F_z)-dependent studies.

$$L_{\text{sscan}}^{\text{CRLS}} = 2a \times \text{res} = \text{res} \times \left(\frac{6RF_z}{\varepsilon} \right)^{1/3} \quad (7)$$

We have used the term “ideal” quite ambiguously to describe $L_{\text{sscan}}^{\text{CRLS}}$, the most appropriate scan size for defect generation. It is expected and empirically validated that the generated defects will be more *uniformly* (relative to overlapping trials) distributed over the wear area before the advent of other varieties of defects. This allows for the design of experiments to probe these low-density species (typically <1 defect within the tip–sample contact).^[14]

To evaluate the effects of scan overlap we must account for the additional history overlap imparts to the surface; achieved by estimating a scan correction (scan_{cor}) for overlapping studies. The scan_{cor} determines the additional number of scans contributed by overlap to the contact history and therefore can be used to estimate the number of scan cycles required to achieve an equivalent degree of wear, under identical loads, *without* scan overlap. The scan_{cor} is arrived at naturally by association to the force of overlap within overlapping contacts. The Hertz model defines the pressure distribution $p(r)$ in terms of *r*, the distance from the center of contact via Eq. 8.^[144]

$$\begin{aligned} F_z &= \int_0^{2\pi} \int_0^a p(r)r dr d\theta \\ &= \frac{1.5F_z}{\pi a^2} \int_0^{2\pi} \int_0^a \left(1 - \frac{r^2}{a^2} \right)^{1/2} r dr d\theta \\ &= \frac{2p_0 \pi a^2}{3} \end{aligned} \quad (8)$$

Here p_0 is the maximum Hertz pressure within the contact. Once the boundary of the overlapping area is defined (Fig. 5), the force of overlap can be calculated. The scan_{cor} is collectively calculated in terms of $F_{\text{ovlp}}^{\text{Total}}$, the total force within all successive overlapping contact areas. $F_{\text{ovlp}}^{\text{Total}}$ is formulated from a geometric breakdown of overlapping circles of radii *a* (Fig. 5) and leads to the three integrals in Eq. 9, which have been converted to Cartesian coordinates. The $(F_z \times \text{res})$ term normalizes *each experimental scan* and the functions *A*, *B*, and *C* are given in Fig. 5 (see equation below).

$$\text{scan}_{\text{cor}} = 1 + \frac{2 \times \sum_{m_1}^{m_i} \{\text{res} - m_y\} \left(\frac{1.5F_z}{\pi a^2} \right) \left[\int_0^{a \sin(\theta)} \int_0^{\sqrt{a^2 - x^2}} p(x, y) dy dx - \int_A^{a \sin(\theta)} \int_0^B p(x, y) dy dx + \int_0^C \int_0^{-B} p(x, y) dy dx \right]}{\text{res} \times F_z} \quad (9)$$

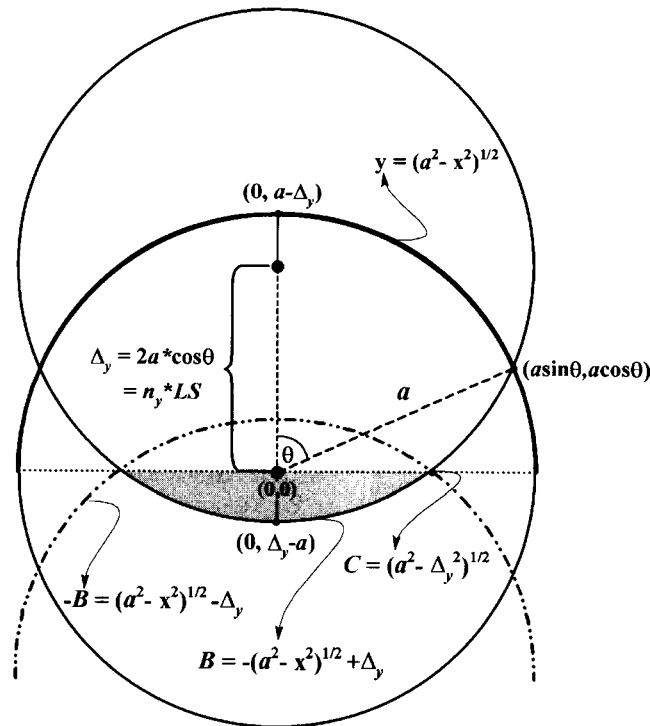


Fig. 5 Geometry of overlapping scans according to Hertzian contact mechanics theory.

The center-to-center distance (Δ_y) along the slow scan axis for successive scans is referenced to the first scan line ($n_0=0$) and is known a priori; n_y is a positive integer corresponding to the n th line step from n_0 as shown in Fig. 6. The series is truncated at n_i ($n_i=2a/LS$) because overlap does not exist for the i th successive scan where

$\Delta_i \geq 2a$. For simplicity, the summation is redefined in terms of m_y having an integer range of $[m_1, m_i]$ with $m_i=n_{i-1}$ because the 1 in Eq. 9 accounts for n_0 . For the interested reader, more details on the theoretical workup can be found in Ref. [145]. We can now utilize the general, material independent result ($scan_{cor}$ given in

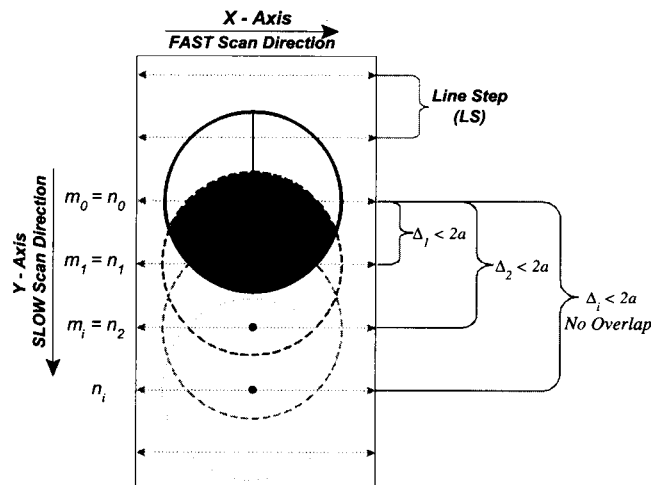


Fig. 6 Definition of elements used for $scan_{cor}$ analysis of sequential raster lines.

Eq. 10) to explore how CRLS analysis is applied to previous wear trials with mica.

$$\text{scan}_{\text{cor}}(\theta, m_y) = 1 + \sum_{\theta(m_1)}^{\theta(m_2)} \left[\frac{\text{res} - m_y}{\text{res}} \right] \times \left(1.011 \exp \frac{-(\theta - 92.83)^2}{34.67^2} \right) \quad (10)$$

Completing the correction simply requires multiplying the experimental number of scans containing overlap ($N_{\text{scans}}^{\text{Exp}}$) with scan_{cor} ($\text{scan}_{\text{cor}} \times N_{\text{scans}}^{\text{Exp}} = N_{\text{scans}}^{\text{Cor}}$). Importantly, CRLS can be tested directly because it can predict wear for “paired” trials. In such circumstances, an experimental trial with overlap is taken as the primary trial from which the CRLS prediction and the secondary nonoverlapping experiments are based. Experimentally, the secondary trials are conducted at a Hertz mean pressure (p_m) equivalent to the primary run over a region with $L_{\text{sscans}}^{\text{CRLS}}$ defined by Eq. 7. Therefore, the nonoverlapping secondary wear trials consist of $N_{\text{scans}}^{\text{Cor}}$ over a ($L_{\text{sscans}}^{\text{CRLS}} \times L_{\text{fscan}}$) nm^2 region. The surface damage from both instances can be evaluated and compared with F_{adh} measurements, topography, and frictional force microscopy. In theory, the two wear experiments have “identical” scan history within this Hertzian approximation. Deviations from CRLS behavior are expected, however, because the tenets of elastic contact mechanics do not include inelastic energy dissipation pathways natural to a wearing contact. Numerical and experimental results clearly demonstrate that the systematic error attributed to scan overlap is considerable and affects fundamental wear processes acting at the tip–surface contact.^[145] Work is currently under way to establish the relationship between scan overlap and defect nucleation and growth.

WEAR OF MICA SURFACES

There have been many theoretical and experimental studies on wear of oxides and the generation and propagation of defects within condensed matter. Here we shall describe a few examples of crystalline systems within the context of tip induced defect nucleation and wear of mica surfaces in solution. The examples will focus on studies of defect nucleation that have revealed the prototypical behavior of what is to be expected (and what is detectable with AFM) of a surface reconstructing under the influence of an AFM tip. At the most fundamental level of defect nucleation, this includes *terminal* surface bond rupture for covalent systems as well as removal of ions from ionic surfaces.

Native Mica Surfaces

Now we will briefly describe adhesion and wear of mica surfaces using silicon-nitride-based AFM tips. The complete experimental details are described elsewhere.^[142] In these studies, oxidized and hydroxylated silicon nitride tips were used.^[102,122] Under these conditions, the silicon nitride tip chemistry then varies with pH similar to that of silica,^[146] where a neutral silanol-covered surface exists at the isoelectric point between pH 2 and 3, with a gradual surface charge increase via the formation of an anionic surface species with increasing pH ($\sim 0.004\text{--}2$ charges/ nm^2) over the range of pH 3–10.^[66,78] In aqueous solution, the adhesive force (F_{adh}) vs. pH for native mica with an oxidized and hydroxylated silicon nitride tip is shown in Fig. 7. This pH dependence on adhesion is similar to that found for silica surfaces under the same conditions, with a shift in peak adhesion from $\text{pH} \sim 4.5$, for silica/silica, to $\text{pH} \sim 6$ for the silica/mica interaction.^[66] Based on this profile, alterations in adhesion, friction, and topography under various loads for three pH ranges (pH 2–3, 5–6, and >8) can be assessed and related to the interfacial chemistry.

Typical of silicates, for the highest pH conditions ($\text{pH} \geq 8$), the mica surface undergoes rapid wear.^[78–81,85] Even under low loads (Hertz mean pressure, $p_m \sim 1.2$ GPa) wear scars 0.22 nm in depth are formed. With additional scans (>10) wear scars of 1.0 nm or more are rapidly formed (Fig. 8). Upon removal of a single repeat layer (1.0-nm-deep feature), the friction in the wear scar is equivalent to that of the contiguous unworn mica surface, indicating that we have progressed from the outermost oxygen-terminated layer to the next chemically equivalent repeat layer. This is a general observation for mica wear at any pH and has also been observed by Salmeron

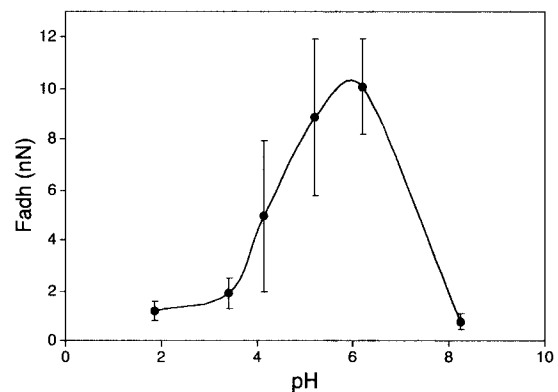


Fig. 7 Mean F_{adh} vs. pH for muscovite mica with a Si_3N_4 tip. Error bars correspond to the first standard deviation from the >180 force distance curves collected for each point.

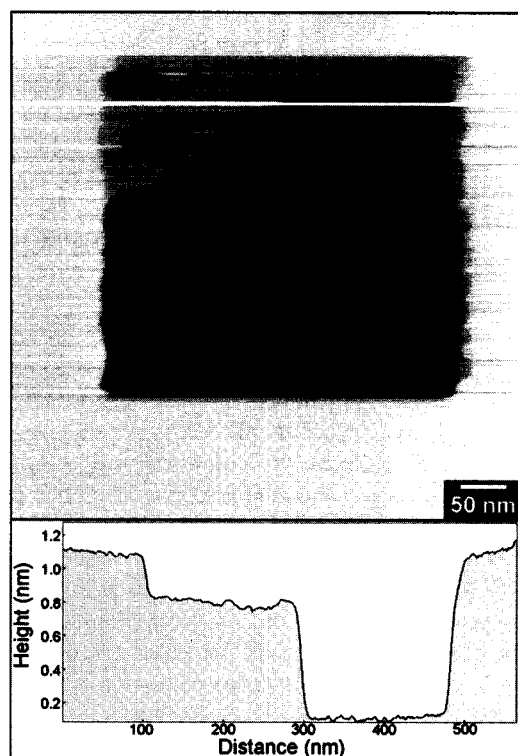


Fig. 8 Topographic AFM images of a worn mica surface at pH 8 and the corresponding line trace across the surfaces showing both 1.0- and 0.22-nm wear regions. (View this art in color at www.dekker.com.)

et al. under humid conditions.^[14,16] Comparison of the threshold forces for removal of the $\text{SiO}_3/\text{AlO}_3$ tetrahedral layer, i.e., generating 0.22-nm wear scars, illustrates the tribochemical influence hydroxide ions have on hydrolysis of surface bonds. Table 1 summarizes the threshold pressures and the ab initio calculated activation energies (E_a) for water, acid, and base-catalyzed Si–O–M hydrolysis^[147,148] Once the MO_3 (M=Si or Al) basal fragment is removed, the underlying aluminite (gibbsite) layer is exposed and should carry a net positive charge for $\text{pH} \leq 10$.^[149,150] This is another “model” property of mica and the details on how this affects the tip–sample contact during friction imaging can be found in Ref. [142].

Conducting wear trials at pH 5 under lower loads ($p_m \sim 0.74$ GPa; ca. $1/2 p_{\text{thresh}}$), the surface friction in the imaged region is observed to *decline* (Fig. 9A) relative to the unworn surface, before any noticeable wear (topographical) on the nanometer scale. This decrease in friction can be attributed to the accumulation of negative surface charge both on the tip and at the imaged surface through OH^- insertion into strained Al–O–Si and Si–O–Si bonds, yielding surface anions, such as siloxy (Si-O^-) groups.^[83,86] Analysis of the surface topography reveals

a discernible increase by ~ 0.05 nm (Fig. 9B), which is near the noise-level limit of ± 0.03 nm. This height increase would be consistent with capping of the surface dangling bonds by OH^- and H^+ as the bonds are ruptured. Adhesion measurements, as summarized in Table 2, within the native and worn (“induced”) region show a marked shift to lower adhesive forces for the worn surface, which is expected for the proposed repulsive tip–sample interaction.

Although not a common observation, several groups have reported surface charging with little to no topography changes during wear experiments. Using the nano-scale Kelvin probe, capable of measuring variations in surface potential (work function mapping), DeVecchio and Bhushan have observed electron-deficient regions within the “zero-wear” regime for single-crystal aluminum under ambient conditions (RH $45 \pm 5\%$).^[73] The topography and potential maps are given in Fig. 10 and illustrate the charging effect before catastrophic failure of the surface.^[73] While studying the frictional properties of halide crystals (KF, KCl, and KBr) in UHV, Carpick et al. observed the evolution of “mysterious” high-friction regions for all crystal surfaces on AFM imaging. Table 2 provides a summary of the tribological properties of mica and the halide crystals. An interesting characteristic of the halide systems is that for KBr the increased friction was not accompanied with a change in topography; however, topographic contrast on the order of 0.2 nm was found to simultaneously occur for the KF crystal. It is

Table 1 Threshold pressures for mica wear under solution conditions, and ab initio calculated activation energies (E_a) for acid-, base-, and H_2O -catalyzed hydrolysis

Conditions	$p_{\text{thresh}}^{[148]}$ (GPa)	Hydrolysis activation energy (E_a , kcal/mol)
Mica wear pH 3	2.1	–
Mica wear pH 5	1.5	–
Mica wear pH 8	1.2	–
Si–O–Si (OH catalyzed)	–	$2-8^{[148]}$
Si–O–Al (H^+ catalyzed)	–	$16^{[147]}$
Si–O–Si (H^+ catalyzed)	–	$24^{[147]}$
Si–O–Al (H_2O catalyzed)	–	$26^{[147]}$
Si–O–Si (H_2O catalyzed)	–	$29^{[147,160]}$

Threshold pressures (p_{thresh}) were calculated with Hertz continuum mechanics theory. p_{thresh} corresponds to the gross deformation (abstraction) regime that is defined by removal of SiO_3 and AlO_3 basal tetrahedral units.

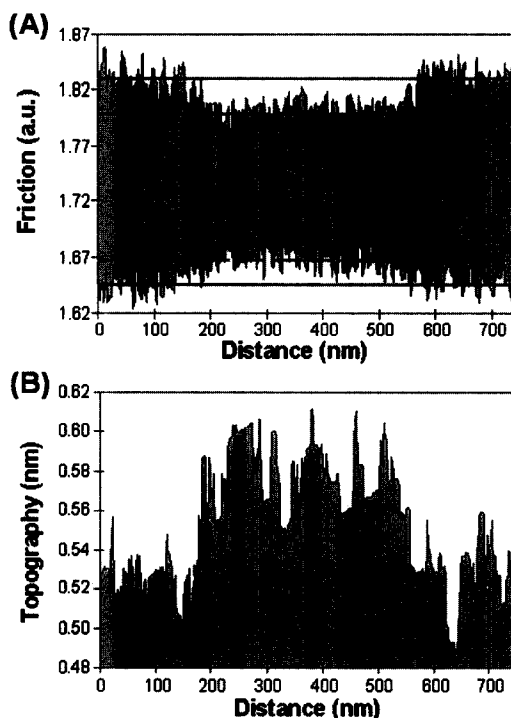


Fig. 9 Friction (A) and topography (B) cursor profiles of the native and worn mica surface following defect nucleation (charging) of a (400×400) nm² region under pH 5 conditions. The friction and topography profiles, respectively, indicate that the worn surface has become *negatively* charged and has *expanded* in height by ~ 0.05 nm with respect to the unworn (neighboring) mica surface.

believed that “defects” are triggered by the AFM contact; however, it is not clear why localization of the high-friction regions occurs and why the high- and low-friction regions have nearly identical adhesive forces. Further experiments are needed to address these questions and will be valuable contributions toward bridging simulation and experiment.^[151–153]

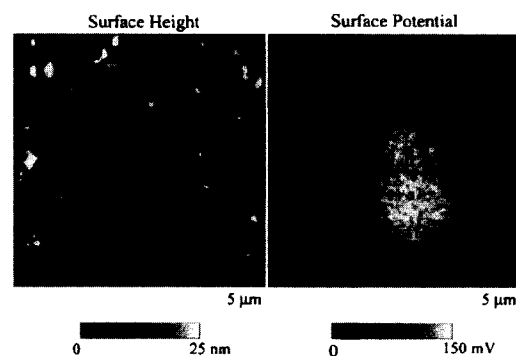


Fig. 10 Topography (left) and surface potential (right) micrographs of single-crystal aluminum postwear trial under low loads. Although very little topographic contrast is present, the surface potential detects an electron deficient domain (bright central region) corresponding to the nucleation regime, i.e., pregress deformation of the surface. (From Ref. [73].)

For mica, under pH 5–6 imaging conditions, the tip induced surface charges have a temporal stability between 10 and 45 min, depending on the number of subsequent scans. Lattice-resolved images within a charged region, even with negligible topographic and friction contrast, portray a transforming mica lattice with two lattice constants. One periodicity corresponds to the native surface (0.52 nm) whereas the other corresponds to the defective, reconstructed surface (0.3 nm). This transition has been monitored in situ by scanning at a load $\sim 75\%$ of the threshold force for SiO₃ abstraction. Exemplary friction micrographs of an in situ reconstruction, at pH 5 and under a load of 9 nN (p_m of 1.25 GPa), are given in Fig. 11. The progression from the 0.52- to the 0.3-nm periodicity (Fig. 11) provides explicit evidence as well as a characteristic structure of the metastable “nucleation” wear regime before the advent of gross deformation. An additional benefit of this in situ reconstruction is the ability to observe the transition regime, where a mixed

Table 2 Tribological properties of mica and halide crystals

Specimen	Anion radius (nm)	Native periodic (nm)	Reconstructed periodicity (nm)	Nucleation height (nm)	$F_{adh}^{Induced}/F_{adh}^{Native}$	$F_f^{Induced}/F_f^{Native}$
Mica ^a	–	0.52 ^b	0.3	$\leq 0.05 \pm 0.03$	0.38–0.75 ^c	0.74–1 ^c
KF ^d	0.136	0.378	–	0.2 ± 0.03	0.98	2.3
KCl ^d	0.181	0.445	–	0.04 ± 0.02	0.93	1.79
KBr ^d	0.195	0.467	–	< 0.02	0.94	1.24

^aFrom Refs. [142] and [145] with topography, friction, and adhesion data corresponding to the defect nucleation regime.

^bFor micas (001) crystal plane; $F_{adh}^{Induced}/F_{adh}^{Native}$ is the ratio of force of adhesion measurements within the wear-induced region to the native surface; $F_f^{Induced}/F_f^{Native}$ is the force of friction ratio of measurements within the wear-induced region to the native surface.

^cDepends strongly on pH and the extent of surface charging.

^dFrom Ref. [141].

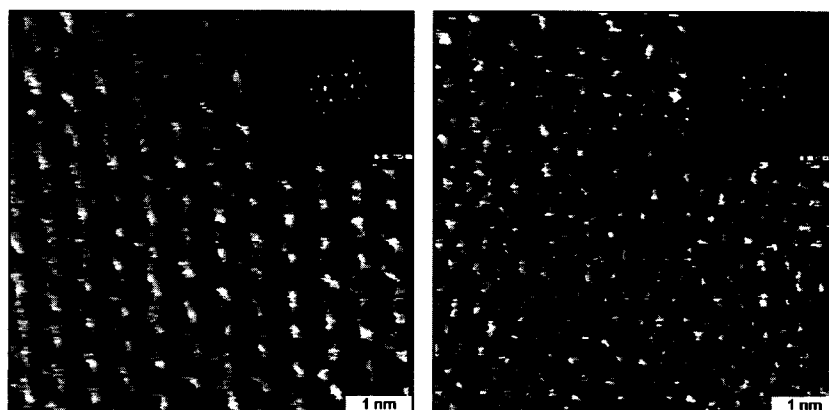


Fig. 11 Frictional force images of in situ tribochemical surface reconstruction of the native mica lattice from a 0.52- (left) to a 0.3-nm (right) periodicity under the local stress of an AFM tip. The 2-D FFT inserts clearly illustrate the lattice reconstruction. This progression occurs over several scans and leaves no wear of the surface.

population of the two discrete surface species are observed.^[142] Such information may find applications in calculating the kinetic parameters of the reconstructing surface.

The lattice-resolved reconstruction clarifies that the change in the observed structure at the outermost surface is due to scission of the surface Si–O–Si and Al–O–Si bonds, along with the concomitant insertion of OH[−] and H⁺ to terminate the surface. Appearance of the 0.3-nm lattice is intriguing, however, because AFM only gives a characteristic periodicity. The origin is difficult to assign unequivocally, although a simple geometric argument correlates well with AFM results.^[142] There are interesting corollaries to work on high-silica zeolites,^[83] silica,^[154] cristobalite,^[155] and kaolinite^[156] that lend support to our current interpretation of the reconstruction; that is, hydrogen bonding is contributing significantly to the stability of the reconstructed surface.^[156] For instance, Koller et al. have examined the siloxy–silanol (SiO[−]···HOSi) defect interaction in high-silica zeolites and found that six-member rings are able to form stable conformations with multiple defects.^[83]

For the lowest pH conditions (pH < 3), wear of the surface is inhibited even though the surface is still immersed in water. In fact, the surface shows no wear under *identical loads* with over 8 times the number of scans required for wear at pH 5–6. Clearly, this is because of insufficient amounts of OH[−] in the water to catalyze the Si–O–Si or Al–O–Si bond scission needed to initiate wear. Only after the load is increased to 23 nN ($p_m \sim 2.1$ GPa) is any noticeable wear observed (in the limit of 10 scans). Interestingly the threshold force of ~ 70 –80 nN ($p_m \sim 2.25$ GPa), previously determined by Kopta and Salmeron with monolayer coverage of water on mica, is

consistent with the range of our determinations in acidic solutions.^[14]

Comparing the surface wear at pH 3, 5–6, and 8 (Table 1) shows that load (the local stress field) plays a more significant role under conditions where the OH[−] concentrations are the lowest. Again, this is justified by the necessity to strain the bridging oxygen bonds more and induce cleavage in the absence of OH[−] mediated bond scission. The critical load for this transition must then be linked with the minimum stress needed to facilitate bond scission in the presence of a particular OH[−] concentration.

A brief comparison of mica wear^[14,16,142,145] to the tip induced dissolution of calcite is instructive because there are distinct differences between these two systems. Dickinson, Langford, Kim, Park, Hariadi, and Scudiero^[74–77] have elegantly explored calcite and brushite dissolution in supersaturated solutions with AFM. They have found strong correlations between theoretical and experimentally determined activated volumes and realistic activation energies using a relatively straightforward model. Application of a similar model to mica has had some difficulties with agreement between empirically fitted material constants and their “known” values.^[14] There is a fundamental difference between mica and calcite that may be limiting the model’s success. The basal mica plane is a covalent network of bridging oxygen bonds, which require scission in order for defect nucleation to occur. On the other hand, the nucleating stage for calcite (an ionic crystal) involves the displacement of individual surface ions into solution (separating ion pairs). As demonstrated by Dickinson, calcite wear does not exhibit a critical load where dissolution suddenly begins (Fig. 12). This is in stark

Wear Track Growth Rate vs Contact Force During Repeated Linear Scanning

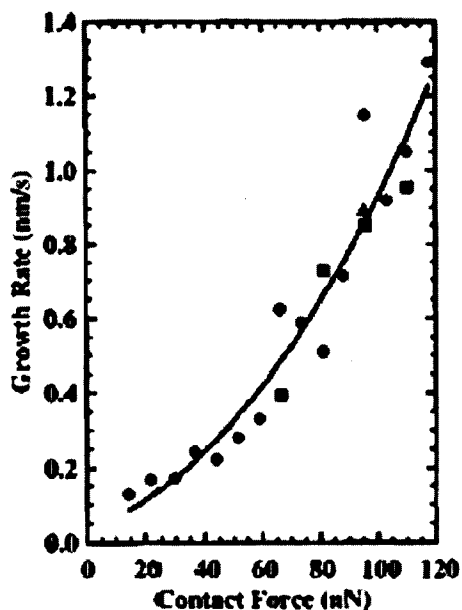


Fig. 12 AFM scanning induced wear track growth of calcite as a function of applied load. Notice the absence of a critical load for dissolution, indicating the growth is reaction limited. This is unlike mica, which exhibits a threshold force in the abstraction regime for removal of SiO_3 molecular fragments. (From Ref. [77].)

contrast to mica, where in UHV and under $3 \leq \text{pH} \leq 8$ conditions, a critical threshold pressure is observed, thus indicating that mechanical stress accounts for a significant portion of the energy required to cleave the surface bonds, and comparisons between the two systems should be conducted with caution, especially relating to adaptation of models.

Mica Surfaces Functionalized with Alkylsilanes

There have been few frictional studies of modified mica surfaces by AFM. Alkylsilanes in the form of triethoxy- or trichlorosilanes can form mono- and multilayers on the mica surface. The formation of monolayers of alkylsilanes on mica and silicon surfaces has been heavily investigated especially for use as potential lubricant and protectant films in MEMS devices.^[92,93,96,157,158] Unlike reactions of alkylsilanes on hydroxylated silicon surfaces, alkylsilane monolayers on mica do not form covalent bonds to the substrate, but rather become organized via an interconnected network of $-\text{Si}-\text{O}-\text{Si}-$ linkages between nearest neighbors. This produces monolayers with relatively lower packing densities as compared to other

alkane-based SAMS such as alkanethiols on Au.^[159] A key difficulty in the formation of alkylsilane monolayers is the precise control over the amount of water present during film formation. Sufficient water is required to carry out the condensation reactions on the surface for monolayer formation without inducing the production of micelles among unreacted alkylsilanes. Long-range ordered structures are in general not observed for alkylsilane films on mica surfaces.

Wear of the mica surface is inhibited by the presence of an alkylsilane film. The friction response of the surface, however, is highly dependent on the amount of water present in the environment during wear. The presence of water above 50% relative humidity rapidly increases the friction as a function of load, much as it does for the native mica surface as described above.^[61] This impact of water on the frictional properties of the nominally hydrophobic coated surface clearly shows that defects within the films can provide sufficient access of water to the underlying surface-film interface to catalyze film breakdown even under relatively low loads (~ 10 nN) as compared to the wear of the native surface (~ 75 nN).

CONCLUSION

The area of nanotribology of oxides and the probing of defect nucleation at the atomic level by AFM is just beginning. Continuing developments in AFM technology via enhanced noncontact methodologies is advancing the ability of the AFM to probe even single atomic defects at crystal surfaces on nonconducting substrates. In this chapter we have described how detailed control of the imaging environment and of the chemistry at the tip and sample surfaces can allow for atomic-level details of defect nucleation to be assessed and probed in situ before the onset of gross wear. This has permitted examination of tribochemically and mechanically enhanced wear processes of mica to be explored. We have also outlined a methodology for assessing the scan history dependence on wear of surfaces. Many avenues of oxide wear and charge nucleation at surfaces are unexplored and deserve attention, including the impact of temperature on wear at the nanoscale.

ACKNOWLEDGMENTS

We acknowledge support for JH from The National Science Foundation (IGERT DGE-9972892) and the American Chemical Society Petroleum Research Fund (34792-G5). We also gratefully acknowledge Dr. Jayne

Garno for comments on the work, as well as providing the images in Fig. 3.

REFERENCES

1. Binnig, G.; Quate, C.F.; Gerber, C. Atomic force microscope. *Phys. Rev. Lett.* **1986**, *56*, 930–933.
2. Mate, C.M.; McClelland, G.M.; Erlandsson, R.; Chiang, S. Atomic-scale friction of a tungsten tip on a graphite surface. *Phys. Rev. Lett.* **1987**, *59*, 1942–1945.
3. Burnham, N.A.; Colton, R.J. Measuring the nano-mechanical properties and surface forces of materials using an atomic force microscope. *J. Vac. Sci. Technol., A, Vac. Surf. Films* **1989**, *7*, 2906–2913.
4. Nyffenegger, R.M.; Penner, R.M. Nanometer-scale surface modification using the scanning probe microscope: Progress since 1991. *Chem. Rev.* **1997**, *97*, 1195–1230.
5. Carpick, R.W.; Salmeron, M. Scratching the surface: Fundamental investigations of tribology with atomic force microscopy. *Chem. Rev.* **1997**, *97*, 1163–1194.
6. Bhushan, B.; Israelachvili, J.N.; Landman, U. Nanotribology—Friction, wear and lubrication at the atomic-scale. *Nature* **1995**, *374*, 607–616.
7. Landman, U.; Luedtke, W.D.; Burnham, N.A.; Colton, R.J. Atomistic mechanisms and dynamics of adhesion, nanoindentation, and fracture. *Science* **1990**, *248*, 454–461.
8. Dedkov, G.V. Experimental and theoretical aspects of the modern nanotribology. *Phys. Status Solidi, A Appl. Res.* **2000**, *179*, 3–75.
9. Singer, I.L. Friction and energy-dissipation at the atomic-scale—A review. *J. Vac. Sci. Technol., A, Vac. Surf. Films* **1994**, *12*, 2605–2616.
10. Tang, H.; Joachim, C.; Devillers, J. Interpretation of atomic-force microscopy images—The mica (001) surface with a diamond tip apex. *J. Vac. Sci. Technol., B* **1994**, *12*, 2179–2183.
11. Erlandsson, R.; Hadziioannou, G.; Mate, C.M.; McClelland, G.M.; Chiang, S. Atomic scale friction between the muscovite mica cleavage plane and a tungsten tip. *J. Chem. Phys.* **1988**, *89*, 5190–5193.
12. Carpick, R.W.; Agrait, N.; Ogletree, D.F.; Salmeron, M. Measurement of interfacial shear (friction) with an ultrahigh vacuum atomic force microscope. *J. Vac. Sci. Technol., B* **1996**, *14*, 1289–1295.
13. Carpick, R.W.; Agrait, N.; Ogletree, D.F.; Salmeron, M. Variation of the interfacial shear strength and adhesion of a nanometer-sized contact. *Langmuir* **1996**, *12*, 3334–3340.
14. Kopta, S.; Salmeron, M. The atomic scale origin of wear on mica and its contribution to friction. *J. Chem. Phys.* **2000**, *113*, 8249–8252.
15. Miyake, S. Atomic-scale wear properties of muscovite mica evaluated by scanning probe microscopy. *Appl. Phys. Lett.* **1994**, *65*, 980–982.
16. Hu, J.; Xiao, X.D.; Ogletree, D.F.; Salmeron, M. Atomic-scale friction and wear of mica. *Surf. Sci.* **1995**, *327*, 358–370.
17. Hagen, T.; Grafstrom, S.; Ackermann, J.; Neumann, R.; Trautmann, C.; Vetter, J.; Angert, N. Friction force microscopy of heavy-ion irradiated mica. *J. Vac. Sci. Technol., B* **1994**, *12*, 1555–1558.
18. Qian, L.M.; Luo, J.B.; Wen, S.W.; Xiao, X.D. The experimental rules of mica as a reference sample of AFM/FFM measurement. *Chin. Sci. Bull.* **2001**, *46*, 349–352.
19. Xu, L.; Salmeron, M. Effects of surface ions on the friction and adhesion properties of mica. *Langmuir* **1998**, *14*, 2187–2190.
20. Wei, Z.Q.; Wang, C.; Bai, C.L. Investigation of nanoscale frictional contact by friction force microscopy. *Langmuir* **2001**, *17*, 3945–3951.
21. Hoshi, Y.; Kawagishi, T.; Kawakatsu, H. Velocity dependence and limitations of friction force microscopy of mica and graphite. *Jpn. J. Appl. Phys.* **2000**, *39*, 3804–3807.
22. Piner, R.D.; Mirkin, C.A. Effect of water on lateral force microscopy in air. *Langmuir* **1997**, *13*, 6864–6868.
23. Schwarz, U.D.; Zworner, O.; Koster, P.; Wiesendanger, P. Quantitative analysis of the frictional properties of solid materials at low loads. 2. Mica and germanium sulfide. *Phys. Rev., B* **1997**, *56*, 6997–7000.
24. Tsujimichi, K.; Tamura, H.; Hirofani, A.; Kubo, M.; Komiyama, M.; Miyamoto, A. Simulation of atomic force microscopy images of cleaved mica surfaces. *J. Phys. Chem., B* **1997**, *101*, 4260–4264.
25. Qian, L.M.; Xiao, X.D.; Wen, S.Z. Tip in situ chemical modification and its effects on tribological measurements. *Langmuir* **2000**, *16*, 662–670.
26. Gyalog, T.; Bammerlin, M.; Luthi, R.; Meyer, E.; Thomas, H. Mechanism of atomic friction. *Eur. Lett.* **1995**, *31*, 269–274.
27. Christenson, H.K. Adhesion and surface-energy of mica in air and water. *J. Phys. Chem.* **1993**, *97*, 12034–12041.
28. Teschke, O.; de Souza, E.F. Dielectric exchange: The key repulsive or attractive transient forces

- between atomic force microscope tips and charged surfaces. *Appl. Phys. Lett.* **1999**, *74*, 1755–1757.
29. Knarr, R.F.; Quon, R.A.; Vanderlick, T.K. Direct force measurements at the smooth gold/mica interface. *Langmuir* **1998**, *14*, 6414–6418.
 30. Vakarelski, I.U.; Ishimura, K.; Higashitani, K. Adhesion between silica particle and mica surfaces in water and electrolyte solutions. *J. Colloid Interface Sci.* **2000**, *227*, 111–118.
 31. Weisenhorn, A.L.; Maivald, P.; Butt, H.J.; Hansma, P.K. Measuring adhesion, attraction, and repulsion between surfaces in liquids with an atomic-force microscope. *Phys. Rev., B* **1992**, *45*, 11226–11232.
 32. Maw, W.; Stevens, F.; Langford, S.C.; Dickinson, J.T. Single asperity tribochemical wear of silicon nitride studied by atomic force microscopy. *J. Appl. Phys.* **2002**, *92*, 5103–5109.
 33. Liu, E.; Blanpain, B.; Celis, J.P.; Roos, J.R. Comparative study between macrotribology and nanotribology. *J. Appl. Phys.* **1998**, *84*, 4859–4865.
 34. Pashley, R.M. DLVO and hydration forces between mica surfaces in Li^+ , Na^+ , K^+ , and Cs^+ electrolyte-solutions—A correlation of double-layer and hydration forces with surface cation-exchange properties. *J. Colloid Interface Sci.* **1981**, *83*, 531–546.
 35. Raviv, U.; Laurat, P.; Klein, J. Time dependence of forces between mica surfaces in water and its relation to the release of surface ions. *J. Chem. Phys.* **2002**, *116*, 5167–5172.
 36. Kjellander, R.; Marcelja, S.; Pashley, R.M.; Quirk, J.P. A theoretical and experimental-study of forces between charged mica surfaces in aqueous CaCl_2 solutions. *J. Chem. Phys.* **1990**, *92*, 4399–4407.
 37. Teschke, O.; Ceotto, G.; de Souza, E.F. Dielectric exchange force: A convenient technique for measuring the interfacial water relative permittivity profile. *Phys. Chem. Chem. Phys.* **2001**, *3*, 3761–3768.
 38. Israelachvili, J.N. *Intermolecular and Surfaces Forces*; Academic Press: New York, 1992.
 39. Basu, S.; Sharma, M.M. Measurement of critical disjoining pressure for dewetting of solid surfaces. *J. Colloid Interface Sci.* **1996**, *181*, 443–455.
 40. Toikka, G.; Hayes, R.A. Direct measurement of colloidal forces between mica and silica in aqueous electrolyte. *J. Colloid Interface Sci.* **1997**, *191*, 102–109.
 41. Tabor, D.; Winterton, R.H.S. The direct force measurement of normal and retarded van der Waals forces. *Proc. R. Soc. Lond., A Math. Phys. Eng. Sci.* **1969**, *312*, 435–450.
 42. Hutter, J.L.; Bechhoefer, J. Measurement and manipulation of van-der-Waals forces in atomic-force microscopy. *J. Vac. Sci. Technol., B* **1994**, *12*, 2251–2253.
 43. Pashley, R.M.; Israelachvili, J.N. Molecular layering of water in thin-films between mica surfaces and its relation to hydration forces. *J. Colloid Interface Sci.* **1984**, *101*, 511–523.
 44. Xu, L.; Salmeron, M. An XPS and scanning polarization force microscopy study of the exchange and mobility of surface ions on mica. *Langmuir* **1998**, *14*, 5841–5844.
 45. Purton, J.A.; Allan, N.L.; Blundy, J.D. Impurity cations in the bulk and the {001} surface of muscovite: An atomistic simulation study. *J. Mater. Chem.* **1997**, *7*, 1947–1951.
 46. Nishimura, S.; Biggs, S.; Scales, P.J.; Healy, T.W.; Tsunematsu, K.; Tateyama, T. Molecular-scale structure of the cation modified muscovite mica basal-plane. *Langmuir* **1994**, *10*, 4554–4559.
 47. Snowdeniff, D.; Price, P.B.; Nagahara, L.A.; Fujishima, A. Atomic-force-microscopic observations of dissolution of mica at sites penetrated by keV/nucleon ions. *Phys. Rev. Lett.* **1993**, *70*, 2348–2351.
 48. Terashima, H. Adsorption of polystyrene to mica/cyclohexane interfaces at the theta-temperature. *Phys. Chem. Chem. Phys.* **2000**, *2*, 5252–5258.
 49. Heuberger, M.; Luengo, G.; Israelachvili, J.N. Tribology of shearing polymer surfaces. 1. Mica sliding on polymer(PnBMA). *J. Phys. Chem., B* **1999**, *103*, 10127–10135.
 50. Cantrell, W.; Ewing, G.E. Thin film water on muscovite mica. *J. Phys. Chem., B* **2001**, *105*, 5434–5439.
 51. *Modern Tribology Handbook*; Bhushan, B., Ed.; CRC Press: Boca Raton, 2001.
 52. *Nanotribology: Critical Assessment and Research Needs*; Hsu, S.M., Ying, Z.C., Eds.; Kluwer Academic: Boston, 2003.
 53. Deer, W.A.; Howie, R.A.; Zussman, J. *Sheet Silicates*; Longmans, Green and Co.: London, 1962.
 54. Wyckoff, R.W.G. *Crystal Structures*; Interscience: New York, 1971.
 55. Woodward, J.T.; Ulman, A.; Schwartz, D.K. Self-assembled monolayer growth of octadecylphosphonic acid on mica. *Langmuir* **1996**, *12*, 3626–3629.
 56. Eastman, T.; Zhu, D.M. Adhesion forces between surface-modified AFM tips and a mica surface. *Langmuir* **1996**, *12*, 2859–2862.
 57. Demirel, A.L.; Granick, S. Transition from static to kinetic friction in a model lubricated system. *J. Chem. Phys.* **1998**, *109*, 6889–6897.

58. Barthel, E.; Roux, S. Velocity-dependent adherence: An analytical approach for the JKR and DMT models. *Langmuir* **2000**, *16*, 8134–8138.
59. Wurger, A. Comment on "relationship between friction and molecular structure: Alkylsilane lubricant films under pressure". *Phys. Rev. Lett.* **1999**, *83*, 1696.
60. Kopta, S.; Barrera, E.; Ogletre, D.F.; Charych, D.H.; Salmeron, M. Comment on "relationship between friction and molecular structure: Alkylsilane lubricant films under pressure"—Kopta et al. reply. *Phys. Rev. Lett.* **1999**, *83*, 1697.
61. Barrera, E.; Kopta, S.; Ogletre, D.F.; Charych, D.H.; Salmeron, M. Relationship between friction and molecular structure: Alkylsilane lubricant films under pressure. *Phys. Rev. Lett.* **1999**, *82*, 2880–2883.
62. Lio, A.; Charych, D.H.; Salmeron, M. Comparative atomic force microscopy study of the chain length dependence of frictional properties of alkanethiols on gold and alkylsilanes on mica. *J. Phys. Chem., B* **1997**, *101*, 3800–3805.
63. Tian, F.; Xiao, X.D.; Loy, M.M.T.; Wang, C.; Bai, C.L. Humidity and temperature effect on frictional properties of mica and alkylsilane monolayer self-assembled on mica. *Langmuir* **1999**, *15*, 244–249.
64. Chen, Y.L.; Helm, C.A.; Israelachvili, J.N. Measurements of the elastic properties of surfactant and lipid monolayers. *Langmuir* **1991**, *7*, 2694–2699.
65. Sterthaus, R.; Wegner, G. Ultrathin layers of polyelectrolytes on mica: Preparation, characterization, and electrokinetic surface potential. *Langmuir* **2002**, *18*, 5414–5421.
66. Batteas, J.D.; Quan, X.H.; Weldon, M.K. Adhesion and wear of colloidal silica probed by force microscopy. *Tribol. Lett.* **1999**, *7*, 121–128.
67. Miyake, S. Improvement of mechanical properties of nanometer period multilayer films at interfaces of each layer. *J. Vac. Sci. Technol., B* **2003**, *21*, 785–789.
68. Prioli, R.; Reigada, D.C.; Freire, F.L. Nanoscale friction and wear mechanisms at the interface between a boron carbide film and an atomic force microscope tip. *J. Appl. Phys.* **2000**, *87*, 1118–1122.
69. Reigada, D.C.; Prioli, R.; Jacobsohn, L.G.; Freire, F.L. Boron carbide films deposited by a magnetron sputter-ion plating process: Film composition and tribological properties. *Diamond and Related Materials* **2000**, *9*, 489–493.
70. Sundararajan, S.; Bhushan, B. Micro/nanotribological studies of polysilicon and SiC films for MEMS applications. *Wear* **1998**, *217*, 251–261.
71. Prioli, R.; Reigada, D.C.; Freire, F.L. The role of capillary condensation of water in the nanoscale friction and wear properties of boron carbide films. *J. Appl. Phys.* **2000**, *88*, 679–682.
72. Adams, J.B.; Hector, L.G.; Siegel, D.J.; Yu, H.L.; Zhong, J. Adhesion, lubrication and wear on the atomic scale. *Surf. Interface Anal.* **2001**, *31*, 619–626.
73. DeVecchio, D.; Bhushan, B. Use of a nanoscale Kelvin probe for detecting wear precursors. *Rev. Sci. Instrum.* **1998**, *69*, 3618–3624.
74. Scudiero, L.; Langford, S.C.; Dickinson, J.T. Scanning force microscope observations of corrosive wear on single-crystal brushite ($\text{CaHPO}_4 \cdot 2\text{H}_2\text{O}$) in aqueous solution. *Tribol. Lett.* **1999**, *6*, 41–55.
75. Dickinson, J.T.; Hariadi, R.F.; Langford, S.C. Nanometer scale investigations of chemical mechanical polishing mechanisms using scanning force microscopy. *Ceram. Trans.* **1999**, *102*, 213–232.
76. Park, N.S.; Kim, M.W.; Langford, S.C.; Dickinson, J.T. Tribological enhancement of CaCO_3 dissolution during scanning force microscopy. *Langmuir* **1996**, *12*, 4599–4604.
77. Park, N.S.; Kim, M.W.; Langford, S.C.; Dickinson, J.T. Atomic layer wear of single-crystal calcite in aqueous solution using scanning force microscopy. *J. Appl. Phys.* **1996**, *80*, 2680–2686.
78. Iler, R.K. *The Chemistry of Silica*; Wiley-Interscience: New York, 1979.
79. Schmitz, I.; Schreiner, M.; Friedbacher, G.; Grasserbauer, M. Tapping-mode AFM in comparison to contact-mode AFM as a tool for in situ investigations of surface reactions with reference to glass corrosion. *Anal. Chem.* **1997**, *69*, 1012–1018.
80. Fischer, T.E.; Mullins, W.M. Chemical aspects of ceramic tribology. *J. Phys. Chem.* **1992**, *96*, 5690–5701.
81. Zirl, D.M.; Garofalini, S.H. Mechanism of alkali adsorption on silica surfaces. *Phys. Chem. Glasses* **1989**, *30*, 155–159.
82. Hunger, M.; Freude, D.; Pfeifer, H.; Schwieger, W. MAS NMR-studies of silanol groups in zeolites ZSM-5 synthesized with an ionic template. *Chem. Phys. Lett.* **1990**, *167*, 21–26.
83. Koller, H.; Lobo, R.F.; Burkett, S.L.; Davis, M.E. $\text{SiO}^- \cdots \text{HOSi}$ hydrogen-bonds in as-synthesized high-silica zeolites. *J. Phys. Chem.* **1995**, *99*, 12588–12596.
84. Ruiz, J.M.; McAdon, M.H.; Garces, J.M. Aluminum complexes as models for Brønsted acid sites in zeolites: Structure and energetics of $[\text{Al}(\text{OH})_4]^-$, $[\text{Al}(\text{H}_2\text{O})_6]^{3+}$, and intermediate monomeric species $[\text{Al}(\text{OH})_x(\text{H}_2\text{O})_{n-x} \cdots m\text{H}_2\text{O}]_{3-x}$ obtained by hydrolysis. *J. Phys. Chem., B* **1997**, *101*, 1733–1744.

85. Xu, H.; Van Deventer, J.S.J. Ab initio calculations on the five-membered alumino-silicate framework rings model: Implications for dissolution in alkaline solutions. *Comput. Chem.* **2000**, *24*, 391–404.
86. Sokol, A.A.; Catlow, C.R.A.; Garces, J.M.; Kuperman, A. Local states in microporous silica and aluminum silicate materials. I. Modeling structure, formation, and transformation of common hydrogen containing defects. *J. Phys. Chem., B* **2002**, *106*, 6163–6177.
87. Katsuki, F.; Kamei, K.; Saguchi, A.; Takahashi, W.; Watanabe, J. AFM studies on the difference in wear behavior between Si and SiO₂ in KOH solution. *J. Electrochem. Soc.* **2000**, *147*, 2328–2331.
88. Pal, S.; Banerjee, S. Friction-induced microstructure growth. *J. Phys., D Appl. Phys.* **2001**, *34*, 253–256.
89. Lin, X.Y.; Creuzet, F.; Arribart, H. Atomic-force microscopy for local characterization of surface acid–base properties. *J. Phys. Chem.* **1993**, *97*, 7272–7276.
90. Zembala, M.; Adamczyk, Z.; Warszyski, P. Influence of adsorbed particles on streaming potential of mica. *Colloids Surf., A Physicochem. Eng. Asp.* **2001**, *195*, 3–15.
91. Sniogowski, J.J.; de Boer, M.P. IC-compatible polysilicon surface micromachining. *Annu. Rev. Mater. Sci.* **2000**, *30*, 299–333.
92. Maboudian, R.; Ashurst, W.R.; Carraro, C. Tribological challenges in micromechanical systems. *Tribol. Lett.* **2002**, *12*, 95–100.
93. Maboudian, R.; Carraro, C. Surface engineering for reliable operation of MEMS devices. *J. Adhes. Sci. Technol.* **2003**, *17*, 583–591.
94. Malek, C.G.K.; Das, S.S. Adhesion promotion between poly(methylmethacrylate) and metallic surfaces for LiGA evaluated by shear stress measurements. *J. Vac. Sci. Technol., B* **1998**, *16*, 3543–3546.
95. Miller, S.L.; Rodgers, M.S.; La Vigne, G.; Sniogowski, J.J.; Clews, P.; Tanner, D.M.; Peterson, K.A. Failure modes in surface micromachined microelectromechanical actuation systems. *Microelectron. Reliab.* **1999**, *39*, 1229–1237.
96. Komvopoulos, K. Surface engineering and microtribology for microelectromechanical systems. *Wear* **1996**, *200*, 305–327.
97. Carpick, R.W.; Ogletree, D.F.; Salmeron, M. Lateral stiffness: A new nanomechanical measurement for the determination of shear strengths with friction force microscopy. *Appl. Phys. Lett.* **1997**, *70*, 1548–1550.
98. Timoshenko, S.P.; Goodier, J.N. *Theory of Elasticity*; McGraw-Hill: New York, 1987.
99. Cleveland, J.P.; Manne, S.; Bocek, D.; Hansma, P.K. A nondestructive method for determining the spring constant of cantilevers for scanning force microscopy. *Rev. Sci. Instrum.* **1993**, *64*, 403–405.
100. Sader, J.E.; Larson, I.; Mulvaney, P.; White, L.R. Method for the calibration of atomic-force microscope cantilevers. *Rev. Sci. Instrum.* **1995**, *66*, 3789–3798.
101. Neumeister, J.M.; Ducker, W.A. Lateral, normal, and longitudinal spring constants of atomic-force microscopy cantilevers. *Rev. Sci. Instrum.* **1994**, *65*, 2527–2531.
102. Tortonese, M.; Kirk, M. Characterization of application specific probes. *SPIE Proceedings—Micromachining and Imaging*, **1997**, *3009*, 53–60.
103. Albrecht, T.R.; Akamine, S.; Carver, T.E.; Quate, C.F. Microfabrication of cantilever styli for the atomic force microscope. *J. Vac. Sci. Technol., A, Vac. Surf. Films* **1990**, *8*, 3386–3396.
104. Siedle, P.; Butt, H.J.; Bamberg, E.; Wang, D.N.; Kuhlbrandt, W.; Zach, J.; Haider, M. Determining the form of atomic-force microscope tips. *Inst. Phys. Conf. Ser.* **1993**, *130*, 361–364.
105. Ogletree, D.F.; Carpick, R.W.; Salmeron, M. Calibration of frictional forces in atomic force microscopy. *Rev. Sci. Instrum.* **1996**, *67*, 3298–3306.
106. Sader, J.E. Parallel beam approximation for V-shaped atomic-force microscope cantilevers. *Rev. Sci. Instrum.* **1995**, *66*, 4583–4587.
107. Sader, J.E.; Chon, J.W.M.; Mulvaney, P. Calibration of rectangular atomic force microscope cantilevers. *Rev. Sci. Instrum.* **1999**, *70*, 3967–3969.
108. Senden, T.J.; Ducker, W.A. Experimental-determination of spring constants in atomic-force microscopy. *Langmuir* **1994**, *10*, 1003–1004.
109. Torii, A.; Sasaki, M.; Hane, K.; Okuma, S. A method for determining the spring constant of cantilevers for atomic force microscopy. *Meas. Sci. Technol.* **1996**, *7*, 179–184.
110. Hazel, J.L.; Tsukruk, V.V. Friction force microscopy measurements: Normal and torsional spring constants for V-shaped cantilevers. *J. Tribol.* **1998**, *120*, 814–819.
111. Hutter, J.L.; Bechhoefer, J. Calibration of atomic-force microscope tips. *Rev. Sci. Instrum.* **1993**, *64*, 1868–1873.
112. Walters, D.A.; Cleveland, J.P.; Thomson, N.H.; Hansma, P.K.; Wendman, M.A.; Gurley, G.; Elings, V. Short cantilevers for atomic force microscopy. *Rev. Sci. Instrum.* **1996**, *67*, 3583–3590.
113. Miyatani, T.; Fujihira, M. Bending of a rectangular cantilever of an atomic force microscope as a

- function of position along length. *Jpn. J. Appl. Phys.* **1997**, *36*, 5280–5281.
114. Levy, R.; Maaloum, M. Measuring the spring constant of atomic force microscope cantilevers: Thermal fluctuations and other methods. *Nanotechnology* **2002**, *13*, 33–37.
 115. Cain, R.G.; Biggs, S.; Page, N.W. Force calibration in lateral force microscopy. *J. Colloid Interface Sci.* **2000**, *227*, 55–65.
 116. Green, C.P.; Sader, J.E. Torsional frequency response of cantilever beams immersed in viscous fluids with applications to the atomic force microscope. *J. Appl. Phys.* **2002**, *92*, 6262–6274.
 117. Maugis, D. *Contact, Adhesion and Rupture of Elastic Solids*; Cardona, M., Fulde, P., von Klitzing, K., Merlin, R., Queisser, H.-J., Stromer, H., Eds.; Springer-Verlag: Berlin, 2000.
 118. Johnson, K.L. *Contact Mechanics*; Cambridge University Press: Cambridge, 1987.
 119. Villarrubia, J.S. Morphological estimation of tip geometry for scanned probe microscopy. *Surf. Sci.* **1994**, *321*, 287–300.
 120. Westra, K.L.; Mitchell, A.W.; Thomson, D.J. Tip artifacts in atomic-force microscope imaging of thin-film surfaces. *J. Appl. Phys.* **1993**, *74*, 3608–3610.
 121. Goss, C.A.; Brumfield, J.C.; Irene, E.A.; Murray, R.W. Imaging and modification of Au(111) monatomic steps with atomic-force microscopy. *Langmuir* **1993**, *9*, 2986–2994.
 122. Sheiko, S.S.; Moller, M.; Reuvekamp, E.M.C.M.; Zandbergen, H.W. Calibration and evaluation of scanning-force-microscopy probes. *Phys. Rev., B* **1993**, *48*, 5675–5678.
 123. Atamny, F.; Baiker, A. Direct imaging of the tip shape by AFM. *Surf. Sci.* **1995**, *323*, L314–L318.
 124. Schneir, J.; Villarrubia, J.S.; McWaid, T.H.; Tsai, V.W.; Dixon, R. Increasing the value of atomic force microscopy process metrology using a high-accuracy scanner, tip characterization, and morphological image analysis. *J. Vac. Sci. Technol., B* **1996**, *14*, 1540–1546.
 125. Dongmo, L.S.; Villarrubia, J.S.; Jones, S.N.; Renegar, T.B.; Postek, M.; Song, J.F. Experimental test of blind tip reconstruction for scanning probe microscopy. *Ultramicroscopy* **2000**, *85*, 141–153.
 126. Jarausch, K.F.; Stark, T.J.; Russell, P.E. Silicon structures for in situ characterization of atomic force microscope probe geometry. *J. Vac. Sci. Technol., B* **1996**, *14*, 3425–3430.
 127. Markiewicz, P.; Goh, M.C. Atomic-force microscope tip deconvolution using calibration arrays. *Rev. Sci. Instrum.* **1995**, *66*, 3186–3190.
 128. Markiewicz, P.; Goh, M.C. Simulation of atomic-force microscope tip-sample sample-tip reconstruction. *J. Vac. Sci. Technol., B* **1995**, *13*, 1115–1118.
 129. Odin, C.; Aime, J.P.; Elkaakour, Z.; Bouhacina, T. Tip finite-size effects on atomic-force microscopy in the contact mode—Simple geometrical considerations for rapid estimation of apex radius and tip angle based on the study of polystyrene latex balls. *Surf. Sci.* **1994**, *317*, 321–340.
 130. Xu, L.; Yao, X.W.; Zhang, L.P.; Li, M.Q.; Yang, F.J. Effects of the long-range macroscopic forces on atomic-force-microscope images. *Phys. Rev., B* **1994**, *49*, 2875–2877.
 131. Xu, S.; Amro, N.A.; Liu, G.Y. Characterization of AFM tips using nanografting. *Appl. Surf. Sci.* **2001**, *175*, 649–655.
 132. Bietsch, A.; Schneider, M.A.; Welland, M.E.; Michel, B. Electrical testing of gold nanostructures by conducting atomic force microscopy. *J. Vac. Sci. Technol., B* **2000**, *18*, 1160–1170.
 133. Trenkler, T.; Hantschel, T.; Stephenson, R.; De Wolf, P.; Vandervorst, W.; Hellemans, L.; Malave, A.; Buchel, D.; Oesterschulze, E.; Kulisch, W.; Niedermann, P.; Sulzbach, T.; Ohlsson, O. Evaluating probes for “electrical” atomic force microscopy. *J. Vac. Sci. Technol., B* **2000**, *18*, 418–427.
 134. Sekimoto, M.; Yoshihara, H.; Ohkubo, T. Silicon nitride single-layer X-ray mask. *J. Vac. Sci. Technol.* **1982**, *21*, 1017–1021.
 135. Johnson, K.L.; Kendall, K.; Roberts, A.D. Surface energy and the contact of elastic solids. *Proc. R. Soc. Lond., A Math. Phys. Eng. Sci.* **1971**, *324*, 301–313.
 136. Derjaguin, B.V.; Muller, V.M.; Toporov, Y.P. Effect of contact deformations on adhesion of particles. *J. Colloid Interface Sci.* **1975**, *53*, 314–326.
 137. Maugis, D. Adhesion of spheres—The JKR–DMT transition using a Dugdale model. *J. Colloid Interface Sci.* **1992**, *150*, 243–269.
 138. Greenwood, J.A. Adhesion of elastic spheres. *Proc. R. Soc. Lond., A Math. Phys. Eng. Sci.* **1997**, *453*, 1277–1297.
 139. Weihs, T.P.; Nawaz, Z.; Jarvis, S.P.; Pethica, J.B. Limits of imaging resolution for atomic force microscopy of molecules. *Appl. Phys. Lett.* **1991**, *59*, 3536–3538.
 140. Adamson, A.W. *Physical Chemistry of Surfaces*; Wiley & Sons: New York, 1990.
 141. Carpick, R.W.; Dai, Q.; Ogletree, D.F.; Salmeron, M. Friction force microscopy investigations of potassium halide surfaces in ultrahigh vacuum: Structure, friction and surface modification. *Tribol. Lett.* **1998**, *5*, 91–102.

142. Helt, J.M.; Batteas, J.D. Wear of mica under aqueous environments: Direct observation of defect nucleation by AFM. *Langmuir*, to be submitted.
143. Hsu, S.M.; Zhang, J.; Yin, Z.F. The nature and origin of tribochemistry. *Tribol. Lett.* **2002**, *13*, 131–139.
144. Hertz, H. On the contact of elastic solids. *J. Reine Angew. Math.* **1881**, *92*, 156–171.
145. Helt, J.M.; Batteas, J.D. The contact radius–line step relationship: Importance in atomic force microscopy wear experiments. *J. Chem. Phys.* to be submitted.
146. Bousse, L.; Mostarshed, S. The zeta-potential of silicon-nitride thin-films. *J. Electroanal. Chem.* **1991**, *302*, 269–274.
147. Xiao, Y.T.; Lasaga, A.C. Ab-initio quantum-mechanical studies of the kinetics and mechanisms of silicate dissolution— $H^+(H_3O^+)$ catalysis. *Geochim. Cosmochim. Acta* **1994**, *58*, 5379–5400.
148. Batteas, J.D.; Weldon, M.K.; Raghavachari, K. Bonding & Inter-Particle Interactions of Silica Nanoparticles: Probing Adhesion at Asperity-Asperity Contacts. In *Nanotribology: Critical Assessment and Research Needs*; Hsu, S.M., Ying, Z.C., Eds.; Kluwer Academic: Boston, 2003; 387–398.
149. Hiemstra, T.; Yong, H.; Van Riemsdijk, W.H. Interfacial charging phenomena of aluminum (hydr)oxides. *Langmuir* **1999**, *15*, 5942–5955.
150. Kavanagh, B.V.; Posner, A.M.; Quirk, J.P. Effect of polymer adsorption on properties of electrical double-layer. *Faraday Discuss.* **1975**, *59*, 242–249.
151. Shluger, A.L.; Rohl, A.L.; Wilson, R.M.; Williams, R.T. Atomistic modeling of imaging of ionic surfaces with a scanning force microscope. *J. Vac. Sci. Technol., B* **1995**, *13*, 1155–1162.
152. Loppacher, C.; Bennewitz, R.; Pfeiffer, O.; Guggisberg, M.; Bammerlin, M.; Schar, S.; Barwich, V.; Baratoff, A.; Meyer, E. Experimental aspects of dissipation force microscopy. *Phys. Rev., B* **2000**, *62*, 13674–13679.
153. Gnecco, E.; Bennewitz, R.; Gyalog, T.; Loppacher, C.; Bammerlin, M.; Meyer, E.; Guntherodt, H.J. Velocity dependence of atomic friction. *Phys. Rev. Lett.* **2000**, *84*, 1172–1175.
154. Pelmenchikov, A.; Leszczynski, J.; Pettersson, L.G.M. Mechanism of dissolution of neutral silica surfaces: Including effect of self-healing. *J. Phys. Chem., A* **2001**, *105*, 9528–9532.
155. Pelmenchikov, A.; Strandh, H.; Pettersson, L.G.M.; Leszczynski, J. Lattice resistance to hydrolysis of Si–O–Si bonds of silicate minerals: Ab initio calculations of a single water attack onto the (001) and (111) beta-cristobalite surfaces. *J. Phys. Chem., B* **2000**, *104*, 5779–5783.
156. Benco, L.; Tunega, D.; Hafner, J.; Lischka, H. Upper limit of the O–H···O hydrogen bond. AB initio study of the kaolinite structure. *J. Phys. Chem., B* **2001**, *105*, 10812–10817.
157. Maboudian, R. Surface processes in MEMS technology. *Surf. Sci. Rep.* **1998**, *30*, 209–270.
158. Maboudian, R.; Ashurst, W.R.; Carraro, C. Self-assembled monolayers as anti-stiction coatings for MEMS: Characteristics and recent developments. *Sens. Actuators, A, Phys.* **2000**, *82*, 219–223.
159. Ulman, A. Formation and structure of self-assembled monolayers. *Chem. Rev.* **1996**, *96*, 1533–1554.
160. Kubicki, J.D.; Xiao, Y.; Lasaga, A.C. Theoretical reaction pathways for the formation of $[Si(OH)_5]^{1-}$ and the deprotonation of orthosilicic acid in basic solution. *Geochim. Cosmochim. Acta* **1993**, *57*, 3847–3853.



Microgel Dispersions: Colloidal Forces and Phase Behavior

Jianzhong Wu

University of California, Riverside, California, U.S.A.

Zhibing Hu

University of North Texas, Denton, Texas, U.S.A.

INTRODUCTION

In many aspects, colloidal particles suspended in a liquid behave like large idealized atoms that exhibit liquid, glass, and crystal phases similar to those observed in atomic systems.^[1-6] Phase transitions in colloidal systems have been intensively studied over the last decade not only because of the theoretical interest for addressing fundamental questions about the nature of liquids, crystals, and glasses, but also for many practical applications of colloids.^[7-11] In recent years, colloidal dispersions have been used extensively for the fabrication of nanostructured materials such as photonic crystals, catalysts, membranes, and ceramics, and for device applications.^[11-16] Current uses of colloidal particles as the building blocks of materials rely mostly on empirical approaches. Meanwhile, present knowledge on the structural and thermodynamic properties of colloidal dispersions is primarily based on an effective one-component model (OCM) where colloidal particles are represented by hard spheres and all remaining components in the dispersion, including solvent molecules, small ions, and polymers, are represented as a continuous medium.^[17-23] Although the OCM approach is attractive because of its simplicity, application to practical systems is often limited by incomplete understanding of colloidal forces.^[24-28]

Amid numerous conventional colloids, aqueous dispersions of poly-*N*-isopropylacrylamide (PNIPAM) microgel particles, first synthesized by Pelton and Chibante^[29] in 1986, are of special interest for studying phase transitions and for the fabrication of colloid-based advanced materials.^[30-36] Nearly monodispersed PNIPAM particles can now be routinely prepared in a wide range of colloidal sizes (50 nm up to 1 μm) and with a variety of physiochemical characterizations.^[35,37] Because the size of PNIPAM particles is temperature-sensitive,^[38] crystallization at different colloidal volume fractions can be conveniently measured by varying temperatures. By tuning the preparation conditions and the composition of the aqueous solution, the interaction potential between

microgel particles can vary from star-polymer-like to hard-sphere-like potential for short-range repulsion, from electrostatically neutral to highly ionizable for long-range electrostatic interactions, and from essentially no attraction to strong attraction for van der Waals forces.^[36,39] Furthermore, steric repulsion can be introduced by grafting polymers on the surface of PNIPAM particles.^[40] The versatility in interaction potential makes PNIPAM microgel particles attractive for studying a broad variety of interesting phenomena in colloidal systems.^[32,41-44] Although the practical values of PNIPAM particles have been long recognized, most previous studies on the physiochemical properties of PNIPAM dispersions have focused on particle preparations, swelling, rheology, and light (neutron) scattering measurements.^[35,36,45-47] Little work has been reported on the relationship between the temperature-dependent interparticle potential and the phase behavior of PNIPAM dispersions. Unlike that in a conventional colloidal system, the interparticle potential in aqueous dispersions of PNIPAM microgel particles is sensitive to temperature changes. Consequently, the phase diagram of PNIPAM dispersions may be noticeably different from those for ordinary colloids where, in most cases, the interparticle potential is essentially invariant with temperature.

In this chapter, we report our recent investigations on the colloidal forces and phase behavior of neutral PNIPAM particles dispersed in pure water.^[48-50] We will first discuss thermodynamic methods for the characterization of colloidal forces based on dynamic and static light scattering measurements. The analytical expression of colloidal forces allows us to construct a theoretical phase diagram that can be compared with that obtained from spectroscopic measurements. In particular, we will illustrate how the volume transition of PNIPAM particles affects the interaction potential and determines a novel phase diagram that has not been observed in conventional colloids. Finally, we discuss briefly the kinetics of crystallization in an aqueous dispersion of PNIPAM particles.

COLLOIDAL FORCES BETWEEN MICROGEL PARTICLES

Qualitatively, the pair potential between neutral microgel particles includes a short-range repulsion that is similar to the interaction between two polymer-coated surfaces, and a longer-ranged van der Waals-like attraction that arises from the difference in the Hamaker constants of the particle and the solvent.^[51,52] To obtain a quantitative expression for the interparticle potential that covers a broad range of temperature, we assume that the interaction potential can be represented by a Sutherland-like function that includes a hard-sphere repulsion and a van der Waals attraction. A similar potential was used Senff and Richtering^[43,53] for representing the phase behavior and rheological properties of PNIPAM microgel dispersions. Fig. 1 shows that the relative zero shear viscosity of PNIPAM dispersion can be approximately represented by that for hard spheres. Besides, as shown later, the kinetics of microgel crystallization also resembles that for hard spheres.

The variation of microgel diameter as a function of temperature is related to the swelling of microgel particles. The classical theory of gel swelling, proposed many years ago by Flory,^[54] asserts uniform distributions of polymer segments and crosslinking points throughout the polymer network. However, recent experiments based on nuclear magnetic resonance (NMR) and light scattering

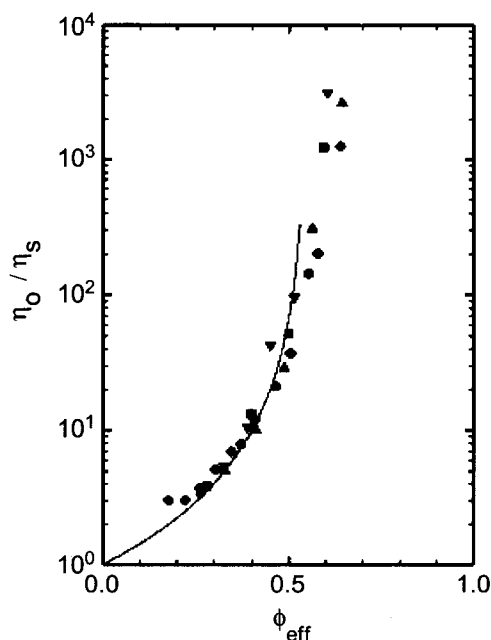


Fig. 1 Relative zero shear viscosity at different temperatures vs. the effective volume fraction. The line represents the master curve of hard-sphere suspensions. (From Refs. [43] and [53].)

investigations suggest the heterogeneous nature of PNIPAM particles.^[51,55] To take into account the heterogeneity, we use an empirical modification of the Flory–Rehner theory proposed by Hino and Prausnitz.^[56] This theory has been applied successfully to describing the volume transitions of bulk PNIPAM gels. Because the physics for the volume transition is irrelevant to the particle size as long as the surface effect is unimportant, and because the effect of the osmotic pressure of dispersion on the swelling of an individual particle is negligible,^[42] we assume that the same thermodynamic model for bulk polymer gels is also applicable to microgel particles.

According to the modified Flory–Rehner theory,^[56] the polymer volume fraction within the particle ϕ is determined from:

$$\begin{aligned} & \ln(1 - \phi) + \phi + \chi\phi^2 + \frac{\phi_0}{m} \\ & \times \left[\left(\frac{\phi}{\phi_0} \right)^{1/3} - \left(\frac{\phi}{\phi_0} \right)^{5/3} + \left(\frac{\phi}{2\phi_0} \right) \right] \\ & = 0 \end{aligned} \quad (1)$$

where m is the average number of segments between two neighboring crosslinking points in the microgel network, and ϕ_0 is the polymer volume fraction in the reference state where the conformation of network chains is closest to that of unperturbed Gaussian chains. Approximately, ϕ_0 is equal to the volume fraction of polymers within the microgel particles at the condition of preparation. The Flory polymer–solvent energy parameter χ is given empirically as a function of temperature T and polymer volume fraction ϕ :^[56]

$$\begin{aligned} \chi &= \frac{3}{1 - 0.65\phi} \\ & \times \left[2 \ln \left(\frac{5001}{1 + 5000 \exp(2458.867/T)} \right) - \frac{4566.468}{T} \right] \end{aligned} \quad (2)$$

At a given temperature, Eq. 1 can be solved to find the polymer volume fraction ϕ from which the diameter of PNIPAM particles (σ) is calculated:

$$\frac{\sigma}{\sigma_0} = \left(\frac{\phi_0}{\phi} \right)^{1/3} \quad (3)$$

where σ_0 is the particle diameter at the reference state. In this work, we fit the average chain length m and the volume fraction of polymer ϕ_0 at the reference state to the diameters of microgel particles obtained from static and dynamic light scattering measurements. Because the osmotic pressure of microgel dispersion is small in

comparison to the gel swelling pressure, the microgel particle concentration has a negligible effect on the chemical potential of water. As a result, the size of microgel particles should be insensitive to the overall concentration of colloidal dispersions.

The van der Waals attraction beyond the hard-sphere diameter may be represented by a power law potential:

$$u_A(r) = -\frac{H}{r^n} \quad (4)$$

where H is the Hamaker constant. We assume that $n=8$ in considering that the range of attraction between colloidal particles (relative to the particle size) is shorter than that between atomic molecules. The calculated results are not sensitive to a small change in n if the Hamaker constant is obtained by fitting to osmotic second virial coefficients from static light scattering experiments. Because the interparticle attraction arises from the dispersion forces between polymeric segments from different particles, the Hamaker constant of microgel particles is approximately given by:^[57]

$$H \propto \rho_m^2 \quad (5)$$

where ρ_m represents the number density of polymeric groups within each particle. The proportionality constant in Eq. 5 is independent of temperature and polymeric group density ρ_m . Following Eqs. 4 and 5, we obtain the attractive potential because of the van der Waals forces:

$$\frac{u_A(r)}{kT} = -k_A \left(\frac{T_0}{T}\right) \left(\frac{\sigma_0}{\sigma}\right)^{6+n} \left(\frac{\sigma}{r}\right)^n \quad (6)$$

where k_A is a dimensionless constant, and T_0 is the reference temperature that is introduced for the purpose of dimensionality. In Eq. 6, the parameters T_0 , σ_0 , and k_A are temperature-independent and they can be obtained by fitting to osmotic second virial coefficients from static light scattering measurements. An osmotic second virial coefficient in a colloidal dispersion is defined as:

$$B_2 = 2\pi \int_0^\infty [1 - e^{-u(r)/kT}] r^2 dr \quad (7)$$

where r stands for the center-to-center distance between colloidal particles, k is the Boltzmann constant, and $u(r)$ is the interparticle potential.

The particle size and the osmotic second virial coefficients of microgel dispersions can be conveniently measured using static and dynamic light scattering. To correlate the radius of PNIPAM gel particles as a function of temperature, we combine the radius of gyration R_g with the hydrodynamic radius R_H from static and dynamic light scattering measurements, respectively. By assuming that

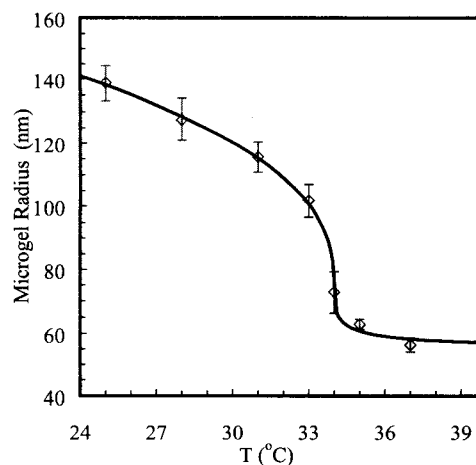


Fig. 2 Radius of PNIPAM particles vs. temperature. The points are averages from dynamic and static light scattering measurements with the error bars showing the differences between the two. The line is calculated from Eqs. 1–3.

the microgel particles are homogeneous spheres, we define the effective radius:

$$R = (\sqrt{5/3}R_g + R_H)/2 \quad (8)$$

This effective radius is introduced to represent the excluded volume of microgel particles as required in phase equilibrium calculations. Fig. 2 presents the radius of microgel particles near the volume transition temperature (approximately at 34.3°C). The error bars give the difference between the hydrodynamic radius and that calculated from the radius of gyration. The solid line is calculated by using the modified Flory–Rehner theory (Eqs. 1–3). In the calculation of the particle radius, the polymer fraction at the condition of preparation $\phi_0=0.0884$, the average number of segments between two neighboring crosslinking points $m=34$, and the particle radius at the preparation condition $R_0=125.8$ nm are obtained by fitting to the experimental data. These model parameters are in good agreement with experiments.

Fig. 3 presents the reduced osmotic second virial coefficients (B_2/B_2^{HS}) for PNIPAM microgel particles dispersed in water. Here the open circles are data points from static light scattering measurements and the line is calculated using Eqs. 6 and 7, with the molecular weight $M_w=1.73 \times 10^7$ g/mol and the proportionality constant $k_A=6.43 \times 10^{-5}$ obtained by fitting to the experimental data. The hard-sphere second virial coefficient is related to the particle diameter σ by $B_2^{\text{HS}}=(2\pi/3)\sigma^3$. A positive osmotic second virial coefficient means that the overall interparticle potential is repulsive; otherwise, it is attractive. Fig. 3 indicates that below the volume transition

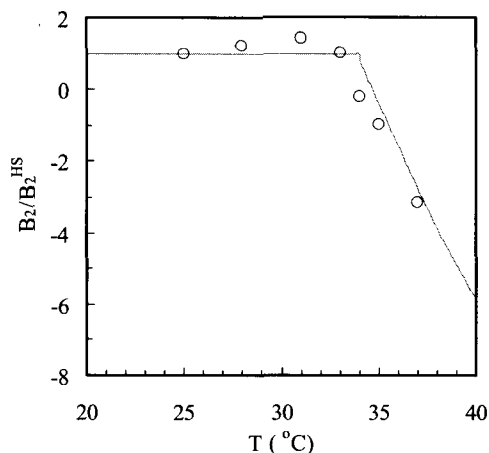


Fig. 3 The reduced osmotic second virial coefficients (B_2/B_2^{HS}) for PNIPAM particles dispersed in pure water. Points are from static light scattering and the line is calculated from Eq. 7 normalized by the second virial coefficient $B_2^{\text{HS}} = (2\pi/3)\sigma^3$ for the corresponding hard spheres. (View this art in color at www.dekker.com.)

temperature, the PNIPAM particles behave essentially like hard spheres. In this case, the microgel particles are in the swollen state and they contain up to 97% of water by volume. As a result, the van der Waals attraction between colloidal particles is negligible because of the close match in the Hamaker constants of the particle and the water. The reduced osmotic second virial coefficient exhibits a sharp change at the volume transition temperature, beyond which it turns to negative, indicating an increase in the van der Waals attraction as the particles collapse. Fig. 3 suggests that with temperature-dependent size and energy parameters, the Sutherland-type function captures the essential features of the interaction potential between microgel particles.

Because the number density of polymeric segments within each particle is closely related to the particle size, we expect that the attraction between microgel particles is highly temperature-sensitive. Fig. 4 shows the reduced energy parameter $\epsilon/(kT)$ near the volume transition temperature as obtained by correlation with the osmotic second virial coefficients from experiments. Experimental values for this parameter are not included because it is difficult to make a direct (or indirect) measurement of the reduced energy parameter. But the credibility of calculated results is implied in the comparison of osmotic second virial coefficients, as shown in Fig. 3. Remarkably, the energy parameter increases by over six orders of magnitude as temperature changes from 24°C to 36°C, with the sharpest increase at the volume transition temperature of 34°C.

THERMODYNAMIC MODELS FOR PHASE EQUILIBRIUM CALCULATIONS

To calculate the phase diagram, we need to have the thermodynamic models for both fluid and crystalline phases, as well as the structure of the crystal. It has been shown before by small-angle neutron scattering measurements that even at low crosslinker concentrations, aqueous dispersions of PNIPAM microgel particles crystallize like hard-sphere liquids.^[42] Fig. 5 indicates that the structure factor of the colloidal crystal is well represented by that for a face centered cubic (fcc) structure. Therefore it is reasonable to assume that hard spheres provide a good reference system for representing the thermodynamic properties of microgel dispersions. Because the van der Waals attraction between microgel particles is short-ranged compared to the particle size, a first-order perturbation theory is appropriate for both phases. The higher-order terms are insignificant when the perturbation potential is short-ranged.^[58]

The Helmholtz energy of the fluid phase includes a hard-sphere contribution that is given by the Carnahan–Starling equation of state, and a perturbation that takes into account the van der Waals attraction. In dimensionless units, the Helmholtz energy is given by:

$$\frac{F}{NkT} = \ln(\eta) - 1 + \frac{4\eta - 3\eta^2}{(1 - \eta)^2} + 12\eta \int_1^\infty x^2 g_F^{\text{HS}}(x) \frac{u_A(x)}{kT} dx \quad (9)$$

where N represents the total number of particles, $\eta = \pi\rho\sigma^3/6$ is the particle packing fraction, ρ is the

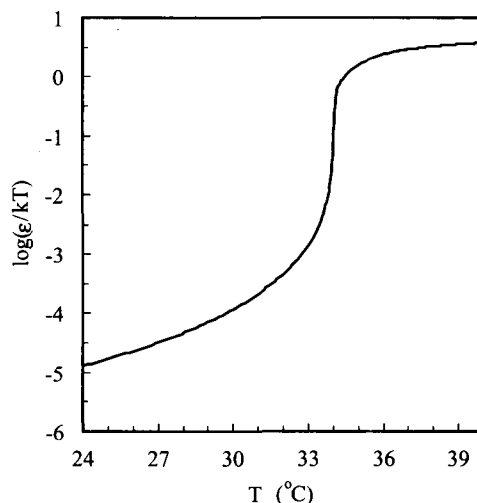


Fig. 4 The reduced energy parameter (ϵ/kT) for interparticle potential between PNIPAM particles near the volume transition temperature.

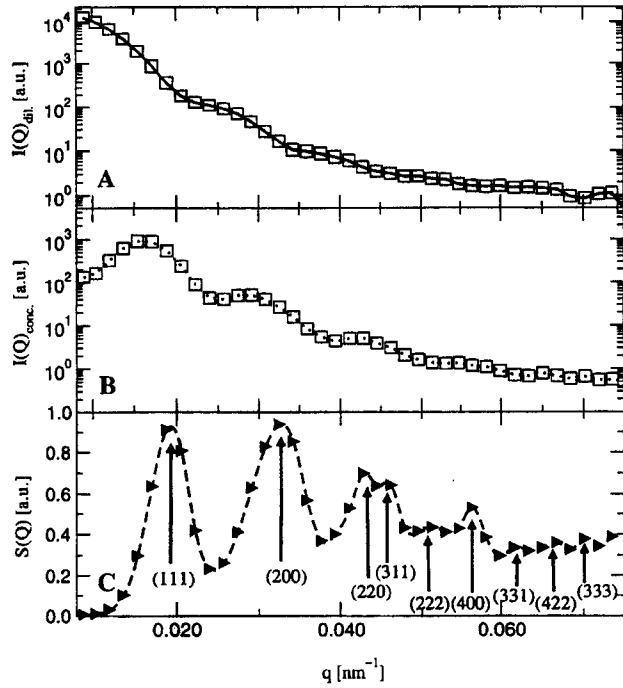


Fig. 5 (A) Neutron scattering profile for a dilute microgel dispersion. (B) Scattering profile for a colloidal crystal of microgel particles. (C) Structure factor of the crystal. The Bragg peaks are interpreted according to the fcc lattice. (From Ref. [42].)

particle number density, and $g_{\text{F}}^{\text{HS}}(r)$ is the hard-sphere radial distribution function. For convenience, we correlate the integral in Eq. 9 as a function of particle packing fraction using the radial distribution function $g_{\text{F}}^{\text{HS}}(r)$ obtained from the Percus–Yevick equation.^[59]

$$I_{\text{F}}(\eta) \equiv \int_1^{\infty} x^{-6} g^{\text{HS}}(x) dx = 0.027224\eta^2 + 0.1642\eta + 0.2007 \quad (10)$$

The quadric form as given in Eq. 10 is applicable to the reduced density $\rho\sigma^3 < 0.6$. Replacement of the integral in Eq. 9 with $I_{\text{F}}(\eta)$ gives:

$$\frac{F}{NkT} = \ln(\eta) - 1 + \frac{4\eta - 3\eta^2}{(1 - \eta)^2} - 12\eta I_{\text{F}}(\eta)\varepsilon^* \quad (11)$$

where:

$$\varepsilon^* = \frac{\varepsilon}{kT} = k_{\text{A}} \left(\frac{T_0}{T} \right) \left(\frac{\sigma_0}{\sigma} \right)^{6+n} \quad (12)$$

Other thermodynamic properties can be derived from Eq. 11 following standard thermodynamic relations.

To describe the thermodynamic properties of the solid phase, we follow a perturbation approach similar to that for the fluid phase. The Helmholtz energy in-

cludes a contribution from the reference hard-sphere crystal and a perturbation taking into account the van der Waals attraction:

$$\frac{F}{NkT} = \frac{F^{\text{HS}}}{NkT} + 12\eta \int_1^{\infty} x^2 g_{\text{S}}^{\text{HS}}(x) \frac{u_{\text{A}}(x)}{kT} dx \quad (13)$$

where $g_{\text{S}}^{\text{HS}}(r)$ is the radial distribution function of the hard-sphere solid. As in a hard-sphere system, an aqueous dispersion of PNIPAM microgel particles forms a face centered cubic lattice in the solid phase even when the particles are at low crosslinking density (“softer” particles).^[42]

According to an improved cell theory,^[60] the Helmholtz energy of the hard-sphere solid is given by:

$$\frac{F^{\text{HS}}}{NkT} = - \ln \left[\frac{8}{\sqrt{2}} \left((\rho/\rho_0)^{1/3} - 1 \right) \right] \quad (14)$$

Compared with the original cell model proposed many years ago by Lennard-Jones and Devonshire,^[61] the improved cell model introduces a factor of 8, taking into account the fact that the neighboring particles share partially the free space. Unlike the original cell model, the modified cell model provides accurate freezing and melting densities for the fluid–solid transition of uniform hard spheres. The hard-sphere radial distribution function $g_{\text{S}}^{\text{HS}}(r)$ can be calculated using a modified Gaussian model for density distributions.^[49] Using the radial distribution function $g_{\text{S}}^{\text{HS}}(r)$ for the hard-sphere solids, we numerically integrate the perturbation term in Eq. 13. The final expression for the Helmholtz energy of the solid phase is given by:

$$\frac{F}{NkT} = - \ln \left[\frac{8}{\sqrt{2}} \left((\rho/\rho_0)^{1/3} - 1 \right) \right] - 12\eta I_{\text{S}}(\rho)\varepsilon^* \quad (15)$$

where:

$$I_{\text{S}}(\rho) \equiv \int_1^{\infty} x^{-6} g_{\text{S}}^{\text{HS}}(x) dx = 0.451\rho^2 - 0.5253\rho + 0.5514 \quad (16)$$

Eq. 16 is applicable for the solid phase with the reduced density $0.95 < \rho\sigma^3 < 1.27$.

EQUILIBRIUM PHASE DIAGRAM

Once we have an expression for the Helmholtz energy, the chemical potential μ and the osmotic pressure P can be derived following standard thermodynamic relations:

$$\mu = \left(\frac{\partial F}{\partial N} \right)_{T,V} \quad (17)$$

$$P = - \left(\frac{\partial F}{\partial V} \right)_{T,N} \quad (18)$$

where “V” stands for the total volume. A fluid–fluid coexistence curve is obtained from the criteria of phase equilibrium:

$$\mu^\alpha = \mu^\beta \quad (19)$$

$$P^\alpha = P^\beta \quad (20)$$

where “ α ” and “ β ” designate two distinguishable fluid phases. To calculate the pressure and the chemical potential in the fluid phase, the Helmholtz energy is given by Eq. 11. For each temperature, we solve for equilibrium densities ρ^α and ρ^β using Eqs. 19 and 20. If no solution is found, the temperature is above the critical temperature for fluid–fluid equilibrium; in this case, there is only one fluid phase.

For fluid–solid equilibrium, we also use Eqs. 19 and 20. But now, for phase α , we use Eq. 11 for the liquid-phase Helmholtz energy, whereas we use Eq. 15 for the solid-phase Helmholtz energy for phase β . Again, we search for densities ρ^α and ρ^β that satisfy both equations of phase equilibrium (i.e., Eqs. 19 and 20).

To calibrate the thermodynamic models proposed in this work, we first consider the phase behavior of a Yukawa system that is often used to represent colloidal dispersions with weak attractive interactions. Fig. 6 compares the fluid–solid as well as metastable fluid–fluid coexistence curves from simulation^[62] and from the

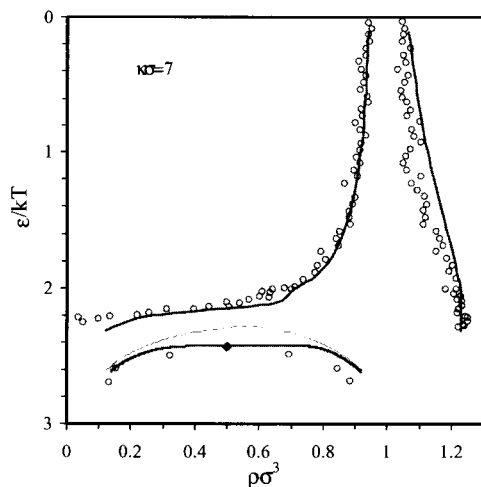


Fig. 6 The phase diagram of a typical colloidal system with weak attractive forces. The points are from simulation data for Yukawa potential. (From Ref. [62].) The lines are from the theory. (View this art in color at www.dekker.com.)

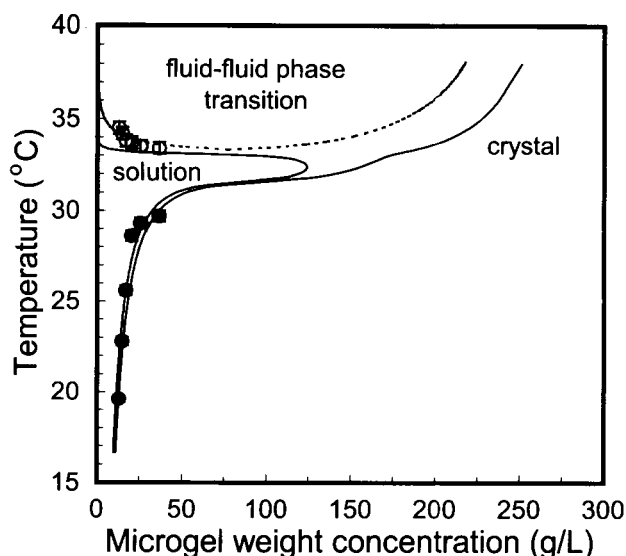


Fig. 7 The phase diagram of aqueous dispersions of PNIPAM particles determined from turbidity measurements (symbols) and from the thermodynamic perturbation theory with an empirical correction of temperature (lines). The filled and open circles represent the melting and the second phase separation temperatures, respectively.

perturbation theory. The agreement is satisfactory except near the critical point of the fluid–fluid equilibrium where the long-range fluctuations become significant. An improved prediction in this region can be achieved by applying the renormalization group theory.^[63] Fig. 6 indicates that at high temperature, the system is dominated by short-range repulsion and it exhibits freezing transition similar to that for hard spheres, whereas at low temperature, freezing occurs at dilute conditions and is separated by a metastable liquid–liquid equilibrium.

Fig. 7 shows the calculated phase diagram of PNIPAM microgel dispersion using the first-order perturbation theories for fluid and solid phases. Also shown in this figure are results determined from a UV–VIS spectrometer. In this calculation, the calculated temperature is rescaled empirically by $T' = T(15/R_g)^{0.005}$ to match the experimental results quantitatively. The discrepancy is probably because of the slight size difference (~ 2 nm) between the microgel samples used in light scattering and in phase diagram measurements. Nevertheless, the theory and the experiment agree, at least semiquantitatively.

The phase diagram shown in Fig. 7 differs drastically from that of a conventional colloidal dispersion, or that of a colloid polymer mixture.^[64] Below the volume transition temperature, the coexistence phases at the freezing and melting points have close particle densities, similar to that observed in a hard-sphere system. However, above the volume transition temperature, fluid–solid transition

spans over a wide gap of particle concentrations. At high temperature, the fluid phase at the freezing point is highly dilute, whereas the solid phase at the melting point is highly concentrated. Interestingly, this phase diagram indicates that the microgel dispersion can freeze at temperatures both above and below the gel volume transition temperature. For instance, according to this phase diagram, a microgel dispersion with 7 g/L particle concentration is in the fluid state at 34.5°C; it becomes a solid of similar density when the temperature drops to about 34°C, and the dispersion will be separated into a dilute solution and a solid of much higher density (about 17 g/L) at about 35.3°C. The dashed line in Fig. 7 shows a metastable fluid–fluid coexistence curve with a low critical solution temperature. This coexistence curve is reminiscent of that for an aqueous solution of uncrosslinked PNIPAM polymer. Because of strong hydrogen bonding with water molecules from CO and NH groups, PNIPAM can be dissolved in water at low temperature. In this case, the isopropyl groups along the PNIPAM chain are caged by water molecules. When the temperature is increased, the cages of water molecules are partially melted, resulting in entropy increases. As a result, on increase of the temperature, the hydrophobic attraction caused by the isopropyl groups and the polymer backbone become more important and the solubility of PNIPAM in water drops.

KINETICS OF CRYSTALLIZATION

As shown in Fig. 3, light scattering measurements indicate that when the particles are in the swollen state, the osmotic second virial coefficients of PNIPAM microgel dispersions are essentially the same as those for hard spheres. The nucleation kinetics confirms further that the swollen PNIPAM particles behavior like hard spheres. We find that the kinetics of microgel crystallization can be represented quantitatively by the classical nucleation theory (CNT).

The classical theory of nucleation and crystal growth has been adapted by Russel^[65] to hard-sphere colloids, and extended and evaluated numerically by Ackerson and Schatzel.^[66] According to the CNT,^[67] the crystal nucleation rate per unit volume I depends exponentially on the Gibbs energy barrier in the formation of a critical nucleus ΔG_{crit} :

$$I = \zeta \exp(-\Delta G_{\text{crit}}/k_{\text{B}}T) \quad (21)$$

where the kinetic prefactor ζ is usually expressed as $A\phi^{5/3}(1-\phi/\phi_{\text{g}})^{2.6}$, where A is a constant independent of the particle volume fraction ϕ , and ϕ_{g} is the glass transition concentration. The critical Gibbs energy of nucle-

ation is related to the difference in the chemical potentials of the solution and the crystal $\Delta\mu$, the solution–solid interfacial tension γ , and the number density of the crystalline phase ρ_{s} :

$$\Delta G_{\text{crit}} = \frac{16\pi}{3} \frac{\gamma^3}{[\rho_{\text{s}}\Delta\mu]^2} \quad (22)$$

In most applications of the CNT to analyze crystal nucleation experiments, the parameter A in the kinetic prefactor and the interfacial tension are treated as adjustable variables.

In Fig. 8, we compare the rate of nucleation per unit volume in the microgel dispersion investigated in this work with previous studies for hard-sphere-like colloids.^[7,68–70] Also shown in Fig. 8 are calculated results from CNT using A and γ as adjustable parameters, as well as the predictions of CNT with the kinetic prefactor and the fluid–solid interfacial tension obtained from Monte Carlo simulations.^[71] In these calculations, the chemical potentials of the fluid and solid phases are calculated from Eqs. 11 and 15. Fig. 8 indicates that although the rate of nucleation for microgel dispersions is close to previous investigations on well-established hard-sphere-like colloids and it agrees well with CNT using $\log_{10}(A) = -5.96$

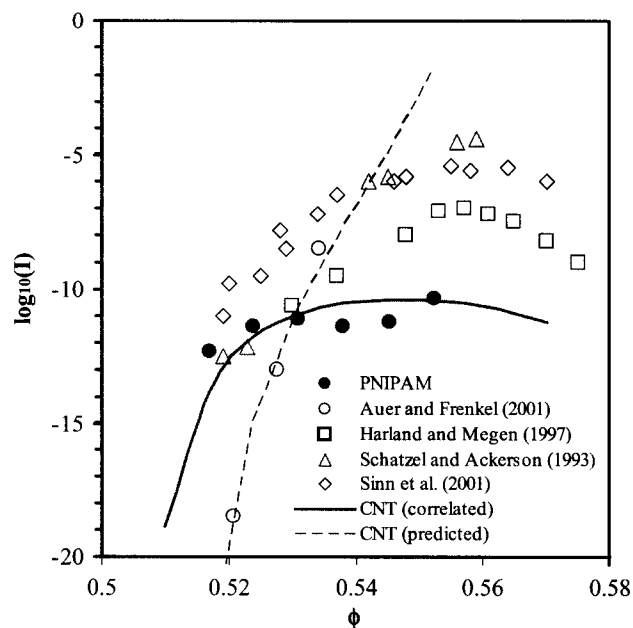


Fig. 8 The nucleation rates per unit volume as a function of the particle volume fraction in an aqueous dispersion of PNIPAM microgel particles and in various hard-sphere systems. The solid line is calculated from CNT with the prefactor A and the fluid–solid interfacial tension γ as adjustable parameters. The dashed line is the prediction of the CNT using A and γ from Monte Carlo simulation. (View this art in color at www.dekker.com.)

and $\gamma/k_B T = 0.45$, it significantly deviates from simulation results for hard spheres. Similar observations have been reported by Schatzel and Ackerson for crystallization kinetics in a model hard-sphere system consisting of polymethyl methacrylate particles coated with a thin layer of hydroxystearic acid suspended in a mixture of decalin and tetralin.^[68]

CONCLUSION

The volume transition of PNIPAM particles significantly affects the interaction potential and determines a novel phase diagram that has not been observed in conventional colloids. Because both particle size and attractive potential depend on temperature, PNIPAM aqueous dispersion exhibits phase transitions at a fixed particle density by either increasing or decreasing temperature. At low temperature, freezing occurs at large particle volume fractions, similar to that in a hard-sphere system; whereas at high temperature, the freezing occurs at low particle concentration, driven by the strong van der Waals attraction caused by the collapsed microgel particles. Although the kinetics of nucleation in PNIPAM microgel dispersions is similar to that for hard-sphere-like colloids, it deviates significantly from the prediction of the CNT using the kinetic prefactor and the fluid–solid interfacial tension obtained from recent simulations for the crystal nucleation of hard spheres.

In many aspects, the phase behavior of colloidal dispersions reassembles that for simple fluids. However, a noticeable difference is that unlike the vapor–liquid equilibrium of a simple fluid, the equilibrium between a dilute and a concentrated colloidal dispersion is often metastable. Although that difference, arising from the short-ranged solvent-mediated attraction between colloidal particles, is now well-documented, not much attention has been given to other features that are unique in colloidal systems. Temperature-dependent potential, as shown in this work, is special in colloidal systems. Because the interparticle potential is strongly temperature-dependent, the phase behavior of PNIPAM dispersions differs remarkably from that for simple fluids or for conventional colloids. In future work, it might be interesting to investigate other features that are special to colloidal dispersions, including the multibody effect on the phase behavior and dissimilarity of interparticle potentials in different phases.

ACKNOWLEDGMENTS

J. W. gratefully acknowledges the financial support from the University of California Directed Research and Development. Z. H. gratefully acknowledges the financial

support from the National Science Foundation (grant no. DMR-0102468), and the U.S. Army Research Office (grant no. DAAD19-01-1-0596). We thank G. Huang and B. Zhou for their help.

REFERENCES

1. Weeks, E.R.; Crocker, J.C.; Levitt, A.C.; Schofield, A.; Weitz, D.A. Three-dimensional direct imaging of structural relaxation near the colloidal glass transition. *Science* **2000**, *287*, 627–631.
2. Russel, W.B.; Saville, D.A.; Schowalter, W.R. *Colloidal Dispersions*; Cambridge University Press: Cambridge, New York, 1989.
3. Pusey, P.N. In *Liquid, Freezing, and the Glass Transition*; Les Houches, J.P., Levesque, H.D., Zinn-Justin, J., Eds.; Elsevier: Amsterdam, 1990.
4. Schatzel, K.; Ackerson, B.J. Observation of density fluctuations during crystallization. *Phys. Rev. Lett.* **1992**, *68*, 337–340.
5. Cheng, Z.D.; Chaikin, P.M.; Zhu, J.X.; Russel, W.B.; Meyer, W.V. Crystallization kinetics of hard spheres in microgravity in the coexistence regime: Interactions between growing crystallites. *Phys. Rev. Lett.* **2002**, *8801*, art. no. 015501; pp. 5501, U5110–U5112.
6. Arora, A.K.; Tata, B.V.R. Interactions, structural ordering and phase transitions in colloidal dispersions. *Adv. Colloid Interface Sci.* **1998**, *78*, 49–97.
7. Pusey, P.N.; van Megen, W. Phase behavior of concentrated suspensions of nearly hard colloidal spheres. *Nature* **1986**, *320*, 340–341.
8. Denton, A.R.; Lowen, H. Stability of colloidal quasicrystals. *Phys. Rev. Lett.* **1998**, *81*, 469–472.
9. Cheng, Z.D.; Zhu, J.X.; Russel, W.B.; Chaikin, P.M. Phonons in an entropic crystal. *Phys. Rev. Lett.* **2000**, *85*, 1460–1463.
10. Pham, K.N.; Puertas, A.M.; Bergenholtz, J.; Egelhaaf, S.U.; Moussaid, A.; Pusey, P.N.; Schofield, A.B.; Cates, M.E.; Fuchs, M.; Poon, W.C.K. Multiple glassy states in a simple model system. *Science* **2002**, *296*, 104–106.
11. Xia, Y.N.; Gates, B.; Yin, Y.; Lu, Y. Monodispersed colloidal spheres: Old materials with new applications. *Adv. Mater.* **2000**, *12*, 693–713.
12. Blanco, A.; Chomski, E.; Grabtchak, S.; Ibisate, M.; John, S.; Leonard, S.W.; Lopez, C.; Meseguer, F.; Miguez, H.; Mondia, J.P.; Ozin, G.A.; Toader, O.; van Driel, H.M. Large-scale synthesis of a silicon photonic crystal with a complete three-dimensional bandgap near 1.5 micrometres. *Nature* **2000**, *405*, 437–440.
13. Velev, O.D.; Tessier, P.M.; Lenhoff, A.M.; Kaler,

- E.W. Materials—A class of porous metallic nanostructures. *Nature* **1999**, *401*, 548.
14. Dabbs, D.M.; Aksay, I.A. Self-assembled ceramics produced by complex-fluid templation. *Annu. Rev. Phys. Chem.* **2000**, *51*, 611–622, pp. 601–U623.
 15. Giannelis, E.P.; Krishnamoorti, R.; Manias, E. Polymer–silicate nanocomposites: Model systems for confined polymers and polymer brushes. *Adv. Polym. Sci.* **1999**, *138*, 107–147.
 16. Godovsky, D. Device applications of polymer-nanocomposites. *Adv. Polym. Sci.* **1999**, *153*, 163–205.
 17. Frenkel, D. Colloidal systems—Playing tricks with designer “atoms”. *Science* **2002**, *296*, 65–66.
 18. Noro, M.G.; Frenkel, D. Extended corresponding-states behavior for particles with variable range attractions. *J. Chem. Phys.* **2000**, *113*, 2941–2944.
 19. Likos, C.N. Effective interactions in soft condensed matter physics. *Phys. Rep.* **2001**, *348*, 268–439.
 20. Dijkstra, M.; van Roij, R.; Evans, R. Effective interactions, structure, and isothermal compressibility of colloidal suspensions. *J. Chem. Phys.* **2000**, *113*, 4799–4807.
 21. Rosenbaum, D.; Zamora, P.C.; Zukoski, C.F. Phase behavior of small attractive colloidal particles. *Phys. Rev. Lett.* **1996**, *76*, 150–153.
 22. Asherie, N.; Lomakin, A.; Benedek, G.B. Phase diagram of colloidal solutions. *Phys. Rev. Lett.* **1996**, *77*, 4832–4835.
 23. Quesada-Perez, M.; Callejas-Fernandez, J.; Hidalgo-Alvarez, R. Interaction potentials, structural ordering and effective charges in dispersions of charged colloidal particles. *Adv. Colloid Interface Sci.* **2002**, *95*, 295–315.
 24. Hansen, J.P.; Lowen, H. Effective interactions between electric double layers. *Annu. Rev. Phys. Chem.* **2000**, *51*, 209–242.
 25. Attard, P. Recent advances in the electric double layer in colloid science. *Curr. Opin. Colloid Interface Sci.* **2001**, *6*, 366–371.
 26. Ninham, B.W. On progress in forces since the DLVO theory. *Adv. Colloid Interface Sci.* **1999**, *83*, 1–17.
 27. Walz, J.Y. The effect of surface heterogeneities on colloidal forces. *Adv. Colloid Interface Sci.* **1998**, *74*, 119–168.
 28. Ruckenstein, E. Attraction between identical colloidal particles caused by collective electrostatic repulsion. *Adv. Colloid Interface Sci.* **1998**, *75*, 169–180.
 29. Pelton, R.H.; Chibante, P. Preparation of Aqueous Lattices with *N*-isopropylacrylamide. *Colloids Surfaces.* **1986**, *20*, 247–256.
 30. Weissman, J.M.; Sunkara, H.B.; Tse, A.S.; Asher, S.A. Thermally switchable periodicities and diffraction from mesoscopically ordered materials. *Science* **1996**, *274*, 959–960.
 31. Debord, J.D.; Eustis, S.; Debord, S.B.; Lofye, M.T.; Lyon, L.A. Color-tunable colloidal crystals from soft hydrogel nanoparticles. *Adv. Mater.* **2002**, *14*, 658–662.
 32. Debord, J.D.; Lyon, L.A. Thermoresponsive photonic crystals. *J. Phys. Chem., B* **2000**, *104*, 6327–6331.
 33. Okubo, T.; Hase, H.; Kimura, H.; Kokufutata, E. Thermosensitive colloidal crystals of silica spheres in the presence of gel spheres of poly(*N*-isopropyl acrylamide). *Langmuir* **2002**, *18*, 6783–6788.
 34. Debord, S.B.; Lyon, L.A. Influence of particle volume fraction on packing in responsive hydrogel colloidal crystals. *J. Phys. Chem., B* **2003**, *107*, 2927–2932.
 35. Pelton, R. Temperature-sensitive aqueous microgels. *Adv. Colloid Interface Sci.* **2000**, *85*, 1–33.
 36. Saunders, B.R.; Vincent, B. Microgel particles as model colloids: Theory, properties and applications. *Adv. Colloid Interface Sci.* **1999**, *80*, 1–25.
 37. Kawaguchi, H. Functional polymer microspheres. *Prog. Polym. Sci.* **2000**, *25*, 1171–1210.
 38. Hirotsu, S.; Hirokawa, Y.; Tanaka, T. Volume-phase transitions of ionized *N*-isopropylacrylamide gels. *J. Chem. Phys.* **1987**, *87*, 1392–1395.
 39. Fernandez-Nieves, A.; Fernandez-Barbero, A.; Vincent, B.; de las Nieves, F.J. Charge controlled swelling of microgel particles. *Macromolecules* **2000**, *33*, 2114–2118.
 40. Laukkanen, A.; Hietala, S.; Maunu, S.L.; Tenhu, H. Poly(*N*-vinylcaprolactam) microgel particles grafted with amphiphilic chains. *Macromolecules* **2000**, *33*, 8703–8708.
 41. Gao, J.; Hu, Z.B. Optical properties of *N*-isopropylacrylamide microgel spheres in water. *Langmuir* **2002**, *18*, 1360–1367.
 42. Hellweg, T.; Dewhurst, C.D.; Bruckner, E.; Kratz, K.; Eimer, W. Colloidal crystals made of poly(*N*-isopropylacrylamide) microgel particles. *Colloid Polym. Sci.* **2000**, *278*, 972–978.
 43. Senff, H.; Richtering, W. Temperature sensitive microgel suspensions: Colloidal phase behavior and rheology of soft spheres. *J. Chem. Phys.* **1999**, *111*, 1705–1711.
 44. Hu, Z.B.; Wang, C.J.; Chen, Y.Y.; Zhang, X.M.; Li, Y. Spinodal decomposition in *N*-isopropylacrylamide gel. *J. Polym. Sci., B, Polym. Phys.* **2001**, *39*, 2168–2174.
 45. Gilanyi, T.; Varga, I.; Meszaros, R.; Filipcsei, G.; Zrinyi, M. Characterisation of monodisperse poly(*N*-isopropylacrylamide) microgel particles. *Phys. Chem., Chem. Phys.* **2000**, *2*, 1973–1977.
 46. Saunders, B.R.; Crowther, H.M.; Morris, G.E.; Mears, S.J.; Cosgrove, T.; Vincent, B. Factors affecting the swelling of poly(*N*-isopropylacrylamide) microgel particles: Fundamental and commer-

- cial implications. *Colloids Surf., A Physicochem. Eng. Asp.* **1999**, *149*, 57–64.
47. Wu, C.; Zhou, S.Q.; Auyeung, S.C.F.; Jiang, S.H. Volume phase transition of spherical microgel particles. *Angew. Makromol. Chem.* **1996**, *240*, 123–136.
 48. Hu, Z.B.; Tang, S.J.; Cheng, C.D.; Wu, J.Z. Crystallization kinetics of thermosensitive colloids probed by transmission spectroscopy. *Phys. Rev. Lett.* **2003**. submitted for publication.
 49. Wu, J.Z.; Huang, G.; Hu, Z.B. Inter-particle potential and the phase behavior of temperature-sensitive microgel dispersions. *Macromolecules* **2003**, *36*, 440–448.
 50. Wu, J.Z.; Zhou, B.; Hu, Z.B. Phase behavior of thermally responsive microgel colloids. *Phys. Rev. Lett.* **2003**, *90*, art. no. 048304.
 51. Varga, I.; Gilanyi, T.; Meszaros, R.; Filipcsei, G.; Zrinyi, M. Effect of cross-link density on the internal structure of poly(*N*-isopropylacrylamide) microgels. *J. Phys. Chem., B* **2001**, *105*, 9071–9076.
 52. Berli, C.L.A.; Quemada, D. Prediction of the interaction potential of microgel particles from rheometric data. Comparison with different models. *Langmuir* **2000**, *16*, 10509–10514.
 53. Senff, H.; Richtering, W. Influence of cross-link density on rheological properties of temperature-sensitive microgel suspensions. *Colloid Polym. Sci.* **2000**, *278*, 830–840.
 54. Flory, P.J. *Principles of Polymer Chemistry*; Cornell University Press: Ithaca, 1953.
 55. Guillermo, A.; Addad, J.P.C.; Bazile, J.P.; Duracher, D.; Elaissari, A.; Pichot, C. NMR investigations into heterogeneous structures of thermosensitive microgel particles. *J. Polym. Sci., B, Polym. Phys.* **2000**, *38*, 889–898.
 56. Hino, T.; Prausnitz, J.M. Swelling equilibria for heterogeneous polyacrylamide gels. *J. Appl. Polym. Sci.* **1996**, *62*, 1635–1640.
 57. Israelachvili, J.N. *Intermolecular and Surface Forces*, 2nd Ed.; Academic Press: London, 1992.
 58. Gil Villegas, A.; Galindo, A.; Whitehead, P.J.; Mills, S.J.; Jackson, G.; Burgess, A.N. Statistical associating fluid theory for chain molecules with attractive potentials of variable range. *J. Chem. Phys.* **1997**, *106*, 4168–4186.
 59. Hansen, J.P.; McDonald, I.R. *Theory of Simple Liquids*, 2nd Ed.; Academic Press: London, 1986.
 60. Wu, J.Z.; Prausnitz, J. Phase equilibria in a system of “breathing” molecules. *Fluid Phase Equilib.* **2002**, *194*, 689–700.
 61. Hirschfelder, J.D., C.F. Curtis, and R.B. Bird, *Molecular Theory of Gases and Liquids*. Wiley: New York, **1964**.
 62. Hagen, M.H.J.; Frenkel, D. Determination of phase diagrams for the hard-core attractive Yukawa system. *J. Chem. Phys.* **1994**, *101*, 4093–4097.
 63. Lue, L.; Prausnitz, J.M. Renormalization-group corrections to an approximate free-energy model for simple fluids near to and far from the critical region. *J. Chem. Phys.* **1998**, *108*, 5529–5536.
 64. Poon, W.; Pusey, P.; Lekkerkerker, H. Colloids in suspense. *Phys. World* **1996**, *9*, 27–32.
 65. Russel, W.B. On the dynamics of the disorder order transition. *Phase Transit.* **1990**, *21*, 127–137.
 66. Ackerson, B.J.; Schatzel, K. Classical growth of hard-sphere colloidal crystals. *Phys. Rev., E* **1995**, *52*, 6448–6460.
 67. Harland, J.L.; van Meegen, W. Crystallization kinetics of suspensions of hard colloidal spheres. *Phys. Rev., E* **1997**, *55*, 3054–3067.
 68. Schatzel, K.; Ackerson, B.J. Crystallization of hard-sphere colloids. *Phys. Scr., T* **1993**, *49A*, 70–73.
 69. Sinn, C.; Heymann, A.; Stipp, A.; Palberg, T. Measurements in concentrated suspensions: Solidification kinetics of hard-sphere colloidal suspensions. *Prog. Colloid Polym. Sci.* **2001**, *118*, 266–275.
 70. Vanmegen, W.; Underwood, S.M. Glass-transition in colloidal hard-spheres—Mode-coupling theory analysis. *Phys. Rev. Lett.* **1993**, *70*, 2766–2769.
 71. Auer, S.; Frenkel, D. Prediction of absolute crystal-nucleation rate in hard-sphere colloids. *Nature* **2001**, *409*, 1020–1023.

Microweighing in Supercritical Carbon Dioxide

You-Ting Wu
Christine S. Grant

North Carolina State University, Raleigh, North Carolina, U.S.A.

INTRODUCTION

Carbon dioxide (CO₂), when heated and pressurized above its critical temperature (31°C) and pressure (7.377 MPa), is identified as being in a fourth, supercritical state with properties intermediate between liquid and gas (Table 1). At the critical point, the interface of CO₂ liquid and vapor starts to vanish (Fig. 1). Supercritical CO₂ (scCO₂) has liquid-like densities providing good solvent capability, gas-like viscosities, and diffusivities to benefit mass transport, and a nonhazardous nature for the environment. Because of these properties and other advantages of CO₂ over organic solvents such as low surface tension and low cost, scCO₂ has received increasing industrial and research attention in a variety of processes such as extraction,^[3,4] cleaning,^[5,6] polymer synthesis,^[7,8] and more recently microelectronics processing.^[9,10] CO₂ has been proposed to serve as an energy-efficient and environmentally benign solvent platform.^[11] The real-time monitoring of the time-dependent mass change is crucial to understanding, characterizing, designing, and controlling the aforementioned processes. However, this monitoring presents a number of challenges because of the difficulty in applying various detection methods under high-pressure conditions.

In this chapter, two microweighing techniques in sc CO₂, gravimetric and piezoelectric, are reviewed. A comparison is made between two representatives of these techniques: the magnetic suspension balance (gravimetric) and the quartz crystal microbalance (QCM, piezoelectric). The QCM theory in high-pressure fluids is briefly introduced, followed by a summary of recent research which includes 1) the experimental verification of QCM theory; 2) the scCO₂ adsorption on metal surfaces; and 3) the dissolution of polymer films for applications in scCO₂-based lithography processes. Finally, the application of QCM in absorption, solubility, and other surface-specific processes in scCO₂ will be reviewed to highlight the versatility of the QCM technique.

MICROWEIGHING TECHNIQUES: GRAVIMETRIC AND PIEZOELECTRIC

Many important physical and chemical processes can be monitored by observing the associated mass changes. Currently, two microweighing techniques, gravimetric and piezoelectric, have been widely used as an analytical tool for research and applied applications. Gravimetric microbalances are the most direct technique to measure mass variations at the microgram level. However, in a number of cases, most conventional gravimetric microbalances such as spring, beam, and torsional balances are not designed for the operation under extreme conditions. The extreme conditions are usually defined as conditions of high pressures (>1450 psi), viscous fluids, and/or high temperatures. In order to adapt the conventional gravimetric balances to work under extreme pressures, some researchers^[12,13] have designed a high-pressure container to include both the microbalance and the sample. This not only greatly increases the system expenses, structural complexity, and operational difficulties, but also sacrifices the capability under high temperatures (>125°C) because of the microbalance working conditions. Jwayyed et al.^[13] modified a commercial high-pressure microbalance (Cahn C-1000 balance) by redesigning the container (nipple shape with 30 cm o.d. and 25 cm height) for use in scCO₂. They were only able to extend the pressure limit from 1600 to 3000 psi.

In recent years, some researchers^[14,15] have been able to design a unique balance, a magnetic suspension balance (MSB), for mass measurements under extreme conditions (>3000 psi). The MSB takes advantage of the principle of magnetic coupling to isolate the balance from the sample that is contained in a small pressure cell (Fig. 2), while maintaining most features of the traditional microbalances. Using this magnetic suspension coupling, the measured force is transmitted from the pressure cell to the microbalance that is located in the ambient environment. Such novel design eliminates the large container, enables the capability of mass determinations under

Table 1 Physical properties of gas, liquid, and supercritical fluid (order of magnitude)

	Density (g/cm ³)	Diffusivity (cm ² /sec)	Viscosity (g/cm/sec)
Gas	1×10^{-3}	1×10^{-1}	1×10^{-4}
Liquid	1.0	5×10^{-6}	1×10^{-2}
Supercritical fluid	3×10^{-1}	1×10^{-3}	1×10^{-4}

Source: From Ref. [5], with permission of William Andrew Publishing.

extreme conditions, and makes realistic applications of gravimetric techniques in CO₂-based processes. The MSB has primarily been applied to determine the adsorption/absorption and diffusivity of scCO₂ in addition to other solutes on/in bulk solid materials under static conditions.^[16–22] Applications of MSB for other chemical processes and applications under dynamic (flowing) conditions are rarely found in the literature.

Piezoelectric quartz crystal resonators take advantage of the electric polarization that occurs when the crystal is subjected to a mechanical stress.^[23] Several different devices operate using the piezoelectric technique according to the modes of electromechanical coupling, such as modes of thickness shear, face shear, and surface acoustic wave.^[24] The AT-cut thickness-shear mode resonator, commonly referred to QCM, is the most widely used piezoelectric mass sensor.^[25] The QCM consists of a thin quartz disk with two metal electrodes plated on its two opposite surfaces (Fig. 3). The QCM is a powerful microweighing tool for detecting in situ the mass changes to the ng/cm² level of sensitivity. In the last decade, there has been increased application of the QCM for studies of a wide range of chemical processes and chemistries on surfaces and in thin films.^[23–29] There are few difficulties for QCM applications under extreme conditions, because of the rigidity and chemical inertness of the quartz crystals and the elimination of any connection except the supply of electricity. Rigid electrical leads are commonly used to hold the crystal in place and excite the sensor that is contained in the pressure cell (Fig. 4). The QCM has been applied to many scCO₂-based processes and chemistries in bulk phases or at surface films; they will be summarized later in the following sections.

Table 2 summarizes a comparison of the performance of MSB with QCM for the microweighing in scCO₂. As can be seen, the QCM is a more powerful and versatile microweighing tool in scCO₂ than the MSB, mainly owing to its low cost, conceptual simplicity, high mass sensitivity, wide range of applications, rapid time response, and miniature and simple construction. In particular, the nanogram-level sensitivity enables the QCM as a possible technique that can be utilized to study interfacial processes related to nanotechnologies and nanomaterials.

QUARTZ CRYSTAL MICROBALANCE THEORY IN HIGH-PRESSURE FLUIDS

Fundamentals

As the QCM is piezoelectric, an external electrical potential applied across the electrodes produces internal mechanical stress. This stress induces an acoustic wave that propagates through the crystal and meets minimum impedance when the thickness of the crystal is a multiple of a half wavelength of the acoustic wave. A resonant oscillation is achieved by including the crystal into an oscillation circuit in which the electric and the mechanical oscillation are close to the fundamental frequency (F_0) of the crystal.^[25,26]

When a crystal is immersed in a fluid, any frequency shift from its fundamental value (F_0) in vacuum can be observed because of contributions from 1) mass sorption or desorption from the crystal surface; 2) pressure; 3) density and viscosity of the fluid surrounding the crystal; and 4) surface roughness of the crystal. The following expression has been established to describe changes in the crystal frequency, ΔF , due to the aforementioned effects:^[30]

$$\Delta F = F - F_0 = \Delta F_m + \Delta F_p + \Delta F_n + \Delta F_r \quad (1)$$

where F is the measured frequency of quartz, ΔF_m relates to mass loading, ΔF_p is dependent on pressure, ΔF_n

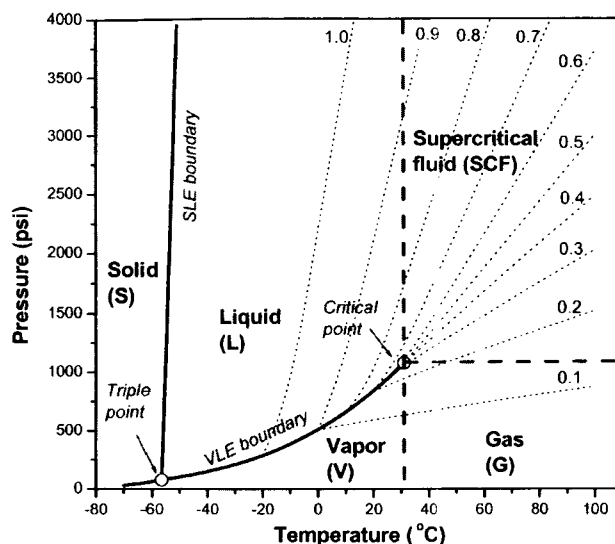


Fig. 1 Phase diagram for CO₂ with constant density lines (dot lines, g/cm³). Above the critical point (31°C and 1070 psi), the vapor–liquid equilibrium (VLE) boundary vanishes, and the supercritical state is observed. The dash lines do not represent a boundary, but for the convenience to distinguish different states of CO₂. (View this art in color at www.dekker.com.)

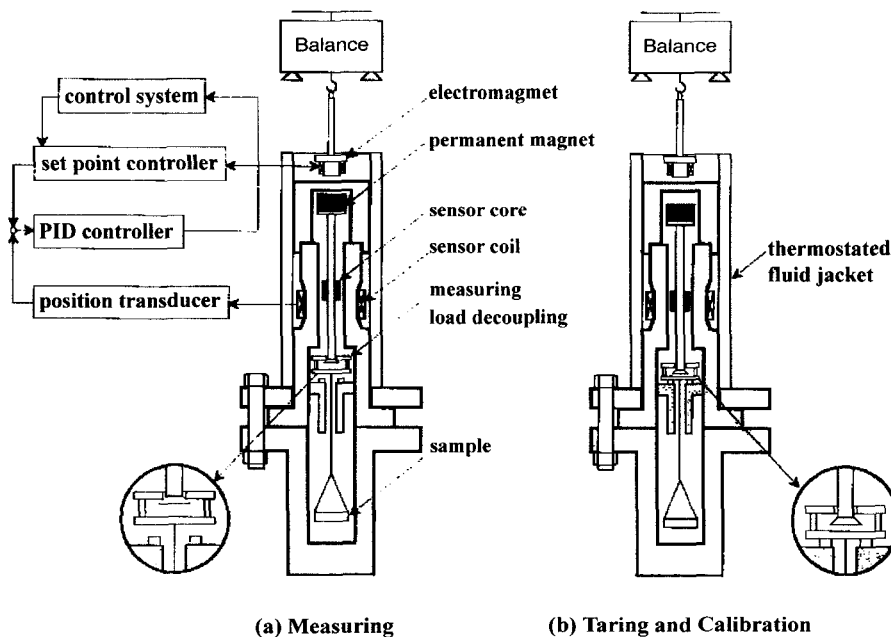


Fig. 2 A typical magnetic suspension balance (MSB). (From Ref. [21].)

changes with density and viscosity, and ΔF_r is a function of surface roughness.

According to the well-known Sauerbrey equation,^[31] ΔF_m is directly proportional to the mass loading on the crystal:

$$\Delta F_m = -2nF_0^2 \Delta m / (\mu_q \rho_q)^{1/2} = -C_m \Delta m \quad (2)$$

where μ_q is the shear modulus of quartz, ρ_q is the density of the crystal, Δm is the film mass per real surface area, n is the number of faces of the crystal exposed, and C_m is the mass sensitivity of QCM, which is a function of the characteristic properties (F_0 , μ_q , and ρ_q) of the quartz crystal. Eq. 2 applies only if the adsorbed mass is much less than the mass of the crystal and it assumes this mass is firmly attached to the surface; hence the material moves together with the crystal. Such conditions are assumed to be fulfilled in cases of coated solid films and self-assembled monolayers.

The pressure dependence of frequency, ΔF_p , increases with increasing pressure linearly, as shown by Stockbridge^[32] for gases up to 15 psi. Susse^[33] described a similar relationship for liquids up to 1.5×10^4 psi. Thus ΔF_p can be written as:

$$\Delta F_p = F_0 \alpha P = C_p P \quad (3)$$

where α is the proportionality constant and C_p is the pressure sensitivity of QCM crystal, both of which are independent of the type of fluid in contact with the crystal.

The viscosity and density contribution, ΔF_η , describes the interaction of the vibrating crystal with a Newtonian viscous fluid. The interaction leads to an additional

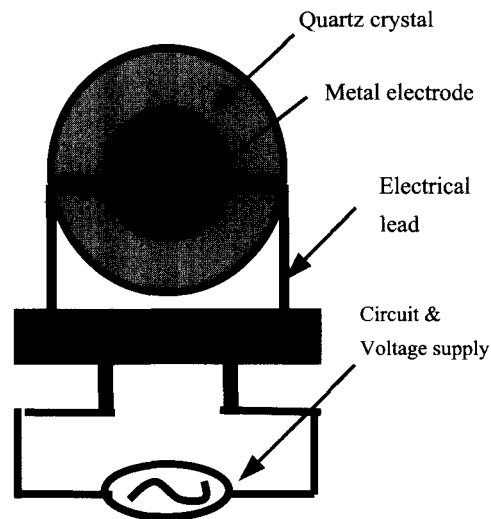


Fig. 3 Schematic view of a piezoelectric QCM crystal (only one side shown). A typical 5-MHz QCM from International Crystal Manufacturing consists of a thin quartz crystal (0.85 cm diameter) sputtered with a metal electrode (0.35 cm diameter) on each side. Both sides should be exposed to $scCO_2$ because of high pressure. (View this art in color at www.dekker.com.)

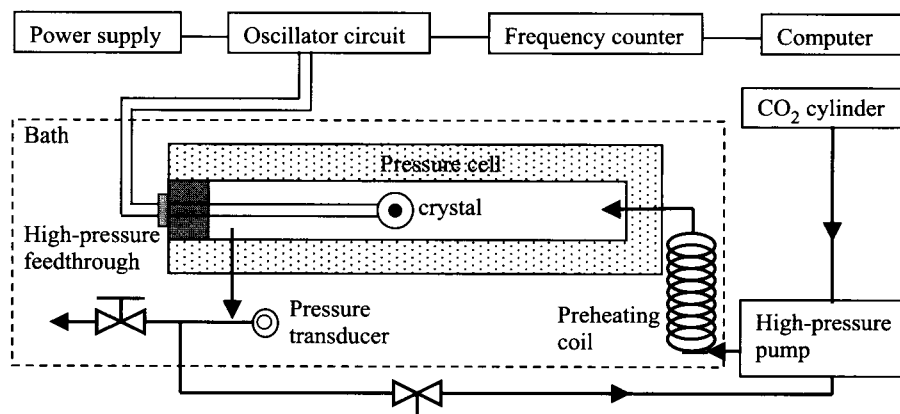


Fig. 4 Schematic view of an experimental setup of QCM measurement system in scCO₂. (From Ref. [50].)

loading of the crystal, causing a decrease in frequency. ΔF_η is expressed to be proportional to the square root of the product of viscosity and density of the surrounding fluid:^[32,34,35]

$$\Delta F_\eta = -0.5C_m(\pi F_0)^{-1/2}(\rho_f \eta_f)^{1/2} \quad (4)$$

where ρ_f and η_f are the absolute density and viscosity of the fluid, respectively.

Roughness Effect

A common feature of the approaches to QCM theory as reviewed by Thompson et al.^[27] is the neglect of microscopic properties of interfaces and surface roughness.^[36] This leads to deviations of most experimental frequency shift data from the predictions by these approaches. Buttry and Ward^[23] and Schumacher et al.^[37]

observed that up to 80% of the observed frequency shifts for a crystal in contact with a liquid could be attributed to roughness effects.

As the microscopic properties of crystal–fluid interfaces change with the surface morphology, a predictive analytical expression for the roughness contribution to frequency, ΔF_r , is not available. Urbakh and Dai-kin^[36,38,39] formulated a model for surface roughness, assuming that a rough surface can be characterized by the average height (h), lateral length (a), and distance (l) between the inhomogeneities of the surface (Fig. 5). They incorporated this model into a framework of perturbation theory^[36,38] and derived a general relationship for ΔF_r as:

$$\Delta F_r = -0.5C_m(\pi F_0)^{-1/2}(\rho_f \eta_f)^{1/2} \Psi(a, \delta, a/l, h/a) \quad (5)$$

where Ψ is a scaling function, related to three dimensionless factors, a/δ , a/L , and h/a ; δ is the decay length of

Table 2 Comparison of two microweighing methods

Characteristics	Gravimetric: MSB ^[21]	Piezoelectric: QCM ^[24]
Mass sensitivity	10^{-5} – 10^{-6} g ^[13]	$< 10^{-9}$ g
Time resolution of response	5×10^{-2} sec ^[13] (need fine damping control system)	$< 10^{-3}$ sec
Measuring variables	Gravity	Frequency and/or impedance
Calculations	Simple	Simple
Construction	Complex, especially the designing of the magnetic coupling and fine damping control system	Very simple
Size	Medium size when comparing with the QCM	Miniature size (0.5–2.5 cm diameter)
Calibration	Required to correct buoyancy	Not necessary ^[25]
Cost	Expensive	Cheap ($< \$30$ a QCM crystal) ^a
Operation conditions	Mainly static; ^[13] extreme conditions	Both static and dynamic; extreme conditions
Applications	Mainly for processes and chemistries in bulk phases	For processes and chemistries both in bulk phases and at thin films

^aPrice information was obtained from International Crystal Manufacturing.

fluid velocities,

$$\delta = [\eta_f / (\pi F_0 \rho_f)]^{1/2} \quad (6)$$

In particular, if one assumes a slowly varying roughness ($h/a \ll 1$ and $h/\delta \ll 1$) for the crystal surface with a limit of $a/\delta \ll 1$ or $a/\delta \gg 1$, the scaling function Ψ is proportional to the ratio a/δ .^[36] Reformulating Eq. 5 yields:

$$\Delta F_r = -0.5 C_m C_r \rho_f \quad (7)$$

where $C_r = \Psi \delta$ is defined as the frequency-roughness correlation factor. This factor is only a function of surface roughness (h and a), provided that the assumptions above are fully established. Otherwise, C_r should be additionally viewed as a weak function of δ .

EXPERIMENTAL EXAMINATION OF QUARTZ CRYSTAL MICROBALANCE THEORY AND ADSORPTION OF CO₂ ON METAL SURFACES

As the frequency of a QCM crystal exposed to a high-pressure fluid is affected by different factors, it is critical to accurately separate out each influencing factor. Experimental verification of QCM theory enables the calculation of the actual mass change on the crystal surface. The investigation of CO₂ adsorption on metal electrodes of blank crystals is a required initial step for the successful use of the QCM technique to investigate the chemical and physical properties of surface films in scCO₂.

Separation of Contributions to Frequency

As the microscopic properties of crystal-fluid interfaces complicate the QCM frequency behavior, a unique strategy^[40] to verify the QCM theory in scCO₂ is to experimentally establish a relationship between the microscopic properties of crystal surfaces and frequency

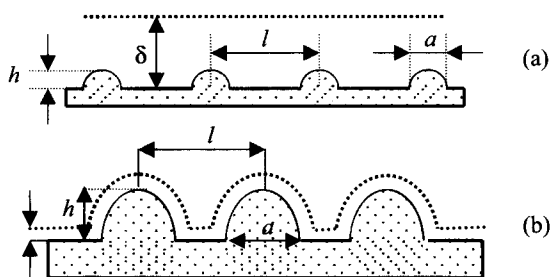


Fig. 5 Two types of ideal surface roughness. (a) Slightly rough, $h/\delta \ll 1$; (b) strongly rough, $h/\delta \gg 1$. (From Ref. [40].)

shifts. In a study reported here, the surface roughness of QCM crystals (three gold and three silver 5-MHz crystals; Table 3) was characterized using an AFM technique. Three groups of QCM experiments were performed on the six crystals to separate the following different contributions to QCM frequency: ΔF_p , ΔF_m , ΔF_η , and ΔF_r . The first set of experiments performed on Ag-polished and Ag-rough crystals utilized helium, the lightest inert gas considered nonabsorbing ($\Delta F_m=0$) on metals, to determine ΔF_p and ΔF_η . To evaluate the roughness contribution of frequency, ΔF_r , the second set of experiments utilized N₂, another nonabsorbing gas on the metal surfaces at room temperatures (i.e., ΔF_m negligibly small). The last group of experiments was conducted using low-density gaseous CO₂ ($<0.2 \text{ g cm}^{-3}$), an adsorbing gas at room temperatures, to test the adsorbed masses of CO₂ on the metal surfaces.

The first set of experiments in helium indicated that the frequency shifts of the smoothest silver crystal (Ag-polished) could be accurately predicted with the QCM theory for pressure and viscosity (Eqs. 3 and 4) by neglecting the roughness effect. However, for the roughest silver crystal (Ag-rough), about 10% of the total frequency shifts could not be theoretically predicted with Eqs. 3 and 4. The variations in the prediction were attributed to the roughness effect. This is consistent with the experimental findings by Tsionsky et al.^[30] who investigated frequency shifts of gold and nickel crystals in He, H₂, Ar, and N₂.

The second set of experiments in nitrogen showed that the roughness effect had a significant influence on the frequency even for the smoothest silver and gold crystals. The experimental roughness contribution, ΔF_r , was calculated by subtracting theoretical ΔF_p and ΔF_η from the experimental ΔF (Eq. 1). The resulting ΔF_r was plotted as a function of theoretical N₂ density; the corresponding frequency shift corrected in this manner was found to be a nearly linear function of density, indicating the precision of the theoretical expression of ΔF_r (Eq. 7). Therefore the frequency-roughness correlation factor, C_r , can be obtained by correlating ΔF_r with the N₂ density (ρ_f) or the decay length (δ), using Eqs. 8a and 8b,

$$C_r = a_1(1 + b_1 \rho_f) \quad (8a)$$

$$C_r = a_2 + b_2 \delta \quad (8b)$$

where a and b are the constants assumed to be independent of the type of fluid. The values of a and b for each crystal are also shown in Table 3. Eqs. 8a and 8b represent accurate predictions of C_r with most correlation coefficients better than 0.999. Eq. 8a is only applicable to gases because of the neglect of the influence of viscosity, while

M

Table 3 Some characteristic properties of six different QCM crystals

Crystals	RMS roughness ^a (10 ⁻⁷ cm)	H (10 ⁻⁷ cm)	a (10 ⁻⁷ cm)	l (10 ⁻⁷ cm)	C _r (10 ⁻⁵ cm) ^b	
					Eq. 8a	Eq. 8b
Ag-polished	3.7	12	180	190	1.32(1-2.65ρ _f)	0.398+4.96 × 10 ⁴ δ
Ag-unpolished	26	85	1410	2180	1.79(1-3.48ρ _f)	0.322+7.44 × 10 ⁴ δ
Ag-rough ^c	647	1030	-	-	7.28(1-1.27ρ _f)	5.16+1.05 × 10 ⁵ δ
Au-polished	2.8	8	110	120	1.37(1-2.23ρ _f)	0.595+4.10 × 10 ⁴ δ
Au-unpolished	115	210	1370	2120	3.22(1-2.37ρ _f)	1.41+9.17 × 10 ⁴ δ
Au-rough ^c	681	1090	-	-	6.88(1-1.51ρ _f)	3.99+1.63 × 10 ⁵ δ

^aThe rms roughness is defined as the root mean square (or standard deviation) of the Z values within a given AFM image area with respect to the average Z value.

^bThe units for ρ_f and δ are g/cm³ and cm, respectively.

^cLack of data for a and l because of no apparent periodic inhomogeneities in the AFM images of the strongly rough crystals.

Source: From Ref. [40].

Eq. 8a is suitable for dense gases (ρ_f>0.2 g/cm³) and liquids.^[40] C_r was found to be dependent primarily on the rms roughness of crystals and, to a lesser degree, on a and l.^[40]

In the last group of experiments, the frequency shifts (ΔF) of all six crystals in gaseous CO₂ (pressure <1000 psi) were measured to evaluate the amount of CO₂ adsorbed on the metal surfaces. The CO₂ adsorption was calculated from ΔF_m that was obtained by subtracting the theoretical ΔF_p, ΔF_η, and ΔF_r from ΔF, using Eqs. 1 to 4, 7, and 8a. As can be seen (Fig. 6), all six crystals with different surface roughness values adsorbed similar amounts of gaseous CO₂ per real surface area, which agrees well with the adsorption theory. This is additional evidence of the accuracy of the reformulated QCM theory by including the roughness contribution. It also implies that the a and b values obtained in N₂ are independent of the type of fluid.

Adsorption of Supercritical CO₂ on Metal Surfaces

Several researchers have determined the mechanisms of adsorption of scCO₂ on metal surfaces. Otake et al.^[41] determined the mass of CO₂ adsorbed onto rough silver QCM electrodes at 40°C and at pressures up to 5800 psi. They concluded that scCO₂ mass adsorption on metal surfaces could approach values as high as 25 μg/cm². Guigard et al.^[42] evaluated the adsorption of CO₂ on rough gold electrodes at 40°C and 45°C and at pressures up to 1500 psi. They found the similar maximum amount of CO₂ adsorption as by Otake et al. However, these researchers all neglected the roughness contribution to frequency in the calculation. In order to fully account for the roughness contribution, the Wu research group

examined in greater detail the scCO₂ adsorption on metal surfaces.^[40]

The frequency shifts of Ag-polished and Ag-rough crystals (Fig. 7) in scCO₂ were measured to evaluate the amount of CO₂ adsorbed on the surfaces (Fig. 8). The calculation procedure is the same as in the gaseous CO₂. As the CO₂ density and the amount of adsorbed CO₂ increase with increasing pressure, the holes and valleys between the inhomogeneities on the crystal surface are gradually filled (Fig. 8, inset), which causes a gradual decrease of surface roughness.^[36] Therefore C_r was corrected for the overestimation of the roughness

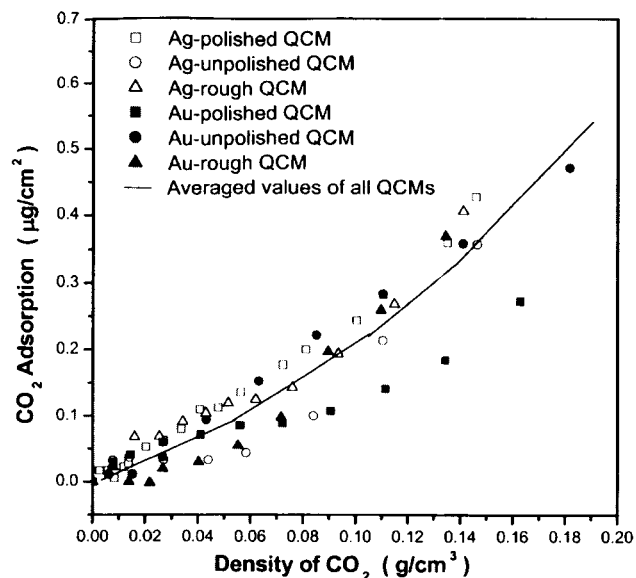


Fig. 6 Adsorption of gaseous CO₂ on silver and gold surfaces at 40°C, using the C_r values calculated with Eq. 8b. (From Ref. [40].) (View this art in color at www.dekker.com.)

contribution,^[40]

$$C_r = (a_2 + b_2\delta)\xi/\xi_0 \quad (8c)$$

where ξ and ξ_0 are the roughness in centimeters of the original substrate surface and the modified surface by the absorbed molecules, respectively. ξ is a function of thickness (or mass) of absorbed molecular layers. Analysis showed that it was appropriate to predict scCO₂ adsorption on the Ag-polished crystal by neglecting the roughness contribution ($C_r=0$ or $\xi=0$), when the density was larger than 0.4 g cm⁻³ (Fig. 8). This was because the quantity (2.4 μg/cm²) of CO₂ mass absorbed at the density of 0.4 g cm⁻³ could smooth the surface of Ag-polished crystal.^[40]

For the Ag-rough crystal, calculation showed that the two limits of $\xi/\xi_0=1.0$ and 0.75 could fit the adsorption data of the Ag-polished crystal well in the regions of low and high densities (<0.4 and >0.7 g/cm³; Fig. 8). It was concluded that the use of rough QCM crystals (rms roughness >10 nm) required careful attention in scCO₂ adsorption studies, because of the variation of C_r .^[40] Only very smooth QCM crystals (several nanometers or less) are capable of accurately determining the adsorption of scCO₂ on the metal surfaces without considering the surface roughness contribution. The adsorption of scCO₂ on the silver and gold surfaces at 40°C ranges to 3.6 μg/cm², but not up to 25 μg/cm² as determined by Otake et al.^[41] and Guigard et al.^[42] who used very rough crystals and neglected the roughness contribution.

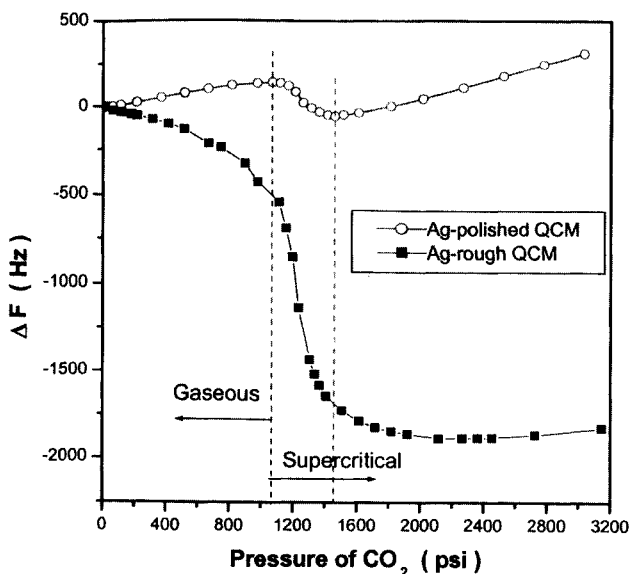


Fig. 7 Frequency shift of Ag-polished and Ag-rough crystals in gaseous and scCO₂ at 40°C as a function of pressure. (From Ref. [40].) (View this art in color at www.dekker.com.)

APPLICATIONS OF QUARTZ CRYSTAL MICROBALANCE FOR DISSOLUTION STUDY OF POLYMER FILMS IN SUPERCRITICAL CO₂

Polymer dissolution (or polymer desorption) in solvents is an important phenomena in polymer science and engineering. Applications of polymer dissolution or desorption are found in several areas such as microlithography, controlled drug delivery, and plastics recycling.^[43] For example, the successful implementation of a microlithography process requires technical information on the dissolution of photoresist polymer films in specific solvents during 1) the development of the resist images and 2) the stripping of the remaining films after the lithography process.^[44] Hinsberg et al.^[45,46] and Ito^[47] applied the QCM techniques to determine the dissolution rate of novolac and poly(4-hydroxystyrene) films in aqueous developer solutions at atmospheric pressure. Mueller et al.^[48] have used the QCM to investigate the diffusivity of casting organic solvents in photoresist films for the evaluation of the influence of the solvents on the polymer dissolution behavior. These researchers demonstrated that the QCM technique was a particular attractive tool for the evaluation of the dissolution of polymer films in organic and aqueous solutions.

The dissolution kinetics of polymer films in scCO₂ provides useful technical information for the development of scCO₂-based interfacial processes that require excellent control of surface properties (e.g., thickness and morphology) at the micro- and nanometer scales. The recently proposed surface processing of microelectronics in scCO₂^[9] is a typical field that requires information on polymer film dissolution. However, a search of the literature in this specific area revealed that there have been a very limited number of studies on the polymer dissolution kinetics in scCO₂ by the use of QCM technique. To date, the number of dissolution studies of polymer films in scCO₂ by other online techniques, e.g., interferometry,^[49] is also limited. This is probably due to the lack of various detection techniques at extreme conditions and to the situation of such scCO₂-based processes being in the stages of early development. Nevertheless, Wu and Grant^[50] have utilized the QCM for the evaluation of polymer film dissolution in scCO₂.

Based on the availability and applicability of the reformulated QCM theory in scCO₂, the dissolution study of polymer films in scCO₂ was achieved utilizing the experimental high-pressure QCM apparatus (Fig. 4). Fig. 9 represents a typical experimental run using a Si-polished QCM crystal to evaluate the dissolution kinetics of poly(FOMA-r-THPMA) films (low MW polymer) at 60°C and 2400 psi. The fundamental frequency (F_0 ; Fig. 9) of the

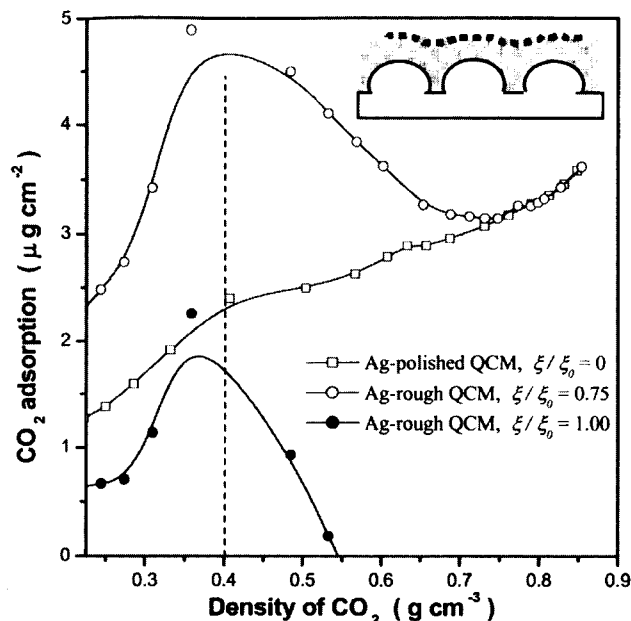


Fig. 8 Adsorption of scCO_2 at 40°C on Ag-polished and Ag-rough QCM crystals. The inset on the upper right corner demonstrates how the adsorbed mass may alter the surface morphology. (From Ref. [40].) (View this art in color at www.dekker.com.)

blank crystal was determined in vacuum ($P=0$ psi). The crystal was removed from the vessel and the polymer film was cast onto the crystal by dip-coating in an 8 wt.% polymer-trifluorotoluene solution. After drying the film in vacuum for 30 min the stable frequency (F_1 ; Fig. 9) of the coated crystal was measured. The total polymer mass (m_0) coated on the crystal corresponded to the frequency difference of ($F_1 - F_0$). CO_2 was gradually pumped into the vessel via steep changes in pressure (see abrupt steep changes in frequency curve in Fig. 9) and the frequency data ($F_{2,i}$, $i=1$ to 4) were continually recorded. As the polymer was insoluble at pressures lower than 1700 psi at 60°C , this set of frequency data at elevated pressures were used to evaluate the swelling (or CO_2 absorption) of film and CO_2 diffusivity in the polymer film. After the frequency of the crystal became stable at the last steep change in pressure ($P=1520$ psi), the CO_2 pressure was instantaneously raised to the required experimental pressure (2400 psi) by adding more CO_2 into the vessel. The QCM frequency went through a minimum value (F_3) and increased rapidly, indicating the removal of polymer film from the crystal surface. The minimum frequency is the point at which CO_2 absorption (film swelling) and film dissolution are balanced. Therefore in the example presented here, the dissolution of polymer film in scCO_2 consists of two steps: 1) absorption-dominating and 2) dissolution-dominating. After the polymer film dissolved in scCO_2 at 2400 psi and 60°C for 10 min, the CO_2 in the

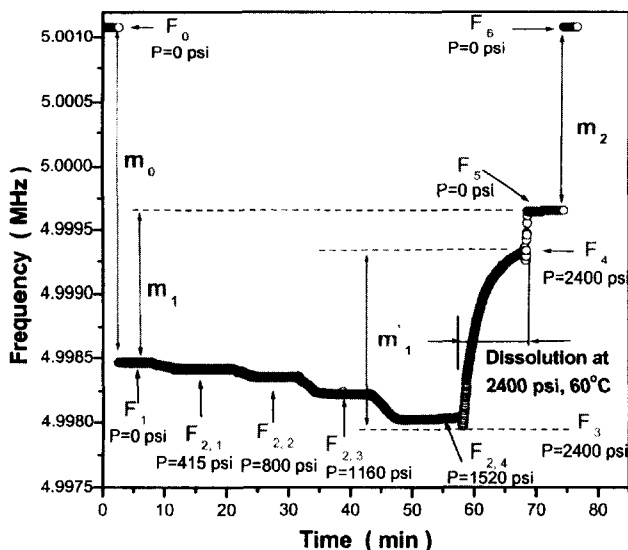
vessel was rapidly released and the QCM frequency (F_5) was measured again in vacuum. The remaining polymer film was removed by dissolution in pure trifluorotoluene (TFT), and excess TFT was dried off in vacuum. The original fundamental frequency ($F_6 = F_0$) of the crystal was recovered, indicating complete polymer removal. On the polymer dissolution graph, the line from F_3 to F_4 represents the dissolution curve that can be used to evaluate the kinetics. Wu and Grant^[50] have evaluated the dissolution kinetics of poly(FOMA-r-THPMA) films under the conditions that will be required for static film-developing and stripping in the microelectronics processing. Studies are currently underway to evaluate the dissolution kinetics of polymer films in a flowing scCO_2 environment.

ADDITIONAL QUARTZ CRYSTAL MICROBALANCE APPLICATIONS IN SUPERCRITICAL CO_2

Absorption of Supercritical CO_2 and Other Analytes in Solid Films

The absorption and solubility of scCO_2 or other analytes in solid films are important properties that can be used to understand many scCO_2 -based processes and chemistries. The swelling of polymer films in scCO_2 is a typical example of absorption processes. The QCM determination of absorption is realized by modification of the QCM surface with a coating that can interact with a desired analyte in a way that the mass and thickness of the coating are increased (Fig. 10A). To date, researchers^[51-53] have successfully used the QCM technique to investigate the absorption of scCO_2 in polymers at elevated pressures with high performance. There are a limited number of QCM studies on the absorption of an analyte other than CO_2 into a solid film, where both the analyte and the solid film are contained in a scCO_2 environment.

Interestingly, based on the QCM, some dual techniques have been developed to measure other absorption-relevant physical properties. Hattori et al.^[54,55] combined vapor-liquid partition chromatography with a piezoelectric QCM to measure vapor-liquid equilibrium (VLE) ratios of benzene and toluene at an infinite dilution state in a scCO_2 -poly(vinyl acetate) system. The QCM indicated the solubility of organic solutes in the polymer phase while the chromatography analyzed the concentrations of solutes in the scCO_2 phase. Good VLE data were obtained with this dual technique. Nakamura et al.^[56] reported the determination of adsorption isotherms of scCO_2 on several proteins and polysaccharides by a combination of two different microbalances, gravimetric and piezoelectric. The QCM was used to measure the absorption of CO_2 into the proteins and polysaccharides; the absolute adsorption



Symbol	ΔF	Note
m_0	$F_1 - F_0$	Polymer mass initially coated
m_1	$F_5 - F_1$	Polymer mass removed
m_1	$F_4 - F_3$	Mass change during dissolution
m_2	$F_6 - F_5$	Polymer mass not removed during dissolution
—	$F_{2,i} - F_1$	CO ₂ adsorption during step-pressurizing
—	$F_5 - F_4$	CO ₂ desorption during the release of CO ₂

Fig. 9 A typical experimental QCM determination for the dissolution of poly(FOMA-r-THPMA) film in scCO₂ at 2400 psi and 60°C under static conditions. Detailed explanation in the text. (From Ref. [50].) (View this art in color at www.dekker.com.)

could be accurately calculated from the gravimetric data by subtracting the absorption contribution.

Precision Cleaning and Dissolution Using Supercritical CO₂

The QCM determination in cleaning and dissolution processes typically involves the partial or complete removal of a film or coating from the QCM surface by a liquid, gas, or a fluid in the supercritical state (Fig. 10B). Precision cleaning and precision decontamination can be defined as processes that result in a surface contaminant level of less than 10 $\mu\text{g}/\text{cm}^2$.^[57] However, most precision cleaning processes require a contaminant level of less than 1 $\mu\text{g}/\text{cm}^2$.^[58] A majority of recently developed scCO₂-based precision cleaning processes are found in the

microelectronic industry. Some typical examples are 1) the decontamination of micromechanical devices;^[59] 2) the initial removal of impurities such as organic soils and fingerprints from silicon wafers; 3) the stripping of resists from metallized silicon surfaces without damaging thin metallization patterns;^[60] and 4) the direct development of resist films.^[10,61] More recently, the scCO₂-drying of organic or aqueous rinse liquids from micro-electro-mechanical systems (MEMS) or other silicon structures were proposed to prevent the collapse of the fine features on the surfaces.^[62,63] The QCM is capable of monitoring the mass changes in all these CO₂-based precision-cleaning processes at the nanogram scale.

Solubility of Chemicals in Supercritical CO₂

A thermodynamic property that is essential to any application of supercritical fluids is chemical solubility. The application of the QCM in the determination of solubility (Fig. 10B) is, in principle, very close to the approach used for cleaning and dissolution studies. A critical difference is the amount of time required for the attainment of phase equilibrium. The QCM method is ideally suited for solutes that exhibit low solubility, or for measurements conducted at low scCO₂ densities, a condition in which many solutes have low solubility. This is because the QCM theory (Eq. 2) is considered accurate provided the mass of a coating does not exceed 2% of the crystal mass.^[23] Guigard et al.^[42] have applied the QCM technique to determine the solubilities of two metal chelates, bis(acetylacetonato) copper and bis(thenoyltrifluoro-acetonato) copper, in scCO₂ and described the methodology in detail. They found that the solubilities measured by the QCM were in excellent agreement with the four sets of literature values obtained using other techniques, with a standard deviation of 25%.^[42] This level of discrepancy is actually encouraging because of the extreme low solubility values on the order of 10⁻⁵ mole fraction. Besides metal chelates, the QCM method can be extended to determine the solubilities of natural products (e.g., herbal medicines), photoresists, polymers, fats, biomaterials, and many other chemicals of interest for CO₂-based processes. This is especially true in cases in which the traditional detection methodologies (e.g., spectroscopic techniques) are limited due to either their low sensitivity or the complexity of the associated apparatuses under extreme pressure conditions.

Molecular Recognition in Supercritical CO₂

Molecular recognition is of interest for biological processes because most biomolecules show selectivity and specificity when interacting with other species. This particular microweighing methodology involves either



directly coating host molecules (insoluble in $scCO_2$) on the surface of a QCM crystal (Fig. 10A) or modifying the surface with a self-assembled monolayer (SAM) (Fig. 10D). The SAM can be formed using thiols or other chain-like molecules that have two active groups at the two ends of the chain. The $-SH$ group of the thiol or one end of the chain-like molecule is attached to the QCM surface, while the $-OH$ group or the other end is grafted with the receptor molecule. When guest or donor molecules are supplied into the vessel together with CO_2 , they are bonded to the host or receptor molecules via molecular interactions, resulting in a mass increase of the coating. Naito et al.^[64,65] successfully demonstrated two examples of molecular recognitions in $scCO_2$ using the QCM technique. In the first system, ethyl acetate and ethanol were selectively bound to anthracene-bis(resorcinol)tetraol that was coated on the crystal surfaces. In the second situation, nucleobases such as 9-ethyladenine and 2-pyrrolidone were recognized at different extents by thymine that was immobilized on the thiol-modified QCM surfaces. The equilibrium constants and the associated kinetics of molecular binding were easily obtained by the use of the QCM technique.

Evaluation of Deposition in Supercritical CO_2

Chemicals either previously dissolved in the $scCO_2$ phase or produced via reactions of other CO_2 -soluble chemicals may deposit onto surfaces, due to solubility variations with temperature and pressure or the insoluble characteristics. The dynamic mass of deposited surface films can be detected in situ using the QCM method (Fig. 10C). For example, the QCM technique can be directly used to evaluate the deposition of metals (e.g., copper and nickel) on silicon wafers.^[66] The metals were generated via the hydrogen reduction of organometallic compounds that are dissolved in a $scCO_2$ carrier. This deposition process was named as chemical fluid deposition (CFD), and the deposition of metals on pattern features less than 100 nm wide has been demonstrated using such CFD technique.^[66]

Polymer Foaming in Supercritical CO_2

In recent years, $scCO_2$ -based polymer foaming has been of particular importance in the production of low dielectric films in electronics manufacturing and tissue engineering scaffolds for biological purposes.^[67] Upon removal of the $scCO_2$ phase, the absorbed CO_2 is released from swollen polymer networks, resulting in free-standing porous foams. The foams have cell diameters of less than 1 μm and the process accomplishes density reductions of

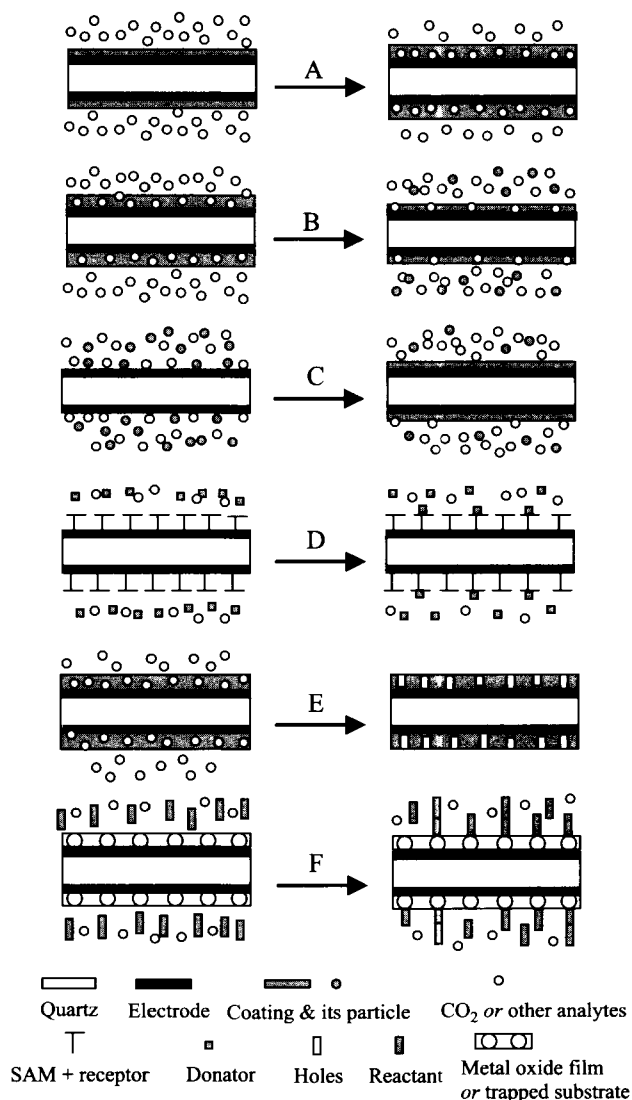


Fig. 10 Schematic representations of some typical $scCO_2$ -based processes or chemistries that can be investigated using the QCM. (A) Absorption or molecular recognition; (B) cleaning, developing, stripping, drying, dissolution, or solubility in $scCO_2$; (C) deposition; (D) molecular recognition; (E) foaming; (F) surface reaction, or polymerization.

97% relative to the parent polymers.^[68] Quartz crystal microbalance can act as a useful tool for detecting the dynamic mass changes associated with such foaming processes (Fig. 10E). The dynamic mass changes can be correlated with the structure and morphology of the foams by evaluation using microscopic techniques, such as SEM and AFM. The combination of the QCM microweighing with the microscopic techniques can provide a comprehensive understanding of the foaming processes.

Surface Reactions in Supercritical CO₂

Reactions or polymerizations on metal oxide surfaces or other surfaces immobilized with active groups can be followed by detecting the mass increase on the surfaces with the QCM technique (Fig. 10F). When treated with acids, the metal oxide surfaces provide OH active groups to promote immobilization. The silylation of native oxide silicon surfaces in the preparation of coating for hydrophobic photoresists^[69] is a typical example of surface reactions in scCO₂. Supercritical CO₂ has been utilized as a carrier of silane reagents, thereby reducing the consumption of chemicals and improving the rate of surface coverage.

CONCLUSION

Two techniques, MSB and QCM, have been developed primarily as microweighing tools for wide use under extreme conditions. In the literature, the MSB has been utilized mainly for the determination of adsorption/absorption and diffusivity of scCO₂ in bulk polymers under static conditions. When compared to the MSB technique, the QCM has found a wider range of applications for many scCO₂-based static or dynamic processes both in the bulk phase and at the surface film. This is primarily because of the intrinsic attributes of the QCM approach, such as the nanogram-level mass sensitivity, millisecond-level time resolution, miniature and simple construction, and low cost. The QCM can be successfully developed into a submicroweighing tool in scCO₂ by the careful examination of the QCM theory in high-pressure fluids. Although the QCM has applications in various CO₂-based processes and chemistries, such as dissolution, solubility, adsorption/absorption, and molecular recognition, the reported efforts and application areas in the literature are limited to date. It is evident from the progress reviewed in this chapter that the QCM demonstrates great potential for use in scCO₂.

Because scCO₂ is a "green" solvent, it is expected that the use of this solvent in nanoscale processing will increase significantly in the next few decades. The complete scope of the QCM in actual nanoscale processing has not been realized either. Hence the QCM will serve as an excellent analytical tool for developmental studies on emerging nanotechnologies and nanomaterials.

ACKNOWLEDGMENTS

This material is based upon work supported in part by the Science and Technology Center of the National Science

Foundation under Agreement No. CHE-9876674. We acknowledge the DeSimone group at the University of North Carolina, Chapel Hill (UNC), the Carbonell group and Kenan Center at the NC State University for technical assistance and facility utilization. Finally, we acknowledge Professor Scott Wallen and Michael Hurrey at UNC for their contributions in AFM experiments.

REFERENCES

1. DeSimone, J.M. Practical approaches to green solvents. *Science* **2002**, *297* (5582), 799–803.
2. McCoy, M. Industry intrigued by CO₂ as solvent—'Green' processes based on supercritical carbon dioxide are moving out of the lab. *Chem. Eng. News* **1999**, *77* (24), 11–13.
3. Mchugh, M.A.; Krukonic, V.J. *Supercritical Fluid Extraction: Principles and Practice*, 2nd Ed.; Butterworth-Heinemann Stoneham, UK, 1993.
4. Marsal, A.; Celma, P.J.; Cot, J.; Cequier, M. Supercritical CO₂ extraction as a clean degreasing process in the leather industry. *J. Supercrit. Fluids* **2000**, *16* (3), 217–223.
5. McHardy, J.; Sawan, S.P. *Supercritical Fluid Cleaning: Fundamentals, Technology, and Applications*; Noyes Publications: Westwood, NJ, 1998.
6. Purtell, R.; Rothman, L.; Eldridge, B.; Chess, C. Precision parts cleaning using supercritical fluids. *J. Vac. Sci. Technol., A: Vac. Surf. Films* **1993**, *11* (4), 1696–1701.
7. Desimone, J.M.; Guan, Z.; Elsbernd, C.S. Synthesis of fluoropolymers in supercritical carbon-dioxide. *Science* **1992**, *257* (5072), 945–947.
8. Cooper, A.I. Polymer synthesis and processing using supercritical carbon dioxide. *J. Mater. Chem.* **2000**, *10* (2), 207–234.
9. Weibel, G.L.; Ober, C.K. An overview of supercritical CO₂ applications in microelectronics processing. *Microelectron. Eng.* **2003**, *65* (1–2), 145–152.
10. Sundararajan, N.; Yang, S.; Ogino, K.; Valiyaveetil, S.; Wang, J.G.; Zhou, X.Y.; Ober, C.K.; Obendorf, S.K.; Allen, R.D. Supercritical CO₂ processing for submicron imaging of fluoropolymers. *Chem. Mater.* **2000**, *12* (1), 41–48.
11. Taylor, D.K.; Carbonell, R.; DeSimone, J.M. Opportunities for pollution prevention and energy efficiency enabled by the carbon dioxide technology platform. *Annu. Rev. Energy Environ.* **2000**, *25*, 115–146.
12. Wong, B.; Zhang, Z.; Handa, Y.P. High-precision

- gravimetric technique for determining the solubility and diffusivity of gases in polymers. *J. Polym. Sci., Part B: Polym. Phys.* **1998**, *36* (12), 2025–2032.
13. Jwayyed, A.M.; Humayun, R.; Tomasko, D.L. High pressure flow gravimetric apparatus for supercritical fluid extraction studies. *Rev. Sci. Instrum.* **1997**, *68* (12), 4542–4548.
 14. Lockemann, C.A.; Riede, T.; Magin, P. An experimental method to determine the sorption and swelling behavior of solids at high pressures. *Process Technol. Proc.* **1996**, *12*, 547–552.
 15. Wagner, W.; Brachthaeuser, K.; Kleinrahm, R.; Loesch, H.W. A new, accurate single-sinker densitometer for temperatures from 233 to 523 K at pressures up to 30 MPa. *Int. J. Thermophys.* **1995**, *16* (2), 399–411.
 16. Herbst, A.; Staudt, R.; Harting, P. The magnetic suspension balance in high pressure measurements of pure gases. *J. Therm. Anal. Calorim.* **2003**, *71* (1), 125–135.
 17. Areerat, S.; Hayata, Y.; Katsumoto, R.; Kegasawa, T.; Egami, H.; Ohshima, M. Solubility of carbon dioxide in polyethylene/titanium dioxide composite under high pressure and temperature. *J. Appl. Polym. Sci.* **2002**, *86* (2), 282–288.
 18. Von Schnitzler, J.; Eggers, R. Mass transfer in polymers in a supercritical CO₂ atmosphere. *J. Supercrit. Fluids* **1999**, *16* (1), 81–92.
 19. Sato, Y.; Takikawa, T.; Yamane, M.; Takishima, S.; Masuoka, H. Solubility of carbon dioxide in PPO and PPO/PS blends. *Fluid Phase Equilib.* **2002**, *194–197*, 847–858.
 20. Sato, Y.; Takikawa, T.; Sorakubo, A.; Takishima, S.; Masuoka, H.; Imaizumi, M. Solubility and diffusion coefficient of carbon dioxide in biodegradable polymers. *Ind. Eng. Chem. Res.* **2000**, *39* (12), 4813–4819.
 21. Sato, Y.; Takikawa, T.; Takishima, S.; Masuoka, H. Solubilities and diffusion coefficients of carbon dioxide in poly(vinyl acetate) and polystyrene. *J. Supercrit. Fluids* **2001**, *19* (2), 187–198.
 22. DeSimone, J.M.; Wojcinski, L.M., III; Kennedy, K.A.; Zannoni, L.; Saraf, M.; Charpentier, P.; Roberts, G.W. The polymerization of fluorinated monomers and the determination of phase equilibria in carbon dioxide. *Polym. Mater. Sci. Eng.* **2001**, *84*, 137.
 23. Buttry, D.A.; Ward, M.D. Measurement of interfacial processes at electrode surfaces with the electrochemical quartz crystal microbalance. *Chem. Rev.* **1992**, *92* (6), 1355–1379.
 24. Ward, M.D.; Buttry, D.A. In situ interfacial mass detection with piezoelectric transducers. *Science* **1990**, *249* (4972), 1000–1007.
 25. Lu, C.; Czanderna, A.W. *Applications of Piezoelectric Quartz Crystal Microbalances; Methods and Phenomena, Their Applications in Science and Technology*, Elsevier New York, 1984; Vol. 7.
 26. O'Sullivan, C.K.; Guilbault, G.G. Commercial quartz crystal microbalances—Theory and applications. *Biosens. Bioelectron.* **1999**, *14* (8–9), 663–670.
 27. Thompson, M.; Kipling, A.L.; Duncanhewitt, W.C.; Rajakovic, L.V.; Cavicvlask, B.A. Thickness-shear-mode acoustic-wave sensors in the liquid-phase—A review. *Analyst* **1991**, *116* (9), 881–890.
 28. Wegener, J.; Janshoff, A.; Steinem, C. The quartz crystal microbalance as a novel means to study cell–substrate interactions in situ. *Cell Biochem. Biophys.* **2001**, *34* (1), 121–151.
 29. O'Sullivan, C.K.; Vaughan, R.; Guilbault, G.G. Piezoelectric immunosensors—Theory and applications. *Anal. Lett.* **1999**, *32* (12), 2353–2377.
 30. Tsionsky, V.; Daikhin, L.; Urbakh, M.; Gileadi, E. Behavior of quartz-crystal microbalance in nonadsorbed gases at high-pressures. *Langmuir* **1995**, *11* (2), 674–678.
 31. Sauerbrey, G. Use of quartz vibration for weighing thin films on a microbalance. *Z. Phys.* **1959**, *155* (2), 206–222.
 32. Stockbridge, C.D. Effects of Gas Pressure on Quartz Crystal Microbalances. In *Vacuum Microbalance Techniques*; Behrmdt, K.H., Ed.; Plenum Press: New York, 1966; 147.
 33. Susse, C. Variation des constantes elastiques du quartz en fonction de la pression jusqu'a 1000-atm. *J. Phys. Radium* **1955**, *16* (4), 348–349.
 34. Kanazawa, K.K.; Gordon, J.G., II. The oscillation frequency of a quartz resonator in contact with a liquid. *Anal. Chim. Acta* **1985**, *175*, 99–105.
 35. Kanazawa, K.K.; Gordon, J.G., II. Frequency of a quartz microbalance in contact with liquid. *Anal. Chem.* **1985**, *57* (8), 1770–1771.
 36. Urbakh, M.; Daikhin, L. Influence of the surface-morphology on the quartz-crystal microbalance response in a fluid. *Langmuir* **1994**, *10* (8), 2836–2841.
 37. Schumacher, R.; Borges, G.; Kanazawa, K.K. The quartz microbalance: A sensitive tool to probe surface reconstructions on gold electrodes in liquid. *Surf. Sci.* **1985**, *163* (1), L621–L626.
 38. Urbakh, M.; Daikhin, L. Roughness effect on the frequency of a quartz-crystal resonator in contact

- with a liquid. *Phys. Rev., B* **1994**, *49* (7), 4866–4870.
39. Daikhin, L.; Urbakh, M. Effect of surface film structure on the quartz crystal microbalance response in liquids. *Langmuir* **1996**, *12* (26), 6354–6360.
 40. Wu, Y.-T.; Akoto-Ampaw, P.-J.; Elbaccouch, M.; Grant, C.S.; Hurrey, M.; Wallen, S.L. Quartz crystal microbalance (QCM) in high pressure carbon dioxide—Experimental examination of QCM theory and adsorption of carbon dioxide on metal surfaces. *Langmuir* **2003**. Submitted.
 41. Otake, K.; Kurosawa, S.; Sako, T.; Sugeta, T.; Hongo, M.; Sato, M. Frequency change of a quartz crystal microbalance at the supercritical condition of carbon dioxide. *J. Supercrit. Fluids* **1994**, *7* (4), 289–292.
 42. Guigard, S.E.; Hayward, G.L.; Zytner, R.G.; Stiver, W.H. Measurement of solubilities in supercritical fluids using a piezoelectric quartz crystal. *Fluid Phase Equilib.* **2001**, *187*, 233–246.
 43. Narasimhan, B.; Peppas, N.A. The physics of polymer dissolution: Modeling approaches and experimental behavior. *Polym. Anal., Polym. Phys.* **1997**, *128*, 157–207.
 44. Dammel, R.; Reiser, A. Recent developments in the dissolution of novolak-based resists. *Polym. Mater. Sci. Eng.* **1993**, *68*, 49–51.
 45. Hinsberg, W.D.; Willson, C.G.; Kanazawa, K.K. Use of a quartz crystal microbalance rate monitor to examine photoproduct effects on resist dissolution. *Proc. SPIE Int. Soc. Opt. Eng.* **1985**, *539*, 6–13.
 46. Hinsberg, W.D.; Willson, C.G.; Kanazawa, K.K. Measurement of thin-film dissolution kinetics using a quartz crystal microbalance. *J. Electrochem. Soc.* **1986**, *133* (7), 1448–1451.
 47. Ito, H. Dissolution behavior of chemically amplified resist polymers for 248-, 193-, and 157-nm lithography. *IBM J. Res. Develop.* **2001**, *45* (5), 683–695.
 48. Mueller, K.E.; Koros, W.J.; Wang, Y.Y.; Willson, C.G. Diffusivity measurements in polymers: Part III. Quartz crystal microbalance techniques. *Proc. SPIE Int. Soc. Opt. Eng.* **1997**, *3049*, 871–878.
 49. Pham, V.Q.; Weibel, G.L.; Rao, N.G.; Ober, C.K. Dissolution rate measurements for resist processing in supercritical carbon dioxide. *Proc. SPIE Int. Soc. Opt. Eng.* **2002**, *4690*, 425–431.
 50. Wu, Y.-T.; Grant, C.S. Evaluation of the dissolution of photoresist polymer films in supercritical carbon dioxide using quartz crystal microbalance. *Langmuir* **2003**. Submitted.
 51. Wang, N.H.; Takishima, S.; Masuoka, H. Solubility measurements of gas in polymer by the piezoelectric-quartz sorption method at high pressures and its correlation. Carbon dioxide+poly(vinyl acetate) and carbon dioxide+ poly(butyl methacrylate) systems. *Kagaku Kogaku Ronbunshu* **1990**, *16* (5), 931–938.
 52. Miura, K.; Otake, K.; Kurosawa, S.; Sako, T.; Sugeta, T.; Nakane, T.; Sato, M.; Tsuji, T.; Hiaki, T.; Hongo, M. Solubility and adsorption of high pressure carbon dioxide to poly(styrene). *Fluid Phase Equilib.* **1998**, *144* (1–2), 181–189.
 53. Aubert, J.H. Solubility of carbon dioxide in polymers by the quartz crystal microbalance technique. *J. Supercrit. Fluids* **1998**, *11* (3), 163–172.
 54. Hattori, K.; Wang, N.H.; Takishima, S.; Masuoka, H. Chromatographic measurement of vapor–liquid equilibrium ratios of organic solvents in supercritical carbon dioxide-poly(vinyl acetate) system. *Process Metall.* **1992**, *7B*, 1671–1676.
 55. Wang, N.H.; Hattori, K.; Takishima, S.; Masuoka, H. Measurement and prediction of vapor–liquid equilibrium ratios for solutes at infinite dilution in carbon dioxide+ poly(vinyl acetate) system at high pressures. *Kagaku Kogaku Ronbunshu* **1991**, *17* (6), 1138–1145.
 56. Nakamura, K.; Hoshino, T.; Suzuki, Y.; Yosizawa, H. Adsorption Isotherms for Supercritical Carbon Dioxide on Proteins and Polysaccharides. In *Proc. Int. Congr. Eng. Food*, 6th Ed.; Blackie: Glasgow, UK, 1994.
 57. Spall, W.D. Supercritical carbon dioxide precision cleaning for solvent and waste reduction. *Int. J. Environ. Conscious Des. Manuf.* **1993**, *2* (1), 81–86.
 58. McHardy, J.; Stanford, T.B.; Benjamin, L.R.; Whiting, T.E.; Chao, S.C. Progress in supercritical CO₂ cleaning. *SAMPE J.* **1993**, *29* (5), 20, 22–27.
 59. Douglas, M.A.; Wallace, R.M. Method of Cleaning and Treating a Micromechanical Device. US patent Number EP0746013, December 4, 1996.
 60. Rubin, J.B.; Davenhall, L.B.; Taylor, C.M.V.; Sivils, L.D.; Pierce, T. Carbon Dioxide-Based Supercritical Fluids as IC Manufacturing Solvents. In *IEEE International Symposium on Electronics and the Environment*; Danvers, MA, 1999.
 61. Lewis, H.G.P.; Weibel, G.L.; Ober, C.K.; Gleason, K.K. E-beam patterning of hot-filament CVD fluorocarbon films using supercritical CO₂ as a developer. *Chem. Vap. Depos.* **2001**, *7* (5), 195.
 62. Namatsu, H. Supercritical drying for water-rinsed resist systems. *J. Vac. Sci. Technol., B: Microelectron. Nanometer Struct.* **2000**, *18* (6), 3308–3312.
 63. Jafri, I.; Busta, H.; Walsh, S.T. Critical point drying

- and cleaning for MEMS technology. Proc. SPIE Int. Soc. Opt. Eng. **1999**, 3880, 51–58.
64. Naito, M.; Sasaki, Y.; Dewa, T.; Aoyama, Y.; Okahata, Y. Effect of solvation on induce-fit molecular recognition in supercritical fluid to organic crystals immobilized on a quartz crystal microbalance. *J. Am. Chem. Soc.* **2001**, 123 (44), 11037–11041.
65. Mori, T.; Naito, M.; Irimoto, Y.; Okahata, Y. Nucleobase molecular recognition in supercritical carbon dioxide by using a highly sensitive 27 MHz quartz-crystal microbalance. *Chem. Commun.* **2000**, (1), 45–46.
66. Blackburn, J.M.; Long, D.P.; Cabanas, A.; Watkins, J.J. Deposition of conformal copper and nickel films from supercritical carbon dioxide. *Science* **2001**, 294 (5540), 141–145.
67. Cooper, A.I. Recent developments in materials synthesis and processing using supercritical CO₂. *Adv. Mater.* **2001**, 13 (14), 1111–1114.
68. Shi, C.; Huang, Z.; Kilic, S.; Xu, J.; Enick, R.M.; Beckman, E.J.; Carr, A.J.; Melendez, R.E.; Hamilton, A.D. The gelation of CO₂: A sustainable route to the creation of microcellular materials. *Science* **1999**, 286 (5444), 1540–1543.
69. Cao, C.; Fadeev, A.Y.; McCarthy, T.J. Reactions of organosilanes with silica surfaces in carbon dioxide. *Langmuir* **2001**, 17 (3), 757–761.

Mineral Nanoparticles: Electrokinetics

Mehmet S. Celik

Istanbul Technical University, Istanbul, Turkey

Bahri Ersoy

Afyon Kocatepe University, Afyon, Turkey

INTRODUCTION

The term “electrokinetics” means the combined effects of motion and electrical phenomena. However, the term “electrokinetic properties” carry a wider connotation including zeta potential (ζ), the structure of electrical double layer (EDL), surface potential, and isoelectric point (iep) phenomena. The electrokinetic properties of a substance, inorganic or organic, are used to explain the mechanism of dispersion and agglomeration in a liquid phase and to identify the adsorption mechanisms of ions or molecules at a solid–liquid interface. Therefore they play an important role in a spectrum of applications including ceramics, food, mining, paper, medicine, water and wastewater treatment, emulsions, biochemistry, and detergents. In this paper, the type and significance of electrokinetic properties of mineral nanoparticles, the mechanism of particle–particle interactions in liquid systems, and the applications of electrokinetic phenomena are presented.

DESCRIPTION OF ELECTROKINETIC PROPERTIES OF MINERAL PARTICLES

Origin of Surface Charge

Each mineral particle in a liquid whether colloidal ($<1 \mu\text{m}$) or nanoparticle ($<100 \text{ nm}$) carries electrokinetic charges depending on the properties of liquid phase such as pH

and ionic strength.^[1–3] The surface charge of minerals can originate as a result of a number of mechanisms discussed below.

Dissociation of surface groups

In most solid minerals, dissociable functional surface groups such as carboxyl ($-\text{COOH}$) and hydroxyl ($-\text{OH}$) are present. These groups may be ionizable depending on the solution pH; a surface is charged either negatively at high pHs or positively at low pHs.

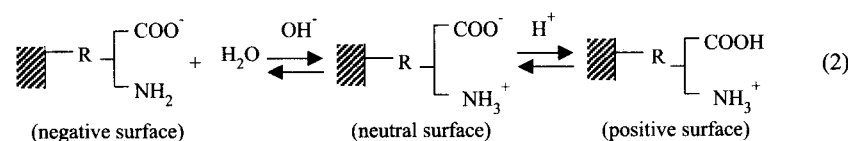
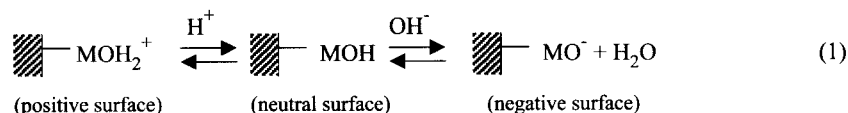
For metal oxides and hydroxides: (see Eq. (1) below), where M represents a metal cation at the surface.

For coal representing a typical hydrophobic mineral—where R represents a hydrocarbon compound constituting the coal structure (see Eq. (2) below).

Consequently, for simple metal oxides and hydroxides, e.g., SiO_2 , Al_2O_3 , Fe_2O_3 , and AlOOH , complex metal oxides including clay minerals^[4–6] and some hydrophobic minerals, e.g., coal,^[7] H^+ , and OH^- ions are considered as the potential determining ions (pdis) (see “Potential Determining, Indifferent, and Specifically Adsorbed Ions” section).

Preferential dissolution of lattice ions

This type of charging mechanism is generally developed in aqueous solutions with some soluble ionic solids, viz., AgI , CaCO_3 , BaSO_4 , and CaF_2 as a result of the preferential release of certain constituent lattice ions from the



solid into liquid phase as a result of hydration and lattice energies.^[8] The concentrations of these ions at equilibrium state are dictated by the solubility product of the solid.^[9] For AgI particles, for instance, the amount of Ag⁺ ions released into water from the particle surface at 25°C is more than that of I⁻ ions. Therefore the surface of AgI particle remains negatively charged. Thus the constituent lattice ions for these minerals are considered as the pdis.

Preferential adsorption of ions from solution

This mechanism is most commonly observed and results from the differences in the affinity of two phases for some ions. Some specific ions (see "Potential Determining, Indifferent, and Specifically Adsorbed Ions" section) can strongly adsorb on a solid surface and charge the particle, or, vice versa, a charged particle can become noncharged through such adsorption, e.g., adsorption of H⁺ and OH⁻ on oxide minerals (Eqs. 3 and 4 in the case of SiO₂), Ag⁺ and I⁻ adsorption on silver iodide particles, and Al³⁺ and HDTMA⁺ (hexadecyltrimethylammonium) adsorption on clinoptilolite.^[10] It should be noted that especially for H⁺ and OH⁻ ions, it is difficult to distinguish whether the charging of a particle is generated from the adsorption or dissociation of these ions. (see below).^[2]

Isomorphic substitutions

Almost all clay and zeolite minerals that are generally characterized as aluminum silicates exhibit negative charges in water, which results from the substitutions within the crystal lattice of Al³⁺ for Si⁴⁺ or Mg²⁺ for Al³⁺.^[11-14] Consequently, negative charges are developed in the lattice to compensate the so-called exchangeable cations, i.e., Na⁺, K⁺, and Ca²⁺ entering the crystal structure. When such minerals come in contact with water, some of these cations can easily dissociate, leading to negatively charged surfaces.

Accumulation and transfer of electrons

Besides ion transfer, as explained above, electron transfer is also possible between solid and liquid phases depending on differences in the electron affinities of the two phases. Also, some molecules of dipole character may be oriented

at the solid-liquid interface leading to charged surfaces,^[2,3] this is mostly observed at the metal-solution interface.

Electrical Double Layer and Double-Layer Models

When a mineral particle is immersed in a liquid, a surface charge will be developed through one of the mechanisms discussed above. Let us imagine a negatively charged solid particle in an electrolyte solution; while the oppositely charged counterions will congregate in the vicinity of the particle, coions having the same sign with that of the particle will be repelled from the surface as a result of electrostatic interactions. Thus a charged surface layer (layer 1) and an ionic layer (layer 2) all the way to the bulk water constitute the electrical double layer with a thickness usually ranging from a few angstroms to a few hundred angstroms. To examine the structure of EDL, different models have been proposed.^[3,15] These models are introduced below.

Helmholtz compact layer model

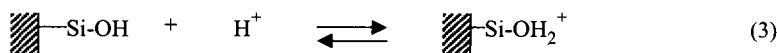
The earliest model of the EDL, in which a rigid layer away from the surface in solution consists of oppositely charged ions, was proposed in 1879 by Helmholtz.^[16] Also, the surface charge of particle is equal to that of rigid layer. Because this model ignores the disrupting effect of thermal agitation, it is unreasonable. This model is known as a molecular condenser model owing to its similarity to a parallel plate condenser.^[11] Using the law of distribution of EDL, the potential ψ (V) across the double layer for this capacitor is

$$\psi = \sigma d / \epsilon \epsilon_0 \quad (5)$$

where σ is the charge density per unit area of a plate (C/m²), ϵ (dimensionless) is the dielectric constant of the medium, and ϵ_0 is the permittivity of free space (8.854 × 10⁻¹² C²/J m).

Gouy-Chapman diffuse double-layer model

This is independently known as the Gouy-Chapman model. They expressed that, in addition to the electrostatic attraction of counterions to the charged surface, some of them tend to diffuse toward the bulk solution because of



their thermal motion. Note that the EDL theory can be developed for different solid geometries such as flat plate, sphere, and cylinder. Because most studies for organic and inorganic solids in liquids assume the flat plate geometry,^[17,18] here we also consider the flat plate to simplify the structure of EDL. The theory of Gouy–Chapman is based on the two fundamental equations: Poisson and Boltzmann.^[16] The Poisson equation (Eq. 6) for a flat surface given below is related to the potential distribution of an electric charge relative to the distance from the surface in a medium.

$$d^2\psi/dx^2 = \psi_{(x)} = -\rho_{(x)}/\epsilon\epsilon_0 \quad (6)$$

where $\psi_{(x)}$ is the double-layer potential (V) at a point located a distance x from the surface, $\rho_{(x)}$ is the charge density per unit volume (C/m^3) at the same point.

The Boltzmann equation is given by

$$n_i = n_i^0 \exp(-z_i e \psi / kT) \quad (7)$$

where n_i is the number of ions of type i per unit volume near the surface or in diffuse layer, n_i^0 is the number of ions of type i per unit volume in the bulk solution, z_i is the valence number of i including its sign, e is the electronic charge (1.602×10^{-19} C), k is the Boltzmann constant (1.381×10^{-23} J/K), and T is the absolute temperature (K). The term $z_i e \psi$ signifies the electrostatic (or coulombic) work required to bring the ion, i , from the bulk of the solution (where $x \rightarrow \infty$ and $\psi_0 = 0$) to a position where the potential is ψ .

The volume charge density near the surface is

$$\rho = \sum e z_i n_i = \sum e z_i n_i^0 \exp(-z_i e \psi / kT) \quad (8)$$

Substituting Eq. 8 into Eq. 6 yields the Poisson–Boltzmann equation (Eq. 9).

$$d^2\psi/dx^2 = (-1/\epsilon\epsilon_0) \sum e z_i n_i^0 \exp(-z_i e \psi / kT) \quad (9)$$

Eq. 9 shows a nonlinear differential equation without an explicit general solution but can be analytically solved by the Debye–Huckel approximation provided that $z_i e \psi < kT$, i.e., the potential (ψ) $< 25.7/z_i$ mV throughout the EDL. Thus Eq. 9 is converted to the following form^[16]

$$d^2\psi/dx^2 = \kappa^2 \psi \quad (10)$$

where κ is known as the Debye–Huckel parameter with a unit of reciprocal length (m^{-1}) and given by

$$\kappa = \left[\left(e^2 \sum n_i^0 z_i^2 \right) / (\epsilon\epsilon_0 kT) \right]^{1/2} \quad (11)$$

For water at 25°C, Eq. 11 becomes

$$\kappa = 3.288I^{1/2} \quad (12)$$

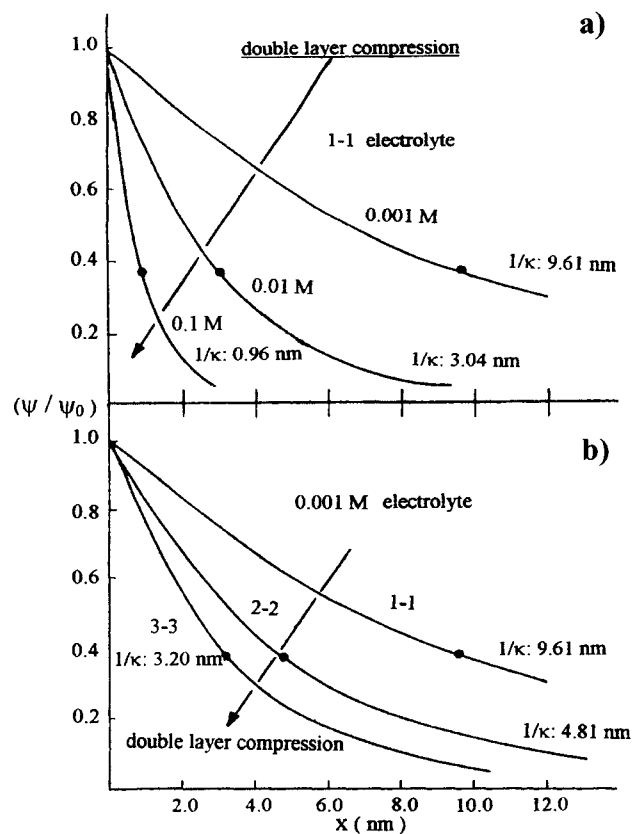


Fig. 1 Variation of electrical double-layer thickness with electrolyte concentration. (From Ref. [16].)

where I is the ionic strength ($I = 1/2 \sum c_i z_i^2$) of the solution and c_i is the concentration of an ion, i in mol/L, and z_i is the valence number of i . Note that the inverse of κ , $1/\kappa$, is a very important term in the stability of colloidal particles and is called as “the electrical double-layer thickness.” When the distance from surface reaches the value of $1/\kappa$, the double-layer (DL) potential (ψ) equals ψ_0/e ($e = 2.7182$). Eq. 12 clearly shows that the double-layer thickness is basically dependent on the ion concentration and the valency of the ion. An increase in both parameters results in a decrease in double-layer thickness and potential as shown in Fig. 1.

For surface potentials (ψ_0) < 25 mV, the solution of Eq. 10 yields^[13]

$$\psi = \psi_0 \exp(-\kappa x) \quad (13)$$

where x is the distance from surface and κ is the Debye–Huckel parameter. For high surface potentials, i.e., $z_i e \psi > kT$, the exact solution of Eq. 9 is required. The solution given by Gouy (1910) and Chapman (1913), for the case of a symmetrical electrolyte ($z_{i+} = -z_{i-} = z$, such as

NaCl, CaSO₄; and $n_{i+}^0 = n_{i-}^0 = n^0$) and some mathematical manipulations, becomes^[16]

$$\tanh(z e \psi / k T) = \tanh(z e \psi_0 / k T) \exp(-\kappa x) \quad (14)$$

or

$$\gamma = \gamma_0 \exp(-\kappa x)$$

where $\gamma = \tanh(z e \psi / 4 k T)$ and $\gamma_0 = \tanh(z e \psi_0 / 4 k T)$.

Evidently, although Eq. 14 is relatively more complex than Eq. 13, it has wider applicability. The surface

charge density (σ_0) of a particle in a liquid is given elsewhere.^[3]

Stern–Grahame model

The Gouy–Chapman model of EDL includes some unrealistic cases. For example, the ions are assumed as point charges and any specific effects related to the ion size are neglected. Therefore the adsorption densities on the solid surface calculated for moderate surface potentials and ionic strength values are so high that they are physically

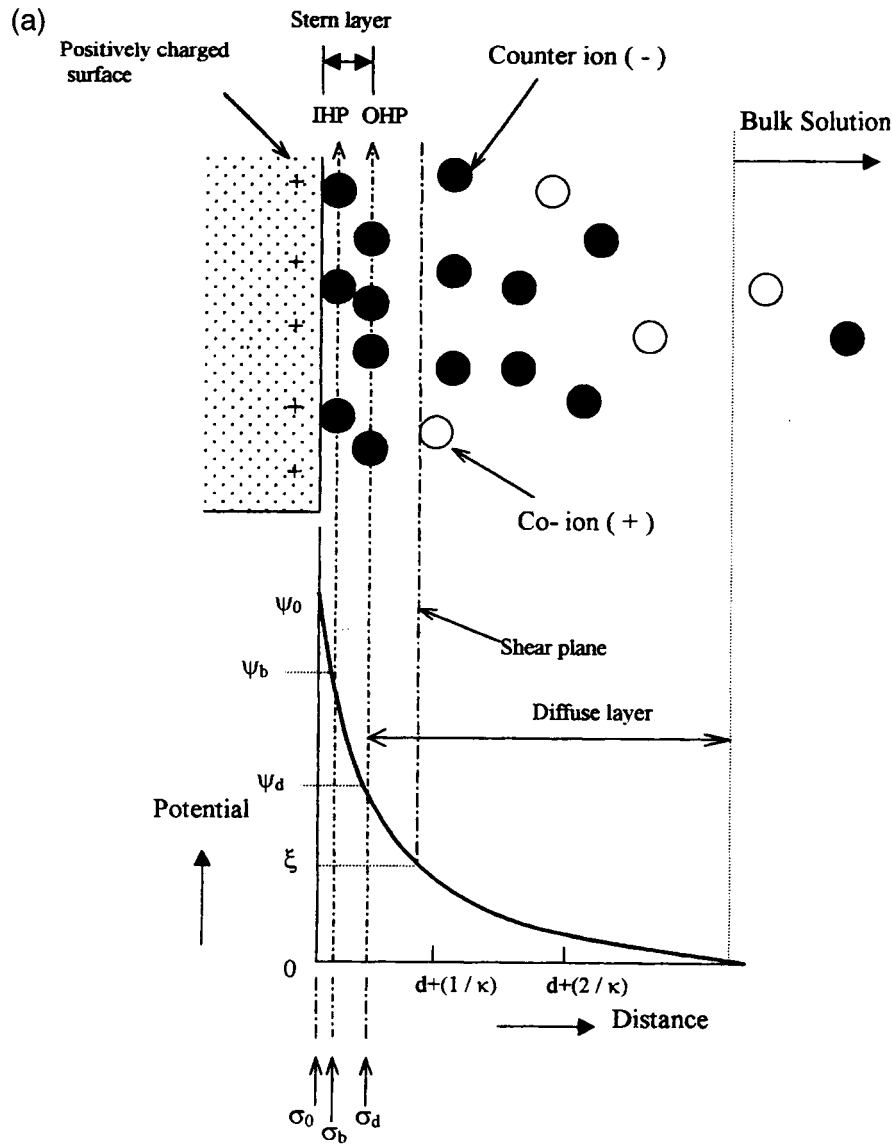


Fig. 2 The Stern–Grahame model represented by (a) by low concentration of specifically adsorbed ions and (b) by higher concentration of the specifically adsorbed ions.

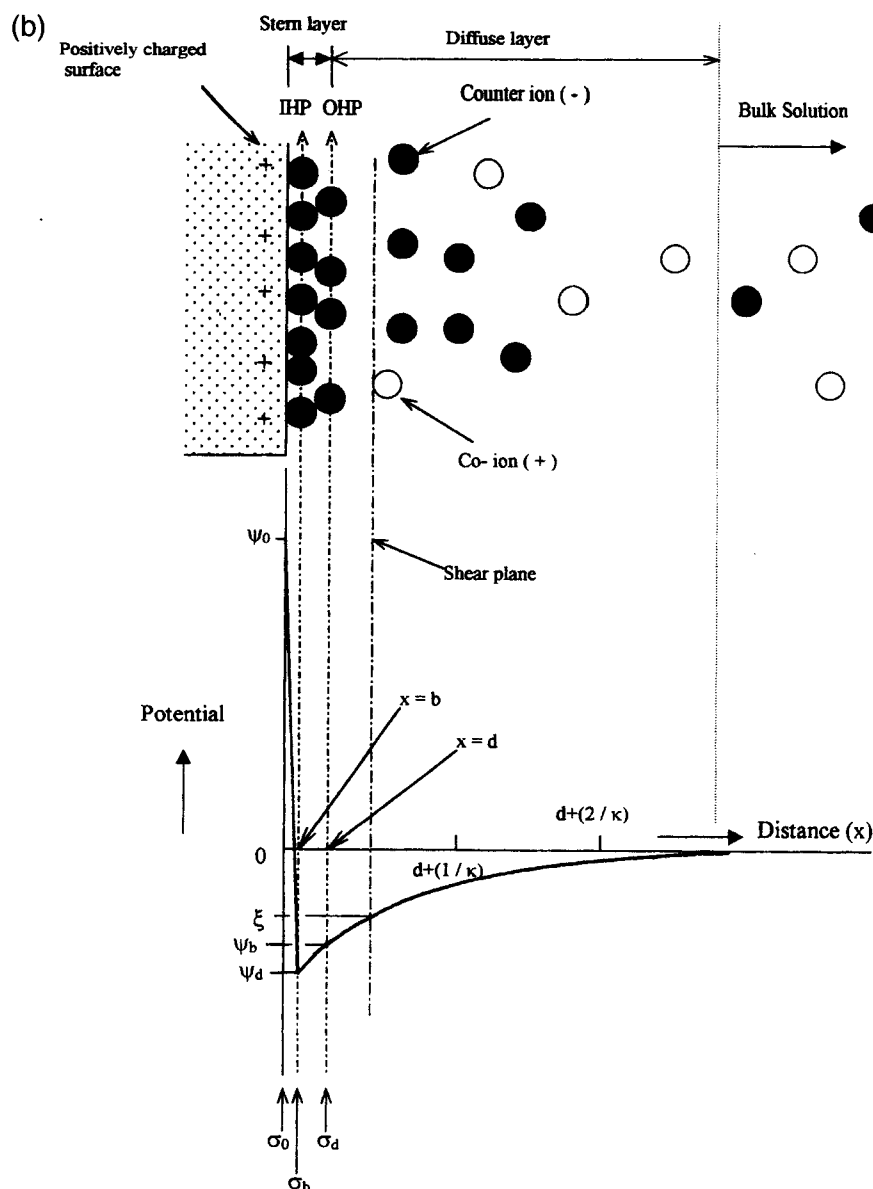


Fig. 2 (Continued).

impossible. Also, the solvent is assumed to have continuous properties everywhere in solution; however, its properties such as the dielectric constant and the viscosity may be different in the EDL and the bulk solution.

Stern (1924)^[19] modified the Gouy–Chapman model with an adsorbed layer of ions of thickness d , which is usually considered as 0.3–0.5 nm. This layer, assumed to be held fixed at the surface, is called the Stern layer. Thus the ion distribution in solution around the charged particle is divided into two parts: the Stern layer, which is the identical form in the Helmholtz model and consists of

specifically adsorbed ions, and the diffuse (or Gouy) layer. The double layer in Fig. 2 essentially shows three layers, i.e., the layer of charged solid surface, the Stern layer, and the diffuse layer, but in the literature the commonly used term is “double layer.” Also, there is a shear plane in the diffuse layer at which the double layer potential (ψ) is called the zeta (ξ) potential.

Grahame^[19] further divided the Stern layer into two parts: inner Helmholtz plane (IHP) and outer Helmholtz plane (OHP) (Fig. 2a,b). At the b plane, there are specifically adsorbed unhydrated ions known as the IHP,

while that of the closest approach to the more weakly adsorbed hydrated ions at d is known as the OHP, the onset of the diffuse layer. This model, known as the Stern–Grahame model, is usually represented with low amounts of specifically adsorbed ions (Fig. 2a) while the modified version (Fig. 2b) incorporates the specifically adsorbed ions. In the former, the sign of particle surface cannot be reversed, but it is possible in the latter. The potential distribution in the diffuse layer for a symmetrical electrolyte (Eq. 14) can be rewritten as;

$$\tanh(ze\psi/4kT) = \tanh(ze\psi_d/4kT) \exp[-\kappa(x - d)] \quad (15)$$

Note that, in the case of electrolyte concentrations less than 0.1 M, the zeta (ζ) potential can be used instead of ψ_d . The composition of the double layer is usually inferred from a comparison between σ_0 and σ_d or ψ_0 and ψ_d , then computed by some model. The following equation has a reasonably wide applicability if the amount of specifically adsorbed ions is low.

$$(\theta/1 - \theta) = (c_i/55.5) \exp[-(z_i e \psi_b + \Phi)/kT] \quad (16)$$

where $\theta = \sigma_b/\sigma_0$ ($0 \leq \theta \leq 1$), σ_b and σ_0 are charge densities at the IHP and at the surface (in C/cm^2), and Φ stands for the specific adsorption free energy in units of kT and ψ_b is the potential at the IHP, c_i is the bulk concentration of ion

i (mol/L). Eq. 16 is an extension of the familiar Langmuir equation.^[2]

Potential Determining, Indifferent, and Specifically Adsorbed Ions

Potential determining ions (pdi) are the major ions responsible for the establishment of the surface charge of particle.^[3] Their activities in the liquid play a crucial role in the generation of potential difference across a solid–liquid interface. They are also able to reverse the sign of z_p of the solid. As a simple recipe, for a cation to be the pdi, it must make the surface more positive upon increasing the cation concentration. Similarly, for an anion to be the pdi, it must impart the surface more negative charges with increasing anion concentration. While the pdi for ionic solids such as AgI, BaSO₄, and CaCO₃, etc. are the lattice constituent ions, i.e., Ag⁺, I⁻, Ba²⁺, SO₄²⁻, Ca²⁺, CO₃²⁻, H⁺ and OH⁻ ions are for metal oxides and hydroxides, silicate or clay minerals, some hydrophobic minerals (e.g., coal), and some synthetic polymers with sulfate groups.^[1,3,5,6] Fig. 3 clearly shows the difference in the behavior of a positively charged alumina surface toward (a) pdi: H⁺ and OH⁻; (b) the indifferent ions Cl⁻, and NO₃⁻, Na⁺, and Ba²⁺; and (c) the specifically adsorbed ions SO₄²⁻ and S₂O₃²⁻. For metal oxides, for example, the surface potential is

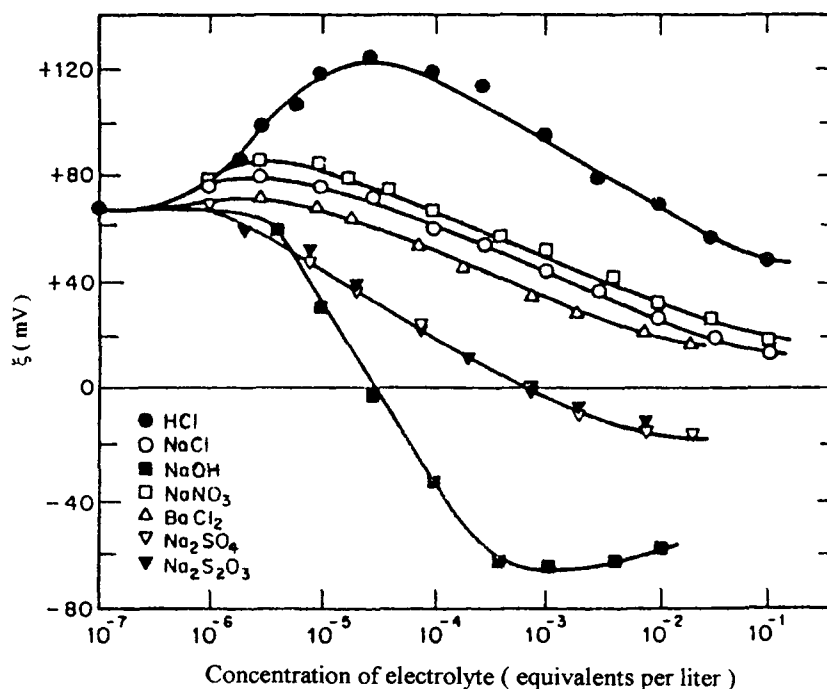


Fig. 3 Zeta potential profile of a positively charged alumina surface in the presence of various ions. (From Ref. [3].)

determined by the activities of pdis and expressed by Nernst-like equation

$$\psi_0 = (RT/F) \ln(a_{\text{H}^+}/a_{\text{H}^+}^0) \quad (17)$$

where F is the Faraday constant, a_{H^+} is the activity of H^+ , and $a_{\text{H}^+}^0$ refers to the point of zero charge (pzc). The operational formula for aqueous solutions at 25°C is

$\psi_0 = 0.059 \text{ V} (\text{pH}^0 - \text{pH})$, where pH^0 refers to the pzc.^[19] For AgI, Eq. 17 can be written as

$$\psi_0 = (RT/F) \ln(a_{\text{Ag}^+}/a_{\text{Ag}^+}^0) \quad (18)$$

Indifferent ions are those that cannot specifically adsorb in the Stern layer of the EDL and unable to reverse the sign of surface charge of the particle but only compress the

Table 1 iep and pzc of some typical natural and synthetic minerals

Mineral	Typical formula	iep or pzc	Reference
<i>Metal oxides and hydroxides</i>			
Corundum	Al_2O_3	pH 3 ^a	[5]
Quartz	SiO_2	pH 2.2 ^a	[22]
Hematite	Fe_2O_3	pH 3 ^a , pH 7.1 ^b	[23]
Rutile	TiO_2	pH 4.7 ^a	[5]
Zirconium	ZrO_2	pH 10 ^a	[5]
Diaspore	$\gamma\text{-AlO(OH)}$	pH < 2 ^a	[5]
Goethite	$\alpha\text{-FeOOH}$	pH 3.2 ^a	[5]
<i>Metal sulfides</i>			
Pyrite	FeS_2	pH 6.5 ^a	[24]
Chalcopyrite	CuFeS_2	pH 1.8 ^b	[25]
Sphalerite	ZnS	pH 2 ^b	[25]
Silver sulfide	Ag_2S	pAg 10.2 ^b	[3]
<i>Soluble ionic minerals</i>			
Calcite	CaCO_3	pH 8 ^a	[26]
Fluorite	CaF_2	pCa 3 ^b	[3]
Silver iodide	AgI	pAg 5.6 ^b	[3]
<i>Complex minerals</i>			
Colemanite	$\text{Ca}_2\text{B}_6\text{O}_{11} \cdot 5\text{H}_2\text{O}$	pH 10.5 ^a	[21]
Kaolinite	$\text{Al}_2\text{Si}_2\text{O}_5(\text{OH})_4$	pH 3.8 ^a	[11]
Dolomite	$\text{CaMg}(\text{CO}_3)_2$	pH 8 ^a	[27]
Fluorapatite	$\text{Ca}_5(\text{PO}_4)(\text{F},\text{OH})$	pH 6 ^b	[28]
Wolframite	$(\text{FeMn})\text{WO}_4$	pH 2.5 ^a	[29]
<i>Hydrophobic minerals</i>			
Coal	C	pH 1.5 ^a –4.8 ^a	[7,30]
Anthracite	C	pH 3.3 ^a	[31]
Talc	$\text{Mg}_3(\text{Si}_4\text{O}_{10})(\text{OH})_2$	pH 1.9 ^b	[1]
Sulfur	S	pH 2 ^b	[1]
Molybdenite	MoS_2	pH 1 ^b	[1]
<i>Synthetic minerals and mineral mixtures (composites)</i>			
Silicon carbide	SiC	pH 3.3 ^a	[32]
Silicon	Si	pH 2.4 ^a	[32]
Hematite	$\alpha\text{-FeOOH}$	pH 7.8 ^b	[33]
Boehmite	AlOOH	pH 9.2 ^{a,c}	[34]
Carbon (fiber)	C	pH 4.5 ^a	[35]
Rutile	TiO_2	pH 5.9 ^a	[36]
Mixed metal oxide (40% Ni + 60% Co) ^c		pH 9.5 ^b	[37]
Mixed metal oxide (50% SiO_2 + 50% Al_2O_3) ^d		pH 5.2 ^b	[38]

^aThe iep.

^bThe pzc.

^cSamples of Ni and Co mixed oxide in the form of powders were synthesized by thermal decomposition of the nitrates at 400°C . Forty and sixty percent means the weight ratio of the composite material.

^dAs starting materials, AlCl_3 and tetraethyl orthosilicate were used. They were mixed in an autoclave, and were calcined afterward at 500°C .

electrical double layer. For example, monovalent ions such as Na^+ and Cl^- are indifferent ions for colemanite,^[21] and Na^+ , Cl^- , NH_4^+ , NO_3^- , CaOH^+ , MgOH^+ , $\text{Al}(\text{OH})^+$, and $\text{Al}(\text{OH})^{2+}$ are indifferent ions for clinoptilolite (natural zeolite).^[10] Indifferent ions, which usually decrease the double-layer thickness ($1/\kappa$), are used in electrokinetic studies to determine the point of zero charge (pzc) or isoelectric point (iep) of minerals (Fig. 3).

Specifically adsorbed ions possess special affinity for the solid surface through coulombic and noncoulombic forces. These noncoulombic forces may be chemical in nature, i.e., involving some degree of covalent bonding with surface atoms or be more physical, e.g., van der Waals forces between the ion and the surface or between the hydrocarbon chains of surfactant ions adsorbed.^[3]

Isoelectric Point and/or Point of Zero Charge

Although the isoelectric point (iep) and the point of zero charge (pzc) are identical by definition, there are some differences between them. The iep or pzc of some typical minerals are given in Table 1. While the pzc denotes the state in which the net surface charge of the solid is zero, the iep describes the condition at which the potential at the shear plane, i.e., the zp obtained from electrokinetic measurements is zero; the iep and pzc are the same in the absence of the specific adsorption. But the pzc of a mineral need not coincide with the iep in most cases as seen in Table 1.

The iep of a mineral is directly obtained by electrokinetic measurements (see "Potential Determining, Indifferent, and Specifically Adsorbed Ions" section) against pH, usually in the presence of indifferent electrolytes (or ions) of various molarities seen in Fig. 4. This figure indicates that 1) KNO_3 is an indifferent electrolyte for this system and 2) the iep in this case is the same as the pzc. The pzc is experimentally determined usually by potentiometric titration method of the adsorbed pdi.^[40] For example, for oxides, hydroxides, and silicates, the surface charge density at pzc, σ_0 , can be expressed as

$$\sigma_0 = F(\Gamma_{\text{H}^+} - \Gamma_{\text{OH}^-}) = 0 \quad (19)$$

where Γ_{H^+} , and Γ_{OH^-} are analytical surface excess for H^+ and OH^- ions, respectively. Here it must be noted that iep and pzc of minerals depend on the heterogeneity of mineral surface and pretreatments of minerals such as leaching, washing, and ultrasonic scrubbing.^[11,23,30,41] Interestingly, the iep of particularly semisoluble salt-type minerals has been found to vary with the solids concentration.^[21]

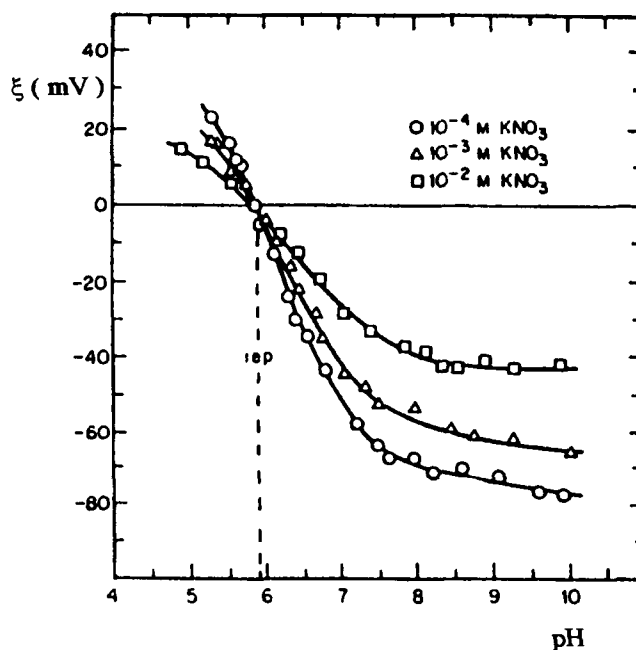


Fig. 4 Determination of the iep by electrokinetic measurements against pH in the presence of indifferent electrolytes of various molarities. (From Ref. [39].)

Zeta Potential (zp)

Zeta (ξ) potential is an intrinsic property of a mineral particle in a liquid. It determines the strength of the EDL repulsive forces between particles and identifies the stability of a colloidal system. The zp is known as the measurable surface potential of a particle, viz., the potential at the shear plane. There is no direct experimental method for determining both the surface potential (ψ_0) and Stern layer potential (ψ_d).^[3] So far, the exact position of the shear plane within the diffuse layer of the EDL could not be determined, but it is assumed that the position of the shear plane is very close to the outer Helmholtz plane (OHP).^[11] The ξ potential is fairly close to the Stern potential, ψ_d , in magnitude, and definitely less than the potential at surface, ψ_0 .

METHODS OF ZETA POTENTIAL MEASUREMENTS

Electrokinetic measurements using electrophoresis, electroosmosis, streaming potential, and sedimentation potential can be interpreted to yield a quantity known zeta or electrokinetic potential.^[3,42] Of these four techniques, the electrophoresis is perhaps the best known and most

commonly used technique to measure the z_p of minerals. While the electrophoresis technique with modifications is extended for the measurement of very fine particles such as nanoparticles (<100 nm) and colloidal particles (<1 μm), other techniques are usually employed for larger particles. The size of mineral particles is independent of the charge and only identifies the measurement technique.

Electrophoresis

When a charged mineral particle in a conducting liquid is applied an electrical field, it moves toward the oppositely charged electrode (relative to its charge). This is called electrophoresis. The method is based on the mobility (U) of the particle under the applied electrical field (E). The electrophoretic mobility of the particle represents the velocity (v) per unit electric field (E) and is given by

$$U \text{ (mobility)} = \text{speed/electric field} = v/E \\ = (\text{m/sec.})/(\text{V/m}) \quad (20)$$

The mobility of particle is converted to the z_p by the Henry equation

$$U = (\xi\varepsilon/1.5\eta)f(\kappa a) \quad (21)$$

where ξ is the zeta potential, ε is the dielectric constant of the medium relative to the vacuum, η is the viscosity of the medium, $f(\kappa a)$ is the corrector factor depending on the product of κ (Debye-Huckel parameter), and a is the particle radius. For very small particles in dilute solution where the thickness of the DL ($1/\kappa$) is large, $\kappa a \ll 1$ and $f(\kappa a) = 1$ (Huckel equation). For large particles in more concentrated solution, $\kappa a \gg 1$ and $1/\kappa$ is small, and $f(\kappa a) = 1.5$ (Smoluchowski equation).^[7]

If the particles are invisible, as in the case of some protein molecules, they are tracked by the Tiselius technique.^[3,42] However, for particles of about 0.5 μm in diameter or larger, direct observation is possible using an optic microscope illuminated with a strong light source. An ultramicroscope is useful for particles down to 0.1 μm . An electrical field is applied on the cell consisting of two electrodes and the movement of mineral particles dispersed in a conducting liquid is observed. Thus the rate of movement of particles moving toward the opposite electrode is observed under an optical microscope using a light beam lamp. Particle velocity is measured by timing individual particles on a microscope grid as they move from the start to the finish line. Ten to twenty particles are usually tracked with each traverse taking 3–15 sec. Thus the electrophoretic mobility of the particle is determined and then converted to the z_p using the Smoluchowski equation.

Electrokinetic measurements of nanoparticles can be performed by the Laser Doppler Electrophoresis method (LDE), the Phase Analysis Light Scattering Techniques (PALS), Tiselius technique, the Rotating Prism and Rotating Grating, and zone electrophoresis methods.^[42,43] The LDE and PALS techniques can provide z_p or electrokinetic measurements of many millions of nanoparticles in a few seconds. The LDE is based on the mixing of scattered light from a sample of a suspension of colloidal particles moving in an electric field, with light directly from the source. The scattered light is frequency-shifted by the Doppler effect, and optical mixing of this with the "unshifted" reference beam light leads to a beating at a frequency dependent on the speed of the particles. The limitation of this method arises from the small displacement of the particles because of a low mobility. This problem can be somewhat overcome with the Phase Analysis Light Scattering Technique (PALS). In this technique, phase modulation is applied so that the Doppler frequency of zero mobility particle is equal to the modulation frequency ω_0 . It is possible then to measure the deviation of the actual frequency, present in the scattered light, by performing a phase comparison of the detected signal with the imposed modulator frequency. If the mobility is truly zero, the relative phase of the two will be constant: If a small mobility is present, the relative phase will be shifted, and a small phase shift can be detected by a phase comparator.^[43] At high ionic strengths where the conventional zeta meters fail to function, the PALS technique is becoming useful.

Electroosmosis

This method is based on the measurement of liquid in a capillary (or in a system of capillaries such as a porous plug of compressed solid particles) under an applied electric field. When electric field or potential gradient, E , is applied via the working electrodes on the system, the electrolytes flow in response to the field and drag the liquid along with them. This movement of liquid can be conveniently observed by measuring the movement of a small bubble in the capillary, converting it to the flow rate from which the flow rate the z_p of the solid may be calculated using the following equation.^[9]

$$\xi = 4\pi\eta\lambda V_e/\varepsilon i \quad (22)$$

where V_e is the electroosmosis velocity of the liquid, i is the electric current passing through the capillary, η is the viscosity of the liquid, ε is dielectric constant of the liquid, and λ is the specific conductance of the liquid.

Streaming Potential

Streaming potential method may be considered as the converse of the electroosmosis. Here the electric field instead of the liquid velocity is measured. When a liquid is forced to flow through a capillary tube or porous plug by applying pressure, a potential difference is developed. This potential difference is called the streaming potential. The z_p of the solid (constituting the porous plug) from streaming potential data is given by the following Helmholtz-Smoluchowski equation (Eq. 23).^[19]

$$\xi = 4\pi\eta\lambda E_s/\varepsilon P \quad (23)$$

where E_s is the streaming potential and P is the pressure applied for streaming the liquid. This equation is valid under the conditions where the flow is linear and the pore diameter is much greater than the value of $1/\kappa$.^[3,9]

Sedimentation Potential

This technique may be regarded as the converse of the electrophoresis method. When a particle in a liquid settles through a suspending medium under the gravitational forces, it produces an electric field E . This electric field

is measured by inserting reversible electrode probes at two different heights in the column of settling particles and then $E = \Delta\phi/L$, where $\Delta\phi$ is the potential difference and L is the separation between the electrodes. The E value may be used to calculate the z_p, provided that the particle surface is nonconducting, the particles are of uniform size, and $\kappa a \gg 1$.^[3,9]

$$E = (\xi\epsilon a^3/3\eta\lambda)(m_1 - m_2)ng \quad (24)$$

where a is the radius of the particle, m_1 and m_2 are the densities of particle and liquid respectively, n is the number of solid particles in a unit volume, and g is the gravitational constant.

INTERACTION MECHANISMS BETWEEN MINERAL PARTICLES

DLVO Theory and the Interaction Energy Curves

The DLVO (Derjaguin and Landau, 1941;^[44] Verwey and Overbeek, 1948^[45]) theory explains the stability of colloidal systems including nanosized particles considering

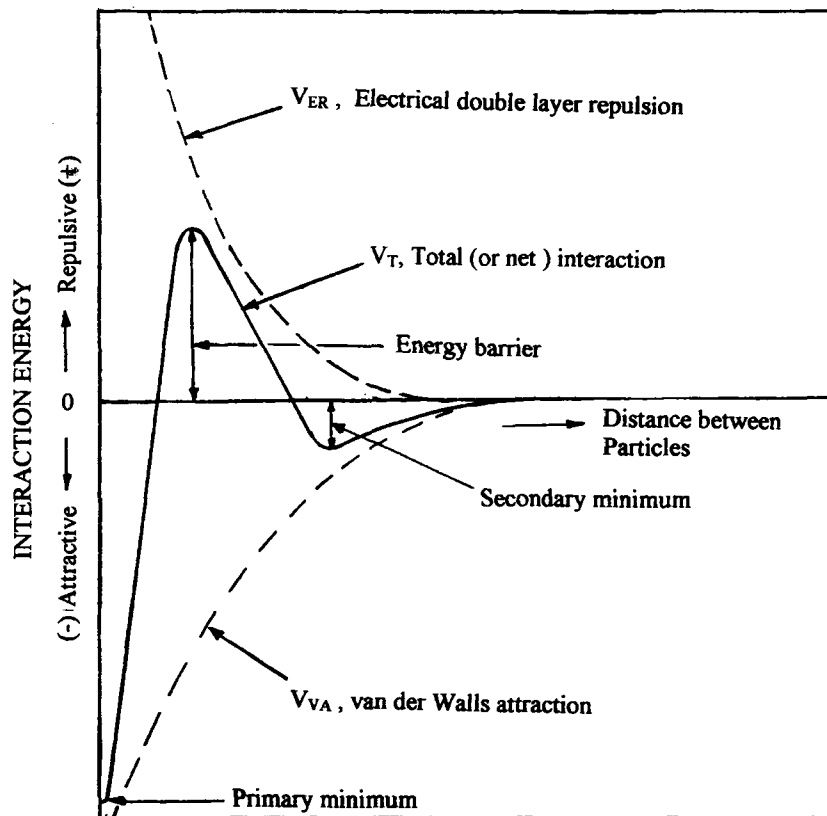


Fig. 5 Repulsive and attractive forces as a function of distance of separation.

the total potential energy of interaction between colloidal particles depending on the distance between them. The total or net interaction energy is equal to the summation of the EDL interaction energy (V_{ER}) and the van der Waals interaction energy (V_{VA}) and given as

$$V_T = V_{ER} + V_{VA} \tag{25}$$

The EDL interaction energy between two colloidal particles in an electrolyte solution results from the overlapping of their diffuse layers; that is, it results from an osmotic pressure of counterions in repulsive character when the two particles have the same sign of charge. But, when they are opposite in charge, the DL interaction energy becomes attractive in character. The van der Waals interaction energy (V_{VA}) between the particles arises from the London-van der Waals forces. If the two particles are identical, the van der Waals interaction is always negative (attractive) but in the case of different particles, this may change depending on the Hamaker constant of the particles and the medium.^[15,46]

For two spherical colloidal particles of equal size, which usually appear in most colloidal systems, the total interaction energy using the DLVO theory is described provided that $a \gg H$ as follows^[15]

$$V_T = 32\pi\epsilon\epsilon_0 a (kT/ze)^2 \chi^2 \exp(-\kappa H) - (Aa/12H) \tag{26}$$

where a is the radius of colloidal particles, H is the shortest distance between them, A is the effective Hamaker constant depending on the Hamaker constants of the particles and the medium, κ is the Debye-Huckel parameter, and χ is given by

$$\chi = \tanh(ze\xi/4kT) \tag{27}$$

Indeed, the right hand of Eq. 27 is identical with the term $\tanh(ze\psi_d/4kT)$ in Eq. 15, only the zeta (ξ) potential instead of ψ_d is used. In Eq. 26, the first term denotes the EDL repulsion energy (V_{ER}) and the second term the van der Waals attraction energy (V_{VA}). Note that here ξ is used as an effective surface potential of the particles. If V_T ,

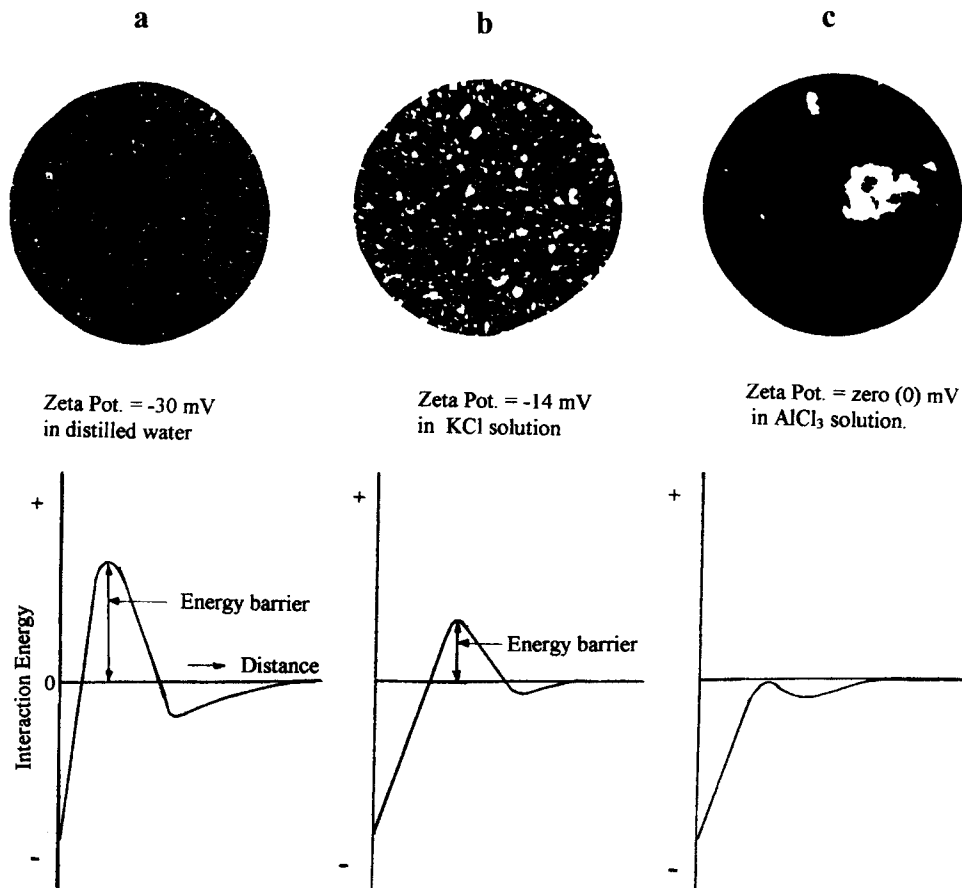


Fig. 6 Total energy of interaction curves for silica particles and their corresponding coagulation behavior. (From Ref. [48].)

V_{ER} , and V_{VA} are plotted as a function of the distance (H), the characteristic curves such as those in Fig. 5 are obtained. Here the V_T value at each distance is obtained by the summation of the V_{ER} and V_{VA} values; that is, the smaller energy is subtracted from the larger energy. If repulsive, the net value is plotted above; if attractive, the net value is plotted below. The V_T curve is then formed. As seen in Fig. 5, both repulsive and attractive interactions become weaker as the separation distance increases. At sufficiently large distances, the particles exert no influence on each other.

If the colloidal particles are very close, the van der Waals attractive forces take over with a resultant negative energy of interaction leading to the coagulation of particles. At contact state, the total interaction energy is known as the primary minimum. There is also another negative attraction energy usually beyond 3 nm known as the aggregation region or the secondary minimum.^[46] But the coagulation in this region is not stable and reversible with respect to the case in the primary minimum.^[9,47] Rheological properties such as thixotropy are closely related to coagulation at the secondary minimum.

If the particles are further away, van der Waals attraction forces sharply decrease because of the large exponent of inverse distance, and the EDL repulsion forces take over with an energy barrier occurring between the particles. If aggregation is required, the height of the energy barrier shown in Fig. 5 should be lowered or removed. Conversely, for a good dispersion, the height of the energy barrier must be enlarged. These two cases can be realized by changing the EDL repulsive forces, as it is perhaps impossible to change the van der Waals forces.

Now we can ask this question, how can we change the EDL repulsive forces? This is possible by changing the z_p of particles through changing parameters such as the type and concentration of electrolyte and solution pH. For example, for negatively charged colloidal silica particles in distilled water at 0, -14, and -30 mV, the photomicrographs of the colloidal silica particles taken by Rosental^[3] are given in Fig. 6a, b, and c, respectively. The total interaction energy (V_T) curves are assumed to correspond to the cases in Fig. 6a, b, and c, respectively. As seen in Fig. 6a, silica particles with a z_p value of -30 mV exhibit dispersion and the height of the energy barrier is considerably high. When KCl is added into water, the z_p of silica particles comes down to the -14 mV (Fig. 6b) as a result of the double-layer compression with a resultant decrease in repulsive energy and in turn in the height of the energy barrier. Consequently, in this system, sometimes the van der Waals attractive forces may become dominant depending on the kinetic conditions and/or the existence of the non-DLVO forces such as hydration, hydrophobic forces, and steric forces. When a trivalent electrolyte, $AlCl_3$, is added into system, the z_p

comes down to zero, which is called the isoelectric point (Fig. 6c), owing to the charge neutralization on the silica surface; the height of the energy barrier disappears and the van der Waals attractive forces become dominant in the system.^[49] Accordingly, the colloidal particles come in contact and coagulate (Fig. 6c).

At the point where the energy barrier just disappears:

$$dV_T/dH = 0 \text{ and } V_T = 0 \quad (28)$$

Applying these conditions to Eq. 26 results in an expression for the critical coagulation (or flocculation) concentration, C_c , for a symmetrical ($z_+ = -z_-$, z is the valence number of electrolyte, e.g., NaCl) electrolyte as follows:

$$C_c = K(P^4/A^2z^6) \quad (29)$$

where K is a constant that depends only on the properties of the dispersion medium and A is the effective Hamaker constant. When the z_p is very high, the term P approaches unity and the critical concentration becomes inversely proportional to the sixth power of the valency, z . This dependence of C_c on $1/z^6$, known as the Schultz-Hardy rule, is consistent with the DLVO theory. For instance, if coagulation occurs at 1 M with a 1:1 electrolyte, it will occur at $1/2^6$ ($\cong 0.016$) M with a 2:2 electrolyte, and at $1/3^6$ ($\cong 0.0014$) M with a 3:3 electrolyte.

APPLICATIONS OF ZETA POTENTIAL AND ELECTROPHORETIC MOBILITY

As mentioned earlier, the z_p is a good indicator to explain the stability mechanisms of different colloidal and emulsion systems, and the adsorption mechanism between any organic or inorganic species at any solid-liquid interface. The term stability, when applied to colloidal dispersions, is a relative term intended to express the resistance of the dispersion to change. In any colloidal system, colloidal particles may have different z_p values depending on the conditions, i.e., solution pH, existence of electrolyte, type, and concentration. The z_p is used mainly in the following areas as an indicator of the dispersion and coagulation of colloidal systems. Therefore it has a wide spectrum of applications, some of which will be briefly mentioned.

The preparation of a well-dispersed clay-water colloidal system in the slip casting molding method requires the z_p of clay particles be sufficiently high to provide repulsion between the particles so that a dense packing with strong material is produced.^[50] In the purification of municipal water and cleaning up of industrial wastes, it is usually necessary to remove solids from dilute suspension. The key to effective colloid removal is the reduction of z_p

of the colloidal particles to zero by adjusting solution pH, and type and concentration of electrolyte.^[11,51]

The pigments in paint, consisting of fine particles or nanoparticles, colored or colorless solid particles, must be dispersed readily to maintain a stable dispersion. The ζ value of pigments in a solvent plays an important role in maintaining a good dispersion.^[52] The pharmaceutical industry often prepares their product by suspending colloidal particles or nanoparticles of the drug uniformly throughout a liquid vehicle. A successful suspension remains stable and enjoys a long shelf life. This is often achieved by producing a stable dispersion that settles very slowly at maximum ζ . Suspensions of paper stocks containing fine particles including filler or pigments are generally regarded as colloidal systems. If fine particles are agglomerated, they will attach to the fiber, leading to better drainage and improvement in total retention at a ζ value of 0 mV.^[53] The EDL repulsive forces and ζ values between colloidal latex particles defining a sol of polymer particles such as polystyrene latex^[50] have a decisive role in the preparation of monodisperse latex.^[54,55]

The ζ measurements are used to determine the optimum conditions for the stability of emulsions. In most emulsion systems such as cream in cosmetic industry (oil in water or water in oil emulsions), mayonnaise in food industry (solid in liquid emulsion), and toothpaste in pharmaceutical industry (solid in liquid emulsion), the stability is achieved through a good control of ζ .^[56] The ζ values of fiber materials are used in the characterization of fiber materials such as carbon, polyethylene, cotton, and polyester in liquids and identifying the adsorption capacity of different organic dye molecules.^[42]

Flotation is a technique widely used in mining industry to separate valuable minerals from their ores or to separate the valuable minerals from each other. Finely ground minerals in water are coupled with an appropriate collector chemical and then floated with air bubbles. The ζ is used to select appropriate collector, elaborate the method of collector adsorption on minerals, and examine activation mechanism of minerals.^[7,8,55]

Electrophoretic deposition is an important technique directly used to produce a thin or thick coating on a conducting base.^[50,57] In this technique, charged particles migrate to an electrode of opposite charge under the influence of an electric field. Untrusting paint coatings on metal surfaces, composite coatings, production of superconductors,^[48] and photocopying by electrodeposition^[58] are further examples of this kind. Differences in electrophoretic mobilities of some proteins induce their separation in biological systems.^[19,40,42,47,52–54,58–61] Similarly, analysis of the blood cells can reveal illness through electrophoretic mobility; a mobility of $-1.1 \mu\text{m sec}^{-1}/\text{V cm}^{-1}$ is reported for fresh human red cells in blood at pH 7.4.^[60] In addition, the intravascular coagulation

diseases of human can be indirectly controlled by ζ .^[48] Bacterial action is also governed by electrical potential.^[62]

Detergency is the ability to remove dirt such as soil and oil adhering to fiber. The dirt removal from fabric by detergent is explained by the heterocoagulation theory including the EDL repulsion and van der Waals attraction energy between two different materials, fabric and dirt.^[59,61] Soil used for agricultural purposes contains an appreciable fraction of colloidal material composed of both lyophobic and lyophilic colloids. When soil is treated with water, the soil must be kept in a flocculated state to impart porosity, a suitable medium for good plant growth; this condition is provided by adding some electrolyte into water. The permeability of oil-producing sandstones is governed by the clay particles present in sandstone material. The migration of clay particles is relevant to the properties of water used in the system and also the electrokinetic properties of clay particles.^[63]

CONCLUSION

It is clear from this review that electrokinetic properties of mineral particles are encountered in all walks of life. Understanding of electrokinetics of mineral nanoparticles in a liquid, in addition to the ionic composition of the solution, requires the knowledge of surface charge, zeta potential, surface potential, structure of EDL at the mineral/liquid interface, and its double-layer thickness. This information is then used to identify the interaction mechanisms between two particles or between a particle surface and a substance (in ionic or nonionic form), and in turn, the stability of solid-liquid system and the adsorption of an ion (or molecule) on a charged or noncharged mineral. Its practical implications are then explained in terms of the DLVO theory.

REFERENCES

1. Leja, J. *Surface Chemistry of Froth Flotation*; Plenum Press: New York, 1983; 341–430. Second Printing.
2. Lyklema, J. Fundamentals of Electrical Double Layers in Colloidal Systems. In *Colloidal Dispersions*; Goodwin, J.W., Ed.; Dorset Press: Amsterdam, 1982; 48–69.
3. Hunter, J.R. *Zeta Potential in Colloid Science, Principles and Applications*; Academic Press: San Diego, 1988; 1–342. Third Printing.
4. Parks, G.A.; de Bruyn, P.L. The zero point of charge of oxides. *J. Phys. Chem.* **1962**, *66*, 967–972.
5. Parks, G.A. The isoelectric points of solid oxides,

- solid hydroxides, and aqueous hydroxo complex systems. *Chem. Rev.* **1965**, *65*, 177–198.
6. Somasundaran, P. Interfacial Chemistry of Particulate Flotation. In *Advances in Interfacial Phenomena*; AIChE Symp. Ser., 1975; Vol. 71, (150), 1–15.
 7. Laskowski, J.S. Coal Flotation and Fine Coal Utilization. In *Developments in Mineral Processing*; Fuerstenau, D.W., Ed.; Elsevier Science B.V.: Amsterdam, 2001; 35–44.
 8. Dobias, B. Salt Type Minerals. In *Flotation Science and Engineering*; Matis, K.A., Ed.; Marcel Dekker Inc.: New York, 1995; 207–259.
 9. Sennet, P.; Olivier, J.P. Colloidal Dispersions, Electrokinetic Effects and the Concept of Zeta Potential. In *Industrial and Eng. Chem., The Interface Symposium*, August 12, 1965; Vol. 57, 32–50.
 10. Ersoy, B.; Celik, M.S. Electrokinetic properties of clinoptilolite with mono and multivalent electrolytes. *Microporous Mesoporous Mater.* **2002**, *55*, 305–312.
 11. Williams, D.J.A.; Williams, K.P. Electrophoresis and zeta potential of kaolinite. *J. Colloid Interface Sci.* **1978**, *65* (1), 80–87.
 12. Fuerstenau, M.C. Oxide and Silicate Flotation. In *Flotation Science and Engineering*; Matis, K.A., Ed.; Marcel Dekker Inc.: New York, 1995; 89–126.
 13. Grim, R.E. *Clay Mineralogy*; Mc-Graw-Hill Book Com. Inc.: New York, 1968, 184–233.
 14. Kraepiel, A.M.L.; Keller, K.; Morel, F.M.M. On the acid-base chemistry of permanently charged minerals. *Environ. Sci. Technol.* **1998**, *32*, 2829–2838.
 15. Gregory, J. Fundamentals of flocculation. *Crit. Rev. Environ. Control* **1989**, *13*, 185–230.
 16. Hiemenz, P.C. *Principles of Colloid and Surface Chemistry*, 2nd Ed.; Marcel Dekker Inc.: New York, 1986; 677–789.
 17. Harding, I.H.; Healy, T.W. Electrical double layer properties of latex colloids. *J. Colloid Interface Sci.* **1985**, *107* (2), 382–398.
 18. Sridharan, A.; Satyamurty, P.V. Potential–distance relationships of clay–water colloidal systems considering the Stern theory. *Clays Clay Miner.* **1996**, *44* (4), 479–484.
 19. Usui, S. Electrical Double Layer. In *Electrical Phenomena at Interfaces, Fundamentals, Measurements and Applications*; Watanabe, A., Ed.; Marcel Dekker Inc.: New York, 1984, 15–46.
 20. Modi, H.J.; Fuerstenau, D.W. Streaming potential studies on corundum in aqueous solutions of inorganic electrolytes. *J. Phys. Chem.* **1957**, *61*, 640–643.
 21. Celik, M.S.; Yasar, E. Electrokinetic properties of some hydrated boron minerals. *J. Colloid Interface Sci.* **1995**, *173*, 181–185.
 22. Fuerstenau, D.W.; Huang, P. The effect of the adsorption of lead and cadmium ions on the interfacial behavior of quartz and talc. *Colloids Surf., A Physicochem. Eng. Asp.* **2001**, *177*, 147–156.
 23. Kulkarni, R.D.; Somasundaran, P. Mineralogical heterogeneity of ore particles and its effects on their interfacial characteristics. *Powder Technol.* **1976**, *14*, 279–285.
 24. Pradeep, T.; Subramanian, S.; Rath, R.K. Surface chemical studies on pyrite in the presence of polysaccharide-based flotation depressants. *J. Colloid Interface Sci.* **2000**, *229*, 82–91.
 25. Parks, G.A. Aqueous Surface Chemistry of Oxides and Complex Oxide Minerals, Isoelectric Point and Zero Point of Charge in Equilibrium Concepts in Natural Water Systems. In *Advances in Chemistry Series*; Gould, R.F., Ed.; American Chemical Society: Washington, DC; Vol. 67, 121–160.
 26. Luevanos, A.M.; Salas, A.U.; Valdivieso, A.L. Mechanisms of adsorption of sodium dodecylsulfonate on celestite and calcite. *Miner. Eng.* **1999**, *12* (8), 919–936.
 27. Pokrovsky, O.S.; Schott, J.; Thomas, F. Dolomite surface speciation and reactivity in aquatic systems. *Geochim. Cosmochim. Acta* **1999**, *63* (19/20), 3133–3143.
 28. Somasundaran, P.; Ananthapadmanabhan, K.P. Physico-chemical aspects of flotation. *Trans. Indian Inst. Met.* **1979**, *32* (1), 177–194.
 29. Xu, Z.; Wang, D.; Hu, Y. A study of interactions and flotation of wolframite with octyl hydroxamate. *Miner. Eng.* **1997**, *10* (6), 623–633.
 30. Celik, M.S.; Somasundaran, P. Effect of pretreatments on flotation and electrokinetic properties of coal. *Colloids Surf.* **1980**, *1*, 121–124.
 31. Unlu, M.; Doga, T.U. Electrokinetic properties of anthracite and morphology of its electrical double layer. *J. Eng. Environ.* **1987**, *11* (1), 62–77.
 32. Rao, R.R.; Roopa, H.N.; Kannan, T.S. Dispersion, slipcasting and reaction nitridation of silicon–silicon carbide mixtures. *J. Eur. Ceram. Soc.* **1999**, *19*, 2145–2153.
 33. Cromieres, L.; Moulin, V.; Fourest, B.; Giffaut, E. Physicochemical characterization of the colloidal hematite/water interface: Experimentation and modelling. *Colloids Surf., A Physicochem. Eng. Asp.* **2001**, *177*, 147–156.
 34. Ersoy, B. Sol–Gel Coating of Al₂O₃–La₂O₃ on Clay Based Substrate and Production of Ceramic Membrane. In M.Sci. Thesis; Dumlupinar University; Turkey, 1996; 66–107.
 35. Springer, J.; Bismarck, A. Characterization of fluorinated PAN-based carbon fibers by zeta

- potential measurements. *Colloids Surf., A Physicochem. Eng. Asp.* **1999**, *159*, 331–339.
36. Webb, J.T.; Bhatnagar, P.D.; Williams, D.G. The interpretation of electrokinetic potentials and the inaccuracy of the DLVO theory for anatase sols. *J. Colloid Interface Sci.* **1974**, *49* (3), 346–361.
37. De Faria, L.D.; Prestat, M.; Koenig, J.F.; Chartier, P.; Trasatti, S. Surface properties of Ni+Co mixed oxides: A study by x-rays, xps, BET and pzc. *Electrochim. Acta* **1988**, *44*, 1481–1489.
38. Tscapek, M.; Tcheicvili, L.; Wasowski, C. The point of zero charge (pzc) of kaolinite and SiO₂ + Al₂O₃ mixtures. *Clay Miner.* **1974**, *10*, 219–229.
39. Wiese, G.R.; Healy, T.W. *J. Colloid Interface Sci.* **1975**, *51*, 427.
40. Takahashi, K. Electrocapillary Measurements. In *Electrical Phenomena at Interfaces, Fundamentals, Measurements and Applications*; Watanable, A., Ed.; Marcel Dekker Inc.: New York, 1984; 147–182.
41. Kulkarni, R.D.; Somasundaran, P. Effect of pre-treatment on the electrokinetic properties of quartz. *Int. J. Miner. Process.* **1977**, *4*, 89–98.
42. Kittaka, S. Electrokinetic Measurements. In *Electrical Phenomena at Interfaces, Fundamentals, Measurements and Applications*; Watanable, A., Ed.; Marcel Dekker Inc.: New York, 1984; 183–224.
43. Rowlands, W.N.; O'Brien, R.W.; Hunter, R.J.; Patrick, V.J. Surface properties of aluminum hydroxide at high salt concentration. *J. Colloid Interface Sci.* **1997**, *188*, 325–335.
44. Derjaguin, B.V.; Landau, L.D. Theory of the stability of strongly charged lyophobic sols and of the adhesion of strongly charged particles in solutions of electrolytes. *Acta Physicochim. URSS* **1941**, *14*, 622–633.
45. Verwey, E.J.W.; Overbeek, J.Th.G. *Theory of the Stability of Lyophobic Colloids*; Elsevier: Amsterdam, 1948; 168.
46. Israelachvili, J.N. *Intermolecular and Surface Forces*, 2nd Ed.; Academic Press: San Diego, 1995; 83–254.
47. Furusawa, K.; Matsumoto, M. Stability Measurement of Disperse Systems. In *Electrical Phenomena at Interfaces, Fundamentals, Measurements and Applications*; Watanable, A., Ed.; Marcel Dekker Inc.: New York, 1984; 225–268.
48. Riddick, T.M. *Control of Colloid Stability Through Zeta Potential*; Zeta-Meter Inc.: New York, 1968; 1–372.
49. Schwarz, J.A.; Driscoll, C.T.; Bhanot, A.K. The zero point of charge of silica-alumina oxide suspensions. *J. Colloid Interface Sci.* **1984**, *97* (1), 55–61.
50. Shanefield, D.S. *Organic Additives and Ceramic Processing*, 2nd Ed.; Kluwer Academic Publishers: Massachusetts, 1996, 131–251.
51. Grutsch, J.F. Wastewater treatment: The electrical connection. *Environ. Sci. Technol.* **1978**, *12* (9), 1023–1027.
52. Kumano, I. Pigments and Paints. In *Electrical Phenomena at Interfaces, Fundamentals, Measurements and Applications*; Watanable, A., Ed.; Marcel Dekker Inc.: New York, 1984, 355–368.
53. Yamada, H. Paper. In *Electrical Phenomena at Interfaces, Fundamentals, Measurements and Applications*; Watanable, A., Ed.; Marcel Dekker Inc.: New York, 1984; 323–338.
54. Usui, S.; Hachisu, S. Interaction of Electrical Double Layers and Colloid Stability. In *Electrical Phenomena at Interfaces, Fundamentals, Measurements and Applications*; Watanable, A., Ed.; Marcel Dekker Inc.: New York, 1984; 47–98.
55. Kydors, K.A.; Matis, K.A. Flotation of Iron Sulfide Minerals: Electrokinetic Aspects. In *Flotation Science and Engineering*; Matis, K.A., Ed.; Marcel Dekker Inc.: New York, 1995; 127–155.
56. Fukushima, S.C. Cosmetics. In *Electrical Phenomena at Interfaces, Fundamentals, Measurements and Applications*; Watanable, A., Ed.; Marcel Dekker Inc.: New York, 1984; 369–386.
57. Ferrari, B.; Moreno, R. Electrophoretic deposition of aqueous alumina slips. *J. Eur. Ceram. Soc.* **1997**, *17*, 549–556.
58. Karasawa, S. Reproduction in Copying and Electrophoretic Display. In *Electrical Phenomena at Interfaces, Fundamentals, Measurements and Applications*; Watanable, A., Ed.; Marcel Dekker Inc.: New York, 1984; 413–436.
59. Suzawa, T. Fibers. In *Electrical Phenomena at Interfaces, Fundamentals, Measurements and Applications*; Watanable, A., Ed.; Marcel Dekker Inc.: New York, 1984; 299–322.
60. Kondo, T. Electrokinetic Phenomena in Biological Systems. In *Electrical Phenomena at Interfaces, Fundamentals, Measurements and Applications*; Watanable, A., Ed.; Marcel Dekker Inc.: New York, 1984; 397–412.
61. Imamura, T.; Tokiwa, F. Detergency. In *Electrical Phenomena at Interfaces, Fundamentals, Measurements and Applications*; Watanable, A., Ed.; Marcel Dekker Inc.: New York, 1984; 269–284.
62. Poortinga, A.T.; Bos, R.; Norde, W.; Busscher, H.J. Electric double layer interactions in bacterial adhesion to surfaces. *Surf. Sci. Rep.* **2002**, *189*, 1–32.
63. Yen, T.F.; Kuo, J.F.; Sharma, M.M. Further investigation of the surface charge properties of oxide surfaces in oil-bearing sands and sandstones. *J. Colloid Interface Sci.* **1987**, *115* (1), 9–16.



Mixed Metal Oxide Nanoparticles

Pramesh N. Kapoor

Ajay Kumar Bhagi

University of Delhi, Delhi, India

Ravichandra S. Mulukutla

Nanoscale Materials, Inc., Manhattan, Kansas, U.S.A.

Kenneth J. Klabunde

Kansas State University, Manhattan, Kansas, U.S.A.

INTRODUCTION

Mixed metal oxide (MMO) nanoparticles (also called heterometal oxide nanoparticles) can play an appreciable role in many areas of chemistry and physics. The unique electronic and magnetic properties obtained when combining two metals in an oxide matrix have been well studied.^[1,2] However, the most common use for MMOs has been in the area of catalysis, and here they have found use both as the catalyst and as catalyst supports.^[3,4] Specifically, MMO containing aluminum has found many opportunities in catalysis.^[5-7]

Mixed metal oxides are also used in many applications in the electronic industry as passive or active components in devices. These exhibit high dielectric, and ferro- or pyroelectric properties, e.g., BaTiO₃, LiNbO₃, KTaO₃, Pb_{1-x}La_xTi_yZr₂O₃, etc. The most remarkable MMO materials are surely the thermal-conducting superconductors based on YBa₂Cu₃O_{7-x}. The technological interest in MMOs such as silica-titania and silica-zirconia arises from their chemical resistance and their thermomechanical or optical properties. SiO₂-TiO₂ glasses and zircon, SrZrO₄, are characterized by very low thermal expansion, which confer them a high thermal-shock resistance. SiO₂-TiO₂ and SiO₂-ZrO₂ glasses have high refractive indices and are wonderful catalysts or catalyst supports.^[8] Owing to their refractoriness, these MMOs are difficult to produce by conventional melting techniques; thus, sol-gel technique is used for their preparation. The homogeneity of binary oxide has great influence on structural evolution of the gels during the heat treatment. Magnesium aluminate spinel (MgAl₂O₄) is expected to have applications as a structural material at high temperatures because it has a high melting point and superior thermal and chemical properties. It is also of technological interest as a refractory material at elevated temperatures. It is important to realize that improved properties are recorded for ceramic materials at nanoscale and these materials are

expected to find the most important place in technology in the coming years.

In this article, we have covered the most important and recent methods of preparation of nanocrystalline MMOs. Special emphasis has been given on sol-gel technique because of its popularity among researchers, resulting in homogeneous and pure MMO nanoparticles. Among physical methods, perhaps flame spray pyrolysis is gaining more importance in recent time. Structure, properties, and applications of MMO nanoparticles have also been discussed. This area of research is wide open and offers scope for development in synthetic and application fields.

SYNTHESIS OF MIXED METAL OXIDE NANOPARTICLES

Developments in the field of MMO nanoparticles have produced many significant and interesting results in all areas investigated. This attracted attention toward the preparation of these potential new materials with variable composition having unique properties. Researches have explored and developed both physical and chemical methods by which such materials can be prepared.

Physical Methods

Several physical aerosol methods have been reported for the synthesis of nanosized particles of ceramic materials. The most successful include gas condensation techniques,^[9-12] spray pyrolysis,^[13,14] thermochemical decomposition of metal-organic precursors in flame reactors,^[15,16] and some other aerosol processes named according to energy sources applied to reach the temperatures required for gas-particle conversion. The experi-

mental details of these physical/aerosol methods have been outlined by Khaleel and Richards.^[17]

Vapor condensation method

It involves two steps. In the first step, a metallic nanophase powder is condensed under an inert convection gas at high pressure, after the supersaturated vapor of metal is obtained inside a chamber. In the second step, the powder is oxidized by allowing oxygen into the chamber. It is a critical step in which the temperature is as high as 1000°C because of the exothermic nature of the reaction. High temperature results in agglomeration into large particles, and often annealing process at high temperature is required for completion of oxidation. Nanoparticles result when supersaturation is achieved above the vapor source. A collection surface cooled by liquid nitrogen is used to collect the particles.

Spray pyrolysis

Some other techniques with slight modifications also work on same principle. They are aerosol thermolysis, evaporative decomposition of solutions, plasma vaporization of solutions, aerosol decomposition, flame pyrolysis, etc. A new broad name suggested for these techniques is flame spray pyrolysis (FSP) technology. The starting materials, or chemical precursors, are usually the appropriate salts, either in solution or in a sol or in suspension form. Aerosol droplets are generated by nebulizer or atomization technique of the starting chemical precursors. These droplets generated undergo evaporation with solute condensation within the droplet followed by drying and thermolysis of precipitate particles at high temperatures forming microporous particles. They are finally sintered to form dense particles. In this technique, various methods are used for atomization, including pressure, two-fluid, electrostatic, and ultrasonic atomizers. These methods give droplets of different sizes (2–15 μm) at various rates of atomization and various droplet velocities. Tal Materials Inc. uses a patented flame spray pyrolysis process developed at the University of Michigan for the direct, large-scale production of inexpensive MMO nanopowders.^[18,19]

The preparation of a variety of nanosized MMO powders from the thermolysis/flame pyrolysis of a new polymer-matrix-based precursor solution has been reported by Pramanic et al.^[20] Spinels such as MgAl₂O₄, CuFe₂O₄, NiFe₂O₄, CoFe₂O₄, ZnFe₂O₄; orthoferrites such as LaFeO₃; NdFeO₃; GdFeO₃; SmFeO₃; garnets such as Y₃Al₅O₁₂, Gd₃Al₅O₁₂, Gd₃Fe₅O₁₂, Sm₃Fe₅O₁₂; and composites such as Fe₂O₃·NiO, Fe₂O₃·CuO, and Fe₂O₃·TiO₂ have been reported.

Thermochemical/flame decomposition of metal–organic precursors

This method is an example of another type of gas condensation technique. In this method, the starting material is a liquid chemical precursor. It is also known as chemical vapor condensation (CVC). It involves vaporization of chemical precursors, which are then oxidized with the help of a fuel–oxidant mixture (propane–O₂ or methane–O₂). It combines the rapid thermal decomposition of a precursor carrier gas stream in a reduced pressure environment with thermophoretically driven deposition of the rapidly condensed product particles on a cold substrate.^[16] The flame temperature varies between 1200 and 3000 K, which allows rapid gas phase chemical reactions. In rapid thermal decomposition of precursor in solution (RTDS), the precursor material dissolved in water undergoes rapid hydrothermal reactions in a near-critical and supercritical water environment. Due to the short residence time and extremely fast quenching rate, the particle growth in the reaction is limited. Both ultrafine metal oxides and MMOs using inexpensive water-soluble precursors are prepared using this method. Some examples of nanocrystalline powders produced using RTDS are (1) Fe₃O₄ (magnetite) having grain size less than 12 nm from FeSO₄/urea as precursors, (2) NiFe₂O₄ (trevorite) having grain size less than 10 nm from Fe(NO₃)₃/Ni(NO₃)₂/urea as precursors, and (3) NiO/ZrO₂ having grain size nearly 10 nm from Ni(NO₃)₂/ZrO(NO₃)₂.

Chemical Methods

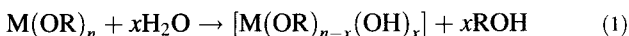
The most potential and successful route for preparing homogeneous ceramic materials is liquid phase chemistry. The most widely used and perhaps most reliable method is the sol–gel method. There are many other wet chemistry methods known, such as microemulsion techniques and precipitation from solutions. Another novel technique is the mechanochemical synthesis method, which involves solid-state chemistry reactions.

Sol–gel technique

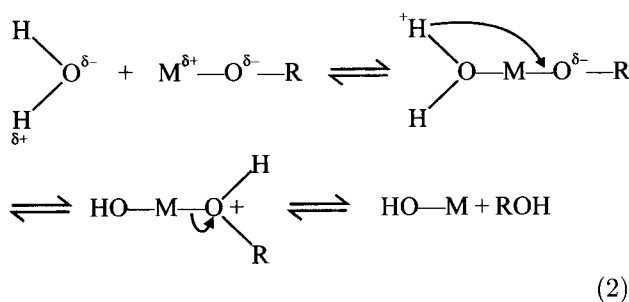
The synthesis of MMOs by sol–gel technique is one of several liquid phase methods that is the most widely employed and has been widely reviewed.^[21–28] Reviews on the preparation of aerogels have also appeared in the literature.^[29,30] Mainly, three routes are used to prepare sol–gel ceramic materials, which are distinguished by the nature of the starting material. They are (1) an aqueous solution of inorganic salt, (2) an aggregate of colloidal particles in a solvent, and (3) a network-forming species

in organic or aqueous solution. The last route is the most acceptable because network formers can be tailor-made or modified to control the chemistry and processing of the gel, and ultimately its morphology. Usually, alkoxides, bimetallic- μ -oxoalkoxides, and heterometallic (double, ter, *tert*-) alkoxides are used as precursors in alcoholic solutions. Other precursors include metal β -diketonates and metal carboxylates.

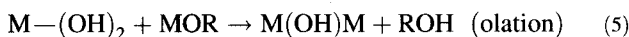
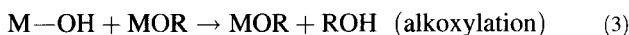
Hydrolysis and condensation of metal alkoxides: The sol-gel route is actually a two-step inorganic polymerization. In the first step, polymerization starts by hydrolysis at the metal-alkoxy linkage yielding alcohol and new reactants, hydroxylated metal centers (M-OH).



The mechanism of this reaction can be outlined as below:

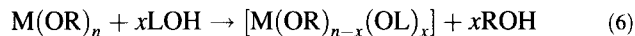


In the second step, condensation or three-dimensional propagation occurs when hydroxylated species condense to form oxypolymers. Polycondensation involves alkoxylation, oxolation, or ololation, a reaction that creates oxygen bridges and releases XOH species (where X=H or R).



The nature of the inorganic framework obviously then determines the relative rates of hydrolysis and condensation at different centers. The rates of hydrolysis and condensation depend upon the nature of metal in terms of its electrophilicity and ability to expand its coordination number.^[31] The hydrolysis rates of transition metal alkoxides are very high, as metal centers are highly electrophilic and exhibit several coordination numbers. This sometimes complicates the problem, especially in the case when heterobimetallic alkoxides are used as precursor, as precipitation occurs at different rates and often instantaneously. One of the suitable ways to overcome this problem is the modification of precursor by reacting alkoxide

with other ligands when the exchange reaction takes place.^[32] This results into a new precursor, which may undergo hydrolysis at a much slower rate.



Thus, at times when alkoxy ligands are quickly removed by hydrolysis, then chelating ligands such as acetyl acetone or other β -diketonates act as terminating agents that limit the condensation reaction.^[33] The major steps involved in sol-gel technique^[21,22] for the preparation of MMOs as outlined in Fig. 1 are:

1. Preparation of a homogeneous solution of pure precursor in an organic solvent, which is miscible with water or the hydrolysis reagent.
2. Preparation of sol from solution by treating the homogeneous solution with H_2O , or H_2O with $HCl/NaOH/NH_4OH$.
3. Allowing the sol to convert into gel by polymerization (aging).
4. Shaping of gel into the desired form or shape followed by drying. In this step, solvent is removed. The manner in which the liquid phase is removed from wet gel determines whether the dried material is a highly porous aerogel or a denser xerogel. A xerogel is formed as the solvent evaporates from the wet gel, resulting in collapse of the wet-gel structure. If the network is compliant, the gel deforms because of capillary forces generated by the liquid phase as it recedes into the body of the gel. Supercritical drying (SCD) or ambient pressure upon wet gels results in

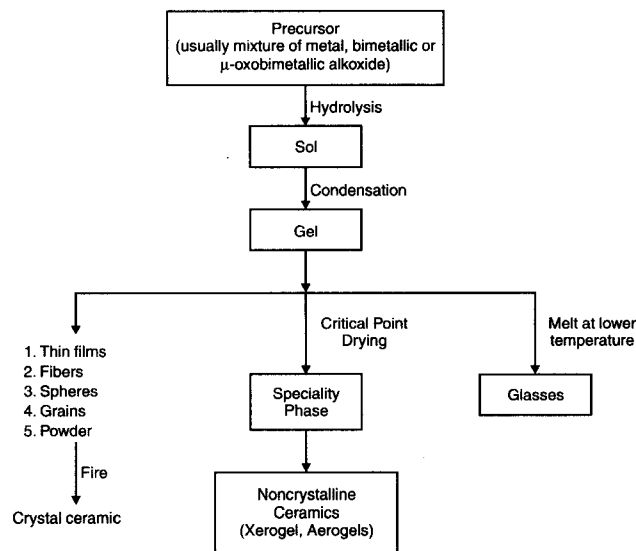


Fig. 1 Steps involved in sol-gel method.

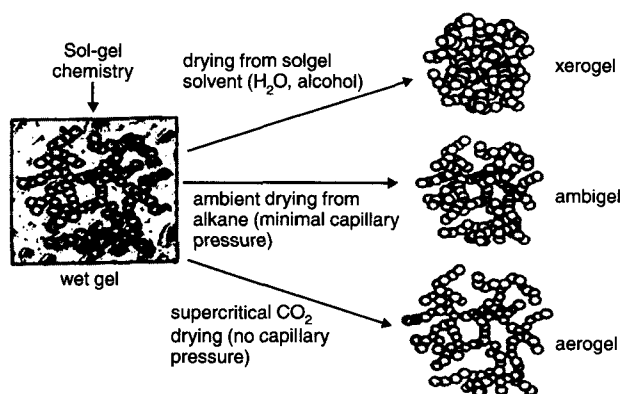


Fig. 2 The method used to extract the pore fluid from a wet gel creates a dry solid with variable porosity: strong capillary forces create a xerogel, weak capillary forces create an ambigel, and zero capillary force creates an aerogel that nominally retains the low-density framework for the wet gel. (Reprinted with permission from Ref. [31].)

aerogels. Aerogels are actually nanoscale mesoporous materials of low density and high surface area.

SCD preserves the porosity by bringing the solvent phase into its supercritical state (a state where no liquid-vapor interface exist), so that capillary pressures do not develop. There are two SCD methods. The sol-gel synthesis of $(\text{Ru}_x\text{Ti}_{1-x})\text{O}_2$ ($x = 0, 0.14, 0.20, 0.32$) involves modification of an alkoxide preparation of TiO_2 with a ruthenium chloride, RuCl_3 , refluxed in ethanol. Monolithic aerogels are formed using SCD method with CO_2 . These were characterized after annealing treatment at 400°C , which removed the chloride and alkoxide. The resulting oxides consisted of ~ 10 nm nanocrystallites of primarily phase-separated TiO_2 and RuO_2 (these rutile phases can form only a solid solution of a few mole percent RuO_2 and TiO_2). These MMO aerogels show surface areas of approximately $85 \text{ m}^2 \text{ g}^{-1}$.^[34]

Ambient pressure method involves surface modifications as well as network strengthening.^[35–38] Surface modification means, for example, that terminal silanols (Si-OH) are replaced by nonreactive groups via silylation or esterification. These modifications inhibit condensation reactions, i.e., conversion of Si-OH centers to Si-O-Si , which locks in structural collapse by sealing compressed pores shut. This allows the porous network to almost retain its original volume. Network strengthening is done by either aging of wet gel in mother liquor (including thermal treatment in water) or soaking it in a precursor alkoxide [such as $\text{Si}(\text{OR})_4$] during washing or aging steps.

One can also use solvents with low surface tension so that pore liquid is exchanged with low-surface-tension solvents just before the ambient-pressure drying. The MMOs so obtained have been named as ambigels and are less porous than the corresponding SCD ceramics but have comparable surface area and pore volume (Fig. 2).^[31] Finally, conversion of the shaped gel to the desired ceramic material by heating takes place at a much lower temperature than the conventional process of melting of oxides together.

Another widely used method for obtaining MMO aerogels is the prehydrolysis route.^[39,40] In this method, two alkoxides with different rates of hydrolysis are used as precursors for obtaining MMO aerogels. However, before mixing these together, the one with the lower rate of hydrolysis is hydrolyzed or partially hydrolyzed separately and then mixed with the other alkoxide solution. This is to avoid phase segregation caused by different rates of hydrolysis. Similarly, hydrolysis of metal alkoxide with faster rate of hydrolysis can be slowed by suit-

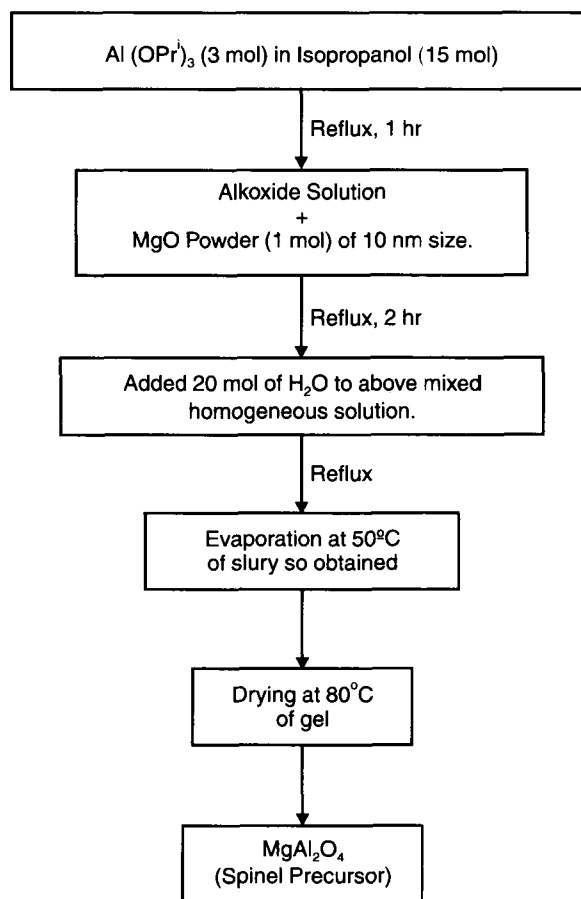


Fig. 3 Preparation route for spinel MgAl_2O_4 precursor.

able complexation. This is done to promote formation of M–O–M' mixed bond, which increases the homogeneity of MMO aerogel. A nonhydrolytic sol–gel route has also been used for preparation of MMO aerogels.^[41] The M–O–M' bridges are obtained by condensation of MX + M'–OR → M–OM + RX. In most cases, these reactions are thermally activated. Actually, the condensation completes with redistribution of the ligands, giving complicated halogenoalkoxides,^[42] which ultimately leads to products after hydrolysis. The surface areas of oxides obtained after calcination was found to be quite high, but a low level of homogeneity on atomic scale was noticed. Syntheses of MgAl₂O₄ spinel and Mg₂SiO₄ spinel forsterite precursor from a heterogeneous alkoxide solution have been reported in the literature.^[43,44] The preparation route is shown in Fig. 3. The obtained precursor was composed of a mixture of boehmite [AlO(OH)] and a mixed hydroxide [Mg₄Al₂(OH)₁₄·3H₂O]. The precursor was converted to a spinel phase through two steps: (1) decomposition of mixed hydroxide at ~400°C and (2) solid-state reaction between MgO (which has decomposed from mixed hydroxide) and γ -Al₂O₃ (which had been converted from boehmite at higher temperature). To prepare almost-monolithic spinel powder, calcination at a temperature of 1300°C was required. Powder that was calcined at 1000°C showed extraordinary sinterability, and fully dense polycrystalline spinel could be obtained at sintering temperature as low as 1400°C.

Synthesis of La_{0.7}Sr_{0.3}MnO₃ (LSMO)/silica hybrid nanocomposites have been reported by Huang et al.^[45] Homogeneous granular mixtures can be obtained through sol–gel chemical route in a single step. The precursors used are the following: (1) complexes of La³⁺, Sr²⁺, and Mn²⁺ with EDTA and (2) tetraethoxysilane (TEOS). Silica is produced by an ammonia-catalyzed method, whereas LSMO is obtained by thermal decomposition of the complex precursors. When hydrolysis of silicon alkoxide to form silica oxyalkoxy oligomers takes place in the LSMO precursor solution, both are formed in the same system. Thus, effective combination of both phases achieves a satisfactory level. The microstructure of the composites can be controlled mainly through the calcination temperature. When calcined at 800°C, silica undergoes some interaction with LSMO, and Si–O–metal bonds are formed. These bonds establish the connection between silica network and LSMO surface.

Synthesis of pure nanocrystalline Al₂O₃/MgO powder has been reported by Carnes et al.^[46] The two Mg and Al alkoxide solutions were mixed in desired molar ratios and then allowed to react with a mixture of water in ethanol to yield a hydroxide gel. Upon solvent removal, a fine powder was obtained, which was then heat-treated under dynamic vacuum. The powder has excellent surface area

(790–830 m²/g) showing a completely amorphous XRD pattern.

Bimetallic- μ -oxoalkoxides as precursors for sol–gel technique: Homogeneously dispersed bimetallic oxides in nanocrystalline form, of the type MAI₂O₄ (where M=Mg, Ca, Mn, Co, Fe, Ni, and Zn) were obtained by preparation of bimetallic- μ -oxo-bridged (Al–O–M–O–Al) alkoxides [(RO)₂Al–O–M–O–Al(OR)₂], which upon thermal dehydration yield oxides [OAl–O–M–O–AlO] such that M is homogeneously dispersed in M and Al₂ ions of empirical formula MAI₂O₄ in nanocrystalline form.^[47] These materials were obtained in high-surface-area forms and were characterized by X-ray diffraction (XRD), electron microscopy (TEM), surface area analyses (BET), and solid-state ²⁷Al NMR. Comparative studies of hydrolysis of μ -alkoxo-bridged alkoxides yielded MMO phases of lower surface area. This method has proved advantageous over other traditional routes. One such method is coprecipitation of metal hydroxides followed by heat treatment at high temperature.

Reverse microemulsion/micelle method

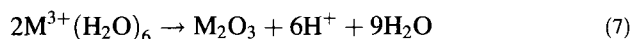
It is a promising route for synthesis of MMO nanoparticles.^[48–50] Surfactants dissolved in organic solvents form spheroidal aggregates called reverse micelles. The polar ends of surfactant molecules organize around small water pools (~100 Å) in the presence of water. This leads to dispersion of aqueous phase in the continuous oil phase. These reverse micelles are used as water solutions of reactive precursors to prepare insoluble nanoparticles. Various reactive precursors such as alkoxides or metal salt mixtures can be used for synthesis of nanoparticles inside the micelles. Solvent removal followed by calcination lead to the final product.

The above method was adopted to prepare the ZnFe₂O₄/TiO₂ nanocomposite.^[51] In this method, ZnFe₂O₄ and TiO₂ were prepared by coprecipitation and controlled hydrolysis methods, respectively. ZnFe₂O₄ was coprecipitated from a mixed solution of Zn(NO₃)₂ and Fe(NO₃)₂ in a 1:2 molar ratio at pH 13 and temperature of 100°C. TiO₂ was precipitated from mixed solution with a volume ratio of Ti(OBu)₄: C₂H₅OH:H₂O ≡ 1:10:100 at pH 2. Both products were washed with deionized water. They were added separately to dodecyl benzene sulphonic acid (DBS), where ZnFe₂O₄ or TiO₂ nanoparticles were capped with a layer of DBS. These then readily dispersed in organic solvents such as benzene or toluene. The capped ZnFe₂O₄ and TiO₂ nanoparticles were mixed in various molar ratios, followed by extraction into toluene. Organic phase was removed by distillation, leaving mixed organic sol of ZnFe₂O₄/TiO₂. This sol was distilled to remove toluene solvent and finally heated at 400°C for

2 hr to burn DBS, leaving behind nanocomposite $\text{ZnFe}_2\text{O}_4/\text{TiO}_2$ material. CoFe_2O_4 nanoparticles were also synthesized by this technique. It uses Co- and Fe-containing surfactants as metal sources.^[52,53]

Low-temperature wet chemical synthesis by precipitation from solutions

It involves dissolving salt precursors, usually chloride, oxychloride, nitrate, etc., in water followed by addition of base solution (NaOH or NH_4OH) to coprecipitate hydroxides. The hydroxide mixtures are calcined to obtain MMO powder. Its disadvantage is poor control of particle size and size distribution, as fast (uncontrolled) precipitation often causes formation of larger particles and not nanoparticles. Mechanistically, in this solvation sheets of water around metal ion are dehydrated under alkaline conditions, e.g.,



The above scheme tells us the importance of alkaline conditions.^[54] As an example, manganese ferrite (MnFe_2O_4) nanoscale particles ranging from 5 to 180

nm have been prepared from Fe^{3+} , Fe^{2+} , and Mn^{2+} aqueous solution.

STRUCTURE AND MORPHOLOGY

Control over structural and morphological properties are most crucial for performance of MMO nanoparticles in various applications. Mixed metal oxides are known to have different structural arrangement of constituent ions. The nature of these ions is important (size and charge) in the final adaptation of geometry; however, control over homogeneity, stoichiometry, phase, and crystallinity largely depend upon structure and reactivity of precursors in homogeneous solutions and their fate in subsequent processing steps. The stoichiometry and homogeneity depend upon the ability of mixed precursors especially on addition of water to form a single molecular species, so that the ions are distributed evenly.

Structural and morphological challenges initiated the search for suitable methods of preparation of various MMO ceramics. Several new and modified methods have been proposed for preparation of numerous ceramic nanoparticles. For example, in a modified aerogel method,

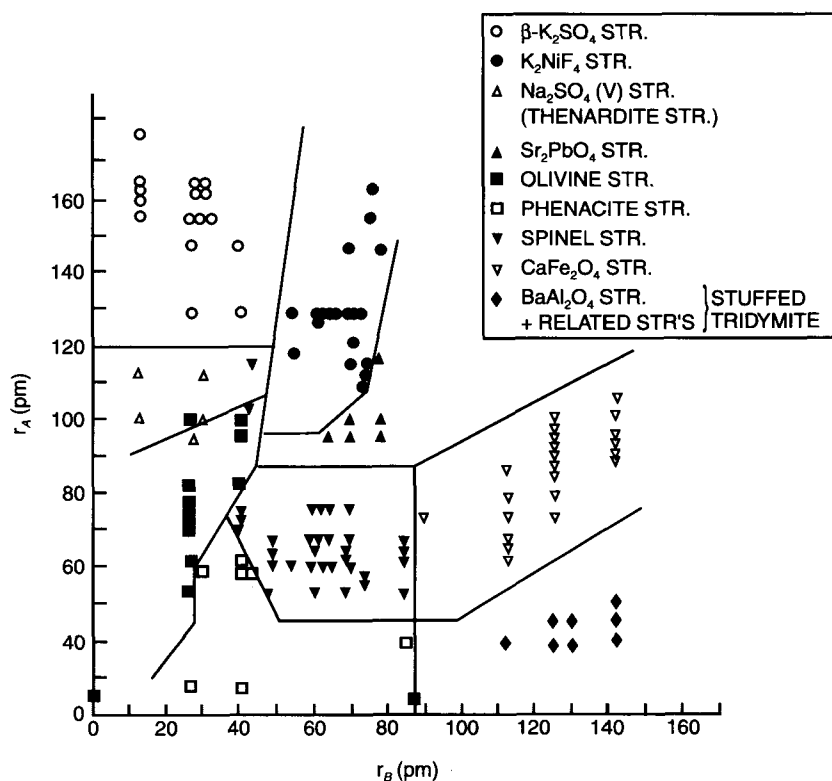


Fig. 4 Classification of the structures of A_2BO_4 ionic minerals as a function of cation radii. (Reproduced with permission from *Treatise on Solid State Chemistry*, Vol. 1, N.B. Hannay, ed., Plenum, New York, Copyright © 1973, Bell Telephone Laboratories, Inc.)

addition of large amount of aromatic hydrocarbons to alcohol–methoxide solutions before hydrolysis to form gel yields ceramic materials with extraordinarily large surface area in comparison to materials obtained without adding it. This is probably because of reduced surface tension of the solvent mixture, which facilitates solvent-removed alcogel–aerogel transformation.^[55,56]

Mixed metal oxide nanoparticles exhibit unusual surface morphologies and possess more reactive surface because of the presence of high concentrations of edge/corner sites and other defects. Morphological studies indicate that the nanocrystals are more polyhedral and thus possess more defects. Such defects could be of the Frankel or Schottky type (vacancies) or may be manifested as unusual configurations of edges, corners, or crystal planes. A ceramic material with high surface area displays 30–40% of the ceramic moieties on the surface, which allows surface gas reactions to approach the stoichiometric range.^[17] As MMOs contain a variety of cations, the prediction of structure simply on the basis of radius ratios of cations and oxide ions becomes complicated. This means some simpler approach is required. For example, take a list of known structures and the radii of the ions present in them. The radii of two of the ions present in a given compound are plotted against each other. This is graphically related to

arithmetic radius ratio approach. It is seen that compounds with similar structures are grouped together. In Fig. 4, compounds of the type $A_2B_4O_4$ (where B is a higher-valent metal than A) are plotted as a function of radii A and B. In these materials, oxide ions form a closed packed array (framework) and sizes of A and B decide how they fit in (sometimes major distortion in closest-packed structure is noticed). On the basis of fields in Fig. 4, one can predict structures of newly discovered ceramic materials with known r_A and r_B values.^[57]

Spinel Structures

It consists of a face-centered cubic arrangement of oxygen ions. A unit cell contains 32 O^{2-} ions, 64 tetrahedral, and 32 octahedral sites, which are occupied by A^{2+} ($A = Mg, Fe, Ca, Zn, \text{etc.}$) and B^{3+} ($B = Al, Fe, \text{etc.}$) cations. The general formula of spinel is written as $A^{II}B_2^{III}O_4$ [where A^{II} is a Group 2 metal ion or transition metal in +2 oxidation state and B^{III} is a Group 3B (B, Al, Ga, In) cation or transition metal ion in +3 oxidation state]. As a unit cell has 32 O^{2-} ion and only 4 are present per molecule (from the formula), then spinel structure has 8 (64/8) tetrahedral and 4 (32/8) octahedral vacancies per molecule of AB_2O_4 . When A^{2+} ions occupy one eighth of a tetrahe-

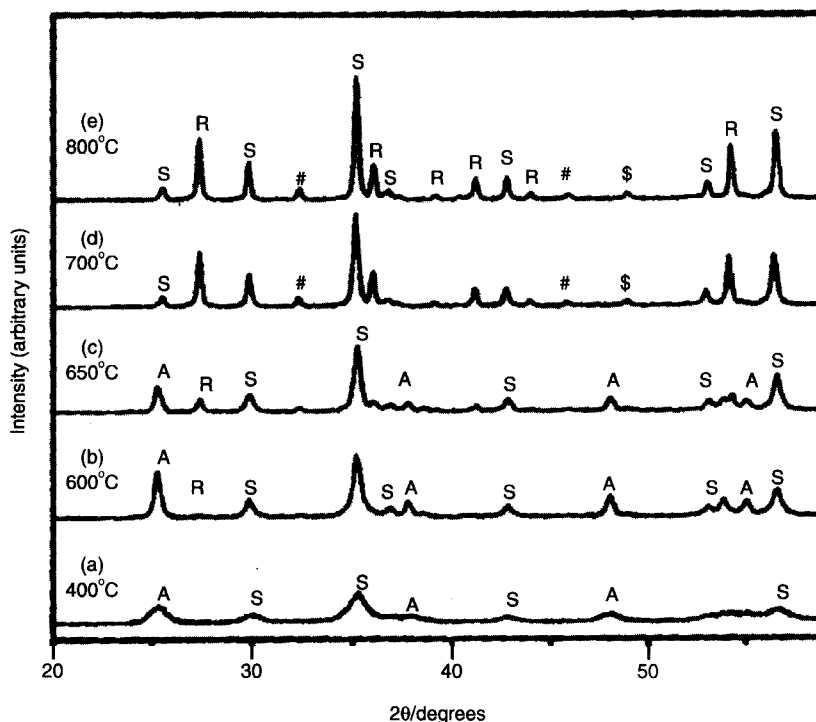
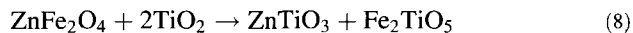


Fig. 5 XRD patterns of the $ZnFe_2O_4/TiO_2$ composite with a molar ratio of $Zn:Ti = 0.1$ after annealing at various temperatures for 2 hr. A = anatase, R = rutile, S = spinel, \$ = Fe_2TiO_5 , # = $ZnTiO_3$. (Reprinted with permission from Ref. [51].)

dral (1 out of available 8) hole and B^{3+} ions occupy half (2 out of available 4) of an octahedral hole, the structure is called "normal" spinel, e.g., $MgAl_2O_4$. This is a very stable arrangement even in terms of coordination, having tetrahedral arrangement about a divalent cation and octahedral arrangement about a trivalent cation. In some cases, one half of B^{3+} ions exchange their positions with A^{2+} ions. This is called "inverse" spinel, e.g., $NiFe_2O_4$. In this arrangement, one eighth of tetrahedral sites are occupied by half of B^{3+} , whereas the rest of B^{3+} ions along with A^{2+} ions occupies half of the octahedral sites. If the general formula for "normal" spinel is written as $(A)[B]_2O_4$ to suggest () and [] representing tetrahedral and octahedral coordination, then the general formula for "inverse" spinel is written as $(B)[AB]O_4$. Many MMOs also have intermediate cation distribution between these two extremes. The general formula for these structure is then written as $(A_{1-x}B_x)[B_{2-x}A_x]O_4$, where x is the "inversion parameter" ($0 < x < 1$).^[58,59]

Nanocomposites of $ZnFe_2O_4$ and TiO_2 were studied by Yuan and Zhang.^[51] TiO_2 (anatase phase) and $ZnFe_2O_4$ (spinel phase) with broad diffractions were recorded [Fig. 5a]. This means that in the composite, TiO_2 and $ZnFe_2O_4$ crystallite phases separate each other, having small size. Fig. 5b and c shows composite begins to form at $600^\circ C$. Anatase to rutile transformation takes place at $700^\circ C$. [Fig. 5d and e]. The strongest peak ($2\theta = 25.3^\circ$) disappears and, simultaneously, two new peaks of phases $ZnTiO_3$ and Fe_2TiO_5 appear. This shows the following solid-phase reaction might be taking place at annealing temperature.



Measurement of grain sizes in comparison with values of TiO_2 and $ZnFe_2O_4$ shows the following: (1) As annealing temperature increases, the grain size of TiO_2 increases. (2) In composite, an increase in temperature has the same effect of growth of $ZnFe_2O_4$ as it does on pure $ZnFe_2O_4$. TEM analysis proved particles are distributed homogeneously and particles grow with uniform sizes.

Perovskite Structures

Perovskite-phase MMO ceramics are important because of changes in their physical properties on application of an external electrical stimulus. These properties include ferroelectric, pyroelectric, piezoelectric, and dielectric behavior. These have led to numerous applications in electromechanical transducers, light modulation, charge storage, nonvolatile memory applications, etc.^[23,24] The class of MMOs having the formula ABO_3 (such as $CaTiO_3$) is called perovskite. The structure of this mineral was first thought to be cubic but later confirmed as

orthorhombic. The truly cubic form is referred to as "ideal perovskite" having a unit cell edge of $\sim 4 \text{ \AA}$ containing one ABO_3 . In perovskite structure, large cation A is surrounded by 12 oxide ions to form cuboctahedral coordination, while B cation is surrounded by 6 oxide ions in an octahedral coordination.

Nanophase powders of $Y_xZr_{1-x}O_{2-x/2}$ have been prepared from a mixture of ZrO_2 and Y_2O_3 powders.^[60] It is shown that depending upon the starting powder mixture composition, the yttrium content in nanophases can be controlled to obtain tetragonal or cubic phases. Tetragonal or a mixture of tetragonal and cubic were observed for low yttria content (3.5 mol% yttria), and cubic for higher yttria contents (19, 54, and 76 mol% yttria). These powders were found to have a most probable grain size of about 10–12 nm, and the grains appeared as isolated single crystals with polyhedral shape. The grain shape appeared to be polyhedral and not too anisotropic. Lattice figures were parallel to surfaces, showing that (100) and (111) face dominates.^[17]

PROPERTIES AND APPLICATIONS OF MIXED METAL OXIDE NANOPARTICLES

Properties of MMO nanoparticles are mainly size dependent, and their chemical and physical properties are unique in comparison to corresponding bulk materials. The study of physical and chemical properties is interesting as it allows gradual transition from atomic or molecular to condensed matter systems. As the particle size decreases, the percentage of atoms residing on the surface increases. This makes MMO nanoparticles more reactive, as atoms/ions are more reactive than their bulk counterparts because of coordinative unsaturation. Because of this and high surface-to-volume ratio, it is not unusual to see unique behavior and characteristics of MMO nanoparticles, including insulating oxides. When strong chemical bonding is present, delocalization varies with size; this in turn can lead to different chemical and physical properties.^[17]

Acid–Base Behavior (Catalysts)

Several oxide composites have been found to be potential catalysts for a variety of important reactions because of different centers present in the same material and their basicity or acidity.^[61,62] This behavior varies from one MMO to another. Some exhibit surface basic behavior and some surface acidic behavior, whereas mixtures show unusual properties. The mixing of two oxides can enhance the catalytic activity many fold because of synergistic

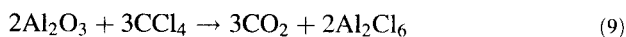
effects, as seen in the mixed aerogel of titania/zirconia. The acid strength increases and active sites are more than pure titania and zirconia. This is probably because of oxide–oxide interaction at molecular level, suggesting that co-gelling two metal oxides is an effective way to bring two oxides in close contact.^[17]

Unusual Adsorptive Properties

Perhaps one of the greatest promises of MMO nanoparticles in chemistry is their ability to chemically adsorb a wide range of organic molecules or inorganic gases that are considered as hazardous environment pollutants. They not only adsorb but also dissociate these to nonhazardous substances on their surface. Carnes et al.^[46] studied the adsorption of CCl₄, SO₂, and paraoxon on both Al₂O₃ and Al₂O₃/MgO.

Reaction of Al₂O₃ and (1/1) Al₂O₃/MgO with CCl₄

The reaction of CCl₄ with Al₂O₃ and Al₂O₃/MgO was carried out to understand the destructive adsorption abilities of the metal oxides toward a model chlorocarbon at elevated adsorption temperatures.



Thermodynamics predicts that the samples containing or being made of MgO will be more reactive than the Al₂O₃ samples.^[31] However, surface area, crystallite size, and morphology play important roles.

Sulfur dioxide adsorption on aluminum and aluminum/magnesium oxide

Adsorption of SO₂ was carried out to learn if the adsorption properties are different for nanocrystals (NC) when compared to commercial microcrystals (MC).^[46] The experimental results showed that at atmospheric pressure and room temperature, SO₂ adsorbed onto NC-Al₂O₃ up to 3.5 molecules SO₂/nm²; similarly, on CM-Al₂O₃ there were 3.5 molecules SO₂/nm² adsorbed, and on NC-(1/1) Al₂O₃/MgO there were 6.8 molecules SO₂/nm², whereas on CM-MgO there were only 0.68 molecules SO₂/nm² adsorbed. These data indicate that NC-Al₂O₃/MgO efficiently adsorb SO₂ in slightly more than one layer. After adsorption, the samples were subjected to dynamic vacuum to remove the physisorbed species. The vacuum treatment removed most of the adsorbed SO₂ from the CM-MgO, whereas the NC-Al₂O₃/MgO sample retained 3.9 chemisorbed molecules of SO₂/nm².

CONCLUSION

Mixed metal oxide nanoparticles can provide great diversity of substances and phenomena. Different metals in their various oxidation states can combine in different ratios to produce a variety of materials. These new materials with variation in physical, chemical, and morphological properties can be exploited in various fields of science and technology. The compression of nanoscale ceramic particles yields more flexible solid objects, apparently because of the multitude of grain boundaries that exist. After further development of compression techniques so that highly densified nonporous MMO nanomaterials can be prepared, these may find uses as replacements for metals in many applications including electrochemistry. These materials, beyond doubt, would be environment friendly, not only by themselves but also as future water purifiers and destructive adsorbents. These MMO nanoparticles are finding use in antichemical/biological warfare, in air purification, and as an alternative to incineration of toxic substances. Mixed metal oxide nanoparticles would also be replacing many heterogeneous catalysts known today because of high surface area, which increases their efficiency many fold. Research on the effect of particle size (percent dispersion as a measure of the fraction of metal atoms on the surface and thus available to incoming reactants) and shape (crystal faces, edges, corners, defects that lead to enhanced surface reactivity) has been and continues to be a potential field. In general, the ability to prepare MMO nanoparticles for use in high surface area catalysis has certain inherent advantages, and further progress is sure to come in the near future. It has been proposed that further work in the area of nanophase ceramics may lead to increased flexibility, less brittleness, and greater strength. It may also be possible to form materials with a large fraction of atoms at grain boundaries, maybe in unique arrangements. It may also be possible to produce binary materials of normally immiscible oxides. This article has explored the synthetic, structural, and application prospects that MMO nanoparticles provide. Although relatively few examples have been chosen, all relevant areas have been covered.

REFERENCES

1. Amigó, R.; Asenjo, J.; Krotchenko, E.; Torres, F.; Tejada, J. Electrochemical synthesis of new magnetic mixed oxides of Sr and Fe: Composition, magnetic properties, and microstructure. *Chem. Mater.* **2000**, *12* (2), 573–579.
2. Rodriguez, J.A.; Hanson, J.C.; Chaturvedi, S.; Maiti, A.; Brito, J.L. Phase transformations and electronic properties in mixed metal oxides; experimental and

- theoretical studies on the behavior of NiMoO₄ and MgMoO₄. *J. Chem. Phys.* **2000**, *112* (2), 935–945.
- Heinz, D.; Hoelderich, W.F.; Krill, S.; Boeck, W.; Huthmacher, K. V₂O₅/TiO₂ catalysts for the vapor-phase oxidation of β-picoline: Influence of the TiO₂ carrier. *J. Catal.* **2000**, *192*, 1–10.
 - Watanabe, H.; Koyasu, Y. New synthesis route for Mo–V–Nb–Te mixed oxide catalyst for propane amoxidation. *Appl. Catal. A* **2000**, *194–195*, 479–485.
 - Corma, A. Inorganic solid acids and their use in acid catalyzed hydrocarbon reactions. *Chem. Rev.* **1995**, *95*, 559–614.
 - Reddy, B.N.; Subrahmanyam, M. Amoxidation of 3-picoline over highly dispersed vanadia on alumina–silica mixed support. *Langmuir* **1992**, *8*, 2072–2073.
 - Kiessling, D.; Went, G.; Hagenau, K.; Schoellner, R. Dimerization of n-butenes on amorphous nickel oxide–alumina/silica catalysts. *Appl. Catal.* **1991**, *71*, 69–78.
 - Andrianainarivelo, M.; Corrin, R.; Laclercq, D.; Mutin, P.H.; Vioux, A. Mixed oxides SiO₂–ZrO₂ and SiO₂–TiO₂ by a non-hydrolytic sol–gel route. *J. Mater. Chem.* **1996**, *6* (10), 1665–1671.
 - Siegel, R.W.; Ramaswami, S.; Hahn, H.; Zongquan, L.; Ting, L.; Grousky, R. Synthesis, characterization, and properties of nanophase titanium dioxide. *J. Mater. Res.* **1988**, *3*, 1367–1372.
 - El-Shall, M.S.; Slack, W.; Vann, W.; Kane, D.; Hanely, D. Synthesis of nanoscale metal oxide particles using laser vapourisation/condensation in diffusion cloud chamber. *J. Phys. Chem.* **1994**, *98* (12), 3067–3070.
 - Nanophase Materials*; Edelstein, A.S., Hadjipayanis, G.C., Siegel, R.W., Eds.; Kluwer Academic Publishers: Dordrecht, 1994; 73–80 and 85–88.
 - Nanotechnology, Molecularly Designed Materials*; Cow, G.M., Gonsalves, K.E., Eds.; American Chemical Society: Washington, DC, 1996; 79–99.
 - Kodas, T.T. *Adv. Mater.* **1989**, *6*, 180.
 - Messing, G.L.; Zhang, S.C.; Jayanthi, G.V. Ceramic powder synthesis by spray pyrolysis. *J. Am. Ceram. Soc.* **1993**, *76* (11), 2707–2726.
 - Nanotechnology, Molecularly Designed Materials*; Cow, G.M., Gonsalves, K.E., Eds.; American Chemical Society: Washington, DC, 1996; 64–78.
 - Skanadan, G.; Chen, Y.I.; Glumac, N.; Kear, B.H. Ceramic powder synthesis by spray pyrolysis. *Nanostruct. Mater.* **1999**, *11* (2), 149–158.
 - Khaleel, A.; Richards, R.M. Ceramics. In *Nanoscale Materials in Chemistry*; Klabunde, K.J., Ed.; Wiley-Interscience: New York, 2001; 85–120.
 - Laine, R.M.; Waldner, K.; Bickmore, C.; Treadwell, D.R. Ultrafine powders by flame spray pyrolysis. U.S. Patent, 5, 958, 361, Sept. 28, 1999.
 - Laine, R.M.; Rand, S.C.; Hinklin, T.; Williams, G. Ultra-fine powders as lasing media. WO 0038282 HOIS 20000629.
 - Pramanik, P.; Roy, J.C.; Sen, A.; Pati, R.K. Novel Chemical Methods for Preparation of Nanosized Oxide Ceramics. In *International Symposium on Metastable, Mechanically Alloyed and Nanocrystalline Materials*, Proceedings of ISMANAM-2000, Oxford, UK, Material Science Forum, 2001; Vols. 360–362, 623–630.
 - Mehrotra, R.C.; Singh, A. Recent Trends in Metal Alkoxide Chemistry. In *Progress in Inorganic Chemistry*; Karlin, K.D., Ed.; John Wiley & Sons Inc., 1997; 239–454.
 - Mehrotra, R.C.; Singh, A.; Tripathi, U.M. Recent advances in alkoxy and aryloxy chemistry of scandium, yttrium and lanthanoids. *Chem. Rev.* **1991**, *91*, 1287–1303.
 - Chandler, E.D.; Roger, C.; Smith, M.J.H. Chemical aspects of solution routes to perovskite-phase mixed-metal oxides from metal–organic precursors. *Chem. Rev.* **1993**, *93*, 1205–1241.
 - Liliane, G.H.P. Heterometallic alkoxides and oxoalkoxides as intermediates in chemical routes to mixed metal oxides. *Polyhedron* **1994**, *13*, 1185–1195.
 - Chemistry of Advanced Materials: An Overview*; Interrante, L.V., Hampden, M.J., Eds.; Wiley-VCH: New York, 1998.
 - Hench, L.L.; West, J.K. Aerogels—Airy materials: Chemistry, structure, and properties. *Chem. Rev.* **1990**, *90*, 33–72.
 - Brinker, C.J.; Scherer, C.W. *Sol–Gel Science*; Academic Press: San Diego, CA, 1990.
 - Narula, C.K. *Ceramic Precursor Technology and Its Applications*; Marcel Dekker: New York, 1995.
 - Husing, N.; Schubert, U. Aerogels—Airy materials: Chemistry, structure, and properties. *Angew. Chem. Int. Ed.* **1998**, *37*, 22–45.
 - Schneider, M.; Baiker, A. Titania-based aerogels. *Catal. Today* **1997**, *35*, 339–365.
 - Rolison, D.R.; Dunn, B. *Electrically Conductive Oxide Aerogels: New Materials in Electrochemistry*; *J. Mater. Chem.*; Royal Chemical Society, 2001; Vol. 11, 963–980.
 - Sanchez, C.; Livage, J.; Henry, M.; Babonneau, F. *J. Non-Cryst. Solids* **1998**, *100*, 65.
 - Ribot, F.; Toledano, P.; Sanchez, C. *Chem. Mater* **1991**, *3*, 759.
 - Swider, K.E.; Hagans, P.L.; Merzbacher, C.I.; Rolison, D.R. Synthesis of ruthenium dioxide–

- titanium dioxide aerogels: Redistribution of electrical properties on the nanoscale. *Chem. Mater.* **1997**, *9*, 1248–1255.
35. Prakash, S.S.; Brinker, C.J.; Hurd, A.J.; Rao, S.M. Silica aerogel films prepared at ambient pressure by using surface derivatisation to reduce reversible drying shrinkage. *Nature* **1995**, *374*, 439–443.
36. Gerben, T. The subcritical preparation of aerogels based on sodium water glass. *J. Sol-Gel Sci. Technol.* **1998**, *13*, 323.
37. Haereid, S.; Anderson, J.; Einarsrud, M.A.; Hua, D.W.; Smith, D.M. *J. Non-Cryst. Solids* **1995**, *185*, 221.
38. Haereid, S.; Nilsen, E.; Einarsrud, M.A. Properties of silica gels aged in TEOS. *J. Non-Cryst. Solids* **1996**, *204*, 228–234.
39. Yoldas, B.E. Formation of titania–silica glasses by low temperature chemical polymerization. *J. Non-Cryst. Solids* **1980**, *38 & 39*, 81–86.
40. Miranda Salvado, I.M.; Fernandez Navarro, J.M. *J. Non-Cryst. Solids* **1992**, *147–148*, 256.
41. Andrianainarivelo, M.; Corriu, R.; Leclercq, D.; Mutin, P.H.; Vionx, A. Mixed oxides $\text{SiO}_2\text{-ZrO}_2$ and $\text{SiO}_2\text{-TiO}_2$ by non-hydrolytic sol–gel route. *J. Mater. Chem.* **1996**, *6* (10), 1665–1671.
42. Bradley, D.C.; Hancock, D.C.; Wardlaw, H. Titanium chloride alkoxides. *J. Chem. Soc.* **1952**, 2773–2778.
43. Shino, T.; Shiono, K.; Miyamoto, K.; Pezzotti, G. Synthesis and characterization of MgAl_2O_4 spinel precursor from a heterogeneous alkoxide solution containing fine MgO powder. *J. Am. Ceram. Soc.* **2000**, *83* (1), 235–237.
44. Shiono, T.; Migamoto, K.; Sugishima, Y.; Okamoto, Y.; Hayashi, K.; Nishikawa, T. Preparation and sinterability of forsterite powders derived from heterogeneous alkoxide solution containing fine MgO powders. *J. Jpn. Soc. Powder Metall.* **1994**, *41* (5), 573–576.
45. Huang, Y.H.; Yan, C.H.; Wang, S.; Luo, F.; Wang, Z.M.; Liao, C.S.; Xu, G.X. Chemical synthesis of $\text{La}_{0.7}\text{Sr}_{0.3}\text{MnO}_3$ /silica homogeneous nanocomposites. *J. Mater. Chem.* **2001**, *11*, 3296–3299.
46. Carnes, C.L.; Kapoor, P.N.; Klabunde, K.J. Synthesis, characterisation and adsorption studies of nanocrystalline aluminium oxide and a bimetallic nanocrystalline aluminium oxide/magnesium oxide. *Chem. Mater.* **2002**, *14*, 2922–2929.
47. Kapoor, P.N.; Heroux, D.; Mulukutla, R.S.; Klabunde, K.J. High surface area homogeneous nanocrystalline bimetallic oxides obtained by hydrolysis of bimetallic- μ -oxoalkoxides. *J. Mater. Chem.*, **2003** *13*, 410–414.
48. Herrig, H.; Hempelmann, R. *Mater. Lett.* **1996**, *27*, 287.
49. Fang, J.; Wang, J.; Ng, S. C.; Chew, C.H. *Nanostruct. Mater.* **1997**, *8* (4), 499.
50. Gan, L.M.; Zhang, L.S.; Chan, H.S.O.; Chew, C.H.; Loo, B.H. A novel method for the synthesis of perovskite-type mixed metal oxides by the inverse microemulsion technique. *J. Mater. Sci.* **1996**, *31*, 1071–1079.
51. Yuan, Z.; Zhang, L. *Synthesis, Characterisation and Photocatalytic Activity of $\text{ZnFe}_2\text{O}_4/\text{TiO}_2$ Nanocomposite*; *J. Mater. Chem.*, 2001; Vol. 11, 1265–1268.
52. Davies, K.J.; Wells, S.; Upadhyay, R.V.; Charles, S.W.; O’Grady, K.; Hilo, M.E.; Meaz, T.; Morep, S. The observation of multi-axial anisotropy in ultra-fine cobalt ferrite particles used in magnetic fluids. *J. Magn. Magn. Mater.* **1995**, *149*, 14–18.
53. Pillai, V.; Shah, D.O. Synthesis of high-coercivity cobalt ferrite particles using water-in-oil microemulsions. *J. Magn. Magn. Mater.* **1996**, *163*, 243–248.
54. Thimmaiah, S.; Rajamathi, M.; Singh, N.; Bera, P.; Meldrum, F.; Chandershekhar, N.; Seshadri, R. A solvothermal route to capped nanoparticles of $\gamma\text{-Fe}_2\text{O}_3$ and CoFe_2O_4 . *J. Mater. Chem.* **2001**, *11*, 3215–3221.
55. Klabunde, K.J.; Stark, J.V.; Koper, O.; Mohs, C.; Khaleel, A.; Glavee, G.; Zhang, D.; Soresen, C.M.; Hadjipanayis, G.C. *Nanophase Materials*; Hadjipanayis, G.C., Siegel, R.W., Eds.; Kluwer Academic Publishers: Dordrecht, 1994; 1–21.
56. Bedilo, A.; Klabunde, K.J. Synthesis of catalytically active zirconia aerogels. *J. Catal.* **1998**, *176*, 448–458.
57. Huheey, J.E. Ionic Bonding and The Nature of Solids. In *Inorganic Chemistry, Principles of Structure and Reactivity*, 2nd Ed., Harper International Edition; Harper & Row Publishers: New York, 1978; 86–87.
58. Bragg, W.H. The structure of the spinel group of crystals. *Philos. Mag.* **1915**, *176* (30), 305–315.
59. Sickafus, K.E.; Wills, J.M. Structure of spinel. *J. Am. Ceram. Soc.* **1999**, *82* (12), 3279–3292.
60. Rouanet, A.; Pichelin, G.; Roucau, C.; Snoeck, E.; Monty, C. *Nanophase Materials*; Hadjipanayis, G.C., Siegel, R.W., Eds.; Kluwer Academic Publishers: Dordrecht, 1994; 85–88.
61. Philipp, R.; Omate, K.; Aoki, A.; Fujimoto, K. On the active site of magnesia/calcium oxide mixed oxide for oxidative coupling of methane. *J. Catal.* **1992**, *134*, 422–433.
62. Stakheev, A.; Yu Shapiro, E.S.; Apijok, J. XPS and XAES study of $\text{TiO}_2\text{-SiO}_2$ mixed oxide system. *J. Phys. Chem.* **1993**, *97*, 5668–5672.

Molecular Assembly of Nanowires

Tomoyuki Akutagawa
Takayoshi Nakamura

Hokkaido University, Sapporo, Japan

Jan Becher

University of Southern Denmark, Odense, Denmark

INTRODUCTION

Fabrication of one-dimensional (1-D) fundamental nanoscale structures from molecular systems through bottom-up approach should be one of the most important steps to realize nanoscale electronic devices.^[1–3] Because 1-D systems are the structures with the lowest dimension that permit efficient electron transport, the nanowires are expected to be critical to functionalize and integrate the nanoscale electronic devices. Nanowires are important units in constructing electronic circuits, particularly in electrical conducting; thus a variety of nanowires have been the focus of extensive studies aimed toward nanoscale electronic systems.^[1–4] At present, a wide range of compounds from inorganic metals, semiconductors, and carbon nanotubes have been employed as nanowires (Fig. 1).^a The diameter, length, and electronic structure of these nanowires varied significantly. The electronic properties of nanowires range from insulating, semiconducting, metallic, to superconducting. Electrical conduction within nanowires is dominated by the carriers at around Fermi level of the band structure, just as in bulk metals and semiconductors (Fig. 1).^[5] Although the electronic density of states along the short axis of nanowire has a discrete character because of the restricted lattice translation, that along the wire direction is approximately represented as the band structure.^[6] The doped polymers, single-walled carbon nanotubes (SWCNTs), semiconductor, and metal nanowires may have Fermi surfaces. On the other hand, DNAs are the insulator with large band gap. Semiconductor nanowires are more important than metal nanowires from the viewpoint of device application.^[7]

Although only a few examples are reported for the preparation of nanowires of molecular assemblies,^[8–10] we consider that these molecular nanowires should have an important role in the complete bottom-up manufacture of the molecular electronics. Such nanowires can be

assembled from π -molecules through molecule-by-molecule π -stacking. The researches in the field of “molecular conductors” will offer a guiding principle in constructing electrical conducting molecular nanowires.^[11–15] The anisotropic charge-transfer (CT) interaction in molecular conductors is advantageous to form the 1-D π - π stacking nanowire structure. In addition, “supramolecular chemistry” will offer powerful tools to fabricate molecular nanowires through the self-assembly process.^[16–18] Appropriate design of molecule to orient and integrate the molecular-assembly nanowires on the substrate surface should be effective to realize molecular-assembly electronic devices. Furthermore, the techniques of “Langmuir–Blodgett (LB) Films” are very useful methods to fabricate nanoscale molecular-assembly structures on a variety of substrate surfaces.^[19–21] To realize molecular-assembly nanoscale devices through bottom-up chemical approach, three types of scientific concepts—molecular conductor, supramolecular chemistry, and surface science—should be linked together.

Molecular Conductors

A large number of molecular conductors, ranging from semiconductors to metals and superconductors, was prepared.^[11–15] In general, a stable organic molecule has a closed-shell electronic structure without conduction carriers, thereby making molecular solids highly insulating. Conduction carriers can be generated via the intermolecular CT interaction between the highest occupied molecular orbital (HOMO) of the electron donor (**D**) and the lowest occupied molecular orbital (LUMO) of the electron acceptor (**A**) molecules. Fig. 2a shows the molecular structures of typical **D** and **A** molecules utilized in the field of molecular conductors. Among them, tetrathiafulvalene (TTF) and 7,7,8,8-tetracyano-*p*-quinodimethane (TCNQ) are the well-known **D** and **A** molecules, respectively, which gave the first molecular metal of $(\text{TTF}^{+0.59})(\text{TCNQ}^{-0.59})$. The degree of CT (δ) in the binary $(\text{D}^{+\delta})(\text{A}^{-\delta})_x$ CT complex depends on the ionization potential of **D** and electron affinity of **A** molecules. The planar

^aRecent progress in nanowires. See special issue of nanowires in Ref. [4].

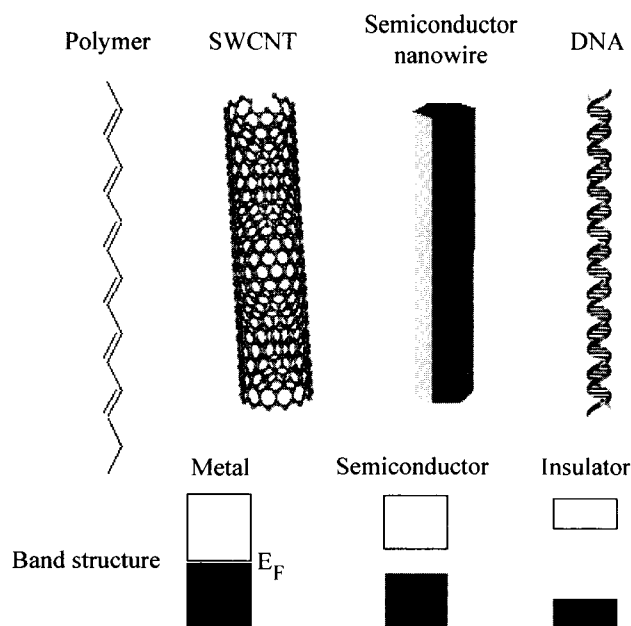


Fig. 1 Nanowires constructed from doped-polymer, SWCNT, semiconductor, and DNA. The electronic band structures of these are illustrated below. (View this art in color at www.dekker.com.)

π -conjugated D and A molecules have a tendency to form the 1-D columnar structure through the π - π stacking interaction, which also formed 1-D π -band structure (Fig. 2b). Because the π -orbitals exist orthogonal to the molecular plane, the direction of π - π interaction is highly anisotropic. Therefore, the 1-D π - π interaction in the molecular conductors is suitable for obtaining molecular nanowires.

Langmuir-Blodgett Technique

Langmuir-Blodgett (LB) method is one of the conventional fabrication techniques of nanoscale thin-film structures utilizing the air-water interface.^[19-21] Fig. 3 illustrates typical procedures to obtain Langmuir monolayer at the air-water interface and the film-forming processes of LB multilayers on substrate. Amphiphilic molecules having hydrophilic and hydrophobic moieties are dissolved into conventional organic solvents, which were spread at the air-water interface. The monolayer with a thickness of molecular scale can form a variety of molecular-assembly structures such as gas-, liquid-, and solid-like short- and long-range orders through the control of surface pressure (F , mN m^{-1}). Increase in the F enhances the magnitude of intermolecular interactions between the molecules. The chemical designs of hydrophilicity and hydrophobicity of the component molecules are important to obtain stable monolayer at the air-water interface.

Stable monolayers at the air-water interface can be transferred onto hydrophilic or hydrophobic substrates via dipping of the substrate. Glass, quartz, CaF_2 , Si, and mica are utilized as typical hydrophilic substrates. The surface wetting of these substrates largely influences the surface morphologies of the transferred LB films. Another conventional deposition technique is the horizontal-lifting method, which directly transfers the monolayer at the air-water interface onto the hydrophobic substrate.

Electrically active thin films have been fabricated by the LB techniques.^[22-24] For example, metallic and semiconducting LB films have been obtained from amphiphilic molecular conductors based on TTF and TCNQ derivatives.^[22-24] Although the LB films possess a periodicity along the film-forming direction, random distribution of two-dimensional crystalline domains on the substrate surface dispels bulk periodicity within the substrate surface. To realize nanoscale electronic devices through bottom-up self-assembly approach, the orientation and size control of these electrical active domains within the substrate surface are two of the important problems that need to be overcome.

Supramolecular Chemistry

The term of supramolecular chemistry is a last key science to realize the bottom-up self-assembly approach.^[16-18] Supramolecule is defined as an entity composed of several or large numbers of molecules, which are connected to each other through the noncovalent weak intermolecular interactions such as van der Waals (dipole-dipole, dipole-induced dipole and dispersion interactions), charge-transfer, hydrogen-bonding interactions, etc. The design of these intermolecular interactions is essential to obtain self-assembly molecular nanowires. Self-assembled supramolecules bearing the desired structure can be achieved by using programmed molecules that are appropriately designed. From the flexibility in supramolecular designs together with the rich physics in molecular conductors, electrical active molecular nanowires are considered as very promising candidates for constructing future nanoscale devices.

A large number of complex supramolecular assemblies have already been constructed.^[16-18] A simple complex between cation and crown ether is one of the typical model systems of supramolecules^[25,26] (Fig. 4). Crown ethers such as 12-crown-4, 15-crown-5, and 18-crown-6 have hydrophilic cavity to bind cation through metal-oxygen interatomic interactions. According to the size of hydrophilic cavity, cations can be selectively included into the cavity. For example, 15-crown-5 and 18-crown-6 molecules show high Na^+ and K^+ affinity, respectively. We already introduced two design concepts of molecular conductors and LB technique to fabricate molecular-assembly nanowires. For an effective design of

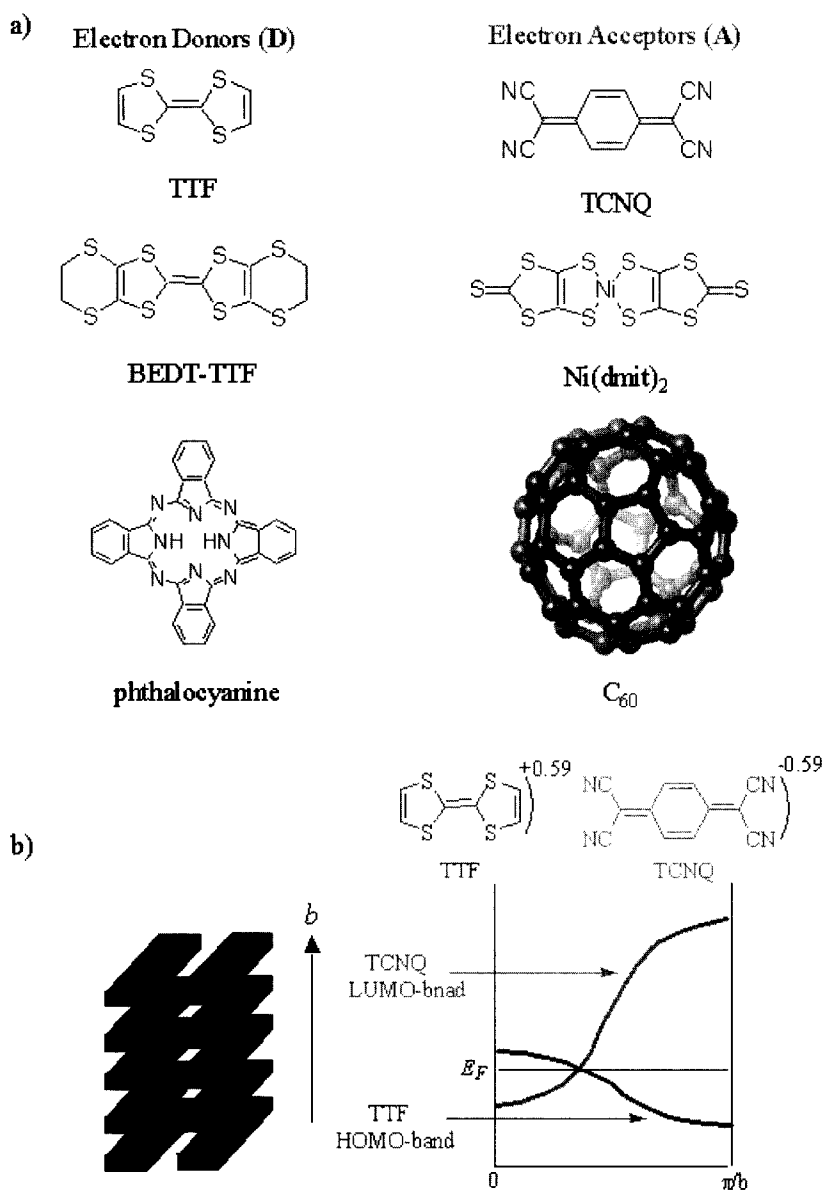


Fig. 2 Molecular structures of typical a) electron donor (D) and acceptor (A) molecules employed in molecular conductors. b) The 1-D columnar structure through the π - π stacking interaction in crystals (left) and metallic 1-D π -band structure of (TTF)(TCNQ) (right). (View this art in color at www.dekker.com.)

molecular nanowires, we further introduced the supramolecular approach to obtain nanowire orientation on the substrate surface.

RESULTS AND DISCUSSION

Design of Molecules for Fabricating Molecular-Assembly Nanowires

Amphiphilic bis(tetrathiafulvalene) [bis(TTF)] macrocycle **1** was designed from the concepts of molecular

conductors, Langmuir-Blodgett films, and supramolecular chemistry.^[27,28] The molecule has two redox-active TTF units that are linked via a [24]crown-8 macrocycle and two long hydrophobic decylthio-chains (Fig. 5). Two TTF units within the molecule **1** can act as electron donor for realizing intermolecular CT interaction with electron acceptors, which forms electrically conducting 1-D π - π stacks. The second structural point is the introduction of two hydrophobic chains ($-\text{SC}_{10}\text{H}_{21}$), which were introduced into one side of the TTF unit. By introducing these hydrophobic chains, the molecule has amphiphilic character to apply the LB technique. The last designing point

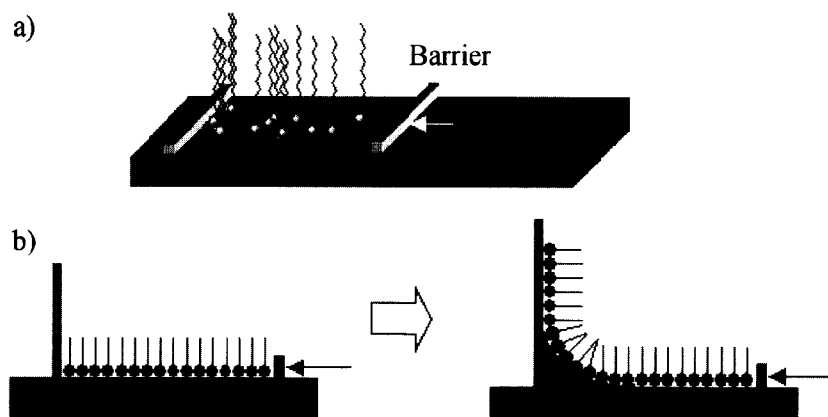


Fig. 3 Langmuir-Blodgett technique to fabricate nanoscale thin-film structures. a) Langmuir monolayer at the air-water interface. Amphiphilic molecule has hydrophilic (red head) and hydrophobic tail. Surface pressure (F , mN m^{-1}) can be controlled by moving barriers. b) Transfer process of Langmuir monolayer onto substrate surface. (View this art in color at www.dekker.com.)

is carried out via the supramolecular approach—the introduction of ion-recognizing crown ether moiety into the molecule. The ion-recognizing property can be employed to fabricate oriented molecular-assembly nanowires on the substrate surface.

Compound **1** was synthesized by the cyanoethyl protected TTF building block.^[29,30] Stepwise deprotection/alkylation procedure was performed by $\text{CsOH} \cdot \text{H}_2\text{O}$ /2,6-bis(2-iodoethoxy)ethane. Because a TTF molecule possesses a two-step redox process ($\text{TTF} \rightarrow \text{TTF}^+$ and $\text{TTF}^+ \rightarrow \text{TTF}^{2+}$),^[11–15] donor **1** possesses a four-step redox process. The cyclic voltammetry (CV) diagram of donor **1** in 1,2-dichloroethane ($\text{C}_2\text{H}_4\text{Cl}_2$) vs. SCE showed the two-step, two-electron oxidation waves at 0.56 and 0.90 V, respectively.^[27,28] The two TTF units in donor **1**, linked via [24]crown-8 unit, independently exhibited redox reaction.

The CT complex between one molecule of donor **1** and two molecules of 2,3,5,6-tetrafluoro-7,7,8,8-tetracyano-*p*-quinodimethane ($\text{F}_4\text{-TCNQ}$), $(\mathbf{1})(\text{F}_4\text{-TCNQ})_2$ was pre-

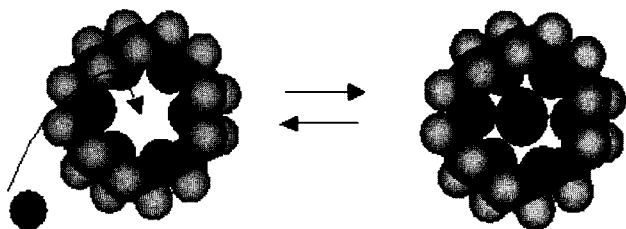


Fig. 4 Supramolecular complex between the cation and crown ether. Cations are complexed into the crown ether cavity through cation-oxygen interactions. (View this art in color at www.dekker.com.)

pared to fabricate oriented molecular-assembly nanowires. The electronic ground state of the CT complexes can be discussed in terms of the differences between the redox potentials, $\Delta E = E_{1/2}(\text{donor}) - E_{1/2}(\text{F}_4\text{-TCNQ})$, for electron donor **1** and $\text{F}_4\text{-TCNQ}$.^[31,32] Partial CT states, $(\text{D}^{+\delta})(\text{A}^{-\delta})$ with $0.5 < \delta < 1$, are necessary for the formation of metallic CT complexes having a segregated-stack structure, which is achieved when ΔE has a value between -0.02 and 0.34 V.^[31,32] Fully ionic $(\text{D}^+)(\text{A}^-)$ and neutral $(\text{D}^0)(\text{A}^0)$ CT complexes are typically observed when $\Delta E < -0.02$ V and $\Delta E > 0.34$ V, respectively. In the case of donor **1** and $\text{F}_4\text{-TCNQ}$ ($E_{1/2}(\mathbf{1}) = 0.73$ V), the ΔE values of CT complex of $(\mathbf{1})(\text{F}_4\text{-TCNQ})_2$ was -0.17 V. Because these values were far from the conditions of partial CT complexes, fully ionic ground state $(\mathbf{1}^{2+})(\text{F}_4\text{-TCNQ}^-)_2$ was expected for the molecular nanowires.

Monolayer of Charge-Transfer Complexes at the Air-Water Interface

The CT complex $(\mathbf{1})(\text{F}_4\text{TCNQ})_2$ was prepared in situ by mixing donor **1** and two equivalent of $\text{F}_4\text{-TCNQ}$ in $\text{CHCl}_3/\text{CH}_3\text{CN}$ (9:1, v/v). Concentration of the spreading solution was fixed at 1 mM with respect to $(\mathbf{1})(\text{F}_4\text{-TCNQ})_2$. Surface pressure (F)-area per molecule (A) isotherms were recorded at 291.5 K with a barrier speed of $50 \text{ cm}^2 \text{ min}^{-1}$. The LB monolayers were transferred onto freshly cleaved mica surfaces by a single up-stroke drawing. Because the macrocyclic moiety may recognize ions introduced into the subphase upon the formation and deposition of the monolayers, the K^+ ions were introduced into the subphase for realizing ion recognition at first.

The F - A isotherms of the floating monolayers of the CT complex of $(\mathbf{1})(\text{F}_4\text{-TCNQ})_2$ on pure water and aqueous

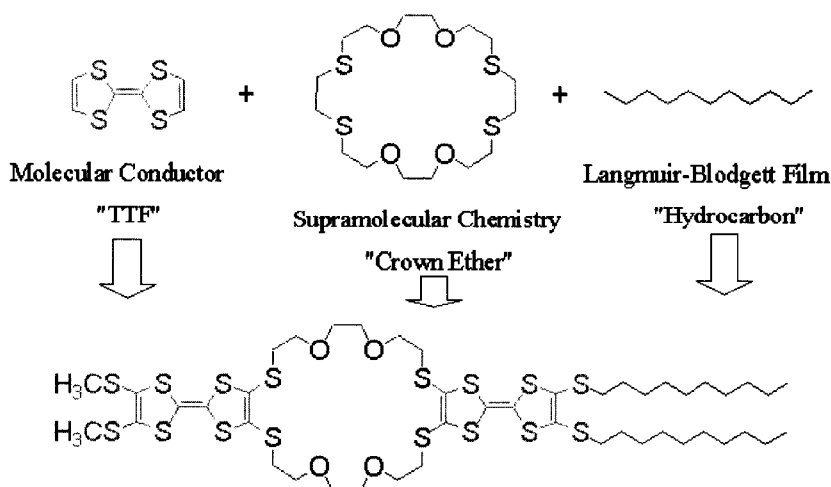


Fig. 5 Molecular design of amphiphilic bis(tetrathiafulvalene) [bis(TTF)] macrocycle **1** from the viewpoints of molecular conductor (TTF), supramolecular chemistry (crown ether), and Langmuir-Blodgett films (hydrocarbons). (View this art in color at www.dekker.com.)

0.01 M KCl subphase are shown in Fig. 6. The surface areas of CT complexes extrapolated at 0 mN m^{-1} on pure water and 0.01 M KCl subphase are almost consistent with each other ($A_0 \sim 1.2 \text{ nm}^2$). Because these values are larger than that of neutral **1** ($A_0 = 0.6 \text{ nm}^2$), the formation of CT complex causes much expansion of the surface area. The films were deposited under a controlled surface pressure of 10 mN m^{-1} , at which point the surface areas of $(\mathbf{1})(\text{F}_4-$

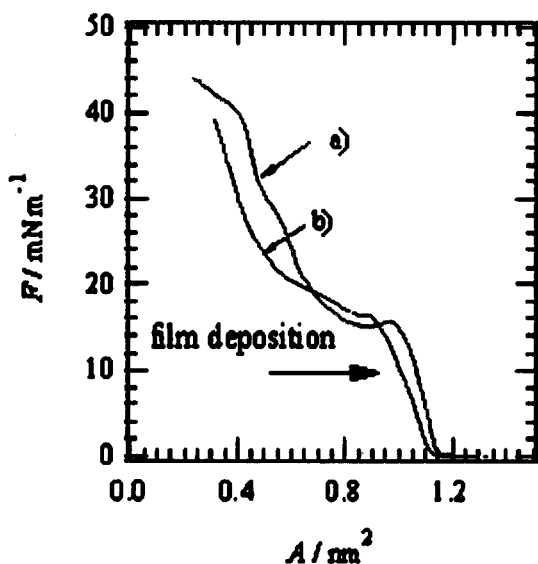


Fig. 6 F - A isotherms of CT complex of $(\mathbf{1})(\text{F}_4\text{-TCNQ})_2$ on a) pure water and b) 0.01 M KCl subphase. The films were transferred at 10 mN m^{-1} . (View this art in color at www.dekker.com.)

$\text{TCNQ})_2$ on pure water and 0.01 M KCl ($A_{10} \sim 1.1 \text{ nm}^2$) were almost identical to each other.

Molecular-Assembly Nanowires on Mica Surface

Fig. 7 shows the surface morphologies of the CT complex of $(\mathbf{1})(\text{F}_4\text{-TCNQ})_2$ that transferred onto freshly cleaved mica by a single withdrawal from monolayer on a) pure water and b) 0.01 M KCl subphase. Although both films showed the formation of molecular-assembly nanowires, significant difference about the nanowire orientation was confirmed between them. Both nanowires had typical width of 50 nm and height of $\sim 2.5 \text{ nm}$. By introducing

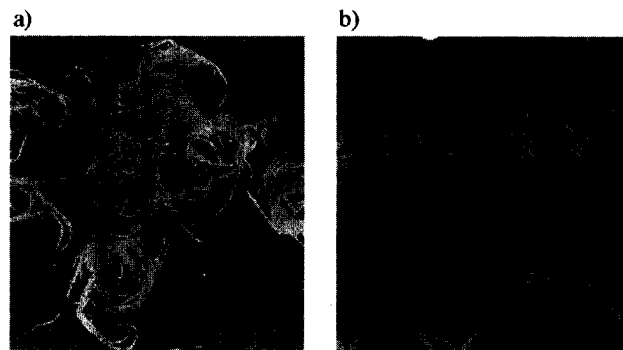


Fig. 7 Surface morphology of transferred nanowires of $(\mathbf{1})(\text{F}_4\text{-TCNQ})_2$ from a) pure water and b) 0.01 M KCl. The scales of AFM images are $10 \times 10 \mu\text{m}^2$. (View this art in color at www.dekker.com.)

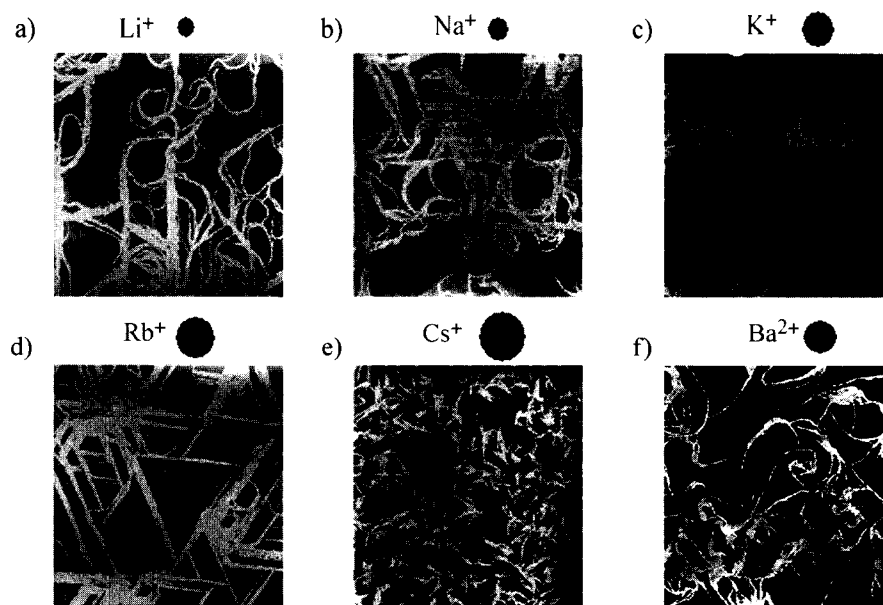


Fig. 8 Surface morphology of transferred nanowires of $(1)(F_4\text{-TCNQ})_2$ on mica from a) LiCl, b) NaCl, c) KCl, d) RbCl, e) CsCl, and f) BaCl_2 containing subphase. The concentration of ions in the subphase was fixed at 0.01 M. The scales of AFM images are $10 \times 10 \mu\text{m}^2$. (View this art in color at www.dekker.com.)

0.01 M KCl into the subphase, the nanowire orientation appeared as network structure connecting the well-developed nanowires to each other. Almost all the nanowires on the mica surface formed an angle of 60° to each other.

Because the F - A isotherm of $(1)(F_4\text{-TCNQ})_2$ between pure water and 0.01 M KCl subphase was almost consistent with each other, the CT complex may not recognize K^+ ion at the air-water interface. Therefore the

orientation of nanowire should occur during the film deposition processes because the orientation direction of the nanowires was consistent with the crystal lattice of mica.^[33,34] The morphology of nanowires on mica surface strongly depended on the cation species that were introduced into the subphase (Fig. 8). When we introduced Li^+ (ion radius $r_i=0.6 \text{ \AA}$) or Na^+ ($r_i=0.95 \text{ \AA}$) into the subphase, although the formation of nanowires were confirmed, the nanowire orientation completely

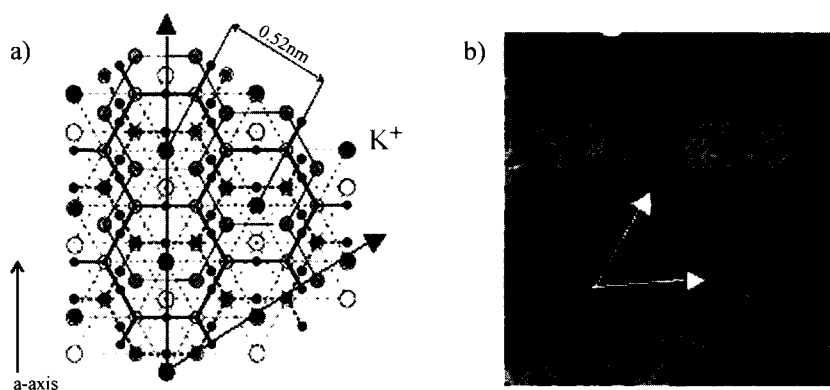


Fig. 9 a) Crystal structure of mica surface. Hexagonal arrays of K^+ sites are indicated by red closed circles. b) Atomic force microscopy (AFM) image of oriented nanowires on mica surface deposited from 0.01 M KCl subphase. The white allows correspond to hexagonal lattice of K^+ site on mica, showing the relation between the nanowire orientation and K^+ array. (View this art in color at www.dekker.com.)

disappeared. Much larger cation of Cs^+ ($r_1=1.69 \text{ \AA}$) yielded the ill-developed molecular nanowires with maximum length of less than $\sim 1 \mu\text{m}$. In the case of Rb^+ ($r_1=1.48 \text{ \AA}$), well-developed oriented nanowires were observed at a typical length of above $2 \mu\text{m}$. The most densely developed oriented nanowires were confirmed by the introduction of K^+ ($r_1=1.33 \text{ \AA}$) into the subphase, which resulted in a typical nanowire dimension of $2.5 \times 50 \times \sim 2000 \text{ nm}^3$. Although Ba^{2+} ($r_1=1.35 \text{ \AA}$) has almost similar ionic radius to that of K^+ , the nanowire orientation completely disappeared on the mica surface.

The difference of the nanowire orientation according to the ions is related with the surface property of mica rather than the ion radius. Mica has a typical composition of $\text{KAl}_3\text{Si}_3\text{O}_{10}(\text{OH})_2$, and vacant potassium sites of sixfold symmetry appear by the cleavage (Fig. 9).^[33,34] These K^+ sites should be negatively charged and attract cations when the mica substrates are immersed in the K^+ -containing subphase. The nanowire orientation may occur by matching of the surface potential of mica surface and that of the nanowires, rather than by ion recognition of individual molecules. The anionic species of $\text{F}_4\text{-TCNQ}$ anion radical should be embedded on K^+ , and nanowires may orient in an epitaxial way through the lattice matching between mica and nanowires. Such recognition mechanism is the most probable explanation for the nanowire orientation. Although the dimension of nanowires is much larger than the unit cell of hexagonal array of K^+ on mica surface, the nanowire orientation was affected by the K^+ array on mica surface.

Fig. 10 shows selected AFM images ($1 \times 1 \mu\text{m}^2$) of oriented molecular-assembly nanowires on mica. As previously mentioned, the nanowires oriented 60° to each other, which provided interesting nanoscale structures such as nanowire tree and triangles. The six-folded

connecting modes of each nanowire form novel nanoscale junction structures, which can apply for constructing the integrated nanoscale electronic circuits.

Molecular-Assembly Structures Within Nanowire

The single crystal of $(2)(\text{F}_4\text{-TCNQ})_2$ were obtained, and here donor **2** is the four-alkyl chain derivative of compound **1**. Assuming a similar molecular packing structure of CT complex between $(2)(\text{F}_4\text{-TCNQ})_2$ and $(1)(\text{F}_4\text{-TCNQ})_2$, we can discuss the molecular-assembly structure in the nanowires based on the crystal structure of $(2)(\text{F}_4\text{-TCNQ})_2$.^[35] Fig. 11 shows the unit cell of $(2)(\text{F}_4\text{-TCNQ})_2$ viewed along the b axis. Donor **2** formed an intramolecular π - π dimer through folding of the flexible 24-crown-8 moiety, in which the π -planes of the two TTF units overlapped at their inner C_3S_5 rings. Along the c axis, the D-A layers are separated by the hydrophobic decylthio chains; moreover, the hydrophilic and hydrophobic layers are alternately arranged. The crystal structure suggests that the direction normal to the substrate surface in the LB film is consistent with the c axis ($c=1.72 \text{ nm}$). As indicated in Fig. 11, which shows the π - π stacking structure within the ab plane, the π - π dimer structure of $\text{F}_4\text{-TCNQ}$ stacked alternately with the intramolecular TTF dimer along the $-a + b$ axis. The π - π stacking sequence between donor **2** and $\text{F}_4\text{-TCNQ}$ was -D-A-A-D-, forming a 1-D mixed-stack structure.

The molecular orientation within the LB films was evaluated by using the polarized ultraviolet-visible-near infrared (UV-vis-NIR) spectra.^[19-21] The polarized UV-vis-NIR spectra of the LB film of $(1)(\text{F}_4\text{-TCNQ})_2$ did not indicate any in-plane anisotropy with the normal incidence, indicating the isotropic distribution of molecular

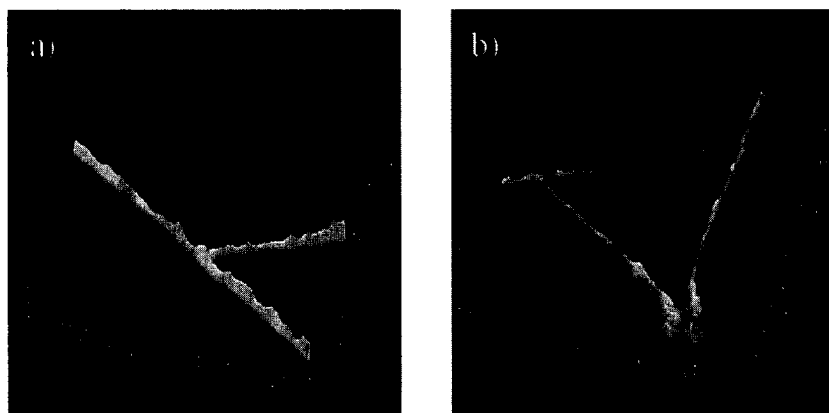


Fig. 10 Selected AFM images of oriented molecular-assembly nanowires. a) Nanowire tree and b) nanowire triangles. Scale of AFM images are $1 \times 1 \mu\text{m}^2$. (View this art in color at www.dekker.com.)

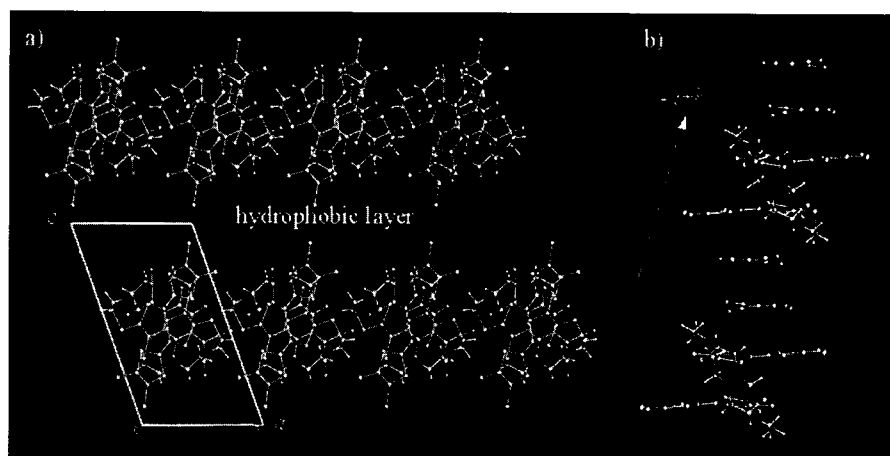


Fig. 11 Crystal structure of CT complex $(2)(F_4\text{-TCNQ})_2$. a) Unit cell viewed along the b axis. b) Alternate π - π stacking structure between donor **2** and $F_4\text{-TCNQ}$ dimer along the $-a+b$ axis. Alkyl chains are omitted. (View this art in color at www.dekker.com.)

orientation within the substrate surface. Two sharp absorptions (B bands) were assigned to the intramolecular transition of the $F_4\text{-TCNQ}^-$ anion radical,^[36] while the C and D bands were assigned to the intramolecular transi-

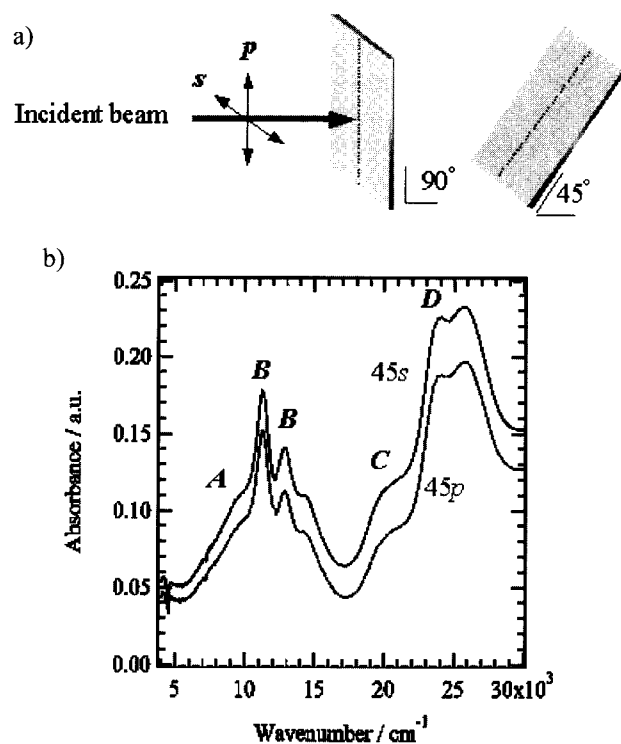


Fig. 12 Polarized UV-vis-NIR spectra of the LB film of $(1)(F_4\text{-TCNQ})_3$. a) Optical arrangements of the substrates to measure the polarized UV-vis-NIR spectra at 90° and 45° incidence. b) Polarized UV-vis-NIR spectra of 45° incidence with p- and s-polarization. (View this art in color at www.dekker.com.)

tions of TTF^+ and $F_4\text{-TCNQ}^-$, respectively.^[37] The broad A bands were assigned to the intramolecular transition of bis(TTF)-macrocycles,^[38-40] which overlapped with the B bands. With 45° incidences (Fig. 12a), the absorption intensity for the s-polarization was larger than that for the p-polarization. Because the intramolecular transition moments of donor **1** and $F_4\text{-TCNQ}$ lie along the long axes of TTF and $F_4\text{-TCNQ}$ molecules, the long axes of donor **1** and $F_4\text{-TCNQ}$ were relatively parallel to the substrate surface.

From the results of X-ray structural analysis and polarized UV-vis-NIR spectra, we constructed the schematic molecular packing model within the nanowire (Fig. 13).^[27,28] The nanowires transferred from K^+ containing subphase had typical dimensions of $2.5 \times 50 \times \sim 1000 \text{ nm}^3$. Considering the molecular size of donor **1**, the nanowire should be composed of 1-2 molecular layers in the height direction and 20-30 molecules in the width direction. Assuming that the nanowire has a local structure similar to that of crystal structure of $(2)(F_4\text{-TCNQ})_2$, the longitudinal direction of the nanowire should correspond to the π - π stacking direction of TTF units and/or $F_4\text{-TCNQ}$ molecules. Therefore, a few thousand molecules are necessary to form over $1\text{-}\mu\text{m}$ -long nanowire, taking into account that the standard π - π stacking distance is around 0.35 nm .

Electrical Conductivity and Magnetic Properties

To estimate the electrical conductivity of nanowires, the temperature-dependent electrical conductivity and paramagnetic susceptibility were measured in the form of the LB film. Fig. 14 shows the temperature-dependent

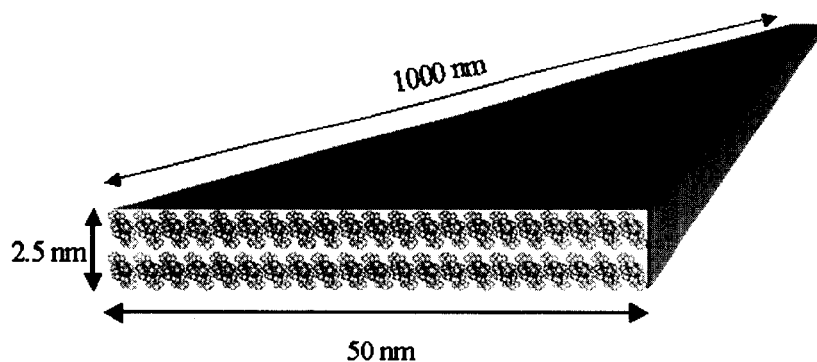


Fig. 13 Possible molecular arrangements within a nanowire. (View this art in color at www.dekker.com.)

electrical conductivity (*right scale*) and paramagnetic susceptibility (*left scale*) of LB film of $(\mathbf{1})(F_4\text{-TCNQ})_2$. The room-temperature electrical conductivity (σ_{RT}) was $1.5 \times 10^{-3} \text{ S cm}^{-1}$ with an activation energy of 0.17 eV. The semiconducting temperature dependence was consistent with that of the mixed-stack arrangement of donor and $F_4\text{-TCNQ}$ dimer. Although the accumulated film should be composed of piles of nanowires and monolayers of $(\mathbf{1})(F_4\text{-TCNQ})_2$, each nanowire may have the same order of electrical conductivity.

The temperature-dependent paramagnetic susceptibility (χ) of the LB films of $(\mathbf{1})(F_4\text{-TCNQ})_2$ was measured

via electron spin resonance (ESR). As shown in Fig. 14, χ increased monotonically with decreasing temperatures, which followed the Curie–Weiss law. The line-shape of the ESR signals could be fitted using Lorentzian. Line width around 0.5 mT did not show anomaly within the measured temperature range. Because g -values for BEDT-TTF^+ cation and $F_4\text{-TCNQ}^-$ anion radicals have been typically observed at 2.0074 and 2.0025, respectively,^[11–15] the g -values (~ 2.004) of the LB films for $(\mathbf{1})(F_4\text{-TCNQ})_2$ were observed in the intermediate range between BEDT-TTF and $F_4\text{-TCNQ}$, which indicated that both the cation and the anion radical species contribute to the paramagnetic susceptibility of the LB films.

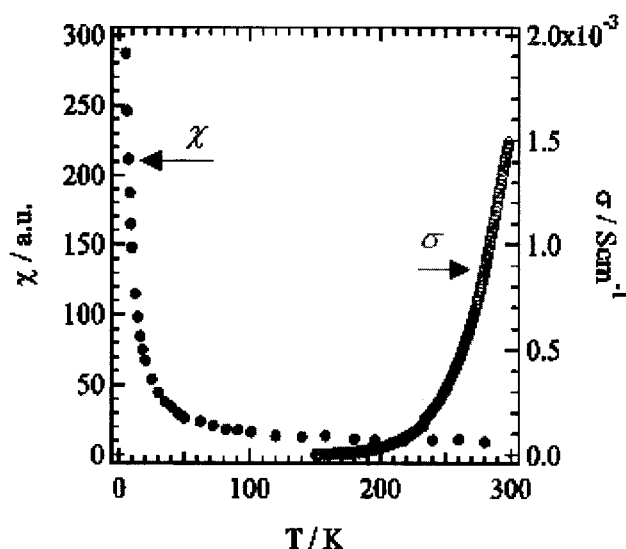


Fig. 14 Temperature-dependent electrical conductivity (*right scale*) and paramagnetic susceptibility (*left scale*) of the LB film of $(\mathbf{1})(F_4\text{-TCNQ})_2$. (View this art in color at www.dekker.com.)

CONCLUSION

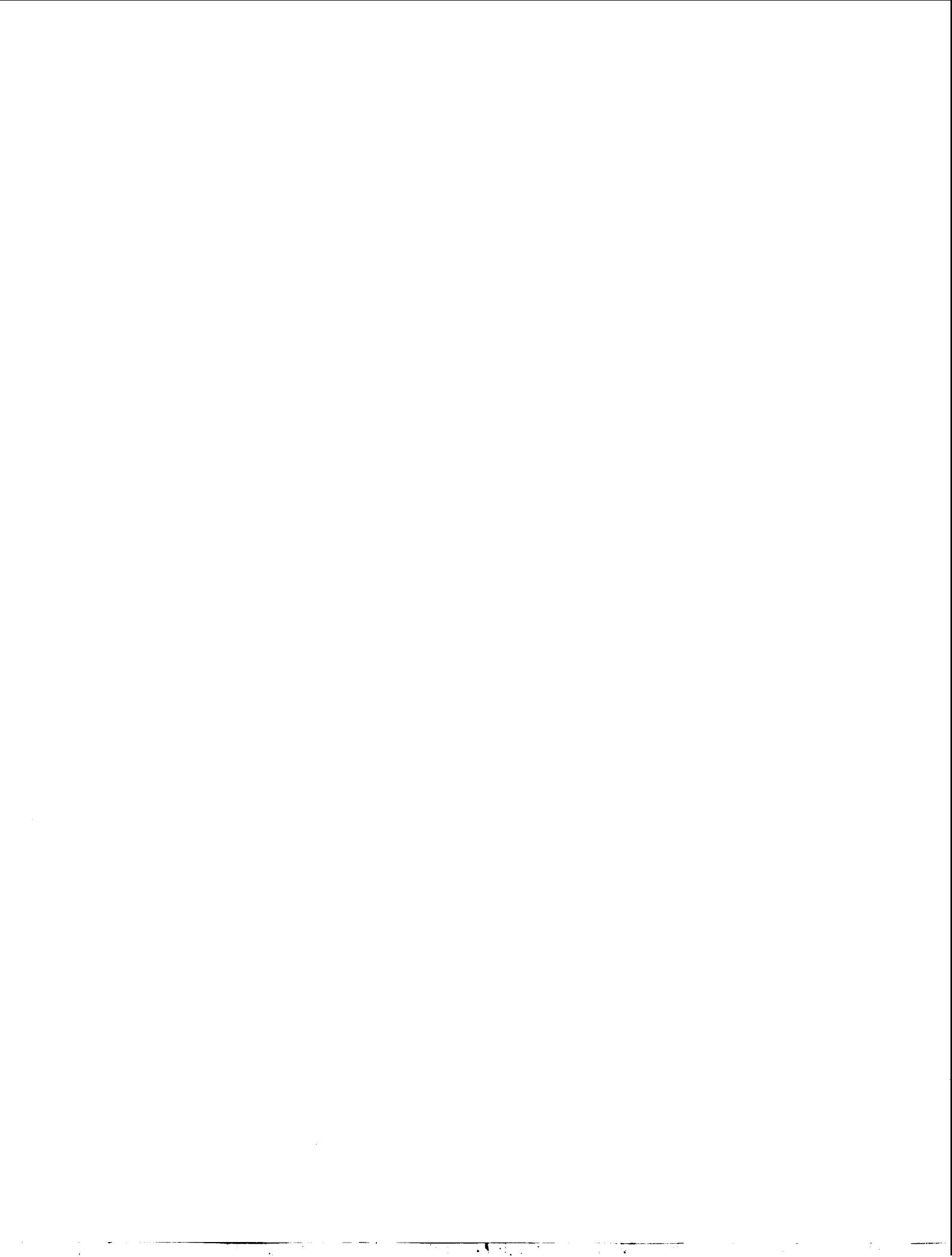
We constructed oriented molecular-assembly nanowires, which are important parts for the fabrication of nanoscale electronic devices. Molecular-assembly nanowires have a potential to fabricate nanoscale electronics in all self-assembly chemical processes. Amphiphilic bis(TTF) macrocycle derivative is one such example, forming self-assembly nanowires oriented on mica surface. This molecule was designed from the viewpoints of: 1) molecular conductor; 2) Langmuir–Blodgett films; and 3) supramolecular chemistry. Designs from the concepts of molecular conductor and Langmuir–Blodgett film are necessary to construct nanoscale electrical conducting, one-dimensional structure. Furthermore, the design of weak intermolecular interactions (ion recognition) from the supramolecular approach should be a key methodology to construct oriented molecular-assembly nanowires. Control of electronic structures of the nanowires may be achieved through careful design of the charge-transfer interactions (electronic dimensionality, bandwidth, carrier concentration, etc.), while a variety of nanoscale

structures such as zero-dimensional nanodots and nanowires should be obtainable from the designs of supramolecular chemistry.

REFERENCES

1. Akutagawa, T.; Nakamura, T. *Semiconductor and Molecular-Assembly Nanowires, Chemistry of Nano-Molecular Systems—Toward the Realization of Molecular Devices*; Sugiura, K., Matsumoto, T., Tada, H., Nakamura, T., Eds.; Springer-Verlag: Berlin, 2002; 122–147.
2. Joachim, C.; Gimzewski, J.K.; Aviram, A. Electronic using hybrid-molecular and mono-molecular devices. *Nature* **2000**, *408*, 541–548.
3. Heath, J.R.; Kuekes, P.J.; Snider, G.S.; Williams, R.S. A defect-tolerant computer architecture: Opportunities for nanotechnology. *Science* **1998**, *280*, 1716–1721.
4. *Adv. Mater.* **2003**, *15* (5).
5. Kittel, C. *Introduction to Solid State Physics*, 6th Ed.; John Wiley: New York, 1986.
6. Ferry, D.K.; Goodnick, S.M. *Transport in Nanostructures*; Ahmed, H., Pepper, M., Broers, A., Eds.; Cambridge Univ. Press: Cambridge, 1997.
7. Hu, J.; Odom, T.W.; Lieber, C.M. Chemistry and physics in one dimension: Synthesis and properties of nanowires and nanotubes. *Acc. Chem. Res.* **1999**, *32*, 435–445.
8. Favier, F.; Liu, H.; Penner, R.M. Size-selective growth of nanoscale tetrathiafulvalene bromide crystallites on platinum particles. *Adv. Mater.* **2001**, *13*, 1567–1570.
9. Nostrum, C.F.; Picken, S.J.; Schouten, A.-J.; Nolte, R.J.M. Synthesis and supramolecular chemistry of novel liquid crystalline crown ether-substituted phthalocyanines: Toward molecular wires and molecular ionoelectronics. *J. Am. Chem. Soc.* **1995**, *117*, 9957–9965.
10. Nostrum, C.F. Self-assembly wires and channels. *Adv. Mater.* **1996**, *8*, 1027–1030.
11. Cowan, D.O. *New Aspects of Organic Chemistry*; Yoshida, Z., Shiba, T., Oshiro, Y., Eds.; Kodansha: Tokyo, 1989.
12. *Organic Conductors*. Farges, J.-P., Ed.; Marcel Dekker: New York, 1994.
13. *Handbook of Organic Conductive Molecules and Polymers*; Nalwa, H.S., Ed.; Wiley: Stuttgart, 1997; Vol. 1.
14. Williams, J.M.; Ferraro, J.R.; Thorn, R.J.; Carlson, K.D.; Geiser, U.; Wang, H.; Kini, A.M.; Whangbo, M.-H. *Organic Superconductors*; Prentice-Hall: New Jersey, 1992.
15. Ishiguro, T.; Yamaji, K.; Saito, G. *Organic Superconductors*, 2nd Ed.; Springer: New York, 1998.
16. Lehn, J.-M. *Supramolecular Chemistry*; VCH: Weinheim, 1995.
17. Vögtle, F. *Supramolecular Chemistry*; Wiley: Tokyo, 1995.
18. Steed, J.W.; Atwood, J.L. *Supramolecular Chemistry*; Wiley: Chichester, 2000.
19. *Langmuir–Blodgett Films*; Roberts, G., Ed.; Plenum Press: New York, 1990.
20. Ulman, A. *An Introduction to Ultrathin Organic Films*; Academic Press: San Diego, CA, 1991.
21. Petty, M.C. *Langmuir–Blodgett Films. An Introduction*; Cambridge University Press: Cambridge, 1996.
22. Nakamura, T. *Handbook of Organic Conductive Molecules and Polymers. Vol. 1 Charge–Transfer Salts, Fullerenes and Photoconductors*; Nalwa, H.S., Ed.; Wiley: Stuttgart, 1997; 728–780.
23. Bryce, M.R.; Petty, M.C. Electrical conductive Langmuir–Blodgett films of charge–transfer materials. *Nature* **1995**, *374*, 771–776.
24. Metzger, R.M. Electrical rectification by a molecule: The advent of unimolecular electronic devices. *Acc. Chem. Res.* **1999**, *32*, 950–957.
25. Weber, E.; Toner, J.L.; Goldberg, I.; Vögtle, F.; Laidler, D.A.; Stoddart, J.F.; Bartsch, R.A.; Liotta, C.L. *Crown Ethers and Analogs*; Patai, S., Rappoport, Z., Eds.; John Wiley & Sons: New York, 1989.
26. Gokel, G.W. *Crown Ethers and Cryptands*; Stoddart, J.F., Ed.; RSC: Cambridge, 1994.
27. Akutagawa, T.; Ohta, T.; Hasegawa, T.; Nakamura, T.; Christensen, C.A.; Becher, J. Formation of oriented molecular nanowires on mica surface. *Proc. Nat. Acad. Sci. U. S. A.* **2002**, *99*, 5028–5033.
28. Nakamura, T.; Ohta, T.; Tatewaki, Y.; Wakahara, K.; Akutagawa, T.; Hasegawa, T.; Christensen, C.A.; Becher, J., submitted for publication.
29. Nielsen, M.B.; Lomholt, C.; Becher, J. Tetrathiafulvalenes as building blocks in supramolecular chemistry II. *Chem. Soc. Rev.* **2000**, *29*, 153–164.
30. Simonsen, K.B.; Svenstrup, N.; Lan, J.; Simonsen, O.; Mørk, P.; Kristensen, C.J.; Becher, J. Sequential functionalisation of bis-protected tetrathiafulvalene-dithiolates. *Synthesis* **1996**, 407–418.
31. Torrance, J.B.; Vazquez, J.E.; Mayerle, J.J.; Lee, V.Y. Discovery of a neutral-to-ionic phase transition in organic materials. *Phys. Rev. Lett.* **1981**, *46*, 253–257.
32. Saito, G.; Ferraris, J.P. Requirements for an

- “organic metal”. *Bull. Chem. Soc. Jpn* **1980**, *53*, 2142–2145.
33. Wyckoff, R.W.G. *Crystal Structures*; Wiley: New York, 1960; Vol. 4.
34. Lima-de-Faria, J. *Structural Mineralogy. An Introduction*; Kluwer: Dordrecht, 1994.
35. Akutagawa, T.; Kakiuchi, K.; Hasegawa, T.; Nakamura, T.; Becher, J., submitted for publication.
36. Torrance, J.B.; Mayerle, J.J.; Bechgaard, K. Comparison of two isostructural organic compounds, one metallic and the other insulating. *Phys. Rev., B* **1980**, *22*, 4960–4965.
37. Jacobsen, C.S. *Optical Properties in Semiconductor and Semimetals. High Conducting Quasi-One-Dimensional Organic Crystals*; Conwell, E., Ed.; Academic Press: New York, 1988; 293–384.
38. Akutagawa, T.; Abe, Y.; Nezu, Y.; Nakamura, T.; Kataoka, M.; Yamanaka, A.; Inoue, K.; Inabe, T.; Christensen, C.A.; Becher, J. Linear pentaiodide in the radical cation salt of a tetrathiafulvalene bisannulated macrocycle. *Inorg. Chem.* **1998**, *37*, 2330–2331.
39. Akutagawa, T.; Abe, Y.; Hasegawa, T.; Nakamura, T.; Inabe, T.; Christensen, C.A.; Becher, J. Tuning of intramolecular π - π overlap mode of tetrathiafulvalene bisannulated macrocycles in the open-shell electronic state. *Chem. Lett.* **2000**, 132–133.
40. Abe, Y.; Akutagawa, T.; Hasegawa, T.; Nakamura, T.; Sugiura, K.; Sakata, Y.; Inabe, T.; Christensen, C.A.; Becher, J. Structures and electronic properties of TTF bisannulated 24-crown-8 charge transfer complexes. *Synth. Met.* **1999**, *102*, 1599–1600.



Molecular Assembly of Organosilanes

Atsushi Takahara

Kyushu University, Fukuoka, Japan

M

INTRODUCTION

Ultrathin films of organosilane have been identified as promising nanocoating for micro- and nanoscale technologies such as electronic devices and micromachines.^[1–3] As the silanol groups of organosilane monolayer prepared from organotrichlorosilane or organotrialkoxysilane strongly interact with the substrate surface, the monolayer is thermally and chemically robust compared with conventional amphiphilic monolayers. Because the chain length of organosilane is approximately 1–3 nm, the organosilane forms a uniform ultrathin film on the substrate surface.

Two methods have been proposed for the preparation of organosilane monolayers. One is chemisorption from organosilane solution,^[4–7] and the other is the Langmuir–Blodgett (LB) method.^[8–22] Fig. 1 shows the film-formation mechanisms of the organosilane by the LB method (a) and the chemisorption method (b). In the case of the LB method Fig. 1a, the toluene solution of organotrichlorosilane was spread on the water surface (pH = 5.8) at a controlled subphase temperature. To attain the quasi-equilibrium state of the monolayer, the monolayer was kept on the water subphase under a given constant surface pressure for 15 min. The monolayer was transferred and immobilized onto the Si-wafer substrate surface by the LB method. In the case of chemisorption Fig. 1b, organosilane molecules were deposited either from the solution or from the vapor phase. It has been clarified that the aggregation state of the organosilane monolayers prepared by the LB method shows a higher packing density than the chemisorbed monolayers.^[15,22]

Organosilane monolayers, which have surfaces terminated by various functional groups, are useful for manipulation of the physicochemical properties of solid surfaces such as wettability, nanotribology, and protein adsorption behavior. A key to fabricating functional organosilane monolayers is controlling the distribution of surface functional groups. Fabricating micro- and nanodevices using a bottom-up approach requires building blocks with a precisely controlled and tunable chemical composition, morphology, and size that can be fabricated virtually at will. The organosilane monolayer is a candidate for such a building block because of its stability and ease of fabrication. Patterned microfeatures of organosilane

monolayers can be fabricated on the substrate, allowing surface physicochemical properties to be area-selectively controlled. Two methods will be discussed in this article. One of them utilizes crystallization of organosilane of the binary component monolayer at the air/water interface.^[8–11] Because the diffusion of organosilane molecules at the air/water interface is slow, macroscopic phase separation is inhibited, even with the alkylsilane and fluoroalkylsilane mixed monolayers. The phase-separated monolayer is transferred to the Si-wafer substrate by the LB method. Another method utilizes photolithography by a vacuum ultraviolet (VUV) ray source.^[23,24] In the case of a VUV source with $\lambda = 172$ nm, photodecomposition of the organic moiety occurs because of the higher photon energy of the VUV ray compared with the bond energy of a typical C–C linkage. Using photolithography, one can prepare a micropatterned surface with various organosilane monolayers by repeating the photodecomposition and chemisorption processes. By changing the shape and area ratio of the patterns of the photomask, this technique enables one to control the area ratio and the wettability gap of different organosilane monolayers.

PATTERNING OF ORGANOSILANE MONOLAYERS VIA CRYSTALLIZATION AT THE AIR/WATER INTERFACE

Formation of Organosilane Monolayers at the Air/Water Interface

Fig. 2 shows the chemical structure of organosilanes used for monolayer preparation. Organotrichlorosilane is primarily used for monolayer preparation at the air/water interface. Lignoseric acid [LA, $\text{CH}_3(\text{CH}_2)_{22}\text{COOH}$] is also used to prepare the mixed monolayers. LA is not polymerized and is also nonreactive against the silicon substrate. The chlorine groups of organosilane on the water surface were found to be substituted by hydroxyl groups. At a surface pressure of $10\text{--}30$ mN m^{-1} , the hydroxyl groups in organosilane molecules reacted with those in adjacent molecules in the case of the highly condensed monolayer, resulting in formation of a polymerized

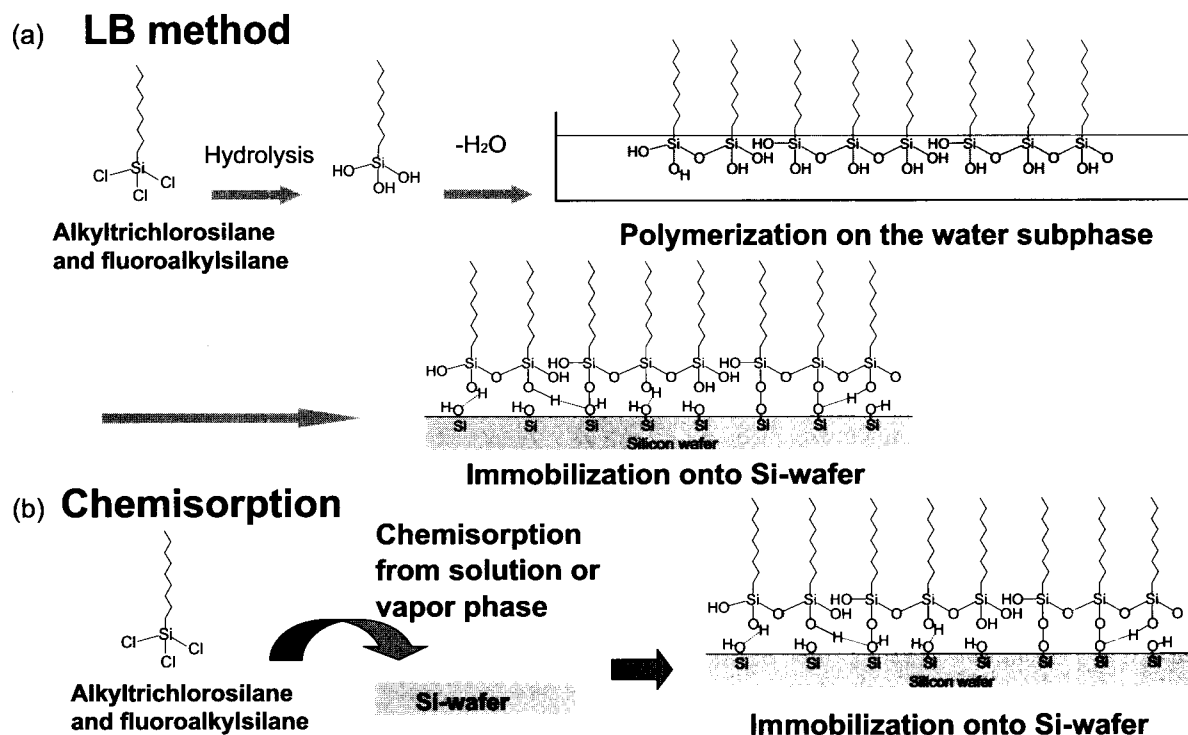
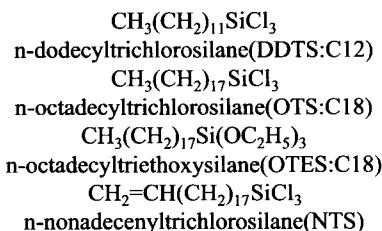
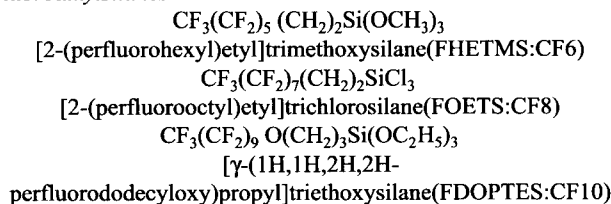


Fig. 1 Film formation mechanism of organosilane by Langmuir–Blodgett (LB) method (a) and chemisorption method (b). (View this art in color at www.dekker.com.)

Alkylsilanes



Fluoroalkylsilanes



Aminosilane

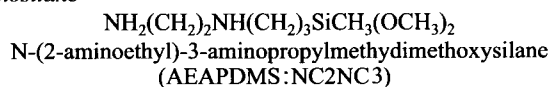


Fig. 2 Chemical structure of organosilanes.

monolayer. The polymerized monolayer was easily transferred onto a Si wafer by the LB method, and the residual hydroxyl groups could be covalently bonded with silanol groups on the Si wafer surface.

Fig. 3 shows the surface pressure–area (π -A) isotherms for the n-octadecyltrichlorosilane (OTS), n-dodecyltrichlorosilane (DDTS), [1H,1H,2H,2H-perfluorododecyloxy]propyltriethoxysilane (FDOPTES), and [2-perfluorooctyl]ethyltrichlorosilane (FOETS) monolayers on the water surface at a subphase temperature of 293 K, as well as electron diffraction (ED) patterns of the monolayers transferred onto the hydrophilic SiO substrate on the EM grid at a surface pressure of approximately 20 mN m^{-1} . The π -A isotherms of the OTS and FDOPTES monolayers showed a steep increase in surface pressure with decreases in the surface area. The molecular occupied areas were determined to be 0.24 and $0.29 \text{ nm}^2 \text{ molecule}^{-1}$ for the OTS and FDOPTES monolayers, respectively. Electron diffraction patterns of both the OTS and the FDOPTES monolayers showed hexagonal crystalline arcs at 293 K. The (10) spacings of the OTS and the FDOPTES monolayers were calculated to be ca. 0.42 and 0.50 nm based on ED patterns, respectively.^[18] These ED results make it clear that the hydrophobic alkyl and fluoroalkyl chains in the crystalline OTS and FDOPTES monolayers were closely packed in the hexagonal crystal lattice at 293 K.

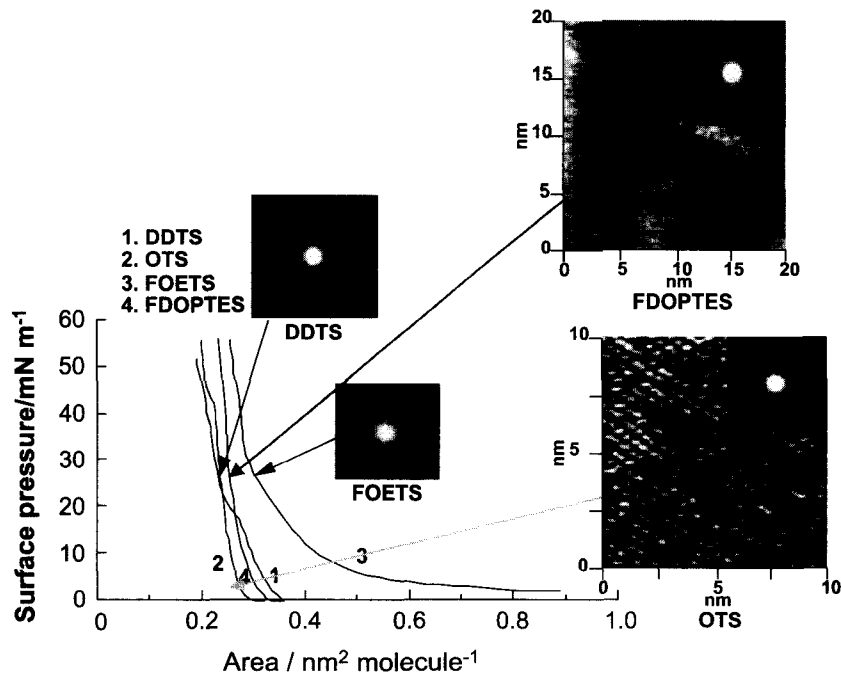


Fig. 3 π - A isotherms for the OTS, DDTs, FDOPTES, and FOETS monolayers on the water surface at a subphase temperature of 293 K, as well as the AFM images and ED patterns of the monolayers transferred onto the substrate at the surface pressure of around 20 mN m^{-1} . (View this art in color at www.dekker.com.)

High-resolution atomic force microscopy (AFM) was applied to observe the molecular arrangement of both the crystalline OTS-C18 and FDOPTES monolayers. Fig. 3 also displays AFM images on a molecular scale for the crystalline OTS-C18 and FDOPTES monolayers transferred onto a Si wafer at a surface pressure of 15 mN m^{-1} at 293 K.^[18] The (10) spacing was evaluated to be ca. 0.42 and 0.50 nm by two-dimensional fast Fourier transform (2-D-FFT). These values are in good agreement with the (10) spacings determined from the ED patterns for the crystalline OTS and FDOPTES monolayers. Thus, it is conceivable that the higher portions (the brighter dots) in the AFM images of Fig. 3 correspond to the individual methyl group of the OTS molecule and the fluoromethyl group of the FDOPTES molecule in the monolayers, respectively. In contrast, the π - A isotherms for the DDTs monolayer and the FOETS monolayer with a shorter alkyl chain showed a gradual increase in surface pressure with decreasing surface area. In general, this can be interpreted as an indication that the monolayer is in a liquid-condensed or liquid-expanded state. In addition, the ED patterns of the DDTs and the FOETS monolayers showed an amorphous halo at 293 K. Hence, it can be envisaged that the chain lengths of hydrophobic groups of the DDTs and the FOETS molecules were not long enough to crystallize on the water subphase at 293 K.

Phase Separation of Mixed Monolayers at the Air/Water Interface

Phase separation is expected to occur in the binary component monolayer of crystalline OTS and amorphous FOETS because of the incompatibility of OTS and FOETS. Fig. 4 shows the π - A isotherm and the AFM image of the scanned area $10 \times 10 \mu\text{m}^2$ for the OTS/FOETS (50/50 mol/mol) mixed monolayer, which was transferred onto the Si wafer substrate by the LB method at a surface pressure of 25 mN m^{-1} . The height profile along the line shown in the AFM image revealed that the brighter and darker portions in the AFM image correspond to the higher and the lower regions of the monolayer surface, respectively. The molecular occupied area (the limiting area) of $0.28 \text{ nm}^2 \text{ molecule}^{-1}$ for the OTS/FOETS (50/50) mixed monolayer appears to be almost equal to the average of the molecular occupied area for the OTS ($0.24 \text{ nm}^2 \text{ molecule}^{-1}$) monolayer and the FOETS ($0.31 \text{ nm}^2 \text{ molecule}^{-1}$) monolayer based on the molar fraction of OTS and FOETS. The OTS/FOETS mixed monolayer can be transferred onto the Si wafer substrate over a wide range of surface pressure. The transfer ratio of the OTS/FOETS mixed monolayer was ca. 1.0 at a surface pressure of 25 mN m^{-1} , indicating that the substrate surface is almost completely covered with the immobilized mixed monolayer. Also, the transfer of the OTS/FOETS mixed

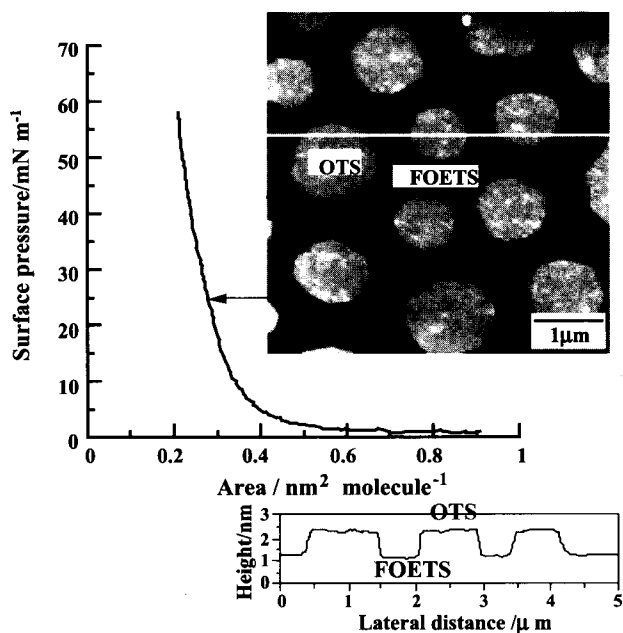


Fig. 4 π -A isotherm and AFM image of the scanned area $10 \times 10 \mu\text{m}^2$ for the OTS/FOETS (50/50) mixed monolayer, which was transferred onto the Si wafer substrate by the LB method at the surface pressure of 25 mN m^{-1} . (View this art in color at www.dekker.com.)

monolayer on the silicon substrate was confirmed by using attenuated total reflection Fourier transform infrared (ATR-FT-IR) spectroscopy and X-ray photoelectron spectroscopy (XPS). Because the area occupied by the circular flat-topped domains increases with increases in the OTS content, it is expected that the circular domains correspond to the OTS domain. The AFM line profile revealed that the circular domains were 1.1–1.3 nm higher than the surrounding area. Because the difference in molecular lengths between OTS and FOETS was ca. 1.3 nm, it can be concluded that the higher circular domains and the surrounding flat matrix regions were composed of OTS and FOETS molecules, respectively. OTS molecules formed circular domains even if the molar percent of OTS molecules was 75%. It is apparent from the ED pattern of the OTS/FOETS (75/25) mixed monolayer that the OTS domain is in a crystalline state, as the ED pattern showed a Debye ring and the magnitude of spacing corresponds to the (10) spacing of the OTS monolayer. In the case of the mixture of fluoroalkane and alkane, macroscopic phase separation was observed. However, in the case of organosilanes at the air/water interface, macroscopic phase separation such as that occurring with coalescence of the crystalline domain is inhibited because of the limited diffusion at the air/water interface.

A similar phase-separated structure was also expected for the mixed monolayer of the crystalline NTS and

amorphous FOETS. Crystallization of the n-nonadecenyl-trichlorosilane (NTS) phase was confirmed by ED.^[17] Fig. 5 shows the AFM images of the mixed NTS/FOETS and carboxylated NTS (NTS_{COOH})/FOETS monolayers. It was clarified that the NTS/FOETS mixed monolayers were in a phase-separated state, and that circular flat-topped domains ca. 1–2 μm in diameter were surrounded by a sealike flat region. The phase separation in the mixed NTS/FOETS can also arise from crystallization of the NTS component. The NTS_{COOH}/FOETS mixed monolayer was prepared through oxidation of the vinyl group of the NTS phase in the NTS/FOETS mixed monolayer.^[17] The NTS_{COOH} monolayer showed high surface free energy, with the magnitude being comparable to that of water. The surface morphology of the NTS/FOETS mixed monolayer was not changed even after oxidation because of the presence of a strong interaction between silanol groups of NTS and the Si wafer. The height difference between the NTS_{COOH} domain and the FOETS matrix phase in the NTS_{COOH}/FOETS mixed monolayer was almost the same as that for the NTS/FOETS mixed monolayer. In addition, an XPS measurement was performed for the NTS/FOETS and the NTS_{COOH}/FOETS mixed monolayers to confirm oxidation of the NTS phase. The larger ratio of oxygen/carbon atoms for the (NTS_{COOH}/FOETS) mixed monolayer than that for the NTS/FOETS monolayer suggests that the vinyl end groups of the NTS molecules were oxidized to carboxyl groups. The magnitude of the lateral force of the NTS_{COOH} phase was higher than that of the FOETS phase in the case of the NTS_{COOH}/FOETS mixed monolayer in contrast to the case of the NTS/FOETS

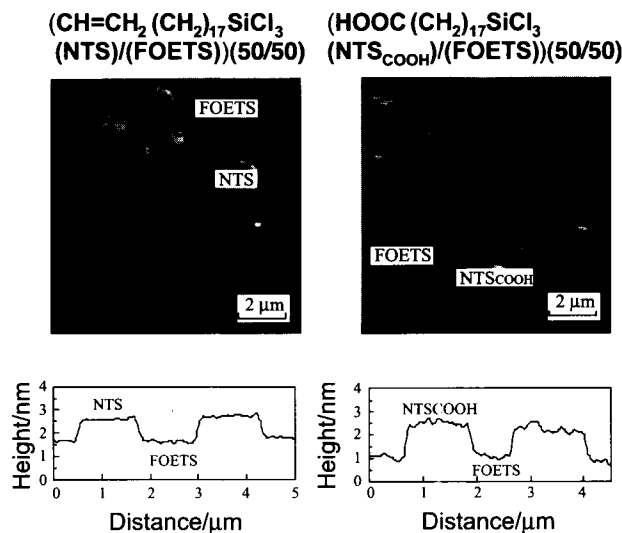


Fig. 5 AFM images of the mixed NTS/FOETS and carboxylated NTS (NTS_{COOH})/FOETS monolayers. (View this art in color at www.dekker.com.)

mixed monolayer. As the NTS_{COOH} phase had hydrophilic carboxyl end groups at the surface, these end groups can presumably form intermolecular hydrogen bonds with neighboring NTS_{COOH} molecules. Therefore, the surface of the outermost NTS_{COOH} phase is expected to show a higher shear strength than that of the NTS phase because of a difficulty in surface deformation. Also, there is a significant contribution of adhesion force between the sample surface and the tip with regard to lateral force. Because the surface free energy of the NTS_{COOH} phase is comparable to that of water, the water capillary force interacting between the NTS_{COOH} monolayer surface and the hydrophilic Si_3N_4 tip could strongly contribute to the adhesion force of the NTS_{COOH} phase. It is therefore conceivable that the NTS_{COOH} phase exhibited higher lateral force than the FOETS phase because of the formation of intermolecular hydrogen bonding and a thicker adsorbed water layer as discussed above. Lateral force microscopic (LFM) and XPS measurements revealed that the phase-separated monolayer with a large surface energy gap was successfully prepared.

To investigate the various types of mixed monolayers, a novel mixed-monolayer system was designed using reactive organosilanes and a nonreactive fatty acid. A phase-separated monolayer can also be prepared from both FOETS and nonpolymerizable and crystallizable amphiphiles such as stearic acid (SA) and lignoceric acid (LA). Fig. 6 shows the AFM images of the LA/ FOETS

(50/50 mol/mol) mixed monolayer Fig. 6a and after extraction of LA with hexane Fig. 6b. The LA/ FOETS mixed monolayer was in a phase-separated state similar to the OTS/FOETS mixed monolayer as shown in Fig. 4. It is reasonable to conclude from Fig. 6a and b that the circular domains are composed of LA molecules, as the circular flat-topped domains were preferentially extracted with hexane. In addition, the FOETS matrix was not extracted with hexane because FOETS molecules were immobilized on the Si wafer surface by the Si–O–Si covalent bond and multiple hydrogen bonding. The electron diffraction of the LA/ FOETS mixed monolayer showed a crystalline diffraction from LA domains. In addition, the circular domain of LA is higher than that of FOETS by 2 nm. Because the bare Si surface with Si–OH groups was exposed to the surface, the Si phase can easily be back-filled by another organosilane through chemisorption from its solution. Thus, various types of surface modification are possible by chemisorption of various organosilanes to the FOETS monolayer with holes shown in Fig. 6b. Fig. 6c shows the AFM topographic image of the OTS/FOETS mixed monolayer prepared by the chemisorption of OTS onto the Si part of the FOETS monolayer. The surface structure of Fig. 6c was very similar to the phase-separated structure observed for the OTS/FOETS mixed monolayer directly prepared by the LB method. The OTS phase is mechanically and chemically very stable because of the polymerization

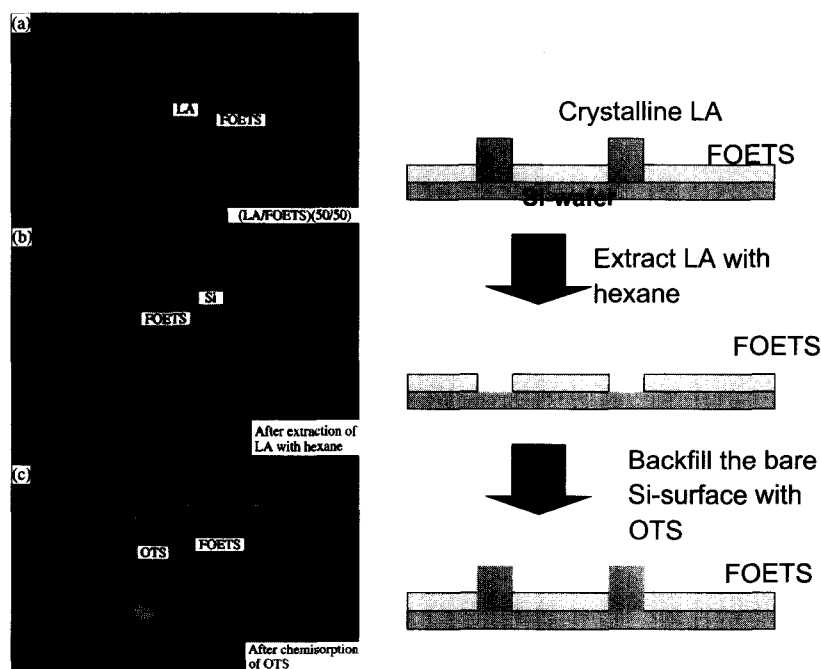


Fig. 6 AFM images of the LA/ FOETS (50/50 mol/mol) mixed monolayer (a), ghost monolayer after extraction of LA with hexane (b), and after backfill of ghost monolayer with OTS (c). (Reproduced from Ref. [13].) (View this art in color at www.dekker.com.)

and anchoring to the Si wafer. However, the domain height of the OTS phase in Fig. 6c was less than that observed for the OTS/FOETS mixed monolayer prepared by the LB method in Fig. 6c. In addition, the surface roughness of the OTS domains prepared by chemisorption was more distinct than that of the OTS domains prepared by the LB method. These results indicate that the OTS monolayer prepared by chemisorption is less ordered than that prepared by the LB method. This was also confirmed by grazing incidence X-ray diffraction (GIXD).^[15,22] However, the abovementioned procedure to backfill the Si portion of the FOETS monolayer by the chemisorption of organosilane could be applicable to the preparation of two-phase monolayers in which the constituents have different surface free energies or surface chemistries.

FABRICATION OF MULTIPHASE ORGANOSILANE MONOLAYERS THROUGH CHEMISORPTION AND PHOTOLITHOGRAPHY

A structural surface that exhibits patterns of varying wettability can be produced by chemisorption and local photodecomposition of organosilanes. Using such patterns as templates for 3-D structures with various topographic and surface properties appears very promising. Site-specific adsorption of microparticles can be achieved by specific interactions between microparticles and a mono-

layer surface. Immobilization of a polymerization initiator on a functional monolayer enables site-specific polymerization, which can result in a large topography change. Fig. 7 summarizes the scheme of fabrication of micro-patterned organosilane monolayers, site-specific polymerization, and immobilization of microparticles on patterned organosilane monolayers. These three processes are described in this section.

Preparation of a Three Component Patterned Organosilane Monolayer

Fig. 8 outlines the essential steps for fabrication of micro-patterned organosilane monolayers. The first step was the preparation of organosilane-grafted Si substrates. The chemical vapor adsorption (CVA) method was used to fabricate the monolayers from organotrialkoxysilane.^[25] Uniform monolayer formation was confirmed by AFM observations. Removal of the monolayer in selected areas by photodecomposition was the next step in the process. In photolithography, irradiation with VUV rays ($\lambda=172$ nm) leads to excitation cleavage of covalent bonds such as C-C, C-H, and Si-C bonds, and formation of surface Si-OH residues.^[25] The magnitude of water contact angle on OTES and FHETES monolayers was measured as a function of irradiation time of VUV light generated from an excimer lamp ($\lambda=172$ nm). VUV irradiation was done under 0.8 mmHg of pressure. Initially, OTES and FHETES monolayers gave water contact angles larger than 100° . However, within 15 min, the angles approached

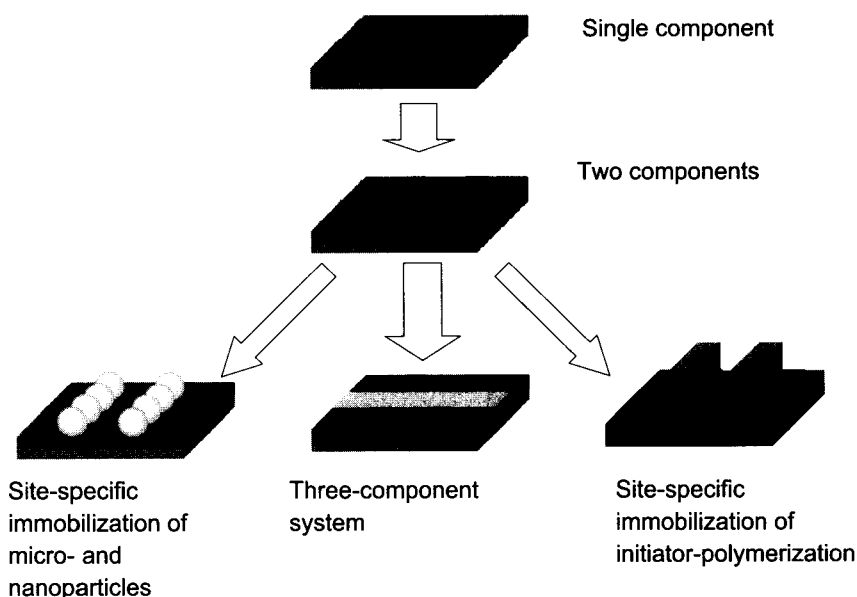


Fig. 7 Schematic representation of surface patterning, site-specific polymerization, and site-specific immobilization of microparticles. (View this art in color at www.dekker.com.)

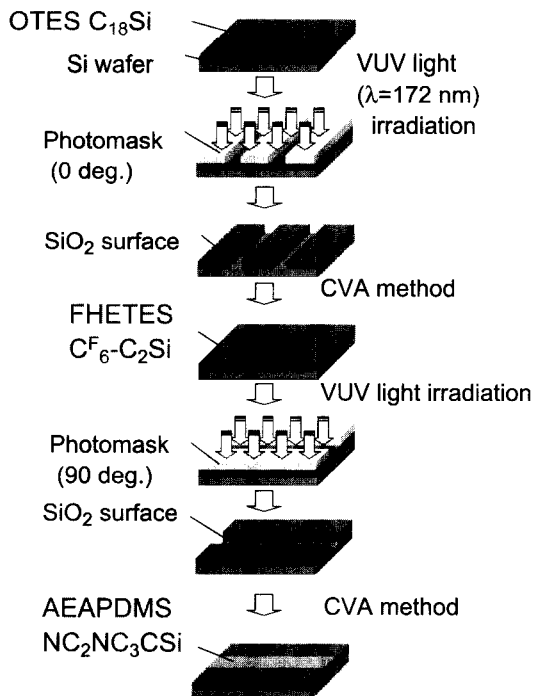


Fig. 8 Schematic representation of site-specific photodecomposition by irradiation with VUV rays and chemisorption. (Reproduced from Ref. [24].) (View this art in color at www.dekker.com.)

0°, which indicates that almost complete removal of a monolayer can be achieved with 15-min irradiation of VUV light. The monolayer removal was also confirmed by XPS measurements. Using a photomask, one can prepare a pattern with the desired shape and a precisely controlled arrangement of surface functional groups. As an example, the preparation and characterization of an n-octadecyltriethoxysilane (OTES), [2-perfluorohexyl]ethyltriethoxysilane (FHETES), [2-aminoethyl]-3-aminopropylmethyldimethoxysilane (AEAPDMS) patterned surface is introduced in this section. The OTES-grafted Si wafer was irradiated for 15 min with VUV light. The second organosilane monolayer, FHETES (molecular length ca. 1.0 nm), was then introduced onto the first patterned surfaces by a similar method with alkylsilane. Formation of a ternary component monolayer requires another photodecomposition and chemisorption process, with the photomask rotated 90° from its position in the first patterning step. The OTES/FHETES sample was then irradiated with VUV, resulting in crossline micropatterns on the substrate surfaces. The third organosilane monolayer, AEAPDMS (molecular length ca. 0.9 nm), was finally introduced onto the second patterned substrate surfaces, again by the CVA method.

XPS and contact angle measurements were used to characterize the changes in the surface chemical compositions of the micropatterned organosilane monolayers. Fig. 9 shows the XPS survey scan spectra of the changes in the surface chemical compositions through the micropatterning process. The OTES monolayer showed C_{1s} , O_{1s} , Si_{2s} , and Si_{2p} peaks at 285, 533, 151, and 100 eV, respectively. The OTES/FHETES patterned Si substrate clearly showed an additional F_{1s} peak at 690 eV, whereas the OTES/FHETES/AEAPDMS grafted Si substrates showed another N_{1s} peak at 400 eV. Decomposition of the FHETES monolayer was revealed by the decreased intensity of the F_{1s} peak. The grafting of organosilane monolayers was also confirmed from C_{1s} and N_{1s} XPS narrow-scan spectra. These results indicate that the three kinds of organosilane molecules were subsequently grafted on the substrate surfaces.

Fabrication of a micropattern with three kinds of surface functional groups was confirmed by Scanning force microscopy (SFM) observation. Fig. 10a and b shows AFM and LFM images of an OTES/FHETES/AEAPDMS three-component micropatterned organosilane monolayer, respectively. Fig. 10c and d shows the line profiles of the white lines in Fig. 10a. These figures show crossline microstructures fabricated on Si-wafer substrates. The widths of the fabricated FHETES and

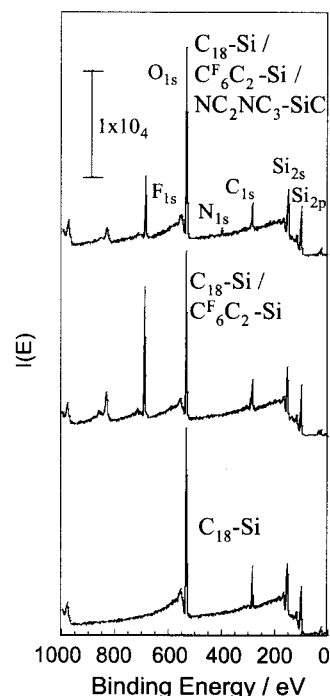


Fig. 9 XPS survey scan spectra of the OTES, OTES/FHETES, and OTES/FHETES/AEAPDMS micropatterned Si substrates (emission angle 45°).

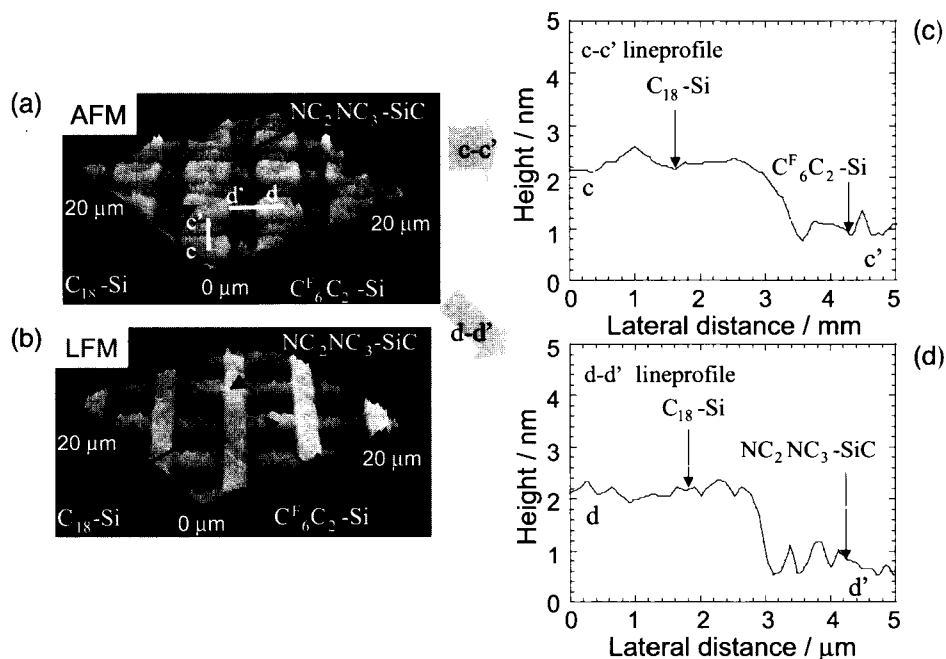


Fig. 10 AFM and LFM images of three-component micropatterned organosilane monolayers. (a) AFM image of an OTES/FHETES/AEAPDMS micropatterned surface; (b) LFM image of an OTES/FHETES/AEAPDMS micropatterned surface; (c), (d) line profiles of white line parts in (a). (Reproduced from Ref. [37].) (View this art in color at www.dekker.com.)

AEAPDMS lines were consistent with the widths of slits in the photomask. In the line profile of the AFM image as shown in Fig. 10c, the height difference between the OTES and FHETES surfaces was ca. 1.4 nm. The height difference corresponds to the difference in the molecular length (ca. 1.3 nm) between OTES and FHETES. In contrast, the height difference between the OTES and AEAPDMS surfaces was ca. 1.5 nm Fig. 10d, corresponding to the difference in the molecular length (ca. 1.4 nm) between OTES and AEAPDMS. The origin of the contrast in the LFM image can be explained by the difference in the surface properties of the three components, i.e., the chain rigidity, crystallinity, and chemistry of terminal functional groups of the organosilane molecules.^[22] AEAPDMS-grafted areas are the brightest of the three components because the terminal amino groups exerted high lateral force due to the strong interaction between the hydrophilic amino group and the Si-OH group of the cantilever tip. The area ratio of the prepared micropatterned monolayer is in accord with that of the target value; that is, the estimated area ratio of OTES/FHETES/AEAPDMS was 4/2/3.

The introduction of a different organosilane component was also confirmed by the measurement of surface free energy. Table 1 shows the surface free energies of uniform or micropatterned organosilane monolayers. The surface free energy was calculated from the contact angles of

water and methylene iodide based on Owens and Wendt's method.^[26] In Table 1, γ_s^d and γ_s^p denote the dispersion and polar components of surface free energy, respectively. The surface free energy of the OTES/FHETES micropatterned surface is smaller than that of the OTES monolayer surface; the decrease can be attributed to the fluoroalkyl groups of FHETES, which are known to decrease surface free energy. On the other hand, the surface free energy, especially the hydrogen-bonding component γ_s^h , extensively increased after the grafting of AEAPDMS; this increase can likely be attributed to the relatively high polarity of amino groups introduced in the grafted AEAPDMS monolayers.^[24] Taken together with

Table 1 Surface free energy of micropatterned organosilane monolayers

Organosilanes	γ_{sv} (mJ m^{-2})	γ_{sv}^d (mJ m^{-2})	γ_{sv}^h (mJ m^{-2})
AEAPDMS	48.5	34.3	14.2
OTES	20.1	18.1	2
FHETES	14.7	13.1	1.6
OTES/FHETES	17.1	15.5	1.6
OTES/FHETES/ AEAPDMS	23.8	19.7	4.1

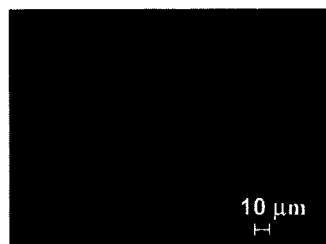


Fig. 11 Environmental scanning electron microscopic image of a water droplet on a monolayer after exposure to water vapor at 273K. (Reproduced from Ref. [37].)

the SFM observation, this stepwise change in surface free energy confirms that the three-component organosilane surfaces had been micropatterned with highly hydrophobic and hydrophilic areas. Our patterning of three-component organosilane monolayers is expected to be a useful template for immobilizing various organic or inorganic materials on Si surfaces.

A laterally structured surface with different wetting properties may be produced by various techniques such as microcontact printing,^[27] micromachining,^[28] photolithography,^[29] and vapor deposition.^[30] If one phase of a micropatterned surface has an affinity toward a certain liquid, the surface can be used as a template for local liquid condensation. A line-patterned high-wettability contrast surface was prepared via the local photodecomposition of an FHETMS monolayer. The advantage of this method is that the height difference of the two phases is less than 2 nm and the topographic effect on wettability can be ignored. The water-droplet formation on the micropatterned surface was directly observed with an environmental scanning electron microscope. First, the Environmental scanning electron microscope (ESEM) sample chamber was evacuated below the saturated vapor pressure (612 Pa) of water at 273 K. The sample surface was then cooled to 273 K and the vapor pressure of the ESEM sample chamber was increased to 700 Pa. Fig. 11 shows the ESEM image of the water droplet on the surface of the FHETMS/Si-OH patterned monolayer during the initial condensation process. The water began to condense on the Si-OH portion of the patterned surface. The size of the water droplet and the number of water droplets increased until the droplets coalesced in a line. Because water has a large surface free energy compared with the FHETMS phase, it is more likely to condense on the higher surface free energy region. After the vapor pressure of the ESEM sample chamber was raised to 1050 Pa, the water droplet began to bridge with droplets on the adjacent line. Because the micropatterning surface can confine liquid in distinct micropatterned regions, the surface can be used for local growth of a crystal of functional

molecules^[31] or as a substrate for ink-jet printing with functional molecules.^[32]

Site-Specific Polymerization of Methacrylate Monomers

The patterned organosilane monolayers introducing an organosilane molecule with a polymerization-initiating unit are useful as template surfaces for site-specific polymerization. An atom transfer radical polymerization (ATRP) unit was immobilized as a monolayer component. Because ATRP is one of the most successful methods for polymerizing a variety of monomers in a controlled fashion,^[33,34] tailor-made surface topography is possible. Several reports have described the formation of polymer thin film by radical polymerization from the immobilized ATRP initiator.^[35,36]

Fig. 12 shows a schematic representation of a site-specific ATRP from a micropatterned monolayer surface.^[37] Before introducing the initiator for ATRP into the organosilane monolayer system, an AEAPDMS monolayer was prepared on a Si wafer substrate surface. The prepared surface terminated by amino groups was treated with 2-bromoisobutyric acid in the presence of a condensation agent. After the modification, the water contact angle of the obtained surface increased from 63° to 69° because of the change in the surface functional groups. Introduction of the initiating unit was further confirmed by an XPS measurement, in which the peaks attributed to Br and carbonyl carbon were observed at 68 and 287.9 eV, respectively. The resulting surface was irradiated by VUV light through a photomask. The LFM image of the patterned surface shows the presence of a pattern corresponding to the line width of the photomask used.

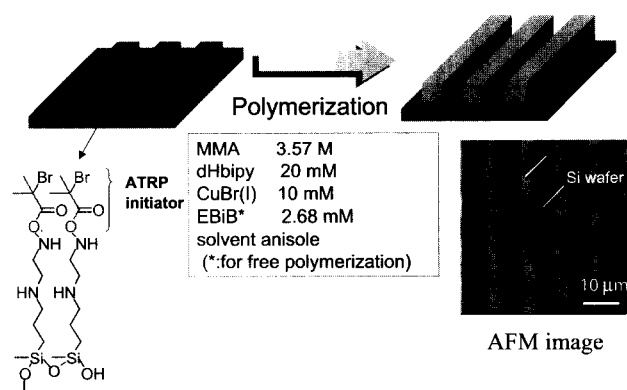


Fig. 12 Schematic representation of the site-specific atom transfer living radical polymerization from a micropatterned monolayer surface and AFM image of line-patterned PMMA ultrathin film. (View this art in color at www.dekker.com.)

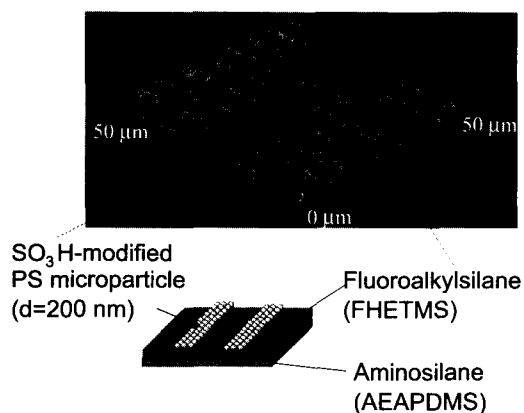


Fig. 13 AFM image of the AEAPDMS/FHETMS monolayer after exposure to the aqueous dispersion of sulfonated PS microparticles. (Reproduced from Ref. [37].) (View this art in color at www.dekker.com.)

Surface-initiated radical polymerization of methyl methacrylate (MMA) was done in the presence of CuBr(I) and 4,4'-di-*n*-heptyl-2,2'-bipyridine in anisole. To control the polymerization process, the corresponding initiator, ethyl 2-bromoisobutyrate, was also added for bulk polymerization. The mixture was degassed, and argon was bubbled through the mixture for 20 min to ensure that oxygen was removed completely. The mixture was heated to 363 K. After several hours, the polymerization solution was cooled to room temperature to terminate the polymerization. The Si wafer was immersed in THF and rinsed with toluene to remove the adsorbed free poly(methyl methacrylate) (PMMA). The PMMA micropattern was observed by AFM.

Fig. 12 also shows the AFM image of the line-patterned PMMA ultrathin film. An AFM image revealed that the site-specific polymerization of methacrylate monomer occurred on the micropatterned surface of the ATRP initiator. The height and width of the PMMA layer is ca. 6–10 nm and ca. 5 μm , respectively. The width estimated from the AFM image is in good agreement with the line width of micropatterns of surface immobilized initiator. The formation of a PMMA layer was further confirmed by an XPS measurement, in which the characteristic peaks attributed to the aliphatic ether and carbonyl carbons were observed at 285, 286.5, and 288.8 eV, respectively.

Site-Specific Adsorption of Charged Microparticles

Two-dimensional alignment of micro- and nanoparticles on a substrate surface might be a promising method for fabricating functional materials, as properties of

micro- and nanoparticles can be adjusted by controlling the size and surface chemistry. Various attempts have been made at the site-specific immobilization of micro- and nanoparticles.^[38,39] In this study, the micropatterned organosilane monolayer with an aminosilane/fluoroalkylsilane line pattern was applied as a template surface for site-specific immobilization of negatively charged microparticles.

FHETMS and AEAPDMS were used as surface modifiers for a Si wafer substrate. The AEAPDMS/FHETMS micropattern (line width, AEAPDMS//FHETMS = 2/4 $\mu\text{m}/\mu\text{m}$) was fabricated by a method similar to that used to yield the multicomponent organosilane monolayer. The Si wafer substrate with a micropatterned surface was then exposed to the aqueous dispersed solution of sulfonated polystyrene (PS) microparticles at pH = ca. 6.0 for 30 min. As shown in Fig. 13, the site-specific immobilization of PS particles was successfully achieved on the micropatterned substrate surface.^[40] An AFM image shows that the layers consisting of adsorbed PS microparticles are ca. 200 nm high and ca. 2 μm wide. The height and width estimated from the AFM image is in good agreement with the diameter of PS microparticles and the line width of AEAPDMS micropatterns, respectively. This result suggests that the sulfonated PS particles were adsorbed on the surface as a monolayer. The site-specific adsorption of PS particles onto the AEAPDMS grafted surfaces can be ascribed to the electrostatic interaction between negatively charged sulfonic acid groups of PS particles and positively charged amino groups of AEAPDMS-grafted surfaces.

CONCLUSION

Patterned microfeatures of organosilane monolayers were fabricated on the substrate by two different methods. One method utilizes the crystallization of a binary component organosilane monolayer at the air/water interface. Another method utilizes the local photodecomposition by VUV light and backfilling of the decomposed area by chemisorption of organosilane monolayers. It was also revealed that micropatterned organosilane monolayers can be used as model surfaces with controlled, area-selective surface nature such as free energy, nanostructure, and chemical composition.

ACKNOWLEDGMENTS

The author wishes to acknowledge Professor T. Kajiyama, Dr. H. Otuska, Dr. K. Tanaka, Dr. K. Kojio, M. Morita, Mr. H. Sakata, and Mr. T. Koga for their helpful discussion. This research was partially supported by Grants-in-Aid for Scientific Research Nos. 12480264

and 1200875189, the COE Research "Design and Control of Advanced Molecular Assembly Systems" (08CE2005), and the 21st-century COE Program, "Functional Innovation of Molecular Informatics" from the Ministry of Education, Culture, Sports, Science and Technology, Japan.

REFERENCES

1. Ulmann, A. *An Introduction to Ultrathin Organic Films: From Langmuir-Blodgett to Self-Assembly*; Academic Press: San Diego, CA, 1991.
2. Tredgold, R.H. *Order in Thin Organic Films*; Cambridge University Press: Cambridge, UK, 1994.
3. *Nanotechnology*; Timp, G., Ed.; Springer: New York, 1999.
4. Sagiv, J. Organized monolayers by adsorption. I. Formation and structure of oleophobic mixed monolayers on solid surfaces. *J. Am. Chem. Soc.* **1980**, *102*, 92–98.
5. Sagiv, J. Organized monolayers by adsorption. II. Molecular orientation in mixed monolayers built on anisotropic polymeric surfaces. *Isr. J. Chem.* **1979**, *18*, 339–345.
6. Wasserman, S.R.; Tao, Y.T.; Whitesides, G.M. Structure and reactivity of alkylsiloxane monolayers formed by reaction of alkyltrichlorosilanes on silicon substrates. *Langmuir* **1989**, *5*, 1074–1087.
7. Parikh, A.N.; Allara, D.L.; Azouz, I.B.; Rondelez, F. An intrinsic relationship between molecular structure in self-assembled n-alkylsiloxane monolayers and deposition temperature. *J. Phys. Chem.* **1994**, *98*, 7577–7590.
8. Ge, S.-R.; Takahara, A.; Kajiyama, T. Aggregation structure and surface properties of immobilized organosilane monolayers prepared by the upward drawing method. *J. Vac. Sci. Technol.* **1994**, *A 12*, 2530–2536.
9. Ge, S.-R.; Takahara, A.; Kajiyama, T. Phase separated morphology of immobilized organosilane monolayer studied by scanning probe microscope. *Langmuir* **1995**, *11*, 1341–1346.
10. Takahara, A.; Kojio, K.; Ge, S.-R.; Kajiyama, T. Scanning force microscopic studies of surface structure and protein adsorption behavior of organosilane monolayers. *J. Vac. Sci. Technol.* **1996**, *A14*, 1747–1754.
11. Kajiyama, T.; Ge, S.-R.; Kojio, K.; Takahara, A. Scanning force microscopic study of surface structure and properties of (alkylsilane/fluoroalkylsilane) mixed monolayer. *Supramol. Sci.* **1996**, *3*, 123–130.
12. Kojio, K.; Ge, S.-R.; Takahara, A.; Kajiyama, T. Molecular aggregation state of n-octadecyltrichlorosilane monolayer prepared at an air/water interface. *Langmuir* **1998**, *14*, 971–974.
13. Takahara, A.; Kojio, K.; Ge, S.-R.; Kajiyama, T. Scanning Force Microscopy of Surface Structure and Surface Mechanical Properties of Organotrichlorosilane Monolayers Prepared by Langmuir Method. In *ACS Symp. Ser.*; Ratner, B.D., Tsukruk, V.V., Eds.; Scanning Probe Microscopy of Polymers, American Chemical Society: Washington, D.C., 1998; Vol. 694, 204–222.
14. Kojio, K.; Takahara, A.; Kajiyama, T. Formation mechanism of n-octadecyltrichlorosilane monolayer prepared at the air/water interface. *Colloids Surf., A* **2000**, *180*, 294–306.
15. Kojio, K.; Takahara, A.; Omote, K.; Kajiyama, T. Molecular aggregation state of n-octadecyltrichlorosilane monolayers prepared by the Langmuir and chemisorption methods. *Langmuir* **2000**, *16*, 3932–3936.
16. Kojio, K.; Takahara, A.; Kajiyama, T. Molecular aggregation state and molecular motion of organosilane monolayers prepared at the air/water interface. *Langmuir* **2000**, *16*, 9314–9320.
17. Kojio, K.; Takahara, A.; Kajiyama, T. Aggregation Structure and Surface Properties of 18-Nonadecyltrichlorosilane Monolayer and Multilayer films Prepared by Langmuir Method. In *ACS Symp. Ser.*; Silicones and Silicon-Modified Materials, American Chemical Society: Washington, D.C., 2000; Vol. 729, 332–352.
18. Kojio, K.; Takahara, A.; Kajiyama, T. Structure and Surface Properties of Immobilized Fluoroalkylsilane and Their Mixed Monolayers. In *ACS Symp. Ser.*; Fluorinated Surfaces, Coatings, and Films, American Chemical Society: Washington, D.C., 2001; Vol. 787, 31–47.
19. Takahara, A.; Ge, S.-R.; Kojio, K.; Kajiyama, T. In situ atomic force microscopic observation of albumin adsorption onto phase-separated organosilane monolayer surface. *J. Biomater. Sci., Polym. Ed.* **2000**, *11*, 111–120.
20. Takahara, A.; Hara, Y.; Kojio, K.; Kajiyama, T. Scanning force microscopic study of protein adsorption on the surface of organosilane monolayers prepared by the Langmuir-Blodgett method. *Macromol. Symp.* **2001**, *167*, 271–284.
21. Takahara, A.; Hara, Y.; Kojio, K.; Kajiyama, T. Plasma protein adsorption behavior onto the surface of phase-separated organosilane monolayers on the basis of scanning force microscopy. *Colloids Surf., B* **2002**, *23*, 141–152.
22. Takahara, A.; Kojio, K.; Kajiyama, T. Effect of aggregation state on nanotribological behaviors of

- organosilane monolayers. *Ultramicroscopy* **2002**, *91*, 203–213.
23. Sugimura, H.; Ushiyama, K.; Hozumi, A.; Takai, O. Micropatterning of alkyl- and fluoroalkylsilane self-assembled monolayers using vacuum ultraviolet light. *Langmuir* **2000**, *16*, 885–888.
 24. Koga, T.; Otsuka, H.; Takahara, A. Fabrication of three-component micropatterned organosilane monolayer by a stepwise photolithography process. *Chem. Lett.* **2002**, *31*, 1196–1197.
 25. Koga, T.; Morita, M.; Sakata, H.; Otsuka, H.; Takahara, A. Surface structure and properties of multi-component micropatterned organosilane monolayers prepared by stepwise photodecomposition and chemisorption process. *Int. J. Nanosci.* *in press*.
 26. Owens, D.K.; Wendt, R.C. Estimation of the surface free energy of polymers. *J. Appl. Polym. Sci.* **1969**, *13*, 1741–1747.
 27. Kumar, A.; Biebuyk, H.A.; Whitesides, G.M. Patterning self-assembled monolayers—Applications in material science. *Langmuir* **1994**, *10*, 1498–1511.
 28. Abbott, N.L.; Folkers, J.P.; Whitesides, G.M. Manipulation of the wettability of surfaces on the 0.1-micrometer to 1-micrometer scale through micromachining and molecular self-assembly. *Science* **1992**, *257*, 1380–1382.
 29. Calvert, J.M. Lithographic patterning of self-assembled films. *J. Vac. Sci. Technol.* **1993**, *B11*, 2155–2163.
 30. Gau, H.; Herminghous, S.; Lenz, P.; Lipowsky, R. Liquid morphologies on structured surfaces: From microchannels to microchips. *Science* **1999**, *283*, 46–49.
 31. Kagan, C.R.; Breen, T.L.; Kosbar, L.L. Patterning organic–inorganic thin-film transistors using micro-contact printed templates. *Appl. Phys. Lett.* **2001**, *79*, 3536–3538.
 32. Calvert, P. Inkjet printing for materials and devices. *Chem. Mater.* **2001**, *13*, 3299–3305.
 33. Wang, J.S.; Matyjaszewski, K. Controlled living radical polymerization—atom-transfer radical polymerization in the presence of transition metal complexes. *J. Am. Chem. Soc.* **1995**, *117*, 5614–5615.
 34. Matyjaszewski, K.; Xia, J. Atom transfer radical polymerization. *Chem. Rev.* **2001**, *101*, 2921–2990.
 35. Ejaz, M.; Ohno, K.; Tsujii, Y.; Fukuda, T. Controlled grafting of a well-defined glycopolymer on a solid surface by surface-initiated atom transfer radical polymerization. *Macromolecules* **2000**, *33*, 2870–2874.
 36. Kong, X.; Kawai, T.; Abe, J.; Iyoda, T. Amphiphilic polymer brushes grown from the silicon surface by atom transfer radical polymerization. *Macromolecules* **2001**, *34*, 1837–1844.
 37. Takahara, A.; Sakata, H.; Morita, M.; Koga, T.; Otsuka, H. Fabrication and characterization of multi-component organosilane nanofilms. *Compos. Interfaces* **2003**, *10*, 489–504.
 38. Masuda, Y.; Itoh, M.; Yonezawa, T.; Koumoto, K. Low-dimensional arrangement SiO₂ particles. *Langmuir* **2002**, *18*, 4155–4159.
 39. Fudouzi, H.; Kobayashi, M.; Shinya, N. Assembly of microsized colloidal particles on electrostatic regions patterned through ion beam irradiation. *Langmuir* **2002**, *18*, 7648–7652.
 40. Koga, T.; Otsuka, H.; Takahara, A. Controlled arrangements of charged microparticles on the patterned monolayer surfaces. manuscript in preparation.

Molecular Computing Machines

M

Yaakov Benenson
Ehud Shapiro

Weizmann Institute of Science, Rehovot, Israel

INTRODUCTION

Biopolymers such as nucleic acids and proteins encode biological data and may be viewed as strings of chemical letters. While electronic computers manipulate strings of 0's and 1's encoded in electric signals, biologically encoded data might, in principle, be manipulated by biochemical means. During the last decade, several approaches to compute with biomolecules were developed, and the field has become known as biomolecular or DNA computing. The approaches varied widely with respect to the model of computation they employed, the problems they attempted to solve, and the degree of human intervention. One approach focused on the application of the Turing machine model and, more generally, string-processing automata to biomolecular information processing. Its goal is to construct computers made of biomolecules that are capable of autonomous conversion of an input data-encoding molecule to an output molecule according to a set of rules defined by a molecular program. Here we survey the field of biomolecular computing machines and discuss possible future directions.

BACKGROUND

The seminal work of Adleman^[1] demonstrated that commonly used biochemical manipulations of DNA can be utilized to solve real-world computational problems and initiated the field of biomolecular computing. In the biomolecular approach to computing, the computational paradigm is chosen to fit the capabilities of biomolecules, rather than adapting the biomolecular machinery to computational schemes borrowed from electronic computers.^[2] The problems initially solved by DNA computing were so-called "combinatorial problems." An example of such a problem is the traveling salesman problem, which is to find the most efficient route through several cities given a distances chart between them, passing through each city exactly once. Solving the problem can be performed by calculating all possible routes that pass exactly once through each city, comparing them and choosing the shortest one. As the number of potential routes is exponential in the size of the problem, this computation may

require an exponential number of steps. More efficient solution methods are not known for the traveling salesman problem and for similar such problems, termed NP-hard. It was hoped that the potential massive parallelism of DNA manipulation could speed up the solution of NP-hard problems. The DNA computing technique employed to solve the traveling salesman problem included 1) generation of all possible solution candidates (e.g., various routes) encoded in DNA strands and selection of the correct ones, 2) their amplification and detection by known molecular biology techniques, and 3) isolation and characterization of the shortest one. Computational problems solved in vitro with variations of this approach encompassed instances of Hamiltonian Path,^[1] SAT,^[3] maximal clique,^[4] and "knight move"^[5] problems. The computer, i.e., the physical system that produced a solution, comprised the biomolecules themselves, the laboratory equipment required to realize their biochemical manipulation, and the laboratory personnel who operated the laboratory equipment, performing the operations required to execute the computation. Therefore while these computing systems used biomolecules for computation, they realized laboratory-scale, rather than molecular-scale, computers.

A second direction in DNA computing, proposed by Winfree,^[6,7] uses self-assembly of DNA tiles.^[8,9] It relies on the mathematical theory of tiling. One result of this theory discovered by Wang^[10] is that aperiodic assembly of appropriately designed tiles emulates the operation of a Turing machine, a universal computer. The tiles have colored edges, and they may be assembled once two adjacent tiles have edges of the same color. DNA tiles^[8] are relatively rigid flat constructs with four sticky ends, with one sticky end emulating one edge of a tile and different sticky ends emulating different colors. DNA tiles make contact through complementary sticky ends, emulating recognition by the same color. Initial breakthrough in this area was achieved by constructing a periodic two-dimensional crystal from DNA tiles, based on Wang assembly rules. The first actual computation performed by this technique was a cumulative XOR (exclusive OR) logical operation on a string of four binary bits.^[9] In this experiment, an input string was built from alphabet tiles (either "0" or "1") and then a second row of tiles

self-assembled upon it. The first tile of the second row contained the result of the XOR operation between the first two bits, and each subsequent tile performed the operation between the intermediate cumulative result and the next unprocessed bit. Besides the potential to realize universal computation through Turing machine emulation, the technique of DNA tiles self-assembly may become a basis for fabrication of smart, aperiodic materials on a nanoscale, as suggested by several recent results.^[11,12]

A third direction in DNA computing is an attempt to realize the vision,^[13] recalled by Adleman in the conclusion to his seminal paper of a programmable, autonomous, molecular-scale computer: "In the future, research in molecular biology may provide improved techniques for manipulating macromolecules. Research in chemistry may allow for the development of synthetic designer enzymes. One can imagine the eventual emergence of a general purpose computer consisting of nothing more than a single macromolecule conjugated to a ribosomelike collection of enzymes that act on it." This paradigm of biomolecular computers is the focus of our review. It views a DNA strand as a string or a tape that functions as the input as well as the memory storage for *automata* such as a finite automaton or a Turing machine.^[13] This paradigm is inspired by the realization that some biomolecular machines in the living cell are essentially simple automata operating on digital information encoded in directional biopolymers.^[14,15] An automaton operates by scanning a tape of symbols one symbol at a time, possibly modifies one symbol in each step, moving to an adjacent symbol and changing its state according to a predefined set of the transition rules. The tape of symbols may be naturally encoded in a polar biopolymer such as DNA or RNA. The transition rules of the machine may be encoded by transition molecules similar to tRNA. A transition, i.e., the physical modification of the input according to the transition rules, may be accomplished, in principle, by a combination of different processing enzymes. Taking this viewpoint, DNA and RNA polymerases, the ribosome, and recombinases can all be viewed as simple molecular automata. For example, RNA polymerase is, mathematically speaking, a so-called finite state transducer, which translates a string over the alphabet {A, T, C, G} into a string over the alphabet {A, U, C, G} according to a simple translation table. An artificial molecular automaton may be able to operate autonomously, realizing a truly molecular-scale computer. Such a computer could have several important applications, discussed below.

The concept of a biomolecular computer was first introduced by Bennett^[13] in 1982 as a hypothetical design for an energy-efficient computer. In this conceptual design, a set of artificial enzymes encoded the transition table of the machine and operated on RNA-based data tape. The design did not include any concrete imple-

mentation details. Several detailed designs were proposed since then. Rothmund^[16] and Smith^[17] proposed models for molecular implementations of Turing machines. Garzon et al.^[18] designed a model of finite automata and Sakamoto et al.^[19,20] implemented a semiautonomous state machine that could perform state transitions.

MOLECULAR AUTOMATA

Automata

Generally, an automaton consists of 1) a data tape divided into cells, each containing a symbol selected from the tape alphabet, and 2) a finite-state device driven by transition rules. The device is positioned over one of the cells and is in one of a finite number of internal states. Depending on the symbol read and the internal state, a transition rule instructs the device to write a new symbol, change state, and move one cell to the left or to the right. The Turing machine^[21] is the most general automaton, capable of writing on the tape as well as moving in either direction. Fig. 1A demonstrates a Turing machine with two symbols and two states, with the upper part of the panel showing the application of one transition rule. Each rule is of the form *initial state, current symbol* → *new state, new symbol, direction of movement* (R=right, L=left). A more restricted, yet important, class of automata is called finite-state acceptors (finite automata for short).^[22] A finite automaton is a unidirectional read-only Turing machine. Its input is a finite string of symbols. It is initially positioned on the leftmost input symbol in a default initial state and, in each transition, moves one symbol to the right, possibly changing its internal state (Fig. 1B is an example of a computation step of a finite automaton). Each of its transition rules specifies a next state based on the current state and current symbol. The computation terminates after the last input symbol is processed. Alternatively, it may suspend without completion when no transition rule applies. Some states are deemed accepting and the automaton accepts an input if there is a computation with this input that ends in an accepting final state. Otherwise, it is said to reject the input.

A finite automaton with two states and an alphabet of two symbols is shown in Fig. 1C. It determines whether a string of symbols over the alphabet {*a*, *b*} contains an even number of *a*'s. On a diagram, an incoming arrow represents an initial state, and a double circle represents an accepting state. Below the diagram, a sample computation over an input *abba* shows the intermediate configurations obtained during the sequential application of the transition rules.

A two-state, two-symbol automaton can have eight possible transition rules. The programming of such an

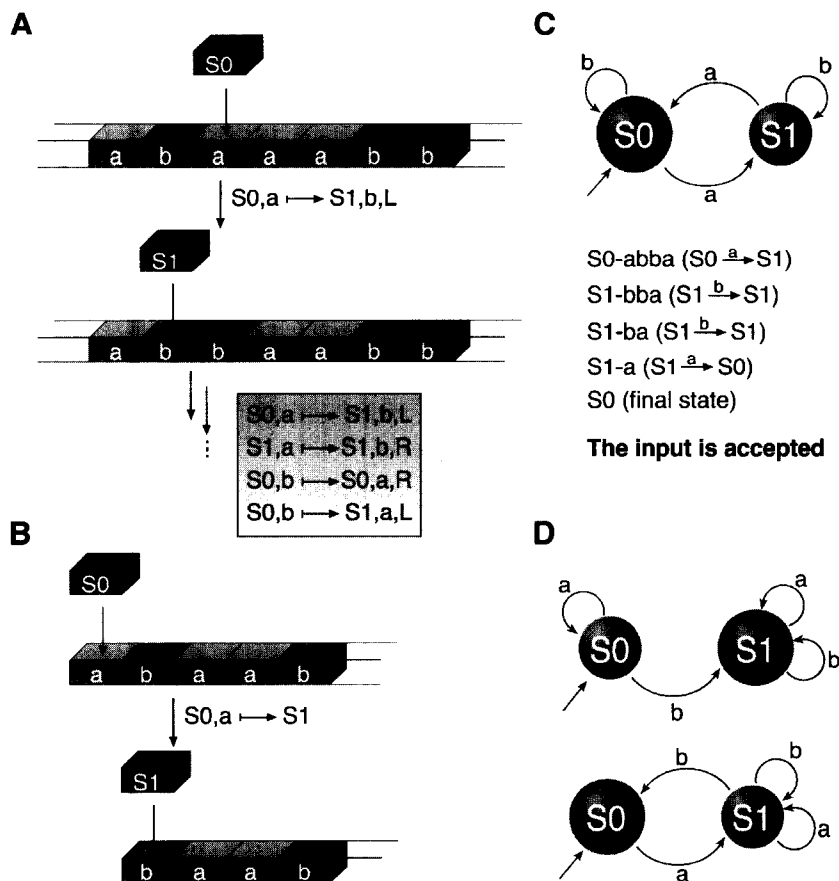


Fig. 1 Examples of automata.

automaton amounts to selecting the transition rules and determining the accepting states. Fig. 1D shows some examples of additional final automata. The topmost automaton determines whether an input string contains at least one *b* symbol. A second one determines if an input string begins with *a* and ends with *b*. It is an example of a nondeterministic automaton with two transitions ($S1, b \rightarrow S0$ and $S1, b \rightarrow S1$) applicable to the same configuration. A computation ending in an accepting state uses $S1, b \rightarrow S1$ for all *b* symbols except the last, and uses $S1, b \rightarrow S0$ for the last *b*.

Early Designs of Molecular Automata

Bennett^[13] described a “truly chemical Turing machine” with a linear tape analogous to RNA, where the internal state and head location are realized by a special chemical modifier attached to one of the nucleotides. Each transition rule is realized by a hypothetical “enzyme” that exclusively recognizes a unique combination of a nucleotide and its modifier, replaces a nucleotide by an output symbol, and attaches a next-state modifier to one of the

adjacent nucleotides, according to the desired head movement (Fig. 2).

In Fig. 2, a transition molecule 7 that recognizes a combination of the symbol *a* and the state S0 loads itself with the molecule for the symbol *b* and a molecule for the state S1. The loaded molecule 2 reversibly attaches itself to a data tape 1. An intermediate complex 3 forms through new chemical bonds between the transition molecule and the symbol *a* and state S0, between the new symbol *b* and the data tape, and between the adjacent symbol *b* and the new state S1 (dotted lines). In the next intermediate 4, the old symbol *a* and state S0 become attached to the transition molecule and are detached from the data tape; the new symbol *b* is inserted into the data tape; the new state S1 attaches to the symbol *b* that lies to the right of the site of newly inserted symbol. The transition molecule 6 dissociates from the completely modified data tape 5 and is subsequently stripped of the attached old state and symbol.

Bennett introduced several logical elements that remain relevant till this day. First, he proposed to encode a data tape in a single biopolymer, using a natural

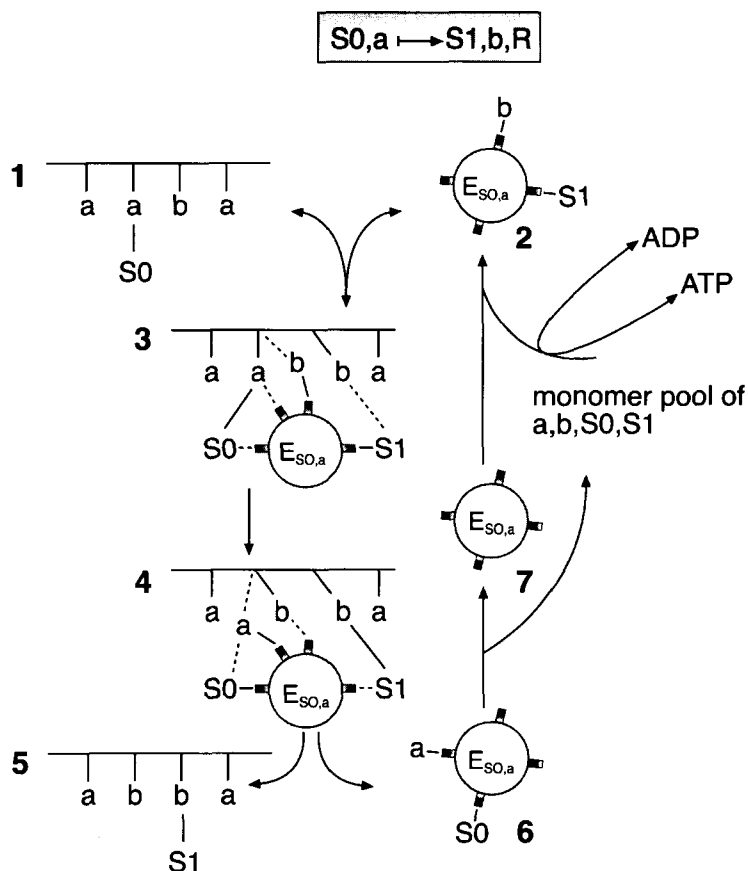


Fig. 2 An example of a single transition performed by Bennett's hypothetical chemical Turing machine. The rule implemented is $S_0, a \rightarrow S_1, b, R$. (From Ref. [13] © Kluwer Academic/Plenum Publishers.)

"alphabet." Second, he introduced the important concept of a "transition molecule," i.e., representation of each transition rule by a separate molecule or molecular assembly.

Following work on molecular automata dealt with realizing this concept. Different ways to encode tape symbols and machine states and to build transition molecules were proposed and various biochemical transition mechanisms were considered.

Rothemund^[16] proposed a detailed design for a molecular Turing machine that utilized a common DNA structural motif known as a "cohesive terminus" or a "sticky end." A sticky end is a short (one to six nucleotides) stretch of single-stranded DNA emerging from the double-stranded DNA molecule of a potentially unlimited length. The advantage of a sticky end as compared with the dsDNA is that it is reactive compared with dsDNA. Molecules with sticky ends may interact once the DNA sequences of their sticky ends are complementary, irrespective to the sequence of their double-stranded part. This technique is extensively used in recombinant DNA

technology. Rothemund's hypothetical computer comprised a data tape and transition molecules made of DNA and hardware containing DNA ligase and restriction enzymes. Ligase is an enzyme that may glue together fragments of DNA that have complementary sticky ends. Restriction enzymes recognize specific locations in the double-stranded DNA and cut inside of near this location, forming two fragments with complementary sticky ends. Rothemund pioneered an encoding system of "frame shifts," where a long stretch of double-stranded DNA encoded a symbol while shorter sticky ends derived from this stretch encoded state-symbol combinations. This entailed a particular design of the transition molecules, using SII-type restriction enzymes that cut DNA outside their recognition sequence. The machine was not designed to be autonomous as it required a number of manual steps to perform a single transition (Fig. 3).

Fig. 3 describes a single transition $S_0, a \rightarrow S_1, b, R$ as implemented by Rothemund's hypothetical Turing machine. In this design, each data symbol is represented by a stretch of dsDNA flanked by invariant left (L) and right

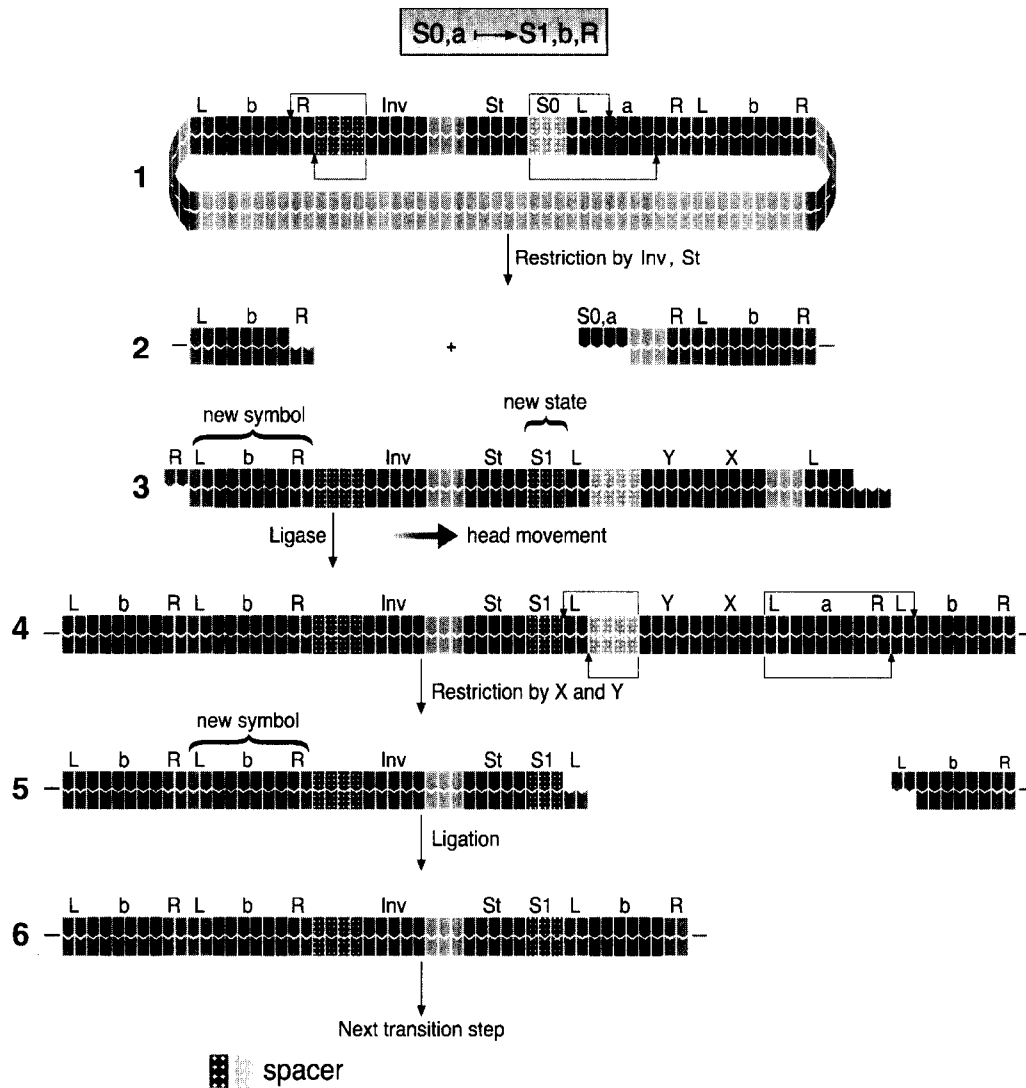


Fig. 3 A single transition $S_0, a \rightarrow S_1, b, R$ as implemented by the Rothmund's hypothetical Turing machine. (From Ref. [16] © American Mathematical Society.)

(**R**) short sequences. The starting circular double-stranded DNA structure **1** represents a data string *bab* and a Turing machine head, located at a symbol *a*. Inside a “head,” there are two SII-type enzyme recognition sites. One is denoted **Inv** and another **St** for “state enzyme.” **Inv** enzyme invariantly cuts in the **R** region of a symbol that lies to the left of the head. **St** enzyme cuts inside the current symbol *a*, and the exact restriction site is determined by the length of a spacer between the **St** recognition site and an **L** region of the current symbol. This spacer is denoted as **S0**.

After double restriction by **Inv** and **St**, the enzymes are removed and a modified data tape **2** with two sticky ends is formed. One is inside the **R** region of the left-most *b* symbol. Another lies within the coding sequence

of a current *a* symbol. Because the exact structure of this sticky ends depends on the state spacer length, it contains information on both the current symbol and the current state. This sticky end is recognized by the transition molecule **3**, which encodes a rule $S_0, a \rightarrow S_1, b, R$. It contains two sticky ends: one recognizes the current state-symbol sticky end of the data tape, and another one recognizes the sticky end within the **R** region of the left-hand symbol. Its dsDNA region contains, from left to right, an encoding for a new symbol *b*, a spacer and a recognition site of the **Inv** enzyme, a recognition site of the **St** enzyme, a new state spacer (**S1** in this case), **L** region, another spacer, two recognition sites of the auxiliary SII-type enzymes **X** and **Y**, and another **L** region.

The solution containing the transition molecules is added to the cleaved data tape **2**. Because real computation would require many different kinds of transition molecules, the existence of an invariant sticky end in a data tape would allow it to react nonselectively with different transition molecules. Therefore the original design contained only right-hand state-symbol specific sticky end. The left-hand sticky end was exposed by yet another restriction enzyme after correct ligation to the state-symbol sticky end and washout of the useless transitions (not shown on the figure). Following double ligation and insertion of the transition molecule, an intermediate structure **4** is formed. At this stage, the new symbol *b* is inserted into the tape. The head is also inserted, with the new state encoded by the new state spacer. However, the previous symbol *a* is regenerated. It needs to be excised by means of the enzymes **X** and **Y**. The enzymes form two complementary sticky ends in the intermediate **5**: one in the **L** region of the right-hand symbol *b*, and another one in the **L** region preinserted in the transition molecule. After their ligation, the next legal configuration **6** is formed. The **St** enzyme is now positioned at the correct distance from the next symbol *b*. Thus this multistep transition process results in an insertion of a new symbol

b, excision of a previous symbol *a*, and change of the machine state from S_0 to S_1 .

Sakamoto et al.^[19,20] described a different approach to biomolecular state machines. While their system implemented only a fixed state-to-state transition scheme, which is not dependent on any input, it had the advantage of semiautonomous operation. The system was experimentally verified and shown to perform several transitions (Fig. 4).

Fig. 4A shows a set of transition rules. Panel B depicts the molecular transition table. Each state is encoded by unique sequence of a ssDNA of 20–30 nt long. A transition between S_1 and S_2 is represented by a concatenation of two sequences, one complementary to S_1 and another one—to S_2 . The “stop” segment does not allow DNA polymerase to pass through. Fig. 4C shows the initial configuration of the machine. A transition table is concatenated to the initial state S_1 . Fig. 4D describes a sample computation. Initial state S_1 is annealed to its complementary counterpart in the rule $S_1 \rightarrow S_2$ of the transition table and then extended by DNA polymerase to form a DNA stretch for S_2 . After denaturation and another annealing, the S_2 stretch is annealed to its counterpart in the rule $S_2 \rightarrow S_3$ and extended to S_3 stretch. The whole

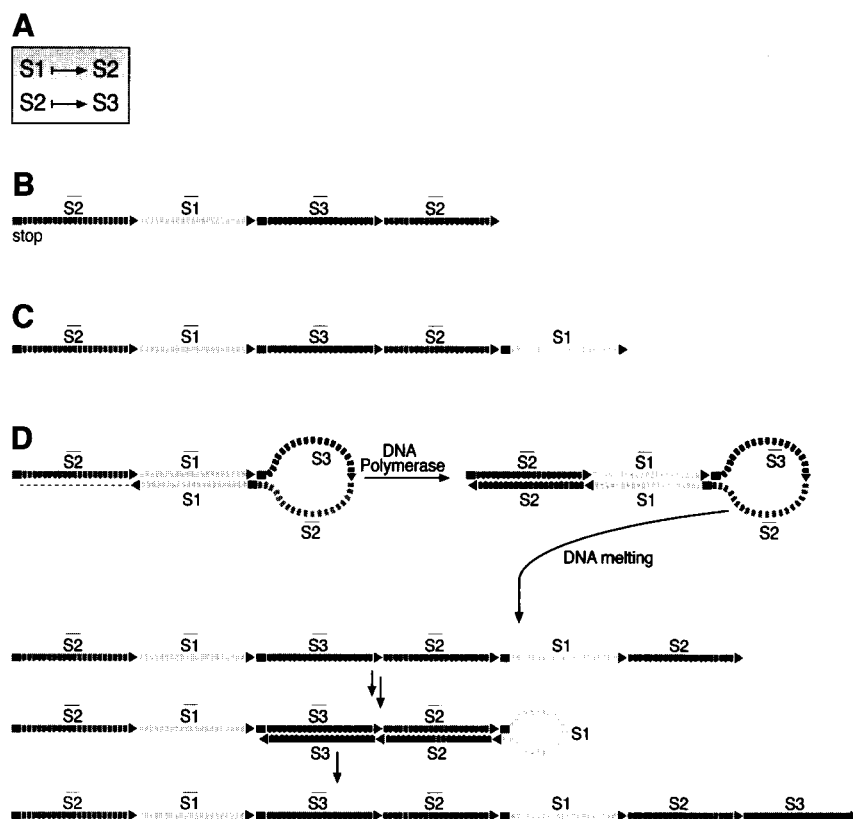


Fig. 4 A molecular state machine of Sakamoto et al.

process is performed in the PCR-like manner, termed "Whiplash PCR" with cycles of denaturing, annealing, and polymerase extension.

Shapiro^[14,15] proposed a detailed logical design for a molecular Turing machine, with an emphasis on a general-purpose programmable computer that may operate in vivo and interact with its biochemical environment. The design was realized in a working mechanical implementation.

The structural blocks of the design proposed by Shapiro are depicted in Fig. 5. The mechanical computer employs a chain of basic building blocks (Fig. 5A), referred to as *alphabet monomers*, to represent the Turing machine's tape (Fig. 5B), and uses another set of building blocks (Fig. 5C), referred to as *transition molecules*, to encode the machine's transition rules. The computer operates on two polymers simultaneously: the *tape polymer*, representing the Turing machine's tape, and the *trace polymer*, which is a byproduct of the computation constructed incrementally from displaced transition molecules and displaced alphabet monomers and has no analog

in the theoretical Turing machine. A transition molecule loaded with an alphabet monomer specifies a computational step of the computer similarly to the way an aminoacyl-tRNA specifies a translation step of the ribosome.^[23] The transition encoding is similar to a Wang tile construction^[10] which is also at the basis of DNA computing via self-assembly.^[6-9] The set of loaded transition molecules constitutes the computer *program* (Fig. 1A). A description of the design and mechanism of operation is shown in Figs. 5 and 6. Fig. 5C shows the formation of a transition molecule and Fig. 5D shows an active transition molecule. An active transition molecule joins the two data polymers. It is embedded in the tape polymer and represents the location of the Turing machine's read/write head as well as the machine's internal state. At the same time, the active transition molecule is the terminal molecule of the trace polymer, representing the most recent transition of the computation. Fig. 5E schematically depicts the computer (hardware). The computer is made of two subunits, referred to as *small* and *large*, each with a tunnel called the *small tunnel* and the *large tunnel*, respectively.

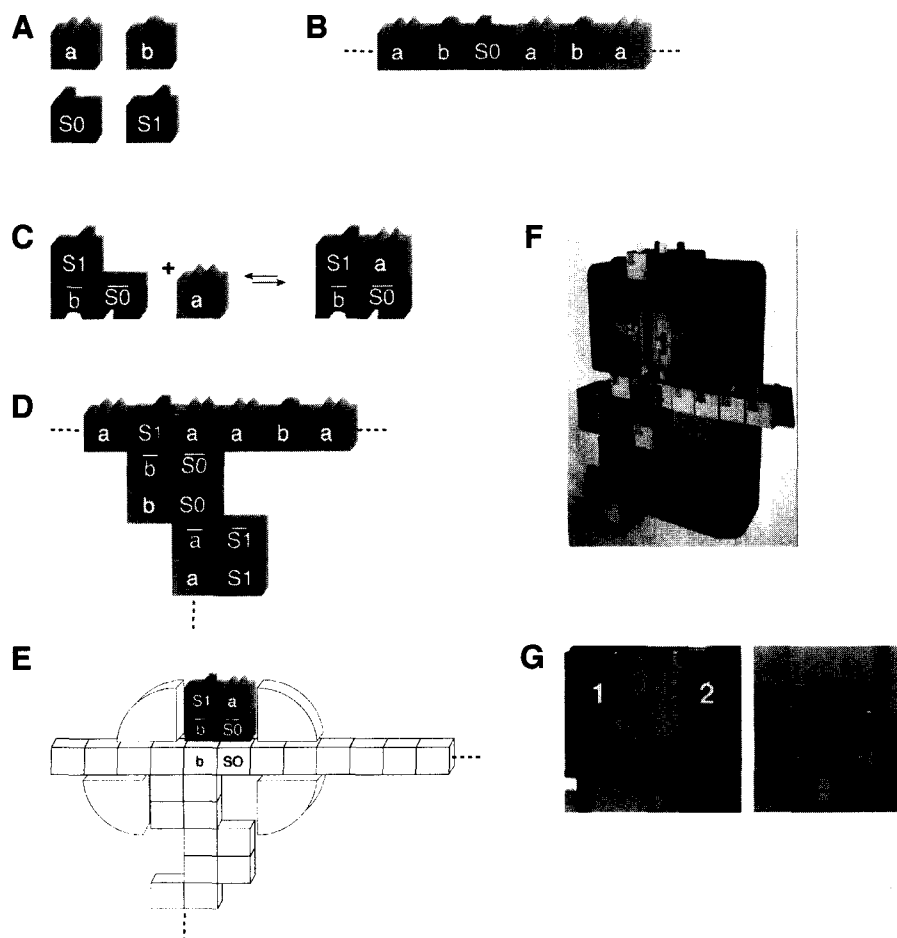


Fig. 5 Structural blocks of the Shapiro's mechanical Turing machine.

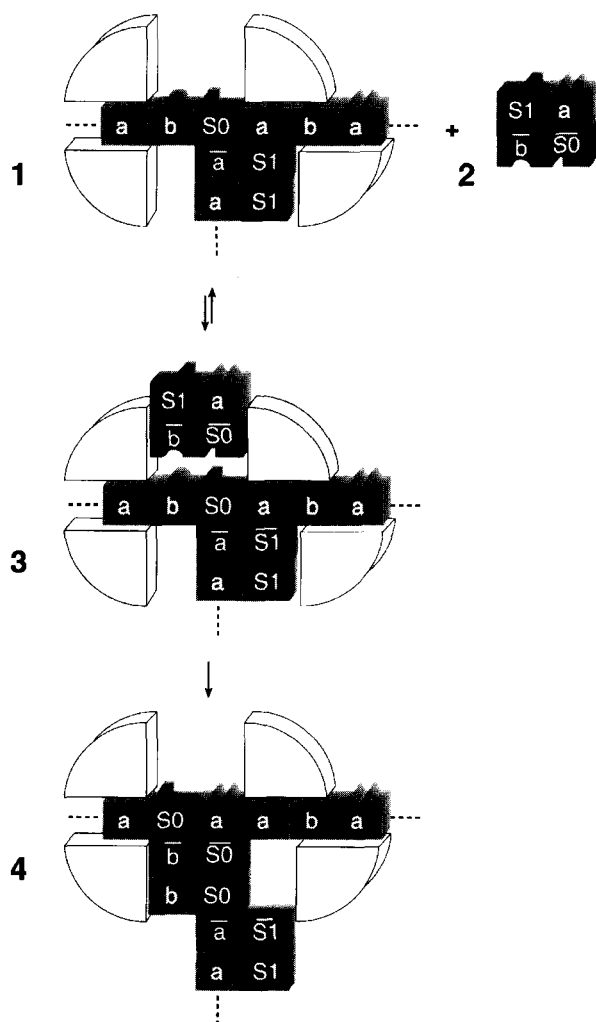


Fig. 6 Operational cycle of the Shapiro's mechanical Turing machine.

The small tunnel provides incoming loaded transition molecules with access to the active transition molecule and to its adjacent alphabet monomer. Access is controlled by gating mechanisms that block transition molecules that are ill-formed or do not match the current state and current tape symbol. These mechanical analogs of allosteric conformational changes open the channel only when a valid incoming transition molecule approaches. The large tunnel holds the active transition molecule and the tail of the trace polymer being constructed.

The actual mechanical computer is $18 \times 29 \times 9$ cm as shown in Fig. 5F. The small tunnel **1** is part of the small subunit and is 2 units wide. The large tunnel **2** is part of the large subunit and is 3 units wide, so that it can accommodate the displaced transition molecule and the new active transition molecules. The small and large subunits

can move one unit sideways relative to each other. Such movement is necessary following a change of direction of the computation. An incoming transition molecule **3** is approaching the active transition molecule **4** and the alphabet molecule to its right. The tape polymer can move left or right 1 unit, aligning the active transition molecule to the left or to the right side of the large tunnel. Such movement is necessary to accommodate consecutive transitions in the same direction. The hardware as well as the data tapes and the incoming transition molecule are shown.

Fig. 5G shows the mechanical implementation of the gating mechanisms, front (left) and back views. Five mechanisms in the small tunnel prevent erroneous transitions from occurring. All mechanisms are based on a spring-loaded bell crank/cam which is connected to a linkage which, in its free state, blocks passage of the approaching transition molecule. Each bell crank/cam checks for a certain condition and, if the condition is met, is rotated. The connected linkage then moves out of the way of the approaching transition molecule, essentially effecting a conformational change in the tunnel. Two mechanisms **1** and **2** detect that the (left or right) transition molecule is loaded with an alphabet molecule. Mechanism **3** detects that the recognition site of the incoming transition molecule matches the state side group of the active transition molecule and the alphabet symbol to its right. Additional two mechanisms check for the blank transition.

The computer operates in cycles (Fig. 6), processing one transition molecule per cycle. In each cycle, an incoming loaded transition molecule **2** that matches the current state and its adjacent alphabet monomer of the data polymer **1** becomes the new active transition molecule and its accompanying alphabet monomer is incorporated into the tape polymer via the intermediate **3**. This is achieved by displacing the currently active transition molecule and the matched alphabet monomer, effectively editing the tape polymer, and elongating the trace polymer by the displaced molecules to form the next configuration **4**. Specifically, when processing a left transition molecule, the computer moves left to accommodate the molecule, if necessary, and displaces the currently active transition molecule and the alphabet monomer to its left by the new molecule. The computer processes a right transition molecule similarly by moving right and displacing the alphabet monomer to the right of the active transition molecule.

The trace polymer created during the computation represents past state changes and head movements, as well as the symbols that were "erased" from the tape during each transition, and as such has several important advantages. First, the trace polymer renders the computer reversible. Because the trace polymer embodies a complete

record of the computation, a molecular implementation of the computer will be subject to the speed/energy consumption tradeoff of reversible devices. Second, computation traces, in general, and the trace polymer, in particular, enable many "software" program analysis and debugging tools,^[24] which are critically needed for large-scale applications. Third, the trace polymer enables "hardware" error detection and correction. One expects that any biomolecular implementation of the computer may exhibit nonnegligible error rate. Such errors can be detected, and possibly also corrected, by cascading several computers along the same trace polymer, each detecting, and possibly also correcting, errors produced by its predecessor.

The most important property of the mechanical computer is that it is reactive.^[25] It can have an ongoing, program-controlled, interaction with its environment. This capability is a result of the biologically inspired architecture of the computer rather than inherited from the theoretical Turing machine, which was conceived as a "batch" computing device that receives its input at the beginning of the computation and produces an output if and when the computation ends. The ribosome, for example, suspends the construction of a polypeptide chain when a required amino acid is unavailable. Similarly, this computer can be "programmed" to suspend until a specific molecule is available. The availability of such a control molecule can be tied to other relevant environmental conditions, thus triggering a computation only when these conditions prevail.

The Turing machine is a nondeterministic computing device in that it can make choices during a computation, and so is the mechanical computer. In a biomolecular implementation, this capability can be used to have the environment affect the course of a computation, based on the relative concentrations of molecules that enable one computational step compared with molecules enabling a different computational step. Using these two capabilities, the computer can be programmed so that both the timing and the course of a computation are affected and controlled by the biochemical environment.

The computer is endowed with an output device as follows. A simple extension to the Turing machine design is an instruction that erases the tape segment to the right of the read/write head. This instruction would mean in this context: "cleave the tape polymer to the right of the active transition molecule and release this tape polymer segment to the environment." With this instruction, the computer can create and release any effectively computable polymer of alphabet monomers, in any number of copies, in the course of a computation. A cleaved tape polymer segment released by one computer can serve as the initial tape for the computation of another com-

puter, or it can be ligated under certain conditions to the tape of another computer, thus enabling parallel processing, communication, and synchronization among multiply operating computers.

The computer design allows it to respond to the availability and to the relative concentrations of specific molecules in its environment and to construct program-defined polymers and release them into the environment. Hence if implemented using biomolecules, the computer can be part of biochemical pathways. In particular, given a biomolecular implementation of the computer that uses ribonucleic acids as alphabet monomers, one can envision how cleaved tape polymer segments can function as messenger-RNA, effecting program-directed synthesis of proteins in response to specific biochemical conditions within the cell. Such an implementation can provide a family of computing devices with broad biological and pharmaceutical applications.

Molecular Finite Automata

Two programmable, autonomous finite automata made of biomolecules were demonstrated by Benenson et al.^[26,27] Both use a DNA molecule as input, DNA molecules as software, encoding the automaton transitions, and DNA-manipulating enzymes as hardware. The differences between the two are the source of energy for the computation and the reuse of software molecules. The first automaton relies on ATP as an energy source and consumes its software molecules during computation, while the second utilizes solely the energy stored in the chemical bonds of its DNA input molecule and its software molecules are reusable. While having similar logical structures, these versions differ in the implementation details. The design of the molecular finite automaton incorporates ideas from designs for molecular Turing machines.^[15,16] The hardware of the first automaton consists of a mixture of the class IIS restriction nuclease *FokI*, T4 DNA ligase, and ATP, while the second automaton utilizes only *FokI*.

The structure of the latter automaton is shown in Fig. 7. Fig. 7A shows the encoding of *a*, *b*, and terminator (sense strands) and the <state, symbol> interpretation of exposed 4-nucleotide sticky ends, the leftmost representing the current symbol and the state S1, similarly the rightmost for S0. Fig. 7B shows the hardware: the *FokI* restriction enzyme, which recognizes the sequence GGATG and cleaves 9 and 13 nucleotides apart on the 5'→3' and 3'→5' strands, respectively. The software comprises eight short double-stranded (ds) DNA molecules, the transition molecules encoding the eight possible transition rules (Fig. 7C). It consists of a <state, symbol> detector (light gray), a *FokI* recognition site (dark gray), and a spacer (intermediate gray) of variable length that determines the

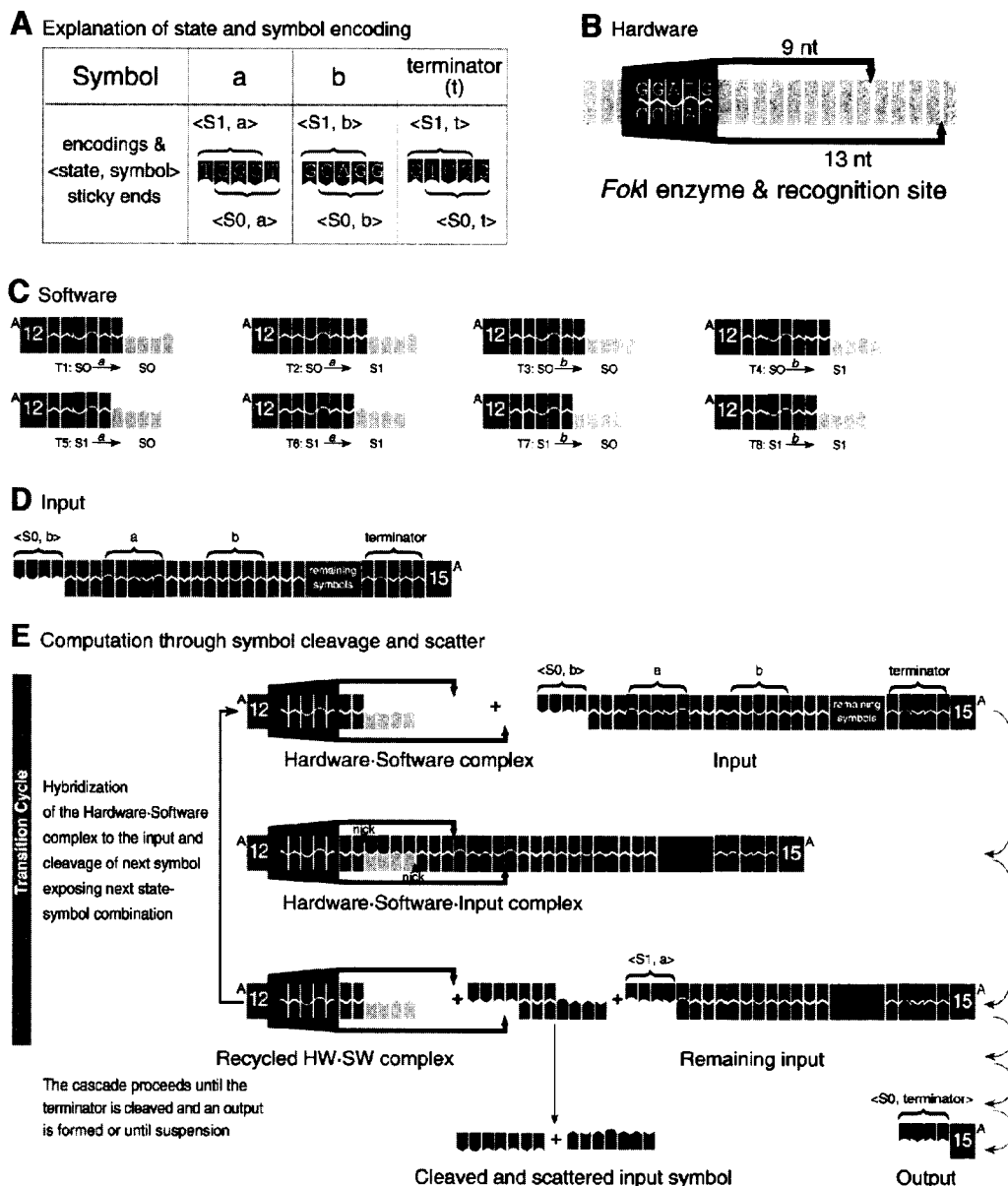


Fig. 7 Design details and mechanism of operation of the molecular automata of Benenson et al. (From Ref. [27] © PNAS.)

FokI cleavage site inside the next symbol, which, in turn, defines the next state. Empty spacers effect S1 to S0 transition, single base-pair (bp) spacers maintain the current state, and 2-bp spacers transfer S0 to S1.

A dsDNA molecule encodes the initial state of the automaton and the input (Fig. 7D), with five to six base pairs (bp) coding for one input symbol (Fig. 7A), with the exposed sticky end at the 5'-terminus encoding the initial state and the first symbol. The ligase-based system may also contain "peripherals," two output-detection molecules of different lengths, each of which can ligate se-

lectively with a different output molecule to form an output-reporting molecule that indicates a final state and can be readily detected by gel electrophoresis. In the ATP-free system, the output is detected by examining the length of the remainder of a processed input molecule. The computation starts when the hardware, software, and input are all mixed together and runs autonomously, if possible till termination. The automaton processes the input as shown in Fig. 7E. The computation proceeds via a cascade of transition cycles. In each cycle, the sticky end of an applicable transition molecule may ligate to

the sticky end of the input molecule, detecting the current state and the current symbol. Alternatively, it may hybridize noncovalently. In both cases, the product is cleaved by *FokI* inside the next symbol encoding, exposing a new four-nucleotide sticky end. The design of the transition molecules ensures that the encodings of the input symbols *a* and *b* are cleaved by *FokI* at only two different "frames",^[16] the leftmost frame encoding the state *S1* and the rightmost frame encoding *S0* (Fig. 7A). The exact next restriction-site and thus the next internal state are determined by the current state and the size of the spacers (Fig. 7C, intermediate gray) in an applicable transition molecule. The computation proceeds until no transition molecule matches the exposed sticky end of the input or until the special terminator symbol is cleaved, forming an output molecule that has a sticky end encoding the final state. In a step extraneous to the computation and analogous to a "print" instruction of a conventional computer, this sticky end may ligate to one of two output detectors and the resultant output reporter may be identified by gel electrophoresis.

The ATP-free automaton has several advantages over the ligase-based version. First, the software molecule used in a transition is recycled because it undergoes no modification. Thus a finite number of software and hardware molecules may, in principle, process an input of any length. Second, much better performance characteristics may be achieved with the ATP-free automaton because the processing does not involve the usually slow ligation step. Using stoichiometric amounts of the software and the hardware molecules, it is possible to process a single symbol in a few seconds. On the other hand, the ligase-based automaton is less structurally restricted. It may utilize different SII-type restriction enzymes as a hardware, including those that require a covalently bonded substrate. More importantly, it was found^[27] that the ability of *FokI* to cleave DNA with its recognition and cleavage sites attached by sticky-end hybridization was limited to specific hybridization complexes. Long spacers and low GC content often resulted in cleaving only one of the input strands, producing a computationally illegal configuration. Correct performance was achieved with short spacers and high GC content of the sticky ends. The final design used the shortest possible spacers of 0, 1, and 2 bp (Fig. 7C), which dictated a particular symbol encoding (Fig. 7A) and the introduction of spacers between the symbols (Fig. 7D). Using ligase may relax some of these constraints.

These molecular automata may be viewed from two perspectives. On one hand, the computations were performed with bulk amounts of the input molecules. Each molecule was processed independently and in parallel,

thus the inputs could potentially be distinct. The parallel character of the computation could be employed in a hypothetical process of screening of DNA libraries. Large libraries of molecules could be filtered through the same software, for a search of certain sequence feature. Traditional approach to the same problem would require (nonparallel) sequencing of the whole library and then running nonparallel computer algorithms on the sequences. To analyze parallel performance of our system, the cumulative number of unit operations in a unit time per unit volume was measured. This would represent an upper limit on the complexity of the libraries that could be analyzed. The parallel performance of the ligase-based version was in the order of 8.3×10^6 operations/sec/ μL , while in the ATP-free case, the performance was improved almost 8000-fold and reached 6.6×10^{10} operations/sec/ μL .

Another approach is to try and scale down the system to run it in a very small compartment such as living cell. Then the question is what are the minimal requirements from the operational system. It is not unfeasible that a mixture of a single input molecule, four software molecules, and one or two *FokI* molecules could form a functioning computer while placed in a sufficiently small volume (to avoid dilution). While such possibility still requires experimental demonstration, it is possible to estimate its characteristics from the process performed in the bulk. Scaling down the concentrations, such a "minimal computer" would fit in a cube with a side length of 100 nm. The size of each component is in the range of several nanometers, with long inputs being tens of nanometers long. Such a computer would be a truly nanoscale computer. A computation on a single input molecule would proceed at a rate of 1000 sec per step in the ligase-based version and about 20 sec in the ATP-free version. While such rates seem slow compared with the electronic computers, they reflect the properties of biological systems. Once these computers would be able to operate in a cell, their performance would be competitive with respect to other cellular processes.

CONCLUSION

The notion of a biomolecular computing machine has evolved gradually over the past decades. Theoretical designs proposed for such machines eventually led to simple molecular computing machines functioning in the test tube. The field may develop in several directions. First, more complex computing machines could be designed and built. This includes general finite automata, string transducers, stack automata, and, ultimately, the Turing machine. Currently, progress in this direction

seems to be hampered by the lack of DNA- and RNA-manipulating enzymes; we hope that an eventual progress in enzyme engineering may supply the tools required to develop more complex machines. Another important issue relevant to many machine designs is symbol encoding. Current experimental realizations utilize artificial alphabet of predesigned DNA sequences. However, the computer should "understand" natural alphabets of either single nucleotides or amino acid codons to be biologically relevant. Designing even the simplest finite automaton that would operate on an arbitrary DNA sequence remains a major challenge. A third future direction is a search for application that would clearly demonstrate qualitative edge of a molecular computer over competing technologies.

We believe that the application potential of autonomous biomolecular computers is not to surpass electronic computers with performance; in fact, it is hard to believe they ever will. The advantage is that biomolecular computers process information encoded in molecules rather than in electric signals. Any *direct* computing over biomolecular inputs could only be performed by the computers of the same format, i.e., made of biomolecules. As we already mentioned, running sequence analysis algorithms on DNA libraries without actually sequencing all library members could be conveniently performed by a molecular state machine whose alphabet is composed of single nucleotides or codons. Another broad range of application may emerge once the molecular computer is successfully "plugged into" cellular molecular environment. By "plugging into" we mean that some of the computer components would be able to respond to certain changes in the environment, affecting the result of the computation. While the most obvious component to communicate with the environment seems to be the software, both the hardware and input could be affected as well. Once the communication between the intracellular compounds and the computer is established, the computer may, in principle, perform complex analysis of the environmental conditions. The complexity of such analysis would increase with the complexity of the computing machine and the sensitivity of the communication channels. However, even the simplest finite automata seem to provide enough computational power to make rather complex diagnostics.

REFERENCES

1. Adleman, L.M. Molecular computation of solutions to combinatorial problems. *Science* **1994**, *266* (5187), 1021–1024.
2. Kari, L. DNA computing: Arrival of biological mathematics. *Math. Intell.* **1997**, *19* (2), 9–22.
3. Lipton, R.J. DNA solution of hard computational problem. *Science* **1995**, *268* (5210), 542–545.
4. Ouyang, Q.; Kaplan, P.D.; Liu, S.; Libchaber, A. DNA solution of the maximal clique problem. *Science* **1997**, *278* (5337), 446–449.
5. Faulhammer, D.; Cukras, A.R.; Lipton, R.J.; Landweber, L.F. Molecular computation: RNA solutions to chess problems. *Proc. Natl. Acad. Sci. U. S. A.* **2000**, *97* (4), 1385–1389.
6. Winfree, E. On the Computational Power of DNA Annealing and Ligation. In *DNA Based Computers: Proceedings of the DIMACS Workshop, April 4, 1995, Princeton University*; Lipton, R.J., Baum, E.B., Eds.; American Mathematical Society: Providence, RI, 1996; 199–221.
7. Winfree, E. Algorithmic Self Assembly of DNA. Ph.D Thesis; Caltech, 1998.
8. Winfree, E.; Liu, F.; Wenzler, L.; Seeman, N.C. Design and self-assembly of two-dimensional DNA crystals. *Nature* **1998**, *394* (6693), 539–544.
9. Mao, C.; LaBean, T.H.; Reif, J.H.; Seeman, N.C. Logical computation using algorithmic self-assembly of DNA triple-crossover molecules. *Nature* **2000**, *407* (6803), 493–496.
10. Wang, H. Proving theorems by pattern recognition. Part II'. *Bell Syst. Tech. J.* **1961**, *40*, 1–41.
11. Feng, L.; Park, S.; Reif, J.; Yan, H. A two-state DNA lattice switched by DNA nanoactuator. *Angew. Chem.* **2003**, *115* (36), 4478–4482.
12. Yan, H.; Park, S.; Finkelstein, G.; Reif, J.; LaBean, T. DNA-templated self-assembly of protein arrays and highly conductive nanowires. *Science* **2003**, *301* (5641), 1882–1884.
13. Bennett, C.H. The thermodynamics of computation—A review. *Int. J. Theor. Phys.* **1982**, *21* (12), 905–940.
14. Shapiro, E. A Mechanical Turing Machine: Blueprint for a Biomolecular Computer. In *Proc. 5th Int. Meeting on DNA Based Computers*; Winfree, E., Giffrod, D., Eds.; DIMACS Series in Discrete Mathematics and Theoretical Computer Science, American Mathematical Society: Providence, RI, 1995; 229–230.
15. Shapiro, E.; Karunaratne, K.S.G. Method and System of Computing Similar to a Turing Machine. US Patent 6,266,569, 2001.
16. Rothmund, P.W.K. A DNA and Restriction Enzyme Implementation of Turing Machine. In *DNA Based Computers: Proceedings of the DIMACS Workshop, April 4, 1995, Princeton University*; Lipton, R.J., Baum, E.B., Eds.; American Mathematical Society: Providence, RI, 1996; 75–119.
17. Smith, W.D. DNA Computers in vivo and in vitro. In *DNA Based Computers: Proceedings of the*

- DIMACS Workshop, April 4, 1995, Princeton University*; Lipton, R.J., Baum, E.B., Eds.; American Mathematical Society: Providence, RI, 1996; 121–185.
18. Garzon, M.; Gao, Y.; Rose, J.A.; Murphy, R.C.; Deaton, R.; Franceschetti, D.R.; Stevens, S.E. In vitro Implementation of Finite-State Machines. In *Automata Implementation: Lecture Notes in Computer Science 1436*; Wood, D., Yu, S., Eds.; Springer: Berlin, 1998; 56–74.
 19. Sakamoto, K.; Kiga, D.; Komiya, K.; Gouzu, H.; Yokoyama, S.; Ikeda, S.; Sugiyama, H.; Hagiya, M. State transitions by molecules. *Biosystems* **1999**, *52* (1–3), 81–91.
 20. Sakamoto, K.; Gouzu, H.; Komiya, K.; Kiga, D.; Yokoyama, S.; Yokomori, T.; Hagiya, M. Molecular computation by DNA hairpin formation. *Science* **2000**, *288* (2469), 1223–1226.
 21. Turing, A.M. On computable numbers, with an application to the Entscheidungsproblem. *Proc. Lond. Math. Soc., II Ser.* **1936**, *42*, 230–265.
 22. Hopcroft, J.E.; Motwani, R.; Ullmann, J.D. *Introduction to Automata Theory, Languages, and Computation*, 2nd Ed.; Addison Wesley: Boston, 2000.
 23. Alberts, B.; Johnson, A.; Lewis, J.; Raff, M.; Roberts, K.; Walter, P. *Molecular Biology of the Cell*, 4th Ed.; Garland: New York, 2002.
 24. Shapiro, E. *Algorithmic Program Debugging*; MIT Press: Cambridge, MA, 1982.
 25. Harel, D.; Pnueli, A. On the Development of Reactive System. In *Logics and Models of Concurrent Systems*; Apt, K.R., Ed.; Springer-Verlag: New York, 1985; 477–498.
 26. Benenson, Y.; Paz-Elizur, T.; Adar, R.; Keinan, E.; Livneh, Z.; Shapiro, E. Programmable and autonomous computing machine made of biomolecules. *Nature* **2001**, *414* (6862), 430–434.
 27. Benenson, Y.; Adar, R.; Paz-Elizur, T.; Livneh, Z.; Shapiro, E. DNA molecule provides a computing machine with both data and fuel. *Proc Natl. Acad. Sci. U. S. A.* **2003**, *100* (5), 2191–2196.



Molecular Designs for Self-Organized Superstructures

Makoto Tadokoro

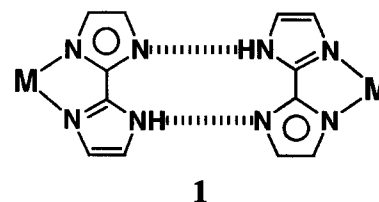
Osaka City University, Osaka, Japan

INTRODUCTION

Molecular arrays with desirable topological networks have recently been realized in crystal by self-organized binding between molecular building blocks with hydrogen-bonding (H-bonding) and metal-coordinating affinities. The coordination bonds and the H-bonds are relatively weak interactions that impart strength, directionality, and complementarity.^[1-6] Such crystal manipulations, often known as crystal engineering, are performed to yield arrays of controlled superstructures providing new functional molecular solids.^[7,8] Thus the self-organization of designed molecules containing certain kinds of complementary H-bonding and coordinating units has stimulated new efforts in the material sciences using, for example, controlled molecular arrays adsorbed to a solid surface,^[9-11] a self-organized molecular assembly with unique cavities,^[12] and an integrated system of molecular device.^[13]

MOLECULAR METAL BUILDING BLOCK

In some molecular systems, it has been possible to control molecular aggregation in the crystal by the di-functional ligands, which bond to metal using coordinate-covalent interactions and to each other using H-bonding interactions.^[14-19] As 2,2'-biimidazole (H₂bim) is a bidentate chelating ligand with multiproton donor sites, it can coordinate to a transition metal with three reversible types of protonated and deprotonated mode: neutral (H₂bim), mono-deprotonated (monoanion, Hbim⁻¹), and di-deprotonated (dianion, bim⁻²) types.^[20] The 2,2'-biimidazolate monoanion (Hbim⁻¹), recently introduced by us, works as such a di-functional bridging ligand not only to form a stable metal-chelate complex but also a new intermolecular complementary H-bonding with two sets of NH donors and N acceptors, as shown in Drawing 1.^[21] Molecular system such as Hbim⁻¹ has not been found in molecular aggregation used for crystal engineering except in our aggregation system.



CONTROLLED CRYSTAL STRUCTURES WITH ANIONIC [Ni(Hbim)₃]⁻

First of all, we have designed a new anionic building block, a tris-biimidazolate nickel (II) complex ([Ni(Hbim)₃]⁻), where the biimidazolate ligand acts as a strong π -conjugated ligand to form three complementary H-bonding sites, which forms a variety of multidimensional superstructures with long-range ordered arrays. The [Ni(Hbim)₃]⁻ is constructed from the nickel (II) center coordinated by three bidentate Hbim⁻ ligands through the lone pairs of the imine nitrogen atoms in the imidazole rings. The [Ni(Hbim)₃]⁻ has an approximate point group D_3 symmetry, whose Δ and Λ isomer are illustrated in Fig. 1. In these cases, the nature of metal anion assembly was affected by the nature and size of the counteranion. Interestingly, synthesis of simple one-pot procedures by mixing the nickel (II) ion, Hbim⁻, and counteranion produces four types of H-bonded crystals 1-4 based on the arrangement of [Ni(Hbim)₃]⁻.^[22] The production of the four types of molecular architecture by one-pot molecular self-organization of the [Ni(Hbim)₃]⁻ evolves from three fundamental factors: 1) three complementary binary H-bonding sites; 2) Δ and Λ optical isomers in the chiral coordination mode; and 3) the kind of counteranions. Fig. 2 shows crystal structures of the four patterns of molecular arrangement, respectively: a) a zero-dimensional (0-D) dot structure with no complementary H-bonds of Hbim⁻, which are blocked by H₂O molecules; b) a 1-D H-bonded zigzag ribbon formed from alternative linkages of H-bonds between the Δ and Λ optical isomers using two of the three Hbim⁻ of [Ni(Hbim)₃]⁻; c) a 2-D H-bonded honeycomb sheet self-organized by alternative H-bonds

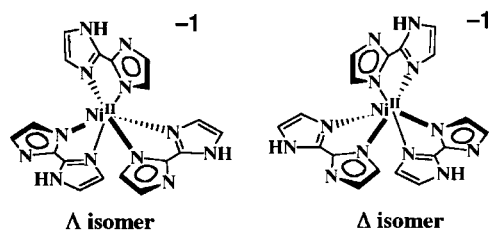


Fig. 1 Λ and Δ isomers of building blocks $[\text{Ni}(\text{Hbim})_3]^-$.

using all three Hbim^- between Λ and Δ isomers of $[\text{Ni}(\text{Hbim})_3]^-$; and d) a 3-D supra cross-catenated network formed from expanded 2-D honeycomb sheets. Each crystal has a different kind of counteraction, such as alkyl ammonium [a tetramethyl ammonium (NMe_4^+) ions for 1, a tetra-*n*-propyl ammonium (N^nPr_4^+) ion for 2, and a tetraethyl ammonium (NEt_4^+) ion for 4] and a crown ether

derivative [a potassium *cis-syn-cis*-dicyclohexano-18-crown-6 ($[\text{K-DCH}(18\text{-crown-6})]^+$) ion for 3]. Therefore our results suggest that the mode of self-organization can be controlled by varying the kind of counteraction, although at this stage the prediction of the cation specificity is difficult. In the present study, we have succeeded systematically in the organization of the $[\text{Ni}(\text{Hbim})_3]^-$ for the creation of 3 with double channels as included microporous crystals, such as an organic zeolite^[23] and a modified zeolite with MOF^[24] [Fig. 3a], and 4 with double-interlocking chains as polycatenate structures [Fig. 3b]. The 3 is constructed from all three H-bonding sites of $[\text{Ni}(\text{Hbim})_3]^-$ with the complementary intermolecular H-bonds. Two of the H-bonding sites in it make a 1-D H-bonded zigzag ribbon like 2. Then the 1-D zigzag ribbons are connected to each other by the remaining H-bonding site to form the 2-D honeycomb sheets along the *ab* plane by the alternate arrangement of Λ and Δ

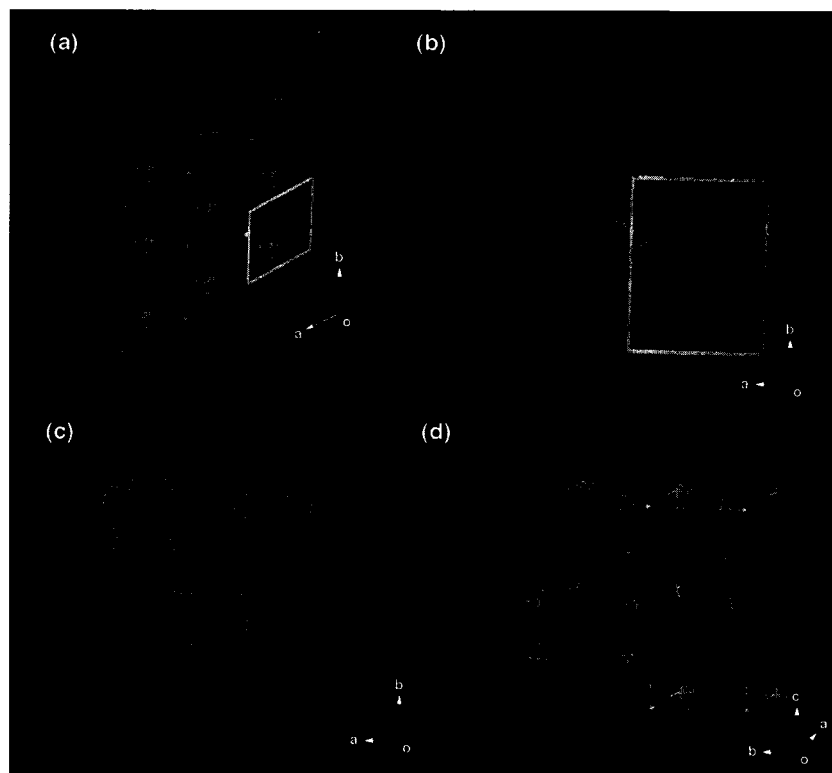


Fig. 2 The crystal structures of the H-bonded building blocks $[\text{Ni}(\text{Hbim})_3]^-$. (a) 0-D Dot structures in 1 formed from $[\text{Ni}(\text{Hbim})_3]^-$ [ball and stick representation of Hbim^- ligands (red) and nickel ions (magenta) along the *c* axis]. The orange ball-and-stick lines and the green spheres are shown for the NMe_4^+ and water molecules, respectively. (b) 1-D Zigzag ribbons in 2 formed from $[\text{Ni}(\text{Hbim})_3]^-$ along the *c* axis. The orange and the green ball-and-stick lines are shown for the N^nPr_4^+ ions and methanol molecules, respectively. (c) Double channel structures built up by 2-D honeycomb sheets in 3 formed from $[\text{Ni}(\text{Hbim})_3]^-$. The inner channels in 3 are constructed by K^+ -crown ether complexes [the ball-and-stick representations of K^+ ions (orange spheres) and crown ethers (green ball-and-stick lines) and the outer channels are constructed by $[\text{Ni}(\text{Hbim})_3]^-$ to form a microporous crystal]. (d) 2-D Expanded honeycomb sheet structure in 4 with $[\text{Ni}(\text{Hbim})_3]^-$ along the *a* axis. The free neutral H_2bim ligands connect 1-D zigzag-ribbon arrays by complementary H-bonding to form an expanded 2-D sheet structure along the *bc* plane. The orange ball-and-stick lines represent NEt_4^+ ions. (View this art in color at www.dekker.com.)

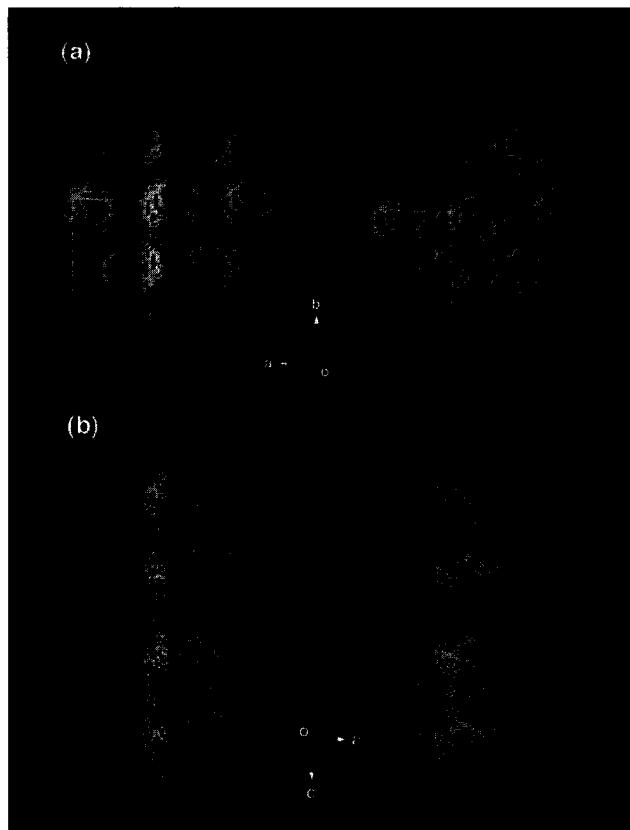


Fig. 3 (a) A perspective stereo view of a microporous structure with a double channel formed by both $[\text{Ni}(\text{Hbim})_3]^-$ and K^+ -crown ether complexes for 3. (b) A portion of the 3-D polycatenate network for 4: red and yellow lines represent the different 2-D expanded honeycomb sheets formed from $[\text{Ni}(\text{Hbim})_3]^-$. The stacking honeycomb sheets in red interlock with the other stacking honeycomb sheets with a perpendicular orientation in yellow to generate a double-interlocking polycatenate structure. (View this art in color at www.dekker.com.)

optical isomers of the six $[\text{Ni}(\text{Hbim})_3]^-$. The 2-D sheet stacks along the c axis to produce the outer channel structures, which are built up by a sequence of the same optical isomers. While 4 takes an interest in the controlled self-organization of 3-D complicated superstructures for supramolecular chemistry.^[25] The inner channels are formed by stacking of two $[\text{K-DCH}(18\text{-crown-6})]^+$ cations facing each other along the c axis. The channel contains methanol and water molecules with H-bondings. The framework structure of 4 has four structural characteristics. First, this has a 1-D zigzag ribbon structure similar to that with 2. Second, free neutral H_2bim ligands connect 1-D ribbon arrays by complementary H-bondings to form an expanded 2-D honeycomb sheet structure along the bc plane. Third, the honeycomb sheets interpenetrate the other honeycomb sheets having the perpendicular orientation to construct a double interlocking catenate structure. Finally, the cate-

nated structure is arranged in 3-D to form an infinite interlocking cross-catenated structure.

Toward Complicated Crystal Structure

A major goal of the field of crystal engineering is to control rationally the assembly of 3-D arrays using intermolecular interactions and specific molecular topologies. We have found that the Cs^+ ion can be used as a new tool to manipulate an H-bonded superstructure built with the $[\text{Ni}(\text{Hbim})_3]^-$. Two of the three Hbim^- in the $[\text{Ni}(\text{Hbim})_3]^-$ can be bound to a Cs^+ ion in crystal 5 by an electrostatic π -bonding interaction, which is not possible for other stable alkali metal ions. Furthermore, a more complicated 3-D superstructure of the double-helical racemate was formed in crystal 6 by cooperative application of an organic cation and the Cs^+ interaction.

Superstructures with many 3-D frameworks have been created in different crystals by a self-assembly process. Most of the 3-D frameworks were developed by employing various topological building blocks as coordination polymers^[26] and as H-bonding polymers.^[27] However, the cooperative construction of 3-D arrays using both the weak H-bonding and coordination interactions has rarely been achieved to date.^[28,29] We explore the effects of alkali metal ions, as well as organic cations, on superstructures formed by $[\text{Ni}(\text{Hbim})_3]^-$. Generally, alkali metal ions with a large polarizability can coordinate to aromatic rings in a multihaptic mode.^[30] Of all the stable alkali metal cations (i.e., Li^+ , Na^+ , K^+ , Rb^+ , and Cs^+), only the Cs^+ ion was found to have a rational electrostatic interaction with $[\text{Ni}(\text{Hbim})_3]^-$. We have prepared not only a 3-D double interlocking polycatenate superstructure of interpenetrated 2-D honeycomb sheets by using such a Cs^+ interaction, but also a double-helical 3-D racemate with (10,3)- a nets by using the cooperative interactions between organic cations and Cs^+ .^[31]

Fig. 4a shows a fragment structure of $\{\text{Cs}[\text{Ni}(\text{Hbim})_3]\}_n$ in 5 formed from the interaction of the Δ and Λ optical isomers of $[\text{Ni}(\text{Hbim})_3]^-$ with Cs^+ as counterions. The three Hbim^- ligands in $[\text{Ni}(\text{Hbim})_3]^-$ are involved in H-bonding interactions forming a 2-D honeycomb sheet with (6,3) nets. Four Cs^+ ions are located in each hexagonal cavity of the sheet constructed by six $[\text{Ni}(\text{Hbim})_3]^-$, and fix the two interpenetrating rods of the other two sheets at an inclination of $\sim 70^\circ$ to create a 3-D polycatenate superstructure with a double interlocking interpenetration [Fig. 4b]. Electrostatic interaction between Cs^+ and the two different optical isomers of $[\text{Ni}(\text{Hbim})_3]^-$ forms a 1-D alternative coordination polymer with the general formula $\{(\Delta)\text{-Cs}[\text{Ni}(\text{Hbim})_3]\text{-}(\Lambda)\text{-Cs}[\text{Ni}(\text{Hbim})_3]\}_n$. Each Δ or Λ optical isomer fixed by two Cs^+ ions participates in the formation of a different interpenetrating sheet, respectively. Such a 3-D double interlocking interpenetration based on $[\text{Ni}(\text{Hbim})_3]^-$ has

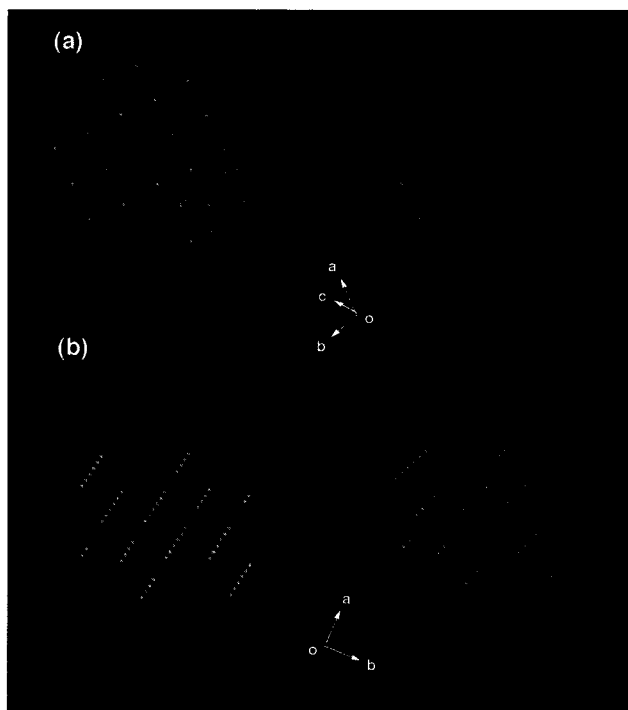


Fig. 4 (a) The stereo view shows two interlocked honeycomb sheets (red and blue) that are linked to each other by Cs^+ ions. The blue and red sheets were built up by alternate linkage between the optical isomers (Δ and Λ) of $[\text{Ni}(\text{Hbim})_3]^-$. Four Cs^+ ions (green spots) are present in each hexagon-cavity formed by the six building blocks. (b) The stereo view shows the whole structure of 4 (red and light blue lines) with the shortest Ni–Ni bonds. The green spots represent Cs^+ ions. The main honeycomb sheet framework forms a twofold interpenetration with (6,3) nets, and as a whole they form a double-interlocking polycatenate structure. (View this art in color at www.dekker.com.)

already been prepared by 4 using an organic NEt_4^+ ion. Moreover, an organic cation can work cooperatively with Cs^+ to manipulate the new superstructure formed in the crystal. The addition of $\text{N}^{\text{Pr}}\text{Pr}_4^+$ ion led 6 with the general formula $\{\text{Cs}[\text{Ni}(\text{Hbim})_3]_2(\text{N}^{\text{Pr}}\text{Pr}_4^+) \cdot \text{MeOH}\}_n$ to form a 3-D double-helical structure of racemate (10,3)-*a* nets having a 1-D column of Cs^+ in the center [Fig. 5a]. The columns of Cs^+ in the 4_1 double helices lie along the *c* axis with Cs–Cs distances of 8.60 and 8.14 Å. The networks of 6 are composed of the Δ – Δ and Λ – Λ dimers with the same optical isomer of $[\text{Ni}(\text{Hbim})_3]^-$ linked by one Cs^+ ion. In other words, each 4_1 strand in the helix is formed by using only one optical isomer of $[\text{Ni}(\text{Hbim})_3]^-$. Furthermore, each helix is H-bonded to four other identical optical isomers by using the Hbim[−] moiety. The 3-D H-bonded network forms an 8_7 chiral double helix with large cavities [Fig. 5b]. The entire racemate structure is created by combining the 4_1 helices into an opposite-handed 8_7 helical structure. The superstructure formation of 6 can be attributed to the cooperative use of $\text{N}^{\text{Pr}}\text{Pr}_4^+$ and Cs^+ cations. The $\text{N}^{\text{Pr}}\text{Pr}_4^+$ occupy the void spaces created by the interpenetration of each independent chiral 3-D net with Δ or Λ isomers of $[\text{Ni}(\text{Hbim})_3]^-$. The use of other alkali metals with $\text{N}^{\text{Pr}}\text{Pr}_4^+$ produces only 1-D zigzag ribbons within 2.

The large ionic radius and high polarizability of Cs^+ ions are important in the formation of this new, more complicated structure. It is believed that the Cs^+ ion is bound to the deprotonated imidazolate site of the Hbim[−] ligand by using electrostatic π -interactions in both 5 and 6. The binding distances range from 3.188(10) to 3.62(1) Å for the Cs–C bond and 3.323(10) to 3.607(8) Å for the Cs–N bond for 5, and 3.368(6) to 3.565(7) Å (Cs–C) and 3.342(5) to 3.643(6) Å (Cs–N) for 6. It is also believed that the crystal structures presented are the first where the structure was formed from an interaction between a Cs^+ ion and an imidazolate ring. The bond distances found in 5

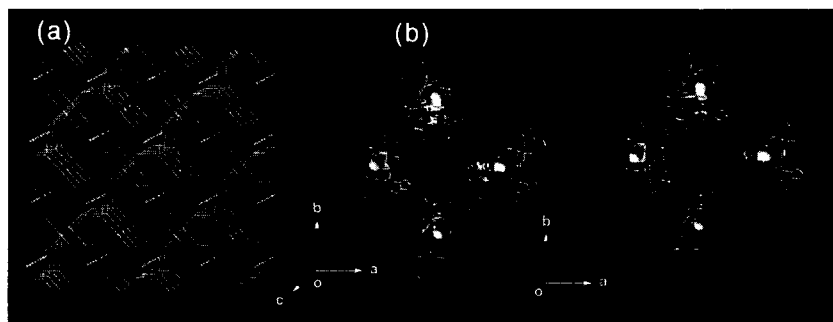


Fig. 5 (a) A perspective view along the *c* axis showing the whole network with (10,3)-*a* nets of 5. The shortest Ni–Ni distances of Λ isomers (red and yellow) and Δ isomers (blue and light blue) of $[\text{Ni}(\text{Hbim})_3]^-$ are shown. Green spots represent Cs^+ ions. They are constructed from each homochiral trinuclear unit with two Δ -isomers or two Λ -isomers of $[\text{Ni}(\text{Hbim})_3]^-$ bound by Cs (I) ions. (b) The perspective stereo view along the *c* axis is shown for a larger right-handed 8_7 helix constructed from four smaller right-handed 4_1 helices. (View this art in color at www.dekker.com.)

and 6 are similar to those in different complexes.^[32–34] This clearly has shown that an electrostatic π -bonding interaction can form between a Cs^+ ion and an imidazolate ring in $[\text{Ni}(\text{Hbim})_3]^-$. Furthermore, when Cs^+ and N^mPr_4^+ were used at the same time, an intricate 3-D racemate structure with (10,3)-*a* nets was formed by the 4_1 double helices wrapping around a 1-D column of Cs^+ ions. Finally, the current work may possibly be a general route to the formation of 2-D and helical structures by controlling the assembly of only D_3 symmetric building blocks with different optical activity.

CONTROLLED CRYSTAL STRUCTURES BY NEUTRAL BIIMIDAZOLATE COMPLEX

We have tried to eliminate the counterion and create a new superstructure with an infinite chain without the effect of counterions on the assembly of metal complexes constructed from H-bonding dimer units such as Drawing 1. In this section, four types of self-organizing superstructures with infinite chains are identified by designing four neutral Hbim^{-1} complexes with altered

metal coordination spheres. As a result, we can systematically produce five types of preprogramming superstructures of a dimer (A), a linear chain (B), a zigzag ribbon (C), a honeycomb sheet (D), and a helical chain (E), respectively, as shown in Fig. 6.^[35]

Classification of multidimensional superstructures has already been performed in organic compounds assembled by intermolecular H-bonding of carboxylic acid derivatives^[36] as well as in coordination polymers by bridging ligands such as oxalate.^[37–40] Carboxylic acid H-bonding and oxalate coordination polymers have been rationally synthesized in a linear chain and a zigzag ribbon, a honeycomb sheet, and other 3-D superstructures. These superstructures afford the classification of the multiaggregation compounds that consist only of H-bonds or coordination bonds. Here we have established a new categorical classification of the superstructures generated by the simultaneous use of both complementary intermolecular H-bondings and stable coordination bondings.

The H-bonded dimer unit through the Hbim^{-1} ligands has been assembled securely and strongly by using neutral complexes containing Hbim^{-1} (Drawing 1). For example, the previously reported neutral $[\text{Cu}^{\text{II}}(\text{Hbim})$

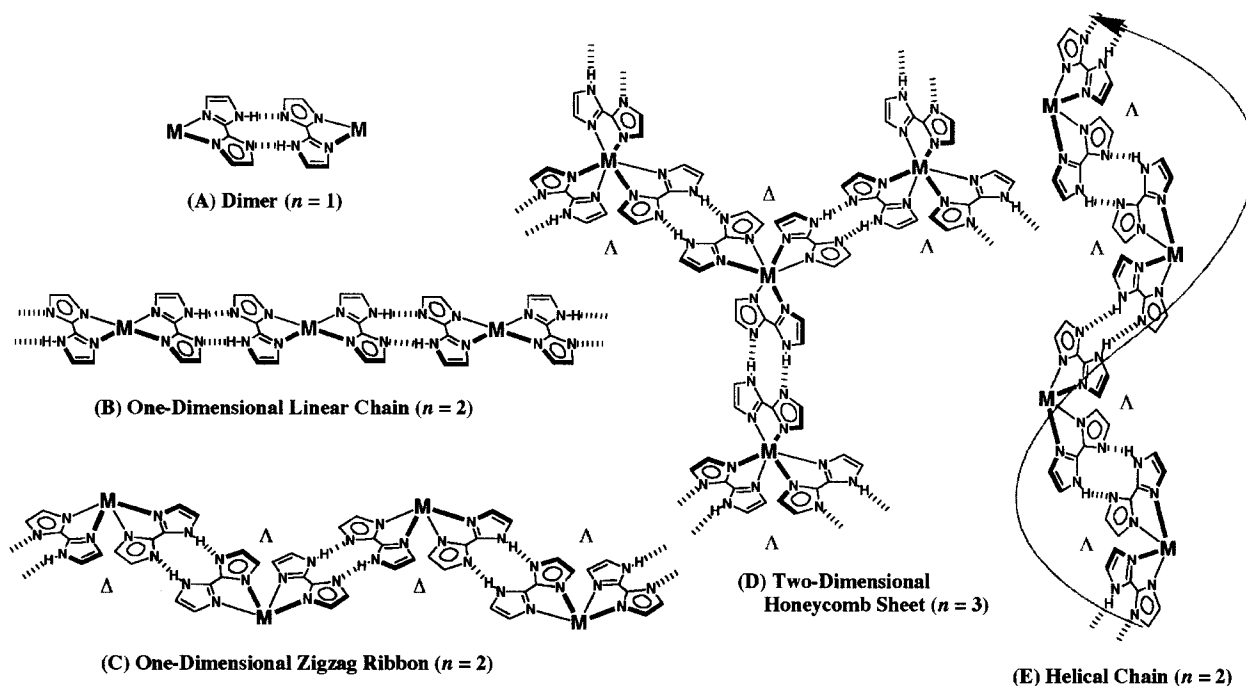


Fig. 6 Schematic representations of multidimensional assemblies formed by transition-metal complexes with controlled configurations and regulated numbers of Hbim^{-1} ligands: (A) “Zero-dimensional dimer” constructed by complementary intermolecular H-bonds between Hbim^{-1} in the metal complexes coordinated by only one Hbim^{-1} ligand. (B) “One-dimensional linear chain” assembled by the metal complexes with *trans*-configuration coordinated by at least two Hbim^{-1} ligands. (C) “One-dimensional zigzag ribbon” assembled by metal complexes with two Hbim^{-1} ligands in *cis*-configuration. (D) “Two-dimensional honeycomb sheet” linked by three intermolecular H-bonds between the metal complexes with three Hbim^{-1} ligands. The sheet is constructed by H-bonding with alternate linkage between different optical isomers of Δ and Λ types. (E) “Helical chain” assembled by intermolecular H-bonding between the same optical isomers of Δ or Λ containing at least two Hbim^{-1} ligands. The symbol n represents the number of Hbim^{-1} ligands coordinated to transition metal ions. (View this art in color at www.dekker.com.)

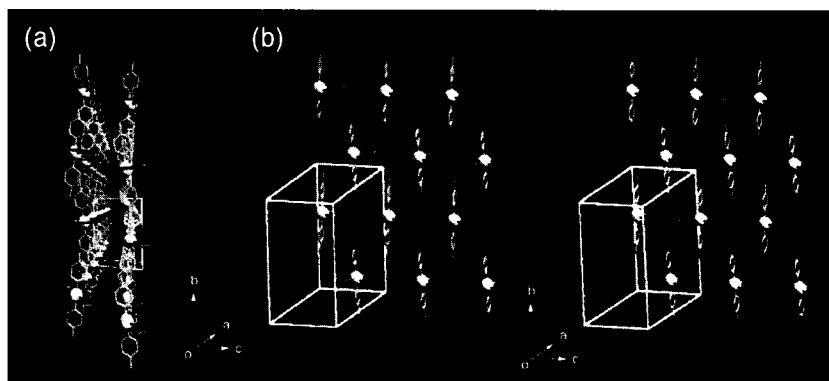


Fig. 7 Arrangement of one-dimensional linear chains in a crystal formed by 7. Three CH_3 groups containing 'Bupy are omitted for clarity. (a) A perspective view of one-dimensional linear chains linked along the a axis and piled along the b axis (color coding: Hbim^{-1} is shown in red, Ni^{2+} green, and 'Bupy blue). (b) A perspective stereo view of linear chains, as viewed along the a axis. (View this art in color at www.dekker.com.)

(Salen NMe_2) formed an H-bonded dimer of type A. In contrast, the positively charged $[\text{Cu}^{\text{II}}(\text{Hbim})(\text{tacn})]^+$ formed an intermolecular H-bonding interaction with ClO_4^- counteranion in preference to self-complementary $\text{NH}\cdots\text{N}$ H-bonding interaction between Hbim^{-1} ligands.^[41] It suggests that the counterions, in particular, the anions with strong H-bonding ability in the ionic complexes, interrupt the formation of the dimer unit. Although counterions such as alkyl ammonium ions in the crystal with the $[\text{Ni}(\text{Hbim})_3]$ have an effect on the superstructures, they do not perturb the complementary H-bondings. Thus these facts indicate that there is no chance of interruption of self-complementary ligand–ligand interactions because of sterically demanding bulky cations and the preferential H-bonding between Hbim^{-1} ligands of anion complexes. From this point, in order to develop the effective self-organization of superstructures, neutral complexes rather than charged ones should be used.

Fig. 7 shows a superstructure with 1-D linear chains of type B in crystal 7 constructed by neutral $[\text{Ni}^{\text{II}}(\text{Hbim})_2(\text{'Bupy})_2]$ ('Bupy=4-*tert*-butyl pyridine) with a *trans* configuration. The blue single crystals of it are obtained from a basic methanol solution by simple one-pot self-organization with Ni^{II} ions, Hbim^{-1} , and 'Bupy. The chain in the crystal along the a axis is composed of infinite links of intermolecular H-bonds of two Hbim^{-1} ligands, located in *equatorial* positions on the distorted octahedron (the range of $\text{NH}\cdots\text{N}$ distances: 2.80–2.82 Å). The two *axial* positions are occupied by two monodentate 'Bupy ligands. Each chain is piled along the b axis to form stacking sheets in the ac plane while fitting each 'Bupy group into the space between the chains. On the other hand, formation of the 1-D linear chains can be altered to that of 1-D zigzag ribbons by changing the direction of intermolecular H-bonding sites in the building blocks. Fig. 8 shows the zigzag ribbon of type C in crystal

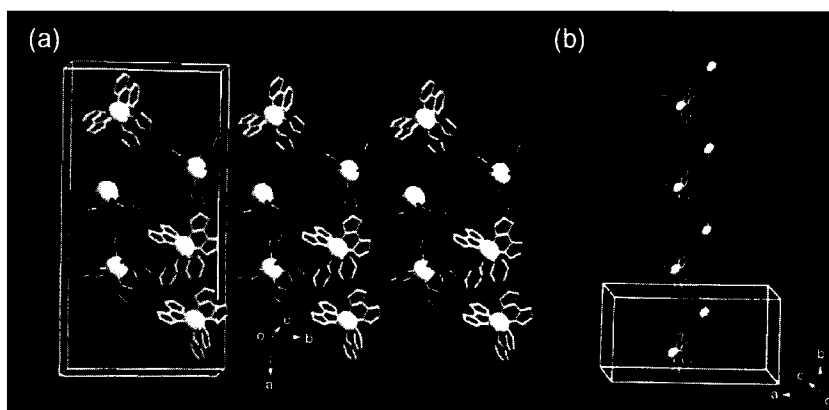


Fig. 8 Arrangement of one-dimensional zigzag ribbons in a crystal formed by 8. (a) A zigzag ribbon structure is formed by alternate linkage between different optical isomers of Δ (red) and Λ (blue) types along the b axis (nickel ions shown in green). The zigzag ribbons are stacked along the a axis. (b) A single chain of a one-dimensional zigzag ribbon is represented along the b axis. (View this art in color at www.dekker.com.)

8 constructed by $[\text{Ni}^{\text{II}}(\text{Hbim})_2(\text{bpy})]$ with the bpy (=2,2'-bipyridine) ligand. The pale orange crystals of $[\text{Ni}^{\text{II}}(\text{Hbim})_2(\text{bpy})]$ are obtained by the same synthetic method of $[\text{Ni}^{\text{II}}(\text{Hbim})_2(\text{Bupy})_2]$ except for the use of bidentate bpy instead of 'Bupy. The zigzag ribbon consists of 1-D ordered arrays along the b axis formed by alternative H-bondings between different optical isomers of Δ and Λ of $[\text{Ni}^{\text{II}}(\text{Hbim})_2(\text{bpy})]$. Two Hbim^{-1} ligands of $[\text{Ni}^{\text{II}}(\text{Hbim})_2(\text{bpy})]$ are used to form the H-bonded zigzag-ribbon networks, but a coordinated bpy does not participate in the formation of the networks (the range of $\text{NH}\cdots\text{N}$ distances: 2.78–2.83 Å). Each bpy residue on the zigzag ribbon is aligned standing alternately parallel to each other and perpendicular to the 1-D main chains. Thus we have demonstrated that we can control linear vs. zigzag 1-D networks by using monodentate and bidentate ligands, respectively.

As shown in Fig. 9a, a neutral racemic complex of $[\text{Ru}^{\text{III}}(\text{Hbim})_3]$ with D_3 symmetry forms a 2-D honeycomb sheet of type D in crystal 9 with (6,3) nets. Compound $[\text{Ru}^{\text{III}}(\text{Hbim})_3]$ is prepared from the precursor complex

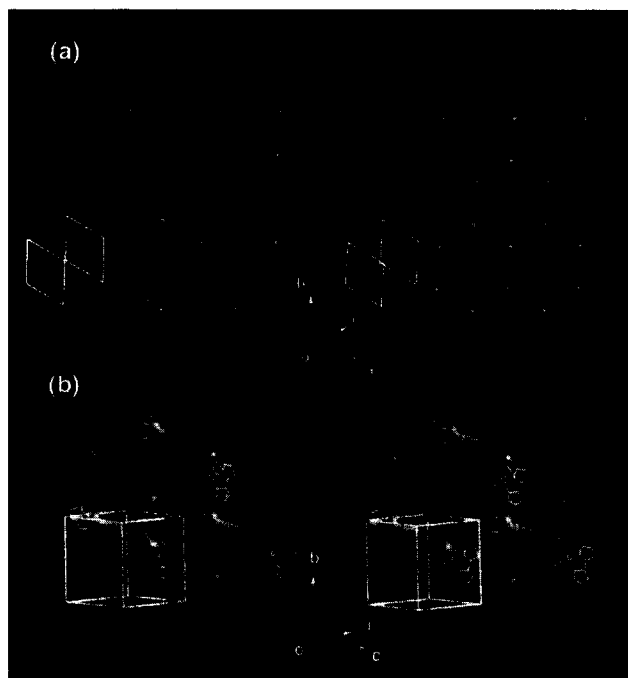


Fig. 9 Arrangement of two-dimensional honeycomb sheets in a crystal formed by 9 (stereo view). (a) A two-dimensional honeycomb sheet is formed by alternate linkage between different optical isomers of Δ (blue) and Λ (red) types (Ru^{3+} ions are shown as magenta spheres). The sheet is constructed by complete H-bonds on three Hbim^{-1} sites of 9. (b) The crystal structure of the single polycatenate network for the crystal of 9. Double-interlocking interpenetrations with the polycatenate structure are formed by two sets of stacked honeycomb sheets that are nearly perpendicular to each other in three dimensions. (View this art in color at www.dekker.com.)

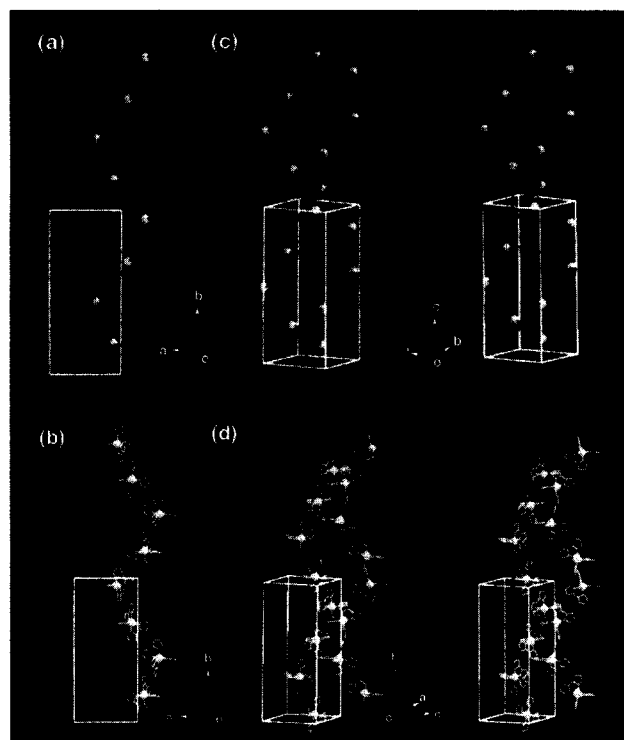


Fig. 10 Arrangement of helical chains in a crystal formed by 10 or 11 (Co^{3+} ions are shown as yellow spheres): (a) and (b) View of each helical chain is represented by the right-handed helix formed by Λ -isomers of 10 in red and the left-handed helix by Δ -isomers of 11 in light-blue along the c axis. (c) Stereo view of two right-handed single helices made up of Λ -isomers 10 (red). The two single helices do not intersect each other and do not form a double helix. (d) Stereo view of two left-handed single helices made up of Δ -isomers of 11 (light blue). (View this art in color at www.dekker.com.)

$[\text{Ru}^{\text{II}}(\text{H}_2\text{bim})_3]^{2+}$ and the desired dark blue single crystals are crystallized from a methanol solution.^[42] All the three Hbim^{-1} sites of $[\text{Ru}^{\text{III}}(\text{Hbim})_3]$ form the complementary intermolecular H-bonds completely. The honeycomb sheet self-organized by $[\text{Ru}^{\text{III}}(\text{Hbim})_3]$ is constructed by using alternative H-bondings between optical isomers of Δ and Λ types of $[\text{Ru}^{\text{III}}(\text{Hbim})_3]$ (the range of $\text{NH}\cdots\text{N}$ distances: 2.79–2.80 Å). Each sheet forms an infinite number of identical sheets and passes each hexagonal cavity created by six $[\text{Ru}^{\text{III}}(\text{Hbim})_3]$ units through the two interpenetrating rods of the other two sheets at an inclination of $\sim 70^\circ$ to give a 3-D polycatenate structure with a double interlocking interpenetration in 9 [Fig. 9b]. The two chiral building blocks of Λ - $[\text{Co}^{\text{III}}(\text{Hbim})_3]$ and Δ - $[\text{Co}^{\text{III}}(\text{Hbim})_3]$ form 1-D helical chains of type E with a right-handed (for crystal 10) [Fig. 10a and c represented by red] and a left-handed (for crystal 11) [Fig. 10b and d represented by light blue] orientation, respectively. The red single crystals 10 and 11 of Λ - and Δ - $[\text{Co}^{\text{III}}(\text{Hbim})_3]$ are crystallized from 2-propanol by the deprotonation reaction of the optically

resolved Λ - and Δ -[Co^{III}(H₂bim)₃](NO₃)₃ precursor complexes, respectively.^[43] Each 1-D helical chain is constructed by employing intermolecular H-bonds between the same optical isomers, which utilize two of three Hbim⁻¹ sites in Λ - or Δ -[Co^{III}(Hbim)₃]. Both helical chains form 4₁ single strands, which have a pitch of ca. 33.4 Å similar to that of the B-DNA double strand. Another residual Hbim⁻¹ site of Δ - and Λ -[Co^{III}(Hbim)₃] is blocked by H-bonds with 2-propanol of crystallization, without using the helical chain construction.

In the case of superstructures on 10 and 11 using all of three sites, a 3-D chiral network with larger porous spaces formed by 8₇ cavities of (10,3)-*a* nets like 6 would be expected to be constructed as found in the crystal with [Ni(Hbim)₃]⁻¹, which has the structure reinforced by a twofold interpenetration and stable double helical structures. In contrast, 10 and 11 do not have any larger porous networks. It has not been obvious to date why large cavities are not constructed by (10,3)-*a* single networks, although two factors, solvent effect and the strength of the H-bonds formed, are anticipated. Öhrstrom and Larsson have shown lately the (10,3)-*a* nets based on single helical H-bonding networks formed from both building blocks of Δ - and Λ -[Co^{III}(Hbim)₃] by using a solvent effect with DMF/H₂O mixed solvent.^[44] Here the two superstructures of a honeycomb sheet and a helical strand built from tris-2,2'-biimidazole complexes with *D*₃ symmetry can be individually prepared by using a racemic compound and an optically resolved ones, respectively.

In summary, we demonstrated the practical structures of A–E in Fig. 6 based on the relationships between specified molecular arrays and molecular building blocks, and identified the four types of new superstructures, B–E, by X-ray analysis. The knowledge from structural data should help provide the preprogramming of new superstructures built from the “neutral” Hbim⁻¹ complexes. Thus we have recently found that the neutral complexes with some Hbim⁻¹ ligands can control the preprogramming superstructures in multidimensionality by using configurations around the coordination sphere, as there is no chance of interruption of self-complementary ligand–ligand interactions because of sterically demanding bulky cations and the preferential H-bonding between Hbim⁻¹ ligands of anion complexes.

CONCLUSION

Crystal engineering techniques using those functionalized molecular building blocks will be utilized in future studies for the creation of new solid-state materials. Thus the building blocks in Fig. 6 would produce the functionalized preprogramming superstructures by introducing additive ligands with physical properties such as

magnetic and photoactive ones to other coordination sites on the arrays of A, B, C, and E. We are now attempting to develop functional solid-state materials using these techniques. Our further study will be aimed at finding the mutual relationship between H-bonded superstructures of [Ni(Hbim)₃]⁻¹ and the kinds or shapes of their component counterions. Thus cations play an important role in predicting the crystal structures and rationalizing the crystal structure engineering in these systems. In addition, the introduction of paramagnetic metal ions and transition metal chromophores into the system of the H-bonding extended arrays may lead to the creation of a new material with interesting magnetic and electronic properties.

ACKNOWLEDGMENTS

This work was supported by a Grant-in-Aid for Scientific Research (Nos. 13440201 and 10146103) on Priority Areas from the Ministry of Education, Science, and Culture, Japan. The authors thank the Analytical Center in Osaka City University, for use of a single-crystal X-ray diffractometer and elemental analyses. I would like to thank Prof. Kazuhiro Nakasuji of the Graduate School of Science of Osaka University for the useful discussion of this manuscript.

REFERENCES

1. Batten, S.R.; Robson, R. Interpenetrating nets: Ordered, periodic entanglement. *Angew. Chem., Int. Ed. Engl.* **1998**, *37*, 1460.
2. Zaworotko, M.J. Superstructural diversity in two dimensions: Crystal engineering of laminated solids. *Chem. Commun.* **2001**, 1.
3. Va idhyanathan, R.; Natarajan, S.; Rao, C.N. Synthesis of a hierarchy of zinc oxalate structures from amine oxalates. *Dalton* **2001**, 699.
4. Kitagawa, S.; Kondo, M. Functional micropore chemistry of crystalline metal complex-assembled compound. *Bull. Chem. Soc. Jpn.* **1998**, *71*, 1739.
5. Holman, K.T.; Pivovar, A.M.; Swift, J.A.; Ward, M.D. Metric engineering of soft molecular host frameworks. *Acc. Chem. Res.* **2001**, *34*, 107.
6. Sherrington, D.C.; Taskinen, K.A. Self-assembly in synthetic macromolecular synthons via multiple hydrogen bonding interactions. *Chem. Soc. Rev.* **2001**, *30*, 83.
7. Desiraju, G.R. Supramolecular synthons in crystal engineering—A new organic synthesis. *Angew. Chem., Int. Ed. Engl.* **1995**, *34*, 2311.

8. Desiraju, G.R. Hydrogen bonds and other intermolecular interactions in organometallic crystals. *Dalton* **2000**, 3745.
9. Oda, R.; Huc, I.; Schmutz, M.; Candau, S.J.; MacKintosh, F.C. Tuning bilayer twist using chiral counterions. *Nature* **1999**, 399, 566.
10. Cai, C.; Müller, B.; Weckesser, J.; Barth, J.V.; Tao, Y.; Bösch, M.M.; Kündig, A.; Bosshard, C.; Biaggio, I.; Günter, P. Model for in-plane directional ordering of organic thin films by oblique incidence organic molecular beam deposition. *Adv. Mater.* **1999**, 11, 750.
11. Höger, S.; Bonrad, K.; Mourran, A.; Beginn, U.; Möller, M. Synthesis, aggregation, and adsorption phenomena of shape-persistent macrocycles with extraannular polyalkyl substituents. *J. Am. Chem. Soc.* **2001**, 123, 5651.
12. Fujita, M.; Umemoto, K.; Yoshizawa, M.; Fujita, N.; Kusakawa, T.; Biradha, K. Molecular paneling via coordination. *Chem. Commun.* **2001**, 509.
13. Joachim, C.; Gimzewski, J.K.; Aviram, A. Electronics using hybrid-molecular and mono-molecular devices. *Nature* **2000**, 408, 541.
14. Burrows, A.D.; Chan, C.-W.; Chowdhry, M.M.; McGrady, J.E.; Mingos, D.M.P. Multi-dimensional crystal engineering of bifunctional metal complexes containing complementary triple hydrogen bonds. *Chem. Soc. Rev.* **1995**, 138, 329.
15. Mitsumi, M.; Toyoda, J.; Nakasuji, K. Metal-pteridine complexes having three-dimensional hydrogen-bonded networks. *Inorg. Chem.* **1995**, 34, 3367.
16. Wilton-Ely, J.D.E.T.; Schier, A.; Mitzel, N.W.; Schmidbaur, H. Structural diversity in gold(I) complexes of 4-sulfanylbenzoic acid. *Dalton* **2001**, 1058.
17. Yang, G.; Zhu, H.-G.; Ling, B.-H.; Chen, X.-M. Syntheses and crystal structures of four metal-organic co-ordination networks constructed from cadmium(II) thiocyanate and nicotinic acid derivatives with hydrogen bonds. *Dalton* **2001**, 580.
18. MacDonald, J.C.; Dorrestein, P.C.; Pilly, M.M.; Foote, M.M.; Lundburg, J.L.; Henning, R.W.; Schuitz, A.J.; Manson, J.L. Design of layered crystalline materials using coordination chemistry and hydrogen bonds. *J. Am. Chem. Soc.* **2000**, 122, 11692.
19. Beatty, A.M. Hydrogen bonded networks of coordination complexes. *CrystEngComm* **2001**, 51, 243.
20. Kaiser, S.W.; Saillant, R.B.; Butler, W.M.; Russussen, P.G. Rhodium and iridium complexes of biimidazole: 1. Mononuclear and dinuclear species. *Inorg. Chem.* **1976**, 15, 2681.
21. Tadokoro, M.; Toyoda, J.; Isobe, K.; Itoh, T.; Miyazaki, A.; Enoki, T.; Nakasuji, K. Dimeric hydrogen-bonded transition metal complex containing bidentate mono-deprotonated 2,2'-biimidazolate ligand. *Chem. Lett.* **1995**, 613.
22. Tadokoro, M.; Isobe, K.; Uekusa, H.; Ohashi, Y.; Toyoda, J.; Tashiro, K.; Nakasuji, K. Cation-dependent formation of superstructures by one-pot self-organization of hydrogen-bonded nickel complexes. *Angew. Chem. Int. Ed.* **1999**, 38, 95.
23. Moore, J.S.; Lee, S. Molecular craft. *Chem. Ind.* **1994**, 556.
24. Rosi, N.L.; Eddaoudi, M.; Kim, J.; O'Keeffe, M.; Yaghi, O.M. Advances in the chemistry of metal-organic frameworks. *CrystEngComm* **2002**, 4, 401.
25. Carlucci, L.; Ciani, G.; Proserpio, D.M.; Sironi, A.A. 1-, 2-, and 3-dimensional polymeric frames in the coordination chemistry of AgBF₄ with pyrazine. The first example of three interpenetrating 3-dimensional triconnected nets. *J. Am. Chem. Soc.* **1995**, 117, 4562.
26. Munakata, M.; Wu, L.P.; Kuroda-Sowa, T. Toward the construction of functional solid-state supramolecular metal complexes containing copper(I) and silver(I). *Adv. Inorg. Chem.* **1999**, 46, 173.
27. Aakeröy, C.B.; Seddon, K.R. The hydrogen bond and crystal engineering. *Chem. Soc. Rev.* **1993**, 26, 397.
28. Chowdhry, M.M.; Mingos, D.M.P.; White, A.J.P.; Williams, D.J. Supramolecular self-assembly of a transition-metal-organo network based on simultaneous coordinate- and hydrogen bond interactions. *Chem. Commun.* **1996**, 899.
29. Munakata, M.; Wu, L.P.; Yamamoto, M.; Kuroda-Sowa, T.; Maekawa, M. Construction of three-dimensional supramolecular coordination copper(I) compounds with channel structures hosting a variety of anions by changing the hydrogen-bonding mode and distances. *J. Am. Chem. Soc.* **1996**, 118, 3117.
30. Lambert, C.; Kaupp, M. "Inverted" sodium-lithium electronegativity: Polarity and metalation energies of organic and inorganic alkali-metal compounds. *Organometallics* **1993**, 12, 853.
31. Tadokoro, M.; Shiomi, T.; Isobe, K.; Nakasuji, K. Caesium(I) mediated 3-D super-structures by one-pot self-organization of hydrogen-bonded nickel complexes. *Inorg. Chem.* **2001**, 40, 5476.
32. Gregory, K.; Bremer, M.; Schleyer, P.R.; Klusener, P.A.A.; Brandsma, L. *N*-Cesio-carbazole·pmda and *N*-potassio-carbazole·pmda (PMDA = *N,N,N',N'',N'''*-pentamethyl-diethylenetriamine). Cation size and multi-hapto bonding. *Angew. Chem., Int. Ed. Engl.* **1989**, 28, 1224.
33. Harder, S.; Prosenc, M.H. The heaviest alkali

- metallocene: Structure of an anionic cesocene triple-decker. *Angew. Chem., Int. Ed. Engl.* **1996**, *35*, 97.
34. Harrowfield, J.M.; Ogden, M.I.; Richmond, W.R.; White, A.H. Calixarene-cupped caesium: A coordination conundrum. *Chem. Commun.* **1991**, 1159.
 35. Tadokoro, M.; Kanno, H.; Kitajima, T.; Umemoto, H.S.; Nakanishi, N.; Isobe, K.; Nakasuji, K. Self-organizing super-structures formed from hydrogen-bonded biimidazolate metal complexes. *Proc. Natl. Acad. Sci. U. S. A.* **2002**, *99*, 4950.
 36. Desiraju, G.R. Chemistry beyond the molecule. *Nature* **2001**, *412*, 397.
 37. Coronado, E.; Galán-Mascarós, J.R.; Gomez-García, C.J.; Laukhin, V. Coexistence of ferromagnetism and metallic conductivity in a molecule-based layered compound. *Nature* **2000**, *408*, 447.
 38. Bénard, S.; Yu, P.; Audié, J.P.; Rivière, E.; Clément, R.; Guilhem, J.; Tchertanov, L.; Nakatani, K. Structure and NLO properties of layered bimetallic oxalate-bridged ferromagnetic networks containing stilbazolium shaped chromophores. *J. Am. Chem. Soc.* **2000**, *122*, 9444.
 39. Andrés, R.; Brissard, M.; Gruselle, M.; Train, C.; Vaissermann, J.; Malezieux, B.; Jamet, J.-P.; Verdager, M. Rational design of three-dimensional (3D) optically active molecule-based magnets: Synthesis, structure, optical and magnetic properties of $\{[\text{Ru}(\text{bpy})_3]^{2+}, \text{ClO}_4^-, [\text{Mn}^{\text{II}}\Delta\text{Cr}^{\text{III}}(\text{ox})_3]^{-}\}_n$ and $\{[\text{Ru}(\text{bpy})_2\text{ppy}]^+, [\text{Mn}^{\text{II}}\text{Cr}^{\text{III}}(\text{ox})_3]^{-}\}_n$, with $\text{M}^{\text{II}} = \text{Mn}^{\text{II}}, \text{Ni}^{\text{II}}$. X-ray structure of $\{[\Delta\text{Ru}(\text{bpy})_3]^{2+}, \text{ClO}_4^-, [\Delta(\text{Mn}^{\text{II}}\Delta\text{Cr}^{\text{III}}(\text{ox})_3)]^{-}\}_n$ and $\{[\Delta\text{Ru}(\text{bpy})_2\text{ppy}]^+, [\Delta(\text{Mn}^{\text{II}}\Delta\text{Cr}^{\text{III}}(\text{ox})_3)]^{-}\}_n$. *Inorg. Chem.* **2001**, *40*, 4633.
 40. Decurtins, S.; Ferlay, S.; Pellax, R.; Gross, M.; Schmalte, H.; Veciana, N. *Supramolecular Engineering of Synthetic Metallic Materials—Conductors and Magnets*; Rovira, C., Amabilino, J.D., Eds.; B. Kluwer Academic Pub., 1999; 175.
 41. Tadokoro, M.; Nakasuji, K. Hydrogen bonded 2,2'-biimidazolate transition metal complexes as a tool of crystal engineering. *Coord. Chem. Rev.* **2000**, *198*, 205.
 42. Rillema, P.; Sahai, R.; Matthews, P.; Edwards, A.K.; Shaver, R.J. Multimetallic ruthenium(II) complexes based on biimidazole and bibenzimidazole: Effect of dianionic bridging on redox and spectral properties. *Inorg. Chem.* **1990**, *29*, 167.
 43. Kanno, H.; Manriki, S.; Yamazaki, E.; Utsuno, S.; Fujita, J. Preparation and resolution of a series of cobalt(III) complexes containing 2,2'-biimidazole and ethylenediamine. *Bull. Chem. Soc. Jpn.* **1996**, *69*, 1981.
 44. Öhrstrom, L.; Larsson, K.; Borg, S.; Norberg, S.T. Crucial influence of solvent and chirality—The formation of helices and three-dimensional nets by hydrogen-bonded biimidazolate complexes. *Chem. Eur. J.* **2001**, *7*, 4805.

Molecular Electronic Logic and Memory

M

Dustin K. James

James M. Tour

Rice University, Houston, Texas, U.S.A.

INTRODUCTION

Electronic logic chips are used in many products today, from cell phones to robotic toys to automobiles and trucks, dishwashers and freezers, thermostats, and coffee makers. The most visible application of course is in our desktop and laptop computers. To enable further miniaturization of the circuitry used in these devices, recent research has focused on developing molecular-based logic and memory. In this chapter, we will review the state of the art in the development and characterization of molecular electronic logic and memory, with discussions of the quantum cellular array approach (QCA) (and the related electrostatic repulsion architecture) and the crossbar approach to building molecular circuits followed by a more in-depth look at very recent results from our laboratory concerning the NanoCell approach to molecular logic and memory.

MOLECULAR ELECTRONICS

The rapidly developing field of molecular electronics is one of the driving forces behind the interest in molecular-based circuits.^[1-9] The limitations of the present “top-down” method of producing semiconductor-based devices have been the subject of debate and conjecture since Gordon Moore’s prediction that the number of components per integrated circuit would double every 18 months.^[10] It is thought that the inherent limitations of the present technology will lead to a dead-end in the next few years. For instance, silicon’s band structure disappears when silicon layers are just a few atoms thick. Lithographic techniques that are used to produce the circuitry on the silicon wafers are limited, in part, by the wavelengths at which they work. However, leaders in the semiconductor manufacturing world are still making advances that appear to be pushing “Moore’s Law” beyond its prior perceived limits. In the commercial technology of 2001, the copper wires in Intel’s Pentium[®] 4 logic chip are 0.13 μm wide.^[11] Intel is developing technology to create logic chips with wires 90 nm wide to be commercialized in 2003.^[12]

For comparison’s sake, a typical molecular electronics candidate synthesized in our laboratory is calculated to be

0.3 nm wide and 2.5 nm in length (Fig. 1).^[5] It would take 300 of these molecules, positioned side by side, to span the 90-nm metal line in the most advanced logic chip in development. The small size of these molecules is emphasized when one considers that 500 g (about 1 mol) would contain 6×10^{23} molecules, or more molecules than the number of transistors ever made in the history of the world. This amount of material could be produced by using relatively small 22-L laboratory reaction flasks. Changing the physical characteristics of this molecule is as easy as changing the raw materials used to make it. The small size, the potential of synthesizing huge numbers in small reactors, and the ease of modification of the physical characteristics of the molecules are good reasons for pursuing molecular electronics research. As an example of how far the technology has come, molecular electronics is discussed in the “Emerging Research Devices” section of the most recent International Technology Roadmap for Semiconductors^[13,14] and molecules that may act as wires are a large part of the emerging technology. Molecular electronics was named the “breakthrough of the year” by *Science Magazine* for 2001.^[15] Instead of replacing the present silicon-based technology, nanoelectronic architectures could prove to be a complement to traditional solid-state devices.^[1,5,16,17]

To take advantage of the ultrasmall size of molecules, one needs an interconnect technology that 1) scales from the molecular dimensions; 2) can be structured to permit the formation of the molecular equivalent of large-scale diverse modular logic blocks as found in very large-scale interconnect (VLSI) architectures; and 3) can be selectively connected to mesoscopically (100 nm scale) defined input/output leads.

The first approach to molecular computing is based on quantum cellular automata (QCA) and related electrostatic information transfers.^[18-20] This method relies on electrostatic field repulsions to transport information throughout the circuitry. One major benefit of the QCA or electrostatics approach is that heat dissipation is less of an issue because only a few or fractions of an electron are used for each bit of information.

The second approach is based on the massively parallel solid-state Teramac computer developed at Hewlett-Packard (HP),^[9,21] and involves building a similarly

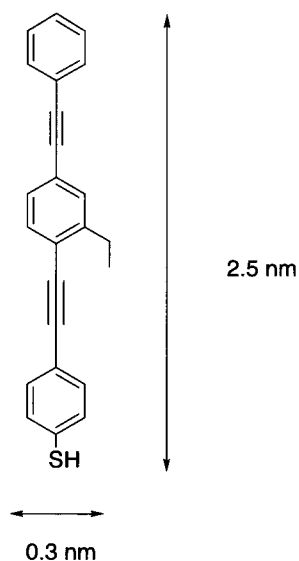


Fig. 1 The dimensions of a typical molecule studied in molecular electronic applications are calculated to be 0.3 nm in width and 2.5 nm in length using molecular mechanics to determine the energy-minimized structure. (From Ref. [5].)

massively parallel computing device using molecular electronics based on crossbar technologies that are proposed to be defect-tolerant. A Teramac-like crossbar-based approach called the “NanoFabric” architecture deals more effectively with the numbers of wires emanating from the array.^[22] When applied to molecular systems, the crossbar approaches propose to use single-walled carbon nanotubes (SWNTs)^[23–27] or synthetic nanowires (NWs)^[28–31] for the crossbars. Logic functions are performed either by sets of crossed and specially doped nanowires, or by molecular switches placed at each crossbar junction.

The third approach involves using molecular scale switches as part of a NanoCell.^[32] The NanoCell relies on disordered arrays of molecular switches to perform logic functions. It does not require that each switching molecule be individually addressed, and furthermore utilizes the principles of chemical self-assembly in construction of the logic circuitry, thereby reducing complexity. While fabrication constraints are greatly eased, programming difficulties increase dramatically.

QUANTUM CELLULAR AUTOMATA (QCA) AND ELECTROSTATIC ARCHITECTURES

Quantum dots have been called “artificial atoms” or “boxes for electrons”^[33] because they have discrete charge states and energy level structures that are similar to atomic systems and can contain from a few thousand to

one electron. They are typically small, electrically conducting regions, 1 μm or less in size, with a variety of geometries and dimensions. Because of the small volume, the electron energies are quantized. No shell structure exists; instead, the generic energy spectrum has universal statistical properties associated with quantum chaos.^[34] Several groups have studied the production of quantum dots.^[35] Heath et al. discovered that hexane solutions of Ag nanoparticles, passivated with octanethiol, formed spontaneous patterns on the surface of water when the hexane was evaporated,^[36] and has prepared superlattices of quantum dots.^[37,38] Lieber has investigated the energy gaps in “metallic” single-walled carbon nanotubes^[23] and has used an atomic force microscope to mechanically bend SWNT to create quantum dots less than 100 nm in length. He found that most metallic SWNT are not true metals, and that by bending the SWNT, a defect was produced that had a resistance of 10–100 k Ω . Placing two defects less than 100 nm apart produced the quantum dots.

In the QCA approach toward molecular electronic computing systems, four quantum dots in a square array are placed in a cell such that electrons are able to tunnel between the dots but are unable to leave the cell.^[39] Coulomb repulsion will force the electrons to occupy dots on opposite corners. The two ground state polarizations are both energetically equivalent and can be labeled logic “0” or “1.” Flipping the logic state of one cell, for instance, by applying a negative potential to a lead near the quantum dot occupied by an electron, will result in the next-door cell flipping ground states in order to reduce Coulomb repulsion. In this way, a line of QCA cells can perform computations.^[40] A QCA fan-out structure has been proposed; however, when the ground state of the input cell is flipped, the energy imposed into the system may not be enough to flip all the cells of both branches of the structure, producing long-lived metastable states and erroneous calculations. Switching the cells using a quasiadiabatic approach prevents the production of these metastable states.^[41]

While the use of quantum dots in the demonstration of QCA is a good first step in reduction to practice, the ultimate goal is to use individual molecules to hold the electrons and pass electrostatic potentials down QCA wires. We have synthesized molecules that were shown by ab initio computational methods to have the capability of transferring information from one molecule to another through electrostatic potentials (Fig. 2). The potentials use a millionth of an electron per bit of information. This is quite attractive because a major consideration in molecular devices is the energy consumption/dissipation needs. Considering the fact that there are 10^8 gates/cm² (in presently sized silicon-based systems) functioning at the rate of 10^{-9} sec (present speeds), those gates afford 10^{17} electrons/sec (~ 0.02 A/cm²) if only one electron per gate

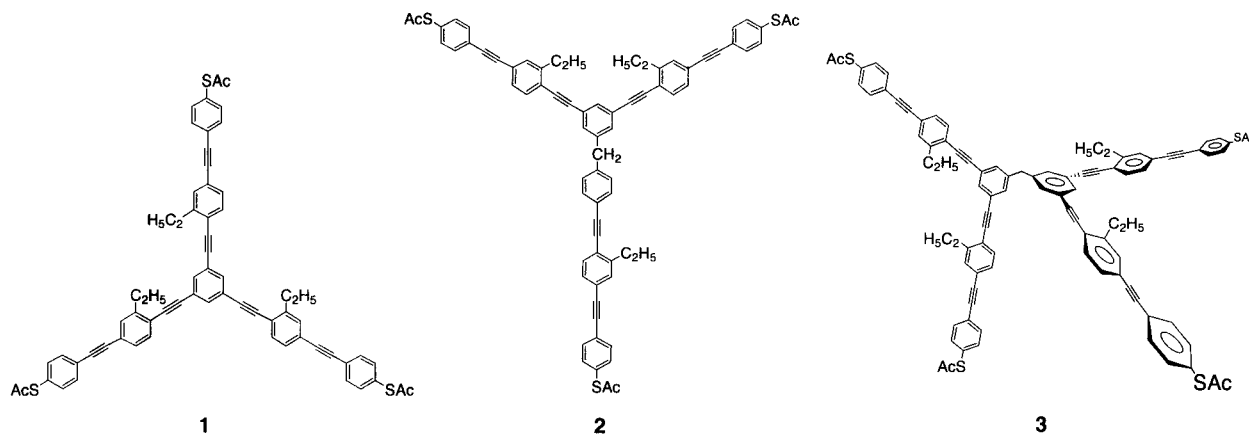


Fig. 2 Three compounds that were synthesized for studies in computing using electrostatic potentials. **1** is a molecular three-terminal junction that could be used as a molecular interconnect. **2** is a molecular-sized switch for which there is a corresponding equivalent of a source, drain, and gate terminals of a bulk solid state FET. **3** can be an active OR or a passive NOR gate if positive logic is used, or an AND or NAND gate if negative logic is used.

is used to transport, indicate, fetch, or represent a binary digit. At this point, heat considerations are already extreme: if the average resistance of the circuit is 30Ω , this represents 20 W/cm^2 . If an increase of several orders of magnitude in performance is expected with molecular circuits, this would imply a proportional increase in power dissipation. Such levels of power dissipation rule out most conventional current or electron transfer methods for practical molecular devices wherein large numbers of devices are densely configured.

Electrostatic interactions are produced by small reshapes of the electron density as a result of the input signals. In turn, electrostatic potential interactions between molecules could transport the information throughout the central processing unit (CPU). When this approach is used, there is no need for electron currents or electron transfers as in present devices; a small change in the electrostatic potential of one molecule could be enough to send the information to another molecule. These perturbations of the electrostatic potential imply a very small amount of charge transfer, substantially less than one electron.

Although we synthesized molecules that included three-terminal molecular junctions, switches, and molecular logic gates to demonstrate the electrostatics methodology, none of the molecules were incorporated into an actual assembly. Because the electrostatics method has major obstacles to overcome before even simple laboratory tests can be attempted, all results were based on computation only. While relatively large quantum dot arrays can be fabricated by using existing methods, a major problem is that placement of molecules in precisely aligned arrays at the nanoscopic level is very difficult to

achieve with accuracy and precision. Another problem is that degradation of only one molecule in the array can cause failure of the entire circuit. There has also been some debate about the unidirectionality (or lack thereof) of QCA designs.^[42–44] Examples of two-dot QCA arrays have yet to be demonstrated using molecules, because addressing the molecular-sized inputs and the recording of a signal based on fractions of an electron are enormous hurdles.

CROSS-BAR ARRAYS

Heath et al.^[9] reported on a massively parallel experimental computer that contained 220,000 hardware defects yet operated 100 times faster than a high-end single processor workstation for some configurations. The solid-state-based (not molecular electronics) Teramac computer, built at HP, relied on its fat-tree architecture for its logical configuration. The minimum communication bandwidth needed in the fat-tree architecture was determined by utilizing Rent's rule, which states that the number of wires coming out of a region of a circuit should scale as the power of the number of devices (n) in that region, ranging from $n^{1/2}$ in two dimensions to $n^{2/3}$ in three dimensions. The HP workers built in excess bandwidth, putting in many more wires than needed. The reason for the large number of wires can be understood by considering a simple city map. To get from point A to point B, one can take local streets, main thoroughfares, freeways, interstate highways, or any combination thereof. If there is a roadblock at any point C between A and B, then renavigation can be assessed by using the map to

arrive to point B. In the Teramac computer, "street blockages" are stored in a defect database; when one device needs to communicate with another device, it uses the database and the map to determine how to get there. Therefore the Teramac design can tolerate defects.

In the Teramac computer (or a proposed molecular computer based on the Teramac design), the wires that comprise the address lines controlling the settings of the configuration switches and the data lines that link the logic devices are the most important and plentiful part of the computer. It is logical that a large amount of research has been performed to develop NWs that could be used in the massively parallel molecular computer. This approach is dependent on precise order in devices with exact arrays of nanostructures, including nanowires or nanotubes, sometimes bridged by molecules, and interfaced with microstructure in order to communicate with the outside world.^[9,18,45] Advancements have been made in the art since our last review,^[3] many of which have been reviewed by Luo et al.^[46] and by us. (See the entry "Molecular Wires," for our review of this related area.)

Lieber has reviewed the work carried out in his laboratory to synthesize and determine the properties of NWs and nanotubes.^[23] He used Au or Fe catalyst nanoclusters to serve as the nuclei for NWs of Si and GeAs with diameters of 10 nm and lengths of hundreds of nanometers. By choosing specific conditions, Lieber was able to control both the length and the diameter of the single crystal semiconductor NW.^[28] Silicon NWs doped with B or P were used as building blocks by Lieber to assemble semiconductor nanodevices. Active bipolar transistors were fabricated by crossing n-doped NWs with p-type wire base. The doped wires were also used to assemble complementary inverter-like structures.

Lieber used Langmuir-Blodgett (LB) techniques to transfer multiple layers of nanowires onto planar substrates, followed by spin coating a photoresist layer onto the lattice.^[47] The photoresist was patterned and developed, and the exposed nanowires were removed by sonication in deionized water. The remaining photoresist covering the nanowire arrays was dissolved in acetone. Large arrays were built.

Yu et al.^[48] reported the synthesis of silicon NWs by chemical vapor deposition using SiH₄ as the Si source and Au or Zn nanoparticles as the catalytic seeds at 440°C. The wires produced varied in diameter from 14 to 35 nm, and were grown on the surface of silicon wafers. After growth, isolated NWs were mechanically transferred to wafers and Al contact electrodes were put down by standard e-beam lithography and e-beam evaporation such that each end of a wire was connected to a metallic contact. In some cases, a gate electrode was positioned at the middle of the wire. Tapping-mode atomic force micros-

copy (AFM) indicated the wire in this case was 15 nm in diameter.

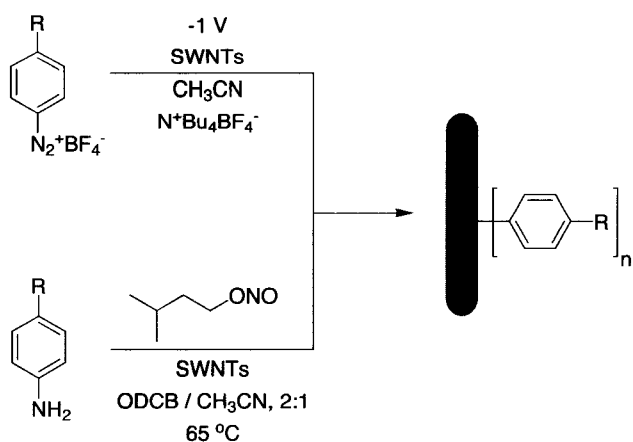
Heath found that annealing the Zn-Si wires at 550°C produced increased conductance attributed to better electrode/nanowire contacts. Annealing Au-Si wires at 750°C for 30 min increased current about 10⁴, an effect attributed to doping of the Si with Au, and lower contact resistance between the wire and Ti/Au electrodes.

More recently, Melosh et al.^[49] reported on a method of obtaining aligned metal and semiconductor nanowires, based on the process of first growing nanowires in a selectively etched GaAs/Al_{0.8}Ga_{0.2}As superlattice, and then releasing them onto a 10-nm epoxy adhesion layer on an oxidized silicon wafer. After heat curing of the epoxy layer, the GaAs template was removed by treatment with KI/H₂O. The wafer was then rinsed with ultrapure water and dried, and the exposed epoxy adhesion layer was removed by using an O₂ plasma etch. This process produced nanowire arrays with center-to-center distances as small as 16 nm and high aspect ratios (up to 10⁶). Multiple cycles produced crossed nanowires with a junction density > 10¹¹ per cm². No molecules were placed at the junctions of the nanowires.

Much research has been performed to determine the efficacy of SWNTs as NWs in molecular computers. One problem with SWNTs is their lack of solubility in common organic solvents. In their synthesized state, individual SWNTs form ropes,^[50] from which it is difficult to isolate individual tubes. In our laboratory, a measure of the solubility of the tubes was seen in 1,2-dichlorobenzene.^[51] An obvious route to higher solubility is to functionalize SWNTs by attachment of soluble groups through covalent bonding. Mickelson et al.^[52] found that fluorinated SWNTs were soluble in alcohols, while Chen et al.^[53] were able to dissolve SWNTs by ionic functionalization of the carboxylic acid groups present in purified tubes.

We have found that SWNTs can be functionalized by electrochemical reduction of aryl diazonium salts in their presence.^[54] Using this method, about 1 in 20 carbon atoms of the nanotube framework are reacted. We have also found that the SWNTs can be functionalized by direct treatment with aryl diazonium tetrafluoroborate salts in solution, or by in situ generation of the diazonium moiety using an alkyl nitrite reagent.^[55] These functional groups give us handles with which we can direct further, more selective derivatization (Fig. 3) and we recently reviewed the area of covalent sidewall derivatization of SWNTs.^[56]

From an electronics perspective, the good thing about SWNTs is that all the carbons on the sidewalls are essentially the same; therefore, there is no location for an electron to localize during electronic transport. However, most of organic synthetic chemistry is predicated upon the ability to distinguish different carbon atoms in a molecule



R = halogen, CO₂CH₃, NO₂, *tert*-butyl, COOH, in addition to

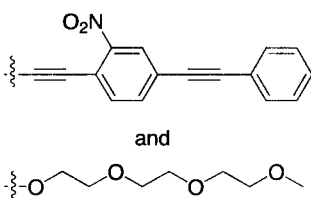


Fig. 3 Reaction of SWNTs with aryl diazonium compounds. Shown are the electrochemical reactions with preformed diazonium salts, and the thermally activated reaction with in situ generated diazonium compounds. Also shown are a number of specific moieties that have been attached via these methods.

based on their subtle electronic and/or steric differences. Thus, from a synthetic perspective, the bad thing about SWNTs is that all the carbons on the sidewalls are essentially the same; therefore, one cannot use the plethora of synthetic techniques that favor formation of one type of carbon-carbon bond over another. However, if one did have a crossbar array of nanotubes, where the voltage between the two tubes could be selectively addressed at discrete locations, then the bridging on the specified cross-junctions might be possible; this has not yet been demonstrated.

Unfortunately, fluorination and other sidewall functionalization methods can perturb the electronic nature of the SWNT. An approach by Smalley et al.^[50,57] and Stoddart and Heath^[27] to increasing the solubility without disturbing the electronic nature of the SWNTs was to wrap polymers around the SWNTs, but leave individual tubes' electronic properties unaffected. Stoddart and Heath found that the SWNT ropes were not separated into individually wrapped tubes; the entire rope was wrapped. Smalley found that individual tubes were wrapped with polymer; the wrapped tubes did not exhibit the roping behavior. Although Smalley was able to demonstrate removal of the polymer from the tubes, it is not clear,

however, how easily the SWNTs can be manipulated and subsequently used in electronic circuits. In any case, the placement of SWNTs into controlled configurations has been, for the most part, a top-down methodology. Significant advances will be needed to take advantage of controlled placement at dimensions that exploit a molecule's small size.

Lieber proposed a SWNT-based nonvolatile random access memory device comprising a series of crossed nanotubes, wherein one parallel layer of nanotubes is placed on a substrate and another layer of parallel nanotubes, perpendicular to the first set, is suspended above the lower nanotubes by placing them on a periodic array of supports.^[24] The elasticity of the suspended nanotubes provides one energy minima, wherein the contact resistance between the two layers is zero, and the switches (the contacts between the two sets of perpendicular NWs) are OFF. When the tubes are transiently charged to produce attractive electrostatic forces, the suspended tubes flex to meet the tubes directly below them, and a contact is made, representing the ON state. The ON/OFF state could be read by measuring the resistance at each junction, and could be switched by applying voltage pulses at the correct electrodes. This theory was tested by mechanically placing two sets of nanotube bundles in a crossed mode and measuring the *I*(*V*) characteristics when the switch was OFF or ON. Although nanotube bundles with random distributions of metallic and semiconductor properties were used, the difference in resistance between the two modes was a factor of 10, enough to provide support for their theory. In another study, Lieber used scanning tunneling microscopy (STM) to determine the atomic structure and electronic properties of intramolecular junctions in SWNTs samples.^[25] Metal-semiconductor junctions were found to exhibit an electronically sharp interface without localized junction states, while metal-metal junctions had a more diffuse interface and low-energy states.

A major problem with using SWNTs or NWs is how to guide them in formation of the device structures, i.e., how to put them where you want them. Lieber has studied the directed assembly of NWs by using fluid flow devices in conjunction with surface patterning techniques, and found that it was possible to deposit layers of NWs with different flow directions for sequential steps.^[28] For surface patterning, Lieber used NH₂-terminated surface strips to attract the NWs; in between the NH₂-terminated strips were either methyl-terminated regions or bare regions, to which the NW had less attraction. Flow control was achieved by placing a poly(dimethylsiloxane) (PDMS) mold, in which channel structures had been cut into the mating surface, on top of the flat substrate. Suspensions of the NWs (GaP, InP, or Si) were then passed through the channels. The linear flow rate was about 6.40 mm/sec. In some cases, the

regularity extended over mm length scales, as determined by scanning electron microscopy (SEM).

In a similar fashion, the assembly of individual SWNTs onto substrates was realized by functionalizing substrate surfaces with polar and nonpolar chemical groups in adjacent areas.^[58] SWNTs deposited from a suspension tended to self-assemble into the polar regions of the substrate, with a lateral-directional force, probably as a result of electrostatic interactions, rotating the SWNTs so that they were confined with the polar area of the substrate. At low concentrations of 0.02 mg/mL, only single nanotubes were found at the center of each microscale polar molecular pattern. Although there was room for more than one SWNT on each patterned area, it was postulated that the hydrophobic surface of the first SWNT prevented additional SWNTs from being attracted to the underlying hydrophilic functionality. A problem with using carbon nanotubes is that they are always formed as mixtures of conducting tubes (0 eV bandgaps), semimetallic or "mod-3" tubes (~1 meV bandgaps), and semiconducting tubes (1 eV bandgaps). Most protocols form semiconducting tubes as ~60–70% of the mixture, therefore, one has to hope that the desired tube type would form or assemble in the desired device region. Of course, for a large array, the formation of the desired structure with the proper tube type is statistically prohibitive. Avouris and coworkers at IBM have developed a method of engineering both multiwalled nanotubes (MWNTs) and SWNTs using electrical breakdown methods.^[59] Shells in MWNT can vary between metallic or semiconductor character. Using electrical current in air to rapidly oxidize the outer shell of MWNTs, each shell can be removed in turn because the outer shell is in contact with the electrodes and the inner shells carry little or no current. Shells are removed until arrival at a shell with the desired properties. We recently published a process for selectively reacting the metallic and semimetallic tubes to the exclusion of the semiconducting tubes.^[60] Therefore there is the hope, within a few years, that macroscopic quantities of homogeneous tube types will become available.

While Lieber has shown that it is possible to use the crossed NWs themselves as switches, Stoddart and Heath have synthesized molecular devices that would bridge the gap between the crossed NWs and act as switches in memory and logic devices.^[61] The UCLA/Caltech researchers have synthesized catenanes and rotaxanes that can be switched between states using redox chemistry. For instance, LB films were formed from the catenane, and the monolayers were deposited on polysilicon NWs etched onto a silicon wafer photolithographically. A second set of perpendicular Ti NWs were deposited through a shadow mask, and the $I(V)$ curve was determined. The data, when compared to controls, indicated that the molecules were acting as solid-state molecular switches.

As yet, however, there have been no demonstrations of combining the Stoddart switches with NWs.

The defect-tolerant approach to molecular computing using crossbar technology faces several hurdles before it can be implemented. Large numbers of nano-sized wires are used to obtain defect tolerance. How are each of these wires going to be accessed by the outside world? Multiplexing, the combination of two or more information channels into a common transmission medium, will have to be a major component of the solution to this dilemma. The directed assembly of the NWs and attachment to the multiplexers will be complicated, nonetheless, HP and CalTech researchers are making strides in this arena. Another hurdle is signal strength degradation as it travels along the NWs. Gain is typically introduced into circuits by the use of transistors. However, placing a transistor at each NW junction is an untenable solution because the silicon transistor would be much larger than the NW junction. Likewise, in the absence of a transistor at each cross point in the crossbar array, molecules with very large ON:OFF ratios will be needed. For instance, if a switch with a 10:1 ON:OFF ratio were used, then 10 switches in the OFF state would appear as an ON switch. Hence isolation of the signal via a transistor is essential. Researchers are hoping to insert diodes to sidestep this hurdle.

Additionally, if SWNTs are to be used as crossbars, connection of molecular switches via covalent bonds introduces sp^3 -hybridized carbon atom linkages at each junction, disturbing the electronic nature of the SWNT and possibly rendering the SWNTs useless in the first place. Noncovalent bonding of the device molecule to the SWNT will probably not provide the conductance necessary for the circuit to operate. Therefore continued work is being carried out to devise and construct crossbar architectures that address these challenges.

THE NANOCCELL

This NanoCell architecture involves an approach where molecular switches are not specifically directed to a precise location and the internal topology is generally disordered. A NanoCell is a two-dimensional (three-dimensional models could also be considered) network of self-assembled metallic particles or islands connected by molecules that show reprogrammable (can be turned ON or OFF) switching and/or memory properties. The NanoCell is surrounded by a small number of lithographically defined access leads at the edges of the NanoCell. Unlike typical chip fabrication, the NanoCell is not constructed as a specific logic gate and the internal topology is, for the most part, disordered. Logic is created in the NanoCell by training it postfabrication, similar in some respects to a field-programmable gate array (FPGA). Even if this

process is only a few percent efficient in the use molecular devices, very high logic densities will be possible. Moreover, the NanoCell has the potential to be reprogrammed, thereby creating a real-time dynamic reconfigurable hard-wired logic. The CPU of the computer would be composed of arrays of NanoCells, wherein each NanoCell would have the functionality of many transistors working in concert. A regular array of NanoCells is assumed to manage complexity, and ultimately, a few NanoCells, once programmed, should be capable of programming their neighboring NanoCells through bootstrapping heuristics. Alternatively, arrays could be programmed one NanoCell at a time via an underlying complementary metal oxide semiconductor (CMOS) platform.

Within the fabricated NanoCell, the input and output leads could be repetitively interchanged based on the programming needs of the system, thereby demonstrating the pliability of the architecture. Naturally, issues of gain will eventually have to be addressed through either an underlying CMOS layer or clocked circuits programmed into the NanoCell.^[62] Even if one CMOS transistor were used for gain at the output from each NanoCell, enormous space savings could be attained because a NanoCell could possess the functionality of numerous transistors working in concert to produce a specified logic function. Furthermore, by capitalizing on the NDR properties of the molecular switches, internal gain elements based on NDR/nanoparticle/NDR stacks (Goto pairs) could be efficacious.^[63,64]

The functionality of a NanoCell depends largely on the $I(V)$ characteristics and placement of its molecular switches with respect to the nanoparticles. We have demonstrated NDR with a large ON:OFF ratio from several types of molecular switches based on nitro-containing OPEs (similar to **4** in Fig. 4). We will exploit this switching behavior (rise, then decline in the current with increased voltage) to build logic devices that exhibit negating functionality such as NAND or XOR responses

from these two-terminal devices because two voltage inputs that are high could set the device into an OFF state (right side of the $I(V)$ curve). Switches that do not exhibit the NDR characteristic cannot provide the negating functionality needed for the NanoCell approach.

The object in programming or training a NanoCell is to take a random, fixed NanoCell and turn its switches ON and OFF until it functions as a target logic device. The NanoCell is then trained postfabrication by changing the states, ON or OFF, of the molecular switches by imposing voltages at the surrounding input/output leads.

NANOCELL MEMORIES

The NanoCell approach, as previously described and simulated,^[1,32] is not dependent on placing molecules or nano-sized metallic components in precise orientations or locations. The internal portions are, for the most part, disordered and there is no need to precisely locate any of the switching elements. The nano-sized switches are added in abundance between the micron-sized input/output electrodes, and only a small percentage of them need to assemble in an orientation suitable for switching. The result of the NanoCell architecture is that the patterning challenges of the input/output structures become far less exacting because standard micron-scale lithography can afford the needed address system. Also, fault tolerance is enormous.^[32] However, programming is significantly more challenging than when using ordered ensembles. We describe here an example in which a NanoCell has been successfully assembled and tested. Remarkably, the NanoCell exhibits reproducible switching behavior with excellent peak-to-valley (PVR) ratios,^[65] peak currents in the milliamperage range and reprogrammable memory states that are stable for more than a week with substantial 0:1 bit level ratios.

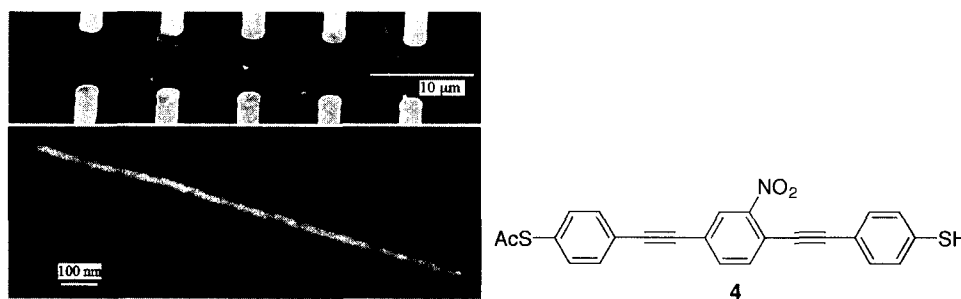


Fig. 4 SEM image of the NanoCell after assembly of the Au nanowires and **4**. The top image shows the five juxtaposed pairs of fabricated leads across the NanoCell, and some Au nanowires are barely visible on the internal rectangle of the discontinuous Au film. The lower image is a higher magnification of the NanoCell's central portion showing the disordered discontinuous Au film with an attached Au nanowire that is affixed via the OPE-dithiol (not observable) derived from **4**.

A NanoCell is a two-dimensional unit of juxtaposed electrodes fabricated atop a Si/SiO₂ substrate. In the embodiment described here, five Au electrode pairs were patterned on opposing sides of the NanoCell (Fig. 4, top). A discontinuous gold film was vapor deposited onto the SiO₂ in the central region (Fig. 4, bottom). The chips were always treated with UV ozone and ethanol-washed immediately prior to use to remove exogenous organics. Electrical measurements of up to 30 V DC confirmed there was ≤ 1 pA conduction across the discontinuous Au film between the five juxtaposed pairs of ~ 5 - μm spaced electrodes. In this study, each juxtaposed pair serves as an independent memory bit address system.

The assembly of molecules and nanowires in the central portion of the NanoCell was then carried out under N₂ to provide a current pathway across the NanoCell. Compounds similar to the mononitro oligo(phenylene ethynylene) (OPE) **4**^[66] have been previously shown to exhibit switching and memory storage effects when fixed between proximal Au probes.^[66,67] Au nanowires (diameter of 30 nm and length of 300–2000 nm, grown in a polycarbonate membrane by electrochemical reduction at 1.2 Coulombs^[68]) were added to a vial containing **4** in CH₂Cl₂. The vial was agitated for 40 min to dissolve the polycarbonate membrane and to form **4**-encapsulated Au nanowires via chemisorption of the thiols to the nanowires.^[69] Because the thiol groups are far more reactive toward Au than thioacetyl groups,^[70] this procedure leaves the latter projecting away from the nanowire surfaces. NH₄OH and ethanol were added, and the vial was agitated for 10 min to remove the acetyl group.^[71] A chip containing 10 NanoCell structures was placed in the vial (active side up), and the vial was further agitated for 27 hr

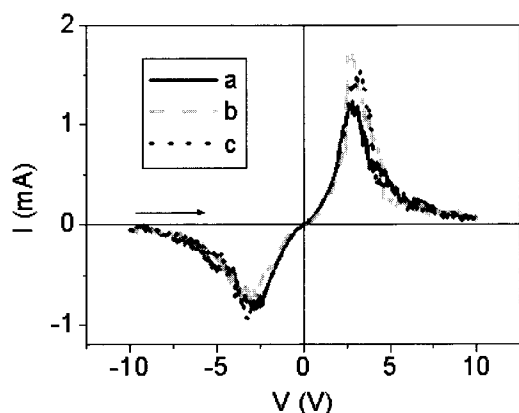


Fig. 5 $I(V)$ characteristics of the NanoCell at 297 K. The curves for a, b, and c are the first, second, and third sweeps, respectively (~ 40 s/scan). The PVRs in c are 23:1 and 32:1 for the negative and positive switching peaks, respectively. The arrow indicates the sweep direction of negative to positive. (View this art in color at www.dekker.com.)

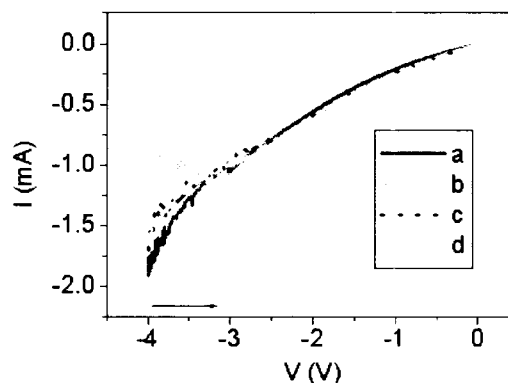


Fig. 6 $I(V)$ characteristics of the NanoCell before (a) and after (b–d) three voltage pulses at -8 V at 297 K. Curves b, c, and d were the first, second, and third scans (after the -8 V reset pulses), respectively. Scans a–d were run at ~ 40 s/scan. The results here are from the same device used to generate the $I(V)$ curve in Fig. 5. (View this art in color at www.dekker.com.)

to permit the nanowires to interlink the discontinuous Au film via the OPEs (Fig. 4). The chip was removed, rinsed with acetone, and gently blown dry with N₂.

The assembled NanoCells were electrically tested on a probe station with a semiconductor parameter analyzer at room temperature (297 K) under vacuum (10^{-5} mm Hg). Typical $I(V)$ characteristics of the NanoCell devices are shown in Fig. 5. Two stable and reproducible switching peaks are observed in a bias range of -10 and $+10$ V. The shape of the $I(V)$ curve is asymmetric because the molecule, as a result of the nitro-group orientation, is asymmetrically oriented, and/or the contacts are likely to be slightly different on each end. After about 300 scans, the switching responses further stabilized in peak voltage; the device showed no degradation to >2000 scans over a 22-hr period of continuous sweeping. Also, after testing, an assembled NanoCell was stored in a capped vial (air) for 2 months with little, if any, signal variations relative to the readings recorded at the initial testing.

A juxtaposed pair of electrodes, as described above, showed little variation in its behavior over several thousand scans. However, there were notable differences when comparing different electrode pairs in that they showed variations in peak current position (occurring typically within a range of 3–15 V), peak current (typically 0.1–1.7 mA), and PVR (typically 5–30). The differences are undoubtedly related to the variations in the conduction pathways of these disordered arrays.

If a voltage sweep is conducted on a NanoCell in a bias range that is up to or not far beyond the peak of the $I(V)$ curve (switching event), a pseudo-linear trace is observed, as shown by curve a (0-state) in Fig. 6. However, if three voltage pulses at -8 V (100 msec width, 104 msec period) are then applied to the same pair of leads, a peak

appears (1-state) in the first scan after the voltage pulses, as shown by curve **b** in Fig. 6. Apparently, the voltage pulses set the system into a new state that is then read by the bias sweep **b**. This is being termed the switch-type memory effect. However, the following scans **c** and **d** produced $I(V)$ responses similar to curve **a**, the scans before the voltage pulses, suggesting that the state set by the voltage pulse was erased after reading it by scan **b**. In other words, the switch-type memory effect has a destructive-read property [as seen with present-day dynamic random-access memory (DRAM)]. A positive voltage pulse, i.e., +8 V, can also set the system into the 1-state. Voltages higher than ± 8 V always worked, but voltages lower than ± 8 V did not reset this particular NanoCell into the 1-state. All of the active NanoCells showed this rewritable behavior, although the magnitudes and set voltages varied between different. Nanocells as described above.

On the same device as shown in Figs. 5 and 6, another type of memory effect was found which has a nondestructive-read, the so-called conductivity-type memory, which operates by the storage of a high- or low-conductivity (σ) state. The difference between the switch-type memory and the conductivity-type memory is based on the voltage-sweep range: -4 to 0 V for the former and -2 to 0 V for the latter. An initially high conductivity state (high σ or 0-state) was observed in a bias range of -2 to 0 V as shown in Fig. 7, curves **a-c**. The high σ state is changed (written) into a low σ state (1-state) upon application of three voltage pulses at -8 V (100 msec width, 104 msec period), as shown by curves **d-f**. The low σ state persists as a stored bit, which is essentially unaffected by successive read sweeps. There is a 400:1 0-state/1-state ratio in current levels between the high and low σ states recorded at -2 V for this NanoCell device. The ratios may vary between different electrode pairs but the ratio here is representative. The highest observed 0:1 ratio was 12,500:1 (198 μ A:16 nA at -2.0 V) for a 5- μ m gap electrode pair, and the lowest observed ratio was 10:1 at the same voltage.

The conductivity-type memory effect is independent of bias sweep directions. Once set into the low σ state upon application of voltage-set (write) pulses, the system holds the low σ state regardless of negative bias sweep from 0 to -2 V or positive bias sweep from 0 to 2 V. Several routes were investigated to erase the stored low σ state (written bit). Voltage pulses at -3 to -4 V (~ 20 pulses at 1 msec pulse width, 10-msec pulse period) reset the memory into the original high σ state (use a voltage pulse that comes near the peak of the switching event, but not far past the peak). Although the overall write, read, erase sequence used in the screening of these devices was rather slow because of the resetting time of the probing electronics, the inherent switching may be on the order of milliseconds, or faster, for each operation if customized elec-

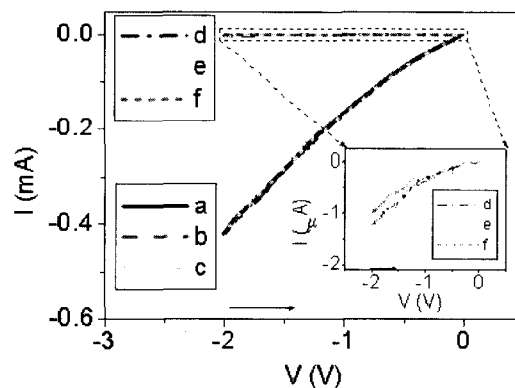


Fig. 7 $I(V)$ characteristics of the NanoCell before (scans a-c) and after (scans d-f) three voltage set-pulses of -8 V at 297 K. The initial high σ state (0-state) is represented by curves a, b, and c, which are the first, second, and third scans before the set-pulse, respectively. The low σ state (1-state) is represented by curves d, e, and f, which are the first, second, and third scans after the -8 V set-pulses, respectively. The inset shows scans d-f in the μ amp range. Scans a-c were run at ~ 40 s/scan. Scans d-f were run at ~ 50 s/scan. This is the same device depicted in Figs. 5 and 6. (View this art in color at www.dekker.com.)

tronics were used. The switch-type and conductivity-type memory effects are shown here in the negative bias regions; however, they apply in the positive bias region as well.

The bit retention time for the switch-type memory is at least 11 days and with $\sim 10\%$ change in the voltage peak position of the curves when compared to the read-tests run seconds after setting the written state; however, there was no decline in the magnitude of the response. The conductivity-type memory persisted for at least 9 days. Over this period, the 0:1 signal magnitudes interestingly increased, although the reset voltages also drifted higher ($\sim 10\%$) over this period. Therefore the two types of memory effects can have much longer retention times, but these are merely the time periods over which they have been tested. Longer durations were not studied. During waiting periods over which these retention times were recorded, the NanoCells had been occasionally exposed to air at 1 atm for periods of up to 30 min, as more samples were moved through the testing chamber. Therefore the stored written states are robust even with short exposure to air. Yields of functioning NanoCells that have been prepared via the protocol described here seemed to be electrode gap-dependent. A NanoCell produced by using the described protocol chip showed 100%, 65%, and 30% yields for devices with 5-, 10-, and 20- μ m spacings between the juxtaposed electrodes, respectively.

The assembled chips were tested in the probe station both in the dark, by covering the observation window with aluminum foil, and in the presence of the room light

with the station's fiber optic observation light projected through the observation window ~ 10 cm above the chip. The same electrical responses were obtained regardless of the lighting, thereby excluding a photoconductive mechanism.

Several control experiments were conducted to investigate the mechanism of action for the NanoCell memories. When the same assembly process was conducted but **4** was not added, all the leads were "open" and no switching behavior was observed over the tested 15 juxtaposed electrodes (5 pairs at 5- μ m spacings, 5 pairs at 10- μ m spacings, and 5 pairs at 20- μ m spacings). Therefore the process is **4**-dependent. When the assembly procedure was conducted but the nanowires were not present (only **4**, polycarbonate devoid of nanowires, CH_2Cl_2 , NH_4OH , and ethanol were added), two out of three juxtaposed 5- μ m spacings showed switching between them; however, the switching effect signal degraded nearly completely after 3–10 scans. Therefore some molecules may have bridged the discontinuous Au film, but the connections were not as abundant or stable. A similar behavior was observed at 10- μ m spacings between the electrodes. When an alkyl system, $\text{AcS}(\text{CH}_2)_{12}\text{SH}$ (**5**),^[72] was substituted for **4** in the standard assembly process, and 30 juxtaposed electrode pairs were studied, 28 showed no device behavior. Interestingly, however, one 5- μ m electrode pair showed the characteristic switching that dissipated after three scans, while a second electrode pair showed reproducible switching behavior but the onset and peak currents occurred at 14 V. Therefore **1** is not unique among molecule types.

Concerning the mechanism underlying the programmable memories, a molecular electronic effect was first considered. Several mechanisms were proposed for molecular electronic switching^[73–75] based upon charging of the molecules, which results in changes in the contiguous structure of the lowest unoccupied molecular orbital (LUMO). This can be accompanied by conformational changes that would modulate the current based on changes in the extended π -overlap. Conversely, as some have pointed out, the so-called "molecular-based" switching might not be an inherently molecular phenomenon, but may result from surface bonding rearrangements that are molecule/metal contact in origin. For example, a sulfur atom changing its hybridization state, or subangstrom shifts between different Au surface atom bonding modes, or molecular tilting.^[76,77] An estimate of the number of molecular junctions between a set of juxtaposed electrode pairs is difficult to gauge; however, based on the size of the nanowires and the Au islands, which can be 0.3–1 μ m long, the number of molecular junctions could be as few as four in a 5- μ m electrode gap. The number of molecules in parallel, per junction, could be as few as 30 or as many as several thousand, based on the nanowire diameters and

lengths. Note that the quantum conductance of each molecule is ~ 0.08 mA/V.

In addition to a molecular electronic process, electrode migration was considered as a cause for the high currents and reset operations that are analogous to filamentary metal memories.^[78–81] To investigate this possibility, the exposed organic material was stripped from a working NanoCell by treating the assembled chip with UV ozone for 10–30 min. Remarkably, the device behavior of the NanoCell remained and often improved. In some cases, the 0:1 bit level ratios for the conductivity memory even increased up to 10^6 :1 (2.53 mA:0.76 nA at -3.0 V). This could suggest that the ozone was not able to reach the small amount of active organic molecules in the key nanodomains that are sandwiched between the nanowires and the Au islands, and that the more exposed leakage routes were destroyed by the ozone. Conversely, it could suggest that, indeed, filamentary metal had grown along the molecules and that these metal filaments were causing the observed switching behavior, with any molecular leakage routes being destroyed by the ozone. It was previously shown by modeling that the NanoCell should exhibit extraordinary defect tolerance because of the abundance of molecules available for switching; furthermore, if one molecule degrades, another could slip into place from the self-assembled monolayers that cover all the surrounding metal surfaces.^[32] Consider also that, at the atomistic level, a molecular change in either conformation or hybridization at the metal–molecule interface, due to voltage changes or charging, could give electronic response characteristics that are analogous to filamentary metals (atoms moving in and out of alignment for current flow), and thereby resemble negative differential resistance-like behavior. In other words, metallic nanofilaments forming during a voltage sweep, then on increasing the voltage, they could exhibit a sudden break, causing a decline in the current.

Additionally, a mechanical motion involving the molecule-covered nanowires was considered. However, it was deemed less likely because of the highly crosslinked nature of the micron-sized matrix.

None of the former data was conclusive enough to exclude either the molecular electronic-based mechanism or the nanofilament mechanism. However, a later finding pointed toward the nanofilament-based mechanism being the dominant or exclusive pathway. As described above, we had never seen the switch-like behavior from the bare chips; they just showed open circuits. As customary to ensure open circuits before we begin the molecule/nanowire assembly, while probing an older chip (4 months storage at room temperature in a FluorowareTM container) from the same lot of chips that was used to prepare the NanoCell described here, we notice switching with magnitudes similar to the levels outlined in Fig. 5. Neither

nanowires nor molecules had been added; it was merely the aged discontinuous Au film vapor-deposited between electrodes. Possibly, while the film had aged, the islands migrated across the gaps sufficiently close together to form nanofilaments upon voltage scanning, and then metal filament breakage occurred at higher voltages, giving responses similar to that shown in Fig. 5. The metallic island migration was not obvious by microscopic analysis of the discontinuous Au films because the resolution needed within the topologically nonplanar arrays cannot be achieved with either SEM or AFM. We carried out $I(V,T)$ (current as a function of voltage and temperature, -2 to 2 V, 280 to 80 K and back to 280 K) measurements to assess the possible conduction mechanism of the high σ conductivity-type memory state on the bare chip. The data suggested "dirty" or modified-metal conduction: metallic conduction with trace impurities. However, in the low conductivity state, only thermionic emission was observed. The same type of $I(V,T)$ measurements on a molecule/nanowire assembled NanoCell showed both a temperature dependence and a non-temperature dependence based on the particular juxtaposed electrode set studied. Albeit confusing, there may be a duality of mechanisms coexisting on the same chip, namely, metallic filaments in the high σ state and molecular phenomena in the low σ state. Further studies are ongoing to better discern this process. Fabrication of NanoCells with more refractory metals such as Pt or Pd will be carried out to further test this point. Additionally, we are currently making chips with a 193 -nm stepper to yield juxtaposed electrode gap spacings of <1 μm with smaller Au-film islands and appropriately sized nanowires, with the hope of attaining higher degrees of consistency between electrode pairs. With the presently sized embodiments, write/erase speeds, and the lack of isolation and fan-out, the NanoCell is not a harbinger for DRAM, flash, or magnetic random access memory (MRAM) replacements. However, it demonstrates the first fabrication of a disordered nanoscale ensemble for high-yielding switching and memory, while mitigating the painstaking task of nanoscale lithography or patterning; thereby furthering the promise of disordered programmable arrays for complex device functionality.

CONCLUSION

Of the three basic approaches to building a molecular computer—QCA, crossbar array, and NanoCell, two approaches appear to be at the forefront of the advancing science—the crossbar array approach and the NanoCell approach. The crossbar approach has seen many advances in the fabrication and assembly of nanowire arrays on surfaces. The NanoCell approach has also been swiftly

advanced, and includes molecules in its assembly, but whether the device properties are due to the molecules themselves or to the formation of metal nanofilaments facilitated by the molecules remains unknown at this time. Work continues on many fronts to advance the idea of using molecules to meet the future computing needs of an ever more complex world. We are amazed and delighted to see this research unfold around us.

ACKNOWLEDGMENTS

We thank the Defense Advanced Research Projects Agency (DARPA) administered by the Office of Naval Research (ONR); the ONR Polymer Program; the US Department of Commerce, National Institute of Standards and Technology; the Army Research Office; NASA; and the Air Force Office of Scientific Research (AFOSR F49620-01-1-0364) for financial support of this work.

REFERENCES

1. Tour, J.M. *Molecular Electronics: Commercial Insights, Chemistry, Devices, Architecture, and Programming*; World Scientific Publishing: New Jersey, 2003.
2. Heath, J.R.; Ratner, M.A. Molecular electronics. *Phys. Today* **2003**, *2003*, 43–49. May.
3. Tour, J.M.; James, D.K. Molecular Electronic Computing Architecture. In *Handbook of Nanoscience, Engineering, and Technology*; Goddard, W.A., III, Brenner, D.W., Lyshevski, S.E., Iafate, G.J., Eds.; CRC Press: Boca Raton, FL, 2002; 4-1–4-28.
4. Ward, M.D. Chemistry and molecular electronics: New molecules as wires, switches, and logic gates. *J. Chem. Educ.* **2001**, *78* (3), 321–328.
5. Tour, J.M. Molecular electronics. Synthesis and testing of components. *Acc. Chem. Res.* **2000**, *33* (11), 791–804.
6. Heath, J.R. Wires, switches, and wiring. A route toward a chemically assembled electronic nanocomputer. *Pure Appl. Chem.* **2000**, *72* (1–2), 11–20.
7. Reed, M.A.; Tour, J.M. Computing with molecules. *Sci. Am.* **2000**, *2000*, 68–75. (June).
8. Overton, R. Molecular electronics will change everything. *Wired* **2000**, *8* (7), 242–251.
9. Heath, J.R.; Kuekes, P.J.; Snider, G.S.; Williams, R.S. A defect-tolerant computer architecture: Opportunities for nanotechnology. *Science* **1998**, *280*, 1716–1721. (12 June).
10. Moore, G.E. Cramming more components onto integrated circuits. *Electronics* **1965**, *38* (8). Avail-

- able on the web. <http://www.intel.com/research/silicon/moorespaper.pdf> (accessed September 2002).
11. Intel press release. <http://www.intel.com/pressroom/archive/releases/20011017man.htm> (accessed September 2002).
 12. Intel press release. <http://www.intel.com/pressroom/archive/releases/20020813tech.htm> (accessed September 2002).
 13. International Technology Roadmap for Semiconductors web pages. <http://public.itrs.net/Files/2001ITRS/PIDS.pdf> (accessed September 2002).
 14. Wang, K.L. Issues of nanoelectronics: A possible roadmap. *J. Nanosci. Nanotechnol.* **2002**, *2* (3–4), 235–266.
 15. Service, R.F. Molecules get wired. *Science* **2001**, *294*, 2442–2443. (21 December).
 16. Carroll, R.L.; Gorman, C.B. The genesis of molecular electronics. *Angew. Chem., Int. Ed.* **2002**, *41*, 4378–4400.
 17. Goldhaber-Gordan, D.; Montemerlo, M.S.; Love, J.C.; Opitek, G.J.; Ellenbogen, J.C. Overview of nanoelectronic devices. *Proc. IEEE* **1997**, *85* (4), 521–540.
 18. Lent, C.S.; Tougaw, P.D. A device architecture for computing with quantum dots. *Proc. IEEE* **1997**, *85* (4), 541.
 19. Tougaw, P.D.; Lent, C.S.; Porod, W. Bistable saturation in coupled quantum-dot cells. *J. Appl. Phys.* **1993**, *74*, 3558.
 20. Tour, J.M.; Kozak, M.; Seminario, J.M. Molecular scale electronics: A synthetic/computational approach to digital computing. *J. Am. Chem. Soc.* **1998**, *120*, 8486.
 21. Heath, J.R. Wires, switches, and wiring: A route toward a chemically assembled electronic nanocomputer. *Pure Appl. Chem.* **2000**, *72*, 11.
 22. Goldstein, S.C.; Budiu, M. Nanofabrics: Spatial Computing Using Molecular Electronics. In *Proc. 28th Annual Int. Symp. On Comp. Arch.*; 2001. June.
 23. Hu, J.; Odom, T.W.; Lieber, C.M. Chemistry and physics in one dimension: Synthesis and properties of nanowires and nanotubes. *Acc. Chem. Res.* **1999**, *32*, 435.
 24. Rueckes, T.; Kim, K.; Joselevich, E.; Tseng, G.Y.; Cheung, C.-L.; Lieber, C.M. Carbon nanotubes-based nonvolatile random access memory for molecular computing. *Science* **2000**, *289*, 94.
 25. Ouyang, M.; Huang, J.-L.; Cheung, C.-L.; Lieber, C.M. Atomically resolved single-walled carbon nanotubes intramolecular junctions. *Science* **2001**, *291*, 97.
 26. Bozovic, D.; Bockrath, M.; Hafner, J.H.; Lieber, C.M.; Park, H.; Tinkham, M. Electronic properties of mechanically induced kinks in single-walled carbon nanotubes. *Appl. Phys. Lett.* **2001**, *78*, 3693.
 27. Star, A.; Stoddart, J.F.; Steuerman, D.; Diehl, M.; Boukai, A.; Wong, E.W.; Yang, X.; Chung, S.-W.; Choi, H.; Heath, C.M. Preparation and properties of polymer-wrapped single-walled carbon nanotubes. *Angew. Chem., Int. Ed. Engl.* **2001**, *40*, 1721.
 28. Huang, Y.; Duan, X.; Wei, Q.; Lieber, C.M. Directed assembly of one-dimensional nanostructures into functional networks. *Science* **2001**, *291*, 630.
 29. Gudiksen, M.S.; Wang, J.; Lieber, C.M. Synthetic control of the diameter and length of single crystal semiconductor nanowires. *J. Phys. Chem., B* **2001**, *105*, 4062.
 30. Cui, Y.; Lieber, C.M. Functional nanoscale electronic devices assembled using silicon nanowire building blocks. *Science* **2001**, *291*, 851.
 31. Chung, S.-W.; Yu, J.-Y.; Heath, J.R. Silicon nanowire devices. *Appl. Phys. Lett.* **2000**, *76*, 2068.
 32. Tour, J.M.; Van Zandt, W.L.; Husband, C.P.; Husband, S.M.; Wilson, L.S.; Franzon, P.D.; Nakanishi, D.P. Nanocell logic gates for molecular computing. *IEEE Trans. Nanotechnol.* **2002**, *1*, 100.
 33. McEuen, P.L. Artificial atoms: New boxes for electrons. *Science* **1997**, *278*, 1729.
 34. Stewart, D.R.; Sprinzak, D.; Marcus, C.M.; Duruoz, C.I.; Harris, J.S., Jr. Correlations between ground state and excited state spectra of a quantum dot. *Science* **1997**, *278*, 1784.
 35. Rajeshwar, K.; de Tacconi, N.R.; Chenthamarashan, C.R. Semiconductor-based composite materials: Preparation, properties, and performance. *Chem. Mater.* **2001**, *13*, 2765.
 36. Sear, R.P.; Chung, S.-W.; Markovich, G.; Gelbart, W.M.; Heath, J.R. Spontaneous patterning of quantum dots at the air–water interface. *Phys. Rev., E* **1999**, *59*, 6255.
 37. Markovich, G.; Collier, C.P.; Henrichs, S.E.; Remacle, F.; Levine, R.D.; Heath, J.R. Architectonic quantum dot solids. *Acc. Chem. Res.* **1999**, *32*, 415.
 38. Weitz, I.S.; Sample, J.L.; Ries, R.; Spain, E.M.; Heath, J.R. Josephson coupled quantum dot artificial solids. *J. Phys. Chem., B* **2000**, *104*, 4288.
 39. Snider, G.L.; Orlov, A.O.; Amlani, I.; Zuo, X.; Bernstein, G.H.; Lent, C.S.; Merz, J.L.; Porod, W.J. Quantum dot cellular automata: Review and recent experiments (invited). *Appl. Phys.* **1999**, *85*, 4283.
 40. Snider, G.L.; Orlov, A.O.; Amlani, I.; Bernstein, G.H.; Lent, C.S.; Merz, J.L.; Porod, W. Quantum-dot cellular automata: Line and majority logic gate. *Jpn. J. Appl. Phys., Part I: Reg. Pap. Short Notes* **1999**, *38*, 7227.

41. Toth, G.; Lent, C.S. Quasiadiabatic switching for metal-island quantum-dot cellular automata. *J. Appl. Phys.* **1999**, *85*, 2977.
42. Orlov, A.O.; Amlani, I.; Toth, G.; Lent, C.S.; Bernstein, G.H.; Snider, G.L. Experimental demonstration of a binary wire for quantum-dot cellular automata. *Appl. Phys. Lett.* **1999**, *74*, 2875.
43. Lent, C.S. Molecular electronics: Bypassing the transistor paradigm. *Science* **2000**, *288*, 1597.
44. Bandyopadhyay, S. Debate response: What can replace the transistor paradigm? *Science* **2000**, *288*, 29 June.
45. Huang, Y.; Duan, X.; Cui, Y.; Lauhon, L.J.; Kim, K.-H.; Lieber, C.M. Logic gates and computations from assembled nanowire building blocks. *Science* **2001**, *294*, 1313.
46. Luo, Y.; Collier, C.P.; Jeppsen, J.O.; Nielsen, K.A.; Delonno, E.; Ho, G.; Perkins, J.; Tseng, H.-R.; Yamamoto, T.; Stoddart, J.F.; Heath, J.R. Two-dimensional molecular electronics circuits. *Chem-PhysChem* **2002**, *3*, 519–525.
47. Whang, D.; Jin, S.; Wu, Y.; Lieber, C.M. Large-scale hierarchical organization of arrays for integrated nanosystems. *Nano Lett.* **2003**, *3*, 1255–1259.
48. Yu, J.-Y.; Chung, S.-W.; Heath, J.R. Silicon nanowires: Preparation, devices fabrication, and transport properties. *J. Phys. Chem., B* **2000**, *104*, 11864.
49. Melosh, N.A.; Boukai, A.; Diana, F.; Geradot, B.; Badolato, A.; Petrof, P.M.; Heath, J.R. Ultra-high density nanowire lattices and circuits. *Science* **2003**, *300*, 112–115.
50. Ausman, K.D.; O'Connell, J.J.; Boul, P.; Ericson, L.M.; Casavant, M.J.; Walters, D.W.; Huffman, C.; Saini, R.; Wang, Y.; Haroz, E.; Billups, E.W.; Smalley, R.E. In *Roping and Wrapping Carbon Nanotubes*, Proceedings of XVth International Winterschool on Electronic Properties of Novel Materials Euroconference, Kirchberg, Tirol, Austria, 2000.
51. Bahr, J.L.; Mickelson, E.T.; Bronikowski, J.J.; Smalley, R.E.; Tour, J.M. Dissolution of small diameter single-wall carbon nanotubes in organic solvents? *Chem. Commun.* **2001**, *2001*, 193.
52. Mickelson, E.T.; Chiang, I.W.; Zimmerman, J.L.; Boul, P.J.; Lozano, J.; Liu, J.; Smalley, R.E.; Hauge, R.H.; Margrave, J.L. Solvation of fluorinated single-wall carbon nanotubes in alcohol solvents. *J. Phys. Chem., B* **1999**, *103*, 4318.
53. Chen, J.; Rao, A.M.; Lyuksyutov, S.; Itkis, M.E.; Hamon, M.A.; Hu, H.; Cohn, R.W.; Eklund, P.C.; Colbert, D.T.; Smalley, R.E.; Haddon, R.C. Dissolution of full-length single-walled carbon nanotubes. *J. Phys. Chem., B* **2001**, *105*, 2525.
54. Bahr, J.L.; Yang, J.; Kosynkin, D.V.; Bronikowski, M.J.; Smalley, R.E.; Tour, J.M. Functionalization of carbon nanotubes by electrochemical reduction of aryl diazonium salts: A bucky paper electrode. *J. Am. Chem. Soc.* **2001**, *123*, 6536.
55. Bahr, J.L.; Tour, J.M. Highly functionalized carbon nanotubes using in situ generated diazonium compounds. *Chem. Mater.* **2001**, *13*, 3823.
56. Bahr, J.L.; Tour, J.M. Covalent chemistry of single-wall carbon nanotubes. *J. Mater. Chem.* **2002**, *12*, 1952–1958.
57. O'Connell, M.J.; Boul, P.; Ericson, L.M.; Huffman, C.; Wang, Y.; Haroz, E.; Kuper, C.; Tour, J.; Ausman, K.D.; Smalley, R.E. Reversible water-solubilization of single-walled carbon nanotubes by polymer wrapping. *Chem. Phys. Lett.* **2001**, *342*, 265.
58. Rao, S.G.; Huang, L.; Setyawan, W.; Hong, S. Large-scale assembly of carbon nanotubes. *Nature* **2003**, *425*, 36–37.
59. Collins, P.G.; Arnold, M.S.; Avouris, P. Engineering carbon nanotubes and nanotubes circuits using electrical breakdown. *Science* **2001**, *292*, 706.
60. Strano, M.S.; Dyke, C.A.; Usrey, M.L.; Barone, P.W.; Allen, M.J.; Shan, H.; Kittrell, C.; Hauge, R.H.; Tour, J.M.; Smalley, R.E. Electronic structure control of single walled carbon nanotube functionalization. *Science* **2003**, *301*, 1519–1522.
61. Pease, A.R.; Jeppesen, J.O.; Stoddart, J.F.; Luo, Y.; Collier, C.P.; Heath, J.R. Switching devices based on interlocked molecules. *Acc. Chem. Res.* **2001**, *34*, 433.
62. Nackashi, D.P.; Franzon, P.D. Moletronics: A circuit design perspective. *Proc. SPIE* **2000**, *4236*, 80.
63. Goto, E. The parametron: A digital computing element which utilizes parametric oscillation. *Proc. IRE* **1959**, *47*, 1304.
64. Ellenbogen, J.C.; Love, J.C. Architectures for molecular electronic computers: 1. Logic structures and an adder designed from molecular electronic diodes. *Proc. IEEE* **2000**, *88*, 386.
65. Chen, J.; Reed, M.A.; Rawlett, A.M.; Tour, J.M. Large on-off ratios and negative differential resistance in a molecular electronic device. *Science* **1999**, *286*, 1550.
66. Yao, Y.; Flatt, A.K.; Maya, F.; Tour, J.M. submitted for review.
67. Chen, J.; Wang, W.; Reed, M.A.; Rawlett, A.M.; Price, D.W.; Tour, J.M. Room-temperature negative differential resistance in nanoscale molecular junctions. *Appl. Phys. Lett.* **2000**, *77*, 1224.
68. Mbindyo, J.K.N.; Mallouk, T.E.; Mattzela, J.B.; Kratochvilova, I.; Razavi, B.; Jackson, T.N.; Mayer, T.S. Template synthesis of metal nanowires contain-

- ing monolayer molecular junctions. *J. Am. Chem. Soc.* **2002**, *124*, 4020.
69. Martin, B.R.; St. Angelo, S.K.; Mallouk, T.E. Interactions between suspended nanowires and patterned surfaces. *Adv. Funct. Mater.* **2002**, *12*, 759.
 70. Tour, J.M.; Jones, L., II; Pearson, D.L.; Lamba, J.S.; Burgin, T.P.; Whitesides, G.W.; Allara, D.L.; Parikh, A.N.; Atre, S. Self-assembled monolayers and multilayers of conjugated thiols, *a,w*-dithiols, and thioacetyl-containing adsorbates. Understanding attachments between potential molecular wires and gold surfaces. *J. Am. Chem. Soc.* **1995**, *117*, 9529.
 71. Cai, L.; Yao, Y.; Yang, J.; Price, D.W., Jr.; Tour, J.M. Chemical and potential assisted assembly of thioacetyl-terminated oligo(phenylene ethynylene)s on gold surfaces. *Chem. Mater.* **2002**, *14*, 2905.
 72. Bain, C.D.; Troughton, E.B.; Tao, Y.-T.; Evall, J.; Whitesides, G.M.; Nuzzo, R.G. Formation of monolayer films by the spontaneous assembly of organic thiols from solution onto gold. *J. Am. Chem. Soc.* **1989**, *111*, 321.
 73. Seminario, J.M.; Derosa, P.A.; Bastos, J.L. Theoretical interpretation of switching in experiments with single molecules. *J. Am. Chem. Soc.* **2002**, *124*, 10266–10267.
 74. Cornil, J.; Karzazi, Y.; Bredas, J.L. Negative differential resistance in phenylene ethynylene oligomers. *J. Am. Chem. Soc.* **2002**, *124*, 3516–3517.
 75. Fan, F.-R.R.; Yang, J.; Cai, L.; Price, D.W.; Dirk, S.M.; Kosynkin, D.; Yao, Y.; Rawlett, A.M.; Tour, J.M.; Bard, A.J. Charge transport through self-assembled monolayers of compounds of interest in molecular electronics. *J. Am. Chem. Soc.* **2002**, *124*, 5550.
 76. Donhauser, Z.J.; Mantooth, B.A.; Kelly, K.F.; Bumm, L.A.; Monnell, J.D.; Stapleton, J.J.; Price, D.W., Jr.; Rawlett, A.M.; Allara, D.L.; Tour, J.M.; Weiss, P.S. Conductance switching in single molecules through conformational changes. *Science* **2001**, *292*, 2303.
 77. Rawlett, A.M.; Hopson, T.J.; Nagahara, L.A.; Tsui, R.K.; Ramachandran, G.K.; Lindsay, S.M. Electrical measurement of a dithiolated electronic molecule via conducting atomic force microscopy. *Appl. Phys. Lett.* **2002**, *81*, 3043.
 78. Buckley, W.D. Process of Making a Filament-Type Memory Semiconductor Device. US Patent 3,980,505, September 14, 1976.
 79. Chesnys, A.; Karpinskas, S.-A.; Urbelis, A. Current–voltage characteristic and parameters of the current filament region of an amorphous gallium telluride–crystalline silicon barrier register structure. *Tech. Phys. (Translation of Zhurnal Tekhnicheskoi Fiziki)* **2002**, *47*, 58.
 80. Simmons, J.G.; Verderber, R.R. Conduction and reversible memory phenomena in thin insulating films. *Proc. R. Soc. Lond., A Math. Phys. Sci.* **1967**, *301*, 77.
 81. Thurstans, R.E.; Oxley, D.P. The electroformed metal–insulator–metal structure: A comprehensive model. *J. Phys., D, Appl. Phys.* **2002**, *35*, 802.

Molecular Electronics: Analysis and Design of Switchable and Programmable Devices Using Ab Initio Methods

M

Pedro A. Derosa
Vandana R. Tarigopula
Jorge M. Seminario

University of South Carolina, Columbia, South Carolina, U.S.A.

INTRODUCTION

The process of scaling down modern semiconductor devices faces serious obstacles, mainly because of device-addressing problems. Practical limitations in fabrication and extraordinary increases in production costs will also be limiting issues. Small molecules, easy to tailor, are the natural candidates to complement semiconductor components in the generation of hybrid circuits, giving birth to a completely new area of electronics, molecular electronics or Moletronics. Experimental characterization is highly challenging, and only a few experiments in which only one molecule is addressed have been performed,^[1–3] because technical possibilities of success become greatly diminished with the minuscule system size. Fortunately, modern quantum-chemistry-theoretical-based computational techniques are able to accurately solve molecular systems using precise natural laws, and this ability increases substantially as systems become smaller.

This review investigates recent results on molecular systems that can potentially be used as electronic devices. It is particularly focused on molecules that can behave as controllable switches (a characteristic that allows programmability) and the theoretical techniques available for their analysis, design, and simulation. Switching has been studied before but not with the purpose of programmability. For instance, Collier et al.^[4] studied switching based on the translation degrees of freedom of mechanical bonds, and more elaborate molecular circuits have been proposed, such as a flash-like, single-electron memory cell;^[5] however, they are hardly useful for a paradigm of a chemically random assembly of molecules governed mostly by thermodynamic and some kinetic controls where programmability features at the level of devices are of paramount importance.^[6] The studies cited focused on electrical features and their correlation to conformational properties, the metallic contacts characterization, and the metal–molecule interface. Determining the correlation between transport characteristics and molecular electronic and geometrical configuration is particularly important, because this correlation provides a mechanism to control electron transport in molecular and atomistic systems.

THEORY-BASED APPROACHES FOR THE CALCULATION OF MOLECULAR SYSTEMS

In this section, we describe several approaches used for the analysis of molecular electronic systems. We briefly summarize the common methods and tools that allow researchers to theoretically characterize, design, model, and simulate moletronics systems.

Methods

The main methods used in moletronics are borrowed from quantum chemistry and solid state physics, and in particular, density functional theory (DFT) is used for discrete and extended systems as well as their interconnection using the Green function (GF) scattering technique.

Ab initio density functional theory for molecules

In the study of molecules presenting highly nonlinear features, the Kohn–Sham molecular orbitals (MOs) can provide a qualitative picture of the molecular mechanisms of operation and how they are affected by its boundaries. The solution of the Schrödinger equation for the system under consideration should provide an exact solution if an exact Hamiltonian is used; however, such a solution is very tedious because of the massive computational resources it demands. One way to bypass this difficulty is to use DFT where the solution of the wave function replaces the solution of the electron density. Electron density is obtained from auxiliary systems of noninteracting electrons whose total electron density is forced to be identical to the electron density of the interacting or real electrons. The advantage of this approach is that the system of noninteracting electrons can be easily separated into individual one-electron MOs, also called Kohn–Sham MOs. Each MO is associated to individual energies that can be roughly correlated with the excitation energies of the molecular system. The shape and energy of these MOs have been widely used in the qualitative explanation of electron transport (*vide infra*) in single molecules. However, the use of MOs is only for qualitative purposes. MOs

from DFT, or any other theory, can never precisely describe the exact wave function of a real system because real electrons are not independent particles. For most practical purposes, DFT calculations using functionals based on ab initio approaches and beyond the local approximation have been very successful in describing the main features of molecular systems with acceptable precision. This fact has converted DFT into the main computational tool in modern quantum chemistry, and into the preferred tool for the study of molecular electronics.

Integration of several tools is often necessary. Single molecules are first treated by using ab initio density functional theory (DFT) as implemented in the Gaussian-98 program,^[7] or its recent version, Gaussian-03.^[8] The molecular geometry is optimized with no constraint (except for special cases) until all eigenvalues of the Hessian matrix are positive, ensuring that the molecule is in a minimum energy configuration. The Becke-3 Perdew-Wang 91 (B3PW91) procedure, which consists of the Becke3 hybrid exchange functional combined with the generalized gradient approximation (GGA) Perdew-Wang-91 correlation,^[9-11] is used in combination with different basis set selected according to the system. In general, systems with metallic atoms are treated using LANL2DZ,^[12-14] an effective core potential and basis set. The LANL2DZ basis set explicitly considers all the valence electrons, rather than just those in last electronic shell. Core electrons are treated in an approximate way by using pseudopotentials that include relativistic effects allowing an excellent description of heavy metal atoms.^[15] The level of theory B3PW91/LANL2DZ has been used in several works, and further details can be found in Refs. [16-20] In some cases, where no metallic atoms are present, 6-31G* basis or higher sets are also used.

Atomic charges are estimated by using Mulliken population analysis, which associates charge to each atom by integrating the basis functions assigned to each individual atom and assigning equally to each atom of each pair their overlap contributions. Mulliken charges can only provide complementary information. Mulliken values do not support conclusions, but provide a qualitative picture of the quantitative results; atomic charges are not expectation values but mere indicators highly dependent on the method and basis set used to solve the Schrödinger equation. Nevertheless, if properly balanced basis sets are used, Mulliken analysis can provide an excellent tool for qualitative analysis and interpretations of charge transfer effects.

Green functions

I - V characteristics are calculated by combining the DFT results with a Green function technique originally

designed for mesoscopic systems.^[21-27] This approach considered the molecule attached to infinite contacts that modify its electronic structure, the new modified electronic structure is, in turn, used to calculate the system (molecule plus contacts) I - V characteristic. The electron transport properties of a molecule under a bias voltage V are described by its Green function, G_M , obtained from the molecular Hamiltonian, $H(V)$, which is obtained by reoptimizing the molecular electronic structure under the presence of an external electrical field. The transport of electrons takes place through the MOs, which are affected by interaction with the contacts and with the applied voltage.^[28,29] MOs may be affected by an applied external field or by the charge state on the molecule. For instance, delocalized MOs can become localized, or vice versa, when the molecule traps one electron. The molecule is in a conducting state (low impedance) if delocalized MOs are available in the energy range for which one contact has occupied levels and the other unoccupied ones. The molecule is in a nonconducting state (high impedance) if those MOs are localized, i.e., they do not connect both ends of the molecule to the contacts. When the molecule is open shell (electrons are unpaired), both α and β spin states are considered to obtain the molecular I - V characteristics.

The Green function is obtained from Eq. 1,

$$G_M = [E\mathbf{1} - H_{MM} - H_{M1}g_1H_{1M} - H_{M2}g_2H_{2M}]^{-1} \quad (1)$$

where subscripts i and j in H_{ij} (submatrices of H in Eq. 2) refer to the molecule (M), contact 1 (1), and contact 2 (2).

$$H = \begin{bmatrix} H_{11} & H_{1M} & H_{12} \\ H_{M1} & H_{MM} & H_{M2} \\ H_{21} & H_{2M} & H_{22} \end{bmatrix} \quad (2)$$

Information about the macroscopic nature of the contacts is introduced by a Green function for a semi-infinite medium (g_i), whereby s , p , and d contributions^[30] to the density of states (DOS) of the Au metal are explicitly considered. Derosa and Seminario represented the metallic contacts by assuming a density of states with s , p , and d contributions, but energy-independent. This approach, although not perfect, was an improvement compared to available applications (see, for example, Refs. [31] and [32]) that considered only an s -character, also energy-independent DOS. These descriptions of the contacts were finally improved by calculating at DFT level, the DOS of a metallic system extended using periodic boundary conditions (vide infra).^[33]

From the molecular Green function, the transmission function (TF), which is the sum of the transmission probabilities of all channels (MOs) available at energy E , is obtained, as described by Eq. 3, and the current is

obtained from Eq. 4,^[25] where f_i is the Fermi–Dirac function for a voltage V_i at contact i ($V = V_2 - V_1$).

$$T(E, V) = \text{trace}[F_1(V)G_M(E, V)F_2(V)G_M^+(E, V)] \quad (3)$$

$$I(V) = \frac{2e}{h} \int_{-\infty}^{\infty} dE T(E, V)[f_1(E, V_1) - f_2(E, V_2)] \quad (4)$$

As a first approximation, the experimental work function of the metal making the contact, -5.31 eV for Au, was used for some calculations of neutral systems.^[34] In previous works,^[29,35] this value was also used to study the anions. An average of the highest occupied molecular orbital (HOMO)–lowest unoccupied molecular orbital (LUMO) midgap energy from several neutral organic molecules attached to Au atoms yielded an energy of -5.2 eV, which is in excellent agreement with the experimental work function of Au. However, the midgap average energy for the single anions and dianions is -1.55 and 0.88 eV, respectively. The HOMO and LUMO energies obtained from DFT is an approximation (with a minus sign) of the ionization potential and the electron affinity of the molecule, respectively. Thus it is not surprising that both energies are higher (in absolute value) for anions than for neutral; however, this situation will not reflect the position of the HOMO–LUMO gap (HLG) relative to the metal Fermi level. This shift in position of the HLG, which was not considered in our original model, was later accounted for to estimate the electrical characteristics of the anion and dianion.

The density of states (DOS) is also obtained from the Green function formalism,^[25] as shown by Eq. 5.

$$\text{DOS}(E, V) = \text{trace}[(i[G_M(E, V) - G_M^+(E, V)])] \quad (5)$$

A full description of this procedure is published elsewhere,^[29] where more detailed information and useful references can be found.

Ab initio calculations for crystals and extended systems

CRYSTAL-98^[36] is used to study the metallic contacts within the linear combination of atomic orbital approximations. Macroscopic properties (band structure, DOS, etc.) are obtained by reproducing the unit cell to infinite, following the rules of the corresponding crystal structure. CRYSTAL-98 is a suite of programs that can calculate the electronic structure, total energy, and wave functions, including its band structure, density of states, electron charge distribution, electron momentum distribution, Compton profile, Mulliken charges, electrostatic potentials, and X-ray structure factors^[37] by using a DFT approach for periodic systems.^[38] The basis set expands the

Bloch functions built $\Psi_k(r)$ by using s , p and d Gaussian functions, as can be observed in Eq. 6.

$$\Psi_k(r+g) = \Psi_k(r) \exp(ik \cdot g) \quad (6)$$

The electron density of the N -electron system^[38] is given by Eq. 7, where θ is the Heaviside step function, and $\varepsilon_i(k)$ is the eigenvalue of the i th crystalline orbital. ε_F is the Fermi energy.

$$\rho(r) = \int_{\text{Brillouin zone}} dk \sum_i^{\text{Occupied bands}} |\varphi_{ki}(r)|^2 \theta(\varepsilon_F - \varepsilon_i(k)) \quad (7)$$

The Bloch functions described above are used to expand the crystalline orbitals that are linear combinations of atom-centered Gaussian-type functions, $\varphi_{ki}(r)$. The coefficients for the linear expansion are adjusted such that $\varphi_{ki}(r)$ are the solutions of the one-particle equations (Eq. 8),

$$\hat{h}_i \varphi_{ki}(r) = \varepsilon_{ki} \varphi_{ki}(r) \quad (8)$$

where \hat{h} is the single particle Hamiltonian operator shown in Eq. 9, which includes the contributions from kinetic, external potential, Coulomb, and exchange-correlation potential operators, respectively.

$$\hat{h}_{KS} = \hat{t} + \hat{v} + \hat{J}[\rho(r)] + \hat{v}_{xc}(r) \quad (9)$$

The exchange-correlation operator is expanded in a basis of Gaussian-type functions, as seen in Eq. 10, where g is the cell (vectors) containing the j th basis function centered at the atomic position s_j .

$$v_{xc}^{i,jg} = \int dr \chi_i(r - s_i) v_{xc}(r) \chi_j(r - s_j - g) \quad (10)$$

This integral is solved analytically because the exchange-correlation potential is expanded with Gaussian auxiliary basis functions, $G_a(r)$; thus the integral is transformed into a linear combination of integrals of the form given by Eq. 11, which is solved only once then stored for subsequent use.

$$g_a^{i,jg} = \int dr \chi_i(r - s_i) G_a(r) \chi_j(r - s_j - g) \quad (11)$$

At each step, the coefficients are recalculated so the exchange-correlation potential fits the analytic form that depends on the charge density. In addition, the exchange potential is calculated by using the Hartree–Fock prescription, yielding a fully nonlocal functional, and when combined with the PW91 correlation functional, yields one of the so-called hybrid functionals. We use the hybrid functional approach with the gradient-corrected PW91 functionals^[10] for the correlation potential together with the SBKJC VDZ ECP (8s 8p 6d)/[4s 4p 3d]^[39,40] ECP and

basis set. The Au bulk is treated as an infinite periodic system with face centered cubic (fcc) crystalline structure, thus realistic density of states for a metal is obtained to construct the Green function for the contacts.

Tools for Molecular Calculations

This section describes tools employing the ab initio based techniques described in the last section.

Nonlinear circuit solver

Recently, an algorithm able to calculate the current-voltage characteristics of combinations of single molecules has been developed.^[6] In general, the algorithm is able to determine all possible solutions of an electrical circuit with devices having highly nonlinear characteristics, such as negative differential resistance or resonant tunneling. The solutions to these circuits are multivalued functions, which cannot be obtained with the traditional programs to solve electrical circuits.

The DFT, GF, and their combination, DFT-GF, provide quantitative information needed for the design and testing of programmable molecular circuits. Once the molecule is characterized, the I - V curve is used as the device characteristic. The analysis is systematically applied branch by branch, such as sweeping a suitable range of currents and determining all compatible voltages from the I - V of the device in the branch, then all possible voltage drops in the branch (each configuring one possible state) are determined by combining voltage drops on each device.

The method does not scale very well at this stage of development; the scaling depends on the number of solutions for each branch and the number of branches. However, this method can systematically solve any combination of molecular devices irrespective of the particular I - V characteristic and provide all possible solutions; this feature is not available in any current software for circuit solution.

Interpretation using molecular orbitals

A powerful technique for the analysis of molecular circuits, i.e., the use of the quantum chemistry techniques, including MOs and their energies, as indexes for the estimation of electron transport was recently introduced into the field of molecular electronics.^[28,29,35] Delocalized MOs are expected to provide a more suitable path for electron transport, because they simultaneously connect the molecule to the metallic atoms at both ends. Thus analyzing MO qualitative predictions on how easy it is for a molecule to conduct electrons can be inferred. MOs can

explain, without calculating the currents, the behavior of several oligomers and the effect of their substituents. Furthermore, using MOs can identify groups in the molecule responsible for a particular observed behavior, information that can be used in the design of new molecular devices; for instance, using them to explain the electrical behavior of π -conjugated organic molecules resembling a resonant tunneling diode.^[28]

Fig. 1 shows some of the conformations studied using DFT. The HOMO-LUMO gap (HLG) energy for planar and rotated π -conjugated organic molecules is reported in this figure at the bottom of the corresponding case. Calculations were extended to include gold clusters at both ends of these molecules. This work determined the mechanism of operation of the molecular resonant tunneling diode (MRTD),^[28] where the electron transport occurs through the lowest unoccupied molecular orbital and so the shape of the LUMO determines the transport characteristics of the molecule presenting negative differential resistance (NDR). These analyses explained qualitatively^[28] the peak found experimentally at 2.1 V at a temperature of 60 K,^[41] and explained the observed reduction in peak voltage as temperature increases. One of the key findings of this research is that Seminario and Derosa analyzed single molecules providing the effect of amplification.^[42] Subsequently, electronic transport was fully investigated, and it was concluded that the molecular chemical potential determines the conduction barrier, and that the molecule becomes charged as the external potential increases.^[33] In earlier studies, Seminario et al.^[28] were able to explain the nonlinear character of the current-voltage (I - V) characteristic of the molecule and its temperature dependence.

The effect of the bias voltage on the electron transmission of a molecular device, negative differential resistance

A bias voltage applied to a molecule attached to metallic contacts has two effects. On one hand, it changes the Fermi level in the contacts; electrons lower their energy on the positive electrode and increase their energy in the negative electrode and, as a result, electrons are available on the negatively polarized contact at energies for which empty states are available in the positive electrode. If these electrons find a delocalized molecular level that connects both ends, electron transport occurs. On the other hand, the electric field created across the molecule affects MOs and can change not only their energy, but also the degree of localization; thus a MO that is localized at zero voltage may become delocalized by the electric field and vice versa.

One of the most interesting effects observed in some of the molecules studied is the negative differential

	(a)	(b)	(c)	(d)
Q = 0				
HLG	3.70	4.68	3.48	4.01
τ	0°	90°	0.4°/2.8°	89.6°/89.7°
Q = -1				
HLG	1.09/1.13	0.53/0.80	1.25/1.17	0.78 ^a
τ	0°	90°	0.2°/1.9°	
Q = -2				
HLG	1.30/1.59	0.10 ^a	0.80/1.02	0.36 ^a
τ	0°		0.1°/1.7°	

Fig. 1 LUMO plots, HLG energies (in eV), and torsion angles (τ) for the optimized neutral and for the vertical and adiabatic structures of the anions. Only one LUMO is shown if the vertical and adiabatic shapes are similar. (See Ref. [28] for further details.)^a Only vertical HLG is shown because the structure becomes planar during the optimization. (View this art in color at www.dekker.com.)

resistance (NDR). NDR means negative slope in the I - V curve. NDR can occur for two main reasons. One is charge or conformational-induced NDR; at a given voltage, the molecule can become charged, or change its structure such that current decreases after the voltage is increased. The other, intrinsic NDR, is produced by a change in the molecular electronic structure that reduces the electron transport capabilities of the MOs involved in

conduction. Intrinsic NDR cannot be predicted if a bias voltage is not included in the calculations and cannot be predicted if the correct chemistry of the molecule is not considered. The current is calculated via Eq. 4 (in the section "Green functions"), where T , the transmission function, would only depend on E if a field is not applied to the molecule to account for the effect of the voltage. In such a case, V only enters in the Fermi

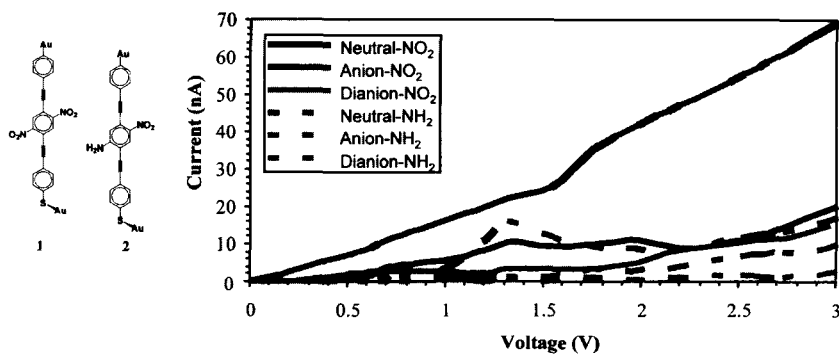


Fig. 2 Current–voltage of the neutrals (blue), anions (red), and dianions (green) for **1** (continuous lines) and **2** (dashed lines). (View this art in color at www.dekker.com.)

factors that control the “window”; as a consequence, the current can only monotonically increase with V , and NDR would not be predicted.

Fig. 2 shows the current-vs.-voltage curve for two test molecules; both molecules have three benzene rings separated by a C–C triple bond group. Molecule **1** (NO_2 in Fig. 2) has two nitro groups as substituents in the central ring; molecule **2** (NH_2) has one nitro and one amino group in the central ring. We used density functional theory (DFT) calculations to explain the electrical behavior of these π -conjugated organic molecules with current–voltage characteristics resembling a resonant tunneling diode.^[33]

Considering the behavior of the neutral of these molecules (blue curve solid and dotted, respectively, for **1** and **2**), intrinsic NDR is observed for **2** at around 1.3 V, while no NDR is observed for **1**. Fig. 3 shows the trans-

mission function at voltages relevant for the observed NDR effect. The NDR is observed between 1 and 1.5 V; the integration range to obtain the current at 1 V is from -5.81 to -4.81 eV (Fig. 3 and Eq. 3), and from -6.06 and -4.56 eV for 1.5 V.

For **2**, a peak in the TF observed between -6.06 and -5.81 eV increases in height and approximately maintains its width when the voltage rises from 1 to 1.3 V (position of the NDR peak). Then the area below TF decreases considerably as the voltage increases further, thus explaining the decrease in the current (NDR). No similar effect is observed for **1**. This effect would have gone unnoticed if an electrical field had not been considered; the observed effect on the TF is entirely attributable to the changes in the molecular electronic structure (changes in MO localization and energy) due to the effect of an external field.

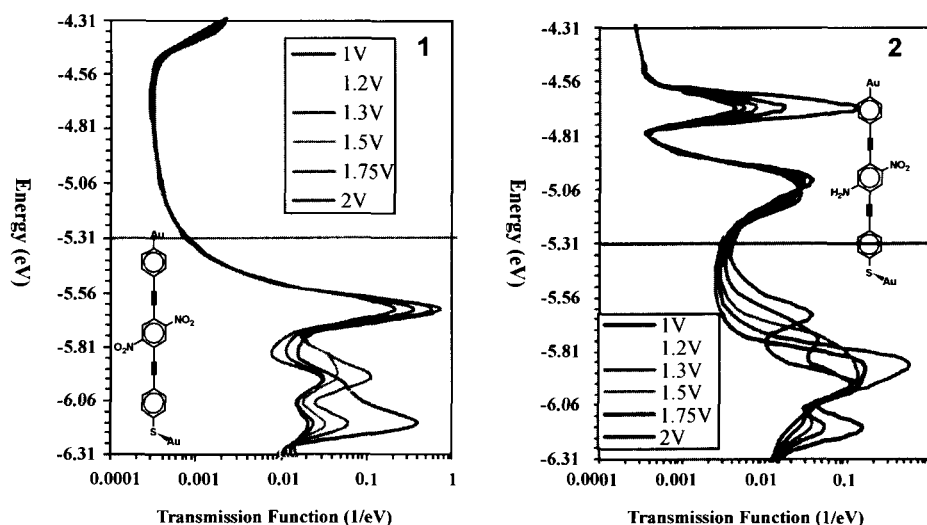


Fig. 3 Transmission function vs. energy of incoming electrons at several bias voltages for the neutral of **1** and **2**. (Adapted from Ref. [33].) (View this art in color at www.dekker.com.)

The need to implement the present methods is attributable to the impossibility of using simple model barriers able to represent the potential of small molecules acting on the conducting electrons. There are two ways that NDR and RT can be obtained from a single molecule. 1) The first is by charging the molecule or changing its geometry. Because the ion of a molecule has totally different characteristics than its neutral, charging a molecule is equivalent to substituting a molecule for another in the circuit. 2) Changing the shape of a molecule, for instance, by rotating a ring with respect to the other, which will very likely change the electron transport characteristics of molecule 2 via the intrinsic resonant tunneling (IRT) inherent to most molecular systems. The former yields sharp changes in the currents, and the latter yields smoother and symmetric curves, such as those in a typical resonance case.

Molecular electrostatic potentials

Molecular electrostatic potential (MEP) is another important piece of information needed to understand the electronic properties of molecules. Areas of the molecule with specific properties (such as electron donation or electron-withdrawing capabilities) can be easily identified from an MEP map; this information is extremely useful in understanding molecular interactions and in molecular design. With MEPs, the well-exploited electronic configuration analysis is able to accurately explain a switching experiment,^[43] complementing the conclusions drawn by experimentalists, with a further explanation that include concepts and all the factors influencing the switching of the molecule, and raising research goals for subsequent experiments.

MEP does not show a smooth behavior across the molecule. For instance, when a bias voltage is applied,

the voltage profile shows a complicated topology, which is very different from monotonous decrease that is expected from simple linear or bilinear devices. An example of an MEP profile across a molecule is shown in Fig. 4. Fig. 4a shows the MEP profile across a single benzene ring at 2 Å above the benzene plane, while b) and c) are two different views of the MEP topology when a bias potential of 2 V is applied across the molecule. This picture dramatically changes the idea that molecules are simple barriers, and indicates that more precise studies should be performed to properly describe electron transport properties in molecules.

Tour et al.^[44,45] have also theoretically determined the first precise electrostatic potential profile obtained on a single molecule in the presence of an external potential source.

Seminario and Derosa have heavily investigated the behavior of benzene rings substituted with nitro and amine groups. It has been already determined that these groups render the negative ions of the ring stable with respect to the neutral state of the same molecule, thus they are able to exist as single, stable molecules. In addition, for some of these molecules, electron transport characteristics are different for the anion than for the neutral state. If this is the case, these molecules are able to behave by themselves as memory devices. Our calculations indicate that some of these molecules are able to store a second electron when bonded to metallic atoms.^[28,33,35] The main advantage of this behavior for molecular electronics is that these molecules present storage characteristics at three levels (charge=0, -1, and -2), therefore they could behave as devices without the need for a control gate because we have one extra state available forming a two-terminal, three-state device that could be substituted for a three-terminal, two-state device.^[35,46]

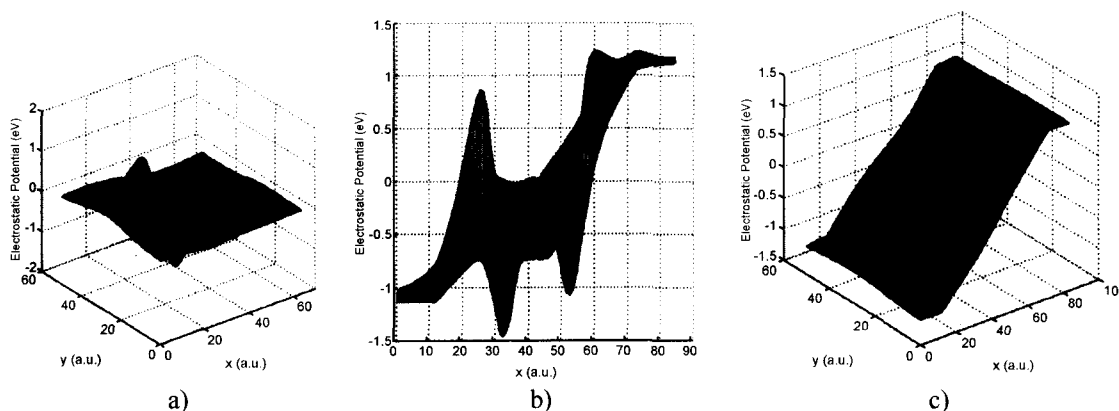


Fig. 4 Molecular electrostatic potential profile at 2 Å above the molecular plane. a) No voltage applied across the molecule; b) side view of the MEP profile when 2 V are applied across the molecule; c) like b) but from a different view angle: view of the MEP profile showing the distribution on the plane. (View this art in color at www.dekker.com.)

APPLICATIONS

The following discussion reviews several applications of the tools and techniques described above.

DFT-Based I - V Calculations

As a preliminary approach to calculating the I - V characteristic of single molecules, a purely ab initio approach for the calculation of molecular current-voltage characteristics was developed.^[17]

This method only uses molecular calculations to estimate the I - V through a molecule, thus formulating a new prescription can obtain current-voltage characteristics via the use of precise quantum chemistry techniques. As shown by the results in Fig. 5, the agreement of calculations^[17] with the experiments on single molecules^[1] is very encouraging. Fig. 5 shows results labeled as Au-S-(p-C₆H₄)-S-Au to be within the two experimental curves exp1 and exp2. This technique does not require any experimental feedback to predict the I - V characteristics. In addition, these studies have determined that the position

of the molecule with respect to the metal tips has a strong effect on the charge transfer process.

NDR and Memory

Some molecules have been found to present a particular response, such as NDR, to an applied voltage. This simply means that above a certain voltage, the current through the device decreases when the applied voltage increases. It is experimentally^[41,47] and theoretically^[28] known the nitroamine molecule **1** shows a strong negative differential resistance; its I - V is characterized by a threshold at low voltage, followed by a steady and pronounced increase in the current until it reaches a maximum, then it sharply decreases. The steady increase in current is partly attributable to the increase in the TF of the neutral molecule, but is mainly a result of a simultaneous charge of the molecule to -1 . The current for the negative ion is relatively small compared to the corresponding current that could be obtained with the neutral state; however, this is in qualitative agreement with the experiment where only 1 nA is obtained at the peak of the curve through ~ 1000 molecules. The

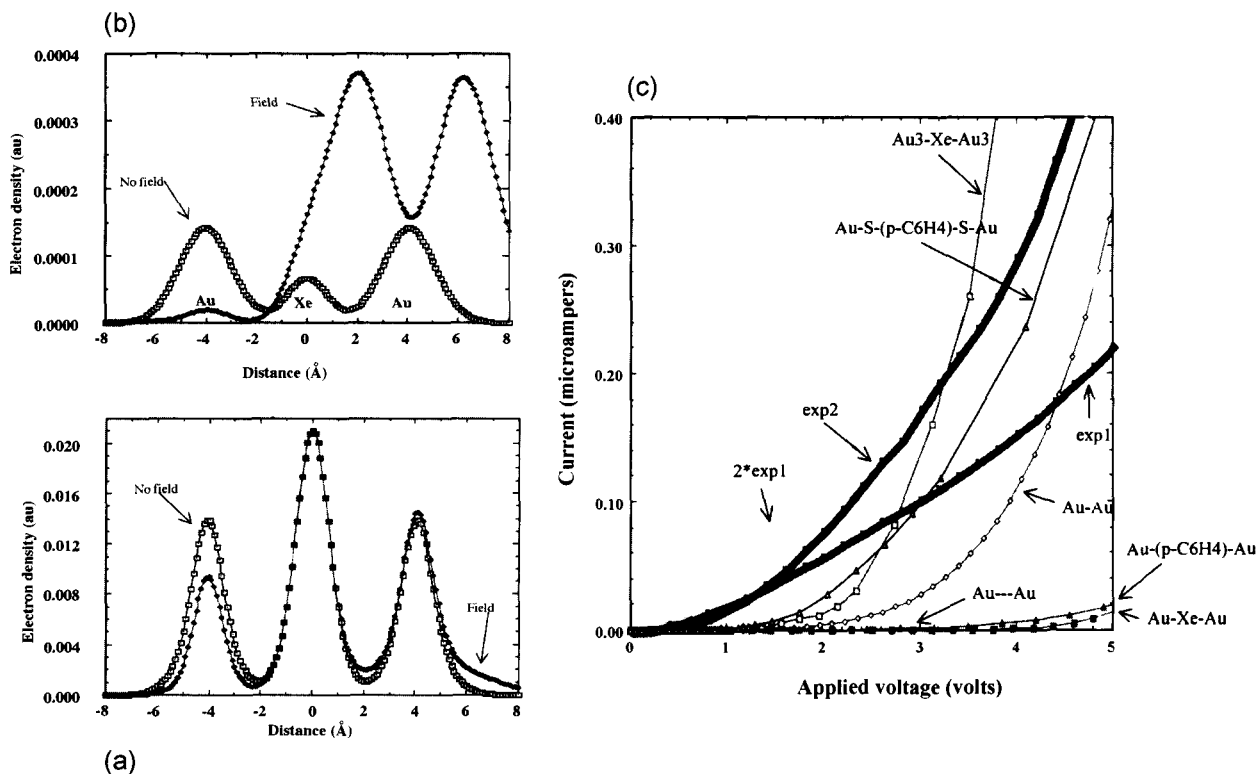


Fig. 5 Panels (a) and (b) show electron densities along parallel axes to the molecule (Au-Xe-Au) axis at 1.5 and 3 Å, respectively. Cases when the external applied field is able to transfer one electron from the Au atom on the right side of the junction to the Au atom on the left side are shown. (c) Molecular $I(V)$ characteristics. exp1 and exp2 correspond to the experimentally determined values of $I(V)$. (Adapted from Ref. [17].) (View this art in color at www.dekker.com.)

sharp drop observed in the experiment is attributable to a second electron charging the molecule, and yielding a current lower than the currents for neutral and anion as shown in Fig. 2. These characteristics, together with the fact that the presence of Au atoms stabilizes the first two anions, make this molecule suitable for use as a memory device. Based on experimental observations,^[41,47] the molecule probably charges with one electron at a voltage between 0.5 and 1.5 V, and most likely one electron is stored at a voltage closer to 0.5 V as a result of the position of the LUMO (Fig. 6), which is accessible for conduction at a bias voltage of 0.6 V, while the second electron is stored at a voltage closer to 1.5 V.

A bias voltage charges (writes) the neutral, and a pulse below 0.5 V allows reading the state of the molecule without altering its charge state—thus the “memory” can be read. If uncharged, the molecule will be in a low impedance state; but if charged, it will be in a high impedance state. The predicted position of the NDR peak is not exactly identical to the experimental observation, probably because of temperature effects^[28] that we had not considered, and the fact that the experimental setting corresponds to a statistical average of ca. 1000 molecules in parallel.

Molecule 2 (dinitro) had not been experimentally tested (to the best of our knowledge); therefore, its characteristics were inferred from this study. Its anion and dianion were also predicted to be stable against electron ejection. If we assume that the molecule remains uncharged for low voltages, a threshold for conduction is observed. The LUMO of this molecule is accessible for conduction of electrons from the metal contacts at bias

voltage of 2V, thus this molecule will not become charged for lower bias voltages. The storage of one electron in this molecule yields a sharp increase of current. If another electron is stored, a sharp decrease takes place.

NDR is expected in the dinitro molecule, although with a different mechanism than for the nitroamine. Unlike the latter, a range of voltages might be predicted in which the dinitro molecule is in a high conductance state, rather than just a peak. As a result, charged and uncharged states can be easily identified. The dinitro molecule can also perform as memory device. Its neutral shows high impedance, while its single ion shows low impedance. A read pulse should be lower than 2 V, the conductance of the neutral and the single charged state are perceptibly different in that range, and the applied voltage is insufficient to charge the molecule if it is uncharged. However, if the write pulse is large enough to doubly charge the molecule, an ambiguity can result, because both neutral and double charge states of the molecule show high impedance.

The nitro groups are known to be electron-withdrawing groups; therefore, when the dinitro is connected to macroscopic tips, electrons are available in the contact flow and could charge the molecule even without an applied voltage, resulting in a current–voltage characteristic that is different from what is expected for the neutral. High conductance is expected at low voltages, with a sudden drop when a second electron is stored. This molecule is stable under the ejection of the second electron, thus keeping the charge until it is forced to discharge. A voltage pulse of more than 2 V writes a non-conducting state in the molecule, and a low voltage pulse

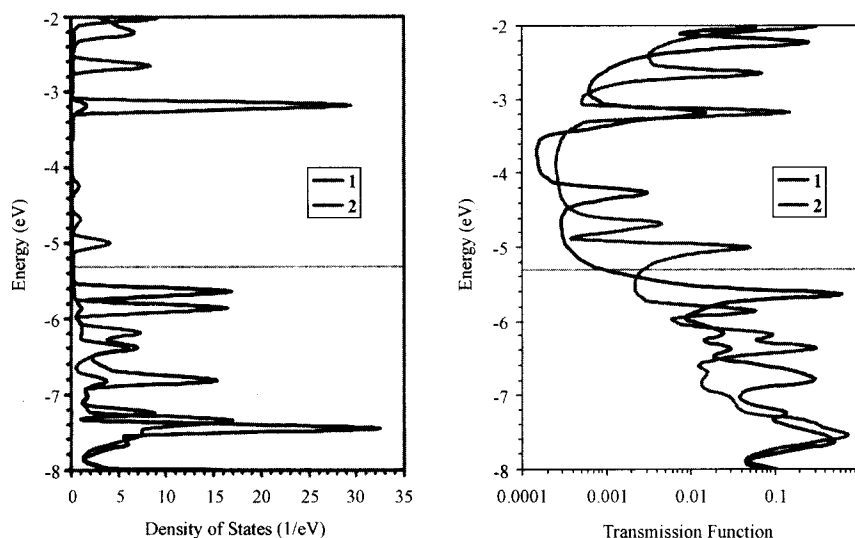


Fig. 6 Density of states (a) and transmission function (b) for the neutral of 1 (blue) and 2 (red). The position of E_F , i.e., the interface between the occupied and unoccupied levels, is a 5.31 eV (light blue). (Adapted from Ref. [33].) (View this art in color at www.dekker.com.)

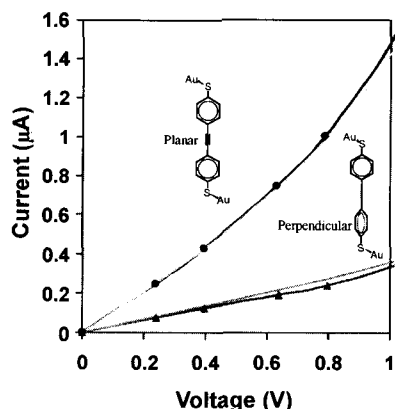


Fig. 7 Demonstration of molecular gain in a thiolane system. (View this art in color at www.dekker.com.)

will read the molecule statically, i.e., without changing its charge state.

Molecular Gain

An interesting manifestation of molecular gain was discovered,^[48] and later calculated by using high levels of theory^[42] considering two different modes of operation of a single molecule with two phenyl rings. The relative position of these rings, perpendicular-or parallel with respect to each other, determines the magnitude of the impedance.

The observed rotational barrier for this molecule is about 0.05 eV, which is the energy needed to shift from the parallel conformation to the perpendicular one. However, when such a shift occurs, the HLG increases to 0.85 eV—in other words, by investing 0.05 eV, the

transmission barrier can be changed to 0.85 eV, which corresponds to an amplification factor of 17.

Another important finding of this calculation is the switching capabilities of this molecule, the coplanar conformation present an impedance of $\sim 50 \text{ K}\Omega$ at 1 V, whereas for the perpendicular conformation, the impedance is almost $3 \text{ M}\Omega$, i.e., ~ 60 times greater (Fig. 7).

Fig. 7 shows the I - V for both conformations, the planar and rotated conformations. The solid line corresponds to the I - V obtained after the application of an electric field to the molecule, the dotted line represents the zero-field approximation, i.e., the Hamiltonian at zero bias is used for the entire voltage range. No significant difference between the two approaches is observed for this molecule up to 1 V. Thus the zero-field approximation, unlike that for other molecules, works fairly well here.

Conducting and Insulating Molecular Devices

Seminario et al.^[49] demonstrated that molecules of nanometer sizes could still be characterized as low- and high-impedance devices by using quantum ab initio techniques. Low-impedance and high-impedance devices are needed as building blocks for circuits and systems in molecular electronics. Small alkanes and polyynes chains with σ and π bonding, respectively, yield a high–low impedance relation of 2 orders of magnitude for changes of 1 nm in length, of 3 orders of magnitude for changes of 1.3 nm in length, and with exponential growth after 0.9 nm. A substantial difference between polyynes and alkanes was observed at small lengths; this difference is unpredictable from what is known about the larger chains.

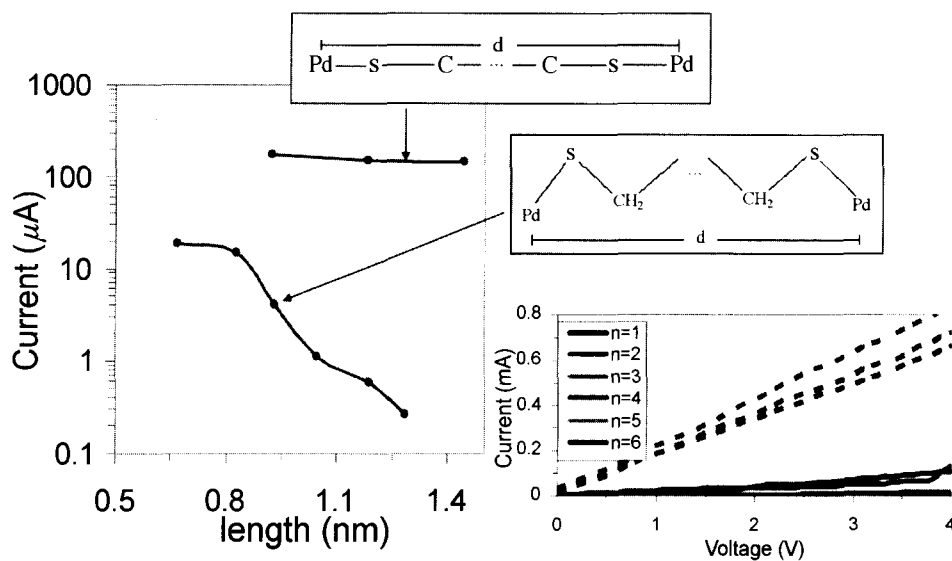


Fig. 8 Variation of the current in the alkanes and polyynes. (View this art in color at www.dekker.com.)

The current in the alkanes is relatively low compared with the current in the polyynes. The current in the polyynes increases linearly with the voltage, as shown in Fig. 8, but it does not change too much with the size of the polyyne.

On the other hand, the current through the alkanes is smaller and it decreases very rapidly with the number of C atoms in the chain. Fig. 8 also shows, in logarithmic scale, the current at 1 V for all cases. While polyynes do not show a significant change with the size of the chain, the current through alkanes decreases rapidly and almost exponentially for the larger alkanes.

A Programmable Diode

In searching for new possible molecular devices, Derosa et al.^[50] studied the molecule depicted in Fig. 9, the molecule 3-nitro-2-(3'-nitro-2'-ethynylpyridine)-5-pyridinethiol (DNDP) has two pyridine rings with a nitro group each in a meta position with respect to the N atom in the pyridine. The two rings are separated by a phenylene group. The neutral state of this molecule has a stable configuration for which the rings are almost perpendicular to each other ($\sim 87^\circ$).

To the best of the author's knowledge, this molecule is the only six-member-rings-based molecule separated by phenylene groups that presents a stable configuration for which the rings are not coplanar. Even more interesting, the anion and dianion for the DNDP are coplanar, thus the same molecule has a stable state with planar and non-planar conformations. Fig. 10 depicts a comparison with other similar molecules: a) is the DNDP, b) shows the same molecule but without the nitro groups, i.e. two pyridine rings separated by a phenylene, c) shows a molecule similar to DNDP but with two phenylene rings instead of pyridines, and d) shows the tolane. The only case where the rings are not parallel is a), the DNDP.

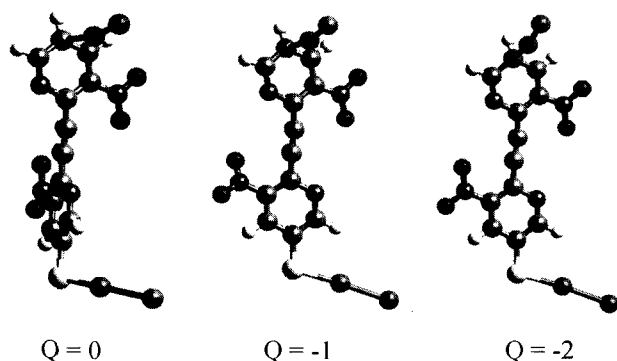


Fig. 9 The dinitro dipyrindine molecule. Neutral (left), anion (center), and dianion (right) are shown. Au, C, H, N, and O atoms are green, gray, white, blue, and red respectively. (View this art in color at www.dekker.com.)

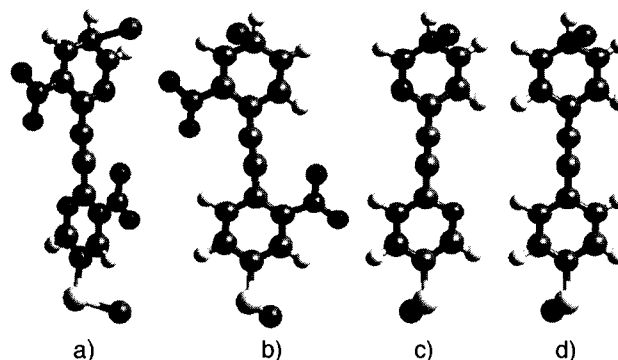


Fig. 10 Comparison between related molecules, all of them consisting of two six-member rings separated by a phenylene group: a) both rings are pyridines and each has a nitro group, b) both rings are pyridines, c) both rings are phenyls and each has a nitro group, d) a tolane molecule. Au, C, H, N, and O atoms are green, gray, white, blue, and red respectively. (View this art in color at www.dekker.com.)

Provided the anion (or the dianion) are low impedance states, a molecule with this characteristic is desirable as a controllable switch—in which switching can be achieved by controlling the charge or the conformation in the molecule. It can also be used as a memory device when connected to two contacts—the molecule can be written by using an external field to control the relative rotation of the rings; this is possible because the presence of the nitro group gives the rings a dipole moment that will interact with the external field. To write a *zero*, we need to induce the noncoplanar conformation; to write a *one*, we need to force the rings to be coplanar and the molecule will grab a charge from the contacts because it is energetically favorable. To read the molecule, we need to sense its current by attaching the molecule ends to contacts: high impedance means zero (rings noncoplanar and the molecule is neutral), low impedance means one (rings coplanar, and the molecule is ionized). Alternatively, this molecule can be a nanoactuator, if we control the charge state; we can induce rotation by charging or discharging the molecule.

The I - V for this molecule was calculated by attaching two Au atoms on one end to a S atom, and attaching another two Au atoms to the other end, directly bonded to the pyridine ring. The I - V curves are shown in Fig. 11, as expected, the neutral is a poor conductor while the anion and dianion conduct very well for positive bias (“+” on the vapor deposited end-top in the figure, and “-” on the self-assembly end) and poorly for negative bias. The different nature of the contacts provides this system with an even more attractive application—it can work as a programmable diode; it will behave as a diode if charged, but it can be turned off if we uncharge the molecule.

The idea of using an external field to induce switching was not born with this molecule, molecules with three

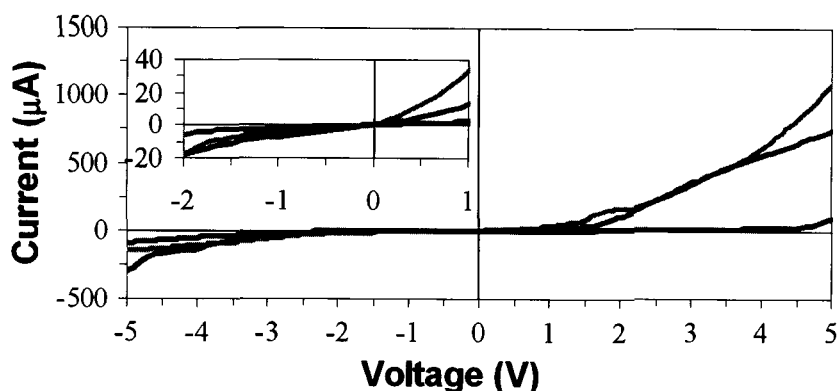


Fig. 11 Current-vs.-voltage curves for the neutral (black), anion (orange), and dianion (blue). The inset shows details at the low voltage range. (View this art in color at www.dekker.com.)

phenyl rings were modified by attaching substituents to give this central ring a finite dipole moment to interact with the external field.^[41,51] Switches based on this idea are schematically represented in Fig. 12.

Metal Alligator Clip Interactions

Several works were devoted to understand the nature of the molecule–contact interface, and several other models have been proposed.^[23,52–57] Through the characterization of different metallic contacts as they interact with the molecular device through different alligator clips, it was demonstrated that the best alligator clip corresponds to S, which is, however, not much better than the isonitryl (NC)

alligator clip. It was predicted that the best metal for the metal–molecule interface corresponds to Pd, followed by Ni and Pt. Cu can be considered intermediate, and the worst cases correspond to Au and Ag (Fig. 13).

The impact of this study has been accepted at several research environments, including experimental ones, in which Pd and Pt have been considered as main substituents for Au, the metal that had been extensively used as contact for many nanotechnology approaches.^[58]

A benzene ring bonded through a S or CN group to six different metallic atoms (Ni, Cu, Pd, Ag, Au, and Pt) at each end was fully studied. The I – V curves were compared with each other, and conclusions were drawn about the best clip–metal combination. For this particular

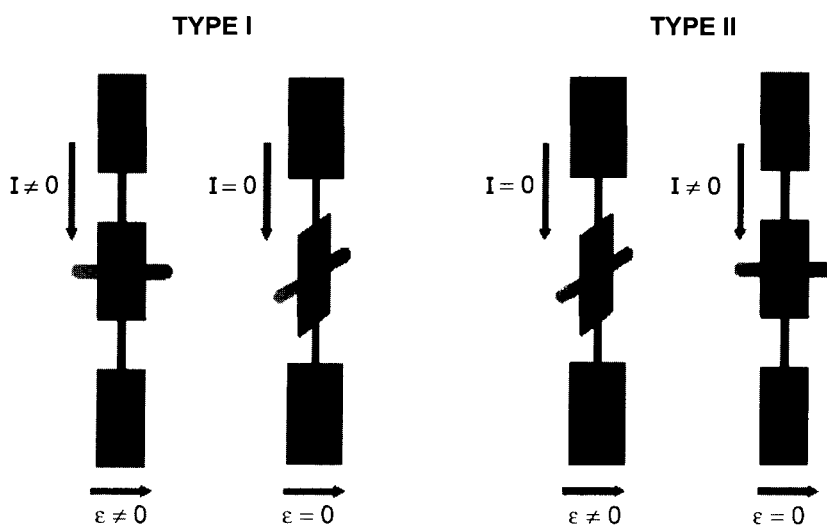


Fig. 12 Complementary molecular field effect transistors (CMoIFETs): The current through molecules is controlled by an external electric field able to rotate the central part of the molecule. To perform an electronic function, complementary types of molecules are required: Type I are ON when no field is applied and OFF when a field is applied, whereas the opposite takes place for type II molecules. (View this art in color at www.dekker.com.)

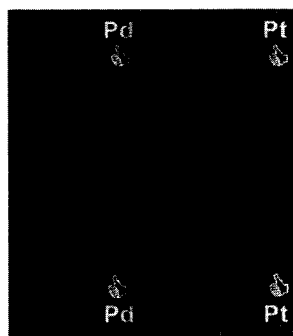


Fig. 13 The study of the molecule–contact interfaces provided information about the best way to interconnect molecular systems. (View this art in color at www.dekker.com.)

calculation, no electric field was applied to the molecule, and complementary calculations indicated that frontier MOs of a single benzene ring are hardly affected by the external field, thus unimportant differences would have been found if a field had been applied.

The Metal–Molecule Interface

Derosa and Seminario also provided the theoretical proof that solved a controversial issue for both experimentalists and theoreticians, which involved the metal–molecule interface geometry.^[29,33] They demonstrated through the geometrical optimization of different systems that the interaction between the clip and the gold surface is achieved through only one Au atom, rather than through two or three Au atoms, i.e., S tends to bond to one Au atom only. The system analyzed was a single benzene ring attached through a S clip to Au atoms (we considered from one Au atom to five Au atoms). Benzene was chosen because it represents the end group of many molecules very commonly used for molecular electronics, a series of phenyl-based oligomers, and provided an insight into the nature of the metal–molecule interface on a self-assembled monolayer, and the metal–molecule interface on a vapor-deposited metal from ab initio DFT.^[59] The analysis is based on the ability of the Kohn–Sham MOs to determine the electron transport characteristics of single molecules when they are attached to metallic contacts. The geometry optimization performed for all the studied systems used a high-accuracy convergence criterion, and one of the best tradeoffs between precision and cost. Furthermore, the theoretical results reasonably reproduce available experimental evidence.

The self-assembly process consists of the deposition of the molecules over a Au surface; thus, the metallic surface suffers minimal perturbations by the presence of the deposited structure. Accordingly, results show that the interaction between the clip and the gold surface is achieved

through only one Au atom, rather than through two or three Au atoms. We predicted a S–Au bond of ~ 2.45 Å and a C–S–Au of $\sim 105^\circ$. Considering S in a hollow site attached to three Au atoms in the exact center of the triangle, it is not compatible with the geometry we predicted; if S–Au is 2.45 Å, then the angle C–S–Au is 137° (Au–Au distance in a crystal is 2.88 Å). On the other hand, if the angle C–S–Au is considered 105° , in agreement with our predictions, then the S–Au distance should be ~ 1.7 Å. Either way, we end up with a very high strain configuration, thus a very unstable bond, which is incompatible with the experimental finding that S is a good clip to attach organic molecules to metal surfaces. S, even when it can be above a triangle of Au atoms, cannot be in the center but mainly attached to one of the Au atoms. In short, even if S is above a triangle of three metal atoms, it will not be in the bare center, but closer to one of the atoms in the triangle; such a Au atom is the one with the highest interaction with the S alligator clip. In some cases, the S clip is bonded to two Au atoms; however, the structure becomes energetically less favorable.

Charge Effect on the Contacts

In a study of the dinitro and nitroamine molecule, Seminario et al.^[33] determined that all the charge transferred from the Au atoms to the molecule is taken from the Au directly connected to the phenyl ring, and almost no charge is taken from or added to the Au bonded to the S. Therefore, there will be substantial differences when S connects the molecule to the Au atoms at both ends. A calculation of nitroamine molecule, but with two Au atoms in the upper ring instead of one, yields a total charge of 0.38 in the two Au atoms. When three Au atoms are connected at each end of the molecule, the S–Au₃ group at the S end is neutral, while the Au₃ group at the other end bears a total charge of 0.48. This structure has two Au atoms directly connected to the S on one end, and one Au atom connected to the aryl ring on the other end. On the S side, the Au atom not directly connected to S has a charge of -0.2 , while the S is positive by the same amount. The Au atoms directly attached to the S are neutral. On the other end, the Au directly attached to the C in the ring holds almost all the charge at that end ($+0.46$), while the other two Au are almost neutral. This indicates that, even when each nitro group can store up to half an electron, the molecule only takes less than half an electron from the contact with no S. When the nitroamine and the dinitro molecules are charged, part of the charge is stored in the Au atoms rather than in the molecule. For dianions, almost one electron for the dinitro and over one electron for the nitroamine are stored in the Au atoms, plus the sulfur. The fact that the Au atoms adsorb part of the charge does not imply that the molecule cannot become

charged with two electrons; in fact, there is no definite limit in the real system where we can distinguish the molecule from the contacts. Certainly, the few first Au atoms making contact to the molecule have to be considered part of the molecule. Most of the charge transferred to the molecule comes from the Au atoms directly attached to the upper ring, irrespective of how many Au atoms are directly connected to the upper ring, or whether there are other Au atoms connected to them. Independently of how the molecule is connected to Au, the amount of charge in the molecule is half of an electron. The Au atoms attached to the upper ring are positive, and compensate the charge in the rest of the molecule. Even if the molecule is not intrinsically charged at 0 V, it can be easily precharged before its use by applying a bias voltage, and therefore this molecule can operate in another mode with two charge states, -1 and -2 .

Geometry Effects of the Metallic Contacts

To make sure that a more detailed representation of the interface geometry does not strongly affect the electrical characteristics of the molecule, the original geometry in the dinitro and nitroamine molecules, described in the previous sections, was modified by adding one H atom bonded to the C on the vapor deposited end and two more Au atoms on the self-assemble monolayer (SAM) side, such that the S atom is on a hollow site of three Au atoms. The geometries for Au-(2'-nitro-4-ethynylphenyl-4'-ethynylphenyl-5'-nitro-1-benzenethiolate)-Au₃ (**1''**) and Au-(2'-amino-4-ethynylphenyl-4'-ethynylphenyl-5'-nitro-1-benzenethiolate)-Au₃ (**2''**) were partially optimized in the following manner: one Au atom is placed randomly close to a fully optimized benzene ring; then the calculation runs until a local minimum is obtained and it is confirmed by a second derivative calculation of the en-

ergy. This full benzene ring plus Au atom system is substituted into the molecules. This forms molecules that are most likely more realistic than those used before. For the S-ended side of the molecule, a triad of Au atoms is optimized and an S atom is placed on the hollow site and optimized with a constraint of C_{3v} symmetry. Such a structure is unstable, thus the constraint is needed to represent a possible (111) surface hollow site of an Au crystal. Next, a benzene ring is attached to the S of the Au₃S system, keeping the Au₃S base fixed and letting the benzene ring to reach its most stable configuration with respect to the Au₃S system.

The addition of a C-H bond to the system does not change the frontier MOs or those around them, as shown in Fig. 14. Therefore electrical characteristics, such as the I - V curve, are not affected. As long as the electronic structure around the Fermi level is the same, drastic changes in the geometry of the system only slightly affect the results. The metal geometry at the interface may add impedance, but the main features, such as NDR, are mostly governed by the molecular conformation in the central ring. This is supported by experiments, which show good reproducibility in the electrical characteristics when measuring several samples of the same molecule. It is expected that the geometry of the vapor deposited Au is different from sample to sample; however, results are reproducible as shown in Ref. [46]. On the other hand, it has been shown that the shape of the I - V curves changes radically when the substituents in the central ring, which are those that strongly modify the frontier MOs, are changed. The substituents determine the nature of the molecular device. Thus the contacts do not affect the main characteristic of the device. Conduction is practically attributable to antibonding orbitals, rather than bonding ones, which are much more stable and much lower in energy than the Fermi energy of the metallic contacts. Neither the H bonded to a C nor the addition of more Au

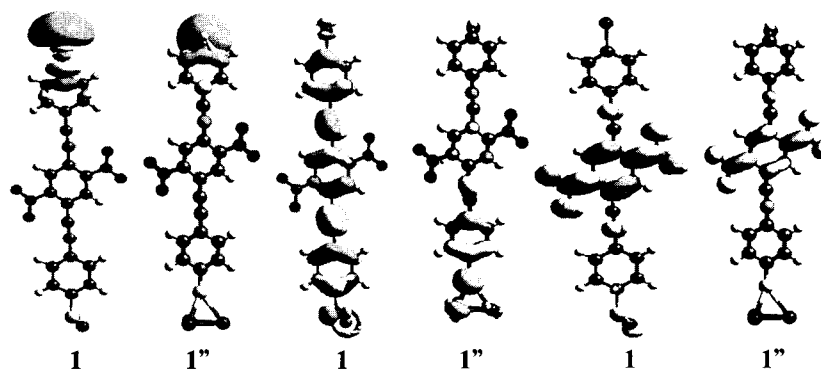


Fig. 14 MOs of **1** and **1''** showing the effects of adding one H and two Au atoms to **1**. (a) LUMO+3 of **1** and HOMO of **1''**, (b) HOMO of **1** and **1''**, (c) LUMO of **1** and **1''**. (Adapted from Ref [33].) (View this art in color at www.dekker.com.)

atoms contribute to the main channels of conduction through the molecule, because they only contribute with very stable bonding or very unstable antibonding MOs, all of them well localized. Nevertheless, the presence of the C–H or C–Au bonds provides marked and contrasting suggestions on how the contacts were created. A cleavage of the C–H bond could lead to strong damage of the nanopore, and this is certainly of paramount importance for a study of metal vapor deposition. On the other hand, the addition of more gold atoms simply increases the number of localized MOs, but they do not contribute to electron conduction.

Although the correct geometry in the experiment is unknown, the authors believe that the geometry with the S symmetrically centered on a hollow site, sometimes used in theoretical calculations, is chemically and physically impossible. This assertion is based on experimental^[1] information and theoretical calculations,^[29] which determine that S should be bonded to just one Au atom. Notice that constraining the geometry is the only way a S atom can be kept in the geometric center of Au triangle—thus confirming our affirmation that this geometry is not realistic. The extended nature of the surface may not be really relevant because the attachment of the molecule to the surface is strongly dominated by local effects. Even assuming that the SAM was performed on a perfect (111) surface, there is evidence that the angles are the correct ones. For instance, an angle of 107° is reported for the bond angle of Au–S–C when alkanes are used.^[60] This is in agreement with calculations yielding 102° in a slightly different environment. There is experimental evidence indicating that the metal–S–C angle is 104° ,^[61] which agrees with the theoretical predictions described in this section. Angles on the order of $\sim 150^\circ$ are certainly a possibility, but they yield substantially less stable structures as observed experimentally^[60] and theoretically.^[29]

In summary, interpreting that S is in a hollow site might lead to confusion. The fact is that S does not position itself symmetrically above the center of an Au₃ triangle. The geometry suggested in this section is compatible and in perfect agreement with the experimental findings that S is on a hollow site. However, the S atom does not remain at the center of the triad. We assume two possible and realistic bond angles for S, 90° and 100° , connecting an oligomer chain, thus making a tilt angle of 30° with the normal to the surface, as is already established experimentally for some alkanes.^[60,62]

Search for Minimum Molecular Programmable Units

Molecular electronics can be developed if we are able to program a RANDOM arrangement of molecules or a

field programmable molecular random array. Preliminary simulations have shown that programming this molecular arrays is possible;^[63–65] however, schemes for implementing these programming techniques still need to be realized and that starts by characterizing the smallest molecular system with programmable features. Present programs for the calculation of current–voltage characteristics of electronic circuits, needed for such demonstrations, are only able to predict single-valued characteristics. A procedure exists to incorporate molecular physics procedures with a practical analysis of molecular circuits having strong nonlinearities.^[6] The highly nonlinear current–voltage (*I–V*) characteristics shown by some molecules open up a complete new set of possibilities for operational circuits. However, the engineering design becomes more complex and new approaches should be developed because traditional tools for circuit analysis are prepared to deal mostly with linear components. Combinations of nonlinear systems yield circuits with multivalued characteristics. Thus determining all the possible states of the circuits is of fundamental importance to characterize operational modes defined as set of states allowed under normal operation. A special signal, usually large in magnitude, above a threshold, can be used to drive this system from one operational mode to another. This flexibility allows more than one *I–V* curve for each device, facilitating the programming of molecular circuits.

The first step in the design flow of moletronics systems is to determine the electrical properties of single molecules. Theoretical methods allow scientists to study systems comprising a molecular system interconnected by small metal clusters. Triangular patterns made of gold clusters interconnecting molecules are expected to be the building blocks of moletronics functional units, for which all of their possible functional states need to be characterized. The analysis of possible configurations allowed by self-assembly procedures needs to be performed to find possible programmable units. When programmable molecular units of a given geometrical structure are found, the candidate molecule goes through the simulation loop until the simulated system yields programmable characteristics, otherwise the molecule is discarded and another, with different *I–V* characteristics, is chosen. Molecules with highly nonlinear current–voltage (*I–V*) curves are preferred because of their ability to create switchable states. The simulation loop, looking for a programmable molecular unit, begins with the proposal of new single molecular devices and their characterization utilizing ab initio principles. The next step is the characterization of simple combinations of series and parallel circuits of a few units, then functional units can be studied. These minimum programmable units are then combined in larger circuits with more versatility, leading to field programmable molecular random arrays.^[65]

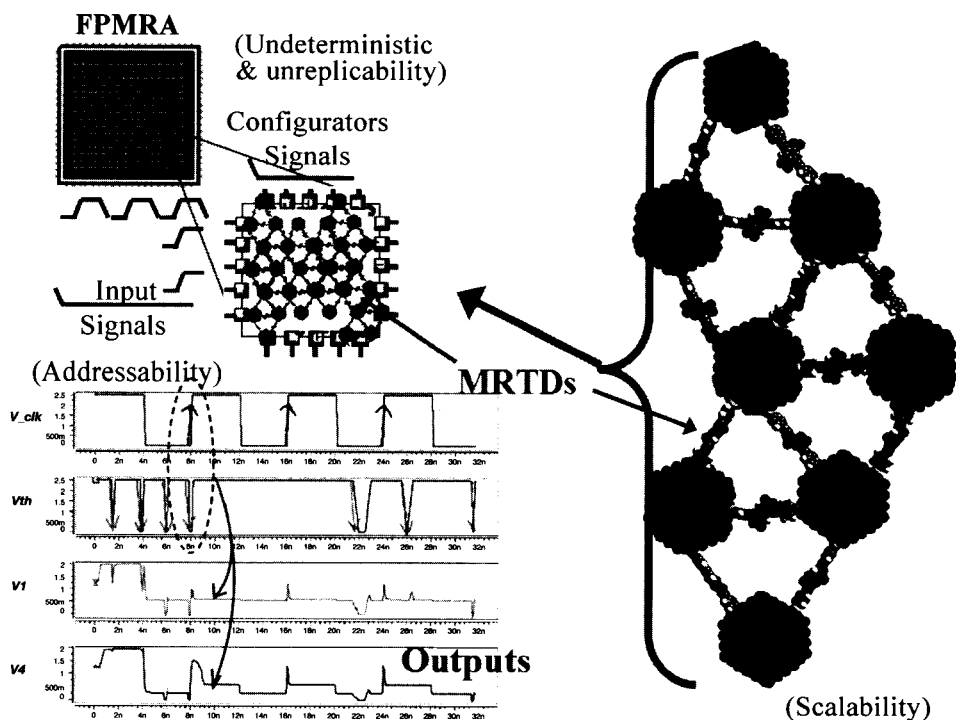


Fig. 15 Design of configurable random molecular logic units. (View this art in color at www.dekker.com.)

Testbed for Molecular Architectures

Having made a considerable effort to characterize the molecular device, a design paradigm for molecular electronics is simulated to demonstrate that clusters of devices showing negative differential molecular impedance can be used as minimum programmable units.^[6,64,66] These molecular-scale resonant tunneling devices show features of multiple-valued logic and memory. The plausibility of programmability of minimum molecular units arranged in triangular structures, which are similar to the (111) surface of a face centered cubic crystal, are shown in Fig. 15. In general, minimum units can be used as multivalued logic blocks.^[64,66,67] Input, output, and control signals can be used to program the molefabric to a specific function, which can be accomplished by using artificial intelligence techniques such as neural networks and evolutionary techniques. Future work is needed to test other individual molecules until an optimum molecule, with adequate I - V characteristics, is found for an efficient learning process of the molefabric.

CONCLUSION

The field of moletronics is certainly exciting. Modern semiconductor devices are already facing complications

with further size reduction, and are now forced to consider quantum mechanical effects as transistor sizes become increasingly smaller. It is believed that the semiconductor industry will soon hit a practical device size limit, and at that point, it will be necessary to pursue alternate computing strategies to further reduce size and power consumption, while providing increased computing power. Moletronics is one such alternative. Because molecules are on the nanometer scale, using them as electrical switches will provide an innate reduction in size, and the high molecular densities that can be achieved should lead to increased computing power. However, it is not expected that moletronics will replace conventional electronics; rather, it will complement it. The small molecular size also introduces many difficulties that must be overcome before moletronic devices can become a reality.

In this article, we have discussed the methods used to calculate the electronic and electron transport properties of moletronic systems with programmability characteristics, as well as some applications of these methods. Theoretical results showed excellent consistency with experiments and explained experimental phenomena that were observed prior to these simulations, and recently theory was also able to predict experimental outcomes before the actual experiment were performed. This predictive capability enables molecular simulations to actually design molecular components and recommend to

experimentalists the most appropriate systems to be tested. Finally, the search for minimum molecular programmable units and how these units may be used for computing purposes were discussed to explain the analysis and design flow of molecular devices.

ACKNOWLEDGMENTS

We acknowledge Angelica Zacarias, Luis Cordova, Cecilia de la Cruz, Suneel Guda, Hernan Figueroa, and Jimena Bastos, who participated in an earlier work being reviewed in this article. We also thank David McClard, Nagendra Vadlamani, and Sridhar Bingi for their assistance with the details of the manuscript. We thank James Tour from Rice University for his invaluable contribution to some of the work referred to in this manuscript. We highly appreciate the support of ARO under grants DAAD19-00-1-(0154, 0592, 0634) and DAAD19-99-1-0085, DARPA/ONR under grant N00014-01-1-0657, and the USC NanoCenter.

REFERENCES

1. Reed, M.A.; Zhou, C.; Muller, C.J.; Burgin, T.P.; Tour, J.M. Conductance of a molecular junction. *Science* **1997**, *278*, 252–254.
2. Llang, W.; Shores, M.P.; Bockrath, M.; Long, J.R.; Park, H. Kondo resonance in a single-molecule transistor. *Nature* **2002**, *417*, 725–729.
3. Park, J.; Pasupathy, A.N.; Goldsmith, J.I.; Chang, C.; Yaish, Y.; Petta, J.R.; Rinkoski, M.; Sethna, J.P.; Abruñas, H.D.; McEuen, P.L.; Ralph, D.C. Coulomb blockade and the Kondo effect in single-atom transistors. *Nature* **2002**, *417*, 722–725.
4. Collier, C.P.; Mattersteig, G.; Wong, E.W.; Luo, Y.; Beverly, K.; Sampaio, J.; Raymo, F.M.; Stoddart, J.F.; Heath, J.R. A [2]catenane-based solid state electronically reconfigurable switch. *Science* **2000**, *289*, 1172–1175.
5. Türel, Ö.; Likharev, K. CrossNet: Possible neuromorphic networks based on nanoscale components. *Int. J. Circuit Theory Appl.* **2003**, *31*, 37–53.
6. Seminario, J.M.; Cordova, L.E.; Derosa, P.A. An ab initio approach to the calculation of current–voltage characteristics of programmable molecular devices. *Proc. IEEE*, **2003**, *91*, 1958–1975.
7. Frisch, M.J.; Trucks, G.W.; Schlegel, H.B.; Scuseria, G.E.; Robb, M.A.; Cheeseman, J.R.; Zakrzewski, V.G.; Montgomery, J.A., Jr.; Stratmann, R.E.; Burant, J.C.; Dapprich, S.; Millam, J.M.; Daniels, A.D.; Kudin, K.N.; Strain, M.C.; Farkas, O.; Tomasi, J.; Barone, V.; Cossi, M.; Cammi, R.; Mennucci, B.; Pomelli, C.; Adamo, C.; Clifford, S.; Ochterski, J.; Petersson, G.A.; Ayala, P.Y.; Cui, Q.; Morokuma, K.; Malick, D.K.; Rabuck, A.D.; Raghavachari, K.; Foresman, J.B.; Cioslowski, J.; Ortiz, J.V.; Stefanov, B.B.; Liu, G.; Liashenko, A.; Piskorz, P.; Komaromi, I.; Gomperts, R.; Martin, R.L.; Fox, D.J.; Keith, T.; Al-Laham, M.A.; Peng, C.Y.; Nanayakkara, A.; Gonzalez, C.; Challacombe, M.; Gill, P.M.W.; Johnson, B.; Chen, W.; Wong, M.W.; Andres, J.L.; Gonzalez, C.; Head-Gordon, M.; Replogle, E.S.; Pople, J.A. *GAUSSIAN-98*; Gaussian Inc.: Pittsburgh, PA, 1998.
8. Frisch, M.J.; Trucks, G.W.; Schlegel, H.B.; Scuseria, G.E.; Robb, M.A.; Cheeseman, J.R.; Montgomery, J.A., Jr.; Vreven, T.; Kudin, K.N.; Burant, J.C.; Millam, J.M.; Iyengar, S.S.; Tomasi, J.; Barone, V.; Mennucci, B.; Cossi, M.; Scalmani, G.; Rega, N.; Petersson, G.A.; Nakatsuji, H.; Hada, M.; Ehara, M.; Toyota, K.; Fukuda, R.; Hasegawa, J.; Ishida, M.; Nakajima, T.; Honda, Y.; Kitao, O.; Nakai, H.; Klene, M.; Li, X.; Knox, J.E.; Hratchian, H.P.; Cross, J.B.; Adamo, C.; Jaramillo, J.; Gomperts, R.; Stratmann, R.E.; Yazyev, O.; Austin, A.J.; Cammi, R.; Pomelli, C.; Ochterski, J.W.; Ayala, P.Y.; Morokuma, K.; Voth, G.A.; Salvador, P.; Dannenberg, J.J.; Zakrzewski, V.G.; Dapprich, S.; Daniels, A.D.; Strain, M.C.; Farkas, O.; Malick, D.K.; Rabuck, A.D.; Raghavachari, K.; Foresman, J.B.; Ortiz, J.V.; Cui, Q.; Baboul, A.G.; Clifford, S.; Cioslowski, J.; Stefanov, B.B.; Liu, G.; Liashenko, A.; Piskorz, P.; Komaromi, I.; Martin, R.L.; Fox, D.J.; Keith, T.; Al-Laham, M.A.; Peng, C.Y.; Nanayakkara, A.; Challacombe, M.; Gill, P.M.W.; Johnson, B.; Chen, W.; Wong, M.W.; Gonzalez, C.; Pople, J.A. *GAUSSIAN-2003*; Gaussian, Inc.: Pittsburgh, PA, 2003.
9. Becke, A.D. Density-functional thermochemistry. III. The role of exact exchange. *J. Chem. Phys.* **1993**, *98*, 5648–5652.
10. Perdew, J.P.; Chevary, J.A.; Vosko, S.H.; Jackson, K.A.; Pederson, M.R.; Singh, D.J.; Fiolhais, C. Atoms, molecules, solids, and surfaces: Applications of the generalized gradient approximation for exchange and correlation. *Phys. Rev., B* **1992**, *46*, 6671–6687.
11. Perdew, J.P.; Wang, Y. Accurate and simple analytic representation of the electron-gas correlation energy. *Phys. Rev., B* **1992**, *45*, 13244–13249.
12. Wadt, W.R.; Hay, P.J. Ab initio effective core potentials for molecular calculations. Potentials for main group elements Na to Bi. *J. Chem. Phys.* **1985**, *82*, 284–298.

13. Hay, P.J.; Wadt, W.R. Ab initio effective core potentials for molecular calculations. Potentials for the transition metal atoms Sc to Hg. *J. Chem. Phys.* **1985**, *82*, 270–283.
14. Hay, P.J.; Wadt, W.R. Ab initio effective core potentials for molecular calculations. Potentials for K to Au including the outermost core orbitals. *J. Chem. Phys.* **1985**, *82*, 299–310.
15. Foresman, J.B.; Frisch, A. *Exploring Chemistry with Electronic Structure Methods*; Gaussian: Pittsburgh, 1996.
16. Seminario, J.M.; Zacarias, A.G.; Tour, J.M. Molecular alligator clips for single molecule electronics. Studies of group 16 and isonitriles interfaced with Au contacts. *J. Am. Chem. Soc.* **1999**, *121*, 411–416.
17. Seminario, J.M.; Zacarias, A.G.; Tour, J.M. Molecular current–voltage characteristics. *J. Phys. Chem., A* **1999**, *103*, 7883–7887.
18. Zacarias, A.G.; Castro, M.; Tour, J.M.; Seminario, J.M. Lowest energy states of small Pd clusters using density functional theory and standard ab initio methods. A route to understanding metallic nanopropes. *J. Phys. Chem., A* **1999**, *103*, 7692–7700.
19. Seminario, J.M.; Zacarias, A.G.; Castro, M. Systematic study of the lowest energy states of Pd, Pd₂, and Pd₃. *Int. J. Quantum Chem.* **1997**, *61*, 515–523.
20. Balbuena, P.B.; Derosa, P.A.; Seminario, J.M. Density functional theory study of copper clusters. *J. Phys. Chem., B* **1999**, *103*, 2830–2840.
21. Mujica, V.; Kemp, M.; Ratner, M.A. Electron conduction in molecular wires. I. A scattering formalism. *J. Chem. Phys.* **1994**, *101*, 6849–6855.
22. Mujica, V.; Kemp, M.; Ratner, M.A. Electron conduction in molecular wires. II. Application to scanning tunneling microscopy. *J. Chem. Phys.* **1994**, *101*, 6856–6864.
23. Yaliraki, S.N.; Kemp, M.; Ratner, M.A. Conductance of molecular wires: Influence of molecule–electrode binding. *J. Am. Chem. Soc.* **1999**, *121*, 3428–3434.
24. Yaliraki, S.N.; Roitberg, A.E.; Gonzalez, C.; Mujica, V.; Ratner, M.A. The injecting energy at molecule/metal interfaces: Implications for conductance of molecular junctions from an ab initio molecular description. *J. Chem. Phys.* **1999**, *111*, 6997–7002.
25. Datta, S. *Electronic Transport in Mesoscopic Systems*; Cambridge University Press: Cambridge, UK, 1995.
26. Samanta, M.P.; Tian, W.; Datta, S.; Henderson, J.I.; Kubiak, C.P. Electronic conduction through organic molecules. *Phys. Rev., B* **1996**, *53*, R7626–R7629.
27. Datta, S.; Tian, W.; Hong, S.; Reifenberger, R.; Henderson, J.; Kubiak, C.P. Current–voltage characteristics of self-assembled monolayers by scanning tunneling microscopy. *Phys. Rev. Lett.* **1997**, *79*, 2530–2533.
28. Seminario, J.M.; Zacarias, A.G.; Tour, J.M. Theoretical study of a molecular resonant tunneling diode. *J. Am. Chem. Soc.* **2000**, *122*, 3015–3020.
29. Derosa, P.A.; Seminario, J.M. Electron transport through single molecules: Scattering treatment using density functional and green function theories. *J. Phys. Chem., B* **2001**, *105*, 471–481.
30. Papaconstantopoulos, D.A. *Handbook of the Band Structure of Elemental Solids*; Plenum Press: New York, 1986.
31. Tian, W.; Datta, S.; Hong, S.; Reifenberger, R.; Henderson, J.I.; Kubiak, C.P. Conductance spectra of molecular wires. *J. Chem. Phys.* **1998**, *109*, 2874–2882.
32. Ventra, M.D.; Kim, S.-G.; Pantelides, S.T.; Lang, N.D. Temperature effects on the transport properties of molecules. *Phys. Rev. Lett.* **2001**, *86*, 288–291.
33. Seminario, J.M.; Zacarias, A.G.; Derosa, P.A. Analysis of a dinitro-based molecular device. *J. Chem. Phys.* **2002**, *116*, 1671–1683.
34. Lide, D.R. *CRC Handbook of Chemistry and Physics*; CRC Press: Boca Raton, 1998. vol. 79th Edition 1998–1999.
35. Seminario, J.M.; Zacarias, A.G.; Derosa, P.A. Theoretical analysis of complementary molecular memory devices. *J. Phys. Chem., A* **2001**, *105*, 791–795.
36. Roetti, C. The CRYSTAL Code. In *Lecture Notes in Chemistry*; Pisani, C., Ed.; Springer-Verlag: Berlin, 1996; Vol. 67, 125–137.
37. Dovesi, R.; Roetti, C.; Causa, M.; Apra, E.; Orlando, R.; Saunders, V.R.; Harrison, N.M. *Crystal 98*, http://www.ccwp.ac.uk/ccwp/cg_crystal.html.
38. Towler, M.D.; Zupan, A.; Causa, M. Density functional theory in periodic systems using local Gaussian basis sets. *Comput. Phys. Commun.* **1996**, *98*, 181–205.
39. Cundari, T.R.; Stevens, W.J. Effective core potentials methods for the lanthanides. *J. Chem. Phys.* **1993**, *98*, 5555–5565.
40. Stevens, W.J.; Krauss, M.; Basch, H.; Jasien, P.G. Relativistic compact effective potentials and efficient, shared-exponent basis-sets for the 3rd-row, 4th-row, and 5th-row atoms. *Can. J. Chem.* **1992**, *70*, 612–630.
41. Chen, J.; Reed, M.A.; Rawlett, A.M.; Tour, J.M. Large on–off ratio negative differential resistance in a molecular electronic device. *Science* **1999**, *286*, 1550–1552.

42. Seminario, J.M.; Derosa, P.A. Molecular gain in a thiolane system. *J. Am. Chem. Soc.* **2001**, *123*, 12418–12419.
43. Donhauser, Z.J.; Mantooh, B.A.; Kelly, K.F.; Bumm, L.A.; Monnell, J.D.; Stapleton, J.J.; Price, D.W., Jr.; Rawlett, A.M.; Allara, D.L.; Tour, J.M.; Weiss, P.S. Conductance switching in single molecules through conformational changes. *Science* **2001**, *292*, 2303–2307.
44. Tour, J.M.; Kosaki, M.; Seminario, J.M. Molecular scale electronics: A synthetic/computational approach to digital computing. *J. Am. Chem. Soc.* **1998**, *120*, 8486–8493.
45. Tour, J.M.; Kozaki, M.; Seminario, J.M. Use of Molecular Electrostatic Potential for Molecular Scale Computation. US Patent 6,259,277, 2001.
46. Reed, M.A.; Chen, J.; Rawlett, A.M.; Price, D.W.; Tour, J.M. Molecular random access memories. *Appl. Phys. Lett.* **2001**, *78*, 3735–3737.
47. Chen, J.; Wang, W.; Reed, M.A.; Rawlett, A.M.; Price, D.W.; Tour, J.M. Room-temperature negative differential resistance in nanoscale molecular junctions. *Appl. Phys. Lett.* **2000**, *77*, 1224–1226.
48. Seminario, J.M.; Zacarias, A.G.; Tour, J.M. Theoretical interpretation of conductivity measurements of thiolane sandwich. A molecular scale electronic controller. *J. Am. Chem. Soc.* **1998**, *120*, 3970–3974.
49. Seminario, J.M.; De La Cruz, C.; Derosa, P.A. Nanometer-size conducting and insulating molecular devices. *Chem. Phys. Lett.* **2003**. Submitted.
50. Derosa, P.A.; Guda, S.; Seminario, J.M. A programmable molecular diode driven by charge-induced conformational changes. *J. Am. Chem. Soc.* **2003**, *125*, 14240–14241.
51. Chen, J.; Calvet, L.C.; Reed, M.A.; Carr, D.W.; Grubisha, D.S.; Bennett, D.W. Electronic transport through metal-1,4-phenylene diisocyanide-metal junctions. *Chem. Phys. Lett.* **1999**, *313*, 741–748.
52. Vondrak, T.; Wang, H.; Winget, P.; Cramer, C.J.; Zhu, X.-Y. Interfacial electronic structure in thiolate self-assembled monolayers: Implication for molecular electronic. *J. Am. Chem. Soc.* **2000**, *122*, 4700–4707.
53. Yaliraki, S.N.; Ratner, M.A. Molecule-interface coupling effects on electronic transport in molecular wires. *J. Chem. Phys.* **1998**, *109*, 5036–5043.
54. Emberly, E.G.; Kirzenow, G. Theoretical study of electrical conduction through a molecule connected to metallic nanocontacts. *Phys. Rev., B* **1998**, *58*, 10911–10920.
55. Selzer, Y.; Salomon, A.; Cahen, D. The importance of chemical bonding to the contact for tunneling through alkyl chains. *J. Phys. Chem., B* **2002**, *106*, 10432–10439.
56. Cahen, D.; Hodes, G. Molecules and electronic materials. *Adv. Mater.* **2002**, *14*, 789–798.
57. Onipko, A.; Klymenko, Y.; Malysheva, L. Conductance of molecular wires: Analytical modeling of connection to leads. *Phys. Rev., B* **2000**, *62*, 10480–10493.
58. Shashidhar, R. *Report to DARPA Moletronics Program*; 2002.
59. Derosa, P.A.; Zacarias, A.C.; Seminario, J.M. Application of Density Functional Theory to the Study and Design of Molecular Electronic Devices: The Metal-Molecule Interface. In *Reviews in Modern Quantum Chemistry*; Sen, K.D., Ed.; World Scientific: Singapore, 2002; 1537–1567.
60. Ulman, A. Formation and structure of self-assembled monolayers. *Chem. Rev.* **1996**, *96*, 1533–1554.
61. Heister, K.; Rong, H.-T.; Buck, M.; Zharnikov, M.; Grunze, M. Odd-even effects at the S-metal interface and in the aromatic matrix of biphenyl-substituted alkanethiol self-assembled monolayers. *J. Phys. Chem., B* **2001**, *105*, 6888–6894.
62. Haag, R.; Rampi, M.A.; Holmlin, R.E.; Whitesides, G.M. Electrical breakdown of aliphatic and aromatic self-assembled monolayers used as nanometer-thick organic dielectrics. *J. Am. Chem. Soc.* **1999**, *121*, 7895–7906.
63. Tour, J.M.; VanZandt, W.L.; Husband, C.P.; Husband, S.M.; Wilson, L.S.; Franzon, P.D.; Nakanishi, D.P. NanoCell logic gates for molecular computing. *IEEE Trans. Nanotechnol.* **2002**, *1*, 100–109.
64. Seminario, J.M.; Cordova, L.E.; Derosa, P.A. Search for minimum molecular programmable units. *Proc. IEEE Nanotechnol. Conf.* **2002**, *2*, 421–424.
65. Seminario, J.M.; Cordova, L.E. Toward multiple-valued configurable random molecular logic units. *Proc. IEEE Nanotechnology Conf.* **2001**, *1*, 146–150.
66. Seminario, J.M.; Derosa, P.A.; Cordova, L.E.; Bozard, B.H. A molecular device operating at terahertz frequencies: Theoretical simulations. *IEEE Trans. Nanotechnol.* **2003**, *in press*.
67. Seminario, J.M. A theory guided approach to molecular electronics: Analysis, design and simulation. *Proc. IEEE Nanotechnol. Conf.* **2003**.



Molecular Manipulator Dynamic Design Criteria

Andrés Jaramillo-Botero

Pontificia Universidad Javeriana, Cali, Colombia

M

INTRODUCTION

The ability to intentionally manipulate three-dimensional (3-D) irregular-shaped matter with atomic precision, abiding to physical laws, is considered as one of the ultimate goals of nanoscience and engineering. Nature has given us a vast assortment of biological molecular machines that demonstrate the viability of this goal, including, among others, the ribosome (which can translate mRNA instructions into proteins) and kinesin, an enzyme that acts as a molecular motor which pulls things toward the outer reaches of the cell. In nerve cells, it is kinesin that pulls vesicles or other cellular materials from the cell body to the nerve endings. These biological systems are primarily “application-specific molecular machines.” They are not universal assemblers that could, in principle, be used in a programmable fashion to perform alternate functions at the molecular level. Self-replicating programmable manufacturing systems able to arrange atoms for multiple “applications” would require a universal assembler with an appropriate end-effector and a corresponding controller. The scope of this entry explores design criteria for such a universal assembler (Fig. 1).

This article reviews the literature on the creation of nanometer-scale spatial positioners, from a kinematic and dynamic standpoint, as one of the basic building blocks for an atomic-scale manipulator (to arrange differently functionalized molecular building blocks into a lattice or any other nanometer-scale object in a specified and complex pattern, it is necessary to introduce positional control). The development of theoretical criteria for the design of reduced constrained dynamic complexity of a nanoscale positioning device (nanomanipulator), based on the equations of motion (EOM) for spatial serially articulated rigid multibodies, is presented in this article. By using a rigid-body semiclassical mechanics approach, it is shown how dynamic complexities, such as coupling and nonlinearities introduced by high-speed operation, complicate the control task and deteriorate performance. The first section of the article introduces the reader to appropriate state space forms of the EOM for a serially coupled set of rigid bodies using internal coordinates. This allows a compact mathematical description of the problem at hand and exposes the intended solution by permitting concise physical insight. The second section develops the

complete set of EOM for both the Newton–Euler and Lagrange–Euler formulations. From the state space equivalence of both methods, the EOM are then expressed as a function of the articulated body inertia operator for the multibody, leading to a highly dependent form of the EOM on this operator. The internal matrix structure of the articulated body inertia is then revealed. The third section presents the analysis that leads to a reduced set of EOM from the structural simplification of the articulated body inertia matrix and develops the general kinematics and mass distribution criteria for doing so. From the resulting analysis, a set of compliant manipulator configurations that could, in principle, be built from carbon nanotubes, linked by direct-driven rotational molecular joints, is shown. Finally, the last section concludes on the obtained results and describes current and future work.

NEED FOR A UNIVERSAL MOLECULAR ASSEMBLER

Today, atomic force microscopy (AFM) provides capabilities that allow scientist to characterize matter at the nanometer-scale (e.g., electrically, mechanically, and chemically) while correlating it to structure.^[1] But perhaps its most notable capability is that of allowing the manipulation of nanometer-scale objects efficiently on 2-D surfaces,^[2,3] making it possible to explore substrate–sample interactions^[4] or the creation of devices incorporating nanometer-scale objects.^[5] Atomic force microscopy is indeed an important tool for the study of nanodevices, but as impressive as it may be, it is not likely to become the type of atomic manipulator expected to permit the aforementioned goal, leading to the shift in paradigm proposed by molecular manufacturing: bottom-up atomic-scale construction. For this, a new set of devices is required to allow for atomic level manipulation in 3-D space, autonomous/commanded self-replication, nanometer/submicrometer-scale size, increased spatial dexterity, and higher operational energy efficiency, among others.

Currently proposed nanoscale molecular devices inherit their design, for the most part, from macroscopic counterparts.^[6,7] Little regard is taken to consider atomic-scale effects (in particular, nonbonded interactions or the

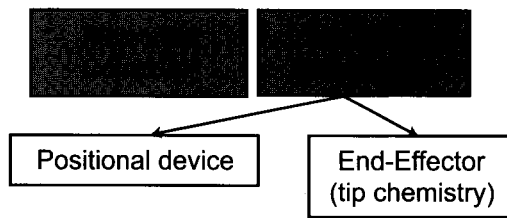


Fig. 1 Universal molecular assembler.

discrete nature of the atoms spherical contact surfaces^[6] other than mere static structural stability of the molecular components or the undesired dynamic properties being ported from the macroscopic systems to the nanoscale that increase controller complexities and, in some cases, impose serious constraints on performance. Nanometer-scale manipulator designs tend to favor particular characteristics (e.g., force magnitude at the end-effector or stretching stiffness—refer to Fig. 2) while sacrificing other properties that are also fundamental at the nanoscale, such as dexterity (for molecular obstacle avoidance), reachable workspace, or operational speed, among others.

New Approach

This article is concerned with the theoretical criteria for the design of a nanoscale positioning device (nanomanipulator), based on the equations of motion (EOM) for spatial serially articulated rigid multibodies, in particular, by using a rigid-body semiclassical mechanics approach. The resulting equations for the corresponding micro-canonical or canonical ensembles make it evident that the

key operator affecting the complexity of the EOM is the articulated body inertia of the system.

This entry analyzes the necessary conditions under which the spatial articulated body inertia operator for the system can be made decoupled (diagonal) and configuration-invariant (independent of joint coordinates). Simplifying its structure via design, by considering the kinematics and mass distribution of the system, proves to be a major advantage for reducing the complexity of the forward dynamics solution (used in molecular simulations) and the inverse dynamics solution (used in the design of appropriate controllers). The proposed devices are presumed to be fully actuated; that is, joint motion depends on an individual actuator, located directly or remotely on the joint origin.

Although some research has been devoted in the past to highly speculative designs and concepts,^[7,9,10] some with adequate functionality (evaluated via molecular simulations using first principles), it is worth pointing out that advances into the design of robust modular mechano-synthesis nanodevices are still very limited. This work provides a new direction in this quest by proposing novel designs for a positioning device for molecular mechano-synthesis with high dexterity, large workspace (ratio to manipulator size), and improved dynamic performance at high speed that could, in principle, be synthesized from modular self-assembled parts. Furthermore, the proposed designs can be actuated at the corresponding joints by existing polymeric muscles at the nanometer scale. It is assumed that arbitrary positioning of atoms in 3-D space requires at least 3 degrees of freedom, while that of complex macromolecules requires a minimum of 6 degrees of freedom to account for the added complexity of arbitrary orientation of manipulated bodies.

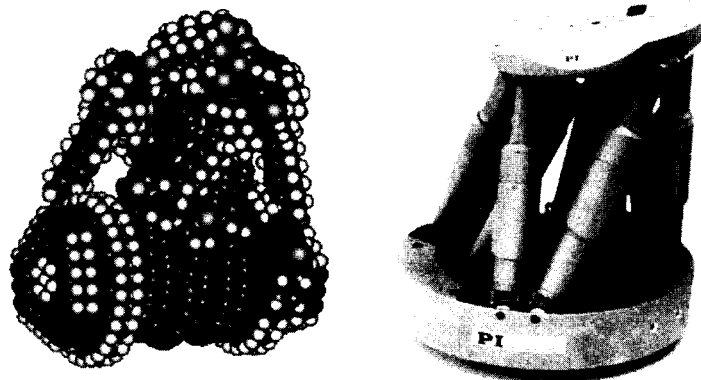


Fig. 2 Nanometer scale Stewart platform manipulator (left picture—©K.E. Drexler, Institute of Molecular Manufacturing—<http://www.imm.org>) and macroscopic commercial counterpart (right picture—by Physik Instrumente GmbH). Both designs trade off controllability (highly coupled designs that limit speed), dexterity (useful in obstacle avoidance), and reachable workspace for higher payload. (View this art in color at www.dekker.com.)

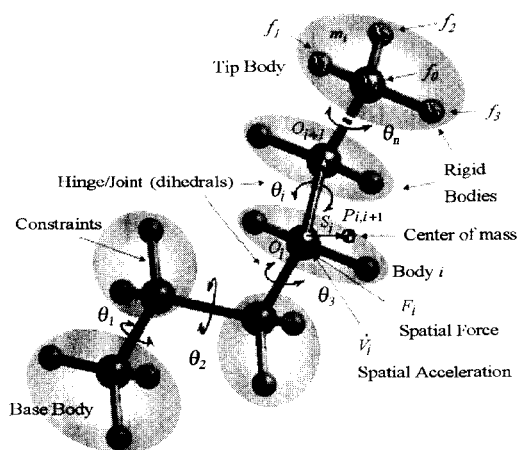


Fig. 3 Rigid body (atomic clusters) molecular system representation. (View this art in color at www.dekker.com.)

The approach presented here considers a semiclassical dynamics formulation of the constrained EOM for a serial set of articulated rigid molecular bodies, analogous in structure to a human manipulator arm. The notion of rigid body is employed at the molecular level in the context of clusters of atoms (refer to Fig. 3) that make up the primary components of the nanoscale positioning device (e.g., a single atom, a phenyl ring, an alpha helix, or even an entire protein domain). In turn, the notion of constrained dynamics comes from introducing constraints on molecular structural properties such as bond lengths and bond angles to shift focus onto the dihedrals that distinguish conformations, in this way reducing the number of atomic degrees of freedom (DOF).

Consequently, the description and analysis of the molecular system are simplified without losing nanoscale properties, and the real-time requirements for control or simulation of the device are significantly reduced (intracluster motions are neglected). Articulated motion comes from clusters interconnected via hinges or joints. Joints do not have to be bonded atomically as shown in Fig. 3.

STATE SPACE REPRESENTATION OF THE EQUATIONS OF MOTION

Assume that the state of the system is known and defined by the collection of generalized coordinates (Q , \dot{Q} , \ddot{Q}) corresponding to effective joint positions, velocities, and accelerations, respectively. Furthermore, assume that the mass distribution of each rigid element of the multibody is completely characterized, given a localized center of mass and a known inertia tensor. It then follows that for a

constrained molecular dynamics model, the EOM under Newton's formulation are represented in state space as

$$F(Q) = M(Q)\ddot{Q} + C(Q, \dot{Q}) + N(Q, \dot{Q}) \quad (1)$$

where F denotes the vector of generalized forces (e.g., torques) applied at the joint, N are any other conservative forces (e.g., potential) acting on each generalized coordinate, M denotes the articulated body inertia matrix, and C denotes the nonlinear velocity-dependent terms of force (e.g., Coriolis, centrifugal, and gyroscopic forces). Solving Eq. 1 leads to a direct calculation of joint actuator forces required for the system to follow a specific spatial trajectory. On the other hand, the dynamics of motion are obtained by solving Eq. 1 for effective joint accelerations,

$$\ddot{Q} = M^{-1}(Q)[F(Q) - C(Q, \dot{Q}) - N(Q, \dot{Q})] \quad (2)$$

This article explores the dependence of both Eqs. 1 and 2 on the articulated body inertia operator M and particular forms of this operator that lead to reduced complexities in both the inverse and forward dynamics solutions expressed above.

Canonical Ensemble

Standard Newtonian dynamics leads to conservation of total energy along a motion trajectory; thus the collection of points for this type of molecular dynamics (MD) describes a microcanonical ensemble (NVE: number of particles, volume, and energy are conserved). To deal with normal experimental conditions, it is necessary to add contact with a heat bath at constant temperature. An appropriate ensemble to simulate these conditions (NVT and NPT) is the canonical ensemble. The corresponding extensions to support a canonical ensemble were carried out by Nosé^[11] and Hoover^[12] for Cartesian dynamics. Nosé introduced an additional time-scaling variable, and its conjugate momentum, into the system to represent its interaction with the heat bath. The resulting EOM drive the velocity changes with time which, in turn, drive the changes in thermal energy (kinetic), leading to its proper canonical description. However, Nosé's EOM involve virtual time, which implies unequal time steps in real time. This is inconvenient for the analysis of dynamic properties of the system (e.g., Fast Fourier Transform (FFT)), so Hoover proposed transforming the Nosé EOM into real variables. A concise form of the Hoover dynamics EOM follows,

$$F(Q) = M(Q)\ddot{Q} + C(Q, \dot{Q}) + \Phi_x^{\text{nb}} + \xi M(Q)\dot{Q} \quad (3)$$

where Φ_x^{nb} is the sum of gradients of the nonbond and external potentials Φ with respect to Cartesian coordinates and ξ denotes the baths friction coefficient. For simulation purposes, the friction coefficient, ξ , is integrated for each time step using a modified leap frog verlet from the

relation between the ratio of instantaneous temperature to bath temperature and the timescale of relaxation of the bath variables.^[13]

It should be noted that Eq. 3 has the same form as that for the microcanonical ensemble (Eq. 1), except that it includes one additional term: a friction term as a result of the atomic interaction with a heat bath.

The Articulated Body Inertia Using Spatial Operator Algebra

This section presents an overview of the development of the EOM for a serial chain multibody (Fig. 3) using spatial operator algebra. For additional detail on spatial algebra in multibody dynamics, see Refs. [14] and [15]. From the equivalence between the Newtonian and Lagrangian formulations, a particular form of the EOM is found to express the nonlinear velocity-dependent terms in C (Eq. 1) as a function of the articulated body inertia of the system, M . This form of the EOM conduces to a straightforward explanation of why altering the structure of M , by design, is critical for the dynamic complexity of the system.

Spatial Transformations

To operate and manipulate 6-D physical quantities on a common coordinate reference frame, 6-D spatial transformation operators are required. For any generic 3-D distance vector from point 1 to point 2, $t_{1,2}$, the translation operator is defined as

$$\hat{T}_{1,2} = \begin{bmatrix} U & \tilde{t}_{1,2} \\ 0 & U \end{bmatrix} \quad (4)$$

where

$$\tilde{t}_{1,2} = \begin{bmatrix} 0 & -t_z & t_y \\ t_z & 0 & -t_x \\ -t_y & t_x & 0 \end{bmatrix} \quad (5)$$

is the skew symmetric equivalent to the vector cross product and U is the 3-D identity matrix.

To simplify notation, a coordinate free form representation of the EOM is adopted, hence the orientation transformation is not made explicit. For an actual implementation of the solution, such an operator is required.

Newton–Euler Formulation

Assuming a base to tip propagation of kinematic parameters (refer to Fig. 3), the spatial (translational and rotational components stacked in a single 6-D operator) velocities (V), from body $i=1 \dots n$, are expressed as

$$V_i = \hat{P}_{i-1,i}^T V_{i-1} + H_i \dot{Q}_i \quad (6)$$

where H_i denotes the projection matrix onto the joint (i) DOF. Differentiating with respect to time results in the spatial accelerations (\dot{V}),

$$\dot{V}_i = \hat{P}_{i-1,i}^T \dot{V}_{i-1} + H_i \ddot{Q}_i + \dot{\hat{P}}_{i-1,i}^T V_{i-1} + \dot{H}_i \dot{Q}_i \quad (7)$$

A reverse (or downward) propagation from body $i = n \dots 1$ of the spatial forces follows to complete the EOM,

$$F_i = \hat{P}_{i,i+1} F_{i+1} + I_i \dot{V}_i + [\dot{I}_i + I_i \dot{S}_{O_i,cm}^T] V_i \quad (8)$$

where the spatial inertia matrix for body i , $I_i \in \mathfrak{R}^{6 \times 6}$, is obtained from the scalar mass and the moments of inertia with respect to a point of interest on the body. Boundary conditions are set accordingly for the type of base (floating/fixed) and for the existence of external forces. Assuming for body i a mass m_i and a tensor of inertia $J_{i,cm}$ about its center of mass, cm, the spatial inertia operator is defined as

$$I_{i,cm} = \begin{bmatrix} J_{i,cm} & 0 \\ 0 & m_i U \end{bmatrix} \in \mathfrak{R}^{6 \times 6} \quad (9)$$

It then follows from the parallel axis theorem that the spatial inertia of the body about the hinge origin, O_i , I_i is given by

$$I_i = \begin{bmatrix} J_{O_i} & m_i \tilde{s}_{O_i,cm} \\ -m_i \tilde{s}_{O_i,cm} & m_i U \end{bmatrix} \quad (10)$$

Finally, spatial forces are projected onto the DOF of each joint to obtain the effective forces,

$$F_i = H_i^T F_i \quad (11)$$

By assuming, for notational simplicity, that EOM are found at the center of mass and by defining higher level physical operators as follows,

$$I = \text{diag}[I_n, I_{n-1}, \dots, I_1] \in \mathfrak{R}^{6n \times 6n}$$

$$H = \text{diag}[H_n, H_{n-1}, \dots, H_1]^T \in \mathfrak{R}^{6n \times m}$$

$$V = [V_n, V_{n-1}, \dots, V_1]^T \in \mathfrak{R}^{6n \times m}$$

$$\dot{Q} = [\dot{Q}_n, \dot{Q}_{n-1}, \dots, \dot{Q}_1]^T \in \mathfrak{R}^{n \times m}$$

$$\dot{V} = [\dot{V}_n, \dot{V}_{n-1}, \dots, \dot{V}_1]^T \in \mathfrak{R}^{6n \times m}$$

$$\ddot{Q} = [\ddot{Q}_n, \ddot{Q}_{n-1}, \dots, \ddot{Q}_1]^T \in \mathfrak{R}^{n \times m}$$

$$F = [F_n, F_{n-1}, \dots, F_1]^T \in \mathfrak{R}^{6n \times m}$$

$$S = \text{diag}[\hat{S}_n, \hat{S}_{n-1}, \dots, \hat{S}_1] \in \mathfrak{R}^{6n \times 6n}$$

$$P = \begin{bmatrix} U & 0 & 0 & \dots & 0 \\ -\hat{P}_{n,n-1} & U & 0 & \dots & 0 \\ 0 & -\hat{P}_{n-1,n-2} & U & \dots & 0 \\ \vdots & \vdots & \ddots & \ddots & \vdots \\ 0 & 0 & \dots & -\hat{P}_{2,1} & U \end{bmatrix} \quad (12)$$

where m is the number of DOF per joint and U is the 6-D identity matrix. Then, Eqs. 6–8 and 11 are rewritten in indexless spatial notation.

$$P^T V = H \dot{Q} \quad (13)$$

Solving for spatial velocities in Eq. 13

$$V = P^{T^{-1}} H \dot{Q} \quad (14)$$

where

$$P^{-1} = \begin{bmatrix} U & 0 & 0 & \dots & 0 \\ \hat{P}_{n-1,n} & U & 0 & \dots & 0 \\ \hat{P}_{n-2,n} & \hat{P}_{n-2,n-1} & U & \dots & 0 \\ \vdots & \vdots & \ddots & \ddots & \vdots \\ \hat{P}_{1,n} & \hat{P}_{1,n-1} & \dots & \hat{P}_{1,2} & U \end{bmatrix} \in \mathfrak{R}^{6n \times 6n} \quad (15)$$

Because $P^{T^{-1}}$ (upper triangular) is nilpotent, $P_{0,n}^{T^{-1}} = 0$, then $P^{T^{-1}} = P^{-1T}$. For simplicity, let $\rho \equiv P^{-1}$, then,

$$V = \rho^T H \dot{Q} \quad (16)$$

From the above equation, it follows that the manipulator Jacobian (J), relating the joint state with the end-effector position and orientation, is given by

$$J = \rho^T H \quad (17)$$

In turn, spatial accelerations are written as follows,

$$\dot{V} = \dot{\rho}^T H \dot{Q} + \rho^T \dot{H} \dot{Q} + \rho^T H \ddot{Q} \quad (18)$$

and the spatial forces expressed with respect to joint origin,

$$PF = \dot{I}V + I\dot{V} - \dot{S}IV \quad (19)$$

Solving for spatial forces,

$$F = \rho[\dot{I}V + I\dot{V} - \dot{S}IV] \quad (20)$$

and from projecting onto the axes of motion from Eq. 11, the effective forces are obtained,

$$F = H^T \rho[\dot{I}V + I\dot{V} - \dot{S}IV] \quad (21)$$

Replacing Eqs. 14 and 18 in Eq. 21,

$$F = H^T \rho[\dot{I}\rho^T H \dot{Q} + I[\dot{\rho}^T H \dot{Q} + \rho^T \dot{H} \dot{Q} + \rho^T H \ddot{Q}] - \dot{S}I\rho^T H \dot{Q}] \quad (22)$$

Grouping terms of \ddot{Q} and \dot{Q} ,

$$F = [H^T \rho I \rho^T H] \ddot{Q} + H^T \rho \times [\dot{I}\rho^T H + I\dot{\rho}^T H + I\rho^T \dot{H} - \dot{S}I\rho^T H] \dot{Q} \quad (23)$$

Recognizing that Eq. 23 is equivalent, in state space, to Eq. 1, then the articulated body inertia operator for the system is given by

$$M = H^T \rho I \rho^T H \quad (24)$$

Clearly, M is strictly dependent only on the kinematics and mass distribution of the multibody. Note that it can also be written in terms of the manipulator Jacobian, from Eq. 17

$$M = JIJ^T \quad (25)$$

The nonlinear-dependent (quadratic in velocity) terms (Coriolis, centrifugal, and gyroscopic) in Eq. 23 are extracted as

$$C = H^T \rho[\dot{I}\rho^T H + I\dot{\rho}^T H + I\rho^T \dot{H} - \dot{S}I\rho^T H] \dot{Q} \quad (26)$$

Lagrange–Euler Formulation

Using the same operators already found, we will express the EOM in terms of the Lagrangian operator, $L=T-U$, where T is the kinetic energy and U is the potential energy.

The kinetic energy of the serial multibody

The kinetic energy for the entire system is the sum of the kinetic energy of each of the links, equivalent to

$$T_i = \frac{1}{2} \sum_{i=1}^n V_i^T I_i V_i \quad (27)$$

This can be expressed in simplified spatial form from the higher level operators in Eqs. 12 and 16, using the above equation,

$$T(Q, \dot{Q}) = \frac{1}{2} \dot{Q}^T H^T \rho(Q) I \rho^T(Q) H \dot{Q} \quad (28)$$

From Eq. 18, it then follows that the kinetic energy is given as a function of M by

$$T(Q, \dot{Q}) = \frac{1}{2} \dot{Q}^T M(Q) \dot{Q} \quad (29)$$

The potential energy of the serial multibody

The potential energy of each link is a function of the geometry of the manipulator. Let $h_i(Q)$ be the height of the center of mass of the i th link (position of the center of mass opposing the direction of gravity). The total potential energy for the manipulator is given by the sum of contributions from each link:

$$U(Q) = \sum_{i=1}^n m_i g h_i(Q) \quad (30)$$

where m_i is the mass of the i th link and g is the gravitational constant. For simplicity, the systems potential energy is denoted in spatial notation as

$$U(Q) = \Phi(Q) \quad (31)$$

No gravity pull is assumed at the nanoscale.

The Lagrangian operator for the serial articulated multibody is then written as

$$L(Q, \dot{Q}) = T - U = \frac{1}{2} \dot{Q}^T M(Q) \dot{Q} - \Phi(Q) \quad (32)$$

Yang and Tzeng^[16] proposed a simple method to "linearize" serial chain robot manipulators based on the Lagrange-Euler formulation. The method consists of eliminating by design the terms in T and U that depend on joint coordinate variables. By doing so, differentiation of both kinetic and potential energy leads to complete independence of the EOM on joint rates (velocity-dependent terms) for simple manipulators of up to 3 DOF and simplified dynamics for higher DOF. Nonetheless, the resulting configurations are still joint-coupled.

Applying variational principles to the Lagrangian operator results in the Lagrange-Euler dynamic EOM,

$$F_i = \frac{d}{dt} \frac{\partial L}{\partial \dot{Q}_i} - \frac{\partial L}{\partial Q_i} \quad (33)$$

where F_i represents the spatial forces acting on the i th joint.

It will be convenient to express the kinetic energy as a sum,

$$L(Q, \dot{Q}) = \frac{1}{2} \sum_{i,j=1}^n M_{ij}(Q) \dot{Q}_i \dot{Q}_j - \Phi(Q) \quad (34)$$

From Eqs. 29-31, the first term in Eq. 33 is given by

$$\begin{aligned} \frac{d}{dt} \frac{\partial L}{\partial \dot{Q}_i} &= \frac{d}{dt} \left(\sum_{j=1}^n M_{ij} \dot{Q}_j \right) \\ &= \sum_{j=1}^n (\dot{M}_{ij} \dot{Q}_j + M_{ij} \ddot{Q}_j) \end{aligned} \quad (35)$$

On the other hand, the first partial derivative of the Lagrangian operator with respect to joint variables is

$$\frac{\partial L}{\partial Q} = \frac{1}{2} \sum_{j,k=1}^n \frac{\partial M_{kj}(Q)}{\partial Q_i} \dot{Q}_k \dot{Q}_j - \frac{\partial \Phi(Q)}{\partial Q_i} \quad (36)$$

Subtracting Eq. 36 from Eq. 35 results in the EOM. Because the potential energy is dependent only on Q , these are not expanded (our interest lays on nonlinear velocity-dependent terms)

$$\begin{aligned} F_i &= \sum_{j=1}^n (\dot{M}_{ij} \dot{Q}_j + M_{ij} \ddot{Q}_j) - \frac{1}{2} \\ &\quad \times \sum_{j,k=1}^n \frac{\partial M_{kj}(Q)}{\partial Q_i} \dot{Q}_k \dot{Q}_j + \frac{\partial \Phi(Q)}{\partial Q_i} \end{aligned} \quad (37)$$

This is expressed in higher-level spatial operators as

$$F = M \ddot{Q} + \dot{M} \dot{Q} - \frac{1}{2} \dot{Q}^T M_Q \dot{Q} + \frac{\partial \Phi}{\partial Q} \quad (38)$$

where M_Q corresponds to the partial derivative of M with respect to joint variables. \dot{M}_{ij} in Eq. 37 can be expanded in terms of partial derivatives to yield

$$\sum_{j=1}^n \dot{M}_{ij}(Q) = \sum_{j,k=1}^n \frac{\partial M_{ij}(Q)}{\partial Q_k} \dot{Q}_k \quad (39)$$

Rewriting Eq. 37 using the above result yields

$$\begin{aligned} F_i &= \sum_{j=1}^n M_{ij}(Q) \ddot{Q}_j + \frac{\partial \Phi(Q)}{\partial Q_i} \\ &\quad + \sum_{j,k=1}^n \left(\frac{\partial M_{ij}}{\partial Q_k} \dot{Q}_j \dot{Q}_k - \frac{1}{2} \frac{\partial M_{kj}(Q)}{\partial Q_i} \dot{Q}_k \dot{Q}_j \right) \end{aligned} \quad (40)$$

From Eq. 37, the nonlinear velocity-dependent terms are given by

$$C(Q, \dot{Q}) = \dot{M} \dot{Q} - \frac{1}{2} \dot{Q}^T M_Q \dot{Q} \quad (41)$$

By inspection, Eq. 37 is equivalent in state space to Eq. 1. It must then follow that Eq. 41 \equiv Eq. 26,

$$H^T \rho [\dot{I} \rho^T H + I \dot{\rho}^T H + I \rho^T \dot{H} - \dot{S} I \rho^T H] \dot{Q} \\ \equiv \dot{M} \dot{Q} - \frac{1}{2} \dot{Q}^T M_Q \dot{Q} \quad (42)$$

The proof of this equality is reached in a straightforward manner from the time derivatives of the spatial operators.

The key issue here is noting the dependence of F on M in Eq. 40. By doing so, the following can be said about simplifying the complexity of F via careful structural design of the multibody.

1. Obtaining a decoupled form of the articulated body inertia operator (i.e., a diagonalized form of it) eliminates joint actuator interactions.
2. Obtaining a configuration-invariant form of the articulated body inertia operator eliminates the dependence of M on joint coordinates (Q), hence nonlinear velocity-dependent terms in the EOM (C) vanish, except nonbonded potential components and friction term.

STRUCTURAL SIMPLIFICATIONS ON M THAT LEAD TO SIMPLIFIED CONSTRAINED DYNAMICS

The existence of a diagonalized composite body inertia form for serially articulated rigid-body spatial manipulators can be proven given that the representing mass operator for the system defines a metric tensor.^[17] If this tensor is made to be metric Euclidean (i.e., with constant coefficients) by design, based on kinematic and mass distribution characteristics, then its configuration manifold is flat and the associated curvature tensor vanishes^[21] (i.e., global diagonalizing transformation exists).

$$R_{hijk} = \frac{1}{2} \\ \times \left[\frac{\partial^2 M_{hk}}{\partial Q_i \partial Q_j} + \frac{\partial^2 M_{ij}}{\partial Q_h \partial Q_k} - \frac{\partial^2 M_{hj}}{\partial Q_i \partial Q_k} - \frac{\partial^2 M_{ik}}{\partial Q_h \partial Q_j} \right] \\ + \sum_l \left[\left\{ \begin{matrix} l \\ ij \end{matrix} \right\} [hk, l] - \left\{ \begin{matrix} l \\ ik \end{matrix} \right\} [hj, l] \right] = 0 \quad (43)$$

where R is the curvature tensor of M , R_{hijk} is the corresponding $n(n+1)/2$ Riemannian symbols of the first kind,^[18] and the quantities

$$[ij, k] \text{ and } \left\{ \begin{matrix} k \\ ij \end{matrix} \right\}$$

are the Christoffel symbols of the first and second kind,^[18] respectively, which are computed from the corresponding first derivatives of the mass matrix operator with respect to the joint angles.

On the other hand, the existence of a configuration-invariant form of the articulated body inertia can be proven and the corresponding criteria can be derived when the first-order partial derivative of the corresponding metric tensor with respect to joint coordinates vanishes ($M_Q = 0$),

$$M_{Q_i} = \frac{\partial H^T}{\partial Q_i} \rho I \rho^T H + H^T \frac{\partial \rho}{\partial Q_i} I \rho^T H + H^T \rho \frac{\partial I}{\partial Q_i} \rho^T H \\ + H^T \rho I \frac{\partial \rho^T}{\partial Q_i} H + H^T \rho I \rho^T \frac{\partial H}{\partial Q_i} \\ = H^T \rho [\tilde{H}_\delta^i \rho I - I \rho^T \tilde{H}_\delta^i] \rho^T H \quad (44)$$

where the matrix \tilde{H}_δ^i is the $6n \times 6n$ matrix whose elements are all zero, except for the 6×6 block corresponding to the \tilde{H}_i at the i th location on the diagonal. The index i corresponds to the joint-angle Q_i with respect to which the sensitivity derivative of the mass matrix M_Q is being taken.

An alternate approach comes from the structure of M . By analytically determining the joint coordinate-dependent terms in M and explicitly eliminating these, or inducing their constancy, through design criteria, configuration invariance can be achieved. Additionally, the off-diagonal terms in M can be explicitly removed by design. Expanding the spatial operator form of M , found in Eq. 24, into its diagonal and off-diagonal components leads to

$$M_{i,i} = H_i^T \left[I_i + \sum_{k=i+1}^n \hat{P}_i^k I_k \hat{P}_i^{kT} \right] H_i \quad (45)$$

$$M_{i,j} = H_i^T \left[\hat{P}_j^i I_j + \sum_{k=j+1}^n \hat{P}_i^k I_k \hat{P}_j^{kT} \right] H_j \quad i > j \quad (46)$$

For a serial chain, M is symmetric positive definite, then, $M_{j,i} = M_{i,j}^T$, $j < i$. Clearly, Eq. 45 cannot be null because of the principal moments of inertia.

Structural Manipulator Building Blocks

Simple two DOF cases can serve as building blocks for more complex articulated multibodies. For 2 DOF arms with open kinematic chain structure, the articulated body inertia cannot be decoupled unless the joint axes are orthogonal to each other (refer to Fig. 4). Possible mass distribution properties for decoupledness assuming joints with a rotational single degree of freedom, r as the distance vector between the two joints, b_i as the direction

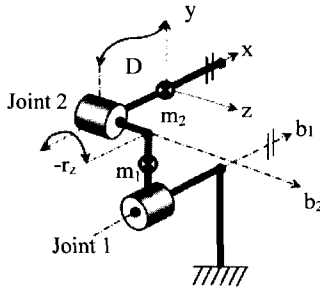


Fig. 4 Schematic of two rotational DOF arm and corresponding kinematic and mass parameters (cylinders indicate rotating joint).

cosines of the joint axes (\$z_i\$ as the joint axis), and a tensor of inertia given by

$$J = \begin{bmatrix} I_{xx} & I_{xy} & I_{xz} \\ I_{yx} & I_{yy} & I_{yz} \\ I_{zx} & I_{zy} & I_{zz} \end{bmatrix} \quad (47)$$

are shown in Fig. 5.

For arms with open kinematic chain structure, the articulated body inertia can only be invariant iff one of the conditions expressed in Fig. 6 or Fig. 7 is met.

The necessary and sufficient conditions for a 2 DOF open kinematic chain structure and mass distribution to possess a decoupled and invariant articulated body inertia are given in Fig. 8. For higher DOF, the above 2 DOF cases can be used as building blocks. On the other hand, one way to relax the orthogonality condition for decoupling is to relocate the actuators to reduce the reaction torques exerted by an actuator. The above configurations assume actuators acting directly on each joint, hence reaction torques are present. From the conditions for decoupling, it can be deduced that decoupling the inertia tensor for more than 2 degrees of freedom requires modification of the structure of the arm mechanism. This was also demonstrated by Asada and Youcef-Toumi^[20] and Youcef-Toumi^[24] for macroscopic manipulators with fixed base. Fig. 8 shows a possible 4 DOF multibar spatial mechanism configuration that can be controlled in a single plane (fixed waist rotation during motion of \$\theta_2, \theta_3\$, and \$\theta_4\$)

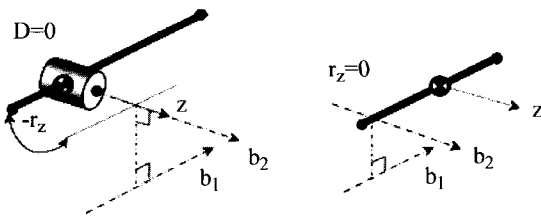


Fig. 5 Decoupled configurations resulting from Fig. 4.

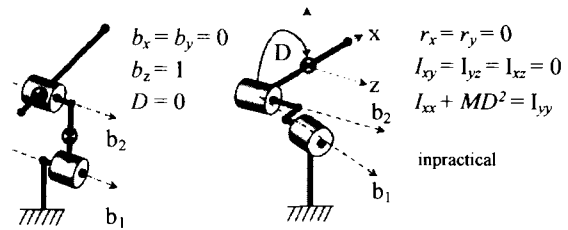


Fig. 6 Invariant configurations resulting from Fig. 4.

with full decoupled and invariant inertia. The rotation of any link is a result of 1 and only 1 actuator [i.e., \$\theta_1(1,4,6), \theta_2(2,5,8), \theta_1(3,7,9)\$].

Thermal Noise and Positional Variance (Uncertainty)

Thermal noise at the molecular level affects the positional accuracy. One of the key issues in achieving good positional accuracy at the nanoscale is controlling temperature or conversely controlling the structural stiffness of the elements that make up the manipulator. The latter is preferred, given the need to operate these nanodevices at room temperature. Because the presented designs have bending forces applied to their structural elements, we wish to evaluate their stiffness with respect to deflection of their ends as a consequence of thermal noise.

This has been shown by Ref. [19] from classical statistical mechanics. Let the probability density function for one position coordinate of a particle, say \$x\$, subject to the potential energy function \$V(x)\$ be \$f_x(x)\$.

$$f_x(x) = \frac{\exp[-V(x)/k_B T]}{\int_{-\infty}^{\infty} \exp[-V(x)/k_B T] dx} \quad (48)$$

where \$k_B = 1.38 \times 10^{23}\$ J/K is the Boltzmann constant and \$T\$ is the temperature. From the potential energy for a simple case, say the harmonic potential.

$$V(x) = \frac{1}{2} k_s x^2 \quad (49)$$

it is shown that the probability density function is Gaussian:

$$f_x(x) = \frac{\exp[-k_s x^2 / 2k_B T]}{\int_{-\infty}^{\infty} \exp[-k_s x^2 / 2k_B T] dx} \quad (50)$$

$$= \frac{1}{\sqrt{2\pi}\sigma_{class}} \exp\left(\frac{-x^2}{2\sigma_{class}^2}\right)$$

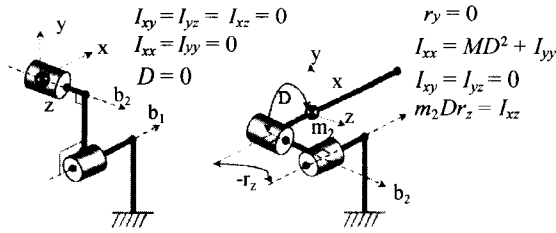


Fig. 7 Decoupled and/or invariant configurations resulting from Fig. 4.

Yielding the classical value for the positional variance (=standard deviation squared=mean square displacement=RMS positional error squared),

$$\sigma^2 = \frac{k_B T}{f_R} \tag{51}$$

showing clearly that thermal noise can be controlled by decreasing the temperature T or by increasing the restoring force f_R (measured by the stiffness k_s).

The positional uncertainty in quantum statistical mechanics for a harmonic oscillator shows that “quantum effects” do not pose a fundamental problem either,

$$\sigma^2 = \frac{\hbar\omega}{k_s} \left[\frac{1}{2} + [\exp(\hbar\omega/kT) - 1]^{-1} \right] \tag{52}$$

Describing the frequency, ω , in terms of the mechanical parameters ($\omega = \sqrt{k_s/m}$) leads to

$$\sigma^2 = \frac{\hbar}{\sqrt{k_s m}} \left[\frac{1}{2} + [\exp(\hbar\omega/kT) - 1]^{-1} \right] \tag{53}$$

Applying Eq. 51 to a cylindrical rod of radius r , length L , and traverse stiffness given by

$$k_s = \frac{3\pi r^4 E}{4L^3} \tag{54}$$

where E is the material’s Young modulus (e.g., $E = 10^{12}$ Pa for diamond), we can deduce that the positional error squared is given as

$$\sigma^2 = \frac{k_B T 4L^3}{3\pi r^4 E} \tag{55}$$

For a rod at room temperature (300 K) of $E = 10^{12}$ N/m² (diamond), $r = 8$ nm, and $L = 50$ nm, the RMS positional error is $\sigma = 0.007$ nm, much less than an atomic diameter. For the quantum mechanical version in Eq. 53, positional variance is again acceptable.

Single-wall carbon nanotubes (SWCN) are good candidates as structural elements. In general, diamondoid structures are favored for nanomechanical systems because of their fundamental physical properties (strength and stiffness, among others).

Consequently, the structural elements that make up the manipulator must be chosen according to the systems kinematics and the calculated positional error of the end-effector. A simple kinematic analysis shows the calculation of the RMS positional error at the end-effector as a function of the propagation of deflections of the composing structural elements because of thermal noise. Using the cylindrical rods defined previously as structural elements for the kinematic configuration found in Fig. 8, and assuming an equal positional variance in all Cartesian coordinates, the worst-case RMS positional error of the manipulator’s end-effector can be computed from Eq. 16 for a joint differential change on all 4 degrees of freedom. Using Denavit–Hartenberg’s (DH) convention for coordinate frame assignment and parameterization,^[22] the Jacobian for such a configuration can be computed algebraically from the kinematics equations,

$$A_1^0 A_2^1 A_3^2 A_4^3 = T_4^0 \tag{56}$$

where

$$A_i^{i-1} = \begin{bmatrix} \cos \theta_i & -\cos \alpha_i \sin \theta_i & \sin \alpha_i \sin \theta_i & a_i \cos \theta_i \\ \sin \theta_i & \cos \alpha_i \cos \theta_i & -\sin \alpha_i \cos \theta_i & a_i \sin \theta_i \\ 0 & \sin \alpha_i & \cos \alpha_i & d_i \\ 0 & 0 & 0 & 1 \end{bmatrix} \tag{57}$$

where a_i and d_i represent the Cartesian distance between joint axes i and $i-1$, α_i is the angle between adjacent joint axis, θ_i is the i th joint angle, and T_4^0 represents the orientation and position of the end-effector with respect to the inertial reference frame.

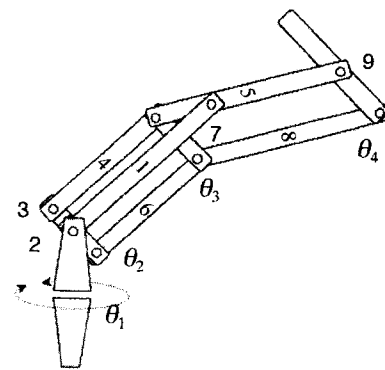


Fig. 8 Four DOF decoupled and invariant inertia manipulator for simultaneous motions involving θ_{2-4} . (View this art in color at www.dekker.com.)

Table 1 Denavit-hartenberg parameters for the manipulator shown in Fig. 8

a_i (rad)	a_i (nm)	θ_i (rad)	d_i (nm)
$\pi/2$	0	θ_1	50
0	50	θ_2	0
0	50	θ_3	0
0	0	θ_4	0

$$T_4^0 = \begin{bmatrix} n_x & o_x & a_x & p_x \\ n_y & o_y & a_y & p_y \\ n_z & o_z & a_z & p_z \\ 0 & 0 & 0 & 1 \end{bmatrix} \quad (58)$$

where n , o , and a represent the 3-D vectors associated with the orientation of the manipulators' end-effector with respect to the inertial frame x , y , and z and p represents the position of the end-effector with respect to the same reference frame. For this particular configuration, the DH parameters are given in Table 1.

The Jacobian can then be calculated from the column vectors that relate the differential Cartesian change of the end-effector with the differential change in each i joints,

$$\frac{dT_n}{d\theta_i} = \begin{bmatrix} -n_x p_y + n_y p_x \\ -o_x p_y + o_y p_x \\ -a_x p_y + a_y p_x \\ n_x \\ n_y \\ n_z \end{bmatrix} \quad (59)$$

Solving Eq. 16 for V , the maximum end-effector differential translational deviation in any given coordinate is 0.028 nm (still less than an atomic diameter). This does not account for the additional error introduced by joint backlash.

CONCLUSION

Two and three DOF configurations with movable base are currently being designed at the molecular level, from modular parts (carbon nanotubes). Decoupled inertia is achievable for manipulators of up to 3 DOF, via structural redesign of the serial chain, while configuration-invariant inertia is manageable for higher DOF systems. These results become the basis for designing manipulators

with reduced complexity dynamics, improved stability, and controllability, given that 1) for a hypothetical fully decoupled system, the dynamic control equations could then be computed under strict parallelism in $O(1)$ with $O(n)$ processors using a single input single output (SISO) controller (given precomputation of Φ_X^{nb}) and/or 2) for a configuration-invariant system, the computation of the inverse mass matrix does not need to be explicitly addressed at every control/integration time step. Having both conditions met results in the following simplified EOM,

$$F = M\ddot{Q} + \Phi_X^{nb} + \xi M\dot{Q} \quad (60)$$

$$\ddot{Q} = M^{-1}[F - \Phi_X^{nb} - \xi M\dot{Q}] \quad (61)$$

where M is diagonal and can be precalculated only once.

ACKNOWLEDGMENTS

This work was performed under partial support of the Institute of Pure and Applied Mathematics (IPAM), an NSF Institute at the University of California at Los Angeles, California.

REFERENCES

1. Falvo, M.R.; Clary, G.; Helser, A.; Paulson, S.; Taylor, R.M., II; Chi, V.; Brooks, F.P., Jr.; Washburn, S.; Superfine, R. Nanomanipulator experiments exploring frictional and mechanical properties of carbon nanotubes. *Microsc. Microanal.* **1998**, *4*, 504–515.
2. Falvo, M.R.; Finch, Chi, V.; Washburn, S.; Taylor, R.M., II; Brooks, F.P., Jr.; Superfine, R. In *The Nanomanipulator: A Teleoperator for Manipulating Material at the Nanometer Scale*. Proc. 5th International Symp. Scie. Eng. Atomically Engineered Matter. World Scientific, Richmond, VA, November 5, 1995.
3. Foster, J.S.; Frommer, J.E.; Arnett, P.C. Molecular manipulation using a tunnelling microscope. *Nature* **1988**, *331*, 324–327.
4. Sheehan, P.E.; Lieber, C.M. Nanotribology and nanofabrication of MoO₃ structures by atomic force microscopy. *Science* **May 24, 1996**, *272*, 1158–1161.
5. Postma, H.W.C.; de Jonge, M.; Yao, Z.; Dekker, C. Electrical transport through carbon nanotube junctions created by mechanical manipulation. *Phys. Rev., B* **2000**, *62* (16), R10653–R10656.

6. Gao, P.; Sweil, S. A six-degree-of-freedom micro-manipulator based on piezoelectric translators. *Nanotechnology* **1999**, *10*, 447–452.
7. Merkle, R. A new family of six degree of freedom positional devices, Ralph Merkle. *Nanotechnology* **June 1997**, *8* (2), 47–52.
8. Cagin, T.; Jaramillo-Botero, A.; Gao, G.; Goddard, W.A., III. Molecular mechanics and molecular dynamics analysis of Drexler–Merkle gears and neon pump. *Nanotechnology* **1998**, *9* (3), 143–152.
9. Montemagno, C.; Bachand, G. Constructing nano-mechanical devices powered by biomolecular motors. *Nanotechnology* **1999**, *10*, 225–231.
10. Sohlberg, K.; Tuzun, R.E.; Sumpter, B.G.; Noid, D.W. Application of rigid-body dynamics and semiclassical mechanics to molecular bearings. *Nanotechnology* **1997**, *8* (1997), 103–111.
11. Nosé, S. *J. Chem. Phys.* **1984**, *81*, 511.
12. Hoover, W.G. *Phys. Rev.* **1985**, *A31*, 1695.
13. Vaidehi, N.; Jain, A.; Goddard, W.A., III. Constant temperature constrained molecular dynamics: The Newton–Euler inverse mass operator method. *J. Phys. Chem.* **1996**, *100*, 10508–10517.
14. Featherstone, R. The calculation of robot dynamics using articulated-body inertias. *Int. J. Rob. Res.* **1983**, *2* (1).
15. Jaramillo-Botero, A.; Crespo, A. *A Unified Formulation for Massively Parallel Rigid Multibody Dynamics of $O(\log_2 N)$ Computational Complexity*; Journal of Parallel and Distributed Computing, Academic Press, June 1, 2002; Vol. 62 (6).
16. Yang, D.C.H.; Tzeng, S.W. Simplification and linearization of manipulator dynamics by the design of inertia distribution. *Int. J. Rob. Res.* **1986**, *5* (3).
17. Spong, M. In *Remarks on Robot Dynamics: Canonical Transformations and Riemannian Geometry*, Proc. IEEE International Conference on Robotics and Automation, Nice, France, 1992; 554–559.
18. Eisenhart, L. *Riemannian Geometry*; Princeton University Press: Princeton, NJ, 1960.
19. Drexler, K.E. *Nanosystems: Molecular Machinery, Manufacturing, and Computation*; Wiley and Sons, 1992.
20. Asada, H.; Youcef-Toumi, K. In *Decoupling of Manipulator Inertia Tensor by Mass Redistribution*, Proceedings ASME Mechanisms Conference, 1984.
21. Bedrossian, N. In *Linearizing Coordinate Transformations and Euclidean Systems*, Workshop on Nonlinear Control of Articulated Flexible Structures, Santa Barbara, CA, Oct. 1991.
22. Denavit, J.; Hartenberg, R.S. A kinematic notation for lower-pair mechanisms based on matrices. *J. Appl. Mech.* **June 1955**, 215–221.
23. Lovelock, D.; Rund, H. *Tensors, Differential Forms, and Variational Principles*; Dover: New York, 1989.
24. Youcef-Toumi. Analysis and design of manipulators with decoupled and configuration-invariant inertia tensors using remote actuation. *Trans. ASME* **1992**, *114*.

Molecular Motor-Powered Nanodevices: Mechanisms for Control

Jacob J. Schmidt
Carlo D. Montemagno

University of California, Los Angeles, California, U.S.A.

INTRODUCTION

Although the biophysical and biochemical properties of motor proteins have been well studied, only recently have attempts been made to develop them as mechanical components in hybrid nanoengineered systems.^[1–4] The motor protein F_1 -ATPase is the smallest rotary motor known and can generate forces compatible with currently producible nanomechanical structures; we have previously fabricated and operated hybrid organic–inorganic nanodevices powered by F_1 -ATPase (Fig. 1).^[4] Control of device activity is a critical aspect in the engineering and deployment of integrated nanomachines. There are a variety of possible control mechanisms, including mechanical, optical, electrical, and chemical. We have previously implemented chemical controls into F_1 -ATPase.^[5] These controls followed from the design and construction of allosteric metal-binding sites that constituted a reversible and repeatable on/off switch of motor activity which was demonstrated in the bulk and at the single molecule level. For biomolecular motor-powered hybrid devices to fully realize their potential, progressing beyond scientific experiments and low-functioning curiosities, the devices and device components should be entirely reimaged from an engineering perspective. Development of a library of controls acting directly on motor proteins, their fuel, the components interfaced with them, or a combination of all of these will be highly useful toward increasing the utility, applicability, and range of operation of engineered biomotors.

In this article, we will address these issues, describing the results of current research in which control of mechanical proteins incorporated into hybrid devices has been addressed for the first time. We will also discuss our recent work in which chemical controls were incorporated into the F_1 -ATPase, able to reversibly start and stop the mechanical motion at the single molecule level. We will conclude with an outlook of the field as a whole and future directions.

MECHANISMS AND STRATEGIES FOR CONTROL OF MOTOR PROTEINS

The F_1 -ATPase is a biomolecular rotary motor deriving its mechanical energy from the hydrolysis of ATP. The

loaded motor has been measured at the single molecule level to generate a constant torque of ~ 40 pN nm while operating at high (50–100%) efficiency.^[6,7] The no-load rotational velocity of F_1 -ATPase has been measured to be over 7800 rpm.^[8] In addition, genetic modification of F_1 -ATPase has allowed the precise (sub-50 nm) positioning of single F_1 -ATPase molecules on engineered nanofabricated substrates of nickel-capped posts.^[4,9] Such advantageous natural and engineered characteristics of F_1 -ATPase make it an ideal candidate for precision orientation and attachment to nanomechanical structures.^[4,10,11]

Potential applications of devices using the F_1 -ATPase and other motor proteins are currently limited because of the lack of control over the motor motion. The capability of the motor to reversibly turn on and off in response to an external signal represents an important first step in rational and useful device design for the next generation of biomolecular devices. Motor activity must be directed for device manipulation and efficient use of fuel. In natural biological systems such as the cell, thousands of proteins work interdependently, regulating themselves and others to ensure that the cell can adapt to changing external conditions, wasting no resources and ensuring that essential functions are carried out. These natural biological control mechanisms of proteins and protein complexes regulate their function in response to a variety of external stimuli: chemical, thermal, and mechanical, among others.

Commonly occurring natural controls include conformational changes in some proteins occurring in certain ranges of pH or ionic strength. These shape changes can alter the catalytic or hydrolytic activity of the protein, slow it down, or affect its interactions with other proteins. These conformational changes can also be induced through the application of electric fields. The advantages of engineering these kinds of responses in motor protein-based hybrid devices draw upon the capability of micro- and nanoelectromechanical systems, MEMS and NEMS, fabrication to place arrays of electrodes at arbitrary positions on a substrate surface. Electric fields produced by such electrodes would give the power to individually address single motors. Electrical control has been shown to exist naturally in the family of porins. Porins are pore proteins that transport water and other solutes across cell



Fig. 1 Depiction of the hybrid nanodevice constructed previously.¹⁴ Electron beam lithography was used to construct 50-nm Ni-capped SiO₂ posts on which individual 10 × His-tagged F₁-ATPase motors were mounted. Ni rods, 75 × 750 nm, were linked to the rotor of the motor through a peptide/biotin/streptavidin/biotin bond. Upon addition of ATP, the rods were observed to rotate using conventional optical microscopy. (View this art in color at www.dekker.com.)

membranes, controlling concentration-dependent properties such as osmolarity and acidity. Some porins have been shown to open and close physically in response to an applied voltage, a shape change that activates and deactivates the proteins' transporting ability.^{112–141} These shape changes are a result of charged or polar groups in the protein responding to an external electric field and, on a small scale, occur in every ligand-receptor binding event. It may be possible to engineer similar responses on other proteins using polar or charged residues to enhance these responses. Proteins not containing the necessary functional groups to respond to the applied fields can be engineered to contain the groups or to further tune their response, much in the same way as the chemical binding sites discussed above were created. Electrical control mechanisms have the promise of addressability, control of activity, and easy interfacing with external instrumentation.

Motor activity can also be controlled without changing the protein conformation. Attachment of cargo presenting variable loads resulting from viscous, electric, or magnetic forces will result in a change of the motor speed for molecular motors with constant torque output, such as F₁-ATPase. Although this will not be possible in every case, it is a powerful and flexible method of motor control. Any moving part attached to the motor, if susceptible to an external field, may be used to increase controllably the drag force experienced by the motor. Work by Noji et al.¹¹⁵ have used this principle to study the rotation characteristics of F₁-ATPase. In these experiments, magnetic beads were attached to F₁-ATPase motors lying on a substrate while observed by optical microscopy. As the rotary shaft of the motor turned, the bead turned with

it. An external magnetic field with controllable direction and magnitude was applied to this system, creating a counterforce opposing the rotation of the motor. Fields large enough to slow and stall the motor were used, with the result that the rotary energy potential of the motor was determined.

There are several different strategies for the implementation of controls into hybrid biomotor devices. In contrast to natural systems, primitive engineered hybrid nanosystems to date have contained only a few proteins removed from their natural environments and therefore also removed from their natural control mechanisms. As a consequence, much regulation of the function of motor proteins is often possible only through regulation of the fuel supply. Fuel-based control techniques are able only to activate motors, with the motors functioning until the fuel is exhausted. In the regime of Michaelis–Menten kinetics (i.e., in a steady state when the substrate concentration is much greater than the enzyme concentration), $V = V_{\max}[S]/(K_M + [S])$, where V is the catalytic turnover rate, V_{\max} is the maximum rate, $[S]$ is the substrate concentration, and K_M is the Michaelis constant. Therefore the enzyme velocity can be controlled by the substrate concentration, for substrate concentrations small compared with K_M (K_M for unloaded F₁-ATPase is 15 μM). There are significant shortcomings with an approach based on the regulation of the fuel supply: other ATP-utilizing molecules will also be affected, there is no differential motor control, and fine control of operational parameters such as speed is not possible.

Recent work in chemical control mechanisms has utilized light-activated “caged” ATP, a chemical derivative of ATP in a nonhydrolyzable form, which is able to release a defined amount of ATP related to the intensity, duration, and location of optical illumination.¹¹⁶ This technique has controlled the operation of kinesin motors for proscribed periods of time as they proceeded along microtubule tracks (Fig. 2).¹¹ Alternative mechanisms of fuel-based control include myosin mutants with engineered binding sites having sensitivities for analogs of ADP with bulky side chains such as *N*⁶-(2-methylbutyl) ADP, allowing differential control between specific motor types.¹¹⁷

Alternatively, chemical control of the motors apart from fuel regulation may be effected through chemical modification of the motor itself. By engineering peptides which bind directly to each other, the motor can be stopped in the presence of the appropriate chemical reagents, as in reversible disulfide cross-linking of kinesin.¹¹⁸ Alternatively, enzyme activity may be altered by engineering metal ion-binding sites (e.g., the addition or substitution of histidine, aspartate, or lysine residues)¹¹⁹ into appropriate regions of the protein. The presence of these metal-binding sites can fix adjacent regions of the protein to each other by introduction of metal ions into these binding sites. This induces strong bonding between the ions and adjacent

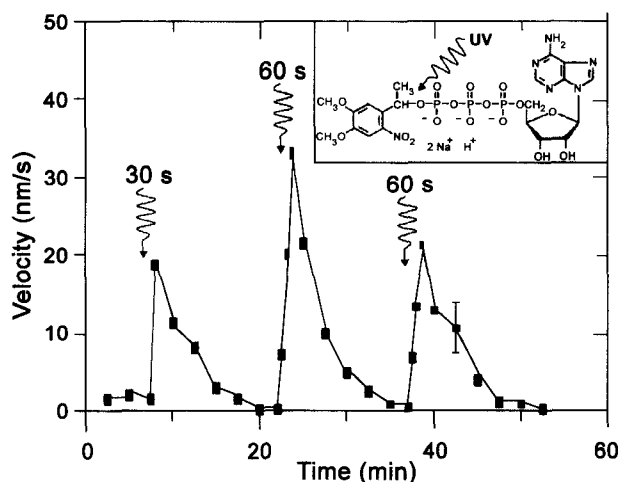


Fig. 2 Average speed of microtubules after exposure of caged ATP to UV light for 30, 60, and 60 sec converting 20%, 30%, and 20% of the initial caged ATP into free ATP. The presence of the ATP-consuming enzyme, hexokinase, leads to a rapid decline of the microtubule velocity. The inset shows the structure of DMNPE-caged ATP. (From Ref. [1].)

residues. Because ions can bind several amino acids simultaneously, it is possible to attach two separate, independent regions to the ion—in effect, altering the local elasticity of these subunits by fixing them to each other. If movement of these regions is necessary for protein activity, this activity can be impaired or entirely halted. This is an illustration of an allosteric control mechanism, a mechanism in which enzyme function is controlled without affecting substrate availability or reactivity. With this aim, we genetically modified the F_1 -ATPase, engineering pockets in the enzyme with high affinity for binding zinc ions. When the protein binds the zinc, it is incapable of performing the conformational changes necessary for rotation of its central shaft, the γ subunit, therefore stopping the motor from further motion.

IMPLEMENTATION OF ALLOSTERIC CHEMICAL CONTROLS INTO F_1 -ATPASE

Isolated F_1 -ATPase is composed of five different subunits with stoichiometry of $\alpha_3\beta_3\gamma\delta\epsilon$. The $\alpha_3\beta_3\gamma$ subcomplex of F_1 -ATPase has been identified as a minimum ATPase-active complex with characteristics and stability similar to native F_1 -ATPase.^[20–22] The X-ray crystallographic structures of the F_1 fragment of the bovine mitochondrial ATPase (BF_1) have revealed the nature of the conformational changes involved in ATP hydrolysis in atomic detail.^[23] The crystal structures of BF_1 show that three α and three β are arranged alternately forming a hexameric ag-

gregate having one nucleotide binding site each, with the long coiled-coil structure of the γ subunit inserted into the central cavity of the ring. There are three catalytic sites, located on β subunits at α/β interfaces, and three non-catalytic sites, located on α subunits at different α/β interfaces. The β subunits assume two conformations in the crystal structures, an open and a closed state, that interconvert via a hinge-bending motion. In the closed state, the β subunit binds ATP (β_T) or ADP (β_D); in the open state, the active site is empty (β_E). The corresponding conformations of the α subunits are designated as α_T , α_D , and α_E . The conformations of α_T , α_D , and α_E are nearly identical. In contrast, the structures of β_T and β_D , which are quite similar to each other, are completely different from that of β_E . The β_T and β_D are in the “closed” conformation, the C-terminal domain of which is elevated, closed to the nucleotide binding domain, while the β_E is in the “open” conformation, with its substrate binding site open.^[23–25] Although β_T and β_D adopt the same overall state, there are structural differences in several surface loops related to the critical role of these states in the rotary motion of this complex.

During ATP synthesis, the three noncatalytic sites are homogeneously liganded with MgAMP-PNP (an ATP analog), whereas the three catalytic sites are heterogeneously bound to ligands during normal enzyme operation. These structural features, in addition to the direct observation of γ rotation in F_1 -ATPase,^[26] strongly support the binding change model established by Boyer.^[27] The rotary mechanism postulated by this model assumes that the sequential participation of the three catalytic sites and alternate interchange of their roles during ATP hydrolysis drive the counterclockwise rotation of the γ subunit.^[28,29] In other words, the intrinsic conformational changes induced by the heterogeneous nucleotide affinities to catalytic sites, coupled with the rotation of γ , are crucially necessary for the catalysis of ATP hydrolysis.

The binding change mechanism suggests that F_1 -ATPase activity can be controlled by blocking the conformational changes necessary for ATP hydrolysis. Because the six α/β interfaces (three interdimer and three intradimer) are all different, and the rotation of the γ subunit relies on sequential interchange between different conformational and substrate ligation states, we hypothesized that reversible inhibition of the catalytic and rotation cycle may be achieved through insertion of secondary metal binding site capable of interfering with the sequential cycle (Fig. 3). When the open/closed conformational interconversion of the β subunits is hindered, the nucleotides that have been bound (MgATP or MgADP) are trapped and free nucleotides are prevented from entering the binding sites. Because the conformational states of α_T , α_D , and α_E are identical, they provide an immobile substrate to which the β subunits can be fixed, physically

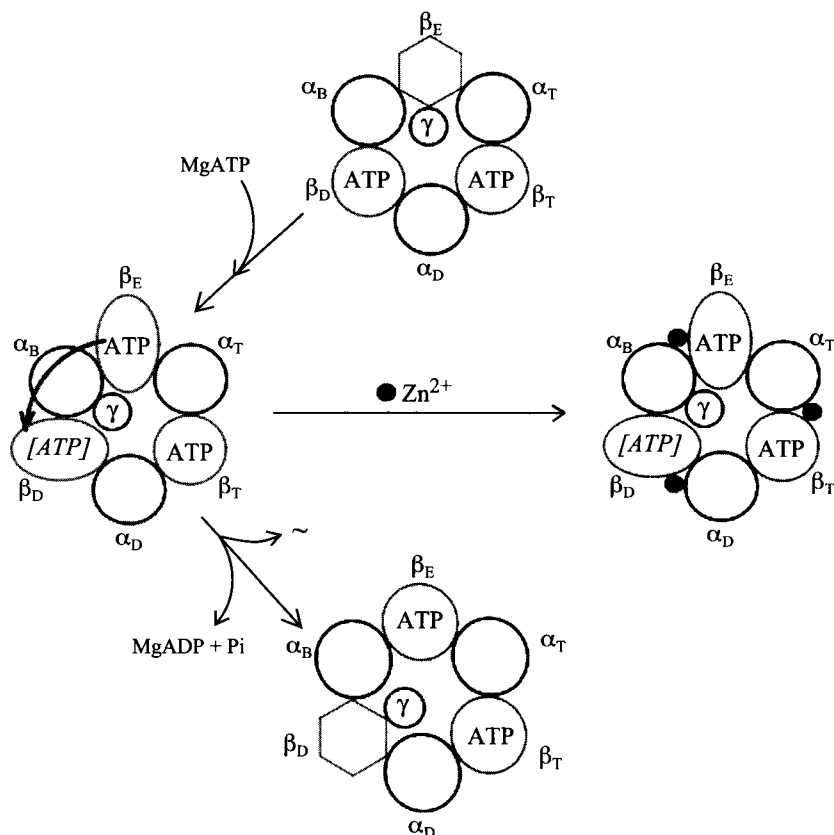


Fig. 3 Model for zinc switch-controlled ATPase. Counterclockwise rotation of the γ subunit from α_E to β_D initiates a conformational change. Blue circles represent α subunits liganded with MgATP (omission of ATP for clarity). Green circles represent β subunits at different states: circles represent β liganded with MgATP, ellipses represent β in the transition from closed to open conformation, and hexagons represent β in open conformation. [ATP] represents the transition state of β_D converting from closed to open conformation. \sim represents the energy released during the hydrolysis. While the zinc binds to the engineered additional binding site, the conformation of $\alpha_3\beta_3\gamma$ is locked in one state, so that neither ATP nor ADP can enter in or exchange out. (View this art in color at www.dekker.com.)

preventing switching between cooperative nucleotide binding sites and the rotational movement of the γ subunit. The effect of this hypothetical conformational lock is to fully inhibit the operation of F_1 -ATPase. Such a site is therefore predicted to function as a classic allosteric inhibitor of enzyme activity^[30] and should provide a chemical switch for the control of motor activity in a nanomechanical device.

Obviously, a strong permanent binding of the α and β subunits directly to each other would permanently immobilize the protein, possibly irreversibly. However, binding them each to a multivalent ligand in effect binds them to each other, accomplishing the same immobilization. Furthermore, removal of the ligands restores the protein to its initial state and reverses the immobilization. With this in mind, we modeled bovine mitochondrial F_1 -ATPase and designed binding sites in the protein intended to have high affinities for zinc ions. We chose to con-

struct an allosteric control element based on a zinc-binding site, as these domains are relatively compact, consisting of three or four amino acids that chelate the metal.^[31] Moreover, computational design methods have been developed that reliably predict and construct de novo metal centers into proteins of known structure.^[32-34] Reversible inhibition of the enzymatic activity may be readily achieved by the addition of extrinsic metal chelators (e.g., 1,10-phenanthroline) that sequester zinc, but not the Mg^{2+} required for ATP binding and hydrolysis. The bovine protein was modeled because the crystal structures of the F_1 -ATPase in empty, ATP-bound, and ADP-bound states are known. Such structures of the F_1 -ATPase from thermophilic *Bacillus* PS3 (TF₁), used in our previous experiments, are not available. However, TF₁ also has a functional asymmetry among the three catalytic subunits, although it does not contain any endogenously bound nucleotide.^[35] Therefore the binding

change model-based design for the fixation of conformational change in bovine F_1 -ATPase is suitable to be applied to TF_1 . The binding sites were produced through the replacement of selected glycine, glutamine, and aspartate residues with histidine.

To design locations for allosterically active zinc-binding sites in BF_1 , we first identified regions in the interfaces that undergo local conformational changes, but are not part of the active site. In collaboration with Hellinga et al.^[36] at Duke University, protoallosteric sites were identified using C_α - C_α double-difference distance maps comparing β_E and β_T structures. These binding sites were placed at locations in each α / β interface having large relative motions during catalytic activity but separate from nucleotide binding sites. The DEZYMER algorithm protein design program^[32] was used to carry out the calculations and refinement of site design for the construction of a tetrahedral zinc center at the interface between each pair of α and β subunits. The idealized tetrahedral zinc primary coordination sphere consists of three histidines and a water molecule. The zinc is allowed to coordinate with either the N_δ or N_ϵ nitrogens of the histidines and is constrained within the plane of the imidazole rings.^[33,37,38] The algorithm predicted a set of sites that were then rank-ordered and examined by inspection. The geometry of the interaction between the metal and the histidine side chains is derived from visual inspections of natural protein structures.^[39] We chose a site located in the interdimer interface between β_D and α_E . This designed site replaces glutamine $\alpha 405$, glycine $\beta 392$, and aspartate $\beta 400$ in BF_1 with histidine residues. The initial design phase yielded a site with approximate tetrahedral geometry. This site was then optimized using a combination of molecular dynamics and conjugate gradient energy minimizations to satisfy the metal coordination geometry resulting in movement of the loop in this region. Mutations were chosen to satisfy both the desired metal binding geometry and the steric compatibility of the protein folding (Fig. 4).

Using site-directed mutagenesis, the peptide replacements were made to the gene encoding a mutant F_1 -ATPase (named DEMHZ) with $10 \times$ His tags on the β subunits and a lone cysteine on the γ subunit, described previously.^[4] The modified α , β , and γ coding sequence of TF_1 , DEMH, which contains five additional mutations as a working wild type, was cloned into the expression plasmid pETBlueTM (Novagen) with a T7 lac promoter. The vector-encoded *NheI* site (3434) was eliminated (gctagc to gcgagc). Three histidines for creating the zinc binding sites were introduced by standard PCR oligonucleotide-directed mutagenesis techniques using Pfu DNA polymerase (Stratagene). Specifically, they are Gln-397-His on α and Gly-398-His and Asp-406-His on β (calculated with the inclusion of the $10 \times$ His tags). Expression of the

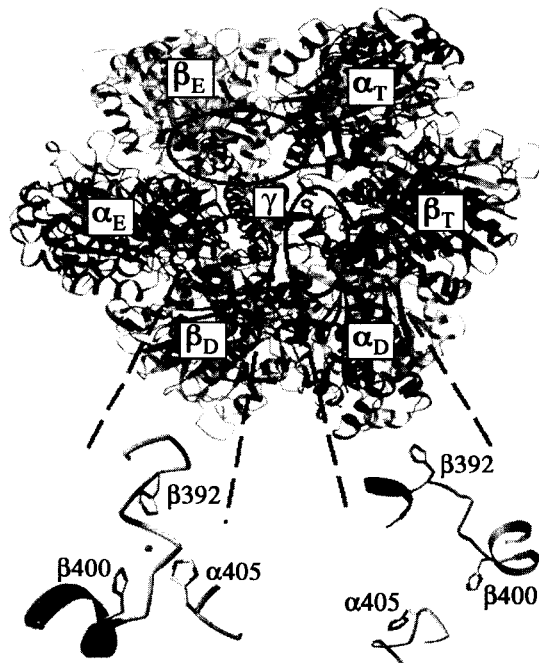


Fig. 4 Molecular model of the computationally designed Zn^{2+} binding site in BF_1 ATPase. The histidines in the three interdimer interface locations are shown in red. The circle indicates the site in the β_D / α_E interface predicted to form a tetrahedral Zn^{2+} -binding site (left insert). The ovals indicate that the sites in the other two interdimer interfaces do not form a geometry predicted to favor metal binding (right insert). (View this art in color at www.dekker.com.)

recombinant protein, DEMHZ, was conducted in *Escherichia coli* TunerTM (λ DE3) pLacI (Novagen).

The mutations on pETBlue-DEMHZ were checked by restriction enzyme digestion and confirmed by DNA sequencing, which failed to reveal any additional mutations or frameshifts. DEMHZ protein was overexpressed in *E. coli* TunerTM (λ DE3) by IPTG induction and purified to homogeneity by Ni-NTA affinity chromatography. There was some concern about the endogenous ATPase genes in the host strain TunerTM (λ DE3) pLacI. However, because the recombinant protein was stable to $100^\circ C$, and the crude lysate was prepared by heating the extracts at $60^\circ C$ for 45 min, the native protein subunits should have denatured completely under such conditions. Moreover, the use of Ni-NTA affinity chromatography also ensured the purification of His-tagged constructs only. So it was very unlikely that chimeric F_1 -ATPase was purified.

Following the generation of the mutant, the motor was grown in large quantities in a bacterial expression system, harvested, and purified. *E. coli* TunerTM (λ DE3) pLacI containing the F_1 -ATPase mutant expression plasmid, pETBlue-DEMHZ, was cultured at $37^\circ C$ in LB medium

(with 1% glucose, 50 $\mu\text{g/ml}$ carbencillin, and 34 $\mu\text{g/ml}$ chloramphenicol). When the growth of this transformant reached the mid-logarithmic phase ($\text{OD}_{600}=0.6$), 1 mM of isopropyl- β -thiogalactopyranoside (IPTG) was added to induce endogenous T7 polymerase, and the cells were cultured successively for 4 hr. Purification of the mutant $\alpha_3\beta_3\gamma$ subcomplex was carried out following the methods by Matsui and Yoshida^[40] with some minor modifications. Cells were harvested by centrifugation at $6000 \times g$ for 20 min at 4°C . The collected cells (7.5 g out of 2 L culture) were resuspended in buffer A (50 mM Tris- SO_4 , 1 mM EDTA), incubated with lysozyme on ice for 30 min. The suspension was disrupted by sonication, and then heated at 60°C for 15 min. The precipitate was removed by centrifugation at $105,000 \times g$ (Beckman JA-30.50) for 15 min. The supernatant was saved and heated at 60°C for 30 min and then centrifuged at $105,000 \times g$ for another 45 min. The supernatant fraction was applied to HiPrep[®] 16/10 DEAE column (Pharmacia) that was pre-equilibrated with buffer A. The column was washed with 200 mL of buffer A containing 150 mM NaCl and eluted with 80 mL of a 300–330 mM linear NaCl gradient. The eluted fractions were concentrated by adding ammonium sulfate to a final concentration of 75% saturation. The resuspended pellet was mixed with nickel-nitrilotriacetic acid (Ni-NTA) Superflow[™] resin (QIAGEN), following a batch purification procedure.^[41] After washing the unbound proteins, the bound proteins (with $10 \times$ His tags) were eluted out with 1 M imidazole. The purity of the DEMHZ was analyzed by sodium dodecyl sulfate-polyacrylamide gel electrophoresis (SDS-PAGE) using a 12% polyacrylamide gel. Protein concentrations of the $\alpha_3\beta_3\gamma$ complex were determined by measuring the absorbance at 280 nm using coefficient factor 0.45 of absorbance for 1 mg/mL of F_1 -ATPase. Steady-state ATPase activity was determined spectrophotometrically at 25°C in the presence of an ATP-regenerating system.^[42]

Bulk ATPase activity assays using an ATP-regenerating coupled enzyme system were performed to determine if Zn(II) could effectively inhibit the activity of the engineered ATPase, as well as the minimum Zn(II) concentration for full activity inhibition. To investigate the zinc effect on the DEMHZ, the indicated amount of ZnSO_4 was added to the assay mixture, which contained 50 mM Tris-HCl (pH 7.4), 100 mM KCl, 2.5 mM phosphoenolpyruvate, 50 $\mu\text{g/ml}$ double enzyme composed of pyruvate kinase and lactate dehydrogenase (Roche), 0.2 mM NADH (Sigma), 2 mM Na_2ATP , and 4 mM MgCl_2 . One unit of activity was defined as the activity that hydrolyzed 1 μmol ATP/sec/ μmol ATPase. Assessment of zinc effect on ATP binding affinity to catalytic sites was carried out in the same assay system, except with a fixed concentration (800 μM) of zinc that could effectively inhibit ATPase activity, and various

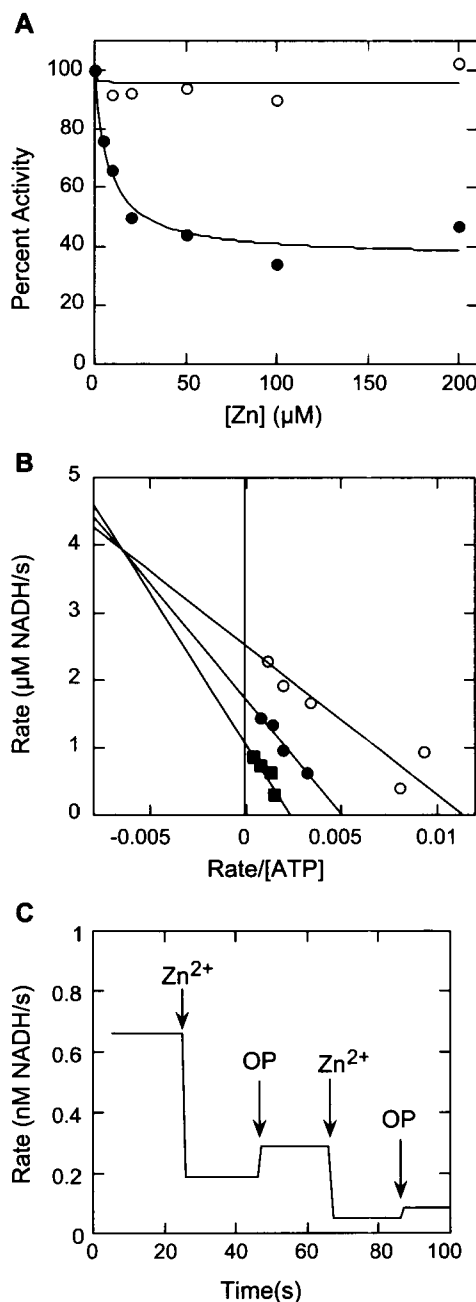


Fig. 5 Steady-state kinetics of ATP hydrolysis in the wild-type and mutant TF₁ enzymes. (A) The effect of Zn^{2+} addition on the activity of wild-type (DEM_H; open circles) and mutant (DEM_{HZ}; closed circles) enzymes. For DEM_{HZ}, Zn^{2+} binding is modeled with a hyperbolic binding isotherm 19, with $^{app}K_d=8.6 \mu\text{M}$. (B) Eadie-Hofstee transformation of the steady-state kinetics of DEM_{HZ} with respect to ATP concentration in the presence of different Zn^{2+} concentrations (open circles, 0 μM ; closed circles, 5 μM ; squares, 200 μM). (C) Two cycles of successive additions of 100 μM Zn^{2+} and 150 μM 1,10-phenanthroline (OP). (From Ref. [5].)

concentrations of ATP. An experiment reversibly activating and deactivating the F_1 -ATPase was carried out by adding 800 μM of zinc and about 10% excess of the specific metal ion chelator 1,10-phenanthroline.

A summary of our previous work comparing ATPase activity of the mutant and wild-type^[5] is shown in Fig. 5. In the absence of Zn^{2+} , DEMH and DEMHZ exhibited similar specific activity, indicating that the histidine mutations did not affect catalysis. Addition of Zn^{2+} to DEMHZ reduced the activity by 60% at saturating concentrations, but did not affect wild-type TF_1 . Zn^{2+} bound hyperbolically with an apparent dissociation constant of $8.6 \pm 1.2 \mu\text{M}$. The Scatchard plot was linear (not shown) and consistent with noncooperative binding of Zn^{2+} . An Eadie–Hofstee transformation of the steady-state kinetics with respect to ATP at various Zn^{2+} concentrations revealed a pattern that is consistent with a linear mixed inhibition mode, in which both $K_m(\text{ATP})$ and V_{max} are affected by Zn^{2+} . This finding is consistent with binding of Zn^{2+} to both the free enzyme and the enzyme–substrate complex,^[43] as expected. Repeated cycles of Zn^{2+} addition followed by chelation with 1,10-phenanthroline demonstrated that the Zn^{2+} inhibition of the enzyme's hydrolytic activity was reversible. This deactivation/re-activation cycle could be repeated many times. Taken together, these data suggest that we have successfully designed a Zn^{2+} -dependent allosteric effector site that reversibly modulates TF_1 activity, as predicted.

Enzyme kinetics derived from these studies indicated that the mutant DEMHZ $\alpha_3\beta_3\gamma$ has much higher propensity than wild type to bind $\text{Zn}(\text{II})$. However, quantification of the effect of the zinc on the mutant and wild-type protein was complicated by the discovery that the coupled enzyme assay itself was affected by the addition of zinc. We also conducted phosphorus colorimetric detection assays, an alternative method of measuring ATPase activity, and found possible effects on wild-type activity, but the sensitivity of that technique was poor and formed a precipitate at certain reagent concentrations. We did not use the P_i release method for measuring ATPase activity because it is not able to monitor rate fluctuations.^[44]

Several conclusions can be made from the data. 1) $\text{Zn}(\text{II})$ did not alter the affinities of catalytic sites of the wild-type $\alpha_3\beta_3\gamma$ complex for ATP significantly, suggested by $K_m=210 \mu\text{M}$ in the presence of zinc vs. $K_m=159 \mu\text{M}$ in the absence of zinc. 2) $\text{Zn}(\text{II})$ has a strong effect on the ATPase activity of the mutant complex. In the presence of $\text{Zn}(\text{II})$, the activity was nearly fully inhibited; however, it was noticed that at low ATP concentrations, a precipitate formed upon addition of $\text{Zn}(\text{II})$, complicating the measurement of ATP hydrolysis rate. Therefore it remains unclear whether $\text{Zn}(\text{II})$ alters the ATP affinity to the mutant $\alpha_3\beta_3\gamma$ complex, apart its direct effect on hydrolysis. 3) ATP hydrolysis of both the mutant and wild-type

$\alpha_3\beta_3\gamma$ complex exhibited negative cooperativity as a function of ATP concentration, as indicated by the Eadie–Hofstee plots, consistent with reported literature.^[24,40] 4) This zinc switch mutant had a K_m (1490 μM) over 9 times bigger than wild-type K_m (159 μM) in the absence of $\text{Zn}(\text{II})$, which might be a result of some intrinsic changes made by introducing the zinc-binding site in the mutant $\alpha_3\beta_3\gamma$ complex. 5) It is possible that $\text{Zn}(\text{II})$ substitutes in a functional manner for Mg^{2+} . If this was true, $\text{Zn}(\text{II})$ competitively bound to ATP as well as to the mutant $\alpha_3\beta_3\gamma$ complex, which led to a full inhibition of ATPase activity of the mutant. The actual number of bound $\text{Zn}(\text{II})$ equivalents to the mutant $\alpha_3\beta_3\gamma$ complex remains to be determined.

To overcome the shortcomings of the bulk activity assays and also demonstrate the ability of the engineered mutation to enable control of the motors on the single molecule level, we observed fluorescent actin filaments attached to individual molecules of TF_1 . A flow chamber was constructed consisting of one (22 \times 40 mm #0) coverslip attached to a microscope slide using double-sided tape. In buffer A (50 mM KCl, 5 mM MgCl_2 , 10 mM MOPS-KOH, pH 7) (1:10), 0.1% Ni-NTA-coated polystyrene beads^[45] (0.22 μm) was infused into the flow cell and incubated for 15 min, resulting in a bead density of several beads in a 5 \times 5 μm^2 area. Nonadherent beads were removed through rinsing 3 times with 2 volumes of buffer B (buffer A + 10 mg/mL BSA). The His-tagged biotinylated ATPase (28 nM) in buffer B was then incubated for 5 min and rinsed 3 \times with 2 volumes of buffer B. Streptavidin (180 nM) in buffer B was incubated for 12–15 min and rinsed 3 \times with 2 volumes of buffer B. Actin filaments (fluorescently labeled with Phalloidin-TRITC, polymerized, and biotinylated^[26]) were diluted to 50 nM in buffer B and incubated in the flow chamber for 12–15 min. The chamber was washed twice with 2 chamber volumes of buffer B and a third wash of 2 chamber volumes of buffer C [buffer B with an oxygen scavenger (0.5% 2-mercaptoethanol, 30 U/mL catalase, 6 mg/mL glucose, and 0.2 mg/mL glucose oxidase) and an ATP regenerating system (2 mM Na_2ATP , 0.2 mg/mL creatine kinase, and 2.5 mM creatine phosphate)]. The actin filaments were observed using a Nikon E800 upright optical microscope in epifluorescent mode. ZnSO_4 (800 μM) in buffer C was added to measure any inhibition on the mutant and wild-type protein. 1,10-Phenanthroline (800 μM) in buffer C was added to determine the reversibility of the zinc switch.

Upon addition of ATP, some filaments were observed to rotate clockwise (as expected because the motors were attached to the top surface and viewed from the motor side “upside-down”), although the majority were stationary or fluctuated around a central position. There were no filaments observed rotating in the counterclockwise direction. The rotating filaments were then incubated with 800 μM

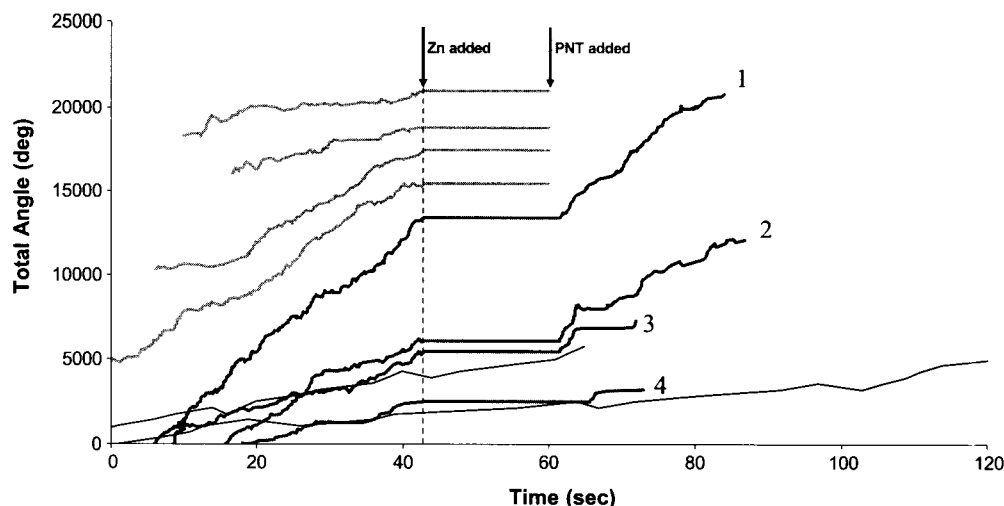


Fig. 6 Measurements of single molecule rotation and control. The movements of rotating fluorescent actin filaments were recorded and digitized. The rotation angle vs. time is shown for eight filaments attached to the mutant ATPase and two filaments attached to motors without the zinc mutation (black lines). The filaments rotated continuously in the presence of ATP. After the addition of $800 \mu\text{M}$ ZnSO_4 (blue arrow), the filaments attached to the mutant motor stopped, whereas the filaments attached to the wild-type motor continued rotating at the same rate. 1,10-Phenanthroline ($800 \mu\text{M}$) was added to the stopped filaments (red arrow), restarting the motor motion. There was an interval of about 3 sec after the addition of both the Zn^{2+} and the phenanthroline in which the filaments were unfocused because of disturbance of the stage position, preventing a more precise determination of the times of cessation and reinitiation of motion. Some filaments dislodged from the surface during the fluid replacement and so rotation data following the PNT addition is not available (green lines). The data for all filaments have been shifted in time to synchronize the Zn^{2+} addition times. There appear to be no lasting effects of the Zn^{2+} on the motors. The rotational rates before Zn^{2+} addition and after Zn^{2+} removal are similar, as linear fits of each of the pink traces show: (1) before Zn^{2+} 0.96 rotations/sec, after Zn^{2+} 0.97 rotations/sec; (2) 0.61, 0.61; (3) 0.36, 0.32; (4) 0.27, 0.19. The differences between the numbers are within the variations of rotational rate of each before Zn addition. The lengths of filaments 1–4 are 1.75, 2.0, 2.25, and 2.25 μm , respectively. (View this art in color at www.dekker.com.)

ZnSO_4 and 2 mM ATP. Some filaments detached from the surface during this buffer exchange, but all rotating filaments (and some fluctuating filaments) remaining were observed to stop after introduction of the Zn. After several minutes, the filaments remained immobilized and $800 \mu\text{M}$ 1,10-phenanthroline, a Zn chelator, and 2 mM ATP were introduced in the chamber. The filaments which were formerly rotating and were not dislodged during the fluid exchange restarted their motion (likewise with the formerly fluctuating filaments). Experiments with the wild-type motor showed no effects resulting from the presence of zinc; rotating filaments continued their motion at the same rate both before and after Zn addition. To verify that the rotation mechanism of the filaments was because of the motor proteins, introduction of 0.5 M imidazole resulted in the detachment of all moving actin filaments in both the wild type and mutant experiments. In addition, although the wild-type motors were not inhibited by zinc, addition of 10 mM sodium azide halted filament rotation. Plots of the rotation angle vs. time for several filaments are shown for both the mutant and wild type in Fig. 6. The process of Zn addition and removal from the mutant protein does not appear to have any permanent effect on

the mechanical properties of the mutant ATPase; that is, the rotation rates before zinc addition and after zinc removal are very close. Furthermore, the mutation to the ATPase has not appeared to alter its mechanical characteristics when compared with the wild type; that is, the motors rotate filaments of the same length at the same rate, indicating that the torque output and efficiency of the motor are unchanged.

CONCLUSION

In summary, we have genetically engineered a zinc switch in the $\alpha_3\beta_3\gamma$ complex of TF_1 . Through introducing or removing the $\text{Zn}(\text{II})$, the conformations of the $\alpha_3\beta_3\gamma$ complex were correspondingly fixed or freed, such that the F_1 -ATPase activity could be turned on and off. This allowed us to switch the nanodevice coupled with this genetically modified F_1 -ATPase on and off in a well-controlled way. Regarding the creation and implementation of control mechanisms in general, each type of control mechanism has unique advantages and disadvantages relative to the intended application. Chemically controlled motors could

result in devices that respond to their environment variables, such as pH, ionic concentration, and temperature, and are not tied to any specific location, although all engineered motors would be affected. Immobile substrate-bound devices may be best served by electrical contacts integrated into the surface; this allows for differential control, in which some devices are operational while others are not. These contacts have the advantages of easy and configurable connections to the outside world and rapid conveyance of signals from the controller to the device. Some proteins can be both electrically and chemically controlled. This flexibility in choices allows the design and application requirements to dictate the components and not vice versa. Exploration and development of artificial protein binding sites, determination of optimal electrode configurations, electric field magnitudes and frequencies, and buffer compositions utilize computational calculations and simulations. These techniques are necessary for screening large numbers of variables and exploring regions of parameter space prohibitive from a cost and time perspective. Establishment of a library of controls and control techniques is a crucial step toward a wider array of useful hybrid bionanodevices.

ACKNOWLEDGMENTS

The tireless work of Haiqing Liu resulted in the successful generation of the mutant, biochemical assays, and single molecule measurements. We also thank Homme Hellinga, Loren Looger, and Shahir Rizk at Duke University for their assistance in binding site design and biochemical assays.

REFERENCES

- Hess, H.; Clemmens, J.; Qin, D.; Howard, J.; Vogel, V. Light-controlled molecular shuttles made from motor proteins carrying cargo on engineered surfaces. *Nano Lett.* **2001**, *1* (5), 235–239.
- Bohm, K.J.; Stracke, R.; Muhlig, P.; Unger, E. Motor protein-driven unidirectional transport of micrometer-sized cargoes across isopolar microtubule arrays. *Nanotechnology* **2001**, *12*, 238–244.
- Hiratsuka, Y.; Tada, T.; Oiwa, K.; Kanayama, T.; Uyeda, T. Controlling the direction of kinesin-driven microtubule movements along microlithographic tracks. *Biophys. J.* **2001**, *81*, 1555–1561.
- Soong, R.K.; Bachand, G.D.; Neves, H.P.; Olkhovets, A.G.; Craighead, H.G.; Montemagno, C.D. Powering an inorganic nanodevice with a biomolecular motor. *Science* **2000**, *290* (5496), 1555–1558.
- Liu, H.; Schmidt, J.J.; Bachand, G.D.; Rizk, S.S.; Looger, L.L.; Hellinga, H.W.; Montemagno, C.D. Control of a biomolecular motor-powered nanodevice with an engineered chemical switch. *Nat. Mater.* **2002**, *1* (3), 173–177.
- Kinosita, K.; Yasuda, R.; Noji, H.; Ishiwata, S.; Yoshida, M. F₁-ATPase: A rotary motor made of a single molecule. *Cell* **1998**, *93* (1), 21–24.
- Noji, H.; Yoshida, M. The rotary machine in the cell, ATP synthase. *J. Biol. Chem.* **2001**, *276*, 1665–1668.
- Yasuda, R.; Noji, H.; Yoshida, M.; Kinosita, K.; Itoh, H. Resolution of distinct rotational substeps by submillisecond kinetic analysis of F₁-ATPase. *Nature* **2001**, *410*, 898–904.
- Soong, R.K.; Stelick, S.J.; Bachand, G.D.; Montemagno, C.D. Evaluating Adhesion Strength of Biological Molecules to Nanofabricated Substrates. In *Technical Proceedings of the Second International Conference on Modeling and Simulation of Microsystems*; Computational Publications: San Juan, Puerto Rico, 1999.
- Montemagno, C.D.; Bachand, G.D. Constructing nanomechanical devices powered by biomolecular motors. *Nanotechnology* **1999**, *10*, 225–331.
- Bachand, G.D.; Montemagno, C.D. Constructing organic/inorganic NEMS devices powered by biomolecular motors. *Biomed. Microdevices* **2000**, *2*, 179–184.
- Muller, D.; Engel, E. Voltage and pH-induced channel closure of porin OmpF visualized by atomic force microscopy. *J. Mol. Biol.* **1999**, *285*, 1347–1351.
- Durell, S.R.; Hao, Y.; Guy, H.R. Structural models of the transmembrane region of voltage-gated and other K⁺ channels in open, closed, and inactivated conformations. *J. Struct. Biol.* **1998**, *121*, 263–284.
- Bainbridge, G.; Gokce, I.; Lakey, J.H. Voltage gating is a fundamental feature of porin and toxin β -barrel membrane channels. *FEBS Lett.* **1998**, *431*, 305–308.
- Noji, H.; Itoh, H.; Adachi, K.; Yoshida, M.; Kinosita, K. Rotary torque of stalled F₁-motor. *Biophys. J.* **2001**, *80* (1 Part 2), 655–651.
- Dantzig, J.A.; Higuchi, H.; Goldman, Y.E. Studies of molecular motors using caged compounds. *Methods Enzymol., Caged Compd.* **1998**, *291*, 307–348.
- Gillespie, P.G.; Gillespie, S.K.H.; Mercer, J.A.; Shah, K.; Shokat, K.M. Engineering of the myosin- β nucleotide-binding pocket to create sensitivity to N⁶-modified ADP analogs. *J. Biol. Chem.* **1999**, *274* (44), 31373–31381.
- Tomishige, M.; Vale, R.D. Controlling kinesin by reversible disulfide cross-linking: Identifying the

- motility-producing conformational change. *J. Cell Biol.* **2000**, *151* (5), 1081–1092.
19. Kasianowicz, J.; Burden, D.; Han, L.; Cheley, S.; Bayley, H. Genetically engineered metal ion binding sites on the outside of a channel's transmembrane β -barrel. *Biophys. J.* **1999**, *76*, 837–845.
 20. Senior, A.E. The proton-translocating ATPase of *Escherichia coli*. *Annu. Rev. Biophys. Chem.* **1990**, *19*, 7–41.
 21. Oster, G.; Wang, H. ATP synthase: Two motors, two fuels. *Structure* **1999**, *7* (4), R67–R72.
 22. Nakamoto, R.K.; Ketchum, C.J.; Kuo, P.H.; Peskova, Y.B.; Al-Shawi, M.K. Molecular mechanisms of rotational catalysis in the F₀F₁ ATP synthase. *Biochim. Biophys. Acta* **2000**, *1458* (2–3), 289–299.
 23. Abrahams, P.; Leslie, A.G.W.; Lutter, R.; Walker, J.E. Structure at 2.8 Å resolution of F₁-ATPase from bovine heart mitochondria. *Nature* **1994**, *370*, 621–628.
 24. Tsunoda, S.P.; Muneyuki, E.; Amano, T.; Yoshida, M.; Noji, H. Cross-linking of two beta subunits in the closed conformation in F₁-ATPase. *J. Biol. Chem.* **1999**, *274*, 5701–5706.
 25. Ren, H.; Dou, C.; Stelzer, M.S.; Allison, W.S. Oxidation of the alpha(3)(beta D311C/R333C) (3)gamma subcomplex of the thermophilic *Bacillus PS3F(1)*-ATPase indicates that only two beta subunits can exist in the closed conformation simultaneously. *J. Biol. Chem.* **1999**, *274* (44), 31366–31372.
 26. Noji, H.; Yasuda, R.; Yoshida, M.; Kinosita, K. Direct observation of the rotation of F₁-ATPase. *Nature* **1997**, *386* (6622), 299–302.
 27. Boyer, P.D. The binding change mechanism for ATP synthase—Some probabilities and possibilities. *Biochim. Biophys. Acta* **1993**, *1140*, 215–250.
 28. Allison, W. F₁-ATPase: A molecular motor that hydrolyzes ATP with sequential opening and closing of catalytic sites coupled to rotation of its subunit. *Acc. Chem. Res.* **1998**, *31*, 819–826.
 29. Kaibara, C.; Matsui, T.; Hisabori, T.; Yoshida, M. Structural asymmetry of F₁-ATPase caused by the g subunit generates a high-affinity nucleotide binding site. *J. Biol. Chem.* **1996**, *271*, 2433–2438.
 30. Perutz, M.F. Mechanism of cooperativity and allosteric regulation in proteins. *Q. Rev. Biophys.* **1989**, *22*, 139–237.
 31. Glusker, J.P. Structural aspects of metal liganding to functional groups in proteins. *Adv. Protein Chem.* **1991**, *42*, 1–76.
 32. Hellinga, H.W.; Richards, F.M. Construction of new ligand-binding sites in proteins of known structure. 1. Computer-aided modeling of sites with predefined geometry. *J. Mol. Biol.* **1991**, *222* (3), 763–785.
 33. Marvin, J.S.; Hellinga, H.W. Conversion of a maltose receptor into a zinc biosensor by computational design. *Proc. Natl. Acad. Sci. U. S. A.* **2001**, *98*, 4955–4960.
 34. Benson, D.; Haddy, A.E.; Hellinga, H.W. Converting a maltose receptor into a nascent binuclear copper oxygenase by computational design. *Biochemistry* **2002**, *41*, 3262–3269.
 35. Shirakihara, Y.; Leslie, A.G.W.; Abrahams, J.P.; Walker, J.E.; Ueda, T.; Sekimoto, Y.; Kambara, M.; Saika, K.; Kagawa, Y.; Yoshida, M. The crystal structure of the nucleotide-free subcomplex of F₁-ATPase from the thermophilic *Bacillus PS3* is a symmetric trimer. *Structure* **1997**, *5* (6), 825–836.
 36. Marvin, J.; Corcoran, E.; Hattangadi, N.; Zhang, J.; Gere, S.; Hellinga, H. The rational design of allosteric interactions in a monomeric protein and its applications to the construction of biosensors. *Proc. Natl. Acad. Sci. U.S.A.* **1997**, *98*, 4366–4371.
 37. Wisz, M.S.; Garrett, C.Z.; Hellinga, H.W. Construction of a family of Cys2His2 zinc binding sites in the hydrophobic core of thioredoxin by structure-based design. *Biochemistry* **1998**, *37*, 8269–8277.
 38. Christianson, D.W.; Cox, J.D. Catalysis by metal-activated hydroxide in zinc and manganese metalloenzymes. *Annu. Rev. Biochem.* **1999**, *68*, 33–57.
 39. Pavletich, N.P.; Pabo, C.O. Zinc finger-DNA recognition: Crystal structure of a Zif268-DNA complex at 2.1 Å. *Science* **1991**, *252*, 809–817.
 40. Matsui, T.; Yoshida, M. Expression of the wild-type and the Cys-/Trp-less $\alpha_3\beta_3\gamma$ complex of thermophilic F₁-ATPase in *Escherichia coli*. *Biochim. Biophys. Acta* **1995**, *1231*, 139.
 41. Qiagen *The QIAexpressionist™. A Hand Book for High-Level Expression and Purification of 6 His-Tagged Protein*; QIAGEN 2000.
 42. Pullman, M.E.; Penefsky, H.S.; Datta, A.; Racker, E. Partial resolution of the enzyme catalyzing oxidative phosphorylation. I. Purification and properties of soluble, dinitrophenol-stimulated adenosine triphosphatase. *J. Biol. Chem.* **1960**, *235*, 3322–3329.
 43. Segel, I.H. *Enzyme Kinetics*; Wiley & Sons: New York, 1975.
 44. Matsui, T.; Muneyuki, E.; Honda, M.; Allison, W.S.; Dou, C.; Yoshida, M. Catalytic activity of the $\alpha_3\beta_3\gamma$ complex of F₁-ATPase without noncatalytic nucleotide binding site. *J. Biol. Chem.* **1997**, *272*, 8215–8221.
 45. Yasuda, R.; Noji, H.; Kinosita, K.; Yoshida, M. F₁-ATPase is a highly efficient molecular motor that rotates with discrete 120 degrees steps. *Cell* **1998**, *93* (7), 1117–1124.

Molecular Probes of Cation–Arene Interactions

George W. Gokel

Washington University School of Medicine, St. Louis, Missouri, U.S.A.

M

INTRODUCTION

The three phases of matter are gas phase, liquid (or condensed), and solid state. In recent years, the stunning advances in computational studies have led some to refer to it in a jocular sense as the fourth: “the computational state.” Some of the studies discussed in this article concern gas phase results determined by mass spectrometry and by calculation. Additionally, data have been derived from solution and solid-state studies. Important inferences can be drawn from computations, work undertaken in the gas phase, in solution, and in the solid state. Significant as all of these methods are, only X-ray crystallographic data permit unambiguous analysis and comparison of structural information. The emphasis of this article is therefore on the evidence for cation– π interactions that is available from solid-state structures.

ISSUES AND INTERACTIONS

The three major species considered in chemistry are anions, cations, and neutral species. Anions are negatively charged and therefore Lewis-basic. Arenes are electron-rich and also considered to be Lewis bases. The interaction between two Lewis bases is usually repulsive rather than attractive. The term “neutral” means uncharged, but a neutral compound may be either Lewis-basic (e.g., dimethyl ether) or Lewis-acidic (e.g., aluminum chloride). Our major concern in this article will be with interactions of the type illustrated in the lower panel of Fig. 1. Such interactions involve the arene’s π -cloud as a Lewis (base) donor and the cation as a Lewis acid. The cation is represented as M^+ , and most of the discussion herein will concern metallic cations. Other cations are certainly possible and will be noted where appropriate (Fig. 1).

Although this article is limited to interactions of cations with arenes, there is much to be considered. Arenes may possess sigma-donors in addition to the π -system that is the primary focus of the present discussion. Sigma-donors may be substituents on the arene or they may be an integral part of the arene. They may enhance the arene’s Lewis basicity or they may detract from it. The top row of Fig. 2 shows benzene, the archetype aromatic,

at the left, followed by pyridine, nitrobenzene, and methoxybenzene (anisole). The nitro group is electron-withdrawing and the methoxy group is electron-donating. Thus nitrobenzene is a weaker π -base than is benzene and anisole is stronger. In both cases, however, the oxygen atoms can function as sigma-donors in their interactions with cations.^[1] The pyridine nitrogen atom is also a good sigma-donor, and its presence in the heterocycle makes the aromatic ring about as weak a π -base as nitrobenzene.

The second line of Fig. 2 shows, from left to right, furan, thiophene, imidazole, and cyclopentadienide anion. The latter is formed by deprotonating cyclopentadiene. When two cyclopentadienide (Cp) anions react with ferrous ion [Fe(II)], ferrocene (third line of Fig. 2) is formed. Ferrocene is the prototype for cyclopentadienyl– π complexes, whether they involve a sandwich structure or only one Cp ring. Organometallic structures of this general type number in the thousands (Fig. 2).

The remaining two structures shown on the third line of Fig. 2 are indole and phenol. Neither is a “simple” arene. Both are important in nature as the side-chain arenes of tryptophan (Trp, W) and tyrosine (Tyr, Y), respectively. The other two arenes that occur as side chains of the common amino acids are imidazole (second line) and benzene (first structure). These arenes are side-chain elements of histidine (His, H) and phenylalanine (Phe, F), respectively. Imidazole is electron-poor and has two potentially sigma-donating nitrogen atoms. As a result, it has not generally been of interest, as a π -donor has not been explored. Interest in the arenes benzene, phenol, and indole, however, has been high. The amino acids phenylalanine, tyrosine, and tryptophan comprise about 8.5% of the amino acids in all known protein structures. Thus along any given protein chain, one amino acid out of every dozen is capable of interacting with ubiquitous sodium, potassium, or other cations (Fig. 3).

GAS PHASE AND COMPUTATIONAL STUDIES

Pioneering studies of the cation–arene interaction were reported by Sunner et al.^[2] in 1981. They used mass spectrometric methods to show that the interaction of K^+ with benzene in the gas phase was similar energetically to

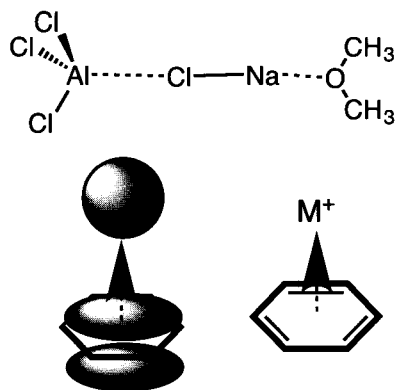


Fig. 1 Lewis acid-base interactions. Top panel: The Lewis acid AlCl_3 interacts with the Lewis base chloride of NaCl while Na^+ interacts with dimethylether. Bottom: Two representations of a cation-pi interaction between a metal cation (M^+) and benzene.

the interaction of this cation with either a molecule of water or of methanol. Similar results were disclosed for Na^+ by Castleman et al.^[3,4] and by Lisy et al.^[5,6] some time later. Fig. 4 shows the presumed orientation of a benzene ring (shown in the CPK i.e., Corey-Pauling-Koltunorspace-filling metaphor) and Na^+ (left) and K^+ ions. Benzene is symmetrical and the ion's position with respect to the pi-cloud is predictable. This is not necessarily the case with more complex arenes such as phenol or indole.

In recent years, a number of computational studies have been conducted,^[7–11] in some cases, in concert with mass spectral analyses^[12–14] (Table 1). In general, the conclusions are the expected and reasonable findings.

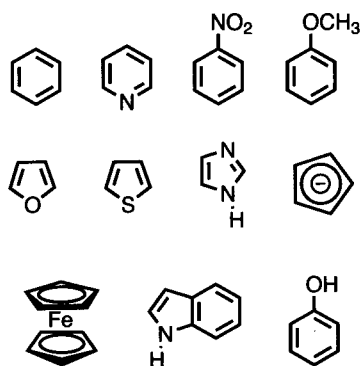


Fig. 2 The top row shows from left to right benzene, the archetype aromatic, pyridine, nitrobenzene, and methoxybenzene (anisole). The second line shows, from left to right, furan, thiophene, imidazole, and cyclopentadienide anion. When two cyclopentadienide (Cp) anions react with ferrous ion $[\text{Fe}(\text{II})]$, ferrocene (third line) forms. It is shown with indole and phenol.

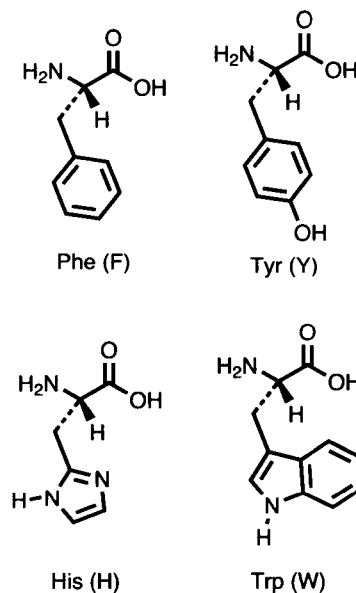


Fig. 3 The four “essential” amino acids that have aromatic side chains. The amino acids are phenylalanine (F), tyrosine (Y), histidine (H), and tryptophan (W).

Smaller cations of like charge, e.g., Na^+ compared with K^+ , interact more strongly with an arene. Likewise, more electron-rich arenes, e.g., indole compared with benzene, are better donors for the same cation.

An example of how mass spectrometry may be used to study cation-pi interactions may be found in the study of pyxophanes.^[15] The diacetylene, **1**, shown in Fig. 5 was prepared so that it would have a pi-rich interior of a size appropriate to bind Na^+ but too small to bind K^+ . These size notions were confirmed by a solid-state structure of **1**. The intriguing pyxophane has a molecular weight of 320 Da, but its $^1\text{H-NMR}$ spectrum shows only two types of protons.

When the electrospray mass spectrum of the pyxophane was determined in the presence of equimolar Na^+ and K^+ , a peak corresponding to $[\mathbf{1} \cdot \text{Na}]^+$ was observed at m/e 343. No peak corresponding to $\mathbf{1} + \text{K}^+$ was observed at m/e 359. This suggested selective pi-complexation of the

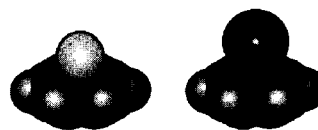


Fig. 4 The presumed orientation of a benzene ring (shown in the CPK metaphor) and Na^+ (left) and K^+ ions. (View this art in color at www.dekker.com.)

Table 1 Values reported for sodium and potassium cation interactions with benzene

Interaction	$-\Delta H$ (kcal/mol)	Method(s) used	Reference
$\text{Na}^+ + \text{C}_6\text{H}_6$	28.0 ± 0.1	Mass spectrometry	[17]
$\text{Na}^+ + \text{C}_6\text{H}_6$	24.7–28.1	Computational methods	[9]
$\text{Na}^+ + \text{CH}_3\text{OH}$	26.6	Mass spectrometry	[17]
$\text{Na}^+ + \text{H}_2\text{O}$	24.0	Mass spectrometry	[17]
$\text{Na}^+ + \text{C}_6\text{H}_6$	21.5–21.8	Mass spectrometry and computational methods	[9,14]
$\text{K}^+ + \text{C}_6\text{H}_6$	18.3	Mass spectrometry and computational methods	[2]
$\text{K}^+ + \text{H}_2\text{O}$	17.9	Mass spectrometry and computational methods	[2]

smaller Na^+ ion by **1** and exclusion of larger K^+ . These structural conclusions are reasonable based on known shapes, sizes, and interactions. Details cannot be known because they simply are not revealed in a mass spectral study. Notwithstanding, a structure was proffered shortly after the results appeared.^[16] The conclusion was based on computational analysis, which is useful and, in this case, seemed reasonable. Thus one gains insight from both studies but actual structural data from neither.

ARENE INTERACTIONS WITH NONMETALLIC CATIONS

Ammonium (R_4N^+), phosphonium (R_4P^+), sulfonium (R_3S^+), and some others are common in nonmetallic cations. Their chemistry is both extensive and important. From the biological perspective, however, ammonium cations are the most important of these. The amine side chain of lysine (Lys, K) is protonated at physiologic pH as is the guanidinium residue of arginine (Arg, R). The potential of nonmetallic cations to interact with arenes was recognized in the early 1980s. Meot-Ner and Deakne^[17] used mass spectrometric studies to explore the interaction between -onium salts and arenes. At about the same time, Burley and Petsko^[18] surveyed the Protein Data Bank (PDB) to see if -onium ion interactions with

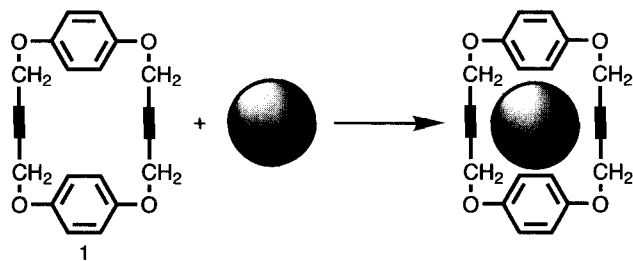


Fig. 5 Diacetylene, **1**, has a pi-rich interior of a size appropriate to bind Na^+ but too small to bind K^+ .

arenes could be identified. They were successful in identifying such interactions, but the structural database was limited.

SOLUTION STUDIES OF ORGANIC CATION-PI INTERACTIONS

Solution studies involving synthetic receptor molecules have also been reported, which confirmed cation- π interactions in aqueous solution.^[19] These have involved several types of receptors, and their function has been studied in various solvents. The receptor shown at the right incorporates the essential elements for studies of this type. It is shown with an included adamantanyltrimethylammonium cation. Receptor **2** is cyclic and contains an internal cavity. It is soluble in water by virtue of its 4 carboxylate anions that are present as cesium salts. The four sides of the receptor system are composed of pi-surfaces. The carboxylates are potential sigma-donors, but they are turned outward. The four oxygen atoms are also potential sigma-donors, but their attachment to an aromatic system enhances the pi-donicity of the arene at the expense of sigma-donation by the oxygen.

The use of water as a solvent has the potential advantage of driving together the organic receptor and substrate. The concern in such systems is that water will so strongly solvate one or both of the components that complexation between them will prove to be too weak to detect. Gas phase studies (mass spectrometry or computation) are unencumbered by solvation issues but may be criticized as unrealistic. This is especially true if inferences in the chemistry are to be applied to biological systems, which function in water.

Modern NMR techniques permit structural information to be obtained from these complexation studies. Nuclear Overhauser enhancements (NOEs) indicate proximity of certain atoms or groups. The aromatic receptors are especially amenable to study by NMR methods as the arenes have shielding and deshielding zones that affect

adjacent nuclei. Numerous examples of and additional details concerning organic receptor molecules that have been studied in solution may be found in a review by Ma and Dougherty (Fig. 6).^[20]

SOLID-STATE STRUCTURAL STUDIES OF CATION-PI INTERACTIONS INVOLVING ANIONIC ARENES

The salt potassium tetraphenylborate [$K^+B^-(C_6H_5)_4$] has been known for many years.^[21] When it crystallizes, it forms a repeating unit that is packed to maximize the stabilizing forces and to minimize any unfavorable steric and electronic interactions. A two-molecule segment of its crystal structure, rendered in mixed ball and stick and CPK metaphor, is shown in Fig. 7. The K^+ ion is nestled in an electron-rich pocket created by two benzene rings of one anion and two from an adjacent anion. The lines at the left of the figure from K^+ to the arene indicate the line of contact between the cation and the arene's centroid. The distance from K^+ to the centroid is 2.986 Å, and the centroid-K-centroid angle is $\sim 100^\circ$.

The boron atom's negative charge is shared among the four benzene rings in each salt, making each arene a stronger donor than it would be if neutral. The packing of the arenes is such that the space between them would probably be empty if the spherical cation failed to occupy it. This structure illustrates many of the issues of interest in cation- π complexation. It is also clear that such precise distance and angle information cannot be gleaned from other analytical methods.

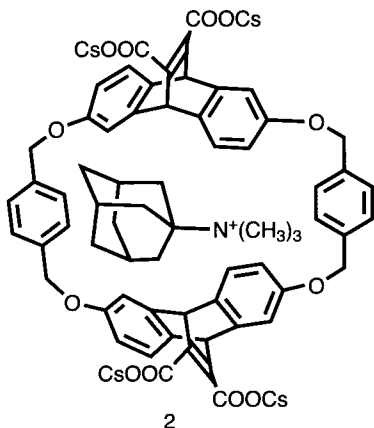


Fig. 6 This figure shows a cyclic receptor (2), with an adamantanyltrimethylammonium cation included in its internal cavity.

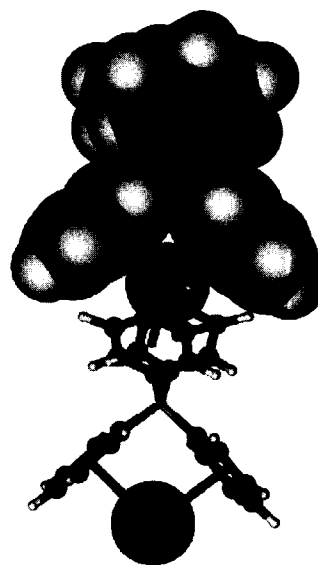


Fig. 7 Rendering of two molecules of $KB(C_6H_5)_4$ showing the cation-anion contacts. The boron atom's negative charge is shared among the four benzene rings in each salt, making each arene a stronger donor than it would be if neutral. (View this art in color at www.dekker.com.)

A number of other salts have been studied that reveal similar results. These include $NaBPh_4$ and $RbBPh_4$. The latter was reported in 1962^[22] and is recorded in the Cambridge Structural Database (CSD) using their six-letter code^a as "RBPBOR." The structure of $NaBPh_4$, which is similar to the K^+ and Rb^+ structures, is recorded in the CSD as ZZZUPI₁₀.

Early efforts to demonstrate cation- π interactions involved using an alkali metal cation as a reducing agent for an arene. Brooks et al. treated 1,4-dihydronaphthalene with *n*-butyllithium to afford dilithium naphthalene as a dark purple solid. Its solid-state structure (CSD code: NAPLIM) is shown in Fig. 8a.^[23] The arene is in contact with two lithium ions, which are present on opposite sides of the naphthalene (Fig. 8). The lithium ions are ~ 2 Å from the benzene ring centroids, and each cation is stabilized by tetramethylethylenediamine. It is interesting to note in this case that the van der Waals thickness of a benzene ring is ~ 3.5 Å and the ionic radius for Li^+ is

^aEach of the CSD's more than 250,000 crystal structures is assigned a unique code, usually consisting of six letters but sometimes followed by a number. Where possible, and especially for early structures, the code was suggestive of the structure as RBPBOR suggests rubidium and tetraphenylborate. As expected, most of the burgeoning number of structures do not have identifiable or suggestive names.

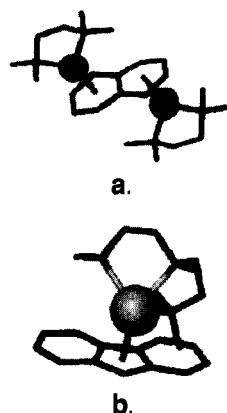


Fig. 8 Dilithium naphthalenide's solid-state structure (CSD code: NAPLIM) is shown in Fig. 7a. The arene is in contact with two lithium ions, which are present on opposite sides of the naphthalenide. A similar approach gives orange crystals of the sodium fluorenyl complex shown in Fig. 7b. (View this art in color at www.dekker.com.)

~ 0.7 Å, suggesting that a Li-arene contact should be about $(1.75 + 0.7 =) 2.45$ Å. In this structure, the distance is ~ 2 Å, suggesting a very strong cation- π interaction.

A similar approach involved treating fluorene with *n*-butylsodium and pentamethyldiethylenetriamine to give orange crystals of the sodium fluorenyl complex shown in Fig. 8b.^[24] The solid-state structure is recorded in the CSD as VOKPUG. It is interesting that the cation- π interaction occurs with the central ring rather than either of the benzene rings. The Na-centroid distance is 2.562 Å. The ionic radius of Na^+ is about 1 Å, so the observed distance is once again shorter than the calculated value of $(1.75 + 1 =) 2.75$ Å.

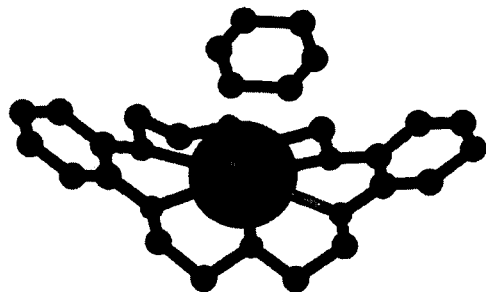


Fig. 9 Crystal structure of potassium cation complexed by dibenzo-18-crown-6 and axially-solvated by neutral benzene. The K^+ ion is pulled out of the plane formed from the 6 oxygen atoms in the crown ether.

SOLID-STATE STRUCTURAL STUDIES OF CATION- π INTERACTIONS INVOLVING NEUTRAL ARENES

The importance of an early and revealing structural study by Hrcir et al.^[25] was not generally recognized at the time it appeared. The K-benzene distance is 3.369 Å. The ionic radius of K^+ is approximately 1.35 Å, giving an expected K^+ -arene contact distance of $(1.75 + 1.35 =) 3.1$ Å. In this example, the K-arene contact is longer than the sum of the van der Waals distances, but the arene is not charged in this case. An interesting feature of this structure is that the K^+ ion is pulled out of the plane formed from the 6 oxygen atoms in the crown ether (Fig. 9).

Many solid-state structures show close contacts between arenes and cations.^[26] One example is found in zeolites, which trap cations and arenes within their intricate molecular structure.^[27] Another is found in numerous calixarene complexes^[28] in which one or more cations are in proximity to the numerous arenes in the receptor molecule.^[29,30]

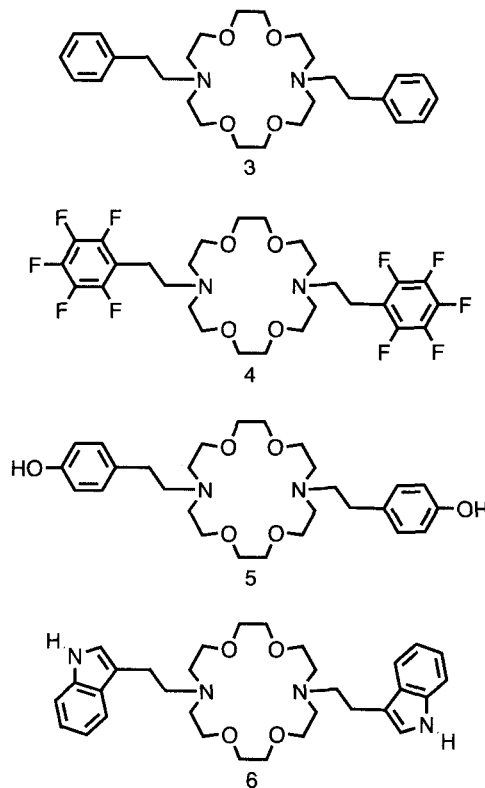


Fig. 10 Bibracchial (two-armed) lariat ethers having arene-terminated side arms: 3, benzene; 4, penta fluoro benzene; 5, phenol; and 6, indole.

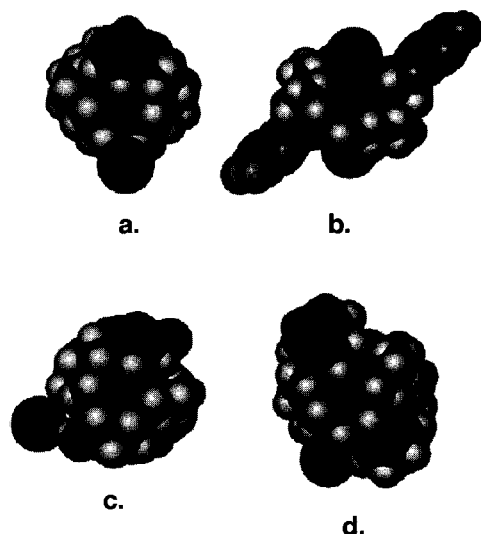


Fig. 11 The solid state structures of **3-6** complexing KI are shown as a-d, respectively. In panel b, the two Lewis acidic arenes are turned away from the macrocycle and the cation interacts directly with iodide anion whereas iodide is excluded from the solvation sphere in a, c, and d. (View this art in color at www.dekker.com.)

LARIAT ETHERS AS MOLECULAR PROBES OF CATION-ARENE INTERACTIONS

Examples of designed cation- π receptor molecules are not yet common. A number of such compounds have been developed for gas phase and solution studies, but these do not provide definitive structural information. On the other hand, a solid-state structure is always suspected on the grounds that packing forces may exert an unexpected influence on the molecular arrangement. Even so, crystal structures are generally persuasive and provide details not available by other methods.

Lariat ethers are crown ethers that have flexible side chains attached to the macroring. Donors present on the side chains may further stabilize cations bound in the macrocycle's cavity. In principle, both sigma- and pi-donors may be incorporated to serve this purpose. Four bibracchial (two-armed) lariat ethers are shown as compounds **3-6** (Fig. 10). Each is a diaza-18-crown-6 macrocycle that has an arene-terminated ethylene sidearm. The arenes on **3**,^[31] **5**,^[32] and **6**^[33] correspond to the side-chain residues of phenylalanine, tyrosine, and tryptophan, respectively. Compound **4**^[34] is structurally very similar to **3**, but the arene is electron-deficient owing to the strong electron-withdrawing effect of fluorine (Fig. 10).

The solid-state structures of **3-6** as their KI complexes are shown in Fig. 11a-d, respectively. In all cases, K^+ is complexed in the crown's central cavity or hole. From the electrostatic perspective, the iodide ion should be the best

anionic donor and it should be in essentially direct contact with the ring-bound cation. Instead, the sidearm arenes appear to be the axial donors in **3**·KI, **5**·KI, and **6**·KI. Such a result might be caused by crystal packing forces. Note that the iodide ion is in approximately the same position in a, c, and d, although H-bond interactions with hydroxyl (c) or amino (d) groups are possible only with **5** and **6**, respectively. The concern about packing forces is dispelled by the result shown in Fig. 9b. In this case, the benzene ring of **3** has been replaced by pentafluorophenyl groups. These are only slightly larger than benzene, but they may be considered pi-acids rather than pi-bases. Thus they are expected *not* to interact with bound K^+ . As shown in Fig. 11, panel b, the two arenes are turned away from the macrocycle and the cation interacts directly with the iodide anion. Two iodide ions are shown in Fig. 11b. They actually comprise part of an infinite chain of $(-K-I)_n$ ion pairs within the crystal (Fig. 11).

To further clarify these interactions, the diaza-18-crown-6 compound (**7**) was prepared that has 2-methoxyethyl and 2-phenylethyl side chains.^[35] The compound and the complex observed by X-ray crystallography are illustrated schematically in Fig. 12. The complex possesses no obvious H-bonding residue in the sidearms, but iodide anion in **7**·KI is excluded from the cation's solvation sphere. Because there is only one arene available to serve as an axial donor, the other site is occupied by the ether oxygen. When a single sidearm is present (*N*-2-phenylethylaza-18-crown-6), iodide occupies the axial position opposite the single arene.^[36]

An interesting feature of the solid-state structural studies is that the bound cation in **6** was closer to the 5-membered ring instead of the more electron-rich 6-membered ring. Computational studies showed a clear

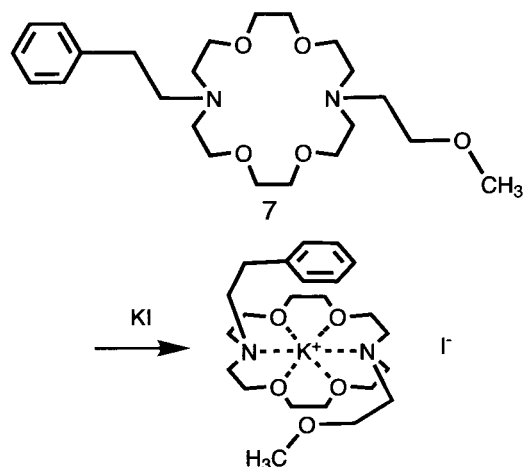


Fig. 12 The diaza-18-crown-6 compound (**7**) was prepared to have 2-methoxyethyl and 2-phenylethyl side chains.

preference for the benzo, rather than the pyrrolo subunit, of indole to serve as the pi-donor. Similar experimental results were observed for both Na⁺ and K⁺ in concert with a variety of counteranions. When the position of attachment between the macrocycle and the arene was moved, benzene became the cation's axial donor.^[37] This suggests that indole is indeed a versatile pi-donor.

CONCLUSION

Arenes are predicted by computational methods to bind cations. The first evidence for such interactions came from mass spectrometric studies conducted in the gas phase. Subsequent studies undertaken with designed receptor molecules gave evidence for cation-arene interactions in various solvents. Recently, numerous solid-state structural data have confirmed these interactions and have provided distance and angle information upon which to base more sophisticated receptor design efforts.

ACKNOWLEDGMENTS

The author gratefully acknowledges that his work in this area has been supported by grants from the National Institutes of Health, the National Science Foundation, and the Petroleum Research Fund.

REFERENCES

1. Nicholas, J.B.; Hay, B.P. Anisole as an ambidentate ligand: Ab initio molecular orbital study of alkali metal cations binding to anisole. *J. Phys. Chem., A* **1999**, *103*, 9815–9820.
2. Sunner, J.; Nishizawa, K.; Kebarle, P. Ion-solvent interactions in the gas phase. The potassium ion and benzene. *J. Phys. Chem.* **1981**, *85*, 1814–1820.
3. Guo, B.C.; Purnell, J.W.; Castleman, A.W., Jr. The clustering reactions of benzene with sodium and lead ions. *Chem. Phys. Lett.* **1990**, *168*, 155–160.
4. Gilligan, J.J.; McCunn, L.R.; Leskiw, B.D.; Herman, Z.; Castleman, A.W., Jr. Associative ionization of excited sodium species with various ligands: Assessing relative bonding strengths of ion-ligand interactions. *Int. J. Mass Spectrom.* **2001**, *204*, 247–253.
5. Cabarcos, O.M.; Weinheimer, C.J.; Lisy, J.M. Competitive solvation of K⁺ by benzene and water: Cation-pi interactions and pi-hydrogen bonds. *J. Chem. Phys.* **1998**, *108*, 5151–5154.
6. Cabarcos, O.M.; Weinheimer, C.J.; Lisy, J.M. Size selectivity by cation-p interactions: Solvation of K⁺ and Na⁺ by benzene and water. *J. Chem. Phys.* **1999**, *110*, 8429–8435.
7. Dunbar, R.C. Binding of Na⁺, Mg⁺, and Al⁺ to the pi faces of naphthalene and indole: Ab initio mapping study. *J. Phys. Chem., A* **1998**, *102*, 8946–8952.
8. Nicholas, J.B.; Hay, B.P.; Dixon, D.A. Ab initio molecular orbital study of cation-pi binding between the alkali-metal cations and benzene. *J. Phys. Chem., A* **1999**, *103*, 1394–1400.
9. Hoyau, S.; Norman, K.; McMahon, T.B.; Ohanessian, G. A quantitative basis for a scale of Na⁺ affinities of organic and small biological molecules in the gas phase. *J. Am. Chem. Soc.* **1999**, *121*, 8864–8875.
10. Wouters, J. Use of theoretical descriptors to characterize cation-pi binding sites in (macro)molecules. *J. Comput. Chem.* **2000**, *21*, 847–855.
11. Hay, B.P.; Nicholas, J.B.; Feller, D. Novel binding modes in tetramethoxycalix[4]arene: Implications for ligand design. *J. Am. Chem. Soc.* **2000**, *122*, 10083–10089.
12. Ryzhov, V.; Dunbar, R.C. Interactions of phenol and indole with metal ions in the gas phase: Models for Tyr and Trp side-chain binding. *J. Am. Chem. Soc.* **1999**, *121*, 2259–2268.
13. Ryzhov, V.; Dunbar, R.C.; Cerda, B.; Wesdemiotis, C. Cation-pi effects in the complexation of Na⁺ and K⁺ with Phe, Tyr, and Trp in the gas phase. *J. Am. Soc. Mass Spectrom.* **2000**, *11*, 1037–1046.
14. Armentrout, P.B.; Rodgers, M.T. An absolute sodium cation affinity scale: Threshold collision-induced dissociation experiments and ab initio theory. *J. Phys. Chem., A* **2000**, *104*, 2238–2247.
15. Behm, R.; Gloeckner, C.; Grayson, M.A.; Gross, M.L.; Gokel, G.W. Pyxophanes: Selective gas phase ion complexation by 1,6,13,18-tetraoxa[6.6]paracyclophane-3,15-diyne. *Chem. Commun.* **2000**, 2377–2378.
16. Yoshida, M.; Tsuzuki, S.; Tamaoki, N. Induced-fit conformational changes in the cation-pi complexes of pyxophane: A DFT study. *Perkin 2* **2001**, 1021–1023.
17. Meot-Ner, M.; Deakyne, C.A. Unconventional ionic hydrogen bonds. 2. NH⁺...pi. Complexes of onium ions with olefins and benzene derivatives. *J. Am. Chem. Soc.* **1985**, *107*, 474–479.
18. Burley, S.K.; Petsko, G.A. Amino-aromatic interactions in proteins. *FEBS Lett.* **1986**, *203*, 139–143.
19. Kearney, P.C.; Mizoue, L.S.; Kumpf, R.A.; Forman, J.E.; McKurdy, A.; Dougherty, D.A. Molecular recognition in aqueous media. New binding studies provide further insights into the cation-pi interaction and related phenomena. *J. Am. Chem. Soc.* **1993**, *115*, 9907–9919.

20. Ma, J.C.; Dougherty, D.A. The cation– π interaction. *Chem. Rev.* **1997**, *97*, 1303–1324.
21. Hoffmann, K.; Weiss, E. Ueber metall-alkyl- und -aryl-verbindungen. XVI. Die krystalstructuren von kaliumtetraphenylborat, $K[B(C_6H_5)_4]$ und tetramethylammonium-tetraphenylborat, $[N(CH_3)_4][B(C_6H_5)_4]$. *J. Organomet. Chem.* **1974**, *67*, 221–228.
22. Ozol, Y.; Vimba, S.; Levins, A. Crystal structure of $RbBPh_4$. *Krystallografiya* **1962**, *7*, 362.
23. Brooks, J.J.; Rhine, W.; Stucky, G.D. π groups in ion pair bonding. Stabilization of the dianion of naphthalene by lithium tetramethylenediamine. *J. Am. Chem. Soc.* **1972**, *94*, 7346–7351.
24. Corbelin, S.; Kopf, J.; Weiss, E. Monomeres, tetrameres und polymeres natriumfluorenid S [$s = Me_2N(CH_2)_2N(Me)(CH_2)_2NMe_2$, $Me_2N(CH_2)_nNMe_2$ ($n = 2, 3$)]. *Chem. Ber.* **1991**, 2417–2422.
25. Hrcir, D.C.; Rogers, R.D.; Atwood, J.L. New bonding mode for a bridging dioxygen ligand: The crystal and molecular structure of [K.dibenzo-18-crown-6][$Al_2Me_6O_2$]. *J. Am. Chem. Soc.* **1981**, *103*, 4277.
26. Gokel, G.W.; Wall, S.L.D.; Meadows, E.S. Experimental evidence for alkali metal cation– π interactions. *Eur. J. Org. Chem.* **2000**, 2967–2978.
27. Hashimoto, S.; Ikuta, S.; Asahi, T.; Masuhara, H. Fluorescence spectroscopic studies of anthracene adsorbed into zeolites: From the detection of cation– π interaction to the observation of dimers and crystals. *Langmuir* **1998**, *14*, 4284–4291.
28. Ikeda, A.; Shinkai, S. On the origin of high ionophoricity of 1,3-alternate calix[4]arenes: π -donor participation in complexation of cations and evidence for metal-tunneling through the calix[4]arene cavity. *J. Am. Chem. Soc.* **1994**, *116*, 3102–3110.
29. Arduini, A.; Casnati, A.; Pochini, A.; Ungaro, R. Recognition of cationic species with synthetic receptors. *Curr. Opin. Chem. Biol.* **1997**, *1*, 467–474.
30. Casnati, A.; Sansone, F.; Ungaro, R. Peptido- and glycolixarenes: Playing with hydrogen bonds around hydrophobic cavities. *Acc. Chem. Res.* **2003**, *36*, 246–254.
31. Meadows, E.S.; De Wall, S.L.; Barbour, L.J.; Gokel, G.W. Alkali metal cation– π interactions observed by using a lariat ether model system. *J. Am. Chem. Soc.* **2001**, *123*, 3092–3107.
32. De Wall, S.L.; Barbour, L.J.; Gokel, G.W. Cation– π complexation of potassium cation with the phenolic sidechain of tyrosine. *J. Am. Chem. Soc.* **1999**, 8405–8406.
33. De Wall, S.L.; Meadows, E.S.; Barbour, L.J.; Gokel, G.W. Solution and solid state evidence for alkali metal, cation– π interactions with indole, the side-chain of tryptophan. *J. Am. Chem. Soc.* **1999**, *121*, 5613–5614.
34. De Wall, S.L.; Meadows, E.S.; Barbour, L.J.; Gokel, G.W. Synthetic receptors as models for alkali metal cation– π binding sites in proteins. *Proc. Natl. Acad. Sci. U. S. A.* **2000**, *97*, 6271–6276.
35. Hu, J.; Barbour, L.J.; Gokel, G.W. Sigma-donor, π -donor, and anion competition in π -complexation of alkali metal cations. *Chem. Commun.* **2002**, 1808–1809.
36. Hu, J.; Barbour, L.J.; Gokel, G.W. Probing alkali metal– π interactions with the side chain residue of tryptophan. *Proc. Natl. Acad. Sci. U. S. A.* **2002**, *99*, 5121–5126.
37. Hu, J.; Barbour, L.J.; Gokel, G.W. The indole sidechain of tryptophan as a versatile π -donor. *J. Am. Chem. Soc.* **2002**, *124*, 10940–10941.

Molecular Simulations of DNA Counterion Distributions

Alexander P. Lyubartsev

Stockholm University, Stockholm, Sweden

INTRODUCTION

One of the remarkable physical properties of a DNA molecule is that it is a strongly charged polyelectrolyte. In solution, DNA dissociates, forming a negatively charged polyion surrounded by an atmosphere of mobile, positively charged counterions. Although positive counterions are attracted to DNA, they screen the negative charge of DNA, decreasing the attractive force for other positive counterions. Additionally, ions of different valency and size interact with DNA in a different manner, leading to effects of competition between ions of different species. There is always a delicate balance of forces forming the equilibrium ion distribution around DNA. The functionality of DNA in the cell is, in a decisive degree, determined by electrostatic forces, which in turn are dependent on the presence of different charged components in the surrounding solution. It is clear that understanding of DNA functionality is impossible without an understanding of electrostatic interactions of DNA with the environment.

The aim of the present review is to show how molecular computer simulations can contribute to our understanding of the basic features of the interaction of DNA with its ionic environment, what kind of information can be obtained by computer simulations, and how this information can be used to bridge experimental and theoretical studies of DNA. First, some common polyelectrolyte models of DNA will be briefly reviewed, and a survey of available computer simulation techniques will be given. Then, applications of computer simulations to describe the ionic environment of DNA on different levels of precision will be discussed: Monte Carlo (MC) and Brownian dynamics (BD) simulations within the continuum dielectric models, molecular dynamics (MD) simulations with explicit treatment of solvent, as well as a combination of these techniques, giving rise to the "multiscale modeling" approach.

Several reviews devoted to different aspects of DNA-ion interactions and computer simulations of DNA have recently appeared.^[1-3] A more general and detailed review of the computer simulation of polyelectrolytes is presented in Ref. [4].

DNA POLYELECTROLYTE MODELS AND THEORIES

A theoretical description of the ionic environment of DNA is not a simple task. In fact, in any condensed matter system, the more detailed and closer to reality the molecular model is, the more complicated (and often including even more approximations) is the theory that has to be applied to obtain meaningful results. There exist several levels of theoretical descriptions of polyelectrolyte systems. In the simplest approach (the so-called "primitive model"), a DNA is presented as a rigid cylinder, and mobile ions as point charges or small rigid charged spheres. Within the primitive model, the solvent is described as a uniform dielectric continuum, described by a dielectric permittivity of this solvent. The interaction between ions is described by the Coulombic potential scaled by the value of the dielectric permittivity.

The most commonly used approach to describe the properties of polyelectrolyte solutions at this level is the Poisson-Boltzmann (PB) (mean field) theory.^[5] This approach implies a Boltzmann distribution of the mobile ion species in the average field of other ions. For a simple cylindrical geometry, the PB equation can be rather easily solved by numerical methods. If the electrostatic potential is small, the exponent term in the standard PB equation may be linearized, resulting in the linearized PB equation that allows an analytical solution. In this context, the counterion condensation (CC) model formulated by Manning^[6] can also be mentioned. According to the CC model, for a highly charged cylindrical polyion, a certain amount of counterions remains in close proximity to the polyion. These counterions neutralize a given fraction of the total polyion charge, whereas the remaining counterions reside in the bulk phase. Because most of the charge of the polyion (76% in the case of DNA) is neutralized, the distribution of ions in the bulk phase may be described by the linearized PB equation. Because of its simplicity, the Manning CC model has had a profound impact on practical, as well as theoretical, studies of polyelectrolyte solutions.

The major problem with theories based on the PB approximation is that the Boltzmann expression for the ion

density cannot be strictly derived from the statistical-mechanical theory; therefore the accuracy of the PB theory should be checked by more rigorous theories, or by simulations. The PB theory neglects the small ion correlations within the model. The effect of correlations can be explained as follows. If a counterion is present at some point near the polyion surface, it will decrease the probability for other counterions to be around it. Therefore near this point, the counterion density will be lower than that given by the PB theory. The decrease in local counterion density causes an effective attractive force (in addition to the mean force) that draws the counterions closer to the polyion surface. Clearly, the effect becomes stronger with increase of the ion valency. Ion correlation effects can considerably change the behavior of the polyelectrolyte systems in quantitative as well as qualitative ways.

There exist a number of liquid state theories, based on integral equations, which go beyond the PB approximation: the hypernetted chain approximation (HNC),^[7,8] the BBGY chain equations,^[9,10] the mean spherical approximation,^[5] the modified PB theory,^[11] as well as some others. A discussion of these theories and a comparison of predictions of such models to both the PB model and that of computer simulations can be found in a recent review.^[12]

More elaborate DNA models may include specific details of its structure. One example is the so-called "grooved" model of DNA,^[13] in which the charged groups of DNA are located outside the cylindrical hard core, on the sites corresponding to the phosphate groups of DNA. In addition, full-atomic molecular models of DNA or other polyelectrolytes in continuum solvent have been considered. In such cases, the PB equation becomes three-dimensional, but its solution is still rather straightforward.^[14,15] Sometimes effects of polarization and hydration are included by considering a distant-dependent and field-dependent dielectric constant. The relevant theory to treat this class of models is the modified PB equation.^[16] Stricter statistical-mechanical theories become too complicated to be of any practical use in this case.

The above-discussed analytical theories have to resort to approximations already at the level of the primitive model. Comparison of theory with experiment is, in such cases, inconclusive; if discrepancies occur, it may be difficult to attribute them to the approximations within the model, or to approximations during the mathematical treatment of the model. Computer simulations can help to answer the questions because they may provide an accurate, asymptotically exact, statistical-mechanical solution for a given model. Moreover, computer simulations allow to treat even more accurate and detailed models, with a proper account of effects caused by hydration, dielectric

saturation, and the molecular structure of the solvent by considering explicit solvent molecules.

The main computer simulation methods are MC and MD. The MC method^[17] is based on a stochastic procedure, which generates molecular configurations with probabilities equal to that in the canonical (or another statistical) ensemble. By calculating simple arithmetic averages over generated molecular configurations, it is possible to define average values of physical properties in the canonical ensemble and to obtain exact (in statistical sense) answers to a statistical-mechanical problem. An important kind of MC simulation technique is the grand canonical Monte Carlo (GCMC) method, which allows to perform simulations in the grand canonical ensemble at constant chemical potential.^[18]

The MC method is very suitable for a description of electrolyte and polyelectrolyte systems within the frame of continuum solvent models (i.e., when solvent molecules are not explicitly included in the simulations). However, for models with explicit solvent molecules, the MC method is not so efficient. The main reason is that in the liquid state, the molecules are closely packed and the fraction of the accepted MC steps becomes too small. For molecular all-atom models of the solvent, the MD simulation scheme is then more efficient.

The MD simulation technique implies a numerical solution of the Newtonian equations of motion for all atoms in the simulated molecular system. At each step of the MD simulation, the coordinates and velocities of the particles are recalculated according to equations of classical mechanics where forces are computed from some predefined expressions, called the force field. The time step is usually chosen at about 10^{-15} sec and a typical MD simulation covers a time interval of 10^{-8} – 10^{-10} sec. In addition to structural and thermodynamic properties, the dynamics of the molecular system can be studied, including time correlation functions, diffusion, and other transport properties.

At present, MD simulation is the most commonly used simulation method for studying molecules and molecular interactions in the liquid state. However, because MD implies simulation of all atoms in the system including solvent molecules, it becomes too expensive for studies of polyelectrolytes. A simplified description of polyelectrolyte systems, in terms of continuum solvent models, is still a preferable option. For such models, either the MC method or the stochastic analogue of MD—BD is used. In BD, the solvent molecules are not explicitly accounted for, but enter the equations of motion for solute molecules by two terms: a friction force and a random force. The third term in forces describes interactions with other solute particles in the system (e.g., other ions or polyions). Because the solvent molecules are not treated explicitly in BD, it allows simulation of substantially larger systems

than full-atomic MD simulation. Moreover, compared with MC simulations, the dynamic properties of the ions can be determined. For example, the effect of polyions on ion diffusion can be studied.

SIMULATION OF COUNTERIONS AROUND DNA WITHIN CONTINUUM SOLVENT MODELS

Evaluation of Analytical Theories

The first attempts of computer simulations of DNA-like polyelectrolytes were made in the beginning of the 1980s using the MC method.^[19,20] More systematic studies, with varying salt concentrations and/or ion type, have been carried out later.^[21–27] The primary objective of these earlier computer simulation studies was to evaluate the applicability of analytical theories describing ionic distributions around DNA. In most of these works, the primitive model was used [i.e., the DNA was modeled as a hard body (cylinder) with a uniform distribution of surface charge, and the ions were represented as point charges or charged hard spheres]. In some of these works, a soft short-range ion–ion or ion–DNA interaction potential,^[23] or a specific location of the charges on the polyion surface^[22] has been used. The main outcome of the early simulations was that the PB approximation is generally valid if only monovalent ions are present in the solution. In subsequent works with more detailed and more accurate (in the sense of longer runs) simulations, it was shown that deviation of the PB theory from the simulations does not exceed 10% for the ion distribution or the electrostatic potential in the relevant range of ion concentrations.

For ions of higher valency and their mixtures, the PB approximation often fails. The typical behavior is that the PB approximation underestimates the ion density in the nearest layer next to the polyion surface, which is a result of neglecting ion–ion correlations. An example is given in Fig. 1, which shows the ion density distributions for a cylindrical model of DNA in the presence of a mixture of divalent counterions and monovalent coions. One can see an increased simulated concentration of counterions compared with the PB result within about 5 Å from the polyion surface. This feature may seem not large on the figure, but given the facts of the logarithmic scale of Y -axis and steep slope of the curve, it results in a noticeable higher affinity of divalent ions to DNA.

An additional attraction of counterions to DNA can be seen more clearly in the “integrated charge” curve, which represents ion distribution integrated from the surface of polyion to some distance r . The sense of this curve is the total counterion charge (per length of the polyion) within the cylinder of radius r around the polyion. An example of

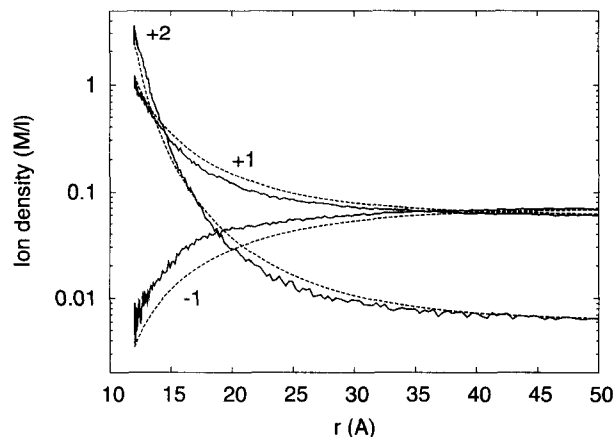


Fig. 1 Ion distribution profile around a cylindrical DNA model for a mixture of divalent and monovalent counterions and monovalent coions, obtained in MC simulation (solid lines) and PB approximation (dashed lines). Radius of all ions in MC simulations, 2 Å. The simulation was set up as in Ref. [37].

the integral charge curve is shown in Fig. 2 for the mixture of monovalent and divalent counterions with monovalent coions.^[23] It is seen that for the given case (0.022 M MgCl_2 and 0.155 M NaCl mixture), the amount of divalent ions within 5 Å from the DNA surface in the PB approximation is underestimated by about 20%. In other cases (e.g., higher concentrations) deviations may reach 40% or even more.

Besides quantitative differences, computer simulations can, in some cases, predict a qualitatively different behavior as compared with the PB model. An example is the so-called “charge reversal” or “overneutralization,” which may happen if the total charge of the counterions in the close vicinity of a polyion exceeds the charge of the polyion itself, which then leads to an alternating sign of the electrostatic potential. Such behavior was typically observed for divalent or higher-valence counterions under certain thermodynamic conditions,^[25] but it may happen even for monovalent ions if the salt concentration is high enough.^[13] The charge reversal cannot be obtained in the PB theory. There is no clear experimental evidence of the charge reversal, except perhaps for a rather old work by Strauss et al.,^[28] who observed a cationic polyion (poly-4-vinylpyridine) moving against the electric field at high salt concentration.

More accurate statistical–mechanical theories, such as the HNC or the modified PB theory, were found to reproduce properties of the ion distributions relatively well even for multivalent ions.^[8,11,23] Fig. 2, reproduced from the work of Murthy et al.,^[23] shows the integral charge computed for a mixture of divalent and monovalent ions by the PB and HNC theories as well as by MC

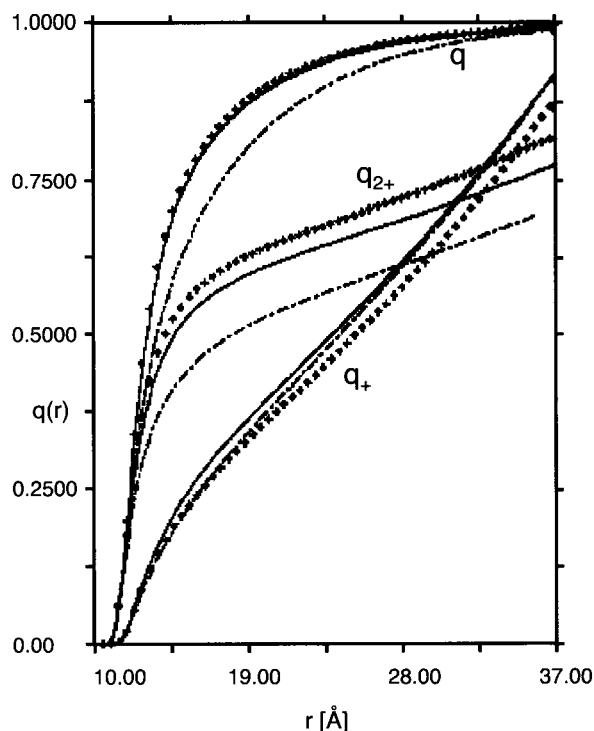


Fig. 2 Radially integrated counterionic (q_{2+} and q_{+}) and total (q) charge for a 0.155 M NaCl and 0.022 M MgCl_2 salt mixture around a cylindrical model of DNA. Points are MC simulation result; dash-dot lines and solid lines are PB and HNC theories, respectively. (From Ref. [23]. © American Chemical Society, 1985.)

simulations. Clearly, the HNC result is much closer to the simulation data than that obtained by the PB theory. The HNC theory, as well as some other more elaborated theories, are able to reproduce even such effects as charge reversal.^[8] However, these theories are difficult to apply in the case of more complicated (noncylindrical) geometries (e.g., for a model with specific location of the charges on the polyion).

Manning condensation theory is often considered as a further simplification of the PB theory. Still, it catches some basic features of ion distributions. Lamm et al.^[27] compared the fraction of electrostatically bound ions using the MC, PB, and CC methods. If the bound fraction of counterions is determined as those residing within a region around the DNA where the electrostatic potential is less than kT , the MC results are found to quantitatively reproduce the bound fraction predicted by the Manning condensation theory. Another interesting feature of ion distribution, also related to the CC theory, is that the concentration of counterions just next to the DNA surface depends very weakly on the salt concentration, and

remains high (a few molars per liter) even at very low salt concentrations. According to the CC theory, a fraction of DNA counterions remains condensed to DNA even at infinite dilution. This feature was also confirmed by the computer simulations.

Dielectric Effects

MC computer simulations within the primitive electrolyte model imply uniform continuum dielectrics with dielectric permittivity of liquid water ($\epsilon \approx 80$). In fact, dielectric permittivity of DNA itself is substantially lower. It is also often argued that because the water molecules around the DNA are strongly oriented in the electrostatic field of DNA, their reorientation mobility is reduced, which must make the dielectric permittivity lower than in the bulk solution. Some estimations show that the effective dielectric constant may be as low as 6–30 in the first one to two molecular layers near a DNA surface^[29,30] compared with the bulk value of about 80. Nonuniform dielectric permittivity is a source of polarization forces, and their effect on ionic distribution is a priori unclear.

MC simulations, incorporating the effect of dielectric discontinuity^[31,32] at the polyion surface and using alternative dielectric saturation models,^[33] have investigated the effects of the assumption of a constant dielectric permittivity, finding minor effects on the counterion distributions. Moreover, the effect may be different—it may drive ions out of the DNA grooves,^[31] or, at the opposite, increase their concentration near the DNA surface,^[32] depending on the details of the DNA model (shape) and the way how the dielectric effects are incorporated.

In fact, at distances on the order of a few angstroms, the concept of dielectric permittivity is not well defined. Within the primitive model, the interaction potential is the Coulombic potential scaled by the value of the dielectric constant. This potential is an approximation of the exact solvent-mediated potentials between the ions in the solution, which in fact represents the free energy of ion–solvent interactions. From this point of view, ϵ in the interaction potential can be regarded as a parameter of the potential, which may differ from the local dielectric constant related, for example, to the water dipole fluctuation or the dielectric response. Evaluation of solvent-mediated potentials may be performed from the all-atom MD simulations, which showed that the effective dielectric constant—as a parameter of the effective potential—remains high even at high-enough salt concentrations and near the DNA surface.^[33,34] The effects caused by an explicit account of the solvent in computer simulations on ion distribution around the DNA will be discussed in more detail below.

Effect of Specific Distribution of Charges

The effects caused by a specific distribution of charges on the polyion surface were studied in a number of works^[13,31,35-38] with applications to DNA. Quite evidently, a different structure of the charge distribution on the polyion may cause a rather different distribution of the ion density in the close vicinity of the polyion. Typically, one puts charges of -1 on the sites corresponding to the phosphate groups of DNA. Additionally, helical grooves may be set, mimicking the minor and major grooves of DNA. In some cases, the DNA is presented with all-atom resolution.^[39]

A detailed study of different ways to mimic helical grooves on DNA was presented by Montoro and Abascal.^[13] These authors observed that specific interactions of ions with DNA (soft repulsion potential), the incorporation of the discrete charge distribution, and the grooved nature of the DNA surface may change the ion density profile around DNA considerably (Fig. 3). For example, in a "groove model" of DNA, in which explicit grooves on DNA were introduced, a double hump on the counterion density profile was observed, which even transformed to a

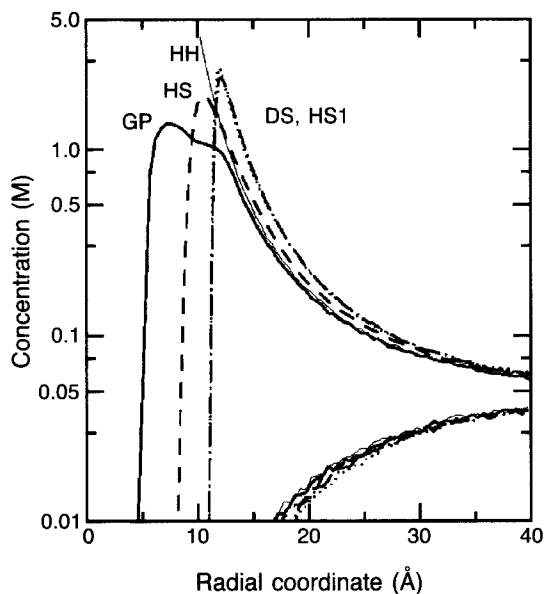


Fig. 3 Ion distribution profiles at 0.05 M monovalent salt, calculated in MC simulations for different DNA models. HH is "homogeneous hard cylinder," HS is "homogeneous soft cylinder" (ions interact with the polyion with repulsive $1/r^9$ potential), HS1 is homogeneous soft cylinder with a displaced axis of short-range repulsion, DS is discretely charged, soft repulsion model with charges located on sites of phosphate groups, GP is grooved DNA model with explicit grooves. (From Ref. [13]. © American Institute of Physics, 1995.)

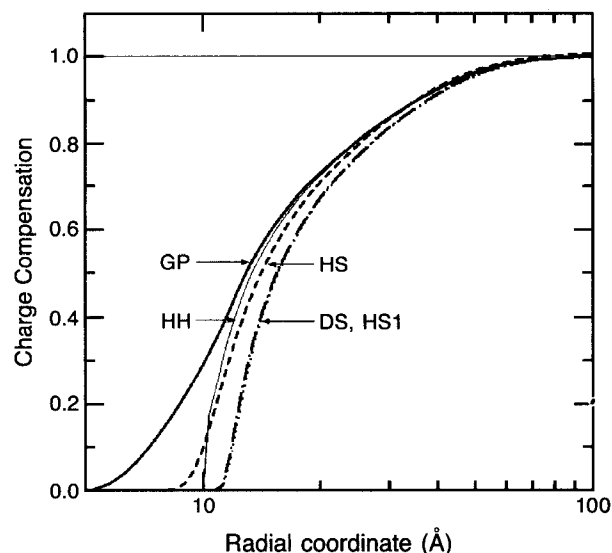


Fig. 4 Integrated charge (charge compensation) function, calculated in MC simulations for different DNA models. Notations are the same as in Fig. 3. (From Ref. [13]. © American Institute of Physics, 1995.)

double maximum at higher concentrations. This is in agreement with BD simulations of a full-atomic description of DNA.^[40,41] In addition, substantial penetration of counterions in the minor and major grooves was observed.^[36] Enhanced concentration of counterions in the grooves (with stronger effect in the minor groove) has been observed also in several works.^[37,38] However, distribution of counterions far from the DNA depends only weakly on the structure of the DNA surface.

An MC study of a DNA model with an all-atom resolution in a continuum solvent was carried out by Mills et al.^[39] for different forms of DNA. It was found that the grooved structure of both A-DNA and the B-DNA affects the details of the ion distribution in the center region of the polyion dramatically. However, the total number of bound ions at a particular added salt value differs only slightly among the conformations.

A general conclusion from the studies on the effect of the specific charge location on DNA is that although it may affect strongly the details in ion distribution near the polyion, the distribution of counterions far from the polyion (at distances more than 20 Å from the DNA axis) remains largely invariant. Furthermore, the integral properties of the ion distribution, such as the amount of ions within a certain distance around the polyion, depend very little on how the charges are located on the polyion surface. This is illustrated in Fig. 4, where the integrated charge is displayed for the same ion distributions as shown in Fig. 3. The integrated charge curves are determined

mostly by the total charge density of the polyion and by the ion composition. The primary reason for the weak sensitivity of the global properties of the ion distribution to the details of charge location is the long-range character of electrostatic interactions, which effectively averages contributions from all the charges of the polyion and makes the total electrostatic field similar to that of a uniformly charged cylinder.

Ion Competition

The interaction of mobile ions with polyions depends strongly on the ion type, charge, and size. Counterions of higher valency are more strongly attracted to polyions than monovalent ions—that is why they force low-valency ions out from the nearest vicinity of the polyelectrolyte. The size of the ions additionally plays a role and becomes especially important in the discussion of the competition of ions of the same valency. Smaller ions can come closer to the polyion surface and lower the electrostatic energy as compared with larger ions. However, within the primitive electrolyte model, the size of ions in simulations is not directly related to their real “crystallographic” sizes. Rather, it is a parameter that, in an average way, takes into account the effective hydration shell of water molecules around the ion. Reasonable values of the ion hydration radii can be obtained by fitting to available experimental data on ion osmotic and activity coefficients.^[42] Other ways of choosing effective ion radii are discussed in a recent work by Banavali and Roux.^[43]

The problem of ion competition has received much attention because of its importance in biological and technological applications. (For more information, see, for example, Ref. [44].) Typically, one determines a “competition coefficient,” which has a sense of an equilibrium constant of the ion exchange process.^[45] The competition coefficient may be determined experimentally from nuclear magnetic resonance (NMR) relaxation measurements,^[45] or from direct ion exchange experiments.^[46,47] The competition parameter may be also determined from computer simulations, or other theoretical approaches in a standard manner: For a given concentration of ions of different species, the ion density profiles are calculated and from these data, the amount of ions of each species within some distance from the polyion surface is obtained. Some uncertainty arises when one tries to define which ions are “bound” and which are “free.” Usually, one considers ions within some cutoff distance r_B from the surface of DNA (which is on the order of a few angstroms) as “bound.” Paulsen et al.^[45] analyzed the dependence of the competition coefficient on the cutoff radius and found that it is almost independent of r_B if r_B is chosen in reasonable limits.

In this way, the competition of ions of several divalent counterions with Na^+ around the DNA was studied in the work^[45] where a comparison of the PB model, MC simulations, and NMR experiments has been made. It was found that simulation results were closer to the experimental data than the PB results. Other studies of the ion competition effects are reported in a number of more recent MC simulations.^[38,48,49] It was shown that the PB approximation underestimates binding of higher-valency ions and that this underestimation increases with ion valency.^[38,45]

In the case of concentrated polyelectrolyte systems (e.g., oriented DNA fibers in equilibrium with a bulk electrolyte solution), the situation is different. The simulation cell, in this case, cannot include the “bulk” solution, so the concentration of the ions in the bulk is not directly known. The problem can be solved by performing GCMC simulations both in the polyelectrolyte gel phase and in the bulk solution (without polyions), at the same chemical potential.^[50] The GCMC approach has been applied for studying the competition of monovalent, divalent, and trivalent ions in a series of works by Korolev et al.^[46,47,51] In these works, competition coefficients of different ions, computed in GCMC simulations, were compared with the experimental ones measured by ion exchange experiments for DNA fibers, which were stabilized by the presence of ethanol. In computer simulations, the presence of ethanol was modeled as a lower (than in pure water) dielectric constant. The competition coefficients for the ions of different valencies and sizes have been computed and a good agreement with the ion exchange measurements has been observed.

Interaction of DNA with Multivalent Ligands

Studies of DNA interacting with complex multivalent molecular ions is of considerable interest because of the role of such ions (e.g., polyamines) in living systems. Additionally, polyamines are often used as condensing agents in the preparation of condensed samples of DNA. Other interesting and important applications are related to binding of charged intercalative drugs to DNA and to protein–DNA binding.

Application of standard polyelectrolyte theories to complex multivalent ions faces additional difficulties related to the spatial distribution of the ion charges and the internal degrees of freedom. In analytical theories, these additional features are usually either ignored^[52] or treated in some approximate manner.^[53,54] In computer simulations, on the contrary, inclusion of the internal structure of the ionic ligand does not pose any principal complications. In Ref. [37], the polyamine spermidine³⁺ was modeled as a chain of three monovalent ions connected by

harmonic bonds. It was shown that because of the effects of the nonlocal charge distribution and internal degrees of freedom, the binding affinity of spermidine to DNA was reduced compared with that of a simple trivalent (metal) ion. The binding was reduced even below the predictions of the PB theory, which generally underestimates the binding affinities of higher valency ions for simple ions. Existing NMR diffusion studies qualitatively confirm this result.^[55]

The binding of an octavalent rodlike ligand to DNA in the presence of monovalent salt has been studied by Olmstedt et al.^[56] using GCMC simulations. Such highly charged ligand binds strongly to DNA, forming a stable complex. A strong reduction in the surface counterion (e.g., Na⁺) concentration over a region including—but extending well beyond—the location of the ligand binding site has been observed.

Brownian Dynamics of Counterions Around DNA

BD simulations allow, alongside ion distribution, computation of dynamic and transport properties of ions. The presence of a polyion makes the diffusion of ions slower than in the bulk solution, because of both the steric obstacles imposed by the polyion and the electrostatic interactions. Thus the retardation of the diffusion provides information on the binding of ions to the polyelectrolyte. An advantage of diffusion studies is that the self-diffusion coefficient is a quantity that is directly available from experiments measuring macroscopic self-diffusion.

The diffusion properties of counterions in the presence of DNA were studied by BD simulations in a number of works.^[40,57,58] The self-diffusion coefficient can also be obtained within the PB mean field approximation, using the PB–Smoluchowski diffusion model.^[59] A comparison of lithium counterion diffusion coefficients determined in BD simulations, in the PB–Smoluchowski model, and in the experiment was performed in Ref. [57]. The comparison of the two polyelectrolyte theories with the experiment clearly demonstrated the effect of ion correlations included in the BD simulations, which substantially improve agreement with the experiment.

Apart from the general interest as to how the presence of DNA affects ion dynamics, such simulations provide valuable information for the interpretation of NMR relaxation experiments. For example, BD may provide data on the time correlation function of the electric field gradients^[40,58] experienced by Na⁺ counterions associated with DNA, for which the NMR quadrupolar relaxation of the ²³Na nuclei is determined by the time-dependent fluctuation of these field gradients.

SIMULATIONS OF COUNTERIONS AROUND DNA WITH EXPLICIT ACCOUNT OF SOLVENT

Molecular Dynamics of DNA

The studies of the ionic environment of DNA discussed above have been carried out within continuum solvent models. The effects of solvent and hydration can be taken into account rather straightforwardly in computer simulations by introducing explicit solvent (water) molecules. However, an all-atom description makes the simulations very time-consuming and reduces the size of the system that can be considered. At the present level of computer power, the maximum number of atoms that can be simulated long enough to obtain meaningful results is on the order 10⁴, which corresponds to a simulation box size of 50–60 Å. This size is not enough to study polyelectrolyte aspects of ion distribution. Still, all-atom simulations are extremely important for understanding ion–DNA interactions in close proximity to the DNA.

The preferable method in all-atom simulations is MD, although the first attempt to simulate such model was performed by the MC method.^[60] Earlier MD simulations of DNA^[61–63] were too short to produce information on ionic distribution. Given the diffusion of counterions around DNA on the order 10⁻⁶ cm/sec², at least nanosecond time scale is needed for the counterions to sample the space around DNA. Such simulations became possible from the second part of 1990s, when a large number of works on MD simulations of DNA, with full-atomic description of solvent and ions, appeared.^[64–71] In the majority of these studies, the main interest was in the DNA molecule itself, investigating DNA backbone structure and dynamics, base stacking, phosphate orientation, overall nucleic acid structure, and so on. (For more information on these issues, the reader is referred to recent reviews.^[3,72]) Below, we shall concentrate on works dealing with MD simulations of ion distributions around DNA. Note first that results on MD simulations are dependent on the force field used. The force fields used in macromolecular simulations are usually empirically parameterized to reproduce some set of experimental results. At present, the most often used force fields for DNA simulations are AMBER^[73] and CHARMM.^[74] It was found that these force fields may give somewhat different DNA structures.^[70] However, the hydration structure and ion distribution are very similar in AMBER and CHARMM simulations.^[71,75] This is because of the fact that these force fields differ mainly by parameters describing intramolecular DNA interactions, whereas parameters describing forces between water, ions, and DNA are almost the same.

Specific Binding of Ions

A major issue in molecular dynamic studies of the ionic environment of DNA is the problem of specific ion binding to different sites on the DNA surface. Whether this binding is sequence-specific or purely electrostatic is still to be determined. X-ray experiments carried out in the 1980s have suggested that there exists a "spin of hydration" of DNA,^[76] which is a sequence of water molecules in the minor and major grooves that is impenetrable to cations. Cations, according to this picture, form a diffuse cloud around, which is defined by electrostatic interactions. However, MD simulations, made in the 1990s, have shown that Na⁺ counterions may intrude the spin of hydration of DNA and substitute for water molecules.^[66-68,77] This was also confirmed by newer, high-resolution X-ray data.^[78]

The question of sequence-specific counterion binding to DNA has a principal importance to our understanding of mechanisms of DNA recognition. When counterions bind to DNA in a sequence-specific manner, they form a mosaic of nonuniform charge distribution depending on the DNA sequence. Moreover, it was supposed that direct ion binding to DNA affects the DNA structure,^[78] although this point of view is under debate.^[79] Molecular computer simulation can provide valuable information to this discussion.

Most of the mentioned MD simulations of DNA have been carried out with Na⁺ counterions. In some works, other counterions were also studied. In Ref. [68], a comparative study of Li⁺, Na⁺, and Cs⁺ around DNA was performed. It was found that these monovalent alkali ions interact with DNA in a very different manner. Li⁺ ions bind almost exclusively to the phosphate groups of DNA. Na⁺ ions bind prevailing bases in the minor groove through one water molecule, although a smaller fraction of ions binds directly to the bases at some specific sites (AT step in the minor groove and guanine bases in the major groove). Cs⁺ ions bind directly to sugar oxygen in the minor groove. It was shown also that the specific character of ion bonding is, to a large extent, determined by the hydration structure of water around DNA. A stronger binding of Li⁺ ions to DNA was also confirmed by NMR studies of the diffusion of Li⁺ and Cs⁺ ions in oriented DNA fibers.^[80]

DNA oligomers d(TpA)₁₂ in the presence of K⁺ counterions were simulated in Ref. [81]. Comparing with Na⁺ counterions, a stronger preference of K⁺ ions to the major groove has been observed.

MD of DNA with divalent ions Mg²⁺ and Ca²⁺ was performed in some recent works.^[63,64,82] However, the slow diffusion of Mg²⁺ ions makes it difficult to perform a reliable estimation of distribution of these ions around the DNA.

Recently, some works appeared on the distribution of multivalent polyamine ions around DNA.^[83-85] It was found that flexible polyamine molecules (spermine or spermidine) have several binding modes, interacting with different sites on the DNA in an irregular manner. That is why polyamine molecules are not seen in X-ray diffractions of DNA. Spermine⁴⁺ ions compete with Na⁺ ions and water molecules in binding to bases in the minor groove, and they influence the structure of the DNA hydration shell in different ways.^[85]

Comparison with Continuum Solvent Models

An interesting question that MD simulation could answer is: How reliable are computations within the continuum solvent model, for example, in the prediction of overall ion density around DNA? The angularly averaged density profile of counterions (Na⁺ mostly) has been calculated in some recent works.^[66-68] At short distances (within 5 Å from the DNA surface), these density profiles are defined mainly by the details of DNA structure and hydration forces. Naturally, the distributions are very different from the density profiles calculated for the cylindrical model of DNA within the continuum solvent model (both in analytical approaches and MC simulations). Such comparison, from Ref. [68], is shown in Fig. 5, where angularly averaged distributions of different monovalent counterions around the DNA are displayed, together with the PB theory result. Introducing details of the DNA structure within the continuum dielectric model may make the counterion distribution closer to that obtained in MD simulations. For example, a maximum in ion density is

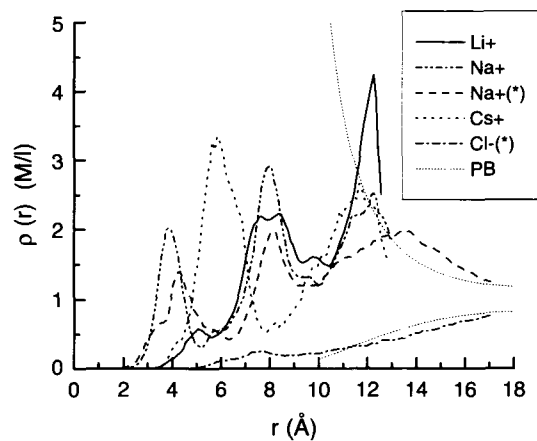


Fig. 5 Density profile of different ions around DNA obtained in all-atom MD simulations. The results marked with (*) are from a simulation with a larger simulation cell than the other data. The thin dotted line shows the PB results with a cell radius corresponding to the system marked (*). (From Ref. [68]. Adenine Press.)

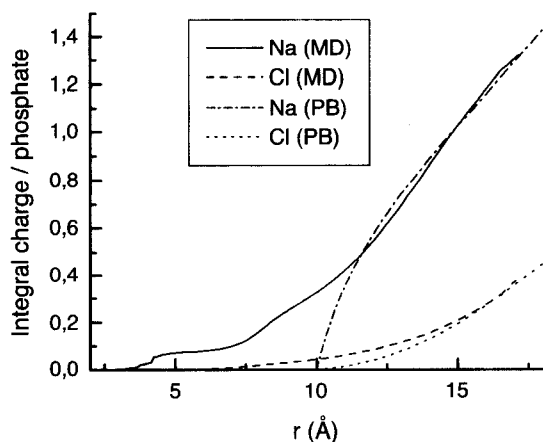


Fig. 6 Integral charge for Na^+ and Cl^- ions per phosphate obtained in all-atom MD simulations and PB approximation. (From Ref. [68]. Adenine Press.)

observed at about 8 Å from the DNA axis, corresponding to a high probability for counterions to be inside the DNA grooves.^[38]

On larger distances from the DNA, the ion distribution, computed in MD simulations, became more similar to that calculated in the PB theory, or obtained in continuum solvent simulations. In addition, the integral charge for Na^+ ions turned out to be very similar already on distances greater than 12 Å from the DNA surface (Fig. 6). This means that cylindrical PB equation, despite many inherent approximations, is still able to evaluate amounts of ions that are attracted (or “nonspecifically” bound) to DNA.

Multiscale Simulation Approach

However, direct simulation of ion density in MD simulation is a tedious task and can be performed only at relatively small distances from the DNA surface. These distances do not include the true “bulk” phase, where neither water nor ions are affected by the electrostatic field of DNA. On the other hand, the problem of finding the ion distribution in the whole range (from the DNA surface to the bulk solution) is the important one. The “bulk” ion concentration in the living cell is determined by the work of ion channels in the membrane; however, only ions that are in close proximity to DNA affect their properties. Although continuum solvent models allow to compute for the ion distribution in the whole range, they contain adjustable parameters, such as the effective ion radius, and are unable to describe the effects of specific ion binding (e.g., specific binding of Li^+ ions to the phosphate groups).

In Refs. [33] and [34], an approach was suggested to link together the two levels of simulations of electrolyte or

polyelectrolyte systems (i.e., the all-atom MD simulations and the MC simulations without explicit solvent). The main idea is that detailed all-atom MD simulations provide information on how to parameterize parameters for the continuum solvent model. In practice, as a first step, an MD simulation of size as large as can be afforded is performed. From this simulation, the radial distribution function (RDF) between ions as well as between ions and some sites of DNA is determined. Then, an inverse MC procedure is performed,^[34,86] which finds the effective interaction potentials that match the RDF obtained in the MD simulations. The great benefit of effective potentials is that they can be used for simulation of the very same system but of substantially larger scale because the solvent molecules are not included. The typical behavior of the effective potentials is that they have a few oscillations at short distances, reflecting the molecular structure of the solvent, and then—at distances of more than 10 Å—approach the Coulombic potential with the dielectric constant of water.^[33,34] The short-range part of the effective potentials is rather ion-specific, thus the specific features of ion–DNA interactions are automatically included in the model.

In Ref. [34], the effective potentials between different alkali ions and DNA have been determined and used for MC simulations of the ion environment of DNA. The computed ion distributions are shown in Fig. 7. One can notice clear similarities with the ion distribution obtained in all-atom MD simulations in Fig. 5. Another interesting observation is that for Na^+ and K^+ ions, the density profiles follow very closely the solution of the PB equation for distances larger than 15 Å from the DNA axis (of course, they were rather different at closer distances).

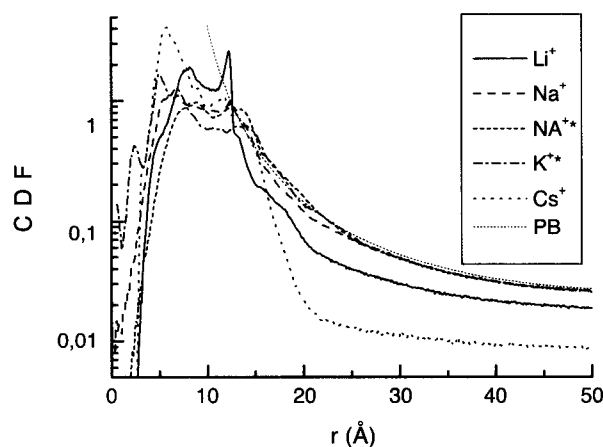


Fig. 7 Density profile of different ions around DNA obtained by MC simulation with effective solvent-mediated potentials. The notations for the curves are the same as in Fig. 5. (From Ref. [34]. American Institute of Physics. Simulation details are given in this reference.)

For two other ions, Li^+ and Cs^+ , the deviations from the solution of the PB equation were more significant because of specific interactions of these ions with DNA. From the simulations, the relative binding affinity of these ions to DNA was determined as $\text{Cs}^+ > \text{Li}^+ > \text{Na}^+ \geq \text{K}^+$, in agreement with the experimental results.

The multiscale modeling approach may be used to take into account solvent and hydration effects in studies of ion binding and competition, as well as of the interaction of DNA with other ligands and proteins. Work in this direction is now in progress.

CONCLUSION

The aim of the present review has been to show that computer simulation techniques are becoming increasingly important in the description of the ionic environment of DNA as well as other properties of biomacromolecular systems. Computer simulations allow us to follow the motion of every atom in the studied system, thus providing very detailed information and contributing to our general understanding of the physical mechanisms that govern the behavior of these biologically, as well as technologically, important systems. With the rapid development of computer technology, allowing larger systems to be studied on a longer time scale and enabling also a more accurate and detailed description of molecular interactions, the importance of molecular simulations in this area will grow further. Furthermore, new developments in experimental techniques including "single-molecule" experiments, as well as an interest in more and more complicated systems related to new areas of biotechnology, biomaterials, and nanotechnology additionally enhance the importance of computer simulation methods.

ACKNOWLEDGMENTS

The author is thankful to Jose Abascal for providing electronic copies of the figures. Many thanks to Lars Nordenskiöld, Aatto Laaksonen, and Nikolai Korolev for stimulating discussions. This work was supported by the Swedish Research Council.

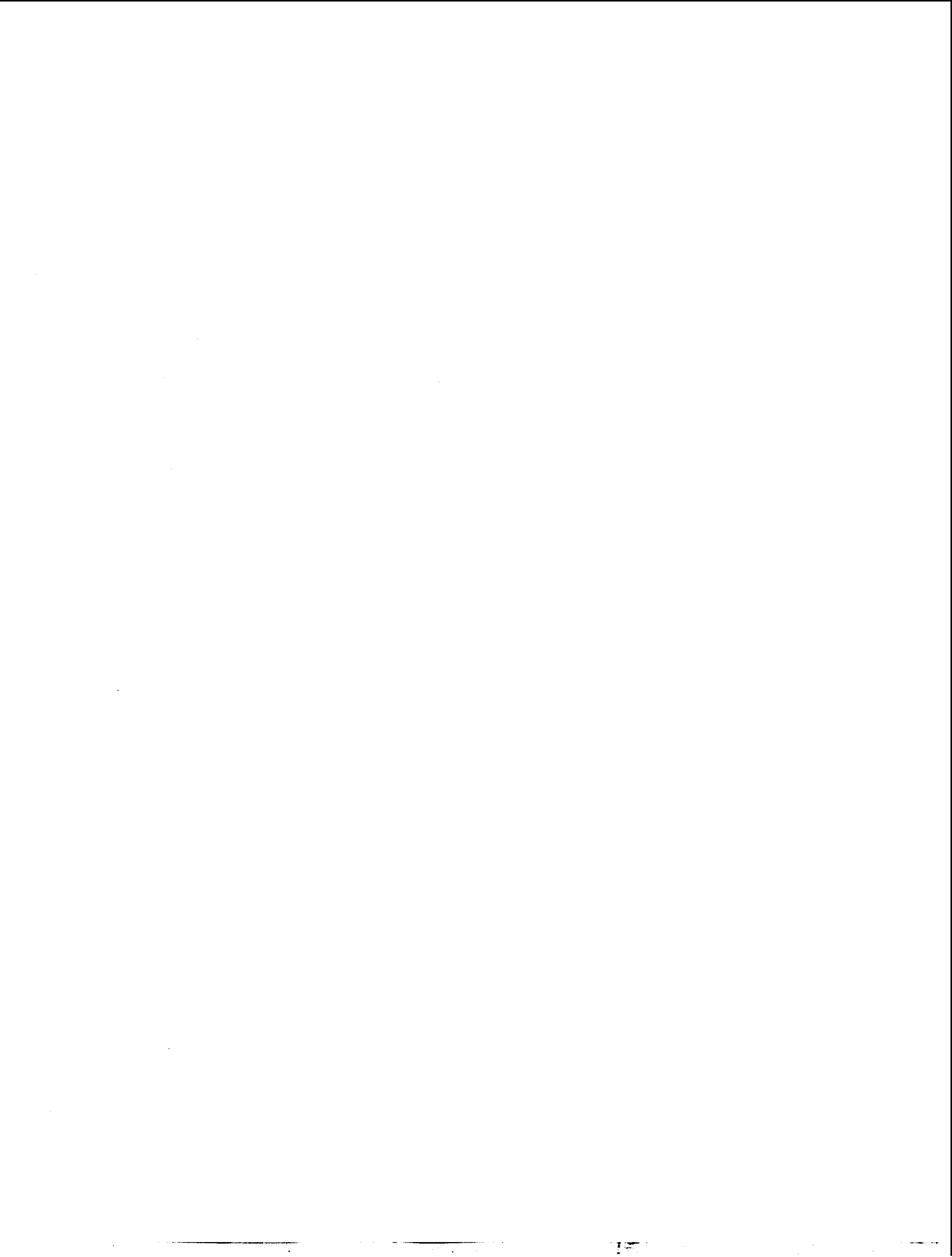
REFERENCES

- Anderson, C.F.; Record, M.T. Salt-nucleic acid interactions. *Annu. Rev. Phys. Chem.* **1995**, *46*, 657-700.
- Jayram, B.; Beveridge, D.L. Modeling DNA in aqueous solutions: Theoretical and computer simulation studies on the ion atmosphere of DNA. *Annu. Rev. Biophys. Biomol. Struct.* **1996**, *25*, 367-394.
- Cheatham, T.E.; Kollman, P.A. Molecular dynamics simulations of nucleic acids. *Annu. Rev. Phys. Chem.* **2000**, *51*, 435-471.
- Lyubartsev, A.P.; Nordenskiöld, L. *Computer Simulations of Polyelectrolytes*; Tripathy, S.K., Kumar, J., Nalwa, H.S., Eds.; Handbook of Polyelectrolytes and Their Applications, American Scientific Publishers, 2002; Vol. 3, 309-326.
- Fixman, M. The Poisson-Boltzmann equation and its application to polyelectrolytes. *J. Chem. Phys.* **1979**, *70* (11), 4995-5005.
- Manning, G.S. Limiting laws and counterion condensation in polyelectrolyte solutions. *J. Chem. Phys.* **1969**, *51*, 924-933.
- Vlachy, V.; McQuarrie, D. A theory of cylindrical polyelectrolyte solution. *J. Chem. Phys.* **1985**, *83* (4), 1927-1932.
- Tovar, E.G.; Losada-Gassou, H.; Henderson, D. Hypernetted chain approximation for cylindrical polyelectrolytes. *J. Chem. Phys.* **1985**, *83* (1), 361-372.
- Croxton, T.; McQuarrie, D.A. The electrical double layer in the Born-Green-Yvon approximation. *Mol. Phys.* **1981**, *42*, 141-151.
- Ramanathan, G.V. Statistical mechanics of electrolytes and polyelectrolytes: II. Counterion condensation on a line charge. *J. Chem. Phys.* **1982**, *77* (8), 4133-4140.
- Outhwaite, C.W. A modified Poisson-Boltzmann equation for the ionic atmosphere around a cylindrical wall. *J. Chem. Soc., Faraday Trans. II* **1986**, *82*, 789-794.
- Vlachy, V. Ionic effects beyond Poisson-Boltzmann theory. *Annu. Rev. Phys. Chem.* **1999**, *50*, 145-165.
- Montoro, J.C.G.; Abascal, J.L.F. Ionic distribution around simple DNA models: I. Cylindrically averaged properties. *J. Chem. Phys.* **1995**, *103* (18), 8273-8284.
- Klein, B.J.; Pack, G.R. Calculation of the spatial distribution of the charge density in DNA environment. *Biopolymers* **1983**, *22*, 2331-2352.
- Cortis, C.M.; Friesner, R.A. Numerical solution of the Poisson-Boltzmann equation using tetrahedral finite-element meshes. *J. Comput. Chem.* **1997**, *18* (13), 1591-1608.
- Gavryushov, S.; Zielenkiewicz, P. Electrostatics of a DNA-like polyelectrolyte: Effects of solvent dielectric saturation and polarization of ion hydration shells. *J. Phys. Chem., B* **1999**, *103* (28), 5860-5868.
- Metropolis, N.; Rosenbluth, A.W.; Rosenbluth,

- M.N.; Teller, A.H.; Teller, E. Equation of state calculations by fast computing machines. *J. Chem. Phys.* **1953**, *21*, 1087–1092.
18. Wood, W.W. *Physics of Simple Liquids*; North-Holland: Amsterdam, 1968.
 19. Vlachy, V.; Dolar, D. Monte Carlo studies of polyelectrolyte solutions at low degrees of polymerization. *J. Chem. Phys.* **1982**, *76* (4), 2010–2014.
 20. Bratko, D.; Vlachy, V. Distribution of counterions in the double layer around a cylindrical polyion. *Chem. Phys. Lett.* **1982**, *90* (6), 434–438.
 21. Mills, P.; Anderson, C.; Record, M.T. Monte Carlo studies of counterions–DNA interactions. Comparison of the radial distribution of counterions with predictions of other polyelectrolyte theories. *J. Phys. Chem.* **1985**, *89*, 3984–3994.
 22. LeBret, M.; Zimm, B. Monte Carlo determination of the distribution of ions around a cylindrical polyelectrolyte. *Biopolymers* **1984**, *23*, 271–286.
 23. Murthy, C.S.; Bacquet, R.J.; Rosicky, P.J. Ionic distribution near polyelectrolytes. A comparison of theoretical approaches. *J. Phys. Chem.* **1985**, *89*, 701–710.
 24. Guldbbrand, L.; Nilsson, L.G.; Nordenskiöld, L. A Monte Carlo simulation study of electrostatic forces between hexagonally packed DNA double helices. *J. Chem. Phys.* **1986**, *85* (11), 6686–6698.
 25. Vlachy, V.; Haymet, A.D.J. A grand canonical Monte Carlo simulation study of polyelectrolyte solutions. *J. Chem. Phys.* **1986**, *84* (10), 5874–5880.
 26. Mills, P.; Anderson, C.; Record, M.T. Grand canonical Monte Carlo calculations of thermodynamic coefficients for a primitive model of DNA–salt solutions. *J. Phys. Chem.* **1986**, *90*, 6541–6548.
 27. Lamm, G.; Wong, L.; Pack, G.R. Monte Carlo and Poisson–Boltzmann calculations of the fraction of counterions bound to DNA. *Biopolymers* **1994**, *34* (2), 227–237.
 28. Strauss, U.P.; Gershfeld, N.L.; Spiera, H. Charge reversal of cationic poly-4-vinylpyridine derivatives in KBr solution. *J. Am. Chem. Soc.* **1954**, *76*, 5909–5911.
 29. Hansen, W.N. The immersed double layer. *J. Electroanal. Chem.* **1983**, *150*, 133–140.
 30. Young, M.A.; Jayaram, B.; Beverige, D.L. Local dielectric environment of B-DNA in solution: Result from a 14 ns molecular dynamics trajectory. *J. Phys. Chem., B* **1998**, *102*, 7666–7669.
 31. Conrad, J.; Troll, M.; Zimm, B. Ions around DNA: Monte Carlo estimates of distribution with improved electrostatic potentials. *Biopolymers* **1988**, *27*, 1711–1732.
 32. Jayaram, B.; Swaminathan, S.; Beveridge, D.L.; Sharp, K.; Honig, B. Monte Carlo simulation studies on the structure of the counterion atmosphere of B-DNA. Variations on the primitive dielectric model. *Macromolecules* **1990**, *23*, 3156–3165.
 33. Lyubartsev, A.P.; Laaksonen, A. Osmotic and activity coefficients from effective potentials for hydrated ions. *Phys. Rev., E* **1997**, *55* (5), 5689–5696.
 34. Lyubartsev, A.P.; Laaksonen, A. Effective potentials for ion–DNA interactions. *J. Chem. Phys.* **1999**, *111* (24), 11207–11215.
 35. Montoro, J.C.G.; Abascal, J.L.F. Discrete charge effects in the structure of ions around polyelectrolyte model. *Mol. Phys.* **1996**, *89* (4), 1071–1086.
 36. Montoro, J.C.G.; Abascal, J.L.F. Ionic distribution around simple B-DNA models: II. Deviations from cylindrical symmetry. *J. Chem. Phys.* **1998**, *109* (14), 6200–6210.
 37. Lyubartsev, A.P.; Nordenskiöld, L. Monte Carlo simulation study of DNA polyelectrolyte properties in the presence of multivalent polyamine ions. *J. Phys. Chem., B* **1997**, *101*, 4335–4342.
 38. Abascal, J.L.F.; Montoro, J.C.G. Ionic distribution around simple B-DNA models: III. The effect of ionic charge. *J. Chem. Phys.* **2001**, *114* (9), 4277–4284.
 39. Mills, P.A.; Rashid, A.; James, T.L. Monte Carlo calculations of ion distributions surrounding the oligonucleotide $d(atatatatat)_2$ in the B, A and wrinkled D conformations. *Biopolymers* **1992**, *32*, 1491–1501.
 40. Guldbbrand, L. The distribution and dynamics of small ions in simulations of ordered polyelectrolyte solutions. *Mol. Phys.* **1989**, *67* (1), 217–237.
 41. Guldbbrand, L.E.; Forester, T.R.; Lynden-Bell, R.M. Distribution and dynamics of mobile ions in systems of ordered B-DNA. *Mol. Phys.* **1989**, *67* (1), 473.
 42. Triolo, R.; Grigera, J.R.; Blum, L. Simple electrolytes in the mean spherical approximation. *J. Phys. Chem.* **1976**, *80* (17), 1858–1861.
 43. Banavali, N.K.; Roux, B. Atomic radii for continuum electrostatics calculations on nucleic acids. *J. Phys. Chem., B* **2002**, *106*, 11026–11035.
 44. Record, M.T.; Zhang, W.; Anderson, C.F. Analysis of effects of salts and uncharged solutes on protein and nucleic acids equilibria and processes: A practical guide to recognizing and interpreting polyelectrolyte effects, Hofmeister effects, and osmotic effects of salts. *Adv. Protein Chem.* **1998**, *51*, 281–353.
 45. Paulsen, M.D.; Anderson, C.F.; Record, M.T. Counterion exchange reactions on DNA: Monte Carlo and Poisson–Boltzmann analysis. *Biopolymers* **1988**, *27*, 1249–1265.

46. Korolev, N.; Lyubartsev, A.P.; Rupprecht, A.; Nordenskiöld, L. Experimental and Monte Carlo simulation studies on the competitive binding of Li^+ , Na^+ and K^+ ions to DNA in oriented DNA fibers. *J. Phys. Chem., B* **1999**, *103*, 9008–9019.
47. Korolev, N.; Lyubartsev, A.P.; Rupprecht, A.; Nordenskiöld, L. Competitive binding of Mg^{2+} , Ca^{2+} , Na^+ and K^+ ions to DNA in oriented fibers: Experimental and Monte Carlo simulation results. *Biophys. J.* **1999**, *77*, 2736–2749.
48. Das, T.; Bratko, D.; Bhuiyan, L.B.; Outhwaite, C.W. Polyelectrolyte solutions containing mixed valency ions in the cell model: A simulation and modified Poisson–Boltzmann theory. *J. Chem. Phys.* **1997**, *107* (21), 9197–9207.
49. Ni, H.; Anderson, C.F.; Record, M.T. Quantifying the thermodynamic consequences of cation ($\text{M}^{2+}, \text{M}^+$) accumulation and anion (X^-) exclusion in mixed salt solutions of polyanionic DNA using Monte Carlo and Poisson–Boltzmann calculations of ion–polyion preferential interaction coefficient. *J. Phys. Chem., B* **1999**, *103*, 3489–3504.
50. Lyubartsev, A.P.; Nordenskiöld, L. Monte Carlo simulation study of ion distribution and osmotic pressure in hexagonally oriented DNA. *J. Phys. Chem.* **1995**, *99*, 10373–10382.
51. Korolev, N.; Lyubartsev, A.P.; Rupprecht, A.; Nordenskiöld, L. Competitive substitution of hexamine cobalt for Na^+ and K^+ ions in oriented DNA fibers. *Biopolymers* **2001**, *58*, 268–278.
52. Wilson, R.W.; Rau, D.C.; Bloomfield, V.A. Comparison of polyelectrolyte theories of the binding of cations to DNA. *Biophys. J.* **1980**, *30*, 317–325.
53. Rouzina, I.; Bloomfield, V.A. Influence of ligand spatial organisation on competitive electrostatic binding to DNA. *J. Phys. Chem.* **1996**, *100*, 4305–4313.
54. Stigter, D.; Dill, K.A. Binding of ionic ligands to polyelectrolytes. *Biophys. J.* **1996**, *71*, 2064–2074.
55. Andreasson, B.; Nordenskiöld, L.; Schultz, J. Interactions of spermidine and methylspermidine with DNA studied by nuclear magnetic resonance self-diffusion measurements. *Biophys. J.* **1996**, *70*, 2847–2856.
56. Olmstedt, M.C.; Bond, J.P.; Anderson, C.F.; Record, M.T. Grand canonical Monte Carlo molecular and thermodynamic predictions of ion effects on binding of an oligocation (L^{8+}) to the center of DNA oligomers. *Biophys. J.* **1995**, *68*, 634–647.
57. Guldbbrand, L.; Nordenskiöld, L. Brownian dynamics simulation of counterion dynamics in cylindrical polyelectrolyte solution. *J. Phys. Chem.* **1987**, *91*, 5714–5718.
58. Reddy, M.R.; Rosky, P.J.; Murthy, C.S. Counterion spin relaxation in DNA solutions: A stochastic dynamics simulation study. *J. Phys. Chem.* **1987**, *91*, 4923–4933.
59. Nilsson, L.G.; Nordenskiöld, L.; Stilbs, P.; Braunlin, W.H. Macroscopic counterion diffusion in solutions of cylindrical polyelectrolytes. *J. Phys. Chem.* **1985**, *89*, 3385–3391.
60. Clementi, E.; Corongiu, G. B-DNA structural determination of Na^+ counterions at different humidities, ionic concentrations, and temperatures. *J. Quant. Chem.* **1982**, *22*, 595–630.
61. Seibel, G.L.; Singh, U.C.; Kollman, P.A. A molecular dynamics simulation of double-helical DNA including counterions and water. *J. Am. Chem. Soc.* **1985**, *82*, 6537–6540.
62. Swaminathan, S.; Ravishanker, G.; Beveridge, D.L. Molecular dynamics of B-DNA including water and counterions: A 140-ps trajectory for d(CGCGAATTCGCG) based on the GROMOS force field. *J. Am. Chem. Soc.* **1991**, *113*, 5027–5040.
63. York, D.M.; Darden, T.; Deerfield, D.; Pedersen, L.G. The interaction of Na(I), Ca(I), and Mg(II) metal ions with duplex DNA: A theoretical modeling study. *Int. J. Quant. Chem.* **1992**, *19*, 145–166.
64. MacKerell, A.D. Influence of magnesium ions on duplex DNA structural, dynamics and solvation properties. *J. Phys. Chem., B* **1997**, *101*, 646–650.
65. Cheatham, T.E., III; Kollman, P. Molecular dynamics simulations highlight the structural differences among DNA:DNA, RNA:RNA, and DNA:RNA hybrid duplexes. *J. Am. Chem. Soc.* **1997**, *119*, 4805–4825.
66. Young, M.A.; Ravishanker, D.; Beveridge, D.L. A 5-nanosecond molecular dynamics trajectory for B-DNA: Analysis of structure, motions and solvation. *Biophys. J.* **1997**, *73*, 2313–2336.
67. Young, M.A.; Jayaram, B.; Beveridge, D.L. Intrusion of counterions into the spine of hydration in the minor groove of B-DNA: Fractional occupancy of electronegative pockets. *J. Am. Chem. Soc.* **1997**, *119*, 59–69.
68. Lyubartsev, A.P.; Laaksonen, A. Molecular dynamics simulations of DNA in solution with different counterions. *J. Biomol. Struct. Dyn.* **1998**, *16* (3), 579–591.
69. Young, M.A.; Beveridge, D.L. Molecular dynamics simulations of an oligonucleotide duplex with adexine tracts phased by a full helix turn. *J. Mol. Biol.* **1998**, *281*, 675–687.
70. Feig, M.; Pettitt, B.M. A molecular simulation picture of DNA hydration around A- and B-DNA. *Biopolymers* **1998**, *48*, 199–209.

71. Feig, M.; Pettitt, B.M. Modelling high-resolution hydration patterns in correlation with DNA sequence and conformation. *J. Mol. Biol.* **1999**, *286*, 1075–1095.
72. Beveridge, D.L.; McConnel, K.J. Nucleic acids: Theory and computer simulation, Y2k. *Curr. Opin. Struct. Biol.* **2000**, *10*, 182–196.
73. Cornel, W.D.; Cieplak, P.; Bayly, C.I.; Gould, I.R.; Merz, K.M.; Ferguson, D.M.; Spellmeyer, D.C.; Fox, T.; Caldwell, J.W.; Kollman, P.A. A second generation force field for the simulation of proteins, nucleic acids, and organic molecules. *J. Am. Chem. Soc.* **1995**, *117*, 5179–5197.
74. MacKerell, A.D.; Bashford, D.; Bellott, M.; Dunbrack, R.L.; Evanseck, J.D.; Field, M.J.; Fischer, S.; Gao, J.; Guo, H.; Ha, S.; Joseph-McCarthy, D.; Kuchnir, L.; Kuczera, K.; Lau, F.T.K.; Mattos, C.; Michnick, S.; Ngo, T.; Nguyen, D.T.; Prodhom, B.; Reiher, W.E.; Roux, B.; Schlenkrich, M.; Smith, J.C.; Stote, R.; Straub, J.; Watanabe, M.; Wiórkiewicz-Kuczera, J.; Yin, D.; Karplus, M. All-atom empirical potential for molecular modeling and dynamics studies of proteins. *J. Phys. Chem., B* **1998**, *102*, 3586–3616.
75. Feig, M.; Pettitt, B.M. Sodium and chlorine ions as part of the DNA solvation shell. *Biophys. J.* **1999**, *77*, 1769–1781.
76. Drew, H.R.; Dickerson, R.E. Structure of a B-DNA dodecamer: III. Geometry of hydration. *J. Mol. Biol.* **1981**, *151*, 535–556.
77. Stefl, R.; Koca, J. Unrestrained molecular dynamics simulations of $[d(AT)_5]_2$ duplex in aqueous solution: Hydration and binding of sodium ions in the minor groove. *J. Am. Chem. Soc.* **2000**, *122*, 5025–5033.
78. McFail-Isom, L.; Sines, C.C.; Williams, L.D. DNA structure: Cations in charge? *Curr. Opin. Struct. Biol.* **1999**, *9*, 298–304.
79. McConnell, K.J.; Beveridge, D.L. DNA structure: What's in charge? *J. Mol. Biol.* **2000**, *304*, 803–820.
80. van Dam, L.; Lyubartsev, A.P.; Laaksonen, A.; Nordenskiöld, L. Self-diffusion and association of Li^+ , Cs^+ , and H_2O in oriented DNA fibers. An NMR and MD simulation study. *J. Phys. Chem., B* **1998**, *102*, 10636–10642.
81. Auffinger, P.; Westhof, E. Water and ion binding around $r(\text{UpA})_{12}$ and $d(\text{TpA})_{12}$ oligomers—Comparison with RNA and DNA $(\text{CpG})_{12}$ duplexes. *J. Mol. Biol.* **2001**, *305*, 1057–1072.
82. Bevan, D.R.; Lee, L.; Pedersen, L.G.; Darden, T.A. Molecular dynamics simulations of the $d(\text{ccaacgttgg})_2$ decamer: Influence of the crystal environment. *Biophys. J.* **2000**, *78*, 668–682.
83. Bryson, K.; Greenall, R.J. Binding sites of the polyamines putrescine, cadaverine, spermidine and spermine on A- and B-DNA located by simulated annealing. *J. Biomol. Struct. Dyn.* **2000**, *18*, 393–412.
84. Korolev, N.; Lyubartsev, A.P.; Nordenskiöld, L.; Laaksonen, A. Spermine: An “invisible” component in the crystals of B-DNA: A grand canonical Monte Carlo and molecular dynamics simulation study. *J. Mol. Biol.* **2001**, *308* (5), 907–917.
85. Korolev, N.; Lyubartsev, A.P.; Laaksonen, A.; Nordenskiöld, L. On the competition between water, sodium ions and spermine in binding to DNA: A molecular dynamics computer simulation study. *Biophys. J.* **2002**, *82*, 2860–2875.
86. Lyubartsev, A.P.; Laaksonen, A. Calculation of effective interaction potentials from radial distribution functions: A reverse Monte Carlo approach. *Phys. Rev., E* **1995**, *52* (4), 3730–3737.



Molecular Switches

Jean-Pierre Launay
Christophe Coudret
Christian Joachim

Centre d'Elaboration de Matériaux et d'Etudes Structurales (CEMES), Centre National de la Recherche Scientifique (CNRS), Toulouse, France

INTRODUCTION

A switch is an ensemble of pieces whose function is to stop and/or establish the electrical current in a circuit.^[1] This 19th century definition of a switch continues to be valid in our days. But because of the requirement of better communication means during the 20th century, the pieces of our modern switches are no more mechanical or electromechanical in nature. In our information society era which uses plenty of communication and computation machines, the many switches constituting those machines are now made of solid-state semiconducting materials. After the relay and the vacuum tube, the microfabricated transistor is the modern reference of an integrated switch at the surface of a silicon wafer. Furthermore, not only electrical current, but also photons flux, magnetic flux, etc. have now their own switches, expanding the possibility of miniaturizing a switch to other types of material, such as dielectrics and ferromagnets.

A human operator was supposed to operate a switch in the 19th century. The increasing complexity of circuitry made this operator to disappear to the benefit of a third electrode per switch. In electronics, a switch is now a three-terminal device. The "on/off" triggering information is generally provided to a given switch by another one inside the circuit, without involving the operator. Taking the transistor as reference for switch performances, there is now a continuous demand for a further reduction of the weight, the size, the power consumption, and the switching time of the solid-state switches.

One solution is to reduce the amount of material required to fabricate a transistor by improving the lithographic technique, engraving a transistor on an always smaller and smaller portion of the surface of a semiconductor wafer. A radically new approach was proposed by Aviram and Ratner in 1974.^[2] Instead of continuing the miniaturization of the transistor at the surface of a wafer by inventing new lithography techniques, why not go all the way down to the atomic scale. Here the next big step is to create switches whose pieces are simple organic molecules and even a few atoms bound together to form a single molecule. Those switches are called molecular switches. In principle, they can

control an electron flux or, for example, a photon flux in a photonic circuit.

What remains unchanged is the kernel of the definition of a switch: whatever the amount of material assembled or bonded to fabricate a switch (a condensed phase, a macromolecule, a few molecules, a single molecule), a switch must have two states (the "on" and "off" states) well separated to ensure the stability of both the "on" and the "off" states. Behind the scene, there is often an internal physical or chemical variable to describe the state of the material assembled to constitute the switch. This is independent of the physical or chemical effect triggering the switch and whatever the flux to be controlled. Along a reaction coordinate proper to each kind of switch, a double-well energy curve can often be plotted (Fig. 1) defining the "on," the "off" states of the switch, and the transition region. But in simple monostable molecular switches, only one well is existing. The well is simply deformed or displaced by the triggering effect. The double-well case gives rise to bistable molecular switches: in a few examples, the same value of the triggering parameter can maintain both the "on" and the "off" state depending on the history of the switching event, i.e., there is a memory effect (note that conventional switches for domestic applications are usually bistable, but electronic switches such as transistors are only monostable). The memory corresponds to a hysteresis effect related to a cooperative phenomenon often obtained with molecular material molecular switches.^[3]

In practice, mainly molecular electronic switches are explored. The reason is that the exchange of information between a given molecular switch and other molecular switches in the same circuit requires communication and interconnections means adapted to the size of ultimately a single molecule. Electrons have a much more practical wavelength than photons for this purpose. Furthermore, a tunnel junction is a very useful source of tunneling electrons where a molecule can be positioned on, like a jumper. Of course, such positioning is still very delicate to perform experimentally, taking into account the necessity to know exactly at the atomic scale the conformation and the exact position of the molecule in the junction. The invention of the scanning tunnel microscope (STM) in 1981^[4] arrived

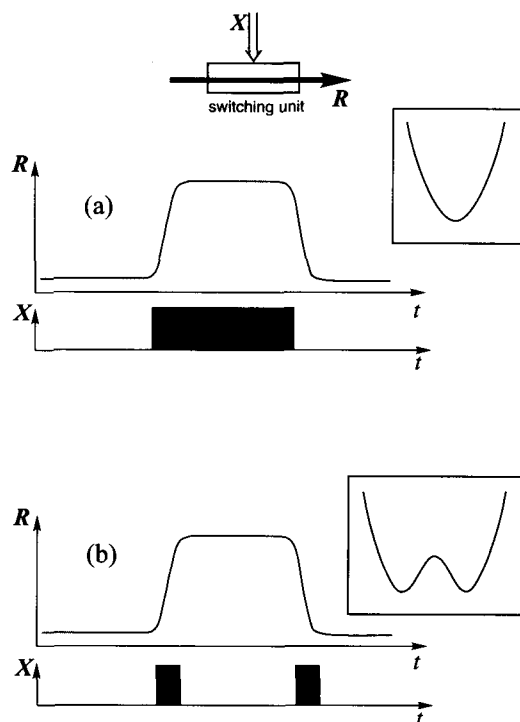


Fig. 1 Topology of a switch. R is the response and X the switching action. (a) Monostable switch: the response comes back to its original value as soon as the switching action ceases; (b) bistable switch: the response remains modified after the end of the switching action (memory effect). Inserts: energy curves describing the state of a switch as a function of an internal coordinate. In the case of the bistable switch, an energy barrier separates the two states, permitting the memory effect. (View this art in color at www.dekker.com.)

exactly on time to show experimentally as early as in 1988^[5] that such electrical interconnection between a single molecule and a macroscopic operator was possible.

Many experiments on molecular switches are still performed by averaging the answer of the molecules over many and even billions of the same type. This increases the signal-to-noise ratio and amplifies the signal to be measured. In those experiments, each molecule is supposed to be noninteracting with the others, so that the switching ability depends only on one class of molecules. Using many instead of one is not only a matter of convenience. This approach can speed up the exploration of new molecular switches, by separating two otherwise intricate problems: obtaining a switching effect and positioning one molecule on a surface.

In this article, we shall consider first “chemical switches,” i.e., systems based on a chemical reaction, or on a cooperative process involving many molecules. Thus although the change in properties between the “on” and “off” states can be spectacular, it is not, in principle, possible to reach the truly monomolecular scale. Then we

shall see the case of monomolecular switches, this latter goal being now strongly boosted by technological and fundamental purposes. There will be two variants: first “intrinsic” molecular switches, i.e., molecules which present a special sensitivity to an external perturbation, with a bistable character, and can be studied in solution, in particular for screening purposes; the second variant will be “surface bound” molecular switches, really interconnected to an electrical circuit, which implies a strong interaction with the surface, so that the switching effect comes actually from the molecule–surface ensemble.

CHEMICAL SWITCHES

Simple Chemical Conversions

A frequently encountered concept of molecular switch in chemistry is based on the abrupt variation of a property linked to a chemical concentration of some species, that could be detected by various optic or electrochemical measurement. In the most common approach, this is achieved by selecting a reversible chemical reaction for which the two processes back and forward are kinetically very fast compared to the time scale of the experiment. This is strongly reminiscent of colored indicators used in classic analytical chemistry. If we consider a set of species A , B , and X , the concentrations of which are controlled by the following equilibrium $A = B + X$, then one can easily show that the concentrations of species A and B (and thus any macroscopic property linked to their concentrations, such as color, etc.) will vary quickly over a limited domain of $-\log [X]$ values. Thus the latter parameter can be used as a control parameter. It is usually pH ($X = \text{H}^+$), it can also be pX for another ion or the potential of an electrode. The switching effect is obtained by circulating around the “threshold” value $-\log K$ (Fig. 2).

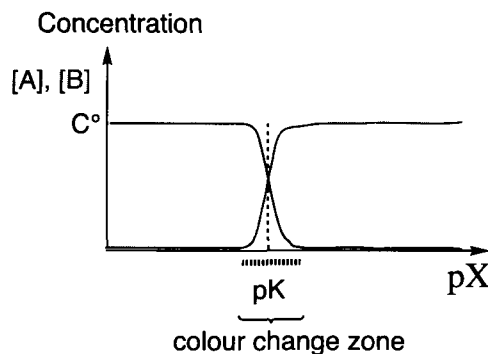


Fig. 2 Abrupt variation of the concentration of a species (and thus of the related macroscopic property) around the threshold value. (View this art in color at www.dekker.com.)

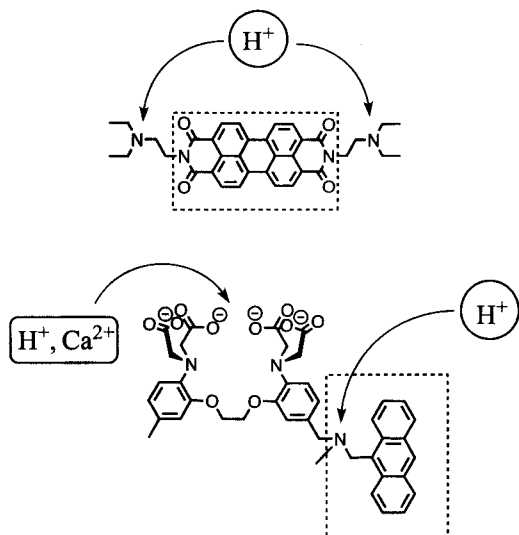


Fig. 3 Switching of fluorescence by either H^+ , (From Ref. [7].) or a combination of H^+ and Ca^{2+} . (From Ref. [8].)

Sophisticated systems have been designed in order to exploit the output signal. One can indeed read out the switching by light (either in absorption, i.e., a color change, or in emission, i.e., a luminescence change) or by an electrochemical way, or by both. Many molecules have been proposed^[6-8] for which an output signal, typically fluorescence, is triggered by chemical stimuli (Fig. 3). When several input conditions must be fulfilled, such systems even behave as logical gates.^[8]

However, as these switches are based on a quantitative conversion of a macroscopic population of molecules, in practice one has to add a sufficient amount of species X to the solution in order to read the signal related to compound A, then to add a chemical that has a better affinity toward X to set free the compound B. Thus a "switching cycle" involves an *ordered* sequence of *irreversible* mixing steps and reversible chemical reactions steps. This leads to the accumulation of the products resulting from the necessary second chemical reaction and of solvent. Thus the intervention of an operator is absolutely necessary, to open or close taps to add chemicals, playing the same role as ancient telephone operators from the 19th century, before the introduction of the third terminal on each switch.

Ways to suppress the use of an external operator have been proposed. First, the states of different switches or molecules can be coupled by the exchange of another chemical species, for instance H^+ .^[9] In addition, it is possible to devise systems based on chemical reactors with reactions far from equilibrium, where several steady states can exist. For instance, in the case of "kinetic bistability,"^[10] an abrupt variation can occur when the system passes through a bifurcation. Finally, the most

spectacular developments would be the control of the state of the switch by an oscillating reaction. Such reactions have been used as a way to design logic gates, based on the propagation of chemical waves in a two-dimensional (2-D) nonstirred reactor containing an excitable media.^[11] This would represent an archetype of a neuronal computer, because a living cell such as a neuron can be viewed as an out-of-equilibrium reactor.

Molecules in Interaction: Cooperativity

A large class of works is related to switching effects involving molecules in interaction, constituting a molecular material. In some circumstances, one can achieve appealing characteristics for information storage, such as a sharp transition and even a hysteresis. The most typical example is given by spin-transition systems.^[3] They involve paramagnetic coordination complexes with two

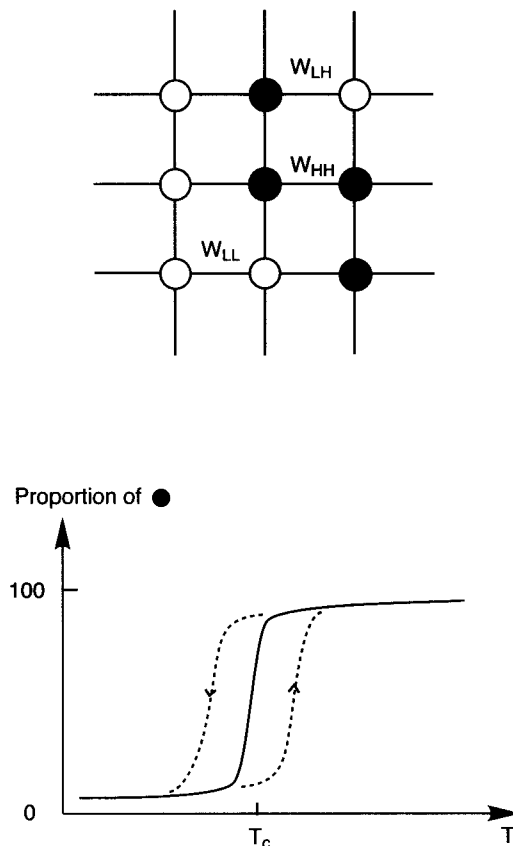


Fig. 4 Cooperativity and abrupt transition. Up: array of interacting molecules, each presenting two states, for instance \circ = low-spin state (L), and \bullet = high-spin state (H). W_{LH} , W_{HH} , and W_{LL} designate the interaction energies between molecules. Bottom: response (proportion of \bullet) as a function of temperature. An abrupt transition occurs, as shown, when the cooperativity parameter is positive, i.e., $\frac{1}{2}(W_{HH} + W_{LL}) > W_{HL}$. In some cases a hysteresis can appear (dotted lines).

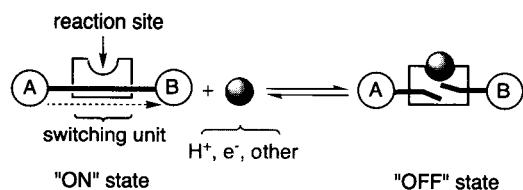


Fig. 5 Switch made of two outer sites and a central switching unit sensitive to a chemical agent. (View this art in color at www.dekker.com.)

possible states, a low-spin one and a high-spin one, the high-spin situation being favored by temperature. If the molecules are without interaction, the state of an individual molecule is governed by Boltzmann statistics, and only a gradual transition occurs when the temperature is raised. But an interesting situation arises when a positive cooperativity occurs, i.e., when the high-spin state of a molecule is favored by the presence of other high-spin state molecules in its vicinity. Then, as shown by a simple model, the transition from low-spin to high-spin can be very sharp, and in some cases, a hysteresis appears, corresponding to a memory effect (Fig. 4). This has been the basis of a number of propositions to realize memory

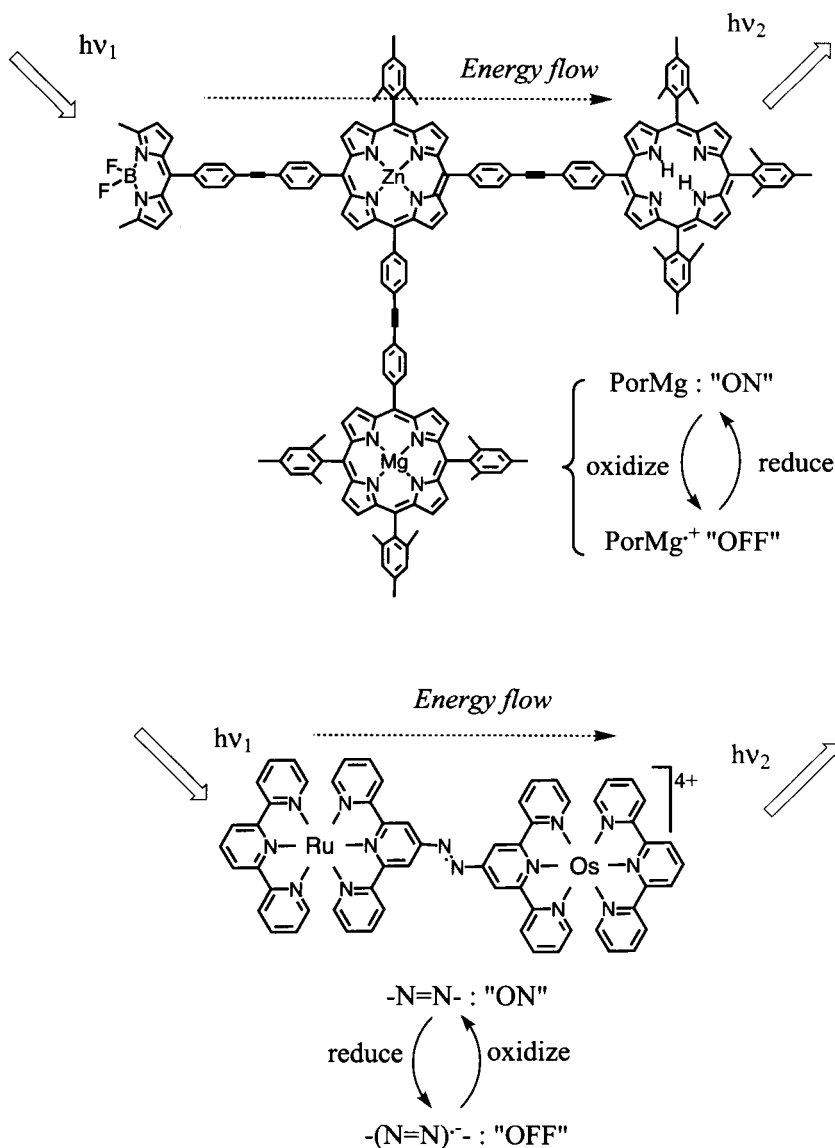


Fig. 6 Switches based on the control of an intramolecular energy flow by a redox group. Up: association of porphyrins. (From Ref. [12].) Bottom: use of an azo group. (From Ref. [13].) (View this art in color at www.dekker.com.)

devices. In particular, the possibility to switch the system state by light, and not only temperature, has greatly expanded the potential for applications.^[3]

However, in such systems, the switching effect relies inherently on the cooperativity parameter, i.e., the presence of many molecules. There is strictly no way to downsize the device to one molecule.

Chemical Bimolecular Reactions Involving a Change of an Intramolecular Process

En route for miniaturization, let us consider now the attempts to switch “on” and “off” an intramolecular transfer process of electrons. In this section we wish to present some examples of switches operated by a bimolecular reaction where the switching unit requires a modification of its composition or electronic configuration (Fig. 5), usually by a *chemical* reaction.

All of the chemical approaches of the problem imply the synthesis of rather complicated molecules made of a pair of groups A, B, the energetic or electronic configuration of which will prove the transfer, and a switching unit able to respond to a chemical stimulation such as an ion complexation, a redox reaction, or even a more “classic” organic chemistry reaction. Following natural phenomena, two types of transfer have also been explored: energy transfer and electron transfer.

Energy is a rather difficult communication vector to control, because, after light absorption by a molecule, creating an electronically excited state, the energy tends to relax as heat to other parts of the molecule or to the surrounding. This dissipation is unavoidable. However, smart molecules have been devised, allowing cascading

the energy through an array of chromophores. The switching effect is then obtained either by uncoupling the chromophores, or most commonly by creating a temporary energy sink. Some examples^[12,13] are given in Fig. 6.

Switching an electron transfer along a molecular wire may sound easier as the electron should not vanish. Among the best systems explored are mixed valence systems, basically composed of at least two almost identical redox centers: they are differing only by one excedentary electron. Hence such a molecule undergoes a permanent intramolecular redox reaction, reflecting the electron quantum exchange between the two sites. This redox process is simply described in terms of a double wellled energy landscape as a function of a reaction coordinate. Switching is now based on changing the coupling between the two redox states. This can be achieved for example by changing the set of molecular orbital of the bridge by an acid–base reaction^[14] or even a Diels–Alder reaction^[15] (Fig. 7).

Finally, for such chemically sensitive switches, although the molecules do not interact with themselves, the input requires a chemical reaction and the output is a population-averaged property. Consequently, these switches will be hardly downsized to a single molecule.

MONOMOLECULAR SWITCHES (I): INTRINSIC MOLECULAR SWITCHES

Model Molecules Studied in Solution

Here we consider molecules for which the barrier is large enough (Fig. 1), defining two states, “on” and “off,” that

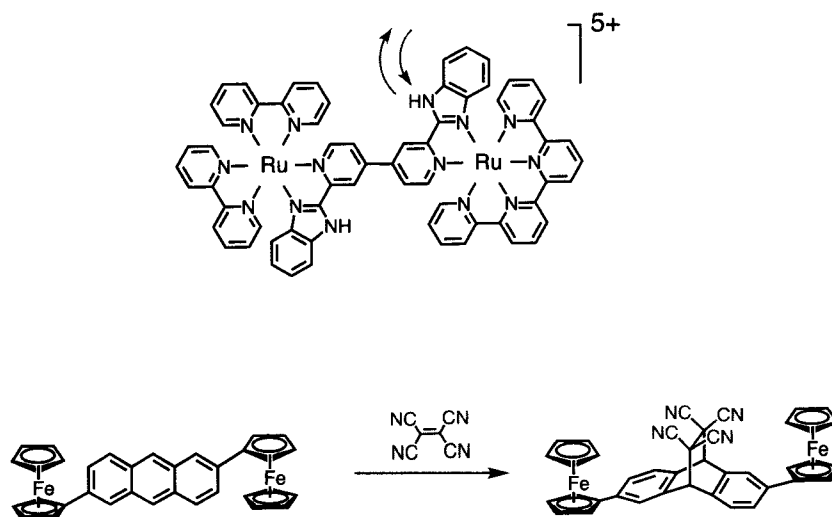


Fig. 7 Switches based on the control of an intramolecular electron transfer by a chemical agent. Up: protonation/deprotonation. (From Ref. [14].) Bottom: adduct formation. (From Ref. [15].) (View this art in color at www.dekker.com.)

we assume of nearby energies. This corresponds to an intrinsic bistability, which persists even when the molecules are isolated. The transformation is actually an isomerization reaction, i.e., a unimolecular process that does not require the reactant molecules, but can be activated by a physical process. The description is based on a simple double-well energetic landscape.

Certain compounds undergo a light-induced one. This usually leads to a deep change in the light absorption properties and is therefore called photochromism. In such a process, a molecule is brought in its Franck–Condon excited state upon absorbing a suitable photon $h\nu_1$ and then starts to relax back to its ground state (Fig. 8). However, for this type of compound two isomeric ground states are available. A careful choice of the system can lead to a quantitative isomerization of the starting compound. An identical process but with another light of energy $h\nu_2$, or if the activation barrier is low, simply heating can be used as a way to reverse the populations.

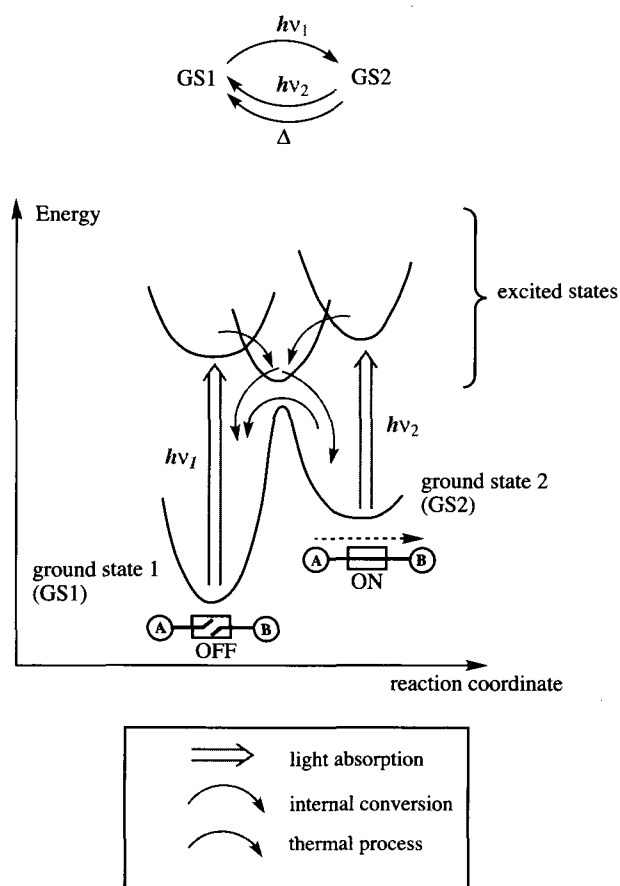


Fig. 8 Potential energy curves involved in photochromic switches. The switching action drives the system from one potential well to the other, via high energy excited states. (View this art in color at www.dekker.com.)

Photochromism has been widely used to demonstrate the basic principle of switching, because the photochemical transformation is an elegant way to transform, at the macroscopic scale, one form into another, and these forms remain usually unchanged after the irradiation. Following the approach mentioned in the previous section, several teams have presented molecules able to switch “on” and “off” an intramolecular “interaction” parameter.

Regarding the switching unit, any photochromic moiety could be used in principle, but the recent work has focused on diarylethene-based molecules, in which a photocyclization/ring reopening process occurs. They present indeed distinct advantages: they show excellent photochromic characteristics (stability, reversibility, quantum yield, etc.), but above all, the two states correspond to very different states of conjugation of an extended framework, thus heralding very different electronic properties, and finally, the geometry does not change very much during the photocyclization process, thus facilitating their incorporation in large supermolecules or assemblies.

The first members of the series were described independently by Irie,^[16] and Gilat et al.,^[17] and this initiated a bunch of studies where photochromism has been associated to other properties. The change in absorption properties between the two photoisomers is already a signature of the large change in delocalization along the molecular skeleton. But, upon connection of redox sites of the pyridinium family, it is possible in addition to modifying the electrochemical properties.^[17] Other variants have been described. For instance, the introduction of a fluorescent unit allows the change in the emission response.^[18] The association with a hyperpolarizable group led to a modification of the nonlinear optical properties.^[19] Chiro-optical switching effects have also been described.^[20] Grafting paramagnetic sites on each side of the central unit allowed the demonstration of switching an intramolecular exchange interaction parameter.^[21] Finally, with redox sites of the Ruthenium-(cyclometallated) family, it has been possible to switch “on” and “off” an intramolecular intervalence electron transfer,^[22] i.e., a process which constitutes for mixed-valence molecules the equivalent of the conductance for a nanojunction (Fig. 9).

Thanks to the versatility of diarylethene chemistry, it is even possible to realize more complex functions than just switching. Playing with electrochemical and photo-physical properties can lead to elaborate responses such as write/read/erase, which could be useful for the realization of molecular-based memories.^[23]

As photochromic compounds are addressed by light, the response is typically the one of an ensemble of molecules, usually without interactions. But it is possible in principle to record signals corresponding to

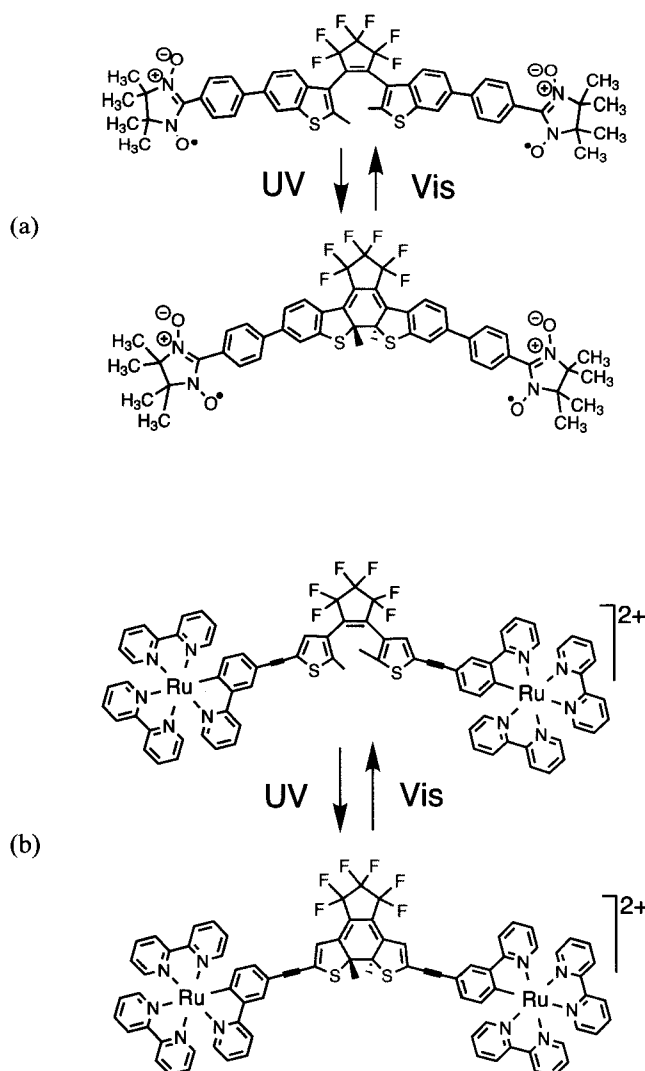


Fig. 9 Photochromic switches based on diarylethenes. (a) Control of an exchange interaction between magnetic centers; (From Ref. [21].) (b) control of an intramolecular electron transfer between redox sites. (From Ref. [22].) (View this art in color at www.dekker.com.)

a unique isolated molecule. This has been achieved quite recently by Irie et al. who observed by confocal microscopy the signal of single molecules of a dithienylethene-bis(phenylethynylantracene) dyad embedded in a polymer film.^[24]

Electrical Studies on an Ensemble of Molecules

In this section, more recent molecules with an intrinsic “bistable” design are presented. They are destined to be supported by a surface, following the recent evolution of the technology to manipulate molecules at the surface of a solid. Therefore they can be triggered from the “on”

to the “off” states by the application of an electric field when sandwiched between two metallic electrodes. As they are chemically designed to be adsorbed on a surface, the ultimate goal here is to electronically connect one molecule at a time. This field was opened by Aviram who synthesized in the 1980s a hemiquinone molecule well adapted to be attached to a surface. The switch was intrinsic and triggered by an electric field with double-well-potential-like characteristics. The first STM measurements were attempted in 1987 in IBM laboratories.^[5] But at that time, the available equipment did not permit to reach a firm conclusion about the switching effect.^[25]

This first experiment was nevertheless a prelude to studies aiming at the demonstration of electronic functions of molecules when disposed as thin monomolecular

layers, in particular rectification. This latter goal was finally achieved by Metzger in 1997.^[26] Since then and in relation to the switching problem, a large number of fascinating families of molecules equipped with different groups have been synthesized for this purpose. For example, the catenanes and rotaxanes molecular switches are based on the concept of "threading," i.e., they contain two parts which cannot separate without breaking a bond.^[27,28] The active parts used to control a motion are donor and acceptor moieties which can be associated through weak interactions, but because these moieties are kept in proximity by the special topology of the molecule and cannot fully separate, the association reaction is actually a monomolecular reaction analogous to an isomerization. Despite the flexibility inherent to large molecules presenting a large number of possible torsions, the number of pertinent conformations they can adopt is relatively limited, typically two, because of the unique topology of the system. They correspond to the location of a mobile part (the "shuttle") in front of two possible "stations" (Fig. 10). Such molecules can be studied first in solution, where the acceptor/donor character of a

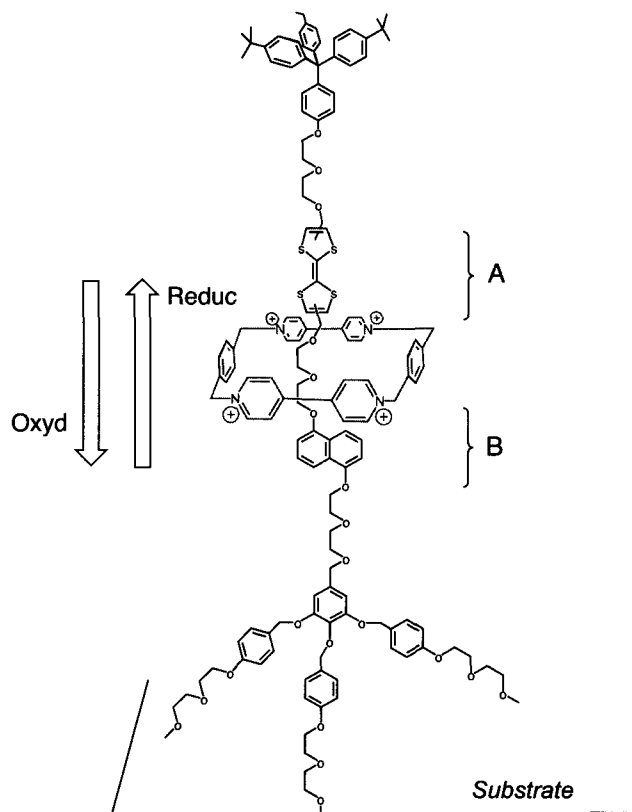


Fig. 10 Molecular shuttle with two stations, A and B. The motion is controlled by the electrochemical oxidation of the TTF unit (station A). (From Ref. [29].) (View this art in color at www.dekker.com.)

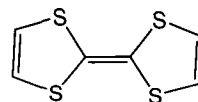


Fig. 11

moiety can be reversed by electrochemistry, and then can be transferred and used in solid-state devices.

Many examples have been described by Luo et al. The active molecules were deposited as Langmuir–Blodgett (LB) monolayers on an *n*-polycrystalline silicon substrate and covered by a Ti/Al top electrode, thus giving a two-terminal device of monomolecular thickness. The response was then probed by a method analogous to the remnant polarization method used for ferroelectric devices, i.e., scanning a voltage range while measuring the current at a low nonperturbing voltage, to avoid capacitance effects.^[29] The basic signature of a switching effect is then the appearance of a hysteresis curve, associated with the existence of two possible conformations with different electron transport properties. Note that the perturbation here is an oxidation/reduction of a moiety, transforming, for instance, a donor tetrathiafulvalene (TTF) (Fig. 11) into an acceptor (TTF⁺). This is basically an electrochemical process, requiring in solution the intervention of a counter ion. It is not clear how such a process occurs in the solid-state device based on a monolayer.

Although several control experiments show that a two-station structure is necessary to obtain a switching effect, the exact interpretation remains obscure, because the molecules contain several other flexible parts, and their exact orientation in the LB layer, as well as the geometry of the contacts with the interfaces, is not readily accessible to experiment.

Another series of molecules was designed and studied by Tour, Reed, et al.^[30,31] They are made of several (phenylene ethynylene) groups with thiol end groups for attachments on electrodes ("alligator clips"). These molecules are then used either in a nanopore cell (Fig. 12), allowing the contacting of an ensemble of molecules (ca. 10³) between a substrate and an evaporated upper electrode. The molecules form a self-assembled monolayer (SAM) and, because of the small size of the pore (30–50 nm), a defect-free ensemble can be expected. The interesting behavior resides in the appearance of a negative differential resistance effect (NDR), an effect tentatively assigned to the rotation of a phenylene group and/or charge injection under the influence of the applied voltage.

Looking further, although these devices are two-terminal ones, they can be of some use in electronics circuitry. The construction of a 2-D crossbar arrangement, with such layers of molecules at the nodes, would give

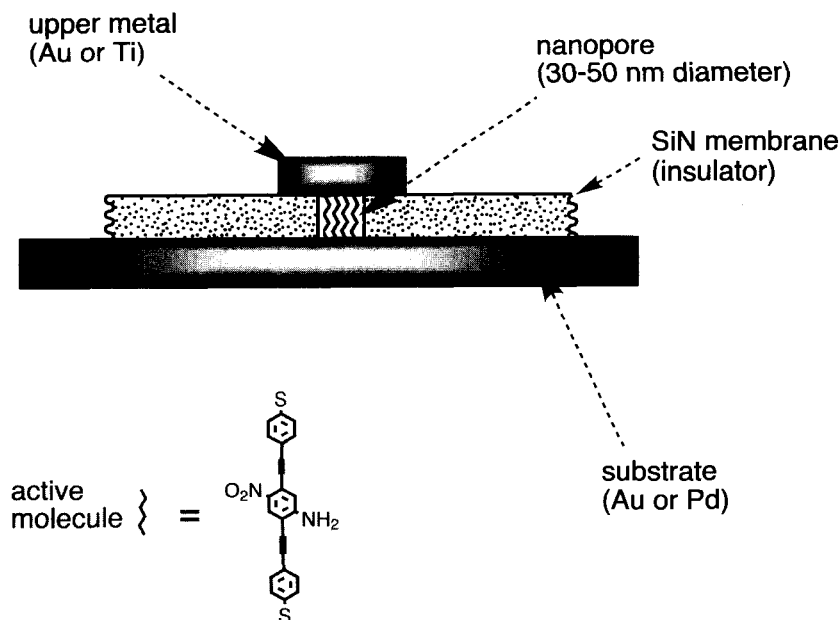


Fig. 12 The “nanopore” setup. Each nanopore is filled by several thousands of active molecules. (From Ref. [30].) (View this art in color at www.dekker.com.)

an electronic circuit with a little amount of molecular material at the node in a defect-tolerant architecture similar to what was proposed in the 1960s.

MONOMOLECULAR SWITCHES (II): SURFACE MOLECULAR SWITCHES

The end of the miniaturization roadmap for molecular switches is a single molecule connected between two, or if possible three, electrodes. This requires an underneath surface that will support the molecule and the nanoelectrodes. The surface can be active or passive in the definition of the molecular switch. The switching ability of the molecule can be intrinsic to the molecule, as mentioned in the previous section, or it can be created by the interaction of the molecule with the surface.

As an example of the first possibility, we can mention the recent experiment by Dulic et al.,^[32] who succeeded in contacting a photochromic switch of the diarylethene family with two electrodes, by the “break-junction” technique. The switching of the nanojunction conductance was observed, but in one direction only (from “on” toward “off”), due to the quenching effect of the metal surface.

We now consider the second possibility, i.e., systems strongly dependent on the interaction with a surface. The first real demonstration that an object of the size of a

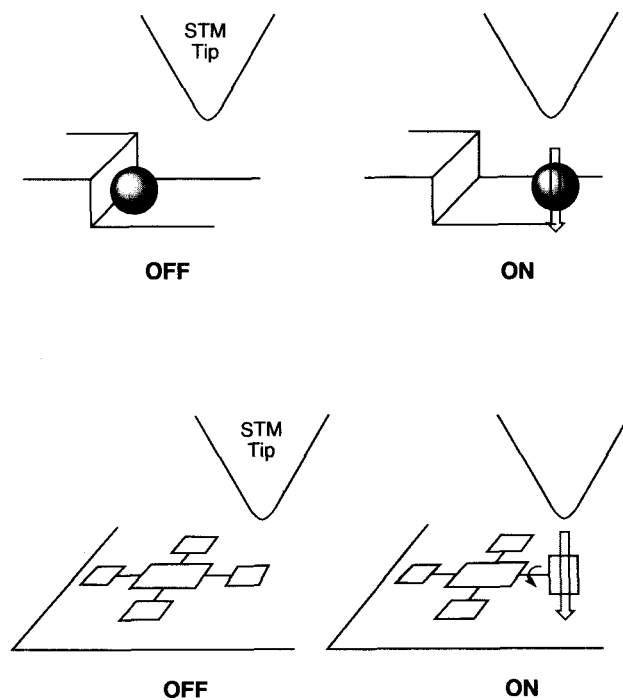


Fig. 13 Atomic and molecular switch on a surface. Up: Eigler’s atomic switch using the positioning of a Xe atom. (From Ref. [33].) Bottom: molecular switch based on the rotation of a porphyrin “leg” out of the molecular plane. (From Ref. [34].) (View this art in color at www.dekker.com.)

single atom can switch “on” and “off” a current was experimentally observed by Eigler et al. using a Xe atom switching back and forth under the tip of an STM at very low temperature.^[33] This is a surface atomic switch whose double-well potential is created on the surface by the van der Waals trap created by the tip apex for the “on” state and by a nearby monoatomic step edge for the “off” state. The tip-apex-to-surface applied electric field is used to pass the atom from one well to the other (Fig. 13).

The first double-well, truly single-molecule switch was experimentally observed in 2001.^[34] It results from a peculiar property of the adsorption of a leg porphyrin molecule on metal surface. On a Cu(100) surface, the four legs of this molecule are almost perpendicular to the surface. On a Cu(111) surface, the four legs are flat on the surface, the central porphyrin being attracted by the 111 surface state of copper. The fabrication procedure was to adsorb the molecule on a Cu(211) surface which presents 111 facets separated by monoatomic steps. Some molecules adsorb on the edge of a step with three legs on the 111 facet and one at the step edge. The three legs are flat but the fourth one is found in a metastable state. Its most stable position is, of course, flat on the lower terrace. But this leg is now a bit too far to the down facet compared to the three others legs. Therefore it prefers to stay perpendicular to the surface (Fig. 13, bottom part). This

creates a double-well potential for the configuration energy of this leg. The barrier can be overcome by pushing on the leg by the tip apex of the STM. The “on” and “off” states are defined for the same altitude of the tip apex on the switching leg. The “on” and “off” electrical resistance of this single intramolecular switch has been measured together with the energy required to switch on/off the leg. The on/off current difference in this molecular switch is due to a control of the electronic coupling between the tip and the surface through the molecular legs. It is large when the leg is perpendicular to the surface and low when parallel.

Another way to change the electronic coupling between the tip and the surface using a single molecule is to change the homo-lumo gap of the molecule. A simple experimental way is to deform the molecule by pressing on it with the tip apex. The C₆₀ single-molecule amplifier is an example of such a device^[35,36] as shown in Fig. 14. Used in its blocked-saturated mode, this is a monostable molecular switch. The C₆₀ device benefits from the high degeneracy of its homo and lumo orbitals, a degeneracy yielding to a low transparency toward electrons because of destructive interference effects through the molecule. By compressing the C₆₀, this degeneracy is raised, giving rise to a very fast increase of the tunnel current through the C₆₀ molecule in this compressed state. A C₆₀ molecular device can be used as a switch but

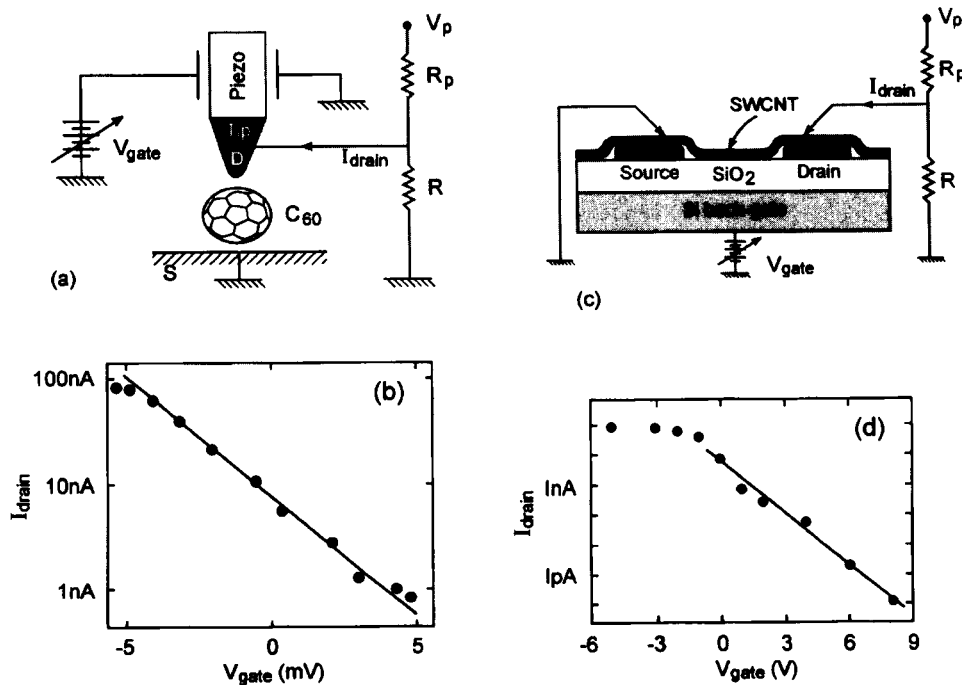


Fig. 14 The variation of the drain-source current intensity as a function of the gate voltage for the original C₆₀ single-molecule amplifier and the original single-carbon nanotube transistor. This variation corresponds to the slope of the passage from an “off” to an “on” state in a mono-stable switch (Fig. 1). (Reproduced with permission from Nature, 2000, 408, p. 541. Copyright 2000, MacMillan Magazines Limited) (View this art in color at www.dekker.com.)

		Response (R)			
		electrical	mechanical	optical	magnetic
Switching action (X)	electrical	○ a ○ b		● k ● l	
	mechanical	● c ● e ⊙ d			
	optical	● f ● g	⊙ j	● m ● n ⊙ o	● q
	chemical	● h ● i		● p	

Fig. 15 Chart of the different types of molecular switches, according to the type of switching action, and the type of response. ●: Experiments performed on a statistical ensemble, leading to a relatively large device; ○: on a few molecules (ca. 1000); ⊙: on one molecule. From the following teams: a: Pease, Luo;^[27,29] b: Tour, Donhauser;^[30,31] c: Joachim and Gimzewski;^[35,36] d: Moresco;^[34] e: Tans;^[39] f: Dulic;^[32] g: Fraysse;^[22] h: Gonzalo;^[15] i: Haga;^[14] j: Hugel;^[40] k: Akasaka;^[13] l: Holten;^[12] m: Irie;^[16] n: Gilat;^[17] o: Irie;^[24] p: Daffy, de Silva;^[7,8] q: Matsuda.^[21] (View this art in color at www.dekker.com.)

also as a transistor. This had opened the way to simulate very complex hybrid molecular circuits made of more than 600 C₆₀ transistors interconnected together by a standard metallic circuit to test how high impedance and low gain transistors may still be used to design simple processors.^[37]

A macromolecular version of the C₆₀ single molecule switch was proposed in 2003 using a single-wall carbon

nanotube positioned on a mesoscopic junction.^[38] To create a monostable switch, the tip of an AFM is brought from the top of the device to deform the tube in the center of the device (Fig. 14). Depending on the chirality of the tube, its band gap can be closed or opened, modifying the resistance of the junction. With a good transconductance, carbon nanotube electronic transistors have also been fabricated using a third top metallic electrode like the grid of a field effect transistor.^[39] Those mesoscopic devices are at the down limit of microelectronics where the source–drain distance of the transistor is of the dimension of a macromolecule.

CONCLUSION

The different approaches of “molecular switches” are displayed in Fig. 15, according to the type of switching action and the type of measured response. In addition, a third characteristic is important, i.e., the scale at which the system works: a large statistical ensemble, a few molecules, or ultimately one. Only in this last case can we expect to take the full benefit of miniaturization and really reach the domain of molecular electronics, where the major question is about the fundamental limits.

Like any devices, a molecular switch is characterized by its performance such as its switching time and the energy required to change the status of the switch. For a single molecular switch interconnected between two electrodes, it has not yet been possible to measure the switching time. This is due to the large resistance of a metal–molecule–metal tunnel junction of the order of 1 GΩ for a single organic molecule, down to a few

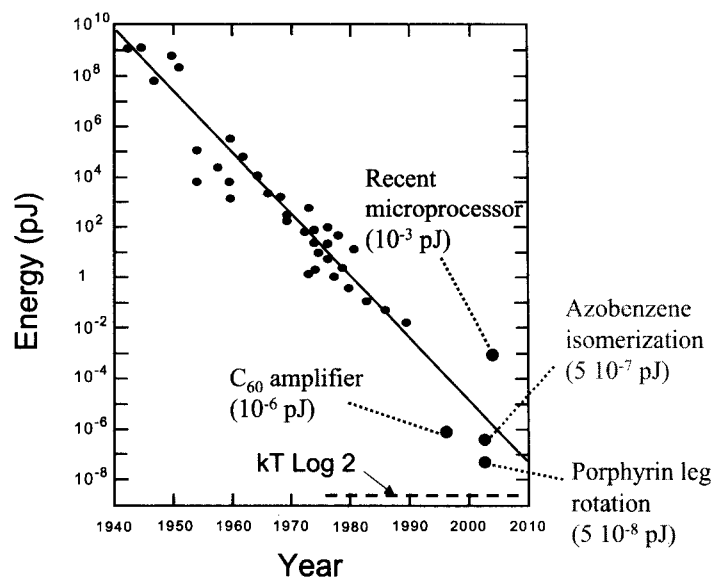


Fig. 16 Switching energy as a function of time. The approach of fundamental limits. (From Ref. [42].) (View this art in color at www.dekker.com.)

megaohms for macromolecule molecular switches such as a single-wall carbon nanotube (SWCNT). The RC constant of the switch is mainly controlled by the product of this resistance by the line capacitance, the latter of the order of a few picofarads. This leads to a minimum observable switching time of a few microsecond. Of course, the isomerization of a single molecule takes less than a few picoseconds. Here it is the way the device is built which sets up the limit, not the intrinsic limitation of the molecule itself.

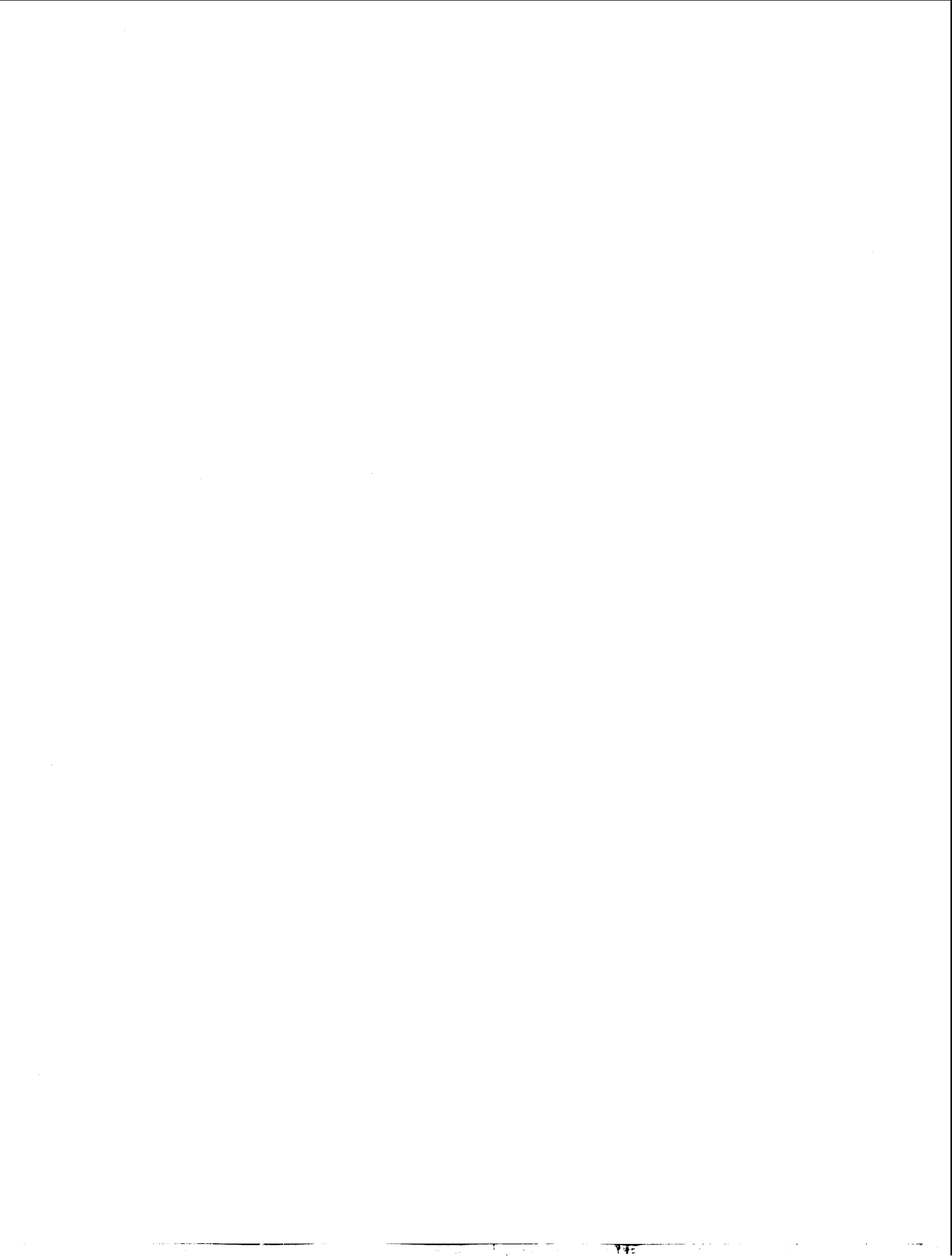
Measuring the energy associated with a single-molecule geometrical change is a technological challenge but has been realized, for instance, with azobenzene molecules by monitoring their mechanical properties.^[40] In the case of a surface electrical molecular switch, the energy required to switch "on" and "off" has been recently measured using a new near-field microscope: the noncontact UHV AFM microscope.^[41] The tip apex of the AFM oscillates on the surface and the tip apex altitude is decreased progressively toward the surface. This permits in a dynamic way to record the interaction force between the tip apex and the surface, giving access to the interaction energy. This instrument was used on the leg porphyrin switch to record the energy required to switch "off" the switch. The tip apex is located on the chosen switchable leg of the molecule and the force-distance curve recorded. The switching energy found is about 5×10^{-20} J (7 kcal/mol), which is four orders of magnitude lower than the state-of-the-art semiconductor technology transistor. It is interesting to report this value on the diagram proposed some years ago by Keyes,^[42] in which the energy dissipated per logic operation is displayed (in logarithmic units) as a function of date (Fig. 16). One sees that the trend toward smaller and smaller energy consumption continues and raises the question of the absolute limit.

Thus aside from its technological applications, a molecular switch is becoming a very interesting nanodevice to study the thermodynamic limits of switching. With a value as low as 7 kcal/mol, one is very close to the $kT \log 2$ limit, considered as the minimum energy necessary to drive any switching device interacting with a thermal bath at a temperature T .^[43]

REFERENCES

1. *The Academic Press Dictionary of Science and Technology*; Academic Press: San Diego, 1991.
2. Aviram, A.; Ratner, M.A. Molecular rectifiers. *Chem. Phys. Lett.* **1974**, *29*, 277–283.
3. Kahn, O.; Martinez, C.J. Spin transition polymers: From molecular materials toward memory devices. *Science* **1998**, *279* (5347), 44–48.
4. Behm, R.J.; Garcia, N.; Rohrer, H. *Scanning Tunneling Microscopy and Related Methods*; Kluwer Academic Publishers: Dordrecht, 1990.
5. Aviram, A.; Joachim, C.; Pomerantz, M. Evidence of switching and rectification by a single molecule effected with a scanning tunneling microscope. *Chem. Phys. Lett.* **1988**, *146*, 490.
6. Rurack, K.; Resch-Genger, U. Rigidization, preorientation and electronic decoupling—The 'magic triangle' for the design of highly efficient fluorescent sensors and switches. *Chem. Soc. Rev.* **2002**, *31* (2), 116–127.
7. Daffy, L.M.; de Silva, A.P.; Gunaratne, H.Q.N.; Huber, C.; Lynch, P.L.M.; Werner, T.; Wolfbeis, O.S. Arenedicarboximide building blocks for fluorescent photoinduced electron transfer pH sensors applicable with different media and communication wavelengths. *Chem. Eur. J.* **1998**, *4* (9), 1810–1815.
8. de Silva, A.P.; McClenaghan, N.D. Proof-of-principle of molecular-scale arithmetic. *J. Am. Chem. Soc.* **2000**, *122* (16), 3965–3966.
9. Raymo, F.M.; Giordani, S. Signal communication between molecular switches. *Org. Lett.* **2001**, *3* (22), 3475–3478.
10. Reckley, J.S.; Showalter, K. Kinetic bistability in the permanganate oxidation of oxalate. *J. Am. Chem. Soc.* **1981**, *103* (23), 7012–7013.
11. Steinbock, O.; Kettunen, P.; Showalter, K. Chemical wave logic gates. *J. Phys. Chem.* **1996**, *100* (49), 18970–18975.
12. Holten, D.; Bocian, D.F.; Lindsey, J.S. Probing electronic communication in covalently linked multiporphyrin arrays. A guide to the rational design of molecular photonic devices. *Acc. Chem. Res.* **2002**, *35* (1), 57–69.
13. Akasaka, T.; Otsuki, J.; Araki, K. Redox-responsive molecular switches based on azoterpyridine-bridged Ru/Os complexes. *Chem. Eur. J.* **2002**, *8* (1), 130–136.
14. Haga, M.-a.; Meser Ali, M.; Koseki, S.; Fujimoto, K.; Yoshimura, A.; Nozaki, K.; Ohno, T.; Nakajima, K.; Stufkens, D.J. Proton-induced tuning of electrochemical and photophysical properties in mononuclear and dinuclear ruthenium complexes containing 2,2'-bis(benzimidazol-2-yl)-4,4'-bipyridine: Synthesis, molecular structure and mixed-valence state and excited-state properties. *Inorg. Chem.* **1996**, *35* (11), 3335–3347.
15. Gonzalo, V.; Coudret, C.; Patoux, C.; Launay, J.P. Modulation of intramolecular electronic coupling in 2,6-diferrocenylanthracene via a Diels–Alder reaction with TCNE. *C. R. Acad. Sci. Ser. IIC* **1999**, *2* (5–6), 321–328.
16. Irie, M. Diarylethenes for memories and switches. *Chem. Rev.* **2000**, *100* (5), 1685–1716.
17. Gilat, S.L.; Kawai, S.H.; Lehn, J.M. Light-triggered

- molecular devices: Photochemical switching of optical and electrochemical properties in molecular wire type diarylethene species. *Chem. Eur. J.* **1995**, *1* (5), 275–284.
18. Fernandez-Acebes, A.; Lehn, J.M. Optical switching and fluorescence modulation properties of photochromic metal complexes derived from dithienylethene ligands. *Chem. Eur. J.* **1999**, *5* (11), 3285–3292.
 19. Majumdar, D.; Lee, H.M.; Kim, J.; Kim, K.S.; Mhin, B.J. Photoswitch and non linear optical switch: Theoretical studies on 1,2-bis-(3-thienyl)-ethene derivatives. *J. Chem. Phys.* **1999**, *111* (13), 5866–5872.
 20. Feringa, B.L.; van Delden, R.A.; Koumura, N.; Geertsema, E.M. Chiroptical molecular switches. *Chem. Rev.* **2000**, *100* (5), 1789–1816.
 21. Matsuda, K.; Matsuo, M.; Mizoguti, S.; Higashiguchi, K.; Irie, M. Reversed photoswitching of intramolecular magnetic interaction using a photochromic bis(2-thienyl)ethene spin coupler. *J. Phys. Chem., B* **2002**, *106* (43), 11218–11225.
 22. Fraysse, S.; Coudret, C.; Launay, J.P. Synthesis and properties of dinuclear complexes with a photochromic bridge: An intervalence electron transfer switching “on” and “off”. *Eur. J. Inorg. Chem.* **2000**, (7), 1581–1590.
 23. Kawai, S.H.; Gilat, S.L.; Ponsinet, R.; Lehn, J.M. A dual-mode molecular switching device: Bisphenolic diarylethenes with integrated photochromic and electrochromic properties. *Chem. Eur. J.* **1995**, *1* (5), 285–293.
 24. Irie, M.; Fukaminato, T.; Sasaki, T.; Tamai, N.; Kawai, T. A digital fluorescent molecular photo-switch. *Nature* **2002**, *420* (6917), 759–760.
 25. Aviram, A.; Joachim, C.; Pomerantz, M. Erratum to «evidence of switching and rectification by a single molecule effected with a scanning tunneling microscope». *Chem. Phys. Lett.* **1989**, *162*, 416.
 26. Metzger, R.M. Unimolecular electrical rectifiers. *Chem. Rev.* **2003**, *103* (9), 3803–3834.
 27. Pease, A.R.; Jeppesen, J.O.; Stoddart, J.F.; Luo, Y.; Collier, C.P.; Heath, J.R. Switching devices based on interlocked molecules. *Acc. Chem. Res.* **2001**, *34* (6), 433–444.
 28. Raehm, L.; Sauvage, J.-P. Molecular machines and motors based on transition metal-containing rotaxanes and catenanes. *Struct. Bond.* **2001**, *99*, 55–78.
 29. Luo, Y.; Collier, C.P.; Jeppesen, J.O.; Nielsen, K.A.; Delonno, E.; Ho, G.; Perkins, J.; Tseng, H.R.; Yamamoto, T.; Stoddart, J.F.; Heath, J.R. Two-dimensional molecular electronics circuits. *Chem-PhysChem* **2002**, *3* (6), 519–525.
 30. Tour, J.M.; Rawlett, A.M.; Kozaki, M.; Yao, Y.X.; Jagessar, R.C.; Dirk, S.M.; Price, D.W.; Reed, M.A.; Zhou, C.W.; Chen, J.; Wang, W.Y.; Campbell, I. Synthesis and preliminary testing of molecular wires and devices. *Chem. Eur. J.* **2001**, *7* (23), 5118–5134.
 31. Donhauser, Z.J.; Mantooth, B.A.; Kelly, K.F.; Bumm, L.A.; Monnell, J.D.; Stapleton, J.J.; Price, D.W.; Rawlett, A.M.; Allara, D.L.; Tour, J.M.; Weiss, P.S. Conductance switching in single molecules through conformational changes. *Science* **2001**, *292* (5525), 2303–2307.
 32. Dulic, D.; van der Molen, S.J.; Kudernac, T.; Jonkman, H.T.; de Jong, J.D.; Bowden, T.N.; van Esch, J.; Feringa, B.L.; van Wees, B.J. One-way opto-electronic switching of photochromic molecules on gold. **2003**, *91*, 207–402.
 33. Eigler, D.M.; Lutz, C.P.; Rudge, W.E. An atomic switch realized with a scanning tunneling microscope. *Nature* **1991**, *352*, 600–603.
 34. Moresco, F.; Meyer, G.; Rieder, K.H.; Tang, H.; Gourdon, A.; Joachim, C. Conformational changes of single molecules induced by scanning tunneling microscopy manipulation: A route to molecular switching. *Phys. Rev. Lett.* **2001**, *86* (4), 672–675.
 35. Joachim, C.; Gimzewski, J.K. An electromechanical amplifier using a single molecule. *Chem. Phys. Lett.* **1997**, *265* (3-5), 353–357.
 36. Joachim, C.; Gimzewski, J.K.; Tang, H. Physical principles of the single-C-60 transistor effect. *Phys. Rev., B* **1998**, *58* (24), 16407–16417.
 37. Ami, S.; Joachim, C. Logic gates and memory cells based on single C60 electromechanical transistor. *Nanotechnology* **2001**, *12*, 44.
 38. Minot, E.D.; Yaish, Y.; Sazonova, V.; Park, J.Y.; Brink, M.; McEuen, P.L. Tuning carbon nanotube band gaps with strain. *Phys. Rev. Lett.* **2003**, *90*, 156401.
 39. Tans, S.J.; Devoret, M.H.; Dai, H.; Thess, A.; Smalley, R.E.; Geerligs, L.J.; Dekker, C. Individual single wall carbon nanotubes as quantum wires. *Nature* **1997**, *386*, 474.
 40. Hugel, T.; Holland, N.B.; Cattani, A.; Moroder, L.; Seitz, M.; Gaub, H.E. Single-molecule optomechanical cycle. *Science* **2002**, *296* (5570), 1103–1106.
 41. Loppacher, C.; Guggisberg, M.; Pfeiffer, O.; Meyer, E.; Bammerlin, M.; Luthi, R.; Schlittler, R.; Gimzewski, J.K.; Tang, H.; Joachim, C. Direct determination of the energy required to operate a single molecule switch. *Phys. Rev. Lett.* **2003**, *90* (6), art. no.-066107.
 42. Keyes, R.W. Miniaturization of electronics and its limits. *IBM J. Res. Develop.* **1988**, *32* (1), 24–28.
 43. Landauer, R. Dissipation and noise immunity in computation and communication. *Nature* **1988**, *335*, 779–784.



Molecular Switches and Unidirectional Molecular Motors: Light-Induced Switching and Motion

M

Richard A. van Delden
Ben L. Feringa

University of Groningen, Groningen, The Netherlands

INTRODUCTION

The fascinating principles exploited by nature to control organization, switching, and motion are a major source of inspiration for the design and synthesis of artificial molecular systems with such functions. The highly efficient retinal *cis-trans* photoisomerization in the process of vision is a superior example of a molecular switch,^[1,2] and the intriguing biomolecular motors^[3] set an extremely high standard for the development of synthetic counterparts. The bottom-up construction of switches and motors, with the realization of machines and robotics of nanosize dimensions as the ultimate goal, offers a formidable challenge to scientists. Synthetic approaches toward artificial machinery have already resulted in several molecular systems whereby switching and/or motion is controlled by means of chemical, electrochemical, photochemical, or thermal input.^[4-6] For instance, molecular propellers,^[7] brakes,^[8] switches,^[9] turnstiles,^[10] ratchets,^[11] and shuttles^[12,13] have been constructed. Catenanes and rotaxanes have shown to be particularly promising systems in the development of molecular machines.^[14-17] Jimenez et al.,^[18] for example, reported the contraction and stretching of a linear rotaxane dimer resembling a natural muscle at work,^[19] and Chia et al.^[20] demonstrated the threading and dethreading of rotaxanes assembled on a surface. Recently, Hugel et al.^[21] reported the first single molecule machine based on photoactive azo dyes.

In this article, we do not attempt to give a complete and detailed overview of all molecular switches and motors developed thus far and the reader is referred to various reviews. Molecular switches, based on a large variety of principles, have been reviewed extensively.^[9] Molecular motors found in nature as well as synthetic counterparts are reviewed elsewhere.^[22] We will focus on systems based on sterically overcrowded alkenes, in which light is used to induce switching or motion, to illustrate several of the key principles involved.

STERICALLY OVERCROWDED ALKENES AS CHIROPTICAL MOLECULAR SWITCHES

In a chiral approach toward molecular switches, the unique properties associated with stereoisomers of chiral photoresponsive molecules are exploited. The two stereoisomers of such photochromic compounds represent the distinct states of a light-switchable digital molecular system (Fig. 1).

Chiroptical techniques offer the attractive feature that the change in chirality of the photochromic system^[23] can be detected. A major advantage of chiroptical switches is that nondestructive readout is feasible by monitoring the change in optical rotation at wavelengths remote from the wavelengths used for switching. Another important advantage of using chiral photochromic compounds is that they can be employed to control other (chiral) properties, e.g., the organization of a liquid crystalline phase.

Chiral Switches Based on Enantiomers

A direct way of controlling chirality in a molecular switching system is by using the interconversion between two enantiomers by chiral light (Fig. 2). Schuster et al.^[24,25] have published switchable systems which function under the influence of circularly polarized light. The switching process we envisioned involves the interconversion of the (*P*)- and (*M*)-enantiomers of helically shaped, inherently dissymmetric alkenes.

The possible photoisomerization steps are the following: 1) irradiation with circularly polarized light (CPL) will lead to a small excess of one of the two enantiomers starting from a racemate; 2) alternating irradiation with (*l*)- and (*r*)-CPL at a certain wavelength will result in a modulation between both enantiomers; and 3) irradiation with linear polarized or unpolarized light results again in a racemic (*P,M*)-mixture.

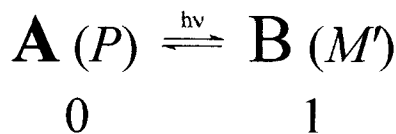


Fig. 1 Chiroptical molecular switch based upon stereoisomers A and B with different chirality.

Decisive factors for a successful molecular switch based on enantiomers are as follows: 1) irradiation with CPL should not cause any photodestruction; 2) the enantiomers should have sufficiently high g -values (g = anisotropy factor); and 3) the quantum efficiency for photoisomerization should be high, as the rate of photoresolution is exponentially related to this quantity. Out of a large number of sterically overcrowded chiral alkenes that were synthesized and resolved, helically shaped alkene **1** meets these requirements (Scheme 1).^[26] The enantiomers of **1** are stable at ambient temperatures and are fatigue-resistant. This overcrowded alkene shows structural resemblance to helicenes, and large CD absorptions and optical rotations are found. A stereospecific photoisomerization takes place that reverses the helicity of the molecules.

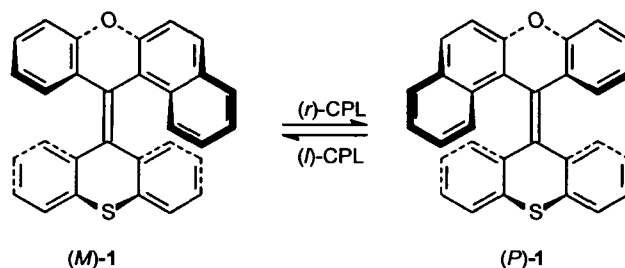
Starting from racemic **1**, switching between photostationary states with small enantiomeric excesses (0.07%) of (*P*)- and (*M*)-**1** was accomplished by irradiation with (*l*)- and (*r*)-CPL, respectively. This demonstrates that chiral light can be used to switch a molecular system from one handedness to the other. Such a switching behavior on the molecular level might have potential in developments toward molecular integrated systems or optical data storage units, for example, by employing liquid crystalline matrices (vide infra). The selectivity of switching is, however, severely limited by the theoretical limitations of the concept.^[27]

Chiral Switches Based on Pseudoenantiomers

A way of circumventing the major limitations predicted and encountered in enantiomeric switches is by the use



Fig. 2 Schematic representation of a molecular switch based on enantiomers.

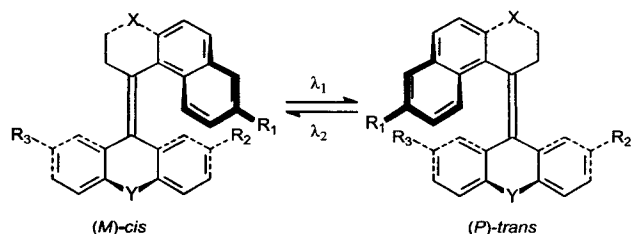


Scheme 1 Circularly polarized light switch based on sterically overcrowded alkene **1**.

of pseudoenantiomeric photochromic molecules. Inspired by the efficient switching of retinal in the human eye,^[28] the design of pseudoenantiomeric chiroptical switches is again based on sterically overcrowded alkenes (Scheme 2).^[29,30] As for **1**, the intrinsic (helical) chirality originates from a distortion of the molecular framework leading to (*M*)- and (*P*)-helices. Both forms of the overcrowded alkene feature a *cis*- and a *trans*-stilbene chromophore in the same molecule. A photochemically induced *cis*-*trans* isomerization results in reversal of the helicity. Because of the near mirror-image relation of the two pseudoenantiomers, such a system offers a way to control molecular chirality merely by changing the wavelength of the light employed.

The first chiroptical switching process was realized with thioxanthene-based alkenes (*M*)-*cis*-**2** and (*P*)-*trans*-**2** (Scheme 3).^[31] Irradiation of enantiomerically pure (*M*)-*cis*-**2** in *n*-hexane solution at 300 nm resulted in a photostationary state consisting of 64% (*M*)-*cis*-**2** and 36% (*P*)-*trans*-**2** because of different UV absorptions of the (*M*)-*cis* and (*P*)-*trans*-isomers (vide infra). Using 250-nm wavelength light, a photostationary state of 68% (*M*)-*cis*-**2** and 32% (*P*)-*trans*-**2** was reached. Alternated irradiation at 250 and 300 nm resulted in a photomodulation between these two photostationary states. It should be noted that after 20 switching cycles, 10% racemization was observed because of a relatively low racemization barrier. A second drawback is the relatively low switching efficiency of this prototype system. Both drawbacks can be overcome by synthetic modification.

It was found that the racemization barriers could be tuned over a range of approximately 50 to above 125 kJ mol⁻¹ by modification of the bridging atoms X and Y in the upper and lower half of the inherently dissymmetric alkenes (Scheme 2).^[32] The effect of increasing the size of X and Y is that the naphthalene unit of the upper half is pushed toward the lower half, and as a consequence, the steric hindrance at the so-called *fjord region* and the barrier for racemization are increased. For instance, going from Y = O to S, the Gibbs energy of activation



Scheme 2 General scheme of a chiroptical molecular switch based on pseudoenantiomers of a sterically overcrowded alkene.

for the racemization process increases from 91.2 to 120.9 kJ mol⁻¹.

In a switching process, which is based on the difference in UV/Vis absorption of two states of a photochromic molecular system, the switching efficiency is linearly related to the ratio of the UV/Vis absorptions of the isomers (following Eq. 1). The ratio of the two extinction coefficients at a certain wavelength, together with the ratio of the quantum yields (Φ) for interconversion of the two forms, determines the photostationary state ratios. The ratio of the two extinction coefficients of a photochromic switch is wavelength-dependent, and this is a decisive factor for the selectivity of the switch.

$$\frac{[cis]}{[trans]} = \frac{\epsilon_{trans} \Phi_{trans \rightarrow cis}}{\epsilon_{cis} \Phi_{cis \rightarrow trans}} \quad (1)$$

To increase the stereoselectivity of the photochromic process, a dimethylamino electron-donating substituent and a nitro electron-withdrawing substituent were introduced in the lower half (Scheme 4).^[33,34] This asymmetric substitution results in relatively large differences in the UV/Vis absorption characteristics of the two pseudoenantiomers (Fig. 3A). Maxima in the ratio of extinction coefficients of the two pseudoenantiomers are found at 365 and 435 nm. With this system, in *n*-hexane, switching between a photostationary state of 90% (*M*)-*cis*-3 and 10% (*P*)-*trans*-3 (435 nm) and 30% (*M*)-*cis*-3 and 70% (*P*)-*trans*-3 (365 nm) is achieved.^[33] It was possible to perform 80 switching cycles without any deterioration or racemization.

Of utmost importance for further applications of chiroptical molecular switches is the pseudoenantiomeric relationship between the two isomers. This pseudoenantiomeric relation is evident from the circular dichroism (CD) spectra of the two forms (Fig. 3B). With this system, molecular chirality can effectively be controlled by changing only the wavelength of light used.

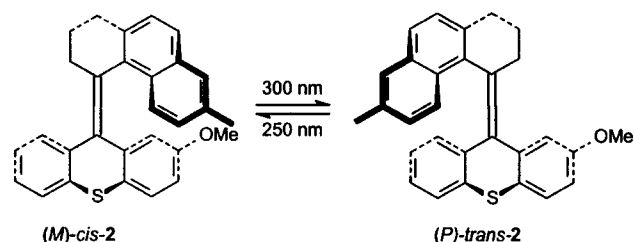
To obtain information on the necessity of both a donor and an acceptor moiety in the same molecule to induce efficient switching, the acceptor-only nitro-substituted

and donor-only dimethylamino-substituted switches **4** and **5**, respectively, were synthesized (Fig. 4). For both compounds, the wavelengths for the most selective switching process are considerably blue-shifted compared with the donor-acceptor switches because of the absence of a charge transfer absorption band, and switching selectivities for both **4** and **5** are lower than for the donor-acceptor substituted analog. Apparently, a combination of donor and acceptor substituents is a prerequisite for selective chiroptical switching in sterically overcrowded alkene systems. Therefore the concept of donor-acceptor substituted switches was further exploited.

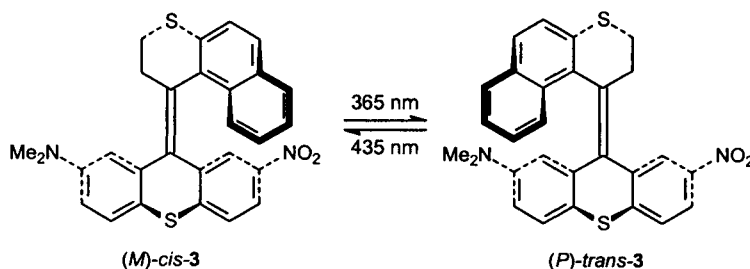
The major drawback of **3**, which becomes of considerable importance especially when the molecule is incorporated in a liquid crystalline matrix, is low solubility and compatibility. Low compatibility leads to severe limitations with respect to the applicability of the system in an organized environment (*vide infra*). Donor-acceptor compound **6** was designed to increase the solubility without interfering with the switching efficiency (Scheme 5).^[35] Although the UV/Vis spectra of **6** are comparable to those of its parent compound **3**, there are subtle differences resulting in slightly different photochemical behavior.

Irradiation of **6** in *n*-hexane solution at the most efficient wavelength of 380 nm resulted in the formation of a photostationary state consisting of 70% (*P*)-*trans*-**6** and 30% (*M*)-*cis*-**6**. Subsequent irradiation at 465 nm resulted in the formation of a photostationary state consisting of 98% (*M*)-*cis*-**6** and 2% (*P*)-*trans*-**6**. This system thus shows nearly quantitative switching to a *cis* photostationary state because of a slight bathochromic shift of the UV/Vis curve of the *trans*-isomer relative to the *cis*-isomer. Although this is only a minor effect, it allows irradiation at the red edge of the spectrum to almost exclusively excite the *trans*-isomer resulting in a near quantitative switching to the *cis* photostationary state.

In another approach to change the photophysical properties of donor-acceptor switches, the relative position of the donor and acceptor substituents can be changed



Scheme 3 The first chiroptical molecular switch based on a sterically overcrowded alkene **2**.



Scheme 4 Donor–acceptor substituted chiroptical molecular switch **3** showing high stereoselectivity.

(Scheme 6).^[36] By introducing a dimethylamino-substituent in the upper half of the switch as in **7**, the difference between the two isomers was expected to increase. In case of (*M*)-*cis*-**7**, where the donor and acceptor substituents are close together, a strong dipolar interaction between the donor and acceptor moieties is expected. The possibility for this direct interaction is absent in case of (*P*)-*trans*-**7**. Nevertheless, efficient photoisomerization was only observed in one direction strongly depending on solvent polarity. In toluene, for example, a remarkable *cis/trans* ratio of 99:1 was found upon irradiation at 435 nm.

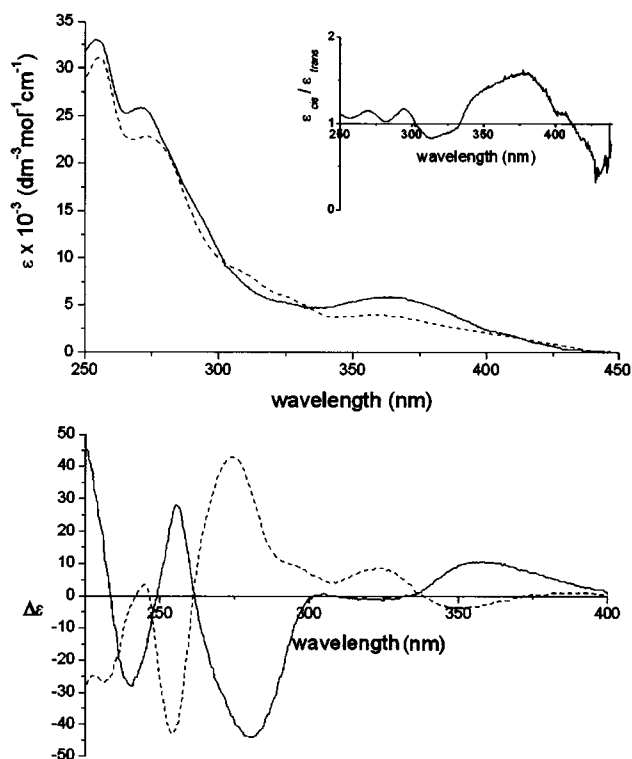


Fig. 3 UV/Vis (top) and CD (bottom) absorption spectra of donor–acceptor switch **3** (inset: the ratio of the two extinction coefficients $\epsilon_{cis}/\epsilon_{trans}$). The solid lines correspond to (*M*)-*cis*-**3** and the dashed graphs correspond to (*P*)-*trans*-**3**.

Switching to a state of excess, (*P*)-*trans*-**7**, however, was only possible in highly polar solvents such as, for example, dichloromethane, and even then, a maximum *trans/cis* ratio of only 55:45 was achieved. Although at certain wavelengths the extinction coefficient of the *cis*-isomer is higher than that of the *trans*-isomer, there is a preference for the *cis*-isomer throughout the entire spectrum and in almost any solvent. Because absorption characteristics are similar to those of **3**, in this case, apparently, the quantum yield ratio is the predominant factor for the switching selectivity. As a result of favorable donor–acceptor interaction in the excited state, a *cis*-like geometry will be preferred leading to a *cis*-ground state only slightly dependent on the wavelength used for excitation. This assumption is supported by the fact that in more polar solvents, where intramolecular dipole interactions become less important, the photostationary states are increasingly shifted to the *trans*-isomer. Compound **7** can, in principle, be used in a write-once type of molecular information storage system where, starting from the *trans*-state, information is written very efficiently with a diastereomeric ratio up to 99:1 (in toluene solution) in preference of the *cis*-state.

Special Molecular Switches

The above examples show that sterically overcrowded alkenes allow control of molecular chirality and offer a

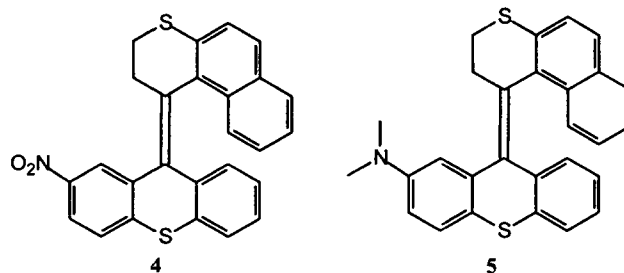
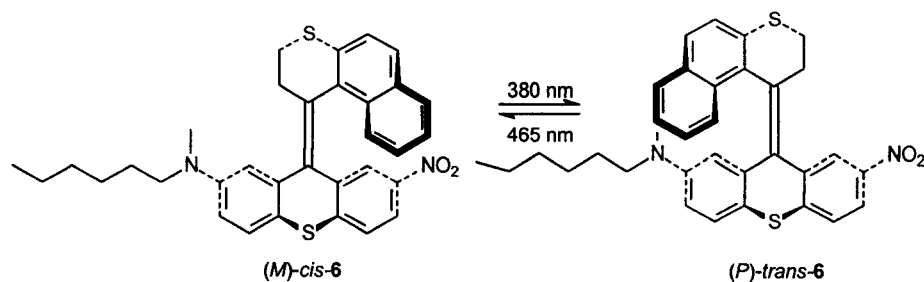


Fig. 4 Simplified analogs of the donor–acceptor switches; acceptor-only compound **4** and donor-only compound **5**.



Scheme 5 *n*-Hexyl modified donor–acceptor switch 6.

binary switch system on a molecular level. The next examples aim to further exploit this chiroptical switching concept toward control over other functions or toward more sophisticated photochromic systems.

Controlled Molecular Rotation

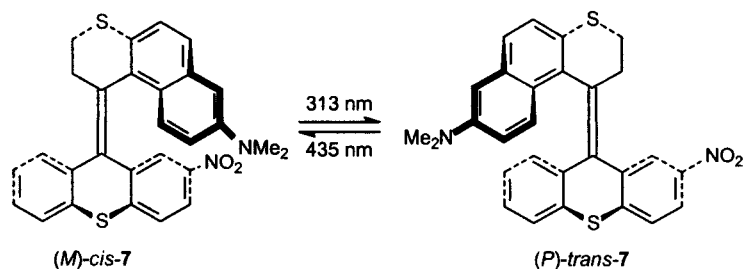
An approach toward a functional switch involves the control of the rotation around a single bond in a photoswitchable molecule modified with a biaryl-type rotor.^[37] Photoisomerization between the (*M*)-*cis*-8 and the (*P*)-*trans*-8 form should cause a distinct difference in rotation rate for the biaryl rotation because steric hindrance on the rotor is completely different for the two pseudoenantiomers (Scheme 7). Dynamic NMR studies revealed barriers for the biaryl rotation of $\Delta G^\ddagger = 4.54$ and 4.71 kJ mol^{-1} for the *cis*- and *trans*-isomer, respectively. In contrast with expectation, but in agreement with semiempirical calculations, the barrier for the *trans*-compound was higher than for the *cis*-compound. The observed isomerizations were attributed to distinct differences in the chiral conformations and steric effects associated with folding in the molecules. Particularly, the methyl groups of the xylyl rotor meet severe steric hindrance of the CH_2 groups of the upper half in *trans*-8, whereas the nearly planar naphthalene moiety in *cis*-8 simply bends away during the rotary

process. This system can be considered a molecular gear but suffers from a small difference in energy barriers and inefficient photoswitching.

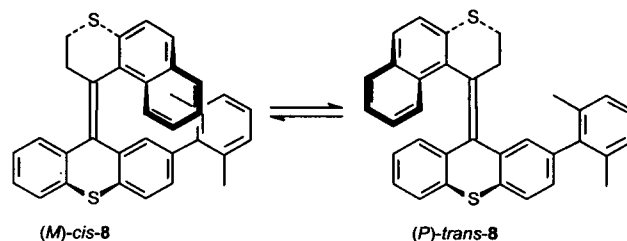
Gated Response and Dual-Mode Photoswitching of Luminescence

Locking of written information is absolutely essential for optical data storage based on molecular switches. Donor–acceptor switch 3, as a result of the presence of a basic dimethylamino-substituent, allows gated photoswitching (Scheme 8).^[34] The photochemical isomerization process of both (*M*)-*cis*-3 and (*P*)-*trans*-3 was effectively blocked by protonation of the dimethylamine moiety which changes the lower half of the molecule from a *push–pull* donor–acceptor system to a *pull–pull* acceptor–acceptor system. The photoisomerization behavior can be restored upon subsequent deprotonation.

This protonation–deprotonation protocol does not only lead to gated response, but also has an effect on the fluorescence of the molecule, leading to a dual-mode photoswitching of luminescence. For (*M*)-*cis*-3 in *n*-hexane, a weak fluorescence is found around 528 nm, whereas for (*P*)-*trans*-3b, a relatively strong fluorescent emission is observed around 531 nm. The fluorescence was found to be highly solvent-dependent. Protonation of these photochromic compounds resulted in complete



Scheme 6 Alternative chiroptical molecular switch 7 with donor group in upper half and acceptor group in lower half of the molecule.



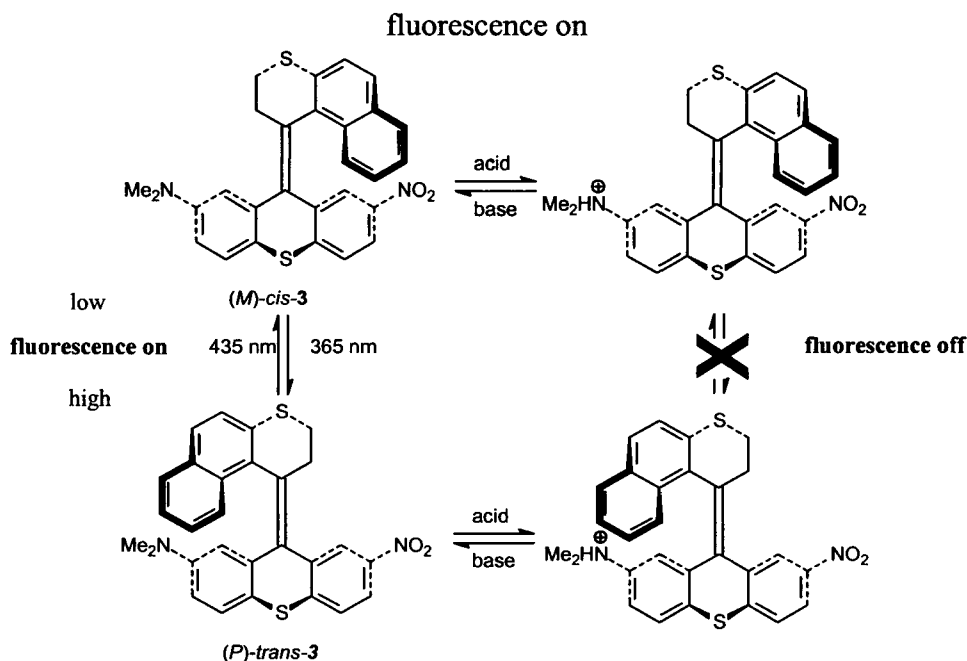
Scheme 7 Controlled intramolecular rotation of a biaryl propeller unit in a chiroptical molecular switch **8**.

quenching of the emission for both forms, whereas after deprotonation, fluorescence intensities were fully recovered. Combined with the photochemical switching, this allows for switching between three fluorescent states *on* (*trans*), *dimmed* (*cis*), and *off* (both protonated forms) by simultaneous use of light and acid/base stimuli. In circularly polarized luminescence studies, it was found that the chirality of the fluorescent excited states strongly depends on the polarity of the solvent.^[38] In *n*-hexane, both (*M*)-*cis*-**3** and (*P*)-*trans*-**3** show circularly polarized luminescence of the same handedness, while in benzene, circular polarization of luminescence is opposite for (*M*)-*cis*-**3** and (*P*)-*trans*-**3**. This remarkable behavior was explained by the existence of a mutual *trans*-like luminescent excited state in *n*-hexane, where in benzene, clearly, *cis*-like as well as *trans*-like excited

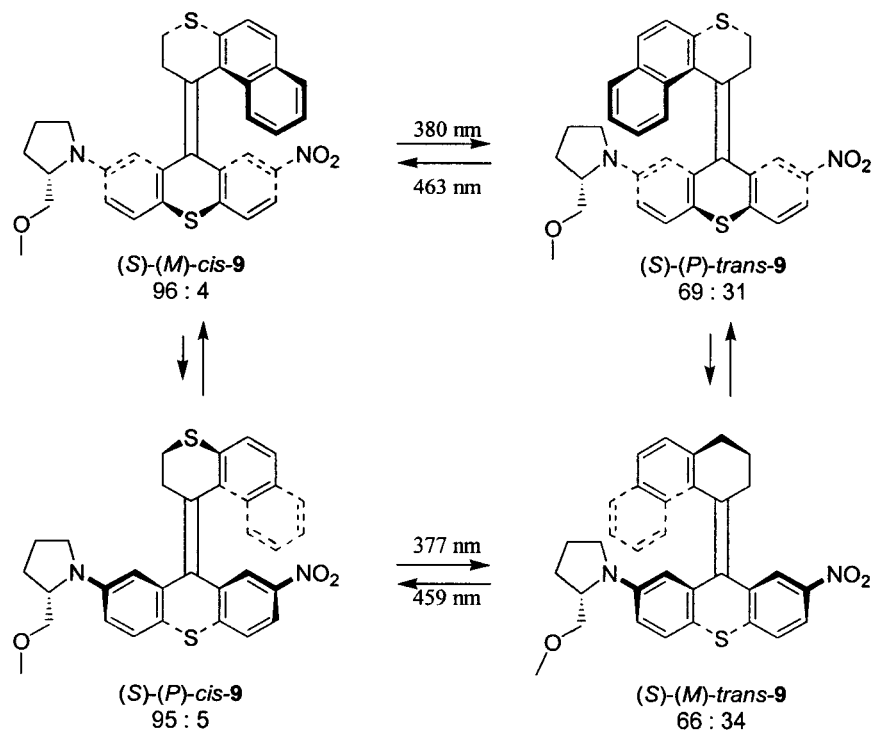
states can be observed. In benzene solution, this system can function as a molecular modulator of circularly polarized luminescence.

Pyrrolidine-Functionalized Molecular Switch

En route toward further functionalization of the switch skeleton in compound **9**, a chiral (*S*)-2-methoxymethylpyrrolidine group was introduced as the electron donor moiety (Scheme 9). The additional stereogenic center in this molecular switch results in four distinct diastereomeric forms. As a result, the two photoequilibria are now different, and a difference in energy for the two separate *cis*- [(*S*)-(*M*)-*cis*-**9**/(*S*)-(*P*)-*cis*-**9**] and *trans*- [(*S*)-(*M*)-*trans*-**9**/(*S*)-(*P*)-*trans*-**9**] isomers of **9** can be anticipated. For both pseudoenantiomeric couples, the ideal



Scheme 8 Gated photoswitching and fluorescence based on reversible protonation.



Scheme 9 Four diastereoisomers of pyrrolidine-based chiroptical switch **9** and the isomerization pathways.

switching wavelengths and photostationary state ratios are summarized in Scheme 9. Switching selectivities are similar for the two diastereomeric bistable switching pairs, and functionalization of the donor part of the molecular switch has only a minor influence on the switching selectivity. This offers attractive possibilities for the use of these switch molecules in multicomponent photoactive materials.

Another interesting feature of **9** when compared with donor-acceptor switch **3** (Scheme 4) is that because of the diastereomeric relation between the respective *cis*- and *trans*-isomers, the thermal helix inversion steps are no longer true racemizations. The steady-state ratios are not 50:50, indicating that there is a small but significant energy difference between the two *cis*- and the two *trans*-forms of **9** (Scheme 9). This effect can be used to induce directionality in molecular rotation which might lead to molecular motors.

Chiroptical Switching in Polymeric Matrices

In order for any molecular switch to be useful in future nanotechnological applications, the system should retain its properties when incorporated in a processable matrix. Incorporation into a polymer matrix would, for example, offer a photoswitchable film for reversible data storage.

For this purpose, a polymer-bound sterically overcrowded alkene **10** was designed (Fig. 5).^[39] Irradiation of thin films of this chiral photochromic polymer results in distinct changes in the CD spectrum, but **10** suffers from low switching selectivity and long irradiation times.

Photochemical switching of polymers doped with sterically overcrowded alkenes revealed that photoswitching was possible in a polymer matrix. The isomerization processes, however, critically depend on the mobility in the matrix. The restrictive polymer matrix slows down this process to a large extent, and more effective applications of the sterically overcrowded alkenes as chiroptical

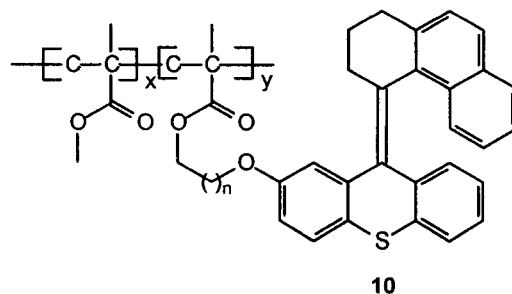


Fig. 5 Polymer-bound chiroptical molecular switch **10** ($n = 1-5$; $x/y \geq 95.3:4.7$).

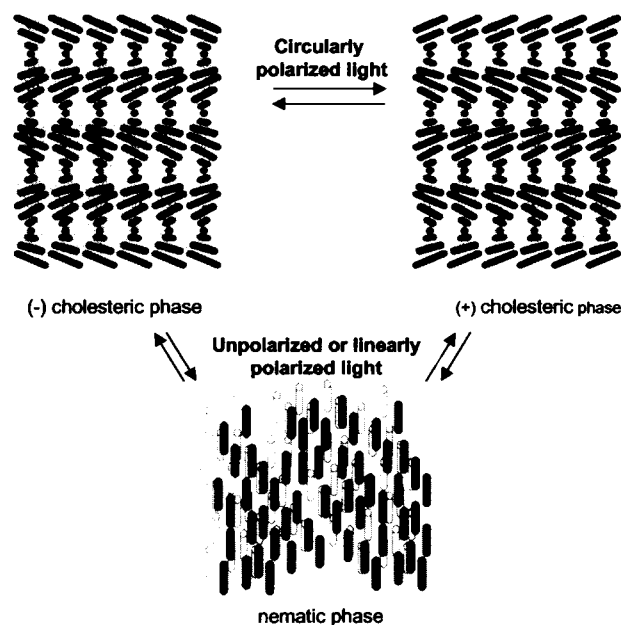
molecular switches were found with more flexible liquid crystalline host materials.

TOWARD APPLICATIONS: SWITCHING OF LIQUID CRYSTALLINE PHASES

Liquid crystals (LCs), which are already widely applied in, for example, display technology, form excellent host materials for chiral molecular switches. When doped with a suitable molecular switch as a guest, liquid crystals offer a processable photoswitchable material, with essential features for application of these systems. Nematic liquid crystals are especially appealing for use in combination with these chiral guest compounds because they are extremely sensitive toward chiral perturbations forming chiral nematic or cholesteric phases. In their cholesteric packing, the mesogenic host molecules amplify the molecular chirality of the guest material resulting in a macroscopic chiral helical packing. Cholesteric phases can be assigned by a helical packing of the mesogens with a certain sign and a certain pitch.^[40–42] This pitch is a measure of the chirality of the system. An important property of cholesteric liquid crystals for potential technological application is that they show unique optical properties when the pitch is of the same magnitude as the wavelengths of visible light. When illuminated with white light, cholesteric phases reflect light of a certain wavelength (color) dependent on the pitch of the LC phase. The interest in colored doped cholesteric phases in the research on chiroptical molecular switches is twofold. When chiroptical molecular switches can induce pitch lengths resembling the dimensions of the wavelength of visible light, a direct color readout of written information is possible. On the other hand, direct tuning of the color of the cholesteric phase opens the opportunity to develop color liquid crystal display materials addressable by light, i.e., color pixel formation.

Enantiomeric Switches in a Liquid Crystal Matrix

A main goal of the research on enantiomeric switches has been the development of a potential liquid crystal photo-trigger based on CPL. Because nematic materials are extremely sensitive to chiral perturbations, changes in LC films can even reflect enantiomeric excesses as small as 0.07% as found for **1**.^[26] Irradiation with (*l*)-CPL (313 nm) of racemic **1** doped in a nematic LC host M15 resulted in the formation of a negative cholesteric phase. The molecular chirality controlled by circularly polarized light is amplified by the liquid crystalline environment. Accordingly, irradiation with (*r*)-CPL (again 313 nm) resulted in a cholesteric phase of opposite positive screw

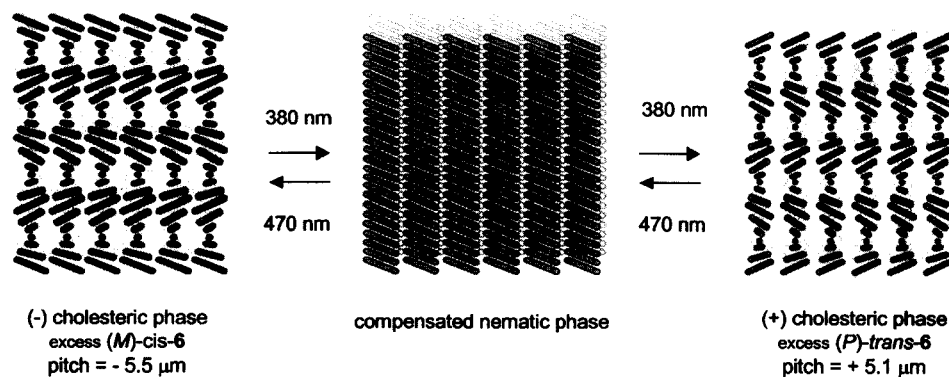


Scheme 10 Schematic representation of CPL switching between different liquid crystalline phases.

sense. The amount of dopant needed to obtain a measurable cholesteric phase is relatively large (20 wt.%) because of the small enantiomeric excesses reached in the photostationary state. Irradiation of the cholesteric film with linear polarized light at 313 nm resulted in an achiral compensated nematic phase. The two chiral influences (*l*- and (*r*)-CPL at the most efficient wavelength stimulate the two extreme photostationary states. Actually, this macroscopic switchable material represents a multistate switch in which the cholesteric phases with intermediate pitches can be addressed by changing, for example, the irradiation time or wavelength (Scheme 10).

Pseudoenantiomeric Switches in a Liquid Crystal Matrix

The photochemical modulation of the helical screw sense and the pitch of a cholesteric phase was also realized with the combination of a nematic liquid crystalline host and donor–acceptor switch **3**.^[43] Different liquid crystals can be used as a host and show comparable results. For example, doping of liquid crystalline compound M15 with (*P*)-*trans*-**3** (2.4 wt.%) converts the nematic phase into a cholesteric phase. Irradiation at 365 or 435 nm of a thin film of this cholesteric phase led to photostationary states with an excess of (*M*)-*cis*-**3** or an excess of (*P*)-*trans*-**3**, comparable to the system in *n*-hexane solution. These two cholesteric phases show different pitches and opposite screw sense (+8.5 and –12.2 μm), as expected from the



Scheme 11 Schematic representation of the switching of the chirality of a doped cholesteric liquid crystal.

pseudoenantiomeric relationship of the two forms of the photoswitchable dopant. Switching efficiencies in a liquid crystalline environment and in solution are more or less equal, but irradiation times have increased. Doping concentrations are, however, limited for this particular system. For this reason, compound **6** with a solubilizing *n*-hexyl tail was synthesized (vide supra) and an increase in compatibility was observed in all tested nematic host materials.

For compound **6**, a cholesteric phase was readily induced by doping with either one of the enantiomerically pure forms of **6** in all tested nematic liquid crystalline hosts. The molecular chirality of the dopant was amplified to provide a macroscopic chirality of the liquid crystalline phase comparable to compound **3**. Using a 2.6-wt.% sample of **6** in M15, for example, switching between cholesteric phases with pitches of +10.1 and -12.0 μm was achieved using 380- and 435-nm light, respectively. A material of choice for further improvement of the system is E7, a commercially applied LC mixture which is liquid crystalline at room temperature. Ideal switching wavelengths in this LC host were determined to be 380 and 470 nm. Using again a 2.6-wt.% sample, switching between cholesteric phases with pitches of +5.1 and -5.5 μm was possible. These values represent the minimum pitches that can be reached for a 2.6-wt.% sample. By changing the irradiation time or the irradiation wavelength, cholesteric phases with intermediate pitches, including a compensated nematic phase, are addressable (Scheme 11).

Controlling the Color of Cholesteric Phases

As indicated above, to obtain colored LC phases, pitches in the range of nanometers are required. Although the dopant concentration for **6** in E7 can be further increased, for LC color application, a different host system

has to be used. For two important reasons, the system of choice was a chiral polymerizable cholesteric acrylate mixture (**11** and **12**) developed by Philips Research (Fig. 6).^[44–47] First of all, because of the presence of a chiral diacrylate, the LC host already shows a colored cholesteric phase. Upon doping with a chiroptical switch, the color of the LC phase only has to be influenced rather than fully induced. A second important property of this system is that because of the presence of an achiral monoacrylate and a chiral diacrylate, this system can undergo photopolymerization when a suitable photoinitiator is present. This photopolymerization process locks the cholesteric phase to generate a stable polymeric matrix reflecting the optical properties of the initial liquid crystal matrix. This could allow stable storage of information. The principle was demonstrated using a mixture of 40% chiral (*S,S*)-diacrylate **11** with 60% achiral monoacrylate **12** (forthwith denoted as **11/12**). This mixture forms a green cholesteric phase with a maximum reflection wavelength of about 440 nm.

Switching properties of **6** were retained in this acrylate mixture.^[35] Upon 435-nm irradiation, a photostationary state was reached with a ratio *cis*-**6**/*trans*-**6** of 67:33. Irradiation at 380 nm resulted in a photostationary state of 31% *cis*-**6** and 69% *trans*-**6**. In all doped cases, the reflection wavelength was red-shifted compared with the undoped mixture.

Switching experiments were performed on an aligned sample with 12.5 wt.% of enantiomerically pure (*M*)-*trans*-**6** in the presence of 1 wt.% of photoinitiator (Irgacure 651) and 1 wt.% of inhibitor (*p*-methoxyphenol) at 435-nm irradiation. At this wavelength, no polymerization is initiated and a *trans* to *cis* isomerization of the chiral dopant is the only process observed. Upon photoisomerization, the reflection band of the LC film was gradually shifted to shorter wavelength. Starting at a reflection wavelength of 666 nm (red), a blue shift of the reflection wavelength to 541 nm (green) was observed at

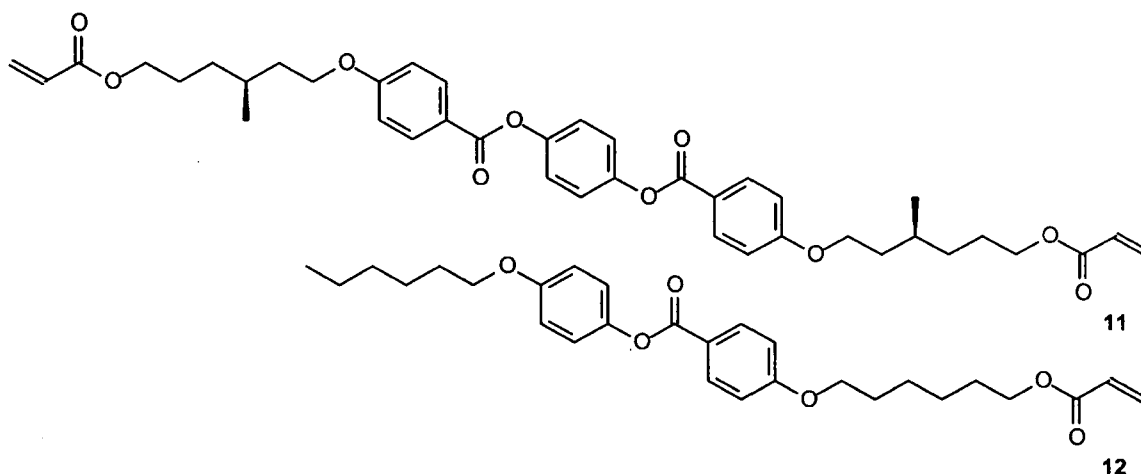


Fig. 6 Photopolymerizable cholesteric mixture of monomeric acrylates 11 and 12.

the photostationary state after about 150 sec of irradiation (Fig. 7). When increasing the irradiation wavelength using a 450-nm cutoff filter, the wavelength of reflection could further be decreased to a value of 526 nm. This blue shift of 140 nm can also be induced directly by >450 nm irradiation of the initial pure (*M*)-*trans*-6 doped film.

Photopolymerization of the LC film was effected by 5-min irradiation at 365 nm in vacuo. At this wavelength, photoisomerization of the dopant is expected to some extent. After the irradiation, the liquid crystalline phase was polymerized and a rigid polymer matrix was obtained. For the 12.5-wt.% sample of pure (*M*)-*trans*-6 in

11/12, photopolymerization resulted in a blue shift of the reflection from 666 nm in the monomeric state to 632 nm for the polymerized state. The photostationary mixture obtained after 450-nm irradiation, which showed a reflection of 526 nm in the monomeric state, gave a polymerized matrix with a 518-nm reflection. The obtained polymeric phases in all cases reflect the photostationary state of the chiral dopant. Furthermore, the polymerized phases are completely inert to prolonged irradiation and the photochemically written color information is effectively locked.

This system constitutes a "write and lock" mechanism for color information (Fig. 7). Writing is performed by

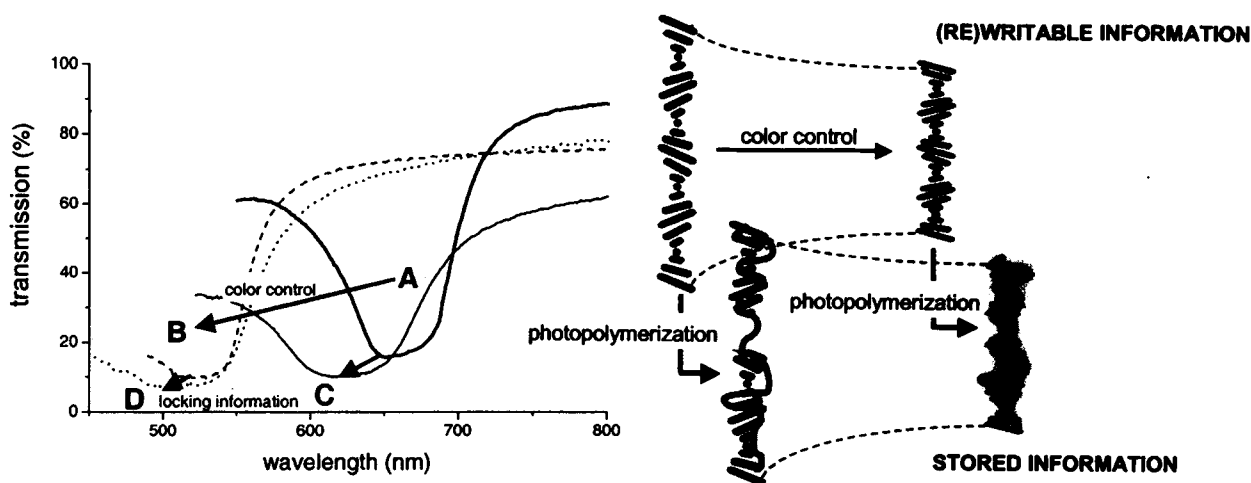


Fig. 7 Color control of LC film: writing and locking information for a 12.5-wt.% sample of (*M*)-*trans*-6 in 11/12. Wavelength of reflection at different stages of the process: A) initial sample; B) photostationary state after 450-nm irradiation; C) polymerized sample after 365-nm irradiation of the initial sample (A); D) polymerized sample after 365-nm irradiation of the photostationary state (B) and a schematic representation of color control and storage of information by photopolymerization of a cholesteric liquid crystal.

light, and cholesteric phases with pitches between 666 and 526 nm can be induced by varying the irradiation time. Color inspection (red to green) offers an easy readout procedure. Further irradiation of this LC phase results in a change in the (*M*)-*trans*-**6** to (*P*)-*cis*-**6** ratio and, as a consequence, a change in the wavelength of reflection (the color) of the LC film, as long as the 450-nm photostationary state is not reached. This monomeric state can be considered a rewritable state. Upon photopolymerization, the LC matrix will harden and the written information is locked. Again, color inspection (orange to green) offers an easy readout procedure which is now absolutely nondestructive. The information is locked and there is no change in cholesteric pitch observed upon further irradiation.

STERICALLY OVERCROWDED ALKENES AS UNIDIRECTIONAL ROTARY MOTORS

The design and synthesis of molecular motors are among the major endeavors in nanoscience. Inevitable motor functions will be needed to power nanomachines, although the design and functioning might be completely different from any known macroscopic or biological motor. We formulated three basic requirements for a molecular motor system: 1) repetitive 360° rotary motion; 2) consumption of energy; and 3) unidirectional rotation. The first chemically driven^[48–50] and photochemically driven unidirectional rotary motors^[51] were reported simultaneously.^[52] Until these accomplishments, no synthetic system could be classified as a molecular motor according to the prerequisites formulated above.

The chiroptical molecular switches already show a unidirectional rotation of about 105° where the direction of the movement is solely governed by the helicity in the initial state, and this process is driven by light. In the design of molecular motors, using sterically overcrowded alkenes as the basic structure, an extension of the rotary movement is necessary and the light-induced motion during the switching event should continue in the same direction. Realizing that these sterically overcrowded alkenes consist of four stereoisomers, i.e., the pseudoenantiomeric forms that constitute the two switching stages and their enantiomers, the possibility of full 360° rotation arises as illustrated briefly for compound **9** (vide supra).

The First Light-Driven Unidirectional Molecular Motor

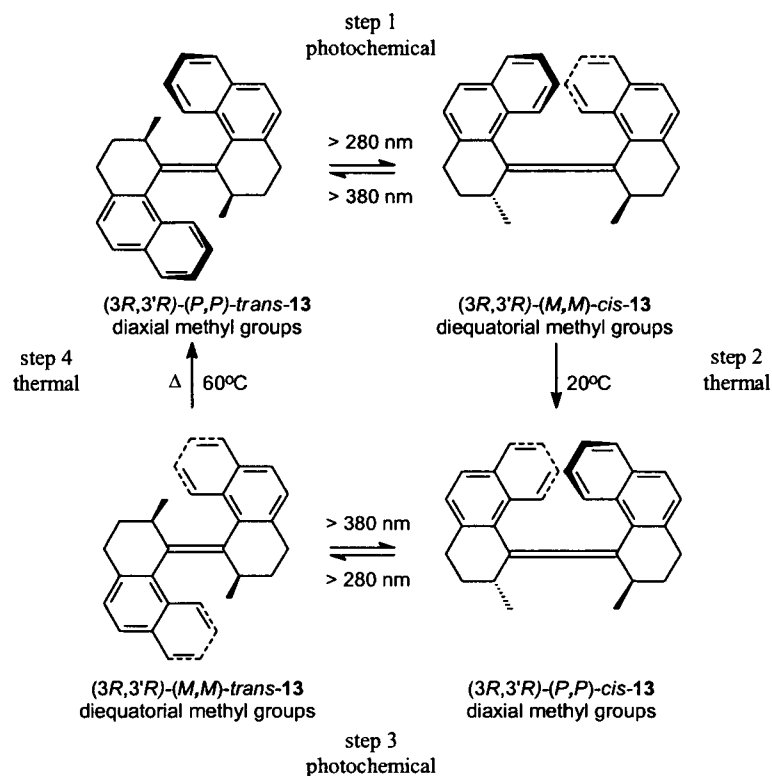
Following extensive study on the thermal and photochemical isomerization processes of biphenanthrylidene,^[53–56] it was demonstrated that the intrinsic

chirality associated with sterically overcrowded alkenes can be used to accomplish unidirectional rotary motion.^[57–59] In compound (3*R*, 3'*R*)-**13** (Scheme 12), the sterically overcrowded alkene skeleton bears two additional stereogenic centers besides the (*P,P*)-helical structure. In its most stable conformation (*P,P*)-*trans*-**13**, the two methyl substituents adopt an energetically favored axial orientation because of steric hindrance (Scheme 12). Irradiation with light ($\lambda \geq 280$ nm) results in an isomerization process (step 1) to form (*M,M*)-*cis*-**13**. Inherent to the nature of such an isomerization, the methyl substituents are forced to adopt an energetically unfavorable equatorial orientation. At room temperature, a fast helix inversion (step 2) takes place resulting in (*P,P*)-*cis*-**13** where the methyl substituents again adopt an axial orientation. A second photoisomerization step (step 3) results in the formation of (*M,M*)-*trans*-**13** with the methyl substituents again in their energetically unfavorable equatorial position. A second helix inversion (step 4) is induced by heating at 60°C and results in the formation of the initial (*P,P*)-*trans*-**13** isomer.

These four discrete steps add up to a full 360° unidirectional rotation of one (rotor) half of the molecule relative to the other (stator) half. Two photochemical energetically uphill isomerizations driving the rotary movement (steps 1 and 3) are each followed by two irreversible energetically downhill thermal helix inversions (steps 2 and 4). The release of internal energy of the system that takes place during helix inversion, to place the methyl substituents again in the more favorable axial orientation, ensures the unidirectionality of the process. The direction of rotation is solely governed by the configuration of the stereogenic centers because this determines the axial or equatorial orientation of the methyl groups. Essential features of the rotating system are the central olefinic bond, the helicity of the overcrowded alkene, the absolute configuration of the stereogenic centers, and the conformational flexibility of the cyclohexenyl rings. Because of the same wavelength used for both photoisomerization steps, a repetitive unidirectional rotation can be induced by continuous irradiation at elevated temperature. This is the first example of a light-driven unidirectional molecular motor as illustrated in Fig. 8.

Second-Generation Molecular Motor

One drawback of the first-generation motor is the thermal requirement of the system, and although photon energy is the driving force, heating to about 60°C is necessary to continue the rotary motion. A second drawback is that this system has little opportunities for structural variation. To overcome these drawbacks, a so-called second-generation motor concept was developed combining the



Scheme 12 Light-driven unidirectional molecular motor **13**.

design versatility of our chiroptical molecular switches with the unique rotary behavior of the first-generation molecular motor (Fig. 9). In this concept, one-half of the molecule (a chiral 2-methyl-2,3-dihydrothiopyran upper part) would function as the rotor part, while the other could be used for adjusting the molecular properties by synthetic modifications. The main question was whether the presence of a single stereogenic center would suffice to induce unidirectional rotation.

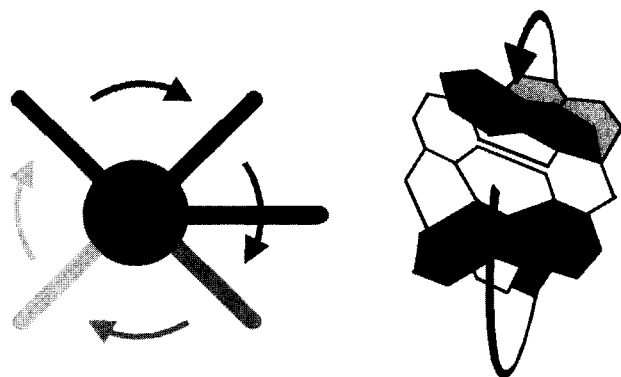


Fig. 8 Continuous unidirectionally rotating molecular motor **13**.

The prototype system that was synthesized is compound (*2'R*)-**14**.^[60] Analogous to the first-generation molecular motor, for **14**, a strong preference for an axial conformation of the methyl group at the stereogenic center was established. This stereochemical feature is essential to achieve unidirectional rotation. Starting from the energetically favored (*2'R*)-(*M*)-*trans*-**14** isomer, by irradiation with 365-nm light, a *trans* to *cis* isomerization was induced. This resulted in the corresponding less stable isomer (*P*)-*cis*-**14**, completely analogous to the first-generation molecular motor. Upon heating to 60°C, the unstable *cis*-isomer (*P*)-*cis*-**14** is converted to the stable (*2'R*)-(*M*)-*cis*-form. A second energetically uphill photoisomerization step yields the unstable (*2'R*)-(*P*)-*trans*-form which, upon heating, reverts again to stable (*2'R*)-(*M*)-*trans*-**14**, completing a full unidirectional 360° rotation of the rotor upper half relative to the stator lower half of the molecule (Scheme 13).

The direction of rotation in this second-generation motor is again dictated by the orientation of the methyl substituent at the stereogenic center. The process is solely driven by two light-induced energetically uphill photoisomerization processes, forcing the methyl substituent in the upper half of the molecule in an energetically unfavorable equatorial conformation. The release of

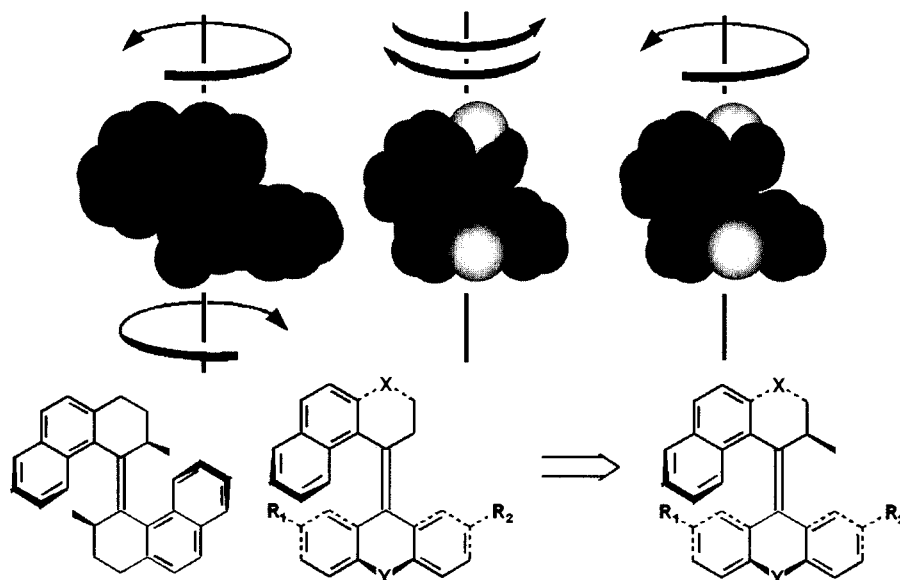


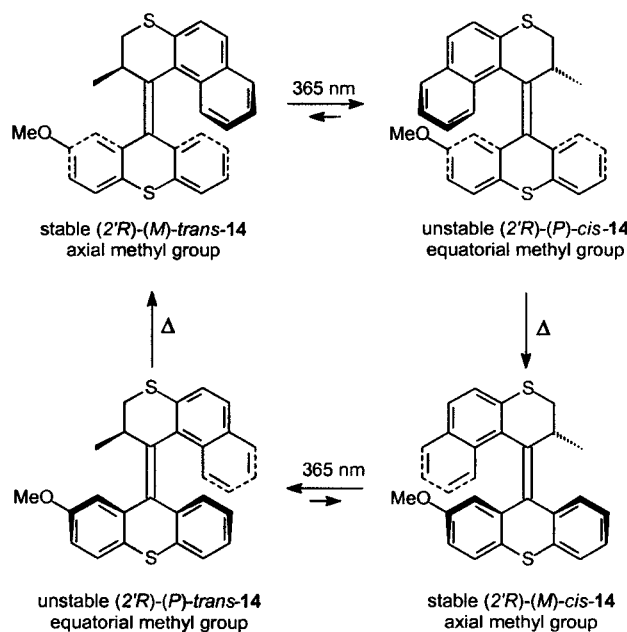
Fig. 9 Design of second-generation motors.

internal energy is accomplished by a helix inversion step where the methyl substituent adopts the favorable axial conformation. These two energetically downhill processes ensure the unidirectionality of the entire rotary motion.

Following this proof of principle, an important objective was to decrease the barrier for the thermal

helix inversion steps to allow rotation at room temperature. The approach focused on modification of the bridging groups X and Y (Fig. 9) to tune the steric hindrance at the fjord region of the molecules. Based on the experience with the molecular switches, compounds **15**, **16**, and **17** were synthesized in which, because of decreased dimensions of the (hetero-)atoms X and Y (O and CH₂ compared with S), helix inversion was expected to be facilitated (Fig. 10).^[61] Changing the sulfur atom (in **15**) for an oxygen atom in the lower half (in **16**) resulted in a decrease in the half-life (in *n*-hexane) at room temperature by a factor of about 8. Replacing a sulfur by a carbon atom in the upper half decreased the half-life by a factor of about 320. This resulted in a motor **17** with a half-life for thermal helix inversion of about 2400 sec at room temperature allowing unidirectional rotation under ambient conditions.

In an attempt to further reduce these energy barriers, a new motor **18** with a tetrahydronaphthalene instead



Scheme 13 First example of unidirectional rotation controlled by a single stereogenic center; the prototype of the second-generation motor **14**.

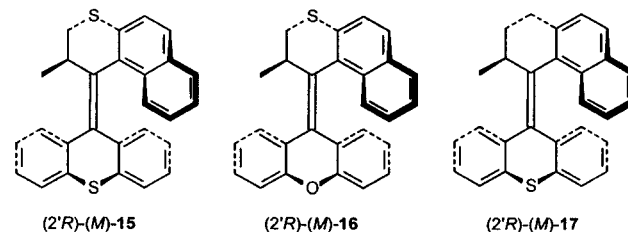


Fig. 10 Second-generation motor: unidirectional rotation controlled by a single stereogenic center and structural modifications that allow control of rotary behavior.

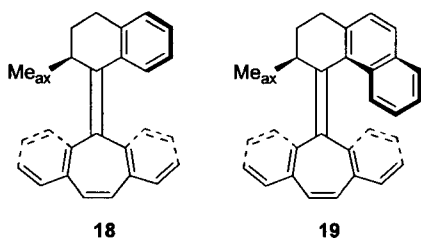


Fig. 11 Tetrahydronaphthalene (**18**) and tetrahydrophenanthrene-based (**19**) motor.

of a tetrahydrophenanthrene upper part used in the other second-generation motors including parent compound **19** was synthesized (Fig. 11).^[62] Counterintuitively, for motor system **18**, the rotary motion is severely slowed down. This remarkable effect was attributed to a higher ground state energy of motor **19** compared with **18**. It is evident that there is a delicate balance between ground-state distortion and steric and electronic effects on the photochemical and thermal isomerization processes in these sterically overcrowded alkenes.

Another objective is the design of a system that can function under the influence of visible light. For this purpose, the absorption of the molecules has to be shifted from the UV region to the visible region. Asymmetric donor–acceptor substitution in **20** was expected to induce a red shift in UV/Vis absorption (Scheme 14).^[63] Fig. 12

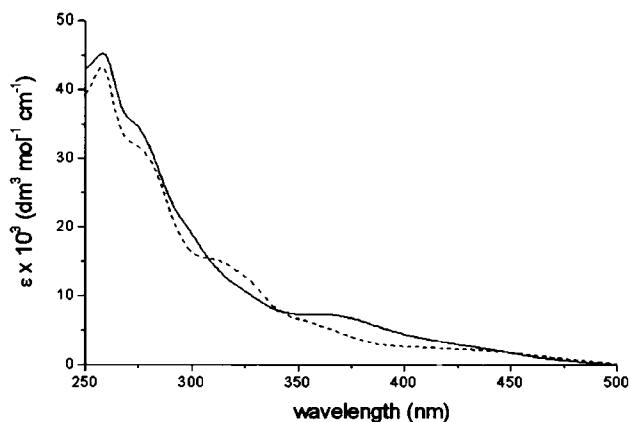
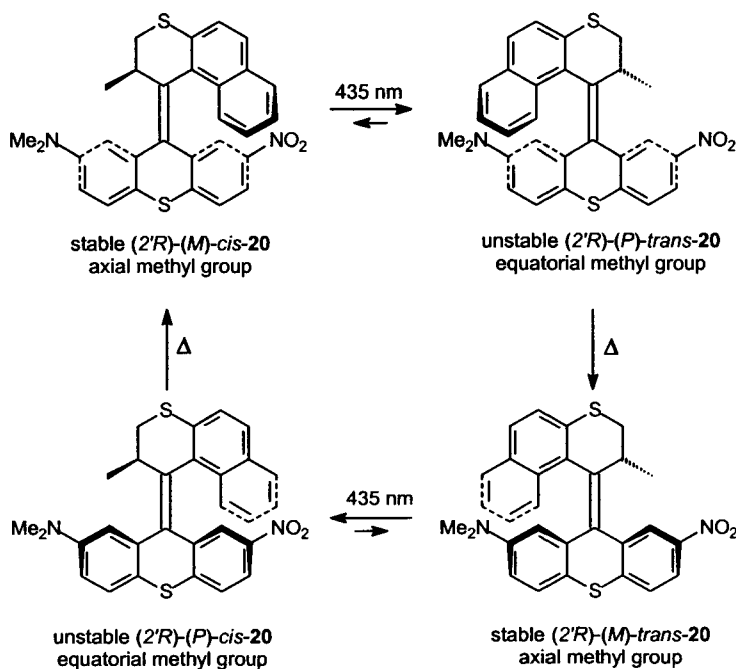


Fig. 12 UV/Vis absorption of *cis*-**20** (solid) and *trans*-**20** (dashed) in chloroform.

clearly shows that the UV/Vis absorption of both isomers of **20** extends to about 500 nm implying the possibility of excitation of these photoisomerizable compounds in the visible region of the spectrum.

Completely analogous to other second-generation motors, irradiation of enantiomerically pure (*2'R*)-(*M*)-*cis*-**20** with visible light of 435 nm resulted in the formation of less stable (*2'R*)-(*P*)-*trans*-**20** (Scheme 14). In this compound, the methyl substituent is forced to adopt an equatorial orientation. Subsequent heating at 50°C



Scheme 14 Visible light-driven unidirectional rotation of donor–acceptor motor **20**.

resulted in the formation of the stable (*2'R*)-(*M*)-*trans*-**20**. Irradiation of (*M*)-*trans*-**20** with visible (435 nm) light induced a second isomerization and the formation of energetically unfavorable (*P*)-*cis*-**24**. Heating the system to 50°C resulted in a helix inversion to form (*M*)-*cis*-**20** again. The combined four-step rotary cycle ensures that compound **20** functions as a molecular motor that can be driven by visible light.

UNIDIRECTIONAL ROTARY MOTION IN A LIQUID CRYSTALLINE ENVIRONMENT

In the first-generation molecular motor, the energy of the irradiation light is used to exert mechanical motion. The next step toward any nanotechnological application of such a motor would be to actually drive other functions or perform work. In addition, for future application of these molecular motors, conservation of the molecular properties in an organized medium is essential. Combining the properties of our first molecular motor **13** with those of liquid crystalline materials is a first step in the direction of a nanotechnological application. The essence of the research is to examine whether the control of molecular rotation that can be exerted by light irradiation can be amplified to control the motion of a large ensemble of molecules and, as a consequence, the macroscopic (chiral) properties in a liquid crystalline phase, thereby allowing indirect macroscopic visualization of rotary motion.

Compound **13** (Scheme 12) efficiently induces cholesteric phases for different mesogenic host compounds. A helical twisting power of $+69 \mu\text{m}^{-1}$, for example, was found for (*P,P*)-*trans*-**13** in E7.^[64] The rotary process in the liquid crystalline matrix was tested using a drop-casted sample of E7 doped with 2.4 wt.% of (*P,P*)-*trans*-**13** and was shown to be analogous to solution experiments (Scheme 12). Unidirectional rotation was proven to be possible in a liquid crystalline matrix. It should be noted, however, that during the heating step, the LC material was in an isotropic stage, and as a consequence, the orientation is temporarily lost. The whole light-driven process is less efficient in a liquid crystal than in solution for two important reasons: 1) the absorption of the LC material reduces the amount of photons that will actually reach the photoisomerizable material, which is evident from the strong dependence of isomerization efficiency on substrate thickness; and 2) because of the absorption of the LC material, the wavelength range that actually reaches the compound is $>340 \text{ nm}$ which causes a shift in the two photoequilibria.

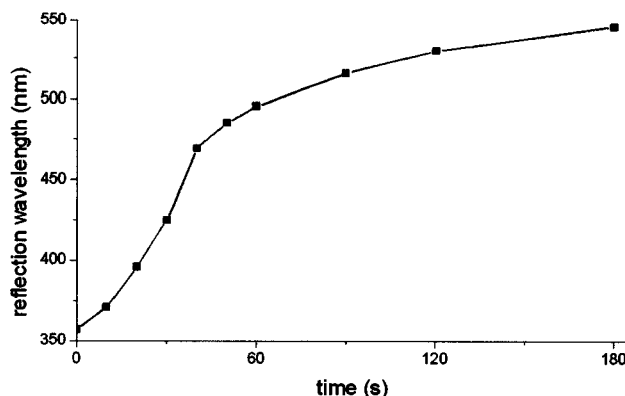


Fig. 13 Wavelength of reflection at a 45° angle of a molecular motor doped LC phase (6.16 wt.% in E7) as a function of time starting from (*P,P*)-*trans*-**13** upon irradiation with $>280 \text{ nm}$.

The high helical twisting powers for (*P,P*)-*trans*-**13** open up the possibility to generate cholesteric phases with pitch lengths in the range of the wavelength of visible light. Doping of E7 with only 6.16 wt.% of (*P,P*)-*trans*-**13** resulted in a violet cholesteric phase with a pitch of 234 nm and a reflection wavelength (at an angle of 45°) of 357 nm. From the ratio and the pitches of the 2.4-wt.% sample discussed above, the helical twisting powers of (*P,P*)-*cis*-**13** and (*M,M*)-*trans*-**13** could be calculated to be $+12$ and $-5 \mu\text{m}^{-1}$, respectively. The dramatic decrease in the helical twisting power going from (*P,P*)-*trans*-**13** to the other isomers is essential for generating light-induced macroscopic changes by unidirectional rotation. Upon irradiation ($\lambda \geq 280 \text{ nm}$) of the violet film of 6.16 wt.% of (*P,P*)-*trans*-**13** in E7, a fast bathochromic shift of the reflection wavelength was induced. In only 80 sec, the color of the film changed from violet via blue, green, yellow, and orange to red as can be readily detected by visual inspection. The time-dependent quantitative change in reflection wavelength measured at a 45° angle is presented in Fig. 13.

After heating the sample to 60°C at any time of irradiation, the (*M,M*)-*trans*-**13** isomer is converted to (*P,P*)-*trans*-**13** with a concomitant hypsochromic shift of the reflection wavelength. Again, during the heating process, the LC material was in an isotropic stage, and as a consequence, the orientation is temporarily lost.

These results show that unidirectional rotary motion could be performed in a LC matrix, as is schematically illustrated in Fig. 14. The light-driven motion in the dopant induces the motion of a large ensemble of rod-like molecules during the reorganization in the LC film. This indirectly allows visual observation of the rotary motion, but, more importantly, shows that rotation on a

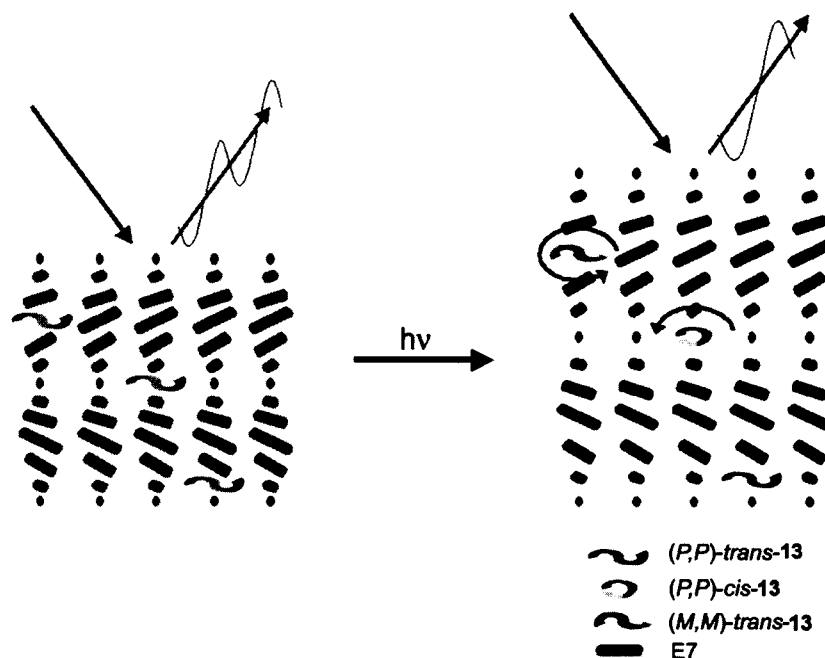


Fig. 14 Schematic representation of unidirectional rotation of the guest molecular motor **13**, the induced elongation of the pitch of the LC host matrix, and the change in reflection wavelength of the light.

molecular level can be used to drive a reorganization of a macroscopic liquid crystalline film. Furthermore, it demonstrates that the molecular motor can perform actual work.

CONCLUSION

It has been shown that chiral sterically overcrowded alkenes are extremely suitable for functioning as molecular switches and motors. Chiroptical switches based on sterically overcrowded alkenes were constructed that could function both in solution as well as in a liquid crystalline matrix. These switches might be used as molecular trigger elements or as reversible data storage units at the molecular level. The first light-driven molecular motors were also based on an overcrowded alkene. By combining two chiral elements (helical structure and stereogenic center) in the same photoactive molecule, the fundamental properties of a molecular motor, energy consumption resulting in unidirectional rotary motion, were demonstrated. This prototype system led to the development of a second-generation of molecular motors for which tuning of the rotation speed and irradiation wavelength was proven to be possible. All the systems developed are still far from actual application, but they offer a solid basis for the development of future

generations of switches and motors to meet the numerous challenges ahead on the road toward nanomechanical machinery.

REFERENCES

1. Astumian, R.D. *Sci. Am.* **2001**, 285, 56.
2. *Molecular Machines and Motors*; Sauvage, J.-P., Ed.; Struct. Bond., Springer: New York, 2001; Vol. 99.
3. Goodsell, D.S. *Our Molecular Nature: The Body's Motors, Machines and Messages*; Springer: New York, 1996.
4. Molecular machines. *Acc. Chem. Res.* **2001**, 34, 409. Special issue.
5. Balzani, V.; Gomez-Lopez, M.; Stoddart, J.F. *Acc. Chem. Res.* **1998**, 31, 405.
6. Sauvage, J.-P. *Acc. Chem. Res.* **1998**, 31, 611.
7. Mislow, K. *Chemtracts, Org. Chem.* **1989**, 2, 151.
8. Kelly, T.R.; Boyer, M.C.; Bhaskar, K.V.; Bebbington, D.; Garcia, A.; Lang, F.; Kim, M.H.; Jette, M.P.A. *J. Am. Chem. Soc.* **1994**, 116, 3657.
9. *Molecular Switches*; Feringa, B.L., Ed.; Wiley-VCH: Weinheim, 2001.
10. Bedard, T.C.; Moore, J.S. *J. Am. Chem. Soc.* **1995**, 117, 10662.

11. Kelly, T.R.; Tellitu, I.; Sestero, J.P. *Angew. Chem., Int. Ed.* **1997**, *36*, 1866.
12. Sauvage, J.-P.; Dietrich-Buchecker, V. *Molecular Catenanes, Rotaxanes and Knots*; Wiley-VCH: Weinheim, 1999.
13. Balzani, V.; Credi, A.; Raymo, F.M.; Stoddart, J.F. Artificial molecular machines. *Angew. Chem., Int. Ed.* **2000**, *39*, 3348.
14. Pease, A.R.; Jeppesen, J.O.; Stoddart, J.F.; Luo, Y.; Collier, C.P.; Heath, J.R. Switching devices based on interlocked molecules. *Acc. Chem. Res.* **2001**, *34*, 433.
15. Bermudez, V.; Capron, N.; Gase, T.; Gatti, F.G.; Kajzar, F.; Leigh, D.A.; Zerbetto, F.; Zhang, S. Influencing intramolecular motion with an alternating electric field. *Nature* **2000**, *406*, 608.
16. Brouwer, A.M.; Frochot, C.; Gatti, F.G.; Leigh, D.A.; Mollier, L.; Paolucci, F.; Rofia, S.; Wurlpel, G.W.H. Photoinduction of fast, reversible translational motion in a hydrogen-bonded molecular shuttle. *Science* **2001**, *291*, 2124.
17. Raymo, F.M.; Stoddart, J.F. Switchable Catenanes and Molecular Shuttles. In *Molecular Switches*; Feringa, B.L., Ed.; Wiley-VCH: Weinheim, 2001; 219.
18. Jimenez, M.C.; Dietrich-Buchecker, C.; Sauvage, J.-P. Towards synthetic molecular muscles: Contraction and stretching of a linear rotaxane dimer. *Angew. Chem., Int. Ed.* **2000**, *39*, 3284.
19. Feringa, B.L. Nanotechnology: In control of molecular motion. *Nature* **2002**, *408*, 151.
20. Chia, S.; Cao, J.; Stoddart, J.F.; Zink, J.I. Working supramolecular machines trapped in glass and mounted on a film surface. *Angew. Chem., Int. Ed.* **2001**, *40*, 2447.
21. Hugel, T.; Holland, N.B.; Cattani, A.; Moroder, L.; Seitz, M.; Gaub, H.E. Single-molecule optomechanical cycle. *Science* **2002**, *296*, 1103.
22. *Molecular Motors*; Schliwa, M., Ed.; Wiley-VCH: Weinheim, 2003.
23. *Photochromism, Molecules and Systems*; Dürr, H., Bouas-Laurent, H., Eds.; Elsevier: Amsterdam, 1990.
24. Lemieux, R.P.; Schuster, G.B. *J. Org. Chem.* **1993**, *58*, 100.
25. Zhang, Y.; Schuster, G.B. *J. Org. Chem.* **1995**, *60*, 7192.
26. Huck, N.P.M.; Jager, W.F.; de Lange, B.; Feringa, B.L. Dynamic control and amplification of molecular chirality by circular polarized light. *Science* **1996**, *273*, 1686.
27. Stevenson, K.L. *J. Am. Chem. Soc.* **1972**, *94*, 6652.
28. Hampp, N. Bacteriorhodopsin as a photochromic retinal protein for optical memories. *Chem. Rev.* **2000**, *100*, 1755.
29. Feringa, B.L.; van Delden, R.A.; ter Wiel, M.K.J. *Molecular Switches*; Feringa, B.L., Ed.; Wiley-VCH: Weinheim, 2001; 123–163. Chapter 5.
30. Feringa, B.L.; van Delden, R.A.; Koumura, N.; Geertsema, E.M. Chiroptical molecular switches. *Chem. Rev.* **2000**, *100*, 1789.
31. Feringa, B.L.; Jager, W.F.; de Lange, B.; Meijer, E.W. *J. Am. Chem. Soc.* **1991**, *113*, 5468.
32. Feringa, B.L.; Jager, W.F.; de Lange, B. Resolution of sterically overcrowded ethylenes; a remarkable correlation between bond lengths and racemization barriers. *Tetrahedron Lett.* **1992**, *33*, 2887.
33. Jager, W.F.; de Jong, J.C.; de Lange, B.; Huck, N.P.M.; Meetsma, A.; Feringa, B.L. *Angew. Chem., Int. Ed. Engl.* **1995**, *34*, 348.
34. Huck, N.P.M.; Feringa, B.L. *J. Chem. Soc., Chem. Commun.* **1995**, 1095.
35. van Delden, R.A.; van Gelder, M.B.; Huck, N.P.M.; Feringa, B.L. Controlling the color of cholesteric liquid-crystalline films by photoirradiation of a chiroptical molecular switch used as dopant. *Adv. Funct. Mater.* **2003**, *13*, 319.
36. van Delden, R.A.; Schoevaars, A.M.; Feringa, B.L. *Mol. Cryst. Liq. Cryst.* **2000**, *344*, 1.
37. Schoevaars, A.M.; Kruizinga, W.; Zijlstra, R.W.J.; Veldman, N.; Spek, A.L.; Feringa, B.L. *J. Org. Chem.* **1997**, *62*, 4943.
38. van Delden, R.A.; Huck, N.P.M.; Warman, J.M.; Meskers, S.C.J.; Dekkers, H.P.J.M.; Feringa, B.L. *J. Am. Chem. Soc.* **2003**, *125*, 15659.
39. Oosterling, M.L.C.M.; Schoevaars, A.M.; Haitema, H.J.; Feringa, B.L. *Isr. J. Chem.* **1996**, *36*, 341.
40. Dunmar, D.; Tonyiyama, K. *Handbook of Liquid Crystals Vol 1: Fundamentals*; Demus, D., Goodby, J., Gray, G.W., Spiess, H.-W., Vill, V., Eds.; Wiley-VCH: Weinheim, 1998; 215–239.
41. Meier, G. *Applications of Liquid Crystals*; Springer Verlag: Berlin, 1975; 1–21.
42. Chandrasekhar, S. *Liquid Crystals*; Cambridge University Press: Cambridge, 1977.
43. Feringa, B.L.; Huck, N.P.M.; van Doren, H.A. *J. Am. Chem. Soc.* **1995**, *117*, 9929.
44. Lub, J.; van der Veen, J.H.; van Echten, E. *Mol. Cryst. Liq. Cryst.* **1996**, *287*, 205.
45. Lub, J.; van der Veen, J.H.; ten Hoeve, W. *Recl. Trav. Chim. Pays-Bas* **1996**, *115*, 321.
46. Hikmet, R.A.M.; Lub, J.; Tol, A.J.W. *Macromolecules* **1995**, *28*, 3313.
47. Hikmet, R.A.M.; Zwerver, B.H.; Lub, J. *Macromolecules* **1994**, *27*, 6722.
48. Kelly, T.R.; de Silva, H.; Silva, R.A. Unidirectional

- rotary motion in a molecular system. *Nature* **1999**, *401*, 150.
49. Kelly, T.R.; Silva, R.A.; de Silva, H.; Jasmin, S.; Zhao, Y. A rationally designed prototype of a molecular motor. *J. Am. Chem. Soc.* **2000**, *122*, 6935.
 50. Kelly, T.R. Progress toward a rationally designed molecular motor. *Acc. Chem. Res.* **2001**, *34*, 514.
 51. Koumura, N.; Zijlstra, R.W.J.; van Delden, R.A.; Harada, N.; Feringa, B.L. Light-driven monodirectional molecular rotor. *Nature* **1999**, *401*, 152–155.
 52. Davis, A.P. Nanotechnology: Synthetic molecular motors. *Nature* **1999**, *401*, 120.
 53. Harada, N.; Saito, A.; Koumura, N.; Uda, H.; de Lange, B.; Jager, W.F.; Wynberg, H.; Feringa, B.L. *J. Am. Chem. Soc.* **1997**, *119*, 7241.
 54. Harada, N.; Saito, A.; Koumura, N.; Roe, D.C.; Jager, W.F.; Zijlstra, R.W.J.; de Lange, B.; Feringa, B.L. *J. Am. Chem. Soc.* **1997**, *119*, 7249.
 55. Harada, N.; Koumura, N.; Feringa, B.L. *J. Am. Chem. Soc.* **1997**, *119*, 7256.
 56. Zijlstra, R.W.J.; Jager, W.F.; de Lange, B.; van Duijnen, P.T.; Feringa, B.L.; Goto, H.; Saito, A.; Koumura, N.; Harada, N. Chemistry of unique chiral olefins. 4. Theoretical studies of the racemization mechanism of *trans*- and *cis*-1,1',2,2',3,3',4,4'-octahydro-4,4'-biphenanthrylidenes. *J. Org. Chem.* **1999**, *64*, 1667.
 57. van Delden, R.A.; ter Wiel, M.K.J.; Koumura, N.; Feringa, B.L. *Molecular Motors*; Schliwa, M., Ed.; Wiley-VCH: Weinheim, 2003; 559–577. Chapter 23.
 58. Feringa, B.L.; Koumura, N.; van Delden, R.A.; ter Wiel, M.K.J. *Appl. Phys., A* **2002**, *75*, 301.
 59. Feringa, B.L. In control of motion: From molecular switches to molecular motors. *Acc. Chem. Res.* **2001**, *34*, 504.
 60. Koumura, N.; Geertsema, E.M.; Meetsma, A.; Feringa, B.L. Light-driven molecular rotor: Unidirectional rotation controlled by a single stereogenic center. *J. Am. Chem. Soc.* **2000**, *122*, 12005.
 61. Koumura, N.; Geertsema, E.M.; van Gelder, M.B.; Meetsma, A.; Feringa, B.L. Second generation light-driven molecular motors. Unidirectional rotation controlled by a single stereogenic center with near-perfect photoequilibria and acceleration of the speed of rotation by structural modification. *J. Am. Chem. Soc.* **2002**, *124*, 5037.
 62. Geertsema, E.M.; Koumura, N.; ter Wiel, M.K.J.; Meetsma, A.; Feringa, B.L. In control of the speed of rotation in molecular motors. Unexpected retardation of rotary motion. *Chem. Commun.* **2002**, 2962.
 63. van Delden, R.A.; Koumura, N.; Schoevaars, A.M.; Meetsma, A.; Feringa, B.L. A donor acceptor substituted molecular motor: Unidirectional rotation driven by visible light. *Org. Biomol. Chem.* **2003**, *1*, 33.
 64. van Delden, R.A.; Koumura, N.; Harada, N.; Feringa, B.L. Supramolecular chemistry and self-assembly special feature: Unidirectional rotary motion in a liquid crystalline environment: Color tuning by a molecular motor. *Proc. Natl. Acad. Sci. U. S. A.* **2002**, *99*, 4945.

Molecular Wires

Dustin K. James
James M. Tour

Rice University, Houston, Texas, U.S.A.

M

INTRODUCTION

Electrical wiring is used all around us in today's world. Metallic wiring 1 cm in diameter facilitates the flow of electrons that power our household lighting, radios, televisions, and other appliances such as computers. Within those appliances and computers, wires 1 mm wide on printed circuit boards connect electronic devices such as resistors, rheostats, and logic chips. Inside those logic chips, wires tenths of a micrometer wide connect solid-state transistors, carved out of silicon, and allow them to act in concert with thousands of similar transistors to carry out computations. This last size reduction nearly reaches what is thought to be the limit of present semiconductor manufacturing technology. To enable further miniaturization, recent research has produced molecular-scale wires, ranging in length from 1 to 100 nm. In this chapter, we will review the state of the art in the synthesis and characterization of molecular wires and examine theoretical work concerning how they are thought to conduct electricity.

Molecular Electronics

The rapidly developing field of molecular electronics is one of the driving forces behind the interest in molecular wires.^[1-8] The limitations of the present "top-down" method of producing semiconductor-based devices have been the subject of debate and conjecture since the prediction of Moore^[9] that the number of components per integrated circuit would double every 18 months. It is thought that the inherent limitations of the present technology will lead to a dead end in the next few years. For instance, silicon's band structure disappears when silicon layers are just a few atoms thick. Lithographic techniques that are used to produce the circuitry on the silicon wafers are limited by the wavelengths at which they work. However, leaders in the semiconductor manufacturing world are still making advances that appear to be pushing "Moore's law" beyond its prior perceived limits. In the commercial technology of 2001, the copper wires in Intel's Pentium[®] 4 logic chip are 0.13 μm wide.^[10] Intel is developing technology to create logic

chips with wires 90 nm wide to be commercialized in 2003.^[11]

For comparison's sake, a typical molecular wire synthesized in our laboratory is calculated to be 0.3 nm wide and 2.5 nm long (Fig. 1).^[4] It would take 300 of these molecules, side by side, to span the 90-nm metal line in the most advanced logic chip in development. The small size of these molecules is emphasized when one considers that 500 g (about 1 mol) of this wire would contain 6×10^{23} molecules, or more molecules than the number of transistors ever made in the history of the world. This amount of material could be produced using relatively small 22-L laboratory reaction flasks. Changing the physical characteristics of this wire is as easy as changing the raw materials used to make it. The small size, the potential of synthesizing huge numbers in small reactors, and the ease of modification of the physical characteristics of the molecules are good reasons for pursuing molecular wire research. As an example of how far the technology has come, molecular electronics is discussed in the "Emerging Research Devices" section of the most recent International Technology Roadmap for Semiconductors^[12,13] and new molecular wires are a large part of the emerging technology. Molecular electronics was named the "breakthrough of the year" by Science^[14] for 2001.

Optoelectronics

Because of their chemical structure, some highly conjugated molecular wires have applications in optoelectronics.^[15-17] Poly(phenylene vinylene)s are being used as components in organic light-emitting diodes (OLEDs) in displays such as those used in cellular phones and other electronic devices. Various other polymeric materials and small molecules are also being used or are in development. These materials are applied in very thin layers about 100 nm thick, with the organic small molecules forming crystalline phases. This is quite different from the molecular electronics field, where it is envisioned that single molecules will eventually be used in circuits. However, much of the literature we will review addresses the optoelectronics applications of the molecular wires, and

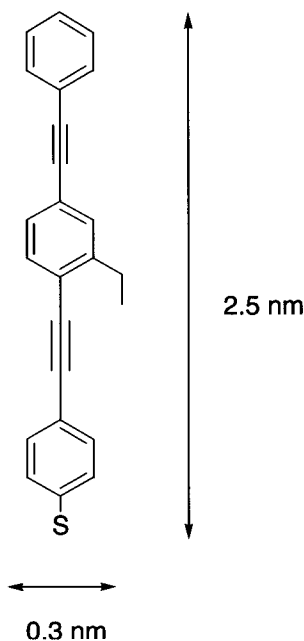


Fig. 1 The dimensions of a typical molecular wire are calculated to be 0.3 nm in width and 2.5 nm in length using molecular mechanics (Spartan) to determine the energy-minimized structure. (From Ref. [4].)

so we have included leading references for that area of research.

MOLECULAR WIRES

In this work, when we say “molecular wires,” we mean discrete molecules, not crystals or films. We accept the statement of Cotton et al.^[18] that linear chains of metal atoms that exist only in the solid state via the stacking of flat molecules, or through the formation of μ -bridged chains of octahedral molecules (such as NbCl_4) should not be called molecular wires. The extremely interesting inorganic crystalline nanowires being developed by Hu et al.,^[19] Chung et al.,^[20] Cui and Lieber,^[21] and Gudixsen et al.^[22] may eventually be used as wiring in molecular electronics-based circuitry, but the fact that they comprise crystalline phases and not discrete molecules precludes their inclusion in this review.

In our survey of the literature, we find two general types of molecular wires. The largest portion of the literature, including most of our work, covers organic molecular wires. A smaller portion of the literature covers organometallic molecular wires. We include what some may call inorganic molecular wires in the organometallic class because of the ease of classification and the small number of inorganic molecular wires in the literature.

Molecular wires are meant to conduct electricity between two points of a circuit. However, a majority of the molecular wires intended for molecular electronics have never been tested in an actual circuit. One reason for this is that it is difficult to do so because of their small size. Another reason is that there is not one generally accepted test-bed that is readily available to all researchers. Rather, there are several different test-beds in the literature,^[23–26] and the results from those molecular wires that have been tested are, in many cases, not comparable. These devices are difficult to make, yields are low, and obtaining reproducible results requires care and patience. Drawing conclusions about the activity of the classes of compounds, or building structure–activity relationships among several classes using the data generated can be a difficult exercise. However, because it has been shown that aromatic thiolates are much higher conducting than alkane thiolates^[27] when bonded to Au surfaces, much attention has focused on conjugated aromatic molecular wires (*vide infra*).

Organic Molecular Wires

Oligo(2,5-thiophene ethynylene)s

Our group has focused on the synthesis of organic molecular wires. One class of compounds synthesized are the oligo(2,5-thiophene ethynylene)s (OTEs), several examples of which are compounds 1–5, as shown in Fig. 2.^[28–31] This class of rigid-rod oligomeric molecular wires was made through an iterative divergent–convergent synthesis method that allowed the quick assembly of the products, doubling their length at each step. The longest molecular wire synthesized was 12.8 nm in length. Note that these wires have thioester groups at one or both ends. When deprotected in situ, the thiol groups enable the molecular wires to adhere to Au (or other metal) surfaces,^[27] thus serving as “alligator clips.” When large numbers of molecular wires bond to Au in a regular packed array, through this self-assembly process, the group of molecules is called a self-assembled monolayer (SAM). The bonding of the S atom to Au enables the flow of electricity from the Au metal Fermi levels through the S molecular orbitals to the molecular orbitals formed by the conjugated portion of the molecule (see “Theory and Measurement of Conduction” and references cited therein for a discussion of this phenomena). The ethynyl units in between the aromatic molecules are used to maintain a maximum overlap of the orbitals and to keep the molecules in a rodlike shape. The various side chains appended to the thiophene cores were intended to increase the organic solvent solubility of the wires. Unfunctionalized rigid rod oligomers of this length suffer from severe solubility problems.

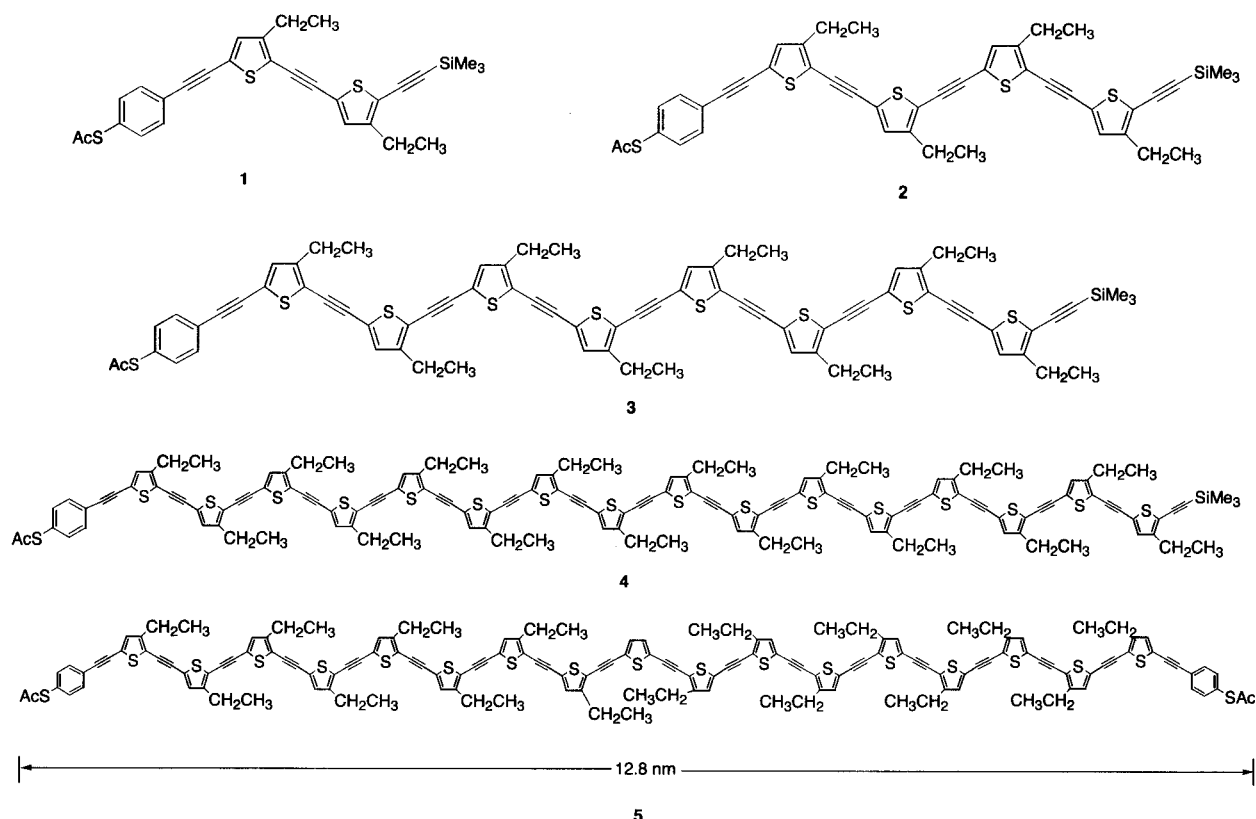


Fig. 2 Oligo(2,5-thiophene ethynylene) molecular wires **1–5** synthesized by the authors. (From Ref. [28].) Note that **1–4** have thioester termini on one end only, whereas molecular wire **5** has thioester termini on both ends. The length of **5** is 12.8 nm for its energy-minimized conformation.

Oligo(1,4-phenylene ethynylene)s

A second class of molecules that has been studied extensively in our laboratory^[32] and by others^[33,34] are the oligo(1,4-phenylene ethynylene)s (OPEs). The molecule shown in Fig. 1 is of this class, as are the molecules shown in Fig. 3. As with the OTEs, the OPEs can be rapidly synthesized using transition metal-catalyzed coupling reactions. In this case, the compounds were synthesized in both solution phase and on a polymer-based solid resin. Compounds **6–9** of Fig. 3 are intermediates that were produced by cleaving the products from the resin using iodomethane and by coupling the resulting aryl iodides to the alligator clip acetyl(4-ethynylthiophenol) using typical transition metal-catalyzed coupling reactions.^[32] The removal of the trimethylsilyl-protecting groups from the alkynes produced compounds **10–12** (from **6**, **7**, and **9**, respectively), and the coupling of the terminal alkyne in each case to acetyl(4-iodothiophenol) produced compounds **13** and **14** (from **10** and **12**, respectively). As in the OTEs, the C₁₂ side chains were used to impart organic solubility to the products. The use of longer side chains such as C₁₆ can result in side-chain interdigitation, leading to insolubility problems rather than increasing solubility.

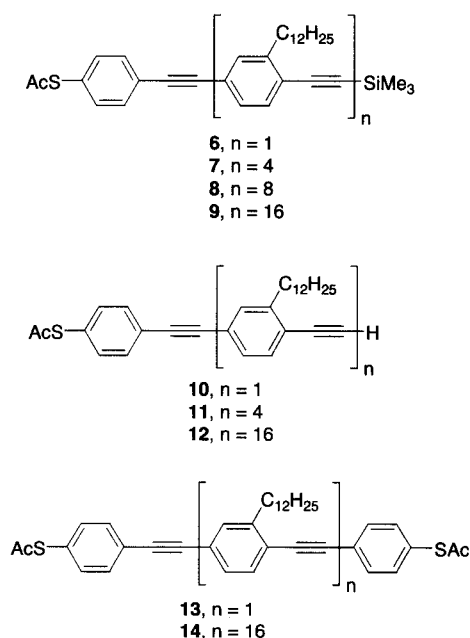


Fig. 3 A series of oligo(phenylene ethynylene)s (OPEs) was synthesized using a polymer support to increase the yields and to facilitate purification. (From Ref. [32].)

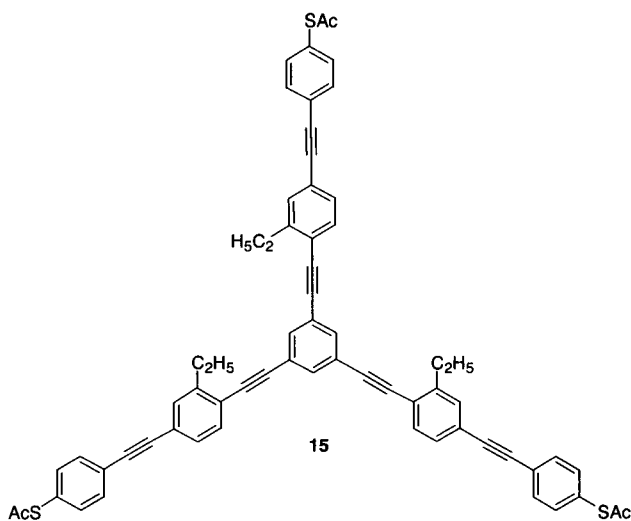


Fig. 4 A three-terminal molecular wire that is functionalized with an alligator clip at each terminus and contains side-chain ethyl groups for solubility. (From Ref. [35].)

In a series of syntheses of molecules in OPE subclasses, we have made products with more than two terminals and derivatives that are meant to test the necessity for a completely conjugated system.^[35] Fig. 4 shows a three-terminal molecular wire **15**. Note that all three terminals are functionalized with a protected thiol alligator clip, and that three of the aromatic nuclei have ethyl side chains to provide additional organic solvent solubility to the molecule. Fig. 5 shows a three-terminal molecular wire **16** that contains an interior methylene group as a possible barrier to current. Fig. 6 shows two four-terminal molecular wires **17** and **18**, each with one methylene group interior current barrier. Fig. 7 shows two four-terminal molecular wires **19** and **20**, each with two methylene group interior current barriers. The unfortunate circumstance is that, presently, no reliable system exists for testing these three-terminal and four-terminal molecular wires, so it is unknown whether or not the interior methylene group barriers are indeed resistant to current. However, the conductance of alkanethiolates (containing no aromatic conjugation whatsoever) on Au surfaces has been determined and has been shown to be less than that of conjugated systems (*vide infra*).

To further explore the organic functionality necessary for molecular wires to carry current, we have synthesized a group of two-terminal molecular wires **21–26**, shown in Fig. 8, which contains interior methylene or ethylene group barriers to electrical conduction, and which could be tested using presently known test-beds.^[35] Each of these was synthesized using relatively straightforward chemistry, a fact that illustrates our earlier claim that it is easy to explore molecular wire space by changing just one

or two aspects of the synthesis. We also synthesized a series of OPEs with different alligator clips to see what effect that variation would have on the conductance of the molecular wire,^[36] and we have developed combinatorial chemistry routes that will be capable of the synthesis of tens to hundreds of new molecular wires at one time.^[37]

When members of the OPE family were functionalized with groups other than aliphatic ones (see Fig. 9), we began to see switching behavior,^[24,38,39] although there is some question about whether the switching behavior results from molecular tilting, modulations in the metal/molecule contact,^[38] or from molecularly inherent features.^[24] In the nanopore,^[24] molecular wire **27** and amine-functionalized **29** had no activity, whereas nitro-functionalized **28** and **30** were both active switches; conversely, analysis by scanning tunneling microscopy (STM)^[38] indicated that all three of **27**, **28**, and **30** underwent conformational-based switching (**29** was not tested in the STM experiment) (see Refs. [1,2] for more information on switching). This underscores that fact that varying test-beds can afford widely different results.

Oligo(phenylene vinylene)s

A third class of compounds that has been studied in our laboratories as well as in others' are the oligo(phenylene vinylene)s (OPVs).^[40–46] As mentioned earlier, the ma-

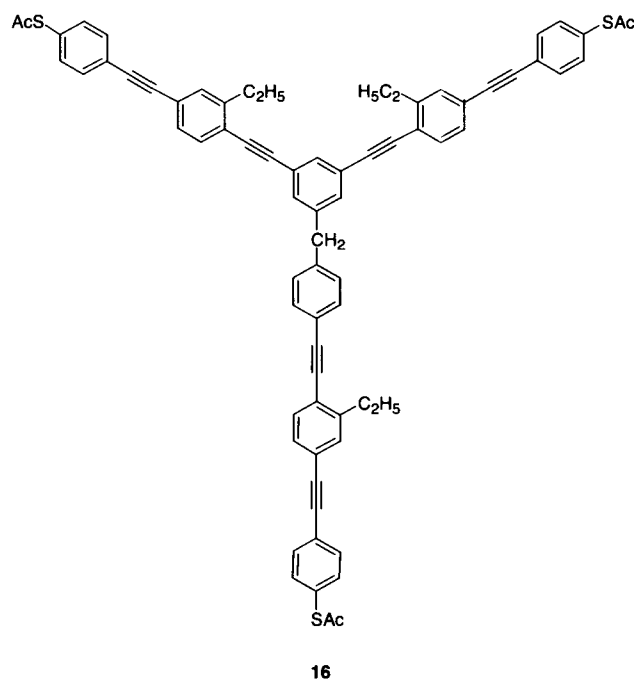


Fig. 5 A three-terminal molecular wire containing an interior methylene group meant to serve as a possible small gate-like barrier to electrical current. (From Ref. [35].)

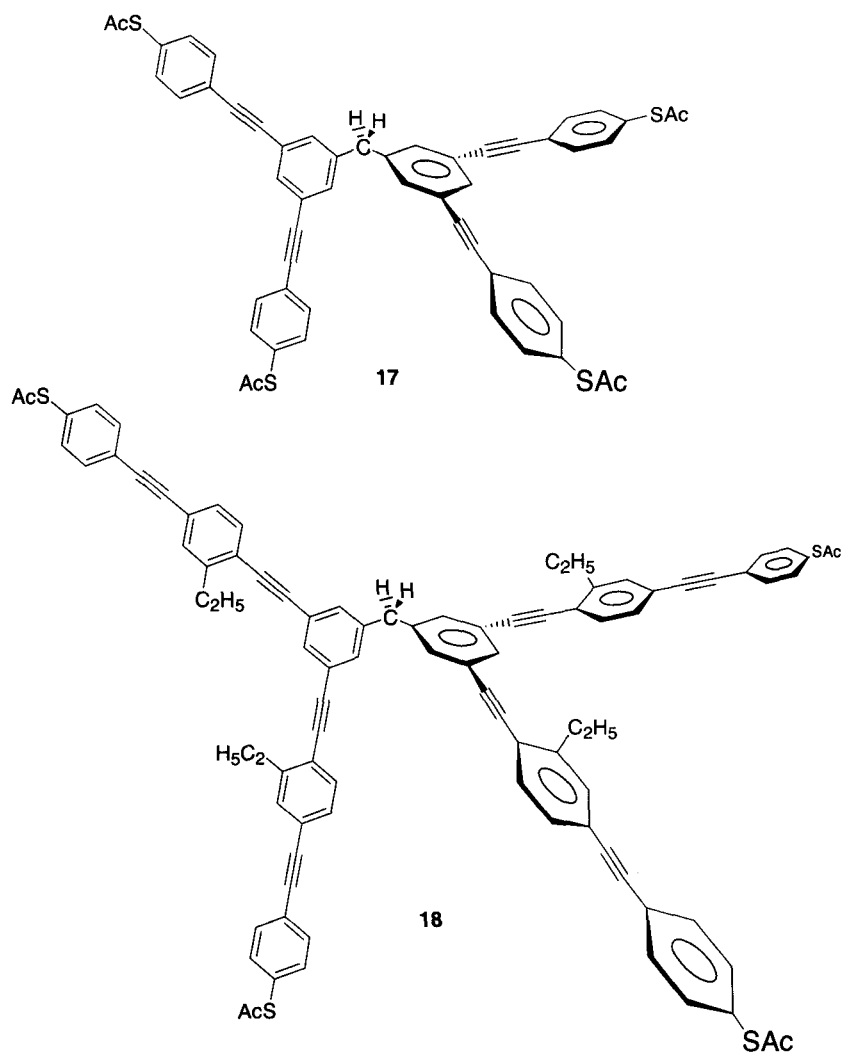


Fig. 6 Two four-terminal molecular wires **17** and **18**, each containing an interior methylene group intended to be a gate-like barrier to current. (From Ref. [35].)

majority of others' works on OPVs have been geared toward applications in the optical and OLED field.^[41-44,46] Our work produced molecular wires targeted for molecular electronics applications, and involved the synthesis of the three OPVs **31-33**, shown in Fig. 10. Note that **31** is unfunctionalized, containing only a protected thiol alli-

gator clip for later SAM formation. After formation of the SAM, Au or other metals would be deposited, under vacuum, for the formation of the top contact to complete the circuit through the π -framework. We functionalized **32** with a nitro group on the interior aromatic core to determine if **32** would then act as a switch. Compound

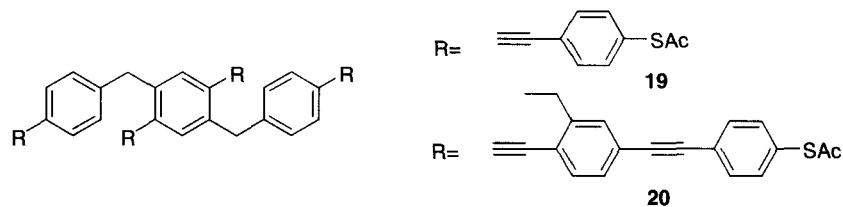


Fig. 7 Two four-terminal molecular wires **19** and **20**, with each terminal having a protected alligator clip and each molecular wire having two interior methylene group current barriers. (From Ref. [35].)

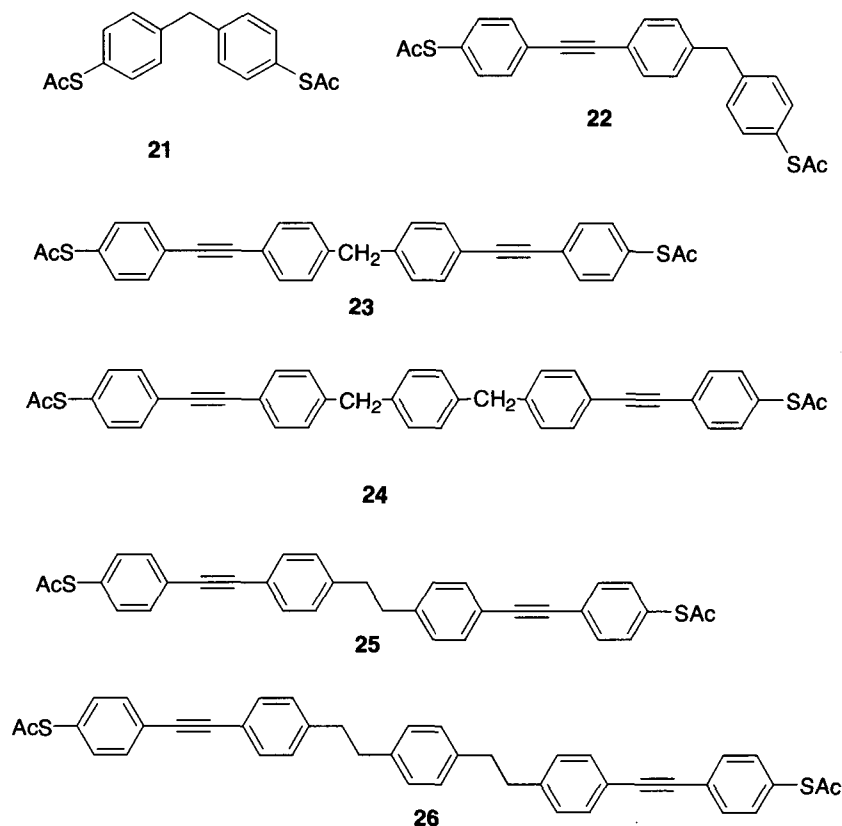


Fig. 8 Molecular wires **21–26**, each containing an interior methylene or ethylene group barrier to conduction. (From Ref. [35].)

32 is undergoing testing in a collaborator's laboratory. Finally, **33** was synthesized with both a nitro functional group and protected thiol groups at both ends so that it could span two Au contacts and form a circuit via a self-assembly process. This type of self-assembly process is

important in our nanocell research program,^[1] and is quite different from the approaches of others, who have not necessarily designed OPVs that are meant to connect two proximal probes, an interface to the present solid state-based technology.

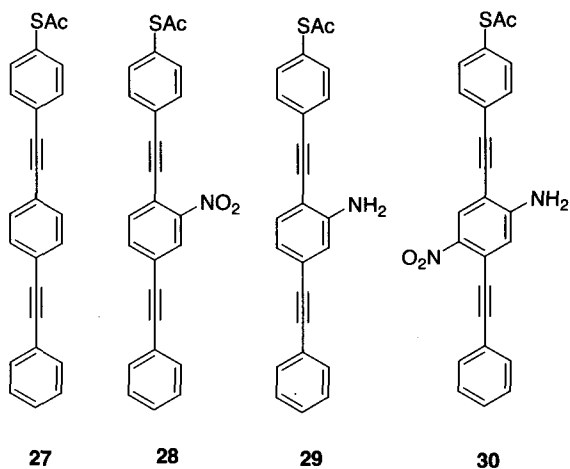


Fig. 9 Unfunctionalized OPE **27** and functionalized OPEs **28–30**. (From Refs. [24] and [38].)

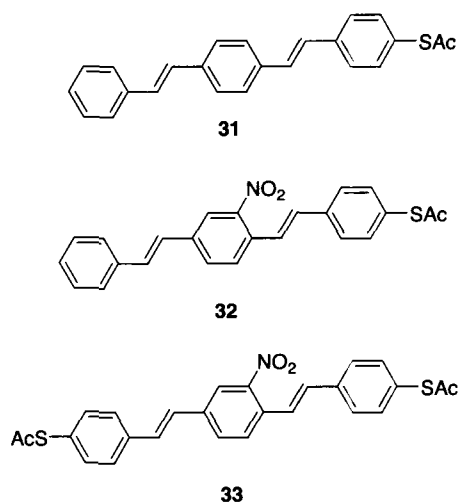


Fig. 10 Three OPVs **31–33** synthesized by the authors. (From Ref. [40].)

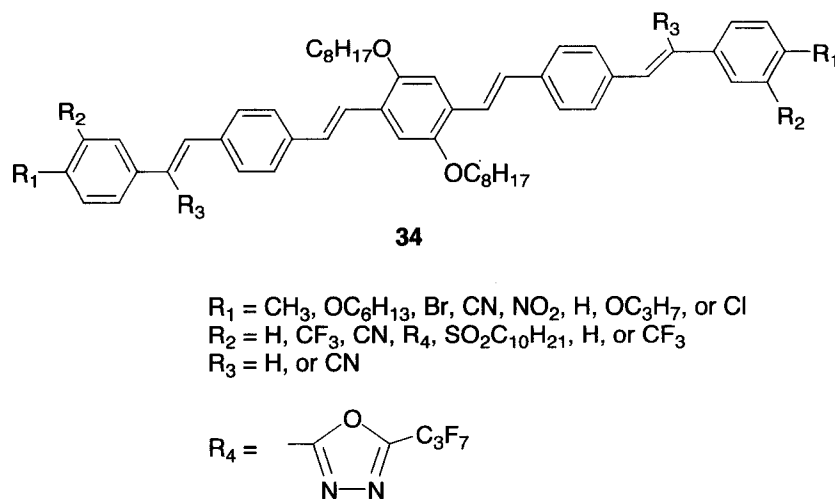


Fig. 11 A series of OPVs **34** synthesized by Detert and Sugiono^[46] to study the effect that variation of substituents R_1 , R_2 , R_3 , and R_4 had on the electronic spectra.

Detert and Sugiono^[46] synthesized a series of readily soluble OPVs shown in Fig. 11 to study their electronic spectra. They found that appending various electron-withdrawing groups to the terminal aromatic rings allowed the tuning of the electron affinity of the chromophore without significant changes in the spectra. When those same substituents were placed on the vinylene segments of the OPV molecules, strong bathochromic shifts were observed. Wong et al.^[42] investigated similar substituent effects. Syamakumari et al.^[41] and Gu et al.^[43] synthesized large assemblies of OPVs attached to

other molecules and measured their optical, electronic, and aggregation behaviors.

Sikes et al.^[45] and Davis et al.^[44] have used OPVs as core components of molecules (Fig. 12) synthesized to test electron tunneling and long distance electron transfer, respectively. Of the compounds Sikes et al. synthesized, **35** spanned the most distance, 3.3 nm. The OPVs were assembled on a Au electrode and the tethered ferrocene redox species at the other end of the OPV bridge was exposed to an aqueous electrolyte. They used laser-induced temperature jump techniques to measure the

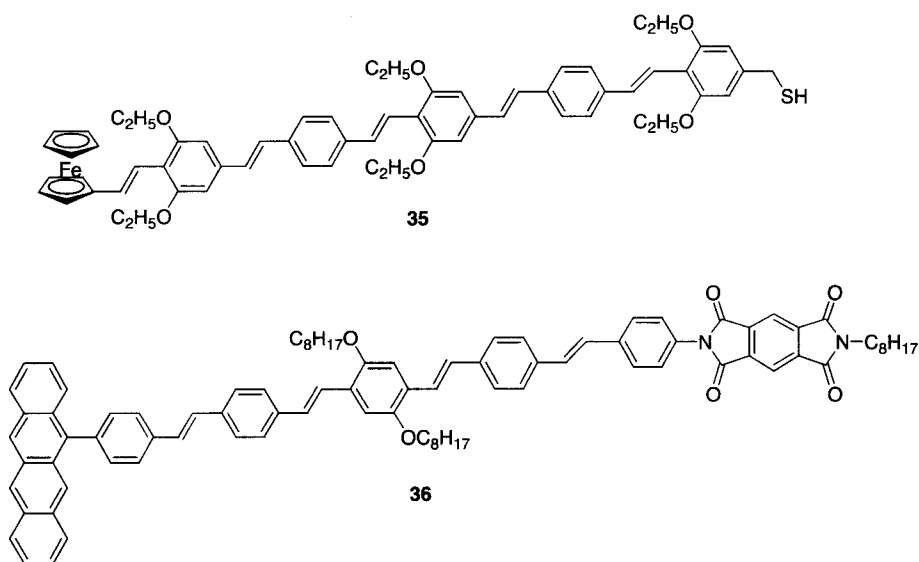
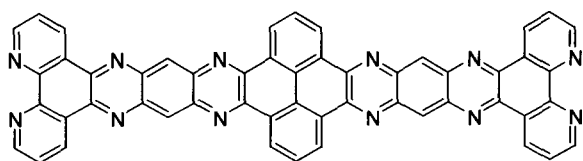
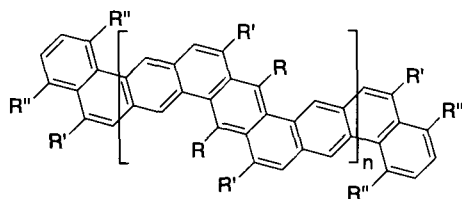


Fig. 12 Sikes et al.^[45] synthesized a series of OPVs including **35** to test electron tunneling whereas Davis et al.^[44] synthesized a series of OPVs including **36** to measure long distance electron transfer.



37



38

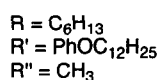


Fig. 13 Gourdon^[49] synthesized the aromatic ladder oligomers oligo(quinoxaline) **37** and the oligo(benzoanthracene) **38**.

rate constants of thermal interfacial electron transfer through the system and observed transfer through the OPV. They found that OPVs up to 2.8 nm in length were good conductors, with the transfer limited by structural reorganization.

In their study of a series of compounds including **36** (Fig. 12), the lengthiest molecule tested, Davis et al.^[44] found that electron transfer over long distances depends critically on the low-frequency torsional motions of the molecular wires (i.e., when the molecules twist and turn, their molecular orbitals do not line up in a fashion that favors fast electron transfer). But their tests were in solution rather than the more device-realistic molecule-surface attached patterns.

Aromatic ladder oligomers

Our group has synthesized a vast array of aromatic ladder polymers^[47,48] for use in conducting polymer and opto-electronic applications. However, we realized that for molecular electronic applications, the molecules we synthesized needed to have defined length and composition to be commercially useful as molecular wires.

As shown in Fig. 13, Gourdon^[49] have synthesized two classes of conjugated ladder oligomers that maintain

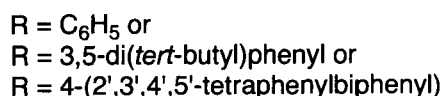
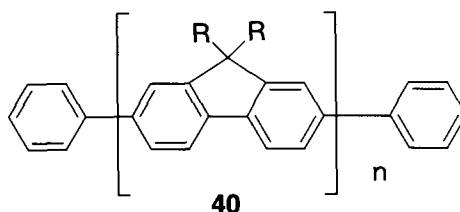
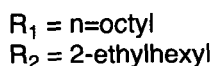
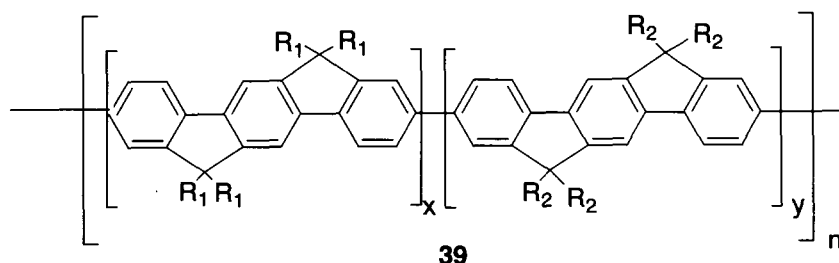


Fig. 14 One-dimensional polyphenylene polymers **39** and **40** that have been synthesized by Grimdale and Müllen.^[54]

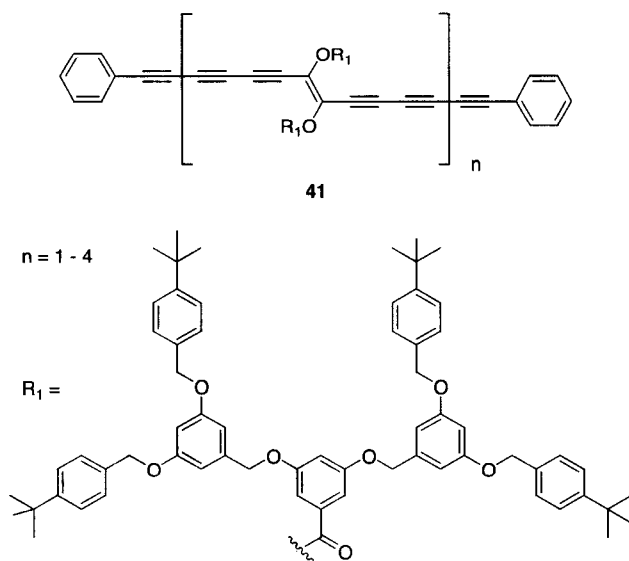


Fig. 15 Encapsulated oligo(pentaacetylene) molecular wire **41** synthesized by Schenning et al.^[55]

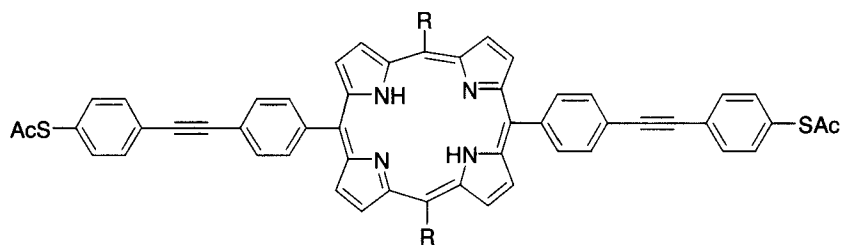
similar guidelines for molecular wires, including a defined length, rigidity, extended π -conjugation for good electron transfer, and good electronic coupling with metallic contacts. The oligo(quinoline) derivative **37** and oligo(benzoanthracene) molecular wire **38** were synthesized using standard condensation and coupling reactions. The oligo(quinoline) **37** has built-in alligator clips in the terminal 1,10-phenanthroline moieties. We have also synthesized molecular wires containing terminal pyridine and other nitrogen-containing functional groups.^[36] Calculations have supported their use as alligator clips.^[50] An iterative crossed divergent-convergent process that leads to rapid growth of the oligomers was developed to synthesize the oligo(benzoanthracene) **38**.

Oligophenylenes and polyphenylenes

The oligophenylene and polyphenylene classes of molecules, possessing a continuous overlap of molecular orbitals through extended conjugation without intervening groups such as alkynes or olefins, has been an active area of research for our group.^[51-53] Grimsdale and Müllen^[54] have synthesized a series of one-dimensional polyphenylenes including polyindeno[1,2-b]fluorene **39** and poly(9,9-diarylfuorene) **40**, shown in Fig. 14. The photoluminescence (PL) spectra of the series of polyindeno[1,2-b]fluorenes **39** all have maxima around 430 nm, making them possible candidates for OLED materials as well as molecular wires, although for applications in molecular electronics, one would normally want to be able to synthesize molecular wires with known lengths and constitutions because of concerns about homogeneity and materials handling. We have synthesized many oligophenylene derivatives^[35,36] and generally find that the torsional twisting caused by the steric hindrance between the hydrogen atoms at the *ortho* positions of adjacent phenyl rings leads to decreased orbital overlap, and possibly lower conductance.

Acetylene oligomers

Schenning et al.^[55] and Livingston et al.^[56] have synthesized the acetylene oligomer class of organic molecular wires. Their work included producing acetylene oligomers that are insulated via dendritic encapsulation (see Fig. 15). They found that the insulated product **41** underwent ready isomerization around the double bond, producing a mixture of *E* and *Z* isomers that made purification of the materials difficult. Oligomeric acetylenic molecular wires that have been encapsulated within zeolites and other mesoporous materials show high electrochemical charge uptake.^[57] Taylor et al.^[58] have



- 42**, R = C₆H₅
43, R = *p*-C₆H₄-CH₃
44, R = *p*-C₆H₄-Br
45, R = *p*-C₆H₄-I

Fig. 16 Porphyrins **42–45** synthesized by the authors. (From Ref. [35].) Zn, Cu, and Co metal atoms were inserted into **42**. Subsequent deprotection of the thiol acetates resulted in no metal ion loss.

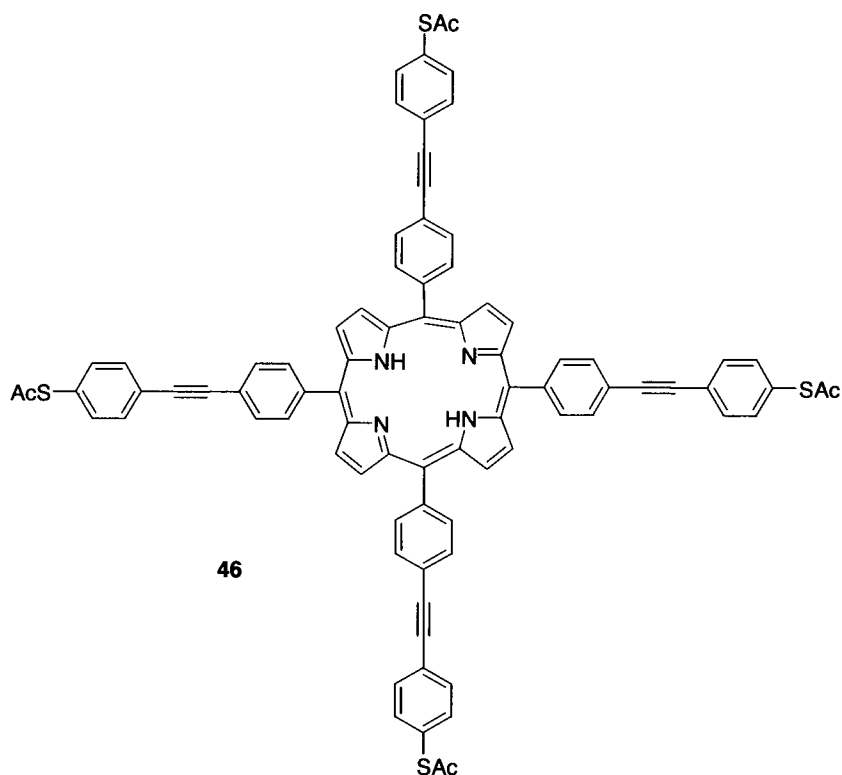


Fig. 17 A four terminal porphyrin-based molecular wire **46** synthesized by the authors. (From Ref. [35].)

published an approach to insulated molecular wires of the oligo(phenylene) class.

Carbon nanotubes

Carbon nanotubes have been attractive candidates for use as molecular wires.^[59,60] The so-called “cross-bar” approach to the development of a molecular electronics-based computer has, as one approach, the use of carbon nanotubes for the wiring between the molecular switches^[5,8] of the circuitry. It is unfortunately difficult to work with carbon nanotubes because of their insolubility in most organic solvents,^[61] and their tendency to form bundles of tubes that are difficult to separate. Several methods for the functionalization of the carbon nanotubes that may make it easier to handle the carbon nanotubes have been developed.^[62,63] However, the same functionalization techniques can also destroy the electrical properties of the molecules.^[2] Calculations by Seifert et al.^[64] indicate that sidewall fluorination of carbon nanotubes could produce products with a wide range of characteristics from insulating to metallic-like behavior. It is possible that nanowires^[19] will be used in the cross-bar computing devices instead of carbon nanotubes because of the easier synthesis and handling of the nanowires.

Organometallic Molecular Wires

We have synthesized molecules in the porphyrin class of molecular wires^[35] and have recently returned to this work.^[65] Fig. 16 shows four porphyrin derivatives made in our laboratories. Zn, Cu, and Co were all inserted into **42** using the corresponding hydrated metal acetates. Deprotection of the thiol acetates by NH_4OH resulted in no loss of metal, as indicated by subsequent nuclear magnetic resonance (NMR) analysis. Although being interesting compounds in and of themselves, **44** and **45** could also be intermediates in the synthesis of more complex molecular

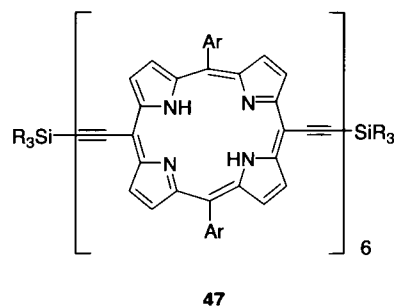


Fig. 18 The porphyrin hexamer **47** synthesized by Anderson,^[67] with six porphyrin units linked through dialkynes.

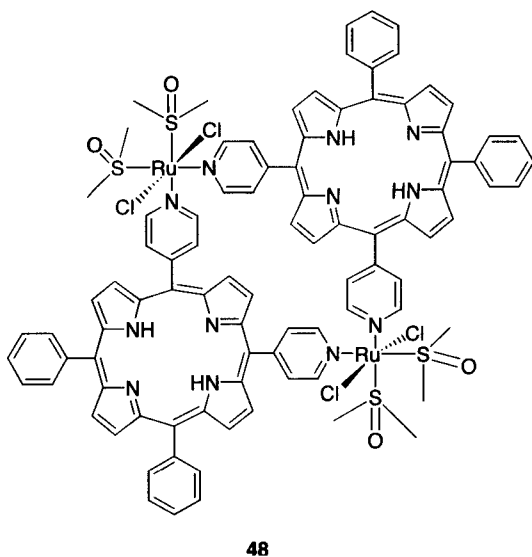


Fig. 19 The porphyrin metallacycle **48** synthesized by Iengo et al.^[68]

wires. A four-terminal porphyrin shown in Fig. 17 was also synthesized.

Ambroise et al.^[66] have published a large body of work concerning the synthesis and testing of molecular “pho-tonic” wires based on porphyrin molecules linked by diaryl ethyne units to light-absorbing dyes. The energy absorbed by the dyes is transmitted through the porphyrin-diaryl-ethyne wires to a free-base porphyrin transmission unit. The quantum efficiency was determined to be very high, from 81% to >99%.

Anderson^[67] has reviewed the synthesis and optoelec-tronic properties of conjugated porphyrin molecular wires.

As with the OPTs, OPEs, and oligomeric acetylenes, alkyne moieties have been used to link porphyrin units to make longer molecular wires, such as **47** in Fig. 18. The estimated length of **47** is 8.3 nm from Si atom to Si atom. Anderson’s work has shown that the electronic behavior of these types of systems can be attributed to strong interporphyrin conjugation in the ground state. This strong interaction is amplified in the excited states, and also in the oxidized and reduced forms of the porphyrin core.

Iengo et al.^[68] have used self-assembly techniques to synthesize large metallacycles of porphyrins. By synthe-sizing porphyrins having two peripheral pyridine appen-dages at either 90° or 180° to each other, and by adding the requisite ionic metallic component such as the RuCl₂ complex of dimethylsulfoxide (DMSO), supramolecular structures are produced. This self-assembly process pro-ceeds with two porphyrin and two RuCl₂ complexes form-ing (as one example) the molecule **48** shown in Fig. 19. The substitution of CO for DMSO in the RuCl₂ raw material forms a similar metallacycle with CO instead of DMSO as Ru ligands. By inserting Zn into the resulting porphyrin core and by exposing the mixture to 4,4’-bi-pyridine (which acts as a ligand for the Zn atoms at the porphyrin cores), a stacked complex was formed. The au-thors envisioned that such complexes, with their extended conjugation and metal centers, could harvest light energy and act as molecular wires.

The self-assembly of inorganic molecular wires in solution has been described by Kimizuku.^[69] However, it is unknown whether this process would produce products usable in constructing devices.

Pyridine ligands are common in organometallic mo-lecular wires,^[70–72] with a review recently appearing.^[73] For instance, Constable et al.^[70] synthesized the molecular wire **49** shown in Fig. 20. The [Ru(terpy)₂]²⁺ salts by

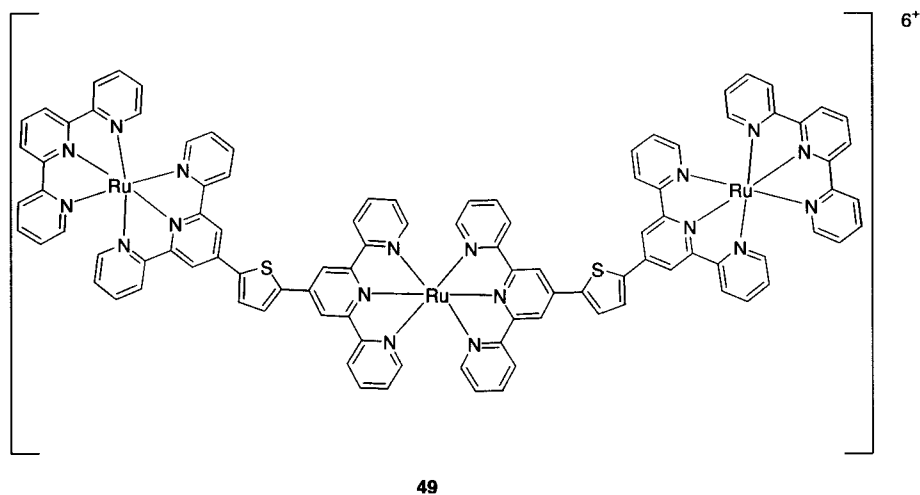


Fig. 20 The molecular wire **49** synthesized by Constable et al.^[70] that showed luminescence because of the presence of 2,5-thiophenediyl spacers.

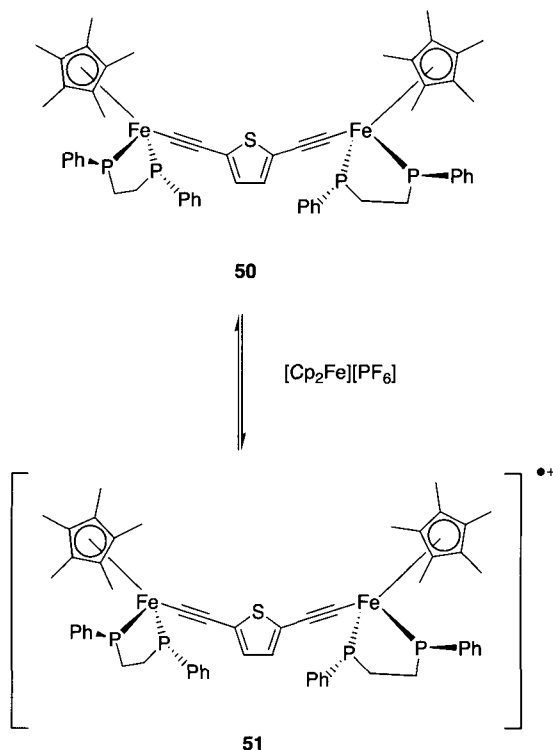


Fig. 21 A mixed-valence complex pair of molecular wires **50** and **51** as synthesized by Stang et al.^[74]

themselves are nonluminescent, whereas adding the 2,5-thiophenediyl spacers produces a molecular wire that is luminescent. Shiotsuka et al.^[71] made a Ru–Au–Ru triad by using a bis- σ -Au-acetylide to connect two Ru complexes. The resulting molecular wire showed an intense emission at 620 nm upon excitation at 360 nm, suggesting some energy transfer from the Au to the Ru site via the π -conjugation offered by the ethynyl units. Berry et al.^[72] synthesized a trinickel complex of the ligand di-2,2'-pyridylamide that had a deep blue color and showed metal–metal bonding interaction in the crystal structure.

An interesting mixed-valence molecular wire pair **50** and **51** synthesized by Stang et al.^[74] is shown in Fig. 21. As we have seen in many of the molecular wires, both the thiophenyl and the alkynyl units are present in this molecular wire.

THEORY AND MEASUREMENT OF CONDUCTION

Theory of Conduction in Molecular Wires

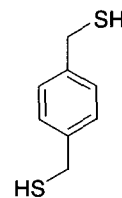
The difficulties in obtaining direct measurements of current in molecular wires have not deterred theoretical chemists from developing models of the conductive process. This has been a very fruitful area of research.

The editors of *Chemical Physics* recently devoted an entire issue to "Transport in Molecular Wires."^[75] We will briefly review the relevant literature here.

The molecular wire–electrode interface

One of the most important aspects of the application of molecular wires is developing a method for contacting the molecular wire with the electrode that will be carrying the current to the molecular wire. Several researchers have examined the theoretical aspects of this connection.^[76–79] Yaliraki et al.^[76] examined the bonding of 1,4-bis(thiomethyl)benzene (**52** in Fig. 22) to metal surfaces using Green's function and the extended Hückel Hamiltonian, and found that, except for the length of the surface bond, conductance through the molecule was not affected by the angle of the S-metal bond to the surface. They found that if Se substituted for S in the molecular wire, the conductance through the wire was larger (O substitution produced conductance of the same magnitude as S). They also found that Au made a better electrode than Ag. Note that a methylene node was between the terminal S atom and the aromatic benzene molecule, unlike other models where the S atom is directly bonded to the aromatic nucleus.

Using ab initio Hartree–Fock calculations, Johansson and Stafström^[77] found that for a benzenethiol bonded to Au, the conducting states of the organic molecular wire interacted directly with the electronic system of the Au substrate, forming an ohmic contact. Onipko et al.^[78] presented a detailed analytical approach to modeling the connection of the contacts to molecular wires that is applicable to a variety of functionalized systems. Seminario et al.^[79] used the Green function coupled with the B3PW91/LANL2DZ level of theory to calculate the behavior of S and isonitrile (–NC) alligator clip bonds to Ni, Cu, Pd, Ag, Pt, and Au. They found that the best metal for the metal–molecule interface was Pd, followed by Ni and Pt. Cu was intermediate whereas Au and Ag were worst. The S-based alligator clip was slightly better than the isonitrile alligator clip. The bond angle of the metal–alligator clip bond did make a difference in the



52

Fig. 22 The structure of 1,4-bis(thiomethyl)benzene **52**, the molecule studied by Yaliraki et al.^[76]

calculated conductance of the molecular wire, apparently because of various levels of overlap with the extended π system of the aromatic nucleus.

The theoretical use of molecular wires to transport spin-dependent information in an area of molecular electronics called "spintronics" has been studied by Emberly and Kirczenow.^[80] Spintronics utilizes the electron's spin degree of freedom as well the charge of the electron to store, transmit, and process data. Based on their calculations, spin valve behavior should be observable in SAMs formed from 1,4-benzenedithiol between two Ni wires (a "break-junction" test-bed).

Recall that in Figs. 5–8 were several examples of synthesized molecules that contained methylene or ethylene group spacers to break up the extended conjugation of the OPEs. Karzazi et al.^[81,82] have published quantum-chemical calculations that were used to describe qualitatively the mechanism leading to resonant tunneling diodes (RTDs) with negative differential resistance (NDR; a switching phenomena) in molecular wires with such spacers as part of their molecular structures. It was theorized that having an ethylene spacer versus a methylene spacer led to better NDR characteristics, with larger on-off ratios.

Conductance theory of molecular wires

A large body of work has been published regarding the theoretical aspects of conductance of molecular wires.^[83–96] We will highlight several aspects of the work here, and invite the reader to explore the cited literature for more information.

Seminario et al.^[83,85,88] and Derosa and Seminario^[87] have used density function theory and Green function theory to model the molecular orbitals of simple 1,4-benzenedithiol and more complex conjugated OPE systems. Calculations show that the highest occupied molecular orbitals (HOMOs) and the lowest unoccupied molecular orbitals (LUMOs) of a system can be localized (i.e., confined to certain atoms of the molecule) or delocalized (i.e., distributed over the entire molecular system depending on the charge). The localization of molecular orbitals will tend to prevent conductance through the molecule, whereas delocalization will tend to favor conductance. The addition of substituents and/or addition or subtraction of electrons from the system can change not only the shape (localization or delocalization) of the LUMOs and HOMOs but their energy levels. Changes in energy levels will affect whether the LUMOs and/or HOMOs overlap with the Fermi levels of the metal contact, also affecting the conduction through the molecules. The values of conductance for these systems with various charges determined by calculation agreed with experimentally derived data. The change in the LUMOs and HOMOs brought about by the injection of electrons into

the molecular system was the reason that they could act as switches, turning on or off to current.

Mujica et al.^[89] have examined the theoretical aspects of molecular rectification.^[97] Rectification occurs when the shape of the forward $I(V)$ curve is not the inverse of the reverse bias $I(V)$ curve when determining the conductance of a molecular wire as related to the applied voltage. The work of Mujica et al. suggested that the rectification is difficult to achieve because the finite voltages in the system cause the deformation of the structure, leading to effectively symmetrical voltage profiles for the forward and reverse biases. Interestingly, many have observed rectification because the two contacts between the ends of the molecular wires are different.

Avouris and Lang^[98] have done an interesting theoretical study on the effect of coadsorption of contaminants on the conductance of molecular wires. Avouris and Lang had observed experimentally that the conductance of semiconducting carbon nanotubes changed when metal/semiconducting nanotube/metal devices were exposed to oxygen. Density function theory was used to determine that adsorption of electropositive Li atoms or electronegative O atoms perturbed the molecular orbitals of biphenyl. This work has wide-ranging implications, as it has been thought that the development of molecular electronics-based computers might not require the ultra pure water (UPW) and expensive clean rooms that the semiconductor manufacturing industry needs to produce the high yields of working devices of the present commercial technology. However, purity of the chemicals and cleanliness of the tools and reaction chambers could be of paramount importance to the commercialization of the molecular wire technology. This calculation also has implications for experimental work, as contamination could easily introduce artifacts and false positives or negatives into laboratory testing.

Granger et al.^[99] have recently predicted that carbon nanotubes and other linear molecular conductors can support electronic states that are localized far from their surface. Hill and McLean^[100] have published experimental evidence for such states around an In nanowire. This work could have implications in answering the question: "Just how close does a molecular wire have to be to a connection to conduct electricity?" Carbon nanotubes or inorganic nanowires placed in near proximity may have electronic effects on circuitry and devices.

Measurement of Conductance in Molecular Wires

A large body of work has also been published concerning the measurement of conductance in molecular wires.^[101–112] We will touch on the highlights in this review.

Reed et al.^[23] and Chen and Reed^[103] have studied the conductance of both single molecules and of SAMs of molecules formed in a nanopore device. Stable and reproducible switching and memory effects were seen in the nanopore devices, with demonstrated NDR and charge storage with bit retention times of greater than 15 min at room temperature.

Patrone et al.^[105] compared the electronic coupling efficiency of S and Se alligator clips on Au surfaces and found Se to be the better coupling link. Rampi and Whitesides^[107] have developed a test-bed for measuring conductance in molecular wires using two metal electrodes sandwiching two SAMs, with the top metal electrode being Hg for convenience of formation. There are three different forms of this test-bed; the first comprises two Hg drops, each covered with the same SAM; the second test-bed comprises a Hg drop covered with a SAM interacting with a SAM formed on Ag; the third test-bed is similar to the first, only with redox-active molecules trapped between the two SAMs to do electrochemical measurements on them.

Avouris^[108] has carried out extensive conductance measurements on carbon nanotubes and has constructed electronic devices containing them, including carbon nanotube field effect transistors (CNTFETs). Nanotubes are known to have either metallic or semiconducting properties. One problem with single-walled nanotube (SWNT) bundles is separating the metallic tubes from the semiconducting tubes. Avouris has developed a process that removes the metallic nanotubes, leaving the semiconducting behind.

Kushmerick et al.^[110] have developed a test-bed device in which a SAM of the molecule of interest is formed on

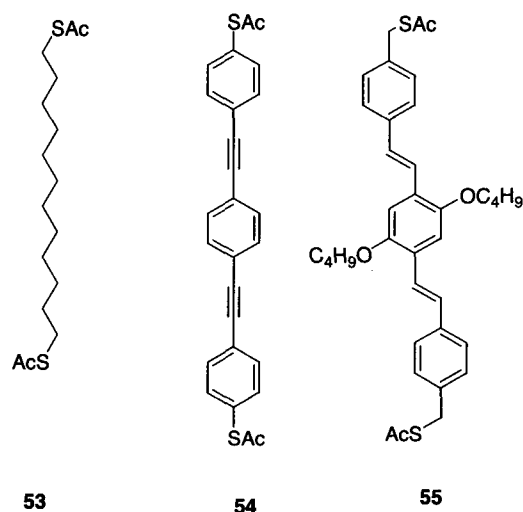
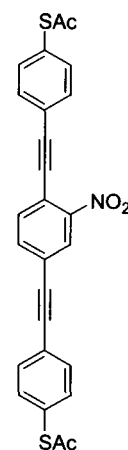


Fig. 23 The molecular wires **53–55** tested by Kushmerick et al.^[110] using a crossed-wire tunnel junction test-bed.



56

Fig. 24 The molecular wire **56**, the conductance of which was tested by Rawlett et al.^[111] using cAFM.

one of two 10- μm Au wires that are crossed, and brought into contact by the Lorentz force (i.e., DC current in one wire deflects it in a magnetic field). Using this device, $I(V)$ characteristics were measured for three molecules **53–55** shown in Fig. 23. Normalizing the conductance of the C_{12} alkanethiol **53** to 1, the conductance of the OPE molecular wire **54** was measured at 15 and the conductance of the OPV molecular wire **55** was measured at 46. Note that **55** has benzylic thioester moieties with methylene barrier groups to disrupt the molecular orbital overlap of the rest of the conjugated system. The researchers attribute the increased conductivity of the OPV molecule to both the increased coplanarity of the molecule (the alkynes in the OPEs allow the phenyl rings to be more freely rotating when compared to the vinylene group-linked OPVs, thus the population of OPE molecules existing in fully conjugated form is lower than the population of OPV molecules existing in fully conjugated form at the same temperature), and to the more regular periodicity of the conjugated molecular backbone of the OPV molecular wire. Compare the short 0.1218-nm alkyne linkage in the OPE molecular wire to the 0.1352-nm vinylene linkage of the OPV molecular wire and the 0.141 ± 0.001 nm periodicity of the π -conjugated molecular backbone.

Rawlett et al.^[111] used conducting atomic force microscopy (cAFM) to measure the conductance of two different molecules that had been inserted into the naturally occurring defect sites of a dodecanethiol SAM on Au. The molecular wires **54** (Fig. 23) and **56** (Fig. 24) constrained to be standing upright, parallel to the surface of the Au, because of the tight packing of the dodecanethiol SAM. Au nanoparticles were attached to the projecting deprotected thiol groups, and the nanoparticle was

contacted by a Au-coated AFM tip to measure the conductance through what are thought to be individual molecules based on evidence not discussed here. Reproducible NDR effects were seen only for molecular wire **56**, not for **54**, indicating that the functionalization of the wire with the $-\text{NO}_2$ group leads to the NDR effect.

Wang et al.^[112] have completed a systematic temperature-dependent study of the conductance of alkanethiolates in SAMs and have shown conclusively that direct tunneling is the dominant transport mechanism.

CONCLUSION

Based on the wealth of literature cited, fully conjugated completely organic aromatic molecular wires are the best candidates for introduction into new electronic devices as replacements for the Al or Cu wiring presently used in logic and memory devices. The OPE and OPV classes of molecular wires with S alligator clips have the highest conductances, both theoretical and measured. Recent data indicate that OPV molecular wires are better than OPE molecular wires. Many more questions remain to be answered, the most important of which is how these molecular wires will be integrated into processes to build the molecular electronic and optoelectronic devices of the future. Problems raised by such integration efforts will likely require several iterations in molecular wire research. As we have pointed out, the beauty of organic chemistry is that simple changes to the raw materials used in synthesizing the molecular wires can yield products with vastly different physical properties. The molecular wire(s) that eventually appears in commercial devices may bear no resemblance to those we have discussed. Thus research in this area can still yield much fruit.

ACKNOWLEDGMENT

We thank DARPA administered by the Office of Naval Research (ONR); the ONR Polymer Program; the U.S. Department of Commerce, National Institute of Standards and Technology; the Army Research Office; NASA; and the Air Force Office of Sponsored Research (AFOSR F49620-01-1-0364) for financial support of this work.

REFERENCES

1. Tour, J.M. *Molecular Electronics: Commercial Insights, Chemistry, Devices, Architecture, and Programming*; World Scientific Publishing: New Jersey, 2003, *in press*.

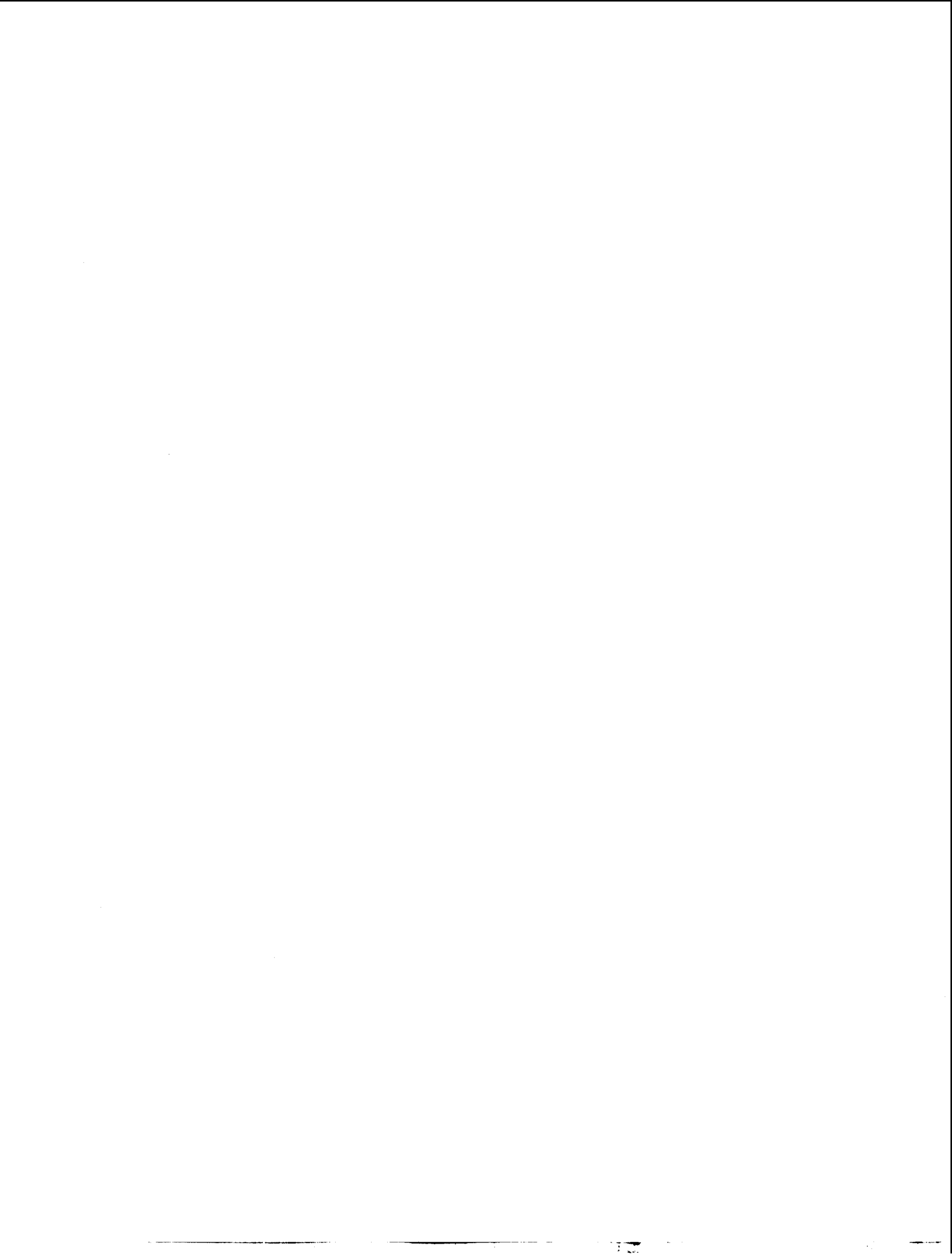
2. Tour, J.M.; James, D.K. Molecular Electronic Computing Architecture. In *Handbook of Nanoscience, Engineering, and Technology*; Goddard, W.A., III, Brenner, D.W., Lyshevski, S.E., Iafate, G.J., Eds.; CRC Press: Boca Raton, FL, 2002; 4-1-4-28.
3. Ward, M.D. Chemistry and molecular electronics: New molecules as wires, switches, and logic gates. *J. Chem. Educ.* **2001**, *78* (3), 321-328.
4. Tour, J.M. Molecular electronics. Synthesis and testing of components. *Acc. Chem. Res.* **2000**, *33* (11), 791-804.
5. Heath, J.R. Wires, switches, and wiring. A route toward a chemically assembled electronic nanocomputer. *Pure Appl. Chem.* **2000**, *72* (1-2), 11-20.
6. Reed, M.A.; Tour, J.M. Computing with molecules. *Sci. Am.* June **2000**, *2000*, 68-75.
7. Overton, R. Molecular electronics will change everything. *Wired* **2000**, *8* (7), 242-251.
8. Heath, J.R.; Kuekes, P.J.; Snider, G.S.; Williams, R.S. A defect-tolerant computer architecture: Opportunities for nanotechnology. *Science* June 12 **1998**, *280*, 1716-1721.
9. Moore, G.E. Cramming more components onto integrated circuits. *Electronics* **1965**, *38* (8). Available on the web: <http://www.intel.com/research/silicon/moorespaper.pdf> (accessed September 2002).
10. Intel press release: <http://www.intel.com/pressroom/archive/releases/20011017man.htm> (accessed September 2002).
11. Intel press release: <http://www.intel.com/pressroom/archive/releases/20020813tech.htm> (accessed September 2002).
12. International Technology Roadmap for Semiconductors web pages: <http://public.itrs.net/Files/2001ITRS/PIDS.pdf> (accessed September 2002).
13. Wang, K.L. Issues of nanoelectronics: A possible roadmap. *J. Nanosci. Nanotech.* **2002**, *2* (3/4), 235-266.
14. Service, R.F. Molecules get wired. *Science* December 21, **2001**, *294*, 2442-2443.
15. Patel, N.K.; Cinà, S.; Burroughes, J.H. High-efficiency organic light-emitting diodes. *IEEE J. Sel. Top. Quantum Electron.* **2002**, *8* (2), 346-361.
16. Popovic, Z.D.; Aziz, H. Reliability and degradation of small molecule-based organic light-emitting devices (OLEDs). *IEEE J. Sel. Top. Quantum Electron.* **2002**, *8* (2), 362-371.
17. Matthews, S.J. Organically grown. *Laser Focus World* **2001**, *37* (8), 169-170, 172, 175.
18. Cotton, F.A.; Daniels, L.M.; Murillo, C.M.; Wang,

- X. Getting the right answer to a key question concerning molecular wires. *Chem. Commun.* **1999**, 1999, 2461–2462.
19. Hu, J.; Odom, T.W.; Lieber, C.M. Chemistry and physics in one dimension: Synthesis and properties of nanowires and nanotubes. *Acc. Chem. Res.* **1999**, 32 (5), 435–445.
 20. Chung, S.-W.; Yu, J.-Y.; Heath, J.R. Silicon nanowire devices. *Appl. Phys. Lett.* **2000**, 76 (15), 2068–2070.
 21. Cui, Y.; Lieber, C.M. Functional nanoscale electronic devices assembled using silicon nanowire building blocks. *Science* February 2, **2001**, 291, 851–853.
 22. Gudixsen, M.S.; Wang, J.; Lieber, C.M. Synthetic control of the diameter and length of single crystal semiconductor nanowires. *J. Phys. Chem., B* **2001**, 105 (19), 4062–4064.
 23. Reed, M.A.; Zhou, C.; Muller, C.J.; Burgin, T.P.; Tour, J.M. Conductance of a molecular junction. *Science* October 10, **1997**, 278, 252–254.
 24. Chen, J.; Reed, M.A.; Rawlett, A.M.; Tour, J.M. Large on–off ratios and negative differential resistance in a molecular electronic device. *Science* November 19, **1999**, 286, 1550–1552.
 25. Ranganathan, S.; Steidel, I.; Anariba, F.; McCreery, R.L. Covalently bonded organic monolayers on a carbon substrate: A new paradigm for molecular electronics. *Nano Lett.* **2001**, 1 (9), 491–494.
 26. Fan, F.-R.F.; Yang, J.; Cai, L.; Price, D.W., Jr.; Dirk, S.M.; Kosynkin, D.V.; Yao, Y.; Rawlett, A.M.; Tour, J.M.; Bard, A.J. Charge transport through self-assembled monolayers of compounds of interest in molecular electronics. *J. Am. Chem. Soc.* **2002**, 124 (19), 5550–5556.
 27. Bumm, L.A.; Arnold, J.J.; Cygan, M.T.; Dunbar, T.D.; Burgin, T.P.; Jones, L., II; Allara, D.L.; Tour, J.M.; Weiss, P.S. Are single molecular wires conducting? *Science* **1996**, 271, 1705–1706.
 28. Pearson, D.L.; Tour, J.M. Rapid syntheses of oligo(2,5-thiophene ethynylene)s with thioester termini: Potential molecular scale wires with alligator clips. *J. Org. Chem.* **1997**, 62 (5), 1376–1387.
 29. Pearson, D.L.; Jones, L., II; Schumm, J.S.; Tour, J.M. Molecular scale electronics. Synthesis and testing. *Synth. Met.* **1997**, 84, 303–306.
 30. Pearson, D.L.; Jones, L., II; Schumm, J.S.; Tour, J.M. In *Synthesis of Molecular Scale Wires and Alligator Clips*, Proceedings of the NATO Advanced Research Workshop on Atomic and Molecular Wires, Les Houches, France, May 6–10, 1996; Joachim, C., Roth, S., Eds.; Kluwer Academic Publishers: Dordrecht, 1997; Vol. 341, 81–87. Applied Science Series E.
 31. Tour, J.M. Molecular wires for electronic applications. *Polym. News* **2000**, 25 (10), 329–336.
 32. Jones, L., II; Schumm, J.S.; Tour, J.M. Rapid solution and solid phase synthesis of oligo(1,4-phenylene ethynylene)s with thioester termini: Molecular scale wires with alligator clips. Derivation of iterative reaction efficiencies on a polymer support. *J. Org. Chem.* **1997**, 62 (5), 1388–1410.
 33. Collman, J.P.; Zhong, M.; Constanzo, S.; Sunderland, C.J.; Aukauloo, A.; Berg, K.; Zeng, L. A practical route to functionalized (phenylethynyl)phenylthiol acetates for self-assembled monolayer studies. *Synthesis* **2001**, 2001, (3), 367–369.
 34. Gu, T.; Nierengarten, J.-F. Synthesis of fullerene–oligophenyleneethynylene hybrids. *Tetrahedron Lett.* **2001**, 42, 3175–3178.
 35. Tour, J.M.; Rawlett, A.M.; Kozaki, M.; Yao, Y.; Jagessar, R.C.; Dirk, S.M.; Price, D.W.; Reed, M.A.; Zhou, C.-W.; Chen, J.; Wang, W.; Campbell, I. Synthesis and preliminary testing of molecular wires and devices. *Chem. Eur. J.* **2001**, 7 (23), 5118–5134.
 36. Dirk, S.M.; Price, D.W., Jr.; Chanteau, S.; Kosynkin, D.V.; Tour, J.M. Accoutrements of a molecular computer: Switches, memory components and alligator clips. *Tetrahedron* **2001**, 57, 5109–5121.
 37. Hwang, J.-J.; Tour, J.M. Combinatorial synthesis of oligo(phenylene ethynylene)s. *Tetrahedron* **2002**, 58, *in press*.
 38. Donhauser, Z.J.; Mantooth, B.A.; Kelly, K.F.; Bumm, L.A.; Monnell, J.D.; Stapleton, J.J.; Price, D.W., Jr.; Rawlett, A.M.; Allara, D.W.; Tour, J.M.; Weiss, P.S. Conductance switching in single molecules through conformational changes. *Science* June 22, **2001**, 292, 2303–2307.
 39. Chen, J.; Wang, W.; Klemic, J.; Reed, M.A.; Axelrod, B.W.; Kaschak, D.B.; Rawlett, A.M.; Price, D.W.; Dirk, S.M.; Tour, J.M.; Grubisha, D.S.; Bennett, D.W. Molecular wires, switches, and memories. *Ann. N.Y. Acad. Sci.* **2002**, 960, 69–99.
 40. Flatt, A.F.; Dirk, S.M.; Henderson, J.C.; Shen, D.E.; Su, J.; Reed, M.A.; Tour, J.M. Synthesis and testing of new end-functionalized oligomers for molecular electronics, submitted for review.
 41. Syamakumari, A.; Schenning, A.P.H.J.; Meijer, E.W. Synthesis, optical properties, and aggregation behavior of a triad system based on perylene and oligo(*p*-phenylene vinylene) units. *Chem. Eur. J.* **2002**, 8 (15), 3353–3361.
 42. Wong, M.S.; Li, Z.H.; Shek, M.F.; Samroc, M.; Samoc, A.; Luther-Davies, B. Synthesis and

- third-order nonlinear optical properties of end-functionalized oligo-phenylenevinylenes. *Chem. Mater.* **2002**, *14* (7), 2999–3004.
43. Gu, T.; Ceroni, P.; Marconi, G.; Armaroli, N.; Nierengarten, J.-F. Synthesis and electronic properties of covalent assemblies of oligophenylenevinylene units arising from a calyx[4]arene core. *J. Org. Chem.* **2001**, *66* (19), 6432–6439.
44. Davis, W.B.; Ratner, M.A.; Wasielewski, M.R. Conformational gating of long distance electron transfer through wire-like bridges in donor–bridge–acceptor molecules. *J. Am. Chem. Soc.* **2001**, *123* (32), 7877–7886.
45. Sikes, H.D.; Smalley, J.F.; Dudek, S.P.; Cook, A.R.; Newton, M.D.; Chidsey, C.E.; Feldberg, S.W. Rapid electron tunneling through oligophenylenevinylene bridges. *Science* February 23, **2001**, *291*, 1519–1523.
46. Detert, H.; Sugiono, E. Soluble oligo(phenylenevinylene)s with electron withdrawing substituents for the use in light emitting diodes. *Synth. Met.* **2000**, *115* (1–3), 89–92.
47. Zhang, C.Y.; Tour, J.M. Synthesis of highly functionalized pyrazines by ortho-lithiation reactions. Pyrazine ladder polymers. *J. Am. Chem. Soc.* **1999**, *121* (38), 8783–8790.
48. Yao, Y.; Tour, J.M. Synthesis of imine-bridged phenylenepyridine ladder polymers. Optical band gap widening through intramolecular charge transfer in planar polymers. *Macromolecules* **1999**, *32* (8), 2455–2461.
49. Gourdon, A. In *Synthesis of Conjugated Ladder Oligomers*, Proceedings of the NATO Advanced Research Workshop on Atomic and Molecular Wires, Les Houches, France, May 6–10, 1996; Joachim, C., Roth, S., Eds.; Kluwer Academic Publishers: Dordrecht, 1997; Vol. 341, 81–87. Applied Science Series E.
50. Billić, A.; Reimers, J.R.; Hush, N.S. Adsorption of pyridine on the gold(111) surface: Implications for “alligator clips” for molecular wires. *J. Phys. Chem., B* **2002**, *106* (26), 6740–6747.
51. Tour, J.M. Soluble oligo- and polyphenylenes. *Adv. Mater.* **1994**, *6* (3), 190–198.
52. Tour, J.M.; John, J.A. Synthesis of polyphenylenes via Bergman cyclization and polymerization of enediyne monomers. *Polym. Prepr. (Am. Chem. Soc., Div. Polym. Chem.)* **1993**, *34* (2), 372–373.
53. Tour, J.M.; Lamba, J.J.S. Synthesis of planar poly(*p*-phenylene) derivatives for maximization of extended π -conjugation. *J. Am. Chem. Soc.* **1993**, *115* (11), 4935–4936.
54. Grimsdale, A.C.; Müllen, K. 1-, 2-, and 3-Dimensional polyphenylenes—From molecular wires to functionalized nanoparticles. *Chem. Rec.* **2001**, *1*, 243–257.
55. Schenning, A.P.H.J.; Arndt, J.-D.; Ito, M.; Stoddart, A.; Schrieber, M.; Siemsen, P.; Martin, R.E.; Boudon, C.; Gisselbrecht, J.-P.; Gross, M.; Gramlich, V.; Diederich, F. Insulated molecular wires: Dendritic encapsulation of poly(triacetylene) oligomers, attempted dendritic stabilization of novel poly(pentaacetylene) oligomers, and an organometallic approach to dendritic rods. *Helv. Chim. Acta* **2001**, *84*, 296.
56. Livingston, R.C.; Cox, L.R.; Gramlich, V.; Diederich, F. 1,3-diethynylallenes: New modules for three-dimensional acetylenic scaffolding. *Angew. Chem., Int. Ed. Engl.* **2001**, *40* (12), 2334–2337.
57. Alvaro, M.; Ferrer, B.; García, M.; Lay, A.; Trinidad, F.; Valenciano, J. Remarkably high electrochemical charge uptake for modified electrodes of polyacetylene molecular wires encapsulated within zeolites and mesoporous MCM-41 aluminosilicate. *Chem. Phys. Lett.* April 26, **2002**, *356*, 577–584.
58. Taylor, P.N.; O’Connell, M.J.; McNeill, L.A.; Hall, M.J.; Aplin, R.T.; Anderson, H.L. Insulated molecular wires: Synthesis of conjugated polyrotaxanes by Suzuki coupling in water. *Angew. Chem., Int. Ed. Engl.* **2000**, *39* (19), 3456–3460.
59. Kong, J.; Franklin, N.R.; Zhou, C.; Chapline, M.C.; Peng, S.; Cho, K.; Dai, H. Nanotube molecular wires as chemical sensors. *Science* January 28, **2000**, *287*, 622–625.
60. Franklin, N.R.; Li, Y.; Chen, R.J.; Javey, A.; Dai, H. Patterned growth of single-walled carbon nanotubes on full 4-inch wafers. *Appl. Phys. Lett.* **2001**, *79* (21), 4571–4573.
61. Bahr, J.L.; Mickelson, E.T.; Bronikowski, M.J.; Smalley, R.E.; Tour, J.M. Dissolution of small diameter single-wall carbon nanotubes in organic solvents? *Chem. Commun.* **2001**, *2001*, 193–194.
62. Bahr, J.L.; Tour, J.M. Covalent chemistry of single-wall carbon nanotubes—A review. *J. Mater. Chem.* **2002**, *12*, 1952–1958.
63. Bahr, J.L.; Tour, J.M. Highly functionalized carbon nanotubes using in situ generated diazonium compounds. *Chem. Mater.* **2001**, *13*, 3823–3824.
64. Seifert, G.; Köhler, T.; Frauenheim, T. Molecular wires, solenoids, and capacitors by sidewall functionalization of carbon nanotubes. *Appl. Phys. Lett.* **2000**, *77* (9), 1313–1315.
65. Ciszek, J.; Tour, J.M. unpublished results.
66. Ambroise, A.; Kirmaier, C.; Wagner, R.W.; Loewe, R.S.; Bocian, D.F.; Holten, D.; Lindsey, J.S. Weakly coupled molecular photonic wires:

- Synthesis and excited state energy-transfer dynamics. *J. Org. Chem.* **2002**, *76* (11), 3811–3826. and references cited therein.
67. Anderson, H.L. Building molecular wires from the colours of life: Conjugated porphyrin oligomers. *Chem. Commun.* **1999**, *1999*, 2323–2330.
 68. Iengo, E.; Zangrando, E.; Minatel, R.; Alessio, E. Metallacycles of porphyrins as building blocks in the construction of higher order assemblies through axial coordination of bridging ligands: Solution- and solid-state characterization of molecular sandwiches and molecular wires. *J. Am. Chem. Soc.* **2002**, *124* (6), 1003–1013.
 69. Kimizuku, N. Toward self-assembling inorganic molecular wires. *Adv. Mater.* **2000**, *12* (19), 1461–1463.
 70. Constable, E.C.; Housecroft, C.E.; Schofield, E.R.; Encinas, S.; Armaroli, N.; Barigelletti, F.; Flamigni, L.; Figgemeier, E.; Vos, J.G. Luminescent molecular wires with 2,5-thiophenediyl spacers linking {Ru(terpy)₂} units. *Chem. Commun.* **1999**, *1999*, 869–870.
 71. Shiotsuka, M.; Yamamoto, Y.; Okuno, S.; Kitou, M.; Nozaki, K.; Onaka, S. Construction of molecular wires based on a gold (I) bis- σ -acetylide building block incorporated into ruthenium(II) polypyridyl complexes. *Chem. Commun.* **2002**, *2002*, 590–591.
 72. Berry, J.F.; Cotton, F.A.; Daniels, L.M.; Murillo, C.A. A trinickel dipyridylamido complex with metal–metal bonding interaction: Prelude to polynickel molecular wires and devices? *J. Am. Chem. Soc.* **2002**, *124* (13), 3212–3213.
 73. Barigelletti, F.; Flamigini, L. Photoactive molecular wires based on metal complexes. *Chem. Soc. Rev.* **2000**, *29* (1), 1–12.
 74. Stang, S.L.; Paul, F.; Lapinte, C. Molecular wires: Synthesis and properties of the new mixed-valence complex [Cp*(dppe)Fe–C \equiv C–X–C \equiv C–Fe(dppe)Cp*][PF₆] (X=2,5-C₄H₂S) and comparison of its properties with those of the related all-carbon-bridged complex (X=–C₄–). *Organometallics* **2000**, *19* (6), 1035–1043.
 75. Transport in Molecular Wires. In *Chem. Phys.*; Hänggi, P., Ratner, M., Yaliraki, S., Eds.; Elsevier Science B.V.: The Netherlands, 2002; Vol. 281, 111.
 76. Yaliraki, S.N.; Kemp, M.; Ratner, M.A. Conductance of molecular wires: Influence of molecule–electrode binding. *J. Am. Chem. Soc.* **1999**, *121* (14), 3428–3434.
 77. Johansson, Å.; Stafström, S. Interactions between molecular wires and a gold surface. *Chem. Phys. Lett.* May 26, **2000**, *322*, 301–306.
 78. Onipko, A.; Klymenko, Y.; Malysheva, L. Conductance of molecular wires: Analytical modeling of connection to leads. *Phys. Rev., B* **2000**, *62* (15), 10480–10493.
 79. Seminario, J.M.; De La Cruz, C.E.; Derosa, P.A. A theoretical analysis of metal–molecule contacts. *J. Am. Chem. Soc.* **2001**, *123* (23), 5616–5617.
 80. Emberly, E.G.; Kirczenow, G. Molecular spintronics: Spin-dependent electron transport in molecular wires. *Chem. Phys.* **2002**, *281*, 311–324.
 81. Karzazi, Y.; Cornil, J.; Brédas, J.L. Negative differential resistance behavior in conjugated molecular wires incorporating spacers: A quantum-chemical description. *J. Am. Chem. Soc.* **2001**, *123* (41), 10076–10084.
 82. Karzazi, Y.; Cornil, J.; Brédas, J.L. Resonant tunneling diodes based on molecular wires incorporating saturated spacers: A quantum-chemical study. *Nanotechnology* **2002**, *13*, 336–340.
 83. Seminario, J.M.; Zacarias, A.G.; Tour, J.M. Molecular current–voltage characteristics. *J. Phys. Chem., A* **1999**, *103* (39), 7883–7887.
 84. Emberly, E.; Kirczenow, G. Electrical conductance of molecular wires. *Nanotechnology* **1999**, *10*, 285–289.
 85. Seminario, J.M.; Zacarias, A.G.; Tour, J.M. Theoretical study of a molecular resonant tunneling diode. *J. Am. Chem. Soc.* **2000**, *122* (13), 3015–3020.
 86. Emberly, E.G.; Kirczenow, G. Current-driven conformational changes, charging, and negative differential resistance in molecular wires. *Phys. Rev., B* **2001**, *64*, 125318-1–125318-5.
 87. Derosa, P.A.; Seminario, J.M. Electron transport through single molecules: Scattering treatment using density functional and green function theories. *J. Phys. Chem., B* **2001**, *105* (2), 471–481.
 88. Seminario, J.M.; Zacarias, A.G.; Derosa, P.A. Theoretical analysis of complimentary molecular memory devices. *J. Phys. Chem. A* **2001**, *105* (5), 791–795.
 89. Mujica, V.; Ratner, M.A.; Nitzan, A. Molecular rectification: Why is it so rare? *Chem. Phys.* **2002**, *281*, 147–150.
 90. Xue, Y.; Datta, S.; Ratner, M.A. First-principles based matrix Green's function approach to molecular electronic devices: General formalism. *Chem. Phys.* **2002**, *281*, 151–170.
 91. Lehmann, J.; Ingold, G.-L.; Hänggi, P. Incoherent charge transport through molecular wires: Interplay of Coulomb interaction and wire population. *Chem. Phys.* **2002**, *281*, 199–209.
 92. Petrov, E.G.; May, V.; Hänggi, P. Controlling

- electron transfer processes through short molecular wires. *Chem. Phys.* **2002**, *281*, 211–224.
93. Ness, H.; Fisher, A.J. Coherent electron injection and transport in molecular wires: Inelastic tunneling and electron–phonon interactions. *Chem. Phys.* **2002**, *281*, 279–292.
94. Nitzan, A.; Galperin, M.; Ingold, G.-L.; Grabert, H. On the electrostatic potential profile in biased molecular wires. *ArXiv Phys.* July 31, **2002**, *1*, 1–6. 0207124.
95. Sendt, K.; Johnston, L.A.; Hough, W.A.; Crossley, M.J.; Hush, N.S.; Reimers, J.R. Switchable electronic coupling in model oligoporphyrin molecular wires examined through the measurement and assignment of electronic absorption spectra. *J. Am. Chem. Soc.* **2002**, *124* (31), 9299–9309.
96. Pourtois, G.; Beljonne, D.; Cornil, J.; Ratner, M.A.; Brédas, J.L. Photoinduced electron-transfer processes along molecular wires based on phenylenevinylene oligomers: A quantum-chemical insight. *J. Am. Chem. Soc.* **2002**, *124* (16), 4436–4447.
97. Zhou, C.; Deshpande, M.R.; Reed, M.A.; Jones, L., II; Tour, J.M. Nanoscale metal/self-assembled monolayer/metal heterostructures. *Appl. Phys. Lett.* **1997**, *71* (5), 611–613.
98. Avouris, P.; Lang, N.D. Effects of coadsorption on the conductance of molecular wires. *Nano Lett.* **2002**. 10.1021/nl020202o.
99. Granger, B.E.; Král, P.; Sadeghpour, H.R.; Shapiro, M. Highly extended image states around nanotubes. *Phys. Rev. Lett.* **2002**, *89* (13), 135506-1–135506-4.
100. Hill, I.G.; McLean, A.B. Strongly anisotropic band dispersion of an image state located above metallic nanowires. *Phys. Rev. Lett.* **1999**, *82* (10), 2155–2158.
101. Lehmann, J.; Kohler, S.; Hänggi, P.; Nitzan, A. Molecular wires acting as coherent quantum ratchets. *Phys. Rev. Lett.* **2002**, *88* (22), 228305-1–228305-4.
102. Weber, H.B.; Reichert, J.; Weigend, F.; Ochs, R.; Beckmann, D.; Mayer, M.; Ahlrichs, R.; Löhneysen, H.V. Electronic transport through single conjugated molecules. *Chem. Phys.* **2002**, *281*, 113–125.
103. Chen, J.; Reed, M.A. Electronic transport of molecular systems. *Chem. Phys.* **2002**, *281*, 127–145.
104. Agraït, N.; Untiedt, C.; Rubio-Bollinger, G.; Vieira, S. Electron transport and phonons in atomic wires. *Chem. Phys.* **2002**, *281*, 231–234.
105. Patrone, L.; Palacin, S.; Bourgoin, J.P.; Laboute, J.; Zambelli, T.; Gauthier, S. Direct comparison of the electronic coupling efficiency of sulfur and selenium anchoring groups for molecules adsorbed onto gold electrodes. *Chem. Phys.* **2002**, *281*, 325–332.
106. Davis, W.B.; Ratner, M.A.; Wasielewski, M.R. Dependence of electron transfer dynamics in wire-like bridge molecules on donor–bridge energetics and electronic interactions. *Chem. Phys.* **2002**, *281*, 333–346.
107. Rampi, M.A.; Whitesides, G.M. A versatile experimental approach for understanding electron transport through organic materials. *Chem. Phys.* **2002**, *281*, 373–391.
108. Avouris, P. Carbon nanotube electronics. *Chem. Phys.* **2002**, *281*, 429–445.
109. Cuniberti, G.; Fagas, G.; Richter, K. Fingerprints of mesoscopic leads in the conductance of a molecular wire. *Chem. Phys.* **2002**, *281*, 465–476.
110. Kushmerick, J.G.; Holt, D.B.; Pollack, S.K.; Ratner, M.A.; Yang, J.C.; Schull, T.L.; Naciri, J.; Moore, M.H.; Shashidhar, R. Effect of bond-length alternation in molecular wires. *J. Am. Chem. Soc.* **2002**, *124* (36), 10654–10655.
111. Rawlett, A.M.; Hopson, T.J.; Nagahara, L.A.; Tsui, R.K.; Ramachandran, G.K.; Lindsay, S.M. Electrical measurements of a dithiolated electronic molecule via conducting atomic force microscopy. *Appl. Phys. Lett.* **2002**, *81* (16), 3043–3045.
112. Wang, W.; Lee, T.; Reed, M.A. Characterization of electron tunneling in self-assembled alkanethiol monolayer devices **2002**. Submitted for publication.



Moore's Law: Performance and Power Dissipation

Laszlo B. Kish

Texas A&M University, College Station, Texas, U.S.A.

INTRODUCTION

Moore's law predicts that the number of transistors in a chip will grow exponentially in time. Exponents giving the best fit of various chip families suggest an 18-month transistor number doubling time. If Moore's law of miniaturization will be followed below the size of 40 nm, physics will impose fundamental and practical limits of performance because of shrinking noise margin, increasing and quickening noise, and increasing power dissipation. It is important to locate the fundamental aspects of the problem, to explore relevant practical problems and possible solutions, and to investigate this situation not only in microelectronics, such as complementary metal oxide semiconductor (CMOS), but also in single-electron transistor (SET)-based nanoelectronics and even in quantum informatics applications. Recent studies show that quantum computers are not satisfactory tools to solve these problems of *general-purpose* data handling, and that the fundamental limits governing classical (CMOS) computers allow a much better performance than possible quantum computers.

FUTURE OUTLOOK

We all have been enjoying the fast growth of speed and memory size of computers during the last decades. Recently, the emerging fields of quantum computing and nanoelectronics have suggested that the future will be even more brilliant.

However, as soon as we confront physical laws and reality with expectations, the future becomes more realistic. In this article, we briefly outline some of the key issues.

GENERAL CONSIDERATIONS

Thermal noise is an omnipresent small-voltage fluctuation on resistors. It has been thought that thermal noise will never be an issue in digital electronics. This view has been reevaluated and changed recently by Kish.^[1] On a parallel resistor-capacitor (RC) unit, the effective thermal noise voltage U_n is given as:

$$U_n = \sqrt{kT/C} \quad (1)$$

and the bandwidth f_c of this noise is:

$$f_c = \frac{1}{2\pi RC} \quad (2)$$

Gaussian noise processes, such as thermal noise, can cross large amplitude levels, provided that sufficiently long time is available. In a logic circuitry, noise amplitudes reaching beyond the noise margin U_{th} cause false bit flips that can result in bit errors. For a single band-limited noise process, the mean frequency $\nu(U_{th})$ of bit errors can be obtained from the Rice formula:^[1]

$$\nu(U_{th}) = \frac{2}{\sqrt{3}} \exp\left(\frac{-U_{th}^2}{2U_n^2}\right) f_c \quad (3)$$

where U_n is the effective noise voltage and f_c is the bandwidth.

So, what happens during miniaturization? In CMOS technology, the resistors are two-dimensional conductors; thus the resistance stays (roughly) constant. Therefore the supply voltage has to be decreased to keep the electrical field and dissipation at acceptable levels. The capacitances decrease. Together, these effects yield the following trends:

- 1) Shrinking noise margin (because U_{th} is only a fraction of the supply voltage)
- 2) Growing noise (because of Eq. 1)
- 3) Growing bandwidth (quickening of the noise; Eq. 2).

All these phenomena (1, 2, and 3) act toward radically increasing the frequency of bit errors via Eq. 3. To have a feeling of the nature of this problem, on Fig. 1, the bit error frequency vs. the noise margin normalized to the noise voltage is shown for different bandwidths (clock frequency) and different numbers of transistor. The practical limit of usability is a certain U_{th}/U_n ratio when the bit error rate is around 1 error/year. Even a 10% decrease of the U_{th}/U_n ratio compared with its critical value yields an error rate increase to 10^5 when we consider all transistors in a modern PC (3×10^9 – 10^{10} transistors).

Utilizing these results and a prediction of the evolution of capacitance and noise margin using present trends,

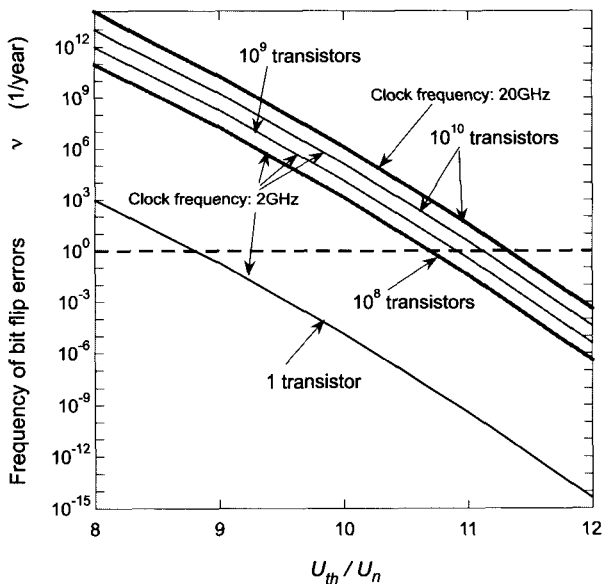


Fig. 1 Bit errors vs. the ratio of noise margin and effective noise voltage. (From Ref. [1].) (View this art in color at www.dekker.com.)

recently, a prediction of the end of Moore's law was reported by Kish^[1] (Fig. 2).

The shrinking noise margin (logic threshold voltage) and the increasing noise margin required by the increasing and quickening noise pose conflicting requirements, which would stop miniaturization in 6–8 years if the trends of the last year continue.

In the rest of this article, we outline the objectives that need further analysis and give some initiatives for extended research in the future.

REFINEMENTS OF PREDICTIONS FOR CMOS TECHNOLOGY

It has been pointed out in Ref. [1] that the prediction was based on strong approximations to keep generality and because of lack of information about certain device parameters. Since Ref. [1] was published, new information from microprocessor makers about some previously unknown parameters has emerged and some new efforts have been made to reduce the supply voltage with a rate less than previously supposed. However, these efforts are controversial because many large-scale users (e.g., in aviation electronics)^[2] would like to increase the rate of supply voltage reduction to improve device failure rate, which has been steadily growing because of high electric fields in chips.

Therefore theoretical efforts have been made on refining the prediction for the bit error problem because of thermal noise. The refined model takes into the account the following aspects:

- Further noise margin decrease because of the opening threshold voltages of the P-type and N-type MOSFET transistors
- Somewhat reduced noise because of parallel gate circuits
- Various supply voltage reduction strategies (predictions are controversial)
- The fact that the internal supply voltage and noise margin of microprocessors in 2002 were already less than supposed in Ref. [1].

Interestingly, preliminary investigations indicate that the size range, where the problems begin, remains the same because the different corrections act in different directions and the effects compensate for each other. Thus the conclusions obtained in the context of Fig. 2 remain the same.

THE CASE OF SINGLE-ELECTRON TRANSISTORS

The next question is the bit error situation of microprocessors based on SETs.^[3] SETs work with tunneling,

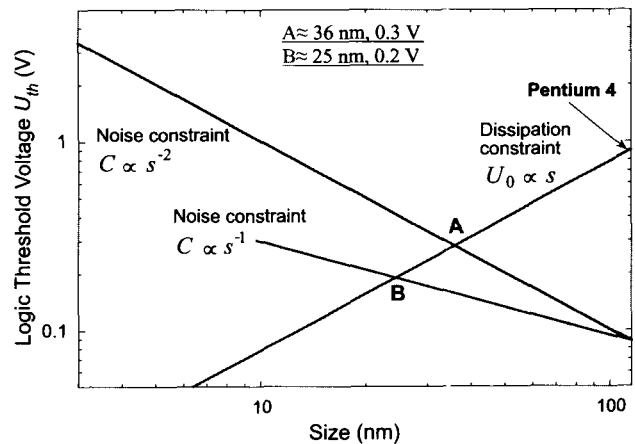


Fig. 2 Prediction of the end of Moore's law. (From Ref. [1].) The technology faces a difficult problem when the upper limit of noise margin set by the dissipation/field constraint and the lower limit of noise margin required by the noise/error constraint cross each other (between points A or B, depending on the evolution of gate oxide thickness). (View this art in color at www.dekker.com.)

which is not dissipative, but the processes coupled to it are dissipative. The electrons at the tunnel junction of a closed SET can be excited by thermal energy fluctuations to the energy level where tunneling can occur and a single electron can cause a single bit error in a SET. Similarly, an open SET can be temporarily shut down by thermal fluctuations. Thus the tentative expectation is that SETs will have a similar nature of bit error characteristics as CMOS. However, the picture is more complex.^[3]

- Instead of a single capacitance, three different capacitances influence bit errors: the two tunnel junction capacitances and the quantum dot capacitance (gate capacitance).
- The noise margin cannot be increased arbitrarily by increasing supply voltage. It has a practical maximum that is equal to the voltage difference between the totally closed and totally open transistors. Higher voltages cause multiple-electron operation mode, and large noise and dissipation.
- There are two different working ranges vs. the quantum dot size: larger sizes (Coulomb blockade controls the current transport) and smaller sizes (<10 nm; quantum confinement effects dominate).

Preliminary studies^[3] show that the requirement for small quantum dot size becomes much harder to satisfy when not only the d.c. characteristics but also the bit errors matter in a microprocessor with 10^8 or more SETs. To have SET-based microprocessors, the characteristic quantum dot size has to be less than 1 nm.

ULTIMATE LIMITS OF ENERGY DISSIPATION VS. PERFORMANCE IN CLASSICAL AND QUANTUM COMPUTING

Heat problems with today's microprocessors have made it very clear that the ultimate and most fundamental questions of viability of the technology are related to power requirement information processing. This is the ultimate question for general-purpose classical or quantum computers. If CMOS and SET fail, it is a natural question if quantum computing and quantum information can help us out and—if yes—how. Because, so far, the existing quantum computing architectures have been neither practical nor general purpose, the only question we may be able to answer is the ultimate limits of performance. Performance includes error rate (accuracy), speed (bandwidth), and power dissipation. It is very important to take temperature into

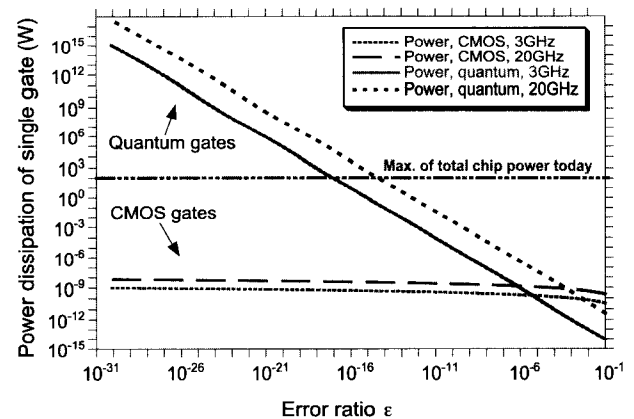


Fig. 3 Minimal power dissipation of a single logical gate, classical (CMOS) and quantum, vs. the error ratio of the gate. (From Ref. [4].) (View this art in color at www.dekker.com.)

account, and to compare the ultimate performance limits of classical and quantum computers at the same temperature.^[4] If it is room temperature, both the classical and quantum computers should be tested at room temperature; if it is the microkelvin temperature range, than the same conditions are required for both.

Recent studies^[5] show that quantum computers have energy requirement problems at high accuracy because of arguments similar to Heisenberg's uncertainty principle. Classical computers perform much better when accuracy is concerned; however, quantum computers can balance this deficiency by a greater speed.^[4] (For a comparison of the energy requirements of a classical and a quantum gate when they run at the same clock frequency, see Fig. 3.^[4])

Realistic estimations^[6] based on existing quantum error correction methods indicate that a general-purpose quantum computer, which would use the best known quantum error correcting methods, would dissipate at least 100 times more energy than its classical counterpart.

Concerning future research aspects, we think that the ultimate focus of this study will not be the accuracy (error rate) of classical and quantum computers, but the energy requirements of processing Shannon information (bit). This aspect induces many new questions, including the problem of computer architectures that are not sensitive to noise. An important question is the energy and complexity requirement of error-correcting coding, and the ultimate measure should be energy requirement vs. Shannon information.

REFERENCES

1. Kish, L.B. End of Moore's law: Thermal (noise) death of integration in micro and nanoelectronics. *Phys. Lett.* **2002**, *305*, 144–149.
2. Huang, B.; Qin, J.; Walters, J.; Bernstein, J.B. Development of Derating Guidelines for Semiconductor Devices. In *Aerospace Vehicle Systems Institute Report*; 2003; unpublished.
3. Kim, J.; Kish, L.B. Can Single Electronic Microprocessors Ever Work at Room Temperature? In *Proceedings of SPIE, Vol. 5115*, Conference on Noise in Nanoelectronics, Sensors and Standards, Santa Fe, NM, June 1–4, 2003; Kish, L.B., Green, F., Innaconne, G., Vig, J., Eds.; 2003; 174–182.
4. Kish, L.B. Moore's Law is Killed by Classical Physics; Can Quantum Information Save It? In *Proceedings of SPIE, Vol. 5115*, Conference on Noise in Nanoelectronics, Sensors and Standards, Santa Fe, NM, June 1–4, 2003; Kish, L.B., Green, F., Innaconne, G., Vig, J., Eds.; 2003; 167–173.
5. Gea-Banacloche, J. Minimum energy requirements for quantum computation. *Phys. Rev. Lett.* **2002**, *89*, 217901.
6. Gea-Banacloche, J.; Kish, L.B. Comparison of energy requirements for classical and quantum information processing. *Fluct. Noise Lett.* **2003**, *3*, C3–C7.

Motor Proteins in Synthetic Materials and Devices

Henry Hess

University of Washington, Seattle, Washington, U.S.A.

George Bachand

Sandia National Laboratories, Albuquerque, New Mexico, U.S.A.

Viola Vogel

University of Washington, Seattle, Washington, U.S.A.

INTRODUCTION

After billions of years of evolution, biological nanomotors and, in particular, motor proteins have achieved a level of performance unmatched by current synthetic nanomotors. Motor proteins in hundreds of specific designs perform a wide range of functions in biology, while achieving more than 50% efficiency in the conversion of chemical energy to mechanical work.^[1,2]

The research discussed in this entry aims at utilizing motor proteins in hybrid “bio/nano” devices to explore the potential of nanomotors in technological applications. Challenges for this approach include the design of suitable synthetic environments, the interfacing of biological components with synthetic structures, the controlled modification of biological motors using recombinant techniques, and in general, the difficulty of engineering at a size scale where random fluctuations due to Brownian motion are an integral part of the system.

At this point, an international group of research teams has utilized a variety of rotational and linear motor proteins to demonstrate the first devices integrating motor proteins. These devices illustrate the important role that motor proteins can play in nanotechnology.

MOTORS IN NANOTECHNOLOGY

Technological revolutions often involve access to new materials, and the mastery of a new material is so fundamental to mankind that historic ages are defined by the state-of-the-art material, hence the “stone age” or “bronze age.” However, some technological revolutions are characterized by the newfound ability of man to convert energy into mechanical work, based, for example, on the invention of the steam engine, which powered the industrial revolution. Can nanotechnology become a revolution of energy conversion in addition to a materials

revolution, driven by a nanomotor, which will power the “Nanofactory” and the “Nanoautomobile” of tomorrow?

Currently, no man-made nanomotor exists that can impact nanotechnology in the way that the steam engine defined the industrial revolution. However, while the first prototypes of synthetic nanomotors are studied,^[3,4] nature provides us with a wide range of biological nanomotors, which have evolved to perform a wide range of functions with an amazing efficiency.^[5] While the center stage is occupied by motor proteins such as myosin, which is, for example, responsible for muscle contraction, biological motor designs include motors based on ribonucleic acid (RNA) pulling on double-stranded deoxyribonucleic acid (DNA) to package it into the protein shell of a virus,^[6] ribosomes moving along RNA while synthesizing a new protein, or even an electrostrictive membrane protein aiding the process of hearing.^[7] The mechanism by which biological motors, in particular motor proteins, generate force is a very active field of research, and significant progress has been made.^[8] Nowadays, motor proteins can be readily isolated and are even commercially available.

Biomolecular motors, in particular motor proteins, are a gift of nature to the nanotechnologist. They can be used in hybrid “bionano” devices to explore the potential of nanomotors. At this point, a small number of prototypical nanodevices based on motor proteins has been assembled, and in the following, we will introduce the biological motors used, and discuss the progress in the design of hybrid devices.

BIOLOGICAL FUNCTIONS OF MOTOR PROTEINS

Motor proteins represent a unique class of enzymes and enzyme complexes that convert chemical energy into mechanical work with relatively high efficiency. In these proteins, energy associated with catalysis (or an electrochemical gradient) is linked to conformational changes in

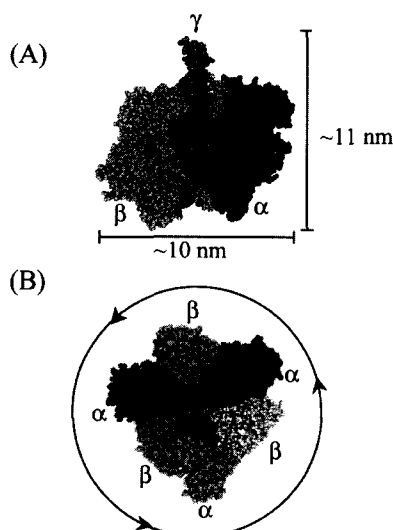


Fig. 1 (A) Side view of the crystal structure of the bovine F_1 -ATPase reported by Braig et al.^[12] Adjacent α and β subunits were removed to show the γ subunit and bound ADP (red). (B) Top of the F_1 -ATPase motor showing the alternating α/β hexamer (stator) and central γ subunit (rotor). The γ subunit rotates counterclockwise in a three-step process during ATP hydrolysis. The F_0 portion of ATP synthase, which inserts into a membrane and converts a proton flow into a rotary motion, is not shown. (View this art in color at www.dekker.com.)

the structure. As with man-made motors, these molecular machines can be categorized as either rotary or linear motors, depending on their mode of translation.

Two true rotary molecular motors were identified, and extensively studied in terms of the biochemical and biophysical properties of these protein complexes. The bacterial flagellar motor is a classic example of a rotary motor used by certain bacteria to move in a fluid environment. The complex uses a proton gradient to propel a large flagellum at speeds of up to 300 rps, and produces a rotary torque in excess of 550 pN nm.^[9] A second rotary motor, ATP synthase (F_0F_1 -ATPase), is a ubiquitous enzyme complex responsible for proton-powered production of adenosine 5'-triphosphate (ATP) in living system.^[10] Translocation of H^+ across a membrane results in the rotation of a central shared subunit, and synthesis of three molecules of ATP per revolution. Moreover, the cytoplasmic F_1 -ATPase domain may independently function as an ATP-fueled rotary motor,^[11] construction of integrated devices with this motor protein will be discussed later (Fig. 1).

A number of linear motors were extensively studied in terms of their biomechanical characteristics,^[8,13,14] as well as their potential use in hybrid nanodevices.^[15] Linear motors can be chosen from three principal families: myosins—moving along actin filaments toward the

barbed end; kinesins—moving along microtubules toward the plus end; and dyneins—moving along microtubules toward the minus end^[16] (Fig. 2).

Actin filaments, which are double-stranded twisted ropes polymerized from 5.5-nm-long actin monomers, are highly flexible and can branch into a dense mesh. Microtubules are stiff, unbranched, proteinaceous tubes with an outer diameter of ~ 30 nm, consisting of 8–18 parallel protofilaments assembled from 8-nm-long tubulin dimers. While motors of the myosin family are the molecular actuators responsible for the contraction of muscles, specialized motors of all families participate in the intracellular transport of membrane organelles and protein complexes. The morphology and biochemistry of the different types of motors is closely coupled to their function. For example, myosin II has evolved to act in

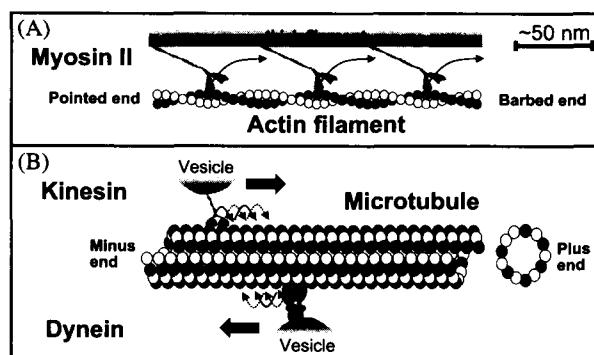


Fig. 2 (A) Myosin II, the myosin type present, e.g., in skeletal muscle, assembles into a thick filament. The collective, unsynchronized motion of the myosin motors along the actin filament causes the contraction of muscle cells. Each myosin motor attaches only intermittently to the actin filament (nonprocessive motion), “running” along with a velocity of up to 8 $\mu\text{m}/\text{sec}$. Actin filaments consist of two helical strands polymerized from actin monomers with a full period of 72 nm. (B) Conventional kinesin is a two-headed motor moving toward the “plus” end of a microtubule. The two heads move in coordinated fashion, covering a distance of 8 nm with each step, hydrolyzing one ATP molecule per step, and generating a maximum force of 7 pN. In vitro, kinesin takes up to 100 steps/sec. At least one of the kinesin heads is attached at any point in time (processive motion). Cytoplasmic dynein is a processive, two-headed motor moving toward the “minus” end of the microtubule. It is a particularly large protein complex, consisting of more than eight subunits with a combined mass of more than 1000 kDa. Microtubules are tubular structures with an outer diameter of 30 nm, which are polymerized from individual tubulin monomers with a length of 8 nm. Microtubules assembled in vitro can reach a length of up to 100 μm . In vivo, microtubules constantly assemble and disassemble; however, the use of drugs like taxol can stabilize microtubules for weeks by slowing the depolymerization. (View this art in color at www.dekker.com.)

a large array of motors in fast skeletal muscle. Consequently, the biochemical cycle of binding ATP, hydrolyzing ATP, and releasing the products adenosine 5'-diphosphate (ADP) and phosphate is tuned toward a short time of attachment to the actin filament (nonprocessive motion). In contrast, the step size of a conventional kinesin motor (transporting as a single motor, e.g., synaptic vesicles) matches exactly the 8-nm spacing between adjacent tubulin binding sites on a protofilament of a microtubule, which, together with a coordinated hydrolysis cycle of the two heads of the motor, facilitates a large number of consecutive steps without detaching from the microtubule (processive motion).^[5]

The large number of natural designs of linear motors for functions ranging from muscle contraction to vesicle transport can serve as a tool chest for hybrid devices. It is also an inspiration for artificial modifications to existing motors, for example, by integrating chemical switches or by changing their processivity.^[17,18,61] Currently, conventional kinesins and microtubules are a motor/filament combination, which is often utilized for reasons related to the robustness of the proteins, the successful expression of kinesin in *Escherichia coli*,^[19] and the easy modification of tubulin.^[20]

MOTOR PROTEINS IN A SYNTHETIC ENVIRONMENT

Controlling the interaction between the motor proteins and the synthetic materials is a major challenge in the design of hybrid devices.^[21] While regions of the surface intended as motor protein-coated tracks or islands have to have a high affinity for protein adsorption, denaturation and concomitant loss of function of the protein after adsorption to the surface has to be avoided as well. It is equally important for the defined positioning of motors in a device to prevent the adsorption of motors to regions surrounding the intended motor protein-rich regions, a challenging task because of the general tendency of proteins to stick to many synthetic surfaces.

A variety of approaches to reduce denaturation were developed, ranging from precoating surfaces with a generic protein (albumin, casein),^[22] which restricts the surface-motor contact to small patches in-between the preadsorbed proteins, to coating the surface with polymer brushes with functionalized ends,^[23] which prevents motor adsorption directly to the surface while providing a designated binding site on the polymer. The most sophisticated approach toward attaching a motor (discussed in more detail in the subsection "Rotational Systems") relied on genetically engineering specific anchor sites into the protein, which connect to a patterned nickel film on the surface.^[11,24] The adsorption of motors

has been selectively prevented by either empirically identifying materials, which together with added detergents in the solution reduce protein adsorption,^[25] or by using surface modification strategies originally developed for nonfouling surfaces.^[26]

The lifetime of hybrid bionanodevices is a frequent concern. To maintain motor proteins in a functional state, the temperature, ionic strength, pH, and salt concentration of the surrounding solution have to be controlled.^[27] Microtubules and actin filaments depolymerize over time,^[28] a process which can be slowed but not entirely prevented. In addition, proteins are subject to degradation by proteases, and they sustain photodamage during observation under the fluorescence microscope. In combination, these factors currently limit the lifetime of actively operating devices to hours or a few days at room temperature. However, for a large number of applications, this lifetime, together with adequate storage at low temperatures before operation, is sufficient.

REGULATING BIOMOLECULAR MOTOR ACTIVITY

A fundamental element in the engineering of biomolecular motor-powered devices and materials is the ability to modulate the activity of the motors. To date, two strategies have been used to regulate the functionality of biomolecular motors in synthetic systems. The first strategy involved the controlled release of caged ATP into solution to modulate the linear translation of conventional kinesin.^[29] Because the density of tethered kinesin was relatively low, an ATP-consuming enzyme, hexokinase, was used to rapidly reduce the liberated ATP in solution, and produce discrete spikes of available ATP. In this manner, the magnitude of velocity and distance could be regulated based on the intensity of light exposure.^[29] This strategy has direct application for controlling any molecular motor that utilizes ATP as a fuel source. A primary advantage in this system is the ability to produce discrete spikes in ATP that, in turn, may be used to regulate the velocity/distance traveled by linear motors, or the speed/number of cycles for rotary motors.

The second strategy for controlling motor functionality involved genetically engineering an allosteric effector site into the catalytic domain of the F₁-ATPase molecular motor.^[30] This site was engineered to bind Zn²⁺ such that the conformation changes necessary for ATP hydrolysis and γ subunit rotation would be reversibly inhibited when the site was occupied; chelation of the Zn²⁺ would subsequently restore activity. In single molecule assays, rotation of all (i.e., 100%) mutated F₁-ATPase was observed in the presence of 800 μ m ZnSO₄, whereas bulk

activity assays indicated a 60% inhibition in catalytic activity at saturating levels of Zn^{2+} . This suggests that the complete inhibition of hydrolytic activity is not requisite for tight control of motor rotation in ATPase. Repeated cycles of Zn^{2+} inhibition, followed by chelation with 1,10-phenanthroline, demonstrated the ability to reversibly control the functionality of the F_1 -ATPase motor.^[30] A unique advantage in this strategy is the ability to tailor the allosteric binding site, which may serve as a recognition element in sensor-type applications.

NANODEVICES

Rotational Systems

The F_0F_1 -ATPase enzyme complex consists of eight subunits (α , β , χ , α , β , γ , ϵ , and δ) that are arranged in two distinct domains, the cytoplasmic F_1 and hydrophobic F_0 domains. The F_1 -ATPase domain can function independently as an ATP-powered rotary motor,^[11,31] and offers a potential source of actuation in nanoscale device architectures.^[24,32] During ATP hydrolysis, the central rotor (i.e., γ subunit) of F_1 -ATPase rotates in response to the conversion of ATP to ADP+ P_i at each of the three catalytic sites. This three-step process that results in rotation of the γ subunit was confirmed by a number of methods.^[32-34] The precise mechanism of mechanical coupling of ATP hydrolysis and rotation of the γ subunit has yet to be determined.

In general, a prerequisite technology for utilizing molecular motors as functional components of nanoscale devices is the ability to interface biological and nonbiological components. To this end, the F_1 -ATPase from thermophilic bacterium *Bacillus* PS3 was genetically engineered to express a 10x histidine (His) tag on the N-terminus of the β subunits.^[24,32] The His-tagged motors were subsequently used to precisely position individual F_1 -ATPase motors on arrays of nanoscale nickel dots.^[35] Because the His-tags were located on the N-terminal of the β subunit, the motors were positioned such that the base of the stator was adjacent to the surface, and the rotor was positioned perpendicular to the surface and fully accessible for attachment of additional components. A single cysteine (Cys) was also engineered at position 107 in the γ subunit to provide a unique chemical "handle" for attaching synthetic cargo.^[24,32] The ability to genetically engineer the motors for specified interactions with synthetic components represents a powerful tool for tailoring the interaction of various components.

As a basic proof-of-principle, a simple device was designed and constructed, in which the F_1 -ATPase motors provided a source of actuation to nanoscale metallic com-

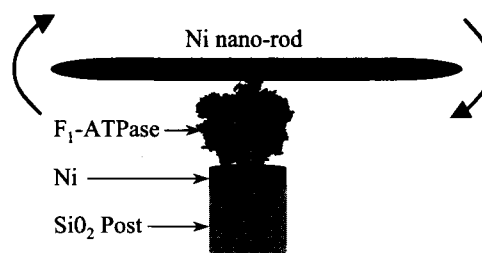


Fig. 3 Schematic representation of the integrated nanodevice that provided a proof-of-principle with regard to actuating nanomechanical devices with a biomolecular motor.^[36] In the presence of ATP, the rotary motor F_1 -ATPase spins the nickel nanorod ($10 \times 150 \times 1000$ nm) with an angular velocity of 4 Hz while providing a torque of 20 pN nm. Elevating the motor on a post reduces the viscous drag on the moving nanorod, which increases near a surface. (View this art in color at www.dekker.com.)

ponents.^[36] This device has three primary components: 1) a lithographically defined surface of Ni posts, 2) F_1 -ATPase motors, and 3) functionalized nanoscale "propellers" (Fig. 3). The device was assembled by sequential addition of individual components; however, yield was relatively poor (i.e., 1%, defined as the number of rotating propellers divided by the number of propellers distributed on the surface). Rotation was initiated with the addition of ATP, and stopped with sodium azide, an inhibitor of ATPase activity. The mean frequency of rotation was 4.8 Hz and directly correlated with the length of the propeller, suggesting that the torque was constant. The work performed by the F_1 -ATPase motor to rotate a propeller through one complete revolution was calculated to be ~ 120 pN nm, with an efficiency of 50%.^[36] The device functioned for over 2 hr, at which point the propeller broke free from the motor. Overall, this experiment demonstrated the ability of this biomolecular motor to function as an actuator in a nanoscale mechanical device.

The force tolerances of these devices were characterized by using dynamic force spectroscopy to understand and potentially design integrated nanodevices with an increased assembly yield and lifetime.^[37] In these experiments, the relative order of bond strengths (strongest to weakest) based on the magnitudes of their lifetimes were: biotin-streptavidin, (His)₆-Ni-NTA, (His)₆-Ni, and (His)₆-gold. Based on these findings, the weakest bond in the F_1 -ATPase-powered devices resides in the interaction between histidine and Ni, and likely represents a critical factor resulting in device failure. Improvements in device assembly and longevity may be engineered through further analysis and redesign of the interaction used to adhere the F_1 -ATPase motors to the substrate, as well as to the propellers (or other components).

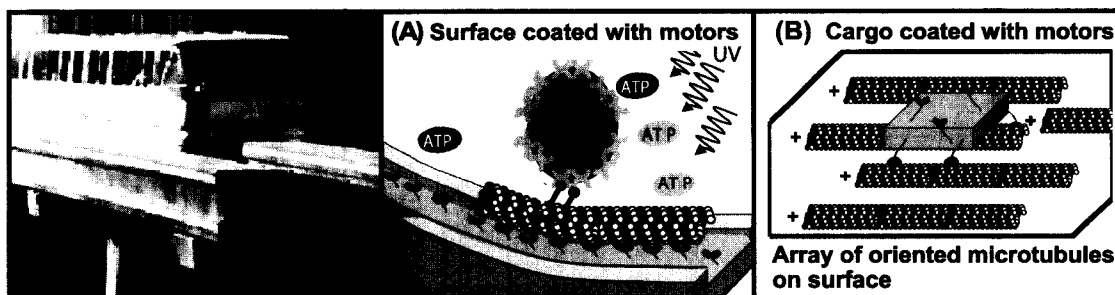


Fig. 4 Nanoscale transport systems based on motor proteins face three principal challenges: guiding the movement, loading the cargo, and controlling the speed.^[15] Two approaches toward guiding the movement have emerged: (A) motor proteins are selectively adsorbed to a structured surface and guide the movement of microtubules or actin filaments serving as shuttle modules, or (B) an oriented array of microtubules is assembled on a surface by adsorption or polymerization and support the directed movement of motor proteins connected to the cargo. Selective loading of cargo and control of movement has been demonstrated for approach (A) by using biotin/streptavidin links for cargo attachment and controlled release of ATP from an inactive, “caged” precursor using UV light. (From Ref. [29]. Copyright 2001 Am. Chem. Soc.) (View this art in color at www.dekker.com.)

Overall, the F_1 -ATPase biomolecular motor represents a highly efficient rotary actuator in integrated, nanomechanical devices. A number of enabling technologies were developed and used to construct a simple nanodevice powered by F_1 -ATPase motors. Further characterization of this device by force measurements of binding strengths has determined the key linkages that likely result in poor assembly yields as well as device failure. As a whole, these data provide a foundation for the continued engineering and analysis of biomolecular motor-powered nanodevices.

Transport Systems

One of the first ideas for a hybrid bionanodevice was a nanoscale transport system, a “molecular shuttle,” with the ability to move single molecules along tracks under user control.^[15] The close analogy to the biological motor protein-based transport mechanisms^[38] provided a clear vision of the feasibility and utility of such a system. Conceptually, a transport system requires solutions to the questions of how to direct the movement, how to load and unload cargo, and how to control the speed of the system.^[29] The guiding issue was addressed with two different approaches (Fig. 4): either the actin filaments or microtubules are selectively immobilized on the surface and support the movement of motors attached to the cargo (bead assay^[39]), or the motors are selectively adsorbed to the surface and move the corresponding filament, which in turn connects to the cargo (gliding assay^[40]).

While the initial experiments by Turner et al.^[41] yielded unpolarized patterns of aligned and immobilized microtubules capable of supporting kinesin motility, later experiments demonstrated polarized alignment of microtubules on surfaces using a variety of methods based on

fluid flow.^[42–44] Kinesin motors nonspecifically bound to the cargo surface then supported the directed transport of micrometer-sized objects across the array of microtubules.

The inverse arrangement, using microtubules as shuttle modules that move across a surface coated with motors and link specifically to the cargo, requires the structuring of the surface in order to create tracks. A variety of strategies including chemical modification,^[45,46] guiding channels,^[29,47] and combinations of surface chemistry and topography^[25,48,49] has been employed to direct the shuttles along predetermined paths. In addition, flow fields^[50] and electric fields^[51] can influence the path of the shuttle. The choice between these guiding strategies is, in large part, determined by the physical properties of the filaments used as shuttles. For example, the large stiffness of microtubules^[52] precludes effective guiding by motors adsorbed in tracks on a chemically modified surface.^[53] Unidirectional motion of the shuttles propelled by surface adsorbed motors can be achieved by suitable track geometries.^[25,53] Conveniently, the orientation of the surface adsorbed motors does not have to be controlled, because the flexible tail region of the kinesin motor allows the motor heads to find a suitable position for microtubule binding independent of the original orientation.^[54,55] Microtubules can be readily functionalized with fluorescent dyes or biotin linkers,^[54] which facilitates the observation of their movement as well as the attachment of cargo if the microtubules are employed as shuttles.

In summary, the basic challenges of guiding, loading, and controlling can be addressed by using a variety of approaches to achieve directed transport, by linking cargo to microtubules or motors, and by controlling motor activity as described in the section on controlling motor functionality. By integrating these approaches, a nanoscale transport system can be assembled and, in the future,

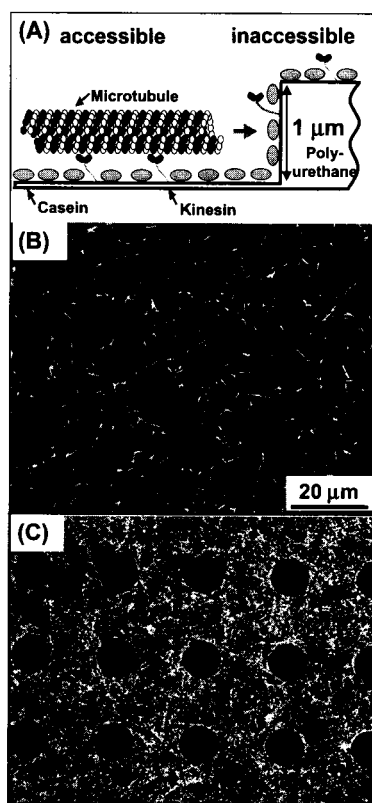


Fig. 5 Fluorescently labeled microtubules transported by surface-adsorbed kinesins can serve as nanoscale probes exploring the surface. The sensitivity of the microtubule path to the topography allows us to image an unknown surface.^[56] This is illustrated in (A), where a microfabricated pattern of 1- μm -high posts divides the surface into an accessible and an inaccessible region, because microtubules move on the bottom surface and are unable to climb a steep incline. Repeated observation of microtubule positions under the fluorescence microscope as shown in (B) yields information about the path of several hundred microtubules. The superposition of 500 images taken every 5 sec reveals the surface topography (C). (From Ref. [56]. Copyright 2002 Am. Chem. Soc.) (View this art in color at www.dekker.com.)

combined with other modular systems such as assembly and packaging stations.

Surface Imaging

The self-propelled movement of microtubules with a diameter of 30 nm on a kinesin-coated surface provides us with a novel nanoscale probe, which can explore a surface in a radically different fashion compared to the tip of a scanning probe microscope. While scanning probe microscopes use a single tip, which scans the surface in a controlled, linear movement, the microtubule movement per se is random. Therefore it is necessary to synthesize an

image of the surface based on the random paths of a large number of microtubules exploring the unknown surface at the same time. A basic implementation of this new approach to surface imaging (Fig. 5) was demonstrated for a surface with a structured topography,^[56] but the research into guiding mechanisms for nanoscale transport systems indicates that the microtubule path is influenced by surface chemistry or fluid flow as well. Despite its limitations due to the sensitivity of the proteins and the optical detection of the microtubule position, the described technique is an example of how the availability of self-propelled nanoprobes enables the implementation of a new scanning method with similarities to mathematical Monte Carlo methods. Nanotechnology is not always "the same but smaller." Instead, sometimes "small is different" (Uzi Landman) applies, which creates opportunities to utilize nanosystems for innovative technologies.

Actuators

While nanoscale transport systems are the technological equivalent to the biological tasks of kinesin in intracellular transport, nanoactuators are inspired by the biological application of myosin motors in muscles. Evidently, molecular motors can be assembled into large arrays and exert many Newtons of force, and it is an interesting question if highly efficient engines built from macroscopic arrays of molecular motors may replace electric motors or heat engines in the future. However, for the purposes of nanotechnology, even single biomolecular

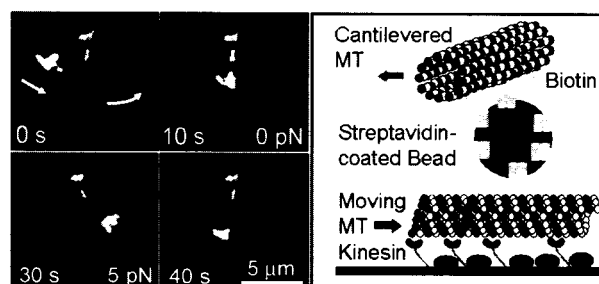


Fig. 6 A microscopic forcemeter for the measurement of intermolecular forces on the order of a few piconewtons can be assembled from microtubules functionalized with ligands, beads coated with receptors, and kinesins (0 and 10 sec). It consists of a cantilevered microtubule that binds to a streptavidin-coated bead loaded onto a microtubule moved by kinesins.^[59] The kinesins push the moving microtubule (30 sec), straining the bond between streptavidin and biotin until it ruptures (40 sec). Observation of the concurrent bending of the cantilevered microtubule allows the determination of the strain forces based on the known stiffness of microtubules. (From Ref. [59]. Copyright 2001 Am. Chem. Soc.) (View this art in color at www.dekker.com.)

motors generate forces, which are sufficient to overcome typical loads.^[57,58]

Recently, a miniaturized forcemeter for the measurement of intermolecular bond strengths was demonstrated.^[59] In this forcemeter, several kinesin motors provide the force to strain the bond between a receptor–ligand pair, while the magnitude of the strain is reflected in the bending of a microtubule attached to the ligand, which serves as a nanoscale cantilevered beam of known stiffness (Fig. 6). The forcemeter with lateral dimensions of less than 10 μm can generate and detect forces on the order of several piconewtons, which is sufficient to rupture most single molecule receptor/ligand bonds within seconds. The strain generated by the action of motor proteins inherently matches the low rate of force application characteristic for *in vivo* conditions, a situation that is difficult to duplicate with other approaches to molecular force measurements.^[60] In addition, the small size of the instrument suggests the assembly of an array of forcemeters, capable of drastically reducing the time required for a statistically significant number of force measurements.

This forcemeter points the way to more sophisticated nanodevices, which aid in the measurement of properties of nanoscale objects, and can play an active role in the assembly and disassembly of nanoscale structures.

CONCLUSION

Motor proteins are fast and versatile nanomotors with high energy efficiency and interface in a very specific manner with “road”-like filaments and various objects serving as “cargo.” At this point, this makes them superior to any man-made nanomotor, and allows us to explore the technological applications of nanomotors in hybrid nanodevices. Inspired by the biological applications of motor proteins in intracellular transport and as actuators, a number of devices have been designed. Challenges regarding the interface between biological and synthetic elements in the hybrid devices are addressed, and artificial elements, such as “anchors” or a “throttle,” are directly integrated into the motor protein. Nature has mastered not only the design of nanoscale functional units but also the integration of these units into the sophisticated multipurpose subcellular or cellular systems. This research attempts to learn nature’s lessons and translate them into valuable engineering.

ACKNOWLEDGMENTS

Partial funding through NASA grant NAG5-8784 is gratefully acknowledged. This work was also partially

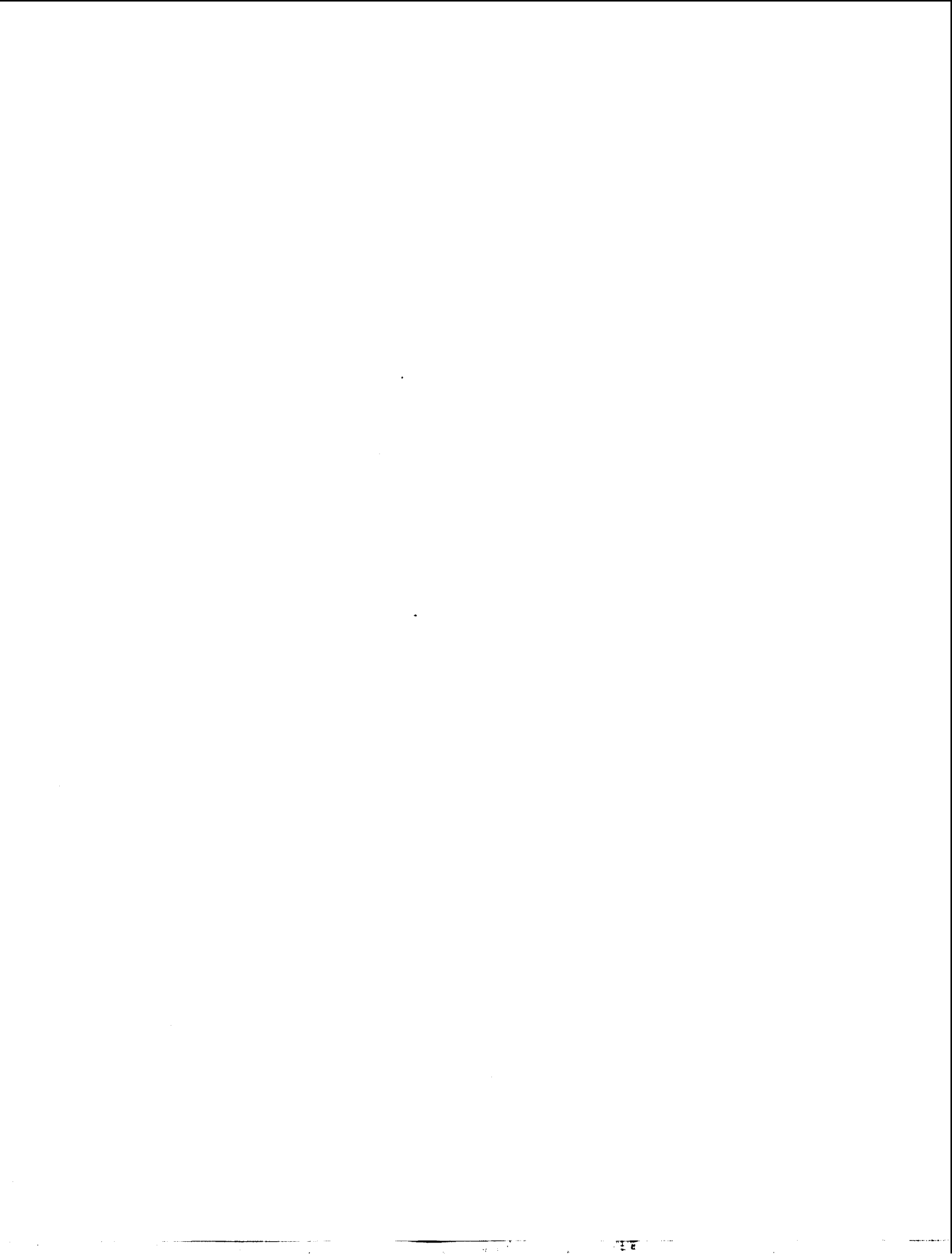
supported through the Materials Science and Engineering Division, Office of Basic Energy Sciences, Department of Energy. Sandia is a multiprogram laboratory operated by Sandia Corporation, a Lockheed Martin Company, for the United States Department of Energy under contract DE-AC04-94AL85000.

REFERENCES

1. Kinosita, K., Jr.; Yasuda, R.; Noji, H.; Adachi, K. A rotary molecular motor that can work at near 100% efficiency. *Philos. Trans. R. Soc. Lond., B Biol. Sci.* **2000**, *355* (1396), 473–489.
2. Kawaguchi, K.; Ishiwata, S. Temperature dependence of force, velocity, and processivity of single kinesin molecules. *Biochem. Biophys. Res. Commun.* **2000**, *272* (3), 895–899.
3. Stoddart, J.F. Molecular machines. *Acc. Chem. Res.* **2001**, *34* (6), 410–411.
4. Feringa, B.L. In control of motion: From molecular switches to molecular motors. *Acc. Chem. Res.* **2001**, *34* (6), 504–513.
5. Howard, J. *Mechanics of Motor Proteins and the Cytoskeleton*; Sindauer: Sunderland, MA, 2001.
6. Smith, D.E.; Tans, S.J.; Smith, S.B.; Grimes, S.; Anderson, D.L.; Bustamante, C. The bacteriophage straight phi29 portal motor can package DNA against a large internal force. *Nature* **2001**, *413* (6857), 748–752.
7. Zheng, J.; Shen, W.; He, D.Z.; Long, K.B.; Madison, L.D.; Dallos, P. Prestin is the motor protein of cochlear outer hair cells. *Nature* **2000**, *405* (6783), 149–155.
8. Vale, R.D.; Milligan, R.A. The way things move: Looking under the hood of molecular motor proteins. *Science* **2000**, *288* (5463), 88–95.
9. DeRosier, D.J. The turn of the screw: The bacterial flagellar motor. *Cell* **1998**, *93* (1), 17–20.
10. Boyer, P.D. A research journey with ATP synthase. *J. Biol. Chem.* **2002**, *277* (42), 39045–39061.
11. Noji, H.; Yasuda, R.; Yoshida, M.; Kinosita, K. Direct observation of the rotation of F1-ATPase. *Nature* **1997**, *386* (6622), 299–302.
12. Braig, K.; Menz, R.I.; Montgomery, M.G.; Leslie, A.G.; Walker, J.E. Structure of bovine mitochondrial F(1)-ATPase inhibited by Mg(2+) ADP and aluminium fluoride. *Struct. Fold. Des.* **2000**, *8* (6), 567–573.
13. Howard, J. Molecular motors: Structural adaptations to biological functions. *Nature* **1997**, *389*, 561–567.
14. Fisher, M.E.; Kolomeisky, A.B. Simple mechanochemistry describes the dynamics of kinesin

- molecules. *Proc. Natl. Acad. Sci. U. S. A.* **2001**, *98* (14), 7748–7753.
15. Hess, H.; Vogel, V. Molecular shuttles based on motor proteins: Active transport in synthetic environments. *Rev. Mol. Biotechnol.* **2001**, *82*, 67–85.
 16. Alberts, B.; Bray, D.; Lewis, J.; Raff, M.; Roberts, K.; Watson, J.D. *Molecular Biology of the Cell*; Garland: New York, 1994.
 17. Thorn, K.S.; Ubersax, J.A.; Vale, R.D. Engineering the processive run length of the kinesin motor. *J. Cell Biol.* **2000**, *151* (5), 1093–1100.
 18. Tomishige, M.; Vale, R.D. Controlling kinesin by reversible disulfide cross-linking. Identifying the motility-producing conformational change. *J. Cell Biol.* **2000**, *151* (5), 1081–1092.
 19. Gilbert, S.P.; Johnson, K.A. Expression, purification, and characterization of the drosophila kinesin motor domain produced in *Escherichia coli*. *Biochemistry* **1993**, *32* (17), 4677–4684.
 20. Hyman, A.A.; Drechsel, D.N.; Kellog, D.; Salser, S.; Sawin, K.; Steffen, P.; Wordeman, L.; Mitchison, T.J. Preparation of modified tubulins. *Methods Enzymol.* **1991**, *196*, 478–485.
 21. *Biopolymers at Interfaces*; Malmsten, M., Ed.; Marcel Dekker: New York, 1998.
 22. Howard, J.; Hunt, A.J.; Baek, S. Assay of microtubule movement driven by single kinesin molecules. *Methods Cell Biol.* **1993**, *39*, 137–147.
 23. deCastro, M.J.; Ho, C.H.; Stewart, R.J. Motility of dimeric ncd on a metal-chelating surfactant: Evidence that ncd is not processive. *Biochemistry* **1999**, *38* (16), 5076–5081.
 24. Bachand, G.; Montemagno, C.D. Constructing organic/inorganic NEMS devices powered by biomolecular motors. *Biomed. Microdevices* **2000**, *2–3*, 179–184.
 25. Hiratsuka, Y.; Tada, T.; Oiwa, K.; Kanayama, T.; Uyeda, T.Q. Controlling the direction of kinesin-driven microtubule movements along microlithographic tracks. *Biophys. J.* **2001**, *81* (3), 1555–1561.
 26. Hoffman, A.S. Non-fouling surface technologies. *J. Biomater. Sci., Polym. Ed.* **1999**, *10* (10), 1011–1014.
 27. Bohm, K.J.; Stracke, R.; Unger, E. Speeding up kinesin-driven microtubule gliding in vitro by variation of cofactor composition and physicochemical parameters. *Cell Biol. Int.* **2000**, *24* (6), 335–341.
 28. Kristofferson, D.; Mitchison, T.; Kirschner, M. Direct observation of steady-state microtubule dynamics. *J. Cell Biol.* **1986**, *102* (3), 1007–1019.
 29. Hess, H.; Clemmens, J.; Qin, D.; Howard, J.; Vogel, V. Light-controlled molecular shuttles made from motor proteins carrying cargo on engineered surfaces. *Nano Lett.* **2001**, *1* (5), 235–239.
 30. Liu, H.; Schmidt, J.J.; Bachand, G.D.; Rizk, S.S.; Looger, L.L.; Hellinga, H.W.; Montemagno, C.D. Control of a biomolecular motor-powered nanodevice with an engineered chemical switch. *Nat. Mater.* **2002**, *1* (3), 173–177.
 31. Yoshida, M.; Muneyuki, E.; Hisabori, T. ATP synthase—A marvelous rotary engine of the cell. *Nat. Rev., Mol. Cell Biol.* **2001**, *2* (9), 669–677.
 32. Montemagno, C.; Bachand, G. Constructing nanomechanical devices powered by biomolecular motors. *Nanotechnology* **1999**, *10*, 225–331.
 33. Yasuda, R.; Noji, H.; Kinosita, K., Jr.; Yoshida, M. F1-ATPase is a highly efficient molecular motor that rotates with discrete 120 degree steps. *Cell* **1998**, *93* (7), 1117–1124.
 34. Adachi, K.; Yasuda, R.; Noji, H.; Itoh, H.; Harada, Y.; Yoshida, M.; Kinosita, K., Jr. Stepping rotation of F1-ATPase visualized through angle-resolved single-fluorophore imaging. *Proc. Natl. Acad. Sci. U. S. A.* **2000**, *97* (13), 7243–7247.
 35. Bachand, G.-D.S., R.-K.; Neves, H.-P.; Olkhovets, A.; Craighead, H.-G.; Montemagno, C.-D. Precision attachment of individual F1-ATPase biomolecular motors on nanofabricated substrates. *Nano Lett.* **2001**, *1* (1), 42–44.
 36. Soong, R.K.; Bachand, G.D.; Neves, H.P.; Olkhovets, A.G.; Craighead, H.G.; Montemagno, C.D. Powering an inorganic nanodevice with a biomolecular motor. *Science* **2000**, *290* (5496), 1555–1558.
 37. Schmidt, J.J.; Jiang, X.; Montemagno, C.D. Force tolerances of hybrid nanodevices. *Nano Lett.* **2002**, web released 9/28/02.
 38. Goldstein, L.S.; Philp, A.V. The road less traveled: Emerging principles of kinesin motor utilization. *Nat. Rev., Mol. Cell Biol.* **1999**, *15*, 141–183.
 39. Block, S.M.; Goldstein, L.S.; Schnapp, B.J. Bead movement by single kinesin molecules studied with optical tweezers. *Nature* **1990**, *348* (6299), 348–352.
 40. Harada, Y.; Yanagida, T. Direct observation of molecular motility by light microscopy. *Cell Motil. Cytoskelet.* **1988**, *10* (1–2), 71–76.
 41. Turner, D.C.; Chang, C.; Fang, K.; Brandow, S.L.; Murphy, D.B. Selective adhesion of functional microtubules to patterned silane surfaces. *Biophys. J.* **1995**, *69*, 2782–2789.
 42. Bohm, K.J.; Stracke, R.; Muhlig, P.; Unger, E. Motor protein-driven unidirectional transport of micrometer-sized cargoes across isopolar microtubule arrays. *Nanotechnology* **2001**, *12* (3), 238–244.
 43. Limberis, L.; Stewart, R.J. Polarized alignment and surface immobilization of microtubules for

- kinesin-powered nanodevices. *Nano Lett.* **2001**, *1* (5), 277–280.
44. Brown, T.B.; Hancock, W.O. A polarized microtubule array for kinesin-powered nanoscale assembly and force generation. *Nano Lett.* **2002**, *2* (10), 1131–1135.
 45. Suzuki, H.; Yamada, A.; Oiwa, K.; Nakayama, H.; Mashiko, S. Control of actin moving trajectory by patterned poly(methylmethacrylate) tracks. *Biophys. J.* **1997**, *72*, 1997–2001.
 46. Nicolau, D.V.; Suzuki, H.; Mashiko, S.; Taguchi, T.; Yoshikawa, S. Actin motion on microlithographically functionalized myosin surfaces and tracks. *Biophys. J.* **1999**, *77* (2), 1126–1134.
 47. Clemmens, J.; Hess, H.; Howard, J.; Vogel, V. Analysis of microtubule guidance by microfabricated channels coated with kinesin. *Langmuir* **2003**, *19* (5), 1738–1744.
 48. Suzuki, H.; Oiwa, K.; Yamada, A.; Sakakibara, H.; Nakayama, H.; Mashiko, S. Linear arrangement of motor protein on a mechanically deposited fluoropolymer thin film. *Jpn. J. Appl. Phys., Part 1* **1995**, *34* (7B), 3937–3941.
 49. Dennis, J.R.; Howard, J.; Vogel, V. Molecular shuttles: Directing the motion of microtubules on nanoscale kinesin tracks. *Nanotechnology* **1999**, *10*, 232–236.
 50. Stracke, P.; Bohm, K.J.; Burgold, J.; Schacht, H.J.; Unger, E. Physical and technical parameters determining the functioning of a kinesin-based cell-free motor system. *Nanotechnology* **2000**, *11* (2), 52–56.
 51. Stracke, R.; Bohm, K.J.; Wollweber, L.; Tuszyński, J.A.; Unger, E. Analysis of the migration behaviour of single microtubules in electric fields. *Biochem. Biophys. Res. Commun.* **2002**, *293* (1), 602–609.
 52. Gittes, F.; Mickey, B.; Nettleton, J.; Howard, J. Flexural rigidity of microtubules and actin filaments measured from thermal fluctuations in shape. *J. Cell Biol.* **1993**, *120* (4), 923–934.
 53. Hess, H.; Clemmens, J.; Matzke, C.M.; Bachand, G.D.; Bunker, B.C.; Vogel, V. Ratchet patterns sort molecular shuttles. *Appl. Phys., A* **2002**, *75*, 309–313.
 54. Hunt, A.J.; Howard, J. Kinesin swivels to permit microtubule movement in any direction. *Proc. Natl. Acad. Sci. U. S. A.* **1993**, *90* (24), 11653–11657.
 55. Hua, W.; Chung, J.; Gelles, J. Distinguishing inchworm and hand-over-hand processive kinesin movement by neck rotation measurements. *Science* **2002**, *295* (5556), 844–848.
 56. Hess, H.; Clemmens, J.; Howard, J.; Vogel, V. Surface imaging by self-propelled nanoscale probes. *Nano Lett.* **2002**, *2* (2), 113–116.
 57. Hunt, A.J.; Gittes, F.; Howard, J. The force exerted by a single kinesin molecule against a viscous load. *Biophys. J.* **1994**, *67*, 766–781.
 58. Meyhofer, E.; Howard, J. The force generated by a single kinesin molecule against an elastic load. *Proc. Natl. Acad. Sci. U. S. A.* **1995**, *92* (2), 574–578.
 59. Hess, H.; Howard, J.; Vogel, V. A piconewton forcemeter assembled from microtubules and kinesins. *Nano Lett.* **2002**, *2* (10), 1113–1115.
 60. Clausen-Schaumann, H.; Seitz, M.; Krautbauer, R.; Gaub, H.E. Force spectroscopy with single biomolecules. *Curr. Opin. Chem. Biol.* **2000**, *4* (5), 524–530.
 61. Tomishige, M.; Vale, R.D. Controlling kinesin by reversible disulfide cross-linking: Identifying the motility-producing conformational change. *J. Cell Biol.* **2000**, *151*, 1081–1092.



Nano-Mesoscopic Interface: Hybrid Devices

Gianfranco Cerofolini

STMicroelectronics, Catania, Italy

INTRODUCTION

The continuous size reduction associated with the development of microelectronics will, sooner or later, face the need of manipulating single molecules, addressing and contacting them to wanted regions of the device. Although the manipulation of individual molecules is already possible using the scanning tunneling microscope and their functional characterization is usually achieved for thiol-terminated molecules grafted to gold electrodes, both the process (individual management by scanning tunnel microscopy) and material (gold) are, however, incompatible with the integrated-circuit (IC) technology. Batch processing requires that the molecules are addressed to (photolithographically predefined) regions by a difference of chemical potentials. In turn, that requires a control of the chemical terminations of the surfaces of the most important IC films. Among them, the unique single crystalline surface is that of the silicon substrate, which makes it the most serious candidate for the growth of ordered functional films. Of the several producible orientations of silicon, the (100) surface is that with the largest applications. In usual technological cases, the (100) surface of silicon is hydrogen-terminated (immediately after aqueous HF etching) or covered by oxo terminations (after the formation of the native oxide). Although neither one nor the other has the necessary chemical and crystalline order required to be a seed for the deposition of molecular devices, they can, however, be used to prepare clean silicon surfaces with 2×1 reconstruction or hydrogen-terminated silicon surfaces with 2×1 or 1×1 reconstruction. Alkenes or alkynes can be used to functionalize the silicon via cycloaddition to the clean 2×1 -reconstructed surface or via hydrosilation on the hydrogen-terminated surfaces.

THE CONCEPTUAL POSSIBILITY OF MOLECULAR ELECTRONICS

With the synthesis of rotaxanes, catenanes, Möbius strips, etc., topological chemistry has changed from a visionary view^[1,2] (one of the founding papers, Ref. [1], circulating as a preprint at the Reaction Mechanisms Conference held in Princeton, NJ, at the end of summer 1960, was

summarily rejected as not being chemistry^[3]) to a consolidated discipline for the synthesis of molecules able to mimic, on a molecular scale, the behavior of macroscopic machines.^[4,5] In a way, those molecules may be considered as molecular machines.

Although the first molecular machines mimicked mechanical machines, a number of molecules able to perform even sophisticated electrical functions have been also synthesized.

Fig. 1 shows an example of molecule^[6] with interesting electrical properties. The molecule is formed by a bipyridinium core, two alkane chains, and two thiol terminations. The bipyridinium core works as a Schmitt trigger, the alkane chains behave as wires, and the thiol terminations provide alligator clips to external electrodes. Once grafted to gold electrodes (through its thiol terminations), the molecule displays or not resonant electronic conduction, according to the charge state on one nitrogen atom in the bipyridinium core: if both nitrogen atoms are positively charged, the molecule does not display conduction; if one nitrogen is reduced (by injection, controlled by an external electrode, of one electron), the molecule displays conduction. In a way, the molecule performs as an electronic device (a Schmitt trigger), but has a size of the order of 3 nm^3 .

The molecule in Fig. 1 is certainly not unique in possessing interesting electronic properties: the review of Ref. [7] reports wires, rectifiers, memories, etc. listing 106 references. The availability of such a molecular scaffold has kindled the interest toward an application of molecular devices for a new electronics—*molecular electronics*.

Molecular electronics has, however, a chance to become interesting for large-volume applications (and thus a potential competitor of microelectronics) only if it goes beyond the current and expected future limits of the IC technology.

MICROELECTRONICS AND THE EVOLUTION OF THE INTEGRATED CIRCUIT

At present (end of 2002 A.D.), ICs have bit density of the order of 10^8 bit cm^{-2} (for microprocessors). This density has been achieved by an increase by a factor of 2 each 18 months (observation known as Moore's law) over the

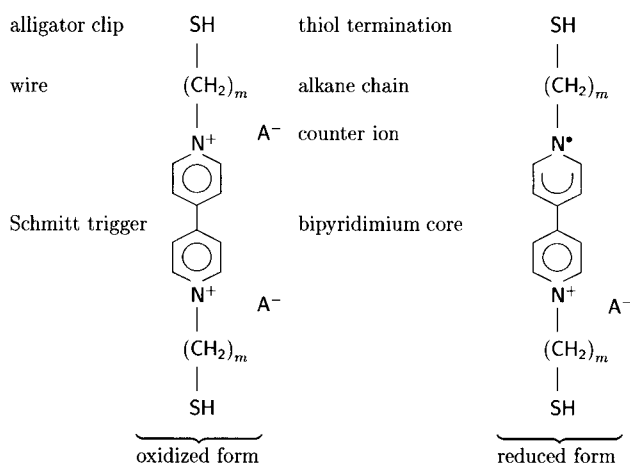


Fig. 1 Attribution of electrical functions to functional groups for an organic molecule behaving as a Schmitt trigger.

past three decades; this (once spontaneous) evolution is expected to continue (although now assisted by a concerted activity planned in the International Technology Roadmap for Semiconductors—the “Roadmap”)^[8] over the next 10 years also.

The IC has, ever since its invention, been characterized by a progressive reduction of vertical and horizontal sizes of its fundamental building block—the metal-oxide semiconductor (MOS) field-effect transistor. Scaling theorems have indicated how to change concentration profiles and boundary conditions to maintain certain wanted characteristics—and this process usually results in an improvement of the others. Today, the MOS transistor (with gate length of 0.13 μm) is nothing but the original MOS transistor (with gate length of ca. 50 μm) suitably scaled.

This top-down route has been relatively easy to run until the minimum feature size L_{litho} , which can be defined via photolithography, has been reduced to the light wavelength. Further improvements have been possible only thanks to masterly combinations of reticle enhancement techniques (optical proximity correction, phase shifting masks, and off-axis illumination) which have allowed the definition of geometries with size lower than the wavelength by a factor of 2–3.

The top-down development of microelectronics sooner or later will be limited by the “physical limit” (i.e., the nonscalability of the MOS transistor below a critical size L_{phys} ^[9]) or by the “photolithographic limit” L_{litho} ^[10]. Which between the above feature sizes will indeed limit the scaling down of ICs is not clear; nor it is clear if the climbing investment cost for production lines (predicted, hitherto correctly, by the second Moore’s law and projected to rise from \$2.5 billion in 2000 to \$15 billion in 2010) will eventually limit the minimum feature size to a value L_{eco} (the “economic limit”).

Let L^* denote the maximum among L_{phys} , L_{litho} , and L_{eco} . At present, it is difficult to make a sensible prediction about the value of L^* ; the Roadmap suggests $L^* \leq 30$ nm (for dynamic random access memory half pitch,^[8]), thus guaranteeing that the quiet revolution of microelectronics will continue over the next 10 years. Because L_{phys} is manifestly higher than the typical molecular size (say, 1 nm), L^* is thus in the interval 1–30 nm.

The closer is L^* to the upper limit of this interval, the sooner microelectronics will become a mature industry. On another side, the closer is L^* to the upper limit, the wider is the room for the development of a new (at present, hypothetical) bottom-up technology, in which the single data-handling devices are molecules^[7] arranged and interconnected to form a truly molecular electronic circuit.

THE HYBRID SOLUTION FOR MOLECULAR ELECTRONICS

The availability of molecular devices able to perform logical operations^[7] does not guarantee per se the possibility of molecular electronics, unless one is able to arrange them in an ordered and accessible way and to probe their states. The fundamental limits posed by quantum mechanics suggest that the connection of the microscopic world of molecules to the macroscopic world of humans or machines will require a stage of amplification of the signal at the mesoscopic level. Because single devices of microelectronic ICs are mesoscopic in nature and may be operated to behave as measurement apparatuses, the most promising architecture is the hybrid one, in which a very dense array of molecular devices is hosted in a silicon-based microelectronic IC, which provides the functions for addressing, reading, and writing, in addition to the input–output power stage.

This point deserves a particular discussion. According to the idea of Bohr,^[11] eventually formalized in the theory of Daneri et al.^[12] the detection of the microscopic state of a system requires the interaction of the microscopic system with a macroscopic apparatus. To act as a measurement device, the composite (microscopic+macroscopic) system must have so many states as the number of microscopic states and must have ergodic properties such as to reproduce the probability distribution of the microscopic state alone.

The analysis of ideal experiments (such as the detection of a particle in a Wilson chamber or in a Geiger counter) shows indeed that typical situations of nuclear physics, in which the microscopic state is characterized by a large energy (compared with the thermal unit $k_{\text{B}}T$, with k_{B} the Boltzmann constant and T the apparatus temperature) concentrated on a few degrees of freedom, are

actually described by the above picture.^[13] That certain ICs may operate as measuring devices is demonstrated by the detection of single photons through p-i-n diodes supplied at a voltage just above the breakdown^[14] and of alpha particles through the soft errors of dynamic random access memories.^[15] The first example is particularly interesting because it applies to a situation in which the event to be detected (the presence of a photon) has an energy (say, 1 eV) not exceedingly higher than the thermal unit (say, 25 meV). This occurrence thus suggests the possibility of using suitable microelectronic devices for the detection of the state (e.g., the oxidation number) of microscopic systems (e.g., molecules) hosted on the IC.

Actually, scanned probe techniques [such as the scanning tunneling microscope (STM)] have already been proven to have the necessary sensitivity to image single electrons in nanostructures^[16] (although “they almost invariably alter the properties of the system they are measuring”^[17]). Even assuming the ability to reduce the STM size in the micrometer length scale (to be compatible with the IC circuitry), its use for the detection and modification of the electronic state of an ordered array of molecules (considered as a molecular memory) will require dramatic changes in circuit architecture. In present ICs, all bits are matrix-ordered and are singularly accessible by specifying row and column; the use of STM as sensing-writing element suggests the need of organizing the memory as a shift register.

The STM is not the unique apparatus able to detect the electronic state of single molecules; in recent years, the single electron transistor has been proven to work. Such a transistor, based on the concept of Coulomb blockade^[18,19] has the advantage over STM to be producible with the methods of the IC technology and not to require dramatic changes in circuit architecture.

This state of affairs suggests that molecular electronics will necessarily involve a combination of microtechnologies and nanotechnologies^[20] and identifies in *self-assembly* (i.e., the deposition of functional molecules in wanted regions of the microelectronic device) and in *grafting* (i.e., the selective bonding of certain groups of the molecules to electrodes in the microelectronic regions) the key problems of molecular electronics. Actually, the few examples of logic devices prepared exploiting the electronic properties of molecules are hybrid devices with photolithographically defined electrodes.^[21–23]

Determining the conductance of individual molecules is a difficult task. The case of DNA is emblematic of this difficulty—depending on the study, DNA is indeed said to be an insulator, semiconductor, conductor, or proximity-induced superconductor.^[24] The usual approach to allow electrical testing of organic molecules is to terminate them with thiol (–SH) groups, which behave as alligator clips to gold. Gold electrodes with parallel-plate geometry are

now currently prepared down to separations of 4 nm. While useful for the determination of the electrical characteristics of the molecules (allowing the assessment of their conduction mechanism), this arrangement is, however, largely incompatible with silicon-based ICs, for which gold should be avoided.

Although it may seem difficult to insert functional molecules between two electrodes with a controlled separation in the nanometer length scale (say, 3 nm), a solution to this problem, fully compatible with the IC technology, has recently been proposed.^[25] The MOS transistor provides indeed a parallel-plane geometry with silicon plates separated by just the gate-oxide thickness—3 nm in the current technology. To allow the insertion of functional molecules therein, it is sufficient to define the gate geometry with an etch sequence formed by a plasma etch of the unmasked polysilicon followed by a wet (aqueous HF) etch of the underlying SiO₂. This process, initiated with a “vertical” attack, does not complete with the total dissolution of the unmasked SiO₂ but rather proceeds laterally overetching a portion of the SiO₂ covered by the polysilicon. The width of the overetched region (the “recessed region”) is controlled by the exposure of the structure to the etching solution. Of course, this is only one of the several possibilities offered by microelectronics, and it is expected that the region hosting the molecular electronics will be obtained exploiting features (such as overetches) hitherto ignored (or even demolished) in IC processing.

Accepting this view, the development of any nanotechnology for data processing does necessarily require the ability to control a number of IC surfaces to allow self-assembly, while still providing the functions of power supply, addressing, sensing, etc. To a large extent, the materials of microelectronics are limited to Si, SiO₂, Si₃N₄, Al, and Ti; of them, only silicon is single crystalline and is thus the most natural candidate as the seed for ordered organic layers.

THE (100) SURFACE OF SILICON AND ITS USUAL CHEMICAL STATES

Silicon surfaces are producible in various orientations: (111), (100), (110), (113), etc. Of them, the (100) surface is the most used in IC processing. In practical conditions, the (100) silicon surface is mainly oxygen-terminated or hydrogen-terminated.

The Surface Resulting After Aqueous HF Etching of Sacrificially Grown SiO₂

Silicon and fluorine combine to form one of the most stable bonds, the Si–F bond energy $E_b[\text{Si–F}]$ being

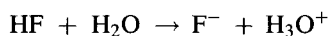
6.9 eV.^[26] It does not surprise, therefore the astonishment when etching by HF-concentrated aqueous solutions of thermally grown SiO₂ was discovered to leave hydrogen-terminated silicon surfaces.^[27]

The first explanation of this fact was given by Ubara et al.^[27] in terms of polarization of Si—Si backbonds to Si—F bonds. Assuming that the strength of the Si—F bond derives from an electrostatic reinforcement because of electron transfer from silicon to fluorine, the ionicity of the Si—F bond polarizes the Si—Si backbonds, which allows an easy insertion of HF into the weakened Si—SiF bond. If this bond is cleaved with the addition of fluorine to the SiF site and of hydrogen to the other silicon atom, the ionicity is increased and so is the polarization of the residual backbonds. Reiterating this argument, one obtains that the formation of a SiF_n moiety becomes easier the higher is *n*, and that the process is concluded with the formation of a volatile molecule, SiF₄, and of hydrogen terminations at the silicon surface.^[27]

This scheme was investigated quantum mechanically on model molecules (such as H₃Si—SiH₂F or H₃SiF) by Trucks et al.^[28] They showed that the activation energy, 1.0 eV, of the process leading to two fluorine atoms attached to the same silicon atom is lower than the activation energy, 1.4 eV, of the process transferring the fluorine to the adjacent silicon atom. Although the Si—H bond is spontaneously destroyed by reaction with HF (the reaction being exothermic by 1.3 eV), an activation energy of 1.2 eV was calculated for this process. Although small, the difference of 0.2 eV, between the activation energies for the destruction of the Si—H bond and that for the attachment of another fluorine atom to fluorinated silicon, is so high as to make the time constant of the former reaction 4 orders of magnitude higher than that of latter reaction. These calculations support therefore the opinion, first formulated by Ubara et al.^[27] that the formation of hydrogen-terminated surfaces is kinetically, rather than thermodynamically, controlled.

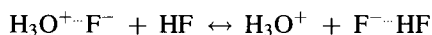
The assumption that undissociated HF is the etching agent is, however, contradicted by the following facts:

1. In diluted aqueous solution, HF is completely dissociated,



its behavior as a weak acid is a result of the reduction of the H₃O⁺ activity resulting from tight ion pairing H₃O⁺···F⁻ between the oxonium and fluoride ions (Ref. [29], Chapter 3).

2. In concentrated aqueous solution, the H₃O⁺ activity is increased because of the formation of the hydrogen-bonded adduct F⁻···HF via the equilibrium



the concentrated aqueous solution does therefore contain undissociated HF, but its binding energy to F⁻ is so high (Eb[F⁻···HF]=2.2 eV; Ref. [30, p. 76]) that the adduct F⁻···HF is considered a well-defined ion HF₂⁻ (Ref. [29], Chapter 3).

3. In gas phase (where the etching species is undissociated HF), the attack results mainly in fluorine-terminated silicon surfaces.^[31]

Following the criticism of Ref. [32] and using the results of high-level quantum mechanical calculation of the stability of the Si—Si bond in relation to its terminations,^[33] Cerofolini thus proposed an ionic route able to account for the observed hydrogen termination resulting after attack by HF-concentrated aqueous solution to thermally oxidized silicon. The route is constituted by three cycles each composed by four consecutive steps, the rate-determining one being F⁻ transfer from the etching solution to the coma of SiF_n termination.^[34] Even the gas-phase attack, leading to fluorine-terminated silicon, seems to be controlled by the presence of adsorbed water.^[31]

The “Native Oxide” and Its Growth Kinetics

An ideally hydrogen-terminated surface is presumed to be indefinitely stable (in the laboratory timescale) in air.

Although the (100) surface resulting after aqueous HF etching of the overlying oxide is expected to be terminated with silicon dihydride, the hydrogen terminations actually form, however, a heterogeneous family of monohydride, dihydride, and trihydride species,^[35,36] and the surface still contains an appreciable amount of silicon—oxygen centers, roughly corresponding to 0.2–0.5 monolayers, depending on the preparation.^[37] Such oxygen-containing centers are responsible for the environmental instability of these surfaces via the oxidation of the backbonds to Si—O bonds; this process, initiated at oxygen defects and mediated by adsorbed water, proceeds with an island growth and is eventually responsible for surface roughening.^[38]

Once the first layer has grown (at a characteristic time τ₁), further oxidation occurs in a layer-by-layer fashion; the characteristic time τ_{*n*} required for the formation of the *n*th layer increasing exponentially with *n* is given by:

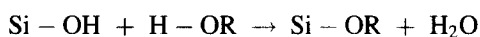
$$\tau_n = \tau_1 a^{n-1}$$

where *a* is a suitable constant.^[37] The native oxide so formed is the final result of a complex oxidation process, in which H₂O and O₂ both play a crucial role.^[37]

Understanding such a behavior is not a trivial task. A microscopic model for it was proposed by Cerofolini et al. in a series of papers in terms of tunneling either of a proton from adsorbed water^[39,40] or of an electron to adsorbed oxygen.^[41,42] The development of the kinetic

description of layer-by-layer growth does not require the detailed knowledge of the tunneling species (for that it suffices to assume that the process is limited by a tunneling-assisted step); rather, the kinetic model provides a practical example for a self-similar process, in which the rates of growth from layer to layer are scaled by a subunitary positive Grossmann factor.^[43]

Grafting of organic molecules to SiO₂ is a relatively simple task.^[44] For that it suffices first to cleave (by immersion in water or in water solutions of ammonia) the surface siloxanic bridges Si–O–Si, thus forming an array of silanols Si–OH, and then to expose the surface to alcohols; grafting occurs via condensation:



Because R can contain practically any functional group, this route seems to offer an interesting possibility for the functionalization of silicon.^[45] However, two factors play against it:

1. No process is known for the preparation of a complete ordered layer of silanols, either at the SiO₂ or silicon surface.
2. The oxo bridge between silicon and carbon undergoes readily hydrolysis, so that the condensation reaction above is somewhat reversible, that renders the grafted species environmentally weak.

It is generally believed that the production of environmentally robust, ordered organic layers requires a preparation of the surface somewhat different from the current ones and a grafting through Si–C bonds.

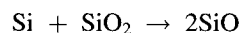
TRYING TO CONTROL THE CHEMICAL AND CRYSTALLINE ORDER OF THE (100) SURFACE OF SILICON

The “technological” surfaces discussed in the previous section do not preserve either the crystalline order of the underlying substrate or its chemical homogeneity; they are not useful as seed for ordered organic layers.

The Clean, 2 × 1-Reconstructed, (100) Silicon Surface

Clean (100) silicon surfaces with 2 × 1 reconstruction [referred to as 2 × 1 (100) Si, in which neighboring pairs of surface atoms form double-bonded dimers, and the dimers are organized in a two-dimensional lattice] can be prepared by suitable heat treatment in an ultrahigh vacuum (UHV) of technological surfaces. If the surface is covered by a native oxide, the oxo groups can be destroyed by heating at high temperature *T* (above

1000°C); in the absence of oxygen, interfacial silicon reacts with SiO₂ forming volatile SiO:



If the surface is mainly hydrogen-terminated (because it is prepared via aqueous HF etching of a sacrificial SiO₂ film), the hydrogen terminations may be demolished at somewhat lower temperature (say, *T* < 800°C) with the formation of H₂.

Experimental evidence for the presence of the double-bonded dimers at the (100) silicon surface can be obtained from the presence of a satellite peak shifted by 0.2 eV toward lower binding energies in the Si 2*p* spectrum obtained by X-ray photoemission spectroscopy (XPS).^[46]

The Hydrogen-Terminated, 2 × 1- or 1 × 1-Reconstructed, (100) Silicon Surfaces

Hydrogen-terminated, 2 × 1-reconstructed, (100)-oriented silicon surfaces [referred to as 2 × 1 (100)H Si, in which the π bond of the surface dimer is broken and the two radicals are saturated by bonding to hydrogen] can be obtained by exposing, without breaking the vacuum, the clean 2 × 1 (100) surface kept at ca. 400°C to a few langmuirs of atomic hydrogen, in turn obtained by the dissociation of H₂ after contact with a hot tungsten filament.

The overall process (requiring a treatment in an UHV and an exposure to atomic hydrogen) is, however, complicated and may be simplified as follows. The surfaces prepared by aqueous HF etching can indeed be used for the preparation of highly ordered hydrogen-terminated surfaces via exposure to an H₂ atmosphere at relatively high temperature. In fact, the oxygen terminations remaining after the HF attack are totally demolished after heating at *T* > 750°C; this treatment destroys the preexisting heterogeneous distribution of trihydride, dihydride, and monohydride terminations and eventually results in monohydride terminations and 2 × 1 reconstruction^[36] or in dihydride terminations and 1 × 1 reconstruction^[47] (for which even the residual σ bond of the surface dimer is broken and the radicals are saturated with hydrogen atoms), according to the process. The surfaces so prepared are flat down to the atomic level.

USING CONTROLLED SURFACES TO FUNCTIONALIZE SILICON

Functionalization of Clean (100) Silicon via Cycloaddition

The clean, 2 × 1-reconstructed, (100) silicon surface can be used to functionalize the silicon via [2+2] or [4+2]

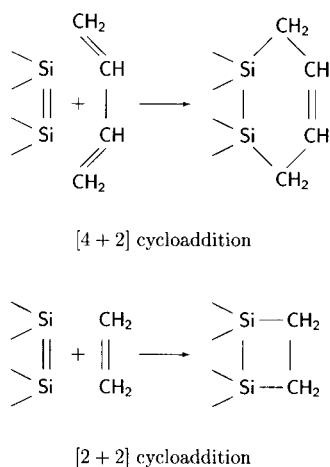


Fig. 2 Addition of an alkene ([2+2] cycloaddition, bottom) or a conjugated diene ([4+2] cycloaddition or Diels–Alder reaction, top) to the clean, 2×1 -reconstructed, (100) silicon surface.

cycloaddition.^[48,49] Fig. 2 sketches both these reactions for the simplest alkene and diene.

Dienes are particularly interesting because, irrespective of whether they undergo [4+2] cycloaddition (as sketched in Fig. 2) or [2+2] cycloaddition (as performed in Ref. [50] using 1,4-cyclohexadiene), they may be used to insert a second functional group (the C=C double bond) on 2×1 (100) Si. An ordered layer of intact functional groups allows the possibility of preparing hybrid organo-silicon devices. Cycloaddition reactions must, however, be carried out in an UHV because the 2×1 (100) Si surface is very reactive and, when exposed to air, forms quickly a disordered native oxide, characterized by the copresence of silanic and silanolic terminations in addition to oxo, peroxy, and perhaps epoxy bridges (Figs. 3 and 4).

Functionalization of Hydrogen-Terminated (100) Silicon via Hydrosilation

In view of its relative inertness, it is not easy to graft organic molecules to hydrogen-terminated silicon. The preferred way for that is the *hydrosilation* reaction (Ref. [29], p. 1255). This reaction occurs between 1-alkenes and hydrogen-terminated silicon.

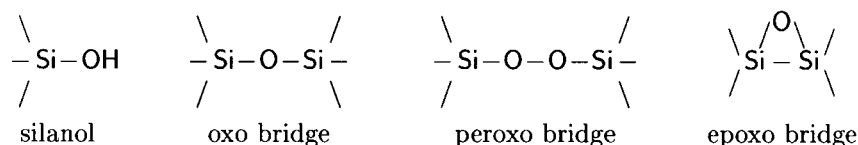


Fig. 3 Silicon–oxygen moieties at the silicon surface.

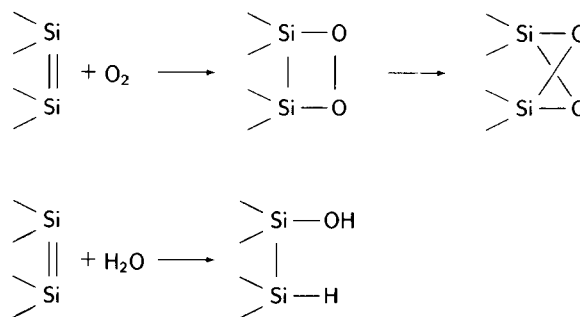


Fig. 4 Expected reactions of water (bottom) and oxygen (top) at the 2×1 (100) Si surface, showing how silanols, peroxy, and oxo centers may be formed after exposure to air of the clean, 2×1 -reconstructed, (100) surface of silicon.

Hydrosilation is a reaction involving hydrogen shift from silicon to a carbon atom involved in the π bond and bond formation between the silicon atom and the other carbon atom (Fig. 5). If the number n of carbon atoms in the alkane chain is small (say, $n < 8$), the alkene hydrosilation occurs only in the presence of a catalyst (H_2PtCl_6)^[44] or after activation (radical formation);^[51] for long chains (say, $n > 10$), the reaction occurs spontaneously at a temperature of about 200°C .^[44,52]

Because hydrosilation involves only one silicon atom, it was mainly studied on the hydrogen-terminated, 1×1 -reconstructed, (111) silicon surface [denoted as 1×1 (111)H Si], and only few works have been devoted to study alkene hydrosilation on 1×1 (100)H Si.^[52,53] The hydrosilation of 1-alkenes at 1×1 (100)H Si is expected to occur according to pathways (I') or (I'') in Fig. 6.

The C=C bond is not unique in undergoing hydrosilation. This reaction is indeed known to occur for the C=N, C=O, and C \equiv C bonds also (Ref. [29], p. 1256).

Although the reactivity of 1-alkynes is similar to that of 1-alkenes, there is, however, an important difference: after the first addition (II), the formed species, **2'** and **2''** in Fig. 6, contain a double bond in the vicinity of another hydrogen termination of silicon, so that the reaction can, in principle, proceed, via (III) or (IV), with the formation of the species **3** or **4**. Understanding the nature of the interfacial species is not without interest: for instance, if the reaction stopped after (II), the silicon surface would be

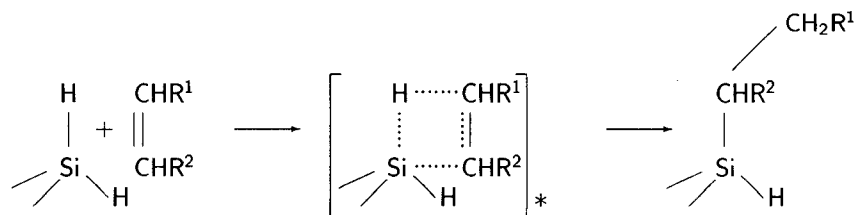


Fig. 5 Hydrosilylation of 1-alkenes as a concerted reaction. One between R^1 and R^2 denotes hydrogen; the other may be either hydrogen or an alkane chain.

equipped with a second reactive group (the $C=C$ group) in addition to the one, if any, carried by R .

The only characterizations we know of the hydrogen-terminated, 1×1 -reconstructed, (100) silicon surface derivatized with 1-alkyne are the ones due to Sieval et al.^[54] and Cerofolini et al.^[55] The first collaboration,

basing their conclusions on infrared spectroscopy and quantum mechanical calculations, arrived to the conclusion that the grafting of 1-hexadecyne at 200°C on the technological hydrogen-terminated surface occurs mainly with the formation of the adducts **3** and **4**. The second collaboration, basing their conclusions on XPS, arrived to the conclusion that the grafting of 1-octyne at 170°C on 2×1 (100)H Si occurs with the formation of the adducts **2**. At the present level of investigation, it is not clear if the different reported behaviors are a result of the nature of the surface, length of the alkyne, or reaction temperature or simply to an inadequate interpretation of the experimental data.

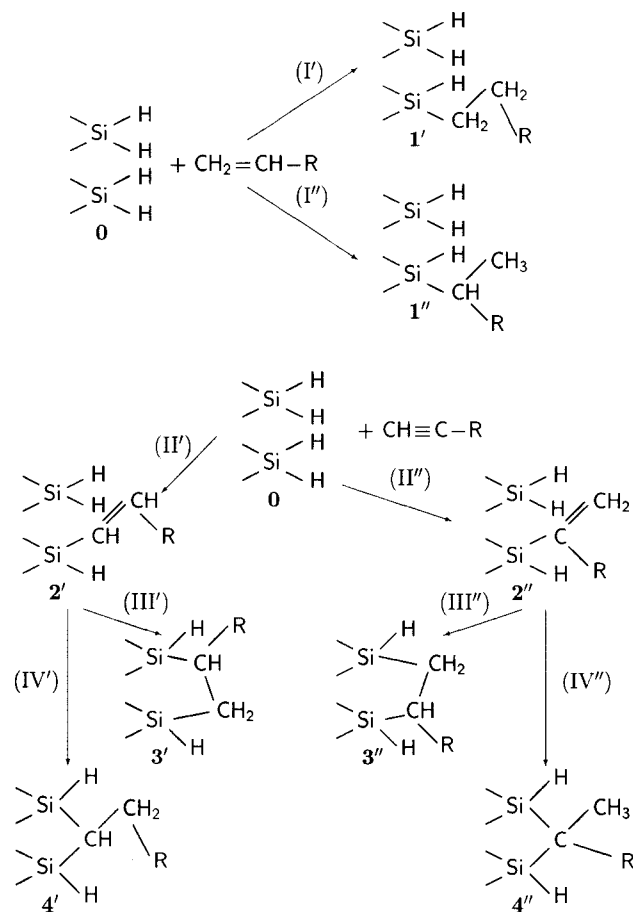


Fig. 6 Hydrosilylation of 1-alkene [pathway (I)] and 1-alkyne [pathway (II)] at the hydrogen-terminated, 1×1 -reconstructed, (100)-oriented, silicon surface; R denotes a suitably terminated alkane chain.

CONCLUSION

The evolution of molecular electronics via the hybrid route requires the functionalization of the (100) surface of silicon. Two states of the (100) silicon surface seem to have the necessary characteristics of crystalline and chemical order required for the deposition of molecular devices with size in the nanometer length scale: the clean 2×1 -reconstructed surface and the hydrogen-terminated 1×1 - or 2×1 -reconstructed surfaces. Alkenes or alkynes may be used for their functionalization: via cycloaddition to the clean surface or via hydrosilylation at the hydrogen-terminated surfaces.

REFERENCES

1. van Gulick, N. Theoretical aspects of the linked ring problem. *New J. Chem.* **1993**, *17*, 619–625.
2. Frisch, H.L.; Wasserman, E. Chemical topology. *J. Am. Chem. Soc.* **1961**, *83*, 3789–3795.
3. Walba, D.M. Preface to van Gulick paper. *New J. Chem.* **1993**, *17*, 618.
4. Lehn, J.-M. *Supramolecular chemistry—Scope and perspectives. Molecules, supermolecules and*

- molecular devices. *Angew. Chem., Int. Ed. Engl.* **1988**, *27*, 89–112.
5. Balzani, V.; Credi, A.; Raymo, F.M.; Stoddart, J.F. Artificial molecular machines. *Angew. Chem., Int. Ed.* **2000**, *39*, 3348–3391.
 6. Gittins, D.I.; Bethell, D.; Schiffrin, D.J.; Nichols, R.J. A nanometre-scale electronic switch consisting of a metal cluster and redox-addressable groups. *Nature* **2000**, *408*, 67–69.
 7. Joachim, C.; Gimzewski, J.K.; Aviram, A. Electronics using hybrid-molecular and mono-molecular devices. *Nature* **2000**, *408*, 541–548.
 8. Semiconductor Industry Association (S.I.A.). *International Technology Roadmap for Semiconductors*; SIA: San Jose, CA, 2001.
 9. Packan, P.A. Pushing the limits. *Science* **1999**, *285*, 2079–2081.
 10. Ito, T.; Okazaki, S. Pushing the limits of lithography. *Nature* **2000**, *406*, 1027–1031.
 11. Bohr, N. The quantum postulate and the recent development of atomic theory. *Nature* **1928**, *121*, 580–590. Reprinted in *Quantum Theory and Measurement*, edited by J.A. Wheeler and W.H. Zurek (Princeton Univ. Press, Princeton, NJ, 1983) pp. 87–126.
 12. Daneri, A.; Loinger, A.; Prosperi, G.M. Quantum theory of measurement and ergodicity conditions. *Nucl. Phys.* **1962**, *33*, 297–319.
 13. Daneri, A.; Loinger, A.; Prosperi, G.M. Further remarks on the relations between statistical mechanics and quantum theory of measurement. *Nuovo Cim., B* **1966**, *44*, 119–128.
 14. McIntyre, R.J. The distribution of gains in uniformly multiplying avalanche photodiodes: Theory. *IEEE Trans. Electron Devices* **1972**, *ED-19*, 703–713.
 15. Cerofolini, G.F.; Ferla, G.; Foglio Para, A. A proposal: Dynamic RAMs as particle detectors. *Nucl. Instrum. Methods* **1980**, *169*, 125–128.
 16. Lemay, S.G.; Janssen, J.W.; van den Hout, M.; Mooij, M.; Bronikowski, M.J.; Willis, P.A.; Smalley, R.E.; Kouwenhoven, L.P.; Dekker, C. Two-dimensional imaging of electronic wavefunctions in carbon nanotubes. *Nature* **2001**, *412*, 617–620.
 17. Woodside, M.T.; McEuen, P.L. Scanned probe imaging of single-electron charge states in nanotube quantum dots. *Science* **2002**, *296*, 1098–1101.
 18. Devoret, M.H.; Schoelkopf, R.J. Amplifying quantum signals with the single-electron transistor. *Nature* **2000**, *408*, 1039–1046.
 19. Postma, H.W.Ch.; Teepen, T.; Yao, Z.; Grifoni, M.; Dekker, C. Carbon nanotube single-electron transistors at room temperature. *Science* **2001**, *293*, 76–79.
 20. Cerofolini, G.F. Beyond Silicon? Perspectives for Molecular Electronics. In *Chemistry for Innovative Materials*; Cerofolini, G.F., Mininni, R.M., Schwarz, P., Eds.; EniChem: Milano, 1991; 84–97.
 21. Collier, C.P.; Wong, E.W.; Belohradsky, M.; Raymo, F.M.; Stoddart, J.F.; Kuekes, P.J.; Williams, R.S.; Heath, J.R. Electronically configurable molecular-based logic gates. *Science* **1999**, *285*, 391–394.
 22. Huang, Y.; Duan, X.; Cui, Y.; Lauhon, L.J.; Kim, K.-H.; Lieber, C.M. Logic gates and computation from assembled nanowire building blocks. *Science* **2001**, *294*, 1313–1317.
 23. Bachtold, A.; Hadley, P.; Nakanishi, T.; Dekker, C. Logic circuits with carbon nanotube transistors. *Science* **2001**, *294*, 1317–1320.
 24. Hipps, K.W. It's all about contacts. *Science* **2001**, *294*, 536–537.
 25. Cerofolini, G.F.; Ferla, G. Toward a hybrid micro-nanoelectronics. *J. Nanopart. Res.* **2002**, *4*, 185–191.
 26. Walsh, R. Bond dissociation energy values in silicon-containing compounds and some of their implications. *Acc. Chem. Res.* **1981**, *14*, 246–252.
 27. Ubara, H.; Imura, T.; Hiraki, A. Formation of Si—H bonds on the surface of microcrystalline silicon covered with SiO_x by HF treatment. *Solid State Commun.* **1984**, *50*, 673–675.
 28. Trucks, G.W.; Raghavachari, K.; Higashi, G.S.; Chabal, Y.J. Mechanism of HF etching of silicon surfaces: A theoretical understanding of hydrogen passivation. *Phys. Rev. Lett.* **1990**, *65*, 504–507.
 29. Cotton, F.A.; Wilkinson, G. *Advanced Inorganic Chemistry*, 5th Ed.; Wiley: New York, NY, 1988.
 30. March, J. *Advanced Organic Chemistry*, 4th Ed.; Wiley: New York, NY, 1992.
 31. Miki, N.; Kikuyama, H.; Kawanabe, I.; Miyashita, M.; Ohmi, T. Gas-phase selective etching of native oxide. *IEEE Trans. Electron Devices* **1990**, *37*, 107–115.
 32. Cerofolini, G.F.; Meda, L. Chemistry at silicon crystalline surfaces. *Appl. Surf. Sci.* **1995**, *89*, 351–360.
 33. Cerofolini, G.F.; Re, N. Chemical Perspectives on Growth and Properties of Ultrathin SiO₂ Layers. In *Fundamental Aspects of Ultrathin Dielectrics on Si-Based Devices*; Garfunkel, E., Gusev, E., Vul, A., Eds.; Kluwer: Dordrecht, 1998; 117–129.
 34. Cerofolini, G.F. A study of the ionic route for hydrogen terminations resulting after SiO₂ etching by concentrated aqueous solutions of HF. *Appl. Surf. Sci.* **1998**, *133*, 108–114.
 35. Niwano, M.; Kageyama, J.; Kinashi, K.; Takashi, I.; Miyamoto, N. Infrared spectroscopy study of initial stages of oxidation of hydrogen-terminated Si

- surfaces stored in air. *J. Appl. Phys.* **1994**, *76*, 2157–2163.
36. Aoyama, T.; Goto, K.; Yamazaki, T.; Ito, T. Silicon (001) surface after annealing in hydrogen ambient. *J. Vac. Sci. Technol., A* **1996**, *14*, 2909–2915.
 37. Morita, M.; Ohmi, T.; Hasegawa, E.; Kawakami, M.; Ohwada, M. Growth of native oxide on a silicon surface. *J. Appl. Phys.* **1990**, *68*, 1272–1281.
 38. Usuda, K.; Kanaya, H.; Yamada, K.; Sato, T.; Sueyoshi, T.; Iwatsuki, M. Scanning tunneling microscopy of hydrogen-terminated Si(111) surfaces at room temperature. *Appl. Phys. Lett.* **1994**, *64*, 3240–3242.
 39. Cerofolini, G.F. Kinetics of tunnel-assisted multilayer chemisorption on homogeneous surfaces. *J. Colloid Interface Sci.* **1994**, *167*, 453–456.
 40. Cerofolini, G.F.; Meda, L.; Falster, R. A Model for Room-Temperature Wet Oxidation of Silicon. In *Semiconductor Silicon 1994*; Huff, H.R., Bergholz, W., Sumino, K., Eds.; The Electrochemical Society: Pennington, NJ, 1994; 379–388.
 41. Cerofolini, G.F.; La Bruna, G.; Meda, L. Gas-phase room-temperature oxidation of (100) silicon. *Appl. Surf. Sci.* **1996**, *93*, 255–266.
 42. Cerofolini, G.F. Room-Temperature Oxidation of Single-Crystalline Silicon. In *Silicon for the Chemical Industry III*; Oye, H.A., Rong, H.M., Ceccaroli, B., Nygaard, L., Tuset, J.K., Eds.; Tapir: Trondheim, 1996; 117–127.
 43. Vlad, M.O.; Cerofolini, G.F.; Ross, J. Temporal logarithmic oscillations in self-similar multilayer aggregation: Shlesinger–Hughes renormalization with application to the tunnel-assisted wet oxidation of silicon. *J. Phys. Chem., A* **1999**, *103*, 4798–4807.
 44. Tertykh, V.A.; Belyakova, L.A. Solid-Phase Hydro-silation Reactions with Participation of Modified Silica Surface. In *Adsorption on New and Modified Inorganic Sorbents*; Dabrowski, A., Tertykh, V.A., Eds.; Elsevier: Amsterdam, 1996; 147–189.
 45. Cleland, G.; Horrocks, B.R.; Houlton, A. Direct functionalization of silicon via the self-assembly of alcohols. *J. Chem. Soc., Faraday Trans.* **1995**, *91*, 4001–4003.
 46. Himpfel, F.J.; McFeely, F.R.; Taleb-Ibrahimi, A.; Yarnoff, J.A.; Hollinger, G. Microscopic structure of the SiO₂/Si interface. *Phys. Rev., B* **1988**, *38*, 6084–6096.
 47. Cerofolini, G.F.; Galati, C.; Lorenti, S.; Renna, L.; Viscuso, O.; Bongiorno, C.; Raineri, V.; Spinella, C.; Condorelli, G.G.; Fragala', I.L.; Terrasi, A. The early oxynitridation stages of hydrogen-terminated (100) silicon after exposure to N₂:N₂O. III. The initial condition. *Appl. Phys., A*, **2003**, *17*, 403–409.
 48. Bent, S.F. Organic functionalization of group IV semiconductor surfaces: Principles, examples, applications, and prospects. *Surf. Sci.* **2002**, *500*, 879–903.
 49. Buriak, J. Organometallic chemistry on silicon and germanium surfaces. *Chem. Rev.* **2002**, *102*, 1271–1308.
 50. Yamashita, Y.; Hamaguchi, K.; Machida, S.; Mukai, K.; Yoshinobu, J.; Tanaka, S.; Kamada, M. Adsorbed states of cyclopentene, cyclohexene, and 1,4-cyclohexadiene on Si(100)(2 × 1): Towards the fabrication of novel organic films/Si hybrid structures. *Appl. Surf. Sci.* **2001**, *169/170*, 172–175.
 51. Lopinski, G.P.; Wayner, D.D.M.; Wolkow, R.A. Self-directed growth of molecular nanostructures on silicon. *Nature* **2000**, *406*, 48–51.
 52. Sieval, A.B.; Demirel, A.L.; Nissink, J.W.M.; van der Maas, J.H.; de Jeu, W.H.; Zuilhof, H.; Sudholter, E.J.R. Highly stable Si–C linked functionalized monolayers on the silicon (100) surface. *Langmuir* **1998**, *14*, 1759–1768.
 53. Sieval, A.B.; Vleemimg, V.; Zuilhof, H.; Sudholter, E.J.R. An improved method for the preparation of organic monolayers of 1-alkenes on hydrogen-terminated silicon surfaces. *Langmuir* **1999**, *15*, 8288–8291.
 54. Sieval, A.B.; Opitz, R.; Maas, H.P.A.; Schoeman, M.G.; Meijer, G.; Vergeldt, F.J.; Zuilhof, H.; Sudholter, E.J.R. Monolayers of 1-alkynes on the H-terminated Si(100) surface. *Langmuir* **2000**, *16*, 10359–10368.
 55. Cerofolini, G.F.; Galati, C.; Reina, S.; Renna, L. Functionalization of the (100) surface of hydrogen-terminated silicon via hydrosilation of 1-alkyne. *Mater. Sci. Eng., C*, **2003**, *23*, 253–257.



Nanoarrays Synthesized from Porous Alumina

Latika Menon

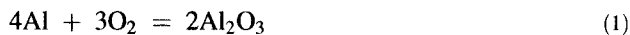
Texas Tech University, Lubbock, Texas, U.S.A.

INTRODUCTION

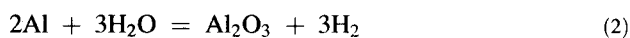
Currently, nanotechnology is concerned with fabrication of useful materials at the nanoscale level for applications in nanodevices. Several methods are being used for nanofabrication,^[1–10] e-beam lithography, interference lithography, cluster method, etc. One commonly used method is the use of membranes with nanosized holes. When the holes are filled up with appropriate materials, it leads to formation of a self-assembled nanoarray. Some commonly used membranes are polycarbonate membranes and nanoporous alumina membranes. Use of porous alumina membranes is particularly noteworthy.^[11] These are aluminum oxide membranes with nanosized cylindrical holes perpendicular to the surface of the film. The membranes are available commercially in some fixed sizes with specific pore diameters. They can also be prepared very easily in the laboratory using electrochemical means. Fabrication conditions can be controlled to achieve desired pore length and diameter, and they can be used in many different ways to prepare a variety of nanostructured materials, magnetic metals and alloys, semiconductor alloys and heterostructures, superconductors, carbon nanotubes, etc. This article briefly reviews some of the ongoing research in the area of nanofabrication using porous alumina templates.

FABRICATION OF NANOPOROUS ALUMINA TEMPLATE

It is well known that a thin (2–5 nm) film of aluminum oxide always forms on the surface of aluminum exposed to air. This is because of oxidation of aluminum in the presence of oxygen and water vapor. The reactions occurring during the process are



and



The oxidation process can be hastened by anodizing or oxidizing aluminum in the presence of an acid. Anodization in a weak acid leads to formation of a nonporous

barrier layer of aluminum oxide. In contrast, a strong acid can partially dissolve aluminum oxide. Anodization in a strong acid (pH < 4) therefore results in a porous aluminum oxide film (commonly known as porous alumina) because of a competing mechanism of oxide growth and partial dissolution of aluminum oxide by hydrogen ions.^[12,13]

In the laboratory, a commercially available aluminum foil is first electropolished to create a clean, shiny, flat surface (roughness ~ 5–10 nm). Electropolishing is carried out under d.c. conditions in an electrolyte commonly called the L1 electrolyte. It consists of 1050 mL ethyl alcohol, 150 mL butyl cellosolve, 93 mL perchloric acid, and 205 mL distilled water. The optimum voltage is of the order of 30–60 V, and the optimum electropolishing time is of the order of 10–30 sec.^[14–16] The electropolished Al surface is then anodized in the presence of an acid. In this process, the Al foil is placed at the anode, while a Pt mesh is used as cathode (Fig. 1). A d.c. voltage is applied across the two electrodes. A moderately strong acid (for example, 15% sulfuric acid, 3% oxalic acid, or 5% phosphoric acid) is used as electrolyte. During the process of anodization, a thin film of nanoporous aluminum oxide forms at the surface of aluminum as shown in the schematic cross-section diagram in Fig. 2.

The pores are cylindrical, straight, and are open at the top. The pores do not grow all the way into the aluminum surface. There is a thin barrier layer of aluminum oxide separating the porous alumina layer from the bottom aluminum layer. The thickness of the barrier layer and the diameter of the pores are controlled by fabrication conditions, namely, the acid used and the voltage applied. Some commonly used acids are 3% oxalic, 15% sulfuric, and 5% phosphoric acid. The smallest pore diameters are obtained by anodization in 15% sulfuric acid at low voltages, and the largest pore diameters are obtained for anodization in 5% phosphoric acid at higher voltages. Pore densities are typically of the order of 10^{10} – 10^{11} pores/cm². Barrier layer thickness is in the range of tens of nanometers. Pore diameters are in the range of 8–200 nm. Theoretical modeling of pore growth and dependence of pore parameters on fabrication conditions are discussed in detail in Refs. [17–19]. The length of the pores is controlled by time of anodization. Increased time of anodization leads to longer pore lengths. Some typical

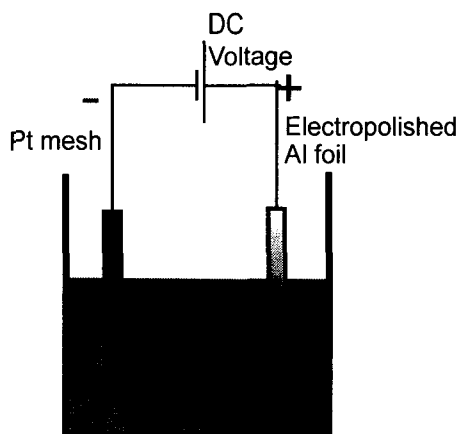


Fig. 1 Schematic diagram showing a typical anodization process.

AFM images of templates prepared by anodization under different conditions are shown in Figs. 3 and 4. The pores are highly ordered over length scales of the order of 5–10 μm . The extent of ordering can be increased slightly by annealing the Al foil prior to anodization and also by carrying out a multistep anodization process.^[20] In a multistep process, Al foil is first anodized for a very long time (typically 12–18 hr). Long time anodization causes the pores to rearrange and reduces the number of defects and dislocations. It also leads to formation of a very thick alumina template. The thick template is dissolved away in a 0.2 M chromic–0.4 M phosphoric acid mixture at 60°C which leaves behind a textured Al surface consisting of an array of ordered bumps. Reanodization of the

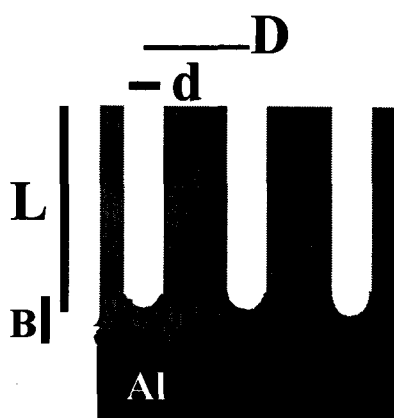


Fig. 2 Schematic cross-sectional diagram of a typical porous alumina template showing the nanoporous layer, the barrier layer and the aluminum layer (L is the pore length, d is the pore diameter, D is the interpore spacing, and B is the thickness of the barrier layer).

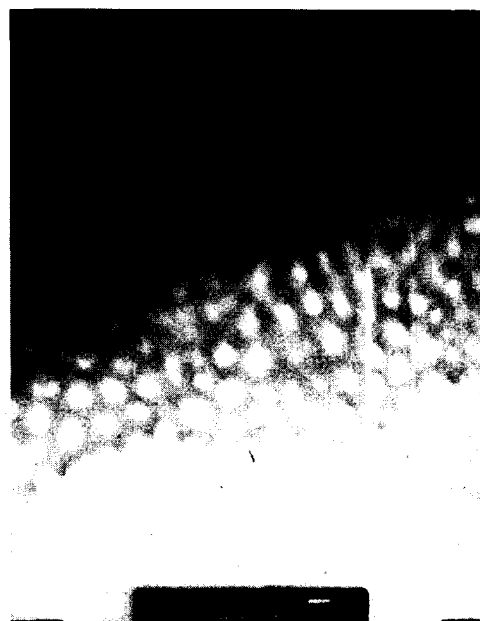


Fig. 3 Transmission Electron Microscope image of a template anodized in 15% sulfuric acid at 10 V showing an array of pores with diameter ~ 10 nm. (View this art in color at www.dekker.com.)

textured Al surface for the desired length of time leads to a well-ordered nanoporous template (Fig. 4). Instead of a multistep anodization process, an initial ordered nanoindentation of the Al surface can also be used to improve the ordering of the subsequent pore array.^[21]

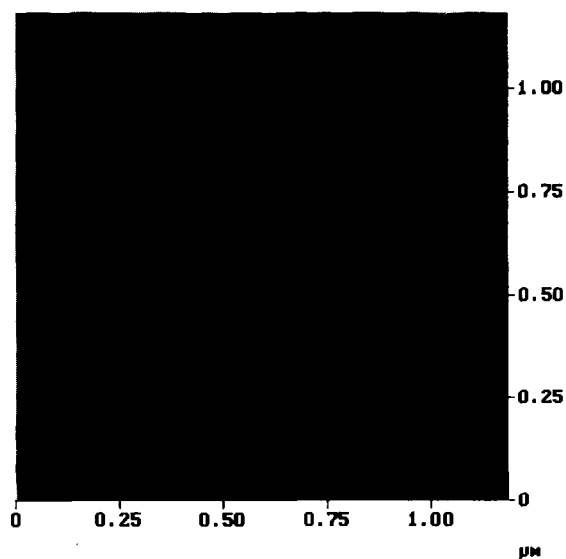


Fig. 4 Atomic force microscopic image of a template anodized in 3% oxalic acid at 40 V showing an array of pores with diameter 50 nm. (View this art in color at www.dekker.com.)

NANOFABRICATION METHODS USING POROUS ALUMINA

Once the templates are fabricated with the desired pore size, they can be used in many different ways to fabricate nanoarrays. Some of these methods are discussed in this section.

Electrodeposition

Alternating current electrodeposition is the simplest way to fill the pores with the appropriate material. For example, to prepare an array of Fe nanowires inside the pores, a 0.1 M aqueous solution of FeSO_4 can be used. Porous alumina and the Pt mesh are the electrodes. An a.c. voltage is applied across the two electrodes. The frequency and voltage are optimized. In the solution, FeSO_4 dissociates into Fe^{2+} ions and $(\text{SO}_4)^{2-}$ ions. During every negative half-cycle, Fe ions are reduced to Fe atoms and deposit inside the pores. Fig. 5 shows a cross-section SEM image of a nanoporous alumina membrane containing Fe nanowires. Using a similar electrodeposition method, nanoarrays of other magnetic metals, for example, Co and Ni, can also be prepared. Alloys, for example, FeCo and CoNi, can be prepared by using an electrolyte

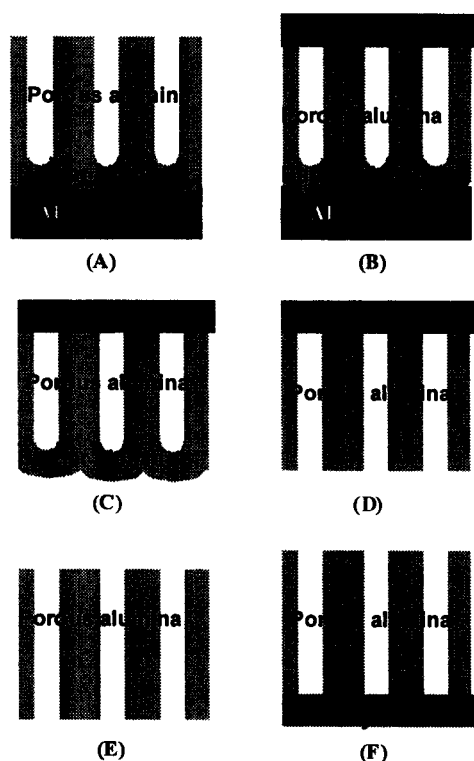


Fig. 5 Sequence of steps to prepare a template in contact with a conducting substrate to achieve d.c. electrodeposition.

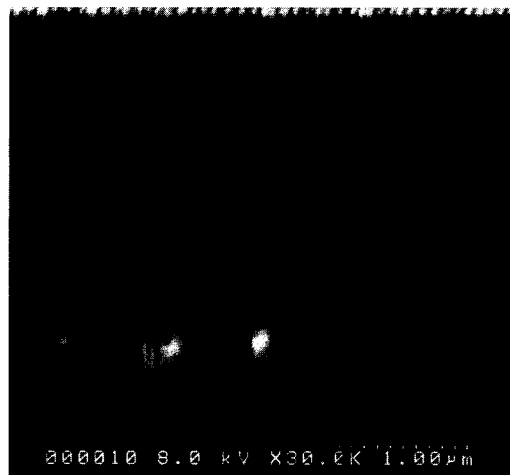


Fig. 6 Scanning electron microscope cross-section image showing an array of pores containing Fe nanowires. Pore diameter ~ 50 nm. (From J. Yun, Texas Tech University.)

containing the appropriate ratio of the constituent materials. The two materials are then subsequently electrodeposited into the pores under optimized a.c. conditions to create alloy nanoarrays. The magnetic properties of Fe, Co, Ni, and FeCo nanoarrays are discussed in "Magnetic Nanoarrays." Other materials, for example, thermoelectric materials such as Bi,^[22] superconducting Pb,^[23] conducting materials Cu and Au,^[24] and conducting polymers,^[25] may also be synthesized inside the pores by using the appropriate electrolyte.

To carry out d.c. electrodeposition, the barrier layer below the pores must be removed. This can be achieved by following the sequence of steps shown in Fig. 6. The top nanoporous layer is first coated with a protective organic layer. The sample is then soaked in 3% HgCl_2 solution to remove the bottom Al layer. This is followed by soaking in 5% phosphoric acid solution for a predetermined length of time to remove the alumina layer at the bottom. The top organic layer is finally removed by soaking in ethyl alcohol solution. This leaves behind a through-hole template. One side is coated with a thin conducting layer, e.g., Au. Using an appropriate electrolyte, nanowires can be deposited inside the pores under d.c. conditions, using a three-terminal setup and a potentiostat. The Pt mesh is used as the counterelectrode, porous alumina is used as the working electrode, and a third electrode, for example, calomel electrode, is used as reference electrode. The voltage between the reference electrode and the alumina is adjusted so that it is higher than the standard reduction potential of the element to be deposited. The standard reduction potentials are obtained from literature. Direct current electrodeposition is particularly useful in the deposition of multilayered nanowires

for applications in Giant Magnetoresistance (GMR) devices and other semiconductor-based spintronic structures. Multilayer nanowires with layers as thin as a few angstroms may be fabricated in porous alumina using electrodeposition.^[26] This is achieved using separate electrolytes for the two components or by using a single electrolyte. The electrolyte is prepared such that it consists of only a trace amount of the nobler element, A, in comparison with the second element, B. The deposition voltage is continually switched between two values, one at which only A is deposited and the other at which both A and B are deposited. By keeping only a trace amount of the nobler metal, A, in the electrolyte, it is ensured that the amount of metal in the AB layer is small, so that its deposition is diffusion-limited. The process may be carried out by adjustment of either the current density (galvanostatic) or the potential (potentiostatic).

Transfer of Porous Alumina onto Substrate

In this method, alumina template is transferred to an appropriate substrate, so that it is in direct contact with the substrate. Several processing steps are necessary to separate the template from the parent aluminum film. The sequence of steps is shown in Fig. 7. The sample is initially anodized for a very short time, sufficient to produce a thin nanoporous layer $\sim 0.1\text{--}0.5\ \mu\text{m}$. A protective organic coating is then applied to the top porous layer. The bottom Al and the barrier alumina layer are etched away in HgCl_2 solution and 5% phosphoric acid solution, respectively. Dry etching methods, for example,

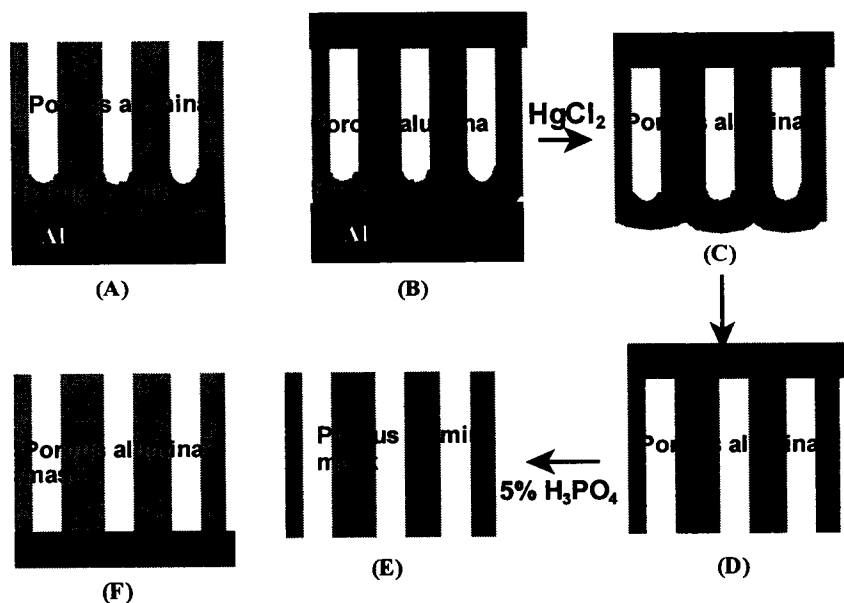


Fig. 7 Sequence of steps to process a nanoporous alumina template for transfer onto a substrate.

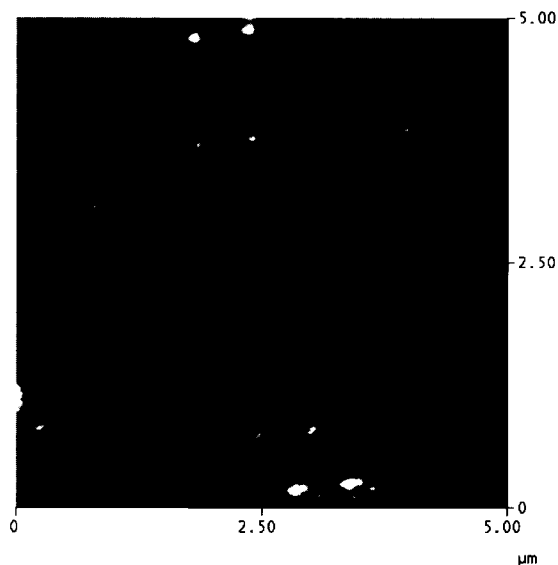


Fig. 8 Atomic force microscopic image showing an array of Co nanodots on a Si substrate. (View this art in color at www.dekker.com.)

plasma etching or focused ion beam milling, may also be used to remove the barrier layer.^[27,28] In the final stage, the organic coating is dissolved away in ethyl alcohol. This leaves behind a thin through-hole nanoporous alumina layer. The layer is carefully transferred onto a substrate, dried, and subsequently used as a mask for deposition of nanoarrays of various materials. Fig. 8 shows an AFM of an array of Co nanodots prepared in this

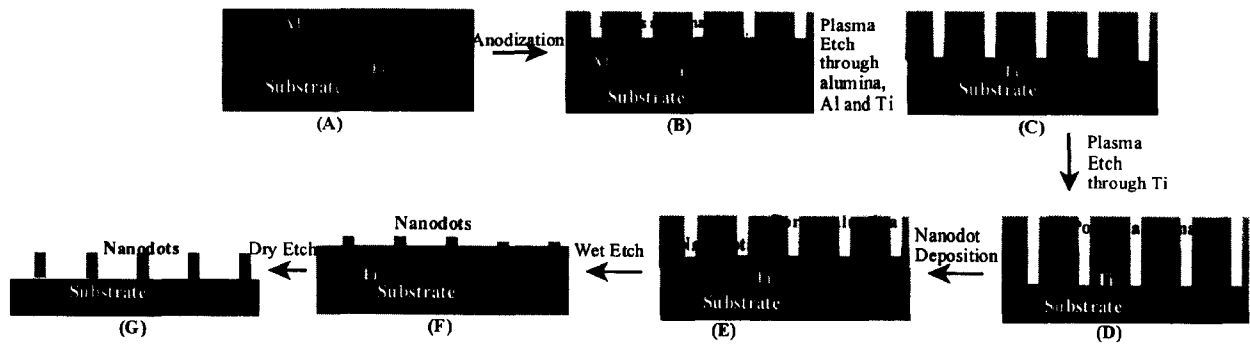


Fig. 9 Sequence of steps to deposit nanoporous alumina template on a substrate.

manner on a Si substrate. One difficulty with this method is the very small area of the prepared masks. This is because of the very small thickness of the masks ($\sim 0.1\text{--}0.5\ \mu\text{m}$) and the very brittle nature of aluminum oxide. This problem can be overcome if porous alumina is directly deposited (instead of being transferred) on a substrate.

Direct Deposition of Porous Alumina on a Substrate

In our laboratory, we have recently demonstrated a novel method to deposit nanoporous alumina template on a substrate.^[29] The method also allows transfer of the nanoporous template pattern onto the bottom substrate. The technique combines anodization process to produce template arrays and plasma etching through the pores. The sequence of steps is shown schematically in Fig. 9. We used silicon wafers as the starting substrate material, although in principle, the method can be extended to any other substrate, for example, epitaxial GaN.^[30] A 5-nm-thick adhesion layer of Ti is deposited onto Si substrate by e-beam evaporation followed by a 1- μm -thick layer of Al. Without the Ti layer, the subsequently deposited nanoporous alumina membrane is found to peel from the Si substrate. The aluminum film is anodized in an acid under d.c. conditions for 2–3 min. A cross-section SEM image of the as-deposited template is shown in Fig. 10. The remaining Al layer following anodization and the alumina layer produced by the anodization process are clearly seen. The presence of a thin barrier layer of alumina (U-shaped barrier) is also seen at the pore bottoms. The thickness of the barrier layer in this case is only of the order of 10–20 nm. One major problem for applications based on this method is posed by etching of this barrier layer to pattern layers directly below. Wet chemical etching methods, such as dilute phosphoric acid, although attempted in the past by other research groups,^[31,32] are not particularly useful. In addition to removing the barrier layer, it also causes pore widening,

thus increasing pore diameter and, in some cases, completely removing the alumina film. We have used plasma etching to anisotropically remove the barrier layer without changing pore diameter. Plasma etching was carried out using a commercial inductively coupled plasma system with reactive ion etching (RIE). Cl_2 diluted with Ar was used as etchant. The etch process required critical control over various parameters, in particular, etch power and etch time. Details of the process are described in Ref. [29]. Cross-section image of the final product after a 60-sec etch at 200-W RIE power is shown in Fig. 11. The pores in the top nanoporous alumina layer can be clearly seen. In addition, the etch has penetrated through the barrier region and continued down through the Al to the Ti adhesion layer. Some of

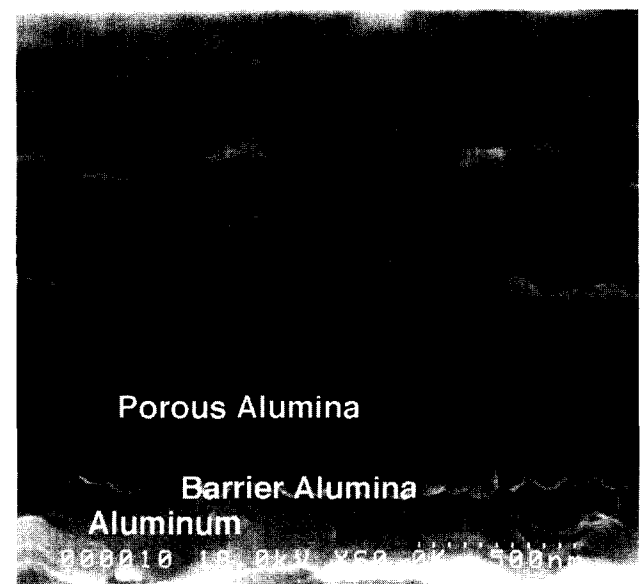


Fig. 10 Left: SEM cross-section image before plasma etch showing nanoporous alumina layer at the top, barrier layer followed by aluminum layer below.

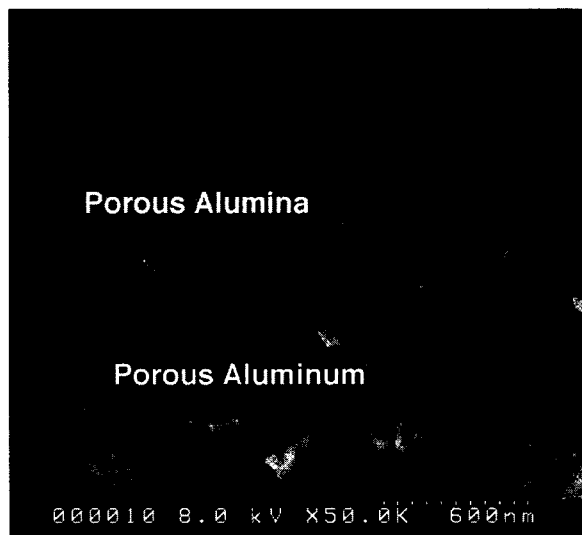


Fig. 11 Right: Cross-section image postplasma etch showing porous alumina layer and the porous aluminum layer below. (From J. Yun, M. Holtz, Texas Tech Univ.)

the Al nanotubes produced by the process have snapped in cleaving, showing the hexagonal shape of the parent hole template. Following breakthrough of the barrier layer, etch time can be varied to control the depth of the aluminum pores. In fact, with the appropriate etchant, the etch can even be continued through the Ti layer into the bottom substrate. In this manner, a nanoporous pattern, which mirrors the pattern on the initial nanoporous alumina template, can be created on any substrate. The top nanoporous alumina layer can easily be removed by soaking in a mixed solution of 0.2 M chromic/0.4 M phosphoric acid. Fig. 12 shows an AFM image of the top view of the aluminum template postremoval of the porous alumina layer. The pore diameter is of the order of 50–60 nm similar to that of the initial alumina film. In the final stage, nanoarrays of various materials can be synthesized by depositing/growing them inside the pores.

SELF-ASSEMBLED NANOARRAYS

Using the various methods discussed, nanoarrays of different materials have been successfully deposited. These include magnetic materials, semiconductor compounds, superconductors, and carbon nanotubes. A brief description of the properties of these nanoarrays is given below.

Magnetic Nanoarrays

Current magnetic recording media are based on magnetic thin films where the information is stored on grains. To

increase data storage density in such media, one must either reduce the size of the grains or reduce the number of grains that constitute each bit. Reducing the number of grains leads to increased noise and decreased size of grains leads to superparamagnetism where thermal energies alone are enough to flip the magnetization direction. These limits depend mainly on the anisotropy constant of the material and the aspect ratio of the grains. For present-day magnetic media, the superparamagnetic limit will be reached at densities of about 100 Gb/in². Patterned media consisting of isolated single-domain islands where each island stores one bit of information are expected to overcome the above problem. It is thought that for such patterned media (with anisotropy constant equal to that of present-day magnetic media), storage densities as high as 1 Tb/in² will be achievable. For such large densities, the size of the islands will have to be around 10 nm. Using porous alumina, one can easily fabricate nanomagnetic islands with feature size down to 10 nm. Materials such as Fe, Co, and Ni electrodeposited into the nanopores serve as a model system for the study of magnetic properties, interactions, and thermal stability of nanometer-sized particles. Several research groups have carried out investigations on the magnetic properties of Fe, Co, and Ni nanowires electrodeposited in porous alumina.^[33–37] The standard synthesis procedure has been to use a.c. electrodeposition. The wires are in the form of cylinders positioned perpendicular to the film plane in a regular array. The wires have been characterized using electron diffraction measurements. Fig. 13 shows a TEM image of Fe nanowires released from alumina template and dispersed onto a substrate. The wire diameter is of the order of 10 nm. High-resolution TEM images of the wires

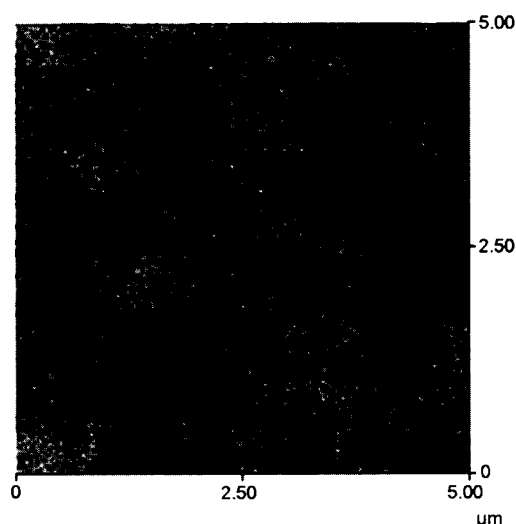


Fig. 12 Top view AFM image showing pores on aluminum layer. (View this art in color at www.dekker.com.)



Fig. 13 Transmission electron microscopic image of Fe nanowires released from porous alumina.

reveal that the wires are polycrystalline in nature with grain sizes ranging from ~ 5 to 50 nm. Electron diffraction image for Fe nanowires is also shown in Fig. 14. Analysis of the image confirms a bcc crystal structure for these nanowires. Similar studies for Co and Ni nanowires

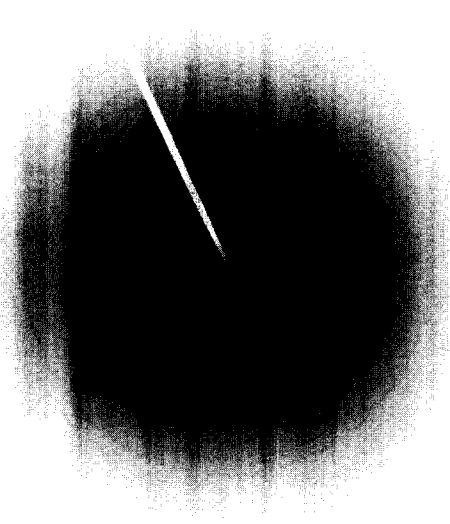


Fig. 14 Electron diffraction image of Fe nanowires. (View this art in color at www.dekker.com.)

reveal an hcp structure for Co and fcc structure for Ni nanowires.^[38,39]

Magnetic properties of these nanowires exhibit strong perpendicular anisotropy. Fig. 15 shows a typical magnetization vs. field image for an array of Fe nanowires electrodeposited inside porous alumina. The diameter of the wires is around 10 nm, and the length is of the order of 1 μ m. In the direction perpendicular to the film plane, the coercivity is very high, about 2341 Oe (remanence ratio 0.96), and in the parallel orientation, the coercivity is only about 300 Oe (remanence ratio 0.055). The nanowires thus possess uniaxial anisotropy with easy axis perpendicular to the film plane. The large anisotropy arises mostly from shape anisotropy because of the cylindrical shape of the nanowires. For a cylinder-shaped entity, the demagnetizing factor for field parallel and perpendicular to the cylinder axis are 0 and 2π , respectively. The shape anisotropy therefore forces the magnetization to be in the axial direction and is given by $2\pi M_s$, where M_s is the saturation magnetization. The anisotropy field can be estimated by extrapolating the magnetization curves using the M_s values for bulk Fe (1710 emu/cm^3) and is estimated to be of the order of 8 kOe for Fe nanowires. These may be compared with theoretically predicted shape anisotropy field of $2\pi M_s$ ($\sim 10.7 \text{ kOe}$ for Fe nanowires) for an infinite cylinder. The large perpendicular coercivity suggests resistance to magnetization reversal. The large perpendicular squareness

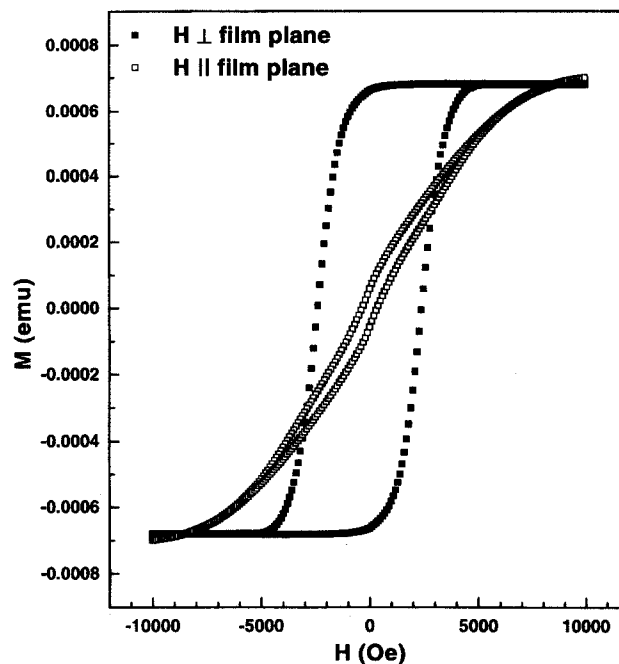


Fig. 15 Magnetization vs. field for an array of Fe nanowires in the perpendicular and parallel direction.

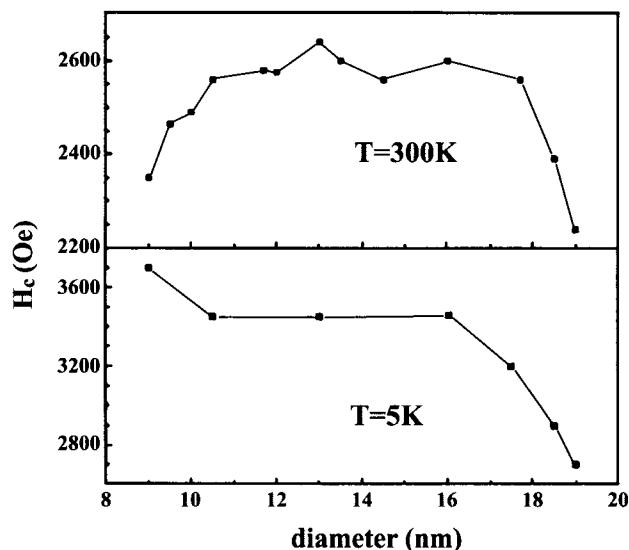


Fig. 16 Coercivity as a function of wire diameter for Fe nanoarrays, at room temperature and at 5 K.

in comparison to the parallel squareness indicates large remanent magnetization. All of these factors, large perpendicular squareness, high remanence, and the large coercivities, may make these materials useful for magnetic recording media.^[40,41] For such applications, it is necessary to investigate the dependence of magnetic properties on size of the nanostructure.

We have carried out a systematic investigation of the magnetic properties of Fe nanowires as a function of length and diameter of nanowires.^[42] For large length of the nanowires, of the order of microns, the coercivity H_c was found to be somewhat independent of length for fixed wire diameter. The coercivity, however, depends critically on the diameter of the wires. In general, the coercivity is found to decrease with increasing wire diameter. For example, Fe nanowires of diameter 32 nm exhibit a coercivity of ~ 2158 Oe which is about 200 Oe smaller than that for wires of diameter 9 nm. The decrease in coercivity is a result of development of multidomain structure in larger nanowires.

An interesting feature is observed for wires with very small diameter, < 13 nm. As seen in Fig. 16, for diameter < 13 nm, the coercivity is found to decrease. The maximum in coercivity therefore occurs at a wire diameter of about 13 nm and has a value of about 2640 Oe. In contrast to the behavior at 300 K, at 5 K, the coercivity exhibits a maximum for the smallest wire diameter investigated, namely, 9 nm (Fig. 16). The coercivity is around 3700 Oe at 5 K. Unlike the behavior at 300 K, for increasing wire diameter, the coercivity continually decreases. The non-monotonic behavior at 300 K, in contrast to that at 5 K,

can be explained as follows. At such small sizes, the wire diameter is much smaller than a single domain. Ferromagnetic domains cannot form and superparamagnetism dominates. Accordingly, the coercivity is low. Indeed, Li and Metzger^[43] reported very small activation volumes, $\sim 1.0 \times 10^{-18}$ cm³, for small diameter Fe nanowires at room temperature. This value is very close to the theoretical superparamagnetic limit.^[44] The superparamagnetic effect will contribute to magnetization at low temperature below blocking temperature leading to the increase of coercivity at 5 K. Magnetic interaction between the wires is an important factor in recording media and can be estimated by measuring the quantity defined as ΔM .

$$\Delta M = I_d(H) - (1 - 2I_r(H)) \quad (3)$$

where $I_r(H)$ is d.c. demagnetization remanence and $I_r(H)$ is isothermal remanence. For isothermal remanent magnetization measurements, the sample was first demagnetized. A magnetic field was then applied and reset to zero and the remanent magnetization was measured. This was carried out for different field values, and the isothermal remanent magnetization curve was obtained as a function of the field. In the case of the d.c. demagnetization curve, the sample was first saturated in a high field of 13 kOe and the remanent magnetization was obtained at various values of the reversal field. Fig. 17 shows the ΔM plots for Fe wires with different diameters. All of them show negative peaks, suggesting presence of magnetostatic interaction.

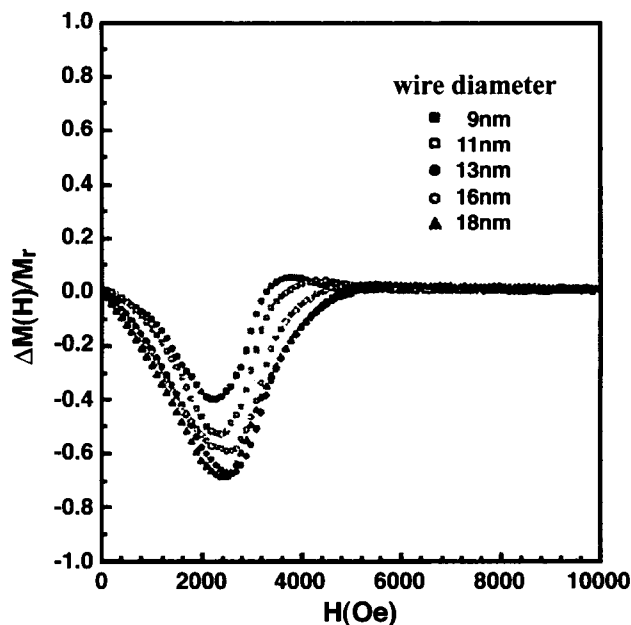


Fig. 17 ΔM plots for Fe nanowires of varying diameter.

Magnetic properties of Co and Ni nanoarrays electro-deposited in porous alumina have also been studied in great detail by various authors. The largest coercivities for Ni nanowires have been reported by Nielsch et al.^[36] They obtained coercivity of ~ 1200 Oe for highly ordered Ni wires of diameter 30 nm with remanence of the order of 100%. The diameter of the wires was varied in the range 30 to 55 nm while keeping the nanowire distance constant (100 nm) and found that the coercivity drops to 600 Oe (remanence $\sim 30\%$) for wires of diameter 55 nm. Magnetic measurements for Co nanowires in anodic alumina templates have been studied extensively by Zeng et al.^[45] For a fixed wire diameter of about 10 nm, as the nanowire length is increased, H_c is found to increase steeply until a constant value of about 2300 Oe is approached at wire lengths of about 200 nm. For larger wire lengths, the coercivity is more or less independent of length. For wire lengths of the order of 500–1000 nm, the coercivity is found to decrease gradually with increasing nanowire diameter. This is accompanied by shearing of the hysteresis loop. Both the decrease of H_c and the shearing of the loop are attributed to magnetostatic interactions.

Time dependence of magnetic properties of Fe, Co, and Ni nanoarrays has been studied.^[46–48] Quantities such as magnetic viscosity and activation volume have been calculated, and models for reversal mechanism in these nanowires have been extensively investigated. Typically, the activation volume for wires with diameter of the order of 10 nm is calculated to be of the order of $\sim 4 \times 10^{-18}$ cm³. This value is much smaller than the physical wire volumes, which indicates that magnetization reversal starts in a small region of wires. Magnetic reversal mechanisms such as coherent rotation and curling treat the wires as perfect homogeneous cylinders. However, the coherent rotation and curling modes are delocalized and could lead to activation volumes much larger than those observed. A more reasonable explanation of the reduced coercivities and thermal activation volumes encountered in electrodeposited nanowires is morphological inhomogeneities. Transmission electron microscopic results indicate a considerable degree of polycrystallinity with crystallite diameter of about 5 nm. Polycrystalline wires can be interpreted as random-anisotropy ferromagnets where interatomic exchange tries to align the local spins, but the exchange stiffness has to compete against random-anisotropy forces associated with the local uniaxial anisotropy. As a consequence, the magnetization processes become localized.^[49] The localization length or physical activation volume strongly depends on crystallite size.

As discussed earlier, in nanowires, magnetic anisotropy originates mainly from shape anisotropy. Large-shaped anisotropies can result from large saturation magnetization, which, in turn, can lead to large coercivity. This

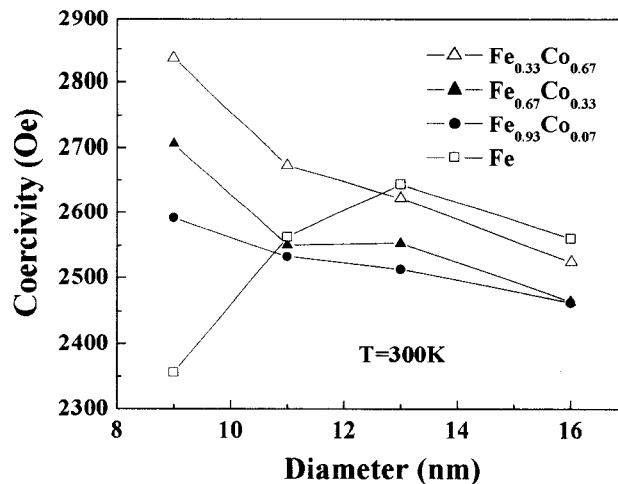


Fig. 18 Variation of coercivity as a function of wire diameter for FeCo alloys.

suggests that large coercivities are expected in FeCo nanowires because in bulk form, these alloys exhibit large saturation magnetization (1950 emu/cm³ for 35 at.% Co) which is larger than both Fe and Co. We have successfully electrodeposited FeCo alloys into the pores.^[50] For these arrays, we did observe coercivity for some FeCo nanowires to be larger than that of Fe and Co. The coercivity is found to be 2600 Oe for Fe_{0.93}Co_{0.07}, 2900 Oe for Fe_{0.67}Co_{0.33}, 2850 Oe for Fe_{0.33}Co_{0.67}, and 2400 Oe for Fe_{0.07}Co_{0.93}. The coercivity is largest for Fe_{0.33}Co_{0.67} and Fe_{0.67}Co_{0.33} samples and is much higher than those obtained for Fe (2400 Oe) and Co (1900 Oe) prepared under similar conditions. As in the case of elemental Fe, Co, and Ni nanoarrays, we obtained very high squareness ratio (~ 1) for most of the samples, suggesting excellent perpendicular magnetization characteristics. Fig. 18 shows the variation of coercivity as a function of diameter of the nanowires for all the Fe_{1-x}Co_x alloys. Length of the nanowires is kept constant in all the samples (~ 3 μ m). It is noted that contrary to the behavior of pure Fe, Fe–Co alloys show no maximum in coercivity as a function of wire diameter, suggesting that the superparamagnetic behavior is eliminated even for the smallest diameter wires (9 nm) used in this study. With increasing Co addition, the saturation magnetization and hence shape anisotropy constant of Fe–Co alloys are increased, which should result in higher energy barrier E (given by KV , where K is the anisotropy constant and V is the volume).

Semiconductor Nanoarrays

Alternating current or direct current electrodeposition can be used to fabricate arrays of semiconducting nanowires/nanodots in porous alumina. Electrochemically, the most

easily fabricated semiconductors are the II–VI semiconductors of the type CdS, CdSe, etc. This can be achieved using three different methods. In the first method used by Moskovits,^[51] a metal capable of forming a semiconductor is first electrodeposited into the pores of alumina. The top surface of the porous aluminum oxide is then etched away in an acid to expose the ends of the metallic array of wires. The deposited metal is then allowed to react with a liquid or gaseous reagent to convert them chemically to a semiconductor. For example, cadmium particles can be converted to CdS by reaction with sulfur vapor or hydrogen sulfide. Gallium particles may be converted to GaAs by reaction with arsine.

In the second method, sulfuric acid is a.c.-electrolyzed causing the sulfide atoms to be deposited in the pores. This is followed by a.c. electrodeposition of Cd into the pores, allowing the S atoms to react chemically with the Cd atoms, causing formation of CdS. Instead of a.c. electrodeposition of Cd, one may simply soak the porous template containing S atoms into a boiling solution of cadmium sulfate.

In the third method, the electrolyte used for the electrodeposition is nonaqueous unlike that used for magnetic materials.^[52,53] For the preparation of semiconductor nanowires of MX (M = Cd, Pb, Zn and X = S, Se, Te), a solution of dimethylsulfoxide containing a salt of M (50 mM) and elemental X (S or Se) is used. For example, CdS is electrodeposited using a 50-mM solution of cadmium perchlorate and 50 mM S in a dimethylsulfate solution. A small amount of lithium perchlorate is also added to improve the conductivity.

We have successfully prepared nanowires of CdS, CdSe, PbSe, ZnSe, etc. using the deposition methods

described above. Details of our studies on these nanoarrays and their possible device applications are discussed in detail in Ref. [54]. Such nanowire arrays can be used to study their electrical properties and thus investigate their potential applications in devices such as diodes, transistors, photodetectors, and light-emitting devices. Semiconductor nanodots and nanowire devices could be the building blocks for digital nanoelectronics, an integrated circuit technology which will permit downscaling to be carried beyond what is currently achievable.

Energetic Nanocomposite Nanoarrays

Energetic materials are a class of substances consisting of an appropriate mixture of a fuel and oxidizer material. When ignited, they release a large amount of energy because of an exothermic reaction. Such materials have several applications, in explosives, propellants, etc. Recently, it has been found that when fabricated in the form of nanocomposites, the energetic properties are highly enhanced.^[55]

Using porous alumina templates, we have developed two novel methods to fabricate these materials. In both methods, a thin film of Al is the fuel material and Fe oxide nanowires are the oxidizer material. Al film is prepared by means of thermal evaporation, while the nanowires are prepared by means of electrodeposition inside nanoporous alumina templates. We have found that presence of aluminum oxide around the wires inhibits direct interaction between Al and iron oxide. The aluminum oxide barrier layer and the aluminum oxide around the wires therefore need to be completely removed. Fig. 19 shows the sequence of steps that we followed to achieve this.^[56]

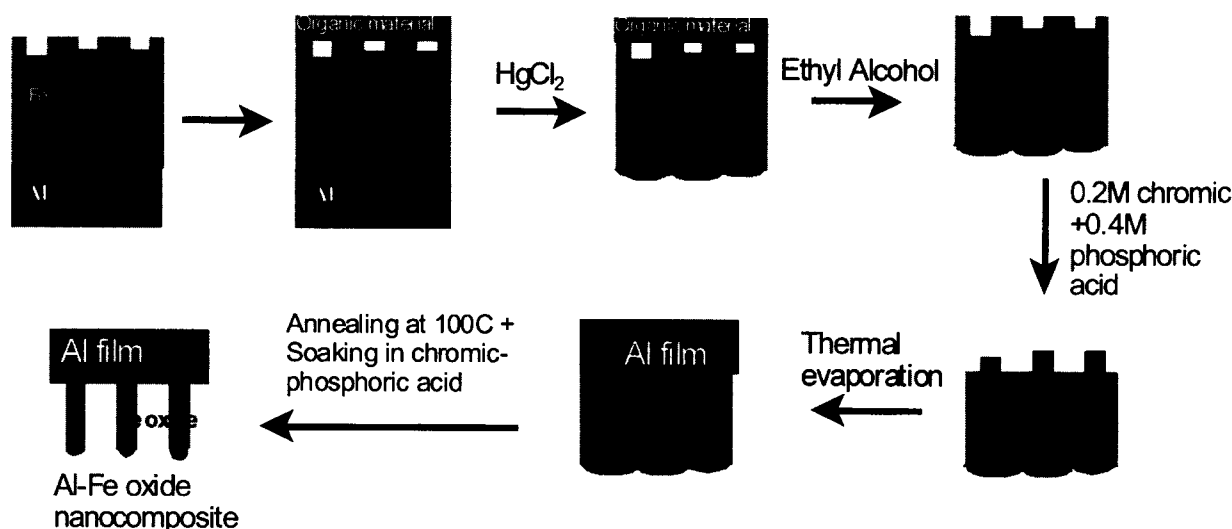


Fig. 19 Sequence of steps to prepare Al-Fe oxide nanocomposites (method 1).

The electrodeposited sample is first coated with a thin organic layer. The sample is then soaked in 3% mercuric chloride solution, which removes the bottom Al layer. The top organic layer protects Fe wires inside the pores from being etched away by mercuric chloride solution. In the next step, the organic layer is removed in ethyl alcohol solution and the sample is dried. The sample is now soaked in a mixture of chromic-phosphoric acid at 60°C to partially etch the pores from the top revealing Fe wires. The sample is rinsed and dried, and a thin film of Al (50 nm) is coated on top by means of thermal evaporation. Al film is therefore in contact with the Fe nanowires. The sample is annealed at 100°C for a few minutes to improve the interface contact between Al and the Fe nanowires. It is then soaked in chromic-phosphoric acid mixture to etch away the remaining aluminum oxide film. This leaves behind an Al film attached to an array of Fe nanowires. The sample is cleaned, dried, and annealed to completely remove trace amounts of water vapor and also to convert Fe nanowires into Fe oxide. In method 2 (see Fig. 20 for sequence of steps), a thin film of photoresist material is deposited on a glass wafer followed by thermal evaporation of a thin layer of aluminum (50-nm thickness). A commercial Al foil is anodized separately under d.c. conditions at 40 V in 3% oxalic acid for 30 min, creating a nanoporous template with pore diameter of the order of 50 nm. Fe nanowires are electrodeposited inside the pores under a.c. conditions. The sample is then soaked in a mixed solution of 0.2 M chromic/0.4 M phosphoric acid at 60°C. The acid mixture dissolves aluminum oxide completely leaving behind the Fe wires in solution. This solution is poured onto the thermally evaporated Al film. The Al film is annealed at 100°C to improve adhesion of Fe nanowires, followed by rinsing and drying to remove traces of the acid. The sample is then soaked in a solution of acetone

to dissolve the photoresist material. This leaves behind the final product, Al-Fe oxide nanocomposite film, which is rinsed in methanol followed by annealing at 100°C for a few minutes to remove all traces of water vapor. Al-Fe oxide nanocomposite prepared using these two methods is found to ignite readily under flame ignition, indicating several possible applications of these materials in explosives, propellants, and other military applications.

Carbon Nanotube Arrays

Carbon nanotubes^[57] can be viewed as rolled-up sheets of graphite with diameters approximately a few nanometers. They can be either metallic or semiconducting, with band gaps that can be controlled by controlling the tube diameter. Several applications are envisioned for these materials. Carbon nanotube electronics are expected to provide a viable alternative to silicon when chip feature sizes cannot be made any smaller using silicon.^[58] Nanotube electronics are also expected to provide great progress in computer miniaturization and computing power. They have potential applications in cold-cathode flat panel displays because of their excellent field emission properties.^[59] Carbon nanotubes can be used to encapsulate other materials such as Fe, Co, etc.^[60] They can be used in infrared imaging, inert membranes for biomedicine, etc. They can be placed on an Scanning Probe Microscopy (SPM) tip to manipulate molecules with sub-angstrom accuracy.^[61] The tips are atomically precise with chemistry similar to C₆₀, and thus serve as functional elements with a wide variety of molecular fragments. Functionalizing carbon nanotube tips will allow mechanical manipulation of many molecular systems on various surfaces with sub-angstrom accuracy.

For several of the applications described above, particularly in nanotube electronics, it is necessary to be

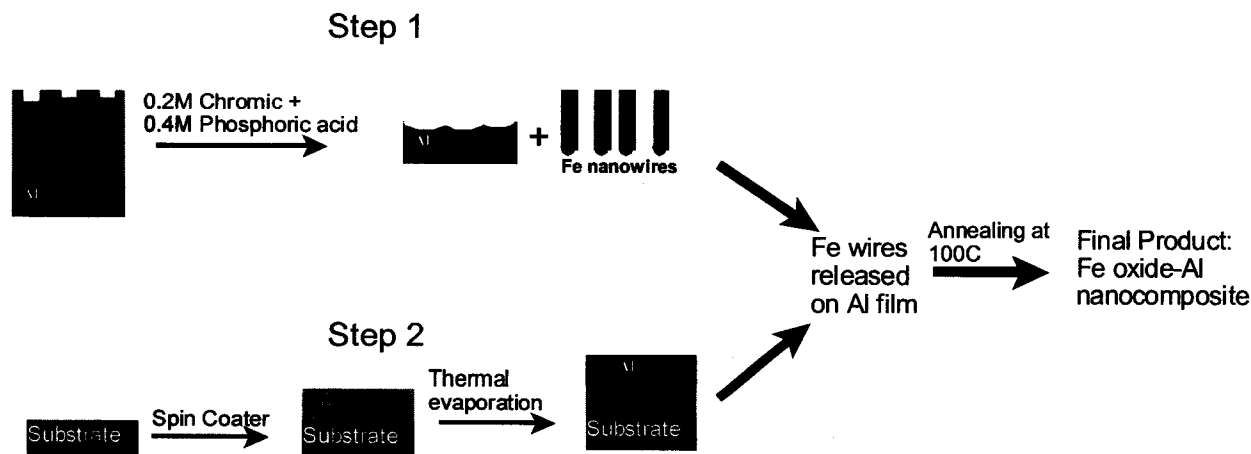


Fig. 20 Sequence of steps to prepare Al-Fe oxide nanocomposite (method 2).

able to control the growth of carbon nanotubes both with respect to size and orientation. Carbon nanotube arrays have been successfully synthesized in ordered porous alumina templates.^[62-66] The diameter and spacing of the carbon nanotubes are controlled by controlling the diameter and interpore spacing in porous alumina. Most of the methods involve initial deposition of Co inside the pores which act as catalyst for the growth of carbon nanotubes. Earliest demonstration of carbon nanotube synthesis in porous alumina was provided by Li et al.^[65,66] A small amount of Co is electrodeposited in the pores, and the templates are heated in a tube furnace at 600°C for 4-5 hr under CO flow (100 cm³/min). The CO flow is then replaced by a mixture of 10% acetylene in nitrogen at a flow rate of 100 cm³/min for about 2 hr at 650°C. The samples are then annealed for 15 hr in nitrogen leading to formation of an array of carbon nanotubes. The carbon nanotubes produced in porous alumina templates have the following common characteristic features: they always grow perpendicular to film plane, are multiwalled, have uniform sizes, and are open-ended. The growth of carbon nanotubes inside pores by catalytic decomposition of organic vapors has been postulated as either base or tip growth.^[67] Scanning electron microscopic studies indicate residual Co/Fe catalyst in the base of the tubes, indicating that a tip growth mechanism could be responsible for the tube growth. It is also thought that the surrounding alumina may also be acting as a catalyst in nanotube growth.^[68]

Field emission characteristics of ordered carbon nanotubes have been investigated.^[63-69] Yuan et al.^[63] demonstrated excellent field emission characteristics for these nanotube arrays. In their measurements, they removed the barrier layer between the aluminum and the porous layer. Field emission was seen to begin at a relatively low electric field (~ 2.8 V/ μ). They measured a very large emission current 0.08 mA/cm² at 3.6 V/mm, much greater than that reported by Davydov et al.^[69] for as-prepared nanotube arrays (in presence of barrier layer). Over a period of 150 hr, no significant reduction in emission current was observed. In contrast, in the presence of the barrier layer, the current density was found to decrease rapidly with time over a period of a few minutes. Another reason for the enhanced field emission may be related to the open-ended nature of the carbon nanotubes, which results in smaller radius of curvature than the closed ends, thus causing electrons to be emitted more easily. In a similar study, Jeong et al.^[70] measured a turn-on field of 1.9-2.1 V/ μ m and a field enhancement factor of 3360-5200. In their samples, the barrier layer is absent and the density of carbon nanotubes was very small, $\sim 10^7$ tips/cm². The intertube distance is therefore higher, minimizing field screening effect and, in turn, enhancing field emission effect.^[71] Field emitter arrays with such high

emitting efficiency are expected to have applications in flat panel displays in the near future. For application in nanoelectronics, it is sometimes necessary to be able to make connections between carbon nanotubes. One solution is to directly prepare T- or Y-junction carbon nanotubes. In general, pores inside nanoporous alumina are straight when the anodization voltage is kept fixed during anodization. However, one can create branched pores inside alumina by changing the anodization voltage during anodization. In particular, Y-shaped pore forms in porous alumina when the anodization voltage is reduced by a factor of 1/2 during the anodization. Li et al.^[66] synthesized Y-junction carbon nanotubes in such templates by using Co as a catalyst and by pyrolysis of acetylene at 650°C. Papadopoulos et al.^[72] obtained electronic transport measurements on both individual and parallel arrays of Y-junction nanotubes synthesized in porous alumina. Nonlinear transport and rectifying behavior was observed. This behavior can be explained in terms of a change in band gap across the junction caused by the change in diameter across the junction. Y-junction carbon nanotubes are thus a realization of semiconductor heterostructures in the nanometer scale. Y-shaped nanotubes and nanowires are expected to have possible applications in room-temperature single electron transistor and spintronic devices.

CONCLUSION

In conclusion, porous alumina is indeed a versatile template. It allows fabrications of a variety of nanostructures in the form of nanoarrays with feature sizes as small as 10 nm. As described in this article, characterization and measurement of appropriate properties of the nanoarrays can be easily carried out. It allows investigation of several fundamental phenomena at the nanoscale level and also allows for investigation of potential applications of nanostructures in future high-performance nanoscale devices.

ACKNOWLEDGMENTS

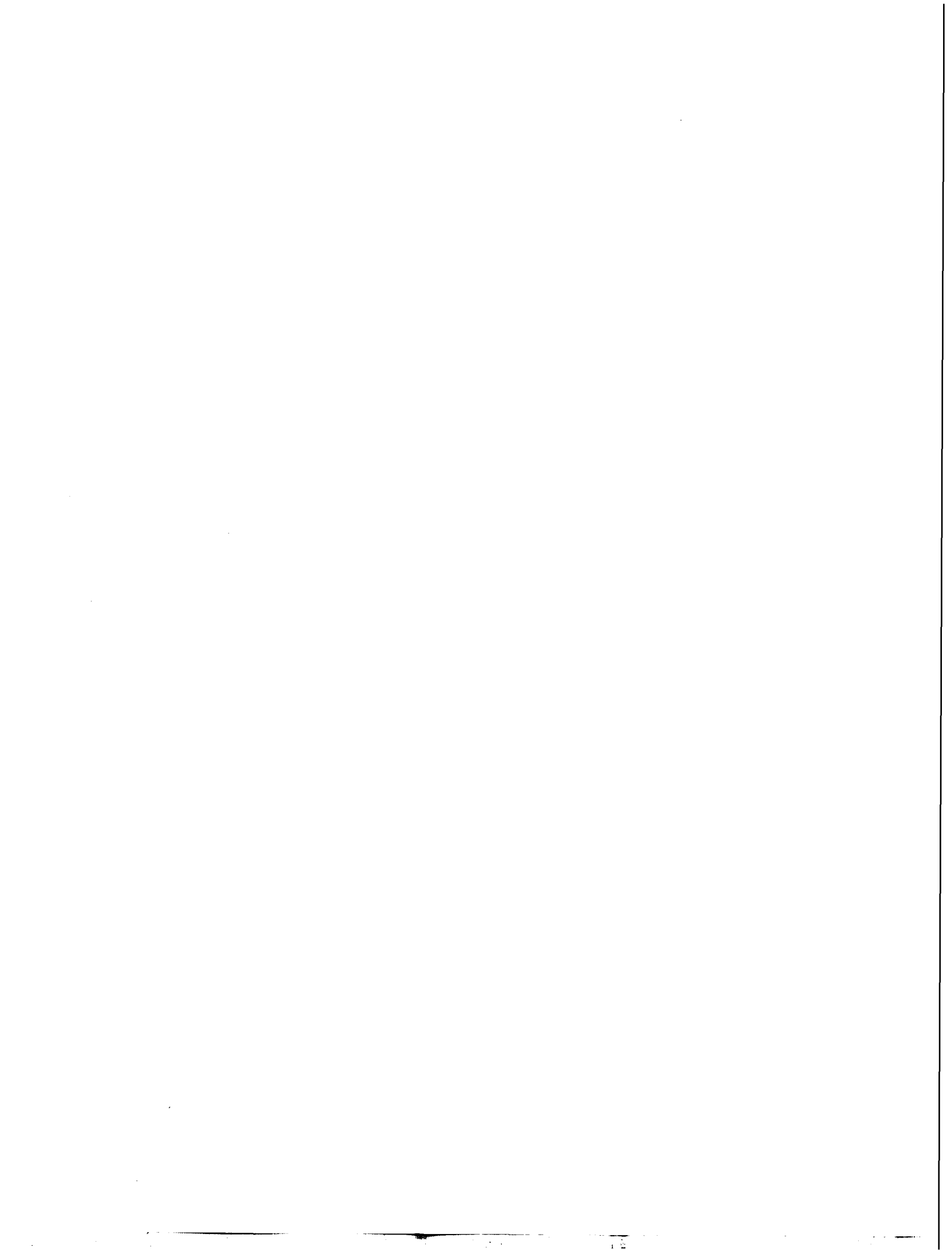
Most of the work described in this article (unless specified) has been carried out by the author and her colleagues at the University of Nebraska-Lincoln and at Texas Tech University, Lubbock. The author would like to thank S. Bandyopadhyay, N. Kouklin, X.Z. Li, P.F. Williams, M. Holtz, K. Zhu, and J. Yun for useful discussions, collaborations, and help with experiments. Several aspects of the work are supported by grants from National Science Foundation, Office of Naval Research, and the Department of Army.

REFERENCES

1. Edelstein, A.S. *Nanomaterials: Synthesis, Properties and Applications*; Edelstein, A.S., Camarata, R.C., Eds.; Institute of Physics Publishers: Bristol, Philadelphia, 1996.
2. Shalaev, V.M.; Moskovits, M. *Nanostructured Materials: Clusters, Composites and their Films*; ACS Symposium Series, American Chemical Society Editions: Washington, DC, 1997; Vol. 679.
3. Fendler, J.H. *Nanoparticles and Nanostructured Films: Preparation, Characterization and Applications*; Wiley-VCH: Weinheim, Germany, 1998.
4. Murray, C.B.; Kagan, C.R.; Bawendi, M.G. Self-organization of CdSe nanocrystallites into three-dimensional quantum dot superlattices. *Science* **1995**, *270*, 1335.
5. Andres, R.P.; Bielefeld, J.D.; Henderson, J.I.; Janes, D.B.; Kolagunta, V.R.; Kubiak, C.P.; Mahoney, W.J.; Osifchin, R.G. Self-assembly of a two-dimensional superlattice of molecularly linked metal clusters. *Science* **1996**, *273*, 1690.
6. Shi, J.; Gider, S.; Babcock, K.; Awschalom, D.D. Magnetic clusters in molecular beams, metals, and semiconductors. *Science* **1996**, *271*, 937.
7. Billas, I.M.L.; Becker, J.A.; Chatelain, A.; de Heer, W.A. Magnetic moments of iron clusters with 25 to 700 atoms and their dependence on temperature. *Phys. Rev. Lett.* **1993**, *71*, 4067.
8. White, R.L.; New, R.M.H.; Pease, R.F.W. Patterned media: A viable route to 50 Gbit/in.² and up for magnetic recording? *IEEE Trans. Magn.* **1997**, *33*, 990.
9. Chou, S.Y.; Wei, M.S.; Krausse, P.R.; Fischer, P.B. Single-domain magnetic pillar array of 35 nm diameter and 65 Gbits/in² density for ultrahigh density quantum magnetic storage. *J. Appl. Phys.* **1994**, *76*, 6673.
10. Ross, C.A.; Smith, H.I.; Savas, T.; Schattenburgh, M.; Farhoud, M.; Hwang, M.; Walsh, M.; Abraham, M.C.; Ram, R.J. Fabrication of patterned media for high density magnetic storage. *J. Vac. Sci. Technol. B*, **1999**, *17*, 3168.
11. Menon, L. Synthesis of Nanowires Using Porous Alumina. In *Advances in Nanophase Materials and Nanotechnology (Vol. Quantum Dots and Nanowires)*; Bandyopadhyay, S., Nalwa, H.S., Eds.; American Scientific Publishers, 2003. (the "Series Editors").
12. Lohregel, M.M. Thin anodic oxide layers on aluminium and other valve metals: High field regime. *Mater. Sci. Eng.* **1993**, *R11*, 243.
13. Keller, F.; Hunter, M.S.; Robinson, D.L. Structural features of oxide coatings on aluminum. *J. Electrochem. Soc.* **1953**, *100*, 411.
14. Bandyopadhyay, S.; Miller, A.E.; Chang, H.-C.; Banerjee, G.; Yuzhakov, V.; Yue, D.-F.; Ricker, R.E.; Jones, S.; Eastman, J.A.; Baugher, E.; Chandrasekhar, M. Electrochemically assembled quasi-periodic quantum dot arrays. *Nanotechnology* **1996**, *7*, 360.
15. Ricker, R.E.; Miller, A.E.; Yue, D.-F.; Banerjee, G.; Bandyopadhyay, S. Nanofabrication of a quantum dot array: Atomic force microscopy of electropolished aluminum. *J. Electron. Mater.* **1996**, *25*, 1585.
16. Bandyopadhyay, S.; Menon, L.; Kouklin, N.; Zeng, H.; Sellmyer, D.J. Electrochemically self-assembled quantum dot arrays. *J. Electron. Mater.* **1999**, *28*, 515.
17. Li, A.P.; Müller, F.; Gösele, U. Polycrystalline and monocrystalline pore arrays with large interpore distance in anodic alumina. *Electrochem. Solid-State Lett.* **2000**, *3*, 131.
18. O'Sullivan, J.P.; Wood, G.C. *Proc. R. Soc. Lond., Ser. A* **1970**, *317*, 511.
19. Jessensky, O.; Müller, F.; Gösele, U. Self-organized formation of hexagonal pore arrays in anodic alumina. *Appl. Phys. Lett.* **1998**, *72*, 1173.
20. Masuda, H.; Fukuda, K. Ordered metal nanohole arrays made by a two-step replication of Honeycomb structures of nanoporous alumina. *Science* **1995**, *268*, 1466.
21. Masuda, H.; Yamada, H.; Satoh, M.; Asoh, H.; Nakao, M.; Tamamura, T. Highly ordered nanochannel-array architecture in anodic alumina. *Appl. Phys. Lett.* **1997**, *71*, 2770.
22. Zhang, Z.; Ying, J.Y.; Dresselhaus, M.S. Bismuth quantum-wire arrays fabricated by a vacuum melting and pressure injection process. *J. Mater. Res.* **1998**, *13*, 1745.
23. Yi, G.; Schwarzacher, W. Single crystal superconductor nanowires by electrodeposition. *Appl. Phys. Lett.* **1999**, *74*, 1746.
24. Hornyak, G.L.; Patrissi, C.J.; Martin, C.R. Fabrication, characterization and optical properties of gold-nanoparticle/porous-alumina composites: The non-scattering Maxwell-Garnett limit. *J. Phys. Chem., B* **1997**, *101*, 1548.
25. Martin, C.R. Nanomaterials—A membrane-based synthetic approach. *Science* **1994**, *266*, 1961.
26. Schwarzacher, W. Metal nanostructures a new class of electronic devices. *Electrochem. Soc. Interface* **1999**, *20*.
27. Liang, J.; Chik, H.; Yin, A.; Xu, J. Two-dimensional superlattices of nanostructures: Nonlithographic formation by anodic alumina membrane template. *J. Appl. Phys.* **2002**, *91* (4), 2544–2546.
28. Kanamori, Y.; Hane, K.; Sai, H.; Yugami, H. 100 nm

- period silicon antireflection structures fabricated using a porous alumina membrane mask. *Appl. Phys. Lett.* **2001**, *78*, 142.
29. Menon, L.; Kanchibotla, B.R.; Patibandla, S.; Aurongzeb, D.; Holtz, M.; Yun, J.; Zhu, K. Anodization and plasma etching of nanopore patterns on a generic substrate. Submitted to *Appl. Phys. Lett.*
 30. Menon, L.; Holtz, M., et al., unpublished.
 31. Rabin, O.; Herz, P.R.; Cronin, S.B.; Lin, Y.-M.; Akinwande, A.I.; Dresselhaus, M.S. Nanofabrication using self-assembled alumina templates. *Mater. Res. Soc. Symp.* **2001**, *636*, D4.7.1.
 32. Huang, Q.; Lye, W.-K.; Longo, D.M.; Reed, M.L. Sub-micron patterned anodic oxidation of aluminum thin films. *Mater. Res. Symp. Proc.* **2001**, *636*, D9.49.1.
 33. AlMawlawi, D.; Coombs, N.; Moskovits, M. Magnetic properties of Fe deposited into anodic aluminum oxide pores as a function of particle size. *J. Appl. Phys.* **1991**, *70*, 4421.
 34. Metzger, R.M.; Konovalov, V.V.; Sun, M.; Xu, T.; Zangari, G.; Xu, B.; Benakli, M.; Doyle, W.D. Magnetic nanowires in hexagonally ordered pores of alumina. *IEEE Trans. Magn.* **2000**, *36*, 30.
 35. Skomski, R.; Zeng, H.; Zheng, M.; Sellmyer, D.J. Magnetic localization in transition-metal nanowires. *Phys. Rev., B* **2000**, *62*, 3900.
 36. Nielsch, K.; Wehrspohn, R.B.; Barthel, J.; Kirschner, J.; Gsele, U.; Fischer, S.F.; Kronmüller, H. Hexagonally ordered 100 nm period nickel nanowire arrays. *Appl. Phys. Lett.* **2001**, *79*, 1360.
 37. Li, F.; Zhang, L.; Metzger, R.M. On the growth of highly ordered pores in anodized aluminum oxide. *Chem. Mater.* **1998**, *10*, 2470.
 38. Strijkers, G.J.; Dalderop, J.H.J.; Broaksteeg, M.A.A.; Swagten, H.J.M.; de Jonge, W.J.M. Structure and magnetization of arrays of electrodeposited Co wires in anodic alumina. *J. Appl. Phys.* **1999**, *86*, 5141.
 39. Zheng, M.; Menon, L.; Zeng, H.; Liu, Y.; Bandyopadhyay, S.; Kirby, R.D.; Sellmyer, D.J. Magnetic properties of Ni nanowires in self-assembled arrays. *Phys. Rev., B* **2000**, *62*, 12282.
 40. Whitney, T.M.; Jiang, J.S.; Searson, P.C.; Chien, C.L. Fabrication and magnetic properties of arrays of metallic nanowires. *Science* **1993**, *261*, 1316.
 41. Iwasaki, S.; Nakamura, Y. An analysis for the magnetization mode for high density magnetic recording. *IEEE Trans. Magn.* **1977**, *MAG-13*, 1272.
 42. Menon, L.; Zheng, M.; Zeng, H.; Bandyopadhyay, S.; Sellmyer, D.J. Size dependence of the magnetic properties of electrochemically self-assembled Fe quantum dots. *J. Electron. Mater.* **2000**, *29*, 510.
 43. Li, F.; Metzger, R.M. Activation volume of a-Fe particles in alumite films. *J. Appl. Phys.* **1997**, *81*, 3806.
 44. Koster, E.; Arnoldssen, T.C. *Magnetic Recording*; Mee, C.D., Daniel, E.D., Eds.; McGraw-Hill: New York, 1987; Vol. 1.
 45. Zeng, H.; Zheng, M.; Skomski, R.; Sellmyer, D.J.; Liu, Y.; Menon, L.; Sellmyer, D.J. Magnetic properties of self-assembled Co nanowires of varying length and diameter. *J. Appl. Phys.* **2000**, *87*, 4718.
 46. Li, F.; Metzger, R.M. Activation volume of a-Fe particles in alumite films. *J. Appl. Phys.* **1997**, *81*, 3806.
 47. Bao, X.; Li, F.; Metzger, R.M. Synthesis and magnetic properties of electrodeposited metal particles on anodic alumite film. *J. Appl. Phys.* **1996**, *79*, 4866.
 48. Liberatos, A.; Chantrell, R.W.; Sterring, E.R.; Lodder, J.C. Magnetic viscosity in perpendicular media. *J. Appl. Phys.* **1991**, *70*, 4431.
 49. Skomski, R.; Zeng, H.; Zheng, M.; Sellmyer, D.J. Magnetic localization in transition-metal nanowires. *Phys. Rev., B* **2000**, *62*, 3900.
 50. Menon, L.; Bandyopadhyay, S.; Liu, Y.; Zeng, H.; Sellmyer, D.J. Magnetic and structural properties of electrochemically self-assembled Fe_{1-x}Cox nanowires. *J. Nanosci. Nanotechnol.* **2001**, *1*, 149.
 51. Moskovits, M. Semiconductors and Method for Their Manufacture. International Patent Publication #5202290, 1993.
 52. Baranski, A.S.; Fawcett, W.R. The electrodeposition of metal chalcogenides. *J. Electrochem. Soc.* **1980**, *127*, 766.
 53. Xu, D.; Shi, X.; Guo, G.; Gui, L.; Tang, Y. Electrochemical preparation of CdSe nanowire arrays. *J. Phys. Chem., B* **2000**, *104*, 5061.
 54. Bandyopadhyay, S. Electrochemically self-assembled nanostructure arrays, appearing in the *Encyclopedia of Nanoscience and Nanotechnology*, Marcel-Dekker Publications.
 55. Pantoya, M.; Granier, J. Modeling Laser Ignition and Heat Propagation in Nanocomposite Thermites. Proceedings of the 8th AIAA/ASME Joint Thermophysics and Heat Transfer Conference. 2002. Paper No. AIAA-2002-3030.
 56. Menon, L., et al., unpublished.
 57. Hellemans, A. IBM researchers devise nanotube ICs. *IEEE Spectrum* **2001**, *38*, 26.
 58. Iijima, S. Helical microtubules of graphitic carbon. *Nature* **1991**, *354*, 56.

59. Rinzler, A.G.; Hafner, J.H.; Nikolaev, P.; Luo, L.; Kim, S.G.; Tomanek, D.; Nordlander, P.; Colbert, D.T.; Smalley, R.E. Unraveling nanotubes: Field emission from an atomic wire. *Science* **1995**, *269*, 1550.
60. Liu, S.; Zhu, J. Carbon nanotubes filled with long continuous cobalt nanowires. *Appl. Phys., A* **2000**, *70*, 673.
61. Dai, H.; Hafner, J.H.; Rinzler, A.G.; Colbert, D.T.; Smalley, R.E. Nanotubes as nanoprobe in scanned probe microscope. *Nature* **1996**, *384*, 147.
62. Suh, J.S.; Lee, J.S. Highly ordered two-dimensional carbon nanotube arrays. *Appl. Phys. Lett.* **1999**, *75*, 2047.
63. Yuan, Z.H.; Huang, H.; Dang, H.Y.; Cao, J.E.; Hu, B.H.; Fan, S.S. Field emission property of highly ordered monodispersed carbon nanotube arrays. *Appl. Phys. Lett.* **2001**, *78*, 3127.
64. Iwasaki, T.; Motoi, T.; Den, T. Multiwalled carbon nanotubes growth in anodic alumina nanoholes. *Appl. Phys. Lett.* **1999**, *75*, 2044.
65. Li, J.; Moskovits, M.; Haslett, T.L. Nanoscale electro-less metal deposition in aligned carbon nanotubes. *Chem. Mater.* **1998**, *10*, 1963.
66. Li, J.; Papadopoulos, C.; Xu, J.M.; Moskovits, M. Highly-ordered carbon nanotube arrays for electronics applications. *Appl. Phys. Lett.* **1999**, *75*, 367.
67. Baker, R.T.K. Catalytic growth of carbon filaments. *Carbon* **1989**, *27*, 315.
68. Thess, A.; Lee, R.; Nikolaev, P.; Dai, H.; Petit, P.; Robert, J.; Xu, C.; Hee Lee, Y.; Kim, S.G.; Rinzler, A.G.; Colbert, D.T.; Scuseria, G.E.; Tomanek, D.; Fischer, J.E.; Smalley, R.E. Crystalline ropes of metallic carbon nanotubes. *Science* **1996**, *273*, 483.
69. Davydov, D.N.; Sattari, P.A.; AlMawlawi, D.; Osika, A.; Haslett, T.L.; Moskovits, M. Field emitters based on porous aluminum oxide templates. *J. Appl. Phys.* **1999**, *86*, 3983.
70. Jeong, S.-H.; Hwang, H.-Y.; Lee, K.-H.; Jeong, Y. Template-based carbon nanotubes and their application to a field emitter. *Appl. Phys. Lett.* **2001**, *78*, 2052.
71. Nilsson, L.; Groening, O.; Emmenegger, C.; Kuettel, O.; Schaller, E.; Schalpbach, L.; Kind, H.; Bonard, J.-M.; Kern, K. Scanning field emission from patterned carbon nanotube films. *Appl. Phys. Lett.* **2000**, *76*, 2071.
72. Papadopoulos, C.; Rakitin, A.; Li, J.; Vedenev, A.S.; Xu, J.M. Electronic transport in Y-junction carbon nanotubes. *Phys. Rev. Lett.* **2000**, *85*, 3476.



Nanoceramics

Abbas Khaleel

United Arab Emirates University, Al-Ain, United Arab Emirates

INTRODUCTION

Ceramics is one of the fields where nanoscience and nanotechnology have shown remarkable progress, producing a variety of advanced materials with unique properties and performance. Nanoceramics is a term used to refer to ceramic materials fabricated from ultrafine particles, i.e., less than 100 nm in diameter. In this field, a great deal of research has been accomplished in the last 20 years and has resulted in significant outcomes that are of great impact academically as well as industrially.

OVERVIEW

Advanced ceramics include inorganic and nonmetallic solid materials composed of polycrystalline sintered bodies, fine powders, single crystals, noncrystalline materials, thin or thick films, and fibers with various morphologies. Systems of metal oxides, carbides, borides and nitrides compose most of the important ceramic materials. Traditional ceramics, or old ceramics, such as tile pottery, are made from minerals such as clay; however, industrial ceramics, or advanced ceramics, are made of highly pure well-chosen materials such as silicon carbide and alumina. Many people think that ceramic materials are used for artistic objects and tableware only. In fact ceramic products are now very important in a wide range of industrial and advanced technical applications in several fields including electronics, medicine, nuclear industry, magnetic applications, and several others.

It has been well proven that the bulk behavior of materials can be dramatically altered when constituted of nanoscale building blocks. Mechanical, magnetic, optical, and other properties of materials have been found to be favorably affected. Hardness and strength, as an example, can be greatly enhanced by consolidating ceramic materials from nanoscale particles. Ductility and superplastic-forming capabilities of nanophase ceramics have now become possible, leading to new processing routes that will be more cost-effective than traditional methods.

In this article, our focus will be on advanced ceramics fabricated from nanometer-sized powders. Preparation, properties, and applications will be the main directions of

focus and a special attention will be given to the effect of the particle size in these materials.

PREPARATION

Remarkable progress in synthetic chemistry has led to significant advances in material science, making possible the synthesis of various substances and materials. The manufacture of ceramics involves heat treatment of tightly squeezed powders. The size of the building block of these powders has been found to affect the properties of the final product. The method of preparation is very often a determining factor in shaping the material and its properties. For example, burning Mg in O₂ (MgO smoke) yields 40–80-nm cubes and hexagonal plates, whereas thermal decomposition of commercial Mg(OH)₂, MgCO₃, and especially Mg(NO₃)₂ yields irregular shapes often exhibiting hexagonal platelets. Surface areas can range from 10 m²/g (MgO smoke) to 150 m²/g for Mg(OH)₂ thermal decomposition. On the other hand, aerogel-prepared Mg(OH)₂ can lead to MgO with surface areas as high as 500 m²/g.

Because the main focus of this article is ceramics fabricated from nanometer-sized building blocks, different methods for preparing ultrafine ceramic powders will be discussed. The steps in manufacturing ceramics from powders, which include molding, extrusion, and densification, will not be discussed here.

Physical Methods

Vapor condensation methods

Gas-condensation techniques to produce nanoparticles directly from a supersaturated vapor of metals are among the earliest methods for producing nanoparticles. They generally involve two steps: First, a metallic nanophase powder is condensed under inert convection gas after a supersaturated vapor of the metal is obtained inside a chamber. Second, the powder is oxidized by allowing oxygen into the chamber (to produce metal oxide powder). A subsequent annealing process at high temperatures is often required to complete the oxidation. The system

consists of a vapor source inside a vacuum chamber containing a mixture of an inert gas, usually argon or helium, mixed with another gas, which is selected based on the material to be prepared. Oxygen is mixed with the inert gas to produce metal oxides. NH_3 is usually used to prepare metal nitrides and an appropriate alkane or alkene, as a source of carbon, is usually used to prepare metal carbides. Nanoparticles are formed when supersaturation is achieved above the vapor source. A collection surface, usually cooled by liquid nitrogen, is placed above the source. The particles are transported to the surface by a convection current or by a combination of a forced gas flow and a convection current, which is set up by the difference in the temperature between the source and the cold surface. Some improved systems involve a way to scrap the nanoparticles from the cold collection surface so that the particles would fall into a die and a unit where they can be consolidated into pellets. Supersaturated vapor can be achieved by many different vaporization methods. The most common techniques include thermal evaporation, sputtering, and laser methods. A variety of nanoscale metal oxides and metal carbides have been prepared using laser-vaporization techniques.

The advantages of vapor condensation methods include versatility, ease in performance and analysis, and high-purity products. On the other hand, they can be employed to produce films and coatings. Furthermore, laser-vaporization techniques allow for the production of high-density, directional, and high-speed vapor of any metal within an extremely short time. Despite the success of these methods, they have the disadvantage that the production cost is still high because of low yields. Heating techniques have other disadvantages that include the possibility of reactions between the metal vapors and the heating source materials.

Spray pyrolysis

This technique is known by several other names including solution aerosol thermolysis, evaporative decomposition of solutions, plasma vaporization of solutions, and aerosol decomposition. The starting materials in this process are chemical precursors, usually appropriate salts, in solution, sol, or suspension. The process involves the generation of aerosol droplets by nebulizing or "atomization" of the starting solution, sol, or suspension. The generated droplets undergo evaporation and solute condensation within the droplet, drying, thermolysis of the precipitate particle at higher temperature to form a microporous particle, and, finally, sintering to form a dense particle.

Different techniques for atomization are employed including pressure, two-fluid, electrostatic, and ultrasonic atomizers. These atomizers differ in droplet size (2–15 μm), rate of atomization, and droplet velocity (1–20 m/sec).

These factors affect the heating rate and residence time of the droplet during spray pyrolysis which, in turn, affect some of the particle characteristics including particle size. For a specific atomizer, particle characteristics, including particle size distribution, homogeneity, and phase composition depend on the type of precursor, solution concentration, pH, viscosity, and the surface tension.

Aqueous solutions are usually used because of their low cost, safety, and the availability of a wide range of water-soluble salts. Metal chloride and nitrate salts are commonly used as precursors because of their high solubility. Precursors that have low solubility or those that may induce impurities, such as acetates that lead to carbon in the products, are not preferred.

The advantages of this method include the production of high-purity nanosized particles, homogeneity of the particles as a result of the homogeneity of the original solution, and the fact that each droplet/particle goes through the same reaction conditions. The disadvantages of spray pyrolysis include the need for large amounts of solvents and the difficulty to scale-up the production. The use of large amounts of nonaqueous solvents increases the production expenses because of the high cost of pure solvents and the need for proper disposal.

Thermochemical/flame decomposition of metalorganic precursors

Flame processes have been widely used to synthesize nanometer-sized particles of ceramic materials. This is another type of gas-condensation technique with the starting material being a liquid chemical precursor. The process is referred to as chemical vapor condensation (CVC). In this process, chemical precursors are vaporized and then oxidized in a combustion process using a fuel-oxidant mixture such as propane-oxygen or methane-air. It combines the rapid thermal decomposition of a precursor-carrier gas stream in a reduced pressure environment with thermophoretically driven deposition of the rapidly condensed product particles on a cold substrate. The flame usually provides a high temperature (1200–3000 K), which promotes rapid gas-phase chemical reactions.

A variety of chemical precursors can be used including metal chlorides, such as TiCl_4 to prepare TiO_2 and SiCl_4 to prepare SiO_2 , metal-alkyl precursors, metal alkoxides, and gaseous metal hydrides, such as silane as a source of silicon to prepare silica. Chlorides have been the most widely used precursors in the industry and the process is sometimes referred to as the "chloride process." The high vapor pressure of chlorides and the fact that they can be safely stored and handled make them excellent potential precursors. The disadvantages of using chloride precursors are the formation of acidic gases and contamination of the products with halide residues. Flame processes are

used industrially to produce commercial quantities of ceramic particulates, such as silica and titania. This is because of the low cost of production as compared to all other methods. The disadvantage of flame synthesis is that the control of particle size (both primary particle and aggregates size), morphology, and phase composition is difficult and limited.

Chemical Methods

Sol-gel technique

The sol-gel process is typically used to prepare nanometer-sized particles of metal oxides. This process is based on the hydrolysis of metal reactive precursors, usually alkoxides in an alcoholic solution, resulting in the corresponding hydroxide. Condensation of the hydroxide by giving off water leads to the formation of a network-like structure. When all hydroxide species are linked, gelation is achieved and a dense porous gel is obtained. The gel is a polymer of a three-dimensional skeleton surrounding interconnected pores. Removal of the solvents and appropriate drying of the gel result in an ultrafine powder of the metal hydroxide. Further heat treatment of the hydroxide leads to the corresponding powder of the metal oxide. As the process starts with a nanosized unit and undergoes reactions on the nanometer scale, it results in nanometer-sized powders. For alkoxides that have low rates of hydrolysis, acid or base catalysts can be used to enhance the process.

When drying is achieved by evaporation under normal conditions, the gel network shrinks as a result of capillary pressure that occurs and the hydroxide product obtained is referred to as xerogel. However, if supercritical drying is applied using a high-pressure autoclave reactor at temperatures higher than the critical temperatures of solvents, less shrinkage of the gel network occurs as there is no capillary pressure and no liquid-vapor interface, which better protects the porous structure. The hydroxide product obtained is referred to as an aerogel. Aerogel powders usually demonstrate higher porosities and larger specific surface areas than analogous xerogel powders.

Sol-gel processes have several advantages over other techniques to synthesize nanopowders of metal oxide ceramics. These include the production of ultrafine porous powders and the homogeneity of the product as a result of homogeneous mixing of the starting materials on the molecular level.

Reverse microemulsions/micelles method

The reverse micelle approach is one of the recent promising routes to nanocrystalline materials including

ceramics. Surfactants dissolved in organic solvents form spheroidal aggregates called reverse (or inverse) micelles. In the presence of water, the polar head groups of the surfactant molecules organize themselves around small water pools (~ 100 Å), leading to dispersion of the aqueous phase in the continuous oil phase.

Reverse micelles are used to prepare nanoparticles by using a water solution of reactive precursors that can be converted to insoluble nanoparticles. Nanoparticle synthesis inside the micelles can be achieved by different methods including hydrolysis of reactive precursors, such as alkoxides, and precipitation reactions of metal salts. Solvent removal and subsequent calcination lead to the final product. Several parameters, such as the concentration of the reactive precursor in the micelle and the weight percentage of the aqueous phase in the microemulsion, affect the properties, including particle size, particle-size distribution, agglomerate size, and the phases of the final ceramic powders. There are several advantages to using this method including the ability to prepare very small particles and the ability to control the particle size. Disadvantages include low production yields and the need to use large amounts of liquids.

Precipitation from solutions

Precipitation is one of the conventional methods to prepare nanoparticles of metal oxide ceramics. This process involves dissolving a salt precursor, usually chloride, oxychloride or nitrate, such as AlCl_3 to make Al_2O_3 , $\text{Y}(\text{NO}_3)_3$ to make Y_2O_3 , and ZrCl_4 to make ZrO_2 , in water. The corresponding metal hydroxides are usually obtained as precipitates in water by adding a base solution such as sodium hydroxide or ammonium hydroxide solution. The remaining counter-ions are then washed away and the hydroxide is calcined after filtration and washing to obtain the final oxide powder. This method is useful in preparing ceramic composites of different oxides by coprecipitation of the corresponding hydroxides in the same solution. Solution chemistry is also used to prepare non-oxide ceramics or pre-ceramic precursors that can be converted to ceramics upon pyrolysis.

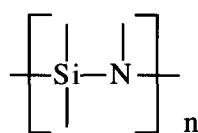
One of the disadvantages of this method is the difficulty in controlling the particle size and size distribution. Very often, fast and uncontrolled precipitation takes place resulting in large particles.

Chemical synthesis of pre-ceramic polymers coupled with physical processing techniques

This method is based on the use of molecular precursors, which facilitates the synthesis of nanomaterials containing phases of desired compositions. It involves a chemical reaction to prepare an appropriate polymer, which is then



Polycarbosilanes



Polysilazanes

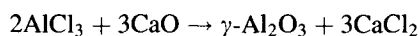
Fig. 1 General structural formulas of polycarbosilanes and polysilazanes.

converted into ceramic material upon pyrolysis. Using chemical reactions to prepare the pre-ceramic polymer not only allows for control of phase compositions but also overcomes the limitation of low production yields of the physical methods. This method has been very useful in preparing nonoxide ceramics such as silicon carbide and silicon nitride. The conversion of an organometallic precursor into a ceramic depends on different parameters such as the molecular structure of the precursor and the pyrolysis conditions (temperature, duration, and atmosphere). Metal carbides and metal nitrides have been obtained by pyrolysis of polymers containing the appropriate elements such as Si or Al and C or N. These polymers are called pre-ceramic polymers and are prepared from simpler chemical precursors. A considerable amount of free carbon from the thermolysis process is very often a problem. Silicon carbide (SiC) and silicon nitride (Si₃N₄) are the most studied ceramic materials prepared via this route. They are usually synthesized by the pyrolysis of polycarbosilanes and polysilazanes, for which general structural formulas are shown in Fig. 1, at temperatures between 1000°C and 1200°C.

Mechanochemical synthesis

Mechanochemical synthesis involves mechanical activation of solid-state displacement reactions. This process has been successfully used recently to make nanoceramic powders such as Al₂O₃ and ZrO₂. It involves the milling of precursor powders (usually a salt and a metal oxide) to form a nanoscale composite of the starting materials,

which react during milling, and subsequent heating, if necessary, to form a mixture of dispersed nanoparticles of the desired oxide within a soluble salt matrix. Nanoparticles of Al₂O₃ (10–20 nm), for example, can be prepared by milling AlCl₃ with CaO.



BONDING CONSIDERATIONS

Understanding chemical bonding and structures in ceramic materials is necessary in order to understand their chemical and physical behavior. When materials are composed of nanometer-sized building blocks, they deviate considerably from structural perfection and stoichiometry. As a result, the number of defects due to edges, corners, f-centers, and other surface imperfections is greatly enhanced, which, in turn, affects several physical and chemical properties as will be discussed below.

A range of cohesive forces contribute to the nature of bonding in ceramic materials including ionic (MgO, Fe_{1-x}O), covalent, metallic, van der Waals, and hydrogen bonding. Ionic compounds are formed when highly electronegative and highly electropositive elements are combined in a lattice. Pure ionic model is a reasonable approximation for some systems while it is a poor approximation for crystals containing large anions and small cations. In such systems, covalent contribution to bonding becomes significant. Van der Waals interactions play a crucial role in many ceramic systems, especially those with layered structures. In many oxide hydrates or hydroxy oxides, hydrogen bonding also contributes to the cohesive energy. For further reading on structure and bonding, the reader is referred to structural inorganic chemistry books.

SELECTED PROPERTIES

Ceramics possess their own chemical, physical, mechanical, and magnetic properties that are different from those of other materials such as metals and plastics. The properties of ceramics depend mainly on the type and the amounts of materials in their composition. However, the size of the building blocks of a ceramic material has been found to play an important role in its properties (see Ref. [1] and references therein).

When materials are prepared from nanometer-sized particles, a significant portion of the atoms become exposed on the surface. As a result, such materials exhibit unique properties that are remarkably different from those of the corresponding bulk. The physical and chemical

properties of nanoparticles show the gradual transition from atomic or molecular to condensed matter systems.

Chemical Properties

Ceramic materials are relatively inert, especially crystalline materials that tend to have perfect structures with minimum amount of defects. Most of the reactivity of these materials involves the surfaces where coordinatively unsaturated as well as defect sites exist. The behavior of the surface toward other species and the nature of interaction depend on the composition and the morphology, which determine the nature and the degree of surface interactions with other substances. Most of the time, interactions are limited to adsorption on the surface, which does not affect the bulk making these materials good corrosion-resistant.

The possibility of preparing ceramic powders in high surface areas with high porosity makes them well desired in some advanced applications. One example is the use of ceramic materials as supports for heterogeneous catalysts. Another example is the use of such materials in biomedical applications, where the surface of nanophase ceramics exhibits a remarkably improved biomedical compatibility compared to conventional ceramics, as discussed below.

Mechanical Properties

Ceramics are very strong materials showing considerable resistance against compression and bending. Some ceramic materials are similar to steel in strength. Most ceramics retain their strength at high temperatures. Silicon carbides and silicon nitrides, as an example, retain their strength at temperatures as high as 1400°C. As a result, such materials are used in high-temperature applications. Many of the physical and mechanical properties are particle-size dependent. As a result, several systems of nanophase ceramics have exhibited quite interesting and favorably enhanced mechanical properties.

Improved sintering and hardness properties

Nanoceramics are processed from nanophase powders by compacting first powders composed of individual ceramic particles (usually less than 50 nm in size) into a raw shape (often called a green body). This compacted powder is then heated at elevated temperatures. Densification occurs as a result of diffusion of vacancies out of pores (to grain boundaries), which lead to shrinkage of the sample. This process is referred to as pressure-less sintering. Fortunately, nanophase powders were found to compact as easily as their analogous submicron particles. To avoid particle size growth, samples have to be sintered at the

lowest temperature possible for a time sufficient to remove the residual porosity and establish coherent grain boundaries. Successful sintering enhances the hardness of the final material.

Experimental evidence shows that nanophase powders densify at faster rates as compared to commercial (submicron) particles.^[1] Faster densification rates allow achieving a given density at smaller grain sizes, before serious growth takes place. As a result of their small particle and pore sizes, nanocrystalline powders sinter to much greater densities than their conventional analogs at the same temperature. This also establishes that nanocrystalline powders, as compared to conventional powders, reach the same density at much lower temperatures. This, of course, eliminates the need for very high temperatures.

One disadvantage that can accompany fast densification though is inhomogeneous heating where the outside layers of the particles densify into a hard impervious shell which constrains the inside of the sample from normal shrinking, leading to some cracking as a result of strain incompatibility. This problem can be avoided by several ways. The most efficient way is to heat the samples slowly to reduce the shrinkage in the outer shell while heat is transported to the inner regions. On the other hand, high-density nanostructured ceramic systems including Y_2O_3 , TiO_2 , and ZrO_2 have been achieved by means of pressure-assisted sintering. Applying some pressure during sintering can increase the densification rate and suppress the particle growth.

Nanoscale powders of nonoxide ceramics such as metal carbides and nitrides show similar behavior. Conventional SiC, as an example, is difficult to sinter. Addition of some additives such as boron or carbon is very often necessary to densify SiC. Ultrafine powder of SiC sinters at lower temperatures and densifies without additives. On the other hand, mechanical properties can be fairly improved by the introduction of metallic nanoparticles dispersed within the matrix grains. Such systems are referred to as nanocomposites. Tungsten, nickel, or molybdenum nanoparticles dispersed within Al_2O_3 matrix grains, as an example, can enhance the mechanical properties of alumina, including the fracture strength and hardness.

Reduced brittleness and enhanced ductility and superplasticity

Superplasticity and ductility refer to the capability of some polycrystalline materials to undergo extensive tensile deformation without necking or fracture. Ceramic brittleness is the biggest technical barrier in practical applications, especially in load-bearing applications. Theoretical and experimental results provide evidence for the possibility that traditional brittle materials can be ductilized by reducing their grain sizes.^[1] When made

from nanoparticles, brittle ceramics can be superplastically deformed at modest temperatures and then heat treated at higher temperatures for high-temperature strengthening.

The capability to synthesize superplastic ceramic materials is now established. Nanocrystalline ceramics deform at faster rates, lower stresses, and lower temperatures. One important use of superplasticity in ceramics is diffusion bonding, where two ceramic parts are pressed together at moderate temperatures and pressures to form a seamless bond through diffusion and grain growth across the interface. Diffusion bonds form more easily in nanocrystalline ceramics than in larger grained ceramics as a result of both the enhanced plastic flow of nanocrystalline ceramics and the larger number of grain boundaries they provide for diffusional flux across the interface.

Electrical Properties

Ceramics include electrical conducting, insulating, and semiconducting materials. Chromium oxide is an electrical conductor, aluminum oxide is an insulator, while silicon carbide behaves as a semiconductor. As a result, ceramic materials have been used in a variety of electronic applications based on their electrical behavior.

Several electrical properties are particle-size and composition dependent. Electrical resistance and dielectric constant, as an example, for some systems increased as a result of small particle size. Conductivity of some mixed oxide ceramics, such as lithium aluminosilicate, is higher than that of their constituent oxides.

Magnetic Properties

Some ceramic materials possess magnetic properties. These include iron oxide-based ceramics and oxides of chromium, nickel, manganese, and barium. Ceramic magnets are known to exhibit high resistance to demagnetization. As a result, several ceramic powders have been employed in a wide range of electronic and magnetic applications as discussed below.

The fabrication of such materials from ultrafine particles can significantly enhance their magnetic behavior. The fact that in nanometer-sized particles a large portion of the atoms are on the surface, where the coordination numbers are less than that for bulk atoms, affects several parameters including unique surface/interface behavior and different band structure, which both lead to magnetism enhancement. It is now well established that one of the requirements to achieve appropriate coercivity and high magnetization saturation is to fabricate such materials in highly divided particles, preferably in the nanometer-sized range, with homogeneity and narrow size distribution. For further reading on nanoscale magnetism,

the reader is referred to Sorensen's chapter "Magnetism" in Ref. [1].

Many other properties are also particle-size dependent. The optical properties, as an example, of some ceramic materials have been found to depend on particle sizes. Nanoparticles of TiO_2 , as an example, are more efficient UV absorber than powders of large particles.

APPLICATIONS

Ceramic materials are of great value in a variety of applications as a result of their unique properties compared to other materials. Because of their electrical and magnetic properties, ceramics are important in several electronic applications, where they are used as insulators, semiconductors, conductors, and magnets. Ceramic materials also have important uses in the aerospace, biomedical, construction, and nuclear industries. In many of these applications, ceramic materials have shown significantly better performance when fabricated from nanometer-sized particles.

Mechanical Applications

Industrial ceramics are widely employed in applications that require strong, hard, and abrasion-resistant materials. Metal-cutting tools, tipped with alumina, and tools made from silicon nitrides for cutting, shaping, grinding, and sanding iron, nickel-based alloys, and other metals are very commonly used. Other ceramics such as silicon nitrides and carbides are used to make components for high-temperature use such as valves and turbocharger rotors. Ceramic materials and metal-based ceramics (cermets) are used to make components for space vehicles, including heat-shield tiles for the space shuttle and nosecones for rocket payloads.

Electrical Applications

Ceramics are used as insulators, semiconductors, and conductors. Aluminum oxide (Al_2O_3), for example, does not conduct electricity at all and is used to make insulators. Other ceramics, such as barium titanate (BaTiO_3), are used as semiconductors in electronic devices. Some copper oxide-based ceramics are superconductive at temperatures higher than those at which metals become superconductive. Superconductivity refers to the ability of a cooled material to conduct an electric current with no resistance. This phenomenon can occur only at extremely low temperatures, which are difficult to maintain. Transition metal nitrides, carbides, and borides are of interest as cathodes in electrochemical applications. This interest stems from the favorable properties of these

Table 1 Examples of electronic ceramics

Functions	Examples of materials	Applications
Insulation	Al ₂ O ₃ , SiC+BeO	IC substrate
Dielectricity	BaTiO ₃	capacitor
Semiconducting	SiC, LaCrO ₃ , SnO ₂ , ZnO+Bi ₂ O ₃	gas defector, thermistor, varistor
Piezoelectricity	ZnO, SiO ₂	piezolighter, piezofilter, surfacewave transducer, piezovibrator, flexible piezodetector
Pyroelectricity	PZT	IR detectors
Ferroelectricity	PLZT	optical shutter, optical memory
Ionic conduction	β-Al ₂ O ₃ , ZrO ₂	Na-S battery, O ₂ sensor
Luminescence	Y ₂ O ₂ S:Eu, ThO ₂ :Nd, Al ₂ O ₃ :Cr	cathode luminescence, IR laser
Light guide	SiO ₂	optical communication fiber
Polarization	PLZT	optical shutter
Soft magnetism	γ-Fe ₂ O ₃ , Zn _{1-x} Mn _x Fe ₂ O ₄	magnetic tape
Hard magnetism	SrO·6Fe ₂ O ₃	magnet seal

PZT: lead zirconate-titanate ceramics. PLZT: lanthanum-modified lead zirconate-titanate ceramics.

materials including electronic conductivity and good thermal conductivity, which when coupled with their mechanical strength and high melting points suggest that such materials can be stable in a range of environments.

Some ceramics such as strontium titanate (SrTiO₃) are employed in the form of thin films as capacitors in several electronic devices because of their capability to store large amounts of electricity in extremely small volumes. Lithium aluminosilicate ceramics have potential applications as solid electrolytes for utilization in solid high-energy density lithium battery systems. Piezoelectric ceramics are now key electronic components for television, FM radio, and the like. Very recently, piezoelectric ceramic displays have been developed in Japan, where microceramic actuators for activating the pixels are used. Piezoelectric effect refers to the appearance of an electric potential across certain faces of a crystal when it is subjected to mechanical pressure.

Other examples of functions and applications of advanced ceramics in the field of electronics are shown in Table 1.^[2]

Magnetic Applications

Iron oxide-based ceramics (ferrites) are widely employed as low-cost magnets in electric motors. Such magnets help in converting electric energy into mechanical energy. Unlike metal magnets, ferrites conduct high-frequency currents, and as a result, they do not lose as much power as metal conductors do. Manganese zinc ferrites are used in magnetic recording heads, and ferric oxides are the active component in several magnetic recording media, such as recording tapes and computer diskettes.

Biomedical Applications and Bioceramics

Some advanced materials are used in the biomedical field to make implants for use within the body. The main requirement of biomaterials for this application is the ability of their surfaces to support new bone growth. Ceramic materials are known to possess exceptional biocompatibility properties with bone cells and tissues. Specially made porous ceramic materials such as alumina, titania, zirconia, and others bind with bone and other natural tissues. Such ceramics are used to make hip joints, dental caps, and bridges. Other advanced ceramics such as hydroxyapatite, Ca₁₀(PO₄)₆(OH)₂, which is the principal component of bones and teeth, have excellent biocompatibility and bone in-growth capabilities and are used in reconstructing fractured bones and as replacement materials.

Recent research on long-term functions of osteoblasts on nanophase ceramics has shown evidence for unique and significant behavior.^[3] Compared to conventional ceramics, nanophase ceramics has shown enhanced osteoblast adhesion and proliferation, alkaline phosphatase synthesis, and concentration of extracellular matrix calcium.

Coatings

Because of its unique hardness and corrosion resistance, ceramic enamel is often used in coating metals. Thin hard wear-resistant coatings of ceramics include materials such as titanium nitride and titanium carbonitride. An emerging class of new hard protecting coatings beyond homogeneous layers of a ceramic nitride material is layered coating structures such as superlattices or multilayers of different nitrides. Such multilayer coating has been successfully applied in several applications such as bearings,

pumps, and compressors. Nonnitride coatings, such as tungsten carbide/carbon, are also of interest because of their high elasticity and chemical inertness.

Several techniques are being employed for protective ceramic coating. These include thermal spraying, chemical vapor deposition (known as CVD), and plasma spraying.

Nuclear Industry

Lithium-based ceramics are now considered as potential solid tritium breeders in nuclear fusion reactors. Potential breeder materials include LiAlO_2 , Li_2O , Li_2ZrO_3 , and Li_4SiO_4 . Solid breeders are safer during operation than liquid lithium systems, which are highly reactive.

CONCLUSION

Nanoceramics is one of the great outcomes of the evolutionary research in the field of nanoscience and nanotechnology, where fabrication of materials from nanometer-sized building blocks has resulted in a wide range of industrially useful materials. Recent research has proven that ceramic materials fabricated from ultrafine powders can be obtained through several physical as well as chemical methods that can be scaled up to produce commercial amounts. These unique materials have exhibited very remarkable behavior as compared with their bulk counterparts. Significant characteristics include chemical, mechanical, magnetic, electrical, and optical properties. As a result, improved performance of ceramic materials has been observed in a variety of applications including chemical, mechanical, magnetic, electrical, and biomedical. The new properties and improved performance of nanoceramics that are being discovered stimulate the development and improvement of ceramic processing, which, in turn, open the doors wide for the use of ceramics in a wide range of new technologies.

Directions of current interests include the preparation and processing of ultrafine (nanometer-sized) powders, the development of new synthetic routes to materials of

homogeneous sintered bodies, and the preparation of ceramics made of several composites.

REFERENCES

1. Khaleel, A.; Richards, R. Ceramics. In *Nanostructured Materials in Chemistry*; Klabunde, K.J., Ed.; John Wiley and Sons, Inc.: New York, 2001; 85–120.
2. Yanagida, H. Electronic Ceramics. In *Fine Ceramics*; Saito, S., Ed.; Elsevier: New York, 1988; 239–261.
3. Webster, T.J.; Ergun, C.; Doremus, R.H.; Siegel, R.W.; Bizios, R. Enhanced functions of osteoblasts on nanophase ceramics. *Biometaterials* **2000**, *21* (17), 1803–1810.

SUGGESTED READING

- Brinker, C.J.; Scherer, W. *Sol-Gel Science*; Academic Press: San Diego, USA, 1990.
- Cow, G.M.; Gonsalves, K.E. *Nanotechnology, Molecularly Designed Materials*; American Chemical Society: Washington, DC, 1996.
- Edelstein, A.S.; Cammarato, R.C. *Nanoparticles: Synthesis, Properties and Applications*; Institute of Physics Publishing: Philadelphia, 1996.
- Hadjipanayis, G.C.; Siegel, R.W. *Nanophase Materials*; Kluwer Academic Publishers: Dordrecht, 1994.
- Ichinose, N.; Ozaki, Y.; Kashu, S. *Superfine Particle Technology*; Springer: London, 1992.
- Interrante, L.V.; Hampden-Smith, M.J. *Chemistry of Advanced Materials: An Overview*; Wiley-VCH: New York, 1998.
- Jolivet, J.-P. *Metal Oxide Chemistry and Synthesis. From Solution to Solid State*; John Wiley and Sons, Ltd.: New York, 2000.
- Narula, C.K. *Ceramic Precursor Technology and Its Applications*; Marcel Dekker, Inc.: New York, 1995.
- Segal, D. *Chemical Synthesis of Advanced Ceramic Materials*; Cambridge University Press: Cambridge, 1989.

Nanocrystal Arrays: Self-Assembly and Physical Properties

Xiao Min Lin

Argonne National Laboratory, Argonne, Illinois, U.S.A.

Raghuveer Parthasarathy

University of Chicago, Chicago, Illinois, U.S.A.

University of California, Berkeley, California, U.S.A.

Heinrich M. Jaeger

University of Chicago, Chicago, Illinois, U.S.A.

INTRODUCTION

Over the last few years, research in the area of nanoscience has blossomed into an independent and highly interdisciplinary area.^[1] Materials in the nanometer scale (size range 10 Å to 1 μm) are typically referred to as nanoparticles, nanocrystals, nanorods, or nanowires, depending on their crystallinity and shape. Here we refer to them simply all as nanocrystals, without distinguishing the differences. The unique material properties in this size range come from several sources: 1) quantum size effects,^[2] where confinement of charge carriers in a small space leads to discrete energy levels; 2) classical charging effects,^[3] which originate from the discrete nature of the electrical charge; and 3) surface/interface effects,^[4] where the properties of surface or interface atoms become much more significant, as the surface-to-volume ratio increases with decreasing of particle size. Many novel properties of single, isolated nanocrystal have been investigated during the past two decades, such as size-dependent optical absorption and luminescence in semiconductors,^[5,6] coulomb blockade phenomena in charge transfer,^[7] or enhanced surface magnetic moments in magnetic nanocrystals.^[8]

By comparison, assemblies of nanocrystals have only begun to be studied in a systematic fashion in recent years. The exciting aspect of nanocrystal arrays is that they form a truly new class of materials, where the basic building blocks are nanocrystals instead of atoms.^[9] The properties of these materials not only depend on which chemical elements are used to form the building blocks, but also depend on how many atoms are in each building block and how strongly coupled these building blocks are. Traditional materials can be either crystalline or amorphous, depending on the arrangement of the constituent atoms. Similarly, nanocrystal arrays can also be ordered or disordered. In the former case, they are referred to as nanocrystal superlattices (NCSs).

The purpose of this article is to introduce several recent developments in the field, focusing on the experimental point of view. In "Formation of Nanocrystal Arrays," experimental issues regarding the formation of nanocrystal arrays will be discussed and, in particular, the conditions for controlled formation by self-assembly. In "Electronic Transport" and "Optical Properties," we consider electronic and optical transport properties of nanocrystal arrays, with the main theme being the collective phenomena in these systems, rather than behavior related to the individual nanocrystal. "Conclusion" contains a brief discussion of outstanding issues and concluding remarks. Because of the limited space, we will focus our article on arrays formed by chemically synthesized nanocrystals only. Therefore lithographically patterned quantum dot arrays will not be discussed. For aspect not covered here and for additional, in depth information on nanocrystal arrays, we refer the reader to Refs. [9–12].

FORMATION OF NANOCRYSTAL ARRAYS

The ultimate goal of nanocrystal self-assembly is the fabrication of highly ordered two-dimensional (2-D) or three-dimensional (3-D) superlattices or other well-defined structures.^[12,13] One of the earliest research efforts in this direction can be found in the work of Bentzon et al.^[14] who observed uniformly sized Fe₂O₃ particles to spontaneously form hexagonal arrays. The discovery of high-temperature routes for high-quality semiconductor nanocrystals synthesis further stimulated the development of this field.^[15] By now, nanocrystals made of metals,^[16–20] semiconductors,^[21,22] and oxides^[14,23,24] have been shown to form ordered NCSs under proper experimental conditions, although the degree of ordering can still vary rather significantly.

In general, the spontaneous formation of nanocrystal superlattices via self-assembly requires the following: 1) a high degree of monodispersity in nanocrystal diameter (typically a relative size deviation in nanocrystal core diameters of less than 5%); 2) a complete coating of core surface with ligand molecules; and 3) suitable physical mechanisms to promote ordered packing. In the following, we discuss the relevant issues associated with the nanocrystal cores, the ligand shells surrounding the cores, and the self-assembly mechanisms.

Nanocrystal Core

There are several different techniques to obtain monodisperse nanocrystals. High-temperature synthesis is the most widely used since Murray et al.^[15] in 1993 obtained high-quality semiconductor nanocrystals by this method. The basic principle behind this kinetically controlled

process was actually proposed quite some time earlier.^[25] The idea is to oversaturate the nucleating species in a very short period of time, so that there is a burst of nucleation sites at the beginning of the chemical reaction (Fig. 1A). If the concentration of the nucleating species is kept below the saturation level afterward, there will be no new nucleation sites. Subsequently, only the existing nucleation sites can grow. By monitoring the growth of particles, different sizes of nanocrystals can be synthesized with high monodispersity. Sugimoto^[26] used this idea to synthesize uniform micron-sized spheres. Murray et al. extended this technique to semiconductor nanocrystals by using a high boiling point solvent (mixture of long chain alkylphosphines, alkylphosphine oxides, and alkylamines). High reaction temperature, necessary to decompose the organometallic precursor, also results in high crystallinity of the final product (Fig. 1B). The relative size distribution of nanocrystals can, furthermore, be "focused" in situ by adjusting the concentration of reaction species during the growth.^[27]

The second technique that is frequently used is the size-selective precipitation method (Fig. 1C).^[28,29] This method exploits the fact that the solubility of nanocrystals in a solvent-nonsolvent mixture is highly size-dependent. By slowly adding a nonsolvent into a polydisperse colloid, large particles typically become destabilized and are the first to precipitate out from the solution, which can be separated and redissolved into the original solvent. Increasing the concentration of nonsolvent gradually causes smaller particles to precipitate. By repeating this process, different fractions become increasingly more monodisperse. Whetten et al.^[20,29] have coupled this process with mass spectroscopy to obtain nanocrystals of highly precise mass.

Different from the above two methods is a recently developed process called digestive ripening which can transform a polydisperse colloid directly into a more monodisperse colloid through a thermodynamic pathway (Fig. 1D). Lin et al.^[30] first demonstrated this process by heating a polydisperse gold colloid in an environment of excess dodecanethiol molecules. The large particles break up into smaller ones upon heating, and the initially polydisperse colloid evolves into a much more uniform system. This is in sharp contrast to the Ostwald ripening process, which favors large particles because of their lower surface energy. Stoeva et al.^[31] recently showed that this process is not limited to the gold colloid synthesized by the inverse micelle technique, but works as well for gold colloid prepared by the solvate metal atom dispersion (SMAD) method. This ripening process explains why thiolated gold colloid typically gives particle sizes in the range of 4–6 nm. Although it has been reported that different thiol-gold ratios can be used to adjust the particle sizes,^[32] they may be formed in

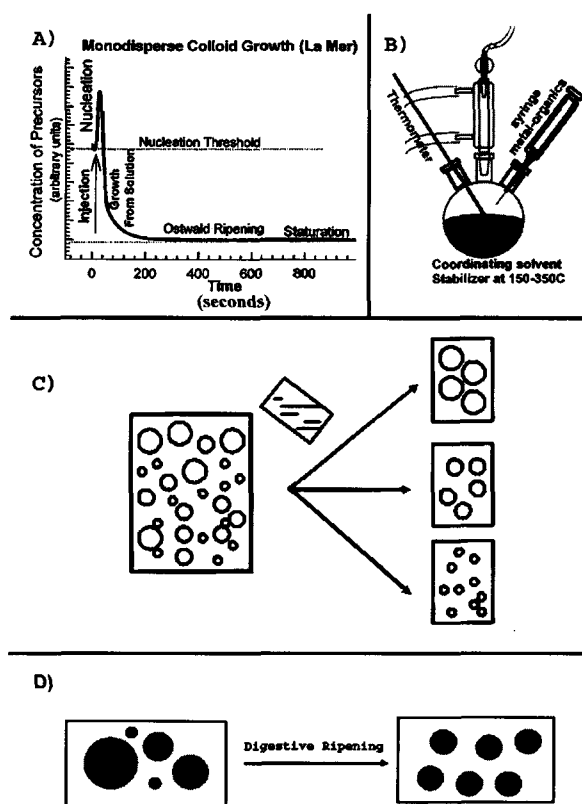


Fig. 1 Schematic diagrams of various approaches to synthesize monodisperse colloidal nanocrystals. A) Nucleation rate diagram of high-temperature synthesis.^[9] B) Experimental setup of high-temperature synthesis.^[9] C) Size-selective precipitation technique through solvent replacement.^[20] D) Digestive ripening process.^[30] (Parts A and B are reprinted with permission from Ref. [9]. Copyright 2000, Annual Review of Materials Science.)

kinetically trapped metastable sizes at room temperature. Reflux heating would eventually drive these particles into thermodynamically favored size ranges.^[33] Although the detailed mechanism behind digestive ripening is still under investigation, it has been speculated that intermolecular interaction and molecular surface interaction might induce a specific ligand packing curvature on the nanocrystal surface, which, in turn, determines the particle size.^[31]

Ligand Shell

In aqueous solution, nanocrystals are typically stabilized by double layers of ions adsorbed on the surface.^[34] Nanocrystals in the organic solvent generally require coating with an organic ligand shell. There has been quite a variety of ligand molecules used in the literature, such as alkanethiol,^[35,36] amine,^[37] and carboxylic acid.^[38] Ligand shells have several functions. First, and most importantly, they prevent nanocrystals from sintering upon colliding in the solution or on the substrate. The resulting steric repulsive force between ligand molecules is essential to the ordered packing of nanocrystals into arrays.^[34] Molecular dynamics simulation by Luedtke and Landman^[39] showed that ligand molecules interdigitate and even bundle together to form a robust structure that separates nanocrystals in the array. Subsequent high-resolution transmission electron microscopy experiments supported this claim.^[40]

An important point is that the array packing order will depend not only on the particle size dispersion, but also on the integrity of the ligand shells. Adsorption of ligand molecules in the solution is a reversible process, and there

is frequent exchange between molecules adsorbed on the nanocrystal surface and molecules in the solution. Therefore repeated precipitation and washing can remove some ligand molecules from nanocrystal surface, which causes incomplete coating of ligand molecules on the surface. Depending on the number of attached ligands and their interactions with those of neighboring nanocrystals, the interparticle spacings will vary when nanocrystals self-assemble on the surface. As a result, for incomplete ligand coating, the average interparticle spacing is typically smaller and has a wider distribution. As shown in Fig. 2, arrays formed by nanocrystals surrounded by an incomplete ligand shell exhibit a much reduced long-range ordering as compared with arrays formed by nanocrystals that have their surface saturated with ligands.^[41]

Ligand molecules can also affect the nanocrystal solubility and induce specific interaction with complimentary molecules adsorbed on other nanocrystals or surface. Alkanethiol with carboxylic acid group on one end can replace straight alkanethiol molecules, therefore allowing nanocrystals synthesized in the organic phase be transferred to aqueous solution.^[38] DNA-labeled nanocrystals can form aggregates when complimentary strands of DNA are added and result in a color change that is easy to detect.^[42] Streptavidin-labeled nanocrystals can form a large array through biotin-streptavidin linkage.^[43]

The physical properties of nanocrystals can also be changed by the ligand molecules. For example, electron-donating ligand such as pyridine or CO can change the unpaired electron density of a magnetic nanocrystal, quenching the magnetic moment of surface atoms attached.^[44] On the other hand, enhanced surface moments were observed for nanocrystals formed in the gas phase without electron-donating ligands on the surface.^[45]

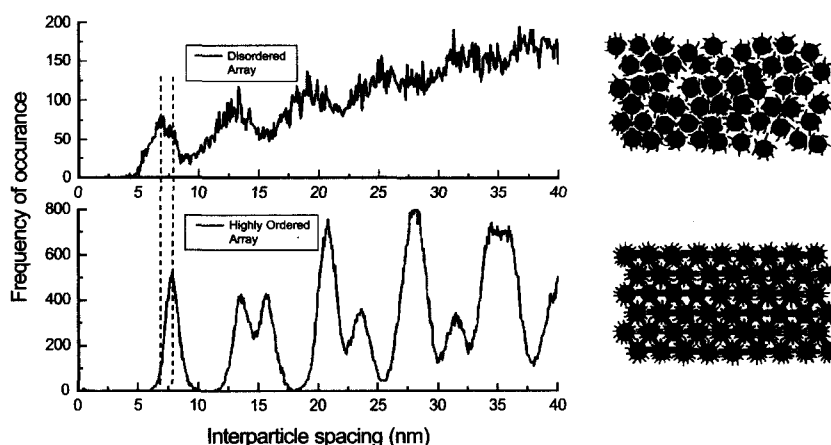


Fig. 2 Interparticle spacings for a highly ordered array formed by monodisperse 5-nm Au nanocrystals with complete ligand shell and for a disordered array formed by the same nanocrystals but with incomplete ligand shells. (Image analysis based on transmission electron micrographs was done by N. Mueggelburg.)

Self-Assembly Mechanism

The driving forces for self-assembly of nanocrystals in solution and on surfaces have been extensively studied in a variety of systems.^[46–51] The mechanisms are, however, quite complicated, depending on the specific materials, the size and shape of the particles, the charges on their surfaces, and on the physical environment during the self-assembly process. They can be roughly categorized into the following types.

1. Entropy-driven systems. Colloidal particles with strong repulsive interaction can crystallize when the concentration of particles exceeds a critical limit.^[46–48] This is because the entropy gain associated with local motions around the regular lattice point compared with motion around random sites is sufficient to compensate the entropy loss arising from long-range ordering. In some cases, the structure of colloidal crystals grown from the surface can also be controlled by prefabricated patterns on the surface.^[49]
2. Attraction-driven systems. For neutral, uncharged particles of sufficiently large size, van der Waals interaction can be strong enough to induce aggregation. At large distance, the attraction force varies as $-AR^6/D^6$, where A is the Hamaker constant, R is the particle radius, and D is the interparticle distance. At

small distance, the functional form changes into $-AR/D$.^[50–52] If the attraction force is the only force that acts upon the particles or it is significantly stronger than any other interaction that is present, it will cause irreversible, diffusion-limited aggregation. Ligand coating on nanocrystal surfaces can act as a “bumper” or buffer layer to prevent such irreversibility. Diffusion of nanocrystals under the influence of the attractive force can lead to formation of large ordered arrays.^[16] Care must be taken to minimize the disruptive effect of solvent dewetting to obtain high-quality arrays (Fig. 3).^[16] Temperature also plays an important role to anneal out some defect sites during the self-assembly process. For a pair of 6-nm gold particles separated by a gap of 1.7 nm (dodecanethiol chain length), a simple calculation shows that the interparticle van der Waals force is roughly 46 meV, which is comparable to the thermal energy at room temperature. Fig. 4 shows the edge of a self-assembled gold nanocrystal array. Particle sizes are more polydisperse at the edge than in the interior of the domain, presumably because of the thermal annealing effect during the assembly process.

3. Other physically driven systems. Assembly of micron spheres and nanocrystals can also be accomplished by electrophoretic deposition.^[53,54] The assembly of particles on the electrode surface is a result of electrohydrodynamic fluid flow arising from an ionic

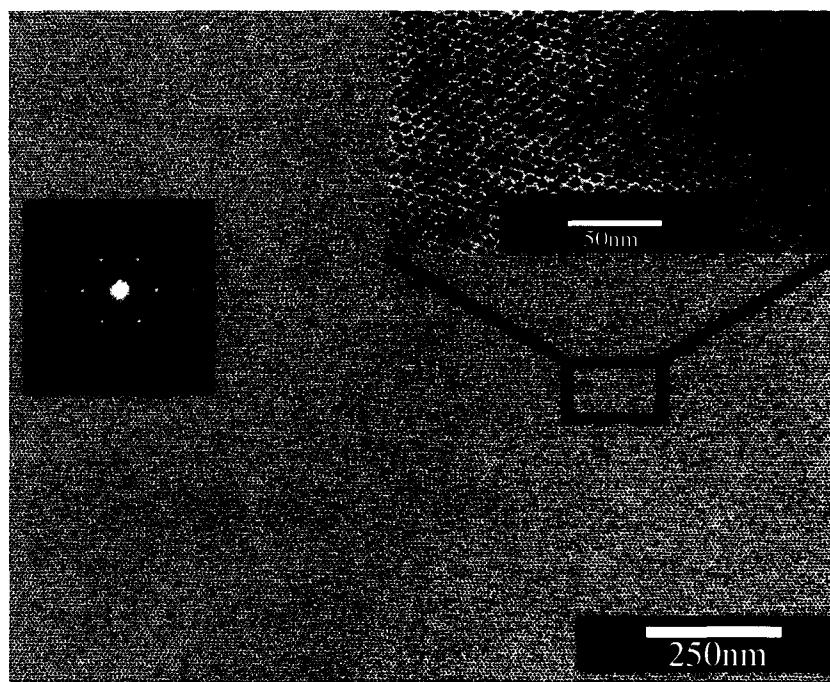


Fig. 3 Long-range-ordered gold nanocrystal superlattices formed on silicon nitride substrate by controlling solvent dewetting. Each individual nanocrystal is about 5 nm in diameter.^[16] Inset shows the Fourier transformation of a small portion of the image.

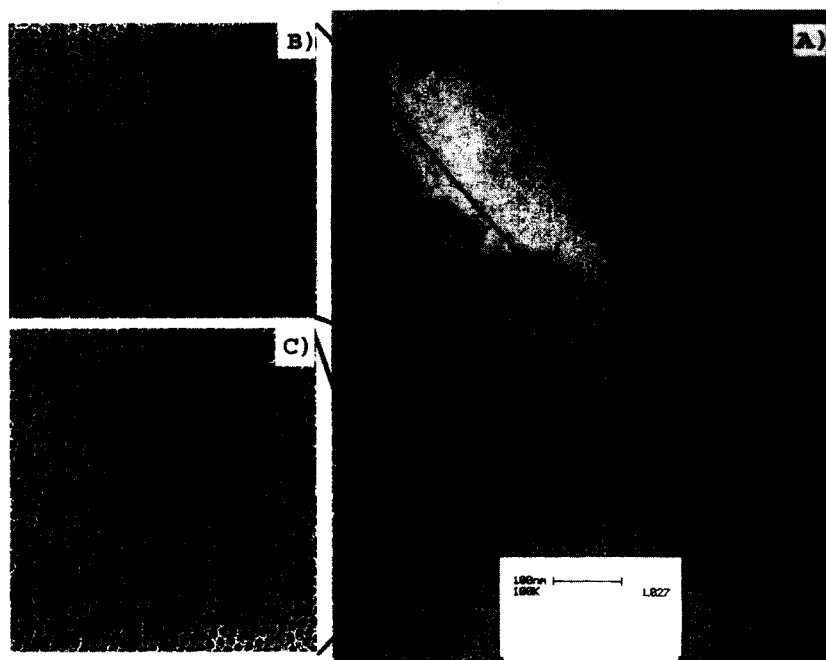


Fig. 4 (A) The edge of self-assembled gold nanocrystal superlattices shows a sharp boundary, indicating that diffusion under the influence of interparticle van der Waals forces is responsible for the assembly process. (B–C) The edge of the domain exhibits a large-size polydispersity in size than the interior of the domain, indicating thermal annealing effect during the assembly process.

current flowing through the solution. By adjusting the electric field strength or frequency, the lateral attraction force between particles can be modulated. This facilitates the reversible formation of two-dimensional fluid and crystalline states on the surface.

ELECTRONIC TRANSPORT

Charge transfer through nanocrystal arrays is of great importance not only because of the fundamental new physics involved in such highly correlated system, but also because the modern electronic components are approaching the size limit of standard photolithography techniques.^[55] Self-assembled structures based on chemically synthesized nanocrystals have the potential to circumvent such limitations and thus be used as alternative future electronic components.^[56]

The transport through individual nanocrystals has been well-studied both theoretically and experimentally (by both scanning tunneling microscopy^[57,58] and two-terminal measurements^[59]). For metal nanocrystal, its main feature is the Coulomb blockade effect, in which transfer of a single electron on or off a nanocrystal is strongly affected by electrostatic interaction with the nanocrystal's

charge. Because of the large number of free electrons in metal nanocrystals, the discrete level spacing as a result of quantum confinement effects is small and becomes significant only at very low temperatures, typically $\ll 1$ K. For semiconductor nanocrystals, the number of free carriers is much smaller and quantum confinement effects, together with the Coulomb blockade, determine transport properties.^[59]

Many-particle systems, on the other hand, are not as well understood and are more complex because of the intricacies of coupling between constituent nanocrystals, effects of structural order and disorder, and charge transfer between nanocrystal cores and ligands. A variety of phenomena have been reported in different systems, including spin-dependent tunneling in magnetic particle assemblies,^[18] hopping-type transport in dithiol linked arrays,^[60] and metal-insulator-like transitions in silver nanocrystal monolayers.^[61–63] Arrays of semiconductor particles exhibit interesting time- and illumination-dependent transport which, furthermore, shows striking slow relaxation behavior, reminiscent of glasses.^[64]

Our own work has focused on weakly coupled metallic nanocrystal system—monolayers of 5 nm diameter 1-dodecanethiol-ligated gold nanocrystals, self-assembled on silicon nitride substrates—and we will begin our discussion with these arrays as our focus.^[65,66] By “weakly

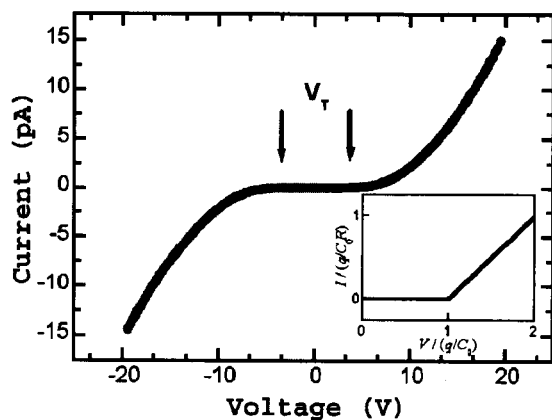


Fig. 5 Current–voltage (I – V) characteristic for a weakly coupled gold nanocrystal superlattice array at low temperature (12 K). The distance between the in-plane electrodes was 330 nm and the array width was 2 μm . The lower inset shows a schematic I – V curve for a single nanocrystal. (From Ref. [65].)

coupled” we mean that the Coulomb blockade energy, associated with the transfer of individual electrons between individual nanocrystals, dominates transport—the Coulomb or single electron charging energies are large compared with $k_B T$, and the electron wavefunctions, consequently, are localized on the scale of single nanocrystals. A typical current–voltage (I – V) curve at 12 K, from an array of length $N \approx 50$ particles separating the electrodes and width $M \approx 270$ particles, is shown in Fig. 5. There is a significant voltage threshold ($V_T = 4.2$ V) below which no current flows. The voltage threshold is the direct consequence of the Coulomb blockade. For each particle, an energetic cost $V_0 \sim e/r = e/C_0$, where r is the particle radius, ϵ is the dielectric constant of the medium surrounding the metal core, and C_0 is the self-capacitance of the metal sphere, must be paid to transport a single electron onto the charged nanocrystal. For the particles in Fig. 5, V_0 is around 100 mV, and V_T arises as the sum of this single electron charging energy over all nanocrystals traversed in crossing from one electrode to the other. V_T grows linearly with array length: $V_T = \alpha N(e/C_0)$, where the parameter α ($\alpha < 1$) accounts for interparticle capacitive coupling and the randomness of the offset charges in the underlying substrate that give rise to the Coulomb blockade repulsion.^[65–68]

Current can flow when the voltage threshold is exceeded—but how, microscopically, do electrons move from nanocrystal to nanocrystal? This can be answered by detailed measurements of the nonlinear current–voltage characteristics as a function of temperature. In the following, we start with a discussion of the low-temperature limit, in which thermal energies can effectively be neglected, and then consider the influence of finite temperatures.

Low-Temperature Limit

There is a distinctive threshold voltage in this temperature range. Beyond the array’s threshold, current rises as a power law in voltage:

$$I \sim M \frac{V_0}{R} \left[\frac{(V - V_T)}{V_T} \right]^\zeta$$

where R is the interparticle resistance, M is the array width, V_0 is the charging voltage (e/C_0), and V_T is the threshold voltage. This power-law form was predicted independently nearly a decade ago by Middleton and

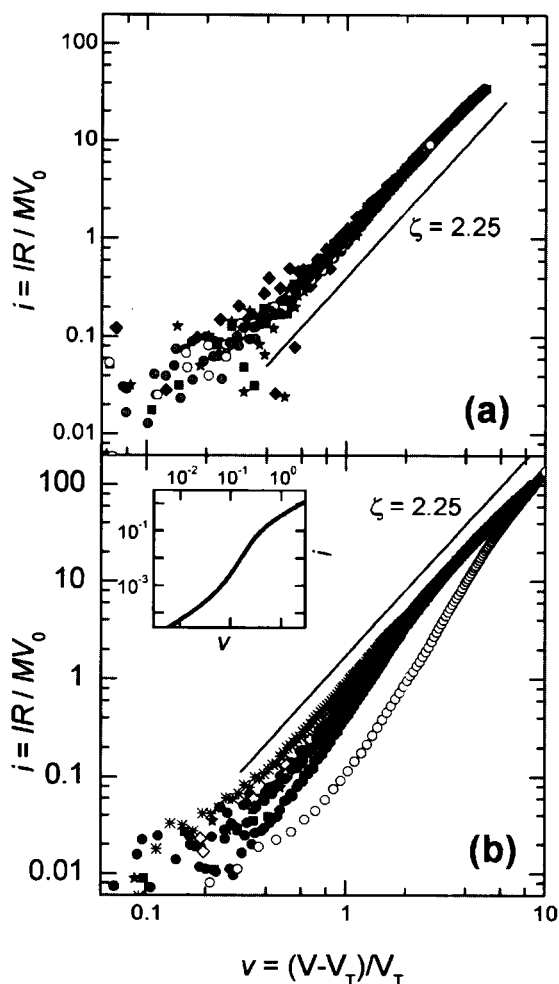


Fig. 6 Log–log plots of I – V curves above the voltage threshold for both highly ordered nanocrystals arrays (a) and disordered nanocrystals array caused by solvent dewetting (b). A single power law with an exponent of 2.25 fits all the highly ordered arrays, while structural disorder causes significant deviations from power-law behavior. Inset to (b) shows simulated I – V curves for parallel one-dimensional chains of nanocrystals with randomly distributed thresholds. (From Ref. [65].)

Wingreen (MW)^[67] and by Roux and Herrmann (RH).^[68] Middleton and Wingreen pointed out that local charge disorder (i.e., random offset charges) gives each nanocrystal a different single-electron charging energy, uniformly distributed in the interval $(0, V_0)$. The path between the electrodes with the lowest total Coulomb blockade cost determines the voltage threshold. Beyond threshold, the applied voltage allows an increasing number of paths to conduct current. As the current–voltage relation in each one-dimensional path is linear, the resulting array I – V curve (beyond threshold) is superlinear. In fact, MW provided an analogy between the branched, meandering flow of current in this sort of arrays to Kardar–Parisi–Zhang (KPZ) models.^[69] This deterministic growth model was originally used to describe interface growth in disordered media, such as cluster formation, liquid front in fluid flow, and surface roughness of growing crystal. From this analogy, MW’s theory gives a value of the scaling exponent: $\zeta=5/3$.

Experiments on highly ordered superlattices show robust power-law scaling (Fig. 6a), in accord with the MW model. However, the measured scaling exponent, $\zeta=2.2$, differs from the theoretical prediction, $\zeta=5/3$. The cause for the discrepancy between theory and experiment remains an open question, although it may arise from dispersity in the interparticle resistances or from inadequacies in the analogy to KPZ-type models.

Structurally disordered arrays display different behavior beyond threshold. Fig. 6 compares ordered arrays with disordered arrays in which voids were caused by solvent dewetting, thereby breaking up the monolayer. Rather than exhibiting robust scaling with a single exponent ζ over

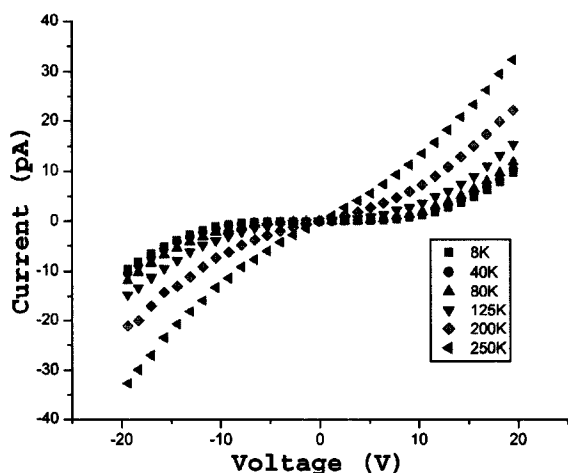


Fig. 7 I – V curves for a gold nanocrystal array as a function of temperature. In the low-temperature limit (below 100 K), a clear threshold exists, with a weak, linear temperature dependence. At high temperatures (above 100 K), there is a finite zero-biased conductance. (From Ref. [70].)

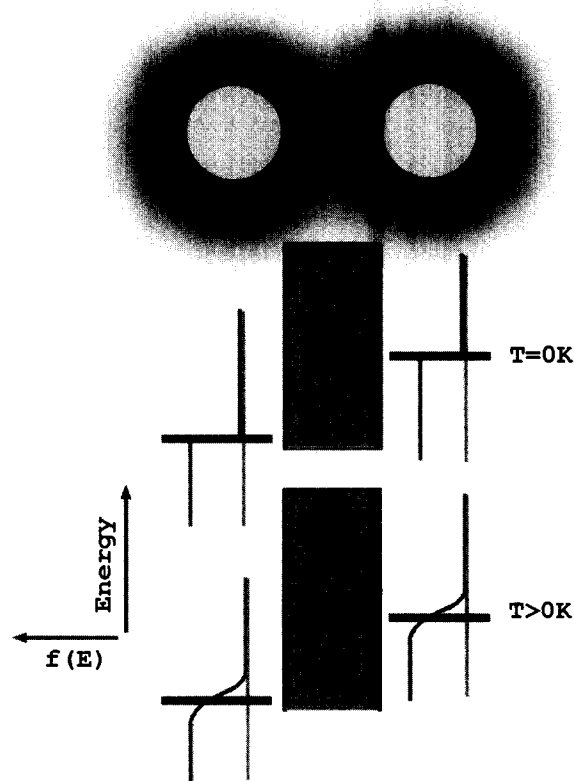


Fig. 8 Schematic diagram of thermally-assisted tunneling at finite temperatures. The offset between energy levels involved in tunneling is caused by the single-electron charging energy. (From Ref. [70].)

several orders of magnitude, the current–voltage data for the disordered samples are not well fit by a single power law and display significant sample-to-sample variations. The lack of scaling behavior can be understood by considering disordered arrays as two-dimensional patches connected by one-dimensional “bottlenecks” which disturb the branching and growth of current-carrying paths. Accurate determination of array scaling exponents thus can only be performed in structurally ordered arrays.

Finite Temperatures

Fig. 7 shows a set of I – V curves measured at different temperatures. A careful examination of this data reveals that, at low temperatures (<100 K), there is a very weak temperature dependence. In this temperature region, the I – V characteristics above V_T appear simply shifted along the voltage axis with increasing temperature, while the current scale is untouched.^[70,71] Based on the experimental results, we can write $V_T(T)=V_T(0)(1-b\frac{k_B T}{e^2/C_0})$, where $V_T(T)$ is the threshold voltage at temperature T and b is a

numerical factor. In other words, temperature contributes energy of order $k_B T$ per nanocrystal, which assists the electrons in “paying” the coulomb blockade cost for transport. Quantitatively, $b=13.9$, both from experiments and from a model of thermally assisted tunneling.^[69] Fig. 8 is a schematic picture of thermally assisted tunneling in metal nanocrystals. This correspondence, combined also with the absence of exponentially activated conduction in this region, implicates as the transport mechanism tunneling from metal core to metal core through large barriers (eV) provided by the ligands.^[69]

At high temperatures, in our array around 100 K, V_T is lowered to zero, and the zero-bias conductance ($g_0=dI/dV$ at $V=0$) is found to obey an Arrhenius form: $g_0=\exp(-U/T)$. In certain other nanocrystal systems, only this exponential form is seen at the temperatures examined.^[60] One must be wary of equating Arrhenius-like conductance with, for example, activated hopping over a barrier, as it also follows from a direct tunneling scenario at temperatures which overwhelm the Coulomb blockade energy.

We have referred to the arrays above as “weakly coupled,” meaning several things: First, the tunneling amplitudes between particles are low, leading to only picoamperes of current flow at biases of several volts. Second, the interparticle capacitances (determined by both the interparticle spacings and the nanocrystal sizes) are less than or equal to the single-particle capacitance C_0 . Third, transport is dominated by coulomb blockade effects, as shown by a finite voltage threshold at low temperatures. Experiments on strongly coupled nanocrystal arrays have also been performed, as we will now discuss.

Interparticle coupling can be increased by the use of more complex conjugated or aromatic ligands^[60] or by compressing arrays in Langmuir–Blodgett troughs. The latter technique has been used extensively by Heath et al.^[61,62] Characteristic of transport data from these systems is the lack of a voltage threshold, i.e., a finite zero-bias conductance, down to the lowest temperatures examined.

The most dramatic feature of compressed nanocrystal monolayers, discovered by Heath’s group, is the appearance of shiny, metallic optical reflectivity beyond a certain critical compression.^[61,62] This has been referred to as a metal-insulator transition; we will discuss it also in the next section in the context of plasmon coupling. At present, simultaneous optical and electronic transport data do not exist. However, a wide range of transport data from these films (transferred from Langmuir troughs onto solid substrates), from compressions at both sides of the optical transition, show resistivity which increases exponentially with decreasing temperature, indicating insulating behavior. Although not technically metallic, the arrays show a rich variety of transport characteristics,

with conductivity (σ) following activated hopping forms [$\sigma\sim\exp(-U/T)$],^[72] variable-range hopping of interacting electron forms [$\sigma\sim\exp(-U/T^{1/2})$],^[73] and other forms depending on variables such as compression and disorder.^[73] We will return to some of the issues raised by these experiments in the final section of this article.

OPTICAL PROPERTIES

The optical properties of small particles have received considerable attention during the past decade because of potential applications in optical sensors^[74] and lasing devices.^[75] Research has mainly focused on semiconductor nanocrystals and their assemblies. Size-dependent optical absorption and photoluminescence as a result of the creation and recombination of excitons have been studied extensively.^[5,6] In nanocrystal arrays, it has been found that interactions between nanocrystals can lead to long-range resonance transfer (LRRT).^[22,76] This process is schematically sketched in Fig. 9. When two different sizes of CdSe nanocrystals, for example, are combined in a mixed nanocrystal array, excitation in the small particles (donors) can resonantly excite large particles (acceptors). If the transferred excitation can be trapped in a low energy state of the large particle, then the reverse process cannot occur and a unilateral energy transfer process has taken place. Photoluminescence (PL) quantum yield (QY) of both the donor and acceptor in a mixed nanocrystal array showed a quenching of QY for the small particles and an

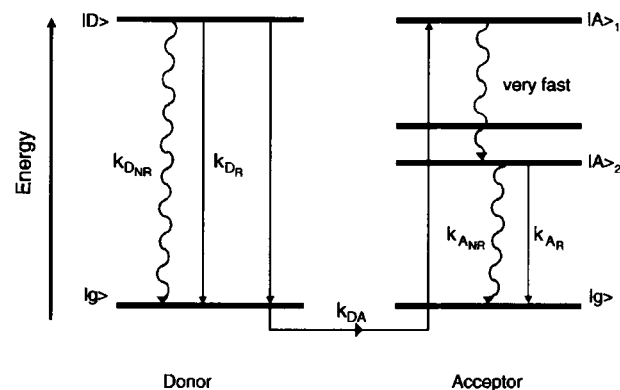


Fig. 9 Schematic diagram of electronic energy transfer between two different size nanocrystals in a close-packed nanocrystal array. The smaller particles that have large bandgaps are donors of excitation, while large particles with smaller bandgaps are acceptors of excitation. Different pathways of both radiative (R) relaxation and nonradiative (NR) relaxation are also indicated. (From Ref. [9]. Copyright 2000, Annual Review of Materials Science.)

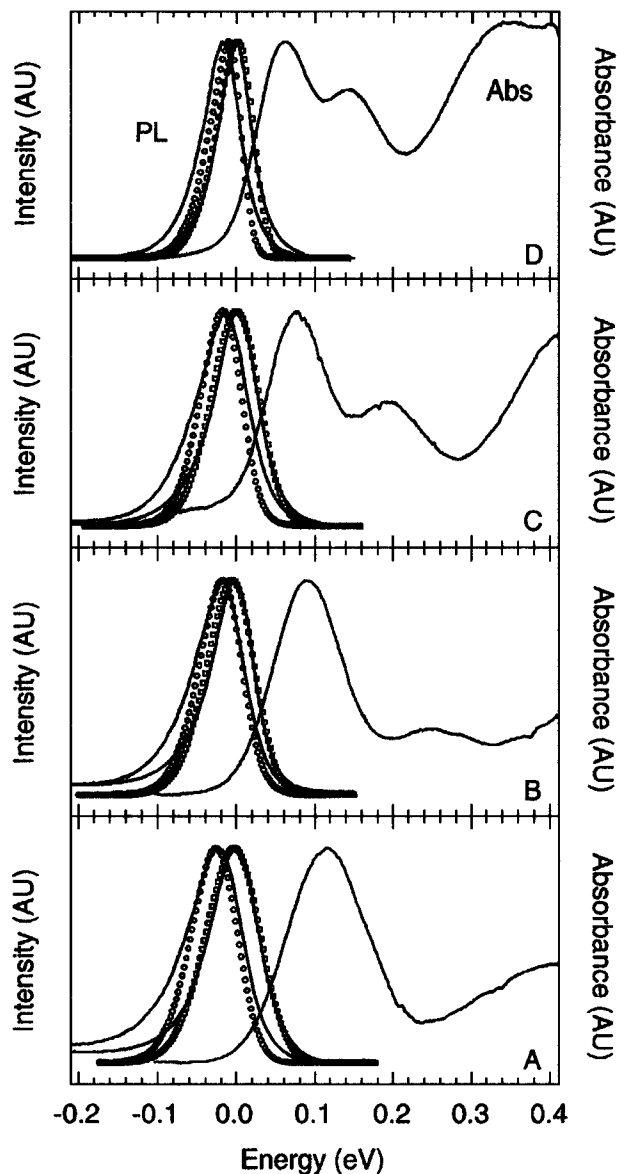


Fig. 10 Absorption and photoluminescence spectra (PLs) for different sizes of CdSe nanocrystals (A) 30.3, (B) 39.4, (C) 48.0, and (D) 62.1 Å diameters. PL spectra for nanocrystals in a close-packed array are red-shifted compared to spectra obtained from particles in solution. Open squares and circles are theoretical fitting curves taking into account the inhomogeneous distribution of emitting energies. (From Ref. [9]. Copyright 2000, Annual Review of Materials Science.)

enhancement for the large particles and thus confirm that the energy transfer process indeed takes place.^[76] Even in a highly uniform nanocrystal array with size deviation less than 5%, the intrinsic inhomogeneity can lead to energy transfer among particles with different sizes. As a result, the PL spectrum of nanocrystals in solid form red-shifts

compared with the same nanocrystals in colloidal form (Fig. 10).

Optical properties of metallic nanocrystals are dominated by surface plasmon phenomena, where spatially confined electrons oscillated in resonance with incident electromagnetic waves. For specific metals, such as silver and gold, the plasmon absorption occurs in the visible wavelength range, giving rise to the visible colors for these colloids. For example, 5-nm gold nanocrystals are deep maroon in color. The frequency-dependent polarizability of a single nanocrystal is given by the Clausius-Mossotti equation:^[77]

$$\alpha_A(\omega) = R^3 \frac{\epsilon(\omega) - \epsilon_m}{\epsilon(\omega) + 2\epsilon_m}$$

where R is the radius of the particle, $\epsilon(\omega)$ is the dielectric function of the particle, and ϵ_m is the dielectric function of the medium. Using the dielectric function of metals, the polarizability of a single nanocrystal is

$$\alpha_A(\omega) = \frac{R^3}{1 - \omega(\omega + i/\tau)/\Omega^2}$$

where $\Omega = \omega_p/\sqrt{3}$ and ω_p is bulk plasmon frequency. The single particle therefore behaves like a harmonic oscillator of frequency Ω and damping constant τ . The dipolar oscillation produces a strong electrical field near the surface, which is responsible for the surface-enhanced Raman scattering (SERS) of small molecules adsorbed on surfaces.^[78] When nanocrystals are brought into close vicinity, interparticle coupling can lead to additional resonances.^[79] Fig. 11 shows, in a schematic diagram, how light at normal incidence can induce a coupled mode where neighboring particles are oscillating in phase. This coupling causes additional absorption peaks in the long

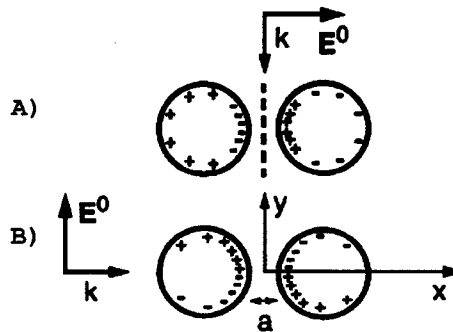


Fig. 11 Schematic diagram of surface plasmons induced by a polarized plane wave incident upon two adjacent nanocrystals from different directions. (A) The external electric field is parallel to the line joining the nanocrystals. (B) The external field is perpendicular to the line joining the nanocrystals. (From Ref. [80]. Copyright 2001, Optical Society of America.)

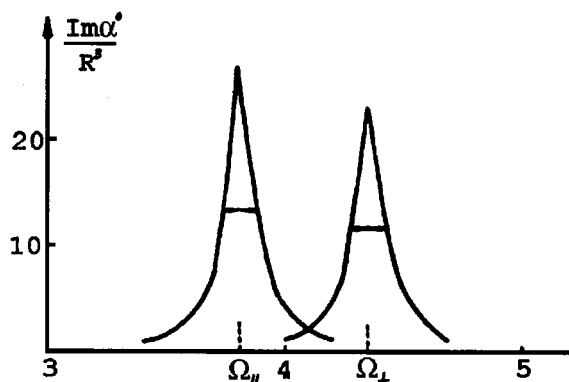


Fig. 12 Calculated imaginary part of the polarizability of nanocrystals arranged on a square lattice. Resonance frequencies Ω_{\perp} and Ω_{\parallel} correspond to surface plasmon oscillations perpendicular and parallel to the plane of nanocrystals. (From Ref. [81]. Copyright 1983, American Physical Society.)

wavelength region. This coupling resonance depends not only on the particle size and interparticle spacing, but also on the polarization of the incident light and the structure of the nanocrystals lattices.^[80] Persson and Liebsch^[81] performed a theoretical calculation of a *p*-polarized light incident on a two-dimensional square lattice (Fig. 12). Two resonant peaks in the imaginary part of the polarizability correspond to coupled plasmon oscillations, either parallel or perpendicular to the array. The frequencies of these resonances are given by:

$$\Omega_{\parallel} = \Omega^2 \left(1 - \frac{1}{2} R^3 U_0 \right)$$

$$\Omega_{\perp} = \Omega^2 (1 + R^3 U_0)$$

where U_0 is a geometric factor that depends on the structure of the array. In the case of disordered particle arrangements, the same calculation based on a coherent potential approximation shows that both of these absorption peaks are broadened. Experiments on disordered nanocrystal arrays confirmed that prediction.^[82]

A promising scheme of utilizing surface plasmons of coupled nanocrystals for optical applications was proposed by Quinten et al.^[83] In their model, a linear chain of metal nanocrystals was used to transmit electromagnetic waves through interparticle dipolar coupling. The field intensity of the transmitted electromagnetic wave depends strongly on the polarization of the incident light. Traditional dielectric optical waveguides have a fundamental wavelength limitation. In comparison, small particle arrays have the potential to become functional units for guiding, modulation, and amplification of light signals on a length scale that is much smaller than the wavelength of light.

In the case of strongly coupled nanocrystal arrays, such as Ag nanocrystal arrays compressed on the Langmuir trough, the optical properties also undergo dramatic changes when metal-insulator-like transitions occur.^[61,62] The real part of the dielectric constant turns negative, indicating more metallic features. However, the derived value of the dielectric constant is about 10 times larger than typical values for an ordinary Ag film. This indicates that the "metallic" state caused by the strong coupling of neighboring nanocrystals is still quite different from the bulk metallic states that we are familiar with.

CONCLUSION

The controlled assembly of nanocrystals into large arrays and superlattices opens the door to a new class of artificial materials whose properties can be tuned by choosing different core materials, by varying the core sizes and shapes, and by tuning the interparticle coupling strength. In particular, the ability to vary independently the properties of the individual nanocrystal building blocks and the type and strength of the interactions between them allows for new and unprecedented control. As a result, materials with electronic or optical properties not obtainable from bulk can be designed "bottom up" by nanocrystal assembly.

At present, the main challenge still lies in our ability to tune all of the key physical parameters of a nanocrystal array at will. As far as electronic transport is concerned, weakly coupled arrays are dominated by single electron Coulomb blockade effects. Strongly coupled arrays, on the other hand, are considerably different. Understanding the strongly coupled state and the transitions between strong and weak coupling are two pressing issues in this field. Experimentally, it is difficult to controllably adjust interparticle couplings. Compression in Langmuir troughs has yielded the fascinating data described above, but it suffers from the disadvantage of simultaneously altering both the voltage and current scales of transport. As nanocrystals are brought closer together, their capacitive coupling increases, lowering the Coulomb blockade cost for electron transport.^[67] Also, the tunneling barrier separating the metal cores narrows, increasing the interparticle tunneling amplitudes. Techniques to independently manipulate these two effects would do much to further our understanding. One possible route is a better grasp of the role of ligands in nanocrystal systems, perhaps designing metal core/ligand particles with specific tunneling rates. (Such feats have been accomplished in the context of electron tunneling through proteins.^[84])

Theoretical studies of Coulomb blockade-dominated array transport have been limited. Even for weakly coupled

arrays, open questions remain, such as the discrepancy between the predicted and observed values of the exponents for the current-voltage scaling relations. For strongly coupled arrays, the paucity of studies is even more pronounced. It is not yet clear to what extent such well-known concepts such as variable-range hopping, metal-insulator transitions, localization, etc. developed for microscopic disorder in semiconductors or disordered thin metal films carry over directly to nanocrystal arrays. For example, it is not obvious that anything besides fixed-range, nearest-neighbor hopping should even occur in metal nanocrystal arrays because of the large, mesoscopic distances involved and because, in contrast to hopping between sharp impurity levels in semiconductors, in metals, at any finite temperatures, the spectrum of available states is broad. Furthermore, the interplay of several types of disorder (random offset charges and variations in the particle size modulating the local charging energy and variations in the particle spacings giving rise to coupling strength disorder) as well as the potentially complex roles played by any electronic states inside the ligands make application of these established, but more microscopic concepts nontrivial.

Controlling the optical response on a nanometer scale is another emerging direction of much promise. With strong coupling between nanocrystals, theoretical models have predicted that coherent transfer of electromagnetic energy along nanocrystal arrays should be possible, despite significant radiative loss. Experiments have not unambiguously demonstrated this phenomenon so far largely because of the difficulty of creating the desired array structures on a very small length scale and also because of current limitations with near-field optical detection schemes.

Several of the recently developed approaches discussed in this article provide new pieces to the expanding toolkit for nanocrystal array assembly: The digestive ripening method can produce size dispersions significantly below 5%; fully ligand-saturated Au nanocrystals can assemble into extended monolayer superlattices with unprecedented degree of long-range order; nanocrystal arrays can be patterned into arbitrary 2-D shapes by electron beam exposure or can be interfaced with lithographically defined electrodes; and the use of membrane substrates allows for transport measurements and, with the same samples, for characterization of the local structural order by transmission electron microscopy.

ACKNOWLEDGMENTS

We would like to thank fruitful discussion with Prof. David Grier about the manuscript. This work has been

supported by the U.S. Department of Energy, BES-Materials Sciences, under Contract W-31-109-ENG-38, University of Chicago-Argonne National Laboratory Consortium for Nanoscience Research (CNR), and by the MRSEC program of National Science Foundation under Award Number DMR-0213745.

REFERENCES

1. *Nanotechnology*, 1st Ed.; Timp, G., Ed.; Springer-Verlag: New York, 1999.
2. Halperin, W.P. Quantum size effects in metal particles. *Rev. Mod. Phys.* **1986**, *58* (3), 533–606.
3. Kastner, M.A. The single-electron transistor. *Rev. Mod. Phys.* **1992**, *64* (3), 849–858.
4. Pool, R. Clusters: Strange morsels of matter. *Science* **1990**, *248*, 1186–1188.
5. Empedocles, S.; Bawendi, M. Spectroscopy of single CdSe nanocrystallites. *Acc. Chem. Res.* **1999**, *32*, 389–396.
6. Nirmal, M.; Brus, L. Luminescence photophysics in semiconductor nanocrystals. *Acc. Chem. Res.* **1999**, *32*, 407–414.
7. Chen, S.; Ingram, R.S.; Hostetler, M.J.; Pietron, J.J.; Murray, R.W.; Schaaff, T.G.; Khoury, J.T.; Alvarez, M.M.; Whetten, R.L. Gold nanoelectrodes of varied size: Transition to molecule-like charging. *Science* **1998**, *280*, 2098–2101.
8. Bucher, J.; Douglass, D.C.; Bloomfield, L.A. Magnetic properties of free cobalt clusters. *Phys. Rev. Lett.* **1991**, *66* (23), 3052–3055.
9. Murray, C.B.; Kagan, C.R.; Bawendi, M.G. Synthesis and characterization of monodisperse nanocrystals and close-packed nanocrystal assemblies. *Annu. Rev. Mater. Sci.* **2000**, *30*, 545–610.
10. Collier, C.P.; Vossmeier, T.; Heath, J.R. Nanocrystal superlattices. *Annu. Rev. Phys. Chem.* **1998**, *49*, 371–404.
11. Pileni, M.P. Nanocrystal self-assembly: Fabrication and collective properties. *J. Phys. Chem., B* **2001**, *105*, 3358–3371.
12. Weller, H. Self-organized superlattices of nanoparticles. *Angew. Chem., Int. Ed. Engl.* **1996**, *35* (10), 1079–1081.
13. Ohara, P.C.; Gelbart, W.M. Interplay between hole instability and nanoparticle array formation in ultrathin liquid films. *Langmuir* **1998**, *14* (12), 3418–3424.
14. Bentzon, M.D.; Wouterghem, J.V.; Morup, S.; Tholen, A.; Koch, C.J.W. Ordered aggregates of ultrafine iron oxide particle: 'Super crystals'. *Philos. Mag., B* **1989**, *60* (2), 169–178.

15. Murray, C.B.; Norris, D.J.; Bawendi, M.G. Synthesis and characterization of nearly monodisperse CdE (E=sulfur, selenium, tellurium) semiconductor nanocrystallites. *J. Am. Chem. Soc.* **1993**, *115*, 8706–8715.
16. Lin, X.M.; Jaeger, C.M.; Sorensen, C.M.; Klabunde, K.J. Formation of long-range-ordered nanocrystal superlattices on silicon nitride substrates. *J. Phys. Chem., B* **2001**, *105* (17), 3353–3357.
17. Wang, Z.L.; Harfenist, S.A.; Vezmar, I.; Whetten, R.L.; Bentley, J.; Evans, N.D.; Alexander, K.B. Superlattices of self-assembled tetrahedral Ag nanocrystals. *Adv. Mater.* **1998**, *10* (10), 808–812.
18. Black, C.T.; Murray, C.B.; Sandstrom, R.L.; Sung, S. Spin-dependent tunneling in self-assembled cobalt-nanocrystal superlattices. *Science* **2000**, *290*, 113.
19. Motte, L.; Billoudet, F.; Lacaze, E.; Douin, J.; Pileni, M.P. Self-organization into 2D and 3D superlattices of nanosized particles differing by their size. *J. Phys. Chem.* **1997**, *101*, 138–144.
20. Whetten, R.L.; Khoury, J.T.; Alvarez, M.M.; Murthy, S.; Vezmar, I.; Wang, Z.L.; Stephens, P.W.; Cleveland, C.L.; Luedtke, W.D.; Landman, U. Nanocrystal gold molecules. *Adv. Mater.* **1996**, *8* (5), 428–433.
21. Murray, C.B.; Kagen, C.R.; Bawendi, M.G. Self-organization of CdSe nanocrystallites into three dimensional quantum dot superlattices. *Science* **1995**, *270*, 1335–1338.
22. Kagan, C.R.; Murray, C.B.; Bawendi, M.G. Electronic energy transfer in CdSe quantum dot solids. *Phys. Rev. Lett.* **1996**, *76*, 1517–1520.
23. Cusack, L.; Rizza, R.; Gorelov, A.; Fitzmaurice, D. Self-assembly and subsequent self-organization of a semiconductor nanocrystallite superlattice. *Angew. Chem., Int. Ed. Engl.* **1997**, *36* (8), 848–851.
24. Yin, J.S.; Wang, Z.L. Ordered self-assembling of tetrahedral oxide nanocrystals. *Phys. Rev. Lett.* **1997**, *79* (13), 2570–2573.
25. Johnson, I.; LaMer, V.K. The determination of the particle size of monodispersed systems by the scattering of light. *J. Am. Chem. Soc.* **1947**, *69*, 1184.
26. Sugimoto, T. Preparation of monodispersed colloidal particles. *Adv. Colloid Interface Sci.* **1987**, *28*, 65.
27. Peng, X.G.; Wickham, J.; Alivisatos, A.P. Kinetics of II–V and III–V colloidal semiconductor nanocrystal growth: “Focusing” of size distribution. *J. Am. Chem. Soc.* **1998**, *120* (21), 5343–5344.
28. Frens, G. Particle size and sol stability in metal colloids. *Kolloid-Z. Z. Polym.* **1972**, *250*, 736–741.
29. Schaaff, T.G.; Knight, G.; Shafiqullin, M.N.; Bor, R.F.; Whetten, R.L. Isolation and selected properties of 10.4 kDa gold: Glutathione cluster compound. *J. Phys. Chem.* **1998**, *102*, 10643–10646.
30. Lin, X.M.; Sorensen, C.M.; Klabunde, K.J. Digestive ripening, nanophase segregation and superlattice formation in gold nanocrystal colloids. *J. Nanopart. Res.* **2000**, *2*, 157–164.
31. Stoeva, S.; Klabunde, K.J.; Sorensen, C.M.; Dragieva, I. Gram-scale synthesis of monodisperse gold colloids by the solvated metal atom dispersion method and digestive ripening and their organization into two- and three-dimensional structure. *J. Am. Chem. Soc.* **2002**, *124* (10), 2305–2311.
32. Leff, D.V.; Ohara, P.C.; Heath, J.R.; Gelbart, W.M. Thermodynamic control of gold nanocrystal size: Experiment and theory. *J. Phys. Chem.* **1995**, *99* (18), 7036–7041.
33. Lin, X.M. From Nanocrystals to Nanocrystal Superlattices: Synthesis and Properties. Ph.D Thesis; Kansas State University, 1999.
34. *Clusters and Colloids, From Theory to Application*; Schmid, G., Ed.; VCH: Weinheim, 1994.
35. Hostetler, M.J.; Wingate, J.E.; Zhong, C.J.; Harris, J.E.; Vachet, R.W.; Clark, M.R.; Londono, J.D.; Green, S.J.; Stokes, J.J.; Wignall, G.D.; Glish, G.L.; Porter, M.D.; Evans, N.D.; Murray, R.W. Alkanethiolate gold cluster molecules with core diameters from 1.5 nm to 5.2 nm: Core and monolayer properties as a function of core size. *Langmuir* **1998**, *14*, 17–30.
36. Brust, M.; Walker, M.; Bethell, D.; Schiffrin, D.J.; Whyman, R. Synthesis of thiol-derivatised gold nanoparticles in a two-phase liquid–liquid system. *J. Chem. Soc. Chem. Commun.* **1994**, 801–802.
37. Brown, L.O.; Hutchison, J.E. Formation and electron diffraction studies of ordered 2-D and 3D superlattices of amine-stabilized gold nanocrystals. *J. Phys. Chem., B* **2001**, *105*, 8911–8916.
38. Schmitt, H.; Badia, A.; Dickinson, L.; Reven, L.; Lennox, R.B. The effect of terminal hydrogen bonding on the structure and dynamics of nanoparticle self-assembled monolayers (SAMs): An NMR dynamics study. *Adv. Mater.* **1998**, *10* (6), 475–480.
39. Luedtke, W.D.; Landman, U. Structure, dynamics, and thermodynamics of passivated gold nanocrystallites and their assemblies. *J. Phys. Chem.* **1996**, *100* (32), 13323–13329.
40. Wang, Z.L.; Harfenist, S.A.; Whetten, R.L.; Bentley, J.; Evans, N.D. Bundling and interdigitation of adsorbed thiolate groups in self-assembled nanocrystal superlattices. *J. Phys. Chem.* **1998**, *103*, 3068–3072.

41. Lin, X.M.; Jaeger, H.M., (unpublished results).
42. Mirkin, C.A.; Letsinger, R.L.; Mucic, R.C.; Storhoff, J.J. A DNA-based method for rationally assembling nanoparticles into macroscopic materials. *Nature* **1996**, *382*, 607–611.
43. Grabar, K.C.; Freeman, R.G.; Hommer, M.B.; Natan, M.J. Preparation and characterization of Au colloid monolayers. *Anal. Chem.* **1995**, *67*, 735–743.
44. Van Leeuwen, D.A.; Van Ruitenbeek, J.M.; De Jough, L.J. Quenching of magnetic moments by ligand–metal interactions in nanosized magnetic metal clusters. *Phys. Rev. Lett.* **1994**, *73*, 1432–1435.
45. Apsel, S.E.; Emmert, J.W.; Deng, J.; Bloomfield, L.A. Surface-enhanced magnetism in nickel clusters. *Phys. Rev. Lett.* **1996**, *76*, 1441–1444.
46. Alder, B.J.; Wainwright, T.E. Phase transition for a hard sphere system. *J. Chem. Phys.* **1957**, *27*, 1208–1209.
47. Van Meegen, W.; Underwood, S.M. Glass transition in colloidal hard spheres: Model coupling theory analysis. *Phys. Rev. Lett.* **1993**, *70*, 2766–2769.
48. Hoover, W.G.; Ree, F.H. Melting transition and communal entropy for hard sphere. *J. Chem. Phys.* **1968**, *49*, 3609–3617.
49. Van Blaaderen, A.; Rue, R.; Wiltzius, P. Template-directed colloidal crystallization. *Nature* **1997**, *385* (6614), 321–324.
50. Bargeman, D.; Van Voorst Vader, F. Van der Waals forces between immersed particles. *J. Electroanal. Chem.* **1972**, *37*, 45–52.
51. Korgel, B.A.; Fitzmaurice, D.A. Condensation of ordered nanocrystal thin film. *Phys. Rev. Lett.* **1992**, *80* (16), 3531–3534.
52. Ohara, P.C.; Leff, D.V.; Heath, J.R.; Gelbart, W.M. Crystallization of opals from polydisperse nanoparticles. *Phys. Rev. Lett.* **1995**, *75* (19), 3466–3469.
53. Trau, M.; Saville, D.A.; Aksay, I.A. Field-induced layering of colloidal crystals. *Science* **1996**, *272*, 706–709.
54. Giersig, M.; Mulvaney, P. Formation of ordered two-dimensional gold colloid lattices by electrophoretic deposition. *J. Phys. Chem.* **1993**, *97*, 6334–6336.
55. Service, R.F. Optical lithography goes to extremes and beyond. *Science* **2001**, *293*, 785–786.
56. Simon, U. Charge transport in nanoparticle arrangements. *Adv. Mater.* **1998**, *10* (17), 1487–1992.
57. Dorogi, M.; Gomez, J.; Osifchin, R.; Andres, R.P.; Reifenberger, R. Room-temperature coulomb blockade from a self-assembled molecular nanostructure. *Phys. Rev., B* **1995**, *52* (12), 9071–9077.
58. Wang, B.; Wang, H.; Li, H.; Zeng, C.; Hou, J.G.; Xiao, X. Tunable single-electron tunneling behavior of ligand-stabilized gold particles on self-assembled monolayers. *Phys. Rev., B* **2000**, *63* (3), 35403–35407.
59. Klein, D.L.; Roth, R.; Lim, A.K.L.; Alivasatos, A.P.; McEuen, P.L. A single-electron transistor made from a cadmium selenide nanocrystals. *Nature* **1997**, *389*, 671–699.
60. Andress, R.P.; Bielefeld, J.D.; Henderson, J.I.; Janes, D.B.; Kolagunta, V.R.; Kubiak, C.P.; Mahoney, W.J.; Osifchin, R.G. Self-assembly of a two-dimensional superlattice of molecularly linked metal clusters. *Science* **1996**, *273*, 1690–1693.
61. Collier, C.P.; Saykally, R.J.; Shinag, J.J.; Henrichs, S.E.; Heath, J.R. Reversible tuning of silver quantum dot monolayers through the metal-insulator transition. *Science* **1997**, *277*, 1978–1981.
62. Markovich, G.; Collier, C.P.; Heath, J.R. Reversible metal-insulator transition in ordered metal nanocrystal monolayers observed by impedance spectroscopy. *Phys. Rev. Lett.* **1998**, *80* (17), 3807–3810.
63. Doty, R.C.; Yu, H.; Shih, C.K.; Korgel, B.A. Temperature-dependent electron transport through silver nanocrystal superlattices. *J. Phys. Chem., B* **2001**, *105* (35), 8291–8296.
64. Leatherdale, C.A.; Kagan, C.R.; Morgan, N.Y.; Empedocles, S.A.; Kastner, M.A.; Bawendi, M.G. Photoconductivity in CdSe quantum dot solids. *Phys. Rev., B* **2000**, *62* (4), 2669–2680.
65. Parthasarathy, R.; Lin, X.M.; Jaeger, H.M. Electronic transport on metal nanocrystal arrays: The effect of structural disorder on scaling behavior. *Phys. Rev. Lett.* **2001**, *87*, 186807–186810.
66. Parthasarathy, R. Electronic Transport in Arrays of Gold Nanocrystals. Ph.D. Thesis; Univ. of Chicago, 2002.
67. Middleton, A.A.; Wingreen, N.S. Collective transport in arrays of small metallic dots. *Phys. Rev. Lett.* **1993**, *71*, 3198.
68. Roux, S.; Herrmann, H.J. Disorder-induced nonlinear conductivity. *Europhys. Lett.* **1987**, *4* (11), 1227–1231.
69. Kardar, M.; Parisi, G.; Zhang, Y.C. Dynamic scaling of interface growth. *Phys. Rev. Lett.* **1986**, *56*, 889–892.
70. Parthasarathy, R.; Lin, X.M.; Eltero, K.; Rosenbaum, T.F.; Jaeger, H.M. *Phys. Rev. Lett.*, *in press*.
71. Bezradin, A.; Westervelt, R.M.; Tinkham, M. Self-assembled chains of graphitized carbon nanoparticles. *Appl. Phys. Lett.* **1999**, *74* (18), 2699–2701.
72. Sampaio, J.F.; Beverly, K.C.; Heath, J.R. DC transport in self-assembled 2D layers of Ag

- nanoparticles. *J. Phys. Chem., B* **2001**, *105* (37), 8797–8800.
73. Beverly, K.C.; Sampaio, J.F.; Heath, J.R. Effects of size dispersion disorder on the charge transport in self-assembled 2-D Ag nanoparticle arrays. *J. Phys. Chem., B* **2002**, *106* (9), 2131–2135.
74. Elghanian, R.; Storhoff, R.C.; Mucic, R.C.; Letsinger, R.L.; Mirkin, C.A. Selective colorimetric detection of polynucleotides based on the distance-dependent optical properties of gold nanoparticles. *Science* **1997**, *277*, 1078.
75. Klimov, V.I.; Mikhailovsky, A.A.; Xu, S.; Malko, A.; Hollingsworth, J.A.; Leatherdale, C.A.; Eisler, H.-J.; Bawendi, M.G. Optical gain and stimulated emission in nanocrystal quantum dots. *Science* **2000**, *290*, 314–317.
76. Kagen, C.R.; Murray, C.B.; Bawendi, M.G. Long-range resonance transfer of electronic excitations in close-packed CdSe quantum-dot solids. *Phys. Rev., B* **1996**, *54*, 8633–8643.
77. Jackson, J.D. *Classical Electrodynamics*, 2nd Ed.; John Wiley & Sons: New York, 1975.
78. *Surface Enhanced Raman Scattering*; Chang, R.K., Furtak, T.E., Eds.; Plenum: New York, 1982.
79. Kreibig, U.; Vollmer, M. *Optical Properties of Metal Clusters*; Springer-Verlag: Berlin, 1995.
80. Kottmann, J.P.; Martin, O.J. Retardation-induced plasmon resonances in coupled nanoparticles. *Opt. Lett.* **2001**, *26* (14), 1096–1098.
81. Persson, B.N.J.; Liebsch, A. Optical properties of two-dimensional systems of randomly distributed particles. *Phys. Rev., B* **1983**, *28* (8), 4247–4254.
82. Yamaguchi, T.; Yoshida, S.; Kinbara Optical effect of the substrate on the anomalous absorption of aggregated silver films. *Thin Solid Films* **1974**, *21*, 173.
83. Quinten, M.; Leitner, A.; Krenn, J.R.; Aussenegg, F.R. Electromagnetic energy transport via linear chains of silver nanoparticles. *Opt. Lett.* **1998**, *23* (17), 1331–1333.
84. Winkler, J.R.; Di Bilio, A.J.; Farrow, N.A.; Richards, J.H.; Gray, H.B. Electron tunneling in biological molecules. *Pure Appl. Chem.* **1999**, *71* (9), 1753–1764.

Nanocrystal Dispersed Platinum Particles: Preparation and Catalytic Properties

Ioan Balint

Romanian Academy, Bucharest, Romania

Akane Miyazaki

Tokyo Institute of Technology, Yokohama, Japan

INTRODUCTION

The synthesis of metal particles with well-controlled shapes and sizes is critical for catalytic applications in structure-sensitive reactions because the rates depend significantly on the metal crystallite size as well as on the orientation of the crystalline planes.^[1] The morphology-catalytic reactivity relationship is generally unclear for the catalysts prepared by classical impregnation method because the resulting metal particles are nonuniform in size and shape, and are often too small to be precisely characterized. Additionally, there is a significant support effect on the catalytic reactivity of the small metal particles.^[2-4] With other preparation methods such as vapor^[5] and metal cluster deposition,^[6] electron beam lithography,^[7] etc., it is possible to control, to some extent, the size, but not the crystallographic orientation, of the metal particles.

The colloid method is one of the most promising ways to obtain relatively monodispersed metal particles with controlled shapes.^[8] Among metals, platinum is a suitable precursor because different shapes of nanoparticles can be prepared by using suitable capping polymers.^[9-11] The NO/CH₄ reaction was chosen to investigate the structure-catalytic reactivity relationship for the well-structured Pt nanoparticles. The conventionally prepared Pt/Al₂O₃ catalysts give relatively high selectivity to NH₃ and CO. Because NO/CH₄ reaction is structure-sensitive, significant improvements in the catalytic behavior are expected through a fine control of the morphology of Pt particles.^[12,13]

The general aim of our work is to bridge the gap existing between the science of clean single crystals surfaces and the world of real catalysis. Particularly, we intend to have a better understanding of the relationship existing between the structure of the supported Pt particles and the catalytic behavior for the NO/CH₄ reaction. From the practical point of view, our scope is to prevent or to considerably reduce the formation of undesired reaction products, such as NH₃, CO, and N₂O. The approach to fulfill the abovementioned goals was to prepare well-

defined Pt nanocrystals having mainly cubic structure, to support them on alumina, and to test their specific catalytic activity for the NO/CH₄ reaction.

EXPERIMENTAL

The synthesis method for the controlled shape colloidal Pt nanoparticles was reported relatively recently.^[10] In principle, the procedure consisted of the reduction of K₂PtCl₄ precursor with H₂ in the presence of polyacrylate capping materials.^[10,11] Morphological control in the synthesis of the well-defined Pt nanoparticles was further optimized by using NIPA (polymer of *N*-isopropylacrylamide) as a capping polymer and by changing the synthesis temperature.^[9] The preparation method followed in the present study consisted of the reduction of K₂PtCl₄ (10⁻⁴ M) with H₂ in the presence of the NIPA polymer (10⁻³ M) in the 10–40°C temperature range.^[9]

The resulting Pt nanocrystals (with mainly cubic shape) were supported by adding, under stirring, 0.1 g of γ -alumina (Aerosil; 100 m² g⁻¹) to 50 ml of colloidal Pt solution to get a final loading of Pt on 1 wt.% alumina. After water was removed from the suspension by freeze-drying, the remaining solid was calcined in air at 500°C for 8 hr to remove the NIPA polymer by decomposition. The calcined catalysts were pelletized, crushed, and sieved. The 335- to 1000- μ m fraction was used for catalytic tests. The Pt colloid as well as the calcined catalyst were characterized by transmission electron microscopy (TEM; Hitachi H-8100). Additionally, the catalysts were characterized by X-ray diffraction (XRD; Rigaku Multiflex diffractometer provided with peak assignment software), by N₂ adsorption for measurement of physical surface (Belsorb 28 SA), and by CO chemisorption for determination of metal surface (Yuasa ChemBET-3000).

For convenience, the alumina-supported, well-structured Pt nanocrystals will be called, hereafter, Pt{100}/Al₂O₃. The activity of the Pt{100}/ γ -Al₂O₃ catalyst (0.05 g) for the NO/CH₄ reaction was tested in flow system by using a quartz microreactor (i.d.=5 mm) operating at

Table 1 The morphology of the Pt particles in different stages (Pt colloid, after deposition on alumina, and after high-temperature aging) as determined by TEM, XRD, and CO chemisorption measurements

Samples	Diameter (nm)								
	Colloidal stage			Active catalyst ^a			Aged catalyst ^b		
	d_{TEM}^c	d_{XRD}^d	d_{CO}^e	d_{TEM}	d_{XRD}	d_{CO}	d_{TEM}	d_{XRD}	d_{CO}
Pt{polycrystalline}/Al ₂ O ₃	—	—	—	2.8	—	2.4	—	—	—
Pt{100}/Al ₂ O ₃	13.6	—	—	13.4	11.7	23	15.1	10.6	21

^aCatalyst working in the NO/CH₄ reaction mixture up to 600°C.

^bCatalyst aged at 950°C for 4 hr in the NO/CH₄ reaction mixture.

^cThe average size was determined from TEM micrographs by counting more than 200 Pt nanoparticles.

^dSize calculated from the broadening of the XRD peak of Pt(111) ($2\theta \approx 40^\circ$).

^eAverage size determined from CO chemisorption data.

atmospheric pressure. The total flow rate of the reactant mixture (1% NO and 0.4% CH₄, balance Ar) was 50 cm³ min⁻¹ standard temperature and pressure (STP). The corresponding gas hour space velocity (GHSV) was 60,000 hr⁻¹.

The analysis of gaseous mixtures was carried out with a gas chromatograph (GL Sciences-320) equipped with a thermal conductivity detector (TCD). N₂, NO, and CH₄ were separated by a molecular sieve 13 × column and the CO₂ and N₂O were separated by a Porapak-Q column.

The activity of well-structured platinum catalysts (Pt{100}/Al₂O₃) was compared with that of a standard catalyst supplied by Engelhard Corporation Japan (lot no. H-T1150-01). The Engelhard catalyst (metal loading, 1 wt.%), hereafter called Pt{polycrystalline}/Al₂O₃, had metal and Brunauer–Emmet–Teller (BET) surface areas of 1.19 (≈44% dispersion) and 114 m² g⁻¹, respectively. The metal particle size, determined from chemisorption and TEM data, were 2.4 and 2.8 nm, respectively (Table 1).

The catalytic behavior in the NO/CH₄ reaction was expressed in terms of conversion, selectivity, and yield.^[12]

RESULTS

The configuration of NIPA thermosensitive polymer changes reversibly with temperature because a hydrophilic–hydrophobic transition takes place at ≈36°C. The influence of capping conditions on the morphology of Pt particles was investigated by carrying out the reduction of K₂PtCl₄ both in hydrophobic and hydrophilic regions (10–40°C). The proportion of Pt cubic to other shapes passed through a maximum (≈70%) for a reduction temperature of 40°C (Fig. 1).

Fig. 2 presents the TEM images of the Pt nanoparticles in different stages. Fig. 2a shows the well-defined cubic Pt nanocrystals, of around 13 nm, in colloidal stage. Analysis

by high-resolution transmission electron microscopy (HRTEM) revealed that the square particles were Pt single crystals with a surface relatively free of defects (smooth surface). The Pt nanoparticle shown in Fig. 2b is bounded by {100} facets because the distance between the adjacent lattice fringes of 0.196 nm corresponds to the interplanar distance of Pt{200}. Other crystallographic orientations (i.e., {111} and {110}) as well as steps and ledges are also possible^[11] at the slightly rounded corners of the cubes. The cubic structure of the Pt nanoparticles was preserved after supporting them on alumina (Fig. 2c). The conversion of the square Pt nanoparticles to other shapes (i.e., irregular, round, and hexagonal) was observed after high-temperature aging (950°C for 4 hr) in the NO/CH₄ mixture (Fig. 2d). The impact of the morphological changes of the supported Pt nanoparticles on the catalytic activity and selectivity for the NO/CH₄ reaction will be analyzed hereafter.

Because the morphology of the Pt nanoparticles changes slightly from batch to batch and the NO/CH₄ reaction is very sensitive to the metal structure, it is our

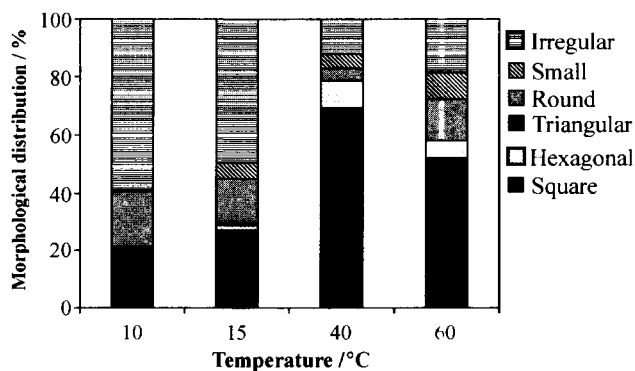


Fig. 1 The relationship between the morphological distribution of the platinum nanoparticles in colloidal stage and the reduction temperature.

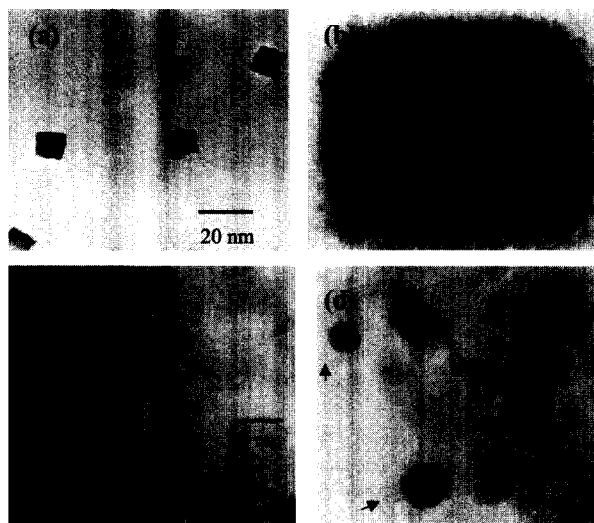


Fig. 2 TEM images of (a) Pt colloid composed mainly of cubic nanoparticles ($\approx 70\%$); (b) high magnification of an individual cubic Pt nanoparticle; (c) alumina-supported Pt nanoparticles; and (d) alumina-supported Pt nanoparticles aged at 950°C for 4 hr in the NO/CH_4 mixture.

standard procedure to characterize the Pt nanoparticles in colloidal stage as well as after deposition on alumina and catalytic tests by TEM, XRD, and CO chemisorption. Table 1 presents the average size of Pt particles in colloidal stage (TEM data), after deposition on alumina and catalytic tests up to 600°C (TEM, XRD, and CO chemisorption data), and after thermal aging (950°C , 4 hr) in the NO/CH_4 reaction mixture (TEM, XRD, and CO chemisorption

data). The average size (d_{TEM}) of the colloidal Pt nanoparticles (≈ 13.6 nm) does not change after deposition on alumina or after catalytic reaction up to 600°C in the NO/CH_4 reaction mixture ($d_{\text{TEM}} \approx 13.4$ nm). Good thermal stability of the alumina-supported Pt nanoparticles is confirmed also by XRD data ($d_{\text{XRD}} \approx 11.7$ nm).

Theoretical calculations, by considering the d_{TEM} average particle size of 13.4 nm, predict a platinum dispersion of around 7%. Such a small dispersion is, in practice, difficult to measure by CO chemisorption. However, we attempted to measure it by using a sensitive chemisorption apparatus, which can generate and measure CO pulses on the order of microliters. The d_{CO} value of ≈ 23 nm, determined for the catalysts working in reaction mixtures up to 600°C , is higher than those determined by TEM ($d_{\text{TEM}} \approx 13.4$ nm) or by XRD ($d_{\text{XRD}} \approx 11.7$ nm) (Table 1). Taking into account the extremely small dispersion, the low metal loading (1% Pt), and the small amount of catalyst (0.05 g) used for metal surface determination, the chemisorption data are quite satisfactory and may be useful especially in revealing the evolution of metal surface area with temperature.

Morphological information regarding the thermally aged catalyst (950°C , 4 hr in the NO/CH_4 mixture) is given in Table 1 (d_{TEM} , d_{XRD} , and d_{CO}), Fig. 2d, as well as in Figs. 3 and 4 (morphological and size distributions, respectively). Apparently, the TEM data indicate a slight increase in particles size from 13.4 to 15.1 nm for the thermally aged Pt nanoparticles (Table 1). In contrast, the XRD and chemisorption data ($d_{\text{XRD}} \approx 10.6$ and $d_{\text{CO}} \approx 21$ nm) suggest a slight decrease in particle size after thermal aging (Table 1). This apparent contradiction, between

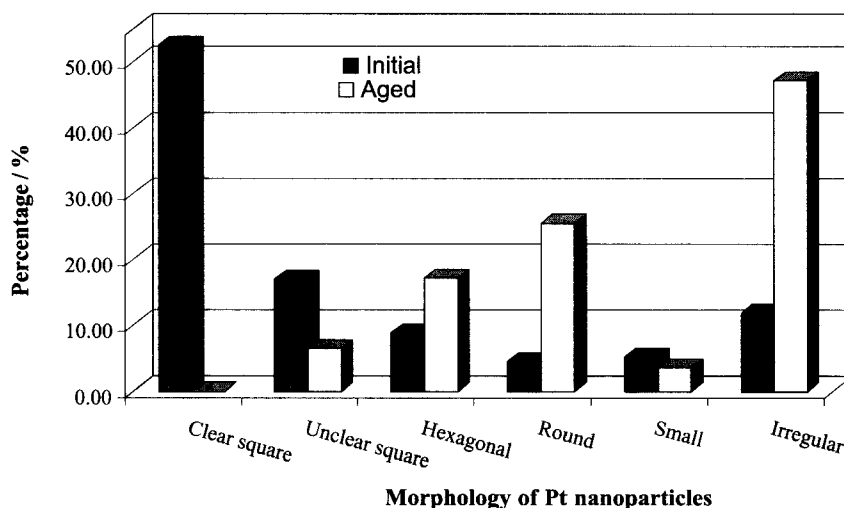


Fig. 3 Morphological distribution of the (I) initial colloidal Pt nanocrystals deposited on $\gamma\text{-Al}_2\text{O}_3$ and (II) alumina-supported Pt nanoparticles subjected to thermal aging at 950°C for 4 hr in the NO/CH_4 reaction mixture. (View this art in color at www.dekker.com.)

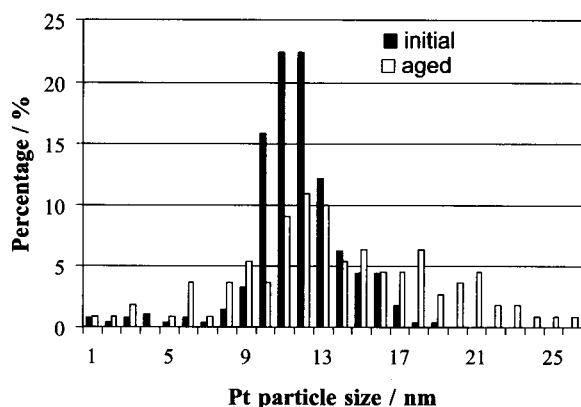


Fig. 4 The size distribution of the (I) colloidal Pt nanoparticles supported on alumina (initial) and (II) alumina-supported Pt nanoparticles subjected to thermal aging at 950°C for 4 hr in the NO/CH₄ mixture.

TEM data on one hand and chemisorption and XRD data on the other hand, will be analyzed later in the "Discussion" section.

The morphologies of the colloidal Pt nanoparticles synthesized at 40°C and of the thermally aged (950°C, 4 hr in the NO/CH₄ mixture) Pt nanoparticles supported on alumina are comparatively presented in Fig. 3. Around 53% and 17% of the colloidal Pt nanocrystals have been found to have "clear square" and "unclear square" shapes, respectively. The "clear square" particles were Pt{100} single crystals with surfaces relatively free of defects (Fig. 2b). The particles with "unclear square" shape were also cubic nanocrystals but with a rough surface (defected surface). Besides cubic, other shapes, such as hexagonal ($\approx 9\%$), round ($\approx 4\%$), small ($\approx 5\%$), and irregular ($\approx 12\%$), have been identified, too.

The initial morphological distribution was significantly altered after thermal aging at 950°C for 4 hr in the NO/CH₄ mixture. The "clear square" and the "unclear square" particles were practically completely converted to irregular ($\approx 47\%$), round ($\approx 25\%$), and hexagonal ($\approx 17\%$).

From the Gaussian-type size distribution of the colloidal Pt nanoparticles, an average particle size of ≈ 13.6 nm was determined (Fig. 4, Table 1). The size distribution of the Pt nanoparticles became apparently broader after thermal aging at 950°C for 4 hr, but the average particle size increased only slightly, from 13.4 to 15.1 nm.

The catalytic activity of Pt{100}/Al₂O₃ for the NO/CH₄ reaction vs. temperature is presented in Fig. 5. The total conversion of NO was achieved for $T \geq 350^\circ\text{C}$. The concentration of N₂O goes through a maximum at 400°C and then decreases with increasing reaction temperature. In the lower-temperature domain (350–500°C),

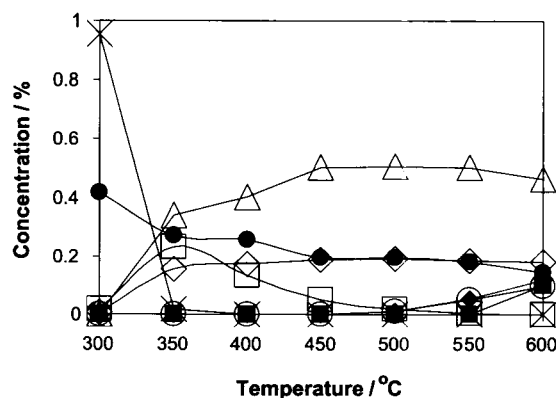


Fig. 5 The conversion of NO to all products as a function of temperature for the Pt{100}/Al₂O₃ catalyst. (x) NO; (●) CH₄; (Δ) N₂; (□) N₂O; (■) NH₃; (◇) CO₂; (◆) CO; and (○) H₂ (reactant mixture: 1% NO, 0.4% CH₄, and balance Ar).

the only product of methane oxidation was CO₂. The formation of CO was observed for $T \geq 500^\circ\text{C}$. Small amounts of NH₃ were detected only in the high-temperature region ($T \geq 550^\circ\text{C}$). Experiments in which the catalyst was cycled up and down in the temperature range of 300–600°C did not show any significant variations in catalytic activity.

The conversion of NO and CH₄ as well as the reaction selectivity to various products are presented in Fig. 6. The reaction selectivity to N₂ reaches a maximum at 550°C ($\approx 99\%$). The selectivity to N₂O has a maximum at 350°C ($\approx 40\%$) and then decreases with increasing reaction temperature. The selectivity to NH₃ increased with increasing reaction temperature from $\approx 1\%$ at 550°C to $\approx 10\%$ at 600°C.

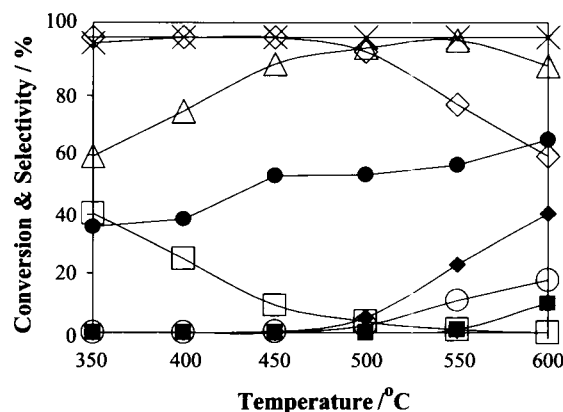


Fig. 6 The temperature dependence of the NO/CH₄ reaction conversion (X) and selectivity (S) for Pt{100}/Al₂O₃ catalysts. (x) X(NO); (●) X(CH₄); (Δ) S(N₂); (□) S(N₂O); (■) S(NH₃); (◇) S(CO₂); (◆) S(CO); and (○) S(H₂) (reactant mixture: 1% NO, 0.4% CH₄, and balance Ar).

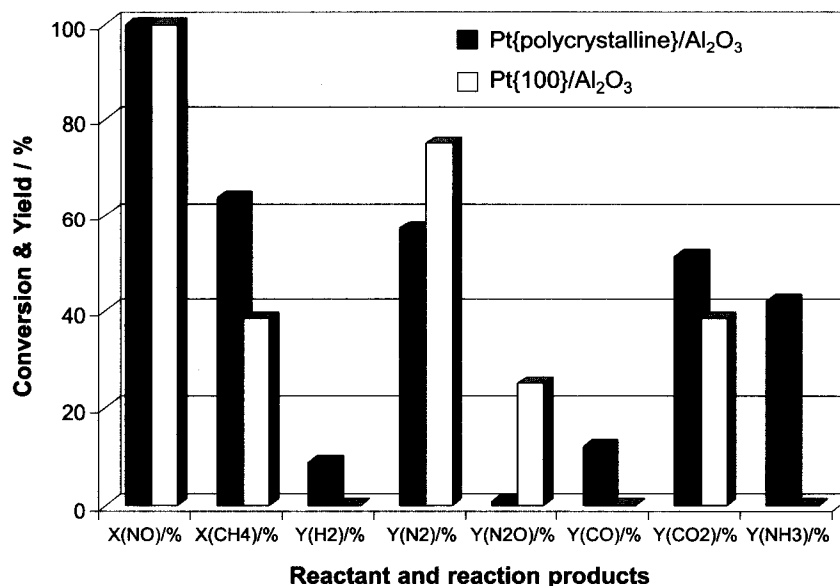


Fig. 7 Comparison between the NO/CH₄ reaction conversion (X) and yield (Y), and the products for Pt{polycrystalline}/Al₂O₃ (Engelhard) and Pt{100}/Al₂O₃ (well-defined Pt nanoparticles) catalysts at 400°C.

The catalytic behavior of Pt{100}/Al₂O₃ for the NO/CH₄ reaction was compared with that of a standard catalyst, Pt{polycrystalline}/Al₂O₃, at 400°C (Fig. 7) and 500°C (Fig. 8). In this manner, the observed differences would be ascribed to the morphological effects of the Pt particles on the NO/CH₄ reaction.

Both catalysts investigated exhibit comparable activity for NO conversion, increasing yield to N₂ (opposite trend for N₂O) and increasing CH₄ conversion with temperature (Figs. 7 and 8).

Interestingly, significantly lower yields to CO and NH₃ were observed for the Pt{100}/Al₂O₃ catalyst compared

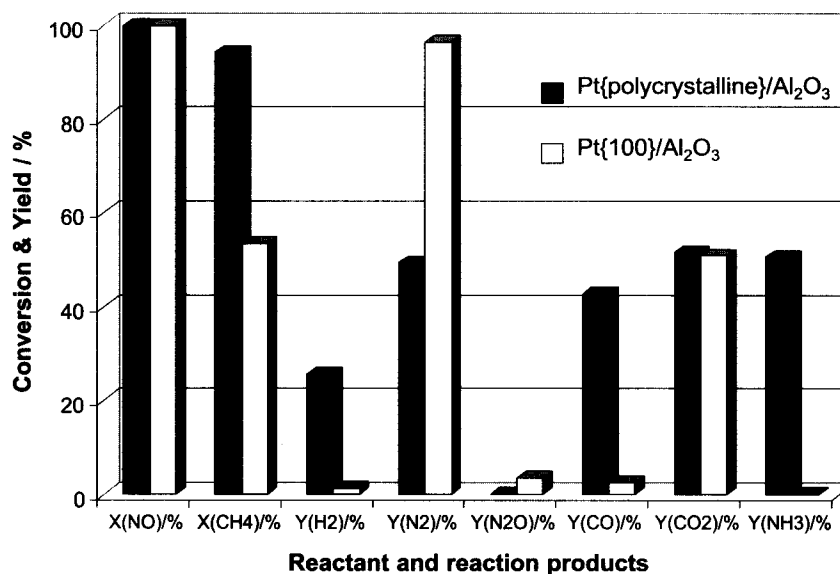


Fig. 8 Comparison between the NO/CH₄ reaction conversion (X) and yield (Y), and the products for Pt{polycrystalline}/Al₂O₃ (Engelhard) and Pt{100}/Al₂O₃ (well-defined Pt nanoparticles) catalysts at 500°C.

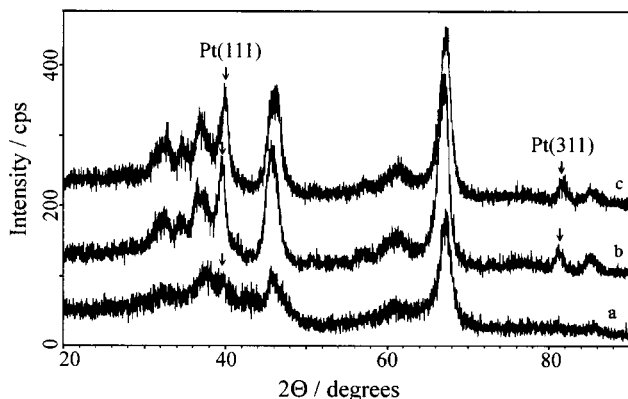


Fig. 9 Comparative XRD patterns for polycrystalline and well-structured platinum particles supported on alumina. Spectrum (a): Pt{polycrystalline}/Al₂O₃ (Engelhard) catalyst used in the NO/CH₄ reaction in the 300–600°C temperature range. Spectrum (b): Pt{100}/Al₂O₃ (well-structured Pt nanoparticles) used in the NO/CH₄ reaction in the 300–600°C temperature range. Spectrum (c): Pt{100}/Al₂O₃ after aging at 950°C for 4 hr in the NO/CH₄ reaction mixture.

with the Pt{polycrystalline}/Al₂O₃ catalyst (Figs. 7 and 8). On the other hand, the well-structured Pt nanoparticles showed higher yield to N₂O.

The XRD pattern of the Pt{polycrystalline}/Al₂O₃ presented in Fig. 9a indicates that Pt particles are too small (≈ 2.4 nm) to give characteristic XRD peaks. The XRD patterns of the Pt{100}/Al₂O₃ catalysts (Fig. 9b and c) exhibit the characteristic XRD reflections of the large, well-crystallized Pt nanoparticles at $2\theta \approx 40^\circ$ and $2\theta \approx 81^\circ$. The average sizes of Pt crystallites, calculated from the XRD peaks at $2\theta \approx 40^\circ$ by using the Debye–Scherer equation, were 11.7 nm for the Pt{100}/Al₂O₃ catalyst working in the NO/CH₄ mixture at the 300–600°C temperature range and 10.7 nm for the same catalyst aged at 950°C for 4 hr in the reaction mixture. The XRD results suggest a remarkable size stability of the alumina-supported Pt nanocrystals.

DISCUSSION

According to ultrahigh vacuum (UHV) investigations, the catalytic activities for numerous reactions vary from one metal crystal face to another.^[14] For example, the NO/H₂ reaction proceeds with significantly different rates over Pt(100) and (110) monocrystals.^[15] Therefore the rate of N₂ formation is at least five times higher on the surface of Pt(100) than on Pt(110). In fact, the studies performed on the clean surfaces predict that a strong structure–catalytic reactivity relationship should also exist in atmospheric pressure conditions.

The first step to better understand the structure–catalytic reactivity relationship is to have a good morphological control (shape and size) of the supported metal nanoparticles and to reduce or eliminate the support effect. In this way, the most important factors responsible for the significant differences observed between the catalytic behaviors of the large, well-defined Pt nanoparticles and the small, polycrystalline Pt particles in the NO/CH₄ reaction can be identified and analyzed more easily. The catalytic tests show that, over the Pt{100}/Al₂O₃ catalyst, the formation of CO and NH₃ is largely prevented, whereas the yield to N₂O increases compared with the Pt{polycrystalline}/Al₂O₃ catalyst.

It is clear that the interaction with the support is minimal in the case of the large (≈ 13 nm) Pt nanoparticles grafted after the formation on alumina. Boudart^[16] observed that the catalytic behavior of particles larger than 5 nm mostly reflects the properties of bulk metals.

The main differences observed between the two catalysts compared are the dominant orientation of the crystallographic facets and the average size of Pt crystallites. The large Pt nanocrystals (≈ 13 nm) of the Pt{100}/Al₂O₃ catalyst were, in majority ($\approx 70\%$), cubic-shaped. In contrast, the conventional Pt{polycrystalline}/Al₂O₃ catalyst had small, round-shaped Pt particles of ≈ 2.4 nm with random crystallographic orientations. The impact of the abovementioned factors, shape and size, on the catalytic behavior for the NO/CH₄ reaction will be discussed later in this work.

Activation of NO

It is rational to consider that the first step of NO conversion is the dissociation from the metal surface.^[17]



The absence of a reductant, which removes the strongly adsorbed O_{ads}, prevents further NO decomposition.^[18,19] We observed that in the absence of CH₄, around 2–5% of NO decomposes for a short time (few minutes) over the reduced Pt{100}/Al₂O₃ catalyst. Burch and Ramli^[20] suggested that the relative activities for various catalysts reflect the ease of catalyst reduction by a reducing agent (i.e., CH₄).

The dissociation of NO over the clean surfaces of metal single crystals has been intensively investigated. The most important conclusions of these studies will be briefly reviewed to explain the catalytic behavior of Pt{100}/Al₂O₃ in the NO/CH₄ reaction:

- (I) The NO dissociation on clean metal surfaces is a coverage-dependent process.^[21] Low NO coverage (typically $\theta < 0.3$) favors the complete dissociation

of NO.^[22] It is likely that in real catalytic conditions, the adsorbed NO will be only partially dissociated because of the high surface coverage. Thus the molecular NO will coexist on the metal surface with N_{ads} and O_{ads} species.

- (II) The dissociation of NO is very sensitive to crystallographic orientation. Desorption studies evidenced that only 5% of the adsorbed NO dissociates from Pt(111) and Pt(110), in contrast with Pt(100), which dissociates by around 50%.^[22] Moreover, the Pt(111) facet is reported to be completely unreactive for NO decomposition at any coverage.^[23] On the other hand, the high-index Pt planes are unusual active for NO decomposition. For example, more than 98% of the adsorbed NO is dissociated from the Pt(410) surface.^[22]

Some studies pointed out that NO dissociates mainly at the steps.^[17] The conventional catalyst, containing small Pt particles with random crystallographic orientation, is rich in high-index planes, edges, kinks, and steps. Therefore it is expected to show high activity for NO decomposition. In contrast, the large Pt nanocrystals have limited activity for NO decomposition because of the low concentration of high-index planes and surface defects. Our assumptions are confirmed by experimental facts. The Pt(100) single crystals are catalytically active but give a dissociation for $\text{NO} \approx 50\%$ under conditions where the polycrystalline Pt samples give a dissociation of 75% for NO.^[22] The activity for NO decomposition should have a great impact on the NO/CH₄ reaction selectivity to N₂O and N₂. We will discuss in detail these aspects in the next paragraph.

In fact, NO can be decomposed not only by metals but also by metal oxides. Winter^[24] investigated the decomposition of NO to over 40 oxides (PtO_x was not included in this screening) and found out that the most active oxides give a conversion of below 50% for NO. In our specific case, we could not provide evidence on the formation of PtO_x species through any experimental method used [temperature-programmed reduction (TPR) and XRD]. Therefore it is safe to state that the bulk PtO_x is not formed over the Pt{100}/Al₂O₃ catalyst and, in consequence, is not involved in the decomposition of NO. On the other hand, we clearly observed that (in the absence of a reductant) the oxygen resulting from NO decomposition poisons the reaction because of the formation of a superficial layer of strongly adsorbed oxygen.^[25]

In practice, NO decomposition can be even more complicated. From single crystal studies, two possible structures have been found for the Pt(100) plane, indicated by (1×1) and (5×2) .^[26] The (1×1) surface has a square structure on a square substrate, whereas the (2×5) surface has a hexagonal structure on the square substrate. The

(1×1) and (5×2) surfaces exhibit different adsorption and catalytic properties.^[27] The dissociation of NO takes place only on the (1×1) phase, whereas the hexagonal one is inert.^[18] However, at present, it is difficult to assess the impact of these structures, observed in UHV conditions, on catalytic behavior at atmospheric pressure.

It is likely that for a real catalyst under steady-state conditions, less active sites (e.g., terraces) will certainly come into play, so the overall reactivity will be the result of weighted contributions from various surface structure elements, dominated by active sites located at steps, edge, and kinks.^[17]

Formation of N₂ and N₂O

There is almost a general agreement in the published literature, from catalytic investigations conducted under atmospheric pressure^[2,28] and studies performed on clean metal surfaces,^[22,23] that N₂ and N₂O are formed via the following reactions:



There are also a few works assuming that N₂O can be an intermediate during the reduction of NO by CH₄.^[29]

Our experimental results strongly support the mechanism for N₂O formation described by Eq. 3. The generation of N₂O is favored over the Pt{100}/Al₂O₃ catalyst because the large, well-defined Pt nanocrystals exhibit low activity for NO decomposition. In contrast, high selectivity to N₂ was observed over the small (≈ 2.4 nm) polycrystalline Pt particles because of the high efficiency shown for NO decomposition (Eq. 2).

The dissociation equilibrium for NO is a temperature-dependent process. As the temperature increases, the reaction is shifted toward the dissociation of NO, thus the most favored reaction becomes the recombination of N_{ads} to give molecular N₂ (Eq. 2 and Fig. 6).

Conversion of CH₄

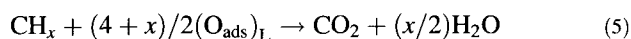
Methane must overcome an activation energy barrier of around 7 kcal mol⁻¹ to chemisorb on metal surfaces, and the barrier height for breaking the C—H bond by kinetic energy is 29 kcal mol⁻¹.^[30] The dissociative adsorption of methane occurs either on the fully reduced Pt, or at mixed sites comprising Pt^{δ-}—Pt^{δ+}, but the fully oxidized Pt surface is less active than the reduced or partially oxidized surface.^[31]



Then the CH_x and H_{ads} surface species are oxidized by the O_{ads} (resulting from NO decomposition) to CO₂ and H₂O

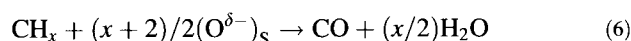
over the Pt{100}/Al₂O₃ catalyst. In other words, the high oxidizing activity of the adsorbed oxygen on the surface of large Pt particles explains the high selectivity to deep oxidation products despite methane excess used in our experiments.

The structure sensitivity of methane oxidation over platinum was explained by the different reactivities of the adsorbed oxygen.^[32] The higher resistance of the large Pt particles against bulk oxidation^[16] explains the enhanced catalytic activity for CH₄ oxidation.^[32] The catalytic activity of the large Pt particles for oxidation reactions was found to be at least one order of magnitude higher than the small, well-dispersed Pt particles.^[33] The chemisorbed oxygen is bound more weakly to the metal surface and therefore is more ready to react with CH_x species.^[34] The oxidation of CH_x on the large Pt nanocrystals (≈13 nm) can be described by the following equation:



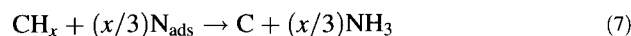
The subscript "L" indicates that the oxygen is adsorbed on large Pt particles. The hydrocarbon continuously removes the pool of O_{ads} then NO dissociation continues, mainly on high index planes and surface defects.

In contrast to the large Pt nanocrystals, the well-dispersed Pt particles, with an average size of 2.4 nm, give high selectivity to CO and NH₃ (Figs. 7 and 8). These results can be explained as follows. The dispersed Pt particles can be successively converted, depending on the temperature, to PtO, PtO₂, and, finally, PtAl₂O₄.^[33,35] Because of the low oxidation activity of O^{δ-} (PtO_x) species, some of the surface CH_x species will undergo only partial oxidation:



The subscript "S" indicates that the O^{δ-} is formed on small Pt particles.

In addition to CO, large amounts of NH₃ are formed during the reduction of NO with CH₄ over the conventional Pt/Al₂O₃^[28] and Pt/SiO₂^[36] catalysts. The selectivity to NH₃ was observed to decrease with increasing oxygen concentration in reactant mixtures. It is likely that the lifetime of the CH_x and H_{ads} species on the small Pt particles is longer because of the low oxidation ability of bulk PtO_x. Therefore the reactions responsible for ammonia formation are favored:



The formation of NH₃ over Pt{100}/Al₂O₃ was greatly reduced because the active oxygen chemisorbed on the

large Pt particles rapidly removes, as do CO₂ and H₂O, the carbonaceous and H species from the surface.

Impact of Platinum Morphological Evolution on Catalytic Behavior

From the aforementioned results as well as from already published works,^[12,13] it is clear that both the size and the facet have a determinant role in the catalytic activity of Pt particles for the NO/CH₄ reaction. Morphological changes of the Pt nanoparticles are expected to take place in reaction conditions. Therefore a closer look was taken on the morphological evolution of the Pt nanoparticles with time in reaction conditions, as well as on the impact of this evolution on the catalytic behavior for the NO/CH₄ reaction.

The catalyst was subjected to an accelerated thermal aging at 950°C for 4 hr in the NO/CH₄ reaction mixture. Then, the catalytic behavior of the aged catalyst was checked again in the low-temperature region (300–600°C). Fig. 10 illustrates the aging effect on the catalytic behavior of alumina-supported Pt nanoparticles. For the sake of simplicity, only yields to the harmful products (N₂O, CO, and NH₃) were compared. The main changes observed after high-temperature aging can be summarized as follows: 1) the production of N₂O and CO decreased significantly (the formation of CO was prevented below 550°C and the yield to N₂O became negligible at T ≥ 400°C); and 2) the formation of NH₃ was completely suppressed (Fig. 10).

From the data presented in Table 1 and Fig. 3, it was found that aging had little effect on particle size, but a significant effect on the shape of Pt nanocrystals. The

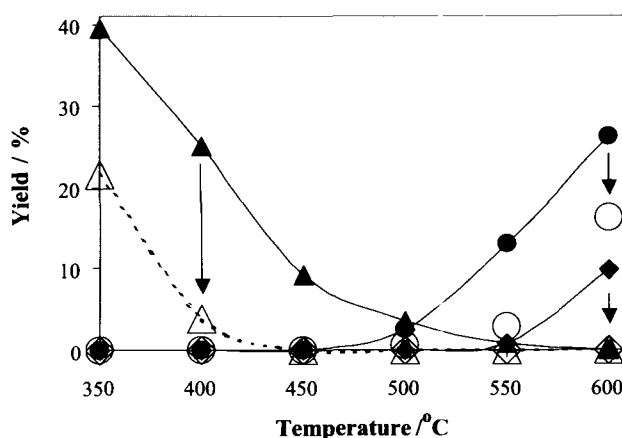


Fig. 10 Comparison between the NO/CH₄ yield to N₂O (Δ, ▲), CO (○, ●), and NH₃ (◇, ◆) for the fresh (open symbols) and high-temperature (950°C, 4 hr) aged (closed symbols) alumina-supported Pt nanoparticles in the 350–600°C temperature range (reactant mixture: 1% NO, 0.4% CH₄, and balance Ar).

larger d_{TEM} value observed for the aged catalyst (≈ 15.1 nm) compared with the fresh catalyst (≈ 13.4 nm) can be explained by the flattening of the Pt particles on the support, rather than by sintering (no sign of particle agglomeration was observed). The flattening of Pt nanoparticles (or the decrease in thickness) is supported also by the decrease in d_{XRD} value from 11.7 to 10.6 nm after aging. As we already discussed, the initially square Pt nanoparticles (relatively free of defects) were converted during thermal aging to irregular-shaped, round-shaped, and hexagonal-shaped particles (Fig. 2d). In other words, the low index facets were gradually shifted at high temperature to higher index planes. It is well known that a rearrangement of the metal surface, called "surface roughening" or "surface melting," can take place (below the melting temperature) if it is heated above some critical temperature. It is relatively common for a surface to show one equilibrium reconstruction at low temperature and to show another equilibrium surface structure upon heating.^[37] In the case of alumina-supported Pt nanoparticles, the process of surface roughening was not a reversible one.

As it was already stressed, the low index Pt planes (i.e., Pt(100))^[19] are less active for NO dissociation compared with higher index planes (i.e., Pt(410))^[22] or surface defects.^[17] The decrease in N₂O yield for thermally aged Pt nanoparticles, rich in surface defects, can be easily explained by taking into account their high activity for NO decomposition (Fig. 10).

The reasons for the significant decrease in CO and NH₃ yields after thermal aging will be given hereafter. As it was already emphasized, the small Pt particles have lower catalytic activity for oxidation reaction because they easily form PtO_x species (bulk oxide).^[33] The oxygen coverage as well as the desorption temperature are significantly higher on the small (≈ 2 nm) Pt particles relative to the large (≈ 8.3 nm) ones.^[38] For our specific case, the CH_x species, formed by the dissociative adsorption of CH₄, will be further oxidized to CO_x by oxygen resulting from the dissociation of NO. The high activity of the restructured Pt nanoparticles (thermally aged) for NO decomposition increases the supply of active oxygen, which rapidly removes surface carbonaceous species such as CO₂. As a consequence, the reaction yield to CO decreases.

The same explanation is valid in the case of ammonia formation. It is accepted that NH₃ is formed in the reactions between N_{ads} and a hydrogen source, either CH_x or H_{ads}.^[28] In fact, a reduction in NH₃ production can be reached if the active surface oxygen rapidly removes the hydrogen sources. The high activity of the restructured (rough) Pt nanoparticles to decompose NO increases the supply of surface oxygen, which can remove, as oxidation products (CO₂ and H₂O), the hydrogen sources (CH_x and H_{ads}) responsible for ammonia formation.

Thus the recombination N_{ads} (Eq. 2) becomes favored and the reaction of ammonia formation (Eqs. 7 and 8) can be prevented.

CONCLUSION

The NO/CH₄ reaction is structure-sensitive, depending both on the size and the shape (facet) of the Pt nanoparticles. The "facet effect" plays an essential role in NO dissociation, and thus is responsible for the reaction selectivity to N₂O and N₂. The "size effect" is responsible for the reaction selectivity to CO and NH₃ by controlling the oxygen catalytic activity.

It is clear that accurate tuning of the supported metals' morphology (size and shape) can bring in future spectacular improvements in the catalytic activity and selectivity for structure-sensitive reactions.

REFERENCES

1. Gates, B.C. Supported metal clusters: Synthesis, structure, and catalysis. *Chem. Rev.* **1995**, *95* (3), 511–522.
2. Argo, A.M.; Odzak, J.F.; Lai, F.S.; Gates, B.C. Observation of ligands effects during alkane hydrogenation by supported metal clusters. *Nature* **2002**, *415* (6872), 623–626.
3. Balint, I.; Miyazaki, A.; Aika, K.-i. Alumina dissolution promoted by CuSO₄ precipitation. *Chem. Mater.* **1999**, *11* (2), 378–383.
4. Balint, I.; Miyazaki, A.; Aika, K.-i. Alumina dissolution during impregnation with PdCl₄²⁻ in the acid pH range. *Chem. Mater.* **2001**, *13* (3), 932–938.
5. Iwasawa, Y. Supported Catalysts From Chemical Vapor Deposition and Related Techniques. In *Preparation of Solid Catalysts*; Ertl, G., Knoezinger, H., Weitkamp, J., Eds.; Wiley-VCH Verlag GmbH: Weinheim, 1999; 427–459.
6. Gates, B.C. Model of metal catalysts: Beyond single crystals. *Top. Catal.* **2001**, *14* (1–4), 173–180.
7. Somorjai, G.A. New model catalysts (platinum nanoparticles) and new techniques (SFG and STM) for studies of reaction intermediates and surface restructuring at high pressures during catalytic reactions. *Appl. Surf. Sci.* **1997**, *121/122*, 1–19.
8. Schmid, G. Cluster and Colloids, From Theory to Applications. In *The Chemistry of Transition Metal Colloids*; New York: Tokyo, 1994; 459–537.
9. Miyazaki, A.; Nakano, Y. Morphology of platinum nanoparticles protected by poly(*N*-isopropylacrylamide). *Langmuir* **2000**, *16* (18), 7109–7111.

10. Ahmadi, T.S.; Wang, Z.L.; Green, T.C.; Henglein, A.; El-Said, M.A. Shape-controlled synthesis of colloidal platinum nanoparticles. *Science* **1996**, *272* (5270), 1924–1926.
11. Wang, Z.L.; Ahmad, T.S.; El-Sayed, M.A. Steps, ledges and kinks on the surfaces of platinum nanoparticles of different shapes. *Surf. Sci.* **1997**, *380* (2–3), 302–310.
12. Balint, I.; Miyazaki, A.; Aika, K.-i. NO reduction by CH₄ over well-structured Pt nanocrystals supported on γ -Al₂O₃. *Appl. Catal., B* **2002**, *37* (3), 217–229.
13. Balint, I.; Miyazaki, A.; Aika, K.-i. Investigation of the morphology–catalytic reactivity relationship for Pt nanoparticles supported on alumina by using the reduction of NO with CH₄ as a model reaction. *Chem. Commun.* **2002**, (10), 1044–1045.
14. Somorjai, G.A. *Introduction to Surface Chemistry and Catalysis*; Wiley: New York, 1994; 319–324, Chapter 4.2.3.
15. Tanaka, K.-i.; Sasahara, A. Reconstructive activation of bimetallic surfaces. Catalytic reduction of NO with H₂ on Pt(100), Pt(110), Rh(100), Rh(110), and bimetallic single crystal surfaces of Rh/Pt(100), Rh/Pt(110), Pt/Rh(100), and Pt/Rh(110). *J. Mol. Catal.* **2000**, *155* (1–2), 13–22.
16. Boudart, M. Heterogeneous catalysis by metals. *J. Mol. Catal.* **1985**, *30* (1–2), 27–38.
17. Zambelli, T.; Winterlin, J.; Trost, J.; Ertl, G. Identification of the “active sites” of a surface catalyzed reaction. *Science* **1996**, *273* (5282), 1688–1690.
18. Walker, A.V.; Gruyters, M.; King, D.A. Modeling the out-of-phase oscillatory catalytic production of N₂O from NO reduction on Pt{100}. *Surf. Sci.* **1997**, *384* (1–3), L791–L797.
19. Comrie, C.M.; Weinberg, W.H.; Lambert, R.M. The adsorption of nitric oxide on platinum (111) and platinum (110) surfaces. *Surf. Sci.* **1976**, *57* (2), 619–631.
20. Burch, R.; Ramli, A. A comparative investigation of the reduction of NO by CH₄ on Pt, Pd, and Rh catalysts. *Appl. Catal., B* **1998**, *15* (1–2), 49–62.
21. Kao, C.T.; Blackman, G.S.; Van Hove, M.A.; Somorjai, G.A.; Chan, C.M. The surface structure and chemical reactivity of rhodium(111)–(2 × 2)–3NO by HREELS and dynamical LEED analysis. *Surf. Sci.* **1989**, *224* (1–3), 77–96.
22. Banholzer, W.F.; Masel, R.I. Nitric oxide decomposition on Pt(410). *J. Catal.* **1984**, *85* (1), 127–134.
23. Root, T.W.; Schmidt, L.D.; Fisher, G.B. Adsorption and reaction of nitric oxide and oxygen on Rh(111). *Surf. Sci.* **1983**, *134* (1), 30–45.
24. Winter, E.R.S. The catalytic decomposition of nitric oxide by metallic oxides. *J. Catal.* **1971**, *22* (2), 158–170.
25. Fritz, A.; Pitchon, V. The current state of research on automotive lean NO_x catalysis. *Appl. Catal., B* **1997**, *13* (1), 1–25.
26. Vovk, E.I.; Smirnov, M.Y.; Zemlyanov, D. NO and deuterium co-adsorption on the reconstructed Pt(100)-hex surface: A temperature programmed reaction study. *Surf. Sci.* **2000**, *453* (1–3), 103–111.
27. Lauterbach, J.; Bonilla, G.; Pletcher, T.D. Non-linear phenomena during CO oxidation in the mbar pressure range: A comparison between Pt/SiO₂ and Pt(100). *Chem. Eng. Sci.* **1999**, *54* (20), 4501–4512.
28. Burch, R.; Ramli, A. A kinetic investigation of the reduction of NO by CH₄ on silica and alumina-supported Pt catalysts. *Appl. Catal., B* **1998**, *15* (1–2), 63–73.
29. Denton, P.; Schuurman, Y.; Giroir-Fendler, A.; Praliaud, H.; Primet, M.; Mirodatos, C. N₂O as an intermediate for the formation of N₂ during SCR (NO): Stationary and transient conditions. *C. R. Acad. Sci., Ser. IIC Chim.* **2000**, *3* (6), 437–441.
30. Hickman, D.A.; Schmidt, L.D. Synthesis gas formation by direct oxidation of methane over Pt monoliths. *J. Catal.* **1992**, *138* (1), 267–282.
31. Burch, R.; Hayes, M.J. C–H bond activation in hydrocarbon oxidation on solid catalysts. *J. Mol. Catal., A* **1995**, *100* (1–3), 13–33.
32. Labalme, V.; Garbowski, E.; Guilhaume, N.; Primet, M. Modifications of Pt/alumina combustion catalysts by barium addition: II. Properties of aged catalysts. *Appl. Catal., A* **1996**, *138* (2), 93–108.
33. Hicks, R.F.; Qi, H.; Young, M.L.; Lee, R.G. Structure sensitivity of methane oxidation over platinum and palladium. *J. Catal.* **1990**, *122* (2), 280–294.
34. Burch, R.; Loader, P.K. Investigation of methane oxidation on Pt/Al₂O₃ catalysts under transient reaction conditions. *Appl. Catal., A* **1995**, *122* (2), 169–190.
35. Hwang, C.-P.; Yeh, C.-T. Platinum-oxide species formed by oxidation of platinum crystallites supported on alumina. *J. Mol. Catal.* **1996**, *112* (2), 295–302.
36. Vartuli, J.C.; Gonzalez, R.D. Ammonia formation in the catalytic reduction of nitric oxide by hydrocarbons: I. Promotional effects of hydrogen. *J. Catal.* **1974**, *32* (3), 470–481.
37. Masel, R.I. *Principles of Adsorption and Reaction on Solid Surfaces*; John Wiley and Sons, Inc.: New York, 1996; 67–68.
38. Putna, E.S.; Vohs, J.M.; Gorte, R.J. Oxygen desorption from α -Al₂O₃(0001) supported Rh, Pt and Pd particles. *Surf. Sci.* **1997**, *391* (1–3), L1178–L1182.

Nanocrystalline Materials: Fatigue

Alexei Yu. Vinogradov

Osaka City University, Osaka, Japan

Sean R. Agnew

University of Virginia, Charlottesville, Virginia, U.S.A.

INTRODUCTION

The processes of damage accumulation and the resulting fracture of materials under cyclic loading at stress levels below the tensile strength are collectively referred to as *fatigue*. These phenomena are quite sensitive to materials structure, including crystal structure grain size, character and distribution of grain boundaries, dislocation density and arrangement, internal stress, texture, surface quality, etc. Additional complexity is introduced by a wide variability of testing and service conditions, including environments. Various factors can be of greater or lesser importance for different aspects of fatigue. However, grain size can be regarded as a key structural factor affecting nearly all aspects of fatigue. This is not surprising because the grain is the elementary structural unit of polycrystalline solids. Furthermore, grain size is known to strongly affect all known mechanisms of inelastic deformation, particularly dislocation slip and deformation twinning. Notably, without plastic deformation mechanisms leading to damage accumulation, there would be no fatigue.

The advent of nanocrystalline materials after the early work by Gleiter^[1] opened new horizons for the discovery and design of new materials with unusual properties, as well as opportunities for scientific investigation of potentially novel mechanisms heretofore unobserved in classical materials systems. The purpose of the present article is to review the state-of-the-art within both of these contexts, as investigations of the fatigue behavior of nanocrystalline (NC) materials have been motivated by the possibility that NC materials will have enhanced fatigue resistance, as compared to their coarse-grained counterparts, as well as basic a desire to understand the fundamental mechanisms of deformation and fracture in nanoscale.

Before discussing the fatigue behavior of NC materials, it is useful to briefly outline why the properties, in general, and fatigue response, in particular, of NC materials are considered unique.

1. Nanomaterials are at the “interface” between amorphous and ordinary crystalline solids. Some authors

(such as Gleiter)^[1] have entertained the notion that their structure might be considered a two-phase composite consisting of small perfect crystalline regions of nanodimensions surrounded by relatively thick glassy-like grain boundaries (Fig. 1). Hence NC materials may inherit some properties from both crystals and glasses, while potentially remaining distinct from both of these extremes.

2. The number of atoms associated with grain boundaries can approach the number of atoms within the grain interior. Another way of stating this is that the volume fraction of grain boundaries can become as large as 50%. Thus the grain boundaries and their specific structure and properties will play a very important role in most, if not all, properties of NC materials.
3. Finally, a grain size of the order 100 nm corresponds to the structural level obtained within severely deformed metals. Specifically, the defects accommodating plastic deformation (dislocations) self-assemble into the collective structures with a characteristic length-scale in tens of nanometers.

A variety of techniques have been developed in the past decade for manufacturing nanomaterials (see Ref. [2] for a review). Among these, some of the more important are inert gas condensation, electrodeposition, devitrification from an amorphous precursor obtained by rapid solidification or ball milling, and severe plastic deformation (SPD) (see entry on “Nanocrystalline Substances: Synthesis and Properties”). The present article emphasizes the latter approach because severe plastic deformation for grain reduction has the advantage of producing of fully dense, bulk ultrafine grain (UFG) and NC materials with desired purity or target composition. In other words, SPD allows one to produce material suitable for investigation of fatigue behavior using classical testing methods and possessing dimensions large enough for structural applications, where fatigue properties are of interest. Among SPD techniques, the equal channel-angular pressing (ECAP) technology introduced by Segal^[3] as a cold (or warm) working technique allows extremely large strains to be imposed on bulk samples without fracture. The

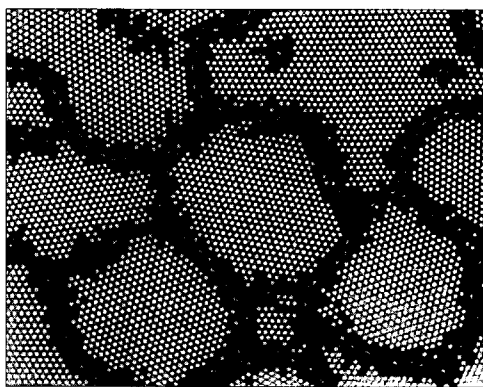


Fig. 1 Schematic presentation of the atomic structure of nano-materials: two-phase composite structure of crystalline grains and disordered glassy-like grain boundaries. (From Ref. [1].)

technique has proven to be capable of fabricating massive samples with a variety of UFG and nanostructures. As the majority of experimental results concerning fatigue of nanocrystals have been obtained on ECAP materials so far, the present review will primarily be concerned with these materials.

ECAP is performed by passing a billet through two intersecting channels of the same cross section. Severe plastic deformation occurs by simple shear on the plane of intersection between the channels. Because the cross-section geometry does not change during processing, ECA pressing can be repeatedly performed through various routes determined by possible rotations of the billet between subsequent passes. With repeated pressing, the material hardens dramatically so that unusually high strengths can be achieved. Ideally, the resultant strain imposed per ECA pass is controlled by the included angle between channels 2θ solely (given sharp die channel corners), and the cumulative shear strain Γ after N passes is $\Gamma = 2N \cot \theta$. The effective strain is given by $\varepsilon_i = 2N \cot \theta / \sqrt{3}$.^[3] Thus when the tool angle $2\theta = 90^\circ$, $\Gamma = 2N$ and the amount of the imposed strain can be substantially higher than is usually attained in standard cold-working procedures, such as rolling.^[3]

BACKGROUND

Fatigue Life Characterization

Total fatigue life of smooth bodies has been conventionally divided into two regions corresponding to the time required for crack nucleation and propagation.^[4,5] The resistance to crack initiation naturally requires strength, while the tolerance to the crack advance requires ductility. The most promising feature of SPD materials, which suggests the possibility of obtaining significantly en-

hanced fatigue properties, is associated with a combination of high strength and good ductility in the nanostructured state.^[2,6,7] Low-cycle fatigue (LCF) and high-cycle fatigue (HCF) regimes are conventionally distinguished in accord with applied strain amplitude. HCF testing corresponds to probing a materials resistance to crack initiation, whereas LCF testing corresponds to assessing the material's defect tolerance. Combining these two regimes, it is convenient to consider the total strain range $\Delta\varepsilon_t$ consisting of two components—elastic $\Delta\varepsilon_{el}$ and plastic $\Delta\varepsilon_{pl}$. The empiric Coffin–Manson relationship relates the total fatigue life (number of cycles to failure N_f) to $\Delta\varepsilon_{pl}/2$ as

$$\frac{\Delta\varepsilon_{pl}}{2} = \varepsilon'_f (2N_f)^c \quad (1)$$

where ε'_f is the fatigue ductility coefficient (which is often found to be approximately equal to the true fracture ductility ε_f in monotonic testing^[4,5]) and c is the fatigue ductility exponent. Similarly, $\Delta\varepsilon_{el}/2$ is related to the number of reversals to failure according to the Basquin law as

$$\frac{\Delta\varepsilon_{el}}{2} = \frac{\sigma'_f}{E} (2N_f)^b \quad (2)$$

where E is the Young's modulus, σ'_f is the fatigue strength (which is supposed to be related to the yield stress or the ultimate tensile strength of the material), and b is the Basquin exponent. Hence the fatigue life under a given total strain is expressed in terms of materials constants ε'_f , σ'_f , c , and b

$$\frac{\Delta\varepsilon_t}{2} = \frac{\sigma'_f}{E} (2N_f)^b + \varepsilon'_f (2N_f)^c \quad (3)$$

Although a simple equivalence of the pair ε'_f and σ'_f to the tensile ductility and σ_{UTS} , respectively, is rarely observed in experiments, the correlation between these pairs of qualities often exists. Eq. 3 is schematically illustrated in Fig. 2 for the fine-grain ECAP AlMgSc alloy. At high strains corresponding to short lives, the plastic strain component is dominant in the total applied strain and the fatigue life is primarily determined by ductility. At long fatigue lives, the elastic strain amplitude is more significant than plastic and fatigue life is dictated by the fracture strength so that the endurance limit increases with strength.^[3,4,8] Unfortunately, in most cases, ductility is sacrificed as the highest strength levels are achieved. This rule holds for most high-strength nanomaterials as well, and those fabricated by inert gas condensation, devitrification from the glassy state, powder compaction, etc. are usually so brittle that their potential is limited. Similarly, the simultaneous enhancement of both HCF and LCF lives is challenging, and inevitably requires a balance between

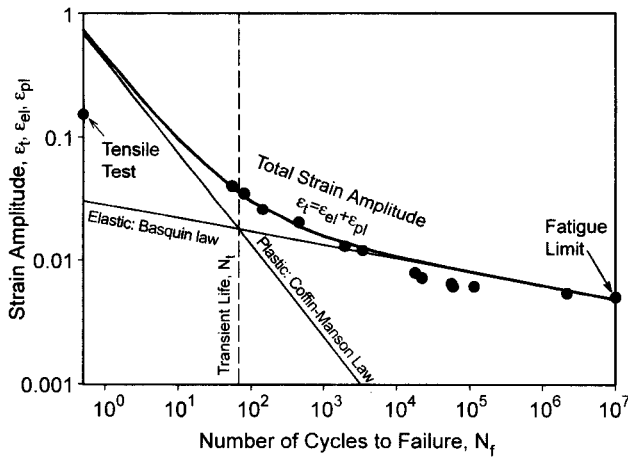


Fig. 2 Strain-life diagram. Solid line corresponds to Eq. 3 with experimentally obtained parameters of Coffin–Manson and Basquin law for the ECAP Al–4.5Mg–0.2Sc–0.2Zr alloy. Experimental points for this alloy are also plotted.

strength and ductility.^[4,8] It has been shown^[5,6,9] that nanomaterials manufactured by severe plastic deformation can, in principle, significantly benefit from spectacular improvement of both the strength and ductility.

For a comprehensive assessment of fatigue response, one also needs to evaluate the crack growth rate under a given stress intensity range ΔK and loading cycle asymmetry $R = \sigma_{\max}/\sigma_{\min}$, where σ_{\max} and σ_{\min} are the maximum and minimum applied stress, respectively. This information is of primary concern for engineering. Furthermore, an in-depth analysis involves characterization of the stress–strain hysteresis loop. In the present review, we briefly address all these issues as they apply to NC materials.

Effect of Grain Size on Fatigue

To describe the effect of grain size d on fatigue, it is necessary to specify how the grain size relates to the material's resistance to crack initiation and propagation, i.e., to quantify the effect of d on fatigue life parameters such as ε_f' , σ_f' , c , b , and the fatigue limit σ_f , defined as the peak cyclic stress below which no fatigue failure occurs prior to 10^7 or 10^8 cycles. The influence of grain size on the fatigue of conventional polycrystalline materials has been investigated and reviewed on many occasions (see, for example, Refs. [4,5,10–14]). Most observations can be summarized in two sentences.

1. The fatigue limit of pure face-centered cubic (f.c.c.) metals is not affected by the grain size.
2. The fatigue strength of materials exhibiting planar slip increases with decreasing grain size and follows the

Hall–Petch relationship, shown below, in the same way as the yield stress in conventional polycrystals.

$$\sigma_f = \sigma_{of} + K_f d^{-1/2} \quad (4)$$

where σ_{of} and K_f empiric materials properties.

It has been concluded that one of the most important fundamental material characteristics governing fatigue is the slip character. During LCF, the wavy-slip materials form a well-defined cell structure, with the cell size being dependent upon the saturation stress and independent of the preliminary strain history.^[4,5,10–12] Materials with a planar slip do not form a cell structure, and the dislocations are arranged in planar arrays extending across a grain. That grain size has a more pronounced effect on the fatigue behavior of planar slip materials has been convincingly demonstrated by Tomson and Backofen^[11] by using pure copper (wavy slip) and α -brass (planar slip). Mughrabi^[14] suggested extending this standpoint to UFG metals as well.

Indeed, the fatigue limit σ_f of UFG wavy slip aluminum alloys is not improved after multiple ECA pressing despite a remarkable enhancement of their monotonic strength, as will be discussed in more detail below. Results on commercial purity copper vary notably from modest to high σ_f improvement, depending, possibly, on fabrication (number of ECA passes, strain path, etc.). However, the independence of the grain size in coarse-grain wavy slip f.c.c. metals appears to be related to a specific cell structure formed during cycling. Because the typical grain/cell size in the SPD metals of 100–300 nm is smaller than the typical fatigue cell size in coarse-grained metals (~ 500 nm), exceptions to the classical rules may be anticipated.

A small grain size can result in more homogeneous deformation, which can retard crack nucleation by reducing stress concentrations and ultimately raise the fatigue limit of the material. It has been reported^[15] that the fatigue limit follows the Hall–Petch relationship with decreasing grain size in the same way as the ultimate tensile strength σ_{UTS} until critical grain size is attained, below which the slope of the $\sigma - d^{-1/2}$ curve is decreased. Consider NC copper with a grain size $d = 20$ nm, $\mu = 45$ GPa, and $b = 2.5 \times 10^{-10}$ m. An estimate of the stress required for dislocation multiplication (where the source length is assumed to be one-half the grain size, d) $\tau \geq 2\mu b/d = 12$ GPa, which is approximately equal to the theoretical strength $\sigma_{\text{theor}} = E/10$, where E is the Young's modulus of the material ($E = 120$ GPa for copper). In other words, dislocation activity within nanocrystalline grains is expected to be extremely difficult, which explains their frequently observed brittleness. On the other hand, there have been suggestions that the plasticity of NC materials may be associated with mechanisms other than perfect dislocation motion. Hence there may be an optimum grain

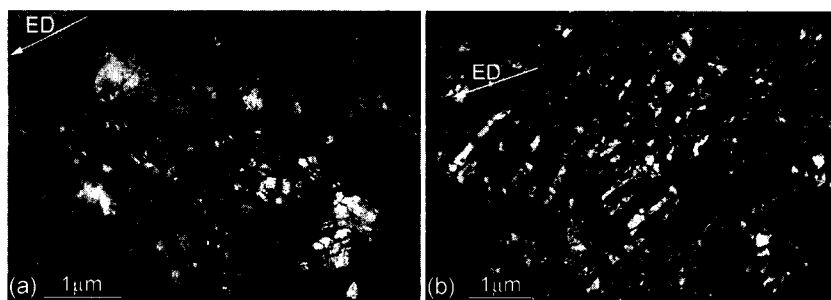


Fig. 3 Bright-field TEM images illustrating the equiaxed (a) and elongated (b) UFG structures after ECAP (Fe–36Ni Invar alloy after 8 and 12 ECA passes, respectively). Arrows indicate the extrusion direction.

size in the nanoscale region, where the maximum monotonic and cyclic strength is reached. Because the volume fraction of grain boundaries is comparable with the volume of grains, for very small grain sizes, there have been numerous suggestions that the deformation might localize within an amorphous grain boundary region, depicted in Fig. 1. Youngdahl et al.^[17] concluded that the deformation of nanocrystalline copper with a mean grain size between 30 and 100 nm produced by gas condensation and compaction occurs as a result of dislocation activity. No evidence for grain boundary sliding or rotation was found in their in situ transmission electron microscopy (TEM) experiments.

Experimental results concerning the cyclic behavior are currently available for various UFG SPD metals such as: 1) pure Cu^[18–28] and Ni^[29]—the most studied representative wavy-slip materials; 2) single-phase solid solutions—AA5056 Al–Mg alloy^[30,31] and Fe–36Ni (Invar) alloy;^[32,33] 3) Ti,^[34,35] which is a typical example of hexagonal close-packed (h.c.p.) metals exhibiting planar-slip; 4) precipitation hardenable CuCrZr alloy,^[36] 6061 Al–Mg alloy,^[37] Al–Mg–Sc alloys,^[38] and low-carbon steel.^[39] Brief reviews of the fatigue life of ECAP metals have been reported.^[16,33] Details of preparation and ECA processing are in the above-cited publications.

STRUCTURE OF ECAP METALS

Before reviewing the cyclic behavior of UFG materials, it is useful to first observe the microstructure prior to and after fatigue. A typical UFG structure after ECAP is shown in Fig. 3a. Let us briefly summarize the microstructural features of nanocrystalline materials fabricated by SPD, which are most relevant to fatigue. (See Ref. [2] for a comprehensive review.)

1. The average grain size ranges from 100 to 350 nm, depending on the particular metal or alloy. The

grain size distribution is often broad, depending on the details of the processing. The largest grains in the grain size distribution can be as large as 1–5 μm after SPD. It is emphasized that the grain boundaries are often hardly visible in TEM bright- or dark-field images.

2. Whether the grains are primarily separated by low- or high-angle boundaries remains an issue of some dispute. Some authors claim high-angle boundaries on the basis of qualitative indications of selected area electron diffraction patterns (SAEDP).^[2] Others have performed more statistical studies using scanning electron microscopy (SEM)-based electron back scattering diffraction (EBSD), or a similar TEM-based Kikuchi pattern analysis.^[40–42]
3. Two major structural types can be distinguished by the grain shape: a rather uniform structure with nearly equiaxed grains (Refs. [1,25] and references therein) (Fig. 3a), and a kind of fragmented structure with significantly elongated grains (Fig. 3b).
4. There is a great deal of stored energy in these systems associated with dislocations and their structures. Despite the very high average dislocation densities (10^{13} – 10^{15} m⁻²) commonly observed in these materials by TEM,^[2,43] it is noted that the interiors of the smaller grains appear to be free of dislocations. Thus it has been surmised that the dislocations may largely be incorporated within the boundaries themselves. These lattice strains associated with these defects are best characterized by using X-ray diffraction techniques associated with the broadening of Bragg peaks,^[29] and frequently identified as root mean squared (rms) strains in that analysis.
5. Because of the large stored energy, microstructural instability is often a hallmark of NC materials. After cyclic deformation, a variety of structural changes have been observed in ECAP metals.
6. The most striking feature of the postfatigue structure pure wavy slip SPD metals is the grain coarsening

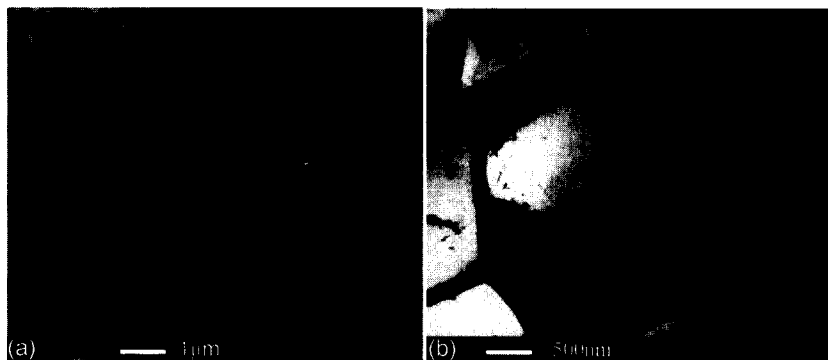


Fig. 4 Abnormal grain growth in cyclically deformed ECAP copper ($\Delta\epsilon_p/2=5 \times 10^{-3}$) (a) and ladder-like dislocation walls formed in the enlarged grains in the course of fatigue (b).

and abnormal grain growth triggered by cyclic deformation (Fig. 4a). This phenomenon has been noticed in many publications dealing with pure Cu and Ni.^[20–25,29,41] Recovery, recrystallization, and grain growth can be largely suppressed by limiting the mobility of grain boundaries as well as controlling the ease of relaxation by dislocation climb or cross-glide. Solid solutions and h.c.p. metals are rather stable and no substantial grain growth is observed in the Invar alloy^[24] (Fig. 5), and Ti after fatigue.^[23] Grain coarsening in the 5056 Al–Mg alloy depends on the processing and can be negligible.^[7]

7. For some materials, the average dislocation density in the central part of the grains may remain unaltered, being of the order of 10^{12} – 10^{15} m^{-2} . However, the grain boundaries themselves appear more distinct after cycling in all materials examined (e.g., Fig. 5). This seems to be the only noticeable structural change in fatigued Ti, Al–Mg, Cu–0.44Cr–0.2Zr, and Invar alloys, and it may be associated with a reduction in the dislocation density in the immediate vicinity of the grain boundaries.

8. A decrease in the internal stresses during the course of fatigue has been carefully demonstrated by Thiele et al.^[29] for UFG Ni, and by Wang et al.^[25] for UFG Cu using the X-ray technique. Some of the changes observed by X-ray diffraction may be associated with grain coarsening as well. The evolution of the grain size distribution calculated from the X-ray peak broadening is shown in Fig. 6 for different stages of fatigue of ECAP Cu.

HIGH CYCLE FATIGUE BEHAVIOR

Tensile and HCF properties of a variety of ECAP materials are summarized in Table 1. The enhancement of HCF life in terms of fatigue limit is achieved for most NC materials, as has been expected merely from the improvement of monotonic strength after grain refinement (“Introduction”). The scatter in experimental data obtained by different researchers on UFG Cu is caused by a variety of manufacturing conditions in different

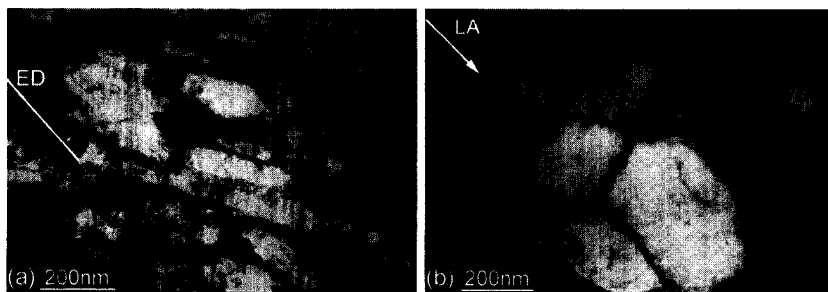


Fig. 5 TEM photos showing the structure of ECAP Invar alloy (8 ECA pressings, compare Fig. 3a) after fatigue at $\Delta\epsilon_p/2=5 \times 10^{-3}$. Low dislocation density is observed in some grains (b). Arrows indicate the loading axis that is aligned with extrusion direction.

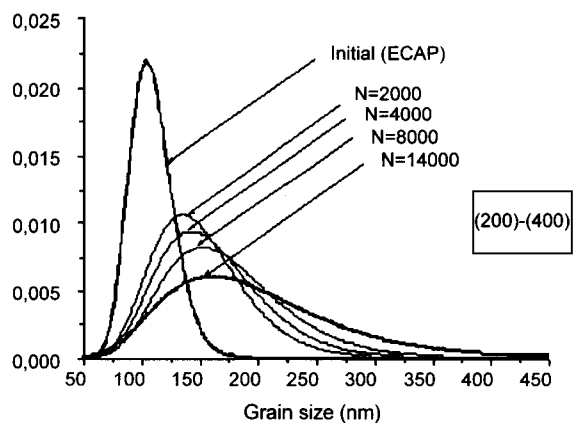


Fig. 6 Evolution of the grain size distribution in UFG Cu subjected to cyclic deformation with $\Delta\epsilon/2=5 \times 10^{-4}$; N —number of cycles. (From Ref. [25].)

laboratories, resulting in a variety of actually imposed strain and resulting microstructures. (Examples of the Wöller plots for two types of ECAP Cu having the equiaxed and elongated grain structure similar to those shown in Fig. 3 are given in Fig. 7a.) As suggested in the

section “Background,” a very pronounced improvement of the fatigue limit is observed in a planar slip material, ECAP Ti, processed at elevated temperature (400°C) and then subjected to further strengthening by cold-rolling to 75% area reduction and annealed for structural stabilization at 300°C for 1–2 hr^[35]. The fatigue limit of 500 MPa in pure SPD titanium is close to that of conventional Ti alloys (Fig. 7b). The impressive improvement of the fatigue strength in the peak-aged ECAP Cu–0.44Cr–0.2Zr alloy^[36] (Fig. 7a) is also worth noting in comparison with other commercial Cu-based alloys and tempers. The combination of affordable electric conductivity, thermal conductivity, and thermal stability with high tensile and fatigue strength make this multifunctional material attractive for a variety of electromechanical applications. The experimental data reveal that the ultimate tensile strength and the fatigue limit of NC SPD metals follow the Hall–Petch relationship^[4] (Fig. 8). Hence it is concluded that NC materials fabricated by SPD generally demonstrate a great potential for enhancement of high cycle fatigue life, in full agreement with the analysis given in the sections “Introduction” and “Background,” Eq. 6, and Fig. 2.

Markushev and Murashkin^[48] have reviewed the effect of grain refinement via SPD on the mechanical properties

Table 1 Grain size and mechanical properties of SPD alloys

Material	Processing	$\sigma_{0.2}$	(MPa)	σ_{UTS} (MPa)	δ (%)	$\sigma_{r,0}$ (MPa)
Cu 99.96%	CR 75%, HT 550°C, 2 hr	35	140	240	46	65
Cu 99.96% ^[41]	ECAP, B 8	0.2 eq	390	440	22	80
Cu–0.44Cr–0.2Zr ^[36]	ECAP Bc, 8, A 500°C, 1 hr	0.16 eq	650	720	1	285
Ti VT1-0	CR	15	380	460	26	240
Ti VT1-0 ^[35]	ECAP Bc, 8 400°C	0.3 eq	640	810	15	380
Ti VT1-0 ^[34]	ECAP Bc, 8 400°C, CR 75%	0.15 el	970	1050	8	420
Fe–36Ni Invar ^[32]	CR 75%	N/A	275	490	40	137
Fe–36Ni Invar ^[32]	ECAP Bc 2,	0.30 eq	570	732	47	280
Fe–36Ni Invar ^[32]	ECAP Bc 8,	0.26 eq	690	790	35	290
Fe–36Ni Invar ^[32]	ECAP Bc 12,	0.18 el	835	912	52	330
5056 Al alloy	O-temper	25	122	290	43	116
5056 Al alloy	H18	—	407	434	10	152
5056 Al alloy ^[31]	ECAP C, 4, 150°C	0.35 el	280	340	25	116
5056 Al alloy ^[31]	ECAP Bc, 8, 110°C	0.22 el	392	442	7	116
6061 Al alloy	O-temper	40–80	150	270	48	40
6061 Al alloy	T6	—	276	310	12	50
6061 Al alloy ^[37]	ECAP, 1, 125°C	el	310	375	20	80
6061 Al alloy ^[37]	ECAP, Bc, 4, 125°C	0.4 eq	380	425	20	<60
Al–4Mg–0.3Sc	Extruded	—	315	415	17	160
Al–1.5Mg–0.2Sc–Zr	ECAP, Bc, 8, 150°C	0.2–0.4	280	280	17	120
Al–3.0Mg–0.2Sc–Zr	ECAP, Bc, 6, 150°C	0.2–0.4	340	360	13	135
Al–4.5Mg–0.2Sc–Zr	ECAP, Bc, 6, 160°C	0.2–0.4	370	400	15	140

d =initial grain size, $\sigma_{0.2}$ =conventional yield stress, σ_{UTS} =ultimate tensile strength, δ =elongation to failure in tension, $\sigma_{r,0}$ =endurance limit based on 10^7 cycles.

CR=cold-rolling, Q=quenching, A=aging, HT=heat treatment; eq and el=equiaxed and elongated grain structure, respectively.

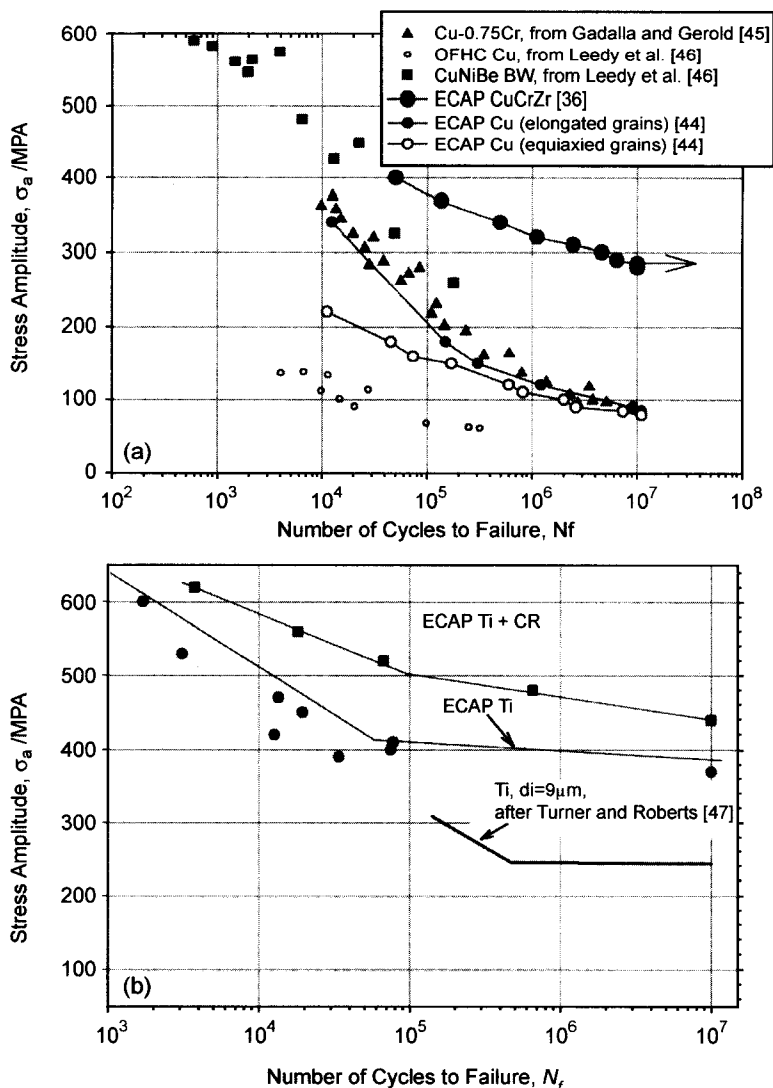


Fig. 7 S-N plots and fatigue limits of ECAP Cu and Cu-0.44Cr-0.2Zr alloy (a) and Ti (b).

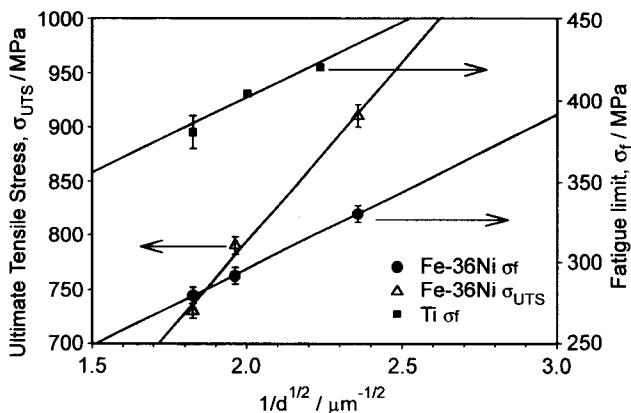


Fig. 8 Hall-Petch behavior of the ultimate tensile strength (for Fe-36Ni alloy) and fatigue limit (for Fe-36Ni and Ti) of ECAP metals.

of commercial Al alloys, and concluded that SPD, in general, is not very effective for strength or fatigue improvement of Al alloys. The results of Chung et al.^[37] on solution treated 6061 Al alloy typify the finding that multiple ECAP does not significantly improve the fatigue limit of Al alloys; however, they demonstrated notable improvement of fatigue limit just after the first pass through the die (note that they did not employ a standard heat treatment for precipitation hardening). Strengthening via grain refinement by SPD may be masked by other strengthening mechanisms on one hand and, on the other, the redistribution of phases and alloying elements can give rise to grain boundary brittleness and loss of ductility at room temperature. It is noted that grain refinement of Al alloys via SPD has proven extremely valuable for inducing superplasticity at elevated temperatures in a large number of alloy systems.^[49,50]

LOW CYCLE FATIGUE BEHAVIOR

At relatively large plastic strain ranges from 10^{-4} to 10^{-2} and short fatigue lives, the cyclic response of UFG materials is described by the Coffin–Manson law.^[1] As illustrated in Fig. 9 for UFG Cu and 5056 Al–Mg alloy. Although the data in Fig. 9a are compiled from the results obtained by different researchers on differently processed samples, one can see a reasonable agreement between these results. Samples in the as-received state after ECAP

demonstrate notable degradation in low cycle fatigue (LCF) life when compared to the ordinary coarse-grain samples. This is not surprising in view of their lower ductility and poor resistance to macroscopic and microscopic plastic instabilities such as necking, shear banding, cracking, etc. Such behavior is typical of metals with low levels of strain hardening (recall Considères criterion). As will be discussed in detail below, a postprocessing heat treatment can significantly improve the LCF properties. Remarkably, UFG Ti obtained by ECAP did not reveal a

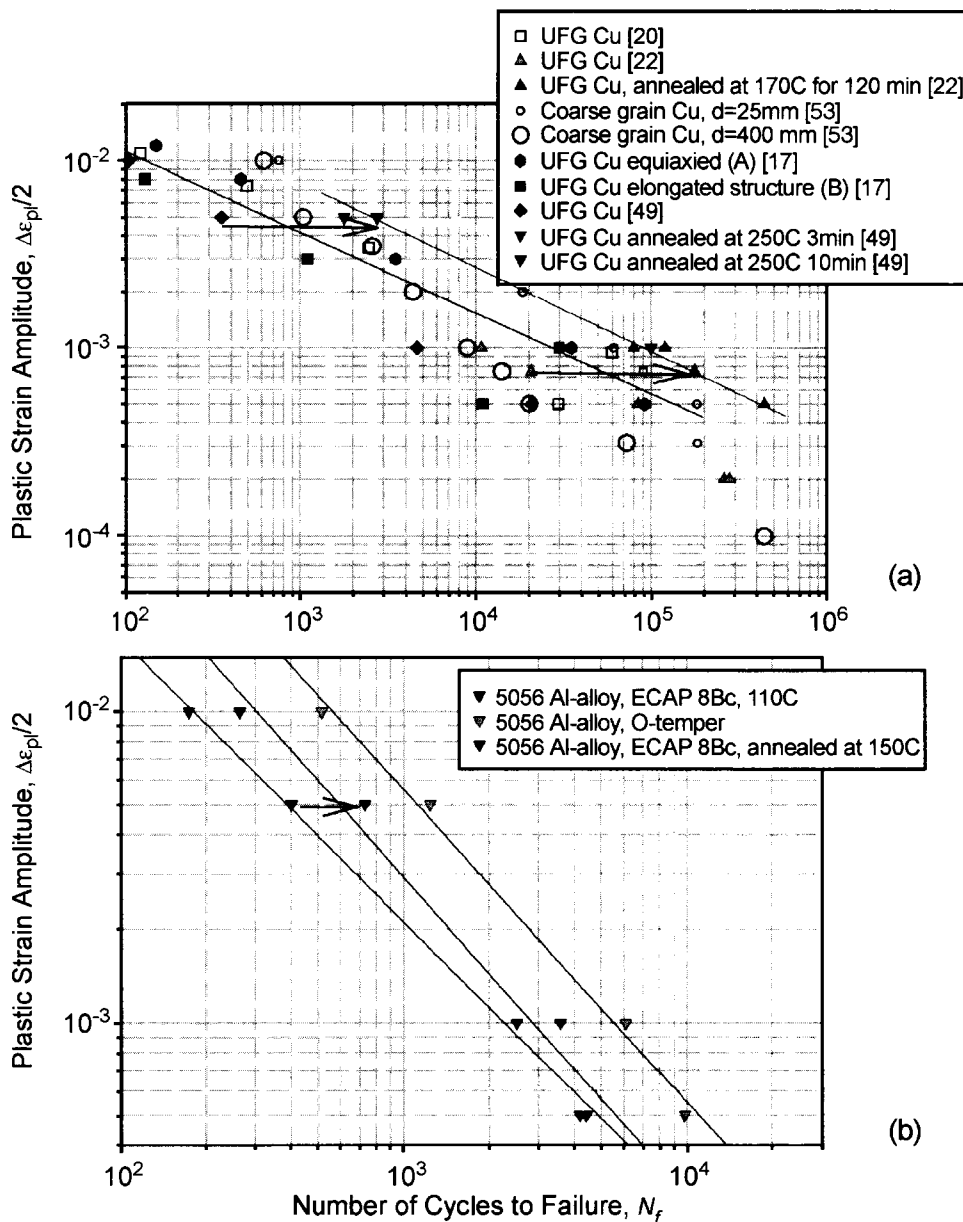


Fig. 9 Coffin–Manson plots for ultrafine grain Cu (a) and 5056 Al–Mg alloy (b) obtained by SPD (reprinted with permission). Arrows indicate the improvement of fatigue life after post-ECAP heat treatment. (From Ref. [30].) (*View this art in color at www.dekker.com.*)

significant degradation in low-cyclic fatigue performance in the plastic strain controlled testing, and the Coffin–Manson lines were practically indistinguishable for the samples before and after ECAP^[35] This result agrees with the general observation in the sections “Introduction” and “Background,” that non-f.c.c. metals can exhibit greater improvement in their fatigue performance if both LCF and HCF regimes is of major concern.

Cyclic Softening and Hardening

The cyclic stress–strain curves (CSSC) of NC materials can be represented by a power law in the same way as for other polycrystalline metals (see Refs. [4,5] and references therein).

$$\sigma_a = K'_b (\Delta \epsilon_{pl}/2)^{n'_b} \quad (5)$$

This relation is essentially the same as that used to describe the monotonic stress–stress curve

$$\sigma = K \epsilon^n \quad (6)$$

where K'_b , n'_b , K , and n are materials constants, and the subscript index b stands for the basic CSSC. Fig. 10 summarizes some currently available cyclic stress strain data for ECAP metals. It has been observed in a former communication^[32] that the slopes of the CSSC in logarithmic scale for the same material (Fe–36Ni Invar alloy) subjected to different number of ECA pressings between 2 and 12 are approximately the same, i.e., the cyclic strain hardening exponent n'_b values are nearly equal for all samples regardless of the preimposed strain. Fig. 11 compares the monotonic and CSSC for ECAP Fe–36 Ni Invar alloy (only the initial part of the tensile stress–strain

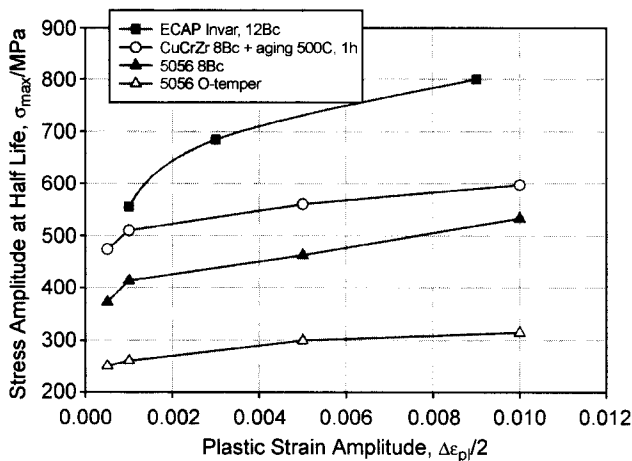


Fig. 10 Basic cyclic stress–strain curves for several UFG ECAP metals.

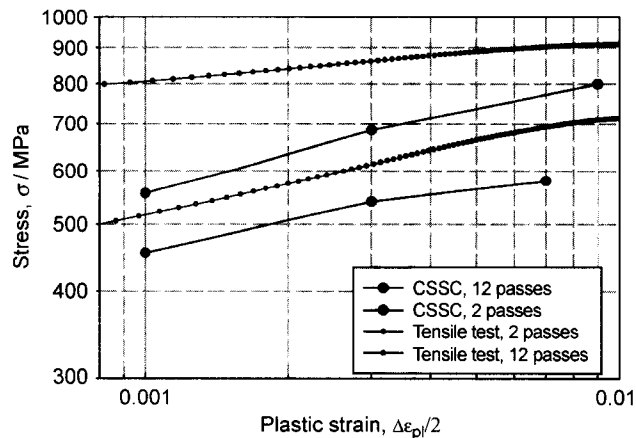


Fig. 11 Fragments of tensile stress–strain curves and CSSC for ECAP Fe–36Ni Invar alloy after 2 and 12 ECA passes. (From Ref. [32].) (View this art in color at www.dekker.com.)

curve is shown). The relative position of the monotonic and cyclic stress–strain curves delivers information on the materials cyclic hardening/softening behavior under different strain amplitudes. In the region of strain amplitudes where the CSSC lies above the monotonic stress–stress curve, the material cyclically hardens.^[5] On the other hand, in the regions where the CSSC is positioned below the monotonic stress–strain curve, the material cyclically softens. Hence it becomes obvious that the ECAP materials are prone to cyclic softening at any imposed plastic strain amplitude.

Softening is common for cyclic deformation of prestrained f.c.c. metals.^[4,5,51] It has been also clearly observed in many ECAP f.c.c. metals such as copper,^[20–22,26] Ni,^[29] single-phase Al–Mg 5056^[30,31] and Fe–36Ni Invar alloys,^[32] and precipitation-hardened

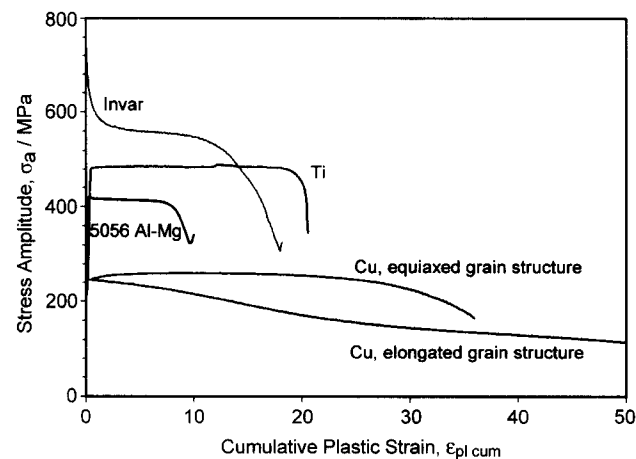


Fig. 12 Cyclic hardening/softening curves of some selected SPD metals with UFG structures. (From Ref. [33].)

Cu_{0.44}Cr_{0.2}Zr alloy.^[36] However, the detailed characteristics of cyclic softening, its phenomenology, and microscopic mechanisms vary broadly depending on the material and processing. Fig. 12 shows the cyclic hardening–softening curves for various NC ECAP metals tested under plastic strain control. The very first investigations of LCF behavior of ECAP materials revealed that the cyclic response strongly depends on processing and the initial UFG structure. Vinogradov et al.^[18] observed no cyclic softening in ECAP Cu under plastic strain amplitudes $\Delta\varepsilon_p/2=5 \times 10^{-4}$ and 10^{-3} . Furthermore, some light hardening was noticed on the early stage of straining (Fig. 12). However, Agnew and Weertman^[20] observed pronounced cyclic softening in similar UFG Cu produced by ECAP. The degree of softening appears to depend on the temperature, time, and plastic strain amplitude, and can vary from material to material.^[23] The mechanism of cyclic softening of UFG f.c.c. metal is largely associated with a complex effect of dislocation recovery, cyclically induced dynamic “recrystallization,” and grain coarsening, which is more pronounced at higher strain amplitudes.^[17–21,23,25,27] Interestingly, cyclic softening and the associated coarsening facilitates the formation of dislocation structures typical for ordinary metals, i.e., cellular and ladder-like dislocation arrangements^[20,23] (Fig. 4b). Thiele et al.^[29] performed a detailed structural investigation of the fatigue-induced structures in UFG Ni and the dependence of the grain size. Using X-ray diffraction peak profile analysis, they detected a reduction of internal stresses in the course of cycling. It was demonstrated that there is a lower threshold grain size d_{th} of 1 μm , above which dislocation patterning takes place with a length scale (~ 500 nm) nearly independent of the initial grain size. For materials with $d < d_{th}$, the cyclic stress–strain curve obeys the Hall–Petch relation.

Not surprisingly, the SPD structure can be stabilized and the rate of cyclic softening can be reduced by: 1) annealing at an intermediate temperature, i.e., reducing the stored strain energy prior to cyclic loading;^[19,22,26,30,33,44] 2) using solid solution alloys instead of pure metals,^[31,32] and 3) precipitation.^[36] The numerous large-scale shear bands, which are observed in the fatigued ECAP Fe–36Ni alloy, may contribute to the cyclic softening in that alloy. Höppel and Mughrabi,^[55] using Vickers microhardness measurements, have convincingly shown that the material in the shear band of a cyclically deformed ECAP Cu sample is softer than its surroundings. The values are in line with the concept of cyclically induced dynamic recrystallization and grain growth.^[22,23,26] Similar measurements have been performed by Vinogradov on the fatigued ECAP Fe–36Ni alloy. It has been demonstrated that the main reason for rapid cyclic softening of the UFG under- or peak-aged CuCrZr alloy (Fig. 12) is related to dislocation cutting of

the fine strengthening precipitates.^[36] The degree of softening is substantially lowered in overaged samples; however, the monotonic mechanical properties (strength and ductility) are degraded in this case.

FATIGUE DAMAGE AND STRAIN LOCALIZATION

Internal stresses in metals increase during monotonic straining, finally leading to microvoid nucleation or crack initiation as the resources of plastic deformation exhaust in local volumes of the material. Thus it may come as a surprise to some readers that the cyclic deformation of UFG metals fabricated by SPD may reduce the level of internal stress (as indicated by X-ray diffraction measures of rms strains^[29] and the general cyclic softening behavior referred to above), yet the end result is still a fatigue fracture. The answer, in its general form, is actually trivial: fracture occurs as a result of inhomogeneity in the plastic deformation manifesting itself as strain localization. The gradients of plastic deformation are often connected with grain boundaries, which may serve as barriers to dislocation motion as well as effective sources and sinks of lattice dislocations. These concepts are supported by atomic force microscopy (AFM) observations of fine traces of plastic deformation in UFG copper and nickel where: 1) dislocation activity is particularly visible at the grain boundaries,^[16,33,52] and 2) dislocation slip is terminated at the grain boundary and is not transferred to an adjacent grain. TEM observations have also demonstrated some reduction of the dislocation density near the grain boundary during fatigue (compare Fig. 5a and b, for example). Reducing the excess dislocation density around grain boundaries may explain the observed cyclic softening and the decrease of root mean square internal stress levels and, ironically, it may ultimately promote intergranular cracking. Fracture surface analysis and the surface crack morphology shows that failure in the SPD metals indeed occurs intergranularly.^[16,32,35]

Strain localization in the ECA-processed materials is frequently observed during both monotonic and cyclic deformation.^[10–15,44] Fig. 13 shows shear bands oriented at 45° to the loading axis in pure Cu after fatigue at $\Delta\varepsilon_p/2=5 \times 10^{-3}$ and 5056 Al–Mg alloy after monotonic deformation. These bands commonly appear shortly after yielding in tensile deformation or at the end of saturation in cyclic testing. Fatigue cracks initiate and propagate along this kind of shear band (Fig. 13a).^[25] Although shear banding is the major form of fatigue damage in wavy-slip UFG materials, these bands play a twofold role in fracture: on one hand, they promote crack nucleation due to strain localization and stress concentration; on the

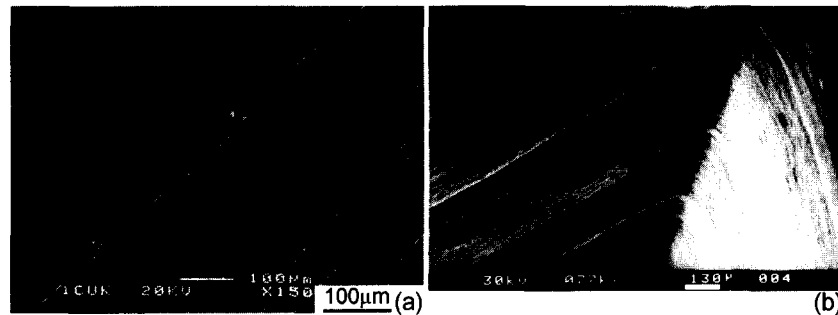


Fig. 13 SEM micrographs showing the shear bands in fatigued ECAP Cu (a) and in the tensile tested ECAP 5056 Al-Mg alloy (b). Final crack propagating along the shear band is shown in (a).

other hand, they reduce the overall elastic stresses, as evidenced by the reduction in stress at the end of saturation in strain controlled tests. Therefore it is unclear if suppression of the susceptibility to shear banding would delay or accelerate fatigue failure because cracking is a likely alternative mechanism for stress relaxation when other plastic mechanisms are exhausted. For instance, in UFG titanium or precipitation-hardened CuCrZr alloy, large-scale shear bands are not observed. However, a large population of surface microcracks is observed on the late stage of fatigue.

The microstructural nature of shear bands has been investigated in detail, at least for UFG Cu. Agnew et al.^[21] observed that the shear bands in UFG copper appear like ordinary persistent slip bands (PSBs) in coarse-grain poly- and single crystals. For instance, the shear bands were removed by electropolishing, and then they reappeared on the same places during subsequent cyclic loading, indicating materials softening associated with shear bands. Furthermore, careful structural observations have shown that the shear bands in UFG copper can have essentially the same ladder-like dislocation structure as the PSBs in ordinary crystals. The TEM image shown in

Fig. 4b demonstrates the dislocation walls separated by dislocation-free channels in fatigued UFG copper. Höppel et al.^[23] investigated the microstructural aspects of shear banding in UFG copper, including the dependence of strain amplitude and temperature, and have found that grain coarsening and shear banding are more pronounced at high strain amplitudes, which agrees with the observed faster cyclic softening. Thus pure f.c.c. UFG metals first exhibit relaxation and coarsening during cyclic softening, along with the formation of the low-energy configurations typical of conventional fatigued crystals, i.e., ordinary PSBs may occur. Finally, microcracks appear to initiate on intrusions and then behave similarly to those in conventional metals.

Although a similar scenario is applicable to those UFG metals exhibiting considerable grain coarsening during cycling,^[16,21–23,29] conflicting observations have been reported by Vinogradov et al.^[54] and Wu et al.,^[27,28] who did not observe any gross structural coarsening in fatigued ECAP Cu. Furthermore, using TEM, SEM, and electron channeling contrast imaging (ECCI), it was shown that the dimensions of protrusions on the surface did not match the dimensions of the grains. In fact,

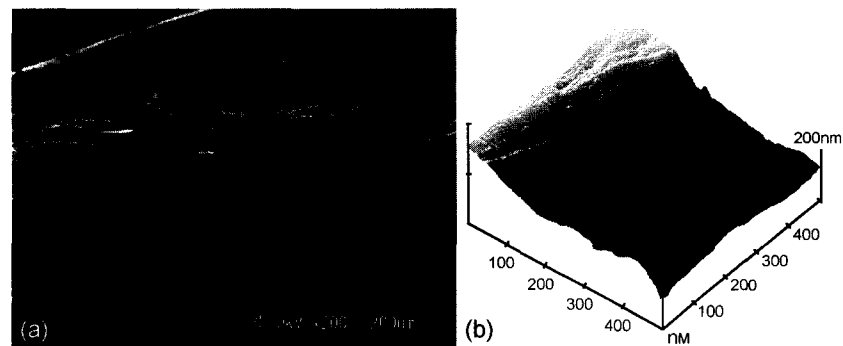


Fig. 14 SEM image of the shear offset on the surface of fatigued Fe-36Ni ($\Delta\epsilon_p/2 = 3 \times 10^{-3}$) (a). AFM image illustrating the large-scale displacement of adjacent grains along the grain boundary in the shear direction (b). The dislocation slip in the grain interior is clearly visible. (View this art in color at www.dekker.com.)

numerous questions remain unanswered as to which elements govern the fatigue behavior in the complex UFG microstructure.

There are at least two kinds of plastic instabilities which manifest themselves in various NC metals under various testing conditions: 1) the PSB-like shear bands that appear during fatigue as a result of slow large-scale structural rearrangement involving grain coarsening as a prerequisite for ladder structure formation; and 2) the shear bands that arise both in monotonic and cyclic testing, and phenomenologically (if not structurally) resemble twinning events. Shear bands of the second kind are not crystallographic and are not microscopically straight (Fig. 14a). They emerge very suddenly at free surfaces along grain boundaries in adiabatic fashion and are accompanied by significant acoustic emissions.^[54,56] The possibility of grain boundary sliding at ambient temperature in UFG SPD materials has been speculated in the literature^[2,43] in terms of enhanced diffusion and grain boundary mobility associated with heavily distorted grain boundaries. However, it is of particular importance to note the traces of dislocation slip of 1–10 nm height in the grain interior (Fig. 14b): that the slip lines are confined to a single grain, and the slip does not transfer through the boundary.^[33] Thus the AFM observations^[16,33,52] highlight the fact that conventional intragranular dislocation activity cannot be neglected as the most important mechanism of plastic deformation of UFG metals.

Shear bands in NCs may emerge to a free surface in a way similar to the shear bands commonly observed in metallic glasses during inhomogeneous plastic flow,^[57] which is also accompanied by intensive acoustic emission,^[58] and the morphology of shear bands in metallic glasses is very similar to that in NCs; however, this similarity may be completely coincidental because the concept of thick amorphous boundaries has not been justified by direct structural observations, particularly for metals fabricated by SPD. Wu et al.^[25,27] and Vinogradov et al.^[54] have found that the shear bands tend to align themselves with the plane of simple shear on the last ECA pressing, i.e., these bands are sensitive to the structure and its inhomogeneities formed during the last pass through the die. This leads to a conclusion that the careful control over processing (strain path, temperature, velocity, etc.) may allow control of the material's resistance to shear banding. Indeed, the nanostructure with equiaxed grains is less susceptible to rapid adiabatic shear banding than the structure with the grains (cells, fragments, etc.) elongated in the direction of last shear. Furthermore, UFG copper manufactured using different die sets (with round and rectangular corner) and different processing routes (but the same number of ECA passes and nearly the same grain size) exhibited different shear

banding susceptibility: the softer UFG copper, which saturated at 120 MPa and then cyclically softened at $\Delta\varepsilon_{pl}=1 \times 10^{-3}$, did not reveal the shear bands during either cyclic or monotonic loading,^[59] while the stronger copper saturated at 250 MPa and demonstrated many shear band on late stage of fatigue at the same plastic strain amplitude.^[18,54]

Annealing of as-processed UFG copper at an intermediate temperature for a short time, which does not give rise to substantial grain growth, resulted in the disappearance of adiabatic shear bands and accompanying acoustic emission.^[56] Despite the considerable difference in the microscopic mechanisms resulting in the two kinds of shear bands, they both appear as precursors of microcracks and serve as a preferred sites of crack nucleation.

FATIGUE CRACK GROWTH

The fatigue life assessment of smooth bodies delivers only indirect information regarding resistance to flaws either pre-existing or forming in the course of cycling. Comprehensive understanding of fatigue properties requires evaluation of the fatigue crack growth. The attention to fatigue crack growth in NC materials is presently growing with the development of processing techniques capable of producing large enough samples from which to make the standard compact tension (CT) or center-cracked-tension (CCT) specimens. The kinetic diagram showing the crack growth rate da/dN vs. the stress intensity factor range ΔK ($\Delta K = Y\Delta\sigma\sqrt{\pi a}$, where Y is the geometrical factor dependent upon the specimen and crack geometry, $\Delta\sigma = \sigma_{max} - \sigma_{min}$ is the applied stress range, and a is the crack length) for a given stress ratio R , and environment is used commonly to quantify the fatigue

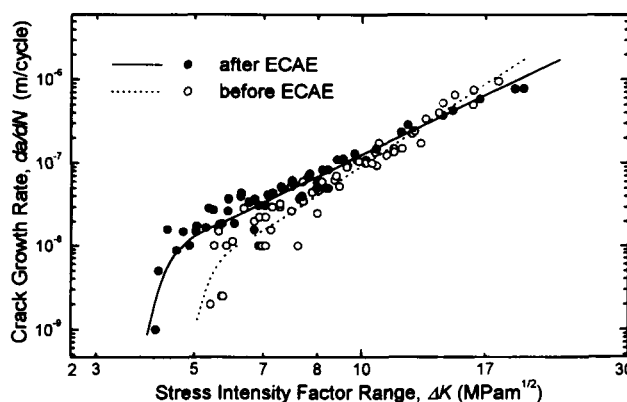


Fig. 15 Crack growth rate diagram of the fine grain ECAE 5056 Al alloy in comparison with its coarse grain O-temper counterpart. (From Ref. [31].)

crack growth behavior. We should underline that the da/dN vs. ΔK plot for NC materials (Fig. 15) exhibits the same stages of a stable crack propagation as those well known for conventional polycrystals, i.e., a stage of slow crack advance in a near threshold region and an intermediate stage, where the Paris relationship

$$\frac{da}{dN} = C(\Delta K)^m \quad (7)$$

(where C and m are materials properties) applies for most materials. Patlan et al.^[30] found that the fatigue threshold ΔK_{th} decreased after ECAP of a nonheat-treatable 5056 Al–Mg alloy (Fig. 15). Chung et al.^[37] demonstrated very similar results for the UFG 6061 Al alloy and UFG ECAP low carbon steel.^[39] It has been shown that the crack growth rate in the near threshold region is higher in the UFG state than in the ordinary polycrystalline state; however, the result is reversed at relatively high stress intensity factor increments ΔK , i.e., da/dN in UFG metals is smaller on the intermediate fatigue stage. Recently, Hanlon et al.^[60] obtained similar results for electro-deposited NC Ni with grain size of 20–40 nm. The lower crack growth resistance in the near threshold regime was attributed to a less tortuous path of the intergranular crack in the UFG structure (Fig. 13a). One can see that the crack propagates nearly perfectly straight on stage I of fatigue and then, as the crack length and the related ΔK value increase, the tortuosity of the crack path increases with numerous deflections and attempts to switch from mode II to mode I.

It has long been established in the fracture mechanics approach that the transition from the near-threshold slow crack growth regime to the intermediate fatigue stage is accompanied by a transition in the crack behavior from being strongly structure sensitive to structure insensitive. Such a transition is often observed when the crack tip cyclic plastic zone r_{cp} , which is estimated as

$$r_{cp} = \lambda \left(\frac{\Delta K}{2\sigma'_y} \right)^2 \quad (8)$$

(where λ is the numerical factor of the order of $1/\pi$ and σ'_y is the cyclic yield stress determined from the CSSC) becomes of the same order as the grain size d .^[4,61] If the stress intensity factor range corresponding to the transition point is denoted as ΔK_T , the last equation yields a transition criterion $r_{cp}(\Delta K_T) \approx d$. However, estimations of a reverse plastic zone radius r_{cp} at the transition point return a r_{cp} value for the materials tested (Cu, 5056, and 6161 Al alloys), which is significantly greater than the average grain size d . For example, taking for A5056 Al–Mg alloy $\sigma'_y = 280$ MPa and the threshold $\Delta K = \Delta K_{th} = 4.3$ MPa m^{1/2},^[31] one obtains $r_{cp} = 7\text{--}8$ μm —which is considerably larger than $d = 0.3\text{--}0.4$ μm . This suggests that a

large number of neighboring grains may be involved into crack tip plasticity, even near threshold. Eq. 8 at the transition point can be simply rearranged as

$$\Delta K_T \sim \sigma'_y \sqrt{d^*} \quad (9)$$

[where d^* is a characteristic scale of a materials structural unit responsible for fracture (grain size, subgrain or cell size, particle size, etc.)], which predicts ΔK_T to increase with d ; this effect is observed in low-carbon steels (for example, Refs [4,61]). Assuming that threshold ΔK_{th} approximately equals ΔK_T , the last relationship is often written in a more general, but less-transparent and less-argued form as

$$\Delta K_{th} = A + B\sqrt{d^*} \quad (10)$$

where A and B denote materials constants. However, observations reported in Refs. [30,37,39,60] show the reduced ΔK_{th} in UFG metals processed by SPD and NC metals, in general. If Eq. 9 were valid for these materials, a shift of ΔK_{th} to lower magnitudes (1 MPa m^{1/2} in the 5065 Al alloy, for example) should be expected, which is far below the observed values (of 4–4.5 MPa m^{1/2} in the same Al alloy). These observations cast some doubt on the general applicability of a simplified plastic zone size concept to explain the fatigue transition behavior of materials. Higo et al.^[62] performed a systematic investigation of ΔK_{th} and da/dN dependence on the grain size and the $\sigma_{0.1}$ yield stress in Cu and Cu–Al alloy with different Al content, i.e., with different stacking fault energy ranged between 5 and 45 mJ m⁻² approximately. In contrast with the linear behavior of Eq. 9, they experimentally observed that the propagation rates were slower in the fine-grained materials and da/dN varied linearly with $d^{-1/2}$ in the same manner as the $\sigma_{0.1}$ yield stress, i.e., followed the Hall–Petch relationship, which is the reverse of Eqs. 9 and 10. These effects were pronounced in alloys with higher Al content, i.e., in planar slip metals where (we have stated) a stronger dependence of fatigue life on the grain size is expected. Thus it is shown that although the fatigue crack growth behavior in NC metals reveals some similarity to that of conventional polycrystals, the quantitative explanation of the fatigue threshold reduction as well as the reduction of the crack growth rate at relatively high ΔK is not straightforward. More experimental data are required in the following areas:

1. crack growth rate dependence on ΔK at different R values for different materials (so far, data are only available for Al alloys);
2. precise investigations of fatigue crack closure; and

- more precise experimental evaluation of the reverse plastic zone are required before the mechanism controlling the fatigue crack behavior will be identified. Despite a somewhat lower tolerance of the NC metals to small and sharp intergranular cracks (at least in Al alloys), these materials demonstrate a better resistance to large cracks, perhaps, because of a smaller plastic zone size, which in turn, according to Eq. 11, appears smaller because of a higher strength and cyclic yield stress.

FATIGUE MECHANISMS IN UFG MATERIALS

The apparent similarity between the CSSCs in the coarse-grain and NC metals, which we have discussed above, suggests that the major deformation mechanisms are also alike for both kinds of materials. Thus before introducing any complication in the modeling of fatigue behavior of NC metals, one should first determine if it is possible to explain the mechanical properties of SPD metals via ordinary dislocation dynamics.

Many discussions have been put forward in the literature about the particular role of grain boundaries in the properties of UFG materials.^[1,2] Obviously, the interfacial energy and higher diffusivity of grain boundaries cannot be disregarded for many phenomena (particularly in nanocrystalline materials). In fatigue of SPD metals, for instance, grain boundaries play a significant role. On one hand, the fine-grained structure usually possesses longer fatigue life—at least under stress controlled cycling—than the coarse-grain one. On the other hand, the grain boundaries appear to contribute to the relatively low stability of the UFG structure and the tendency toward recovery and grain coarsening during cycling. Furthermore, grain boundaries appear to play a role in the frequently observed shear banding as well as crack initiation and propagation. Therefore grain boundaries arguably represent the most critical structural element.

Stress–Strain Response Under Cyclic Loading

Despite the complexity of the nanocrystalline structures, the fatigue behavior of NC metals is, in many ways, more easily described than that of ordinary poly- and single crystals. The main reason for simplification is the lack of dislocation patterning in the UFG structures. Vinogradov et al.^[30,35] have suggested that the shape of a stable hysteresis loop and the cyclic stress–strain curve can be described, at least semiquantitatively, by considering only

the kinetics of the average dislocation density within the framework of a simplified one-parameter model first proposed by Essmann and Mughrabi^[63] for dislocation annihilation. It was assumed that the mobile dislocations initiate at a grain boundary pass through the grain and disappear in the opposite grain boundary. Thus the grain boundaries act as effective sources and sinks for dislocations. Because TEM observations do not reveal any substantial difference between the initial and postfatigued structures, in some UFG metals, it is plausible to suggest that dislocations do not accumulate inside the fine grains during cycling in these cases. Following Essmann and Mughrabi^[63] and Mughrabi,^[64] a kinetic equation for dislocation density, ρ , can be written in its simplest form as

$$\frac{d\rho}{d\gamma} = \frac{2}{bL} - \frac{2}{b}y\rho \quad (11)$$

where L is the slip path of dislocations with the Burgers vector b and y is the so-called annihilation length. The first term on the right-hand side of Eq. 11 describes the rate of dislocation multiplication with the strain increase, while the second term accounts for the strain-induced decrease of dislocation density (dislocation dynamic recovery and annihilation of a general kind). At large enough strains, saturation is attained because of the equilibrium between the dislocation multiplication and annihilation, $d\rho/d\varepsilon = 0$.

To describe the stress–strain relationship, we assume that the shear flow stress, τ , is controlled by the average total dislocation density as

$$\tau = \tau_0 + \alpha\mu b\sqrt{\rho} \quad (12)$$

where τ_0 is the friction stress, α is a geometrical factor of the order of 0.5, and μ is the shear modulus. For numerical estimations, one can take τ_0 as equivalent to the cyclic shear yield stress ($\sigma_0 \approx 240$ MPa). Combining Eqs. 11 and 12 results in an elementary differential equation, which can be solved analytically assuming y and L do not vary with straining. While the assumption concerning the constancy of the annihilation distance seems reasonable, and has been experimentally justified (at least for Cu,^[63]), the assumption regarding L is considerably less obvious. Adopting $L = \text{const}$ condition for the sake of simplicity one can, however, propose a few arguments in a favor of this suggestion. For the cell structure, which is typical of conventional polycrystals, the slip path has been related to the cell diameter. In UFG materials, the grain size is smaller than the typical cell size, and the grain boundaries form the main barriers for dislocation motion. Therefore it is plausible to relate the dislocation mean free path to the

average grain size if the grain size is small enough. Integration of Eq. 14 together with Eq. 12 and $\tau(0)=\tau_0$ as an initial condition yields

$$\tau = \tau_0 + \alpha\mu b \sqrt{\frac{1 - \exp(-2\gamma/b)}{Ly}} \quad (13)$$

The saturation stress τ_s at sufficiently high strain $\gamma \gg b/y$ takes the form

$$\tau_s = \tau_0 + \frac{\alpha\mu b}{\sqrt{Ly}} \quad (14)$$

As an example, a typical ascending part of the stable hysteresis loop of the 5056 Al alloy is plotted in Fig. 16 in the so-called relative coordinates^[5] $\sigma_r - \varepsilon_{pl r}$, where the loop is displaced in such a way that the tip of the compressive half-loop comes to the origin coordinates, and both half-loops are treated as identical. The nonlinear curve fit of experimental points by function (13) with two fitting parameters— L and y —provides a good agreement between the experimental and calculated loops with L and y of $(1.2 \pm 0.6) \times 10^{-7}$ and $(8.4 \pm 3.0) \times 10^{-9}$ m, respectively (Fig. 16). The ordinary relations between shear and nominal stress-strain characteristics— $\sigma = M\tau$ and $\varepsilon = \gamma/M$ with $M \approx 3$ as the geometrical Taylor factor—are adopted. It is worth noting that the mean free pass of dislocations L appears to be of the order of the half-grain (cell) diameter d , which is in fair agreement with the assumptions made above.

Analogously, by using Eq. 14, one can calculate peak stresses, σ_s , at different plastic strain amplitudes examined, giving an approximation of the cyclic stress-strain curve (Fig. 8).^[30,35] Because of the simplicity of

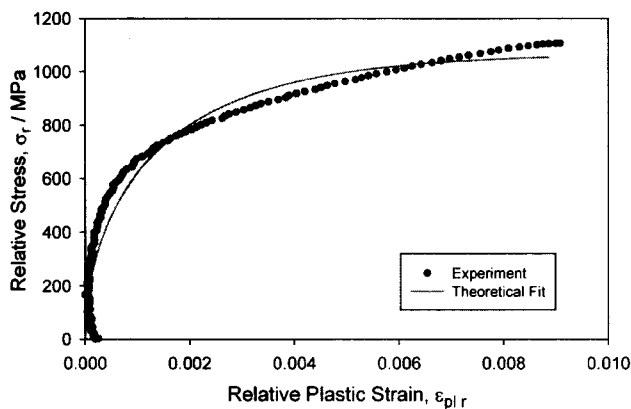


Fig. 16 Results of modeling of the hysteresis loop shape and CSSC of UFG 5056 Al-alloy within the frames of a single-parametric kinetic dislocation model. (From Ref. [30].)

this one-parameter model, the qualitative agreement between experimental results and calculations achieved is surprising. In the low strain limit, formula (14) can be rewritten as

$$\tau = \tau_0 + \alpha\mu b \sqrt{\frac{2\gamma}{bL}} = \tau_0 + \alpha\mu(\gamma b)^{1/2} d^{-1/2} \quad (15)$$

which corresponds to Ashby's expression of the Hall-Petch work-hardening stress $\tau = \tau_0 + kd^{-1/2}$ [τ_0 and $k = k(\gamma)$ are materials properties; compare with Eq. 7], if $L = d/2$. In other words, from Eq. 11, the " $d^{-1/2}$ " dependence of the flow stress recovered theoretically agrees with the experimentally observed Hall-Petch behavior of the CSSC and the fatigue limit.

Thus despite oversimplification, this approach is capable of qualitative explaining such experimental results as

1. saturation of the cyclic stress amplitude,
2. high saturation stress,
3. rapid hardening/softening on the early stage of cycling,
4. shape of the cyclic stress-strain curve and
5. Hall-Petch behavior of the fatigue limit.

More precise modeling would require two (or three) kinds of dislocations to be distinguished—mobile and immobile (the former are responsible the intergranular slip and the latter are attracted to the grain boundaries) as has been suggested by Estrin et al.^[65] for ordinary polycrystals.

Fatigue Life Prediction

The first attempt to model the fatigue life of SPD metal was performed by Ding et al.^[66] They considered the NC metal to be a two-phase composite consisting of a soft matrix representing grain interior and "hard" reinforcement representing the heavily distorted nonequilibrium grain boundaries (or the grain boundary affected zone having a characteristic thickness of 5 nm, which they suggested was experimentally supported by TEM and X-ray structural analysis). The authors suggested the dislocation accumulation to be the main strengthening mechanism in UFG metals; however, the grain boundaries also contribute to the resultant strength. The crack growth rate da/dN was calculated from the fracture mechanics concept assuming da/dN to be proportional to the crack tip opening displacement ($\Delta CTOD$). The $\Delta CTOD$ was related to the J -integral, and the latter was calculated in the cited work with an assumption that within the fatigue damage zone, the local cyclic stress was uniform and equal to the ultimate tensile strength of the UFG material.

The empirical Coffin–Manson and Basquin laws were finally derived as

$$\frac{\Delta \varepsilon_{pl}}{2} = \left[\frac{192C^2}{\lambda \pi^2 F^2} \left(\frac{n'}{n'+1} \right) \left(\frac{\sigma'_y}{K'} \right) \ln \left(\frac{a_f}{a_i} \right) \right]^{\frac{1}{3n'+1}} (2N_f)^{\frac{-1}{3n'+1}}$$

$$\frac{\Delta \sigma}{2} = K' \left[\frac{192C^2}{\lambda \pi^2 F^2} \left(\frac{n'}{n'+1} \right) \left(\frac{\sigma'_y}{K'} \right) \ln \left(\frac{a_f}{a_i} \right) \right]^{\frac{n'}{3n'+1}} (2N_f)^{\frac{-n'}{3n'+1}} \quad (16)$$

where a_i and a_f are the initial and final critical crack length, respectively, λ is a fitting parameter having a sense of the cyclic plastic zone correction factor same as that in Eq. 8, and C and F are the so-called GB constraint and GB strengthening factors respectively, which are introduced as:

$$F \equiv \frac{\sigma_{yUFG}}{\sigma_{yO}}$$

$$C \equiv \frac{1}{2} \frac{\Delta \sigma / 2}{\Delta \sigma_{eff} / 2} \quad (17)$$

where σ_{yUFG} and σ_{yO} denote the yield stresses in the UFG and ordinary polycrystalline materials, respectively, and $\Delta \sigma / 2$ and $\Delta \sigma_{eff} / 2$ are the average steady-state cyclic flow stress amplitude in the bulk of the material and the effective stress amplitude that contributes to local deformation, respectively. A satisfactory agreement between the calculated from Eqs. 16 fatigue life and experimental data was obtained,^[66] demonstrating a potential for fatigue life prediction in frames of the proposed phenomenological approach.

EFFECT OF TEXTURE

It is now understood that crystallographic texture exerts a very strong influence on the cyclic response of polycrystalline metals. For instance, Lukáš and Kunz^[13] first demonstrated that coarse-grain copper saturates at higher stresses than its small grain analog. Llanes and Laird^[67] showed that this effect could be attributed to a strong $\langle 111 \rangle$ – $\langle 100 \rangle$ fiber texture formed in coarse-grain copper during annealing. The SPD processing used to produce most of the materials discussed in this report inevitably results in the formation of at least moderate textures,^[68–70] which can be important for fatigue because of its effect on dislocation mobility, as well as the relative sensitivity of the material to plastic instabilities. Other methods of producing NC materials (e.g., film growth or inert gas condensation) may be more or less prone to these textural issues.

EFFECT OF ENVIRONMENT

It has long been recognized that the environment plays a very important role in fatigue damage, affecting both the crack nucleation and propagation, and a survey of the experimental results concerning the cyclic response of NC materials would not be complete without a few words about environmentally assisted fatigue. Yamasaki et al.^[59] investigated corrosion assisted fatigue of ECAP copper immersed into 1 M NaNO₂ aqueous solution in terms of cyclic hardening/softening behavior and surface morphology. They found that UFG copper possesses a notably better resistance to environmental attack, including corrosion fatigue, when compared to its coarse-grain counterpart. In contrast with coarse-grain Cu, which shows a transgranular fatigue fracture, corrosion fatigue in UFG specimens occurs intergranularly. Because localized corrosion is the most deleterious, the use of NC materials (having boundaries nearly everywhere) is said to be beneficial in the case where mass loss is the same for both sample types. Further improvement of fatigue properties and corrosion fatigue resistance is possible if the instability problem of SPD materials is resolved.

EFFECT OF PROCESSING ON FATIGUE AND OPTIMIZATION OF FATIGUE PERFORMANCE

The most influential SPD processing parameter is the amount of strain imposed. Increasing number of ECA pressings results in increasing monotonic strength and fatigue limit.^[32–34,36] Furthermore, the fatigue properties of UFG metals can be improved by gaining some ductility and reducing constraints for dislocation motion, i.e., by decreasing the tendency for shear banding and strain localization, which is common in many hardened metals. Thus it can be advantageous for fatigue properties to employ materials with a partially recovered structure. The positive effect of heat treatment on LCF has been already revealed in the early fatigue studies of ECAP materials.^[18] It has been shown, via the acoustic emission technique and microscopic surface observations, that susceptibility to shear banding in ECAP Cu decreases dramatically after a short-term (10 min) annealing at relatively low temperature of 250°C,^[56] and LCF life can be improved by a factor of 5–10 after a heat treatment that does not result in any grain growth.^[19,21,23] While ECAP results in considerable reduction of tensile and cyclic ductility, the same materials subjected to a post-ECAP annealing can potentially obtain a higher ductility than its conventional coarse-grain counterpart,^[23,45] and shifts the Coffin–Manson line toward higher fatigue lives (Fig. 9).

Because SPD metals retain some ductility after fabrication, their tensile and high cyclic strength can be additionally improved after postprocessing conventional cold rolling with or without intermediate annealing at moderate temperature. This has been shown for several Al–Mg alloys^[31] and commercial purity Ti^[23,25] as discussed in the section “High Cycle Fatigue Behavior.”

The effect of precipitation in SPD NC metals is complex. On one hand, it has already been mentioned that precipitates can dramatically increase the thermal stability of SPD metals and, on the other, grain boundaries may recover during aging thereby reducing their susceptibility to strain localization and premature cracking. As an example, it has been shown that optimal aging of ECAP UFG Cu–Cr–Zr alloy results in a high-strength structure with 200 nm grain size, which remains fine after subsequent annealing at temperatures as high as 500°C.^[36] Kim et al.^[71] have shown that the one-pass ECA pressing of the solid-solution treated 2024 Al alloy, followed by a low-temperature aging, can impressively enhance both strength and ductility: samples aged at 100°C for 20 hr had the strength $\sigma_{UTS}=715$ MPa, and the total elongation to failure $\delta=16\%$. Chung et al.^[37] have shown that the yield stress and tensile strength of 6061 Al alloy benefit from multiple ECA pressing (four passes) as compared to the one-time-pressed sample (the ECAP of solution treated billets was performed at 125°C and no subsequent heat treatment was applied.) Although the effect of the single ECA pressing of aluminum alloy 6061^[37] is impressive, it is not clear whether it would be impossible to achieve the same strength and ductility in Al alloys after conventional treatment. Hence two principal competing approaches for enhancement of fatigue properties via SPD can be seen: 1) achievement of compromise between strength and ductility in a minimum number of ECA pressings—one wherever possible, i.e., a cost-effective procedure employing relatively small imposed strains; and 2) achievement of maximum possible strength and high cycle fatigue life. The results of Chung et al.^[37] show a lack of correlation between the tensile strength and fatigue limit, i.e., the four-pass sample with higher σ_{UTS} has the fatigue limit lower than the one-time pressed sample. In conclusion, there are still great opportunities for the development of optimum processing scheme for desired fatigue properties of SPD materials.

CONCLUSION

The presently available experimental results concerning the fatigue behavior of NC materials have been reviewed, and the following aspects are highlighted in retrospect to

the available knowledge about the grain size effect on fatigue of conventional materials:

1. The significant enhancement of high cyclic fatigue life has been demonstrated after grain refinement down to submicrocrystalline and nanoscopic size for most materials, depending on the slip mode.
2. Despite the high tensile strength and improved high cyclic fatigue properties on NC and UFG metals, the low cyclic fatigue life appears shorter than that of their coarse-grain counterparts because of some loss in ductility during SPD.
3. Fatigue damage occurs on different scale levels from the intragranular movement of individual dislocations to macroscopic strain localization in the shear bands. The nature of the shear bands on SPD metals has been discussed from the standpoint of the initial ultrafine grain structure and its evolution during cyclic deformation.
4. The susceptibility of the ECAP materials to strain localization and microcracking can be a main factor, which limits their tensile and fatigue ductility and, to a large extent, determines their fatigue performance.
5. Postprocessing annealing has proven to be capable of considerable improvement of LCF performance of SPD metals because of reduction of their susceptibility to strain localization.
6. NC and UFG materials possess lower resistance to crack propagation than their coarse-grain analogs near the threshold.
7. Both grain refinement and dislocation work hardening play an important role in the resultant properties of materials obtained by severe plastic deformation. As a consequence, most of the cyclic properties of NC materials can be rationalized, at least qualitatively, in terms of Hall–Petch and dislocation hardening within a framework of a simple approach involving one- or two-parametric dislocation generation–annihilation kinetics.

The effects of texture, processing, and environment on fatigue life, crack initiation, and propagation in NC materials have been just scarcely studied, and further investigations in this field should be of interest for both potential applications and fundamental issues of fatigue of these materials.

REFERENCES

1. Gleiter, H. Nanostructured materials—State-of-the-art and perspectives. *Z. Metallk.* **1995**, *86*, 78–83.
2. Valiev, R.Z.; Islamgaliev, R.K.; Alexandrov, I.V.

- Bulk nanostructured materials from severe plastic deformation. *Prog. Mater. Sci.* **2000**, *45*, 103–185.
3. Segal, V.M. Materials processing by simple shear. *Mater. Sci. Eng., A* **1995**, *197*, 157–164.
 4. Suresh, S. *Fatigue of Materials*; Cambridge University Press: Cambridge, United Kingdom, 1991.
 5. Polák, J. *Cyclic Plasticity and Low Cycle Fatigue Life of Metals*; Elsevier: The Netherlands, 1991.
 6. Valiev, R.Z. Materials science: Nanomaterial advantage. *Nature* **2002**, *419*, 887–889.
 7. McFadden, S.X.; Mishra, R.S.; Valiev, R.Z.; Zhilyaev, A.P.; Mukherjee, A.K. Low-temperature superplasticity in nanostructured nickel and metal alloys. *Nature* **1999**, *398*, 684.
 8. Landgraf, R.W. The Resistance of Metals to Cyclic Deformation. In *Achievement of High Fatigue Resistance in Metals and Alloys*; ASTM: Philadelphia, 1970; 3–36. ASTM STP 467.
 9. Wang, Y.; Chen, M.; Zhou, F.; Ma, F. High tensile ductility in a nanostructured metal. *Nature* **2002**, *419*, 912–915.
 10. Pelloux, R.M. Effect of Grain Size on Fatigue. In *Ultrafine-Grain Metals*; Burke, J.J., Weiss, V., Eds.; Syracuse Univ. Press, 1970; 231.
 11. Tompson, A.W.; Backofen, W.A. Effect of grain size on fatigue. *Acta Metall.* **1971**, *19*, 597–606.
 12. Plumtree, A.; Abdel-Raouf, H.A. Cyclic stress-strain response and substructure. *Int. J. Fatigue* **2001**, *23*, 177–805.
 13. Lukáš, P.; Kunz, L. Effect of grain size on the high cycle fatigue behaviour of polycrystalline copper. *Mater. Sci. Eng.* **1987**, *85*, 67–75.
 14. Mughrabi, H. On the Grain-Size Dependence of Meta Fatigue: Outlook on the Fatigue of Ultrafine-Grained Metals. In *Investigations and Applications of Severe Plastic Deformation*; Lowe, T.C., Valiev, R.Z., Ed.; NATO Science Series, Kluwer Publishers, 2000; Vol. 3/80, 241–253.
 15. Li, S.X.; Lu, K.; Guo, F.Q.; Chu, R.; Wang, Z. The strength of amorphous and nanocrystalline FeMo-SiB alloys. *Mater. Lett.* **1997**, *30* (4), 305–310.
 16. Vinogradov, A.; Hashimoto, S. Multiscale phenomena in fatigue of ultra-fine grain materials—An overview. *Mater. Trans., JIM* **2001**, *42*, 74–84.
 17. Youngdahl, C.J.; Weertman, J.R.; Hugo, R.C.; Kung, H.H. Deformation behavior in nanocrystalline copper. *Scr. Mater.* **2001**, *44*, 1475–1478.
 18. Vinogradov, A.; Kaneko, Y.; Kitagawa, K.; Hashimoto, S.; Stolyarov, V.; Valiev, R. Cyclic response of ultra-fine grained copper under constant plastic strain amplitude. *Scr. Mater.* **1997**, *36*, 1345–1351.
 19. Vinogradov, A.; Patlan, V.; Kitagawa, K. Acoustic emission and strain localization in ultra-fine grained copper produced by equi-channel angular pressing. *Mater. Sci. Forum* **1998**, *312–314*, 607–612.
 20. Agnew, S.R.; Weertman, J.R. Low-cycle fatigue behavior of ultrafine grain copper. *Mater. Sci. Eng., A* **1998**, *244*, 145–153.
 21. Agnew, S.R.; Vinogradov, A.Yu.; Hashimoto, S.; Weertman, J.R. Overview of fatigue performance of Cu processed by severe plastic deformation. *J. Electron. Mater.* **1999**, *28*, 1038–1044.
 22. Mughrabi, H.; Höppel, H.W. Cyclic Deformation and Fatigue Properties of Ultrafine Grain Size Materials: Current Status and Some Criteria for Improvement of the Fatigue Resistance. In *MRS Proceedings*; MRS: Warrendale, PA, U.S.A., 2001; Vol. 634, B2.1.
 23. Höppel, H.W.; Zhou, Z.M.; Mughrabi, H.; Valiev, R.Z. Microstructural study of the parameters governing coarsening and cyclic softening in fatigued ultrafine-grained copper. *Philos. Mag., A* **2002**, *82*, 1781–1794.
 24. Wu, S.D.; Wang, Z.G.; Jiang, C.B.; Li, G.Y. Scanning electron microscopy-electron channelling contrast investigation of recrystallization during cyclic deformation of ultrafine grained copper processed by equal channel angular pressing. *Philos. Mag. Lett.* **2002**, *82*, 559–565.
 25. Wang, Z.G.; Wu, S.D.; Jiang, C.B.; Liu, S.M.; Alexandrov, I.V. ECA Pressing of Copper Single Crystals and Fatigue-Induced Softening in UFG Metals. In *Fatigue 2002*, Proc. of the 8th Int. Fatigue Congress, Stockholm, Sweden, June 2002; Blom, A.F., Ed.; EMAS: Sweden, 2002; 1541–1547.
 26. Höppel, H.W.; Valiev, R.Z. Optimizing fatigue behaviour in ultrafine-grained metals. *Z. Metallkd.* **2002**, *93*, 641–648.
 27. Wu, S.D.; Wang, Z.G.; Li, G.Y.; Valiev, R.Z. *Fatigue*, Proc. of the 7th Int. Fatigue Congress, Beijing, P.R. China; Wu, X.R., Wang, Z.G., Eds.; Higher Education Press: P.R. China, 1999; Vol. 3, 247–253.
 28. Wu, S.D.; Wang, Z.G.; Jiang, C.B.; Li, G.Y.; Alexandrov, I.V.; Valiev, R.Z. The formation of PSB-like shear bands in cyclically deformed ultra-fine grained copper processed by ECAP. *Scr. Mater.* **2003**, *48*, 1605–1609.
 29. Thiele, E.; Holste, C.; Klemm, R. Influence of size effect on microstructural changes in cyclically deformed polycrystalline nickel. *Z. Metallkd.* **2002**, *93*, 730–736.
 30. Patlan, V.; Vinogradov, A.; Higashi, K.; Kitagawa, K. Overview of fatigue properties of fine grain 5056 Al-Mg alloy processed by equal-channel angular pressing. *Mater. Sci. Eng., A* **2001**, *300*, 171–182.
 31. Vinogradov, A.; Patlan, V.; Kitagawa, K.; Kawazoe,

- M. Fatigue properties of 5056 Al-Mg alloy processed by equal-channel angular pressing. *Nanostruct. Mater.* **1999**, *11*, 925–934.
32. Vinogradov, A.; Kopylov, V.; Hashimoto, S. Enhanced strength and fatigue life of ultra-fine grain Fe-36Ni Invar alloy. *Mater. Sci. Eng., A* **2003**, *355*, 277–285.
 33. Vinogradov, A.; Hashimoto, S. Fatigue of severely deformed metals. *Adv. Eng. Mater.* **2003**, *5*, 351–358.
 34. Stolyarov, V.V.; Alexandrov, I.V.; Kolobov, Yu.R.; Zhu, M.; Zhu, Y.; Lowe, T. *Fatigue'99*, Proc. of the 7th Int. Fatigue Congress, Beijing, P.R. China; Wu, X.R., Wang, Z.G., Eds.; Higher Education Press: P.R. China, 1999; Vol. 3, 1345–1351.
 35. Vinogradov, A.; Stolyarov, V.V.; Hashimoto, S.; Valiev, R.Z. Cyclic behaviour of ultra-fine grain titanium produced by severe plastic deformation. *Mater. Sci. Eng., A* **2001**, *318*, 163–173.
 36. Vinogradov, A.; Suzuki, Y.; Kopylov, V.I.; Patlan, V.; Kitagawa, K. Structure and properties of ultra-fine grain Cu-Cr-Zr alloy produced by equal-channel angular pressing. *Acta Metall.* **2002**, *50*, 1636–1651.
 37. Chung, C.S.; Kim, J.K.; Kim, H.K.; Kim, W.J. Improvement of high-cycle fatigue life in a 6061 Al alloy produced by equal channel angular pressing. *Mater. Sci. Eng., A* **2002**, *337*, 39–44.
 38. Washikita, A.; Kitagawa, K.; Kopylov, V.I.; Vinogradov, A. Fatigue life of fine-grain Al-Mg-Sc alloys produced by equal-channel angular pressing. *Mater. Sci. Eng., A* **2003**, *349*, 318–326.
 39. Kim, H-K.; Choi, M-I.; Chung, C-S.; Shin, D.H. Fatigue properties of ultrafine grained low carbon steel produced by equal channel angular pressing. *Mater. Sci. Eng., A* **2003**, *340*, 243–250.
 40. Agnew, S.R.; Kocks, U.F.; Hartwig, K.T.; Weertman, J.R. Texture Evolution During Equal Channel Angular Forging and Dislocation Boundary Misorientations After Severe Plastic Deformation. In *Proc. 19th Risø Inter. Symp. Mater. Sci.*; Carstensen, J.V., Lefferes, T., Lorentzen, T., Pedersen, O.B., Sørensen, B.F., Winther, G., Eds.; Risø National Laboratory: Roskilde, Denmark, 1998; 201–206.
 41. Mishin, O.V.; Gertsman, V.Y.; Valiev, R.Z.; Gottstein, G. Grain boundary distribution and texture in ultrafine-grained copper produced by severe plastic deformation. *Scr. Mater.* **1996**, *35*, 873–878.
 42. Terhune, S.D.; Swisher, D.L.; Oh-Ishi, K.; Horita, Z.; Langdon, T.G.; McNelley, T.R. An investigation of microstructure and grain-boundary evolution during ECA pressing of pure aluminium. *Metal. Mater. Trans., A* **2002**, *33* (7), 2173–2184.
 43. Valiev, R.Z.; Kozlov, E.V.; Ivanov, Yu.F.; Lian, J.; Nazarov, A.A.; Baudalet, B. Deformation behaviour of ultra-fine-grained copper. *Acta Metall.* **1994**, *42*, 2467–2475.
 44. Hashimoto, S.; Vinogradov, A.; Kaneko, Y.; Kitagawa, K.; Valiev, R. On the cyclic behaviour of ultra-fine grained copper produced by equal-channel angular pressing. *Mater. Forum* **1999**, *312–314*, 593–598.
 45. Gadalla, A.A.; Gerold, V. The fatigue of copper-chromium alloy. *Ind. J. Pure Appl. Phys.* **1980**, *18* (6), 383–386.
 46. Leedy, K.D.; Stubbins, J.F.; Singh, B.N.; Garner, F.A. Fatigue behavior of copper and selected copper alloys for high heat flux applications. *J. Nucl. Mater.* **1996**, *233–237A*, 547–552.
 47. Turner, N.G.; Roberts, W.T. Fatigue behavior of titanium. *Trans. AIME* **1968**, *242*, 1223–1230.
 48. Markushev, M.V.; Murashkin, M.Yu. Mechanical properties of submicrocrystalline aluminium alloys after severe plastic deformation. *Phys. Met. Metallogr.* **2000**, *90*, 506–515.
 49. Komura, S.; Furukawa, M.; Horita, Z.; Nemoto, M.; Langdon, T.G. Optimizing the procedure of equal-channel angular pressing for maximum superplasticity. *Mater. Sci. Eng., A* **2002**, *297*, 111–118.
 50. Komura, S.; Horita, Z.; Furukawa, M.; Nemoto, M.; Langdon, T.G. An evaluation of the flow behavior during high strain rate superplasticity in an Al-Mg-Sc alloy. *Metal. Mater. Trans., A* **2001**, *32A*, 707–716.
 51. Feltner, C.E.; Laird, C. Cyclic stress-strain response of f.c.c. metals and alloys. *Acta Metall.* **1967**, *15*, 1621–1632.
 52. Vinogradov, A.; Hashimoto, S.; Patlan, V.; Kitagawa, K. Atomic force microscopic study of surface morphology of ultra-fine grained materials after tensile testing. *Mater. Sci. Eng., A* **2001**, *319–321*, 862–866.
 53. Muhghrabi, H.; Wang, R. Cyclic Stress-Strain Response and High-Cyclic Fatigue Behaviour of Copper Polycrystals. In *Basic Mechanisms in Fatigue*; Lukáš, P., Polák, J., Eds.; Elsevier: Amsterdam, The Netherlands, 1988; 1–13.
 54. Vinogradov, A.; Patlan, V.; Hashimoto, S.; Kitagawa, K. Acoustic emission during cyclic deformation of ultra-fine grain copper processed by severe plastic deformation. *Philos. Mag., A* **2002**, *82*, 317–335.
 55. Höppel, H.W.; Mughrabi, H. *Proc. of the Second International Conf. on Severely Deformed Metals*; Wiley VCH: Germany, December, 2003.
 56. Vinogradov, A. Acoustic emission in ultra-fine grained copper. *Scr. Mater.* **1998**, *38*, 797–805.
 57. Donovan, P.E.; Stobbs, W.M. The structure of shear bands in metallic glasses. *Acta Metall.* **1981**, *29*, 1419–1436.

58. Vinogradov, A. Classification of acoustic emissions in metallic glasses. *J. Acoust. Emiss.* **1999**, *17*, 1–13.
59. Yamasaki, T.; Miyamoto, H.; Mimaki, T.; Vinogradov, A.; Hashimoto, S. Corrosion Fatigue of Ultra-Fine Grain Copper Fabricated by Severe Plastic Deformation. In *Ultrafine Grain Metals II*; Zhu, Y.T., Langdon, T.G., Mishra, R.S., Semiatin, S.L., Saran, M.J., Lowe, T.C., Eds.; TMS: USA, 2002; 361–370.
60. Hanlon, T.; Kwon, Y.-N.; Suresh, S. Grain size effects on the fatigue response of nanocrystalline metals. *Scr. Mater.* **2003**, *49*, 675–680.
61. Taira, S.; Tanaka, K.; Hoshina, M. Grain Size Effect on Crack Nucleation and Growth in Long-Life Fatigue of Low-Carbon Steel. In *Fatigue Mechanisms*; Fong, J.T., Ed.; ASTM STPUSA1979; Vol. 675, 165–173.
62. Higo, Y.; Pickard, A.C.; Knott, J.F. Effect of grain size and stacking fault energy on fatigue-crack-propagation thresholds in Cu–Al aluminium alloys. *Met. Sci.* **1981**, *15* (6), 233–240.
63. Essmann, U.; Mughrabi, H. Annihilation of dislocations during tensile and cyclic deformation and limits of dislocation densities. *Philos. Mag.*, A **1979**, *40*, 731–756.
64. Mughrabi, H. Dislocation clustering and long-range internal stresses in monotonically and cyclically deformed metal crystals. *Rev. Phys. Appl.* **1988**, *23*, 367–379.
65. Estrin, Y.; Braasch, H.; Brechet, Y. A dislocation density based constitutive model for cyclic deformation. *J. Eng. Mater. Tech. ASME* **1996**, *118* (4), 441–447.
66. Ding, H.Z.; Mughrabi, H.; Höppel, H.W. A low cycle fatigue life prediction model of ultrafine-grained metals. *Fatigue Fract. Eng. Mater. Struct.* **2002**, *25*, 975–984.
67. Llanes, L.; Laird, C. Effect of grain-size and ramp loading on the low amplitude cyclic stress–strain curve of polycrystalline copper. *Mater. Sci. Eng.*, A **1990**, *128* (2), L9–12.
68. Field, R.D.; Hartwig, K.T.; Necker, C.T.; Bingert, J.F.; Agnew, S.R. Equal-channel angular extrusion of beryllium. *Metall. Mater. Trans.*, A **2002**, *23A*, 965–972.
69. Gholinia, A.; Bate, P.; Prangnell, P.B. Modelling texture development during equal channel angular extrusion of aluminium. *Acta Mater.* **2002**, *50*, 2121–2136.
70. Agnew, S.R.; Weertman, J.R. The influence of texture on the elastic properties of ultrafine-grain copper. *Mater. Sci. Eng.*, A **1998**, *242*, 174–180.
71. Kim, W.J.; Chung, C.S.; Ma, D.S.; Hong, S.I.; Kim, H.K. Optimization of strength and ductility of 2024 Al by equal channel angular pressing (ECAP) and post-ECAP aging. *Scr. Mater.* **2003**, *49*, 333–338.

Nanocrystalline Materials: Synthesis and Properties

Alexandr I. Gusev

Russian Academy of Sciences, Yekaterinburg, Russia

INTRODUCTION

The synthesis of nanocrystalline bulk and powder materials is one of the problems facing the modern materials scientist. In recent decades, the interest paid to this problem has grown remarkably because it was found that the properties of nanocrystalline substances change considerably when the size of crystallites decreases below a threshold value.^[1–8] Such changes arise when the average size of crystal grains does not exceed 100 nm and are most pronounced when grains are less than 10 nm in size. Ultrafine-grain substances should be studied considering not only their composition and structure, but also particle size distribution. Ultrafine-grain substances with grains 300 to 40 nm in size on the average are usually referred to as submicrocrystalline, while those with grains less than 40 nm in size on the average are called nanocrystalline. The classification of substances by the size D of their particles (grains) is shown in Fig. 1.

Nanosubstances and nanomaterials may be classified by geometrical shape and the dimensionality of their structural elements. The main types of nanomaterials with respect to the dimensionality include cluster materials, fibrous materials, films and multilayered materials, and also polycrystalline materials whose grains have dimensions comparable in all the three directions (Fig. 2).

The main objective of this paper is to give a general idea about diverse nanocrystalline substances and materials. The chemical composition, the microstructure, the grain size distribution, and, consequently, the properties of nanosubstances largely depend on their production method. It is for this reason that the paper first describes main methods for production of powders and bulk samples in the nanocrystalline state and then considers specific features of the microstructure of nanocrystalline substances. The influence of the nanocrystalline state on properties of various substances and determination of causes of this influence present the objective of the final part of this paper.

BACKGROUND OF FINE MATERIALS

In December 1959, at his talk at the California Institute of Technology, Feynman^[9] stressed the problem of control over the substance in the interval of extremely small

dimensions as an insufficiently explored, but very promising field of science. He noted in particular that "...when we have some control of the arrangement of things on a small scale we will get an enormously greater range of possible properties that substances can have, and of different things that we can do. ...The problems of chemistry...can be greatly helped if our ability to see what we are doing, and to do things on an atomic level, is ultimately developed."

In 1982–1985, Gleiter^[11] proposed a concept of the nanostructure of solids and was the first to realize a method for production of bulk materials with nanometer-sized grains (crystallites). From that time on, bulk and powder substances, which contained nanometer-sized particles, have been called nanocrystalline. Gleiter's works spurred studies into the synthesis, the structure, and the properties of nanocrystalline substances.

Differences in the properties of fine particles from those of bulk materials have been known and used for a relatively long time. Examples are aerosols, dyeing pigments, and glasses colored with colloidal particles of metals. A very significant field of successful application of fine particles is catalysis of chemical reactions. Multilayered nanostructures are used in electronics. These structures represent a crystal, which has, in addition to the usual lattice of periodically arranged atoms, a superlattice comprising alternating layers of different compositions.

Semiconductor nanoheterostructures, which realize quantum-size effects, are of special interest to electronics. Nanoheterostructures, especially double ones, including quantum wells, wire, and dots, allow controlling basic parameters of semiconductors (the energy spectrum, the forbidden gap width, the effective mass, and the mobility of carriers).

DISTINCTIVE PROPERTIES

The density of states $N(E)$ is a continuous function in a three-dimensional (3-D) semiconductor. When the electron gas dimensionality decreases, the energy spectrum becomes split and discrete (Fig. 3). A quantum well is a two-dimensional structure, in which charge carriers are limited to the direction perpendicular to the layers and can move freely in the layer plane. Charge carriers are limited

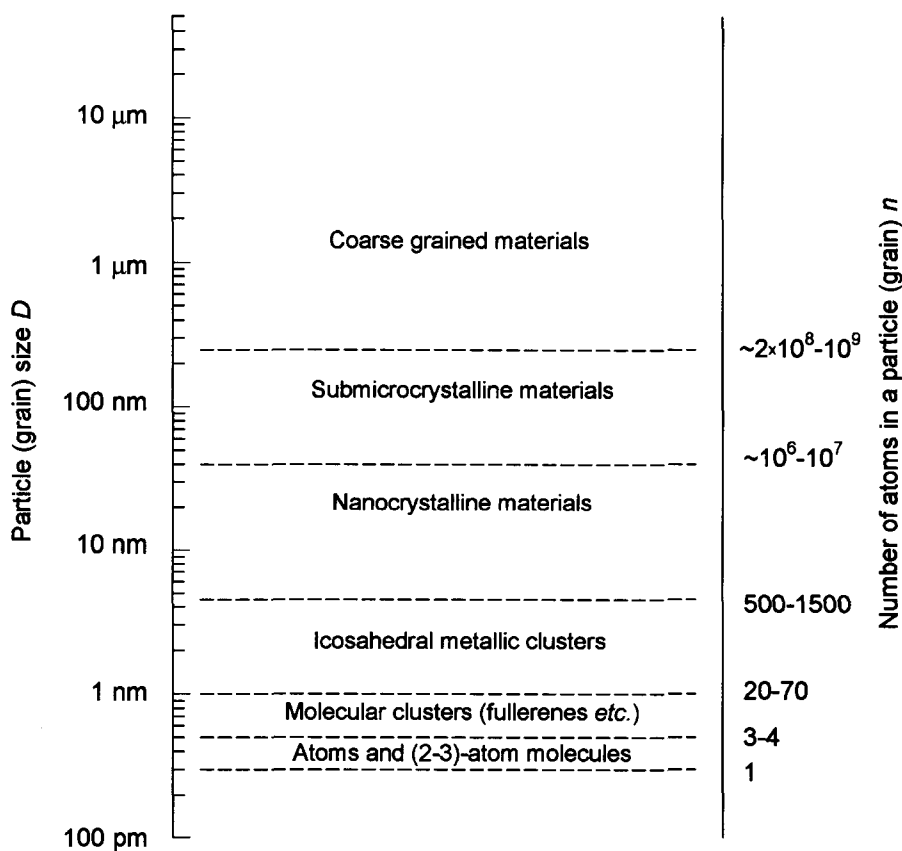


Fig. 1 Classification of substances and materials by their particle (grain) size D .

to two directions in a quantum wire and only move along the wire axis. A quantum dot is a quasi-zero-dimensional ("0" D) structure, in which charge carriers are limited in three directions. The electron energy spectrum of an ideal quantum dot is fully discrete (Fig. 3) and corresponds to the spectrum of a single atom, although a real quantum dot (a "superatom") can include hundreds of thousands of atoms.

A small size of grains determines a large length of grain boundaries. Also, grains may have various atomic defects (vacancies or their complexes, disclinations, and dislocations), whose number and distribution differ from those in coarse grains 5 to 30 μm in size. If dimensions of a solid in one, two, or three directions are comparable with characteristic physical parameters having the length dimensionality (the size of magnetic domains, the electron

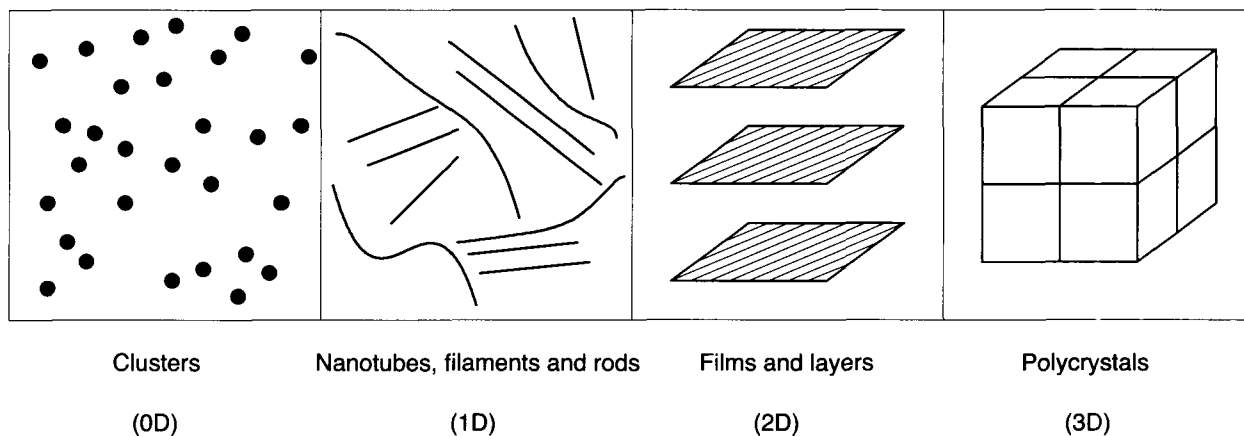


Fig. 2 Types of nanocrystalline materials: 0-D (zero-dimensional) clusters; 1-D (one-dimensional) nanotubes, filaments, and rods; 2-D (two-dimensional) films and layers; 3-D (three-dimensional) polycrystals.

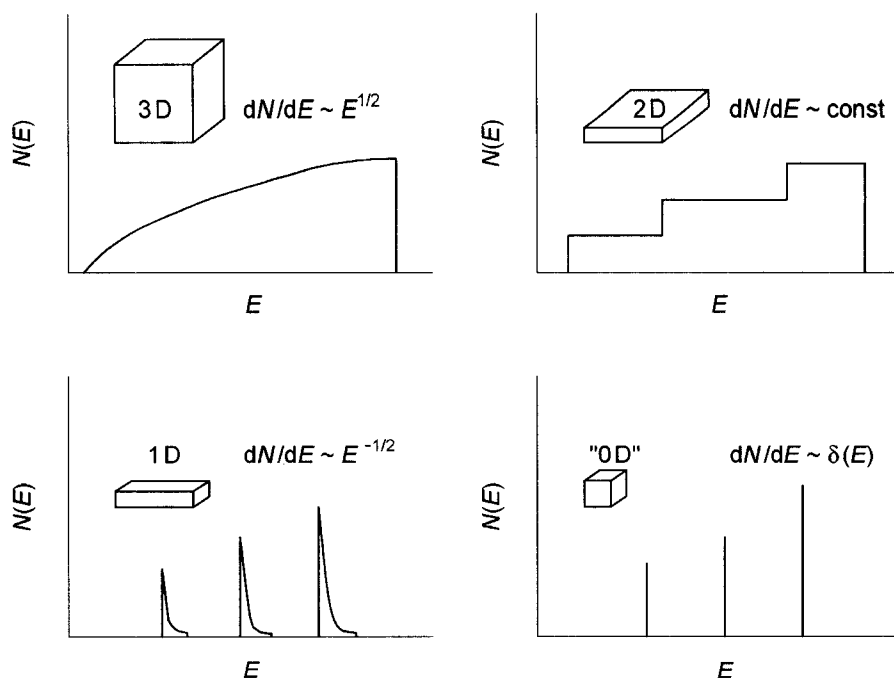


Fig. 3 Density of states of charge carriers of states $N(E)$ as a function of the semiconductor dimensionality: (3-D) three-dimensional semiconductor; (2-D) quantum well; (1-D) quantum wire; (0-D) quantum dot.

free path, the size of excitons, the de Broglie wavelength, etc.), dimensional effects will be observed for the corresponding properties. Thus dimensional effects imply a set of phenomena connected with changes in properties of substances, which are caused by 1) a change in the particle size, 2) the contribution of interfaces to properties of the system, and 3) comparability of the particle size with physical parameters having the length dimensionality. Specific features of the structure of nanocrystalline substances make their properties differ considerably from those of usual polycrystals. Therefore the decrease in the grain size is viewed as an efficient method for adjustment of properties of solids.

Nanocrystalline substances represent a special state of condensed matter, namely, macroscopic ensembles of superfine particles up to several nanometers in size. Properties of nanosubstances are determined by both specific features of separate particles and their collective behavior, which depends on the interaction between nanoparticles.

SYNTHESIS OF NANOCRYSTALLINE POWDERS

Gas Phase Synthesis

Isolated nanoparticles are prepared by the evaporation of a metal, an alloy, or a semiconductor at a controlled

temperature in the atmosphere of a low-pressure inert gas and the subsequent condensation of the vapor near or on a cold surface. The gas phase synthesis provides particles between 2 and several hundreds of nanometers in size. Nanoparticles ≤ 20 nm in size have a spherical shape, while coarser particles are faceted.

The metal may be evaporated from a crucible or fed to the evaporation zone as a wire or a powder. A beam of argon ions serves for the metal evaporation. The energy may be injected via direct heating, passage of an electric current, an electric-arc plasma discharge, inductive heating with currents of high and superhigh frequencies, laser radiation, or electron beam heating. A vacuum, a motionless inert gas, a gas flow, or a plasma jet may serve as the working medium. The composition and the size of nanoparticles may be controlled by changing the atmosphere pressure and composition (an inert gas or a reagent gas) and the temperature gradient between the evaporated substance and the surface, on which the vapor condensates.

Properties of isolated nanoparticles largely depend on the contribution of the surface layer. In the case of a spherical particle with the diameter D and the surface layer thickness δ , the fraction of the surface layer in the total volume of the particle is $\sim 6\delta/D$. When the surface layer thickness equals 3–4 atomic monolayers (0.5–1.5 nm) and the size of nanoparticles is 10–20 nm, the surface layer accounts for up to 50% of the whole substance.

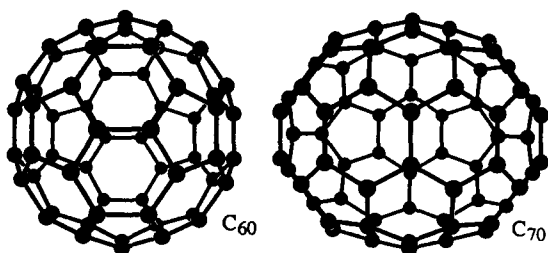


Fig. 4 Structure of most significant fullerenes C_{60} and C_{70} . The C_{60} molecule is shaped like a soccer-ball and its cage is about 0.7 nm in diameter. All fullerenes exhibit hexagonal and pentagonal rings of carbon atoms.

Plasmachemical Technique

Low-temperature (4000–8000 K) nitrogen, ammonium, hydrocarbon, or argon plasma of the arc, glow, high-frequency, or superhigh-frequency discharge is used in the plasmachemical synthesis. Elements, their halogenides, and other compounds serve as the starting material. Particles of plasmachemical powders represent single crystals 10 to 100–200 nm in size. Laser heating provides nanopowders with a narrow particle size distribution. The gas phase synthesis with laser radiation for generation and maintenance of the plasma, in which the chemical reaction takes place, proved to be an efficient method for production of molecular clusters.

Molecular clusters occupy a special place among nanostructured substances. The best known of these structures are the fullerenes,^[10] representing a new allotropic modification of carbon in addition to graphite and diamond.

The C_{60} and C_{70} fullerenes are produced by electric arc sputtering of graphite in the helium atmosphere at a pressure of $\sim 10^4$ Pa. However, electron beam evaporation and laser heating are also used.

A C_{60} molecule has the structure of a truncated regular icosahedron (Fig. 4), where carbon atoms form a closed hollow spherical surface comprising 5- and 6-member rings. Each atom has its coordination number equal to 3 and is located at vertices of two hexagons and one pentagon. Crystallization of C_{60} from a solution or a gas phase leads to appearance of fullerites, which are molecular crystals with a cubic lattice having the constant of 1.417 nm. The C_{70} fullerene is shaped like a closed spheroid (Fig. 4).

In 1992, a stable $Ti_8C_{12}^+$ cluster was discovered^[11] corresponding to a Ti_8C_{12} molecule in the form of a distorted pentagon dodecahedron (Fig. 5). The $Ti_{18}C_{12}$ cluster has the linear dimension of about 0.5 nm. Ti_8C_{12} clusters were produced by the plasmachemical gas phase synthesis in a helium atmosphere using hydrocarbons (methane, ethylene, acetylene, propylene, and benzene) and titanium vapors as reagents. Titanium was evaporated under irradiation from a Nd-laser with a 532-nm wavelength. The Ti_8C_{12} cluster is the first member in the new class of molecular clusters, that is, M_8C_{12} metallo-carbohedrenes, where $M=Zr, Hf, V, Cr, Mo, \text{ or } Fe$.

Precipitation from Colloid Solutions

A standard method for producing nanoparticles from colloid solutions consists of a chemical reaction between the solution components and interruption of this reaction

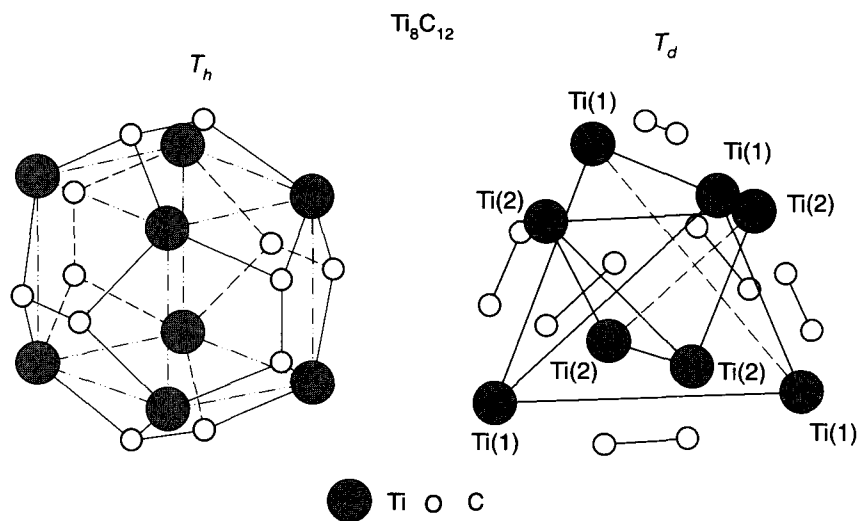


Fig. 5 Dodecahedral structure of the molecular cluster Ti_8C_{12} with the symmetries T_h and T_d taking into account different length of Ti—C and C—C bonds.

at a certain moment of time. After this, the dispersed system changes from the liquid colloid state to the dispersed solid state. For example, nanocrystalline cadmium sulfide CdS is produced by precipitation from a mixture of $\text{Cd}(\text{ClO}_4)_2$ and Na_2S solutions. The solution pH is increased abruptly to stop the growth of CdS particles.

Mixed-composition nanoparticles, i.e., nanocrystalline heterostructures, are synthesized by precipitation from colloid solutions. The core and the shell of a mixed nanoparticle are made of semiconductor substances having different structures of electronic levels. Heterostructures, such as CdSe/ZnS or ZnS/CdSe, HgS/CdS, ZnS/ZnO, and $\text{TiO}_2/\text{SnO}_2$, are formed through a controlled precipitation of one type of semiconductor molecules on presynthesized nanoparticles of a semiconductor of another type.

Precipitation from colloid solutions is highly selective and allows producing stabilized nanoclusters with a very narrow particle size distribution.

Thermal Decomposition and Reduction

Subject to thermal decomposition are elemento- and metallo-organic compounds, carbonyls, formates, oxalates, amides, and imides of metals, which decompose at some temperature and form the synthesized substance. For example, metal powders with particles 100 to 300 nm in size on the average are prepared by pyrolysis of iron, cobalt, nickel, and copper formates in a vacuum or an inert gas at 470–530 K.

Superfine metal powders are also produced by hydrogen reduction of hydroxides, chlorides, nitrates, and carbonates of metals at <500 K. Advantages of this method include a low concentration of impurities and a narrow particle size distribution of powders (Fig. 6).

Mechanical Synthesis

Mechanical synthesis as a method for producing nanopowders may be divided into two categories: mechanical milling and mechanical alloying. Mechanical milling is used both for grinding and amorphization of the starting material. Mechanical alloying requires grinding, mixing, mass transfer, and chemical interaction of powders of several pure elements, compounds, or alloys. Substances in the crystalline and amorphous states may be prepared by mechanical alloying.

Mechanical synthesis is the most efficient method for large-quantity production of nanopowders.

Grinding and mechanical synthesis are performed in high-energy planetary, ball, or vibrating mills. The average size of powder particles is 200 to 5–10 nm. For example, Fe–Ni and Fe–Al nanocrystalline alloys with grains 5 to 15 nm in size were synthesized by grinding of metal powders in a ball vibrating mill during 300 hr.^[8]

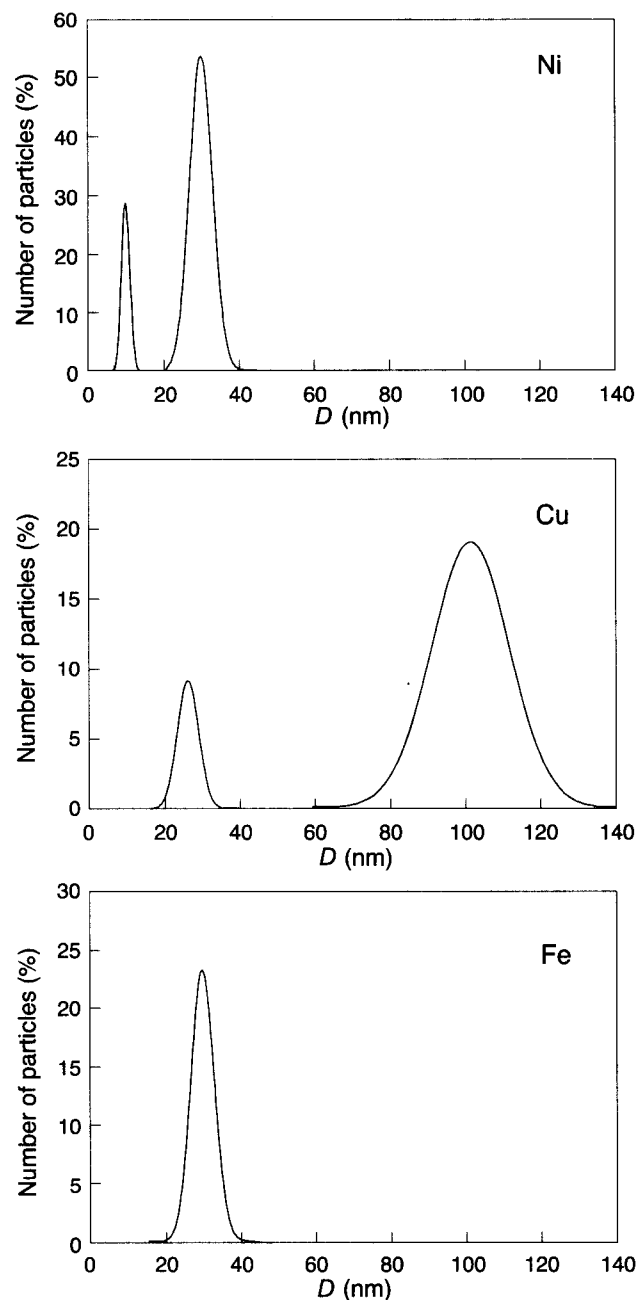


Fig. 6 Typical distributions of metal particles by their size D . The particles were synthesized via reduction of metals from compounds in a hydrogen flow.

Synthesis by Detonation and Electric Explosion

One more type of the mechanical treatment, which provides conditions for synthesis and dispersion of the final product, is a shock wave. Nanocrystalline diamond powders are prepared from mixtures of graphite and metals under the shock wave pressure of a few dozens of

gigapascals. Diamond powders may be produced more conveniently by explosion of organic substances with a high concentration of carbon and a low percentage of oxygen.

Detonation of condensed explosives, which decompose with liberation of free carbon, is used for commercial production of diamond nanopowders. The volume of explosion chambers is not less than 2–3 m³. Synthesized diamond powders consist of cubic particles about 4 nm in size on the average.

Fine powders with particles up to 50 nm in size are produced by an electric explosion of wire when it passes a strong current pulse, 10⁻⁵–10⁻⁷ sec long, having a density of 10⁴–10⁶ A mm⁻².^[12] A wire of diameter 0.1 to 1.0 mm is used. A current pulse quickly heats the metal up to a temperature $T > 10^4$ K (above the melting point) and the overheated metal is dispersed as in explosion. The average size of particles diminishes as the current density grows and the pulse length shortens. Electric explosion in an inert atmosphere provides powders of metals and alloys. Fine powders of oxides, nitrides, carbides, or their mixtures may be synthesized when reagents (O₂+He, N₂, H₂O, and C₁₀H₂₂) are added into the reactor.

Synthesis of Superfine Oxides in Liquid Metals

In this method, molten gallium, lead, or Pb–Bi alloy serve as the working medium. A metal M, whose chemical affinity for oxygen is larger than the oxygen affinity of the molten metal, is dissolved in the melt. Then the dissolved metal M is oxidized by bubbling water vapor or an oxidizing gas mixture (H₂O+Ar) through the melt. Superfine amorphous oxides of metals are formed as a result of selective oxidation. For example, oxidation of aluminum in molten gallium leads to formation of flocks of amorphous Al₂O₃·H₂O. It consists of fibers 5 to 100 nm in diameter, which are spaced 5 to 400 nm. The synthesized material has a porosity of 97–99 vol.% and a specific surface of 30 to 800 m² g⁻¹.

Nanostructured oxides SbO₂, TeO, NiO, GeO₂, SnO₂, In₂O₃, K₂O, ZnO, Ga₂O₃, Na₂O, MnO, Li₂O, Al₂O₃, BaO, SrO, MgO, and CaO may be produced via selective oxidation. The method is also applicable to synthesis of superfine nitrides, sulfides, and halogenides. In this case, a mixture of an inert gas and nitrogen N₂, hydrogen sulfide H₂S, or gaseous gallium or lead chlorides is passed through the melt with a dissolved metal.

Self-Propagating High-Temperature Synthesis

Self-propagating high-temperature synthesis (SHS) represents solid-state burning of reagents (metal and carbon for

carbides or metal in nitrogen for nitrides) at a temperature of 2500 to 3000 K. Usually, the average size of grains in carbides produced by the SHS method is 5 to 20 μm.

A nanosized powder of titanium carbide was prepared by the SHS method using sodium chloride as an inert dilutant.^[13] As titanium and carbon are burning, NaCl forms a melt, which insulates the formed carbide particles and prevents their growth. Also, NaCl dissolves well in water and can be easily separated from the synthesized carbide. The size of titanium carbide particles decreases with growing percentage of NaCl in the initial mixture. The average size of particles is about 100 nm.

Ordering in Nonstoichiometric Compounds as a Method of Producing a Nanostructure

A nanostructure in nonstoichiometric compounds such as MC_y cubic carbides is produced through disorder–order transformations, which take place as phase transitions of the first kind with an abrupt change of the volume.^[14] If a nonstoichiometric compound is cooled quickly from a high temperature, at which the disordered state is at equilibrium, ordering cannot be completed and the compound remains in a metastable disordered state. Because lattice constants of the disordered and ordered phases are different, stresses arise in the sample, leading to the cracking of crystallites at interfaces between the disordered and ordered phases and formation of a nanostructured powder.

The first ordering-induced nanostructure was realized in a nonstoichiometric vanadium carbide.^[15] The initial powder of the VC_{0.875} carbide with grains 1 to 2 μm in size was aged for a long time at 300 K. The aged powder contained agglomerates 5 to 30 μm in size, which were formed by particles measuring about 1 μm. The particles had a complicated structure (Fig. 7). Each entity ~1 μm in size looked like an open rosebud and contained a large number of nanocrystallites in the form of strongly bent plate disks 400 to 600 nm in diameter and 15 to 20 nm thick (Fig. 8). The bulk of the nanocrystallites consisted of the V₈C₇-ordered carbide, while the surface layer about 0.7 nm thick included a great number of vacancy agglomerates.

PREPARATION OF BULK NANOCRYSTALLINE SUBSTANCES

Disorder–Order Transformations

A nanostructure may be produced not only by ordering of powders, but also bulk nonstoichiometric compounds. Bulk samples of the VC_{0.875} carbide were prepared using a hot pressing of a powder of disordered vanadium

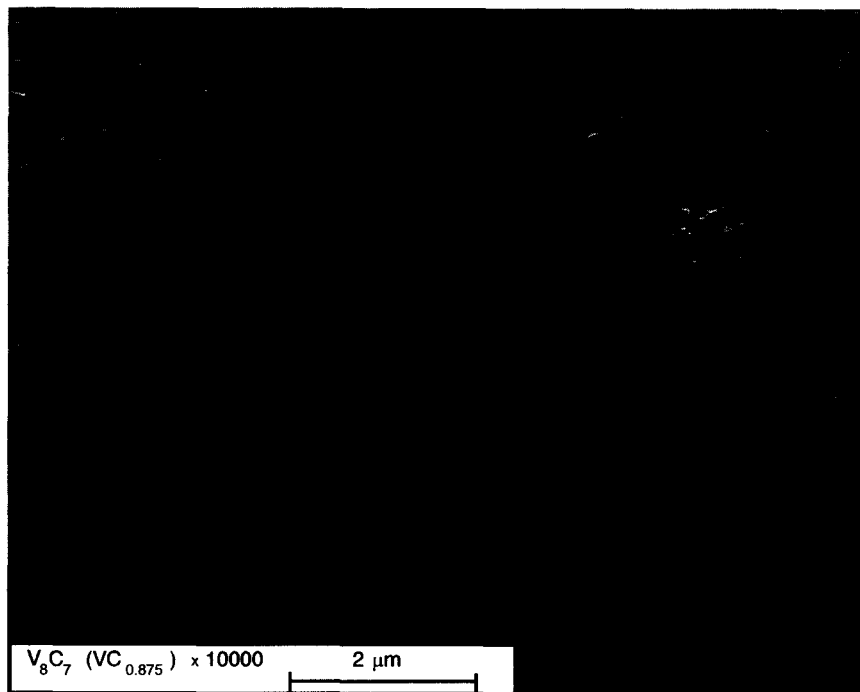


Fig. 7 Microstructure of a powder of the VC_{0.875} vanadium carbide after long-term aging at ambient temperature in an ambient atmosphere (× 10000 magnification). (From Ref. [15].)

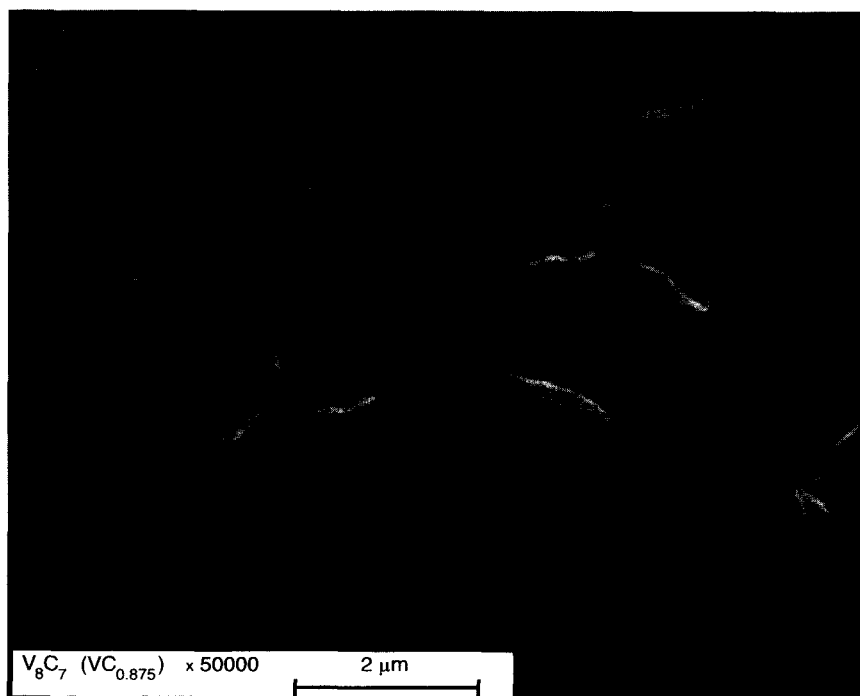


Fig. 8 Morphology of particles of an aged powder of the VC_{0.875} carbide (× 50000 magnification). (From Refs. [15,16].) Particles about 1 μm in size represent a set of nanocrystallites having the shape of bent plate disks 400 to 600 nm in diameter and about 15–20 nm thick.

carbide at a temperature of 2000 K and a pressure of 20–25 MPa.^[16] The size of grains in sintered samples was 10 to 60 μm . The sintered samples were annealed at 1370 K for 2 hr and then were cooled slowly (at a rate of 100 K hr^{-1}) to 300 K or quenched from 1500 to 300 K. The maximum thermal treatment temperature approached the disorder–order transformation temperature T_{trans} and was equal to $T_{\text{trans}} \pm 100$ K. Along with structural reflections, additional weak reflections corresponding to the V_8C_7 -ordered phase appeared in the X-ray diffraction spectrum after both annealing and quenching.

The V_8C_7 -ordered phase was formed thanks to the disorder–order transformation. The grain size of the basic phase did not change upon ordering, but superstructural lines widened because of a small size of domains of the ordered phase. Superstructural reflections widened most for the sample, which was quenched from 1500 K. This means that domains of the ordered phase were smallest in that sample. The size of domains was about 130 nm in annealed samples and ~ 20 nm in samples quenched from 1500 K.

Thus the nanostructure in the bulk nonstoichiometric vanadium carbide represented a set of domains of an ordered phase and was formed thanks to the $\text{VC}_{0.875} \rightarrow \text{V}_8\text{C}_7$ disorder–order phase transformation.

Ordering is an efficient method for creation of a nanostructure in bulk and powder nonstoichiometric compounds. Disorder–order transformations, which are accompanied by changes of the volume, can be used to produce a nanostructure not only in nonstoichiometric compounds, but also in substitutional solid solutions, including alloys.

Compaction of Nanopowders

A method for production of bulk nanocrystalline substances, which was proposed by researchers^[17] in 1981–1986, has been well known. This technology uses the method of evaporation and condensation for production of nanoparticles, which are deposited on the cold surface of a rotating cylinder. Evaporation and condensation are realized in a rarefied inert gas, mostly helium. Particles of the surface condensate are usually faceted. The deposited condensate is removed from the cylinder surface using a special scraper and is placed in a collector. The inert gas is pumped out and the nanocrystalline powder is compacted in a vacuum first at a pressure of ~ 1 GPa and finally at a pressure up to 10 GPa. Bulk nanomaterials prepared by this method contain particles of an average size D from 1–2 to 80–100 nm and have a relative density of 85–97% depending on evaporation and condensation conditions. The absence of contact with the ambient atmosphere during synthesis and compaction of the nanopowder precludes contamination of the bulk samples. For production of bulk nanocrystalline oxides and nitrides,

the metal is evaporated to an oxygen- or nitrogen-containing atmosphere.

Porosity of nanoceramics prepared by compaction of powders is connected with triple junctions of crystallites. It may be decreased and made more uniform by compaction of nanopowders and their sintering at relatively low temperatures $T \leq 0.5T_m$ (T_m being the melting point).

The magnetic pulsed method^[18] is reduced to intensive dry pressing of powders. Pulsed compression waves cause vigorous heating of the powder thanks to the quick release of energy during friction of particles. When the size of particles is small ($D \leq 0.3 \mu\text{m}$), their heating time is shorter than the characteristic length of pulsed compression waves (1–10 μsec). If compression wave parameters are chosen properly, it is possible to realize dynamic hot pressing of nanopowders thanks to their high surface energy. The magnetic pulsed method provides denser samples than steady-state pressing at nearly equal pressures (Fig. 9). Short-time heating reduces recrystallization caused by high temperatures and helps preserving a small size of particles.

A promising method for compaction of ceramic nanopowders without plasticizers is dry cold ultrasonic pressing.^[19] Ultrasound decreases interparticle friction, breaks agglomerates and coarse particles, and improves the volume distribution of particles. Therefore the density of the compact is enhanced, the growth of grains during sintering is limited, and the nanostructure is preserved. Ultrasonic pressing of nanopowders is especially efficient in the production of intricate articles, such as bushes, gear wheels, and spirals (Fig. 10).

Ceramic nanomaterials are sintered using heating with millimeter-range superhigh frequency (SHF) radiation.^[20] Volume absorption of the SHF energy ensures one-time uniform heating of the whole sample and provides sintered ceramics having a homogeneous microstructure. The sintering temperature is 1300 to 2300 K. Microwave sintering of compacts, which had a relative density of 70–80% and were made of a TiO_2 nanopowder with an average size of particles equal to 20–30 nm, allowed producing sinters having a relative density of 97–99% and grains 200 to 220 nm in size on the average.

The existing methods for compaction of nanopowders and sintering of bulk nanomaterials already provide high-density intricate articles. However, it has been so far impossible to maintain the same small size of grains in sintered nanomaterials as in initial nanopowders. To keep the size of grains small, one has to decrease the temperature and duration of sintering and perform the sintering operation under a high pressure.

Film and Coating Deposition

Deposition on a cold or heated surface of a substrate allows making films and coatings, i.e., continuous layers

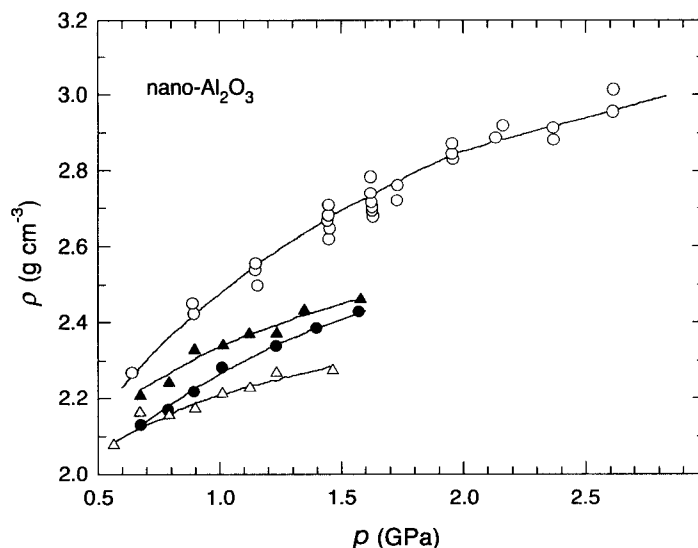


Fig. 9 Pressure dependence of the density ρ of the nanocrystalline oxide $n\text{-Al}_2\text{O}_3$ for steady-state and magnetic pulsed pressing: (1), (2), (3) represent steady-state pressing at temperatures of 300, 620, and 720 K, respectively; (4) represents magnetic pulsed pressing.

of a nanocrystalline substance not more than several micrometers thick. Films may have different compositions and the size of their crystallites may change over a wide interval including the amorphous state and multilayer structures (superlattices). Pressing is not necessary because a bulk layer of a nanomaterial is obtained.

Deposition on a substrate may be realized from vapors, plasma, or a colloid solution. In the case of vapor deposition, a metal is evaporated in a vacuum or an

oxygen- or nitrogen-containing atmosphere and then vapors of the metal or its compound (an oxide or a nitride) are condensed on a substrate. The size of crystallites in the film may be adjusted by varying the evaporation rate and the substrate temperature. Nanostructured films may be produced by deposition from plasma.

Oxide and sulfide semiconductor films are obtained by deposition on a substrate from colloid solutions. Nanostructured films containing nanoparticles of different

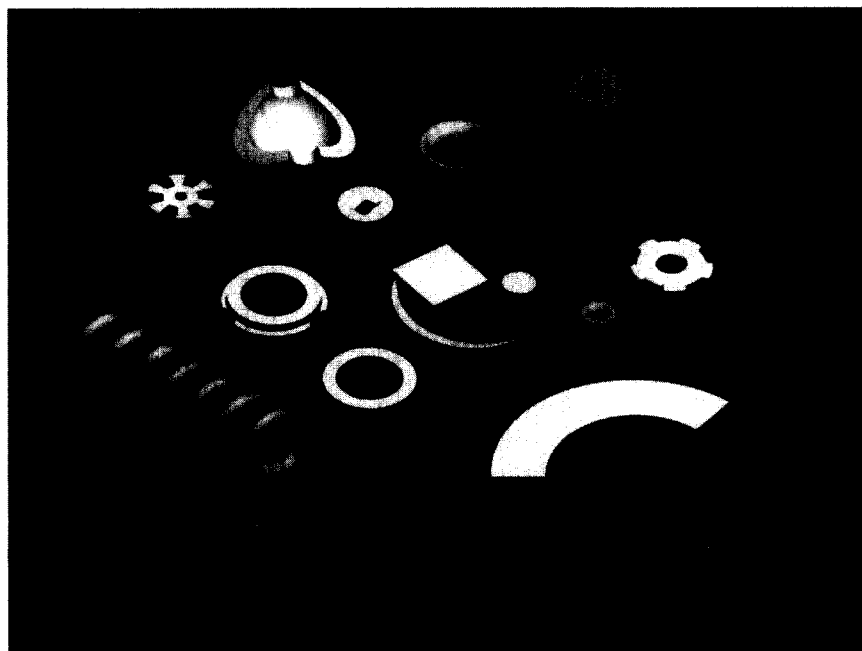


Fig. 10 Ceramic articles synthesized by ultrasonic pressing of nanopowders. (From Ref. [19].)

semiconductors are prepared by the codeposition method. The methods of chemical and physical deposition from a gaseous phase (CVD and PVD) are traditionally used for producing of films.

Nanocrystallization of Amorphous Alloys

Nonporous nanostructured materials are produced by crystallization of amorphous metal alloys. Thin bands of amorphous alloys are made by melt spinning, i.e., quick (at a rate $\geq 10^6$ K sec⁻¹) cooling of the melt on the surface of a rotating disk. Then the amorphous band is annealed to create a nanostructure.

Considerable study currently devoted to crystallization of amorphous alloys in connection with development of soft magnetic materials in Fe-Cu-M-Si-B (M=Nb, Ta, W, Mo, or Zr) systems.^[21] Amorphous alloys of the Fe-Cu-Nb-Si-B system proved to be most successful. Their crystallization at 700–900 K resulted in formation of a uniform nanocrystalline structure. Grains of the α -Fe(Si) phase ~ 10 nm in size and copper clusters about 1 nm in size were uniformly distributed in the amorphous matrix of the alloy.

Crystallization of quickly solidifying amorphous alloys of the Al-Cr-Ce-M (M=Fe, Co, Ni, or Cu) system, which contained over 92 at.% Al, led to formation of a structure including an amorphous phase and Al-rich icosahedral nanoparticles ($D \sim 5$ –12 nm) precipitated in the amorphous phase.^[22] Alloys with this structure possess a high tensile strength (up to 1340 MPa), which approaches the strength of special steels.

Severe Plastic Deformation

Severe plastic deformation applies mostly to plastically deformable materials. In addition to the decrease in the average size of grains to 100–200 nm, it allows producing bulk samples with a nearly pore-free structure, which cannot be prepared by compaction of superfine powders.

The main methods, which are used to considerably refine grains without breakage of samples, are high-pressure torsion and equal-channel angular (ECA) pressing (Fig. 11). The ECA pressing method was proposed in Ref. [23]. As compared with other methods of plastic deformation, this method provides the most uniform structure of substances. The structure and properties of submicrocrystalline materials, which were produced using severe plastic deformation, are described in Ref. [24].

The main feature of the structure of submicrocrystalline materials prepared by deformation methods is nonequilibrium grain boundaries, which are a source of strong stresses. Triple junctions of grains represent one more source of stress. Annealing of submicrocrystalline materials causes changes in their microstructure. Initially, when the annealing temperature equals nearly one-third

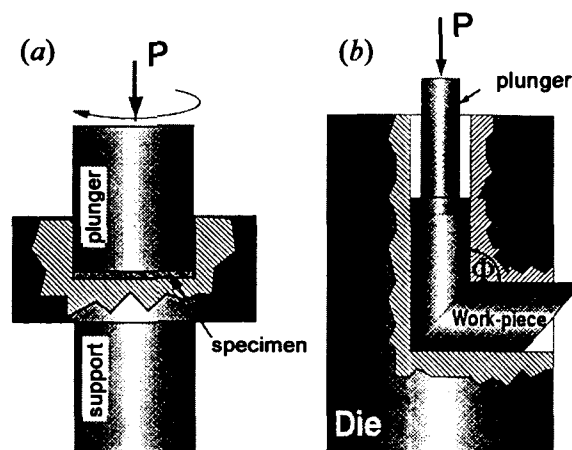


Fig. 11 Schemes of main methods of severe plastic deformation: (From Ref. [24]) (a) high-pressure torsion; (b) equal-channel angular pressing.

of the melting point, stresses are relaxed, grain boundaries acquire a more equilibrium state, and grains grow insignificantly. The further increase in the annealing temperature and time is followed by collective recrystallization, i.e., coarsening of grains.

The method of severe plastic deformation was used to produce a submicrocrystalline structure in such metals as Cu, Pd, Fe, Ni, and Co, aluminum, magnesium, and titanium alloys, and intermetallics. A bulk nanocrystalline sample with grains ~ 30 –40 nm in size was prepared from a coarse ($D \sim 2$ –5 μm) powder of a nonstoichiometric $\text{TiC}_{0.62}$ titanium carbide by the method of high-pressure torsion.^[18]

MICROSTRUCTURE OF BULK NANOCRYSTALLINE SUBSTANCES

In the simplest case, a nanocrystalline substance, which comprises atoms of one species, includes two components with different structures: grains (crystallites) 5 to 20 nm in size and intercrystalline boundaries up to 1.0 nm long. Crystallites have a similar structure and differ by their orientations and sizes only. The structure of interfaces is determined by the type of interatomic interactions and the mutual orientation of adjacent crystallites. It was thought originally that the intercrystalline substance is characterized by a random location of atoms and the absence of the long- and short-range order.^[17] This state was called a gas-like structure, taking into account the location of atoms only.

Later studies showed that the atomic order on interfaces of nanosubstances approaches the atomic order in coarse-grain polycrystals. An example is a comparative study of the structures of coarse-grain palladium and

nanocrystalline palladium n-Pd, which was prepared by evaporation and condensation. This study demonstrated that widening of diffraction reflections for n-Pd was a result of a small size of crystallites and stresses in grains or on interfaces rather than the gas-like structure of the grain-boundary phase or a large number of vacancies in grains.^[25] Pores were detected only at triple junctions and not on the entire length of the interfaces.^[26] The atomic density on intercrystalline boundaries proved to be nearly equal to its counterpart in crystallites.

According to Ref. [27] the coordination number of the first coordination sphere in an as-prepared n-Pd sample was 5–6% smaller than in coarse-grain palladium. However, almost all atoms were located at lattice sites in n-Pd samples, which were aged at room temperature for several months.^[28] It was found^[27,28] that grain boundaries in an as-prepared bulk n-Pd sample were in the equilibrium state with a small short-range order. This state was unstable even at room temperature and the sample acquired a more ordered state during 120–150 days, while the size of crystallites increased from 12 to 25–80 nm.^[29]

Interfaces in compacted nanocrystalline substances may contain three types of defects:^[2] separate vacancies, vacancy agglomerates or nanovoids at triple junctions, and large voids instead of missing crystallites (Fig. 12).

The annihilation of positrons^[2,30] is the most reliable up-to-date method used for the study of free volumes in nanocrystalline substances. It is sensitive to extremely small concentrations of defects in solids, namely, from

10^{-6} to 10^{-3} defects per atom. The capture of positrons by defects allows using the electron–positron annihilation for analysis of interfaces in nanosubstances.

When a positron emitted from a radioactive source gets into a solid, it quickly loses its velocity and energy, which drops to the value corresponding to the crystal temperature. Then the positron diffuses in the substance in the free (delocalized) state and annihilates from this state in the characteristic lifetime τ_f of about 100 psec. During the time τ_f , the positron may move a distance of about 100 nm in defectless solids. Because the size of grains in a nanosubstance is smaller than the length of the positron diffusion in a defect-free grain, virtually all positrons may reach the grain surface and interfaces. If grains contain defects, which capture positrons, only part of positrons reach the grain boundary. Therefore it is possible to obtain information about intragrain defects. After a positron has been captured by a defect, it annihilates from the localized state in a time exceeding τ_f . The longer the lifetime of a positron in a defect is, the larger is the free volume.

Schaefer^[2] and Würschum et al.^[30] have given considerable study to nanomaterials by the electron–positron annihilation method. Vacancies and nanovoids were detected in nanocrystalline metals Al, Cu, Mo, Pd, Fe, and Ni, nanocrystalline silicon Si and zirconium oxide ZrO_2 , and many other materials. The investigations demonstrated that lifetime spectra of positrons usually contain two strong components and one weak component with intensities I_1 , I_2 , and $I_3 = 1 - I_1 - I_2$, which correspond to the lifetime τ_1 , τ_2 , and τ_3 , respectively (Fig. 12). In nanocrystalline metals, the lifetime τ_1 approaches the lifetime of positrons τ_{1V} in lattice monovacancies of coarse-grain metals. Therefore τ_1 is viewed as the lifetime of positrons in vacancy-like free volumes in grain interfaces (interface vacancies). The size of these vacancies corresponds to one or two missing atoms. The positron lifetime τ_2 characterizes annihilation of positrons in three-dimensional vacancy agglomerates (nanovoids) of the size of about 10 missing atoms. A very long lifetime τ_3 corresponds to annihilation of positrons in large voids of the size of missing crystallites.

Generally, the positron annihilation revealed the following: 1) the lifetime of positrons in nanocrystalline metals is longer than the lifetime τ_f of free delocalized positrons; 2) positrons are captured by monovacancies, vacancy complexes, and voids, whose size approaches the size of crystallites; and 3) free vacancy volumes, which capture positrons at low temperatures, belong to interfaces and not to crystallites.

The microstructure of submicrocrystalline substances, which are synthesized using severe plastic deformation, differs from the microstructure of compacted nanocrystalline substances. The main feature of the structure of submicrocrystalline substances is the presence of randomly misoriented nonequilibrium grain boundaries.

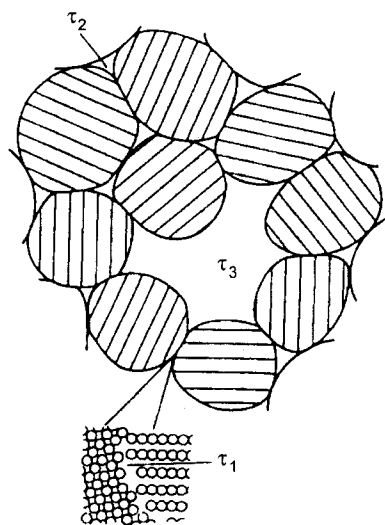


Fig. 12 Two-dimensional schematic model of a nanocrystalline material with microscopic free volumes as detected by positron lifetime spectroscopy: (From Ref. [2]) vacancy-like free volumes (with positron lifetime τ_1) in the interface, nanovoids (agglomerates of about 10 vacancies) at the triple junction of crystallites (τ_2), and a large void (τ_3) of the size of missing crystallites.

Unannealed submicrocrystalline metals and alloys are characterized by extinction contours along grain boundaries, which point to large elastic stresses. Annealing eliminates dislocations from grains, extinction contours vanish, and a stripe contrast, which is typical of the equilibrium state, appears. The relaxation of interfaces is accompanied by growth of grains during annealing.

PROPERTIES OF ISOLATED NANOPARTICLES AND NANOCRYSTALLINE POWDERS

The transition from crystals to nanoparticles is followed by changes in the interatomic distances and lattice constants. For example, when the size of Ag and Au particles decreases from 40 to 10 nm, the lattice constant becomes $\sim 0.1\%$ smaller. When the size of Si particles decreases from 10 to 3 nm, the lattice constant increases by 1.1%. The ambiguity of the dimensional effect may be a result of adsorption of impurities or different chemical compositions of particles. One more possible reason is the structural transformations, which are caused by the decrease in the particle size. Reliable experiments did not reveal shrinkage of the lattice constant as the particle size decreased to 10 nm, whereas shortening of interatomic distances for particles of smaller sizes is real enough as compared with bulk substances.

The most probable reason why the lattice constant of small particles changes as compared with its counterpart in a macroscopic substance consists in uncompensated interatomic bonds of surface atoms and hence the surface relaxation. In the case of nanoparticles, the surface relaxation is a maximum on the surface, decreases toward the center of the particle, and may prove to be oscillating under certain conditions. Thus the lattice constant may either increase or decrease as the size of nanoparticles diminishes.^[7,8]

The melting temperature T_m drops nonlinearly with decreasing size of small particles of Pb, Sn, Bi, In, Ga, Cu, Ag, Au, and Al. For example, the maximum decrease in the melting temperature of Sn, Ga, and Hg clusters ~ 1 nm in size was 152, 106, and 95 K, respectively.^[4] When the radius of CdS colloid nanoparticles was reduced from 4 to 1 nm, T_m dropped nearly by 800 K.^[31] According to Refs. [4] and [8], melting temperatures of bulk crystals and small particles > 10 nm in size differ insignificantly. The melting temperature decreases when the size of nanoparticles becomes less than 10 nm.

Differences in thermodynamic properties of nanoparticles and a bulk substance are a result of changes in the phonon spectrum. The phonon spectrum of small particles contains low-frequency modes, which are absent in spectra of bulk crystals. The phonon spectrum of

nanoparticles is limited by some minimum frequency on the side of low-frequency vibrations. No such limitation exists for bulk samples. Specific features of the vibration spectrum of nanoparticles affect the low-temperature heat capacity in the first place.

A theoretical analysis,^[32] which took into account the quantum-size effect, showed that the low-temperature region ($T \rightarrow 0$) has some temperature T_0 , below which the nanoparticle heat capacity $C_v(r)$ is smaller than the heat capacity C_v of a bulk crystal. At $T > T_0$, the difference $\Delta C = C_v(r) - C_v$ becomes positive, reaches a maximum, and, as the temperature rises further, turns to zero. The difference of the heat capacities $\Delta C = C_v(r) - C_v \rightarrow 0$ with increasing size r of the particle. These conclusions agree with experimental data.^[33] The heat capacity of Ag nanoparticles 10 nm in size had the quantum-size effect in a magnetic field with $B = 6$ T: at $T < 1$ K and $T > 1$ K, the heat capacity of Ag nanoparticles was lower and higher than the heat capacity of bulk silver, respectively. In the absence of the magnetic field, the heat capacity of colloid silver nanoparticles was higher than the heat capacity of bulk Ag over the whole temperature interval studied (Fig. 13).

An examination of phonon densities for coarse-grained Ni and a nanocrystalline nickel powder with particles ~ 10 nm in size showed that the density of phonon states increased in n-Ni as compared with coarse-grained Ni at energies lower than 15 meV.^[34]

Specific features of magnetic properties of nanoparticles are connected with discreteness of electron and phonon states. In particular, the Curie paramagnetism of a nanoparticle can overlap the Pauli paramagnetism at low temperatures. For example, magnetic susceptibility of lithium nanoparticles of diameter 3.2 nm corresponds to the Pauli paramagnetism at high temperatures and obeys the Curie law at low temperatures.^[4] Hg₁₃ clusters are weak paramagnetics in a magnetic field of up to 15 kOe independently of temperature. In a field with $H > 20$ kOe, susceptibility of Hg₁₃ clusters increases to large paramagnetic values at temperatures below 80 K, although mercury is a diamagnetic.^[4]

The phenomenon of superparamagnetism is connected with the small size of ferromagnetic particles. When some critical size D_c is reached, ferromagnetic particles turn to single-domain ones, and, simultaneously, the coercive force H_c becomes a maximum. As the particle size diminishes further, the coercive force drops abruptly to zero as a result of transition to the superparamagnetic state. Typical ferromagnetics acquire the superparamagnetic state when the particle size is less than 1–10 nm.

When the size of Fe nanoparticles decreases from 80 to 8–10 nm, the coercive force H_c increases almost three times. The dimension dependence of H_c for Ni nanoparticles exhibits a maximum corresponding to nanoparticles

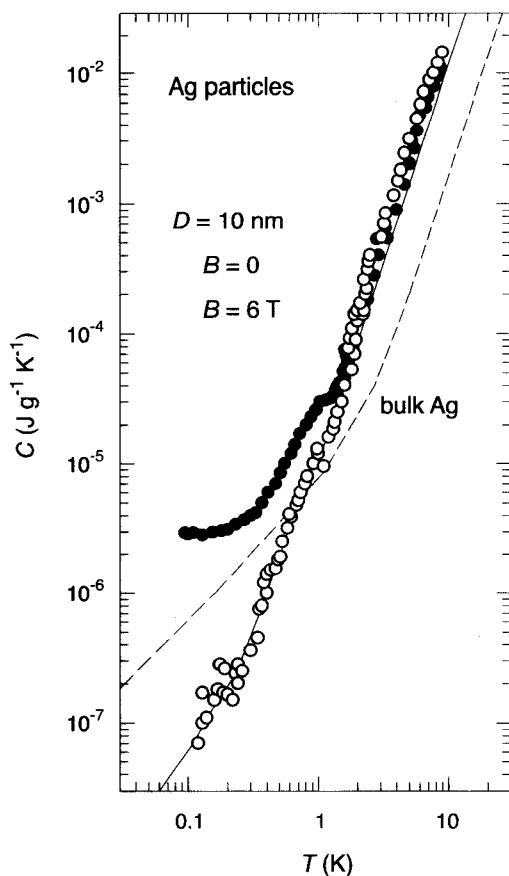


Fig. 13 Specific heat capacity C of colloidal Ag with $D=10$ nm at $T \leq 10$ K. Measurements were made in the absence of a magnetic field and in a magnetic field $B=6$ T. The dashed line shows the specific heat capacity of bulk coarse-grained silver.

15 to 35 nm in diameter. As the particle size diminishes from 15 to 12 nm, H_c decreases nearly 5 times.^[35] An analysis of the saturation magnetization I_s for bulk Ni and a nanocrystalline Ni powder ($D=12, 22$ and 100 nm)^[36] showed that refinement of particles to 12 nm caused an almost twofold decrease in the I_s value as compared with bulk Ni.

Optical dimensional effects show themselves for nanoparticles whose size is smaller than the radiation wavelength and does not exceed 10–15 nm.^[37] When fine-grain metal films absorb light, the visible part of the spectrum contains peaks, which are absent in the spectra obtained for bulk metals. For example, granulated films of Au particles 4 nm in diameter have a maximum absorption at $\lambda=560$ –600 nm. Absorption spectra of Ag, Cu, Mg, In, Li, Na, and K nanoparticles also contain maxima in the optical range.^[4] Differences in absorption spectra of nanoparticles and bulk metals are explained by the fact that the imaginary part of dielectric permeability is inversely proportional to the particle size. The particle

size determines the shape of the low-frequency edge and the absorption bandwidth.

The size of semiconductor nanoparticles is comparable with the Bohr radius of excitons in a macroscopic crystal: the exciton radius changes over broad limits from 0.7 nm for CuCl to 10 nm for GaAs. The decrease in the size of nanoparticles causes displacement of the exciton absorption band to the high-frequency region (“blue” shift). The blue shift is observed for CdS nanoparticles with $D \leq 10$ –12 nm. When the size of ZnO, ZnS, CdS, and CdSe nanoparticles decreases, their luminescence spectra are displaced to the short-wave region.

EFFECT OF THE GRAIN SIZE AND INTERFACES ON PROPERTIES OF BULK NANOSUBSTANCES

Properties of bulk nanomaterials depending on the grain size and the state of grain boundaries have been analyzed in reviews.^[6,38,39]

At 300 K, the microhardness of bulk nanocrystalline substances is usually several times larger than H_V of coarse-grained substances. The growth of H_V was observed with decreasing size of n-Fe and n-Ni grains.^[41] The microhardness H_V of nanocrystalline n-Cu copper ($D \sim 16$ nm) is ~ 2.5 times larger than that of copper with grains 5 μm in size. However, as the size of n-Cu grains diminishes from 16 to 8 nm, H_V decreases by $\sim 25\%$. The decrease in H_V is also observed when n-Pd grains are refined from 13 to 7 nm. The microhardness H_V of Ni-P, TiAlNb, TiAl, and NbAl₃ nanocrystalline alloys drops as the grain size decreases from 60–100 to 6–10 nm.

In a general case, the microhardness of nanosubstances grows as the grain size decreases to some D_c value and drops at $D < D_c$. Mechanical and elastic properties of nanocrystalline metals are determined not only by a small size of grains, but also by the state of interfaces. Therefore contradictory results on the dimension dependence of the microhardness may be due to different structures of interfaces.

Strength properties of nanosubstances are enhanced with decreasing size of grains. The yield stress of nanocrystalline Pd ($D=5$ –15 nm) and Cu ($D=25$ –50 nm) is 2–3 times higher than the yield stress of coarse-grained metals.^[40] The tensile strength of nanocrystalline metals is 1.5–8 times larger than that of coarse-grained metals.^[40,41]

At temperatures from 150 to 300 K, the heat capacity C_p of n-Pd ($D=6$ nm) and n-Cu ($D=8$ nm) is 30–50% and $\sim 10\%$ higher than the heat capacity of coarse-grained bulk Pd and Cu, respectively. In the interval of 0.06 to 10.0 K, the low-temperature heat capacity of compacted nanocrystalline copper n-Cu with grains 6.0 and 8.5 nm in

Table 1 Comparison of heat capacity C_p ($\text{J mol}^{-1} \text{K}^{-1}$) for the nanocrystalline, amorphous, and coarse-grained polycrystalline states of different substances

Material	State					
	Nanocrystalline			Amorphous	Coarse-grained	
	Synthesis method ^a	Crystallite size D (nm)	C_p	C_p	C_p	T (K)
Pd	1	6	37	27	25	250
Cu	1	8	26	—	24	250
Ru	2	15	28	—	23	250
$\text{Ni}_{0.8}\text{P}_{0.2}$	3	6	23.4	23.4	23.2	250
Se	3	10	24.5	24.7	24.1	245

^a1: Compaction of ultrafine powders prepared by evaporation; 2: ball milling; 3: crystallization from the amorphous state.

Source: Ref. [43].

size proved to be 5–10 times larger than the heat capacity of coarse-grained copper. Measurements of the heat capacity of amorphous, nanocrystalline, and coarse-grained selenium Se over the temperature interval from 220 to 500 K^[42] revealed a small increase in the heat capacity of bulk nanocrystalline n-Se as compared with coarse-grained Se at $T < 375$ K. A comparison of the heat capacity of substances in nanocrystalline, amorphous, and coarse-grained states^[43] showed that the heat capacity of samples prepared by compaction of nanopowders is largely different from the heat capacity of substances in the coarse-grain state (Table 1). Oppositely, this difference does not exceed 2% for samples prepared by crystallization from the amorphous state. One may think that most of the excess heat capacity of compacted nanomaterials is a result of a large surface area of interfaces, structural distortions, and impurities.

The thermal expansion coefficient α is proportional to the heat capacity. Therefore the coefficient α of bulk nanosubstances should be higher than α of coarse-grained polycrystals. Indeed, the coefficient α of nanocrystalline copper n-Cu with grains 8 nm in size on the average is twice as large as α of coarse-grained copper.^[44]

A large surface area of interfaces and a high concentration of defects determine an intensive scattering of charge carriers in nanomaterials. A considerable increase in electroresistivity ρ of nanocrystalline Cu, Pd, Fe, and Ni and various alloys with decreasing size of grains has been noted by many researchers. For example, at temperatures $0 < T \leq 275$ K, electroresistivity of n-Cu ($D=7$ nm) is 7 to 20 times larger than ρ of common coarse-grained copper.

The effect of the nanostate on magnetic properties of paramagnetics is well pronounced, e.g., in palladium (Fig. 14).^[8] At 300 K, susceptibilities of nanocrystalline n-Pd and the initial coarse-grained palladium differ by 8%. According to Ref. [8] such a considerable variation of

the susceptibility is a result of the presence of intragrain vacancy complexes in n-Pd, which change the density of electron states at the Fermi level.

The majority of studies into magnetic properties of bulk nanosubstances have dealt with ferromagnetic metals and alloys. A study of submicrocrystalline Ni^[45] has confirmed that the coercive force of plastically deformed ferromagnetics is several times larger than H_c of initial

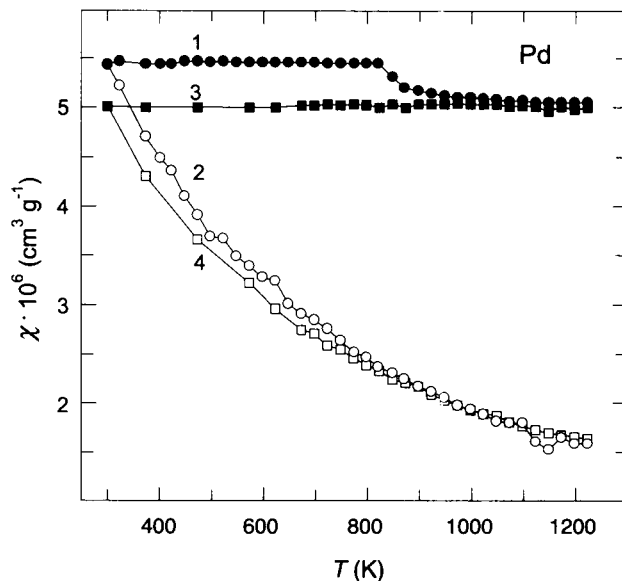


Fig. 14 Magnetic susceptibility χ of nanocrystalline n-Pd and coarse-grained palladium: (From Ref. [8]) (1) annealing $\chi(300, T)$ and (2) temperature $\chi(T)$ dependences of the susceptibility for n-Pd; (3) annealing $\chi(300, T)$ and (4) temperature $\chi(T)$ dependences of the susceptibility for the initial coarse-grained Pd. The annealing dependences $\chi(300, T)$ of the susceptibility (curves 1 and 3) were measured at 300 K after annealing at a temperature T and cooling to 300 K.

metals. However, annealing of submicrocrystalline Ni at $T \leq 470$ K causes a decrease in the coercive force, while the grain size remains unchanged. Annealing at higher temperatures leads to a decrease in H_c and an increase in the grain size. Therefore a large coercive force of submicrocrystalline metals and alloys is equally determined by a nonequilibrium state of interfaces on the one hand and a small size of grains on the other hand. Relaxation of interfaces during annealing and growth of grains cause a decrease in H_c .

CONCLUSION

Studies performed in recent decades have considerably improved our understanding of the effects related to the size of grains (crystallites) in solids. For a long time, studies have been focused on small particles (nanoclusters) whose properties are intermediate between properties of isolated atoms and polycrystalline solids. The advent of methods for production of compact materials having an extremely fine-grain structure with nanometer-sized grains provided conditions for the study of the structure and properties of solids in the nanocrystalline state. Each of those methods has its virtues and drawbacks, and neither of them is universal because each is applicable to a certain range of substances. Because of their specific structure, properties of nanocrystalline substances differ considerably from those of usual polycrystals. An analysis of the available experimental data shows that not only the grain size (as in isolated nanoparticles), but also the structure and the state of interfaces (grain boundaries) play a significant role in a nanocrystalline solid. The separation of surface effects (connected with interfaces) and volume effects (related to the size of particles) is very important for the theoretical interpretation of the experimental results obtained for isolated nanoparticles and bulk nanocrystalline materials.

Extensive studies of nanocrystalline substances and materials have led to appearance of new sciences, namely, nanocrystalline solid-state physics and chemistry. Therefore it is possible to establish tight contacts between nanomaterials and nanotechnologies, which will present the main motive force of the scientific and technological progress in the 21st century.

REFERENCES

- Gleiter, H. Materials with ultrafine microstructure: Retrospectives and perspectives. *Nanostruct. Mater.* **1992**, *1* (1), 1–19.
- Schaefer, H.-E. Interfaces and Physical Properties of Nanostructured Solids. In *Mechanical Properties and Deformation Behavior of Materials Having Ultrafine Microstructure*; Nastasi, M.A., Parkin, D.M., Gleiter, H., Eds.; Kluwer Academic Press: Dordrecht, Netherlands, 1993; 81–106.
- Siegel, R.W. What do we really know about the atomic-scale structures of nanophase materials? *J. Phys. Chem. Solids* **1994**, *55* (10), 1097–1106.
- Petrov, Yu.I. *Clusters and Small Particles*; Nauka: Moscow, 1986 (in Russian).
- Andrievskii, R.A. The synthesis and properties of nanocrystalline refractory compounds. *Russ. Chem. Rev.* **1994**, *63* (5), 411–428.
- Gusev, A.I. Effects of the nanocrystalline state in solids. *Phys. Uspekhi* **1998**, *41* (1), 49–76.
- Gusev, A.I. *Nanocrystalline Materials: Preparation and Properties*; Ural Division of the Russ. Acad. Sci.: Yekaterinburg, 1998 (in Russian).
- Gusev, A.I.; Rempel, A.A. *Nanocrystalline Materials*; Nauka-Fizmatlit: Moscow, 2000 (in Russian).
- Feynman, R.P. There is plenty of room at the bottom: An invitation to enter a new field of physics. <http://www.zyvex.com/nanotech/feynman.html>.
- Kroto, H.W.; Heath, J.R.; O'Brien, S.C.; Curl, R.F.; Smalley, R.E. C_{60} : Buckminsterfullerene. *Nature* **1985**, *318* (6042), 162–163.
- Guo, B.C.; Kerns, K.P.; Castleman, A.W. $Ti_8C_{12}^+$ -metallo-carbohedrenes: A new class of molecular clusters? *Science* **1992**, *255* (5050), 1411–1413.
- Kotov, Yu.A.; Yavorski, N.A. Study of particles forming at electric explosion of conductors. *Fiz. Him. Obrab. Mater.* **1978**, (4), 24–29 (in Russian).
- Nersisyan, H.H.; Lee, J.H.; Won, C.W. Self-propagating high-temperature synthesis of nano-sized titanium carbide powder. *J. Mater. Res.* **2002**, *17* (11), 2859–2864.
- Gusev, A.I.; Rempel, A.A.; Magerl, A.J. *Disorder and Order in Strongly Nonstoichiometric Compounds: Transition Metal Carbides, Nitrides and Oxides*; Springer: Berlin, 2001.
- Rempel, A.A.; Gusev, A.I. Nanostructure and atomic ordering in vanadium carbide. *JETP Lett.* **1999**, *69* (6), 472–478.
- Gusev, A.I.; Tulin, A.A.; Lipatnikov, V.N.; Rempel, A.A. Nanostructure of dispersed and bulk nonstoichiometric vanadium carbide. *Russ. J. Gen. Chem.* **2002**, *72* (7), 985–993.
- Gleiter, H. Nanocrystalline materials. *Prog. Mater. Sci.* **1989**, *33* (4), 223–315.
- Ivanov, V.V.; Kotov, Yu.A.; Samatov, O.M.; Böhme, R.; Karow, H.U.; Schumacher, G. Synthesis and dynamic compaction of ceramic nanopowders

- by techniques based on electric pulsed power. *Nanostruct. Mater.* **1995**, *6* (1–4), 287–290.
19. Khasanov, O.L.; Dvilis, E.S.; Pokholkov, Yu.P.; Sokolov, V.M. Mechanisms of ultrasonic pressing of ceramic nanopowders. *J. Adv. Mater.* **1999**, *5* (3), 69–75.
 20. Bykov, Yu.; Eremeev, A.; Flyagin, V.; Kaurov, V.; Kuftin, A.; Luchinin, A.; Malygin, O.; Plotnikov, I.; Zapevalov, V. The gyrotron system for ceramics sintering. *Ceram. Trans.* **1995**, *59*, 133–140.
 21. Yoshizawa, Y.; Oguma, S.; Yamauchi, K. New iron-based soft-magnetic alloys composed of ultrafine grain structure. *J. Appl. Phys.* **1988**, *64* (10), 6044–6046.
 22. Inoue, A. Preparation and novel properties of nanocrystalline and nanoquasicrystalline alloys. *Nanostruct. Mater.* **1995**, *6* (1–4), 53–64.
 23. Segal, V.M. Materials processing by simple shear. *Mater. Sci. Eng., A* **1995**, *197* (2), 157–164.
 24. Valiev, R.Z.; Aleksandrov, I.V. *Nanostructured Materials Obtained by Severe Plastic Deformation*; Logos: Moscow, 2000 (in Russian).
 25. Fitzsimmons, M.; Eastman, J.A.; Müller-Stach, M.; Wallner, G. Structural characterization of nanometer-sized crystalline Pd by X-ray-diffraction techniques. *Phys. Rev., B* **1991**, *44* (6), 2452–2460.
 26. Ishida, Y.; Ichinose, H.; Kizuka, T.; Suenaga, K. High-resolution electron microscopy of interfaces in nanocrystalline materials. *Nanostruct. Mater.* **1995**, *6* (1–4), 115–124.
 27. Babanov, Yu.A.; Blaginina, L.A.; Golovshchikova, I.V.; Haubold, T.; Boscherini, F.; Mobilio, S. Defects in nanocrystalline palladium. *Phys. Met. Metallogr.* **1997**, *83* (4), 444–451.
 28. Löffler, J.; Weissmüller, J.; Gleiter, H. Characterization of nanocrystalline palladium by x-ray atomic density distribution functions. *Nanostruct. Mater.* **1995**, *6* (5–8), 567–570.
 29. Weissmüller, J.; Löffler, J.; Kleber, M. Atomic structure of nanocrystalline metals studied by diffraction techniques and EXAFS. *Nanostruct. Mater.* **1995**, *6* (1–4), 105–114.
 30. Würschum, R.; Greiner, W.; Schaefer, H.-E. Preparation and positron lifetime spectroscopy of nanocrystalline metals. *Nanostruct. Mater.* **1993**, *2* (1), 55–62.
 31. Goldstein, A.N.; Echer, C.M.; Alivisatos, A.P. Melting in semiconductor nanocrystals. *Science* **1992**, *256* (2062), 1425–1427.
 32. Nonnenmacher, Th.F. Quantum size effect on the specific heat of small particles. *Phys. Lett.* **1975**, *51A* (4), 213–214.
 33. Goll, G.; Löhneyen, H. Specific heat of nanocrystalline and colloidal noble metals at low temperatures. *Nanostruct. Mater.* **1995**, *6* (5–8), 559–562.
 34. Trampenau, J.; Bauszus, K.; Petry, W.; Herr, U. Vibrational behaviour of nanocrystalline Ni. *Nanostruct. Mater.* **1995**, *6* (5–8), 551–554.
 35. Daroczi, L.; Beke, D.I.; Posgay, G.; Kis-Varga, M. Magnetic properties of ball milled nanocrystalline Ni and Fe. *Nanostruct. Mater.* **1995**, *6* (5–8), 981–984.
 36. Yao, Y.D.; Chen, Y.Y.; Hsu, C.M.; Lin, H.M.; Tung, C.Y.; Tai, M.F.; Wang, D.H.; Wu, K.T.; Suo, C.T. Thermal and magnetic studies of nanocrystalline Ni. *Nanostruct. Mater.* **1995**, *6* (5–8), 933–936.
 37. Bohren, C.F.; Huffman, D.R. *Absorption and Scattering of Light by Small Particles*; Wiley-Interscience: New York, 1998.
 38. Andrievskii, R.A.; Glezer, A.M. Size effects in nanocrystalline materials: I. Structure characteristics, thermodynamics, phase equilibria, and transport phenomena. *Fiz. Met. Metalloved.* **1999**, *88* (1), 50–73.
 39. Andrievskii, R.A.; Glezer, A.M. Size effects in nanocrystalline materials: II. Mechanical and physical properties. *Fiz. Met. Metalloved.* **2000**, *89* (1), 91–112 (in Russian).
 40. Neiman, G.W.; Weertman, J.R.; Siegel, R.W. Mechanical behavior of nanocrystalline Cu and Pd. *J. Mater. Res.* **1991**, *6* (5), 1012–1027.
 41. Siegel, R.W.; Fougere, G.E. Mechanical properties of nanophase metals. *Nanostruct. Mater.* **1995**, *6* (1–4), 205–216.
 42. Sun, N.X.; Lu, K. Heat capacity comparison among the nanocrystalline, amorphous and coarse-grained polycrystalline states in elemental selenium. *Phys. Rev., B* **1996**, *54* (9), 6058–6061.
 43. Rupp, J.; Birringer, R. Enhanced specific-heat-capacity (cp) measurements (150–300 K) of nanometer-sized crystalline materials. *Phys. Rev., B* **1987**, *36* (15), 7888–7890.
 44. Birringer, R.; Gleiter, H. Nanocrystalline Materials. In *Encyclopedia of Material Science and Engineering*; Cahn, R.W., Ed.; Pergamon Press: Oxford, 1988; Suppl. Vol. 1, 339–349.
 45. Mulyukov, Kh.Ya.; Korznikova, G.F.; Abdulov, R.Z.; Valiev, R.Z. Magnetic hysteresis properties of submicron grained nickel and their variation upon annealing. *J. Magn. Magn. Mater.* **1990**, *89* (1), 207–213.

Nanocrystallization

John H. Perepezko

University of Wisconsin, Madison, Wisconsin, U.S.A.

INTRODUCTION

This discussion focuses on the development of nanostructured materials through controlled primary crystallization reactions of amorphous alloys. The nanocrystalline state is at the forefront of study in a variety of disciplines involving condensed matter. In broad terms the main activities can be classified into material synthesis strategies, property measurement and evaluation, applications, and computer simulation and modeling. A key attribute of the nanocrystalline state that offers a broad attraction for many disciplines is derived from the nanometer length scale. At this length scale the chemical, biological, physical, mechanical, and structural properties and performance of materials are susceptible to significant changes during synthesis,^[1] and the current computational capabilities allow for effective simulation and analysis of nanocrystalline assemblies.^[2]

The principles that govern the kinetics of microstructural evolution apply directly to other devitrification reactions that yield nanostructured intermetallic phases and quasi-crystalline phases that are also promising in terms of their structural and functional performance. Some of the key issues concerning synthesis and stability are illustrated from the observed behavior in specific amorphous alloys, but the discussion also applies to other similar alloy systems.

OVERVIEW

The nanocrystalline state, where the microstructural size scales are in the 1- to 100-nm range, can be synthesized by a variety of processing routes starting with the vapor, liquid, or solid state.^[1] Although it may be expected that the final nanocrystalline state is independent of the processing route, in practice this is not the case. For example, for deposition from the vapor at the high rates that promote nanocrystalline grain sizes, residual impurities or entrapped gas can be present in the deposit. Similarly, from an initial solid, the nanocrystalline state is often achieved by the mechanical milling of powders. During subsequent consolidation of powders to a bulk form, it is common to incorporate impurities from the medium used for milling and to retain a residual porosity.^[3] The attainment of nanocrystalline structures from

the liquid or vapor requires the attainment of a high crystal nucleation rate, which in turn is promoted by a large undercooling before the onset of crystallization. Actually, there are two pathways that may be followed to achieve the high crystal nucleation density.^[4] If a liquid is rapidly quenched at a rate that happens to coincide with the conditions for a high nucleation rate a nanocrystalline structure is possible by direct quenching.^[5] However, under most conditions of rapid quenching it is difficult to control the processing and the reproducibility. Instead, a direct cooling to an amorphous state and a subsequent low-temperature crystallization treatment is usually preferred as a method of achieving reproducible nanostructure synthesis including the fabrication of nanostructures in bulk sample volumes.^[6-8]

The classes of metallic glasses that provide the most effective routes to nanocrystallization are closely related to two important aspects of solidification that involve kinetic competition: 1) avoidance of crystallization upon cooling of the liquid and 2) the control of crystallization upon heating of the glass. Although there are connections between these aspects, including the common underlying important role of melt undercooling as a measure of liquid metastability, in each case the controlling reactions occur under regimes of different kinetic constraints.^[9] In addition to the closed-system methods involving liquid or vapor quenching, it is recognized that open systems involving continuous deformation^[10] or irradiation^[11] can drive a material toward nanocrystallinity and in some cases to an amorphous structure. In this case, the stored energy due to defects, grain refinement, and solute supersaturation is a measure of the level of metastability that is crucial to consider in the analysis of amorphization and the development of nanostructured microstructures.^[12]

NANOCRYSTALLIZATION REACTIONS

The crystallization behavior of amorphous materials is of central importance in the synthesis of nanostructured materials. The reaction pathways that are operative during crystallization must be identified and controlled to develop successful strategies for the consolidation of amorphous powders or ribbons that can be processed into bulk nanostructured solids. Moreover, the control of the reaction path

during crystallization provides for the option to develop nanoscale structures with different phase selection.

The different reaction paths and product selection options are identified in Fig. 1, which illustrates schematically the free energy relationships between an initial amorphous phase that is considered as an undercooled liquid solution and several crystalline product phases that include stable α and β phases and a metastable γ phase.^[13,14] Within the alloy composition ranges that are usually favored for glass formation there are several types

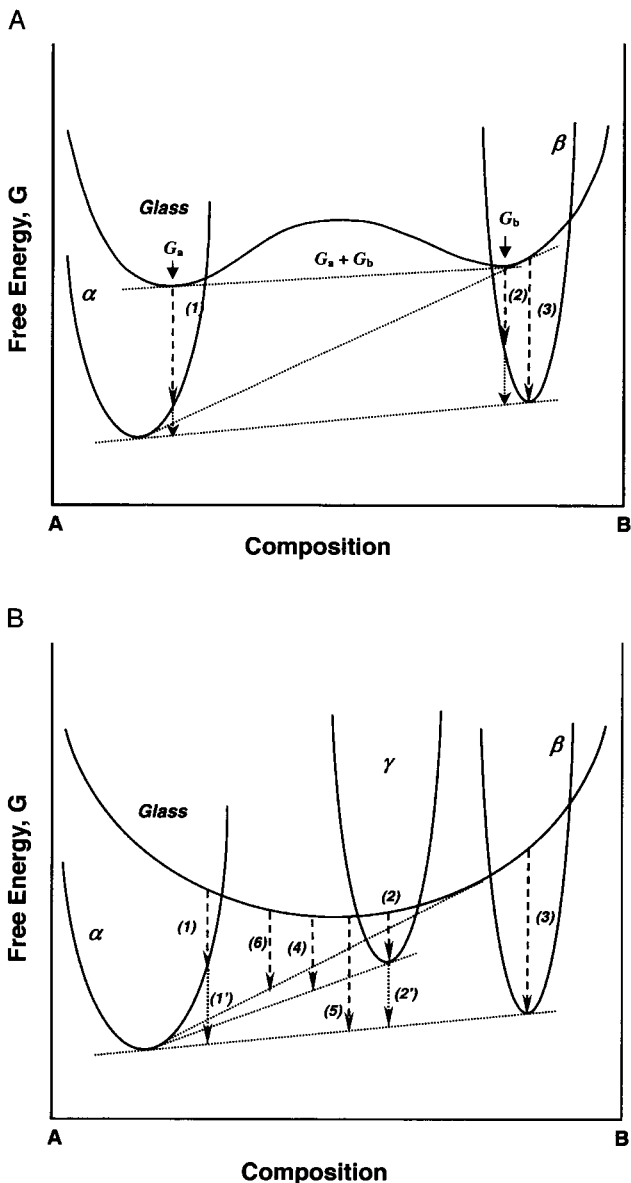


Fig. 1 Schematic free energy vs. composition diagrams illustrating some of the possible nanocrystallization reactions of an amorphous phase. (A) reaction pathways for an alloy with a negative heat of mixing and a metastable γ phase. (B) reaction pathways for an alloy with a positive heat of mixing.

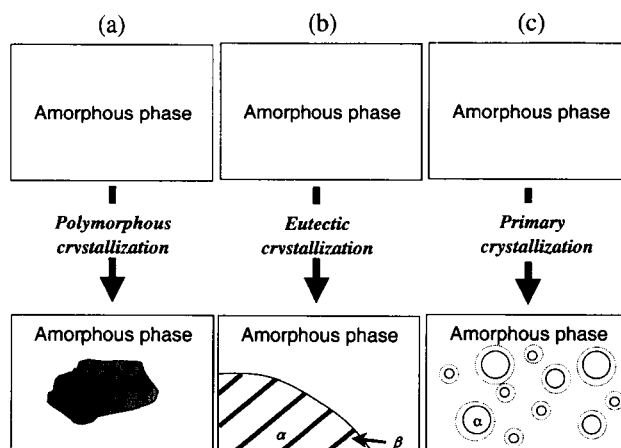


Fig. 2 Schematic illustration of the characteristic microstructural morphologies that develop during nanocrystallization by (a) polymorphic, (b) eutectic, and (c) primary phase reactions. In (c) the dotted curve around primary phase nanocrystals denotes the extent of the solute diffusion field.

of crystallization reactions that can be used to develop nanocrystalline structures during controlled heating or isothermal reaction. One of the simplest reactions is the direct transformation from the glass to a single-phase crystal without composition change as illustrated in Fig. 1A and b by pathways (1) and (2) for either stable or metastable initial product phases. The composition invariant or polymorphic reaction can yield metastable structures such as supersaturated solid solution phases or metastable intermediate phases that can undergo further transformation that is indicated by pathways (1') and (2') in Fig. 1A and b. With primary crystallization, a single phase is the initial product, but the reaction proceeds with a partitioning of solute to yield a solute lean primary crystal and a residual amorphous phase matrix that is enriched in solute.^[6,15-18] The kinetics of primary crystallization is evidently related to the rate of solute diffusion in the amorphous matrix that is necessary to dissipate the solute that is rejected during primary crystal growth.^[19] It is also apparent that primary crystallization does not result in a stable equilibrium product structure that is indicated by the compositions α_e and β_e in Fig. 1A and B. To complete the primary crystallization, a subsequent multiphase crystallization develops either from the nucleation site provided by the primary crystal or directly from the amorphous phase. For example, with eutectic crystallization that is indicated by pathway (3) in Fig. 1A, the product phases (i.e., α and β) often develop by a coupled growth and appear with a lamellar or rod type of regular morphology in a spherulitic pattern.^[8,19] In this case the synthesis of a nanoscale microstructure requires a high density of α and β colonies with an ultrafine lamellar spacing. A schematic illustration of the characteristic microstructural morphologies associated with each of the nanocrystallization

reactions is provided in Fig. 2. Often, under high-undercooling conditions metastable phase reactions can develop as a precursor to the formation of stable crystallization products. For example, as indicated in Fig. 1B, the undercooled liquid or amorphous phase can undergo a phase separation reaction leading to the formation of two liquids with different compositions that are indicated by G_a and G_b in Fig. 1b. At low temperature or high undercooling, limited atomic mobility will result in a fine scale of phase separation that can extend into the nanoscale regime.^[20] Moreover, in some cases the interfaces between the different liquid regions can serve as heterogeneous nucleation sites for subsequent crystallization reactions and establish high nucleation product number densities. In addition, there is evidence that in some systems minor impurity levels can promote the development of phase separation reactions.^[14] Another example of a precursor reaction is the formation of an intermediate phase as a metastable product as illustrated in Fig. 1A for the γ phase.

KINETICS OF NANOCRYSTALLIZATION

One of the key requirements that must be satisfied for the development of a nanoscale microstructure by a crystallization reaction is the attainment of a very high nucleation product number density. The main features of the steady-state nucleation rate kinetics can be described by

$$J_i^s = \Omega_i \exp \left[-\frac{\Delta G^* f(\theta)}{kT} \right] \quad (1)$$

where J_i^s is the steady state nucleation rate on a volume ($i=v$) or surface basis ($i=a$).^[12] Respective values for the prefactor, Ω_i , activation barrier, ΔG^* , and the contact angle function, $f(\theta)$, are used in Eq. 1, and kT is the thermal energy. The expressions for Ω_i involve a product of a nucleation site density on a catalytic surface or volume basis, the number of atoms on a nucleus surface and a jump frequency. For most cases, $\Omega_v = 10^{30}/\eta \text{ cm}^{-3} \text{ sec}^{-1}$ and $\Omega_a = 0.10^{22}/\eta \text{ cm}^{-2} \text{ sec}^{-1}$, with η the liquid shear viscosity (in poise) given by Ref. [6] as

$$\eta = 10^{-3.33} \exp \left[\frac{3.34T_L}{T - T_g} \right] \quad (2)$$

in terms of the liquidus temperature, T_L , and the glass transition, T_g , and ϕ , the fraction of active catalytic sites. The activation barrier for nucleation is given by

$$\Delta G^* = \frac{b\sigma^3}{\Delta G_v^2} \quad (3)$$

where σ is the liquid–solid interfacial energy,^[21] ΔG_v is the driving free energy for nucleation of a unit volume of product phase, and $b=16\pi/3$ for spherical nuclei. With a

planar catalytic surface site and spherical nuclei $f(\theta)=[2-3\cos\theta+\cos^3\theta]/4$. Following the establishment of a supersaturation or undercooling, there is an initial time period during which the nucleation cluster population evolves toward the steady-state distribution.^[22] During this transient period the time-dependent nucleation rate, $J_i(t)$, is given by

$$J_i(t) = J_i^s \left[1 + 2\Sigma(-1)^n \exp \left(-\frac{n^2 t}{\tau} \right) \right] \quad (4)$$

where τ is the time lag or delay time that is estimated by $(n^{*2}/\pi^2\beta)$. The critical nucleus size, n^* , in atoms is obtained from $n^*=4\pi r^{*3}/(3V_a)$ where V_a is the volume per atom and $r^*=-2\sigma/\Delta G_v$ is the critical nucleus radius. The atomic jump frequency, β , can be estimated by D/λ^2 , where D is the diffusion coefficient in the undercooled phase and λ is the jump distance.^[23,24]

To achieve a nanocrystalline microstructure (i.e., with a size scale $\leq 100 \text{ nm}$) in a fully crystallized volume, the nucleation number density should be at least of the order of 10^{21} m^{-3} . Of course, nanocrystallization can be achieved only if there are also restrictions on the kinetics of nanocrystal growth following nucleation.

The kinetic analysis of growth follows different forms that depend on the nature of the solute partitioning associated with phase growth. For example, during polymorphous transformation without solute redistribution, the growth rate, V , is controlled by interface attachment limited kinetics as represented by

$$V = V_0 \exp \left[-\frac{Q_D}{RT} \right] \left(1 - \exp \left[\frac{\Delta G_v}{RT} \right] \right) \quad (5)$$

where V_0 is a prefactor of the order of $5 \times 10^3 \text{ m/sec}$ and Q_D is the activation energy for interface jumps.^[19,25] At low temperature where $\Delta G_v \gg RT$ growth is diffusion controlled as expressed by

$$V = V_0 \exp \left[-\frac{Q_D}{RT} \right] \quad (6)$$

For the case of eutectic reaction where the solute redistribution is limited to the reaction interface

$$V \cong 4D_1 \frac{\delta}{\lambda^2} \quad (7)$$

where D_1 is the interface diffusivity, δ is the thickness of the reaction front, and λ is the lamellar spacing.^[25,26] With these kinetic modes, the reaction is relatively rapid and a metastable microstructure based on nanocrystals and an amorphous phase with the original composition is possible if the kinetics of subsequent decomposition reactions to a more stable phase constitution is sluggish.

When growth requires a redistribution of solute as in primary crystallization, the kinetics are limited by the rate

of diffusion of the rejected solute into the amorphous matrix. For evolving nanocrystals that are isolated from each other the growth rate has the following form

$$V = \frac{\alpha}{2} \sqrt{\frac{D}{t}} \quad (8)$$

where α is a dimensionless factor that is evaluated from the compositions at the particle/matrix interface and the average composition and D will be controlled by the slowest diffusing solute in a multicomponent alloy.^[26] However, at high nucleation densities the isolation can be lost as the diffusion fields from neighboring nanocrystals begin to overlap (i.e., soft impingement).^[25] Under this condition there is a kinetic inhibition to further growth. Concurrent with the growth of nanocrystals, the highly refined sizes indicate that capillarity effects such as Ostwald ripening due to curvature-driven transport (i.e., Gibbs-Thomson effect) can be important.^[25,27]

AMORPHIZATION KINETICS AND TRANSITIONS

The kinetic transition between nanocrystalline products and an amorphous phase is a common structural change

that occurs during solidification with increasing cooling rate as the liquid undercooling approaches T_g . Often, the initiation of the transition is represented by a critical cooling rate and interpreted as a sharp structural change.^[28] However, there are also many reports of mixed crystal/glass phase structures indicating that the transition occurs over a range of cooling rates reflecting the kinetic competition and the probabilistic nature of nucleation.^[29,30] It is useful to note that the glass transition is not a phase transformation in a thermodynamic sense, but it is a kinetic manifestation of the slowing of atomic transport in the liquid with cooling. In fact, the calorimetric glass transition signal is due to the large change in heat capacity that occurs when a liquid becomes configurationally frozen. The slowing of atomic transport is also reflected by an increase in liquid viscosity. The time for the liquid structure to relax during cooling is related to the viscosity, and for typical laboratory measurement conditions T_g corresponds to a viscosity in the range of 10^{12} – 10^{13} P (10^{11} – 10^{12} Pa sec).^[31]

Indeed, following amorphization by rapid melt quenching, many metallic glasses do not exhibit a clear glass transition signal, T_g , upon reheating. Instead, initial exothermic maxima are observed to develop that indicate a multiple-stage crystallization^[5,32,33] as shown in Fig. 3 for an amorphous $\text{Al}_{88}\text{Y}_7\text{Fe}_5$ ribbon after melt spinning and after initial crystallization. The microstructural analysis

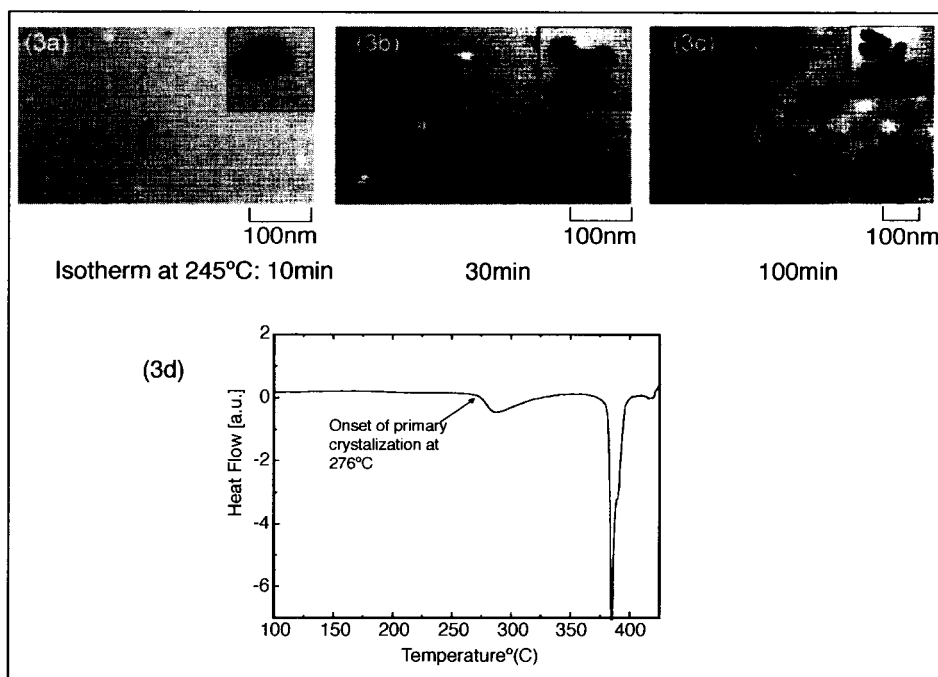


Fig. 3 TEM bright-field images from an $\text{Al}_{88}\text{Y}_7\text{Fe}_5$ melt-spun ribbon that was isothermally annealed at 245°C for (a) 10 min, (b) 30 min, (c) 100 min, and (d) continuous heating differential scanning calorimetry (DSC) trace at 40 K/Min showing a primary crystallization onset at 276°C.

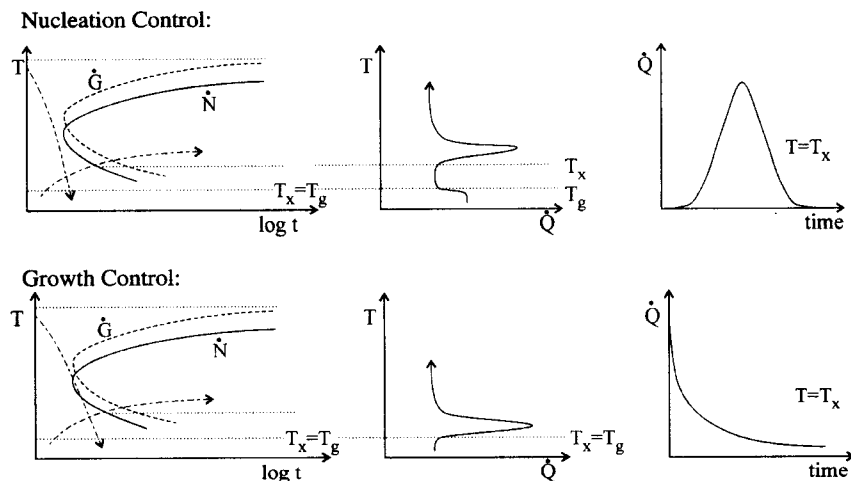


Fig. 4 The principal forms of kinetic control for metallic glass formation.

has established that for many amorphous Al-base alloys that contain transition metal (TM) and rare earth (RE) solutes, the initial crystallization corresponds to primary phase formation (i.e., Al) yielding a sample that contains a high density of nanocrystals within an amorphous matrix.^[5] This behavior is of importance in understanding the kinetic control of glass formation. The two basic strategies to synthesize amorphous alloys are illustrated schematically in Fig. 4. With nucleation control, the undercooling that is achieved during cooling bypasses the nucleation reaction and the nucleation size distribution,^[9] $C(n)$ that may be retained by the cooling does not overlap with the critical nucleation size, n^* , at the crystallization temperature, T_x . As a result, there is no precursor reaction to influence the evolution of crystalline clusters during subsequent thermal treatment. In this way, a clear separation in temperature between the T_g and T_x signals can be observed during reheating of a glass. These kinetic conditions are the basis for bulk glass formation during slow cooling. During isothermal annealing at T_x , the heat evolution rate \dot{Q} exhibits a clear delay before the onset of the nucleation reaction and a peak maximum associated with the completion of nucleation and continued growth. On the other hand, under growth-controlled conditions the cooling rate is insufficient to bypass the nucleation onset completely so that some small fraction of crystallites may form initially, but the rapidly rising viscosity and falling growth rate with continued cooling near T_g prevents rapid cluster growth. In addition, the cluster size distribution that is retained overlaps in size with the critical nucleation size at T_x . In this case, as indicated in Fig. 4, upon reheating a sample with preexisting crystallites (i.e., quenched-in nuclei), rapid crystallization because of the development of quenched-in clusters as well as additional nucleation ensues at T_x , which will essentially coincide

with T_g .^[34] Whereas many of the early metallic glass alloys were synthesized under growth-controlled conditions (i.e., marginal glass formers)^[35] the primary crystallization particle densities in these alloys are of the order of 10^{18} m^{-3} . For the class of amorphous Al- and Fe-base glasses, the primary crystallization number densities range from 10^{21} up to almost 10^{23} m^{-3} . Both of the basic mechanisms for glass formation that are outlined in Fig. 3 can yield a high number density of nanocrystals upon devitrification. With nucleation control, nanostructure development can be achieved by controlled reheating, because the maximum in the growth rate typically occurs at a higher temperature than the maximum in the nucleation rate.^[25] In addition to the two basic synthesis routes outlined in Fig. 4, there is another important distinction between alloys that form bulk glasses and the marginal glass-forming alloys based on the temperature dependence of the liquid viscosity.^[31] The main features of the viscosity behavior are shown in Fig. 5 where “strong” liquids display an Arrhenius type of temperature dependence. A good example of a strong liquid is SiO_2 , but the bulk glass-forming alloys also display strong liquid characteristics.^[31] For the “fragile” liquid behavior shown in Fig. 5 the viscosity is low even in the undercooled regime, but increases sharply upon approaching the glass transition. It appears that the marginal glass-forming alloys exhibit a fragile type of viscosity behavior. It is evident that the transport behavior will impact both the ease of glass formation and the kinetics of nanocrystal development. The different synthesis routes that are shown in Fig. 4 originate from the relative time scales for the onset of nucleation and melt cooling. The transition from growth control to nucleation control can be achieved either by an increase in the cooling rate or by lengthening the time for onset of nucleation, t_n . Because t_n

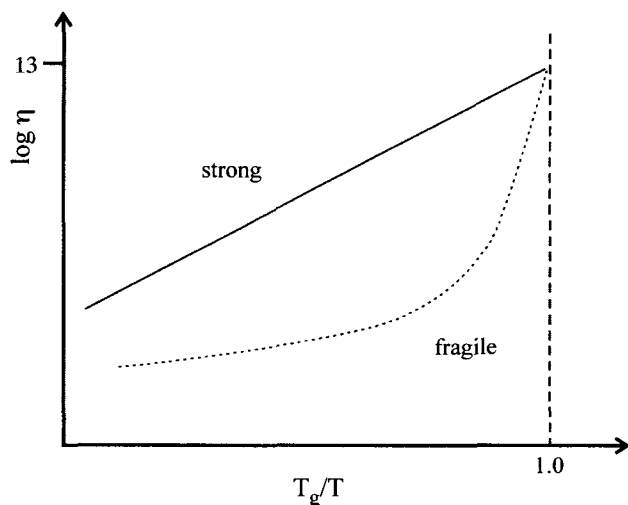


Fig. 5 A schematic illustration of the liquid viscosity behavior vs. T_g/T for strong and fragile glasses.

is related to atomic transport in the liquid, strong liquids with high viscosity are favored for bulk glass formation. It is also apparent that t_n can be lengthened by removing active nucleation sites from the melt. In fact, this is the basis for the effectiveness of melt fluxing, which has been shown to promote bulk glass formation.^[36,37] The actual mechanism for the development of the ultrahigh number densities of nanocrystals is under active study, and proposals based on homogeneous^[38,39] and heterogeneous^[35,40] nucleation and precursor phase separation reactions^[41] are under examination.

The attainment of nanocrystal dispersions of essentially pure Al with ultrahigh number densities is a critical component of the attractive structural performance, but an equally important characteristic is the high thermal stability. One indication of this stability is the wide temperature range between the primary crystallization and final crystallization of between 75° and 100°C in Fig. 3. Within this range, there is a metastable two-phase coexistence involving the Al nanocrystals and the surrounding amorphous matrix with limited coarsening of the microstructure. The sluggish kinetics is related at least in part to the large differences in component atom sizes and diffusivities^[42-44] as well as the onset of impingement of the diffusion fields from neighboring nanocrystals.^[40] Indeed, even at a particle density of 10^{21} m^{-3} the average nanocrystal separation is only about 100 nm. It is also evident that for the Al nanocrystals to grow there is a rejection of solute (i.e., TM and RE) as is typical for primary crystallization reactions. The low solute diffusivities, especially for the large RE atom, act to limit the growth,^[45] and the transport is limited further by the reduced concentration gradient due to impingement as

indicated by the asymmetric primary crystallization exotherm in Fig. 3. In fact, because the amorphous matrix composition will also be enriched in TM and RE components, it is possible to use the solute redistribution during primary crystallization to enhance the stability of the amorphous matrix (i.e., raise T_g).^[15,46] This kinetic restriction inhibits further nanocrystal growth and accounts for the asymmetric crystallization peak and the remarkable thermal stability.

NANOCRYSTALLIZATION DURING MELT QUENCHING

As noted in Fig. 4, it is possible to encounter conditions that represent the maximum nucleation rate (i.e., the minimum time for the onset of nucleation or the nose of the C curve) during continuous cooling. One important requirement to achieve a maximum nucleation density is the removal of potent heterogeneous nucleation sites so that the alloy melt may be cooled to the temperature yielding the maximum nucleation rate without prior crystal formation. For homogeneous nucleation the temperature for a maximum nucleation rate is about $2/3 T_m$.^[12] The schematic illustration in Fig. 4 does not provide a perspective on the sensitivity of the microstructural scale to cooling rate at temperatures near the maximum nucleation rate temperature, but this important feature of nanocrystallization can be developed by considering a melt-quenched nanostructure.

For Nb-rich alloys in the Nb-Si system the main solidification reaction is a eutectic yielding Nb+ Nb_3Si as indicated in the phase diagram in Fig. 6.^[47] The microstructure that is developed following melt spinning is revealed in Fig. 7 for a wedge-shaped sample that was produced by thinning the ribbon of a Nb-25 at.% Si alloy from one side (opposite from the wheel side) the most rapidly cooled region adjacent to the wheel is amorphous. With increasing distance from the chill surface the onset of crystallization is characterized by nanoscale grains with a size of about 15 nm. The fine-grain structure is a mixture of Nb and Nb_5Si_3 , but the size scale increases to about 100 nm over short distance within the 20- μm -thick ribbon before the equiaxed structure evolves into a dendritic morphology.

A common occurrence in the synthesis of nanostructures during rapid solidification is the absence of a phase that according to the equilibrium phase diagram should be present. This occurs when the missing phase is subjected to kinetic limitations in nucleation and/or growth. In the absence of a stable phase, solidification is then governed by a metastable phase diagram. This diagram is constructed from the equilibrium diagram in Fig. 6

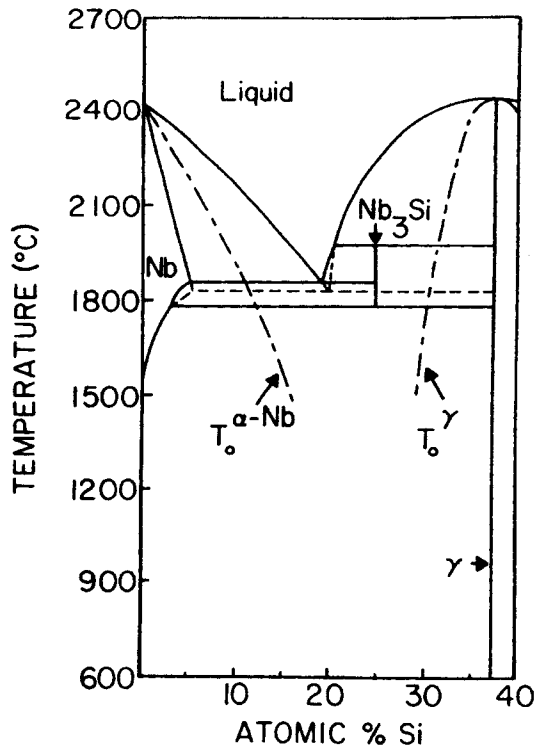


Fig. 6 Phase diagram for the Nb-Si system showing the metastable extension of the Nb₅Si₃ (i.e., γ) liquidus to form a metastable eutectic $L \rightarrow \alpha\text{-Nb} + \text{Nb}_5\text{Si}_3$. This extension is relevant when the Nb₃Si phase is absent. Also shown are approximate T_0 curves for the transformation of liquid to $\alpha\text{-Nb}$ and to γ .

where the Nb₃Si phase is suppressed and where the Nb₅Si₃ (designated γ) liquidus extends below the $L + \text{Nb}_5\text{Si}_3 \rightarrow \text{Nb}_3\text{Si}$ peritectic isotherm and intersects the Nb liquidus to yield a metastable $L \rightarrow \text{Nb} + \text{Nb}_5\text{Si}_3$ eutectic. For alloys near a peritectic reaction, solidification of the high-temperature phase (in this case, Nb₅Si₃) can continue below the peritectic temperature while the remaining liquid develops only slight undercooling with respect to the low-temperature phase (in this case, Nb₃Si). Hence, phases that are ordinarily formed by peritectic reactions may often be absent in nanocrystallization reactions.

A useful method for examining the thermodynamic options available to an alloy undergoing nanocrystallization is to examine the T_0 curves for the various liquid-to-crystal transformations in a system. Schematic T_0 curves are included for the Nb and Nb₅Si₃ (γ) phases in Fig. 6. The T_0 curves place a bound on temperatures and compositions where partitionless solidification is possible.^[13]

Regardless of the level of undercooling that is achieved during rapid quenching, a range of compositions may exist between adjacent T_0 curves where partitionless solidification is impossible and crystal growth must involve the more difficult process of diffusional solute redistribution into a mixture of solid phases.^[48] Because of this difficulty, glass formation or nanocrystallization is most likely in this range, which was observed to be centered near Nb₃Si as indicated in Fig. 6.

The synthesis of a two-phase nanostructure clearly involves copious nucleation. One factor that can increase the opportunity for high nucleation rates is the relatively slow growth for crystals that require solute redistribution. Furthermore, during continuous cooling, the rate of recalescence after the initial nucleation event depends on the crystal growth rate. If it is slow, the melt may be undercooled further, permitting a rapid rise in the nucleation rate.^[12] Moreover, the two-phase nanostructures that are developed during melt spinning identify an important class of metastable microstructure that is available in the form of very high grain densities of the equilibrium phases that were observed to range from 10^{18} to 10^{21} m^{-3} . A high density of grains for a two-phase mixture is metastable because of a high incoherent interphase boundary area. For example, with a grain size of $0.12 \mu\text{m}$ and an interphase boundary energy in the range

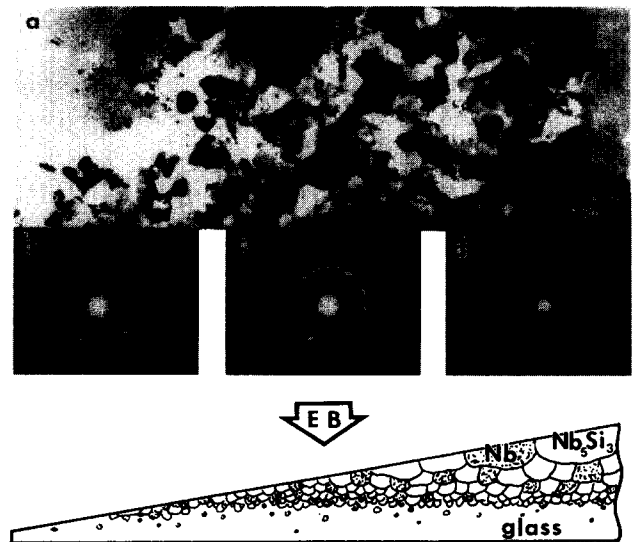


Fig. 7 (a) Microstructure of a Nb-25 at.% Si melt-spun ribbon near the TEM foil edge (the left-hand side of the micrograph) for a specimen polished from one side; (b) SADPs positioned under the areas from which they were taken; (c) a schematic drawing showing the microstructure across the ribbon (EB, electron beam).

of 500–1000 mJ m^{-2} that is typical for incoherent interfaces, the excess free energy due to the polycrystalline grain structure is 120–150 J mol^{-1} . However, for nanoscale grains with a size of 15 nm the free energy increment increases to the range of 800–1600 J mol^{-1} . Thus, with nanostructured grains the level of metastability is comparable with that associated with nonequilibrium crystal structures.^[14]

The devitrification of an amorphous phase is a fairly well recognized approach to the synthesis of a nanocrystalline grain structure. The attainment of an equiaxed grain structure resulting from an isotropic growth is characteristic of a polymorphic type of crystallization reaction. In this sense the evolution of an equiaxed two-phase nanocrystalline grain structure represents a distinct pattern of noncooperative growth that does not appear to be readily achieved by continuous heating or isothermal annealing devitrification treatment. However, the production of a high nucleation density for each phase appears to require a high rate of heat extraction as well as diffusional growth limitations so that the two-phase nanocrystalline structure is limited in spatial extent because of a relatively narrow range of favorable processing conditions.

NANOCRYSTAL CATALYSIS

The limited experimental information available indicates that the nucleation process during primary crystallization of amorphous alloys is usually heterogeneous in nature, but the origin of the active catalytic sites has not been identified in all cases.^[49] For example, it has been established that, with several amorphous Fe alloys, the development of a high density of Fe nanocrystals is strongly promoted by the addition of small amounts of certain solutes such as Cu.^[50] In fact, high-resolution transmission electron microscopy (TEM) and atom probe field ion microscopy (APFIM) observations indicate that Cu solute allows for reactions that act to catalyze Fe nucleation.^[51,52] In amorphous Al-base alloys it appears that a comparable nucleation catalysis behavior can be observed with both soluble and insoluble additions. For example, the addition of 1 at.% Cu to amorphous Al–Ni–Sm has been reported to yield an Al nanocrystal density approaching 10^{23} m^{-3} with diameters of 5–7 nm.^[53] Similarly, the incorporation of insoluble nanosized Pb crystalline particles in an amorphous matrix is effective in catalyzing the crystallization of Al nanocrystals and yields a significant increase in the total number density of nanocrystals.^[54] The catalysis behavior highlights the opportunity for the controlled synthesis of bulk alloys with an ultrahigh number density of nanoscale dispersoids.

MECHANICALLY INDUCED CRYSTALLIZATION OF AMORPHOUS PHASES

One consequence of the metastability of nanocrystalline and amorphous phases is that the structure and properties of the materials can depend on the processing pathway. This pathway dependence offers the chance to obtain phases with novel characteristics that cannot be achieved by melt quenching. For example, nanocrystallization reactions during cold rolling occur after continued folding and rolling of initially crystalline or amorphous multilayer samples, as illustrated schematically in Fig. 8. The repeated folding and rolling process can yield a true strain in the multilayer sample of the order of 100.^[55] The kinetics of this crystallization process appears to be linked to the initial size distribution and density of the quenched-in nuclei in the amorphous matrix. In some cases, for example in melt-spun $\text{Al}_{92}\text{Sm}_8$, the sample fully crystallizes during rolling.^[56] Amorphous alloys that follow the nucleation-controlled solidification pathway and therefore have no significant cluster concentration are considerably more stable against a rolling-induced crystallization reaction.^[57] The observed primary crystallization of marginal glass formers during initial rolling implies an atomic transport of the constituents through the amorphous matrix. Nanocrystals can also be induced by deformation in bulk glass-forming alloys without any thermal annealing.^[58] The redistribution of solute atoms during crystallization appears to be characteristic of a driven system where an athermal mechanical process during shear deformation controls the transport.^[59–61] A more complete understanding of deformation-catalyzed nanocrystallization should also consider the nonequilibrium nature of the rolling process as well as the structural metastability of the amorphous phase. Understanding the nature of shear-induced crystallization is thus not solely a matter of focusing on the processing conditions and their influence on the structural modifications, but necessitates a refined knowledge of the amorphous structure before deformation.

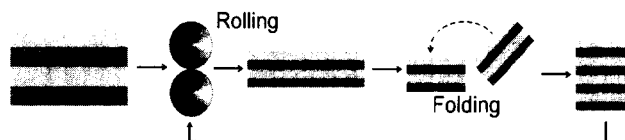


Fig. 8 A schematic illustration of the cold-roll and fold process. A multilayer of elemental foils with foil thicknesses between 7 and 25 μm is reduced by 50% with each rolling pass.

CONCLUSION

The development of nanostructured materials can be achieved in bulk form by the use of amorphous phases as effective precursors. Indeed, the controlled primary crystallization of amorphous alloys yields essentially a nanophase composite of nanocrystalline primary phase dispersed within an amorphous matrix. It is remarkable that the nanocrystal number density can achieve high levels of 10^{21} to 10^{23} m^{-3} at primary phase volume fractions approaching about 30% to yield ultra high strength. An equally remarkable fact is the relative high thermal stability of the nanophase composite. This is truly a novel microstructure that has revealed challenging basic issues on the governing reactions kinetics that control the structure synthesis and performance. At the same time, alternative synthesis routes have been identified based on deformation-induced alloying and glass formation that can be adapted for processing of bulk glasses. The deformation response of amorphous alloys is sensitive to the processing during synthesis and to the influence of quenched-in crystallites.

ACKNOWLEDGMENTS

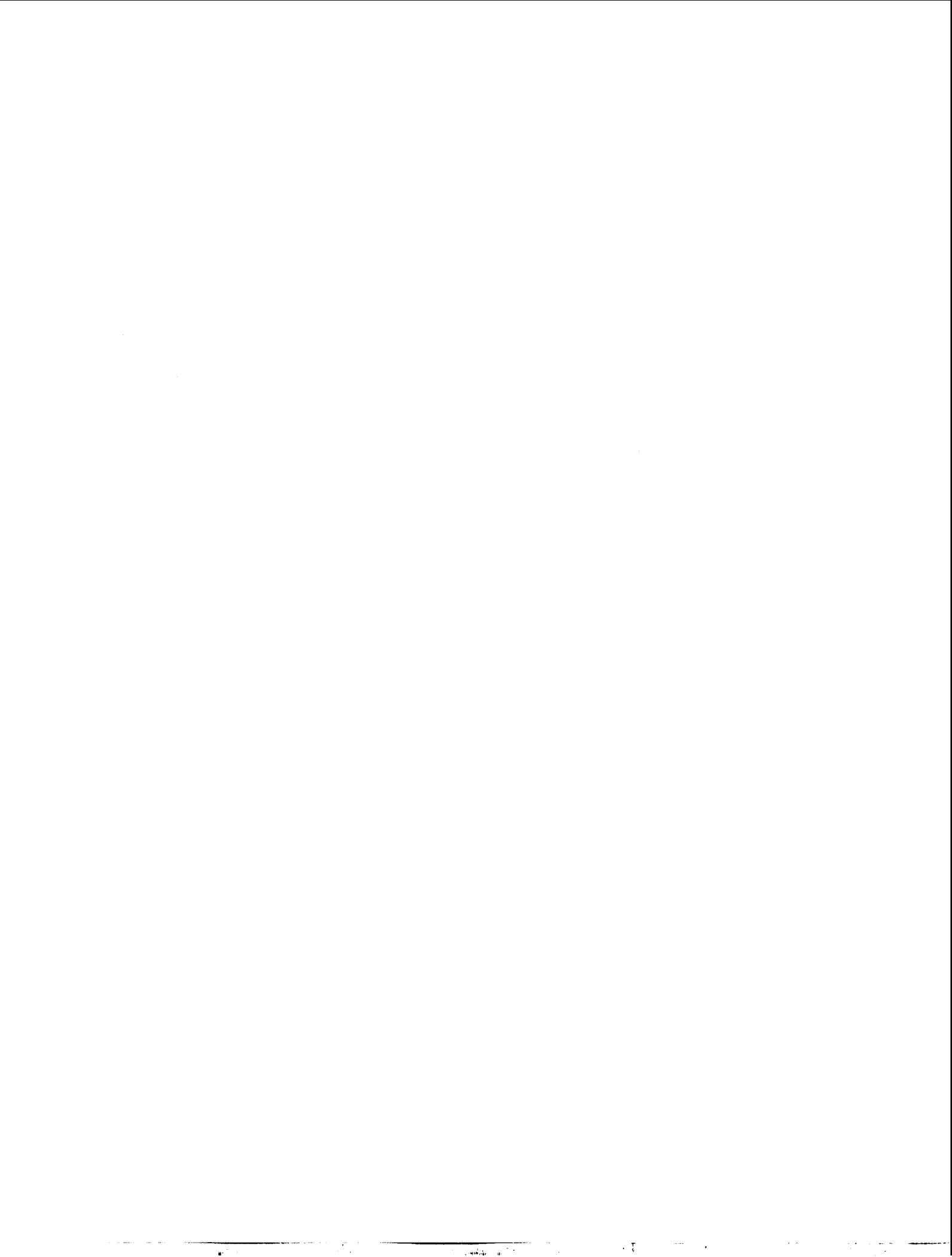
The continued support of the Army Research Office (ARO) and encouragement from Dr. W. Mullins for studies of novel microstructure synthesis during solidification and intense plastic deformation is most gratefully appreciated.

REFERENCES

- Gleiter, H. Nanocrystalline materials. *Prog. Mater. Sci.* **1989**, *33*, 223–315.
- Yanakov, V.; Wolf, D.; Phillot, S.R.; Mukerjee, A.K.; Gleiter, H. Dislocation processes in the deformation of nanocrystalline aluminium by molecular-dynamics simulation. *Nat. Mater.* **2002**, *1*, 45–48.
- Koch, C.C. The synthesis and structure of nanocrystalline materials produced by mechanical attrition: A review. *Nanostruct. Mater.* **1993**, *2*, 109–129.
- Greer, A.L. Crystallization of amorphous alloys. *Metall. Mater. Trans., A* **1996**, *27A*, 549–555.
- Inoue, A. Amorphous, nanoquasicrystalline and nanocrystalline alloys in Al-based systems. *Prog. Mater. Sci.* **1998**, *43*, 365–520.
- Turnbull, D. Metastable structures in metallurgy. *Metall. Trans., A* **1981**, *12*, 695–708.
- Lu, K. Nanocrystalline metals crystallized from amorphous solids: Nanocrystallization, structure and properties. *Mater. Sci. Eng., R Rep.* **1996**, *R16*, 161–221.
- Köster, U.; Schünemann, U. Phase Transformations in Rapidly Solidified Alloys. In *Rapidly Solidified Alloys: Processes, Structures, Properties, Applications*; Liebermann, H.H., Ed.; Marcel Decker, Inc.: New York, 1993; 303–337.
- Perepezko, J.H.; Hebert, R.J. Amorphous aluminum alloys—Synthesis and stability. *J. Metall.* **2002**, *54* (3), 34–39.
- Johnson, W.L. Thermodynamic and kinetic aspects of the crystal to glass transformation in metallic materials. *Prog. Mater. Sci.* **1986**, *30*, 81–134.
- Martin, G.; Bellon, P. Driven alloys. *Solid State Phys.* **1996**, *50*, 189–330.
- Boettinger, W.J.; Perepezko, J.H. Fundamentals of Solidification at High Rates. In *Rapidly Solidified Alloys: Processes, Structures, Properties, Applications*; Liebermann, H.H., Ed.; Marcel Decker, Inc.: New York, 1993; 17–78.
- Baker, J.C.; Cahn, J.W. Thermodynamics of Solidification. In *Solidification*; ASM: Metals Park, OH, 1971; 23–58.
- Perepezko, J.H.; Boettinger, W.J. Use of Metastable Phase Diagrams in Rapid Solidification. In *Alloy Phase Diagrams*; Bennett, L.H., Massalski, T.B., Giessen, B.C., Eds.; Elsevier: New York, 1983; 223–240.
- Allen, D.R.; Foley, J.C.; Perepezko, J.H. Nanocrystal development during primary crystallization of amorphous alloys. *Acta Mater.* **1998**, *46*, 431–440.
- Clavaguera-Mora, M.T.; Clavaguera, N.; Crespo, D.; Pradell, T. Crystallization kinetics and microstructure development in metallic systems. *Prog. Mater. Sci.* **2002**, *47*, 559–619.
- Tsai, A.P.; Kamiyama, T.; Kawamura, Y.; Inoue, A.; Matsumoto, T. Formation and precipitation mechanism of nanoscale Al particles in Al–Ni base amorphous alloys. *Acta Mater.* **1997**, *45*, 1477–1487.
- Hono, K. Nanoscale microstructural analysis of metallic materials by atom probe field ion microscopy. *Prog. Mater. Sci.* **2002**, *47*, 621–729.
- Porter, D.A.; Easterling, K.E. *Phase Transformations in Metals and Alloys*; Chapman and Hall: New York, 1992.
- Kingery, W.D.; Bowen, H.K.; Uhlmann, D.R. *Introduction to Ceramics*, 2nd Ed.; J. Wiley & Sons: New York, 1976.

21. Spaepen, F. Homogeneous nucleation and the temperature dependence of the crystal-melt interfacial tension. *Solid State Phys.* **1994**, *47*, 1–32.
22. Russell, K.C. Nucleation in solids: The induction and steady state effects. *Adv. Colloid Interface Sci.* **1980**, *13*, 205–318.
23. Kashchiev, D. Solution of the non-steady state problem in nucleation kinetics. *Surf. Sci.* **1969**, *14*, 209–220.
24. Kelton, K.F. Crystal nucleation in liquids and glasses. *Solid State Phys.* **1991**, *45*, 75–177.
25. Christian, J.W. *The Theory of Transformations in Metals and Alloys*, 2nd Ed.; Pergamon Press: Oxford, UK, 1975.
26. Kirkaldy, J.S.; Young, D.J. *Diffusion in the Condensed State*; The Institute of Metals: London, 1987.
27. Trivedi, R.K. Theory of Capillarity. In *Lectures on the Theory of Phase Transformations*; Aaronson, H.I., Ed.; TMS: Warrendale, PA, 1999; 135–165.
28. Clavaguera-Mora, M.T. Glass formation in metallic systems. *Ber. Bunsenges. Phys. Chem.* **1998**, *102*, 1291–1297.
29. Perepezko, J.H. Kinetic processes in undercooled melts. *Mater. Sci. Eng., A* **1997**, *226–228*, 374–382.
30. Perepezko, J.H.; Uttormark, M.J. Nucleation-controlled solidification kinetics. *Metall. Mater. Trans., A* **1996**, *27*, 533–547.
31. Angell, C.A. Formation of glasses from liquids and biopolymers. *Science* **1995**, *267*, 1924–1935.
32. Battezzati, L.; Baricco, M.; Schumacher, P.; Shih, W.C.; Greer, A.L. Crystallization behaviour of Al–Sm amorphous alloys. *Mater. Sci. Eng., A* **1994**, *179/180*, 600–604.
33. Foley, J.C.; Allen, D.R.; Perepezko, J.H. Analysis of nanocrystal development in Al–Y–Fe and Al–Sm glasses. *Scr. Mater* **1996**, *35*, 655–660.
34. Chen, L.C.; Spaepen, F. Calorimetric evidence for the microcrystalline structure of “amorphous Al/transition metal alloys.” *Nature* **1988**, *336*, 366–368.
35. Cochrane, R.F.; Schumacher, P.; Greer, A.L. Crystallization of amorphous Al₈₅Ni₁₀Ce₅ alloy. *Mater. Sci. Eng., A* **1991**, *133*, 367–370.
36. Kui, H.W.; Turnbull, D. The melting of Ni₄₀Pd₄₀P₂₀ glass. *Appl. Phys. Lett.* **1985**, *47* (8), 796–797.
37. Drehman, A.J.; Greer, A.L. Kinetics of crystal nucleation and growth in Pd₄₀Ni₄₀P₂₀ glass. *Acta Metall.* **1984**, *32*, 323–332.
38. Greer, A.L. Crystallization kinetics of Fe₈₀B₂₀ glass. *Acta Metall.* **1982**, *30*, 171–192.
39. Omata, S.; Tanaka, T.; Ispida, T.; Sato, A.; Inoue, A. Nucleation and growth kinetics of small crystals in amorphous Al₈₈Ce₂Ni₉Fe. *Philos. Mag., A* **1997**, *76*, 387–412.
40. Perepezko, J.H.; Hebert, R.J.; Tong, W.S. Amorphization and nanostructure synthesis in Al alloys. *Intermetallics* **2002**, *10*, 1079–1088.
41. Gangopadhyay, A.K.; Croat, T.K.; Kelton, K.F. The effect of phase separation on subsequent crystallization in Al₈₈Gd₆La₂Ni. *Acta Mater.* **2000**, *48*, 4035–4043.
42. Hono, K.; Inoue, A.; Sakurai, T. Atom probe analysis of Fe_{73.5}Si_{13.5}B₉Nb₃Cu₁ nanocrystalline soft magnetic material. *Appl. Phys. Lett.* **1991**, *58*, 2180–2182.
43. Hono, K.; Hiraga, K.; Wang, Q.; Inoue, A.; Sakurai, T. The microstructure evolution of a Fe_{73.5}Si_{13.5}B₉Nb₃Cu₁ nanocrystalline soft magnetic material. *Acta Metall.* **1992**, *40*, 2137–2147.
44. Greer, A.L. Stress effects on interdiffusion in amorphous multilayers. *Defect Diffus. Forum* **1996**, *129/130*, 163–180.
45. Hono, K.; Zhang, Y.; Inoue, A.; Sakurai, T. Atom probe studies of nanocrystalline microstructural evolution in some amorphous alloys. *Mater. Trans., JIM* **1995**, *36*, 909–917.
46. Foley, J.C.; Allen, D.R.; Perepezko, J.H. Strategies for the development of nanocrystalline materials through devitrification. *Mater. Sci. Eng., A* **1997**, *226–228*, 569–573.
47. Bendersky, L.; Biancianiello, F.S.; Boettinger, W.J.; Perepezko, J.H. Microstructural characterization of rapidly solidified Nb–Si alloys. *Mater. Sci. Eng.* **1987**, *89*, 151–159.
48. Boettinger, W.J. Growth Kinetic Limitations During Rapid Solidification. In *Rapidly Solidified Amorphous and Crystalline Alloys*; Kear, B.H., Giessen, B.C., Cohen, M., Eds.; North Holland: Amsterdam, 1982; 15.
49. Wu, R.I.; Wilde, G.; Perepezko, J.H. Glass formation and nanostructure development in Al-based alloys. *Mater. Res. Soc. Symp. Proc.* **2000**, *581*, 101–106.
50. Yoshizawa; Oguma, S.; Yamauchi, K. New Fe-based soft magnetic alloys composed of ultrafine grain structure. *J. Appl. Phys.* **1988**, *64*, 6044–6046.
51. Ayers, J.D.; Harris, V.G.; Sprague, J.A.; Elam, W.T.; Jones, H.N. On the formation of nanocrystals in the soft magnetic alloy Fe_{73.5}Nb₃Cu₁Si_{13.5}B₉. *Acta Mater.* **1998**, *46*, 1861–1874.
52. Ohkubo, T.; Kai, H.; Ping, D.H.; Hono, K.; Hirotsu, Y. Mechanism of heterogeneous nucleation of

- alpha-Fe nanocrystals from $\text{Fe}_{89}\text{Zr}_7\text{B}_3\text{Cu}_1$ amorphous alloy. *Scr. Mater.* **2001**, *44*, 971–976.
53. Hong, S.J.; Warren, P.J.; Chun, B.S. Nanocrystallization behaviour of Al–Y–Ni with Cu additions. *Mater. Sci. Eng., A* **2001**, *304–A306*, 362–366.
54. Perepezko, J.H.; Hebert, R.J.; Wu, R.I.; Wilde, G. Primary crystallization in amorphous Al-based alloys. *J. Non-Cryst. Solids* **2003**, *317*, 52–61.
55. Perepezko, J.H.; Hebert, R.J.; Wu, R.I. Nanostructure synthesis and amorphization during cold rolling. *Mat. Sci. Forum* **2002**, *386–388*, 11–20.
56. Hebert, R.J.; Perepezko, J.H. *Mater. Sci. Eng. in press.*
57. Wilde, G.; Sieber, H.; Perepezko, J.H. Glass formation versus nanocrystallization in an $\text{Al}_{92}\text{Sm}_8$ alloy. *Scr. Mater.* **1999**, *40*, 779–783.
58. Kim, J.-J.; Choi, Y.; Suresh, S.; Argon, A.S. Nanocrystallization during nanoindentation of a bulk amorphous alloy at room temperature. *Science* **2002**, *295*, 654–657.
59. Sagel, A.; Sieber, H.; Fecht, H.-J.; Perepezko, J.H. Synthesis of an amorphous Zr–Al–Ni–Cu Alloy with large supercooled liquid region by cold rolling of elemental foils. *Acta Mater.* **1998**, *46*, 4233–4241.
60. Hebert, R.J.; Perepezko, J.H. Significance of the heat of mixing for the amorphization of multilayers by deformation processing. *Mat. Sci. Forum.* **2002**, *386–388*, 21–26.
61. Perepezko, J.H.; Hebert, R.J. Alloying reactions in nanostructured multilayers during intense deformation. *Z. Met.kd. in press.*



Nanocrystals Synthesized in Colloidal Self-Assemblies

M. P. Pileni

Université Pierre et Marie Curie (Paris VI), Paris, France

INTRODUCTION

During this last decade, because of the emergence of a new generation of high-technology materials, the number of groups studying nanomaterials has increased exponentially.^[1,2] The electrical, optical, and magnetic properties of inorganic nanomaterials vary widely with their sizes and shapes. Nanomaterials are used in several domains such as chemistry, electronics, high-density magnetic recording media, sensors, and biotechnology. This is, in part, because of their novel material properties, which differ from both the isolated atoms and the bulk phase. An ultimate challenge in materials research is the creation of perfect nanometer-scale crystallites identically replicated in unlimited quantities in a state than can be readily handled and can behave as pure macromolecular substances. Thus the ability to systematically manipulate these is an important goal in modern materials chemistry. Optimizing this ability requires an understanding of nanocrystal growth, which turns out to be a complex process. The essential first step in the study of their physical properties and the use of nanomaterials in various technologies is their production. Several approaches to manipulate inorganic nanocrystals have been undertaken. The major contribution was to produce spherical nanocrystals with a very low size distribution. Deposition processes include use of microwave plasma,^[3] low-energy cluster beam deposition,^[4] inorganic chemistry,^[5] ball milling,^[6] sonochemical reactions,^[7] sol-gel,^[8] and flame by vapor phase reaction and condensation.^[9] In 1986, we developed a method based on reverse micelles (water-in-oil droplets) to prepare nanocrystals.^[1,2] Normal micelles make it possible to produce ferrite magnetic fluids.^[10]

To control the shapes of nanocrystals, several procedures are now being studied. Hard templates are employed to direct 1-D nanostructure growth. The nanometer-sized pores in membranes and zeolites are utilized to confine the growth of wires.^[11-14] Alternatively, lithography and deposition are combined to create quantum wires on single-crystal surfaces.^[15-17] Electrochemical synthesis is used to produce well-defined nanorods.^[18-20] In 1993 and again in 1995, we were able to partially control the shape of nanocrystals by using colloidal solutions as templates.^[21,22]

In the following, we will concentrate mainly on nanocrystal growth in colloidal self-assemblies and describe discrepancies in the control of size and shape.

COLLOIDAL SELF-ASSEMBLIES OF SURFACTANTS

Direct Micelles

Surfactants are molecules with a polar hydrophilic head (attracted to water) and a hydrophobic hydrocarbon chain (attracted to oil). If a surfactant is solubilized in water, the chains tend to self-associate to form various aggregates.^[23,24] Of course, if the solvent is able to solubilize simultaneously the polar head and the alkyl chains, no aggregates are formed. The shape of the surfactant plays an important role in forming the assembly. If the surfactant molecules have a very large polar head and a small chain, the chains tend to self-associate and form a spherical aggregate that is called a direct micelle. When the direct (or normal) micelle is formed at low concentrations, it is spherical and the length of the hydrocarbon chain and the size of the polar head fix its diameter. On increasing the surfactant concentration, various aggregate shapes are formed. The most commonly used surfactants are sodium dodecyl sulfate [Na(DS)], cetyl trimethyl ammonium chloride (CTAC), or cetyl trimethyl ammonium bromide (CTAB).

Reverse Micelles

If the surfactant has the shape of a champagne cork (small polar head and branched hydrocarbon chains), spherical water-in-oil droplets are formed. These are usually called reverse micelles.^[25] They are a thermodynamically stable mixture of water, oil, and surfactant, where water and oil regions are separated by a surfactant monolayer. Because of the amphiphilic nature of the surfactant, numerous disordered or partially ordered phases are formed, depending on temperature and concentration.^[26] The surfactant most frequently used is sodium di(2-ethylhexyl) sulfosuccinate, usually called Na(AOT). The water/isooctane/Na(AOT) ternary-phase diagram shows a large

zone where the reverse micellar phase is found. In this liquid-like phase, the ratio of water to surfactant concentration $w = [\text{H}_2\text{O}]/[\text{Na}(\text{AOT})]$ determines the reverse micelle size. At w values lower than 15, water mobility is greatly reduced (bound water). Above $w = 15$, the linear increase of the water pool radius r_w with w (from 4 to 18 nm) is explained by a geometrical model,^[27] which assumes a constant area per surfactant molecule and that all surfactant molecules participate in the reverse micelle interface. They are able to exchange their water content during collision between two droplets. The volume of water added to the solution is the only parameter controlling the droplet diameter. Hence, the droplet size remains unchanged in various bulk oil solvents. The intermicellar potential, modeled by an adhesive sphere potential, depends on the particle diameter (d), the attractive range (Δ), and the sticky parameter (τ^{-1}) describing the attractive strength between two droplets.^[28] The latter increases with the length of the bulk oil alkyl chain. It is related to the decrease in percolation threshold with oil chain length, and is explained in terms of an increase in intermicellar droplet interactions. This is caused by penetration of solvent molecules into the interface screening the AOT-alkyl chain interactions. In the case of long-chain oil solvents, steric hindrance does not allow solvent molecules to penetrate the interface, inducing an increase in attractive interactions.^[29–32] The kinetic exchange process^[33] is directly related to the sticky parameter and to the modulus binding of the film at the water-oil interface. Hence, the solvent used tunes the kinetic exchange process: for short-chain solvents, the surfactant alkyl chain is well solvated and the micellar interactions are weak, inducing a low kinetic exchange rate constant. Conversely, large molecules are poor solvents for alkyl chains inducing strong interactions between micelles (i.e., high kinetic rate constants). Hence, by replacing cyclohexane by isooctane as the bulk oil solvent, the kinetic rate constant, at fixed droplet size, increases by a factor of 10.^[34] These two properties (size and exchange process) make it possible by mixing two micellar solutions containing the reactants to produce nanomaterials.

Colloidal Self-Assemblies Made of Divalent Surfactant

Following our paper^[35] in 1991, a great deal of work has been performed with divalent bis(2-ethylhexyl) sulfosuccinate $[\text{X}(\text{AOT})_2]$. We demonstrated that, at low water content, spherical reverse micelles are formed. It was found that, with $\text{Cu}(\text{AOT})_2$, $\text{Co}(\text{AOT})_2$, and $\text{Cd}(\text{AOT})_2$, on increasing the water content, spherical water-in-oil droplets turn into cylinders. This study has been extended by other groups; Eastoe et al.^[36–39] confirm these data and show this for other surfactants such as $\text{Zn}(\text{AOT})_2$,

$\text{Ni}(\text{AOT})_2$, and $(\text{C}_7\text{H}_{14})_4\text{N}(\text{AOT})_2$. In the oil-rich region, the phase behavior of copper(II) bis(2-ethylhexyl)sulfosuccinate $[\text{Cu}(\text{AOT})_2]$ -isooctane-water is known over a wide domain.^[40–43] When the surfactant is not totally solvated, the various structures are governed by the hydration of the head polar group with a progressive increase in the surfactant parameter $s = v_s/a_s l_s$, where v_s , a_s , and l_s are the volume of the surfactant, the surface area, and the length of the alkyl chain, respectively. All these divalent surfactants behave similarly: At low water content, reverse micelles are formed. On increasing the water content, the system evolves to interconnected cylinders, to an equilibrium between lamellae and interconnected cylinders, to an onion-phase region, and, finally, to reverse micelles.^[40–43] Hence, these structures are made with the same surfactant and differ by their shapes. In the region where the head polar group is totally hydrated, spontaneously formed thermodynamically stable emulsions in equilibrium with other microstructure phases are observed. These spontaneous emulsions are comprised of supra-aggregates,^[43]—lamellar spherulites in which the interior and exterior are phases of interconnected cylindrical nanostructures. In another part of the phase diagram, clumps of interdigitated micelles are surrounded by an interconnected cylinder phase. The phase boundaries emerge qualitatively from elementary considerations that require only notions of local and global packing constraints.

SYNTHESES OF NANOCRYSTALS IN SELF-ASSEMBLIES DIFFERING BY THEIR SIZES AND SHAPES

In the oil-rich region, the reactants are confined in the water pool. Because of this, the chemical reaction (i.e., production of nanocrystals) takes place in the supersaturation regime, thus allowing the formation of particles having a very high crystallinity. Such self-assemblies are either droplets (reverse micelles), or bicontinuous phases such as interconnected cylinders or lamellar phases. In aqueous solutions, a functionalized surfactant is used to make normal micelles that are the chemical media for nanocrystal growth. In this case, the reactants are localized at the water-oil interface of the micelles, creating a supersaturation regime.

Syntheses in Reverse Micelles with Formation of Spherical Nanocrystals

Fifteen years ago,^[44] we discovered that reverse micelles are good candidates for templates. Coprecipitation reactions and chemical reduction occur in reverse micelles by

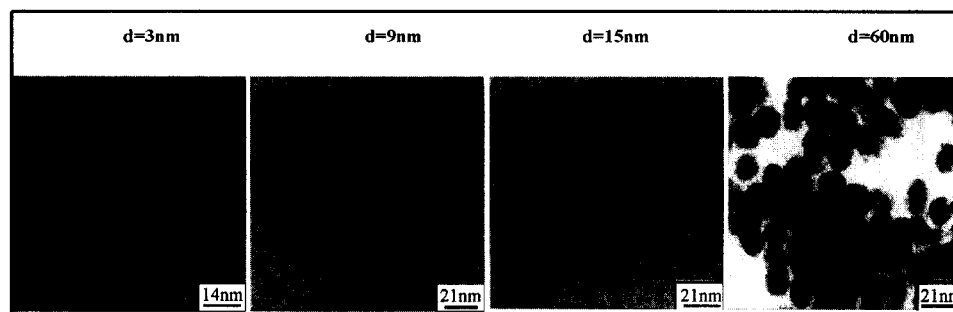


Fig. 1 Change of the copper nanocrystal sizes with the reverse micelle diameter. Reverse micelles are made with 0.1 M Na(AOT) surfactant solubilized in isooctane. One solution contains 10^{-2} M Cu(AOT)_2 , whereas the second one contains 2×10^{-2} M hydrazine. The water content is fixed by the amount of water added to the solution and controls the droplet size. By mixing the two reverse micelles, copper nanocrystals are formed. A drop of solution is deposited on grid and the transmission electron microscopy (TEM) patterns are presented for various water droplet sizes.

using the two properties described above (change in the droplet size with the water content and micellar exchange process). Let us consider A and B solubilized in two micellar solutions. On mixing them and because of the exchange process, A and B are in contact and react. Thus it is possible to fabricate a very wide range of spherical nanomaterials^[1] such as semiconductors, metals, oxides, and various metal and semiconductor alloys. The control of the template size, by changing the water content, enables control of the spherical nanocrystal size.^[21,44] Fig. 1 shows the control of copper nanocrystal size with the water content. It is of interest to note that this nano-reactor makes it possible to produce metal nanocrystals without any detectable oxide. The nanocrystals are characterized by a very high crystallinity when one of the reactants used is a functionalized surfactant (the surfactant has one of the reactants as the counterion). Otherwise, when the two highly hydrated reactants are solubilized in the two droplets, amorphous nanomaterials are formed and metals are produced in their oxide form. The size of the produced material, under the same experimental conditions, is not that of the droplet used as a template.^[1,2] In fact, for II–VI semiconductors^[45] (CdS, CdTe, and CdMnS), the particle size varies from 2 to 4 nm, whereas for metals, it increases from 2 to 6 nm for silver^[46] and from 2 to 10 nm for copper^[21] and silver sulfide.^[47] This control of the particle size is obtained for the smallest water-in-oil droplets (varying from 0.6 to 6 nm), whereas for larger template sizes (from 6 to 12 nm), no changes in the particle size are observed (Fig. 2). This is well demonstrated for large numbers of nanocrystals and is explained in terms of water structure.^[48] An exception is found for silver sulfide nanocrystals with a linear increase in the particle size with that of the template and similar sizes of the droplets and the material.^[47] By changing the

length of the solvent alkyl chain, we know that the droplet size remains the same, whereas the intermicellar interactions change. Syntheses at constant droplet size and in various bulk oil solvents induce a change in the produced nanocrystal size. This is observed for a large variety of nanocrystals and is well demonstrated with copper nanocrystals made in reverse micelles having isooctane and cyclohexane as the bulk phase (Fig. 2). This change in the particle size, keeping the same droplet radius, is explained in terms of efficiency in the exchange control process: Because cyclohexane is a good solvent for surfactant chains, intermicellar interactions between droplets and then the kinetic exchange rate constant are smaller with cyclohexane than isooctane.

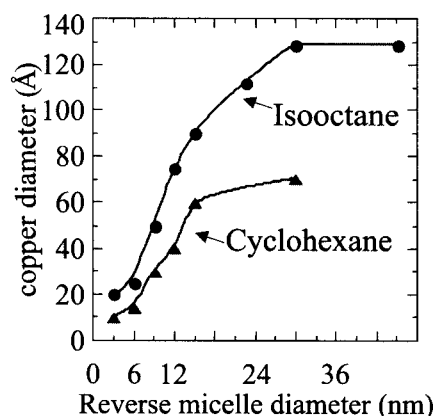


Fig. 2 Variation of the copper nanocrystal size with the droplet diameters by using either isooctane or cyclohexane as the bulk oil solvent. The same procedure as described in Fig. 1 is used. Isooctane is replaced by cyclohexane. From the TEM pattern, the average diameter of nanocrystal sizes is measured. (View this art in color at www.dekker.com.)

Discrepancies in the Use of Reverse Micelles as Templates

The method described above makes it possible to obtain a very large number of spherical nanomaterials, indicating that reverse micelles are efficient templates. However, note that some of them do not exist in the bulk phase and others can never be produced. Hence, in equilibrium states, the solid solubility between Fe and Cu is negligibly small. Their mixing enthalpy is positive and they form no intermetallic compounds even though their atomic radii are quite similar. On the nanoscale, reverse micelles produce Fe/Cu alloys.^[49] With semimagnetic semiconductors^[45] such as $\text{Cd}_y\text{Mn}_{1-y}$, it is possible to include, as in the bulk phase, 50% of Mn^{2+} ions in the CdS matrix, whereas with CdTe, there are no detectable manganese ions in the nanocrystals^[50] and telluride nanorods are formed. No obvious explanations can be given. However, this indicates that physical chemistry in colloidal and homogeneous solutions differs.

The experimental mode used to prepare the nanocrystals is one of the key parameters. This is also described below for controlling nanocrystal shape. Let us consider spherical reverse micelles made of functionalized surfactants such as cadmium bis(2-ethylhexyl) sulfosuccinate [$\text{Cd}(\text{AOT})_2$]. By adding a given amount of water, the water pool diameter reaches 10 nm. By replacing pure water with a solution containing sodium sulfide, spherical CdS nanocrystals are produced. Conversely, bubbling H_2S diluted with nitrogen gas results in formation of flat triangles of CdS nanocrystals^[51] (Fig. 3). High-resolution electron microscopy shows formation of well-defined monocrystals. The formation of flat triangles could be explained by the fact that the nucleation process is slower in using diluted H_2S gas. This enables selective adsorption of hydronium (H^+) on specific faces. Such nanocrystal growth cannot be explained by surfactant impurity:

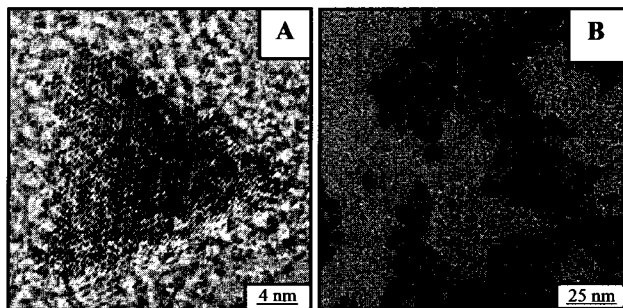


Fig. 3 Triangles of CdS nanocrystals at various enhancements. Reverse spherical micelles of 0.1 M $\text{Cd}(\text{AOT})_2$ solubilized in isoctane at water content equal to 31 are submitted to a slow bubbling of H_2S . CdS nanocrystals are formed.

The same reverse micelles produce spheres and triangles. This shape control by the presence of H^+ in the solution can be related to the formation of cubic platinum nanocrystals^[52] from aqueous solutions containing PtCl_4^{2-} and bubbled with hydrogen (H_2). With time, hydrogen and chloride ions are formed in the solution and a precipitate of cubic platinum nanoparticles appears. It must be noted that the particles are well defined and faceted. Coalescence is prevented by selective adsorption of H^+ or Cl^- on the facets. Other examples in the literature show formation of nonspherical nanoparticles: hence, spherical reverse micelles made of CTAB/butanol/octane produce cubic KMnF_3 nanocrystals.^[53] Details of the synthesis are not given and it is rather difficult to explain which parameter plays the determinant role. However, we have to keep in mind that bromide derivatives of CTAB are present during the synthesis. This will be discussed below. Similarly, elongated and rod-shaped BaCrO_4 and CaCO_3 nanocrystals are produced by using reverse micelles.^[54-57] This could be caused by selective adsorption on various faces during the nanocrystal growth of either reactive products or impurities coming from the preparation of functionalized surfactants used to form reverse micelles. From this, it is reasonable to conclude that reverse micelles can be used as nanoreactors to produce nanoparticles. In most cases, a spherical template produces nanospheres. Hydration of the water pool, procedure mode, and size of the template control the nanocrystal growth. However, production of various species during the chemical reaction and the presence of some impurities prevent the control of spherical particles and induce the formation of nanoparticles having various shapes.

Colloidal Solutions Used as Template to Produce Nanocrystals

Instead of using reverse micelles, let us consider a phase diagram made of a functionalized surfactant such as $\text{Cu}(\text{AOT})_2$ -water-isoctane. The confinement of the reactant is still one of the major parameters. As (already) described above, the phase diagram markedly differs with the water content: At low water content, reverse micelles are formed. On increasing the water content, the system evolves to interconnected cylinders, then to an equilibrium between lamellae and interconnected cylinders, to an onion-phase region, and, finally, to reverse micelles.^[41,42] Hence, the polar volume fraction controls the shape of colloids. To make nanocrystals and to determine if the shape of the template controls that of the nanocrystals, water is replaced by hydrazine in the aqueous solution, keeping the same polar volume fraction colloidal shapes described above. Fig. 4 shows that the shape of the template partially controls that of copper nanocrystals.^[57] The

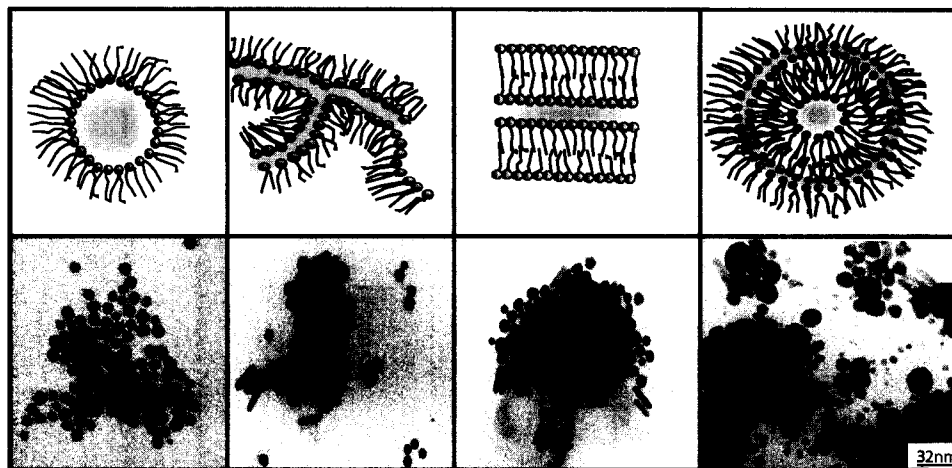


Fig. 4 Change in the shape of copper nanocrystals in various colloidal solutions differing by their structures. The colloidal solution is made of 0.1 M $\text{Cu}(\text{AOT})_2$ in isooctane and hydrazine is injected in the colloidal solution. At low water content (below 3), spherical reverse micelles are formed, inducing formation of spheres. On increasing the water content to $w=5$, interconnected cylinders are produced with the formation of a mixture of spherical and cylindrical copper nanocrystals. In lamellar phase obtained at $w=11$, a mixture of spheres and cylinders is produced, whereas at $w=30$, supra-aggregates are formed and a large variety of copper nanocrystals differing by their shapes are produced. (View this art in color at www.dekker.com.)

crystallinity of these nanomaterials is very high. In the interconnected cylinder region, spheres and cylinders are formed: The cylinder structure is characterized by a fivefold symmetry.^[58] In the region of the phase diagram consisting of an onion phase containing internal and ex-

ternal interconnected cylinders, a large variety of shapes are observed.^[59] This control of the nanocrystal shape by that of the template has been recently confirmed by Simmons et al.^[60] Syntheses of CdS nanoparticles in such colloidal assemblies characterized by various structures

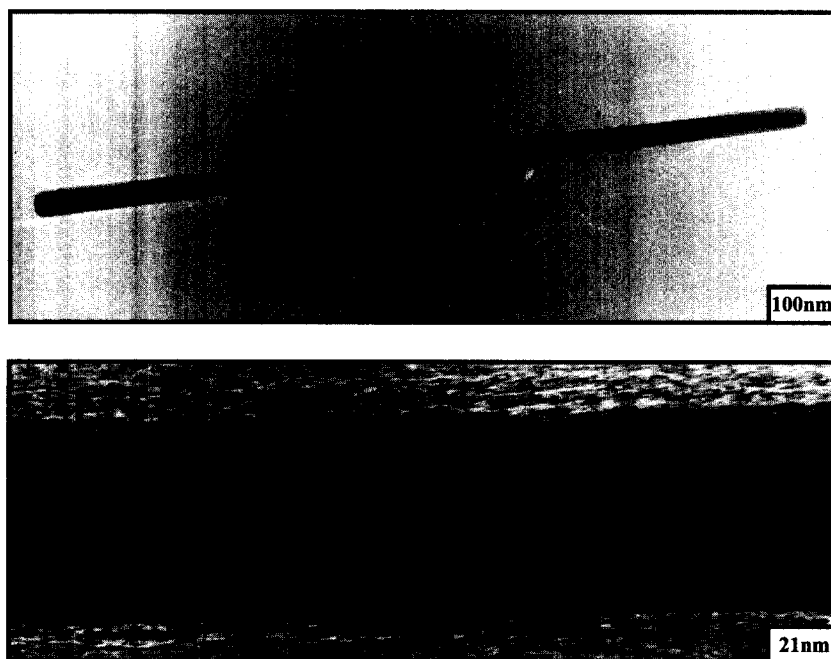


Fig. 5 TEM patterns at various enhancements of copper nanorods. Hydrazine is added to 0.1 M $\text{Cu}(\text{AOT})_2$ solubilized in isooctane in the presence of 10^{-3} M NaCl and copper nanorods are produced at the end of the chemical reduction of Cu^{2+} by hydrazine.

make it possible to vary the morphology of the nanocrystals from spheres to nanorods with a switch in the crystal structure from cubic to hexagonal. However, the role of templates is not as obvious as described above. Adsorption of ions, salts, and molecules has to be taken into account.

Influence of adsorption of ions on nanocrystal growth

Let us consider the system described above [Cu(AOT)₂-isooctane-water]. In the region of interconnected cylinders that are in equilibrium with a lamellar phase, small cylinders are obtained. Addition of a small amount of salt to the colloidal solution gives long copper nanorods with a high crystallinity in fivefold symmetry (Fig. 5)^[61] and an aspect ratio controlled by the concentration of chloride ions in the microphase.^[62,63] It has been demonstrated that this effect is mainly caused by the chloride ions. This is attributed to selective adsorption of these ions on (001) faces and to the fact that the growth is faster on the (111) faces. Formation of these nanorods is not observed, except with bromide, on replacing chloride by other anions^[64] (Fig. 6). Note that with bromide anions, a rather large amount of cubic nanocrystals is formed, whereas with most other anions, mainly spherical objects are produced. From this, it is obvious that adsorption of a given anion enables control of the copper nanocrystal shape. These

data have to be related to those obtained by Esumi et al.,^[65] who produced gold nanorods by UV-visible irradiation of a gold salt solubilized in the bulk phase of normal micelles made of CTAC. The authors claim that direct micelles play the role of the template. It is difficult to understand this role: Gold ions do not interact with the micellar solution and are reduced photochemically. The chloride ions coming from the counterion of the surfactant could play this role, as observed above for copper nanorods produced in the presence of Cl⁻, and allow the gold crystal growth along the 111 direction. These data can also be related to those published by Jana et al.,^[66,67] who produced silver and gold nanorods with an aspect ratio controlled by the ratio of seeds and base concentrations in the presence of the CTAC surfactant. As mentioned, cubic KMnF₃ nanocrystals are formed^[53] from reverse micelles made from the CTAB surfactant and Cu(AOT)₂-H₂O-isooctane solution^[63] in the presence of Br⁻. Similarly, self-assembled monolayers (SAMs) used as templates and immersed in a solution containing bromide ions produce cubic cadmium sulfide nanoparticles.^[68] The environments of these various systems totally differ. The only common factor is the presence of bromide ions during the nanocrystal growth. However, it cannot be claimed that the general principle for growing cubes is that bromide ions have to be present during the process. As mentioned, bubbling hydrogen through an aqueous solution containing PtCl₄²⁻ produces cubic

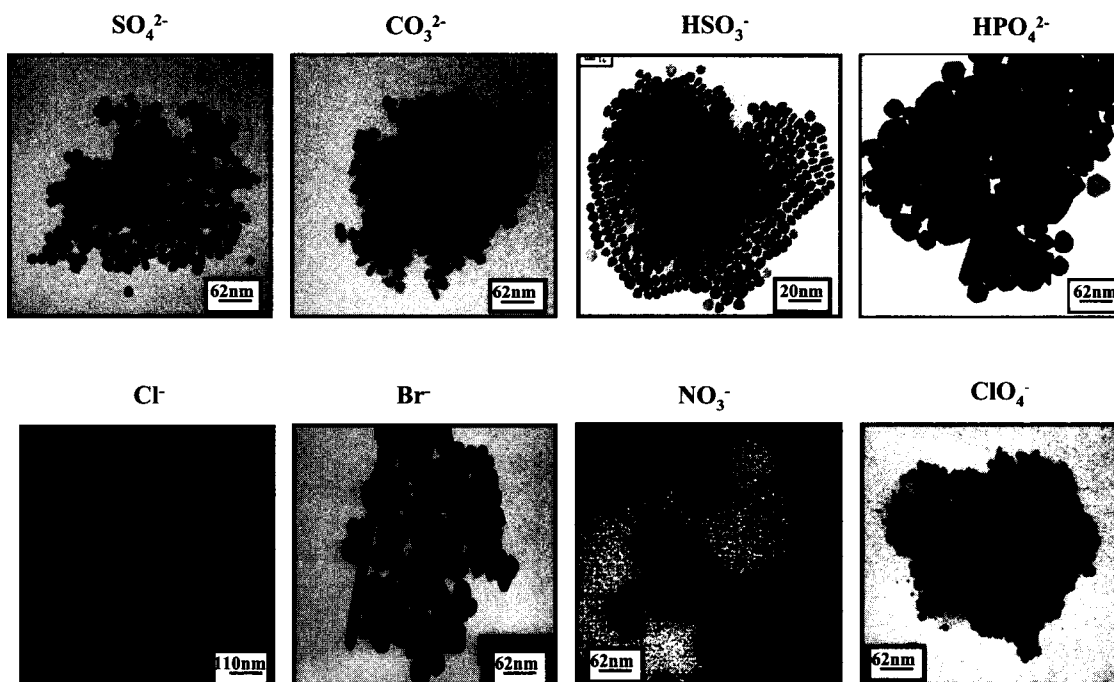


Fig. 6 Change in the copper nanocrystal shape in the presence of various anions, keeping Na⁺ as the cation, [Salt] = 10⁻³ M. The same procedure as described in Fig. 5 is used. NaCl is replaced by Na₂SO₄, Na₂CO₃, NaHSO₃, Na₂HPO₄, NaCl, NaBr, NaNO₃, and NaClO₄.

platinum nanocrystals.^[52] From this, it can be concluded that cubic nanocrystal growth is more related to the presence of ions that absorb selectively than the template.

Influence of molecule adsorption on the nanocrystal growth

Molecules added to the solution can also play a role in the control of particle shape. Nanodisks^[69] are produced in the presence of surfactants that no longer form well-defined templates (aggregates), whereas nanospheres are produced in reverse micelles.^[70] Nanodisk size depends on the amount of hydrazine present in the solution. Note that this is the first example where it is possible to control nanodisk size, and the color of the colloidal solution containing nanodisks evolves from red to gray^[71] (Fig. 7). Because the concentration of the surfactant remains unchanged, to explain the disk formation, we have to take into account the adsorption of hydrazine or/and hydrogen, and hydroxyl ions on the faces. Association of molecules used as additives and salts (together) can also play a role in the control of particle shapes. Polymers and salts are needed to produce PbS nanorods^[72] from functionalized surfactants solubilized in chloroform, whereas spheres are produced in their absence. In the latter case, the surfac-

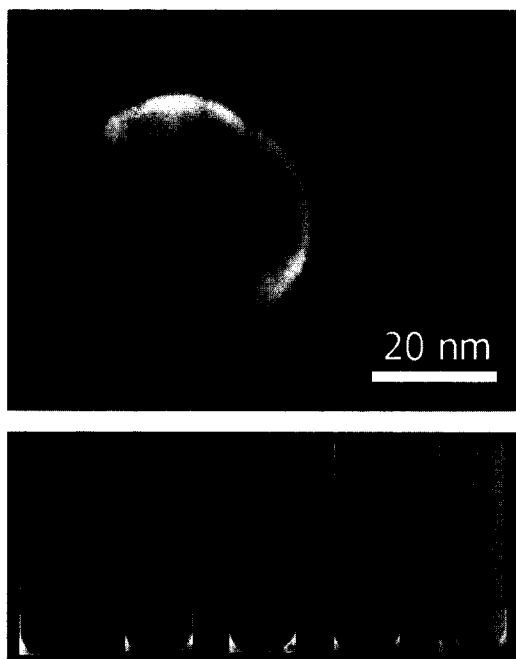


Fig. 7 Silver nanodisks characterized by various absorption spectra caused by change in the nanodisk size while keeping the same aspect ratio. A large volume of hydrazine added to 0.1 M Ag(AOT) is hexane. The relative amount of hydrazine controls the size of nanocrystals. (View this art in color at www.dekker.com.)

tants do not self-assemble in chloroform because the head polar group and the alkyl chains are both soluble in this solvent and act as reactants.

From the literature, a general agreement seems to emerge that control of the nanoparticle shape, via inorganic syntheses, needs to involve a mixture of two surfactants.^[73,74] This has been well demonstrated with various materials such as CdSe, cobalt, and Fe nanorods. The relative ratio of surfactants controls their aspect ratio. However, such claims are not always valid. In fact, the presence of a single surfactant is enough to control the dimensions of silver, gold, and copper nanorods. A convincing experiment showing that the selective adsorption of molecules is one of the major parameters in controlling the particle shape is the production of ZnTe and CdTe nanowires^[75,76] by the solvothermal process. Metals are solubilized in hydrated hydrazine, which is not only an electron transfer medium but also a strong electron donor. These authors claim that in this medium, which is, from my knowledge, a homogeneous solution, hydrazine plays the role of a template.

NORMAL MICELLES USED TO PRODUCE FERRITE NANOCRYSTALS

Fine magnetic particles, dispersed in a suitable liquid carrier (such as water, kerosene, diester, etc.), form a magnetic fluid. Their magnetic properties^[77,78] cannot be analyzed without the inclusion of the effects of size, shape, surface, polydispersity, and interactions between particles. For this reason, a method for synthesizing the particles with good control of these parameters is necessary. Recently, we developed a new procedure to make ferrite nanocrystals that allows changing of the nanocrystal size while keeping the same surface area.^[10,79,80]

Divalent dodecyl sulfate $[X(DS)_2]$ ($X = \text{Fe, Co, Zn}$) is solubilized in aqueous solution and forms mixed oil-in-water micelles. A base is added to the micellar solution, is stirred for 2 hr, and, after centrifugation, the precipitate is washed several times with a solution of 50% water and 50% ethanol to remove the surfactant. Thus the powder obtained consists of ferrite nanocrystals. Depending on the type of ions, X, associated with Fe(DS)_2 stoichiometric solid solutions of ferrite, is obtained. Hence, various materials such as Fe_3O_4 ,^[10,79,80] $\gamma\text{-Fe}_2\text{O}_3$,^[10,79,80] $\text{Co}_x\text{-Fe}_y\text{O}_4$,^[81] and $\text{Co}_x\text{Zn}_y\text{Fe}_2\text{O}_4$ ^[82,83] were produced and the obtained material depends on the relative concentration of the reactants. Note that Fe_3O_4 is the reduced form of $\gamma\text{-Fe}_2\text{O}_3$. Immediately after synthesis, Fe_3O_4 is produced. After a few hours, the Fe^{2+} ions are oxidized to Fe^{3+} and $\gamma\text{-Fe}_2\text{O}_3$ is formed. With this procedure, a large variety of ferrite nanocrystals can be prepared. To obtain an alkaline magnetic fluid, the nanocrystals are dispersed in aqueous

solution, whereas for a neutral fluid, the nanocrystals are coated with citrate ions and dispersed in water.^[81,84] The nanocrystal size distribution is around 20–30%. Changing the surfactant concentration controls the particle size by a factor of 2 or 4. Whatever the fabricated material is, the nanocrystals structure is an inverted spinel. This procedure drastically differs from syntheses in homogeneous solution.^[85–93] The major differences are:

- 1) The reactant concentration is two orders of magnitude lower than that in homogeneous solution.
- 2) A spinel structure can be obtained in the absence of Fe(III) at the starting point of the reaction, whereas the ratio Fe(II)/Fe(III) must be higher than 0.4 in homogeneous solution. In the latter case, with a high Fe(II) salt concentration and without Fe(III) derivatives,^[94–96] the formation of Fe₃O₄ micrometer particles is observed. Their morphology depends critically on parameters similar to those described above (reactant concentrations, pH, ionic strength, etc.). Furthermore, it has been impossible to produce particles in the nanosize range when Fe(II) salt is used for the synthesis.
- 3) Changing the micellar concentration controls the particle size. In homogeneous solution, it is controlled by changing the type of salt (chlorides, nitrates, perchlorates, etc.), Fe(II)/Fe(III) ratio, pH, and ionic strength of the media. Such drastic changes in experimental conditions induce a large modification in the particle interface (hydroxide formations, etc.) and magnetic properties^[92,93] of the nanocrystals. Conversely, using colloidal solutions makes it possible to produce nanocrystals with magnetic properties that do not depend on their coating.^[81]

CONCLUSION

In the last decade, colloidal solutions were assumed to be very efficient templates for controlling particle size and shape. A large number of groups used reverse micelles to control spherical nanoparticles.^[1,2] This makes possible determining the various parameters involved in such processes and demonstrates that they can still be considered as efficient nanoreactors with some discrepancies.^[97] There are fewer reports concerning the control of the particle shape and it is still rather difficult to determine the key parameters. They depend on the adsorption of salts, molecules, and procedure. Crystal growth on the nanoscale seems to follow behavior similar to that of the bulk phase with a marked dependence on pH. The latter is particularly important when some impurities are present in the growth medium because it influences, for example, the formation either of zwitter-ions or complex ions, the efficiency of which is greater than that of the initial impu-

riety. These elements lead to a decrease in the growth rates of certain crystal faces. Most of the changes are based on the existence of a more or less epitaxial adsorption layer on the crystal. This layer is composed of solvents, impurities, or salts. Their precise roles are as yet uncertain. The changes are because of the differences between the growth rates of the various crystallographic faces. From this, it can be concluded that the template is not the key parameter in the shape control.

From these comments, we can ask why templates made of surfactants are quite effective in controlling the formation of nanospheres whereas rather large exceptions are observed for anisotropic shapes. This is probably because of the fact that colloidal templates are highly dynamic. The energy needed to produce spherical nanocrystals is less than that for producing anisotropic nanocrystals. A general method for controlling nanocrystal shapes through soft chemistry has not yet been found, but this does not mean that such a method cannot be discovered. To reach a final conclusion, we need more data and we need to compare the fabrication of anisotropic nanocrystals with various types of materials. Probably other approaches, which have yet to be found, are required. This is suggested by the fact that the fabrications of elongated ferrite nanocrystals in biological media and in vitro are completely different. In biological media, the mechanism of crystal growth is not well known. However, to produce similar nanomaterials in vitro, a very high base concentration is needed and the corresponding pH would induce the destruction of the biological media. This means that other ways exist and have to be discovered.

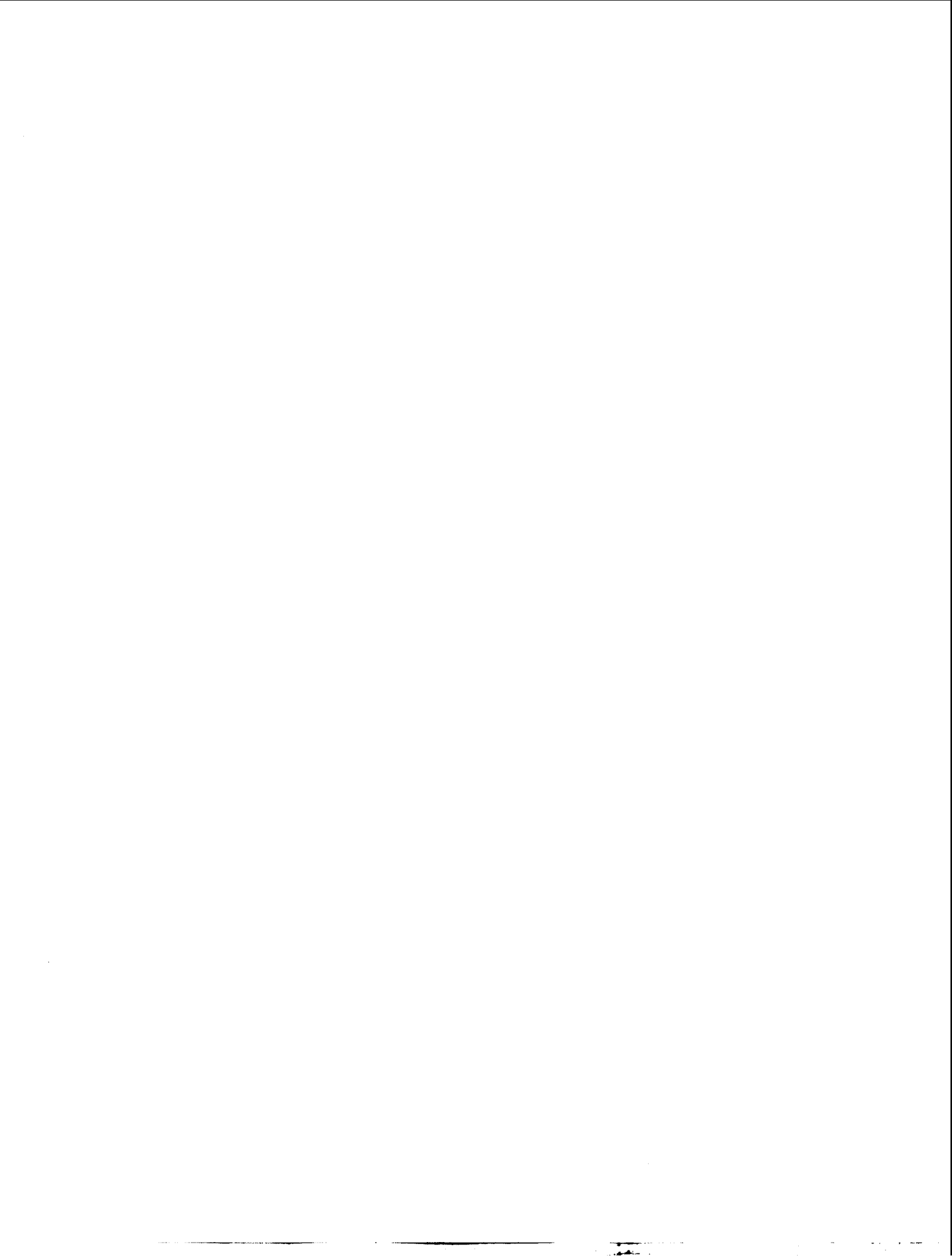
REFERENCES

1. Pileni, M.P. Reverse micelles as microreactors. *J. Phys. Chem.* **1993**, *97* (27), 6961–6973.
2. Pileni, M.P. Nanosized particles made in colloidal assemblies. *Langmuir* **1997**, *13*, 3266–3276.
3. Vollath, D.; Szabo, D.V.; Taylor, R.D.; Willis, J.O. Synthesis and magnetic properties of nanostructured maghemite. *J. Mater. Res.* **1997**, *12*, 2175–2182.
4. Perez, A.; Melinon, P.; Dupuis, V.; Prevel, B.; Bardotti, L.; Tuallion-Combes, J.; Masenelli, B.; Treilleux, M.; Pellarin, M.; Lerme, J.; Cottancin, E.; Broyer, M.; Jamet, M.; Negrier, M.; Tournus, F.; Gaudry, M. Nanostructured materials from clusters: Synthesis and properties. *J. Mater. Trans.* **2001**, *42*, 1460–1470. (Special issue on Nano Metals).
5. Murray, C.B.; Norris, D.J.; Bawendi, M.G. Synthesis and characterization of nearly monodisperse CdE (E = sulfur, selenium, tellurium) semiconductor nanocrystallites. *J. Am. Chem. Soc.* **1993**, *115* (19), 8706–8715.
6. Goya, G.F.; Rechenberg, H.R. Ionic disorder and N^ael

- temperature in ZnFe_2O_4 nanoparticles. *J. Magn. Magn. Mater.* **1999**, *196–197*, 191–192.
7. Shafi, K.V.P.M.; Koltypin, Y.; Gedanken, A.; Prozorov, R.; Balogh, J.; Lendvai, J.; Felner, I.J. Sonochemical preparation of nanosized amorphous NiFe_2O_4 particles. *Phys. Chem., B* **1997**, *101* (33), 6409–6414.
 8. Sugimoto, T.; Shimotsuma, Y.; Itoh, H. Synthesis of uniform cobalt ferrite particles from a highly condensed suspension of b-FeOOH and b-Co(OH)₂ particles. *Powder Technol.* **1998**, *96*, 85–89.
 9. Elmore, W.C. Ferromagnetic colloid for studying magnetic structures. *Phys. Rev.* **1938**, *54*, 309–310.
 10. Moumen, N.; Pileni, M.P. Control of the size of cobalt ferrite magnetic fluid. *J. Phys. Chem.* **1996**, *100* (5), 1867–1873.
 11. Martin, A. Nanomaterials—A membrane-based synthetic approach. *Science* **1994**, *266*, 1961–1966.
 12. van der Zande, B.M.I.; Bohmer, M.R.; Fokkink, L.G.J.; Schonenberger, C. Aqueous gold sols of rod-shaped particles. *J. Phys. Chem., B* **1997**, *1* (6), 852–854.
 13. Cepak, V.M.; Martin, C.R. Preparation and stability of template-synthesized metal nanorod sols in organic solvents. *J. Phys. Chem., B* **1998**, *102* (49), 9985–9990.
 14. Molares, M.E.T.; Buschmann, V.; Dobrev, D.; Neumann, R.; Scholz, R.; Schuchert, I.U.; Vetter, J. Single-crystalline copper nanowires produced by electrochemical deposition in polymeric ion track membranes. *Adv. Mater.* **2001**, *13*, 62–65.
 15. Namatsu, H.; Kurihara, K.; Nagase, M.; Makino, T. Fabrication of 2-nm-wide silicon quantum wires through a combination of a partially-shifted resist pattern and orientation-dependent etching. *Appl. Phys. Lett.* **1997**, *70*, 619–621.
 16. Wang, J.; Thompson, D.A.; Robinson, B.J.; Simmons, J.G. Molecular beam epitaxial growth of InGaAs/InGaAsP quantum wires on V-grooved InP substrates with (III) sidewalls. *J. Cryst. Growth* **1997**, *175–176*, 793–798.
 17. Nepijko, S.A.; Ievlev, D.N.; Schulze, W.; Urban, J.; Ertl, G. Growth of rodlike Ag nanoparticles by vapor deposition of small clusters. *ChemPhysChem* **2000**, *1*, 140–142.
 18. Yu, Y.Y.; Chang, S.S.; Lee, C.L.; Wang, C.R.C. Gold nanorods: Electrochemical synthesis and optical properties. *J. Phys. Chem., B* **1997**, *101* (34), 6661–6664.
 19. Huang, L.M.; Wang, H.T.; Wang, Z.B.; Mitra, A.; Bozhilov, K.N.; Yan, Y.S. Nanowire arrays electro-deposited from liquid crystalline phases. *Adv. Mater.* **2002**, *14*, 61–64.
 20. Wang, Z.L.; Gao, R.P.; Nikoobakht, B.; El-Sayed, M.A. Surface reconstruction of the unstable {110} surface in gold nanorods. *J. Phys. Chem., B* **2000**, *104* (23), 5417–5420.
 21. Lisiecki, I.; Pileni, M.P. Synthesis of copper metallic clusters using reverse micelles as microreactors. *J. Am. Chem. Soc.* **1993**, *115* (10), 3887–3896.
 22. Tanori, J.; Pileni, M.P. Change in the shape of copper nanoparticles in ordered phases. *Adv. Mater.* **1995**, *7*, 862–864.
 23. *Surfactant in Solution*; Mittal, K., Lindman, B., Eds.; Plenum: New York, 1984.
 24. *Surfactant in Solution*; Mittal, K., Lindman, B., Eds.; Plenum: New York, 1987.
 25. Pileni, M.P. *Structure and Reactivity in Reverse Micelles*; Pileni, M.P., Ed.; Elsevier, 1989.
 26. Mitchell, D.; Ninham, B. Micelles, vesicles and microemulsions. *J. Chem. Soc., Faraday Trans.* **1981**, *77*, 601–629.
 27. Pileni, M.P.; Zemb, T.; Petit, C. Solubilization by reverse micelles: Solute localization and structure perturbation. *Chem. Phys. Lett.* **1985**, *118*, 414–420.
 28. Robinson, B.H.; Toprakcioglu, C.; Dore, J.C.; Chieux, P. Small-angle neutron-scattering study of microemulsions stabilized by aerosol-OT. *J. Chem. Soc., Faraday Trans.* **1992**, *80*, 13–27.
 29. van Dijk, M.A. Dielectric study of percolation phenomena in a microemulsion. *Phys. Rev. Lett.* **1985**, *55* (9), 1003–1005.
 30. Huang, J.S. Surfactant interactions in oil continuous microemulsions. *J. Chem. Phys.* **1985**, *82* (1), 480–484.
 31. Lemaire, B.; Bothorel, P.; Roux, D. Micellar interactions in water-in-oil microemulsions: I. Calculated interaction potential. *J. Phys. Chem.* **1983**, *87* (6), 1023–1028.
 32. Huang, J.S.; Safran, S.A.; Kim, M.W.; Grest, G.S.; Kotlarchyk, M.; Quirke, N. Attractive interactions in micelles and microemulsions. *Phys. Rev. Lett.* **1984**, *53*, 592–595.
 33. Jain, T.K.; Cassin, G.; Badiali, J.P.; Pileni, M.P. Relation between exchange process and structure of AOT reverse micellar system. *Langmuir* **1996**, *12* (10), 2408–2411.
 34. Fletcher, P.D.I.; Robinson, B.H. Dynamic processes in water in oil microemulsions. *Ber. Bunsenges. Phys. Chem.* **1981**, *85*, 863–867.
 35. Petit, C.; Lixon, P.; Pileni, M.P. Structural study of divalent metal bis(2-ethylhexyl) sulfosuccinate aggregates. *Langmuir* **1991**, *7* (11), 2620–2625.
 36. Eastoe, J.; Fragneto, G.; Robinson, B.H.; Towey, T.F.; North, A.N.; Leng, K.F.J. Variation of surfactant counterion and its effect on the structure on properties of aerosol-OT based water-in-oil microemulsions. *J. Chem. Soc., Faraday Trans.* **1992**, *88*, 461–471.
 37. Eastoe, J.; Steytler, C.; Robinson, B.H.; Heenan,

- R.K.; North, A.N.; Dore, J.C. Structure of cobalt aerosol-OT reversed micelles studied by small-angle scattering methods. *J. Chem. Soc., Faraday Trans.* **1994**, *90*, 2479–2504.
38. Eastoe, J.; Robinson, B.H.; Heenan, R.K. Water-in-oil microemulsions formed by ammonium and tetrapropylammonium salts of Aerosol OT. *Langmuir* **1993**, *9* (11), 2820–2824.
 39. Eastoe, J.; Towey, T.F.; Robinson, B.H.; Williams, J.; Heenan, R.K. Structures of metal bis(2-ethylhexylsulfosuccinate) aggregates in cyclohexane. *J. Phys. Chem.* **1993**, *97* (7), 1459–1463.
 40. Tanori, J.; Pileni, M.P. Control of the shape of copper metallic particles by using a colloidal system as template. *Langmuir* **1997**, *13* (4), 639–646.
 41. Lisiecki, I.; Andre, P.; Filankembo, A.; Petit, C.; Tanori, J.; Gulik-Krzywicki, T.; Ninham, B.W.; Pileni, M.P. Mesostructured fluids: 1. Cu(AOT)₂-H₂O-isooctane in oil rich regions. *J. Phys. Chem., B* **1999**, *103* (43), 9168–9175.
 42. Lisiecki, I.; Andre, P.; Filankembo, A.; Petit, C.; Tanori, J.; Gulik-Krzywicki, T.; Ninham, B.W.; Pileni, M.P. Mesostructured fluids: 2. Microstructure and supra-aggregation. *J. Phys. Chem., B* **1999**, *103* (43), 9176–9189.
 43. André, P.; Filankembo, A.; Lisiecki, I.; Petit, C.; Tanori, J.; Gulik-Krzywicki, T.; Ninham, B.W.; Pileni, M.P. Supra-aggregation: Microphase formation in complex fluids. *Adv. Mater.* **2000**, *12*, 119–123.
 44. Petit, C.; Pileni, M.P. Synthesis of cadmium sulfide in situ in reverse micelles and in hydrocarbon gels. *J. Phys. Chem.* **1998**, *92* (8), 2282–2286.
 45. Pileni, M.P. II–VI Semiconductors made by soft chemistry syntheses and optical properties. *Catal. Today* **2000**, *58*, 151–166.
 46. Petit, C.; Lixon, P.; Pileni, M.P. In situ synthesis of silver nanocluster in AOT reverse micelles. *J. Phys. Chem.* **1993**, *97* (49), 12974–12983.
 47. Motte, L.; Billoudet, F.; Pileni, M.P. Self-assembled monolayer of nanosized particles differing by their sizes. *J. Phys. Chem.* **1995**, *99* (44), 16425–16429.
 48. Motte, L.; Lisiecki, I.; Pileni, M.P.; Bellisent, M.C.; Dore, J.C. Role of Water Molecules in the Growth of Nanosize Particles in Reverse Micelles. In *Hydrogen Bond Networks*; Kluwer Academic Publishers, 1994; 447–454.
 49. Duxin, N.; Brun, N.; Bonville, P.; Colliex, C.; Pileni, M.P. Nanosized Fe–Cu–B alloys and composites synthesized in diphasic systems. *J. Phys. Chem., B* **1997**, *101* (44), 8907–8913.
 50. Inger, D.; Pileni, M.P. Limitations in producing nanocrystals using reverse micelles as nanoreactors. *Adv. Funct. Mater.* **2001**, *11*, 136.
 51. Pinna, N.; Weiss, K.; Urban, J.; Pileni, M.P. Triangular CdS nanocrystals: Structural and optical studies. *Adv. Mater.* **2001**, *13*, 261–264.
 52. Henglein, A.; Giersig, M. Reduction of Pt(II) by H₂: Effects of citrate and NaOH and reaction mechanism. *J. Phys. Chem., B* **2000**, *104* (29), 6767–6772.
 53. Agnoli, F.; Zhou, W.L.; O'Connor, C.J. Synthesis of cubic antiferromagnetic KMnF₃ nanoparticles using reverse micelles and their self-assembly. *Adv. Mater.* **2001**, *13*, 1697–1699.
 54. Li, M.; Schnablegger, H.; Mann, S. Coupled synthesis and self-assembly of nanoparticles to give structures with controlled organization. *Nature* **1999**, *402*, 393–395.
 55. Hopwood, J.D.; Mann, S. Synthesis of barium sulfate nanoparticles and nanofilaments in reverse micelles and microemulsions. *Chem. Mater.* **1997**, *9* (8), 1819–1828.
 56. Hammond, S.J.R.; Robinson, B.H. Formation and morphology of calcium sulfate nanoparticles and nanowires in water-in-oil microemulsions. *Langmuir* **1999**, *15* (6), 1993–2002.
 57. Pileni, M.P. Mesostructured fluids in oil-rich regions: Structural and templating approaches. *Langmuir* **2001**, *17* (24), 7476–7486.
 58. Lisiecki, I.; Sack-Kongehl, H.; Weiss, K.; Urban, J.; Pileni, M.P. Annealing process of anisotropic copper nanocrystals. *Langmuir* **2000**, *16* (23), 8802–8808.
 59. Tanori, J.; Pileni, M.P. Control of the shape of copper metallic particles by using a colloidal system as template. *Langmuir* **1997**, *13* (4), 639–646.
 60. Simmons, B.A.; Li, S.; John, V.T.; McPherson, G.L.; Bose, A.; Zhou, W.; He, J. Morphology of CdS nanocrystals synthesized in a mixed surfactant system. *Nano Lett.* **2000**, *2* (4), 263–268.
 61. Lisiecki, I.; Filankembo, A.; Sack-Kongehl, H.; Weiss, K.; Pileni, M.-P.; Urban, J. Structural investigations of copper nanorods by high-resolution TEM. *Phys. Rev., B* **2000**, *61*, 4968–4974.
 62. Pileni, M.P.; Tanori, J.; Filankembo, A.; Dedieu, J.D.; Gulik-Krzywicki, T. Template design of microreactors with colloidal assemblies: Control the growth of copper metal rods. *Langmuir* **1998**, *14* (26), 7359–7363.
 63. Filankembo, A.; Giorgio, S.; Lisiecki, I.; Pileni, M.P. Is the anion major parameter in the shape control of nanocrystal? *J. Phys. Chem., B* **2003**, *107*, 7492–7500.
 64. Filankembo, A.; Pileni, M.P. Is the template of self-colloidal assemblies the only factor that controls nanocrystal shapes? *J. Phys. Chem., B* **2000**, *104* (25), 5865–5868.
 65. Esumi, K.; Matsuhisa, K.; Torigoe, K. Preparation of rodlike gold particles by UV irradiation using cationic micelles as a template. *Langmuir* **1995**, *11* (9), 3285–3287.

66. Jana, N.R.; Gearheart, L.; Murphy, C.J. Wet chemical synthesis of silver nanorods and nanowires of controllable aspect ratio. *Chem. Commun.* **2001**, (7), 617–618.
67. Jana, N.R.; Gearheart, L.; Murphy, C.J. Wet chemical synthesis of high aspect ratio cylindrical gold nanorods. *J. Phys. Chem., B* **2001**, *105* (19), 4065–4067.
68. Chen, C.-C.; Lin, J.-J. Controlled growth of cubic cadmium sulfide nanoparticles using patterned self-assembled monolayers as a template. *Adv. Mater.* **2001**, *13*, 136–139.
69. Maillard, M.; Giorgio, S.; Pileni, M.P. Silver nanodisks. *Adv. Mater.* **2002**, *14*, 1084.
70. Courty, A.; Lisiecki, I.; Pileni, M.P. TE vibration of self-organized silver nanocrystals. *J. Chem. Phys.* **2002**, *116*, 8074–8078.
71. Maillard, M.; Giorgio, S.; Pileni, M.P. Tuning the size of silver nanodisc with similar aspect ratio: Synthesis and optical properties. *J. Phys. Chem., B* **2003**, *107*, 2466–2469.
72. Wang, S.; Yang, S. Preparation and characterization of oriented PbS crystalline nanorods in polymer films. *Langmuir* **2002**, *16* (2), 389–397.
73. Manna, L.; Scher, E.C.; Alivisatos, A.P. Synthesis of soluble and processable rod-, arrow-, teardrop-, and tetrapod-shaped CdSe nanocrystals. *J. Am. Chem. Soc.* **2000**, *122* (51), 12700–12706.
74. Puntès, V.F.; Krishnan, K.M.; Alivisatos, A.P. Colloidal nanocrystal shape and size control: The case of cobalt. *Science* **2001**, *291* (5511), 2115–2117.
75. Li, Y.; Ding, Y.; Wang, Z. A novel chemical route to ZnTe semiconductor nanorods. *Adv. Mater.* **1999**, *11*, 847–850.
76. Li, Y.; Liao, H.; Ding, Y.; Fan, Y.; Zhang, Y.; Qian, Y. Solvothermal elemental direct reaction to CdE (E=S, Se, Te) semiconductor nanorod. *Inorg. Chem.* **1999**, *38* (7), 1382–1387.
77. Berkowitz, A.E.; Lahut, J.A.; Jacobs, I.S.; Levinson, L.M.; Forester, D.W. Spin pinning at ferrite–organic interfaces. *Phys. Rev. Lett.* **1975**, *34*, 594–597.
78. Gangopadhyay, S.; Hadjipanayis, G.C.; Sorensen, C.M.; Klabunde, K.J. Effect of particle size and surface chemistry on the interactions among fine metallic particles. *IEEE Trans. Magn.* **1993**, *29*, 2619–2621.
79. Moumen, N.; Bonville, P.; Pileni, M.P. Control of the size of cobalt ferrite magnetic fluids: Mössbauer spectroscopy. *J. Phys. Chem.* **1996**, *100* (34), 14410–14416.
80. Feltin, N.; Pileni, M.P. New technique for synthesizing iron ferrite magnetic nanosized particles. *Langmuir* **1997**, *13* (15), 3927–3933.
81. Ngo, A.T.; Bonville, P.; Pileni, M.P. Nanoparticles of $\text{Co}_x\text{Fe}_y[\text{O}_4]$: Syntheses and properties. *Eur. Phys. J., B* **1999**, *9*, 583–592.
82. Hocheplied, J.F.; Bonville, P.; Pileni, M.P. Nonstoichiometric zinc ferrite nanocrystals: Syntheses and unusual magnetic properties. *J. Phys. Chem., B* **2000**, *104* (5), 905–912.
83. Hocheplied, J.F.; Pileni, M.P. Magnetic properties of mixed cobalt–zinc ferrite nanoparticles. *J. Appl. Phys.* **2000**, *87* (5), 2472–2478.
84. Ngo, A.T.; Bonville, P.; Pileni, M.P. Spin canting and size effects in nanoparticles of nonstoichiometric cobalt ferrite. *J. Appl. Phys.* **2001**, *89* (6), 3370–3376.
85. Jolivet, J.P.; Massart, R.; Fruchart, J.M. Synthèse et étude physicochimique de colloïdes magnetiques non surfactes en milieux aqueux. *Nouv. J. Chim.* **1983**, *7*, 325–331.
86. Rosensweig, R.E.; Kaiser, R.; Miskolczy, G. Viscosity of magnetic fluid in a magnetic field. *J. Colloid Interface Sci.* **1969**, *29*, 680–686.
87. Khalafalla, S.E.; Reimers, G.W. Preparation of dilution-stable aqueous magnetic fluids. *IEEE Trans. Magn. Magn.* **1980**, *16*, 178–183.
88. Sato, T.; Kuroda, C.; Saito, M.; Sugihara, M. In *Ferrites: Proceeding of the International Conference*; Hoshino, Y., Ida, S., Sugimoto, M., Eds.; University of Tokyo Press: Tokyo, Japan, 1971; 72.
89. Nakatsuka, K.; Jeyadevan, B. Initial susceptibilities of magnetic fluids dispersing Mn–Zn ferrite and cobalt ferrite particles. *IEEE Trans. Magn. Magn.* **1994**, *16*, 4671–4673.
90. Vandenberghe, R.E.; Vanleerberghe, R.; De Grave, E.; Robbrecht, G. Preparation and magnetic properties of ultra-fine cobalt ferrites. *J. Magn. Magn. Mater.* **1980**, *15*, 1117–1118.
91. Davies, K.J.; Wells, S.; Charles, S.W. The effect of temperature and oleate adsorption on the growth of maghemite particles. *J. Magn. Magn. Mater.* **1993**, *122*, 24–28.
92. Charles, S.W.; Davies, K.J.; Wells, S.; Upadhyay, R.V.; O’Grady, K.; El Hilo, M.; Meaz, T.; Morup, S. The observation of multi-axial anisotropy in ultrafine cobalt ferrite particles used in magnetic fluids. *J. Magn. Magn. Mater.* **1995**, *149*, 14–18.
93. Jolivet, J.P.; Belleville, P.; Tronc, E.; Livage, J. Influence of Fe (II) on the formation of the spines iron oxide in alkaline medium. *Clays Clay Miner.* **1992**, *40*, 531–539.
94. Matijevec, E. Preparation and properties of uniform size colloids. *Chem. Mater.* **1993**, *5* (4), 412–426.
95. Sugimoto, T.; Matijevec, E. Formation of uniform spherical magnetite particles by crystallization from ferrous hydroxide gels. *Colloid Interface Sci.* **1980**, *74*, 227–243.
96. Domingo, C.; Rodriguez-Cemente, R. The pathways to spinel iron oxides by oxidation of iron (II) in basic media. *Mater. Res. Bull.* **1991**, *26*, 47–55.



Nanodiamonds

Jean-Yves Raty

University of Liège, Sart-Tilman, Belgium

Giulia Galli

Lawrence Livermore National Laboratory, Livermore, California, U.S.A.

INTRODUCTION

Carbon is everywhere around us. Its stable crystalline phase is graphite, but under some circumstances, it can be converted into its most interesting phase for applications—diamonds. Naturally, a diamond is produced inside the Earth's mantle by a high-pressure–high-temperature phase transformation of graphite. It is metastable and that is the reason why it can be recovered in mines after having migrated toward the most external shells of the Earth.

Its unsurpassed hardness, excellent transport properties, transparency, and inertness make a diamond a material of choice for many industrial applications. Synthetic diamond, produced by a high-pressure–high-temperature treatment of graphite, or by ion bombardment, is now commonly used in industries. But what happens to the carbon phase diagram when the sample size reaches the order of several nanometers?

OVERVIEW

After the discovery of diamond inclusions (several nanometers in size) in some meteorites that had fallen on Earth, some groups have theoretically studied the relative stability of graphite and diamond as a function of particle size.

The first attempt to understand the stability of diamonds at the nanoscale was published by Badziag et al.^[1] They computed the binding energy of diamond-like and graphite-like carbon clusters using fixed energy values for carbon–carbon and carbon–hydrogen bonds. They found that below a size of 3–6 nm and a number of 100–21000 carbon atoms, diamond clusters become more stable than their graphitic counterparts. After that precursor study, several groups tried to model the relative diamond-to-graphite stability with more sophisticated models. A charged cluster model was presented by Hwang et al.^[2] and Jang and Hwang.^[3] At that time, the crossover between diamond and graphite was predicted to occur for clusters containing 400 atoms. In comparison with Ref. [1], the model used there was purely electrostatic. Other charge lattice calculations by Gamarnik^[4] predict

the reversal of stability to occur between 4.3 and 10.2 nm, depending on the temperature. It is worth noting that although these models have totally different ingredients and neglect the detailed structure of the clusters, such as specific surface structure or different degrees of hydrogen surface passivation, they reach the same conclusion that a diamond becomes more stable than graphite below 3–10 nm. Indeed, diamonds of several nanometers in diameter have been found or produced in a large variety of environments, as we will discuss in “Nanodiamond Sources.” Then, we will present an overview of the properties of nanodiamonds, both as isolated particles and as assemblies in films, and we will show how promising these carbon nanoparticles are for tomorrow's applications.

NANODIAMOND SOURCES

Nanodiamonds in the Sky

Nanoscale diamonds were discovered in 1987 by Lewis et al.^[5] in meteorites. Not all meteorites contain diamonds. At this time, nanodiamonds have been found in specific types of meteorites, the so-called “carbonaceous chondrites.” Two major sources of nanodiamonds are the “Allende” chondrite (C3V type), which weighed several tons when it fell on Mexico in 1969, and also other types of chondrites, such as the Murchison meteorite (type C2).

The nanodiamonds found in these meteorites have a lognormal size distribution, with a median diameter of 26 Å, corresponding to roughly 1060 atoms. The shape of the distribution has been interpreted to be caused by growth followed by partial conversion of small grains to larger ones. The particles were shown to contain impurities, mainly hydrogen, nitrogen, and oxygen, principally in –COOH groups.^[6] It is worth noting that in some cases, such as C2-type chondrites, a diamond (in its nanoscale form) is up to five times more abundant than graphite. Further analysis of meteoritic nanodiamonds by Amarti et al.^[7] revealed the nanodiamond content of the C2 meteorite to be ~400 ppm and attributed the shape of the size distribution to a condensation process.

The major question arising from those discoveries is: How and when were those diamonds produced? Daulton et al.^[8] performed a detailed high-resolution transmission electron microscopy (HRTEM) study of a large quantity of nanodiamonds coming from meteorites, as well as those produced by means of detonation or chemical vapor deposition (CVD). Their work concludes that meteoritic diamond features (morphology, type of eventual twinning) are much closer to the low-hydrogen-pressure CVD process than to the high-temperature-high-pressure detonation.

These findings are of much interest to the astrophysicists community because chondrites are primitive meteorites that formed *before* the solar system. Their structure and content provide information on nuclear and chemical processes in stars and in the interstellar medium. There still remained some doubts about the fact that the nanodiamonds found in the meteorites are actually presolar.^[9] Dai et al.^[10] have studied other nanodiamonds, with structural features similar to the meteoritic samples, which have been found in interplanetary dust particles originating from comets or asteroids. They found that there are very few nanodiamonds in those particles—infinitely fewer than in chondrites. Because comets are objects that formed earlier in the solar system than meteorites, this seems to indicate that the nanodiamonds found in the meteorites are not presolar at all.

This hypothesis is corroborated by the discovery of unexpected lines in the infrared spectra of 12 warm supergiants,^[11,12] which are also carbon-rich protoplanetary nebulae. A broad absorption line centered at 21 μm wavelength was attributed to large polycyclic aromatic hydrocarbon (PAH) molecules or some partially hydrogenated fullerenes,^[13] before being attributed to nanodiamonds by Hill et al.^[14] In that study, the observed infrared absorption from the interstellar dust is shown to be comparable to either nitrogen-rich nanodiamonds, or to nanodiamonds containing vacancies and/or interstitial atoms. They also noticed that some absorption features could be explained by the relaxation of part of the nanodiamonds surface toward sp^2 carbon configuration. By fitting the absorption spectra with those of terrestrial diamonds, they estimate the size of these interstellar nanodiamonds to be around 2.6 and 3 nm, exactly as for meteoritic diamonds.

Other hydrogenated nanodiamond signatures have been indirectly evidenced by Van Kerkhoven et al.^[15] around some other types of stars. In those objects, the nanodiamonds are thought to be hydrogen-terminated, with some surface reconstructions, and could have a size ranging between 1 and 10 nm. The main conclusion of that study is that the nanodiamonds are produced in situ in the disks of stellar objects. Thus they should be present everywhere. The authors suggest that nanodiamonds are indeed present everywhere in space, but remain undetected because of

the dehydrogenation of their surface for reconstruction, with the surface carbon getting sp^2 -bonded.

Nanodiamonds in Detonation Soots

As one can see, nature seems to favor the appearance of diamond nanoparticles. But it is not only in the cosmos that nanodiamonds can be found.

Indeed, pure trinitrotoluene (TNT) detonation has been shown to produce, among other carbon structures, nanocrystalline (NC) diamonds with diameters of about 10 nm.^[16] By mixing TNT with some other solids such as RDX (cyclotrimethylene trinitramine— $\text{C}_3\text{H}_6\text{N}_6\text{O}_6$), TATB, or NIGU, and by detonating the mixture in an inert gas atmosphere, most spheroidal diamond particles produced were 4 nm in diameter.^[17] Because of those first studies, the synthesis of nanodiamonds by detonation has been optimized and detonation-produced diamonds are now even commercially available. These nanodiamonds are often called “ultra dispersed diamond” (UDD) because of their very narrow size distribution. A thermodynamic model has been proposed by Viecelli et al.^[18] in which the nanodiamond formation is produced from nanometric liquid droplets. Aleksenski et al.^[19] performed a structural study of UDD using X-ray diffraction and small angle X-ray scattering. They evidenced a diamond cluster core of about 43 Å, the surface of which is covered by a mixture of sp^2 -bonded and sp^3 -bonded carbons. The authors could explain their small-angle X-ray scattering (SAXS) measurement with a model in which the diamond core is surrounded by onionlike carbon shells and nanosized graphite platelets. The thickness of these surrounding shells seems to be much dependent on the type of detonation synthesis (dry technology—gas cooling, or wet technology—water cooling). Baidakova et al.^[20] further analyzed the fractal dimension of the external shells of nanodiamonds. On annealing, they show that the diamond content of the particles decreases from 1200 K in favor of the formation of graphite flakes on the surface of particles and in favor of onion shells at temperatures 1300 K and higher. Similar transformations occur under electron beam annealing as well. Fig. 1 shows the evolution of the electron energy loss spectroscopy (EELS) of a UDD nanoparticle as a function of exposure time. The spectra rapidly evolve from diamond-like to amorphous-like because of heating produced by the electron beam.

Other detonation-produced (TNT+RDX) nanodiamonds were analyzed by Chen et al.^[21] In their study, the particles were almost perfectly spherical and 4–6 nm in diameter, but some larger (~ 15 nm) spherical particles were also present. The composition analysis evidenced 87–90% carbon, 0.5–1% hydrogen, 1.6–2.5% nitrogen, and 6–10% oxygen. The authors explained the spherical shape of the particles as a consequence of the recrystallization of a liquidlike carbon droplet during the

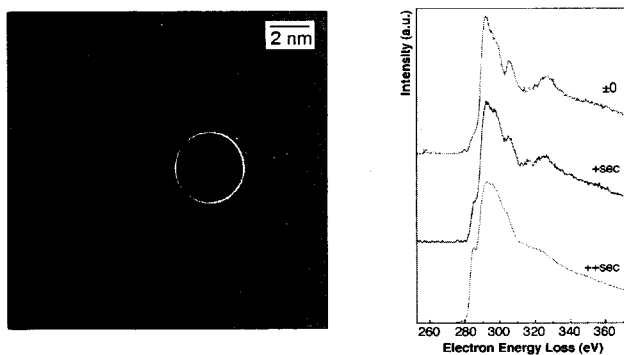


Fig. 1 Electron energy loss spectroscopy of a single nanodiamond particle. (Courtesy of T. Van Buuren and J. Plitzko.) Left: HRTEM picture of the UDD powder. The particle under study (~ 3 nm in diameter) is designated by the circle. The reader can notice the enhanced atomic planes. Right: EELS spectra as a function of exposure time. (View this art in color at www.dekker.com.)

detonation. The structure was shown to be diamond, with a small proportion of sp^2 -bonded carbon atoms.

The small UDD nanocrystals often aggregate in larger conglomerates, as shown in the study of Aleksenskii et al.,^[22] with small distortion of the initial spherical particle shape (Fig. 2).

The structure and defects of UDD have been extensively studied. In Ref. [24], infrared spectroscopy evidences O–H, C–H, C=C, C=O, and C–O–C groups. Other surface groups are evidenced by nuclear magnetic resonance (NMR). The electron spin resonance measurement indicates that nitrogen is not present as a substitutional (paramagnetic) site inside the particle's core. However, another group^[25] has measured a high concentration of paramagnetic centers. These are attributed to \dangling C–C bonds located at the interface between

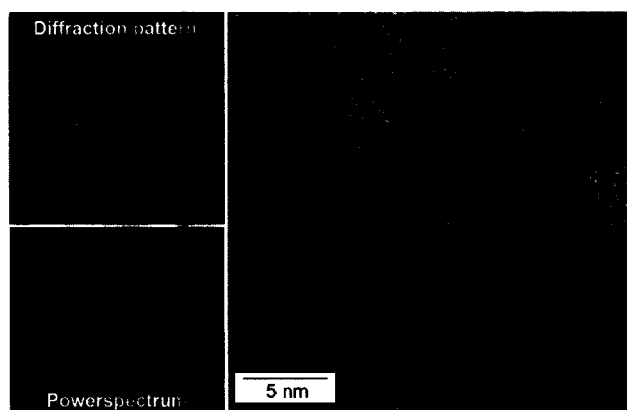


Fig. 2 Electron diffraction pattern (top left), power spectrum (bottom left), and HRTEM picture of the edge zone of a conglomerate of nanodiamonds (UDD). (From Ref. [23].)

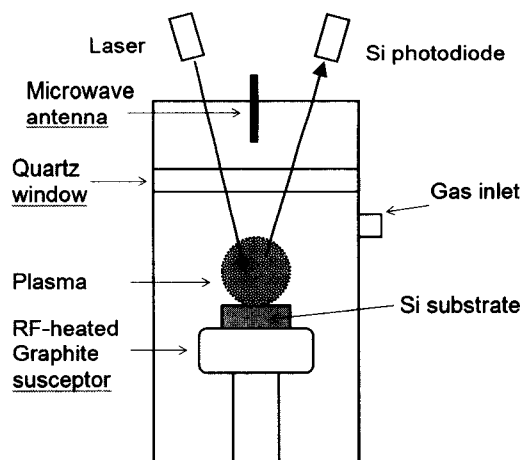


Fig. 3 Schematic representation of a plasma CVD reactor used in ultrananocrystalline diamond films production. (From Ref. [27].) (View this art in color at www.dekker.com.)

the diamond core and the graphene sheets forming the surface. A similar paramagnetism has been observed in Ref. [26].

Nanodiamond CVD Production

In the process of optimizing the CVD technique for the generation of high-quality diamond films, it was shown that, under some conditions, the deposited film was no more a microcrystals assembly, but a smooth film of much smaller diamond particles (Fig. 3).

A typical CVD experiment would involve the injection of a mixture of methane and hydrogen gas in a plasma reactor. The diamond film, with variable morphologies, is deposited on a silicon substrate.^[28] Under certain conditions of relative CH_4/H_2 concentrations and substrate temperature, it has been observed that the diamond film consisted of much smaller particles. The CVD-deposited diamonds films are distinguished into three categories: microcrystalline diamonds (0.5–10 μm), nanocrystalline diamonds (50–100 nm), and ultrananocrystalline (UNC) diamonds (2–5 nm). Garcia et al.^[29] reported diamond particles of 50 nm diameter by applying a negative d.c. bias voltage during the first minutes of the deposition from a mixture of 4% CH_4 in H_2 . The nanometric diamonds appear to be the first stage of diamond growth as long deposition times show them coalesce to form a microcrystalline diamond film. Gruen et al. managed to optimize the gas concentration to generate UNC diamonds.^a Replacing the major part of hydrogen by argon (typical

^aA complete review of ultrananocrystalline diamond properties and potential applications can be found in Ref. [27].

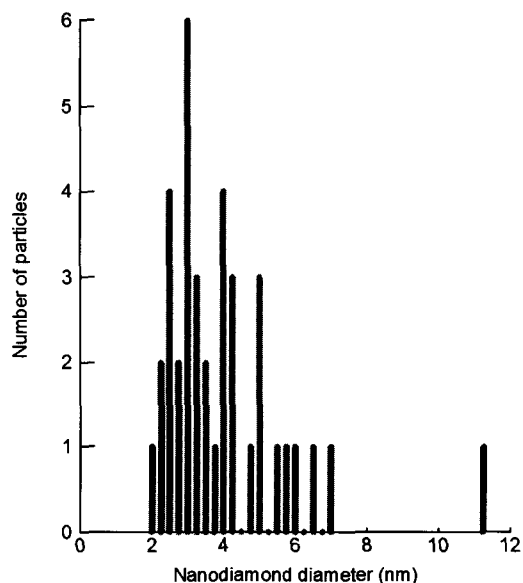


Fig. 4 Size histogram obtained from the analysis of an HRTEM image of an ultrananocrystalline diamond film where C_{60} was used as a substitute to CH_4 in the CVD reactor. (From Ref. [31].) (View this art in color at www.dekker.com.)

1% hydrogen) in the plasma causes the deposition of a smooth film of nanoparticles of only a few nanometers in size (Fig. 4).^[30] Those UNC films contain only 2–5% of sp^2 -bonded carbons in grain boundaries and less than 1% hydrogen.

Different plasma CVD techniques are used to produce diamond films. Nanocrystalline diamond crystals with a

typical size of 50–100 nm are produced by hollow cathode arc plasma CVD, or direct current glow discharge-assisted CVD, among many other experiments.^[32] In that last study, a detailed analysis of the proportion of nanodiamonds to graphite shows that up to 75% of carbon is present in the film as sp^3 -bonded carbon in 3- to 5-nm diamond crystals. The remaining sp^2 -bonded atoms are mostly present in the form of a thin graphite layer (150–200 nm) present between the substrate and the UNC diamond, as well as in grain boundaries. This UNC film has been shown to be stable up to 950°C.^[33]

NANODIAMOND STRUCTURES

Nanodiamonds that are produced under those very different conditions of atmosphere, temperature, and pressure have similar size distributions. In particular, extraterrestrial nanodiamonds, detonation nanodiamonds, and ultrananocrystalline diamonds have sizes that typically range between 2 and 5 nm (Fig. 4).

The crystallinity of nanodiamonds has been tested by diffraction, but is also directly observable by electron microscopy (enhanced atomic planes in Figs. 1 and 2 transmission electron micrographs). A complete crystallographic study of nanodiamonds produced in the three ways we have described (meteoritic, detonation, and CVD-UNC nanodiamonds) has been performed by Daulton et al.^[8] in an attempt to determine the origin and synthesis mechanism of meteoritic diamonds. In all those types of nanodiamonds, twinning is often observed,

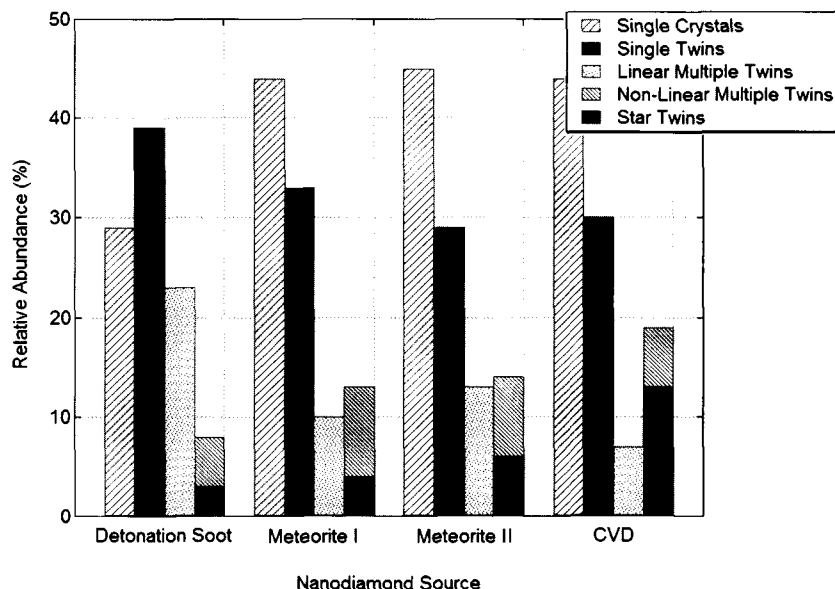


Fig. 5 Distribution of different twinning types in nanodiamonds from various origins. The meteoritic diamond originated from the Murchison meteorite (I) and the Allende meteorite (II). One can note the similarity in the twinings in meteoritic and CVD nanodiamonds. (From Ref. [8].) (View this art in color at www.dekker.com.)

preferentially for the largest particles. Twinning can take different forms, from simple twins, to multiple, to even fivefold star twins. However, the shape of the nanoparticles is globally spherical (Fig. 5).

The structure of the nanodiamond surface is little known. sp^2 -bonded carbon may be present at the surface and in UNC diamond film grain boundaries.^[34] Hydrogen is present in all three varieties of nanodiamonds, but other impurities have been evidenced in detonation-produced and extraterrestrial nanodiamonds.

Maillard-Schaller et al.^[35] have measured the impurity content of detonation-produced nanodiamonds by Raman and X-ray photoelectron spectroscopy (XPS). The major impurity is oxygen. The nitrogen content of their samples is 1–2% and traces of N, Fe, S, and Ar are also found. H_2 plasma treatment of the nanodiamonds deposited on a Si substrate by electrophoresis causes oxygen impurities to leave the sample, whereas the nitrogen content remains the same. The sp^3/sp^2 content of the diamonds is unchanged by the high-temperature treatment.

NANODIAMOND PROPERTIES

Very few theoretical studies of single nanodiamonds properties have been performed. Halicioglu^[36] relaxed spherical nanometric diamond slabs with Brenner potentials. The so-formed structures exhibit inward relaxation from the top surface layers, the interatomic distance between neighboring atoms decreasing from the center of the cluster to the surface. They also noticed significant variations in relative cohesive energy with respect to bulk diamond. Recently, an *ab initio* molecular dynamics simulation, a parameter-free technique that solves quantum mechanical equations with great accuracy, was used

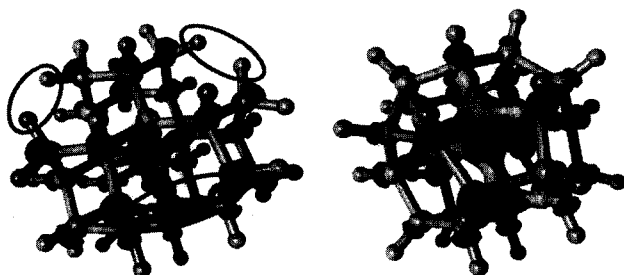


Fig. 6 Structure of a 0.7-nm 29-carbon atom cluster. Left: The fully hydrogenated cluster. Right: The result of surface reconstruction induced by the removal of six pairs of hydrogen atoms (circled on the left). Carbon atoms are in light grey; hydrogen atoms are in dark grey. The isosurfaces represent the lowest unoccupied molecular orbital (LUMO; here located on the C—H bonds) and the highest occupied molecular orbital (HOMO; here located at the center of the cluster) drawn at 30% of their maximal value. (View this art in color at www.dekker.com.)

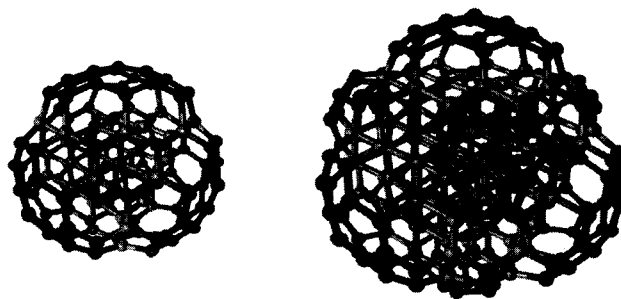


Fig. 7 C_{147} and C_{275} bucky diamonds. The diamond core atoms are represented in light grey. (From Ref. [23].) (View this art in color at www.dekker.com.)

to simulate the structure and to compute the electronic and optical properties of nanodiamonds.^[23] Contrary to classical treatment, the quantum simulation of nanodiamonds yields an expansion of the cluster volume with respect to bulk diamonds. That tensile stress is at the opposite of what is observed in Si or Ge nanoparticles. The surface reconstruction of nanodiamonds has been shown to strongly affect electronic structure, as shown in Fig. 6.

When the totality of hydrogen is removed from the cluster, the surface is shown to sometime reconstruct in a specific way, forming the so-called “bucky diamonds.” These structures consist of a diamond core the surface of which is reconstructed in a fullerene-like manner (Fig. 7).

The optical properties of nanodiamonds have been studied mostly by X-ray techniques. The X-ray emission and absorption spectra of detonation nanodiamonds are

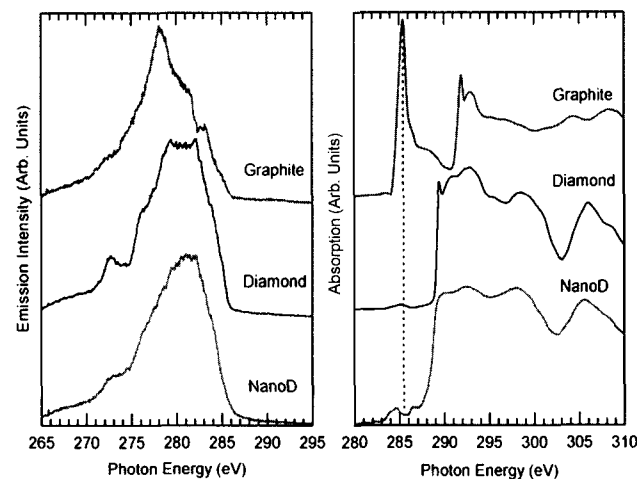


Fig. 8 X-ray emission (left) and absorption (right) spectra from highly oriented pyrolytic graphite (HOPG), bulk diamonds, and detonation-produced nanodiamonds (4 nm average size). (From Ref. [23].) (View this art in color at www.dekker.com.)

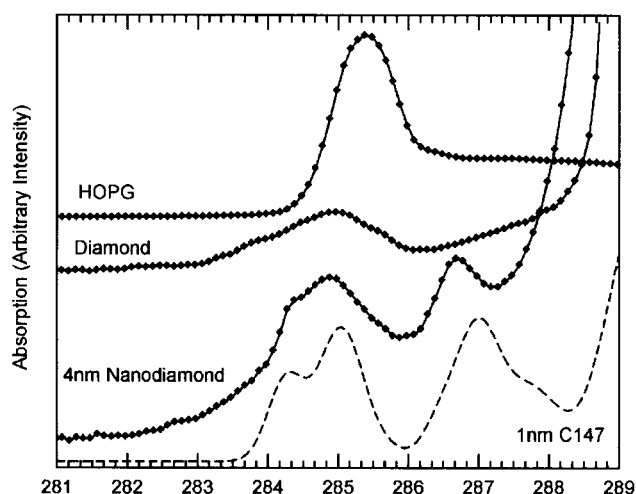


Fig. 9 Detail of the pre-edge X-ray absorption spectra of HOPG, bulk diamonds, and detonation nanodiamonds vs. the X-ray energy in electron volts. The density of unoccupied states computed *ab initio* from a C_{147} bucky diamond is shown for comparison (dashed line). (From Ref. [23].)

very similar to those of bulk diamonds and are totally different from graphite (Fig. 8).

The differences between bulk diamonds and nanodiamonds are exciton broadening (289.3 eV) and a shallower secondary minimum (302 eV). However, there

are some pre-edge features in the nanodiamond absorption spectrum that are not caused by impurities and are reproducible (Fig. 9). These features could be the signature of specific surface reconstructions such as in bucky diamonds.

Other information can be obtained from Fig. 8: There is no shift in valence and conduction band maximum and minimum in comparison with bulk diamonds. This indicates that quantum confinement does not affect the electronic structure for particles 4 nm and larger. This property can also be observed on computed absorption spectra from Fig. 10.

The optical properties of UDD layers have been studied optically and by XPS by Aleksenskii et al.^[37] The band gap is measured to be 3.5 eV, with many energy levels present in the nanodiamonds band gap and contributing to a broad luminescence band (380–520 nm). The optical absorption of the material is attributed to threefold coordinated atoms on the surface. The unannealed sample contains 8% N and 22% O, mainly under the form of nitrate ions attached to the particle's surface.

The electron transport in ultradisperse diamonds deposited on quartz substrates has been measured by He et al.^[40] The conductivity of the films is shown to decrease with annealing. Surprisingly, it is semiconducting at high temperature but the temperature dependence of the conductivity is negative at lower temperatures. This behavior is attributed to conduction through surface

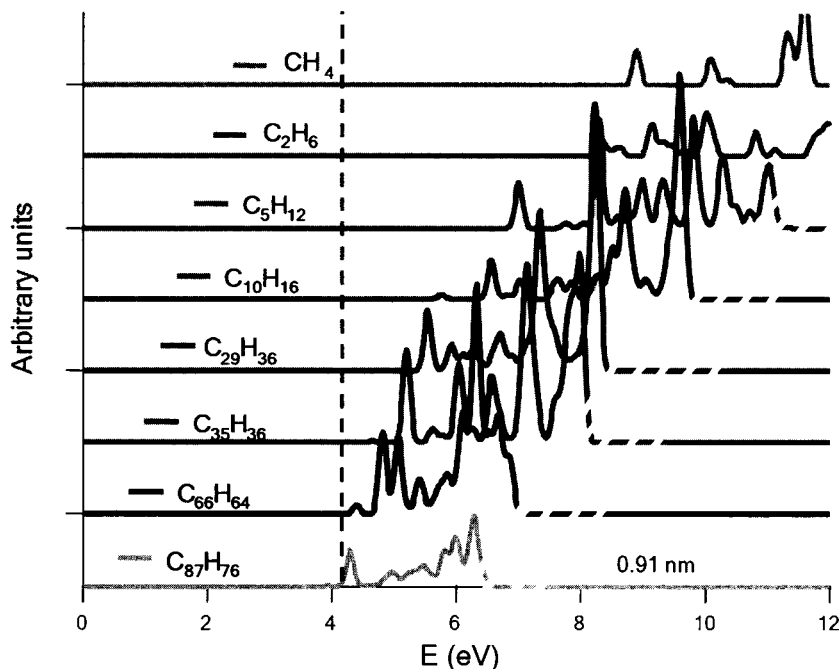


Fig. 10 Optical spectra of carbon clusters ranging from methane to 1-nm nanodiamonds. The spectra are computed using the time-dependent local density approximation on *ab initio*-relaxed cluster geometries. (From Refs. [38] and [39].) The dashed line shows the bulk absorption threshold computed with the same method (4.23 eV for an experimental value of 5.5 eV). (View this art in color at www.dekker.com.)

conduction (π -type because of graphite-like sheets) at low temperature and through diamond core σ -type conduction at higher temperature.

An interesting property of a hydrogenated diamond surface is its "negative electron affinity," the ability of an electron that is excited in the conduction band to freely leave the material. Nanodiamonds have smaller bandgaps than bulk diamond, and for that reason are excellent candidates for low-threshold electron emission devices. The additional requirement is that the electron affinity is small, or even negative. The electron emission of the UDD film from Ref. [40] is strong and has a low field threshold (3.2 V/ μm). It has been attributed to grain boundaries of nanodiamond films, rather than substrates. A similar field emission study was performed on ultrananocrystalline diamond films by Krauss et al.^[41] The emission is again attributed to conduction through the grain boundaries–vacuum interface. With moderate heating (200–300°C), the photoemission yield is increased by a factor of 5.^[42] When the hydrogenated UNC film is exposed to air, electron affinity is actually shown to become negative. A similar negative electron affinity has been measured after treating a film of deposited nanodia-

monds obtained from detonation, but only after treating the film with H_2 plasma, which removes most of the impurities, except nitrogen.^[35]

NANODIAMOND NITROGEN N-DOPING

A very promising way to have nanodiamond films incorporated in technological applications is by doping them with nitrogen. The goal is to introduce carrier levels into the diamond gap (this level is located 1.7 eV below the conduction band minimum in bulk diamonds) to increase conductivity and to lower the electron emission voltage threshold. Nitrogen is a major impurity of natural diamond. As we said before, nanodiamonds produced by detonation contain a high percentage (1–2%) of nitrogen. This nitrogen is brought into the diamonds from the trinitrotoluene reactant and cannot be removed from the nanoparticles.^[35] The precise location of the nitrogen atoms in the nanoparticles is uncertain, but several magnetic studies have been unable to see any trace of substitutional nitrogen (known as P1 center).^[24] This is surprising as nitrogen is present in N-doped

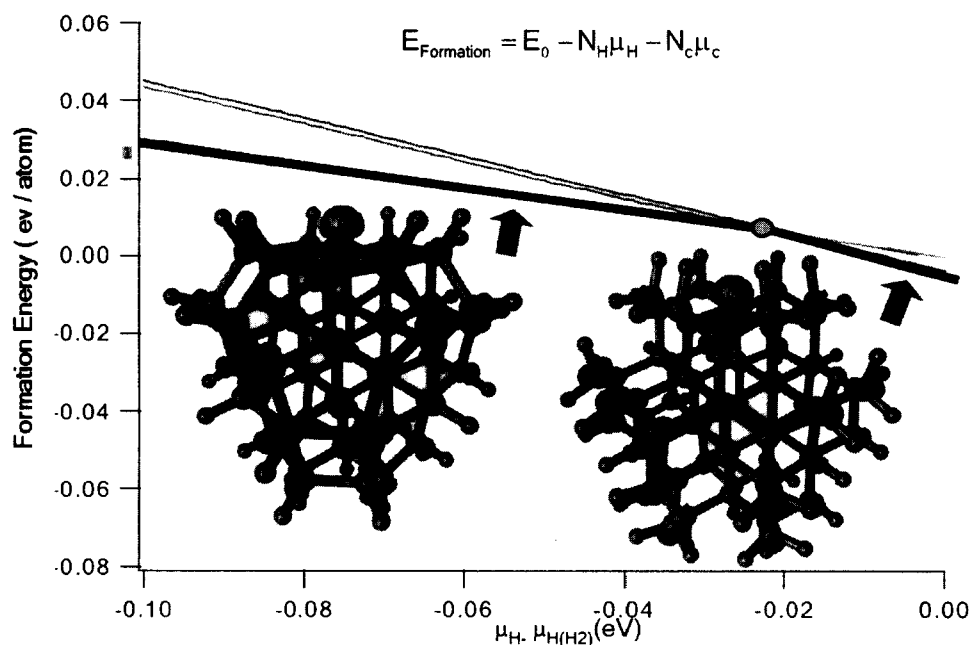


Fig. 11 Formation energy of 66 carbon atom clusters containing one nitrogen impurity atom as a function of the hydrogen chemical potential μ_{H} (eV). This energy is the difference between the cluster's total energy and the energy the same number of carbon and hydrogen atoms (N_{C} and N_{H}) would have in their most stable form (here we consider diamond and the H_2 molecule). The origin of μ_{H} (eV) is taken as the energy of one hydrogen atom in the H_2 molecule. The thick black segments indicate the most stable structures. The stable configurations are the $\text{C}_{65}\text{H}_{65}\text{N}$ and $\text{C}_{65}\text{H}_{39}\text{N}$ clusters. In these, the nitrogen atom is substitutional in the particle's surface. Above ~ -0.02 eV, the stable structure is a fully hydrogenated cluster in which the nitrogen atom (in blue) sits on the surface. Below this energy (this would correspond to a higher temperature and/or a lower hydrogen pressure), the stable structure has a partially reconstructed surface in which the nitrogen resides. The $\text{C}_{65}\text{H}_{66}\text{N}$ and $\text{C}_{65}\text{H}_{40}\text{N}$ clusters in which the nitrogen atom is substitutional to a core carbon atom are never stable (thin lines). The isosurfaces are drawn at 30% of the maximal value of the HOMO (on the nitrogen atom) and LUMO (on C–H bonds), respectively. (View this art in color at www.dekker.com.)

CVD-produced microcrystals as a substitute to core carbon atoms.^[43] A theoretical study of the grain boundaries of UNC diamonds in the presence of nitrogen impurities has been performed by Zapol et al.^[44] This tight-binding density functional study shows that nitrogen substitution to carbon in the grain boundary is energetically more favorable than in the crystal's core. The conductivity increase of the N-doped film is then attributed to an increase in threefold coordinated carbon atoms caused by the nitrogen impurity. A recent ab initio molecular dynamics study^[39] shows that for small diamond clusters, nitrogen is preferentially present as a substitute to surface carbon. The tensile stress evidenced in those nanoparticles^[23] facilitates nitrogen inclusion in comparison to bulk diamonds, where intentional nitrogen doping has proven to be difficult. Nitrogen incorporation is shown to require more and more energy with increasing particle size (Fig. 11).

Nitrogen doping of UNC films has been studied by Bhattacharyya et al.^[45] Doping is achieved by introducing nitrogen gas (1–20%) into the mixture fed to the CVD reactor. They achieved the highest carrier concentration and electrical conductivity ever measured for a phase-pure diamond thin film. The increase of N₂ gas concentration causes larger grain boundaries and larger grains to be deposited, and increases the conductivity up to 143 Ω⁻¹ cm⁻¹. This large conductivity is attributed to the large proportion of nitrogen atoms in the grain boundaries. The optical and emission properties of N-doped UNC diamond films are still under investigation. A theoretical study^[39] has compared the energy gap of hydrogen-terminated nanodiamonds clusters and clusters including various nitrogen impurities on the surface as a function of size. The variation is faster for reconstructed surfaces because of the size evolution of the surface curvature. For nonreconstructed surfaces, the curvature changes little with cluster size and the energy gap remains almost constant and smaller than for H-terminated clusters (Fig. 12).

NANODIAMONDS FOR THE FUTURE

Nanodiamonds are very promising materials for application, especially under the form of ultrananocrystalline diamond thin films. An extensive review of UNC film properties and potential applications can be found in Ref. [27]. We have cited the perspectives offered in field-induced and light-induced induced emission by nitrogen-doped UNC films. They could be used to produce bright, low-voltage (cold) cathodes. They may be used in the future as microelectromechanical system (MEMS) materials. Pioneer devices have been successfully produced by Krauss et al.^[46] The exceptional hardness, fracture strength, and inertness of the films,

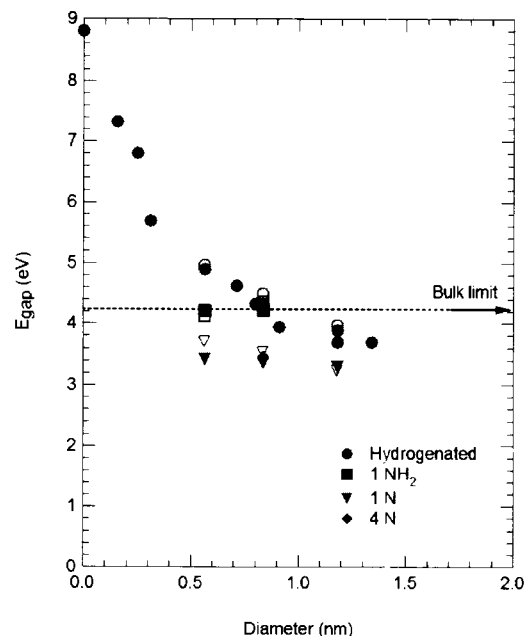


Fig. 12 Computed HOMO–LUMO energy gaps for various nanodiamond structures. Red circles: Hydrogenated nanoclusters; black squares: nanodiamonds with a NH₂ surface group; green triangle: one surface substitutional nitrogen; pink diamond: four surface substitutional nitrogen atoms. The filled symbols represent the nonreconstructed, maximally hydrogenated nanodiamonds; the empty symbols represent (100) reconstructed surfaces. (View this art in color at www.dekker.com.)

together with a smooth surface, make UNC a unique material for miniaturized mechanical systems and devices, such as cantilevers, gears, etc. The hydrogen termination of the surface also brings a “natural lubricant” to the moving devices.

UNC diamonds also have potential applications in optoelectronics, as photonic switches, electronic devices (pn junctions), etc. They are on their way to being commercially used as surface acoustic wave devices. Recent experiments have even used UNC films as support to attach ADN.^[47] These devices have proven to be extremely stable and have opened the way to the integration of biology in electronics.

CONCLUSION

Nanodiamonds have unique, fascinating properties, as isolated particles or in thin films, but many aspects still have to be understood. The interaction between nanodiamonds is largely unknown. The most intriguing fact is that all types of nanodiamonds have similar features and size distributions (independently of the production type), extreme pressure and temperature, and low-pressure CVD, and are around stars. Indeed, everywhere where

scientists have looked for carbon nanostructures with a high-resolution microscope, they found nanodiamonds. Would they not be everywhere around us?

ACKNOWLEDGMENTS

This work was performed under the auspices of the US Department of Energy at the University of California/Lawrence Livermore National Laboratory under contract no. W-7405-Eng-48. J. Y. R. acknowledges support from the FNRS.

REFERENCES

1. Badziag, P.; Verwoerd, W.S.; Ellis, W.P.; Greiner, N.R. Nanometre-sized diamonds are more stable than graphite. *Nature* **1990**, *343*, 244–245.
2. Hwang, N.M.; Hahn, J.H.; Yoon, D.Y. Charged cluster model in the low pressure synthesis of diamond. *J. Cryst. Growth* **1996**, *162*, 55–68.
3. Jang, H.M.; Hwang, N.M. Theory of the charged cluster formation in the low pressure synthesis of diamond: Part II. Free energy function and thermodynamic stability. *J. Mater. Res.* **1998**, *13*, 3536–3549.
4. Gamarnik, M.Y. Energetical preference of diamond nanoparticles. *Phys. Rev., B* **1996**, *54*, 2150–2156.
5. Lewis, R.S.; Tang, M.; Wacker, J.F.; Anders, E.; Steel, E. Interstellar diamonds in meteorites. *Nature* **1987**, *326*, 160–162.
6. Lewis, R.S.; Anders, E.; Draine, B.T. Properties, detectability and origin of interstellar diamonds in meteorites. *Nature* **1989**, *339*, 117–121.
7. Amarti, S.; Lewis, R.S.; Anders, E. Interstellar grains in meteorites: I. Isolation of SiC, graphite and diamond; size distributions of SiC and graphite. *Geochim. Cosmochim. Acta* **1994**, *58*, 459–470.
8. Daulton, T.L.; Eisenhour, D.D.; Bernatowicz, T.J.; Lewis, R.S.; Buseck, P.R. Genesis of presolar diamonds: Comparative high-resolution transmission electron microscopy study of meteoritic and terrestrial nanodiamonds. *Geochim. Cosmochim. Acta* **1996**, *60*, 4853–4872.
9. Koscheev, P.; Gromov, M.D.; Mohapatra, R.K.; Ott, U. History of trace gases in presolar diamonds inferred from ion-implantation experiments. *Nature* **2001**, *412*, 615–617.
10. Dai, Z.R.; Bradley, J.P.; Joswiak, D.J.; Brownlee, D.E.; Hill, H.G.M.; Genge, M.J. Possible in situ formation of meteoritic nanodiamonds in the early solar system. *Nature* **2002**, *418*, 157–159.
11. Buss, R.H.; Cohen, M.; Tielens, A.G.; Werner, M.W.; Bergman, J.D.; Witteborg, F.C.; Rank, D.; Sanford, S.A. Hydrocarbon emission features in the infrared spectra of warm supergiants. *Astrophys. J.* **1990**, *365*, L23–L26.
12. Volk, K.; Kwok, S.; Hrivnak, B.J. High-resolution infrared space observatory spectroscopy of the unidentified 21 micron feature. *Astrophys. J.* **1999**, *516*, L99–L102.
13. Justanont, K.; Barlow, M.J.; Skinner, C.J.; Roche, P.F.; Aitken, D.K.; Smith, C.H. Mid-infrared spectroscopy of carbon-rich post-AGB objects and detection of the PAH molecule chrysene. *Astron. Astrophys.* **1996**, *309*, 612–628.
14. Hill, H.G.; Jones, A.P.; d'Hendecourt, L.B. Diamonds in carbon-rich proto-planetary nebulae. *Astron. Astrophys.* **1998**, *336*, L41–L44.
15. Van Kerkhoven, C.; Thielens, A.G.; Waelkens, C. Nanodiamonds around HD 97048 and Elias 1. *Astron. Astrophys.* **2002**, *384*, 568–584.
16. Van Thiel, M.; Ree, F.H. Properties of carbon clusters in TNT detonation products: The graphite diamond transition. *J. Appl. Phys.* **1987**, *62*, 1761–1767.
17. Greiner, N.R.; Philips, D.S.; Johnson, J.D.; Volk, F. Diamonds in detonation soots. *Nature* **1998**, *333*, 440–442.
18. Viecelli, A.; Bastea, S.; Glosli, J.N.; Ree, F.H. Phase transformation of nanometer size carbon particles in shocked hydrocarbon and explosives. *J. Chem. Phys.* **2001**, *115*, 2730–2736.
19. Aleksenski, A.E.; Baidakova, M.V.; Vul', A.Ya.; Siklitsky, V.I. The structure of diamond nanoclusters. *Phys. Solid State* **1999**, *41*, 740–743.
20. Baidakova, M.V.; Siklitsky, V.I.; Vul', A.Ya. Ultradisperse-diamond nanoclusters. Fractal structure and diamond-graphite phase transition. *Chaos Solitons Fractals* **1999**, *10*, 2153–2163.
21. Chen, P.W.; Ding, Y.S.; Chen, Q.; Huang, F.L.; Yun, S.R. Spherical nanometer-sized diamond obtained from detonation. *Diamond Relat. Mater.* **2000**, *9*, 1722–1725.
22. Aleksenskii, A.E.; Osipov, V.Yu.; Dideikin, A.T.; Vul', A.Ya.; Adriaenssens, G.J.; Afanas'ev, V.V. Ultradisperse diamond cluster aggregation studied by atomic force microscopy. *Tech. Phys. Lett.* **2000**, *26*, 819–821.
23. Raty, J.Y.; Galli, G.; Van Buuren, T.; Bostedt, C.; Terminello, L. Quantum confinement and fullerene-like surface reconstructions in nanodiamonds. *Phys. Rev. Lett.* **2003**, *90*, 037401–037404.
24. Iakoubovskii, K.; Baidakova, M.V.; Wouters, B.H.; Stesmans, A.; Adriaenssens, G.J.; Vul', A.Ya.; Grobet, P.J. Structure and defects of detonation synthesis nanodiamonds. *Diamond Relat. Mater.* **2000**, *9*, 861–865.

25. Shames, A.I.; Panich, A.M.; Kempinski, W.; Alenskenskii, A.E.; Baidakova, M.V.; Dideikin, A.T.; Osipov, V.Yu.; Siklitski, V.I.; Osawa, E.; Osawa, M.; Vul', A.Ya. Defect and impurities in nanodiamonds: EPR, NMR and TEM study. *J. Phys. Chem. Solids* **2002**, *63*, 1993–2001.
26. Belobrov, P.I.; Gordeev, S.K.; Petrakovskaya, E.A.; Falaleev, O.V. Paramagnetic properties of nanodiamonds. *Dokl., Phys.* **2001**, *46*, 459–462.
27. Butler, J.E.; Windischmann, H. Developments in CVD-diamond synthesis during the past decade. *MRS Bulletin* **1998**, *23*, 22–27.
28. Fayette, L.; Marcus, B.; Mermoux, M.; Tourillon, G.; Laffon, K.; Parent, P.; Le Norm, F. Local order in CVD diamond films: Comparative Raman, x-ray diffraction and x-ray absorption near-edge studies. *Phys. Rev., B* **1998**, *57*, 14123–14132.
29. Garcia, M.M.; Jimenez, I.; Gomez-Aleixandre, C.; Abella, J.M.; Sanchez, O.; Terminello, L.J.; Himpsel, F.J. X-ray absorption spectroscopy and atomic force microscopy study of bias-enhanced nucleation of diamond films. *Appl. Phys. Lett.* **1998**, *72*, 2105–2107.
30. Jiao, S.; Sumant, A.; Kirk, M.A.; Gruen, D.M.; Krauss, A.R.; Auciello, O. Microstructure of ultrananocrystalline diamond films grown by microwave Ar-CH₄ plasma chemical vapor deposition with or without H₂. *J. Appl. Phys.* **2001**, *90*, 118–122.
31. Qin, L.C.; Zhou, D.; Krauss, A.R.; Gruen, D. TEM characterization of nanodiamonds thin films. *Nanostruct. Mater.* **1998**, *10*, 649–660.
32. Heiman, A.; Gouzman, I.; Christiansen, S.H.; Strunk, H.P.; Comtet, G.; Hellner, L.; Dujardin, G.; Edrei, R.; Hoffman, A. Evolution and properties of nanodiamonds films deposited by direct current glow discharge. *J. Appl. Phys.* **2001**, *89*, 2622–2630.
33. Hoffman, A.; Heiman, A.; Christiansen, S.H. Mechanism of diamond film formation by stress relaxation on a preferentially oriented basal plane graphitic precursor. *J. Appl. Phys.* **2001**, *89*, 5769–5773.
34. Koblinski, P.; Wolf, D.; Phillpot, S.R.; Gleiter, H. Role of bonding and coordination in the atomic structure of grain boundaries of diamond and silicon. *J. Mater. Res.* **1998**, *13*, 1077–1099.
35. Maillard-Schaller, E.; Kuettel, O.M.; Diederich, L.; Schlapbach, L.; Zhirnov, V.V.; Belobrov, P.I. Surface properties of nanodiamonds films deposited by electrophoresis on Si(100). *Diamond Relat. Mater.* **1999**, *8*, 805–808.
36. Halicioglu, T. Properties of diamond and diamond-like clusters in nanometric dimensions. *Phys. Status Solidi, B* **1997**, *199*, 345–350.
37. Aleksenskii, A.E.; Osipov, V.Yu.; Vul', A.Ya.; Ber, B.Ya.; Smirnov, A.B.; Melekhin, V.G.; Adriaenssens, G.J.; Iakoubovskii, K. Optical properties of nanodiamonds layers. *Phys. Solid State* **2001**, *43*, 145–150.
38. Gonze, X.; Beuken, J.M.; Caracas, R.; Detraux, F.; Fuchs, M.; Rignanese, G.M.; Sindic, L.; Verstraete, M.; Mikami, M.; Ghosez, P.; Raty, J.Y.; Allan, D.C. First principles computation of material properties: The ABINIT software project. *Comput. Mater. Sci.* **2002**, *25*, 478–492.
39. Raty, J.Y.; Galli, G.; Hood, R.Q. In press.
40. He, D.; Shao, L.; Gong, W.; Xie, E.; Xu, K.; Chen, G. Electron transport and electron field emission of nanodiamonds synthesized by explosive detonation. *Diamond Relat. Mater.* **2000**, *9*, 1600–1603.
41. Krauss, A.R.; Auciello, O.; Ding, M.Q.; Gruen, D.M.; Huang, Y.; Zhirnov, V.V.; Givargizov, E.I.; Breskin, A.; Chechen, R.; Shefer, E.; Konov, V.; Pimetov, S.; Karabutov, A.; Rakhimov, A.; Suetin, N. Electron field emission for ultrananocrystalline diamond film. *J. Appl. Phys.* **2001**, *89*, 2958–2967.
42. Piantanida, G.; Breskin, A.; Chechik, R.; Katz, O.; Laikhtman, A.; Hoffman, A.; Coluzza, C. Effect of moderate heating on the negative electron affinity and photoyield of air-exposed hydrogen-terminated chemical vapor deposited diamond. *J. Appl. Phys.* **2001**, *89*, 8259–8264.
43. Nokhrin, S.; Rosa, J.; Vanecek, M.; Badalyan, A.G.; Nesladek, M. EPR study of preferential orientation of crystallites in N-doped high quality CVD diamond. *Diamond Relat. Mater.* **2001**, *10*, 480–484.
44. Zapol, P.; Sternberg, M.; Curtiss, L.A.; Fraunheim, Th.; Gruen, D.M. Nitrogen impurities in ultrananocrystalline diamond grain boundaries. *Mater. Res. Symp. Proc.* **2000**, *593*, 483–487.
45. Bhattacharyya, S.; Auciello, O.; Birrel, J.; Carlisle, J.A.; Curtiss, L.A.; Coyette, A.N.; Gruen, D.M.; Krauss, A.R.; Schlueter, J.; Sumant, A.; Zapol, P. Synthesis and characterization of highly conducting nitrogen-doped ultrananocrystalline diamond films. *Appl. Phys. Lett.* **2001**, *79*, 1441–1443.
46. Krauss, A.R.; Auciello, O.; Gruen, D.M.; Jayatissa, A.; Sumant, A.; Tucek, J.; Mancini, D.C.; Moldovan, N.; Erdemir, A.; Ersoy, D.; Gardos, M.N.; Busmann, H.G.; Meyer, E.M.; Ding, M.Q. Ultrananocrystalline thin films for MEMS and moving mechanical assembly devices. *Diamond Relat. Mater.* **2001**, *10*, 1952–1961.
47. Yang, W.; Auciello, O.; Butler, J.E.; Cai, W.; Carlisle, J.A.; Gerbi, J.E.; Gruen, D.M.; Knickerbocker, T.; Lasseter, T.L.; Russel, J.N.; Smith, L.M.; Hamers, R.J. DNA modified nanocrystalline diamond thin-films as stable, biologically active substrates. *Nat. Mater.* **2002**, *1*, 253–257.

Nanoencapsulation of Bioactive Substances

Yury E. Shapiro

Bar-Ilan University, Ramat-Gan, Israel

INTRODUCTION

Nanoencapsulation is one of the most important subcategories of controlled-release bionanotechnology. Normally, active substances are encapsulated in submicrometer-sized devices made of barrier materials. These materials are designed to control the rate of release. This concept has been largely inspired by spontaneous assembling of the phospholipid liposomes as a model of biological membranes.^[1] As in Nature, one has to develop preparations of nanovehicles that allow precise control over their structure and morphology. In this context, the self-assembled superstructures of surfactants (micelles, liposomes)^[2] and/or polymers (nanoparticles) have proven to be valuable tools.^[3]

Nanoparticles may be defined as being submicrometer (from 10 to 1000 nm) colloidal systems generally, but not necessarily, made of polymers (biodegradable or not).^[4-6] Depending on the process used for their preparation, two different types of nanoparticles can be obtained, namely, nanospheres and nanocapsules. Unlike nanospheres (matrix systems where the bioactive substance is dispersed throughout the particles), nanocapsules exhibit a membrane-wall structure with an aqueous or oily core containing the bioactive substance. Thus, nanocapsules may be considered as a "reservoir" or "envelop" system. Because nanoparticles have very high surface areas, the active substance may also be adsorbed or conjugated onto the surface.^[6] At present, micellar/liposomal systems have also been included under the term "nanoparticles."

Another type of nanometer-sized carriers is an inclusion complex or clathrate, which can be assembled by inclusion of bioactive substances into molecular cavities of the so-called cavitands,^[7] or dendrimers.^[8,9] Natural examples of such internal-cavity-containing molecules are cyclodextrins, which are used widely for preparation of various drug formulations.^[10] The outer diameter of molecular nanocapsules is in the range of 3–50 nm. The nanometer size ranges of liposomes, nanoparticles, and clathrates offer certain distinct advantages for drug delivery. Because of their subcellular size, they can penetrate deep into tissues through fine capillaries, cross the fenestration present in the epithelial lining (e.g., liver), and generally are taken up efficiently by the cells to

perform the so-called intracellular trafficking.^[6,11,12] This allows direct delivery of therapeutic agents to target sites in the body followed by the controlled release.^[13]

CONTROLLED RELEASE

Controlled-release nanotechnology can solve a variety of problems regarding the effective delivery of a bioactive compound to a target to achieve good local and systemic tolerance during and after application.^[14] In controlled-release systems, a drug or some other active agent is incorporated into a self-assembled carrier. The main condition of success is to design tissue-friendly and biodegradable accompanying materials.^[4-6] The delivery carriers are usually required for the following reasons: 1) many effective drugs are characterized by poor aqueous solubility and need to be solubilized; 2) many drugs, such as proteins, are very fragile and need a microenvironment providing protection from hydrolysis or enzymatic degradation; 3) many drugs are highly toxic and require a carrier to shield tissues until the drug release at the targeted tissue occurs; 4) the release itself has to be designed to allow controlling; and 5) targeted delivery of drug can be attained by conjugating a specific vector to the carrier.^[15]

The rate of releasing the agent depends on the nature of the carrier as well as various environmental factors (such as nature of solvent, osmotic pressure, temperature, pH of media, and so on). The controlled release, depending on rate of releasing, can be classified as triggered, pulsing, or sustained. The rate of delivery of any bioactive substance to a target tissue or reaction site is highly critical. Key advantages to the use of this technology are prolonged activity, fewer doses, fewer undesirable side effects, and reduced toxicity.^[5]

Three mechanisms of controlled release can be considered: diffusion controlled (through membranes and from matrices), chemically controlled (erosion and cleavage of polymer chain or spacer connecting bioactive agent with carrier, if any), and solvent activated (osmotic pressure and swelling). Each mechanism has certain advantages and must be selected for design of carrier depending on the agent to be released as well as the

conditions required to yield favorable release. Recently, significant effort has been devoted to develop nanotechnology for controlled drug delivery devices because it offers a suitable means of delivering low molecular weight drugs, as well as macromolecules such as peptides, proteins, DNA, or genes by either localized or targeted delivery to the tissue of interest.^[6,11,16,17]

LIPOSOMES

Liposomes (or vesicles) are topologically closed nano-sized lamellar aggregates of highly ordered lipid molecules that are normally dispersed in a hydrophilic solvent, typically water. The aggregates may be formed by the combination of both polar and nonpolar residues in the same lipid molecule, which is described as amphiphilic. In aqueous medium the amphiphilic molecules arrange the ordered micellar or lamellar structures depending on the concentration, in which the hydrophobic regions are brought into proximity with each other while the polar groups are exposed to water. The amphiphiles are capable of forming a variety of phases due to steric factors such as head group size, variation in the number of acyl chains, or to electrostatic effects arising from attractive or repulsive forces between adjacent polar head groups.^[18] The different phases can interconvert, either by inward or outward migration of particular amphiphiles changing their shape. Heating, for example, increases the dynamic motion of hydrocarbon chains, effectively broadening the nonpolar region. Changes in pH can affect an ionization of polar head groups and so alter their diameter, as can changes in their hydration level.^[19] Thus, bilayer to nonbilayer transition can take place, resulting in loss of membrane barrier function. These transitions can be exploited to design liposomal carrier systems with preset release properties that are triggered by changes in their microenvironment.^[19]

Normal micelles, which have only short-range order, form spontaneously when the amphiphiles are added to water. The liquid crystalline phases, which exhibit long-range order, like lamellar (cubic) and normal hexagonal phases, do not disperse spontaneously. When the lamellar phase is diluted with excess aqueous phase, it converts into spherical liposomes (Fig. 1),^[2] which are widespread carriers for drugs, cosmetics, and many other types of actives.^[19] Because of the presence of the aqueous core and the hydrophobic lipid bilayers, liposomes can accommodate both hydrophilic and hydrophobic actives. The liposomes can be constructed with widely different physical structures, lipid composition, and surface properties, thus enabling a great deal of control over entrapment and release of their contents.

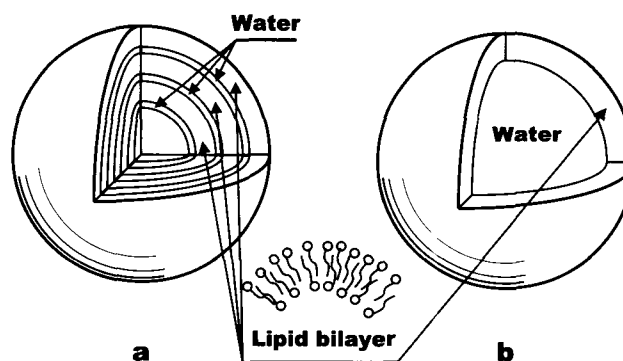


Fig. 1 Schematic structure of liposomes: (a) multilamellar vesicles, MLV, and (b) small and large unilamellar vesicles, SUV and LUV.

Three kinds of liposomes are in common use. Large spherical liposomes, each consisting of numerous concentric bilayers, alternating with layers of water, are known as multilamellar vesicles (MLVs) (Fig. 1a).^[2] The MLVs are simple to produce, but the volume available for solute entrapment is limited. By gentle swirling, individual lamellae are able to detach to form large unilamellar vesicles (LUVs) (Fig. 1b).^[20] Because the interior of LUVs is not occupied by internal lamellae, there is ample space for incorporation of actives. This also means that cells taking up LUVs are less subject to lipid overload. However, LUVs are more fragile than MLVs. In general, MLVs and LUVs vary in their outer diameter, from 100 nm up to 10 μm . Their large size range is considered to be a drawback for many medical applications requiring parenteral administration because it leads to rapid clearance from the bloodstream by the cells of the reticuloendothelial system (RES).

Small unilamellar liposomes (SUVs), with outer diameter in the range of 20–100 nm,^[21] can be obtained by ultrasonication of MLVs.^[18] Because of their small size, clearance from the systemic circulation is significantly reduced, but SUVs have a much lower capacity for drug entrapment, typically less than 1% of the material available.

Preparation of Liposomes

Multilamellar vesicles

Multilamellar vesicles (Fig. 2a) may be prepared from natural or synthetic lipids by suspending them in an aqueous solution maintained at a temperature above the melting point T_c of the lipid. For unsaturated phospholipids such as egg and soy phosphatidylcholine, which have T_c values below 0°C, this can be done by stirring in

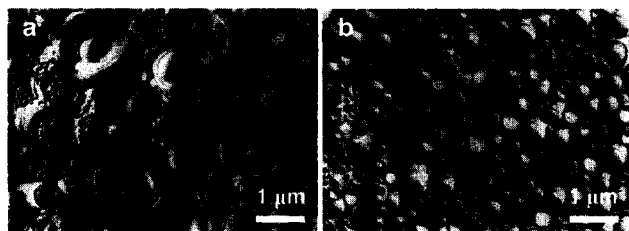


Fig. 2 Freeze-fracture transmission electron micrographs of liposomes: (a) MLV constituted from 0.1 M mixture of tetradecyldimethylaminoxide/tetradecyltrimethyl ammonium bromide/hexanol=9/1/20, and (b) SUV prepared from 3wt.% didodecyldimethyl ammonium bromide in water. (From Hoffmann, H.; Thunig, C. et al. *Langmuir* **1994**, *10* (11), 3972–3981. Copyright 1994, ACS.)

an inert atmosphere of nitrogen or argon to avoid lipid oxidation.^[2] A small amount of the active solution is entrapped within the interlamellar spaces when lipid is hydrated, followed by the liposome formation. The loaded liposomes can be separated from nonencapsulated solute using centrifugation or dialysis.

The encapsulation efficiency can be increased by inclusion of a charged amphiphile, such as phosphatidylglycerol or phosphatidic acid, at a molar ratio of 10–20%, or by preliminary freeze-drying of the lipid from an organic solution followed by formation of an expanded foam with an increased surface area, which increases the amount of aqueous phase that can be incorporated.^[22] The most advanced method, which was designed to achieve high levels of entrapment, particularly of sensitive biomacromolecules such as proteins and nucleic acids, is dehydration/rehydration method.^[23] It allows a prolongation of exposure of solute to the lipid before its final lamellar structure has been fixed. This may be achieved by preparing MLVs in water followed by converting these to SUVs. Thus, when SUVs are mixed with a solution of the active to be entrapped, most of the amphiphile is directly exposed to the solute. At this stage, water is removed by freeze-drying to produce the vesicles in a metastable state enriched with active. Following the hydration stage, the liposomes are diluted with an isotonic buffer^[23] to provide an osmotic gradient between the internal and external phases and avoid redistribution of active, and finally washed to remove the nonencapsulated material.

Lipids dissolved in organic solvents can be hydrated in solution without prior solvent removal. If the solvent is water miscible, such as ethanol or propylene glycol, it may be removed at the end of MLV preparation by dialysis or filtration. Water-immiscible solvents such as ether, chloroform, or methylene chloride may also be used, then later removed through evaporation. High-capacity multi-

vesicular liposomes were created in w/o/w double emulsion, containing active in the inner entrapped aqueous phase.^[24] Composition and conditions are chosen such that each droplet of the organic chloroform–ether disperse phase contains multiple droplets of the initial aqueous solution of active. The organic solvents are removed under a nitrogen flow, wherein the lipid is deposited around the internal aqueous, drug-containing nanodroplets, which form separate compartments within a single liposome. The method allows encapsulation efficiencies of up to 90%, but requires specialized lipids and rather complex preparation conditions.

Different technology has been applied so far to produce a new solid lipid carrier system, the so-called solid lipid nanoparticles (SLNs).^[25–28] It is rather effective for encapsulating drugs that are poorly soluble in both aqueous and organic media.^[25] Solid lipid nanoparticles combine the advantages of both liposomes and polymer nanoparticles. In SLNs the liquid lipid in emulsion is replaced by a solid lipid, e.g., high-melting glycerides (trilaurin, tribehenin) or waxes (cetyl palmitate); the particles are stabilized against aggregation by natural emulsifiers (lecithin), synthetic surfactants (Miranol, Plantaren, Tween 80), or sterically stabilizing polymers (Pluronic F68).^[26,27] To prepare SLN dispersions, melted lipid mixed with an active was added to a surfactant solution of distilled water at elevated temperature. After stirring, the crude preemulsion was homogenized under high pressure between 500 and 1500 bar, applying several homogenization cycles.^[26,27] Mean particle size of prepared SLNs ranged from 100 to 300 nm.

Within SLNs, actives with a melting point below the melting point of the lipid matrix preferentially distribute to the surface of the particles.^[27] Wide-angle X-ray scattering investigations suggested that good entrapment efficacy in SLNs can be achieved with lipids of low crystalline order and metastable polymorphs of the β' form.^[28] This allows optimization of lipid composition in favor of formation of this metastable polymorph.

Small unilamellar vesicles

Small unilamellar vesicles (Fig. 2b) can be formed easily by high-power probe or bath sonication of MLVs in an inert atmosphere by cooling to dissipate local overheating^[18] and avoid disruption of lipid molecules. Alternatively, MLVs can be converted into SUVs by use of high-pressure homogenization, such as in the case of SLN, or extrusion. High-pressure extrusion involves forcing MLVs through porous membranes^[29] at temperatures above T_c . As a result, lamellar fragments break away and close to form small vesicles of similar diameter to that of the pore. A particular advantage of the method is that the disruptive effects of sonication are avoided. Rapid

injection of an ethanol solution of lipid into an aqueous solution also leads to production of vesicles 30 to 110 nm in diameter.^[30] This method has two disadvantages as compared to sonication: high polydispersity and dilute suspension of liposomes obtained. Acidic phospholipids such as phosphatidic acid and phosphatidylglycerol are able to form unilamellar liposomes simply by transiently increasing the pH.^[18] However, this process is critical to ionic strength, presence of other lipid components, and rate of titration.

Large unilamellar vesicles

Methods for preparing LUVs fall into two categories. The first involves removal of a lipid solubilizing agent, whereas the second applies physical modification of preformed bilayer. In the first case, the lipid is initially dissolved by an aqueous solution of the surfactant (either ionic—cholate, deoxycholate, or nonionic—Triton 100, octylglucoside) to form mixed lipid–surfactant micelles followed by removal of the surfactant by dialysis, diafiltration, or gel chromatography.^[31] With another method, a volatile solvent such as diethyl ether, petroleum ether, or dichlorofluoromethane containing dissolved lipid is infused slowly into the aqueous phase, which is maintained at a temperature above the boiling point of the solvent so that bubbles are formed.^[32] The lipid molecules form a multilayer around the vapor–water interphase, and as the solvents evaporate, uni- and oligolamellar liposomes with the size range of 100–400 nm remain in dispersion. Encapsulation efficiencies up to 46% were reported.

In the more advanced reverse-phase evaporation method, the w/o emulsion containing excess lipid in the organic phase (diethyl ether) is subject to rotary evaporation. At this stage the emulsion inversion takes place. This involves collapse of inverted micelles so that their aqueous contents form the new continuous phase, while their lipid components convert into a vesicular form.^[33] In the absence of cholesterol, these vesicles have an outer diameter in the range of 50–500 nm, whereas with 50 mol% cholesterol, mean diameter is about 500 nm. High encapsulation efficiencies up to 65% can be achieved using hydrophilic solutes.

Physical modification of existing bilayers involves the above-mentioned extrusion method, which is effective for obtaining both SUVs and LUVs, and exposure of SUVs to alternate cycles of freezing and thawing. These procedures lead to fusion of the SUVs followed by formation of LUVs.^[29] An elegant method using fusion is based on electrostatic effect. SUVs composed of negatively charged phospholipids are mixed with calcium ions, which cause the vesicles to aggregate and then fuse.^[34] This results in formation of “cochleate cylinders,” which are rolled-up portions of lipid bilayer.

Chelation of Ca^{2+} by adding EDTA results in conversion of the cochleates to LUVs.

Applications of Liposomes

Liposomes have been widely investigated as delivery systems for treatment of cancer, as well as bacterial, fungal, viral, and parasitic diseases.^[35] Liposome-based gene transfection systems have been promoted as means to achieve the transfection efficacy of viral constructs without any associated risks. Liposomes themselves can serve as immunological adjuvants. They are applied as vehicles to deliver various radioisotopes and contrast agents for use in diagnostic imaging. In general, several beneficial properties of the liposomal form of drugs and the ways of providing their targeted delivery are essential for polymer nanoparticles as well. However, because of the noncovalent interactions responsible for their formation liposomes have only limited stability and are subject to structural changes.^[18]

Efficiency of both the liposomal forms and nanoparticles depends on the rate of releasing of an active substance and their clearance from the blood. Compounds with low molecular weight release rapidly. Depending on molecular weight and the ability to withstand enzymatic attack, drugs could then act either locally (e.g., hydrolysis of stored sucrose by liposomal fructofuranosidase) or, after diffusion through the lysosomal membrane, in other cell compartments (e.g., inhibition of DNA-directed RNA synthesis by liposomal actinomycin D).^[35] It was shown that the rate of clearance of injected liposomes from the blood is rather rapid, dose dependent, and biphasic. Neutral MLVs and SUVs exhibit a slower rate of clearance than charged MLVs.^[35] Understanding of liposomal fate and behavior led to several proposed applications. The most important fact is that liposomes with entrapped material were shown to end up in the fixed macrophages of the RES, mainly in the liver and spleen.^[36] Fast blood clearance is the principal obstacle to use of liposomes for drug delivery via the parenteral route. Liposome clearance can be substantially reduced by inclusion of monosialoganglioside GM_1 , hydrogenated phosphatidylinositol, or PEG-substituted phosphatidylethanolamine into the bilayer.^[37] The same effect may be achieved by PEG coating of liposomes—PEGylation.^[38] This modification hampers detection by the RES, and led to their being called StealthTM liposomes. The long-circulating PEGylated liposomes are considered suitable for targeted drug delivery to tumors and inflammatory foci, as well as for diagnostic imaging applications, e.g., magnetic resonance and scintigraphic imaging.

Two types of targeting are under way: passive and active. Passive targeting is limited in its scope, leads to the rather wide distribution of the drug-filled liposomes in

tissues, and depends dramatically on time of circulation. Thus, tremendous efforts are being directed at present toward the development of control together with modification of the liposome surface with molecules having recognition properties. Typical examples of such modification are antigenic determinants, including various types of membrane receptors, or antibodies (either intact or as active fragments), other proteins, lipoproteins, glycoproteins, and so on, which may associate with bilayers as they do in the living cells. One such way is ligand-coupling strategy, which was originally realized with tumor-specific antibodies, known as immunoliposomes.^[39] Most of the subsequent studies have used chemical coupling to link a targeting moiety to an amphiphilic molecule inserted into the liposome bilayer. The most widely used approach involves the use of heterobifunctional cross-linking reagents for introducing thiol-ether-based linkages between the lipid anchor and the ligand (e.g., immunoglobulin).^[40]

The way in which liposomes induce immune responses to antigens associated with them is still not clear, but has been attributed to a depot mechanism and the ability of liposomes and antigen content to migrate to regional lymph nodes. A novel concept, namely, production of the required vaccine antigen by the host cells *in vivo*, promises to alter vaccination, especially where vaccines are either ineffective or unavailable. The concept entails the direct injection of antigen-encoding plasmid DNA, which, after its uptake by cells, finds its path to the nucleus where it transfects the cells.^[41] Antigen so produced is recognized by the host as foreign and then subjected to pathways leading to protective immunity. Simple mixing of antigen-encoding plasmid DNA or DNA itself and cationic SUV leads to neutralization of polyanionic nucleic acid chain to form a compact nanostructure, known as a lipoplex.^[42] Each of these nanoparticles carries a small net positive charge, which enables them to interact with the negatively charged cell membranes and gain entry by receptor-mediated endocytosis to perform transfection.

POLYMER NANOSPHERES

Manufacture of Nanospheres

The first approaches used to produce polymer nanoparticles were derived from the field of latex engineering. These methods were based on *in situ* polymerization of monomers.^[43,44] Despite the actual technological advances, polymerization-based methods have some drawbacks and limitations. Thus, alternative methods based on the dispersion of well-characterized preformed polymers or natural biopolymers^[4,5] have been proposed.^[45] Together with polymerization-based methods, these new

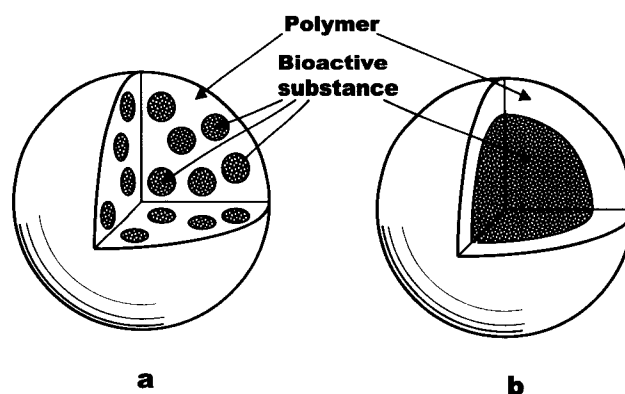


Fig. 3 Schematic structure of polymer nanoparticles: (a) nanospheres and (b) nanocapsules.

techniques allow the production of both nanospheres and nanocapsules (Fig. 3).

Polymerization methods

Two different approaches have been considered for the preparation of nanospheres by polymerization methods, depending on whether a monomer to be polymerized is emulsified in a nonsolvent phase (emulsion polymerization) or dissolved in a solvent that is a nonsolvent for the resulting polymer (dispersion polymerization).^[44]

In two types of emulsion polymerization, either conventional (*o/w* emulsion) or inverse (*w/o* emulsion), the monomer is emulsified in the nonsolvent phase with surfactant, leading to the formation of monomer-swollen micelles and stabilized monomer droplets. The polymerization reaction takes place in the presence of an initiator that creates free reactive monomer radicals. These collide with the unreactive monomers and initiate polymer chain growth, or nucleation.^[44] The reaction stops when full consumption of monomer or initiator is achieved. The drug to be incorporated to the nanospheres may be present during the polymerization process. Two different mechanisms of nucleation were considered. First, the so-called micellar polymerization mechanism treats the monomer-swollen micelles as the site of nucleation and propagation.^[46,47] In this case, monomer droplets serve as monomer reservoirs. The monomer molecules reach the micelles by diffusion through the continuous phase. The second mechanism is valid for monomers that are sufficiently soluble in the continuous phase. In this case, homogeneous nucleation followed by propagation can occur directly in this phase, leading to formation of oligomers.^[47] When the oligomers have reached a certain length, they form primary particles stabilized by surfactant molecules present in the system. In the case of inverse emulsion polymerization, when we deal with *w/o*

system, the water-soluble monomers cannot diffuse from the micelles through the organic phase because of their low partition coefficient. The resulting nanospheres contain fewer polymer chains and a narrower size distribution as compared to the conventional emulsion polymerization.^[48]

Both the conventional and inverse emulsion polymerization reactions were applied for the production of biodegradable poly(alkyl cyanoacrylate) (PACA) nanospheres.^[49,50] In the case of conventional emulsion polymerization, the alkyl cyanoacrylate monomer is added to an aqueous acidic solution of surfactant under vigorous stirring to polymerize it following the anionic mechanism. Drug is dissolved in the polymerization medium either before the addition of monomer or at the end of the polymerization reaction. Nanospheres (Fig. 4a) are sedimented by ultracentrifugation of the obtained suspension. In the case of inverse emulsion polymerization, drug is dissolved in a small amount of water or hydrophilic solvent and emulsified in an organic phase (e.g., isooctane, cyclohexane, and hexane) in the presence of surfactants. Alkyl cyanoacrylate monomers are then added directly or dissolved in an organic solvent to the preformed w/o emulsion under stirring.^[49] The system becomes milky, and nanospheres with a diameter of 200–300 nm with a narrow polydispersity are formed.

Dispersion polymerization deals with polymerization of monomers dissolved in an aqueous medium that acts as a precipitant for the polymer to be formed. Nucleation is induced in the aqueous monomer solution,^[51] and the presence of stabilizers or surfactants is not absolutely necessary for the formation of nanospheres.

As mentioned earlier, polymerization methods have significant limitations, especially for formation of nanospheres.^[45] First, it is very difficult to predict the molecular weight of the resulting material. This is a

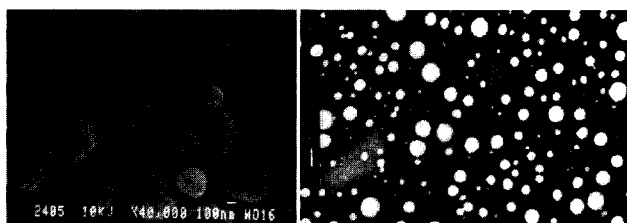


Fig. 4 (a) Electron scanning micrograph of insulin-loaded poly(ethylcyanoacrylate) nanospheres obtained by a polymerization technique. (From Radwan, M.A.; Aboul-Enein, H.Y. *J. Microencapsul.* **2002**, *19* (2), 225–235. Copyright 2002, Taylor & Francis, Ltd.) (b) Transmission electron micrograph of procaine hydrochloride loaded poly(lactide-co-glycolide) nanospheres obtained by precipitation method. (From Govender, T.; Stolnik, S. et al. *J. Control. Release* **1999**, *57* (2), 171–185, Copyright 1999, Elsevier.)

major drawback because the molecular weight influences the biodistribution and release of the polymer carrier. Second, the presence of free radicals or numerous H⁺ ions generated by anionic polymerization process can inhibit drug activity. Third, the presence of toxic unreacted monomer, initiator, and surfactant molecules requires time-consuming and, sometimes, inefficient procedures for their elimination.

Dispersion of preformed polymers

Among the numerous synthetic polymers available for the preparation of nanospheres, the most commonly used are polyesters such as poly(lactic acid) (PLA), poly(glycolic acid) (PGA), poly(lactic-co-glycolic acid) (PLGA), poly(ϵ -caprolactone) (PLG), and poly(β -hydroxybutyrate) (PHB).^[4,5] Under physiological conditions, polyesters are generally degraded by hydrolysis into products that are well tolerated by various tissues.

Solvent Evaporation Method. In this method, a polymer is dissolved in an organic solvent (dichloromethane, chloroform, or ethyl acetate).^[52] A drug is dissolved or dispersed into the polymer solution, and this mixture is then emulsified into an aqueous solution to make an o/w emulsion by using a surfactant such as gelatin, poly(vinyl alcohol) (PVA), polysorbate-80, poloxamer-188, etc. After the formation of emulsion, the organic solvent is evaporated either by heating or continuous stirring.^[53] The double emulsion method, dealing with w/o/w emulsions, may also be used to prepare nanospheres containing water-soluble drugs.^[54] Both these methods apply high-speed homogenization or sonication, which are not quite appropriate for large-scale production. In this pursuit, the following approaches have been attempted.

Spontaneous Emulsification (Solvent Diffusion) Method. In a modified version of the solvent evaporation method, the water-soluble solvent (acetone or methanol) along with the water-insoluble organic solvent (dichloromethane or chloroform) was used as an oil phase.^[55] Because of the spontaneous diffusion of the water-soluble solvent, an interfacial turbulence is created between the two phases leading to the formation of smaller particles. As the concentration of water-soluble solvent increases, a considerable decrease in particle size can be achieved.

Salting-Out Method. The salting-out technique replaces chlorinated solvents with water-miscible acetone.^[56] An aqueous phase saturated with electrolytes (e.g., magnesium salts) and containing PVA as a stabilizing and thickening agent is added under stirring to an acetone solution of polymer. The miscibility of both phases is prevented by the saturation of the aqueous phase with

electrolytes, according to a salting-out phenomenon. The addition of the aqueous phase is continued until a phase inversion occurs and an o/w emulsion is formed. Then, a sufficient amount of water is added to disrupt the equilibrium between the two phases and allow complete diffusion of acetone into water followed by polymer precipitation in the form of nanospheres. Other solvents (e.g., tetrahydrofuran) as well as nonelectrolytic salting-out agents (e.g., sucrose) could also be appropriate.¹⁵⁷¹ A variety of polymers can be used with this technique including PLA, methacrylic acid copolymers, and cellulose derivatives.

Emulsification-Diffusion Method. This method formally resembles the previous method, but its originality is in using benzyl alcohol as an organic solvent.¹⁵⁸¹ An aqueous phase containing PVA as a stabilizing and thickening agent is added to a solution of polymer in benzyl alcohol under stirring. With an excess of water, an o/w emulsion is obtained because benzyl alcohol has low miscibility with water. The precipitation of the polymer occurs due to the diffusion of benzyl alcohol into water, leading to the formation of nanospheres. By increasing the content of PVA in the external phase, it was possible to produce nanoparticles as small as 70 nm in diameter. The polymers used were PLA, PLGA, PCL, and methacrylic acid copolymers.

Direct Precipitation Method. This technique involves the use of polymer solution in an organic solvent that is completely miscible with the aqueous phase (acetone, ethanol, or acetonitrile) and allows nanospheres to be obtained after addition of water (with or without a surfactant) under stirring¹⁵⁹¹ (Fig. 4b). After precipitation of nanoparticles, the solvent is removed by vaporization under vacuum. Applications of this method are limited to drugs that are highly soluble in polar solvents but insoluble in water.

Supercritical Fluid Technology. Conventional methods such as in situ polymerization and solvent evaporation often require the use of toxic solvents and surfactants. Supercritical fluids allow attractive alternatives for the nanoencapsulation process because these are environmentally friendly solvents.¹⁶⁰¹ The commonly used methods of supercritical fluid technology are the rapid expansion of supercritical solution (RESS)¹⁶¹¹ and the supercritical antisolvent (SAS) method.¹⁶²¹ A supercritical fluid is a substance that is used in a state above the critical temperature and pressure where gases and liquids can coexist. It is able to penetrate materials such as gas, and to dissolve materials such as liquid. For example, use of carbon dioxide or water in the form of a supercritical fluid allows substitution for an organic solvent.

In the RESS method,¹⁶¹¹ a polymer is solubilized in a supercritical fluid and the solution is expanded through a nozzle. Thus, the solvent power of supercritical fluid dramatically decreases and the solute eventually precipitates. A uniform distribution of drug inside the polymer matrix, e.g., PLA nanospheres, can be achieved only for low-molecular-mass (<10,000) polymers because of the limited solubility of high-molecular-mass polymers in supercritical fluids.¹⁶³¹ In the SAS method,¹⁶²¹ the solution is charged with the supercritical fluid in the precipitation vessel containing a polymer in an organic solvent. At high pressure, enough antisolvent will enter into the liquid phase so that the solvent power will be lowered and the polymer precipitates. After precipitation, the antisolvent flows through the vessel to strip the residual solvent. When the solvent content has been reduced to the desired level, the vessel is depressured and the solid nanoparticles are collected.

POLYMER NANOCAPSULES

Manufacture of Nanocapsules

In general, all the methods for preparation of nanocapsules (Fig. 3b) are based on the self-assembly approach, which resembles aggregation of lipid molecules in aqueous solution into liposomes (Fig. 1).

Surface polymerization method

To overcome the instability of liposomes, lipids that are functionalized with polymerizable groups can be polymerized within vesicular structures.¹⁶⁴¹ Because of the polymerization reaction, the individual lipid molecules are interconnected via covalent bonds that stabilize the wall-forming membrane considerably. However, nanocapsules prepared from reactive lipids are rather costly.

In an analogous fashion to the lipids, amphiphilic block copolymers can also aggregate in aqueous solution to vesicular structures.¹⁶⁵¹ Block copolymer liposomes are significantly more stable than those formed from lipids due to the larger size and the lower dynamics of the underlying polymer molecules. Nevertheless, similarly to lipids they are held together solely by noncovalent interactions. Analogously to the reactive lipids, the block copolymer molecules could also be modified with polymerizable groups. Such block-copolymer-based nanocapsules can be expected to possess great potential for encapsulation and controlled release, because the physical properties of their polymer walls can be controlled by the block length or the chemical constitution of the underlying polymer molecules. So far only a few papers dealing with such nanocapsules have appeared.^{166,1671} In one of them

the formation of vesicles from poly(isoprene)-*b*-poly-(2 cinnamoyl methacrylate) (PI-PCEMA) diblock copolymer in hexane-tetrahydrofuran mixtures was used as a starting stage.^[66] The PCEMA blocks were photo-cross-linked and then the PI blocks had to be hydroxylated to make water-soluble nanocapsules. Diameter of the nanocapsules was in the range of 50–60 nm. A rather simple one-step procedure has been used to prepare vesicles of poly(2-methyloxasoline)-*b*-poly(dimethylsiloxane)-*b*-poly(2-methyloxasoline) in aqueous solution.^[67] The underlying triblock copolymers were modified with methacrylate end groups without disturbing the vesicles in water, which were cross-linked under UV irradiation. Diameter of the obtained nanocapsules could be controlled in the range of 50–500 nm.

A similar concept uses just the geometry of the vesicular aggregates as a template. The interfacial polymerization of monomeric surfactants is an advanced method of this type of technique used for the preparation of nanocapsules.^[68–74] For example, for the preparation of nanocapsules containing α -chymotrypsin, the reverse hydrated micelles from *N,N*-diallyl-*N,N*-didodecyl ammonium bromide (DDAB) in cyclohexane entrapping enzyme in the inner aqueous cavities were polymerized by UV irradiation. After precipitation in acetone, these nanocapsules were dispersed in the aqueous medium with the aid of ionic (AOT) or nonionic (Brij-97) surfactants. Nuclear magnetic resonance spectroscopy data suggested that thereby bilayer nanocapsules with an average outer diameter of 20 nm were formed.^[68] Their inner monolayer was made up of the two-dimensional poly-DDAB network, and the outer monolayer was composed of surfactant molecules.^[69,70]

Another way used the ability of liposomes to solubilize hydrophobic monomers such as styrene,^[71,72] alkylacrylates, or alkylmethacrylates^[3,73,74] within a bilayer. Their subsequent free-radical or UV-initiated polymerization led to the formation of a two-dimensional polymer network entrapped in the interior of the membrane (Fig. 5). The different compartments provided by the self-assembly of the lipid molecules generally serve only as a templates, which, similar to the previous case, control both the size and shape of the resulting nanocapsules. It was shown that the cross-linked polymer nanocapsules formed in vesicular dispersions are able to retain their structure even after isolation from the lipid matrix.^[74]

Based on the method proposed for preparation of the PACA nanospheres,^[49] PACA nanocapsules, consisting of a polymer envelope surrounding an oily core, were prepared.^[75] The monomer molecules located at the surface of the oil nanodroplets, on contact with aqueous hydroxide anions, immediately polymerized at the water-oil interface, followed by the formation of a polymer wall



Fig. 5 Cryotransmission electron micrograph of poly(acrylic acid) hollow nanospheres obtained by polymerization method. (From Sauer, M.; Meier, W. RSC Chem. Commun. **2001**, No. 1, 55–56; reproduced by permission of The Royal Society of Chemistry.)

with a mean thickness of about 3 nm.^[75] It was later shown that the PACA nanocapsule morphology depends on the pH of the aqueous phase, composition of the organic phase, and emulsification conditions.^[76] This dependence results in formation of a mixture of nanocapsules and nanospheres. When aprotic water-miscible organic solvents such as acetone or acetonitrile were used, only true nanocapsules were obtained.

Template approach

A similar way for producing polymer nanocapsules is to assemble a preformed polymer wall around a template particle or an oil nanodroplet that can be subsequently removed.^[3] The most convenient approach is to use an oppositely charged polyelectrolyte self-assembly at charged core surfaces.^[77] Not all of the ionic groups of the adsorbed polyelectrolyte are consumed by the electrostatic interactions with the surface. As a result, the original surface charge is usually overcompensated by the adsorbed polymer. Hence, the surface charge of the coated particle changes its sign and is now available for the adsorption of a polyelectrolyte of again opposite charge. Such sequential deposition produces ordered polyelectrolyte multilayers. The thickness of the wall is controlled by the number of deposition steps. To avoid a polyelectrolyte-induced particle flocculation, the rather low particle concentrations and the removal of nonadsorbed polyelectrolyte after each step are necessary. Weakly cross-linked melamine formaldehyde particles have been used as template core particles.^[3] Exposure of the coated

particles to an acidic solution of pH <1.6 dissolves the core without affecting the layered polyelectrolyte wall.

Functionalized polystyrene latex nanoparticles carrying surface charges are also suitable templates for the polyelectrolyte self-assembly technique. Inorganic particles were incorporated into the adsorbed walls by a sequential adsorption of SiO₂ nanoparticles with negative surface charge and cationic poly(*N,N*-diallyl-*N,N*-dimethyl ammonium chloride) (PDDAC).^[78] Layers with a thickness ranging from tens to hundreds of nanometers could be prepared. Removing the polystyrene core leaves SiO₂/PDDAC nanocomposite capsules. Nevertheless, the long-term stability of such polyelectrolyte walls in biological fluids (e.g., in blood plasma), or in media of high ionic strength, may be rather limited.

Coacervation method

This method uses the phenomenon of polymer-polymer incompatibility to form nanocapsules. The wall-forming polymer is dissolved in a solvent and to this solution a second polymer (called the phase inducer) is introduced followed by the formation of a two-phase system. The smartest complex coacervation process uses the interaction of two oppositely charged polyelectrolytes in water to form a polymer-rich coating solution called a coacervate.^[79,80] If drug nanoparticles or nanodroplets are then added, the phase, rich with the coating polymer, engulfs the drug being encapsulated, thereby forming embryo capsules. Cooling the system causes the coacervate to gel via network formation. Gelatin is a primary polymer component of most coacervation systems.

More rigid nanocapsules can be prepared by a combination of coacervation and emulsion/suspension polymerization approaches. For example, the polymerization of divinylbenzene (DVB) in toluene/DVB swollen polystyrene latex particles or in polystyrene containing toluene droplets leads to the formation of poly-DVB nanocapsules due to limited compatibility of the chemically different polymers in solution followed by a microphase separation and the formation of a poly-DVB wall around a toluene-polystyrene core.^[81] After evaporation of the internal toluene a cavity remains in the core.

Survival of the polymer walls after removing the solid or liquid core is the general goal of the coacervation method. A rather elegant approach to remove the core under mild conditions has recently been demonstrated.^[82] First, the core of the particles was formed by a low-molecular-weight poly(dimethylsiloxane) around which a cross-linked organosilicon wall was formed in a second step. The poly(dimethylsiloxane) core was removed quantitatively by ultrafiltration. The remaining organosil-

icon envelopes obviously had rather high porosity allowing fast releasing the low molecular weight bioactives.

Applications of Nanoparticles

Nanoparticles used as pharmaceutical forms must satisfy the following conditions: they must be free of any toxic impurities, easy to store and administer, and sterile if parenteral use is expected. One of the most promising applications of nanoparticles is their use as parenteral carriers for anticancer drugs based on their ability to accumulate in a number of tumors.^[83,84] The encapsulation of a variety of anticancer drugs (e.g., doxorubicin, 5-fluorouracil, dactinomycin, and methotrexate), immunomodulators (muramyl dipeptide-L-alanyl-cholesterol), or antisense oligonucleotides mainly within PACA nanoparticles enhanced their efficacy against experimental tumors in comparison to the free drug.^[84] A reduction of the general toxicity of anticancer drugs was also achieved. The most effective application of anticancer drug-loaded nanoparticles may be their use in the treatment of hepatic metastases. The incorporation of magnetic subnanoparticles into drug-containing nanoparticles and subsequent electromagnetic guidance has been shown to improve antimetastatic efficiency by facilitating access to extravascular tumors.^[83] Two other methods to achieve tumor-specific targeting were by using nanoparticles coated with either monoclonal antibodies, in order to recognize specific cell determinants,^[84] or with PEG, to increase the blood circulation time of nanoparticles.^[85]

The nanoparticles of PACA have gained wide popularity recently despite some major drawbacks such as the use of low-pH media and cytotoxicity.^[86] To overcome these, derivatives of poly(methylidenemalonate) were prepared, i.e., poly(ethyl-2-(ethoxycarbonyl) methylenecarbonyl acrylate)^[87] and poly(ethyl-2-(ethoxycarbonyl) ethyl methylene malonate-co-ethylene oxide).^[88] These polymers are associated with both the hydrophilic and hydrophobic functionalities providing long-time circulation of nanoparticles in blood and sustained release.

Intracellular infections are another field of application of nanoparticles. It is known that antibiotics exhibit either poor ability to penetrate the infected cells or decreased activity in intracellular compartments. PACA nanoparticles loaded with ampicillin showed high efficacy against *Listeria monocytogenes* and *Salmonella typhimurium* infections.^[89] They are suitable for the specific transport of antiviral agents. Recently, PACA nanoparticles loaded with the protease inhibitor saquinavir were shown to be effective in HIV-infected human macrophage cultures.^[90] The same nanoparticles loaded with primaquine, and even without any drug within, treat parasitic infections such as visceral leishmaniasis.^[89] The

void nanoparticles themselves have immunomodulation activity. This fact opens new prospects in the field of parasitic infections as well as in the treatment of other infections or tumors.

Nanoparticles increase the oral bioavailability of the peptide and protein drugs. For example, enhanced oral bioavailability was reported for insulin (Fig. 4a), dicumarol, and plasmid DNA encapsulated into adhesive nanoparticles made of polyanhydride copolymers of fumaric and sebacic acids.^[6] The use of nanoparticles is prospective for oral delivery antigens because of their ability to control the release of proteins and to protect them from enzymatic degradation in the gastrointestinal tract. The very slow degradation rate of PMMA nanoparticles is particularly appropriate for vaccine purposes because it provides prolonged contact between the antigen and the immunocompetent cells. At the same time, coating the nanocapsules with monoclonal antibodies is expected to increase the level of absorption of entrapped vaccines and, therefore, the immune response.^[90] These investigations allow one to create new generations of effective vaccines for oral immunization.

Depending on the rate of desired release, the PACA, PLA, and PLGA nanoparticles can be applied for intramuscular, subcutaneous, and topical administration. For example, the topical use of nanoparticles by the ocular route has been investigated for the treatment of chronic diseases such as glaucoma. Because of their low viscosity in suspensions, these systems can be administered as eye drops providing the sustained drug delivery.^[91]

MOLECULAR INCLUSION COMPLEXES

Molecular inclusion complexes of the host-guest type provide unprecedented "molecular nanoencapsulation" of drugs.^[10] The most advanced among them are inclusion complexes of α -, β -, and γ -cyclodextrins^[7] and dendrimers.^[8,9]

Cyclodextrins comprise a family of cyclic oligosaccharides. Three major cyclodextrins have a shape of a bracelet built up from glucopyranose units (6 units for α -, 7 for β -, and 8 for γ -cyclodextrin) (Fig. 6a). The diameter of the inner cavity varies for α -, β -, and γ -cyclodextrin from 0.5 to 0.8 nm. In an aqueous solution, the slightly apolar cyclodextrin cavity is occupied by water molecules that are energetically unfavored, and therefore may be readily substituted by appropriate "guest" molecules that are less polar than water. One or a few cyclodextrin molecules can entrap one or more "guest" molecules. Most frequently, the host/guest ratio is 1:1; however, 2:1, 1:2, 2:2 (Fig. 6c-e), or even more complicated associations, such as rotoxanes, exist.^[7] The formerly hydrophobic guest, upon complexation, becomes hydrophilic and effectively protected against any type of reaction, except that with cyclodextrin hydrolysis. The formed inclusion complexes can be isolated as stable crystalline substances.

Natural cyclodextrins, however, have relatively low solubility, both in water and organic solvents, which thus limits their use in pharmaceutical formulations. Recently, various kinds of cyclodextrin derivatives have been

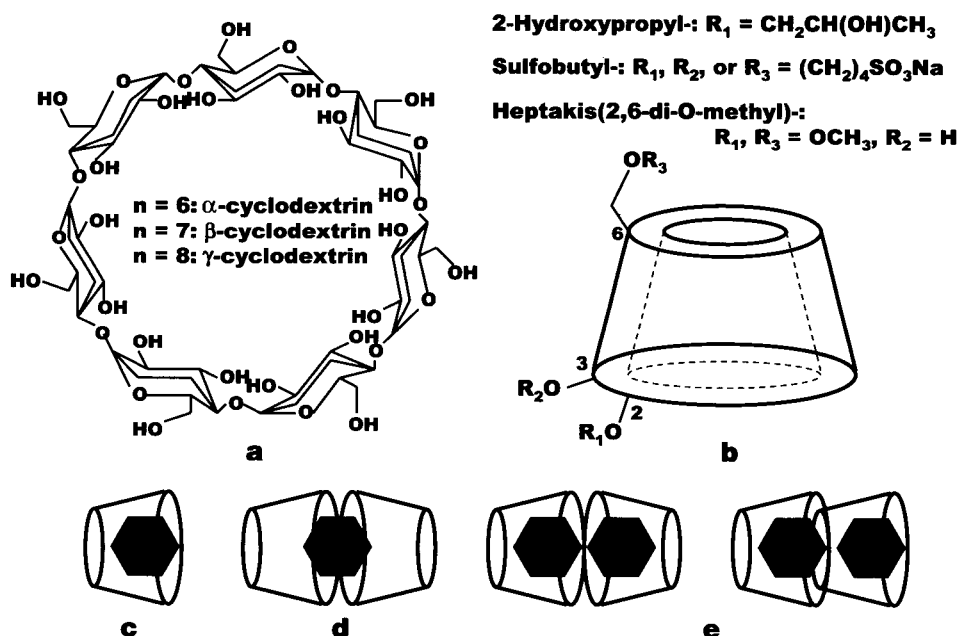


Fig. 6 Chemical structure of cyclodextrins (a), the schematic representation of their O-derivatives (b), and the possible inclusion

prepared to extend the physicochemical properties and inclusion capacity of natural cyclodextrins as novel drug carriers.^[10] To elongate the actual cyclodextrin cavity or enhance solubility, substituents are attached to the primary or secondary hydroxyl groups situated on the two rims of the molecular bracelet. This elongation may be hydrophobic if acyl or hydroxyalkyl groups are attached. At present, the acetylated, hydroxypropylated, and sulfobutylated derivatives, mainly of β - and γ -cyclodextrins, can be considered as drug carriers^[10] (Fig. 6b).

Dendrimers are highly branched cascade molecules that emanate from a central core through a stepwise, repetitive reaction sequence.^[8] Such a molecule consists of three topologically different regions: a small initiator core of low density and multiple branching units, the density of which increases with increasing distance from the core, thus eventually leading to a rather densely packed shell (Fig. 7). Dendritic shielding actually amounts to an encapsulation that can create a distinct microenvironment around the core moiety and hence affect its properties. Dendrimers with amphiphilic core-shell structures were shown to look like "unimolecular micelles."^[92] Dendrimers that have internal cavities with a dense outer shell may be synthesized by controlling the last step. This has been demonstrated by the preparation of a fifth-generation poly(propyleneimine) dendrimer.^[93] Because of their outer shell, these molecules can be regarded as dendritic compartments that are capable of retaining guest molecules entrapped during synthesis. If the surface *tert*-butyl groups were removed guest molecules could diffuse out of the compartments. The compact dendrimer topology is promising for both the controlled release^[93] and confined biochemical nanoreactors.^[8]

Dendrimers are, generally, not hollow polymer particles. Recently, elegant synthetic protocols have been developed that form the inner cavity directly from dendritic precursors. One of them is based on a polyether dendrimer

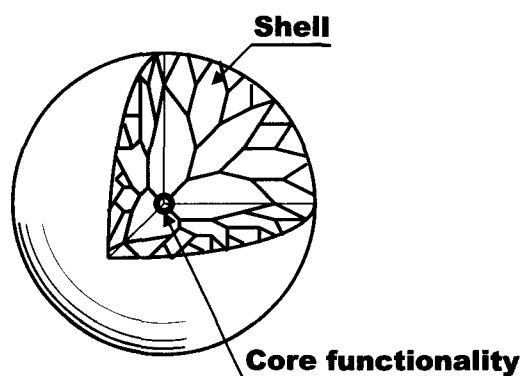


Fig. 7 Schematic structure of a spherical dendrimer of the fifth generation.

with a trimesic acid ester core.^[94] The molecular nanocapsules were formed by selective cross-linking of homoallyl ether groups at the surface of the dendrimer and subsequent degradation of the core region by hydrolysis (Fig. 8). An attractive possibility offered by this method is that the remaining functional groups in the interior of the carrier system could serve as "endoreceptors" available for molecular recognition. This approach allows control over size and geometry of the formed nanocapsules, but preparation is rather refined. This is still a limiting factor for possible applications of dendrimers as drug carriers.

Applications of Molecular Inclusion Complexes

The metabolic fate of natural cyclodextrins and their derivatives given orally has been thoroughly investigated and their lack of toxicity has been demonstrated.^[10] However, the intravenous or intramuscular administration of some β -cyclodextrin derivatives like heptakis(2,6-di-*O*-methyl)- β -cyclodextrin in rats and rabbits increased blood urea nitrogen, creatinine, and transaminases, indicating some kidney and liver failure, while those for 2-hydroxypropyl-, 6-*O*-maltosyl- β -cyclodextrin, and β -cyclodextrin sulfate at the same dosage remained within normal limits.^[10] Another drawback of cyclodextrins as drug carriers is their ability to induce human erythrocytes to change their biconcave shape to monoconcave and induce lysis at higher concentrations because cyclodextrins are able to solubilize the biomembrane components. When we deal with the inclusion complex, or when the cyclodextrin cavity is modified by chemical derivatization, the effect on cell membranes can be dramatically mitigated. The above-mentioned 2-hydroxypropyl- and sulfobutyl- β -cyclodextrin were generally found to be safe when administered parenterally in animals and humans.^[95]

One of the most important functions of cyclodextrins is to enhance the aqueous solubility of included drugs. The degree of substitution markedly influences the solubilization. In general, hydroxyalkylated, sulfated, and sulfoalkylated cyclodextrins and their complexes have lower aqueous solubility than parent cyclodextrins.^[10] When mono- or disaccharides are bounded to one or two primary hydroxyl groups of cyclodextrins through the α -1,6-glycosidic bond, their solubility in water increases. It is remarkable that the enzymatically prepared branched cyclodextrins have higher affinity to drugs and bioavailability along with weak hemolytic activity.^[96]

In oral delivery, hydrophilic and hydrophobic cyclodextrin derivatives are useful for immediate- and sustained-release type formulations. The hydrophilic cyclodextrins have been extensively applied to enhance the oral bioavailability of steroids, cardiac glycosides,

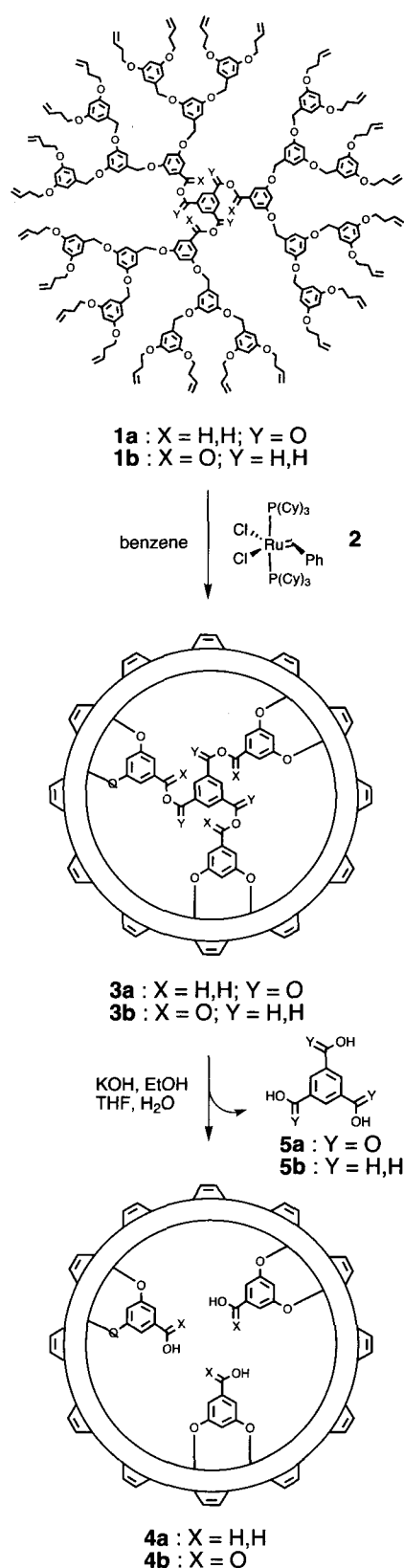


Fig. 8 Preparation of a cored dendrimer. (From Ref. [94] Copyright 1999, ACS.)

anti-inflammatory drugs, barbiturates, antiepileptics, neuroleptics, antidiabetics, vasodilators, etc.^[10,96-99] Recently, highly hydrophilic cyclodextrin derivatives, such as 2-hydroxypropyl-, 6-*O*-maltosyl-, and sulfobutyl- β -cyclodextrin have been used to obtain an immediate-release formulation, which is readily dissolved in the gastrointestinal tracts, providing an enhancement of oral bioavailability of poorly water-soluble drugs.^[99] On the other hand, alkylated and acylated derivatives are useful as slow-release carriers for water-soluble drugs. Among them heptakis(2,6-di-*O*-ethyl)-, heptakis(2,3,6-tri-*O*-ethyl)-, and heptakis(2,3,6-tri-*O*-butanoyl)- β -cyclodextrin were the first slow-release carriers to be used in conjunction with diltiazem, isosorbide dinitrate, and salbutamol.^[10]

The cyclodextrin vehicles are effective in ophthalmic formulations because they do not irritate the ocular surface resulting in a fast washout of the instilled drug. Hydrophilic 2-hydroxypropyl- and sulfobutyl- β -cyclodextrin are nontoxic to the eye and well tolerated in aqueous eye drops with low viscosity. They do not penetrate the corneal barrier, but enhance the ocular bioavailability of included lipophilic drugs like dexamethasone acetate.^[100]

Cyclodextrins improve the solubility and stability of drugs in topical preparations onto the skin, thus enhancing the transdermal penetration of drugs and sustaining the drug release along with lowering their toxicity.^[10] In general, hydrophilic cyclodextrins and their complexes penetrate through the skin inefficiently. However, when cyclodextrins are applied under occlusive dressing conditions, they are able to permeate the skin.^[10] For example, transdermal delivery of prostaglandin E₁, which is unstable and poorly permeable into the skin, in complex with a penetration enhancer, 1-[2-(decylthio)ethyl]azacyclopentane-2-one, with the aid of 6-*O*-(carboxymethyl)-*O*-ethyl- β -cyclodextrin, leads to the treatment of peripheral vascular disorders as an alternative to parenteral injections.^[101]

Cyclodextrins are effective for providing the targeted drug delivery.^[10] It is known that the specific delivery of neuropharmaceuticals to the brain is obscured by the presence of the blood-brain barrier. Inclusion complexes with cyclodextrins are able to solve the permeability problem, as it was shown for inclusion complexes of psychotropic agents (phenazepam, gidazepam).^[97,98] Another example is the conjugate of *N*-leucine-enkephalin and 6-amino-6-deoxy- β -cyclodextrin.^[102] Both types of prodrugs provide brain targeting followed by the sustained release. In general, the substituents introduced at primary hydroxyl groups of cyclodextrins through a spacer of appropriate length are self-included within the cavity. However, the enkephalin conjugate can accommodate other guest molecules (e.g., dothiepine) because the self-inclusion is restricted due to steric hindrance.

CONCLUSION

It is clear that biology has much to offer nanotechnology in demonstrating how to organize, functionalize, and assemble new molecular and submolecular materials and tools to design nanosize carriers for bioactive substances. From the chemical point of view, it is important to synthesize newer polymers and surfactants to match the hydrophilic and hydrophobic properties of the bioactive substances. Implementation of cavitands for formation of inclusion complexes can dramatically increase the loading capacity of carriers in combination with polymer nanoparticles and liposomes. Their new amphiphilic derivatives are capable of forming nanospheres and nanocapsules, presenting a high loading capacity toward both hydrophobic and hydrophilic drugs without any polymerization process. In order to provide the targeted delivery and controlled release of the bioactive substance, designing the carriers with tailored surface characteristics based on specific peptide, protein, polynucleotide, or polysaccharide motifs with preordained functions becomes the regular strategy.

REFERENCES

- Dworkin, J.P.; Deamer, S.A.; Sandford, S.A.; Allamandola, L.J. Self-assembling amphiphilic molecules. *Proc. Natl. Acad. Sci. U. S. A.* **2001**, *98* (3), 815–819.
- Bangham, A.D.; Standish, M.M.; Watkins, J.C. Diffusion of univalent ions across the lamellae of swollen phospholipids. *J. Mol. Biol.* **1965**, *13* (1), 238–252.
- Meyer, W. Polymer nanocapsules. *Chem. Soc. Rev.* **2000**, *29* (5), 295–303.
- Jagur-Grodzinski, J. Biomedical application of functional polymers. *React. Funct. Polym.* **1999**, *39* (2), 99–138.
- Uhrich, K.E.; Cannizzaro, S.M.; Langer, R.S.; Shakesheff, K.M. Polymeric systems for controlled drug release. *Chem. Rev.* **1999**, *99* (11), 3181–3198.
- Panyam, J.; Labhasetwar, V. Biodegradable nanoparticles for drug and gene delivery to cells and tissue. *Adv. Drug Deliv. Rev.* **2003**, *55* (3), 329–347.
- Szejtli, J. Introduction and general overview of cyclodextrins chemistry. *Chem. Rev.* **1998**, *98* (5), 1743–1753.
- Hecht, S.; Fréchet, J.M.J. Dendritic encapsulation of function: Applying nature's site isolation principle from biomimetics to material science. *Angew. Chem., Int. Ed.* **2001**, *40* (1), 74–91.
- Gorman, C.B.; Smith, J.C. Structure–property relationship in dendritic encapsulation. *Acc. Chem. Res.* **2001**, *34* (1), 60–71.
- Uekama, K.; Hirayama, F.; Irie, T. Cyclodextrin drug carrier systems. *Chem. Rev.* **1998**, *98* (5), 2045–2076.
- Jung, T.; Kamm, W.; Breitenbach, A.; Kaiserling, E.; Xiao, J.X.; Kissel, T. Biodegradable nanoparticles for oral delivery of peptides. *Eur. J. Pharm. Biopharm.* **2000**, *50* (2), 147–160.
- Song, C.; Labhasetwar, V.; Cui, X.; Underwood, T.; Levi, R.J. Arterial uptake of biodegradable nanoparticles for intravascular local drug delivery. *J. Control. Release* **1998**, *54* (2), 201–211.
- Kreuter, J. Drug targeting with nanoparticles. *Eur. J. Drug Metab. Pharmacokinet.* **1994**, *19* (3), 253–256.
- Handbook of Pharmaceutical Controlled Release Technology*; Wise, D.L., Ed.; Marcel Dekker, Inc.: New York, 2000.
- Yang, L.; Alexandridis, P. Physicochemical aspects of drug delivery and release from polymer-based colloids. *Curr. Opin. Colloid Interface Sci.* **2000**, *5* (1–2), 132–143.
- Moghimi, S.M.; Hunter, A.C.; Murray, J.C. Long-circulating and target specific nanoparticles: Theory to practice. *Pharmacol. Rev.* **2001**, *53* (2), 283–318.
- Carino, G.P.; Jacob, J.S.; Mathiowitz, E. Nanosphere based oral insulin delivery. *J. Control. Release* **2000**, *65* (1–2), 261–269.
- Lasic, D.D. *Liposomes: From Physics to Applications*; Elsevier: Amsterdam, 1993.
- Kirby, C.J.; Gregoriadis, G. Liposomes. In *Encyclopedia of Controlled Drug Delivery*; Mathiowitz, E., Ed.; John Wiley & Sons, Inc.: New York, 1999; Vol. 1, 461–492.
- Reeves, J.P.; Dowben, R.M. Formation and properties of thin-walled phospholipid vesicles. *J. Cell Physiol.* **1969**, *73* (1), 49–60.
- Shapiro, Yu.E. Paramagnetic hydrophilic probing of the colloid systems by NMR spectroscopy. *Russ. Chem. Rev.* **1988**, *57* (8), 717–729.
- New, R.R.C. *Liposomes, A Practical Approach*; Oxford IRL Press: New York, 1990.
- Liposome Technology*, 2nd Ed.; Gregoriadis, G., Ed.; CRC Press: Boca Raton, FL, 1993.
- Kim, S.; Turker, M.S.; Chi, E.Y.; Sela, S.; Martin, G.M. Preparation of multivesicular liposomes. *Biochim. Biophys. Acta* **1983**, *728*, 339–348.
- Müller, R.H.; Jacobs, C.; Kayser, O. Nanosuspensions as particulate drug formulations in therapy. *Adv. Drug Deliv. Rev.* **2001**, *47* (1), 3–19.
- Müller, R.H.; Lucks, J.S. Arzneistoffträger aus

- festen Lipidteilchen-feste Lipid Nanosphären (SLN). European Patent 0,605,497, April 1, 1993.
27. Schwarz, C.; Mehnert, W.; Lucks, J.S.; Müller, R.H. Solid lipid nanoparticles (SLN) for controlled drug delivery. *J. Control. Release* **1994**, *30* (1), 83–96.
 28. Jenning, V.; Gohla, S.H. Encapsulation of retinoids in solid lipid nanoparticles (SLN). *J. Microencapsul.* **2001**, *18* (2), 149–158.
 29. Szoka, F.; Olson, F.; Health, T.; Vail, W.; Mayhew, E.; Papahadjopoulos, D. Preparation of unilamellar liposomes of intermediate size by a combination of reverse phase evaporation and extrusion through polycarbonate membranes. *Biochim. Biophys. Acta* **1980**, *601*, 559–571.
 30. Batzri, S.; Korn, E.D. Single bilayer liposomes prepared without sonication. *Biochim. Biophys. Acta* **1973**, *298*, 1015–1019.
 31. Kagava, Y.; Racker, E. Partial resolution of the enzymes catalyzing oxidative phosphorylation. *J. Biol. Chem.* **1971**, *246* (17), 5477–5487.
 32. Deamer, D.W.; Bangham, A.D. Large liposomes by an ether vaporization method. *Biochim. Biophys. Acta* **1976**, *443*, 629–634.
 33. Szoka, F.; Papahadjopoulos, D. Procedure for preparation of liposomes with large internal aqueous space and high capture by reverse-phase evaporation. *Proc. Natl. Acad. Sci. U. S. A.* **1978**, *75* (9), 4194–4198.
 34. Papahadjopoulos, D.; Vail, W.J.; Jacobson, K.; Poste, G. Cochleate lipid cylinders: Formation by fusion of unilamellar lipid vesicles. *Biochim. Biophys. Acta* **1975**, *394*, 483–491.
 35. *Liposomes as Drug Carriers: Recent Trends and Progress*; Gregoriadis, G., Ed.; John Wiley & Sons: Chichester, U.K., 1988.
 36. Gregoriadis, G.; Ryman, B.E. Liposomal localization of β -fructofuranosidase-containing liposomes injected into rats—Some implications in treatment of genetic disorders. *Biochem. J.* **1972**, *129* (1), 123–133.
 37. *Targeting of Drugs: Strategies for Stealth Therapeutic Systems*; Gregoriadis, G., McCormack, B., Eds.; Plenum Press: New York, 1998.
 38. Klibanov, A.L.; Maruyama, K.; Torchilin, V.P.; Huang, L. Amphipathic PEGs effectively prolong the circulation time of liposomes. *FEBS Lett.* **1990**, *268* (1), 235–237.
 39. Neerunjun, D.; Gregoriadis, G.; Hunt, R. Fate of a liposome-associated agent injected into normal and tumor-bearing rodents. *Life Sci.* **1977**, *21* (3), 357–370.
 40. Wolff, B.; Gregoriadis, G. The use of monoclonal anti-Thy₁ IgG₁ for targeting of liposomes to AKR-A cells. *Biochim. Biophys. Acta* **1984**, *802* (2), 259–273.
 41. Chattergoon, M.; Boyer, J.; Weiner, D.B. Genetic immunization: A new era in vaccines and immune therapeutics. *FASEB J.* **1997**, *11* (10), 753–763.
 42. Felgner, P.L.; Ringold, G.M. Cationic liposome-mediated transfection. *Nature* **1989**, *337*, 387–388.
 43. Durbin, D.P.; El-Aasser, M.S.; Poehlein, G.W.; Vanderhoff, J.W. Influence of monomer pre-emulsification on formation of particles from monomer drops in emulsion polymerization. *J. Appl. Polym. Sci.* **1979**, *24* (3), 703–707.
 44. Lovell, P.A.; Lovell, P.; El-Aasser, M.S. *Emulsion Polymerization and Emulsion Polymers*; John Wiley & Sons, Inc.: New York, 1997.
 45. De Jaeghere, F.; Doelker, E.; Gurny, R. Nanoparticles. In *Encyclopedia of Controlled Drug Delivery*; Mathiowitz, E., Ed.; John Wiley & Sons, Inc.: New York, 1999; Vol. 2, 641–664.
 46. Shapiro, Yu.E.; Dozorova, N.P.; Mironova, N.M.; Balyberdina, T.G. Influence of emulsifier on the microstructure of copolymers of butadiene with methyl methacrylate. *Macromol. Comp. (Russia)* **1981**, *23A* (6), 1374–1380.
 47. Vanderhoff, J.W. Mechanism of emulsion polymerization. *J. Polym. Sci., Polym. Symp.* **1985**, *72*, 161–198.
 48. Carver, M.T.; Hirsch, E.; Wittmann, J.C.; Fitch, R.M.; Candau, F. Percolation and particle nucleation in inverse microemulsion polymerization. *J. Phys. Chem.* **1989**, *93* (12), 4867–4873.
 49. Couvreur, P.; Kante, B.; Roland, M. Possible uses of microdisperse forms as intracellular vehicles. *Pharm. Acta Helv.* **1978**, *53* (12), 341–347.
 50. Krause, H.-J.; Schwarz, A.; Rohdewald, P. Interfacial polymerization, a useful method for the preparation of poly(methylcyanoacrylate) nanoparticles. *Drug Dev. Ind. Pharm.* **1986**, *12* (4), 527–552.
 51. Shen, S.; Sudol, E.D.; El-Aasser, M.S. Dispersion polymerization of methyl methacrylate—Mechanism of particle formation. *J. Polym. Sci., A, Polym. Chem.* **1994**, *32* (6), 1087–1100.
 52. Gurny, R.; Peppas, N.A.; Harrington, D.D.; Banker, G.S. Development of biodegradable and injectable lattices for controlled release of potent drugs. *Drug Dev. Ind. Pharm.* **1981**, *7* (1), 1–25.
 53. Scholes, P.D.; Coombes, A.G.A.; Illum, L.; Davis, S.S.; Vert, M.; Davies, M.C. The preparation of sub-500 nm poly-(lactide-co-glycolide) microspheres for site-specific drug delivery. *J. Control. Release* **1993**, *25* (1–2), 145–153.
 54. Zambaux, M.F.; Bonneaux, F.; Gref, P.; Maincent, P.; Dellacherie, E.; Alonso, M.J.; Labrude, P.;

- Vigneron, C. Influence of experimental parameters on the characteristics of poly(lactic acid) nanoparticles prepared by double emulsion method. *J. Control. Release* **1998**, *50* (1–3), 31–40.
55. Niva, T.; Takeushi, H.; Hino, T.; Kunou, N.; Kawashima, Y. Preparations of biodegradable nanospheres of water-soluble and insoluble drugs with D,L-lactide/glycolide copolymer by a novel spontaneous emulsification solvent diffusion method and the drug release behavior. *J. Control. Release* **1993**, *25* (1–2), 89–98.
56. Bindschaedler, C.; Gurny, R.; Doelker, E. Process for Preparing a Powder of Water-Insoluble Polymer Which Can Be Re-dispersed in a Liquid Phase. U.S. Patent 4,968,350, November 6, 1990.
57. Allemann, E.; Gurny, R.; Doelker, E. Preparation of aqueous polymeric nanodispersions by a reversible salting-out process. *Int. J. Pharm.* **1992**, *87* (1–3), 247–253.
58. Leroux, J.C.; Allemann, E.; Doelker, E.; Gurny, R. New approach for the preparation of nanoparticles by an emulsification–diffusion method. *Eur. J. Pharm. Biopharm.* **1995**, *41* (1), 14–18.
59. Couvreur, P.; Roland, M.; Speiser, P. Biodegradable Submicroscopic Particles Containing a Biologically Active Substance. U.S. Patent 4,329,332, May 11, 1982.
60. Tom, J.W.; Debenedetti, P.G. Particle formation with supercritical fluids. *J. Aerosol Sci.* **1991**, *22* (5), 555–584.
61. Tom, J.W.; Debenedetti, P.G. Formation of biodegradable polymeric microspheres and microparticles by rapid expansion of supercritical solution. *Biotechnol. Prog.* **1991**, *7* (5), 403–411.
62. Mawson, S.; Johnston, K.P.; Combes, J.R.; DeSimone, J.M. Formation of poly(1,1,2,2-tetrahydroperfluorodecyl acrylate) submicron fibers and particles from supercritical carbon dioxide solutions. *Macromolecules* **1995**, *28* (9), 3182–3191.
63. Soppimath, K.S.; Aminabhavi, T.M.; Kulkarni, A.R.; Rudzinski, W.E. Biodegradable polymeric nanoparticles as drug delivery devices. *J. Control. Release* **2001**, *70* (1–2), 1–20.
64. Ringsdorf, H.; Schlarb, B.; Venzmer, J. Molecular architecture and function of polymeric oriented systems. *Angew. Chem., Int. Ed.* **1988**, *27* (1), 113–158.
65. Discher, B.M.; Won, Y.-Y.; Ege, D.S.; Lee, J.C.-M.; Bates, F.S.; Discher, D.E.; Hammer, D.A. Polymersomes: Tough vesicles made from diblock copolymers. *Science* **1999**, *284*, 1143–1146.
66. Ding, J.; Liu, G. Water-soluble hollow nanospheres as potential drug carriers. *J. Phys. Chem., B* **1998**, *102* (31), 6107–6113.
67. Nardin, C.; Hirt, T.; Leukel, J.; Meier, W. Polymerized ABA triblock copolymer vesicles. *Langmuir* **2000**, *16* (3), 1035–1041.
68. Shapiro, Yu.E.; Pykhteeva, E.G.; Fyodorova, G.V. Activity of α -chymotrypsin immobilized into poly(*N,N*-diallyl-*N,N*-didodecyl ammonium bromide) nanocapsules. *Bioorganic Chem. (Russia)* **1997**, *23* (3), 174–182.
69. Shapiro, Yu.E.; Pykhteeva, E.G.; Levashov, A.V. ^1H NMR self-diffusion in polymer–surfactant nanocapsules and cryogels with enzyme. *J. Colloid Interface Sci.* **1998**, *206* (1), 168–176.
70. Shapiro, Yu.E.; Pykhteeva, E.G. Immobilization of α -chymotrypsin into the poly(*N,N*-diallyl-*N,N*-didodecyl ammonium bromide)/surfactant nanocapsules. *Appl. Biochem. Biotechnol.* **1998**, *74* (2), 67–84.
71. Kurja, J.; Nolte, R.J.M.; Maxwell, I.A.; German, A.L. Free-radical polymerization of styrene in dioctadecyldimethyl ammonium bromide vesicles. *Polymer* **1993**, *34* (10), 2045–2049.
72. Morgan, J.D.; Johnson, C.A.; Kaler, E.W. Polymerization of equilibrium vesicles. *Langmuir* **1997**, *13* (24), 6447–6451.
73. Poulain, N.; Nakache, E.; Pina, A.; Levesque, G. Nanoparticles from vesicle polymerization. *J. Polym. Sci., A, Polym. Chem.* **1996**, *34* (5), 729–737.
74. Hotz, J.; Meier, W. Vesicle-templated polymer hollow spheres. *Langmuir* **1998**, *14* (5), 1031–1036.
75. Al Khouri-Fallouh, N.; Roblot-Treupel, L.; Devisaguet, J.P.; Puiseux, F. Development of new process for the manufacture of polyisobutylcyanoacrylate nanocapsules. *Int. J. Pharm.* **1986**, *28* (2–3), 125–135.
76. Puglisi, G.; Fresta, M.; Giammona, G.; Ventura, C.A. Influence of the preparation conditions of poly(ethyl cyanoacrylate) nanocapsule formation. *Int. J. Pharm.* **1995**, *125* (2), 283–287.
77. Donath, E.; Sukhorukov, G.B.; Caruso, F.; Davis, S.A.; Möhwald, H. Novel hollow polymer shells by colloid-templated assembly of polyelectrolytes. *Angew. Chem., Int. Ed.* **1998**, *37* (16), 2201–2205.
78. Caruso, F.; Caruso, R.A.; Möhwald, H. Nanoengineering of inorganic and hybrid hollow spheres by colloidal templating. *Science* **1998**, *282*, 1111–1114.
79. Nihant, N.; Grandfils, C.; Jerome, R.; Teyssie, P. Microencapsulation by coacervation of poly(lactide-*co*-glycolide). *J. Control. Release* **1995**, *35* (2–3), 117–125.
80. Chan, L.W.; Heng, P.W.S. Effect of poly(vinylpyrrolidone) and ethylcellulose on alginate micro-

- spheres prepared by emulsification. *J. Microencapsul.* **1998**, *15* (4), 409–420.
81. Okubo, M.; Konishi, Y.; Minami, H. Production of hollow polymer particles by suspension polymerization. *Colloid Polym. Sci.* **1998**, *276* (7), 638–642.
 82. Emmerich, O.; Hugenberg, N.; Schmidt, M.; Sheiko, S.S.; Baumann, F.; Deubzer, B.; Weis, J.; Ebenhoch, J. Molecular boxes based on hollow organosilicon materials. *Adv. Mater.* **1999**, *11* (15), 1299–1300.
 83. Couvreur, P.; Grislain, L.; Lenaert, V.; Brasseur, F.; Guiot, P.; Biernacki, A. Biodegradable Polymeric Nanoparticles as Drug Carrier for Antitumor Agents. In *Polymeric Nanoparticles and Microspheres*; Guiot, P., Couvreur, P., Eds.; CRC Press: Boca Raton, FL, 1986; 27–93.
 84. Brigger, I.; Dubernet, C.; Couvreur, P. Nanoparticles in cancer therapy and diagnosis. *Adv. Drug Deliv. Rev.* **2002**, *54* (5), 631–651.
 85. Allemann, E.; Rousseau, J.; Brasseur, N.; Kudrevich, S.V.; Lewis, K.; van Lier, J.E. Photodynamic therapy of tumors with hexafluoro zinc phthalocyanine formulated in PEG-coated poly(lactic acid) nanoparticles. *Int. J. Cancer* **1996**, *66* (6), 821–824.
 86. Lherm, C.; Muller, R.H.; Puiseux, F.; Couvreur, P. Alkylcyanoacrylate drug carriers: II. Cytotoxicity of cyanoacrylate nanoparticles with different alkyl chain length. *Int. J. Pharm.* **1992**, *84* (1), 13–22.
 87. Breton, P.; Roy, D.; Marchal-Heussler, L.; Seguin, C.; Couvreur, P.; Lescure, F. New Poly(methylidene malonate 2.1.2) Nanoparticles: Recent Developments. In *Targeting of Drugs, Advances in System Constructs*; Gregoriadis, G., McCormack, B., Poste, G., Eds.; Plenum Press: New York, 1994; Vol. 4, 161–172.
 88. Bru-Magniez, N.; Larras, V.; Riess, G.; Breton, P.; Couvreur, P.; Roques-Carmes, C. Novel Surfactant Copolymers Based on Methylidene Malonate. *Int. Patent PCT WO 99/38898*, 1999.
 89. Kreuter, J. Drug Targeting with Nanoparticles. In *Colloidal Drug Delivery Systems*; Kreuter, J., Ed.; Marcel Dekker, Inc.: New York, 1994; 219–343.
 90. Bender, A.R.; von Briesen, H.; Kreuter, J.; Duncan, I.B.; Rubsamen Waigman, H. Efficiency of nanoparticles as a carrier system for antiviral agents in human immunodeficiency virus-infected human monocytes/macrophages in vitro. *Antimicrob. Agents Chemother.* **1996**, *40* (6), 1467–1471.
 91. Le Broulais, C.A.; Treupelacar, L.; Phodes, C.T.; Sado, P.A.; Leverge, R. New ophthalmic drug delivery system. *Drug Dev. Ind. Pharm.* **1995**, *21* (1), 19–50.
 92. Sunder, A.; Krämer, M.; Hanselmann, R.; Mülhaupt, R.; Frey, H. Molecular nanocapsules based on amphiphilic hyperbranched polyglycerols. *Angew. Chem., Int. Ed.* **1999**, *38* (23), 3552–3555.
 93. Jansen, J.F.G.A.; Meijer, E.W.; De Brabander van den Berg, E.M.M. The dendritic box: Shape-selective liberation of encapsulated guests. *J. Am. Chem. Soc.* **1995**, *117* (15), 4417–4418.
 94. Wendland, M.S.; Zimmerman, S.C. Synthesis of cored dendrimers. *J. Am. Chem. Soc.* **1999**, *121* (6), 1389–1390.
 95. Thompson, D.O. Cyclodextrins-enabling excipients: Their present and future in pharmaceuticals. *Crit. Rev. Ther. Drug Carr. Syst.* **1997**, *14* (1), 1–104.
 96. Yamamoto, M.; Hirayama, F.; Uekama, K. Improvement of stability and dissolution of prostaglandin E₁ by maltosyl- β -cyclodextrin in lyophilized formulation. *Chem. Pharm. Bull.* **1992**, *40* (3), 747–751.
 97. Andronati, S.A.; Shapiro, Yu.E.; Yakubovskaya, L.N.; Gorbatyuk, V.Ya.; Andronati, K.S.; Krasnoschyokaya, S.P. Inclusion compounds of psychotropic agents and cyclodextrins. *J. Incl. Phenom. Mol. Recognit. Chem.* **1996**, *24* (1–2), 175–186.
 98. Shapiro, Yu.E.; Gorbatyuk, V.Ya.; Yakubovskaya, L.N.; Andronati, K.S.; Andronati, S.A. Spatial structure of clathrates of the 1,4-benzodiazepine derivatives and β -cyclodextrin. *J. Struct. Chem. (Russia)* **1996**, *37* (5), 847–890.
 99. *New Trends in Cyclodextrins and Derivatives*; Duchêne, D., Ed.; Editions de Santé: Paris, 1991.
 100. Jarho, P.; Urtti, A.; Pate, D.W.; Suhonen, P.; Järvinen, T. Increase in aqueous solubility, stability and in vitro corneal permeability by hydroxypropyl- β -cyclodextrin. *Int. J. Pharm.* **1996**, *137* (2), 209–216.
 101. Adachi, H.; Irie, T.; Uekama, K.; Manako, T.; Yano, T.; Saita, M. Combination effects of *O*-carboxymethyl-*O*-ethyl- β -cyclodextrin and penetration enhancer HPE-101 on transdermal delivery of prostaglandin E₁ in hairless mice. *Eur. J. Pharm. Sci.* **1993**, *1* (3), 117–123.
 102. Djedaini-Pilard, F.; Desalos, J.; Perly, B. Synthesis of a new molecular carrier: *N*-(Leu-enkephalin)yl 6-amido-6-deoxy-cyclomaltoheptaose. *Tetrahedron Lett.* **1993**, *34* (14), 2457–2460.

Nanoengineered Capsules with Specific Layer Structures

Lars Dähne

Capsulation Nanoscience AG, Berlin, Germany

Claire S. Peyratout

Max Planck Institute of Colloids and Interfaces, Potsdam, Germany

INTRODUCTION

Encapsulation techniques gained great importance during the last decades to protect, store or release materials in well-defined ways. As in other technical fields, the miniaturization of capsules progressed parallel to the development of new materials and techniques. At the present time, microcapsules are already used in many technical applications in the pharmaceutical, cosmetic, food, textile, adhesive, printing, and agricultural industries.^[1–5]

Several approaches are used to fabricate nanocapsules:^[6] first, one can use aggregates of lipid molecules in spherically closed bilayer structures, the so-called vesicles or liposomes.^[7,8] These relatively unstable structures can be stabilized by cross-linking. In a similar fashion, amphiphilic block copolymers in aqueous solution can also aggregate to vesicular structures.^[9]

Other approaches to prepare capsules concern suspension and emulsion polymerization techniques around latex particles,^[10,11] dendrimers or hyperbranched polymers.^[12,13] Finally, one can cover a sacrificial template core with a membrane permeable for the products of core dissolution. Based on this approach, a new type of microcapsule prepared from polyelectrolytes (PE) was developed 5 years ago using the layer-by-layer (LbL) technology for encapsulating dissolvable templates in the micrometer and nanometer range (see Fig. 1).^[14] The LbL technology enables the nanometer-precise assembling of multilayers. A wide variety of materials can be combined yielding capsules, which can have simultaneously several functions in the capsule wall as well as an adjustable semipermeability. Furthermore, the inner and outer capsule surface can be easily functionalized by biological or chemical binding sites, and the interior can be filled with macromolecules or with precipitates of low molecular weight agents. Monodispersity of the capsules can be achieved by using monodisperse templates.

PREPARATION OF POLYELECTROLYTE CAPSULES

LbL Method on Planar Substrates

In polymer thin films research, the most influential domain in the use of noncovalent interactions is the electrostatic layer-by-layer assembly.^[15–18] This 11-year-old technique^[8] is based on the alternating adsorption of multiply charged cationic and anionic species driven by electrostatic interactions (Fig. 1). During the self-assembly process of a polyion to an oppositely charged surface, the polymer adsorption proceeds until the surface charge is reversed. This allows in a next step the adsorption of a counterpolyion. The alternating adsorption of polycations and polyanions can be repeated at will. Because of the self-limitation of the process, the amount of polymer adsorbed in one step is constant and yields for usual polyelectrolytes a layer thickness of 1.5 to 3 nm.^[19–21]

Diverse charged functional polymers have been successfully assembled into thin films by LbL (see reviews^[19–21] and references therein) and comprise conducting and light-emitting polymers, nonconjugated redox-active polymers, reactive polymers, polymers bearing nonlinear optically active dyes, liquid crystalline polyelectrolytes, temperature-sensitive and switchable polymers, and dendrimers. A variety of colloidal objects have also been placed in multilayer films, such as stable colloidal dispersions of charged silica, metal oxides, polyoxometalates, semiconductors, and fullerenes, as well as metal colloids, metallosupramolecular complexes, charged latex spheres, microcrystallites, clay platelets, or charged inorganic sheets. In addition, natural polyelectrolytes such as nucleic acids, proteins, polysaccharides, as well as certain charged supramolecular biological assemblies have been used for LbL.

In principle, all of these materials can also be combined for the preparation of polyelectrolyte capsules. However,

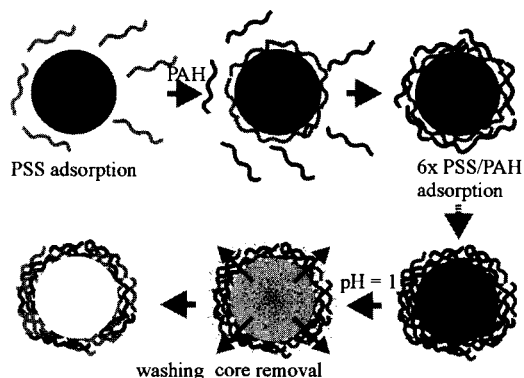


Fig. 1 Preparation of hollow polyelectrolyte capsules: scheme of the polyelectrolyte deposition process and of subsequent MF-core decomposition. (View this art in color at www.dekker.com.)

restrictions exist. First, assembling of polyelectrolytes on colloids does not allow a drying step after each layer, as it is often described with planar films. Second, colloidal suspensions in the nanometer- and micrometer-size range have to be stabilized against coagulation, which requires charged and hydrophilic surfaces. Third, the dissolution process of the templating core requires special conditions such as low pH, organic solvents, or oxidative environment. Fourth, the permeability of the LbL wall has to be tuned to allow the permeation (evacuation) of core dissolution products.

LbL Technology on Colloidal Particles

As mentioned above, the initial colloidal substrate as well as each of the PE species have to be sufficiently charged to ensure adsorption and to prevent flocculation.^[22–26] Moreover, it has to be ensured that the concentration of the adsorbing polyelectrolyte is large enough to provide saturation conditions. Incomplete covering yields charge differences within one colloidal batch followed by coagulation. Excess polyelectrolyte molecules must be removed before adding the next PE to avoid formation of complexes in solution (Fig. 1). This separation can be achieved either by centrifugation or filtration.^[27] Centrifugation yields often problems with resuspension, difficulties for smaller particles of low density to settle, loss of materials, and a lengthy process. The filtration method yields problems in filling the filters, in turn producing low yields. However, this method can be practically scaled-up and automated.^[27] In particular, cross-flow filtration can solve the problems of small-scale batches.

Removal of the Templates

The decomposition of the encapsulated template is a key step for the capsule fabrication (Fig. 1). Several templates

have been used for the capsule preparation such as weakly cross-linked melamine-formaldehyde lattice,^[14] organic^[28–30] and inorganic crystals,^[31,32] silica particles, polystyrene lattice,^[33] metal nanoparticles and nanorods,^[34–36] and biological templates.^[37–39] None of them has all qualities required for a “perfect” core, i.e., stability toward the LbL process, insensitivity of the multilayers structure at template dissolution conditions, and residues-free dissolution.

The majority of capsules have been prepared up to now with weakly polymerized, monodisperse melamine formaldehyde (MF) templates, produced in the size range from 300 to 10000 nm (Microparticle GmbH, Germany). The template can be dissolved in 0.1 M HCl within seconds into MF oligomers.^[40] During the decomposition of the MF core, the capsules swell as demonstrated on a sample made with 6 layers of poly(allylamine) (PAH) and 6 layers of poly(styrenesulfonate) (PSS) (Fig. 2). This swelling is caused by an elevation of the internal osmotic pressure induced by dissolved MF oligomers inside the capsules.^[40] The capsules show a higher permeability as expected from planar and unstressed polyelectrolyte films of the same material and thickness. Presumably, the high mechanical pressure during the dissolution process induces pores in the capsule wall that determine the permeability more than the intrinsic diffusion properties of the polyelectrolyte films do.^[41]

To reduce the permeability of MF capsules, further polyelectrolyte layers can be assembled after the dissolution of the core, resulting in a closing of the pores and a decrease of the permeability.^[42] Another disadvantage of MF capsules is given by cytotoxic MF residues. Otherwise, the presence of MF residues was exploited for trapping water-soluble substances.^[43–45] However, this encapsulation method is not controlled enough for viable applications.

Colloidal polystyrene (PS) latices have been used as core, which can be dissolved in tetrahydrofuran (THF).^[46] The swelling of PS in THF leads to a large volume

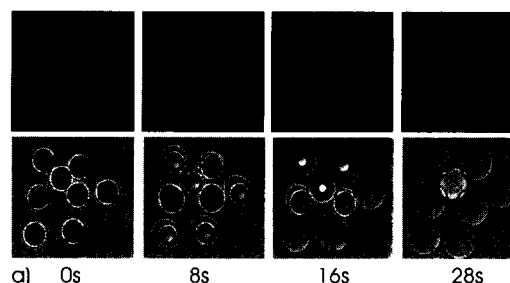


Fig. 2 Swelling of capsules during the dissolution of MF templates encapsulated in 6 PAH/PSS bilayers in 0.1 M HCl (top confocal micrograph: fluorescence of the labelled wall, bottom: transmission micrograph). (View this art in color at www.dekker.com.)

increase that is directly often responsible for a high percentage of capsule fractures.

Red blood cells present an alternative to MF particles: they are available in nonspherical shapes, are quasi-monodisperse, and are inexpensive.^[37] Moreover, the encapsulation of cells and cellular materials may have important applications in biotechnology and medicine. The decomposition of the biological templates is achieved by using a pH 12 sodium hypochlorite solution. However, under these harsh conditions, the polyelectrolyte wall is partly oxidized.^[43]

A current development is the use of inorganic crystals such as CdCO_3 , CaCO_3 , or MnCO_3 as templates, which can be prepared in the range between 3 and 8 μm . The dissolution is performed under mild conditions, and the products leave the capsule interior without problem.

Silicon dioxide particles have been used recently as templates and subsequently dissolved in hydrofluoric acid. SiO_2 particles are available over a broad size range and high monodispersity. The core is decomposed in 1 M HF within few seconds into SiF_6^{2-} ions, which leave the capsule wall without problems. Confocal imaging of this dissolution process does not show any swelling of the capsule wall. Hence the mechanical stress applied onto the wall during the dissolution is negligibly small, and the polyelectrolyte layer structure is kept almost unchanged. Indeed, such capsules exhibit a lower permeability than capsules based on MF templates.

PROPERTIES OF SIMPLE HOLLOW POLYELECTROLYTE CAPSULES

Diameter

In general, the capsules size matches the template diameter. The size of hollow capsules ranges generally between 500 nm and 5 μm , but it can be extended below 100 nm and up to 15 μm . However, for too thin walls or

too large diameters, deviations from the spherical shape are reported.

Wall Thickness

The wall thickness depends on the layer number and the material. The mostly used combination of PAH/PSS yields a thickness of around 4 nm per layer pair. These values have been measured by scanning force microscopy (SFM) on hollow capsules, dried on a mica substrate. During the drying process, the capsules collapse like an inflatable plastic ball after complete loss of the air. The thickness of the dry double wall can be taken directly from the profile of the atomic force microscopy (AFM) image (Fig. 3).

Surface Charge

The outer surface charge of the capsules is simply determined by the last layer. The charge of the inner layer is assumed to correspond to the first layer on the former template. For example, in case of MF-templated capsules, the first layer PSS should result in a negative inner-layer surface. However, it is not quite clear how far adsorbed residues of positively charged MF oligomers influence the inner surface.

Capsule Permeability

Capsule permeability has been tackled by two approaches. One approach consists in encapsulating soluble materials and in measuring their release from the fluorescence interior. Another approach consists in adding a fluorescence-labeled substance to the outer solution of a hollow capsules suspension and in monitoring the penetration into the capsules by means of confocal laser scanning microscopy (CLSM). Using fluorescence-labeled PAH molecules, first rough estimations gave a cutoff of 5000 g/mol for capsules prepared from $(\text{PSS}/\text{PAH})_4$ on MF

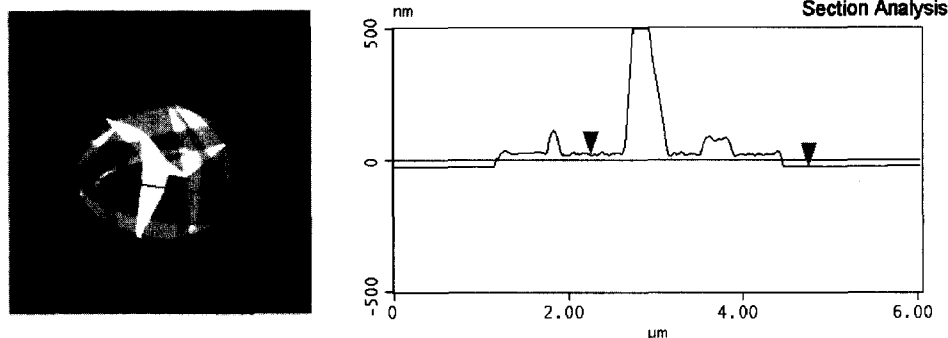


Fig. 3 Scanning force microscopy image of a $(\text{PAH}/\text{PSS})_4$ capsule, dried on mica and the corresponding height profile. (View this art in color at www.dekker.com.)

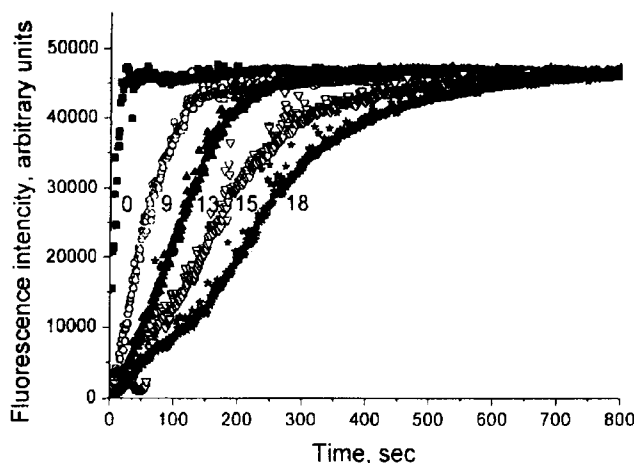


Fig. 4 Release of fluorescein from encapsulated fluorescein crystals into a buffer solution as a function of the layer number. (From Ref. [29].)

cores.^[14] In case of fast permeating smaller molecules, fluorescence recovery after photobleaching (FRAP) experiments have been performed. The dyes in the interior were bleached and the fluorescence recovery has been measured which is connected with the diffusion of fluorescence molecules from the outside to the interior.^[42]

For the first approach, several fluorescent dyes were used as model and coated with various numbers of PSS/PAH multilayers under conditions of low solubility of the materials.^[29,32,47] Results on PSS/PAH-encapsulated fluorescein reveal an increase of the release rate with pH and ionic strength and a decrease with the layer number (Fig. 4).^[47] The diffusion coefficient per layer was determined to be approximately 10^{-16} m²/sec in the presence of salt.

Similar results obtained with ibuprofen release studies support a model of two release channels, one by diffusion and one by pressure through pore-like structures presumably formed during the dissolution process.^[48–52] Further studies showed that the permeability depends strongly on the polyelectrolyte material as known from planar films.^[51] PAH/PSS MF capsules are less permeable than poly(diallyldimethylamine)/PSS capsules.^[49]

The permeability depends furthermore on the environment such as ionic strength, pH and temperature.^[55–62] It was reported that the permeability of PSS/PAH capsule could be controlled by pH^[53] and ionic strength.^[63,76] Capsules could be switched between an open (low pH or high ionic strength) and a closed state (high pH or low ionic strength). This was exploited for the encapsulation of macromolecules under mild conditions.

Mechanical Stability

Hollow capsules maintain a spherical shape up to a diameter of 15 μ m although the wall thickness is only 30 nm. The resistance against pressure was quantified by addition of polyelectrolytes to a capsule suspension. Because of the impermeability of the capsules for these molecules, high osmotic pressure from the outside modifies the capsules shape. Above a specific concentration of outside polymer or a critical pressure P_c , a shape transition from a spherical to a sickle shape was observed (Fig. 5). From this observation, an elasticity modulus between 500 and 700 Mpa was calculated. This value is comparable to macroscopic plastic materials, and reflect a high degree of local interactions between the polyanion and the polycation.^[64,65]

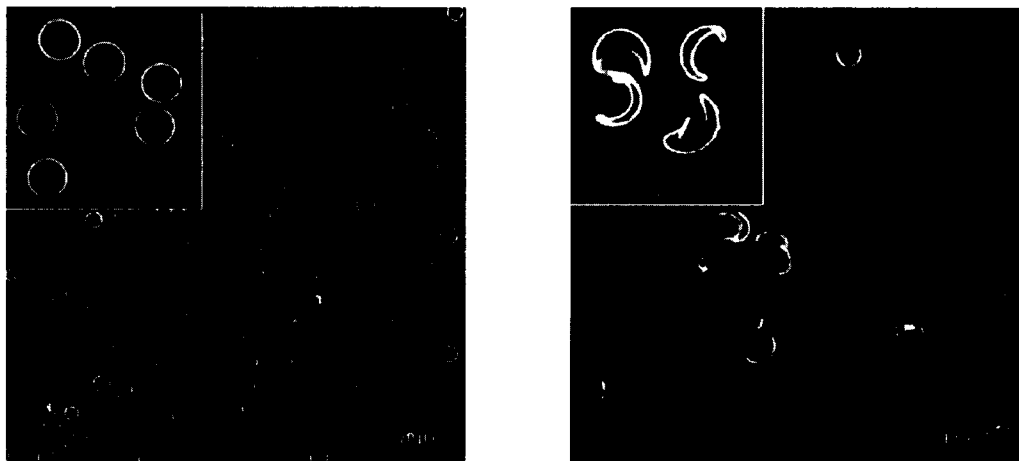


Fig. 5 Transformation of the spherical capsules to a sickle shape under the osmotic pressure of an outer PSS solution. (From Refs. [64] and [65].)

The elasticity of capsules was investigated by loading microcapsules with 1 M PSS solution and decreasing the polyelectrolyte concentration outside. This leads to a swelling of the capsules proportional to the concentration difference.^[72] Higher pressure caused the capsules to break. In contrast, at smaller swelling, a partly reversible elastic behavior was reported.^[66] The investigation of the MF core dissolution, where a reversible swelling of the capsule was observed, also points to an elastic behavior (see Fig. 2).^[40,67]

The deformability and osmotic properties of hollow PSS/PAH microcapsules assembled on the decomposable template MF were studied by means of the micropipette video microscopic technique.^[68] The microcapsules reacted to micropipette suction with plastic deformation. The upper limit value of the plastic modulus D_p was evaluated at roughly 5 kPa. Addition of lipids yields a high degree of plasticity, at least in the range of the applied mechanical forces.^[68]

Physicochemical Stability

Standard PAH/PSS capsules are stable in aqueous solution between pH 0 and 13 and at high ionic strength. PAH/PSS capsules were also suspended in various organic media by a gradual solvent exchange with a preservation of shell stability and integrity.^[53,69] The stability in organic solvents renders possible the preparation of oil-in-water or water-in-oil emulsions without employing any surfactants. The obtained microdrops are highly stable and have a high degree of monodispersity.^[69]

Combinations of weak polyelectrolytes or of materials with only small amount of charges are more sensitive against pH and ion strength, which lead to strong enhancement of the permeability up to the dissolution of the LbL capsules.

MODIFICATION OF THE POLYELECTROLYTE CAPSULES

Because of the variable applicability of the LbL process, the capsules can be widely modified. This concerns the interior, the wall, and the inner and outer surface of the capsule wall.

Permanent Filling of the Interior with Functional Macromolecules

In most cases, precipitation of low molecular weight materials in presence of hollow capsules happens on the wall surface or in the bulk solution but not as desired in the interior of capsules.^[70,71] A solution to tackle this

problem is offered by immobilization of functional macromolecules in the capsule interior. They result in different physical properties of capsule interior and bulk solution and induce preferably precipitation inside the capsules. Three approaches have been followed to immobilize macromolecules permanently in the capsule interior (Fig. 6).

In the ship-in-bottle approach, monomers are incubated together with empty preformed shells (Fig. 6a).^[72] After diffusion of monomers and initiator inside the shell, the polymerization is started inside and outside the capsule. The resulting polymers are trapped, and after washing, capsules filled with high polymer concentrations are isolated. This is demonstrated in Fig. 7a, where PSS copolymerized with acrylrhodamine is shown. The polymer concentration in the interior can be up to 1 monomolar, although the high osmotic pressure attained induce a remarkable capsule swelling. A drawback of this efficient method is the limitation to synthetic polymers.

For the encapsulation of preformed polymers or biomacromolecules, two other approaches have been developed. In one method, polymers are precipitated with complex-forming auxiliaries or alone under specific

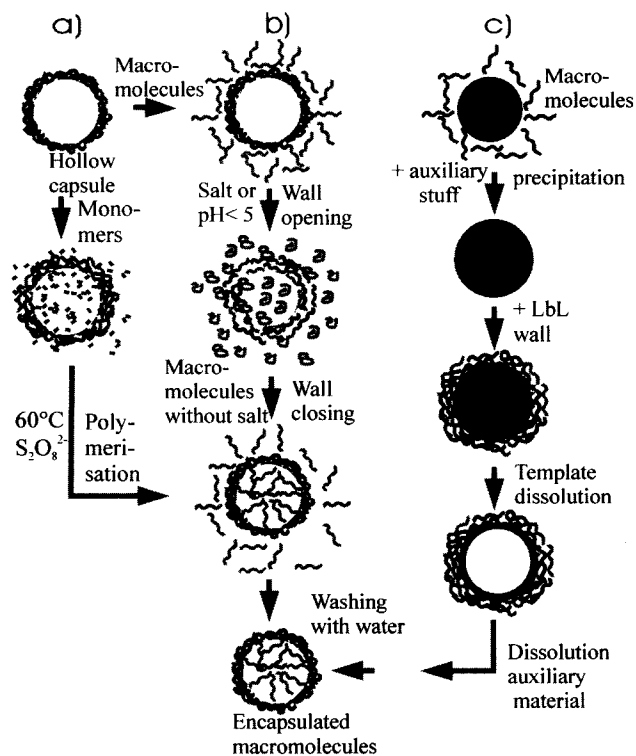


Fig. 6 Methods to immobilize macromolecules in the capsule interior: a) ship in bottle synthesis, b) loading by switching the permeability, c) loading by controlled precipitation. (View this art in color at www.dekker.com.)

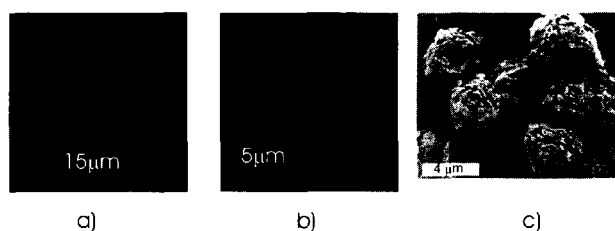


Fig. 7 Confocal laser scanning images of capsules: a) filled with PSS-rhodamine copolymer 0.5 M;^[72] b) capsules after complexation of PSS in the interior with fluorescent pseudoisocyanine J-aggregates;^[54] c) scanning electron microscopy image of CaCO₃ crystals grown in the capsule interior by enzymatic reaction. (From Ref. [72,54,83].) (View this art in color at www.dekker.com.)

conditions onto the melamine core (Fig. 6c).^[66] Onto this initial layer, stable classical LbL polyelectrolyte multilayers are assembled. The core is removed, the initial layers are dissolved under specific conditions, and the auxiliaries are washed away. Then the inside of the capsules is filled with the polymer.^[73] This approach requires for each application specific conditions under which the desired polymer can be precipitated and is difficult to implement practically.

Another approach for encapsulation consists in loading preformed capsules by switching the shell wall permeability through variation in environmental conditions, such as pH^[41,74,75] or ionic strength (Fig. 6b).^[76] In the capsule open state, surrounding macromolecules can diffuse into the interior. Switching the pH or ion strength back, the capsule wall closes and the macromolecules in the interior are captured. This method can only be

performed with specifically designed capsules of suitable permeability. Furthermore, only low polymer concentrations can be achieved.

Capsules filled with functional polymers or with biomolecules can fulfill many tasks:

1. A gradient of the physicochemical properties between the outer and inner solution such as pH, ion strengths, polarity, charge distribution (Donnan potential), etc. can be used for the accumulation or selective precipitation of low molecular weight substances in the capsules. For example, if PSS-filled capsules (Fig. 7b) are placed in a mixture of water and nonpolar solvents, the water content in the vicinity of the entrapped polyelectrolytes increases. This effect has been used for encapsulation of poorly water-soluble drugs.^[77] Several dyes and inorganic salts, such as fluorescein, rhodamine, calcium carbonate, and barium carbonate, were precipitated inside PE capsules by using such gradients.^[70,71] Electrostatic adsorption in polymer-filled shells has been used to trap semiconductor nanocrystals, iron oxide, or nanosized magnetic ferrite particles.^[78–80]
2. The incorporation of polymer-bound catalysts or biocatalysts results in microreaction containers. Small molecular weight educts can diffuse into the capsules and react with the catalyst, and the products are released.
3. The capsule wall can prevent poisoning or destruction of biocatalysts because large molecules such as polymers, enzymes, and bacteria cannot enter the capsules. The concept of macromolecule encapsulation in MF microshells by opening and closing pores was applied to enzymes. For instance, α -chymotrypsin

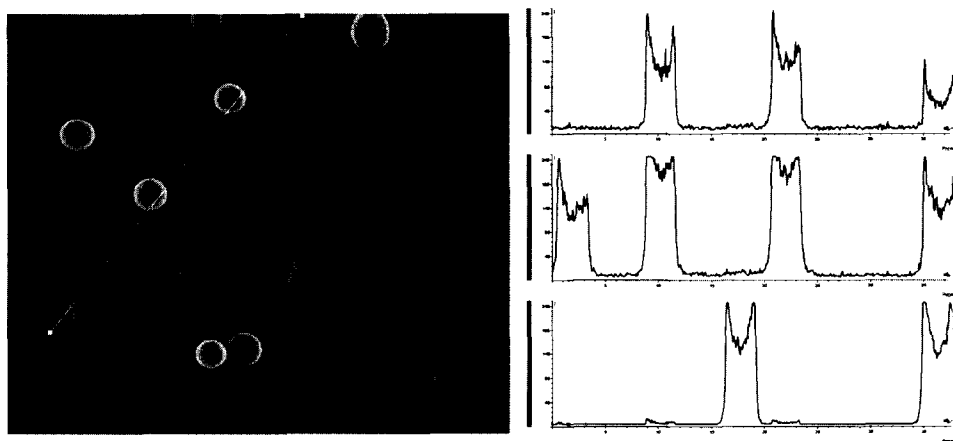


Fig. 8 Combinatorial library of (PAH/PSS)₅ capsules with different combinations of dye molecules (fluorescein, rhodamine, Cy5, and pyrene) covalently linked to the PAH layers in the capsule wall; the right image shows the fluorescence intensity along a line through the dye tagged capsules. One can clearly differentiate the dye constituents and their amount. (View this art in color at www.dekker.com.)

was encapsulated in hollow PSS/PAH shells by method 3. The protein in the capsules retained a high activity (50–60%) and long storage stability.^[81]

Urease was also encapsulated into PSS/PAH shell using a similar approach: the pore-controlling factor was, in this case, the solvent choice.^[82] Ethanol was added to a urease/microshells suspension and opened the pores.^[44,45] Using these urease-loaded PAH/PSS capsules, calcium carbonate was synthesized exclusively inside of the capsules (Fig. 7c). The carbonate anions were generated inside of the capsules by a urease-catalyzed urea decomposition. Addition of calcium ions produced precipitation of calcium carbonate, which completely filled the capsule volume. Because of the easiness in varying experimental parameters, such as the wall thickness, internal composition, and influx, these PE capsule-based systems can be used to study fundamental aspects of biomineralization processes.^[83]

Encapsulation of enzyme crystals or aggregates with the LbL technique^[84,85] has been performed for chymotrypsin^[86] and lactate dehydrogenase. The encapsulated lactate dehydrogenase exhibits increased lifetimes due to higher stability to denaturation and is not substrate-inhibited.^[87]

Modification of the Wall

So far, the most and best-studied polyelectrolyte association on surfaces, core shells, and capsules has been poly(allylamine)/poly(styrenesulfonate). Nevertheless, shells based on other synthetic polyelectrolytes such as poly(diallyldimethylamine), poly(ethyleneimine), or Nafion have recently been synthesized.^[49,88] Because of the potential applications in the pharmaceutical industry, there are increasing activities in the area of naturally occurring polyelectrolytes: recently, LbL capsules containing carrageenan,^[89] dextran sulfate,^[63] chitosan/chitosan sulfate,^[90] sodium alginate, carboxymethyl cellulose,^[48] or protamine^[91] were reported. In contrast to planar films from biomolecules, the preparation of polyelectrolyte capsules is limited because of the harsh conditions used for the dissolution of the core. However, the development of new templates such as CaCO₃ particles extends the preparation possibilities. Decomposable hollow capsules based on deoxyribonucleic acid (DNA) and spermidine (SP) were already prepared.^[33]

Several functionalities can be easily introduced in the capsule wall using polymers, which were labeled before the assembly process. Capsules with increased stability have been prepared by cross-linking of water-soluble ionene precursor polymers yielding luminescent conjugated oligofluorenes.^[46] A copolymer of poly(aniline) and PSS was introduced to obtain walls with reducing

properties.^[92] By using polymers presenting photoreactive diazo groups, the ionic bonds between the negative PSS and the positive diazoresin are converted to covalent cross-links. Cross-linked hollow capsules are mechanically more stable in various chemical environments than their ionically linked counterparts.^[93] Photochromic hollow shells using an azobenzene-containing polymer were produced.^[89]

The use of hollow or filled capsules for combinatorial purposes requires a tagging of the capsule wall. Polymers with covalently bound fluorescent dyes have been incorporated in the capsule walls. A luminescent library of (PAH/PSS)₅ capsules were prepared by assembling four different dyes, each covalently attached in several PAH layers. Different layer combinations yielded 16 tagged capsules (Fig. 8). The intermediate layers minimize perturbing interactions between the layers. Although all capsules have the same size and properties, they can easily be distinguished by multichannel confocal fluorescence microscopy or by flow cytometry.^[94]

Water-insoluble organic dyes were incorporated in capsule walls by depositing them in nonaqueous solution alternatively with polyelectrolytes in aqueous solution.^[95] Using different fluorescent dyes, a two-step energy transfer cascade in the wall of hollow microcapsules was constructed.^[96,97] The dyes were assembled in such a way that fluorescence resonance energy transfer through the capsule wall from outside to inside happened. Nanoporous capsule walls or shell-in-shell structures have been constructed by consecutive alternating adsorption of polyelectrolytes and SiO₂ on melamine formaldehyde particles, followed by removal of MF cores with HCl acid and of the sandwiched SiO₂ particle layers between indestructible PAH/PSS walls with HF. The inner and outer shell could be distinguished by labeling the inner shell with fluorescein and the outer shell with rhodamine B. Although the distance between the two shells is only 50 nm, confocal microscopy could resolve this difference (Fig. 9).^[98] The two shell walls are separated by an intermediate PAH solution; which acts as an osmotic pressure buffer and yields higher mechanical stability against outside pressure.^[98]

Several inorganic materials can be prepared as charged nanoparticles. SiO₂, TiO₂, laponite,^[99] and CdTe nanoparticles have been used for the preparation of capsules.^[100–102] Incorporation of colloidal dispersion of charged silica nanobeads as one of the wall components led to composite organic/inorganic colloidal materials.^[103–105] Depending on the method chosen to remove the core, one obtains either a hollow inorganic/organic hybrid wall by dissolution of the MF core in HCl or a hollow silica sphere by thermal decomposition of the organic compounds.^[106,107] Calcination of a composite between core-shell silica and gold nanoparticles

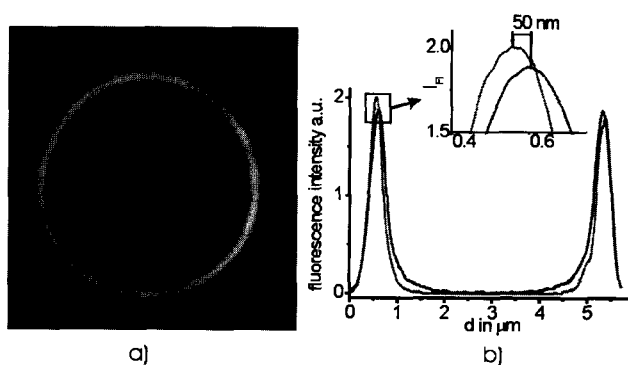


Fig. 9 Confocal image of a shell in shell structure. The outer shell is labeled by fluorescein and the inner shell is labeled by rhodamine; the right image shows the distance between both shells, analyzed by two-color imaging. (From Ref. [98].) (View this art in color at www.dekker.com.)

(Au@SiO₂)/PDADMAC deposited onto polymer spheres gave rise to hollow spheres of Au@SiO₂.^[110] Noble metals, such as silver, were incorporated either inside the capsule or in the capsule wall.^[92]

Functional nanoparticles were incorporated into capsules to introduce magnetic, fluorescent, or catalytic properties. Superparamagnetic magnetite (Fe₃O₄) was mounted as a component of the shell wall^[108–111] or as a part of the capsule interior.^[79]

The combination of lipids and PE capsules creates an artificial system, mimicking biological membranes. Confocal microscopy images of capsules coated with fluorescent lipids demonstrated, within the resolution of the instrument, a homogeneous coverage of the capsule surface by lipid bilayers or multilayers.^[112] The permeability for polar substances decreased remarkably after deposition of the lipid bilayer onto the hollow PE capsules. However, studies on electrical properties showed an increase in conductivity with the bulk electrolyte concentration, which was attributed to the presence of pores or defects in the lipid film.^[113]

Modification of the Surface

The outer surface of polyelectrolyte capsules can be functionalized using in the last assembling step a polyelectrolyte which contains the desired function. The simplest example to tune the surface charge is the choice of a cationic or anionic polyelectrolyte. A more sophisticated application is the introduction of a high density of coupling sites, where subsequent functionalization can be performed. The commonly used chemical surface groups such as carboxyl or amino functions can be easily

introduced by using poly(acrylic acid) or poly(allylamine). The disadvantage of the last layer is its stability in solution. While the inner layers of LbL films are fully immobilized, the outermost layer equilibrates in a solution because of the high charge density. Hence some of the polymer chains containing functional groups get lost under extreme conditions such as high or low pH, high ionic strength, etc. This problem can be solved by cross-linking the last layer.

CONCLUSION

One important milestone in the fast development of the LbL polyelectrolyte films^[114,115] was their use in 1998 for the preparation of hollow capsules. These closed LbL films extended remarkably the application fields of the method. The large versatility and modularity of the LbL capsules led to a fast development in the last 5 years as demonstrated on the selected examples in this review.

The LbL capsules will not substitute all other encapsulation technologies, but due to their specific properties, they can contribute to new applications especially in high technology fields. These properties are summarized in the following paragraph, together with the actual drawbacks and problems:

The capsule preparation is simple and does not need expensive equipment, but the procedures are rather time-consuming. In addition, an upscaling of the process is under way, but not solved yet.

The selection of arbitrary templates allows the preparation of capsules in a wide size range, with a well-defined shape and a high monodispersity, but the ideal template has not been found yet. Therefore, the LbL film is stressed during the core dissolution, leading to changes in permeability, size and internal structure as well as to remaining residues of the templates.

The capsules exhibit semipermeable properties, which can be tuned in a broad region by the layer number, the material, or subsequent crosslinking. However, the permeability could not be lowered enough for the encapsulation of small water-soluble molecules.

PSS/PAH capsules possess an extremely high physicochemical stability against aggressive media, like acids, bases, high salt contents and organic solvents. But also instable capsules can be designed, which decompose under defined circumstances and release their interior.

Interior, wall and outer surface of LbL capsules can be more easily modified than in other capsule systems. The nanometer precise deposition of functionalized layers and intermediate layers allows the combination

of many different functions in one capsule without cross-reactions.

Due to the short time of the capsule development and the almost infinite possibilities to vary parameters in the preparation process, there are still many open questions, but also a very high potential for further important developments in this field. Especially in the bio-sciences, many surprises can be expected due to the potential of the capsules to serve as model systems for cells, viruses etc. The use of PE shells as biomimetic systems is under research as for example combinations of capsules and lipid bilayers equipped with ion channels. Research on modifications of the capsule surface in order to recognize specific biological materials or interfaces is started. The use of the capsules as micro-vessels for DNA amplification (PCR) or as non-viral gene transfection systems is planned. One important step is the further miniaturization down to 30 nm which has been recently achieved without aggregation.^[118]

REFERENCES

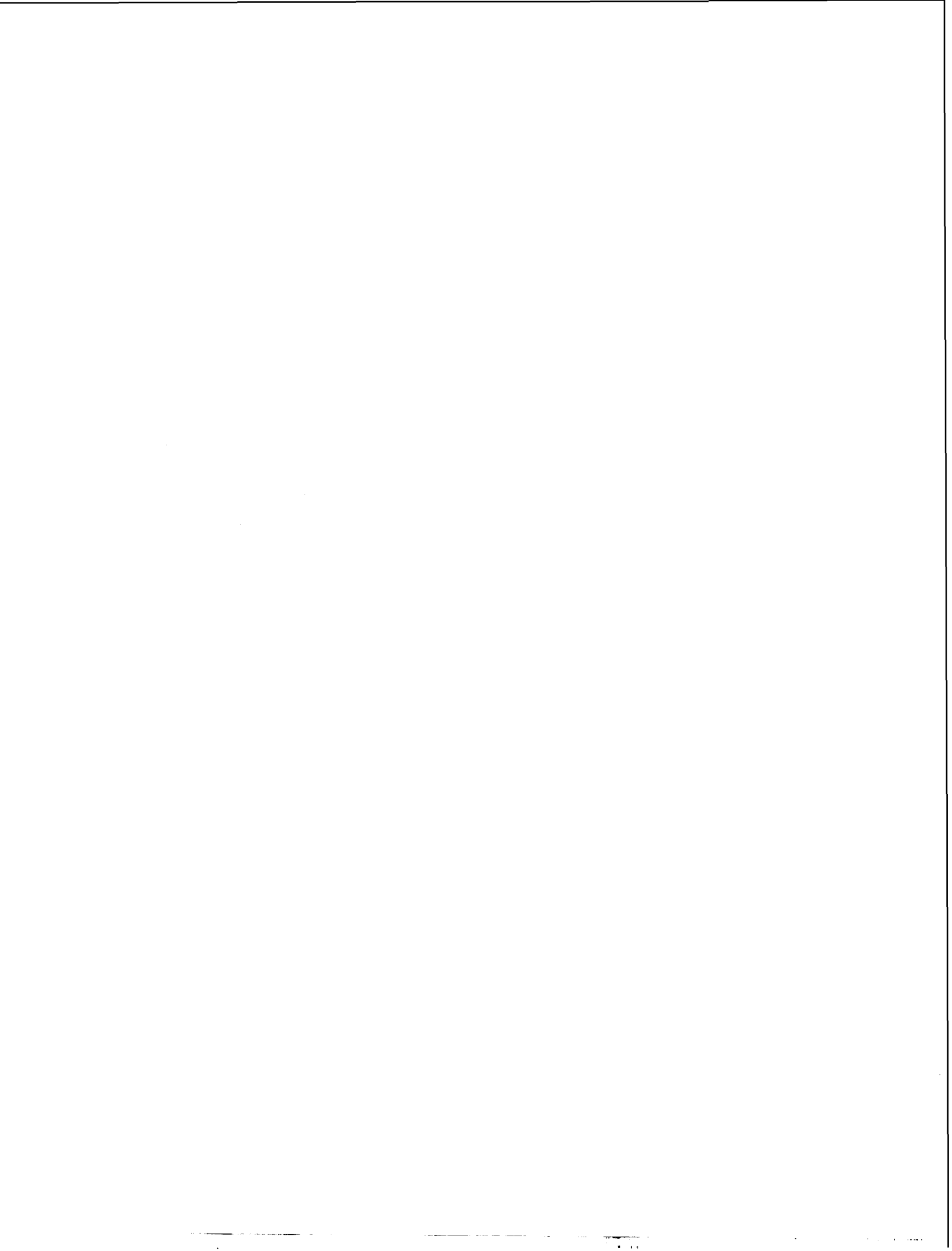
1. Brannonpeppas, L. Controlled-release in the food and cosmetics industries. *ACS Symp. Ser.* **1993**, 520, 42–52.
2. Jung, J.; Perrut, M. Particle design using supercritical fluids: Literature and patent survey. *J. Supercrit. Fluids* **2001**, 20 (3), 179–219.
3. Rafler, G. Mikropartikel in Forst und Landwirtschaft. *Spektrum Wiss.* **1994**, 122–124.
4. Schleicher, L.; Green, B.K. *Manifold Record Material*. US-Patent US2730456, January 10, 1956.
5. Wasan, K.M. Formulation and physiological and biopharmaceutical issues in the development of oral lipid-based drug delivery systems. *Drug Dev. Ind. Pharm.* **2001**, 27 (4), 267–276.
6. Meier, W. Polymer nanocapsules. *Chem. Soc. Rev.* **2000**, 29 (5), 295–303.
7. Lutz, S.; Essler, F.; Panzner, S. Serum Stable Nanocapsules from Liposomal Templates. In *Controlled Release Society 29th Annual Meeting*; 2002.
8. Decher, G.; Hong, J.D.; Schmitt, J. Buildup of ultrathin multilayer films by a self-assembly process 3. In *Consecutively Alternating Adsorption of Anionic and Cationic Polyelectrolytes on Charged Surfaces*. *Thin Solid Films* **1992** 210 (1–2), 831–835.
9. Forster, S.; Plantenberg, T. From self-organizing polymers to nanohybrid and biomaterials. *Angew. Chem., Int. Ed.* **2002**, 41 (5), 689–714.
10. Renken, A.; Hunkeler, D. Microencapsulation: A review of polymers and technologies with a focus on bioartificial organs. *Polimery* **1998**, 43 (9), 530–539.
11. Hunkeler, D. Polymers for bioartificial organs. *Trends Polym. Sci.* **1997**, 5 (9), 286–293.
12. Manna, A.; Imae, T.; Aoi, K.; Okada, M.; Yogo, T. Synthesis of dendrimer-passivated noble metal nanoparticles in a polar medium: Comparison of size between silver and gold particles. *Chem. Mater.* **2001**, 13, 1674–1681.
13. Sunder, A.; Kramer, M.; Hanselmann, R.; Muhlaupt, R.; Frey, H. Molecular nanocapsules based on amphiphilic hyperbranched polyglycerols. *Angew. Chem., Int. Ed. Engl.* **1999**, 38, 3552–3555.
14. Donath, E.; Sukhorukov, G.B.; Caruso, F.; Davis, S.A.; Moehwald, H. Novel hollow polymer shells by colloid-templated assembly of polyelectrolytes. *Angew. Chem., Int. Ed.* **1998**, 37 (16), 2202–2205.
15. Decher, G. Layered nanoarchitectures via directed assembly of anionic and cationic molecules. In *Comprehensive Supramolecular Chemistry*; Sauvage, J.-P., Ed.; Pergamon Press: Oxford, 1996; 507–552.
16. Decher, G. Fuzzy nanoassemblies: Toward layered polymeric multicomposites. *Science* **1997**, 277 (5330), 1232–1237.
17. Decher, G.; Eckle, M.; Schmitt, J.; Struth, B. Layer-by-layer assembled multicomposite films. *Curr. Opin. Colloid Interface Sci.* **1998**, 3 (1), 32–39.
18. Knoll, W. Self-assembled microstructures at interfaces. *Curr. Opin. Colloid Interface Sci.* **1996**, 1 (1), 137–143.
19. Bertrand, P.; Jonas, A.; Laschewsky, A.; Legras, R. Ultrathin polymer coatings by complexation of polyelectrolytes at interfaces: Suitable materials, structure and properties. *Macromol. Rapid Commun.* **2000**, 21, 319–348.
20. Arys, X.; Jonas, A.; Laschewsky, A.; Legras, R. *Supramolecular Polymers*; Marcel Dekker: New York, 2000; 505–563.
21. Decher, G. Polyelectrolyte multilayers, an Overview. In *Multilayer Thin Films*; Decher, G., Schlenoff, J.B., Eds.; Wiley VCH: New York/Bassel, 2003; 1–46.
22. Moehwald, H.; Lichtenfeld, H.; Moya, S.; Voigt, A.; Baumler, H.; Sukhorukov, G.; Caruso, F.; Donath, E. From polymeric films to nanoreactors. *Macromol. Symp.* **1999**, 145, 75–81.
23. Moehwald, H. From Langmuir monolayers to nanocapsules. *Colloids Surf., A Physicochem. Eng. Asp.* **2000**, 171 (1–3), 25–31.
24. Moehwald, H.; Donath, E.; Sukhorukov, G.B.

- Smart Capsules. In *Multilayer Thin Films*; Wiley VCH: New York, 2003; 363–392.
25. Sukhorukov, G.B. Designed Nano-Engineered Polymer Films on Colloidal Particles and Capsules. In *Novel Methods to Study Interfacial Layers*; Miller, M.R., Ed.; Elsevier Science, 2001; 384–414.
 26. Sukhorukov, G.B. Multilayer Hollow Microspheres. In *MML Series*; Citus Books, 2002; 111–147.
 27. Voigt, A.; Lichtenfeld, H.; Sukhorukov, G.B.; Zastrow, H.; Donath, E.; Baumler, H.; Moehwald, H. Membrane filtration for microencapsulation and microcapsules fabrication by layer-by-layer polyelectrolyte adsorption. *Ind. Eng. Chem. Res.* **1999**, *38* (10), 4037–4043.
 28. Caruso, F.; Yang, W.J.; Trau, D.; Renneberg, R. Microencapsulation of uncharged low molecular weight organic materials by polyelectrolyte multilayer self-assembly. *Langmuir* **2000**, *16* (23), 8932–8936.
 29. Antipov, A.A.; Sukhorukov, G.B.; Donath, E.; Moehwald, H. Sustained release properties of polyelectrolyte multilayer capsules. *J. Phys. Chem., B* **2001**, *105* (12), 2281–2284.
 30. Trau, D.; Yang, W.J.; Seydack, M.; Caruso, F.; Yu, N.T.; Renneberg, R. Nanoencapsulated microcrystalline particles for superamplified biochemical assays. *Anal. Chem.* **2002**, *74* (21), 5480–5486.
 31. Dai, Z.F.; Voigt, A.; Donath, E.; Moehwald, H. Novel encapsulated functional dye particles based on alternately adsorbed multilayers of active oppositely charged macromolecular species. *Macromol. Rapid Commun.* **2001**, *22* (10), 756–762.
 32. Petrov, A.I.; Gavryushkin, A.V.; Sukhorukov, G.B. Effect of temperature, pH and shell thickness on the rate of Mg^{2+} and $Ox(2-)$ release from multilayered polyelectrolyte shells deposited onto microcrystals of magnesium oxalate. *J. Phys. Chem., B* **2003**, *107* (3), 868–875.
 33. Schuler, C.; Caruso, F. Decomposable hollow biopolymer-based capsules. *Biomacromolecules* **2001**, *2* (3), 921–926.
 34. Gittins, D.I.; Caruso, F. Multilayered polymer nanocapsules derived from gold nanoparticle templates. *Adv. Mater.* **2000**, *12* (24), 1947–1948.
 35. Gittins, D.I.; Caruso, F. Tailoring the polyelectrolyte coating of metal nanoparticles. *J. Phys. Chem., B* **2001**, *105* (29), 6846–6852.
 36. Mayya, K.S.; Gittins, D.I.; Dibaj, A.M.; Caruso, F. Nanotubules prepared by templating sacrificial nickel nanorods. *Nano Lett.* **2001**, *1* (12), 727–730.
 37. Neu, B.; Voigt, A.; Mitlohner, R.; Leporatti, S.; Gao, C.Y.; Donath, E.; Kiesewetter, H.; Moehwald, H.; Meiselman, H.J.; Baumler, H. Biological cells as templates for hollow microcapsules. *J. Microencapsul.* **2001**, *18* (3), 385–395.
 38. Diaspro, A.; Silvano, D.; Krol, S.; Cavalleri, O.; Gliozzi, A. Single living cell encapsulation in nano-organized polyelectrolyte shells. *Langmuir* **2002**, *18* (13), 5047–5050.
 39. Donath, E.; Moya, S.; Neu, B.; Sukhorukov, G.B.; Georgieva, R.; Voigt, A.; Baumler, H.; Kiesewetter, H.; Moehwald, H. Hollow polymer shells from biological templates: Fabrication and potential applications. *Chem. Eur. J.* **2002**, *8* (23), 5481–5485.
 40. Gao, C.Y.; Moya, S.; Lichtenfeld, H.; Casoli, A.; Fiedler, H.; Donath, E.; Moehwald, H. The decomposition process of melamine formaldehyde cores: The key step in the fabrication of ultrathin polyelectrolyte multilayer capsules. *Macromol. Mater. Eng.* **2001**, *286* (6), 355–361.
 41. Sukhorukov, G.B.; Antipov, A.A.; Voigt, A.; Donath, E.; Moehwald, H. pH-Controlled macromolecule encapsulation in and release from polyelectrolyte multilayer nanocapsules. *Macromol. Rapid Commun.* **2001**, *22* (1), 44–46.
 42. Ibarz, G.; Daehne, L.; Donath, E.; Moehwald, H. Resealing of polyelectrolyte capsules after core removal. *Macromol. Rapid Commun.* **2002**, *23* (8), 474–478.
 43. Moya, S.; Daehne, L.; Voigt, A.; Leporatti, S.; Donath, E.; Moehwald, H. Polyelectrolyte multilayer capsules templated on biological cells: Core oxidation influences layer chemistry. *Colloids Surf., A Physicochem. Eng. Asp.* **2001**, *183*, 27–40.
 44. Gao, C.Y.; Liu, X.G.; Shen, J.C.; Moehwald, H. Spontaneous deposition of horseradish peroxidase into polyelectrolyte multilayer capsules to improve its activity and stability. *Chem. Commun.* **2002**, (17), 1928–1929.
 45. Gao, C.Y.; Donath, E.; Moehwald, H.; Shen, J.C. Spontaneous deposition of water-soluble substances into macrocapsules: Phenomenon, mechanism and application. *Angew. Chem., Int. Ed. Engl.* **2002**, *41* (20), 3789–3793.
 46. Park, M.K.; Xia, C.J.; Advincula, R.C.; Schutz, P.; Caruso, F. Cross-linked, luminescent spherical colloidal and hollow-shell particles. *Langmuir* **2001**, *17* (24), 7670–7674.
 47. Shi, X.Y.; Caruso, F. Release behavior of thin-walled microcapsules composed of polyelectrolyte multilayers. *Langmuir* **2001**, *17* (6), 2036–2042.

48. Qiu, X.P.; Leporatti, S.; Donath, E.; Moehwald, H. Studies on the drug release properties of polysaccharide multilayers encapsulated ibuprofen microparticles. *Langmuir* **2001**, *17* (17), 5375–5380.
49. Qiu, X.P.; Donath, E.; Moehwald, H. Permeability of ibuprofen in various polyelectrolyte multilayers. *Macromol. Mater. Eng.* **2001**, *286* (10), 591–597.
50. Mendelsohn, J.D.; Barrett, C.J.; Chan, V.V.; Pal, A.J.; Mayes, A.M.; Rubner, M.F. Fabrication of microporous thin films from polyelectrolyte multilayers. *Langmuir* **2000**, *16* (11), 5017–5023.
51. Shiratori, S.S.; Rubner, M.F. pH-Dependent thickness behavior of sequentially adsorbed layers of weak polyelectrolytes. *Macromolecules* **2000**, *33* (11), 4213–4219.
52. Hiller, J.; Mendelsohn, J.D.; Rubner, M.F. Reversibly erasable nanoporous anti-reflection coatings from polyelectrolyte multilayers. *Nat. Mater.* **2002**, *1*, 59–63.
53. Antipov, A.A.; Sukhorukov, G.B.; Leporatti, S.; Radtchenko, I.L.; Donath, E.; Moehwald, H. Polyelectrolyte multilayer capsule permeability control. *Colloids Surf., A Physicochem. Eng. Asp.* **2002**, *198*, 535–541.
54. Peyratout, C.S.; Daehne, L. Preparation of photosensitive dye aggregates and fluorescent dye nanocrystals in microreaction containers. *Adv. Mater.* **2003**, *15* (20), 1722–1726.
55. Harris, J.J.; Stair, J.L.; Bruening, M.L. Layered polyelectrolyte films as selective, ultrathin barriers for anion transport. *Chem. Mater.* **2000**, *12*, 1941–1946.
56. Harris, J.J.; Bruening, M.L. Electrochemical and in situ ellipsometric investigation of the permeability and stability of layered polyelectrolyte films. *Langmuir* **2000**, *16* (4), 2006–2013.
57. Steitz, R.; Leiner, V.; Siebrecht, R.; v. Klitzing, R. Influence of the ionic strength on the structure of polyelectrolyte films at the solid/liquid interface. *Colloids Surf., A Physicochem. Eng. Asp.* **2000**, *163*, 63–70.
58. Lvov, Y.; Decher, G.; Moehwald, H. Assembly, structural characterization, and thermal behavior of layer-by-layer deposited ultrathin films of poly(vinylsulfite) and poly-(allylamine). *Langmuir* **1993**, *9* (2), 481–486.
59. Dubas, S.T.; Schlenoff, J.B. Polyelectrolyte multilayers containing a weak polyacid: Construction and deconstruction. *Macromolecules* **2001**, *34* (11), 3736–3740.
60. Fery, A.; Schoeler, B.; Cassagneau, T.; Caruso, F. Nanoporous thin films formed by salt-induced structural changes in multilayers of poly(acrylic acid) and poly-(allylamine). *Langmuir* **2001**, *17* (13), 3779–3783.
61. Farhat, T.R.; Schlenoff, J.B. Ion transport and equilibria in polyelectrolyte multilayers. *Langmuir* **2001**, *17*, 1184–1192.
62. Antipov, A.A.; Sukhorukov, G.B.; Moehwald, H. Influence of the ionic strength on the polyelectrolyte multilayers permeability. *Langmuir* **2003**, *19*, 2444–2448.
63. Georgieva, R.; Moya, S.; Hin, M.; Mitlohner, R.; Donath, E.; Kiesewetter, H.; Moehwald, H.; Baumler, H. Permeation of macromolecules into polyelectrolyte microcapsules. *Biomacromolecules* **2002**, *3* (3), 517–524.
64. Gao, C.; Donath, E.; Moya, S.; Dudnik, V.; Moehwald, H. Elasticity of hollow polyelectrolyte capsules prepared by the layer-by-layer technique. *Eur. Phys. J., E* **2001**, *5*, 21–27.
65. Gao, C.Y.; Leporatti, S.; Moya, S.; Donath, E.; Moehwald, H. Stability and mechanical properties of polyelectrolyte capsules obtained by stepwise assembly of poly(styrenesulfonate sodium salt) and poly(diallyldimethyl ammonium) chloride onto melamine resin particles. *Langmuir* **2001**, *17* (11), 3491–3495.
66. Radtchenko, I.L.; Sukhorukov, G.B.; Leporatti, S.; Khomutov, G.B.; Donath, E.; Moehwald, H. Assembly of alternated multivalent ion/polyelectrolyte layers on colloidal particles. Stability of the multilayers and encapsulation of macromolecules into polyelectrolyte capsules. *J. Colloid Interface Sci.* **2000**, *230* (2), 272–280.
67. Gao, C.Y.; Moya, S.; Donath, E.; Moehwald, H. Melamine formaldehyde core decomposition as the key step controlling capsule integrity: Optimizing the polyelectrolyte capsule fabrication. *Macromol. Chem. Phys.* **2002**, *203* (7), 953–960.
68. Baumler, H.; Artmann, G.; Voigt, A.; Mitlohner, R.; Neu, B.; Kiesewetter, H. Plastic behaviour of polyelectrolyte microcapsules derived from colloid templates. *J. Microencapsul.* **2000**, *17* (5), 651–655.
69. Moya, S.; Sukhorukov, G.B.; Auch, M.; Donath, E.; Moehwald, H. Microencapsulation of organic solvents in polyelectrolyte multilayer micrometer-sized shells. *J. Colloid Interface Sci.* **1999**, *216* (2), 297–302.
70. Sukhorukov, G.; Daehne, L.; Hartmann, J.; Donath, E.; Moehwald, H. Controlled precipitation of dyes into hollow polyelectrolyte capsules based on

- colloids and biocolloids. *Adv. Mater.* **2000**, *12* (2), 112–115.
71. Sukhorukov, G.B.; Susha, A.S.; Davis, S.; Leporatti, S.; Donath, E.; Hartmann, J.; Moehwald, H. Precipitation of inorganic salts inside hollow micrometer-sized polyelectrolyte shells. *J. Colloid Interface Sci.* **2002**, *247* (1), 251–254.
 72. Daehne L.; Leporatti, S.; Donath E.; Moehwald, H. Fabrication of micro reaction cages with tailored properties. *J. Am. Chem. Soc.* **2001**, *123* (23), 5431–5436.
 73. Radtchenko, I.L.; Sukhorukov, G.B.; Moehwald, H. Incorporation of macromolecules into polyelectrolyte micro- and nanocapsules via surface controlled precipitation on colloidal particles. *Colloids Surf., A Physicochem. Eng. Asp.* **2002**, *202* (2–3), 127–133.
 74. Sukhorukov, G.B.; Brumen, M.; Donath, E.; Moehwald, H. Hollow polyelectrolyte shells: Exclusion of polymers and donnan equilibrium. *J. Phys. Chem., B* **1999**, *103* (31), 6434–6440.
 75. Khopade, A.J.; Caruso, F. Stepwise self-assembled poly(amidoamine) dendrimer and poly(styrenesulfonate) microcapsules as sustained delivery vehicles. *Biomacromolecules* **2002**, *3* (6), 1154–1162.
 76. Ibarz, G.; Daehne, L.; Donath, E.; Moehwald, H. Smart micro- and nanocontainers for storage, transport, and release. *Adv. Mater.* **2001**, *13* (17), 1324–1327.
 77. Radtchenko, I.L.; Sukhorukov, G.B.; Moehwald, H. A novel method for encapsulation of poorly water-soluble drugs: Precipitation in polyelectrolyte multilayer shells. *Int. J. Pharm.* **2002**, *242* (1–2), 219–223.
 78. Gaponik, N.; Radtchenko, I.L.; Sukhorukov, G.B.; Weller, H.; Rogach, A.L. Toward encoding combinatorial libraries: Charge-driven microencapsulation of semiconductor nanocrystals luminescing in the visible and near IR. *Adv. Mater.* **2002**, *14* (12), 879–882.
 79. Shchukin, D.G.; Radtchenko, I.L.; Sukhorukov, G.B. Synthesis of nanosized magnetic ferrite particles inside hollow polyelectrolyte capsules. *J. Phys. Chem., B* **2003**, *107* (1), 86–90.
 80. Radchenko, I.L.; Giersig, M.; Sukhorukov, G.B. Inorganic particle synthesis in confined micron-sized polyelectrolyte capsules. *Langmuir* **2002**, *18*, 8204–8208.
 81. Tiourina, O.P.; Antipov, A.A.; Sukhorukov, G.B.; Larionova, N.L.; Lvov, Y.; Moehwald, H. Entrapment of alpha-chymotrypsin into hollow polyelectrolyte microcapsules. *Macromol. Biosci.* **2001**, *1* (5), 209–214.
 82. Lvov, Y.; Antipov, A.A.; Mamedov, A.; Moehwald, H.; Sukhorukov, G.B. Urease encapsulation in nanoorganized microshells. *Nano Lett.* **2001**, *1* (3), 125–128.
 83. Antipov, A.A.; Shchukin, D.G.; Fedutik, Y.A.; Zhanaveskina, I.; Klechkovskaya, V.; Sukhorukov, G.B.; Moehwald, H. Urease-catalyzed carbonate precipitation inside the restricted volume of polyelectrolyte capsules. *Macromol. Rapid Commun.* **2003**, *24* (3), 274–277.
 84. Caruso, F.; Trau, D.; Moehwald, H.; Renneberg, R. Enzyme encapsulation in layer-by-layer engineered polymer multilayer capsules. *Langmuir* **2000**, *16* (4), 1485–1488.
 85. Jin, W.; Shi, X.Y.; Caruso, F. High activity enzyme microcrystal multilayer films. *J. Am. Chem. Soc.* **2001**, *123* (33), 8121–8122.
 86. Balabushevitch, N.G.; Sukhorukov, G.B.; Moroz, N.A.; Volodkin, D.V.; Larionova, N.I.; Donath, E.; Moehwald, H. Encapsulation of proteins by layer-by-layer adsorption of polyelectrolytes onto protein aggregates: Factors regulating the protein release. *Biotechnol. Bioeng.* **2001**, *76* (3), 207–213.
 87. Bobreshova, M.E.; Sukhorukov, G.B.; Saburova, E.A.; Elfimova, L.I.; Shabarchina, L.I.; Sukhorukov, B.I. Lactate dehydrogenase in interpolyelectrolyte complex. Function and stability. *Biofizika* **1999**, *44* (5), 813–820.
 88. Dai, Z.F.; Moehwald, H. Highly stable and biocompatible Nafion-based capsules with controlled permeability for low-molecular-weight species. *Chem. Eur. J.* **2002**, *8* (20), 4751–4755.
 89. Jung, B.D.; Hong, J.D.; Voigt, A.; Leporatti, S.; Daehne, L.; Donath, E.; Moehwald, H. Photochromic hollow shells: Photoisomerization of azobenzene polyionene in solution, in multilayer assemblies on planar and spherical surfaces. *Colloids Surf., A Physicochem. Eng. Asp.* **2002**, *198*, 483–489.
 90. Berth, G.; Voigt, A.; Dautzenberg, H.; Donath, E.; Moehwald, H. Polyelectrolyte complexes and layer-by-layer capsules from chitosan/chitosan sulfate. *Biomacromolecules* **2002**, *3* (3), 579–590.
 91. Tiourina, O.P.; Sukhorukov, G.B. Multilayer alginate/protamine microsized capsules: Encapsulation of alpha-chymotrypsin and controlled release study. *Int. J. Pharm.* **2002**, *242* (1–2), 155–161.
 92. Antipov, A.A.; Sukhorukov, G.B.; Fedutik, Y.A.; Hartmann, J.; Giersig, M.; Moehwald, H. Fabrication of a novel type of metallized colloids and hollow capsules. *Langmuir* **2002**, *18* (17), 6687–6693.
 93. Pastoriza-Santos, I.; Scholer, B.; Caruso, F. Core-shell colloids and hollow polyelectrolyte capsules

- based on diazoresins. *Adv. Funct. Mater.* **2001**, *11* (2), 122–128.
94. Härmä, H. Particle technologies in diagnostics. *Technol. Rev.* **2002**, *126*, 1–30.
95. Dai, Z.F.; Voigt, A.; Leporatti, S.; Donath, E.; Daehne, L.; Moehwald, H. Layer-by-layer self-assembly of polyelectrolyte and low molecular weight species into capsules. *Adv. Mater.* **2001**, *13* (17), 1339–1342.
96. Dai, Z.F.; Daehne, L.; Donath, E.; Moehwald, H. Mimicking photosynthetic two-step energy transfer in cyanine triads assembled into capsules. *Langmuir* **2002**, *18* (12), 4553–4555.
97. Dai, Z.F.; Daehne, L.; Donath, E.; Moehwald, H. Downhill energy transfer via ordered multichromophores in light-harvesting capsules. *J. Phys. Chem., B* **2002**, *106* (44), 11501–11508.
98. Dai, Z.F.; Daehne, L.; Moehwald, H.; Tiersch, B. Novel capsules with high stability and controlled permeability by hierarchic templating. *Angew. Chem., Int. Ed.* **2002**, *41* (21), 4019–4022.
99. Caruso, R.A.; Susha, A.; Caruso, F. Multilayered titania, silica, and laponite nanoparticle coatings on polystyrene colloidal templates and resulting inorganic hollow spheres. *Chem. Mater.* **2001**, *13* (2), 400–409.
100. Caruso, F. Nanoengineering of particle surfaces. *Adv. Mater.* **2001**, *13* (1), 11–22.
101. Caruso, F. Generation of complex colloids by polyelectrolyte-assisted electrostatic self-assembly. *Aust. J. Chem.* **2001**, *54* (6), 349–353.
102. Caruso, F. Engineering of Core-Shell Particles and Hollow Capsules. In *Nano-Surface Chemistry*; Rosoff, M., Ed.; Marcel Dekker: New York, 2002; 505–526.
103. Caruso, F.; Lichtenfeld, H.; Giersig, M.; Moehwald, H. Electrostatic self-assembly of silica nanoparticle—Polyelectrolyte multilayers on polystyrene latex particles. *J. Am. Chem. Soc.* **1998**, *120* (33), 8523–8524.
104. Caruso, F.; Moehwald, H. Preparation and characterization of ordered nanoparticle and polymer composite multilayers on colloids. *Langmuir* **1999**, *15* (23), 8276–8281.
105. Caruso, F. Hollow capsule processing through colloidal templating and self-assembly. *Chem. Eur. J.* **2000**, *6* (3), 413–419.
106. Caruso, F.; Caruso, R.A.; Moehwald, H. Nanoengineering of inorganic and hybrid hollow spheres by colloidal templating. *Science* **1998**, *282* (5391), 1111–1114.
107. Caruso, F.; Caruso, R.A.; Moehwald, H. Production of hollow microspheres from nanostructured composite particles. *Chem. Mater.* **1999**, *11* (11), 3309–3314.
108. Sukhorukov, G.B.; Donath, E.; Moya, S.; Susha, A.S.; Voigt, A.; Hartmann, J.; Moehwald, H. Microencapsulation by means of step-wise adsorption of polyelectrolytes. *J. Microencapsul.* **2000**, *17* (2), 177–185.
109. Voigt, A.; Buske, N.; Sukhorukov, G.B.; Antipov, A.A.; Leporatti, S.; Lichtenfeld, H.; Baumler, H.; Donath, E.; Moehwald, H. Novel polyelectrolyte multilayer micro- and nanocapsules as magnetic carriers. *J. Magn. Magn. Mater.* **2001**, *225* (1–2), 59–66.
110. Caruso, F.; Spasova, M.; Susha, A.; Giersig, M.; Caruso, R.A. Magnetic nanocomposite particles and hollow spheres constructed by a sequential layering approach. *Chem. Mater.* **2001**, *13* (1), 109–116.
111. Caruso, F.; Susha, A.S.; Giersig, M.; Moehwald, H. Magnetic core-shell particles: Preparation of magnetite multilayers on polymer latex microspheres. *Adv. Mater.* **1999**, *11* (11), 950–953.
112. Moya, S.; Donath, E.; Sukhorukov, G.B.; Auch, M.; Baumler, H.; Lichtenfeld, H.; Moehwald, H. Lipid coating on polyelectrolyte surface modified colloidal particles and polyelectrolyte capsules. *Macromolecules* **2000**, *33* (12), 4538–4544.
113. Georgieva, R.; Moya, S.; Leporatti, S.; Neu, B.; Baumler, H.; Reichle, C.; Donath, E.; Moehwald, H. Conductance and capacitance of polyelectrolyte and lipid-polyelectrolyte composite capsules as measured by electrorotation. *Langmuir* **2000**, *16* (17), 7075–7081.
114. The principle of electrostatic multilayer deposition was first described in Iler, R.K. Multilayers of colloidal particles. *J. Colloid Interface Sci.* **1966**, *21*, 569–594.
115. Decher, G. Polyelectrolyte Multilayers, an Overview. In *Multilayer Thin Films*; Decher, G., Schlenoff, J.B., Eds.; Wiley VCH: New York, 2003; 1–46.
116. Shenoy, D.B.; Sukhorukov, G.B.; Moehwald, H. Layer-by-layer engineering of biocompatible. Decomposable core-shell structures. *Biomacromolecules* **2003**, *4* (2), 265–272.
117. Tiourina, O.P.; Radtchenko, I.; Sukhorukov, G.B.; Moehwald, H. Artificial cell based on lipid hollow polyelectrolyte microcapsules: Channel reconstruction and membrane potential measurement. *J. Membr. Biol.* **2002**, *190* (1), 9–16.
118. Daehne, L.; Moehwald, H.; Decher, G.; Sukhorukov, G.; Lvov, Y. private communication.



Nanoengineered Polymer Microcapsules

Gleb B. Sukhorukov

Max-Planck-Institute of Colloids and Interfaces, Potsdam/Golm, Germany

INTRODUCTION

The nanoengineering of colloidal surfaces and the design of functional colloid particles are currently interesting topics of applied chemistry and biochemistry in the field engaged in developing new materials with tailored properties. Research on composite colloidal particles (core-shell structures with size ranging from 1 to 1000 nm) has created interest because of various applications expected in the areas of coatings, electronics, photonics, catalysis, biotechnology, sensorics, medicine, ecology, and others. In general, the research on core-shell structure and encapsulation implies the formation of a colloidal core of defined content and size, and the preparation of a shell providing the required stability, permeability, compatibility, release of core material, and catalytic or affinity properties. Tailoring the different components of one particle becomes important to develop these functionalized colloids (i.e., to combine several properties in one core-shell structure). The desired properties may be adjusted to facilitate the interaction of the core with different solvents or cell membranes. The shell may also have magnetic, optical, conductive, or targeting properties for directing and manipulating the core containing bioactive materials.

A major task in the development of advanced drug formulations deals with the elaboration of delivery systems for providing the sustained release of bioactive materials. Mostly, these systems comprise polymer particles in the size range of 50 nm–100 μ m. Drug molecules are embedded in polymer matrices, or in core-shell structures. In the latter case, the shell permeability or degradation rate determines the release rate of the bioactive core material. The composition of the shell may additionally provide certain functionalities.

This review is devoted to the literature on recently introduced novel pathways to fabricate nanoengineered core-shell structures, which can employ a great variety of substances as shell constituents and can be incorporated into hollow spheres. The way the shells are assembled on colloids resembles the formation of ultrathin polymer films by layer-by-layer (LbL) adsorption on macroscopic flat support, an idea proposed by Iler^[1] in 1966 and later developed by Lee et al.^[2] In 1991, Decher and Hong^[3] proposed a method of forming polyelectrolyte films by

using the alternate adsorption of polycations and polyanions. A crucial factor for polyionic LbL assembly is the change of the sign of the surface charge on polyelectrolyte adsorption. Beginning in 1998, this strategy of LbL assembly of charged species was transferred to coat micron-sized and submicron-sized colloidal particles (Fig. 1).^[4] The idea emerged to employ the nanoengineered properties of multilayers as shell structures formed on colloidal particles.

MULTILAYER ASSEMBLY ON COLLOIDAL PARTICLES

The main problem in applying the LbL technology to coat surfaces of colloidal particles is how to separate the remaining free polyelectrolytes from the particles prior to the next deposition cycle. Today, there are several approaches for that difficulty, including centrifugation, filtration protocols for washing particles with adsorbed polyelectrolytes, and the so-called sequential adding of polyelectrolytes at matched concentrations. For details of these approaches, their advantages, and their drawbacks, refer to Sukhorukov et al.^[4] Donath et al.^[5] and Voigt et al.^[6] It should be mentioned that the filtration method^[6] is the only method applicable for scaling up the coating of different colloidal particles in large volumes. The monitoring of the process of film formation (i.e., charge reversal and continuous layer growth) was followed at each step by electrophoresis, dynamic light scattering, single particle light scattering (SPLS), and fluorescent intensity measurements.^[4,7] Fig. 2 illustrates the typical particle charge (ζ -potential) changes recorded on layer deposition for polycation/polyanion pairs. The ζ -potential alternates between positive and negative values, indicating the successful recharging of the particle coated with the adsorbed polyelectrolyte multilayer on each layer deposition. The evidence for sequential layer growth has been obtained by means of SPLS.^[4,6] In Fig. 3, the intensity distribution of the control naked particles is compared with particles coated with eight layers assembled by filtration technique. From the shift of the peak of the intensity distribution, the adsorbed mass can be derived. These data can be converted into a layer thickness of the adsorbed polyion multilayers, assuming a given refractive

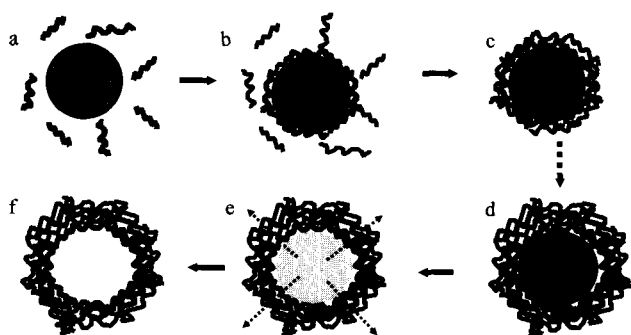


Fig. 1 Consecutive adsorption of positively (gray) and negatively (black) charged polyelectrolytes onto negatively charged colloid particles (a–e). After dissolution of colloidal core (e), a suspension of polyelectrolyte capsules is obtained (f).

index.^[4] The increase of polyelectrolyte film thickness is proportional to the layer number (Fig. 3, bottom). Mean polyelectrolyte layer thickness was found to be 1.5 nm for the case of polystyrene sulfonate (PSS) and polyallylamine (PAH) alternatively assembled from 0.5 M NaCl. It should be noted that the average layer thickness of polyelectrolyte multilayers strongly depends on the kind of polyelectrolytes and the salt concentration used at polyelectrolyte assembly. More rigid polymers and an increased salt concentration lead to a thicker adsorption layer.^[8]

Multilayer assembly can be performed not only on solid particles such as silica, PS latex particles, or organic

crystals, but also on “soft” particles formed just before multilayer buildup, such as protein aggregates and the compact form of DNA. The micron-sized aggregates of proteins (lactate dehydrogenase^[9] and chemotrypsin^[10]) were applied as templates for polyelectrolyte multilayer assembly. The polyelectrolyte multilayer coating of these aggregates captures the proteins inside the capsules and, at the same time, provides a selective barrier for the diffusion of different species (substrates, inhibitors) from the exterior. The concept of polyelectrolyte multilayer assembly on aggregates is similar to that on the surface of colloidal particles.^[4] Here, instead of solid colloidal particles, the preformed protein aggregates have been used as templates for polyelectrolyte multilayer assembly. As shown in Ref. [10], the chemotrypsin aggregates in high-salt solution form particles of 100–300 nm. After these particles are covered with a polyelectrolyte layer, the capsule can be transferred to a low-salt solution, where chemotrypsin is captured by a polyelectrolyte shell. The method of LbL shell formation on protein aggregates provides encapsulation efficiency close to 100%. Indeed, one can always find a condition for protein aggregation (for instance, it usually happens at the isoelectric point). The subsequent release of proteins from the shell can be controlled by certain polyelectrolyte compositions. It makes such systems very suitable as drug delivery systems with controlled-release properties.

The assembly of three polyelectrolyte layers was performed also on condensed DNA particles with size of about 50–100 nm. A certain polymer composition used for

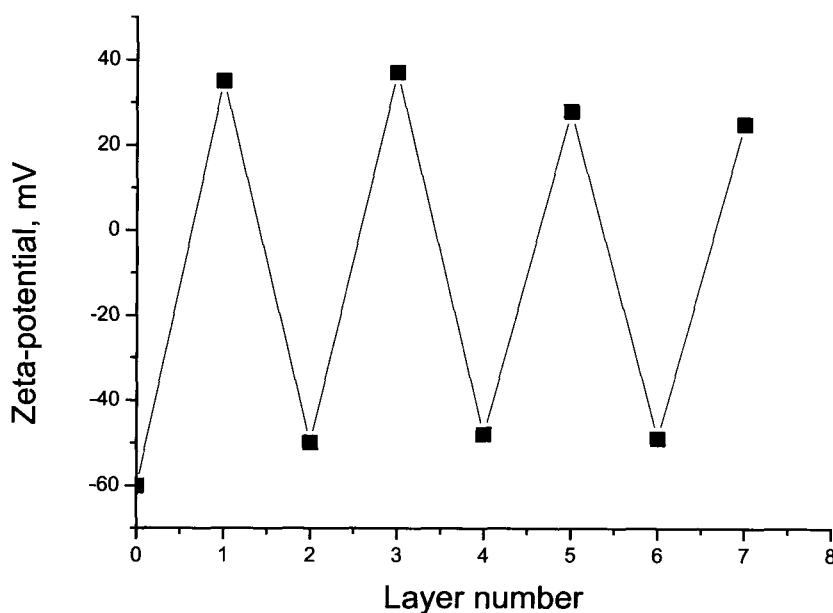


Fig. 2 ζ -Potential as a function of layer number for PSS/PAH alternatively coated polystyrene latex particles. Particle diameter = 640 nm.

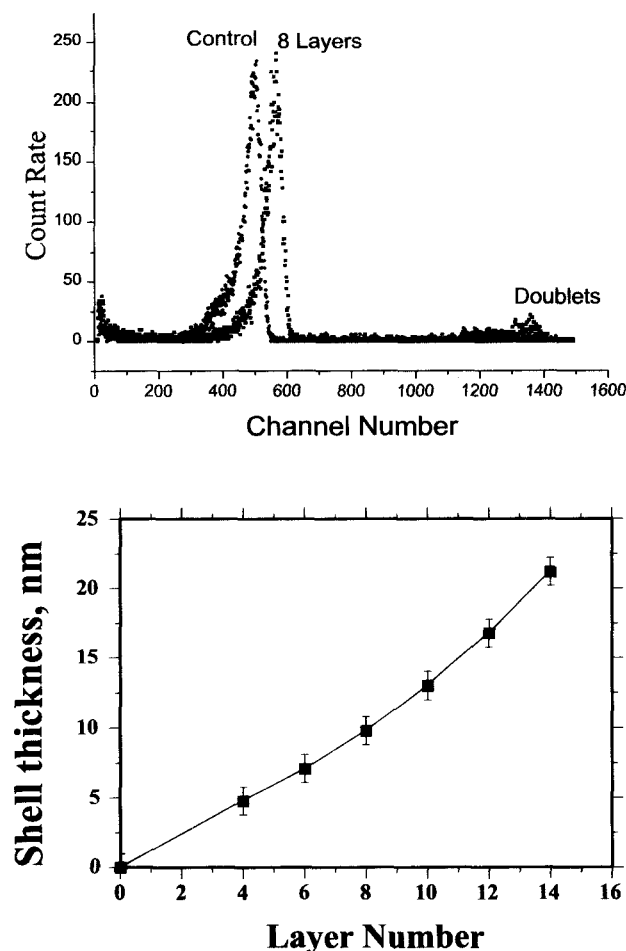


Fig. 3 Top: Normalized light scattering intensity distributions (SPLS) of PAH/PSS-coated polystyrene sulfate latex particles ($\varnothing=640$ nm). Particles with eight layers are compared with uncoated ones. Bottom: Shell thickness as a function of layer number. (View this art in color at www.dekker.com.)

coating DNA particles provides stable suspension^[11,12] and facilitates the uptake of these particles by biological cells, with the outermost layer bearing certain receptors. Sequential gene expression of cells after the uptake of such particles has been illustrated.^[12,13]

The method of LbL adsorption of oppositely charged macromolecules onto colloidal particles has been applied already for different templates with sizes ranging from 50 nm to tens of microns, such as organic and inorganic colloid particles, protein aggregates, emulsion droplets, biological cells, and drug nanocrystals. Various materials (e.g., synthetic polyelectrolytes, chitosan and its derivatives, proteins, DNA, lipids, multivalent dyes, and magnetic nanoparticles) have been used as layer constituents to fabricate the shell. The possibility of using different materials allows the shell to adjust its design based on the required stability biocompatibility and affinity properties

of the capsules. The most commonly used methods to monitor LbL deposition on monodisperse PS latex particles for various substances are the SPLS method and microelectrophoresis. Inorganic [magnetite, silica, titania, and fluorescent quantum (Q) dots] nanoparticles,^[14–16] lipids,^[17–19] and proteins (albumin, immunoglobulin, and others)^[7,20,21] were incorporated as building blocks for shell formation on colloidal particles. In Schuler and Caruso,^[21] the construction of enzyme multilayer films on colloidal particles for biocatalysis was demonstrated. The enzyme multilayers were assembled on submicrometer-sized polystyrene spheres via the alternate adsorption of poly(ethyleneimine) and glucose oxidase. The high surface area of particles coated with biomultilayers was subsequently utilized in enzymatic catalysis. The step-by-step coating of different lipids alternated with polyelectrolytes was performed by the adsorption of preformed vesicles onto the capsule surface. As was shown by Moya et al.^[18] the lipids form a bilayer structure on the surface of polyelectrolyte multilayers. The fabrication of inorganic shells on colloidal particles envisages the application of such core-shell structures in catalysis and colloidal band gap crystals.^[14,16] Introducing magnetic particles into the shell composition opens the possibility of manipulating them by applying external field.^[15,17]

COLLOIDAL CORE DECOMPOSITION AND FORMATION OF HOLLOW CAPSULE

Different colloidal cores can be decomposed after multilayers are assembled on their surface. If the products of core decomposition are small enough to be expelled out of polyelectrolyte multilayers, the process of core dissolution leads to the formation of hollow polyelectrolyte shells (Fig. 1d–f). Up to now, various colloidal templates, such as organic templates [melamine formaldehyde (MF) particles, poly-D,L-lactic acid (PLA), or poly-D,L-lactic-co-glycolic acid (PDLA) microparticle and nanoparticle organic crystals], and inorganic cores, such as carbonate or silica oxide microparticles and biological cells, have all been used as templates for hollow capsule fabrication. Decomposition can be performed by different means, such as low pH for MF and carbonate particles,^[22] organic water-miscible solvents for PLA, PDLA, or organic crystals,^[23] and HF treatment for silica oxide microparticles, and strong oxidizing agents (NaOCl) for biological cells with same the MF particles.^[24,25]

The formation of hollow capsules was more intensively studied on MF particles.^[5,26] These particles dissolve onto oligomers at 0.1 M NaCl and in some water-miscible solvents such as DMF or DMSO. Subjecting the coated eight PSS/PAH layers of MF particles to low pH results in solubilization of the core. The MF oligomers, which have

a characteristic cross-sectional extension of about 2–3 nm, are expelled from the core and permeate through the polyelectrolyte layers, forming the shells. This observation is consistent with the finding that polyelectrolyte-coated MF particles are readily permeable to molecules of a few nanometers in size.^[4] The MF oligomers are finally separated from the hollow shells by centrifugation or filtration protocols.

The fabricated hollow polyelectrolyte capsules were characterized using scanning electron microscopy (SEM), transmission electron microscopy (TEM), atomic force microscopy (AFM), and confocal fluorescent microscopy techniques.^[5–7,17,24,27] An AFM image of hollow polyelectrolyte capsules is shown in Fig. 4. The numerous folds and creases observed are attributed to the collapse of the hollow capsules under drying. The shells are flattened and some spreading is noticed. The diameter of the capsules shown in Fig. 4 is larger than the diameter of the templated MF particle (5 μm). This increase in diameter is ascribed to collapsing and adhesive forces attracting the polyelectrolyte shell to the surface. From the AFM image, it was also deduced^[27] that the thickness of the polyelectrolyte film is on the order of 20 nm for the eight-layer polyelectrolyte film. This value is consistent with SPLS data on layer thickness obtained for polyelectrolyte-coated polystyrene particles (Fig. 3). Nevertheless, Gao et al.^[26] reported on the rest of the core materials found in polyelectrolyte shells after MF particles decomposition.

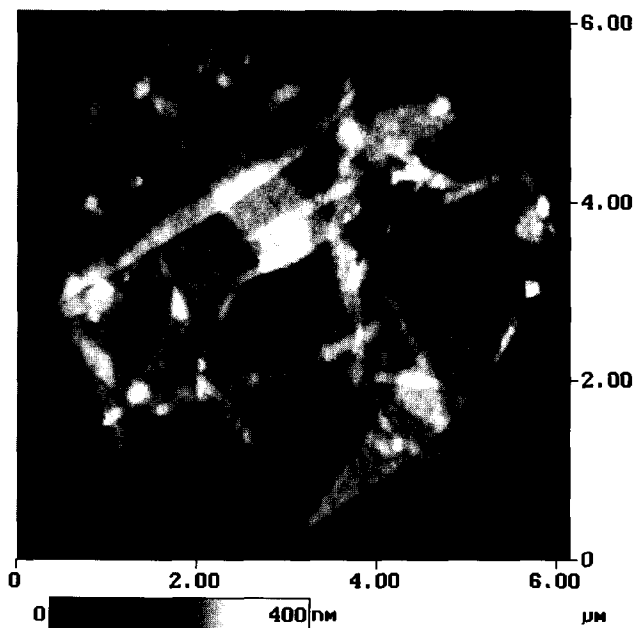


Fig. 4 Atomic force microscopy image of the capsules composed of eight PSS/PAH layers templated on MF particles.

The nature of the colloid does not significantly affect the thickness of the polyelectrolyte layers. It should be noted that the polyelectrolyte capsules completely repeat the shape of the templating colloids, as was shown by the example of echinocyte cells, which have starlike shape.^[24] The choice of the core is determined by concrete tasks. For instance, carbonate cores are decomposable at $\text{pH} < 4$; they are convenient to fabricate into hollow capsules composed of biological polymers. Calcium and manganese carbonate crystals were used as core materials for the fabrication of hollow polyelectrolyte capsules by means of LbL assembly in Ref. [28]. The use of inorganic templates is a significant step toward the biocompatibility of polyelectrolyte multilayer capsules. Scanning electron microscopy and energy-dispersive X-ray (EDX) measurements proved the purity of the capsules from the core materials.

Another study proposed the use of decomposable biocompatible templates composed of PLA and PDLA.^[23] These particles were used to build a shell composed of biocompatible polyelectrolytes. Uniform, complete coating with oppositely charged polyelectrolyte pairs was achieved for different combinations investigated. After core dissolution in water-miscible organic solvents such as acetone, stable hollow capsules with tailored properties were obtained. The results reported in Ref. [23] demonstrate that polyester microparticles could serve as viable alternative components to conventionally employed templates to derive hollow capsules with shape and shell thickness exploring a “biofriendly” process. The only drawback of such particles is some polydispersity in the size, but for many uses, this parameter is not important.

At present, hollow polyelectrolyte capsules with diameters varying from 0.2 to 10 μm and with wall thicknesses from a few to tens of nanometers were obtained. Many compounds, such as synthetic and natural polyelectrolytes, dyes, and inorganic nanoparticles, were used as layer constituents to build the hollow capsules. Uniform inorganic and hybrid inorganic–organic hollow microspheres have been produced by coating colloidal core templates with alternating layers of oppositely charged nanoparticles and polymers, and thereafter removing the core by heating to 500°C.^[14,29] Hollow rigid silica spheres were obtained by calcination of polymer latex spheres coated with multilayers of silica nanoparticles (SiO_2) bridged by polycations.

Permeability and Release Properties

The potential use of polyelectrolyte coating on colloidal particles as depot systems for controllable release requires data on the permeation of small molecules (molecular weights up to 500) through polyelectrolyte walls. To achieve sustained-release properties for shells, it would be advantageous to be able to decrease the layer permeability

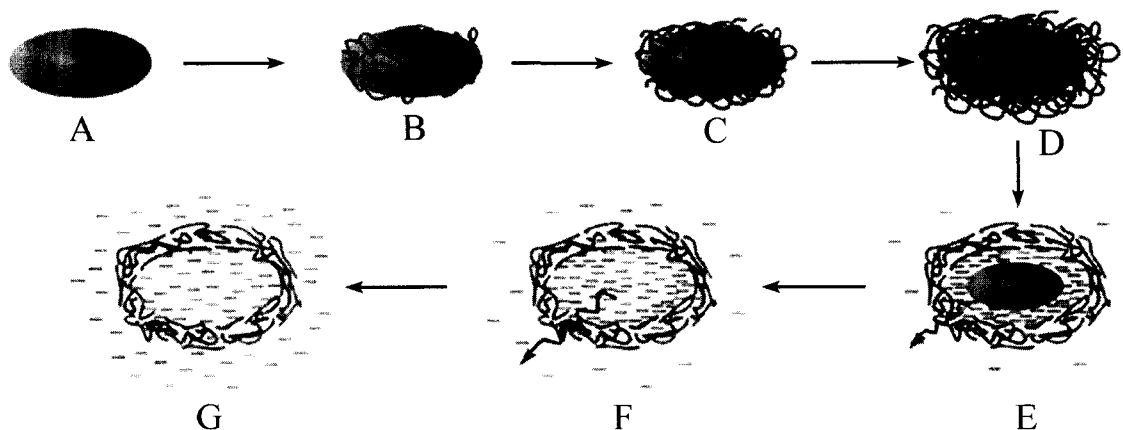


Fig. 5 Scheme of the polyelectrolyte multilayer deposition process and of the subsequent core dissolution. The initial steps (A, B) involve stepwise shell formation on a fluorescein core. After the desired number of polyelectrolyte layers is deposited, the coated particles are exposed to pH=8 (C) and core dissolution with fluorescein penetration into the bulk is initiated, resulting finally in fully dissolved cores and remaining empty capsules (D). (View this art in color at www.dekker.com.)

for small polar molecules once they are encapsulated. The small polar fluorescent markers, such as fluorescein, are reasonable models for permeability study. The formation of thicker capsule walls composed of polyelectrolyte multilayers with increasing layer number might be a way to decrease permeation. Verification of this approach was performed in Ref. [30]. Microparticles of fluorescein of about 5 μm in size were covered with a different number of PSS/PAH polyelectrolyte layers in conditions where fluorescein is not soluble, pH=2. It should be noted here that when pH=2, both polyelectrolytes are strongly charged, and hence the resulting multilayer films possess the same amount of amino and sulfur groups. After multilayer formation, core dissolution was initiated by a pH change and monitored by increasing fluorescence in the bulk. The scheme on Fig. 5 illustrates coating fluorescein particles and subsequent fluorescein release when the particles become soluble. After LbL adsorption (Fig. 5A–C), core dissolution is initiated by changing the pH from 2 to 8 (Fig. 5D) and is completed after a certain period of time (Fig. 5E).

Fluorescein particles rapidly dissolve at pH 8. Thus the idea was to slow down the rate of core dissolving by covering the particles with polyelectrolyte multilayers. Shell walls consisting of a different number of layers were fabricated and examined with regard to their fluorescein permeability behavior. Fluorescence spectroscopy is a convenient tool for the determination of the core dissolving rate because the fluorescence of the core is completely suppressed as a consequence of the self-quenching of the dye. On releasing the dye into the bulk, fluorescence intensity increases. Thus the rate of dissolving can be directly followed by measuring the fluorescence increase in the sample.

Fig. 6 shows typical time-dependent fluorescence curves obtained by switching the pH to 8. Fluorescein particles covered by layers of different thickness (9, 13, 15, and 18 layers) are compared with controls demonstrating the dissolving of naked fluorescein particles. As shown on release profiles after a comparatively short induction period, the rate of dissolving becomes constant before the fluorescence in the bulk finally levels off. The initially slowly increasing fluorescence is related to the start of core dissolving. At this stage of the process, the structure of the polyelectrolyte multilayer may change because of the nascent osmotic pressure coming from dissolved fluorescein molecules. Shortly after the beginning of core dissolution, the concentration of fluorescein inside the capsules becomes constant and almost saturated because a steady-state situation between progressing core dissolution and permeation is established. One may further assume a constant concentration gradient between the shell interior and the bulk because the bulk solution can be assumed as being infinitely diluted. Therefore the rate of fluorescein penetration through the polyelectrolyte layers to the bulk becomes constant. Indeed, a linear increase of the fluorescence is observed. This state corresponds to the stage of dissolution depicted in Fig. 5. The slope of the linear region decreases with the number of polyelectrolyte layers. Obviously, an increasing number of adsorbed layers reduce the fluorescein penetration. After the core is completely dissolved, the fluorescein concentration inside the shell equilibrates with the bulk. The driving force for diffusion decreases and the release levels off.

In Antipov et al.^[30] the permeability value was found to be on the order of 10^{-8} m/sec. Assuming a single polyelectrolyte layer thickness of 2 nm, the permeability

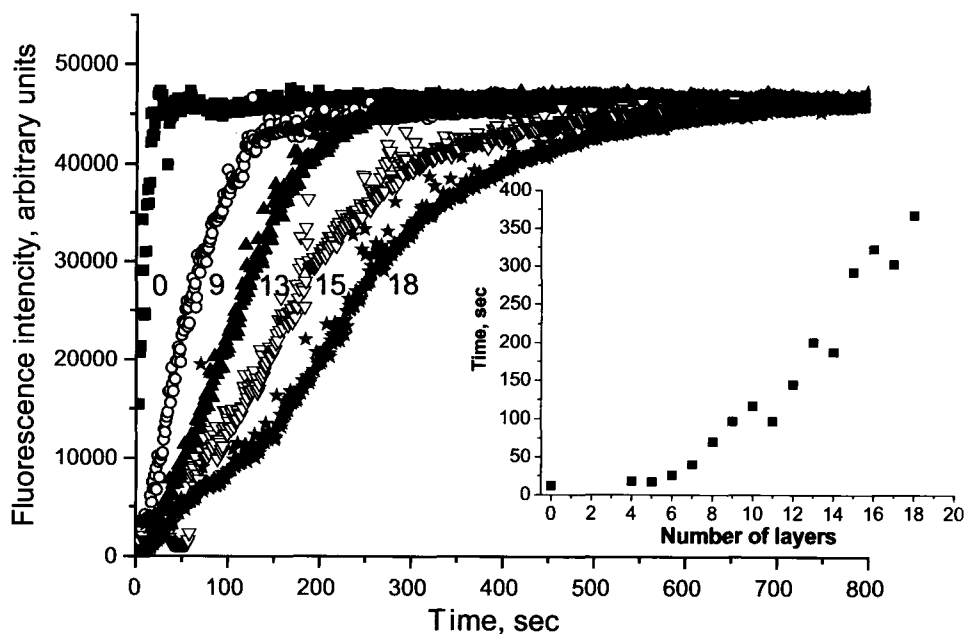


Fig. 6 Fluorescence increase on time, obtained by dissolving fluorescein particles covered with shells of different thickness (9, 13, 15, and 18 layers), compared with naked (0) fluorescein particles. Inset: Time dependence of core decomposition time on the number of layers in the shells.

can be converted into a diffusion coefficient (D) by multiplying the permeability with the shell wall thickness. The calculated diffusion coefficients are on the order of 10^{-15} m²/sec.

If the permeability of the polyelectrolyte multilayer is provided by diffusion through the entangled polymer network, it should scale with the inverse of the layer thickness. The behavior of the time of complete release as a function of the number of layers is shown in Fig. 6 (inset). As can be seen in Fig. 6, the increasing layer number sustains the fluorescein release. This effect becomes remarkable when the layer number exceeds eight, which corresponds to 15- to 20-nm-thick shell. This finding is consistent with observations^[13] where it was shown that the conformation of the first eight layers differs from that of further assembled layers. These deeper layers are more dense and result in a fivefold reduction of the estimated diffusion coefficient. Naturally, these data are only particular to the case of PSS/PAH layers, and the permeation might be different if the capsules are made of other polyelectrolytes. Nevertheless, the tendency to sustain the penetration of small molecules with layer number is demonstrated.

Polyelectrolyte complexes are known to be very sensitive to the presence of salt.^[31] Therefore the permeability coefficient of polyelectrolyte multilayers is influenced by ionic strength. In the presence of small ions,

ionic couples in multilayers are partially dissolved, which makes the polyelectrolyte film more penetrable for solutes.^[32] Permeability coefficient data derived from release curves show a dramatic change of an increase of one order of magnitude in NaCl concentration change from 1 to 500 mM.^[33]

Thus the polyelectrolyte multilayer shells with enough number of layers assembled around cores consisting of low-molecular-weight compounds provide barrier properties for release under conditions where the core is dissolved. Increasing the shell thickness to more than 20 nm might cause barrier difficulties for low-molecular-weight compounds passing through the capsule wall. Multilayer coating on microparticles and nanoparticles is a promising approach for the fabrication of systems with prolonged-release and controlled-release properties. The release can be adjusted with the number of assembled polyelectrolyte layers. A large variety of synthetic polyelectrolytes with different properties, polysaccharides, and other biopolymers used for multilayer assembly may provide many possibilities to fine-tune the release properties of shells with biocompatibility and possibility of using various cores. The assembly of shells by LbL technique opens new pathways for biotechnological applications, where controlled release and sustained release of a substance are required. Many problems connected with drug formulation, release, and delivery;

controlling concentrations in the organism; and the periodicity of its reception might be solved by the formation of shells on precipitates and nanocrystals. This approach has been already explored for drug formulations with controlled-release properties of biocompatible shells.^[34,35] It seems to be not difficult to add targeting properties to the polyelectrolyte layer. This way, the affinity of polyelectrolyte multilayer-coated drugs to specific or injured tissues can be increased.

Thermal treatment of polyelectrolyte capsules results in the reduction of permeability coefficients. As investigated in Ref. [36], the permeability coefficient of hollow capsules templated on MF cores can be decreased by two orders of magnitude. Thermal annealing of the capsules causes polyelectrolyte rearrangements, which leads to a more compact structure. Some defects in polyelectrolyte shells because of core dissolution processes can be repaired.

Macromolecules Encapsulation

Basically, the multilayer polyelectrolyte capsules have semipermeable properties. If the film thickness is about 10–20 nm, small molecules can penetrate whereas high-molecular-weight compounds are excluded. However, there are several approaches to introduce macromolecules inside hollow polyelectrolyte capsules, when the core is decomposed. The first approach is opening and closing the pores in capsule walls in a controllable way. One can cause segregation in polyelectrolyte multilayers either by pH or solvent change. Indeed, polyelectrolyte multilayers undergo transition at a certain pH at about the pK of

charged groups. This transition works on segregation because of the accumulation of charges by a network of entangled polyelectrolytes. As a result, such segregation leads to the formation of pores large enough for macromolecules to penetrate the capsule wall.^[22,37] This process is completely reversible. Changing the pH back, the capsules become nonpermeable for polymers again (Fig. 7). Thus the captured polymers stay inside. Several macromolecules, such as albumin, chemotrypsin, and dextran, have been encapsulated by this protocol.^[37,38] The reversed segregation in polyelectrolyte multilayers can be introduced also by solvent mixtures such as water–ethanol, as was demonstrated by Lvov et al.^[39] for encapsulation of proteins.

Another approach for encapsulation consists of the precipitation of polymers onto surfaces of colloid particles before the main multilayer buildup. The precipitated materials are harvested on the surface of particles. The proper choice of the concentration of particles, polymers, and the speed of heterocoagulation allows a smooth coverage of colloidal particles to form by precipitating polymers. A polyelectrolyte LbL shell is formed on particles already covered by precipitated polymers. After formation of the stable outer shell, the colloidal template could be decomposed. The polymer molecules underneath the stable shell can be dissolved in the shell interior. In fact, this approach comprises of three stages (Fig. 8): 1) precipitation of polymers on a colloidal surface (Fig. 8a–c); 2) capture of precipitated polymers on colloidal particles by stable shell formation (Fig. 8d); and 3) decomposition of the core; the products of decomposition are expelled through capsule wall, whereas the polymers dissolve and

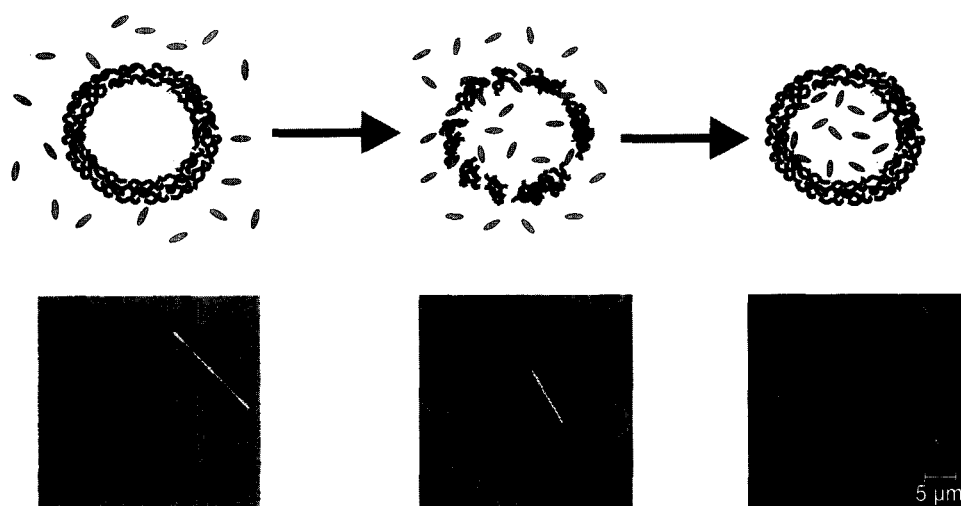


Fig. 7 Permeation and encapsulation of dextran FITC into polyion multilayer capsules. Left, $pH > 7$; middle, $pH < 6$; and right, the capsule with encapsulated dextran FITC again at $pH > 7$. (View this art in color at www.dekker.com.)

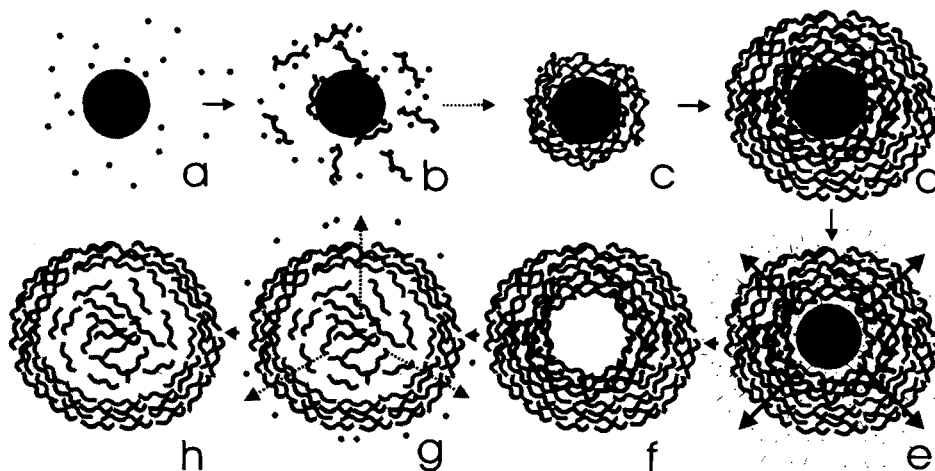


Fig. 8 A schematic illustration of the preparation of a capsule loaded with polyelectrolytes.

float in the capsule interior (Fig. 8e–h). This approach has been tested for encapsulation of noncharged polysaccharides (i.e., dextran and polyelectrolyte as PSS and PAH).^[40] Dextran was precipitated by adding ethanol drop by drop whereas polyelectrolytes formed an insoluble complex with multivalent ions such as Me^{3+} and CO_3^{2-} for PSS and PAH, respectively. Some swelling of the capsule after polymer dissolution into the interior was observed because of osmotic pressure. Naturally, the amount of loaded polymers per capsule is the amount of all added polymers divided by the number of colloidal particles harvesting precipitating polymers. The possible loss of used polymers because of breakage of capsules did not exceed 10–15%. The described procedure allows the dosage of macromolecular contents in the capsule in tiny (less than nanograms) amounts.

To summarize the approaches on how to encapsulate the macromolecules by precipitation and then to capture by LbL shell fabrication, the positive and negative features should be stressed. In fact, encapsulation via precipitation could reach encapsulation efficiency close to 100%. Indeed, for encapsulation via harvesting of polymers on colloidal particles as described above, we have achieved about 80–90% encapsulation efficiency.^[40] The more important peculiarities of using initial colloidal templates as polymer collectors are as follows: 1) the size distribution is determined by original templates; 2) the amount of loaded polymers can be dosed and homogeneously distributed in each capsule; and 3) there are possibilities to load the capsule with several different substances. The last point has not yet been demonstrated, but one expects no significant difficulties in composing a multicomponent shell, and precipitating on the surface of colloidal particles several macromolecules, sequentially or at the same time, if they could be precipitated at the

same condition. One has to consider only the compatibility of conditions for each precipitation step and further LbL fabrication of stable polyelectrolyte shells. The captured macromolecules are kept in the capsule interior until it is nonpermeable for macromolecules. This might be utilized for fabricating enzyme microreactors when the substrates and reaction products diffuse through the capsule wall freely. The loaded macromolecules might be released after a certain pH or salt treatment.

PHYSICOCHEMICAL REACTIONS INSIDE POLYELECTROLYTE CAPSULES

Caused by pH Gradient

The capsule wall has semipermeable properties that allow for different physicochemical properties of the capsule interior compared to the exterior. Incorporation of polymers into the capsule allows the use of such capsules with modified inner volume for providing chemical reactions only in the capsule interior. Here we describe two possible ways for the precipitation of dyes as drug model substances within capsule interiors loaded with polymers. Precipitation occurs, then solubility dramatically decreases. One can establish polarity or pH gradient through the capsule wall when the capsules are filled with certain polymers. Indeed, the presence of a polyelectrolyte on only one side of the membrane might significantly change such properties as pH value. For instance, if a polyanion is placed inside capsule, the pH value inside has to be acidic due to electroneutrality because H^+ ions compensate for negative charges of polyanions. The resulting pH has to be closer to the $\text{p}K$ value of charged groups of polyelectrolytes. This situation on pH gradient is considered in

more details in Refs. [41] and [42]. Here we give an illustration for the precipitation of carboxytetramethylrhodamines (CRs) inside the capsule. Carboxytetramethylrhodamine has pH-dependent solubility and becomes nonsoluble at pH lower than 3.5. In the presence of capsules filled with PSS maintaining a pH value near 2.5, the CR molecules penetrate the capsule wall and, when facing lower pH, begin to precipitate. Here we provide typical SEM images of CR precipitates formed in the capsules (Fig. 9). The capsules look filled with solid materials.

As was shown previously, the encapsulated polyelectrolytes can establish pH gradient through the capsule wall. In particular, the capsules containing PAH have more basic pH than that in the outer solution. This method has been utilized for the selective synthesis of magnetic, 20-nm Fe_3O_4 nanoparticles^[43] and nonmagnetic, elongated, 250-nm hematite Fe_2O_3 ^[42] particles inside the polyelectrolyte capsules filled with polycations. The iron oxide particles were visualized by TEM (Fig. 10). The structure of the particles depends on the given $\text{Fe}^{2+}/\text{Fe}^{3+}$ ratio in the outer solution as was proven by wide-angle X-ray scattering (WAXS) measurements. These revealed diffraction peaks corresponding to Fe_2O_3 and Fe_3O_4 lattices. Besides magnetite, different ferrites (CoFe_2O_4 , ZnFe_2O_4 , and MnFe_2O_4) were synthesized from corresponding salts exclusively inside polyelectrolyte capsules of 6 μm diameter.^[43] Polyelectrolyte capsules with synthesized ferrite (magnetite) particles possess enough magnetic activity to be easily manipulated in water solu-

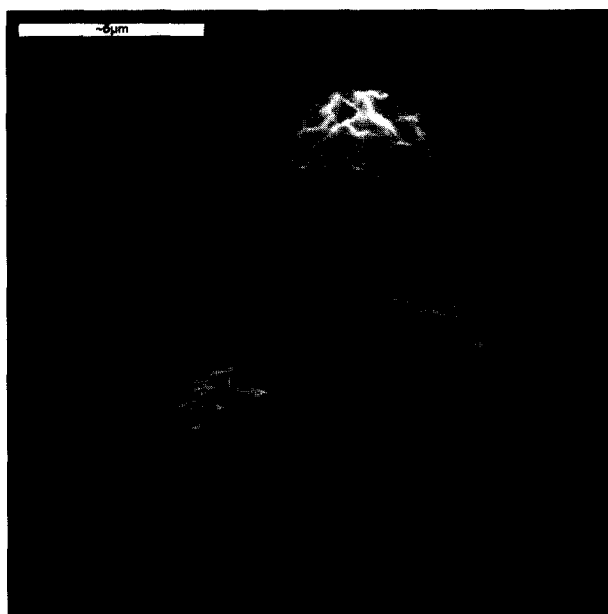


Fig. 9 Scanning electron microscopy image of CR precipitates formed in capsules loaded with PSS.



Fig. 10 Transmission electron microscopy image of Fe-based precipitates (240-nm elongated iron oxide particles) in capsules filled with PAH.

tion by an external magnetic field. The SEM images demonstrate that capsules with synthesized nanoparticles keep a bulky shape on drying, which is apparently because of the formation of rigid walls presenting inorganic nanoparticles glued to organic polymers.

Caused by Polarity Gradient

Another way to fill the capsule with small molecules is by establishing a polarity gradient of hydrophilic polymers. These capsules were suspended in a water/organic solvent mixture to keep a higher water content in the interior because of the hydrophilicity of encapsulated polyelectrolytes.^[44] With the preparation of a water/acetone or water/acetone mixture with an overall high ratio of organic solvents, one can dissolve many poor water-soluble (PWS) molecules. However, inside the capsule, we have media with low solubility and PWS molecules should precipitate there. At slow evaporation of organic solvents, the PWS molecules are collected in the capsule interior because of lower solubility there. Finally, one has an aqueous suspension of capsules containing precipitates of organic molecules.^[44] Scanning electron microscopy images of capsules filled with PWS are similar to the image shown in Fig. 9. Incidentally, we found that the precipitates formed inside the capsules did not show any X-ray diffraction signals unless later annealed. Hence they are either amorphous or exist as nanocrystallites. This is a highly desirable feature for many drug applications because it facilitates dissolution and hence release.

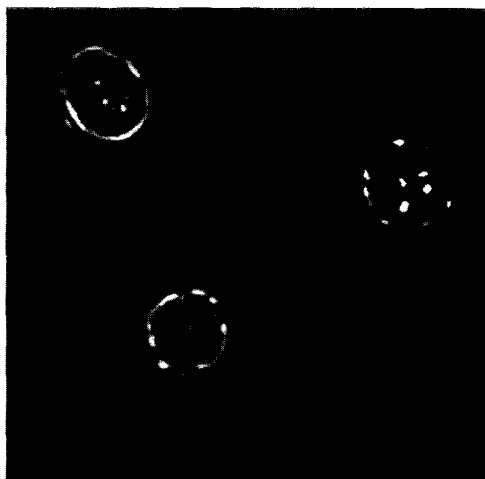
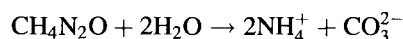


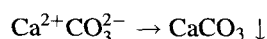
Fig. 11 Optical microscopy image of urease-catalyzed CaCO_3 crystal growth inside 5- μm polyelectrolyte capsules.

ENZYMATIC REACTIONS

In Lvov et al.^[39] and Antipov et al.^[45] the encapsulation of urease by solvent variation and its enzymatic activity were demonstrated. Urease catalyzes the reaction:



In the presence of Ca^{2+} ions, calcium carbonate is formed:



Carbonate ions generated by urease in the capsule interior immediately react with calcium ions and freely diffuse

through the capsule wall. As shown by Antipov et al.^[45] calcium carbonate crystals presumably grow within the capsule interior until they occupy the whole capsule lumen (Fig. 11). The formation of calcium carbonate particles might also occur outside of the capsule because of the diffusion of carbonates, but in certain conditions, calcium carbonate particles might be found almost only inside the capsule. As investigated by electron diffraction, the lattices of calcium carbonate grown within the capsule interior exhibit vaterite structure. Remarkably, there was no growth of calcium carbonates over the capsule wall. Thus the microcapsules with an imported enzyme can be a suitable model to mimic inorganic processes in biological cells.

Another illustration of enzymatic reactions inside capsules has been reported in Ref. [38]. A proteolytic enzyme, α -chemotrypsin, was homogeneously distributed in the capsule interior with a concentration of 50 g/L. Encapsulated chemotrypsin was found to retain a high physiological activity of about 70%, as shown with fluorescent products.

CONCLUSION

The uniformity, simplicity, and versatility of possible applications are significant points of the abovedescribed technology. The particular aspects coming from the basic concept of the technology are outlined in Fig. 12. As an initial matrix, we have a colloidal template. Organic and inorganic particles, drug nanocrystals, biological cells, protein aggregates, emulsion droplets, and, in fact, any

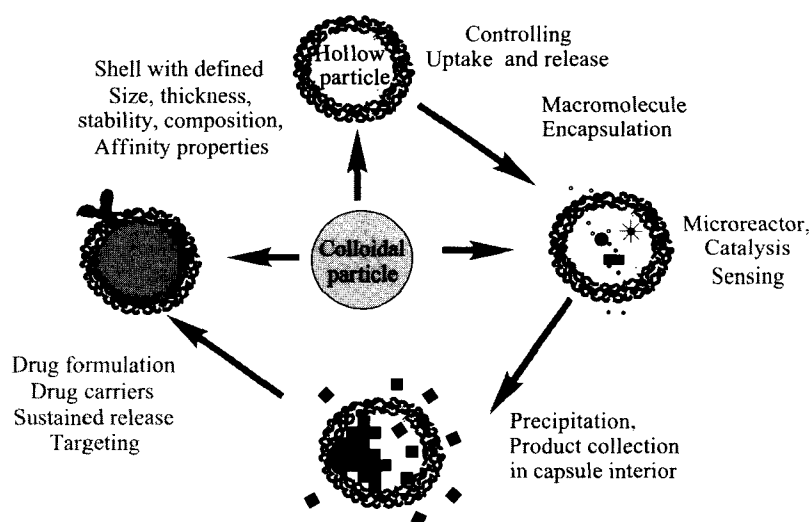


Fig. 12 Comprehensive illustration of applications of stepwise shell formation on colloidal particles. (View this art in color at www.dekker.com.)

colloidal particles ranging in size from 50 nm to tens of microns are possible templates to fabricate shells. The shell can be composed of a variety of materials. The choice of polymers to build the shell is determined by application to reach the desired stability and comparability. Actually, one could choose the proper line to pursue certain tasks using the scheme in Fig. 12 to achieve the desired characteristics of core-shell structures or capsules.

Selective shell permeability makes it possible to keep macromolecules in the capsules. Macromolecules can be incorporated into the inner volume of the capsule by different means, either through their aggregation in the solution or precipitation onto the surface of collecting colloidal particles, followed by their capture through the formation of stable polyelectrolyte shells afterward, or the opening and closing of pores in the capsule wall by pH, salt, and solvent. These approaches to load macromolecules into the capsules differ by the size of capsules, their monodispersity, low or high macromolecule concentrations in the capsules, encapsulation efficiency, and possibilities to incorporate several substances in one capsule. Of course, the macromolecules can be incorporated as layer constituents during shell buildup. Layer-by-layer deposition on colloidal particles at fabrication could supply the LbL degradation of components afterward. One could find the optimum time scale for this process as well. Generally speaking, one also has to choose the most profitable way according to the aims these capsules are supposed to serve. Talking about encapsulation of enzymes, it should be stressed that selective permeability provides the elaboration of enzymatic microreactors where the proteins are placed into the capsule interior, whereas substrates and products of the one-step or multistep enzymatic reactions in the capsules can readily penetrate the capsule wall. In addition, the encapsulated enzymes have higher stability and are protected by the outer shell against high-molecular-weight inhibitors and proteolytic agents. The capsules themselves can be easily withdrawn from one solution, washed, and placed in another by filtration or centrifugation, or they can be driven by applying magnetic fields if the magnetite particles were used as layer constituents. We did not mention here any chemical treatment of the capsules after they have been assembled. Obviously, further modifications, such as cross-linking, can significantly change the properties of the capsules, such as permeability or stability.

The capsules might be used as combinatorial libraries. For instance, Gaponik et al.^[46] modified the polyelectrolyte capsules with different semiconductor luminescent nanoparticles (Q-dots). A variety of possibilities to impart fluorescent fingerprint characteristics (labelling with defined mixtures of different Q-dots) open an avenue to make many experiments with capsules in one pot. Indeed, the capsules of each functionality, size, or

composition discriminated by unique fluorescent characteristics can be followed at the same time in *in vitro* or *in vivo* testing.

Fundamental research on these capsules should be mentioned. They represent a unique system to study the chemical and physical phenomena in micron-sized and submicron-sized volumes. In comparison with liposomes, the polyelectrolyte capsules, besides their higher stability, give the possibility of varying the content of the inner volume in a controllable way. Defined inner composition allows chemical reactions in restricted volumes, which has been demonstrated up to now only as precipitation reactions for small organic molecules and inorganic salts in the capsule interior. There are no doubts that such a philosophy might be expanded further. Selective permeability and related solubility, pH, and temperature are background parameters to modify the capsule interior. The complexity provides more possibilities. For example, if one establishes a different pH in the capsules loaded with different enzymes to achieve the optimal conditions for catalytic reactions in each capsule, these capsules might either exchange intermediate products or selectively collect them in each tape of capsules. These capsules might be a device to study single-molecule effects. Indeed, the concentration of substances 10^{-7} M means about one molecule of this substance in capsules of 300 nm diameter. Defined inputs into the interior could register discrete chemical reactions occurring in the capsule interior.

The polyelectrolyte capsules could serve also as support for lipid bilayers. As shown in Refs. [19] and [47], lipid bilayers assembled on polyelectrolyte capsules reduce the permeation for small ions. Thus there are perspectives to reconstitute channel formers into the lipid bilayer supported by polymeric shells and to use this as a stable model. Such research might aim to construct artificial cells, cell compartments, or artificial organs because of the emerging possibilities to introduce different substances into the capsule and build the shell (i.e., "membrane") using a variety of compatible materials. The hollow and loaded capsules are novel types of cages for compartmentalization of materials, and are good models for research on biomineralization.

Mimicking the processes in biological cells and cell compartments foresees the involvement of a number of enzymes, which work together at the same time. The method of controllable opening and closing pores provides also a possibility to encapsulate several proteins at the same time and at certain concentrations in the capsules to catalyze sequential enzymatic reactions (for instance, glucose oxidation by glucose oxidase followed by utilization of hydrogen peroxide by peroxidase). The loaded enzyme, as we showed, might be released out of the capsule after a certain pH treatment, which

N

could find some applications for systems with controlled release.

A wide range of possible uses, interplays of several approaches, the solving of different problems, and the focus on fundamental and application aspects in diverse areas of life and material sciences attract interest and stimulate further research on the development of approaches for nanoengineering surfaces of colloidal particles and polymeric capsules.

ACKNOWLEDGMENT

The author expresses his gratitude to Prof. Dr. H. Möhwald (MPI Colloids and Interfaces, Potsdam) for continuous support of the work on this topic and stimulating discussions. Dr. E. Donath is acknowledged for fruitful collaboration over the years. Members of the group at MPI—Dr. A. Voigt, Dr. D. Shchukin, Dr. K. Glinel, Dr. D. Shenoy, Dr. O. Tiourina, I.L. Radtchenko, and A.A. Antipov—are thanked for providing a creative atmosphere, collaboration, and help in the research on nanoengineered polymeric microcapsules.

REFERENCES

1. Iler, R.K. Multilayers of colloidal particles. *J. Colloid Interface Sci.* **1966**, *21*, 569–572.
2. Lee, H.; Kepley, L.J.; Hong, H.G.; Akhter, S.; Mallouk, T.E. Adsorption of ordered zirconium phosphonate multilayer films on silicon and gold surfaces. *J. Phys. Chem.* **1988**, *92*, 2597–2601.
3. Decher, G.; Hong, J.-D. Build up of ultrathin multilayer films by a self-assembly process: I. Consecutive adsorption of anionic and cationic bipolar amphiphiles. *Macromol. Chem., Macromol. Symp.* **1991**, *46*, 321–327.
4. Sukhorukov, G.B.; Donath, E.; Lichtenfeld, H.; Knippel, E.; Knippel, M.; Budde, A.; Mohwald, H. Layer-by-layer self-assembly of polyelectrolytes onto colloidal particles. *Colloids Surf., A* **1998**, *137*, 253–266.
5. Donath, E.; Sukhorukov, G.B.; Caruso, F.; Davis, S.; Möhwald, H. Novel hollow polymer shells: Fabrication, characterization and potential applications. *Angew. Chem., Int. Ed. Engl.* **1998**, *37*, 2201–2205.
6. Voigt, A.; Lichtenfeld, H.; Zastrow, H.; Sukhorukov, G.B.; Donath, E.; Möhwald, H. Membrane filtration for microencapsulation and microcapsules fabrication by layer-by-layer polyelectrolyte adsorption. *Ind. Eng. Chem. Res.* **1999**, *38*, 4037–4043.
7. Sukhorukov, G.B.; Donath, E.; Davis, S.A.; Lichtenfeld, H.; Caruso, F.; Popov, V.I.; Möhwald, H. Step-wise polyelectrolyte assembly on particle surfaces—A novel approach to colloid design. *Polym. Adv. Technol.* **1998**, *9*, 759–767.
8. Lvov, Y.M.; Decher, G.; Möhwald, H. Assembly, structural characterization, and thermal behaviour of layer-by-layer deposited ultrathin films of poly(vinyl sulfate) and poly(allylamine). *Langmuir* **1993**, *9*, 481–486.
9. Bobreshova, M.E.; Sukhorukov, G.B.; Saburova, E.A.; Elfimova, L.I.; Sukhorukov, B.I.; Sharabchina, L.I. Lactate dehydrogenase in interpolyelectrolyte complex. Function and stability. *Biophysics* **1999**, *44*, 813–820.
10. Balabushevitch, N.G.; Sukhorukov, G.B.; Moroz, N.A.; Larionova, N.I.; Donath, E.; Möhwald, H. Encapsulation of proteins by layer-by-layer adsorption of polyelectrolytes onto protein aggregates: Factors regulating the protein release. *Biotechnol. Bioeng.* **2001**, *76*, 207–213.
11. Trubetskoy, V.S.; Loomis, A.; Hagstrom, J.E.; Budker, V.G.; Wolff, J.A. Layer-by-layer deposition of oppositely charged polyelectrolytes on the surface of condensed DNA particles. *Nucleic Acids Res.* **1999**, *27*, 3090–3095.
12. Finsinger, D.; Remy, J.S.; Erbacher, P.; Koch, C.; Plank, C. Protective copolymers for nonviral gene vectors: Synthesis, vector characterization and application in gene delivery. *Gene Ther.* **2000**, *7*, 1183–1192.
13. Dallüge, R.; Haberland, A.; Zaitsev, S.; Schneider, M.; Zastrow, H.; Sukhorukov, G.; Böttger, M. Characterization of structure and mechanism of transfection-active peptide–DNA complexes. *Biochim. Biophys. Acta* **2002**, *1576*, 45–52.
14. Caruso, F. Hollow capsule processing through colloidal templating and self-assembly. *Chem. Eur. J.* **2000**, *6*, 413–419.
15. Caruso, F.; Susa, A.S.; Giersig, M.; Mohwald, H. Magnetic core-shell particles: Preparation of magnetite multilayers on polymer latex microspheres. *Adv. Mater.* **1999**, *11*, 950–953.
16. Rogach, A.; Sucha, A.; Caruso, F.; Sukhorukov, G.; Kornovski, A.; Kershaw, S.; Möhwald, H.; Eychmüller, A.; Weller, H. Nano- and microengineering: 3D colloidal photonic crystals prepared from submicron sized polystyrene latex spheres pre-coated with luminescent polyelectrolyte/nanocrystal shells. *Adv. Mater.* **2000**, *12*, 333–336.
17. Sukhorukov, G.B.; Donath, E.; Moya, S.; Susa,

- A.S.; Voigt, A.; Hartmann, J.; Möhwald, H. Microencapsulation by means of step-wise adsorption of polyelectrolytes. *J. Microencapsul.* **2000**, *17*, 177–185.
18. Moya, S.; Donath, E.; Sukhorukov, G.B.; Auch, M.; Bäuml, H.; Lichtenfeld, H.; Möhwald, H. Lipid coating on polyelectrolyte surface modified colloidal particles and polyelectrolyte capsules. *Macromolecules* **2000**, *33*, 4538–4544.
 19. Georgieva, R.; Moya, S.; Leporatti, S.; Neu, B.; Bäuml, H.; Reichle, C.; Donath, E.; Mohwald, H. Conductance and capacitance of polyelectrolyte and lipid–polyelectrolyte composite capsules as measured by electrorotation. *Langmuir* **2000**, *16*, 7075–7081.
 20. Caruso, F.; Fiedler, H.; Haage, K. Assembly of beta-glucosidase multilayers on spherical colloidal particles and their use as active catalysts. *Colloids Surf., A* **2000**, *169*, 287–293.
 21. Schuler, C.; Caruso, F. Preparation of enzyme multilayers on colloids for biocatalysis. *Macromol. Rapid Commun.* **2000**, *21*, 750–753.
 22. Antipov, A.A.; Sukhorukov, G.B.; Leporatti, S.; Radtchenko, I.L.; Donath, E.; Möhwald, H. Polyelectrolyte multilayer capsule permeability control. *Colloids Surf., A* **2002**, *198–200*, 535–541.
 23. Shenoy, D.; Antipov, A.A.; Sukhorukov, G.B.; Möhwald, H. Layer-by-layer engineering of biocompatible, decomposable core-shell structures. *Biomacromolecules* **2003**, *4*, 265–272.
 24. Neu, B.; Voigt, A.; Mitlöchner, R.; Leporatti, S.; Donath, E.; Gao, C.Y.; Kiesewetter, H.; Möhwald, H.; Meiselman, H.J.; Bäuml, H. Biological cells, as templates for hollow microcapsules. *J. Microencapsul.* **2001**, *18*, 385–395.
 25. Georgieva, R.; Moya, S.; Hin, M.; Mitlohner, R.; Donath, E.; Kiesewetter, H.; Mohwald, H.; Bäuml, H. Permeation of macromolecules into polyelectrolyte microcapsules. *Biomacromolecules* **2002**, *3*, 517–524.
 26. Gao, C.; Moya, S.; Lichtenfeld, H.; Casoli, A.; Fiedler, H.; Donath, E.; Möhwald, H. The decomposition process of melamine formaldehyde cores: The key step in the fabrication of ultrathin polyelectrolyte multilayer capsules. *Macromol. Mater. Eng.* **2001**, *286*, 355–361.
 27. Leporatti, S.; Voigt, A.; Mithöhner, R.; Sukhorukov, G.B.; Donath, E.; Möhwald, H. Scanning force microscopy investigation of polyelectrolyte nano- and microcapsule wall texture. *Langmuir* **2000**, *16*, 4059–4063.
 28. Antipov, A.A.; Shchukin, D.; Fedutik, Y.A.; Petrov, A.I.; Sukhorukov, G.B.; Möhwald, H. Carbonate microparticles for hollow polyelectrolyte capsules fabrication. *Colloids Surf., A*, *in press*.
 29. Caruso, F.; Caruso, R.A.; Mohwald, H. Nanoengineering of inorganic and hybrid hollow spheres by colloidal templating. *Science* **1998**, *282*, 1111–1114.
 30. Antipov, A.A.; Sukhorukov, G.B.; Donath, E.; Möhwald, H. Sustained release properties of polyelectrolyte multilayer capsules. *J. Phys. Chem., B* **2001**, *105*, 2281–2286.
 31. Klitzing, R.V.; Mohwald, H. A realistic diffusion model for ultrathin polyelectrolyte films. *Macromolecules* **1996**, *29*, 6901–6907.
 32. Kabanov, V.; Zezin, A. Soluble interpolyelectrolyte complexes as a new class of synthetic polyelectrolytes. *Pure Appl. Chem.* **1984**, *56*, 343–350.
 33. Qiu, X.P.; Donath, E.; Mohwald, H. Permeability of ibuprofen in various polyelectrolyte multilayers. *Macromol. Mater. Eng.* **2001**, *286*, 591–597.
 34. Ai, H.; Jones, S.A.; de Villiers, M.M.; Lvov, Y. Nano-encapsulation of furosemide microcrystals for controlled drug release. *J. Control. Release* **2003**, *86*, 59–68.
 35. Antipov, A.A.; Sukhorukov, G.B.; Möhwald, H. Influence of the ionic strength on the polyelectrolyte multilayers permeability. *Langmuir* **2003**, *19*, 2444–2448.
 36. Ibarz, G.; Dahne, L.; Donath, E.; Mohwald, H. Controlled permeability of polyelectrolyte capsules via defined annealing. *Chem. Mater.* **2002**, *14*, 4059–4062.
 37. Sukhorukov, G.B.; Antipov, A.A.; Voigt, A.; Donath, E.; Möhwald, H. Incorporation of macromolecules into polyelectrolyte micro- and nanocapsules via surface controlled precipitation on colloidal particles. *Macromol. Rapid Commun.* **2001**, *22*, 44–46.
 38. Tiourina, O.P.; Sukhorukov, G.B. Multilayer alginate/protamine microcapsules: Encapsulation of alpha-chymotrypsin and controlled release study. *Int. J. Pharm.* **2002**, *242*, 155–161.
 39. Lvov, Y.; Antipov, A.A.; Mamedov, A.; Mohwald, H.; Sukhorukov, G.B. Urease encapsulation in nanoorganised microshells. *Nano Lett.* **2001**, *1*, 125–128.
 40. Radtchenko, I.L.; Sukhorukov, G.B.; Mohwald, H. Incorporation of macromolecules into polyelectrolyte micro- and nanocapsules via surface controlled precipitation on colloidal particles. *Colloids Surf., A* **2002**, *202*, 127–133.
 41. Sukhorukov, G.B.; Donath, E.; Brumen, M.;

- Mohwald, H. Hollow polyelectrolyte shells: Exclusion of polymers and Donnan equilibrium. *J. Phys. Chem., B* **1999**, *103*, 6434–6440.
42. Radtchenko, I.L.; Gierzig, M.; Sukhorukov, G.B. Inorganic particle synthesis in confined micron-sized polyelectrolyte capsules. *Langmuir* **2002**, *18*, 8204–8208.
 43. Shchukin, D.; Radtchenko, I.L.; Sukhorukov, G.B. Synthesis of nanosized magnetic ferrite particles inside hollow polyelectrolyte capsules. *J. Phys. Chem., B* **2003**, *107*, 86–90.
 44. Radtchenko, I.L.; Sukhorukov, G.B.; Mohwald, H. A novel method for encapsulation of poorly water-soluble drugs: Precipitation in polyelectrolyte multilayer shells. *Int. J. Pharm.* **2002**, *242*, 219–223.
 45. Antipov, A.A.; Shchukin, D.; Fedutik, Y.; Zhanavskina, I.; Klechkovskaya, V.; Sukhorukov, G.B.; Möhwald, H. Urease-catalyzed carbonate precipitation inside restricted volume of polyelectrolyte capsules. *Macromol. Rapid Commun.* **2003**, *24*, 274–277.
 46. Gaponik, N.; Radtchenko, I.L.; Sukhorukov, G.B.; Weller, H.; Rogach, A.L. Toward encoding combinatorial libraries: Charge-driven microencapsulation of semiconductor nanocrystals luminescing in the visible and near IR. *Adv. Mater.* **2002**, *14*, 879–882.
 47. Tiourina, O.P.; Radtchenko, I.L.; Sukhorukov, G.B.; Möhwald, H. Artificial cell based on lipid hollow polyelectrolyte microcapsules: Channel reconstruction and membrane potential measurement. *J. Membr. Biol.* **2002**, *190*, 9–16.

Nanofilms in Giant Magnetoresistance Heads

Edward Grochowski

Robert E. Fontana, Jr.

IBM Almaden Research Center, San Jose, California, U.S.A.

INTRODUCTION

The magnetic hard disk drive has become the foremost data storage device for computer applications based on cost, capacity, performance, and miniature form factor. Although it is a mechanical, rotating disk storage device, power requirements are minimal, usually a few watts; reliability over a wide range of operating environments, from below 0°C to well over 100°C, is excellent; and costs are less than \$0.01 per megabyte. Throughout its 46-year history, hard disk drives have been the recipient of significant technological innovations which have added to the usefulness of this device, and data density on the disk surface, areal density, has increased nearly 35 million times in this period (Fig. 1).^[1]

The principal magnetic components in a drive are the media or disks, and a recording head that reads and writes data (Fig. 2). These data are recorded in the form of magnetized regions on the media within a deposited thin film of magnetic alloy normally consisting of chromium, cobalt, platinum, and a fourth component as boron. Data are distributed geometrically on a series of concentric rings, or tracks, whose location has been predetermined by a process called formatting. Along these tracks, bits of data are magnetically written by an inductive element in the head, and subsequently sensed or read by the giant magnetoresistive element that is an integral part of the head structure. Fig. 3 is a schematic of the writing process with a projection of the bit length and track width for a 100 Gb/in.² areal density. Writing involves a magnetic reorienting of the very small alloy micrograins in the media, and the interface between two magnetized bits is shown in Fig. 3. To maintain an adequate signal-to-noise ratio, a large number of grains are required per bit, nearly 1000 grains. Increasing areal density involves reducing bit dimensions, requiring smaller grain diameters. In the case of 100 Gb/in.², a grain diameter of 5 nm is projected.

Fig. 4 illustrates the history of magnetic recording head design since 1970. The transition from a ferrite, wire-wound inductive head to a thin film head in late 1970s to early 1980s was driven by progressive areal density increases. In both of these early designs, an inductive element performed both read and write

functions. As areal density increased beyond 0.10 Gb/in.², this inductive element proved inadequate to maintain an acceptable signal-to-noise ratio in reading and, in addition, the read amplitude was velocity-dependent. A second element was added to recording heads, a simple magnetoresistive (MR) [or anisotropic magnetoresistive (AMR)] sensor that now separated read and inductive write parts of the head, but shared common elements or layers of the structure. The MR element used a nickel-iron (NiFe) ferromagnetic film that consequently changed resistance when experiencing a magnetic field originating from stored bits on the rotating disk media. This modification allowed the write element to be more easily built with fewer copper coil turns than inductive heads that perform both read and write operations.

As areal densities continued to increase beyond 10 Gb/in.², scaling of the MR element to smaller dimensions based on reading submicrometer tracks also reduced signal amplitude. A new read sensor technology was required.^[2,3]

GMR HEAD DEFINITION

In 1988, a new magnetoresistive effect was discovered in Germany and France, identified as the giant magnetoresistive (GMR) effect, using multilayers of chromium and iron synthesized by molecular beam epitaxy. When this Cr/Fe structure was tested at liquid helium, cryogenic temperatures in very strong magnetic fields of several thousand Oersteds, or about 100 times greater than what would be obtained from a rotating magnetic media in a disk drive, the result was a resistance change of as much as 50%.^[4] This newly observed behavior was of great interest to magnetic recording scientists. An application of GMR as a sensor element to magnetic recording would be very valuable at high data densities, where scaling sensor dimensions into the nanometer range could still yield a readable room temperature signal amplitude, or resistance change in the presence of a magnetic field of a magnitude experienced with a recorded disk.

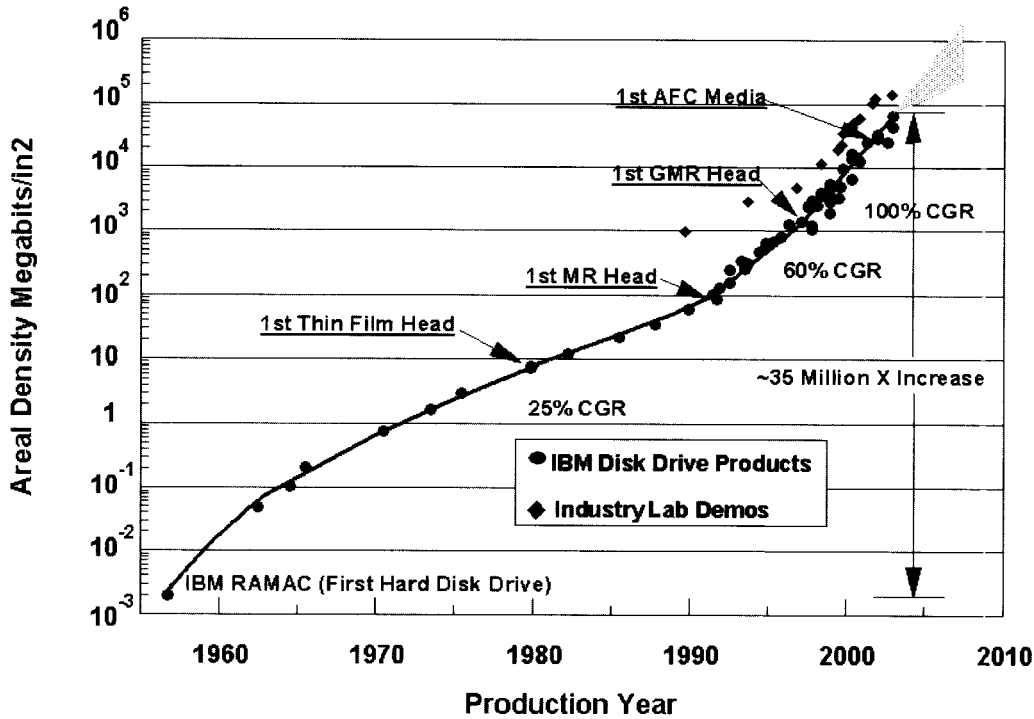


Fig. 1 Hard disk areal density trend. (View this art in color at www.dekker.com.)

Subsequently, IBM researchers demonstrated that the origin of the GMR effect arose from electron spin scattering in ferromagnetic materials. Using conventional vacuum sputtering techniques, unique thin film structures were shown to exhibit the GMR effect at disk drive

operating temperatures and in low magnetic fields.^[5] Whereas in the early investigations, a strong antiparallel (AP) coupling within the Cr/Fe layers was the origin of GMR, IBM researchers found that the interaction of a magnetically fixed or pinned ferromagnetic layer and a

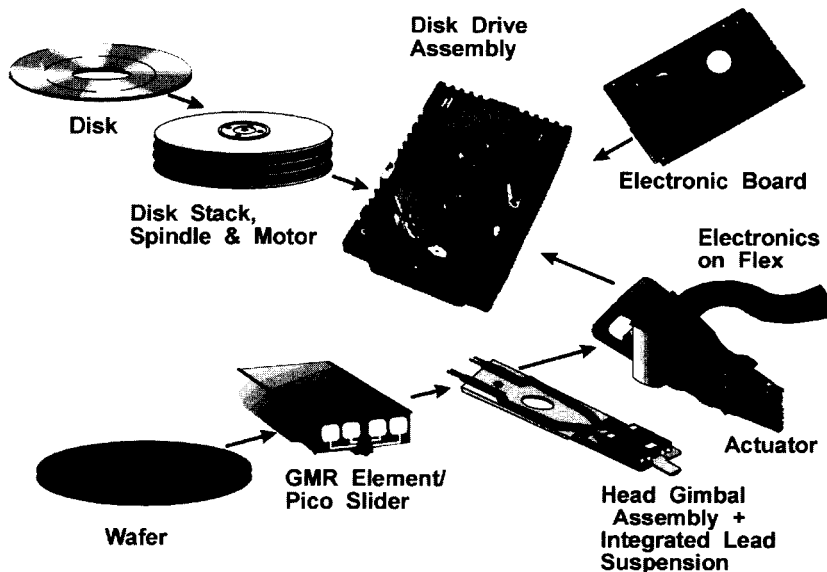


Fig. 2 Magnetic hard disk drive components. (View this art in color at www.dekker.com.)

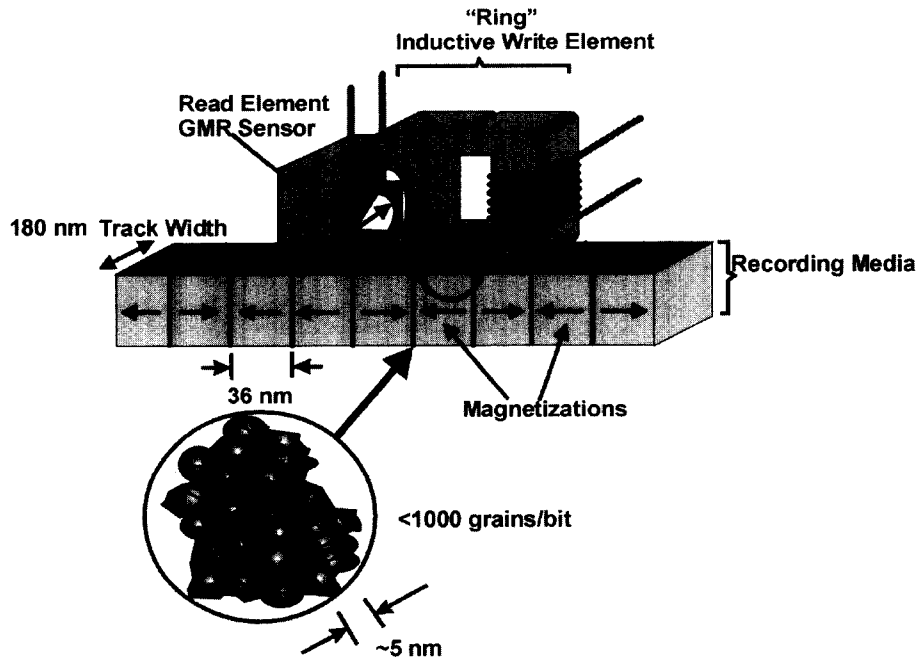


Fig. 3 Magnetic recording basics at 100 Gb/in². (View this art in color at www.dekker.com.)

magnetically free ferromagnetic layer separated by a highly conductive, nonmagnetic spacer also produced the GMR effect. This free layer was free to rotate, responding to external magnetic fields from the disk, while the pinned

layer remained magnetically fixed. Control of the spin-dependent current and a valve-like similarity to tunneling between ferromagnetic layers prompted the label “spin valve” for this structure.^[6]

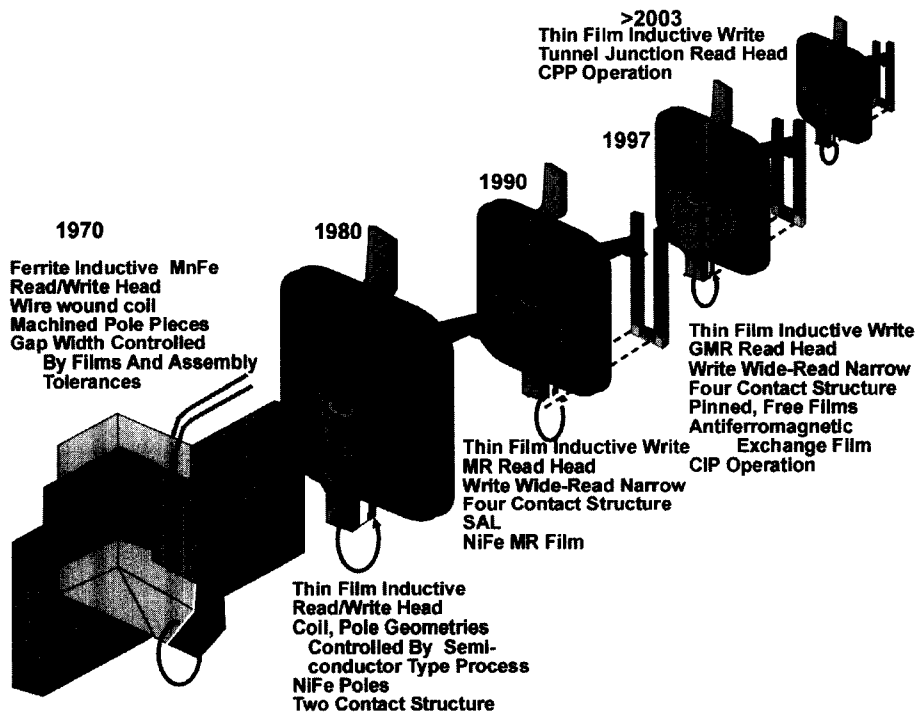


Fig. 4 The evolution of magnetic read/write sensors. (View this art in color at www.dekker.com.)

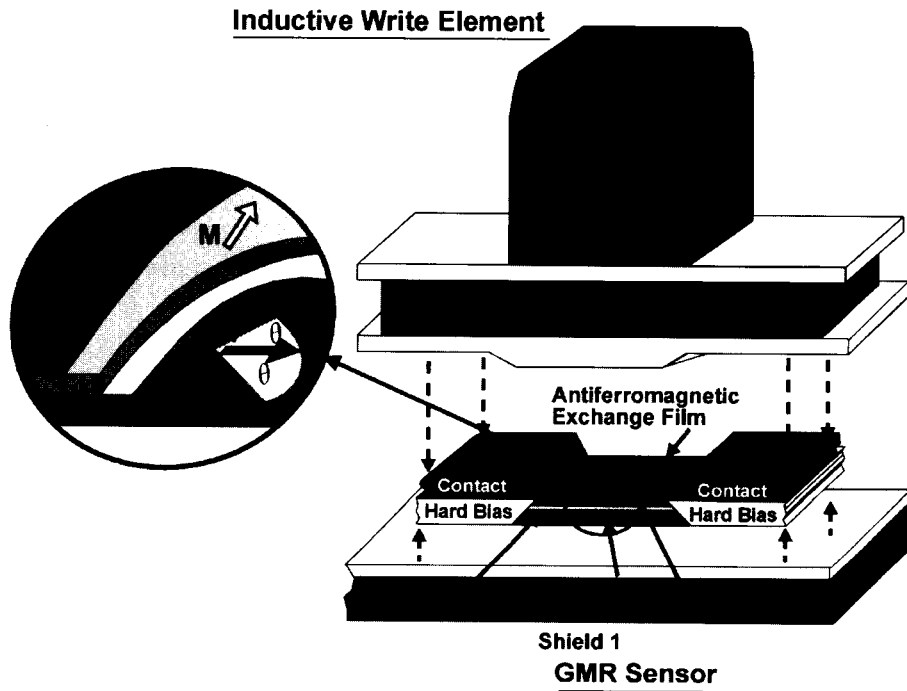


Fig. 5 GMR read sensor with section of inductive write element. (View this art in color at www.dekker.com.)

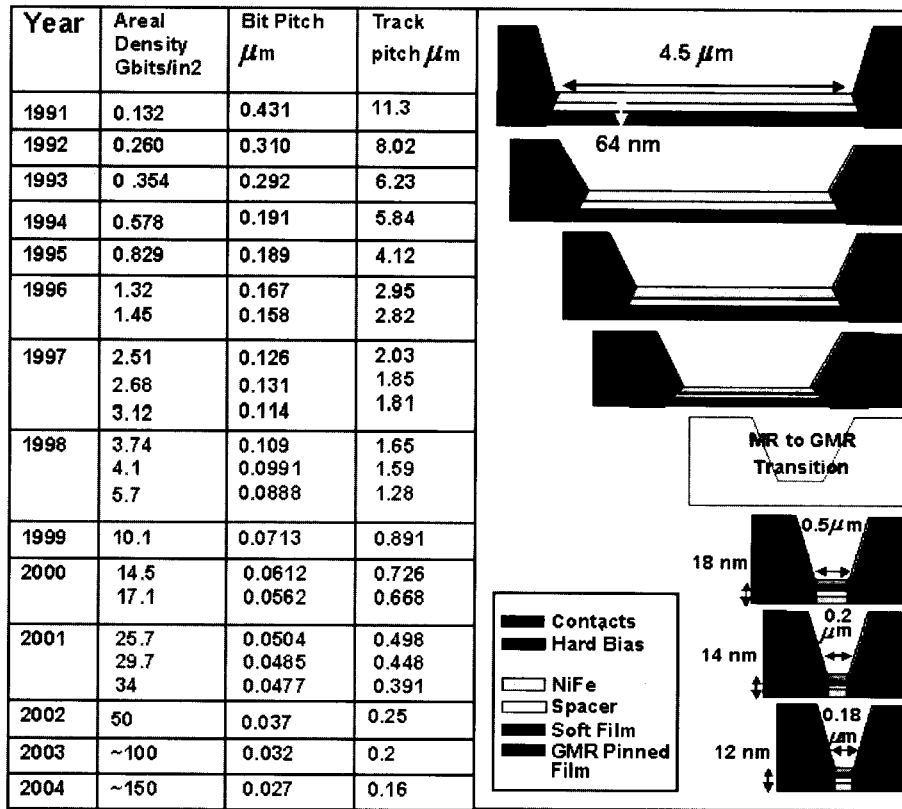


Fig. 6 MR/GMR read head evolution. (View this art in color at www.dekker.com.)

The GMR effect varies as the cosine of the angle of magnetizations between pinned and free layers (Fig. 5), varying as

$$\cos(\theta_{\text{free}} - \theta_{\text{pinned}}) = \sin(\theta_{\text{free}}) \quad (1)$$

Considering that $\theta_{\text{pinned}} = \pi/2$

Therefore the voltage of a spin valve, GMR sensor with width W , height h , resistance R , and a relative term called magnetoresistance $(\Delta R/R)_{\text{GMR}}$ with current I passing through the structure is given by:

$$V_{\text{GMR}} = I\{R + (W/2h)(\Delta R/R)\eta \sin \theta_{\text{free}}\} \quad (2)$$

where η is an efficiency factor which includes any misalignment of the magnetization based on demagnetizing effects.

Fig. 6 shows the read head progress for the transition to giant magnetoresistive heads (GMR) and the accompanying bit pitch and track pitch evolution including projections for future years. These advanced GMR read elements could be composed of multiple films with a total thickness of as small as $0.01 \mu\text{m}$ with a contact-contact spacing of less than $0.2 \mu\text{m}$. These ultrasmall dimensions qualify GMR sensors as nanotechnology devices.

Both MR and GMR read head electrical resistance depends on a magnetic field produced by the recorded information on the disk. In the previous MR heads, this resistance change occurs in a single NiFe film, while in GMR heads, this resistance change occurs in multiple films. Whereas in a conventional NiFe MR film, the resistance change is maintained as a linear response to the disk's field based on the close interaction of a magnet-

ically soft adjacent layer (SAL), and the GMR response is intrinsically linear.^[7]

There are four fundamental film types in a conventional GMR structure, although some of these films may be comprised of multiple subfilms. Fig. 5 is a cross section of a GMR read sensor and overlying inductive write element through the air bearing surface (ABS). The plane of this figure is parallel with the disk media. A GMR or free film has a variable magnetization that changes under the influence of the disk's magnetic field. The second film is a very thin conducting spacer, usually copper, with a thickness less than the mean free path of electrons. This film allows electrical current to pass easily to the third film, also a GMR film, which has a fixed or pinned magnetization. The fourth film is a pinning film which maintains the fixed magnetization of the third film through the process of antiferromagnetic exchange coupling. Typical antiferromagnetic exchange films contain the element manganese alloyed with either iridium, platinum, or iron. In contact with both ends of the GMR film stripe is a magnetically hard region, usually composed of an alloy of chromium, platinum, cobalt, and boron. These regions maintain a stability to the GMR sensor by suppressing magnetic domain noise through the use of a longitudinal bias applied to both ends of the GMR multifilm region.

THE GMR EFFECT

GMR read sensors exploit the quantum nature of electrons, which have two spins, spin up and spin down.

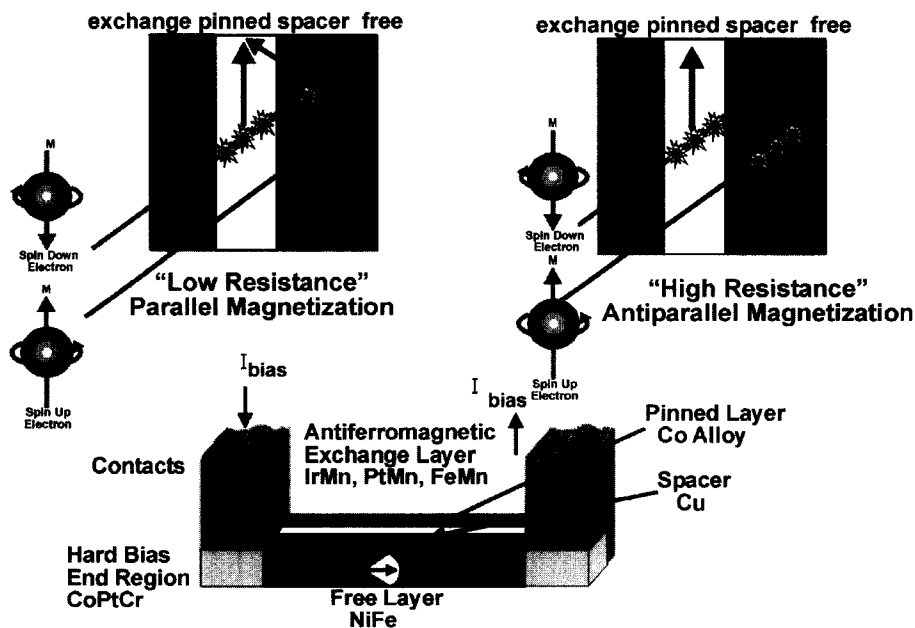


Fig. 7 GMR/spin valve operation. (From Ref. [2].) (View this art in color at www.dekker.com.)

Referring to Fig. 7, a view of a GMR sensor with ABS perpendicular to the plane of the page, the multilayer structure is indicated with antiferromagnetic exchange layer, pinned layer, spacer and GMR free layer with hard bias, stabilizing end regions, and electrical contacts. The electrical conductivity of this multilayer structure is proportional to the mean free path of electrons and the density of electrons in the films' materials. The mean free path is the distance an electron travels before a scattering event occurs, i.e., the loss of momentum through collisions with phonons or magnons within the material's lattice. Therefore, electrical conductivity depends on the amount of electron scattering that occurs within the multilayer structure. Electron spin generates a magnetic dipole, analogous to the magnetic dipole originating from electrical current flowing within a loop of conducting wire. Electron scattering can be observed to be more prevalent in films having an opposing magnetization, i.e., mean free paths of electrons are spin-dependent.^[8]

Conductivity depends on the ability of electrons to traverse the entire multilayer structure, without collisions, and both spin up and spin down electron mean free paths are determined by the relative orientations of the magnetizations within each film. In Fig. 7, if these magnetizations are all parallel, as would be the case if the free NiFe layer senses a magnetic field originating from the disk media, the spin up electron's path through the free layer, across the Cu spacer, and penetrating far into the pinned layer results in a low resistance (high conductivity). Spin down electrons undergo collisions in both free and pinned

layers and do not add to the conductivity. In fact, spin down electrons would not be able to penetrate far beyond the spacer layer before colliding. If all the magnetizations are antiparallel, as would be the case when no magnetic field from the media is present and the magnetization of the free layer is reversed, the distance of both spin up and spin down electrons is reduced by collisions so that neither can penetrate far beyond the spacer layer. This is the high resistance case. It can be demonstrated that the difference in conductivity between parallel and antiparallel cases for the GMR sensor can be expressed as:

$$\Delta C_{\text{total}} = \alpha(\lambda^+ - \lambda^-)^2 \quad (3)$$

where C is the sensor conductivity, α is a proportionality constant, λ^+ is the mean free path of electrons with spin parallel to the magnetization, and λ^- is the mean free path antiparallel. Typical GMR sensors exhibit conductivity changes of 10% from antiparallel to parallel states, although values larger than 20% have been reported in the laboratory.^[10]

INTERNAL MAGNETIC FIELDS IN GMR STRUCTURES

Fig. 8 demonstrates a GMR/spin valve linear voltage response to a changing external disk media magnetic field, which is the read process in magnetic recording. To design an efficient GMR read structure, the full linear portion of

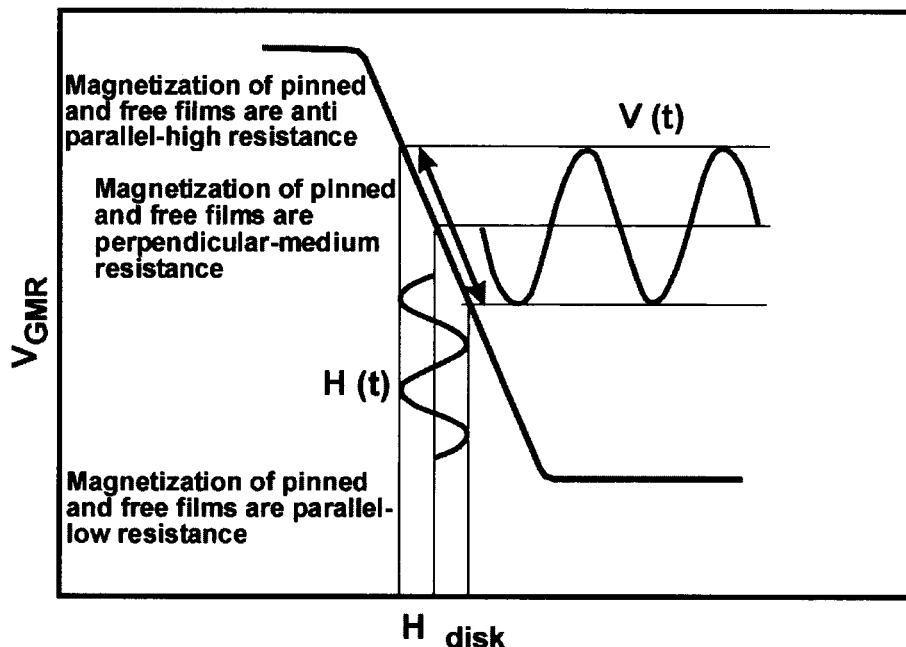
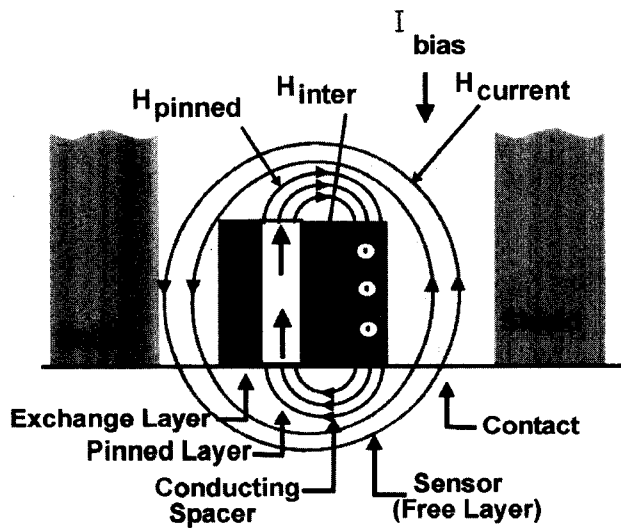


Fig. 8 Spin valve response to disk magnetic field. (View this art in color at www.dekker.com.)



$$H_{\text{pinned}} + H_{\text{inter}} + H_{\text{current}} = 0$$

Key: Electrons shared between layers

Fig. 9 Spin valve head (GMR) internal magnetic fields. (View this art in color at www.dekker.com.)

this curve is the operating response region, and is obtained by matching the free layer magnetic moment with the magnetic flux originating from the disk media.

$$M_{st} \sim M_r d \tag{4}$$

where M_s is the magnetization and t is thickness of the GMR free layer and, conversely, M_r and d are the magnetization and the thickness of the disk media layer. The GMR voltage, and therefore $\sin \theta_{\text{free}}$, is proportional to the time-varying disk field $H(t)$ applied along the structure's transverse direction. The free layer magnetization is normally oriented 90° to this field, along the longitudinal direction of the sensor when no disk field is present, previously shown in Fig. 5. For this magnetic field "balancing" between GMR and disk moments to be effective, the net of all other magnetic forces within the GMR free layer must be zero, as shown in Fig. 9. This design objective is often referred to as the "proper bias" of the GMR read head, so that

$$H_{\text{pinned}} + H_{\text{inter}} + H_{\text{elect}} = 0 \tag{5}$$

where H_{pinned} is the magnetostatic field arising from the pinned layer, H_{inter} is the spacer coupled field between pinned and free layers, and H_{elect} is the normal induced field arising from electrical sense current flowing within the free layer. Also shown in Fig. 9 are the shield structures that function to isolate the GMR sensor from

adjacent disk media magnetic fields, assuring that only one specific magnetized region of transition is read at a time. In many GMR designs, the overlying inductive head P_1 element also serves as one side of the shield structure (Fig. 5).

GMR STABILIZATION

Figs. 5–7 show a magnetic hard bias region contiguous to the GMR element which adds a longitudinal magnetic bias to the structure. As in MR read heads, complex multidomain regions within the NiFe free layer must be prevented from forming within the thin film. These regions would promote Barkhausen induced noise effects in the GMR sensor read back signal. Unlike the prior MR read head structures, in GMR read heads, only the free layer must make contact with the hard bias end regions because the pinned and exchange regions have a fixed magnetization in a direction perpendicular to the current flow (transverse direction). During processing, the pinned and exchange layer's magnetization is oriented by heating beyond the "blocking temperature," i.e., the temperature above which magnetization reverts to a very low value (Fig. 10). A cooling cycle in a transverse magnetic field determines the final pinned layer's magnetic orientation. As the hard bias end regions are also magnetically oriented, but in the longitudinal direction, the alloy selection for this film as well as the pinned layer is critical, based on blocking temperatures. Usually, an alloy of CoPtCr is selected for the hard bias region because its longitudinal magnetization is not affected by the thermal cycle required to set the pinned layer's transverse orientation. In addition, the pinned layer's blocking temperature must still be high

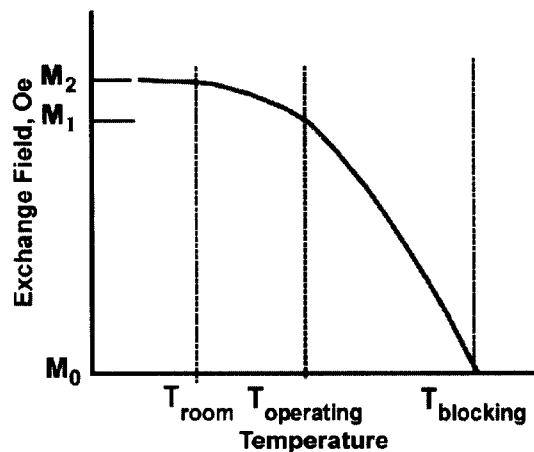


Fig. 10 The blocking temperature. (View this art in color at www.dekker.com.)

Table 1 Comparison of antiferromagnets for GMR/spin valves

Antiferromagnet	Blocking temperature [C]	Exchange energy [erg/cm ²]	Critical thickness [Å]
Ni ₄₅ Mn ₅₅	375	0.24	300
Ni ₄₉ Mn ₅₁	340	0.20	300
α -Fe ₂ O ₃	320	0.10	<500
Cr ₄₀ Mn ₄₀ Pt ₂₀	300	0.12	250
Pt ₂₀ Pd ₃₀ Mn ₅₀	300	0.12	250
Ir ₂₀ Mn ₈₀	280	0.15	80
Ru ₁₂ Rh ₈ Mn ₈₀	225	0.17	100
Ni ₅₀ O ₅₀	210	0.12	350
Fe ₅₀ Mn ₅₀	180	0.11	110

(From Ref. [1].)

enough to remain stable during heat cycling in subsequent process operations. Table 1 shows the blocking temperature for some common antiferromagnetic alloys used in GMR heads.

ANTIFERROMAGNETIC EXCHANGE COUPLING

Exchange coupling is a principal mechanism that determines GMR head operation, and it may be considered as the interaction between a ferromagnet (NiFe in this case) in contact with an antiferromagnet, with sample compositions as shown in Table 1. Referring to Fig. 11, a ferromagnetic material is defined as one in which all atomic dipole moments line up in the same direction; whereas in antiferromagnetic materials, the moments of adjacent atoms line up in opposite directions. In the former material, there is a net magnetic moment while in the latter there is no net macroscopic moment. Exchange may be defined as the tendency for neighboring atomic dipoles to line parallel or antiparallel to each other, and it results from the overlap of orbiting electrons in neighboring atoms. Exchange may occur within the same material or in two different adjacent materials. In the latter case, because exchange principally occurs across distances between atoms in a solid, it can be considered a near-neighbor phenomenon and is critically dependent on the quality and purity of the interface.

If an antiferromagnetic film is deposited onto a ferromagnetic film by vacuum sputtering, a clean, contaminant-free interface results, and the atoms align themselves by exchange so that a permanent biasing layer is created, which maintains the ferromagnet oriented in a constant direction. The B/H hysteresis loop of a ferromagnet/antiferromagnet structure is shifted by an amount H_x and is

a direct measure of the amount of exchange coupling occurring across the interface. The ideal antiferromagnetic material would basically be an insulator with a high exchange energy, a high blocking temperature for process stability with a narrow blocking temperature range and distribution, and with a small critical thickness.^[6]

MORE COMPLEX GMR STRUCTURES

In a nanolayer GMR structure, thin (as small as a monolayer) films of Co or Fe are added to NiFe free layer / Cu spacer interface, resulting in an increase in the GMR signal amplitude up to 50%. These nanolayer films are believed to reduce the spin-dependent scattering at the interface by improving the interfacial purity of the NiFe, which could be lost by mixing with Cu during the sputtering process. The nanolayers may be added to the NiFe free layer, or the pinned layer, or both, and many GMR read head structures attain higher GMR amplitudes through the use of nanolayers.

In a dual spin valve or dual GMR structure, the NiFe free layer is surrounded with two Cu spacers, as well as two pinned and antiferromagnetic exchange layers in an almost symmetrical configuration. This can be considered

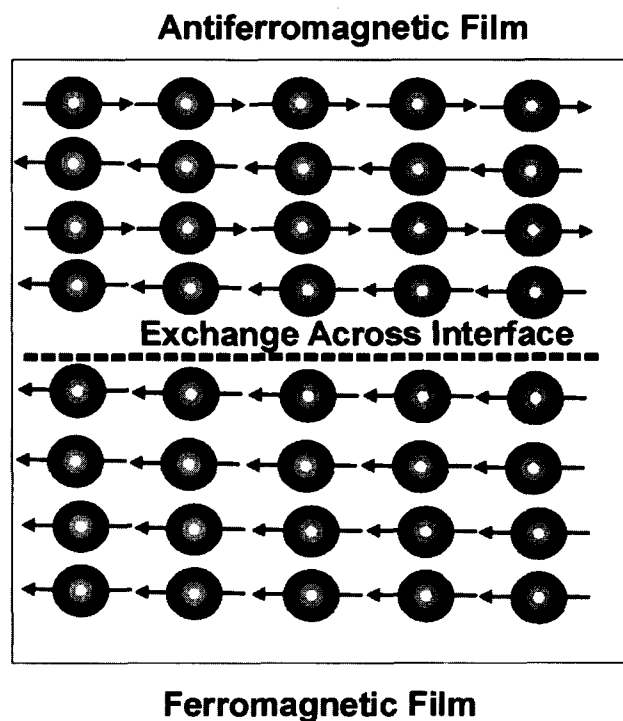


Fig. 11 Ferromagnetic/antiferromagnetic interface structure. (From Ref. [11].) (View this art in color at www.dekker.com.)



as a combination of two simple GMR structures, back-to-back and sharing a common free layer. In this case, a majority of electrons originating from this free layer can now reach a pinned layer, eliminating any electrons from these layers that do not participate in the GMR effect. It is estimated that an increase in the GMR amplitude reaches up to 33% for the dual structure. In addition, because the GMR structures are mirror images of each other, the current induced field is effectively cancelled so that proper biasing may occur independent of applied current. Conversely, because more films are involved in the dual GMR structure, the resulting resistance of the structure is lower, and this may lead to a lower overall GMR signal.

Depositing an additional layer of ruthenium or rhodium within the pinned layer was shown to stabilize the magnetization of this film and enhance the exchange field. This could allow the use of many more antiferromagnets, which previously did not have adequate fields, but had other beneficial characteristics such as higher blocking temperatures or better insulation properties. Based on the phenomenon of antiparallel (AP) coupling, the pinned layer now consists of two ferromagnetic films separated by the AP-spacer layer. This increased stabilization can also be the result of decreasing the demagnetizing field in the pinned layer, thereby reducing any rotation of the magnetization. It is estimated that a 25- to 100-times improvement in pinned layer stabilization results from AP pinning and, as areal density increases necessitate narrower and shorter GMR structures, this technique is expected to become more prevalent in read heads.

The use of a thin interposed layer of a nonmagnetic metal, such as ruthenium, to create a coupling effect between two ferromagnetic layers to retain opposite magnetic orientations was recently extended to the magnetic disk structure.^[12,13] This media structure, termed antiferromagnetic coupled (AFC) media, was demonstrated to exhibit good magnetic stability as areal density increases beyond 30 Gb/in.², thereby delaying the effects of superparamagnetism. The latter phenomenon occurs when metal grains within the media become so small that the energy required to create or erase the bits of magnetically stored information is the thermal energy (kT , where k is the Boltzmann constant and T is the operating temperature of the disk drive) of the environment.^[14] Ruthenium thicknesses of 6C (about three atomic layers) are commonly used because coupling strength oscillates with film thickness. It was found that at a thickness of maximum strength, electron waves in this ruthenium spacer constructively interfere and allow the magnetically polarized energy from one interface through to the other ferromagnetic layer. The AFC medium is projected to find application in magnetic storage for many years to come.

GMR PROCESSING-LITHOGRAPHY

Fig. 1 indicated a 100% growth rate in areal density for magnetic recording since 1997, based on the use of GMR read sensors, in effect doubling this parameter every year.

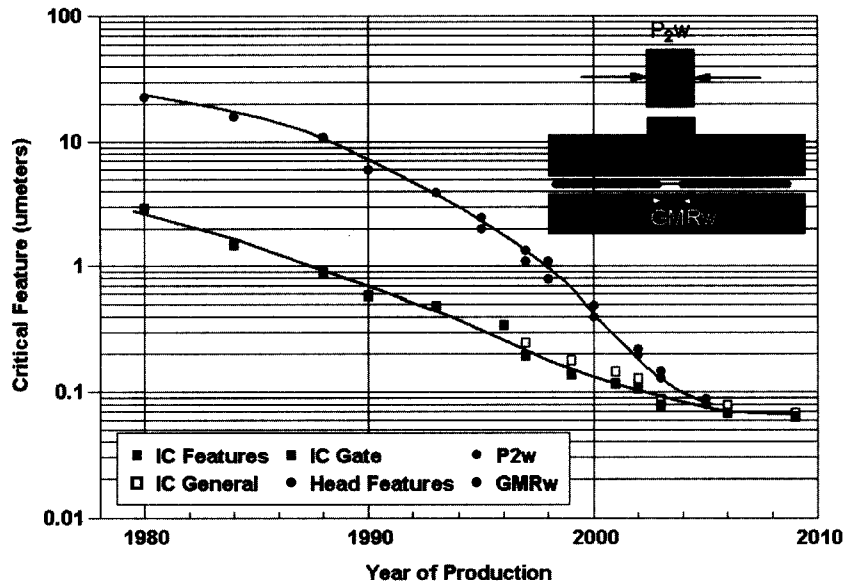


Fig. 12 Lithographic critical feature roadmap for GMR heads and semiconductor IC. (View this art in color at www.dekker.com.)

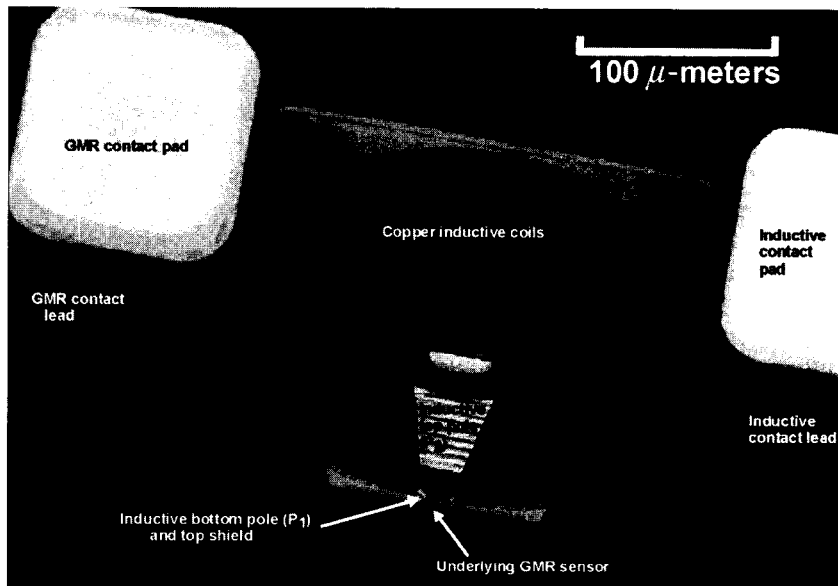


Fig. 13 Partial microphotograph of inductive write, GMR read head. (View this art in color at www.dekker.com.)

This density increase in magnetic recording originates from a shrinking in the bit cell area, which results from lithographic and processing improvements. This is in contrast to the integrated circuit (IC) field in which the transistor count in an IC device doubles every 1.5 years (roughly 60% growth rate). In the latter case, only about one-third of this increase originates from a transistor cell

area or lithographic improvements. This is shown in Fig. 12, where historical IC, general IC, and IC gate features are compared with historical magnetic recording head, inductive write head width, and GMR element length. The critical head dimensions, P2w (or write width) determines the track width and GMRw, the read width for the track.^[17]

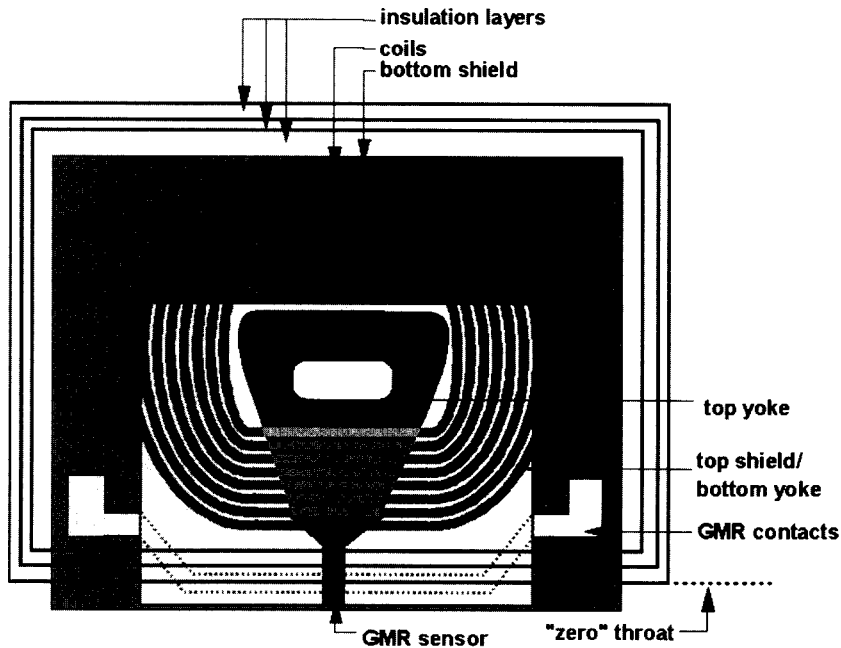


Fig. 14 Thin film head, top view. (View this art in color at www.dekker.com.)

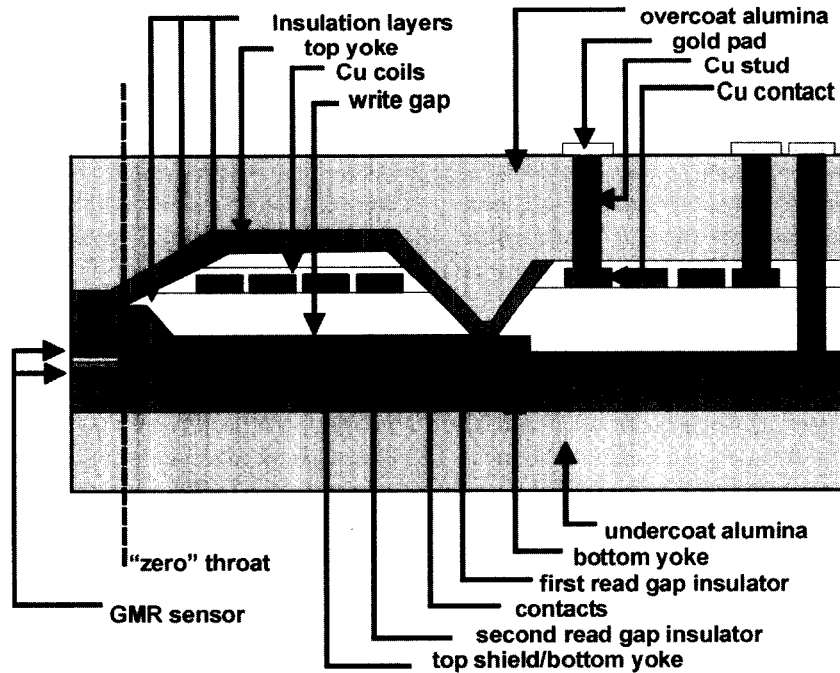


Fig. 15 Thin film head, side-section view. (View this art in color at www.dekker.com.)

It is convenient to describe the fundamentals of processing for both inductive write element and GMR read sensor, which are both integrated into a single read/write structure. The actual head processing is similar to thin film integrated circuit processing, and consists of a

sequence of patterning by application of photoresist, masking and exposure operations (lithography), film deposition, and localized material removal by etching to create the various layers and structures. In addition, the use of lift-off operations, as well as highly directional

Ph = Photo Pl = Plating Dp = Deposition Pa = Patterning	
Bottom Yoke or Shield	$2Ph + Pl + 2Dp + 1Pa = 6$
Gap(s)	$Ph + 3Dp + Pa = 5$
Top Shield	$2Ph + Pl + 2Dp + 1Pa = 6$
Sensor/Stabilization/Contacts	$2Ph + 6Dp + 2Pa = 10$
Coil(s) + Insulators	$4Ph + Pl + 2Dp = 7$
Top Yoke	$2Ph + Pl + 2Dp + 1Pa = 6$
Contacts, Studs, Pads	$3Ph + 3Pl + 6Dp = 12$
Overcoat	$1Dp + Pa = 2$
Total Processes	54

Fig. 16 Inductive write/GMR read process operations. (View this art in color at www.dekker.com.)

etching as special techniques for the control of vertical and horizontal dimensions of critical features, is required at these feature sizes and topographies. Fig. 13 is a top view microphotograph of the head structure and Fig. 14 identifies the principal parts as seen from this view. It can be seen that only the overlying inductive write element is visible. In Fig. 15, the actual vertical structure is indicated, in which the GMR sensor is first formed by successive depositions followed by a series of insulators and metal films which comprise the inductive element. The total device structure consists of the order of 20 layers, ranging in thickness from as thin as 1–2 nm in the GMR sensor to 3–4 μm for the pole tip of the inductive write element. Progressively higher areal densities were achieved by reducing both critical thicknesses and horizontal dimensions of the head structure in a process referred to as scaling. Over the past 10 years, areal density has increased by a factor of 400, which has required a GMR sensor thickness decrease of a factor of 10–15, the sensor width MRw decreased by a similar factor, and the inductive pole tip width P2w scaled down also by a similar factor. It can be projected that further areal densities increases, which are expected as the norm in magnetic recording although probably not retaining the previous 100% growth, will involve continual decreases in these critical dimensions well into the subnanometer range for vertical GMR dimensions, and into the submicrometer range for the horizontal dimension of P2w.

An outline of typical processing operations for both inductive and GMR structures for the read/write head is shown in Fig. 16. There are four fundamental, generic operations which involve specific equipment and process-

es, and these are very similar to those employed in IC processes. Photo, involving the application of a photo-sensitive resist film and its subsequent exposure by a photo mask and UV light source; plating, or electroplating, the formation of a relatively thick metal film by an electrolytic process (this operation usually requires the preformation of a metal seed film to complete the electric circuit prior to plating); deposition, usually referring to a vacuum sputtering operation in which very thin metal films are accurately formed with precise control of composition, magnetic orientation, and crystallographic structure; and finally, patterning, which denotes the formation of elements of the head by either subtractive etching or “a lift-off” process. The latter can be illustrated by an example of the formation of the inductive pole structure, or P2w, as shown in Fig. 17. This material removal technique is applied to maintain tight control of vertical walls of a very small horizontal pattern, which is usually of the order of μm thick, i.e., has a high aspect ratio of as much as 10:1. As soon as the seed layer is applied and resist pattern formed in Fig. 17, the thick P2 NiFe film is electroplated. The center region is protected with a new field removal resist and exposed.

After stripping this resist and etching both field film and seedlayer, the final pole region remains. The particular topography of this P2 film originates from the requirement that the inductive yokes must encircle the copper coils and insulator layers, as shown in Fig. 15. This yoke topography for the head conforms to the multiple layers of polymers and coils, and the resulting head topography can be greater than 10 μm . “Zero throat” in this figure refers to the point at which the

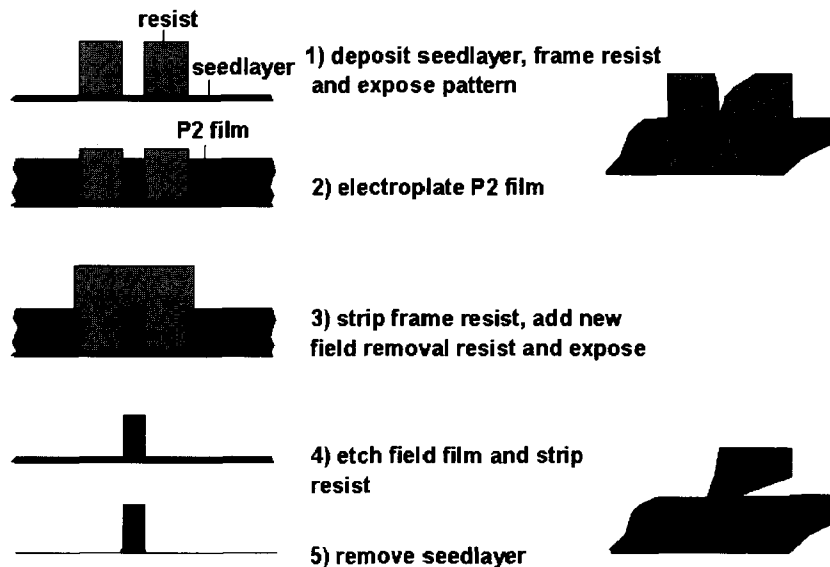


Fig. 17 Inductive head P2w processing. (View this art in color at www.dekker.com.)

inductive throat begins and is defined by the edge of one of the polymer insulators.

this structure. Subsequent processing and layers form the inductive write element.

GMR PROCESS

For the formation of a GMR sensor, referring to Fig. 15, the GMR gap consists of two dielectric layers which electrically isolate the contacts and sensor from the surrounding shield and inductive element. Furthermore, these electrical contacts and sensor are connected via a contiguous junction process in which a degree of geometric overlapping results. The horizontal dimensions for MRw, as well as the previous example of frame plating for P2w, require a fine-line lithographic equipment and process to form the images. These sensor dimensions define a trackwidth capability on the disk and, as areal density evolves to increased levels, these dimensions become progressively smaller. The contiguous junction process uses a critical lithography step with about 1 μm thick resist to form this trackwidth by a similar process to P2w—the use of a resist mask to protect the active GMR region during the subtractive removal of sensor material to define the GMR dimensions. This etching process, shown in Fig. 18, is a resist structure which exhibits a reentrant or negative wall angle and, therefore, subsequent depositions of contact metal and hard bias stabilization films do not completely seal the resist edges. This allows the resist “stencil” to be removed in this lift-off process based on the exposure of the undercut region by the dissolving in the appropriate solvent. The stencil is actually floated away in this solvent, leaving the GMR sensor defined by

FUTURE SCALING OF GMR NANOLAYER SENSORS

As was previously indicated, areal density increases require further reduction in MRw by scaling of MRw in an evolutionary trend described in Fig. 6. The process challenge is to create submicrometer openings with a controlled undercut in the resist images. For example, if a future trackwidth is 0.3 μm, this would result in a 0.1-μm undercut, which also would be the base dimension of the resist structure overhang, a dimension that could reduce the structural integrity of this resist structure at its base. In addition, this overhang also determines the amount of contact to sensor overlap at the junction region, inferring that the read sensor trackwidth is fixed by both the image resist as well as control of the undercut. Future GMR sensor processing must address both image size in the resist, as determined by the exposure tool and process, as well as image profile in the resist.

The above discussion addresses track density, but another important factor for future GMR structures is scaling of thickness of the GMR sensor to higher linear (bit) densities. The GMR sensor layer thickness must be decreased to allow it to be saturated by progressively smaller magnetic transitions originating from the disk. In addition, the shield separation above and below the GMR sensor is determined by two dielectric thicknesses—top and bottom. At today’s areal densities of 40 Gb/in.², shield

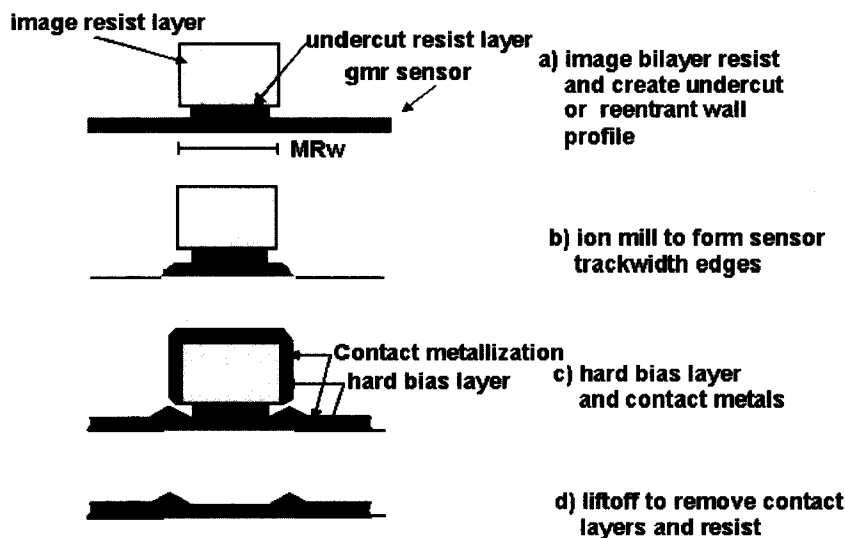


Fig. 18 GMR head MRw processing. (View this art in color at www.dekker.com.)



separations are approximately 70 nm; and the films that comprise a GMR sensor, the NiFe free layer, spacer layer, pinned layer, and antiferromagnetic exchange layer are about 2, 2, 2, and 15 nm, respectively. The latter would not be expected to scale to a smaller thickness because this value is determined by antiferromagnetic coupling to the pinned layer. Future areal density increases require that top and bottom insulating layers must be reduced to less than 25 nm, and that GMR free, spacer, and pinned films must all be less than 2 nm. It will be a challenge to demonstrate insulating layers with a high degree of electrical integrity. It does seem reasonable that this challenge will be met.

POTENTIAL DESIGN CHANGES IN GMR SENSORS

As future scaling requirements reduce the vertical dimensions of GMR sensors, a reduction in the width of this element can also be expected. It is proposed that there is a critical width dimension, as well as a critical NiFe thickness, where the GMR effect is reduced to a very low value, i.e., the $\Delta R/R$ of the sensor approaches a value where the resulting signal-to-noise ratio does not permit accurate reading of the data. One solution to this reduced GMR effect is to pass the sense electrical current normal to the sensor as opposed to a longitudinal direction, along the long axis of the element. This type of device, known as current perpendicular to the sensor's plane (CPP), is a significant excursion for today's current in-plane (CIP) GMR devices, and is being studied in many laboratories. A variation of this concept is to replace the metallic spacer with a very thin insulator, of the order of a few angstroms in thickness. In this structure, known as a tunnel valve or tunnel junction device, current carriers are able to tunnel through the thin insulator film when magnetizations on either side are parallel, and are prevented from tunneling in the antiparallel case. Preparing a very thin insulator that is pin hole-free is a significant process challenge. The CPP read device may become important as areal densities increase well beyond 100 Gb/in².

CONCLUSION

The GMR nanotechnology was shown to enable large areal density increases in magnetic hard disk drives, which have occurred rapidly in the past 5–10 years.^[18,19] Based on the importance of magnetic storage to the computer age, a significant research-and-development effort is

being maintained on a worldwide basis to enhance the read capability of GMR technology for higher areal densities, and this involves the exploration of new magnetic materials, scaling down sensor horizontal and vertical dimensions, and finally, considering alternative structures based on today's GMR sensors.

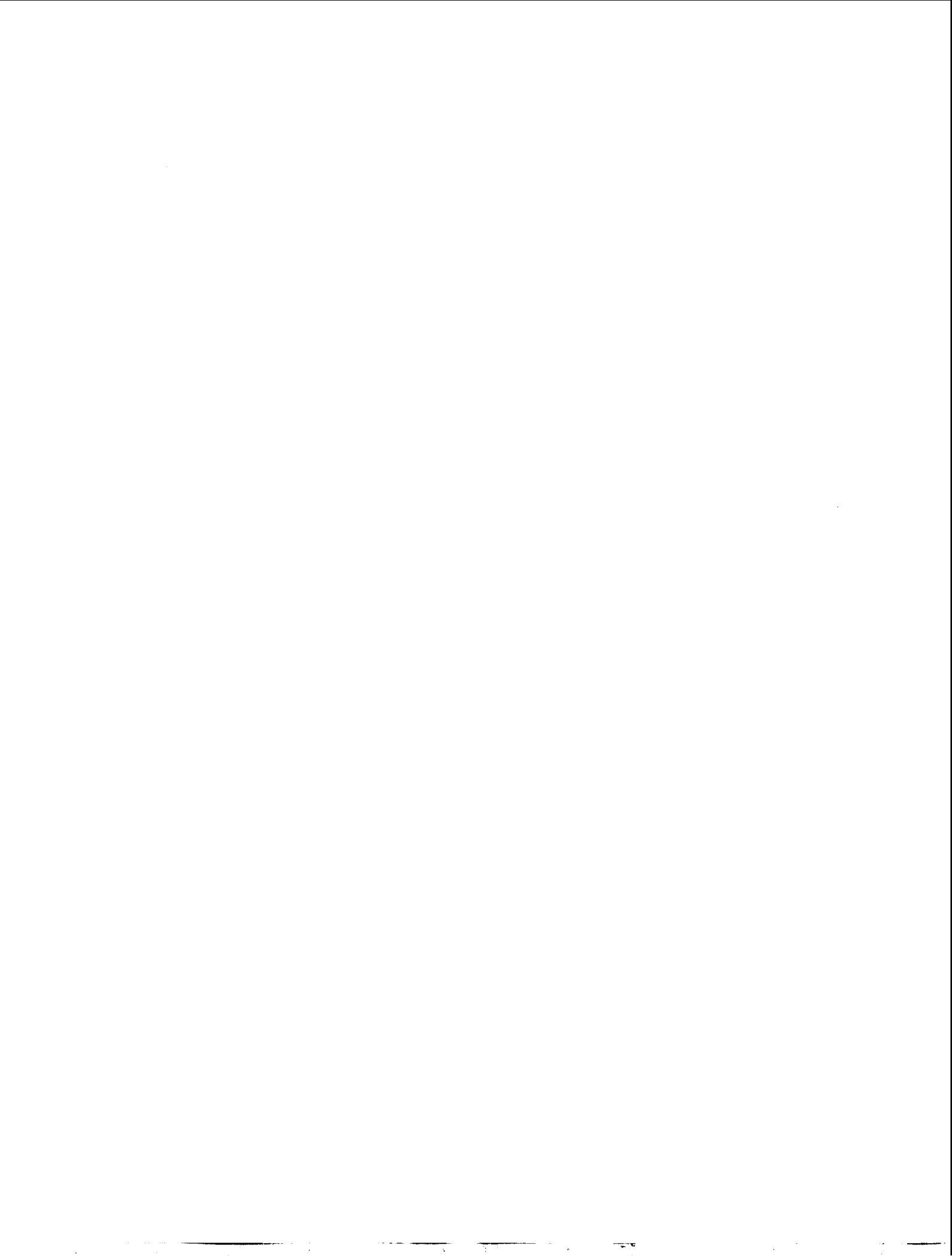
ACKNOWLEDGMENT

The authors would like to express their appreciation to Bruce Gurney, of the IBM Almaden Research Center, for his scientific contributions to this manuscript and for his review of the final document, and for the research efforts of Dr. Gurney and many other IBM Almaden colleagues for their contributions to GMR. Additionally, the graphics and document support of Michael Xu, also of Almaden, is acknowledged.

REFERENCES

1. <http://www.storage.ibm.com/hdd/technology/grochows/grocho01.htm> (accessed November 2002).
2. Gurney, B.; Grochowski, E. Spin valve sensors take up where MR heads leave off. *Data Storage* **1998**, *5* (10), 59.
3. Grochowski, E. Magnetoresistive head technology and areal density growth. *Insight* **1995**, *8* (4), 4.
4. Baibich, M.; Broto, J.; Fert, A.; Van Dau, F.; Petroff, F.; Eitenne, P.; Creuzet, G.; Friederich, A.; Chazelas, J. Giant magnetoresistance of (001) Fe/(001) Cr magnetic superlattices. *Phys. Rev. Lett.* **1988**, *61* (21), 2472.
5. Parkin, S.; More, N.; Roche, K. Oscillations in exchange coupling and magnetoresistance in metallic superlattice structures: Co/Ru, Co/Cr and Fe/Cr. *Phys. Rev. Lett.* **1990**, *64* (19), 2304.
6. Gurney, B.; Carey, M.; Tsang, C.; Williams, M.; Parkin, S.; Fontana, R., Jr.; Grochowski, E.; Pinarbasi, M.; Lin, T.; Mauri, D. Spin Valve Giant Magnetoresistive Sensor Materials for Hard Disk Drives. In *Datatech*, 4th Ed.; 2000; 87.
7. Gurney, B.; Speriosu, V.; Wilhoit, D.; Lefakis, H.; Fontana, R., Jr.; Heim, D.; Dovek, M. Can spin valves be reliably deposited for magnetic recording applications? *J. Appl. Phys.* **1998**, *81* (8), 3998.
8. Gurney, B.; Speriosu, V.; Lefakis, H.; Wilhoit, D.; Need, O. Direct measurement of spin-dependent conduction-electron mean free paths in ferromagnetic metals. *Phys. Rev. Lett.* **1993**, *71* (24), 4023.

9. Gurney, B.; Wilhoit, D.; Speriosu, V.; Sanders, I. Influence of Au and Ag at the interface of sputtered giant magnetoresistance Fe/Cr multi-layers. *IEEE Trans. Magn.* **1990**, *26* (5), 2747.
10. Speriosu, V.; Herman, D., Jr.; Sanders, I.; Yogi, T. Magnetic thin films in recording technology. *IBM J. Res. Develop.* **1990**, *34* (6), 884.
11. Lin, T.; Mauri, D. Field-anneal effects on magnetic and magnetoresistive properties of Fe-Mn, Ir-Mn and NiO spin valves. *IEEE Trans. Magn.* **1999**, *35* (5), 2607.
12. Margulies, D.; Fullerton, E.; Schabes, M.; Do, H.; Grochowski, E.; Carey, M.; Gurney, B.; Moser, A.; Best, M.; Rubin, K.; Rosen, H.; Doerner, M.; Mirzamaani, M.; Tang, K. Antiferromagnetically Coupled Magnetic-Medium Structure Extends Areal Density for Hard Disk Drives. In *Datatech*, 7th Ed.; 2001; 9.
13. Fullerton, E.; Margulies, D.; Schabes, M.; Carey, M.; Gurney, B.; Moser, A.; Best, M.; Zeltzer, G.; Rubin, K.; Rosen, H. Antiferromagnetically coupled magnetic media layers for thermally stable high density recording. *Appl. Phys. Lett.* **2000**, *77* (23), 3806.
14. Charap, S.; Lu, P.; He, Y. Thermal stability of recorded information at high densities. *IEEE Trans. Magn.* **1997**, *33* (1), 978.
15. Tsang, C.; Fontana, R., Jr.; Lin, T.; Heim, D.; Gurney, B.; Williams, M. Design, fabrication, and performance of spin valve read heads for magnetic recording applications. *IBM J. Res. Develop.* **1998**, *42* (1), 103.
16. Dieny, B.; Speriosu, V.; Parkin, S.; Gurney, B.; Wilhoit, D.; Mauri, D. Giant magnetoresistance in soft ferromagnetic multi-layers. *Phys. Rev., B* **1991**, *43* (1), 1297.
17. Fontana, R., Jr.; MacDonald, S.; Santini, H.; Tsang, C. Process considerations for critical features in areal density thin film magnetoresistive heads: A review. *IEEE Trans. Magn.* **1999**, *35* (2), 806.
18. Thompson, D.; Best, J. The future of magnetic data storage technology. *IBM J. Res. Develop.* **2000**, *44* (3), 311.
19. Grochowski, E.; Thompson, D. Outlook for maintaining areal density growth in magnetic recording. *IEEE Trans. Magn.* **1994**, *30* (6), 3797.
20. Ashar, K. *Magnetic Disk Drive Technology*; IEEE Press: New York, NY, 1997.



Nanofiltration Separations

Eric M. V. Hoek

Anna Jawor

University of California, Riverside, California, U.S.A.

INTRODUCTION

The term “nanofiltration” (NF) generally refers to a class of pressure-driven membrane separation processes whereby nanometer- or larger-sized substances may be selectively removed from a carrier fluid. The name “nanofiltration” is derived from two phrases. The prefix “nano” means 1 billionth. Hence, 1 nm has a value of 10^{-9} m or 10 Å. The suffix “filtration” refers to a process whereby solutes are physically separated from a solvent by passing the solution through a semipermeable barrier or medium.^[1] The review that follows intends to introduce the reader to the basic concepts of nanofiltration separations, the material properties of NF membranes, the common applications of NF separations, the theory and models describing NF separation performance, and some performance limitations.

NANOFILTRATION BASICS

Membrane processes are advanced filtration processes, which utilize separation properties of finely porous polymeric or inorganic films and are used in a wide range of industrial processes to separate biological macromolecules, colloids, ions, solvents, and gases. The development and application of membrane separation processes is one of the most significant recent advances in chemical, environmental, and biological process engineering. Membrane processes are commonly distinguished based on the main driving force, which is applied to accomplish the separation. An overview of the driving forces and related membrane separation processes is given in Table 1.^[2]

Nanofiltration falls into the category of pressure-driven membrane processes, and it fills an important gap between ultrafiltration (UF) and reverse osmosis (RO). Ultrafiltration processes are intended to remove all particles, colloids, and large macromolecules, while passing small macromolecules and dissolved substances. Reverse osmosis membranes are designed to separate all dissolved solutes from their carrier solvent down to monovalent ions, dissolved metals, and organics above a few hundred daltons (Da). Nanofiltration was originally conceived to

perform water softening (i.e., removal of divalent ions in water production), but more generally intends to remove, selectively, a particular solute (e.g., divalent ion) while allowing another solute (e.g., monovalent ion) to pass with the solvent through the membrane. Fig. 1 provides another perspective of various pressure-driven filtration processes and the substances they are intended to remove.

In nanofiltration processes, a selective separation takes place across a semipermeable separation layer, which is formed over the top of a porous support. The driving force of the separation process is the pressure difference between the feed (retentate) and the filtrate (permeate) side of the separation layer of the membrane. The size of NF membrane pores in combination with the surface electrical properties allows divalent ions and uncharged solutes larger than a few thousand daltons to be highly retained, while monovalent ions and low-molecular weight organics are reasonably well transmitted. The nominal *molecular weight cutoff* for many commercially available nanofiltration membranes ranges from a few hundred to a few thousand daltons.^[3] These characteristics make NF membranes extremely useful in the fractionation and selective removal of many dissolved solutes from complex process streams. Other advantages include high flux and low energy consumption (because of low operating pressure requirement), as well as reduced environmental impact compared with conventional processes such as evaporation and extraction.^[4]

MATERIALS

Nanofiltration membranes are characterized by pore diameters of about 5 Å to 5 nm and operating pressure between 5 and 40 bars. Because they significantly reject many ions, NF membranes are often wrongly categorized as “loose RO” membranes. The most notable difference between RO and NF is the ability of NF to highly reject multivalent ions, while significantly passing monovalent ions. Another distinctive feature of NF membranes is their ability to reject uncharged, dissolved materials and positively charged ions according to the size and shape of the molecule in question. These selective separation

Table 1 Driving forces and their related membrane separation processes

Driving force	Membrane process
Pressure difference	Microfiltration, ultrafiltration, nanofiltration, reverse osmosis
Chemical potential difference	Pervaporation, dialysis, gas separation, liquid membranes
Electrical potential difference	Electrodialysis, membrane electrolysis
Temperature difference	Membrane distillation

capabilities are directly related to the membrane material properties.

It is widely known that retained organic and colloidal matter may adhere strongly to polymeric surfaces through non-covalent interactions—such as those arising from van der Waals, electrostatic, and acid–base properties of the polymer materials—and cause severe performance decline.^[5–12] Nanofiltration membranes often become “fouled” by dissolved organic and colloidal

matter, which is ubiquitous in many natural and industrial waters. Hence one of the challenges from a materials perspective is to create a membrane with optimal pore size, surface charge, and hydrophilic nature to effect a highly selective separation with low energy consumption, while minimizing the adhesion for fouling materials.

The array of membrane materials to select from includes polysulfone, polyethersulfone, sulfonated polyethersulfone, cellulose acetate and its derivatives, polyethylene, polypropylene, polyvinyl alcohol derivative, polyamide, polyacrylonitrile, polyvinylidene fluoride, organo-mineral complexes, ceramic, alumina, and other metal oxides.^[13–18] The polysulfone materials dominate UF/MF applications for water and wastewater treatment, while contemporary RO/NF membrane usage is almost entirely limited to polyamide-based thin-film composites. Although cellulose acetate (CA) technology predates other membrane types and remains relatively inexpensive to purchase and install, the use of cellulose acetate membranes has largely been displaced by polyamide thin-film composite membranes today. Across the range of possible materials, there are two basic material types: integrally skinned asymmetric layers and thin-film composites.

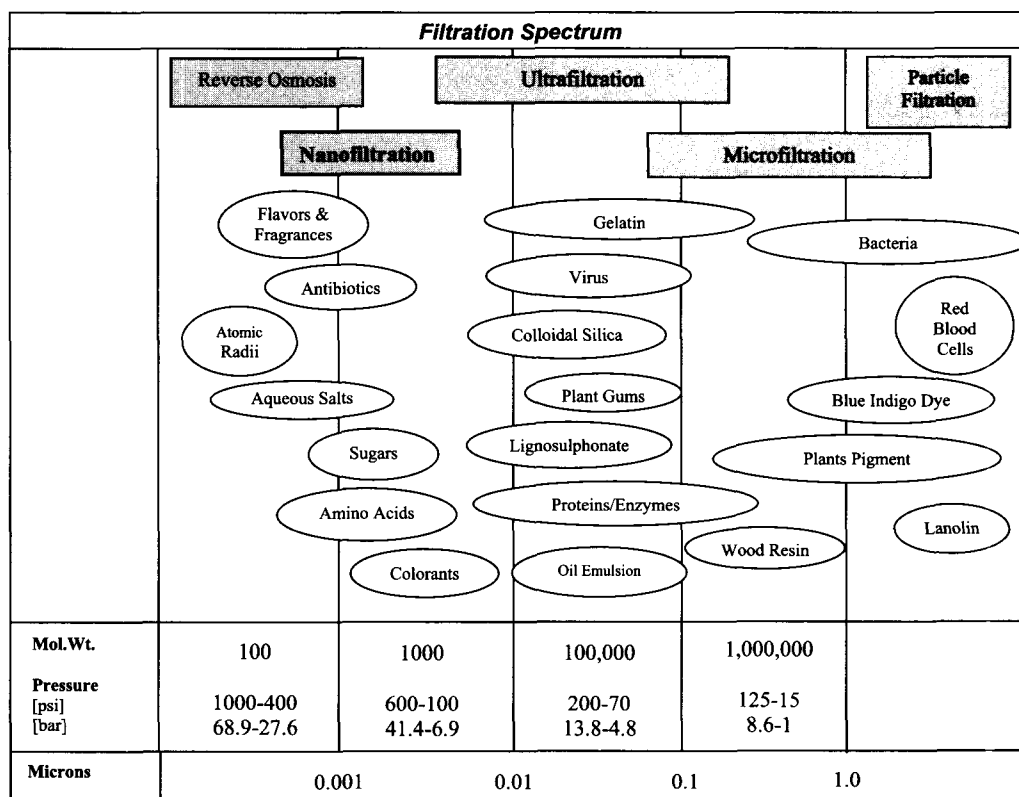


Fig. 1 Diagram known as the “filtration spectrum,” indicating schematically the place of nanofiltration among other common pressure-driven filtration processes. (View this art in color at www.dekker.com.)

Integrally Skinned Asymmetric Membranes

Polymeric asymmetric membranes may be prepared through a phase inversion technique. Phase inversion is a process whereby a polymer is transformed in a controlled manner from a liquid to a solid state.^[16] The cross section of an integrally skinned, asymmetric phase-inversion membrane is schematically illustrated in Fig. 2a. The most popular phase-inversion membranes may be constructed from cellulose acetate (CA), cellulose diacetate (CD), regenerated cellulose (RC), polysulfone (PS), polyethersulfone (PES), sulfonated PS or PES, polyacrylonitrile (PAN), or polyvinylidene fluoride (PVDF). Scanning electron microscope (SEM) images of PAN and PS membrane cross sections are presented in Fig. 2b and c, respectively.

Polysulfone membranes formed by phase inversion are used as microfiltration or ultrafiltration membranes, or as the support layer upon which a thin-film composite RO or NF membrane is formed. However, because we have defined nanofiltration as a process by which nanometer-sized or larger-sized substances are removed from a liquid feed, any material used to perform such a separation may be considered a "nanofiltration membrane." A characteristic of the PS membranes is that an increasing degree of sulfonation correlates with increasing water permeabil-

ity and salt rejection.^[19,20] Dense-skinned phase inversion membranes composed of cellulosic materials typically function as reverse osmosis membranes.

Organic Thin-Film Composite Membranes

In 1978, efforts to improve the performance of "poly" membranes by Cadotte et al.^[21] yielded composite membranes having excellent combinations of high salt rejection and water permeability. Cadotte et al.'s ideas were developed at FilmTec Corporation into a reverse osmosis/nanofiltration membrane product designated as "FT30." The FT30 membrane is a thin-film composite membrane consisting of three layers: a polyester support web, a microporous (polysulfone) interlayer, and an ultrathin polyamide barrier (skin layer) on top. Fig. 3a provides a schematic illustration of a generic thin-film composite (TFC) membrane construction resembling that of FT30.

There are several clones of the FT30 membrane that are now commercially available; some are made under license from FilmTec and others are made by other proprietary synthetic routes. The skin layer of NF membranes may be as thin as 50 nm in cross section up to several hundred nanometers. The composite structure of two commercial NF membranes can be seen in the field emission SEM

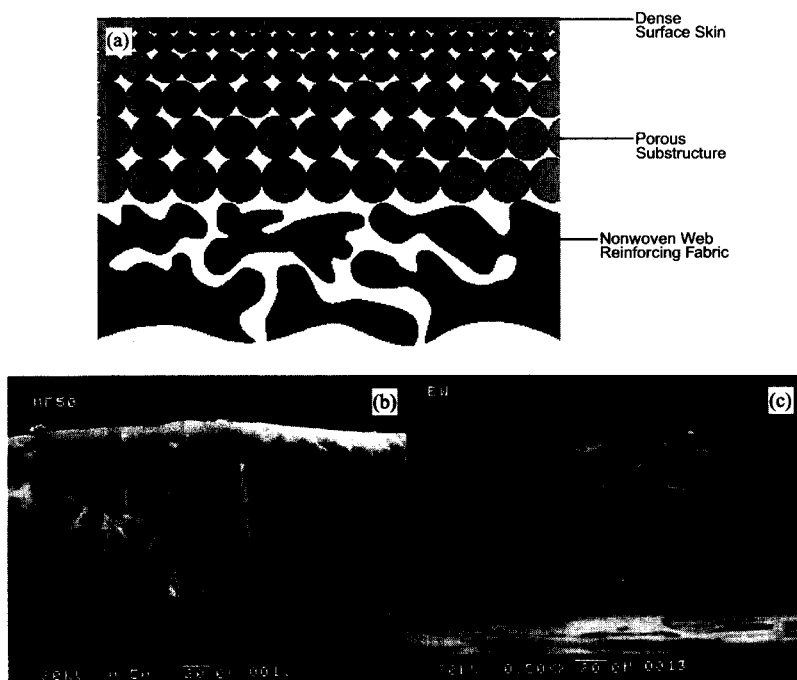


Fig. 2 Cross-section illustration of (a) an integrally skinned asymmetric membrane, plus SEM cross sections of dense-skinned (b) polyacrylonitrile and (c) polysulfone membranes manufactured by GE-Osmonics Inc. Note: illustration in (a) was adapted from Ref. [60].

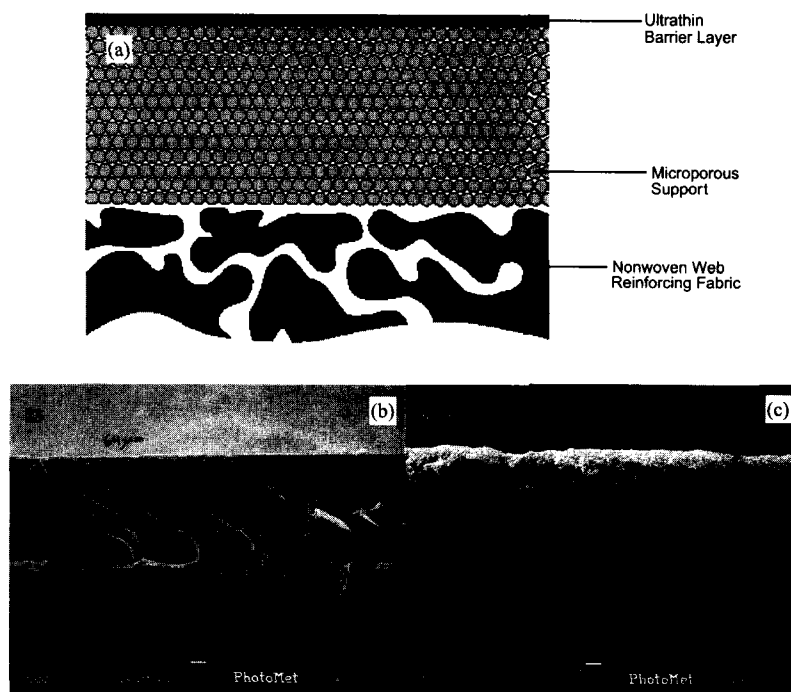


Fig. 3 Cross-section illustration of (a) thin-film composite membrane, plus SEM cross sections of two commercially available polyamide membranes manufactured by (b) GE-Osmonics Inc. and (c) Dow-FilmTec. Note: illustration in (a) was adapted from Ref. [60].

images of Fig. 3b and c. The surface properties of TFC membranes have been studied extensively, largely in efforts to understand the role of surface properties on separation performance and fouling. In particular, studies focusing on surface charge/potential, hydrophobicity, and roughness dominate the literature (see ‘‘Membrane Properties and Performance’’).

Inorganic Thin-Film Composite Membranes

Ceramic composite membranes have been used in a number of industrial separations. They are synthesized from dispersions of silica, titania, or other metal oxide nanoparticles that are forced to agglomerate on the surface of a similar metal oxide microparticle layer. After initial formation, the material is usually sintered at high temperature to form a continuous layer. The base material of construction makes ceramic membranes particularly well suited for treating high-temperature or acidic/caustic wastewaters, as well as for high-fouling industrial streams. The extreme heat tolerance and chemical resistance of ceramics allows repeated cycles of use, cleaning with harsh physical or chemical treatments, and reuse that are unachievable with polymeric membrane materials. However, to date, ceramic membranes are much too expensive to be used in applications requiring

large membrane surface area (such as water production or municipal wastewater treatment), so their use has been limited to specialty industrial separations.^[22,23]

In principle, the cross-sectional structure of ceramic nanofiltration membranes has much the same look as organic TFC membranes. Fig. 4 is an SEM photo of an

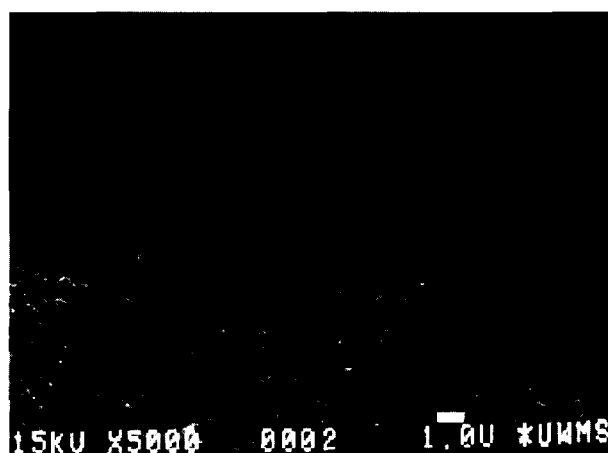


Fig. 4 Scanning electron microscope image of ceramic composite membrane showing three distinct layers of TiO₂ nanoparticle construction: dense skin layer over top of nanoporous support and microporous structural support layers.

experimental thin-film composite ceramic membrane (courtesy of Marc Anderson of the University of Wisconsin). There are three distinct layers. A thin film comprised of small titanium dioxide (TiO_2) nanoparticles, a middle support layer made from larger TiO_2 nanoparticles, and

a structural base formed from much larger TiO_2 particles. One of the current goals in ceramic membrane material research and development is to create a membrane with UF-like permeability, but NF-like selectivity. This may be achieved by taking advantage of nanoparticles

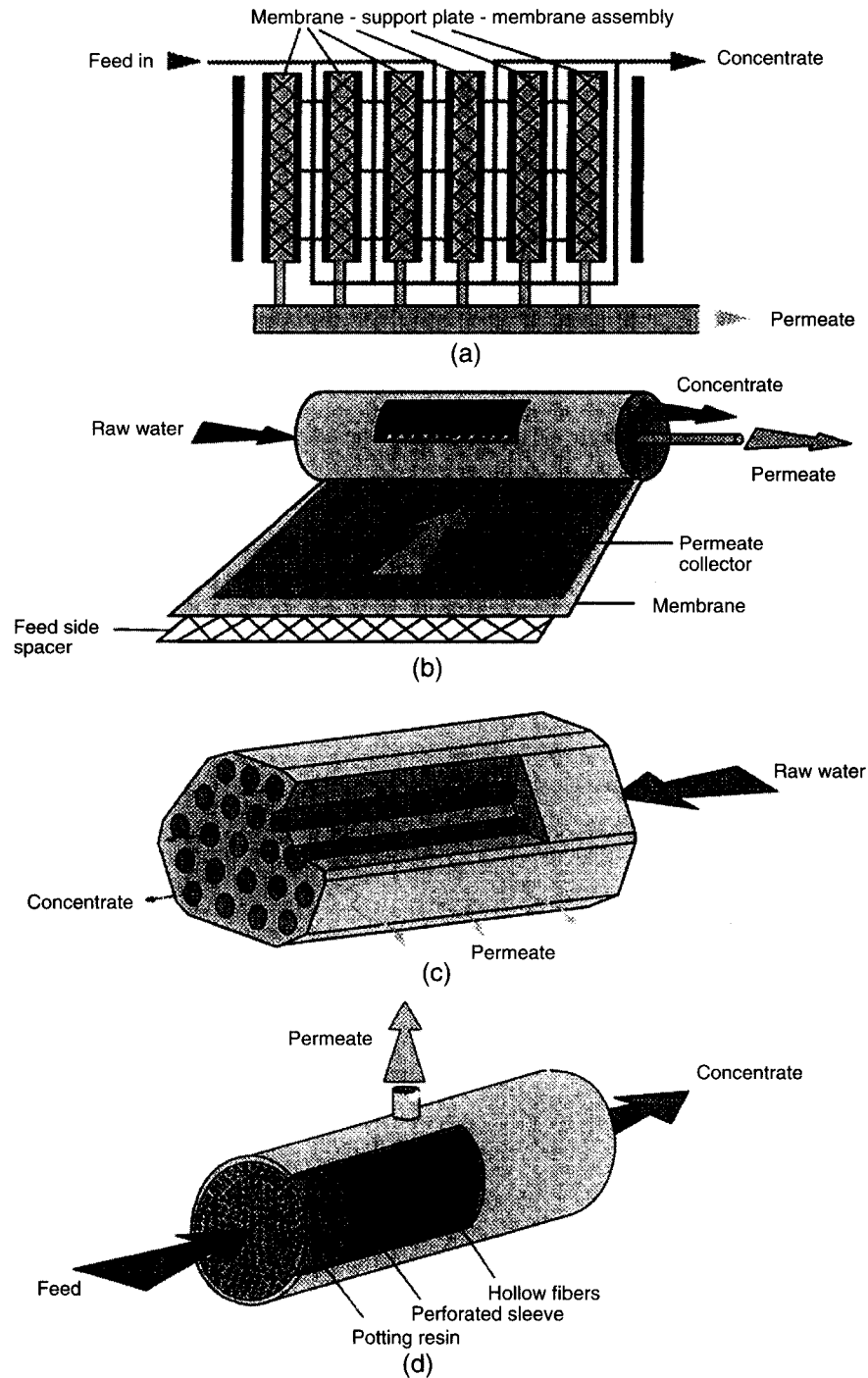


Fig. 5 Schematic representation of the four principle membrane modules: (a) plate-and-frame; (b) spiral-wound; (c) tubular; (d) hollow-fiber. (From Ref. [61].)

with high surface charge density sintered to maintain more open pore structures than the pores in polymeric NF membranes.

Nanofiltration Element Design

Membrane modules are available in spiral-wound, plate-and-frame, hollow-fiber, and tubular configurations as depicted in Fig. 5. Almost all NF membranes used today employ the spiral-wound configuration. In a spiral-wound element (SWE), the membrane leaves are sealed and wrapped around a permeate collection tube. An open mesh spacer separates the active layers of membrane material on the feed side, while a similar spacer lies between the backsides of the membranes and serves as a channel for the treated water to travel to the permeate collection tube. A significant amount of research was performed in the past to optimize the design of feed spacers used in SWEs, and the currently available elements perform quite well. Generally, a thicker feed spacer is used for high fouling waters to prevent clogging of the channel cross section, which can result in a significant tangential pressure drop.

APPLICATIONS

Currently, the reduction of hardness (i.e., Ca^{2+} and Mg^{2+}) and dissolved organics from water are among the most important applications for nanofiltration membranes. However, the selective properties of NF membranes make them suitable for a wide array of unconventional applications. An important example is recovery of heavy metals (e.g., Ni, Fe, Cu, Zn, etc.) and reclamation of wastewaters from metalworking plants and textile mills. More recently, NF membranes have been adopted for use in the biotechnology and pharmaceutical industries for purification of small bioactive organic molecules such as antibiotics or separation of small organic components from biological liquids (e.g., lactic acid separation from fermentation broths, amino acid removal from protein hydrolysates, or removal of organics from municipal wastewater).^[2] Timmer^[2] provided a concise summary of the various applications for nanofiltration membranes that have been reported to date. This summary has been reproduced in Table 2.

PERFORMANCE

The performance of nanofiltration membranes is defined by solvent and solute permeability, as well as fouling resistance. The summary that follows considers the roles

Table 2 Overview of nanofiltration applications in various industries (From Ref. [2])

Industry	Application
Water production	Recovery of LiOH during treatment of battery waste Removal of degreasing agents from water Removal of precursors of disinfection byproducts Hardness removal Removal of natural organic matter (a.o. color) Removal of pesticides Removal of heavy metals (As, Pb), Fe, Cu, Zn, and silica Treatment of brackish water
Food	Demineralization of whey Demineralization of sugar solutions Recycle of nutrients in fermentation processes Separation of sunflower oil from solvent Recovery of cleaning-in-place solutions Recovery of regeneration liquid from decoloring resins in sugar industry Effluent treatment
Textile and paper	Purification of organic acids Removal of dyes from wastewater Removal of amino acids Recovery of water and salts from wastewater Recovery and reuse of chromium(III) and chromium(II) Recovery of water from wastewater or wastewater treatment effluent Recovery of bleaching solution
Chemical	Sulfate removal preceding chlorine and NaOH production CO ₂ removal from process gasses Preparation of bromide Recovery of caustic solutions in cellulose and viscose production CaSO ₄ precipitation Separation of heavy metals from acid solutions Removal of metal sulfates from wastewater Cleaning of machine rinsing solutions Removal of nickel Recovery of Cu-ions from ore extraction liquids Al ³⁺ removal from canning industry wastewater
Agriculture	Removal of phosphate, sulfate, nitrate, and fluoride Removal of algal toxins Purification of landfill leachate Removal of selenium from drainage water

of membrane material properties, operating conditions, and fouling, but begins by defining NF performance and the fundamental mechanisms governing NF membrane separations. Finally, mechanisms of NF membrane fouling are discussed and the role of membrane material properties on separation performance and fouling is reviewed.

Defining NF Separation Performance

When an external pressure is imposed on a liquid adjacent to a nanofiltration membrane, the liquid will flow through the membrane in proportion to the applied pressure. Liquid flow through a NF membrane is described as a solvent flux (J_v), which is given by a Darcy-type relation such as

$$J_v = \frac{\Delta p_{\text{eff}}}{\mu R_{\text{tot}}} \quad (1)$$

in which Δp_{eff} is the effective trans-membrane pressure, μ is the permeate viscosity, and R_{tot} is the total hydraulic resistance toward solvent flow.

Dissolved solutes also flow toward the membrane by the convective flow of their carrier solvent. If the membrane inhibits transport of the solute, it will be retained at the feed side of the membrane. The distribution of a noncharged solute at the membrane / solution interface is determined by steric exclusion. Because of its size, a solute only has access to a fraction of the total surface area of a pore, and a separation between multiple solutes can only be accomplished if the solutes are different in size.^[2,14,24]

For charged solutes, two additional distribution mechanisms contribute to the separation. First, Donnan exclusion has a pronounced effect on the separation of charged solutes by NF membranes. Because of the slightly charged nature of the membrane, solutes with an opposite charge compared with the membrane (counterions) are attracted, while solutes with a similar charge (co-ions) are repelled. At the membrane surface, a distribution of co-ions and counterions will occur, thereby causing an additional separation. Second, because of the charge of the membrane and the dipole momentum of water, water molecules may exhibit polarization in the pore.^[25] This polarization results in a decrease of the dielectric constant inside the pore, thereby making it less favorable for a charged solute to enter. However, even in a situation that the dielectric constant inside the pore is equal to that of water, a change in electrostatic free energy of the ion occurs when the ion is transferred from the bulk into the pore,^[26] which can also cause ion exclusion.

After the solute distributes at the membrane / solution interface, it is transported through the membrane by convection and diffusion. At the permeate side, a second

distribution process occurs, which determines the permeate concentration. The actual, or intrinsic, rejection by a nanofiltration membrane is given by

$$R_s = 1 - \frac{C_p}{C_m} \quad (2a)$$

where C_p is the permeate solute concentration and C_m is the membrane surface solute concentration. However, there is no accurate method of determining the actual membrane surface solute concentration. Because the feed and permeate solute concentrations can be measured, the solute retention is typically described by

$$R_o = 1 - \frac{C_p}{C_b} \quad (2b)$$

where R_o represents the observed solute retention and C_b represents the bulk salt concentration. Retained solutes accumulate at the membrane surface in a concentrated layer and thus diffuse back into the bulk in proportion to the concentration gradient, and hence a concentration profile develops. This phenomenon is called concentration polarization.

The performance of NF membranes has been studied extensively in terms of membrane properties, operating conditions, module geometry, and treatment train configuration. Of considerable importance are the influences of membrane filter geometry and crossflow hydrodynamics on concentration polarization (CP). Concentration polarization influences nanofiltration performance via two mechanisms. First, CP enhances the passage of retained solutes by increasing the chemical potential gradient driving diffusive transport through the membrane, and second, elevated salt concentrations at the membrane surface reduce electrostatic forces that originate from the membrane surface charge and which tend to reduce foulant deposition. Accumulation of a fouling deposit layer on the membrane surface creates an additional hydraulic resistance to permeation (over that of the membrane alone) and enhances concentration polarization.^[27,28]

Solute Transport Model

Determining the significance of various solute transport mechanisms—diffusion, convection, and electromigration—on NF membrane performance is most rigorously accomplished by coupling a model of solute transport through the membrane based on the extended Nernst-Planck (NP) equation with a CP model based on the convective-diffusion equation.^[29] However, knowledge of the actual charge density of the membrane pores is required to make appropriate use of the NP model, and this is rather difficult to determine for real membranes. In addition, a cumbersome numerical scheme is required to

solve the set of equations that result from coupling the local NP model with a local CP model based on the solution of the convection–diffusion equation. Coupling the solution–diffusion model and a simple mass transfer model (film theory) provides a reasonable and analytical solute transport and CP model.^[30–32] While the application of a stagnant film model to membrane separations may be debated, the model provides quite reasonable prediction of NF separation performance.

The starting point for the mathematical description of NF membrane performance is the solution–diffusion model. The model assumes that solute permeation is driven by the gradient in chemical potential of the solute across the membrane.^[30] Thus the flux (J) of an individual component (i) is represented mathematically by

$$J_i = -L_i \frac{d\mu_i}{dx} \quad (3)$$

where $d\mu_i/dx$ is the gradient in chemical potential of component i and L_i is a coefficient of proportionality linking this chemical potential driving force with flux. The chemical potential is written as

$$d\mu_i = RTd \ln(\gamma_i c_i) + v_i dp \quad (4)$$

where c_i is the molar concentration of component i , γ_i is the activity coefficient linking concentration with activity, p is the pressure, and v_i is the molar volume of component i . Following the applicable assumptions for reverse osmosis, the combination of Eqs. 3 and 4 leads to a Fick's law type of relation that is ultimately reduced to

$$J_i = B\Delta C_w = BC_w R_i \quad (5)$$

where B is the solute permeability of the membrane.^[30] When the transport equation is expressed in terms of solvent flux (J_v), the equation is generally written as

$$J_v = A(\Delta P - \Delta\pi_m) \quad (6)$$

where ΔP is the applied pressure and $\Delta\pi_m$ is the osmotic pressure at the membrane surface because of concentration of rejected ionic species at the surface of the membrane. The parameter A is the pure solvent permeability of the membrane, which is the inverse of the intrinsic membrane resistance, R_m .

Solute Concentration Polarization Model

The buildup in concentration of rejected solutes at the membrane–liquid interface results in the formation of a concentrated mass boundary (“film”) layer, called the *salt concentration polarization layer*. At steady state, the solute flux through the film is constant and is related to the solvent flux through the membrane (J_v) via the fol-

lowing one-dimensional, steady-state mass balance within the film layer:

$$-J_v C - D \frac{dC}{dy} = J_v C_p \quad (7)$$

where C is the local solute concentration, D is the solute diffusivity, C_p is the solute permeate concentration, and y is the distance normal to the membrane surface.^[31] Integrating over the solute concentration polarization layer thickness (δ_s) with the appropriate boundary conditions ($y=0$, $C=C_m$; $y=\delta_s$, $C=C_b$) results in the classic film theory equation,

$$J_v = \frac{D}{\delta_s} \ln \left(\frac{C_m - C_p}{C_b - C_p} \right) = k \ln \left(\frac{C_m - C_p}{C_b - C_p} \right) \quad (8)$$

where C_m is the membrane surface solute concentration, C_b is the bulk solute concentration, C_p is the permeate solute concentration, and the ratio of solute diffusivity (D) to the solute concentration polarization layer thickness (δ_s) is set equal to the solute mass transfer coefficient (k). This expression can be rearranged to provide a direct calculation of the concentration polarization factor (C_m/C_b) as

$$\frac{C_m}{C_b} = (1 - R_0) + R_0 \exp \left(\frac{J_v}{k} \right) \quad (9)$$

For laminar flow in a thin rectangular channel, the mass transfer coefficient is often related to a Sherwood number (Sh) through a relationship such as

$$k = Sh \frac{D}{d_h} = 1.85 \left(Re Sc \frac{d_h}{L} \right)^{1/3} \frac{D}{d_h} \quad (10)$$

where Re is the Reynolds number, Sc is the Schmidt number, d_h is the channel hydrodynamic diameter, and L is the channel length.^[30–32] By expanding the individual components,

$$Re = \frac{\rho u d_h}{\mu}; Sc = \frac{\mu}{\rho D}; d_h \cong 2H \quad (11)$$

Eq. 10 can be rearranged to reveal the mass transfer coefficient's dependence on flow rate, channel geometry, and solute type via

$$k = 0.808 \left(\frac{\gamma_0 D^2}{L} \right)^{1/3} \quad (12a)$$

Here γ_0 indicates the wall shear rate, which is defined by $\gamma_0 = 6Q/WH^2$, where Q is the volumetric feed flow rate, W is the crossflow channel width, and H is the channel height.^[32] From Eq. 12a, it becomes clear that the mass transfer coefficient represents the velocity with which a solute migrates away from the membrane surface (back into the bulk) as a function of solute diffusivity, tangential

convection, and filter geometry. This explains the enhanced performance obtained from optimizing channel geometry and crossflow hydrodynamics.

An alternative solute mass transfer coefficient has been derived for laminar flow through thin-rectangular channel with a turbulence promoting feed spacer, such as is used in a nanofiltration spiral-wound element, the mass transfer coefficient may be written as

$$k = 0.31 \left(\frac{\gamma_0 D_3^4}{\nu^{\frac{1}{3}}} \right)^{\frac{1}{2}}, \quad (12b)$$

where ν is the kinematic solution viscosity. Rearranging the film theory equation provides an estimation of the *trans*-membrane osmotic pressure. The resulting expression is

$$\Delta\pi_m = C_b R T R_o \exp\left(\frac{J_v}{k}\right) \quad (13)$$

Thus osmotic pressure is directly proportional to bulk solute concentration, solute rejection, solvent flux, and solute mass transfer. More importantly, $\Delta\pi_m$, R_o , C_b , and J can be measured experimentally, so the effective mass transfer coefficient can easily be determined and compared with prediction by Eq. 13.

Fouling and Nanofiltration Performance

Most municipal, industrial, and natural waters contain complex mixtures of dissolved, macromolecular colloidal, and particulate matter. Conventional processes used to pretreat NF feed waters fail to remove submicron colloids, macromolecules and dissolved matter. This matter accumulates at the membrane surface and results in severe performance decline—a phenomenon known as *fouling*. Fouling of NF membranes may result in loss of both *solvent flux and solute retention*. A review of fouling studies reveals that the foulants of greatest concern for nanofiltration (NF) separations are colloidal matter consisting of organics, silica, clays, metal oxides (specifically iron and manganese), and microorganisms.^[33–42] Fouling may be further categorized into *reversible* and *irreversible* fouling. Flux and solute retention may decline because of solution chemistry effects, concentration polarization, or colloid cake layer formation. The original membrane performance may be recovered by simply flushing the membrane with clean water, and hence these types of fouling are considered reversible. Irreversible fouling is defined as a decline in performance that can only be recovered through harsh chemical cleaning, but often only partially recovered. Frequent chemical cleaning of membranes degrades polymeric thin films, and hence reduces the life span of membranes in many applications. Further-

more, it decreases process efficiency because of the reduced flux and enhanced solute passage, requiring higher applied pressures and larger membrane area. This makes fouling a very important parameter in process design.

Fouling Mechanisms and Models

Interactions between accumulated dissolved and colloidal matter at a NF membrane surface result in several potential fouling mechanisms. Fouling by dissolved organics and sparingly soluble salts is difficult to describe quantitatively, but colloidal fouling is better understood. Because colloids fall within the approximate size range of 10 nm to 10 μ m and NF membrane “pores” are no more than a few nanometers in diameter, pore-blocking mechanisms are considered negligible. Thus the major fouling mechanisms discussed below include the hydraulic pressure drop across the foulant deposit (cake) layer and enhanced osmotic pressure effects, which were recently shown to be the predominant fouling mechanism for RO and NF membranes.^[28] Most practical nanofiltration processes operate with a constant flux, so this convention will be used to describe fouling mechanisms. The objective is to be able to describe the transient applied pressure required to maintain a constant flux in light of the various transient mechanisms of fouling.

The total system pressure is a combination of the trans-membrane hydraulic (Δp_m), the trans-membrane osmotic ($\Delta\pi_m$), and the trans-cake hydraulic (Δp_c) pressure drops and may be expressed mathematically as

$$\Delta P_{\text{total}} = \Delta p_m + \Delta\pi_m + \Delta p_c \quad (14)$$

The *trans*-membrane hydraulic pressure drop is determined by rearranging Eq. 1 to obtain

$$\Delta p_m = J_v \mu R_m \quad (15)$$

Hence by analogy, the trans-cake hydraulic pressure drop may be described from

$$\Delta p_c = J_v \mu R_c, \quad (16)$$

where R_c is the hydraulic resistance offered by the cake layer to the pure solvent.

The cake resistance may be described through the Carman–Kozeny equation, as a function of specific cake resistance (per unit thickness) and cake layer thickness,

$$R_c = r_c \delta_c = \frac{180(1 - \epsilon)^2}{d_f^2 \epsilon^3} \delta_c \quad (17a)$$

or specific cake resistance (per unit mass) and cake layer mass per unit membrane area,

$$R_c = \alpha_c M_c = \frac{180(1 - \epsilon)}{\rho_f d_f^2 \epsilon^3} M_c \quad (17b)$$

Here ε is the cake layer porosity, d_f represents the nominal foulant diameter, and ρ_f is the nominal foulant particle density. In most existing models, it is assumed that the specific cake resistance is constant in time and across the cake layer thickness and only the foulant layer thickness (or mass) changes with time.

It was recently experimentally demonstrated that diffusion of rejected salt ions was hindered within colloid deposit layers formed over nanofiltration membranes.^[28,43] In addition, it was suggested that tangential flow may be hindered within a foulant deposit layer, further reducing solute mass transfer within the deposit layer. The result was elucidation of a single mechanism—"cake-enhanced concentration polarization"—capable of describing the majority of observed flux decline, as well as the observed decline in salt rejection because of colloidal fouling of NF (and RO) membranes.

The overall mass transfer coefficient was considered the sum of two mass transfer coefficients, one describing salt back-diffusion from the membrane surface through the cake layer, and one through the remainder of the salt CP layer. Incorporating the hindered mass transfer coefficient into Eq. 13 yields

$$\Delta\pi_m^* = f_{os} C_b R_o \exp \left[\frac{J_v}{k} + J_v \delta_c \left(\frac{1 - \ln(\varepsilon^2)}{D_{\infty} \varepsilon} - \frac{1}{D_{\infty}} \right) \right] \quad (18)$$

where $\Delta\pi_m^*$ is termed the "cake-enhanced osmotic pressure."

The term in parentheses in Eq. 18 is derived by considering a thin cake layer, in which the tangential flow field is stagnant within the cake, and it represents diffusion through the cake and into the bulk.^[44] This concept is illustrated in Fig. 6. The reduced salt diffusivity

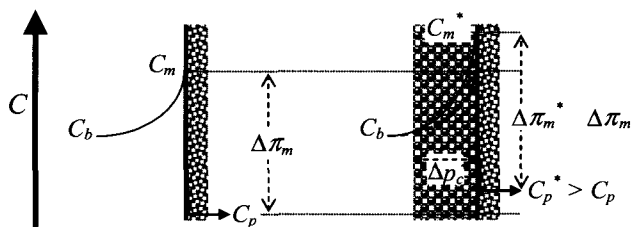


Fig. 6 Conceptual illustration of enhanced concentration polarization because of foulant accumulation in crossflow nanofiltration. The bulk tangential flow velocity, U_0 , and the salt ion diffusion coefficient are critical parameters in determining mass transfer in the salt concentration polarization layer. Tangential flow and salt ion back-diffusion may be locally hindered in the presence of a foulant deposit layer, thus enhancing the membrane surface salt concentration and trans-membrane osmotic pressure. (View this art in color at www.dekker.com.)

in the cake layer is expressed as $\varepsilon D_{\infty} / \tau$, with the tortuosity, τ , being approximated as $1 - \ln(\varepsilon^2)$.^[45-47] Note that in the absence of a foulant deposit layer, Eq. 18 reduces to Eq. 13 as the term in brackets reduces to J_v/k .

Combining the trans-membrane hydraulic, trans-cake hydraulic, and (cake-enhanced) trans-membrane osmotic pressure drops allows direct estimation of the total applied pressure needed to maintain a constant flux as a function of increasing deposit thickness. Of course, a priori knowledge of potential foulants is not always possible, which makes prediction of fouling phenomena difficult without some experimentation or pilot testing. Furthermore, physical or chemical polydispersity of foulants in many NF applications makes rigorous prediction of fouling behavior practically impossible. Perhaps the most important implication of enhanced concentration polarization is that an elevated solute concentration at the membrane surface may enhance solute transport through the membrane. Therefore, fouling can have severe consequences for NF separations subject to permeate water quality regulation if the separation is not designed with consideration of fouling.

Membrane Properties and Performance

Nanofiltration membranes may be constructed of any number of polymeric organic or inorganic materials, but they most commonly appear as polyamide thin-film composites. Commercially available polyamide NF membranes have charged, reasonably hydrophilic surfaces, which naturally repel co-ions, and to maintain electro-neutrality at the membrane / solution interface, counterions are also prevented from passing through the membrane. The degree of ion exclusion increases with increasing co-ion valence because of increased electrostatic repulsion by the membrane. However, the degree of ion exclusion also decreases with increasing counterion valence because high valence counterions tend to screen out membrane surface charge. Moreover, high electrolyte concentrations cause the membrane charge to be more effectively shielded by the counterions, thus reducing the selectivity of the membrane.^[48] The rejection of sodium chloride with NF varies from 0% to 50% according to the feed concentration and electrolyte composition.

Hirose et al.^[49] suggested an approximately linear relationship between membrane surface roughness and permeate flux for cross-linked aromatic polyamide TFC membranes, where permeability increased with increasing surface roughness. The linear relationship was attributed to surface unevenness of the TFC membrane skin layer, which resulted in enlargement of the effective membrane area. This is the explanation offered by most membrane manufacturers. However, Kwak et al.^[15] showed that substitution of bisphenol biphenyl rings with either methyl

or halogen strongly influenced rejection and permeability of aromatic polyester TFC membranes. Higher flux and lower rejection were associated with the smoother membrane surfaces obtained from methyl substitution, while lower flux and higher rejection were associated with the rougher membrane surfaces resulting from halogen substitution.

Additional work by Kwak and Ihm,^[50] coupling nuclear magnetic resonance (NMR) spectroscopy and atomic force microscopy (AFM), showed an important relationship between proton spin-lattice relaxation times and permeability, regardless of surface morphological features. This indicates that membrane morphology (especially the increased surface area because of roughness) is not solely responsible for the low-pressure, high-flux performance of polyamide membranes. In fact, it suggests that the structure and thickness of the thin-film polymer network determine membrane permeability.

Membrane Properties and Fouling

Physical and chemical properties of NF membranes (i.e., permeability, salt retention, "pore" size, etc.) control the rate and extent of colloidal fouling.^[18,28,43,44] The high hydraulic resistance of NF membranes enables substantial foulant deposit layers to form before fouling is detected, and rejection of ionic solutes exacerbates fouling by screening electrostatic interactions.^[43] Other recent studies suggest that membrane surface properties also influence fouling resistance of NF membranes.^[6,10,12,13,15,16,49-51] Several investigations of NF membrane fouling have explored the roles of membrane pore size, surface roughness, electrokinetic surface properties, membrane hydrophobicity/hydrophilicity, and specific chemical functionality.^[51-53] Various analytical techniques have been employed for evaluating specific physical and chemical surface properties of membranes,

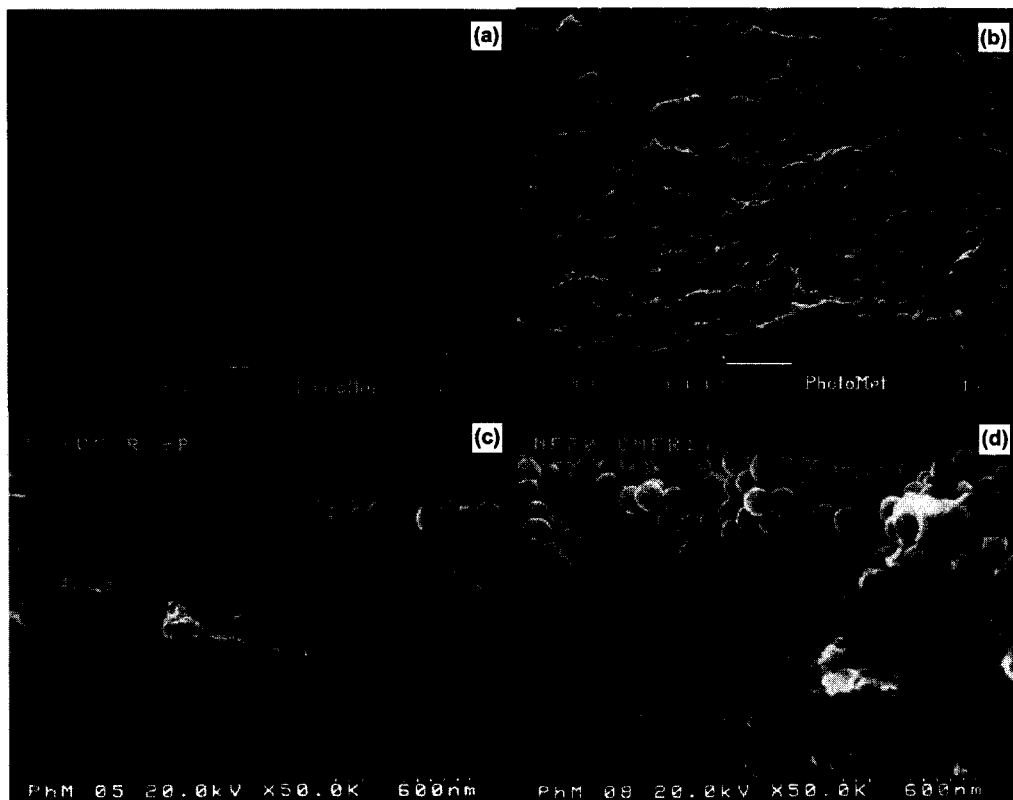


Fig. 7 Field-emission scanning electron microscope (FESEM) images of two commercially available nanofiltration membranes with RMS roughness values of (a) 12.8 nm and (b) 56.5 nm taken from Ref. [43]. Additional (a) and (b) membrane properties include zeta potentials of -18 and -25 mV (at 10 mM and pH 7), pure water contact angles of 51.9 and 51.7, hydraulic resistances of 3.26×10^{10} and 3.13×10^{10} Pa s/m, and salt rejections of 35% and 83% (at 30 gallons per square foot of membrane per day, gfd, and 10 mM NaCl), respectively. Field-emission scanning electron microscope images of fouled NF membranes in (c) and (d) show the membranes from (a) and (b), respectively, accumulate different amounts of colloidal foulants when the same feed suspension was filtered through the membranes under identical operating conditions. The membrane in (b) with significantly rougher and more negatively charged surface appears to attract a thicker deposit layer of 100 nm silica colloids than the smoother membrane in (a).

including Raman spectroscopy (structure),^[13] electron spin resonance (solute mobility in membrane polymer matrix and pores),^[13] AFM, SEM, and TEM (surface morphology, structure, and pore size),^[10,13,15,16,50,54,55] streaming potential (membrane surface zeta potential),^[56,57] NMR spectroscopy (permeability),^[50] (hydrophobicity) contact angle,^[18] and X-ray photoelectron spectroscopy (XPS, surface chemical functional groups).^[58,59]

Field-emission scanning electron microscope (FESEM) images of two commercially available nanofiltration membranes are shown in Fig. 7. The two membranes exhibit RMS roughness values of (a) 12.8 and (b) 56.5 nm (taken from Ref. [43]). Additional properties of membranes (a) and (b) include zeta potentials of -18 and -25 mV (at 10 mM and pH 7), pure water contact angles of 51.9 and 51.7, hydraulic resistances of 3.26×10^{10} and 3.13×10^{10} Pa s/m, and salt rejections of 35% and 83% (at 30 gfd and 10 mM NaCl), respectively. Field-emission scanning electron microscope images in Fig. 7c and d are of the membranes from (a) and (b), respectively, after filtration of identical 200 mg/L suspensions of 100-nm spherical silica colloids in a 10 mM NaCl solution. Different masses of colloidal foulants accumulate on the membrane surfaces even when operating conditions (i.e., flux, crossflow, temperature, etc.) were constant.

It is not entirely clear why these membranes attract different amounts of the colloidal foulant. It has been suggested that subtle differences in physicochemical surface properties and salt rejections may control the initial rate of deposition.^[10] Differing salt rejections will yield different membrane surface salt concentrations (all other conditions being equal), and thus repulsive electrostatic interactions are suppressed creating more favorable conditions for foulant deposition. In this case, the membrane in (b) and (d) had higher salt rejection, which may have countered the slightly greater membrane zeta potential. It has also been suggested that membrane surface roughness may decrease electrostatic repulsive interactions, further enhancing colloidal foulant deposition.

CONCLUSION

Nanofiltration separations are performed in many industries and for many applications. The key material properties of nanofiltration membranes are their selectivity, which may derive from various combinations of size, charge, and dielectric exclusion. The most common nanofiltration membranes are comprised of a thin, dense polymer film polymerized over the top of a porous membrane cast on a fabric support. The most common nanofiltration module type is the flat-sheet, spiral-wound element design. The performance of NF separations is

defined by the solvent permeability and the difference between various solute permeabilities. Fouling is a major concern in most industrial and water treatment applications of nanofiltration separations because it leads to higher operating costs, deterioration of NF thin films, and decreased selectivity. Overall, nanofiltration separations offer low-cost, environmentally friendly, semiselective separation capability for a host of applications and are a promising nanotechnology.

REFERENCES

1. Cheremisinoff, N.P. *Liquid Filtration*; 1998. Butterworth-Heinemann, USA.
2. Timmer, J.M.K. Doctoral Dissertation; Technische Universiteit Eindhoven: Eindhoven, Netherlands, 2001.
3. Meadows, D.M.; Wadley, S.; Buckley, C.A. Evaluation of nanofiltration for recovery of brine from sugar liquor decolourising resin regeneration waste. *Water Sci. Technol.* **1992**, *25*, 339–350.
4. Lu, X.; Bian, X.; Shi, L. Preparation and characterization of NF composite membrane. *J. Membr. Sci.* **2002**, *210*, 3–11.
5. Bowen, W.R.; Hilal, N.; Lovitt, R.W.; Wright, C.J. Direct measurement of interactions between adsorbed protein layers using an atomic force microscope. *J. Colloid Interface Sci.* **1998**, *197*, 348–352.
6. Bowen, W.R.; Doneva, T.A. Atomic force microscopy studies of membranes: Effect of surface roughness on double-layer interactions and particle adhesion. *J. Colloid Interface Sci.* **2000**, *229*, 544–549.
7. Brant, J.A.; Childress, A.E. Assessing short-range membrane–colloid interactions using surface energetics. *J. Membr. Sci.* **2002**, *203*, 257–273.
8. Brant, J.A.; Childress, A.E. Membrane–colloid interactions: Comparison of extended DLVO predictions with AFM force measurements. *Environ. Eng. Sci.* **2002**, *19*, 413–427.
9. Hoek, E.M.V.; Bhattacharjee, S.; Elimelech, M. Effect of surface roughness on colloid–membrane DLVO interactions. *Langmuir* **2003**, *19*, 4836–4847.
10. Vrijenhoek, E.M.; Elimelech, M.; Hong, S. Influence of membrane surface properties on initial rate of colloidal fouling of reverse osmosis and nanofiltration membranes. *J. Membr. Sci.* **2001**, *188*, 115–128.
11. Zhu, X.H.; Elimelech, M. Fouling of reverse-osmosis membranes by aluminum-oxide colloids. *J. Environ. Eng.-ASCE* **1995**, *121*, 884–892.
12. Zhu, X.; Elimelech, M. Colloidal fouling of reverse

- osmosis membranes: Measurements and fouling mechanisms. *Environ. Sci. Technol.* **1997**, *31*, 3654–3662.
13. Khulbe, K.C.; Matsuura, T. Characterization of synthetic membranes by Raman spectroscopy, electron spin resonance, and atomic force microscopy: A review. *Polymer* **2000**, *41*, 1917–1935.
 14. Mulder, M. *Basic Principles of Membrane Technology*, 2nd Ed.; Kluwer Academic Publishers: Dordrecht, NL, 1996.
 15. Kwak, S.Y.; Yeom, M.O.; Roh, I.J.; Kim, D.Y.; Kim, J.J. Correlations of chemical structure, atomic force microscopy (AFM) morphology, and reverse osmosis (RO) characteristics in aromatic polyester high-flux RO membranes. *J. Membr. Sci.* **1997**, *132*, 183–191.
 16. Kim, J.Y.; Lee, H.K.; Kim, S.C. Surface structure and phase separation mechanism of polysulfone membranes by atomic force microscopy. *J. Membr. Sci.* **1999**, *163*, 159–166.
 17. Petersen, R.J. Composite reverse osmosis and nanofiltration membranes. *J. Membr. Sci.* **1993**, *83*, 81–150.
 18. Combe, C.; Molis, E.; Lucas, P.; Riley, R.; Clark, M.M. The effect of CA membrane properties on adsorptive fouling by humic acid. *J. Membr. Sci.* **1999**, *154*, 73–87.
 19. Bowen, W.R.; Doneva, T.A.; Yin, H.B. Polysulfone-sulfonated poly(ether ether) ketone blend membranes: Systematic synthesis and characterisation. *J. Membr. Sci.* **2001**, *181*, 253–263.
 20. Bowen, W.R.; Doneva, T.A.; Yin, H.B. The effect of sulfonated poly(ether ether ketone) additives on membrane formation and performance. *Desalination* **2002**, *145*, 39–45.
 21. Cadotte, J.; Forester, R.; Kim, M.; Petersen, R.; Stocker, T. Nanofiltration membranes broaden the use of membrane separation technology. *Desalination* **1988**, *70*, 77–88.
 22. Faibish, R.S.; Cohen, Y. Fouling-resistant ceramic-supported polymer membranes for ultrafiltration of oil-in-water microemulsions. *J. Membr. Sci.* **2001**, *185*, 129–143.
 23. Faibish, R.S.; Cohen, Y. Fouling and rejection behavior of ceramic and polymer-modified ceramic membranes for ultrafiltration of oil-in-water emulsions and microemulsions. *Colloids Surf., A* **2001**, *191*, 27–40.
 24. Cheryan, M. *Ultrafiltration and Microfiltration Handbook*; Technomic, 1998.
 25. Bontha, J.R.; Pintauro, P.N. Water orientation and ion solvation effects during multicomponent salt partitioning in a nafion cation exchange membrane. *Chem. Eng. Sci.* **1994**, *49*, 3835–3851.
 26. Glueckauf, E. The distribution of electrolytes between cellulose acetate membranes and aqueous solution. *Desalination* **1976**, *18*, 155–172.
 27. Carter, J.W.; Hoyland, G.; Hasting, A.P.M. Concentration polarisation in reverse osmosis flow systems under laminar conditions. Effect of surface roughness and fouling. *Chem. Eng. Sci.* **1974**, *29*, 1651–1658.
 28. Hoek, E.M.V.; Kim, A.S.; Elimelech, M. Influence of crossflow membrane filter geometry and shear rate on colloidal fouling in reverse osmosis and nanofiltration separations. *Environ. Eng. Sci.* **2002**, *19*, 357–372.
 29. Bhattacharjee, S.; Kim, A.S.; Elimelech, M. Concentration polarization of interacting solute particles in cross-flow membrane filtration. *J. Colloid Interface Sci.* **1999**, *212*, 81–99.
 30. Wijmans, J.G.; Nakao, S.; Van Den Berg, F.R.; Troelstra, F.R.; Smolders, C.A. Hydrodynamic resistance of concentration polarization boundary layers in ultrafiltration. *J. Membr. Sci.* **1985**, *22*, 117–134.
 31. Zydney, A.L.; Colton, C.K. A concentration polarization model for the filtrate flux in cross-flow microfiltration of particulate suspensions. *Chem. Eng. Commun.* **1986**, *47*, 1–21.
 32. Blatt, W.F.; Dravid, A.; Michaels, A.S.; Nelson, L. Solute Polarization and Cake Formation in Membrane Ultrafiltration: Causes, Consequences, and Control Techniques. In *Membrane Science and Technology: Industrial, Biological, and Waste Treatment Processes*; Flinn, J.E., Ed.; Plenum Press: Columbus, OH, 1970.
 33. Porter, J.J. Recovery of polyvinyl alcohol and hot water from the textile wastewater using thermally stable membranes. *J. Membr. Sci.* **1998**, *151*, 45–53.
 34. Liew, M.K.H.; Fane, A.G.; Rogers, P.L. Fouling of microfiltration membranes by broth-free antifoam agents. *Biotechnol. Bioeng.* **1997**, *56*, 89–98.
 35. Kelley, S.T.; Zydney, A.L. Protein fouling during microfiltration: Comparative behavior of different model proteins. *Biotechnol. Bioeng.* **1997**, *55*, 91–100.
 36. Hagen, K. Removal of particles, bacteria and parasites with ultrafiltration for drinking water treatment. *Desalination* **1998**, *119*, 85–91.
 37. Fu, L.T.; Dempsey, B.A. Optimizing Membrane Operations with Enhanced Coagulation of toc for Drinking Water Treatment. In *Optimizing Membrane Operations with Enhanced Coagulation of toc for Drinking Water Treatment*; Abstracts of Papers of the American Chemical Society, American Chemical Society: ENVR, 1996; 13.

38. Potts, D.E.; Ahlert, R.C.; Wang, S.S. A critical review of fouling of reverse osmosis membranes. *Desalination* **1981**, *35*, 235–264.
39. Tchobanoglous, G.; Darby, J.; Bourgeois, K.; Mcardle, J.; Genest, P.; Tylla, M. Ultrafiltration as an advanced tertiary treatment process for municipal wastewater. *Desalination* **1998**, *119*, 315–321.
40. Van Houtte, E.; Verbauwhede, J.; Vanlerberghe, F.; Demunter, S.; Cabooter, J. Treating different types of raw water with micro- and ultrafiltration for further desalination using reverse osmosis. *Desalination* **1998**, *117*, 49–60.
41. Vera, L.; Villarroel-Lopez, R.; Delgado, S.; Elmaleh, S. Cross-flow microfiltration of biologically treated wastewater. *Desalination* **1997**, *114*, 65–75.
42. Hong, S.K.; Elimelech, M. Chemical and physical aspects of natural organic matter (NOM) fouling of nanofiltration membranes. *J. Membr. Sci.* **1997**, *132*, 159–181.
43. Hoek, E.M.V. Ph.D. Dissertation; Yale University: New Haven, CT, 2002.
44. Hoek, E.M.V.; Elimelech, M. Cake-enhanced concentration polarization: A new fouling mechanism for salt rejecting membranes. *Environ. Sci. Technol.* **2003**, *17*, 5581–5588.
45. Maxwell, J.C. *Treatise on Electricity and Magnetism*; Clarendon Press, 1881.
46. Cussler, E.L. *Diffusion: Mass transfer in Fluid Systems*, 2nd Ed.; Cambridge University Press: Cambridge, UK, 1984.
47. Boudreau, B.P. The diffusive tortuosity of fine-grained unlithified sediments. *Geochim. Cosmochim. Acta* **1996**, *60*, 3139–3142.
48. Mickley, M.C. A charged ultrafiltration membrane for water softening. *IDA J.* **1985**, *1*, 1–13.
49. Hirose, M.; Ito, H.; Kamiyama, Y. Effect of skin layer surface structures on the flux behaviour of RO membranes. *J. Membr. Sci.* **1996**, *121*, 209–215.
50. Kwak, S.Y.; Ihm, D.W. Use of atomic force microscopy and solid-state NMR spectroscopy to characterize structure–property–performance correlation in high-flux reverse osmosis (RO) membranes. *J. Membr. Sci.* **1999**, *158*, 143–153.
51. Elimelech, M.; Zhu, X.; Childress, A.E.; Hong, S. Role of membrane surface morphology in colloidal fouling of cellulose acetate and composite aromatic polyamide reverse osmosis membranes. *J. Membr. Sci.* **1997**, *127*, 101–109.
52. Zhu, X.H.; Elimelech, M. Colloidal fouling of reverse osmosis membranes—Measurements and fouling mechanisms. *Environ. Sci. Technol.* **1997**, *31*, 3654–3662.
53. Riedl, K.; Girard, B.; Lencki, R.W. Influence of membrane structure on fouling layer morphology during apple juice clarification. *J. Membr. Sci.* **1998**, *139*, 155–166.
54. Knoell, T.; Safarik, J.; Cormack, T.; Riley, R.; Lin, S.W.; Ridgway, H. Biofouling potentials of microporous polysulfone membranes containing a sulfonated polyether–ethersulfone/polyethersulfone block copolymer: Correlation of membrane surface properties with bacterial attachment. *J. Membr. Sci.* **1999**, *157*, 117–138.
55. Bowen, W.R.; Doneva, T.A. Atomic force microscopy studies of membranes: Effect of surface roughness on double-layer interactions and particle adhesion. *J. Membr. Sci.* **2000**, *229*, 544–549.
56. Childress, A.E.; Elimelech, M. Effect of solution chemistry on the surface charge of polymeric reverse osmosis and nanofiltration membranes. *J. Membr. Sci.* **1996**, *119*, 253–268.
57. Childress, A.E.; Elimelech, M. Relating nanofiltration membrane performance to membrane charge (electrokinetic) characteristics. *Environ. Sci. Technol.* **2000**, *34*, 3710–3716.
58. Ferjani, E.; Mejdoub, M.; Roudesli, M.S.; Chehimi, M.M.; Picard, D.; Delamar, M. Xps characterization of poly(methylhydrosiloxane)-modified cellulose diacetate membranes. *J. Membr. Sci.* **2000**, *165*, 125–133.
59. Beverly, S.; Seal, S.; Hong, S. Identification of surface chemical functional groups correlated to failure of reverse osmosis polymeric membranes. *J. Vac. Sci. Technol.* **2000**, *18*, 1107–1113.
60. Filmtec. *Why Filmtec Thin-Film Composite RO Membranes Outperform Cellulose Acetate Membranes in Water Purification Service*: Filmtec Corporation. Dow FilmTech website; <http://www.pacificro.com/DeFilmWh.pdf>, (accessed July 1998).
61. Mallevalle, J., Odendaal, P.E., Wiesner, M.R., Eds.; *Water Treatment Membrane Processes*. McGraw Hill: New York, NY, 1996.

Nanolithography: Length-Scale Limitations

Takashi Ito

Fujitsu Ltd., Tokyo, Japan

INTRODUCTION

Lithography is one of the fundamental technologies by which nanoscale patterns required for the fabrication and integration of nanodevices are generated. Lithographic requirements are becoming increasingly severe. In the semiconductor industry, the past three decades have seen the critical length-scales of component devices decrease by several orders of magnitude, from 15 μm in the case of the first integrated circuit, to less than 130 nm routinely obtained today. The phenomenal rate of decrease in size seems to reach the limitation of conventional optical lithography. The exposure wavelength, photoresist performance, and equipment determine the lithography limitation. The size of the constituent atoms imposes a fundamental limit on the minimum length scale that can be ultimately attained. This article first provides an overview of the fundamentals of optical lithography. It is shown how minimum attainable device dimensions are intimately related to the wavelength of light used. Then, several techniques under investigation for further enhancing the resolution of this workhorse of the microelectronics industry are described. As the options available to industry are not all “optical,” the discussions cover the various nonoptical lithographic techniques currently being explored.

TECHNOLOGY OVERVIEW OF LITHOGRAPHY

Fig. 1 illustrates how the lithographic options vary as the critical device dimension decreases, and provides estimates of the timescales on which decisions may need to be made regarding which options to adopt.^[1] Optical lithography technology has been traditionally used by reducing wavelengths of light sources from mercury lamps to excimer lasers such as KrF and ArF excimer lasers, and probably F₂ and Ar₂ lasers in the future. Phase shift masks (PSM) and immersion configuration can extend the resolution limit for each optical lithography. Extreme ultraviolet (EUV) of wavelengths ranging from 11 to 14 nm is used as extension of the optical method. Nonoptical lithography with proximity X-ray (PXL), electron beam (EBL), and ion beam (IPL) have a potential for finer patterns (as opposed to those produced via optical methods)

because of their shorter wavelengths. Electron-beam projection lithography (EPL), which uses mask projection technique, projects to be most promising. However, electron beam direct writing (EBDW) has a drawback on its throughput. Nanoimprint is a simple technique just like paper printing. A shift by the microelectronics industry to any nonoptical lithographic technique will require the introduction of a new infrastructure of tools, materials, and processing technologies, resulting in huge research and development costs.

PROJECTION OPTICAL LITHOGRAPHY

Key elements of a practical lithographic system are essentially the same for all technologies—optical and nonoptical. As shown in Fig. 2, they include the following: 1) A set of “masks” containing the patterns of components to be fabricated in and/or on the substrate, the tools for making the masks, and the metrology for ensuring precise dimensions and pattern overlay. 2) An energy source (e.g., a light source) for transferring the pattern from a mask to the substrate. 3) A medium—known as a “photoresist” or “resist”—for recording the pattern on the substrate following exposure to the source, and which allows subsequent processing of material in and/or on the underlying substrate. 4) Procedures for reliable detection of pattern defects, which clearly becomes more challenging as the critical dimensions decrease. The lithographic process—especially projection optical lithography—is closely related to the developing process in print photography, where the photographic negative plays the role of the mask, and the photographic emulsion on the print is the resist.

Resolution Limits

The resolution limit in conventional projection optical lithography is largely determined by the well-known Rayleigh’s equation. The resolution (minimum resolvable feature) R and the corresponding depth of focus (DOF) are given by the following:^[2]

$$R = k_1 \lambda / \text{NA}$$

$$\text{DOF} = k_2 \lambda / \text{NA}^2$$

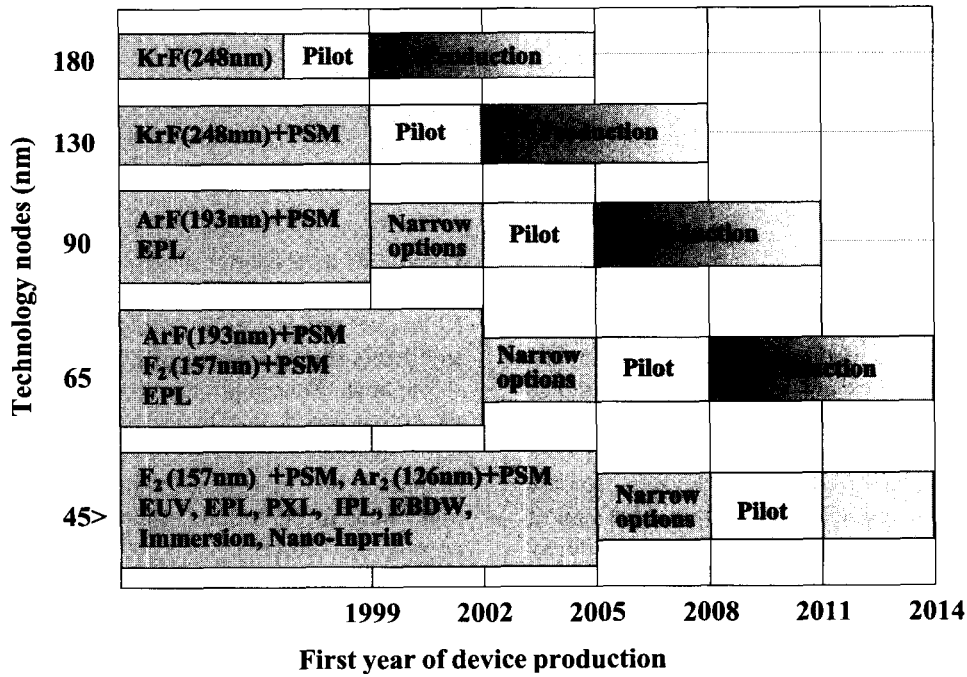


Fig. 1 Technology options of lithography.

Here λ is the exposure wavelength, NA is the numerical aperture of the optical system, and k_1 and k_2 are constants that depend on the specific resist material, process technology, and image-formation technique used. Fig. 3 shows the evolution of projection optical lithography. It

compares the required minimum feature size and the wavelength of the exposure light. At the beginning of the introduction of the projection system, the required minimum feature size was relatively large compared to the wavelength of the exposure light. Then low-NA lens

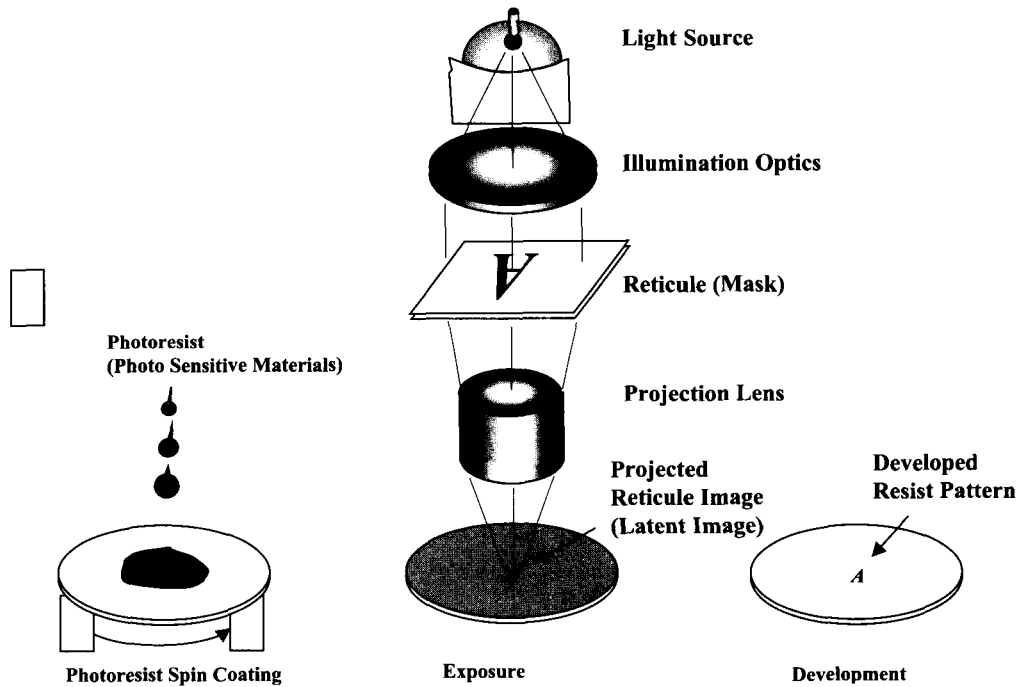


Fig. 2 Principle of lithography. (View this art in color at www.dekker.com.)

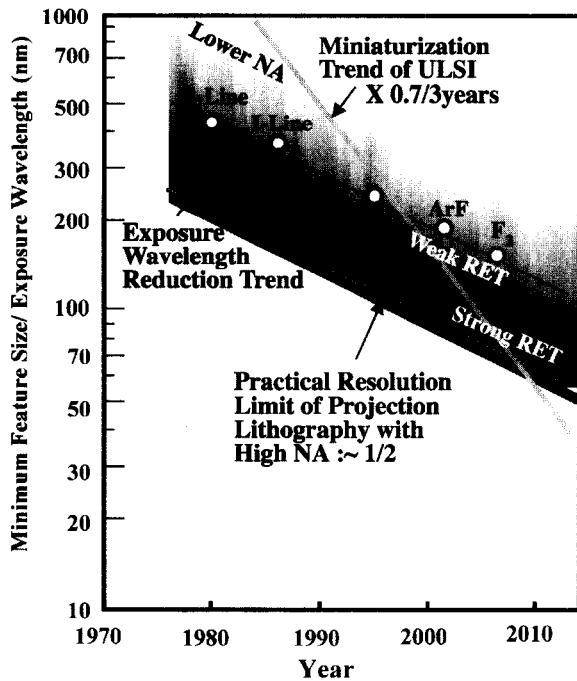


Fig. 3 Trend minimum feature size and exposure wavelength for optical lithography. Practical resolution limit is reduced to approximately half of wavelength with extremely higher NA and resolution enhancement techniques. Miniaturization exceeds the wavelength reduction trend for ULSI manufacturing. (View this art in color at www.dekker.com.)

system was used. However, as the miniaturization requirement of the semiconductor devices is faster than the reduction rate of the wavelength of exposure light, higher resolution was required. Therefore, to obtain higher resolutions, shorter-wavelength light and lens systems with larger numerical apertures are required. In general, the minimum feature size that can be obtained is almost the same as (or slightly smaller than) the wavelength of light used for the exposure, for which one needs a relatively large numerical aperture (typically ≥ 0.5). In such high-NA lens systems, the depth of focus becomes very small, and so the exposure process becomes sensitive to slight variations in the thickness and absolute position of the resist layer.^[3] The smaller the depth of focus, the more rapidly a focused beam diverges on moving away from the focal point. With the recent introduction of a “chemical mechanical polishing” technology, the topographic variations of substrate surfaces have been reduced, making it possible to use extremely large NA systems; however, the margin for error becomes extremely small under such high-NA exposure conditions.

Resolution Enhancement

To improve the resolution of an optical lithography system without introducing other impractical constraints (on, e.g., wafer smoothness), several resolution-enhancement strategies were proposed.^[4-6] Fig. 4 shows a schematic view of

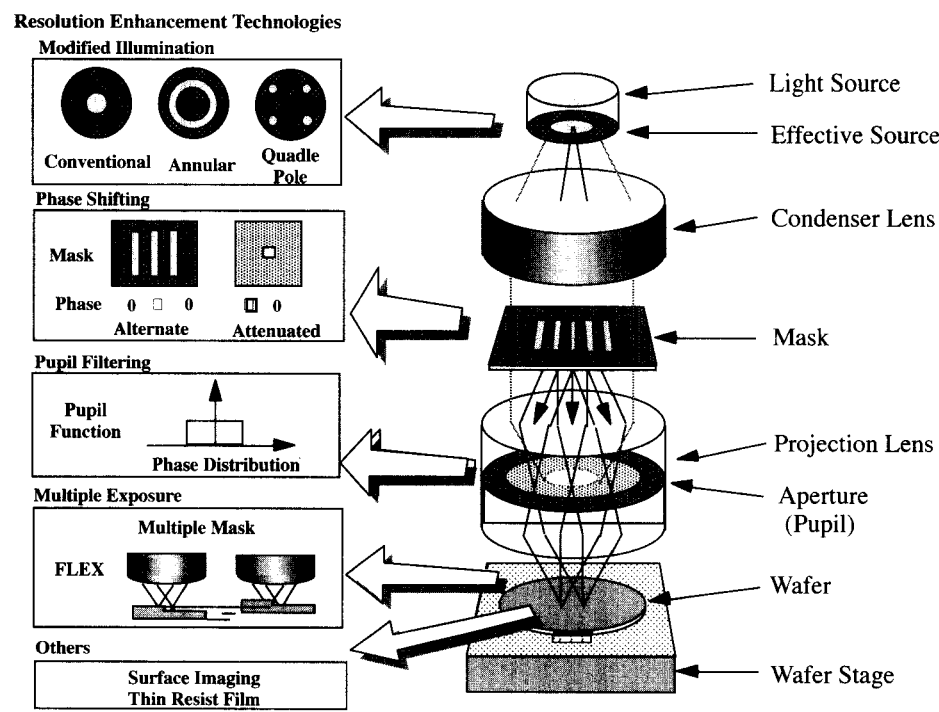


Fig. 4 Schematic view of exposure optical system and various resolution enhancement technologies for each stage of the system. (View this art in color at www.dekker.com.)

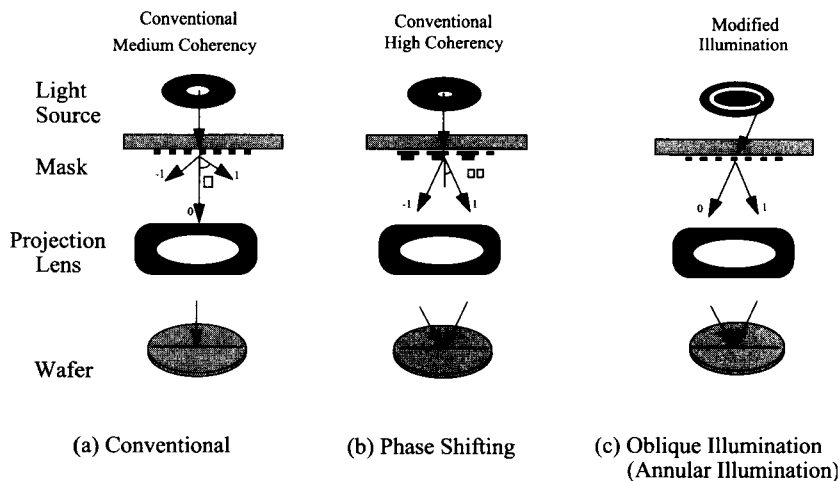


Fig. 5 Grating pattern image formation. (View this art in color at www.dekker.com.)

a typical projection optical-exposure system. Such a system consists of several subsystems, and resolution-enhancement ideas can be applied at various points. These may take the form of modified illumination at the light source, phase shifting of the wave front in the mask plane, and/or filtering with an aperture (pupil) at the projection lens. Some basic ideas of resolution enhancement are illustrated in Fig. 5, which compares image formation in: a) the conventional setup with b) phase shifting and c) modified illumination.

Consider the case when the image on the mask is a simple grating. In the conventional system (a), several diffracted light rays are generated by the grating. Zero-th order light proceeds straight through the system, and several rays of higher order are generated with diffraction angles of θ (first order), 2θ (second order), 3θ (third order) and so on, with $\theta \sim \lambda/a$ for small θ (where a is the grating periodicity). Near the resolution limit, only the zero-th order and first-order rays pass through the lens pupil. Now consider case (b), where the phase of the light passing through the grating mask is modified to have a periodicity twice that of the grating itself. (Phase shifting also requires a higher degree of coherency in the source light compared to the conventional case.) The transmitted wave front is in turn modified, such that the zero-th order light is canceled out and the diffraction angle of the first-order rays halved to 0.5θ . As a result, the spatial frequency of the patterns that can be imaged is doubled (or, put in another way, the resolvable grating periodicity is halved). Although both the opaque pattern and the phase modifications on a real mask will be considerably more complex than a simple grating, this example nevertheless serves to illustrate the substantial improvement in resolution that can be achieved by this approach.

Fig. 6 shows an example of resist patterns formed by using KrF (248 nm) light and a phase shift mask: structures having half the wavelength of the exposure light are clearly visible.

Next, we consider oblique (or off-axis) illumination, as shown in (c). Zero-th order light no longer passes through the center of the pupil, but at an angle to the vertical. The first-order rays again emerge at angles of $\pm\theta$ with respect to the zero-th order ray. And at the resolution limit, one of these passes through the side of the lens pupil opposite to that of the zero-th order ray, while the other diffracted ray is blocked. Therefore the result is geometrically equivalent to the phase-shifted case (b), and again leads to a doubling of the spatial frequency of the images that can be resolved. At present, the most advanced mass-produced LSI circuits have a critical dimension of 90 nm. This is achieved by using partially coherent light from ArF excimer laser with a wavelength of 193 nm, in combination with some resolution-enhancement techniques such

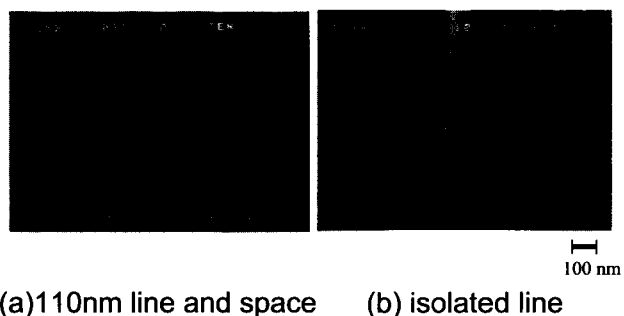


Fig. 6 An example of resolution enhancement technology and the effect of phase shifting technology.

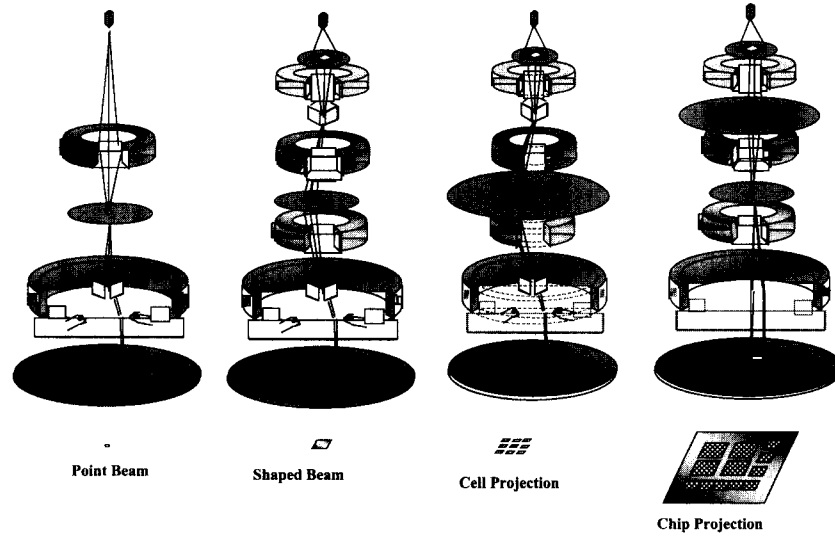


Fig. 7 Various electron beam writing systems; simple point electron beam, shaped electron beam, patterned cell projection, and chip pattern projection. (View this art in color at www.dekker.com.)

as off-axis illumination, phase shift mask, and optical proximity correction, as well as advanced resist systems. To further reduce the critical dimension, wavelength reduction is being actively pursued using F₂ and Ar₂ excimer lasers (wavelengths of 157 and 126 nm, respectively). The combination of shorter-wavelength light and resolution-enhancement techniques may ensure optical lithography's position as the most productive lithographic technology for nanofabrication of length-scale of even less than 50 nm.

ELECTRON BEAM LITHOGRAPHY

Electron beam lithography—in which a beam of electrons, rather than photons, is used as the exposure source—has

extremely high-resolution capabilities combined with a large depth of focus. To date, it has been mainly used in the production of masks and reticles for optical lithography. But it has also been used in the fabrication of very fine-scale devices for fundamental and device-verification studies, and also in the small-scale production of the specialized very high frequency devices. However, in the context of mass-produced integration circuitry, the greatest problem of electron beam lithography is the low throughput capability of the system. While using a finely focused electron beam makes it possible to delineate extraordinarily fine patterns, writing of chip-scale patterns with a single electron beam is a slow process. According to the pattern complexity, the exposure time for the mask writing also becomes very long. Accordingly, there has been considerable interest in developing techniques to

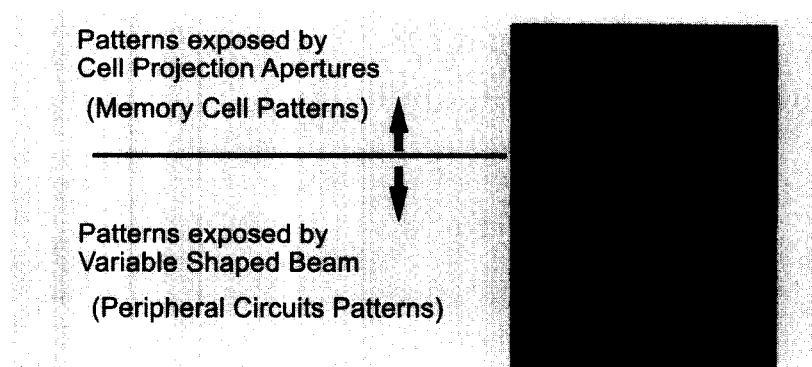


Fig. 8 Resist patterns delineated by cell projection system.

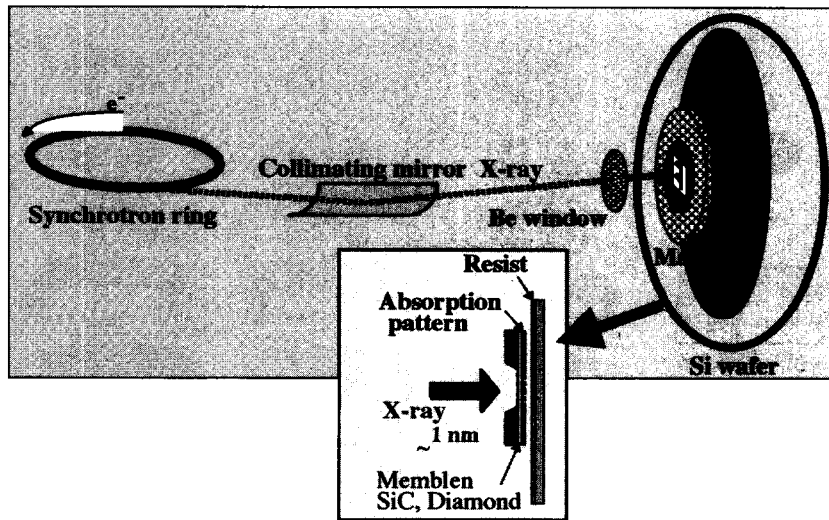


Fig. 9 System of proximity X-ray lithography. X-ray is generated from a synchrotron ring, reflects on a collimating mirror, and irradiates a wafer through a mask. The mask is made of SiC membrane or diamond and absorption pattern. (View this art in color at www.dekker.com.)

expand the throughput of electron beam lithography, and these have generally involved finding ways to enlarge and make the electron beam parallel. Fig. 7 shows various electron-beam writing procedures.

The electron projection lithography (EPL), such as cell projection or chip projection, is one such approach that makes use of parallel exposure. Specifically, in a conventional variable-shaped beam system, the maximum size of the electron beam is sufficient to encompass a mask containing the pattern of several memory cells, which have a repetitive structure. So if such a mask is used in place of the second aperture of the shaped beam system, the pattern can be projected on the substrate in a single exposure. Fig. 8 shows a resist pattern produced by this

approach: the periodically arrayed patterns at the top are produced by exposure using a cell-projection aperture, whereas the random wiring patterns at the bottom were written by using a variable-shape aperture. But even with this system, throughput remains a critical issue.

A more promising approach to improve throughput is to use a projection optical setup, geometrically equivalent to that used in optical lithography: an image of the desired pattern is projected from a mask. Most notable of the recent attempts to utilize mask projection are scattering angular limited projection electron beam lithography (SCALPEL), developed by Bell Laboratories; projection reduction exposure with variable axis immersion lenses (PREVAIL), developed by IBM; and low-energy electron

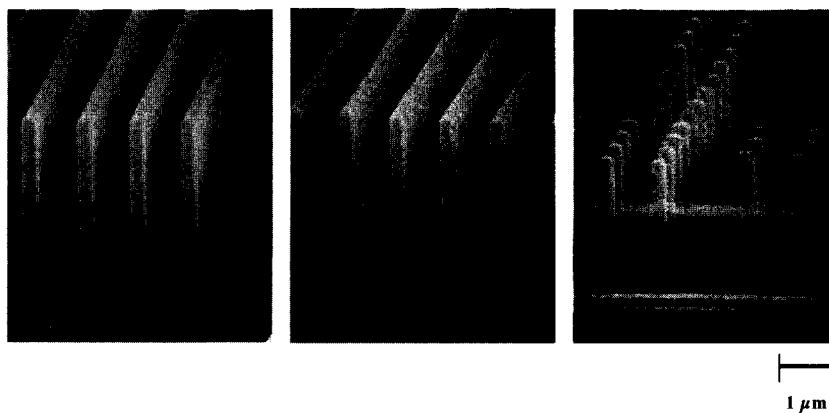


Fig. 10 Resist patterns on different substrates. (Courtesy of NTT-AT.)

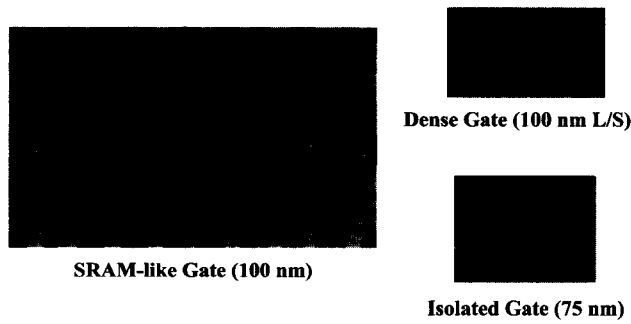


Fig. 11 Examples of polysilicon patterns transferred with X-ray lithography. SRAM-like gate, dense gate, and isolated gate patterns are shown.

beam proximity projection lithography (LEEPL) (see Refs. [7] and [8]). These approaches will be used in conjunction with optical lithography.

PROXIMITY X-RAY LITHOGRAPHY

Proximity X-ray lithography is essentially a form of “shadow printing”—a mask is held in close proximity to the substrate surface, and the image is simply produced on exposure by the shadow of the mask on the surface. Proximity techniques were used in the early days of optical lithography, but have long since been superseded by projection techniques: the former are more susceptible to resolution-limiting diffraction effects. Resolution is less of an issue with proximity printing using X-rays, as the wavelengths used are so much smaller.

The exposure system of the PXL is shown in Fig. 9. A synchrotron is used as the source of X-ray radiation; recently, sources of synchrotron radiation have been developed that can store currents as high as 500 mA with electron folding lifetimes longer than 10 hr, which should be stable enough for practical usage. The X-ray is first collimated by using a silicon carbide mirror, before passing through a transparent window of beryllium into a chamber containing the mask and wafer. Alignment of the sample uses a vertical X–Y stage, in contrast to the horizontal stages used in most other lithographic techniques. The X-ray used has a wavelength of about 1 nm. The mask is prepared on a membrane of silicon carbide or diamond, and a layer of Ta (patterned by direct-write electron beam lithography) serves to absorb the X-rays and so generate the shadow on the semiconductor wafer. The final image exposed by PXL is limited by the electron-beam-made mask.

Fig. 10 shows a series of typical patterns produced in the resist layer following X-ray exposure and subsequent

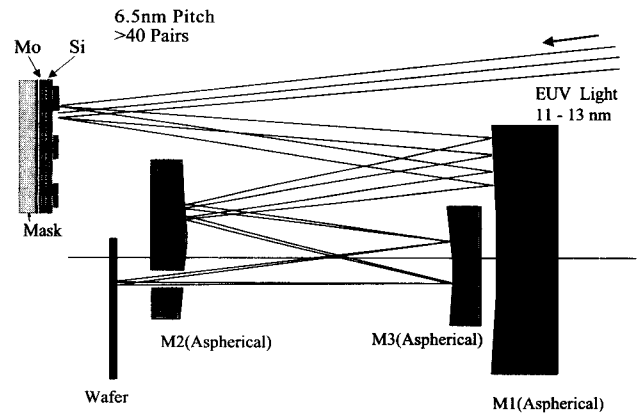


Fig. 12 Concept of EUVL optics. (View this art in color at www.dekker.com.)

development.^{19]} The patterns shown were formed on stepped substrates, and exhibited critical dimensions as small as 150 nm with a distribution of less than 10 nm (3σ). Fig. 11 shows poly silicon patterns transferred from resist patterns with PXL. Dry etching technique was inevitably used to transfer the resist patterns to poly silicon ones.

EXTREME ULTRAVIOLET LITHOGRAPHY

Extreme ultraviolet (EUVL) lithography is a promising candidate for achieving critical dimensions of 50 nm and

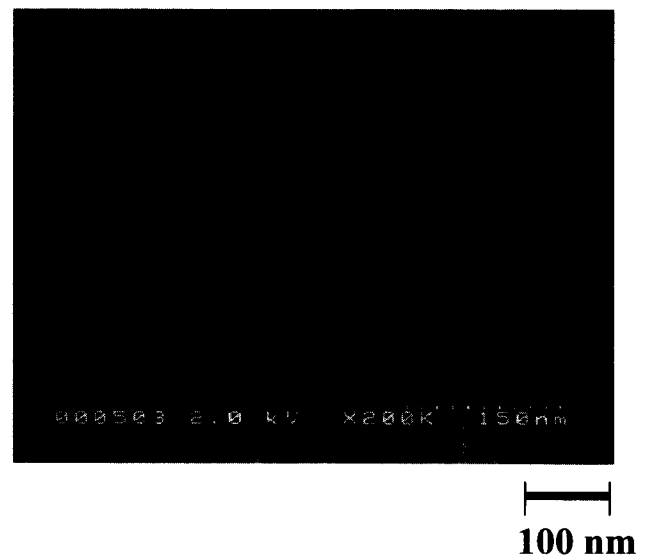


Fig. 13 40-nm line-and-space resist patterns delineated by EUV exposure system.

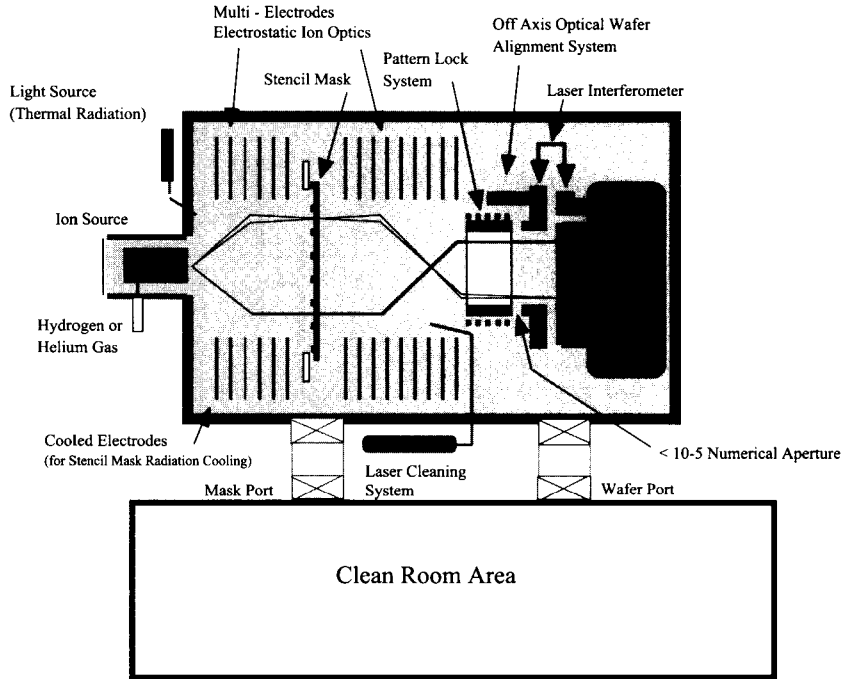


Fig. 14 Schematic top view of ion projection lithography system. (View this art in color at www.dekker.com.)

below.^[10] This approach utilizes the same principle of conventional optical projection lithography and also obeys Rayleigh's equation (shown earlier). But now, the exposure wavelength is in the range 11–13 nm, which introduces its own problems. Fig. 12 shows the concept of EUV optics. First, as the absorption of light in this short-wavelength regime is very strong, lens-based refractive

optics cannot be used in this lithographic system: an all-reflective optic system must therefore be employed. A second difficulty relates to the mirrors themselves. A conventional mirror surface cannot be used at these wavelengths, so one must resort to multilayer structures that rely on interference effects to achieve reflectivity. And even then, the resulting reflectivities are rather low,

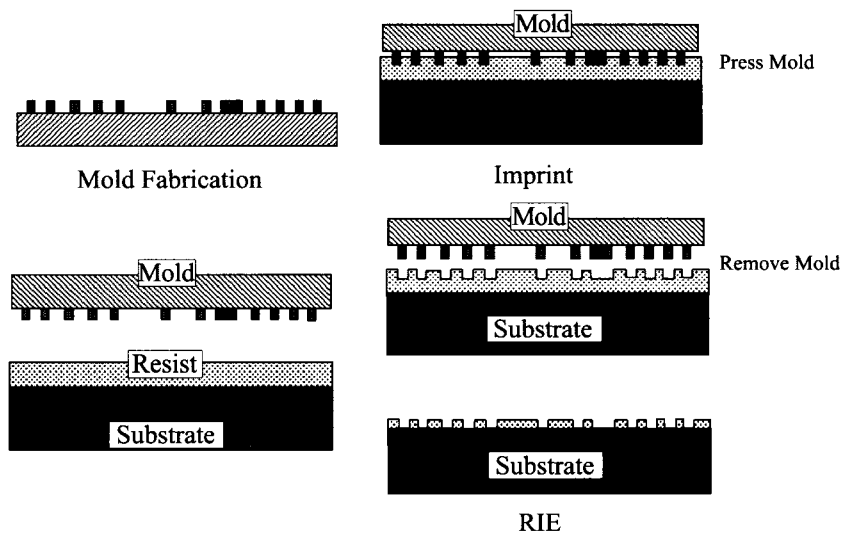


Fig. 15 Process of nanoimprint lithography. (View this art in color at www.dekker.com.)

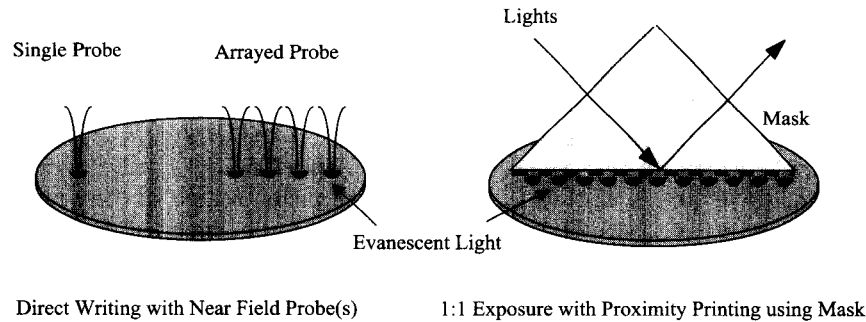


Fig. 16 Concept of near field optical lithography using evanescent light. Direct writing on the left side and proximity printing on the right side. (View this art in color at www.dekker.com.)

typically 60–70% at 13 nm. Accordingly, the number of mirror surfaces in the system needs to be kept as low as possible—6 or fewer—to avoid significant reductions in the light intensity level.

In the case of multilayer mirror optics, the requirement of fewer optical elements means that aspherical mirrors must be introduced to achieve such capabilities. Such aspherical mirrors need to be extremely precise, with figure errors and surface roughness less than 0.1–0.2 nm. As such, an extremely high precision metrology system needs to be developed if this approach to lithography is to become viable.

The source of EUV light is another problematic issue.^[11] At present, the best candidate is a laser-produced plasma of xenon gas. But the energy conversion ratio of laser light (from a YAG laser) to EUV light is so small that lasers of enormous power are required to achieve practical EUV exposure intensities. Therefore, different strategies, such as the use of electrical discharge lamps, are being explored for providing practical light sources for EUV lithography.^[12] Fig. 13 shows an example of resist line-space patterns of 40 nm delineated by an experimental EUV exposure system. The result features its promising lithographic candidate for nanofabrication.

EMERGING TECHNOLOGIES

Several other approaches are proposed for delineating patterns below 100 nm. The configuration of the ion beam projection lithography (IPL) is schematically shown in Fig. 14. The ion beam can be used to avoid deep penetration of the incident ions because of their weight compared to electrons. The principle of the nanoimprint lithography is schematically shown in Fig. 15. It is just a printing of patterns. The near-field optical lithography recently appearing is shown in Fig. 16. The technique uses evanescent light. Direct writing with a near-field probe

and exposure with proximity printing with a mask are realized to limited applications. Limitations of those technologies to fine patterns are currently under investigation. IPL is one of the candidates of the next-generation lithography for production. Whereas the latter two approaches are good techniques to delineate nanostructures for the investigation of nanometer devices.

CONCLUSION

Optical lithography is a fundamental process in the manufacture of highly integrated microelectronic circuitry. But with the relentless commercial drive for ever smaller, faster, and cheaper components, the existing technology are rapidly being pushed to their limits. However, optical lithography has far from reached the end of the road, and will continue to be used for some years, adopting light sources of smaller wavelengths (such as F₂ or Ar₂ excimer lasers) and optical techniques for further enhancing resolution. Depending on requirements for images and costs, possible next-generation lithographic technologies using nonoptical sources are being actively explored. Whether the future of lithography lies with X-rays, electron beams or extreme ultraviolet light is far from clear at present. Critical issues remain to be solved with all of these alternative approaches. It is the time of length-scale limitation when those developments are abandoned. The requirement of nanoscale patterning will make those emerging technologies practical ones.

ACKNOWLEDGMENT

The author would like to thank Dr. S. Okazaki, Association of Super-Advanced Electronics Technologies for discussions and supplying data.

REFERENCES

1. *International Technology Roadmap for Semiconductors*, 1999 Ed.; Inter. SEMATECH, Ed.; Semiconductor Industry Association (SIA): New York, USA.
2. Klein, M.V.; Furtak, T.E. *OPTICS*; John Wiley & Sons: New York, USA, 1986; 398.
3. Okazaki, S. Resolution limits of optical lithography. *J. Vac. Sci. Technol.* **1991**, *B9* (6), 2829–2833.
4. Levenson, M.D., et al. Improving resolution in photolithography with a phase-shifting mask. *IEEE Trans.* **1982**, *ED-29/10*, 1828–1836.
5. Terasawa, T., et al. 0.3 μm optical lithography using a phase shifting mask. *Proc. SPIE* **1989**, *1088*, 25–33.
6. Matsuo, K., et al. High resolution optical lithography system using oblique incidence illumination. *Technol. Dig. IEDM '91* **1991**, 970–972.
7. Berger, S.D., et al. Projection electron beam lithography: A new approach. *J. Vac. Sci. Technol.* **1991**, *B9* (6), 2996–2999.
8. Utsumi, T. Low-energy E-beam proximity lithography (LEEPL). *Jpn. J. Appl. Phys.* **1999**, *38* (12B), 7046–7051.
9. Deguchi, K., et al. Patterning characteristics of a chemically-amplified negative resist in synchrotron radiation lithography. *Jpn. J. Appl. Phys.* **1992**, *31*, 2954–2958.
10. Kinoshita, H., et al. Soft x-ray reduction lithography using multilayer mirrors. *J. Vac. Sci. Technol.* **1989**, *B7* (6), 1648–1651.
11. Kubiak, G.D., et al. High power extreme-ultraviolet source based on gas jets. *Proc. SPIE* **1998**, *3331*, 81–89.
12. Silfvast, W.T., et al. High power plasma discharge source at 13.5 nm and 11.4 nm for EUV lithography. *Proc. SPIE* **1999**, *3676*, 272.

Nanomaterials and Molecular Devices: De Novo Design Theory

Kwang S. Kim
P. Tarakeshwar
Han Myoung Lee

Pohang University of Science and Technology, Pohang, South Korea

INTRODUCTION

The immense potential of functional nanomaterials in the fields of communication, information storage, materials, and biological sciences has heightened the quest to obtain them. In this quest, the “bottoms-up” approach, with its emphasis on chemical methods, has proven to be of more value than the classical “top-down” approach. Design strategies based on quantum theoretical methods are particularly suited to accelerate the “bottoms-up” approach, because of their ability to predict the properties of these nanomaterials to a high degree of accuracy. In the course of this article, we show how the pursuit for small, fast, and powerful nanoelectronic and nanomechanical devices, chemical/biochemical sensors/monitors, DNA chips, etc. can be vastly facilitated using an approach based on de novo theoretical design.

The first step in this process is to obtain a detailed insight of intermolecular interactions prevailing in these nanomaterials. This is because most physical phenomena, such as molecular recognition,^[1] nanorecognition,^[2] molecular clustering/aggregation,^[2] self-assembly,^[3,4] and self-synthesis,^[5] are the result of competitive and cooperative effects of several types of interatomic, intramolecular, and intermolecular interactions.^[6,7]

Based on a thorough understanding of various interaction forces and mechanisms, one can design molecular clusters, inorganic/metal clusters, endo-/exo-hedral fullerenes/nanotubes, nonlinear optical materials, ionophores/receptors/sensors, polypeptides/membranes/enzymes, organic nanotubes/nanowires, photo/electro-nanodevices, and nanomechanical molecular devices. In the course of this article, we show how the above strategy helped design novel and experimentally viable ionophores,^[8–12] organic nanotubes,^[4–6] nanowires,^[5] molecular flippers,^[13] and molecular switches,^[14] etc.

INTERMOLECULAR FORCES

The intricacies of most intermolecular interactions can be obtained from the study of molecular clusters.^[15–18]

These diverse intermolecular interactions can broadly be classified as: 1) H-bonding, 2) ionic interactions, 3) intermolecular interactions involving π systems, 4) metallic interactions, and 5) interactions involving quantum species.

DESIGN AND DEVELOPMENT OF FUNCTIONAL MOLECULES, NANOMATERIALS, AND NANODEVICES

In the following account, we discuss the strategies employed to design nanoclusters, nanowires, ionophores, receptors, sensors, carbon-based nanomaterials, organic nanotubes, encapsulated nanowires, nonlinear optical switches, and nanomechanical devices.

Nanoclusters and Nanowires

Clusters, in addition to offering several ways of making new materials, are a fundamental subject for understanding the intrinsic nature of materials.^[15,16] The investigation of H-bonded clusters,^[18–22] metal clusters,^[23–25] and clusters containing π systems^[26–29] not only provides the necessary information for nanomaterial design but also highlights some of the important similarities and differences in their structures and properties. In this discussion, we focus our attention on noble metal clusters and metal nanowires. Theoretical investigations of these noble metal clusters, to a large extent, depend on the ability of the theoretical method to describe metallic interactions. In particular, the ability of the method to accurately describe relativistic effects is vital to the success of the design strategy. Small noble metal clusters^[23–25,30–33] are of particular interest because the dominance of quantum effects in such small dimensions alludes to the emergence of several interesting characteristics, such as their catalytic properties, etc. While most studies were concentrated on pure metallic clusters, it has recently been realized that mixed metallic clusters exhibit unique electronic, magnetic, optical, and mechanical properties. For example, mixed clusters of gold and silver have been found to

exhibit enhanced optical nonlinearity over the corresponding bulk metals. Another advantage of studying these mixed clusters is that they help understand the mechanism of alloying. A recent example of the utility of theoretical methods is illustrated in the case of gold–tungsten clusters, wherein theoretical calculations were able to accurately predict the structures and properties, before they were experimentally identified.^[24,25]

One of the highlights of neutral and anionic gold and silver clusters is that they exhibit an even–odd oscillation in their stability and electronic properties.^[23] Owing to the spin pairing, the clusters having an even number of atoms tend to be more stable in the neutral state, while those having an odd number of atoms tend to be more stable in the anionic state. Since the 6s orbital energy of Au is almost as low as 5d orbitals due to the relativistic effect, the strong s–d hybridization in Au favors one-dimensional and two-dimensional structures in the case of the gold clusters. This explains the ductility of small gold clusters. In contrast, silver clusters exhibit a strong preference to exist as three-dimensional structures with spherical coordination because the valence orbitals are predominantly of the s-type. A similar argument can also be employed to explain the low coordination number of the Au atom in the gold clusters as compared to the Ag atom in the silver clusters. This preference in coordination reflects itself in the location of the Au and Ag atoms in the corresponding binary clusters of gold and silver, with the Au atoms being located on the boundary, while Ag atoms are generally located in the inner side (Fig. 1). In the anionic systems of both pure and mixed clusters, there is a marked tendency to adopt low-dimensional conformations as compared to the corre-

sponding neutral clusters. However, in the mixed clusters, the conformational preferences are strongly correlated to the number of Au and Ag atoms in the cluster. Given the higher energy of the Ag 5s as compared to the Au 6s orbital, electron transfers from Ag to Au atoms are found in the mixed clusters. This together with the predilection for Au atoms to be located on the boundary indicates that the core of the mixed clusters is positively charged, while the surface is negatively charged. The easy formation of the mixed gold–silver clusters and as a consequence their alloys is due to the significant electrostatic stabilization accruing from the charge transfer from Au to Ag atoms.

In order to obtain more insight into the role of dimensionality, we extend the clusters to nanowires, thin-films, and the bulk systems.^[34] Toward low-dimensional structures, there is a strong sharpening of the d bands, which vastly enhances the corresponding density of states and raises the band edges. This strong preference for lower-dimensional structures is in consonance with the experimental observation that the interatomic interactions progressively become stronger in low-coordinated systems. In our discussion of gold clusters, the presence of an excess charge promotes linearity.^[23] Interestingly, it was experimentally noted that a wire of at least four gold atoms suspended between two gold electrodes is linear.^[35,36] However, theoretical calculations of a free-standing, one-dimensional gold wire indicate that a two-dimensional structure is more stable.^[37] Therefore a subject of intense interest in the recent past is on methods to obtain one-dimensional gold nanowires. It would be useful to modulate the charge transfer in gold alloy nanowires by injecting s electrons into gold wire without

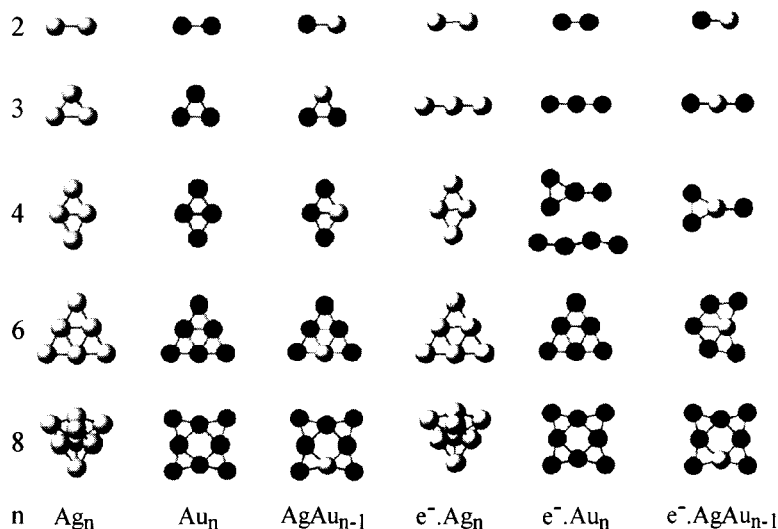


Fig. 1 Predicted lowest-energy conformers of neutral and anionic clusters of pure silver ($Ag_{2-4,6,8}$), pure gold ($Au_{2-4,6,8}$), and gold–silver alloys ($AgAu_{1-3,5,7}$).

distorting its band structure.^[38] The s band of the alloying metal should therefore possess similar energy levels as the 6s orbital of gold. Of all the s band metals, beryllium, magnesium, zinc, cadmium, and mercury have their valence energy levels closest to that of the 6s orbital of gold, and hence can form alloys with gold. Then, density functional calculations were carried out on free-standing, infinite monoatomic gold wires alloyed with both magnesium and zinc. In the alloy chains, the locations of the gold and zinc (or magnesium) atoms were alternated and investigated as both one- and two-dimensional structures. In sharp contrast to pure gold nanowires, the one- and two-dimensional structures of both gold–magnesium and gold–zinc alloys exhibit distinct minima in the plots of the cohesive energy, indicating that both forms are energetically accessible. We note that both zinc 4s and magnesium 3s bands display p character near the Fermi energy. This sp hybridization, which is absent in pure gold nanowires, favors a linear structure in the case of these alloyed nanowires.

Ionophores, Receptors, and Chemical Sensors

The design and synthesis of receptors capable of binding anionic or cationic guests are of crucial importance because of their potential applications in environmental and biological processes. Unlike nanoclusters and nanowires, the theoretical challenge in these systems is to describe the interactions of an organic system with a charged metal, or another organic cation. Furthermore, one has to take into account the role of the environment in modulating the binding characteristics. The environment could either be solvents, molecules, or other ions.

We begin our discussion of ionophore/receptor design with one of the seemingly intractable problems of contemporary biochemistry: the selective recognition of the ammonium cation (NH_4^+).^[8,39] Much of the problem is due to the nearly equivalent sizes of NH_4^+ and the potassium cation (K^+).^[40] In the following account, we show on how we circumvent the problem and were successful in identifying a series of receptors with improved selectivity and affinity for NH_4^+ .^[8] The first step in the receptor design was that high selectivity for NH_4^+ could be achieved with cation– π interactions,^[40–42] if the receptors have an optimal space to capture NH_4^+ and exhibit strong interactions toward NH_4^+ . However, the ionic radius of K^+ is nearly similar to that of NH_4^+ , so spatial differentiation is not useful. Therefore we take advantage of the differences in coordination numbers. K^+ favors a coordination number of six, while NH_4^+ favors only four. Furthermore, one has also to take into account the directional H-bonds involving NH_4^+ cations, to describe the higher selectivity for NH_4^+ over K^+ . Our initial calculations indicated that a benzene-based tripodal system with imidazoline arms (Fig. 2a) possesses vacant sites for the interaction with only one solvent molecule, while the K^+ ion has three vacant sites for three solvent molecules. In order to maximize the affinity and selectivity of these receptors for NH_4^+ , it becomes important to maximize the π -electron density of the receptor. Indeed, receptors with enhanced π -electron density by trimethylated phenyl ring with the strong proton-withdrawing subunits exhibit much higher affinities and selectivities.

Given this background, an extended concept has been applied to the receptor design for a biologically important molecule, acetylcholine.^[9] The receptor should have higher affinity and selectivity for acetylcholine over NH_4^+ .

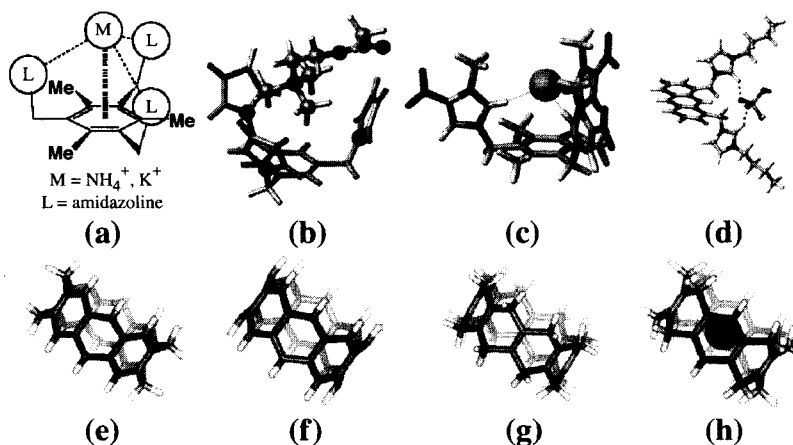


Fig. 2 Receptors for NH_4^+ (a), acetylcholine (b), Cl^- (c), H_2PO_4^- (d), and structures of collarenes (e), cyclacenes (f), beltene (g), and Rb^+ -complexed [8]beltene (h).

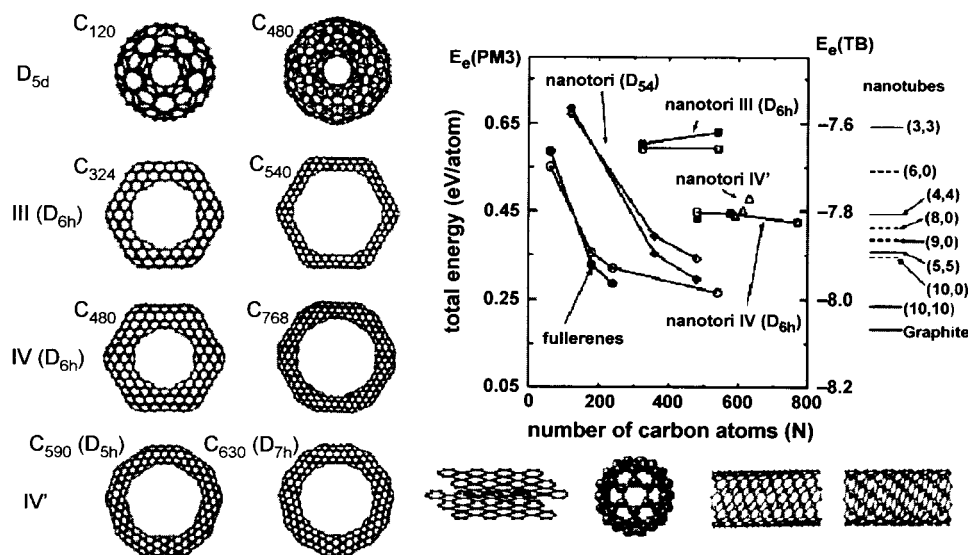


Fig. 3 Optimized structures of various types of carbon nanotube tori and their stability compared with grapheme, fullerene, and nanotubes. (From Ref. [51].)

This requires enhanced dispersion interactions and diminished ionic interactions, which is met by replacing the imidazole arms of the NH_4^+ receptors with pyrrole (Fig. 2b). These theoretical inferences were confirmed by experiments.

Interactions involving anions are very different from those of cations. As anions are more polarizable and hence more susceptible to polar solvents than cations, it becomes important to take into account solvent effects. Based on molecular dynamics simulations combined with *ab initio* calculations, highly selective anionophores have been designed.^[10–12] Enhanced dipole moments (Fig. 2c) were employed by attaching a strategically placed electron-withdrawing group.^[10] This approach would also aid in the design of novel functional molecular systems and biologically important chemosensors. Utilizing the $\text{CH}^+ \dots \text{X}^-$ H-bonds, fluorescent photoinduced electron transfer chemosensors for the recognition of H_2PO_4^- have also been designed and synthesized (Fig. 2d). In addition, we have also been successful in designing cyclopeptides as amphi-ionophores.^[43,44]

It would be appealing to explore the possibility of carbon-based materials being used as ionophores.^[45–47] Belt-shape carbocyclic-conjugated systems (annulenes, beltenes, cyclacenes, and collarenes) are closely related to other carbon-based systems containing curved surfaces. These include fullerenes and carbon nanotubes. The ion binding characteristics of these carbon materials have been unraveled through *ab initio* calculations, Monte Carlo, and molecular dynamics simulations of collarenes (benzene rings linked by methylene linkages), cyclacenes (composed only of benzene rings), and beltenes (ethene groups linked by methylene linkages), and their com-

plexes with various cations (alkali, alkaline-earth metal, and organic cations) in both the gas and aqueous phases (Fig. 2e–h). Additionally, suitable substituents could also enhance their binding affinities and selectivities. In particular, the designed molecules could be modified to be soluble in polar solvents by adding hydrophilic groups on the edges of the molecules.

Carbon-Based Nanomaterials

Since the discovery of fullerenes and carbon nanotubes, much effort has gone into the discovery of other interesting allotropes of carbon with unusual structural characteristics and novel physical properties.^[48–50] Toward this end, the geometries, electronic structures, and energetics of small carbon nanotori were investigated employing both tight-binding and semiempirical quantum chemical methods.^[51] It should be mentioned here that the very large size of these carbon-based materials precludes the use of high-level quantum methods. One therefore has to take recourse to the use of semiempirical or tight-binding methods. As can be seen from Fig. 3, the structures and electronic properties of the smallest nanotori exhibit interesting metal, semiconductor, and insulator characteristics depending on nanotube building blocks.

An interesting offshoot in the context of carbon-based nanomaterials is the role of external perturbations in modulating their physical and chemical characteristics. These perturbations can include cations or neutral atoms. In this context, we examined the magnetic properties of exohedral fullerenes of alkali-metal fullerides (A_xC_{60} , $\text{A}=\text{Na}, \text{K}, \text{Rb}, \text{Cs}$)^[52,53] and the spin properties of endohedral fullerenes ($\text{A}-\text{C}_{60}$, $\text{A}=\text{N}, \text{P}, \text{As}, \text{O}, \text{S}$)^[54–57] (Fig. 4). The

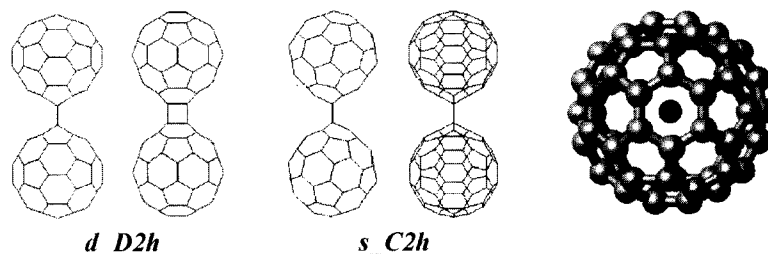


Fig. 4 Ground triplet ($d_{D_{2h}}$) and excited singlet ($s_{C_{2h}}$) states of $(C_{60})_2^{2-}$ with two views (for the alkali cation-doped exohedral fullerenes), and N-containing endohedral fullerene.

most interesting aspect of the experimental investigation of endohedral fullerenes was the fact that the encapsulated nitrogen, which possesses three unpaired electrons and is paramagnetic in nature, is totally inert within C_{60} . Our calculations, however, indicated that the interaction observed in the case of $N-C_{60}$ is predominantly dispersive in nature. These systems are interesting because endohedral fullerenes containing paramagnetic atoms could be utilized to design quantum computers.^[58]

Organic Nanotubes

There are several advantages in using hydrogen bonds to design nanomaterials,^[4-6,59] and in particular nanotubes, because these nanotubes have potential applications as

artificial biological channels, drug delivery, nanochemical reactors, etc.^[60-63] One of the spectacular aspects of a recent report on the self-assembly of an organic nanotube from nontubular units of calix[4]hydroquinone (CHQ) was that the theoretical design preceded the actual experiment of synthesis and investigation of the X-ray structure.^[4-6] Apart from highlighting the robustness of the theoretical approach, this study also provided several insights into the mechanism of self-assembly of CHQ nanotubes.

In the absence of water, for each CHQ monomer, the number of dangling H atoms is 4, while in the presence of water, these dangling H atoms of CHQs form chains $HQ-(water-HQ-HQ-)_n$ water. Although the strength of one-dimensional short H-bonding interaction (~ 10 kcal/

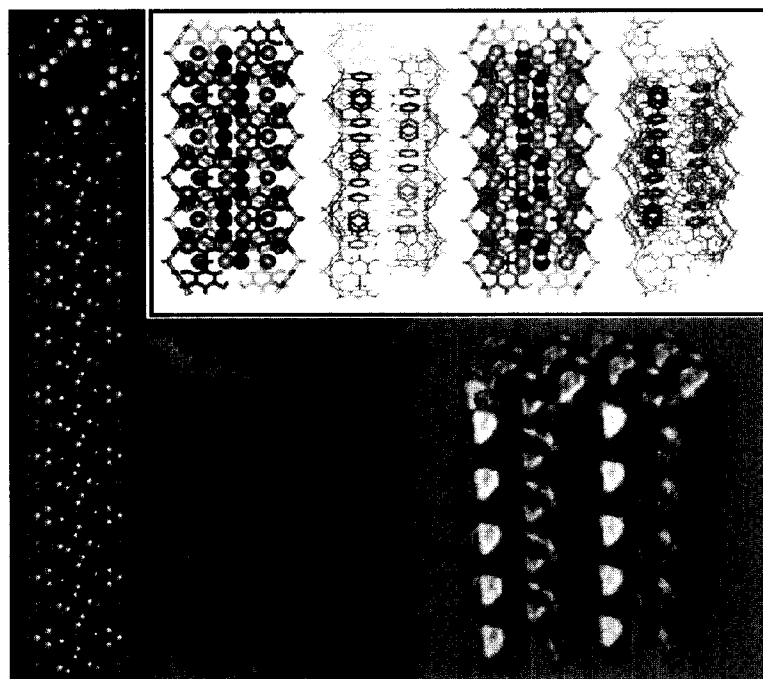


Fig. 5 Calix[4]hydroquinone nanotubes: structure, longitudinal one-dimensional H-bond relay vs. intertubular π - π stacking, the HREM image of a single nanotube, and the water-accessible surface of the tubes. Each tube has four pillar frames of short H-bonds, and the pore size is $8 \times 8 \text{ \AA}^2$. The unit cell is drawn by the dashed lines. (From Ref. [4].)

mol) is similar to or slightly stronger than the strength of the π - π stacking interaction, the assembly along the one-dimensional short H-bonds relay should be much more favorable because the number of H-bonds is three times the number of π - π stacks. Indeed, in experiments with water, CHQs are assembled to form long tubular structures with four infinitely long, short strong H-bond arrays. The CHQ tubes assemble to form long tubular structures in the presence of water, which in turn, form bundles with intertubular π - π stacking interactions (Fig. 5), resulting in crystals with well-ordered two-dimensional arrays of pores. The structures of these pores were utilized for the synthesis of encapsulated nanowires,^[5] which would be described in the next section. A needle-like nanotube bundle exhibits the infinitely long one-dimensional H-bonding network between hydroxyl groups of CHQs and water molecules and well-ordered intertubular π - π stacking pairs (Fig. 5). The geometries of the calculated π - π stacks are very close to the π - π stacks in the X-ray structure.

Encapsulated Metallic Nanowires

As was mentioned earlier, CHQ nanotubes arrays can be utilized in promising templates for nanosynthesis. Redox reaction of the nanotube in the presence of silver nitrate leads to the formation of a silver nanowire arrays in the pores (pore size of $8 \times 8 \text{ \AA}^2$) of the CHQ nanotube. The wires exist as uniformly oriented three-dimensional arrays of ultrahigh density. The driving force for the formation of these nanowires is the free energy gain due to the reduction-oxidation process.^[64,65] The resulting nanowire is composed of four dumbbells, each of which

contains two silver atoms, superimposed on one another and crisscrossed in their length.

The theoretical characterization of the reduced form of the CHQ nanotube was carried out using plane-wave pseudopotential methods.^[66] Our calculations indicated that upon reduction with silver nitrate, the CHQ nanotubes get transformed to the corresponding calix[4]quinone-hydroquinone (CQHQ) nanotubes, whose band gaps of 0.3 eV indicate that they are semiconducting in nature. The gross structural feature of CQHQ nanotubes is similar to that of CHQ nanotubes, with well-ordered H-bond arrays and intertubular π - π stacking pairs. In the CQHQ nanotubes, there are only two infinitely long one-dimensional H-bond arrays per nanotube because two hydroxyl groups are transformed to the corresponding reduced forms. Simultaneously, silver cations get transformed to metallic silver. Upon reduction of the CHQ nanotubes, the silver atoms are located within the reduced CQHQ nanotube (Fig. 6). In the case of 2/2 nanowire, the predicted cohesive energy is 2.4 eV, which is 0.9 eV smaller than the bulk value. The encapsulation of a silver nanowire within the CQHQ nanotube leads to several additional states in the band gap region, which are similar to that of an isolated silver nanowire. In this case two *s* channels cross the Fermi energy level, which indicates the existence of quantum conductance.

Nonlinear Optical Switches and Right-/Left-Handed Helices of Polypeptides

We had talked about harnessing the interaction of photons, electrons, protons, or charged species with molecular

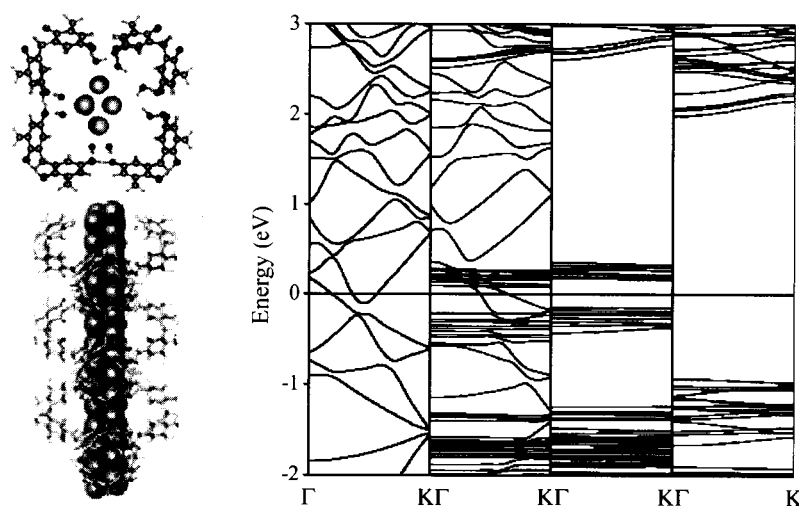


Fig. 6 Top and side views of a silver nanowire inside a calix[4]quinone-hydroquinone (CQHQ) nanotubes (left figures), and the band structures of an isolated silver nanowire (left—first on the right figure), a silver nanowire encapsulated in a CQHQ nanotube (second), a CQHQ nanotube (third), and a calix[4]hydroquinone (CHQ) nanotube (last). (From Ref. [66].)

systems in the design of new nanodevices. While photochemical and electrochemical switching devices have been extensively investigated, most of the photochemical switching devices are limited to the linear regime. However, it would be of interest to use nonlinear optical properties for an efficient memory device. In investigations of the interaction of photons with matter, it is essential that the employed theoretical method should be capable of characterizing both open-shells and excited states. The theoretical investigations of 1,2-bis-(3-thienyl)-ethene derivatives indicate that after photoswitching, the resulting π -conjugated closed forms exhibit highly nonlinear optical properties.^[67] The substitution of suitable donors and acceptors on certain strategic positions of these ethene derivatives, however, makes the closed form nonlinear optically active and the resulting molecular system behaves as an efficient nonlinear optical switch. It should be noted that the above discussion on nonlinear optical devices involves the breaking and formation of bonds. It is interesting to explore the possibility of devices, which rely entirely on conformational or enantiomeric changes.

Peptides are well-known biological systems, whose conformational characteristics are well understood. To date, the conventional wisdom was that a polypeptide can exist only as right-handed helix. However, calculations reveal the feasibility of a left-handed helix.^[68] Most of these calculations on these peptide systems were carried out using molecular dynamic simulations based on empirical potentials. The calculations indicate that the diameter of the left-handed helix is larger than the conventional right-handed helix. The left-handed helix is stabilized when the terminal residues are charged, because the dipole moments of carbonyl groups for the former are aligned opposite to those of the latter. Thus a molecular dynamics simulation of a poly-alanine peptide capped with neutral amino and methyl groups ($\text{CH}_3\text{-(Ala)}_n\text{-NH}_2$) under neutral terminal charge conditions yielded a right-handed α -helix pattern, in about ~ 1.8 nsec. However, when the terminals are charged ($\text{NH}_3^+\text{-(Ala)}_{30}\text{-COO}^-$), a left-handed λ -helix is formed in about ~ 4.0 nsec. During the formation of the left-handed λ -helix, helix-nucleation first occurs at the terminal sites (in particular, near the N-terminus in the case of the left-handed λ -helix) and it promotes the propagation of the helix pattern along the segment. It should be noted that in both the molecular dynamics simulations, only the terminal composition is different. Therefore the handedness of the final conformation is related to the terminal charge conditions. The propagation of the helix pattern along the segment clearly shows that sequential local interactions determine the nascent folding patterns of the protein. The initial folding in the left-handed λ -helix arises from the electrostatic interactions of the positively charged NH_3^+ group with the adjacent carbonyl dipole moiety, followed by the dipole-

dipole interactions between two adjacent carbonyl moieties. These results were further confirmed with more accurate calculations using a density functional approach. The preceding discussion implies that a transition between left-handed and right-handed helix motifs can be triggered by the presence of charged species near the end of the helix terminals. Such a possibility holds immense promise in the development of novel chiral switches.

Nanodevices

Up to now, our discussion was only centered on static systems. However, the quest for nanodevices implies that one has to induce motion in a system using external or internal means. The external means could include changes in pH, radiation, etc. We discuss one such device (a molecular flipper), which has been designed, synthesized, and characterized.^[13] The flipping/flapping motion, in the case of designed device, is due to the changes in edge-to-face and face-to-face aromatic interactions.^[69,70] It is interesting to note that this conformational change can be electrochemically controlled by reduction/oxidation of the quinone moiety in the molecular system.

The strategy for the design of nanodevices is to harness the subtle changes in the π -electron densities of a quinone moiety as results of changes in the electronic environment.^[70,71] Quinones are particularly suited for this endeavor because their electronic characteristics can be electrochemically or photochemically controlled. Based on a theoretical investigation of the conformational characteristics of *p*-benzoquinone-benzene complexes, we found that the energy difference between the stacked and edge-to-face conformations of cyclophane molecules (Fig. 7) is substantial. Thus if one could subtly control the

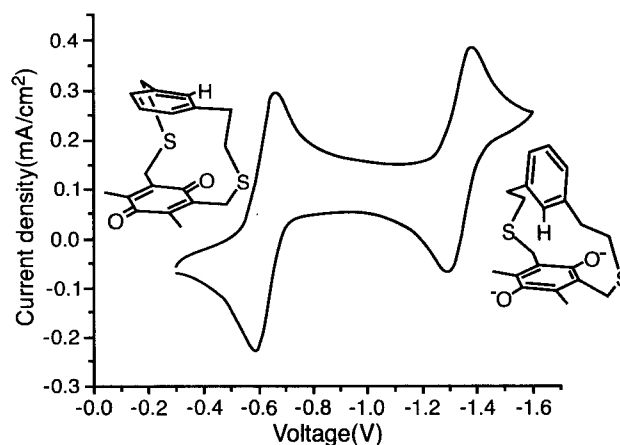


Fig. 7 Cyclic voltammogram of MHQC(left)/MQC(right) (1 mM) in acetonitrile with tetrabutylammonium dihydrogen phosphate (0.1 M) at 25°C (scan rate 100 mV/sec). (From Ref. [13].)

conformational characteristics of 2,11-dithio[4,4]meta-metaquinocyclophane (MQC) (stacked conformer is 7 kcal/mol more stable than the edge-to-face conformer) and 2,11-dithio[4,4]metametahydroquinocyclophane (MHQC) (edge-to-face is 9 kcal/mol more stable than the edge-to-face conformer) by electrochemical and/or photochemical means, we can have a very interesting model of a potential molecular device. The cyclic voltammograms of MQC exhibit two clear reversible redox reactions (Fig. 7). In aprotic media, quinones exhibit two reduction peaks separated by 0.7 V, which corresponds to the formation of a radical anion species and a dianion species of quinones, respectively. This is in agreement with the reduction characteristics of MQC. Two well-separated reduced states of MQC are formed in the aprotic solvent of acetonitrile upon reduction. Therefore the electronic states of MQC and MHQC can be easily transformed into each other by simple electrochemical control of the redox reaction, which results in large conformational flapping motions due to a preference for the stable conformation caused by the change in the electronic state of the quinone moiety.

Thus a cyclophane system composed of quinone and benzene rings exhibits a flapping motion involving squeezing and thrusting motions in the presence of solvent molecules by electrochemical redox process. This case illustrates a promising pathway of harnessing the differences in the relative magnitudes of different kinds of intermolecular interactions to design a nanomechanical device. The large flapping/flipping motion from the edge-to-face and stacked conformations and vice versa is a first step toward a propelling molecular vessel or a molecular flipper that can be electrochemically or photochemically controlled. It could be applied to design molecular hinges, molecular switches, and eventually to design mobile nanomechanical devices.

CONCLUSION

In the course of this article, we have illustrated using several examples from our work that knowledge of interaction forces, together with a judicious choice of theoretical methods, can be employed in the de novo design of functional nanomaterials and nanodevices. The knowledge of interaction forces could also be utilized for the development of novel functional molecular systems having the capacity of controlled assembly. We have discussed the design and synthesis of several functional molecular systems such as nanowires/nanotubes, ionophores/receptors/sensors, electron/proton/molecular tweezers, molecular vehicles, and molecular-robots/bio-nanorobots. We expect that some of the ideas gleaned from our work would find utility in the search for molecular nanoelectronic/mechanical devices, quantum computing devices, biomolec-

ular sensors, and nanosurgery. Although this research field is still in the embryonic stage, the advent of fast computers and extremely powerful programs should revolutionize the design and development of nanomaterials and nanodevices in the near future. One of the advantages of the present work is that it also helps obtain an enhanced understanding of the processes in the macroscopic world.

ACKNOWLEDGMENTS

This work was supported by the Korean Ministry of Science and Technology under the Creative Research Initiatives Program.

REFERENCES

1. *Comprehensive Supramolecular Chemistry*; Atwood, J.L., Davis, J.E.D., MacNicol, D.D., Vögtle, F., Lehn, J.-M., Eds.; Elsevier: Amsterdam, 1996; Vols. 1–11.
2. Tarakeshwar, P.; Kim, K.S. Nanorecognition. In *Encyclopedia of Nanoscience and Nanotechnology*; Nalwa, H.S., Ed.; American Science Publishers: California, 2003.
3. Kuhn, H.; Försterling, H.-D. *Principles of Physical Chemistry: Understanding Molecules, Molecular Assemblies and Supramolecular Machines*; John Wiley & Sons Inc.: New York, 1999.
4. Hong, B.H.; Lee, J.Y.; Lee, C.-W.; Kim, J.C.; Bae, S.C.; Kim, K.S. Self-assembled organic nanotube arrays with infinitely long one-dimensional H-bonds. *J. Am. Chem. Soc.* **2001**, *123* (43), 10748–10749.
5. Hong, B.H.; Bae, S.C.; Lee, C.-W.; Jeong, S.; Kim, K.S. Ultrathin single-crystalline silver nanowire arrays formed in an ambient solution phase. *Science* **2001**, *294* (5541), 348–351.
6. Kim, K.S.; Suh, S.B.; Kim, J.C.; Hong, B.H.; Lee, E.C.; Yun, S.; Tarakeshwar, P.; Lee, J.Y.; Kim, Y.; Ihm, H.; Kim, H.G.; Lee, J.W.; Kim, J.K.; Lee, H.M.; Kim, D.; Cui, C.; Youn, S.J.; Chung, H.Y.; Choi, H.S.; Lee, C.-W.; Cho, S.J.; Jeong, S.; Cho, J.-H. Assembling phenomena of calix[4]hydroquinone nanotube bundles by one-dimensional short hydrogen bonding and displaced π - π stacking. *J. Am. Chem. Soc.* **2002**, *124* (47), 14268–14279.
7. Braga, D.; Grepioni, F. Intermolecular interactions in nonorganic crystal engineering. *Acc. Chem. Res.* **2000**, *33* (9), 601–608.
8. Oh, K.S.; Lee, C.-W.; Choi, H.S.; Lee, S.J.; Kim,

- K.S. Origin of the high affinity and selectivity of novel receptors for NH_4^+ over K^+ : Charged hydrogen bonds vs. cation- π interaction. *Org. Lett.* **2000**, *2* (17), 2679–2681.
9. Yun, S.; Ihm, H.; Kim, H.G.; Lee, C.-W.; Banyopadhyay, I.; Oh, K.S.; Gong, Y.J.; Lee, J.W.; Yoon, J.; Lee, H.C.; Kim, K.S. Molecular recognition of fluoride anion: Benzene-based tripodal imidazolium receptor. *J. Org. Chem.* **2003**, *68* (6), 2467–2470.
 10. Yun, S.; Kim, Y.-O.; Kim, D.; Kim, H.G.; Ihm, H.; Kim, J.K.; Lee, C.-W.; Lee, W.J.; Yoon, J.; Oh, K.S.; Yoon, J.; Park, S.-M.; Kim, K.S. Rational design of biologically important chemosensors: A novel receptor for selective recognition of acetylcholine over ammonium cations. *Org. Lett.* **2003**, *5* (4), 471–474.
 11. Ihm, H.; Yun, S.; Kim, H.G.; Kim, J.K.; Kim, K.S. Tripodal nitro-imidazolium receptor for anion binding driven by (C-H) $^+$ -X $^-$ hydrogen bonds. *Org. Lett.* **2002**, *4* (17), 2897–2900.
 12. Kim, S.K.; Singh, N.J.; Kim, S.J.; Kim, H.G.; Kim, J.K.; Lee, J.W.; Kim, K.S.; Yoon, J. A new fluorescent photo-induced electron transfer chemosensor for the recognition of H_2PO_4^- . *Org. Lett.* **2003**, *5* (12), 2083–2086.
 13. Kim, H.G.; Lee, C.-W.; Yun, S.; Hong, B.H.; Kim, Y.-O.; Kim, D.; Ihm, H.; Lee, J.W.; Lee, E.C.; Tarakeshwar, P.; Park, S.-M.; Kim, K.S. An electrochemically controllable nanomechanical molecular system utilizing edge-to-face and face-to-face aromatic interactions. *Org. Lett.* **2002**, *4* (22), 3971–3974.
 14. Majumdar, D.; Lee, H.M.; Kim, J.; Kim, K.S. Photoswitch and nonlinear optical switch: Theoretical studies on 1,2-bis-(3-thienyl)-ethene derivatives. *J. Chem. Phys.* **1999**, *111* (13), 5866–5872.
 15. Kim, K.S.; Tarakeshwar, P.; Lee, J.Y. Molecular clusters of π -systems: Theoretical studies of structures, spectra and origin of interaction energies. *Chem. Rev.* **2000**, *100* (11), 4145–4185.
 16. *Clusters of Atoms and Molecules*; Haberland, H., Ed.; Springer-Verlag: Berlin, 1994.
 17. Castleman, A.W., Jr.; Bowen, K.H., Jr. Clusters: Structure, energetics, and dynamics of intermediate states of matter. *J. Phys. Chem.* **1996**, *100* (31), 12911–12944.
 18. Tarakeshwar, P.; Lee, H.M.; Kim, K.S. Insights from Theoretical Investigations of Aqueous Clusters. In *Reviews of Modern Quantum Chemistry*; Sen, K.D., Ed.; World Scientific: Singapore; 2002; 1642–1683.
 19. Lee, H.M.; Suh, S.B.; Lee, J.Y.; Tarakeshwar, P.; Kim, K.S. Structures, energies, vibrational spectra, and electronic properties of water monomer to decamer. *J. Chem. Phys.* **2000**, *112* (22), 9759–9772.
 20. Lee, H.M.; Suh, S.B.; Lee, J.Y.; Tarakeshwar, P.; Kim, K.S. Structures, energies, vibrational spectra, and electronic properties of water monomer to decamer. *J. Chem. Phys.* **2001**, *114* (7), 3343.
 21. Lee, H.M.; Suh, S.B.; Kim, K.S. Structures, energies, and vibrational spectra of water undecamer and dodecamer: Ab initio study. *J. Chem. Phys.* **2001**, *114* (24), 10749–10756.
 22. Lee, H.M.; Suh, S.B.; Kim, K.S. Structures, energies, and vibrational spectra of water undecamer and dodecamer: Ab initio study. *J. Chem. Phys.* **2001**, *115* (15), 7331.
 23. Lee, H.M.; Maofa, G.; Sahu, B.R.; Tarakeshwar, P.; Kim, K.S. Geometrical and electronic structures of gold, silver, and gold-silver binary clusters: Origins of ductility of gold and gold-silver alloy formation. *J. Phys. Chem., B* **2003**, *107* (37), 9994–10005.
 24. Pyykkö, P.; Runeberg, N. Icosahedral W-Au $_{12}$: A predicted closed-shell species, stabilized by aurophilic attraction and relativity and in accord with the 18-electron rule. *Angew. Chem. Int. Ed.* **2002**, *41* (12), 2174–2176.
 25. Li, X.; Kiran, B.; Li, J.; Zhai, H.-J.; Wang, L.-S. Experimental observation and confirmation of icosahedral W-Au $_{12}$ and Mo-Au $_{12}$ molecules. *Angew. Chem. Int. Ed.* **2002**, *41* (24), 4786–4789.
 26. Brutschy, B. The structure of microsolvated benzene derivatives and the role of aromatic substituents. *Chem. Rev.* **2000**, *100* (11), 3891–3920.
 27. Muller-Dethlefs, K.; Hobza, P. Noncovalent interactions: A challenge for experiment and theory. *Chem. Rev.* **2000**, *100* (1), 143–168.
 28. Tarakeshwar, P.; Choi, H.S.; Kim, K.S. Olefinic vs. aromatic π -H interaction: A theoretical investigation of the nature of interaction of first-row hydrides with ethene and benzene. *J. Am. Chem. Soc.* **2001**, *123* (14), 3323–3331.
 29. Manojkumar, T.K.; Choi, H.S.; Tarakeshwar, P.; Kim, K.S. Ab-initio studies of neutral and anionic *p*-benzoquinone-water clusters. *J. Chem. Phys.* **2003**, *118* (19), 8681–8686.
 30. Schwerdtfeger, P. Gold goes nano—From small clusters to low-dimensional assemblies. *Angew. Chem. Int. Ed.* **2003**, *42* (17), 1892–1895.
 31. Yoon, J.; Kim, K.S.; Baeck, K.K. Ab initio study of the low-lying electronic states of Ag $_3^-$, Ag $_3$, and Ag $_3^+$: A coupled-cluster approach. *J. Chem. Phys.* **2000**, *112* (21), 9335–9342.
 32. Häkkinen, H.; Moseler, M.; Landman, U. Bonding in Cu, Ag, and Au clusters: Relativistic effects, trends, and surprises. *Phys. Rev. Lett.* **2002**, *89* (3), 033401(1-4).

33. Negishi, Y.; Nakamura, Y.; Nakajima, A.; Kaya, K. Photoelectron spectroscopy of gold–silver binary cluster anions (Au_nAg_m ; $2 \leq n+m \leq 4$). *J. Chem. Phys.* **2001**, *115* (8), 3657–3663.
34. Nautiyal, T.; Youn, S.J.; Kim, K.S. Effect of dimensionality on the electronic structure of Cu, Ag, and Au. *Phys. Rev., B* **2003**, *68* (4), 033407(1–4).
35. Ohnishi, H.; Kondo, V.; Takayanagi, K. Quantized conductance through individual rows of suspended gold atoms. *Nature* **1998**, *395* (6704), 780–783.
36. Yanson, A.I.; Bollinger, G.R.; van den Brom, H.E.; Agrait, N.; van Ruitenbeek, J.M. Formation and manipulation of a metallic wire of single gold atoms. *Nature* **1998**, *395* (6704), 783–785.
37. Rodrigues, V.; Fuhrer, T.; Ugarte, D. Signature of atomic structure in the quantum conductance of gold nanowires. *Phys. Rev. Lett.* **2000**, *85* (19), 4124–4127.
38. Geng, W.-T.; Kim, K.S. Linear monatomic wires stabilized by alloying: Ab initio density functional calculations. *Phys. Rev., B* **2003**, *67* (4), 233403(1–4).
39. Bühlmann, P.; Pretsch, E.; Bakker, E. Carrier-based ion-selective electrodes and bulk optodes: 2. Ionophores for potentiometric and optical sensors. *Chem. Rev.* **1998**, *98* (4), 1593–1688.
40. Kim, D.; Hu, S.; Tarakeshwar, P.; Kim, K.S.; Lisy, J.M. Cation– π interactions: A theoretical investigation of the interaction of metallic and organic cations with alkenes, arenes, and heteroarenes. *J. Phys. Chem., A* **2003**, *107* (8), 1228–1238.
41. Kim, K.S.; Lee, J.Y.; Lee, S.J.; Ha, T.-K.; Kim, D.H. On binding forces between aromatic ring and quaternary ammonium compound. *J. Am. Chem. Soc.* **1994**, *116* (16), 7399–7400.
42. Ma, J.C.; Dougherty, D.A. The cation– π interaction. *Chem. Rev.* **1997**, *97* (5), 1303–1324.
43. Cui, C.; Cho, S.J.; Kim, K.S. Cation affinities of [16]starand model—Comparison with 12-crown-4: Crucial role of dipolar moiety orientations. *J. Phys. Chem., A* **1998**, *102* (7), 1119–1123.
44. Suh, S.B.; Cui, C.; Son, H.S.; U., J.S.; Won, Y.; Kim, K.S. Novel amphi-ionophore in aqueous solution: Cyclohexaaryl. *J. Phys. Chem., B* **2002**, *106* (8), 2061–2064.
45. Choi, H.S.; Suh, S.B.; Cho, S.J.; Kim, K.S. Ionophores and receptors using cation– π interactions: Collarenes. *Proc. Natl. Acad. Sci. U. S. A.* **1998**, *95* (21), 12094–12099.
46. Choi, H.S.; Kim, K.S. Structures, magnetic properties, and aromaticity of cyclacenes. *Angew. Chem. Int. Ed.* **1999**, *38* (15), 2256–2258.
47. Choi, H.S.; Kim, D.; Tarakeshwar, P.; Suh, S.B.; Kim, K.S. A new type of ionophore family utilizing the cation–olefin π interaction: Theoretical study of [n] beltenes. *J. Org. Chem.* **2002**, *67* (6), 1848–1851.
48. Dresselhaus, M.S.; Dresselhaus, G.; Eklund, P.C. *Science of Fullerenes and Carbon Nanotubes*; Academic Press: San Diego, 1996.
49. Dunlap, B.I. Connecting carbon tubules. *Phys. Rev., B* **1992**, *46* (3), 1933–1936.
50. Itoh, S.; Ihara, S.; Kitakami, J. Toroidal form of carbon C_{360} . *J. Phys. Rev., B* **1993**, *47* (3), 1703–1704.
51. Oh, D.-H.; Park, J.M.; Kim, K.S. Structures and electronic properties of small carbon nanotube tori. *Phys. Rev., B* **2000**, *62* (3), 1600–1603.
52. Kim, K.S.; Park, J.M.; Kim, J.; Suh, S.B.; Tarakeshwar, P.; Lee, K.H.; Park, S.S. Dimer to monomer phase transition in alkali–metal fullerenes: Magnetic susceptibility changes. *Phys. Rev. Lett.* **2000**, *84* (11), 2425–2428.
53. Oszlányi, G.; Bortel, G.; Faigel, G.; Tegze, M.; Gránágy, L.; Pekker, S.; Stephens, P.W.; Bendele, G.; Dinnebier, R.; Mihály, G.; Jánossy, A.; Chauvet, O.; Forró, L. Dimerization in KC_{60} and RbC_{60} . *Phys. Rev., B* **1995**, *51* (18), 12228–12232.
54. Park, J.M.; Tarakeshwar, P.; Kim, K.S.; Clark, T. Nature of the interaction of paramagnetic atoms ($A = {}^4\text{N}, {}^4\text{P}, {}^3\text{O}, {}^3\text{S}$) with π systems and endohedral fullerenes $A\text{-C}_{60}$. *J. Chem. Phys.* **2002**, *116* (24), 10684–10691.
55. Almeida Murphy, T.; Pawlik, Th.; Weidinger, A.; Höhne, M.; Alcalá, R.; Spaeth, J.-M. Observation of atomlike nitrogen in nitrogen-implanted solid C_{60} . *Phys. Rev. Lett.* **1996**, *77* (6), 1075–1078.
56. Mauser, H.; van Eikema Hommes, N.J.R.; Clark, T.; Hirsch, A.; Pietzak, B.; Weidinger, A.; Dunsch, L. Stabilization of atomic nitrogen inside C_{60} . *Angew. Chem. Int. Ed.* **1997**, *36* (24), 2835–2838.
57. Lu, J.; Zhang, Z.; Zhao, X. Electronic structures of endohedral N-C_{60} , O-C_{60} and F-C_{60} . *Chem. Phys. Lett.* **1999**, *312* (2–4), 85–90.
58. Ardavan, A.; Austwick, M.; Benjamin, S.C.; Briggs, G.A.D.; Dennis, T.J.S.; Ferguson, A.; Hasko, D.G.; Kanai, M.; Khlobystov, A.N.; Lovett, B.W.; Morley, G.W.; Oliver, R.A.; Pettifor, D.G.; Porfyrakis, K.; Reina, J.H.; Rice, J.H.; Smith, J.D.; Taylor, R.A.; Williams, D.A.; Adelman, C.; Mariette, H.; Hamers, R.J. Nanoscale solid-state quantum computing. *Philos. Trans. R. Soc., Math. Phys. Eng. Sci.* **2003**, *361* (1808), 1473–1485.
59. Chin, D.N.; Zerkowski, J.A.; MacDonald, J.C.; Whitesides, G.M. *Organized Molecular Assemblies in the Solid State*; Whitesell, J.K., Ed.; John Wiley & Sons Inc.: New York, 1999; 185.
60. Bong, D.T.; Clark, T.D.; Granja, J.R.; Ghadiri, M.R.

- Self-assembling organic nanotubes. *Angew. Chem. Int. Ed.* **2001**, *40* (6), 988–1011.
61. Muchado, V.G.; Baxter, P.N.W.; Lehn, J.-M. Self-assembly in self-organized inorganic systems: A view of programmed metallosupramolecular architectures. *J. Braz. Chem. Soc.* **2001**, *12* (4), 431–462.
62. Prins, L.G.; Reinhoudt, D.N.; Timmerman, P. Noncovalent synthesis using hydrogen bonding. *Angew. Chem. Int. Ed.* **2001**, *40* (13), 2382–2426.
63. Hof, F.; Craig, S.L.; Nuckolls, C.; Rebek, J. Molecular encapsulation. *Angew. Chem. Int. Ed.* **2002**, *41* (9), 1488–1508.
64. Braun, E.; Eichen, Y.; Sivan, U.; Ben-Yoseph, G. DNA-templated assembly and electrode attachment of a conducting silver wire. *Nature* **1998**, *391* (6669), 775–778.
65. Taton, T.A.; Mirkin, C.A.; Letsinger, R.L. Scano-metric DNA array detection with nanoparticle probes. *Science* **2000**, *289* (5485), 1757–1760.
66. Suh, S.B.; Hong, B.H.; Tarakeshwar, P.; Youn, S.J.; Jeong, S.; Kim, K.S. Electronic structure of silver subnanowires in self-assembled organic nanotubes: Density functional calculations. *Phys. Rev., B (Rapid Commun.)* **2003**, *67* (24), 241402(1-4).
67. Majumdar, D.; Lee, H.M.; Kim, J.; Kim, K.S. Photoswitch and nonlinear optical switch: Theoretical studies on 1,2-bis-(3-thienyl)-ethene derivatives. *J. Chem. Phys.* **1999**, *111* (13), 5866–5872.
68. Son, H.S.; Hong, B.H.; Lee, C.-W.; Yun, S.; Kim, K.S. A new type of helix pattern in poly-alanine peptide. A new type of helix pattern in polyalanine peptide. *J. Am. Chem. Soc.* **2001**, *123* (3), 514–515.
69. Hong, B.H.; Lee, J.Y.; Cho, S.J.; Yun, S.; Kim, K.S. Theoretical study of the conformations and strain energies of [*n,n*]metaparacyclophanes: Indication of stable edge-to-face and displaced face-to-face conformers for *n*=4. *J. Org. Chem.* **1999**, *64* (15), 5661–5665.
70. Lee, J.Y.; Kim, K.S.; Mhin, B.J. Intramolecular charge transfer of pi-conjugated push-pull systems in terms of polarizability and electronegativity. *J. Chem. Phys.* **2001**, *115* (20), 9484–9489.
71. Lee, J.Y.; Mhin, B.J.; Kim, K.S. New quantum chemical parameter for the substituent effect in benzene based on charge flux. *J. Phys. Chem., A* **2003**, *107* (19), 3577–3579.

Nanomaterials: Manufacturing, Processing, and Applications

N

Pramod K. Sharma

Weifang Miao

Anit Giri

Srikanth Raghunathan

Nanomats, Inc., North Huntingdon, Pennsylvania, U.S.A.

INTRODUCTION

The particles with small size in the range from a few to several tens of nanometers are called quasi zero-dimensional mesoscopic system, quantum dots, quantized or Q-particles, etc.^[1] The reason that nanoscale materials and structures are so interesting is that size constraints often produce qualitatively new behavior. Nanotechnology arises from the exploitation of new properties, phenomena, processes, and functionalities that matter exhibits at intermediate sizes between isolated atoms or molecules (~ 1 nm) and bulk materials (over 100 nm). As opposed to the microscale, the nanoscale is not just another step toward miniaturization, but is a qualitatively new scale. Hence quantum and size phenomena are allowed to manifest themselves either at a purely quantum level or in a certain admixture of quantum and classical components. At the foundation of nanosystems lie the quantum manifestations of matter that become relevant. Consequently, instead of being a limitation or an elusive frontier, quantum phenomena have become the crucial enabling tool for nanotechnology. Extensive research on semiconductor quantum dots has shown that these particles have properties halfway between macroscopic (bulk) and microscopic (molecular-like) substances and have recently aroused great interest in laser, photochemistry, and nonlinear optics.^[2-4] Bawendi et al.^[3] have observed a number of discrete electronic transitions and LO-phonon progression which were cleanly resolved for the first time in nanometer-scale cluster in CdSe. Jungnickel and Henneberger^[5] have described the luminescence properties of semiconductor nanocrystals and the carrier processes that are relevant for the light emission. Their study was concentrated on nanocrystal of size ≈ 5 nm, and hence observed strong carrier confinement. A size dependence in the luminescence efficiency of ZnS:Mn nanocrystals has also been observed by Bargava et al.^[6] and stated that the Mn^{2+} ion d-electron states act as efficient luminescent centers while interacting with s-p electronic states of the host nanocrystals. They showed that this electronic interaction provides an effective energy transfer path and leads

to high luminescent efficiencies at room temperature and hence suggested that nanocrystals doped with optically active luminescent centers may create new opportunities in the study and application of nanoscale material structures.

Because nanomaterials possess unique, beneficial chemical, physical, and mechanical properties, they can be used for a wide variety of applications. This review primarily focuses on the synthesis, properties, and applications of nanomaterials. It has been proven that the particles at the nanometer level have improved quality with respect to their potential application that include, but are not limited to, various structural, optical, electrical, mechanical, and catalytic activity, biomedical, next-generation computer chips, kinetic energy (KE) penetrators with enhanced lethality, better insulation materials, low-cost flat-panel displays, elimination of pollutants, tougher and harder cutting tools, high-sensitivity sensors, high-power magnets, future weapon platforms, aerospace, large lasting satellites, longer-lasting medical implants, corrosion resistance, etc. Fig. 1 shows the improvements in the final properties of the nanomaterials.

SYNTHESIS OF NANOMATERIALS

There are several methods that can be used to synthesize solids. Solids can be also prepared in various forms as fibers, films, foams, ceramics, powders, single crystals, and nanoparticles. However, those solids, which are not thermodynamically stable, may be much more difficult to prepare and may require special methods. The oldest and widely used method is the solid-state routing of synthesizing metal oxides. In this traditional technique, the powder reactants are mixed together, pressed into pellets or some other shape, and then heated in a furnace for prolonged periods. However, this method is not very sophisticated because of the following reasons:

- It requires a high temperature to react the reactants.
- Slow diffusion of ions.
- Unhomogenized reaction mixtures.

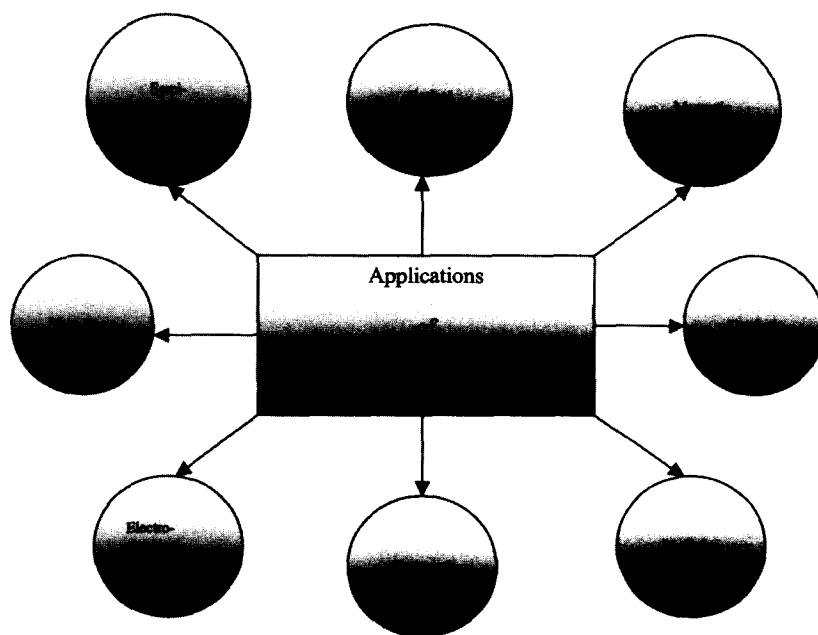


Fig. 1 Applications of nanomaterials. (View this art in color at www.dekker.com.)

- Impure final product because of unreacted reactants.
- Large particle size and bimodal particle size distribution.
- Defects, e.g., points/line/twinning.
- Metal oxides with unusual oxidation states cannot be prepared, e.g., vanadates and tungstates.
- Low surface area.

Solids with nanosize particle size cannot be prepared by traditional method simply because the reactants are not mixed on the atomic scale. All the alternative methods, e.g., hydrothermal, sol-gel, Pechini, CVD, and microwave, described in the rest of this section address this problem by achieving atomic scale mixing of reactants, in gas, liquid, or even solid phases. Most of these are low-temperature methods, although finally firing may be required at high temperatures especially for ceramic-type products. These methods enable the final product with the following characteristics:

- Nanosize particles.
- Narrow particle size distribution.
- High surface area.
- Homogenous.
- Pure.
- Improved properties.

Hydrothermal Synthesis

Hydrothermal methods are becoming a popular technique to precipitate mixed metal oxides directly from either

homogeneous or heterogeneous solution. Hydrothermal method utilizes water under pressure and at temperatures above its normal boiling point as a means of speeding up the reactions between solids.^[7] Water is an excellent solvent because of its high dielectric constant. This decreases with rising temperature and increases with rising pressure, with temperature effect predominating. In addition, the high dielectric constant of water is confirmed to a region of low temperature and high densities (pressure). This property is mainly responsible for increasing the solubility of many sparingly soluble compounds under hydrothermal conditions leading to many useful chemical reactions such as hydrolysis, precipitation, coprecipitation, and crystal growth.

Hydrothermal reactions are usually performed in closed vessels. The pressure-temperature relations of water at constant volume are shown in Fig. 2. The reactants are either dissolved or suspended in a known amount of water and are transferred to acid digestion reactors or autoclaves (Fig. 3). Under hydrothermal conditions, reactants otherwise difficult to dissolve can go into solution and reprecipitate.

Hydrothermal reaction is a single-step process for preparing several oxides and phosphates.^[7-9] Oguri et al.^[10] obtained narrow size distribution of spherical submicron titanium hydrous oxide, which could be readily transformed into polycrystalline anhydrous anatase with spherical morphology. Fine particles of ferroelectric lead titanate with high Curie temperature were prepared via hydrothermal technique.^[11] Kutty and Balachandran synthesized lead zirconate titanate (PZT) in better compositional

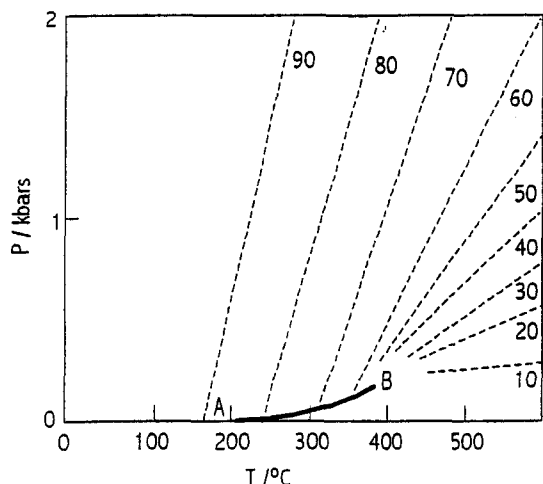


Fig. 2 Pressure–temperature relations for water at constant volume. (From Basic Solid State Chemistry by A. R. West, John Wiley and Sons, Ltd, NY, 1999.)

homogeneity and sinterability. This technique was further used for the fabrication of nanocrystalline metal oxides. Sharma et al.^[12] have synthesized nanosize α -alumina using hydrothermal method with particle size of 10 nm. Quantum size particles (<10 nm) of Y_2O_3 could also be achieved by this technique at 170°C using seeds^[12] and are shown in Fig. 4. This method was further employed for the fabrication of several other metal oxides, e.g., ZnO, TiO_2 , and ZrO_2 , with nanosize particles.^[12–15]

Sol–Gel Synthesis

In sol–gel synthesis, the precursors, which are essentially the starting compounds for the preparation of a colloid,

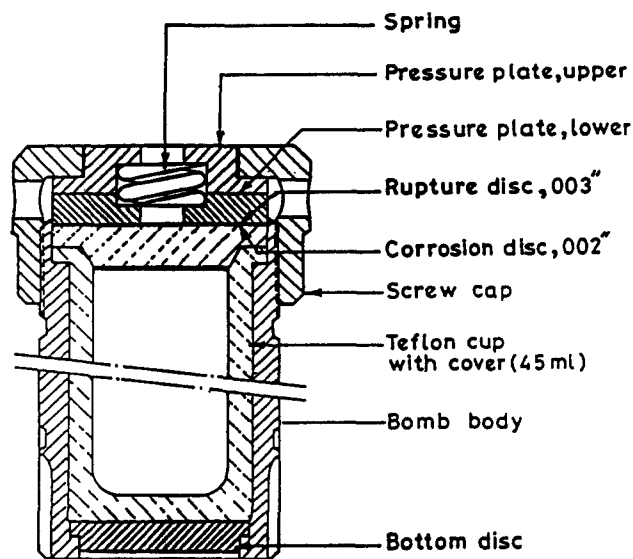


Fig. 3 Schematic diagram of an autoclave.

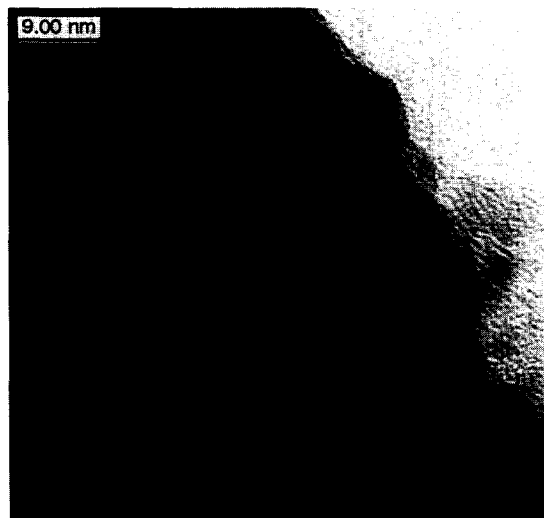


Fig. 4 Hydrothermally prepared nanosize yttria. (View this art in color at www.dekker.com.)

consist of a metal or metalloid element surrounded by various links called ligands. These ligands do not include another metal or metalloid atom, but may be inorganic, such as aluminum nitrate [$Al(NO_3)_2$], or organic, such as aluminum butoxide [$Al(OC_4H_9)_3$]. Metal alkoxides are more widely used than any other precursors because metal alkoxides react readily with water. However, for some nonsilicates, especially for transition-metal-oxide gels, inorganic precursors are used. The transition-metal-oxide gels are also used for obtaining thin-film ferroelectric materials such as barium titanate, electrochromic WO_3 films, and semiconducting V_2O_5 films.^[16–20] Fig. 5 is the high-resolution transmission electron microscopy (HRTEM) of α - Al_2O_3 derived by sol–gel method.

A gel can be classified as aquagel, alcogel, xerogel, and aerogel depending on the nature of the medium that is contained within the gel's three-dimensional network of particles. An aquagel is a gel wherein water is contained within its interstices. An alcogel is a gel in which the water is replaced by alcohol substitution. When the gel is in as-dried condition, it is called a xerogel. If the gel is supercritically dried (a drying process in which a medium is replaced, by another medium, under controlled conditions so that the gel structure does not collapse), then the resulting gel is termed an aerogel, where the fluid trapped in the gel interstices is air. The techniques used to preserve the gel structure include freeze-drying. This apparatus is called the freeze-dryer and is used commercially to preserve foodstuffs such as instant coffee powders, dry milk powder, and nondairy coffee creamer, has been used to synthesize materials, and is available in large sizes. This method has also been used to synthesize dispersion-strengthened alloy and composite systems.^[18] The rationale behind the preservation of the open



Fig. 5 High-resolution transmission electron microscopy of α -alumina synthesized by sol-gel process. (From Ref. [29].) (View this art in color at www.dekker.com.)

structure of the aquagel or alcogel is to facilitate the accelerated expulsion of the fluid trapped at the interstices of the gel, which is made of a continuous, three-dimensional network of nanocrystalline particles, during the metal deposition process in a fluidized-bed reactor. The open structure (greater grain boundary area) of the aerogel lends itself to processing at very low temperatures unlike its commercial counterparts. This method is also useful in the hydrogen reduction, carburization, nitridation, and a host of other surface treatment processes. A schematic of the aerogel is depicted in Fig. 6.

The specific advantages of the sol-gel synthesis technique are as follows:

- Sol-gel synthesis is a very viable alternative method to produce nanocrystalline elemental, alloy, and composite powders in an efficient and cost-effective manner.
- Almost any combination of materials could be synthesized at very low temperatures.
- Greater control of material chemistry and homogeneity is possible.
- Sol-gel synthesized powders could be processed, such as for coating, carburization, and nitridation, at substantially lower temperatures.
- Nanocrystalline powders could be consolidated at much lower pressures and temperatures.
- Enhanced densification of high-temperature materials without the low-temperature binders, which are detrimental to their performance under extreme conditions, is also possible via sol-gel synthesis of nanocrystalline materials.

- Thermomechanical processing of the components could be accomplished at significantly lower processing conditions.
- Processes, such as infiltration, could be carried out uniformly because of the continuous, three-dimensional network of nanocrystalline particles.

However, there are several factors that affect the sol-gel chemistry, but among them, the pH of the aqueous solution plays important roles in the particle morphology, stability, and the particle size of the final reaction products. During the polymerization process, the three-dimensional networks of particles serve as nuclei for further growth. This growth proceeds by a mechanism called Ostwald ripening whereby particles dissolve and reprecipitate on larger, less-soluble nuclei. Ostwald ripening ceases to exist when the difference in solubility between the smallest and largest particles becomes negligible. Nevertheless, this growth continues to larger sizes at higher temperatures. Europium-doped yttrium oxide ($\text{Eu:Y}_2\text{O}_3$) was synthesized by a sol-gel method in the presence of Tween-80 and ϵ -caprolactam in pH range 4–10. It has been observed that the variation in surface area, pore size, and pore volume of the final product was strongly dependent on the initial pH of the solution. The powder with a large surface area ($\sim 230 \text{ m}^2/\text{g}$) and low pore diameter ($\sim 16 \text{ nm}$) was obtained when the powder was processed at $\text{pH} \sim 4$. The crystallite sizes of the

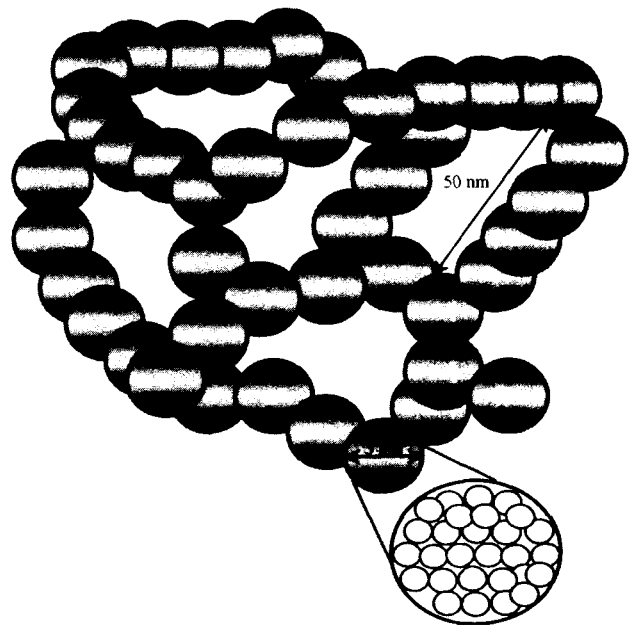
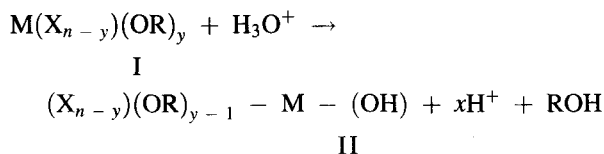


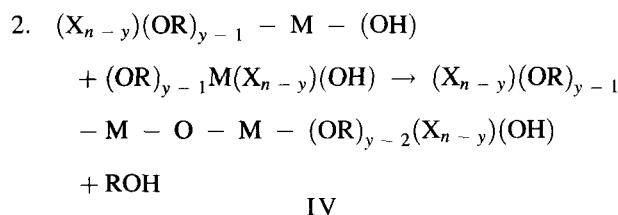
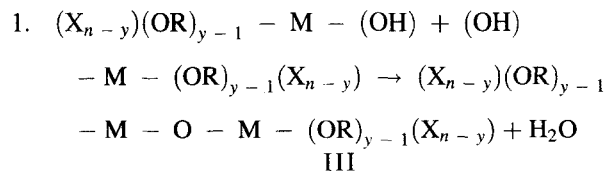
Fig. 6 A schematic of an aerogel structure. (View this art in color at www.dekker.com.)

powders processed at pH~4 and 10 were found to be 35 and 198 nm, respectively.

At low pH, the reaction rate of the hydrolysis is governed by the hydronium ion in solution ($\text{H}_2\text{O} + \text{H}^+ \rightarrow \text{H}_3\text{O}^+$) and is also observed by Sakka and Kamiya^[21] (described below). In this reaction, the amount of water is small because of the rapid formation of H_3O^+ . Cagle and Keefer have stated that the hydrolysis/condensation in low pH condition is relatively controlled and selective, thus generating relatively more linear polymers of metal.^[22-24] Hydrolysis can be represented by the following equation



Condensation can take place by any of the following two equations:



The linear polymerization can be explained by a simple steric argument: monomers (II) are more readily hydrolyzed than dimers (III or IV), which are, in turn, more readily hydrolyzed than middle groups in chains. Therefore the reaction polymerization at low pH is expected to be a linear chain (III or IV) with low cross-links and is also suggested by Pope and Mackenzie.^[25]

At high pH, the reaction is governed by the hydroxyl ions (OH). Although the initial growth leads to linear

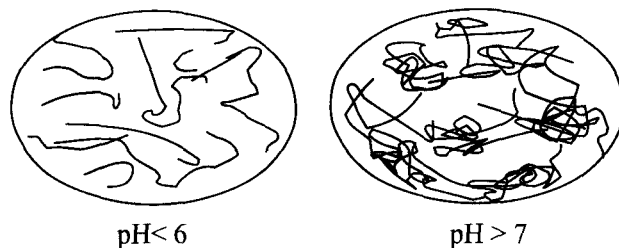
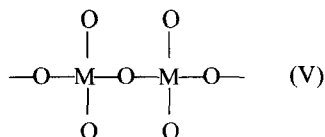


Fig. 7 Schematic diagram of polymeric network in different

chains, because of the high concentration of OH ions, it results in the cyclization because the probability of intermolecular reaction is higher than intramolecular reaction.^[26] At high pH value, hydrolysis/condensation is uncontrolled and unselective, which leads to highly branched polymers. It also generates larger interconnected particles.^[26-28] The polymeric chain at high pH is larger than the one at low pH. At high pH, the most probable metal-oxygen polymeric network formed in the chain is the structure V as shown in Fig. 7. Nevertheless, the larger interstices at pH>7 result in larger grains, as shown in Fig. 7. Thus the crystallite size of the powder at pH>7 (198 nm at pH~10) was smaller than the powder at pH<7 (35 nm at pH~4). At pH~10, a cube-like morphology of the particles is seen in Fig. 8. In contrast, the morphology at pH~4 has totally changed into polygonal shape with size of 40 nm (shown in Fig. 8).

Modified sol-gel synthesis:

Microemulsions as microreactors

Microemulsion-based sol-gel synthesis is a versatile technique to prepare materials with novel microstructures, in particular, ultrafine (nanosize) powders, e.g., TiO_2 , Al_2O_3 , ZrO_2 , etc.^[30-32] A microemulsion may be defined as a thermodynamically stable, optically isotropic solution of two immiscible liquids (e.g., water and oil) consisting of microdomains of one or both liquids stabilized by an interfacial film of surfactants.^[33,34] The surfactant molecule generally has a polar (hydrophilic) head group and a long chained aliphatic (hydrophobic) tail. Such molecules optimize their interactions by residing at the oil / water interface, thereby considerably reducing the interfacial tension. In water-in-oil microemulsion, the aqueous phase is dispersed as microdroplets (typically 10–25 nm in size) surrounded by a monolayer of surfactant molecules in the continuous hydrocarbon phase. The aqueous cores of microemulsions containing soluble metal salts are used as microreactors for the synthesis of nanoparticles. Because of the dynamic nature of the microdroplets, the exchange mechanism involves coalescence and fusion of

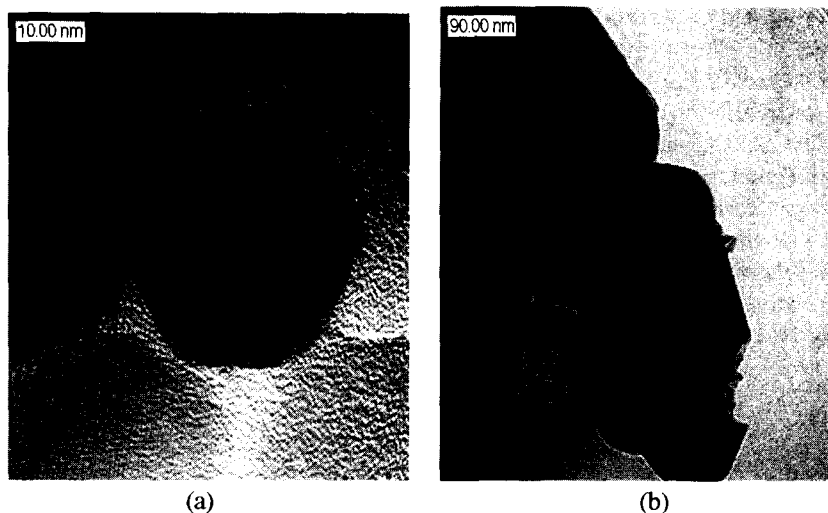


Fig. 8 High-resolution transmission electron microscopy of Eu-doped yttria at pH (a) 4 and (b) 10. (View this art in color at www.dekker.com.)

the droplets upon collision, which then disintegrate into droplets, and this process occurs continuously in the microemulsion.^[35] If two reactants, A and B, are dissolved in the aqueous core of two identical water-in-oil microemulsions, upon mixing, they will form a precipitate, AB. The growth of these particles in microemulsion is suggested to involve interdrop exchange and nuclei aggregation.^[36,37] Recently, this method has been applied for the fabrication of cubic BaTiO₃ (please refer to Fig. 9).



Fig. 9 Nanosize metal oxides synthesized by microemulsion-mediated sol-gel.

Polymerized Complex Method

Wet chemical method using polymeric precursor based on the Pechini process has been employed to prepare a wide variety of ceramics oxides.^[38] The process offers several advantages for processing ceramic powders such as direct and precise control of stoichiometry, uniform mixing of multicomponents on a molecular scale, and homogeneity. In this process, an alpha hydroxycarboxylic acid, preferentially citric acid, is used to chelate various cations by forming a polybasic acid. In the presence of a polyhydroxy alcohol, normally ethylene glycol, these chelates react with the alcohol to form ester and water by-products. When the mixture is heated, polyesterification occurs in the liquid solution and results in a homogenous sol, in which metal ions are uniformly distributed throughout the organic polymeric matrix. When excess solvents are removed, an intermediate resin is formed. This resin gives metal oxides on burning. All the organic matter removes on heat treatment.

In polymerized complex method, several metal ions in a solution could be first chelated to form metal complexes and then polymerized to form a gel, which seems to be one of the most suitable among several other chemical solution processes of nanocrystalline particles because rigidly fixed cations are homogeneously dispersed in the polymer network and have few chances to segregate even during pyrolysis. This method has been already successfully applied to prepared highly pure samples of various double oxides such as BaTiO₃,^[39] Y₆WO₁₂,^[40] mixed-cation oxides,^[41] and even for various superconductors^[42] with multiple cationic compositions.

Chemical Vapor Deposition

Chemical vapor deposition (CVD) may be defined as the deposition of a solid on a heated surface from a chemical reaction in the vapor phase. It is a versatile process suitable for the manufacturing of coatings, powders, fibers, and monolithic components. It is possible to produce most metals, metal oxides, and nonmetallic elements such as carbon and silicon as a large number of compounds including carbides, nitrides, oxides, intermetallics, and many others. The main advantage of CVD is that the deposition rate is high and thick coatings or nanoparticles can be readily obtained. The process is generally competitive and, in some cases, more economical than the physical vapor deposition (PVD). Additionally, it is not restricted to a line of sight deposition, which is a general characteristic of sputtering, evaporation, and other PVD processes. However, two major areas of applications of CVD have rapidly developed the last 20 years or so, namely, in the semiconductor industry and in the metallurgical coating industry which includes cutting tool fabrication. Very recently, the CVD process has been given enormous attention owing to the possibility of mass production of monodisperse nanoscale powders; however, the mechanism of powder synthesis kinetics is still not clear.^[43-46] Kim et al.^[46] have synthesized nanosize TiO_2 powders using CVD. Carbon nanotubes have also synthesized by CVD method using Fe-Mo nanoparticles.^[47]

Microwave Synthesis

Recently, there has been a growing interest in heating and sintering of ceramics by the microwave energy.^[48,49] The interest in the use of microwave processing spans a

number of fields from food processing to medical applications to chemical applications. A major area of research in microwave processing of ceramics includes microwave material interaction, dielectric measurement, microwave equipment design, new material development, sintering, joining, and modeling. Therefore the microwave processing of ceramics has emerged as a successful alternative to conventional processing. Nevertheless, microwave method not only offers the advantages of a uniform heating at lower temperature and time than the conventional method, but also provides an economic method of processing. The microwave energy has been already successively utilized in the fabrication of ceramics as well as carbon fibers at low temperature and time. Varadan et al.^[50] and Sharma et al.^[51] have synthesized various electroceramics such as barium strontium titanate (BST) and lead zirconate titanate (PZT) by microwave. Fig. 10 shows the schematic diagram of a typical domestic microwave unit used by Sharma et al. These materials are observed to have improved mechanical, electrical, and electronic properties. Until recently, microcoiled carbon fibers with large surface area have also been fabricated by using microwave aid.^[52]

Fig. 11 shows a schematic diagram of a microwave chemical deposition unit used for the fabrication of carbon nanotubes and coils. It consists of microwave magnetron, circulator, four-stub tuner, waveguide, cavity, etc. The microwave power can be adjusted from 0 to 3000 W at a frequency of 2.45 GHz. The function of circulator was to prevent power reflected by the load, thus preventing overheating of the magnetron. The forward and reflected powers were determined by a power meter that is helpful in determining impedance matching. The four-stub tuner, consisting four threaded stubs spaced at $3/8$ wavelength apart, was another part to optimize impedance matching.

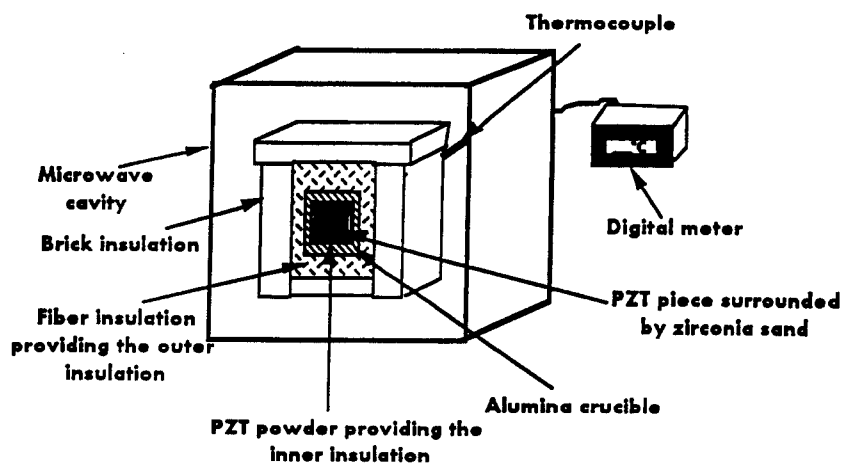


Fig. 10 Schematic diagram of microwave used for the powder.

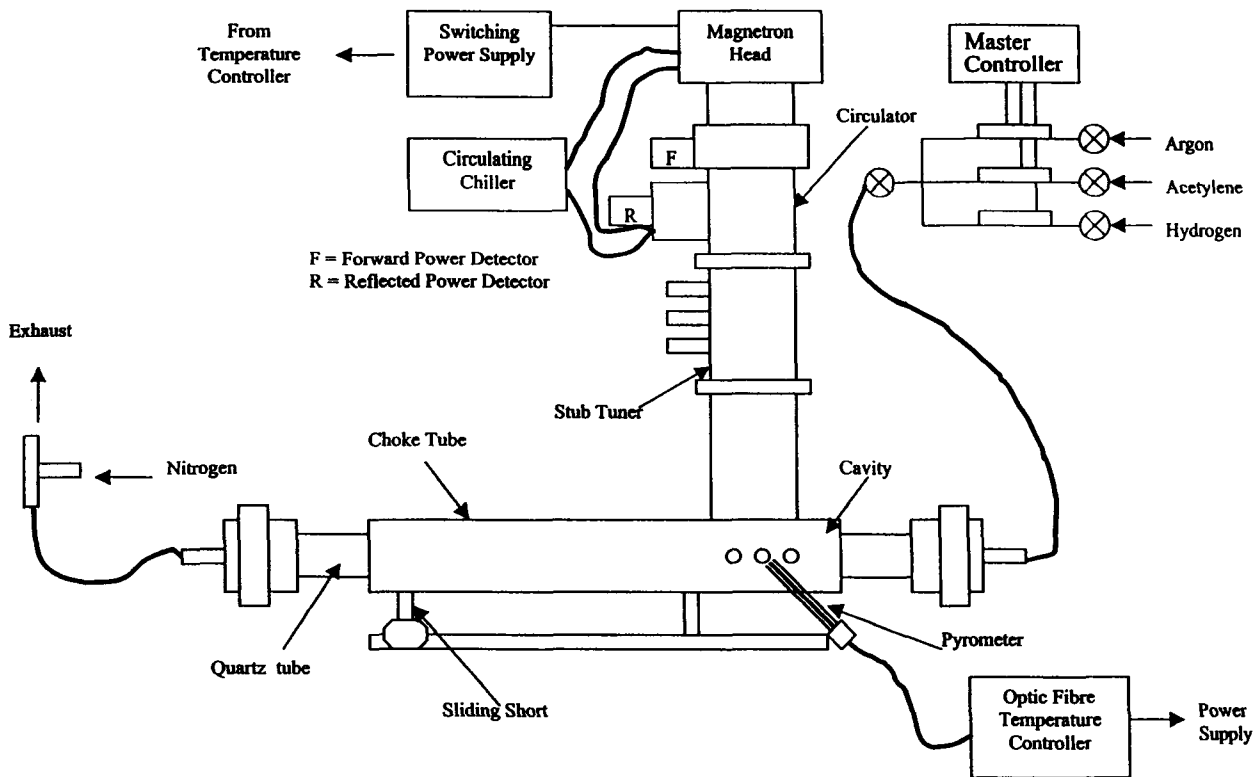


Fig. 11 Schematic diagram of the microwave chemical vapor deposition of carbon nanotubes.

These stubs were adjusted properly, and the four-stub tuner became a matching network which maximized the power transmitted to the load by matching the source impedance to that of the load. As an important part of cavity, sliding short was used to adjust the length of the cavity such that it could resonate at 2.45 GHz. High field intensities could be attained when the cavity resonates. A

quartz tube, which was the reaction chamber, passed through the cavity. Reaction gases were introduced from one end of the quartz tube and exhausted at the other end. The flow rates were controlled by a set of flow controller. In this microwave CVD system, SiC was chosen as substrate because of its high loss tangent; thus it could absorb microwave energy effectively. A fibrous



Fig. 12 Transmission electron microscopy of the CNTs obtained from microwave.

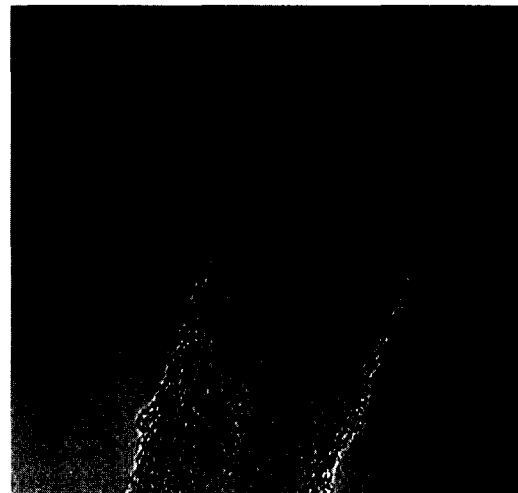


Fig. 13 High-resolution transmission electron microscopy of MWCNT from microwave CVD.

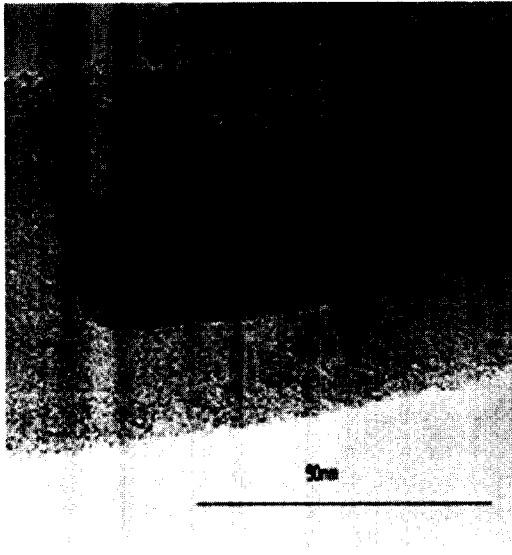


Fig. 14 High-resolution transmission electron microscopy of MWNTs with Encapsulated Co.

morphology with a hollow tube inside was obtained. The diameter of these Multi-wall nano tubes (MWNT) ranges from 20 to 30 nm as shown in Figs. 12–14.

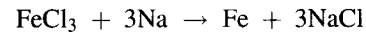
High-Energy Ball Milling Processes

Ball milling has been utilized in various industries to perform size reduction for a long time. Recently, materials with novel microstructures and properties have been synthesized successfully via high-energy ball milling processes.^[53,54] Although different terms have been used to describe the high-energy ball milling processes, three terms are generally used to distinguish powder particle behavior during milling: mechanical alloying (MA), mechanical milling (MM), and mechanochemical synthesis (MS). Mechanical alloying is referred to when mixtures of powders are milled together. In this case, materials transfer is involved to obtain a homogeneous alloy. Mechanical milling describes a milling process when no material transfer is involved; that is, only powder with uniform composition is milled. Mechanochemical synthesis, on the other hand, is a special MA process where chemical reactions between the powders take place during milling. The unique feature of MS process is that grain refinement and chemical reactions take place at low temperatures under far-from-equilibrium conditions.

A wide variety of nanostructure (grain size in the range of 1–100 nm) materials have been synthesized via MA and MM techniques.^[53–55] However, MA and MM are not capable of synthesizing nanoscale powders primarily because of cold welding and agglomeration during milling. In other words, individual powders synthesized by MA

and MM usually contain many nanosize grains and may show rather low specific surface area values.

It has been shown more recently that the nanocomposite mixtures formed during mechanochemical reactions can be further processed into nanoscale particles.^[56–58] For instance, nanocomposite of Fe and NaCl was obtained by milling FeCl₃ and sodium metal according to the following reaction:



On dissolution of the soluble NaCl phase by a simple washing process after milling, Fe nanoparticles with relatively narrow particle size distribution can be obtained.^[56] The synthesis of ultrafine oxide powders with particle size of 10–50 nm has also been reported.^[59,60]

There are some inherent advantages in processing nanomaterials via high-energy ball milling techniques, such as excellent versatility, scalability, and cost-effectiveness. Therefore high-energy ball milling techniques are well suited for manufacturing large quantity of nanomaterials. A major concern of ball milling techniques is the powder contamination. While the contamination is mainly caused by the wear of milling media and container, the level of contamination depends on factors such as milling time, milling intensity, and milling atmosphere. Attempts have been made in recent years to minimize the powder contamination during ball milling. For example, using the same material for the container and grinding media as the powder being milled will help reduce the contamination.

PROPERTIES OF NANOMATERIALS

Optical Properties

It is well known that the yttrium oxide (Y₂O₃) has its application in the lighting industry for Eu:Y₂O₃, the red phosphor of the trichromatic fluorescent lamps.^[61] Because of a ⁵D₀→⁷F₂ transition within europium, Eu:Y₂O₃ shows luminescence properties and emits red light with a wavelength of 611 nm.^[62] The rare earth ions, such as Eu³⁺ and Nd³⁺, show sharp emissions based on electron transitions within the 4f manifold. Furthermore, their emission is found to be highly dependent on the local environment of rare earth ions. Therefore the fluorescence of Eu³⁺ ions can be used as a probe to investigate the local surrounding in the host, e.g., yttria, alumina, and mullite.

Effect of particle size on fluorescence behavior (⁵D₀→⁷F₂ transition) of Eu³⁺ in the yttria powder was studied by Sharma et al.^[63] The most noteworthy feature of Fig. 15 is the sensitivity of ⁵D₀→⁷F₂ peak (614 nm) with the particle size. It has been observed that the peak emission intensity of ⁵D₀→⁷F₂ transition increases

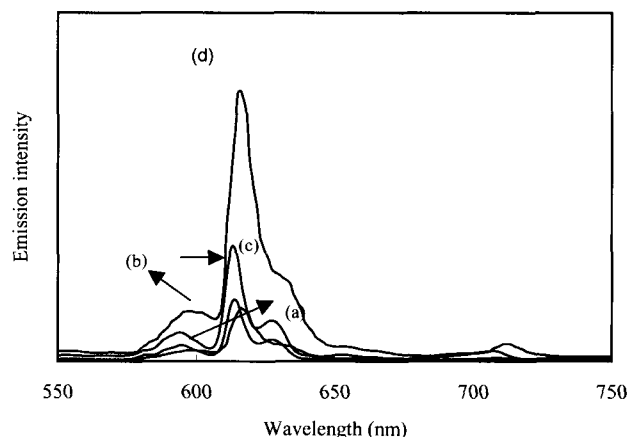


Fig. 15 Emission spectra of powder with the particle size (a) 6 μm , (b) 1 μm , (c) 0.2 μm , and (d) 0.01 μm .

approximately fivefold as the average particle size decreases from 6 μm to 10 nm. This suggests that the emission intensity of fluorescence varies inversely as the particles size increases. Its behavior was expected from the quantum-confinement model as described by Bawendi et al.^[64] and Alivisatos et al.^[65] Goldburt et al.^[66] have observed high efficiency in Tb-doped Y_2O_3 nanocrystals which was measured at 18% as compared with 16% in the bulk and stated that the nonradiative contribution decreases with decrease in particle size. The size dependence of the fluorescence emission intensity can also be demonstrated in terms of number of particles per unit area facing toward the incident light as described by Iwasaki et al.^[67] Increasing surface area of smaller particles (refer Table 1) leads to enhancement in the fluorescence intensity.^[67] All spectral features were found to be unchanged except the intensity of the peak centered at 395 nm, which was found to be enhanced and shifted to lower wavelength (higher energy level) as the particle size decreased. This shift in excitation spectra with particle size is the evidence of quantum confinement. Gallagher et al.^[68] have reported a shift of 60 nm in the excitation peak at the maximum emission from Mn^{2+} doped in ZnS nanocrystals to shorter

wavelength with decrease in particle size because of quantum-confined ZnS.

Electrochromic devices

An electrochromic device consists of materials in which an optical absorption band can be introduced or an existing band can be altered by the passage of current through the materials or by the application of an electric field. Nanocrystalline materials, such as tungstic oxide ($\text{WO}_3 \cdot \text{H}_2\text{O}$) gel, are used in very large electrochromic display devices. The reaction governing electrochromism (a reversible coloration process under the influence of an electric field) is the double injection of ions (of protons, H^+) and electrons, which combine with the nanocrystalline tungstic acid to form a tungsten bronze. These devices are primarily used in public billboards and ticker boards to convey information. Electrochromic devices are similar to liquid-crystal display (LCD) commonly used in calculators and watches. However, electrochromic devices display information by changing color when a voltage is applied. When the polarity is reversed, the color is bleached. The resolution, brightness, and contrast of these devices greatly depend on the tungstic acid gel's grain size. Hence nanomaterials are being explored for this purpose. Using nanostructure materials, color change will be faster and uniform. Additionally, the number of cycles of coloration and bleaching can be enhanced. Recently, Ntera Inc. has developed an electrochromic display technology called NanoChromicsTM using nanostructure film electrodes. The nanostructure films are derived from sol-gel precursors and formulated to suit the particular coating application method.

Catalytic Properties

Some of \$10 trillion worth of chemicals and materials are produced each year through catalytic processes, according to industry estimates and published in Chemical and Engineering News. Most of these processing deal with the microscopic size of the particle with diameters measuring

Table 1 Comparison of Li-MO₂ in microparticle and nanoparticle size

Properties	LiNiO ₂ ^[74]		LiMnO ₂ ^[75]		LiCoO ₂ ^[77]		Li[Cu _{1-x} Fe _x]O ₂	
	Micro	Nano	Micro	Nano	Micro	Nano	Micro	Nano
Crystallite size	830 nm	300 nm	≈ microns	5–50 nm ^[75]	1.67 μm ^[74]	60 nm	≈ microns	<50 nm ^[80]
Capacity (mAh/g)	90 ^[11]	205 ^[11]	130 ^[76]	250	87 ^[11] ; 140 ^[78] ; 126 ^[79] ;	167 ^[11]	140 ^[11]	230 ^[11]
Potential (V)	4.2	4.2	4.1	3.8	4.1 ^[78] ; 3.9 ^[79]	4.2	4.1	4.2

no more than a few billionths of a meter. In catalysis, the goal is to design catalysts with certain features that help boost catalytic performance. It is anticipated that this goal will be more closely approached through tailoring a catalyst particle via nanoparticle synthesis and assembly, so that it performs only specific chemical conversions, performs at high yield, and does so with greater energy efficiency. It has been established that the nanostructures have higher surface area than do conventional materials. The high surface areas can be attained either by fabricating small particles or clusters where the surface-to-volume ratio of each particle is high (category I) or by creating materials where the void surface area (pores) is high compared with the amount of bulk support materials (category II). Materials such as highly dispersed supported metal catalysts and gas phase clusters fall into the first category, and microporous (nanometer-pored) materials such as zeolites, high surface area metal oxides, porous carbon, and amorphous silica fall into category II. The nanostructure approach to high surface area materials may have significant impact in petrochemical process, biosensors, gas sensors, absorption and adsorption phenomena, gas storage, energy storage, battery performance, biological reactions, etc.

Electrochemical Properties

Lithium-based rechargeable batteries have been proposed for a wide variety of extremely demanding applications. These applications include, but are not limited to, electric vehicle (EV), start-light-ignition (SLI), portable electronics, and personal communications devices. The lithium battery technology can be generally classified as cathode, anode, and electrolyte technology (liquid-electrolyte and solid-electrolyte types). Although variation in cathode materials for lithium has been recognized as a highly flexible and versatile technological approach for the production of high-energy density batteries, none of the existing battery technology is capable of satisfying the energy- and power-density requirements in the aforementioned applications. The widespread use of battery is severely hampered by poor performance of cathode materials of Li-ion battery because of the following characteristics:

- Micron-size particles.
- Small surface area.
- Unstable structure during cycling.
- Inadequate mechanical strength.
- Costly precursors, high-temperature stability.

Furthermore, the aforementioned characteristics are the primary factors that deprive the overall performance of the battery, which include the following

- Inferior electrochemical stability.
- Inferior mechanical properties.
- Greater toxicity.
- Low power-to-energy ratio.
- High costs.
- Low cycle life.
- Low calendar life.
- Poor thermal management capabilities.
- Inferior manufacturability.
- Potential hazards, especially of the liquid electrolytes, because of leakage, deposition, and explosion.

To obviate the aforementioned deficiencies associated with cathode materials, researchers have developed a new class of material using nanoparticles of different cathode materials based on metal oxides, which will exceed, or meet, the above performance requirements.

Furthermore, it is now well established that the limitations in the rate capabilities of Li-ion batteries are caused by slow solid-state diffusion of Li within the electrode materials.^[69–72] As a result, there is tremendous interest in the development of *nanostructure* Li-ion battery cathode electrodes. These batteries can store two to three times more energy per unit weight and volume than the one with micron-particle-size electrode.^[73] Table 1 represents the improvement in the Li-ion battery.

Energy Storage

Recent interest in the use of hydrogen as a multipurpose fuel has emphasized the necessity of reliable storage system for this element. LaNi₅ alloy stores up to 1.6%, while FeTi stores up to 1 wt.% of hydrogen in the form of metal hydride. The hydrogen capacity in these host materials was quite low, and hence research was focused on the storage of hydrogen in molecular sieves especially in natural and synthetic zeolites.^[81] CsA-zeolite was found to have hydrogen storage capacity of –6 wt.%. On the other hand, it is also well known that the carbon nanotubes (CNTs) have the capacity of hydrogen storage.^[81–83] Dillon et al.^[82] reported that the SWNTs with low purity could adsorb 5 wt.% of H₂ at 133 K and 0.040 MPa. This value of hydrogen storage was enhanced to 8 wt.% for highly pure Single wall nano tubes (SWNT) in the studies of Ye et al.^[81] However, temperature was reduced to 80 K and pressure was increased to 7.18 MPa. At room temperature, the hydrogen capacity was only 4 wt.% at 10 MPa.

Biomedical

Biomolecule/inorganic interactions can be used to produce ceramics with increased toughness. Fundamental studies of biomineralization, in which an organic

substance (usually protein or peptide or lipid) interacts with an inorganic phase (e.g., calcium carbonate or hydroxyapatite), have led to the bioinspired synthesis of composite materials. Hydroxyapatite (HAp), a major inorganic component of bone, has been used extensively for biomedical implant applications and bone regeneration because of its bioactive, biodegradable, and osteoconductive properties. However, the application of pure HAp is very limited because of its brittleness. Because the natural bone is a composite mainly consisting of nano-sized needlelike HAp crystals and collagen fibers, many efforts have been made to modify by polymers such as polylactic acid, collagen, chitosen, and polyethylene and have received much attention in the field of medical applications because of their excellent biocompatibility and biodegradability.^[84] Additionally, the following materials are used in various applications of biomedical, biotechnical, and bioengineering.

Nano-ZnO

1. Biosensor: Nanoparticles of ZnO can sense the toxic and hazardous gas such as H₂, SF₆, and gasoline in shorter time because of high surface area.
2. Neutralizes biochemical use in biological weapons because high surface area of nanostructured ZnO is highly reactive and able to degrade toxic biochemical (e.g., naphthalene, anthracene, phenol, chlorophenol, and polyaromatic hydrocarbons) use in biological weapons.

Nano-MgO and nano-TiO₂

Nano-MgO and nano-TiO₂ neutralize the biological immune buildings, e.g., bacteria and virus, which are used as biological warfare agents.

Magnetic nanoparticles of Iron

Magnetic particles coated with biocompatible polymers dispersed in water could be used as

- Site-specific drug delivery after being attached with drug molecules to the magnetic particles.
- Magnetic tourniquet. In this case, a person with blood loss because of injury could be injected with the magnetic particles dispersed in water. Then a magnet could be placed on the injury site. The magnetic particles will agglomerate there and hence would prevent the blood from flowing out.

Biodegradable nanosilica

Biodegradable nanosilica can be used for drug delivery. It is important for an inorganic material to be used as a drug

delivery agent; it should be biodegradable, nanosized, porous, and nontoxic. Nanostructured silica can be a good candidate for a drug delivery agent, which can easily degrade and would not provide any side effect. This kind of drug delivery system will be extremely valuable for the instant wound therapy of any injured person.

Protein tagging using nanoluminescent particles

Protein tagging is an experimental strategy in which a tag such as a probe (luminescent lanthanides, e.g., Eu, Sm, etc.) is attached to primary sequence of a protein. The size of the tag used for attachment to the loops of a protein must be extremely small.

This strategy can also be used in:

- Cancer therapy: to block interactions such as enzyme substrate interactions or interaction of a toxin with a specific cell or a component of a cell.
- Drug delivery: for delivery of protein drugs to cells.

CdS and ZnS semiconductor quantum dots

Immunosensor, bioanalytical, and biolabels: Semiconductor quantum dots are highly light-absorbing luminescent nanoparticles, whose absorbance onset and emission maximum shift to higher energy with decreasing particle size because of quantum confinement effect.

Quantum dots can conjugate with antibodies using an engineered adapter protein and are new types of reagents for immunosensors and bioanalytical applications.

Nanogold particles

- Labeling of target molecules especially protein with nanogold particles has revolutionized the visualization of cellular or tissue components by electron microscopy or atomic force microscopy.
- As a bioconjugate: with DNA, it can detect the active site of DNA and can be used in disease diagnostics.

Nanoparticles in gene therapy

Nanoparticles are now also being used as a delivery mechanism in gene therapy. Nanoparticles can be employed to insert good DNA into specific sites to replace faulty genes in such disorders as cystic fibrosis.

Textile

Another huge industry that will be impacted by nanotechnology is the textiles industry. Companies are working on "smart" fabrics that can change their physical

properties according to surrounding conditions or even monitor vital signs. The incorporation of nanoparticles and capsules in clothing offers some promise, and nanotubes would make extremely light and durable materials. Fabrics are already being marketed that are highly resistant to water, stains, and wrinkling.

Magnetic Properties

Ferromagnetic nanomaterials have potential advantages over existing materials in numerous applications in soft magnets,^[85] hard magnets,^[86] magnetic recording,^[87,88] etc. The study and exploitation of magnetism at the nanometer scale have been exceptionally active research areas over the past two decades. Ferromagnetic nanoparticles (usually referred to as magnetic nanoparticles) have generated great interest because of their size-dependent magnetic properties. The ferromagnetic interaction leads to parallel spins on adjacent atoms. However, the exchange forces responsible are short range, and magneto static forces dominate at great distances. Magnetic domains arise spontaneously in bulk ferromagnets to minimize their overall energy. The typical sizes of the domains are in nanometer-size range. Below a certain size, which is in the nanometer range, it is energetically favorable for a particle to be monodomain.

The coercivity of magnetic materials has a striking dependence on their size. It increases with the reduction of particle size in the nanometer range going through a maximum at the single domain size, and then decreases again for very small particles because of thermal effects and becomes zero at the superparamagnetic particle size. Iron, which is a soft magnetic material with coercivity about 20 Oe at room temperature, could be made "hard" with a coercivity of 540 Oe when the particle size is reduced to about 12 nm.^[89] Remarkably low coercivity of the order of a few millioersteds along with high saturation magnetization and permeability has been achieved in $\text{Fe}_{74}\text{Si}_{15}\text{B}_7\text{Cu}_1\text{Nb}_3$ nanocrystalline magnetic alloy where α -Fe(Si) nanocrystallites of size ~ 10 nm are embedded in an amorphous matrix.^[90] These materials were synthesized by melt spinning followed by annealing. The nanocrystallites, whose dimension is less than the exchange length, are exchange-coupled with randomly oriented easy axes of magnetization. The combination of random orientation and averaging over multiple grains makes the preference for magnetization in a particular direction, and therefore the effective magnetic anisotropy and hence coercivity are small.^[91,92] Several other nanocrystalline soft magnetic alloys based on Fe(Co)-Si-B have been studied.^[93]

R-Fe-B (R=Nd, Pr, Dy, Pr) alloys, prepared using melt-spinning, exhibited very high coercivity in the range 10–100 kOe.^[86] In these permanent or hard magnets, the large coercivity is a result of the highly anisotropic tetragonal $\text{R}_2\text{Fe}_{14}\text{B}$ phase, which were produced in the nanoscale size during melt spinning or subsequent crystallization. Several other permanent magnets, e.g., SmCo_5 , $\text{Sm}_2\text{Co}_{17}$, $\text{Sm}_2\text{Fe}_{17}\text{N}_{2.6}$, etc., with high coercivity have been made with nanosized microstructure.^[86] Another class of hard magnetic material is called nanocomposite permanent magnet or exchange-coupled magnet where the nanocomposite consisting of a hard magnetic material such as $\text{Nd}_2\text{Fe}_{14}\text{B}$ and a soft magnetic phase such as α -Fe are coupled through exchange interaction.^[94,95] This leads to high coercivity and high remanence to saturation magnetization ratio and hence high maximum energy product values. In these magnets, the crystallite size needs to be less than 20 nm for exchange coupling to occur. Most of these nanocomposite magnets have been prepared by melt spinning and mechanical alloying.^[96,97] Recently, a chemical synthesis has been proposed with the potential for making three-dimensional magnets with high maximum energy product.^[98] First, $\text{Fe}_{58}\text{Pt}_{42}$ and Fe_3O_4 nanoparticles of 4-nm size are mixed and allowed to self-assemble. When it was heated and chemically reduced, FePt (hard)- Fe_3Pt (soft) nanocomposite is formed. The particles are 5 nm in size. The maximum energy product is 20.1 MGOe compared with 13 MGOe for FePt alone. This is an exciting new development that shows promise for making strong magnets.^[99] Moreover, 4-nm particles of $\text{Fe}_{52}\text{Pt}_{48}$ (synthesized by very similar chemical route) that self-assembled into arrays when annealed exhibited a coercivity of 1800 Oe.^[100] These $\text{Fe}_{52}\text{Pt}_4$ nanocrystal assemblies are smooth ferromagnetic films, and initial magnetic recording experiments suggested that it could support high-density magnetization reversal transitions or bits. A key requirement for magnetic recording at areal density in the terabits per square inch regime is a medium with nanometer-size, magnetically isolated grains with moderately high writable coercivity.^[87,88] With these 4-nm $\text{Fe}_{52}\text{Pt}_{48}$ self-assembled particles, it might be possible to achieve magnetic recording at areal density in the terabits per square inch range.

tragonal $\text{R}_2\text{Fe}_{14}\text{B}$ phase, which were produced in the nanoscale size during melt spinning or subsequent crystallization. Several other permanent magnets, e.g., SmCo_5 , $\text{Sm}_2\text{Co}_{17}$, $\text{Sm}_2\text{Fe}_{17}\text{N}_{2.6}$, etc., with high coercivity have been made with nanosized microstructure.^[86] Another class of hard magnetic material is called nanocomposite permanent magnet or exchange-coupled magnet where the nanocomposite consisting of a hard magnetic material such as $\text{Nd}_2\text{Fe}_{14}\text{B}$ and a soft magnetic phase such as α -Fe are coupled through exchange interaction.^[94,95] This leads to high coercivity and high remanence to saturation magnetization ratio and hence high maximum energy product values. In these magnets, the crystallite size needs to be less than 20 nm for exchange coupling to occur. Most of these nanocomposite magnets have been prepared by melt spinning and mechanical alloying.^[96,97] Recently, a chemical synthesis has been proposed with the potential for making three-dimensional magnets with high maximum energy product.^[98] First, $\text{Fe}_{58}\text{Pt}_{42}$ and Fe_3O_4 nanoparticles of 4-nm size are mixed and allowed to self-assemble. When it was heated and chemically reduced, FePt (hard)- Fe_3Pt (soft) nanocomposite is formed. The particles are 5 nm in size. The maximum energy product is 20.1 MGOe compared with 13 MGOe for FePt alone. This is an exciting new development that shows promise for making strong magnets.^[99] Moreover, 4-nm particles of $\text{Fe}_{52}\text{Pt}_{48}$ (synthesized by very similar chemical route) that self-assembled into arrays when annealed exhibited a coercivity of 1800 Oe.^[100] These $\text{Fe}_{52}\text{Pt}_4$ nanocrystal assemblies are smooth ferromagnetic films, and initial magnetic recording experiments suggested that it could support high-density magnetization reversal transitions or bits. A key requirement for magnetic recording at areal density in the terabits per square inch regime is a medium with nanometer-size, magnetically isolated grains with moderately high writable coercivity.^[87,88] With these 4-nm $\text{Fe}_{52}\text{Pt}_{48}$ self-assembled particles, it might be possible to achieve magnetic recording at areal density in the terabits per square inch range.

CONCLUSION

This review highlighted on the fabrication of nanomaterials by various methods e.g. chemical, physical and mechanophysical. The various properties e.g. chemical, physical, mechanical, magnetic, optical and electrical, of nanomaterials have discussed in detail. Nanostructured materials exhibit novel and technologically attractive properties, which can be exploited for a variety of applications which include, but are not limited to the biomedical, energy, displays, insulations, elimination of pollutants, catalysis, microelectronics, high power magnets, sensors, aerospace, weapons, automobiles etc.

REFERENCES

1. Khairutdinov, R.F.; Rubtsora, N.A.; Costa, S.M.B. Size effect in steady-state and time-resolved luminescence of quantized MoS₂ particle colloidal solutions. *J. Lumin.* **1996**, *68*, 299.
2. Kortan, A.A.; Hull, R.; Opila, R.L.; Bawendi, M.G.; Steigerwald, M.L.; Carrol, P.J.; Bruce, L.E. Nucleation and growth of cadmium selenide on zinc sulfide quantum crystallite seeds, and vice versa, in inverse micelle media. *J. Am. Chem. Soc.* **1990**, *112*, 1327.
3. Bawendi, M.G.; Wilson, W.L.; Rothberg, L.; Carroll, P.J.; Jedju, T.M. Electronic structure and photoexcited-carrier dynamics in nanometer-size CdSe clusters. *Phys. Rev. Lett.* **1990**, *65*, 1623.
4. Alivisatos, A.P.; Harris, A.L.; Lennox, N.J.; Steigerwald, M.L.; Bruce, L.E. Electronic states of semiconductor clusters: Homogeneous and inhomogeneous broadening of the optical. *J. Chem. Phys.* **1988**, *89*, 4001.
5. Jungnickel, V.; Henneberger, F. Luminescence related processes in semiconductor nanocrystals—The strong confinement regime. *J. Lumin.* **1996**, *70*, 238.
6. Bargava, R.N.; Gallagher, D.; Hong, X.; Nurmikko, A. Optical properties of manganese-doped nanocrystals of ZnS. *Phys. Rev. Lett.* **1994**, *72*, 416.
7. Rabenau, A. *Chem. Intl. Ed. Eng.* **1985**, *24*, 1026.
8. Clearfield, A. Hydrothermal synthesis of selected phosphates and molybdates. *Prog. Cryst. Growth Charact.* **1991**, *21*, 1.
9. Haushalter, R.C.; Mundi, L.A. Reduced molybdenum phosphates: Octahedral-tetrahedral framework solids with tunnels, cages, and micropores. *Chem. Mater.* **1992**, *4*, 31.
10. Oguri, Y.; Riman, R.E.; Bowen, H.K. Processing of anatase prepared from hydrothermally treated alkoxy-derived hydrous titania. *J. Mater. Sci.* **1988**, *23*, 2897.
11. Cheng, H.; Ma, J.; Qiang, D. Hydrothermal synthesis of PbTiO₃ from PbO and TiO₂. *J. Mater. Sci. Lett.* **1996**, *15*, 1245.
12. Sharma, P.K.; Jilavi, M.H.; Nass, R.; Schmidt, H. Seeding effect in hydrothermal synthesis of nanosize yttria. *J. Mater. Sci. Lett.* **1998**, *17*, 883.
13. Sharma, P.K.; Jilavi, M.H.B.; Nass, R.; Schmidt, H. Hydrothermal synthesis of nanosize alpha-Al₂O₃ from seeded aluminum hydroxide. *J. Am. Ceram. Soc.* **1998**, *10*, 883.
14. Kimel, R.A. Thesis; The Pennsylvania State University, 2002; 8.
15. Yang, J.; Mei, S.; Ferreira, J.M.F. Hydrothermal synthesis of nanosized titania powders: Influence of peptization and peptizing agents on the crystalline phases and phase transitions. *J. Am. Ceram. Soc.* **2000**, *83*, 1361.
16. Raghunathan, S.; Bourell, D.L. Synthesis and evaluation of advanced nanocrystalline tungsten-based materials. *P/M Sci. Technol. Briefs* **1999**, *1*, 9.
17. Raghunathan, S. In *Tungsten and Tungsten-Based Alloys and Composites for High Heat Flux Duty*, Proceedings of the APMI/MPIF PM²TEC Conference, Nashville, TN, May 16–19, 1993.
18. Raghunathan, S. Synthesis, Consolidation, and High-Temperature Deformation Characteristics of Nanocrystalline Tungsten and Tungsten-Based Alloy and Composite Powders. Ph.D. Dissertation; The University of Texas at Austin, October, 1991.
19. Raghunathan, S.; Persad, C.; Bourell, D.L.; Marcus, H.L. *Mater. Sci. Eng.* **1991**, *A131*, 243.
20. Persad, C.; Raghunathan, S. *Mater. Res. Soc. Symp. Proc.* **1988**, *120*, 23.
21. Sakka, S.; Kamiya, K. The sol-gel transition in the hydrolysis of metal alkoxides in relation to the formation of glass fibers and films. *J. Non-Cryst. Solids* **1992**, *48*, 31.
22. Cagle, P.C.; Klemperer, W.G.; Simmons, C. A Molecular Architecture and its Role in Silica Sol-Gel Polymerization. In *Better Ceramics Through Chemistry III*; Zelinski, B.J.J., Brinker, C.J., Clark, D.E., Ulrich, D.R., Eds.; Mater. Res. Soc. Symp., Proc., 1990; Vol. 180, 29. Pittsburgh, PA.
23. Keefer, K.D. *Silicon-Based Polymer Science; A Comprehensive Resource*; Zeigler, J.M., Gordon, F.W., Eds.; Adv. Chem. Ser., Am. Chem. Soc.: Washington, DC, 1990; Vol. 224, 228.
24. Kelts, L.W.; Effinger, N.J.; Melpoder, S.M. Sol-gel chemistry studied by ¹H and ²⁹Si nuclear magnetic resonance. *J. Non-Cryst. Solids* **1996**, *83*, 353.
25. Pope, E.J.A.; Mackenzie, J.D. Sol-gel processing of silica II. The role of the catalyst. *J. Non-Cryst. Solids* **1986**, *87*, 185.
26. Klemperer, W.G.; Ramamurthi, S.D. Molecular Growth Pathways in Silica Sol-Gel Polymerization. In *Better Ceramics Through Chemistry III*; Brinker, C.J., Clark, D.E., Ulrich, D.R., Eds.; Mater. Res. Soc. Symp. Proc., 1988; Vol. 121, 1. Pittsburgh, PA.
27. Chen, Y-W.; Yen, T-M.; Li, C. Preparation of alumina-zirconia materials by the sol-gel method from metal alkoxides. *J. Non-Cryst. Solids* **1995**, *185*, 49.
28. Liu, C.; Zhong, H.; Komarnani, S.; Pantano, C.G. *J. Sol-Gel Sci. Technol.* **1994**, *1*, 141.
29. Sharma, P.K.; Varadan, V.V.; Varadan, V.K. Effect of tween-80 on the control of particle size and shrinkage properties of nanoscale-alumina synthesized by sol-gel processing. *J. Am. Ceram. Soc.* **2002**, *85*, 2584.

30. Scolan, E.; Sanchez, C. Synthesis and characterization of surface-protected nanocrystalline titania particles. *Chem. Mater.* **1998**, *10*, 3217.
31. Lin, C.P.; Wen, S.B. Variations in a boehmite gel and oleic acid emulsion under calcinations. *J. Am. Ceram. Soc.* **2002**, *85*, 1467.
32. Ramamurthi, S.D.; Xu, Z.; Pyne, D.A. Nanometer-sized ZrO_2 particles prepared by a sol-emulsion-gel method. *J. Am. Ceram. Soc.* **1990**, *73*, 2760.
33. De Gennes, P.G.; Taupin, C. Microemulsions and the flexibility of oil/water interfaces. *J. Phys. Chem.* **1982**, *86*, 2294.
34. Leung, R.; Hou, M.J.; Manohar, C.; Shah, D.O.; Chun, P.W. *Macro- and Microemulsions*; Shah, D.O., Ed.; American Chemical Society: Washington, DC, 1981; 325.
35. Eicke, H.F.; Shepherd, J.C.W.; Steinemann, A. J. *Colloid Interface Sci.* **1976**, *56*, 168.
36. Fendler, J.H. Atomic and molecular clusters in membrane mimetic chemistry. *Chem. Rev.* **1987**, *87*, 877.
37. Sugimoto, T. Preparation of monodispersed colloidal particles. *Adv. Colloid Interface Sci.* **1987**, *28*, 65.
38. Pechini, M.P. US Pat. No 3330697, July 11, 1967.
39. Kumar, S.; Messing, G.L.; White, W.B. *J. Am. Ceram. Soc.* **1993**, *76*, 617.
40. Yoshimura, M.; Ma, J.; Kakihana, M. Low-temperature synthesis of cubic and rhombohedral Y_6WO_{12} by a polymerized complex method. *J. Am. Ceram. Soc.* **1998**, *81*, 2721.
41. Lessing, P.A. *Am. Ceram. Soc. Bull.* **1989**, *68*, 1002.
42. Kakihara, M.; Yoshimura, M.; Mazaki, H.; Yasuoka, H.; Borjesson, L. *J. Appl. Phys.* **1992**, 3904.
43. Cheng, W.; Skendan, G.; Denforth, S.C.; Kear, B.H.; Hahn, H. Chemical vapor processing and applications for nanostructured ceramic powders and whiskers. *Nanostruct. Mater.* **1994**, *4*, 507.
44. Ennis, B.J.; Green, J.; Davis, R. *Chem. Eng. Process.* **1994**, 34.
45. Kear, B.H.; Skandan, G. Thermal spray processing of nanoscale materials: Davos, Switzerland, August 4–8, 1997. *Nanostruct. Mater.* **1997**, *8*, 765.
46. Kim, S.Y.; Yu, J.H.; Lee, J.S. The characteristics of nanosized TiO_2 powders synthesized by chemical vapor condensation. *Nanostruct. Mater.* **1999**, *12*, 471.
47. Li, Y.; Liu, J.; Wang, Y.; Wang, Z.L. Preparation of monodispersed Fe–Mo nanoparticles as the catalyst for CVD synthesis of carbon nanotubes. *Chem. Mater.* **2001**, *13*, 1008.
48. Krage, M.K. Microwave sintering of ferrites. *Am. Ceram. Soc. Bull.* **1981**, *60*, 1232.
49. Roy, R.; Komarneni, S.; Yang, L.J. Controlled microwave heating and melting of gels. *J. Am. Ceram. Soc.* **1985**, *68*, 392.
50. Selmi, F.; Komarneni, S.; Varadan, V.K.; Varadan, V.V. Microwave sintering of Sb-doped SnO_2 . *Mater. Lett.* **1990**, *10*, 235.
51. Sharma, P.K.; Varadan, V.V.; Varadan, V.K. Dielectric and piezoelectric properties of microwave sintered PZT. *Smart Struct. Mater.* **2001**, *10*, 878.
52. Xi, J.; Sharma, P.K.; Varadan, V.V.; Varadan, V.K.; Pradhan, B.K.; Eser, S. Mater, thermal, Raman and surface area studies of microcoiled carbon fiber synthesized by CVD microwave system. *J. Phys. Chem.* **2002**, *76*, 217.
53. Koch, C.C.; Smith, A.P.; Bai, C.; Spontak, R.J.; Balik, C.M. Nonequilibrium processing of polymer materials by mechanical attrition. *Mater. Sci. Forum* **1992**, *88*, 49.
54. Suryanarayana, C. Mechanical alloying and milling. *Prog. Mater. Sci.* **2001**, *46*, 1.
55. Miao, W.F.; Ding, J.; McCormick, P.G.; Street, R. A comparative study of mechanically alloyed and mechanically milled $Nd_{10}Fe_{84}B_6$. *J. Appl. Phys.* **1996**, *79*, 2079.
56. Ding, J.; Miao, W.F.; McCormick, P.G.; Street, R. Mechanochemical synthesis of ultrafine Fe powder. *Appl. Phys. Lett.* **1995**, *67*, 3804.
57. McCormick, P.G. Application of mechanical alloying to chemical refining (Overview). *Mater. Trans., JIM* **1995**, *36*, 161.
58. McCormick, P.G.; Froes, F.H. The Fundamentals of mechanochemical processing. *J. Metallurg.* **1998**, *50*, 61.
59. Ding, J.; Tsuzuki, T.; McCormick, P.G. Ultrafine alumina particles prepared by mechanochemical/thermal processing. *J. Am. Ceram. Soc.* **1996**, *79*, 2956.
60. Gopalan, S.; Singhal, S.C. Mechanochemical synthesis of nano-sized CeO_2 . *Sci. Mater.* **2000**, *42*, 993.
61. Mishra, K.C.; Berkowitz, J.K.; Johnson, K.H.; Schmidt, P.C. Electronic structure and optical properties of europium activated yttrium oxide phosphor. *Phys. Rev., B* **1992**, *45*, 10902.
62. Wickersheim, A.; Lefever, R.A. *J. Electrochem. Soc.* **1964**, *111*, 47.
63. Sharma, P.K.; Jilavi, M.H.; Nass, R.; Schmidt, H. Effect of solvent, host precursor, dopant concentration and crystallite size on the fluorescence properties of Eu(III) doped yttria. *Opt. Mater.* **1998**, *10*, 161.
64. Bawendi, M.G.; Kortan, A.R.; Steigerwald, M.L.; Bruce, L.E. X-ray structural characterization of larger CdSe semiconductor clusters. *J. Chem. Phys.* **1989**, *91*, 7282.
65. Alivisatos, A.P.; Harris, A.L.; Carroll, M.L.; Steigerwald, M.L.; Bruce, L.E. Electron–vibration coupling in semiconductor clusters studied by resonance Raman spectroscopy. *J. Chem. Phys.* **1989**, *90*, 3463.

66. Goldburt, E.T.; Kulkarni, B.; Bhargava, R.N.; Taylor, J.; Liberta, M. Size dependent efficiency in Tb doped Y_2O_3 nanocrystalline phosphor. *J. Lumin.* **1997**, *72-74*, 190.
67. Iwasaki, S.; Ida, T.; Kimura, K. Blue-Green photoluminescence from ultrafine colloidal Si particles in 2-propanol. *Jpn. J. Appl. Phys.* **1996**, *35*, L-551.
68. Gallagher, D.; Heady, W.E.; Racz, J.M.; Bhargava, R.N. Homogeneous precipitation of doped zinc sulfide nanocrystals for photonic applications. *J. Mater. Res.* **1995**, *10*, 870.
69. Bruce, P.G. Solid-state chemistry of lithium power sources. *Chem. Commun.* **1997**, *19*, 1817.
70. Che, G.; Jirage, K.B.; Fisher, E.R.; Martin, C.R.; Yoneyama, H. Chemical-vapor deposition-based template synthesis of microtubular TiS_2 battery electrodes. *J. Electrochem. Soc.* **1997**, *144*, 4296.
71. Whittingham, M.S. U.S. Patent 4,009,052, 1973.
72. Whittingham, M.S. *Science* **1976**, *192*, 1126.
73. Ching, S.; Petrovay, D.J.; Jorgensen, M.L.; Suib, S.L. Sol-gel synthesis of layered birnessite-type manganese oxides. *Inorg. Chem.* **1997**, *36*, 883.
74. Chang, C.C.; Kim, J.Y.; Kumta, P.N. Influence of crystallite size on the electrochemical properties of chemically synthesized stoichiometric $LiNiO_2$. *J. Electrochem. Soc.* **2002**, *149*, A1114.
75. Im, D.; Manthiram, A. Nanostructured lithium manganese oxide cathodes obtained by reducing lithium permanganate with methanol. *J. Electrochem. Soc.* **2002**, *149*, A1001.
76. Bruce, P.G.; Armstrong, A.R.; Gitzendanner, R.L. *J. Electrochem. Soc.* **1999**, *9*, 193.
77. Liu, J.; Wen, Z.; Gu, Z.; Wu, M.; Lin, Z. Synthesis by an EDTA-based soft-chemistry route and characterization of nanosized $LiCoO_2$ cathode materials. *J. Electrochem. Soc.* **2002**, *149*, A1405.
78. Cho, J.; Kim, Y.J.; Park, B. $LiCoO_2$ Cathode material that does not show a phase transition from hexagonal to monoclinic phase. *J. Electrochem. Soc.* **2001**, *148*, A1110.
79. Lu, C.H.; Yeh, P.Y. Surfactant effects on the microstructure and electrochemical properties of emulsion-derived lithium cobalt oxide powders. *Mater. Sci. Eng.* **2001**, *B84*, 243.
80. Kim, J.; Manthiram, A. Synthesis and lithium intercalation properties of nanocrystalline lithium iron oxides. *J. Electrochem. Soc.* **1999**, *146*, 4371.
81. Ye, Y.; Ahn, C.C.; Witham, C.; Fultz, B.; Liu, J.; Rinzler, A.G.; Colbert, D.; Smith, K.A.; Smalley, R.E. Hydrogen adsorption and cohesive energy of single-walled carbon nanotubes. *App. Phys. Lett.* **1999**, *74*, 2307.
82. Dillon, A.C.; Jones, K.M.; Bekkedahl, T.A.; Kiang, C.H.; Bethune, D.S.; Heben, M.J. Storage of hydrogen in single-walled carbon nanotubes. *Nature* **1997**, *386*, 377.
83. Liu, C.; Fan, Y.Y.; Liu, M.; Cong, H.T.; Cheng, H.M.; Dresselhaus, M.S. Hydrogen storage in single walled carbon nanotubes at room temperature. *Science* **1999**, *286*, 1127.
84. Chen, F.; Wang, Z.C.; Lin, C.J. Preparation and characterization of nano-sized hydroxyapatite particles and hydroxyapatite/chitosan nano-composite for use in biomedical materials. *Mater. Lett.* **2002**, *57*, 858.
85. Herzer, G. Nanocrystalline soft magnetic materials. *J. Magn. Magn. Mater.* **1996**, *157/158*, 133.
86. Hadjipanayis, G.C. Nanophase hard magnets. *J. Magn. Magn. Mater.* **1999**, *200*, 373.
87. Weller, D.; Doerner, M.F. Extremely high-density longitudinal magnetic recording media. *Annu. Rev. Mater. Sci.* **2000**, *30*, 611.
88. Bate, G. Magnetic recording materials since 1975. *J. Magn. Magn. Mater.* **1991**, *100*, 413.
89. Giri, A.K.; Julian, C.; Gonzalez, J.M. Coercivity of Fe- SiO_2 nanocomposite materials prepared by ball milling. *J. Appl. Phys.* **1994**, *76*, 6573.
90. Yoshizawa, Y.; Oguma, S.; Yamauchi, K. New Fe-based soft magnetic alloys composed of ultrafine grain structure. *J. Appl. Phys.* **1988**, *64*, 6044.
91. Herzer, G. Grain structure and magnetism of nanocrystalline ferromagnets. *IEEE Trans. Magn.* **1989**, *25*, 3327.
92. Herzer, G. Grain size dependence of coercivity and permeability in nanocrystalline ferromagnets. *IEEE Trans. Magn.* **1990**, *26*, 1397.
93. Yoshizawa, Y. Magnetic properties and microstructure of nanocrystalline Fe-based alloys. *Mater. Sci. Forum* **1999**, *307*, 51.
94. Kneller, E.F.; Hawig, R. The exchange-spring magnet: A new material principle for permanent magnets. *IEEE Trans. Magn.* **1991**, *27*, 3588.
95. Skomski, R.; Coey, J.M.D. Giant energy product in nanostructured two-phase magnets. *Phys. Rev., B* **1993**, *48*, 15812.
96. McCormic, P.G.; Miao, W.F.; Smith, P.A.I.; Ding, J.; Street, R. Mechanically alloyed nanocomposite magnets. *J. Appl. Phys.* **1998**, *83*, 6256.
97. Coey, J.M.D. Permanent magnetism. *Solid State Commun.* **1997**, *102*, 101.
98. Zeng, H.; Li, J.; Liu, J.P.; Wang, Z.L.; Sun, S. Exchange-coupled nanocomposite magnets by nanoparticles self-assembly. *Nature* **2002**, *420*, 395.
99. Sellmyer, D.J. Strong magnets by self-assembly. *Nature* **2002**, *420*, 374.
100. Sun, S.; Murray, C.B.; Weller, D.; Folks, L.; Moser, A. Monodisperse FePt nanoparticles and ferromagnetic FePt nanocrystal superlattices. *Science* **2000**, *287*, 1989.

Nanomaterials: New Trends

Richard Silbergitt

RAND Corporation, Arlington, Virginia, U.S.A.

INTRODUCTION

This paper reviews recent trends in the development and characterization of nanomaterials, which we define as materials with a nanoscale component or structure that exerts a significant influence on properties or function. The trends that we discuss are part of a larger trend in technological development toward integration of disciplines such as physics, chemistry, materials science and engineering, and biology, as well as toward the development of multifunctional materials compatible with increasingly complex environments.^[1] We identify three principal trends that provide the organizational framework for the paper:

1. Integration of organic and biological materials with nanoscale inorganic and polymeric materials (*bionanomaterials*).
2. Incorporation of nanoscale components into materials to improve functionality (*nanocomposites*).
3. Use of “top-down” (e.g., lithography) and “bottom-up” (e.g., self-assembly) processing approaches, sometimes in combination, to produce novel nanoscale structures (*functional nanostructures*).

Each of these trends is discussed in a separate section, with references to the recent (e.g., since 2000) literature. Considering the continuing rapid evolution of this research area, the references are intended to be illustrative rather than comprehensive. The discussed trends are aimed at developing materials to be used in new devices, components, and products, so while a detailed discussion of these items is outside the scope of this paper, we do examine the possible implications of trends in nanomaterials for applications with potential societal effects.^[2] Specifically, we examine possible high-growth and low-growth developments and drivers and barriers to achieving each, as well as the possible synergistic influences that these developments might exhibit. In this discussion, we follow the approach described in Ref. [1].

BIONANOMATERIALS

Fig. 1 schematically illustrates the domain of bionanomaterials. This is the intersection of nanomaterials, which

introduces scale effects to influence materials function, and biomaterials, which introduces biology into materials function at a variety of scales. It incorporates concepts, methods, raw materials, and instrumentation from nanoscience and nanotechnology as well as biology and bioengineering to develop new functional materials at the nanoscale. In some cases, the design and assembly of these materials is based on approaches that imitate or build upon phenomena or mechanisms that occur in nature, which is indicated in Fig. 1 by the inverted arrow labeled “biomimetic design/assembly.” These biomimetic approaches are sometimes aimed at developing materials with biological function and application, e.g., an encapsulant for targeted drug delivery. But biomimetics can also be applied to the design and assembly of nanoscale materials for nonbiological applications, e.g., electronic or optoelectronic materials, or catalysts.

Biomimetic Approaches

Recent use of biomimetic approaches includes the use of motor proteins to shuttle molecules along bioengineered tracks,^[3] the use of “sticky-ended” cohesion of complementary DNA molecules to assemble nanostructures,^[4] the use of block copolymers of polypeptides to form ordered silica structures,^[5] and the design of self-assembling synthetic substitutes for the collagen proteins that form templates for bone growth.^[6] A number of recent reviews describe biologically motivated materials design and assembly approaches with a broad range of applications including catalysis, drug design and delivery, tissue engineering, energy collection, storage, conversion and transport, sensing and actuation, bioassays, chemical and biological agent detection, and electronics.^[7–9]

Supramolecular Materials

Supramolecular materials (assemblies of molecules that are built up through molecular, noncovalent, forces) have emerged as a key ingredient in achieving function at the nanoscale.^[10] These materials can be self-assembled into nanoscale structures such as disks, strips, cylinders, and ribbons to which biologically active materials can be attached.^[11] Selective cleaving of the self-assembling ends can also be used to obtain functionalized nanoporous

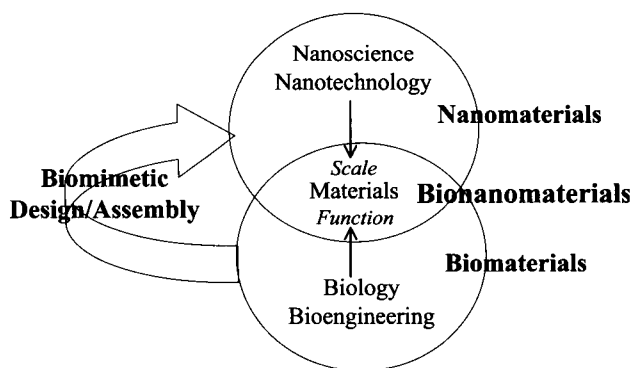


Fig. 1 Schematic illustration of the domain of bionanomaterials.

materials.^[12] The biological self-assembly process itself has also been adapted for nonbiological materials assembly, as molecules based on short peptide sequences taken from fibrinogen (an active ingredient in coagulation) have been used to direct the self-assembly of polyethylene glycol.^[13] In efforts to link biologically driven assembly to electronic devices, peptides with highly specific binding properties to semiconductor heterostructures have been experimentally demonstrated^[14] and designed using computational algorithms.^[15]

Dendrimers (supramolecular materials with a branched tree structure) are being developed and tailored as vehicles for encapsulating drugs for targeted delivery or even strands of DNA for gene therapy, as well as to ‘harvest’ sunlight and transfer the energy into the center of the molecule where it might be used in optoelectronic or photovoltaic applications.^[16] Dendrimers based on liquid crystals have also been proposed for optoelectronic applications,^[17] and a liquid crystal phase with a very large unit cell, containing 30 dendrimers, has recently been demonstrated.^[18]

A possible alternative to dendrimers for encapsulation is afforded by nanocompartments formed from lipid bilayer membranes^[19] or vesicles formed from copolymers containing hydrophobic and hydrophilic blocks.^[20] Complexes of closed lipid bilayer membranes and DNA show promise for gene delivery without use of viruses, although much remains to be learned about the relationship between the supramolecular structures formed by these complexes and their efficiency of gene transfer and expression.^[21]

Biomaterialization

Living organisms form mineralized crystals of many types, often containing complex multifunctional structures (e.g., mollusk shell, sea urchin skeleton, biogenic silica), sometimes with features that have not been incorporated in synthetic materials.^[22] The development of such

biomineralized crystals has been shown to depend on both stereochemical recognition of surface step edges by amino acids and resultant changes in free energy of the growing crystal surface,^[23] linking biological, physical, and chemical interactions in the formation of biominerals with varied asymmetric structures.^[24] Biomineralization principles have recently been used to fabricate a large micropatterned single crystal of calcite from a patterned amorphous calcium carbonate template, with oriented nucleation induced by a self-assembled monolayer of alkanethiol on gold or silver.^[25]

Nanoparticle Probes

One of the first successful applications of bionanomaterials is the use of DNA-tagged nanoparticles for bioassays and biosensors. This has been accomplished through the observation of electrical changes due to binding of the target species to oligonucleotides functionalized with gold nanoparticles^[26] and through the fluorescence of semiconductor nanocrystals linked to oligonucleotides.^[27]

Biomedical Applications

Recent bionanomaterials studies aimed at biomedical applications include the development of nanomaterials linking radioactive atoms to monoclonal antibodies for tumor-specific radiation therapy^[28] and the incorporation of nanoparticles into cement used for orthopedic implants to reduce inflammatory reaction.^[29] Several university centers in the United States and Europe are focused on biomedical applications such as diagnostics, drug delivery, and implants and prostheses,^[30] including work on dendrimers, nanomembranes, and biologically driven motors.^[31] A recent very thoughtful review argues that it is the research effort itself in areas related to nanomedicine that will produce useful results in the near term, rather than the achievement of specific biomedical application objectives.^[32]

Whether the bionanomaterials trends highlighted above will lead to revolutionary advances in technology or merely to continued incremental improvements is impossible to predict. Fig. 2 schematically illustrates two possible paths—a high-growth path under which nanomaterials pervasively affect biology and medicine and a low-growth path under which the continued integration of biology, materials, and nanoscience leads to technological advances in specific areas of opportunity. There are currently strong drivers toward the high-growth path, in particular the high level of scientific interest and available resources, including partnerships between academic, governmental, and commercial institutions, resulting from the U.S. National Nanotechnology Initiative (NNI) and similar initiatives in Europe and Japan, as well as strong societal interest in and fascination with nanoscience and

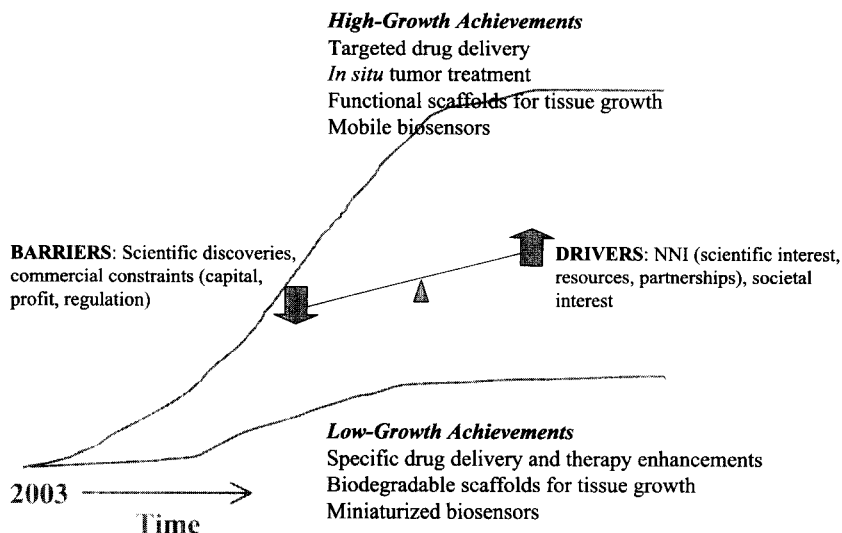


Fig. 2 Possible growth paths for bionanomaterials applications. (View this art in color at www.dekker.com.)

nanotechnology. However, there are also strong barriers that, if not overcome, will push toward the low-growth path, in particular the need for major scientific discoveries and commercial constraints such as the availability of capital, the need to show profit, and regulatory requirements.

The following are some of the significant scientific questions that need to be addressed to progress along either path:

- Can integration of functional biological materials into nanoscale materials systems be reproducibly scaled?
- Can biological function be sufficiently retained in synthetic bionanomaterials to allow high-accuracy molecular recognition and targeting?
- Can encapsulation schemes for bionanomaterials be implemented on a cost-effective commercial scale?
- Can short-term or long-term compatibility of synthetic bionanomaterials in the human body be demonstrated?
- Can effective methods for determining unintended side effects of bionanomaterials be developed and implemented?

The rate at which progress is made in addressing these questions will determine the timescale in Fig. 2, in addition to whether progress is toward the high-growth or the low-growth path.

NANOCOMPOSITES

The incorporation of nanoscale components into materials to improve function is perhaps currently the most advanced area of nanomaterials. A growing number of commercial entities already produce nanoparticles with an

estimated world market near \$500 million in 2000 and growth projected in applications such as conductive and magnetic coatings, optical fibers, phosphors, biological labels, orthopedic materials, sunscreens, catalysts, and scratch-resistant coatings.^[33,34] From the perspective of the chemical industry, nanocomposites can be separated into those that incorporate nanoscale clays, nanoscale oxides or metals, and carbon nanotubes.^[35] We will adopt a slight generalization of this approach and organize the following discussion around polymer nanocomposites (based on nanoscale silicates including clays); composites incorporating metal, oxide, and semiconductor nanoparticles and nanocrystals; nanoscale coatings and films based on these; and composites incorporating carbon nanotubes or semiconductor nanowires.

Polymer Nanocomposites

The interest in polymer nanocomposites stems from the fact that the dispersion of a relatively small amount (e.g., <5%) of a layered silicate such as clay can provide significantly improved properties, including strength, barrier properties, reduced water absorption, and reduced flammability, so long as the clay is exfoliated or intercalated into layers of nanoscale thickness.^[36–38] Recent experimental work^[39] demonstrates the positive influence of dispersed silicate nanolayers on both the crystalline morphology and mechanical properties of the nanocomposite, and recent theoretical work^[40] suggests that the toughening mechanisms may be similar to those postulated for biological structural materials such as spider silk and abalone adhesive. Silicate-based nanocomposites have also been made from aerospace epoxy material and

demonstrated both to have improved mechanical properties and appropriate viscosity and cure kinetics to remain suitable for standard composite molding techniques such as resin transfer molding.^[41]

Nanoparticle and Nanocrystal Composites

Advances in and approaches to the characterization of the electrical, magnetic, optical, and chemical properties of isolated and assembled nanoscale particles and crystals and attempts to use them to improve materials and device function are described in a recent series of articles.^[42] Nanomaterials investigated include Co, Ni, Fe, and magnetic alloy nanoparticles for magnetic device applications;^[43] CdSe^[44] and Mn-doped ZnS^[45] nanocrystals for optical and laser applications; nanoscale Au and Ag for optoelectronic applications;^[46] and nanoparticles capped with organic materials for electronic applications.^[47]

An alternative approach to incorporating functional Fe nanoparticles into electronic devices consists of introducing Fe₂O₃ nanoparticles externally produced onto a Si wafer and annealing in ultrahigh vacuum.^[48] Glass ceramics consisting of SnO₂ nanocrystals dispersed in SiO₂ have also been studied as potential nonlinear materials for all-optical switching devices.^[49]

Mulvaney^[46] shows that optical properties of Au and Ag nanoparticles depend on shape. Both size and geometric shape of Au and Ag nanoparticles have been shown to be controllable through solution-phase chemistry, yielding Ag nanocubes and Au nanoboxes with a truncated cubic shape.^[50]

With respect to catalytic applications, capped metallic nanoparticles have been demonstrated to avoid aggregation on electrode surfaces and show catalytic activity on both metal and Pt-doped polymer substrates,^[51] while semiconductor nanoclusters have been demonstrated to enable the photooxidation of the toxic aromatic organic material pentachlorophenol.^[52] A novel synthesis route to a porous composite nanostructure including catalytic metal oxide nanoparticles uses aqueous solutions of metal salts together with an aqueous dispersion of synthetic clay and surfactants.^[53]

Nanoscale Coatings and Films

All of the nanoparticle and nanocrystal material types mentioned in the previous section have been implemented as nanoscale coatings or films. FePt nanoparticles were synthesized and self-assembled into nanocrystal superlattices and annealed into ferromagnetic films that are mechanically robust and support high-density magnetization reversal transitions required for magnetic data storage.^[54] Ni nanoparticles were also epitaxially grown on a TiN thin-film matrix and exhibited significantly

higher coercivity than randomly oriented Ni particles.^[55] A quantum-dot light-emitting diode was fabricated by sandwiching a monolayer of CdSe (ZnS) nanocrystals between two organic thin films, using phase separation between these films and the organic materials capping the nanocrystals.^[56] Films of Au nanoparticles functionalized with aromatic molecules were spin coated onto interdigitated electrode structures and used as vapor sensors.^[57]

Nanoscale coatings and films have been demonstrated to produce enhancements of a variety of technologically important properties. Nanoporous films of PbZr_xTi_{1-x}O₃ (PZT) allow tailoring of dielectric properties to increase the figure of merit for pyroelectric applications.^[58] Thin films of optical polymers with nanoscale corrugated surfaces provide an alternative approach to antireflection coatings.^[59] Nanostructured hydroxyapatite coatings provide improved adhesion and corrosion resistance for medical implants.^[60] Nanocrystalline Al₂O₃ coatings on glass substrates provide increased hardness with no degradation of optical properties.^[61] Nanoscale coatings also provide the possibility of controlled gradients in mechanical properties that may provide new design options for damage-resistant materials surfaces.^[62]

Nanotube and Nanowire Composites

Carbon nanotubes are exceedingly interesting materials both from a scientific viewpoint and because their unique combination of properties (high conductivity, high tensile strength, high temperature capability, plus nanoscale dimensionality) make them suitable, in principle, for many important commercial applications. As described in a recent review,^[63] carbon nanotubes are already in use as an additive to graphite in a majority of the lithium ion batteries found in cell phones and laptop computers; are anticipated to enter the commercial flat-panel display market as field emitters in 2003; have many additional potential applications including conductive plastics, high-performance fibers for composite materials, and flexible sensors for gas detection; and could be enabling materials for new nanoelectronic technologies. In this paper, we will constrain our discussion to aspects of nanotube research related to the formation of composite materials in which the nanotubes improve functionality.

The simplest version of the carbon nanotube, a cylindrically rolled sheet of hexagonally arrayed carbon atoms, or single-walled carbon nanotube (SWNT), has been produced in strands of macroscopic length,^[64] and micrometer-long crystals consisting of ordered arrays of aligned SWNTs have also been produced.^[65] Composite materials with a nanocrystalline Al₂O₃ matrix and reinforcement by ropes of SWNTs that form a network at the grain boundaries have recently been fabricated^[66] by ball-milling to mix the Al₂O₃ powders and nanotubes,

followed by consolidation using the low-temperature spark plasma sintering process. The best of these composites, fully dense with 10 vol.% SWNTs, had a fracture toughness of $9.7 \text{ MPa m}^{1/2}$, almost three times that of pure Al_2O_3 of the same grain size. Peigney^[67] suggests that the high toughness of these Al_2O_3 -carbon nanotube composites results from the combination of high-quality starting materials, homogeneous dispersion without damaging the nanotubes, and the relatively short time and low temperature required for spark plasma sintering. This work demonstrates that carbon nanotubes can be used as reinforcement for ceramic matrix composites. The next steps toward application will include investigation of larger specimens than the $19 \times 2\text{--}4 \text{ mm}$ disks reported in Ref. [66].

Another type of composite material that can be formed from nanotubes involves the incorporation of fullerenes (e.g., C_{60}) inside the nanotube^[68] to form the so-called peapods. It has been demonstrated^[69] that fullerenes containing metal atoms inside the cage of carbon atoms that make up the fullerene molecule can also be encapsulated inside single-walled carbon nanotubes in a one-dimensional array of "peapods." Such an arrangement with Gd atoms inside C_{82} molecules, which are then encapsulated inside single-wall carbon nanotubes, has been shown to behave as an array of quantum dots, with proposed potential application for quantum well-based electronic and optoelectronic devices.^[70] Another composite nanotube material with potential application is a column of liquid Ga inside a carbon nanotube, which is proposed as a nanothermometer based on the increase in height of the Ga meniscus with increasing temperature.^[71]

Semiconductor nanowires are actively being developed as an alternative to carbon nanotubes for nanoelectronic device applications.^[72] Superlattice structures have been developed in nanowires, in which the semiconductor material changes along the long axis of the nanowire, allowing designed changes in the electronic properties. Such composite nanomaterials have been produced using GaP, GaAs, and InP;^[73] Si and SiGe;^[74] and InAs and InP.^[75] These materials are proposed for applications including nanobarcodes, LEDs, and thermoelectric devices.

Whether the nanocomposites trends highlighted above will lead to revolutionary advances in technology or merely to continued incremental improvements is impossible to predict. Fig. 3 schematically illustrates two possible paths—a high-growth path under which nanocomposite materials are pervasively applied throughout society and a low-growth path under which the use of nanocomposites leads to incremental improvements in specific technology areas. There are currently strong drivers toward the high-growth path, in particular the demonstrated property improvements already achieved with nanoparticle composites in such areas as catalysis and surface strengthening, as well as the presence of an active commercial sector and existing markets. However, there are also barriers that, if not overcome, will push toward the low-growth path, in particular the need for continuing engineering improvements and commercial constraints such as the availability of capital, the need to show profit, and regulatory requirements.

The following are some of the significant technical issues that need to be addressed to progress along either path:

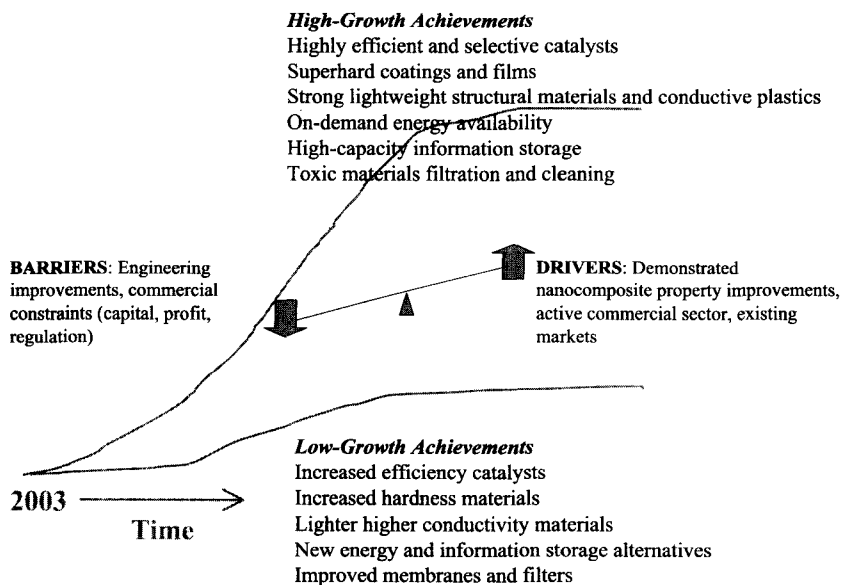


Fig. 3 Possible growth paths for nanocomposites applications. (View this art in color at www.dekker.com.)

- Functionalization of nanoscale components and maintenance of that function in the composite material.
- Design and implementation of effective interfaces between the nanoscale components and the composite matrix.
- Demonstration of reproducible composite behavior and long-term stability.
- Scaling up the nanocomposite for cost-effective production while retaining the property improvements.

The rate at which progress is made in addressing these issues will determine the timescale in Fig. 3, in addition to whether progress is toward the high-growth or the low-growth path.

FUNCTIONAL NANOSTRUCTURES

Perhaps the most fundamental type of functional nanostructure is a microscopic composite with multiple phases formed in situ during processing. As discussed by Ma,^[76] metal alloys with nanoscale grain size typically have increased strength, but lack plasticity necessary for forming or to avoid catastrophic failure in load-bearing applications, and several different approaches to increasing ductility and toughness in such alloys employ a *nonuniform or composite microstructure*. He *et al.*^[77] described an alloy design and solidification process leading to as-cast Ti-based alloys with an in situ composite microstructure consisting of a nanocrystalline matrix and a ductile dendritic phase. The presence of the dendritic phase is shown to increase the plasticity of the material by preventing the propagation of bands of shear stress that, if allowed to grow, could cause catastrophic failure. Thus this type of microscopic composite combines the increased strength of the nanoscale grain size with good ductility and a high elastic-strain limit, and was produced with conventional casting methods, suggesting that the approach may have more general potential for strong, yet tough, metal alloys. The combination of nanoscale grains with microscale dendrites in this material emphasizes the fact that useful nanomaterials do not have to be exclusively nanoscale.

Nanofabrication Methods

A variety of different approaches to fabricate nanostructured materials are described in a recent set of articles,^[78] including the use of lithographic patterns to induce or guide a self-assembly process,^[79] applications of lithography using “soft” materials such as organic elastomers,^[80] and the use of an atomic force microscope tip to

“write” nanostructures onto a gold substrate with alkanethiol “ink”, namely, dip-pen nanolithography.^[81] Another nanofabrication method uses metallic mask membranes fabricated from nanochannel glass (a glass matrix with uniform arrays of hollow channels as small as 20 nm) to produce regular arrays of magnetic dots for magnetic storage application.^[82] A recent study compared ferroelectric nanostructures fabricated via self-assembly of dispersed nanoparticles synthesized from a microemulsion and via electron beam lithography of a polymer precursor layer,^[83] with the self-assembly approach producing droplets in the 50–60 nm range (which the authors argued was several times too large for self-assembly), while the lithographic approach produced arrays of 60–70 nm particles with spacing down to 150 nm.

The stability of fabricated nanostructures under application conditions can be an important issue. Nanoscale features produced on a Cu crystal by ion sputtering under ultrahigh vacuum were demonstrated to be stabilized at room temperature in air for a week or more (far longer than needed to serve as a useful process step) by an oxidation treatment.^[84] The authors noted that without the oxidation treatment, the stability of such nanoscale features is limited by thermally activated diffusion to about 200 K. Feedback-controlled ion beam sputtering has been used to “sculpt” a 5-nm pore in a Si₃N₄ membrane, which was then used as a detector for a single DNA molecule.^[85] The authors suggest that this nanofabrication method could be used to fabricate slits, trenches, crosses, and other structures for nanoscale semiconductor devices.

Nanofabrication via Self-Assembly

Self-assembly phenomena have been used both to form templates for fabricating nanostructures and to assemble the nanostructure itself. Dynospheres (latex particles 0.5 μm in diameter suspended in water) were self-assembled into regular arrays that were used as a mask to deposit arrays of Ni nanoparticles.^[86] Polymethylmethacrylate (PMMA) spheres were self-assembled in trenches in Si wafers to form a three-dimensional photonic crystal.^[87] Nanowires of single-crystal Si that self-align to form a structure suitable for photoemission applications were grown from a thermally evaporated Ni film subjected to magnetron sputtering of Si.^[88] An Al film deposited on a Si or SiO₂ substrate was anodized to produce a hexagonally ordered nanoporous Al₂O₃ structure.^[89] A large variety of topological structures have been produced in mesoporous SiO₂ by combining sol gel and emulsion chemistry with molecular self-assembly.^[90]

Self-assembled nanostructured films have been shown to possess useful chemical and optical properties. A self-assembled monolayer of hexadecanethiol on a gold surface was shown to block the interaction of the surface

with neutral molecules such as water and volatile sulfuric compounds, enhancing its effect as a selective detector of mercury vapor.^[91] Self-assembled multilayer superlattice films containing chromophoric organic molecules were shown to be useful for optical switching based on their large second-order nonlinear optical response.^[92]

Self-Assembly with Diblock Copolymers

Films of copolymers consisting of two distinct blocks [e.g., polystyrene (PS) and PMMA] spontaneously assemble into ordered domains with morphology principally depending on the molecular weight ratio of the constituent polymers, allowing the formation of nanoscale tailored polymer dot arrays via chemical removal of one of the blocks. These polymer dot arrays can then be used as templates or masks to form nanoscale dot arrays of metals or insulators on silicon and other substrates.^[93] Incorporation of metal nanoclusters synthesized in situ from decomposition of precursors within one of the copolymer blocks was demonstrated to produce patterned structures with selective phase separation and particle confinement.^[94] Arrays of Co nanowires with application as ultrahigh-density magnetic data storage media have also been fabricated using nanoporous films derived from diblock copolymers.^[95] Combining a diblock copolymer of polystyrene and polyethylene oxide with a dilute homogeneous solution of a silica precursor leads to a mesostructured silica film that can be calcined to produce closed-cell mesoporous silica films with potential application as low dielectric constant insulators.^[96] Control of optical energy transfer was demonstrated by embedding

semiconducting polymers into the pores of such a silica film, suggesting their potential application in optoelectronics as well.^[97]

Whether the functional nanostructures trends highlighted above will lead to revolutionary advances in technology or merely to continued incremental improvements is impossible to predict. Fig. 4 schematically illustrates two possible paths—a high-growth path under which advances in functional nanostructure fabrication lead to a broad range of new materials and devices and a low-growth path under which functional nanosystems penetrate existing markets in an incremental fashion. There are currently strong drivers toward the high-growth path, in particular the continuing integration of top-down and bottom-up fabrication approaches and the increasingly interdisciplinary nature of research in this area. However, there are also strong barriers that, if not overcome, will push toward the low-growth path, in particular the need for continuing scientific advances, the need to address scale-up issues, and commercial constraints such as the availability of capital, the need to show profit, and regulatory requirements.

The following are some of the significant scientific issues that need to be addressed to progress along either path:

- Retention of microscopic nanostructures under application conditions.
- Reproducible, scalable, cost-effective fabrication of designed nanostructures.
- Demonstration of nanostructure function in macroscopic materials and devices.
- Demonstration of long-term nanostructure functional stability.

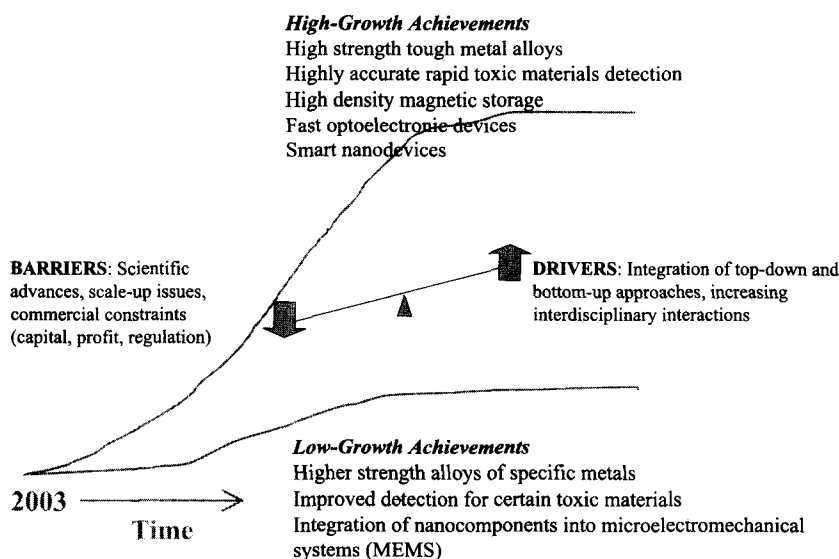


Fig. 4 Possible growth paths for functional nanostructure applications. (View this art in color at www.dekker.com.)

Table 1 Synergisms between nanomaterials applications

	Targeted drug delivery	In situ tumor treatment	Mobile biosensors	Super membranes and catalysts	Superhard coatings and films	Cheap energy storage	High-strength tough metal alloys	Fast precise toxic materials detection	Smart nanodevices
Targeted drug delivery		Facilitates	Spur development	–	–	–	–	Counter chemical and bio agents	Smart drug delivery
In situ tumor treatment	–		Spur development	–	–	–	–	–	–
Mobile biosensors	Facilitates	Facilitates		Blood filters	–	–	–	–	Smart biosensors
Super membranes and catalysts	–	–	Blood filters		–	Improved energy conversion	–	Counter chemical and bio agents	Improved chemical processes
Superhard coatings and films	–	–	Facilitates	–		Facilitates	Long-life structural materials	–	–
Cheap energy storage	–	Facilitates	Facilitates	Improved energy conversion	Spur development		–	Counter chemical and bio agents	Portable power
High-strength tough metal alloys	–	–	–	–	Long-life structural materials	Facilitates		Facilitates	Facilitates
Fast precise toxic materials detection	Counter chemical and bio agents	–	Facilitates	Counter chemical and bio agents	–	Counter chemical and bio agents	–	–	Counter chemical and bio agents
Smart nanodevices	Smart drug delivery	Facilitates	Smart biosensors	Improved chemical processes	–	Portable power	Facilitates	Counter chemical and bio agents	

The rate at which progress is made in addressing these issues will determine the timescale in Fig. 4, in addition to whether progress is toward the high-growth or the low-growth path.

SYNERGISTIC INFLUENCES

The development of certain nanomaterials trends will in some cases exert a synergistic influence on the development of other trends. Table 1 illustrates some of these potential effects for possible high-growth applications of the nanomaterials trends discussed above. Three application developments are considered for each nanomaterials area. Targeted drug delivery, in situ tumor treatment, and mobile biosensors are the bionanomaterials developments considered. Super membranes and catalysts, superhard coatings and films, and cheap energy storage are the nanocomposites developments considered. High-strength tough alloys, fast precise toxic materials detection, and smart nanodevices are the functional nanostructures developments considered. Where the presence of one development could facilitate the other development, e.g., targeted drug delivery and in situ tumor treatment, the word "facilitates" is shown in the appropriate box. This effect is not always symmetric. For example, the presence of in situ tumor treatment would not facilitate targeted drug delivery. In some cases, synergism between the two developments would improve function, e.g., smart nanodevices together with super membranes and catalysts would lead to improved chemical processes. In other cases, the synergism might lead to an entirely new capability, as for example targeted drug delivery and smart nanodevices would enable smart drug delivery. For the purposes of this analysis, we assumed that the synergisms leading to improved function or new capabilities were symmetric. The boxes in Table 1 with dashes indicate no synergism between the two developments.

The following paragraphs briefly summarize the synergisms listed in Table 1 (symmetric synergisms are only discussed once).

Targeted drug delivery: facilitates in situ tumor treatment by providing a mechanism; spurs development of mobile biosensors by providing an application; together with fast precise toxic materials detection could provide detection coupled with treatment for chemical or biological (CB) agents; together with smart nanodevices could provide smart drug delivery.

In situ tumor treatment: spurs development of mobile biosensors by providing an application.

Mobile biosensors: facilitate targeted drug delivery and in situ tumor treatment by providing locations; together with super membranes and catalysts could provide the basis for blood filters; together with smart nanodevices could provide smart biosensing.

Super membranes and catalysts: together with cheap energy storage could provide a means for improved energy conversion; together with fast precise toxic materials detection could provide both for detection and filtering or destruction of CB agents; together with smart nanodevices could provide a means for improving the selectivity and yield of chemical processes that involve separations or catalysis.

Superhard coatings and films: could facilitate mobile biosensors and cheap energy storage by providing protection from damaging materials or hostile environments; together with high-strength tough metal alloys could provide long-life structural materials.

Cheap energy storage: could facilitate in situ tumor treatment and mobile biosensors by providing cost-effective power sources; could spur development of superhard coatings and films by providing an application; together with fast precise toxic materials detection could provide a means for detection and destruction of CB agents; together with smart nanodevices could provide on-demand portable power sources.

High-strength tough metal alloys: can facilitate cheap energy storage, fast precise toxic materials detection, and smart nanodevices by providing functional structural materials.

Fast precise toxic materials detection: facilitates mobile biosensors by providing the mechanism for the biosensor.

Smart nanodevices: facilitate in situ tumor treatment by providing a means for treatment delivery to the tumor site; facilitate high-strength tough metal alloys by providing a possible means for fabrication.

ACKNOWLEDGMENTS

The author is extremely grateful to Frank Gac, John Gilman, Eric Landree, Parry Norling, Fyl Pincus, Stephen Rattien, Ulrich Strom, and Julia Warner for providing reference materials for this paper, and to Philip Antón and Fyl Pincus for their insightful reviews of the draft and several useful suggestions that were incorporated into the final version. The author also acknowledges the financial support of the Rand Corporation for the development of this work.

REFERENCES

1. Antón, P.S.; Silbergliitt, R.; Schneider, J. *The Global Technology Revolution: Bio/Nano/Materials Trends and Their Synergies with Information Technology by 2015*; 2001. RAND MR-1307-NIC, available to the public at <http://www.rand.org/publications/MR/MR1307>.
2. National Science and Technology Council (NSTC/

- Subcommittee on Nanoscale Science, Engineering and Technology (NSET). *Societal Implications of Nanoscience and Nanotechnology*; Roco, M.C., Bainbridge, W.S., Eds.; 2001. Available to the public at <http://www.nano.gov> or <http://itri.loyola.edu/nano/NSET.Societal.Implications/>.
3. Vogel, V. Reverse engineering: Learning from proteins how to enhance the performance of synthetic nanosystems. *MRS Bull.* **2002**, *27* (2), 972–978.
 4. Seeman, N.C.; Belcher, A.M. Emulating biology: Building nanostructures from the bottom up. *PNAS* **2002**, *99* (Suppl. 2), 6451–6455.
 5. Cha, J.N.; Stucky, G.D.; Morse, D.E.; Deming, T.J. Biomimetic synthesis of ordered silica structures mediated by block copolypeptides. *Nature* **2000**, *403*, 289–292.
 6. Taton, T.A. Boning up on biology. *Nature* **2001**, *412*, 491–492.
 7. Ball, P. Natural strategies for the molecular engineer. *Nanotechnology* **2002**, *13*, R15–R18.
 8. Bashir, R. DNA-mediated artificial nanobiostucture: State of the art and future directions. *Superlattices Microstruct.* **2001**, *29* (1).
 9. Asefa, T.; Coombs, N.; Grondey, H.; Jaroniec, M.; Kruk, M.; MacLachlan, M.J.; Ozin, G.A. Bio-inspired nanocomposites: From synthesis toward potential applications. *Mater. Res. Symp. Proc.* **2002**, *707*, AA5.5.1/HH5.5.1–AA5.5.12/HH5.5.12.
 10. Supramolecular materials. *MRS Bull.* **2000**, *25* (4), 26–58. Edited by J.S. Moore.
 11. Stupp, S.I.; Pralle, M.U.; Tew, G.N.; Li, L.; Sayar, M.; Zubarev, E.R. Self-assembly of organic nano-objects into functional materials. *MRS Bull.* **2000**, *25* (4), 42–48.
 12. Ikkala, O.; ten Brinke, G. Functional materials based on self-assembly of polymeric supramolecules. *Science* **2002**, *295*, 2407–2409.
 13. Seal, B.L.; Panitch, A. Biologically-based self-assembling hydrogels. *Mater. Res. Soc. Symp. Proc.* **2002**, *724*, N3.2.1–N3.2.6.
 14. Whaley, S.R.; English, D.S.; Hu, E.L.; Barbara, P.F.; Belcher, A.M. Selection of peptides with semiconductor binding specificity for directed nanocrystal assembly. *Nature* **2000**, *405*, 665–668.
 15. Lustig, S.R.; Jagota, A. Selectivity of polypeptide binding to nanoscale substrates. *Mater. Res. Soc. Symp. Proc.* **2002**, *724*, N4.6.1–N4.6.6.
 16. Fréchet, J.M.J. Nanostructure Synthesis: Functional Polymers and Dendrimers. In *Nanoscience and Nanotechnology: Shaping Biomedical Research*; NIH Bioengineering Consortium (BECON) Symposium Report, 2000, accessed on Feb. 5, 2003 at http://www.becon1.nih.gov/becon_symposia.htm.
 17. Percec, V.; Glodde, M.; Bera, T.K.; Miura, Y.; Shlyanovskaya, I.; Singer, K.D.; Balagurusamy, V.S.K.; Helney, P.A.; Schnell, I.; Rapp, A.; Splett, H.-W.; Hudson, S.D.; Duan, H. Self-organization of supramolecular helical dendrimers into complex electronic materials. *Nature* **2002**, *417*, 384–387.
 18. Ungar, G.; Liu, Y.; Zeng, X.; Percec, V.; Cho, W.-D. Giant supramolecular liquid crystal lattice. *Science* **2003**, *299*, 1208–1211.
 19. Kisak, E.T.; Coldren, B.; Zasadzinski, J.A. Nanocompartments enclosing vesicles, colloids, and macromolecules via interdigitated lipid bilayers. *Langmuir* **2002**, *18*, 284–288.
 20. Gravano, S.M.; Borden, M.; von Werne, T.; Doerffler, E.M.; Salazar, G.; Chen, A.; Kisak, E.; Zasadzinski, J.A.; Patten, T.E.; Longo, M.L. Poly(4-(aminomethyl)styrene)-*b*-polystyrene: Synthesis and unilamellar vesicle formation. *Langmuir* **2002**, *18*, 1938–1941.
 21. Safinya, C.R. Structures of lipid–DNA complexes: Supramolecular assembly and gene delivery. *Curr. Opin. Struct. Biol.* **2001**, *11*, 440–448.
 22. Weiner, S.; Addadi, L.; Wagner, H.D. Materials design in biology. *Mater. Sci. Eng., C* **2000**, *11*, 1–8.
 23. Orme, C.A.; Noy, A.; Wierzbicki, A.; BcBride, M.T.; Grantham, M.; Teng, H.H.; Dove, P.M.; DeYoreo, J.J. Formation of chiral morphologies through selective binding of amino acids to calcite surface steps. *Nature* **2001**, *411*, 775–779.
 24. Addadi, L.; Weiner, S. Crystals, asymmetry and life. *Nature* **2001**, *411*, 753–755.
 25. Aizenberg, J.; Muller, D.A.; Grazul, J.L.; Hamann, D.R. Direct fabrication of large micropatterned single crystals. *Science* **2003**, *299*, 1205–1208.
 26. Park, S.-J.; Taton, T.A.; Mirkin, C. Array-based electrical detection of DNA with nanoparticle probes. *Science* **2002**, *295*, 1503–1506.
 27. Gerion, D.; Parak, W.J.; Williams, S.C.; Zanchet, D.; Micheel, C.M.; Alivisatos, A.P. Sorting fluorescent nanocrystals with DNA. *J. Am. Chem. Soc.* **2002**, *124*, 7070–7074.
 28. McDevitt, M.R.; Ma, D.; Lai, L.T.; Simon, J.; Borchardt, P.; Frank, R.K.; Wu, K.; Pellegrini, V.; Curcio, M.J.; Miederer, M.; Bander, N.H.; Scheinberg, D.A. Tumor therapy with targeted atomic nanogenerators. *Science* **2001**, *294*, 1537–1540.
 29. Shortkroff, S.; Turell, M.B.; Rice, K.; Thornhill, T.S. Cellular response to nanoparticles. *Mater. Res. Symp. Proc.* **2002**, *704*, W11.5.1–W11.5.6.
 30. Malsch, I. Biomedical applications of nanotechnology. *Ind. Phys.* **June/July 2002**, *8* (3), 15–17.
 31. Voss, D. Nanomedicine nears the clinic. *Technol. Rev.* **January/February 2000**, *103* (1), 60–64.

32. Haberzetti, C.A. Nanomedicine: Destination or journey? *Nanotechnology* **2002**, *13*, R9–R13.
33. Rittner, M.N. Nanostructured materials. *Am. Ceram. Soc. Bull.* **March 2002**, *81* (3), 33–36.
34. Thayer, A.M. Nanotech offers some there, there. *Chem. Eng. News* **November 26 2001**, *79* (48), 13–16.
35. Wood, A.; Scott, A. Nanomaterials a big market potential. *Chem. Week* **October 16 2002**, 17–21.
36. Vaia, R.A.; Giannelis, E.P. Polymer nanocomposites: Status and opportunities. *MRS Bull.* **2001**, *26* (5), 394–401.
37. Alexandre, M.; Beyer, G.; Henrist, C.; Cloots, R.; Rulmont, A.; Jérôme, R.; Dubois, P. “One-pot” preparation of polymer/clay nanocomposites starting from Na⁺ montmorillonite. 1. Melt intercalation of ethylene-vinyl acetate copolymer. *Chem. Mater.* **2001**, *13*, 3830–3832.
38. VanderHart, D.L.; Asano, A.; Gilman, J.W. NMR measurements related to clay-dispersion quality and organic-modifier stability in nylon-6/clay nanocomposites. *Macromolecules* **2001**, *34* (12), 3819–3822.
39. Reynaud, E.; Shah, D.; Giannelis, E.P. Correlation between nanostructure and crystalline morphology and mechanical response in nylon 6 nanocomposites. *Mater. Res. Soc. Symp. Proc.* **2003**, *734*, B5.10.1–B5.10.9.
40. Gersappe, D. Molecular mechanisms of failure in polymer nanocomposites. *Phys. Rev. Lett.* 29 July **2002**, *89* (5), 058301-1–058301-4.
41. Chen, C.; Curliss, D. Processing, dynamic studies and properties of exfoliated aerospace epoxy-organoclay nanocomposites. *Mater. Res. Soc. Symp. Proc.* **2002**, *703*, V1.2.1–V1.2.6.
42. New aspects of nanocrystal research. *MRS Bull.* **2001**, *26* (12), 981–1019. Edited by L.M. Liz-Marzán and D.J. Norris.
43. Murray, C.B.; Sun, S.; Doyle, H.; Betley, T. Monodisperse 3d transition-metal (Co, Ni, Fe) nanoparticles and their assembly into nanoparticle superlattices. *MRS Bull.* **2001**, *26* (12), 985–991.
44. Klimov, V.I.; Bawendi, M.G. Ultrafast carrier dynamics, optical amplification, and lasing in nanocrystal quantum dots. *MRS Bull.* **2001**, *26* (12), 998–1004.
45. Shim, M.; Wang, C.; Norris, D.J.; Guyot-Sionnest, P. Doping and charging in colloidal semiconductor nanocrystals. *MRS Bull.* **2001**, *26* (12), 1005–1008.
46. Mulvaney, P. Not all that’s gold does glitter. *MRS Bull.* **2001**, *26* (12), 1009–1014.
47. Schiffrin, D.J. Capped nanoparticles as potential electronic components with nanoscale dimensions. *MRS Bull.* **2001**, *26* (12), 1015–1019.
48. Prabhakaran, K.; Shafi, K.V.P.M.; Ulman, A.; Ogino, T. Multi-functionalization of silicon by nanoparticles through “plug and play” approach. *Mater. Res. Soc. Symp. Proc.* **2002**, *703*, V3.17.1–V3.17.6.
49. Chiodini, N.; Paleari, A.; DiMartino, D.; Spinolo, G. SnO₂ nanocrystals in SiO₂: A wide-band-gap quantum-dot system. *Appl. Phys. Lett.* **2002**, *81* (9), 1702–1704.
50. Sun, Y.; Xia, Y. Shape-controlled synthesis of gold and silver nanoparticles. *Science* **2002**, *298*, 2176–2179.
51. Maye, M.M.; Luo, J.; Lou, Y.; Ly, N.K.; Chan, W.-B.; Phillip, E.; Helpel, M.; Zhong, C.J. Investigating catalytic properties of composite nanoparticle assemblies. *Mater. Res. Soc. Symp. Proc.* **2002**, *703*, V10.6.1–V10.6.6.
52. Wilcoxon, J.P. Catalytic photooxidation of pentachlorophenol using semiconductor nanoclusters. *J. Phys. Chem., B* **2000**, *104*, 7334–7343.
53. Zhu, H.Y.; Lu, G.Q. Molecular engineered porous nanocomposites of metal oxide and clay using surfactants. *Mater. Res. Soc. Symp. Proc.* **2002**, *703*, V1.5.1–V1.5.10.
54. Sun, S.; Murray, C.B.; Weller, D.; Folks, L.; Moser, A. Monodisperse FePt nanoparticles and ferromagnetic FePt nanocrystal superlattices. *Science* **2000**, *287*, 1902–1903.
55. Zhou, H.; Kvit, A.; Kumar, D.; Narayan, J. Nickel nanocomposite thin films. *Mater. Res. Soc. Symp. Proc.* **2002**, *703*, V9.12.1–V9.12.6.
56. Coe, S.; Woo, W.-K.; Bawendi, M.; Bulović, V. Electroluminescence from single monolayers of nanocrystals in molecular organic devices. *Nature* **2002**, *420*, 800–803.
57. Zhang, H.-L.; Evans, S.D.; Henderson, J.R.; Miles, R.E.; Shen, T.-H. Vapour sensing using surface functionalized gold nanoparticles. *Nanotechnology* **2002**, *13*, 439–444.
58. Suyal, G.; Seifert, A.; Setter, N. Pyroelectric nanoporous films: Synthesis and properties. *Appl. Phys. Lett.* **2002**, *81* (6), 1059–1061.
59. Ibn-Elhaj, M.; Schadt, M. Optical polymer thin films with isotropic and anisotropic nano-corrugated surface topologies. *Nature* **2001**, *410*, 796–799.
60. Zhang, Z.; Dunn, M.F.; Xiao, T.S.; Tomsia, A.P.; Saiz, E. Nanostructured hydroxyapatite coatings for improved adhesion and corrosion resistance for medical implants. *Mater. Res. Soc. Symp. Proc.* **2002**, *703*, V7.5.1–V7.5.6.
61. Cayton, R.H.; Brotzman, R.W., Jr. Nanocomposite coatings—Applications and properties. *Mater. Res. Soc. Symp. Proc.* **2002**, *703*, V8.1.1–V8.1.6.
62. Suresh, S. Graded materials for resistance to contact

- deformation and damage. *Science* **2001**, *292*, 2447–2451.
63. Ouellette, J. Building the nanofuture with carbon tubes. *Ind. Phys.* **December 2002/January 2003**, *8* (6), 18–21.
 64. Zhu, H.W.; Xu, C.L.; Wu, D.H.; Wei, B.Q.; Vajtai, R.; Ajayan, P.M. Direct synthesis of long single-walled carbon nanotube strands. *Science* **2002**, *296*, 884–886.
 65. Schlittler, R.R.; Seo, J.W.; Gimzewski, J.K.; Durkan, C.; Saifullah, M.S.M.; Welland, M.E. Single crystals of single-walled carbon nanotubes formed by self-assembly. *Science* **2001**, *292*, 1136–1139.
 66. Zhan, G.-D.; Kuntz, J.D.; Wan, J.; Mukherjee, A.K. Single-wall carbon nanotubes as attractive toughening agents in alumina-based nanocomposites. *Nat. Mater.* **2003**, *2*, 38–42.
 67. Peigney, A. Tougher ceramics with nanotubes. *Nat. Mater.* **2003**, *2*, 15–16.
 68. Smith, B.W.; Monthieux, M.; Luzzi, D.E. Encapsulated C₆₀ in carbon nanotubes. *Nature* **1998**, *396*, 323–324.
 69. Hirahara, K.; Suenaga, K.; Bandow, S.; Kato, H.; Okazaki, T.; Shinohara, H.; Iijima, S. One-dimensional metallofullerene crystal generated inside single-walled carbon nanotubes. *Phys. Rev. Lett.* **2000**, *85*, 5384–5387.
 70. Lee, J.; Kim, H.; Kahng, S.-J.; Kim, G.; Son, Y.-W.; Ihm, J.; Kato, H.; Wang, Z.W.; Okazaki, T.; Shinohara, H.; Kuk, Y. Bandgap modulation of carbon nanotubes by encapsulated metallofullerenes. *Nature* **2002**, *415*, 1005–1008.
 71. Gao, Y.; Bando, Y. Carbon nanothermometer containing gallium. *Nature* **2002**, *415*, 599.
 72. Appell, D. Wired for success. *Nature* **2002**, *419*, 553–555.
 73. Gudixsen, M.S.; Lauhon, L.J.; Wang, J.; Smith, D.C.; Lieber, C.M. Growth of nanowire superlattice structures for nanoscale photonics and electronics. *Nature* **2002**, *415*, 617–620.
 74. Wu, Y.; Fan, R.; Yang, P. Block-by-block growth of single-crystalline Si/SiGe superlattice nanowires. *Nano Lett.* **2002**, *2* (2), 83–86.
 75. Björk, M.T.; Ohlsson, B.J.; Sass, T.; Persson, A.I.; Thelander, C.; Magnusson, M.H.; Deppert, K.; Wallenberg, L.R.; Samuelson, L. One-dimensional steeplechase for electrons realized. *Nano Lett.* **2002**, *2* (2), 87–89.
 76. Ma, E. Controlling plastic instability. *Nat. Mater.* **2003**, *2*, 7–8.
 77. He, G.; Eckert, J.; Löser, W.; Schultz, L. Novel Ti-base nanostructure-dendrite composite with enhanced plasticity. *Nat. Mater.* **2003**, *2*, 33–37.
 78. Emerging methods for micro- and nanofabrication. *MRS Bull.* **2001**, *26* (7), 506–546. Edited by C.A. Mirkin and J.A. Rogers.
 79. Chou, S.Y. Nanoimprint lithography and lithographically induced self-assembly. *MRS Bull.* **2001**, *26* (7), 512–517.
 80. Love, J.C.; Anderson, J.R.; Whitesides, G.M. Fabrication of three-dimensional microfluidic systems by soft lithography. *MRS Bull.* **2001**, *26* (7), 523–528.
 81. Mirkin, C.A. Dip-pen nanolithography: Automated fabrication of custom multicomponent, sub-100-nanometer surface architectures. *MRS Bull.* **2001**, *26* (7), 535–538.
 82. Cheng, B.; Yang, K.; Justus, B.L.; Yeh, W.J. Regular array of magnetic nano-dots prepared by nanochannel glass replica masks. *Mater. Res. Soc. Symp. Proc.* **2002**, *721*, E5.6.1–E5.6.5.
 83. Bhattacharyya, S.; Chattopadhyay, S.; Alexe, M. Fabrication of isolated ferroelectric nanostructures. *Mater. Res. Soc. Symp. Proc.* **2003**, *740*, I10.3.1–I10.3.6.
 84. Sekiba, D.; Bertero, S.; Buzio, R.; de Mongeot, F.B.; Boragno, C.; Valbusa, U. Fabrication of stable nanopatterns on metals. *Appl. Phys. Lett.* **2002**, *81* (14), 2632–2634.
 85. Li, J.; Stein, D.; McMullan, C.; Branton, D.; Aziz, M.J.; Golovchenko, J.A. Ion-beam sculpting at nanometre length scales. *Nature* **2001**, *412*, 166–169.
 86. Ng, V.; Lee, Y.V.; Chen, B.T.; Adeyeye, A.O. Nanostructure array fabrication with temperature-controlled self-assembly techniques. *Nanotechnology* **2002**, *13*, 554–558.
 87. Ferrand, P.; Egen, M.; Griesebock, B.; Ahopelto, J.; Müller, M.; Zentel, R.; Romanov, S.G.; Sotomayor Torres, C.M. Self-assembly of three-dimensional photonic crystals on structured silicon wafers. *Appl. Phys. Lett.* **2002**, *81* (15), 2689–2691.
 88. Ji, C.; Gulians, E.A.; Abeysinghe, D.; Anderson, W.A. Self-organized Si nanowires with room-temperature photo-emission. *Mater. Res. Soc. Symp. Proc.* **2002**, *728*, S3.34.1–S3.34.6.
 89. Cai, A.; Zhang, H.; Hua, H.; Zhang, Z. Direct formation of self-assembled nanoporous aluminum oxide on SiO₂ and Si substrates. *Nanotechnology* **2002**, *13*, 627–630.
 90. Zhao, D.; Yang, P.; Huo, Q.; Chmelka, B.F.; Stucky, G.D. Topological construction of mesoporous materials. *Curr. Opin. Solid State Mater. Sci.* **1998**, *3*, 111–121.
 91. Mirsky, V.M.; Vasjari, M.; Novotny, I.; Rehacek, V.; Tvarozek, V.; Wolfbeis, O.S. Self-assembled

- monolayers as selective filters for chemical sensors. *Nanotechnology* **2002**, *13*, 175–178.
92. Wang, G.; Zhu, P.; Marks, T.J.; Ketterson, J.B. Ultrafast frequency-selective optical switching based on thin self-assembled organic chromophoric films with a large second-order nonlinear response. *Appl. Phys. Lett.* **2002**, *81* (12), 2169–2171.
93. Black, C.T.; Guarini, K.W.; Sandstrom, R.L.; Yeung, S.; Zhang, Y. Formation of nanometer-scale dot arrays from diblock copolymer templates. *Mater. Res. Soc. Symp. Proc.* **2002**, *728*, S4.9.1–S4.9.8.
94. Tadd, E.H.; Bradley, J.; Goldberg, E.P.; Tannenbaum, R. Self-assembly of metal nanoclusters in block co-polymers. *Mater. Res. Soc. Symp. Proc.* **2002**, *703*, V2.1.1–V2.1.10.
95. Ursache, A.; Bal, M.; Goldbach, J.T.; Sandstrom, R.L.; Black, C.T.; Russell, T.P.; Tuominen, M.T. Terabit density cobalt nanowire arrays with tunable magnetic properties. *Mater. Res. Soc. Symp. Proc.* **2002**, *721*, E3.3.1–E3.3.6.
96. Yu, K.; Smarsly, B.; Brinker, J. Closed-cell mesostructured porous silica films templated by PS-*b*-PEO without additional microporosity. *Mater. Res. Soc. Symp. Proc.* **2002**, *728*, S1.9.1–S1.9.7.
97. Nguyen, T.-Q.; Wu, J.; Doan, V.; Schwartz, B.J.; Tolbert, S.H. Control of energy transfer in oriented conjugated polymer–mesoporous silica composites. *Science* **2000**, *288*, 652–656.



Nanomaterials: Recent Advances in Technology and Industry

Ganesh Skandan

Amit Singhal

NEI Corporation, Piscataway, New Jersey, U.S.A.

INTRODUCTION

The emerging field of Nanotechnology, including nanomaterials, nanoscale devices, and nanobiotechnology, has been purported to impact every aspect of our life in the decades to come. The race to capitalize on Nanotechnology, "the next big thing," began in the wake of the abating Internet mania in the year 2000, although basic and applied research on various aspects of this field has been intensely pursued since the early 1990s. For a comprehensive review of scientific advances in this field during the 1990s, the reader is referred to the World Technology Evaluation Center Report.^[1] We should all remember that studies in catalysis and small metal particles began more than a century ago and represents one of the most significant applications of nanomaterials to date. In many instances, Nanotechnology has been referred to as a "disruptive technology," the elegant and pithy phrase coined by Harvard professor, Clayton Christensen.^[2] With the rapid influx of venture capital into the up-and-coming Nanotechnology industry (although it is a far cry from the investment activity that was seen in the mid-1990s with the then emerging internet industry), start-ups are realizing the need for sustainable competitive advantage in what is now becoming a crowded space. Given the scientific evidence so far, the potential for Nanotechnology to beneficially impact various aspects of our life and society exists, but attempting to predict them all at this stage is futile.

To put this field in perspective to the uninitiated, it has often been mentioned that Nanotechnology today is in the same state computers were in the 1960s.^[1] Perhaps, a more apt comparison should be to the Industrial Revolution that began in the late eighteenth century. The Industrial Revolution enabled products that were already in use to be made cheaper, faster, and of uniform and of predictable quality.^[3,4] The Nanotechnology Revolution underway has the potential to impact the performance of existing products, but not so much in terms of cost. At the same time, Nanotechnology has the potential to make possible new products that would otherwise not be possible. All of this has spawned the growth of Nanotechnology as an industrial sector, while in reality it is an

aggregate of several different industries brought together in ways never seen before. Accordingly, it is helpful to compare this new industrial sector to the several industries that came into existence during and after the Industrial Revolution: railroad, automobile, commercial aviation, and most recently, internet. Several hundreds of companies came into existence in the initial stages of each of these industries: there was a time when there was a large number of companies with *motor works* being the common suffix for a majority of them.^[4] This is much the same today with the word *nano* being the prefix in the name of the company. Based on information garnered by market research entities such as CMP Cientifica,^[5] Business Communication Company,^[6] and Nanobusiness Alliance,^[7] the number of companies worldwide that are active in nanotechnology at the present time can be estimated to be in excess of 400. As it has happened in all of these industries, the initial flurry of activity fades in a few years as the companies come to grips with the realities of the market forces. The start-ups burn through the invested capital, and either close shop or morph into a company with a different objective. The stage had been set by the year 2001 for this story line to be repeated in the Nanotechnology industry, except that the financial climate has been dismal since that time, with investment capital becoming a scarce commodity.

Just as it is said that beauty lies in the eyes of the beholder, an objective definition for Nanotechnology depends on the aspect of the field that the person is involved with. To an oncologist working with nanotechnology, it could mean targeted drug delivery to cure certain specific types of cancer, while to a scientist involved with computing, Nanotechnology could refer to molecular switches. The purpose of this article is to look at technological and commercial advances made to date in the area of Nanomaterials either enabling new products or improving existing products. The focus is on products having the potential to beneficially impact present markets, as opposed to a number of markets that may emerge in the future. Moreover, special emphasis is given on applications where the presence of nanoscale features adds certain functionality, instead of simply providing a high-surface-area template.

OVERVIEW

In a broad sense, Nanomaterials include nanoscale particles (metal/ceramic/metalloid/organic particles or composites thereof, nanotubes, and buckyballs), nanoparticles dispersed (or suspended) in a liquid, or nanoparticles dispersed in a polymeric material, either as a coating or a bulk material. A distinction between functional and nonfunctional nanoscale features needs to be drawn: by nonfunctional nanoscale features, we mean that the nanoparticle simply acts as a high surface area support for a second-phase material, and does not possess any intrinsic functionality. A good example is a ceramic catalyst support, such as a honeycomb structure, in which catalytically active metallic nanoparticles are embedded in the high-surface-area ceramic material. As alluded to earlier, such high-surface-area materials have been in existence for decades. On the other hand, functional nanoparticles are those where the nanoparticles themselves perform a certain function, as a result of their particular crystalline structure, or the lack thereof; e.g., particles having gas sensing capabilities because of their ability to undergo redox reactions.

A few nanomaterials companies made rapid progress (measured in terms of the ability to raise capital and build substantial manufacturing capability) in the mid- to late 1990s, with the anticipation that they will be ready if and when the market emerges. Most of them have found out that either the anticipated markets never materialized, or the products they envisioned did not meet the cost requirement of the targeted industry. A case in point was a company that was initially funded by a U.S. government small business innovative research (SBIR) initiative. The company's manufacturing technology was unique, and the nanopowder product had a sufficient number of distinguishing features from the state-of-the-art, especially with respect to performance. The company attracted investment (initially backed by venture capital and later by large corporations in the same market sector), and a full-scale production facility was commissioned within 5 years of obtaining seed capital. However, the well-funded company failed to make any impact on the market because the market was driven by cost, and not by performance. The company's product was superior and more expensive, but the market had no need for a better product, as the available product at that time more than met what the majority of customers desired. The metrics of comparison had shifted from performance to cost. It was too late by the time management realized the market forces in play, and the company had to close down its production facility by the start of the new millennium, and abandon its forays into nanomaterials, at least for the moment. The lesson here is that while nanotechnology can lead to a better product, it may not necessarily lead to a

"business" because the mass market is not ready to pay a higher price for an improved product. To extend this thought further, it may so happen that, while a particular product developed by a company is superior in performance to an existing product, the sales volume generated may be too small to support a large-scale manufacturing infrastructure. It appears that the maximum potential exists for products that are just not improved, but enabled solely by the use of nanomaterials.

The initial part of this article will describe advances made by small and large corporations in producing a variety of nanopowders, because nanopowders provide the all-important building block for forming nanostructured materials. The discussion will be limited to technologies that were successfully developed into, at least, a quasi-commercial operation. As it turns out, the roots of a vast number of nanopowder synthesis processes are either a university or some other research laboratory. However, synthesis processes that are still practiced only in a research environment are excluded from the discussion. Furthermore, the discussion will be restricted to ceramic and metal nanoparticles. Carbon-based materials (e.g., fullerenes/bucky balls, single-wall carbon nanotubes, and multiwall carbon nanotubes) and chalcogenide nanotubes, and organic nanoparticles are beyond the scope of the present discussion.

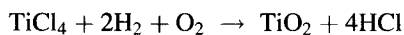
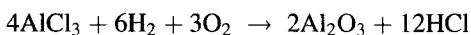
The second part will describe the activities of companies involved in commercializing nanomaterials for specific applications, where substantial value is added to nanoparticles by way of surface treatment or incorporation into a host matrix. Also included are work performed at corporations that purchase nanoparticles from the open market and incorporate them into an end product. This section will also detail the activities of a few companies that are vertically integrated, i.e., they synthesize their own raw nanomaterials and integrate them into a component or a device. However, such vertical integration is not common in the materials industry.

The final section is a reflection on the past decade of nanomaterials development, and a prognosis of where things are likely to be by the end of the decade.

PART I: NANOPOWDER PRODUCTION

Two of the pioneers in production of nanopowders of single-phase oxides (e.g., SiO_2 , TiO_2 , Al_2O_3 , Fe_2O_3 , and ZrO_2) are located on either side of the Atlantic Ocean: Degussa Corporation, headquartered in Europe, and Cabot Corporation in the United States. Both companies have been in production of nanopowders for several decades now, accounting for much of the "nanopowder sales" figures quoted in reports by some market research analysts.

Over the years, Degussa and Cabot have steadily made incremental improvements in particle characteristics, such as reduction in aggregate size and altering surface characteristics to suit specific applications. The Degussa Process, called the AEROSIL[®] process,^[8] involves hydrolysis of gaseous metallic chlorides under the influence of water, which develops during the oxyhydrogen reaction, which, in turn, leads to a high-temperature reaction zone. Example reactions are as follows:



Nanoparticles of titanium dioxide, produced by Degussa, are sold as Degussa P25, and are an extremely well characterized nanopowder. The powder has a surface area of $\sim 50 \text{ m}^2/\text{g}$, with a primary particle size of 21 nm. Fig. 1 shows a transmission electron microscopic (TEM) image of TiO_2 nanopowders. The purity of the oxides is in general $>99\%$, and in some cases, the purity is in excess of 99.9%. The reason for the high purity is that the chloride byproduct is cleaned relatively well through distillation. These nanopowders are used in a number of commercial applications, some of which are: aluminum oxide used in ink jet papers (smoothing and sealing), cable insulation (improvement in dielectric strength), photo resists for production of integrated circuits (ICs) (rheology); titanium dioxide in ultraviolet (UV) protecting gels (transparent, yet 100% UV protection); zirconium oxide in IC substrate boards (higher resolution), battery separators (filler), and polystyrene (free flow aid).

High-surface-area SiO_2 has been the flagship product of Cabot Corporation (in addition to carbon black, which itself is a nanostructured powder, given the high surface area of the powder particles). Cab-o-sil[®] is the trade name of Cabot's SiO_2 nanopowders, an electron micrograph of which is shown in Fig. 2.^[9] Nanoparticles of SiO_2 are produced by a flame process, which substantially resembles the Degussa process described above. An experimental grade of aluminum oxide is also produced by Cabot using the same process, with a surface area of

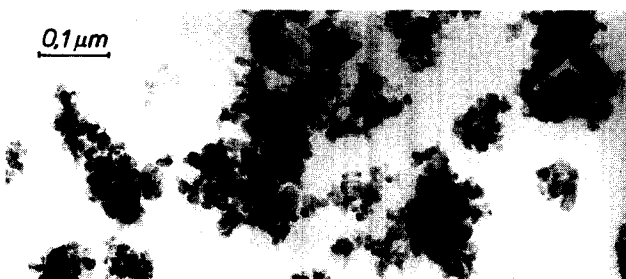


Fig. 1 TEM image of Degussa's P25 titanium dioxide powder.

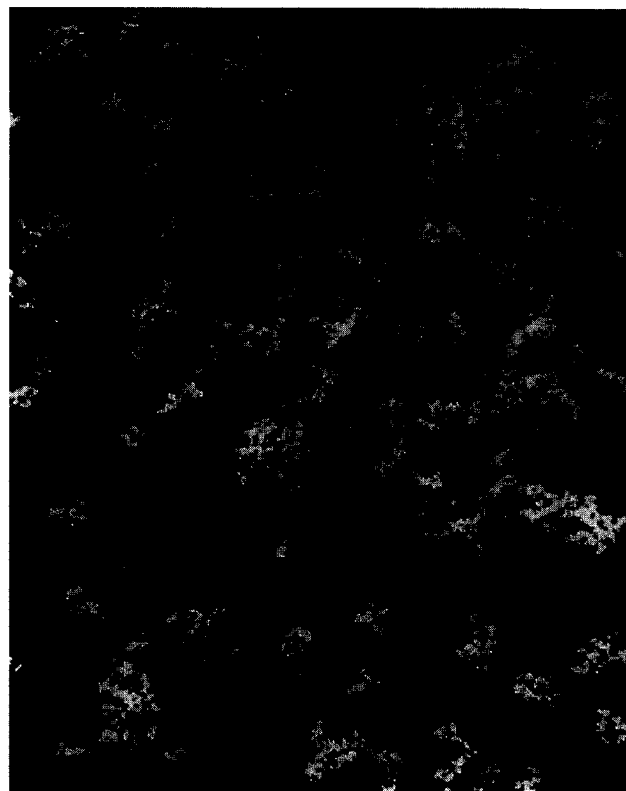


Fig. 2 Electron micrograph of nanoparticles of SiO_2 , produced by Cabot Corporation.

$\sim 55 \text{ m}^2/\text{g}$. The reported average aggregate length, which is different from the aggregate size measured by a typical instrument, such as Coulter N4 plus or a Horiba LA 920, is 150–170 nm.

Interestingly enough, unlike conventional materials development—where a unique material is often developed in response to either an actual or a perceived need—the above-described oxide nanopowders have largely found use in new markets as soon as they became available in large quantities. For example, the production process for synthesis of nanoparticles of aluminum oxide was developed well before the powders began to be used in inkjet papers. Moreover, nanopowders of aluminum oxide, titanium oxide, and silicon dioxide have been commoditized over the years by the two industry giants mentioned above, thereby leaving little room for nanopowder-producing neophytes to use their approach to penetrate well-established markets. A further discussion on the barrier to entry is presented in the final section of the article.

Baikowski International,^[10] a company based in France with operations in the United States as well as in Japan, also provides nanoparticles of aluminum oxide with exceptional purity: $\geq 99.99\%$ (in addition to micron- and

submicron-size particles). The powders have a high surface area, $\sim 120 \text{ m}^2/\text{g}$. Some grades of such high-surface-area powders have an aggregate size as small as $\sim 0.3\text{--}0.4 \mu\text{m}$. The company exclusively produces aluminum oxide, and caters largely to the lighting (for producing translucent ceramics) and polishing (chemical mechanical polishing) industries.

The perceived need for spherical nanoparticles, and with a lower degree of aggregation than what was commercially available, prompted extensive research into new synthesis processes at universities and national laboratories. As soon as a basic research showed promise, the technologies were transferred to a private entity [usually with the aid of federal funds in the form of either SBIRs, or its sister program, small business technology transfer (STTRs)], often located near the originating research institution. The start-ups were the so-called "spin-off" nanomaterial companies. Two such companies in the early days of the Nanotechnology industry were Nanophase Technologies Inc. in Illinois, and Nanodyne Inc. in New Brunswick, although Nanophase Technologies Inc. was funded by equity investment very early on in the life of the company. Nanophase Technologies (NASDAQ: NANX), which evolved from research activity at Argonne National Laboratory in the outskirts of Chicago, focused on the production of oxide nanoparticles, including such commonly used oxides as aluminum oxide, titanium dioxide, and zinc oxide, as well as a number of not so commonly used materials, such as yttrium oxide, copper oxide, and cerium oxide. The synthesis process, schematically shown in Fig. 3, is based on high rate evaporation of metals followed by oxidation in the gas phase.^[11] The process yields nanoparticles on a commercial scale with a spherical morphology (in many cases) and with minimal aggregation, which was different from the nanopowders available at that time, although

the surface areas were comparable. As of the writing of this article, all of the compositions mentioned above are available in tonnage quantities. The strategy to market these products appears to be to sell the nanopowders to larger chemical manufacturers, as opposed to directly providing it to the end user; e.g., the biggest customer of Nanophase Technologies is BASF.^[12]

Nanodyne Inc. was a spin-off from Rutgers—The State University of New Jersey, the basis for the technology being intellectual property and prior research that was carried out at Exxon Corporation. The hallmark of the Nanodyne synthesis approach, shown schematically in Fig. 4, was that existing and commercially available processing technologies (e.g., fluidized bed and rotary furnaces) were used to produce nanostructured materials that were protected by a structure of matter patent. The sole focus of the company was to produce ultrafine grained powders of WC/Co. Research had shown that fine-grained WC/Co materials possessed improved hardness without the usual accompanying loss in toughness, and this provided the impetus to commercialize ultrafine grained WC/Co for tool bits.^[13] A pilot plant was first built in New Brunswick, NJ, with investment from venture capitalists (Ampersand and CMEA). Later, Union Miniere (now Umicore) bought out the interests of all the shareholders, and a semifull-scale production plant was constructed in North Carolina. Unfortunately, the plant was shut down not too long after it was commissioned,^[14] and Nanodyne Inc. went into the history books as one of the first casualties of the Nanotechnology industry.

Just about the time that nanopowders were coming in vogue in the United States, a company called Advanced Powder Technology (APT) was founded in Australia.^[15] Unlike the vapor-phase approaches that were being championed by many companies in the United States, APT developed a patented solid state process that

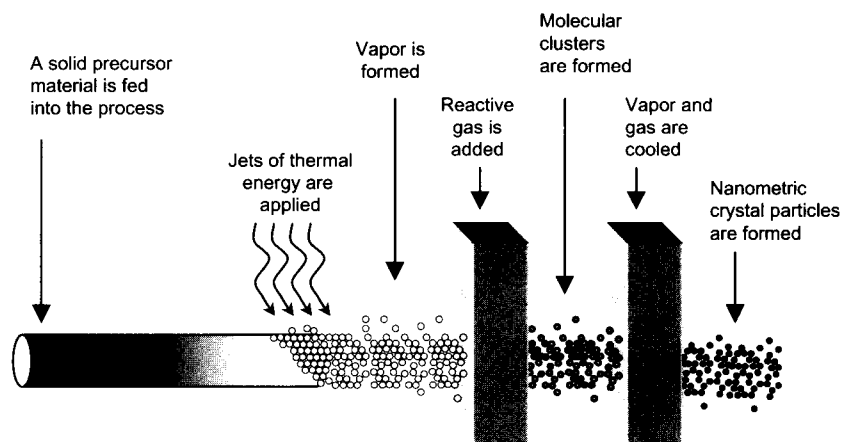


Fig. 3 Schematic showing the vapor-phase process practiced at Nanophase Corporation.

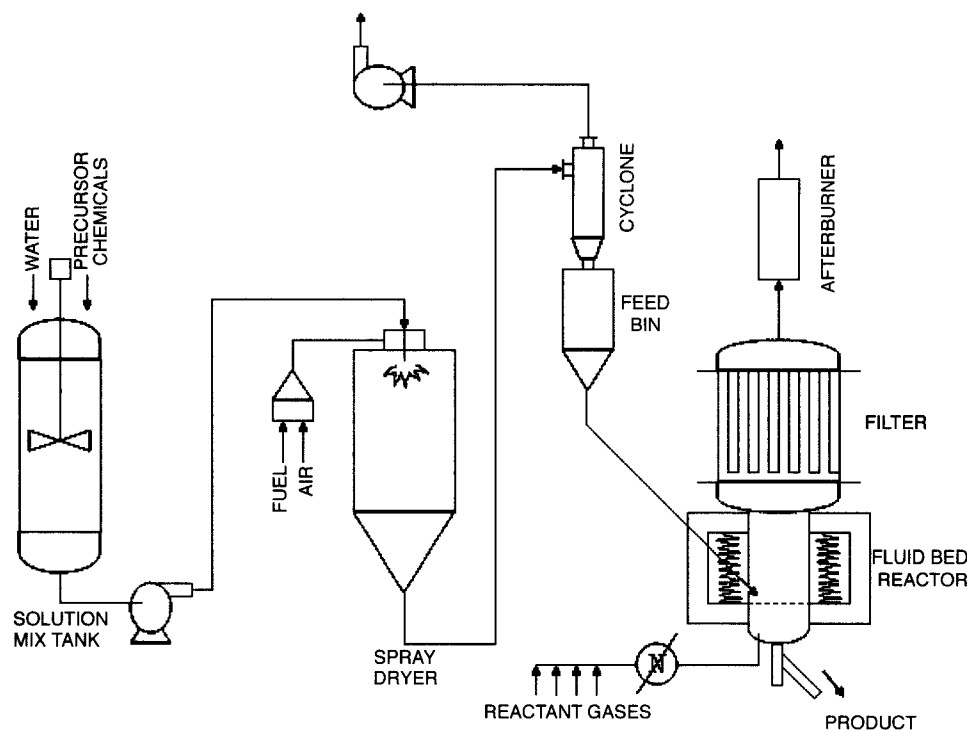


Fig. 4 Schematic of the spray conversion process, developed by Nanodyne Inc.

combined a milling operation. Dry milling was used to induce chemical reactions through ball-powder collisions that resulted in nanoparticles forming within a salt matrix. Particle size is defined by the chemistry of the reactant mix, milling, and heat treatment condition. Particle agglomeration is minimized by the salt matrix, which is then removed by a simple washing procedure. While reducing the size of particles by milling had been known for a very long time, APT was among the first to reduce the particle size to the nanoscale. A joint venture with Samsung Corporation was announced in 2001. One of the major products was cerium oxide, which has generally been an expensive material and was scarcely available in a nanopowder form. The technology has also been extended to other compositions, such as zinc oxide.

During the mid- to late 1990s, alternative vapor-phase technologies to what was practiced at Nanophase Technologies was developed by a number of companies, including NEI Corporation, the company that the authors work for. At NEI, a process called combustion flame-chemical vapor condensation (CF-CVC) was developed to produce oxide nanoparticles,^[16] the origins of which were in a process invented at Rutgers University.^[17,18] The CF-CVC process, shown schematically in Fig. 5, utilized a flat flame in a reduced pressure environment as the heat source for pyrolyzing vapors of metalorganic precursors.

The geometry of the flame insured that the pyrolysis was uniform, and the condensation of the pyrolyzed species into nanoparticles was rapid. The end result was the formation of high-surface-area nanoparticles with a narrow primary particle size distribution, combined with one of the smallest aggregate sizes among nanopowders available in the market. For example, titanium dioxide nanopowders had a surface area of $\sim 65\text{--}75\text{ m}^2/\text{g}$ with an aggregate size (as measured by Coulter N4 Plus) of $\sim 0.1\text{--}0.12\text{ }\mu\text{m}$. Aluminum oxide nanopowders had a surface area of $\sim 120\text{ m}^2/\text{g}$ with an aggregate size of only $\sim 0.125\text{ }\mu\text{m}$.^[19,20]

Significant progress in developing new methods of nanopowder synthesis was made at Nanomaterials Research Corporation (NRC) toward the late 1990s. The production system was based on a patented process^[21] utilizing ultrarapid thermal quenching of high-temperature vapors through a boundary layer converging-diverging nozzle. A suspension of precursor material, which was, for the most part, generated from a fluidized bed of micron size metal particles, was continuously fed to a thermal reaction zone and vaporized under conditions that minimized superheating and favored nucleation of the resulting vapor. The expansion ahead of the nozzle led to rapid condensation, and minimization of nanoparticle coalescence. The process produced metals, intermetallics,

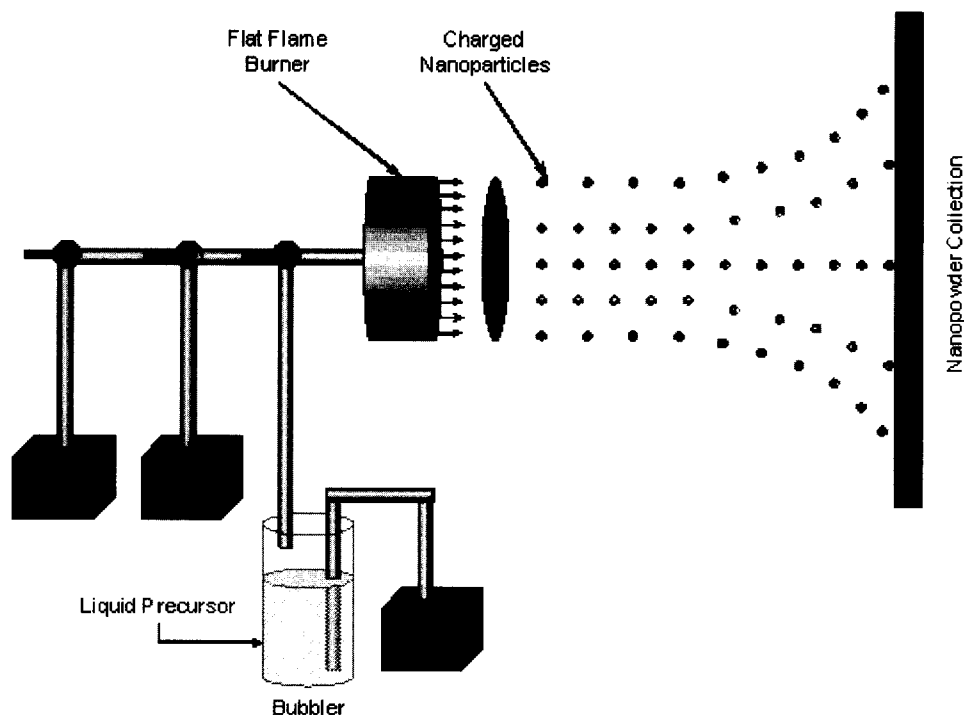


Fig. 5 Schematic layout of the CF-CVC process, developed at NEI Corporation.

single-phase and multicomponent oxides, and even some nonoxides. Subsequently, NRC, which was mostly funded through a number of SBIR programs until then, spun off a separate entity called NanoProducts Inc. A partnership with a major Japanese powder equipment company, Hosokawa Micron Corp., was announced in 2001 for scale-up of the nanopowder synthesis process.^[22] Production is said to be commencing in Japan, as well as in the United States. NRC has also developed other gas-phase nanopowder synthesis processes, similar to the one described above, some of them utilizing chemical precursors such as acetates and nitrates.

Meanwhile, through the 1990s, the process of spinning off nanopowder- and nanomaterial-producing companies from universities continued in the United States. One such company that came into existence in the mid-1990s was TAL Materials, located in Michigan, which focused on a process based on combustion of precursors in a flame.^[23] However, unlike many of the processes described above, the TAL Materials technology did not require the precursors to be vaporized. The precursors were pyrolyzed in a tubular reactor, and high-surface-area nanopowders were collected downstream.^[24] The company, which was still in its infancy at the time this article was being written, has focused on multicomponent oxide particles for value-added applications in lasers, and of the like.^[25]

Nanoscale Materials Inc.^[26] (formerly known as Nantek Inc.), which started operating in 1995, was spun out of Kansas State University—the first commercial spin-off from this university. The company sells an array of oxide nanoparticles, mostly single phase, under the trade name NanoActive™. The powders are characterized by an extremely small feature size, resulting in enormously high surface areas. Accordingly, applications that can benefit from a very high surface area are ideal users of NanoActive™. According to the company, their oxide powders have shown utility in a variety of applications, including destructive adsorption, purification of air and water, scrubbing of acid gases, and sequestering of odors and toxic gases.

Unlike many of its competitors, which emerged from transitioning of a research activity into a business in nanomaterials, Altair Nanomaterials evolved from being a leaseholder on titanium ore mines in the Tennessee Valley to a manufacturer of oxide (and some nonoxide) nanoparticles, titanium dioxide in particular.^[27] The Altair process is a solution-based process, wherein particles are precipitated and milled to be reduced to a smaller size while in suspension.^[28] As of the writing of this article, initial sales into the thermal spray market had been reported, along with success in animal trials of a phosphate powder for treatment of a kidney disease. Altair is a publicly traded company (NASDAQ: ALTI),

and the total sales volume of nanopowders appears to be in the tens of thousands of dollars per quarter.

Nanotechnologies, Inc.,^[29] based in Texas, and Technanogy^[30] in California (both backed by venture capital funding), were relative newcomers to the business of producing nanopowders. Both companies championed vapor phase processes, where a plasma source was used to vaporize metallic materials. The initial emphasis for both companies was on aluminum nanoparticles, with the objective of using them as rocket fuel, and as a component in the primer for bullets. Neither of these two applications seems to have held up to their initial promise, presumably because of cost considerations. Nanotechnologies Inc. has also initiated the development of oxide nanoparticles, and recently announced collaboration with AirProducts Inc. and Essilor, a manufacturer of eyeglasses.

Argonide Corporation^[31] came into existence in the early 1990s, after transferring nanopowder production technology from Russia. A wire of the desired material is exploded in a continuous manner within a controlled atmosphere. A variety of metals including tungsten, aluminum, and oxide nanopowders are produced by the process.^[32]

The path followed by a majority of companies has been somewhat self-directed, as opposed to being directed by the needs of the customer. As a result, considerable emphasis has been placed on the production of single-phase oxide nanopowders, such as aluminum oxide, titanium oxide, zinc oxide, and cerium oxide. This has been driven more by what their individual technologies can offer, and less by what the specific needs of an application are. Accordingly, an additional step of converting the single-phase oxide nanopowders into a useful form has become necessary, which reduces the importance of the starting material, which in turn requires it to be relatively inexpensive. Many nanopowder-producing companies have an eventual price target of ~\$10/lb; it remains to be seen if such a low price is attainable, and even if so, to what extent it remains a viable business for small companies.

In contrast to passive or nonfunctional nanoparticles, i.e., where the internal crystal structure does not contribute to a particular physical phenomenon, functional nanoparticles present significant opportunities for enhancing the properties of a product. Three prominent examples include: 1) multicomponent nanoparticles of electronic oxide ceramics; 2) nanocomposite electrodes for lithium-ion batteries; and 3) active materials for chemical gas sensors and biochemical activity. Processing of these materials is particularly challenging, given the complexity of the material systems, thus it is not surprising that there are very few companies active in these areas, although the market opportunity is immense.

Barium titanate, and variations thereof, is perhaps the most widely used electronic ceramic material. As such, this has prompted the nanomaterials community to investigate the potential benefits of nanostructured barium titanate. It is most commonly used as a sintered high dielectric material (both thick films and bulk). Accordingly, many companies have made several attempts in developing fine particles of barium titanate. One of the most widely practiced synthesis methods has been the hydrothermal process, where precursors are allowed to react at relatively low temperatures, but at well above ambient pressures. TPL Inc. (Albuquerque, NM) has reportedly scaled a process for producing tonnage quantities of ultrafine multicomponent oxide powders belonging to the titanate family.^[33]

NEI Corp. has developed processes for producing nanostructured powders of compositions used as electrodes in rechargeable lithium-ion batteries, and related energy storage devices.^[34-36] Rechargeable lithium-ion batteries present a market opportunity for nanomaterials as three aspects of this class of energy storage device need improvement: energy density, rate capability, and cost. The ability to stabilize structures that are intrinsically of high energy density (example shown below) in a nanoparticle has the potential of inducing improvements in energy density. The rate capabilities of rechargeable batteries can be enhanced by reducing the particle size of electrode materials, because it is well established that the rate capabilities of lithium-ion batteries are limited by solid-state diffusion of lithium ions within the electrode materials.^[37] Furthermore, compositions that utilize relatively inexpensive compositions (i.e., based on iron rather than cobalt) become viable cathode materials when the particle size is reduced to the nanoscale.

Macrocrystalline layered lithium manganese oxide, which has a theoretical energy density twice that of the presently used lithium cobalt oxide, suffers from structural instability during electrochemical cycling, and as a result, exhibits significant capacity decline. Moreover, the rate capability is less than desirable. NEI Corp. is developing nanostructured and doped layered lithium manganese oxide. Fig. 6 shows the charge/discharge curves of the sample under a low current density. The first charge capacity and discharge capacity were within 15% of the theoretical value. When the current density was raised to 22.5 mA/g during charge and discharge, the discharge capacity dropped, but did not show any capacity fade. Furthermore, development work is underway to increase the discharge capacity at high current densities.

Sensing an opportunity in gas detection instruments needed for industrial health and safety, environmental monitoring, and process control, Nanomaterials Research Corporation spent considerable effort in producing single-phase and doped oxide nanoparticles and

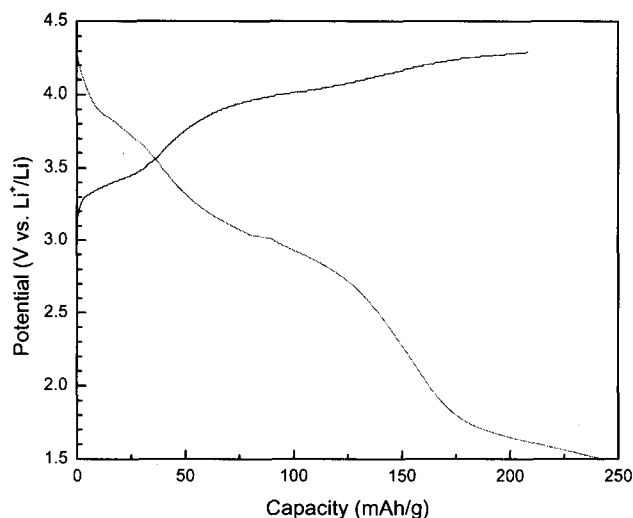


Fig. 6 A charge/discharge curve of a nano- $\text{LiMn}_x\text{M}_{1-x}\text{O}_2$ cathodes in a Li-test cell at a current density of 2.7 mA/g. (View this art in color at www.dekker.com.)

integrating them into gas sensors.^[38] Fig. 7 shows a comparison of the sensitivity of coarse-grained and nanostructured powders. NEI Corp. made initial forays into this market using its low-pressure flame deposition (LPFD) process, which is a high rate process for depositing and sintering nanoparticles in situ on a substrate.^[39,40] The process leads to a porous nanoparticulate thick film structure, which is a desired morphology for gas sensor applications. However, the company did not obtain sufficient traction from the end users of such a technology, and has subsequently shelved the process.

PART II: VALUE-ADDED NANOMATERIALS AND NANOMATERIALS-ENABLED PRODUCTS

In the materials business, the idea of not just producing nanopowders, but also integrating in-house synthesized nanoparticles into a final end product is generally believed to be a good strategy. The argument is that, although nanoparticles have properties that are uniquely distinct from their coarser counterparts, they are still a "raw material," and so do not carry much more value than a commodity. NanoGram was perhaps the first company to build a business on this concept, and have taken it to the extreme. The company, which was founded in the early 1990s with venture capital backing, concentrated on a laser pyrolysis process as the predominant nanopowder synthesis method. A substantial amount of intellectual property was created in the "use" of nanoparticles for a

host of applications, including lithium batteries and chemical mechanical polishing. For example, NanoGram was the first to patent the use of nanoparticles of vanadium oxide as cathode materials for a lithium battery,^[41] although sol-gel derived vanadium oxide xerogels (which are, by definition, nanostructured materials) have been shown to possess significantly higher capacity than coarse particles of vanadium oxide.^[42] The laser nanoparticle synthesis process was subsequently modified to directly deposit nanostructured films at high rates on substrates.^[43] Using this and other nanocomposite technologies, forays were made into the optical waveguide business at the turn of the millennium. The company appears to be deft at changing course as the market evolves. Recently, a new spin-off called NanoGram Devices Corporation has been formed to commercialize energy storage devices for the medical industry.

Another example of a vertically integrated company is Photon-X (Malvern, PA).^[44] The company was established through a sizable venture capital investment. Among the first products envisioned were optical amplifier modules that support high capacity systems, but consume considerably less power with a smaller footprint than conventional products. These amplifier modules were based on new waveguide materials utilizing optical polymers and their nanocomposites. The company has combined materials innovations with new and improved optical designs that enable a reduction in the number of pump lasers for amplifiers. Reducing the number of pump lasers significantly reduces the electrical power consumption. Right from the start, the company's goal was to be the provider of amplifier modules, made from building blocks that are all developed and fabricated in-house.

InMat Inc., a New Jersey-based start-up, is among a handful of companies that have released their products in the commercial market.^[45] The technology and some of the principals of InMat originated from Hoechst

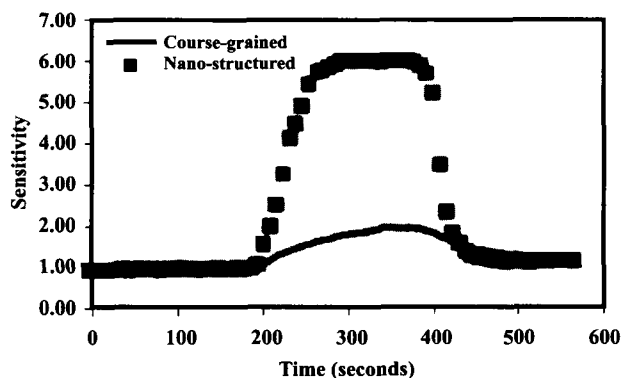


Fig. 7 Data showing the difference in the sensitivity between coarse grained and nanostructured materials.

Research, which had ceased operations in New Jersey in the mid-1990s. The basic technology is a composite formulation consisting of butyl rubber with a dispersion of exfoliated clay particles. The exfoliated layers of clay have nanometer dimensions along the *c* axis, and hence the material is a nanocomposite, which has the unique feature of reducing permeability of air by as much as 200%, while maintaining the flexibility of butyl rubber. As an example, a coating of the nanocomposite is applied to a tennis ball,^[46] thereby increasing its life span. The company is working on establishing its presence into the tire industry and chemically protective gloves, both of which can benefit from rubbers that are less permeable.

Along similar lines, at NEI Corporation, efforts are underway to commercialize transparent polymer nanocomposite coatings that are also hard and scratch-resistant. Innovations have centered on increasing the refractive index, altering the thickness of the coating between 1 and 25 μm (as required by the application), and introducing additional functionalities such as electrical conductivity.^[47]

There are also several examples of companies where nanomaterials form an integral part of the final product. For example, Konarka Technologies,^[48] based in Massachusetts, has built upon dye-sensitized solar cells invented by Grätzel more than 10 years ago.^[49] The core of the dye-sensitized technology consists of nanometer-scale crystals of titanium dioxide semiconductor coated with a monolayer of light-absorbing dye and embedded in an electrolyte between the front and back electrical contacts. The dye absorbs the photon in light. The company claims to be using low-cost raw materials and an inexpensive manufacturing technology to bring this nanomaterial-enabled photovoltaic technology to market.

NanoMagnetics^[50] (UK) has used nanoparticulate magnetic films to produce a data-recording density of ~ 6 Gbit/in.² According to the company, this should eventually lead to a density of several Tbits per square inch. NanoMagnetics realized the importance of a uniform grain size in the film, and has used a protein molecule called ferritin as the cage in which a cobalt-platinum metal alloy is deposited. The advantage in using a protein molecule is that they are always of the same size: a 12-nm-diameter cage with an 8-nm cavity. This way, the size of the alloy nanoparticle is limited to the size of the cavity.

There are also instances where nanomaterials constitute a critical component of the process. A case in point is Reactive Nanotechnologies Inc., which is building upon intellectual property generated at University of Maryland, and claims to have developed a new method of joining that replaces current processes of soldering and brazing, as well as opens up new applications in the areas of metal-to-ceramic joining.^[51] The principle of joining employed

by Reactive Nanotechnologies Inc. is based on a self-propagating exothermic reaction. Two dissimilar components are sandwiched with a stack of alternating layers of elements (with a thickness of several hundred nanometers)—say aluminum and nickel—that undergo an exothermic reaction. The reaction between the two metals is initiated at one end, and propagates rapidly through to the other end. The advantage of the approach is that the components being bonded are not sensitive to the high temperature. The company envisions opportunities in the microelectronics market for application of its technology. A similar (but not competing) technology has been developed by SusTech Darmstadt in Germany.^[52] The microwave curable adhesive system works on the principle that nanoparticulate ferrites pick up energy from electromagnetic AC fields, convert it into heat, and pass to the immediate surrounding.

A noticeable trend has emerged, in which large corporations are buying out (or exclusively licensing the intellectual property) small companies that have forayed into areas of interest to the large corporations, although there may not be any significant sales.^[53] One notable example is the purchase by DuPont Titanium Technologies, a wholly owned subsidiary of DuPont, of a fledgling company called NanoSource Technologies in July 2002. NanoSource Technologies Inc., which was founded in 1999, entered into an exclusive licensing agreement with Tekna Plasma Systems Inc. (Sherbrooke, Quebec, Canada) to produce nanoparticles of titanium dioxide. Moreover, the company had announced in January 2001 that it had developed a first-of-its-kind polymer coating for the surface of titanium dioxide nanoparticles that would make it usable in cosmetic applications.^[54]

PART III: FUTURE PERSPECTIVES

Given the recent flurry of activity in nanomaterials both in the academia and the industry, one can only conclude that there is still plenty of ground to cover. With the federal governments of advanced and developing nations apportioning increasingly large sums of money each year for research in nanomaterials and nanotechnology, we are most likely still away from seeing the peak in research output. In fact, in our judgment, the biggest breakthroughs are yet to come. In just the past few years, nanomaterials have already penetrated the consumer market, even if the sales volume in dollar terms is only in the tens of millions of dollars. Higher-volume applications requiring larger quantities of nanomaterials take a longer amount of time to be qualified for use, and we can expect to see them incorporated in products over the next several years. At the same time, it is quite difficult to clearly predict where

the greatest commercial advances are going to be, and how they will manifest themselves in products. While significant advances in nanotechnology are routinely announced in technical and trade journals, transferring them into applications requires overcoming a number of barriers. Most notable among them are the lack of reproducibility of results reported from various laboratories, and the fact that results are often obtained from nonstandardized tests, making real-life comparisons difficult. To add to all of this, progress in nanomaterials is often at odds with the human nature of inflating what is achievable in the near term, but not envisioning what can be achieved in the distant future.

Interest in specialized nanomaterials and functionalized complex nanoparticles is growing. However, the demand for single-phase and multicomponent oxide powders of commonly used compositions is, at best, tepid. This is because oxide nanopowders, even with excellent particle characteristics such as small primary particle size and small amount of aggregation, do not possess sufficient distinguishing features from the powders that have been available since the latest blitz in this field. In other words, the market has been commoditized, and so does not present new opportunities. Therefore, it is exceptionally difficult for a small company to make much progress as a profitable enterprise.

Another likely scenario is that nanomaterials will be used in a large number of products, where the addition of a relatively small quantity leads to a major change in the properties and performance of the end product. The value-added nanomaterial with functionalized surfaces is likely to possess a unique functionality. Because the additive will impact a large enough market, it will justify the investment in the process technology. The challenge at the hands of companies, particularly the smaller companies in this field, is to identify such applications and team up with the right partners so that it becomes a win-win situation for both parties.

CONCLUSION

Although the number of small nanomaterials companies throughout the world is quite large, each at various stages of commercialization, only a handful of companies are likely to withstand the test of time 10 years from now. Those without sustainable competitive advantage will lose the support of their investors (including federal sources of funding) and cease to exist. On the other hand, those that are wildly successful in certain segments of the market are likely to become takeover targets of large companies dominating that particular niche of the industry.

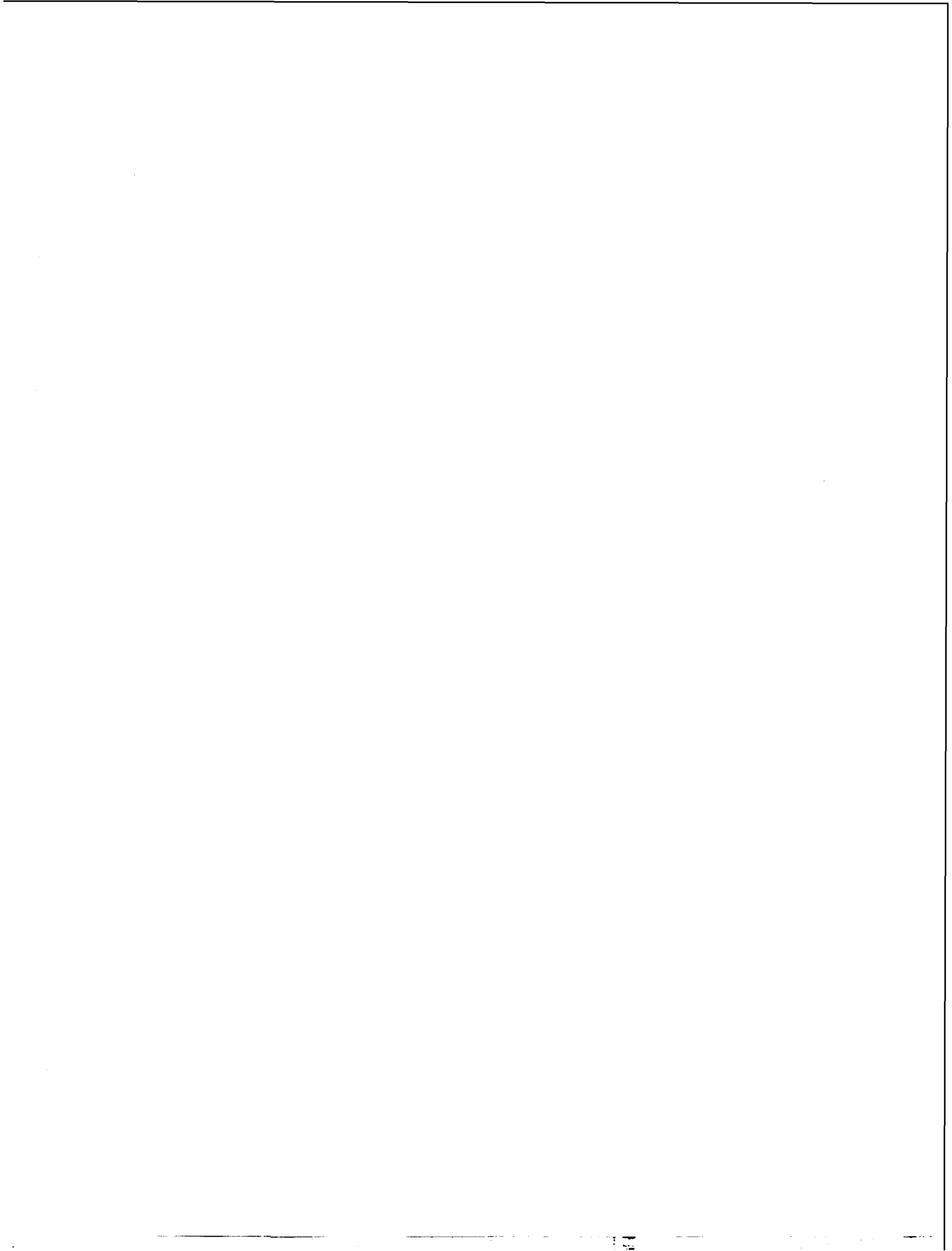
The companies cited in this article do not represent ALL the companies working in this area, but to the

authors' knowledge, they represent examples of the transition from science to technology.

REFERENCES

1. Workshop Report on R & D Status and Trends in Nanoparticles, Nanostructured Materials and Nanodevices in the United States. In *Proc. of the May 8-9, 1997 Workshop*.
2. Christensen, C.M. *The Innovator's Dilemma*, 1st Ed.; HarperBusiness: New York, NY.
3. Drucker, P.F. *Innovation and Entrepreneurship*, 1st Ed.; HarperBusiness: New York, NY, 2000.
4. Drucker, P.F. *Managing in the Next Society*, 1st Ed.; St. Martin's Press: New York, NY, 2002.
5. www.CMP-cientifica.com.
6. www.bccresearch.com.
7. www.nanobusiness.org.
8. *Technical Literature*, Degussa Corporation: Germany.
9. *Technical Literature, Cab-o-Sil[®] Untreated Fumed: USA Silica: Properties and Function*; Cabot Corporation: USA.
10. www.baikowski.com.
11. Ford, Q. *Ceram. Ind.* **1998**, 31.
12. Lu, S. *Proc. of the American Ceramic Society, Annual Meeting; 2003, in press*.
13. McCandlish, L.; Kear, B. Chemical processing and properties of nanostructured WC-Co materials. *Nanostruct. Mater.* **1993**, 3, 19.
14. *Nanoparticle News*; Rittner, M., Ed.
15. www.aptpowders.com.
16. Glumac, N.; Chen, Y.-J.; Skandan, G.; Kear, B.H. Scalable high-rate production of non agglomerated nanopowder in low pressure flames. *Mater. Lett.* **1998**, 34, 148-153.
17. US Patent No. 5,514,356.
18. US Patent No. 5,876,683.
19. www.neicorporation.com.
20. Skandan, G.; Singhal, A. *Met. Powder Rep.* **1999**, 54 (5), 18.
21. US patent number 5,788,738.
22. www.ceramicbulletin.org/newsarchive.asp.
23. www.talmaterials.com.
24. Bickmore, C.; Walder, K.; Baranwal, R.; Hinklin, T.; Treadwall, D.; Laine, R. J. *Eur. Ceram. Soc.* **1998**, 18, 287.
25. Laine, R. *Proc. of the Nanoparticle 2002 Conference, New York*.
26. www.nanoscalematerials.com.
27. www.altairnanomaterials.com.
28. Sabacky, B. *Proc. of the Nanoparticle 2000 Conference*.
29. www.nanoscale.com.

30. www.technanogy.net.
31. www.argonide.com.
32. Tepper, F. Nanosize powders produced by electro-explosion of wire and their potential applications. *Powder Metall.* **2000**, *43* (4), 320.
33. www.tplinc.com.
34. Singhal, A.; Skandan, G.; Amatucci, A.; Pereira, N. In *Nanostructured Electrodes for Rechargeable Li Rechargeable*, Proceedings Volume of Electrochemical Society—Workshop on Interfaces, Phenomena and Nanostructures in Lithium Batteries, Argonne, Dec. 11–13, 2000.
35. *Nanoparticle News*; Business Communications Company.
36. Singhal, A.; Skandan, G. *Proc. of the Conference on Rechargeable Batteries, France. In press.*
37. Sides, C.R.; Li, N.; Patrissi, C.J.; Scrosati, B.; Martin, C.R. Nanoscale materials for Li-ion batteries. *MRS Bull.* **2002**, *27* (8), 604.
38. Hooker, S. *Proc. of the Nanoparticle 2000 Conference.*
39. Skandan, G.; Glumac, N.; Chen, Y.-J.; Cosandey, F.; Heims, E.; Kear, B. Low pressure flame deposition of nanostructured oxide films. *J. Am. Ceram. Soc.* **1998**, *81*, 2753.
40. Skandan, G.; Singhal, A. *Mater. Technol.* **1998**, *13* (4), 149.
41. US Patent of Nanogram.
42. Sol-gel paper on vanadium oxide, take from Hosokawa Micron file.
43. Kambe, N. *Proc. of the Nanoparticle 2002 Conference.*
44. www.photon-X.net.
45. www.inmat.com.
46. http://www.smalltimes.com/document_display.cfm?document_id=2997.
47. http://www.smalltimes.com/document_display.cfm?document_id=5884.
48. www.konarkatech.com.
49. Graetzel patents.
50. www.nanomagnetics.com.
51. www.reactivenanotech.com.
52. www.sustech.de.
53. http://www.smalltimes.com/document_display.cfm?document_id=4173.
54. www.nanosource.com.



Nanoparticles: Generation, Surface Functionalization, and Ion Sensing

Jason J. Davis
Paul D. Beer

University of Oxford, Oxford, United Kingdom

INTRODUCTION

During the past decade or so, considerable interest has grown in the potential commercial and technological exploitation of nanoscale materials in analytical chemistry.^[1] A particular focus of this interest has been the utilization of specific size-dependent electronic, optical, or magnetic properties. Nanoparticles are crystalline clusters (metallic, semiconducting, or insulating) composed of a few hundred to a few thousand atoms and are, characteristically, of nanometer dimension. One consequence of this size is that many of their properties are dominated by their surface rather than by the bulk volume^[2] and, indeed, this fact alone can make these structures very amenable to chemical or environmental influence, or “tuning.” Their nanometer diameter is also the same order of magnitude as the de Broglie wavelength of electrons/holes at room temperature and this, then, can lead to a quantization of electronic/hole energy levels, a phenomenon that has led to the term “quantum dots” (QD). The energy-level spacings are related to particle size.^[3] Although the term “nanoparticles” has been coined only at a time when advances in microscopy have allowed us to resolve them as such, nanoparticles have been in use for many years; for example, Faraday carried out pioneering work with gold nanoparticles, and some of the intense colors evident in stained glass arise from the presence of nanometer-sized oxide clusters.

Gold nanoparticles received substantial attention during the past decade or so. The potential technical importance of monolayer-protected metal nanoparticles in developing nanoscale optoelectronic devices, (bio)chemical sensors, corrosion-resistant materials, and new catalysts has made them one of the primary targets of highly intensive, nanoparticle-based research activity. To date, for example, both single electron and nonlinear optical devices have been constructed from these materials.^[4–6] In addition to utilizing the optical and electronic properties inherent in metallic structures, the magnetic characteristics of suitable particles have also been of some interest, particularly in consideration of separation tech-

nologies. For example, nanoparticles of iron oxide (Fe_3O_4) can be suitably modified with a biological moiety of interest, e.g., a cell and their “superparamagnetic” properties used in magnetic field modulated manipulations/separation.^[7] The possible use of magnetic nanoparticles as contrast agents in magnetic resonance imaging has also been cited.^[8] Through suitable surface chemical modification, it should be possible to generate magnetic nanoparticles with a propensity to concentrate in particular tissue (or cellular) regions allowing, e.g., enhanced image contrast generation between diseased or cancerous cells and healthy cells. To date, these have both been shown to be more effective than conventional magnetic resonance imaging (MRI) agents (such as gadolinium complexes) and capable of allowing in vivo cellular tracking.^[9]

This report will aim to outline the general properties of metallic and semiconducting nanoparticles, their modification and possible application in high-sensitivity, selective ion sensing. There is no universally adopted definition as to what constitutes a nanoparticle, but we will be concerned here with the properties and utilization of particles < 100 nm in diameter. Although more progress has been made in the functionalization of metallic (notably gold and silver) particles, the properties and potential utilization of semiconducting particles will also be discussed.

METALLIC NANOPARTICLES

Although metal colloids have been known since the mid-18th century, only during the past decade or so has it been possible to controllably generate homogeneous samples and to subsequently scrutinize them at levels of resolution comparable to particle size.^[10,11] Although much of the seminal (and applied) work in this field has been carried out with gold, nanometer-sized metal particles of silver,^[12] platinum,^[13] iridium, and palladium^[14] have also been prepared. Although recent work has recognized that nanoparticle shape (in addition to size) greatly influences

physical and chemical properties,^[15,16] this topic will not be discussed here.

Synthesis and Characterization

Metal nanoparticles can be formed through laser vaporization of metallic rods. However, this method is not generally amenable to either scaling up or subsequent chemical modification strategies. Interestingly, with particles prepared under such conditions, certain "magic numbers" of constituent atoms are evident,^[17] an observation consistent with nonbulk, "atomistic" character. Perhaps the most practical and flexible means of nanoparticle generation is by chemically reductive routes in solution. As "bare" metallic nanoparticles are typically unstable in solution, controlled surface functionalization (either during or after synthesis—see below) has been key. Aqueous phase citrate reduction of HAuCl_4 has been, perhaps, the major workhorse in this area; subsequently, surface-bound citrate moieties can be readily displaced by thiolated organics in the formation of monolayer-protected metallic clusters (MPCs). A breakthrough in this field was the demonstration by Brust and coworkers^[11] of a solvent-based, high-concentration, monodisperse synthesis through a surfactant catalyst-based phase transfer of chloroaurate ions (typically with subsequent reduction by a borohydride). Most conveniently, chloroaurate reduction is carried out in the presence of alkanethiols,^[11] and, to a large extent, it is possible to control nanoparticle size through the relative ratios of tetrachloroaurate and thiol. In essence, these capped nanoparticles behave like large organic molecules, in that they can be separated from solution in powdered form, redissolved in solvent, and recrystallized as required. The surface functionalization afforded by these preparative methods stabilizes the particles to aggregation and further allows their properties to be influenced by the structure of the monolayer-forming molecules. In addition, this functionalization can be utilized in mediating surface-confinement (e.g., self-assembly of the nanoparticle itself onto an underlying solid support). Analogous chemistry can be used in the formation of other particles—chloroplatinate reduction yields, for example, platinum nanoparticles.

Properties

Metal nanoparticles have extraordinary size-dependent optical properties, not present in the bulk metal. Specifically, nanoparticles of silver, gold, and copper show distinct and well-defined plasmon absorption in the visible spectrum, an absorption characterized by an extremely large

molar adsorption coefficient. These unique optical, electrical, and surface chemical characteristics are controllable through both particle size and aggregation,^[18,19] and can also be "tuned" to a degree by the nature of the surface functionalization.^[20–22] Interestingly, the effect that the size-dependent electrical characteristics of nanoparticles can have on the properties of surface-confined molecules has recently been resolved in a ^{13}C NMR study.^[23]

Although diffraction analyses have shown that nanoparticles adopt the same crystal structure as the bulk metal, this appears to be less the norm as the particle size falls. For example, gold nanoparticles can adopt an icosahedral structure quite different to the bulk face-centered cubic arrangement. The valence and conduction band density of states (DOS) of these particles undergo significant variance with size; specifically, the initially continuous DOS is progressively replaced by discrete energy levels, the spacing of which increases with decreasing particle size (Fig. 1). As this spacing exceeds thermal energy, a "band gap" effectively opens up in the metal. At smaller sizes still, discrete, energetically separated, quanta are resolvable. These size effects are observable in both metallic and semiconducting particles, although, in the latter, "quantum dot" behavior can be observed at comparatively large (tens of nanometers) particle size.

From the perspective of developing derived electroanalytical devices, the redox properties of nanoparticles have been of some interest. The redox behavior of MPCs has been probed both diffusively in solution^[24,25] and in surface-confined mono- or multilayer films.^[26–30] Again, as soon as nanoparticles fall below a finite size (<1 nm), available electronic states become quantized and, electrochemically, this has the effect of the particle behaving, in essence, as a multivalent redox species.^[31] The specific electrostatic charging of the metallic core of monolayer protected nanoparticles has also been referred to as quantized double layer charging.^[20] The ability of these

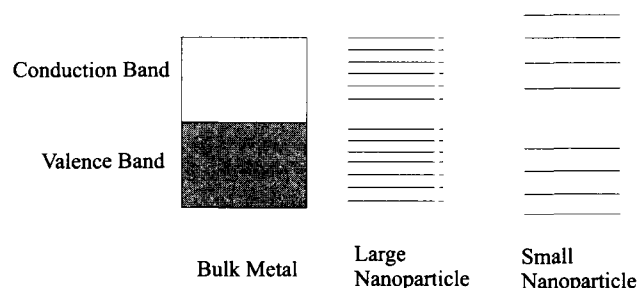


Fig. 1 Schematic layout showing the progression from metallic band structure to quantized electronic structure as nanoparticle dimensions fall.

films to mediate current flow is of obvious application to the development of sensors.

Postsynthesis Nanoparticle Functionalization

Although it is commonly advantageous to modify nanoparticles as they are created, the covalent attachment of molecules to the surface of a nanoparticle is, generally, a dynamic process in which the surface-confined molecules are in dynamic equilibrium with those in the surrounding solution. Because of this, it is possible to displace surface bound molecules with those for which surface-confinement is more thermodynamically favorable—for example, it is possible to displace short chain alkane thiols with those of longer chain.^[32] The use of terminally functionalized alkanethiols facilitates the controlled introduction of surface chemistry into generated nanoparticles—they can be rendered anionic, cationic, hydrophobic and/or suitable for coupling to other molecules or surfaces.

Biomodification

Although the electron scattering propensity of metallic nanoparticles makes them useful biotagging markers,^[33,34] the association of nanoparticles with biomolecules further brings with it the possibility of using them in highly sensitive optical or electrical bioassays. To date, methods have been developed where protein, antibodies, and oligonucleotides can be robustly anchored to particles. Nanoparticles heavily functionalized with oligonucleotides have been used as probes in a variety of DNA detection methods and as elemental building blocks in materials synthesis schemes based upon the sequence-specific hybridization properties of DNA.^[35–37] Typically, the direct adsorption of protein or enzyme onto bare metallic surfaces is accompanied by gross change in protein fold (denaturation) and loss of biological activity. Interestingly, several recent studies have indicated biostability at colloidal metal surfaces.^[38]

SEMICONDUCTING NANOPARTICLES

Much excitement has recently surrounded the potential optical utilization of spherical semiconducting nanocrystals (typically 15–120 Å in diameter),^[39,40] such as those composed of cadmium sulfide,^[40] cadmium selenide, or gallium arsenide.^[41] As with metallic nanoparticles, the dimensions lead to very interesting optical and electronic properties arising from the confinement of excitons (electron/hole pairs) within the particle, and their subsequent quantized behavior. These properties have led to

novel research activity associated with the development of quantum computers, laser diodes, and solar cell technology. The semiconducting band gap associated with these particles is tunable through diameter control at the point of synthesis—the smaller the particle, the greater the energy level spacing between quantized levels; in the case of fluorescence, the absorption and emission peaks shift to longer wavelengths with increasing particle size.^[36]—2.5 nm CdSe particles, for example, fluoresce in the green, while 7-nm equivalents fluoresce in the red.^[36] The potential use of these structures as fluorescent labels has been a core focus during the past 2–3 years; the advantages they hold over more traditional organic fluorophore labels are marked. The fact that equally sized quantum dots made of different materials give rise to different emission/absorption frequencies means that quantum dots are tunable fluorophores. They have wider excitation and narrower emission spectra than conventional organic dye molecules; the former is desirable because several probes with different emission peaks can be excited with a single source, decreasing the number of equipment that might be needed to perform imaging (in fact, QDs can be excited efficiently at any wavelength shorter than that of their emission peak^[36]). A narrow emission spectra reduces spectral cross-talk between different detection channels; in other words, fluorophores of differing emission peaks appear clearer and more distinct from each other. Additionally, these dots also suffer considerably less from the problems of photobleaching inherent in organic dyes and have an associated higher quantum yield (thus they appear “brighter”).^[42] These quantum yields can be further increased by surrounding the dot with an epitaxially grown layer of larger band gap semiconducting material. For example, cadmium selenide dots can be capped with zinc sulfide. These so-called, “core-shell nanocrystals” have associated quantum yields that can be as high as 80%.^[43]

Synthesis

Semiconducting dots are typically synthesized in organic solvent at high temperature from metallic salt and insulator precursors (e.g., a cadmium salt with powdered selenium) in the presence of a stabilizing surface-active agent. As a direct result of this method of forming (stabilized and solubilized) quantum dots, freshly made particles are generated with a surface coating, commonly trioctyl phosphine oxide (TOPO). As with metallic nanoparticles, it appears that the electrical properties of particles are strongly affected by geometry as well as size.^[44] Likewise, as properties are size-dependent, it is

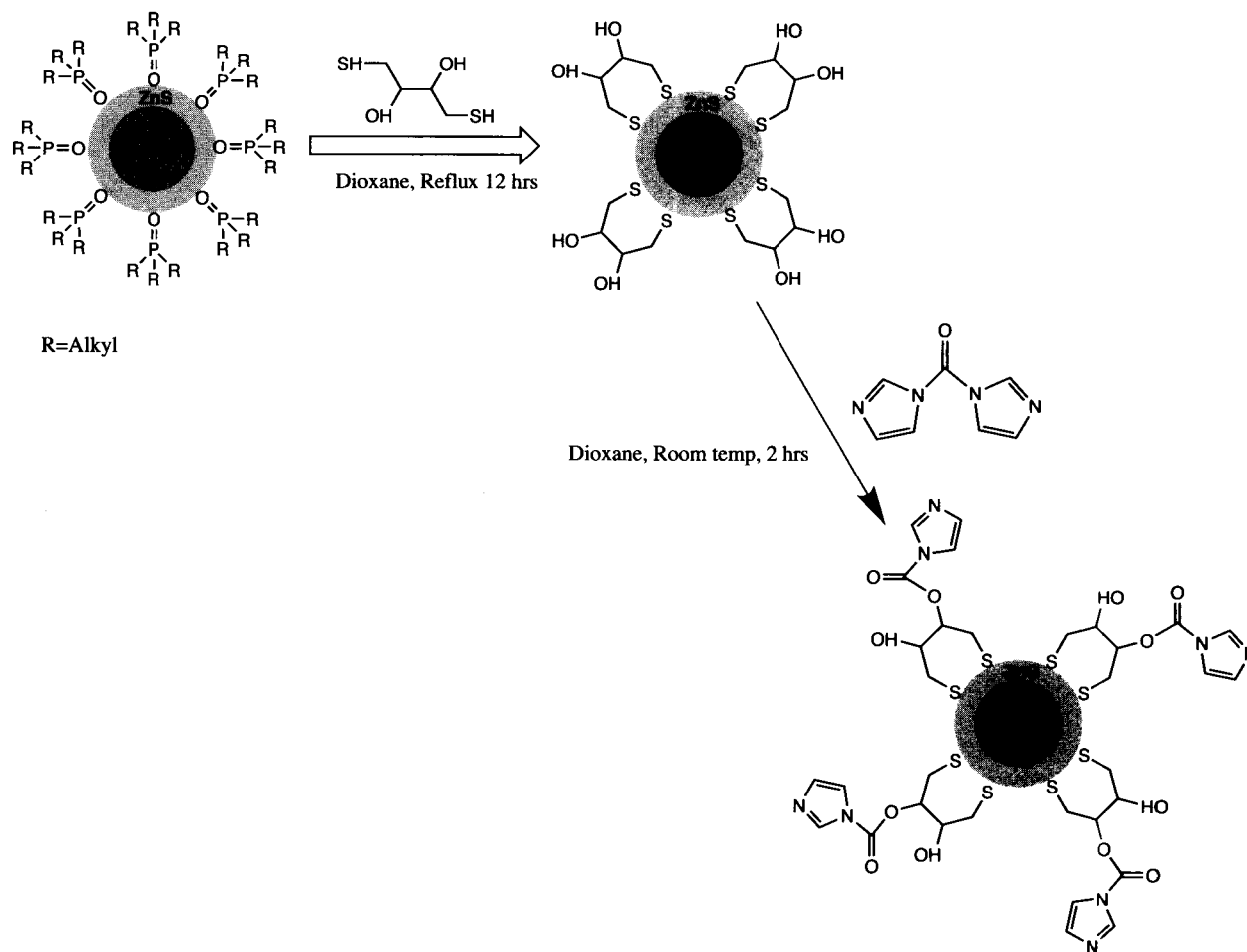


Fig. 2 Functional self-assembly on the surface of semiconducting quantum dots can be used to render them both water soluble and amenable to subsequent (bio)chemical functionalization.

clearly advantageous to ensure that size distributions are as narrow as possible in any sample.

Functionalization

Commonly, quantum dots (and nanoparticles in general) are functionalized by utilizing capping molecules with thiol groups. These capping molecules attach to the surface of the quantum dot by binding at the sulfur atom. This is simple to achieve experimentally: normal procedure involves adding the cap to a colloidal dispersion of quantum dots in an organic solvent and then heating.^[45] Monodentate binding leads to stable isolable products, but bidentate binding has also been used^[46] and, theoretically, gives a more stable cap/surface interaction. To utilize the fluorescent characteristics of these structures in biological media they must, of course, be made water-soluble, and capping with a hydrophilic thiol is one means of achieving this (Fig. 2). A more involved (but ultimately more stable)

method of aqueous solubilization is achievable through surface silanization.^[42] As well as allowing solubility refinements, these surface functionalization methodologies can, subsequently, also be used in either coupling of the quantum dots to other molecules (biomolecules, for example) or their surface assembly.^[47]

THE SURFACE-ASSEMBLY OF NANOPARTICLES

To make use of the intrinsic physiochemical properties of these particles in the development of novel electronic and/or optical devices, methods must be established whereby controlled (many of the potentially useful properties are strongly perturbed on aggregation) assembly on solid surfaces can be achieved.^[48,49] In recent years, a variety of methods have been reported whereby mono (two-dimensional) and multilayers (three-dimensional) of

both metallic^[31,50,51] and semiconducting^[52–54] particles have been generated (with various degrees of control and homogeneity) and characterized. The “new physics” associated with these surfaces has opened up tremendous opportunities for both fundamental research and new applications.^[32,55–58] Although many groups have utilized physical methods of depositing particles, covalent,^[59,60] or ionic^[61,62] assembly offers more control^[63–69] (Fig. 3). The assembly of nanoparticle films can also be electrochemically modulated in cases where the particles are initially decorated with redox-active moieties.^[70] A number of biomolecule-mediated nanoparticle assembly strategies have also been proposed for both metallic and semiconducting particles.^[37,45,71]

Because the most useful quantum dot surfaces are those generated from closely packed (although not physically in contact) colloids, considerable efforts have been expended

in attempts to control this, something which is easiest to achieve if particle–surface interactions are maximized (ideally at the expense of particle–particle interactions).^[72]

In a typical, well-packed 10-nm nanoparticle adlayer, there are 1×10^{10} – 1×10^{11} colloids/cm², depending on edge-to-edge distance. These assembled adlayers are conveniently analyzed at angstrom levels of resolution, by electron microscopy or scanning probe microscopy.

The immobilization of colloidal nanoparticles onto optically transparent electrode surfaces [such as indium tin oxide (ITO)], on which optoelectrochemical analyses can be performed, has also been demonstrated.^[73] Electrochemical studies have resolved electron transfer rate constants between nanoparticles and underlying electrode surfaces of the order of 100 sec^{-1} ^[74] and, predictably, this shows significant dependence on the alkanethiol modification of the particles.^[75] Uosaki et al.^[62] demonstrated

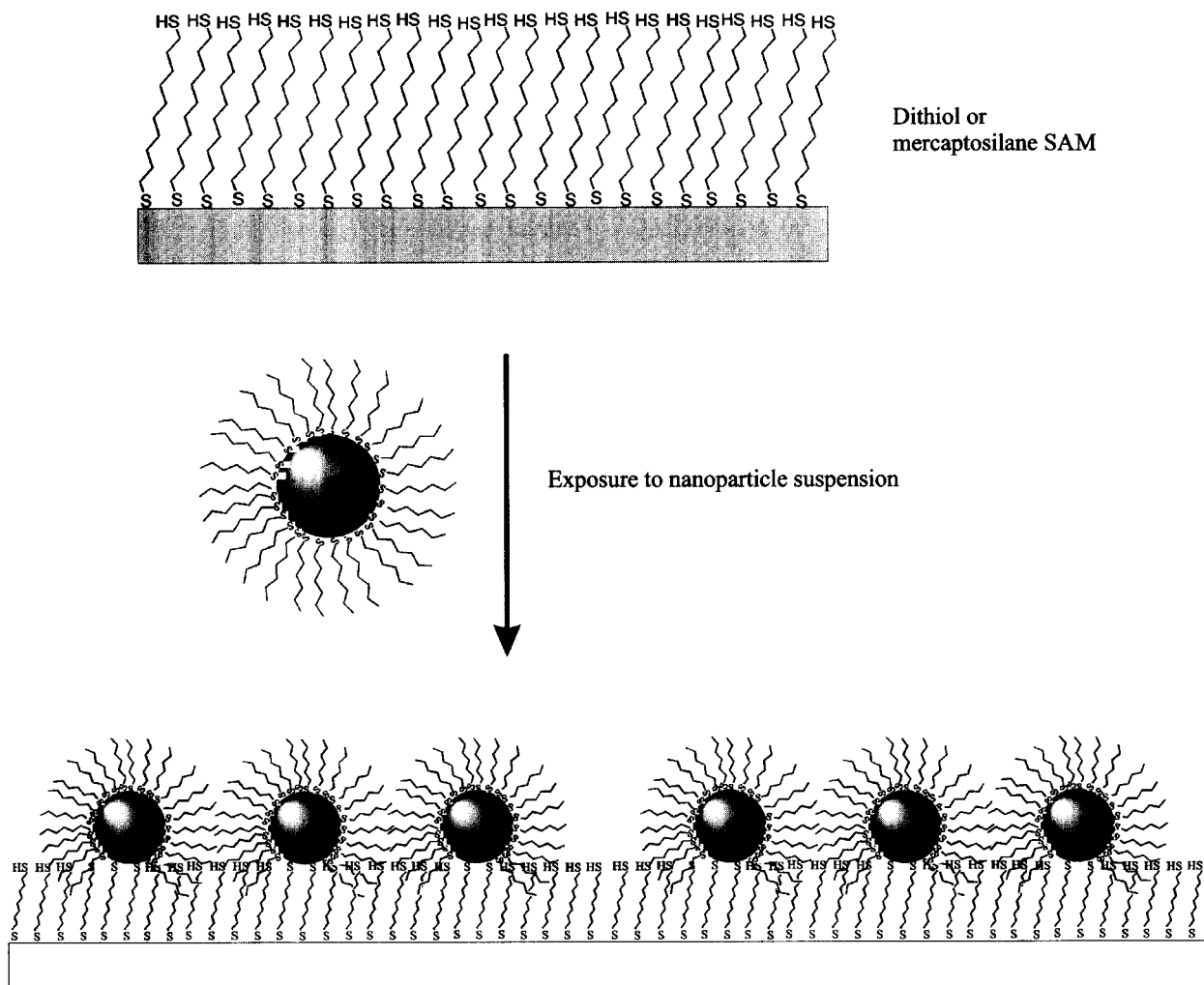


Fig. 3 Schematic representation of a covalent surface assembly protocol for the immobilization of monolayer-capped gold nanoparticles on a functionalized gold electrode surface. (View this art in color at www.dekker.com.)

that, in addition to the strong electronic coupling between surface-confined nanoparticles and their underlying support, fast electron transfer is possible from redox-active moieties attached to gold particles and the underlying electrode. Even in multilayer films, (thermally activated hopping) electron transfer is effectively "channeled" to/from the underlying support via intervening particles. The sensitivity of these electrochemical characteristics to environment is of direct relevance to the generation of derived sensing systems.

ION SENSING AT NANOPARTICLE SURFACES

The development of molecular receptors designed to selectively recognize and sense charged or neutral guest species of biological and environmental importance is a highly topical research field. The "reporting" of recognition may be through "physical change," such as an interfacial mass change associated with bonding (detectable through piezoelectric devices). One may imagine that the "interaction" (binding) and "signaling" regions of a sensor are distinct, and that the monitored signal—be it optical, electrochemical, or otherwise in nature—is reliably and reproducibly perturbed by specific interactions occurring at the neighboring binding site. With electrochemical sensors, perturbation of a voltammetrically monitored electron transfer process, achieved by localization of a redox-active group (e.g., ferrocene) in the vicinity of the receptor, may be achieved by one or a combination of through-space and through-bond interactions. Optical sensing can be achieved through perturbation of an optical signal, typically by equivalent mechanisms. We will focus here on optical and electrochemical transduction where specific molecular association is accompanied by a change in the monitored optical or electrochemical signals derived from the sensor. Such changes can facilitate qualitative or quantitative analyte determination.

Supramolecular chemistry may be defined as the investigation of molecular systems in which the components are reversibly associated by noncovalent intermolecular interaction. From a sensing perspective, such systems may be loosely described as comprising of a "host" sensor and a "guest" analyte species, the latter being neutral, cationic, or anionic. The binding intermolecular forces include electrostatics (ion-ion, ion-dipole, and dipole-dipole), hydrogen bonding, π - π stacking interactions, dispersion and induction forces (van der Waals), and hydrophobic or solvatophobic effects. Individually, these interactions are relatively weak, but in combination they lead to thermodynamically stable complexes, the formation of which can be utilized in the generation of ion sensors.

Cation Sensing

The binding of a cation at a receptor site can be achieved through electrostatic ion-ion or ion-dipole interactions. In general, it is advantageous to utilize polydentate receptor sites that, for well-known thermodynamic reasons (chelate and macrocyclic effects), exhibit increased cation binding affinity. Oxygen-containing crown ethers were the first macrocyclic ligands synthesized which bound alkali metal cations with high selectivity (tunable through structure/geometry). Cryptand and spherand receptor molecules are more highly organized and can accordingly associate very strongly with specific s-block cationic analytes. Through the incorporation of redox-active moieties into these receptors, sensory systems electrochemically responsive to, e.g., lithium,^[76] sodium,^[77] and potassium,^[78] as well as larger cations (some of considerable environmental concern), such as rubidium and cesium,^[79] has also been achieved.

Anion Sensing

The physiological and environmental importance of inorganic anions has fuelled a considerable amount of interest in anion recognition and sensing.^[80] For example, nitrates and phosphates are present in low concentrations in wastewater, but high levels are a contributing factor to eutrophication and, accordingly, are of environmental significance. Although substantial progress has been made in the development of specific, sensitive, cation receptors, similar work with anions has been hindered by their characteristic small charge density (relative to isoelectronic cations) and, subsequently, general low binding affinity. The additional effects of competitive solvation mean that aqueous-phase anion recognition remains a considerable challenge. The design and construction of receptors that can selectively recognize and sense anionic guest species via a macroscopic physical response is thus a current area of chemical sensor technology receiving considerable attention.^[81] Anions are excellent electron pair donors, so they will strongly interact with suitable electron pair acceptors, the simplest of these being an electropositive hydrogen atom capable of forming a hydrogen bond. The directionality of hydrogen bonds introduces the possibility of designing receptors with specific shapes, capable of differentiating between anionic guests of different geometry. Again, by combining a binding site with redox-active moiety, electroanalytical methods can be applied to anion sensing. In recent work, the redox-active ferrocene moiety was used in the electrochemical sensing of anions, both in organic and aqueous media.^[81,82] Transduction of anion binding is achieved by through-space and through-bond stabilization of the higher (Fe^{III} in the case of ferrocenium)

oxidation state and, in voltammetric experiments, this is observable through a cathodic shift in the ferrocene/ferrocenium electrochemical half-wave potential. Acyclic, macrocyclic, and calixarene amide-functionalized ferrocene derivatives have all been subsequently shown to undergo substantial cathodic perturbations of the respective metallocene redox couple in the presence of a variety of anions of biological and environmental importance. These molecular sensors are capable of detecting Cl^- , Br^- , H_2PO_4^- , ReO_4^- , and CH_3CO_2^- (down to low micromolar levels) with, in some cases, the strength of binding correlating with basicity of the anionic guest.

Surface-Confined Chemical Sensors

Self-assembled monolayers (SAMs) can be formed from the exposure of a pristine metallic surface to suitably functionalized molecules, which subsequently form ordered, two-dimensional crystalline arrays; the degree of ordering being dependent on molecular structure and size, substrate morphology, coverage, temperature, and solvent. By combining molecular-scale recognition with such assembly, it is possible to develop a powerful means of generating interfaces capable of analyte detection under a variety of conditions. The "surface tethering" of receptors yields a number of specific additional advantages; efficiency, in terms of quantity of material required, is high; the sensor can be portable, robust, and capable of

being used in a variety of environments. In addition to this, and as discussed below, the preorganization of molecular receptors at a surface enhances the thermodynamic driving force associated with receptor/analyte binding and, therefore, both binding affinity and detection limits.^[83]

Recent work has shown that the introduction of a surface-anchoring thiol moiety into a redox-active anion sensor allows the generation of robust sensing molecular arrays capable of analyte detection in a variety of polar and nonpolar environments. Specifically, by incorporating hydrogen bond donor amide groups and directly linking these functionalities to a redox-active ferrocene unit, hydrogen-bond mediated anion recognition is accompanied by a significant perturbation in the electrochemical characteristics of the monolayer. Strikingly, the anion binding affinities associated with such SAMs are, in some cases, orders-of-magnitude greater than those associated with the same receptors free in solution. This "surface amplification," which can lead to the development of highly effective sensors, is attributable to two things: 1) The "macrocyclic effect" is the entropy- and enthalpy-driven increased thermodynamic stability of a complex formed between an ion (usually cationic) and a multidentate macrocyclic ligand in comparison to the equivalent complex formed with open chain (noncyclic) ligands. By "preorganizing" the host pseudo macrocycle on a surface, and thereby restricting its vibrational and

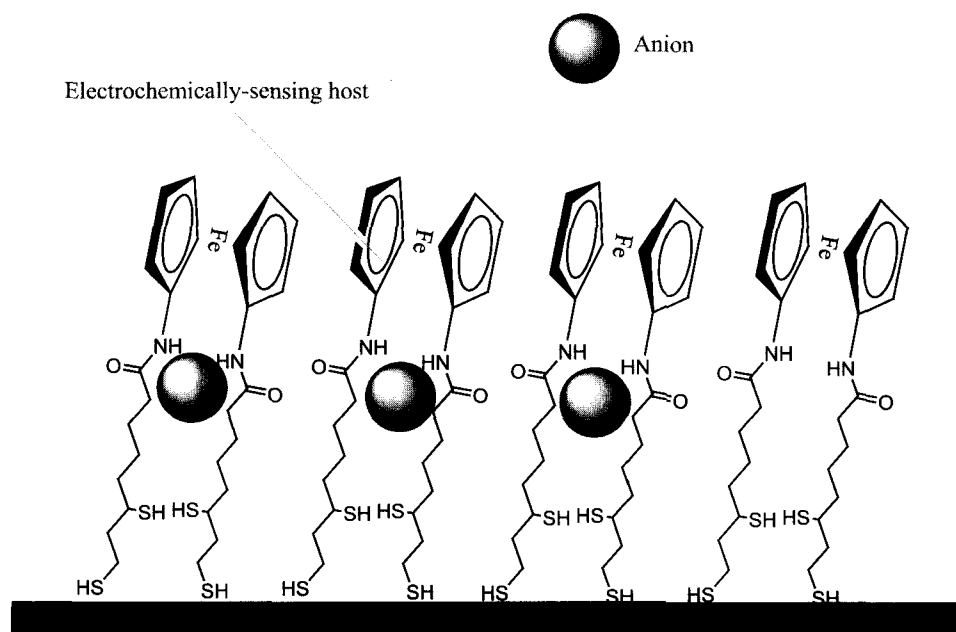


Fig. 4 Schematic representation of a self-assembling, hydrogen-bonding ferrocene amide capable of electroanalytical anion sensing. With the specific receptors shown, hydrogen phosphate anion recognition cathodic shifts in the ferrocene half-wave potential are >290 mV in magnitude—greater, to our knowledge, than anything reported to date. (From Ref. [81].) (View this art in color at www.dekker.com.)

rotational degrees of freedom, the entropic driving force accompanying complex formation is further increased. 2) The comparatively low dielectric constant of the SAM receptor binding site is also likely to significantly enhance anion binding efficacy. The ability to tune both geometry and binding affinity of the host molecular receptor allows one to achieve highly selective sensing. For example, the SAMs shown in Fig. 4 are able to sense dihydrogen phosphate in the presence of more than a 10,000-fold molar excess of halide in solvent. Functional surfaces of this type are able to detect low levels of perchlorate anion (a model for pertechnetate, an environmentally important radioactive waste product of the nuclear and radiopharmaceutical industries) in *aqueous* solution. By increasing both receptor binding affinity and electroanalytical detection sensitivity, it should be possible to extend this aqueous sensing to more basic anions.

Nanoparticle Sensors

The optical and/or electrical/electrochemical properties of metallic or semiconducting nanoparticles and their arrays can be applied to molecular sensing in a variety of ways.

One can envisage the role of the nanoparticles being one or combinations of the following:

- 1) Acting as structural template to preorganize the binding site/receptors—in this case, transduction is not from the particle itself.
- 2) Utilizing the nanoparticle optical properties (plasmon absorption or fluorescence) in transduction—the optical properties of gold nanoparticles (both in solution and surface-confined), for example, are highly sensitive to both the dielectric properties of the intermediate environment and aggregation.
- 3) Making use of nanoparticle conductance in either the electrochemical sensing of molecular binding at mono- or multilayer films, or in recognition-mediated change in film conductance.

Perhaps the least technically challenging, but nonetheless demonstrably powerful, use of nanoparticles in sensing lies with colorimetric assays. Additionally, nanoparticle arrays have considerable potential in vapor-phase analyte detection, Raman, and optical or electrochemical recognition.

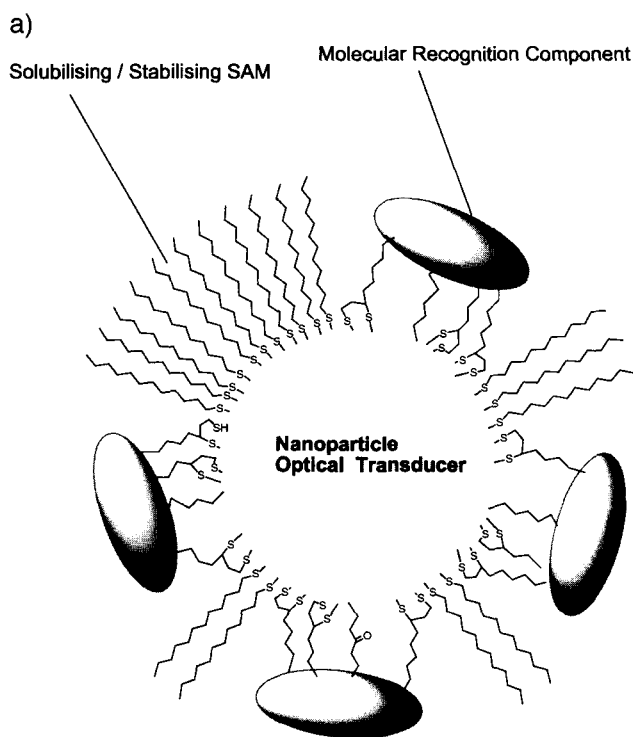


Fig. 5 a) Diagrammatic representation of a nanoparticle appropriately functionalized such that its properties are stable, it is soluble in an appropriate environment, and labeled with a molecular receptor/chemical or biochemical recognition agent. The latter may be a coordination site, oligonucleotide or antibody, for example. b) Place exchange of solubilizing alkyl thiols with a thiolated crown ether produces nanoparticle species that are sensitive to cations; 18-crown-6 and 15-crown-5 ether modified nanoparticles are sensitive to low levels of potassium. Thiolated carboxylic acid modified colloids are sensitive to the presence of heavy metal cations. (From Refs. [87] and [88].) (View this art in color at www.dekker.com.)

b)

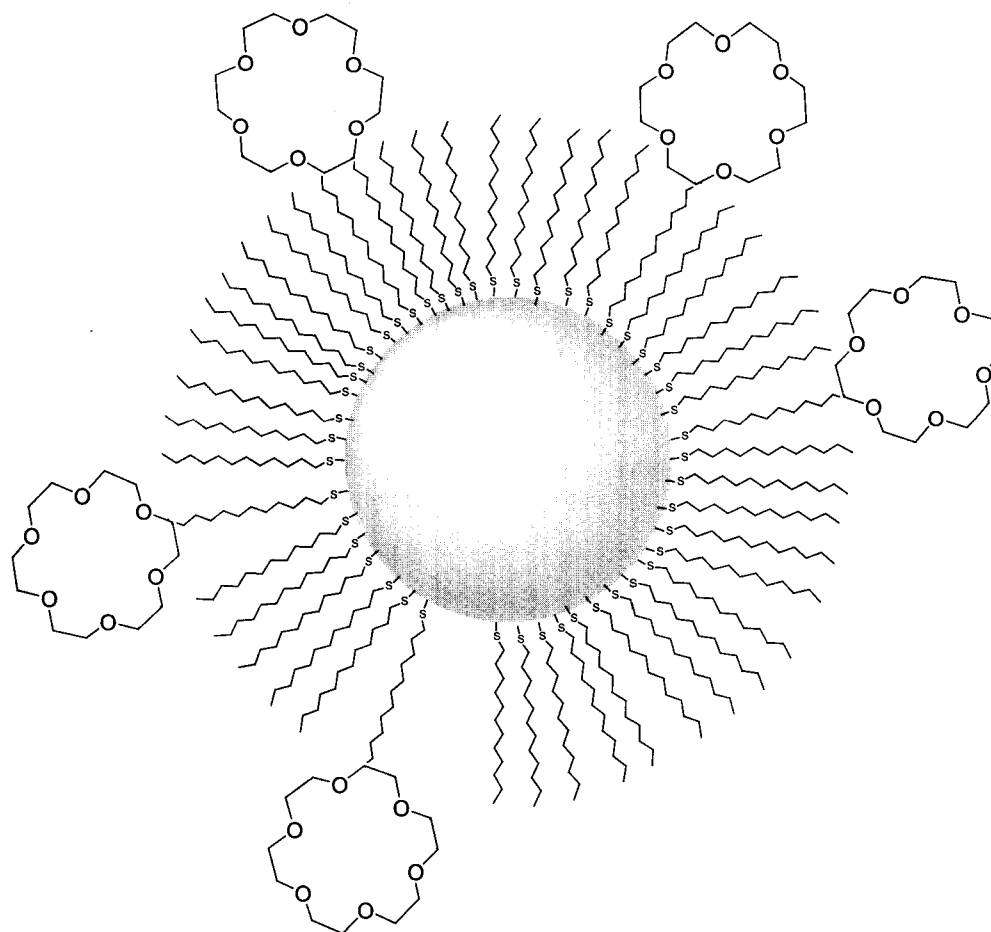


Fig. 5 (Continued).

Colorimetric sensing

As mentioned earlier, gold nanoparticles exhibit characteristic plasmon absorptions that typically give their solutions a pink coloration. The sensitivity of this visible absorption (note: stable nanoparticle suspensions do not appreciably scatter visible light) to aggregation can be utilized in the nanoparticle equivalent of the latex agglutination test,^[84] in which analyte-mediated color change is readily detectable through the use of standard UV-visible spectroscopy. Perhaps the best example of this has been recently demonstrated by Mirkin and coworkers in high-sensitivity colorimetric detection of DNA.^[85] In this work, gold nanoparticles were surface-functionalized with thiolated single-stranded DNA. In the presence of *femtomolar* levels of the complementary DNA, subsequent hybridization-mediated agglutination leads to a visible red-to-purple color change. Colorimetric immunoassays have also been developed based on either anti-

body or antigen nanoparticle functionalization.^[86] Related colorimetric titrations have recently been extended to the generation of ion-sensing systems. Specifically, by self-assembly of appropriately functionalized receptors on nanoparticles, cation- or anion-mediated linking or aggregation can be spectroscopically monitored (Fig. 5). In using self-assembling thiolated crown ethers, Lin et al.^[87] were able to construct colorimetric assays, based on standard, proximity-linked, coupling of plasmons, for potassium, with detection limits down to low micromolar level. Similarly, cadmium-, mercury-, and lead-responsive assays have been developed.^[88]

Vapor phase sensing

The initially Ohmic, thermally activated, conductance properties of MPC films are sensitively dependent on the separation of, and intervening medium between, the

particles. The “intercalation” of organic vapor into such films leads to a detectable decrease in the conductance. Although this phenomenon appears to be highly dependent on the structural aspects of the nanoparticle film, it may be applicable to the generation of highly robust sensors.^[89] To date, several research groups have demonstrated fast, reversible, and highly sensitive (<5 ppm in some cases) responses to a variety of solvent vapors.^[90] Although the mechanisms of vapor sensitivity are poorly understood, the phenomenon has been qualitatively considered in terms of both film swelling and dielectric change.^[91,92]

SERS—Raman sensing at surfaces

The Raman scattering attainable from an adsorbate on a rough metal surface is greatly enhanced over the attain-

able rate on flat substrates. This enhancement, observable on “active metals,” is greatest when the surface roughness is of the order of tens of nanometers and, although not fully understood, is associated with the ability of such surfaces to enhance/focus electromagnetic radiation. Although it is nearly 20 years since the discovery of surface-enhanced Raman scattering of molecules adsorbed at suitable roughened metallic interfaces,^[93,94] where up to 10^6 -fold enhancements over the adsorbate natural Raman scattering can be observed, the generation of suitable roughened surfaces by etching or deposition methods suffers from reproducibility issues. Through the surface-confinement of nanoparticles, homogeneous surfaces of precisely appropriate roughness can be reproducibly fabricated. Furthermore, the plasmon characteristics of colloids appear to further magnify signal enhancement.^[48] The use of colloidal gold or silver nanoparticles in enhancing the spectroscopic data attainable from

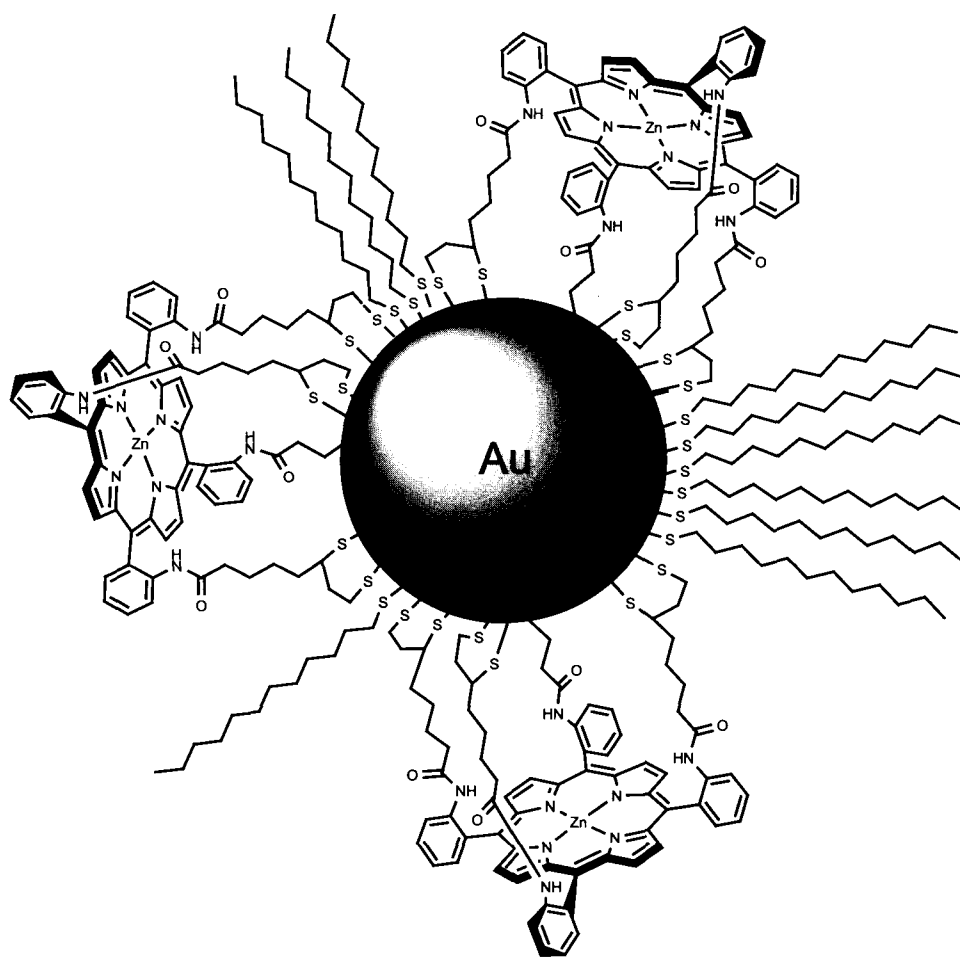


Fig. 6 Schematic of an anion-sensing zinc porphyrin nanoparticle. The tetrapodal porphyrin is anchored to the nanoparticle surface through disulfide moieties. Note, for reasons of clarity, that the relative sizes of nanoparticle and porphyrin are false. (From Ref. [82].)

interfaces has been demonstrated,^[95,96] where million-fold enhancements leading, in some cases, to attomolar sensitivity, have been observed.^[97]

Electroanalytical sensing

Through the functionalization of colloidal gold nanoparticles with self-assembling amidoferrocenes, Astruc et al.^[98,99] were able to demonstrate the establishment of an effective redox probe for dihydrogen phosphate and hydrogen sulfate in an organic solvent medium. This work makes use of the diffusive nature of solubilized nanoparticles, the facile access of anions to the hydrogen-bonding receptor site, and the reliable electrochemical communication with redox-active units confined to the particle surface. Although additional preorganizational effects were noted in these studies, they pave the way to others in which the controlled assembly of redox-active molecular or ionic receptors on nanoparticles (free in solution or assembled in arrays on a surface) may lead to highly effective electroanalytical devices.

Plasmon and optical sensing

Plasmon resonance sensors are ubiquitous in the study of interfacial (bio)molecular interactions and function by detecting changes in local refractive index with high sensitivity.^[100] The collective oscillation of electrons responsible for the characteristic plasmon absorption of metallic nanoparticles is highly sensitive to changes in local (surface) refractive index.^[101,102] In view of the associated local enhancement of electromagnetic field, one may propose that such a surface can act as an "antenna" for interfacial processes such as molecular recognition. By utilizing the environmental sensitivity of appropriately functionalized nanoparticles, one might envisage the development of related SPR sensors of nanometer ("molecular level") dimension. Because we have observed that it is possible to modify nanoparticles surfaces with SAMs, the terminal functionality of which is flexible, it is possible to generate stable colloids which are sensitive to/reactive to different species^[103] (Fig. 5). In pursuit of this and related optical goals, several groups have recently generated nanoparticles functionalized with molecular recognition moieties.^[20,82,99,104]

As a specific example, and with the aim of producing optical and redox-active nanoparticle anion sensors, the synthesis of a new amide-disulfide functionalized zinc metalloporphyrin has been reported.^[82] This compound can be self-assembled on to gold nanoparticles to produce a novel anion-selective optical sensing system (Fig. 6). In this work, the nanoparticle itself is utilized as a diffusive

Table 1 Association constant ($\log k$) data for anion binding by Zn porphyrin receptor both assembled on the surface of a nanoparticle and free in solution

Anion	Particle free Zn porphyrin	Particle bound Zn porphyrin
Cl ⁻	>6	>6
Br ⁻	4.12	4.97
I ⁻	3.21	4.00
NO ₃ ⁻	2.41	3.22
H ₂ PO ₄ ⁻	>6	>6
ClO ₄ ⁻	0	0
*Cl ⁻	<2	4.3
*H ₂ PO ₄ ⁻	2.5	4.1

*Data obtained in DMSO at 298 K.

"template" on which the receptor is "preorganized." The zinc Lewis acid and hydrogen bond-mediated recognition of halide, nitrate, or dihydrogen phosphate by the zinc metalloporphyrin center is associated with a perturbation of the porphyrin optical spectrum. What makes this particularly striking is the ability of the nanoparticle to generate a solution-phase, but preorganized, receptor of high analyte binding affinity. As discussed in the previous section, the combined enthalpic and entropic factors associated with the monolayer-based, receptor site and its surrounding low dielectric are such that binding constants are enhanced by more than 2 orders of magnitude in comparison to the nonparticle-confined receptor (Table 1). Significantly, this enhanced binding affinity is such that anion recognition in a mixed aqueous/solvent system, a challenging situation because of the competitive solvation of the anion, is possible. By further tailoring the receptor site chemical and geometric properties, it should be possible to generate yet more powerful sensing systems. Because functionalized SAMs can be similarly generated on semiconducting nanoparticles, sensing systems based on, e.g., a recognition-based perturbation of fluorescence may be feasible.

CONCLUSION

The potential impact of nanoscale science and technology on our lives is considerable. In recent years, much progress has been made in both generating and analyzing nanoscale material. To exploit some of the striking properties observed in matters of such dimensions, methods must be developed where homogeneous samples of material can be produced in useful quantities and incorporated into functional devices. In this article, we have attempted to summarize recent progress made in characterizing and

utilizing the size-dependent properties of nanoparticles and quantum dots. Specifically, we have outlined and demonstrated methods by which the environmental sensitivities inherent in these structures can be used in sensing technologies. Although interest in generating smaller analytical devices for been around for some time, only in recent years has it been possible to make use of the specific functional properties that are apparent at the nanometer scale. The ability to selectively and sensitively detect ions is of considerable environmental, clinical, and chemical importance. Through designed functionalization of nanoparticles with receptor moieties, it is possible to construct derived optical or electroanalytical assays. We have specifically introduced methodologies whereby nanoparticle-based ion assays can be developed. Through further refinement of nanoparticle functionalization, manipulation, and interrogation, the creation of a vast number of novel and highly responsive sensory devices seems feasible.

ACKNOWLEDGMENTS

The authors wish to acknowledge support from the Engineering and Physical Sciences Research Council (EPSRC) and The Royal Society.

REFERENCES

1. Martin, C. Membrane-based synthesis of nanomaterials. *Chem. Mater.* **1996**, *8*, 1739.
2. Alivisatos, A. Semiconductor clusters, nanocrystals, and quantum dots. *Science* **1996**, *271*, 933.
3. Bawendi, M.; Steigerwald, M.; Brus, L. The quantum mechanics of larger semiconductor clusters ("quantum dots"). *Annu. Rev. Phys. Chem.* **1990**, *41*, 477.
4. Klein, D.; Roth, R.; Lim, A.; Alivisatos, A.; McEuen, P. A single-electron transistor made from a cadmium selenide nanocrystal. *Nature* **1997**, *389*, 699.
5. Wang, B.; Wang, H.; Li, H.; Zeng, C.; Hou, J.; Xiao, X. Tunable single-electron tunneling behavior of ligand-stabilized gold particles on self-assembled monolayers. *Phys. Rev., B* **2001**, *63*, 6303.
6. Novak, J.; Brousseau, L.; Vance, F.; Johnson, R.; Lemon, B.; Hupp, J.; Feldheim, D. Nonlinear optical properties of molecularly bridged gold nanoparticle arrays. *J. Am. Chem. Soc.* **2000**, *122*, 12029.
7. Miltenyi, S.; Muller, W.; Weichel, W.; Radbruch, A. High gradient magnetic cell separation with MACS. *Cytometry* **1990**, *11*, 231.
8. Hahn, P.; Stark, D.; Lewis, J.; Saini, S.; Elizondo, G.; Weissleder, R.; Fretz, C.; Ferrucci, J. First clinical trial of a new superparamagnetic iron oxide for use as an oral gastrointestinal contrast agent in MR imaging. *Radiology* **1990**, *175*, 695.
9. Yeh, T.; Zhang, W.; Ildstad, S. In vivo dynamic MRI tracking of rat T-cells labeled with superparamagnetic iron-oxide particles. *Magn. Reson. Med.* **1995**, *33*, 200.
10. Sato, T.; Ahmed, H.; Brown, D.; Johnson, B.F.G. Single electron transistor using a molecularly linked gold colloidal particle chain. *J. Appl. Phys.* **1997**, *82*, 696.
11. Brust, M.; Fink, J.; Bethell, D.; Schiffrin, D.J.; Kiely, C.J. Synthesis and reactions of functionalized gold nanoparticles. *J. Chem. Soc., Chem. Commun.* **1995**, *16*, 1655.
12. Murthy, S.; Bigioni, T.P.; Wang, Z.L.; Khoury, J.T.; Whetten, R.L. Liquid-phase synthesis of thiol-derivatized silver nanocrystals. *Mater. Lett.* **1997**, *12*, 321.
13. Yee, C.; Scotti, M.; Ulman, A.; White, H.; Rafailovich, M.; Sokolov, J. One-phase synthesis of thiol-functionalized platinum nanoparticles. *Langmuir* **1999**, *15*, 4314.
14. Yee, C.K.; Jordan, R.; Ulman, A.; White, H.; King, A.; Rafailovich, M.; Sokolov, J. Novel one-phase synthesis of thiol-functionalized gold, palladium, and iridium nanoparticles using superhydride. *Langmuir* **1999**, *15*, 3486.
15. Jin, R.; Cao, Y.; Mirkin, C.; Kelly, K.; Schatz, G.; Zheng, J. Photoinduced conversion of silver nanospheres to nanoprisms. *Science* **2001**, *294*, 1901.
16. Huang, T.; Murray, R. Visible luminescence of water-soluble monolayer-protected gold clusters. *J. Phys. Chem., B* **2001**, *105*, 12498.
17. Duncan, M.; Rouvray, D. Microclusters. *Sci. Am.* **1989**, *261*, 110.
18. Henglein, A.; Lilie, J. Storage of electrons in aqueous solution: The rates of chemical charging and discharging the colloidal silver microelectrode. *J. Am. Chem. Soc.* **1981**, *103*, 1059.
19. Kopple, K.; Meyerstein, D.; Meisel, D. Mechanism of the catalytic hydrogen production by gold sols. Hydrogen/deuterium isotope effect studies. *J. Phys. Chem.* **1980**, *84*, 870.
20. Templeton, A.; Wuelfing, W.P.; Murray, R.W. Monolayer-protected cluster molecules. *Acc. Chem. Res.* **2000**, *33*, 27.

21. Markovich, G.; Collier, C.P.; Henrichs, S.E.; Remacle, F.; Levine, R.D.; Heath, J.R. Architectonic quantum dot solids. *Acc. Chem. Res.* **1999**, *32*, 415.
22. Chen, S.; Ingram, R.S.; Hostetler, M.J.; Pietron, J.J.; Murray, R.W.; Schaaff, T.G.; Khoury, J.T.; Alvarez, M.M.; Whetten, R.L. Gold nanoelectrodes of varied size: Transition to molecule-like charging. *Science* **1998**, *280*, 2098.
23. Zelakiewicz, B.; Dios, A.d.; Tong, Y. ^{13}C NMR spectroscopy of ^{13}C -labeled octanethiol-protected Au nanoparticles: Shifts, relaxations, and particle-size effect. *J. Am. Chem. Soc.* **2003**, *125*, 18.
24. Hicks, J.F.; Templeton, C.A.; Chen, S.; Sheran, K.M.; Jasti, R.; Murray, R.W.; Debord, J.; Schaaff, T.G.; Whetten, R.L. The monolayer thickness dependence of quantized double-layer capacitances of monolayer-protected gold clusters. *Anal. Chem.* **1999**, *71*, 3703.
25. Quinn, B.M.; Liljeroth, P.; Kontturi, K. Interfacial reactivity of monolayer-protected clusters studied by scanning electrochemical microscopy. *J. Am. Chem. Soc.* **2002**, *124*, 12915.
26. Gittins, D.I.; Bethell, D.; Nichols, R.J.; Schiffrin, D.J. Redox-connected multilayers of discrete gold particles: A novel electroactive nanomaterial. *Adv. Mater.* **1999**, *11*, 737.
27. Chen, S. Self-assembling of monolayer-protected gold nanoparticles. *J. Phys. Chem., B* **2000**, *104*, 663.
28. Hicks, J.F.; Zamborini, F.P.; Osisek, A.J.; Murray, R.W. The dynamics of electron self-exchange between nanoparticles. *J. Am. Chem. Soc.* **2001**, *123*, 7048.
29. Chen, S. Electrochemical studies of Langmuir-Blodgett thin films of electroactive nanoparticles. *Langmuir* **2001**, *17*, 6664.
30. Jhaveri, S.D.; Lowy, D.A.; Foos, E.E.; Snow, A.W.; Ancona, M.G.; Tneder, L.M. Self-assembling monolayer formation of glucose oxidase covalently attached on 11-aminoundecanethiol monolayers on gold. *J. Chem. Soc., Chem. Commun.* **2002**, *14*, 1544.
31. Chen, S.; Murray, R.W.; Feldberg, S.W. Quantized capacitance charging of monolayer-protected Au clusters. *J. Phys. Chem., B* **1998**, *102*, 9898.
32. Ingram, R.; Hostetler, M.; Murray, R. Poly-heterofunctionalized alkanethiolate-stabilized gold cluster compounds. *J. Am. Chem. Soc.* **1997**, *119*, 9175.
33. Schultz, S.; Smith, D.R.; Mock, J.J.; Schultz, D.A. Single-target molecule detection with nonbleaching multicolor optical immunolabels. *Proc. Natl. Acad. Sci. U. S. A.* **2000**, *97*, 996.
34. Moller, R.; Csaki, A.; Kohler, J.M.; Fritzsche, W. Electrical classification of the concentration of bioconjugated metal colloids after surface adsorption and silver enhancement. *Langmuir* **2000**, *17*, 5426.
35. Mirkin, C.; Letsinger, R.; Mucic, R.; Storhoff, J. A DNA-based method for rationally assembling nanoparticles into macroscopic materials. *Nature* **1996**, *382*, 607.
36. Bruchez, M.; Moronne, M.; Gin, P.; Weiss, S.; Alivisatos, A. Semiconductor nanocrystals as fluorescent biological labels. *Science* **1998**, *281*, 2013.
37. Taton, T.; Mucic, R.; Mirkin, C.; Letsinger, R. The DNA-mediated formation of supramolecular mono- and multilayered nanoparticle structures. *J. Am. Chem. Soc.* **2000**, *122*, 6305.
38. Brown, K.; Fox, A.; Natan, M. Morphology-dependent electrochemistry of cytochrome *c* at Au colloid-modified SnO_2 electrodes. *J. Am. Chem. Soc.* **1996**, *118*, 1154.
39. Mattoussi, H., et al. Properties of CdSe nanocrystal dispersions in the dilute regime: Structure and interparticle interactions. *Phys. Rev., B* **1998**, *58*, 7850.
40. Murray, C.; Norris, D.; Bawendi, M. Synthesis and characterization of nearly monodisperse CdE (E=sulfur, selenium, tellurium) semiconductor nanocrystallites. *J. Am. Chem. Soc.* **1993**, *115*, 8706.
41. Olshavsky, M.; Goldstein, A.; Alivisatos, A. Organometallic synthesis of gallium-arsenide crystallites, exhibiting quantum confinement. *J. Am. Chem. Soc.* **1990**, *112*, 9438.
42. Gerion, D.; Pinaud, F.; Williams, S.; Weiss, S.; Alivisatos, A. Synthesis and properties of biocompatible water-soluble silica-coated CdSe/ZnS semiconductor quantum dots. *J. Phys. Chem., B* **2001**, *105*, 8861.
43. Peng, X.; Schlamp, M.; Kadanavich, A.; Alivisatos, A. Epitaxial growth of highly luminescent CdSe/CdS core/shell nanocrystals with photostability and electronic accessibility. *J. Am. Chem. Soc.* **1997**, *119*, 7019.
44. Hu, J.; Li, L.; Yang, W.; Manna, L.; Wang, L.; Alivisatos, A. Linearly polarized emission from colloidal semiconductor quantum rods. *Science* **2001**, *292*, 2060.
45. Mitchell, G.; Mirkin, C.A.; Letsinger, R.L. Programmed assembly of DNA functionalized quantum dots. *J. Am. Chem. Soc.* **1999**, *121*, 8122.

46. Mattoussi, H.; Mauro, J.; Goldman, E.; Anderson, G.; Sundar, V.; Mikulec, F.; Bawendi, M. Self-assembly of CdSe-ZnS quantum dot bioconjugates using an engineered recombinant protein. *J. Am. Chem. Soc.* **2000**, *122*, 12142.
47. Zanchet, D.; Micheel, C.; Parak, W.; Gerion, D.; Alivisatos, A. Electrophoretic isolation of discrete Au nanocrystal/DNA conjugates. *Nano Lett.* **2001**, *1*, 32.
48. Shipway, A.; Katz, E.; Willner, I. Nanoparticle arrays on surfaces for electronic, optical, and sensor applications. *ChemPhysChem* **2000**, *1*, 18.
49. Gudiksen, M.; Leuhon, L.; Wang, J.; Smith, D.; Leiber, C. Growth of nanowire superlattice structures for nanoscale photonics and electronics. *Nature* **2002**, *415*, 617.
50. Zamborini, F.; Hicks, J.; Murray, R. Quantised double layer charging of nanoparticle films assembled using carboxylate/(Cu²⁺ or Zn²⁺)/carboxylate bridges. *J. Am. Chem. Soc.* **2000**, *122*, 4514.
51. Templeton, A.; Zamborini, F.; Wuelfing, W.; Murray, R. Controlled and reversible formation of nanoparticle aggregates and films using Cu²⁺-carboxylate chemistry. *Langmuir* **2000**, *16*, 6682.
52. Ogawa, S.; Hu, K.; Fan, F.; Bard, A. Photoelectrochemistry of films of quantum size lead sulfide particles incorporated in self-assembled monolayers on gold. *J. Phys. Chem., B* **1997**, *101*, 5707.
53. Nakanishi, T.; Ohtani, B.; Shimazu, K.; Uosaki, K. Layer-by-layer self-assembly of composite films of CdS nanoparticle and alkanedithiol on gold: An x-ray photoelectron spectroscopic characterization. *Chem. Phys. Lett.* **1997**, *278*, 233.
54. Nakanishi, T.; Ohtani, B.; Uosaki, K. Fabrication and characterization of CdS-nanoparticle mono- and multilayers on a self-assembled monolayer of alkanedithiols on gold. *J. Phys. Chem., B* **1998**, *102*, 1571.
55. Yamada, M.; Quiros, I.; Mizutani, J.; Kubo, K.; Nishihara, H. Preparation of palladium nanoparticles functionalized with biferrocene thiol derivatives and their electro-oxidative deposition. *Phys. Chem. Chem. Phys.* **2001**, *3*, 3377.
56. Quiros, I.; Yamada, M.; Mizutani, J.; Kubo, K.; Kurihara, M.; Nishihara, H. Preparation of alkanedithiolate-protected palladium nanoparticles and their size dependence on synthetic conditions. *Langmuir* **2002**, *18*, 1413.
57. Yamada, M.; Nishihara, H.J. Electrochemical construction of an alternating multi-layered structure of palladium and gold nanoparticles attached with biferrocene moieties. *J. Chem. Soc., Chem. Commun.* **2002**, *21*, 2578.
58. Murata, M.; Yamada, M.; Fujita, T.; Kojima, K.; Kurihara, M.; Kubo, K.; Kobayashi, Y.; Nishihara, H. Structural conversion and spin separation in bis(ferrocenylethynyl)anthraquinones triggered by proton-coupled intramolecular electron transfer. *J. Am. Chem. Soc.* **2001**, *123*, 12903.
59. Bakkers, E.; Marsman, A.; Jenneskens, L.; Vanmaekelbergh, D. Distance-dependent electron transfer in Au/spacer/Q-CdSe assemblies. *Angew. Chem., Int. Ed. Engl.* **2000**, *39*, 2297.
60. Pethkar, S.; Aslam, M.; Mulla, I.; Ganeshan, P.; Vijayamohan, K. Preparation and characterisation of silver quantum dot superlattice using self-assembled monolayers of pentanedithiol. *J. Mater. Chem.* **2001**, *11*, 1710.
61. Sagara, T.; Kato, N.; Kakashima, N. Electroreflectance study of gold nanoparticles immobilized on an aminoalkanethiol monolayer coated on a polycrystalline gold electrode surface. *J. Phys. Chem., B* **2002**, *106*, 1205.
62. Uosaki, K.; Kondo, T.; Okamura, M.; Song, W. Electron and ion transfer through multilayers of gold nanoclusters covered by self-assembled monolayers of alkylthiols with various functional groups. *Faraday Discuss.* **2002**, *121*, 373.
63. Kiely, C.J.; Fink, J.; Brust, M.; Bethell, D.; Schiffrin, D.J. Spontaneous ordering of bimodal ensembles of nanoscopic gold clusters. *Nature* **1998**, *396*, 444.
64. Sun, S.H.; Murray, C.B.; Weller, D.; Folks, L.; Moser, A. Monodisperse FePt nanoparticles and ferromagnetic FePt nanocrystal superlattices. *Science* **2000**, *287*, 1989.
65. Jin, J.; Iyoda, T.; Cao, C.S.; Song, Y.L.; Jiang, L.; Li, T.J.; Zhu, D.B. Self-assembly of uniform spherical aggregates of magnetic nanoparticles through—Interactions. *Angew. Chem. Int. Ed. Engl.* **2001**, *40*, 2135.
66. Gittins, D.I.; Bethell, D.; Nichols, R.J.; Schiffrin, D.J. Diode-like electron transfer across nanostructured films containing a redox ligand. *J. Mater. Chem.* **2000**, *10*, 79.
67. Caruso, F.; Mohwald, H. Preparation and characterization of ordered nanoparticle and polymer composite multilayers on colloids. *Langmuir* **1999**, *15*, 8276.
68. Pardo-Yissar, V.; Katz, E.; Lioubashevski, O.; Willner, I. Layered polyelectrolyte films on Au electrodes: Characterization of electron-transfer features at the charged polymer interface and application for selective redox reactions. *Langmuir* **2001**, *17*, 1110.
69. Caruso, F.; Spasova, M.; Saigueirino-Maceira, V.;

- Liz-Marzan, L.M. Multilayer assemblies of silica-encapsulated gold nanoparticles on decomposable colloid templates. *Adv. Mater.* **2001**, *13*, 1090.
70. Yamada, M.; Tadera, T.; Kubo, K.; Nishihara, H. Electrochemical deposition of ferrocene derivative-attached gold nanoparticles and the morphology of the formed film. *J. Phys. Chem., B* **2003**, *107*, 3703.
71. Gerion, D.; Parak, W.; Williams, S.; Zanchet, D.; Micheel, C.; Alivisatos, A. Sorting fluorescent nanocrystals with DNA. *J. Am. Chem. Soc.* **2002**, *124*, 7070.
72. Chu, L.; Yang, S. Contributions of r-1, r-2, r-3 terms of the full dipole fields associated with Raman scattering enhancement from CN molecules adsorbed on a 2-D array of Ag spheroids. *J. Appl. Phys.* **1985**, *57*, 453.
73. Doron, A.; Katz, E.; Willner, I. Organization of Au colloids as monolayer films onto ITO glass surfaces: Application of the metal colloid films as base interfaces to construct redox-active monolayers. *Langmuir* **1995**, *11*, 1313.
74. Hicks, J.; Zamborini, F.; Murray, R. Dynamics of electron transfers between electrodes and monolayers of nanoparticles. *J. Phys. Chem., B* **2002**, *106*, 7751.
75. Chen, S.; Pei, R. Ion-induced rectification of nanoparticle quantized capacitance charging in aqueous solutions. *J. Am. Chem. Soc.* **2001**, *123*, 10607.
76. Plenio, H.; Diodone, R. Complexation of Na⁺ in redox-active ferrocene crown ethers, a structural investigation, and an unexpected case of Li⁺ selectivity. *Inorg. Chem.* **1995**, *34*, 3964.
77. Shephard, D.; Johnson, B.; Matters, J.; Parson, S. Novel redox-active ruthenium cluster crown compounds capable of host-guest chemistry. *J. Chem. Soc. Dalton Trans.* **1998**, *14*, 2289.
78. Beer, P.; Gale, P.; Chen, Z.; Drew, M.; Powell, H. New ionophoric calix[4]diquinones: Coordination chemistry, electrochemistry, and x-ray crystal structures. *Inorg. Chem.* **1997**, *36*, 5880.
79. Webber, P.; Beer, P.; Chen, G.; Felix, V.; Drew, M. Bis(calix[4]diquinone) receptors: Cesium- and rubidium-selective redox-active ionophores. *J. Am. Chem. Soc.* **2003**, *125*, 5774.
80. Beer, P.; Gale, P. Anion recognition and sensing: The state of the art and future perspectives. *Angew. Chem., Int. Ed. Engl.* **2001**, *40*, 486.
81. Beer, P.; Davis, J.; Drillsma-Milgrom, D.; Szemes, F. Anion recognition and redox sensing amplification by self-assembled monolayers of 1,1-bis(alkyl-N-amido)ferrocene. *J. Chem. Soc., Chem. Commun.* **2002**, *16*, 1716.
82. Beer, P.D.; Cormode, D.P.; Davis, J.J. Porphyrin-functionalised nanoparticle anion sensors. **2003**, submitted.
83. Davis, J.J.; Beer, P.D.; Szemes, F.S.; Drillsma-Milgrom, D. *J. Chem. Soc., Chem. Commun.* **2002**, 1716.
84. Bangs, L.B. New developments in particle-based immunoassays: Introduction. *Pure Appl. Chem.* **1996**, *68*, 1873.
85. Elghanian, R.; Storhoff, J.; Mucic, R.; Letsinger, R.; Mirkin, C. Selective colorimetric detection of polynucleotides based on the distance-dependent optical properties of gold nanoparticles. *Science* **1997**, *277*, 1078.
86. Erp, R.V.; Gribnau, T.C.J.; Van Sommeren, A.P.G. Application of a sol particle immunoassay to the determination of affinity constants of monoclonal antibodies. *J. Immunoass.* **1991**, *12*, 425.
87. Lin, S.; Liu, S.; Lin, C.; Chen, C. Recognition of potassium ion in water by 15-crown-5 functionalized gold nanoparticles. *Anal. Chem.* **2002**, *74*, 330.
88. Kim, Y.; Johnson, R.; Hupp, J. Gold nanoparticle-based sensing of "spectroscopically silent" heavy metal ions. *Nano Lett.* **2001**, *1*, 165.
89. Zamborini, F.; Leopold, M.; Hicks, J.; Kulesza, P.; Malik, M.; Murray, R. Electron hopping conductivity and vapor sensing properties of flexible network polymer films of metal nanoparticles. *J. Am. Chem. Soc.* **2002**, *124*, 8958.
90. Vossmeier, T.; Guse, B.; Besnard, I.; Bauer, R.; Mullen, K.; Yasuda, A. Gold nanoparticle/polyphenylene dendrimer composite films: Preparation and vapor-sensing properties. *Adv. Mater.* **2002**, *14*, 238.
91. Zhang, H.; Evans, S.; Henderson, J.; Miles, R.; Shen, T. Vapour sensing using surface functionalized gold nanoparticles. *Nano Technol.* **2002**, *13*, 439.
92. Evans, S.; Johnson, S.; Cheng, Y.; Shen, T. Vapour sensing using hybrid organic-inorganic nanostructured materials. *J. Mater. Chem.* **2000**, *10*, 183.
93. Blatchford, C.G.; Campbell, J.R.; Creighton, J.A. Plasma resonance-enhanced Raman scattering by absorbates on gold colloids: The effects of aggregation. *Surf. Sci.* **1982**, *120*, 435.
94. Tran, C.D. Subnanogram detection of dyes on filter paper by surface-enhanced Raman scattering spectrometry. *Anal. Chem.* **1984**, *56*, 824.

95. Soper, S.A.; Ratzhlaff, K.L.; Kuwana, T. Surface-enhanced resonance Raman spectroscopy of liquid chromatographic analytes on thin-layer chromatographic plates. *Anal. Chem.* **1990**, *62*, 1438.
96. Grabar, C.C.; Griffith-Freeman, R.; Hommer, M.B.; Natan, M.J. Preparation and characterization of Au colloid monolayers. *Anal. Chem.* **1995**, *67*, 735.
97. Duyne, R.P.v.; Haller, K.L.; Altkorn, R.I. Spatially resolved surface enhanced Raman spectroscopy: Feasibility, intensity dependence on sampling area and attomole mass sensitivity. *Chem. Phys. Lett.* **1986**, *126*, 190.
98. Labande, C.; Astruc, D. Colloids as redox sensors: Recognition of H_2PO_4^- and HSO_4^- by amidoferrocenylalkylthiol-gold nanoparticles. *J. Chem. Soc., Chem. Commun.* **2000**, *12*, 1007.
99. Labande, A.; Ruiz, J.; Astruc, D. Supramolecular gold nanoparticles for the redox recognition of oxoanions: Syntheses, titrations, stereoelectronic effects, and selectivity. *J. Am. Chem. Soc.* **2002**, *124*, 1782.
100. Brochman, J.; Nelson, B.; Corn, R. Surface plasmon resonance imaging measurements of ultrathin organic films. *Annu. Rev. Phys. Chem.* **2000**, *51*, 41.
101. Malinsky, M.; Kelly, K.; Schatz, G.; Duyne, R.v. Chain length dependence and sensing capabilities of the localized surface plasmon resonance of silver nanoparticles chemically modified with alkanethiol self-assembled monolayers. *J. Am. Chem. Soc.* **2000**, *123*, 1471.
102. Bright, R.; Musick, M.; Natan, M. Preparation and characterization of Ag colloid monolayers. *Langmuir* **1998**, *14*, 5695.
103. Weisbecker, C.S.; Merritt, M.V.; Whitesides, G.M. Molecular self-assembly of aliphatic thiols on gold colloids. *Langmuir* **1996**, *12*, 3763.
104. Jensen, T.R.; Malinsky, M.D.; Haynes, C.L.; Van Duyne, R.P. Nanosphere lithography: Tunable localized surface plasmon resonance spectra of silver nanoparticles. *J. Phys. Chem., B* **2000**, *104*, 10549.

Nanoparticles: Synthesis in Polymer Substrates

Bai Yang

Junhu Zhang

Jilin University, Changchun, People's Republic of China

INTRODUCTION

Advanced materials composed of inorganic nanoparticles are currently one of the most dynamic areas of scientific research. These particles represent significant fundamental and commercial interest with a wide range of applications including the next generation of optics, electronics, catalysts, and sensors. In the past 20 years, with the increasing developments in nanoengineering, nanoelectronics, and nanobioelectronics, functional building blocks with which to construct microstructures and devices are under intensive investigation. Increasing attention has been paid to metal or semiconductor nanoparticles, which have also been called nanocrystals, nanoclusters, quantum dots, and Q particles.

Nanoparticles are in the size range of 1–100 nm, which lies between single atoms or molecules and bulk materials, and their chemical and physical properties differ markedly from those of the bulk solids. The reasons for these properties can be attributed to high surface area and quantum size effect, which is caused by the reduced size in three dimensions. One typical example is that the melting temperature of nanoparticles strongly depends on the particle size and is substantially lower than the bulk melting temperature. The melting point of 2.5-nm Au nanoparticles is $\sim 40\%$ lower than that of bulk gold. Similar behavior has been observed for CdS nanoparticles. At the same time, with the decrease in the number of atoms in the particles, their electronic properties also start to change. This is the so-called quantum size effect, which can be observed as a blue shift in the optical band gap or exciton energy. When the size of particles is reduced to nanometer scale, the number of atoms at the surfaces or grain boundaries of the crystalline regions is comparable to the number of those that are in the crystalline lattice itself. Physical and chemical properties, which are usually determined by the molecular structure of the bulk lattice, become increasingly dominated by the defect structure of the surface. During the preparation of nanoparticles, engineering of the size and surface structure is of both theoretical and practical importance, because it leads to mechanical, chemical, electrical, optical, magnetic, electro-optical, and magneto-optical properties that are substantially different from those observed for the corre-

sponding bulk materials. Chemists, biologists, and materials scientists have studied and reviewed the preparation and characterization of metal and semiconductor nanoparticles in detail, focusing on their physical and chemical properties.^[1–24]

Nanoparticles can be synthesized from a variety of materials with controllable sizes, shapes, and structures, but because of their high specific surface area and low surface energy, nanoparticles are not stable in ambient circumstances, and they must be incorporated in certain kinds of materials. Materials such as reverse micelles and surfactant vesicles,^[25] glass,^[26,27] zeolites,^[28,29] and polymers^[30–34] have been used as the substrate to prepare composite materials containing nanoparticles. During the preparation of such materials, the substrate not only can prevent the nanoparticles from aggregation, but also can accurately control their size and surface structure. In addition, in applications for optical, electrical, and magnetic devices, nanoparticles are mostly used in the form of thin films. Currently, such films can be made by spin coating,^[35–37] spraying,^[38,39] chemical deposition,^[40–42] electrical deposition,^[43–46] Langmuir–Blodgett (LB) technique,^[47–51] and layer-by-layer self-assembly (LBL) method.^[51–57]

In this article, we will focus on the preparation of nanoparticles in polymer matrices and the assembly of nanoparticles at interfaces.

PREPARATION OF NANOPARTICLES IN POLYMER MATRICES

Polymers have been considered one of the most important matrix materials for the preparation and application of nanoparticles because of their mechanical, optical, electrical, and thermal properties.^[30–34] In polymer networks, movements of nanometer-sized particles are restricted by the polymer chains, so aggregation is avoided and the nanoparticles are stabilized by the polymer networks. The size and size distribution of the particles can also be controlled by the concentration and density of metal ions. In order to prepare nanoparticles in polymer networks, the metal ions should be previously dispersed in the polymer

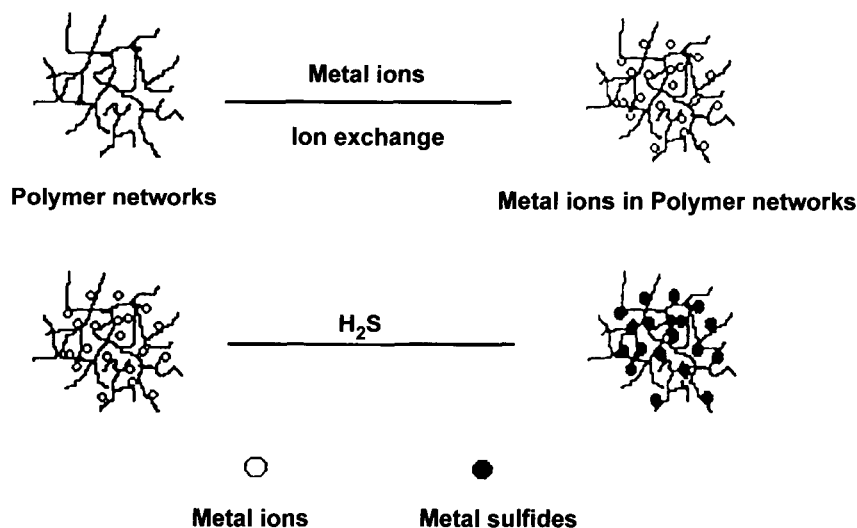


Fig. 1 Scheme for the assembly of metal sulfide nanoparticles in polymer networks. (From Ref. [64].)

networks. There have been two methods for the incorporation of metal ions into polymer networks.

The first method involves the introduction of metal ions into polymer networks by a metal-ion-containing monomer. PbS nanoparticles with an average size of 4.0 nm have been prepared in polymer networks by H₂S treatment of a copolymer of styrene and lead methacrylate.^[58,59] The concentration of the metal ions could be controlled by altering the relative proportion of the two monomers. Infrared (IR) measurements and the variations of the molecular weight of the copolymer before and after reacting with H₂S implied that there exist Pb–OOC bonds on the surface of the nanoparticles. PbS nanoparticles act as cross-linking agents, and the interaction of the polymer with the nanoparticles gives a surface chemical modification of the PbS nanoparticles, which strongly affects the optical properties of the nanoparticles.

The second method involves the introduction of metal ions into polymer networks by ion-exchange adsorption.^[60–65] As shown in Fig. 1,^[64] cross-linked polymer networks were formed by polymerization of styrene with a cross-linking agent. Then the polymerisate was sulfonated by sulfuric acid, and the product could be immersed in an aqueous solution that contained metal salts to adsorb metal ions into the polymer networks by exchange with H⁺ of –SO₃H. By varying the duration of the ion exchange and the concentration of the metal salt solution, we can control the concentration of the metal ions. The metal-ion-containing polymer networks could be dissolved in an organic solvent and then treated with H₂S gas, after which the solution turns yellow but without precipitation, which shows the formation of CdS nanoparticles. The resulting nanoparticles had a narrow particle size distribution. By

this method, CdS, Cu-doped ZnS, and Cu₂S/CdS/ZnS nanoparticles could also be prepared. All these results indicated that the polymer networks could effectively prevent the particles from growing and aggregating.

Metal or semiconductor nanoparticles may also be prepared in situ in the microdomain space formed in block copolymers.^[66–71] Block copolymers exhibit phase separation, which may help isolate the nanoparticles as they form. When a copolymer is used as the matrix for nanoparticles, the particle size is controlled by the composition of the copolymer and the concentration of metal ions. Nafion film, which is a type of ionic polymer and can adsorb metal ions by ion exchange, has also been used to prepare nanoparticles.^[72–75] Similarly, the size of the nanoparticles can be controlled by the initial metal ion concentration and subsequent thermal annealing treatment.

THIN FILMS OF NANOPARTICLES

Nanoparticles in LB Films

Transferring a well-packed monolayer from aqueous solution surfaces to solid substrates was demonstrated about 60 years ago by the Langmuir–Blodgett (LB) technique. Surfactant structures have also been used for direct assembly of metallic, semiconducting, and magnetic nanoparticles. This organization can be accomplished by adsorbing particles electrostatically to charged surfactant headgroups or by in situ generation of particles beneath monolayers at the air–water interface.^[47–51,76–83] Surfactant monolayers with attached nanoparticles can be transferred to solid supports using standard LB techniques.

Monolayers of surfactants have proven to be versatile as templates for the in situ growth of thin nanoparticle films. These monolayers are formed from a range of naturally occurring and synthetic surfactants or from a mixture of suitable surfactants, and their two-dimensional phase behavior and structure are well understood. Fendler and Meldrum have described the formation of sulfide semiconductor nanoparticulate films under a Langmuir monolayer of surfactants as follows:^[51] After the spreading of surfactant monolayer on the air–water interface of the metal ion solution with an atmosphere of H₂S, metal sulfide bonds formed at a large number of sites at the monolayer–aqueous interface. Well-separated nanoparticles of metal sulfide then formed and coalesced into interconnected arrays of semiconductor nanoparticles and a porous semiconductor particulate film composed of particles 20–40 Å thick and 30–80 Å in diameter. Once the first layer of semiconductor nanoparticulate film formed, subsequent layers were deposited up to a plateau thickness beyond which the film cannot grow. The presence of a monolayer with an appropriate surface charge is essential to the formation of the sulfide semiconductor nanoparticulate film. In the absence of a monolayer, infusion of H₂S over an aqueous metal ion solution resulted in the formation of large, irregular, and polydispersed metal sulfide particles, which precipitated in the bulk solution before settling to the bottom of the trough. Furthermore, the nanoparticulate film could not form under positively charged monolayers.

Thin films of nanoparticles can also be fabricated by spreading surfactant-stabilized nanoparticles on aqueous solutions and then transferring them to solid substrates by the LB technique. The technique can be regarded as analogous to monolayer formation from simple surfactants. Nanoparticulate films were formed at the air–water interface by dispersing surfactant-stabilized nanoparticles on an aqueous subphase, which was contained in a Langmuir trough. There are many intrinsic benefits to this method. The nanoparticles are prepared before the incorporation into the films, allowing one to control their dimensions, physical properties, and the particle size and distribution. Gao et al. have reported the fabrication of Fe₂O₃/polymer composite film using the LB method.^[77] Methacrylic acid was used as the surfactant to prepare Fe₂O₃ nanoparticles by the microemulsion method in a system of water–toluene. After a cross-linking agent together with an initiator were added into the organosol and reacted under ultrasonic stirring, an organic–inorganic composite microgel was obtained. This composite microgel showed good amphiphilic properties and could be transferred onto solid substrates from a pure water interface using the LB technique. Infrared and UV–visible (UV–vis) spectra of the film showed the presence of some

residual vinyl groups, which means that the microgel could be further polymerized. Polymerization of surfactant in the composite films improved the stability of the LB film.

Assembly of Nanoparticle Monolayers

Solution-based approaches to surface assembly of metal and semiconductor nanoparticles typically involve electrostatic or covalent binding of the particle to a surface-bound molecular or polymeric thin film.^[84–90] Self-assembly of metal nanoparticle monolayers on polymer-coated substrates yields macroscopic surfaces that are highly active for surface-enhanced Raman scattering (SERS).^[85–87] Nanoparticles are bound to the substrate through multiple bonds between the colloidal metal and functional groups on the polymer such as cyanide (CN), amine (NH₂), and thiol (SH). Self-assembly of nanoparticles onto the oppositely charged substrate surface is governed by a delicate balance of the adsorption and desorption equilibria. The efficient adsorption of one monolayer of nanoparticles onto the oppositely charged substrate surface is the objective of the immersion step. Preventing the desorption of the nanoparticles during the rinsing process is of equal importance. The optimization of the self-assembly in terms of maximizing the adsorption of nanoparticles from their dispersions and minimizing their desorption upon rinsing requires the correct selection of stabilizers and the careful control of the kinetics of the processes.

The deposition process may also be performed on a substrate modified by an LB film, which may give a charged surface. As we have reported,^[91] one monolayer of PbI₂ nanoparticles can be adsorbed on a substrate modified by LB films through electrostatic interactions. First, we transferred two layers of Y-type LB film of stearic acid onto some hydrophilic substrates, which allowed one layer of bipolar pyridinium to be adsorbed onto the carboxylic surface of the LB film. Finally, we deposited one layer of anionic PbI₂ after the bipolar pyridinium. The structure of the self-assembled monolayer film is shown in Fig. 2. Substrates such as Si, CaF₂, quartz, glass, Ag, and Au are widely used for LB processes, so LB film-covered slides can provide a wide range of substrates for a self-assembled monolayer of nanoparticles. In order to observe the PbI₂ nanoparticles monolayer in the self-assembled film with transmission electron microscopy (TEM), a copper grid covered with a very thin layer of formvar was used as the LB film substrate. A TEM photograph of the self-assembly film shows that all the PbI₂ nanoparticles are round and closely packed, but without any large aggregates. As a comparison, one droplet of the PbI₂ solution was dropped onto the

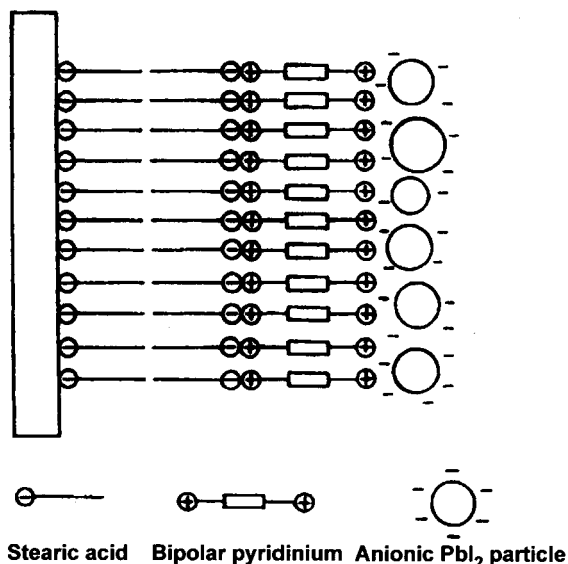


Fig. 2 Scheme for one monolayer of PbI_2 nanoparticles in the stearic acid-bipolar pyridinium- PbI_2 four layer structure. (From Ref. [91].)

grid and blown dry with N_2 . TEM measurements showed that the small particles had aggregated into large ones during the evaporation in the sample preparation. This contrast proves that the bipolar pyridinium film interacts with the nanoparticles strongly and can effectively keep the small particles from aggregating.

Covalent attachment strategies often take advantage of the reactivity of the outer shell atoms in the nanoparticles. Many metallic and semiconductor nanoparticles (Au, Ag, CdS, CdSe) have a high affinity for amine and/or thiol moieties.^[54] For example, Colvin et al. have covalently attached CdS nanoparticles to Au and Al substrates using bifunctional cross-linkers.^[84] Natan and coworkers have assembled Au and Ag nanoparticles on $-\text{NH}_2$ and $-\text{SH}$ terminated organosilane polymers on silica substrates.^[85,87] The kinetics of this surface-assembly reaction have been investigated in some detail, affording control over the number of particles on the surface.

Alternatively, close-packed monolayers of alkanethiol-stabilized nanoparticles have been formed by solvent evaporation.^[17,18] Self-assembled arrays involve self-organization of size-selected nanoparticles encapsulated in protective, compact organic coatings into monolayers, thin films, and superlattices. A key step in this process is the fabrication of size- and shape-controlled nanoparticle superlattices that can grow large enough for technological applications. In this case, the length of the organic ligand defines the distance between particles. This distance has a pronounced effect on the electronic properties of the resulting structure. Particles that can be self-assembled are

usually smaller than 10 nm in size, and it is in this size range that many exciting and unusual physical properties are enhanced.

Layer-by-Layer Assembly of Nanoparticles

The LBL method developed by G. Decher is one of the most promising new methods of thin film deposition, and it is often used for oppositely charged polymers.^[92-94] Recently, it has also been successfully applied to thin films of nanoparticles and other inorganic materials,^[51-57] such as Au,^[95-97] Ag,^[98-101] CdS,^[102] PbS,^[103] Fe_3O_4 ,^[104-106] CdSe,^[107-109] HgTe,^[110] TiO_2 ,^[111] SiO_2 ,^[112-114] and others.^[115-119] Its simplicity and universality combined with the resulting high quality of coatings and uniform distribution of nanoparticles open broad perspectives for this technique both in research and in industry. Compared with other techniques for the fabrication of thin films of nanoparticles, the LBL method has two main advantages: 1) simplicity (the relative ease of preparation and versatility have contributed to the rapid development of this method), 2) universality (tolerance of the substrate shapes and materials and the dual, organic-inorganic nature of the coating).

The LBL assembly of nanoparticles can be described as the sequential adsorption of monolayers of nanoparticles on positively charged layers of a polyelectrolyte. Interestingly, purely inorganic LBL films were described more than 30 years ago.^[120] The deposition of the films can be performed in a cyclic manner, which is made possible by the overcompensation of surface charge, which often takes place when polyelectrolytes and other high molecular weight species are adsorbed onto a solid-liquid interface. The construction of an LBL film of nanoparticles requires four simple steps:^[52] 1) prime a cleaned substrate by absorbing a layer of surfactant or polyelectrolyte onto its surface; 2) immerse the primed substrate in a dilute aqueous solution of a cationic or anionic polyelectrolyte for the optimized length of time for adsorption of a monolayer; 3) rinse and dry the substrate; 4) immerse the polyelectrolyte monolayer covered substrate in a dilute dispersion of oppositely charged semiconductor nanoparticles, also for the optimized length of time for adsorption of a monolayer of nanoparticles. These four operations complete the self-assembly of one polyelectrolyte-nanoparticle bilayer, and by repeating them, multilayered self-assembly films of polyelectrolyte and nanoparticles can be fabricated. The electrostatic attraction between semiconductor colloids and a layer of polyelectrolytes ensures the facile adsorption. At the same time, the electrostatic repulsion between similarly charged species in solution limits the thickness of the newly formed thin layer of nanoparticles.

Our group has reported several kinds of LBL films of nanoparticles,^[121–133] among which we have also fabricated a CdS nanoparticle/cationic polyelectrolyte multilayer film based on electrostatic interactions.^[122] An aqueous solution of CdS nanoparticles was prepared by the addition of mercaptoacetic acid as a stabilizer agent. Infrared measurements imply that mercaptoacetic acid was chemically modified on the surface of CdS nanoparticles through thiol groups, with carboxylic acid groups pointing to the solvent, and the carboxylic acid group was in a state of COO^- , which made it possible to use the surface-modified CdS nanoparticles as the negatively charged species in the LBL assembly process. A quartz substrate covered with aminopropylsilane was prepared by treating with the vapor of 3-aminopropyltriethoxysilane and then reacted with HCl solution to become positively charged. Then, using the LBL method, negatively charged nanoparticles and positively charged polyelectrolyte could be alternatively deposited on the substrate. The structure of the LBL film is shown in Fig. 3. UV-vis absorption spectroscopy was used to monitor the LBL assembly process, and the similarity of the absorption spectra of the alternating films to that of the CdS nanoparticles in the visible region implies that the CdS nanoparticles were successfully assembled in the alternating film. In the UV-vis spectra (Fig. 4) of multilayer films with different numbers of layers, a linear increase of the absorbance of CdS nanoparticles could be observed, which indicates that the oppositely charged species were deposited equivalently in different steps during the LBL process. The deposition process was also monitored by

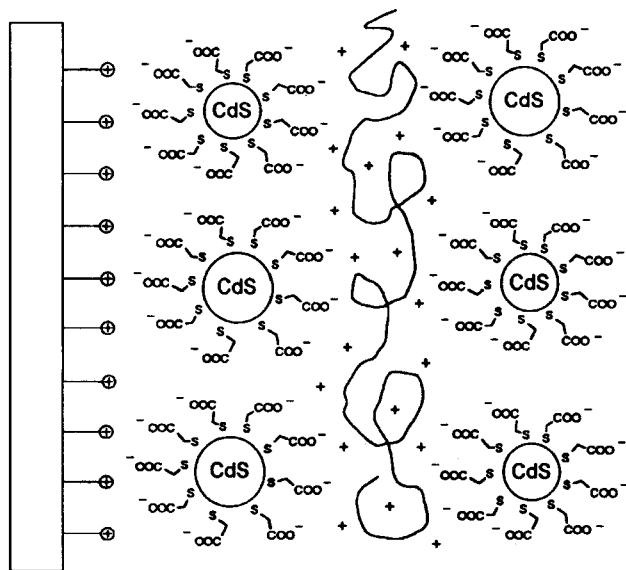


Fig. 3 Scheme for the assembly of CdS nanoparticles in LBL films. (From Ref. [122].)

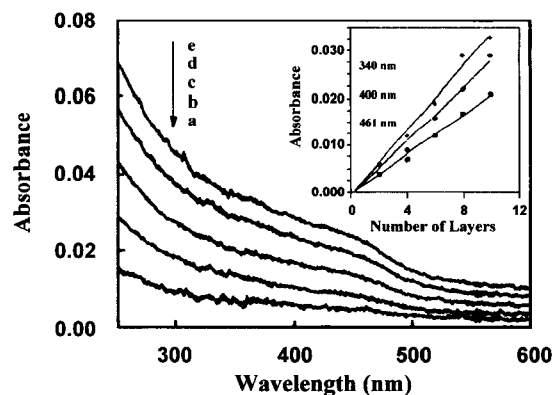


Fig. 4 UV-vis absorption spectra of the LBL films of CdS nanoparticles and a cationic polyelectrolyte with different numbers of layers. Inset: absorbance vs. number of layers at 340, 400, and 461 nm. (From Ref. [122].)

quartz crystal microbalance (QCM), which can detect the adsorption of the charged species in the LBL films. The QCM results of the LBL film in different steps also show a uniform deposition process.

The driving force of the LBL process of nanoparticles could be not only electrostatic interactions, but also coordinative interactions^[134,135] or hydrogen bonds.^[136,137] As is well known, there exist typical coordinate complexations between pyridine and some transition metals. Based on coordinative bonds, CdS nanoparticles with general Cd-rich surfaces could be assembled in LBL films by alternating deposition with poly(4-vinylpyridine) (PVP). The construction of CdS/PVP multilayer film is shown in Fig. 5. The substrate was modified first to create a surface covered with pyridine groups. The resulting substrate was then dipped into a colloidal CdS solution to adsorb one layer of CdS nanoparticles. After being washed, the substrate was transferred to the PVP solution to adsorb one PVP layer. The CdS/PVP multilayer films were prepared by repeating the above steps. UV-vis spectra were used to monitor the self-assembly process, confirming a stepwise and uniform assembly process. The driving force for the CdS/PVP multilayer film was identified by IR spectroscopy. By comparing IR spectra of pure PVP and the multilayer film (Fig. 6), a new peak at 1610 cm^{-1} appeared in the spectrum of the multilayer film. Since the coordinate complexation between pyridine groups and metal ions usually exhibits this band because of the formation of coordination bonds, we considered that CdS nanoparticles were assembled into the multilayer film based on the formation of coordinative bonds between the surface Cd atoms of CdS nanoparticles and the pyridine groups of PVP. We also found that CdS nanoparticles that have S-rich surfaces could not be

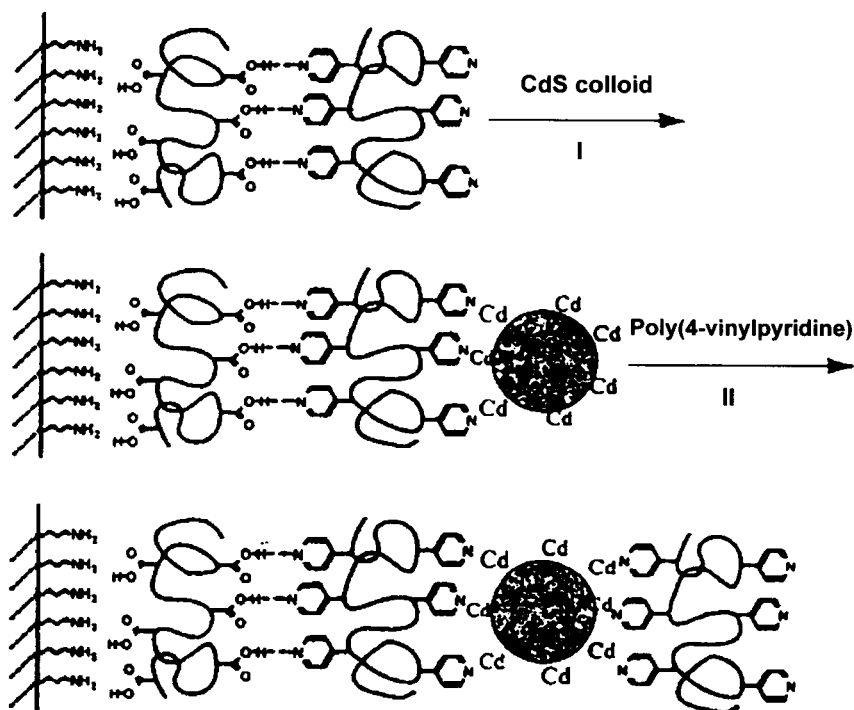


Fig. 5 Scheme for the build-up of alternating films of PVP/CdS nanoparticles based on coordinative bonds. (From Ref. [134].)

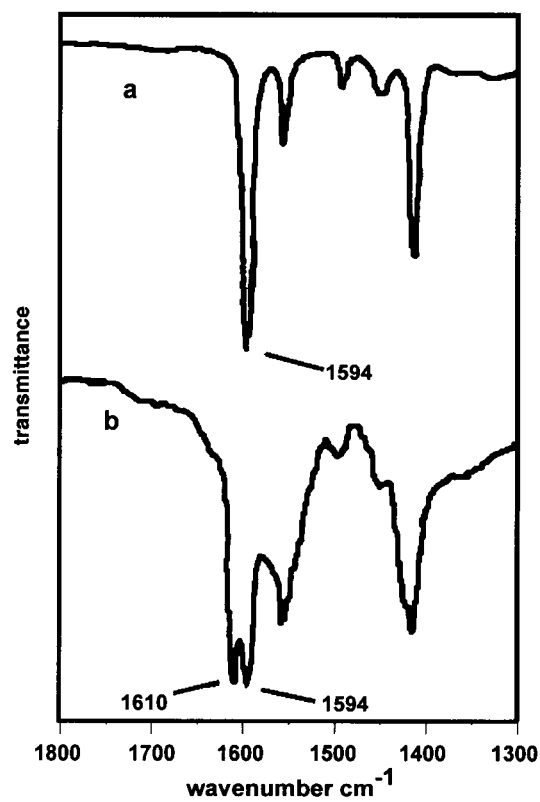


Fig. 6 Infrared spectra of (a) pure PVP and (b) PVP/CdS multilayers. (From Ref. [134].)

assembled with PVP, which ensures the driving force to be coordinative bonds.

It has recently been reported that nanoparticles could also be formed in situ in LBL films of polyelectrolytes.^[138–141] Silver nanoparticles were prepared in situ within poly(acrylic acid) (PAA) and poly(allylamine hydrochloride) (PAH) multilayer films. Carboxylic acid groups in the PAH/PAA-based multilayers bind silver cations by ion exchange with the acid protons. Subsequent reduction forms metallic nanoparticles. Because PAA has a pH-dependent degree of ionization, the multilayer film can be fabricated with different concentrations of free acid groups that are available to bind silver cations depending on the multilayer assembly pH. The nanoparticle size and silver concentration can be controllably increased by reducing the assembly pH of PAH/PAA-based multilayers. Furthermore, because the metal-binding carboxylic acid groups are reprotonated upon nanoparticle formation, the synthesis methodology can be repeatedly cycled to incorporate more silver cations, which increases the size and concentration of silver nanoparticles.

Recently, the LBL process has been applied to the surface modification of colloidal microspheres, which represent attractive building blocks from which to create ordered and complex materials. Möhwald and coworkers have demonstrated the LBL assembly of polyelectrolytes on the surface of colloidal latex spheres.^[142,143] The main advantage of this LBL process is that the film thickness on the colloidal spheres could be fine-tuned by altering the number of layers deposited and the solution conditions from which the polymers are adsorbed. More recently, nanoparticles of SiO₂, Ag, and Au have also been assembled on the surface of colloidal microspheres.^[24,144–150] Assembly of nanoparticles on the surface of colloidal microspheres resulted in the formation of nanoparticle-coated microspheres. By removing the colloidal microspheres template through calcination or dissolution, hollow spheres of metal or silica were formed, which may find applications in catalysis, sensing, optics, and separations.

CONCLUSION

With the development of nanoscience and nanotechnology, nanosized building blocks as nanoparticles will attract more and more attention. In both bulk and film structures, nanoparticles can be stabilized and assembled. We have introduced the incorporation of polymers as the substrates for nanoparticles and the assembly of nanoparticles in thin film structures such as LB films, self-assembled monolayers, and LBL multilayers, which have proved to have potential applications in optics, electron-

ics, magnetics, catalysis, and sensors. Research will now focus on controlling the size, shape, and surface structure of nanoparticles, as well as fabricating new nanostructured materials and looking for new applications. The assembly of nanoparticles on microscale substrates such as patterned surfaces or microspheres, and the physical and chemical properties of single nanoparticles continue to invite our scrutiny.

REFERENCES

1. Kayanuma, Y. Quantum-size effects of interacting electrons and holes in semiconductor microcrystals with spherical shape. *Phys. Rev., B* **1988**, *38* (14), 9797–9805.
2. Bard, A.J. Semiconductor particles and arrays for the photoelectrochemical utilization of solar energy. *Ber. Bunsenges. Phys. Chem.* **1988**, *92* (11), 1187–1194.
3. Steigerwald, M.L.; Brus, L.E. Synthesis, stabilization, and electronic structure of quantum semiconductor nanoclusters. *Annu. Rev. Mater. Sci.* **1989**, *19*, 471–495.
4. Henglein, A. Small-particle research: Physicochemical properties of extremely small colloidal metal and semiconductor particles. *Chem. Rev.* **1989**, *89* (8), 1861–1873.
5. Steigerwald, M.L.; Brus, L.E. Semiconductor crystallites: A class of large molecules. *Acc. Chem. Res.* **1990**, *23* (6), 183–188.
6. Wang, Y. Nonlinear optical properties of nanometer-sized semiconductor clusters. *Acc. Chem. Res.* **1991**, *24* (5), 133–139.
7. Wang, Y.; Herron, N. Nanometer-sized semiconductor clusters: Materials synthesis, quantum size effects, and photophysical properties. *J. Phys. Chem.* **1991**, *95* (2), 525–532.
8. Nair, S.V.; Ramaiah, L.M.; Rustagi, K.C. Electron states in a quantum dot in an effective-bond-orbital model. *Phys. Rev., B* **1992**, *45* (11), 5969–5979.
9. Schmid, G. Large clusters and colloids: Metals in the embryonic state. *Chem. Rev.* **1992**, *92* (8), 1709–1727.
10. Weller, H. Quantized semiconductor particles: A novel state of matter for materials science. *Adv. Mater.* **1993**, *5* (2), 88–95.
11. Weller, H. Colloidal semiconductor Q-particles—Chemistry in the transition region between solid-state and molecules. *Angew. Chem., Int. Ed.* **1993**, *32* (1), 41–53.
12. Linsebigler, A.L.; Lu, G.Q.; Yates, Y.T., Jr. Photocatalysis on TiO₂ surfaces: Principles,

- mechanisms, and selected results. *Chem. Rev.* **1995**, *95* (3), 735–758.
13. Henglein, A. Electronics of colloidal nanometer particles. *Ber. Bunsenges. Phys. Chem.* **1995**, *99* (7), 903–913.
 14. Alivisatos, A.P. Semiconductor cluster, nanocrystals, and quantum dots. *Science* **1996**, *271*, 933–937.
 15. Alivisatos, A.P. Perspectives on the physical chemistry of semiconductor nanocrystals. *J. Phys. Chem.* **1996**, *100* (31), 13226–13239.
 16. Henglein, A. Nanoclusters of semiconductors and metals, colloidal nano-particles of semiconductors and metals: Electronic structure and processes. *Ber. Bunsenges. Phys. Chem.* **1997**, *101* (11), 1562–1572.
 17. Wang, Z.L. Structural analysis of self-assembling nanocrystal superlattices. *Adv. Mater.* **1998**, *10* (1), 13–30.
 18. Wang, Z.L. Transmission electron microscopy of shape-controlled nanocrystals and their assemblies. *J. Phys. Chem., B* **2000**, *104* (6), 1153–1175.
 19. Templeton, A.C.; Wuelfing, W.P.; Murray, R.W. Monolayer-protected cluster molecules. *Acc. Chem. Res.* **2000**, *33* (1), 27–36.
 20. Link, S.; El-Sayed, M.A. Spectral properties and relaxation dynamics of surface plasmon electronic oscillations in gold and silver nanodots and nanorods. *J. Phys. Chem., B* **1999**, *103* (40), 8410–8426.
 21. El-Sayed, M.A. Some interesting properties of metals confined in time and nanometer space of different shapes. *Acc. Chem. Res.* **2001**, *34* (4), 257–264.
 22. Gehr, R.J.; Boyd, R.W. Optical properties of nanostructured optical materials. *Chem. Mater.* **1996**, *8* (8), 1807–1819.
 23. Schärfl, W. Crosslinked spherical nanoparticles with core-shell topology. *Adv. Mater.* **2000**, *12* (24), 1899–1908.
 24. Caruso, F. Nanoengineering of particle surfaces. *Adv. Mater.* **2001**, *13* (1), 11–22.
 25. Fendler, J.H. Atomic and molecular clusters in membrane mimetic chemistry. *Chem. Rev.* **1987**, *87* (5), 877–899.
 26. Ekimov, A.I.; Efros, A.L.; Onushchenko, A.A. Quantum size effect in semiconductor microcrystals. *Solid State Commun.* **1985**, *56* (11), 921–924.
 27. Jain, R.K.; Lind, R.C. Degenerate 4-wave mixing in semiconductor-doped glasses. *J. Opt. Soc. Am.* **1983**, *73* (5), 647–653.
 28. Wang, Y.; Herron, N.J. Optical-properties of CdS and PbS clusters encapsulated in zeolites. *J. Phys. Chem.* **1987**, *91* (2), 257–260.
 29. Moller, K.; Bein, T.; Herron, N.; Mahler, W.; Wang, Y. Encapsulation of lead sulfide molecular clusters into solid matrices. Structural analysis with X-ray absorption spectroscopy. *Inorg. Chem.* **1989**, *28* (15), 2914–2919.
 30. Wang, Y.; Suna, A.; Mahler, W.; Kasowski, R. PbS in polymers. From molecules to bulk solids. *J. Chem. Phys.* **1987**, *87* (12), 7315–7322.
 31. Ziolo, R.F.; Giannelis, E.P.; Weinstein, B.A.; O'Horo, M.P.; Ganguly, B.N.; Mehrotra, V.; Russell, M.W.; Huffman, D.R. Matrix-mediated synthesis of nanocrystalline γ -Fe₂O₃: A new optically transparent magnetic material. *Science* **1992**, *257*, 219–222.
 32. Cahn, R.W. Nanostructures come of age. *Nature* **1992**, *359*, 591–592.
 33. Moffitt, M.; Eisenberg, A. Size control of nanoparticles in semiconductor-polymer composites. I. Control via multiplet aggregation numbers in styrene-based random ionomers. *Chem. Mater.* **1995**, *7* (6), 1178–1184.
 34. Beecroft, L.L.; Ober, C.K. Nanocomposite materials for optical applications. *Chem. Mater.* **1997**, *9* (6), 1302–1317.
 35. De, G.T. Sol-gel synthesis of metal nanoclusters-silica composite films. *J. Sol-Gel Sci. Technol.* **1998**, *11* (3), 289–298.
 36. Fan, H.Y.; Zhou, Y.Q.; Lopez, G.P. Stepwise assembly in three dimensions: Preparation and characterization of layered gold nanoparticles in porous silica matrices. *Adv. Mater.* **1997**, *9* (9), 728–731.
 37. Barnes, K.A.; Karim, A.; Douglas, J.F.; Nakatani, A.I.; Gruell, H.; Amis, E.J. Suppression of dewetting in nanoparticle-filled polymer films. *Macromolecules* **2000**, *33* (11), 4177–4185.
 38. Salata, O.V.; Dobson, P.J.; Hull, P.J.; Hutchison, J.L. Fabrication of PbS nanoparticles embedded in a polymer film by a gas-aerosol reactive electrostatic deposition technique. *Adv. Mater.* **1994**, *6* (10), 772–775.
 39. Schulz, D.L.; Pehnt, M.; Rose, D.H.; Urgiles, E.; Cahill, A.F.; Niles, D.W.; Jones, K.M.; Ellingson, R.J.; Curtis, C.J.; Ginley, D.S. CdTe thin films from nanoparticle precursors by spray deposition. *Chem. Mater.* **1997**, *9* (4), 889–900.
 40. Gorer, S.; Hodes, G. Nanostructure and Size Quantization in Chemical Solution Deposited Semiconductor Films. In *Studies in Surface Science and Catalysis: Semiconductor Nanoclusters—Physical, Chemical, and Catalytic Aspects*; Kamat, P.V., Meisel, D., Eds.; Elsevier Science B.V.: Netherlands, 1997; Vol. 103, 297–320.
 41. Gorer, S.; Albuyaron, A.; Hodes, G. Chemical

- solution deposition of lead selenide films—A mechanistic and structural study. *Chem. Mater.* **1995**, *7* (6), 1243–1256.
42. Pastoriza-Santos, I.; Serra-Rodríguez, C.; Liz-Marzán, L.M. Self-assembly of silver particle monolayers on glass from Ag^+ solution in DMF. *J. Colloid Interface Sci.* **2000**, *221*, 236–241.
 43. Rajeshwar, K.; Tacconi, N.R. Electrodeposition and Characterization of Nanocrystalline Semiconductor Films. In *Studies in Surface Science and Catalysis: Semiconductor Nanoclusters—Physical, Chemical, and Catalytic Aspects*; Kamat, P.V., Meisel, D., Eds.; Elsevier Science B.V.: Netherlands, 1997; Vol. 103, 321–351.
 44. Zoval, J.V.; Stiger, R.M.; Biernacki, P.R.; Penner, R.M. Electrochemical deposition of silver nanocrystallites on the atomically smooth graphite basal plane. *J. Phys. Chem.* **1996**, *100* (2), 837–844.
 45. Zoval, J.V.; Biernacki, P.R.; Penner, R.M. Implementation of electrochemically synthesized silver nanocrystallites for the preferential SERS enhancement of defect modes on thermally etched graphite surfaces. *Anal. Chem.* **1996**, *68* (9), 1585–1592.
 46. El-Kouedi, M.; Sandrock, M.L.; Seugling, C.J.; Foss, C.A. Electrochemical synthesis of asymmetric gold–silver iodide nanoparticle composite films. *Chem. Mater.* **1998**, *10* (11), 3287–3289.
 47. Zhao, X.K.; Yuan, Y.X.; Fendler, J.H. Size-quantized semiconductor particles formed at monolayer surfaces. *J. Chem. Soc., Chem. Commun.* **1990**, 1248–1252.
 48. Zhao, X.K.; Xu, S.Q.; Fendler, J.H. Ultrasmall magnetic particles in Langmuir–Blodgett films. *J. Phys. Chem.* **1990**, *94* (6), 2573–2581.
 49. Zhao, X.K.; Fendler, J.H. Size quantization in semiconductor particulate films. *J. Phys. Chem.* **1991**, *95* (9), 3716–3723.
 50. Zhao, X.K.; Fendler, J.H. Semiconductor particles formed at monolayer surfaces. *Langmuir* **1991**, *7* (3), 520–524.
 51. Fendler, J.H.; Meldrum, F.C. The colloid chemical approach to nanostructured materials. *Adv. Mater.* **1995**, *7* (7), 607–632.
 52. Fendler, J.H. Self-assembled nanostructured materials. *Chem. Mater.* **1996**, *8* (8), 1616–1624.
 53. Schmid, G.; Chi, L.F. Metal clusters and colloids. *Adv. Mater.* **1998**, *10* (7), 515–526.
 54. Feldheim, D.L.; Keating, C.D. Self-assembly of single electron transistors and related devices. *Chem. Soc. Rev.* **1998**, *27* (1), 1–12.
 55. Shipway, A.N.; Katz, E.; Willner, I. Nanoparticle arrays on surfaces for electronic, optical, and sensor applications. *Chem., Phys. Chem.* **2000**, *1* (1), 18–52.
 56. Shipway, A.N.; Willner, I. Nanoparticles as structural functional units in surface-confined architectures. *Chem. Commun.* **2001**, 2035–2045.
 57. Fendler, J.H. Chemical self-assembly for electronic applications. *Chem. Mater.* **2001**, *13* (10), 3196–3210.
 58. Gao, M.Y.; Yang, Y.; Yang, B.; Bian, F.L.; Shen, J.C. Synthesis of PbS nanoparticles in polymer matrices. *Chem. Commun.* **1994**, 2779–2780.
 59. Gao, M.Y.; Yang, Y.; Yang, B.; Shen, J.C. Effect of the surface chemical modification on the optical properties of polymer-stabilized PbS nanoparticles. *Faraday Discuss.* **1995**, *91* (22), 4121–4125.
 60. Huang, J.M.; Yang, Y.; Yang, B.; Liu, S.Y.; Shen, J.C. Synthesis of the CdS nanoparticles in polymer networks. *Polym. Bull.* **1996**, *36* (3), 337–340.
 61. Huang, J.M.; Yang, Y.; Yang, B.; Liu, S.Y.; Shen, J.C. Preparation and characterization of $\text{Cu}_2\text{S}/\text{CdS}/\text{ZnS}$ nanocomposite in polymeric networks. *Polym. Bull.* **1996**, *37* (5), 679–682.
 62. Huang, J.M.; Yang, Y.; Xue, S.H.; Yang, B.; Liu, S.Y.; Shen, J.C. Photoluminescence and electroluminescence of $\text{ZnS}:\text{Cu}$ nanocrystals in polymeric networks. *Appl. Phys. Lett.* **1997**, *70* (18), 2335–2337.
 63. Yang, Y.; Huang, J.M.; Yang, B.; Liu, S.Y.; Shen, J.C. Electroluminescence from ZnS/CdS nanocrystals/polymer composite. *Synth. Met.* **1997**, *91* (1–3), 347–349.
 64. Huang, J.M.; Yang, Y.; Yang, B.; Liu, S.Y.; Shen, J.C. Assembly and applications of the inorganic nanocrystals in polymer networks. *Thin Solid Films* **1998**, 327–329, 536–540.
 65. Yang, Y.; Huang, J.M.; Liu, S.Y.; Shen, J.C. Preparation, characterization and electroluminescence of ZnS nanocrystals in a polymer matrix. *J. Mater. Chem.* **1997**, *7* (1), 131–133.
 66. Moffitt, M.; McMahon, L.; Pessel, V.; Eisenberg, A. Size control of nanoparticles in semiconductor–polymer composites. 2. Control via sizes of spherical ionic microdomains in styrene-based diblock ionomers. *Chem. Mater.* **1995**, *7* (6), 1185–1192.
 67. Sankaran, V.; Cummins, C.C.; Schrock, R.R.; Cohen, R.E.; Silbey, R.J. Small PbS clusters prepared via ROMP block copolymer technology. *J. Am. Chem. Soc.* **1990**, *112* (19), 6858–6859.
 68. Sankaran, V.; Yue, J.; Cohen, R.E.; Schrock, R.R.; Silbey, R.J. Synthesis of zinc sulfide clusters and zinc particles within microphase-separated domains of organometallic block copolymers. *Chem. Mater.* **1993**, *5* (8), 1133–1142.
 69. Selvan, S.T.; Spatz, J.P.; Klok, H.A.; Möller, M.

- Gold-polypyrrole core-shell particles in diblock copolymer micelles. *Adv. Mater.* **1998**, *10* (2), 132–134.
70. Bronstein, L.M.; Sidorov, S.N.; Valetsky, P.M.; Hartmann, J.; Cölfen, H.; Antonietti, M. Induced micellization by interaction of poly(2-vinylpyridine)-block-poly(ethylene oxide) with metal compounds. Micelle characteristics and metal nanoparticle formation. *Langmuir* **1999**, *15* (19), 6256–6262.
71. Hashimoto, T.; Harada, M.; Sakamoto, N. Incorporation of metal nanoparticles into block copolymer nanodomains via in-situ reduction of metal ions in microdomain space. *Macromolecules* **1999**, *32* (20), 6867–6870.
72. Hilinski, E.F.; Lucas, P.A. A picosecond bleaching study of quantum-confined cadmium sulfide microcrystallites in a polymer film. *J. Chem. Phys.* **1988**, *89* (6), 3435–3441.
73. Kuczynski, J.P.; Milosavljevic, B.H.; Thomas, J.K. Photophysical properties of cadmium sulfide in nafion film. *J. Phys. Chem.* **1984**, *88* (5), 980–984.
74. Kakuta, N.; White, J.M.; Campion, A.; Bard, A.J.; Fox, M.A.; Webber, S.E. Surface analysis of semiconductor-incorporated polymer systems. 1. Nafion and CdS-nafion. *J. Phys. Chem.* **1985**, *89* (1), 48–52.
75. Wang, Y.; Suna, A.; McHugh, J. Optical transient bleaching of quantum-confined CdS clusters: The effects of surface-trapped electron-hole pairs. *J. Chem. Phys.* **1990**, *92* (11), 6927–6939.
76. Peng, X.G.; Zhang, Y.; Yang, J.; Zou, B.S.; Xiao, L.Z.; Li, T.J. Formation of Nanoparticulate Fe₂O₃-stearate multiplayer through the Langmuir-Blodgett method. *J. Phys. Chem.* **1992**, *96* (8), 3412–3415.
77. Gao, M.Y.; Peng, X.G.; Shen, J.C. Polymer Langmuir-Blodgett film of organic-inorganic (Fe₂O₃) composite microgel. *Thin Solid Films* **1994**, *248*, 106–109.
78. Peng, X.G.; Lu, R.; Zhao, Y.Y.; Qu, L.H.; Chen, H.Y.; Li, T.J. Control of distance and size of inorganic nanoparticles by organic matrices in ordered LB monolayers. *J. Phys. Chem.* **1994**, *98* (28), 7052–7055.
79. Nakaya, T.; Li, Y.J.; Shibata, K. Preparation of ultrafine particle multilayers using the Langmuir-Blodgett technique. *J. Mater. Chem.* **1996**, *6* (5), 691–697.
80. Kang, Y.S.; Risbud, S.; Rabolt, J.; Stroeve, P. Brewster angle microscopy study of a magnetic nanoparticle/polymer complex at the air/water interface. *Langmuir* **1996**, *12* (18), 4345–4349.
81. Nabok, A.V.; Richardson, T. Cadmium sulfide nanoparticles in Langmuir-Blodgett films of calixarenes. *Langmuir* **1997**, *13* (12), 3198–3210.
82. Li, L.S.; Qu, L.H.; Wang, L.J.; Lu, R.; Peng, X.G.; Zhao, Y.Y.; Li, T.J. Preparation and characterization of quantum-sized PbS grown in amphiphilic oligomer Langmuir-Blodgett monolayers. *Langmuir* **1997**, *13* (23), 6183–6187.
83. Lefebure, S.; Ménager, C.; Cabuil, V.; Assenheimer, M.; Gallet, F.; Flament, C. Langmuir monolayers of monodispersed magnetic nanoparticles coated with a surfactant. *J. Phys. Chem., B* **1998**, *102* (15), 2733–2738.
84. Colvin, V.L.; Goldstein, A.N.; Alivisatos, A.P. Semiconductor nanocrystals covalently bound to metal surfaces with self-assembled monolayers. *J. Am. Chem. Soc.* **1992**, *114* (13), 5221–5230.
85. Freeman, R.G.; Grabar, K.C.; Allison, K.J.; Bright, R.M.; Davis, J.A.; Guthrie, A.P.; Hommer, M.B.; Jackson, M.A.; Smith, P.C.; Walter, D.G.; Natan, M.J. Self-assembled metal colloid monolayers: An approach to SERS substrates. *Science* **1995**, *267*, 1629–1632.
86. Chumanov, G.; Sokolov, K.; Gregory, B.W.; Cotton, T.M. Colloidal metal films as a substrate for surface-enhanced spectroscopy. *J. Phys. Chem.* **1995**, *99* (23), 9466–9471.
87. Bright, R.M.; Musick, M.D.; Natan, M.J. Preparation and characterization of Ag colloid monolayers. *Langmuir* **1998**, *14* (20), 5695–5701.
88. Bandyopadhyay, K.; Patil, V.; Vijayamohan, K.; Sastry, M. Adsorption of silver colloidal particles through covalent linkage to self-assembled monolayers. *Langmuir* **1997**, *13* (20), 5244–5248.
89. Patil, V.; Mayya, K.S.; Sastry, M. Long-term stability of self-assembled monolayers of an aromatic bifunctional molecule during adsorption of silver colloidal particles. *Langmuir* **1999**, *15* (19), 6587–6590.
90. Patolsky, F.; Ranjit, K.T.; Lichtenstein, A.; Willner, I. Dendritic amplification of DNA analysis by oligonucleotide-functionalized Au-nanoparticles. *Chem. Commun.* **2000**, 1025–1026.
91. Gao, M.Y.; Zhang, X.; Yang, B.; Shen, J.C. A monolayer of PbI₂ nanoparticles adsorbed on MD-LB film. *Chem. Commun.* **1994**, 2229–2230.
92. Decher, G. Fuzzy nanoassembled: Toward layered polymeric multicomposites. *Science* **1997**, *277*, 1232–1237.
93. Bertrand, P.; Jonas, A.; Laschewsky, A.; Legras, R. Ultrathin polymer coatings by complexation of polyelectrolytes at interfaces: Suitable materials, structure and properties. *Macromol. Rapid Commun.* **2000**, *21* (7), 319–348.

94. Hammond, P.T. Recent explorations in electrostatic multiplayer thin film assembly. *Curr. Opin. Colloid Interface Sci.* **2000**, *4* (6), 430–442.
95. Schmitt, J.; Decher, G.; Dressick, W.J.; Brandow, S.L.; Geer, R.E.; Shashidhar, R.; Calvert, J.M.; Schmitt, J. Metal nanoparticle/polymer superlattice films: Fabrication and control of layer structure. *Adv. Mater.* **1997**, *9* (1), 61–65.
96. Blonder, R.; Sheeney, L.; Willner, I. Three-dimensional redox-active layered composites of Au–Au, Ag–Ag and Au–Ag colloids. *Chem. Commun.* **1998**, 1393–1394.
97. Musick, M.D.; Keating, C.D.; Lyon, L.A.; Botsko, S.L.; Peña, D.J.; Holliway, W.D.; McEvoy, T.M.; Richardson, J.N.; Natan, M.J. Metal films prepared by stepwise assembly. 2. Construction and characterization of colloidal Au and Ag multilayers. *Chem. Mater.* **2000**, *12* (10), 2869–2881.
98. Cassagneau, T.; Fendler, J.H. Preparation and layer-by-layer self-assembly of silver nanoparticles capped by graphite oxide nanosheets. *J. Phys. Chem., B* **1999**, *103* (11), 1789–1793.
99. Pastoriza-Santos, I.; Koktysh, D.S.; Mamedov, A.A.; Giersig, M.; Kotov, N.A.; Liz-Marzán, L.M. One-pot synthesis of Ag@TiO₂ core-shell nanoparticles and their layer-by-layer assembly. *Langmuir* **2000**, *16* (6), 2731–2735.
100. Kometani, N.; Tsubonishi, M.; Fujita, T.; Asami, K.; Yonezawa, Y. Preparation and optical absorption spectra of dye-coated Au, Ag, and Au/Ag colloidal nanoparticles in aqueous solutions and in alternate assemblies. *Langmuir* **2001**, *17* (3), 578–580.
101. Malynych, S.; Luzinov, I.; Chumanov, G. Poly(vinyl pyridine) as a universal surface modifier for immobilization of nanoparticles. *J. Phys. Chem., B* **2002**, *106* (6), 1280–1285.
102. Hu, K.; Brust, M.; Bard, A.J. Characterization and surface charge measurement of self-assembled CdS nanoparticle films. *Chem. Mater.* **1998**, *10* (4), 1160–1165.
103. Kotov, N.A.; Dékány, I.; Fendler, J.H. Layer-by-layer self-assembly of polyelectrolyte–semiconductor nanoparticle composite films. *J. Phys. Chem.* **1995**, *99* (35), 13065–13069.
104. Liu, Y.J.; Wang, A.B.; Claus, R.O. Layer-by-layer electrostatic self-assembly of nanoscale Fe₃O₄ particles and polyimide precursor on silicon and silica surfaces. *Appl. Phys. Lett.* **1997**, *71* (16), 2265–2267.
105. Aliev, F.G.; Correa-Duarte, M.A.; Mamedov, A.; Ostrander, J.W.; Giersig, M.; Liz-Marzán, L.M.; Kotov, N.A. Layer-by-layer assembly of core-shell magnetite nanoparticles: Effect of silica coating on interparticle interactions and magnetic properties. *Adv. Mater.* **1999**, *11* (12), 1006–1010.
106. Mamedov, A.A.; Kotov, N.A. Free-standing layer-by-layer assembled films of magnetite nanoparticles. *Langmuir* **2000**, *16* (13), 5530–5533.
107. Gao, M.Y.; Richter, B.; Kirstein, S. White-light electroluminescence from self-assembled Q-CdSe/PPV multiplayer structures. *Adv. Mater.* **1997**, *9* (10), 802–805.
108. Gao, M.Y.; Richter, B.; Kirstein, S.; Möhwald, H. Electroluminescence studies on self-assembled films of PPV and CdSe nanoparticles. *J. Phys. Chem., B* **1998**, *102* (21), 4096–4103.
109. Cassagneau, T.; Mallouk, T.E.; Fendler, J.H. Layer-by-layer assembly of thin film zener diodes from conducting polymers and CdSe nanoparticles. *J. Am. Chem. Soc.* **1998**, *120* (31), 7848–7859.
110. Rogach, A.L.; Koktysh, D.S.; Harrison, M.; Kotov, N.A. Layer-by-layer assembled films of HgTe nanocrystals with strong infrared emission. *Chem. Mater.* **2000**, *12* (6), 1526–1528.
111. Liu, Y.J.; Wang, A.B.; Claus, R. Molecular self-assembly of TiO₂/polymer nanocomposite films. *J. Phys. Chem., B* **1997**, *101* (8), 1385–1388.
112. Ariga, K.; Lvov, Y.; Onda, M.; Ichinose, I.; Kunitake, T. Alternately assembled ultrathin film of silica nanoparticles and linear polycations. *Chem. Lett.* **1997**, 125–126.
113. Lvov, Y.M.; Rusling, J.F.; Thomsen, D.L.; Papadimitrakopoulos, F.; Kawakami, T.; Kunitake, T. High-speed multiplayer film assembly by alternate adsorption of silica nanoparticles and linear polycation. *Chem. Commun.* **1998**, 1229–1230.
114. Hattori, H. Anti-reflection surface with particle coating deposited by electrostatic attraction. *Adv. Mater.* **2001**, *13* (1), 51–54.
115. Keller, S.W.; Kim, H.N.; Mallouk, T.E. Layer-by-layer assembly of intercalation compounds and heterostructures on surfaces: Toward molecular “beaker” epitaxy. *J. Am. Chem. Soc.* **1994**, *116* (19), 8817–8818.
116. Kleinfeld, E.R.; Ferguson, G.S. Stepwise formation of multilayered nanostructural films from macromolecular precursors. *Science* **1994**, *265*, 370–373.
117. Lvov, Y.; Ariga, K.; Ichinose, I.; Kunitake, T. Assembly of multicomponent protein films by means of electrostatic layer-by-layer adsorption. *J. Am. Chem. Soc.* **1995**, *117* (22), 6117–6123.
118. Rosidian, A.; Liu, Y.J.; Claus, R.O. Ionic self-assembly of ultrahard ZrO₂/polymer nanocomposite thin films. *Adv. Mater.* **1998**, *10* (14), 1087–1091.

119. Ostrander, J.W.; Mamedov, A.A.; Kotov, N.A. Two modes of linear layer-by-layer growth of nanoparticle-polyelectrolyte multilayers and different interactions in the layer-by-layer deposition. *J. Am. Chem. Soc.* **2001**, *123* (6), 1101-1110.
120. Iler, R.K. Multilayers of colloidal particles. *J. Colloid Interface Sci.* **1966**, *21*, 569-594.
121. Gao, M.Y.; Gao, M.Y.; Zhang, X.; Yang, Y.; Yang, B.; Shen, J.C. Constructing PbI₂ nanoparticles into a multiplayer structure using the molecular deposition (MD) method. *Chem. Commun.* **1994**, 2777-2778.
122. Gao, M.Y.; Zhang, X.; Yang, B.; Li, F.; Shen, J.C. Assembly of modified CdS particles/ cationic polymer based on electrostatic interactions. *Thin Solid Films* **1996**, 284-285, 242-245.
123. Sun, Y.P.; Hao, E.C.; Zhang, X.; Yang, B.; Gao, M.Y.; Shen, J.C. Monolayer of TiO₂/PbS coupled semiconductor nanoparticles. *Chem. Commun.* **1996**, 2381-2382.
124. Hao, E.C.; Yang, B.; Yu, S.; Gao, M.Y.; Shen, J.C. Formation of orderly organized cubic PbS nanoparticles domain in the presence of TiO₂. *Chem. Mater.* **1997**, *9* (7), 1598-1600.
125. Sun, Y.P.; Hao, E.C.; Zhang, X.; Yang, B.; Shen, J.C.; Chi, L.F.; Fuchs, H. Buildup of composite films containing TiO₂/PbS nanoparticles and polyelectrolytes based on electrostatic interaction. *Langmuir* **1997**, *13* (19), 5168-5174.
126. Hao, E.C.; Yang, B.; Zhang, J.H.; Zhang, X.; Sun, J.Q.; Shen, J.C. Assembly of alternating TiO₂/CdS nanoparticle composite films. *J. Mater. Chem.* **1998**, *8* (6), 1327-1328.
127. Hao, E.C.; Sun, Y.P.; Yang, B.; Zhang, X.; Liu, J.M.; Shen, J.C. Synthesis and photophysical properties of ZnS colloidal particles doped with silver. *J. Colloid Interface Sci.* **1998**, *204* (2), 369-373.
128. Sun, J.Q.; Hao, E.C.; Sun, Y.P.; Zhang, X.; Yang, B.; Zou, S.; Shen, J.C.; Wang, S.B. Multilayer assemblies of colloidal ZnS doped with silver and polyelectrolytes based on electrostatic interaction. *Thin Solid Films* **1998**, 327-329, 528-531.
129. Hao, E.C.; Sun, H.P.; Zhou, Z.; Liu, J.Q.; Yang, B.; Shen, J.C. Synthesis and optical properties of CdSe and CdSe/CdS nanoparticles. *Chem. Mater.* **1999**, *11* (11), 3096-3102.
130. Hao, E.C.; Qian, X.M.; Yang, B.; Wang, D.J.; Shen, J.C. Assembly and photoelectrochemical studies of TiO₂/CdS nanocomposite film. *Mol. Cryst. Liq. Cryst.* **1999**, *337*, 181-184.
131. Hao, E.C.; Yang, B.; Ren, H.; Qian, X.M.; Xie, T.F.; Shen, J.C.; Li, D.M. Fabrication of composite film comprising TiO₂/CdS and polyelectrolytes based on ionic attraction. *Mater. Sci. Eng., C* **1999**, *10*, 119-122.
132. Hao, E.C.; Zhang, H.; Yang, B.; Ren, H.; Shen, J.C. Preparation of luminescent polyelectrolyte/Cu-doped ZnSe nanoparticle multilayer composite films. *J. Colloid Interface Sci.* **2001**, *238* (2), 285-290.
133. Zhang, H.; Yang, B.; Wang, R.B.; Zhang, G.; Hou, X.L.; Wu, L.X. Fabrication of a covalently attached self-assembly multilayer film based on CdTe nanoparticles. *J. Colloid Interface Sci.* **2002**, *247* (2), 361-365.
134. Hao, E.C.; Wang, L.Y.; Zhang, J.H.; Yang, B.; Zhang, X.; Shen, J.C. Fabrication of polymer/inorganic nanoparticles composite films based on coordinative bonds. *Chem. Lett.* **1999**, 5-6.
135. Xiong, H.M.; Cheng, M.H.; Zhou, Z.; Zhang, X.; Shen, J.C. A new approach to the fabrication of a self-organizing film of heterostructured polymer/Cu₂S nanoparticles. *Adv. Mater.* **1998**, *10* (7), 529-532.
136. Hao, E.C.; Lian, T.Q. Layer-by-layer assembly of CdSe nanoparticles based on hydrogen bonding. *Langmuir* **2000**, *16* (21), 7879-7881.
137. Hao, E.C.; Lian, T.Q. Buildup of polymer/Au nanoparticle multilayer thin films based on hydrogen bonding. *Chem. Mater.* **2000**, *12* (11), 3392-3396.
138. Dante, S.; Hou, Z.Z.; Risbud, S.; Stroeve, P. Nucleation of iron oxy-hydroxide nanoparticles by layer-by-layer polyionic assemblies. *Langmuir* **1999**, *15* (6), 2176-2182.
139. Joly, S.; Kane, R.; Radzilowski, L.; Wang, T.; Wu, A.; Cohen, R.E.; Thomas, E.L.; Rubner, M.F. Multilayer nanoreactors for metallic and semiconducting particles. *Langmuir* **2000**, *16* (3), 1354-1359.
140. Dai, J.H.; Bruening, M.L. Catalytic nanoparticles formed by reduction of metal ions in multilayered polyelectrolyte films. *Nano Lett.* **2002**, *2* (5), 497-501.
141. Wang, T.C.; Rubner, M.F.; Cohen, R.E. Polyelectrolyte multiplayer nanoreactors for preparing silver nanoparticle composites: Controlling metal concentration and nanoparticle size. *Langmuir* **2002**, *18* (8), 3370-3375.
142. Donath, E.; Sukhorukov, G.B.; Caruso, F.; Davis, S.A.; Möhwald, H. Novel hollow polymer shells by colloid-templated assembly of polyelectrolytes. *Angew. Chem. Int. Ed.* **1998**, *37* (16), 2202-2205.
143. Sukhorukov, G.B.; Donath, E.; Davis, S.; Lichten-

- feld, H.; Knippel, E.; Knippel, M.; Budde, A.; Möhwald, H. Layer-by-layer self assembly of polyelectrolytes on colloidal particles. *Colloids Surf. A* **1998**, *137*, 253–266.
144. Caruso, F.; Lichtenfeld, H.; Giersig, M.; Möhwald, H. Electrostatic self-assembly of silica nanoparticle–polyelectrolyte multilayers on polystyrene latex particles. *J. Am. Chem. Soc.* **1998**, *120*, 8523–8524.
145. Caruso, F.; Caruso, R.A.; Möhwald, H. Nanoengineering of inorganic and hybrid hollow spheres by colloidal templating. *Science* **1998**, *282*, 1111–1114.
146. Caruso, F.; Möhwald, H. Preparation and characterization of ordered nanoparticle and polymer composite multilayers on colloids. *Langmuir* **1999**, *15* (23), 8276–8281.
147. Caruso, R.A.; Susha, A.S.; Caruso, F. Multilayered titania, silica, and laponite nanoparticle coatings on polystyrene colloidal templates and resulting inorganic hollow spheres. *Chem. Mater.* **2001**, *13* (2), 400–409.
148. Gittins, D.I.; Susha, A.S.; Schoeler, B.; Caruso, F. Dense nanoparticulate thin films via gold nanoparticle self-assembly. *Adv. Mater.* **2002**, *14* (7), 508–512.
149. Cassagneau, T.; Caruso, F. Contiguous silver nanoparticle coatings on dielectric spheres. *Adv. Mater.* **2002**, *14* (10), 732–736.
150. Dong, A.G.; Wang, Y.J.; Tang, Y.; Ren, N.; Yang, W.L.; Gao, Z. Fabrication of compact silver nanoshells on polystyrene spheres through electrostatic attraction. *Chem. Commun.* **2002**, 350–351.



Nanostructure and Dynamic Organization of Lipid Membranes

J. Gaudioso
D. Y. Sasaki

Sandia National Laboratories, Albuquerque, New Mexico, U.S.A.

INTRODUCTION

Cell membranes define the size and shape of the cell. In addition to this structural role, the membrane has a crucial regulatory role determining what information, nutrients, and waste can permeate this barrier. The cell membrane consists of a lipid bilayer and proteins, which can be either transmembrane or associated with one leaflet of the bilayer. The dynamic organization of proteins and lipids into domains (e.g., rafts) within the bilayer is important for multiple cellular processes, such as recognition and signaling events.

The chemical recognition process occurring on the surface of membranes is the basis of a versatile and specific sensor system for the cell. Lipid bilayer systems that mimic certain aspects of cell membrane function have been employed in biosensor schemes and continue to generate great interest in the nanotechnology field. Chemical recognition events can also cause structures to form, providing a mechanism for creating controllable, dynamic nanoscale architectures. The two main platforms for studying the dynamic properties of membranes for both nanotechnology and nanoscience applications are vesicular structures, called liposomes, and supported lipid bilayers.

This article aims to illustrate the importance of dynamic nanoscale structures in biological and model biological membranes. Applications of such structures for drug screening, biosensors, and microanalysis will be discussed. The emphasis will be on understanding what triggers structural reorganization on the nanoscale and how the temporal and spatial aspects of such reorganization can be controlled. The sophistication of the nanoscale machinery of the cell membrane offers many lessons that can be applied to the emerging field of nanotechnology.

LIPIDS, LIPOSOMES, AND SUPPORTED BILAYERS

Lipids are amphiphilic molecules, having a hydrophobic tail and a polar head group (Fig. 1A). Most commonly the tail consists of two fatty acid chains with an even number

of carbon atoms (14–18 atoms long) and with various degrees of unsaturation.^[1] In biological membranes, the key components are phospholipids, which have a phosphate at the head group position that is connected to the hydrophobic tails through a glycerol backbone. Often, another moiety, such as choline, serine, or inositol, is attached to the phosphate to form PC, PS, or PI-type lipids, respectively.^[2]

In an aqueous solution, these amphiphilic lipids self-assemble into liposomes (Fig. 1B).^[2] The spherical bilayer structure minimizes unfavorable interactions of the hydrophobic tail region with the water. The head group and tails determine the properties of the bilayer membrane, such as fluidity, charge density, and permeability. As recognized by Singer and Nicolson,^[3] the membrane is a fluid mosaic of lipids and proteins. This fluid-mosaic model does not, however, preclude the existence of structured regions (domains or rafts) within the lipid bilayer. In fact, it is the membrane's fluidity that enables the creation of dynamic nanoscale structures. The lipids can exist in three distinct phases: a tightly packed, ordered gel phase, an intermediate liquid ordered phase, and a disordered liquid phase. The transition temperature for gel to liquid phase transitions (T_g) decreases with decreasing chain length and degree of unsaturation. The steric hindrances, electrostatic charge, and hydrogen bonding of the head groups can also affect the transition temperature as well as the phase separation within the membrane. Such phase-separated domains (e.g., rafts) can undergo compositional fluctuations.^[4] It is key to recognize that under physiological conditions, the membrane is a heterogeneous,^[4] nonequilibrium^[5] system.

As previously mentioned, liposomes and supported bilayers are the two main systems of interest. Supported lipid bilayers can be prepared by the classic Langmuir–Blodgett method. Alternately, liposomes can be fused with surfaces to form supported bilayers.^[6] The fusion schemes for hydrophilic surfaces outlined in Fig. 2A and C result in opposite orientations of membrane faces and any incorporated proteins. In Fig. 2C, the orientation of the leaflets toward the bulk aqueous solution is preserved upon fusion. In the mechanism detailed in Fig. 2A, however, the orientation of the leaflets is reversed; that is,

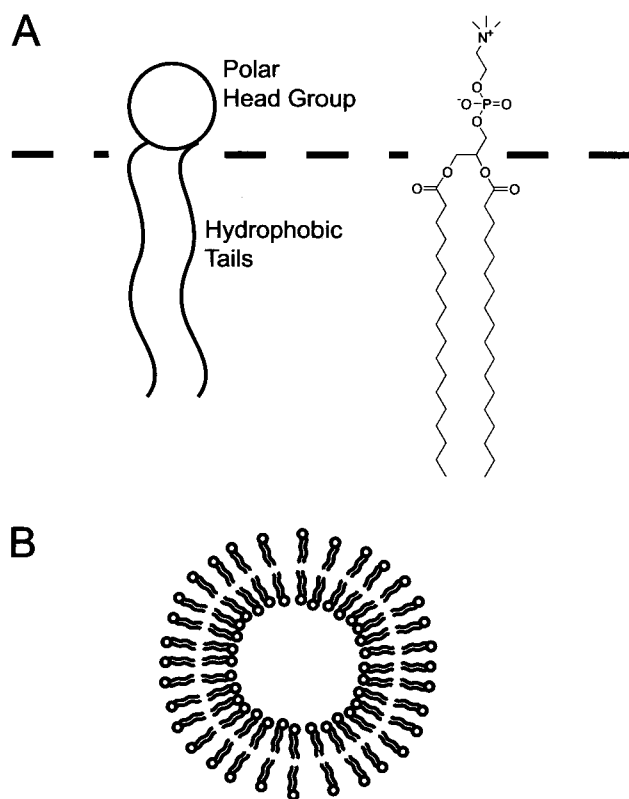


Fig. 1 (A) Cartoon of a lipid molecule showing the hydrophobic tail region and polar head group and the chemical structure for a typical lipid (1,2-Distearoyl-*sn*-Glycerol-3-Phosphocholine, DSPC). (B) The liposome (or vesicle) that spontaneously forms when lipids are placed in aqueous solutions.

the inside leaflet of the liposome becomes the top leaflet of the supported bilayer. Vesicle fusion to hydrophobic surfaces (Fig. 2B) can also be accomplished but the liposomes must rupture resulting in attachment and spreading of the two leaflets of the lipid bilayer. Liposome composition, surface chemistry, vesicle size, temperature, osmotic pressure, and the presence of calcium ions are all factors that influence vesicle fusion.^[7,8] Typically, supported bilayers formed by vesicle fusion maintain a thin layer of water (~ 10 Å) between the substrate and the adjacent membrane surface.^[9–11] This supported bilayer structure is very stable (days to months) in an aqueous environment, but unstable in the presence of detergents or in air. The lateral mobility of lipids within the bilayer is maintained enabling the molecules in the membrane to diffuse over long distances.

There is a suite of tools available for the characterization of nanoscale structures in lipid bilayers. For a description of standard methods for general liposome characterization, the reader is referred to the relevant

chapters in the book by D.D. Lasic^[11] and the book edited by R.R.C. New.^[12] Fluorescence microscopy provides a means to attain real-time data on the dynamical structures occurring in lipid bilayer systems. Single-molecule sensitivity is achievable. Fluorescence resonance energy transfer (FRET) between a fluorescently tagged donor component and a fluorescently tagged acceptor component yields accurate distance information for short length scales. In fluorescence recovery after photobleaching (FRAP), an area on the bilayer surface is photobleached and then monitored for recovery of fluorescence intensity. The fluorescence recovery is due to fluorescently labeled molecules diffusing into the bleached area and can thus be used to measure diffusion rates to evaluate lateral fluidity.

Spatial resolution of fluorescence techniques are, however, diffraction limited to a few hundred nanometers. Unfortunately, this length is often the same size as the dynamic structures. The atomic force microscope (AFM), on the other hand, can be used to characterize features in supported bilayers with subnanometer resolution.^[12] The AFM typically requires about a minute to capture an image. Thus it is suitable for imaging relatively static systems, or slow dynamics. Fluorescence and AFM imaging are the two techniques most relevant to the work discussed in this article, but other methods, including neutron scattering and nuclear magnetic resonance (NMR) spectroscopy,^[13] have also been applied toward dynamic nanostructures in bilayer systems.

Computer simulations are also an effective tool for understanding dynamic nanostructures in bilayer membranes.^[14] Nielsen and coworkers simulated binary mixtures of lipid bilayers revealing dynamic microphase separations with length scales of tens of nanometers.^[4] They further showed that this nanoscale structure affects the functional properties of the membrane. Through simulations and theoretical modeling, Gil et al. analyzed protein organization in lipid bilayers.^[5] The lateral organization of transmembrane proteins can be explained by the properties of the lipid bilayer. Hydrophobic matching between lipids and the hydrophobic region of proteins can lead to an enrichment of one lipid species near the protein. As such, the lipids can mediate protein attraction or repulsion. Also, the wetting of a protein by one lipid component can lead to larger protein organization patterns.

DYNAMIC NANOSTRUCTURES IN BIOLOGICAL AND MODEL BIOLOGICAL MEMBRANES

In this section, a few examples will be given to illustrate the importance of dynamic nanostructures in biological systems. Rafts, domains, and hierarchical structures are

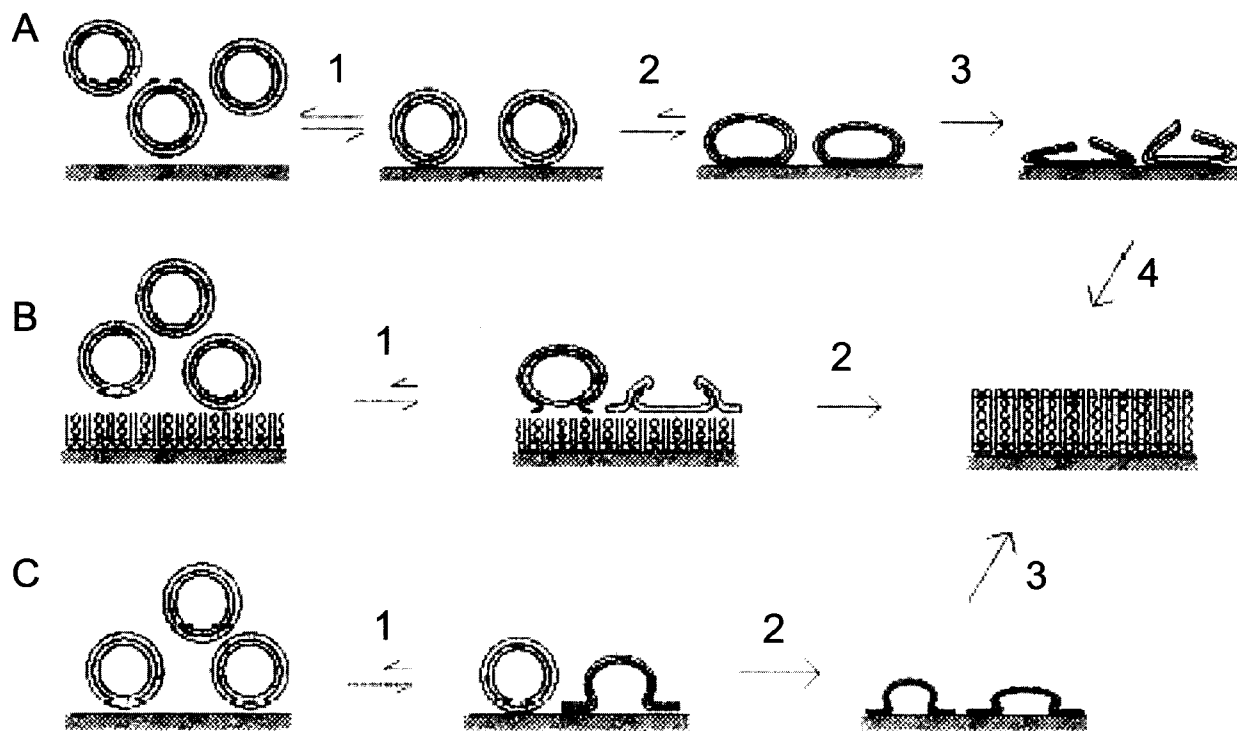


Fig. 2 Schematic representation of the possible mechanisms for planar bilayer formation from liposomes on hydrophilic and hydrophobic surfaces. The drawings are not drawn to scale. Lipid molecules on the support are enlarged approximately 50-fold compared to a liposome. (A) Vesicle fusion on a hydrophilic surface with the leaflet orientation reversed. (B) Vesicle fusion on a hydrophobic surface. (C) Vesicle fusion on a hydrophilic surface with the leaflet orientation preserved. (From Ref. [7]. Copyright 1997 Elsevier Science B.V.)

prevalent in the cell membrane and are the predominant sites of biological activity. Subczynski and Kusumi^[15] reviewed the three types of rafts (Fig. 3) found, to date, in plasma membranes. In unstimulated cells there are small, unstable (lifetimes of less than 1 msec) lipid rafts (a, a', and a'' in Fig. 3) that may have associated proteins. When receptor molecules in these unstable rafts react with ligands, they can create stabilized rafts (Fig. 3b) with lifetimes of minutes. The coalescence of these two types of rafts creates transient confinement zones (TCZs), which serve as signaling rafts (Fig. 3c) by assembling the necessary constituents to switch on a downstream signaling pathway.

Such dynamic nanostructures have been shown to be important in a variety of biological systems. Sheets et al. explain how the organization of the plasma membrane likely exerts spatio-temporal control on immunoglobulin E receptor-mediated signal transduction.^[16] Lipid rafts also play a key role in the immunological synapse.^[17-19] The T-cell antigen receptors (TCR) are located in rafts and they become cross-linked by ligand binding. The cross-linking induces raft aggregation, causing colocalization of signaling proteins. This activates the phosphorylation of

tyrosine residues on membrane-associated proteins and starts downstream signaling.

Because the biological membrane is a complex entity, most structure and function studies are performed on simpler, well-defined model membrane systems of liposomes and supported bilayers. For example, in studies of lipid raft formation, ternary mixtures of saturated lipids, unsaturated lipids, and cholesterol have been found to spontaneously form rafts over a wide range of specific lipid species and concentrations.^[20-22] In these studies, micron-sized domains were imaged via fluorescence microscopy techniques. Nanostructural features in lipid bilayers can also be revealed with AFM, although the domain shape and size have been shown to be somewhat dependent on the substrate and bottom leaflet of the supported bilayer.^[23,24]

Not only do lipid-lipid interactions cause domain formation but lipid-protein interactions can also induce nanoscale structures to form. Rinia et al. reported that transmembrane WALP proteins perturb the bilayer, creating striated domains of 25 nm to 10 μ m with the nanoscale striations spaced at 7.5-nm intervals.^[25] Furthermore, the specific physical properties of the bilayer components can modulate enzyme activity. Honger and

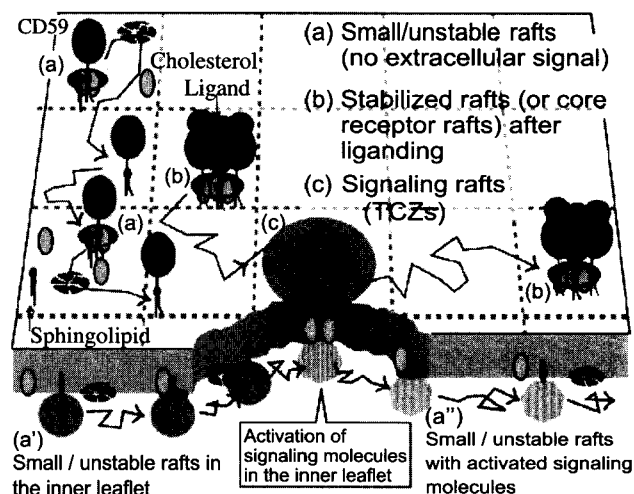


Fig. 3 Three types of rafts found thus far in the plasma membrane. The first type (a) is prevalent in the absence of extracellular stimulation. They are small (perhaps consisting of several molecules) and unstable (the lifetimes may be less than 1 msec) and may be the kind of raft that monomeric GPI-anchored proteins associate with. The second type of raft (b) may appear when receptor molecules form oligomers upon liganding or cross-linking. The receptors may be GPI-anchored receptors or transmembrane receptors with some affinity to cholesterol and saturated alkyl chains. Oligomerized receptors may then induce small but stable rafts around them, perhaps due to the slight reduction in the thermal motion around the cluster and the subsequent assembly of cholesterol. Given the rather stable oligomerization of the receptor molecules, the second type of raft may be stable for minutes, although the associated raft-constituent molecules may be exchanged frequently between the raft and the bulk domains. Such receptor-associated rafts are called "core-receptor rafts." The third type of raft (c) may be formed around these core receptor rafts (although the core receptor rafts may be undergoing diffusion). Here they are called "signaling rafts," because they are likely to be directly involved in downstream signaling from the receptor molecules, by assembling signaling molecules through the (transient and/or more stable) coalescence of rafts that may contain one or two signaling molecules. Small/unstable rafts are also likely to exist in the inner leaflet of the membrane (a') and could coalesce with the core receptor rafts (b and c), where the signaling molecule in the inner leaflet is activated, which might also leave from the signaling rafts (c and a''). (From Ref. [15]. Copyright 2003 Elsevier Science B.V.) (View this art in color at www.dekker.com.)

coworkers demonstrated that phospholipase A₂ enzyme activity correlates with the degree of microheterogeneity within the bilayer.^[26]

Protein binding to receptor lipids in model membranes can also induce a membrane reorganizational process.^[27] Concanavalin A (Con A) protein was found to bind to bilayers composed of the mannosamine-functionalized lipid PSMU and distearylphosphatidylcholine (DSPC).

Initially, PSMU forms aggregates in DSPC, but slowly disperses following Con A adsorption to the membrane surface and binding to the mannosamine head groups. Dispersal is attributed to Con A–Con A steric interactions, distance between receptor sites, and possible protein insertion events.

Another example of a molecular recognition-induced lipid reorganization was developed by Song and co-workers to detect biotoxins.^[28,29] Fluorescently tagged receptors are dispersed in a fluid lipid matrix of palmitoyl, 9-octadecenenoyl phosphatidylcholine (POPC). The dispersed receptors exhibit strong fluorescence. Specific, multivalent binding of the toxin to its receptors brings the fluorophores in close proximity, causing a strong decrease in fluorescence intensity due to self-quenching. Nonspecific binding of toxins to lipid bilayers can also be used in a biosensing scheme that employs optical evanescence.^[30] Pattern analysis and comparison to standards are required to assign the identity of the bound toxin, but the method is rapid and can be used for multiple toxins. The original work analyzed the binding of six different protein toxins.

DYNAMIC NANOSTRUCTURES AS NANOTECHNOLOGY BUILDING BLOCKS

The same specificity of chemical recognition events that alter the nanostructures of biological membrane systems can be utilized to make rapid and sensitive chemical sensors. In a manner similar to the Con A-induced dispersion, the Sasaki lab has developed several synthetic receptor systems for metal ions, Hg²⁺,^[31] Cu²⁺,^[32] and Pb²⁺,^[33] that are sensitive to parts per billion (ppb) levels of the analyte. In all of these cases, a receptor is synthesized with a head group specific for the metal ion of interest and with a pyrene label in the lipid tail. The receptor naturally aggregates in the DSPC lipid matrix, yielding a large pyrene excimer fluorescence peak. Once the receptors chelate the metal ions they disperse, and the monomer fluorescence peak grows in intensity while the excimer diminishes. Binding of the metal ions gives the receptor head groups a net charge; electrostatic repulsion causes their dispersal into the matrix. The AFM can capture before and after images showcasing these controllable dynamic nanostructures. Fig. 4A shows an AFM image of a supported bilayer consisting of a receptor lipid (18-crown-6 ether functionalized lipid, PS18C6) embedded in a matrix lipid (DSPC). Islands and filaments of PS18C6-rich regions are clearly visible. These nanostructures decrease in size and intensity upon the addition of Pb²⁺ ions (Fig. 4B) and removal of the ions leads to a reaggregation of the PS18C6 lipids. Fluorescence measurements indicate this reorganization occurs within seconds. The undefined dynamic nanostructures provide a starting point for the

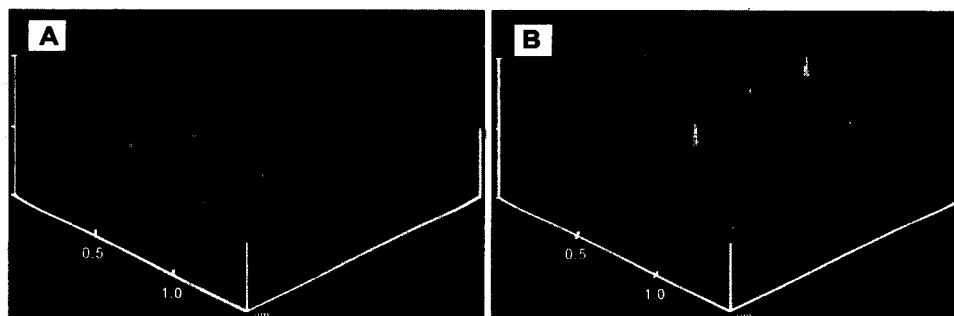


Fig. 4 AFM topographic images of a 20% PS18C6/DSPC bilayer supported on a mica surface demonstrating the actuation of the film from aggregated to dispersed states with Pb^{2+} ions. The membrane in the (A) initial state, then (B) after addition of 0.1 mM $\text{Pb}(\text{NO}_3)_2$. All solutions were aqueous saline (0.1 M NaCl). (From Ref. [33]. Copyright 2002 American Chemical Society.)

development of reversible nanoscale architectures controlled by chemical recognition events.

The Boxer laboratory has pioneered the field of micropatterning supported lipid bilayers. Because this work

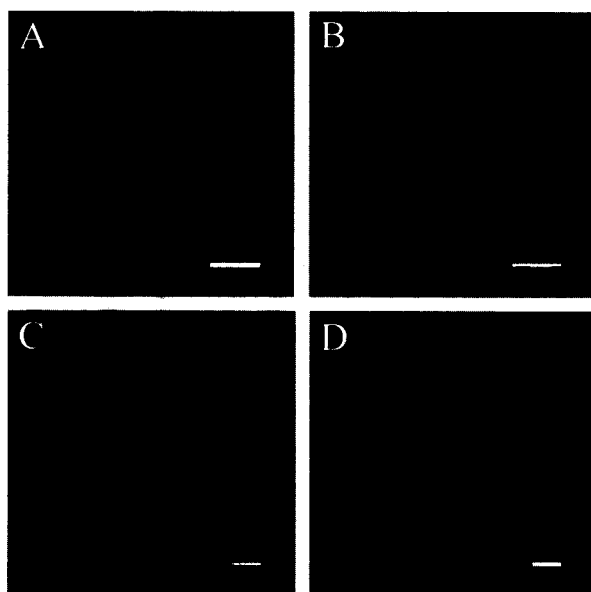


Fig. 5 Epifluorescence images of supported membranes patterned by printing proteins. In each panel the protein is TR-BSA and is colored red, while the supported membrane regions are 2% NBD-PE-doped egg PC and are colored green (note: for the color version of the image visit www.dekker.com). The scale bars are each 20 μm across. (A) 20- μm bilayer regions separated by 15- μm protein; (B) 10- μm bilayer regions separated by 5- μm protein grids; (C,D) 40- μm bilayer regions separated by 10- μm protein grids. In panel C an octagonal spot was photobleached for 30 sec centered on the middle corral. After irradiation ceased, the lipids mix freely within each corral, creating corrals of uniform but intermediate fluorescence intensity, as seen in (D) after 360 sec of recovery. (From Ref. [40]. Copyright 2000 American Chemical Society.) (View this art in color at www.dekker.com.)

has been the subject of several excellent reviews,^[34–36] it will only be briefly described here. The fluid bilayers are patterned into micron-sized features by creating barriers to lateral diffusion through methods as diverse as scratching,^[37] using polymer stamps to blot away lipids^[38] or to microcontact print barriers,^[38] and microfluidic manipulation of the lipid bilayer.^[39] The supported bilayers in Fig. 5 were patterned by microcontact printing of protein (TR-BSA) barriers. After printing the proteins, vesicle fusion was used to form the supported bilayers of fluorescently doped egg-PC lipids. The bilayers only fuse to and occupy regions free of adsorbed proteins. The patterned surfaces contain the lipids within their micron-sized corrals as demonstrated by FRAP measurements (Fig. 5C and D). Although the development of these tools for patterning supported lipid bilayers has been focused on the micron scale, the tools can be scaled down into the nanoscale arena. The polymer stamps used for blotting or microcontact printing can be created with nanoscale

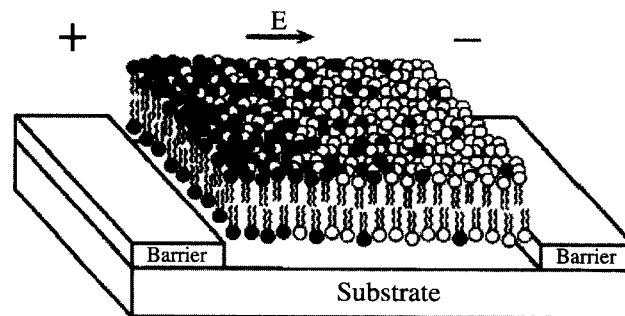


Fig. 6 Schematic diagram of an electric field-induced reorganization of lipids in a confined patch of supported bilayer membrane. A two-component system is shown in which the negatively charged lipid (shaded) builds up a concentration gradient toward the anode side of the corral. This represents an equilibrium distribution where the field-induced drift is balanced by diffusion. (From Ref. [42]. Copyright 1998 National Academy of Sciences, U.S.A.)

features by using advanced photolithography or electron beam lithography and, likewise, microfluidics can be scaled to nanofluidics.

The lipids within the patterned supported bilayers can be dynamically controlled on a submicron scale. The application of an electric field tangentially to the plane of the supported bilayer induces a reorganization of the charged

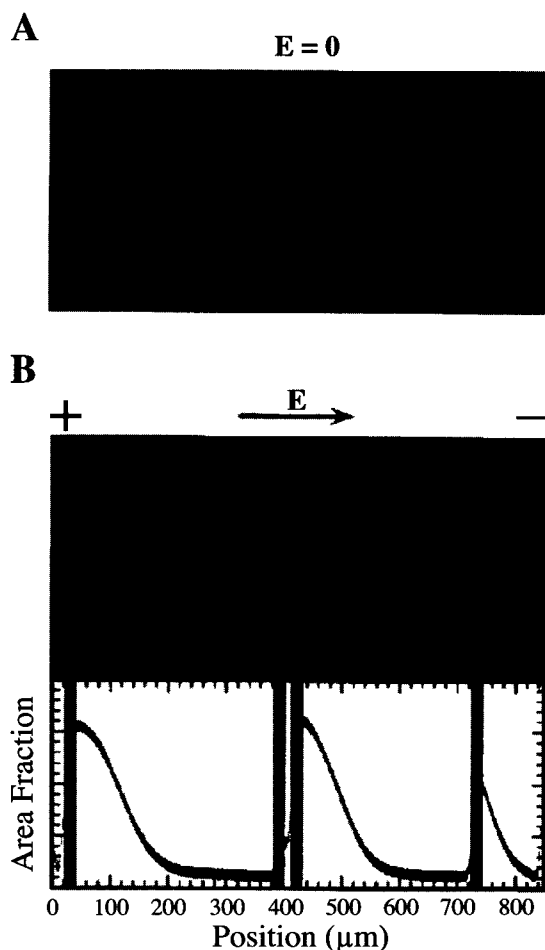


Fig. 7 (A) Epifluorescence image of several corrals of fluid membrane separated by scratch boundaries. The membrane is of uniform composition in the absence of an electric field. Fluorescence is from 1 mol% of *N*-(Texas Red sulfonyl)-1,2-dihexadecanoyl-*sn*-glycero-3-phosphoethanolamine, triethylammonium salt doped into this egg-PC (90%) and DOPS (9%) membrane. (B) Epifluorescence image of a steady-state molecular reorganization induced by an applied field of 25 V/cm. The negatively charged components have built up concentration gradients toward the anode. A trace of the fluorescence intensity across the image is depicted below with the scratch boundaries marked with gray bars. The concentration profiles can be observed to a greater extent in the larger corrals. (From Ref. [41]. Copyright 1997 National Academy of Sciences, U.S.A.)

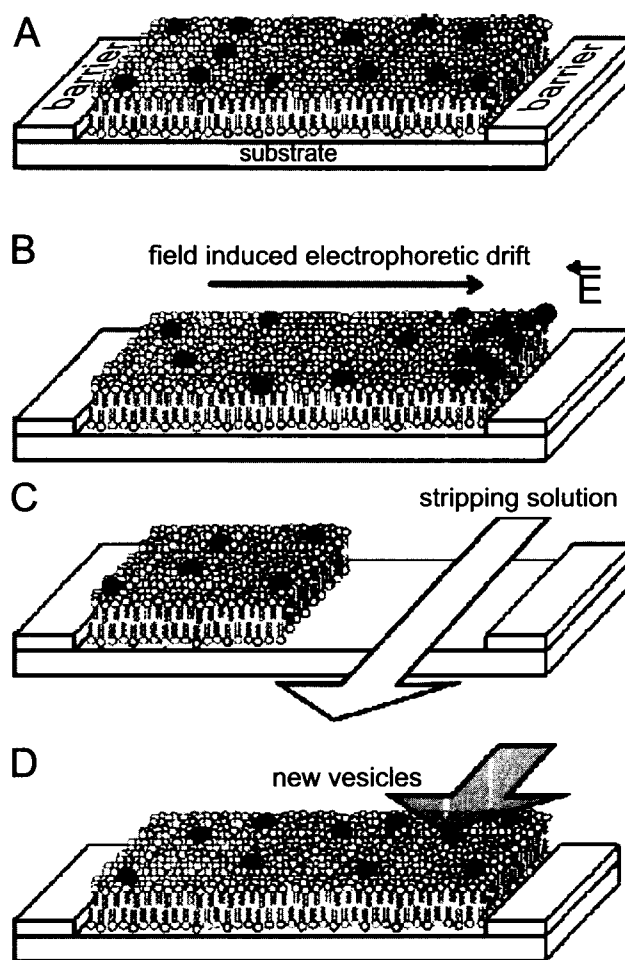


Fig. 8 Micropatterning, electrophoresis, and stripping of lipid bilayers. (A) Schematic diagram of a supported lipid bilayer confined or corralled by microfabricated barriers. Mobile species, illustrated by lipids with red and green head groups, freely diffuse and mix, approaching a uniform concentration across the extent of the lipid bilayer. (B) Application of an electric field induces manipulation of charged membrane components (the red lipids) and represents one method of manipulating a lipid bilayer after formation; the neutral lipids (green) do not respond to this applied field and remain homogeneous in the corral. (C) A stream of stripping solution is flowed over part of the surface under laminar flow conditions, leaving an open region on the substrate. (D) A new lipid bilayer, which could contain new biomolecular species, indicated by the lipid with blue head groups is introduced. The relative sizes and organizations of the components in these drawings are for illustrative purposes only and are not to scale. (From Ref. [39]. Copyright 2003 American Chemical Society.) (View this art in color at www.dekker.com.)

components in a confined patch of membrane^[40,41] as illustrated schematically in Fig. 6. The equilibrium concentration profile is a balance of the field-induced reorganization and Brownian diffusion. The concentration profile will be steeper for larger species, such as dimers and larger molecular aggregates, as these species will be slower diffusing.^[40] Electric field manipulation takes an initially uniform membrane patch (Fig. 7A) and induces a concentration gradient (Fig. 7B) that can be dynamically reversed by switching the applied electric field. The behavior of charged species in the bilayer in response to an applied field can also be exploited to separate mixtures of membrane-associated molecules. Boxer and van Oudenaarden designed a geometrical Brownian ratchet that consists of an array of asymmetric patterned barriers on a solid support.^[42] The barriers rectify the lateral Brownian motion of the molecules within the membrane inducing the various molecular species (with different diffusion coefficients) to follow distinct trajectories through the device. This application of Brownian ratchets to bilayers

offers a promising way to separate membrane proteins in their native conformations.

The composition of the patterned bilayer corrals can be changed after preparation. Fig. 8 details a process of applying a field to concentrate a charged species near one of the barriers (field-induced reorganization; Fig. 8B). The charged species is then selectively removed with the microfluidic flow of a stripping solution (Fig. 8C);^[39] thus a new bilayer species can now be introduced (Fig. 8D). Laminar flow could be used to strip sections of the patterned bilayer, carrying the species downstream to compartments on the microfluidic chip for compositional analysis. An alternate method for changing the lipid composition after patterning uses membrane-coated beads to deliver the new species to areas of opposite charge.^[43] The beads adhere to the patterned corral through an electrostatic attraction and some lipid exchange between the beads and the patterned supported bilayer occurs. This may provide a novel mechanism for incorporating membrane proteins or glycolipids into prepatterned bilayer arrays.

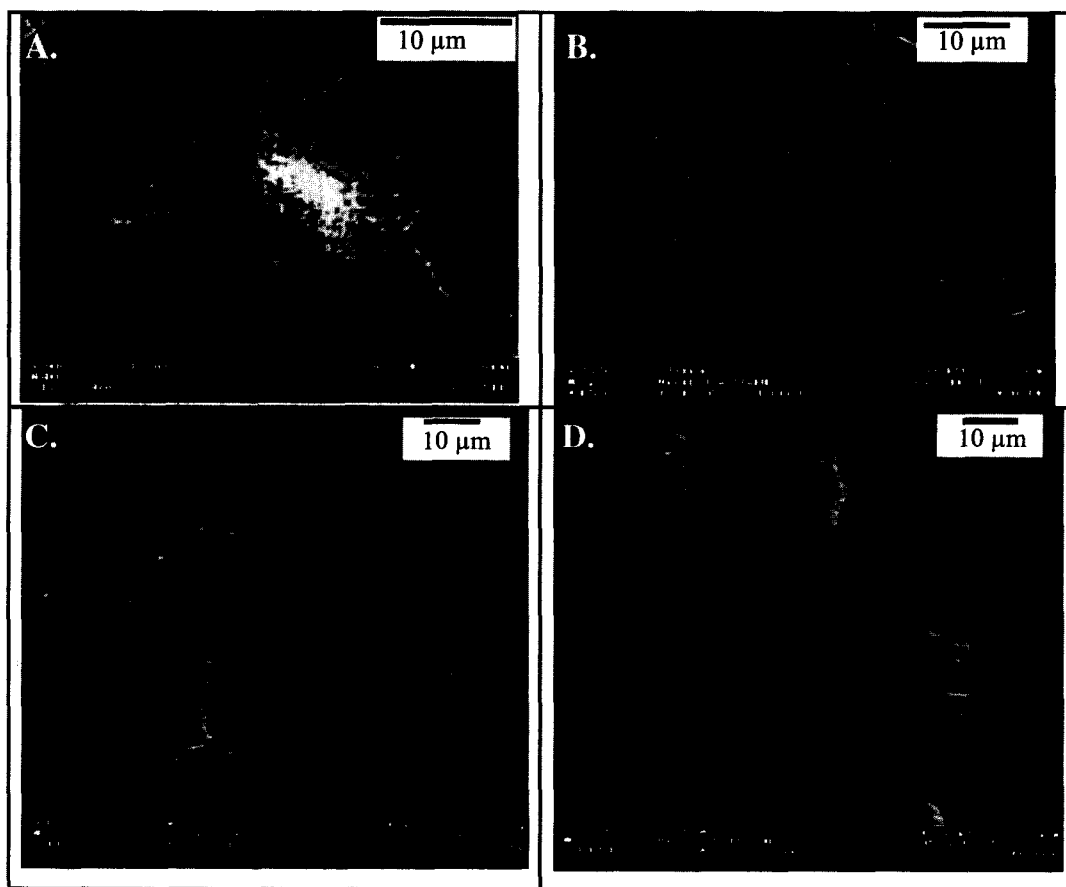


Fig. 9 SEM images of RBL cells. (A) Resting RBL on a plain silicon surface with lamellipodia randomly spreading on the oxidized silicon substrate. Magnification: $\times 3000$. (B) Stimulated RBL at the corner of four patterned squares of lipids. Magnification: $\times 2100$. (C,D) Stimulated RBL over patterned lines of lipids. Magnification: $\times 1250$, $\times 1250$. (C) shows gray lines where the haptened lipids were patterned. (From Ref. [46]. Copyright 2003 American Chemical Society.)

These micropatterned supported bilayers have multiple applications for cell culturing and drug discovery. For example, fibronectin protein barriers for the lipid bilayers create well-defined surfaces for studying cell adhesion.^[44] In addition, cell spreading can be controlled and, conceivably, directed by tuning the dimensions and geometries of the patterned bilayer. Proteins can also be included in the patterned bilayer. The incorporation of antigens creates an anisotropic environment for the study of localized stimulation of rat basophilic leukemia (RBL) mast cells.^[45] Scanning electron microscopy (SEM) images (Fig. 9) clearly show that RBL cell adhesion and spreading is directed by the underlying patterned supported bilayer. This method of incorporating components

in the membrane should extend to the localized confinement of other cellular receptors and provide a means to study their induced cellular responses.

Today, membrane-bound proteins account for 50% of current drug targets.^[46] Yet, membrane proteins are among the most difficult to study because the protein usually requires the membrane for it to remain in its native, active conformation. Patterned membrane microarrays provide a method for studying protein-protein or protein-small molecule (e.g., drug) interactions.^[47] Membrane microarrays maintain the functionality of living cell membranes while providing the simplicity and controllability of an array. The array of membrane patches can be patterned with any of the techniques mentioned above.

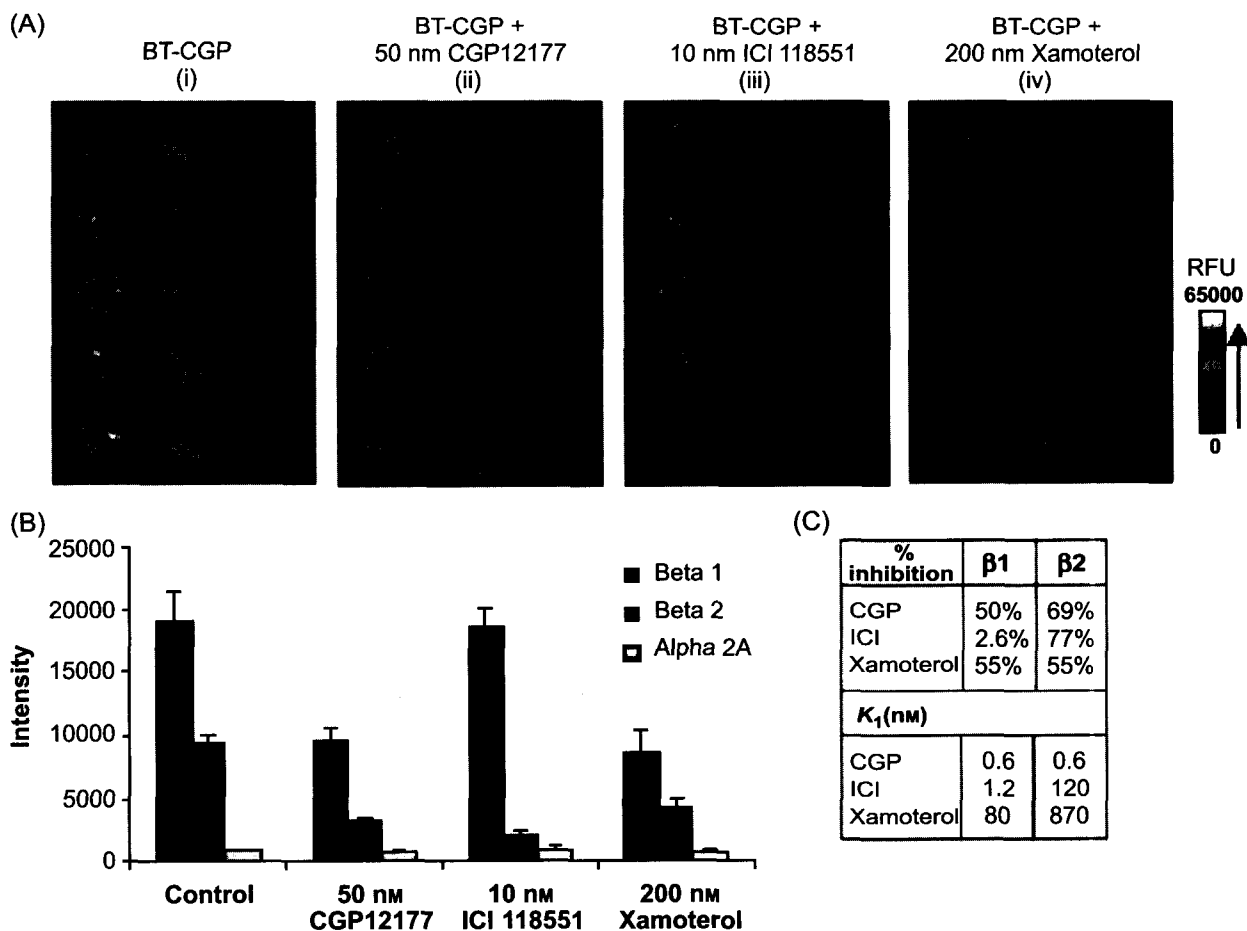


Fig. 10 Demonstration of the use of GPCR microarrays for determining the selectivity of compounds among the different subtypes of a receptor. Each microarray consists of three columns; each column contains, from left to right, five replicate microspots of the $\beta 1$, $\beta 2$, and $\alpha 2A$ adrenergic receptors, respectively. (A) Fluorescence false-color images (from left to right) of the array incubated with solutions containing BT-CGP (5 nM) and mixtures of BT-CGP (5 nM) with CGP 12177 (50 nM), ICI 118551 (10 nM), and xamoterol (200 nM) to the array. (B) Histogram analysis of the images in (A) showing the relative fluorescence intensities (RFU) of the arrays incubated with BT-CGP or mixtures of BT-CGP and inhibitors. (C) Table showing the amounts of inhibition and the K_i values for the inhibitors used in the experiment. (From Ref. [49]. Copyright 2002 Wiley-VCH.) (View this art in color at www.dekker.com.)

The patches can also be printed with a quill-pin printer. This technique has been successfully demonstrated for G-protein coupled receptor (GPCR) proteins.^[46,48] GPCRs consist of seven transmembrane helices. The binding of a ligand to the extracellular side of the transmembrane helices activates a G protein on the intracellular side. The affinity of the GPCR for its ligand depends on the presence of a G protein complexed to the intracellular side. Thus it is important for G proteins to be in the membrane microarray, which is achieved with the quill-pin method. Fig. 10 shows GPCR microarray results for the determination of the affinity of a series of compounds for $\beta 1$, $\beta 2$, and $\alpha 2A$ subtypes of the adrenergic receptor. The BT-CGP ligand is known to be specific for β -subtypes and the GPCR microarray clearly shows this specificity (Fig. 10Ai) as only the $\beta 1$ and $\beta 2$ receptor spots show fluorescence. When the BT-CGP ligand is incubated with a microarray in the presence of an inhibitor (e.g., CGP 12177, ICI 118551, or Xamoterol), the percent binding inhibition can be determined.

CONCLUSION

In recent years, it has become clear that nature takes advantage of dynamic nanoscale structures in many cellular signaling pathways. As mentioned, this serves as a sensitive sensor system for the cell. The ability to monitor nanoscale features in biological systems has provided new insights into the mechanisms of this membrane activity. This article has described progress that the field of nanotechnology has made in mimicking this complex yet robust cellular component. Dynamic aggregates can be used as the basis for chemical and biosensing elements with very high sensitivity and selectivity. Spatial and temporal control of dynamic nanoscale structures in lipid membranes may serve as unique nanobuilding blocks and template scaffolds in bottom-up architectures. Advances in fabrication technology should soon enable supported lipid bilayers to be patterned at the nanoscale and, as discussed, physical methods (electric fields and fluid flows) are already in place for dynamically controlling the lipids in a patterned corral. The near future should bring efforts to combine physical control with chemical control to create more complex dynamic nanoscale structures with lipid membranes for nanotechnology applications.

ACKNOWLEDGMENTS

Sandia is a multiprogram laboratory operated by Sandia Corporation, a Lockheed Martin Company, for the

U.S. Department of Energy under contract DE-AC04-94AL85000 and supported by the Office of Basic Energy Sciences.

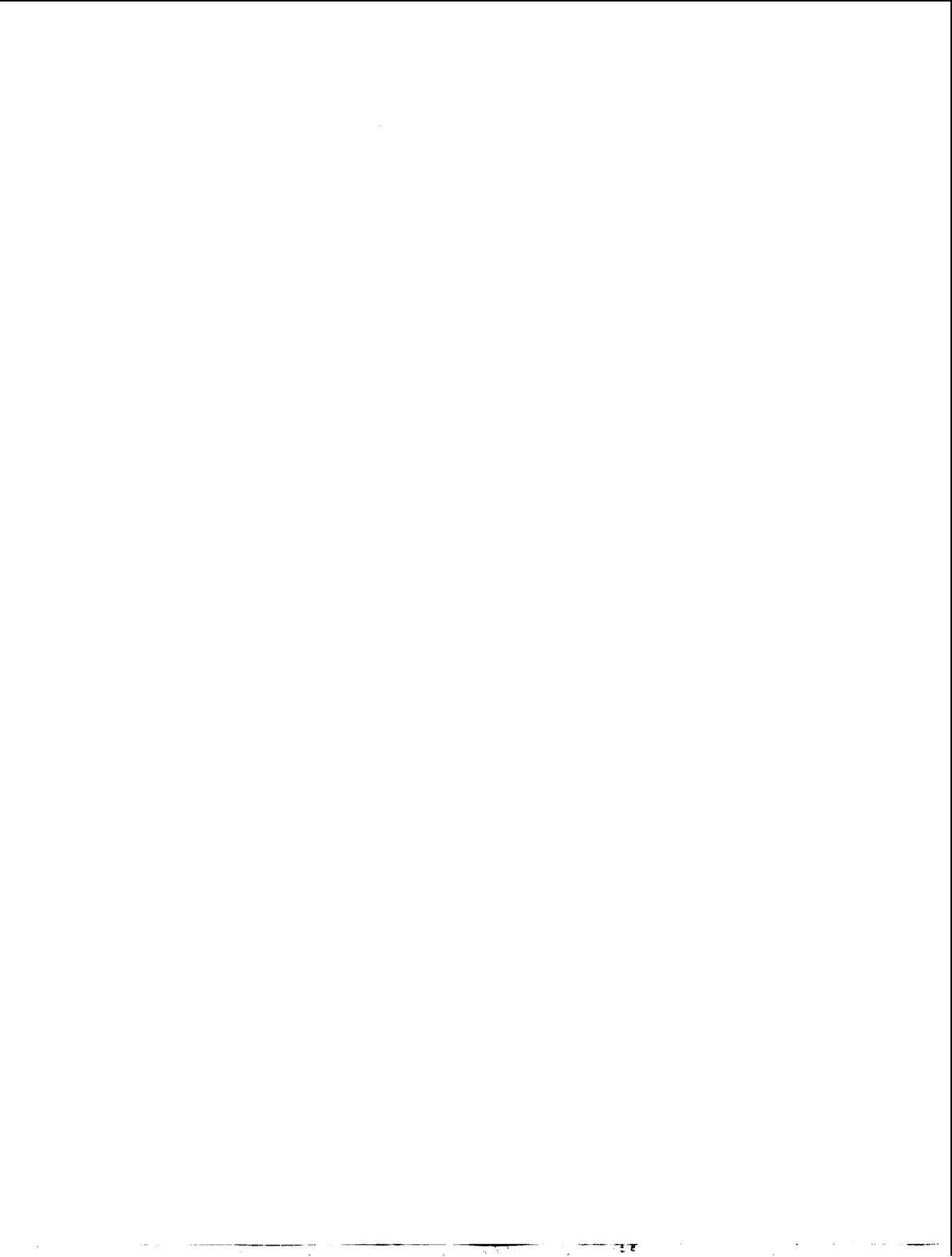
REFERENCES

1. Lasic, D.D. *Liposomes: From Physics to Applications*; Elsevier Science: New York, 1993; 575.
2. New, R.R.C. *Liposomes—A Practical Approach*; IRL Press: New York, 1990; 301.
3. Singer, S.J.; Nicolson, G.L. The fluid mosaic model of the structure of cell membranes. *Science* **1972**, *175*, 720–731.
4. Nielsen, L.; Vishnyakov, A.; Jorgensen, K.; Bjornholm, T.; Mouritsen O. Nanometre-scale structure of fluid lipid membranes. *J. Phys., Condens. Matter* **2000**, *12* (8A), A309–A314.
5. Gil, T.; Ipsen, J.; Mouritsen, O.; Sabra, M.; Sperotto, M.; Zuckermann, M. Theoretical analysis of protein organization in lipid membranes. *Biochim. Biophys. Acta, Rev. Biomembr.* **1998**, *1376* (3), 245–266.
6. McConnell, H.M.; Watts, T.H.; Weis, R.M.; Brian, A.A. Supported planar membranes in studies of cell-cell recognition in the immune system. *Biochim. Biophys. Acta* **1986**, *864* (1), 95–106.
7. Puu, G.; Gustafson, I. Planar lipid bilayers on solid supports from liposomes—Factors of importance for kinetics and stability. *Biochim. Biophys. Acta, Biomembr.* **1997**, *1327* (2), 149–161.
8. Reimhult, E.; Hook, F.; Kasemo, B. Intact vesicle adsorption and supported biomembrane formation from vesicles in solution: Influence of surface chemistry, vesicle size, temperature, and osmotic pressure. *Langmuir* **2003**, *19* (5), 1681–1691.
9. Bayerl, T.M.; Bloom, M. Physical-properties of single phospholipid-bilayers adsorbed to micro glass beads—A new vesicular model system studied by H2 nuclear magnetic resonance. *Biophys. J.* **1990**, *58* (2), 357–362.
10. Johnson, S.J.; Bayerl, T.M.; McDermott, D.C.; Adam, G.W.; Rennie, A.R.; Thomas, R.K.; Sackmann, E. Structure of an adsorbed dimyristoylphosphatidylcholine bilayer measured with specular reflection of neutrons. *Biophys. J.* **1991**, *59* (2), 289–294.
11. Koenig, B.; Kruger, S.; Orts, W.; Majkrzak, C.; Berk, N.; Silverton, J.; Gawrisch, K. Neutron reflectivity and atomic force microscopy studies of a lipid bilayer in water adsorbed to the surface of a silicon single crystal. *Langmuir* **1996**, *12* (5), 1343–1350.
12. Muller, D.J.; Schoenenberger, C.A.; Schabert, F.;

- Engel, A. Structural changes in native membrane proteins monitored at subnanometer resolution with the atomic force microscope: A review. *J. Struct. Biol.* **1997**, *119* (2), 149–157.
13. Bloom, M.; Bayerl, T.M. Membranes studied using neutron scattering and NMR. *Can. J. Phys.* **1995**, *73* (11–12), 687–696.
 14. Scott, H. Modeling the lipid component of membranes. *Curr. Opin. Struct. Biol.* **2002**, *12* (4), 495–502.
 15. Subczynski, W.; Kusumi, A. Dynamics of raft molecules in the cell and artificial membranes: Approaches by pulse EPR spin labeling and single molecule optical microscopy. *Biochim. Biophys. Acta, Biomembr.* **2003**, *1610* (2), 231–243.
 16. Sheets, E.; Holowka, D.; Baird, B. Membrane organization in immunoglobulin E receptor signaling. *Curr. Opin. Chem. Biol.* **1999**, *3* (1), 95–99.
 17. Grakoui, A.; Bromley, S.; Sumen, C.; Davis, M.; Shaw, A.; Allen, P.; Dustin, M. The immunological synapse: A molecular machine controlling T cell activation. *Science* **1999**, *285* (5425), 221–227.
 18. Blanchard, N.; Hivroz, C. The immunological synapse: The more you look the less you know... *Biol. Cell* **2002**, *94* (6), 345–354.
 19. Magee, T.; Pirinen, N.; Adler, J.; Pagakis, S.; Parmryd, I. Lipid rafts: Cell surface platforms for T cell signaling. *Biol. Res.* **2002**, *35* (2), 127–131.
 20. Veatch, S.L.; Keller, S.L. Organization in lipid membranes containing cholesterol. *Phys. Rev. Lett.* **2002**, *89* (26), 268101–268104.
 21. London, E. Insights into lipid raft structure and formation from experiments in model membranes. *Curr. Opin. Struct. Biol.* **2002**, *12* (4), 480–486.
 22. Silvius, J. Role of cholesterol in lipid raft formation: Lessons from lipid model systems. *Biochim. Biophys. Acta, Biomembr.* **2003**, *1610* (2), 174–183.
 23. Tamm, L.; Bohm, C.; Yang, J.; Shao, Z.; Hwang, J.; Edidin, M.; Betzig, E. Nanostructure of supported phospholipid monolayers and bilayers by scanning probe microscopy. *Thin Solid Films* **1996**, *285*, 813–816.
 24. Tokumasu, F.; Jin, A.; Feigenson, G.; Dvorak, J. Nanoscopic lipid domain dynamics revealed by atomic force microscopy. *Biophys. J.* **2003**, *84* (4), 2609–2618.
 25. Rinia, H.; Kik, R.; Demel, R.; Snel, M.; Killian, J.; van der Eerden, J.; de Kruijff, B. Visualization of highly ordered striated domains induced by transmembrane peptides in supported phosphatidylcholine bilayers. *Biochemistry* **2000**, *39* (19), 5852–5858.
 26. Honger, T.; Jorgensen, K.; Biltonen, R.; Mouritsen, O. Systematic relationship between phospholipase A(2) activity and dynamic lipid bilayer microheterogeneity. *Biochemistry* **1996**, *35* (28), 9003–9006.
 27. Bondurant, B.; Last, J.; Waggoner, T.; Slade, A.; Sasaki, D. Optical and scanning probe analysis of glycolipid reorganization upon Concanavalin A binding to mannose-coated lipid bilayers. *Langmuir* **2003**, *19* (5), 1829–1837.
 28. Song, X.; Nolan, J.; Swanson, B. Optical signal transduction triggered by protein–ligand binding: Detection of toxins using multivalent binding. *J. Am. Chem. Soc.* **1998**, *120* (19), 4873–4874.
 29. Song, X.; Nolan, J.; Swanson, B. Optical biosensor based on fluorescence resonance energy transfer: Ultrasensitive and specific detection of protein toxins. *J. Am. Chem. Soc.* **1998**, *120* (44), 11514–11515.
 30. Puu, G. An approach for analysis of protein toxins based on thin films of lipid mixtures in an optical biosensor. *Anal. Chem.* **2001**, *73* (1), 72–79.
 31. Sasaki, D.; Padilla, B. Dithioamide metal ion receptors on fluorescent lipid bilayers for the selective optical detection of mercuric ion. *Chem. Commun.* **1998**, (15), 1581–1582.
 32. Last, J.; Waggoner, T.; Sasaki, D. Lipid membrane reorganization induced by chemical recognition. *Biophys. J.* **2001**, *81* (5), 2737–2742.
 33. Sasaki, D.; Waggoner, T.; Last, J.; Alam, T. Crown ether functionalized lipid membranes: Lead ion recognition and molecular reorganization. *Langmuir* **2002**, *18* (9), 3714–3721.
 34. Boxer, S. Molecular transport and organization in supported lipid membranes. *Curr. Opin. Chem. Biol.* **2000**, *4* (6), 704–709.
 35. Groves, J.; Ulman, N.; Boxer, S. Micropatterning fluid lipid bilayers on solid supports. *Science* **1997**, *275* (5300), 651–653.
 36. Groves, J.T.; Boxer, S.G. Micropattern formation in supported lipid membranes. *Acc. Chem. Res.* **2002**, *35* (3), 149–157.
 37. Cremer, P.; Groves, J.; Kung, L.; Boxer, S. Writing and erasing barriers to lateral mobility into fluid phospholipid bilayers. *Langmuir* **1999**, *15* (11), 3893–3896.
 38. Hovis, J.; Boxer, S. Patterning barriers to lateral diffusion in supported lipid bilayer membranes by blotting and stamping. *Langmuir* **2000**, *16* (3), 894–897.
 39. Kam, L.; Boxer, S. Spatially selective manipulation of supported lipid bilayers by laminar flow: Steps

- toward biomembrane microfluidics. *Langmuir* **2003**, *19* (5), 1624–1631.
40. Kung, L.; Kam, L.; Hovis, J.; Boxer, S. Patterning hybrid surfaces of proteins and supported lipid bilayers. *Langmuir* **2000**, *16* (17), 6773–6776.
 41. Groves, J.; Boxer, S.; McConnel, H. Electric field-induced reorganization of two-component supported bilayer membranes. *Proc. Natl. Acad. Sci. U. S. A.* **1997**, *94* (25), 13390–13395.
 42. Groves, J.; Boxer, S.; McConnell, H. Electric field-induced critical demixing in lipid bilayer membranes. *Proc. Natl. Acad. Sci. U. S. A.* **1998**, *95* (3), 935–938.
 43. van Oudenaarden, A.; Boxer, S.G. Brownian ratchets: Molecular separations in lipid bilayers supported on patterned arrays. *Science* **1999**, *285* (5430), 1046–1048.
 44. Sapuri, A.; Baksh, M.; Groves, J. Electrostatically targeted intermembrane lipid exchange with micro-patterned supported membranes. *Langmuir* **2003**, *19* (5), 1606–1610.
 45. Kam, L.; Boxer, S. Cell adhesion to protein-micropatterned-supported lipid bilayer membranes. *J. Biomed. Mater. Res.* **2001**, *55* (4), 487–495.
 46. Orth, R.; Wu, M.; Holowka, D.; Craighead, H.; Baird, B. Mast cell activation on patterned lipid bilayers of subcellular dimensions. *Langmuir* **2003**, *19* (5), 1599–1605.
 47. Fang, Y.; Frutos, A.; Webb, B.; Hong, Y.; Ferrie, A.; Lai, F.; Lahiri, J. Membrane biochips. *BioTechniques* **2002**, *33*, 62–65.
 48. Groves, J. Membrane array technology for drug discovery. *Curr. Opin. Drug Discov. Dev.* **2002**, *5* (4), 606–612.
 49. Fang, Y.; Frutos, A.; Lahiri, J. G-protein-coupled receptor microarrays. *ChemBioChem* **2002**, *3* (10), 987–991.





Nanostructure of Ionic Amphiphilic Block Copolymer Monolayer at Air / Water Interface

Emiko Mouri

Hideki Matsuoka

Kyoto University, Kyoto, Japan

INTRODUCTION

Amphiphilic diblock copolymers,^[1,2] which have hydrophilic and hydrophobic chains, self-assemble to form a monolayer at the air / water interface and a micelle in selective solvents. The diblock copolymer monolayer system is of great importance and interest from the scientific and technological points of view. The relationship between the fundamental molecule structure and properties, such as length and stiffness of each chain, hydrophilicity–hydrophobicity balance, and the nanostructure of monolayer formed, is an important aspect in establishing a tailor-made polymer assembly at the surface and interface. Furthermore, the hydrophilic chain in the polymer monolayer is an excellent model system of the “polymer brush,”^[3] which is useful in surface modification, colloid stabilization, etc.

OVERVIEW

We have been studying amphiphilic diblock copolymer monolayers at the air / water interface by in situ X-ray^[4–9] and neutron reflectometry.^[10] In recent years, our interest has been focused on ionic amphiphilic diblock copolymer monolayer systems that form an ionic polymer brush in water subphase.^[6,8,9] The long-range electrostatic interaction and osmotic pressure inside the ionic polymer brush are important for the monolayer nanostructure, in addition to short-range steric forces and conformational effects that are usually seen in the neutral brush. This situation causes a large variety of brush structures. Elucidation of the polymer brush nanostructure will enable on-demand control of surface structure and a wide-range application of the polymer brush system.

The diblock copolymer chosen for the investigation is composed of a fluid-like, very flexible hydrophobic chain and a weak polyacid chain, poly(1,1-diethylsilacyclobutane)_m-*block*-poly(methacrylic acid)_n [poly(Et₂SB-*b*-MAA)].^[11] The fluid-like nature of Et₂SB makes it possible to form a polymer monolayer with smooth interface between air and hydrophobic layer with 3–5 Å roughness.^[6] Furthermore, the electron density contrast between

Et₂SB and MAA is larger than that in the general diblock copolymer system. Merited by these two, a suitable system for X-ray reflectivity measurement could be achieved by this diblock copolymer.

The nanostructure of the polymer monolayer has been systematically investigated as a function of hydrophilic chain length, surface pressure, and pH.^[6,8,9] Interesting features are as follows: 1) The hydrophobic layer thickness takes a minimum as a function of hydrophilic chain length at any surface pressure studied.^[6] 2) The hydrophilic layer under the water is not a simple layer but is divided into two layers, i.e., a “carpet”-like dense MAA layer near the water surface and a polyelectrolyte brush layer.^[9] 3) The thickness of this dense layer is about 10–20 Å independent of surface pressure and polymerization degree of PMAA in the range studied.^[9] Phenomenon 1) can be explained by reasonable speculation based on 2) and 3).

The above-mentioned phenomena (1–3) have not been predicted or reported before except for one case.^[31,32] By combining precision synthesis of diblock copolymers, in situ and high-resolution X-ray reflectivity (XR) measurement, and highly quantitative analysis, we have clarified the nanostructure of polymer self-assembly at the interfaces.

IN SITU X-RAY REFLECTIVITY EXPERIMENT

The X-ray reflectivity (XR) technique has been attracting attention as a useful tool for the in situ investigation of the surface nanostructure in laboratory-scale experiments.^[12–14] The usefulness and powerfulness of the neutron reflectivity (NR) technique have also been widely recognized, and novel NR instruments have been constructed^[10] although NR is still regarded as a special technique because of the limitation of experimental facilities.

X-ray reflectivity measurements were performed with an RINT-TTR-MA (Rigaku Corp., Tokyo, Japan) apparatus in which the X-ray generator and detector vertically rotate around the sample stage. The Langmuir–Blodgett (LB) trough (length 130 mm × width 60 mm), made of

aluminum coated with Teflon[®] (USI System, Fukuoka, Japan), was mounted on the sample stage to study the water surface system. Details of the XR apparatus and data treatment have been fully described elsewhere.^[15-17] Data analysis is based on the theory of Parrat^[18] and Sinha et al.^[19] The measurements were performed under specular conditions; that is, the incident and reflection angles were kept equal. The specular reflectivity of X-ray provides information on an electron-density variation normal to the surface in the order of angstroms. The scattering vector q in specular reflectivity is defined by $q = 4\pi\sin\theta/\lambda$, where θ is the incident or reflection angle from the sample surface, and λ is the wavelength of the incident X-rays, which was 1.5406 Å (Cu K_{α1}).

AMPHIPHILIC DIBLOCK COPOLYMER AND POLYMER BRUSH

Amphiphilic diblock copolymers have both hydrophilic and hydrophobic chains in one molecule. It is possible to design diblock copolymer amphiphiles with large hydrophilic and hydrophobic parts in contrast with amphiphilic small molecules whose hydrophilic and hydrophobic parts are both short. Because of the large hydrophobicity due to the long hydrophobic chain, the diblock copolymer forms a polymer monolayer on water with dangling hydrophilic chain. The long hydrophilic chain in the monolayer forms a "polymer brush" in the water subphase.

The brush structure is mainly characterized by brush thickness, brush density, and density profile in the brush. Theoretical predictions, especially for charged brush, have been made since the early 1990s.^[20-22] In the past two decades, experimental studies on the polymer brush have been greatly promoted by advances in reflectometry^[12-14] and methods of surface graft polymerization.^[23]

The polymer brush in water has been mainly studied on either the hydrophilic chain in diblock copolymer monolayer at air / water interface or grafted polymer chain from a solid substrate immersed in water. The advantages of the monolayer at the air / water interface are as follows: 1) The graft length and polydispersity can be precisely controlled and characterized in the polymerization procedure of a diblock copolymer. 2) The graft density can be easily and freely controlled by changing the surface pressure after spreading a diblock copolymer on a water surface if the sample is insoluble to the subphase. On the other hand, if the sample is not perfectly insoluble, it might be anticipated that the π -A isotherm gives only apparent graft density. An estimation of the solubility and its effect on the monolayer is needed. The solubility problem in our case can be solved by a simple calculation from density and thickness of the hydrophobic layer.^[6]

For a grafted polymer chain from a solid substrate, once a well-characterized sample is prepared, the same graft density is always maintained regardless of subphase condition, i.e., pH and salt concentration. However, simultaneous control of graft density and chain length is still difficult, and special instruments and efforts are needed for their characterization.

In the course of polymer brush studies, a neutral diblock copolymer system has been studied by reflectometry from the preliminary stage.^[24-29] The polyethylene-oxide (PEO) brush in the water subphase is a well-studied representative system.^[26-29] Many investigations on the polyelectrolyte brush have been performed since the late 1990s.^[6,30-37] In the polyelectrolyte brush systems, the grafted polymer system is often introduced instead of the monolayer system at the air / water interface.^[33-36] This trend owes much to the progress of living radical polymerization.^[23] However, as described above, the diblock copolymer system has many advantages. Furthermore, the diblock copolymer system is suitable for investigating the relationships between the monolayer structure and the hydrophilic-hydrophobic balance that has not yet been systematically studied either experimentally or theoretically. We believe that detailed discussions on the monolayer structure at the air / water interface and the interesting features related to the hydrophilic-hydrophobic balance are possible only when the diblock copolymer system is utilized.

MONOLAYER STRUCTURE INVESTIGATED BY X-RAY REFLECTOMETRY

Monolayer Preparation

Three polymer samples with different MAA (hydrophilic) chain lengths and a constant Et₂SB (hydrophobic) chain

Table 1 Characterization of poly(Et₂SB)_m-b-poly(MAA)_n

Et ₂ SB:MAA ($m^a:n^b$)	M_n^c	M_w/M_n^d
40:10	6,300	1.16
45:60	11,200	1.18
43.81	12,800	1.12

^aNumber-average degree of polymerization of the poly (Et₂SB) segment determined by ¹H-NMR.

^bNumber-average degree of polymerization of the poly (tBMA) segment (before hydrolysis) determined by ¹H-NMR.

^cNumber-average molecular weight of the block copolymer determined by ¹H-NMR.

^dPolydispersity index determined by gel permeation chromatography (GPC) relative to polystyrene standard before hydrolysis.

Source: Ref. [6]. Copyright 2002 by the American Chemical Society.

length were synthesized by anionic polymerization.^[6,11] The characteristics of the samples are summarized in Table 1. A polymer monolayer was prepared by spreading the sample solution [1 mg/mL tetrahydrofuran (THF) solution] on the water surface in a Langmuir trough. After solvent evaporation, the surface was compressed to reach the desired surface pressure at which XR measurements were carried out.

Nanostructure of Polymer Monolayer—Carpet/Polymer Brush Double-Layer Formation in Hydrophilic Layer

The XR profiles of poly(Et₂SB-*b*-MAA) monolayer on water surface are shown in Fig. 1. The profiles had clear, high-order Kiessig fringes that were rarely observed in profiles on water surface systems mainly because of surface roughness and low contrast. Such clear profiles enabled highly quantitative data analysis and detailed discussion on the monolayer structure in the Å scale.^[6,9]

In principle, if the monolayer is composed of two discrete layers with a thickness of d_1 and d_2 , the reflectivity profile should be represented as a superimposition of three cosine curves with a frequency of d_1 , d_2 , and $(d_1 + d_2)$, on the decay of -4 power governed by Fresnel's law. The cosine curve is amplified by each electron density contrast between layers. The sufficient density contrast between each layer enables us to detect three kinds of frequencies. However, in a poly(Et₂SB-*b*-MAA) system, the Et₂SB hydrophobic layer is more enhanced in the reflectivity curves because this layer has larger electron density contrast than the MAA hydrophilic layer. As a result, the frequency of fringes in the observed curves reflects the thickness of the Et₂SB layer, but the profile contains a contribution from the MAA layer. In fact, the small fringes that originated from the whole layer including the MAA layer were found in a $m:n = 43:81$ sample around $q = 0.05 \text{ \AA}^{-1}$.

The monolayer structure was determined by model fitting of the XR profiles. The amphiphilic diblock copolymer monolayer on water is supposed to be composed of hydrophobic and hydrophilic layers. Therefore a two-box model, which has two discrete layers with interface roughness between layers, is applied first to reproduce experimental data. A three-box model was applied if there was not sufficient agreement by the two-box model.^[8,9]

As is indicated in Fig. 1 by lines, a three-box model was needed to reproduce the XR profiles for the $m:n = 43:81$ monolayer above 20 mN/m. The small fringe at a lower q pointed above could not be reproduced by the two-box model. Profiles for the other two samples were

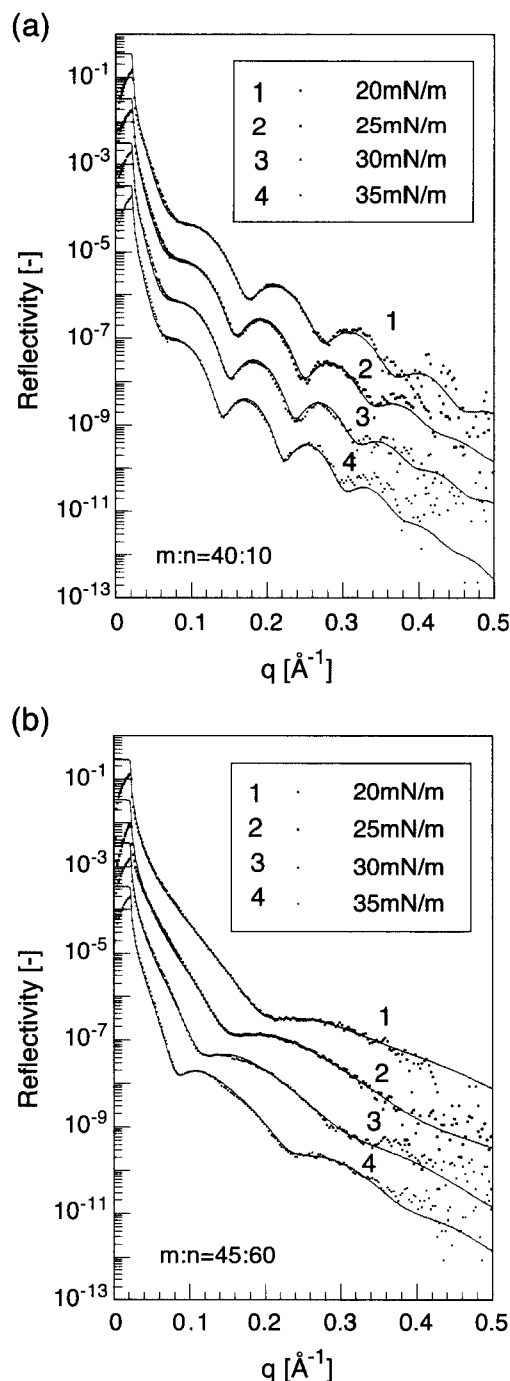


Fig. 1 X-ray reflectivity profiles for poly(Et₂SB)_{*m*}-*b*-poly(MAA)_{*n*} monolayer on water. (a) $m:n = 40:10$, (b) $m:n = 45:60$, (c) $m:n = 43:81$. Each profile was shifted downward by one decade for clarity. The solid lines are the best-fit curves by the two-box model ($m:n = 40:10, 45:60$) and the three-box model ($m:n = 43:81$). (a,b)—From Ref. [6]. Copyright 2002 by the American Chemical Society. c—From Ref. [9]. Copyright 2003 by John Wiley & Sons, Inc.)

(Continued)

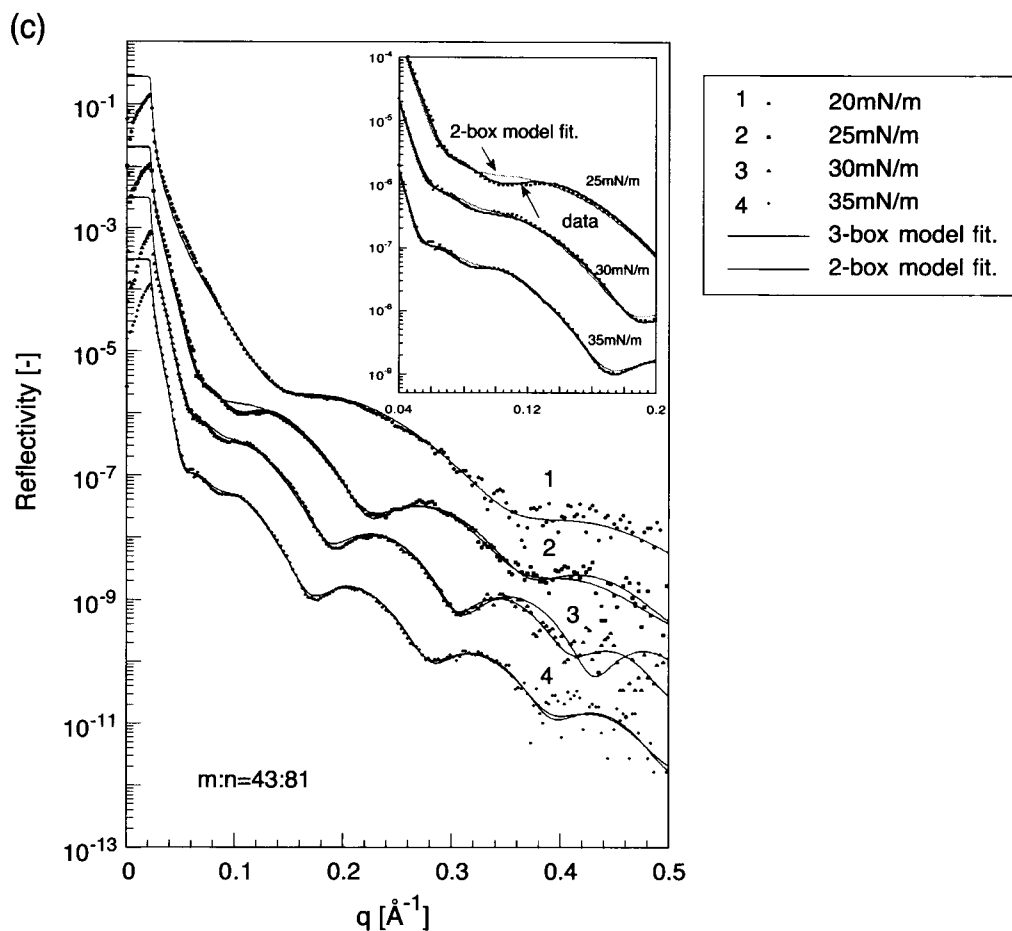


Fig. 1 (Continued).

well reproduced by a two-box model at any surface pressure studied.

The density profiles obtained by the three-box model fitting are shown in Fig. 2. The $m:n=43:81$ monolayer [Fig. 2c] above 20 mN/m was found to be composed of an Et₂SB layer and two MAA layers: The MAA layer was divided into two MAA layers, an upper layer and a lower layer. The upper MAA layer just beneath the Et₂SB layer has a higher density than the lower MAA layer. The lower layer has a lower density and has a large roughness at the interface with a water subphase. This means that this MAA layer has a diffuse structure like a polymer brush. So we call the former a *dense MAA layer* and the latter a *diffuse MAA layer*. The diffuse layer is, in principle, the “brush layer.” A schematic figure of the monolayer structure is also shown in Fig. 3. The thickness of the dense MAA layer is about 15 Å and its density is almost the same as the bulk density of MAA. The surface pressure and chain length dependence of the monolayer structure will be discussed in the following section.

Effect of Surface Pressure—Transition from Carpet Layer to Carpet/Polymer Brush Double Layer

X-ray reflectivity measurements were carried out at different surface pressures, i.e., at different grafting densities (number of polymer chains per unit area), by compressing the monolayer. Brush density was from 0.1 to 0.8 nm⁻² in the surface pressure range studied.^[6,9]

The distinguishing feature shown in Fig. 2 is that the existence of the MAA dense layer with 10–20 Å thickness is independent of surface pressure. The maximum density of the dense MAA layer in contact with water surface, i.e., contact with a hydrophobic Et₂SB layer, is almost the same as the bulk MAA density. The dense layer seems to have an important role in determining the monolayer structure as discussed in the following section.

In Fig. 2c, the transition from a carpet-like dense layer to a dense/diffuse double layer as the surface pressure increases is clearly visualized. At a low surface pressure (20 mN/m), the brush layer cannot be seen by XR; that is,

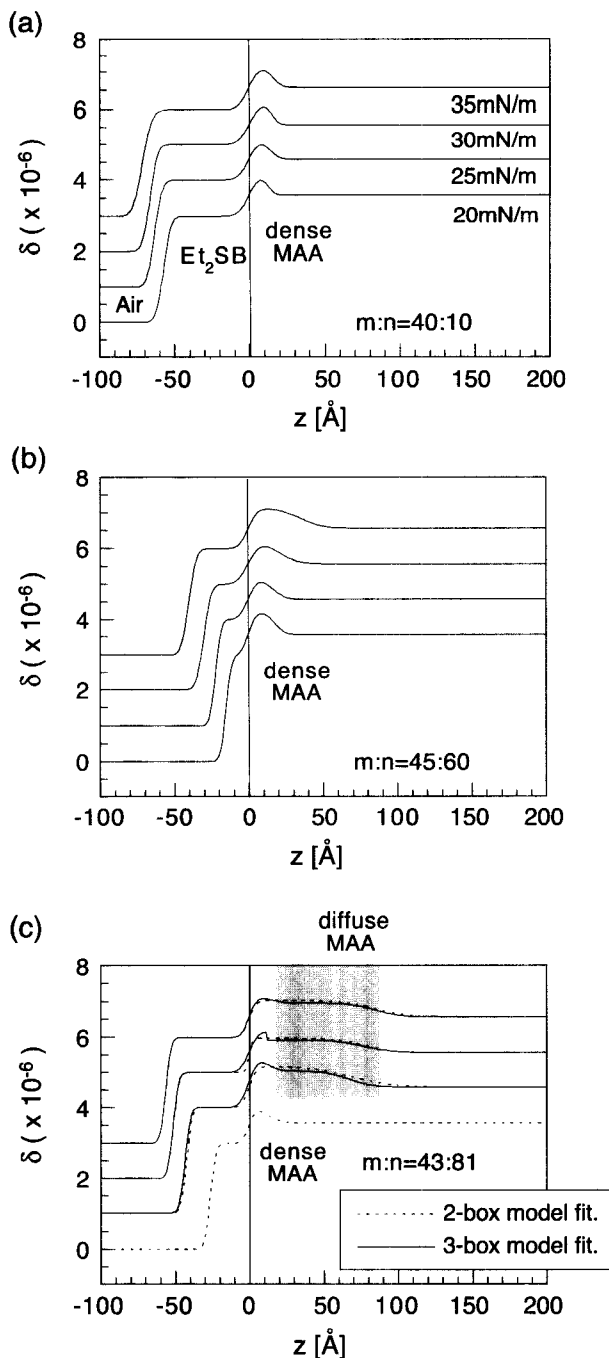


Fig. 2 Density (δ) profiles for poly(Et_2SB) $_m$ - b -poly(MAA) $_n$ on water. (a) $m:n = 40:10$, (b) $m:n = 45:60$, (c) $m:n = 43:81$. δ is proportional to electron density, and defined by r.i. = $1 - \delta - i\beta$, where r.i. is the refractive index. Each profile was shifted upward by one decade for clarity. The order of the profiles is consistent from (a) to (c). (a,b—From Ref. [6]. Copyright 2002 by the American Chemical Society. c—From Ref. [9]. Copyright 2003 by John Wiley & Sons, Inc.)

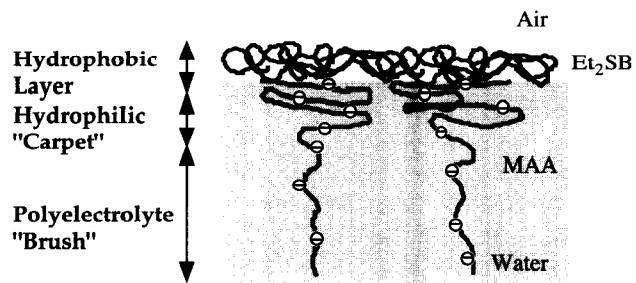


Fig. 3 Schematic representation of the "carpet" layer and the brush layer in poly(Et_2SB) $_{43}$ - b -poly(MAA) $_{81}$ monolayer. (View this art in color at www.dekker.com.)

almost no brush layer exists. By an increase of the surface pressure, the MAA brush layer was formed in addition to the dense layer, and the thickness of the diffused brush layer increased with a further increase of surface pressure.

The density difference between the dense MAA layer and the diffuse MAA layer was largest at 25 mN/m, at which the density of the dense MAA layer was also at maximum. The MAA fraction that contributed to the dense MAA layer was calculated to be 40% at 25 mN/m with an assumption that the MAA bulk density was 1.22 g/cm³.

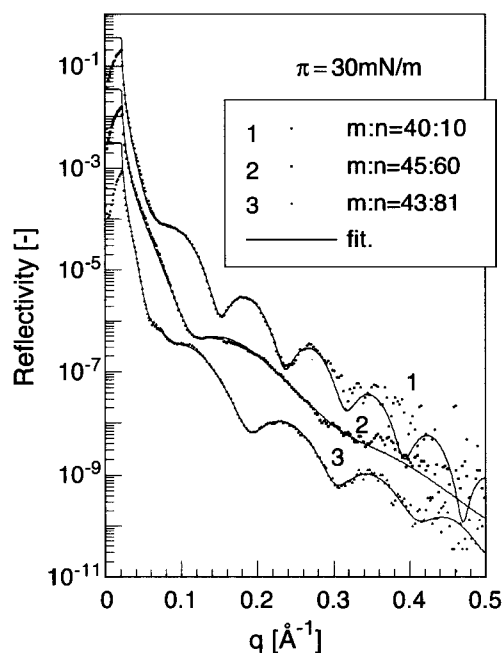


Fig. 4 X-ray reflectivity profiles for poly(Et_2SB) $_m$ - b -poly(MAA) $_n$ on water at 30 mN/m. (1) $m:n = 40:10$, (2) $m:n = 45:60$, (3) $m:n = 43:81$. Each profile was shifted downward by one decade for clarity. The solid lines are the best-fit curves obtained by the two-box model ($m:n = 40:10, 45:60$) and the three-box model ($m:n = 43:81$).

The density difference became smaller as surface pressure increased beyond this point. At the same time, the brush layer formed and its thickness increased as the surface pressure increased.

From these observations, a possible interpretation of the structural change is that a part of the MAA chains is no longer necessary in dense layer above 20 mN/m and they are pushed out to the water subphase and then joined to make a polyelectrolyte brush. In this sense, the dense layer plays a role similar to a "carpet" or "cushion" for the Et₂SB hydrophobic layer on water.

Effect of Hydrophilic Chain Length— Minimum Hydrophobic Layer Thickness and Discrete Layers in the Hydrophilic Layer

The XR profiles for all three samples at 30 mN/m are compared in Fig. 4. As mentioned above, the period of the

fringe corresponds to the hydrophobic Et₂SB layer thickness. It is obvious that the period of the profile for $m:n = 45:60$ (middle MAA length) is the longest, which means that the Et₂SB layer for the sample is the thinnest. The same tendency was observed at any other surface pressure studied.^[6,9]

In Fig. 5, the MAA chain length dependence of each layer thickness is shown. The Et₂SB layer showed an interesting phenomenon: The Et₂SB thickness at the same surface pressure takes a minimum at a medium MAA length at every surface pressure studied [Fig. 5a]. The variation of MAA layer thickness with MAA unit length is also interesting. The thickness variation of the three samples with different hydrophilic chain length ($m:n = 40:10, 45:60, 43:81$) in Fig. 5 showed that the thickness of this dense layer is 10–20 Å independent of surface pressure and polymerization degree of PMAA in the range studied. It is also confirmed in the density profiles in

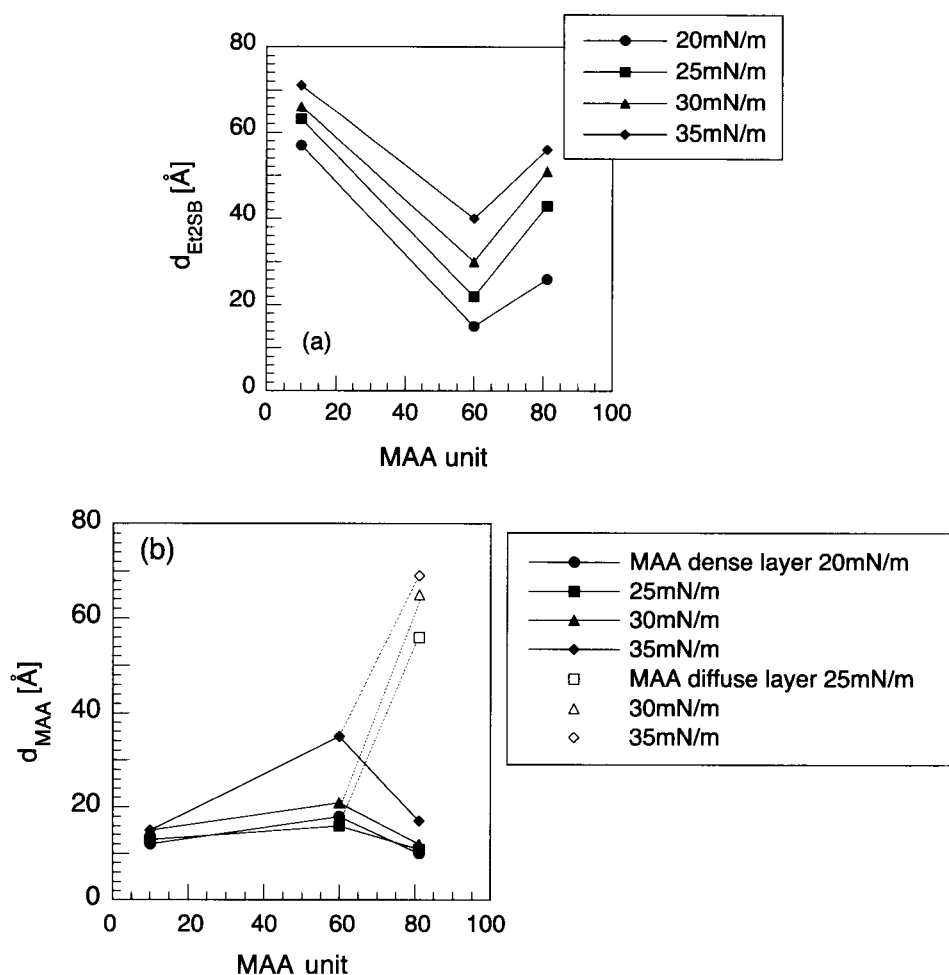


Fig. 5 Thickness variation of the hydrophobic and hydrophilic layers with MAA length. (a) Et₂SB layer and (b) MAA layer. The MAA layer in the $m:n = 43:81$ sample was well reproduced by two discrete layers, a dense MAA layer and a diffuse MAA layer. (From Ref. [9]. Copyright 2003 by John Wiley & Sons, Inc.)

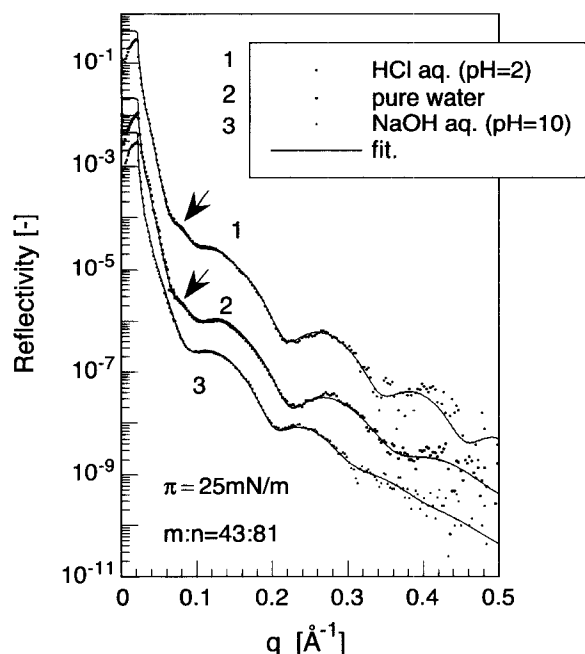


Fig. 6 X-ray reflectivity profiles for poly(Et₂SB)₄₃-b-poly(MAA)₈₁ monolayer on various pH subphases at 25 mN/m. (1) pH 2, (2) pH 7 (pure water), (3) pH 10. Each profile was shifted downward by one decade for clarity. The solid lines are the best-fit curves obtained by the two-box model (pH 10) and the three-box model (pH 2, pH 7). (From Ref. [8]. Copyright 2003 by IUCr.)

Fig. 2. For $m:n = 45:60$ sample, slightly larger thickness, i.e., 18–35 Å, was observed. It is fair to say that we could not distinguish the dense and the short diffuse MAA layers from the XR profiles in this case.

The independence of the thickness in MAA layer just beneath the Et₂SB layer, i.e., dense layer, is interesting because the number of MAA units largely varies from 10 to 80 units. Although the data are not shown here, our newly synthesized samples with different chain lengths ($m:n = 30:20$ to $30:90$) also have a dense layer with a thickness of 10–20 Å.^[32] A thickness of about 15 Å might be the “critical thickness” for a dense layer, or for a dense layer–brush layer transition.

On the other hand, a well-established polyelectrolyte brush is formed only for the $m:n = 43:81$ polymer monolayer. For $m:n = 40:10$ and $m:n = 45:60$ polymer monolayer, only dense MAA layer is formed.

The minimum hydrophobic layer thickness can be related to the double-layer formation in the hydrophilic layer. To explain the Et₂SB layer thickness variation, it is reasonable to consider that the MAA layer has two opposite effects, positive and negative, on surface pressure, and that the formation of a dense MAA layer and diffuse MAA layer in $m:n = 43:81$ monolayer is the key

point. For a small n sample, $m:n = 40:10$, because the MAA contribution to surface pressure is small, much surface compression is needed to achieve the surface pressure desired. This results in the largest thickness of Et₂SB layer. For the medium n sample, $m:n = 45:60$, a *positive* contribution of MAA chain due to its layer size to the surface pressure appears. Hence at the same surface pressure, the Et₂SB layer becomes thinner. For the large n sample, $m:n = 43:81$, a *negative* contribution due to brush formation appears in addition to the *positive* contribution mentioned above. An increase in Et₂SB layer thickness should be observed to compensate for the negative contribution. At this stage, it is not clear whether the dense and the diffuse MAA layers directly correspond to the positive and the negative contributions to surface pressure, respectively. However, it is reasonable to think that the layer near the surface should contribute to a larger increase in surface pressure (a decrease in surface energy) than the brush layer in the subphase.

Effect of pH on the Monolayer Structure—Anomalous pK_a at the Surface

The hydrophilic chain of the diblock copolymer is a weak polyacid, which enabled us to control the monolayer structure by pH. Hence the pH dependence of the monolayer nanostructure was investigated by changing the pH of the subphase.^[6,8]

A marked structural change by pH was observed especially for the $m:n = 43:81$ monolayer. Fig. 6 shows the XR profiles for $m:n = 43:81$ monolayer at different pHs. The fringe with a short period, which was notable for pH 2 and 7 (pure water), was not observed for the profile on the subphase of pH 10. Density profiles (Fig. 7) obtained by

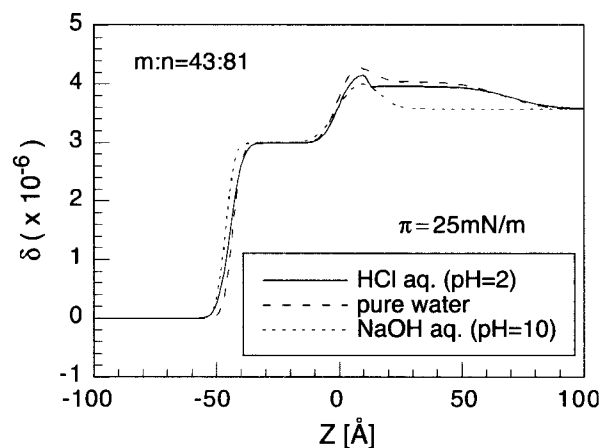


Fig. 7 Density (δ) profiles for poly(Et₂SB)₄₃-b-poly(MAA)₈₁ monolayer on various pH subphases at 25 mN/m. (1) pH 2 (solid line), (2) pH 7 (dashed line), (3) pH 10 (dotted line). (From Ref. [8]. Copyright 2003 by IUCr.)

model fitting of the XR profiles indicate that the brush layer was not detected for the $m:n=43:81$ sample on pH 10 subphase (dotted line) at 25 mN/m, at which the carpet/brush layer formation was detected for acid (solid line) and neutral (dashed line) conditions. Taking the block ratio into consideration, a highly diffused brush should be formed by alkaline condition. Because of the low contrast between the brush layer and water subphase coming from the low volume fraction of the polymer chain in the brush layer, the brush layer could not be detected by XR measurements.

The variation in hydrophobic and hydrophilic layer thickness with pH for all three samples is summarized

in Fig. 8. Almost the same monolayer structure was obtained at acidic (pH 2) and neutral (pure water) conditions, but significant differences were found on the monolayer on subphase of pH 10. For the shortest MAA chain samples, the thickness of the Et₂SB layer in monolayer at pH 10 is explicitly larger than those in acidic and neutral conditions at the same surface pressure. For the long MAA polymer, the carpet/brush structure in the monolayer was not observed and only a dense carpet layer was detectable. Obviously, the observed change of nanostructure with pH is a result of the change of the degree of ionization of carboxylic acid on the hydrophilic chain.

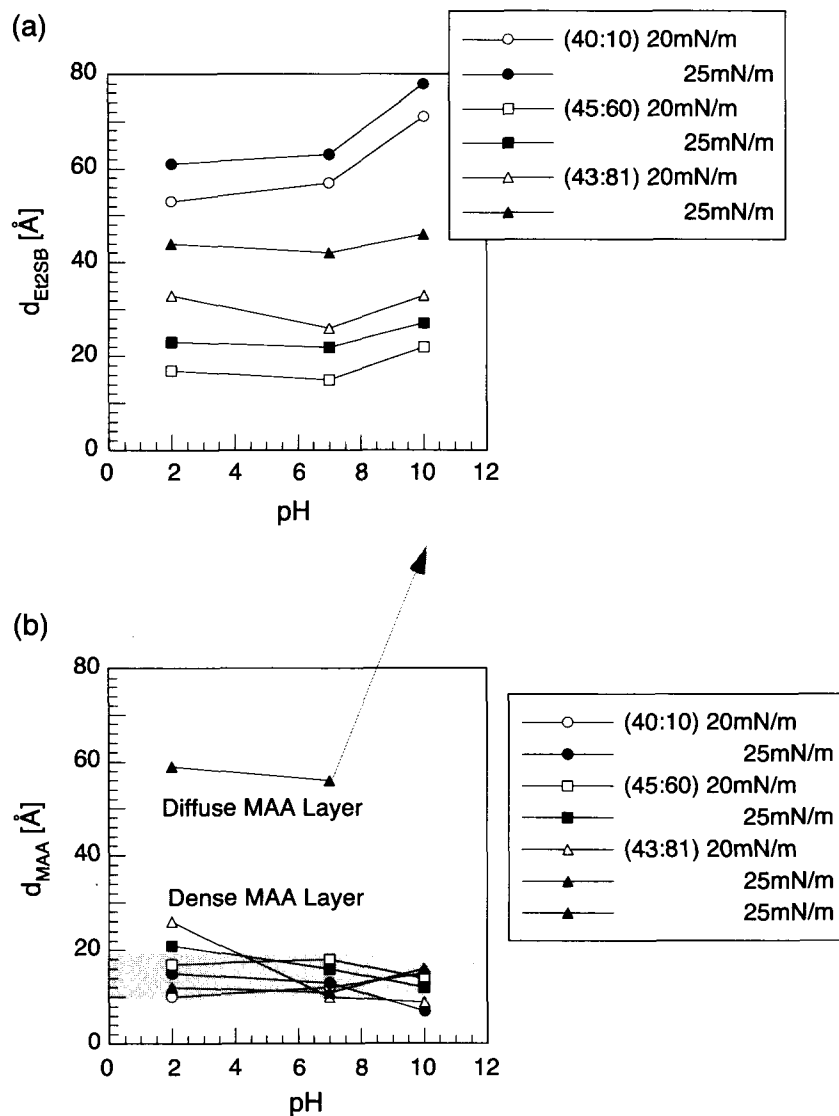


Fig. 8 Thickness variation of the hydrophobic and hydrophilic layers with pH at 20 and 25 mN/m. (a) Et₂SB layer and (b) MAA layer. The $m:n=43:81$ monolayer was well described by a three-box model at pH 2 and pH 7 but well reproduced by a two-box model at pH 10. Considering the $m:n$ block ratio, the diffuse MAA layer should exist at pH 10 in a very diffused form as indicated by the arrow.

In general, a drastic change is expected at the pH around pK_a , which is $pH=4-5$ in bulk solution for carboxylic acids. However, in this system, at the air/water interface, the change occurs between neutral pH and $pH=10$. This means that the pK_a value of the carboxylic groups on the polymer chain in the monolayer is higher than that for bulk state, and it should be located between 7 and 10. This is one of the special characteristics of the surface. The possible origin of this anomalous pK_a at the surface might be an anomalous structure of water, which shows two-dimensional packing of molecules such that the density of polymer chain in the brush is high. This should be clarified in future works.

Comparison with Proposed Theory

Theoretical studies on the structure of the polyelectrolyte brush with variable charges (e.g., weak polyacid) have been carried out as a function of grafting density and ionic strength.^[20-22] The variation of brush thickness with grafting density and ionic strength is not monotonic and is categorized into several regimes. The regimes are characterized by the ratio α/α_b , where α is the degree of dissociation in brush and α_b is the degree of dissociation in bulk. For a brush of weak polyacid in a salt-free solution

as in our system, α is considered to be very small compared to α_b , and categorized into neutral brush regime. In this regime, the brush is expected to behave like a neutral brush.^[21,22] However, our observation of the two discrete MAA layers seems to be characteristic of the polyelectrolyte brush. In addition, the two discrete layers have not been observed in a neutral brush system. These discrepancies are simply because of the oversimplification of the theoretical model: To theoretically describe the polymer brush, the interaction between the brush and the substrate surface (grafted surface) should be taken into account.

The "Real" Nanostructure of Polymer Monolayer and Polymer Brush

The surface pressure and chain length dependencies of the monolayer structure are schematically summarized in Fig. 9.^[6,9] The density profiles are described besides drawings. As also indicated in Fig. 9, the value of the area per molecule is largest for middle n sample. Similarly, the hydrophobic layer thickness is thinnest for the middle n sample. The polymer monolayer formed by the samples with a shorter MAA length is composed of a hydrophilic layer and a dense MAA layer, i.e., without a well-established brush layer at any surface pressure. For the

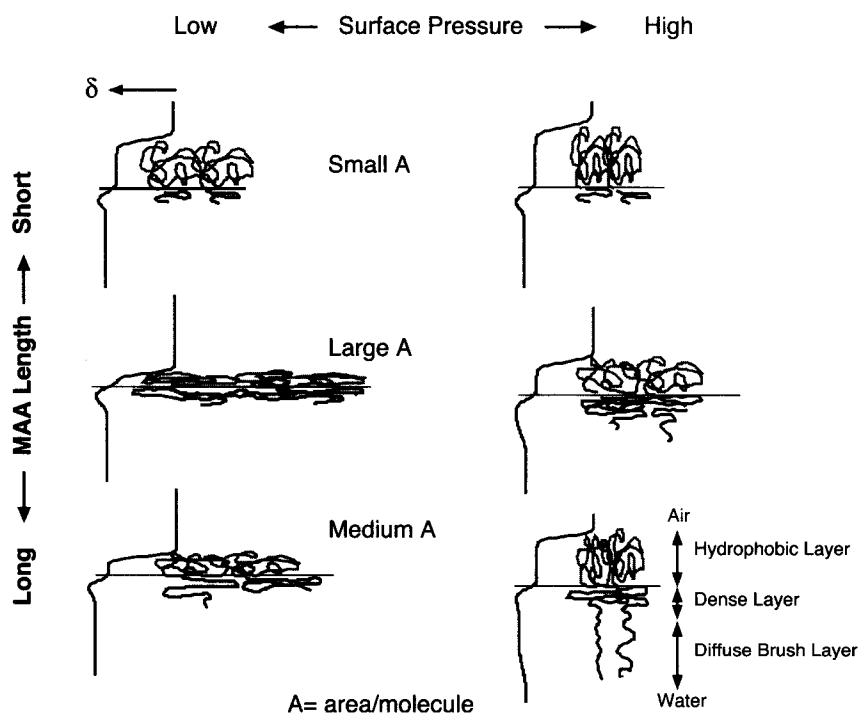


Fig. 9 Schematic representation of the dense layer and the brush layer in poly(Et_2SB)_m-*b*-poly(MAA)_n monolayer on water surface as functions of the surface pressure and the hydrophilic PMAA length. Density profiles are also shown beside the drawings. (From Ref. [9]. Copyright 2003 by John Wiley & Sons, Inc.)

monolayer of a longer MAA sample, a similar situation is observed at a lower surface pressure. With increasing surface pressure, long MAA chains extend to the subphase to form a brush layer that has a lower density than the dense layer.

CONCLUSION

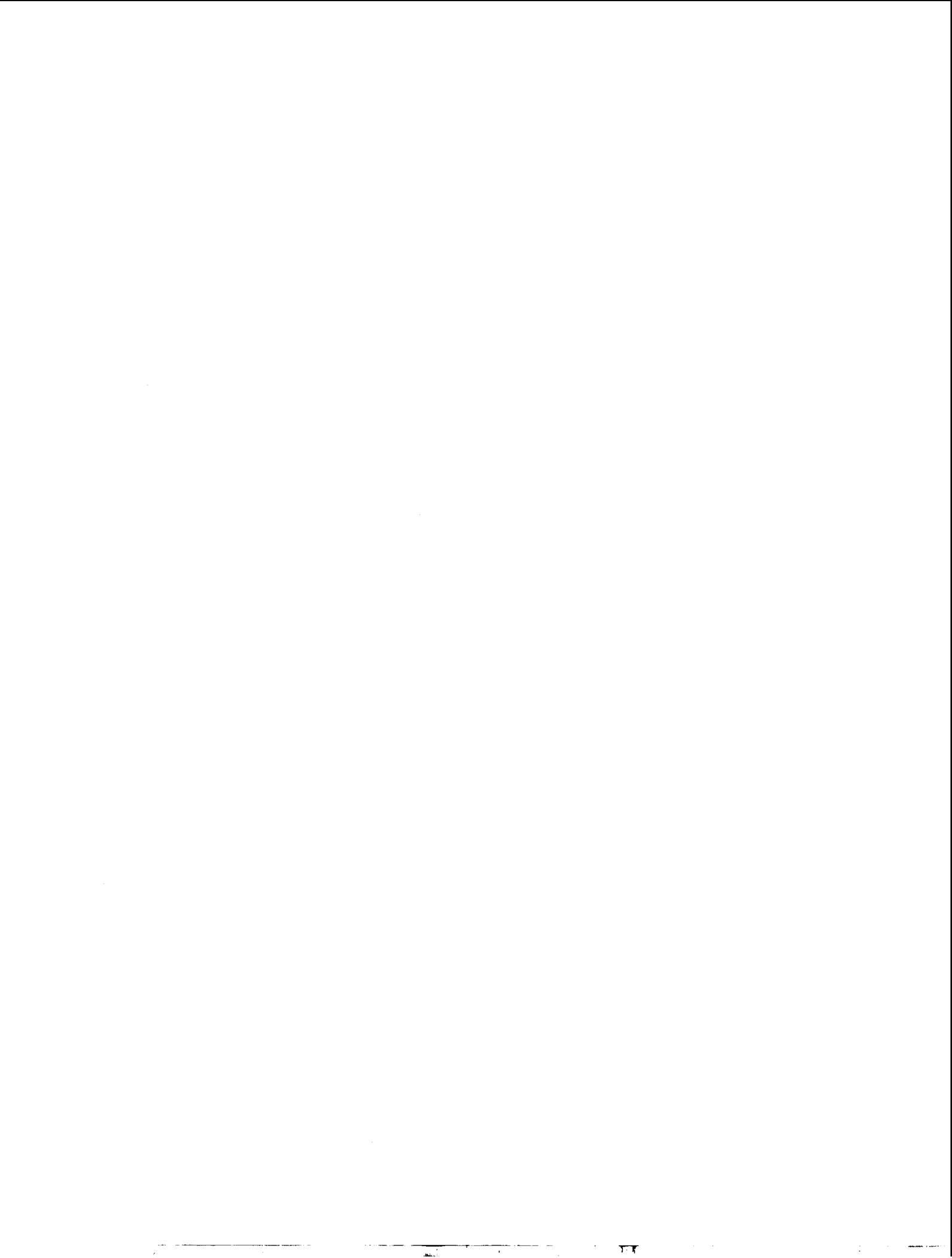
The nanostructure of a monolayer of the ionic amphiphilic diblock copolymer, poly(1,1-diethylsilacyclobutane)-*block*-poly(methacrylic acid) [poly(Et₂SB-*b*-MAA)], at the air / water interface was investigated by in situ XR as a function of surface pressure, MAA chain length, and pH. The MAA brush under the water surface was found to be composed of two parts: a dense layer with a higher density and a diffuse layer with a lower density. The dense layer is always formed independent of MAA chain length, surface pressure, and pH. By contrast, the diffuse layer is formed in addition to the carpet layer only when the hydrophilic chain length is long enough and the surface pressure, i.e., the brush density, is also high enough at lower pHs. At pH 10, the diffuse layer was not observed in the studied range. The dense layer thickness was found to be almost constant at 10–20 Å, independent of surface pressure and MAA chain length. Furthermore, the discrete MAA structure could be an explanation for the interesting observation that the MAA chain length dependence of the thickness of Et₂SB layer showed a minimum at a critical MAA chain length. Either dense or diffuse layer structure and minimum thickness has never been expected in a theoretical study, which indicate the great importance of the in situ experimental study.

We found several new aspects of the diblock copolymer monolayer structure in this study. In situ studies are essential for identifying the carpet/brush double-layer structure and anomalous pK_a. Systematical in situ investigation should clarify the nature of polyelectrolyte brush and make it possible to design and control its structure totally by chain length, chain length ratio, pH, and salt concentration. These findings are expected to contribute to the development of fundamental polymer surface chemistry and of polymer surface nanomaterials.

REFERENCES

1. Hamley, I.W. *The Physics of Diblock Copolymers*; Oxford University Press, 1998; 131–220.
2. Alexandridis, P.; Lindman, B. *Amphiphilic Block Copolymers*; Elsevier: Amsterdam, 2000; 57–190.
3. Milner, S.T. Polymer brushes. *Science* **1991**, *251*, 905–914.
4. Kago, K.; Matsuoka, H.; Yoshitome, R.; Mouri, E.; Yamaoka, H. The importance of a direct in situ evaluation of an amphiphilic diblock copolymer monolayer. The similarity and difference between its nanostructures on water and on solid substrates examined by x-ray reflectometry and atomic force microscopy. *Langmuir* **1999**, *15* (12), 4295–4301.
5. Nakano, M.; Deguchi, M.; Endo, H.; Matsumoto, K.; Matsuoka, H.; Yamaoka, H. Self-assembly of poly(1,1-diethylsilabutane)-*block*-poly(2-hydroxyethyl methacrylate) block copolymer. 2. Monolayer at the air–water interface. *Macromolecules* **1999**, *32* (19), 6088–6092.
6. Mouri, E.; Wahnes, C.; Matsumoto, K.; Matsuoka, H.; Yamaoka, H. X-ray reflectivity study of anionic amphiphilic carbosilane block copolymer monolayers on a water surface. *Langmuir* **2002**, *18* (10), 3865–3874.
7. Matsumoto, K.; Mizuno, U.; Matsuoka, H.; Yamaoka, H. Synthesis of novel silicon-containing amphiphilic diblock copolymers and their self-assembly formation in solution and at air/water interface. *Macromolecules* **2002**, *35* (2), 555–565.
8. Mouri, E.; Matsumoto, K.; Matsuoka, H. Effect of pH on the nanostructure of an amphiphilic carbosilane/methacrylic acid block copolymer at air / water interface. *J. Appl. Crystallogr.* **2003**, *36* (3), 722–726.
9. Mouri, E.; Matsumoto, K.; Matsuoka, H. “Carpet”-like dense layer formation in polyelectrolyte brush at air / water interface. *J. Polym. Sci., B* **2003**, *41* (16), 1921–1928.
10. Torikai, N.; Furusaka, M.; Matsuoka, H.; Matsushita, Y.; Shibayama, M.; Takahara, A.; Takeda, M.; Tasaki, S.; Yamaoka, H. Instrumental design and performance of a new pulsed-neutron reflectometer (ARISA) at KENS for studying free surfaces. *Appl. Phys., A* **2002**, *74*, S264–S266.
11. Matsumoto, K.; Wahnes, C.; Mouri, E.; Matsuoka, H.; Yamaoka, H. Synthesis of anionic amphiphilic carbosilane block copolymer: Poly(1,1-diethylsilacyclobutane)-*block*-methacrylic acid). *J. Polym. Sci., A* **2001**, *39* (1), 86–92.
12. *X-ray and Neutron Reflectivity: Principles and Applications*; Daillant, J., Gibaud, A., Eds.; Springer, 1999; 3–194.
13. Tolan, M. *X-ray Scattering from Soft-Matter Thin Films: Materials Science and Basic Research*; Springer Tracts in Modern Physics, Springer, 1999; Vol. 148, 33–86.
14. Als-Nielsen, J.; McMorrow, D. *Element of Modern X-ray Physics*; Wiley, 2000; 61–103.
15. Yamaoka, H.; Matsuoka, H.; Kago, E.; Eckelt, J. X-ray reflectivity study of fine structure of thin

- polymer films and polymer assembly at interface. *Physica, B* **1998**, *248*, 280–283.
16. Kago, K.; Matsuoka, H.; Endo, H.; Eckelt, J.; Yamaoka, H. X-ray reflectivity study of polymer assembly at air–water interface. *Supramol. Sci.* **1998**, *5*, 349–355.
 17. Matsuoka, H.; Mouri, E.; Matsuomoto, K. Direct in situ investigation of the nanostructure of molecular and macromolecular assemblies at air / water interface by x-ray reflectometry. *Rigaku J.* **2001**, *18*, 54–68.
 18. Parratt, L.G. Surface studies of solids by total reflection of X-rays. *Phys. Rev.* **1954**, *95* (2), 359–369.
 19. Sinha, S.K.; Sirota, E.B.; Garoff, S.; Stanley, H.B. X-ray and neutron scattering from rough surfaces. *Phys. Rev., B* **1988**, *38* (4), 2297–2311.
 20. Wittmer, J.; Joanny, J.F. Charged diblock copolymers at interfaces. *Macromolecules* **1993**, *26* (11), 2691–2697.
 21. Israëls, R.; Leermakers, F.A.M.; Fleer, G.J. On the theory of grafted weak polyacids. *Macromolecules* **1994**, *27* (11), 3087–3093.
 22. Zhulina, E.B.; Birshtein, T.M.; Borisov, O.B. Theory of ionizable polymer brushes. *Macromolecules* **1995**, *28* (5), 1491–1499.
 23. Patten, T.E.; Xia, J.; Abernathy, T.; Matyjaszewski, K. Polymers with very low polydispersities from atom transfer radical polymerization. *Science* **1996**, *272*, 866–868.
 24. Auroy, P.; Auvray, L.; Leager, L. Structures of end-grafted polymer layers: A small-angle neutron scattering study. *Macromolecules* **1991**, *24* (9), 2523–2528.
 25. Kent, M.S.; Lee, L-T.; Farnoux, B.; Rondelez, F. Characterization of diblock copolymer monolayers at the liquid–air interface by neutron reflectivity and surface tension measurement. *Macromolecules* **1992**, *25* (23), 6240–6247.
 26. Bijsterbosch, H.D.; de Haan, V.O.; de Graaf, A.W.; Mellema, M.; Leermakers, F.A.M.; Stuart, M.A.C.; van Well, A.A. Tethered adsorbing chains: Neutron reflectivity and surface pressure of spread diblock copolymer monolayers. *Langmuir* **1995**, *11* (11), 4467–4473.
 27. Dewhurst, P.F.; Lovell, M.R.; Jones, J.L.; Richards, R.W.; Webster, J.R.P. Organization of dispersions of a diblock copolymer of polystyrene and poly(ethylene oxide) at the air–water interface. *Macromolecules* **1998**, *31* (22), 7851–7864.
 28. Faure, M.C.; Bassereau, P.; Lee, L.T.; Menelle, A.; Lheveder, C. Phase transitions in monolayers of PS–PEO copolymer at the air–water interface. *Macromolecules* **1999**, *32* (25), 8538–8550.
 29. Wesemann, A.; Ahrens, H.; Steitz, R.; Förster, S.; Helm, C.A. Internal interface of a compressed PEE–PEO diblock copolymer monolayer. *Langmuir* **2003**, *19* (3), 709716.
 30. Su, T.J.; Styrkas, D.A.; Thomas, R.K.; Baines, F.L.; Billingham, N.C.; Armes, S.P. Neutron and x-ray reflectivity studies of water-soluble block and statistical copolymers adsorbed at the air–water interface. *Macromolecules* **1996**, *29* (21), 6892–6900.
 31. Ahrens, H.; Förster, S.; Helm, C.A. Polyelectrolyte brushes grafted at the air / water interface. *Macromolecules* **1997**, *30* (26), 8447–8451.
 32. Ahrens, H.; Förster, S.; Helm, C.A. Charged polymer brushes: Counterion incorporation and scaling relations. *Phys. Rev. Lett.* **1998**, *81* (19), 4172–4175.
 33. Tran, Y.; Auroy, P.; Lee, L.T. Determination of the structure of polyelectrolyte brushes. *Macromolecules* **1999**, *32* (26), 8952–8964.
 34. Tran, Y.; Auroy, P.; Lee, L.T.; Stamm, M. Polyelectrolyte brushes: Counterion distribution and complexation properties. *Phys. Rev., E* **1999**, *60* (6), 6984–6990.
 35. Currie, E.P.K.; Sieval, A.B.; Fleer, G.J.; Stuart, M.A.C. Polyacrylic acid brushes: Surface pressure and salt-induced swelling. *Langmuir* **2000**, *16* (22), 8324–8333.
 36. Biesalski, M.; Rühle, J. Scaling laws for the swelling of neutral and charged polymer brushes in good solvents. *Macromolecules* **2002**, *35* (2), 499–507.
 37. Mouri, E.; Matsumoto, K.; Matsuoka, H. To be submitted.



Nanostructured Catalysts

Ravichandra S. Mulukutla

Nanoscale Materials, Inc., Manhattan, Kansas, U.S.A.

INTRODUCTION

Practicing green chemistry has become more important over the last decade, reflecting the design, development, and implementation of chemical products and processes to reduce or eliminate the use and generation of substances hazardous to human health and the environment. Some of the principles of green chemistry^[1] are as follows: 1) It is better to prevent waste than to treat or clean up waste after it has been created. 2) Synthetic methods should be designed to maximize the incorporation of all materials used in the process into the final product. 3) The use of auxiliary substances, solvents, separation agents, and others should be avoided; when used these substances should be innocuous. 4) Employ catalysts or catalytic reagents as selective as possible and that are superior to stoichiometric reagents. Hence, the application of catalysts in chemical reactions and more so the impact of nanostructured catalysts is the scope of this article; a few examples will be discussed pertaining to the topic. A catalyst is considered to be active in any given chemical process if it shows high conversion, is selective to the desired products, is stable for a prolonged period of time, and has good mechanical strength. Out of all the concerns, conversion and selectivity dictate the fate of the catalyst in a larger way as it can significantly change the economics of the process. High conversion can be achieved in general if the catalyst species is not sintered during the reaction and selectivity is achieved from the specific crystal structure of the catalytic active metal or the metal oxide precursor. Hence, controlling the catalyst species at molecular level is possible if catalysts were fabricated at nanometer scale. From the definition, particles of between 1 and 10 nm in size have definite crystal structure at nanometer level, and hence the application of nanostructured materials as catalysts can drastically change the conversion and selectivity in the chemical processes. This article describes in detail how nanostructured catalysts affect the catalytic process in comparison to bulk catalysts. More examples can be found in the book chapter written by Klabunde and Mulukutla.^[2]

NANOSTRUCTURED CATALYSTS FOR SELECTIVE PROCESSES

Selectivity in a chemical reaction is defined as the production of one molecule out of many other thermodynamically feasible product molecules. There is an enormous opportunity, for to understand selectivity is very important, and it is less understood than activity.^[3] On the nanometer scale, bifunctional catalysis has been documented as playing a major role in selectivity. On nanostructured catalysts reactant molecules undergo chemical change to produce intermediates. These reaction intermediates will then diffuse a certain distance to other sites where they undergo further rearrangements to produce the final product, which then desorbs. In this case, selectivity changes markedly with conversion. As can be seen from Fig. 1, nanostructured catalysts can be divided into two classes: the first category is composed of nanoparticles of metals supported on metal oxides or molecular sieves and the second includes high-surface-area nanocrystalline metal oxides themselves as catalysts or catalyst supports. Examples for each category are shown and will be described in detail in the following sections.

NANOPARTICLE SUPPORTED CATALYSTS

Nanoparticle catalysts can be designed and synthesized from various methodologies.^[4] The most attractive and appropriate methods involve nanoparticles of metals or metal oxides supported on inert oxides, molecular sieves, and polymers.

Gold Nanoparticle Catalysts

Gold nanoparticle catalysts have attracted wide attention because of their wide applications in CO oxidation, epoxidation of propylene, water-gas-shift reaction, hydrogenation of unsaturated hydrocarbons, and liquid phase selective oxidation.^[5] It is well known that gold is a poor

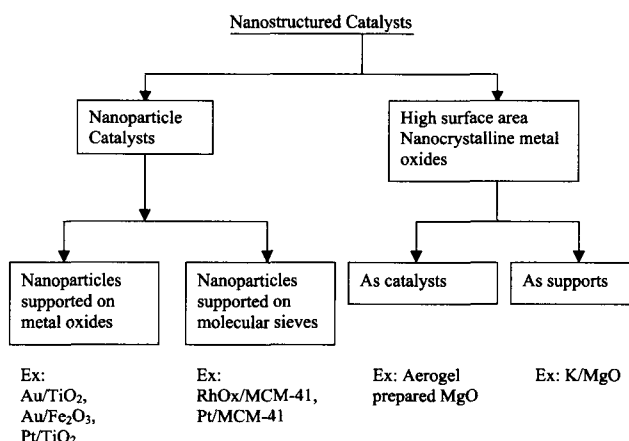


Fig. 1 Classification of nanostructured catalysts.

catalyst in the bulk form, whereas gold nanoparticles supported on oxides exhibit high catalytic activity. A schematic representation of gold nanoparticles supported on oxides is shown in Fig. 2a.

Zhong and Maye^[4] demonstrated a novel approach involving monolayer-encapsulated metal nanoparticles in a core-shell nanostructured assembly as shown in Fig. 2b.

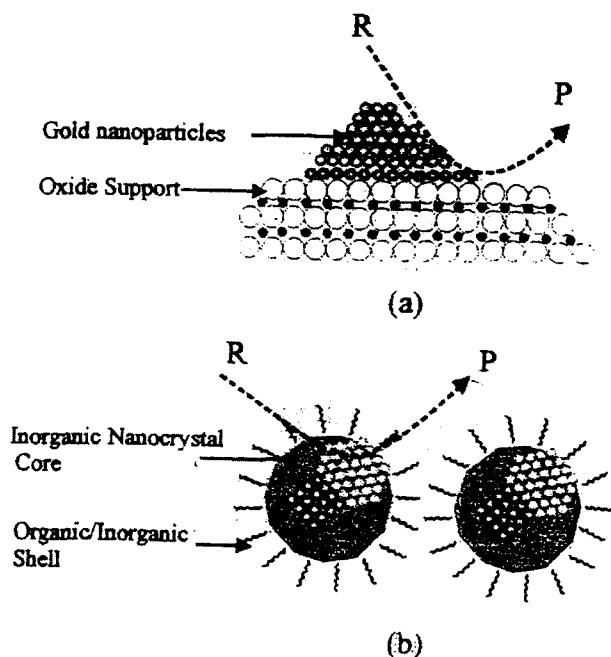


Fig. 2 Schematic representation of nanoparticle catalysts.^[2] (a) Oxide-supported nanoparticle catalyst, (b) core-shell nanoparticle catalyst. (Reprinted with permission from Ref. [4]. Wiley-VCH Verlag GmbH.)

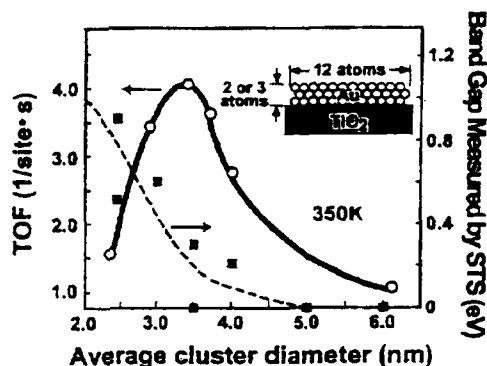


Fig. 3 Turnover frequencies and bandgaps measured by STM as a function of the diameter of Au islands deposited on TiO₂. (Reprinted with permission from Ref. [5]. Elsevier Science B.V. © 2001.)

The core-shell assembled nanostructure undergoes structural or morphological changes during catalytic activation and reaction within both the individual core-shell structure and the collective network environment. The monolayer encapsulation imparts the nanoparticles with shell reactivity and processibility dictated by functional groups in a three-dimensional framework.

Valden et al. reported Au/TiO₂ catalyst^[6] and demonstrated the change in turnover frequency (TOF) of CO oxidation with the change in the diameter of Au islands. As can be seen from Fig. 3, the CO oxidation reaches a maximum at an Au cluster diameter of 3.5 nm, where Au partially loses its metallic nature. They have suggested that this transition might be correlated to the high catalytic activity.

Hayashi and coworkers^[7] found that Au supported on TiO₂ could catalyze epoxidation of propylene in the gas phase containing O₂ and H₂. There are several factors that influence the catalytic activity of the reaction. The most important is the method of preparation, as shown in Fig. 4. The Au/TiO₂ was prepared by either an impregnation method or a deposition precipitation method. The impregnation method did not result in selective oxidation, but instead complete oxidation to H₂O and CO₂, whereas the direct precipitation method led to epoxidation with selectivities above 90%. The difference in the structure of the catalysts prepared by the different methods influences the selectivity. The impregnation method produces large, spherical Au particles with sizes of about several tens of nanometers in diameter, whereas the direct precipitation method results in small hemispherical Au particles strongly contacted with TiO₂ support. This is a very interesting example of how structure and size of the nanoparticles affects the selectivity of the reaction.

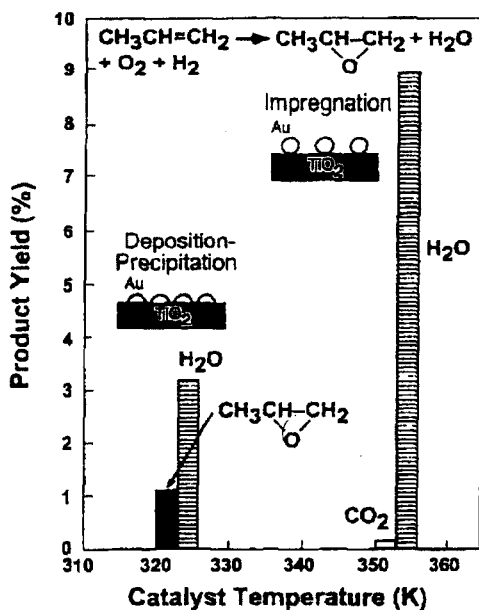


Fig. 4 Epoxidation of propylene over Au/TiO₂ prepared by different methods. (Reprinted with permission from Ref. [5]. Elsevier Science B.V. © 2001.)

Platinum Nanoparticle/MCM-41 Catalysts

Over the last three decades, there have been considerable efforts to synthesize platinum nanoparticle supported catalysts and attempts to study the selectivity in various organic reactions. A classical example is the work of Junges et al.,^[8] who prepared Pt nanoparticles on MCM-41 and applied the catalyst for low-temperature carbon monoxide oxidation. In this work, three methods were employed to synthesize Pt-MCM-41: 1) incipient wetness, 2) ion exchange, and 3) in situ methods. The Pt particle sizes obtained with the three preparation methods varied substantially. For the in situ loading the final average particle size was around 4–6 nm, and TEM observation revealed that the 4-nm-sized particles are located in the pore channels of the MCM-41, while the larger particles might be present on the external surface of MCM-41. The samples synthesized by ion exchange method resulted in 10-nm-sized particles. The incipient wetness impregnation resulted in 2-nm-sized Pt particles with total Pt loading up to 2% mass. All three catalysts were evaluated for CO oxidation with air in an open flow reactor at gas hourly space velocity 25,000 hr⁻¹. The synthetic methods, which resulted in different sizes of Pt particle, had a strong influence on the catalytic performance. The best performance was observed on the samples prepared by incipient wetness, where 50% conversion

was achieved at a temperature of 85°C due to the Pt nanoparticles around 2 nm, which resulted in high conversion. The other two catalysts showed 50% conversion between 110° and 130°C. The work on Pt nanoparticle catalysts provided ample evidence that nanoparticles of Pt can exhibit high rates for CO conversion.

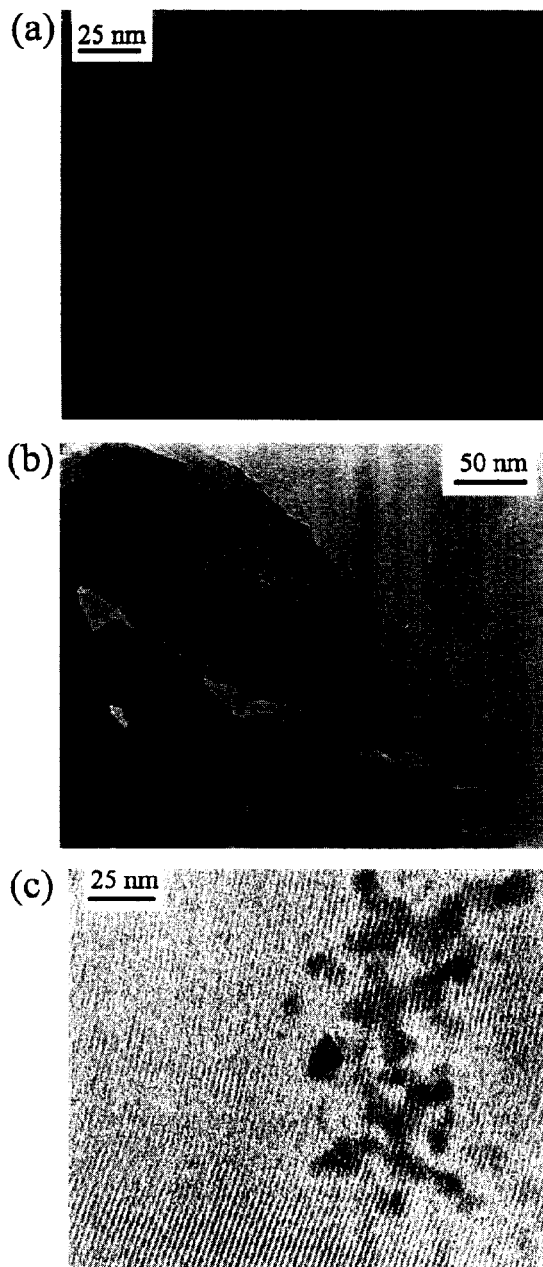


Fig. 5 TEM photographs of (a) Rh-MCM-41-A-200; (b) Rh-MCM-41-B-200, and (c) Rh-su-MCM-41-200. (Reprinted with permission from Ref. [12]. Elsevier Science B.V. © 2002.)

RhOx Nanoparticle/MCM-41

Mulukutla et al.^[9–12] synthesized RhOx nanoparticles in the MCM-41 molecular sieve via a sol–gel method. As shown in Fig. 5, assorted sizes of RhOx nanoparticles were prepared by changing the conditions of the synthesis. The size and location of the resulting rhodium oxide particles varied with the hydrothermal synthesis conditions as shown in TEM photographs in Fig. 5. The RhOx nanoparticles in Rh-MCM-41-A with Si/Rh=200 (Fig. 5a) grew to 6- to 8-nm RhOx particles and they seemed to be located in the bulk of MCM-41. The local structure of MCM-41 might have been destroyed because the particle sizes were larger than the MCM-41 pore diameter (3.2 nm). The argument for RhOx on the surface has been ruled out from the comparison with the MCM-41 supported RhOx sample (Fig. 5c) with a similar Rh loading. Furthermore, the RhOx particles in Rh-MCM-41-A (Fig. 5a) were orthorhombic, whereas the RhOx particles supported on the MCM-41 surface were hexagonal, demonstrating the different locations between the two samples.

The Rh-MCM-41-B with Si/Rh = 200 (Fig. 5b) possessed <3-nm-sized RhOx particles, which were smaller than the MCM-41 with pore diameter of 3.4 nm. TEM photograph of Fig. 5b depicts that the RhOx particles are located in the pore channels of MCM-41. Fig 5c is a TEM photograph of the Rh-su-MCM-41 having Si/Rh = 200, where rhodium oxides are observed as aggregates of about 10-nm size, while the MCM-41 pore channels are clearly visible.

RhOx nanoparticles in the MCM-41 with different particle sizes, structures, and locations in the MCM-41

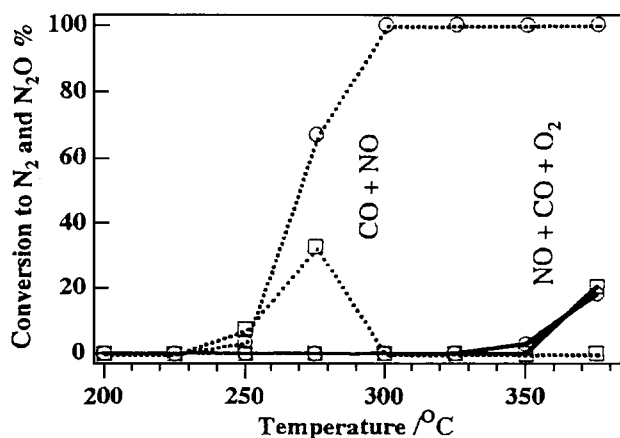


Fig. 6 The NO conversion to N₂ and N₂O against reaction temperature on the Rh-MCM-41-B catalyst; (O) N₂, (□) N₂O, (—) NO+CO+O₂, (- - -) CO+NO. (Reprinted with permission from Ref. [11] Acta Materialia Inc. Published by Elsevier Science Ltd. © 2001.)

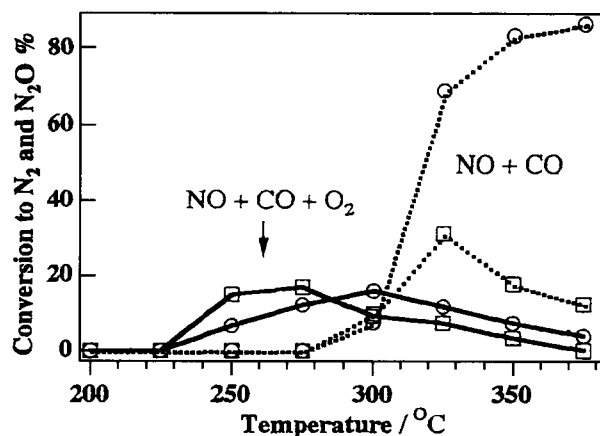


Fig. 7 The NO conversion to N₂ and N₂O against reaction temperature on the Rh-MCM-41-A catalyst; (O) N₂, (□) N₂O, (—) NO+CO+O₂, (- - -) CO+NO. (Reprinted with permission from Ref. [11]. Acta Materialia Inc. Published by Elsevier Science Ltd © 2001.)

were used as catalysts for NO–CO reactions. The NO reduction with CO was performed in the presence and absence of O₂. On the Rh-MCM-41-B catalyst, the NO conversion to N₂ and N₂O in the absence of O₂ began between 275°C and 300°C as shown in Fig. 6. The conversion to N₂O reached a maximum of 30% at 325°C. The selectivity to N₂ increased with temperature and reached 92% at 375°C. Excess oxygen (4%) was added to the stream of NO and CO, which resulted in unexpected promotion of the NO conversion to N₂ and N₂O as shown in Fig. 6. The reaction in the presence of O₂ proceeded at 250°C, whereas it did not proceed below 275°C in the absence of O₂. The promotion phenomenon by excess O₂ is of interest and it may be attributed to the nanosized rhodium oxide precursors in the pore channels of MCM-41. The excess O₂ usually poisons the Rh catalysis since O₂ oxidizes CO to CO₂ very rapidly. It was concluded that under the reaction conditions NO conversion was promoted in the NO–CO reaction in the presence of excess O₂ on the Rh-MCM-41-B catalyst.

Fig. 7 depicts the NO conversion to N₂ and N₂O on the Rh-MCM-41-A catalyst with and without O₂. At 275°C there was about 75% conversion to N₂ and the rest was N₂O, and at the higher temperatures the selectivity toward N₂ was 100%. However, the presence of O₂ in the stream dramatically suppressed the conversion of NO, and the NO conversion to N₂ and N₂O began above 375°C. Thus, the Rh-MCM-41-A catalyst, which had RhOx particles of the size of 6–8 nm exhibited a negative effect of excess O₂ on the NO conversion. These results are entirely different from those observed with the

Rh-MCM-41-B catalyst. NO conversion to N_2 and N_2O in the NO-CO reaction on the RhOx supported on MCM-41 (Rh-su-MCM-41) catalyst exhibited a negative effect by excess O_2 . This feature resembles that observed with the Rh-MCM-41-A catalyst. This observation on the nanostructured RhOx-MCM-41 is emphasized to show that the active sites in different locations and particles sizes play a significant role in the catalytic reaction of NO-CO in presence of O_2 .

NANOCRYSTALLINE METAL OXIDE AS CATALYSTS/CATALYST SUPPORTS

Synthesis of high-surface-area nanocrystalline alkaline metal oxides has drawn much attention because of their high surface area and adsorption capacity compared to their commercial analogues. Some examples are MgO, CaO, TiO_2 , and Al_2O_3 . The extraordinary properties of these nanocrystalline oxides are due to the morphological features of the small crystallites possessing higher populations of reactive surface sites such as edges, corners, and ion vacancies. It has been proposed that some of these nanocrystalline metal oxides, because of their defective sites, might have catalytic properties and that they can be used as catalyst supports because they have high surface area. The following are some examples where nanocrystalline MgO exhibited catalytic properties. In addition, it has been used as support for synthesizing superbase catalysts.

Aerogel-Prepared MgO

Utamapanya et al.^[13] prepared nanocrystalline MgO through an aerogel method using supercritical drying and were successful in obtaining high surface areas in the range of 400–500 m^2/g with crystallite sizes of about 3 nm. The nanocrystalline MgO obtained is referred to as AP-MgO.

Chlorination of Hydrocarbons with Aerogel-Prepared MgO

Aerogel-prepared MgO, when exposed to Cl_2 gas at atmospheric pressure and room temperature, exothermally formed an extremely reactive AP-MgO- Cl_2 adduct; 15% Cl_2 by weight was adsorbed on the surface.^[14] The chlorine adduct was able to chlorinate hydrocarbons in a batch reactor. The normal forms of MgO did not react with Cl_2 gas. Richards et al.^[15] performed further investigation on the characterization of the AP-MgO- Cl_2 adduct, conducting pulse reactions and demonstrating the

catalytic behavior of AP-MgO in the chlorination of hydrocarbons. The XPS characterization of AP-MgO- Cl_2 indicated that the binding energy for Cl 2p is 198.2 eV and this value corresponds to monochloro compounds similar to NaCl and KCl. Hence, the chlorinated species on the surface of AP-MgO is not $MgCl_2$. As shown in Fig. 8a, the chlorination of propane conducted over AP-MgO at temperatures from 0° to 200°C proceeded in normal light. The expected products were 1-chloropropane, 2-chloropropane, and 1,2-dichloropropane. Fig. 8b shows the reaction data conducted without AP-MgO where the reaction proceeded with the help of normal light. As noted, the selectivity to 1,2-dichloropropane up to 60% was observed when the reaction was conducted at 200°C with AP-MgO, with simultaneous decrease of the 2-chloropropane. The selectivity was not affected in the case of a blank reaction.

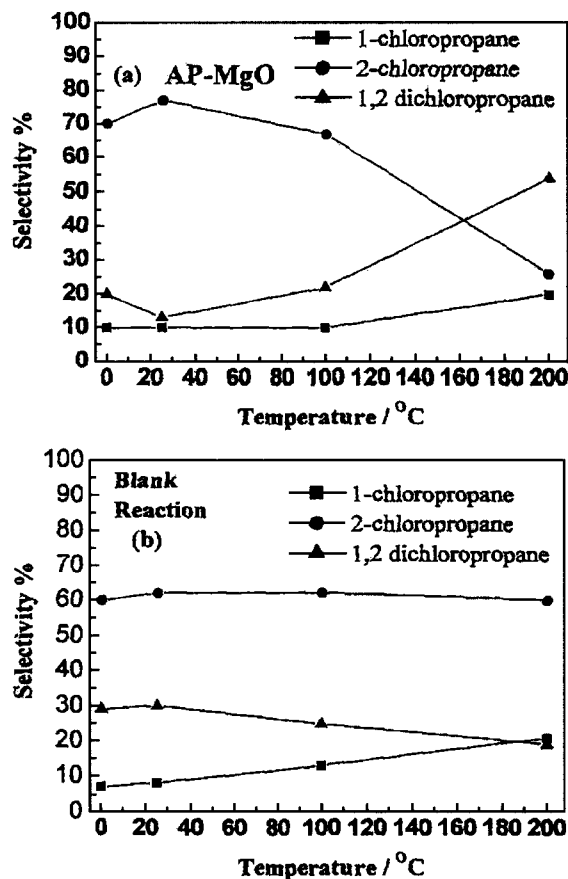


Fig. 8 Chlorination of propane (a) with AP-MgO catalyst. (b) Blank reaction. (Reprinted with the permission from Ref. [15]. Acta Materialia Inc. Published by Elsevier Science Ltd © 2001.)

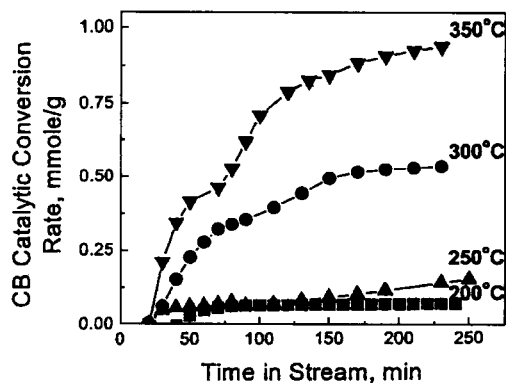


Fig. 9 Kinetics of chlorobutane conversion at different temperatures. (Reprinted with permission from Ref. [17]. American Chemical Society © 2001.)

Dehydrochlorination of 1-Chlorobutane with Aerogel-Prepared MgO

Mishakov et al.^[16] and Fenelonov et al.^[17] evaluated nanocrystalline MgO for dehydrochlorination of 1-chlorobutane. Exposure of AP-MgO to 1-chlorobutane at 200–350°C resulted in both stoichiometric and catalytic dehydrochlorination to form isomers of butene and simultaneous topochemical conversion of MgO to MgCl₂. The resulting MgCl₂ was believed to be an active catalyst for the dehydrochlorination reaction. As shown in Fig. 9, the conversion of chlorobutane at different temperatures over time established the formation of active MgCl₂ from AP-MgO. The formation of such an active catalyst species on the surface of nanocrystalline MgO was possible only with AP-MgO. Hence, this work is a striking example of how a high-surface-area catalytic species such as MgCl₂ can be formed from a nanocrystalline MgO.

Potassium/Aerogel-Prepared MgO

The high surface area of AP-MgO in the range of 350–500 m²/g can be used as a support. Sun and Klabunde^[18] prepared potassium metal-doped nanocrystalline MgO, which exhibited high activity in base-catalyzed isomerization and alkylation. It was established that 10 wt.% of K-doped AP-MgO showed 100% conversion to isomerized products from 2,3-dimethyl-1-butene at room temperature in 30 min. However, the use of commercial analogues and lower-surface-area MgO did not result in such high conversions. The edges/corners on the polyhedral crystallites of high-surface-area MgO are responsible for creating superbasic sites to obtain a highly active isomerization catalysts.

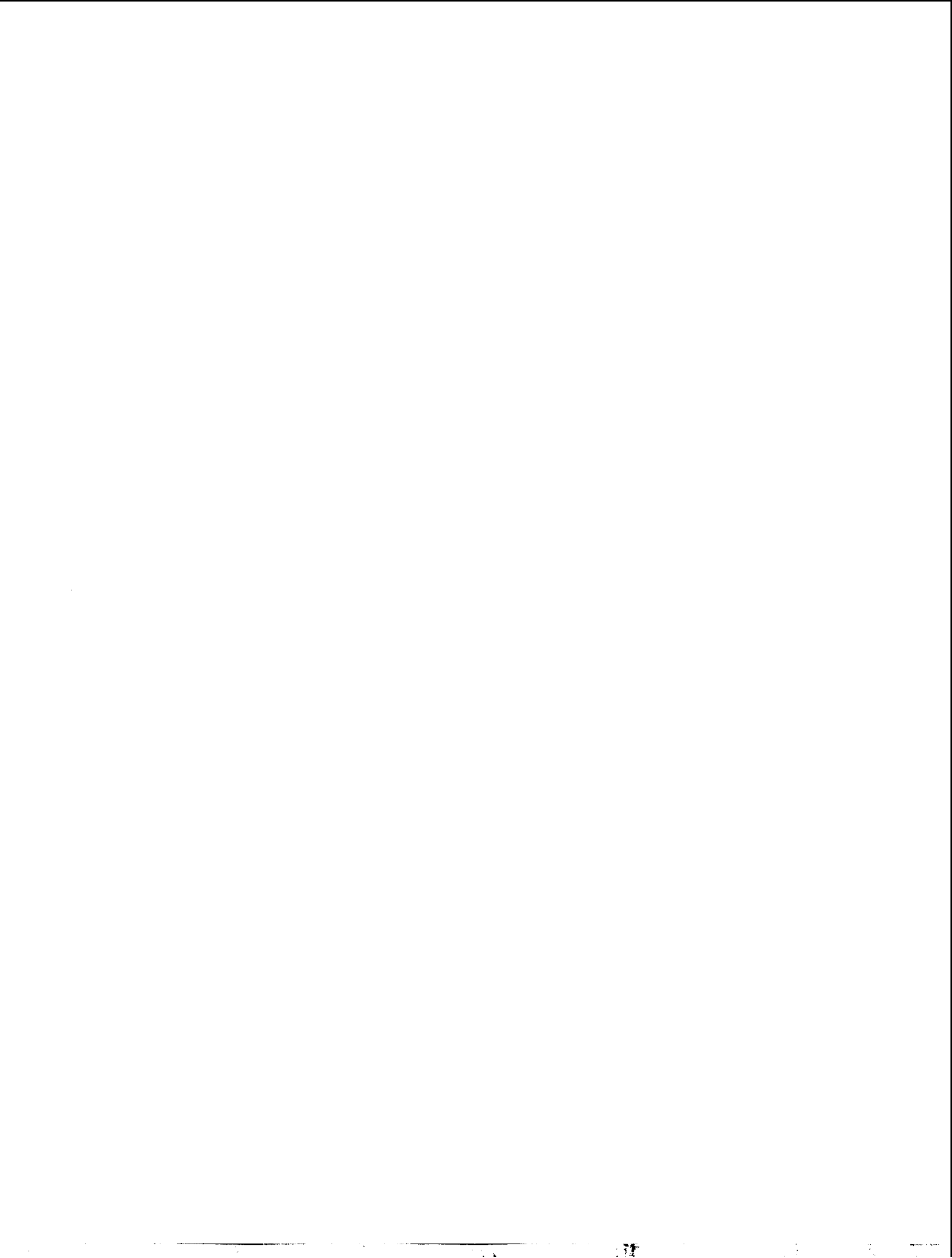
CONCLUSION

This article demonstrates that nanostructured catalysts can be designed by several methods. The prominent ways are synthesizing metal nanoparticles supported on metal oxides and sol-gel method of generating metal/metal oxide nanoparticles in MCM-41 molecular sieves. Nanocrystalline metal oxides with high surface area, which were prepared from aerogel methods, can be used as catalysts or catalyst supports. The examples show that nanostructured catalysts have a significant influence on the conversion and selectivity of the chemical reactions. Control and understanding of particle size and structure of the catalytic active species is the most important factor in achieving the difference between the catalytic property of nanostructured catalysts vs. bulk catalysts.

REFERENCES

1. Anastas, P.T.; Warner, J.C. *Green Chemistry: Theory and Practice*; Oxford University Press: New York, 1998.
2. Klabunde, K.J.; Mulukutla, R.S. Chemical and Catalytic Aspects of Nanocrystals. In *Nanoscale Materials in Chemistry*; Klabunde, K.J., Ed.; John Wiley & Sons, Inc., 2001; 223–261, Chap. 7.
3. Somorjai, G.A.; Borodko, Y.G. Research in nanosciences—Great opportunity for catalysis science. *Catal. Letters* **2001**, *76* (1–2), 1–5.
4. Zhong, C.-J.; Maye, M.M. Core-shell assembled nanoparticles as catalysts. *Adv. Mater.* **2001**, *13*, 1507–1511.
5. Haruta, M.; Date, M. Advances in the catalysis of Au nanoparticles. *Appl. Catal.* **2001**, *222*, 427–437.
6. Valden, M.; Lai, X.; Goodman, D.W. *Science* **1998**, *281*, 1647.
7. Hayashi, T.; Tanaka, K.; Haruta, M. *J. Catal.* **1998**, *78*, 566.
8. Junges, U.; Jacobs, W.; Voigt-Martin, I.; Krutzsch, B.; Schuth, F. MCM-41 as a support for small platinum particles: A catalyst for low-temperature carbon monoxide oxidation. *J. Chem. Soc., Chem. Commun.* **1995**, 2283–2284.
9. Mulukutla, R.S.; Asakura, K.; Namba, S.; Iwasawa, Y. Nanosized rhodium oxide particles in the MCM-41 mesoporous molecular sieve. *Chem. Commun.* **1998**, 1425–1426.
10. Mulukutla, R.S.; Asakura, K.; Kogure, T.; Namba, S.; Iwasawa, Y. Synthesis and characterization of rhodium oxide nanoparticles in mesoporous MCM-41. *Phys. Chem., Chem. Phys.* **1999**, *1*, 2027–2032.
11. Mulukutla, R.S.; Shido, T.; Asakura, K.; Iwasawa,

- Y. Nanoparticles of RhOx in the MCM-41: A novel catalyst for NO-CO reaction in excess O₂. *Scr. Mater.* **2001**, *44*, 1695-1698.
- Mulukutla, R.S.; Shido, T.; Asakura, K.; Kogure, T.; Iwasawa, Y. Characterization of rhodium oxide nanoparticles in MCM-41 and their catalytic performances for NO-CO reactions in excess O₂. *Appl. Catal., A Gen.* **2002**, *228*, 305-314.
 - Utamapanya, S.; Klabunde, K.J.; Schlup, J.R. Nanoscale metal oxide particles/clusters as chemical reagents. Synthesis and properties of ultrahigh surface area magnesium hydroxide and magnesium oxide. *Chem. Mater.* **1991**, *3*, 175-181.
 - Sun, N.; Klabunde, K.J. Nanocrystal metal oxide-chlorine adducts: Selective catalysts of chlorination of alkanes. *J. Am. Chem. Soc.* **1999**, *121*, 5587-5588.
 - Richards, R.; Mulukutla, R.S.; Mishakov, I.; Chesnokov, V.; Volodin, A.; Zaikovski, V.; Sun, N.; Klabunde, K.J. Nanocrystalline ultra high surface area magnesium oxide as a selective base catalyst. *Scr. Mater.* **2001**, *44*, 1663-1666.
 - Mishakov, I.; Bedilo, A.; Richards, R.; Chesnokov, V.; Volodin, A.; Zaikovskii, V.; Buyanov, R.A.; Klabunde, K.J. Nanocrystalline MgO as a dehydrohalogenation catalyst. *J. Catal.* **2002**, *206*, 40-48.
 - Fenelonov, V.B.; Melgunov, M.S.; Mishakov, I.V.; Richards, R.M.; Chesnokov, V.V.; Volodin, A.M.; Klabunde, K.J. Changes in texture and catalytic activity of nanocrystalline MgO during its transformation to MgCl₂ in the reaction with 1-chlorobutane. *J. Phys. Chem., B* **2001**, *105*, 3937-3941.
 - Sun, N.; Klabunde, K.J. High activity solid super base catalysts employing nanocrystals of metal oxides: Isomerization and alkylation catalysis, including conversion of propylene-ethylene mixtures to pentenes and heptenes. *J. Catal.* **1999**, *185*, 506-512.



Nanostructured Catalytic Materials: Design and Synthesis

Hua Chun Zeng

National University of Singapore, Singapore

INTRODUCTION

Natural and manmade catalytic materials are among the oldest “nanostructured materials” known long before the era of nanoscience and nanotechnology. The classic heterogeneous catalysts consist of active nanoscale metal component(s) and solid carriers,^[1] namely, “inert” oxide supports such as alumina, silicates, or magnesium oxide, to increase the reaction surface area and metal utilization. Conventional processing techniques for fabrication of supported catalysts contain one or more of the following steps: impregnation, precipitation, coating, rewashing, ion-exchange, pulverization, drying, and calcination, etc.^[2] Nanoscale metal clusters or particles can be thus formed on the oxide carriers after these processes. It is now well known that the particle size, local composition, and structure (shape) of nanoscale catalysts determine the ultimate catalytic activity and selectivity. For example, it has been demonstrated that the activity of TiO₂-supported gold particles is very sensitive to their size (2 to 3 nm) in the CO oxidation reaction with oxygen at ambient conditions.^[3] It is also well known that the structure and composition of nanocatalysts may change under the reaction conditions, and thus their performance could be time-dependent. Nonetheless, prevailing catalyst preparation still remains largely as a technological art rather than a science, although surface science has significantly deepened our general understanding of heterogeneous catalysis using single-crystal model catalysts.^[4]

Over the past 15 to 20 years, we have witnessed exciting advances in the design and synthesis of low-dimensional nanostructured materials, ranging from fullerenes, carbon nanotubes, supramolecular assemblies, mesoporous structures, to various organic-inorganic hybrid materials. Taking advantage of the rapid development in nanoscience and nanotechnology, a wide range of synthetic techniques are now in place. For example, nanostructured materials can be prepared with constrained or unconstrained synthetic methods, in which inorganic or organic templates (e.g., porous oxides, organic ligands, well-oriented crystal planes, and supramolecule-directing agents) are commonly employed. With these newer approaches and knowledge, a huge variety of nanostructured catalytic materials have been designed and synthesized, which will be the main review topic of the present article.

With the emphasis on catalytic prospect, the objective of this article thus aims at introducing various design and synthesis strategies for this new class of materials. Future challenges and research directions in this area will also be addressed.

DESIGN AND SYNTHESIS OF NANOSTRUCTURED CATALYTIC MATERIALS

Because of the advances in nanostructured catalytic materials and assembling methodologies, we may have to reexamine the roles of each component in the traditional heterogeneous catalysts and redevelop the technology. In fact, a practical solid catalyst is normally not a simple chemical compound, but a highly organized multicomponent materials system (e.g., active components and carrier). In this regard, a modern view of solid catalysts is different from the traditional one. An organized assembly of catalytic materials can be considered as a “catalyst device”,^[5] and the ways of chemical and structural organizations in the device will give profound impacts on its ultimate performance. In the foreseeable future, a transformation from the traditional catalyst preparation to a more sophisticated “assembly” technology is anticipated in view of the rapid progress of this field. As the first steps toward this end, nonetheless, various nanocomponents with desired chemical and structural properties and organization programmability must be fabricated and investigated for the constitution of a nanocatalyst “toolbox.” In the following sections, we will look into the current trends of research in this important area.

Architectures of Porous Materials

Many significant progresses in porous materials have been made over the past two decades, which extends the commonly known zeolites (chemical formula $M_{x/n}^{n+}[(AlO_2)_x(SiO_2)_y]^{x-} \cdot zH_2O$, where M^{n+} represents a metal cation; pore diameter < 1 nm) from microporous regime (pore diameter < 2 nm) to mesopores (2–10 nm),^[6] large mesopores (> 10 nm), and macropores (> 50 nm). In particular, crystalline VPI-5 with uniform pores larger than 1.0 nm had been synthesized for the first time in 1988,

as illustrated in Fig. 1.^[7] Subsequently, periodic mesoporous solids were discovered by Mobil researchers in 1992.^[8] These ordered porous materials with large pore openings had significantly enhanced our ability in utilizing intrapore chemical reactivity and space confinement for catalytic reactions, sorption processes, ion exchange, as well as materials synthesis, including architectures for growth and organization of functional nanomaterials. For example, hexagonal MCM-41 and cubic MCM-48 (Mobil codes) can be prepared with cationic surfactants under basic conditions. These mesoporous silicates together with various modifications (i.e., with metal cations via ion exchange, complexation, and direct “planting”)^[9] allow us to tailor chemical and thermal properties to meet different working environments. For instance, isomorphous substitution and postsynthesis incorporation of active metal species are the two major methods for metal introduction to mesoporous silica.^[10] Furthermore, surface functionalization with organic groups will change the chemical properties of the surfaces, forming hybrid inorganic–organic mesoporous silicates.

In the latter cases, the mesopores of the prepared solids can be viewed as nanoscopic reactors, separators, or host templates for chemical processes and nanostructured materials fabrication.

Various methods have been developed to introduce organic surface groups onto the mesoporous hosts, on the basis of chemical reactions between the hydroxyl-covered surfaces and reactive silane coupling agents. For example, covalent grafting, coating, and co-condensation reactions are common methods to tailor surface properties these days.^[11] In grafting processes, surface modification with organic ligands and functional groups is normally carried out by silylation that takes place on free and geminal silanol groups [i.e., $\equiv\text{Si}-\text{OH}$ and $=\text{Si}(\text{OH})_2$] under dry conditions. On the other hand, coating provides a means to introduce organics onto hydrated pore surfaces where a monolayer of water is present to form organosilanes. Compared to the above two methods, the co-condensation process is a more direct method. The surface organic functional groups can be anchored together with the formation of mesoporous silicates under so-called “one pot”

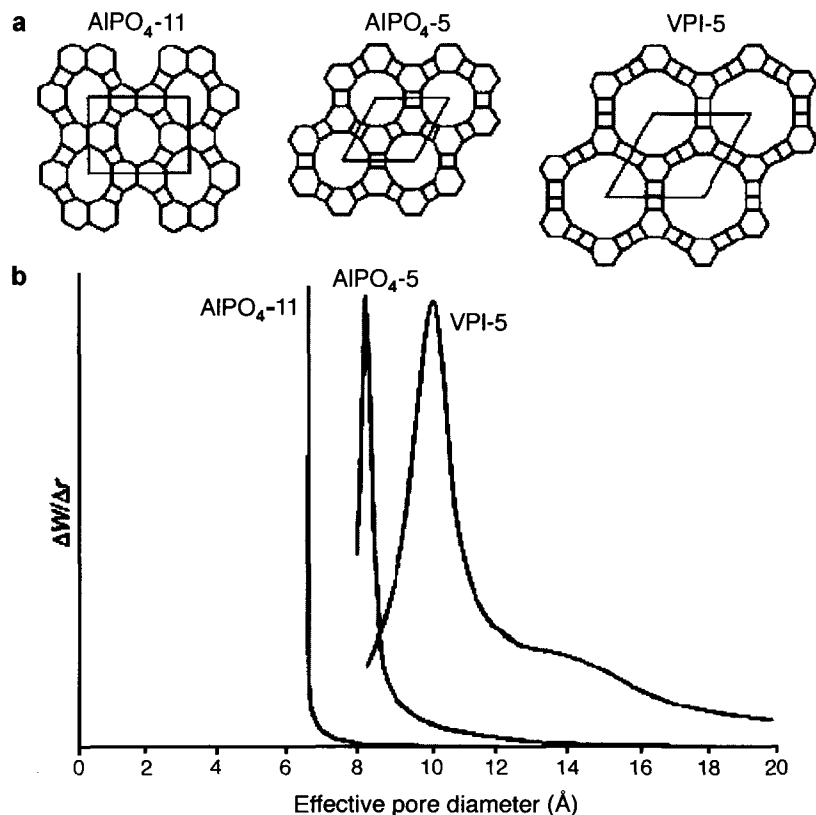


Fig. 1 (a) Pore characteristics in some representative aluminophosphates $\text{AlPO}_4\text{-11}$, $\text{AlPO}_4\text{-5}$, and VPI-5. (b) Measured pore sizes by argon adsorption techniques, noting that the VPI-5 shows a pore diameter greater than 1.0 nm. (From Ref. [7].) (View this art in color at www.dekker.com.)

synthetic conditions.^[12] These organic–inorganic hybrids possess a number of advantages for catalytic applications that organic polymers and amorphous/nonporous silica counterparts do not have.^[11] In many cases, space confinement and stabilization of the catalyst in the mesoporous solid can be attributed to the observed enhancement of catalytic activity. These materials have demonstrated utility as catalysts in acid/base catalysis, oxidations, reductions, enantioselective catalysis, stereospecific polymerizations, and fine chemicals synthesis.^[11] Rich inclusion chemistry of this class of materials with guest species in the internal space had been reviewed recently.^[9]

Over the past decade, increasing research activities have been shown in the fabrication of hierarchical porous structures that possess ordered pores ranging from micro- to macroscale. There have been a number of techniques developed.^[7] For example, microporous colloidal particles have been used for shape-, film-casting to prepare a range of hierarchical porous structures. On the other hand, bulk dissolution and restructuring of preexisting oxides have been used to fabricate shaped hierarchical structures of zeolite. Furthermore, structures with mesoporosity can be prepared by using surfactants as structuring directing agents.^[7] In addition to these approaches, new film formation methods allow us to fabricate various zeolite and molecular sieve layers and membranes. In recent years, pore sizes of ordered mesoporous oxides have been extended up to 10 nm with the use of block copolymers, and from 100 nm to 1 μm with latex spheres as templating structures.^[13,14] For example, nonionic polyethylene oxide surfactants were used to prepare wormhole-like, MSU-type SBA-*n* and CMI-1 mesoporous materials. With decaoxyethylene-cetyl-ether or polyoxyethylene(6)tridecyl-ether surfactants, hierarchical macroporous metal oxides had been synthesized without using polymeric sphere template.^[13] It is believed that the macro-mesostructured metal oxides were formed through an intermediate phase of supermicelles (the length in the micrometer range and the diameter in the submicrometer range) and mesostructured nanoparticles of metal oxides. The removal of the organic components resulted in the formation of hierarchical mesoporous–macroporous structures.^[13] The approach had been successfully applied to ZrO_2 , Nb_2O_5 , Ta_2O_5 , Al_2O_3 , and CeO_2 oxide systems, and the networks of the pores can be preserved at elevated temperatures to meet catalytic applications. Very recently, hierarchical and self-similar growth of self-assembled mesophase crystals in micrometer size had been investigated with the assistance of glass substrate. Ordered octahedral crystal building units can be assembled into various high-ordered stack structures via edge-sharing. It is found that the large structures are formed through stepwise nucleation from the edges of the previous crystals.^[15]

In addition to the general interest in the synthesis and design of micro-, meso-, and macroporous materials, there are interests in the preparation of single-site molecular receptors in silica matrix for specific adsorption and catalysis applications. Using molecular imprinting techniques, both microporosity and chemical functionality have been achieved for this new class of organic–inorganic hybrid materials. Typically, bulk-imprinted silica with hydrophilic framework can be prepared via copolymerization of the imprint organosilane(s) with a silica source (normally, silicon alkoxides such as tetraethyl orthosilicate, TEOS), followed by a mild thermal treatment.^[16] Fig. 2 shows a flowchart of this type of synthesis, where organic functional groups (such as amines) can be immobilized into the silica matrix possessing high specific surface area. The imprinted silicas can act as shape-selective base catalysts,^[17] and the hydrophilic framework prepared in this way offers an interesting potential to stabilize polar reactive intermediates and transition states at the active sites.^[16]

Finally, it should be mentioned that the mesoporous materials can be used as traditional high-surface-area catalytic supports for active metal loading. On the other hand, nanostructured metallic catalysts encapsulated can nucleate the expansion of the mesopore channels. For example, prefabricated gold and platinum nanoparticles had been investigated to tune the pore size of the mesoporous silica (SBA-15) that are grown around them (e.g., in the range of 9.2 to 11.6 nm).^[18]

Other important applications of the porous materials include template synthesis of nanostructured catalytic materials used as either individual (freestanding) catalysts or basic building blocks for self-assembly, as will be discussed in subsequent sections.

Designs of Layered Organic–Inorganic Nanohybrids

In recent years, layered organic–inorganic materials have attracted increasing research attention not only because of the fundamental interest in general supramolecular chemistry, but also because of their potential usage as precursors for catalytic nanomaterials processing. There are two basic types of clay materials: cationic and anionic clays. The cationic clays, which have been investigated extensively over the past decades, were conventional catalysts used in oil cracking before the replacement of zeolites in 1964.^[19] They have been used in many industrial chemical processes such as isomerization, liquid refining, and Friedel–Crafts alkylation, including some emerging environmental technologies (such as cation exchange and waste carriers).^[19] In this class of materials, cations are located in the lamellar space (interlayer space) formed by negatively charged aluminosilicate layers. As

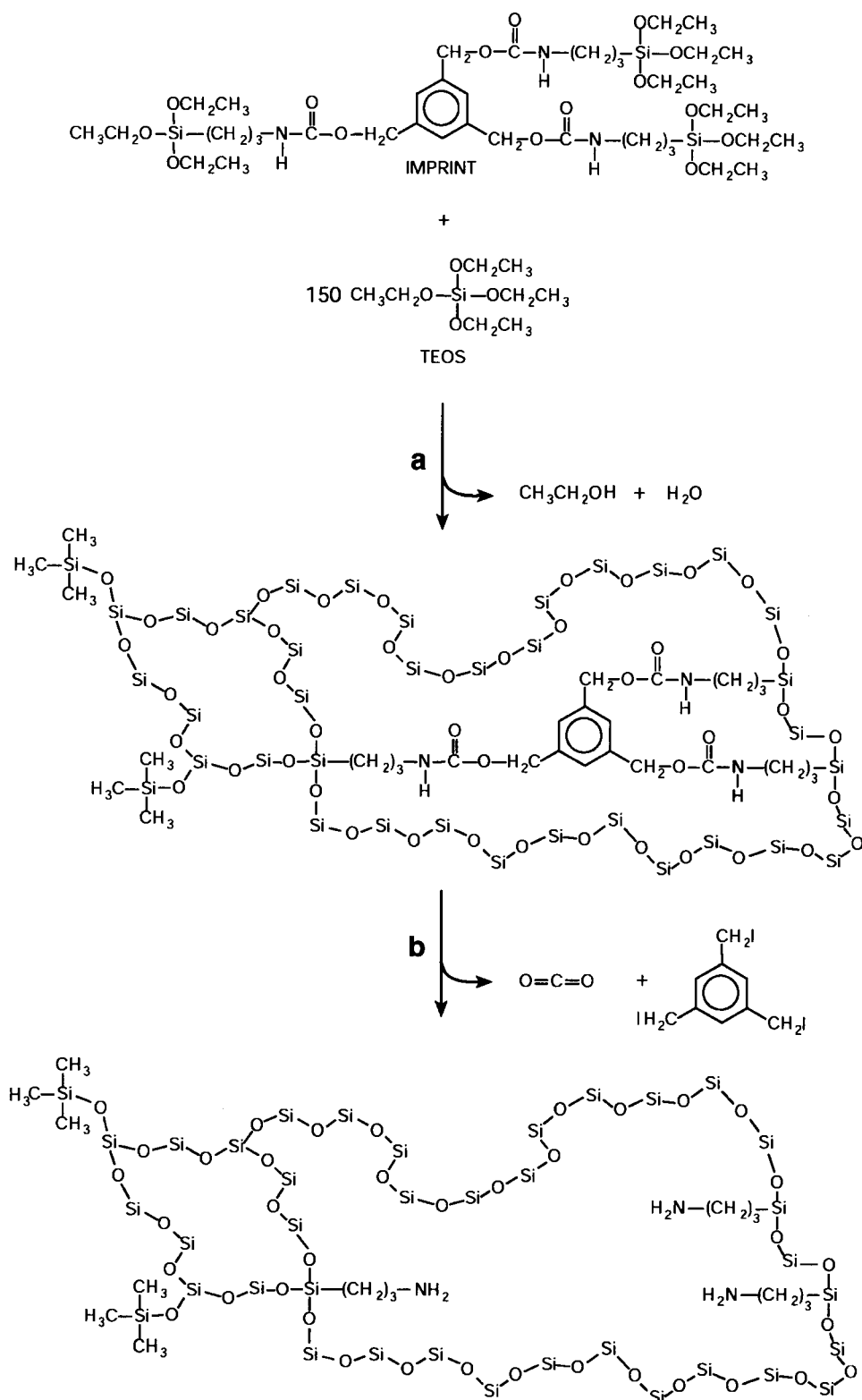


Fig. 2 Process of molecular imprinting in bulk silica. (a) Sol-gel hydrolysis and condensation catalyzed by HCl. (b) Removal of the aromatic core and creation of a cavity with spatially organized aminopropyl groups covalently anchored to the pore surfaces. (From Ref. [17].)

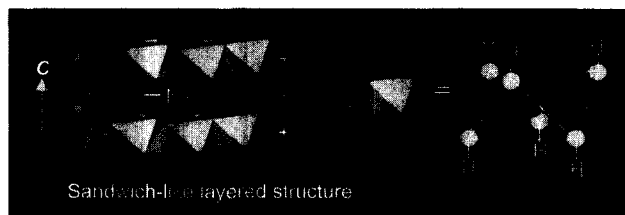


Fig. 3 The hydroxalcalite-like anionic-clays have a layered structure similar to that of brucite [$\text{Mg}(\text{OH})_2$] but with some positive charges. To maintain the electrical neutrality for the solid, intercalation of anions (e.g., nitrate and carbonate or even DNA) into the interbrucite layers (i.e., interlayer space) occurs, which leads to a hydroxalcalite-like structure. (View this art in color at www.dekker.com.)

they are generally prepared starting from the natural minerals, these clays and modified clay catalysts promise widespread industrial applications in the future owing to the low cost. Similar to cationic clays, anionic clays also have alternate lamellar structures, but with an opposite charge arrangement. Anionic clays are mainly synthetic. The preparation is relatively simple and inexpensive; they can be synthesized primarily with coprecipitation, anion exchange, and structure reconstruction methods. Hydroxalcalite-like compounds (HTLcs), for example, have been investigated extensively over the past decade, and they have been widely used as catalysts, flame retardants, molecular sieves, anion adsorbents, ion-exchangers, and medicine stabilizers.^[20] The sheet-like structure containing cations can be derived from layered $\text{Mg}(\text{OH})_2$ (brucite) structure. When divalent cations are partially substituted by trivalent ones, positive charges will be built-up within the octahedron sheets. For solid charge neutrality, anions have to be intercalated into the interlayer space, as illustrated in Fig. 3. The HTLcs have a chemical formula of $[\text{M}_1^{II-x}\text{M}_x^{III}(\text{OH})_2]^{x+}(\text{A}_x^{n-}) \cdot m\text{H}_2\text{O}$ (where M =metal, A =interlayer anions),^[20] whose properties can be tuned with variations of cationic brucite-like sheets and anionic interlayer species. For example, organics- and polymer-containing HTLcs should be viewed as supramolecular assemblies or nanocomposites composed of organic parts (anionic) and inorganic molecular sheets (cationic).^[21] It is important to realize that the intercalative ability in these alternately arranged layers is based on electrostatic interaction, and the inorganic parts are dissolvable in acidic environment while the organic parts are removable by ionic exchange or oxidation at elevated temperatures. Furthermore, layer charge density can be tuned with the content of M^{III} cations in the synthesis. The basal spacing (the distance between two brucite-like sheets) depends on the size of the intercalants. For instance, large-sized biomolecular anions (up to several nanometers), such as nucleoside monophos-

phates and deoxyribonucleic acid (DNA), have been intercalated into the interlayer space of $\text{Mg}_{0.68}\text{Al}_{0.32}(\text{OH})_2\text{NO}_3_{0.32} \cdot 1.2\text{H}_2\text{O}$ (a pristine HTlc).^[22] Because of their synthetic versatility in compositional tailoring, this class of organic-inorganic hybrids has been used as precursor compounds for the synthesis of functionalized metal-oxide nanomaterials and nanocomposites after the thermal removal or conversion of polymeric intercalants.^[23] The chemical nature of the intercalated anions, such as oxidative or nonoxidative, had been investigated with respect to thermal reactions, in which nanostructured Co_3O_4 spinel oxides were formed from $\text{Co}^{II}\text{Co}^{III}$ -HTlc precursors.^[24] Nanocrystalline $\text{Co}_{3-x}\text{Al}_x\text{O}_4$ can also be incorporated into the $\gamma\text{-Al}_2\text{O}_3$ matrix via the simultaneous formation of catalyst and support from the $\text{Co}^{II}\text{Co}^{III}$ -HTlc and alumina xerogel.^[25]

In addition to the above bulk materials preparations, organic-inorganic hybrid materials can also be prepared into thin films to meet new applications. The major synthetic methods employed in this area are sol-gel-based techniques, intercalation reactions, layer-by-layer assembly (e.g., Langmuir-Blodgett technique and electrostatic self-assembly), and evaporation techniques, as exemplified in Fig. 4.^[26] Although the primary objective of these film-fabrication developments is for organic-inorganic electronics, it is believed the hybrid structures prepared can be extended to catalytic applications, including chemical sensors, in the near future.

Very recently, single-crystal bulk organic-inorganic hybrids had been investigated for the fabrication of catalytic nanocomposites and large-scale organization of

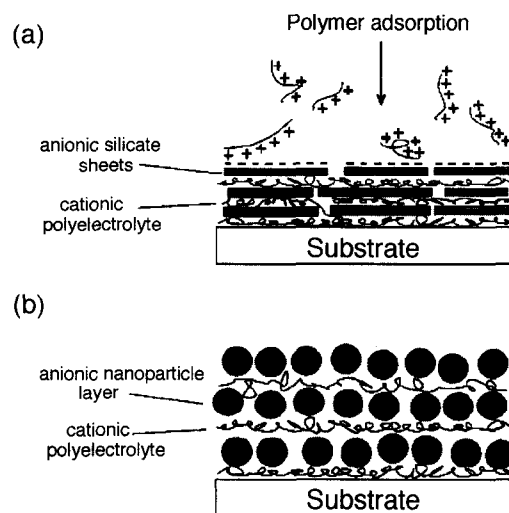


Fig. 4 (a) Electrostatic assembly of anionic inorganic layers and cationic organic layers. (b) A similar assembly of (a) but with negatively charged layers formed from nanoparticles (e.g., CdSe or CdS). (From Ref. [26].)

catalysts under high-temperature environments.^[27,28] In particular, individual MoS₂ (used in hydrosulfurization) layers can be converted from direct sulfidation of single-molecular sheets of MoO₃ supported with organic “pillars” in the interlamellar layers. As there has been a large variety of metal-oxide-organic hybrids available nowadays, this method provides a new means for the indirect synthesis of lamellar organic-inorganic catalytic hybrid materials consisting of building units of transition metal dichalcogenides.^[27] To make the catalytic materials usable in high-temperature environments, large-scale organization of metal-oxide nanostructures in a controllable manner at elevated temperatures is highly desirable but particularly challenging, because of the difficulties in controlling the interconnectivity among individual crystallites due to random nucleation and grain growth upon heating. An organized condensation of single-molecular MoO₃ sheets can be achieved with a controlled removal of the organic intercalants.^[28] This controlled condensation takes place within the space provided by the pristine organic-inorganic hybrid single-crystals. In this sense, the role of precursor crystal can be viewed as a microscopic “green compact” analogous to the macroscopic one in ceramic processing.^[28] These new types of catalyst organization may be useful for microreactor systems where fluid stream stability is crucial, because the stacking of nanostructured catalysts can be controlled to reduce flow resistance.

In addition to the above chemical conversion and organization of nanostructured catalytic materials, organic-inorganic hybrids have also been used in the preparation of freestanding nanostructured materials. For example, catalytically important materials such as tungsten oxide nanowires, tungsten disulfide nanotubes, and VO_x-nanotubes had also been prepared from organic-inorganic hybrid precursors that were preorganized in the forms of lamellar mesostructures.^[29–31] The final nanostructures are formed either with high-temperature processing or with hydrothermal treatment. These synthesized individual inorganic nanostructures will be the subject of the next section.

Nanobuilding Blocks and Mesoscale Self-Organizations

The research in low-dimensional catalytic materials has blossomed in many new directions since Iijima’s discovery of carbon nanotubes in 1991.^[32] For example, syntheses of low-dimensional catalytic nanostructures of MoS₂, WS₂, MoO₃, TiO₂, V₂O₅, ZrO₂, Co₃O₄, ZnO, etc. have been carried out,^[33–41] together with fabrications of nanostructured catalyst carriers such as MgO, Al₂O₃, and SiO₂.^[42–44] While many significant breakthroughs have been made for

the metal oxides and chalcogenides, the search for new types of nanostructures and self-assemblies continues, aiming at complementary functionalities and performances. Technologically, many known catalytic materials are expected to gain better utilizations, because of their new properties and possible high catalytic activities in the nanometer regime (quantum confinement effect).^[39] Discrete, freestanding nanostructures can be viewed as basic structural units or construction building blocks; they can be used individually or collectively (after a proper organization/assembly, will be addressed soon) in heterogeneous catalysis and chemical-sensing applications.

Many synthetic strategies have been developed for the fabrication of nanostructures. For example, metal oxide nanoparticles (zero-dimension, 0-D) can be prepared rather routinely via sol-gel methods^[45] and direct precipitation.^[46] A great variety of core-shell nanostructures (0-D) have also been prepared via sol-gel and other coating methods (e.g., layer-by-layer deposition) with the assistance of removable inner-core supports.^[47] On the other hand, one-dimensional (1-D) nanomaterials can be fabricated with the following techniques. 1) Utilizing intrinsic structural anisotropy: Inorganic materials with low structural symmetries can be prepared into 1-D morphology along certain crystallographic axes.^[37,40] The unidirectional growths can be further manipulated

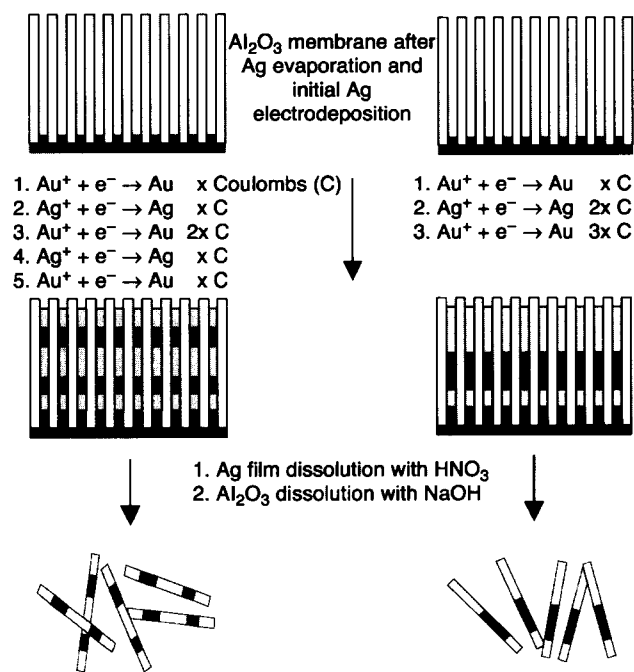


Fig. 5 Synthesis of barcoded 1-D materials with alumina membrane template where 1-D channels are parallel to each other. (From Ref. [50].) (View this art in color at www.dekker.com.)

with the assistance of inorganic salts or ionic/nonionic organic surfactants present in the solution synthesis.^[48] 2) **Template-directed growth:** In addition to the soft templates (such as self-assembled molecular structures, e.g., micelles discussed in the previous sections), this method utilizes solid templates for growth depositions or chemical insertions. For example, nonporous single-crystalline NaCl substrate and porous supports such as zeolites, MCM-41, and anodic alumina membranes (with parallel 1-D channels) have been used in the synthesis of 1-D nanostructures,^[49] including semiconductor metallic barcodes (Fig. 5).^[50] The resultant nanostructures can be harvested by template-removal. In certain cases, however, the template can become a part of the resulting 1-D nanostructures. These latter cases had recently been demonstrated in the synthesis of 1-D bimorph composites of TiO₂-SnO₂ and Co_{0.05}Ti_{0.95}O₂-SnO₂,^[51] and in the preparation of Ag/MoO₃ catalytic nanostructures.^[52] 3) **Surfactant-assisted synthesis:** Preferred electrostatic and chemical interactions between organic surfactants and certain crystallographic surfaces will restrict the growth along certain directions, resulting in the kinetic control of the growth anisotropy. This method had been investigated extensively for metals (e.g., Au) and semiconductor nanomaterials such as CdSe, ZnSe, CdS, and ZnS in recent years.^[53,54] 4) **Oriented attachment:** This growth mechanism had recently been investigated for the synthesis of 1-D materials such as ZnO nanorods and β -Co(OH)₂ nanoplatelets, respectively, from smaller building blocks.^[55,56]

Individual nanostructure units can be used as model catalysts or chemical-sensing devices. For example, a gas sensor for NO₂ detection had been developed with a single nanoribbon of SnO₂. In the illuminated state (UV light), photo-generated holes recombine with trapped electrons at the SnO₂ surface, desorbing NO₂ and increasing the sensing current.^[57] The general advantages of nanodevices are small size, fast response, and high sensitivity. If required, 2-D- or even 3-D nanostructures can be further constructed from starting 0-D- or 1-D subunits via meso-scale self-assembly processes. There have been numerous investigations in this area using organic surfactants.^[40,41] As illustrated in Fig. 6, direct crystallite coupling via oriented attachment process provides another possible means to serve this purpose.^[58] More examples in this area can be found in the literatures.^[55,59] Unlike the layered nanostructures (2-D), self-assembled 2-D nanostructures must possess different properties, because of the presence of discrete low-dimensional subunits and organic capping molecules within the assemblies. The retention or removal of these organizing agents is an important issue in catalytic applications, as the presence of organic components will change the inorganic nature of catalysts (hybridization). Future detailed comparisons for different design strategies are urgently needed.

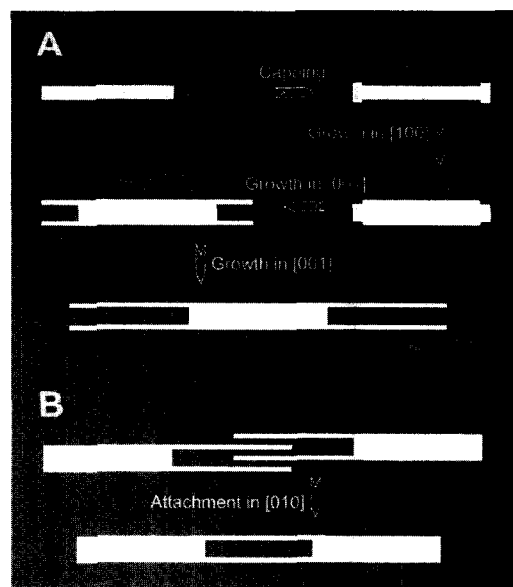


Fig. 6 (A) Flowchart of synthesis of forklike α -MoO₃ nanostructures via manipulating growth directions with TiO₂ capping. (B) Oriented attachment between two forklike nanostructures along the [010] direction (perpendicular to the paper). (From Ref. [58].) (View this art in color at www.dekker.com.)

In addition to the ordered organic-inorganic assemblies, nanoarchitectures of multifunctional catalysts can be further achieved by introducing dispersible organic-capped inorganic nanostructures into 3-D gel matrixes, which will also create the necessary chemical functionality and porosity in addition to the better material utilization. In particular, structurally shaped (or faceted) nanocatalysts may provide predesigned active catalytic sites for the desired chemical reactions, although they may appear to be random in the composite matrixes.

Interfacial Engineering and Self-Assembly

Our understanding of the catalyst carrier has now gone beyond its supporting role; various levels of participation of carriers in catalytic reactions have been known in atomic and molecular scales.^[60] As mentioned earlier, the surface functionalities of catalytic materials (in either planar or spherical form) can be further modified with the guide of nanochemistry principles^[61] and a wide range of surface-engineering processes available.^[47] In addition to metal single-crystal surfaces that have been investigated extensively over the past three decades, the synergetic effects of catalyst-carrier systems have been investigated with model catalysts, which may be closer to the reality of a heterogeneous catalytic reaction environment. Taking

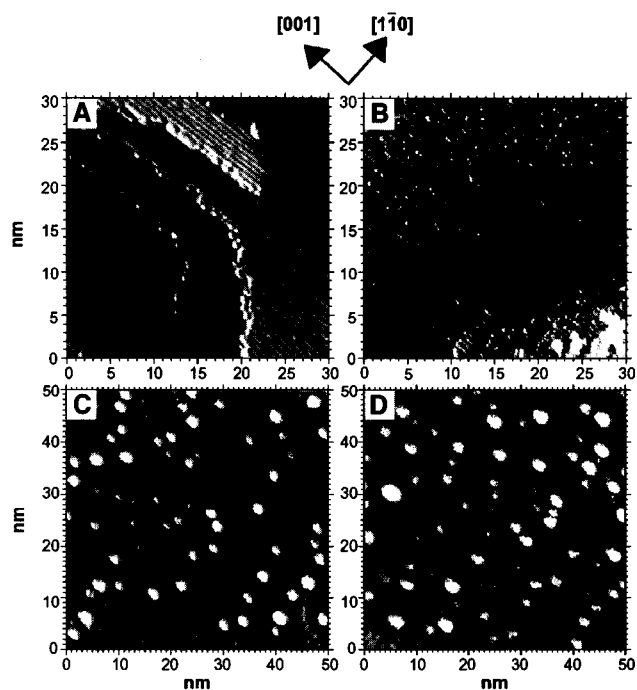


Fig. 7 Scanning tunneling microscopic images of $\text{TiO}_2(110)-(1 \times 1)$: (A) clean surface before oxygen exposure, and (B) after oxygen exposure at 650 K. Scanning tunneling microscopic images of $\text{Au/TiO}_2(110)-(1 \times 1)$: (C) before CO:O_2 exposure, and (D) after CO:O_2 exposure at 300 K. (From Ref. [3].)

advantage of the electron beam lithography technique, for example, metal nanoparticles have been arrayed on silicon surface at predesignated locations.^[62] Pt and Ag nanoparticle arrays were prepared at different interparticle distances. By varying the particle size and distances between particles, the structural factors responsible for the selectivity and activity in diverse catalytic reactions had been investigated.^[62] Other versions of model catalysts on oxidized silicon wafers have also been fabricated by spin-coating technique in recent years.^[63] These wafer-supported catalytic metal and metal-oxide thin films have been tested under catalytic reaction conditions and investigated with state-of-the-art surface analytical techniques. Various catalyst systems have been studied over the past few years.^[63] In view of its versatility, this evaluation approach is expected to be suitable for the characterization of various nanostructured catalytic materials that can be prepared into colloidal suspensions for spin-coating.

Apart from electron/ion beam lithography techniques, nanoelectrochemical patterning process and photolithography methods have also been widely used in the fabrication of substrate patterns for the deposition of nanostructured materials. These processes have been conducted in both vapor-phase (e.g., chemical vapor deposition) and

liquid phase (e.g., solution growth), producing various patterned 2-D nanostructures on the supports. For example, the hierarchical self-assembly of gold nanoparticles onto an organic bilayer template pattern on silicon had been demonstrated.^[64] Furthermore, ordered porous structures had been fabricated by self-assembly of zeolite nanocrystals on micropatterned silicate film surfaces.^[65] Without demanding pretreatments, single-crystal surfaces have recently been proven to be suitable for nanoparticle self-aligned growth. In particular, a hexagonal superlattice of anatase TiO_2 nanospheres has been arranged on $\alpha\text{-MoO}_3(010)$ surface without any surfactants and surface patterns,^[66] noting that both TiO_2 and $\alpha\text{-MoO}_3$ are important catalysts in this material combination. With well-developed surface science techniques, in-depth investigations of supported nanostructured catalysts can be further pursued. Elegant examples in this area have been reported in the literature, as shown in Figs. 7 and 8 for the investigations on CO

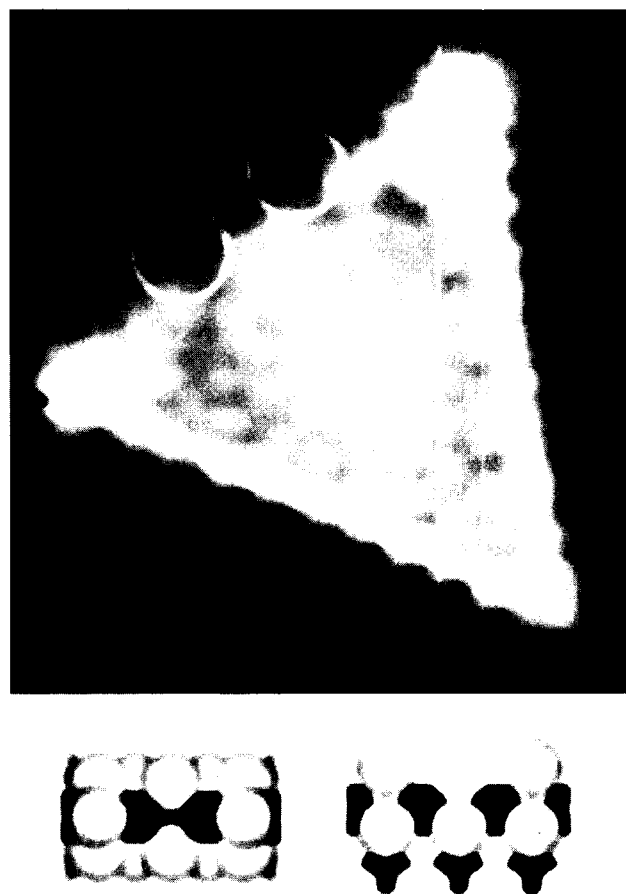


Fig. 8 A scanning tunneling microscopic image of a MoS_2 nanocluster exposed to atomic hydrogen at 600 K, which resulted in the formation of S vacancies (circled). Models below: side and top views of S vacancies. (From Ref. [67].) (View this art in color at www.dekker.com.)

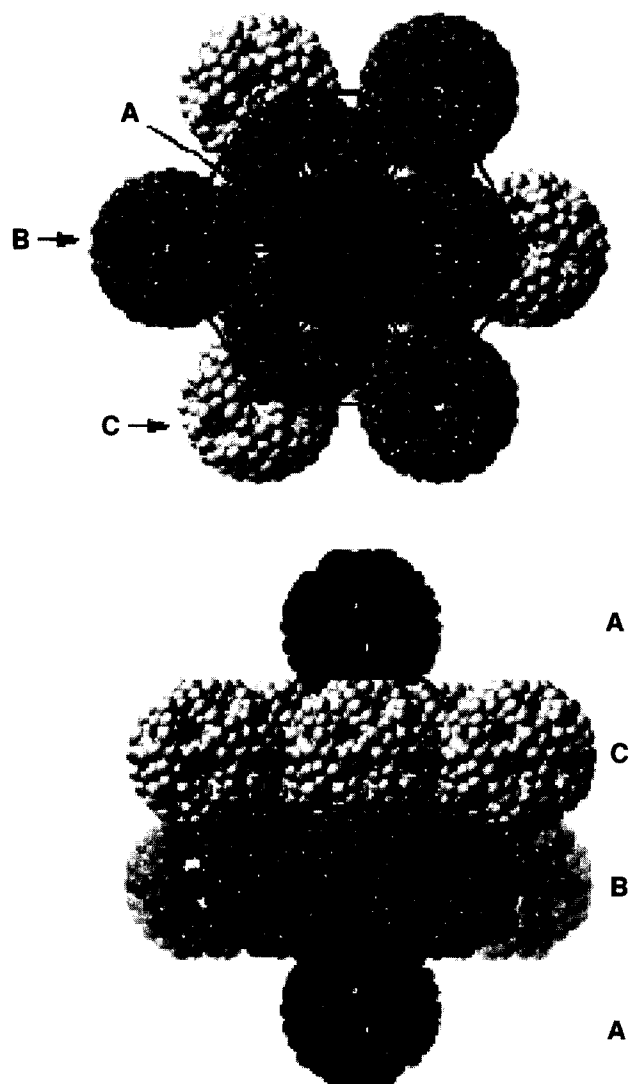


Fig. 9 Packing of ball-like anions $\{[\text{Mo}_2\text{V}_4\text{O}_4(\text{CH}_3\text{COO})]_{30} \{(\text{Mo})\text{Mo}_5\text{O}_{21}(\text{H}_2\text{O})_6\}_{12}\}^{42-}$ in the crystal lattice (space filling model viewed along $[111]$ (top) and perpendicular to $[111]$ (bottom)). (From Ref. [70].)

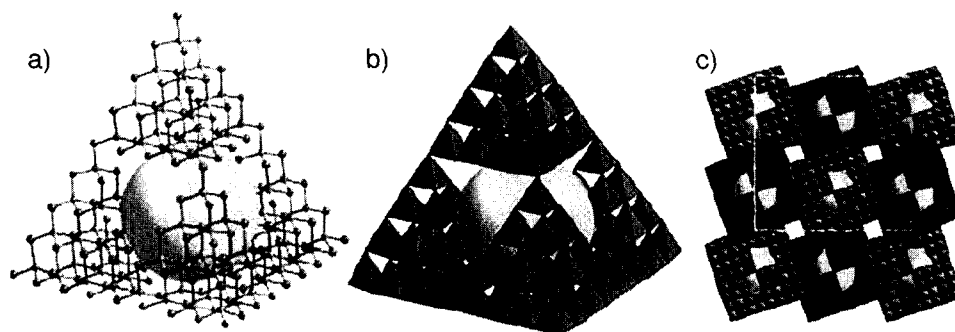


Fig. 10 Models of the $[\text{Cd}_{16}\text{In}_{64}\text{S}_{134}]^{44-}$ anionic clusters: a) a ball-and-stick model, b) the same view as a) shown as metal-centered tetrahedra, and c) crystal packing of the clusters, viewed along the c axis (the unit cell is framed). The large sphere indicates the central cavity. (From Ref. [71].) (View this art in color at www.dekker.com.)

oxidation and hydrodesulfurization.^[3,67] On the (110) surface of TiO_2 , Au particles show high activity at 2–3 nm for CO oxidation. However, Au particles in the Au– TiO_2 composite aerogel retain high activity for the same reaction at a size of 6 nm, because of an increase in the interfacial contact area of the gold with multiple domains of TiO_2 in the aerogel matrix.^[68] The catalytic bifunctionality of an active composite can thus be explored when the support and catalyst have comparable sizes (within a factor of 2).^[68]

Similar to vertical arrays of carbon nanotubes, catalytic materials have also been prepared into 2-D arrays, but with an extruding direction perpendicular to the surface. Recently, ZnO nanorods and GaN nanotubes had been prepared with gold nanoparticle catalysts in the vapor phase and with a subsequent thermal treatment to remove inner templates (e.g., in the synthesis of GaN nanotubes, ZnO nanorods were used as templates);^[69] the diameter of the prepared 1-D nanostructures is proportional to the size of metal catalysts in the synthesis. This method is now widely used in the synthesis of 1-D-nanostructures, including the control of periodic chemical component variation along a nanostructure.

Superpolyhedral Clusters and Their Organizational Forms

Compared with the nanobuilding blocks discussed above, inorganic super fullerene and polyhedral clusters, which have been synthesized in recent years, are generally much smaller but with more distinct geometrical features. This class of materials is formed from even smaller metal–ligand polyhedra, such as tetrahedrons, octahedrons through edge-, corner-sharing, etc. On the other hand, these super inorganic “molecules” can be further packed into repeated arrangements, giving away larger crystallites. Fig. 9 shows a representative packing of this type of superclusters.^[70] Instead of oxygen in zeolites, basic

units of tetrahedrons can now be extended to sulfur, noting that the ionic radius of S^{2-} is much larger than that of O^{2-} . For example, metal sulfides can now be prepared into supertetrahedral clusters with a large cavity, as shown in Fig. 10 for $[Cd_{16}In_{64}S_{134}]^{44-}$ (3.1 nm in edge length).^[71] A great variety of this type of superpolyhedral clusters and molecules has been prepared nowadays and has been reviewed recently.^[72] One common feature in these superpolyhedral clusters is their inner cavity. If treated as nanobuilding blocks in their further architectures, the superclusters with inner space will create even more complex structures in addition to their chemical complexity in nanoconfinement regime. Many of these solids show a semiconducting character.^[72] Apart from the assembly shown in Fig. 9, there have existed a great number of organization schemes of inorganic clusters with organic counterparts.^[45] These tailor-made organic-inorganic nanocomposites could be potential candidates for future heterogeneous catalysis applications.

CONCLUSION

We have examined various design and synthesis strategies for the fabrication of nanostructured catalytic materials. Generally speaking, nanostructured "kits-and-parts" as well as their organization methodologies have been available to constitute a nanocatalyst toolbox, i.e., they are ready for direct usage or further assembly. To transform "catalytic materials" to real custom "catalysts", however, a large research endeavor is needed, and this includes systematic investigations on multicomponent assemblies and resultant chemico-physical properties, including hierarchical pore structures. It is noted that the catalytic performance of these materials remains largely untested, despite the significant progress in materials research. While traditional methods will still dominate the industrial-scale catalyst processing at the present time, we are beginning to see nanostructured catalytic materials in practical applications of "chemical plant/laboratory-on-a-chip" and chemical-sensing technology where the amount of catalysts required is small, and supported type catalysts may not be needed. For larger-scale industrial chemical processes, for instance, it is believed that the traditional "metal ions impregnation" can be replaced with "nanostructures impregnation," as the nanobuilding blocks can be prepared into colloidal suspensions for metal loading on general catalyst supports. Furthermore, nanoarchitectures of these building units can be achieved with the well-developed sol-gel technology. Perhaps, simultaneous formation of nanobuilding blocks and supporting oxide matrix should be considered as a next level of architectures, where the catalyst and support could be better integrated in the new-generation catalysts.

REFERENCES

1. Bell, A.T. The impact of nanoscience on heterogeneous catalysis. *Science* **2003**, *299*, 1688–1691.
2. Stiles, A.B.; Koch, T.A. *Catalyst Manufacture*, 2nd Ed.; Marcel Dekker: New York, USA, 1995.
3. Valden, M.; Lai, X.; Goodman, D.W. Onset of catalytic activity of gold clusters on titania with the appearance of nonmetallic properties. *Science* **1998**, *281*, 1647–1650.
4. Somorjai, G.A. From surface materials to surface technology. *MRS Bull.* **1998**, *23*, 11–29.
5. de Jong, K.P. Assembly of solid catalysts. *Cat. Technol.* **1998**, *2*, 87–95.
6. Férey, G. Microporous solids: From organically templated inorganic skeletons to hybrid frameworks ... ecumenism in chemistry. *Chem. Mater.* **2001**, *13*, 3084–3098.
7. Davis, M.E. Ordered porous materials for emerging applications. *Nature* **2002**, *417*, 813–821.
8. Kresge, C.T.; Leonowicz, M.E.; Roth, W.J.; Vartuli, J.C.; Beck, J.S. Ordered mesoporous molecular sieves synthesized by a liquid-crystal template mechanism. *Nature* **1992**, *359*, 710–712.
9. Moller, K.; Bein, T. Inclusion chemistry in periodic mesoporous hosts. *Chem. Mater.* **1998**, *10*, 2950–2963.
10. Morey, M.S.; Stucky, G.D.; Schwarz, S.; Fröba, M. Isomorphic substitution and postsynthesis incorporation of zirconium into MCM-48 mesoporous silica. *J. Phys. Chem., B* **1999**, *103*, 2037–2041.
11. Stein, A.; Melde, B.J.; Schroden, R.C. Hybrid inorganic-organic mesoporous silicates—Nanosopic reactors coming of age. *Adv. Mater.* **2000**, *12*, 1403–1419.
12. Sayari, A.; Hamoudi, S. Periodic mesoporous silica-based organic-inorganic nanocomposite materials. *Chem. Mater.* **2001**, *13*, 3151–3168.
13. Blin, J.-L.; Léonard, A.; Yuan, Z.-Y.; Gigot, L.; Vantomme, A.; Cheetham, A.K.; Su, B.-L. Hierarchically mesoporous/macroporous metal oxides templated from polyethylene oxide surfactant assemblies. *Angew. Chem., Int. Ed.* **2003**, *42*, 2872–2875.
14. Yi, G.-R.; Moon, J.H.; Manoharan, V.N.; Pine, D.J.; Yang, S.-M. Packings of uniform microspheres with ordered macropores fabricated by double templating. *J. Am. Chem. Soc.* **2002**, *124*, 13354–13355.
15. Tian, Z.R.; Liu, J.; Voigt, J.A.; McKenzie, B.; Xu, H. Hierarchical and self-similar growth of self-assembled crystals. *Angew. Chem., Int. Ed.* **2003**, *42*, 414–417.
16. Bass, J.D.; Katz, A. Thermolytic synthesis of

- imprinted amines in bulk silica. *Chem. Mater.* **2003**, *15*, 2757–2763.
17. Katz, A.; Davis, M.E. Molecular imprinting of bulk, microporous silica. *Nature* **2000**, *403*, 286–289.
 18. Kónya, Z.; Puentes, V.F.; Kiricsi, I.; Zhu, J.; Alivisatos, A.P.; Somorjai, G.A. Nanocrystal templating of silica mesopores with tunable pore sizes. *Nano Lett.* **2002**, *2*, 907–910.
 19. Vaccari, A. Preparation of catalytic properties of cationic and anionic clays. *Catal. Today* **1998**, *41*, 53–71.
 20. Cavani, F.; Trifirò, F.; Vaccari, A. Hydrotalcite-type anionic clays: Preparation, properties and applications. *Catal. Today* **1991**, *11*, 173–301.
 21. Leroux, F.; Besse, J.-P. Polymer interleaved layered double hydroxides: A new emerging class of nanocomposites. *Chem. Mater.* **2001**, *13*, 3507–3515.
 22. Choy, J.H.; Kwak, S.Y.; Jeong, Y.J.; Park, J.S. Inorganic layered double hydroxides as nonviral vectors. *Angew. Chem., Int. Ed.* **2000**, *39*, 4042–4045.
 23. Xu, Z.P.; Xu, R.; Zeng, H.C. Sulfate-functionalized carbon/metal-oxide nanocomposites from hydroxide-like compounds. *Nano Lett.* **2001**, *1*, 703–706.
 24. Xu, R.; Zeng, H.C. Mechanistic investigation on self-redox decomposition of cobalt-hydroxide-nitrate compounds with different nitrate anion configurations in interlayer space. *Chem. Mater.* **2003**, *15*, 2040–2048.
 25. Sampathar, J.T.; Zeng, H.C. Synthesis of $\text{Co}^{\text{II}}\text{Co}^{\text{III}}\text{Al}_x\text{O}_4\text{-Al}_2\text{O}_3$ nanocomposites via decomposition of $\text{Co}_{0.73}\text{Co}_{0.27}^{\text{III}}(\text{OH})_{2.00}(\text{NO}_3)_{0.23}(\text{CO}_3)_{0.02}\cdot 0.5 \text{H}_2\text{O}$ in sol-gel derived $\gamma\text{-Al}_2\text{O}_3$ matrix. *Chem. Mater.* **2001**, *13*, 4722–4730.
 26. Mitzi, D.B. Thin-film deposition of organic-inorganic hybrid materials. *Chem. Mater.* **2001**, *13*, 3283–3298.
 27. Wei, X.M.; Zeng, H.C. Sulfidation of single molecular sheets of MoO_3 pillared by bipyridine in nanohybrid $\text{MoO}_3(4,4'\text{-bipyridyl})_{0.5}$. *Chem. Mater.* **2003**, *15*, 433–442.
 28. Wei, X.M.; Zeng, H.C. Large-scale organizations of MoO_3 nanoplatelets with single-crystalline $\text{MoO}_3(4,4'\text{-bipyridyl})_{0.5}$. *J. Phys. Chem., B* **2003**, *107*, 2619–2622.
 29. Li, X.-L.; Liu, J.-F.; Li, Y.-D. Large-scale synthesis of tungsten oxide nanowires with high aspect ratio. *Inorg. Chem.* **2003**, *42*, 921–924.
 30. Li, Y.D.; Li, X.L.; He, R.R.; Zhu, J.; Deng, Z.X. Artificial lamellar mesostructures to WS_2 nanotubes. *J. Am. Chem. Soc.* **2001**, *124*, 1411–1416.
 31. Krumeich, F.; Muhr, H.-J.; Niederberger, M.; Bieri, F.; Schnyder, B.; Nesper, R. Morphology and topochemical reactions of novel vanadium oxide nanotubes. *J. Am. Chem. Soc.* **1999**, *121*, 8324–8331.
 32. Iijima, S. Helical microtubules of graphitic carbon. *Nature* **1991**, *354*, 56–58.
 33. Tenne, R.; Margulis, L.; Genut, M.; Hodes, G. Polyhedral and cylindrical structures of tungsten disulfide. *Nature* **1992**, *360*, 444–446.
 34. Tenne, R.; Homyonfer, M.; Feldman, Y. Nanoparticles of layered compounds with hollow cage structures. *Chem. Mater.* **1998**, *10*, 3225–3238.
 35. Che, G.L.; Lakshmi, B.B.; Fisher, E.R.; Martin, C.R. Carbon nanotubule membranes for electrochemical energy storage and production. *Nature* **1998**, *393*, 346–349.
 36. Rao, C.N.R.; Cheetham, A.K. Science and technology of nanomaterials: Current status and future prospects. *J. Mater. Chem.* **2001**, *11*, 2887–2894.
 37. Patzke, G.R.; Krumeich, F.; Nesper, R. Oxidic nanotubes and nanorods—Anisotropic modules for a future nanotechnology. *Angew. Chem., Int. Ed.* **2002**, *41*, 2446–2461.
 38. Kovtyukhova, N.I.; Mallouk, T.E. Nanowires as building blocks for self-assembling logic and memory circuits. *Chem. Eur. J.* **2002**, *8*, 4355–4363.
 39. Rao, C.N.R.; Kulkarni, G.U.; Thomas, P.J.; Edwards, P.P. Size-dependent chemistry: Properties of nanocrystals. *Chem. Eur. J.* **2002**, *8*, 29–35.
 40. Xia, Y.; Yang, P.; Sun, Y.; Wu, Y.; Mayers, B.; Gates, B.; Yin, Y.; Kim, F.; Yan, H. One-dimensional nanostructures: Synthesis, characterization, and applications. *Adv. Mater.* **2003**, *15*, 353–389.
 41. Cölfen, H.; Mann, S. Higher-order organization by mesoscale self-assembly and transformation of hybrid nanostructures. *Angew. Chem., Int. Ed.* **2003**, *42*, 2350–2365.
 42. Tang, C.; Bando, Y.; Sato, T. Oxide-assisted catalytic growth of MgO nanowires with uniform diameter distribution. *J. Phys. Chem., B* **2002**, *106*, 7449–7452.
 43. Pu, L.; Bao, X.; Zou, J.; Feng, D. Individual alumina nanotubes. *Angew. Chem., Int. Ed.* **2001**, *40*, 1490–1493.
 44. Jung, J.H.; Ono, Y.; Hanabusa, K.; Shinkai, S. Creation of both right-handed and left-handed silica structures by sol-gel transcription of organogel fibers comprised of chiral diaminocyclohexane derivatives. *J. Am. Chem. Soc.* **2000**, *122*, 5008–5009.
 45. Sanchez, C.; Soler-Illia, G.J. de A.A.; Ribot, F.; Lalot, T.; Mayer, C.R.; Cabuil, V. Designed hybrid organic-inorganic nanocomposites from functional

- nanobuilding blocks. *Chem. Mater.* **2001**, *13*, 3061–3083.
46. Feng, J.; Zeng, H.C. Size-controlled growth of Co_3O_4 nanocubes. *Chem. Mater.* **2003**, *15*, 2829–2835.
47. Caruso, F. Nanoengineering of particle surfaces. *Adv. Mater.* **2001**, *13*, 11–22.
48. Lou, X.W.; Zeng, H.C. Hydrothermal synthesis of $\alpha\text{-MoO}_3$ nanorods via acidification of ammonium-heptamolybdate-tetrahydrate. *Chem. Mater.* **2002**, *14*, 4781–4789.
49. Lakshmi, B.B.; Patrissi, C.J.; Martin, C.R. Sol-gel template synthesis of semiconductor oxide micro- and nanostructures. *Chem. Mater.* **1997**, *9*, 2544–2550.
50. Nicewarner-Peña, S.R.; Freeman, R.G.; Reiss, B.D.; He, L.; Peña, D.J.; Walton, I.D.; Cromer, R.; Keating, C.D.; Natan, M.J. Submicrometer metallic barcodes. *Science* **2001**, *294*, 137–141.
51. He, R.; Law, M.; Fan, R.; Kim, F.; Yang, P. Functional bimorph composite nanotapes. *Nano Lett.* **2002**, *2*, 1109–1112.
52. Dong, W.; Feng, S.; Shi, Z.; Li, L.; Xu, Y. A well-confined redox route to silver nanoparticles on the surface of MoO_3 . *Chem. Mater.* **2003**, *15*, 1941–1943.
53. Wang, Z.L.; Gan, R.P.; Nikoobakht, B.; El-Sayed, M.A. Surface reconstruction of unstable {110} surface in gold nanorods. *J. Phys. Chem., B* **2000**, *104*, 5417–5420.
54. Trindade, T.; O'Brien, P.O.; Pickett, N.L. Nanocrystalline semiconductors: Synthesis, properties, and perspectives. *Chem. Mater.* **2001**, *13*, 3843–3858.
55. Pacholski, C.; Korowski, A.; Weller, H. Self-assembly of ZnO from nanodots to nanorods. *Angew. Chem., Int. Ed.* **2002**, *41*, 1188–1191.
56. Sampanthar, J.T.; Zeng, H.C. Arresting butterfly-like intermediate nanocrystals of $\beta\text{-Co(OH)}_2$ via ethylenediamine-mediated synthesis. *J. Am. Chem. Soc.* **2002**, *124*, 6668–6675.
57. Law, M.; Kind, H.; Messer, B.; Kim, F.; Yang, P. Photochemical sensing of NO_2 with SnO_2 nanoribbon nanosensors at room temperature. *Angew. Chem., Int. Ed.* **2002**, *41*, 2405–2408.
58. Lou, X.W.; Zeng, H.C. Complex $\alpha\text{-MoO}_3$ nanostructures with external bonding capacity for self-assembly. *J. Am. Chem. Soc.* **2003**, *125*, 2697–2704.
59. Liu, B.; Zeng, H.C. Hydrothermal synthesis of ZnO nanorods in the diameter regime of 50 nm. *J. Am. Chem. Soc.* **2003**, *125*, 4430–4431.
60. Campbell, C.T.; Parker, S.C.; Starr, D.E. The effect of size-dependent nanoparticle energetics on catalyst sintering. *Science* **2002**, *298*, 811–814.
61. Ozin, G.A. Nanochemistry: Synthesis in diminishing dimensions. *Adv. Mater.* **1992**, *4*, 612–649.
62. Somorjai, G.A. The development of molecular surface science and the surface science of catalysis: Berkeley contribution. *J. Phys. Chem., B* **2000**, *104*, 2969–2979.
63. Loos, J.; Thune, P.C.; Niemantsverdriet, J.W.; Lemstra, P.J. Polymerization and crystallization of polyethylene on a flat model catalyst. *Macromolecules* **1999**, *32*, 8910–8913.
64. Hoepfener, S.; Maoz, R.; Cohen, S.R.; Chi, L.; Fuchs, H.; Sagiv, J. Metal nanoparticles, nanowires, and contact electrodes self-assembled patterned monolayer templates—A bottom-up chemical approach. *Angew. Chem., Int. Ed.* **2002**, *41*, 1036–1040.
65. Huang, L.; Wang, Z.; Sun, J.; Miao, L.; Li, Q.; Yan, Y.; Zhao, D. Fabrication of ordered porous structures by self-assembly of zeolite nanocrystals. *J. Am. Chem. Soc.* **2000**, *122*, 3530–3531.
66. Yang, H.G.; Zeng, H.C. Self-aligned growth of hexagonal TiO_2 nanosphere arrays on $\alpha\text{-MoO}_3$ (010) surface. *Chem. Mater.* **2003**, *15*, 3113–3120.
67. Helveg, S.; Lauritsen, J.V.; Lægsgaard, E.; Stensgaard, I.; Nørskov, J.K.; Clausen, B.S.; Topsøe, H.; Besenbacher, F. Atomic-scale structure of single-layer MoS_2 nanoclusters. *Phys. Rev. Lett.* **2000**, *84*, 951–954.
68. Rolison, D.R. Catalytic nanoarchitectures—The importance of nothing and the unimportance of periodicity. *Science* **2003**, *299*, 1698–1701.
69. Goldberger, J.; He, R.R.; Zhang, Y.F.; Lee, S.W.; Yan, H.Q.; Choi, H.J.; Yang, P.D. Single-crystal gallium nitride nanotubes. *Nature* **2003**, *422*, 599–602.
70. Müller, A.; Krickemeyer, E.; Bögge, H.; Schmidtman, M.; Peters, F. Organizational forms of matter: An inorganic super fullerene and Keplerate based on molybdenum oxide. *Angew. Chem., Int. Ed.* **1998**, *37*, 3360–3363.
71. Li, H.; Kim, J.; O'Keeffe, M.; Yaghi, O.M. $[\text{Cd}_{16}\text{In}_{64}\text{S}_{134}]^{44-}$: 31-Å tetrahedron with a large cavity. *Angew. Chem., Int. Ed.* **2003**, *42*, 1819–1821.
72. Férey, G. Supertetrahedra in sulfides: Matter against mathematical series? *Angew. Chem., Int. Ed.* **2003**, *42*, 2576–2579.

Nanostructured Composites Using Carbon-Derived Fibers

Peter M. A. Sherwood

Kansas State University, Manhattan, Kansas, U.S.A.

INTRODUCTION

This entry discusses the importance of nanostructure and especially interfacial chemical interactions in the formation of composites where an appropriate matrix material is strengthened by a carbon fiber. Such composites have mechanical and other properties that are especially dependent upon the surface chemistry of the fibers; in other words, the nanostructure of the surface region has a dramatic impact on these properties. The focus of the article will be upon the types of fiber currently used in composite production, with an emphasis upon the surface chemistry of carbon fibers determined by X-ray photoelectron spectroscopy (XPS) in the core and valence band region.

CARBON FIBERS

Fibers find a number of important practical applications. Fibers themselves may be woven into a structure that can be one, two-, or three-dimensional. The surface chemistry of the fibers is important when the fibers are used to generate a fabric, which may require treatment such as dyeing. This chapter will focus on carbon fibers. Carbon fibers are light and strong fibers, which consist of largely graphitic character. The microstructure of the fibers can vary considerably depending upon their production, although on a nanoscale dimension the untreated fibers consist largely of graphite. The principal use for these fibers is to employ them to construct a composite which involves a matrix which is often an epoxy resin or plastic.

The remarkable feature of composites composed of a fiber and a matrix is that the surface chemistry of the fiber has a dramatic impact on the mechanical and other properties of the composite. For example, in carbon fiber composites with an epoxy resin matrix the load that can be sustained without fracture for the same fiber and matrix can be increased by a factor of three by changing the surface chemistry of the outer 5 to 10 Å of the carbon fiber surface.

Carbon is known in three principal allotropic forms, graphite, diamond, and fullerenes. Graphite materials have extensive applications associated with their high thermal and electrical conductivity and their negligible

thermal expansion. In addition, they are one of the lightest refractory materials known and possess biocompatible characteristics.

Perfect graphite has continuous planar hexagonal sheets of carbon atoms with six-member carbon rings with each sheet separated by 3.354 Å from the adjoining sheets. Many less-ordered forms of carbon are known such as pyrolytic carbon where the hexagonal sheets have only short-range order, with intersheet separations that differ from those of perfect graphite.

Carbon fibers were first made in the form of carbon filaments by heating cellulose fibers, an approach used by Thomas Edison.^[1] Carbon fibers of the type of such value today are high modulus fibers. These fibers were developed independently by Bacon,^[2,3] Shindo,^[4] and Watt,^[5] who all used a process of continual stretching of the precursor material as it was carbonized during heat treatment.

Commercial carbon fibers are derived from two principal sources. The first source is based upon textile fibers, especially polyacrylonitrile. The second source is based upon mesophase pitch. In both cases an initial fiber is heated and stretched leading to decomposition to form carbon in a form which may be more or less graphitic-like. Residual molecules of the precursor may be left; for example, the fiber may contain nitrogen if the precursor was polyacrylonitrile. Carbon fiber manufacturers can vary the stretching and heating conditions to yield a fiber with the desired properties (such as the fiber modulus). A third source of carbon fiber has been less well used and is based upon fibers produced when hydrocarbon gas mixtures pass over a catalyst at high temperatures. These fibers have potential, but there are production difficulties associated with the formation of continuous fiber lengths (referred to as a "tow") and reproducible fiber diameters. Fibers formed from the two principal sources are generally sold with particular "tow" sizes (such as 3000 fibers and 12,000 fibers) and very substantial lengths.

It has long been recognized that carbon fibers must be surface treated in order that they can be used for composite production. Early attempts to use untreated fibers led to composites with very disappointing composite properties. Various, commercially confidential, methods were developed for surface treating the fibers. These

methods are nearly always made an integral part of the carbon fiber production process, the treatment plant being included in the carbon fiber production line. Most manufacturers sell fibers with surface treatment "tuned" to the matrix application. Thus a particular type of treatment is recommended for epoxy matrices, and a different treatment for phenolic matrices. The particular treatment methods are not reported. In addition to surface treatment, fibers are generally subjected to a thin coating of a polymeric material known as a "size." This practice is conducted so that the fiber "tows" are easier to handle. In fact, the extent to which fiber surface treatment and sizing impacts the final composite properties is not well understood. The so-called "tuning" of surface treatment to a particular matrix is frequently not based upon a complete understanding of the factors involved. It is the purpose of this chapter to address this matter in more detail.

A very full discussion of the synthesis and other important details of carbon fibers can be found elsewhere (e.g., Ref. [6]).

CARBON FIBER SURFACE CHEMISTRY AND TOPOGRAPHY

Carbon fibers can be produced with a range of surface chemistry and topography. Most commercial carbon fibers, with the exception of those specially prepared for high absorption characteristics, have a relatively low surface area. This is deliberate and a feature of the production process, which may lead to grooves on the fibers resulting from the original production process for the fibers, which involves the extrusion of a polymer (such as polyacrylonitrile) or a pitch to produce the fiber.

When a fiber is placed in a matrix material such as a polymer or resin, the initial first step is the wetting of the fiber by the matrix material. This wetting is assisted if there is some chemical or physical interaction between the fiber and the matrix material. The first key step in the process is thus the wetting of the fiber that allows the fiber to come into contact with the matrix, and then the possible chemical interaction between the fiber and the matrix. Interaction between the fiber and the matrix can involve both chemical and physical interaction.

Carbon fibers are surface treated by processes that nearly always lead to the oxidation of the carbon fiber surface. These processes may involve gas-phase oxidants such as ozone, liquid oxidants such as sodium hypochlorite, and electrochemical oxidation in various electrolytes. Plasma oxidation may also be conducted, although in practice it presents practical problems as a result of the need to pass the fibers without damage into a very low pressure region with the plasma gas. These surface treat-

ments result in two major changes on the carbon fiber surfaces, namely, a change in the fiber surface chemistry and a change in the fiber surface topography. Unfortunately, it is not possible to separate these two factors in a simple way. This is because the surface treatment methods change both the surface chemistry and topography at the same time. Fig. 1 illustrates this situation for a high-modulus carbon fiber based upon pitch.^[7] The atomic force microscope (AFM) data for this fiber change substantially as one compares the AFM data (a) for the carbon fiber (which was neither surface treated nor sized by the manufacturer) before treatment with the fiber after treatment. Before treatment the fiber shows a smooth surface with striations, which are associated with the production of the mesophase pitch fibers, used in the production process. When the fiber is subjected to surface treatment resulting from the galvanostatic electrochemical oxidation of the fiber in 1 M nitric acid at 0.5 A for 10 sec, the surface topography clearly changes. Some pitting of the

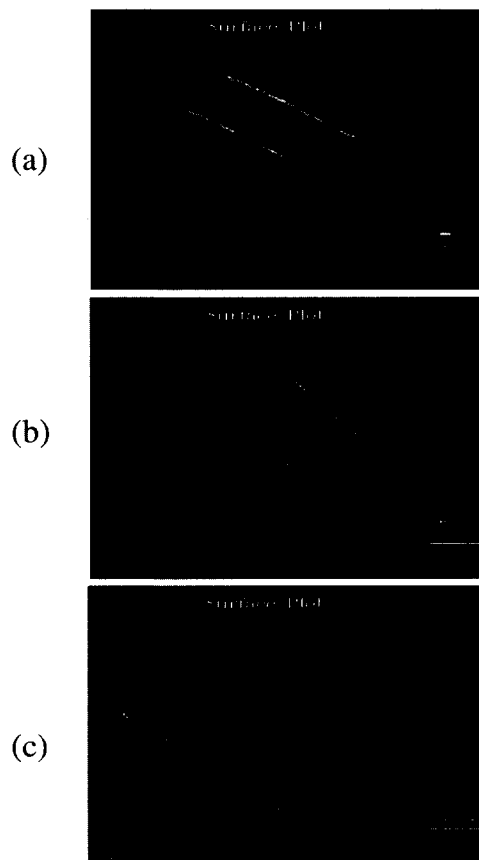


Fig. 1 Atomic force microscope images of (a) a high-modulus pitch-based carbon fiber that was neither surface treated nor sized, (b) the same carbon fibers after electrochemical oxidation in 1 M nitric acid at 0.5 A for 10 sec, and (c) same as (b) but oxidized for 1 min. (View this art in color at www.dekker.com.)

surface can be observed, but the original surface striations from the production process are clearly visible. When the galvanostatic oxidation is conducted for 1 min rather than 10 sec the surface topography changes substantially, with all the original surface striations being lost.

The changes in surface topography produced by the surface treatment are quite clear, and in fact it is clear from the AFM image that the topographical features show differences on a nanoscale dimension.

It is interesting to examine whether there are any changes that arise in the surface chemistry, and not surprisingly one finds that the surface is oxidized by the electrochemical treatment. There are many ways to examine the changes that arise in surface chemistry (for a review, see, for example, Refs. [8] and [9]). One especially powerful method is the use of XPS. This chapter will focus on this technique for the following reasons. The technique is normally nondestructive, the information comes from the outer 10–100 Å of the surface, is atomic (i.e., the atomic numbers of the elements in the surface region can be identified), and provides chemical details. It will be shown below that the topographical changes seen in Fig. 1 are also associated with chemical changes, and these chemical changes can be identified by XPS.

X-RAY PHOTOELECTRON SPECTROSCOPY

X-ray photoelectron spectroscopy [which is sometimes referred to as electron spectroscopy for chemical analysis (ESCA)] is a mature surface analytical probe that is one of a number of ultra-high vacuum surface analysis techniques. The experiment involves placing the sample of interest in an ultra-high vacuum (10^{-9} to 10^{-10} Torr) and then exposing the surface to soft X-rays. This leads to the emission of photoelectrons from both the core and valence band region. The X-ray light used is normally a soft X-ray, typically Mg K α (1253.6 eV) or Al K α (1486.6 eV), the latter source having the advantage that it can be obtained in monochromatic form using a range of commercial X-ray monochromators. As the energy of the photon is known and the energy of the photoelectron measured, the binding energy that holds the electron into the material is simply obtained by the difference in the photon and photoelectron energy with suitable corrections for sample work function and any charging effects. The core region readily provides information about the type of atom present because core electrons normally come at very distinct binding energies, and an examination of an overall spectrum (i.e., a spectrum collected over a wide energy range, typically 1000 or more electron volts) leads to the easy identification of the elements present. Closer examination of the core region obtained by obtaining photoelectron data over a narrow energy range (typically

around 15 eV) allows energy shifts that are characteristic of chemical differences to be identified. It took about 60 years from the first photoelectron spectroscopy experiments before it was realized that core electrons, which take no part in chemical bonding, do in fact give rise to a chemical shift. The reason for this shift is that while the core electrons are strongly attracted to the positively charged atomic nucleus, they are also repelled by the outer valence electrons (the electrons that take part in chemical bonding), leading to a small but readily detectable chemical shift. When the author first started in this field in 1972 it was hoped that chemical shifts might be quite substantial, allowing subtle chemical differences to be determined. It became clear over the past 30 years that these shifts, while very useful, are sometimes small and it is not uncommon for compounds with different chemistry to exhibit similar chemical shifts as a result of a “canceling out” of the principal factors that determine the chemical shift. In fact, the main factors are the charge on the atom from which the photoelectron is ejected, the charge on the surrounding atoms, and the difference in extra atomic relaxation energy between different compounds containing the atom of interest. Atomic charge is a useful but very subjective quantity, because while the nuclear charge (the number of protons in the nucleus) is known exactly, the electronic charge is not clearly defined when it comes to the valence electrons because these electrons are shared between different atoms involved in chemical bonding. Nevertheless, simple models based upon atomic charge have proved very useful for the prediction of core chemical shifts in XPS (see, for example, Ref. [10]).

Fig. 2 illustrates the type of information that can be obtained for a simple carbon compound, and how a simple calculation model can explain the spectrum. The experimental data are for the compound *N*-methyl-2-pyrrolidone (NMP), frozen as a solid from the gas phase by forming the solid on a liquid-nitrogen-cooled plate.^[11] Two peaks can readily be seen in the C1s region, the peak at higher binding energy being due to the carbon atom (No. 4) associated with the C=O (where No. 11 is the oxygen atom) group in the molecule. The spectrum can be understood by examination of the calculated spectrum obtained using the relaxation potential model, which suggests that the four remaining carbon atoms form the low binding energy peak around 285 eV. In fact, the observed shift of around 3–3.5 eV from the C–H carbons is typical for the carbon atom of the >C=O group in a wide range of carbon compounds. Fig. 2 indicates that it is expected that the shift between some inequivalent atoms will be small (such as between carbon atoms 1, 3, 5, and 6). The experimental data have been fitted to a number of component peaks. The curve fitting of XPS data is an important approach to the analysis of core XPS data, and

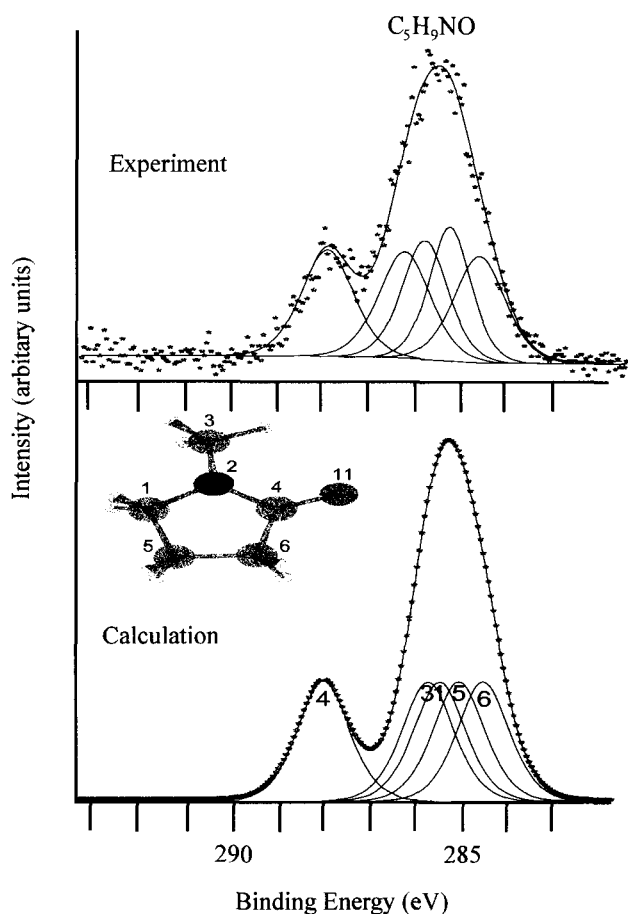


Fig. 2 X-ray photoelectron spectrum of frozen NMP in the C1s region showing the experimental and calculated spectrum. The calculated spectrum shows the component peak positions obtained from a molecular orbital cluster calculation, with the peak areas obtained by adjusting the number of electrons associated with each atomic orbital type by the orbital's photoelectron cross section.

the method has proved a valuable method for extracting chemical information in a wide range of systems. Of course, any curve fitting process is approximate, and there is never a unique answer. The best approach is to use a combination of well-developed fitting procedures, where the understanding of the peak shape and position is good, and combine this approach with a situation where the chemical environment changes and the fitted spectra have to be conducted in a consistent manner.

It is useful at this stage to return to the carbon fiber sample discussed in the previous section. The X-ray photoelectron spectrum observed in this case shows the significant *chemical* changes that accompany the *topographical* changes discussed above. Fig. 3 shows the core

and valence band region observed^[7] for the three samples indicated by (a), (b), and (c) in Fig. 1.

The overall XPS spectrum shows that the surface is practically entirely carbon, which is expected for an untreated and unsized fiber. The detailed O1s region can be seen to be of very low intensity. The detailed C1s region shows some very small amounts of surface functionality that can be seen from the curve fitted features at high binding energy of the principal C1s graphitic peak around 285 eV. In fact, the width and fine details of this peak can be associated with not only residual surface functionality, but also the degree of graphitic character of the carbon fiber.^[12,13] The 10-sec electrochemical treatment gives the spectra shown in (b). Now a dramatic increase can be seen in the amount of oxygen with respect to carbon. The detailed C1s region now shows an additional peak shifted by about 2 eV from the graphitic peak at around 285 eV. In addition, other features can be fitted to the C1s region. The O1s region shows a single intense peak. The 60-sec treatment shown in (c) shows a significant increase in the amount of oxygen, with the detailed C1s region showing the peak at 287 eV now showing the greatest intensity.

These results can be understood in terms of the oxidation of the carbon fiber at the edge sites to form a C/O functionality that lies between a $>C=O$ and a $>C-OH$ functionality. This grouping, which will be referred to as the "bridged structure," can be represented as shown in Fig. 4.

The C-O groups can be seen to have the intermediate functionality described above. The "main peak" is represented by the carbon atoms attached to the oxygen

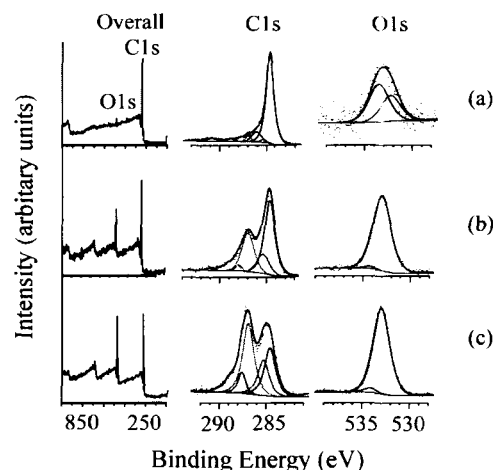


Fig. 3 X-ray photoelectron spectra of the fibers described in Fig. 1. The overall region identifies the O1s and C1s features which are expanded and curve fitted in the separate C1s and O1s regions.

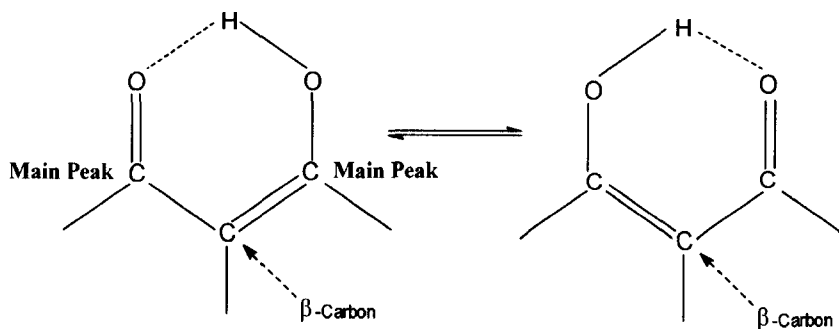


Fig. 4 Representation of the hydrogen-bridged oxide structure (HBS) unit showing the location of the “ β ” and “main” carbon atoms.

atoms, and this is the peak that corresponds to the feature at 287 eV. The β -carbon peak arises at about 0.7 eV to higher binding energy of the principal graphitic feature around 284.6 eV. It is interesting to note that the principal form of oxidized carbon is the bridged structure of Fig. 4. A number of authors suggest that oxidized carbon forms a stable carboxylic acid surface functionality, but the author finds that while this type of functionality is formed in certain cases it never is very intense, and this type of functionality frequently decomposes with the loss of carbon dioxide. The author has conducted extensive studies of the surface chemistry of these systems, and in nearly all cases the types of functionality described above are found.^[8]

Core XPS is a very valuable approach to the study of the chemistry of carbon fiber surface, but the approach is not always able to distinguish between different surface functionalities. For example, it is not possible to distinguish between $>C-OH$ and $>C-O-C<$ functionality. As noted above the “chemical shifts” obtained with XPS are dependent upon electrostatic effects. The valence band region contains electrons whose energy is determined by the mixing of atomic orbitals to give molecular orbitals that are involved in the chemical bonding of the materials under study. This region gives “shifts” whose position depends upon the chemical bonding and thus depends upon factors different from those that give rise to the core shifts. The author has found that this region complements the core region and can often distinguish between subtle chemical differences. For example, it is possible to distinguish between $>C-OH$ and $>C-O-C<$ functionality. In oxidized carbon systems the $C2s$ and $O2s$ atomic orbitals strongly mix to give molecular orbitals when C/O functionality is present, with shifts that are the reverse to those found in the core region. For example $>C-OH$ functionality occurs at higher binding energy to $>C=O$ functionality in the core $O1s$ region, but the reverse is true in the principally $O2s$ valence band region around 25 eV

finding energy. Using model calculations it is possible to predict the changes in the valence band region that would arise when different surface functionalities are present. Fig. 5 shows the predicted valence band XPS spectra for a series of oxidized carbon species that are represented by a D_{6h} -symmetry-substituted coronene structure with different functionalities with the molecular orbitals calculated by multiple scattered wave $X\alpha$ calculations.^[14,15] The calculations predict a different separation between the principally $O2s$ region around 25 eV and the principally $C2s$ region around 18 eV. Note how this separation is predicted to be significantly larger for the $-C-O-C-$ functionality than for the $-C-OH$ functionality. This has allowed the author to distinguish between these two groups experimentally.^[16] It should also be noted that the calculations predict that the $-COOH$ carboxylic acid functionality should give rise to two separated peaks in the valence band region.

The Effect of Size and Initial Surface Treatment

Most carbon fibers used in practical applications have a surface that is sized and initially surface treated by the manufacturer. The presence of this initial surface treatment and size can have a significant impact on the interaction of the fiber with a matrix. To illustrate this point consider taking a commercially surface-treated fiber and the same fiber with the commercial surface treatment removed. Let us now apply an oxidative surface treatment to both fibers, which involves potentiostatic treatment in 1 M nitric acid for 20 min.^[17] The $C1s$ XPS data for both experiments are shown in Fig. 6, where “untreated” refers to the commercially surface-treated fiber with the surface treatment removed.

The fiber with no surface treatment can be seen to exhibit steadily increasing C/O functionality with the

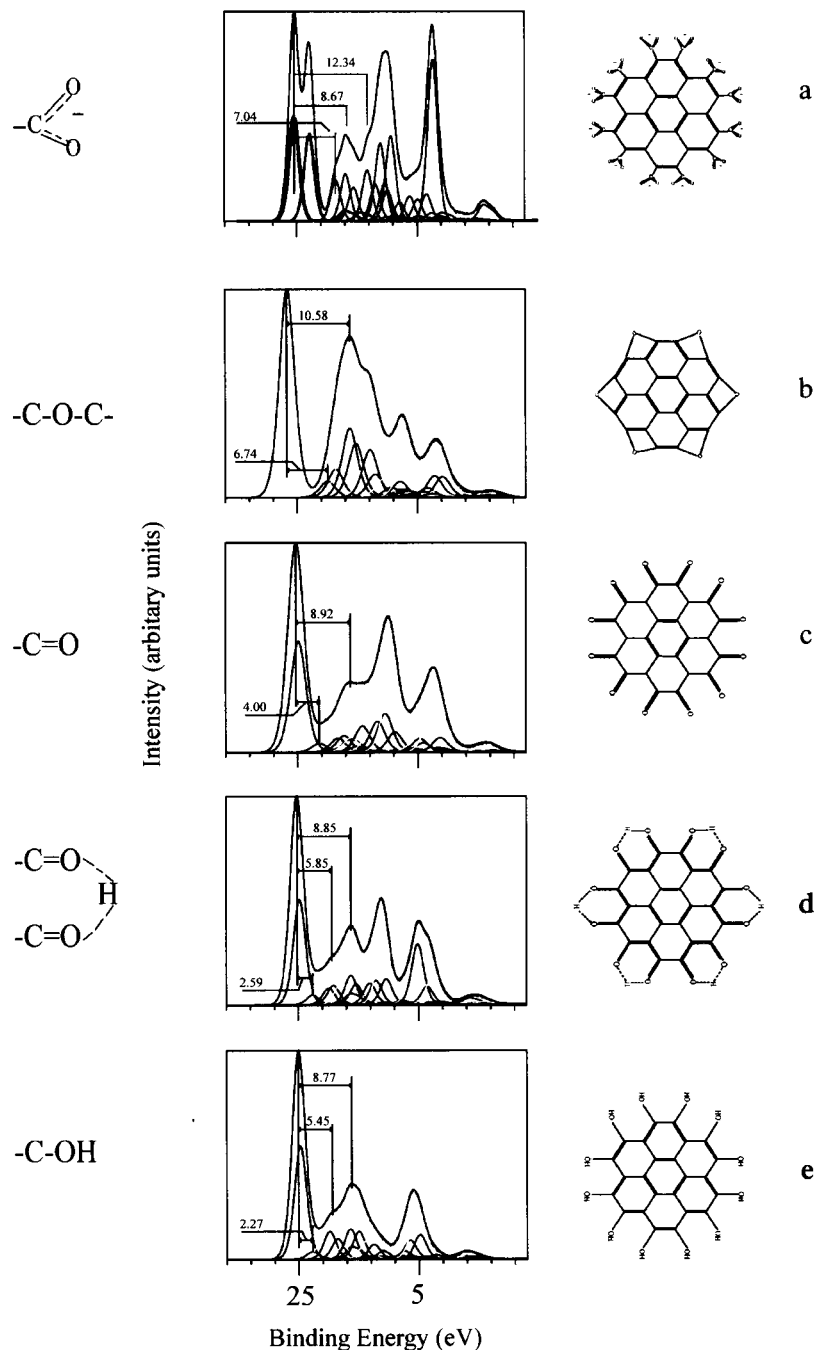


Fig. 5 Calculated X-ray photoelectron valence band spectra of model compounds used to represent typical oxidized carbon fiber surfaces. (a) carboxyl, (b) epoxide, (c) carbonyl, (d) bridged, and (e) hydroxide functional groups.

“bridged structure” of Fig. 4 appearing as a separate peak at higher binding energy (286.7 eV) than the C1s graphitic peak at 284.6 eV. Note how the corresponding “beta” peak of Fig. 4 is shown with half the intensity as the “bridged structure” at 285.3 eV. At 1.5 and 2.0 V,

additional features at 288.1 eV can be seen due to $>\text{C}=\text{O}$ surface functionality and 288.8 eV due to $-\text{CO}_2\text{H}$ functionality. Note how the curve fitting includes the nonlinear background in the fit, and note also how the fit has to be consistent over the whole range of

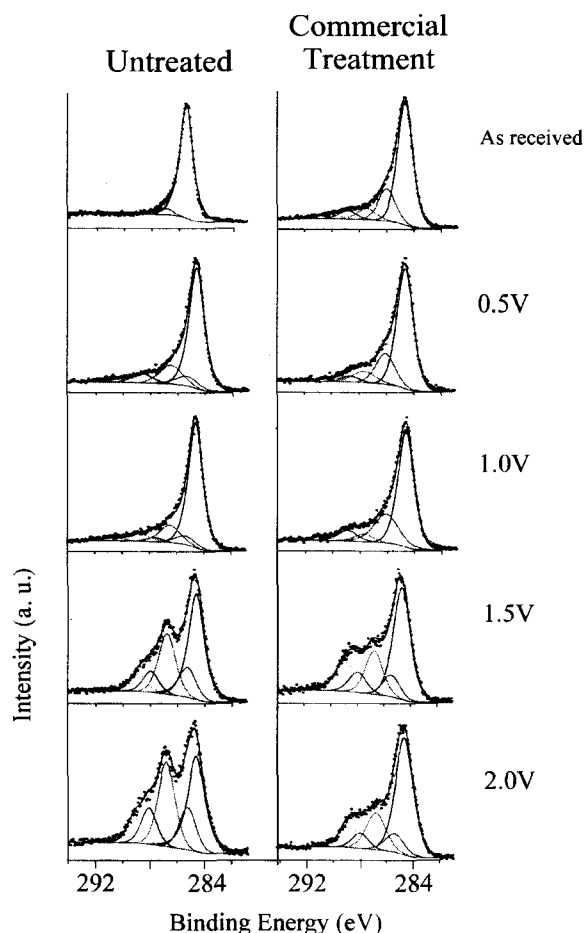


Fig. 6 X-ray photoelectron spectra of the C1s region of an IM7 commercially surface-treated carbon fiber before and after electrochemical oxidation under potentiostatic conditions in 1 M nitric acid for 20 min. The voltages shown are with respect to the saturated calomel electrode. The “untreated” sample is the IM7 commercially surface-treated sample with the surface treatment removed by heating. (From Ref. [17].)

spectra, an illustration of the curve fitting approach discussed above.

In contrast, the spectra for the commercially treated sample show marked differences on electrochemical oxidation from the untreated fiber. The differences are particularly striking at 1.5 and 2.0 V; in fact, the amount of oxidation at 2.0 V seems to be less than that at 3.0 V.

The principal lesson that one can learn from these results is the importance of a well-defined and untreated surface as a precursor for chemical interaction.

The presence of size on a carbon fiber surface might seem to be a simple matter to remove before the fiber was used to form a composite. Solvent extraction would seem the appropriate approach, but in fact while the size is

generally applied in a solvent solution, the removal of the size by solvent is not straightforward. In fact, the surface chemistry is dominated by the size, and solvent extraction does not remove all the size, with significant interaction occurring between the size and the underlying surface treatment. The higher the level of surface treatment the more difficult it is to remove the size.^[7,18]

MONITORING THE BURIED FIBER-MATRIX INTERFACE

The purpose of surface treatment of carbon fibers is to increase the wetting of the fiber by the matrix and to allow chemical and physical interaction with the matrix material. The interfacial chemistry that occurs between the fiber and the matrix, which has seen to be based on a

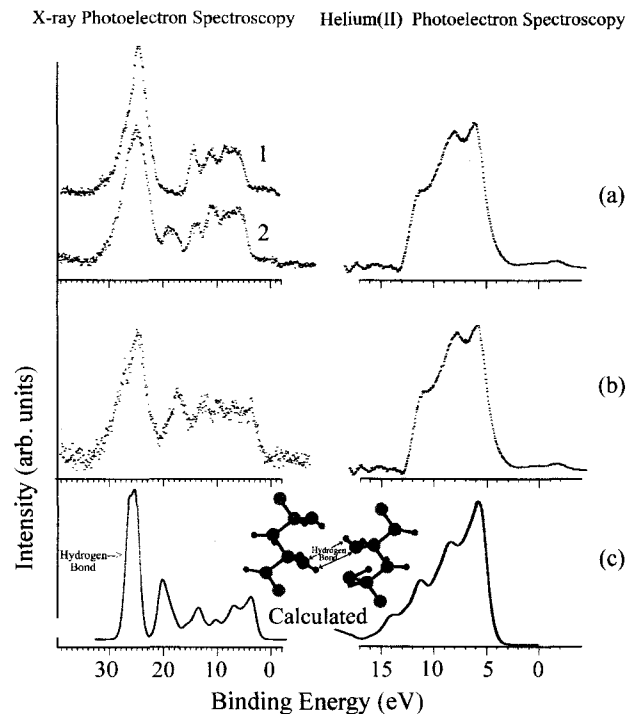


Fig. 7 Valence band photoelectron spectra using X-ray and UV radiation. (a) shows the valence band region for a sample of aluminum with an oxide-free phosphate film, coated with a very thin film of polyvinyl alcohol (PVA). In the X-ray photoelectron spectra for (a), “1” is the valence band spectrum for the orthophosphate film on aluminum without any overlying PVA, and “2” the spectrum with the PVA film. (b) shows the valence band region for polyvinyl alcohol. (c) shows the calculated valence band region for polyvinyl alcohol generated from a band structure calculation. (From Ref. [19].)



nanoscale topography on the fiber surface, will be very important in final composite performance.

The author has approached the challenge of examination of this buried interface by developing a technique where photoelectron spectroscopy can be used to probe this interface by placing a very thin layer of the matrix onto the fiber. The matrix layer is so thin that the interfacial region can be probed by XPS. The outer surface region can also be examined and ultraviolet photoelectron spectroscopy (UPS) can be used for this purpose. Fig. 7 illustrates this approach by showing the valence band spectra for a thin film of polyvinyl alcohol placed on an oxide-free orthophosphate coating on metallic aluminum.^[19] The coating is so thin that the underlying aluminum can be seen, the Al2p region showing two features one because of metallic aluminum and the other because of aluminum orthophosphate, suggesting a film thickness for the phosphate film of about 20 Å. Fig. 7(a) shows the valence band region using X-ray light and UV light. The spectrum in (a) is identical to that in (b), which is for a sample of polyvinyl alcohol when He(II) UV light is used. This confirms that the outer film region is polyvinyl alcohol because the photoelectrons generated by UV light have a much smaller escape depth than those generated by X-ray light. The valence band region in Fig. 7(a) for X-ray light is quite different from that of

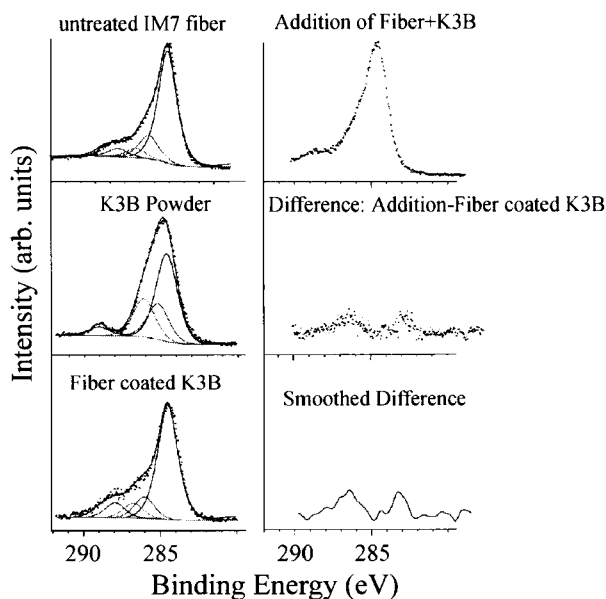


Fig. 8 X-ray photoelectron spectra of the C1s region for (a) as-received IM7 fibers; (b) K3B powder; (c) fibers in part (a) dip-coated with K3B solution; (d) addition of parts (a) and (b); (e) difference of parts (d) and (c); (f) smoothed version of part (e). The intensity scales for parts (d)–(f) are the same.

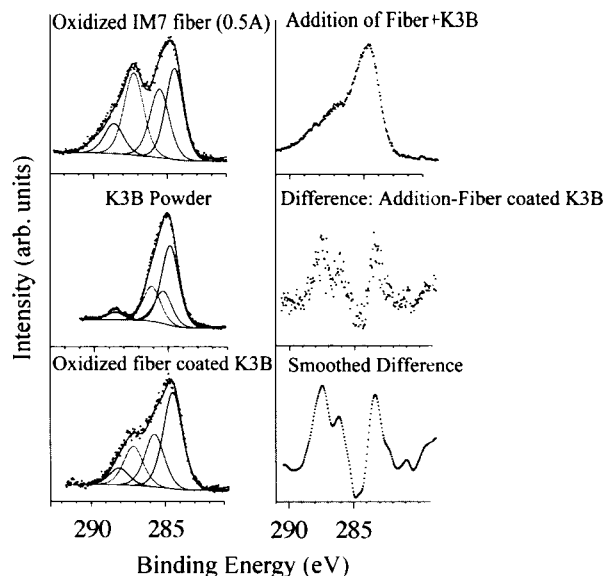


Fig. 9 X-ray photoelectron spectra of the C1s region for (a) IM7 fibers galvanostatically oxidized in 1 M nitric acid at 0.5 A for 40 sec; (b) K3B powder; (c) fibers in part (a) dip-coated with K3B solution; (d) addition of parts (a) and (b); (e) difference of parts (d) and (c); (f) smoothed version of part (e). The intensity scales for parts (d)–(f) are the same. (From Ref. [11].)

polyvinyl alcohol shown in Fig. 7(b) and that of aluminum orthophosphate (Fig. 7(a)).^[11] If the valence band spectrum of polyvinyl alcohol is added to that of the aluminum orthophosphate film, the spectra do not superimpose and this can be demonstrated by using difference spectra.^[19] Also, an additional peak is seen in the C1s region for the PVA-coated phosphate film.

In a carbon fiber system this buried interface can be probed using this approach. For example, the polyimide matrix material K3B is valuable as a matrix that can withstand higher temperatures than a typical epoxy resin matrix. Unfortunately, it is not easy to obtain a chemical interaction between the carbon fibers and this matrix. It is possible to see chemical interaction when a particular surface oxidation is conducted on the carbon fibers. Fig. 8 shows the C1s core region for an untreated IM7 carbon fiber, for K3B, and for a thin film of K3B on this fiber. The difference spectrum (Fig. 8(e) and 8(f)) between the spectrum with the thin K3B film (thin enough to probe the interface region) and the sum of the carbon fiber and K3B spectrum shows no significant difference. In other words, there has been no chemical interaction at the interface. When the untreated IM7 carbon fibers are electrochemically oxidized under galvanostatic conditions at 0.5 A in 1 M nitric acid for 40 sec, and the process repeated, then

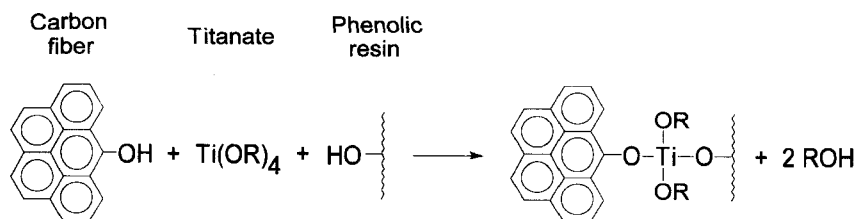


Fig. 10 Reaction scheme between tetrakis(2-ethylhexyl) titanate (TOT) and an oxidized carbon fiber surface.

the corresponding difference spectrum does indeed show a difference, indicating a chemical reaction between the carbon fiber surface and the K3B (Fig. 9).

When a carbon fiber surface does not chemically react with the matrix material, then a “coupling agent”—another molecule that reacts with both the carbon fiber surface and the matrix—can be used. X-ray photoelectron spectroscopy can be used to monitor the effectiveness of this approach. For example, one can use a titanium alkoxide coupling agent (tetrakis(2-ethylhexyl) titanate,

TOT) to couple a surface-treated carbon fiber to a phenolic resin. Fig. 10 shows the way in which the coupling agent acts.

The valence band XPS spectrum can be used to show that the interface between the coupling agent and the fiber and matrix is as suggested. Fig. 11 shows the difference spectrum for the difference between the XPS spectrum of a thin film of a phenolic resin on an E-120 pitch-based carbon fiber electrochemically oxidized in 1 M orthophosphoric acid, and the same situation but with TOT added to the resin. The surface treatment in this case leads to the formation of -C-OH functionality on the fiber surface. Hence the reaction scheme in Fig. 10. The smoothed difference spectrum in Fig. 11 was obtained using the background-subtracted spectra. It can be seen that the difference spectrum gives good agreement with the spectrum calculated for the $\text{Ti(OCH}_3)_4$ molecule based upon a multiple scattered wave $X\alpha$ calculation.^[20] The five features identified in the outer valence band region are in good agreement with the difference spectrum. The difference spectrum also gives evidence of the presence of oxidized titanium (TiO_2). This can be seen when one considers that the calculated spectrum for TiO_2 (based upon a multiple scattered wave $X\alpha$ calculation on the TiO_6^{8-} cluster) suggests that the peak identified as “2” in this calculation would fill the valley between peaks 1 and 2 and 3–5 in the calculated spectrum of $\text{Ti(OCH}_3)_4$. Thus the presence of TiO_2 is consistent with the features observed in the valence band spectrum.

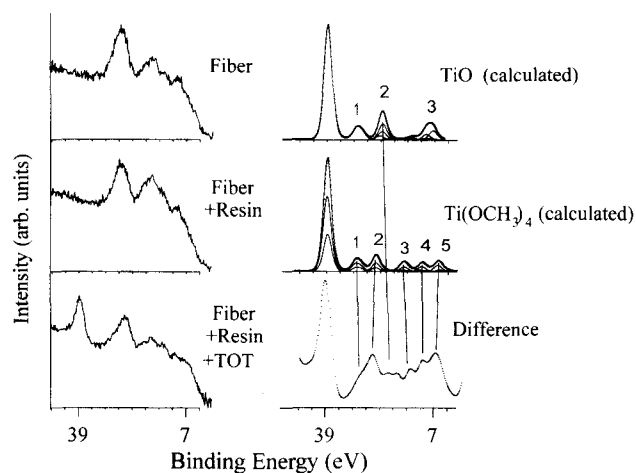


Fig. 11 X-ray photoelectron spectra in the valence band region for E-120 pitch-based carbon fibers. The experimental valence band spectra of the fiber which was surface treated by galvanostatic oxidation in 1 M orthophosphoric acid at 0.5 A for 30 sec is shown (indicated as “fiber”), together with the fiber with a very thin coating of a phenol-formaldehyde resin (indicated as “fiber+resin”), and a fiber where the resin coating contains tetrakis(2-ethylhexyl) titanate (TOT) (indicated as “fiber+resin+TOT”). The difference spectra between “fiber+resin+TOT” and “fiber+resin” are shown where a nonlinear background was removed from both the spectra and the difference spectra were smoothed. The difference spectra are compared with the calculated valence band spectrum for $\text{Ti(OCH}_3)_4$ and TiO_2 calculated by multiple scattered wave $X\alpha$ calculations.

NANOTUBES AND COMPOSITES

Carbon nanotubes have considerable potential for composite fabrication. In recent years there have been an enormous number of important developments in this area. There are many recent reviews and books on this area (e.g., Ref. [21]). The interest in nanotubes as the “ultimate carbon fiber” arises from the very desirable mechanical properties with the potential for a very high Young’s modulus which can be close to that of

the in-plane value for perfect graphite, some 10 to 100 times greater than currently available carbon fibers. Single-wall nanotubes have good flexibility unlike carbon fibers, and thus composites with such nanotubes would be unlikely to fracture when exposed to compressive stress along the axis of the fiber, in contrast to carbon fibers reinforced composites.

There has been little success so far in replacing carbon fibers with carbon nanotubes in composite fabrication. The principal problem is the difficulty of getting good interaction between the carbon nanotube and the matrix. This chapter has focused strongly on this issue, because it is so important in the development of practical composites. We have seen how this interaction can be studied and achieved in this chapter. Further discussion of this issue can be found elsewhere (e.g., Ref. [21]). It is likely that the interfacial interaction issues, and other issues associated with the differences between carbon fibers and nanotubes such as the tendency of the latter to aggregate, will limit the use of nanotubes in composite applications.

CONCLUSION

The surface chemistry associated with the buried interface between a carbon fiber (or carbon nanotube) and the matrix plays a very important role in determining the practical performance of the chosen composite. The surface treatment methods available change both the nanostructure and the chemistry at the interface. Surface science methods, especially XPS, have a very valuable role to play in probing and understanding this interaction.

ACKNOWLEDGMENTS

This material is based upon work supported by the National Science Foundation under grant No. CHE-0137502. The U.S. Government has certain rights in this material.

REFERENCES

1. Edison, T.A. Electric Lamp. U.S. Patent 223,898, January 27, 1880.
2. Bacon, R. Growth, structure, and properties of graphite whiskers. *J. Appl. Phys.* **1960**, *31* (2), 283–290.
3. Bacon, R.; Tang, M.M. Carbonization of cellulose

- fibers: II. Physical property study. *Carbon* **1964**, *2* (3), 220–221.
4. Shindo, A. *Graphite Fiber*, Osaka Kogyo Gijutsu Shikensho Hokoku No. 317, 1961; Government Industrial Research Institute, Osaka, Japan, 1–317.
5. Watt, W. Carbon work at the royal aircraft establishment. *Carbon* **1972**, *10* (2), 121–143.
6. Dresselhaus, M.S.; Dresselhaus, G.; Sugihara, K.; Spain, I.L.; Goldberg, H.A. *Graphite Fibers and Filaments*; Springer Series in Materials Science, Springer-Verlag: Berlin, 1988; Vol. 5.
7. Wang, Y.-Q.; Zhang, F.-Q.; Sherwood, P.M.A. X-ray photoelectron spectroscopic study of carbon fiber surfaces: 23. Interfacial interactions between polyvinyl alcohol and carbon fibers electrochemically oxidized in nitric acid solution. *Chem. Mater.* **1999**, *11* (9), 2573–2583.
8. Sherwood, P.M.A. Surface analysis of carbon and carbon fibers for composites. *J. Electron Spectrosc. Relat. Phenom.* **1996**, *81* (8), 319–342.
9. Drzal, L.T. The surface composition and energetics of type A graphite fibers. *Carbon* **1977**, *15* (4), 129–138.
10. Sherwood, P.M.A. Analysis of the x-ray photoelectron spectra of transition metal compounds using approximate molecular orbital theories. *J. Chem. Soc., Faraday Trans. II* **1976**, *72* (10), 1791–1804.
11. Viswanathan, H.; Wang, Y.-Q.; Audi, A.A.; Allen, P.J.; Sherwood, P.M.A. X-ray photoelectron spectroscopic studies of carbon fiber surfaces: 24. Interfacial interactions between polyimide resin and electrochemically oxidized PAN-based carbon fibers. *Chem. Mater.* **2001**, *13* (5), 1647–1655.
12. Viswanathan, H.; Rooke, M.A.; Sherwood, P.M.A. X-ray photoelectron spectroscopic studies of carbon-fiber surfaces: 21. Comparison of carbon fibers electrochemically oxidized in acid using achromatic and monochromatic XPS. *Surf. Interface Anal.* **1997**, *25* (6), 409–417.
13. Xie, Y.; Sherwood, P.M.A. X-ray photoelectron spectroscopic studies of carbon fiber surfaces: 11. Differences in the surface chemistry and bulk structure of different carbon fibers based on poly(acrylonitrile) and pitch and comparison with various graphite samples. *Chem. Mater.* **1990**, *2* (3), 293–299.
14. Xie, Y.; Sherwood, P.M.A. X-ray photoelectron spectroscopic studies of carbon fiber surfaces: 13. Valence-band studies of oxidized fibers interpreted by Xa calculations. *Chem. Mater.* **1991**, *3* (1), 164–168.
15. Weitzsacker, C.L.; Sherwood, P.M.A. X-ray photoelectron spectroscopic studies of carbon-fiber

- surfaces: 19. Surface chemical changes during electrochemical oxidation in base. *Surf. Interface Anal.* **1995**, 23 (7&8), 531–538.
16. Xie, Y.; Wang, T.; Franklin, O.; Sherwood, P.M.A. X-ray photoelectron spectroscopic studies of carbon fiber surfaces: Part XVI. Core-level and valence-band studies of pitch-based fibers electrochemically treated in ammonium carbonate solution. *Appl. Spectrosc.* **1992**, 46 (4), 645–651.
17. Wang, Y.-Q.; Viswanathan, H.; Audi, A.A.; Sherwood, P.M.A. X-ray photoelectron spectroscopic studies of carbon fiber surfaces: 22. Comparison between surface treatment of untreated and previously surface-treated fibers. *Chem. Mater.* **2000**, 12 (4), 1100–1107.
18. Weitzsacker, C.L.; Bellamy, M.; Sherwood, P.M.A. Studies of the effect of size on carbon fiber surfaces. *J. Vac. Sci. Technol., A* **1994**, 12 (4, part 2), 2392–2397.
19. Wang, Y.-Q.; Sherwood, P.M.A. Interfacial interactions of polymer coatings with oxide-free phosphate films on metal surfaces. *J. Vac. Sci. Technol., A* **2003**, 21 (4), 1120–1125.
20. Wang, T.; Sherwood, P.M.A. X-ray photoelectron spectroscopic studies of carbon fiber surfaces: 20. Interfacial interactions between phenolic resin and electrochemically oxidized carbon fibers using titanium alkoxide coupling agents and their effect on oxidation behavior. *Chem. Mater.* **1995**, 7 (5), 1031–1040.
21. Dresselhaus, M.S.; Dresselhaus, G.; Avouris, P. *Carbon Nanotubes Synthesis, Structure, Properties and Applications*; Topics in Applied Physics, Springer-Verlag: Berlin, 2001; Vol. 80.

Nanostructured Materials Synthesized by Deposition of Metals on Microtubule Supports

Silke Behrens

Institute of Technical Chemistry, Karlsruhe, Germany

Eberhard Unger

Institute of Molecular Biotechnology, Jena, Germany

INTRODUCTION

Compared to bulk materials, nanoscale materials, with their large surface areas and possible quantum confinement effects, possess distinct electronic, optical, and chemical properties.^[1-3] Therefore the synthesis of defined nanostructures is of potential interest in various fields including catalysis or microelectronics. In catalysis, for example, interesting applications for metal nanoparticles emerge from an enhanced activity, good selectivity (controllable by surface modifiers), and synergistic effects in bimetallic catalysts.^[4,5] In electronics, a fundamental concept for miniaturization is the handling of single charges by means of single electron tunneling (SET) in ordered one-, two-, or three-dimensional arrangements of metal or semiconductor clusters.^[6] Inspired by the unique physical and chemical properties, much effort has been made to tailor defined one-, two-, or three-dimensional nanostructures ranging from ordered nanoparticle arrays to nanowires.^[7,8]

In biology, nanostructures are familiar objects. Biological components exhibit size dimensions from the nanometer to the micrometer size range together with exceptional molecular recognition capabilities and functionalities for distinct biochemical transformations and translocations. However, many of these biomolecules do not possess the required physical or chemical properties. DNA, for example, has the appropriate recognition capabilities, but poor electric characteristics prevent its direct use in electric circuits.^[9] On the other hand, inorganic materials such as metals or semiconductors display, for example, the desired electric or optical properties, but their controlled deposition into defined nanostructures is difficult by conventional methods. Recently, the unique features of biological systems have been explored as building blocks for bottom-up assembly or controlled deposition of novel inorganic materials and devices with advanced structures and functionalities.^[10-12] For example, the specific recognition properties of oligonucleotides^[13,14] or antibodies^[15] have been exploited for assembling metal nanoparticles into well-ordered three-

dimensional aggregates. The protein cages of viruses have been used as a template for a controlled deposition and organization of metallic nanoparticles.^[16] Motivated by future electronic applications, researchers used DNA to control the deposition of metals^[17] and create conductive nanowires consisting of silver,^[18] gold,^[19] palladium,^[20] platinum,^[21] and copper.^[22]

In this article we address the template-directed deposition of metals on microtubule supports for fabricating metal nanostructures ranging from regular arrays of nanoclusters to continuous nanowires.

GENERATING NANOSTRUCTURES ON BIOLOGICAL SUPPORTS

Biotemplating strategies take advantage of the characteristic dimensions of biological support, ranging from a few nanometers up to several micrometers. The structure of these biostructures is well defined for a controlled deposition of inorganic materials. Moreover, the surface of these biomolecular components reveals specific patterns of surface functionalities, e.g., amino acid residues or the bases of nucleic acids that are able to bind metal ions or nanoparticles by formation of metal-ligand complexes or electrostatic interaction. In this approach, the biostructure serves as a functionalized scaffold where the metal is generated in situ and shaped into a nanostructure with its morphology dependent on that of the biotemplate.

The basic concept of a surface-controlled, heterogeneous metallization of a biotemplate consists essentially of several steps: First, appropriate metal ions are bound to the biomolecule, creating reactive sites and thus providing activation of defined sites at the biotemplate. Second, the metal ion/biomolecule adducts are treated with a reducing agent establishing metal nuclei attached to the biostructure. In another strategy, nanoparticles that were previously obtained by a homogeneous nucleation process in solution are attached to the surface functionalities of the biotemplate. Once small metal seeds cover the biotemplate, the metal growth proceeds autocatalytically by

consuming the educt feedstock from solution. The final metal coating does not necessarily have to consist of the same metal as the first formed metal nuclei or bound metal seeds, as has been shown by several groups.^[19,23–25] Within this concept, homogeneous cluster nucleation or heterogeneous background metallization—if the reduction is carried out on a substrate—should be suppressed as much as possible as it leads to unspecific deposition of the metal. Many metal deposition techniques require special reaction conditions influenced by various parameters including applied temperature, educt concentration, the reduction potential of the reducing agent, and, in general, the presence of nonnative chemicals. As a consequence, the biomolecular structure used needs to exhibit a sufficient physical and chemical stability toward these nonnative conditions for metal deposition.

STRUCTURAL FEATURES AND PROPERTIES OF MICROTUBULE TEMPLATES

Microtubules, ubiquitously present in eukaryotic cells, are proteinaceous filaments with a diameter of about 25 nm and several micrometers in length.^[26] As part of the cytoskeleton, microtubules are involved in a variety of cellular functions including maintenance of the cellular shape, segregation of the genetic material during mitosis and meiosis, intracellular transport of organelles as well as cell motility. The repeating unit of these polymeric structures is the $\alpha\beta$ -tubulin heterodimer, 4–5 nm in diameter and 8 nm in length, and a M_w of approximately 55,000 each. Microtubules assembled *in vitro* are typically composed of 12 to 14 protofilaments consisting of longitudinally connected heterodimers with a strict $\alpha\beta$ -alternation. Neighboring heterodimers are tilted by approximately 1 nm with respect to the long axis of the microtubule resulting in a helical array of tubulin subunits. *In vitro*, microtubules can be assembled from tubulin at physiological temperature, pH, and ionic strength in the presence of the cofactors guanosine-5'-triphosphate and magnesium ions. The assembly of microtubules is reversible. At 0°C microtubules depolymerize into the heterodimers, a feature actually exploited to purify microtubule protein from porcine brain by applying several temperature-dependent centrifugation cycles. Even at the assembly–disassembly steady state where the average length of microtubules in solution is constant, microtubules are highly dynamic. They constantly polymerize and depolymerize, both *in vivo* and *in vitro*. Application of such protein assemblies as template or support for inorganic materials, however, requires a certain stability regarding the dynamic structural properties and the exposure of the biomolecules to nonphysiological conditions such as metal

ion precursors or elevated temperatures. Therefore we used taxol which suppresses the dynamic instability of microtubules or glutaric dialdehyde which cross-links the tubulin subunits. Treatment with glutaric dialdehyde results in stabilized microtubules remaining intact in the presence of metal ion precursors and up to temperatures of approximately 90°C.

Microtubules are very promising as biotemplates because of their favorable geometric aspect ratio (with a thickness of 25 nm and lengths up to several micrometers) and the variety of potential metal-binding sites at their surface. Moreover, depending on the assembly conditions, tubulin is able to form not only microtubules but also various other polymorphic assemblies with different geometries, among them sheets, ribbons, spirals, or rings.^[27]

CONTROL OF METAL NANOSTRUCTURES BY MICROTUBULE SUPPORTS

It is possible to conjugate Au nanoparticles to biological components and, eventually, control their arrangement into one- to three-dimensional structures with interesting physical properties. Conjugation of Au nanoparticles to biological reporter molecules such as antibodies has long been known to be connected with electron-dense tags for biological samples in transmission electron microscopy (TEM).^[28,29] Mirkin and coworkers prepared three-dimensional Au colloid aggregates revealing, for example, unusual optical^[13,30] and electric^[31] properties.

We examined the surface of microtubules as a template to guide the assembly of Au nanoparticles into tube-like superstructures. The Au particles could easily be connected to microtubule supports by simply incubating the Au nanoparticles with the protein assembly. By this method, the microtubule surface was densely decorated by Au nanoparticles. The particles, however, were not arranged in a geometrically regular pattern but were randomly distributed over the whole surface of the biomolecular support. Fig. 1 shows Au particles, ~5 nm in size, arranged along the backbone of a single microtubule. The conjugation of Au particles to protein surfaces may depend upon several phenomena: It is well known that Au atoms bind to protein surfaces via a covalent bond to S atoms occurring, e.g., in amino acid side chains of methionine or cysteine.^[32] Cysteine or methionine residues, however, are not located in freely accessible parts of the tubulin molecule on the outside surface of a microtubule. Besides this, at pH 6.8, often used for assembly of microtubules, the surface of a microtubule (isoelectric point: pI 4.2^[33]) displays a net negative charge which should result in the repulsion of the likewise negatively charged Au particles. However, nonspecific electrostatic binding could occur at domains positively charged at this

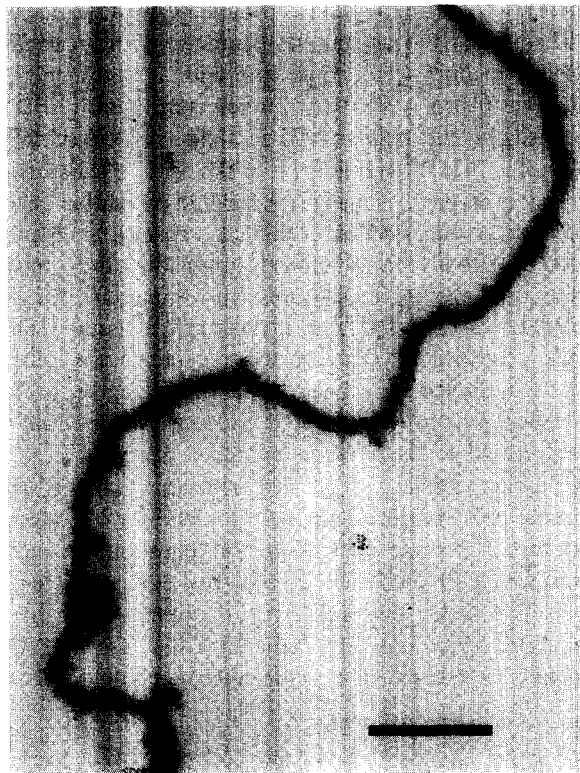


Fig. 1 Transmission electron micrograph of Au particles, 5 nm in size, bound to a single microtubule filament by simple mixing of the biostructure with the preformed Au nanoparticles (scale bar, 250 nm). The particles are randomly distributed over the microtubule surface.

pH, e.g., lysine residues which could cause a random distribution of particles over the surface of the biomolecule.^[34] By another strategy, ~2-nm Au particles attached to microtubule backbones were directly nucleated in situ from HAuCl_4 in the presence of microtubule templates. As a result, the microtubule surface got densely covered by small, 2.3-nm Au particles. The distribution of particles over the microtubule surface, however, was not completely random, but bore some resemblance to the helical arrangement of the tubulin subunits within the protein assembly (Fig. 2), a feature pronounced in a higher gear for nucleation of palladium on microtubules (see below; Fig. 3).

Metal properties, e.g., catalytic activity and selectivity, and optical and electric properties can be altered by combination with a second metal.^[35] Bimetallic Au/Pd particles in the size range of 3 to 60 nm have been synthesized by a seed-growth mechanism and stabilized by microtubule supports: In a first step, the Au nanoparticles were linked to the protein surface and, in a second step, these Au seeds were covered with Pd by reduction of Na_2PdCl_4 with trisodium citrate at 70°C.^[81] The formation

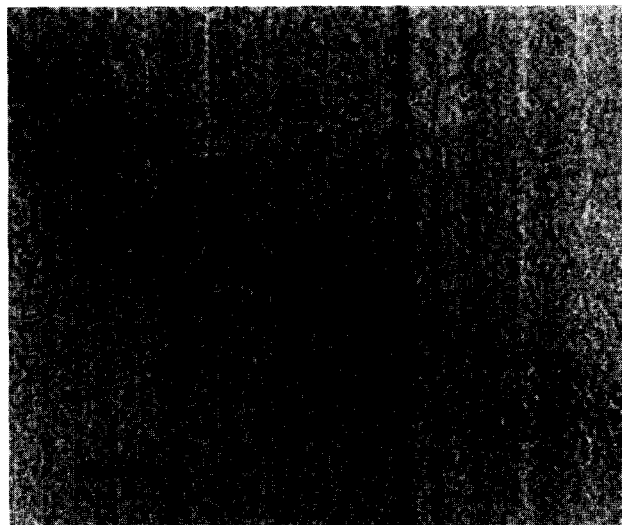


Fig. 2 Transmission electron micrograph of a single microtubule densely covered by Au nanoparticles, 2.3 nm in size. The particles were directly nucleated in situ with sodium borohydride in the presence of the microtubule template (scale bar, 150 nm).

of the bimetallic Pd/Au particles was confirmed by energy dispersive X-ray analysis (EDX). The product of a typical synthesis contained both bimetallic Pd/Au particles and a few Pd particles nucleated directly on the Au-free parts of the protein surface. Examining the catalytic activity by hydrogenation of crotonic acid as a test reaction, we found that the obtained microtubule-supported Au/Pd particles revealed a high catalytic activity under very mild reaction conditions (atmospheric pressure and 25°C) in aqueous reaction medium. Within the size range of the particles

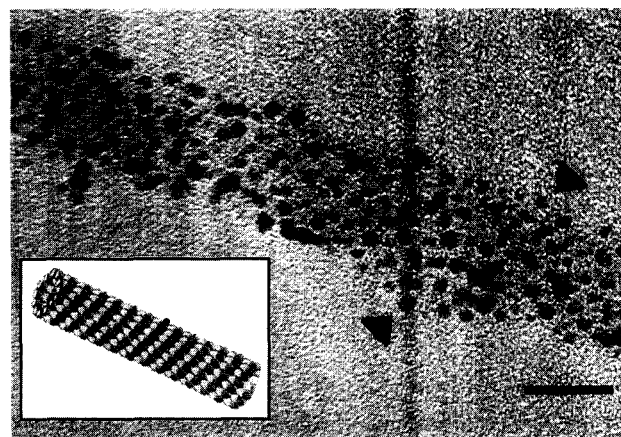


Fig. 3 Transmission electron micrograph of Pd particles, 3.1 nm in size, nucleated on the surface of a microtubule (scale bar, 20 nm). The particles reflect the arrangement of the helical template. (From Ref. [36]. Copyright 2002, Wiley-VCH.)

investigated (particle diameter, 3.8 to 61.8 nm), an increase in catalytic activity with decreasing particle diameter was observed.

Microtubules also promote directly the in situ formation of regular nanoparticle arrays with defined patterns when coupled with an appropriate chemical reaction and, as a support, provide some stabilization of the attached particles. Small monometallic Pd nanoparticles were nucleated in situ after incubation with a Pd ion precursor.^[36] After incubation, the adsorbed metal ions could be subsequently reduced to form ordered arrays of Pd nanoparticles along the backbone of the microtubule reflecting the tubulin pattern in an isomolecular fashion. Depending on the kind of reducing agent used, particles with different sizes were obtained. Reduction with trisodium citrate at 90°C yielded particles having 1.9 nm in diameter. Applying a dimethylamine reduction bath at room temperature allowed the synthesis of slightly larger Pd particles with a mean particle diameter of 3.1 nm. Fig. 3 shows Pd particles on a microtubule obtained by reduction with dimethylamine borane. The particles were mainly attached to the surface of the biotemplate resulting

in densely covered microtubule filaments. High-resolution TEM revealed the crystalline character of the particles. Lattice spacings were consistent with a pure metallic palladium phase, which was further confirmed by EDX. Interestingly, the obtained Pd particle arrays resembled closely the helical arrangement of the tubulin subunits in the protein assembly. The preferential Pd deposition on the biotemplate suggests that in this case specific molecular interactions between functional groups on the protein surface and the Pd in solution were important for the formation of the superlattice arrays. We assume that, firstly, precursor Pd (II) ions were bound to the protein surface, followed by a heterogeneous surface-controlled nucleation process, and, finally, yielding nanosized particles attached to the protein template. The surface of a microtubule consists of defined patterns of amino acid residues providing various active sites for metal ion binding and particle nucleation. The question, however, arises which of these amino acid residues are actually involved in metal ion binding and the process of particle formation. According to the hard acids and bases (HSAB) principle after Parr and Pearson, Pd^{II} is a soft metal ion

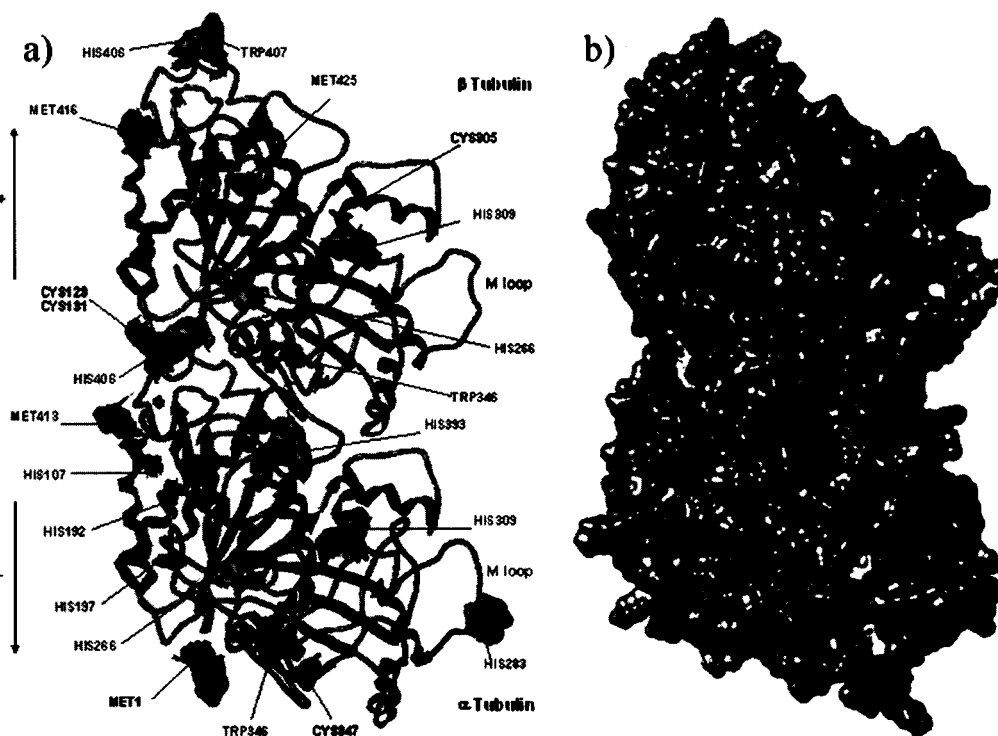


Fig. 4 a) Ribbon diagram of $\alpha\beta$ -tubulin as seen from the outside of a microtubule for selected N and S containing amino acids (cysteine: red; methionine: blue, histidine: green; and tryptophane: orange). b) The solvent accessible surfaces (Connolly surface) for the whole tubulin molecule (gray) and for the selected amino acids remaining freely accessible on the outer surface after assembly into microtubules. The histidine residues (α : 309, 393, and 406; β : 309) are centrally positioned and easily accessible. These histidine residues should be the preferred sites for Pd^{II} binding and particle nucleation. (From Ref. [36]. Copyright 2002, Wiley-VCH.) (*View this art in color at www.dekker.com.*)

and, thus, is expected to bind to soft donor ligands such as to the N or S atoms in the side chains of tryptophan, histidine, cysteine, and methionine. Some of the amino acids, e.g., lysine and arginine, are protonated at the applied pH, so that they are excluded as donor ligands. Fig. 4a shows a schematic diagram of the $\alpha\beta$ -tubulin as seen from the outside of a microtubule. It displays the selected amino acids tryptophan, histidine, cysteine, and methionine at the microtubule outside surface. Tubulin assembly into microtubules involves two types of contacts: head-to-tail binding forming the protofilaments and lateral contacts between the protofilaments. As a consequence, some of the amino acids located in the periphery of the tubulin molecule will be covered after tubulin assembly. Fig. 4b shows the solvent accessible surfaces (Connolly surface) for the remaining amino acids. Some of the shown amino acids are located in channels or only parts of them are exposed to the surface of the molecule. As a result, only four histidine residues are actually centrally positioned on both α - and β -tubulin at the microtubule's outer surface, and should be freely accessible. We therefore suggest that these histidine residues are potential sites for the binding of Pd ions and Pd particle nucleation. In fact, histidine is a typical metalbinding residue in peptides due to the deprotonated N3 atom in the imidazole ring.^[37-39] By varying, the experimental conditions it was possible to control the Pd coating of the template. If the reservoir of metal ions present was increased, the Pd clusters on the template grew and were further connected to generate a quasi-continuous coverage of the microtubule surface with palladium aggregates.

The assumption that these metal clusters were heterogeneously grown in situ, after binding of Pd(II) ions selectively at the histidine sites, was supported by theoretical simulations of Ciacchi and coworkers.^[40] They investigated the heterogeneous nucleation of Pt clusters on DNA and proteins by means of first principles molecular dynamics simulations. They found that Pt dimers formed from a Pt^{II} complex, covalently bound to a biopolymer, and a free Pt^{II} complex after a single reduction step. The imidazole ring, which is a structural feature of both histidine and the purine bases guanine and adenine, was a key residue at the biopolymer surface to induce the formation of these platinum dimers. The formation of Pt dimers was only possible in the presence of strong donor ligands such as purine DNA bases or histidine amino acids, and appeared to be forbidden in the homogeneous dimer formation reaction leading to a weaker Pt-Pt bond. Because of the delocalized electronic states on the heterocyclic ligands, the biopolymer-bound Pt atoms and dimers accepted reducing electrons more easily than the free complexes or dimers in solution and, moreover, the initially formed Pt-Pt bonds were stabilized. Thus the presence of these ligand systems contributed to enhanc-

ing the reaction rate of the heterogeneous cluster nucleation channel. The first-formed Pt nuclei developed then into bigger particles consuming the feedstock of metal complexes in solution and hindering the homogeneous formation of metal particles. As a result, the kinetics of the reduction and deposition process was locally enhanced at the surface of the biopolymer. Thus such a preferential heterogeneous particle growth on an activated biotemplate permits a certain degree of control over the metallization process.

In addition to Au and Pd, other noble metals such as Rh, Ru, and Ag have been used in material synthesis with this type of microtubule template. Fig. 4 displays small Rh nanoparticles on a microtubule obtained by in situ reduction with NaN₃. For electroless metal plating with Ni or Co, the surface of the template had to be previously activated with noble metal atoms or clusters. Kirsch and coworkers deposited about 10-nm-thick Ni or Co coats on microtubule templates, which yielded magnetic nanowires with an outer diameter of 50 to 60 nm.^[24,25] In a first step, the microtubule surface was activated by adsorption of a molecular Pd catalyst. In a second step, Ni or Co was deposited onto the activated microtubules by applying an electroless metallization bath with dimethylamine borane as reducing agent. In their experiments they found clear evidence that nucleation of Ni crystallites started exclusively at the catalytic surface of the Pd catalyst.

CONCLUSION

The interdisciplinary field emerging between biotechnology and materials science for the production of nanoscale materials is a rapidly growing field. Our results illustrate the potential of protein assemblies as biological components with their unique chemical and topological features for the controlled deposition of metals into well-defined, protein-supported nanostructures. In the interplay, the biological and inorganic components provide structure-directing properties and, furthermore, the biological support stabilizes the resulting nanostructure. Au colloids, for example, have been pursued as building blocks for the formation of wire-like structures through manipulation by microtubule templates. When coupled with an appropriate chemical reaction, microtubules promote the in situ formation of ordered arrays of metal nanoparticles resembling the arrangement of the protein molecules within the assembly. Preferential heterogeneous particle growth on the biotemplate permits control over the metallization process on the nanometer scale. Depending on the reaction conditions, the composites formed range from the isomolecular decoration of every protein molecule with one nanoparticle to the complete coating of the whole protein assembly. Although many examples exist where metallic

nanoparticles and materials have successfully been deposited on biomolecules,^[10,11] there still remains a great demand for new, mild, and selective chemical deposition techniques. One of the major advantages associated with this type of protein assemblies as biological template is that it will enable the future design of various patterns of nanomaterials, e.g., ring structures exploiting the great diversity in size and shape of biomolecular tools, e.g., the polymorphic tubulin assemblies. A variety of technical obstacles still have to be solved ranging from the currently limited availability of large amounts of the biological building blocks to the improvement of analytical techniques. Because of the very low amount of material used in single nanodevices, the costs of the protein components should normally not limit application. A decrease in production costs will be required, however, for scale-up of both purification techniques and artificial syntheses. Biomolecular structures modified by genetic engineering and combined with an appropriate metal deposition technique will allow producing advanced materials on the nanometer scale with, for example, novel electronic, optical, magnetic, or catalytic properties.

REFERENCES

- Weller, H. Quantized semiconductor particles: A novel state of matter for materials science. *Adv. Mater.* **1993**, *5* (2), 88–95.
- Murray, C.B.; Norris, D.J.; Bawendi, M.G. Synthesis and characterization of nearly monodisperse CdE (E=S, Se, Te) semiconductor nanocrystallites. *J. Am. Chem. Soc.* **1993**, *115*, 8706–8715.
- Henglein, A. Small-particle research: Physicochemical properties of extremely small colloidal metal and semiconductor particles. *Chem. Rev.* **1989**, *89*, 1861–1873.
- Bönnemann, H.; Brijoux, W. Potential applications of nanostructured metal colloid; Braunstein, P., Oro, L.A., Raithby, P.R., Eds.; *Metal Clusters in Chemistry*, Wiley-VCH: Weinheim, Germany, 1999; Vol. 2, 913–931.
- Schmid, G.; Maihack, V.; Lantermann, F.; Peschel, S. Ligand-stabilized metal clusters and colloids: Properties and applications. *J. Chem. Soc., Dalton Trans.* **1996**, 589–595.
- Simon, U. Charge transport in nanoparticle arrangements. *Adv. Mater.* **1998**, *10* (17), 1487–1492.
- Xia, Y.; Yang, P.; Sun, Y.; Wu, Y.; Mayers, B.; Gates, B.; Yin, Y.; Kim, F.; Yan, H. One-dimensional nanostructures: Synthesis, characterization, and applications. *Adv. Mater.* **2003**, *15* (5), 353–389.
- Behrens, S.; Rahn, K.; Habicht, W.; Böhm, K.J.; Rösner, H.; Dinjus, E.; Unger, E. Nanoscale particle arrays induced by highly ordered protein assemblies. *Adv. Mater.* **2002**, *14* (22), 1621–1625.
- Dekker, C.; Ratner, M. Electronic properties of DNA. *Phys. World* **2001**, *14*, 29–33.
- Niemeyer, C.M. Biomolecules meet nanoparticles. *Angew. Chem., Int. Ed.* **2001**, *40*, 4128–4158.
- Dujardin, E.; Mann, S. Bio-inspired materials chemistry. *Adv. Mater.* **2002**, *14*, 775–788.
- Storhoff, J.J.; Mirkin, C.A. Programmed material synthesis with DNA. *Chem. Rev.* **1999**, *99*, 1849–1862.
- Mirkin, C.; Letsinger, R.; Mucic, R.; Storhoff, J. A DNA-based method for rationally assembling nanoparticles into macroscopic materials. *Nature* **1996**, *382*, 607–608.
- Cao, Y.; Jin, R.; Mirkin, C.J. DNA-modified core-shell Ag/Au nanoparticles. *Am. Chem. Soc.* **2001**, *123*, 7961–7962.
- Connolly, S.; Fitzmaurice, D. Programmed assembly of gold nanocrystals in aqueous solution. *Adv. Mater.* **1999**, *11*, 1202–1205.
- Dujardin, E.; Peet, C.; Stubbs, G.; Cluver, J.N.; Mann, S. Organization of metallic nanoparticles using tobacco mosaic virus templates. *Nano Lett.* **2003**, *3* (3), 413–417.
- Richter, J. Metallization of DNA. *Physica, E* **2003**, *16*, 157–173.
- Braun, E.; Eichen, Y.; Sivan, U.; Ben-Yoseph, G. DNA-templated assembly and electrode attachment of a conducting silver wire. *Nature* **1998**, *391*, 775–778.
- Keren, K.; Krueger, M.; Gilad, R.; Ben-Yoseph, G.; Sivan, U.; Braun, E. Sequence-specific molecular lithography on single DNA molecules. *Science* **2002**, *297*, 72–75.
- Richter, J.; Seidel, R.; Kirsch, R.; Mertig, M.; Pompe, W.; Plaschke, J.; Schackert, H.K. Nanoscale palladium metallization of DNA. *Adv. Mater.* **2000**, *12*, 507–510.
- Mertig, M.; Ciacchi, L.C.; Seidel, R.; Pompe, W. DNA as a selective metallization template. *Nano Lett.* **2002**, *2*, 841–844.
- Monson, C.F.; Wolley, A.T. DNA-templated construction of copper nanowires. *Nano Lett.* **2003**, *3*, 359–363.
- Ford, W.; Harnack, O.; Yasuda, A.; Wessels, J. Platinated DNA as precursors to templated chains of metal nanoparticles. *Adv. Mater.* **2001**, *13*, 1793–1797.
- Kirsch, R.; Mertig, M.; Pompe, W.; Wahl, R.; Sadowski, G.; Böhm, K.J.; Unger, E. Three-dimensional metallization of microtubules. *Thin Solid Films* **1997**, *305*, 248–253.

25. Mertig, M.; Kirsch, R.; Pompe, W. Biomolecular approach to nanotube fabrication. *Appl. Phys.*, A **66**, 723–727.
26. Nogales, E. Structural insights into microtubule function. *Ann. Rev. Biochem.* **2000**, *69*, 277–302.
27. Unger, E.; Böhm, K.J.; Vater, W. Structural diversity and dynamics of microtubules and polymorphic tubulin assemblies. *Electron Microsc. Rev.* **1990**, *3*, 355–395.
28. Roth, J. The silver anniversary of gold: 25 years of the colloidal gold marker system for immunocytochemistry and histochemistry. *Histochem. Cell Biol.* **1996**, *106*, 1–8.
29. Hermann, R.; Walther, P.; Müller, M. Immunogold labeling in scanning electron microscopy. *Histochem. Cell Biol.* **1996**, *106*, 31–39.
30. Storhoff, J.; Lazarides, A.; Mucic, R.; Mirkin, C.A.; Letsinger, R.; Schatz, G. What controls the optical properties of DANN-linked gold nanoparticle assemblies? *J. Am. Chem. Soc.* **2000**, *122*, 4640–4650.
31. Park, S.; Lazarides, A.; Mirkin, C.; Brazis, P.; Kannewurf, C.; Letsinger, R. The electrical properties of gold nanoparticle assemblies linked by DNA. *Angew. Chem., Int. Ed.* **2000**, *39*, 3845–3848.
32. Gole, A.; Dash, C.; Ramakrishnan, V.; Sainkar, S.R.; Mandale, A.B.; Rao, M.; Sastry, M. Pepsin-gold conjugates: Preparation, characterization, and enzymatic activity. *Langmuir* **2001**, *17*, 1674–1679.
33. Stracke, R.; Böhm, K.J.; Wollweber, L.; Tuszynski, J.A.; Unger, E. Analysis of the migration behaviour of single microtubules in electric fields. *Biochem. Biophys. Res. Commun.* **2002**, *293*, 602–609.
34. Keating, C.; Kovaleski, K.; Natan, M. Heightened electromagnetic fields between nanoparticles: Surface enhanced Raman scattering from metal–cytochrome c–metal sandwiches. *J. Phys. Chem., B* **1998**, *102*, 9414–9425.
35. Lee, A.F.; Baddeley, C.J.; Hardacre, C.; Ormerod, R.M.; Lambert, R.M. Structural and catalytic properties of novel Au/Pd bimetallic colloid particles: EXAFS, XRD, and acetylene coupling. *J. Phys. Chem.* **1995**, *99*, 6096–6102.
36. Behrens, S.; Rahn, K.; Habicht, W.; Böhm, K.J.; Rösner, H.; Dinjus, E.; Unger, E. Nanoscale particle arrays induced by highly ordered protein assemblies. *Adv. Mater.* **2002**, *14* (22), 1621–1625.
37. Djuran, M.I.; Milinkoviæ, S.U. Hydrolysis of amide bond in histidine-containing peptides promoted by chelated amino acid palladium (II) complexes: Dependence of hydrolytic pathway on the coordination modes of the peptides. *Polyhedron* **1999**, *18*, 3611–3616.
38. Appelton, T.G.; Pesch, F.J.; Wienken, M.; Menzer, S.; Lippert, B. Linkage isomerism in square–planar complexes of platinum and palladium with histidine and derivatives. *Inorg. Chem.* **1992**, *31* (21), 4410–4419.
39. Parac, T.N.; Kostiaë, N.M. Effects of linkage isomerism and acid–base equilibria on reactivity and catalytic turnover in hydrolytic cleavage of histidyl peptides coordinated to palladium (II). Identification of the active complex between palladium (II) and the histidyl residue. *J. Am. Chem. Soc.* **1996**, *118*, 5946–5951.
40. Ciachi, L.C.; Mertig, M.; Seidel, R.; Pompe, W.; De Vita, A. Nucleation of platinum clusters on biopolymers: A first principles study of the molecular mechanisms. *Nanotechnology* **2003**, *14*, 840–848.



Nanostructured Materials Synthesized by Mechanical Attrition

Carl C. Koch

North Carolina State University, Raleigh, North Carolina, U.S.A.

INTRODUCTION

A wide variety of techniques are being used to synthesize nanostructured materials including inert gas condensation, rapid solidification, electrodeposition, sputtering, crystallization of amorphous phases, and chemical processing.^[1] Mechanical attrition—ball milling of powders—is a technique that has also been used widely for preparation of nanostructured materials.^[2,3] The term “mechanical attrition” can be subdivided into “mechanical milling,” which is the milling of single composition powders, often elements, and “mechanical alloying,” which involves milling of dissimilar powders such that material transfer occurs during milling. Unlike many of the methods for synthesis of nanostructured materials, mechanical attrition produces its nanostructures not by cluster assembly, but by the structural decomposition of coarser-grained structures as the result of severe plastic deformation. This has become a popular method to fabricate nanocrystalline materials because of several factors: the simplicity of the process, the relatively inexpensive equipment (on the laboratory scale) needed, and the applicability to essentially all classes of materials. A major advantage of mechanical attrition is the possibility for easily scaling up to tonnage quantities of material for various applications. The disadvantages that are often cited are contamination from the milling media and/or atmosphere, and the need, for many applications, to consolidate the powder product without coarsening the nanocrystalline microstructure.

A number of reviews concerned with the synthesis of nanostructured materials by mechanical attrition have been published in recent years, e.g., those of Koch,^[2,4] Fecht,^[5] Suryanarayana and Koch,^[1] and Fecht.^[3] This article will serve to update these previous reports. The details of the mechanical attrition processes, equipment used, etc. has been covered in a number of reviews (e.g., Ref. [4]), and will not be repeated here. The phenomenology of the development of nanoscale microstructures by mechanical attrition will be reviewed for the various classes of materials including single-phase metals, metallic alloys, brittle materials, and multiphase materials. Several mechanisms proposed for the development of a nanoscale microstructure will then be described with reference to recent experimental observations. Finally, a

brief discussion of the problems associated with mechanical attrition as a processing method will be presented. These are powder contamination and the need to consolidate the powders into bulk form without coarsening the nanoscale microstructure.

PHENOMENOLOGY—EXPERIMENTAL OBSERVATIONS

Single-Phase Elements—Mechanical Milling

Mechanical attrition has been found to refine grain size of all solid elements studied to the nanoscale. However, the minimum grain size achieved is dependent on a number of process variables as well as properties of the element. The minimum grain size obtainable by milling has been attributed to a balance between the defect/dislocation structure introduced by the plastic deformation of milling and its recovery by thermal processes.^[6] It has been found that the minimum grain size induced by milling scales inversely with the melting temperature of the group of fcc structure metals studied.^[6] These data are plotted in Fig. 1, along with data for other metals and carbon (graphite).^[2] For these data, only the lower melting point metals show a clear inverse dependence of minimum grain size on melting temperature. The minimum grain size for elements with higher melting temperatures (larger than melting temperature for Ni) exhibits essentially constant values with melting temperature for given crystal structure classes. For these elements, it appears that d_{\min} is in the order: fcc < bcc < hcp. However, before explanations for the above based on the strain hardening response, twinning, or other fundamental differences in deformation behavior for the various metallic crystal structures can be considered, it should be pointed out that a number of variables can influence the values of the minimum grain size attained by ball milling. First of all, most of the measurements reported in Fig. 1 are based on the analysis of X-ray line broadening measurements. It is now well established that such measurements are subject to difficulty in terms of absolute quantitative values for grain sizes. Variability among analysis techniques for X-ray line

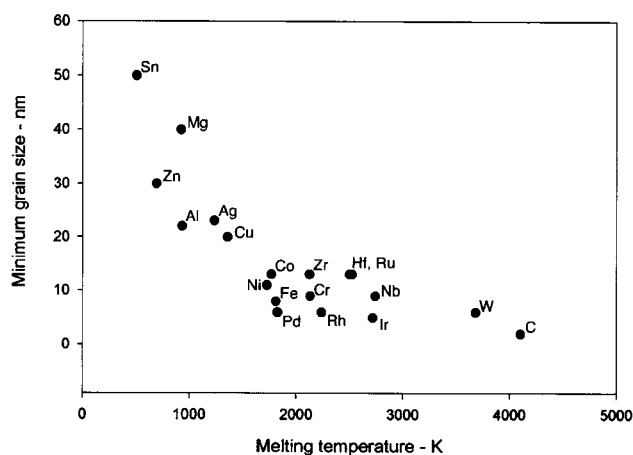


Fig. 1 Minimum nanocrystalline grain size for ball milled elements vs. their melting temperature. (From Refs. [2,6–8].)

broadening, as well as comparisons between these X-ray line broadening results and those from transmission electron microscopy (TEM) measurements, can be significant. However, most of the data in Fig. 1 are obtained from the Cal Tech group, Professor W. L. Johnson and coworkers,^[6,7] or from Oleszak and Shingu.^[8] Both of these groups used the approach of Williamson and Hall^[8a] to estimate the crystallite size and root-mean-square (rms) strain from the X-ray line broadening. Although the mill energies and contamination levels were very different in these studies, remarkable agreement for minimum grain size, d , is found for Al, Cu, Ni, and Fe. Oleszak and Shingu^[8] found a lower d value for W (5.5 nm) than the value (9 nm) obtained by Fecht et al.^[7] The Cal Tech group used a high-energy shaker mill (Spex 8000), while Oleszak and Shingu used a conventional horizontal low-energy ball mill. The metallic impurity level (Fe) from the shaker mill is much larger (~ 2 at.% Fe) than that from the conventional ball mill ($< 0.1\%$ Fe). Conversely, the reported oxygen concentrations were about 4 times higher for powders milled in the conventional mill than for those from the shaker mill. The observation that the minimum nanocrystalline grain sizes for a number of elements milled in a low-energy mill are comparable to those milled in a high-energy mill is contrary to the conclusions previously reported after milling TiNi in a high-energy Spex shaker mill and a lower-energy vibratory mill.^[9] After about 10 h in the Spex mill, the grain size (determined by both TEM and X-ray line broadening analysis) decreased to about 4–5 nm. At longer milling times, an amorphous structure was observed. Milling for 100 h in the vibratory mill resulted in a grain size of about 15 nm. It was originally assumed that this value represented a saturation to the minimum grain size obtainable in the lower energy mill. However, in the

light of the work of Oleszak and Shingu, it is likely that the d_{\min} was not obtained at 100 h in the lower-energy mill, and that continued milling may have further reduced the grain size. These results suggest that total strain, rather than milling energy or ball–powder–ball collision frequency, is responsible for determining the minimum nanocrystalline grain size. This is different from ball milling-induced amorphization or disordering, where it appears that the energy and frequency of ball–powder–ball collisions determine the final structures formed in “driven systems.” However, it is consistent with observations of nanocrystallites formed by high strain values using other noncyclic deformation methods.^[10] These results suggest that mill energy per se is not critical to the final microstructure, although, naturally, the kinetics of the process are dependent on the energy, and times for attaining the same microstructure can be several orders of magnitude longer in the low-energy mills than in high-energy mills.

Milling temperature has been observed to affect the rate at which the nanocrystalline structure develops. The milling time at which a given grain size was attained in a TiNi intermetallic compound was a function of milling temperature.^[9] In this case, amorphization occurred at a “critical” grain size of about 4–5 nm, thus the final nanocrystalline grain size at each milling temperature could not be determined. Shen and Koch^[11] also observed smaller nanocrystalline grain sizes in both Cu and Ni milled at -85°C compared with samples milled at room temperature. For example, for Cu, $d = 26 \pm 3$ nm for room temperature milling and $d = 17 \pm 2$ nm for milling at -85°C . Evidence for smaller nanocrystalline grain sizes formed by milling at low temperatures have now been observed in a number of materials including the intermetallic compound CoZr^[12] and elemental Zn.^[13]

Metallic Alloys—Mechanical Alloying

While the majority of studies of nanocrystalline materials synthesized by ball milling have been on single-composition materials—i.e., either elemental metals, intermetallic compounds, or metal alloys—there have been a number of studies on mechanical alloying of dissimilar powders that result in nanoscale microstructures. First, the alloy effect on nanocrystalline grain size on nanocrystalline alloys will be discussed. These include both alloys made by mechanical alloying of dissimilar powders or milling of alloy powders. It has been suggested that the ultimate grain size achievable by milling is determined by the minimum grain size that can sustain a dislocation pileup within a grain and by the rate of recovery during milling.^[6] To estimate the composition dependence of grain size after milling, one may use the formula

suggested by Nieh and Wadsworth.^[14] The minimum distance, L , between dislocations is given by $L=3Gb/\pi(1-\nu)h$, where G is shear modulus, b is Burgers vector, ν is Poisson ratio, and h is hardness. Indeed, if this is related to the formation of a minimum nanocrystalline grain size, then this nanocrystalline grain size is inversely proportional to hardness, and therefore, in most cases, to composition. In fact, a decreasing nanocrystalline grain size with solute concentration is observed in nanocrystalline alloy systems exhibiting solid solution hardening, such as Cu (Fe), Ti (Cu), Nb (Cu), Cu (Ni), and Cu (Co).^[15] Also consistent with this is the essentially constant nanocrystalline grain size in Ni (Co), where hardness does not change significantly with composition^[11] and the increased grain size in nanocrystalline Ni (Cu), Fe (Cu), and Cr (Cu), which exhibit an apparent solid solution softening effect.^[15] However, the influence of alloying elements on the hardness of the nanocrystalline solid solutions is different from that in conventional polycrystalline solid solutions. The hardness of nanocrystalline solid solutions depends on both solid solution hardening and grain boundary hardening, while the latter makes the major contribution to total hardness. The increase in hardness resulting from the solid solution hardening effect in nanocrystalline alloys is of the same magnitude as that in conventional grain size polycrystalline alloys. However, the addition of alloying elements into the matrix for nanocrystalline alloys may have a strong influence on the grain boundary energy and grain boundary diffusion coefficient and thus on the deformation and recovery mechanisms of the nanocrystalline alloys formed by mechanical attrition. The different deformation and recovery behaviors are responsible for the various grain sizes obtained by milling and thus for the decreased or increased grain boundary hardening effects for the various nanocrystalline solid solutions.

Nanocrystalline grains are observed during the mechanical alloying of dissimilar component powders. Klassen et al.^[16] followed the phase formation and microstructural development during the mechanical alloying of Ti and Al powder blends of overall composition $Ti_{25}Al_{75}$. TEM revealed nanocrystalline grains of partially ordered $L1_2$ phase with a crystallite size of 10–30 nm in the alloy layers at the interface between the pure Ti and Al lamellae at the very early stages of the milling process. The alloy phase that develops between the pure powder components consists of nanocrystalline grains, presumably because of the multiple nucleation events and the slow growth occurring at the relatively low temperatures (100–200°C above ambient) during milling. Trudeau et al.^[17] prepared nanocrystalline FeTi by both low milling energy mechanical alloying (MA) of elemental Fe and Ti powders and mechanical milling (MM) of FeTi compound powders. Higher mill energies resulted in

amorphization. The grain size of the MM Fe/Ti steadily decreases with milling time, while that for the MA Fe/Ti initially increases and then decreases to values essentially identical to those for the milled samples. This effect is illustrated in Fig. 2.

Brittle Materials

The first materials subjected to mechanical alloying were combinations of ductile metals and brittle oxide powders, or with both components ductile metals. It was not clear that, if both components were brittle, the welding of the dissimilar powders believed to be required for the alloying to occur would take place. It might be expected that brittle components would simply fracture during milling and be reduced in size to the limit of comminution observed in the grinding of brittle mineral powders. However, it has been found that ball milling of nominally brittle materials can lead to alloying of brittle components, e.g., Si and Ge,^[18] and the introduction of significant plastic deformation and high dislocation densities in brittle compounds, e.g., Nb_3Sn .^[19] Si and Ge are completely brittle at room temperature, and yet complete solid solutions of Si–Ge alloys were obtained across the binary phase diagram. Thus alloying on the atomic scale was observed by mechanical alloying of brittle components. Nb_3Sn is an extremely brittle intermetallic compound that elastically fractures until tested at temperatures above about 1400°C. However, ball milling Nb_3Sn can produce large amounts of plastic deformation, as observed by TEM of the milled powder. The dislocations so produced then induce a

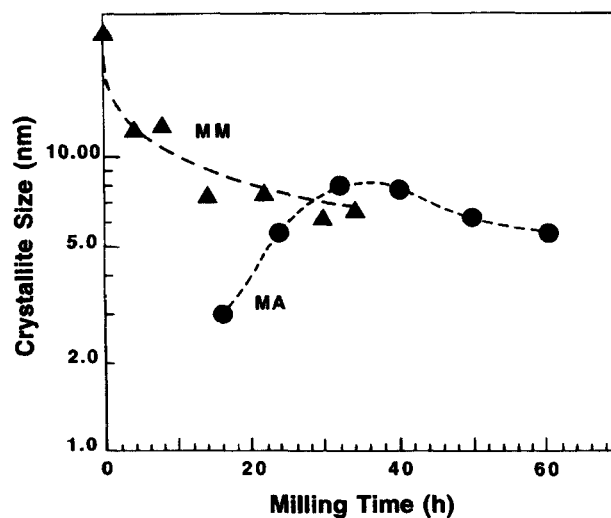


Fig. 2 Crystallite size for FeTi intermetallic phase for low-energy (●) mechanical alloying of Fe and Ti powders, and (▲) mechanical milling of the FeTi compound powders. (From Ref. [17].)

nanocrystalline grain structure similar to that formed in milled ductile metals. It is not yet clear how ball milling can produce large plastic deformation in materials that are very brittle under uniaxial stress conditions. It is suggested that the high hydrostatic stress component, which may exist in the powders during milling, can favor plastic deformation over fracture and allow a large dislocation density to be generated.^[19] Mechanical attrition was also found to induce nanocrystalline microstructures in brittle ceramics, such as ZrO_2 , and ceramic powder mixtures, such as Fe_2O_3/Cr_2O_3 and ZrO_2/Y_2O_3 .^[3]

Polymer Blends

The application of mechanical attrition to polymeric materials was initiated by Shaw.^[20] To fracture the polymer particulates, and on the microscopic level the polymer chains, milling was conducted at temperatures below the glass transition temperature of the given polymer. Shaw's group has studied a number of homopolymers such as polyamide, polyethylene, acrylonitrile-butadiene-styrene, polypropylene, and polystyrene. Refinement of the microstructure typically occurred and milling-induced structural and property changes were noted that were very material-specific. Subsequently, others have studied milling-induced changes in the structure of several semicrystalline and amorphous homopolymers.^[21] For example, in poly(ethylene terephthalate) (PET), milling promotes an oriented amorphous morphology in both high- and low-crystallinity PET. Molecular weight, glass transition temperature, and impact strength have been used to probe the milling-time-dependent molecular and property evolution of several homopolymers, e.g., poly(methylmethacrylate) (PMMA) and polyisoprene (PI). Milling of PMMA resulted in monotonic decreases in molecular weight and glass transition temperature, reflecting the milling-induced scission of the polymer chains. PI exhibited much different behavior in that the decrease in glass transition temperature, T_g , given by $\Delta T_g = T_{g,0} - T_g(t_m)$, where $T_{g,0}$ is the glass transition temperature of the unmilled polymer, first increased and then decreased, as illustrated in Fig. 3. In this case, cryomilled PI does not exhibit a monotonic increase in ΔT_g , but instead shows a sharp maximum at relatively short milling times (2 h), followed by a drop to almost zero before again increasing slightly for longer milling times. This unusual, but reproducible, behavior strongly suggests that the PI chains undergo chemical crosslinking during cryomilling. In such a case, we imagine a dynamic competition between chains breaking (causing a decrease in molecular weight) and crosslinking (promoting an increase in molecular weight) under the nonequilibrium conditions of milling. Sol-gel analysis and Fourier

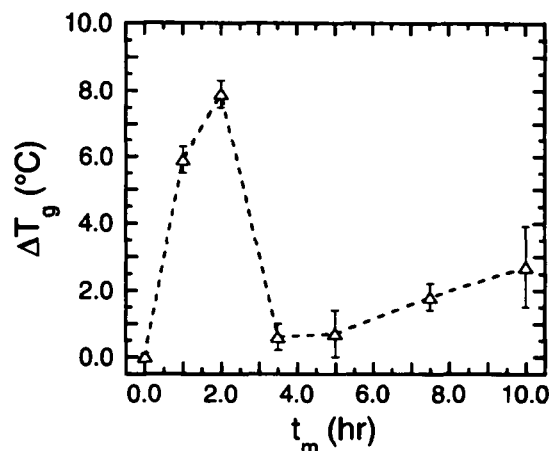


Fig. 3 Dependence of ΔT_g on milling time, t_m , for cryomilled polyisoprene. (From Ref. [21].)

transform infrared (FTIR) spectroscopy yielded further evidence for milling-induced crosslinking in PI. Mechanical attrition was also performed at cryogenic temperatures to incorporate PI into PMMA.^[22] A number of experimental techniques were used to study the structure of these normally immiscible polymer mixtures. TEM clearly showed that the solid-state blending by mechanical attrition of polymeric materials can yield nanoscale dispersions of immiscible polymers. The strong evidence for free radical formation and crosslinking induced by milling suggests many possibilities for the design of novel new polymeric materials with nanoscale microstructures. Incorporation of inorganic dispersoids in polymeric materials at the nanoscale by mechanical attrition is an area of research not yet fully explored.

Nanocomposites

Nanoscale precipitates or dispersoids used to strengthen structural materials have been commonly used for about a century. However, the combination of nanoscale second phases in a nanocrystalline matrix are new microstructures and mechanical attrition is a particularly suited synthesis method for such materials. Because equilibrium solid solubility limits can be significantly enhanced by mechanical attrition of systems of limited mutable solubilities^[23] to form nanocomposites, the immiscible nature of the component phases must be strong. Metals with very different atomic sizes such as Pb and Al can form nanocomposites^[24] as well as covalently or ionic bonded compounds in metallic matrices, such as $\gamma-Al_2O_3$ and AlN in Fe.^[25]

Metalloid second phases in nanocrystalline grain size matrices have been produced via the method of

cryomilling. This technique of reactive milling of metals in liquid nitrogen was first developed by Huang et al.^[26] for Al, and has since been applied to several other metallic materials. The cryomilling of elemental Al and Ni powders in liquid nitrogen resulted in a nanoscale grain size for the Ni-base matrix of about 6 to 11 nm. Continued cryomilling in nitrogen resulted in a reaction between N, O, and the Al, which depleted the Al content of the matrix until, at long cryomilling times (170 h), the structure consisted of nanocrystalline Ni with AlN and γ -Al₂O₃ nanoscale dispersions. Similar to the results they obtained from their work on Al, the presence of the nanoscale dispersoids resulted in a marked inhibition of grain growth even on annealing at high temperatures. The Ni-based nanocrystalline grain size containing the nitride and oxide dispersoids maintained a nanoscale grain structure with limited grain growth (grain size distribution of mostly about 11 nm, with some grains up to 300 nm) after annealing at 1373 K. The same material milled in argon was found to have extensive grain growth to about 1 μ m grain size after annealing at this temperature. These results demonstrated the effectiveness of nanoscale second phases in a nanoscale matrix to impede grain growth.

MECHANISMS FOR NANOCRYSTAL SYNTHESIS BY MECHANICAL ATTRITION

Single-Phase Metals by Mechanical Attrition

The first description of the evolution of a nanoscale grain structure during mechanical milling of elemental metals was given by Fecht and coworkers and summarized, for example, in Ref. [5] The basis of this first model was a study of the nanocrystallization of AlRu and Ru by mechanical attrition.^[27] The structure/microstructure of AlRu as a function of milling time was followed by analysis of X-ray line broadening to estimate average grain size and lattice strain and TEM and high-resolution TEM (HRTEM) to directly observe the microstructural development. The TEM and HRTEM studies showed that, at the early stages of milling, the deformation was localized within shear bands that are approximately 0.5–1 μ m wide. The shear bands contain a high dislocation density. At a given strain, these dislocations begin to annihilate and recombine to small-angle grain boundaries separating individual cells or grains. Small grains, 8–12 nm in diameter, observed within the shear bands and electron diffraction patterns suggest that the misorientation angles between the grains are relatively small. At longer milling times, the grain size steadily decreased, consistent with the X-ray results, and the shear bands coalesced. The small-angle boundaries were replaced

by higher-angle boundaries, implying grain rotation, as reflected by the disappearance of texture in the electron diffraction patterns, as well as the random orientation of the grains observed from the lattice fringes in HRTEM. Fecht summarized the observed phenomenology of nanocrystallization by mechanical attrition into the following three stages:

- Stage 1. Deformation localization in shear bands containing a high dislocation density.
- Stage 2. Dislocation annihilation/recombination/rearrangement to form a cell/subgrain structure with nanoscale dimensions—further milling extends this structure throughout the sample.
- Stage 3. The orientation of the grains becomes random, that is, low angle grain boundaries disappear as high angle grain boundaries replace them, by presumably grain boundary sliding, rotation.

From evidence of the atomic-level lattice strain and the stored enthalpy as a function of reciprocal grain size (or milling time), it was concluded that two different regimes can be distinguished, i.e., dislocation vs. grain boundary deformation mechanisms.^[5] The lattice strain in the fcc elements studied by Eckert et al.,^[6] milled in a high-energy shaker mill, was found to increase continuously with decreasing grain size, and reach a maximum value at the smallest grain size. This is in contrast to the earlier observation on Ru and AlRu, which indicated a maximum in strain vs. $1/d$,^[28] and the more recent study of Oleszak and Shingu^[8] on a low-energy mill, which also shows a broad maximum in strain vs. $1/d$ for a number of elements including several fcc elements. The lattice strain values available from the literature are plotted against reciprocal grain size, $1/d$, in Fig. 4. With the exception of Ru, the data for increasing lattice strain with $1/d$ appear to fall on a common relatively narrow band before decreasing from the maximum strain values. However, these data are obtained from several groups using mills with various energy levels and possible differences in milling temperature. It has been demonstrated^[11] that lower milling temperature resulted in larger values for lattice strain for Cu and Ni. However, the data from the low-energy mill^[8] should be self-consistent and exhibit interesting behavior. That is, the strain rises with decreasing grain size, reaches a maximum, and then decreases to low values for the smallest nanocrystalline grain sizes. A maximum in strain with $1/d$ was previously explained by either a change in deformation mechanism from dislocation generation and movement to grain boundary sliding, grain rotation,^[27] or, in brittle intermetallics to fracture after the strain maximum is reached.^[17] A problem with the first mechanism is that the nanocrystalline grain size continues to decrease after the strain maximum is reached,

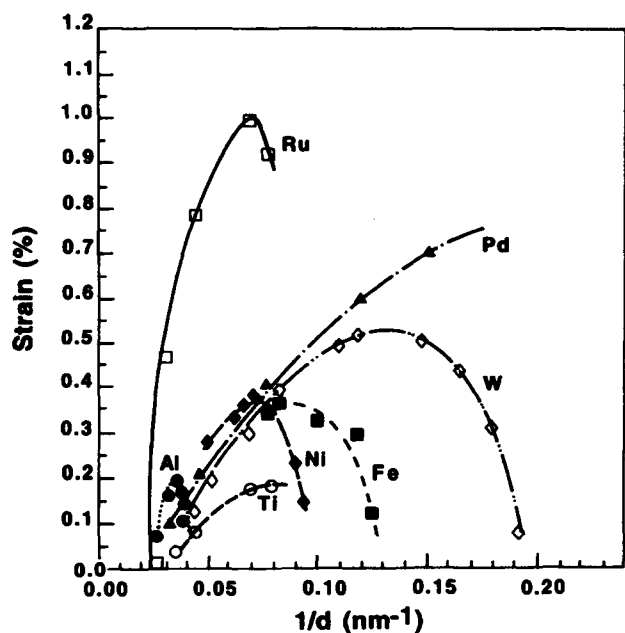


Fig. 4 Lattice strain vs. reciprocal grain size. (From Ref. [2].)

and grain boundary sliding and rotation presumably cannot result in grain size reduction. There is no clear evidence at present for the fracture mechanism, which would also presumably result in a finer particulate distribution.

Additional information to help explain the mechanism of nanocrystalline formation comes from measurements of stored enthalpy. Maxima in stored enthalpy vs.

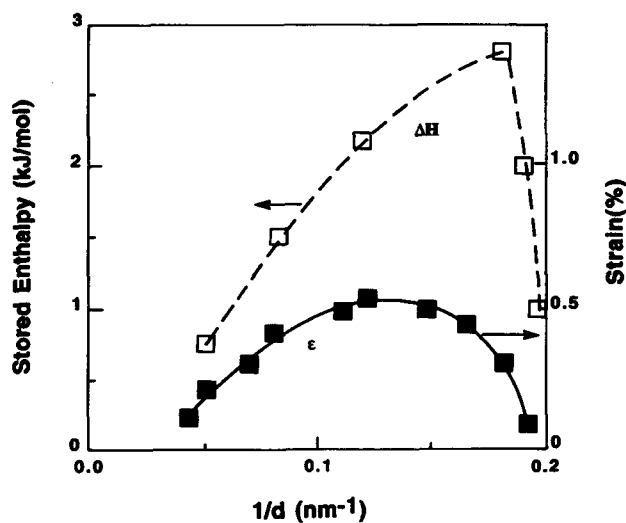


Fig. 5 Stored enthalpy (ΔH) and lattice strain (ϵ) vs. reciprocal grain size for W. (From Refs. [2,8].)

$1/d$ are typically observed.^[6,8,28] However, the maximum in stored enthalpy is often found at smaller grain sizes than the strain maximum, as illustrated in Fig. 5 for W.^[8] Here the maximum in strain occurs at $d = 8.3$ nm, while the maximum in stored enthalpy is at $d = 5.5$ nm. Several suggestions have been offered to explain the maxima in stored enthalpy with $1/d$, including decreasing strain^[8,28] or impurity pickup during milling.^[28] The latter is an unlikely explanation for samples obtained by low-energy milling,^[8] where metallic impurity contamination is negligible. It is stated that the stored enthalpy comes mainly from grain boundaries^[27,28] and grain boundary strains. Stress relaxation may be responsible for the maxima,^[8] but, as noted above, the strain and stored enthalpy maxima do not necessarily coincide.

While the general concepts described above for synthesis of elemental metal nanocrystalline structures by mechanical attrition are likely to have some validity, questions still remain especially regarding the maxima in lattice strain and stored enthalpy, and the mechanism of grain refinement. Several recent experimental studies as well as suggested alternate mechanisms will now be discussed.

Recent studies of the synthesis of nanocrystalline Zn by milling at liquid nitrogen temperatures (cryomilling) have provided evidence for an alternate mechanism for making nanoscale grains.^[29,30] In most previous studies, the progress of nanocrystallization as a function of milling time was followed by X-ray diffraction line broadening analysis, which gives an average grain size. The grain size so determined typically exhibits monotonically decreasing values with milling time. This is also the case for cryomilled Zn, as illustrated in Fig. 6. This average grain size decreases rapidly for the early milling times, and then saturates to a value of about 20 nm for the longer times. However, to study the change in grain size distribution with milling time, an extensive study using TEM was carried out.^[29] It was surprising to observe a large

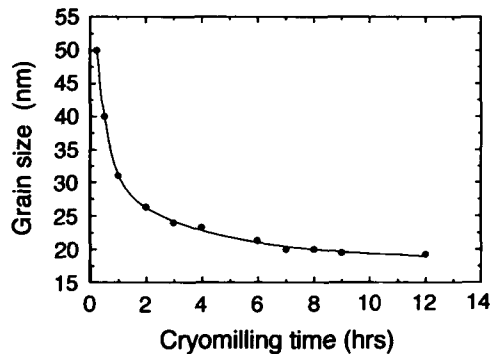
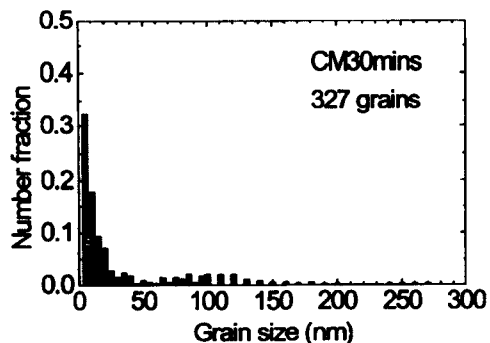
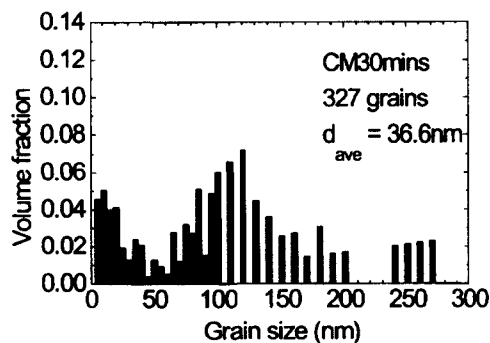


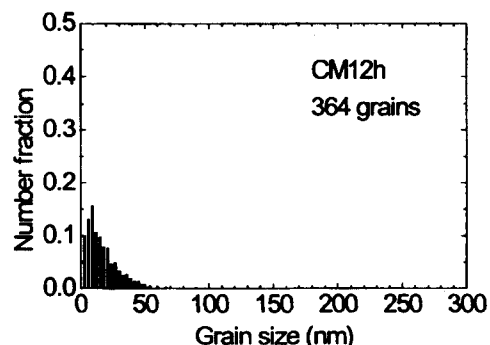
Fig. 6 Average grain size for cryomilled Zn vs. milling time. (From Ref. [29].)



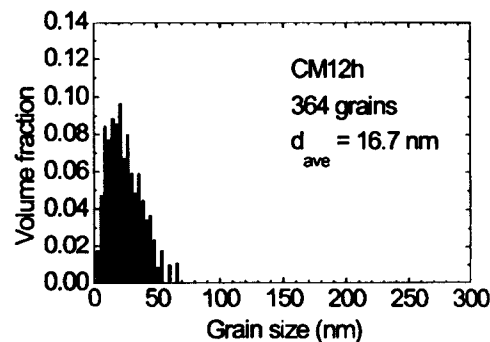
A



a



E



e

Fig. 7 The number fraction and volume fraction of grain size at cryomilling times: 30 min (A, a) and 12 h (E, e). (From Ref. [29].)

fraction of very small grain sizes (less than 5 nm) even in the very early stages (e.g., 0.5 h) of cryomilling. The grain size distribution was found to be essentially bimodal for the shorter milling times, as shown in Fig. 7A and a for 0.5 h of milling, and then collapsed to one peak at longer milling times, and finally narrowed to a tighter distribution at the longest times, as seen in Fig. 7E and e for a milling time of 12 h. These distributions were determined from dark-field TEM micrographs, as shown in Fig. 8a and b for the samples milled 0.5 and 12 h, respectively. From Figs. 7 and 8, it is observed that at short milling times, grains of about 250 nm size exist together with small grains of less than 10 nm. It was suggested that the very small grains formed at the early milling times might have been caused by a dynamic recrystallization (DRX) phenomenon. Dynamic recrystallization refers

A



B

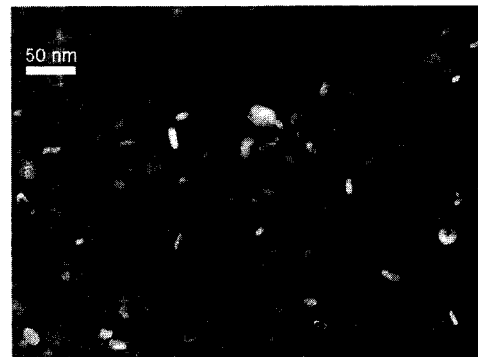


Fig. 8 A) TEM dark field image for Zn cryomilled for 30 min. B) TEM dark field image for Zn cryomilled for 12 h. (From Ref. [29].)

to the occurrence of crystallization during deformation. The mechanisms and transformation kinetics for both static and dynamic recrystallization have been reviewed by Doherty et al.^[31] It appears that DRX can occur as a nucleation and growth process, or as a recovery process. Many issues related to the transformation kinetics for DRX remain unresolved, and the underlying mechanisms are not well understood. However, it is assumed that the high dislocation densities possible by deformation at low temperatures and the nucleation sites probably provided by shear banding are consistent with cryogenic temperature milling of, e.g., Zn, in the high strain, high strain rate deformation which occurs. Evidence for the possibility of dynamic recrystallization playing a role in the synthesis of nanocrystalline grain sizes in metals is dramatically observed in the oscillatory hardness behavior with cryomilling time in Zn.^[32] This oscillatory hardness behavior is illustrated in Fig. 9. The dramatic oscillatory hardness changes with milling times at cryogenic temperatures are not reflected in the hardness data for samples milled at room temperature. They are also not related to any artifact, such as porosity, as shown by the essentially constant, and nearly theoretical, density of the samples. Transmission electron microscopy showed that large variations in the dislocation density and grain-size distribution occurred during cryomilling. The observations suggest that dynamic recrystallization takes place in larger grains (>50 nm), when the dislocation density due to strain hardening reaches a critical level to nucleate DRX. A reaction-rate model was developed which accounts for

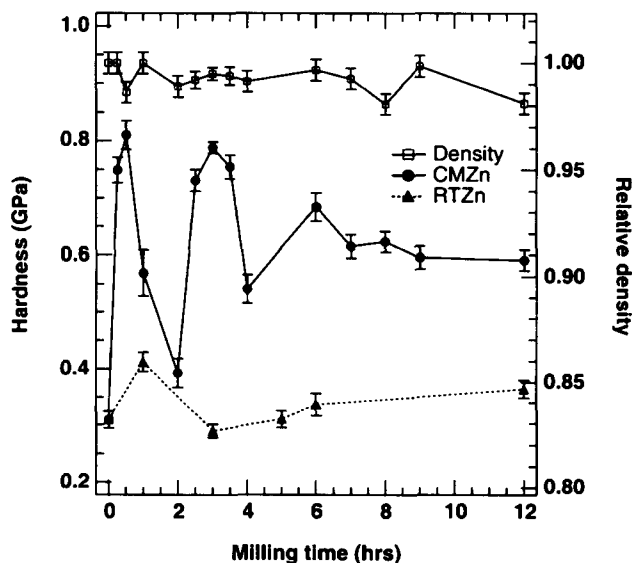


Fig. 9 Hardness vs. milling time for Zn milled at 100 K (solid circles) and at room temperature (solid triangles). The relative densities for the cryomilled samples are indicated by open squares. (From Ref. [32].)

the DRX effect and the observed oscillations in hardness. Good agreement was obtained with the experimental data. These results imply that in special circumstances, i.e., where conditions are right to nucleate DRX, the dynamic recrystallization reaction may also contribute to the synthesis of a nanoscale grain microstructure. In analogy to "continuous recrystallization,"^[31] the mechanism proposed by Fecht and coworkers, in which dislocation structures continuously rearrange themselves during deformation in a recovery-like fashion that ends in high-angle boundaries, nanocrystalline grains, can sometimes be also formed by a "discontinuous" DRX process.

He and Laverna^[33] offered an alternative explanation for the synthesis of nanoscale microstructures in cryomilled Inconel 625 alloy. This Ni-base alloy was milled in liquid nitrogen to form a nanocrystalline grain structure. TEM observations indicated that grains in the cryomilled powder were deformed into elongated grains containing a high density of deformation faults. With continued milling, the elongated grains fractured into small nanoscale fragments. The occurrence of the elongated grains and their subsequent fragmentation were attributed to repeated strain fatigue and fracture caused by the cyclic impact loading in random directions, along with cold welding. A high density of mechanical nanoscale twins was also observed.

While most of the studies on the development of nanocrystalline grain structures by mechanical attrition have involved observing the microstructure as a function of milling time, and presumably, total average strain, Tao et al.^[34] recently investigated the microstructure of a pure Fe plate that had been subjected to surface mechanical attrition. In this case, the milling balls were impacted on the surface of the Fe plate by vibratory motion, such that the surface layer was subjected to high-strain-rate plastic deformation. The degree of plastic deformation was highest at the surface of the plate and decreased, eventually to zero, as distance from the surface into the plate increased. The structure and microstructure of the deformed Fe was then studied by X-ray diffraction line broadening analysis as the plate was progressively etched, layer by layer, and by scanning electron microscopy (SEM), TEM, and HRTEM observations of the cross sections of the surface layers. X-ray diffraction results showed that the grain size was a minimum at the surface and increased with depth, while the microstrain was a maximum at the surface and dropped to about zero at a depth of 60 μm . From the electron microscopy, the surface-treated layer could be subdivided into several sections in terms of grain (or cell) size. From the top surface these were:

- Section 1. Nanostructured regime: $\sim 0\text{--}15\ \mu\text{m}$;
- Section 2. Submicron-sized regime: $\sim 15\text{--}40\ \mu\text{m}$;
- Section 3. Micron-sized regime: $\sim 40\text{--}60\ \mu\text{m}$.

Beyond a depth of 60 μm , the original Fe matrix showed some evidence of plastic deformation but no grain refinement. At the regions adjacent to the strain-free matrix, homogeneously distributed dislocation lines are observed, and the dislocation density increases as the distance from the surface decreases. In addition, dense dislocation walls (DDWs) are observed, with spacing in the micron range and parallel to each other along $\{110\}$ planes. Dislocation tangles are also observed and in some regions the dislocation density is high. With decreasing depth, into Section 3, most original grains are subdivided into micron-sized cells, which are either roughly equiaxed or lamellar. The misorientation of these cells of DDWs are small, typically less than 1° . At still smaller depths, that is in Section 2, the cell sizes are found to decrease with elongated cells several microns long and about 200–400 nm thick. Some equiaxed cells are also seen that are ~ 200 –500 nm in size. Finally, near the surface, where the deformation strain and strain rates are maximum, nanocrystalline microstructures are observed. Equiaxed nanocrystalline grains are observed near the surface, while at the bottom of Section 1, lamellar nanoscale grains are observed. However, inside the lamellar grains, smaller equiaxed grains are also present. Based on these extensive microstructural observations, the sequence of nanocrystalline formation was summarized as follows. Formation of DDWs and dislocation tangles (DTs) first occur, then the DDWs and DTs transform into subboundaries with small misorientations. Finally, the subboundaries and subgrains evolve into nanocrystalline grains with large misorientation angles between them. It was suggested that, for the synthesis of nanocrystalline grains during plastic deformation, high strain rates were necessary as well as large strains. This suggestion is consistent with observations of plastic-deformation-induced grain refinement at high strains, while lower strain rates such as equal channel angular pressing or cold rolling typically produce grain sizes no smaller than about 100–200 nm. However, it may be at variance with the results of low-energy milling experiment, where similar minimum grain sizes have been observed to those produced by high-energy milling.^[8] More studies along the lines of the above are needed to clarify the mechanism for synthesis of nanocrystalline metals by mechanical attrition.

Nanocrystallization Mechanisms for Milling of Dissimilar Elements

The proposed mechanism for nanocrystallization on milling of dissimilar elements that form an intermediate phase, e.g., TiAl from Ti and Al powders,^[16] was the biasing of nucleation vs. growth of the new phase at the relatively low temperatures of milling, as described earlier in this paper. However, milling of dissimilar metals that do not form intermediate phases can also form nanoscale

microstructures and the mechanism must be different. Zghal et al.^[35] reported the results of milling the normally immiscible Cu–Ag and Ni–Ag systems. The Cu–Ag microstructure after milling at lower temperatures exhibits a pronounced texture and a complex microstructure. Milling at higher temperature produced small equiaxed nanoscale grains, which were the result of dynamic recrystallization. In the case of Ni–Ag, which has a larger positive heat of mixing than Cu–Ag, complete mixing was not possible, and a nanocomposite was formed. It was suggested that, as texture was not observed in the Ni-rich phase, which featured smaller grain size (5–10 nm), full mixing of the components cannot take place because of the differences in their mechanical properties.

More studies are needed to clarify the diverse possible mechanisms for nanocrystallization by mechanical attrition of dissimilar powders.

PROBLEMS: CONTAMINATION AND POWDER CONSOLIDATION

A serious problem with the milling of fine powders is the potential for significant contamination from the milling media (balls and vial) or atmosphere. If steel balls and containers are used, iron contamination can be a problem. It poses a most serious risk for the highly energetic mills, e.g., the Spex shaker mill, and depends on the mechanical behavior of the powder being milled, as well as its chemical affinity for the milling media. For example, milling Ni to attain the minimum grain size in a Spex mill resulted in Fe contamination of 13 at.%, while the Fe contamination in nanocrystalline Cu similarly milled was only ≤ 1 at.%.^[15] Lower-energy mills result in substantially less, often negligible, Fe contamination. Other milling media, such as tungsten carbide or ceramics, can be used, but contamination from such media is also possible. Interstitial element (oxygen, nitrogen) contamination can be controlled by milling and subsequent powder handling in a pure inert gas atmosphere, with care taken that the milling vial is leak-free during processing.

Powder consolidation to theoretical density of nanocrystalline materials prepared by mechanical attrition without significant coarsening is necessary for many property measurements, e.g., mechanical behavior, and for applications requiring bulk materials. There is no room in this paper to adequately review the escalating efforts in this important field. However, a number of successes have been documented by both conventional and innovative methods and are reviewed by Groza.^[36] For the special case of very ductile, relatively low melting temperature metals such as Zn and Al, it has been found that, in the absence of a process control agent during milling, cold welding can dominate the process and the powders can be “consolidated” into spherical-shaped balls that can be up

to 6–8 mm in diameter.^[37] Thus in situ consolidation can be attained in these cases during milling. Disks can be formed from the spherical samples via compression. Such disks are suitable for mechanical tests such as miniaturized disk bend tests or small-size tensile samples.

CONCLUSION

Mechanical attrition of powders is a simple and versatile method to prepare nanocrystalline microstructures in a variety of materials including metals, ceramics, polymers, intermetallics, and composites. The mechanism for formation of nanoscale grains by severe plastic deformation induced by ball milling, in general, involves the competition between defect production and defect recovery by thermal processes. The details by which this occurs are still not completely defined. In most cases, a continuous buildup of dislocation density and the rearrangement of dislocations into first cells, and then small equiaxed grains, occur. In some cases, there is evidence for discontinuous dynamic recrystallization. More systematic TEM studies on a variety of materials are needed to confirm the mechanism. Problems of powder contamination during processing must be considered, but can be minimized. Consolidation of the powders with nanoscale microstructures into bulk structures is a topic that requires further attention.

ACKNOWLEDGMENTS

The author's research on nanocrystalline materials has been supported over the years by the U.S. National Science Foundation under grants number DMR-9203479, DMR-9508797, DMR-9871980, and DMR-201474.

REFERENCES

1. Suryanarayana, C.; Koch, C.C. *Nanostruct. Mater.* In *Non-Equilibrium Processing of Materials*; Suryanarayana, C., Ed.; Pergamon, Elsevier Science Ltd.: Oxford, UK, 1999; 313.
2. Koch, C.C. Synthesis of nanostructured materials by mechanical milling: Problems and opportunities. *Nanostruct. Mater.* **1997**, *9*, 13.
3. Fecht, H.J. Nanostructured Materials and Composites Prepared by Solid State Processing. In *Nanostructured Materials: Processing, Properties, and Applications*; Koch, C.C., Ed.; William Andrew Publishing: Norwich, NY, 2002; 73.
4. Koch, C.C. The synthesis and structure of nanocrystalline materials produced by mechanical attrition: A review. *Nanostruct. Mater.* **1993**, *2*, 109.
5. Fecht, H.J. Nanostructure formation by mechanical attrition. *Nanostruct. Mater.* **1995**, *6*, 33.
6. Eckert, J.; Holzer, J.C.; Krill, C.E., III; Johnson, W.L. Structural and thermodynamic properties of nanocrystalline fcc metals prepared by mechanical attrition. *J. Mater. Res.* **1992**, *7*, 1751.
7. Fecht, H.J.; Hellstern, E.; Fu, Z.; Johnson, W.L. Nanocrystalline metals prepared by high-energy ball milling. *Metall. Trans., A* **1990**, *21A*, 2333.
8. Olesak, D.; Shingu, P.H. Nanocrystalline metals prepared by low energy ball milling. *J. Appl. Phys.* **1996**, *79*, 2975.
- 8a. Williamson, G.K.; Hall, W.H. X-ray line broadening from filed aluminum and wolfram. *Acta Metall.* **1953**, *1*, 22.
9. Yamada, K.; Koch, C.C. The influence of mill energy and temperature on the structure of the TiNi intermetallic after mechanical attrition. *J. Mater. Res.* **1993**, *8*, 1317.
10. Lowe, T.C.; Valiev, R.Z. Producing nanoscale microstructures through severe plastic deformation. *JOM* **2000**, *52*, 27.
11. Shen, T.D.; Koch, C.C. The influence of dislocation structure on formation of nanocrystals by mechanical attrition. *Mater. Sci. Forum* **1995**, *179-181*, 17.
12. Pathak, D.K. Effect of Milling Temperature on the Amorphization of Intermetallic Compounds by Mechanical Milling. Ph.D. Dissertation; North Carolina State University: Raleigh, NC, 1995.
13. Zhang, X. Synthesis and Characterization of Nanocrystalline Zn. Ph.D. Dissertation; North Carolina State University: Raleigh, NC, 2001.
14. Nieh, T.G.; Wadsworth, J. Hall-Petch relation in nanocrystalline solids. *Scr. Metall. Mater.* **1991**, *25*, 955.
15. Shen, T.D.; Koch, C.C. Formation, solid solution hardening and softening of nanocrystalline solid solutions prepared by mechanical attrition. *Acta Mater.* **1996**, *44*, 753.
16. Klassen, T.; Oehring, M.; Bormann, R. The early stages of phase formation during mechanical alloying of Ti-Al. *J. Mater. Res.* **1994**, *9*, 47.
17. Trudeau, M.L.; Schultz, R.; Zaluski, L.; Hosatte, S.; Ryan, D.H.; Doner, C.B.; Tessier, P.; Strom-Olsen, J.O.; Van Neste, A. Nanocrystalline iron-titanium alloys prepared by high energy mechanical deformation. *Mater. Sci. Forum* **1992**, *21*, 305.
18. Davis, R.M.; Koch, C.C. Mechanical alloying of brittle components: Silicon and germanium. *Scr. Metall.* **1987**, *21*, 305.
19. Cho, Y.S.; Koch, C.C. Structural evolution in Nb₃Sn

- during mechanical attrition. *Mater. Sci. Eng., A* **1991**, *A141*, 139.
20. Shaw, W.J.D. Current understanding of mechanically alloyed polymers. *Mater. Sci. Forum* **1998**, *19*, 269–272.
 21. Koch, C.C.; Smith, A.P.; Bai, C.; Spontak, R.J.; Balik, C.M. Nonequilibrium processing of polymeric materials by mechanical attrition. *Mater. Sci. Forum* **2000**, *49*, 343–346.
 22. Smith, A.P.; Ade, H.; Balik, C.M.; Koch, C.C.; Smith, S.D.; Spontak, R.J. Cryogenic mechanical alloying of poly(methyl methacrylate) with polyisoprene and poly(ethylene-alt-propylene). *Macromolecules* **2000**, *33*, 2595.
 23. Suryanarayana, C. Mechanical Alloying. In *Non-Equilibrium Processing of Materials*; Suryanarayana, C., Ed.; Pergamon, Elsevier Science Ltd.: Oxford, UK, 1999; 49.
 24. Zhu, M.; Li, B.L.; Gao, Y.; Li, L.; Luo, K.C.; Sui, H.X.; Li, Z.X. Microstructure characteristics of nanophase composite synthesized by mechanical alloying of immiscible Pb–Al and Fe–Cu systems. *Scr. Mater.* **1997**, *36*, 447.
 25. Perez, R.J.; Huang, B.; Lavernia, E.J. Effect of In-Situ Formation of Nanoscale γ -Al₂O₃ and AlN on Thermal Stability of Cryomilled Nanocrystalline Fe. In *Metastable Phases and Microstructure*; Bormann, R., Mazzone, G., Shull, R.D., Averbach, R.S., Ziolo, R.F., Eds.; MRS Symp. Proc., Materials Research Society: Warrendale, Pennsylvania, USA, 1996; Vol. 400, 31.
 26. Huang, B.; Vallone, J.; Luton, M.J. The effect of nitrogen and oxygen on the synthesis of B2 NiAl by cryomilling. *Nanostruct. Mater.* **1995**, *6*, 631.
 27. Hellstern, E.; Fecht, H.-J.; Garland, C.; Johnson, W.L. Mechanism of achieving nanocrystalline AlRu by ball milling. *Mater. Res. Soc. Symp. Proc.* **1989**, *132*, 137.
 28. Hellstern, E.; Fecht, H.-J.; Fu, Z.; Johnson, W.L. Structural and thermodynamic properties of heavily mechanically deformed Ru and AlRu. *J. Appl. Phys.* **1989**, *65*, 305.
 29. Zhang, X.; Wang, H.; Narayan, J.; Koch, C.C. Evidence for the formation mechanism of nanoscale microstructures in cryomilled Zn powder. *Acta Mater.* **2001**, *49*, 1319.
 30. Zhang, X.; Wang, H.; Kassem, M.; Narayan, J.; Koch, C.C. Origins of stored enthalpy in cryomilled nanocrystalline Zn. *J. Mater. Res.* **2001**, *16*, 3485.
 31. Doherty, R.D.; Hughes, D.A.; Humphries, F.J.; Jonas, J.J.; Jensen, D.J.; Kassner, M.E.; King, W.E.; McNelley, T.R.; McQueen, H.J.; Rollett, A.D. Current issues in recrystallization: A review. *Mater. Sci. Eng., A* **1997**, *A238*, 219.
 32. Zhang, X.; Wang, H.; Scattergood, R.O.; Narayan, J.; Koch, C.C. Modulated oscillatory hardening and dynamic recrystallization in cryomilled nanocrystalline Zn. *Acta Mater.* **2002**, 3995.
 33. He, J.; Lavernia, E.J. Development of nanocrystalline structure during cryomilling of Inconel 625. *J. Mater. Res.* **2001**, *16*, 2724.
 34. Tao, N.R.; Wang, Z.B.; Tong, W.P.; Sui, M.L.; Lu, J.; Lu, K. An investigation of surface nanocrystallization mechanism in Fe induced by surface mechanical attrition treatment. *Acta Mater.* **2002**, 4603.
 35. Zghal, S.; Bhattacharya, P.; Twesten, R.; Wu, F.; Bellon, P. Structural and chemical characterization of Cu–Ag and Ni–Ag nanocomposites synthesized by high energy ball milling. *J. Metastable Nanocryst. Mater.* **2002**, *13*, 165.
 36. Groza, J.R. Nanocrystalline Powder Consolidation Methods. In *Nanostruct. Mater.: Processing, Properties, and Applications*; Koch, C.C., Ed.; William Andrew Publishing: Norwich, NY, 2002; 115.
 37. Zhang, X.; Wang, H.; Kassem, M.; Narayan, J.; Koch, C.C. Preparation of bulk ultrafine-grained and nanostructured Zn, Al, and their alloys by in situ consolidation of powders during mechanical attrition. *Scr. Mater.* **2002**, *46*, 661.

Nanostructured Materials Synthesized by Mechanical Means

H.-J. Fecht

University of Ulm, Ulm, Germany

Mechanical attrition, mechanical alloying, and other methods of extreme plastic deformation (high pressure torsion, equal channel angular pressing) have been developed as versatile alternatives to other physical and chemical processing routes in preparing nanophase materials. Here several examples are discussed including the deformation-induced nanophase formation in powder particles, in thin foil sandwich structures, and at the surface of alloys exposed to friction-induced wear leading to the formation of nanocrystals and, in some cases, amorphous nanostructures. This opens exciting perspectives in preparing nanostructured materials with a number of different interface types in terms of structure (crystalline/crystalline, crystalline/amorphous) as well as atomic bond (metal/metal, metal/semiconductor, metal/ceramic etc.). It is expected that the study of nanostructure formation by mechanical means in the future not only opens new processing routes for a variety of advanced nanophase materials but also improves the understanding of technologically relevant deformation processes on a nanoscopic level.

INTRODUCTION

Internal interfaces in materials are extended defects, such as grain boundaries and interphase boundaries, which can be found in almost every natural or artificially produced material or man-made structure.^[1] In general, the correlation between the atomic structure and the energy of interfaces can be described by their respective excess free volume,^[2] which can be minimized by the formation of closely packed structural units of atoms so that interfaces with low index planes and low index atomic rows are parallel to each other.^[3,4] However, the experimental evidence concerning structure–energy correlations of internal interfaces, in particular under thermodynamic equilibrium conditions where entropic effects should be taken into account, remains unclear because of the inherent experimental difficulties and the generally small interface-to-volume ratio in conventional polycrystals.

Decreasing the grain size of a material to a few nanometers leads to a drastic increase of the number of grain boundaries (or other internal interfaces) reaching typical densities up to 10^{19} interfaces per cubic centimeter. The large number of atoms located in these interfaces in comparison with the crystalline part scales roughly with the reciprocal grain size and corresponds approximately to $3\delta/d$, δ being the width of the interface, typically 0.8–1.2 nm.^[5] For example, for a material with a grain or domain size of 5 nm, about 50% of the overall atoms deviate from ideal lattice site positions and become influenced by the grain boundaries. At the same time, the energy (and other properties) of the material is being increased in proportion to the level of atomic disorder of the material, i.e., in proportion to the overall grain boundary area. Nanostructured materials have therefore attracted considerable scientific interest for more than a decade because of their unusual and sometimes unexpected physical (electronic, magnetic, mechanical, optical) and chemical (catalytic) properties.^[6]

Besides the synthesis of clusters, thin films, multilayers, and coatings from the gas or liquid phase, chemical methods such as sol–gel processes and electrodeposition are common methods of synthesizing nanostructured materials. As a versatile alternative, however, mechanical methods have been developed which allow to fabricate nanostructured materials in large quantities with a broad range of chemical compositions and atomic structural arrangements.^[7,8] These methods can, for example, be applied to powder samples, thin-foil sandwiches, and to the surface of bulk samples in order to produce nanostructures at surfaces as discussed below. As a result, a wide range of metals, alloys, intermetallics, ceramics, and composites can be prepared in an amorphous, nanocrystalline, or quasicrystalline state. Because of the broad range of possible atomic structures very different properties in comparison with conventional materials are obtained. For example, nanostructured particles prepared by mechanical attrition can exhibit unusually high values in hardness,^[9,10] enhanced hydrogen solubility,^[11] giant-magnetoresistance effects,^[12] magnetic spin-glass behavior,^[13] etc.

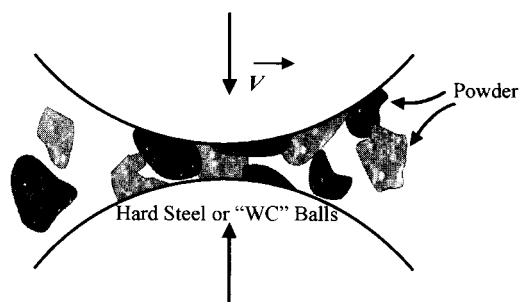


Fig. 1 Schematic sketch of the process of mechanical attrition and the corresponding shear action of metal powders. (View this art in color at www.dekker.com.)

EXPERIMENTAL

A variety of mechanical milling devices have been developed for different purposes.^[14] The basic process of mechanical attrition is illustrated in Fig. 1. Powder particles with typical particle diameters of about 20–100 μm are placed together with a number of hardened steel or WC-coated balls in a sealed container, which is shaken violently. Consequently, plastic deformation at high strain rates ($\sim 10^3$ – 10^4 sec^{-1}) occurs within the particles and the average grain size can be reduced to a few nanometers after extended milling. The temperature rise during this process is modest and is generally estimated to be ≤ 100 to 200°C . The collision time corresponds to typically 2 msec.

High-energy milling forces can be obtained by using high frequencies and small amplitudes of vibration. Ball mills (e.g., SPEX model 8000), which are preferable for small batches of powder, i.e., $\approx 10 \text{ cm}^3$, are sufficient for research purposes. As the kinetic energy of the balls is a function of their mass and velocity, dense materials (steel or tungsten carbide) are preferable to ceramic balls. During mechanical attrition contamination by the milling tools (Fe) and atmosphere (trace elements of O_2 , N_2 in rare gas) can be problematic. By minimizing the milling time and using the purest metal powders available, a thin coating of the milling tools by the respective powder material is generally obtained, which reduces Fe-contamination levels of less than typically 1 at.%. Atmospheric contamination can be minimized or eliminated by sealing the vial with a flexible “O”-ring after the powder has been loaded in an inert gas glove box. Small experimental ball mills can also be enclosed completely in an inert gas glove box. As a consequence, oxygen and nitrogen contamination can be limited to less than 300 ppm. In this respect, the nanoscaled powder material obtained has often a higher purity than materials synthesized by alternative methods, such as chemical processes or inert gas evaporation and condensation. In addition, the struc-

tural contributions of small pores occurring during compaction of small clusters can be safely neglected.^[15]

An alternate route to producing samples with high levels of both plastic deformation and interfacial area is cold rolling of layered elemental sheets.^[16] Each deformation cycle consists typically of rolling the multilayered sandwich to a thickness of approximately 80 μm and subsequent folding as shown in Fig. 2. Here the large increase in interfacial area is created internally with absolutely negligible contamination at ambient temperature.

As a further example of more technical relevance, the development of high-speed ICE trains reaching velocities of more than 300 km/hr is also a materials challenge concerning the mechanical integrity and safety required for the railway tracks (high-strength steel with composition Fe–0.8 at.% C–1.3 at.% Mn).^[17] In particular, the interaction and slip between wheel and rail has to be optimized and is controlled by sophisticated electronics. On the steel surface where the local pressure typically is exceeding 1.0–1.5 GPa, solid-state transformations have been observed which are caused by friction-induced shear forces and have strong similarities with mechanical attrition of powder samples.

EXPERIMENTAL RESULTS

Nanostructure Formation

During mechanical milling or attrition the metal powder particles are subjected to severe plastic deformation from collisions with the milling tools. Consequently, plastic deformation at high strain rates ($\sim 10^3$ – 10^4 sec^{-1}) occurs within the particles and the average grain size can be reduced to a few nanometers after extended milling. As such, the metal particle is plastically deformed with most of the mechanical energy expended in the deformation process being converted into heat, but the remainder being stored in the metals, thereby raising its internal energy.^[18,19]

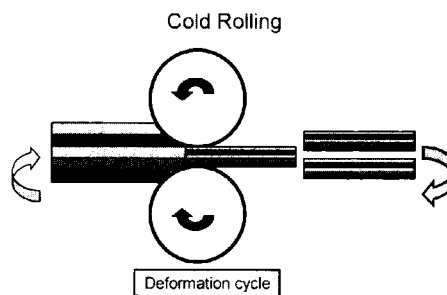


Fig. 2 Schematic sketch of the process of cold rolling of elemental foils. (View this art in color at www.dekker.com.)

The microstructural changes as a result of mechanical attrition can be followed by X-ray diffraction methods averaged over the sample volume. The X-ray diffraction patterns exhibit an increasing broadening of the crystalline peaks as a function of milling time. The peak broadening is caused by size as well as internal strain effects.^[20,21] The average coherently diffracting domain size (grain or crystal size) and the microstrain as a function of milling time are obtained from the integral peak widths assuming Gaussian peak shapes. Based on the method of X-ray analysis applied (Scherrer formula,^[22] Williamson and Hall method at full width at half maximum, or integral peak width at half maximum,^[23] Warren–Averbach analysis,^[24] etc.) the weighting of the grain size distribution is different and therefore the average grain size can vary by a factor of two. Further evaluation by TEM and small angle X-ray or neutron diffraction improves the accuracy of the data.

After corrections for K_{α} and instrumental broadening, the line broadening due to the small crystal size is constant in K -space and is given by $\Delta K = 0.9 (2\pi/d)$, where d is the average domain or grain diameter. The strain broadening corresponds to $\Delta K = A \langle e^2 \rangle^{1/2} K$ with A being a constant depending on the strain distribution ($A \approx 1$ for a random distribution of dislocations^[25] and $\langle e^2 \rangle^{1/2}$ being the rms strain). Additional defects which might contribute to the peak broadening, such as stacking faults, can be safely neglected in all cases discussed here. However, for some metals with very small stacking fault energies, e.g., Co, the contribution of stacking faults to the peak broadening can be considerable, but is clearly the exception.

As a result, it is generally found that in the very beginning mechanical attrition leads to a fast decrease of the average grain size to 40–50 nm. Further refinement occurs slowly to about 10–15 nm after extended milling. The average atomic level strain is reaching values up to 0.7% as shown in Fig. 3 for the milling of Fe powders.

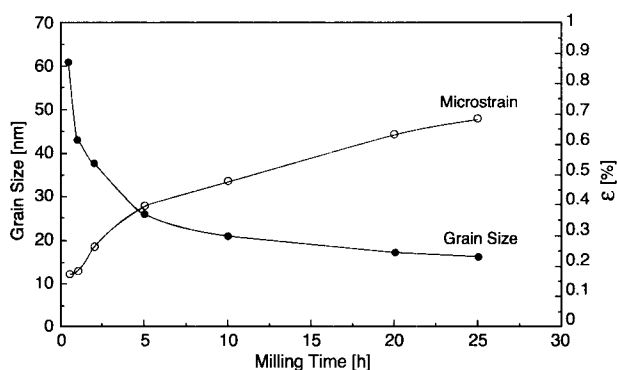


Fig. 3 The average grain size and microstrains as a function of milling time for iron powder determined from X-ray line broadening.

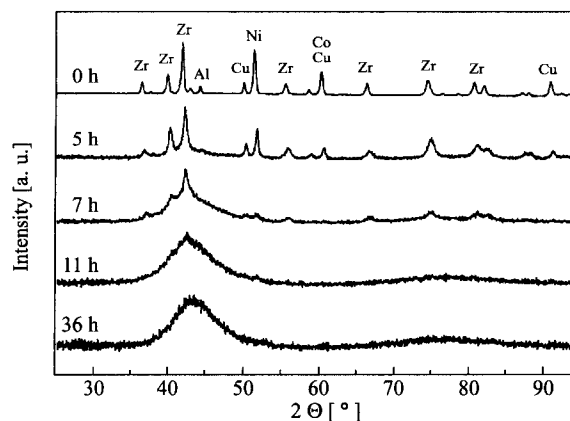


Fig. 4 X-ray spectra for mechanically alloyed $Zr_{60}Al_{10}Ni_9Cu_{18}Co_3$ powder samples exhibiting the transformation from the initially crystalline powder mixture to an amorphous glass-like structure.

From a combination of X-ray, electron, and neutron diffraction, the elemental processes leading to the grain size refinement include three basic stages:^[26]

- (i) Initially, the deformation is localized in shear bands consisting of an array of dislocations with high density (up to 10^{16} per m^2). Here the dislocation cell size dimensions are basically a function of the acting shear stress τ resulting in an average cell size dimension L of $L = 10 Gb/\tau$ with G being the shear modulus and b the Burgers vector.
- (ii) At a certain strain level, these dislocations annihilate and recombine to small angle grain boundaries separating the individual grains. The subgrains formed via this route are already in the nanometer-size range.
- (iii) The orientations of the single-crystalline grains with respect to their neighboring grains become completely random. Thus the microstructure becomes identical with the microstructure of samples produced by the noble gas condensation and compaction and exhibiting a largely reduced number of internal pores.

Extended Solid Solutions and Metallic-Glass Formation

Extended solid solutions far beyond the thermodynamic equilibrium have generally been noted in the course of mechanical milling of alloys. In addition, for phase mixtures with negative enthalpies of mixing and large (>15%) atomic size mismatch solid-state amorphization is observed. During this process long-range solute diffusion and solute partitioning are suppressed and therefore

highly metastable amorphous and nanocrystalline states become accessible.

For example, during mechanical alloying of 75 at.% Zr and 25 at.% Al the formation of a supersaturated hcp (α -Zr) solid solution was observed prior to the solid-state-amorphization reaction.^[27] However, in all cases of binary alloys it remained unclear whether indeed a metallic glass has been formed or just a material with "X-ray amorphous structure". More recently, a similar phase transformation sequence has been investigated in a mechanically alloyed multicomponent elemental $Zr_{60}Al_{10}Ni_9Cu_{18}Co_3$ powder mixture with an alloy composition that is known to form a bulk metallic glass when cooled from the liquid state.^[28] These multicomponent alloys are considerably more stable than binary alloys and can be heated above the glass transition temperature before crystallization sets in. The X-ray spectra at different stages of the milling process are characterized by the successive disappearance of the elemental Al, Co, Cu, and Ni peaks and a simultaneous shift of the Zr peaks to higher scattering angles, corresponding to a decrease in the lattice constant of the hcp-Zr as a result of the rapid dissolution of the smaller atoms, such as Cu, Ni, Co, and Al in the (α -Zr) matrix^[29] as shown in Fig. 4.

An alternate route to producing samples with high levels of both plastic deformation and interfacial area is by cold rolling of layered elemental sheets in an inert gas atmosphere with subsequent folding between each deformation cycle. In this case, the large increase in interfacial area is created internally with negligible contamination. In contrast to mechanical alloying of powder samples the uncertainty in the temperature during processing is removed as the sample is in firm contact with the massive

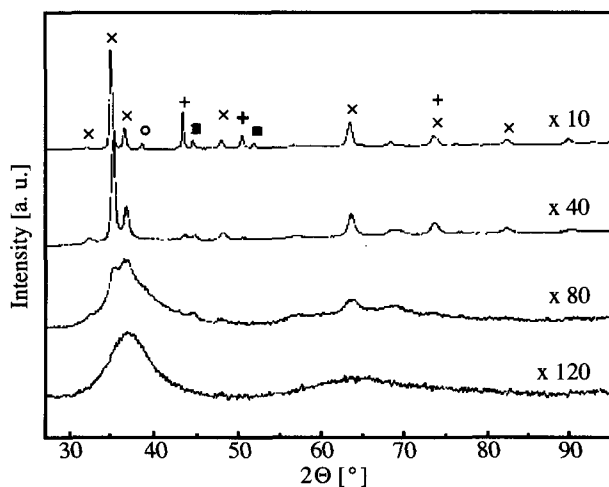


Fig. 5 XRD profiles showing development of a metallic glass by cold rolling of elemental foils of Zr, Al, Cu, and Ni (\times : Zr, \circ : Al, $+$: Cu, \blacklozenge : Ni).

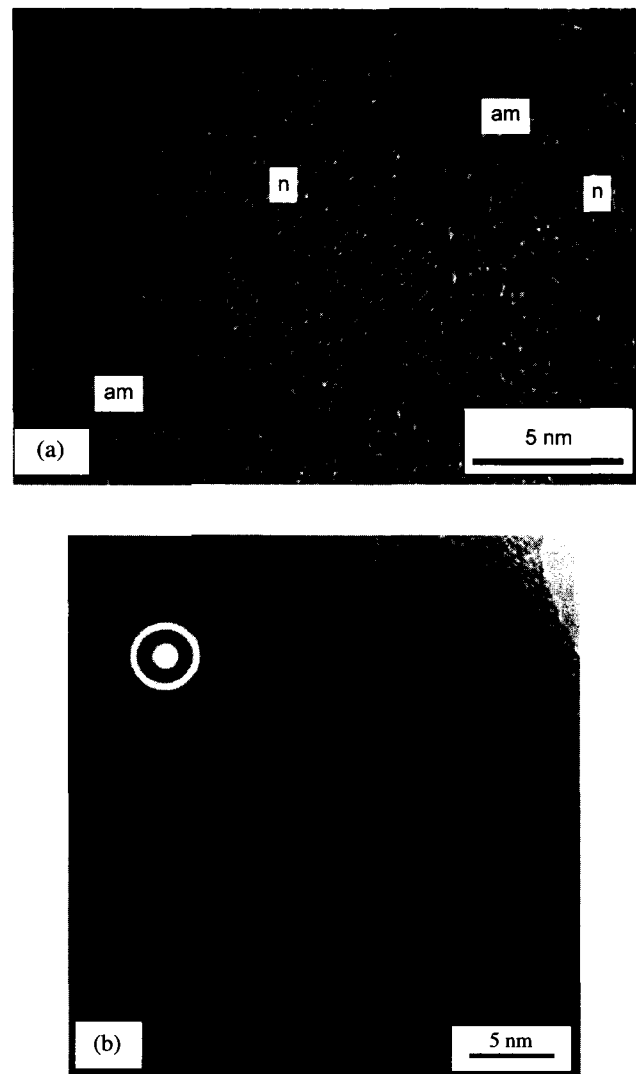


Fig. 6 High-resolution TEM micrograph of a cold-rolled multilayered sample exhibiting a remaining nanocrystalline Zr-rich crystallite surrounded by an amorphous matrix (a) after 80 cycles of deformation and (b) a fully amorphous sample after 120 cycles.

rolls and deformation can be performed at a low strain rate in order to maintain ambient temperatures.

This approach has been used to examine amorphous phase formation in several binary alloys such as Zr-Ni and Cu-Er.^[30,31] In the prior work on amorphous phase formation, deformation rates in excess of 1 sec^{-1} were employed and some annealing was needed to complete the amorphization reaction.^[32] In contrast, fully amorphous foils of a multicomponent $Zr_{65}Al_{7.5}Cu_{17.5}Ni_{10}$ alloy have been synthesized at ambient temperatures from a layered array of individual elemental sheets by repeated low strain rate (0.1 sec^{-1}). Fig. 5 exhibits the X-ray diffraction

patterns from the Zr–Al–Ni–Cu foils taken after 10, 40, 80, and 120 deformation cycles. High resolution TEM analysis exhibits further evidence that a true amorphous phase has been formed when some nanocrystallites of Zr are still present after 80 cycles as shown in Fig. 6a. The sample becomes fully amorphous after 120 cycles (Fig. 6b). However, structural features and corresponding contrast variations of the order of about 2 nm (Fig. 6b) are apparent and typical for a small-scale phase separation.

Thermal Stability

As a result of the cold work considerable energy has been stored in the powder particles. Therefore thermodynamically these materials are far removed from their equilibrium configuration and a large driving force toward equilibrium exists. The stored energy is released during heating to elevated temperatures due to recovery, relaxation processes within the grain boundaries, and grain growth. As a consequence, during annealing at elevated temperatures, relaxation and grain-growth processes will occur leading to a concomitant increase of the grain size.

This behavior has been investigated for a number of materials and presented here in detail for iron. For extended periods of milling time a fast decrease of the average grain size to nanometer dimensions is observed with a stationary average grain size $d=15$ nm and 0.7% microstrain as mentioned above. The enthalpy release during differential scanning calorimetry (DSC) heating experiments spreads over the entire temperature range of the scan as shown in Fig. 7. The very broad signal does not exhibit any distinct peaks but a further increase of the exothermic signal for $T>550$ K.

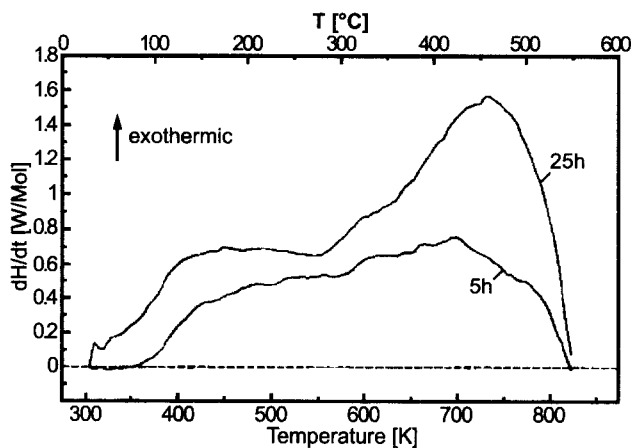


Fig. 7 Exothermal DSC heating scan at 10 K/min of iron powder after mechanical attrition for 5 and 25 hr showing two stages of heat release (below and above ca. 550 K).

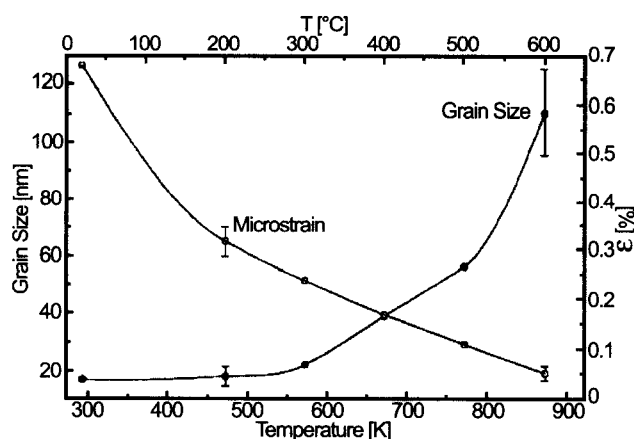


Fig. 8 Dependence of the stationary grain size and microstrain of (initially) nanocrystalline Fe-powder milled for 25 hr on annealing as a function of temperature.

X-ray diffraction of powder samples annealed for 80 min at each temperature revealed the evolution of grain size and strain as a function of annealing temperature as shown in Fig. 8. The microstrain is decreasing rapidly below 550 K whereas the grain size remains nearly constant in this range. As such, the enthalpy release during the first exotherm in Fig. 7 is only related to relaxation and not to grain growth. Grain growth starts to become significant above about 570 K. Furthermore, it has been found that after a fast increase at early times the average grain size d changes from 15 to about 30–40 nm. The average grain size remains constant for $t \geq 2400$ sec and reaches values of 100–200 nm at temperatures about 870 K.

As such, two regimes with and without grain growth can be clearly distinguished. As the influence of lattice point defects and lattice dislocations is negligible, the enthalpy release can be clearly assigned to the existence of grain boundaries. The reduction of the microstrains is

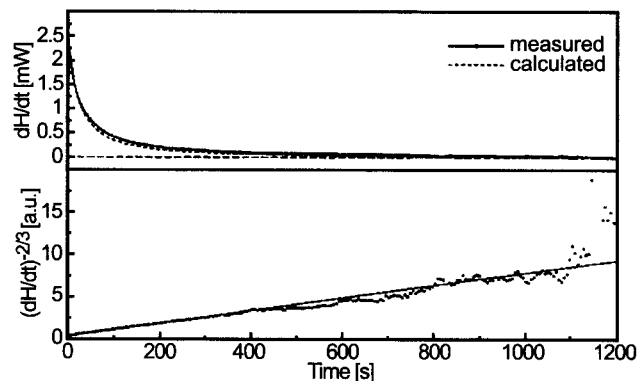


Fig. 9 Isothermal exothermic DSC curve at 500°C of nanocrystalline iron (upper part) and plot of $(dH/dt)^{-2/3}$ vs. time (lower part).

probably caused by grain boundary relaxation and annihilation of secondary grain boundary dislocations. Based on elastic theory it is estimated that this contribution to the overall energy is less than about 10%.

Further isothermal DSC measurements allow to analyze the grain-growth processes in nanocrystalline Fe. For example, the isothermal DSC curve shown in the upper part of Fig. 9 was measured at 770 K after annealing the sample at 670 K and heating to 770 K at a rate of 50 K/min. A monotonically decreasing signal typical for grain growth is observed. Similar signals are observed at 470, 570, and 670 K and clearly differ from those measured in isothermal recrystallization processes controlled by nucleation and growth in conventional polycrystalline metals which are described by Johnson–Mehl–Avrami-type models.^[33] Fig. 9 does not exhibit the expected maximum related to an incubation time for nucleation, but shows only a decrease in the signal.

Furthermore, $(dH/dt)^{-2/3}$ should scale linearly with time when normal parabolic grain-growth behavior is assumed.^[34] This assumption is well approximated for $t < 1200$ sec as shown in the lower part of Fig. 9. The upper part of Fig. 9 includes a fit to the measured DSC signal assuming parabolic grain growth and a grain boundary energy of 1.2 J/m^2 in agreement with theoretical estimates for fully relaxed large-angle grain boundaries in bcc-Fe.^[35]

DISCUSSION

Elemental Metals

The energies finally stored during mechanical attrition largely exceed those resulting from conventional cold working of metals and alloys (cold rolling, wire drawing, extrusion, etc.). During conventional deformation, the excess energy is rarely found to exceed 1–2 kJ/mol and therefore is never more than a small fraction of the enthalpy of fusion ΔH_f . In the case of mechanical attrition, however, the energy determined can reach values typical for crystallization enthalpies of metallic glasses corresponding to about 40% ΔH_f .^[36]

A simple estimate demonstrates that these energy levels cannot be achieved by the incorporation of defects which are found during conventional processing. In the case of pure metals, the contribution of point defects (vacancies, interstitial) can be safely neglected because of the high recovery rate at the actual processing temperature. Even taking nonequilibrium vacancies into account which can form as a consequence of dislocation annihilation up to concentrations of 10^{-3} , such contributions are energetically negligible in comparison.

The maximum dislocation densities that can be reached in heavily deformed metals are less than 10^{16} m^{-2} which

would correspond to an energy of less than 1 kJ/mol. Therefore it is assumed that the major energy contribution is stored in the form of grain boundaries and related strains within the nanocrystalline grains which are induced through grain boundary stresses.

Other detailed studies are obtained from cold rolling and torsion,^[37] wire drawing,^[38] and cyclic deformation^[39] processes resulting in an asymptotic saturation of the flow stresses. This is considered as a result of the simultaneous occurrence of dislocation multiplication and annihilation leading to a saturation of the dislocation density. In particular, under cyclic deformation slip becomes highly localized in so-called persistent slip bands (shear bands). These lie parallel to the primary glide plane and are separated by regions containing the original matrix structure. These bands consist of dense walls of dislocations, largely screw dislocations having a density $\sim 10^{13} \text{ m}^{-2}$. The closest spacing between screw dislocations of opposite sign is ~ 50 nm, the minimum distance before annihilation occurs. For edge dislocations which are more relevant for the deformation of fcc crystals this critical annihilation length is found to be 1.6 nm for Cu. As such, it has been concluded that the annihilation of dislocations can set a natural limit to the dislocation densities which can be achieved by plastic deformation (typically less than 10^{13} m^{-2} for screw dislocations and 10^{16} m^{-2} for edge dislocations).^[7] Steady-state deformation is observed when the dislocation multiplication rate is balanced by the annihilation rate.

It is expected that the shear modulus of the grain boundary regions is lowered by about 40% when the “volume-fraction” of the grain boundaries becomes comparable to that of the crystals.^[1,38,39] Localized deformation then proceeds by the dilatation of the grain-boundary layers similar to superplastic behavior^[40] with the undeformed crystallites moving in a “sea” of dilated grain boundaries.

Extended Solid Solutions

Mechanical attrition has also gained much attention as a nonequilibrium process resulting in solid-state alloying reactions beyond the equilibrium solubility limit for a broad range of alloys, intermetallics, ceramics, and composites.^[41,42] In the case of mechanical attrition of a binary powder mixture, amorphous phase formation can occur by intermixing of the atomic species on an atomic scale, thus driving the crystalline solid solution outside of its stability range against “melting” resulting in solid-state amorphization.^[43] This process is considered as a result of both mechanical alloying^[44] and the incorporation of lattice defects into the crystal lattice.^[45]

The formation of extended solid solutions during mechanical attrition of systems with negative heat of mixing

can be explained in terms of milling-induced interdiffusion reactions.^[46] In this regard the action of deformation (i.e., “driven system”) and especially shearing processes in causing atomic-scale mixing has been clarified recently.^[47] This can be considered as an athermal process that yields a high level of homogenization of the component atoms provided that sufficient deformation is applied. In fact, Monte Carlo simulations indicate that deformation can yield a solid solution even in alloy systems with a positive enthalpy of mixing. In this case, the driven system action, characterized by a “forcing parameter” as the frequency ratio between forced and thermally activated jumps, results in a behavior that is similar to that resulting from an enhanced diffusivity characteristic of a high-temperature, high-entropy state with extended solubilities.

An alternate route to producing samples with high levels of both plastic deformation and interfacial area is by cold rolling of layered elemental sheets which are folded between each deformation cycle. In this case, the large increase in interfacial area is created internally with absolutely negligible contamination. Similarly, in contrast to mechanical attrition the uncertainty in the temperature during processing is removed as the sample is in firm contact with the massive rolls and deformation can be performed at a low strain rate to maintain ambient temperatures. This approach has been used to examine amorphous-phase formation in several binary alloys such as Zr–Ni,^[48] Cu–Er,^[49] and Al–Pt^[50] and also for the preparation of bulk Fe/Ag nanomultilayers with giant magnetoresistance.^[51]

In the prior work on amorphous-phase formation, deformation rates in excess of 1 sec^{-1} were employed and some annealing was needed to complete the amorphization reaction. Fully amorphous foils of a multicomponent $\text{Zr}_{65}\text{Al}_{7.5}\text{Cu}_{17.5}\text{Ni}_{10}$ alloy have been synthesized at ambient temperatures from a layered array of individual elemental sheets by repeated low-strain-rate (0.1 sec^{-1}) cold

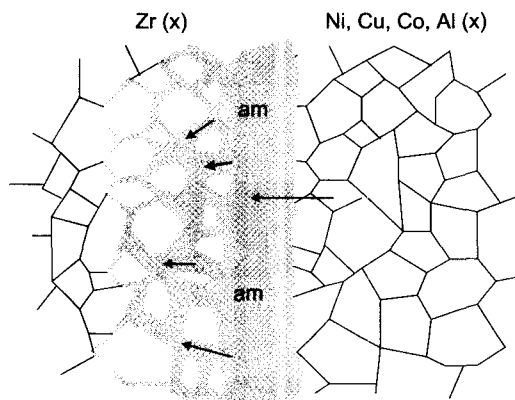


Fig. 10 Schematics of solid-state amorphization reaction at an intermediate stage.

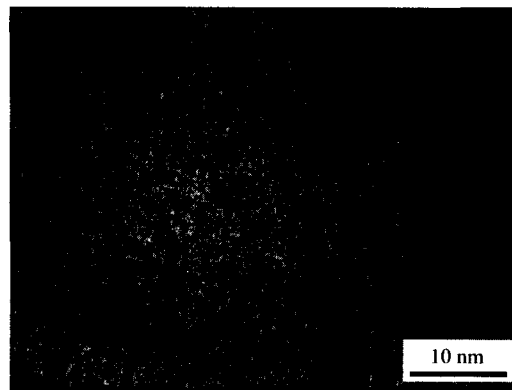


Fig. 11 High-resolution TEM micrograph of a glassy $\text{Zr}_{60}\text{Al}_{10}\text{Ni}_9\text{Cu}_{18}\text{Co}_3$ alloy slowly (10 K/sec) cooled from the liquid state.

rolling.^[52] Fig. 5 shows X-ray diffraction patterns from the Zr–Al–Ni–Cu foils taken after 10 (a), 80 (b), and 120 (c) deformation cycles. High-resolution TEM analysis exhibits further evidence that a true amorphous phase has been formed as shown in Fig. 6.

The detailed X-ray and electron diffraction experiments revealed that the crystal-to-glass transition was preceded by a rapid solution of smaller atoms such as Cu, Ni, Co, and Al in the α -Zr matrix to supersaturation levels with a concomitant reduction in grain size to values below 30 nm as schematically shown in Fig. 10.

As a final product, a fully amorphous Zr–Al–Ni–Cu–Co samples were obtained with structural and thermal properties identical to a metallic glass of the same composition produced by liquid undercooling. Fig. 11 exhibits

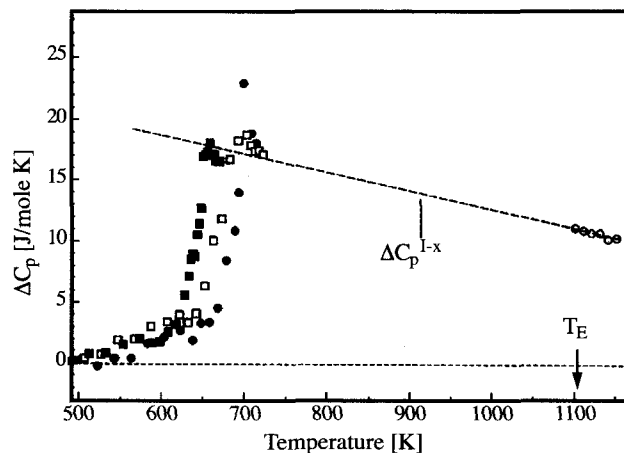


Fig. 12 Thermal analysis exhibiting the difference in heat capacity of the sample material $\text{Zr}_{60}\text{Al}_{10}\text{Ni}_9\text{Cu}_{18}\text{Co}_3$ in comparison with the thermodynamically stable crystalline configuration for amorphous mechanically alloyed powder, bulk metallic glass, and foil stacks (black squares: mechanically alloyed powder, open circles: liquid cooling, closed circles: cold rolling).

a high-resolution TEM image of a fully amorphous, metallic glass with identical composition produced from the liquid state. Whereas structural features on the scale of 2 nm have been observed in the amorphous phase formed in the solid state (Fig. 6b), such contrast variations typical for small-scale phase separation have not been observed by cooling from the liquid phase. This structurally homogeneous state is thermodynamically closer to the equilibrium, albeit metastable.

Surprisingly, thermal analysis of cold-rolled amorphous samples and amorphous powder samples prepared by mechanical alloying also reveals a distinct glass transition at $T_g=647$ K and about 620 K, respectively, as shown in Fig. 12 (followed by a sharp exothermic crystallization peak at 745 K which is not shown here). As such, it is worthy to note that very similar to amorphization reactions observed in mechanically alloyed Zr-based powder mixtures of similar composition the initial stage of cold rolling is characterized by the dissolution of solute into Zr along with a reduction in grain size to about 30 nm before the onset of the crystal-to-glass transition. The formation of similar amorphous phases from two inherently different initial states, i.e., the solid and the liquid state, suggests that compositionally induced static disorder in a mechanically driven system can lead to the same final glassy state which is conventionally derived from freezing the dynamic disorder of a liquid out to a glass.

Nanocrystallization of Surfaces

Many microscopic processes occurring during mechanical attrition and mechanical alloying of powder particles exhibit common features with processes relevant in tribology and wear. For example, the effects of work hardening, material transfer, and erosion during wear situations result in similar microstructures of the wear surface as observed during mechanical attrition.^[53,54] In particular, during sliding wear, large plastic strains and strain gradients are created near the surface. Typical plastic shear strain rates can correspond here to several 10^3 sec^{-1} .

Close to the surface of wear scars as well as in the wear debris of Cu, nanocrystalline structures have been observed by high-resolution electron microscopy with an average grain size of 4–5 nm.^[55] Within the interior of the grains no defects were observed suggesting that most of the defects are absorbed by the grain boundaries because of their proximity. However, this type of plastic deformation at high strain rates does not seem to be limited to metals and alloys,^[56] but has been observed in ceramics^[57] and diamond^[58] as well.

During sliding wear a special tribo layer develops on the surface of a sliding component being subjected to large plastic strains. This surface layer often is called the

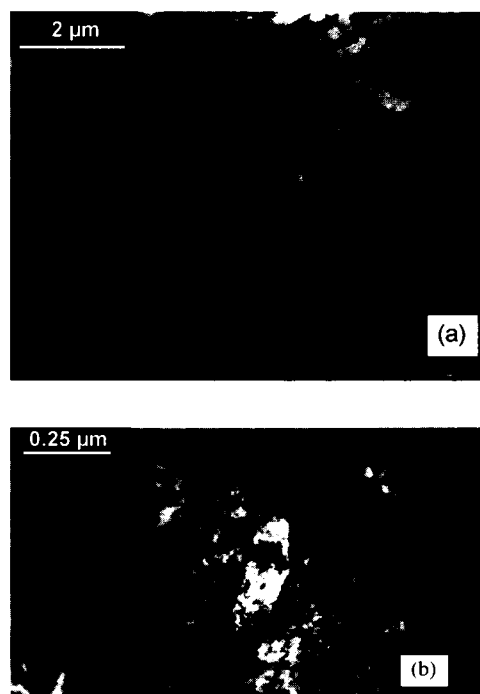


Fig. 13 TEM bright field images (a) of the nanostructured surface layer and (b) the initial pearlitic steel sample.

Beilby layer which, for a long time, was thought to be amorphous because its microstructure could not be resolved with the instruments commonly used.^[59] There are indeed some systems in which truly amorphous layers are produced by sliding,^[60] but in most cases the subsurface layer with a thickness of several micrometers has a nanocrystalline structure.

Corresponding X-ray diffraction and TEM results indicate that the average grain size of the extremely deformed surface layer corresponds to about 20 nm, whereas a gradient in grain size is observed further away from the surface reaching values up to 200 nm.^[61] For example, Fig. 13 exhibits TEM micrographs and the corresponding diffraction patterns of the initial pearlitic structure (a) in comparison with the nanocrystalline layer near the surface (b).

Corresponding X-ray diffraction and TEM results indicate that the average grain size of the extremely deformed surface layer is decreased to about 20 nm, whereas a gradient in grain size is observed further away from the surface where values up to 200 nm are reached.^[62,63] As a consequence, hardness measurements have been performed by nanoindentation and conventional methods as shown in Fig. 14a and b as a function of deformation and also temperature. This remarkable increase in hardness and mechanical strength of regions near the surface by a factor of 4–5 is clearly related to the fact that the average grain size is drastically decreased by the continuous

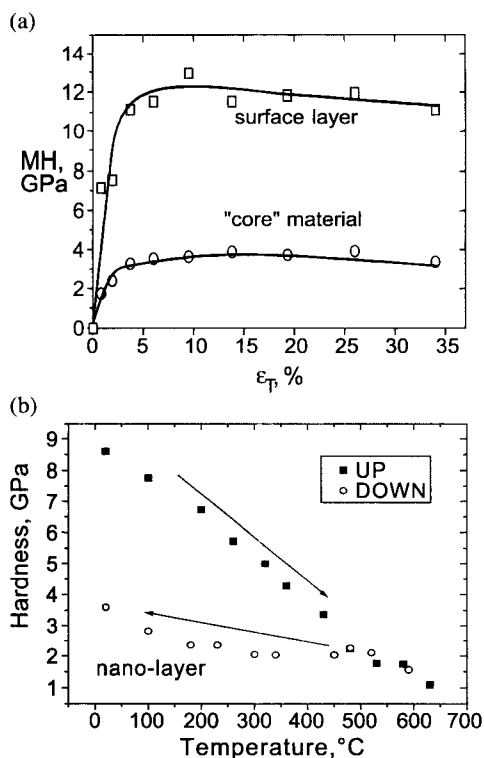


Fig. 14 Microhardness of the nanostructured surface layer of a high-speed railway track and the pearlitic material (core) as a function of total deformation during measurements with indenters of (a) variable pyramid angle and (b) "in situ" as a function of temperature. (Courtesy of Y. Millman.)

deformation process as found by TEM analysis and X-ray diffraction. The apparent hysteresis seen in Fig. 14b is an indication that the microstructure is drastically changed during thermal annealing resulting in considerable grain growth and (re-) precipitation of Fe-carbides and concomitant mechanical softening.^[64]

CONCLUSION

Severe plastic deformation, which can be achieved by a number of different methods, leads to a refinement of the microstructure to a nanometer scale. The correlation of structural and thermal analysis reveals that the defect structure after long milling times is composed of a network of large angle grain boundaries. These grain boundaries are formed by reorganization of dislocations produced in the initial step of the deformation process. Because of the high density of grain boundaries and the large amounts of stored enthalpy, relaxation processes of the heavily deformed structure and grain growth start at rather low temperatures. In some cases with large chem-

ical driving force (large negative enthalpies of mixing, "deep eutectics") the formation of a glass-like state with a distinct glass transition temperature is observed. However, this state obtained by solid-state processing exhibits a distinct underlying disordering on the scale of 2 nm not observed in glassy alloys with identical composition produced from the liquid.

Furthermore, many microscopic processes occurring during mechanical attrition and mechanical alloying of powder particles exhibit common features with processes relevant in tribology and wear. For example, the effects of work hardening, material transfer, and erosion during wear situations result in similar nanostructured layers of a wear surface as observed during mechanical attrition. Typical plastic shear strain rates can correspond here to several 10^3 . As such, the study of extreme plastic deformation processes not only is opening new processing routes for a variety of advanced nanostructured materials but also improves the understanding of technologically relevant deformation processes, e.g., surface wear, on a nanoscopic level which often limit the lifetime of technical components.

ACKNOWLEDGMENTS

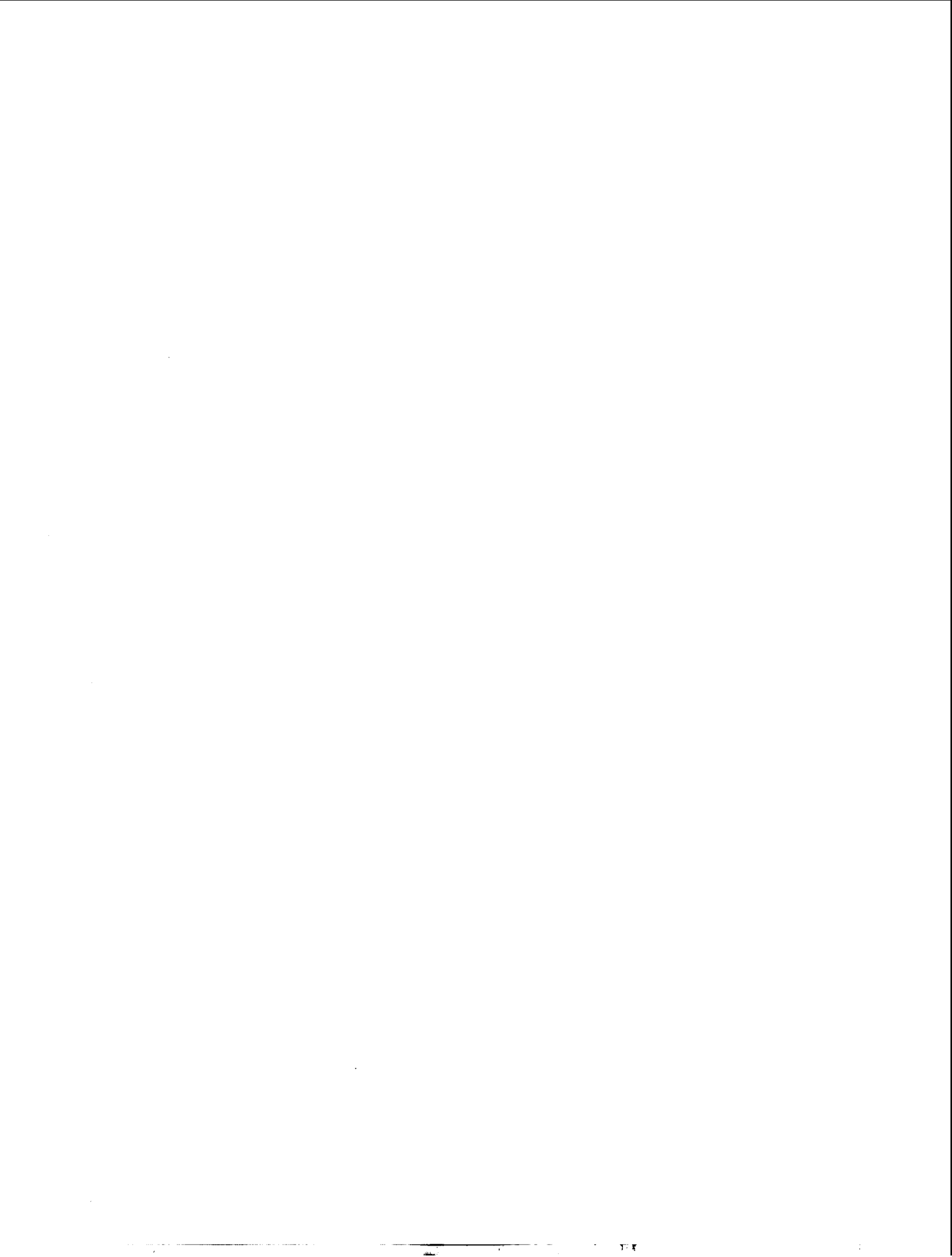
The financial support by the Deutsche Forschungsgemeinschaft (G.W. Leibniz program, grant Fe 313/11-1; Network "Funktionelle Nanostrukturen," project B6) and the collaboration with W.L. Johnson, J.H. Perepezko, A. Sagel, R. Wunderlich and I. Manna are gratefully acknowledged.

REFERENCES

- Lojkowski, W.; Fecht, H.-J. The structure of intercrystalline interfaces. *Prog. Mater. Sci.* **2000**, *45*, 339.
- Fecht, H.-J. Intrinsic instability and entropy stabilization of grain boundaries. *Phys. Rev. Lett.* **1990**, *65*, 610.
- Fecht, H.-J.; Gleiter, H. A lock-in model for the atomic structure of interphase boundaries between metals and ionic crystals. *Acta Metall.* **1985**, *33* (4), 557.
- Gleiter, H. *Physical Metallurgy*; Cahn, R.W., Haasen, P., Eds.; Elsevier: Amsterdam, 1983; 650.
- Kuwano, H.; Ouyang, H.; Fultz, B. A Mössbauer spectrometry study of nanophase Cr-Fe synthesized by mechanical alloying: A measurement of grain boundary width. *Nanostruct. Mater.* **1992**, *1*, 143.
- Gleiter, H. Nanocrystalline materials. *Prog. Mater. Sci.* **1989**, *33*, 223.

7. Fecht, H.-J. *Nanomaterial Synthesis, Properties and Applications*; Edelstein, A., Camarata, B., Eds.; Institute of Physics Publishing: Bristol, 1996; 89.
8. Fecht, H.-J. Nanostructured Materials and Composites Prepared by Solid State Processing. In *Nanostructured Materials*; Koch, C.C., Ed.; Noyes Publications: New York, USA, 2002; 73.
9. Koch, C.C. The synthesis and structure of nanocrystalline materials produced by mechanical attrition: A review. *Nanostruct. Mater.* **1993**, *2*, 109.
10. Kehrel, A.; Moelle, C.; Fecht, H.J. *Nanophase Materials*; Hadjipanayis, G.C., Siegel, R.W., Eds.; Kluwer Academic Publishers: Dordrecht, Basten, London, 1994; 287.
11. Moelle, C.; Fecht, H.J. Thermodynamic properties and phase stability of nanocrystalline metals and hydrides. *Nanostruct. Mater.* **1993**, *3*, 93.
12. Yasuna, K.; Terauchi, M.; Otsuki, A.; Ishihara, K.N.; Shingu, P.H. Bulk metallic multilayers produced by repeated press-rolling and their perpendicular magnetoresistance. *J. Appl. Phys.* **1997**, *82*, 2435.
13. Zhou, G.F.; Bakker, H. Spin-glass behavior of amorphous Co₂Ge synthesized by mechanical milling. *Phys. Rev. Lett.* **1994**, *72*, 2290.
14. Kuhn, W.E.; Friedmann, I.L.; Summers, W.; Szegvari, A. *ASM Metals Handbook*; Powder Metallurgy, Metals Park: Ohio, 1985; Vol. 7, 56.
15. Schaefer, H.-E.; Würschum, R.; Gessmann, T.; Stöckl, G.; Scharwaechter, P.; Frank, W.; Valiev, R.Z.; Fecht, H.-J.; Moelle, C. Diffusion and free volumes in nanocrystalline Pd. *Nanostruct. Mater.* **1995**, *6*, 869.
16. Johnson, W.L. Thermodynamic and kinetic aspects of the crystal to glass transformation in metallic materials. *Prog. Mater. Sci.* **1986**, *30*, 81.
17. Baumann, G.; Fecht, H.-J.; Liebelt, S. Formation of white-etching layers on rail treads. *Wear* **1996**, *191*, 133.
18. Fecht, H.-J.; Hellstern, E.; Fu, Z.; Johnson, W.L. Nanocrystalline metals prepared by high-energy ball milling. *Metall. Trans.* **1990**, *21A*, 2333.
19. Miani, F.; Fecht, H.-J. Evaluating the mechanochemical power transfer in the mechanosynthesis of nanophase Fe-C and Fe-Cu powders. *Int. J. Refract. Met. Hard Mater.* **1999**, *17*, 133.
20. Williamson, G.K.; Hall, W.H. X-ray line broadening from filed aluminium and wolfram. *Acta Metall.* **1953**, *1* (1), 22.
21. Wagner, C.N.J.; Boldrick, M.S. The structure of amorphous and nanocrystalline metals and alloys. *J. Mater. Sci. Eng.* **1991**, *A133*, 26.
22. Guinier, A. *X-Ray Diffraction*; W.H. Freeman and Company: San Francisco, 1963; 121.
23. Fecht, H.-J.; Moelle, C. Properties of nanophase materials synthesized by mechanical attrition. *Mater. Res. Soc. Symp. Proc.*, Nanophase Nanocomposite Mater. II **1997**, *457*, 113.
24. Warren, B.E.; Averbach, B.L. The effect of cold-work distortion on X-ray diffraction. *J. Appl. Phys.* **1950**, *21*, 595.
25. Friedel, J. *Dislocations*; Pergamon Press: Oxford, 1964; 418.
26. Fecht, H.-J.; Han, G.; Fu, Z.; Johnson, W.L. Metastable phase formation in the Zr-Al binary system induced by mechanical alloying. *J. Appl. Phys.* **1990**, *67*, 1744.
27. Sagel, A.; Wunderlich, R.K.; Perepezko, J.H.; Fecht, H.-J. Glass formation in a multicomponent Zr-based alloy by mechanical attrition and liquid undercooling. *Appl. Phys. Lett.* **1997**, *70*, 580.
28. Sagel, A.; Wanderka, N.; Wunderlich, R.K.; Schubert-Bischoff, N.; Fecht, H.-J. Early stages of solid-state amorphization reaction during mechanical alloying of a multicomponent Zr-powder mixture. *Scripta Mater.* **1998**, *38*, 163.
29. Samwer, K.; Fecht, H.-J.; Johnson, W.L. *Glassy Metals III*; Topics in Applied Physics, Beck/Güntherodt, Springer Verlag: Berlin, 1994; Vol. 72, 6.
30. Atzmon, M.; Unruh, K.M.; Johnson, W.L. Formation and characterization of amorphous erbium-based alloys prepared by near-isothermal cold-rolling of elemental composites. *J. Appl. Phys.* **1985**, *58*, 3865.
31. Bourdeaux, F.; Yavari, A.R. Amorphization by solid-state reaction of crystalline aluminum and platinum multilayers prepared by cold rolling. *J. Appl. Phys.* **1990**, *67*, 2385.
32. Chen, L.C.; Spaepen, F. Analysis of calorimetric measurements of grain growth. *J. Appl. Phys.* **1991**, *69*, 679.
33. Tschöpe, A.; Birringer, R.; Gleiter, H. Calorimetric measurements of the thermal relaxation in nanocrystalline platinum. *J. Appl. Phys.* **1992**, *71*, 5391.
34. Wolf, D. Atomic structure and energy of twist boundaries in fcc-metals. *Philos. Mag.* **1990**, *A62*, 447.
35. Haessner, F.; Hemminger, W. Recrystallization of highly textured materials. *Z. Metallk.* **1978**, *69*, 553.
36. Lloyd, D.J.; Kenny, D. The stress-strain behavior of copper over a large strain range. *Scripta Metall.* **1978**, *12* (10), 903.
37. Grosskreutz, J.C.; Mughrabi, H. *Constitutive Equations in Plasticity*; Argon, A.S., Ed.; MIT Press: Cambridge, MA, 1971; 251.
38. Gilman, J.J. Mechanical behavior of metallic glasses. *J. Appl. Phys.* **1975**, *46*, 1625.

39. Donovan, P.E.; Stobbs, W.M. The shear band deformation process in microcrystalline Pd₈₀Si₂₀. *Acta Metall.* **1983**, *31*, 1.
40. Hatherly, M.; Malin, A.S. Shear bands in deformed metals. *Scripta Metall.* **1984**, *18*, 449.
41. Schwarz, R.B.; Johnson, W.L. Solid state amorphization transformation. *J. Less-Common Met.* **1988**, *140*, 1.
42. Shingu, P.H. Mechanical alloying. *Mat. Sci. Forum* **1992**, *188-189*, 88.
43. Fecht, H.-J.; Fu, Z.; Johnson, W.L. Specific-heat anomaly during vitrification of hydrided Fe₂Er single crystals. *Phys. Rev. Lett.* **1990**, *64*, 1753.
44. Fecht, H.J.; Johnson, W.L. Entropy and enthalpy catastrophe as a stability limit for crystalline material. *Nature* **1988**, *334*, 50.
45. Fecht, H.J. Defect-induced melting and solid-state amorphization. *Nature* **1992**, *356*, 133.
46. Koch, C.C. *Materials Science and Technology*; Cahn, R.W., Haasen, P., Kramer, E.J., Eds.; VCH: Weinheim, 1991; Vol. 15, 193.
47. Bellon, P.; Averback, R.S. Nonequilibrium roughening of interfaces in crystals under shear: Application to ball milling. *Phys. Rev. Lett.* **1995**, *74*, 1819.
48. Atzmon, M.; Verhoeven, J.D.; Gibson, E.D.; Johnson, W.L. Formation and growth of amorphous phases by solid-state reaction in elemental composites prepared by cold working. *Appl. Phys. Lett.* **1984**, *45*, 1052.
49. Atzmon, M.; Unruh, K.M.; Johnson, W.L. Formation and characterization of amorphous erbium-based alloys prepared by near-isothermal cold-rolling of elemental composites. *J. Appl. Phys.* **1985**, *58*, 3865.
50. Bourdeaux, F.; Yavari, A.R. Amorphization by solid-state reaction of crystalline aluminum and platinum multilayers prepared by cold rolling. *J. Appl. Phys.* **1990**, *67*, 2385.
51. Yasuna, K.; Terauchi, M.; Otsuki, A.; Ishihara, K.N.; Shingu, P.H. Magnetic effects in multi-layered structures. *Appl. Phys. Lett.* **1997**, *82*, 2435.
52. Sagel, A.; Sieber, H.; Fecht, H.J.; Perepezko, J.H. Amorphization of Zr-Al-Ni-Cu during cold rolling of elemental foils at ambient temperatures. *Philos. Mag. Lett.* **1998**, *77*, 109.
53. Ivanisenko, Y.V.; Baumann, G.; Fecht, H.-J.; Safarov, I.M.; Korznikov, A.V.; Valiev, R.Z. Nanostructured and hardness of white layer at the surface of railroad rails. *Phys. Met. Metallogr.* **1997**, *83*, 303.
54. Fecht, H.-J. Nanostructure formation by mechanical attrition. *Nanostruct. Mater.* **1995**, *6*, 33.
55. Ganapathi, S.K.; Rigney, D.A. An HREM study of the nanocrystalline material produced by sliding wear processes. *Scripta Metall.* **1990**, *24*, 1675.
56. Doyle, F.D.; Aghan, R.L. *Metall. Trans., B* **1975**, *6*, 143.
57. Porat, R.; Berger, S.; Rosen, A. Sintering behaviour and mechanical properties of nanocrystalline WC/Co. *Mat. Sci. Forum* **1996**, *225-227*, 629.
58. Humble, P.; Hannink, R.H.-J. *Nature* **1978**, *273*, 37.
59. Beilby, G. *Aggregation and Flow of Solids*; Macmillan: London, 1921.
60. Askenazy, P. Deformation-Induced Amorphization of Cu-Ti Intermetallics. Ph.D. Thesis; California Institute of Technology, 1992.
61. Bürkle, G. Ph.D. Thesis; University of Ulm, 2003.
62. Lojkowski, W.; Djahanbakhsh, M.; Bürkle, G.; Gierlotka, S.; Zielinski, W.; Fecht, H.-J. Nanostructure formation on the surface of railway tracks. *J. Mater. Sci. Eng., A* **2001**, *303*, 197.
63. Milman, Yu.V.; Chugunova, S.I.; Goncharova, I.V.; Djahanbakhsh, M.; Bürkle, G.; Lojkowski, W.; Fecht, H.-J. The mechanical properties of the nanocrystalline layer on the surface of railway tracks. *J. Mater. Sci. Eng., A* **2001**, *303*, 209.
64. Ivanisenko, Y.; Valiev, R.Z.; Fecht, H.-J. *Scripta Mater.* **2003**, *in press*.



Nanostructured Materials Synthesized in Supercritical Fluid

Yuehe Lin

Pacific Northwest National Laboratory, Richland, Washington, U.S.A.

Xiang-Rong Ye

Pacific Northwest National Laboratory, Richland, Washington, U.S.A.

University of Idaho, Moscow, Idaho, U.S.A.

Chien M. Wai

University of Idaho, Moscow, Idaho, U.S.A.

INTRODUCTION

Supercritical fluid (SCF) approach is a novel and emerging technology to generate nanomaterials in small areas, high-aspect-ratio structures, complicated surfaces, and poorly wettable substrates with high uniformity, high homogeneity, and minimum environmental problems.

Through hydrogen reduction of metal- β -diketone complexes in supercritical CO_2 , a rapid, convenient, and environmentally benign approach has been developed to synthesize a variety of nanostructured materials: 1) metal (Pd, Ni, and Cu) nanowires and nanorods sheathed within multiwalled carbon nanotube (MWCNT) templates; 2) nanoparticles of palladium, rhodium, and ruthenium decorated onto functionalized MWCNTs. These highly dispersed nanoparticles are expected to exhibit promising catalytic properties for a variety of chemical or electrochemical reactions; 3) Cu, Pd, or Cu-Pd nanocrystals deposited onto SiO_2 or SiC nanowires (NWs). Different types of nanostructures were achieved, including nanocrystal-NW, spherical aggregation-NW, shell-NW composites, and "mesoporous" metals supported by the framework of NWs.

BACKGROUND

Supercritical fluid synthesis and processing of nanostructured materials have attracted an increased attention during the past decade.^[1-6] SCFs exhibit a novel hybrid of liquid-like and gas-like properties. They have appreciable densities and can dissolve solid compounds like liquid solvents yet they have low viscosities, low surface tension, and high diffusivities like gases. As a result of their high compressibility, SCFs offer a convenient means of accessing a wide range of solvent properties

without physically changing the solvent. Because of these unusual properties, the synthesis and processing of nanostructured materials using SCFs show significant advantages over conventional processes: 1) SCFs facilitate permeation, diffusion, and penetration to small areas, high-aspect-ratio structures, complicated surfaces, and poorly wettable substrates to attain high uniformity and homogeneity, therefore being capable of fabricating nanostructured materials which are difficult to accomplish through traditional methods; 2) SCFs allow higher concentrations of starting materials than chemical vapor deposition (CVD) does and provide diffusivities higher than liquid solvents do, therefore SCF synthesis and processing could be very fast; 3) the solvent strength of a SCF can be varied by manipulation of fluid temperature and pressure, thus allowing a degree of control and rapid separation of products which is not possible using conventional solvents; and 4) some SCFs, such as supercritical CO_2 (scCO_2), leave no solvent residues and are recyclable, thus being environmentally benign. Furthermore, unreacted materials, by-products, and contaminants in SCFs can be easily removed from the system; therefore products of high purity can be obtained. The synthesis and processing of nanostructured materials such as nanoparticles, nanowires, nanorods, nanotubes, nanocomposites, and thin solid films with nanoscale thickness have been achieved through a number of SCF physical and chemical transformations in which a SCF can act as a medium either for transporting solute species or for chemical reactions, or both. In some cases, the SCF itself can also take part in the reactions. Table 1 summarizes the typical SCF approaches to a variety of nanostructured materials.^[1-6] The aim of this article is to show how to use SCFs in the synthesis and processing of nanostructured materials templated by MWCNTs and nanowires (NWs).

Table 1 Typical SCF approaches to nanostructured materials

	Nanoparticles, nanowires, nanorods nanotubes, nanocomposites	Thin films
Physical transformation	Rapid expansion of supercritical solutions (RESS) Supercritical-assisted nebulization and atomization Physical impregnation in SCFs without expansion Supercritical antisolvent precipitation Supercritical drying processes Size-selective supercritical dispersion and dissolution Physical deposition processes in SCFs	Physical RESS deposition Physical deposition in SCFs
Chemical transformation	RESS into liquid solvents Hydrothermal reactions Water-in-SCF microemulsion reactions Arrested precipitation in SCFs SCF-liquid-solid approach	SCF transport and chemical deposition SCF transport chemical vapor deposition SCF immersion deposition SCF chemical deposition Chemical fluid deposition SCF Deposition of Self-Assembled Monolayers Electrodeposition in SCFs Hydrothermal leaching

Because of their exceptional electrical and mechanical properties caused by quantum confinement effects, one-dimensional carbon nanotubes (CNTs) and NWs have stimulated a growing interest over the past decade for their application potential as interconnects and building blocks for functional nanodevices.^[7-10] CNTs also have other possible uses including storage of hydrogen and other gases, membrane materials for batteries and fuel cells, anodes for Li-ion batteries, capacitors, and chemical filters.^[11-13] Modification of CNTs and NWs to produce nanocomposites provides an attractive strategy to expand, improve, or alter their properties and functions as well as their promising applications.^[14-25]

Because of their small size, high chemical stability, high-aspect-ratio cavities, and large surface-area-to-volume ratio, CNTs have been considered as templates for confining and directing the growth of metallic nanowires, nanorods or tubular structures, or as supports for metal nanoparticles which can be impregnated in the cavities or attached to the external walls of the CNTs.^[26-36] The produced metal/CNT composites can be used as catalysts, sensors, semiconductor devices, data storage, and processing devices, contrast agents in magnetic resonance imaging, new reinforced metal-nanofiber materials, and in xerography.^[26,27,35,37-41] Metal impregnation in the hollow interiors of the CNTs can be achieved in situ during CNT growth by incorporating the metals or metal precursors along with the carbon source. Although Fe, Co, Ni, Ti, Cu, and certain lanthanide and transition-metal carbides have been successfully trapped in CNTs using

this method, harsh conditions such as high temperature or arc evaporation are usually required, and impurities could be produced as encapsulated carbon clusters and soot.^[42-44] Capillary drawing of low-melting metals into cavities of CNTs provides a simple approach for metal loading,^[28,45] however, CNTs are not wetted by liquids with surface tensions higher than 100–200 mN m⁻¹, thereby excluding most metals and other elements in the periodic table.^[46] The most promising and flexible approach to metal loading is then to deposit metals into the cavities or onto the external walls of CNTs through a chemical reaction such as CVD or wet chemical process.^[13,15,26,29-32,35,36,47-55] However, by virtue of the small inner diameter and the extremely high aspect ratio of CNTs, this approach requires high temperatures or extensive reaction times for filling metals into the inner cavities of CNTs, and, consequently, the percentage of filled CNTs often is low. The CVD procedure may suffer from the limited volatility of metal precursors and the resulting low-vapor-phase concentration and mass-transfer-limited reactions, in addition to the high temperature for the decomposition or reduction of metal precursors. In the case of wet chemical procedures, a hindrance could be the slow process for concentrating and impregnating reactants into the cavity of CNTs. As the pristine surface of the CNTs is rather inert and poorly hydrophilic, this approach also results in unsatisfactory adhesion and coverage control of metal nanoparticles coated onto the outer walls of CNTs, and metal agglomeration into fewer larger particles as well.^[53,54] For most of the catalytic

applications, catalyst particles loaded on the exterior of the CNTs are preferred because they are more accessible to the reactant molecules than those encapsulated inside the internal channels. In order to obtain a specific nucleation of metals on the outer surface with good adhesion and control, functionalization of CNTs before metal deposition is required and can be accomplished by chemical treatments using a myriad of oxidants, such as HNO_3 , KMnO_4 , OsO_4 , $\text{HNO}_3/\text{H}_2\text{SO}_4$, and RuO_4 to generate $-\text{COOH}$, $-\text{OH}$, and other functional groups on the external walls of CNTs.^[15,31,32,36,55,56] Also, one-step or two-step sensitization-activation methods have been used for introducing catalytic nuclei (often Pd-Sn alloys or Pd nuclei) to the otherwise noncatalytic CNT surface to achieve a better metal loading through electroless deposition.^[13,30] However, the known wet chemical processes usually involve tedious and time-consuming treatment of CNTs and generate aqueous wastes.

Considerable efforts have also been spent to the modification of NWs to produce hybrid nanocomposites, in which NWs were decorated with nanoparticles, or sheathed by thin films, shells, and molecular layers, and most methods for modifying are solution-based.^[17-25]

Based on hydrogen reduction of metal- β -diketone complexes in supercritical CO_2 , we have developed a rapid, direct, and clean approach for the modification of MWCNTs and NWs to achieve nanocomposites as follows: metal nanowires or nanorods sheathed within MWCNT templates, MWCNTs decorated with catalytic metal nanoparticles, NWs decorated with metal nanocrystals, spherical aggregations of metal nanocrystals strung up by NWs, NWs wrapped by metallic shells, and "mesoporous" metals supported by the framework of NWs.^[57-59]

HYDROGEN REDUCTION OF METAL- β -DIKETONE COMPLEXES IN scCO_2

Hydrogen reduction of metal precursors such as metal- β -diketone complexes in scCO_2 has proven to be one of the most successful approaches for synthesizing sterically stabilized metal nanocrystals.^[60,61] scCO_2 reactions and particle nucleation occur in the presence of organic capping ligands, which bind to the surface of the agglomerates to form monolayers and quench further growth, providing size control and nanocrystal stabilization. Moreover, the steric stabilization of nanocrystals in scCO_2 varies with the tunable density and solvation power of scCO_2 , enabling reversible stabilization and destabilization of colloidal dispersion, which could improve many aspects of nanocrystal processing,

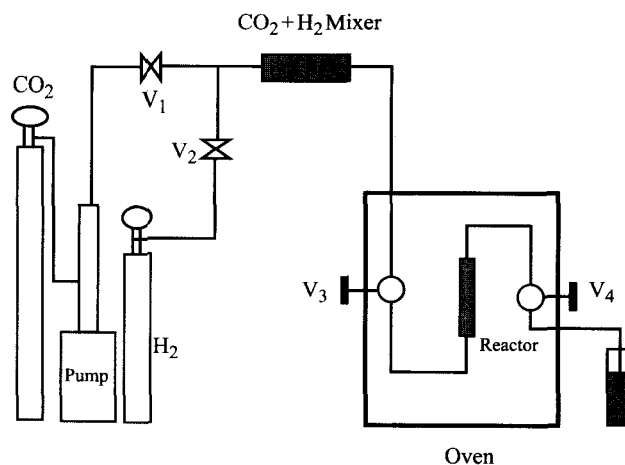


Fig. 1 Schematic drawing of the experimental apparatus.

such as size-selective separation, synthesis, and self-assembly. Robust, highly crystallized, relatively size-monodisperse, and sterically stabilized silver, iridium, and platinum nanocrystals ranging in diameter from 20 to 120 Å were synthesized in scCO_2 by reducing metal- β -diketone complexes with H_2 in the presence of fluorinated thiol ligands.

Hydrogen reduction of metal- β -diketone complexes in scCO_2 has also been demonstrated as an effective method to deposit metal films into high-aspect-ratio structures of inorganic and polymer substrates as well as into mesoporous solids.^[62-67] Herein a metal- β -diketone complex is dissolved into scCO_2 and a heated substrate (or mesoporous solid) is exposed to the solution. H_2 is then mixed into the solution and initiates a chemical reaction involving the precursor, thereby yielding metal films onto the substrate.

Likewise, hydrogen reduction of metal- β -diketone complexes in scCO_2 can be applied to the modification of MWCNTs and NWs using a typical experimental setup shown in Fig. 1.^[57-59] The MWCNTs have diameters of about 20–30 nm and lengths of about 2–3 μm . Two types of NWs, SiO_2 , and SiC NWs, 40 to 110 nm in diameter, several tens of micrometers in length, and randomly oriented on silicon substrates, were subjected to modification. MWCNTs, SiO_2 , or SiC NWs on silicon substrates were loaded in a 3.47-mL high-pressure stainless steel reactor along with a metal- β -diketone complex. Following precursor loading, valve V_1 was closed while valves V_2 , V_3 , and V_4 were opened and H_2 at 3 atm was allowed to flow through the reactor for 5 min to expel the air inside. Valves V_2 , V_3 , and V_4 were then closed, and V_1 was opened to charge the H_2 - CO_2 mixer with 80 atm of CO_2 . After mixing of H_2 and CO_2 , valve V_3

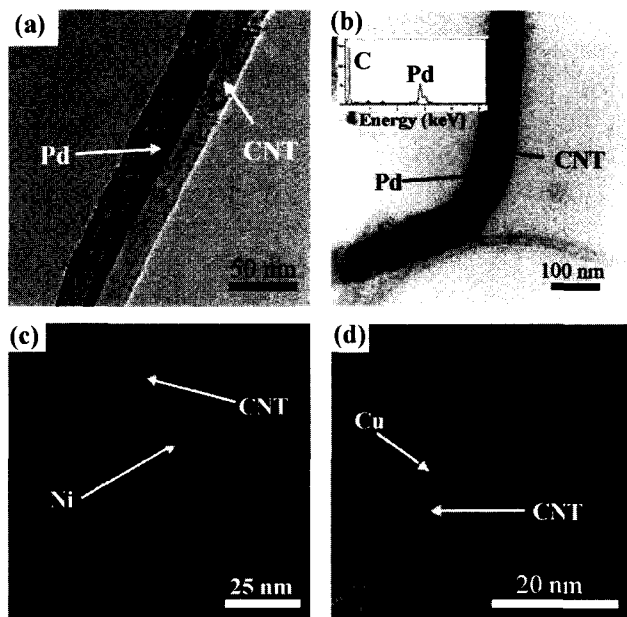


Fig. 2 TEM images of metal nanowires or nanorods impregnated in MWCNT templates. (a,b) Palladium. (c) Nickel. (d) Copper. (From Ref. [57].)

was opened forcing the mixture into the reactor. Valves V_1 and V_3 were then closed for the dissolution of the precursor in the CO_2 solution. To ensure complete dissolution, the reactor was left undisturbed for 30 min. After that, the reactor was heated gradually to the desired temperature and kept at this constant temperature for 5–10 min. After the reaction, the reactor was cooled to 35°C and vented slowly by opening V_4 . Neat CO_2 flow was used to flush the reactor twice to remove the possible unreacted

species and by-products. The reactor was then opened to recover the modified MWCNTs or NWs.

METAL NANOWIRES AND NANORODS SHEATHED WITHIN MWCNTS

Unfunctionalized MWCNTs were used as the templates for confining and directing the growth of metal nanowires and nanorods caused by the hydrogen reduction of metal- β -diketone complexes in scCO_2 . The metal- β -diketone complexes used were $\text{M}(\text{hfa})_2 \cdot x\text{H}_2\text{O}$ ($\text{M}=\text{Pd}$, Ni , and Cu ; hfa =hexafluoroacetylacetonate), and the temperatures of hydrogen reduction were 80 – 150°C , 250°C , and 250°C for filling palladium, nickel, and copper into MWCNTs, respectively. Transmission electron microscopy (TEM) observation of many different views of the product revealed several forms of foreign materials inside the MWCNTs. The amount of filled MWCNT out of the total number of nanotubes is estimated at about 10%. Fig. 2a and b shows the TEM images of nanowires or nanorods sheathed within carbon nanotubes. The nanowires are 7–9 nm in diameter and can be more than 200 nm in full length. The diameter of nanowires corresponds to the inner diameter of the MWCNTs and varies along the wires due to the fluctuation in the MWCNT diameter. The nanowires can be straight or curved, depending upon the curvature of the CNT wrapping. Fig. 2b also shows several segments of nanowires or nanorods that have been filled into the MWCNT. A typical energy dispersive X-ray spectrum (EDS) conducted on an individual nanowire or nanorod in the TEM is shown as an inset in Fig. 2b. It confirms that the nanowires and nanorods were made purely of palladium. Similarly, nanowires and nanorods of nickel or copper can also be developed within the

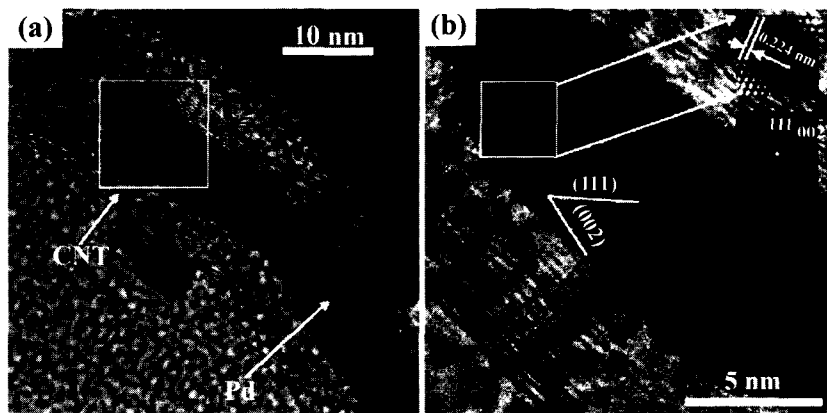


Fig. 3 (a) HRTEM images of a Pd nanorod sheathed within a MWCNT, revealing that the Pd nanorod is crystalline with a fcc structure, (b) enlarged section of (a) showing that the imaging zone axis is $[110]$. (From Ref. [57].)

channels of MWCNT templates, as shown in Fig. 2c and d.

Fig. 3a shows a high-resolution transmission electron microscopy (HRTEM) image of a Pd nanorod sheathed by a MWCNT, revealing that the Pd nanorod is composed of segments of single crystals. The region marked by a dashed square in Fig. 3a was further enlarged and is shown in Fig. 3b. Fourier transform and Fourier filtered HRTEM image are shown as insets in Fig. 3b. The HRTEM image processing indicates that this segment of Pd nanorod possesses the face centered cubic (fcc) structure with a measured lattice constant of 0.38 nm, which is comparable with the reported lattice constant of 0.3887 nm.

Similar to CVD and some wet chemical processes for MWCNT decoration, nucleation of metals as nanoparticles on the outside of MWCNTs occurred unavoidably in supercritical CO_2 along with metal filling. As has been reported, the defects in the MWCNT structure can provide favored sites for nucleation and growth of particles. Therefore besides the pure nanowire (or nanorod)/MWCNT composites, nanowire(or nanorod)/MWCNT/nanoparticle composites are also observed. As shown in Fig. 3a, a couple of palladium nanoparticles were attached to the exterior surface of the MWCNT sheathing the nanowire. Based on our experiment, we can somehow

adjust the outside or inside loading preference of a metal by functionalization of MWCNTs. Metal deposition occurs only on the external walls of functionalized MWCNTs.

MWCNTS DECORATED WITH CATALYTIC METAL NANOPARTICLES

Functionalization of MWCNTs

The functionalization of MWCNTs was performed by dispersing and refluxing 0.5 g of MWCNTs in 40 mL of concentrated H_2SO_4 - HNO_3 mixture (1:1 v/v ratio) for 6 hr to form a dark-brown suspension. The reaction mixture was then diluted with distilled water to 200 mL and stirred for several hours, cooled down to room temperature, and filtered. The recovered black solid was washed several times with distilled water and finally dried at room temperature in vacuum. Previous X-ray photoelectron spectroscopy (XPS) and diffusion reflectance infrared Fourier transform (DRIFT) studies revealed that the surfaces of functionalized MWCNTs become covered with carboxylic ($-\text{COOH}$), Carbonyl ($>\text{C}=\text{O}$), and hydroxyl ($-\text{COH}$) groups^[31,32,68] These functional groups have been demonstrated to provide favorite

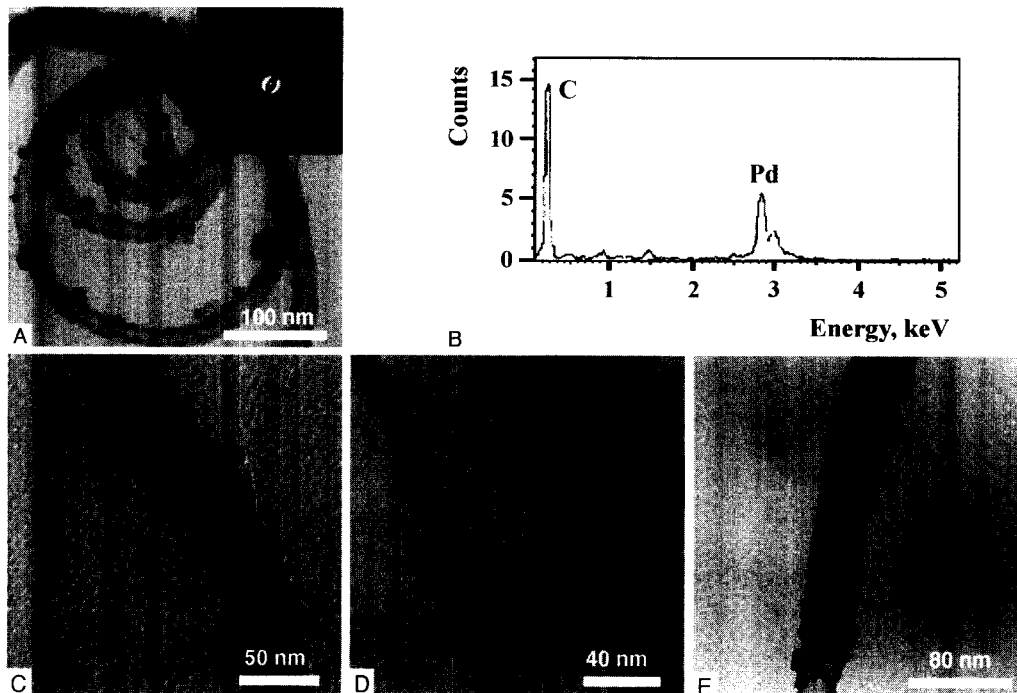


Fig. 4 TEM images and EDX spectroscopy of MWCNTs decorated with Pd nanoparticles after hydrogen reduction of (A) 10 mg, (C) 20 mg, (D) 30 mg and (E) 50 mg $\text{Pd}(\text{hfa})_2$. (From Ref. [58].)

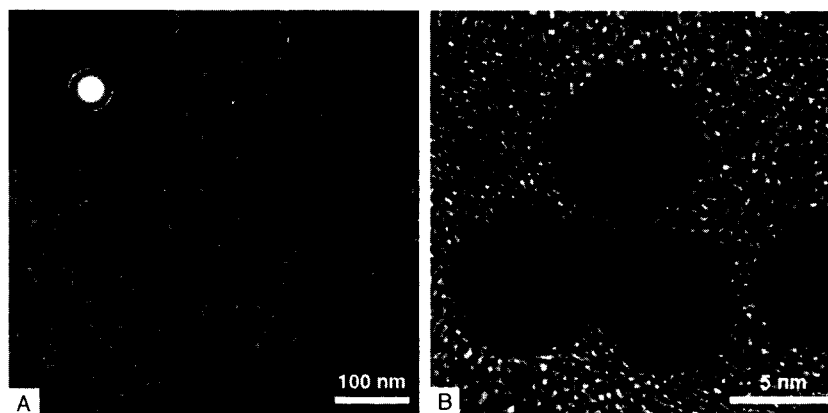


Fig. 5 (A) TEM and (B) HRTEM images of MWCNTs decorated with Rh nanoparticles.

nucleation sites for metal nanoparticle growth and to stabilize the nanoparticles by increasing the nanoparticle–CNT interaction.

Functionalized MWCNTs Decorated with Catalytic Palladium Nanoparticles

Modification of 10 mg of functionalized MWCNTs was carried out through hydrogen reduction of $\text{Pd}(\text{hfa})_2 \cdot x\text{H}_2\text{O}$ at 80°C . A bright field TEM micrograph of the MWCNTs after scCO_2 deposition using 10 mg of $\text{Pd}(\text{hfa})_2 \cdot x\text{H}_2\text{O}$ is shown in Fig. 4A. Well-dispersed, spherical particles were anchored onto the external walls of MWCNTs, and the size range of these particles was about 5–10 nm. A selected area electron diffraction (SAED) pattern on a nanoparticle is shown as an inset in Fig. 4A, and the bright rings with occasional bright spots signify the crystalline nature of the nanoparticle. EDS examination confirmed the presence of Pd in the nanoparticles decorating MWCNTs (Fig. 4B). For comparison, a commercial Pd on activated carbon catalyst sample was also examined by TEM, and the results showed numerous very large Pd particles irregularly distributed on carbon surfaces. The MWCNT appears to provide a unique template for decoration of nanometer-sized Pd metal particles on the carbon surfaces. By increasing the amount of $\text{Pd}(\text{hfa})_2$ precursor, the loading density of Pd nanoparticles on the outer walls of CNTs can be increased (Fig. 4C to E).

Functionalized MWCNTs Decorated with Catalytic Rhodium Nanoparticles

$\text{Rh}(\text{acac})_2 \cdot x\text{H}_2\text{O}$ (acac=acetylacetonate) was used as the metal precursor in the hydrogen reduction reaction for loading Rh nanoparticles onto functionalized MWCNTs. The adopted temperature for the reduction was 250°C . A

representative TEM image of MWCNTs decorated with Rh nanoparticles is displayed in Fig. 5A. A high and homogeneous dispersion of nanoparticles with a uniform distribution of particle sizes centered around 3–5 nm can be distinguished. The nanoparticles are comparable in size to the diameter of MWCNTs and are crystalline in nature as indicated by the SAED pattern given as an inset in Fig. 5A. The HRTEM image shown in Fig. 5B verifies that Rh nanoparticles are crystallites with visible lattice fringes.

Functionalized MWCNTs Decorated with Catalytic Ruthenium Nanoparticles

Decoration of Ru nanoparticles onto functionalized MWCNTs was performed by using $\text{Ru}(\text{acac})_3 \cdot x\text{H}_2\text{O}$ as the metal precursor for hydrogen reduction at 250°C . Fig. 6 presents the TEM images of highly dispersed Ru nanoparticles attached on MWCNTs, with very tiny diameters around 1 nm and a uniform distribution throughout the full length of MWCNTs. The SAED pattern exhibits a set of diffraction rings from Ru metal. The diffraction did not appear as clear spots, but as concentric rings, each of which consists of a large number of very small spots, suggesting that the nanoparticles are composed of many fine crystallites. EDS spectrum of the nanocomposite shows emission from Ru, indicating the chemical identity of nanoparticles as Ru containing.

Chemical States of Metal Nanoparticles Decorated onto Functionalized MWCNTs

The chemical composition of the nanoparticles deposited onto functionalized MWCNTs was analyzed by XPS.

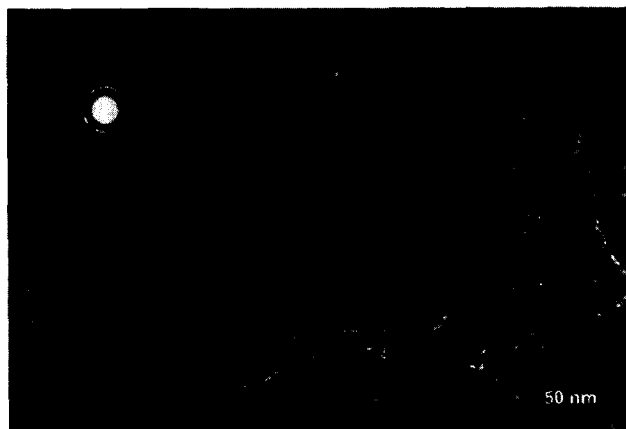


Fig. 6 TEM image of highly dispersed Ru nanoparticles attached on MWCNTs.

Survey XPS spectra of the decorated MWCNTs provide results similar to those from EDS. In addition to peaks of C, O, and Si resulting from the MWCNTs and background (MWCNTs were dispersed onto silicon substrates for XPS analysis), each survey XPS spectrum shows strong peaks of Pd, Rh, or Ru. No other heterolement including fluorine was detected, implying no byproducts or unreacted precursors are present in the nanocomposites.

The states of MWCNT-supported palladium, rhodium, and ruthenium nanoparticles can be more clearly identified through high-resolution XPS analysis. A typical high-resolution XPS spectrum of the Pd-decorated MWCNTs is shown in Fig. 7A. The binding energies, 335.3 eV for $\text{Pd}_{3d_{5/2}}$ peak and 340.6 eV for $\text{Pd}_{3d_{3/2}}$ peak, are in accordance with those reported for Pd^0 .^[69] Furthermore, the peaks are asymmetric, having a line shape typical of metallic Pd.^[69] All these imply that the palladium in the nanoparticles is zero-valent. No significant changes were observed in the binding energies or intensities of the Pd_{3d} XPS core levels after exposing the palladium-decorated MWCNTs to air for 1 month, which demonstrates the stability of the palladium nanoparticles.

Fig. 7B displays the high-resolution Rh_{3d} core level XPS spectrum of MWCNTs coated with Rh nanoparticles. The spectrum shows a low-energy band $\text{Rh}_{3d_{5/2}}$ at 307.3 eV, and a high-energy band $\text{Rh}_{3d_{3/2}}$ centering at 312.1 eV. As the $\text{Rh}_{3d_{5/2}}$ and $\text{Rh}_{3d_{3/2}}$ peaks for rhodium metal lie at 307.2 and 312.0 eV, respectively,^[69] this indicates that Rh is also in the zero-valent state in Rh nanoparticle-MWCNT composites.

For MWCNTs decorated with ruthenium nanoparticles, the high-resolution Ru_{3d} XPS spectrum has been obscured by the C_{1s} spectrum. The deconvoluted spectrum shown in Fig. 7C gives broad bands that can be curve-fitted into two pairs of Ru_{3d} peaks, therefore two chemically

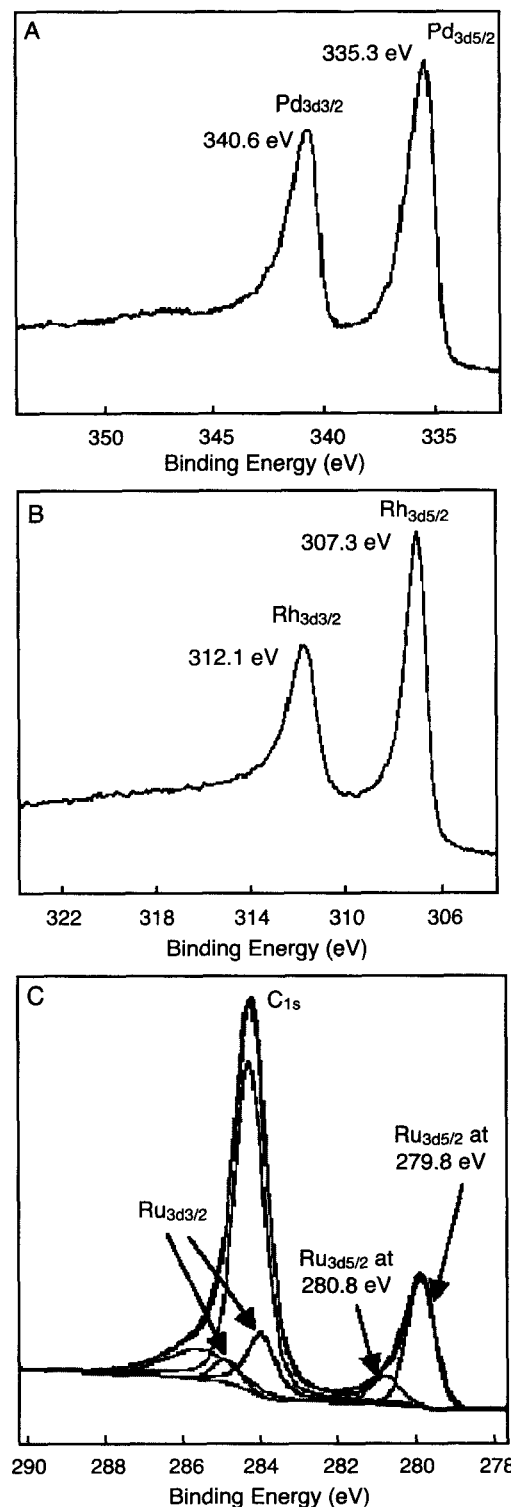


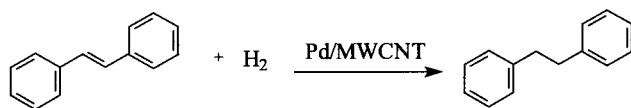
Fig. 7 High-resolution (A) Pd_{3d} , (B) Rh_{3d} , and (C) Ru_{3d} XPS spectra of MWCNTs decorated with Pd, Rh, or Ru nanoparticles. (View this art in color at www.dekker.com.)

different Ru entities can be identified: the dominant pair with a $\text{Ru}_{3d5/2}$ peak at 279.8 eV corresponds well with the 3d5/2 and 3d3/2 lines of element Ru^0 , indicating that the majority of ruthenium loaded on MWCNTs is present as metallic Ru; the minor pair showing a $\text{Ru}_{3d5/2}$ peak at 280.8 eV can be assigned to Ru oxides. The presence of Ru oxides is responsible for the strong interaction between highly dispersed Ru nanoparticles and oxygen-containing groups on the functionalized MWCNTs and could also be resulted from the slight oxidation of Ru nanoparticles upon exposure of samples to ambient air.

Promising Applications of the Metal–MWCNT Nanocomposites in Catalysis

Chemistry in ecologically benign solvents is of increasing interest in recent years. Most solvents used in organic syntheses for heterogeneous or homogeneous catalysis are coming under close scrutiny because of their toxicity and waste generation. There is a great push in industry today to replace these solvents with environmentally friendly solvents such as liquid or supercritical CO_2 . We have recently reported that palladium nanoparticles dispersed by a water-in- CO_2 microemulsion are very effective catalysts for hydrogenation of a number of olefins.^[70] However, separation of products from the surfactants and reuse of the catalyst are potential technical difficulties associated with the microemulsion technique. Developing effective heterogeneous catalysts that can be reused for chemical synthesis in liquid or supercritical CO_2 is currently of great interest to the chemical industry. The Pd nanoparticle–MWCNT composite may provide an effective catalyst for chemical synthesis in a green solvent that allows easy separation of products and minimizes waste solvent generation.

The catalytic capability of the Pd–MWCNT composite was tested for hydrogenation of a CO_2 -soluble olefin *trans*-stilbene in liquid CO_2 :



In this test, stilbene was dissolved in a mixture of 5 atm H_2 and 100 atm of CO_2 to make a 0.033 mol/L solution. The solution was pumped into a 6.94-mL stainless steel vessel loaded with 5 mg of the Pd–MWCNT composite (reported in Fig. 4C) at room temperature (23°C). Ultrasonication was applied to the vessel for 10 sec to disperse the catalyst. The product was trapped in CDCl_3 at different times and analyzed by proton NMR (Bruker,

AMX 300). According to our NMR results, conversion of stilbene to 1,2-diphenylethane was about 80% and 96% after 5 and 10 min of reaction, respectively.

A number of noble metal–carbon fiber or metal porphyrin–graphite composites have been demonstrated to catalyze electrochemical reactions significantly.^[13,71,72] The Pd–MWCNT nanocomposite was also tested for its electrocatalytic activity in oxygen reduction that is important in fuel cell applications. For comparison, graphite powder, MWCNTs, and Pd–MWCNT (Fig. 4C) were mixed individually with mineral oil to make three different carbon paste working electrodes. Cyclic voltammetry measurements were conducted at room temperature in a three-compartment electrochemical cell. The electrolyte was 1.0 M H_2SO_4 saturated with oxygen. The potential was cycled between +0.60 and -0.10 V at 40 mV/sec. As shown in Fig. 8, essentially no O_2 reduction was observed over the potential window for the carbon paste electrodes of bare MWCNT and graphite powder. In contrast, for the Pd–MWCNT electrode, a very large O_2 reduction wave was observed at potentials characteristic for Pd electrocatalysis. The enhancement of the cathodic current indicates a high electrocatalytic activity of the Pd–MWCNT electrode for the reduction of oxygen.

The highly dispersed Rh and Ru nanoparticles on MWCNTs are also expected to be potential catalysts for a variety of reactions.^[26,73] As a catalyst for the hydrogenation of *trans*-cinnamaldehyde and the hydroformylation of hex-1-ene in the liquid phase, Rh-supported MWCNTs were found to be very selective toward C=C double-bond hydrogenation and the production of linear and branched aldehydes, respectively.^[73] However, Ru nanoparticles anchoring on MWCNTs showed an unexpected increase in selectivity (up to 92%) for cinnamyl alcohol in liquid-phase hydrogenation of cinnamaldehyde.^[26]

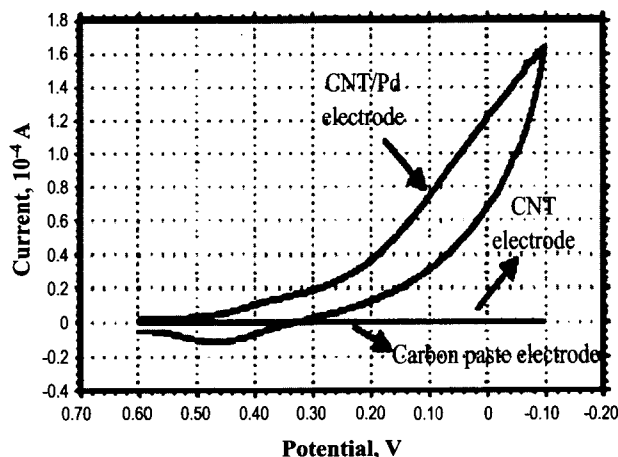


Fig. 8 Cyclic voltammograms of oxygen reduction in 1.0 M H_2SO_4 . (From Ref. [58].)

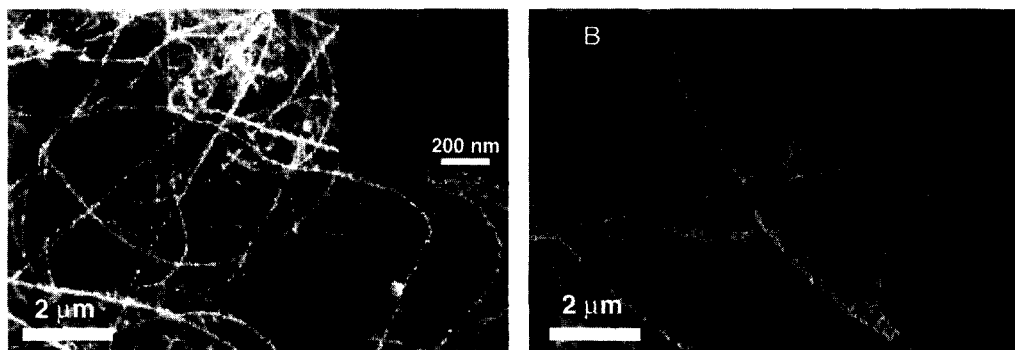


Fig. 9 SEM images of SiO₂ NWs after copper deposition from supercritical CO₂ solutions of (A) 2.0×10^{-3} (B) 2.7×10^{-2} mol/L Cu(hfa)₂. (From Ref. [59].)

METAL–NW NANOCOMPOSITES

Metal–SiO₂ NW Composites

Modification of SiO₂ NWs was performed by hydrogen reduction of Cu(hfa)₂·xH₂O in scCO₂ at 250°C and 80°C, respectively. Typical SEM images of SiO₂ NWs after copper deposition are shown in Fig. 9, and three types of nanostructures are clearly visible. When a lower precursor concentration (2.0×10^{-3} mol/L) was used in the experiment, discrete Cu nanoparticles were found to randomly anchor to the SiO₂ NWs (inset of Fig. 9A). As the concentration of the precursor increased to 2.7×10^{-2} mol/L, the NWs became thicker after coating, wrapped by shells of densely packed Cu nanoparticles. The average outside diameter of the wire-shell composite structures can be up to 400 nm, indicating that the shells were composed of multilayers of Cu nanoparticles. The rough surfaces of the composites suggested that the copper coating was polycrystalline. We believe that the Cu nanoparticles were nucleated in the SCF medium and then deposited onto the SiO₂ NW surfaces to form

the coated layer. Noticeable from the SEM images is also the aggregation of the Cu nanocrystals to form larger structures, most of which were sphere-like and “strung” up by the NWs. The inset in Fig. 9A shows a TEM image of a nanoparticle-decorated NW. Cu nanoparticles with different sizes, ranging from several to 50 nm in diameter, strung onto the SiO₂ NWs.

Metal Alloy–SiC NW Composites

In principle, a number of metal precursors can be used as starting materials as long as they are soluble in CO₂, and metals other than palladium and copper, or metal alloys can be coated on the SiO₂ NWs to form nanocomposites. Furthermore, NWs suitable for the SCF fabrication process are not limited to SiO₂. Such hydrogen reduction of metal precursors in supercritical CO₂ may provide a general and clean process to modify NWs with metallic nanoparticles. Fig. 10 describes Cu–Pd alloy nanoparticles attached to SiC NWs through hydrogen reduction of a mixture of Cu(hfa)₂·xH₂O (95%) and Pd(hfa)₂·xH₂O

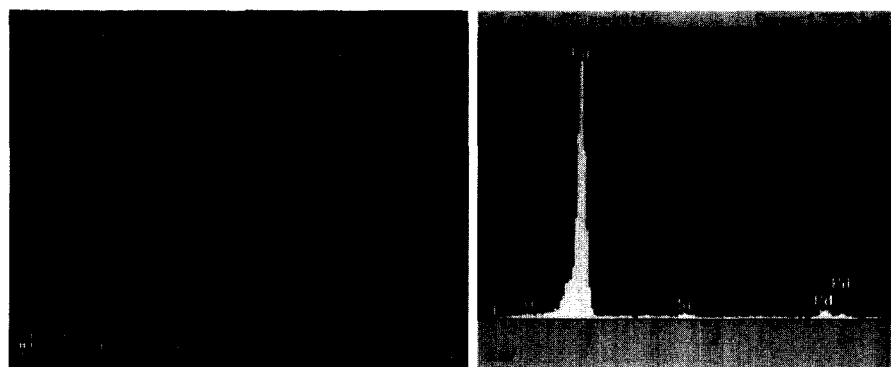


Fig. 10 Cu–Pd–SiC nanocomposites. (a) SEM image of Cu–Pd nanocrystals supported by SiC NWs, (b) EDS of the nanocomposites. (View this art in color at www.dekker.com.)

(5%) in scCO_2 at 80°C . Some aggregated balls of metals are also observed.

CONCLUSION

SCF approach is a novel and emerging technology to generate nanomaterials in small areas, high-aspect-ratio structures, complicated surfaces, and poorly wettable substrates with high uniformity, high homogeneity, and minimum environmental problems.

Through hydrogen reduction of metal- β -diketone complexes in supercritical CO_2 , a rapid, convenient, and environmentally benign approach has been developed to synthesize a variety of nanostructured materials: 1) metal (Pd, Ni, and Cu) NWs and nanorods sheathed within MWCNT templates; 2) nanoparticles of palladium, rhodium, and ruthenium decorated onto functionalized MWCNTs. These highly dispersed nanoparticles are expected to exhibit promising catalytic properties for a variety of chemical or electrochemical reactions; 3) Cu or Cu-Pd nanocrystals deposited onto SiO_2 or SiC NWs. Different types of nanostructures were achieved, including nanocrystal-NW, spherical aggregation-NW, shell-NW composites, and "mesoporous" metals supported by the framework of NWs.

ACKNOWLEDGMENTS

This work was supported by a LDRD program at Pacific Northwest National Laboratory (PNNL) and the Idaho-NSF-EPSCoR and ARO-DEPSCoR programs. Ye also acknowledges a PNNL fellowship to work at PNNL. The work was partially performed at the Environmental Molecular Sciences Laboratory, a national scientific user facility sponsored by the U.S. DOE's Office of Biological and Environmental Research and located at PNNL. PNNL is operated for the Department of Energy by Battelle.

REFERENCES

- Darr, J.A.; Poliakoff, M. New directions in inorganic and metal-organic coordination chemistry in supercritical fluids. *Chem. Rev.* **1999**, *99*, 495-541.
- Cansell, F.; Chevalier, B.; Demourgues, A.; Etourneau, J.; Even, C.; Garrabos, Y.; Pessey, V.; Petit, S.; Tressaud, A.; Weill, F. Supercritical fluid processing: A new route for materials synthesis. *J. Mater. Chem.* **1999**, *9*, 67-75.
- Cooper, A.I. Recent developments in materials synthesis and processing using supercritical CO_2 . *Adv. Mater.* **2001**, *13*, 1111-1114.
- Cooper, A.I. Materials HIPE-creating nanostructures using SCFs. *Mater. World* **2002**, *10* (1), 24-26.
- Schiffirin, D.J. Capped nanoparticles as potential electronic components with nanoscale dimensions. *MRS Bull.* **2001**, *26*, 1015-1019.
- Ye, X.R.; Wai, C.M. Making nanomaterials in supercritical fluids: A review. *J. Chem. Educ.* **2003**, *80*, 198-204.
- Ajayan, P.M. Nanotubes from carbon. *Chem. Rev.* **1999**, *99*, 1787-1800.
- Hu, J.; Odom, T.W.; Lieber, C.M. Chemistry and physics in one dimension: Synthesis and properties of nanowires and nanotubes. *Acc. Chem. Res.* **1999**, *32*, 435.
- Lieber, C.M. The incredible shrinking circuit. *Sci. Am.* **2001**, *285* (3), 59.
- Cobden, D.H. Molecular electronics: Nanowires begin to shine. *Nature* **2001**, *409*, 32-33.
- Saito, S. Carbon nanotubes for next-generation electronics devices. *Science* **1997**, *278*, 77-78.
- Baum, R.M. Nurturing nanotubes. *Chem. Eng. News.* **1997**, *75* (26), 39.
- Liu, Z.L.; Lin, X.H.; Lee, J.Y.; Zhang, W.D.; Han, M.; Gan, L.M. Preparation and characterization of platinum-based electrocatalysts on multiwalled carbon nanotubes for proton exchange membrane fuel cells. *Langmuir* **2002**, *18*, 4054-4060.
- Lin, Y.; Rao, A.M.; Sadanadan, B.; Kenik, E.A.; Sun, Y.P. Functionalizing multiple-walled carbon nanotubes with aminopolymers. *J. Phys. Chem., B* **2002**, *106*, 1294-1298.
- Tsang, S.C.; Chen, Y.K.; Harris, P.J.F.; Green, M.L.H. A simple chemical method of opening and filling carbon nanotubes. *Nature* **1994**, *372*, 159-162.
- Banerjee, S.; Wong, S.S. Synthesis and characterization of carbon nanotube-nanocrystal heterostructures. *Nano Lett.* **2002**, *2*, 195-200.
- Osterloh, F.E.; Martino, J.S.; Hiramatsu, H.; Hewitt, D.P. Stringing up the pearls: Self-assembly, optical and electronic properties of CdSe- and Au-LiMo₃Se₃ nanoparticle-nanowire composites. *Nano Lett.* **2003**, *3*, 125-129.
- Sun, X.H.; Sammynaiken, R.; Naftel, S.J.; Tang, Y.H.; Zhang, P.; Kim, P.S.; Sham, T.K.; Fan, X.H.; Zhang, Y.F.; Lee, C.S.; Lee, S.T.; Wong, N.B.; Hu, Y.F.; Tan, K.H. Ag nanostructures on a silicon nanowire template: Preparation and X-ray absorption fine structure study at the Si K-edge and Ag L_{3,2}-edge. *Chem. Mater.* **2002**, *14*, 2519-2526.
- Sun, X.H.; Li, C.P.; Wong, N.B.; Lee, C.S.; Lee, S.T.; Teo, B.K. Reductive growth of nanosized ligated metal clusters on silicon nanowires. *Inorg. Chem.* **2002**, *41*, 4331-4336.

20. Wen, X.G.; Yang, S.H. Cu₂S/Au core/sheath nanowires prepared by a simple redox deposition method. *Nano Lett.* **2002**, *2*, 451–454.
21. Yin, Y.D.; Lu, Y.; Sun, Y.G.; Xia, Y.N. Silver nanowires can be directly coated with amorphous silica to generate well-controlled coaxial nanocables of silver/silica. *Nano Lett.* **2002**, *2*, 427–430.
22. Kovtyukhova, N.T.; Martin, B.R.; Mbindyo, J.K.N.; Smith, P.A.; Razavi, B.; Mayer, T.S.; Mallouk, T.E. Layer-by-layer assembly of rectifying junctions in and on metal nanowires. *J. Phys. Chem., B* **2001**, *105*, 8762–8769.
23. Duan, X.F.; Huang, Y.; Lieber, C.M. Nonvolatile memory and programmable logic from molecule-gated nanowires. *Nano Lett.* **2002**, *2*, 487–490.
24. Li, C.P.; Sun, X.H.; Wong, N.B.; Lee, C.S.; Lee, S.T.; Teo, B.K. Silicon nanowires wrapped with Au film. *J. Phys. Chem., B* **2002**, *106*, 6980–6984.
25. Li, C.Z.; Sha, H.; Tao, N.J. Adsorbate effect on conductance quantization in metallic nanowires. *Phys. Rev., B* **1998**, *58*, 6775–6778.
26. Planeix, J.M.; Coustel, N.; Coq, B.; Brotons, V.; Kumbhar, P.S.; Dutartre, R.; Geneste, P.; Bernier, P.; Ajayan, P.M. Application of carbon nanotubes as supports in heterogeneous catalysis. *J. Am. Chem. Soc.* **1994**, *116*, 7935–7936.
27. Calvert, P. Strength in disunity. *Nature* **1992**, *357*, 365.
28. Ajayan, P.M.; Iijima, S. Capillarity-induced filling of carbon nanotubes. *Nature* **1993**, *361*, 333–334.
29. Li, J.; Moskovits, M.; Haslett, T.L. Nanoscale electroless metal deposition in aligned carbon nanotubes. *Chem. Mater.* **1998**, *10*, 1963–1967.
30. Ang, L.M.; Hor, T.S.A.; Xu, G.Q.; Tung, C.H.; Zhao, S.; Wang, J.L.S. Electroless plating of metals onto carbon nanotubes activated by a single-step activation method. *Chem. Mater.* **1999**, *11*, 2115–2118.
31. Yu, R.; Chen, L.; Liu, Q.; Lin, J.; Tan, K.L.; Ng, S.C.; Chan, H.S.O.; Xu, G.Q.; Hor, T.S.A. Platinum deposition on carbon nanotubes via chemical modification. *Chem. Mater.* **1998**, *10*, 718–722.
32. Ebbesen, T.W.; Hiura, H.; Bisher, M.E.; Treacy, M.M.J.; Shreeve-Keyer, J.L.; Haushalter, R.C. Decoration of carbon nanotubes. *Adv. Mater.* **1996**, *8*, 155–157.
33. Pradhan, B.K.; Toba, T.; Kyotani, T.; Tomita, A. Inclusion of crystalline iron oxide nanoparticles in uniform carbon nanotubes prepared by a template carbonization method. *Chem. Mater.* **1998**, *10*, 2510–2515.
34. Kyotani, T.; Tsai, L.; Tomita, A. Formation of platinum nanorods and nanoparticles in uniform carbon nanotubes prepared by a template carbonization method. *Chem. Commun.* **1997**, 701–702.
35. Che, G.; Lakshmi, B.B.; Martin, C.R.; Fisher, E.R. Metal-nanocluster-filled carbon nanotubes: Catalytic properties and possible applications in electrochemical energy storage and production. *Langmuir* **1999**, *15*, 750–758.
36. Lordi, V.; Yao, N.; Wei, J. Method for supporting platinum on single-walled carbon nanotubes for a selective hydrogenation catalyst. *Chem. Mater.* **2001**, *13*, 733–737.
37. Freemantle, M. Filled carbon nanotubes could lead to improved catalysts and biosensors. *Chem. Eng. News* **1996**, *74* (29), 62.
38. Cook, J.; Sloan, J.; Green, M.L.H. Carbon nanotube chemistry. *Chem. Ind.* **1996**, *16*, 600–603.
39. Ebbesen, T.W. Carbon nanotubes. *Phys. Today* **1996**, *49* (6), 26–32.
40. Kong, J.; Franklin, N.R.; Zhou, C.W.; Chapline, M.G.; Peng, S.; Cho, K.J.; Dai, H.J. Nanotube molecular wires as chemical sensors. *Science* **2000**, *287*, 622–625.
41. Kong, J.; Chapline, M.G.; Dai, H.J. Functionalized carbon nanotubes for molecular hydrogen sensors. *Adv. Mater.* **2001**, *13*, 1384–1386.
42. Sen, R.; Govindaraj, A.; Rao, C.N.R. Metal-filled and hollow carbon nanotubes obtained by the decomposition of metal-containing free precursor molecules. *Chem. Mater.* **1997**, *9*, 2078–2081.
43. Guerret-Piecourt, C.; Le Bouar, Y.; Loiseau, A.; Pascard, H. Relation between metal electronic structure and morphology of metal compounds inside carbon nanotubes. *Nature* **1994**, *372*, 761–765.
44. Liu, S.W.; Zhu, J.J.; Mastai, Y.; Felner, I.; Gedanken, A. Preparation and characteristics of carbon nanotubes filled with cobalt. *Chem. Mater.* **2000**, *12*, 2205–2211.
45. Ugarte, U.; Chatelain, A.; de Heer, W.A. Nanocapillarity and chemistry in carbon nanotubes. *Science* **1996**, *274*, 1897–1899.
46. Dujardin, E.; Ebbesen, T.W.; Hiura, H.; Tanigaki, K. Capillarity and wetting of carbon nanotubes. *Science* **1994**, *265*, 1850.
47. Chu, A.; Cook, J.; Heeson, R.J.R.; Hutchison, J.L.; Green, M.L.H.; Sloan, J. Filling of carbon nanotubes with silver, gold, and gold chloride. *Chem. Mater.* **1996**, *8*, 2751–2754.
48. Matsui, K.; Pradhan, B.K.; Kyotani, T.; Tomita, A. Formation of nickel oxide nanoribbons in the cavity of carbon nanotubes. *J. Phys. Chem., B* **2001**, *105*, 5682–5688.
49. Che, G.L.; Lakshmi, B.; Fisher, E.R.; Martin, C.R. Carbon nanotubule membranes for electrochemical energy storage and production. *Nature* **1998**, *393*, 346–349.

50. Hsu, W.K.; Trasobares, S.; Terrones, H.; Terrones, M.; Grobert, N.; Zhu, Y.Q.; Li, W.Z.; Escudero, R.; Hare, J.P.; Kroto, H.W.; Walton, D.R.M. Electrolytic formation of carbon-sheathed mixed Sn-Pb nanowires. *Chem. Mater.* **1999**, *11*, 1747–1751.
51. Govindaraj, A.; Satishkumar, B.C.; Nath, M.; Rao, C.N.R. Metal nanowires and intercalated metal layers in single-walled carbon nanotube bundles. *Chem. Mater.* **2000**, *12*, 202–205.
52. Hsin, Y.L.; Hwang, K.C.; Chen, F.R.; Kai, J.J. Production and in-situ metal filling of carbon nanotubes in water. *Adv. Mater.* **2001**, *13*, 830–833.
53. Xue, B.; Chen, P.; Hong, Q.; Lin, J.; Tan, K.L. Growth of Pd, Pt, Ag and Au nanoparticles on carbon nanotubes. *J. Mater. Chem.* **2001**, *11*, 2378–2381.
54. Chen, P.; Wu, X.; Lin, J.; Tan, K.L. Synthesis of Cu nanoparticles and microsized fibers by using carbon nanotubes as a template. *J. Phys. Chem., B* **1999**, *103*, 4559–4561.
55. Lago, R.M.; Tsang, S.C.; Lu, K.L.; Chen, Y.K.; Green, M.L.H. Filling carbon nanotubes with small palladium metal crystallites: The effect of surface acid groups. *J. Chem. Soc., Chem. Commun.* **1995**, 1355–1356.
56. Hwang, K.C. Efficient cleavage of carbon graphene layers by oxidants. *J. Chem. Soc., Chem. Commun.* **1995**, 173–174.
57. Ye, X.R.; Lin, Y.; Wang, C.M.; Wai, C.M. Supercritical fluid fabrication of metal nanowires and nanorods templated by multi-walled carbon nanotubes. *Adv. Mater.* **2003**, *15*, 316–319.
58. Ye, X.R.; Lin, Y.; Wai, C.M. Decorating catalytic palladium nanoparticles on multi-walled carbon nanotubes in supercritical CO₂. *Chem. Commun.* **2003**, 642–643.
59. Ye, X.R.; Zhang, H.F.; Lin, Y.; Wang, L.S.; Wai, C.M. Modification of SiO₂ nanowires with metallic nanocrystals from supercritical CO₂. *J. Nanosci. Nanotech.* **2004**, *4*, 62–65.
60. Shah, P.S.; Husain, S.; Johnston, K.P.; Korgel, B.A. Nanocrystal arrested precipitation in supercritical carbon dioxide. *J. Phys. Chem., B* **2001**, *105*, 9433–9440.
61. Shah, P.S.; Husain, S.; Johnston, K.P.; Korgel, B.A. Role of steric stabilization on the arrested growth of silver nanocrystals in supercritical carbon dioxide. *J. Phys. Chem., B* **2002**, *106*, 12178–12185.
62. Watkins, J.J.; Blackburn, J.M.; McCarthy, T.J. Chemical fluid deposition: Reactive deposition of platinum metal from carbon dioxide solution. *Chem. Mater.* **1999**, *11*, 213–215.
63. Long, D.P.; Blackburn, J.M.; Watkins, J.J. Chemical fluid deposition: A hybrid technique for low-temperature metallization. *Adv. Mater.* **2000**, *12*, 913–915.
64. Blackburn, T.M.; Long, D.P.; Watkins, J.J. Reactive deposition of conformal palladium films from supercritical carbon dioxide solution. *Chem. Mater.* **2000**, *12*, 2625–2631.
65. Blackburn, J.M.; Long, D.P.; Cabanas, A.; Watkins, J.J. Deposition of conformal copper and nickel films from supercritical carbon dioxide. *Science* **2001**, *294*, 141–145.
66. Fernandes, N.E.; Fisher, S.M.; Poshusta, J.C.; Vlachos, D.G.; Tsapatsis, M.; Watkins, J.J. Reactive deposition of metal thin films within porous supports from supercritical fluids. *Chem. Mater.* **2001**, *13*, 2023–2031.
67. Cabanas, A.; Blackburn, J.M.; Watkins, J.J. Deposition of Cu films from supercritical fluids using Cu(I)- β -diketonate precursors. *Microelectron. Eng.* **2002**, *64*, 53–61.
68. Dai, L.; Griesser, H.J.; Mau, A.W.H. Surface modification by plasma etching and plasma patterning. *J. Phys. Chem., B* **1997**, *101*, 9548–9554.
69. Moulder, J.F.; Stickle, W.F.; Sobol, P.E.; Bomben, K.D. *Hand Book of X-ray Photoelectron Spectroscopy*; Chastain, J., Ed.; Perkin-Elmer: Eden Prairie, MN, 1992.
70. Ohde, H.; Wai, C.M.; Kim, H.; Kim, J.; Ohde, M. Hydrogenation of olefins in supercritical CO₂ catalyzed by palladium nanoparticles in a water-in-CO₂ microemulsion. *J. Am. Chem. Soc.* **2002**, *124*, 4540–4541.
71. Steigerwalt, E.S.; Deluga, G.A.; Lukehart, C.M. Pt-Ru/carbon fiber nanocomposites: Synthesis, characterization, and performance as anode catalysts of direct methanol fuel cells. A search for exceptional performance. *J. Phys. Chem., B* **2002**, *106*, 760–766.
72. Collman, J.P.; Chng, L.L.; Tyvoll, D.A. Electrocatalytic reduction of dioxygen to water by iridium porphyrins adsorbed on edge plane graphite electrodes. *Inorg. Chem.* **1995**, *34*, 1311–1324.
73. Giordano, R.; Serp, P.; Kalck, P.; Kihn, Y.; Schreiber, J.; Marhic, C.; Duvail, J.-L. Preparation of rhodium catalysts supported on carbon nanotubes by a surface mediated organometallic reaction. *Eur. J. Inorg. Chem.* **2003**, 610–617.

Nanostructured Ultrastrong Materials

N

Nicholas A. Kotov

Oklahoma State University, Stillwater, Oklahoma, U.S.A.

Arif A. Mamedov

Oklahoma State University and Nomadics, Inc., Stillwater, Oklahoma, U.S.A.

Dirk M. Guldi

University of Notre Dame, Notre Dame, Indiana, U.S.A.

Zhiyong Tang

University of Michigan, Ann Arbor, Michigan, U.S.A.

Maurizio Prato

Università di Trieste, Trieste, Italy

James Wicksted

Oklahoma State University, Stillwater, Oklahoma, U.S.A.

Andreas Hirsch

Friedrich Alexander Universität Erlangen-Nürnberg, Erlangen, Germany

INTRODUCTION

The mass–strength ratio is of exceptional importance for different applications. Critical parts of various moving vehicles from satellites to aircrafts to cars depend on strength and toughness of the materials they are made of, while strict limitations on the weight of the different components are placed by the launch technology. Single-walled carbon nanotubes (SWNT) present significant potential as the basic material for space applications. The exceptional mechanical properties of SWNTs^[1–6] have prompted intensive studies of their composites. These qualities can also be used in a variety of other technologies from automotive to military and medical. However, the present composites have shown only a moderate strength enhancement when compared to other hybrid materials.^[7–9] Although substantial advances have been made,^[10] the mechanical characteristics of SWNT-doped polymers are noticeably below their highly anticipated potential. Pristine SWNTs are well known for poor solubilization, which leads to phase segregation of composites. Severe structural inhomogeneities result in the premature failure of the hybrid SWNT–polymer materials. The connectivity with and uniform distribution within the matrix are essential structural requirements for the strong SWNT composites.^[11–13] Here we show that a new processing approach based on sequential layering of chemically modified nanotubes and polyelectrolytes can

greatly diminish the phase segregation and render SWNT composite highly homogeneous. Combined with chemical cross-linking, this processing leads to drastically improved mechanical properties. The tensile strength of the composites is several times higher than that of SWNT composites made via mixing; it approaches values seen for hard ceramics. The universality of the layering approach applicable to a wide range of functional materials makes possible successful incorporation of SWNT into a variety of composites, imparting them required mechanical properties.

The thin-film membranes that are obtained as a result of the layer-by-layer process can be used as an intermediate or as a component of ultrastrong laminates. At the same time, the prepared membranes can also be utilized in the as-prepared form for space and biomedical technologies because of the combined strength and multiple functionalities of the SWNT membranes.

RESULTS AND DISCUSSION

Single-walled carbon nanotube composites are typically prepared by blending, in situ polymerization, and extrusion. After extensive surface modification, such as grafting or polymer wrapping,^[12–14] the phase segregation from a macromolecular matrix is smaller than for pristine SWNT, but still remains high owing to vastly different

molecular mobilities of both components. Very intense research on appropriate surface modification of SWNT is currently under way in many groups around the world. Nevertheless, most common loadings of nanotubes in the polymer matrix are within the 1–15 wt.% range, whereas more than 50% of the SWNT content is needed for materials with special mechanical performance without compromising the homogeneity of the composite at the nanometer level. This high loading of the nanotubes is particularly important when both electrical and mechanical qualities of the nanotubes are going to be utilized.

The phase segregation between dissimilar materials can be circumvented by applying a new deposition technique often called layer-by-layer assembly (LBL).^[15] It is based on the alternating adsorption of monolayers of individual components attracted to each other by electrostatic and van der Waals interactions and can be carried out with a variety of polyelectrolytes and other compounds with high molecular weight. The immobilization of the macromolecular compounds and strong interdigitation of the nanometer-thick film allows for the close-to-perfect molecular blending of the components.^[16,17]

The SWNT–polyelectrolyte composites produced in this study were assembled onto a solid support via alternate dipping of a solid substrate (glass slides, Si wafers) into dispersions of SWNT and polyelectrolyte solutions.^[18–20] The individual assembly steps, i.e., adsorption of SWNT and polyelectrolyte monolayers, were interlaced by rinsing steps to remove the excess of assembling materials. When the LBL procedure was complete, the multilayer films were lifted off the substrate to obtain uniform freestanding membranes, which can be handled as regular composites.^[21] Such films make possible straightforward testing of their mechanical properties. It is important to note that large-area membranes for space telescopes and similar applications can similarly be made by deposition on the substrates of appropriate size.

Single-walled carbon nanotubes were produced by laser ablation and subsequently purified via acid treatment. They were manufactured by laser vaporization of carbon rods doped with Co, Ni, and FeS in an atmosphere of Ar:H₂. It needs to be pointed out that the standard SWNT products made by HiPCO and other methods contain significant amount of soot, graphite flakes, and remnants of the catalyst, which need to be removed before the assembly. The quality of the dispersion directly affects the mechanical performance of the resulting composite.

A suspension of SWNT raw material was refluxed in 65% HNO₃ and subsequently purified by centrifugation. Supplemented by sonication, this treatment results in the partial oxidation of ca. 5% of the total number of carbon atoms both in caps and walls of SWNT.^[22] A similar type of dispersion can also be made following other methods, such as polymer wrapping the nanotubes and chemical

derivatization. Optimization of the aqueous nanotube dispersions should be considered as one of the most critical direction of the optimization of the carbon nanotube composites and speed and quality of their processing in the composites.

The presence of carboxylic acid groups affords the preparation of metastable SWNT dispersions after 1-min sonication in deionized water without any additional surfactant. Thus-prepared, negatively charged SWNT with a zeta potential of -0.08 V can be layer-by-layer assembled with positively charged polyelectrolyte, such as branched poly(ethyleneimine) (PEI; Mw=70,000) (Fig. 1). Because the overall negative charge of the SWNT used here was fairly small, a layer of SWNT was replaced with a layer of poly(acrylic acid) (PAA; Mw=450,000) after every fifth deposition cycle (Fig. 1). These additional layers improve the linearity of the deposition process and present a convenient chemical anchor for subsequent chemical modification. For the same reasons, a single PEI/PAA bilayer was deposited on a bare glass or Si substrate before the SWNT assembly. The assembly conditions of the entire procedure (pH, ionic strength, concentrations, etc.) were optimized so that the dipping cycles can be repeated as many times as needed with linear growth of the multilayers (Fig. 2a). This enables the preparation of films with any desirable thickness and architecture tailored to different applications. The ionic conditions of LBL assembly were the following: 1% solution of PEI at pH 8.5; 1% PAA at pH 6 (pH 3 for wafer coating); SWNT at pH 6.8. All solutions were made in 18 M Ω deionized (DI) water without addition of any extra salt or other low molecular weight electrolyte. Deionized water was also used for rinsing at pH 8.5, adjusted by NaOH. Wafers and glass slides were cleaned in piranha solution, rinsed with DI water,

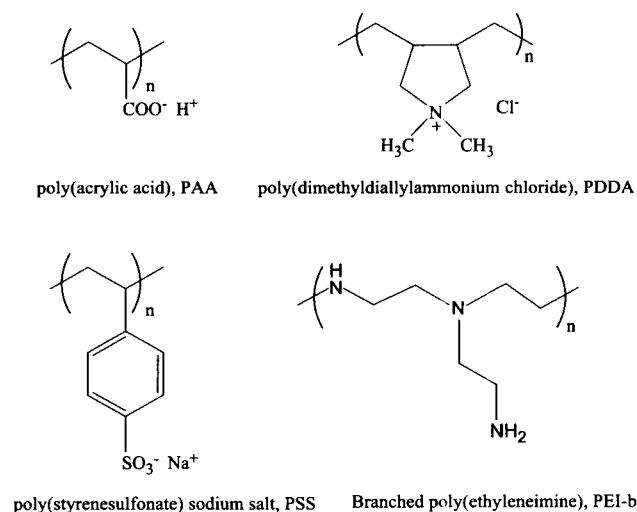


Fig. 1 Common polyelectrolytes used for LBL process.

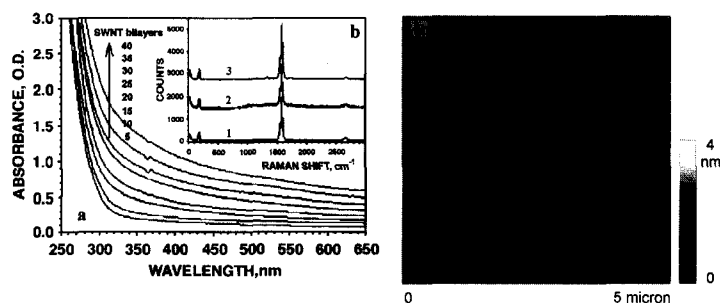


Fig. 2 Structural characterization of SWNT multilayers. (a) Sequential UV-vis spectra of a glass substrate in the course of the LBL deposition of SWNT. The spectra were taken for a total number of (PEI/SWNT) bilayers indicated in the graph. (b) Raman scattering spectra of SWNT dispersion (1), LBL film on a glass substrate (2), and freestanding film (3). (c) Tapping mode AFM image (DI, Multimode IIIA) of a Si wafer bearing (PEI/PAA)(PEI/SWNT)₅. (From Refs. [18,19].)

sonicated for 15 min, and again thoroughly rinsed with DI water. After that, they were coated with a precursor layer: PEI (10 min)+PAA(15 min, pH 3), followed by the deposition of (PEI/SWNT)₅. The layer sequence of (PEI/PAA)(PEI/SWNT)₅ was repeated until the desirable thickness was obtained. Exposure times of 10 and 60 min was used for polyelectrolytes and SWNT baths, respectively.^[18,19]

Multilayer stacks with a cumulative structure of [(PEI/PAA)(PEI/SWNT)₅]₆ and [(PEI/PAA)(PEI/SWNT)₅]₈ containing 30 and 40 (PEI/SWNT) bilayers, respectively, were typically used in this study.

We are currently investigating other methods of SWNT dispersion in water to avoid excessive damage to the SWNT wall, for example, wrapping the nanotubes with copolymers, which can work equally well on the SWNT and multiwalled carbon nanotubes (MWNT). For some applications, MWNTs can be the preferred materials because of their lower cost.

Similarly to other polyelectrolyte LBL systems,^[15] a submonolayer of SWNT is deposited in each deposition cycle. The final morphology of the multilayers can be described as a mixture of individual carbon nanotubes and their 4–9-nm bundles intricately interwoven together in a fine fabric (Fig. 2c). Two important structural characteristics should be pointed out. Single-walled carbon nanotubes uniformly cover the entire surface of the substrate without any evidence of phase separation. Also, the presence of oxidized flat graphite sheets and other forms of carbon colloids in our experiments was very small. Both these factors contributed to the mechanical properties of the composites. The quality of the nanotube material was also assessed by Raman spectroscopy. (Raman measurements were performed in a backscattering configuration with 50 mW of 514.5-nm laser light incident on the samples). The characteristic Raman peaks for SWNTs, e.g., the radial breathing mode at $\sim 182\text{ cm}^{-1}$ and the tangential C–C stretching modes located at $\sim 1560\text{ cm}^{-1}$

(G1 mode) and $\sim 1583\text{ cm}^{-1}$ (G2 mode), were very sharp and narrow, indicating the high uniformity of the SWNT and low level of impurities present in the films. A barely visible peak at $\sim 1340\text{ cm}^{-1}$ (D mode) revealed the presence of residual amounts of disordered carbon structures. Using the correlation between the frequency of the radial breathing mode, ν , and the SWNT diameter, d , expressed as $d=223.75/\nu$,^[23] a value of $d=1.2\text{ nm}$ is obtained, which is in a good agreement with the SWNT diameters obtained from atomic force microscopy (AFM) images of many individual nanotubes. From these images, the length of the nanotubes was estimated to be 2–7 μm .

Poly(ethyleneimine) was utilized as the LBL partner of SWNT because of the terminal $-\text{NH}_2$ and backbone $-\text{NH}-$ groups in the main chain and branches suitable for the subsequent chemical modification of the composite.^[24] The PEI chains can be cross-linked 1) with each other and 2) with carboxyl groups on SWNT and PAA. Chemical stitching increases the connectivity of the polyelectrolyte matrix with SWNT, and therefore, the load transfer in the composite.^[13] We used here the combination of both modification pathways. Partial covalent SWNT–PEI–PAA cross-linking was achieved by heating the films to 130°C after the deposition of each layer, resulting in amide bonds between a variety of protonated and nonprotonated functional groups of PEI, PAA, and SWNT complementing the intrinsic ionic cross-linking of the LBL films.^[25] Subsequently, the film was exposed to glutaraldehyde at room temperature. The sample was cross-linked in 0.5% glutaraldehyde solution in phosphonate buffer (0.054M Na_2HPO_4 , 0.013 M NaH_2PO_4 , pH 7.4) for 1 hr at room temperature. To remove unreacted glutaraldehyde, the film was rinsed with tap water for $3 \times 10\text{ min}$ and then with DI water the same number of times. This reaction produces a tight network of polymeric chains and nanotubes connected by dialdehyde linkages. It was found that if only 1% of all carbon atoms of SWNT are chemically bonded to the

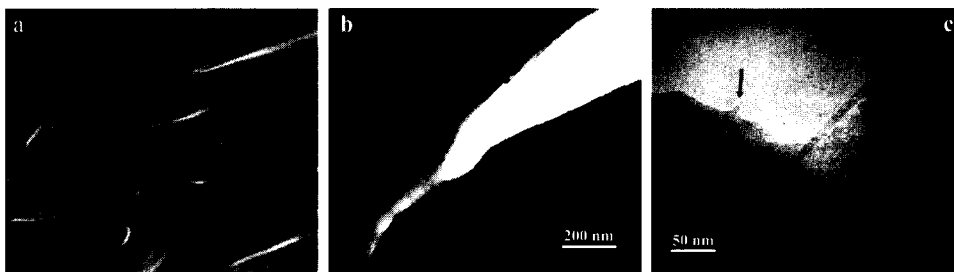


Fig. 3 Electron microscopy of the rupture region in SWNT multilayers. (a) Scanning electron microscopic image of the surface and broken edges of [(PEI/PAA)(PEI/SWNT)₅]₈. (b, c) Transmission electron microscopic images of ruptured areas of the freestanding films. The arrows indicate the likely stubs of the broken nanotube bundles. They were identified as such because 1) their diameters are both equal to that of the actual SWNT bundle bridging the gap and 2) their mutual positioning presents a virtually perfect match with the expected location of the ends of a bundle broken during gap opening.

polymer matrix, such cross-linking drastically increases the shear between them by an order of magnitude.^[13] Therefore a 5% density of -COOH groups on the SWNT surface cited above should be sufficient to obtain good connectivity with the polyelectrolyte matrix. Note that these groups are not completely utilized at the moment because of the relatively low temperature of the amide bond cross-linking step.

The mechanical properties of the LBL-assembled SWNT thin films were studied in their freestanding form prepared by the chemical delamination from the substrate.^[21] Multilayers of SWNT were separated from the silicon wafers by immersion into 0.5% aqueous HF for 3 min. The Raman scattering spectrum of the separated film is almost identical to that of the supported film and original nanotubes (Fig. 2b), demonstrating that the structure of SWNT remains mostly unaltered during cross-linking and delamination. The breathing mode frequency shifts from 185 cm⁻¹ in the assembled film to 182 cm⁻¹ in the cross-linked, self-standing films, indicating a small expansion of the tube diameters.^[18,19]

The delaminated thin films (Fig. 3a) can be easily handled in a variety of ways. They can be made of any desirable size or shape determined only by the dimensions of the substrate. The films that we routinely prepare in this study were ca. 1 × 3 cm. Assemblies with a structure of [(PEI/PAA)(PEI/SWNT)₅]₆ and [(PEI/PAA)(PEI/SWNT)₅]₈ displayed an SWNT content of 50 ± 5 wt.% as calculated from carbon and nitrogen energy-dispersive X-ray analysis (EDAX) peak integrals. Previously reported composites made with modified SWNT revealed strong inhomogeneities even at SWNT loadings as low as 6–8%.^[8,9] The cross-sectional image of the freestanding film (Fig. 4a,b) clearly demonstrates the absence of micron-scale inhomogeneities although the occasional inclusion of round 30–60 nm particles can be seen (possibly dust). The slight variations in the gray-scale contrast between different strata show the actual variations in SWNT distribution within the sample. They originate

from small deviations in SWNT adsorption conditions, such as dispersion concentration and pH, during the buildup procedure. In scanning electron microscopy (SEM) (Fig. 3a), the surface of the sample also appears smooth and continuous. Typically, the separation of single-walled or multiwalled carbon nanotubes and their bundles in mixed polymer composites can be observed as whiskers clearly visible in transmission electron microscopy (TEM) and SEM images.^[4,26] The TEM examination of the initial stages of rupturing showed that virtually no fiber pullout occurs in the LBL multilayers (Fig. 3b). This can be contrasted by extensive nanotube pullout reported before by several groups.^[4,26] For many TEM images obtained in different areas of the self-standing films, we were able to observe only one SWNT bundle bridging the break region (Fig. 3c). The same image also shows two broken carbon fiber stubs embedded in the walls of the crack (marked by arrows in Fig. 3c). In total, the microscopy results indicate the efficient load transfer in the LBL composite. Similar films are currently prepared from the multiwalled carbon nanotubes utilizing the polymer wrapping (Fig. 5).

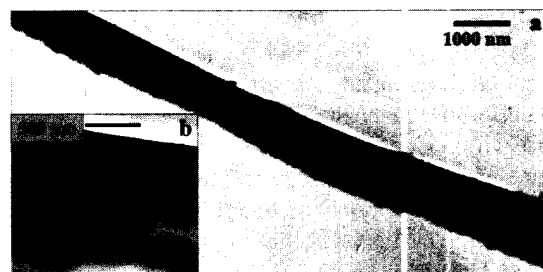


Fig. 4 Transmission electron microscopic examination of the homogeneity of the SWNT LBL film. Survey (a) and close-up (b) TEM images of SWNT film cross sections. The top and bottom sides of the film are slightly different in roughness: The one that was adjacent to the flat substrate is smoother than the "growth" surface of the film. (From Refs. [18,19].)

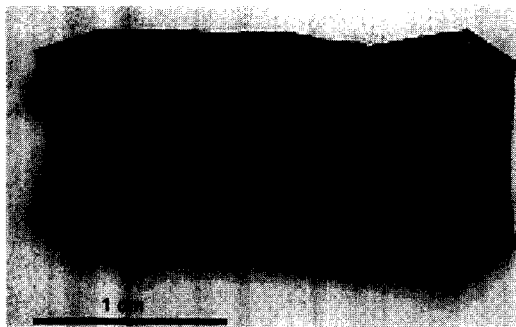


Fig. 5 Optical photograph of the free-standing LBL films made from multiwalled carbon nanotubes. (View this art in color at www.dekker.com.)

The mechanical properties of the layered composites were tested on a custom-made thin-film, tensile-strength tester (McAllister Inc.) recording the displacement and applied force by using pieces cut from [(PEI/PAA)(PEI/SWNT)₅]₆ and [(PEI/PAA)(PEI/SWNT)₅]₈ freestanding films. The tester was calibrated on similar pieces made from cellulose acetate membranes and Nylon threads. [(PEI/PAA)(PEI/SWNT)₅]₆ and [(PEI/PAA)(PEI/SWNT)₅]₈ samples had an average TEM thickness of 0.75 and 1.0 μm , respectively. Their typical stress (σ) vs. strain (ϵ) curves differed quite markedly from stretching curves previously seen for SWNT composites^[10] and for LBL films solely made from polyelectrolytes, (PEI/PAA)₄₀, obtained by the same assembly procedure (Fig. 6b). They displayed a characteristic wave-like pattern, gradual increase of $d\sigma/d\epsilon$ derivative, and the complete absence of the plateau region for high strains corresponding to plastic deformations (Fig. 6a). The latter

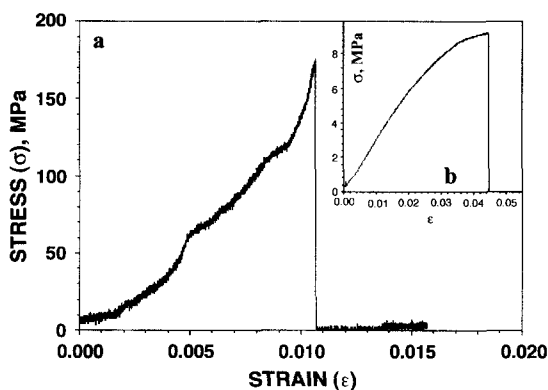


Fig. 6 Typical tensile-strength curves of the SWNT LBL films. Stress-strain dependence for (a) [(PEI/PAA)(PEI/SWNT)₅]₈ and (b) a similar free-standing multilayer film solely made from polyelectrolytes. The dependence of the mechanical properties of the cross-linked LBL composites on humidity was tested in the range of relative humidity of 30–100%, $T=298^\circ\text{C}$, and was found to be negligible. (From Refs. [18,19].)

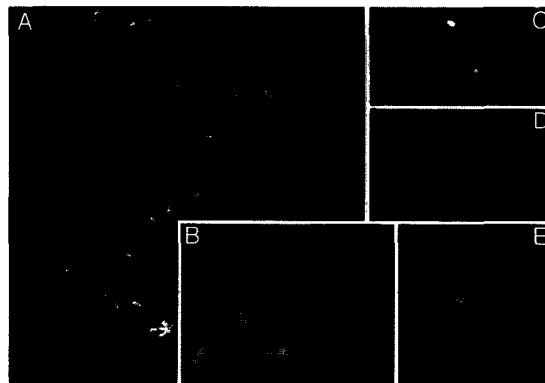


Fig. 7 Atomic force microscopy of rarified PDDA films. (A) Overview of adsorbed PDDA molecules ($2 \times 2 \mu\text{m}$, mica). (B) Cluster of PDDA molecules ($360 \times 230 \text{ nm}$, Si wafer). (C) Fully extended PDDA chain ($350 \times 170 \text{ nm}$). (D) Partially coiled PDDA chain ($160 \times 80 \text{ nm}$, mica). (E) Typical highly coiled conformation of PDDA chain ($100 \times 110 \text{ nm}$). (From Ref. [29].)

correlates well with the enhanced connectivity of SWNT with the polymer matrix (Fig. 3). Other mentioned stretching features indicate the reorganization of the layered composite under stress. A process similar to the sequential breakage of cross-linked parts of coiled molecules (see AFM image in Fig. 2) observed in natural nanocomposites, such as seashells and bones,^[27,28] is likely to be responsible for the wave-like pattern and the increase of the stretching curve slope. This statement can be substantiated by the AFM investigation of the single molecules of a polyelectrolyte adsorbed to the substrate (Fig. 7). Atomic force microscopy images of poly-(diallyldimethylammonium) chloride (PDDA) (Fig. 7) polycation adsorbed to silicates revealed the actual conformation of macromolecules at the organic–inorganic interface. Similarly to PEI, this polyelectrolyte has a positive charge when adsorbed to silica or glass. Coiling of PEI is expected to be even stronger than that of PDDA because the latter has intrinsically strong propensity to form a rod-like structure because of its greater charge. The intentionally rarified submonolayers of polycation were made from 2×10^{-7} wt.% solutions to resolve single chains (Fig. 7A). These are intricately entangled to form a continuous film at higher concentrations. Adsorbed polyelectrolyte were found to be present in the film in different conformational states: extended (Fig. 7C), partially coiled (Fig. 7D), and tightly coiled (Fig. 7E). The length of the macromolecules in extended conformation, 350–400 nm (Fig. 7C), coincides with that expected for poly(diallyldimethylammonium) chloride with $M_w=200,000$. As can be seen from Fig. 7A, most of the molecules (>75%) are present in the tightly coiled conformation. Moreover, the AFM examination of the clusters of the macromolecules molecules (Fig. 7B) demonstrates

that this is apparently the preferential conformation of the polyelectrolyte in densely packed films made at higher concentrations used for multilayer preparation.^[29]

Considering the complexity of the deformation process, the assessment of elastic and inelastic behavior in each part of the curve will be carried out upon detailed microscopic investigation. Meanwhile, the values of $d\sigma/de$ exceeding 50 GPa should be noted.

The comparison with stretching curves of polyelectrolytes (Fig. 6b) shows that the incorporation of nanotubes in the LBL structure resulted in the transfer of the SWNT strength to the entire assembly. The stretching curves of the SWNT multilayers display a clear break point. The ultimate tensile strength, T , was found to be 220 ± 40 MPa with some readings being as high as 325 MPa. This is several times to an order of magnitude greater than the tensile strength of strong industrial plastics with $T=20$ – 66 MPa.^[30] It is also substantially higher than the tensile strength of carbon fiber composites made by mixing: Polypropylene filled with 50 vol.% carbon fibers has $T=53$ MPa.^[31] A recent study on SWNT–poly(vinylalcohol) ribbons with axially aligned nanotubes reported a tensile strength of 150 MPa.^[10] The T values obtained for SWNT LBL films are in fact close to those of ultrahard ceramics and cermets such as tungsten monocarbide ($T=340$ MPa), silicon monocarbide ($T=300$ MPa), and tantalum monocarbide ($T=290$ MPa).^[30] Such strength and failure strain greater than in cermets (ca. $>1\%$ in SWNT LBL vs. 0.2 – 0.6% in carbides) displayed by an organic composite is quite remarkable.

The tensile strength of single carbon nanotubes was experimentally determined to be between 13 and 50 GPa.^[26,32] The lower values obtained for the SWNT multilayers should be mainly attributed to the contribution of polyelectrolytes and some uncertainty in the actual cross-section area at the break point and a degree of cross-linking. The mixing law predicts that polyelectrolyte matrix with $T=9$ MPa makes negligible contribution to the strength of the composite while taking about 50% of its volume fraction. [SWNT is $d=1.14$ g/cm³. Because the density of the polyelectrolytes used for the preparation of the multilayers (i.e., PDDA $d=1.04$ g/cm³; PAA $d=1.14$ g/cm³) is almost the same, the volume fraction of SWNT in the composite can be considered to be equal to the mass fraction.] Additionally, the decrease of the mechanical strength of the nanotubes in the process of ionic functionalization (estimate 15%)^[33] should also be considered as a factor affecting the strength of these composites. These issues are pointed out as means of further optimization of the multilayers. Tuning of their molecular structure and composition should lead to vast improvement of their mechanical properties that could possibly approach those of pristine carbon nanotubes.

It is also interesting to compare the T values for SWNT composite films to those obtained for other LBL films

made with other inorganic components such as montmorillonite platelets, M , and nanoparticles, NP , for instance 8–10-nm magnetite nanoparticles. The freestanding films $(PDDA/NP)_{40}$ and $(PDDA/NP/PDDA/M)_{40}$ made according to Ref. [21] revealed T equal to 40 and 72 MPa, respectively. In conjunction with the tensile strength data (see above), it can be concluded that inorganic or SWNT components act as a molecular armor in the layered composites significantly reinforcing them. The molecular organization of the material made possible the transfer of a part of their strength to the entire assembly.

CONCLUSION

The technology of the preparation of nanocomposites described above should be considered as an effective tool in developing new ultrastrong materials. High structural homogeneity and interconnectivity of the structural components of the LBL films combined with high SWNT loading leads to significant increase of the strength of nanocomposites, being somewhat weaker than some other organic and carbon fiber materials but at the same time being far beyond their potential as ultrastrong composites. The described technique minimizes the structural defects originating from phase segregation and opens a possibility for the molecular design of layered hybrid structural materials from different polymers and other nanoscale building blocks. The prepared freestanding membranes can serve as a unique component for a variety of technologies. One of its great advantages over other technologies is the ability to prepare ultrathin ultrastrong membranes with minimal heterogeneity. We expect these composite materials to be used initially in high-value applications, most possibly as a critical part of a space or biomedical device. Once the carbon nanotubes become less expensive and the LBL processing becomes a routine operation, the same composites can be utilized in more high-volume products such as building construction materials and car components. At the same time, the less-expensive alternatives to the ultrastrong composites with comparable performance can be developed from carbon- or ceramics-based nanomaterials.

REFERENCES

1. Wong, E.W.; Sheehan, P.E.; Lieber, C.M. Nano-beam mechanics: Elasticity, strength, and toughness of nanorods and nanotubes. *Science* (Washington D.C.) **1997**, *277*, 1971–1975.
2. Popov, V.N.; Van Doren, V.E.; Balkanski, M. Elastic properties of single-walled carbon nanotubes. *Phys. Rev.*, **B 2000**, *61*, 3078–3084.

3. Baughman, R.H.; et al. Carbon nanotube actuators. *Science* (Washington D.C.) **1999**, *284*, 1340–1344.
4. Qian, D.; Dickey, E.C.; Andrews, R.; Rantell, T. Load transfer and deformation mechanisms in carbon nanotube-polystyrene composites. *Appl. Phys. Lett.* **2000**, *76*, 2868–2870.
5. Yu, M.F.; et al. Strength and breaking mechanism of multiwalled carbon nanotubes under tensile load. *Science* (Washington D.C.) **2000**, *287*, 637–640.
6. Salvétat, J.P.; et al. Elastic modulus of ordered and disordered multiwalled carbon nanotubes. *Adv. Mater.* (Weinheim, Germany) **1999**, *11*, 161–165.
7. Shaffer, M.S.P.; Windle, A.H. Fabrication and characterization of carbon nanotube/poly(vinyl alcohol) composites. *Adv. Mater.* (Weinheim, Germany) **1999**, *11*, 937–941.
8. Haggenueller, R.; Gommans, H.H.; Rinzler, A.G.; Fischer, J.E.; Winey, K.I. Aligned single-wall carbon nanotubes in composites by melt processing methods. *Chem. Phys. Lett.* **2000**, *330*, 219–225.
9. Watts, P.C.P.; et al. A low resistance boron-doped carbon nanotube-polystyrene composite. *J. Mater. Chem.* **2001**, *11*, 2482–2488.
10. Vigolo, B.; et al. Macroscopic fibers and ribbons of oriented carbon nanotubes. *Science* **290**, 1331–1334.
11. Salvétat, J.P.; et al. Elastic and shear moduli of single-walled carbon nanotube ropes. *Phys. Rev. Lett.* **1999**, *82*, 944–947.
12. Chen, J.; et al. Dissolution of full-length single-walled carbon nanotubes. *J. Phys. Chem., B* **2001**, *105*, 2525–2528.
13. Frankland, S.J.V.; Caglar, A.; Brenner, D.W.; Griebel, M. Molecular simulation of the influence of chemical cross-links on the shear strength of carbon nanotube-polymer interfaces. *J. Phys. Chem., B* **2002**, *106*, 3046–3048.
14. Star, A.; et al. Preparation and properties of polymer-wrapped single-walled carbon nanotubes. *Angew. Chem., Int. Ed.* **2001**, *40*, 1721–1725.
15. Decher, G. Fuzzy nanoassemblies toward layered polymeric multicomposites. *Science* **1997**, *277*, 1232–1237.
16. Wu, A.; Yoo, D.; Lee, J.K.; Rubner, M.F. Solid-state light-emitting devices based on the tris-chelated ruthenium(II) complex: 3. High efficiency devices via a layer-by-layer molecular-level blending approach. *J. Am. Chem. Soc.* **1999**, *121*, 4883–4891.
17. Mamedov, A.A.; Belov, A.; Giersig, M.; Mamedova, N.N.; Kotov, N.A. Nanorainbows. Graded semiconductor films from quantum dots. *J. Am. Chem. Soc.* **2001**, *123*, 7738–7739.
18. Mamedov, A.A.; Kotov, N.A.; Prato, M.; Guldi, D.; Wicksted, J.P.; Hirsch, A. Molecular design of strong SWNT/polyelectrolyte multilayers composites. *Nat. Mater.* **2002**, *1*, 190–194.
19. Mamedov, A.A.; Guldi, D.M.; Prato, M.; Kotov, N.A. Layer-by-Layer Assembly of Carbon Nanotubes. In *Abstracts of Papers*, 223rd ACS National Meeting, Orlando, FL, United States, April 7–11, 2002.
20. Rouse, J.H.; Ounaies, Z.; Lellehei, P.T.; Siochi, E.J. Incorporation of Carbon Nanotubes Within Stepwise Assembled Polyelectrolyte Films. In *Abstracts of Papers*, 223rd ACS National Meeting, Orlando, FL, United States, April 7–11, 2002.
21. Mamedov, A.A.; Kotov, N.A. Free-standing layer-by-layer assembled films of magnetite nanoparticles. *Langmuir* **2000**, *16*, 5530–5533.
22. Mawhinney, D.B.; et al. Surface defect site density on single walled carbon nanotubes by titration. *Chem. Phys. Lett.* **2000**, *324*, 213–216.
23. Rols, S.; et al. Diameter distribution of single wall carbon nanotubes in nanobundles. *Eur. Phys. J., B* **2000**, *18*, 201–205.
24. Westenhoff, S.; Kotov, N.A. Quantum dot on a rope. *J. Am. Chem. Soc.* **2002**, *124*, 2448–2449.
25. Sullivan, D.M.; Bruening, M.L. Ultrathin, ion-selective polyimide membranes prepared from layered polyelectrolytes. *J. Am. Chem. Soc.* **2001**, *123*, 11805–11806.
26. Li, F.; Cheng, H.M.; Bai, S.; Su, G.; Dresselhaus, M.S. Tensile strength of single-walled carbon nanotubes directly measured from their macroscopic ropes. *Appl. Phys. Lett.* **2000**, *77*, 3161–3163.
27. Thompson, J.B.; et al. Bone indentation recovery time correlates with bond reforming time. *Nature* (London) **2001**, *414*, 773–776.
28. Smith, B.L.; et al. Molecular mechanistic origin of the toughness of natural adhesives, fibers and composites. *Nature* (London) **1999**, *399*, 761–763.
29. *CRC Materials Science and Engineering Handbook*; CRC: Boca Raton, FL, 1992.
30. Fu, S.Y.; et al. Hybrid effects on tensile properties of hybrid short-glass-fiber- and short-carbon-fiber-reinforced polypropylene composites. *J. Mater. Sci.* **2001**, *36*, 1243–1251.
31. Yu, M.F.; Files, B.S.; Arepalli, S.; Ruoff, R.S. Tensile loading of ropes of single wall carbon nanotubes and their mechanical properties. *Phys. Rev. Lett.* **2000**, *84*, 5552–5555.
32. Garg, A.; Sinnott, S.B. Effect of chemical functionalization on the mechanical properties of carbon nanotubes. *Chem. Phys. Lett.* **1998**, *295*, 273–278.
33. Tang, Z.; Kotov, N.A.; Magonov, S.; Ozturk, B. *Nat. Mater.* **2003**, *2* (6), 413–418.



Nanostructures Based on Conducting Polymers

Shaun F. Filocamo

Mark W. Grinstaff

Boston University, Boston, Massachusetts, U.S.A.

INTRODUCTION

Nanotechnology is an emerging field that studies fundamental nanoscale processes and the exploitation of those processes in the development and function of nanodevices.^[1] To date, development has been hampered by the need for materials and processes that can perform reproducibly at the nanometer scale. Although at present nanodevice development is dominated by materials made from SiO₂ or metals, these materials can suffer from a lack of processability.^[2] As an alternative that has met with some success, organic-based materials can be easily processed by a variety of methods including spin coating, evaporation, and printing.^[3] Organic and organic/inorganic hybrid materials have been developed for organic light-emitting diodes (OLEDs), field-effect transistors, and other devices.^[4-6] However, organic devices usually suffer from a short lifetime as a consequence of poor mechanical and thermal stability associated with small organic molecules.^[5] Although organic/inorganic hybrid materials have better mechanical and thermal stability,^[7-9] there still exists an inherent lack of component compatibility, leading to difficulties in processing, and intercomponent communication.^[9]

A promising class of materials for nanodevice application is conducting polymers (Fig. 1). Their thermal and environmental stability facilitates use in devices for photochemical and electrochemical applications,^[10-12] and their physical and chemical properties can be easily tailored for specific functions.^[13,14] When conducting polymers were first introduced, their poor solubility in common processing solvents limited their versatility.^[11] However, this issue has been addressed through modifying the backbone of the polymer with side chains, such as alkyl and alkoxy groups. With this approach, processing of these materials in either aqueous or organic media has expanded the utility of conducting polymers in OLEDs, electrochromic displays, and coatings for more sensitive materials.^[6,15-17] Numerous articles are found in the literature reporting devices in the micrometer regime made with conducting polymers.^[2,3,18-21]

Although Moore's law predicts a doubling in the number of transistors per chip approximately every 18 months,^[22] the limits of traditional patterning techniques

are threatening to hinder this advancement. The feature size required to continue this trend is in the <100 nm regime, where control over feature size is critical and difficult to achieve. New procedures and variations on current methods need to be developed to break this regime barrier. In this article, we will review current approaches to creating conducting polymer nanopatterns, from "template synthesis" to lithography. We discuss the advantages and disadvantages of each method and highlight the unique nanostructures formed with these techniques. These materials are likely to enhance the emerging field of nanoelectronics, while complementing current technology.

TEMPLATE SYNTHESIS

The first reported patterning of conducting polymer nanostructures used template synthesis, a method developed by Penner and Martin^[23] in the mid-1980s. They reported the electrochemical polymerization of pyrrole in the pores of a polycarbonate membrane. Template synthesis, as the name implies, utilizes the microporous or nanoporous structure of materials as a template for the electrochemical or oxidative synthesis of conducting polymer nanotubules and nanofibrils.^[24] This technique can also be used to form nanotubes and nanofibrils of metals, carbon, and semiconductors.^[24,25]

Template Materials

The most common template materials used are "track-etch" membranes and alumina membranes.^[26] Track-etch membranes are formed by bombarding a nonporous membrane with nuclear fission fragments.^[27] These membranes are typically polycarbonate or polyester. The tracks that are formed are subsequently chemically etched to produce pores in the material. The size of the uniform pores can be as small as 10 nm in diameter with pore densities as high as 10⁹ pores/cm².^[26] The bombardment occurs randomly, which, at small pore diameters and high pore densities, can cause intersections of the pores.^[26] If these intersections are not desired, alumina or other membranes can be used because the processes used to form these membranes are more controlled.

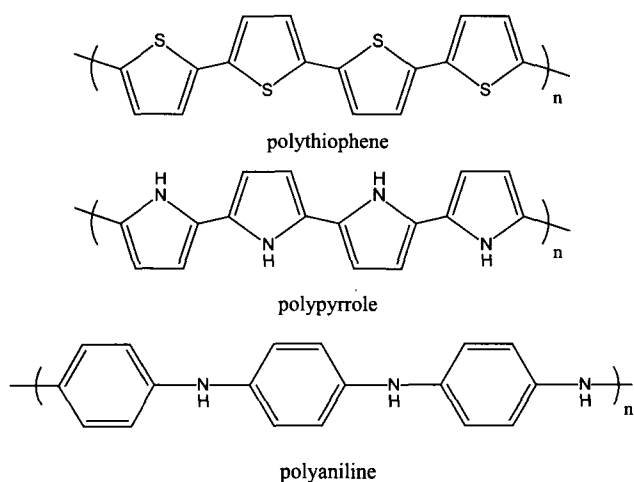


Fig. 1 Examples of conducting polymers.

Porous alumina membranes are formed from the anodization of Al metal in acidic solution. The uniform pores are cylindrical, with pore densities as high as 10^{11} pores/cm² and a size range from >100 down to <5 nm.^[26] Because of the nature of pore formation in the alumina membranes, interconnects do not develop between pores,^[25] affording a template material that can form

isolated nanostructures. Membranes, including SiO₂, zeolites, and other nanoporous solids, have also been used as template materials, although to a lesser extent.^[25]

Mechanism for Template Synthesis

The polymerization mechanism for conducting polymers using template synthesis is either electrochemical or oxidative. The most common electrochemical method is to plate one surface of the membrane with a conducting metal thin film and use this film as the anode in an electroplating process.^[28] The polymer first nucleates on the walls of the pore, and subsequent deposition yields a well-ordered polymer outer layer that becomes more disordered as the tubule wall thickens.^[29] In the oxidative method, the template is immersed in a solution containing monomer and a polymerization reagent, such as an aqueous iron(III) salt.^[30,31] The deposition occurs in a manner similar to the electrochemical method, resulting in a similar polymer-order gradient for the nanostructures (Fig. 2).

Physical Properties of Conducting Polymer Nanotubules/Nanofibrils

Early studies of polypyrrole chain order in nanofibrils (closed tubules) used polarized infrared absorption

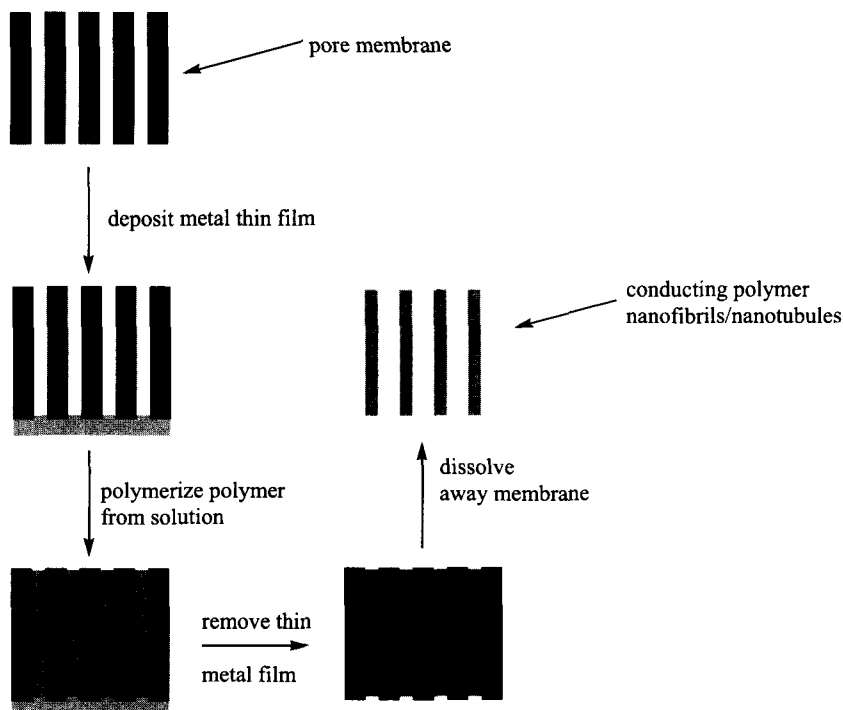


Fig. 2 Schematic of template synthesis. (View this art in color at www.dekker.com.)

spectroscopy (PIRAS) to examine a range of fibril diameters from 30 to 600 nm. In addition, X-ray diffraction was used to observe 30 and 400 nm fibrils.^[32] In the X-ray diffraction studies, 400-nm fibrils showed diffractograms similar to amorphous conducting polymer, while the 30-nm fibrils exhibited diffractograms similar to stretched polymer, suggesting an alignment of the polymer chains in these small-diameter fibrils.^[32]

The PIRAS experiment supported the X-ray diffraction evidence that polymer chain alignment in a fibril increases as the diameter decreases. In a typical PIRAS experiment, the absorbance is measured for light polarized parallel and perpendicular to the major axis of a material (Fig. 3). In the case of a polymer fibril, if the polymer chain alignment is completely random, then the absorbance of light parallel to the pore axis will be the same as the absorbance of light perpendicular to the pore axis and will give a dichroic ratio (ratio of absorbances parallel and perpendicular to the pore axis) of 1. Smaller fibrils had dichroic ratios significantly different from 1, with the fibrils preferentially absorbing one polarization over another.^[32] Amorphous polymer and large-diameter fibrils do not absorb polarized light preferentially, giving dichroic values very close to 1.^[32,33]

Polarized infrared absorption spectroscopy experiments were also performed on polycarbonate membranes; the polycarbonate was also found to be stretch-oriented.^[32] Studies have shown that conducting polymers can be induced to align with the orientation of the substrate.^[34-36] This orientation is lost as the thickness of the deposited polymer film grows. Similarly, the outer walls of conducting polymer tubules and fibrils deposited in stretch-oriented polycarbonate membranes align with the axis of the membrane, but this alignment is slowly lost as polymerization continues and the walls thicken. Wall thickness is controlled by the polymerization time.^[25]

The thickness of the polymer walls is also correlated with the conductivity of the tubule. While thick-walled nanotubules had conductivities similar to bulk material, the narrow-walled nanotubules had significantly higher values.^[35] One explanation for this phenomenon is that the alignment in the polymer chains increases the conjugation length of the polymer, enhancing the electronic properties of the material. As the walls thicken, the overall randomness of the structure increases, decreasing the conjugation length and hence the conductivity.^[35] This method provides a means to control the conductivity of the material through polymerization time. It has been postulated that the walls in a polycarbonate membrane nucleate the ordered polymer in two ways: 1) as the polymerization commences, the polycationic oligomers forming are not as soluble as the monomer units and 2) there is a coulombic attraction between the anionic walls of the membrane and the forming cationic polymer.^[26]

Recently, this "greater ordering" claim has been disputed. Most of the above studies of polypyrrole nanotubules were performed with a polycarbonate membrane; Mativetsky and Datars^[37] used an alumina membrane to form nanotubules of polypyrrole oxidatively and found the tubules to have a highly irregular morphology. Indeed, PIRAS studies with alumina membranes have shown no preferential polarized absorption (dichroic ratios near 1).^[37] Because there are no charged sites in an alumina membrane, the nucleation occurs more randomly in the alumina pores. Polypyrrole then grows radially outward from each nucleation site until it encounters an obstacle: that of the pore wall or another "polypyrrole mass," disrupting order. Although Mativetsky and Datars^[37] were not able to measure conductivity directly, their measurements suggest that the conductivity of these random fibrils is comparable to the fibrils of similar size formed from a polycarbonate

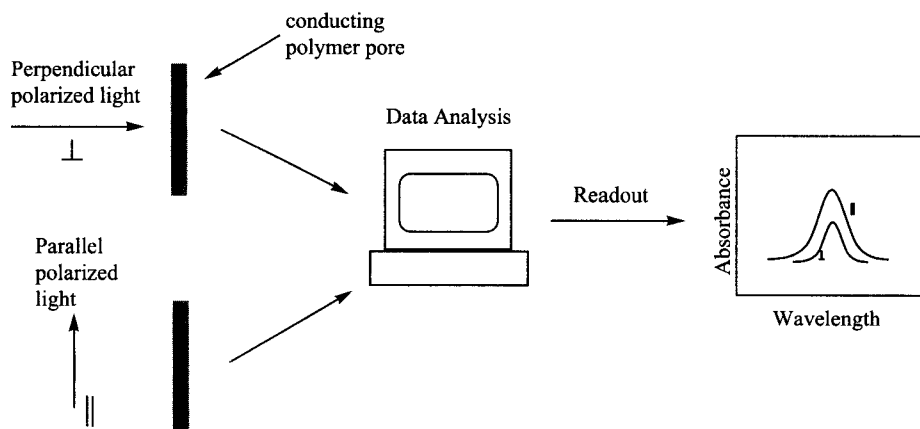


Fig. 3 Schematic of a typical PIRAS experiment. (View this art in color at www.dekker.com.)

membrane. They therefore concluded that the enhanced conductivity of these nanotubes is not a result of increased order imposed by the polycarbonate walls.

Applications of Template Synthesis

Conducting polymer nanofibrils and nanotubes have a wide variety of potential applications. They are highly permeable, and studies have shown that they can be highly selective for certain gas mixtures; the high-density conducting polymer fibrils could be used as a gas permeation membrane.^[38] Conducting polymer nanotubes are also well suited for encapsulated sensors because the polymerization process can be stopped at any time, thus controlling the size of the cavity. Researchers have encapsulated a variety of enzymes and chemical species in thin-walled tubes and have found that their activity is greater than that of enzymes trapped in a thin polymer film.^[30,39,40] These reactions could be carried out in aqueous or organic solvents because the conducting polymer "microreactor" is isolated from the environmental surroundings by the walls of the conducting polymer, utilizing the relative insolubility of the polymer in common solvents.^[30] The surface area for enzyme/substrate interaction can be adjusted by changing the porosity of the membrane, producing a microreactor with a high loading capability.^[30]

With the enhanced conductive properties of these materials, numerous groups have reported using nanotubes

to form a variety of novel systems. For example, Granstrom et al.^[41] polymerized 3,4-ethylene-dioxythiophene (EDOT) in polycarbonate membranes with pore sizes of 10 nm and 100 nm for the preparation of a hole-injection contact in a polymeric light-emitting diode (PLED). An electroluminescent layer was spin-coated on the surface of the membrane, followed by an Al/Ca layer for the electron-injecting contact. Although the PLED tested had a very low efficiency, with optimization, the authors believed that increased efficiencies up to 1–10% could be obtained.^[41] The advantage of this technique is in the sheer quantity of nano-LEDs that can be formed at one time.

In other applications, polyaniline tubes have been studied for use as microscale/nanoscale transistors and for field emission because of their excellent switching properties and mechanical stability (Fig. 4).^[42,43] Polymer composites have been made to blend physical properties, and many have been found to enhance desirable characteristics, such as conductivity and "rectification effect."^[31,44–46]

Inverse Opal Formation

A variation of template synthesis is to use microspheres and nanospheres of polymers as templates for the formation of macroporous 2-D and 3-D polymer structures, called inverse opals. A typical experiment involves assembling a template of colloidal microspheres or nanospheres on a conductive metal electrode surface by slow evaporation from a weight percent solution of colloidal particles on an electrode surface. The particles of materials such as poly(styrene) or silica will assemble themselves as the solvent evaporates. Once the structure is dry and mechanically immobilized, it is immersed in a solution containing the desired monomer units. Electropolymerization of the conducting polymer has been favored in the literature over the oxidative method, with many groups citing a greater control over the polymer growth rate and deposition than with the oxidative method (Fig. 5).^[47,48] The templates are then etched (silica) or dissolved away (colloidal polymer), leaving conducting polymer patterned into a "honeycomb" structure.

This technique has been used to create nanostructures of polypyrrole,^[47–49] polyaniline,^[49–51] polythiophene,^[47,49] and poly(phenylenevinylene) (PPV).^[52] Nanostructure sizes as low as 50 nm have been reported with polypyrrole,^[48] where it was found that the pore size can be controlled by the amount and time of applied voltage and by the size of the colloidal particle utilized. Han et al.^[50] used polystyrene nanospheres that were coated with increasing layers of a polyelectrolyte (PE) to see what effect the size of the nanoparticle would have on the resulting conducting polymer film (Fig. 6). The

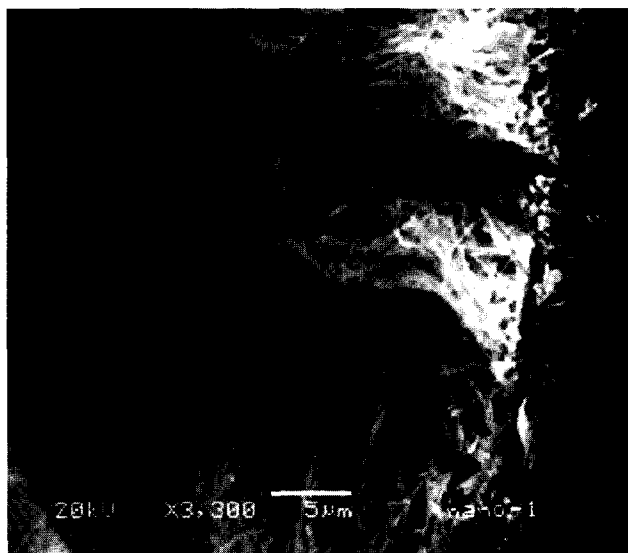


Fig. 4 Scanning electron microscope image of polyaniline nanofibrils formed from a porous alumina membrane using template synthesis. (From Ref. [42]. Copyright (2001), with permission from Elsevier Science.)

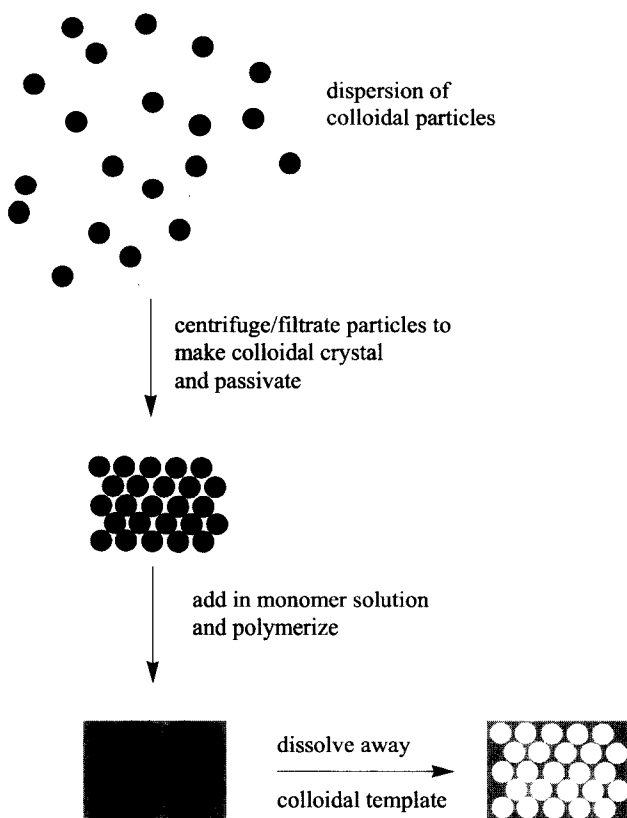


Fig. 5 Schematic of “inverse opal” synthesis. (View this art in color at www.dekker.com.)

pore size actually decreased upon increasing the number of PE layers, leveling off after 4 PE layers, and the structure shrank less upon extraction of the template, improving mechanical stability.^[50]

The tunability of these systems has attracted interest in the field of photonic bandgap crystals.^[47,51,52] They have been shown to exhibit the property of reflecting certain wavelengths of light, spanning the visible and near-infrared (NIR) regions of the spectrum. The conductivities of these 2-D and 3-D structures are similar to those of bulk conducting polymer.^[49]

LITHOGRAPHY AND MASK TECHNIQUES

Lithography is the process of writing a free-form or replicated pattern on a surface by electrical (applied voltage), photochemical (UV, X-ray beam), or physical (diamond etching) means. Lithography has been very successful at creating structures at the micrometer scale, but there are significant challenges and obstacles to forming structures of <100 nm in dimension. Ultimately, the lithography techniques developed must be reliable, accurate, and

efficient. Development over the past 10 years has dealt with these issues, and the next few sections describe these advances. As nanolithography is still a relatively young field, many of the techniques described below are unoptimized.

Solvent-Assisted Micromolding

Solvent-assisted micromolding (SAMIM) is a “soft lithography” technique that provides a simple, fast way to form patterns on a surface. The mold is made out of an elastomeric material [usually poly(dimethylsiloxane) (PDMS)]; it is coated by wetting the mold itself with a thin layer of a solvent appropriate for the polymer or precursor substrate. The mold is then brought into contact with the substrate, and the solvent dissolves (or swells) the substrate, allowing the substrate to flow into the recesses of the mold. As the solvent evaporates, the polymer hardens, but maintains the shape of the mold (Fig. 7).^[53] Kim et al.^[54] first utilized this method to form features down to 50 nm in height and 60 nm in width on polymeric photoresists. Solvent-assisted micromolding was used to create polymeric light-emitting diodes (PLEDs) using a precursor to poly(phenylenevinylene) (PPV) and methanol as a solvent.^[55] Although the features formed were larger than 100 nm, the potential of this technique to form very small devices of interest has been demonstrated.

Micromolding in Capillaries

Micromolding in capillaries (MIMIC) is a technique related to SAMIM. A prepatterned stamp made out of an

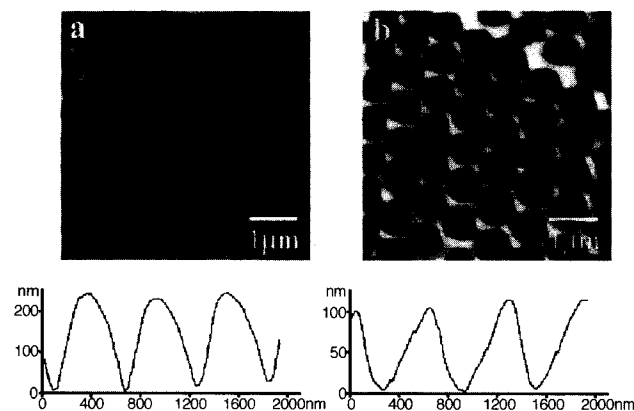


Fig. 6 a) Assembly of PS particles with 2 PE layers on a Au surface. b) Polyaniline honeycomb nanostructure formed in the interstitial voids of the particles. (From Ref. [50]. Copyright (2002) American Chemical Society.) (View this art in color at www.dekker.com.)

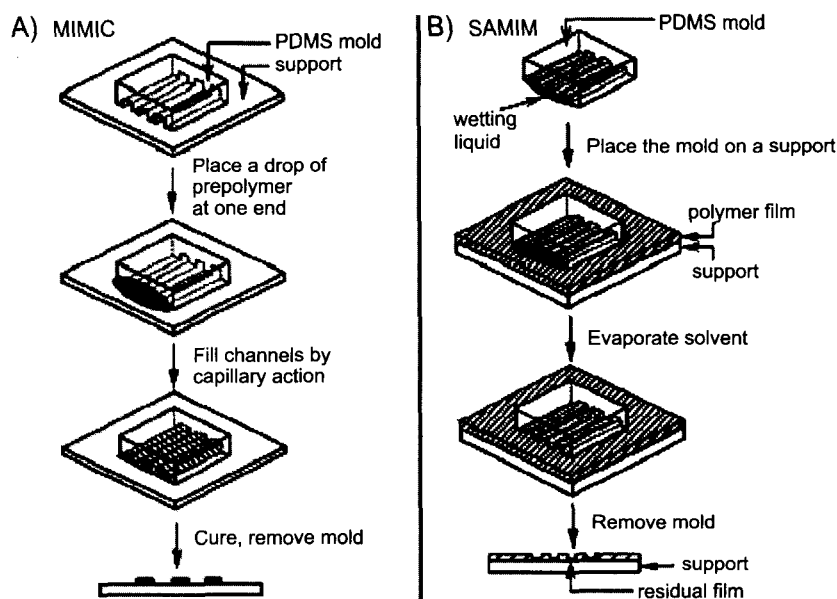


Fig. 7 A) Schematic of MIMIC. B) Schematic of SAMIM. (From Ref. [53] by Annual Reviews.)

elastomer such as PDMS is placed on a clean, flat substrate and a drop of solution of the desired patterning material is placed at the edge of the stamp. Through capillary action, the drop migrates into the grooves of the stamp. As the solution dries, the material is patterned on

the substrate, and the stamp is subsequently removed.^[53] This technique has been used to form nanowire and nanodot patterns of poly(3,4-ethylenedioxythiophene) (PEDOT) doped with poly(4-styrenesulfonate) (PEDOT-PSS).^[56] By varying the size of the capillary channel and

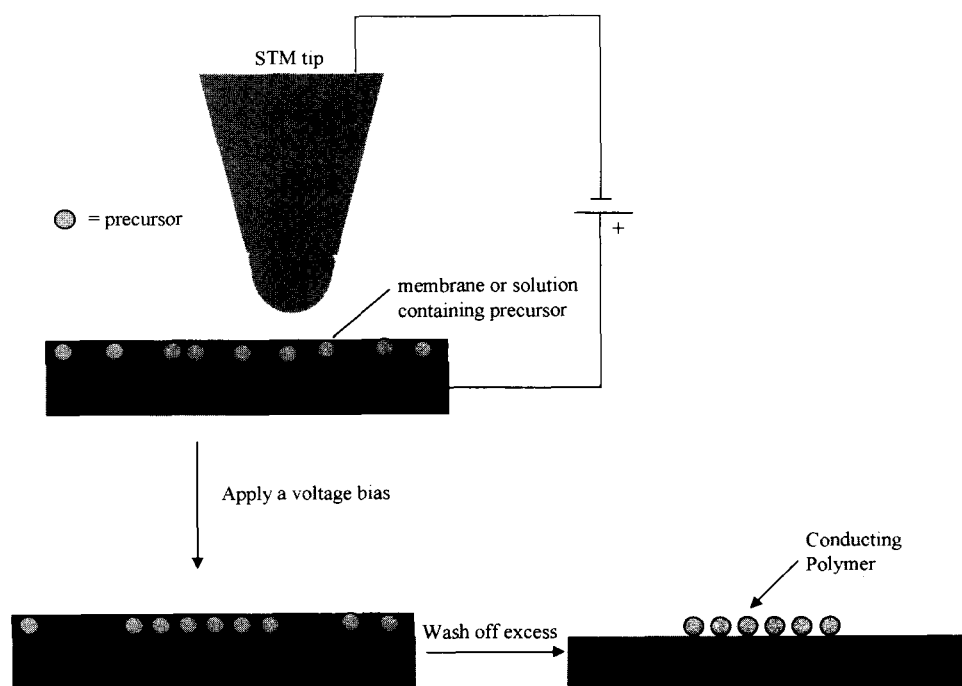


Fig. 8 Schematic of a typical STM lithography experiment. (View this art in color at www.dekker.com.)

the solution concentration, nanowires of 6 nm in height and nanodots of 10 nm in height were formed on the substrate.^[56]

Scanning Tunneling Microscopy Lithography

Scanning Tunneling Microscopy (STM) and related techniques have been used for surface modification for about 15 years. The first example of conducting polymer deposition was reported by Wu et al.^[57] using a scanning electrochemical microscope (SECM), “which maintains a constant faradaic current between a tip electrode and a metal surface electrode.” In this procedure, Nafion™ film was first deposited on the Pt surface and immersed in an anilinium sulfate solution to saturate the film. In this system, the platinum is the surface electrode and tungsten is used as the tip electrode. A positive potential was applied to the Pt surface to oxidize the aniline at the Pt / Nafion interface, and deposition of the resulting polymer was localized around the tip electrode (Fig. 8). The features formed were larger than 100 nm, which was attributed to tip size, thickness of the Nafion film, and electric field distribution. Control over these parameters was predicted to give smaller features.^[57] Borgwarth et al.^[58] utilized SECM to form polythiophene by oxidizing bromide to bromine, which locally diffused to the conductive substrate and oxidatively polymerized the thiophene monomer.

Using a gold electrode, Yang et al.^[59] reported the formation of polypyrrole nanostructures from a tetrafluoroborate/pyrrole solution. The Pt/Ir STM tip was coated with Apiezon™ to insulate most of the tip, helping to control the size of the nanofeature deposited on the surface. Polymer dots were deposited on the surface, and then the ability to remove the polymer dots was demonstrated by “blasting” the polymer dot from the surface with higher voltage.^[59] This technique was used to “write” the word *science* using dots of 5–10 nm in diameter (Fig. 9). The variation in diameter was attributed



Fig. 9 The word “science” formed using STM nanolithography. (From Ref. [59]. Copyright (1995) American Chemical Society.)

to thermal evaporation and consequent concentration of monomer solution during operation, and to the local variation of surface roughness, affecting the movement of the tip as it maintains a constant distance above the surface.^[59] A polymer line with a width of 10 nm and a circle with a diameter of 6 nm were formed by controlling the translation of the tip on the surface using a simple computer program.^[59]

Highly oriented pyrolytic graphite (HOPG) has also been used as the conductive surface for forming conducting polymer nanostructures with an STM tip. Yaniv and McCormick^[60] reported nanofeatures as small as 50 nm in diameter and 4 nm in height, formed from a 0.1 M KCl/0.1 M pyrrole solution. They found that no deposition occurred with potentials below 7.5 V, and control of the features could only be achieved with pulses below 100 nsec. Above this pulse duration, deposition became scattered over the scanned area.^[60] Nyffenegger and Penner^[61] studied qualitatively the mechanism of nanostructure formation using a similar setup. They concluded that the bias pulse forms defects in the basal plane of the HOPG within a few microseconds, and then aniline monomer diffuses to the edge of the defect and is oxidized. As this process proceeds, the cationic aniline oligomers become insoluble and nucleate in the defect.^[61]

Atomic Force Microscope Lithography

The first example of atomic force microscopy (AFM) being used for patterning conducting polymer nanostructures was reported by Cai et al.^[62] The electrochemical polymerization of pyrrole and aniline on an HOPG substrate was locally altered using an AFM tip. Depending on when the AFM scanning was activated, the amount of polymer could be decreased or enhanced in the scanning area. When the AFM tip is scanned over the surface before the application of a potential, any oligomers that are formed once the potential is applied are “swept” to the edges of the scanning area. Indeed, there is an enhancement in the amount of polymer at the edges of the scanning area. When the AFM tip is scanned after polymerization has commenced, the vertical force exerted on the developing polymer both creates a denser film and forces oligomers downward toward the polymer, increasing the local concentration of oligomers and thus the rate of polymerization.^[62]

Dip-pen nanolithography (DPN) was developed by Piner et al.^[63] and, as the name suggests, it uses the AFM tip as a pen, dipped in the desired patterning material. The AFM tip is then brought in close proximity to the surface. A water meniscus forms, which facilitates transport of the material from the tip to the surface. This method has been utilized to pattern a variety of materials to the surface

such as DNA and thiols.^[63–65] The Noy group utilized this method to deposit poly[2-methoxy-5-2'-ethylhexyloxy-1,4-phenylenevinylene] (MEH-PPV) on a glass surface.^[66] The method was coupled with scanning confocal microscopy to obtain luminescent images of the deposited polymer nanostructures. Although the deposition was successful, more studies are needed to determine the extent of nanowire alignment and continuity.^[66]

A technique that combines aspects from previous STM tip techniques is electrochemical dip-pen nanolithography (E-DPN), which has been used to deposit metal and conducting polymer nanostructures on a surface.^[67,68] The tapping mode AFM tip is dipped in the desired monomer or metal salt solution, and as the tip engages the surface in a preprogrammed pattern, a potential is applied between the tip and the surface. This potential reduces the metal salt or electrochemically polymerizes the monomer and deposits the resulting nanostructure on the surface through the meniscus (Fig. 10).^[67,68] In this way, polymers of 3,4-ethylenedioxythiophene,^[68] pyrrole, and aniline^[69] have been formed and deposited on a Si(111) surface with feature sizes as small as 30 nm in width and up to 5 nm in height.

The size of the nanostructures formed depends on a variety of factors, including humidity, speed of translation, and applied voltage, and it has been found that these factors are monomer-dependent. For example, it is easier to draw lines of polyaniline at lower humidity, while other polymers were less affected by the humidity. Aniline has a measurable solubility in water at 25°C (1 g in 28.6-mL water), and upon formation of the water meniscus, capillary action could disperse the aniline before a voltage is applied.

The height of the line can be controlled by the speed of translation of the tip as it deposits.^[68] Two lines of

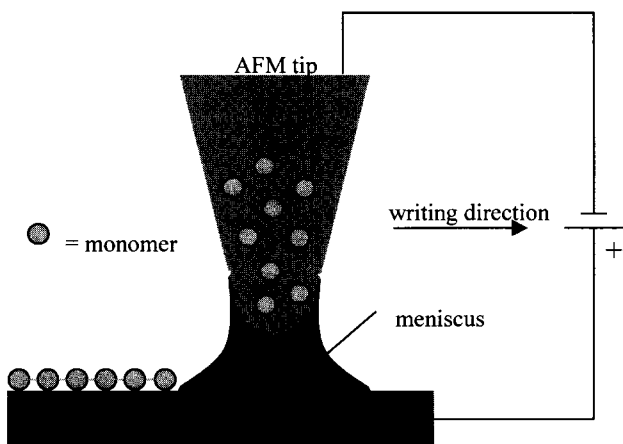


Fig. 10 Schematic of E-DPN. (View this art in color at www.dekker.com.)

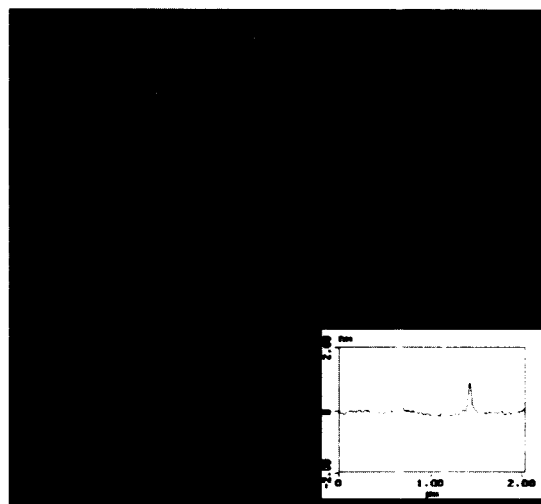


Fig. 11 Atomic force microscope image of PEDOT lines drawn at 10 and 1 nm/sec. Inset shows height difference of the two lines. (From Ref. [67]. Copyright (2001) American Chemical Society.) (View this art in color at www.dekker.com.)

poly(ethylenedioxythiophene) (PEDOT) were drawn at 10 and 1 nm/sec, and the line drawn at 1 nm/sec was significantly higher than the line drawn at 10 nm/sec (Fig. 11). Applied voltage along with humidity controls the width of the line. A larger water meniscus covers a larger surface area, leading to a larger area of deposition.

The voltage applied depends, in part, on the potential of the monomer being used and on the native oxide layer that exists on the Si wafer. As the thickness of the oxide layer increases, so does the necessity of higher voltages for polymerization and deposition. Bias voltages ranged from -7 to -15 V. At such a high bias voltage, it is important to ensure that polymer, and not SiO_2 , is being deposited.

After depositing PEDOT, an oxide layer was formed next to the polymer, and etching studies were performed. Upon exposure to HF, the SiO_2 was etched from the surface, but the PEDOT line remained. Conversely, when exposed to a strongly oxidizing solution of 1:2 H_2O_2 : H_2SO_4 , the PEDOT line was removed while the SiO_2 remained. Similar etching studies were performed with polyaniline and polypyrrole, and the results were consistent with the PEDOT studies. Interconnects also have been formed with a single polymer and with two different polymers using this technique. The ability to pattern these nanostructures precisely will be important toward the development of nanodevices.

Masks

Seo et al.^[70] reported a mask method for the formation of polypyrrole micropatterns and nanopatterns using

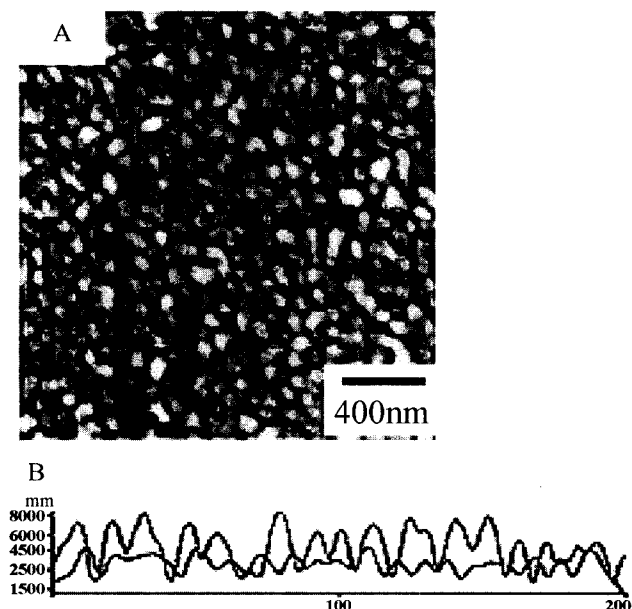


Fig. 12 A) Atomic force microscope image of nanopatterns formed with polypyrrole on PS-*b*-4PV nanometer-separated domains. B) Cross section showing height difference before (blue) and after (red) polypyrrole formation. (From Ref. [69]. Copyright (2002) American Chemical Society.) (View this art in color at www.dekker.com.)

domains formed from polymer blends and block copolymers as the template. It is known that in thin films of polystyrene (PS) and poly(4-vinylpyridine) (4PV), microphase-separated domains are formed, and that thin films of block poly(styrene-*b*-4-vinylpyridine) (PS-*b*-4PV) form nanometer-separated domains.^[70] The mask is formed from protonating the pyridine ring and immersing in a solution of sodium dodecyl sulfate (SDS), which will form a bilayer with the pyridine and itself through ionic and hydrophobic interactions, respectively. Although SDS forms a monolayer with the PS through hydrophobic interactions, the polypyrrole nucleates preferentially on PS and displaces the SDS monolayer, but cannot displace the SDS bilayer. Using this method, nanopatterns as small as 50 nm were obtained (Fig. 12).^[70] The pattern formed is not well defined, and additional research is needed to control pattern size and alignment.

CONCLUSION

The ability to pattern nanostructures has opened up the field of nanoelectronics, and conducting polymers will play a significant role in the development of this field. The

complementarity of these techniques is already apparent and represents a strength in the field. At the nanoscale, control and quantity will be immensely important, highlighting the advantages of both template synthesis and lithography. Today, template synthesis can afford numerous repetitive nanostructures, and lithography can yield nanostructures with precise size at a specific location. Unfortunately, most of the lithography techniques that work so effectively at the micrometer scale have yet to break the nanoscale barrier because of physical limits and methods used to form lithographic masks. Template synthesis is still a "bulk synthesis" technique because it has not been demonstrated that this technique can accurately deposit one or a few nanostructures.

Numerous applications have already been demonstrated for these new materials, from encapsulators for biosensors to photonic bandgap crystals. In addition, the potential for use in fabrication of nanodevice components and interconnects is great, although high-throughput methods may be some years away. The success of many research groups in circumventing the current chemical, physical, and engineering challenges has encouraged an increasing number of researchers to study fundamental nanoscale processes. Such further research and innovation will likely lead to nanoelectronics playing an integral role in the development of future commercial applications.

ACKNOWLEDGMENTS

The authors would like to thank the Army Research Office (Grant 2000-ARG-0041) and NSF. M.W.G. gratefully acknowledges the NSF Career Award, the Dreyfus Foundation for a Camille Dreyfus Teacher-Scholar, and the Alfred P. Sloan Foundation for a Research Fellowship.

REFERENCES

1. Xia, Y.; Rogers, J.A.; Paul, K.E.; Whitesides, G.M. Unconventional methods for fabricating and patterning nanostructures. *Chem. Rev.* **1999**, *99* (7), 1823–1848.
2. Gurunathan, K.; Murugan, A.V.; Marimuthu, R.; Mulik, U.P.; Amalnerkar, D.P. Electrochemically synthesized conducting polymeric materials for applications towards technology in electronics, optoelectronics and energy storage devices. *Mater. Chem. Phys.* **1999**, *61*, 173–191.
3. Bao, Z.; Rogers, J.A.; Katz, H.E. Printable organic and polymeric semiconducting materials and devices. *J. Mater. Chem.* **1999**, *9*, 1895–1904.

4. Tour, J.M. Conjugated macromolecules of precise length and constitution. Organic synthesis for the construction of nanoarchitectures. *Chem. Rev.* **1996**, *96* (1), 537–553.
5. Armonk, J.; Mitzi, D.B.; Chondroudis, K.; Kagan, C.R. Organic–inorganic electronics. *IBM J. Res. Develop.* **2001**, *45* (1), 29–45.
6. Dodabalapur, A. Organic light emitting diodes. *Solid State Commun.* **1997**, *102* (2–3), 259–267.
7. Walcarius, A. Electrochemical applications of silica-based organic–inorganic hybrid materials. *Chem. Mater.* **2001**, *13* (10), 3351–3372.
8. Yano, S.; Iwata, K.; Kurita, K. Physical properties and structure of organic–inorganic hybrid materials produced by sol-gel process. *Mater. Sci. Eng., C* **1998**, *6*, 75–90.
9. Mitzi, D.B. Thin-film deposition of organic–inorganic hybrid materials. *Chem. Mater.* **2001**, *13* (10), 3283–3298.
10. Kumar, D.; Sharma, R.C. Advances in conductive polymers. *Eur. J. Polym. Chem.* **1998**, *34* (8), 1053–1060.
11. Heeger, A.J. Semiconducting and metallic polymers: The fourth generation of polymeric materials. *J. Phys. Chem., B* **2001**, *105* (36), 8475–8491.
12. MacDiarmid, A.G. Polyaniline and polypyrrole: Where are we headed? *Synth. Met.* **1997**, *84*, 27–34.
13. McCullough, R.D. The chemistry of conducting polythiophenes. *Adv. Mater.* **1998**, *10* (2), 93–116.
14. Stanforth, S.P. Catalytic cross-coupling reactions in biaryl synthesis. *Tetrahedron* **1998**, *54*, 263–303.
15. Rosseinsky, D.R.; Mortimer, R.J. Electrochromic systems and the prospect for devices. *Adv. Mater.* **2001**, *13* (11), 783–793.
16. Le Barny, P.; Dentan, V.; Facoetti, H.; Vergnolle, M.; Veriot, G.; Servet, B.; Pribat, D. Application of organic electroluminescent materials in visualization. *C. R. Acad. Sci. Paris.* **2000**, *1* (4), 493–508.
17. Tallman, D.E.; Spinks, G.; Dominis, A.; Wallace, G.G. Electroactive conducting polymers for corrosion control. *J. Solid State Electrochem.* **2002**, *6*, 73–84.
18. Granlund, T.; Nyberg, T.; Roman, L.S.; Svensson, M.; Inganas, O. Patterning of polymer light-emitting diodes with soft lithography. *Adv. Mater.* **2000**, *12* (4), 269–273.
19. Jager, E.W.H.; Smela, E.; Inganas, O. Microfabricating conjugated polymer actuators. *Science* **2000**, *290*, 1540–1545.
20. Urban, G. Microstructuring of organic layers for microsystems. *Sens. Actuators* **1999**, *74*, 219–224.
21. Hohnholz, D.; MacDiarmid, A.G. Line patterning of conducting polymers: New horizons for inexpensive, disposable electronic devices. *Synth. Met.* **2001**, *121*, 1327–1328.
22. Weldon, M.K.; Queeney, K.T.; Eng, J., Jr.; Raghavachari, K.; Chabal, Y.J. The surface science of semiconductor processing: Gate oxides in the ever-shrinking transistor. *Surf. Sci.* **2002**, *500*, 859–878.
23. Penner, R.M.; Martin, C.R. Controlling the morphology of electronically conductive polymers. *J. Electrochem. Soc.* **1986**, *133* (10), 2206–2207.
24. Martin, C.R. Membrane-based synthesis of nanomaterials. *Chem. Mater.* **1996**, *8* (8), 1739–1746.
25. Huczko, A. Template-based synthesis of nanomaterials. *Appl. Phys., A Mater. Sci. Eng.* **2000**, *70*, 365–376.
26. Hulteen, J.C.; Martin, C.R. A general template-based method for the preparation of nanomaterials. *J. Mater. Chem.* **1997**, *7* (7), 1075–1087.
27. Fleisher, R.L.; Price, P.B.; Walker, R.M. *Nuclear Tracks in Solids*; University of California Press: Berkeley, CA, 1975.
28. Chakarvarti, S.K.; Vetter, J. Template synthesis—A membrane based technology for generation of nano-/micro materials: A review. *Radiat. Meas.* **1998**, *29* (2), 149–159.
29. Jerome, C.; Demoustier-Champagne, S.; Legras, R.; Jerome, R. Electrochemical synthesis of conjugated polymer wires and nanotubes. *Chem. Eur. J.* **2000**, *6* (17), 3089–3093.
30. Parthasarathy, R.V.; Martin, C.R. Enzyme and chemical encapsulation in polymeric microcapsules. *J. Appl. Polym. Sci.* **1996**, *62*, 875–886.
31. Lu, M.; Li, X.-H.; Li, H.-L. Synthesis and characterization of conducting copolymer nanofibrils of pyrrole and 3-methylthiophene using the template-synthesis method. *Mater. Sci. Eng., A* **2002**, *334*, 291–297.
32. Cai, Z.; Lei, J.; Liang, W.; Menon, V.; Martin, C.R. Molecular and supermolecular origins of enhanced electronic conductivity in template-synthesized polyheterocyclic fibrils. 1. Supermolecular effects. *Chem. Mater.* **1991**, *3* (5), 960–967.
33. Liang, W.; Martin, C.R. Template-synthesized polyacetylene fibrils show enhanced supermolecular order. *J. Am. Chem. Soc.* **1989**, *112* (26), 9666–9668.
34. Wittmann, J.C.; Smith, P. Highly oriented thin-films of poly(tetrafluoroethylene) as a substrate for

- oriented growth of materials. *Nature* **1991**, *352* (6334), 414–417.
35. Martin, C.R. Nanomaterials: A membrane-based synthetic approach. *Science* **1994**, *266*, 1961–1966.
 36. Yuan, G.-L.; Kuramoto, N. Chemical synthesis of optically active polyaniline in the presence of dextran sulfate as molecular template. *Chem. Lett.* **2002**, *5*, 544–545.
 37. Mativetsky, J.M.; Datars, W.R. Properties of alumina membrane-templated polypyrrole nanostructures. *Solid State Commun.* **2002**, *122*, 151–154.
 38. Kuwabata, S.; Martin, C.R. Investigation of the gas-transport properties of polyaniline. *J. Membr. Sci.* **1994**, *91*, 1–12.
 39. Koopal, C.G.L.; Feiters, M.C.; Nolte, R.J.M.; de Ruyter, B.; Schasfoort, R.B.M.; Czajka, R.; Van Kempen, H. Polypyrrole microtubules and their use in the construction of a third generation biosensor. *Synth. Met.* **1992**, *51*, 397–405.
 40. Martin, C.R.; Parthasarathy, R.V. Polymeric microcapsule arrays. *Adv. Mater.* **1995**, *7* (5), 487–488.
 41. Granstrom, M.; Berggren, M.; Inganas, O. Micrometer- and nanometer-sized polymeric light-emitting diodes. *Science* **1995**, *267*, 1479–1481.
 42. Wang, C.; Wang, Z.; Li, M.; Li, H. Well-aligned polyaniline nano-fibril array membrane and its field emission property. *Chem. Phys. Lett.* **2001**, *341*, 431–434.
 43. Sukeerthi, S.; Contractor, A.Q. A study of polyaniline microtubules: Toward superior transducing abilities. *Chem. Mater.* **1998**, *10* (9), 2412–2418.
 44. Fu, M.; Chen, F.; Zhang, J.; Shi, G. Electrochemical fabrication of aligned microtubular heterojunctions of poly(*p*-phenylene) and polythiophene. *J. Mater. Chem.* **2002**, *12*, 2331–2333.
 45. Li, X.; Zhang, X.; Li, H. Preparation and characterization of pyrrole/aniline copolymer nanofibrils using the template-synthesis method. *J. Appl. Polym. Sci.* **2001**, *81*, 3002–3007.
 46. Yang, J.; Hou, J.; Zhu, W.; Xu, M.; Wan, M. Substituted polyaniline–polypropylene film composites: Preparation and properties. *Synth. Met.* **1996**, *80*, 283–289.
 47. Cassagneau, T.; Caruso, F. Semiconducting polymer inverse opals prepared by electropolymerization. *Adv. Mater.* **2002**, *14* (1), 34–38.
 48. Sumida, T.; Wada, Y.; Kitamura, T.; Yanagida, S. Electrochemical preparation of macroporous polypyrrole films with regular arrays of interconnected spherical voids. *Chem. Commun.* **2000**, *17*, 1613–1614.
 49. Bartlett, P.N.; Birkin, P.R.; Ghanem, M.A.; Toh, C.-S. Electrochemical syntheses of highly ordered macroporous conducting polymers grown around self-assembled colloidal templates. *J. Mater. Chem.* **2001**, *11* (3), 849–853.
 50. Han, S.; Briseno, A.L.; Shi, X.; Mah, D.A.; Zhou, F. Polyelectrolyte-coated nanosphere lithographic patterning of surfaces: Fabrication and characterization of electropolymerized thin polyaniline honeycomb films. *J. Phys. Chem., B* **2002**, *106* (25), 6465–6472.
 51. Wang, D.; Caruso, F. Fabrication of polyaniline inverse opals via templating ordered colloidal assemblies. *Adv. Mater.* **2001**, *13* (5), 350–353.
 52. Deutsch, M.; Vlasov, Y.A.; Norris, D.J. Conjugated-polymer photonic crystals. *Adv. Mater.* **2002**, *12* (16), 1176–1180.
 53. Xia, Y.; Whitesides, G.M. Soft lithography. *Annu. Rev. Mater. Sci.* **1998**, *28*, 153–184.
 54. Kim, E.; Xia, Y.; Zhao, X.-M.; Whitesides, G.M. Solvent-assisted microcontact molding: A convenient method for fabricating three-dimensional structures on surfaces of polymers. *Adv. Mater.* **1997**, *9* (8), 651–654.
 55. Rogers, J.A.; Bao, Z.; Dhar, L. Fabrication of patterned electroluminescent polymers that emit in geometries with feature sizes into the submicron range. *Appl. Phys. Lett.* **1998**, *73* (3), 294–296.
 56. Zhang, F.; Nyberg, T.; Inganas, O. Conducting polymer nanowires and nanodots made with soft lithography. *Nano Lett.* **2002**, *2* (12), 1373–1377.
 57. Wu, Y.-M.; Fan, F.-R.F.; Bard, A.J. High resolution deposition of polyaniline on Pt with the scanning electrochemical microscope. *J. Electrochem. Soc.* **1989**, *136* (3), 885–886.
 58. Borgwarth, K.; Ricken, C.; Ebling, D.G.; Heinze, J. Surface characterization and modification by the scanning electrochemical microscope (SECM). *Ber. Bunsenges. Phys. Chem.* **1995**, *99* (11), 1421–1426.
 59. Yang, R.; Evans, D.F.; Hendrickson, W.A. Writing and reading at nanoscale with a scanning tunneling microscope. *Langmuir* **1995**, *11* (1), 211–213.
 60. Yaniv, D.R.; McCormick, L.D. Polypyrrole nanoplating on HOPG utilizing an STM tip (biosensor fabrication). *Nanotechnology* **1992**, *3* (1), 44–47.
 61. Nyffenegger, R.M.; Penner, R.M. Nanometer-scale electropolymerization of aniline using the scanning tunneling microscope. *J. Phys. Chem.* **1996**, *100* (42), 17041–17049.
 62. Cai, X.W.; Gao, J.S.; Xie, Z.X.; Xie, Y.; Tian, Z.Q.;

- Mao, B.W. Nanomodification of polypyrrole and polyaniline on highly oriented pyrolytic graphite electrodes by atomic force microscopy. *Langmuir* **1998**, *14* (9), 2508–2514.
63. Piner, R.D.; Zhu, J.; Xu, F.; Hong, S.H.; Mirkin, C.A. "Dip-pen" nanolithography. *Science* **1999**, *283* (5402), 661–663.
 64. Maynor, B.W.; Li, Y.; Liu, J. Au "ink" for AFM "dip-pen" nanolithography. *Langmuir* **2001**, *17* (9), 2575–2578.
 65. Demers, L.M.; Ginger, D.S.; Park, S.J.; Li, Z.; Chung, S.W.; Mirkin, C.A. Direct patterning of modified oligonucleotides on metals and insulators by dip-pen nanolithography. *Science* **2002**, *296* (5574), 1836–1838.
 66. Noy, A.; Miller, A.E.; Klare, J.E.; Weeks, B.L.; Woods, B.W.; DeYoreo, J.J. Fabrication of luminescent nanostructures and polymer nanowires using dip-pen nanolithography. *Nano Lett.* **2002**, *2* (2), 109–112.
 67. Li, Y.; Maynor, B.W.; Liu, J. Electrochemical AFM "dip-pen" nanolithography. *J. Am. Chem. Soc.* **2001**, *123* (9), 2105–2106.
 68. Maynor, B.W.; Filocamo, S.F.; Grinstaff, M.W.; Liu, J. Direct-writing of polymer nanostructures: Poly(thiophene) nanowires on semiconducting and insulating surfaces. *J. Am. Chem. Soc.* **2002**, *124* (4), 522–523.
 69. Filocamo, S.F.; Maynor, B.M.; Liu, J.; Grinstaff, M.W. Submitted.
 70. Seo, I.; Pyo, M.; Cho, G. Micrometer to nanometer patterns of polypyrrole thin films via microphase separation and molecular mask. *Langmuir* **2002**, *18* (20), 7253–7257.

Nanostructures Based on Layered Transition Metal Chalcogenides

Russell R. Chianelli

Myriam Perez De la Rosa

The University of Texas, El Paso, Texas, U.S.A.

INTRODUCTION

The discovery of carbon nanotubes by Ijima^[1] initiated a new area of materials science. Following Ijima's discovery, Tenne et al.^[2] later found layered sulfides (MoS₂ and WS₂) to form nanotubes and other fullerene-type structures. Nanoparticles based on layered transition metal sulfides (LTMS) are of special interest because of their diverse applications. Layered transition metal sulfides have been extensively studied because of their crucial role in the petroleum and chemical industry. MoS₂-based and WS₂-based catalysts have been used for sulfur and nitrogen removal from petroleum feedstock.^[3] In addition, MoS₂ is used as a lubricant additive.^[4] Related compounds of TiS₂, as well as MoS₂, can work as cathodes in lithium nonaqueous batteries^[5,6] and possess interesting and useful intercalation chemistry.^[7] WS₂, WSe₂, TiS₂, MoS₂, MoSe₂, and MoTe₂ are all semiconductors with unusual properties and potential electronic applications.^[8]

The structure of MoS₂, WS₂, and ReS₂ consists of a two-dimensional layered closed-packed sulfur arrangement with a transition metal sandwiched between each layer. Weak van der Waals interlayer forces occur between stacked "sandwiches" that allow easy, low-strength shearing.^[9,10] These materials are highly folded and distorted in nature, forming commonly known "rag" and "tubular" structures. Layered transition metal sulfide materials appear as morphological analogs of fullerenes exhibiting structures described as inorganic fullerenes (IFs), single sheets, folded sheets, nanocrystals, and nested IFs, also known as "onion crystals" or "Russian dolls."

Fullerene-related nanoparticles of MoS₂ can be obtained by electron beam irradiation,^[11] laser ablation^[12] of MoS₂ bulk powder, and arc discharge.^[13] Scanning tunneling microscope electrical pulses over amorphous MoS₃ nanoparticles lead to the formation of closed MoS₂ shell IF (a few layers thick) and amorphous MoS₃.^[14] Inorganic fullerene nanoparticles have been synthesized recently by a variety of methods. Others have reported the gas-phase synthesis of fullerene-like structures of WS₂^[2] and MoS₂^[15] and nested fullerenes of MoS₂.^[16] Complex WS₂ nanostructures have been obtained by template growth by Whitby et al.^[17] The preparation and optical

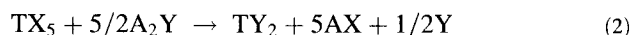
characterization of crystalline nanoparticles prepared by intercalation and ultrasonic fragmentation of bulk crystals have also been studied.^[18-20] Divigalpitiya et al.^[21-23] have reported the synthesis and preliminary characterization of composites based on single sheets of MoS₂. Wilcoxon et al.^[24] Wilcoxon and Samara,^[25] and Parsapour et al.^[26] have reported the growth of MoS₂ nanoparticles using micelle techniques.

SYNTHESIS OF LAYERED TRANSITION METAL SULFIDES

A variety of methods have been used to synthesize LTMS. In general, poorly crystalline dichalcogenides are prepared by heating under hydrogen sulfide flow. The highly folded material is prepared by heating several grams of amorphous MoS₂ for 2 hr at 400°C in a stream of H₂ mixed with 15% H₂S. As a result, the structure denoted as "poorly crystalline" and "raglike" LTMS is obtained.^[27-29] The "rag" structure consists of stacked but highly folded and disordered MoS₂ layers (Fig. 1). The number of stacks and the dimensions of the layers can vary by changing the preparation conditions. The general reaction scheme of low-temperature metaphorical reaction in a solution is:



where T=transitional metal, X=salt anion (Cl, carboxylate, etc.), A=alkali-like cation (Li⁺, Na⁺, NH₄⁺, etc.), and Y=chalcogenides anion. Redox reactions tend to occur because the transition metal ions and the chalcogenides exist in several oxidation states:

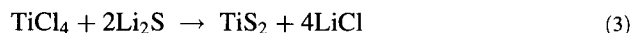


The great stability that the oxides and hydroxides lend to the transition metal salt eliminates the need for an aqueous environment. Moreover, hydroxylic solvents, in general, are very reactive and can serve as solvents for TX₄ or TX₅. Poor reaction between hydrogen sulfide and the transition metal salt does not allow for direct synthesis



Fig. 1 Folded and disorder sheets of MoS₂. (From Ref. [28].)

of TY₂ species. This is why alkali chalcogenides must be used. Even in the absence of oxygen in air or water, the reaction of TiCl₄ with H₂S is unfavorable at temperatures lower than 400°C. These are highly reactive ionic sources of chalcogenides and the reaction readily proceeds at room temperature. Lithium sulfide was found to be the most convenient source of sulfide ion:



For precipitation at room temperature, tetrahydrofuran and ethyl acetate are suitable solvents. Dark precipitates are obtained and easily filtered. Repeated washings with the solvent completely remove LiCl excess. To obtain crystalline TiS₂, further heating at 400–600°C is required in a sealed quartz tube under an inert atmosphere. This example illustrates the synthesis of TiS₂ but it can be applied to any other transition metal sulfide.

WS₂, ReS₂, and OsS₂ can be prepared by heating amorphous sulfides at 400°C in a stream of H₂ mixed with 15% H₂S. The structure of the ReS₂ poorly crystalline structure is the most likely material for the production of large amounts of nanotubes and fullerene-like materials. Recently, tetraalkylammonium thiomolybdates have been used to incorporate carbon into the extremely disordered materials and it is believed that this impurity increases the ability of the MoS₂ to fold.^[30–32]

NESTED INORGANIC FULLERENE ONION-LIKE STRUCTURE

Carbon fullerene onion-like structures have been obtained under high electron irradiation using transmission electron microscopy (TEM).^[33] Tenne et al.^[2] and Margulis et al.^[34] have also observed fullerene onion-like structures in layered materials including WS₂ and MoS₂. Electron-irradiated MoS₂ crystals at 0.5 MeV energy were studied by Yacaman et al. using high-

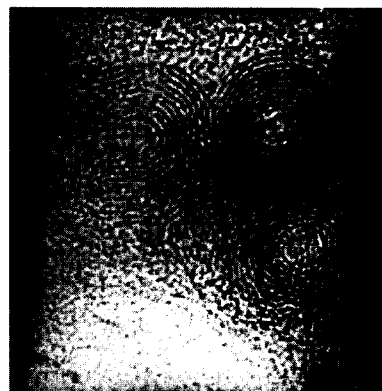


Fig. 2 Onion-like structures in MoS₂. (From Ref. [11].)

resolution electron microscopy. The irradiated MoS₂ crystals presented two main features: onion layers with fullerene-like structures, and others with their planes rotated with respect to each other by well-defined angles.^[11] In the case of carbon, onion-like structures tend to be rounded.^[33] However, the layered materials onion-like structures are faceted near the center and rounded at the edges, as illustrated in Fig. 2. MoS₂ layers in onion-like structures are not evenly spaced (Fig. 3). Another interesting feature of these structures is illustrated in Fig. 4, where a relative rotation of the MoS₂ layers around an axis perpendicular to the basal plane can be clearly seen.

In a different approach, IFs such as IF-MoS₂ have also been synthesized using high-temperature methods that occur above 650°C. These methods involve such techniques as growth from the gas phase in which MoO₃ in the vapor phase is reacted with H₂S in a carrier gas (Scheme 1). The gas-phase reactor synthesis has achieved great control over the nanoparticles growth parameters.

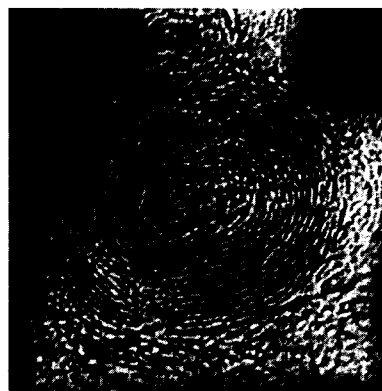


Fig. 3 High-resolution transmission electron microscopy image of MoS₂ onion-like structure. Fourier transform of the structure is shown in the inset. (From Ref. [11].)

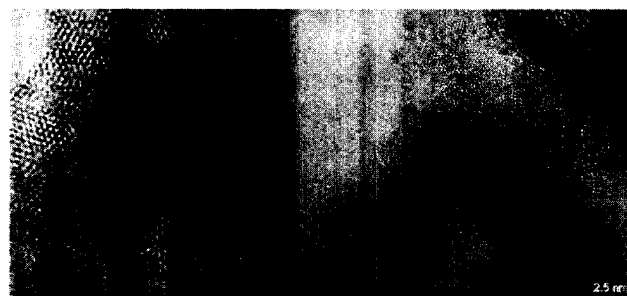
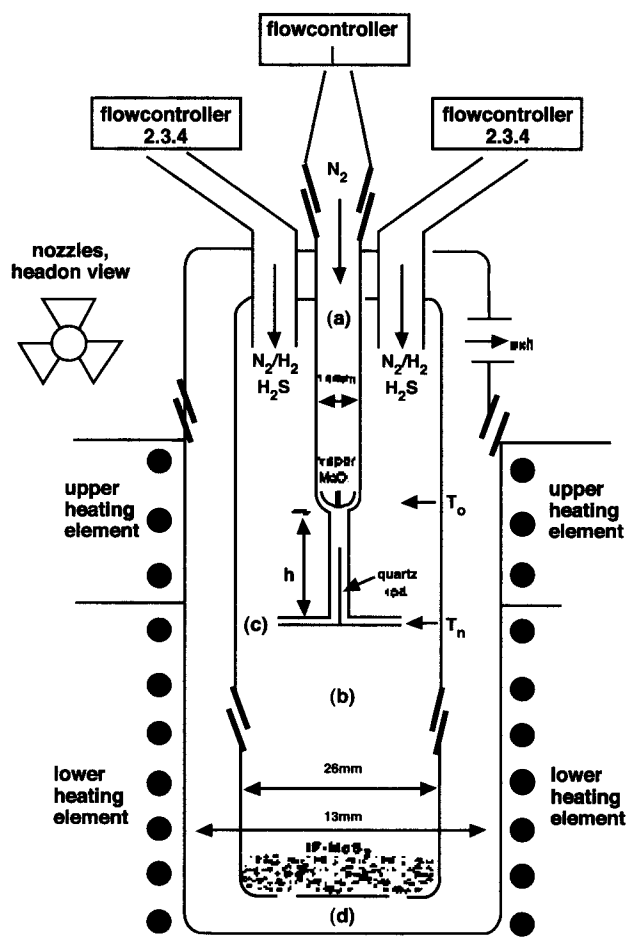


Fig. 4 Irradiated MoS₂ that illustrated a relative rotation of 10° by the layers on MoS₂ around an axis perpendicular to the image: (a) low magnification; and (b) high magnification. (From Ref. [11].)



Scheme 1 (A) Vertical gas-phase reactor for synthesis of MoS₂ fullerene-like nanoparticles: (a) inner tube; (b) middle tube; (c) nozzles; (d) external tube. (B) Closer look at the inner reactor (a). (From Ref. [35].)

This process consists of MoO₃ powder placed in the inner part of the reactor, (a) which is heated to 780°C. Molecular clusters (MoO₃)₃ are formed and carried down through the reactor by N₂ gas. Hydrogen gas diffuses through the nozzles (c) from the outer reactor (b) and starts to react with the molecular clusters. The mild reduction conditions yield reduced MoO_{3-x} clusters, which are less volatile and form MoO_{3-x} nanosize particles at the low part of (a). The suboxide nanoparticles reach a size less than 5 nm before the sulfidization step. The coated oxide nanoparticles are swept by the carrier gas outside the reactor (a). Because the nanoparticles are surface-passivated, they land on the ceramic filter (d) and the oxide-to-sulfide conversion continues within the core without coalescence of the nanoparticles. The gas-phase reactor synthesis process generates pure IF-MoS₂ phase and the control over the size and shape of the nanoparticles is quite good.^[35] A characteristic image of three IF nanoparticles produced in the gas-phase reactor is illustrated in Fig. 5.

MoS₂ fullerene-like nanoparticles can also be produced by a combination of sonochemistry and electrochemistry, recently termed sonoelectrochemistry. Sonoelectrochemical formation of nanoscale metal powders has been achieved by applying an electric current pulse to nucleate the electrodeposit, followed by a burst of ultrasonic energy that removes the metal particles from the sonic probe cathode.^[36] Mastai et al. used the known process for cathodic electrodeposition of MoS₂ from solutions of thiomolybdate ions. Normally amorphous MoS₂ is deposited and becomes crystalline after heat treatment, forming a highly textured film.^[36] Fig. 6 illustrates TEM images of the sonoelectrochemically prepared MoS₂ particles at different orientations with respect to the electron beam. The curved and closed nature of the structures can be observed at different angles. The authors could not state if

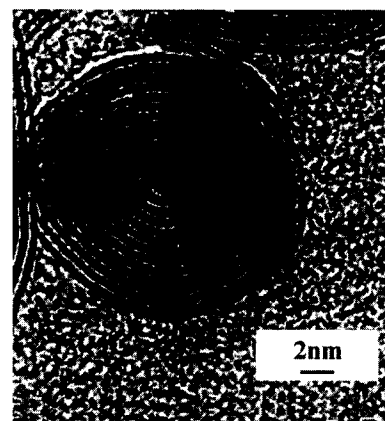


Fig. 5 “Russian doll” structures obtained by gas-phase synthesis. (From Ref. [15].)

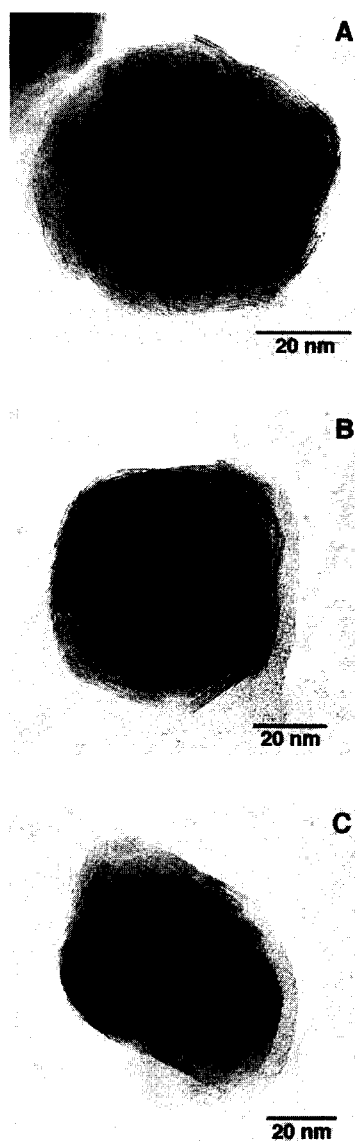


Fig. 6 Transmission electron microscopy images of the same MoS_2 particles taken with the sample rotated in the sample rotated in the direction of the electron beam at an angle of (A) $+45^\circ$; (B) 0° ; and (C) -45° . (From Ref. [36].)

the structures are made up of MoS_2 sheets entirely, are hollow, or contain a core of another material (i.e., MoO_2 , amorphous MoS_2). However, the presence of MoS_2 planes inside the closed structures, but oriented in various directions (Fig. 6C), suggests that the structures are hollow to some extent, as stated by Mastai et al.

They suggested an interesting mechanism to explain the closed curved structure. Amorphous MoS_2 is suspected to be formed by electrodepositing onto the sonic probe cathode. The deposit is then removed from the probe surface by a sonic shock wave. The deposit could be found in a spheroid or planar structure because

nucleating electrodeposits are often nanoparticulates. The effect of the shock wave is not enough to crystallize the deposit according to the authors. They concluded that the cause of the crystallization, and possibly bending, which normally require high temperatures, is the collapse of cavitation bubbles. Cavitation bubble nucleation is favored at a surface, either of the sonic probe itself or of MoS_2 , which was previously removed from the probe surface. The bubble can then grow with the MoS_2 attached to it. During collapse, the high temperature at the surface of the bubble can cause crystallization.^[36] The authors presented two cases to describe the crystallization of the particle. If the original amorphous particle was spheroidal, then the final crystallized particle is likely to maintain a related morphology. If the original particle, as removed from the probe, is closer to two-dimensional, curvatures and closures may occur around the collapsing bubble (the bubble then determines the shape of the structure), or the temperature from the bubble surface into the solution should cause a temperature gradient across the particle, which could also cause curvature. The closure is energetically preferred because of bond energy released by removing reactive edges. The less common nanotube formation could occur if the nucleated deposit were filamentary, or, more likely, if the bubble collapse occurred at the electrodeposit that was still on the electrode surface.^[36] In that case, the effect of the bubble collapse is asymmetric, which could lead to an asymmetric-shaped structure of the final product. Sonochemical reactions that take place inside the collapsing bubble result always in amorphous products because of fast cooling rates ($>10^{10}$ K/sec).^[36]

On the other hand, amorphous or crystalline materials are produced by aqueous ionic reactions that take place in the 2000-nm ring surrounding the collapsing bubble. When operated separately, electrochemistry or sonochemistry yields amorphous MoS_2 . The proposed mechanism, involving the collapse of the cavitation bubble, logically explains the crystallization of this amorphous compound and (bending and closure) considers that the amorphous particle is not already related to the final shape and size.

Ultrasonic radiation not only induces crystallization and shape control reactions, but it can also induce chemical reactions. The combination of electrochemical and sonic processes provides many experimental variables, which allow to control particle size and shape distribution, and will probably be applicable to the formation of closed structures of other layered compounds that can be prepared by electrochemical techniques.^[36]

MoS_2 NANOTUBES

Microtubes of MoS_2 have been grown by Remskar et al.^[37] MoS_2 nanotubes produced using a template have been reported by Zelenski and Dorhout.^[38] A low-temperature



Fig. 7 Scanning electron microscopy images of the surface of electrochemically produced Al_2O_3 . (A) Low-magnification picture of the cross-section band structure. (B) High-magnification picture of the pores. (From Ref. [40].)

method developed by Prasad et al.^[39] produced MoS_2 from solution-phase precursors within the porous membrane of electrochemically generated Al_2O_3 . MoS_2 nanotubes were obtained using Prasad et al.'s method and characterized by high-resolution electron microscopy (HREM) and electron diffraction by Chianelli et al.^[40] MoS_2 nanotubes were prepared using nonporous alumina templates produced by ionization of aluminum. To obtain the nanotubes, a solution-phase precursor of $(\text{NH}_4)_2\text{MoS}_4$ in dimethylformide (DMF) was prepared. Small pieces of alumina template were immersed into the solution for a few seconds. The templates were dried at 70°C on a hot plate until the solvent evaporated. The samples were loaded into a quartz tube, which was placed into a furnace and treated with a mixture of 10% H_2/N_2 at 450°C . The MoS_2 nanotubes were then removed from the templates and characterized by high-resolution transmission electron microscopy (HRTEM). Computational calculations were carried out to study the properties of the MoS_2 nanotubes. A minimum diameter was determined to indicate the structural stability of the MoS_2 nanotubes.^[40]

In Fig. 7A, and B, two images of the Al_2O_3 template used to produce the MoS_2 nanotubes are illustrated. The figure shows low-magnification and high-magnification

scanning electron microscopy (SEM) pictures of the surface and the cross section of the template. The cross-section band structure illustrates pores of 25 nm in diameter in uniform distribution (Fig. 7A). The pore length was about 25 μm wide and 250 μm long, as observed in Fig. 7B. The MoS_2 nanotubes were grown in the pores of the templates. A characteristic high-resolution image of a nanotube is illustrated in Fig. 8. The nanotube shown is approximately 260 nm long. An interplanar average distance of about 6.25 \AA and an interplanar distance of about 2.74 \AA (100 plane) were determined by measuring the (002) planes of the MoS_2 structure at the border of the tubes using higher-magnification micrographs.^[40] This value is larger than the 6.16 \AA expected for crystalline MoS_2 . It should be noted that the (002) planes are not seen in the interior part of the tube indicating normal contrast for a tubular structure. A 2H- MoS_2 nanotube structure was determined by electron diffraction. The (002) reflection also showed an expansion to 6.22 \AA of the lattice parameter as already mentioned. It was noted that the tube is not continuous, but it is split in several sections, each one with a diameter from 15 to 30 nm and a length between 150 and 500 nm. Commonly, the sections of the tube are ellipsoidal. However, in some cases, the shape is distorted as in the last section of the long tube (Fig. 8). The planes of the nanotubes are bent in a similar fashion as the bending of carbon nanotubes previously reported.^[41] A computer-generated model of a MoS_2 nanotube including two layers built using Cerius² (molecular simulation program, ACCELRY S Corporation) is shown in Fig. 9. The MoS_2 in trigonal prismatic coordination was used as a starting model. As the minimum energy configurations were searched, stable configurations for cylinders of different sizes were calculated. Analyzing the Mo-S distances, two groups

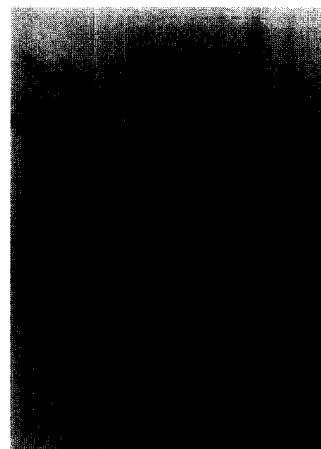


Fig. 8 High-resolution transmission electron microscopy image of a section of a MoS_2 tube. (From Ref. [40].)

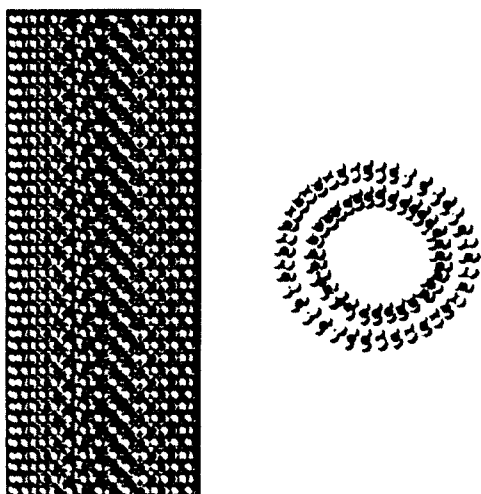


Fig. 9 Molecular model (Cerius²) of MoS₂ nanotube formed by two layers. (From Ref. [40].)

of measurements were reported. One group contains the interior Mo—S distances [Mo—S (int)] and the other contains the exterior Mo—S distances [Mo—S (ext)]. The mean distance for the Mo—S interior bond is 2.65 Å and the mean distance for the exterior bond is 2.75 Å. The calculation implied that MoS₂ nanotubes of this diameter are not stable because bending to form a tube of this diameter requires stretching of the Mo—S bonds well beyond their normal length of 2.41 Å.^[40] The mean distance for six tubes of various diameters between 20 and 120 Å was also calculated and plotted in Fig. 10.^[40] The mean values of both the interior and the exterior Mo—S bonds approach the single crystal value of 2.41 Å. Chianelli et al. stated that below a value of approximately

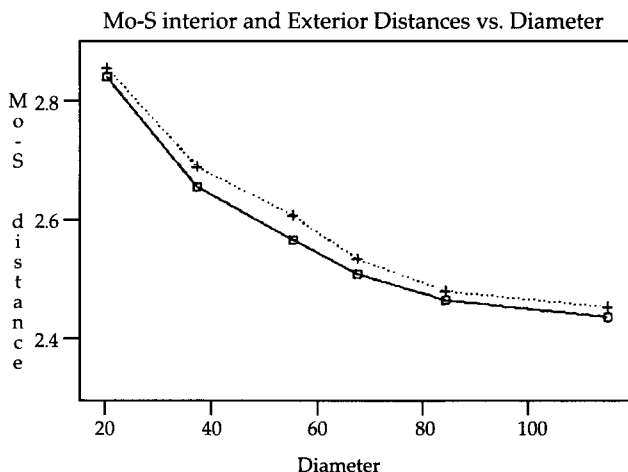


Fig. 10 Interior and exterior distances as a function of tube diameter. (From Ref. [40].)

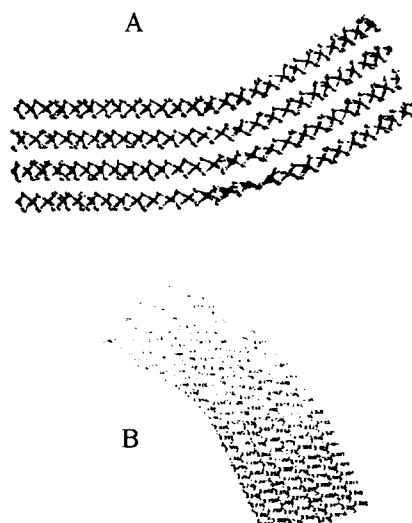


Fig. 11 (A) Model of a bent sheet (30°) of MoS₂ (with four layers). (B) Atoms' position measurements for a similar sheet. (From Ref. [40].)

120 Å, the tubes might be highly unstable because of bond strain. They have reported MoS₂ nanotubes containing bending zones that, in the case of MoS₂ crystals, are often observed on the edges of the surface.^[20] Hence "bent zones" are important to understanding the behavior of MoS₂ sheets. Fig. 11A and B presents the model of a bent sheet of MoS₂ comprised of four layers of MoS₂. Examination of the values of the S—S and Mo—Mo distances shows a very large distortion that clearly appears in the bending zone. In comparison with the distances in the straight sections of the sheet, an increase of 20% in the distance between neighboring atoms is observed. This strongly emphasizes the instability of bent layers as the radius of curvature is reduced.

Synthetic nanotubes, lubricants, and catalysts all exhibit similar bending phenomena. Yacaman et al. reported that even in the case of MoS₂ crystals, a bending effect is often observed at the edges of the crystal surface. Their study showed that although large MoS₂ nanotubes can be synthesized, their minimum size is limited by the strain induced by stretched Mo—S bonds that are required to close tubes with diameters less than approximately 10 nm. Tenne et al.^[21] earlier reported the synthesis of WS₂ nanotubes with diameters in the range of 10 nm. However, a close examination of their published micrographs reveals that the "nanotubes" become broken and discontinuous as the diameter becomes smaller, in agreement with Yacaman et al.'s study. This is in contrast to nanotubes of carbon that can exist down to very small diameters because of the change in carbon bonding, which is natural in fullerene-based materials. Layered materials such as MoS₂ and WS₂ cannot be formed into small nanotubes unless a change in

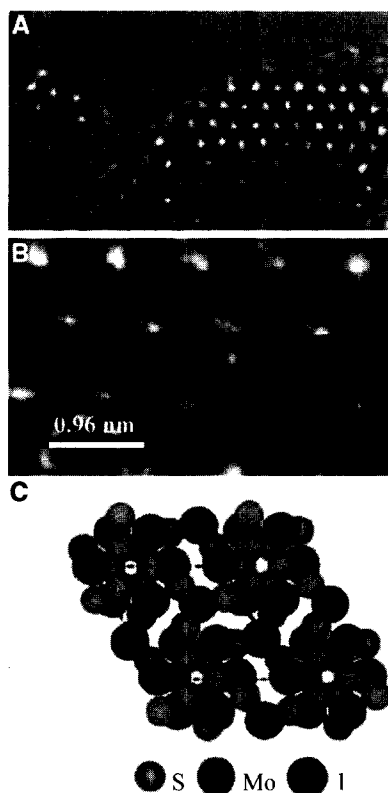


Fig. 12 The cross section of a $(\text{MoS}_2)\text{-I}_x$ TEM image of (A) hexagonal structure of the tubes. (B) High-resolution view of the structure. The insert shows an image simulation for zone $[001]$. (C) A model structure perpendicular to the nanotube axis (gray, S; dark gray, Mo; black, I). (From Ref. [42].)

Mo—S bond occurs. A change from six coordinates to a lower metal coordination might result in smaller-diameter nanotubes; however, this phenomenon has not yet been reported, but is possibly based on the known chemistry of Mo and S. Furthermore, the nanotubes made by the template method are not infinitely long but break into sections, giving the shape of a “Spanish chorizo,” a term coined by Yacaman et al. Calculations indicate that, in principle, there is no structural energetic reason for a nanotube not to grow infinitely. The total energy of the nanotube will be minimized by the distortion from the edge to the center described in “Nested Inorganic Fullerene onion-like Structure.” Nevertheless, HRTEM images clearly show that two sections of the tube are in contact, but each one is preserving its corresponding layers. Therefore it is very likely that the sections are produced as a result of growth kinetics.

MoS_2 single-wall nanotubes (SWNTs) were grown by a catalyzed transport reaction involving C_{60} as a growth promoter.^[42] Remskar et al. show that the MoS_2 nanotubes grow in twisted chiral bundles of identically

structured molecules stacked together with interstitial iodine. The nanotubes were found to vary in length but not in diameter. The chemical composition of the bundles was determined by energy-dispersive x-ray spectroscopy (EDX) and x-ray fluorescence spectrometry to be $(\text{MoS}_2)\text{-I}_x$ with $x \sim 1/3$. However, the authors did not find C_{60} incorporated into the structure using energy electron loss spectrometer (EELS). The bundles possess a hexagonal close-packed structure of identical nanotubes along the longitudinal direction revealed by HRTEM. The center-to-center distance between two tubes was found to be 0.961(1) nm, as seen in Fig. 12. A complex electron diffraction pattern shows a slightly distorted hexagonal symmetry, as illustrated in Fig. 13C. Perpendicular to the bundle axis, a period of 0.83 nm is dominant.^[42] The period is equal with regard to the period 0.27 nm belonging to the hexagonal pattern. Another strong peak located close to the (030) spot is caused by a period of 0.30(1) nm. Two strong periods of 0.20(1) and

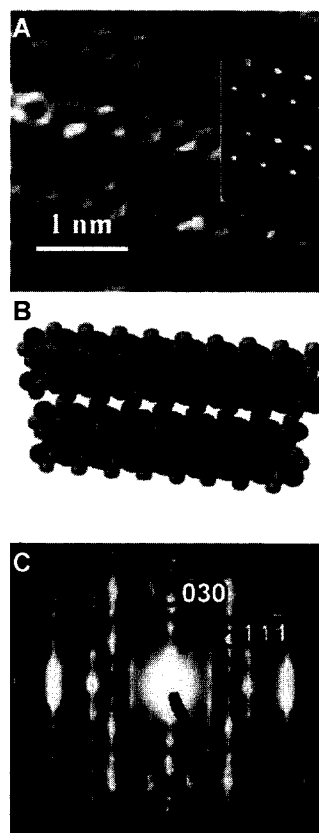


Fig. 13 The $(\text{MoS}_2)\text{-I}_x$ TEM image and electron diffraction in zone $[101]$. (A) High-resolution image with image simulation revealing ordered stacking of nanotubes; bright spots correspond to the positions of molybdenum atoms. (B) Model structure of the tubes. (C) Corresponding electron diffraction pattern indexed in accordance with the model structure. (From Ref. [42].)

0.30(1) nm are present along the axis. The transition electron diffraction (TED) data were confirmed by x-ray diffraction where intense peaks were found corresponding to interlayer distances of 0.832(1), 0.351(1), 0.314(1), 0.308(1), 0.279(1), and 0.20(1) nm.^[42] Remskar et al. proposed a model (3,3) armchair nanotube structure illustrated in Figs. 12C and 13B. The distance between sulfur and molybdenum atoms in the nanotube is nearly of the same distance in platelike MoS₂. The close position of molybdenum and sulfur atoms in neighboring layers perpendicular to the nanotube axis requires at least 25% extension of the unit cell along the tube axis to avoid overlap of the covalent radii.^[42] The distance between the layers was determined to be 0.20 nm by diffraction patterns. The unit cell of the hexagonal close-packed nanotubes within a bundle was found to be 0.40 nm along the bundle axis and 0.96 nm perpendicular to the bundle axis. Their van der Waals diameter corresponds approximately to the distance between the closest sulfur atoms on adjacent nanotubes [0.35(1) nm]. Iodine atoms are inserted in interstitial trigonal voids between the nanotubes, creating one-dimensional rows along the bundle axis. The periodicity of possible sites for iodine position along the bundle is 0.40 nm, which is slightly less than the van der Waals distance for iodine (0.43 nm). The observed HRTEM images are in agreement with their simulations using the symmetry operations of group P6₃(C₆6).^[42] The authors found C₆₀ to be essential in the growth process, but a detail mechanism is not clear at the moment.

ZrSe₂ AND SnS₂ FILAMENT-LIKE NANOPARTICLES

Filament-like nanoparticles of ZrSe₂ and SnS₂ were obtained by microwave plasma process.^[43] Synthesis is performed using microwaves with a frequency of 0.915 or 2.45 GHz.^[44] The reaction takes place inside a quartz tube passing a monomode microwave cavity.^[45] The precursor compounds are vaporized outside of the reaction zone and introduced to the reaction gas in front of the plasma zone, where the nanoparticles are formed. The reaction gas is preheated to avoid the precipitation of the precursor. The reaction was performed under a pressure of 30 mbar using 0.915-GHz plasma. The reaction temperature was set at 260°C or 580°C. The flow rate of the gas was adjusted to obtain a residence time of the particles of about 8 msec in the reaction zone at a temperature of 580°C, and about 4 msec at 260°C. Further reduction of the reaction temperature is obtained by using 2.45-GHz microwaves. Vollath et al. were able to perform the reaction at a temperature as low as 160°C. Gas pressure was set to 10 mbar. The residence time of the particles in the reaction zone was about 2 msec. The reaction temperature was determined

directly after the reaction zone. Because microwave plasma was a nonequilibrium system, the true temperature of the particles during the formation was different. The reaction products were collected on cooled surfaces. Sulfide synthesis used H₂S as a carrier. The metals were introduced in the form of SnCl₄. Elemental sulfur was obtained along with the nanoparticles. To evaporate the sulfur excess, the reaction product was heated up to 120–140°C in a vacuum. The selenide samples were prepared using argon 4 vol.% H₂ as plasma gas. Selenium was introduced in the form of SeCl₄. Fine particles of selenides are extremely sensitive to humidity; therefore the specimens were handled under argon gas prior to electron microscopy data collection. Filament-like morphology is a characteristic example of ZrSe₂ small particles, as illustrated in Fig. 14. The filaments are randomly bent and knotted together. At higher magnifications, the lattice planes clearly show the same bends and twists as the particles (Fig. 15). The fringes in the micrograph represent the Se–Zr–Se {0002} layers with a distance of 0.36 nm close to the reported value of 0.3095 nm.^[46] This filament-like structure is not unique for ZrSe₂ and also appears in the case of SnS₂ structures (Fig. 16). The distance of the lattice fringes for SnS₂ is 0.56 nm, which corresponds to the {0001} planes (JCPDS value, 0.589 nm).^[47] The reduced number of dislocation-like structures is the main difference between the SnS₂ and ZrSe₂ structures. In addition to these filament-like structures, ZrSe₂ exhibited onion-like crystal structures with varying distances between the lattice planes, as shown in Fig. 17. The distance between the lattice fringes was determined to be 0.34 nm. The lattice images (Figs. 16 and 18) show layered structures containing defects and varying distances between the planes. ZrSe₂ tends to recrystallize in the electron microscope; therefore it cannot be completely ruled out that the particles are crystallized under the electron beam of the microscope. The electron diffraction pattern obtained

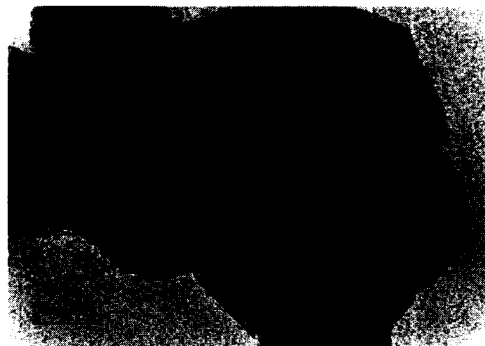


Fig. 14 Filament-like zirconium selenide particles. (From Ref. [43].)

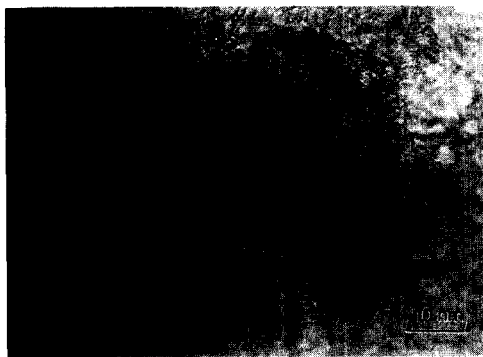


Fig. 15 Filament-like structures of zirconium selenide particles at higher magnification. The lattice fringes distance is 0.36 nm. (From Ref. [43].)

from the SnSe_2 samples shows a pattern similar to SnS_2 ^[47,48] with a 1.5% expansion from 0.589 to 0.598 nm for the {0001} spacing, whereas the lattice parameter in the a -direction shows no expansion. Table 1 compares the diffraction patterns for the two SnS_2 phases according to JCPDS tables with experimental values. The first diffraction line of the (00*i*) type shows a maximum intensity at 0.589 nm, corresponding to the β - SnS_2 structure. However, the diffraction line observed at 0.306 nm is not allowed for β - SnS_2 . This line is allowed for the ordered polytype of the β -structure. Considering these observations, the authors may be tempted to conclude that the nanoparticles synthesized within this study represent a structural transition from the β - SnS_2 structure to its ordered polytype.

The ZrSe_2 nanoparticle structures are not so subtle. The material has obviously a layered structure but the diffraction pattern, shown in Fig. 18, does not agree with ZrSe_2 and ZrSe_3 of the selenide phases with layered structures.



Fig. 16 SnS_2 filaments, synthesized at 200°C. The lattice fringes distance is 0.56 nm, corresponding to the {0002} planes. The filaments have a length of around 30 nm and a width of 3–4 nm. (From Ref. [43].)



Fig. 17 onion-like zirconium selenide particle formed under electron microscope observation. (From Ref. [43].)

The electron diffraction pattern indicates a broad distribution of the distances between the lattice planes. Assuming an expanded c -axis of 0.676 nm instead of 0.619 nm, the diffraction patterns disagree significantly with the hexagonal ZrSe_2 structure.^[46] The second zirconium–selenium phase with layered structure is Zr_2Se_3 ,^[49] given that a c -axis expansion from the JCPDS value of 1.251–1.351 nm has to be assumed. Furthermore, this assumed expansion in the c -axis still does not match the actual diffraction pattern with the published pattern. Assuming an 8% or 9% expansion in the van der Waals bond, the c -axis may still be reasonable. If a similar expansion is also assumed in the a -direction, the diffraction pattern obtained with the nanosized particles fits relatively well with the published diffraction pattern for ZrSe_2 or Zr_2Se_3 . Undoubtedly, this may not be a valid description of the actual structure because expanding in the a -direction means an elongation of the covalent bonds. Table 2 summarizes the results of measured d -values and shows the possible calculated indices, based on a c -axis and a -axis expansion.

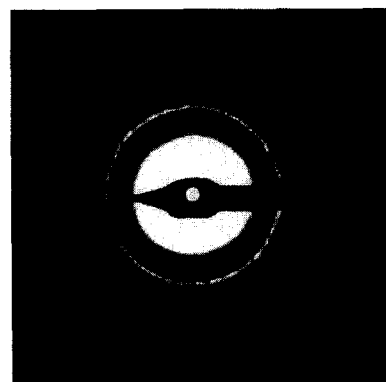


Fig. 18 Zirconium selenide electron diffraction. (From Ref. [43].)

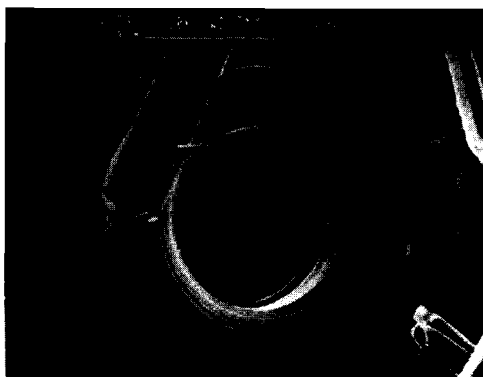


Fig. 19 Structure of trichalcogenide-NbSe₃ shown. (From Ref. [50].)

POTENTIAL USE OF LAYERED TRANSITION METAL CHALCOGENIDES AS MICROMACHINE COMPONENTS

Recently, transition metal trichalcogenides have been synthesized at high temperatures in a variety of shapes. Trichalcogenides such as NbSe₃, TiS₃, and others have layered as well as chainlike structures.^[50] These objects exhibit unusual morphologies larger than atomic scales; Fig. 19 shows an example. Morphologies observed include “wheels,” “tubes,” “rods,” and numerous other shapes. The ability to synthesize shapes such as these from materials that can be metals, magnets, semiconductors, and insulators has led to speculations regarding the construction of micromachines. For example, the “wheel,” if magnetic, might be incorporated into a microelectric motor. In another example, a microbattery might be constructed based on the intercalating abilities of the LTCM. Fabrication seems feasible, but reproducible synthesis in

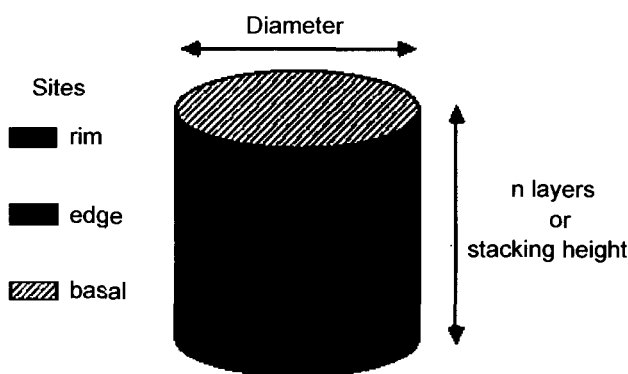


Fig. 20 “Rim/edge” model. (From Ref. [51].) (View this art in color at www.dekker.com.)

Nanostructures Based on Layered Transition Metal Chalcogenides

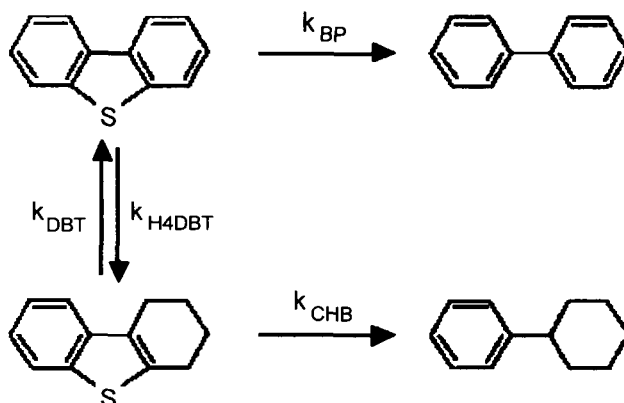


Fig. 21

large uniform quantities remains a problem; however, possibilities for micromachine devices seem extensive.

NANOPARTICULATE HETEROGENEOUS CATALYSIS

Heterogeneous catalysis used in the petroleum refining and chemical industries is an obvious example of widely applied nanoparticles. Traditionally, the industries have relied successfully on empirical methods for synthesizing these materials, but have not applied the understanding of nanoparticles to make further improvements. MoS₂ may be used as an example to show how understanding of nanoparticles leads to improvements in catalytic activity and selectivity.

Catalysts based on MoS₂ have been widely used in the petroleum refining industry since World War II. Usually the MoS₂ is mixed with a second component such as Co or



Fig. 22

Ni to improve activity.^[3] These very successful catalysts were largely discovered and developed empirically. Recently, much progress has been made in understanding their catalytic properties from a nanoparticulate point of view.^[51]

Several issues have become clear and are probably applicable to other heterogeneous catalysts:

1. Commercial catalysts, because they are made at relatively low temperatures, appear in a highly folded and disordered form such as that described above. This is disadvantageous because maximum activity is obtained on catalysts that are well crystallized, and a major unrealized challenge is to cheaply make nanocrystals of these commercial catalysts in large quantities in a supported form.
2. In the case of MoS₂, the selectivity of the reaction is determined by the "stack height" of the crystallites, as indicated in Fig. 20. The industrially important hydrodesulfurization (HDS) reaction, indicated in Fig. 21, occurs along two pathways that take place on different parts of the crystal. The first pathway leading to cyclohexylbenzene occurs only on the "rim" sites, and the second pathway leading to biphenyl occurs on the "rim" and "edge" sites. Thus the aspect ratio of the nanoparticles must be controlled to positively affect the selectivity of the reaction, and the diameter of the crystallite must be made as small as possible to maximize the activity. All these must be accomplished with as much crystalline order as can possibly be retained.
3. Working catalysts are "promoted" with a second metal such as Co or Ni. This metal usually occurs as a second component, such as Co₉S₈ that interacts at the MoS₂ edge plane and can form an interface with it. It is at this interface that the promotion effect occurs by setting up an interaction at the junction of the two materials. A high-resolution electron micrograph of such an interaction is shown in Fig. 22.^[52] It is a further challenge to synthesize these complex nanophase materials in an optimum form in commercial quantities.

THE STRUCTURE AND POTENTIAL ROLE OF ATMOSPHERIC NANOPARTICLES IN PHOTOCATALYTIC AND THERMAL PRODUCTION AND ATMOSPHERIC POLLUTANTS

Nanoparticles are now being recognized as playing a potentially important role in the complex physical and

chemical process that occurs above heavily polluted cities.^[53] Atmospheric aerosols occurring in these areas are found to be complex materials that have the potential to accelerate important ozone-forming reactions both photocatalytically and thermocatalytically. In addition, because the particles are small enough to inhale, they represent a considerable health hazard. The aerosols consist of two intermixed components: the first consists of amorphous carbonaceous materials of variable composition with "fullerene-like" materials dispersed throughout; the second is an inorganic material consisting of nanoparticles of oxides and sulfides "supported" on clay minerals. These inorganic components have all of the characteristics of an airborne photocatalyst. Nanoparticles of Fe₂O₃, MnO₂, and FeS₂ have demonstrated catalytic properties, particularly when occurring in the nanoparticles range as they do in the subject aerosol materials. These materials have band gaps that occur in the broad solar spectrum, enhancing the photocatalytic adsorption of solar radiation beyond that of the wider band gap aluminosilicate and titanate materials that also occur in aerosols. In addition, the materials are acidic and probably are coated with moisture when suspended in air, further enhancing the catalytic ability to crack hydrocarbons and create free radicals. Although this area is still being studied, nanoparticulates appear to play an important, but as yet undetermined, environmental role.

CONCLUSION

The layered transition metal sulfur structure encloses the significance of the fundamental and applied chemistry of molybdenum disulfide. Their properties and crucial catalytic uses of unpromoted and promoted systems are strongly dependent both on the weak van der Waals interlayer interactions and on the nature of the sites defined by its layered structure. Complete understanding of the catalytic properties of MoS₂ requires more information on the edge planes that terminate the anisotropic layers, which are the location of catalytically active sites. Further progress in developing this understanding will enhance the ability to improve the catalysts' effectiveness for HDS processes. The combination of chemical synthesis and physical processes provides many experimental variables that allow control of particle size and shaping distribution, and will probably be applicable to the formation of closed structures of other layered compounds. It is a further challenge to synthesize these complex nanophase materials in an optimum form in commercial quantities.

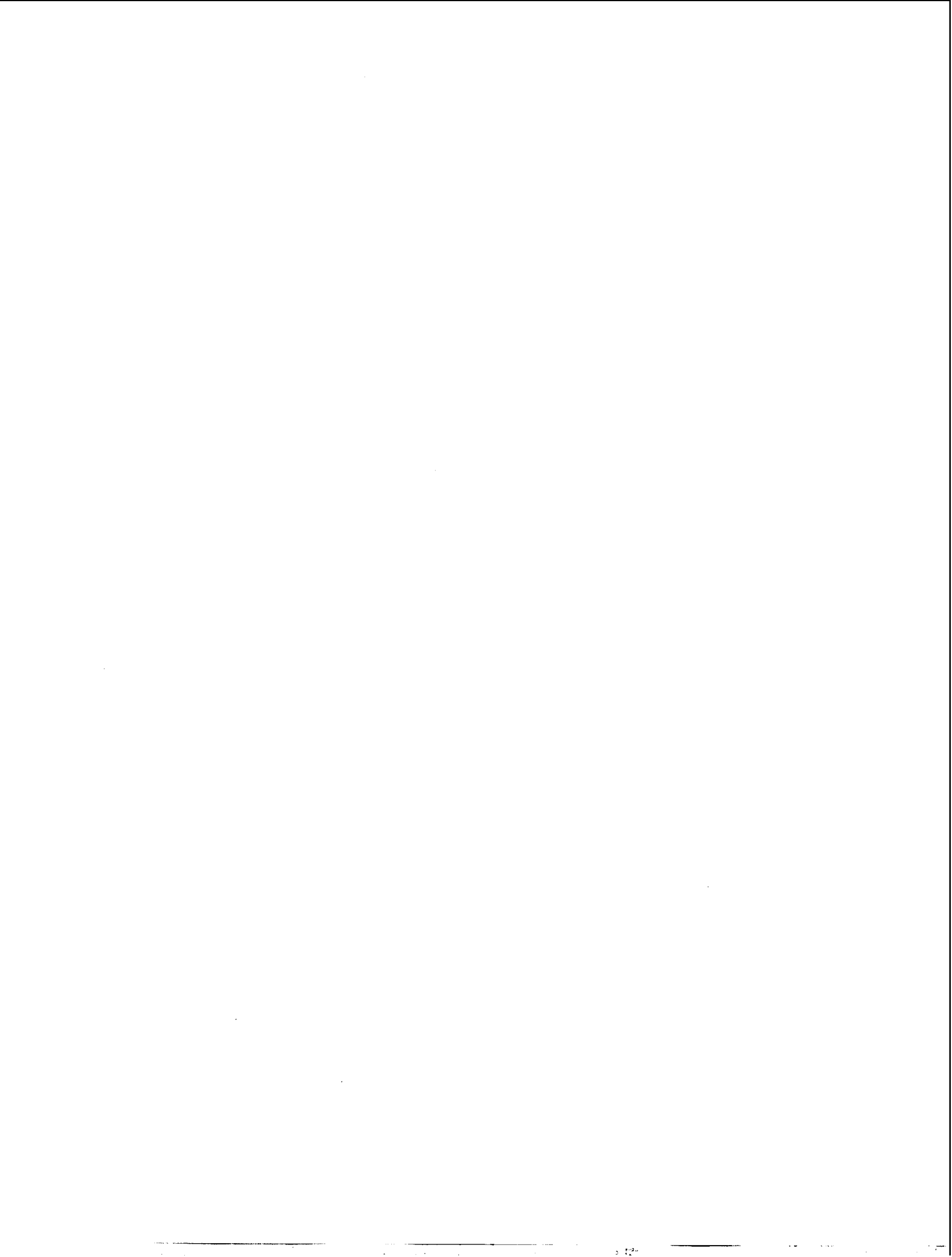
ACKNOWLEDGMENTS

The authors would like to thank the U.S. Department of Energy (DOE) Gateway Initiatives, United States.

REFERENCES

- Ijima, S. Single-shell carbon nanotubes of 1-nm diameter. *Nature* **1993**, *363* (6430), 603–605.
- Tenne, R.; Margulis, L.; Genut, M.; Hodes, G. Polyhedral and cylindrical structures of tungsten disulfide. *Nature* **1992**, *360* (6403), 444–446.
- Weiser, O.; Landa, S. *Sulfide Catalysts: Their Properties and Applications*; Oxford, 1973.
- Hilton, M.R.; Fleischauer, P.D. On the use of a Brale indenter to evaluate the cross-sectional morphology of sputter-deposited molybdenum disulfide solid lubricant films. *Thin Solid Films* **1989**, *172* (2), L81–L83.
- Whittingham, M.S. Electrical energy storage and intercalation chemistry. *Science* **1976**, *192* (4244), 1126–1127.
- Tributsch, H. Photoelectrochemical behavior of layer-type transition metal dichalcogenides. *Faraday Discuss. Chem. Soc.* **1981**, *70*, 190–200.
- Intercalation Chemistry*; Whittingham, M.S., Jacobson, A.J., Eds.; Academic Press: New York, 1982.
- Wilson, J.A.; Yoffe, A.D. Transition metal dichalcogenides. Discussion and interpretation of the observed optical, electrical, and structural properties. *Adv. Phys.* **1969**, *18* (73), 193–335.
- Singer, I.L. *Fundamentals of Friction: Macroscopic and Microscopic Processes*; Singer, I.L., Pollock, H.M., Eds.; Kluwer: Dordrecht, 1992; 237.
- Bowedn, F.P.; Tabor, D. *Friction: An Introduction to Tribology 91*; Anchor: Garden City, NY, 1973.
- Yacaman, M.J.; Lopez, H.; Santiago, P.; Galvan, D.H.; Garzon, I.L.; Reyes, A. Studies of MoS₂ structures produced by electron irradiation. *Appl. Phys. Lett.* **1996**, *69* (8), 1065.
- Parrilla, P.A.; Dillion, A.C.; Jones, K.M.; Riker, G.D.; Shultz, L.; Ginley, D.S.; Heben, M.J. The first true inorganic fullerenes? *Nature* **1999**, *397* (6715), 114.
- Dresselhaus, M.D.; Dresselhaus, G.; Eklund, P.C. *Science of Fullerenes and Carbon Nanotubes*; Academic Press, Inc.: New York, 1996; 1–6; 110–116.
- Homyonfer, M.; Mastai, Y.; Hershinkel, M.; Volterra, V.; Hutchison, J.L.; Tenne, R. Scanning tunneling microscope induced crystallization of fullerene-like MoS₂. *J. Am. Chem. Soc.* **1996**, *118* (33), 7804–7808.
- Zak, A.; Feldman, Y.; Alperovich, V.; Rosentsveig, R.; Tenne, R. Growth mechanism of MoS₂ fullerene-like nanoparticles by gas-phase synthesis. *J. Am. Chem. Soc.* **2000**, *122* (45), 11108–11116.
- Feldman, Y.; Wasserman, E.; Srolovitz, D.J.; Tenne, R. High-rate, gas-phase growth of MoS₂ nested inorganic fullerenes and nanotubes. *Science* **1995**, *267* (5195), 222–225.
- Whitby, R.L.D.; Hsu, W.K.; Boothroyd, C.B.; Kroto, H.W.; Walton, D.R.M. Tungsten disulfide coated multi-walled carbon nanotubes. *Chem. Phys. Lett.* **2002**, *359* (1, 2), 121–126.
- Lu, E.; Persans, P.D.; Ruppert, A.F.; Chianelli, R.R. Preparation and characterization of molybdenum disulfide microcrystals in colloidal dispersion. *Mater. Res. Soc. Symp. Proc.* **1990**, *164*, 153–158. (*Mater. Issues Microcryst. Semicond.*)
- Roxlo, C.B.; Deckman, H.W.; Dunsmuir, J.H.; Ruppert, A.F.; Chianelli, R.R. Surface disorder and exfoliation in lithographically textured molybdenum disulfide. *Mater. Res. Soc. Symp. Proc.* **1987**, *82*, 481–485. (*Charact. Def. Mater.*)
- Chianelli, R.R.; Ruppert, A.F.; Yacaman, M.J.; Vazquez-Zavala, A. HREM studies of layered transition metal sulfide catalytic materials. *Catal. Today* **1995**, *23* (3), 269–281.
- Divigalpitiya, W.M.R.; Frindt, R.F.; Morrison, S.R. Inclusion systems of organic molecules in restacked single-layer molybdenum disulfide. *Science* **1989**, *246* (4928), 369–371.
- Divigalpitiya, W.M.R.; Frindt, R.F.; Morrison, S.R. Oriented films of molybdenum trioxide. *Thin Solid Films* **1990**, *188* (1), 173–179.
- Divigalpitiya, W.M.R.; Frindt, R.F.; Morrison, S.R. Molecular composite films of molybdenum disulfide and styrene. *J. Mater. Res.* **1991**, *6* (5), 1103–1107.
- Wilcoxon, J.P.; Samara, G.; Newcomer, P. Optical features of nanosize iron and molybdenum sulfide clusters. *Mater. Res. Soc. Symp. Proc.* **1995**, *358*, 277–281. (*Microcryst. Nanocryst. Semicond.*)
- Wilcoxon, J.P.; Samara, G.A. Strong quantum-size effects in a layered semiconductor: MoS₂ nanoclusters. *Phys. Rev., B Condens. Matter* **1995**, *51* (11), 7299–7302.
- Parsapour, F.; Kelley, D.F.; Craft, S.; Wilcoxon, J.P. Electron transfer dynamics in MoS₂ nanoclusters: Normal and inverted behavior. *J. Chem. Phys.* **1996**, *104* (13), 4978–4987.
- Chianelli, R.R.; Prestridge, E.B.; Pecoraro, T.A.; DeNeufville, J.P. Molybdenum disulfide in the poorly crystalline “rag” structure. *Science* **1979**, *203* (4385), 1105–1107.

28. Chianelli, R.R. Amorphous and poorly crystalline transition metal chalcogenides. *Int. Rev. Phys. Chem.* **1982**, *2* (2), 127–165.
29. Chianelli, R.R. Fundamental studies of transition metal sulfide hydrodesulfurization catalysts. *Catal. Rev., Sci. Eng.* **1984**, *26* (3–4), 361–393.
30. Chianelli, R.R.; Ruppert, A.F.; Behal, S.K.; Kear, B.H.; Wold, A.; Kershaw, R. The reactivity of molybdenum disulfide single crystal edge planes. *J. Catal.* **1985**, *92* (1), 56–63.
31. Passaretti, J.D.; Chianelli, R.R.; Wold, A.; Dwight, K.; Covino, J. Preparation and properties of the systems cobalt rhodium sulfide ($\text{Co}_{1-x}\text{Rh}_x\text{S}_2$), cobalt ruthenium sulfide ($\text{Co}_{1-x}\text{Ru}_x\text{S}_2$), and rhodium ruthenium sulfide ($\text{Rh}_{1-x}\text{Ru}_x\text{S}_2$). *J. Solid State Chem.* **1986**, *64* (3), 365–371.
32. Chianelli, R.R. Pecoraro, T.A. U.S. Patent 42884422, 1981.
33. Ugarte, D. Curling and closure of graphitic networks under electron-beam irradiation. *Nature* **1992**, *359* (6397), 707–709.
34. Margulis, L.; Salitra, G.; Tenne, R.; Tallanker, M. Nested fullerene-like structures. *Nature* **1993**, *365* (6442), 113–114.
35. Tenne, R. Fullerene-like materials and nanotubes from inorganic compounds with a layered (2-D) structure. *Colloids Surf., A Physicochem. Eng. Asp.* **2002**, *208* (1–3), 83–92.
36. Mastai, Y.; Homyonfer, M.; Gedenken, A.; Hodes, G. Room temperature sonochemical synthesis of molybdenum sulfide fullerene-like nanoparticles. *Adv. Mater.* **1999**, *11* (12), 1012.
37. Remskar, M.; Skraba, Z.; Cleton, F.; Sanjines, R.; Levy, F. MoS_2 as microtubes. *Appl. Phys. Lett.* **1996**, *69* (3), 351–353.
38. Zelenski, C.M.; Dorhout, P.K. Template synthesis of near-monodisperse microscale nanofibers and nanotubes of MoS_2 . *J. Am. Chem. Soc.* **1998**, *120* (4), 734–742.
39. Prasad, T.P.; Diemann, E.; Muller, A. Thermal decomposition of ammonium dithiomolybdate, ammonium tetrathiomolybdate, ammonium dithiotungstate, and ammonium tetrathiotungstate. *J. Inorg. Nucl. Chem.* **1973**, *35* (6), 1895–1904.
40. Chianelli, R.R.; Berhault, G.; Santiago, P.; Mendoza, D.; Espinosa, A.; Ascencio, J.A.; Yacaman, M.J. Synthesis, fundamental properties and applications of nanocrystals, sheets, nanotubes and cylinders based on layered transition metal chalcogenides. *Mater. Technol. (Poulton-le-Fylde, UK)* **2000**, *15* (1), 54–61.
41. Curl, R.F.; Kroto, H.W.; Smalley, R.E. The 1996 Nobel prizes in science. *Sci. Am.* **1997**, *276* (1), 14–16, 18.
42. Remskar, R.; Mrzel, A.; Skraba, Z.; Jesih, A.; Ceh, M.; Demsar, J.; Stadelmann, P.; Levy, F.; Mihailovic, D. Self-assembly of subnanometer-diameter single-wall MoS_2 nanotubes. *Science* **2001**, *292*.
43. Vollath, D.; Seith, B.; Szabo, D.V. Nanoparticles from compounds with layered structures. *Acta Mater.* **2002**, *48*, 953–967.
44. Vollath, D.; Seith, B.; Szabo, D.V. German Patent application P 196 28 357.4, 1996.
45. Vollath, D.; Mobius, A. First World Congress on Microwave Processing, Florida, 1987. paper XVII-4.
46. van Arkel, A.E. *Physica* **1924**, pp. 4, 300 (JCPDS 3-1189).
47. NBS Monogr. **1971**, pp. 9, 25 (JCPDS 23-677).
48. Guenter, J.R.; Oswald, H.R. *Naturwissenschaften* **1968**, pp. 55, 177 (JCPDS 21-1231).
49. Salomons, W.; Wiegers, G.A. *Recl. Trav. Chim.* **1968**, pp. 87, 1339 (JCPDS 37-1492).
50. Trumbore, F.A.; Ter Haar, L.W. Unusual crystal growth morphologies in the niobium–selenium system. *Chem. Mater.* **1989**, *1* (5), 490–492.
51. Chianelli, R.R.; Daage, M.; Ledoux, M.J. Fundamental studies of transition metal sulfide catalytic materials. *Adv. Catal.* **1994**, *40*, 177–232.
52. Cruz-Reyes, J.; Avalos-Borja, M.; Farias, M.H.; Fuentes, S. Hydrodesulfurization catalysts prepared by two methods analyzed by transmission electron microscopy. *J. Catal.* **1992**, *137* (1), 232–242.
53. Yacaman, M.J.; Chianelli, R.R. In *The Structure and Potential Role of Atmospheric Nanoparticles*, Proceedings of the WERC/HSRC Meeting, Albuquerque, NM, April 23–25, 1997.



Nanostructures Derived from Phase-Separated Polymers

Michael R. Bockstaller
Edwin L. Thomas

Massachusetts Institute of Technology, Cambridge, Massachusetts, U.S.A.

INTRODUCTION

The field of polymer-based materials continues its enormous growth covering a wide range of products from disposable coffee cups to car bumpers to biomedical devices. The increased emphasis on enhancement of properties via materials with structures of components engineered on the nanoscale has opened up many new opportunities. For example, blending different polymers while retaining their individual properties in the composite is an effective way of engineering new nano- and microstructural materials from a limited palette of commodity polymers. At present five major reasons for the technological importance of polymer multicomponent systems can be identified: 1) improvements in material performance via synergistic interactions (e.g., temperature resistance, modulus, adhesion); 2) realizing desired processing conditions (e.g., melt viscosity, softening point, solvent resistance); 3) recycling industrial or municipal scrap polymers; 4) adjusting product composition to customer specifications by mixing of different batches; and 5) dilution of high-performance polymers for cost reduction.

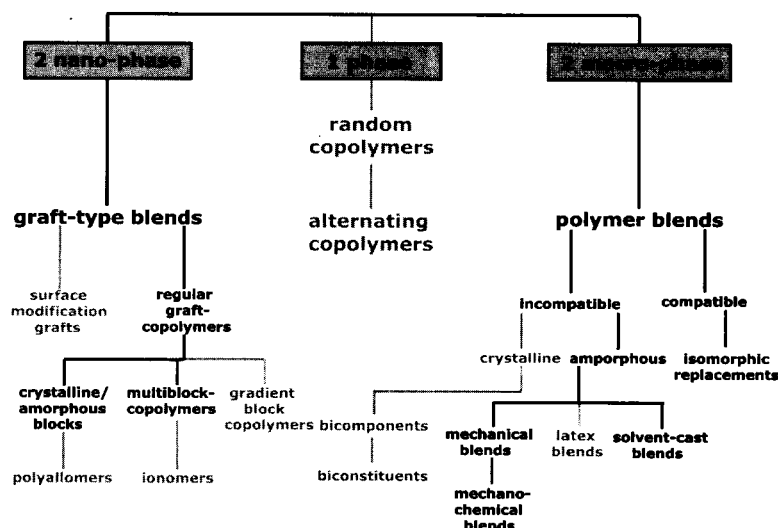
Despite their great industrial relevance, there exists no formally accepted nomenclature for multicomponent polymer systems. A possible classification scheme is provided in Scheme 1. Understanding and controlling the mechanisms of phase separation and nanostructure formation in polymer systems allows one to tailor the performance of these materials to a manifold of applications. For example, co-continuous blends of high- and low-melting point polymers where the low-melting point component is the majority component facilitate to dramatically increase thermal and mechanical properties such as toughness, stress at break, or high-temperature creep resistance while retaining ease of processability. Recent research suggests possible future applications of multicomponent polymer systems that are more far-reaching. Nanostructures based on block copolymer-homopolymer blends are currently studied as a platform for photonic materials with possible use in integrated optics or in thin films as nonlithographic route toward controlled patterning of 100-nm feature sizes. The future technological impact of the latter type of applications will crucially depend on the ability to control structure

formation on multiple length scales by strategic design of chemical groups as well as integrating synthetic design with specific processing pathways that increase the likelihood of attaining a targeted structure.

This article reviews polymer phase behavior and nanostructure formation beginning with a discussion of molecular architecture, equilibrium thermodynamics, and phase separation dynamics. The second part describes recent achievements to control the structure formation processes over macroscopic dimensions. The interplay of relevant balancing forces in self-organization processes is discussed aiming to give the reader some intuition about how molecular details and processing conditions can be used in order to control structure formation. In the third part, new research areas will be presented in which polymer-based nanostructures are likely to have major technological impact. Throughout, examples will focus on synthetic polymers that either are of high industrial interest or that suitably represent characteristics of a broad range of macromolecules but leaving out the complex structure formation processes found in natural biopolymers.

MOLECULAR ARCHITECTURE AND PHASE DIAGRAM

The term *polymer* means “many units” and designates a large molecule made up of smaller repeating units, the number of which determines the degree of polymerization N . Other basic quantities characterizing a polymer chain are the molecular weight $M=Nm$, with m being the molecular weight of a single repeat unit, and its radius of gyration R_G which scales as $N^{1/2}$ for flexible chains in their melt state. As a rule of thumb, molecular weights of common-type flexible polymers of $M \sim 10^5$ g/mol correspond to an effective size of the polymer chain of $R_G \sim 10$ nm. The inherent length scale in the nanometer range renders polymer materials naturally attractive for nanoeengineering purposes. Depending on the synthetic procedure, the repeating unit of a linear polymer may comprise a single identifiable precursor such as in poly(styrene) (PS) or might be composed of the residues of several



Scheme 1 Multicomponent polymer system classification scheme. The types of polymer systems relevant to this text are marked in black.

smaller molecules as in poly(hexamethylene-adipamide) (Nylon-6,6). Table 1 shows the chemical structures of a small selection of polymers relevant to this article. Next to the linear chain architecture, synthetic strategies have been developed to also obtain well-defined star- or branched molecular structures. For a detailed discussion of methods for polymer synthesis the reader is referred to Refs. [1] and [2]. A small subset of the wealth of architectures is shown in Scheme 2. Depending on molecular architecture, degree of polymerization, and temperature, the physical state of polymeric materials can vary between viscous liquid, glassy, semicrystalline, or liquid crystalline. Crystallization processes, which require a highly regular stereochemistry of the polymer, and the associated hierarchy of structures are beyond the scope of this article and will only be briefly mentioned.

Homopolymer Blends

The equilibrium phase behavior of a mixture of two linear polymers A and B was first derived by Flory^[3] and Huggins.^[4] According to the Flory–Huggins theory, the change in free energy upon mixing ΔG_m for a binary polymer blend is given by

$$\frac{\Delta G_m}{k_B T} = \frac{\phi_A}{N_A} \ln \phi_A + \frac{\phi_B}{N_B} \ln \phi_B + \phi_A \phi_B \chi \quad (1)$$

with k_B denoting the Boltzmann constant, T the temperature, $N_{A/B}$ the degree of polymerization (the number of mers of A and B), $\phi_{A/B}$ the volume fraction of polymers A and B, and χ the Flory–Huggins segment–segment interaction parameter. As large chains assume fewer

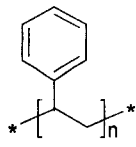
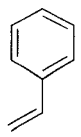
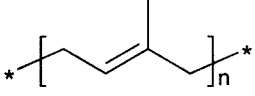
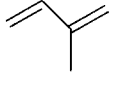
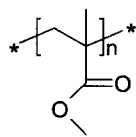
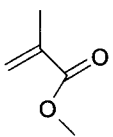
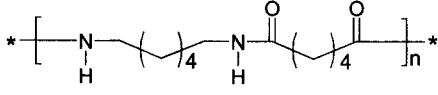
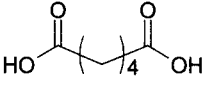
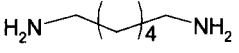
mixed configurational states, the entropic contribution (first two terms in Eq. 1) decreases with increasing molecular weight of the polymers. The phase behavior of binary polymer blends is then largely determined by the value of χ that is fixed by the particular choice of the repeating units of polymers A and B. χ parameters can often be expressed as a linear function of $1/T$, i.e., $\chi(T) = \alpha + \beta/T$; values for α and β have been tabulated for a variety of monomers.^[5] Given a binary polymer mixture, the phase behavior can be predicted by the calculation of the spinodal and binodal that are given by the criteria of stability (Eq. 2) and thermodynamic equilibrium (Eq. 3), respectively.

$$\frac{\partial^2}{\partial \phi_A^2} \Delta G_m = 0 \quad (2)$$

$$\frac{\partial}{\partial \phi_A} \Delta G_m(\phi_A)^{\text{phase 1}} = \frac{\partial}{\partial \phi_A} \Delta G_m(\phi_A)^{\text{phase 2}} \quad (3)$$

The binodal and spinodal curves meet in the critical point that is given for a symmetric polymer blend with equal molecular volumes ($N_A v_A = N_B v_B$, v_i denoting the volume of monomer i) by $\phi_c = 1/2$ and $\chi_c = 2/N$. A typical phase diagram for a binary mixture of symmetric linear homopolymers is shown in Fig. 1. Depending on the sign and temperature dependence of χ , different types of phase behavior can be distinguished, the most important are referred to as: upper critical solution temperature (UCST, mixing upon heating), which is found for positive χ and $d\chi/d(1/T) > 0$, as well as lower critical solution temperature (LCST, mixing upon cooling), which is found for negative χ and $d\chi/d(1/T) < 0$. In a

Table 1 Structure and nomenclature of selected polymers

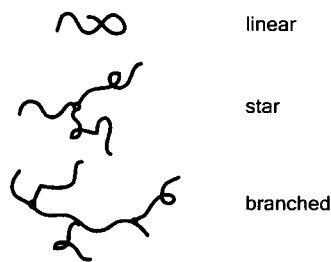
Structure	Monomer	Nomenclature (abbreviation)
		Poly(styrene) (PS)
		Poly(isoprene) (PI)
		Poly(methylmethacrylate) (PMMA)
	 	Poly(hexamethylene adipamid) (Nylon-6,6)

few experimental systems, closed-loop behavior has been observed, i.e., low-temperature LCST and high-temperature UCST.^[6] Table 2 shows a list of some homopolymers that are frequently found in industrial applications and their mixing behavior.

Mechanisms of phase separation in homopolymer blends

There are two major mechanisms of phase separation that have been identified and that occur in different parts of the phase diagram as shown in Fig. 1: nucleation and growth (NG) and spinodal decomposition (SD). NG occurs in the metastable region of the phase diagram (the area between binodal and spinodal) and is characterized by the following steps: 1) initial formation of spherical

fragments of the more stable phase (requires activation barrier); 2) growth of nuclei by first diffusion of material from the supersaturated continuum followed by droplet-droplet coalescence and Ostwald-ripening. Spinodal decomposition, which is the commonly observed mechanism for phase separation in homopolymer blends, occurs in the unstable region of the phase diagram and is characterized by initial small-amplitude composition fluctuations that increase with time and result in interconnected phase morphologies at intermediate stages of phase separation. Co-continuous polymer blends have been the subject of intense research as they generally exhibit superior mechanical properties. Co-continuous interconnected morphologies are commonly induced either by arresting SD or by mechanical mixing of polymer mixtures. Such systems often suffer the problem that they tend to move toward the equilibrium macro-phase-separated structure. Blending of homopolymers in the presence of appropriately chosen graft copolymers has been shown to be a versatile alternative to mechanical mixing, facilitating the stabilization of co-continuous blends by increasing the thermodynamic stability and flexibility of the interface.^[7] Fig. 2 shows the microstructure of a poly(ethylene)/poly(amide) co-continuous blend and the associated enhancement of elastic and tensile properties. Note that the elastic modulus increases by order of magnitudes in the case of the co-continuous blend with regard to its phase separated counterpart.

**Scheme 2** Selection of homopolymer architectures.

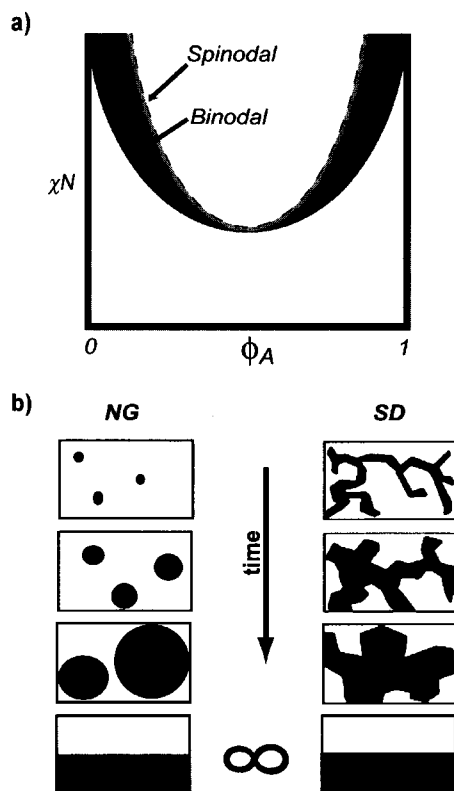


Fig. 1 a) Phase diagram of a symmetric homopolymer blend ($N_A = N_B$). Shaded area indicates metastable region. b) Schematic of the mechanism of phase separation in the metastable (nucleation and growth, NG) and unstable (spinodal decomposition, SD) region of the phase diagram. (View this art in color at www.dekker.com.)

Block Copolymers

Block copolymers consist of two distinct polymer chains that are covalently linked together to form a chain. The large variety of block configurations that can be constructed using modern synthetic methods can be classified based on the number of chemically distinct blocks as well as linear vs. branched connectivity of the blocks within a copolymer as indicated in Scheme 3. As structure formation processes of most of these systems are still under discussion, this article will focus on the current understanding of the simplest and most studied system—linear amorphous diblock copolymers. For excellent review articles in this field we refer the reader to Refs [8–10].

Because block copolymers are single-component systems, they cannot macrophase separate in the melt like a pair of linear homopolymers does. Instead, block copolymers segregate on a local scale. The decrease of A–B segment contacts by local segregation is often

referred to as microphase separation. The enthalpy gain obtained by the local segregation process is counterbalanced by an associated loss in system entropy that results from the localization of the block joints at the intermaterial dividing surface (IMDS) and the necessary stretching of the polymer chains away from the IMDS in order to maintain uniform density. As the entropic contribution can be shown to scale as N^{-1} with $N = N_A + N_B$, it is again the product χN that dictates the microphase-separation process. Three different limiting regimes exist for diblock copolymer melts: 1) the disordered state with unperturbed Gaussian chain statistics ($R_G \sim N^{1/2}$) which is found for $\chi N \ll 1$; 2) the ordered state in the weak segregation limit ($\chi N \sim 10$) with sinusoidal composition fluctuations representing a periodic microstructure; and 3) the ordered state in the strong segregation limit ($\chi N \gg 10$) where strong repulsive forces between segments of A and B result in sharp interfaces separating nearly pure A and B domains with pronounced stretching of the block chains ($R_G \sim N^{2/3}$). Below the order–disorder transition temperature, enthalpic effects become more influential and the block copolymer microphase separates. The product χN and the compositional parameter $f = N_A / (N_A + N_B)$ determine one of seven phases that represent free-energy minima for the ensemble of molecular configurations. The following sequence of phases has been observed for PS–PI diblocks: $f_{PS} < 0.17$, body-centered cubic (BCC); $0.17 < f_{PS} < 0.28$, hexagonal; $0.28 < f_{PS} < 0.34$, bicontinuous (double gyroid); $0.34 < f_{PS} < 0.62$, lamellar; $0.62 < f_{PS} < 0.66$, inverse double

Table 2 Mixing behavior of selected homopolymer blends

Polymer 1	Polymer 2	Miscibility
Poly(styrene)	Poly(butadiene)	no
Poly(styrene)	Poly(methyl methacrylate)	no
Poly(styrene)	Poly(dimethyl siloxane)	no
Nylon-6,6	Poly(ethylene-propylene)	no
Poly(propylene)	Poly(ethylene)	no
Poly(styrene)	Poly(vinyl methylether)	yes
Poly(styrene)	Poly(dimethyl phenyleneoxide)	yes
Poly(ethylene oxide)	Poly(acrylic acid)	yes
Poly(vinylchloride)	Poly(butylene terephthalate)	yes
Poly(methyl methacrylate)	Poly(vinylidene fluoride)	yes

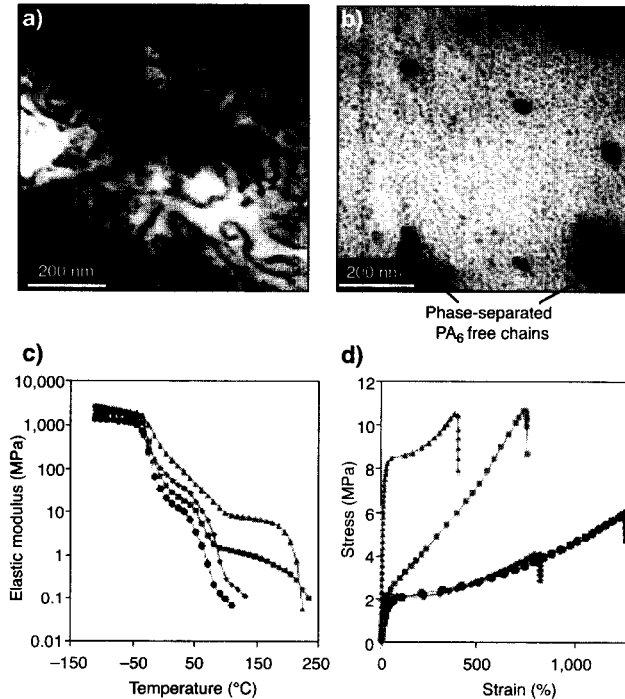
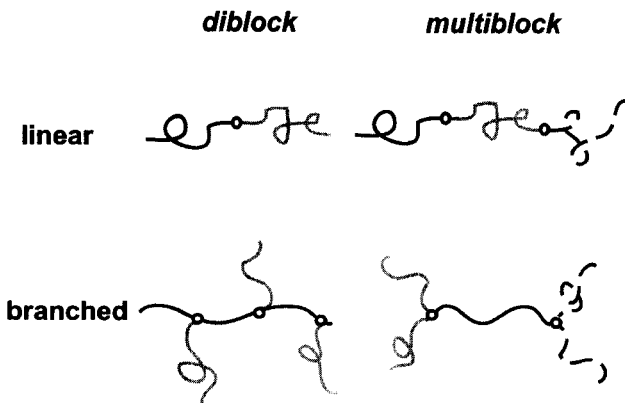


Fig. 2 Transmission electron micrographs of a) co-continuous nanostructured blend (80/20 ratio poly(ethylene)/Nylon-6,6); b) phase separated blend. c) and d) show the increase of elastic modulus and stress-strain properties for co-continuous phase formation. Triangles: co-continuous (80/20), squares: micellar blend (80/20), diamonds: macrophase separated blend, circles: poly(ethylene). (From Ref. [8]. Copyright 2002, Macmillan Publishers Ltd.) (View this art in color at www.dekker.com.)

gyroid; $0.66 < f_{PS} < 0.77$ inverse hexagonal; $f_{PS} > 0.77$, inverse BCC. Depending on the packing frustration self-consistent field calculations also suggested the formation of a double diamond and a perforated lamellar



Scheme 3 Selection of di- and multiblock copolymer architectures. (View this art in color at www.dekker.com.)

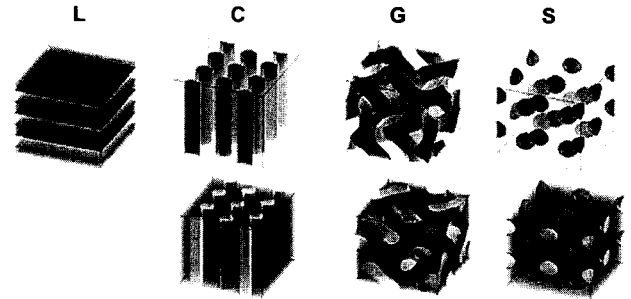
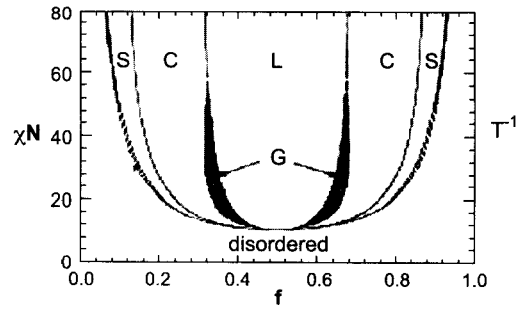


Fig. 3 Phase diagram of a symmetric block copolymer ($N_A = N_B$). L: lamellar phase, C: cylindrical phase, G: gyroid phase, S: spherical phase (cubic body centered). (More information about minimal surfaces: <http://www.msri.org/publications/sgp/jim/images/stills/mini/index.html>.) (View this art in color at www.dekker.com.)

structure between the well-established lamellar and cylinder phases, but these microdomain geometries are considered to be only metastable and will not be discussed here. A phase diagram along with a schematic of the different periodic microstructures found as a function of χN and f for a typical diblock copolymer is shown in Fig. 3. Fig. 4 demonstrates the observation of the above mentioned morphologies via electron micrographs of PS-PI diblock copolymers.

Block copolymer-homopolymer blends

A natural continuation of the research mentioned above is the study of block copolymer/homopolymer blends. Structure formation in blends of homopolymers and block copolymers is determined by the interplay of macrophase separation of the homopolymer and the microphase separation of the block copolymer. Which effect predominates depends on the relative lengths of the respective polymers and on the composition of the blend. In binary blends, low-molecular weight homopolymer is solubilized within a microphase-separated block copolymer structure at low concentrations. Increasing the molecular weight of the homopolymer such that it approaches that of the block

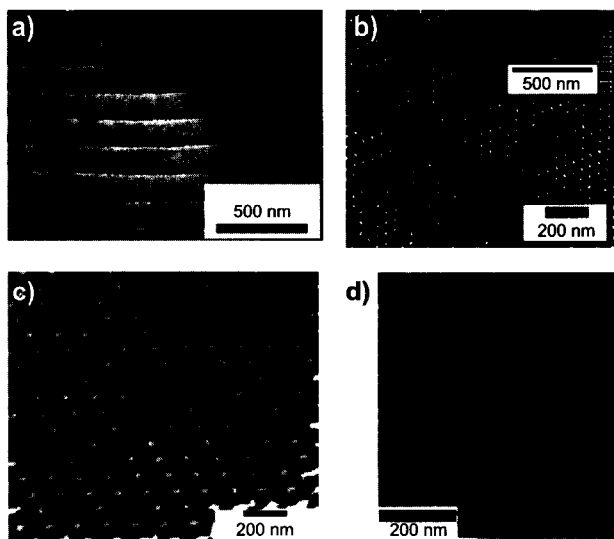


Fig. 4 Transmission electron micrographs of a) lamellar; b) hexagonal cylindrical viewing direction along cylinder axis, inset: viewing direction perpendicular to cylinder axis; c) gyroid [view direction along (110)] and d) BCC spherical phase of poly(styrene-*b*-isoprene) copolymer [along (100)]. For all micrographs, the isoprene block was stained with Osmiumtetroxide to enhance contrast.

copolymer leads to an increasing tendency for segregation of the homopolymer to the center of the domain. If the molecular weight of the homopolymer exceeds the one of the block copolymer, macrophase separation tends to predominate.^[11]

Binary block copolymer blends

Binary block copolymer blends offer another route toward nanoscale structures. Binary blends of triblock (ABC) and diblock (ac) copolymers, with the upper and lower case characters distinguishing the chemical composition and molecular weight of the respective blocks, were extensively studied because of their potential to microphase separate into *noncentrosymmetrical* morphologies. These nanostructures are of high technological interest, as the absence of centrosymmetry implies macroscopic polarization that is associated with many useful properties such as piezo- and pyroelectricity and second-order nonlinear optical activity. Theoretical studies on the formation of noncentrosymmetric morphologies were performed for the case of lamellar structure and suggest that noncentrosymmetrical morphologies require sufficient asymmetry between the Aa and Cc domains. Fig. 5 shows a schematic of possible lamellar morphologies in blends of ABC and ac block copolymers along with an

excellent electron micrograph providing noncentrosymmetrical lamellar structure obtained by blending a poly(styrene-*b*-butadiene-*b*-*tert*-butylmethacrylate) triblock copolymer with poly(styrene-*b*-*tert*-butylmethacrylate) diblock copolymer.^[12]

STRATEGIES FOR CONTROLLING THE SELF-ORGANIZATION PROCESSES

Mechanical behavior can be readily tuned when, e.g., glassy mesostructures are formed in a rubbery matrix, and indeed, glassy-rubbery block copolymers are used for various applications as advanced engineering materials. However, the possible impact of block copolymer

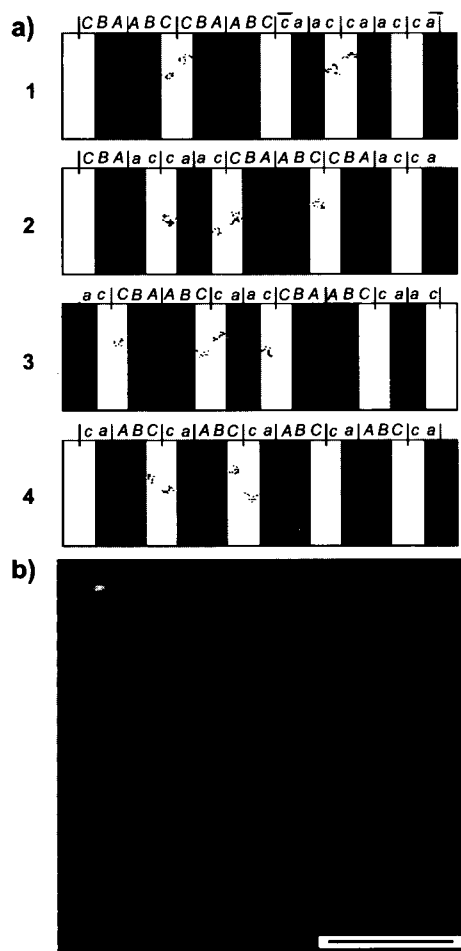


Fig. 5 a) Diagram of the possible lamellar morphologies of ABC/ac block copolymer blends. 1: Macrophase separation, 2: random sequence, 3: centrosymmetric sequence, 4: noncentrosymmetric sequence. b) Transmission electron micrograph of the noncentrosymmetric blend. Scale bar: 250 nm. (From Ref. [13]. Copyright 1999, Macmillan Publishers Ltd.)

nanostructures that are envisioned is much more far-ranged. The emerging challenges that have to be resolved involve the extension of hierarchically ordered structures to larger length scales and the development of new processing technologies that allow to control the ordering process at various length scales. In the following sections, several approaches will be presented that address these challenges. 1) Strategic design of the molecular architecture, e.g., by introducing anisotropic groups that introduce configurational constraints to the self-assembling process; 2) by exploiting the effect of external fields on the self-assembly process; or 3) by using surface energetics and selective polymer–substrate interactions to guide the system to the desirable global geometries.

Techniques Involving Molecular Architecture

Structure formation in rod–coil block copolymer systems

If one block in a coil–coil block copolymer is substituted by a polymer type that exhibits highly restricted conformational freedom, a rod–coil block copolymer is obtained. The interest in rod–coil block copolymers is fueled by the extraordinary wealth of morphologies that are found in rod–coil systems, which can result in novel functional materials with intriguing optical or electronic properties. This spectrum of domain morphologies is due to the delicate interplay between liquid crystallinity of the rod block combined with the phase separated microdomain morphologies. Rod–coil block copolymers also provide an excellent example of *designer nanoscale materials* as the rod blocks represent active sites that can be addressed by external fields (flow, electric, magnetic), providing a means to guide the system into well-defined macroscopically ordered states. A rod-like conformation of a polymer is induced either by step-wise coupling of rigid mesogenic units to form low-molecular weight oligomeric rods or in macromolecular systems by creating a rigid polymer backbone with alternating conjugation, by steric hindrance of side groups attached to each repeating unit or by the formation of helical secondary structures. The asymmetry in the rigidity of the respective rod vs. coil blocks significantly increases the Flory–interaction parameter χ , such that rod–coil block copolymers microphase separate already at low weight fractions of the rod component. The hierarchical order from the nano- to the microscale results as a consequence of the mutual repulsion of the dissimilar blocks and the packing constraints that are imposed by the connectivity as well as the tendency toward orientational ordering of the rod block.

Currently, there exists no general theoretical framework that can account for the complex phase behavior thus observed in rod–coil copolymer systems. Three examples will be provided that represent some of the new morphologies that are encountered in rod–coil block copolymer systems. For excellent review articles of this field we refer the reader to Refs. [13] and [14].

Stupp et al. reported the formation of large, well-organized supramolecular structures (10² kDa) by self-assembly of rod–coil *oligomers* consisting of an elongated mesogenic rods with volume filling fractions ranging from 0.19 to 0.36 and a coil-like poly(isoprene) (PI) part.^[15] Depending on the rod filling fraction, the formation of a strip morphology ($f_{\text{rod}}=0.36$) or a hexagonal superlattice structure ($f_{\text{rod}}=0.25$) was observed. Substituting the poly(isoprene) coil block by a (styrene)₉-*b*-(isoprene)₉ oligomer was reported to result in the formation of mushroom-like assemblies containing about $N=100$ rod–coil oligomers that self-organize into superlattice domains. A schematic of the proposed structure is given in Fig. 6.

Chen et al. investigated the structures formed in *high-molecular* rod–coil block copolymer systems consisting of poly(hexylisocyanate) with $N=900$ as the rod block and poly(styrene) with $N=300$ as the coil block.^[16] Depending on the volume fraction of rod component, the formation of three different morphologies was reported. These were explained to occur as the result of microphase separation of the blocks and crystallization of the rods during solvent evaporation. For a volume filling fraction of the rod

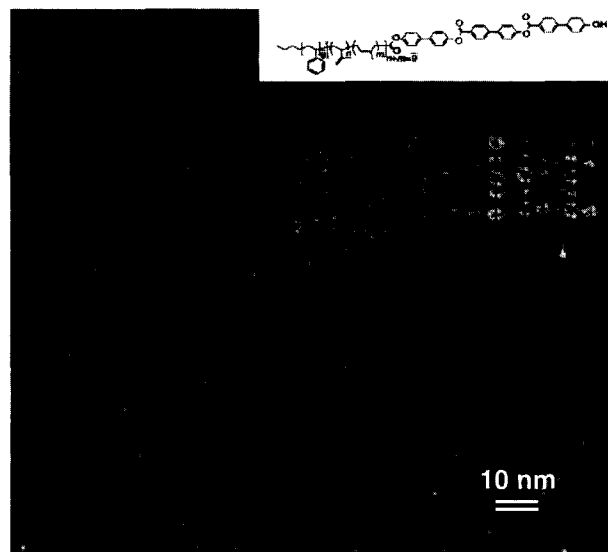


Fig. 6 Transmission electron micrograph revealing superlattice of regularly shaped aggregates. Inset: Suggested mushroom-like morphology of the aggregate. (From Ref. [16]. Copyright 2001, American Association for the Advancement of Science.)

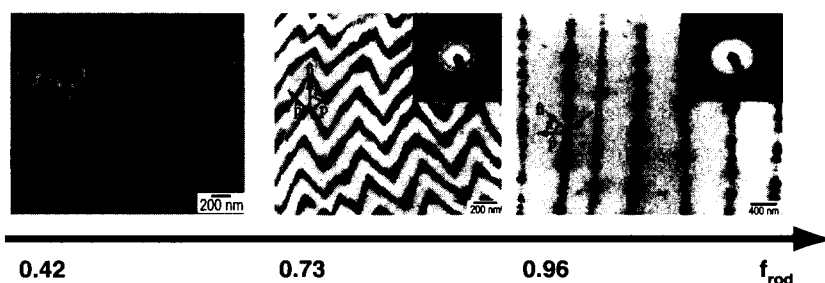


Fig. 7 Transmission electron micrographs of the morphologies of the PHIC-PS rod-coil block copolymer: wavy-lamellar ($f_{\text{PHIC}}=0.42$), zigzag ($f_{\text{PHIC}}=0.89$) and bilayer arrowhead ($f_{\text{PHIC}}=0.96$). The dark regions correspond to PS (stained with Rutheniumoxide). (From Ref. [17]. Copyright 2001, American Association for the Advancement of Science.) (View this art in color at www.dekker.com.)

component $f_{\text{rod}}=0.42$, the formation of a wavy lamellar structure was observed, in which the rod blocks are tilted with respect to the layer normal by about 60° . For $f_{\text{rod}}=0.73$ a novel “zigzag” morphology was observed in which the rod and coil blocks are arranged in a zigzag fashion and the rod blocks are tilted with respect to the layer normal by 45° . For even higher rod filling fractions ($f_{\text{rod}}>0.96$) an “arrowhead-like” pattern formation was observed. Fig. 7 shows electron micrographs of the observed morphologies. The complexity of the structure formation process in rod-coil systems is indicated by the pronounced effect of solvent on the structures depicted in Fig. 7. Well-oriented zigzag patterns were observed only when toluene was used, whereas the use of chloroform as a solvent resulted in more disordered arrangement of the zigzags. The observed difference can be understood as the quality of the solvent determines the onset of microphase separation of the blocks as well as the onset of liquid crystallization of the rod blocks. As a consequence, rod-coil morphologies often do not represent equilibrium structures but rather kinetically trapped states. Park et al. have continued the study of microstructure formation in

rod-coil block copolymers and demonstrated the formation of long-range periodic domain walls yielding a hierarchical morphology with order on multiple length scales consisting of interchain crystals of the rod blocks (1.5 nm), block copolymer microdomains (55 nm), and periodic Neel domain walls ($\sim 1 \mu\text{m}$).^[17] This study is remarkable for two reasons. First, the block copolymer-poly(3-(triethoxysilyl)propylisocyanate-*b*-styrene) (PIC-PS) employed in their study contains reactive groups as part of the isocyanate rod blocks. These entities allow the polymer to be covalently tethered to inorganic substrates after microstructure formation. Second, by directional solvent evaporation, the authors demonstrated unidirectional alignment of domain wall patterns on the centimeter length scale while maintaining interchain and microdomain ordering. A pair of atomic force micrographs of the observed hierarchical rod-coil structure are shown in Fig. 8.

Effect of Mechanical and Electric Fields

Polymeric materials can undergo dramatic changes in their structure in response to external fields. This provides opportunities to direct distinct alignments of polymeric nanostructures through processing. Polymer engineers have long exploited processing to increase properties (e.g., fiber production) through increase of crystallinity and chain orientation. For many envisioned applications of polymer-based nanostructures, it is of special importance to be able to produce functional macroscopic materials with uniform large-scale orientation. In general, self-assembly processes alone do not result in globally ordered structures but rather heterogeneous morphologies consisting of randomly oriented grains within which the domains have homogeneous alignment. The possibility to induce global order in block copolymer microstructures by flow field alignment was pioneered by Keller et al. in extruded polymer materials and a variety of other flow methods have been developed, such as roll-casting and

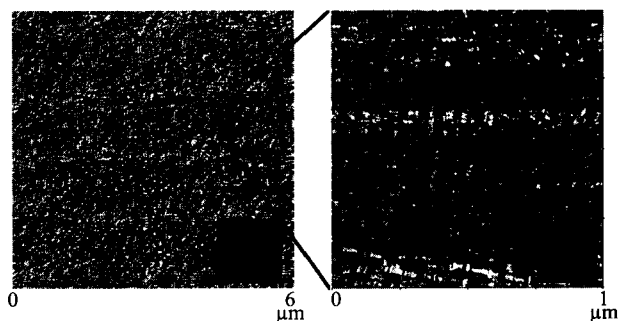


Fig. 8 Tapping mode atomic force micrographs of the hierarchical structure formation of PS-PIHC thin films after casting on silica substrate. The insets show Fourier-transformed images. (View this art in color at www.dekker.com.)

extensional flow.^[18-20] Kornfield et al. studied the influence of oscillatory shear on the alignment of lamellar morphology forming block copolymers by in situ rheo-optical methods that allow monitoring the alignment of the lamellae as a function of applied shear rate and amplitude.^[19] It was argued that with increasing shear rate three different frequency regimes can be distinguished for layered microstructured block copolymers in which the polymer domains have dissimilar viscoelastic properties. Two characteristic frequencies that determine the effect of oscillatory shear on the alignment of lamellar samples were identified: a lower frequency limit ω_d that is associated with the lifetime of fluctuations on a layered structure and a higher frequency limit ω_c that reflects the dynamics of conformational distortions of single polymer chains. It was found that oscillatory strain shearing induces parallel alignment with respect to the shear

direction for $\omega < \omega_d$, perpendicular alignment for $\omega_d < \omega < \omega_c$, and parallel alignment for $\omega_c < \omega$.

For cylindrical microdomain forming coil-coil block copolymers subjected to steady or oscillatory shear, parallel orientation, i.e., the cylinder axes are aligned along the flow direction, was found to be the usual orientational state. However, by anchoring liquid crystalline side groups to a coil-coil block copolymer, Osuji et al. could demonstrate that the strong interaction of the mesogens with the applied flow field can force the cylindrical microdomains to align *transverse* to the flow direction.^[21] In their study of the effect of oscillatory mechanical shear on the microstructure formation of a PS-PI block copolymer in which each isoprene block was functionalized with a mesogenic group, the authors concluded that the invariant homogeneous anchoring of the mesogens with respect to the IMDS results in the

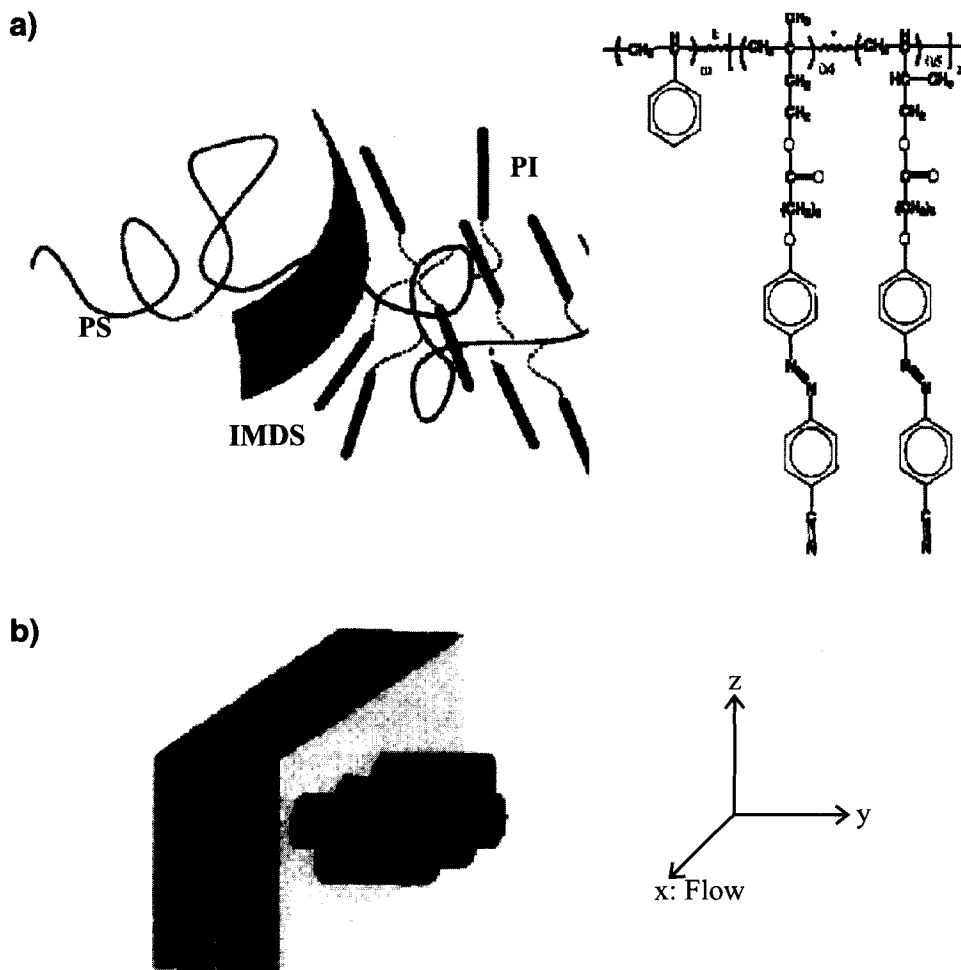


Fig. 9 Schematic structural model of the transverse alignment of cylindrical microdomains and smectic layers. Flow is along *x*- and vorticity is along *y* direction. The model represents a compromise structure in which cylinders are transverse and smectic layers are perpendicular, but the boundary condition for the mesogens are maintained homogeneous. (From Ref. [22].)

transverse cylindrical orientation under shear. A schematic of the proposed structural model of perpendicular smectic layers and transverse cylindrical microdomains is given in Fig. 9.

Amundson et al.^[22] presented a detailed mechanistic study of the effect of electrical fields on the structure evolution in lamellar block copolymer systems. By applying electrical fields of 1.8 MV/m to a symmetric PS-PMMA diblock copolymer while heating the polymer above glass transition temperature, a significant increase in orientation of the lamellae along the electric field direction could be observed. The ordering effect of the electric field could be explained by the orientational dependence of the systems free-energy in the presence of the external field. The situation is similar to the effect of an oscillatory shear-field when $\omega < \omega_d$. The external field raises the free-energy associated with lamellar compression or splay and hence causes movement and annihilation of defect walls and disclination lines. A schematic of the defect movement along with electron micrographs of the films with and without electric field alignment is shown in Fig. 10. Recently, Thurn-Albrecht et al. applied a similar procedure to align cylindrical PS-PMMA block copolymers using electric field strengths of 40 MV/m.^[23]

Thin Film Morphologies

Whereas bulk morphologies of microphase-separated block copolymers are often typified by grains of ordered domains that are randomly oriented with respect to each other, thin films can sometimes exhibit highly ordered domains. This orientation can be understood as a direct result of the surface and interfacial energy minimization. The possible applications of block copolymer thin films have been widely recognized and constitute a very active current field of research. An excellent introduction to the field is the recent review article by Fasolka and Mayes.^[24] Of the various microdomain types, the most investigated is the lamellar. Most theoretical work regarding the physics of thin film morphology was done for the case of symmetrical boundary conditions that is realized, e.g., when the film is located in between two identical substrates. It was found that for films with thickness greater than the lamellar thickness, $t > L$, the lamellae orient parallel to the substrate surface. As a result of the surface substrate boundary conditions the most energetically compatible block is expressed at each of the surfaces. Depending on which block wets the respective surface, one distinguishes between symmetric (same block wets each surface) and antisymmetric (different blocks wet the two surfaces) wetting. The equilibrium conditions for stability of symmetric films are then given as $t = nL$, with n being an integer, and $t = (n + 1/2)L$ for antisymmetric wetting. It was proposed that the

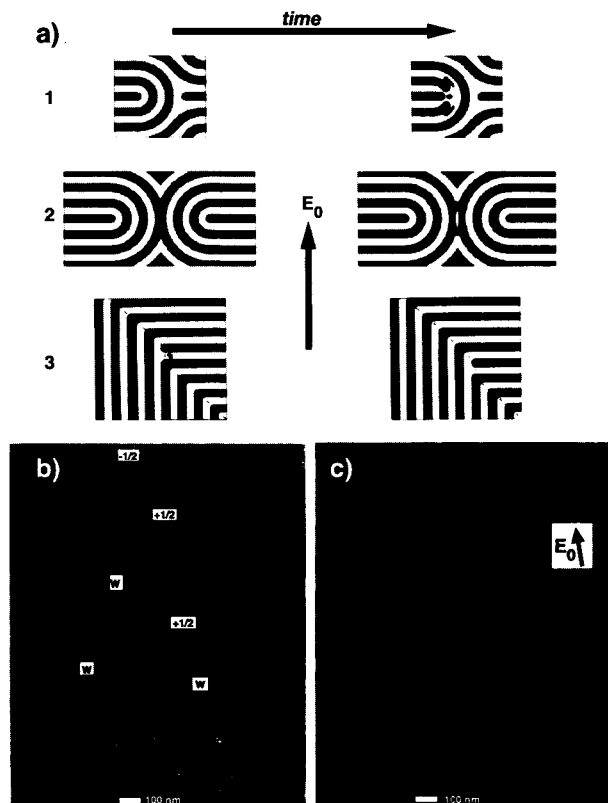


Fig. 10 a) Movement of the disclination lines and wall defects occurring by glide and climb of edge dislocations and creation of pores. 1: Disclination lines approach by perforation of layer; 2: focal conic loop forms island that grows by climb motion along the disclination loop; 3: through combination of climb and glide motion an edge dislocation propagates along a wall defect. b) Transmission electron micrographs of PS-PMMA perpendicular to field direction and c) parallel to field direction. (From Ref. [23].)

entropic penalty that is imposed on chains when surface-parallel lamellae are constrained to film thicknesses incommensurate with integer multiples of L can induce the perpendicular lamellar orientation if the entropic penalty exceeds the enthalpic gain from preferential wetting. A summary of possible thin film morphologies is given in Fig. 11.

Although the assumption of symmetric boundary conditions simplifies the analysis, many practical thin film situations exhibit asymmetric boundary conditions, e.g., supported film systems. In supported film systems, the polymer-substrate interfacial energy of a given type of monomer can differ from its surface energy by an order of magnitude. The presence of asymmetric boundary conditions can therefore result in new morphological trends not found in the symmetric case, e.g., the formation of hybrid structures involving parallel as well as perpendicular alignment. At the time of writing no theoretical model has

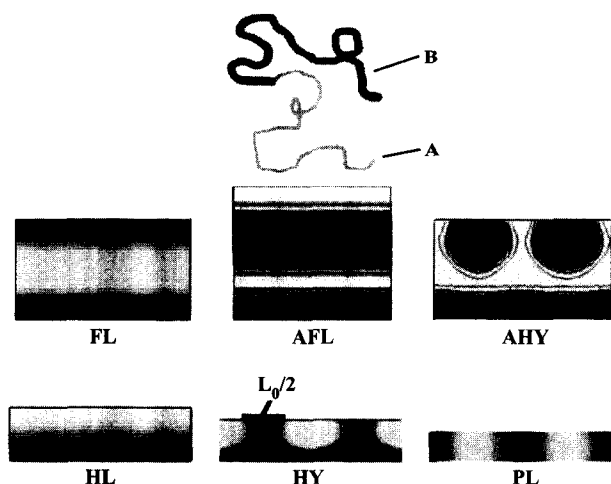


Fig. 11 Diblock copolymer thin film morphologies as a function of boundary conditions. A-block is gray, B-block is black. L_0 : film thickness, FL: symmetric surface-parallel lamellae, AFL: antisymmetric surface-parallel lamellae, AHY: antisymmetric hybrid structure, HL: half-lamellae, HY: symmetric hybrid structure, PL: surface-perpendicular lamellae. (From Ref. [24]. Copyright 2001, Annual Reviews.) (View this art in color at www.dekker.com.)

been developed that could accurately account for many of the experimental observations. This is in part due to the finite roughness and deformability of most surfaces on the molecular scale that represents a major problem in the

application of the theoretical models mentioned above to real supported films.

Epitaxial crystallization of block copolymer thin films

Epitaxy denotes the oriented overgrowth of one crystalline material upon the surface of another. In general, this process requires an approximate agreement in lattice spacings of the two components. Epitaxy is a traditional method of material science used to control registration and orientation. Block copolymers that contain one crystallizable block are of great interest as the crystallization provides an additional driving force for the microphase separation. The resulting morphology is the result of the interplay between segregation and crystallization process and is therefore process-path dependent, resulting in new opportunities to control the structure formation process by directing the crystallization process. Epitaxial methods were shown to be particularly interesting in controlling the orientation of microphase-separated block copolymer domains over large areas. De Rosa et al. recognized that because of crystallographic matching of poly(ethylene) and benzoic acid crystals, the poly(ethylene) blocks of a semicrystalline poly(ethylene-*b*-ethylenepropylene-*b*-ethylene) triblock copolymer can be epitaxially crystallized onto crystals of benzoic acid thereby directing the microphase separation process.^[25] Electron micrographs depicting the microstructure of the block copolymer

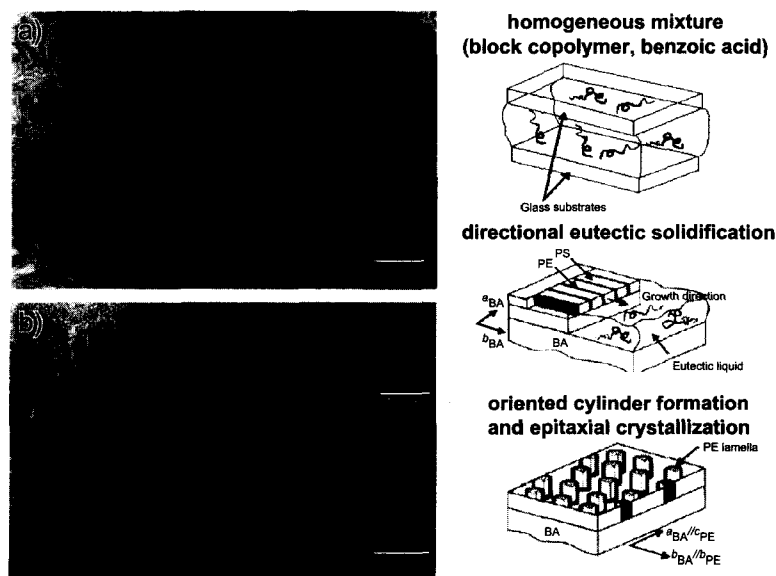


Fig. 12 Transmission electron micrographs of a) solvent-cast and b) directionally solidified/epitaxially crystallized PS-PE copolymer. PE domains form pseudo-hexagonal lattice of perpendicular-oriented cylinders. The styrene blocks have been stained with Rutheniumtetroxide for contrast enhancement. The inset in b) shows magnified region demonstrating the noncircular shape of the PS-PE interface resulting from the 15% smaller domain spacing of benzoic acid in *b* direction. (From Ref. [25]. Copyright 2000, Macmillan Publishers Ltd.)

thin film with and without epitaxial direction are shown in Fig. 12. Epitaxial control over the microphase separation process continues to attract much attention as it opens a new dimension to the control of nanostructure formation: crystal orientation on the 1–10-nm length scale as well as microstructure orientation on the 10–100-nm length scale.

TRENDS IN EXPLOITING POLYMER-BASED NANOSTRUCTURES

Recent advances in understanding the formation of nanostructures based on self-assembled microphase separated block copolymers and the external parameters that afford global ordering of these structures have resulted in applications that capitalize on the specific structural characteristics rather than on a volume averaged behavior. Microphase separated block copolymers have been studied extensively as an alternative approach to conventional lithographic techniques to produce highly ordered nanostructures with possible applications such as a high-

density magnetic recording device or a photonic band-gap material. In the following we present some examples of the new directions in this area of research.

Block Copolymers as Photonic Band Gap Materials

As block copolymers self-assemble into periodic one-, two-, or three-dimensional equilibrium structures, optical effects such as photonic band gaps can be obtained when the molecular weight of the block copolymer is high enough such that the domain spacing is of the order of the wavelength of light (typically $M \sim 10^6$ g/mol). Photonic band gaps denote frequency regions in which light of certain polarization and propagation direction cannot propagate through the material.^[26] As the synthesis and processing of high molecular weight polymers is delicate, the first observation of a self-assembled polymer-based photonic material was not published until 1999.^[27] Various techniques have been developed in order to solve the eminent problem of the inherently low dielectric contrast between typical polymers. Methods such as selective deposition of high index nanocrystals within the polymer scaffold^[28] or selective etching of one of the domains^[29] can raise the dielectric contrast. It could be shown that even for high molecular weight copolymers the double gyroid microdomain morphology can be obtained, indicating pathways to three-dimensional photonic crystals that combine a full photonic band gap with the advantageous mechanical properties of polymeric materials and the ease of self-assembly. Fig. 13b shows a scanning electron micrograph of a double gyroid obtained from high molecular weight PS-PI after selective etching of the PI matrix using UV/ozone.^[29]

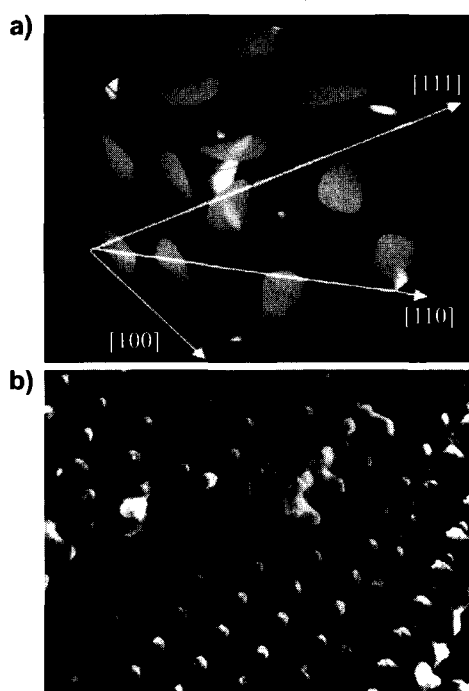


Fig. 13 a) Schematic model of the double-gyroid morphology showing two interpenetrating networks (here: PS) embedded in the matrix material (here: air). Scanning electron micrograph of a free-standing interconnected PS network obtained from a high molecular weight double-gyroid PS-PI block copolymer after selective UV/ozone etching of the PI domain. (View this art in color at www.dekker.com.)

Block Copolymer Lithography

The typical length scale of microphase separation, 10–100 nm, is particularly interesting as it provides a versatile alternative to conventional photolithographic techniques for surface structuring. Possible applications for regular texturing of a surface at the 10-nm length scale are the fabrication of high-storage magnetic recording media, DNA electrophoresis membranes or microoptical elements. Of particular interest is the combination of the controlled structure formation on the nanometer length scale with the distinct chemical nature of the respective blocks. Lopes and Jaeger demonstrated the selective decoration of the PS domains of a cylindrical microstructure forming PS-PMMA diblock copolymer by evaporation of gold on top of the spin-casted polymer thin film.^[30] The dense packing of gold nanocrystals on the PS domains allowed for the

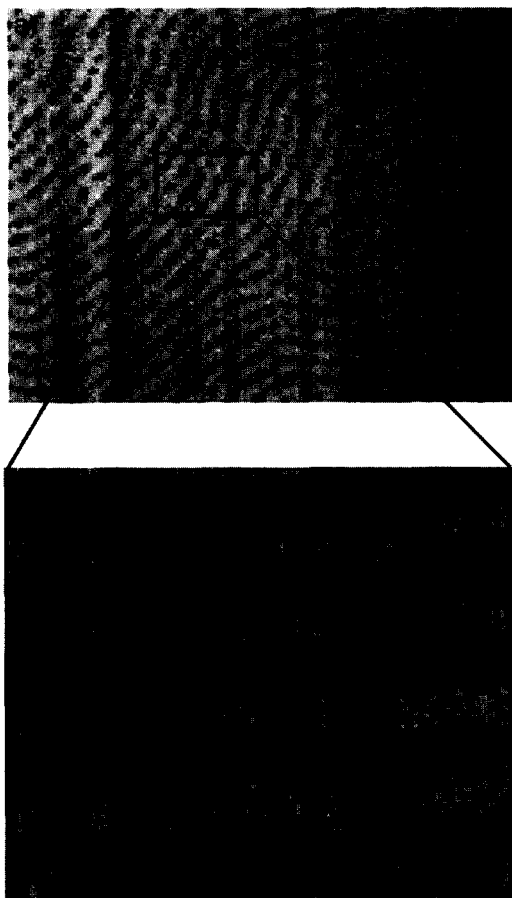


Fig. 14 a) Metal nanochain and nanowire formation after vapor-deposition of Au onto a thin film of cylindrical PS-PMMA block copolymer and annealing for 1 min at 180°C under Ar atmosphere. Au highly selectively decorates the PS domain. b) Magnification of a) demonstrating individual nanocrystal array formation. Scale bars: 200 nm. (From Ref. [30]. Copyright 2001, Macmillan Publishers Ltd.)

formation of a regular pattern of conducting nanowires 50 nm in width which are of great interest as interconnects, gratings, or for biosensor applications. A schematic of the described structure formation process along with electron micrographs of the resulting structures is shown in Fig. 14. Block copolymer lithography has also been studied as possible alternative to conventional lithographic techniques for the fabrication of high-density magnetic storage media. For example, Cheng et al. demonstrated that single-domain ferromagnetic cobalt dots can be fabricated using self-assembled block copolymer lithography.^[31] In their study, the authors took advantage from the significantly different etching rates of organic-inorganic block copolymers when exposed to a reactive ion beam, allowing the selective

etching of one component from the microstructure while converting the inorganic-containing block to a ceramic. A thin film of spherical microdomain morphology forming poly(styrene-*b*-ferrocenyldimethylsilane) (PS-PFS) block copolymer was cast on a layered cobalt-tungsten-silica substrate and the PFS domains used as a mask for subsequent reactive ion etching. A schematic of the procedure as well as a scanning electron micrograph of the obtained nanodot arrays is shown in Fig. 15.

Inorganic-Organic Mesostructures from Block Copolymer Phases

At present, great attention is being paid to the preparation of complex inorganic-organic hybrid materials with long-range order that could find possible applications in catalysis, membrane, and separation technology. Two major synthetic approaches can be distinguished: 1) the in situ synthesis of inorganic particles within a block copolymer domain that has been loaded with a suitable precursor reagent and 2) the simultaneous self-assembly of the block copolymer in the presence of ex situ synthesized nanoparticles that are surface-tailored in order to allow preferential sequestration within a target domain.

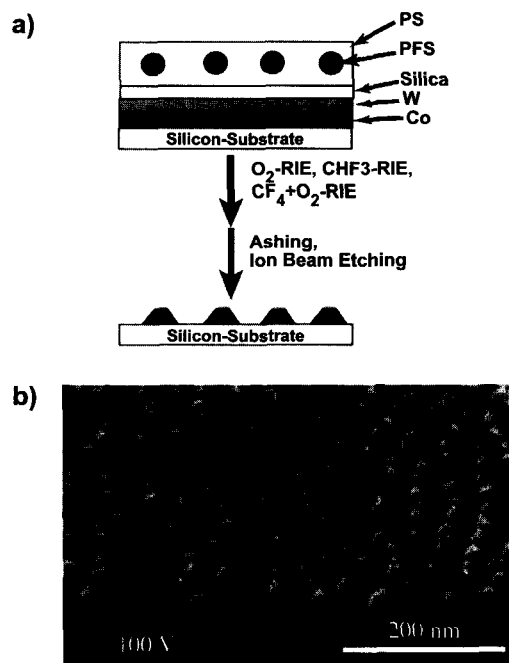


Fig. 15 a) Schematic of the sequential reactive ion etch process (see text for details). b) Tilted scanning electron micrograph showing Co-nanodot arrays obtained after complete etching of the PS-PFS block copolymer. (From Ref. [31]. Copyright 2001, Wiley Interscience.) (View this art in color at www.dekker.com.)

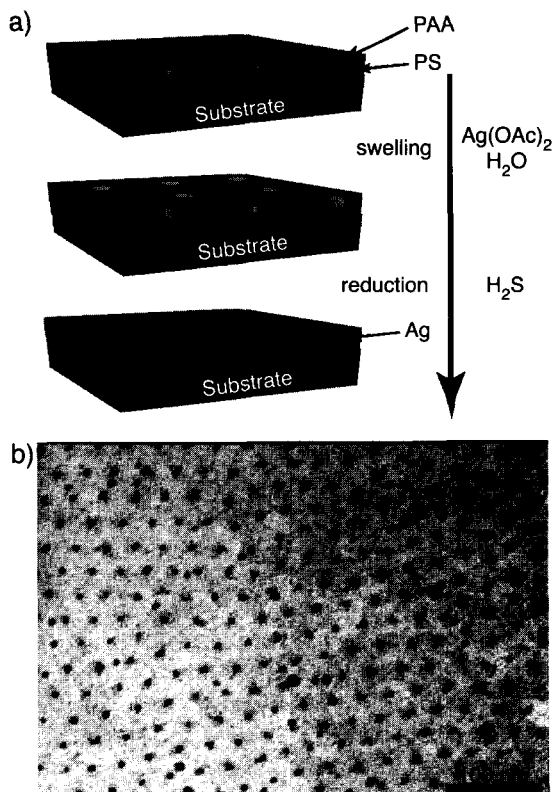


Fig. 16 a) Schematic of the nanoreactor approach. 1: Thin film cast of spherical PS-PAA; 2: selective swelling of PAA spheres with metal precursor; 3: formation of metal nanocrystals by reduction of metal precursor. b) Transmission electron micrograph of thin film demonstrating hexagonal array of Ag nanodots within PS matrix. (From Ref. [32]. Copyright 2002, American Chemical Society.) (View this art in color at www.dekker.com.)

Whereas the first approach facilitates higher volume filling fractions of the inorganic material, the second approach allows better control of the structural characteristics of the sequestered component. Micropatterned solid particles in a block copolymer matrix were produced by Bootongkong et al. in a nanoreactor scheme, in which the hydrophilic domain of a poly(styrene-*b*-acrylic acid) block copolymer is pre-loaded with a metal salt that is reduced in a second reaction step.^[32] The procedure is outlined in Fig. 16. The authors demonstrated that the block copolymer nanoreactor scheme might be applied to a wide variety of metal (Pd, Cu, Au, Ag) as well as semiconductor (PbS) nanocrystals. Whereas the block copolymer nanoreactor scheme results in the formation of discrete or interconnected nanocrystals dispersed within the respective block copolymer domain, Templin et al. demonstrated that by swelling of the poly(ethylene oxide)

domain of a poly(ethylene oxide-*b*-isoprene) block copolymer with an inorganic precursor followed by hydrolysis and calcination, continuous inorganic nanorelief structures can be obtained.^[33] The authors also described the formation of the “plumber’s nightmare” morphology for the hybrid material, which is an uncommon bicontinuous morphology for block copolymers and which was explained by subtle differences in the phase behavior of hybrid vs. neat block copolymer structures. In contrast to the abovementioned in situ approaches, ex situ methodologies become advantageous when precise control of the structural features of the inorganic component becomes relevant to the desired function of the hybrid material or the geometrical characteristics of the inorganic component cannot be obtained through in situ synthesis. For example, Ha and Thomas studied the incorporation of “two-dimensional” clay sheets into lamellar PS-PI block copolymer microstructures.^[34] The authors demonstrated that by decorating the mineral’s surface with poly(styrene), individual clay sheets can be preferentially sequestered within the polystyrene domain of the block copolymer. The resulting nanocomposite materials exhibit

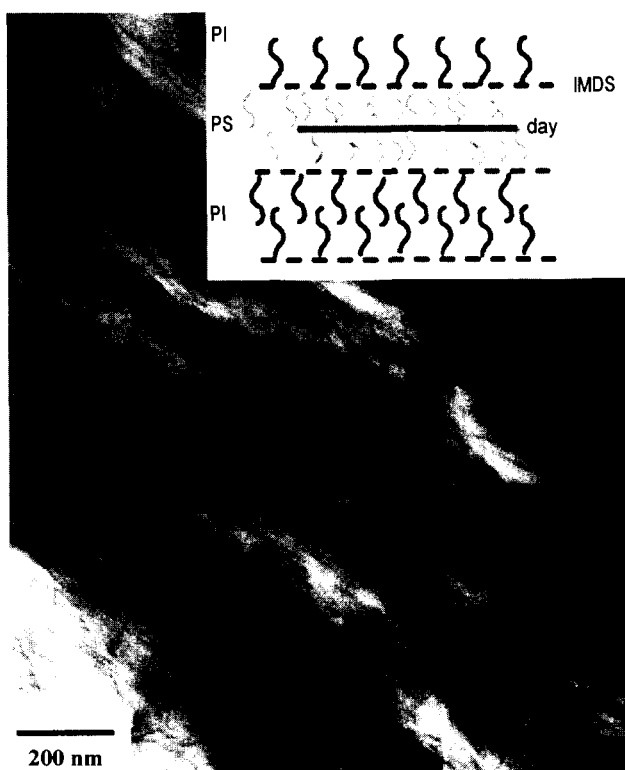


Fig. 17 Transmission electron micrograph of exfoliated clay-PS-PI nanocomposite (no stain). Individual PS-decorated clay sheets are sequestered within PS layers. Inset: Schematic of the composite structure. (View this art in color at www.dekker.com.)

highly anisotropic mechanical and permeability properties. An electron micrograph of the nanocomposite material revealing single-layer clay sheets sequestered within the poly(styrene) domains is shown in Fig. 17. The development of surface decoration techniques that allow for molecular level dispersion of the inorganic component within the polymer matrix represents a major advancement in the field as the inclusion of single-sheet (exfoliated) mineral layers permits to downscale the amount of inorganic component by an order of magnitude (only 2 wt.% inorganic is needed) while providing the advantageous material properties.

The control of the composites' architecture on the nanometer scale is of special importance for future research in this area as it facilitates to dramatically decrease the switching speed in these materials which is diffusion limited, scaling as the square of the feature size. At present, research focus is on the development of next-generation actuator materials that capitalize from both the mechanical and optical characteristics of the sequestered component as well as the rapid dynamic response to external stimulus that results from the architectural control on the molecular level.

ACKNOWLEDGMENTS

This material is based upon work supported by, or in part by, the Alexander von Humboldt Foundation (Feodor-Lynen program) as well as the U.S. Army Research Laboratory and the U.S. Army Research Office under Contract DAAD-19-02-0002. We thank Dr. J.-W. Park, A.M. Urbas, and Y.-H. Ha for their contribution of electron and atomic force micrographs to this work.

REFERENCES

- Hiemenz, P.C. *Polymer Chemistry: The Basic Concepts*; Marcel Dekker: New York, 1984.
- Hadjichristidis, N.; Pitsikalis, M.; Pispas, S.; Iatrou, H. Polymers with complex architecture by living anionic polymerization. *Chem. Rev.* **2001**, *101*, 3747–3792.
- Flory, P.J.J. Thermodynamics of high polymer solutions. *Chem. Phys.* **1941**, *9*, 660.
- Huggins, M.L.J. Solutions of long chain compounds. *Chem. Phys.* **1941**, *9*, 440.
- Balsara, N.P.; Fetters, L.J.; Hadjichristidis, N. Thermodynamic interactions in model polyolefin blends obtained by small-angle neutron scattering. *Macromolecules* **1992**, *25* (23), 6137.
- Ryu, D.Y.; Jeong, U.; Kim, J.K.; Russel, T.P. Closed-loop phase behavior in block copolymers. *Nat. Mater.* **2002**, *1*, 114–117.
- Pernot, H.; Baumert, M.; Court, F.; Leibler, L. Design and properties of co-continuous nanostructured polymers by reactive blending. *Nat. Mater.* **2002**, *1*, 54–58.
- Bates, F.S. Polymer-polymer phase behavior. *Science* **1991**, *251*, 898–905.
- Bates, F.S.; Fredrickson, G.H. Block copolymer thermodynamics. *Annu. Rev. Phys.* **1990**, *41*, 525–557.
- Hamley, I.W. *The Physics of Block Copolymers*; Oxford University Press: New York, 1998.
- Winey, K.I.; Thomas, E.L.; Fetters, L. Swelling a lamellar diblock copolymer with homopolymer—Influences of homopolymer concentration and molecular weight. *Macromolecules* **1991**, *24* (23), 6182–6188.
- Goldacker, T.; Abetz, V.; Stadler, R.; Eruhimovich, I.; Leibler, L. Non-centrosymmetric superlattices in block copolymer blends. *Nature* **1999**, *398*, 137–139.
- Lee, M.; Cho, B.-K.; Zin, W.-C. Supramolecular structures from rod-coil block copolymers. *Chem. Rev.* **2001**, *101*, 3869–3892.
- Klok, H.-A.; Lecommandoux, S. Supramolecular materials via block copolymer self-assembly. *Adv. Mater.* **2001**, *13* (16), 1217–1229.
- Stupp, S.I.; LeBonheur, V.; Walker, K.; Li, L.S.; Huggins, K.E.; Keser, M.; Amstutz, A. Supramolecular materials: Self-organized nanostructures. *Science* **1997**, *276*, 384–389.
- Chen, J.T.; Thomas, E.L.; Ober, C.K.; Mao, G.P. Self-assembled smectic phases in rod-coil block copolymers. *Science* **1996**, *276*, 343–346.
- Park, J.-W.; Thomas, E.L. Multiple ordering transitions: Hierarchical self-assembly of rod-coil block copolymers. *Adv. Mater.* **2003**, *15* (7–8), 585–588.
- Honeker, C.C.; Thomas, E.L. Perpendicular deformation of a near-single-crystal triblock copolymer with a cylindrical morphology. *Macromolecules* **2000**, *33* (25), 9407–9417.
- Chen, Z.-R.; Kornfield, J.A.; Smith, S.D.; Grothaus, J.T.; Satkowski, M.M. Pathways to macroscale order in nanostructured block copolymers. *Science* **1997**, *277*, 1248–1253.
- Keller, A.; Pedemonte, E.; Willmouth, F.M. Macro lattice from segregated amorphous phases of a three block copolymer. *Colloid Polym. Sci.* **1970**, *238*, 385–389.
- Osuji, C.; Zhang, Y.; Mao, G.; Ober, C.K.; Thomas, E.L. Transverse cylindrical microdomain orientation

- in a LC diblock copolymer under oscillatory shear. *Macromolecules* **1999**, *32*, 7703–7706.
22. Amundson, K.; Helfand, E.; Quan, X.; Smith, S.D. Alignment of block copolymer microstructures. *Macromolecules* **1994**, *27* (22), 6559–6570.
 23. Thurn-Albrecht, T.; Schotter, J.; Kastle, G.A.; Emley, N.; Shibauchi, T.; Krusin-Elbaum, L.; Guarini, K.; Black, C.T.; Tuominen, M.T.; Russell, T.P. Ultrahigh-density nanowire arrays grown in self-assembled diblock copolymer templates. *Science* **2000**, *290*, 2126–2129.
 24. Fasolka, M.J.; Mayes, A.M. Block copolymer thin films: Physics and applications. *Annu. Rev. Mater. Res.* **2001**, *31*, 323–355.
 25. De Rosa, C.; Park, C.; Thomas, E.L.; Lotz, B. Microdomain patterns from directional eutectic solidification and epitaxy. *Nature* **2000**, *405*, 433–437.
 26. Joannopoulos, J.D.; Meade, R.D.; Winn, J.N. *Photonic Crystals*; Princeton University Press: New Jersey, 1995.
 27. Fink, Y.; Urbas, A.M.; Bawendi, M.G.; Joannopoulos, J.D.; Thomas, E.L. Block copolymers as photonic bandgap materials. *J. Lightwave Technol.* **1999**, *17* (11), 1963–1969.
 28. Bockstaller, M.R.; Kolb, R.; Thomas, E.L. Metallo-dielectric photonic crystals based on diblock copolymers. *Adv. Mater.* **2001**, *13* (23), 1783–1786.
 29. Urbas, A.M.; Maldovan, M.; Thomas, E.L. Bicontinuous cubic photonic crystal in a block copolymer system. *Adv. Mater.* **2002**, *14* (24), 1850–1853.
 30. Lopes, W.A.; Jaeger, H.M. Hierarchical self-assembly of metal nanostructures on diblock copolymer scaffolds. *Nature* **2001**, *414*, 735–738.
 31. Cheng, J.Y.; Ross, C.; Chan, V.Z.-H.; Thomas, E.L.; Lammertink, R.G.H.; Vansco, G.J. Formation of cobalt magnetic dot array via block copolymer lithography. *Adv. Mater.* **2001**, *13* (15), 1174–1178.
 32. Boontongkong, Y.; Cohen, R.E. Cavitated block copolymer micellar thin films: Lateral arrays of open nanoreactors. *Macromolecules* **2002**, *35* (9), 3647–3652.
 33. Templin, M.; Franck, A.; Du Chesne, A.; Leist, H.; Zhang, Y.; Ulrich, R.; Schaedler, V.; Wiesner, U. Organically modified aluminosilicate mesostructures from block copolymer phases. *Science* **1997**, *278*, 1795–1798.
 34. Ha, Y.H.; Thomas, E.L. Deformation behavior of roll-cast layered silicate/triblock copolymer nanocomposites. *Macromolecules* **2002**, *35* (11), 4419–4428.

Nanostructures Replicated by Polymer Molding

Daniel B. Wolfe
J. Christopher Love
George M. Whitesides

Harvard University, Cambridge, Massachusetts, U.S.A.

INTRODUCTION

This article discusses materials and techniques used to generate polymer replicas of nanostructures by molding, embossing, and printing. Nanostructures are defined as those that have lateral dimensions of less than 100 nm. The effect of spatially confining materials to these dimensions gives rise to physical, electronic, mechanical, magnetic, and optical properties, e.g., quantum behavior,^[1,2] superparamagnetism,^[3] depressed melting point,^[4,5] and increased hardness,^[6,7] that differ, at times significantly, from those of microstructures and macrostructures.

The fabrication and characterization of nanostructures are important for applications in optics,^[8] computation,^[9] data storage,^[10,11] specialty materials,^[7] and biology.^[12] Most processes for producing electrically, magnetically, and optically functional devices containing nanostructures include four basic steps: 1) fabrication of a "master" (i.e., a substrate from which replicas are formed); 2) replication of the master; 3) transfer of the replica into a functional material (e.g., semiconductor or metal); and 4) registration of the pattern of a master (the same as or different than the one used originally) with that of the replica for multilayer structures. This article focuses on the polymers and the molding techniques useful for the second step of this process.

OVERVIEW

Why Replication of Nanostructures into Polymers?

Replication of nanostructures into photosensitive polymers by photolithography is routine in fundamental and applied research and in commercial manufacturing.^[13] The process replicates features from a photomask that is prepared by a serial lithographic technique such as electron-beam lithography,^[14,15] focused-ion milling,^[16-18] or scanning probe lithography.^[19-21] The fabrication of masters by these techniques is slow (~ 10 hr/cm²) because each feature in the mask is drawn individually. The lateral

dimensions of the structures that can be patterned by photolithography are limited by the wavelength of the illumination source; state-of-the-art, 157-nm sources can fabricate features as small as 50 nm.^[22] The techniques for making masters and for sub-100-nm photolithography require specialized, expensive equipment; such equipment is readily accessible in industry, but is not commonly available in academic research laboratories.

Advantages and Disadvantages of Replication of Nanostructures into Polymers

Replication of nanostructures by the molding of polymers shares the attractive feature of photolithography (that is, it can replicate all the features on a master in one step), but with a much lower limit, in principle, for the lateral dimensions of features (~ 1 nm) than that for photolithography. This limit is set by the size of the molecules in the replica. The molding of polymers has four advantages over photolithography: 1) the techniques can replicate nanostructures over large areas (> 1 m²); 2) the dimensions of the features replicated into polymers are not distorted by problems common to photolithographic techniques (e.g., variations in focus, intensity, and exposure dose); 3) the materials and the facilities necessary are inexpensive and readily accessible; and 4) the process may be compatible with low-cost manufacturing processes (e.g., roll-to-roll processing).

The replication of nanostructures by molding in polymers has seen only limited commercial applications to date. Replication of sub-10-nm features is still difficult to obtain reproducibly over large areas because of lateral collapse of the features in the polymeric replica. Defect densities are currently too high for use in most high-performance electronic devices; no defects must be observed over an area of several square centimeters for commercial applications. The process of replication does not reduce the dimensions of features; that is, the dimensions of the features defined in the master must be the same as those desired in the replica. This characteristic differs from photolithography where dimensions in a mask can be reduced optically.

POLYMER MATERIALS AND PROPERTIES FOR USE IN REPLICAS

Table 1 summarizes some of the types of polymers used to replicate masters by molding and the properties relevant to molding. Two properties that influence the quality of a polymer replica are the coefficient of thermal expansion of the master and the polymer and the dimensional change in the polymer during curing. The dimensions of features defined in masters or replicas made of polymers with large coefficients of thermal expansion can be distorted by changes in the temperature. The polymer replica also can shrink during curing because of evaporation of solvents, cross-linking of the polymer, and/or thermal expansion of the polymer (for heat-based curing)^[23] These processes can also yield replicas with distorted features.

Some processes of replication reshape thin films of polymers by softening them at elevated temperatures; the temperature at which the polymer softens is the glass transition temperature (T_g). Low glass transition temperatures (i.e., $45^\circ\text{C} < T_g < 150^\circ\text{C}$) can minimize distortions of the critical dimensions of the features because of thermal expansion of the master during heating and thermal contraction of the replica during cooling. Temperatures within this range also make the process compatible with a wide range of substrate materials (e.g., polymers and low-melt glasses).

Mechanical instabilities in the polymers can lead to vertical and lateral collapse of the features in the replica. The elasticity or the tensile modulus of the material used to make the replica determines the importance of these distortions. They are significant for nanostructures defined in polymers that have a low tensile modulus (< 2 MPa), and they limit the minimum dimension (> 300 nm) and the minimum aspect ratio (0.4; height/width) of the features these polymers (e.g., derivatives of polydimethylsiloxane (PDMS) such as 184-PDMS and s-PDMS) can replicate.^[24–26] A number of groups have developed formulations of PDMS (e.g., *h*-PDMS and *hv*-PDMS) that have a medium to high elastic modulus (4–10 MPa).^[23,27,28] These formulations of PDMS are particularly useful for the replication of nanostructures, as they can replicate features with lateral dimensions as small as 30 nm and with vertical dimensions as small as 2 nm.^[27,29]

The process removing a rigid replica from a rigid master can damage the fragile nanostructures defined on each surface. The physical toughness of the polymer is an indication of how much stress it can tolerate before cracking. The potential for damage to the features in the master and in the replica decreases when using a polymer with a tensile strength of > 0.1 MPa (e.g., PDMS) as the material for the replica. Polymers with a high toughness tend to have a low tensile modulus.

Table 1 Properties of polymers used commonly in replication

	Tensile modulus (MPa)	Toughness (MPa)	Surface free energy (dyn/cm ²)	Coefficient of linear thermal expansion (ppm/°C)	Glass transition temperature (°C)	Method of curing	Commercially available
Poly(dimethylsiloxane) (PDMS)							
184-PDMS ^a	1.8 ^[23]	4.77 ^[23]	21.6	260–310 ^b	N/A	Heat	Yes
<i>h</i> -PDMS ^[27]	8.2 ^[23]	0.02 ^[23]	~20	450 ^[27]	N/A	Heat	No
<i>hv</i> -PDMS ^[23]	3.4 ^[23]	0.13 ^[23]	~20	300 ^[23]	N/A	UV-light	No
s-PDMS ^c	0.6 ^[23]	0.41 ^[23]	~20	–	N/A	UV-light	Yes
Poly(methyl methacrylate)	2200–3100 ^d	195 ^d	36.5	50–90 ^d	85–105°C ^c	N/A	Yes
Poly(vinylchloride)	2400–4100 ^d	65	39	50–100 ^d	75–105°C ^c	N/A	Yes
Poly(styrene)	2300–3300 ^d	36.52 ^d	33	50–83 ^d	74–100°C ^c	N/A	Yes
Poly(urethane)	20–70 ^e	75–80 ^e	28–30	30–60	N/A	UV-light	Yes
Novalac	~6000–9000	~100–110	43.6	30–50	~120°C ^c	N/A	Yes
Photoresist							

^aSylgard 184 available from Dow Corning.

^bDow Corning technical data sheet for Sylgard 184.

^cRMS-033 available from Gelest.

^dModern Plastics Encyclopedia 1999, p B158 to B216.

^eNorland Optical Adhesives technical data sheets.

The surface free energy of the polymer is a parameter that determines the ease of release of the polymer replica from the master and thus the damage to the replicated nanostructures during this process. PDMS is a useful material for use in replicas because it has a low surface free energy (~ 21.6 dyn/cm).^[30] After molding, the surface energy of PDMS replica can be lowered further to ~ 12 dyn/cm by coating the surface with a fluoro-silane;^[31,32] this process makes the surface properties of the stamp similar to poly(tetrafluoroethylene) (Teflon[®]).

TECHNIQUES FOR THE REPLICATION OF NANOSTRUCTURES BY THE MOLDING OF POLYMERS

Replica Molding

Replica molding is a technique used routinely to fabricate macroscale and microscale objects, e.g., compact disks, digital versatile disks (DVD), holograms, and plastic parts, by molding a polymer against ceramic, metallic, or rigid plastic masters (Fig. 1). Typically, the surface of the master is modified chemically to lower its surface free energy by coating it with a fluorinated molecule or polymer; this layer facilitates the separation of the master from the replica after molding. Damage to the nanostructures defined in the master and/or the replica occurs most commonly during this separation. The use of elastomeric polymers in replica molding helps to minimize damage to the nanostructures, especially in the replica, during separation because of the toughness and elasticity of the polymers. An example of replica molding into PDMS is the replication of rings of photoresist into a composite polymer made of a thin layer (40 μm) of *h*-PDMS and a thick layer (>1 mm) of 184 PDMS (Fig. 2).

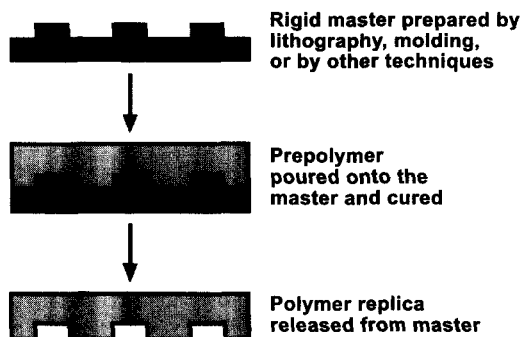


Fig. 1 Scheme for replica molding. (View this art in color at www.dekker.com.)

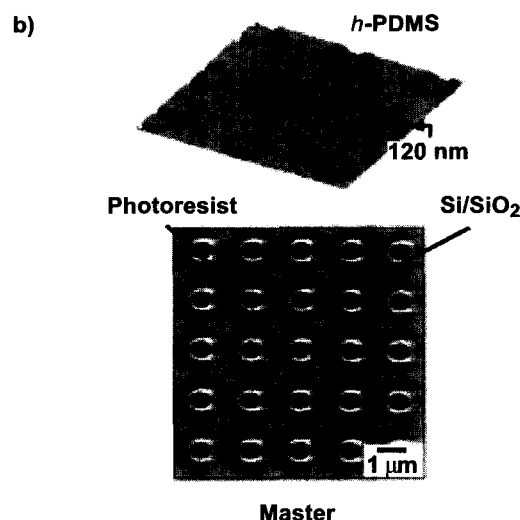
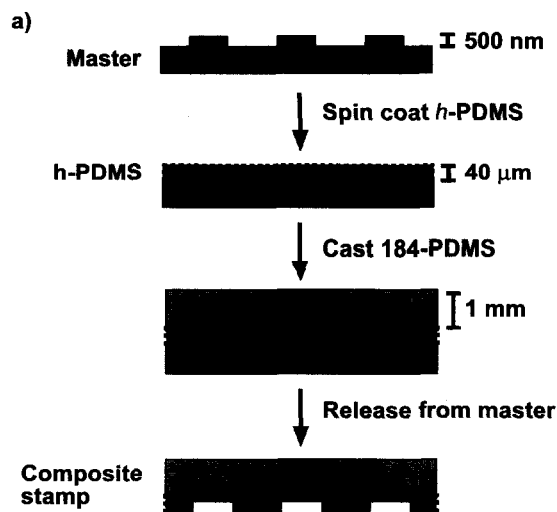


Fig. 2 a) Scheme for replica molding a master into a *h*-PDMS/184 PDMS composite polymer. b) An atomic force micrograph of the replica (top) and a scanning electron micrograph of the master (bottom). The scheme and images in (b) are reproduced with permission from the *American Chemical Society*. (From Ref. [28].) (View this art in color at www.dekker.com.)

The composite PDMS structure can replicate sub-100-nm features by molding and can be removed easily from a master without damaging the nanostructures on either surface.^[27,28]

Soft Lithography

Soft lithography is a suite of techniques that use a PDMS-based stamp—prepared by replica molding—as the master

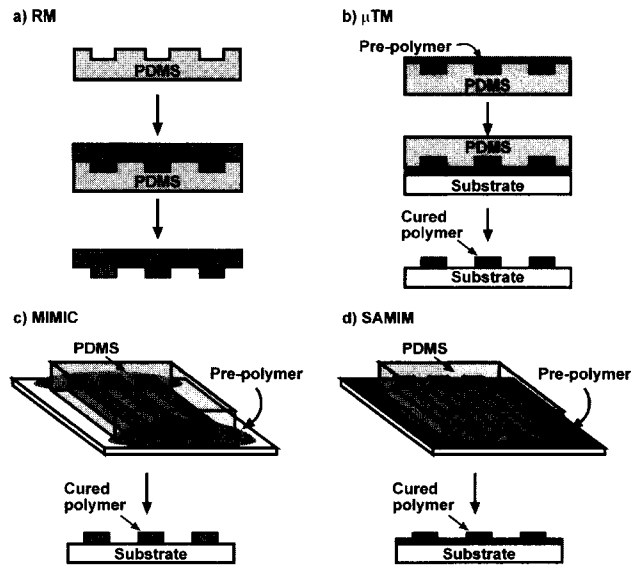


Fig. 3 Schematic illustrations of the procedures used in the corresponding soft lithographic techniques. (View this art in color at www.dekker.com.)

(Fig. 3).^[13,31,32] Replica molding (RM),^[33] microtransfer molding (μ TM),^[34] micromolding in capillaries (MIMIC),^[35] and solvent-assisted micromolding (SAMIM)^[36] are four soft-lithographic techniques that replicate features by the molding of polymers. For many of these techniques, the inherent low surface free energy of PDMS is enough to permit the stamp to be separated from the replica without the need of a release layer.

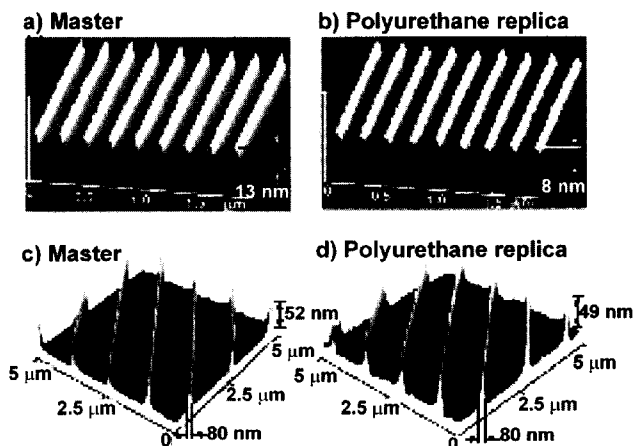


Fig. 4 Atomic force micrographs of (a) a chrome master and (b) a polyurethane replica of the master produced by replica molding. The images in this figure are reproduced with permission from *Advanced Materials*. (From Ref. [33].)

Replica molding

The soft lithographic version of replica molding uses a PDMS stamp as the master instead of a rigid material (Fig. 3a). Fig. 4 shows the replica molding of nanostructures into an UV-curable polyurethane. The PDMS stamp can be used repeatedly; no measurable difference in feature quality is observed after successive replication into polyurethane more than 20 times from the same stamp.

Microtransfer molding

Microtransfer molding prepares a replica by first filling the recessed regions of the stamp with a curable prepolymer (Fig. 3b). The excess prepolymer is scraped from the surface of the stamp using a thin slab of PDMS; this scraping process does not remove the excess polymer completely, and, often, a thin film of excess polymer remains on the replica. The filled stamp is placed onto a rigid substrate under slight pressure. The prepolymer is cured by the appropriate technique, and the mold is removed manually. This technique is well suited for UV-curable materials because the PDMS stamp is optically transparent above ~ 290 nm.

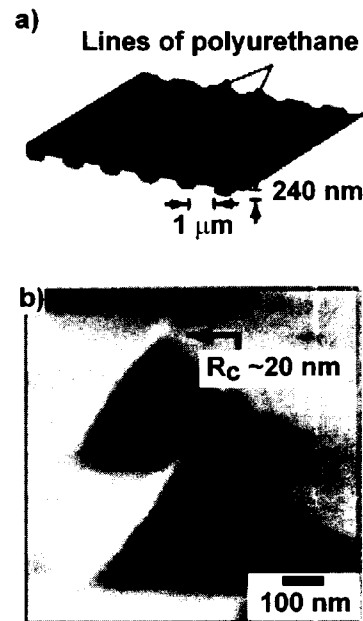


Fig. 5 (a) Atomic force micrograph of lines of photoresist patterned by MIMIC. (b) Scanning electron micrograph of Novalac photoresist patterned by SAMIM. The images are reproduced with permission from *The American Chemical Society*. (From Ref. [28].)

Micromolding in capillaries

Micromolding in capillaries uses capillarity to fill channels in a PDMS stamp with a photocurable or thermally curable polymer (Fig. 3c). A PDMS-based stamp is placed in conformal contact with a surface. The stamp is topographically patterned with a series of channels that extend from one end of the stamp to the other. A drop of liquid prepolymer placed at one end of the stamp fills the channels by capillarity. The polymer is cured once the entire channel network is filled. The replication of nanochannels in a 184-PDMS stamp is difficult because the channels tend to collapse when the stamp is placed in contact with a surface.^[28] Composite stamps of *h*-PDMS and 184-PDMS overcome this limitation and can be used to replicate features with critical dimensions below 300 nm (Fig. 5a). Unlike μ TM, this technique does not produce an excess polymer film on the replica.

Solvent-assisted micromolding

Solvent-assisted micromolding is similar operationally to traditional embossing techniques, but it uses solvent to reshape a polymer rather than elevated temperatures, and it uses an elastomeric stamp instead of a rigid master (Fig. 3d). Elastomeric stamps are especially useful in embossing because the stamp conforms to the surface of the polymer and contacts uniformly over large areas. The stamp is wet with a solvent for the polymer that is to be molded and placed in contact with a thin film of this polymer. The solvent is allowed to evaporate, and the stamp is removed to reveal the replica in the polymer. Air bubbles and voids in the replica as a result of poor evaporation of the solvent before removal of the stamp are not observed because the stamp is gas-permeable. This process has been demonstrated for a number of polymers including: Novalac photoresists, poly(styrene), poly(methylmethacrylate), cellulose acetate, poly(vinyl chloride), and precursors to conjugated organic polymers.^[36] An example of nanostructures prepared by this technique is in Fig. 5b. The molded structure can also act as its own optical element for further size reduction of the features.^[37]

Advantages and disadvantages of soft lithography

The advantages of soft lithography are that: 1) it uses inexpensive materials and equipment; 2) it can replicate over large areas and on nonplanar surfaces; 3) it uses stamps that are compatible with a large number of polymers; and 4) it uses stamps that are gas-permeable. The disadvantages are that: 1) the PDMS molds are not compatible with many organic solvents or high temperatures; 2) the softness of PDMS can cause distortions in molded

structures; 3) the use of PDMS-based stamps requires careful temperature control because of the high coefficient of thermal expansion; that is, small changes in temperature can change the dimensions of the nanostructures; and 4) the registration of multilayer patterns is difficult.

Imprint Lithographies

Step-and-flash imprint lithography (developed by Willson et al.^[38-41]) and nanoimprint lithography (developed by Chou et al.^[42-44]) are two forms of imprint lithography that are used for the replication of nanostructures into polymers. Both techniques work by placing a topographically patterned, rigid master in contact with a formable material coated on a rigid surface. The rigid master is prepared by photolithographic replication of the features into a polymer that is coated on a rigid substrate (e.g., quartz and silicon). The structures are transferred into the substrate by etching.

Step-and-flash imprint lithography

Step-and-flash imprint lithography uses a low-viscosity, photocurable polymer as the material for the replica (Fig. 6)^[41] The low viscosity of the polymer eliminates the need for high temperatures and pressures. A quartz master is placed in contact with the photocurable polymer under slight pressure. Flood illumination through the backside of the master cures the polymer replica. The

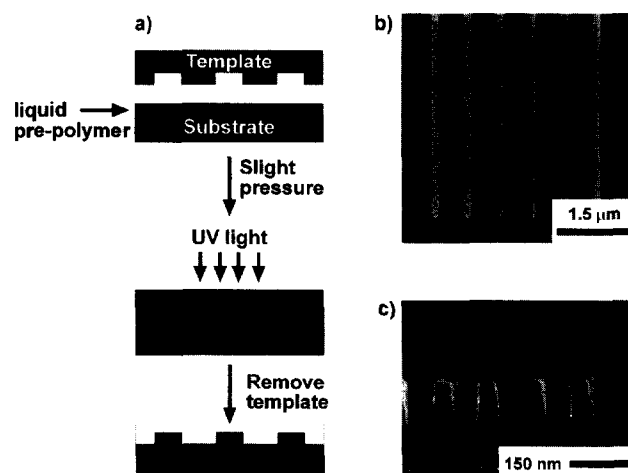


Fig. 6 a) Schematic illustration of step-and-flash imprint lithography. b) Scanning electron micrograph of lines of polymer on a silicon substrate patterned by the technique. c) Scanning electron micrograph of the cross-section of the lines in (b). The images in (b) and (c) are reproduced with permission from *Proceedings of the SPIE*. (From Ref. [45]). (View this art in color at www.dekker.com.)

master is transparent to the wavelengths necessary to cure the polymer. Treatment of the surface of the master with a fluorosilane lowers its surface free energy and facilitates the removal of the master from the replica. The technique can replicate features with lateral dimensions greater than 30 nm and with aspect ratios as high as 8:1 (for 50-nm lines).^[41,45] Step-and-flash lithography is "self-cleaning" because particulates on the surface of the master are trapped in the replica during the curing process. Repeated use of a master actually lowers the density of defects in the replica.^[46]

The advantages of step-and-flash imprint lithography are that: 1) it is a room-temperature technique and is therefore not subject to thermal- or pressure-induced deformations of the nanostructures; 2) it is a rapid process (<5 min/cycle);^[40,47] and 3) it uses optically transparent masters that permit alignment of the replica with underlying features. The disadvantages are that: 1) the masters are more difficult to prepare than those used in soft lithography; 2) the replication of nonplanar masters is difficult;^[48] and 3) the technique is not good for the replication of isolated, recessed features in the master.^[41]

Nanoimprint lithography

Nanoimprint lithography differs from step-and-flash imprint lithography in that it reshapes a polymer at temperatures above its glass transition point, e.g., 90–100°C, and requires high pressures, e.g., 50–100 bar (Fig. 7).^[43,44] The high temperatures lower the viscosity of the polymer enough to fill the master uniformly. The replica and mold

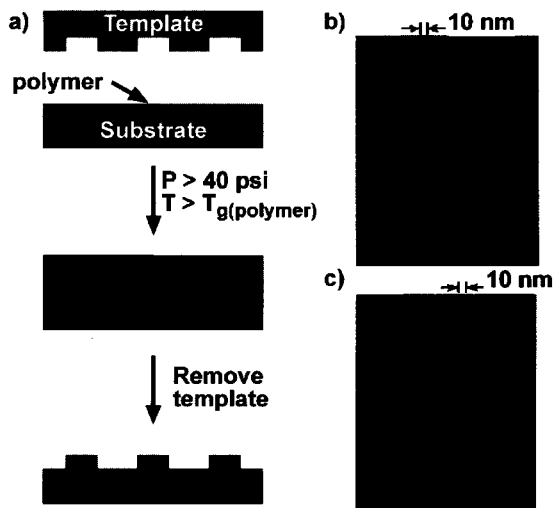


Fig. 7 a) Schematic illustration of the process used in nanoimprint lithography. b) Scanning electron micrograph of the SiO₂ master. c) Scanning electron micrograph of the polymer replica of the master in (b) made by nanoimprinting. The images in (b) and (c) are reproduced by permission of *MRS Bulletin*. (From Ref. [43].) (View this art in color at www.dekker.com.)

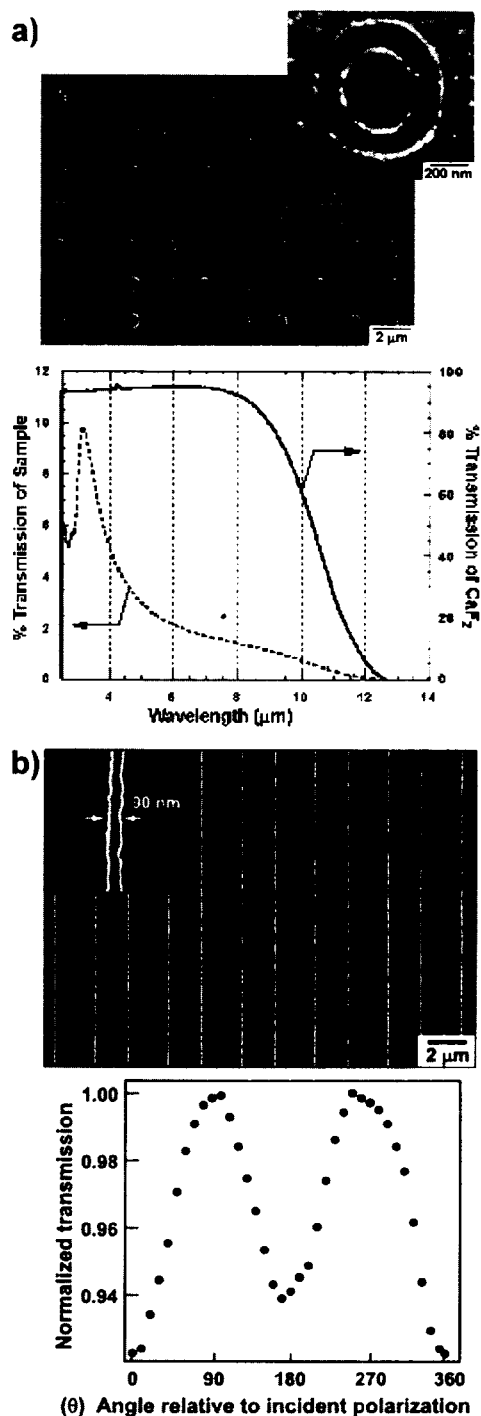


Fig. 8 a) Scanning electron micrograph of rings of nickel formed by lift-off of a photoresist patterned by phase-shifting photolithography and the corresponding transmission spectrum as a function of wavelength for the sample and the CaF₂ substrate. b) Lines of palladium formed by lift-off of photoresist patterned by phase-shifting photolithography and the corresponding plot of the intensity of the transmitted light as a function of angle of polarization. Figure (a) is reproduced with permission from *The Optical Society of America*. Figure (b) is reproduced with permission from *The American Chemical Society*. (From Ref. [28,62].)

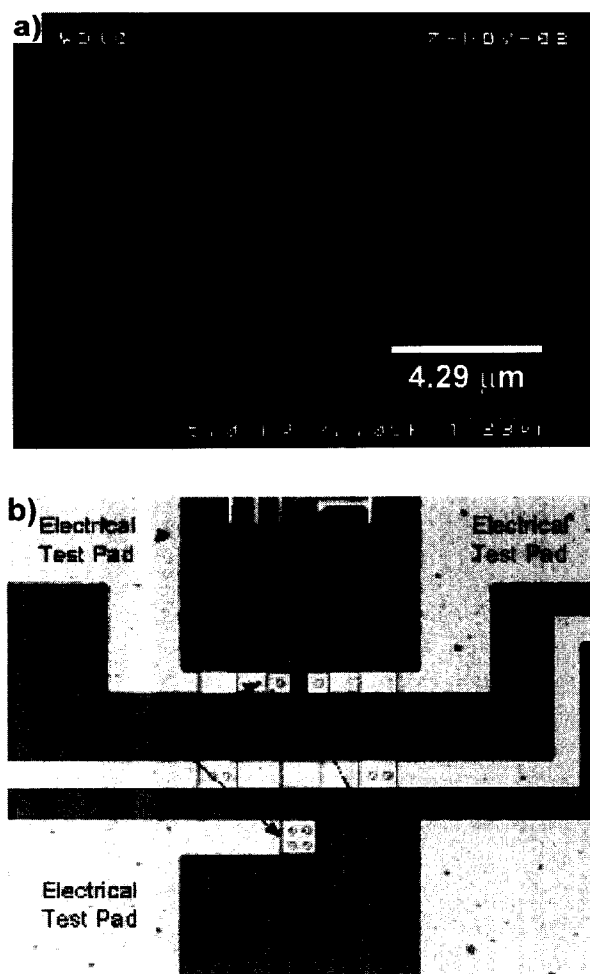


Fig. 9 a) Scanning electron micrograph of a polymer gate made by step-and-flash imprint lithography. b) Optical micrograph of the complete MOSFET device that incorporates the polymer gate in (a). The images are reproduced with permission from *Proceeding of the SPIE*. (From Ref. [77].) (View this art in color at www.dekker.com.)

are allowed to cool before separation. The technique can replicate nanostructures as small as 10 nm and aspect ratios as large as 10:1.^[43] Transparent masters can be used to permit multilevel registration of replicas. Nanoimprint lithography can be carried out in a sequential, step-by-step process similar to that of step-and-flash. The fidelity of replication of nanostructures with critical dimensions of less than 50 nm is poor over large areas because the polymer chains in the materials used in the replicas tend to relax and spread over distances of tens of nanometers.^[47] These factors can only be corrected by designing the original master to account for polymer shrinkage in the processing steps. Another disadvantage of nanoimprinting is that it requires 10–15 min per replication for the heating and cooling cycles; this interval is 3–5 times longer

than that necessary for the entire replication process for step-and-flash imprint lithography and some soft lithographic techniques.^[47]

Uses for Polymeric Replicas with Nanostructures

Replication of nanostructures into polymers is used to make electronic,^[49–59] optical,^[60–64] and mechanical^[65–69] devices. Single-layer, subwavelength, optical elements, e.g., frequency-selective surfaces (Fig. 8a), are one example of such a device fabricated by soft lithography.^[37,62,70,71] A master was replicated into Novalac photoresist by solvent-assisted micromolding. The replica acted as a photomask, and the edges of the raised features were transferred into the underlying photoresist upon exposure to UV-light. The PDMS replica prepared by standard replica molding was used to fabricate polarizers by a similar, phase-shifting lithography technique (Fig. 8b).^[70] The PDMS replicas can also be used to replicate nanostructures into metals by microcontact printing. This process uses the PDMS replica as a stamp to print an organic molecule selectively onto a metal surface. This molecule acts as an etch resist and permits the selective etching of unprotected regions. This technique was used to fabricate polarizers,^[28] hydrogen-gas sensors,^[72] transistors,^[50,52] and microelectromechanical systems (MEMS) devices.^[69,73] The imprint lithographies use the polymer replica as an etch resist to transfer the pattern of the replica into a functional material. These techniques have been used to make photonic crystals,^[74] polarizers,^[75,76] photodetectors,^[56] and transistors (Fig. 9).^[58,59,77]

CONCLUSION

Although replication will not replace the techniques used currently for the preparation of masters, it is extremely useful as a research tool for the rapid prototyping of devices using nanostructures. The combination of the two techniques could enable the fabrication of nanostructures to become routine and cost-effective. Polymeric replicas containing nanostructures may be most useful in the process of fabricating low-cost, low-to-medium performance optical and electronic devices (e.g., RF-ID tags, large area displays, optical filters, and polarizers). Efforts to improve the capabilities of replication will lead to the fabrication of new devices based on the unique properties of nanostructures.

REFERENCES

1. Bukowski, T.J.; Simmons, J.H. Quantum dot research: Current state and future prospects. *Crit.*

- Rev. Solid State Mater. Sci. **2002**, *27* (3 and 4), 119–142.
2. Alivisatos, P. Colloidal quantum dots. From scaling laws to biological applications. *Pure Appl. Chem.* **2000**, *72* (1–2), 3–9.
 3. Sun, X.-C. Microstructure characterization and magnetic properties of nanomaterials. *Mol. Phys.* **2002**, *100* (19), 3059–3063.
 4. Jiang, Q.; Yang, C.C.; Li, J.C. Melting enthalpy depression of nanocrystals. *Mater. Lett.* **2002**, *56* (6), 1019–1021.
 5. Wu, Y.; Yang, P. Melting and welding semiconductor nanowires in nanotubes. *Adv. Mater.* **2001**, *13* (7), 520–523.
 6. Ohji, T. Strengthening mechanisms of nanocomposites. *Mater. Integr.* **2000**, *13* (11), 3–8.
 7. Koch, C. Bulk behavior of nanostructured materials. *Nanostruct. Sci. Technol.* **1999**, 93–111.
 8. Chung, S.-J.; Kim, K.-S.; Lin, T.-C.; Shen, Y.; Markowicz, P.; He, G.S.; Prasad, P.N. Nanophotonics: Nanoscale optical interactions. *Mol. Cryst. Liq. Cryst. Sci. Technol., Sect. A* **2002**, *374*, 59–66.
 9. Tsu, R. Challenges in nanoelectronics. *Nanotechnology* **2001**, *12* (4), 625–628.
 10. Menon, A.K.; Gupta, B.K. Nanotechnology: A data storage perspective. *Nanostruct. Mater.* **2000**, *11* (8), 965–986.
 11. Kirk, K.J. Nano-magnets for sensors and data storage. *Contemp. Phys.* **2000**, *41* (2), 61–78.
 12. Taton, T.A. Nanostructures as tailored biological probes. *Trends Biotechnol.* **2002**, *20* (7), 277–279.
 13. Whitesides, G.M.; Love, J.C. The art of building small. *Sci. Am.* **2001**, *285* (3), 32–41.
 14. Gibson, J.M. Reading and writing with electron beams. *Phys. Today* **1997**, 56–61.
 15. Pease, R.F.W. Nanolithography and its prospects as a manufacturing technology. *J. Vac. Sci. Technol., B* **1992**, *10* (1), 278–285.
 16. Li, H.-W.; Kang, D.-J.; Blamire, M.G.; Huck, W.T.S. Focused ion beam fabrication of silicon print masters. *Nanotechnology* **2003**, *14* (2), 220–223.
 17. Lehrer, C.; Frey, L.; Petersen, S.; Ryssel, H. Limitations of focused ion beam nanomachining. *J. Vac. Sci. Technol., B* **2001**, *19* (6), 2533–2538.
 18. Longo, D.M.; Benson, W.E.; Chraska, T.; Hull, R. Deep submicron microcontact printing on planar and curved substrates utilizing focused ion-beam fabricated printheads. *Appl. Phys. Lett.* **2001**, *78* (7), 981–983.
 19. Crommie, M.F.; Lutz, C.P.; Eigler, D.M. Confinement of electrons to quantum corrals on a metal surface. *Science* **1993**, *262* (5131), 218–220.
 20. Mirkin, C.A. Dip-pen nanolithography: Automated fabrication of custom multicomponent, sub-100-nanometer surface architectures. *MRS Bull.* **2001**, *26* (7), 535–538.
 21. Sulchek, T.; Grow, R.J.; Yaralioglu, G.G.; Minne, S.C.; Quate, C.F.; Manalis, S.R.; Kiraz, A.; Aydine, A.; Atalar, A. Parallel atomic force microscopy with optical interferometric detection. *Appl. Phys. Lett.* **2001**, *78* (12), 1787–1789.
 22. Itani, T.; Wakamiya, W.; Cashmore, J.; Gower, M. 157-nm lithography with high numerical aperture lens for sub-70 nm node. *Microelectron. Eng.* **2003**, *67–68*, 39–46, (Complete).
 23. Choi, K.M.; Rogers, J.A. A photocurable poly-(dimethylsiloxane) chemistry designed for soft lithographic molding and printing in the nanometer regime. *J. Am. Chem. Soc.* **2003**, *125* (14), 4060–4061.
 24. Delamarche, E.; Schmid, H.; Michel, B.; Biebuyck, H. Stability of molded polydimethylsiloxane microstructures. *Adv. Mater.* **1997**, *9* (9), 741–746.
 25. Hui, C.Y.; Jagota, A.; Lin, Y.Y.; Kramer, E.J. Constraints on microcontact printing imposed by stamp deformation. *Langmuir* **2002**, *18* (4), 1394–1407.
 26. Rogers, J.A.; Paul, K.E.; Whitesides, G.M. Quantifying distortions in soft lithography. *J. Vac. Sci. Technol., B* **1998**, *16* (1), 88–97.
 27. Schmid, H.; Michel, B. Siloxane polymers for high-resolution, high-accuracy soft lithography. *Macromolecules* **2000**, *33* (8), 3042–3049.
 28. Odom, T.W.; Love, J.C.; Wolfe, D.B.; Paul, K.E.; Whitesides, G.M. Improved pattern transfer in soft lithography using composite stamps. *Langmuir* **2002**, *18* (13), 5314–5320.
 29. Gates, B.G.; Whitesides, G.M. Unpublished work.
 30. *Siloxane Polymers*; Clarson, S.J., Semlyen, J.A., Eds.; Prentice Hall: Englewood Cliffs, NJ, 1993.
 31. Xia, Y.; Whitesides, G.M. Soft lithography. *Angew. Chem., Int. Ed. Engl.* **1998**, *37* (5), 550–575.
 32. Xia, Y.; Whitesides, G.M. Soft lithography. *Annu. Rev. Mater. Sci.* **1998**, *28*, 153–184.
 33. Xia, Y.; McClelland, J.J.; Gupta, R.; Qin, D.; Zhao, X.-M.; Sohn, L.L.; Celotta, R.J.; Whitesides, G.M. Replica molding using polymeric materials: A practical step toward nanomanufacturing. *Adv. Mater.* **1997**, *9* (2), 147–149.
 34. Zhao, X.-M.; Xia, Y.; Whitesides, G.M. Fabrication of three-dimensional micro-structures: Microtransfer molding. *Adv. Mater.* **1996**, *8* (10), 837–840.
 35. Xia, Y.; Kim, E.; Whitesides, G.M. Micromolding of polymers in capillaries: Applications in micro-fabrication. *Chem. Mater.* **1996**, *8*, 1558–1567.
 36. Kim, E.; Xia, Y.; Zhao, X.-M.; Whitesides, G.M.

- Solvent-assisted microcontact molding: A convenient method for fabricating three-dimensional structures on surfaces of polymers. *Adv. Mater.* **1997**, *9* (8), 651–654.
37. Odom, T.W.; Thalladi, V.R.; Love, J.C.; Whitesides, G.M. Generation of 30–50 nm structures using easily fabricated, composite PDMS masks. *J. Am. Chem. Soc.* **2002**, *124* (41), 12112–12113.
 38. Bailey, T.C.; Johnson, S.C.; Sreenivasan, S.V.; Ekerdt, J.G.; Willson, C.G.; Resnick, D.J. Step and flash imprint lithography: An efficient nanoscale printing technology. *J. Photopolym. Sci. Tech.* **2002**, *15* (3), 481–486.
 39. Colburn, M.; Grot, A.; Amistoso, M.N.; Choi, B.J.; Bailey, T.C.; Ekerdt, J.G.; Sreenivasan, S.V.; Hollenhorst, J.; Willson, C.G. Step and flash imprint lithography for sub-100-nm patterning. *Proc. SPIE Int. Soc. Opt. Eng.* **2000**, *3997*, 453–457. (Emerging Lithographic Technologies IV).
 40. Colburn, M.; Johnson, S.; Stewart, M.; Damle, S.; Bailey, T.C.; Choi, B.; Wedlake, M.; Michaelson, T.; Sreenivasan, S.V.; Ekerdt, J.; Willson, C.G. Step and flash imprint lithography: A new approach to high-resolution patterning. *Proc. SPIE Int. Soc. Opt. Eng.* **1999**, *3676*, 379–389. (Pt. 1, Emerging Lithographic Technologies III).
 41. Colburn, M.; Bailey, T.; Choi, B.I.; Ekerdt, J.G.; Sreenivasan, S.V.; Willson, C.C. Development and advantages of step-and-flash lithography. *Solid State Technol.* **2001**, *44* (7), pp. 67, 68, 71, 73–76, 78.
 42. Chou, S.Y.; Krauss, P.R.; Renstrom, P.J. Nanoimprint lithography. *J. Vac. Sci. Technol., B* **1996**, *14* (6), 4129–4133.
 43. Chou, S.Y. Nanoimprint lithography and lithographically induced self-assembly. *MRS Bull.* **2001**, *26* (7), 512–517.
 44. Chou, S.Y.; Krauss, P.R.; Renstrom, P.J. Imprint lithography with 25-nanometer resolution. *Science* **1996**, *272* (5258), 85–87.
 45. Resnick, D.J.; Bailey, T.; Dauksher, W.J.; Mancini, D.; Nordquist, K.J.; Ainley, E.; Gehoski, K.; Baker, J.H.; Johnson, S.; Meissl, M.; Sreenivasan, S.V.; Ekerdt, J.; Willson, C.G. High resolution templates for step and flash imprint lithography. *Proc. SPIE Int. Soc. Opt. Eng.* **2002**, *4688*, 205.
 46. Bailey, T.; Smith, B.; Choi, B.J.; Colburn, M.; Meissl, M.; Sreenivasan, S.V.; Ekerdt, J.G.; Willson, C.G. Step and flash imprint lithography: Defect analysis. *J. Vac. Sci. Technol., B* **2001**, *19* (6), 2806–2810.
 47. Sotomayor Torres, C.M.; Zankovych, S.; Seekamp, J.; Kam, A.P.; Clavijo Cedeno, C.; Hoffmann, T.; Ahopelto, J.; Reuther, F.; Pfeiffer, K.; Bleidiesel, G.; Gruetzner, G.; Maximov, M.V.; Heidari, B. Nanoimprint lithography: An alternative nanofabrication approach. *Mater. Sci. Eng., C* **2003**, *C23* (1–2), 23–31.
 48. Ruchhoeft, P.; Colburn, M.; Choi, B.; Nounu, H.; Johnson, S.; Bailey, T.; Darmle, S.; Stewart, M.; Ekerdt, J.; Sreenivasan, S.V.; Wolfe, J.C.; Willson, C.G. Patterning curved surfaces: Template generation by ion beam proximity lithography and relief transfer by step and flash imprint lithography. *J. Vac. Sci. Technol., B* **1999**, *17* (6), 2965–2969.
 49. Deng, T.; Goetting, L.B.; Hu, J.; Whitesides, G.M. Microfabrication of half-wave rectifier circuits using soft lithography. *Sens. Actuators, A* **1999**, *75*, 60–64.
 50. Hu, J.; Beck, R.G.; Deng, T.; Westervelt, R.M.; Maranowski, K.D.; Gossard, A.C.; Whitesides, G.M. Using soft lithography to fabricate GaAs/AlGaAs heterostructure field effect transistors. *Appl. Phys. Lett.* **1997**, *71* (14), 2020–2022.
 51. Hu, J.; Beck, R.G.; Westervelt, R.M.; Whitesides, G.M. The use of soft lithography to fabricate arrays of Schottky diodes. *Adv. Mater.* **1998**, *10*, 574–577.
 52. Jeon, N.L.; Hu, J.; Whitesides, G.M.; Erhardt, M.K.; Nuzzo, R.G. Fabrication of silicon MOSFETs using soft lithography. *Adv. Mater.* **1998**, *10* (17), 1466–1469.
 53. Rogers, J.A. Rubber stamping for plastic electronics and fiber optics. *MRS Bull.* **2001**, *26* (7), 530–534.
 54. Koide, Y.; Such, M.W.; Basu, R.; Evmenenko, G.; Cui, J.; Dutta, P.; Hersam, M.C.; Marks, T.J. Hot microcontact printing for patterning ITO surfaces. Methodology, morphology, microstructure, and OLED charge injection barrier imaging. *Langmuir* **2003**, *19* (1), 86–93.
 55. Zhang, F.; Nyberg, T.; Inganaes, O. Conducting polymer nanowires and nanodots made with soft lithography. *Nano Lett.* **2002**, *2* (12), 1373–1377.
 56. Yu, Z.; Schablitsky, S.J.; Chou, S.Y. Nanoscale GaAs metal-semiconductor-metal photodetectors fabricated using nanoimprint lithography. *Appl. Phys. Lett.* **1999**, *74* (16), 2381–2383.
 57. Guo, L.; Krauss, P.R.; Chou, S.Y. Nanoscale silicon field-effect transistors fabricated using imprint lithography. *Appl. Phys. Lett.* **1997**, *71* (13), 1881–1883.
 58. Austin, M.; Chou, S.Y. Fabrication of nanocontacts for molecular devices using nanoimprint lithography. *J. Vac. Sci. Technol., B* **2002**, *20* (2), 665–667.
 59. Austin, M.D.; Chou, S.Y. Fabrication of 70 nm channel length polymer organic thin-film transistors using nanoimprint lithography. *Appl. Phys. Lett.* **2002**, *81* (23), 4431–4433.
 60. Yang, P.; Wirnsberger, G.; Huang, H.; Cordero,

- S.R.; McGehee, M.D.; Scott, B.; Deng, T.; Whitesides, G.M.; Chmelka, B.F.; Buratto, S.K.; Stucky, G.D. Mirrorless lasing from mesostructured waveguides patterned by soft lithography. *Science* **2000**, *287* (5452), 465–467.
61. Schueller, O.J.A.; Zhao, X.-M.; Whitesides, G.M.; Smith, S.P.; Prentiss, M. Fabrication of liquid-core waveguides by soft lithography. *Adv. Mater.* **1999**, *11* (1), 37–41.
 62. Paul, K.E.; Zhu, C.; Love, J.C.; Whitesides, G.M. Fabrication of mid-infrared frequency-selective surfaces (FSS) using soft lithography. *Appl. Opt.* **2001**, *40* (25), 4557–4561.
 63. Love, J.C.; Wolfe, D.B.; Jacobs, H.O.; Whitesides, G.M. Microscope projection photolithography for rapid prototyping of masters with micron-scale features for use in soft lithography. *Langmuir* **2001**, *17* (19), 6005–6012.
 64. Xia, Y.; Kim, E.; Zhao, X.-M.; Rogers, J.A.; Prentiss, M.; Whitesides, G.M. Complex optical surfaces by replica molding against elastomeric masters. *Science* **1996**, *273*, 347–349.
 65. Brittain, S.; Paul, K.; Zhao, X.-M.; Whitesides, G. Soft lithography and microfabrication. *Phys. World* **1998**, *11* (5), 31–36.
 66. Schueller, O.J.A.; Brittain, S.T.; Whitesides, G.M. Fabrication of glassy carbon microstructures by soft lithography. *Sens. Actuators, A* **1999**, *72*, 125–139.
 67. Xu, B.; Arias, F.; Whitesides, G.M. Making honeycomb microcomposites by soft lithography. *Adv. Mater.* **1999**, *11* (6), 492–495.
 68. Xu, B.; Arias, F.; Brittain, S.T.; Zhao, X.-M.; Grzybowski, B.; Torquato, S.; Whitesides, G.M. Making negative Poisson's ratio microstructures by soft lithography. *Adv. Mater.* **1999**, *11* (14), 1186–1189.
 69. Yang, H.; Deschatelets, P.; Brittain, S.T.; Whitesides, G.M. Fabrication of high performance ceramic microstructures from a polymeric precursor using soft lithography. *Adv. Mater.* **2001**, *13* (1), 54–58.
 70. Rogers, J.A.; Paul, K.E.; Jackman, R.J.; Whitesides, G.M. Generating ~ 90 nanometer features using near-field contact-mode photolithography with an elastomeric phase mask. *J. Vac. Sci. Technol., B* **1998**, *26* (1), 59–68.
 71. Paul, K.E.; Prentiss, M.G.; Whitesides, G.M. Patterning spherical surfaces at the two-hundred-nanometer scale using soft lithography. *Adv. Funct. Mater.* **2003**, *13* (4), 259–263.
 72. Wolfe, D.B.; Love, J.C.; Paul, K.E.; Chabinyk, M.L.; Whitesides, G.M. Fabrication of palladium-based microelectronic devices by microcontact printing. *Appl. Phys. Lett.* **2002**, *80* (12), 2222–2224.
 73. Jackman, R.J.; Brittain, S.T.; Adams, A.; Wu, H.; Prentiss, M.G.; Whitesides, S.; Whitesides, G.M. Three-dimensional metallic microstructures fabricated by soft lithography and microelectrodeposition. *Langmuir* **1999**, *15* (3), 826–836.
 74. Guo, L.J.; Cheng, X.; Chao, C.Y. Fabrication of photonic nanostructures in nonlinear optical polymers. *J. Mod. Opt.* **2002**, *49* (3/4), 663–673.
 75. Yu, Z.; Deshpande, P.; Wu, W.; Wang, J.; Chou, S.Y. Reflective polarizer based on a stacked double-layer subwavelength metal grating structure fabricated using nanoimprint lithography. *Appl. Phys. Lett.* **2000**, *77* (7), 927–929.
 76. Wang, J.; Schablitsky, S.; Yu, Z.; Wu, W.; Chou, S.Y. Fabrication of a new broadband waveguide polarizer with a double-layer 190 nm period metal-gratings using nanoimprint lithography. *J. Vac. Sci. Technol., B* **1999**, *17* (6), 2957–2960.
 77. Smith, B.; Stacey, N.A.; Donnelly, J.P.; Onsongo, D.M.; Bailey, T.C.; Mackay, C.J.; Sreenivasan, S.V.; Banerjee, S.K.; Ekerdt, J.; Willson, C.G. Employing step and flash imprint lithography for gate level patterning of a MOS FET device. *Proc. SPIE Int. Soc. Opt. Eng.* **2003**, *5037*, 1029–1034.

Nanotube Sensors

Marc Wirtz

PPG Industries, Inc., Monroeville, Pennsylvania, U.S.A.

Charles R. Martin

University of Florida, Gainesville, Florida, U.S.A.

INTRODUCTION

We have been exploring the transport and electrochemical properties of nanotube membranes prepared by the template method,^[1-3] a general approach for preparing nanomaterials. This method entails synthesis or deposition of the desired material within the cylindrical and monodisperse pores of a nanopore membrane or other solid. We have used polycarbonate filters, prepared via the “track-etch” method,^[4] and nanopore aluminas, electrochemically prepared from Al foil,^[5] as our template materials. Cylindrical nanostructures with monodisperse diameters and lengths are obtained, and depending on the membrane and synthetic method used, these may be solid nanowires or hollow nanotubes. We and others have used this method to prepare nanowires and tubes composed of metals,^[5-12] polymers,^[13-15] semiconductors,^[16,17] carbons,^[18,19] and Li⁺ intercalation materials.^[20-22] It is also possible to prepare composite nanostructures, both concentric tubular composites, where an outer tube of one material surrounds an inner tube of another,^[23,24] and segmented composite nanowires.^[25]

One application for these nanotube membranes is in electroanalytical chemistry where the membrane is used to sense analyte species.^[26,27] In that work, membranes containing gold nanotubes with inside diameters that approached molecular dimensions (1–4 nm) were used.^[26] The Au nanotube membrane was placed between two salt solutions and a constant transmembrane potential was applied. The resulting transmembrane current, associated with migration of ions through the nanotubes, was measured. When an analyte molecule whose diameter was comparable to the inside diameter of the nanotubes was added to one salt solution, this molecule partitioned into the nanotubes and partially occluded the pathway for ion transport. This resulted in a decrease in the transmembrane ion current, and the magnitude of the drop in current was found to be proportional to the concentration of the analyte.^[26]

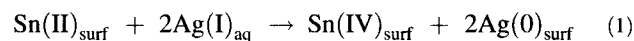
In the experiment discussed above, a baseline transmembrane ion current was established, and the analyte molecule, in essence, turned off this current. It occurred to us that there might be an advantage in doing the opposite,

i.e., starting with an ideally zero current situation and having the analyte molecule switch on the ion current. In other words, we would like to make a synthetic membrane that mimics the function of a ligand-gated ion channel. An example is the acetylcholine-gated ion channel,^[28] which is closed (“off” state) in the absence of acetylcholine but opens (and supports an ion current, “on” state) when acetylcholine binds to the channel. To accomplish this, the off state was obtained by making gold and alumina membranes hydrophobic, and the on state was obtained by introducing ions and electrolyte into the membrane.^[29] Ions were introduced by either partitioning a hydrophobic ionic species (e.g., a drug or a surfactant) into the membrane.

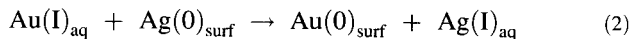
MEMBRANE PREPARATION AND ANALYSIS

Commercially available track-etched polycarbonate filters are used as the templates to prepare the Au nanotubes. The track-etch process^[4] entails bombarding a solid material (in this case a ~10- μ m-thick polycarbonate film) with a collimated beam of high-energy nuclear fission fragments to create parallel damage tracks in the film. The damage tracks are then etched into monodisperse cylindrical pores by exposing the film to a concentrated solution of aqueous base. The diameter of the pores is determined by the etch time and the etch-solution temperature. Membranes with pore diameters ranging from as small as 10 nm to as large as ~10 μ m are commercially available. The membranes used for these studies had nominal pore diameters of 30 nm and contained 6×10^8 pores per square centimeter of membrane surface area.

The electroless plating method is used to deposit the Au nanotubes^[7,30] within the pores of these membranes. Briefly, the template membrane is first “sensitized” by immersion into a SnCl₂ solution, which results in deposition of Sn(II) onto all of the membrane’s surfaces (pore walls and membrane faces). The sensitized membrane is then immersed into a AgNO₃ solution, and a surface redox reaction occurs (Eq. 1), which yields nanoscopic metallic Ag particles on the membrane surfaces.



(The subscripts surf and aq denote species adsorbed to the membrane surfaces and species dissolved in solution, respectively.) The membrane is then immersed into a commercial gold plating solution and a second surface redox reaction occurs, which yields Au nanoparticles on the surfaces (Eq. 2).



These surface-bound Au nanoparticles are good autocatalysts for the reduction of Au(I) to Au(0) using formaldehyde as the reducing agent. As a result, Au deposition begins at the pore walls, and Au tubes are obtained within the pores.^[7,9,30,31]

ESTIMATION OF THE NANOTUBE INSIDE DIAMETER

We used a gas-transport method to obtain an estimate of the inside diameter (i.d.) of the template-synthesized Au nanotubes.^[7] Briefly, the tube-containing membrane is placed in a gas-permeation cell, and the upper and lower half-cells are evacuated. The upper half-cell is then pressurized, typically to 20 psi (138 kPa) with H₂, and the pressure-time transient associated with leakage of H₂ through the nanotubes is measured using a pressure transducer in the lower half-cell. The pressure-time transient is converted to gas flux (Q , mol s⁻¹), which is related to the radius of the nanotubes (r , cm) via.^[7]

$$Q = 4/3(2\pi/MRT)^{1/2}(nr^3\Delta P/l) \quad (3)$$

where ΔP is the pressure difference across the membrane (dyn cm⁻²; 1 dyn = 10⁻⁵ N), M is the molecular weight of the gas, R is the gas constant (erg K⁻¹ mol⁻¹; 1 erg = 10⁻⁷ J), n is the number of nanotubes in the membrane sample, l is the membrane thickness (cm), and T is the temperature

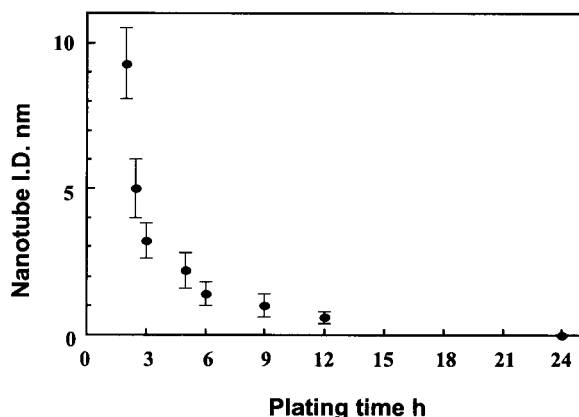


Fig. 1 Variation of the nanotube effective inside diameter with plating time.

(K). At long plating times, membranes containing nanotubes with i.d.'s of molecular dimensions are obtained (Fig. 1).

CHEMICAL SENSING WITH THE Au NANOTUBE MEMBRANES

These Au nanotube membranes have been used as sensors for the determination of ultratrace concentrations of ions and molecules.^[26,27] In this case, the nanotube membrane was allowed to separate two salt solutions, a constant transmembrane potential was applied, and the resulting transmembrane current was measured. When an analyte of comparable dimensions to the inside diameter of the nanotubes was added to one of the salt solutions, a decrease in transmembrane current was observed. The magnitude of this drop in transmembrane current (Δi) is proportional to the analyte concentration.

CALIBRATION CURVES AND DETECTION LIMITS

As in the transport experiments, a U-tube cell was assembled with the nanotube membrane separating the two halves of the cell. The two half-cells were filled with the desired electrolyte and an electrode was placed into each half-cell. Three different sets of electrodes and electrolytes were used. The first set consisted of two Pt plate electrodes, and the electrolyte used in both half-cells was 0.1 M KF. The second set consisted of two Ag/AgCl wires, and the electrolyte used in both half-cells was 0.1 M KCl. The third set consisted of two Ag/AgI wires immersed in 0.1 M KI.

As noted above, the experimental protocol used with these cells was to immerse the electrodes into the appropriate electrolyte and apply a constant potential between the electrodes. The resulting transmembrane current was measured and recorded on an $X-t$ recorder. After obtaining this baseline current, the anode half-cell was spiked with a known quantity of the desired analyte (Fig. 2). This resulted in a change in the transmembrane current, Δi (Fig. 3). A potentiostat was used to apply the potential between the electrodes and measure the transmembrane current. The transmembrane potential used was on the order of 0.5 V.^[26,27]

Plots of $\log \Delta i$ vs. $\log[\text{analyte}]$ for the analytes Ru(bpy)₃²⁺, MV²⁺, and quinine (Fig. 2) were obtained using Ag/AgCl electrodes and 0.1 M KCl as the electrolyte in both half-cells (Fig. 4). For these experiments, a membrane with 2.8-nm i.d. Au nanotubes was used. A log-log format is used for these "calibration curves" because of the large dynamic range (spanning as

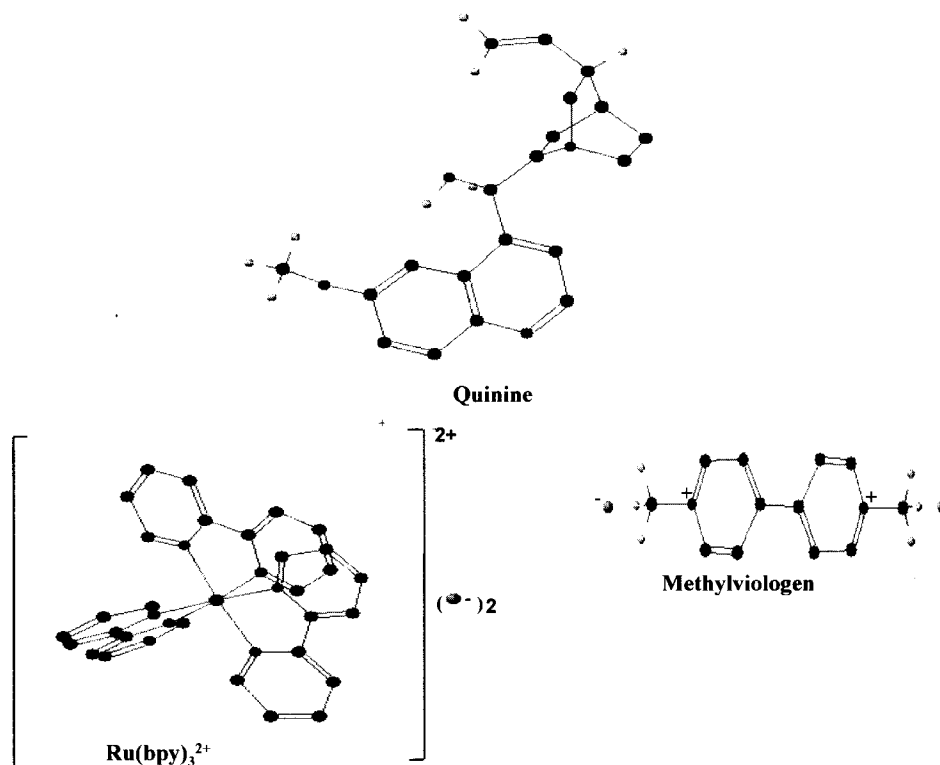


Fig. 2 Chemical structures and approximate relative sizes of the three “big molecule/small molecule” pairs used in the molecular filtration experiments. Quinine, MV²⁺, and Ru(bpy)₃²⁺ were also used as analytes in the sensor work. (View this art in color at www.dekker.com.)

much as 5 orders of magnitude in analyte concentration) obtained with this cell. Analogous calibration curves were obtained for the other electrode/electrolyte systems investigated. The detection limits^[26] obtained are shown

in Table 1. For the divalent cationic electrolytes, the detection limits were lowest (best) in the Ag/AgI/KI cell and worst in the Pt/KF cell. The detection limit for quinine was the same in both the Ag/AgI/KI and Ag/AgCl/KCl cells. In general, the detection limit decreases as the size of the analyte molecule increases (Fig. 2). Finally, the

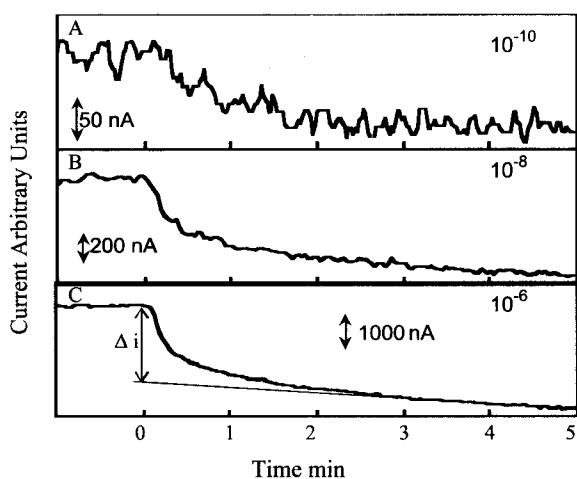


Fig. 3 Nanotube membrane sensor current–time transients associated with spiking the anode half cell with the indicated concentrations of Ru(bpy)₃²⁺. Tube i.d.=2.8 nm; Ag/AgCl/KCl cell: Δi determined as shown in C.

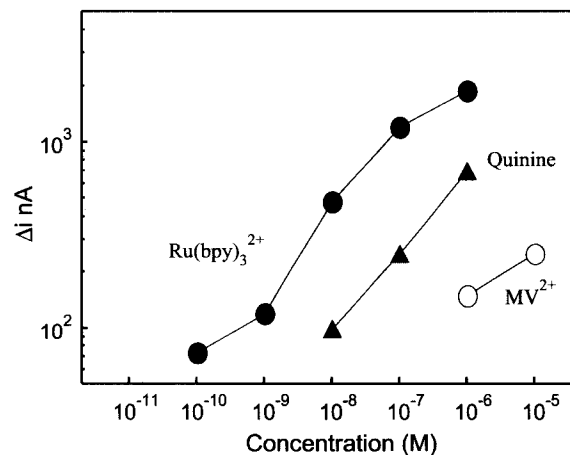


Fig. 4 Calibrations curves for the indicated analytes. Membrane and cell are as described in Fig. 3.

Table 1 Detection limits obtained for the three different electrode/electrolyte systems studied (nanotubule i.d.)

Cell	Analyte	Detection limit (M)
Pt/KF	Ru (bpy) ₃ ²⁺	10 ⁻⁹
Ag/AgCl/KCl	Ru (bpy) ₃ ²⁺	10 ⁻¹⁰
	Quinine	10 ⁻⁸
	MV ²⁺	10 ⁻⁶
	2-naphthol	10 ⁻⁶
Ag/AgI/KI	Ru (bpy) ₃ ²⁺	10 ⁻¹¹
	Quinine	10 ⁻⁸
	MV ²⁺	10 ⁻⁷
	2-naphthol	10 ⁻⁶

detection limits obtained (down to 10⁻¹¹ M) are extraordinary and compete with even the most sensitive of modern analytical methods.

The majority of the quinine in both the KCl and KI solutions is present as the monoprotonated (monocationic) form. Perhaps the reason the detection limits for Ru(bpy)₃²⁺ and MV²⁺ are lower in the Ag/AgI/KI cell while the detection limit for quinine is the same in both this cell and the Ag/AgCl/KCl cell has to do with the difference in charge of these analytes (predominantly monocationic vs. dicationic). To explore this point, the detection limits for a neutral analyte, 2-naphthol, were obtained in both the Ag/AgI/KI and Ag/AgCl/KCl cells. Like quinine, the detection limit for this neutral analyte was the same in both cells (10⁻⁶ M) (Table 1).

In the membrane transport studies, it was shown that Ru(bpy)₃²⁺ and MV²⁺ come across such membranes as the ion multiples Ru(bpy)₃²⁺(X⁻)₂ and MV²⁺(X⁻)₂ (X⁻=anion).^[7] In the KI cell, the ion multiple contains two larger (relative to chloride) iodide anions. Perhaps the larger size of the iodide ion multiple accounts for the lower detection limit in the KI-containing cell. If this is true, then the difference between the quinine cation paired with one I⁻ vs. this cation paired with one Cl⁻ is not great enough to cause the detection limit for this predominantly monovalent analyte to be significantly different in the Ag/AgI/KI vs. the Ag/AgCl/KCl cells (Table 1).

The final variable to be investigated is the effect of nanotube inside diameter on detection limit. To explore this parameter, membranes with nanotube inside diameters of approximately of 3.8, 2.8, 2.2, 1.8, and 1.4 nm were prepared and used in the Ag/AgI/KI cell.^[26] Calibration curves for the analytes Ru(bpy)₃²⁺, MV²⁺, and quinine were generated as before, and detection limits were obtained from these calibration curves. Fig. 5 shows plots of detection limits for these three different analytes vs. the

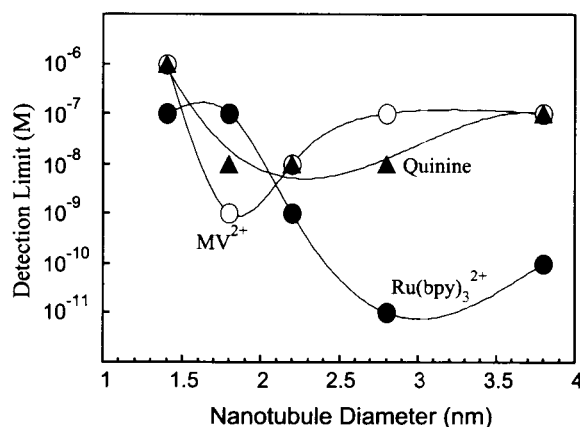
nanotube inside diameter in the membrane used. A minimum in this plot is observed for each of the three analytes.

The nanotube membrane that produces the minimum (best) detection limit depends on the size of the analyte. These molecules decrease in size in the order Ru(bpy)₃²⁺>quinine>MV²⁺. The nanotube membrane that yields the lowest detection limit follows this size order; that is, the nanotube diameters that produce the lowest detection limit for Ru(bpy)₃²⁺, quinine, and MV²⁺ are 2.8, 2.2, and 1.8 nm, respectively. For the roughly spherical analytes, the optimal tube diameter is a little over twice the diameter of the molecule.

MOLECULAR-SIZE-BASED SELECTIVITY

The data presented above show a strong correlation between detection limit and the relative sizes of the nanotube and the analyte molecule (Fig. 5). This indicates that this device should show molecular-size-based selectivity. This is not surprising given the transport studies previously discussed. To explore size-based selectivity, a series of solutions were prepared containing decreasing concentrations of the analyte species, but containing a constant (higher) concentration of an interfering species. The interfering species was smaller than the analyte species. The response of the nanotube membrane (nanotube diameter=2.8 nm) to these solutions was then measured starting from lowest to highest concentration of the analyte species.

The small pyridine molecule was used as the first interfering species. When present at a concentration of 10⁻⁴ M, pyridine offered very little interference for any of the analytes Ru(bpy)₃²⁺, MV²⁺, or quinine. The detection limits in the presence of 10⁻⁴ M pyridine were 10⁻¹⁰ M

**Fig. 5** Detection limits for MV²⁺, quinine, and Ru(bpy)₃²⁺ vs. i.d. of the nanotubes used in the sensor.

for $\text{Ru}(\text{bpy})_3^{2+}$, 10^{-6} M for MV^{2+} , and 10^{-7} M for quinine, within an order of magnitude of the detection limit with no added interfering species (Table 1). In other words, this nanotube membrane sensor can detect 10^{-10} M $\text{Ru}(\text{bpy})_3^{2+}$ in the presence of 6 orders of magnitude higher pyridine concentration.

A second set of experiments was performed using the larger MV^{2+} as the interfering species. Now at low concentrations of analyte, there is a region where the device produces a constant response as a result of the constant concentration (10^{-4} M) of this interfering species; that is, the much higher concentration of the MV^{2+} swamps the response of the device. However, as the concentration of $\text{Ru}(\text{bpy})_3^{2+}$ increases, there is a concentration range where the device responds to this analyte species without interference from the MV^{2+} . This concentration range begins at concentrations of $\text{Ru}(\text{bpy})_3^{2+}$ above 10^{-8} M. That is, the size-based selectivity is such that the larger analyte species, $\text{Ru}(\text{bpy})_3^{2+}$, can be detected down to 10^{-8} M in the presence of 4 orders of magnitude higher concentration of the smaller interfering species, MV^{2+} .

SYNTHETIC ION CHANNEL PORES

We have conducted experiments that provide proof of the basic concept that an analyte molecule can switch on an ion current in a synthetic membrane-based ion-channel mimic.^[29] The membrane used for most experiments was a commercially available microporous alumina filter. The pores in this membrane were made hydrophobic by reaction with an 18-carbon (C_{18}) alkyl silane. When placed between two salt solutions, the pores in this C_{18} -derivatized membrane are not wetted by water, yielding the off state of the membrane. When exposed to a solution containing a sufficiently high concentration of a long-chain ionic surfactant (the analyte), the surfactant molecules partition into the hydrophobic membrane, and ultimately cause the pores to flood with water and electrolyte. As a result, the membrane will now support an ion current, and the ion channel-mimetic membrane is switched to its on state. Cationic drug molecules can also switch this membrane from the off to the on state.

MEMBRANE PREPARATION AND A.C. IMPEDANCE EXPERIMENTS WITH 1-DODECANESULFONIC ACID ANALYTE

The alumina membranes were Anopore[®] (Whatman Inc., Clifton, New Jersey) that had nominally 200-nm-diameter pores and were 60- μm thick. The alumina membranes

were modified with octadecyltrimethoxysilane.^[29] The membrane assembly was mounted between the halves of a U-tube permeation cell, and both half-cells were filled with ~ 20 mL of 0.1 M KCl. A Ag/AgCl working electrode was immersed into one half-cell solution, and a Pt counter electrode and a Ag/AgCl reference electrode were placed in the other half-cell.^[32,33]

Alternating current impedance measurements proved to be a useful way to demonstrate the analyte-induced switching of the membrane between the off and on states. The uppermost curve in Fig. 6 is the Nyquist plot for a C_{18} -modified alumina membrane with 0.1 M KCl solutions, and no analyte (1-dodecanesulfonic acid, DBS) on either side of the membrane. As per prior investigations of ion-channel and ion-channel-mimetic membranes,^[34,35] the impedance data were interpreted in terms of the equivalent circuit shown in the inset of Fig. 6, where R_s is the solution resistance, R_m is the membrane resistance, and C is the membrane capacitance. The dashed curve is the best fit to the experimental data, from which the R_m (Fig. 7) and C values were obtained. Also shown in Fig. 6 are impedance data after spiking the half-cell electrolyte solutions to the indicated concentrations with the analyte (DBS).

In the absence of DBS, the membrane resistance is very large, >50 M Ω as opposed to ~ 5 Ω for the alumina membrane before modification with the C_{18} silane.

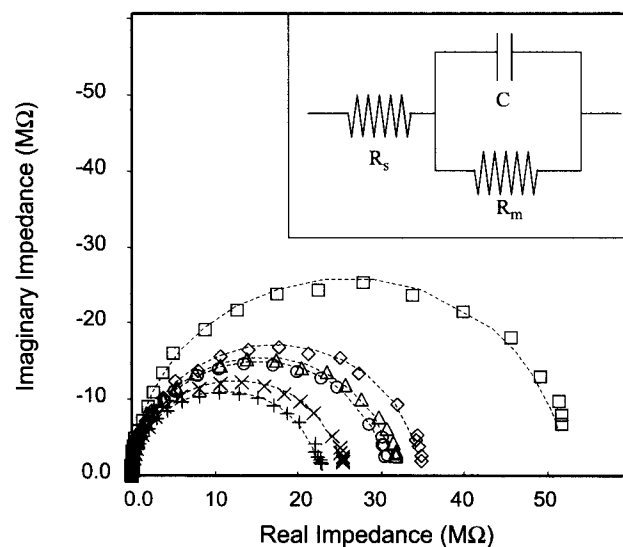


Fig. 6 Nyquist plots for a C_{18} -modified alumina membrane upon exposure to increasing concentrations of DBS in 0.1 M KCl. The points are the experimental data. The lines are calculated data obtained using the equivalent circuit shown in the inset. Concentrations of DBS were as follows: \square = 0 nM; \blacklozenge = 1.4 nM; \triangle = 3 nM; \circ = 10 nM; \times = 40 nM; $+$ = 100 nM.

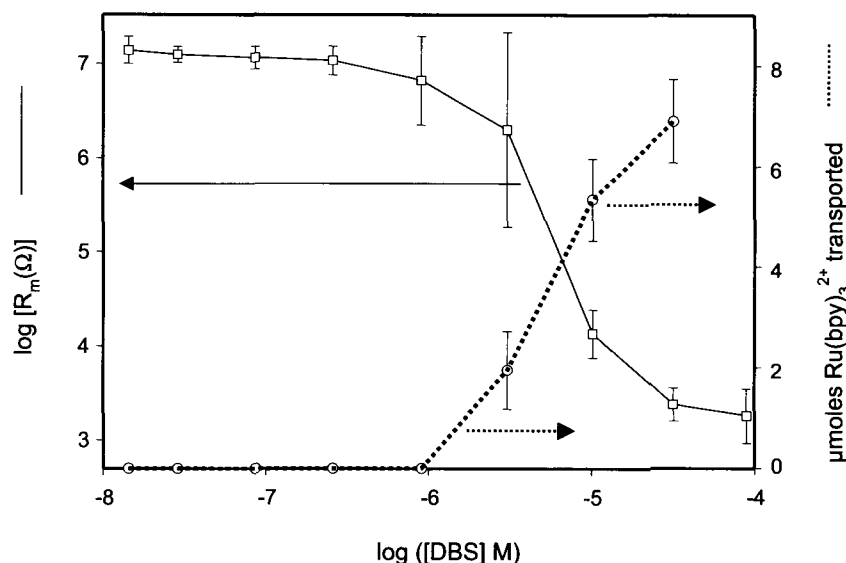


Fig. 7 Plots of log membrane resistance (left y axis) and micromoles $\text{Ru}(\text{bpy})_3^{2+}$ transported across the membrane (right y axis) vs. $\log[\text{DBS}]$ for a C_{18} -modified alumina membrane. The error bars represent the standard deviation of three separate experiments.

Transport experiments (vide infra) show that this is because the very hydrophobic C_{18} -modified pores are not wetted by water. This is supported by contact angle measurements on the membrane surface, where a water contact angle of $130(+8)^\circ$ was obtained for the C_{18} -treated alumina membrane as opposed to $\sim 8(+1)^\circ$ for the untreated membrane.

While over the concentration range 10^{-9} to 10^{-7} M, there is some drop in membrane resistance with increasing DBS concentration (Fig. 8), R_m remains very large (>20 M Ω). However, over the DBS concentration range between 10^{-6} and 10^{-5} M, there is a precipitous,

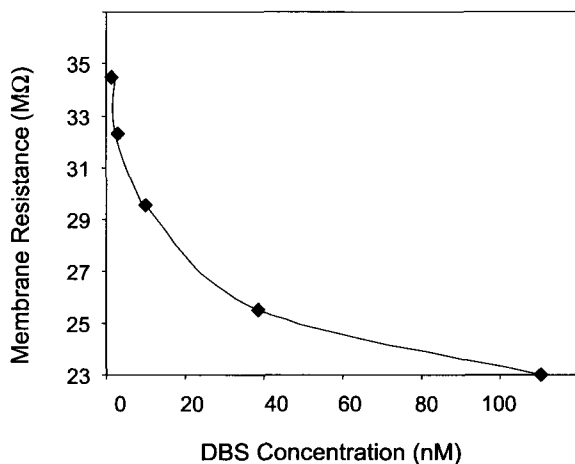


Fig. 8 Plot of membrane resistance vs. DBS concentration.

4-order-of-magnitude, drop in R_m (Fig. 7). This drop signals the analyte-induced switching of the membrane from the off to the on states.

TRANSPORT EXPERIMENTS

These were conducted by mounting the membrane between the two halves of a U-tube permeation cell and adding 0.1 M KCl to each half-cell. The feed half-cell was also 50 μM in either $\text{Ru}(\text{bpy})_3^{2+}$ or naphthalene disulfonate (NDS^{2-}), the permeate ions. An increment of the analyte surfactant (for these experiments DBS) was added to both the feed and permeate half-cells and permeation was allowed to occur for 24 hr. After this time, the permeate half-cell was sampled and the UV absorbance was used to determine the moles of the permeate ion transported. The permeate solution was then returned to the permeate half-cell and a second increment of DBS was added. Permeation was again allowed to occur for 24 hr and the amount of permeate ion transport was again determined. This process was repeated for various DBS concentrations over the range from 10^{-8} to 10^{-4} M.

The data obtained for $\text{Ru}(\text{bpy})_3^{2+}$ transport are shown in Fig. 7. At DBS concentrations below 10^{-6} M, there is no detectable $\text{Ru}(\text{bpy})_3^{2+}$ in the permeate solution. It is important to emphasize that each permeation data point in Fig. 7 corresponds to an additional 24 hr of permeation time. Hence by the time the DBS concentration was increased to 9×10^{-7} M, the total permeation time was 5 days. The inability to detect $\text{Ru}(\text{bpy})_3^{2+}$ in the permeate

solution after 5 days of permeation shows that over the DBS concentration range 0 to $\sim 10^{-6}$ M, the pores in the C_{18} membrane are not wetted by water, making the rate of $Ru(bpy)_3^{2+}$ transport immeasurably small. These data again show that at DBS concentrations below 10^{-6} M, the membrane is in the off state.

At DBS concentrations above 10^{-6} M, $Ru(bpy)_3^{2+}$ transport is switched on, and flux increases with concentration of DBS for concentrations above this value. The impedance and transport data tell a consistent story about the effect of DBS on the C_{18} -derivatized membrane (Fig. 7). At low DBS concentrations ($< 10^{-6}$ M) where the membrane resistance is in the $10^7 \Omega$ range, $Ru(bpy)_3^{2+}$ is not transported. The sudden drop in R_m at DBS concentrations above $\sim 10^{-6}$ M is seen in the transport experiments as an abrupt switching on of $Ru(bpy)_3^{2+}$ transport across the membrane.

X-RAY PHOTOELECTRON SPECTROSCOPY

X-ray photoelectron spectroscopy (XPS) was used to show that the prototypical analyte dodecylbenzene sulfonate (DBS) is present on the C_{18} -modified alumina surface after exposure of the membrane to DBS solution. However, the XPS cross section for S from the DBS proved too weak to obtain unambiguous evidence; furthermore, O, C, and Na^+ (the counterion for the DBS) are ubiquitous, and therefore not useful as probes to prove that DBS is present on the surface. For this reason, we used a surface ion-exchange reaction to replace Na^+ with Cs^+ as the counterion for the surface-bound DBS. We then used XPS to look for the presence of Cs^+ on the C_{18} -modified surface that had been treated with DBS, using an identical surface that was exposed to the Cs^+ solution but not to DBS as the control.

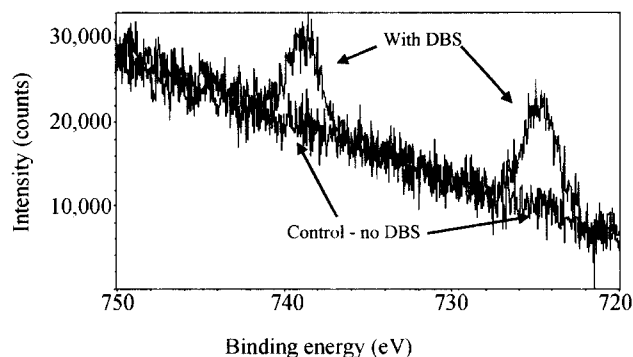


Fig. 9 X-ray photoelectron spectroscopy data for a C_{18} -modified alumina-membrane surface that was exposed to a DBS solution and then to a Cs^+ solution and for an identical surface that was exposed to Cs^+ but not to DBS.

Fig. 9 shows XPS data for a C_{18} -modified membrane that had been exposed to an aqueous 2.0 mM solution of Na^+ -DBS, rinsed, exposed to a 100 mM aqueous solution of $CsNO_3$, and then extensively rinsed again. The Cs 3d peaks at 724 and 738 eV are clearly evident.^[36] This may be contrasted to the control surface—a C_{18} -modified alumina membrane that was exposed to the Cs^+ solution but not to DBS—where no Cs signal is seen (Fig. 9). These data show that exposure of the membrane to DBS results in partitioning of this analyte species onto the C_{18} -modified surface.

MEASUREMENTS OF ION CURRENT

While the transport experiments show that the analyte DBS can switch on ion (e.g., $Ru(bpy)_3^{2+}$ and NDS^{2-}) transport across the membrane, we also wanted to obtain a direct measure of the ion current. To do this, a constant transmembrane potential of 1.5 V was applied and the resulting transmembrane ion current was measured. The current was monitored for 30 min and then the half-cell solutions were spiked with DBS to a total concentration of 10^{-9} M. The current was again measured for 30 min and the half-cells were spiked again with DBS. This process was repeated for various DBS concentrations over the range from 10^{-9} to $10^{-3.5}$ M.

Fig. 10 shows the measured ion current vs. time data; at the indicated times, the electrolyte solutions were spiked to the indicated concentrations with DBS. The ion-current data show the same general trend as both the impedance and transport data—at concentrations below $\sim 10^{-6}$ M, the ion current is at a very low baseline value and at concentrations above $\sim 10^{-6}$ M, the ion current abruptly switches on. In addition, the $10^{-5.5}$ M datum shows that the transition from the low-current to the high-current state very abruptly occurs.

Both the impedance and ion-current data show that when the membrane is in the off state, some small baseline current does flow across the membrane. It is important to note that the resistance value for the off state obtained by the impedance and ion current measurements are essentially identical. As shown in Fig. 6, the impedance measurement yields a value of $\sim 10^7 \Omega$. The ion current in the off state is $\sim 1.5 \times 10^{-7}$ A, which for a 1.5 V transmembrane potential yields a membrane resistance of $\sim 10^7 \Omega$. However, the issue left to resolve is—what is supporting this baseline ion current when the membrane is in the off state? At this point, we cannot say other than to suggest that this current results from some surface conduction process that occurs along the pore walls when the pores are devoid of water. In the absence of DBS, this surface conduction process may involve residual surface hydroxyl sites. The impedance data (Fig. 6) indicate that

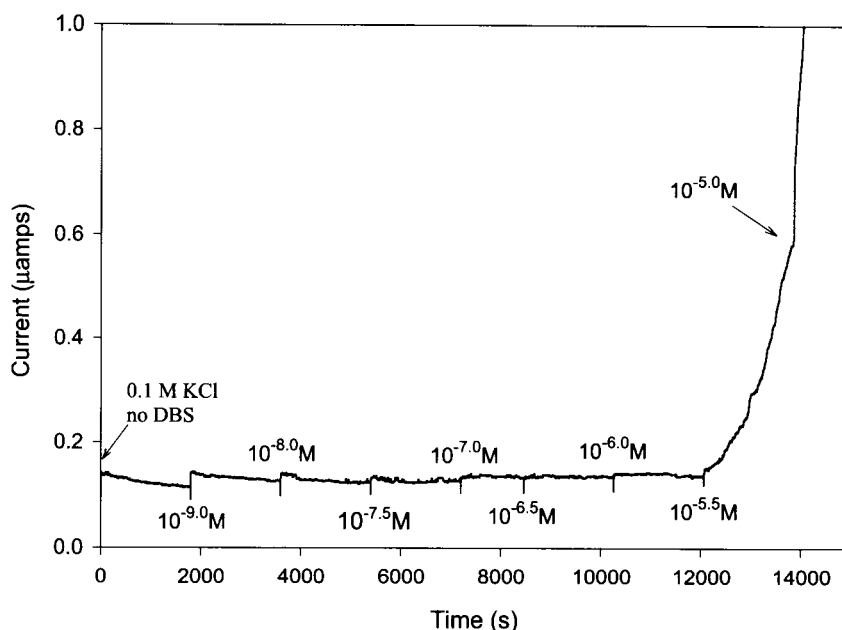


Fig. 10 Ion current through a C_{18} -modified alumina membrane vs. time. The contacting solution phases were spiked with the indicated concentrations of DBS at the indicated times. The electrolyte was 0.1 M KCl. A constant transmembrane potential of 1.5 V was applied.

in the presence of DBS, the surfactant itself is involved in the conduction process.

DETECTION OF DRUG MOLECULES

To explore the role of the hydrophobic effect in driving the analyte species into the C_{18} -derivatized alumina membrane, we investigated the effect of hydrophobic cationic drug molecules on the membrane resistance. The molecules and their molecular weights are amiodarone

(645 g mol⁻¹), amitriptyline (278 g mol⁻¹), and bupivacaine (288 g mol⁻¹) (Fig. 11). Because its molecular weight is more than double those of the other drugs and because it contains very hydrophobic iodo substituents, amiodarone is by far the most hydrophobic of these molecules. If the hydrophobic effect is responsible for driving molecules into the C_{18} -derivatized membrane, then the transition from the off to the on state would occur at lowest concentrations for amiodarone, and this is what is experimentally observed (Fig. 11). There is only a 3% difference in the molecular weights of amitriptyline and bupivacaine; however, bupivacaine presents two additional opportunities for hydrogen bonding with water—the lone pairs on the carbonyl group and the lone pair of the nonprotonated nitrogen. For this reason, bupivacaine is much more hydrophilic, and it would be expected to be the mostly poorly detected of the three drugs; Fig. 11 shows that this is also experimentally observed.

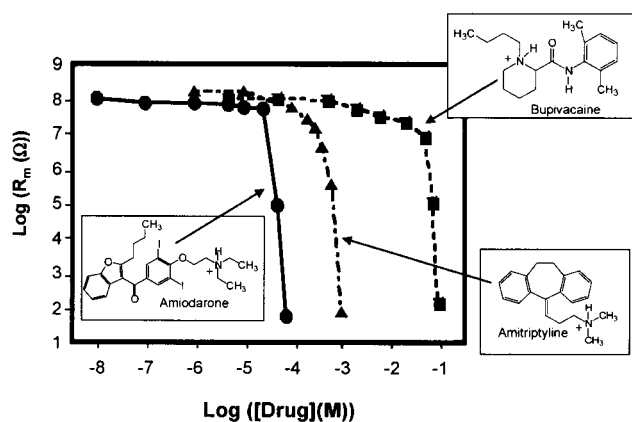


Fig. 11 Plots of log membrane resistance vs. log[Drug] for the indicated drugs and a C_{18} -modified alumina membrane.

CONCLUSION

We have described a highly sensitive method of electroanalysis based on Au nanotube membranes. In addition, we have also shown that synthetic micropore and nanotube membranes can mimic the function of ligand-gated ion channels; that is, they can be switched from an off state to an on state in response to the presence of a chemical stimulus. This concept of ion-channel mimetic

sensing, as originally proposed by Umezawa's group,^[32] has been of considerable interest in analytical chemistry.^[37–40] There is also considerable appeal in using naturally occurring and genetically engineered protein channels as sensors (Ref. [41], and references therein). Such research at the bio/nano interface is of great current interest in our group.

ACKNOWLEDGMENT

Aspects of this work were supported by the Office of Naval Research and the National Science Foundation.

REFERENCES

- Martin, C.R. Nanomaterials—A membrane-based synthetic approach. *Science* **1994**, *266*, 1961–1966.
- Hulteen, J.C.; Martin, C.R. A general template-based method for the preparation of nanomaterials. *J. Mater. Chem.* **1997**, *7* (7), 1075–1087.
- Martin, C.R.; Mitchell, D.T. Nanomaterials in analytical chemistry. *Anal. Chem.* **1998**, *70*, 322A–327A.
- Fleischer, R.L.; Price, P.B.; Walker, R.M. *Nuclear Tracks in Solids*; University of California Press: Berkeley, CA, 1975.
- Hornyak, G.L.; Patrissi, C.J.; Martin, C.R. Fabrication, characterization and optical properties of gold-nanoparticle/porous-alumina composites: The non-scattering Maxwell–Garnett limit. *J. Phys. Chem., B* **1997**, *101*, 1548–1555.
- Nishizawa, M.; Menon, V.P.; Martin, C.R. Metal nanotubule membranes with electrochemically switchable ion-transport selectivity. *Science* **1995**, *268*, 700–702.
- Jirage, K.B.; Hulteen, J.C.; Martin, C.R. Nanotubule-based molecular-filtration membranes. *Science* **1997**, *278*, 655–658.
- Hulteen, J.C.; Martin, C.R. Introducing chemical transport selectivity into gold nanotubule membranes. *J. Am. Chem. Soc.* **1998**, *120*, 6603–6604.
- Jirage, K.B.; Hulteen, J.C.; Martin, C.R. Effects of thiol chemisorption on the transport properties of gold nanotubule membranes. *Anal. Chem.* **1999**, *71*, 4913–4918.
- Hou, Z.; Abbott, N.L.; Stroeve, P. Self-assembled monolayers on electroless gold impart pH-responsive transport of ions in porous membranes. *Langmuir* **2000**, *16*, 2401–2404.
- Tourillon, G.; Pontinnier, L.; Levy, J.P.; Langlais, V. Electrochemically synthesized Co and Fe nano-wires and nanotubes. *Electrochem. Solid-State Lett.* **2000**, *3*, 20–23.
- Schonenberger, C.; van der Zande, B.M.I.; Fokkink, L.G.J.; Henry, M.; Schmid, C.; Kruger, M.; Bachtold, A.; Huber, R.; Birk, H.; Staufer, U. Template synthesis of nanowires in porous polycarbonate membranes: Electrochemistry and morphology. *J. Phys. Chem., B* **1997**, *101*, 5497–5505.
- Martin, C.R. *Handbook of Conducting Polymers*, 2nd Ed.; Reynolds, J.R., Skotheim, T., Elsebaumer, R., Eds.; Marcel Dekker, Inc., 1997; 409–421.
- Demoustier-Champagne, S.; Stavaux, P.-Y. Effect of electrolyte concentration and nature on the morphology and the electrical properties of electro-polymerized polypyrrole nanotubules. *Chem. Mater.* **1999**, *11*, 829–834.
- Sukeerthi, S.; Contractor, Q. Molecular sensors and sensor arrays based on polyaniline microtubules. *Anal. Chem.* **1999**, *71*, 2231–2236.
- Lakshmi, B.B.; Patrissi, C.J.; Martin, C.R. Sol–gel template synthesis of semiconductor oxide micro- and nanostructures. *Chem. Mater.* **1997**, *9*, 2544–2550.
- Lakshmi, B.B.; Dorhout, P.K.; Martin, C.R. Sol–gel template synthesis of semiconductor nanostructures. *Chem. Mater.* **1997**, *9*, 857–862.
- Che, G.; Lakshmi, B.B.; Martin, C.R.; Fisher, E.R. Metal nanocluster-filled carbon nanotubules: Catalytic properties and possible applications in electrochemical energy storage and production. *Langmuir* **1999**, *15*, 750–758.
- Che, G.; Fisher, E.R.; Martin, C.R. Carbon nanotubule membranes for electrochemical energy storage and production. *Nature* **1998**, *393*, 346–349.
- Patrissi, C.J.; Martin, C.R. Sol–gel-based template synthesis and Li-insertion rate performance of nanostructured vanadium pentoxide. *J. Electrochem. Soc.* **1999**, *146*, 3176–3180.
- Li, N.; Patrissi, C.J.; Martin, C.R. Rate capabilities of nanostructured LiMn₂O₄ electrodes in aqueous electrolyte. *J. Electrochem. Soc.* **2000**, *147*, 2044–2049.
- Che, G.; Jirage, K.B.; Fisher, E.R.; Martin, C.R.; Yoneyama, H. Chemical-vapor deposition-based template synthesis of microtubular TiS₂ battery electrodes. *J. Electrochem. Soc.* **1997**, *144*, 4296–4302.
- Cepak, V.M.; Hulteen, J.C.; Che, G.; Jirage, K.B.; Lakshmi, B.B.; Fisher, E.R.; Martin, C.R. Fabrication and characterization of concentric tubular composite micro- and nanostructures using the template synthesis method. *J. Mater. Res.* **1998**, *13*, 3070–3080.
- Cepak, V.M.; Hulteen, J.C.; Che, G.; Jirage, K.B.;

- Lakshmi, B.B.; Fisher, E.R.; Martin, C.R. Chemical strategies for template syntheses of composite micro and nanostructures. *Chem. Mater.* **1997**, *9*, 1065–1067.
25. Martin, B.R.; Dermody, D.J.; Reiss, B.D.; Fang, M.; Lyon, L.A.; Natan, M.J.; Mallouk, T.E. Orthogonal self-assembly on colloidal gold–platinum nanorods. *Adv. Mater.* **1999**, *11*, 1021–1025.
 26. Kobayashi, Y.; Martin, C.R. Highly-sensitive methods for electroanalytical chemistry based on nanotubule membranes. *Anal. Chem.* **1999**, *71*, 3665–3672.
 27. Kobayashi, Y.; Martin, C.R. Toward a molecular coulter counter. *J. Electroanal. Chem.* **1997**, *431*, 29–33.
 28. Voet, D.; Voet, J.G. *Biochemistry*, 2nd Ed.; Wiley: New York, 1995; 1297–1298.
 29. Steinle, E.D.; Mitchell, D.T.; Wirtz, M.; Lee, S.B.; Young, V.Y.; Martin, C.R. Ion channel mimetic micropore and nanotube membrane sensors. *Anal. Chem.* **2002**, *74*, 2416–2422.
 30. Menon, V.P.; Martin, C.R. Fabrication and evaluation of nanoelectrode ensembles. *Anal. Chem.* **1995**, *67*, 1920–1928.
 31. Kang, M.; Martin, C.R. Investigations of potential-dependent fluxes of ionic permeates in gold nanotubule membranes prepared via the template method. *Langmuir* **2001**, *17*, 2753–2759.
 32. Armstrong, R.D.; Covington, A.K.; Evans, G.P. Mechanistic studies of the valinomycin-based potassium-selective electrode using ac impedance methods. *J. Electroanal. Chem.* **1983**, *159*, 33–40.
 33. Xie, S.-L.; Cammann, K. Apparent ion-exchange current densities at valinomycin based potassium ion-selective PVC membranes obtained with an AC-impedance method. *J. Electroanal. Chem.* **1987**, *229*, 249–263.
 34. Zhang, W.; Spichiger, U.E. An impedance study of Mg^{2+} -selective membranes. *Electrochim. Acta* **2000**, *45*, 2259–2266.
 35. Ding, L.; Li, J.; Dong, S.; Wang, E. Supported phospholipid membranes: Comparison among different deposition methods for a phospholipid monolayer. *J. Electroanal. Chem.* **1996**, *416*, 105–112.
 36. *Handbook of X-Ray Photoelectron Spectroscopy*; Muilenberg, G.E., Ed.; Perkin-Elmer Corporation: Eden Prairie, 1978.
 37. Sugawara, M.; Kojima, K.; Sazawa, H.; Umezawa, Y. Ion-channel sensors. *Anal. Chem.* **1987**, *59*, 2842–2846.
 38. Xiao, K.P.; Bühlmann, P.; Umezawa, Y. Ion-channel-mimetic sensing of hydrophilic anions based on monolayers of a hydrogen bond-forming receptor. *Anal. Chem.* **1999**, *71*, 1183–1187.
 39. Wu, Z.; Tang, J.; Cheng, Z.; Yang, X.; Wang, E. Ion channel behavior of supported bilayer lipid membranes on a glassy carbon electrode. *Anal. Chem.* **2000**, *72*, 6030–6033.
 40. Katayama, Y.; Ohuchi, Y.; Yang, X.; Wang, E. The design of cyclic AMP recognizing oligopeptides and evaluation of its capability for cyclic AMP recognition using an electrochemical system. *Anal. Chem.* **October 1, 2000**, *72* (19), 4671–4674.
 41. Bayley, H.; Martin, C.R. Resistive-pulse sensing from microbes to molecules. *Chem. Rev., Sens. Them. Issue* **2000**, *100*, 2575–2594.

Index

- ABC-type chloride channel, chloride-conducting membrane protein, 3699
- Acetamide phosphonic acids, self-assembled, on mesoporous silica, 1055–1057
- Acetate method, magnetic nanomaterial synthesis, 1691–1693
- Achiral bulk crystal structures, chiral surfaces from, 1118–1120
- Acid-catalyzed methylamine synthesis, 640
- Acoustic phonons, in self-assembled multiple germanium structures, 3208–3209
- Actinides, 1130
- Adenosine-triphosphate, 2202
- Adenoviruses, 327–328
- Adhesion between surfaces coated with self-assembled monolayers
- adhesion hysteresis, 5
 - alkylsilane self-assembled monolayers
 - on mica, 6–8
 - on silica, 4–6
 - alkylthiol self-assembled monolayers, on gold, 3–4
 - humidity, capillary condensation, 1–3
 - pulloff forces, 4
- Adhesion of cell on substrate, 11–21
- adhesion energy, bidimensional osmotic pressure, 12
 - application, 17–19
 - aspiration pressure, 16, 18
 - immobile receptors, substrate with, 12
 - ligand-receptor interaction, 12
 - macroscopic adhesion energy, molecular binding energy, 12–13
 - model, 11–12
 - experimental verification, 13–17
- Adsorbate-induced formation, naturally chiral surfaces, 1120
- Adsorbed polymer layer; nanoparticle with metallation, 2912–2913
- polymer colloids, 2912–2913
- Adsorption of polymers, proteins, 23–34
- chemical heterogeneity, 28–32
 - flexible polymer adsorption, 29
 - globular protein adsorption, 29–32
 - modeling, 23–24
 - nanometer scale physical heterogeneity, 25–28
 - simulation studies, 24–25
- Advanced Powder Technology, 2465
- Advectus Life Sciences, 256
- Aerogels, templating, for tunable nanoporosity, 3843–3851
- drying methods, 3845–3849
 - evaporative drying, 3846–3847
 - removal of template material, 3849
 - supercritical drying, 3847–3849
 - sol-gel synthesis, 3843–3844
 - tailoring nanoporous material, 3849–3850
 - template materials, 3844–3845
- Aerosol nanoparticle
- Brownian coagulation, 36–37
 - coagulation, 35–44
 - of monodisperse aerosols, 35–36
 - coagulation equation, 36
 - coagulation in nanoparticle synthesis, 43
 - moment method, 42–43
 - sectional method, 40–41
 - self-preserving solution, 41–42
 - solutions, 40–43
- collision kernels, 36–39
- Brownian coagulation, 36–37
 - electrostatic coagulation, 39
 - gravitational coagulation, 37–38
 - turbulent coagulation, 38–39
- electrostatic coagulation, 39
- gravitational coagulation, 37–38
- turbulent coagulation, 38–39
- Aerospace applications, epoxy layered-silicate nanocomposites, 45–54
- aerospace epoxy nanocomposites, 46
 - layered organosilicate, 45–46
 - layered silicate, 45–46
 - morphology characterization, 46–47
 - morphology development, 49–50
 - different curing agents, 50–51
 - primer layer for aircraft coating, 51–52
 - processing, 49–50
 - properties of, 47–49
- AFOSR. *See* Air Force Office of Sponsored Research
- Air Force Office of Sponsored Research, 2191
- Aircraft coating, silicate nanocomposites as primer layer, 51–52
- Air-water interface
- charge-transfer complexes at, 2022–2023
 - crystallization, organosilane monolayers, 2031–2036
 - ionic amphiphilic block copolymer monolayer, nanostructure, 2519–2529
 - molecular assembly organosilanes, mixed monolayers, phase separation, 2033–2036
- Alanine, 266
- properties of, 3082
- Albumin, properties of, 3082
- Alcohol detection, 368
- Aldol, on lab-on-a-chip micro reactor, 1556
- Alexgel applications, rocket propulsion, 1942–1943
- hydrocarbon-based liquid rocket engines, 1942
 - hydrocarbon-based RBCC systems, 1942
 - liquid hydrogen engines, 1943
 - pulse detonation engines, 1942–1943
- Alkali metal clusters, in zeolite pores, 229–230
- Alkali metal oxides, in zeolite pores, 227–229
- Alkanethiolate, self-assembled monolayer modification, vacuum conditions, 3321–3322
- atomic chlorine modification, 3322–3323
- Alkenes, sterically overcrowded, as unidirection rotary motors, 2169–2173
- Alkylsilane self-assembled monolayers
- on mica, 6–8
 - on silica, 4–6
- Alkylthiol self-assembled monolayers on gold, 3–4
- Allophane, 1149
- Allosteric chemical controls, implementation of, 2115–2120
- Alloys, binary, nanoporosity, 893–902
- Alnis Biosciences, 256
- Alpha subunit (wild type), properties of, 3082
- Alpha-ketoesters, hydrogenation, on platinum, 1116
- Alternating current chaining, colloidal crystals, assembly by, 1035–1036
- Aluminum
- hydrothermal extraction from zeolite lattice, 636
 - nanocrystalline oxide, surface chemistry of, 3795–3804
 - surface free energy, 1573
- Aluminum alloy, orthopedic implant, 269
- Aluminum oxides, 1149
- Aluminum surfaces, pattern anodization, 83–88
- anodization cell, 83–84
 - bulk aluminum sheets
 - evaporated aluminum films on glass, 86–87
- Amide bands, isotope-labeled proteins, sum frequency generation studies, 3758–3759
- Amide clusters supported in zeolites, 230
- Amide synthesis, on lab-on-a-chip micro reactor, 1556
- Amino acid
- charge, hydrophobicity, surface tension, 266
 - in proteins, 266
 - residues of, properties of, 3082
- Aminopropylmethyldimethoxysilane, 2037
- Aminopropyl-triethoxysilane, 2847
- Amorphous carbon forms, structuring of, 417–420
- Amphiphiles, bolaform, layer-by-layer assembly, 1607–1622
- Amplifiers, rare earth-doped, 2861–2862
- Amyotrophic lateral sclerosis, 2783

This is an inclusive index for all five volumes. Volume breaks are as follows: Volume 1: pages 1–892; Volume 2: pages 893–1796; Volume 3: pages 1797–2676; Volume 4: pages 2677–3296; Volume 5: pages 3297–3980.

- Anaerobic organisms, bioremediation, 332
 Anaerobic processes, bioremediation, 332
 Anatase, energetic parameters, 1148
 Anion exchanger, 3699
 Anion recognition, biomimetic macrocyclic receptors for, 295-309
 charged receptors, 295-300
 hydrogen bonding receptors, 301-306
 metal centers, carboxylate coordination to, 300-301
 Anion templated palladium cage, 59
 Anion templated self-assembly, inorganic compounds, 55-68
 cobalt, 55-57
 hexa-molybdenum-based complex, 59
 hexanuclear silver array, route of, 63
 iron, 55
 molybdenum, 59
 nickel, 57-59
 oxo-vanadium, structure of, 56
 palladium, 59-62
 palladium cage, route of formation of, 62
 palladium-based molecular triangle, crystal structure of, 61
 platinum, 59-62
 silver, 62-66
 tetrafluoroborate templated nickel square, 59
 vanadium, 55
 x-ray crystal structure, chloride complex, 64
 Anion-templated rotaxane synthesis, 75
 Vogtle's, 72
 Anion-templated self-assembly, organic compounds, 69-81
 Gale's "anion-anion" assembled solid-state polymer, x-ray crystal structure, 77
 Gale's diamidopyrrole ligand, 77
 guanidinium-appended porphyrins, 76
 Hamilton's self-assembled solid-state hydrogen-bonded structure, ribbon arrangement of, 70
 Kruger's double helicite, molecular structure of, 76
 Mendoza's tetraguanidinium strand, double helicite structure self-assembly, 70
 Schalley's "stopping" rotaxane synthesis, anion template, 73
 Anisotropy, quantum rods made of cadmium selenide
 dielectric properties, 3259-3260
 optical properties, 3256-3259
 Anodes, lithium ion batteries, 427-429
 Anodization
 nanoarrays, electrochemical self-assembly, 1075
 patterned on aluminum surfaces, 83-88
 anodization cell, 83-84
 bulk aluminum sheets
 evaporated aluminum films on glass, 86-87
 Anodization cell, custom-built, 84
 Antibodies
 with infinite binding affinity, 89-94
 irreversible binding, 91
 multivalent binding, 89-91
 nanoparticle-labeled, luminescence of, 1647-1653
 Antibody-based fiber optic nanobiosensors, 2761
 Anticancer drug delivery across blood-brain barrier, 256
 Antidot lattices, chaotic transport in
 Aharonov-Bohm oscillation, 654-664
 Altshuler-Aronov-Spivak oscillation, 657-658
 commensurability peaks, 650-654
 magnetic focusing, leading to fundamental commensurability peak, 651
 scattering, from two adjacent antidots, 652
 scattering matrix formalism, 658-664
 triangular antidot lattices, 656-657
 Antigens, nanoparticle-labeled, luminescence of, 1647-1653
 Antimicrobial nanoemulsions, 256
 Apatite, surface free energy, 1573
 APT. *See* Advanced Powder Technology
 Arginine, 266
 properties of, 3082
 Armchair single-walled carbon nanotubes, 3607-3608
 Aromatics alkylation, mesoporous materials, 1807
 Artificial self-assembling systems, 289-291
 Artificial transmembrane ion channels, 3444-3445
 Asparagine, 266
 properties of, 3082
 Aspartic acid, 266
 properties of, 3082
Aspergillus oryzae, imaging, 134
 Atmosphere, environmental nanoparticle in, 1151
 Atmospheric nanoparticle, 95-107
 formation, growth, 100-104
 coagulation, 103
 condensational growth, 100-102
 homogeneous nucleation, 102-103
 physicochemical properties, 97-100
 chemical composition, 99-100
 physical characterization, 97-98
 size distributions, 95
 sources, 95-96
 Atom probe field ion microscopy, 2312
 Atom transfer radical polymerization, 2039
 Atom trapping, metal-oxide interface, oxide vacancies, nucleation, 1900-1901
 Atomic force microscope lithography, 2621-2622
 Atomic force microscope nanolithography, on organized molecular films, 109-118
 anodization AFM nanolithography, 111-116
 constructive nanolithography, 110-111
 current sensing AFM, nanolithography using, 111
 dip-pen nanolithography, 109-110
 nanografting lithography, 110
 Atomic force microscopy, 119-131, 284, 351, 2033, 2070, 2101, 2278, 2357, 2409, 2508, 2552, 2609, 2621, 2687, 2705, 2783, 2899
 direct force measurement of liposomes, 933-942
 dynamic, heterogeneous surfaces, 987-1000
 receptor-ligand interactions, dynamic measurements, 995
 steric forces, dynamic measurements, 994-995
 tapping mode atomic force microscope, 988-991
 hydrogen-bonded nanostructures studies, 155-167
 imaging artifacts, 143-153
 scanner artifacts, 150-151
 metal ion sorption, 169-178
 microbial cell surfaces, 133-142
 probing DNA, 120-124
 probing polysaccharides, 125-127
 probing proteins, 124-125
 protein adsorption, 3041-3064
 adsorbed protein structure, 3048-3049
 adsorption mechanisms, 3054-3060
 artifacts, 3044-3045
 atomic force microscopy techniques, 3042
 electrostatic effects, 3054-3055
 force interactions, 3051-3054
 growth mechanisms, 3056-3058
 kinetics, 3055-3056
 measurement techniques, 3041-3042
 multilayer formation, 3058
 nonuniform surfaces, 3049-3051
 protein structure, 3058-3060
 supramolecular organization, 3045-3048
 small amplitude, 3641-3654
 Atomic hydrogen, carbon nanotube electrodes, 429
 Atomic scale
 data storage on, 1477
 heterogeneous catalysts, 179-193
 Attenuated total reflection Fourier transform infrared, 2034
 Axle molecules, threaded through macrocycles, 195-204
 daisy-chain polyrotaxane, 195
 equilibrium constants, 198-203
 chain length, branching, effects of, 200-202
 pseudo-[2]-rotaxane formation, 197-198
 solvent, effect of, 198-200
 steric effects, 200
 substituent effects, 200
 terminal groups, influence of, 202-203
 molecular threading, 195-197
 riveted polyrotaxane, 195
Bacillus cereus, nanoparticle decontamination, 244
Bacillus subtilis, nanoparticle decontamination, 244
 Bacterial biosensor development, targets for, 347
 Bacteriophage M13, 324
 Bacteriorhodopsin, properties of, 3082
 Bacterium detection, porous silicon microcavities, 345-349
 Barcoded nanowire, 205-212
 assays using, 208
 barcoded rods, nonfluorescent bioassay using, 208
 biological multiplexing, 207-209
 bulk metals, reflectance values for, 207
 characterization, 206-207
 nanoelectronics, 207
 nanowire synthesis, 205
 reflectance image of nanowire, 206
 striped nanowire synthesis, 205-206
 synthesis, 205-206
 tagging, nonbiological, 209
 uses for, 207-209
 Barium strontium titanate, 2441
 Barrier properties, ordered multilayer polymer nanocomposites, 213-224
 multilayered polymer-polymer nanocomposites, 220-221
 polymer-layered aluminosilicate nanocomposites, 214-220

- Basic nanostructured catalysts, 225–234
 basicity, defined, 225–226
 historical perspective, 225
 nanostructured materials, 226–232
 carbogenic molecular sieves, 231–232
 hydrocalcite, 232
 mesoporous (alumino) silicates, 230–231
 zeolites, 227–230
- Batteries, carbon nanotubes, 514
- BD. *See* Brownian dynamics
- Bending modulus
 composite nanowires, 1776–1778
 nanobelt, 1780–1781
 of oxide nanobelts, 1778–1781
- Benzaldehyde, surface tension, 1573
- Benzene, surface tension, 1573
- Bernoulli's law, ferrohydrodynamic, 1735
- Beta-ketoesters, hydrogenation, on nickel, 1115–1117
- Bicontinuous liquid crystalline nanoparticle, cubosomes, 881–892
 cubic phase, 881–883
 cubosome manufacture, 885–886
 hexagonal liquid crystalline phase, 889
 monoolein, molecular structure of, 882
 other liquid crystalline phases, formation of, 89
 sponge phase, 889
 systems forming, 886–887
- Bilayers, supported, 2507–2508
- Bimetallic nanoparticle
 iron-group element composed of, 1875
 platinum-group element, composed of, 1875
 platinum-group elements composed of, 1874–1875
- Binary alloys, nanoporosity, 893–902
- Binding kinetics on biosensor surfaces, fractal analysis of, 1191–1202
 dual-fractal analysis, 1193
 single-fractal analysis, 1192–1193
 surface plasmon resonance biosensor, 1191–1192
- Bioactive substances, nanoencapsulation of, 2339–2354
 controlled release, 2339–2340
 liposomes, 2340–2343
 molecular inclusion complexes, 2348–2350
 polymer nanocapsules, 2345–2348
 polymer nanospheres, 2343–2345
- Bioaugmentation, 332
- Biocatalytic single enzyme nanoparticle, 235–245
 catalytic stability, 237–238
 enzyme stabilization approaches, 236
 kinetics, 238
 mass transfer, 238
 methacryloxpropyltrimethoxysilane, 236
 synthesis, 235–236
 transmission electron microscopy, 236–237
- Biocompatibility, nanobiomedical implants, 265–266
- BioDelivery Sciences, 256
- Bioelectrochemical sensors, 513–514
- Bioengineering, hybrid nanostructures for, 355–356
- Biofiltration, 335–336
- Bioinertness, proposed mechanism for, 399
- Biological membranes, halide transport through, structural base, 3697–3711
- Biological sensors, electrically functional microstructures from, 1032–1034
- Biological weapon decontamination, by nanoparticle, 241–245
- Biomedical applications, 247–261
 cell-substratum contact sites, 249
 diagnostic relevance, 248
 diagnostic systems, nanotechnology in, 251–253
 dip-pen nanolithography, 247
 miniaturization, controlled drug delivery devices, 254–256
 nanobiotechnology companies, 256
 nanomedicine, 247–248
 nanoscale, 247
 nanotechnology, cellular, tissue engineering, 248–251
 research challenges, 254
 therapeutic relevance, 248
 therapeutics, nanotechnology in, 253–256
- Biomedical implants from nanostructured materials, 263–275
 amino acid
 charge, hydrophobicity, surface tension, 266
 in proteins, 266
 characteristics, 265
 fibrous encapsulation, newly implanted materials, 263–264
 future developments, 272–273
 hydroxyapatite fibers, 266
 implant biocompatibility, 265–266
 nanophase ceramics, as nanobiomedical implants, 266–269
 nanophase materials, surface properties of, 265
 nanophase metals, as nanobiomedical implants, 269
 nanophase polymers, as nanobiomedical implants, 269–270
 nanoscale surface, potential implants, 266
 nanostructured composites, as nanobiomedical implants, 270–272
 potential risks, 272
 soft tissue wound healing, sequential events of, 264
 surface-enhanced Raman scattering technique, 268
- Bio-microarrays, based on functional nanoparticle, 277–286
 dip coating of nanoparticle, 279
 ethylene glycol dimethacrylate, 281
 layer-by-layer technique, 283–284
 lithographic microstructuring, particle deposition, 278
 methacrylic acid, 281
 microarrayer, 284
 microcontact printing, 284
 of nanoparticle layer, 279
 microspotting, of nanoparticle layer, 281
 microstructured surface preparation, 277–283
 nanoparticle, applied in microarray preparation, 281–282
 patterned monolayers of functional nanoparticle, 282–283
- photoablation, 278–279
 photolithography, 284
 protein binding polymer nanoparticle, 282
 surface activation, 277–278
- Biomimetic macrocyclic receptors, for carboxylate anion recognition, 295–309
 charged receptors, 295–300
 hydrogen bonding receptors, 301–306
 metal centers, carboxylate coordination to, 300–301
- Biomimetic self-assembling systems, 287–294
 artificial self-assembling systems, 289–291
 constrained self-assembly, 289–290
 dynamic self-assembling systems, 291
 hierarchical self-assembly, 290
 self-healing structures, 290–291
 shape complementarity, recognition by, 290
- Biomineralization, 2452
- Biomolecular, polymeric nanostructures, scanning probe lithography, 2973–2983
- Biomolecular nanostructures, scanning probe lithography, 2973–2983
- Biomolecular structure at interfaces, 310–319
- Biomolecules, analytical techniques for detection of, 351–352
- Bionanomaterials, 2451–2453
 biomineralization, 2452
 nanoparticle probes, 2452
 supramolecular materials, 2451–2452
- Bionanoparticle, 321–330
 adenoviruses, 327–328
 cowpea chlorotic mottle virus, 322–323
 cowpea mosaic virus, 324–327
 ferritins, 321–322
 gene delivery, 327–328
 M13 bacteriophage, 324
 tobacco mosaic virus, 323–324
- BioOral nanococheleates, 256
- Bioremediation, environmental contaminants, 331–341
 anaerobic organisms, 332
 bioaugmentation, 332
 biostimulation, 332
 environmental pollutants, 331–334
 hydrocarbons, 331–333
 metals, 334
 polycyclic aromatic hydrocarbons, 333–334
 Exxon Valdez oil spill bioremediation project, 336–338
 lessons from, 337–338
 techniques, 334–336
 biofiltration, 335–336
 groundwater bioremediation, 334–335
 phytoremediation, 336
- BioSante Pharmaceuticals, 256
- Biosensor platform, components of, 251
- Biosensor surface
 binding kinetics on, fractal analysis of, 1191–1202
 dual-fractal analysis, 1193
 single-fractal analysis, 1192–1193
 surface plasmon resonance biosensor, 1191–1192
 engineering of, 351–360

- Biosensors**
 based on carbon nanotubes, 361–373
 for chemical warfare agent detection, 375–388
 air, detection of chemical warfare agents in, 375, 377–378, 380–381, 383–386
 cell chamber, 379
 fluorescence measurements, 379
 water, detection of chemical warfare agents in, 375–379, 381–383, 385, 386
 water quality monitoring, toxic agents used for, chemical structures, 379
 porous silicon microcavities, 343–350
 bacterial biosensor development, targets for, 347
 bacterium detection, 345–349
 DNA detection, 344
 lipopolysaccharide, structure of, 347
 virus detection, 344–345
- Bioseparations, nanotube membranes for,** 3663–3664
- Biostimulation,** 332
- Biosurfaces,** 389–403
 bioinertness, 389
 cell adhesion, resisting, 390–391
 D-mannitol-terminated self-assembled monolayers, adsorption of protein on, 397
 D-mannonic 1,5-lactone, 2, 401
 polymer polydimethylsiloxane elastomers, 395
 polymer-colloidal science, 391–392
 polyol-terminated self-assembled monolayers, 395–398
 protein adsorption, resisting, 389–390
 tools for measuring, 394–395
- Biphenylthiol, electrostatic surface potential,** 692
- Birefringence in quantum dot arrays,** 3101–3105
 numerical estimates, 3102–3105
 planar array, 3105
- Bloch bands, expansion in linear combination of,** 3216–3217
- Bloch law,** 1670–1673
- Block copolymer, templating polymer crystal growth using,** 3853–3865
 amorphous systems, block copolymer phase separation, 3853–3854
 large areas, patterning semicrystalline block copolymers over, 3862–3863
 moderately-segregated systems, 3860–3861
 rubbery block copolymers, strongly-segregated semicrystalline, 3861–3862
 semicrystalline systems, microphase separation in, 3854–3855
 semicrystalline-glassy block copolymers, crystallization in nanoscale environments, 3855
 semicrystalline-poor block copolymers, 3855–3858
 semicrystalline-rich block copolymers, 3858–3860
 semicrystalline-rubbery systems, 3860
- Block copolymer micelle coronas,** 2906–2907
 nanoparticle formation in, metallation, 2903–2907
- Block copolymer nanoparticle,** 405–414
 dilute solution, 405–407
 enantiomeric lactide sequences in solution, 407–412
- Block-type carbon nanotube electrodes,** 426
- Blood-brain barrier, anticancer drug delivery across,** 256
- Boehmite, energetic parameters,** 1148
- Bolaform amphiphiles, layer-by-layer assembly,** 1607–1622
- Bonding, nanoceramics,** 2240
- Bonding nature of carbon atoms,** 475–476
- Bovine pancreatic trypsin inhibitor,** 2819
- Brain, gene delivery, polymer nanoparticle for,** 2945
- Brillouin zone, graphite electron,** 479
- Bronsted acid sites,** 636
- Brookite, energetic parameters,** 1148
- Brownian, gravitational coagulation kernels, compared,** 38
- Brownian coagulation, collision kernels,** 36–37
- Brownian dynamics,** 2131
 counterions around DNA, 2137
- Buckminster fullerene C₆₀,** 1225
- Bulk enantiomorphous crystals, surfaces of,** 1117–1118
- Bulk ferromagnetic materials, magnetic properties,** 1718–1719
- Bulk nanocrystalline substances, microstructure,** 2298–2300
- Cadmium selenide**
 quantum dots made of, 3167–3176
 formation of, 3168–3170
 microphotoluminescence, 3170–3171
 optical properties, 3170–3174
 selectively excited photoluminescence, 3171–3174
 quantum rods made of, anisotropy, optical properties, 3256–3259
- Cadmium sulfide nanocrystals,** 787–796
 optical, electronic properties, 789–790
 quantum mechanics/molecular mechanics calculations, 793–795
 semiconductor nanocrystals, 787
 semiempirical calculations, 791–793
- Calcite, surface free energy,** 1573
- Calcium phosphate, orthopedic implant,** 269
- Calix-4-hydroquinone,** 2427
- Calixarenes,** 1312–1313, 1337–1340
- Cambridge Structural Database,** 2126
- Cancer, drug delivery across blood-brain barrier,** 256
- Canonical Monte Carlo simulation, electrical double layer formation,** 1006–1007
- Capacitors, carbon nanotubes,** 537–546
 capacitor performance, 538
 conducting polymer composites, 543–545
 multiwalled nanotubes, 540–543
 single-walled nanotubes, 539–540
- Capillaries, micromolding in,** 2619–2621
- Capillary condensation, adhesion, self-assembled monolayers,** 1–3
- Capillary electrophoresis separation, single-walled carbon nanotubes,** 3617–3628
- Capillary forces, assembly of electrical circuits by,** 1026–1027
- Capsules, hollow,** 870–875
- Carbogenic molecular sieves,** 231–232
- Carbon atom, cohesive energy per, carbon-related structures,** 478
- Carbon forms structured by energetic species,** 415–424
 amorphous carbon forms, structuring of, 417–420
 crystalline carbon forms, structuring, 422–423
- ion beam structuring,** 416–417
 ordered forms, structuring of, 420–422
- Carbon fullerenes,** 1447
- Carbon monoxide oxidation, gold nanoparticle on titania,** 1299–1301
- Carbon nanotube chemistry,** 1473–1476
- Carbon nanotube electrodes,** 425–434
 atomic hydrogen, 429
 block-type carbon nanotube electrodes, 426
 electrochemical capacitors, 425–427
 electrochemical sensors, actuators, electrodes in, 430–431
 functionalization of carbon nanotubes, 427
 molecular hydrogen, 429
 secondary hydrogen battery, fuel cells, electrodes in, 429–430
 secondary lithium ion batteries, anodes, 427–429
- Carbon nanotube field effect transistors,** 2190
- Carbon nanotube interconnects,** 435–459
 interconnect architectures, integration in, 441–442
 internanotube contacts, 439–441
 junctions, crossed-tube, 439–441
 synthesis, 435–439
 directed, 437–439
 nondirected, 436–437
- Carbon nanotube-conducting polymer composites**
 Raman spectroscopy studies, 3267–3279
 charge transfer, 3274–3277
 interfacial interactions, 3270–3274
 shear field processing, 3270
 in supercapacitors, 447–459
 polymer composite, conducting, 447–449
 prototype devices, 454–455
 supercapacitors, 449–451
- Carbon nanotube/polymer nanocomposites,** 2923–2925
 electrical properties, 2924–2925
 mechanical properties, 2924
 optical properties, 2924–2925
- Carbon nanotubes,** 475–492, 507, 1203–1211
 atoms, foreign
 doping by, 486–489
 intercalation, 486–489
 biosensors based on, 361–373
 carbon, fibrous forms of, 481–486
 carbon atoms, bonding nature of, 475–476
 chemistry, 493–506
 chemically functionalized carbon nanotubes, applications of, 501–502
 covalent functionalization, 496–500
 noncovalent functionalization, 500–501
 purity evaluation, 494–495
 reactivity, 495–496
 structure of, 493–494
 cohesive energy per carbon atom, carbon-related structures, 478
 disordered carbons, 476–480
 electrochemical modification, 507–517
 actuators, 514
 batteries, 514
 (bio) electrochemical sensors, 513–514
 bulk electrodes, 507–509
 covalent modification, 509–510
 electrochemical applications, 513–514
 film electrodes, 507
 fuel cells, 514
 hydrogen storage, 514
 microbundle electrodes, 508
 nanotube electrodes, 507–509

- Carbon nanotubes (*cont.*)
 noncovalent modification, 510–512
 paper electrodes, 507
 paste electrodes, 507
 powder microelectrodes, 507
 single-nanotube electrode, 509
 electronic switches, 1104–1107
 electro-osmotic flow control in membranes, 519–528
 electrochemical derivatization, effect on electroosmotic flow, 525–526
 electroosmotic flow, effect of applied current density on, 522–523
 electroosmotic flow velocity, 522
 ionic strength, effect on electroosmotic flow, 523–524
 solution pH, effect on electroosmotic flow, 524–525
 transport properties, carbon nanotube membranes, 521–522
 foreign molecules
 doping by, 486–489
 intercalation, 486–489
 fullerene solid, 1207–1209
 doped fullerenes, 1208
 polymerization, 1209
 superconductivity, 1208–1209
 functionalization of, 427
 gas adsorption, 547–556
 confined spaces, matter in, 550–551
 gas chemisorption, carbon nanotubes, 551
 gas physisorption, 547–549
 gas storage capacity, 549–550
 graphite, fibrous forms of, 481–486
 graphite Brillouin zone, graphite electron, 479
 graphites, 476–480
 hydrogen chemisorption, 529–536
 armchair nanotubes, models of, 530
 chemisorption studies, 532–534
 hydrogen storage, 534–535
 investigations of hydrogen adsorption, 531–535
 models, 530–531
 nanotube small cluster model, 532
 nanotube structure, 529–530
 physisorption studies, 532
 hydrogen storage, 557–566
 room temperature, 560–564
 single-walled carbon nanotubes, 557
 sorption mechanisms, 559–560
 temperature-programmed-desorption system, 558
 ice nanotubes inside, 1415–1424
 continuous freezing, 1420–1422
 experiments, 1423–1424
 freezing, 1417–1422
 freezing into ice nanotube, 1418–1420
 melting behavior, 1417–1422
 phase diagram, 1422–1423
 simulations, 1423–1424
 structure, 1415–1417
 molecular modeling, 461–473
 molecular properties, 1205–1207
 electrical conduction in, 1206–1207
 electronic states in C₆₀, 1205–1206
 nanotubes, electrical conduction in, 1206–1207
 molecular structure, 1203–1204
 within multilayered polyelectrolyte films, 567–574
 multi-wall carbon nanotubes, 480–481
 optical properties, 575–586
 optical absorption, 580–586
 parameters, 577
 resonance Raman process, 583–586
 van Hove singularities, 576–580
 oxidation, 496
 single-wall carbon nanotubes, 480–481
 single-walled, 3605–3615, 3629–3639
 actuation upon charge injection, 3610–3611
 graphite intercalation compounds, 3610–3611
 armchair, 3607–3608
 capillary electrophoresis separation, 3617–3628
 chiral, 3608
 density functional theory study, field emission properties, 3597–3604
 electronic properties, 3608–3610
 geometry of, 3607–3608
 graphene, structures from, 3629–3630
 helical, rotational symmetries, 3631–3633
 translational symmetries, 3630–3631
 zigzag, 3608
 supramolecular mechanics, 587–601
 coalescence of nanotubes, as reversed failure, 597–598
 elastic shell model, supramolecular morphology changes, 591–593
 failure, relaxation mechanisms, 593–596
 linear elastic properties, 588–589
 strength-failure evaluation, kinetic approach, 596–597
 supramolecular scale, tensegrity at, 598–599
 van der Waals interactions, 589–591
 synthesis, 1204–1205
 thermal properties, 603–610
 vapor-grown carbon fibers, 484–486
 Carbon orthopedic implant, 269
 Carbon paste electrodes, modified,
 electrochemical sensors based on, 1053–1057
 Carbon (pyrolytic), orthopedic implant, 269
 Carbon structures, ferromagnetism in, 1661–1662
 Carbonates, 1149
 Carbon-based nanomaterials, design, 2426–2427
 Carbon-derived fibers, nanostructured
 composites using, 2551–2561
 carbon fibers, 2551–2552
 surface chemistry, 2552–2553
 composites, 2559–2560
 fiber-matrix interface, buried, monitoring, 2557–2559
 nanotubes, 2559–2560
 x-ray photoelectron spectroscopy, 2553–2557
 Carboxylate anion recognition, biomimetic
 macrocyclic receptors for, 295–309
 charged receptors, 295–300
 hydrogen bonding receptors, 301–306
 metal centers, carboxylate coordination to, 300–301
 Carboxytetramethylrhodamines, 2377
 Carrier lateral transport, quantum dot lasers, 3121
 Catalysis, by supported gold nanoclusters, 611–620
 adsorbate binding energies, 614–615
 catalyst deactivation, 618
 catalytic properties, 613–614
 characterization, 612–613
 cluster sintering, 618
 cluster sublimation energies, 616–618
 electronic properties, 615–616
 model catalysts, 612–618
 synthesis, 612
 Catalyst, nanocrystalline metal oxide as, 2535–2536
 Catalyst nanostructures, x-ray absorption studies, 3953–3972
 catalyst deactivation, 3964–3966
 by coking, 3965–3966
 cycles, 3966
 by poisoning, 3965
 by sintering, 3965
 catalyst preparation, 3956–3960
 catalyst regeneration, cycles, 3966
 future developments, 3966
 heterogeneous catalysts, 3955–3956
 structural characterization, 3960–3964
 Catalysts
 heterogeneous, atomic scale studies, 179–193
 metal nanoparticle as, 1869–1880
 bimetallic nanoparticle, formation of, 1876
 C–C bond formation, 1878–1879
 characterization, 1873–1874
 hydration, 1878
 iron-group element, composed of, 1875
 oxidation, 1878
 platinum-group elements, composed of, 1874–1875
 preparation, 1871–1874
 reduction, 1876–1877
 structure control, 1874–1876
 visible-light-induced hydrogen generation, 1877
 nanoparticle supported, 2531–2535
 nanostructured, 226–232, 2531–2537
 basic, 225–234
 basicity, defined, 225–226
 carbogenic molecular sieves, 231–232
 historical perspective, 225
 hydrotalcite, 232
 mesoporous (alumino) silicates, 230–231
 zeolites, 227–230
 Catalytic applications, polymerization catalysts, 1803
 Catalytic cracking, mesoporous materials, 1803–1804
 Catalytic functions, zeolite membranes, 1162–1163
 Catalytic processes, over supported nanoparticle, 621–632
 Catalytic properties
 micro-, mesoporous nanomaterials, 633–647
 nanocrystal dispersed platinum particles, 2259–2268
 transition metal oxides, 1913–1914

- Catenanes
 hydrogen bonding, self-assembly directed by, 3405-3406
 switchable, computational analysis, 797-805
 binding site selectivity origin of, 801
 catenane systems dynamics, 799-801
 co-conformational isomerism, 801-802
 structural fundamentals, 798-799
- Cation-arene interactions, molecular probes, 2123-2130
- Cation-chloride cotransporter, 3699
- Cavitand-based coordination cages, self-assembly of, 3415-3430
 enlarged nitrile-based coordination cages, 3422-3423
 nitrile-based coordination cages, 3417-3422
 pyridine-based coordination cages, 3423-3426
- Cell adhesion, resisting, 390-391
- Cell surface receptors, biologically functionalized tips for probing of, 138
- Cell-substratum contact sites, 249
- Cellular delivery, micro-/nanoscale needles for, 254-255
- Cellulose, surface free energy, 1573
- Cellulose acetate, 2400, 2401
- Cellulose nitrate, surface free energy, 1573
- Ceramics
 functionalization of surface layers on, 1277-1285
 alkali-resistant surface layer, 1283-1284
 gradient titanilayer, photocatalytic fiber with, 1283
 new process, 1277-1279
 photocatalytic fiber, 1279-1283
 surface gradient structures, 1277
 mesoporous, functionalization of, 1126-1127
 nanophase, as nanobiomedical implants, 266-269
- Cethyl trimethyl ammonium bromide, 2317
- Cethyl trimethyl ammonium chloride, 2317
- Cetyltrimethylammonium bromide, 2898
- Chain polymerization, controlled, polymer nanowires by, 2951-2958
 photopolymerization, 2953
 scanning tunneling microscope, 2954-2955
 self-ordered molecular layer, 2951-2953
- Channel lattices, nanosized, heterogeneous surfaces with, 1357-1367
- Chaotic transport in antidot lattices, 649-666
 Aharonov-Bohm oscillation, 654-664
 Altshuler-Aronov-Spivak oscillation, 657-658
 commensurability peaks, 650-654
 magnetic focusing, leading to fundamental commensurability peak, 651
 scattering, from two adjacent antidots, 652
 scattering matrix formalism, 658-664
 triangular antidot lattices, 656-657
- Charge carrier dynamics, nanoparticle, 667-682
 metal nanoparticle, charge carrier dynamics of, 673-675
 semiconductor nanoparticle, charge carrier dynamics in, 667-673
- Charge transfer in metal-molecule heterostructures, 683-698
 Moore's law, 683
- Charge transport properties, multilayer nanostructures, 699-707
 nanoscale multilayer structures, 699-700
- Chemical deposition, formation of electrical circuits by, 1027-1028
- Chemical force microscopy, 2709
- Chemical imaging, 2703-2712
- Chemical selectivity, 1505-1514
 interfacial phenomena and, 1505-1514
 molecular interactions, 1506-1511
 molecular organization, 1508-1511
 molecular recognition, at interfaces, 1505-1506
 molecular structure, 1506-1508
 surfaces, chemical selectivity of, 1506-1511
- Chemical sensors
 design theory, 2425-2426
 electrically functional microstructures from, 1031-1032
- Chemical switches, 2146-2149
 chemical bimolecular reactions, 2149
 molecules in interaction, 2147-2149
 simple chemical conversions, 2146-2147
- Chemical synthesis, lab-on-a-chip micro reactors for, 1547-1564
- Chemical transport reactions, inorganic nanotubes synthesized by, 1457-1466
 applications, 1465
 crystal flakes, instability against bending, 1459-1460
 interlayer distances, nanotube chirality, 1460-1461
 lattice structure, 1458-1459
 multiwall nanotubes, 1457-1461
 nucleation, 1458-1459
 plate-like crystal structures, 1457-1458
 silver, nanotube alloyed with, 1461-1465
 stacking-order, tube diameter and, 1460
- Chemical warfare agent, 381
 structures of, 242, 378
- Chemical warfare agent decontamination, by nanoparticle, 241-242
- Chemical warfare agent detection biosensors for, 375-388
 in air, 375, 377-378, 380-381, 383-386
 cell chamber, 379
 fluorescence measurements, 379
 toxic agents, 379
 in water, 375-379, 381-383, 385-386
 water quality monitoring, toxic agents used for, chemical structures, 379
 sensor response to, 385
- Chemically functionalized carbon nanotubes, applications of, 501-502
- Chemirecurrents, sensors based on, 3527-3537
- Chemiresistor sensors, metal nanoparticle monolayers, 1864-1865
- Chip-detection, DNA-conjugated metal nanoparticle
 marker application, for DNA chip readout, 959
 molecular nanotechnology, 959-960
 networks in solution based, 955-956
 preparation, 955
 solid substrates, immobilization onto, 956-958
 surface immobilization of DNA, 957
 whole substrate incubation, immobilization technique, 958
- Chiral, pseudo-chiral molecules at interfaces, self-assembly, 3431-3438
- Chiral nanostructures
 enantioselectivity on surfaces with, 1113-1123
 surfaces with, enantioselectivity, 1113-1123
 achiral bulk crystal structures, chiral surfaces from, 1118-1120
 bulk chiral materials, surfaces based on, 1117-1118
 chiral organic modifiers, surfaces templated with, 1115-1117
 chiral surfaces, 1114-1115
 molecules, chirality of, 1113-1114
 solids, chirality of, 1113-1114
 surfaces, chirality of, 1113-1114
 technological impact of chiral surfaces, 1120-1121
- Chiral organic modifiers, surfaces templated with, 1115-1117
- Chiral pair self-assembled monolayers, scanning tunneling microscopy, 3305-3313
 iodination products of oleic acid, elaidic acid, monolayer of, 3309-3311
 oleyl alcohol iodination product monolayer, 3307-3309
- Chiral single-walled carbon nanotubes, 3608
- Chiral switches based on enantiomers, 2159-2160
- Chiral switches based on pseudoenantiomers, 2160-2162
- Chiral templates, 1116-1117
- Chirality in gold nanoclusters, 1292-1293
- Chiroptical molecular switches, sterically overcrowded alkenes as, 2159-2166
- Chiroptical switching, in polymeric matrices, 2165-2166
- Chitosan, polymeric gene carrier, 2943
- Chlorella* biosensor, 377, 381-382
- Chloride channel, 3699
- Chloride complex, x-ray crystal structure, 64
- Chloride pumps, conversion of proton pumps to, 3707
- Chloride-conducting membrane proteins, Saier nomenclature, 3699
- Chloroform, surface tension, 1573
- Chromophore-receptor systems, 2749
- Circuit, integrated, 2211-2212
- Citrate method, magnetic nanomaterial synthesis, 1685-1686
- Classical computing, limits of energy dissipation vs. performance, 2199
- Clay, in soil, 1149
- Clay surfaces, polymer brushes from, 2959-2971
- Clay-nanoparticle polymer composites, 3000-3001
- Closed-shell carbon clusters, magnetic properties of, 1655-1656
- Cluster sublimation energies, gold nanoclusters, 616-618
- Coagulation, 35-44
 atmospheric nanoparticle, 103
 of monodisperse aerosols, 35-36
- Coagulation equation, aerosol nanoparticle, 36
 solutions, 40-43
 coagulation in nanoparticle synthesis, 43
 moment method, 42-43
 sectional method, 40-41
 self-preserving solution, 41-42
- Coating of titanium dioxide, on stainless steel, 3918-3925
- Coatings, nanoceramics, 2243-2244
- Cobalt
 anion templated system, 55-57
 tungsten carbide, nanocomposites, 3943-3952
- Cobalt alloys, orthopedic implant, 269
- Cobalt/chromium multilayers, thin film structural transition, 3740
- Cobalt/copper multilayers, thin film structural transition, 3738-3739

- Cobalt/manganese multilayers, thin film structural transition, 3739
- Cohesive energy, per carbon atom, carbon-related structures, 478
- Coking, catalyst nanostructures deactivation, 3965–3966
- Collagen, properties of, 3082
- Collision kernels, 36–39
- Brownian coagulation, 36–37
- electrostatic coagulation, 39
- gravitational coagulation, 37–38
- turbulent coagulation, 38–39
- Colloid solutions, nanocrystalline powders precipitation, 2292–2293
- Colloid systems, 709–715
- colloids, 709–710
- micelles, 710–711
- nanocrystals, superlattices, 711–714
- nanoreactors, schematic of, 712
- Colloidal assembly, fabrication of electrical circuits via, 1026–1031
- Colloidal crystals
- assembly by alternating current chaining, dielectrophoretic forces, 1035–1036
- assembly by electrophoretic forces, 1034–1035
- Colloidal germanium nanoparticle, 717–723
- Colloidal gold films
- tunable nanocrystal distribution, 1515–1523
- electrostatic interactions, particle deposition, 1515–1517
- gold nanocrystals, 1517–1518
- kinetics, nanocolloidal gold adsorption, 1519–1520
- nanocolloidal gold suspension, 1517
- quantitative analysis, 1520–1521
- saturation coverages, 1518–1519
- size distribution, 1517–1518
- spatial distribution, 1518–1519
- tunable nanocrystal distribution in, 1515–1523
- electrostatic interactions, particle deposition, 1515–1517
- gold nanocrystals, 1517–1518
- kinetics, nanocolloidal gold adsorption, 1519–1520
- nanocolloidal gold suspension, 1517
- quantitative analysis, 1520–1521
- saturation coverages, 1518–1519
- size distribution, 1517–1518
- spatial distribution, 1518–1519
- Colloidal gold nanocrystals, tumor necrosis factor bound to, vector with docking site for gene therapy, 256
- Colloidal micro nanostructures, assembled on patterned surfaces, 725–738
- 3-D colloid assembly, 726–728
- fundamental interactions in colloid systems, 725–726
- planar surfaces, 728–729
- structured colloid assemblies, 729–736
- Colloidal nanometals, as fuel cell catalyst precursors, 739–759
- metal salt reduction method, 741–743
- wet chemical reduction, 741–748
- Colloidal nanoparticle, 717–723
- electrokinetic characterization, 773–786
- composite particles, synthetic process of, 778–785
- concentrated dispersion, 775–778
- diluted suspension, measurements of particles in, 773–775
- model molecular surfaces, aggregation patterns, 761–772
- Colloidal particle, solid, liquid, interfacial forces between, 1491–1503
- deformable interfaces, interactions involving, 1493–1494
- direct measurement, 1494–1498
- deformable surfaces, 1496–1497
- force curve analysis, 1497–1498
- surface force measurement, 1494–1496
- interfacial forces, 1491–1493
- surface forces measurement, 1491
- Colloidal particles
- electrically functional microstructures from, 1031–1034
- biological sensors, 1032–1034
- chemical sensors, 1031–1032
- quantum electronics nanoparticle devices, 1034
- multiplayer assembly on, 2369–2371
- Colloidal self-assemblies, nanocrystals synthesized in, 2317–2327
- direct micelles, 2317
- divalent surfactant, 2318
- ferrite nanocrystals, 2323–2324
- reverse micelles, 2317–2318
- self-assemblies differing by sizes, shapes, 2318–2323
- Colloidal suspensions, electrical field-induced forces in, 1025–1026
- Combustion flame-chemical vapor condensation, 2469
- Complementary molecular field effect transistors, 2092
- Composite nanowires, bending modulus of, 1776–1778
- Composites, nanostructured, using carbon-derived fibers, 2551–2561
- carbon fibers, 2551–2552
- surface chemistry, 2552–2553
- fiber-matrix interface, buried, monitoring, 2557–2559
- nanotubes, 2559–2560
- x-ray photoelectron spectroscopy, 2553–2557
- Computational analysis, 823–844
- computational analysis
- computational analysis, normal mode, simplified, 824
- normal mode, 824
- Hessian matrix evaluation, 827
- multiparticle soft matter systems, 828–829
- coupled rotational modes, 829
- indifferent modes, 828–829
- particle vibrational modes, 829
- spectator modes, 829
- normal mode, 824
- simplified, 824
- sparse matrix diagonalization, 827–828
- switchable catenanes, 797–805
- switchable rotaxanes, 807–821
- Computer-aided design, DNA-based nanoinstruments, 833–844
- measurement principle, 834–836
- polyacrylamide gels, detection of DNA deformation in, 841
- solution, DNA deformation measured in, 836–841
- at surfaces, detection of DNA deformation, 841–843
- Computing, limits of energy dissipation vs. performance, 2199
- Condensational growth, atmospheric nanoparticle, 100–102
- Conducting polymers, nanostructures based on, 2615–2626
- atomic force microscope lithography, 2621–2622
- capillaries, micromolding in, 2619–2621
- inverse opal formation, 2618–2619
- lithography, 2619–2623
- mask techniques, 2619–2623
- masks, 2622–2623
- polarized infrared absorption spectroscopy, 2616–2617
- scanning tunneling microscopy lithography, 2621
- solvent-assisted micromolding, 2619
- template synthesis, 2615–2619
- Conduction in molecular wires, 2188–2189
- Conductivity, thermal, nanoceramics, 3867–3872
- Confocal laser scanning microscopy, 2357
- Constructive nanolithography, 110–111
- Contacting nanowires, nanoarrays, electrochemical self-assembly, 1076
- Continuous water quality monitoring, experimental apparatus, 379
- Continuum solvent models, DNA counterion distributions, 2133–2127, 2138–2139
- Controlled chain polymerization, polymer nanowires by, 2951–2958
- photopolymerization, 2953
- scanning tunneling microscope, 2954–2955
- self-ordered molecular layer, 2951–2953
- Controlled drug delivery
- miniaturization devices, 254–256
- nanoscale polymer carriers, 255–256
- Coordination framework topology, multimodal ligands, 845–853
- coordination framework design, 845–846
- coordination polymers, 848–852
- three-dimensional architectures, 848–849
- two-dimensional architectures, 849–852
- coordination preferences, 847–848
- multimodal ligands vs. unimodal ligands, 846–847
- Copolymers, block
- nanoparticle, 405–414
- dilute solution, 405–407
- enantiomeric lactide sequences in solution, 407–412
- templating polymer crystal growth using, 3853–3865
- amorphous systems, block copolymer phase separation, 3853–3854
- large areas, patterning semicrystalline block copolymers over, 3862–3863
- moderately-segregated systems, 3860–3861
- rubbery block copolymers, strongly-segregated semicrystalline, 3861–3862

- Copolymers, block (*cont.*)
 semicrystalline systems, microphase separation in, 3854–3855
 semicrystalline-glassy block copolymers, crystallization in nanoscale environments, 3855
 semicrystalline-poor block copolymers, 3855–3858
 semicrystalline-rich block copolymers, 3858–3860
 semicrystalline-rubbery systems, 3860
 Copper ions, equilibrium state of adsorption, 174
 Core-shell hydrogel nanoparticle, 855–864
 environmentally responsive microgels, 855
 fluorescence analysis, 860–862
 mechanical interactions between core, shell, 858–859
 shell thickness dependence, 859–860
 synthesis, 855–837
 thermodynamic properties, 857–858
 Core-shell latex particles, preformed, complexation of, 2901
 Core-shell nanospheres, 865–879
 composite capsules, 875
 hollow capsules, nanobottles, 870–875
 inorganic, 872–875
 polymer, 871–872
 nanosized core-shell spheres, 866–870
 with inorganic, composite shell, 868–870
 with polymer shell, 866–868
 rare earth complex, encapsulation in nanobottles, 875–876
 silica nanobottles, preparation procedure of, 874
 Cortical bone, orthopedic implant, 269
 Corundum, energetic parameters, 1148
 Counterion condensation, 2131
 Counterions around DNA
 Brownian dynamics, 2137
 solvent simulations, 2137–2140
 Covalent functionalization, carbon nanotubes, 496–500
 Covalent immobilization, surface engineering, 354–355
 Covalent/ionic self-assembly, nonlinear optical film fabrication, 3473–3474
 Cowpea chlorotic mottle virus, 322–323
 Cowpea mosaic virus, 324–327
 Cross-linked polyvinylpyrrolidone, hydrogel nanoparticle synthesized by, 1403–1414
 ultrafine poly(N-vinyl pyrrolidone) nanoparticle, 1406–1412
 Cryofracture, transmission electron microscopy after, 980
 Cryo-transmission electron microscopy, 2771
 Crystal fibers, photonic, 2853–2867
 Crystal matrix, pseudoenantiomeric switches in, 2166–2167
 Crystal structures, molecular designs for, 2057–2061
 neutral biimidazole complex, 2061–2064
 Crystalline carbon forms, structuring, 422–423
 Crystallization, organosilanes, molecular assembly, organosilane monolayers, at air-water interface, 2031–2036
 Crystallization at air-water interface, organosilane monolayers, 2031–2036
 Crystallization kinetics, microgel dispersions, 1973–1974
 Crystallization structure, intercalated polypropylene nanocomposites, 1485–1486
 Crystals, liquid, protein binding event detection, 1635–1646
 CSD. *See* Cambridge Structural Database
 Cubic phase structure, cubosomes, 881–883
 Cubosomes, 882
 bicontinuous liquid crystalline nanoparticle, 881–892
 cubic phase particles, 883
 cubic phase structure, 881–883
 cubosome manufacture, 885–886
 hexagonal liquid crystalline phase, 889
 monoolein, molecular structure of, 882
 other liquid crystalline phases, formation of, 89
 sponge phase, 889
 systems forming, 886–887
 Cyanide, 2495
 Cyano, to carboxylic termination conversion, self-assembled silane monolayers, 3345–3359
 Cyanobacterium biosensor, 377
 Cyanogels, spin-coated, 3667–3674
 film characterization, 3669
 preparation, 3669
 Cyclic peptides, self-assembly, hydrogen-bonded nanotubes, 3439–3457
 application status, peptide nanotubes, 3450–3454
 Cycloaddition, on lab-on-a-chip micro reactor, 1556
 Cyclophane hosts, 1318–1321
 Cysteine, 266
 properties of, 3082
 Cytimmune Sciences, 256
 Daisy-chain polyrotaxane, 195
 DARPA. *See* Defense Advanced Research Projects Agency
 Data storage on atomic scale, 1477
 Dealloying, nanoporous metals formed by, 893–896
 Decontamination, by nanoparticles, 241–245
 biological weapons, 241–245
 chemical warfare agents, 241–242
 Defect reduction techniques, quantum dot lasers, 3117–3118
 Defense Advanced Research Projects Agency, 2077
 Defensin, 3699
 Dehydration, on lab-on-a-chip micro reactor, 1556
 Dendrimers, nanoparticle formation in, metallation, 2907–2909
 Dendritic nanocatalysts, 903–911
 Density functional methods, silicon nanocrystals, quantum confinement, 3567–3570
 Density functional theory, 2086
 Deoxyribonucleic acid. *See* DNA
 Derjaguin–Landau–Verwey–Overbeek theory, 169, 171–172, 3807–3809
 surface forces, nanoparticle, 3807–3809
 Design theory, nanomaterials, molecular devices, 2423–2433
 Detonation, nanocrystalline powders, 2292–2294
 Detoxification of nerve agents, 243
 Diacetylene derivatives, photoreactive bolaform amphiphiles, 1612–1615
 Diagnostic systems, nanotechnology in, 247–261
 Dialkyldimethylammonium bromide, 2769
 Diamidopyrrole ligand, Gale's, 77
 Diaspore, energetic parameters, 1148
 Diazo coupling, on lab-on-a-chip micro reactor, 1556
 Diazotization, on lab-on-a-chip micro reactor, 1556
 Diblock copolymers, self-assembly with, 2457–2459
 Diblock/particle mixtures, nanoparticle-polymer mixtures, supramolecular networks synthesized in, 3786–3787
 Dibutyl sulfide, structure of, 378
 Dielectric effects, DNA counterion distributions, 2134
 Dielectrophoretic forces, colloidal crystals, assembly by, 1035–1036
 Differential scanning calorimetry, 2587
 Diffraction, structural color from, 3717–3719
 Diffusion reflectance infrared Fourier transform, 2599
 Digermane, 1170–1172
 Diiodomethane, surface tension, 1573
 Dimensionally graded semiconductor nanoparticle films, 913–921
 Dimeric copper-complexed rotaxane, 817
 Dimethylaminophenylazobenzoic acid, 2763
 Dimethylformide, 2631
 Dimethylsulfoxide, 2187
 Dinuclear triple-stranded helicates, template-directed assembly, 3831–3842
 Dip coating of nanoparticle, 279
 Dip-pen nanolithography, 109–110, 247, 923–931, 2621, 2975–2978
 direct-write, 2978–2979
 Direct force measurement of liposomes, by atomic force microscopy, 933–942
 Direct measurement determination, surface forces, nanoparticle, measurement techniques
 atomic force microscopy, 3811–3812
 for nanoparticle, 3812–3816
 surface force apparatus, 3810–3811
 total internal reflection microscopy, 3811
 Direct micelles, 2317
 Disilane, 1170–1172
 Dissipation of power, performance and, (Moore's law)
 limits of energy dissipation vs. performance, 2199
 predictions for CMOS technology, 2198
 single-electron transistors, 2198–2199
 Distearylphosphatidylcholine, 2510
 Distributed Bragg, 2874
 Dithiol linked 3-D assemblies, 3826
 Divalent surfactant, colloidal self-assemblies, nanocrystals synthesized in, 2318
 Divinylbenzene, 2347
 D-mannitol-terminated self-assembled monolayers, adsorption of protein on, 397
 D-mannonic 1,5-lactone, 2, 401
 DNA, 2201, 2361
 atomic force microscopy, 120–124
 functionalized emulsions, interactions with, 977–986
 applications, 984–985
 DNA counterion distributions, molecular simulations, 2131–2143
 analytical theory evaluation, 2133–2134
 continuum solvent models, 2133–2127
 compared, 2138–2139

- DNA counterion distributions, molecular simulations (*cont.*)
 counterions around DNA
 Brownian dynamics of, 2137
 simulations of, solvent, 2137–2140
 dielectric effects, 2134
 ion competition, 2136
 ions, specific binding of, 2138
 molecular dynamics of DNA, 2137
 multiscale simulation, 2139–2140
 multivalent ligands, interaction of DNA with, 2136–2137
 polyelectrolyte models, 2131–2133
 specific distribution of charges, 2135–2136
- DNA damage, electrochemical toxicity sensors, electroanalytical methods for detecting, 1065–1068
- DNA detection, porous silicon microcavities, 344
- DNA hybridization, electronic control, 963–975
- DNA toxicity detection, combining bioactivation with, 1068–1070
- DNA-based nanoinstruments, computer-aided design, 833–844
 measurement principle, 834–836
 polyacrylamide gels, detection of DNA deformation in, 841
 solution, DNA deformation measured in, 836–841
 at surfaces, detection of DNA deformation, 841–843
- DNA-conjugated metal nanoparticle, chip-detection
 immobilization onto solid substrates, 956–958
 marker application, for DNA chip readout, 959
 molecular nanotechnology, 959–960
 networks in solution based, 955–956
 preparation, 955
 surface immobilization of DNA, 957
 whole substrate incubation, immobilization technique, 958
- DNA-nanoemulsions complexes, 977–986
- Dodecane, surface tension, 1573
- Dodecyltrimethylammonium bromide, 2901
- Dolomite, surface free energy, 1573
- Dots, quantum. *See* Quantum dots
- Double helicate, Kruger's, molecular structure of, 76
- Double layer formation, electrical, 1001–1014
 canonical Monte Carlo simulation, 1006–1007
 Gouy–Chapman theory, 1003–1004
 grand canonical Monte Carlo simulation, 1004–1006
 nonprimitive model, 1006–1007
 primitive model, grand canonical Monte Carlo simulation, 1007–1008
- Double-hydrophilic block copolymers, 2897–2899
- Drug delivery, 256
 fullerene-based, 256
 miniaturization devices, 254–256
 nanobiotechnology in, 247–261
 nanoparticulate platform for, 256
 nanoscale polymer carriers, 255–256
- Drying methods, templating aerogels for tunable nanoporosity, 3845–3849
 evaporative drying, 3846–3847
 removal of template material, 3849
 supercritical drying, 3847–3849
- Dual-mode photoswitching of luminescence, 2163–3164
- Dual-mode resonance, nanobelts, 1779–1780
- Ductility, structural nanomaterials, 3728–3730
- Dynamic atomic force microscopy, heterogeneous surfaces, 987–1000
 receptor-ligand interactions, dynamic measurements, 995
 steric forces, dynamic measurements, 994–995
 tapping mode atomic force microscope, 988–991
- Dynamic nanostructures
 biological membranes, 2508–2510
 as nanotechnology building blocks, 2510–2515
- Dynamic random-access memory, 2075
- Egg yolk phosphatidylcholine, 933
- Elastic shell model, carbon nanotubes, supramolecular morphology changes, 591–593
- Elasticity of cell walls, force spectroscopy, 137
- Electric field-induced mechanical resonance
 nanobest, nanowire, dynamic bending modulus, nonlinear effect, 1774–1776
 nanowires, nanobelts, dynamic bending modulus, 1773–1776
 experimental method, 1773–1774
 fundamental resonance frequency, 1774–1776
- Electrical applications, nanoceramics, 2242–2243
- Electrical conductivity, molecular assembly of nanowires, 2026–2027
- Electrical double layer formation, 1001–1014
 canonical Monte Carlo simulation, 1006–1007
 Gouy–Chapman theory, 1003–1004
 grand canonical Monte Carlo simulation, 1004–1006
 in nanopores, 1004–1007
 nonprimitive model, 1006–1007
 canonical Monte Carlo simulation, 1008–1012
 primitive model, 1004–1006
 grand canonical Monte Carlo simulation, 1007–1008
 surface properties, 1001–1003
- Electrical double layer model, mineral nanoparticle, 1992
- Electrically conducting polymeric nanostructures, one-dimensional, 1015–1024
 molecular interactions as "soft" templates, 1017–1018
 synthesized on surfaces, 1019–1020
 using "solid" templates, 1015–1017
- Electrically conductive inks, metallic nanopowders, 1929–1930
- Electrically conductive pastes, metallic nanopowders, 1929–1930
- Electrically functional nanostructures, 1025–1042
- Electrochemical capacitors, 425–427
- Electrochemical deposition, formation of electrical circuits by, 1027–1028
- Electrochemical dip-pen nanolithography, 2622
- Electrochemical heavy metal detection, 1131
- Electrochemical Langmuir trough, 1043–1049
 examples of application, 1045–1048
 molecular conformation, 1045–1046
 open grids, 1046–1048
- Electrochemical modification, carbon nanotubes, 507–517
 bulk electrodes, 507–509
 covalent modification, 509–510
 electrochemical applications, 513–514
 actuators, 514
 batteries, 514
 (bio) electrochemical sensors, 513–514
 fuel cells, 514
 hydrogen storage, 514
 film electrodes, 507
 microbundle electrodes, 508
 nanotube electrodes, 507–509
 noncovalent modification, 510–512
 paper electrodes, 507
 paste electrodes, 507
 powder microelectrodes, 507
 single-nanotube electrode, 509
- Electrochemical sensors, 1063–1072
 actuators, electrodes in, 430–431
 based on functionalized nanoporous silica, 1051–1061
 for selective adsorption of metal species, 1053
 based on modified carbon paste electrodes, 1053–1057
- DNA damage, electroanalytical methods for detecting, 1065–1068
- DNA detection, combining bioactivation with, 1068–1070
- DNA electrochemistry, 1065–1066
- enzyme-DNA films, 1063–1065
- microelectrode array modified with functionalized nanoporous silica thin film, 1057–1059
 toxicity sensing, electrochemical methods for, 1066–1068
- Electrochemical synthesis, 746–747
- Electrochemically self-assembled nanoarrays, 1073–1085
 electrochemical self-assembly, 1073–1076
 anodization, 1075
 contacting nanowires, 1076
 electrodepositing compound semiconductor, 1075
 electrodepositing metal, 1075
 nanofabrication, 1073
 quantum dot image processors, 1079–1084
 dot capacitance, 1084
 interdot resistance, 1082
 measurements of circuit parameters, 1082
 negative differential resistance, 1082–1084
 quantum dot based neuromorphic architectures, 1080–1081
 self-assembling neural network, 1082
 "superdot" for image-processing applications, 1084
 quantum wire based room temperature infrared photodetectors, 1076–1079
 origin of photoresponse, 1077–1079

- Electrochemistry of DNA, 1065–1066
- Electrodepositing compound semiconductor, nanoarrays, electrochemical self-assembly, 1075
- Electrodepositing metal, nanoarrays, electrochemical self-assembly, 1075
- Electrokinetic characterization, colloidal nanoparticle, 773–786
- composite particles, synthetic process of, 778–785
- concentrated dispersion, 775–778
- diluted suspension, measurements of particles in, 773–775
- Electrokinetics, mineral nanoparticle, 1991–2005
- double-layer model, 1992
- electrical double layer model, 1992
- electroosmosis, 1999
- electrophoresis, 1999
- electrophoretic mobility, applications of, 2002–2003
- ions, 1996–1998
- isoelectric point, 1998
- mineral particle interaction mechanisms, 2000–2002
- point of zero charge, 1998
- properties, 1991–1998
- sedimentation potential, 1000
- streaming potential, 2000
- surface charge, origin of, 1991–1992
- zeta potential, 1998
- applications of, 2002–2003
- measurement, 1998–2000
- Electroluminescence, optical characterization, self-formed quantum dots, 3232–3234
- Electron back scattering diffraction, 2272
- Electron beam direct writing, 2413
- Electron beam lithography, 2413
- Electron beam projection lithography, 2413
- Electron energy loss spectroscopy, 2330
- Electron microscopy imaging techniques, environmental, geological science, 1087–1097
- analytical techniques, 1088–1089
- examples, 1089–1095
- gold nanocrystals, in gold ore deposit, 1091–1093
- heavy element colloids, at Nevada test site, 1091
- lead in early archean zircon, 1093–1095
- uranium nanocrystals, in atmospheric particulates, 1089–1091
- conventional techniques, 1087–1088
- Electron projection lithography, 2418
- Electron spin resonance, 2027
- Electronic artifacts, atomic force microscopy, 151
- Electronic control, DNA hybridization, 963–975
- Electronic coupling in vertically aligned quantum dots, 3135–3143
- coupled quantum dots, 3140–3143
- electronic coupling in quantum dot columns, 3138–3140
- quantum dots columns, 3135–3137
- theory, 3137
- Electronic nanostructures, metal nanoparticle self-assembly into, 1829–1840
- electronic applications, 1830–1833
- fabrication of ordered arrays, 1834–1838
- 1-D arrays, 1838
- 2-D arrays, 1835–1838
- 3-D arrays, 1835
- molecularly protected nanoparticle, 1829
- synthesis, 1833–1834
- Electronic switches, 1099–1111
- carbon nanotubes, 1104–1107
- molecular actuators, 1107–1109
- nanoparticle, 1099–1101
- quantum dots, 1099–1101
- switches, 1101–1104
- Electroosmosis, 1999
- Electroosmotic flow velocity, carbon nanotubes, 522
- Electro-osmotic membrane flow control, carbon nanotubes, 519–528
- electrochemical derivatization, effect on electroosmotic flow, 525–526
- electroosmotic flow
- effect of applied current density on, 522–523
- velocity, 522
- ionic strength, effect on electroosmotic flow, 523–524
- solution pH, effect on electroosmotic flow, 524–525
- transport properties, carbon nanotube membranes, 521–522
- Electrophilic substitution, fullerenes, 1217
- Electrophoresis, 1999
- Electrospinning, polymer nanofibers prepared by, 2931–2938
- concentration of polymer in solution, 2934
- electrical conductivity, 2933–2934
- electrospun nanofibers, applications of, 2935–2936
- electrospun polymer systems, 2934
- fiber formation, 2933–2934
- structure formation, 2934–2935
- surface free energy, 2933
- Electrostatic coagulation, collision kernels, 39
- Electrostatic forces, nanoparticle, determined by direct measurement, 3807
- Electrostatic surface potential, 686–695
- Ellipsometer, 284
- Ellipsometry, spectroscopic. *See* Spectroscopic ellipsometry
- Empirical pseudopotential method, silicon nanocrystals, quantum confinement, 3564–3567
- Emulsions, functionalized, DNA interactions with, 977–986
- Enamine, on lab-on-a-chip micro reactor, 1556
- Enantiomeric switches, in liquid crystal matrix, 2166
- Enantiomerically pure compounds, surfaces of, 1117
- Enantiomers, chiral switches based on, 2159–2160
- Enantiomorphous crystals, bulk, surfaces of, 1117–1118
- Enantiomorphous heteroepitaxial growth, metals on chiral oxides, 1120
- Enantioselectivity
- naturally chiral metal surfaces, 1120
- surfaces with chiral nanostructures, 1113–1123
- achiral bulk crystal structures, chiral surfaces from, 1118–1120
- bulk chiral materials, surfaces based on, 1117–1118
- chiral organic modifiers, surfaces templated with, 1115–1117
- importance of, 1114–1115
- molecules, chirality of, 1113–1114
- naturally chiral metal surfaces, 1120
- solids, chirality of, 1113–1114
- surfaces, chirality of, 1113–1114
- technological impact of chiral surfaces, 1120–1121
- types of, 1115–1120
- on surfaces with chiral nanostructures, 1113–1123
- Encapsulated metallic nanowires, design, 2428
- End functionalization, 496–497
- Endohedral fullerene complexes, dynamics of, 1472–1473
- Endohedral hydrogen physisorption, 531
- Energetic parameters, environmental nanoparticle, 1148
- Energetics, metallic nanopowders, 1927–1928
- Energy dispersive x-ray, 2565
- Energy electron loss spectrometer, 2633
- Energy-dispersive x-ray, 2372, 2633
- Enlarged nitrile-based coordination cages, self-assembly of, 3422–3423
- Environmental applications, molecular self-assembly, 1125–1135
- actinides, 1130
- electrochemical heavy metal detection, 1131
- heavy metal assay, 1130–1131
- nanoscience, 1126–1128
- mesoporous ceramics, functionalization of, 1126–1127
- nanostructured materials, 1126
- self-assembled monolayers, 1127–1128
- nuclear assay methods, enhancement of, 1131–1133
- oxometallate anions, 1129
- radiocesium, 1129–1130
- soft heavy metals, 1128–1129
- sorber materials, self-assembled monolayers as, 1128–1129
- x-ray fluorescence, 1130–1131
- Environmental catalysts based on nanocrystalline zeolites, 1137–1145
- assembly, 1139–1140
- hydrothermal synthesis, 1137–1138
- nanocrystalline zeolite materials, 1140–1142
- environmental remediation, 1141–1142
- hydrocarbons, partial oxidation reactions of, 1140–1141
- organic contaminants, photocatalytic decomposition, 1142
- self assembly, 1137–1140
- synthesis, 1137–1140
- templating methods, 1138–1139
- Environmental contaminants, bioremediation, 331–341
- anaerobic organisms, 332
- anaerobic processes, 332
- bioaugmentation, 332
- biostimulation, 332
- environmental pollutants, 331–334
- hydrocarbons, 331–333
- metals, 334
- polycyclic aromatic hydrocarbons, 333–334
- Exxon Valdez oil spill bioremediation project, 336–338
- lessons from, 337–338
- techniques, 334–336
- biofiltration, 335–336
- groundwater bioremediation, 334–335
- phytoremediation, 336

- Environmental nanoparticle, 1147–1155
 in atmosphere, 1151
 beyond earth, 1152
 in deep earth, 1151–1152
 energetic parameters, 1148
 in minerals, 1149
 physical chemistry, 1147–1148
 in rocks, 1151–1152
 in sediments, 1151–1152
 in soil, 1148–1151
 in water, 1148–1151
- Environmental scanning electron microscope, 2039
- Environmental science, electron microscopy
 imaging techniques, 1087–1097
 analytical techniques, 1088–1089
 examples, 1089–1095
 gold nanocrystals, in gold ore deposit, 1091–1093
 heavy element colloids, at Nevada test site, 1091
 lead in early archaean zircon, 1093–1095
 uranium nanocrystals, in atmospheric particulates, 1089–1091
 conventional techniques, 1087–1088
- Enzymatic synthesis, polyphenols, polyaromatic amines, 3374–3375
- Enzyme-based fiber optic nanobiosensors, 2762–2763
- Enzyme-DNA films, electrochemical toxicity sensors, 1063–1065
- Epithelial chloride channel, 3699
- Epoxy layered-silicate nanocomposites, aerospace applications, 45–54
 aerospace epoxy nanocomposites, 46
 layered organosilicate, 45–46
 layered silicate, 45–46
 morphology characterization, 46–47
 morphology development, 49–50
 different curing agents, 50–51
 primer layer for aircraft coating, 51–52
 processing, 49–50
 properties of, 47–49
- Escherichia coli*, nanoparticle decontamination, 244
- Esterification, on lab-on-a-chip micro reactor, 1556
- Ethane preferred conformation, 1167–1173
- Ethanol, surface tension, 1573
- Ethyl acetate, surface tension, 1573
- Ethylene glycol, surface tension, 1573
- Ethylene glycol dimethacrylate, 281
- Ethylenediaminetetraacetic acid, 2841
- Ethylene-dioxythiophene, 2618
- Europium-based cubane structure, 64
- Evaporative drying, templating aerogels for tunable nanoporosity, 3846–3847
- Excited state properties, configuration interaction methods, 3570–3571
- Excited state transitions, quantum dot lasers, 3114–3116
- Exfoliation, 3019–3020
 intercalated polypropylene nanocomposites, 1485
- Exohedral hydrogen physisorption, 531
- Explosives, metallic nanopowders, 1928–1929
- Extended x-ray absorption fine structure, 170
- Exxon Valdez oil spill bioremediation project, 336–338
 lessons from, 337–338
- Fabricating molecular-assembly nanowires, 2021–2022
- Fast Fourier Transform, 2103
- Fatigue properties, structural nanomaterials, 3730–3731
- Ferrite nanocrystals, 2323–2324
- Ferritins, 321–322
- Ferrohydrodynamic Bernoulli's law, 1735
- Ferromagnetic molecular TDAE-C₆₀, 1656–1657
- Fiber optic chemical nanosensors, 2759–2761
- Fiber optic nanobiosensors, 2761–2763
- Fiber optic nanoimaging
 probe fabrication, 2763–2764
 sensors, 2763–3764
- Fiber-matrix interface, buried, monitoring, 2557–2559
- Fibrinogen, properties of, 3082
- Fibrous encapsulation, newly implanted materials, 263–264
- Fibrous forms of carbon, 481–486
- Field emission scanning electron microscopy, 2410, 2804
- Film electrodes, carbon nanotubes, 507
- Films, nanoparticle, semiconductor, dimensionally graded, 913–921
- Finite-size scaling, mesoscopic thermodynamics, 3900
- First light-driven unidirectional molecular motor, 2169
- Flame atomic absorption spectrometry, 170
- Flame spray pyrolysis, 2008
- Flexible polymer adsorption, 29
- Fluorescein isothiocyanate, 2762
- Fluorescence confocal scanning laser microscopy, 2847
- Fluorescence measurements, chemical warfare agent detection biosensors, 379
- Fluorescence near-field scanning optical microscopy, 2706–2707
- Fluorescence recovery after photobleaching, 2508
- Fluorescence resonance energy transfer, 2508
- Fluoride templated helix, Gale's, crystal structure of, 77
- Fluorination, on lab-on-a-chip micro reactor, 1556
- Fluorine-19 nuclear magnetic resonance spectroscopy, 1181–1182
- Fluorine-like sarin, decontamination by nanoparticle, 241
- Fluorofullerenes, 1175–1190
 chemical properties, 1184–1186
 addition reactions, 1185
 oxafuorofullerenes formation, 1184–1185
 substitution reactions, 1185–1186
 physical properties, 1182–1184
 fluorofullerene ions, 1184
 solubilities in organic solvents, 1182–1184
 thermodynamic properties, 1184
 structural characterization of, 1178–1182
 fluorine-19 nuclear magnetic resonance spectroscopy, 1181–1182
 x-ray crystallography, 1178–1181
- synthesis of, 1176–1178
- Fluorophore-receptor systems, 2750–2751
- Fluorophore-spacer-receptor systems, 2751
- Force gradient atomic resolution imaging, 3650
- Force spectroscopy, 135–140
 elasticity of cell walls, 137
 microbial cell surfaces, 133–142
 principle of, 135–136
 spatially resolved force spectroscopy, 136–137
- Foreign molecules
 doping by, 486–489
 intercalation, 486–489
- Formamide, surface tension, 1573
- Formate method, magnetic nanomaterial synthesis, 1693–1694
- Fourier transform ion cyclotron resonance mass spectroscopy, 1381
- Fractal analysis, binding kinetics on biosensor surfaces, 1191–1202
 dual-fractal analysis, 1193
 single-fractal analysis, 1192–1193
 surface plasmon resonance biosensor, 1191–1192
- Fracture, structural nanomaterials, 3730
- Free radical fluorination, on lab-on-a-chip micro reactor, 1556
- Fuel cell catalyst precursors, colloidal nanometals as, 739–759
 metal salt reduction method, 741–743
 wet chemical reduction, 741–748
- Fuel cells
 carbon nanotubes, 514
 secondary hydrogen battery, electrodes in, 429–430
- Fuels, nanometal powder, 1937–1942
 aluminized gels, development, 1939–1940
 "combustion" in nitrogen, 1942
 gelled aluminized propellants, mechanisms of combustion of, 1938–1939
 hybrid propellants, Alex as additive to, 1938
 ignition delay measurements, 1940
 liquid propellants, Alex as additive to, 1938
 small rocket engine tests, 1942
 solid propellants, Alex as additive to, 1937–1938
- Fullerene C₇₀, 1225–1226
- Fullerene C₇₆, 1226
- Fullerene C₇₈, 1226
- Fullerene C₈₀, 1226–1227
- Fullerene C₈₂, 1228
- Fullerene C₈₄, 1227–1229
- Fullerene C₈₆, 1229
- Fullerene C₈₈, 1229
- Fullerene C₉₀, 1230
- Fullerene carbon nanotubes, 3657
- Fullerene chemistry, 1471–1473
- Fullerene solid, magnetism, 1208–1209
- Fullerene-based drug delivery, 256
- Fullerenes, 1203–1211, 1213–1221, 1235–1249
 amorphous sp² carbon, 1244–1245
 applications, 1219
 chemical reactivity, 1214–1219
 cycloadditions, 1215–1216
 electrophiles, addition of, 1216–1217
 electrophilic substitution, 1217
 higher fullerenes, 1218–1219
 hydrogenation, 1215

- Fullerenes (*cont.*)
 metal complexes, 1217–1218
 multiple additions, 1217
 nucleophiles, addition of, 1216
 oxidation, 1215
 radicals, addition of, 1216
 fullerene solid, 1207–1209
 doped fullerenes, 1208
 polymerization, 1209
 superconductivity, 1208–1209
 graphene topology, 1238–1245
 historical background, 1235–1237
 inorganic, 3933–3942
 molecular properties, 1205–1207
 electronic states in C₆₀, 1205–1206
 nanotubes, electrical conduction in, 1206–1207
 molecular structure, 1203–1204
 nanotubes, 1240–1241
 nuclear magnetic resonance spectra, identification of isomers based on, 1223–1234
 periodic schwarzites, 1241–1244
 polymerization of, 1657
 structure, 1213–1214
 synthesis, 1214
 synthesis, 1204–1205
 topology vs. total energy, 1245–1246
 van der Waals interactions with, 1473
- Functional nanostructures, 2456
 diblock copolymers, self-assembly with, 2457–2459
 nanofabrication, via self-assembly, 2456–2457
- Functionalized nanoporous silica, electrochemical sensors based on, 1051–1061
 for selective adsorption of metal species, 1053
- Functionalized polysilsesquioxane colloids, metallation, nanoparticle formation in, 2910–2911
- Gale's "anion–anion" assembled solid-state polymer, x-ray crystal structure, 77
- Gale's diamidopyrrole ligand, 77
- Gale's fluoride templated helix, crystal structure of, 77
- Gas adsorption, carbon nanotubes, 547–556
 confined spaces, matter in, 550–551
 gas chemisorption, carbon nanotubes, 551
 gas physisorption, 547–549
 gas storage capacity, 549–550
- Gas phase synthesis, nanocrystalline powders, 2291
- Gated response, dual-mode photoswitching of luminescence, 2163–3164
- Gel permeation chromatography, 2739
- Gene delivery
 bionanoparticle, 327–328
 polymer nanoparticle for, 2939–2949
 active targeting, 2944
 brain, 2945
 chitosan, 2943
 liver, 2945
 lung, 2945
 muscle, 2944–2945
 nanoparticle formation, 2939–2940
 nonviral systems, delivery obstacles for, 2940–2941
 passive targeting, 2944
 poly(2-dimethylamino)ethyl methacrylate, 2943
 polyamidoamine dendrimers, 2943
 polyethylenimine, 2941–2943
 poly-L-lysine, 2941
 polymeric gene carriers, 2941–2944
 polyphosphoester, 2943–2944
 targeting, 2944
 tumor, 2945
 in vivo application, 2944–2946
- Gene therapy, vector with docking site for, 256
- Geological science, electron microscopy imaging techniques, 1087–1097
 analytical techniques, 1088–1089
 examples, 1089–1095
 gold nanocrystals, in gold ore deposit, 1091–1093
 heavy element colloids, at Nevada test site, 1091
 lead in early archaic zircon, 1093–1095
 uranium nanocrystals, in atmospheric particulates, 1089–1091
 conventional techniques, 1087–1088
- Germanium, colloidal nanoparticle, 717–723
- Germanium nanoparticle, colloidal, 717–723
- Giant magnetoresistance effect, 1674–1675
- Glassy phase, nanostructured alloys with, 1397–1400
- Globular protein adsorption, 29–32
- Glucose, surface free energy, 1573
- Glucose detection, 366–367
- Glutamic acid, properties of, 3082
- Glutamine, 266
 properties of, 3082
- Glycerol, surface tension, 1573
- Glycine, 266
 properties of, 3082
- Glycolate method, magnetic nanomaterial synthesis, 1694–1695
- Glycoluril, 1314–1316, 1340–1342
- Goethite, energetic parameters, 1148
- Gold
 alkylthiol self-assembled monolayers on, 3–4
 nanotube alloyed with, 1461–1465
 photochemistry, membrane-coated nanoparticle, 2835–2843
- Gold films, colloidal, tunable nanocrystal distribution, 1515–1523
 electrostatic interactions, particle deposition, 1515–1517
 kinetics, nanocolloidal gold adsorption, 1519–1520
 quantitative analysis, 1520–1521
 saturation coverages, 1518–1519
 spatial distribution, 1518–1519
- Gold nanoclusters, 1287–1296
 chirality in, 1292–1293
 layer-by-layer assembly of, modified with self-assembled monolayers, 1581–1590
 structural properties of, 1288–1291
 supported, catalysis by, 611–620
 adsorbate binding energies, 614–615
 catalyst deactivation, 618
 catalytic properties, 613–614
 characterization, 612–613
 cluster sintering, 618
 cluster sublimation energies, 616–618
 electronic properties, 615–616
 model catalysts, 612–618
 synthesis, 612
 thiol-passivated gold nanoclusters, structural properties of, 1291–1292
- Gold nanocrystals, 1517–1518
 nanocolloidal gold suspension, 1517
 size distribution, 1517–1518
- Gold nanoparticle
 assembly, surface plasmon spectra, 3819–3830
 layer-by-layer assembly of, 1625–1628
 on titania, 1297–1304
 carbon monoxide oxidation, 1299–1301
 catalytic activity, 1297
 decomposition of sulfur dioxide on, 1301–1302
- Gold surface, supramolecular aggregates, with controlled size, shape on, 3775–3777
- Gouy–Chapman theory, electrical double layer formation, 1003–1004
- Grain size, nanocrystalline materials, 2301–2303
- Grand canonical Monte Carlo simulation, electrical double layer formation, 1004–1006
- Graphene topology, fullerenes, 1238–1245
- Graphite Brillouin zone, graphite electron, 479
- Graphite electron, Brillouin zone, 479
- Graphite intercalation compounds, single-walled carbon nanotubes, 3610–3611
- Graphites, 476–480
- Gravitational, Brownian coagulation kernels, compared, 38
- Gravitational coagulation, collision kernels, 37–38
- Green function, 2081
- Groundwater bioremediation, 334–335
- Guanidinium-appended porphyrins, 76
- Gun propellants, metallic nanopowders, 1929
- Halide transport through biological membranes, structural base, 3697–3711
- Halide-specific membrane transport systems, 3698
- Halobacterium halobium*, atomic force microscopy, 170
- Halorhodopsin, 3703–3707
- Hamilton's self-assembled solid-state hydrogen-bonded structure, ribbon arrangement of, 70
- Heavy metal assay, 1130–1131
- Hectorite, 215
- Helices of polypeptides, design theory, 2428–2429
- Hematite
 energetic parameters, 1148
 surface free energy, 1573
- Hemoglobin, properties of, 3082
- Heptane, surface tension, 1573
- Hessian matrix evaluation, 827
- Heterogeneous catalysts, atomic scale studies, 179–193
- Heterogeneous catalytic reactions, high-resolution mass spectrometry, 1381–1391
 Fourier transform ion cyclotron resonance mass spectroscopy, 1381
 laser ablation, 1383–1384
 zeolite/silica mass spectroscopy research, 1384–1385

- Heterogeneous surfaces, dynamic atomic force microscopy, 987–1000
 receptor-ligand interactions, dynamic measurements, 995
 steric forces, dynamic measurements, 994–995
 tapping mode atomic force microscope, 988–991
- Hewlett-Packard, 2067
- Hexadecanethiol, 2869
- Hexadecyltrimethylammonium, 1992
- Hexagonal close-packed, 2815
- Hexagonal liquid crystalline phase, cubosomes, 889
- Hexa-molybdenum-based complex, anion templated system, 59
- Hexanuclear silver array, route of, 63
- Hierarchical self-assembly, 290
- Hierarchically imprinted nanostructures, separation of metal ions, 1369–1379
 molecular imprinting, 1369
- High-cycle fatigue, 2270
- High-resolution electron microscopy, 2631
- High-resolution mass spectrometry, heterogeneous catalytic reactions, 1381–1391
 Fourier transform ion cyclotron resonance mass spectroscopy, 1381
 laser ablation, 1383–1384
 zeolite/silica mass spectroscopy research, 1384–1385
- High-resolution transmission electron microscopy, 2260, 2330, 2437, 2575, 2599, 2631, 2804
- High-temperature synthesis, nanocrystalline powders, 2294
- Histidine, 266
 properties of, 3082
- HIV, anti-HIV dendrimer, 256
- Hollow capsule, 870–875
 colloidal core decomposition, 2371–2376
 nanobottles, inorganic, 872–875
 polymer, 871–872
- Hollow spheres, polyelectrolyte-surfactant complex nanoparticle, 2900–2901
- Homogeneous nucleation, atmospheric nanoparticle, 102–103
- HOMO-LUMO gap, 2084
- Honeycomb lattice, of nanotube, 576
- Human fibronectin, surface free energy, 1573
- Humidity, adhesion of surfaces coated with self-assembled monolayers, 1–9
 adhesion, 1–3
 hysteresis, 5
 alkylsilane self-assembled monolayers
 on mica, 6–8
 on silica, 4–6
 alkylthiol self-assembled monolayers, on gold, 3–4
 pulloff forces, 4
- Hybrid bilayer membranes, infrared spectroscopy, 312–317
- Hybrid devices, 2211–2219
- Hybrid magnetic materials, 1723
- Hybrid methods, application in nanochemistry, 1471–1477
- Hybrid nanostructures for bioengineering, 355–356
- Hybrid quantum mechanics, molecular mechanics methods, 1469
- Hybridization, DNA, electronic control, 963–975
- Hydrocarbon-based liquid rocket engines, Alexgel applications, 1942
- Hydrocarbon-based RBCC systems, Alexgel applications, 1942
- Hydrocarbons, environmental pollutants, 331–333
- Hydrocracking, mesoporous materials, 1805
- Hydrodemetallation, mesoporous materials, 1805–1806
- Hydrodesulfurization, 2637
- Hydrofluoric acid, 2758
- Hydrogel nanoparticle core-shell, 855–864
 environmentally responsive microgels, 855
 fluorescence analysis, 860–862
 mechanical interactions between core, shell, 858–859
 shell thickness dependence, 859–860
 synthesis, 855–837
 thermodynamic properties, 857–858
 synthesized by cross-linked polyvinylpyrrolidone, 1403–1414
 ultrafine poly(N-vinyl pyrrolidone) nanoparticle, 1406–1412
- Hydrogen, atomic, carbon nanotube electrodes, 429
- Hydrogen battery, electrodes in, 429–430
- Hydrogen bonding, self-assembly directed by, 3399–3413
 catenanes, 3405–3406
 cyclic assemblies, 3401–3403
 helical structures, 3406–3408
 hydrogen-bonded polymers, 3409
 molecular capsules, boxes, 3403–3405
 molecular self-assembly, 3399
 rotaxanes, 3405–3406
 self-assembly of nanotubes, 3408–3409
 simple systems, 3400
- Hydrogen chemisorption, carbon nanotubes, 529–536
 armchair nanotubes, models of, 530
 hydrogen storage, 534–535
 investigations of hydrogen adsorption, 531–535
 chemisorption studies, 532–534
 physisorption studies, 532
 models, 530–531
 nanotube small cluster models, 532
 nanotube structure, 529–530
- Hydrogen cyanide
 chemical structure, 379
 generation, on lab-on-a-chip micro reactor, 1556
- Hydrogen production, semiconductor nanoparticle, 2845–2846
- Hydrogen storage, carbon nanotubes, 514, 557–566
 room temperature, 560–564
 single-walled carbon nanotubes, 557
 sorption mechanisms, 559–560
 temperature-programmed-desorption system, 558
- Hydrogenation
 alpha-ketoesters on platinum, 1116
 beta-ketoesters on nickel, 1115–1117
- fullerenes, 1215
 on lab-on-a-chip micro reactor, 1556
- mesoporous materials, 1806
- Hydrogen-bonded nanostructures, atomic force microscopy, 155–167
- Hydrogen-bonded nanotubes, self-assembly, cyclic peptides, 3439–3457
 application status, peptide nanotubes, 3450–3454
- Hydrogen-bonded polymers, self-assembly and, 3409
- Hydrogen-bonding, 2057
- Hydroisomerization, mesoporous materials, 1806
- Hydrophilic-hydrophobic block ionomers, reverse core-shell structures by complexation of, 2899–2900
- Hydrophobic pocket
 self-assembly synthesis, 1329–1355
 synthesis, 1305–1327
- Hydrophobicity, amino acid, 266
- Hydrotalcite, 232
- Hydro-talcite-like compounds, 2543
- Hydrothermal extraction of aluminum, from zeolite lattice, 636
- Hydroxyapatite, 266, 2446
- Hydroxyquinoline ligands, triple-stranded helicates, dinuclear, template-directed assembly, 3838–3840
- Hypernetted chain, 2132
- Ice nanotubes inside carbon nanotubes, 1415–1424
 continuous freezing, 1420–1422
 experiments, 1423–1424
 freezing, 1417–1422
 melting behavior, 1417–1422
 phase diagram, 1422–1423
 simulations, 1423–1424
 structure, 1415–1417
- Image processors, quantum dot, 1079–1084
 dot capacitance, 1084
 interdot resistance, 1082
 measurements of circuit parameters, 1082
 negative differential resistance, 1082–1084
 quantum dot based neuromorphic architectures, 1080–1081
 self-assembling neural network, 1082
 "superdot" for image-processing applications, 1084
- Imidazolium threads, 75
- Imide clusters supported in zeolites, 230
- Implants, biomedical, 263–275
 amino acid
 charge, hydrophobicity, surface tension, 266
 in proteins, 266
 biocompatibility, 265–266
 characteristics, 265
 fibrous encapsulation, newly implanted materials, 263–264
 future developments, 272–273
 hydroxyapatite fibers, 266
 nanophase ceramics, as nanobiomedical implants, 266–269
 nanophase materials, surface properties of, 265
 nanophase metals, as nanobiomedical implants, 269

- Implants, biomedical (*cont.*)
 nanophase polymers, as nanobiomedical implants, 269–270
 nanoscale surface, potential implants, 266
 nanostructured composites, as nanobiomedical implants, 270–272
 potential risks, 272
 soft tissue wound healing, sequential events of, 264
 surface-enhanced Raman scattering technique, 268
- In situ electron microscopy techniques, 1425–1438
 aberration correction, electron optics, 1436–1437
 analytical techniques for, 1435–1436
 catalysis studies, 1430–1432
 electrical property studies, 1427–1428
 examples, 1426–1435
 irradiation effects studies, 1432–1433
 magnetic studies, 1426–1427
 mechanical property studies, 1428–1430
 quantum dot studies, 1433–1435
 specialized apparatus for in situ studies, 1435
 thin film growth studies, 1433–1435
- In situ free radical polymerization, 2961–2966
 In situ intercalative polymerization, 216
 In situ living polymerization, 2966–2967
 In situ polymerization, methods of, 2961–2967
- Incident photon to photocurrent efficiency, 2841–2842
- Indium arsenide islands on silicon, 1439–1446
 Indium tin oxide, 2481
 Indium-doped tin oxide, 2841
- Inelastic light scattering, quantum dots, 3155–3166
 electronic ground state, 3156–3158
 GaAs–AlGaAs deep-etched quantum dots, 3161–3162
 InAs self-assembled quantum dots, 3162–3165
 electron quantum-dot atoms, 3162–3163
 scattering mechanisms, 3159–3161
- Infinite binding affinity, 89–94
- Infrared near-field microscopy, 2708–2709
- Infrared spectroscopy
 biomolecular structure at interfaces, 310–319
 hybrid bilayer membranes, 312–317
- Injectable nanospheres, for therapeutic, diagnostic agents, 256
- Inks, electrically conductive, metallic nanopowders, 1929–1930
- Inorganic compounds, anion templated self-assembly, 55–68
 cobalt, 55–57
 hexa-molybdenum-based complex, 59
 hexanuclear silver array, route of, 63
 iron, 55
 molybdenum, 59
 nickel, 57–59
 oxo-vanadium, structure of, 56
 palladium, 59–62
 cage, route of formation of, 62
 palladium-based molecular triangle, crystal structure of, 61
 platinum, 59–62
 silver, 62–66
 tetrafluoroborate templated nickel square, 59
 vanadium, 55
 x-ray crystal structure, chloride complex, 64
- Inorganic fullerene, 3933–3942
- Inorganic fullerene-like nanoparticle, 1450–1451
- Inorganic nanoparticle, tribology, 3933–3942
- Inorganic nanotubes, 1447–1455
 applications, 1452–1453
 beyond carbon, 1447–1449
 carbon fullerenes, 1447
 inorganic fullerene-like nanoparticle, 1450–1451
 properties, 1451–1452
 synthesis, 1449–1450
 synthesized by chemical transport reactions, 1457–1466
 applications, 1465
 crystal flakes, instability against bending, 1459–1460
 gold, nanotube alloyed with, 1461–1465
 interlayer distances, nanotube chirality, 1460–1461
 lattice structure, 1458–1459
 multiwall nanotubes, 1457–1461
 nucleation, 1458–1459
 plate-like crystal structures, 1457–1458
 silver, nanotube alloyed with, 1461–1465
 stacking-order, tube diameter and, 1460
- Inorganic thin-film composite membranes, 2402–2404
- In-plane structured electrodes, 730
- Institute of Pure and Applied Mathematics, 2110
- Integrally skinned asymmetric membranes, 2401
- Integrated circuit, 2211–2212
- Integrated methods, application in nanochemistry, 1471–1477
- Interaction of DNA with multivalent ligands, 2136–2137
- Intercalated polypropylene nanocomposites, 1483–1490
 clay intercalation, 1485
 crystallization structure, 1485–1486
 exfoliation structure, 1485
 kinetics, 1485–1486
 mechanical properties, 1487–1488
 rheology, 1486–1487
 synthesis, 1484–1485
- Intercalative free radical polymerization, using traditional initiators, 2961–2964
- Interconnects, carbon nanotube, 435–459
 interconnect architectures, integration in, 441–442
 internanotube contacts, 439–441
 junctions, crossed-tube, 439–441
 synthesis, 435–439
 directed, 437–439
 nondirected, 436–437
- Interfaces
 biomolecular structure at, 310–319
 molecular orientation at, sum frequency generation vibrational spectroscopy studies, 3749–3760
 nano-mesoscopic, 2211–2219
 silicon, 2213–2215
 pseudo-chiral, chiral molecules, self-assembly, 3431–3438
 water structure at, 389–403
 bioinertness, 389
 cell adhesion, resisting, 390–391
 D-mannitol-terminated self-assembled monolayers, adsorption of protein on, 397
 D-mannonic 1,5-lactone, 2, 401
 polymer polydimethylsiloxane elastomers, 395
 polymer-colloidal science, 391–392
 polyol-terminated self-assembled monolayers, 395–396, 396–398
 protein adsorption, re-issuing, 389–390
 tools for measuring, 394–395
- Interfacial forces between solid colloidal particle, liquid, 1491–1503
 deformable interfaces, interactions involving, 1493–1494
 direct measurement, 1494–1498
 deformable surfaces, 1496–1497
 force curve analysis, 1497–1498
 surface force measurement, 1494–1496
 interfacial forces, 1491–1493
 surface forces measurement, 1491
- Interfacial phenomena, 1505–1514
 molecular recognition, at interfaces, 1505–1506
 surfaces, chemical selectivity of, 1506–1511
 molecular interactions, 1506–1511
 molecular organization, 1508–1511
 molecular structure, 1506–1508
- Interference, structural color from, 3714–3717
- Intermaterial dividing surface, 2644
- Intracellular chloride channel, 3699
- Intrinsic molecular switches, 2149–2153
- Inverse opal formation, 2618–2619
- Ion beam lithography, 2413
- Ion beam projection lithography, 2421
- Ion competition, DNA counterion distributions, 2136
- Ion sensing, nanoparticle, 2477–2492
 at nanoparticle surfaces, 2482–2487
- Ionic amphiphilic block copolymer monolayer, nanostructure
 air–water interface, 2519–2529
 at air–water interface, 2519–2529
- Ionic strength, carbon nanotubes, effect on electroosmotic flow, 523–524
- Ionic strength effects, tunable nanocrystal distribution in colloidal gold films, 1515–1523
 electrostatic interactions, particle deposition, 1515–1517
 gold nanocrystals, 1517–1518
 nanocolloidal gold suspension, 1517
 size distribution, 1517–1518
 kinetics, nanocolloidal gold adsorption, 1519–1520
 quantitative analysis, 1520–1521
 saturation coverages, 1518–1519
 spatial distribution, 1518–1519
- Ionophores, design, 2425–2426
- Ions
 mineral nanoparticle, 1996–1998
 specific binding, DNA counterion distributions, 2138
- Ion-sensitive fiber optic nanosensors, 2760–2761
- IPAM. *See* Institute of Pure and Applied Mathematics
- Iron, anion templated system, 55
- Iron oxide nanoparticle, 1525–1532
 aligned magnetic nanoparticle, thin films with, 1527
 application, 1529–1531
 catalysis, 1530
 coercive force, 1528–1529
 composites, 1526–1527
 electromagnetic functions, 1531
 ferrites, 1526–1527
 functions, 1529–1531
 magnetic inks, 1530–1531
 magnetic properties, 1528–1529

- Iron oxide nanoparticle (*cont.*)
 Mossbauer spectra, 1529
 orientation, 1527–1528
 patterning, 1527–1528
 pure oxides, preparation, 1525–1526
 saturation magnetization, 1528–1529
 in situ patterning, 1528
 two-dimensional array, 1527–1528
- Iron oxides, 1149
- Iron-group element, composed of bimetallic nanoparticle, 1875
- Iron/nickel multilayers, thin film structural transition, 3739
- Iron/ruthenium multilayers, thin film structural transition, 3738
- Irreversible gold nanocrystal deposition, 3461–3466
- Island nucleation
 capture zone areas, distribution of, 1540–1541
 irreversible island formation, behavior of models, 1536–1538
 algorithm for simulation, 1537
 analyses, 1537–1538
 model prescription, 1536–1537
 island nucleation positions, 1543–1544
 nucleation impact of, 1541–1543
 nucleation rate, 1538–1540
 positions, 1543–1544
 predictions of, 1533–1545
- Isoelectric point, mineral nanoparticle, 1998
- Isoleucine, 266
 properties of, 3082
- Isomer identification, based on nuclear magnetic resonance spectra, fullerenes, 1223–1234
- Isopropyl- β -thiogalactopyranoside, 2118
- Isotope-labeled proteins, amide bands, sum frequency generation studies, 3758–3759
- Isotropic nanocomposite permanent magnets based on α -Fe/Nd₂Fe₁₄B, 1752–1754
 based on α -Fe/Sm-Co, 1755
 based on α -Fe/Sm-Fe-C, 1755
 based on α -Fe/Sm-Fe-N, 1755
- Jarosite-alunite, 1149
- Kartree-Fock method, silicon nanocrystals, quantum confinement, 3570–3571
- Kruger's double helicate, molecular structure of, 76
- Kumada coupling, on lab-on-a-chip micro reactor, 1556
- Lab-on-a-chip micro reactors for chemical synthesis, 1547–1564
 micro reactor fabrication, 1548–1549
 reaction control principles, 1549–1555
 reactions performed, 1555–1561
- Lactococcus lactis*, imaging, 135
- Lactose, surface free energy, 1573
- Lagrange-Euler formulation, molecular manipulator dynamic design criteria, 2105–2107
- Landau-Ginzburg mesoscopic functional, 3897–3898
- Langevin magnetization, ferrofluid magnetization, 1734
- Langmuir trough, electrochemical, 1043–1049
 examples of application, 1045–1048
 molecular conformation, 1045–1046
 open grids, 1046–1048
- Langmuir-Blodgett film, vesicles, at silicon-water interface, 2783
- Langmuir-Blodgett formation, polymer/single-walled carbon nanotube films, 571
- Langmuir-Blodgett surface modification method, 352–353
- Langmuir-Blodgett technique, 2020
- Large unilamellar vesicles, 2340
- Laser Doppler electrophoresis, 1999
- Laser-based deposition technique, nanoparticle patterning, 1565–1579
 optical field inside system, 1567–1569
 particle dynamics, 1570–1572
 setup optimization of system, 1569–1570
 solid-liquid interactions during, 1572–1578
 solid-liquid interfacial energy, 1572–1573
 suspensions, 1574–1575
 transported droplets, 1575–1577
- Lasers, rare earth-doped, 2861–2862
- Lateral force microscopic, 2035
- Lattice, antidot, chaotic transport in
 Aharonov-Bohm oscillation, 654–664
 Altshuler-Aronov-Spivak oscillation, 657–658
 commensurability peaks, 650–654
 magnetic focusing, leading to fundamental commensurability peak, 651
 scattering from two adjacent antidots, 652
 scattering matrix formalism, 658–664
 triangular antidot lattices, 656–657
- Lattice thermal conductivity, nanoceramics, 3867–3868
- Layer-by-layer assembly
 gold nanoclusters, modified with self-assembled monolayers, 1581–1590
 nanoparticle, 2496–2499
 thin films, mixed nanoparticle, 1623–1633
- Layer-by-layer surface modification method, 352–353
- Layer-by-layer technique, bio-microarray, 283–284
- Layered double hydroxides
 brucite-like layers, 3387
 crystallization, 3389–3390
 interlayer anions, 3387–3388
 morphology, 3389–3390
 multiple phases, 3387–3398
 polytype, 3388–3389
 self-assembly, 3387–3398
 stacking, 3388–3389
 structure, 3387
 superlattice formation, 3389
- Layered double hydroxide-surfactant interactions, nanocomposite formation, 3390–3396
- Layered transition metal chalcogenides, 2617–2639
- Layered transition metal sulfides, 2617
- Lead zirconate titanate, 2436, 2441
- Lens-shaped quantum dots, self-assembled, applications, 3220–3223
- Lepidocrocite, energetic parameters, 1148
- Leucine, 266
 properties of, 3082
- Lewis acid sites, 636–637
- Lewisite, decontamination by nanoparticle, 242
- Ligand-gated ion channel family, neurotransmitter receptors, 3699
- Ligand-receptor systems
 with different affinities, binding curves for, 90
 with infinite binding affinity, 89–94
- Light olefin-paraffin alkylation, 1806–1807
- Light scattering, inelastic, quantum dots, 3155–3166
 electronic ground state, 3156–3158
 GaAs-AlGaAs deep-etched quantum dots, 3161–3162
 InAs self-assembled quantum dots, 3162–3165
 electron quantum-dot atoms, 3162–3163
 scattering mechanisms, 3159–3161
- Light-driven unidirectional molecular motor, 2169
- Light-emitting diodes, 1037
- Light-induced switching, motion and, 2159–2176
- Light-polymerized fullerenes, ferromagnetism in, 12657–1659
- Limits of energy dissipation vs. performance, 2199
- Linear scaling methodology, 1468–1469
- Linewidth enhancement factor, quantum dot lasers, 3120–3121
- Lipid membranes
 dynamic organization of, 2507–2517
 nanostructure, 2507–2517
- Lipid nanoparticle, 256
- Lipopolysaccharide, structure of, 347
- Liposomes, 2507–2508
 direct force measurement, by atomic force microscopy, 933–942
 nanocapsulation, 2340–2343
- Liquid, solid colloidal particle, interfacial forces between, 1491–1503
 deformable interfaces, interactions involving, 1493–1494
 direct measurement, 1494–1498
 deformable surfaces, 1496–1497
 force curve analysis, 1497–1498
 surface force measurement, 1494–1496
 interfacial forces, 1491–1493
 surface force measurement, 1491
- Liquid crystal matrix
 enantiomeric switches, 2166
 pseudoenantiomeric switches in, 2166–2167
- Liquid crystalline environment, unidirectional rotary motion, 2173–2174
- Liquid crystalline nanoparticle, bicontinuous, cubosomes, 881–892
 cubic phase structure, 881–883
 cubosome manufacture, 885–886
 hexagonal liquid crystalline phase, 889
 monoolein, molecular structure of, 882
 other liquid crystalline phases, formation of, 89
 sponge phase, 889
 systems forming, 886–887

- Liquid crystalline nanoparticle, bicontinuous, cubosomes (*cont.*)
- Liquid crystalline phases, switching of, 2166–2169
- Liquid crystals, protein binding event detection, 1635–1646
- Liquid hydrogen engines, Alexgel applications, 1943
- Liquid metals, superfine oxides, nanocrystalline powders, 2294
- Liquid monopropellants, rocket propulsion, 1936
- Liquid rocket engines, rocket propulsion, 1935–1936
- Lithium ion batteries, anodes, 427–429
- Lithium reactivity
through conversion processes, 2796
through insertion processes, 2791–2795
- Lithographic microstructuring, particle deposition, 278
- Lithography, conducting polymers, 2619–2623
- Live chemical warfare agents, sensor response to, 385
- Liver, gene delivery, polymer nanoparticle for, 2945
- Living free radical polymerization, 2967
- Low-temperature wet-chemical synthesis, precipitation from solutions, 1911
- Luminescence
dual-mode photoswitching of, 2163–3164
nanoparticle-labeled antibodies, antigens, 1647–1653
- Luminescence properties of quantum dots, thermal effect on, 3873–3881
bulk semiconductors, optical properties of, 3873–3874
carriers transfer between quantum dots, 3877–3879
recombinations
in quantum dots, 3875–3877
in simple confined systems, 3875
- Lung, gene delivery, polymer nanoparticle for, 2945
- Lysine, 266
properties of, 3082
- Lysozyme, properties of, 3082
- Macrocycles, axle molecules threaded through, 195–204
daisy-chain polyrotaxane, 195
equilibrium constants, 198–203
chain length, branching, effects of, 200–202
pseudo-[2]-rotaxane formation, 197–198
solvent, effect of, 198–200
steric effects, 200
substituent effects, 200
terminal groups, influence of, 202–203
molecular threading, 195–197
riveted polyrotaxane, 195
- Maghemite, energetic parameters, 1148
- Magnesium, nanocrystalline oxide, surface chemistry of, 3795–3804
- Magnetic applications, nanoceramics, 2243
- Magnetic field sensor, 700
- Magnetic liquid crystals, 1724
- Magnetic nanomaterials, 1665–1681
Bloch law, 1670–1673
chemical design, 1683–1699
combustion method, ferrites obtained by, 1695–1696
complexation method for synthesis of, 1683–1685
effect of particle shape, 1673
fabrication of, 1665–1668
giant magnetoresistance effect, 1674–1675
interparticle interactions, 1673–1674
magnetic domain, 1668–1670
magnetization temperature/size dependence, 1670–1673
polynuclear coordination compounds, thermal decomposition of, 1685–1695
properties, 1668–1676
quantum tunneling, magnetization, 1675–1676
superparamagnetism, 1668–1670
surface effects, 1673–1674
synthesis, 1683–1699
acetate method, 1691–1693
citrate method, 1685–1686
formate method, 1693–1694
glycolate method, 1694–1695
magnetic nanoparticle, 1701–1713
malonate method, 1689–1691
oxalate method, 168–1689
properties, 1665–1681
tartarate method, 1686–1688
- Magnetic nanoparticle, 1715–1730
applications, 1725–1726
capsules, 1724
characterization, 1724–1725
interactions between particles, 1725
nature of surface coverage, 1725
particle size, 1724–1725
colloidal dispersion, 1720–1723
phase behavior, 1721–1722
processes, 1720–1721
properties, 1722–1723
emulsions, 1724
hybrid magnetic materials, 1723
latex, 1724
liposomes, 1724
magnetic properties, 1718–1720
bulk ferromagnetic materials, 1718–1719
magnetic properties of fine particles, 1719–1720
preparation procedures, 1716–1718
chemical nature of particles, 1716
maghemite particles, 1716–1717
magnetite particles, 1716–1717
metallic particles, 1717–1718
other ferric oxides, 1717
polydispersity of samples, 1718
- Magnetic nanoparticle in fluid suspension, 1731–1748
application to power transformer cooling, 1738
bacterial threads of nanomagnets, 1743
biomedical applications, 1740–1743
bacterial threads of nanomagnets, 1743
drug delivery, 1741–1742
immunoassays, 1742
magnetic resonance imaging, 1742–1743
magnetocytolysis, 1741
separations, 1742
drug delivery, 1741–1742
ferrofluid colloidal stability, 1732
ferrofluid composition, 1731–1732
ferrofluid magnetization, 1733–1735
Langevin magnetization characteristic, 1734
magnetization relaxation time constants, 1733–1734
magnetocaloric effect, 1734
magneto-optical effects, 1734–1735
ferrofluid preparation, 1732–1733
ferrofluid synthesis, 1731–1733
ferrofluid colloidal stability, 1732
ferrofluid composition, 1731–1732
ferrofluid preparation, 1732–1733
ferrohydrodynamic Bernoulli's law, 1735
ferrohydrodynamics, 1735–1738
application to power transformer cooling, 1738
ferrohydrodynamic Bernoulli's law, 1735
fluid instabilities, 1735–1736
rotating magnetic field torque-driven phenomena, 1736–1738
fluid instabilities, 1735–1736
immunoassays, 1742
Langevin magnetization characteristic, 1734
magnetic resonance imaging, 1742–1743
magnetization relaxation time constants, 1733–1734
magnetocaloric effect, 1734
magnetocytolysis, 1741
magneto-optical effects, 1734–1735
microelectromechanical systems, 1738–1740
nanoelectromechanical systems, applications to, 1738–1740
rotating magnetic field torque-driven phenomena, 1736–1738
separations, 1742
- Magnetic properties, 1722
molecular assembly of nanowires, 2026–2027
nanocomposite permanent magnets, 1749–1760
anisotropic nanocomposite permanent magnet films, 1755–1756
based on alpha-Fe/Nd₂Fe₁₄B, 1752–1754
based on alpha-Fe/Sm-Fe-C, 1755
based on alpha-Fe/Sm-Fe-N, 1755
based on Fe-B/Nd₂Fe₁₄B, 1754–1755
coercivity, 1750
critical sizes, 1749–1750
exchange coupling, 1749–1750
"exchange-spring" behavior, 1751
fabrication techniques, 1752
isotropic nanocomposite permanent magnets
maximum energy product, 1750
micromagnetically assessed magnetic properties, 1750–1751
remanence, 1750
utilization, 1756–1757
nanoparticle assemblies, 1761–1771
- Magnetic random access memory, 2077
- Magnetic resonance imaging, 2477, 2783
- Magnetospirillum gryphiswaldense*, imaging, 137
- Malonate method, magnetic nanomaterial synthesis, 1689–1691
- Maltose, surface free energy, 1573
- Manganese oxides, 1149
- Mask techniques, conducting polymers, 2619–2623
- Masks, conducting polymers, 2622–2623
- Mechanical alloying, nanostructured materials synthesized by, 2572–2573
- Mechanical attrition, nanostructured materials synthesized by, 2571–2581
brittle materials, 2573–2574
contamination, 2579–2580
mechanical alloying, 2572–2573
mechanical milling, 2571

- Mechanical attrition, nanostructured materials synthesized by (*cont.*)
 mechanisms, 2575–2579
 nanocomposites, 2574–2575
 polymer blends, 2574
 powder consolidation, 2579–2580
 single-phase metals, 2575–2579
- Mechanical synthesis, nanocrystalline powders, 2293
- Mechanosynthesis, nanophase powders, 1787–1785
 industrial trends, 1793–1794
 kinetics, 1789–1791
 mechanical aspects, 1788–1789
 mechanosynthesis of Fe₃C, 1792–1793
 thermodynamics, 1789
- Melamine formaldehyde, 2356, 2371
- Membrane-coated nanoparticle, photochemistry, 2835–3852
 gold, 2835–2843
 metal particles, 2835–2843
 semiconductor nanoparticle, 2843–3846
 hydrogen production, 2845–2846
 photocurrents, photoelectrochemical cells, 2845
 spectral sensitization, 2844
 silica particles, 2846–2847
- Membranes
 electro-osmotic flow control in, carbon nanotubes, 519–528
 lipid, nanostructure, 2507–2517
- Memory, molecular electronic, 2067–2080
- Mendoza's tetraguanidinium strand, double helicate structure self-assembly, 70
- Mercaptohexadecanoic acid, 923
- Mesoporous (alumino) silicates, 230–231
- Mesoporous ceramics, functionalization of, 1126–1127
- Mesoporous materials, 1797–1811
 applications, 1802–1803
 catalytic applications, 1803–1807
 catalytic cracking, 1803–1804
 hydrocracking, 1805
 hydrodemetallation, 1805–1806
 hydrogenation, 1806
 hydroisomerization, 1806
 light olefin-paraffin alkylation, 1806–1807
 olefin disproportionation, 1806
 oligomerization catalysts, 1804–1805
 refining catalysts, 1803
 discovery of, 1797–1800
 functional product development, challenges, 1802
 nitrogen oxides, catalytic decomposition of, 1807–1808
 petrochemical catalysis, 1807
 aromatics alkylation, 1807
 phase transfer catalysts, 1807
 polymer encapsulation, biomolecular approach to, 3383–3384
 separations, application to, 1808
 synthesis development, 1800–1802
- Mesoporous nanomaterials, catalytic properties, 633–647
- Mesoporous silica
 self-assembled acetamide phosphonic acids on, 1055–1057
- thiol-terminated self-assembled monolayer on, 1054–1055
- Mesoscopic thermodynamics, 3893–3904
 complex fluids, competition of mesoscales in, 3900–3902
 finite-size scaling, 3900
 fluctuations, role of, 3895
 Landau–Ginzburg mesoscopic functional, 3897–3898
 percolation, 3902
 susceptibility, 3899–3900
- Metal clusters on oxides, 1813–1820
 cluster morphology, 1815–1816
 gold on TiO₂, 18181–1819
 metal deposition, 1814–1815
 palladium on Al₂O₃, 1816–1818
 substrate preparation, 1813–1816
- Metal ion separation, nanostructures, hierarchically imprinted, 1369–1379
- Metal ion sorption, 170–171
 atomic force microscopy, 169–178
- Metal nanoparticle
 charge carrier dynamics of, 673–675
 DNA-conjugated
 marker application, for DNA chip readout, 959
 molecular nanotechnology, 959–960
 networks in solution based, 955–956
 preparation, 955
 solid substrates, immobilization onto, 956–958
 surface immobilization of DNA, 957
 whole substrate incubation, immobilization technique, 958
 protected with monolayers, 1859–1867
 chemiresistor sensors, 1864–1865
 gas chromatographic phases, 1863–1864
 sorptive properties, 1861–1863
 vapor sorption, 1861–1863
 receptor-modified, 1841–1850
 anions, recognition of, 1844
 as catalysts, 1847–1848
 cations, recognition of, 1844
 fabrication of networks in, 1846–1847
 redox-active species, recognition of, 1843–1844
 rotaxanes on, 1846
 surfaces of, molecular recognition at, 1842–1844
 as templates, 1845–1846
 self-assembly into electronic nanostructures, 1829–1840
 1-D arrays, 1838
 2-D arrays, 1835–1838
 3-D arrays, 1835
 electronic applications, 1830–1833
 fabrication of ordered arrays, 1834–1838
 molecularly protected nanoparticle, 1829
 synthesis, 1833–1834
 in supercritical carbon dioxide solutions, 1851–1858
 microemulsions, 1852
 rapid expansion, supercritical solutions, 1851–1852
 reactive supercritical fluid processing, 1852
 silver nanoparticle, 1853–1855
 silver sulfide nanoparticle, 1855–1856
- Metal nanoparticle as catalysts, 1869–1880
 bimetallic nanoparticle, formation of, 1876
 bimetallic nanoparticle
 iron-group element, composed of, 1875
 platinum-group elements, composed of, 1874–1875
 structure control, 1874–1876
 C–C bond formation, 1878–1879
 characterization, 1873–1874
 hydration, 1878
 oxidation, 1878
 preparation, 1871–1874
 reduction, 1876–1877
 visible-light-induced hydrogen generation, 1877
- Metal nanoparticle ensembles, collective optical properties, 1821–1828
 clusters of, 1822–1823
 linear arrays of, 1823
 metal, metallodielectric nanoparticle, 3-D superlattices of, 1825–1826
 nanoparticle assembly fabrication, 1821–1826
 surface plasmons, 1821
 two-dimensional arrays of, 1823–1825
- Metal nanoparticle in supercritical carbon dioxide solutions, 1851–1858
 microemulsions, 1852
 rapid expansion, supercritical solutions, 1851–1852
 reactive supercritical fluid processing, 1852
 silver nanoparticle, 1853–1855
 silver sulfide nanoparticle, 1855–1856
- Metal nanoparticle protected with monolayers, 1859–1867
 chemiresistor sensors, 1864–1865
 gas chromatographic phases, 1863–1864
 sorptive properties, 1861–1863
 vapor sorption, 1861–1863
- Metal nanostructures, photoexcitation synthesis, 1881–1894
 metal-dot deposition onto metal surface, photoinduced, 1886–1887
 nanoscale structural characteristics of, 1885–1886
 near-infrared optical response, metal thin film, 1890–1891
 photoinduced anisotropic agglomeration, gold nanoparticle, 1881–1885
 silver nanoparticle, photoinduced structural changes of, 1887–1890
- Metal oxide, nanocrystalline, as catalysts/catalyst supports, 2535–2536
- Metal oxide nanoparticle, 1905–1919
 adsorptive properties, 1914
 applications, 1912–1915
 bonding, 1905–1907
 mechanical properties, 1914–1915
 metal oxide surfaces, acid/base behavior of, 1912–1914
 physical properties, 1914–1915
 properties, 1912–1915
 structure, 1905–1907
 defects, 1906–1907
 synthesis, 1907–1912
 chemical methods, 1909–1912
 physical/aerosol methods, 1907–1909
- Metal oxide nanoribbons, 461–473

- Metal-functionalized dendrimer catalysts, comparison of, 904
- Metallamacrocyclic receptors, ion-pairs, 3504–3509
- Metallation, polymer colloids, 2903–2915
adsorbed polymer layer, nanoparticle with, 2912–2913
block copolymer micelles, nanoparticle formation in, 2903–2907
dendrimers, nanoparticle formation in, 2907–2909
functionalized polysilsesquioxane colloids, nanoparticle formation in, 2910–2911
nanoparticle formation inside, 2903–2911
nanoparticle formed on, 2911–2912
polyelectrolyte microgels, nanoparticle in, 2909–2910
- Metallic nanoparticle, 2477–2479
- Metallic nanopowders, 1921–1933
alloying reactions, pressed pellets, 1929
applications, 1927–1930
energetics, 1927–1928
explosives, 1928–1929
gun propellants, 1929
nanostructures, 1930
pyrotechnics, 1929
rocket propellants, 1928
self-heating synthesis, 1929
chemical properties, 1924–1927
electroexploded, characteristics, 1924
handling, 1931
inks, electrically conductive, 1929–1930
nanometal processes, 1921–1924
pastes, electrically conductive, 1929–1930
physical properties, 1924–1927
rocket propulsion, 1935–1945
Alexgel applications, 1942–1943
aluminized gels, development, 1939–1940
"combustion" in nitrogen, 1942
environmental issues, 196–1937
gelled aluminized propellants, mechanisms of combustion of, 1938–1939
hybrid propellants, Alex as additive to, 1938
hydrocarbon-based liquid rocket engines, 1942
hydrocarbon-based RBCC systems, 1942
ignition delay measurements, 1940
liquid hydrogen engines, 1943
in liquid monopropellants, 1936
liquid propellants, Alex as additive to, 1938
for liquid rocket engines, 1935–1936
nanometal powder fuels, 1937–1942
pulse detonation engines, 1942–1943
small rocket engine tests, 1942
solid propellants, Alex as additive to, 1937–1938
for solid rocket engines, 1935
safety, 1931
shipping of, 1931
- Metallic nanopowders low-temperature sintering, 1930
- Metallic semiconductor nanoparticle, polymer-nanoparticle composites, 3001
- Metallic tips, with near-field Raman spectroscopy, 2695–2702
- Metal-molecule heterostructures, charge transfer in, 683–698
- Metal-oxide interface, 1895–1904
defects, role of, 1899–1900
kinetics, 1898–1899
oxide vacancies, nucleation at, 1900–1903
atom trapping, 1900–1901
cluster stability, impact on, 1901–1903
thermodynamics, 1897–1898
- Metals
as environmental pollutants, 334
nanophase, as nanobiomedical implants, 269
quantum dots made of, 3177–3202
core-shell particles, 3191–3192
ligand binding, effect of alloying on, 3192–3194
metal nanoclusters, 3194
nanocluster characterization, 3180–3183
nanocluster matter, 3198–3199
nanocluster synthetic methods, 3179–3180
nanocluster/ligand binding studies, 3184–3185
optical properties, core-shell nanocrystals, 3187–3191
quantum dot arrays, 3194–3198
synthesis optimization, 3183
synthetic variables, 3185–3187
- Metametahydroquinocyclophane, 2430
- Metaquinocyclophane, 2430
- Methacrylic acid, 281
- Methacryloxpropyltrimethoxysilane, 236
- Methanol, surface tension, 1573
- Methanospirillum hungatei*, imaging, 137
- Methionine, 266
properties of, 3082
- Methoxy-ethylhexyloxy-phenylenevinylene, 2622
- Methyl parathion, chemical structure, 379
- Methylmethacrylate, 2040
- Mica, alkylsilane self-assembled monolayers on, 6–8
- Mica surface
charge nucleation, 1947–1965
molecular-assembly nanowires on, 2023–2025
quantitative measurements, 1949–1955
adhesion measurements, 1951
cantilevers, calibration of, 1949–1950
contact radius-line step analysis, 1952–1955
probe tip characterization, 1950–1951
wear, 1952
scanned probe methodologies, 1948–1949
atomic force microscopy, 1948–1949
lateral force measurements, 1949
wear, 1947–1965
alkylsilanes, 1959
native mica surfaces, 1955–1959
- Micelles, 710–711
polymer synthesis, 3381–3382
- Micro reactors, lab-on-a-chip, for chemical synthesis, 1547–1564
- Microarray preparation, nanoparticle applied in, 281–282
- Microarrayer, 284
- Microarrays, biomedical, based on functional nanoparticle, 277–286
dip coating of nanoparticle, 279
ethylene glycol dimethacrylate, 281
layer-by-layer technique, 283–284
lithographic microstructuring, particle deposition, 278
methacrylic acid, 281
microarrayer, 284
microcontact printing, 284
of nanoparticle layer, 279
microspotting, of nanoparticle layer, 281
microstructured surface preparation, 277–283
nanoparticle, applied in microarray preparation, 281–282
patterned monolayers of functional nanoparticle, 282–283
photoablation, 278–279
photolithography, 284
protein binding polymer nanoparticle, 282
surface activation, 277–278
- Microbial cell surfaces, force spectroscopy, 133–142
- Microbial rhodopsins, 3699
- Microbundle electrodes, carbon nanotubes, 508
- Microchip-based delivery systems, 256
- Microcontact printing, 284, 2869–2870
of nanoparticle layer, 279
- Microcrystalline peptide nanotubes, 3442
- Microelectrode array, modified with functionalized nanoporous silica thin film, 1057–1059
- Microgel dispersions, 1967–1976
colloidal forces, 1968–1970
crystallization kinetics, 1973–1974
equilibrium phase diagram, 1971–1973
phase equilibrium calculations, 1970–1971
- Micro-/nanoelectromechanical sensors, 252
- Microporous nanomaterials, catalytic properties, 633–647
- Microscopy techniques, in situ electron, 1425–1438
aberration correction, electron optics, 1436–147
analytical techniques for, 1435–1436
catalysis studies, 1430–1432
electrical property studies, 1427–1428
examples, 1426–1435
irradiation effects studies, 1432–1433
magnetic studies, 1426–1427
mechanical property studies, 1428–1430
quantum dot studies, 1433–1435
specialized apparatus for in situ studies, 1435
thin film growth studies, 1433–1435
- Micro-sized ring self-assembly, nanoparticle, 3282–3284
thermocapillary mechanisms, 3282–3283
wetting mechanisms, 3283–3284
- Microspotting, of nanoparticle layer, 281
- Microstructured surfaces for DNA immobilization, 958
- Microtubule supports, deposition of metals on nanostructures synthesized, 2653–2659
- Microweighing in supercritical carbon dioxide, 1977–1990
gravimetric technique, 1977–1978
microweighing methods, comparison of, 1980
piezoelectric technique, 1977–1978
polymer films in supercritical CO₂, dissolution study, 1983–1984
quartz crystal microbalance theory, 1981–1983
high-pressure fluids, 1978–1981
- Milling, mechanical, nanostructured materials synthesized by, 2571
- Mineral nanoparticle, electrokinetics, 1991–2005
description, 1991–1998
double-layer model, 1992
electrical double layer model, 1992
electroosmosis, 1999
electrophoresis, 1999
electrophoretic mobility, applications of, 2002–2003
ions, 1996–1998

- Mineral nanoparticle, electrokinetics (*cont.*)
 isoelectric point, 1998
 mineral particle interaction mechanisms, 2000–2002
 point of zero charge, 1998
 properties, 1991–1998
 sedimentation potential, 1000
 streaming potential, 2000
 surface charge, origin of, 1991–1992
 zeta potential, 1998–2000, 2002–2003
 applications of, 2002–2003
 measurement, 1998–2000
- Mineral particle interaction mechanisms, 2000–2002
- Minerals, soil, 1149
- Miniaturization, controlled drug delivery devices, 254–256
- Mitochondrial, plastid porin, 3699
- Mitochondrial carrier, 3699
- Mixed metal oxide nanoparticle, 2007–2017
- Mixed nanoparticle, thin films, layer-by-layer assembly of, 1623–1633
- Modified carbon paste electrodes, electrochemical sensors based on, 1053–1057
- Molded nanostructures, photonic applications, 2869–2878
- Molds, high-resolution, 2869–2873
- Molecular actuators of electronic switches, 1107–1109
- Molecular assembly of nanowires, 2019–2029
 air–water interface, charge-transfer complexes at, 2022–2023
 electrical conductivity, 2026–2027
 fabricating molecular-assembly nanowires, 2021–2022
 Langmuir–Blodgett technique, 2020
 magnetic properties, 2026–2027
 mica surface, molecular-assembly nanowires on, 2023–2025
 molecular conductors, 2019–2020
 molecular-assembly structures within, 2025–2026
 nanowire, molecular-assembly structures within, 2025–2026
 supramolecular chemistry, 2020–2021
- Molecular assembly organosilanes, 2031–2042
 chemisorption, fabrication of monolayers through, 2036–2040
 mixed monolayers, at air–water interface, phase separation, 2033–2036
 organosilane monolayers, at air–water interface
 formation of, 2031–2033
 via crystallization, 2031–2036
- Molecular beacon-based fiber optic nanobiosensors, 2761–2762
- Molecular computing machines, 2043–2055
- Molecular conductors, 2019–2020
- Molecular designs for self-organized superstructures, 2057–2066
 controlled crystal structures, 2057–2061
 by neutral biimidazole complex, 2061–2064
 molecular metal building block, 2057
- Molecular devices, design theory, 2423–2433
- Molecular dynamics of DNA, 2137
- Molecular electronic logic, memory, 2067–2080
- Molecular electronics, 2211–2219
 ab initio methods, switchable, programmable devices, 2081–2099
 integrated circuit, 2211–2212
 silicon, 2213–2215
- Molecular inclusion complexes, nanocapsulation, 2348–2350
- Molecular manipulator dynamic design criteria, 2101–2111
 Lagrange–Euler formulation, 2105–2107
 Newton–Euler formulation, 2104–2105
- Molecular mechanics methods, 1469
- Molecular modeling, carbon nanotubes, 461–473
- Molecular motor
 second-generation, 2169–2173
 unidirectional, 2159–2176
 light-driven, 2169
- Molecular motor-powered nanodevices, 2113–2122
 allosteric chemical controls, implementation of, 2115–2120
 motor proteins, control of, 2113–2115
- Molecular orbital, 2081
- Molecular orientation at interfaces, sum frequency generation vibrational spectroscopy studies, 3749–3760
- Molecular probes, cation–arene interactions, 2123–2130
- Molecular recognition at interfaces, 1505–1506
- Molecular resonant tunneling diode, 2084
- Molecular rotation, controlled, 2162
- Molecular self-assembly, environmental, sensing applications, 1125–1135
 actinides, 1130
 electrochemical heavy metal detection, 1131
 heavy metal assay, 1130–1131
 nanoscience, 1126–1128
 mesoporous ceramics, functionalization of, 1126–1127
 nanostructured materials, 1126
 self-assembled monolayers, 1127–1128
 nuclear assay methods, enhancement of, 1131–1133
 oxometallate anions, 1129
 radiocesium, 1129–1130
 soft heavy metals, 1128–1129
 sorbent materials, self-assembled monolayers as, 1128–1129
 x-ray fluorescence, 1130–1131
- Molecular simulations, DNA counterion distributions, 2131–2143
 analytical theory evaluation, 2133–2134
 continuum solvent models, 2133–2127
 compared, 2138–2139
 counterions around DNA
 Brownian dynamics of, 2137
 simulations of, solvent, 2137–2140
 dielectric effects, 2134
 DNA polyelectrolyte models, 2131–2133
 ion competition, 2136
 ions, specific binding of, 2138
 molecular dynamics of DNA, 2137
 multiscale simulation, 2139–2140
 multivalent ligands, interaction of DNA with, 2136–2137
 specific distribution of charges, 2135–2136
- Molecular switches, 2145–2157, 2159–2176
 chemical switches, 2146–2149
 chemical bimolecular reactions, 2149
 molecules in interaction, 2147–2149
 simple chemical conversions, 2146–2147
 chiroptical, sterically overcrowded alkenes as, 2159–2166
 intrinsic, 2149–2153
 pyrrolidine-functionalized, 2164–2165
 surface, 2153–2155
- Molecular wires, 2177–2195
 conductance, measurement of, 2189–2191
 conduction, measurement of, 2188–2191
 electronics, molecular, 2177
 optoelectronics, 2177–2178
 organic molecular wires, 2178–2186
 organometallic molecular wires, 2186–2188
 theory of conduction in, 2188–2189
- Molecular-assembly structures within nanowire, 2025–2026
- Molecularly protected nanoparticle, 1829
- Molecules, chirality of, 1113–1114
- Molten polymer, intercalation by, 216
- Molybdenum, anion templated system, 59
- Monodisperse aerosol particles, coagulation of, 36
- Monolayer on mesoporous silica, thiol-terminated self-assembled, 1054–1055
- Monolayers, metal nanoparticle protected with, 1859–1867
 chemiresistor sensors, 1864–1865
 gas chromatographic phases, 1863–1864
 sorptive properties, 1861–1863
 vapor sorption, 1861–1863
- Monoolein, molecular structure of, 882
- Monoolein–water system, aqueous phase behavior of, 883
- Monophenyl thiol, electrostatic surface potential, 692
- Monosaccharides, phase transfer through noncovalent interactions, 2825–2833
- Montmorillonite, 215
- Moore's law, 2197–2200
 charge transfer in metal–molecule heterostructures, 683
 limits of energy dissipation vs. performance, 2199
 predictions for CMOS technology, 2198
 single-electron transistors, 2198–2199
- Motor proteins
 control of, 2113–2115
 in synthetic materials, 2201–2209
- Multilayer nanostructures, charge transport properties, 699–707
- Multilayer polymer nanocomposites, ordered, barrier properties, 213–224
 multilayered polymer–polymer nanocomposites, 220–221
 polymer-layered aluminosilicate nanocomposites, 214–220
- Multilayered polyelectrolyte films, carbon nanotubes within, 567–574
- Multimodal ligands, coordination framework topology, 845–853
 coordination framework design, 845–846
 coordination polymers, 848–852
 three-dimensional architectures, 848–849
 two-dimensional architectures, 849–852
 coordination preferences, 847–848

- multimodal ligands vs. unimodal ligands, 846-847
- Multiparticle soft matter systems, computational analysis, 828-829
- coupled rotational modes, 829
- indifferent modes, 828-829
- particle vibrational modes, 829
- spectator modes, 829
- Multiphase nanostructured alloys, 1395-1396
- Multiphoton absorption, three-dimensional nanofabrication, 3905-3915
- Multiplayer assembly, on colloidal particles, 2369-2371
- Multiscale simulation, DNA counterion distributions, 2139-2140
- Multivalent ligands, interaction of DNA with, 2136-2137
- Multiwalled nanotubes, 1457-1461
- Multiwalled carbon nanotubes, super capacitors, 540-543
- Muscle, gene delivery, polymer nanoparticle for, 2944-2945
- Mustard gas
- decontamination by nanoparticle, 241-243
- detoxication of, 242-243
- structure of, 378
- Muti-wall carbon nanotubes, 480-481
- Myoglobin, properties of, 3082
- N*-methyl-2-pyrrolidinone, 2553
- NaI-symporter, 3699
- Nanoarray
- electrochemically self-assembled, 1073-1085
- anodization, 1075
- contacting nanowires, 1076
- dot capacitance, 1084
- electrochemical self-assembly, 1073-1076
- electrodepositing compound semiconductor, 1075
- electrodepositing metal, 1075
- interdot resistance, 1082
- measurements of circuit parameters, 1082
- nanofabrication, 1073
- negative differential resistance, 1082-1084
- quantum dot based neuromorphic architectures, 1080-1081
- quantum dot image processors, 1079-1084
- quantum wire based room temperature infrared photodetectors, 1076-1079
- self-assembling neural network, 1082
- "superdot" for image-processing applications, 1084
- synthesized from porous alumina, 2221-2235
- Nanobelt
- bending modulus, 1780-1781
- dual-mode resonance of, 1779-1780
- mechanical properties of, 1773-1786
- as nanocantilevers, 1782-1783
- oxide, bending modulus, 1778-1781
- structurally controlled nanowires, 1778-1779
- NanoBio, 256
- Nanobiomedical. *See* Biomedical
- Nanobiosensor, 2757-2768
- antibody-based fiber optic, 2761
- enzyme-based fiber optic, 2762-2763
- fiber optic, 2761-2763
- molecular beacon-based fiber optic, 2761-2762
- optical, 2757-2768
- Nanobiotechnology companies, 256
- drug delivery applications, 247-261
- Nanobottle, 870-875
- inorganic, 872-875
- polymer, 871-872
- rare earth complex encapsulation in, 875-876
- silica, preparation procedure of, 874
- Nanobridge, thermal properties of, 3883-3891
- breaking, 3887-3890
- initial structures, 3884
- melting, 3887-3890
- oscillations, 3884-3886
- Nanocantilever, nanobelts as, 1782-1783
- NanoCap micellar nanoparticle, for water-insoluble drugs, 256
- Nanocapsule
- oil-filled, 2739-2747
- polymer, 2345-2348
- NanoCarrier, 256
- Nanocatalyst, dendritic, 903-911
- Nanoceramics, 2237-2244
- applications, 2242-2244
- bioceramics, 2243
- biomedical applications and bioceramics, 2243
- coatings, 2243-2244
- electrical applications, 2242-2243
- magnetic applications, 2243
- mechanical applications, 2242
- nuclear industry, 2244
- bonding, 2240
- preparation, 2237-2240
- chemical methods, 2239-2240
- physical methods, 2237-2239
- properties of, 2240-2242
- chemical properties, 2241
- electrical properties, 2242
- magnetic properties, 2242
- mechanical properties, 2241-2242
- thermal conductivity, 3867-3872
- grain boundaries, scattering by, 3869-3870
- inclusions, reductions by, 3871
- increasing, 3871-3872
- interaction processes, 3868
- lattice thermal conductivity, 3867-3868
- radiative component, 3870
- reductions, 3868-3869
- thin layers, reductions by, 3871
- wave scattering by obstacles, 3870
- Nanocluster
- design, 2423-2425
- gold, 1287-1296
- palladium, 2803-2811
- preparation, 2803-2811
- silicon, simulation, 3551-3562
- simulation, silicon, 3551-3562
- computational methods, 3552-3553
- impurity atom, 3553-3554
- multiple oxygen termination, 3555
- oxygen passivation, 3554-3555
- surface passivation, 3553-3555
- Nanocolloidal film
- self-assembly of, 3459-3469
- kinetics, irreversible gold nanocrystal deposition, 3461-3466
- Nanocomposite film, 2454, 3826-3827
- Nanocomposite multilayer polymer, ordered, barrier properties, 213-224
- Nanocomposite permanent magnet, magnetic properties of, 1749-1760
- anisotropic nanocomposite permanent magnet films, 1755-1756
- coercivity, 1750
- critical sizes, 1749-1750
- exchange coupling, 1749-1750
- "exchange-spring" behavior, 1751
- fabrication techniques, 1752
- isotropic nanocomposite permanent magnets based on alpha-Fe/Nd₂Fe₁₄B, 1752-1754
- based on alpha-Fe/Sm-Co, 1755
- based on alpha-Fe/Sm-Fe-C, 1755
- based on alpha-Fe/Sm-Fe-N, 1755
- based on Fe-B/Nd₂Fe₁₄B, 1754-1755
- maximum energy product, 1750
- micromagnetically assessed magnetic properties, 1750-1751
- remanence, 1750
- utilization, 1756-1757
- Nanocomposites, 2453-2456
- nanocrystal composites, 2454
- nanoparticle, 2454
- nanoscale coatings, 2454
- nanotube, 2454-2456
- nanowire composites, 2454-2456
- polymer nanocomposites, 2453-2454
- Nanocrystal
- cadmium sulfide, 787-796
- optical, electronic properties, 789-790
- quantum mechanics/molecular mechanics calculations, 793-795
- semiconductor nanocrystals, 787
- semiempirical calculations, 791-793
- ferrite, 2323-2324
- superlattices, 711-714
- synthesized in colloidal self-assemblies, 2317-2327
- direct micelles, 2317
- divalent surfactant, 2318
- ferrite nanocrystals, 2323-2324
- reverse micelles, 2317-2318
- self-assemblies differing by sizes, shapes, 2318-2323
- Nanocrystal arrays, self-assembly, physical properties, 2245-2258
- Nanocrystal dispersed platinum particles, 2259-2268
- NanoCrystal Technologies, 256
- Nanocrystalline materials, 2289-2304
- bulk nanocrystalline substances, 2294-2298
- fatigue, 2269-2288
- grain size, 2301-2303
- interfaces on properties of, bulk nanosubstances, 2301-2303
- microstructure, bulk nanocrystalline substances, 2298-2300
- nanocrystalline powders
- colloid solutions, precipitation from, 2292-2293
- detonation, 2292-2294
- gas phase synthesis, 2291
- mechanical synthesis, 2293
- nonstoichiometric compounds, 2294
- plasmachemical synthesis, 2292
- self-propagating high-temperature synthesis, 2294
- superfine oxides, in liquid metals, 2294
- synthesis, 2291-2294
- thermal decomposition, 2293
- properties of, 2289-2291
- Nanocrystalline oxide
- aluminum, surface chemistry of, 3795-3804
- as catalysts/catalyst supports, 2535-2536
- magnesium, surface chemistry of, 3795-3804

- Nanocrystalline powder
 colloid solutions, precipitation from, 2292–2293
 detonation, 2292–2294
 electric explosion, 2292–2294
 gas phase synthesis, 2291
 mechanical synthesis, 2293
 plasmachemical synthesis, 2292
 reduction, 2293
 self-propagating high-temperature synthesis, 2294
 synthesis, 2291–2294
 thermal decomposition, 2293
- Nanocrystalline zeolite, environmental catalysts based on, 1137–1145
 assembly, 1139–1140
 hydrothermal synthesis, 1137–1138
 materials, 1140–1142
 environmental remediation, 1141–1142
 hydrocarbons, partial oxidation reactions of, 1140–1141
 organic contaminants, photocatalytic decomposition, 1142
 self assembly, 1137–1140
 synthesis, 1137–1140
 templating methods, 1138–1139
- Nanocrystallization, 2305–2315
- NanoCure System, anticancer drug delivery across blood-brain barrier, 256
- Nanodevice design, 2423–2425, 2429–2430
- Nanodiamond, 2329–2338
- Nanoelectromechanical sensors, 252
- Nanoencapsulation, bioactive substances, 2339–2354
 controlled release, 2339–2340
 liposomes, 2340–2343
 molecular inclusion complexes, 2348–2350
 polymer nanocapsules, 2345–2348
 polymer nanospheres, 2343–2345
- Nanoengineered capsule, with specific layer structures, 2355–2367
- Nanoengineered polymer microcapsules, 2369–2382
- Nanofabrication
 three-dimensional, using multiphoton absorption, 3905–3915
 via self-assembly, 2456–2457
- Nanofiber, polymer, prepared by electrospinning, 2931–2938
 concentration of polymer in solution, 2934
 electrical conductivity, 2933–2934
 electrospun nanofibers, applications of, 2935–2936
 electrospun polymer systems, 2934
 fiber formation, 2933–2934
 structure formation, 2934–2935
 surface free energy, 2933
- Nanofiller, surface modification of, 2919–2920
- Nanofilm, in giant magnetoresistance heads, 2383–2397
- Nanofiltration
 element design, 2404
 separations, 2399–2412
- Nanogranular phase, high strength alloys containing, 1393–1402
 glassy phase, nanostructured alloys with, 1397–1400
 mechanical properties, 1395–1400
- multiphase nanostructured alloys, 1395–1396
 nanoquasicrystalline alloys, 1396–1397
 nanostructure formation, 1393–1395
 single-phase nanocrystalline alloys, 1395
- Nanoindentation, hardness of nanobelt by, 1781–1782
- Nanoinstrument, DNA-based, computer-aided design, 833–844
 measurement principle, 834–836
 polyacrylamide gels, detection of DNA deformation in, 841
 solution, DNA deformation measured in, 836–841
 at surfaces, detection of DNA deformation, 841–843
- Nanolayered cobalt, thin film structural transition, on gallium arsenide, 3738
- Nanolayered copper, palladium thin film, on tungsten substrate, thin film structural transition, 3740
- Nanolayered thin film. *See* Thin film
- Nanolithography
 atomic force microscope, organized molecular films, 109–118
 anodization AFM nanolithography, 111–116
 constructive nanolithography, 110–111
 current sensing AFM, nanolithography using, 111
 dip-pen nanolithography, 109–110
 nanografting lithography, 110
 dip-pen, 923–931
 length-scale limitations, 2413–2422
- Nanomaterial. *See also under* type of nanomaterial
 bionanomaterial, 2451–2453
 biomineralization, 2452
 nanoparticle probes, 2452
 supramolecular materials, 2451–2452
 design theory, 2423–2433
 functional nanostructures, 2456
 diblock copolymers, self-assembly with, 2457–2459
 nanofabrication, via self-assembly, 2456–2457
 magnetic, 1665–1681
 combustion method, ferrites obtained by, 1695–1696
 complexation method for synthesis of, 1683–1685
 effect of particle shape, 1673
 fabrication of, 1665–1668
 giant magnetoresistance effect, 1674–1675
 magnetic domain, 1668–1670
 magnetization temperature/size dependence, 1670–1673
 polynuclear coordination compounds, thermal decomposition of, 1685–1695
 properties, 1668–1676
 quantum tunneling, magnetization, 1675–1676
 surface effects, 1673–1674
 synthesis, 1683–1699
- nanocomposites, 2453–2456
 nanoparticle, 2454
 nanoscale coatings, 2454
 nanotube, 2454–2456
 polymer nanocomposites, 2453–2454
- processing, 2435–2450
 structural, 3723–3735
 ductility, 3728–3730
 elevated temperature behavior, 3731–3732
 fabrication, 3723–3725
 fatigue properties, 3730–3731
 fracture, 3730
 strength, 3726–3728
 wear, 3731
 technology advances, 2465–2475
 trends, 2451–2463
 two-phase, 3730
- Nanomaterials Research Corporation, 2469
- NanoMed Pharmaceuticals, 256
- Nanomedicine, 247–248
- Nano-mesoscopic interface, 2211–2219
 integrated circuit, 2211–2212
 molecular electronics, 2211
 silicon, 2213–2215
- Nanometal, colloidal, as fuel cell catalyst precursors, 739–759
 metal salt reduction method, 741–743
 wet chemical reduction, 741–748
- Nanometer scale physical heterogeneity, 25–28
- NanoMill technology, nanocrystals, 256
- Nanomolding, 2872–2873
- Nanoparticle, 2454, 2477–2492. *See also under* specific type of nanoparticle
 assembly of electrical circuits from, 1028–1031
 biological weapon decontamination, 241–245
 block copolymers, 405–414
 dilute solution, 405–407
 charge carrier dynamics, 667–682
 metal nanoparticle, charge carrier dynamics of, 673–675
 semiconductor nanoparticle, charge carrier dynamics in, 667–673
 direct measurement determination, surface forces, 3805–3817
 Derjaguin–Landau–Verwey–Overbeek theory, 3807–3809
 electrostatic forces, 3807
 measurement techniques, 3810–3816
 steric force, 3809–3810
 van der Waals force, 3805–3807
 electronic switches, 1099–1101
- Nanoparticle assemblies, magnetic properties, 1761–1771
- Nanoparticle composite models, 2925
- Nanoparticle film, semiconductor, dimensionally graded, 913–921
- Nanoparticle manipulation, electrical displays based on, 1036–1037
- Nanoparticle patterning, laser-based deposition technique, 1565–1579
 optical field inside system, 1567–1569
 particle dynamics, 1570–1572
 setup optimization of system, 1569–1570
 solid-liquid interactions during patterning, 1572–1578
 solid-liquid interfacial energy, 1572–1573
 suspensions, 1574–1575
 transported droplets, 1575–1577
- Nanoparticle probe, 2452
- Nanoparticle sensor, 2484–2487
- Nanoparticle supported catalysts, 2531–2535

- Nanoparticle suspension, phase behavior of, 2813–2824
 hard sphere behavior, 2814–2816
 soft repulsions, 2816–2817
 weakly attractive suspensions, 2817–2821
- Nanoparticle-based optical nanosensors, 2764–2765
- Nanoparticle-filled polymer properties, 2920–2923
 electrical properties, 2923
 mechanical properties, 2920–2922
 optical properties, 2922–2923
 thermal properties, 2922
- Nanoparticle-labeled antibodies, antigens, luminescence of, 1647–1653
- Nanoparticle-polymer mixtures, supramolecular networks synthesized in, 3785–3793
 binary particle systems, 3790–3792
 diblock/particle mixtures, morphology of, 3786–3787
 models, 3786–3788
 particle size, 3788–3790
 solid polymeric composites, micromechanical behavior of, 3787–3788
- Nanoparticulate platform, for drug delivery, 256
- Nanophase ceramics, as nanobiomedical implants, 266–269
- Nanophase material, surface properties of, 265
- Nanophase metal, as nanobiomedical implants, 269
- Nanophase polymer, as nanobiomedical implants, 269–270
- Nanophase powder, mechanosynthesis, 1787–1785
 industrial trends, 1793–1794
 kinematic, mechanical aspects, 1788–1789
 kinetics, 1789–1791
 mechanical aspects, 1788–1789
 mechanosynthesis of Fe₃C, 1792–1793
 thermodynamics, 1789
- Nanopore sensor, 252
- Nanoporosity
 binary alloys, 893–902
 tunable, templating aerogels for, 3843–3851
 drying methods, 3845–3849
 sol-gel synthesis, 3843–3844
 tailoring nanoporous material, 3849–3850
 template materials, 3844–3845
- Nanoporous anodic aluminum oxide, optical anisotropy in, 3685–3695
 anodization, aluminum thin-film samples, 3685–3686
 spectroscopic ellipsometry, 3688–3693
- Nanoporous metals, formed by dealloying, 893–896
- Nanopowder, metallic, 1921–1933
 alloying reactions, pressed pellets, 1929
 applications, 1927–1930
 energetics, 1927–1928
 explosives, 1928–1929
 gun propellants, 1929
 nanostructures, 1930
 pyrotechnics, 1929
 rocket propellants, 1928
 self-heating synthesis, 1929
 chemical properties, 1924–1927
 electroexploded, characteristics, 1924
 handling, 1931
 inks, electrically conductive, 1929–1930
 nanometal processes, 1921–1924
 pastes, electrically conductive, 1929–1930
 physical properties, 1924–1927
- rocket propulsion, 1935–1945
 Alexgel applications, 1942–1943
 aluminized gels, development, 1939–1940
 "combustion" in nitrogen, 1942
 environmental issues, 196–1937
 gelled aluminized propellants, mechanisms of combustion, 1938–1939
 hybrid propellants, Alex as additive to, 1938
 hydrocarbon-based liquid rocket engines, 1942
 hydrocarbon-based RBCC systems, 1942
 ignition delay measurements, 1940
 liquid hydrogen engines, 1943
 in liquid monopropellants, 1936
 liquid propellants, Alex as additive to, 1938
 for liquid rocket engines, 1935–1936
 nanometal powder fuels, 1937–1942
 pulse detonation engines, 1942–1943
 small rocket engine tests, 1942
 solid propellants, Alex as additive to, 1937–1938
 for solid rocket engines, 1935
 safety, 1931
 shipping of, 1931
- Nanoquasicrystalline alloys, 1396–1397
- Nanoreactor, schematic of, 712
- Nanoribbon, 467–470
 metal oxide, 461–473
- Nanoscale, 247
 charge transport, 702–705
 Nanoscale charge storage, 702
 Nanoscale coatings, 2454
 Nanoscale polymer carriers, for controlled drug delivery, 255–256
- Nanoscale ring self-assembly, ring structures, 3284–3285
- Nanoscale site control, semiconductor, quantum dots, 3247–3249
- Nanoscale surface, potential implants, 266
- Nanoscale tribology, 3927–3931
 applications, 3927–3930
 computer simulations, nanotribological behavior, 3929–3930
 experimental characterization, nanotribological behavior, 3928–3929
- Nanosensor
 fiber optic chemical, 2759–2761
 ion-sensitive fiber optic, 2760–2761
 nanoparticle-based optical, 2764–2765
 optical, 2757–2768
 nanobiosensors, 2757–2768
 quantum dot-based, 2764
- Nanoshaving, scanning probe lithography, 2975
- Nanoshells, for optical therapies, 256
- Nanosized channel lattices, heterogeneous surfaces with, 1357–1367
 regular nanochannel lattice, 1357–1360
 wetting instability models, 1360–1361
- NanoSpectra Biosciences, 256
- Nanosphere
 core-shell, 865–879
 composite capsules, 875
 hollow capsules, nanobottles, 870–875
 nanosized core-shell spheres, 866–870
 rare earth complex, encapsulation in nanobottles, 875–876
 silica nanobottles, preparation procedure of, 874
- polymer, 2343–2345
- Nanostructure
 based on conducting polymers, 2615–2626
 atomic force microscope lithography, 2621–2622
 capillaries, micromolding in, 2619–2621
 inverse opal formation, 2618–2619
 lithography, 2619–2623
 mask techniques, 2619–2623
 masks, 2622–2623
 polarized infrared absorption spectroscopy, 2616–2617
 scanning tunneling microscopy lithography, 2621
 solvent-assisted micromolding, 2619
 template synthesis, 2615–2619
- based on layered transition metal chalcogenides, 2617–2639
- derived from phase separated polymers, 2641–2656
- electronic, metal nanoparticle self-assembly into, 1829–1840
 1-D arrays, 1838
 2-D arrays, 1835–1838
 3-D arrays, 1835
 electronic applications, 1830–1833
 fabrication of ordered arrays, 1834–1838
 molecularly protected nanoparticle, 1829
 synthesis, 1833–1834
- hierarchically imprinted, separation of metal ions, 1369–1379
- ionic amphiphilic block copolymer monolayer air-water interface, 2519–2529
 at air-water interface, 2519–2529
- metal, photoexcitation synthesis, 1881–1894
 metal-dot deposition onto metal surface, photoinduced, 1886–1887
 nanoscale structural characteristics of, 1885–1886
 near-infrared optical response, metal thin film, 1890–1891
 photoinduced anisotropic agglomeration, gold nanoparticle, 1881–1885
 silver nanoparticle, photoinduced structural changes of, 1887–1890
- metallic nanopowders, 1930
 replicated by polymer molding, 2657–2666
 stability on surfaces, 3675–3683
 synthesized, by deposition of metals on microtubule supports, 2653–2659
- Nanostructure formation, 1393–1395
- Nanostructured catalyst, 2531–2537
 basic, 225–234
 basicity, defined, 225–226
 historical perspective, 225
 nanostructured materials, 226–232
 nanostructured materials
 carbogenic molecular sieves, 231–232
 hydrotalcite, 232
 mesoporous (alumino) silicates, 230–231
 zeolites, 227–230
- Nanostructured composite
 as nanobiomedical implants, 270–272
 using carbon-derived fibers, 2551–2561
 carbon fibers, 2551–2552
 composites, 2559–2560
 fiber-matrix interface, buried, monitoring, 2557–2559
 nanotubes, 2559–2560
 surface chemistry, 2552–2553
 x-ray photoelectron spectroscopy, 2553–2557

- Nanostructured material
 synthesized by mechanical attrition, 2571–2581
 brittle materials, 2573–2574
 contamination, 2579–2580
 mechanical alloying, 2572–2573
 mechanical milling, 2571
 mechanisms, 2575–2579
 nanocomposites, 2574–2575
 polymer blends, 2574
 powder consolidation, 2579–2580
 single-phase metals, 2575–2579
 synthesized by mechanical means, 2583–3593
 synthesized in supercritical fluid, 2595–2606
- Nanostructured surface, protein binding event detection, 1635–1646
- Nanostructured ultrastrong materials, 2607–2613
- Nanotechnology, cellular, tissue engineering, 248–251
- Nanotemplate engineering, for drug, vaccine delivery systems, 256
- Nanotransfer printing, 2870–2872
- Nanotribological behavior
 computer simulations, 3929–3930
 experimental characterization, 3928–3929
- Nanotube, 2454–2456, 2559–2560
 for biotechnology, biocatalysis, 3655–3666
 bioseparations, nanotube membranes for, 3663–3664
 fullerene carbon nanotubes, 3657
 peptide nanotubes, 3657–3660
 self-assembling lipid microtubes, 3656–3657
 template-synthesized nanotubes, 3660–3664
- carbon, 461–610, 1203–1211. *See also* Carbon nanotube
 fullerene solid, 1207–1209
 ice nanotubes inside, 1415–1424
 molecular properties, 1205–1207
 molecular structure, 1203–1204
 single-walled, 3605–3615, 3629–3639
 synthesis, 1204–1205
- carbon-derived fibers, nanostructured composites using, 2559–2560
- formation of, 60
- fullerenes, 1240–1241
- inorganic, synthesized by chemical transport reactions, 1457–1466
 applications, 1465
 crystal flakes, instability against bending, 1459–1460
 gold, nanotube alloyed with, 1461–1465
 interlayer distances, nanotube chirality, 1460–1461
 multiwall nanotubes, 1457–1461
 nucleation, 1458–1459
 plate-like crystal structures, 1457–1458
 silver, nanotube alloyed with, 1461–1465
 stacking-order, tube diameter and, 1460
- nanoparticle composite models, 2925
 organic, design theory, 2427–2428
 protein, as building blocks, 3065–3077
 single-walled carbon, field emission properties, density functional theory study, 3597–3604
 unrolled honeycomb lattice of, 576
- Nanotube electrode, carbon, 425–434
 atomic hydrogen, 429
 block-type carbon nanotube electrodes, 426
 electrochemical capacitors, 425–427
 electrochemical sensors, actuators, electrodes in, 430–431
 functionalization of carbon nanotubes, 427
 molecular hydrogen, 429
 secondary hydrogen battery, fuel cells, electrodes in, 429–430
 secondary lithium ion batteries, anodes, 427–429
- Nanotube interconnect, carbon, 435–459
 interconnect architectures, integration in, 441–442
 internanotube contacts, 439–441
 junctions, crossed-tube, 439–441
 synthesis, 435–439
 directed, 437–439
 nondirected, 436–437
- Nanotube self-assembly, hydrogen bonding, self-assembly directed by, 3408–3409
- Nanotube sensor, 2667–2676
- Nanotube surface functionalization, 1251–1268
 chemical functionalization strategies, 1263–1264
 inorganic interfaces, 1255–1258
 sidewall functionalization, 1252–1255
 solubilization, 1258–1261
 tube manipulation, 1264
- Nanowire, 467–470, 2068, 2595
 barcoded, 205–212
 barcoded rods, nonfluorescent bioassay using, 208
 biological multiplexing, 207–209
 bulk metals, reflectance values for, 207
 characterization, 206–207
 nanoelectronics, 207
 nanowire synthesis, 205
 reflectance image of nanowire, 206
 striped nanowire synthesis, 205–206
 tagging, nonbiological, 209
 uses for, 207–209
- composite, bending modulus of, 1776–1778
 design theory, 2423–2425
 encapsulated metallic, design theory, 2428
 mechanical properties of, 1773–1786
 molecular assembly of, 2019–2029
 air–water interface, charge-transfer complexes at, 2022–2023
 electrical conductivity, 2026–2027
 fabricating molecular-assembly nanowires, 2021–2022
 Langmuir–Blodgett technique, 2020
 magnetic properties, 2026–2027
 mica surface, molecular-assembly nanowires on, 2023–2025
 molecular conductors, 2019–2020
 nanowire, molecular-assembly structures within, 2025–2026
 supramolecular chemistry, 2020–2021
- polymer
 by controlled chain polymerization, 2951–2958
 fabrication of, 929–930
- Nanostructured catalytic materials, design, 2539–2550
- Naturally chiral surfaces, roughening of, 1119–1120
- Near-field microscopy techniques, 2677–2686
 Near-field Raman spectroscopy, 2687–2702
 metallic tips, 2695–2702
 micro-Raman, contrasted, 2692–2693
 Near-field scanning optical lithography, 2979–2980
 Near-field scanning optical microscopy, 351, 2687, 2703–2712, 2758–2759
 Near-field surface-enhanced resonance Raman spectroscopy, 2759
 Negative differential resistance, 2084–2085, 2152
 Nerve agents, detoxification of, 243
 Neuromorphic architectures, quantum dot based, 1080–1081
 Neutral biimidazolone complex, controlled crystal structures, 2061–2064
 Newton–Euler formulation, molecular manipulator dynamic design criteria, 2104–2105
- Nickel
 anion templated system, 57–59
 beta-ketoesters, hydrogenation, 1115–1117
 hydrogenation of beta-ketoesters on, 1115–1117
 Nickel-nitritriacetic acid, 2118
 Nicotinamide threads, 75
 Niobium/titanium multilayers, thin film structural transition, 3740–3741
 Niobium/zirconium multilayers, thin film structural transition, 3738
 Nitration, on lab-on-a-chip micro reactor, 1556
 Nitrile-based coordination cages, self-assembly of, 3417–3422
 N-octanol, surface tension, 1573
 Nonadecyltrichlorosilane, 2034
 Nonbiological tagging, 209
 Noncovalent functionalization, carbon nanotubes, 500–501
 Nonlinear near-field spectroscopy, 2709
 Nonlinear optical materials, self-assembly of organic films for, 3471–3480
 characterization, 3474–3476
 chromophore deposition, orientation, 3476–3478
 covalent/ionic self-assembly, nonlinear optical film fabrication, 3473–3474
 Nonlinear optical switches, design, 2428–2429
 Nonlinear transmission lines, 2680
 Nonstoichiometric compounds, nanocrystalline powders, 2294
 Nonviral systems, delivery obstacles for, 2940–2941
Nostoc commune biosensor, 377
 NRC. *See* Nanomaterials Research Corporation
 Nuclear assay methods, enhancement of, 1131–1133
 Nuclear industry, nanoceramics, 2244
 Nuclear magnetic resonance, 2136, 2186, 2409, 2508, 2826
 Nuclear Overhauser enhancements, 2125
 Nucleation
 homogeneous, atmospheric nanoparticle, 102–103
 island, predictions of, 1533–1545
 irreversible island formation, behavior of models, 1536–1538
 island nucleation process, 1538–1544

- Nucleation (*cont.*)
 of nanoparticle, in ultrathin polymer films, 2713–2719
 in ultrathin polymer films, 2713–2719
 Nucleobase-porphyrin derivatives, 2721–2729
 Nucleobase-substituted oligopyrrolic macrocycles, 2721–2738
 Nucleoside-substituted oligopyrrolic macrocycles, 2721–2738
- Octadecyltrichlorosilane, 2032
 Octadecyltriethoxysilane, 2037
 Office of Naval Research, 2077, 2191
 Off-specular scattering, vesicles, at silicon–water interface, 2775
 Oil-filled nanocapsules, 2739–2747
 Oily carriers, 1720
 Olefin disproportionation, mesoporous materials, 1806
 Olefins, thermoplastic, 3025–3026
 Oligomerization catalysts, mesoporous materials, 1804–1805
 Oligo(phenylene ethynylene), 2074
 Oligo(phenylene vinylene)s, 2180
 Oligopyrrolic macrocycles, 2721–2738
 One-dimensional electrically conducting polymeric nanostructures, 1015–1024
 molecular interactions as "soft" templates, 1017–1018
 synthesized on surfaces, 1019–1020
 using "solid" templates, 1015–1017
 ONR. *See* Office of Naval Research
 On-tube junctions, 440–441
 Optical absorption, carbon nanotubes, 580–586
 resonance Raman process, 583–586
 Optical anisotropy, nanoporous anodic aluminum oxide, 3685–3695
 anodization, aluminum thin-film samples, 3685–3686
 spectroscopic ellipsometry, 3688–3693
 Optical characterization
 self-assembled thin films, 3361–3371
 colloidal assemblies, 3364–3370
 effective medium theories, 3365–3366
 ellipsometric spectra, 3365
 gold colloid preparation, 3362–3364
 spectroscopic ellipsometry on thin island films, 3364–3365
 thin island film theory, 3366–3370
 self-formed quantum dots, 3230–3234
 electroluminescence, 3232–3234
 photoluminescence, 3230–3232
 time-resolved photoluminescence, 3232
 Optical force microscopy, 284
 Optical molecular devices, 2749–2756
 Optical nanosensors, 252–253, 2757–2768
 evolution of, 2757–2759
 nanobiosensors, 2757–2768
 Optical phonons, in self-assembled multiple germanium structures, 3204–3207
 Optical properties
 carbon nanotubes, 575–586
 metal nanoparticle ensembles, 1821–1828
 clusters of, 1822–1823
 linear arrays of, 1823
 metal, metallodielectric nanoparticle, 3-D superlattices of, 1825–1826
 nanoparticle assembly fabrication, 1821–1826
 surface plasmons, 1821
 two-dimensional arrays of, 1823–1825
- Optical therapies, nanoshells for, 256
 Optical waveguide lightmode spectroscopy, protein adsorption kinetics, under applied electric field, 3033
 Optically active structures, field-driven assembly, electrical functionality, 1034–1037
 Optoelectronics, 2177–2178
 Ordered multilayer polymer nanocomposites, barrier properties, 213–224
 multilayered polymer–polymer nanocomposites, 220–221
 polymer-layered aluminosilicate nanocomposites, 214–220
 Ordered vesicles, at silicon–water interface, 2769–2777
 Organellar chloride channel, 3699
 Organic compounds, anion-templated self-assembly, 69–81
 Gale's "anion–anion" assembled solid-state polymer, x-ray crystal structure, 77
 Gale's diamidopyrrole ligand, 77
 guanidinium-appended porphyrins, 76
 Hamilton's self-assembled solid-state hydrogen-bonded structure, ribbon arrangement of, 70
 Kruger's double helicate, molecular structure of, 76
 Mendoza's tetraguanidinium strand, double helicate structure self-assembly, 70
 Schalley's "stopping" rotaxane synthesis, anion template, 73
 Organic film self-assembly, for nonlinear optical materials, 3471–3480
 characterization, 3474–3476
 chromophore deposition, orientation, 3476–3478
 covalent/ionic self-assembly, nonlinear optical film fabrication, 3473–3474
 Organic molecular wires, 2178–2186
 Organic nanotubes, design, 2427–2428
 Organic thin-film composite membranes, 2401–2402
 Organic-based solar cells, 2879–2895
 Organized molecular films, atomic force microscope nanolithography, 109–118
 anodization AFM nanolithography, 111–116
 constructive nanolithography, 110–111
 current sensing AFM, nanolithography using, 111
 dip-pen nanolithography, 109–110
 nanografting lithography, 110
 Organofullerenes in water, 2779–2789
 Organometallic half-sandwich complexes, 3503–3504
 Organometallic molecular wires, 2186–2188
 Organophosphorus compound detection, 367–368
 Organosilanes, molecular assembly, 2031–2042
 chemisorption, fabrication of monolayers through, 2036–2040
 mixed monolayers, at air–water interface, phase separation, 2033–2036
 organosilane monolayers, at air–water interface
 formation of, 2031–2033
 via crystallization, 2031–2036
 Outer Helmholtz plane, 1995
 Oxafullerenes formation, 1184–1185
 Oxalate method, magnetic nanomaterial synthesis, 168–1689
- Oxidation, of carbon nanotubes, 496
 Oxide, 2791–2801
 Oxide nanobelts, bending modulus, 1778–1781
 Oxide nanoparticle, 2791–2801
 alloying reactions, 2796–2798
 electrolyte, 2798–2799
 lithium reactivity
 through conversion processes, 2796
 through insertion processes, 2791–2795
 Oxide polymorphs, energetic parameters for, 1148
 Oxide vacancies, nucleation. metal-oxide interface, 1900–1903
 atom trapping, 1900–1901
 cluster stability, impact on, 1901–1903
 Oxides, metal clusters on, 1813–1820
 cluster morphology, 1815–1816
 gold on TiO₂, 1818–1819
 metal deposition, 1814–1815
 palladium on Al₂O₃, 1816–1820
 substrate preparation, 1813–1816
 Oxometallate anions, 1129
 Oxo-vanadium, structure of, 56
 Oxygen passivation, silicon nanocluster simulation, 3554–3555
 Oxyhydroxide polymorphs, energetic parameters for, 1148
- Pacific Northwest National Laboratory, 2604
 Palladium, molybdenum, 59–62
 Palladium cage, route of formation of, 62
 Palladium carbonyl acetate, 2806
 Palladium nanoclusters, 2803–2811
 preparation, 2803–2811
 Palladium thin film, on tungsten substrate, thin film structural transition, 3740
 Palladium-based molecular triangle, crystal structure of, 61
 Palmitoyl, 9-octadecenoyl phosphatidylcholine, 2510
 Paper electrodes, carbon nanotubes, 507
 Paraoxon
 decontamination by nanoparticle, 242
 detoxification of, 243
 Paraquat, chemical structure, 379
 Partial oxidation of ammonia, on lab-on-a-chip micro reactor, 1556
 Paste electrodes, carbon nanotubes, 507
 Pastes, electrically conductive, metallic nanopowders, 1929–1930
 Pattern anodization, on aluminum surfaces, 83–88
 anodization cell, 83–84
 bulk aluminum sheets
 evaporated aluminum films on glass, 86–87
 Patterned substrate-driven synthesis, 438–439
 Patterned surfaces, colloidal micronanostructures assembled on, 725–738
 3-D colloid assembly, 726–728
 fundamental interactions in colloid systems, 725–726
 planar surfaces, 728–729
 structured colloid assemblies, 729–736
 PEBBLEs sensors, 2764
 Pentameric circular helicate, chloride-templated assembly of, 57
 Peptide nanotubes, 3657–3660
 Percolation, mesoscopic thermodynamics, 3902
 Perfluorododecyloxy propyltriethoxysilane, 2032
 Perfluorohexyl-ethyltriethoxysilane, 2037
 Perfluorooctyl]ethyltrichlorosilane, 2032

- Performance, power dissipation and, (Moore's law), 2197–2200
 limits of energy dissipation vs. performance, 2199
 predictions for CMOS technology, 2198
 single-electron transistors, 2198–2199
- Periodic schwarzites, fullerenes, 1241–1244
- Phase analysis light scattering, 1999
- Phase separated polymers, nanostructures derived from, 2641–2656
- Phase transfer
 on lab-on-a-chip micro reactor, 1556
 monosaccharides through noncovalent interactions, 2825–2833
- Phase transfer catalysts, 1807
- Phenylalanine, 266
 properties of, 3082
- Phenylenediacrylic acid amphiphile derivatives, 1610–1611
 photoreactive bolaform amphiphiles, 1610–1611
- Phonons in self-assembled multiple germanium structures, quantum dots, 3203–3211
- Phospholemmann, 3699
- Phospholipid sensors, 2764–2765
- Photoablation, 278–279
- Photochemical generation of singlet oxygen, on lab-on-a-chip micro reactor, 1556
- Photochemical isomerization, bolaform amphiphiles, 1615–1620
 azobenzene containing chromophores, 1615–1618
 photochemical isomerization, ionic strength, 1619–1620
- Photochemistry, membrane-coated nanoparticle, 2835–2842
 gold, 2835–2843
 metal particles, 2835–2843
 semiconductor nanoparticle, 2843–2846
 hydrogen production, 2845–2846
 photocurrents, photoelectrochemical cells, 2845
 spectral sensitization, 2844
 silica particles, 2846–2847
- Photocyanation, on lab-on-a-chip micro reactor, 1556
- Photoexcitation synthesis, metal nanostructures, 1881–1894
 metal-dot deposition onto metal surface, photoinduced, 1886–1887
 nanoscale structural characteristics of, 1885–1886
 near-infrared optical response, metal thin film, 1890–1891
 photoinduced anisotropic agglomeration, gold nanoparticle, 1881–1885
 silver nanoparticle, photoinduced structural changes of, 1887–1890
- Photoinduced electron transfer, 2751
- Photolithography, 284
 fabrication of multiphase organosilane monolayers through, 2036–2040
- Photoluminescence, 2252
 optical characterization, self-formed quantum dots, 3230–3232
- Photoluminescence of silica-based nanoscale materials, 1476–1477
- Photomultiplier tube, 2760
- Photon correlation spectroscopy, 284, 2739
- Photonic active structures, field-driven assembly, electrical functionality, 1034–1037
- Photonic crystal fiber, 2853–2867
- Photoreactive bolaform amphiphiles, 1610–1615
 diacetylene derivatives, 1612–1615
 layer-by-layer assembly, 1607–1622
 phenylenediacrylic acid amphiphile derivatives, 1610–1611
- Photovoltaic cells, 1037
- Photovoltaics, organic-based solar cells, 2879–2895
- Phyllosilicates, commonly used, 215
- Physical vapor deposition, 2889
- Physicochemical properties, atmospheric nanoparticle, 97–100
 chemical composition, 99–100
 physical characterization, 97–98
- Physisorption, gas, carbon nanotubes, 547–549
- Phytantriol, aqueous phase progression of, in excess water, 888
- Phytoremediation, 336
- Piezoelectric technique, microweighing in supercritical carbon dioxide, 1977–1978
- Pinned orbits, examples of, 650
- Plasmachemical synthesis, nanocrystalline powders, 2292
- Platinum
 alpha-ketoesters, hydrogenation, 1116
 hydrogenation of alpha-ketoesters on, 1116
 molybdenum, 59–62
 morphological evolution, impact on catalytic behavior, 2266–2267
- Platinum particles, nanocrystal dispersed, 2259–2268
- Platinum/cobalt multilayers, thin film structural transition, 3739
- Platinum-group element, composed of bimetallic nanoparticle, 1874–1875
- PNNL. *See* Pacific Northwest National Laboratory
- Poisoning, catalyst nanostructure deactivation, 3965
- Poisson–Boltzman equation, 169
- Polarized infrared absorption spectroscopy, 2616–2617
- Pollution, environmental, 331–334
 bioremediation, 331–341
 anaerobic, 332
 bioaugmentation, 332
 biostimulation, 332
 environmental pollutants, 331–334
 Exxon Valdez oil spill bioremediation project, 336–338
 hydrocarbons, 331–333
 techniques, 334–336
 Exxon Valdez oil spill bioremediation project, lessons from, 337–338
 hydrocarbons, 331–333
 metals, 334
 pollutants
 metals, 334
 polycyclic aromatic hydrocarbons, 333–334
 polycyclic aromatic hydrocarbons, 333–334
 techniques
 biofiltration, 335–336
 groundwater bioremediation, 334–335
 phytoremediation, 336
- Poly(2-dimethylamino)ethyl methacrylate, polymeric gene carrier, 2943
- Poly(3,4-ethylenedioxythiophene), 2620
- Poly(3-hexylthiophene), 2884
- Poly(4-aminobutyl)-L-glycolic acid, 2943
- Poly(4-styrenesulfonate), 2620
- Poly(acrylic acid), 2499, 2718
- Polyacrylonitrile, 2401
- Poly(alkyl cyanoacrylate), 2344
- Polyamidoamine dendrimers, 2943
- Polyampholytes, complexation of, 2900
- Polyaromatic amines, enzymatic synthesis, 3374–3375
- Polycyclic aromatic hydrocarbons, 333–334, 2330
- Poly-(dialkyldimethylammonium) chloride, 2347, 2611, 2715
- Poly(dimethylsiloxane), 2071, 2619, 2658
- Polyelectrolyte capsules, physicochemical reactions inside, 2376–2377
- Polyelectrolyte films, layer-by-layer assembly, 1591–1605
 catalyst applications, 1598–1600
 biocatalytic multilayer assemblies, 1598–1600
 inorganic catalysts, multilayer assemblies bearing, 1600
 membrane preparation, 1591–1592
 polyelectrolyte multilayers, materials transport across, 1592–1598
 alcohol/water mixtures, pervaporation of, 1592–1594
 gas permeation, 1592
 ion permeation, 1594–1596
 organic compounds, enantiomers, separation, 1596
 proteins, fouling behavior, separation of, 1596–1597
 salt transport under nanofiltration, 1596
- Polyelectrolyte microgels, nanoparticle in, metallation, 2909–2910
- Polyelectrolyte models, DNA, 2131–2133
- Polyelectrolytes, multilayer formation on colloid particles, 782–784
- Polyelectrolyte-surfactant complex, 2897–2902
 hollow spheres, 2900–2901
- Polyethersulfone, 2401
- Polyethylene, surface free energy, 1573
- Poly(ethylene oxide), conformation at different solid/liquid polymer interfaces, 3752
- Poly(ethylene oxide)-b-poly(L-lysine), 2899
- Poly(ethylene oxide)-b-poly(sodium methacrylate), 2897
- Poly(ethylene oxide)-g-poly(ethylene imine), 2898
- Poly(ethylene terephthalate), 2574
- Poly(ethylenedioxythiophene), 26222
- Polyethylene-oxide, 2520
- Polyethylenimine, 2941–2943
- Polyfunctional nanoparticle, 256
- Poly(glycolic acid), 2344
- Polyisobutylene, surface free energy, 1573
- Poly(lactic acid), 2344
- Poly(lactic-co-glycolic acid), 2344
- Poly-L-lysine, 2941
- Polymer brushes from clay surfaces, 2959–2971

- Polymer colloid surface, nanoparticle formed on, metallation, 2911–2912
- Polymer colloids, metallation, 2903–2915
- adsorbed polymer layer, nanoparticle with, 2912–2913
 - block copolymer micelles, nanoparticle formation in, 2903–2907
 - dendrimers, nanoparticle formation in, 2907–2909
 - functionalized polysilsesquioxane colloids, nanoparticle formation in, 2910–2911
 - nanoparticle formation inside, 2903–2911
 - polyelectrolyte microgels, nanoparticle in, 2909–2910
 - polymer colloid surface, nanoparticle formed on, 2911–2912
- Polymer encapsulation, in mesoporous materials, biomolecular approach to, 3383–3384
- Polymer molding, 2657–2666
- Polymer nanocapsules, 2345–2348
- Polymer nanocomposites, 2453–2454
- particle, carbon nanotube fillers, 2917–2930
- Polymer nanofibers prepared by electrospinning, 2931–2938
- concentration of polymer in solution, 2934
 - electrical conductivity, 2933–2934
 - electrospun nanofibers, applications of, 2935–2936
 - electrospun polymer systems, 2934
 - fiber formation, 2933–2934
 - structure formation, 2934–2935
 - surface free energy, 2933
- Polymer nanoparticle for gene delivery, 2939–2949
- nanoparticle formation, 2939–2940
 - nonviral systems, delivery obstacles for, 2940–2941
 - polymeric gene carriers, 2941–2944
 - chitosan, 2943
 - poly(2-dimethylamino)ethyl methacrylate, 2943
 - polyamidoamine dendrimers, 2943
 - polyethylenimine, 2941–2943
 - poly-L-lysine, 2941
 - polyphosphoester, 2943–2944
 - targeting, 2944
 - active targeting, 2944
 - passive targeting, 2944
 - in vivo application, 2944–2946
 - brain, 2945
 - liver, 2945
 - lung, 2945
 - muscle, 2944–2945
 - tumor, 2945
- Polymer nanospheres, 2343–2345
- Polymer nanowires
- controlled chain polymerization, 2951–2958
 - photopolymerization, 2953
 - scanning tunneling microscope, 2954–2955
 - self-ordered molecular layer, 2951–2953
 - fabrication of, 929–930
- Polymer polydimethylsiloxane elastomers, 395
- Polymer scaffolds, 2985–2986
- Polymer substrates, synthesis of nanoparticle, 2493–2505
- Polymer synthesis
- in micelles, 3381–3382
 - in novel surfactant gel mesophase, 3378–3381
 - in reverse micelles, 3375–3378
- Polymer-clay nanocomposites, 2959–2971
- Polymer-colloidal science, 391–392
- Polymeric, biomolecular nanostructures, scanning probe lithography, 2973–2983
- protein grafting, 2974
 - self-assembled affinity templates, 2973
 - surface-initiated polymerization, 2973–2974
- Polymeric light-emitting diode, 2618, 2619
- Polymeric matrices, chiroptical switching in, 2165–2166
- Polymeric nanostructures, electrically conducting, one-dimensional, 1015–1024
- molecular interactions as "soft" templates, 1017–1018
 - synthesized on surfaces, 1019–1020
 - using "solid" templates, 1015–1017
- Polymerized fullerenes
- ferromagnetism, 1662
 - magnetic behavior, 1655–1664
 - closed-shell carbon clusters, magnetic properties of, 1655–1656
 - ferromagnetic molecular TDAE-C₆₀, 1656–1657
 - fullerenes, polymerization of, 1657
 - light-polymerized fullerenes, ferromagnetism in, 12657–1659
 - pressure-polymerized fullerenes, ferromagnetism in, 1659–1660
- Polymer-mediated self-assembly of nanoparticle, 2985–2998
- catalytic applications, 2987–2990
 - highly organized polymer-nanoparticle assemblies, 2994–2996
 - nanoparticle assemblies, organized, 2990–2994
 - nanoparticle building blocks, 2986–2987
 - polymer scaffolds, 2985–2986
- Polymer-nanoparticle composites, 2999–3014
- catalysis, composites for, 3008–3010
 - clay-nanoparticle polymer composites, 3000–3001
 - with metallic, semiconductor nanoparticle, 3001
 - ordered assemblies, 3005–3008
 - polymer growth, 3001–3005
- Polymers, adsorption of, 23–34
- chemical heterogeneity, 28–32
 - flexible polymer adsorption, 29
 - globular protein adsorption, 29–32
 - modeling, 23–24
 - nanometer scale physical heterogeneity, 25–28
 - simulation studies, 24–25
- Polymethylmethacrylate, 2456, 2679
- surface free energy, 1573
- Poly(methylmethacrylate), 2040, 2574
- Polynuclear coordination compounds, thermal decomposition of, 1685–1695
- Polyol-terminated self-assembled monolayers, 395–398
- Polypeptides, helices of, design theory, 2428–2429
- Polyphenols, enzymatic synthesis, 3374–3375
- Poly(phenylenevinylene), 2618, 2619, 2877
- Polyphosphoester, 2943–2944
- Polypropylene, 3015–3025
- barrier, 3023
 - crystallization, 3020
 - electrical properties, 3025
 - flammability, 3024–3025
 - hat deflection temperature, 3025
 - mechanical properties, 3020–3023
 - rheology, 3023
 - structure, 3015–3020
 - thermal stability, 3024–3025
- Polypropylene nanocomposites, intercalated, 1483–1490
- clay intercalation, 1485
 - crystallization structure, 1485–1486
 - exfoliation structure, 1485
 - kinetics, 1485–1486
 - mechanical properties, 1487–1488
 - rheology, 1486–1487
 - synthesis, 1484–1485
- Polysaccharides, atomic force microscopy, 125–127
- Polysilsesquioxane colloids, metallation, nanoparticle formation in, 2910–2911
- Polystyrene, surface free energy, 1573
- Poly(styrenesulfonate), 2715
- Polyvinyl alcohol, surface free energy, 1573
- Polyvinyl chloride, surface free energy, 1573
- Polyvinylpyrrolidone, cross-linked, hydrogel nanoparticle synthesized by, 1403–1414
- ultrafine poly(N-vinyl pyrrolidone) nanoparticle, 1406–1412
- Porous alumina, nanoarrays synthesized from, 2221–2235
- Porous silicon microcavity, 343–350, 344
- bacterial biosensor development, targets for, 347
 - bacterium detection, 345–349
 - DNA detection, 344
 - lipopolysaccharide, structure of, 347
 - virus detection, 344–345
- Porphyrin surface, supramolecular aggregates, with controlled size, shape on, 3775–3777
- Porphyritic films, self-organized, on surfaces, 3484–3489
- Porphyritic materials, self-assembly on surfaces, 3481–3502
- applications, 3484
 - porphyrinoids, 3481–3483
 - self-assembled porphyritic materials on surfaces, 3489–3493
 - self-organized porphyritic films on surfaces, 3484–3489
 - supramolecular chemistry, 3483
 - supramolecular systems on surfaces, 3483–3484
- Porphyrinoids, 3481–3483
- Powder consolidation, nanostructured materials synthesized by, 2579–2580
- Powder microelectrodes, carbon nanotubes, 507
- Powders
- nanocrystalline
 - detonation, 2292–2294
 - electric explosion, 2292–2294
 - synthesis, 2292–2294
 - nanophase, mechanosynthesis, 1787–1785
- Power transformer cooling, 1738
- Predictions, CMOS technology, 2198
- Preformed core-shell latex particles, complexation of, 2901
- Pressure-polymerized fullerenes, ferromagnetism in, 1659–1660
- Printed nanostructures, photonic applications, 2869–2878
- Printing
- microcontact, 2869–2870
 - nanotransfer, 2870–2872

- Programmable devices, molecular electronics, 2081–2099
- Proline, 266
properties of, 3082
- Propellants, gun, rocket, metallic nanopowders, 1928, 1929
- Propulsion, rocket, metallic nanopowders, 1935–1945
- Alexgel applications, 1942–1943
hydrocarbon-based liquid rocket engines, 1942
hydrocarbon-based RBCC systems, 1942
liquid hydrogen engines, 1943
pulse detonation engines, 1942–1943
environmental issues, 196–1937
in liquid monopropellants, 1936
for liquid rocket engines, 1935–1936
nanometal powder fuels, 1937–1942
aluminized gels, development, 1939–1940
"combustion" in nitrogen, 1942
gelled aluminized propellants, mechanisms of combustion of, 1938–1939
hybrid propellants, Alex as additive to, 1938
ignition delay measurements, 1940
liquid propellants, Alex as additive to, 1938
small rocket engine tests, 1942
solid propellants, Alex as additive to, 1937–1938
for solid rocket engines, 1935
- Protein adsorption
atomic force microscopy study, 3041–3064
adsorbed protein structure, 3048–3049
adsorption mechanisms, 3054–3060
artifacts, 3044–3045
atomic force microscopy techniques, 3042
electrostatic effects, 3054–3055
force interactions, 3051–3054
growth mechanisms, 3056–3058
kinetics, 3055–3056
measurement techniques, 3041–3042
multilayer formation, 3058
nonuniform surfaces, 3049–3051
protein structure, 3058–3060
supramolecular organization, 3045–3048
chemical heterogeneity
flexible polymer adsorption, 29
globular protein adsorption, 29–32
principles of, 3087–3088
resisting, 389–390
thermodynamics of, 3088
- Protein adsorption kinetics, 3088
under applied electric field, 3031–3039
impedance measurements, 3032
local pH effects, 3038
optical waveguide lightmode spectroscopy, 3033
protein charge heterogeneity, 3038
quartz crystal microbalance, 3033
reflectometry, 3032–3033
solvent interfacial structure, 3038
surface-bound counterions, 3037
total internal reflection fluorescence, 3033
- Protein binding polymer nanoparticle, 282
- Protein interactions
nanophase materials for enhancing, 3090–3093
properties influencing, 3088–3090
with surfaces, 3087–3090
properties influencing, 3088–3090
protein adsorption, 3087–3088
protein orientation, principles of, 3088
- Protein nanotubes, as building blocks, 3065–3077
arrangement, 3067–3071
coating, 3065–3067
mechanical motion, 3071–3073
sensing, 3071
- Protein orientation, principles of, 3088
- Protein structure, 3079–3087
primary protein structure, 3079–3080
quaternary structure, 3086–3087
secondary structure, 3080
tertiary structure, 3080–3086
- Proteins
adsorption of, 23–34
chemical heterogeneity, 28–32
modeling, 23–24
nanometer scale physical heterogeneity, 25–28
simulation studies, 24–25
atomic force microscopy, 124–125
properties of, 3082
- Proximity x-ray lithography, 2413, 2419
- Pseudochiral, chiral, molecules, self-assembly at interfaces, 3431–3438
- Pseudoenantiomeric switches, in liquid crystal matrix, 2166–2167
- Pseudoenantiomers, chiral switches based on, 2160–2162
- Pseudomonas putida*, imaging, 139
- Pseudorotaxane crystal structure, 74
- P-type ATPases, chloride-conducting membrane protein, 3699
- Pulse detonation engines, Alexgel applications, 1942–1943
- Purity evaluation, carbon nanotubes, 494–495
- Pyramidal quantum dots, applications, 3218–3220
- Pyridine-based coordination cages, self-assembly, 3423–3426
- Pyrolytic carbon, orthopedic implant, 269
- Pyrotechnics, metallic nanopowders, 1929
- Pyrazole synthesis, on lab-on-a-chip micro reactor, 1556
- Pyrrolidine-functionalized molecular switch, 2164–2165
- Quantum chemical methods, extended systems, 1468–1471
- Quantum computing, limits of energy dissipation vs. performance, 2199
- Quantum confinement, silicon nanocrystals, 3563–3574
excited state properties, 3564–3573
density functional methods, 3567–3570
empirical pseudopotential method, 3564–3567
Kartree–Fock method, 3570–3571
passivated silicon nanocrystals, 3572–3573
tight binding method, 3567
- Quantum dot arrays
birefringence in, 3101–3105
electromagnetic properties, 3097–3107
- Quantum dot image processors, 1079–1084
dot capacitance, 1084
interdot resistance, 1082
measurements of circuit parameters, 1082
negative differential resistance, 1082–1084
quantum dot based neuromorphic architectures, 1080–1081
self-assembling neural network, 1082
"superdot" for image-processing applications, 1084
- Quantum dot lasers, 3109–3126
advantages of, 3109–3110
defect reduction techniques, 3117–3118
excited-state transitions, 3114–3116
high-power operation, 3121–3122
linewidth enhancement factor, 3120–3121
quantum dot array, equilibrium vs. nonequilibrium carrier distribution in, 3111–3112
reduced carrier lateral transport, 3121
temperature characteristics, 3118–3119
threshold current density, 3116–3117
time-response, 3119–3120
vertical cavity surface emitting lasers, 3122–3123
- Quantum dot polarizability, 3099–3100
nonlocality, 3100–3101
physical interpretation, 3100
- Quantum dot-based nanosensors, 2764
- Quantum dot-based neuromorphic architectures, 1080–1081
- Quantum dots
electronic coupling, 3127–3154
electronic switches, 1099–1101
inelastic light scattering, 3155–3166
electron quantum-dot atoms, 3162–3163
electronic ground state, 3156–3158
GaAs–AlGaAs deep-etched quantum dots, 3161–3162
InAs self-assembled quantum dots, 3162–3165
scattering mechanisms, 3159–3161
luminescence properties of, thermal effect on, 3873–3881
bulk semiconductors, optical properties of, 3873–3874
carriers transfer between quantum dots, 3877–3879
recombinations in quantum dots, 3875–3877
recombinations in simple confined systems, 3875
self-assembled, 3227–3235
electroluminescence, 3232–3234
electron diffraction, 3229
electron microscopy, 3229
electronic structures, 3213–3225
fabrication methods, 3227
lens-shaped dots, 3220–3223
optical characterization, 3230–3234
optical properties, 3213–3225
photoluminescence, 3230–3232
pseudopotential techniques, 3214–3217
pyramidal quantum dots, 3218–3220
single-particle Hamiltonian solution, 3215–3217
strain profile, 3214–3215
structural characterization, 3227
time-resolved photoluminescence, 3232

- Quantum dots (*cont.*)
 "two-body" interactions calculation, 3217
 x-ray scattering, 3229-3230
 self-assembled multiple germanium structures, phonons in, 3203-3211
 acoustic phonons, 3208-3209
 optical phonons, 3204-3207
 semiconductor, atomic ordering, 3237-3246
 Quantum dots made of cadmium selenide, 3167-3176
 formation of, 3168-3170
 microphotoluminescence, 3170-3171
 optical properties, 3170-3174
 selectively excited photoluminescence, 3171-3174
 Quantum dots made of metals, 3177-3202
 core-shell particles, 3191-3192
 ligand binding, effect of alloying on, 3192-3194
 metal nanoclusters, 3194
 nanocluster characterization, 3180-3183
 nanocluster matter, 3198-3199
 nanocluster synthetic methods, 3179-3180
 nanocluster/ligand binding studies, 3184-3185
 optical properties, core-shell nanocrystals, 3187-3191
 quantum dot arrays, 3194-3198
 synthesis optimization, 3183
 synthetic variables, 3185-3187
 Quantum electronics nanoparticle devices, electrically functional microstructures from, 1034
 Quantum Hall effect, single-electron transistor microscopy, 3301-3302
 Quantum rods made of cadmium selenide, anisotropy, 3255-3265
 dielectric properties, 3259-3260
 optical properties, 3256-3259
 Quantum tunneling, magnetic nanomaterials, 1675-1676
 Quantum wire based room temperature infrared photodetectors, 1076-1079
 origin of photoresponse, 1077-1079
 Quantum wire junctions, two-dimensional array, 658
 Quartz, 1149
 Quartz crystal microbalance theory, microweighing in supercritical carbon dioxide, 1981-1983
 Radiocesium, 1129-1130
 Raman near-field microscopy, 2707-2708
 Raman spectroscopy, 2690-2691
 carbon nanotube-conducting polymer composites, 3267-3279
 charge transfer, 3274-3277
 interfacial interactions, 3270-3274
 shear field processing, 3270
 Rare earth complex, encapsulation in nanobottles, 875-876
 Rare earth-doped lasers, amplifiers, 2861-2862
 Reactivity, carbon nanotubes, 495-496
 Receptor ₁-chromophore-receptor ₂ systems, 2749-2750
 Receptor ₁-spacer ₁-fluorophore-spacer ₂-receptor ₂ systems, 2753-2755
 Receptor-ligand interactions, dynamic measurements, 995
 Receptor-modified metal nanoparticle, 1841-1850
 anions, recognition of, 1844
 as catalysts, 1847-1848
 cations, recognition of, 1844
 fabrication of networks in, 1846-1847
 redox-active species, recognition of, 1843-1844
 rotaxanes on, 1846
 surfaces of, molecular recognition at, 1842-1844
 as templates, 1845-1846
 Receptors, design theory, 2425-2426
 Redox-responsive receptors, self-assembly of, 3503-3511
 metallamacrocyclic receptors, ion-pairs, 3504-3509
 organometallic half-sandwich complexes, 3503-3504
 Refraction, structural color from, 3713-3714
 Resonant probes, 2682-2683
 Resorcinarenes, 1308-1312, 1329-1337
 Reverse micelles, 2317-2318
 polymer synthesis, 3375-3378
 Ring structures from nanoparticles, 3281-3288
 micro-sized ring self-assembly, 3282-3284
 thermocapillary mechanisms, 3282-3283
 wetting mechanisms, 3283-3284
 nanoscale ring self-assembly, 3284-3285
 magnetostatic mechanisms, 3285
 polymer films, 3285
 self-assembly of macroscopic rings, 3281-3282
 Risk assessment, 3289-3295
 nature's complexity, matching, 3292-3293
 punctuated equilibrium, understanding, 3291-3292
 technologies, 3290-3291
 transformation of, 3290-3292
 Rocket propulsion, metallic nanopowders, 1935-1945
 Alexgel applications, 1942-1943
 hydrocarbon-based liquid rocket engines, 1942
 hydrocarbon-based RBCC systems, 1942
 liquid hydrogen engines, 1943
 pulse detonation engines, 1942-1943
 environmental issues, 196-1937
 in liquid monopropellants, 1936
 for liquid rocket engines, 1935-1936
 nanometal powder fuels, 1937-1942
 aluminized gels, development, 1939-1940
 "combustion" in nitrogen, 1942
 gelled aluminized propellants, mechanisms of combustion of, 1938-1939
 hybrid propellants, Alex as additive to, 1938
 ignition delay measurements, 1940
 liquid propellants, Alex as additive to, 1938
 small rocket engine tests, 1942
 solid propellants, Alex as additive to, 1937-1938
 for solid rocket engines, 1935
 Rotary motion, unidirectional, in liquid crystalline environment, 2173-2174
 Rotary motors, unidirection, sterically overcrowded alkenes as, 2169-2173
 Rotaxanes
 hydrogen bonding, self-assembly directed by, 3405-3406
 switchable, computational analysis of, 807-821
 Roughening, naturally chiral surfaces, 1119-1120
 Rubbery block copolymers, templating polymer crystal growth using, strongly-segregated semicrystalline, 3861-3862
 Ruthenium/iridium multilayers, thin film structural transition, 3740
 Rutile
 energetic parameters, 1148
 surface free energy, 1573
Saccharomyces carlsbergensis, imaging, 138
Saccharomyces cerevisiae, imaging, 134, 137
 Saier, chloride-conducting membrane proteins, 3699
 Salts, in soil, 1149
 Saponite, 215
 Sarin
 decontamination by nanoparticle, 241, 242
 structure of, 378
 Scanner artifacts, atomic force microscopy, 150-151
 Scanning electrochemical microscope, 2621
 Scanning electron micrograph, 2758
 Scanning electron microscope, 2401
 Scanning electron microscopy, 2072, 2272, 2372, 2514, 2578, 2610, 2631, 2740
 Scanning far-infrared microscopy, 2678-2680
 Scanning near-field infrared microscopy, 2678-2680
 Scanning near-field microwave microscopy, 2680-2683
 coaxial waveguides, 2681
 Scanning near-field optical microscopy, 2677-2678
 apertureless probes, 2677-2678
 fiber probes, 2677
 integrated probes, 2678
 Scanning probe lithography
 dip-pen nanolithography, direct-write, 2978-2979
 nanografting, 2975
 polymeric, biomolecular nanostructures, 2974-2978
 dip-pen nanolithography, 2975-2978
 nanoshaving, 2975
 near-field scanning optical lithography, 2979-2980
 Scanning single-electron transistor microscopy, 3297-3303
 imaging with, 3299-3302
 quantum Hall effect, 3301-3302
 surface charge patterns, 3300
 single-electron transistor
 nature of, 3297-3298
 as scanning device, 3298-3299
 Scanning thermal microscopy, 2680
 Scanning tunneling microscope, 2145, 2213
 Scanning tunneling microscopy, 351, 2071, 2180, 2621, 2677, 2695, 2709
 chiral pair self-assembled monolayers, 3305-3313
 iodination products of oleic acid, elaidic acid, monolayer of, 3309-3311
 oleyl alcohol iodination product monolayer, 3307-3309
 Scanning tunneling microscopy lithography, 2621
 Scanning tunneling microscopy-based microwave microscopy, 2681
 Scattering, structural color from, 3720-3721
Scenedesmus subspicatus biosensor, 376

- Schalley's "stoppering" rotaxane synthesis, anion template, 73
- Second-generation molecular motor, 2169–2173
- Sedimentation potential, 1000
- Sediments, environmental nanoparticle, 1151–1152
- Selectivity, chemical, interfacial phenomena and, 1505–1514
- molecular recognition, at interfaces, 1505–1506
- surfaces, chemical selectivity of, 1506–1511
- molecular interactions, 1506–1511
- molecular organization, 1508–1511
- molecular structure, 1506–1508
- Self-assembled acetamide phosphonic acids on mesoporous silica, 1055–1057
- Self-assembled monolayers
- effect of humidity, adhesion between surfaces coated with, 1–9
- layer-by-layer assembly of gold nanoclusters modified with, 1581–1590
- modification under vacuum conditions, 3315–3329
- alkanethiolate, 3321–3322
- atomic chlorine modification, 3322–3323
- atomic radicals, chemical modification with, 3319–3323
- electron-induced modification, 3317–3319
- radical modification, 3317
- sample preparation, 3317
- surface analysis, 3317
- vapor-phase metallization, 3317, 3323–3326
- x-ray-induced modification, 3317–3319
- surface nanostructure, wetting, 3331–3344
- Self-assembled multiple germanium structures, phonons in, quantum dots, 3203–3211
- acoustic phonons, 3208–3209
- optical phonons, 3204–3207
- Self-assembled nanoarrays, electrochemically, 1073–1085
- electrochemical self-assembly, 1073–1076
- anodization, 1075
- contacting nanowires, 1076
- electrodepositing compound semiconductor, 1075
- electrodepositing metal, 1075
- nanofabrication, 1073
- quantum dot image processors, 1079–1084
- dot capacitance, 1084
- interdot resistance, 1082
- measurements of circuit parameters, 1082
- negative differential resistance, 1082–1084
- quantum dot based neuromorphic architectures, 1080–1081
- self-assembling neural network, 1082
- "superdot" for image-processing applications, 1084
- quantum wire based room temperature infrared photodetectors, 1076–1079
- origin of photoresponse, 1077–1079
- Self-assembled silane monolayers, conversion of cyano to carboxylic termination, 3345–3359
- Self-assembled solid-state hydrogen-bonded structure, Hamilton's, ribbon arrangement of, 70
- Self-assembled thin films, optical
- characterization, 3361–3371
- colloidal assemblies, 3364–3370
- effective medium theories, 3365–3366
- ellipsometric spectra, 3365
- spectroscopic ellipsometry on thin island films, 3364–3365
- thin island film theory, 3366–3370
- gold colloid preparation, 3362–3364
- single-particle optical characterization, 3362–3364
- substrates, 3362
- Self-assembling lipid microtubes, 3656–3657
- Self-assembling systems, biomimetic, 287–294
- artificial self-assembling systems, 289–291
- constrained self-assembly, 289–290
- dynamic self-assembling systems, 291
- hierarchical self-assembly, 290
- self-healing structures, 290–291
- shape complementarity, recognition by, 290
- Self-assembly
- cavitand-based coordination cages, 3415–3430
- enlarged nitrile-based coordination cages, 3422–3423
- nitrile-based coordination cages, 3417–3422
- pyridine-based coordination cages, 3423–3426
- chiral, pseudochiral molecules at interfaces, 3431–3438
- cyclic peptides, hydrogen-bonded nanotubes, 3439–3457
- application status, peptide nanotubes, 3450–3454
- hydrogen-bonded nanostructures, 155–157
- layered double hydroxides, 3387–3398
- nanocolloidal gold films, 3459–3469
- kinetics, irreversible gold nanocrystal deposition, 3461–3466
- two-three-dimensional nanostructure, for electronic applications, 3513–3525
- Self-assembly directed by hydrogen bonding, 3399–3413
- catenanes, 3405–3406
- cyclic assemblies, 3401–3403
- helical structures, 3406–3408
- hydrogen-bonded polymers, 3409
- molecular capsules, boxes, 3403–3405
- molecular self-assembly, 3399
- rotaxanes, 3405–3406
- self-assembly of nanotubes, 3408–3409
- simple systems, 3400
- Self-assembly monolayers
- immobilization on, 355
- surface modification method, 352–353
- Self-assembly of macroscopic rings, nanoparticle, 3281–3282
- Self-assembly of nanoparticle, polymer-mediated, 2985–2998
- catalytic applications, 2987–2990
- highly organized polymer-nanoparticle assemblies, 2994–2996
- nanoparticle assemblies, organized, 2990–2994
- nanoparticle building blocks, 2986–2987
- polymer scaffolds, 2985–2986
- Self-assembly of organic films, nonlinear optical materials, 3471–3480
- characterization, 3474–3476
- chromophore deposition, orientation, 3476–3478
- covalent/ionic self-assembly, nonlinear optical film fabrication, 3473–3474
- Self-assembly of porphyrinic materials, on surfaces, 3481–3502
- applications, 3484
- porphyrinoids, 3481–3483
- self-assembled porphyrinic materials, 3489–3493
- self-organized porphyrinic films, 3484–3489
- supramolecular chemistry, 3483
- supramolecular systems, 3483–3484
- Self-assembly of redox-responsive receptors, 3503–3511
- metallamacrocyclic receptors, ion-pairs, 3504–3509
- organometallic half-sandwich complexes, 3503–3504
- Self-formed quantum dots, 3227–3235
- fabrication methods, 3227
- structural characterization, 3227
- electron diffraction, 3229
- electron microscopy, 3229
- x-ray scattering, 3229–3230
- Self-heating synthesis, metallic nanopowders, 1929
- Self-organized porphyrinic films on surfaces, 3484–3489
- Self-organized superstructures, molecular designs for, 2057–2066
- controlled crystal structures, 2057–2061
- by neutral biimidazolone complex, 2061–2064
- molecular metal building block, 2057
- Self-propagating high-temperature synthesis, nanocrystalline powders, 2294
- Semiconducting bolaform amphiphiles, layer-by-layer assembly, 1607–1622
- Semiconducting nanoparticle, 2479–2480
- Semiconductor, quantum dots
- atomic ordering, 3237–3246
- nanoscale site control, 3247–3249
- optical properties, 3252–3253
- site-controlled self-organization, 3247–3254
- mechanism of, 3249–3250
- three-dimensional site control, 3250–3252
- Semiconductor nanocrystals, cadmium sulfide nanocrystals, 787
- Semiconductor nanoparticle
- charge carrier dynamics in, 667–673
- layer-by-layer assembly of, 1628–1629
- photochemistry, 2843–3846
- Semiconductor nanoparticle films, dimensionally graded, 913–921
- Semicrystalline-glassy block copolymers, templating polymer crystal growth using, crystallization in nanoscale environments, 3855
- Semicrystalline-poor block copolymers, templating polymer crystal growth using, 3855–3858
- Semicrystalline-rich block copolymers, templating polymer crystal growth using, 3858–3860

- Semicrystalline-rubbery systems, templating polymer crystal growth using, 3860
- Sensing applications, molecular self-assembly, 1125–1135
- actinides, 1130
 - electrochemical heavy metal detection, 1131
 - heavy metal assay, 1130–1131
 - nanoscience, 1126–1128
 - mesoporous ceramics, functionalization of, 1126–1127
 - nanostructured materials, 1126
 - self-assembled monolayers, 1127–1128
 - nuclear assay methods, enhancement of, 1131–1133
 - oxometallate anions, 1129
 - radiocesium, 1129–1130
 - soft heavy metals, 1128–1129
 - sorbent materials, self-assembled monolayers as, 1128–1129
 - x-ray fluorescence, 1130–1131
- Sensors. *See also* Biosensors
- nanoparticle, 2484–2487
 - nanotube, 2667–2676
- Sensors based on chemi-currents, 3527–3537
- Separations, nanofiltration, 2399–2412
- Sequential adsorption, nanoscale domains, 3539–3549
- Serine, 266
- properties of, 3082
- Shell thickness dependence, core-shell hydrogel nanoparticle, 859–860
- Shipping of metallic nanopowders, 1931
- Sidewall functionalization, 497–500
- Silane monolayers, self-assembled, conversion of cyano to carboxylic termination, 3345–3359
- Silane self-assembled monolayers, 3539–3549
- Silica
- alkylsilane self-assembled monolayers on, 4–6
 - mesoporous
 - self-assembled acetamide phosphonic acids on, 1055–1057
 - thiol-terminated self-assembled monolayer on, 1054–1055
- Silica mass spectroscopy research, heterogeneous catalytic reactions, 1384–1385
- Silica particles, photochemistry, 2846–2847
- Silica surface functionalization, 1269–1272
- chemical reactions used to produce, 1270–1271
 - in chromatography, 1271–1272
 - immobilized enzymes, functionalized silica surfaces, 1273–1274
 - metal complex catalysts, anchored on silicas, 1272–1273
 - in polymers, dispersion media, 1274–1275
 - in solid-phase extraction, 1271–1272
- Silica-based nanoscale materials, photoluminescence of, 1476–1477
- Silicate nanocomposites, epoxy layered, aerospace applications, 45–54
- aerospace epoxy nanocomposites, 46
 - layered organosilicate, 45–46
 - layered silicate, 45–46
 - morphology characterization, 46–47
 - morphology development, 49–50
 - different curing agents, 50–51
 - primer layer for aircraft coating, 51–52
 - processing, 49–50
 - properties of, 47–49
- Silicon, 2213–2215
- indium arsenide islands on, 1439–1446
- Silicon microcavities, porous, 343–350
- bacterial biosensor development, targets for, 347
 - bacterium detection, 345–349
 - DNA detection, 344
 - lipopolysaccharide, structure of, 347
 - virus detection, 344–345
- Silicon nanocluster simulation, 3551–3562
- computational methods, 3552–3553
 - emission gaps via stokes shift, 3557–3560
 - impurity atom, 3553–3554
 - multiple oxygen termination, 3555
 - oxygen passivation, 3554–3555
 - surface passivation, 3553–3555
 - surface reconstructions, 3555–3557
- Silicon nanocrystals, quantum confinement, 3563–3574
- excited state properties, 3564–3573
 - density functional methods, 3567–3570
 - empirical pseudopotential method, 3564–3567
 - Kartree–Fock method, 3570–3571
 - passivated silicon nanocrystals, 3572–3573
 - tight binding method, 3567
- Silicon nanoparticle, 67–673
- Silicon-water interface, ordered vesicles, 2769–2777
- Silicotungstic acid, 2819
- Silver
- formation of cages, polymers with, 62–66
 - nanotube alloyed with, 1461–1465
- Silver halide nanoparticle, 673
- Silver nanoparticle assembly, surface plasmon spectra, 3819–3830
- Simulants, 381
- Single enzyme nanoparticle, biocatalytic, 235–245
- catalytic stability, 237–238
 - enzyme stabilization approaches, 236
 - kinetics, 238
 - mass transfer, 238
 - methacryloxypropyltrimethoxysilane, 236
 - synthesis, 235–236
 - transmission electron microscopy, 236–237
- Single molecule spectroscopy, 3575–3596
- detection methods, 3576–3580
 - spatial selection, 3577–3579
 - spectral selection, 3577
 - historical perspective, 3576
 - materials characterization, 3580–3590
 - verification, 3580
- Single molecules
- mechanical properties of, 139–140
 - superconducting nanowires templated by, 3761–3773
 - fabrication of, 3763–3765
 - properties of, 3761–3763
 - transport measurements, 3765–3771
- Single nanoparticle spectroscopy, 3821–3822
- Single-electron transistor microscopy, 3297–3303
- imaging with, 3299–3302
 - quantum Hall effect, 3301–3302
 - surface charge patterns, 3300
 - nature of single-electron transistor, 3297–3298
 - single-electron transistor as scanning device, 3298–3299
- Single-electron transistors, 2198–2199
- Single-layer quantum dot ensembles, 3128–3135
- island formation, 3128–3129
- Single-molecule force microscopy, 119–131
- Single-nanotube electrode, carbon nanotubes, 509
- Single-phase nanocrystalline alloys, 1395
- Single-walled carbon nanotubes, 2019, 2068, 2109, 3605–3615, 3629–3639
- actuation upon charge injection, 3610–3611
 - graphite intercalation compounds, 3610–3611
 - armchair, 3607–3608
 - capillary electrophoresis separation, 3617–3628
 - chiral, 3608
 - density functional theory study, field emission properties, 3597–3604
 - electronic properties, 3608–3610
 - field emission properties. density functional theory study, 3597–3604
 - geometry of, 3607–3608
 - graphene, structures from, 3629–3630
 - helical, rotational symmetries, 3631–3633
 - hydrogen storage, 557
 - super capacitors, 539–540
 - translational symmetries, 3630–3631
 - zigzag, 3608
- Single-walled nanotubes, 2190, 2633
- Sintering, catalyst nanostructures deactivation, 3965
- Size distributions, atmospheric nanoparticle, 95
- Size exclusion chromatography, 3180–3182
- Small amplitude atomic force microscopy, 3641–3654
- Smart nanotubes for biotechnology, biocatalysis, 3655–3666
- bioseparations, nanotube membranes for, 3663–3664
 - fullerene carbon nanotubes, 3657
 - peptide nanotubes, 3657–3660
 - self-assembling lipid microtubes, 3656–3657
 - template-synthesized nanotubes, 3660–3664
- Soft heavy metals, 1128–1129
- Soft tissue wound healing, sequential events of, 264
- Soil, nanoparticle in, 1148–1151
- Soil minerals, 1149
- Solar cells, organic-based, 2879–2895
- Sol-gel synthesis, templating aerogels for tunable nanoporosity, 3843–3844
- Sol-gel technique, 1909–1910
- Solid colloidal particle, liquid, interfacial forces between, 1491–1503
- deformable interfaces, interactions involving, 1493–1494
 - direct measurement, 1494–1498
 - deformable surfaces, 1496–1497
 - force curve analysis, 1497–1498
 - surface force measurement, 1494–1496
 - interfacial forces, 1491–1493
 - surface forces measurement, 1491
- Solid polymeric composites, micromechanical behavior of, nanoparticle-polymer mixtures, 3787–3788
- Solid rocket engines, rocket propulsion, 1935
- Solids, chirality of, 1113–1114
- Solid-state hydrogen-bonded structure, self-assembled, Hamilton's, ribbon arrangement of, 70
- Solvent-assisted micromolding, 2619
- Soman, decontamination by nanoparticle, 241–242
- Sorbent materials, self-assembled monolayers as, 1128–1129

- Sorption of metal ions, 170–171
- Spatially resolved force spectroscopy, 136–137
- Spectroscopic ellipsometry
optical anisotropy, nanoporous anodic aluminum oxide, 3688–3693
on thin island films, 3364–3365
- Spectroscopy, single molecule, 3575–3596
detection methods, 3576–3580
spatial selection, 3577–3579
spectral selection, 3577
historical perspective, 3576
materials characterization, 3580–3590
verification, 3580
- Spin-coated cyanogels, 3667–3674
film characterization, 3669
preparation, 3669
- Spinel, energetic parameters, 1148
- Spirulina subsalsa* biosensor, 377
- Spotting of DNA, immobilization technique, 958
- Spray pyrolysis, 1908
- Stainless steel
orthopedic implant, 269
titanium dioxide coatings, 3918–3925
- Stamps, high-resolution, 2869–2873
- StarPharma, 256
- Steric force, nanoparticle determined by direct measurement, 3809–3810
- Sterically overcrowded alkenes, as unidirection rotary motors, 2169–2173
- Streaming potential, 2000
- Structural color, 3713–3722
by diffraction, 3717–3719
from interference, 3714–3717
from refraction, 3713–3714
by scattering, 3720–3721
- Structural nanomaterials, 3723–3735
ductility, 3728–3730
elevated temperature behavior, 3731–3732
two-phase nanomaterials, 3732
fabrication, 3723–3725
processing, 3723–3725
fatigue properties, 3730–3731
fracture, 3730
strength, 3726–3728
wear, 3731
- Structural transitions in thin films, 3737–3747
cobalt/chromium multilayers, 3740
cobalt/copper multilayers, 3738–3739
cobalt/manganese multilayers, 3739
iron/nickel multilayers, 3739
iron/ruthenium multilayers, 3738
nanolayered cobalt, on gallium arsenide, 3738
nanolayered copper, palladium thin film, on tungsten substrate, 3740
niobium/titanium multilayers, 3740–3741
niobium/zirconium multilayers, 3738
platinum/cobalt multilayers, 3739
ruthenium/iridium multilayers, 3740
titanium nitride/aluminum nitride multilayers, 3740
titanium/fcc metal multilayers, 3741–3743
titanium/silver multilayers, 3737
- Submicron resolution, two-photon absorption polymerization, microstructures fabricated by, 3909–3912
- Sulfate permease, 3699
- Sulfate-polyacrylamide gel electrophoresis, 2118
- Sum frequency generation vibrational spectroscopy studies, molecular orientation at interfaces, 3749–3760
- Supercapacitors
carbon nanotube-conducting polymer composites in, 447–459
polymer composite, conducting, 447–449
prototype devices, 454–455
supercapacitors, 449–451
carbon nanotubes, 537–546
capacitor performance, 538
conducting polymer composites, 543–545
multiwalled nanotubes, 540–543
single-walled nanotubes, 539–540
for storage of energy, 537–546
- Superconducting nanowires, templated by single molecules, 3761–3773
fabrication of, 3763–3765
properties of, 3761–3763
transport measurements, 3765–3771
- Supercritical carbon dioxide
metal nanoparticle, 1851–1858
microemulsions, 1852
rapid expansion, supercritical solutions, 1851–1852
reactive supercritical fluid processing, 1852
silver nanoparticle, 1853–1855
silver sulfide nanoparticle, 1855–1856
microweighing, 1977–1990
gravimetric technique, 1977–1978
microweighing methods, comparison of, 1980
piezoelectric technique, 1977–1978
polymer films in supercritical CO₂, dissolution study, 1983–1984
quartz crystal microbalance theory, 1981–1983
- Supercritical drying, templating aerogels for tunable nanoporosity, 3847–3849
- Supercritical fluid, nanostructured materials synthesized in, 2595–2606
- Superfine oxides, in liquid metals, nanocrystalline powders, 2294
- Superlattices, nanocrystals, 711–714
- Superparamagnetism, magnetic nanomaterials, 1668–1670
- Superstructures, self-organized, molecular designs for, 2057–2066
controlled crystal structures, 2057–2061
by neutral biimidazole complex, 2061–2064
molecular metal building block, 2057
- Supported bilayers, 2507–2508
- Supramolecular aggregates
atomic force microscopy, 155
with controlled size, shape, on solid surfaces, 3775–3784
- Supramolecular chemistry, molecular assembly of nanowires, 2020–2021
- Supramolecular materials, 2451–2452
- Supramolecular mechanics, carbon nanotubes, 587–601
coalescence of nanotubes, as reversed failure, 597–598
elastic shell model, supramolecular morphology changes, 591–593
failure, relaxation mechanisms, 593–596
linear elastic properties, 588–589
strength-failure evaluation, kinetic approach, 596–597
supramolecular scale, tensegrity at, 598–599
van der Waals interactions, 589–591
- Supramolecular networks, synthesized in nanoparticle-polymer mixtures, 3785–3793
binary particle systems, 3790–3792
diblock/particle mixtures, morphology of, 3786–3787
models, 3786–3788
particle size, 3788–3790
solid polymeric composites, micromechanical behavior of, 3787–3788
- Supramolecular scale, tensegrity at, carbon nanotubes, 598–599
- Surface charge, mineral nanoparticle, origin of, 1991–1992
- Surface engineering, biosensors, 351–360
biomolecules, analytical techniques for detection of, 351–352
protein immobilization, 353–356
surface patterning, 356–357
- Surface forces, nanoparticle determined by direct measurement, 3805–3817
Derjaguin–Landau–Verwey–Overbeek theory, 3807–3809
electrostatic forces, 3807
measurement techniques, 3810–3816
atomic force microscopy, 3811–3812
for nanoparticle, 3812–3816
surface force apparatus, 3810–3811
total internal reflection microscopy, 3811
steric force, 3809–3810
van der Waals force, 3805–3807
- Surface molecular switches, 2153–2155
- Surface nanostructure, self-assembled monolayers, wetting, 3331–3344
- Surface patterning, biosensor applications, 356–357
- Surface plasmon spectra, silver, gold nanoparticle assemblies, 3819–3830
- Surface-assembly of, 2480–2482
- Surface-enhanced Raman scattering technique, 268
- Surface-initiated free radical polymerization, using cationic initiator derivatives, 2964–2966
- Surfaces
chemical selectivity of, 1506–1511
molecular interactions, 1506–1511
molecular organization, 1508–1511
molecular structure, 1506–1508
stability of nanostructures on, 3675–3683
- Surfaces coated with self-assembled monolayers, adhesion, 1–9
adhesion hysteresis, 5
alkylsilane self-assembled monolayers on mica, 6–8
on silica, 4–6
alkylthiol self-assembled monolayers, on gold, 3–4
capillary condensation, 1–3
pulloff forces, 4
- Surfactant gel mesophase, polymer synthesis, 3378–3381
- Suspensions, nanoparticle, phase behavior of, 2813–2824

- Switchable, programmable devices, molecular electronics, 2081–2099
- Switchable catenanes, computational analysis, 797–805
binding site selectivity origin of, 801
catenane systems dynamics, 799–801
co-conformational isomerism, 801–802
structural fundamentals, 798–799
- Switchable rotaxanes, computational analysis of, 807–821
- Switches
chiral
based on enantiomers, 2159–2160
based on pseudoenantiomers, 2160–2162
electronic, 1099–1111
carbon nanotubes, 1104–1107
molecular actuators, 1107–1109
nanoparticle, 1099–1101
quantum dots, 1099–1101
switches, 1101–1104
enantiomeric, in liquid crystal matrix, 2166
molecular, 2145–2157, 2159–2176
chemical bimolecular reactions, 2149
chemical switches, 2146–2149
chiroptical, sterically overcrowded alkenes as, 2159–2166
intrinsic, 2149–2153
molecules in interaction, 2147–2149
pyrrolidine-functionalized, 2164–2165
simple chemical conversions, 2146–2147
surface, 2153–2155
nonlinear optical, design theory, 2428–2429
pseudoenantiomeric, in liquid crystal matrix, 2166–2167
- Switching
chiroptical, in polymeric matrices, 2165–2166
liquid crystalline phases, 2166–2169
- Synthesis in polymer substrates, 2493–2505
- Tabun, structure of, 378
- Tagging, nonbiological, 209
- Tantalum, orthopedic implant, 269
- Tapping mode atomic force microscope, 988–991
- Targesome, 256
- Tartarate method, magnetic nanomaterial synthesis, 1686–1688
- Temperature-programmed-desorption system, hydrogen storage, 558
- Template synthesis, conducting polymers, 2615–2619
- Template-directed assembly, dinuclear triple-stranded helicates, 3831–3842
- Template-synthesized nanotubes, 3660–3664
- Templating aerogels for tunable nanoporosity, 3843–3851
drying methods, 3845–3849
evaporative drying, 3846–3847
removal of template material, 3849
supercritical drying, 3847–3849
sol-gel synthesis, 3843–3844
tailoring nanoporous material, 3849–3850
template materials, 3844–3845
- Templating polymer crystal growth using block copolymers, 3853–3865
amorphous systems, block copolymer phase separation, 3853–3854
large areas, patterning semicrystalline block copolymers over, 3862–3863
moderately-segregated systems, 3860–3861
rubbery block copolymers, strongly-segregated semicrystalline, 3861–3862
- semicrystalline systems, microphase separation in, 3854–3855
- semicrystalline-glassy block copolymers, crystallization in nanoscale environments, 3855
- semicrystalline-poor block copolymers, 3855–3858
- semicrystalline-rich block copolymers, 3858–3860
- semicrystalline-rubbery systems, 3860
- Tensegrity at supramolecular scale, carbon nanotubes, 598–599
- Tetracyano-P-quinodimethane, 2019
- Tetradecylammonium bromide, 2898
- Tetraethoxysilane, 2846
- Tetraethyl orthosilicate, 2541
- Tetrafluoroborate templated nickel square, anion templated system, 59
- Tetraguanidinium strand
double helicate structure self-assembly, 70
Mendoza's, double helicate structure self-assembly, 70
- Tetrahedral cage, 57
- Tetrahydrofuran, 2356
- Tetramelamine, atomic force microscopy, 156
- Tetramers, nanoparticle, 3822
- Tetrarosettes, atomic force microscopy, 156
- Tetrathiafulvalene, 2019, 2021, 2152
- Therapeutic devices, nanotechnology in, 247–261
- Therapeutics, nanotechnology in, 253–256
- Thermal conductivity
carbon nanotubes, 606–609
nanoceramics, 3867–3872
grain boundaries, scattering by, 3869–3870
inclusions, reductions by, 3871
increasing, 3871–3872
interaction processes, 3868
lattice thermal conductivity, 3867–3868
radiative component, 3870
reductions, 3868–3869
thin layers, reductions by, 3871
wave scattering by obstacles, 3870
- Thermal decomposition
nanocrystalline powders, 2293
polynuclear coordination compounds, 1685–1695
- Thermal effect, luminescence properties of quantum dots, 3873–3881
carriers transfer between quantum dots, 3877–3879
on optical properties of bulk semiconductors, 3873–3874
on recombinations in quantum dots, 3875–3877
on recombinations in simple confined systems, 3875
- Thermal properties of nanobridges, 3883–3891
breaking, 3887–3890
initial structures, 3884
melting, 3887–3890
oscillations, 3884–3886
- Thermodynamics, at meso-, nanoscale, 3893–3904
complex fluids, competition of mesoscales in, 3900–3902
finite-size scaling, 3900
fluctuations, role of, 3895
- Landau-Ginzburg mesoscopic functional, 3897–3898
mesoscale susceptibility, 3899–3900
nanoparticle, building, 3895–3896
percolation, 3902
- Thermomorphic allylic amination, 907
- Thermoplastic olefins, 3025–3026
- Thin films
mixed nanoparticle, layer-by-layer assembly of, 1623–1633
structural transformations, 3737–3743
structural transitions in, 3737–3747
cobalt/chromium multilayers, 3740
cobalt/copper multilayers, 3738–3739
cobalt/manganese multilayers, 3739
iron/nickel multilayers, 3739
iron/ruthenium multilayers, 3738
nanolayered cobalt, on gallium arsenide, 3738
nanolayered copper, palladium thin film, on tungsten substrate, 3740
niobium/titanium multilayers, 3740–3741
niobium/zirconium multilayers, 3738
platinum/cobalt multilayers, 3739
ruthenium/iridium multilayers, 3740
titanium nitride/aluminum nitride multilayers, 3740
titanium/fcc metal multilayers, 3741–3743
titanium/silver multilayers, 3737
- Thin island film theory, 3366–3370
- Thiocyanine, 2840
- Thiol-passivated gold nanoclusters, structural properties of, 1291–1292
- Thiol-terminated self-assembled monolayer on mesoporous silica, 1054–1055
- Threading of axle molecules through macrocycles, 195–204
daisy-chain polyrotaxane, 195
equilibrium constants, 198–203
chain length, branching, effects of, 200–202
pseudo-[2]-rotaxane formation, 197–198
solvent, effect of, 198–200
steric effects, 200
substituent effects, 200
terminal groups, influence of, 202–203
molecular threading, 195–197
riveted polyrotaxane, 195
- Three-dimensional nanofabrication, using multiphoton absorption, 3905–3915
- Threonine, 266
properties of, 3082
- Threshold current density, quantum dot lasers, 3116–3117
- Tight binding method, silicon nanocrystals, quantum confinement, 3567
- Time-resolved laser fluorescence spectroscopy, 170
- Time-resolved photoluminescence, optical characterization, self-formed quantum dots, 3232
- Tips, metallic, with near-field Raman spectroscopy, 2695–2702
- Tissue engineering, 247–261
nanotechnology for, 272
- Titania, gold nanoparticle on, 1297–1304
carbon monoxide oxidation, 1299–1301
decomposition of sulfur dioxide on, 1301–1302
- Titanium, orthopedic implant, 269
- Titanium dioxide coatings, on stainless steel, 3918–3925

- Titanium nitride/aluminum nitride multilayers, thin film structural transition, 3740
- Titanium/fcc metal multilayers, thin film structural transition, 3741–3743
- Titanium/silver multilayers, thin film structural transition, 3737
- Tobacco mosaic virus, 323–324
- Toluene, surface tension, 1573
- Total internal reflection fluorescence, protein adsorption kinetics, under applied electric field, 3033
- Total internal reflection microscopy, surface forces, nanoparticle determination, 3811
- Toxicity sensing, electrochemical methods for, 1066–1068
- Trabecular bone, orthopedic implant, 269
- Transdermal delivery, micro-/nanoscale needles for, 254–255
- Transistors, single-electron, 2198–2199
- Transition metal oxides, catalytic properties of, 1913–1914
- Transmission electron microscopic, 2467
- Transmission electron microscopy, 236–237, 2272, 2312, 2372, 2495, 2572, 2598, 2610, 2628, 2714, 2740, 2898, 3182–3183
after cryofracture, 980
- Transport properties, carbon nanotube membranes, 521–522
- Tribology, inorganic nanoparticle, 3933–3942
- Tribology at nanoscale, 3927–3931
applications, 3927–3930
computer simulations, nanotribological behavior, 3929–3930
experimental characterization, nanotribological behavior, 3928–3929
- Tributylamine, structure of, 378
- Triethoxybenzamide dendrimer, structure of, 907
- Trimers, nanoparticle, 3822
- Trimethoxymethylsilanes, 2847
- Trinitrotoluene, 2330
- Trioctyl phosphine oxide, 2479
- Triphenylthiol, electrostatic surface potential, 692
- Triple-stranded helicates, dinuclear, template-directed assembly, 3831–3842
- Tryptophan, 266
properties of, 3082
- Tryptophan synthase, properties of, 3082
- Tumor, gene delivery, polymer nanoparticle for, 2945
- Tumor necrosis factor, bound to colloidal gold nanocrystals, 256
- Tunable nanocrystal distribution, colloidal gold films, 1515–1523
electrostatic interactions, particle deposition, 1515–1517
gold nanocrystals, 1517–1518
nanocolloidal gold suspension, 1517
size distribution, 1517–1518
kinetics, nanocolloidal gold adsorption, 1519–1520
quantitative analysis, 1520–1521
saturation coverages, 1518–1519
spatial distribution, 1518–1519
- Tunable nanoporosity, templating aerogels for, 3843–3851
drying methods, 3845–3849
evaporative drying, 3846–3847
removal of template material, 3849
sol-gel synthesis, 3843–3844
supercritical drying, 3847–3849
tailoring nanoporous material, 3849–3850
template materials, 3844–3845
- Tungsten carbide-cobalt nanocomposites, 3943–3952
- Turbulent coagulation, collision kernels, 38–39
- Two-photon absorption polymerization, submicron resolution, microstructures fabricated by, 3909–3912
- Tyrosine, 266
properties of, 3082
- Ultra pure water, 2189
- Ultrafast scanning tunneling microscopy, 2682
- Ultrafine poly(N-vinyl pyrrolidone) nanoparticle, 1406–1412
- Ultrananocrystalline, 2331
- Ultrathin polymer films, nucleation of nanoparticle, 2713–2719
- Ultraviolet photoelectron spectroscopy, 2558
- Unidirectional rotary motors, sterically overcrowded alkenes as, 2169–2173
- Unidirectional molecular motor
light-driven, 2169
light-induced switching, 2159–2176
- Unidirectional rotary motion, in liquid crystalline environment, 2173–2174
- Vacuolating cytotoxin, 3699
- Vacuum conditions, self-assembled monolayer modification under, 3315–3329
alkanethiolate, 3321–3322
atomic chlorine modification, 3322–3323
atomic radicals, chemical modification with, 3319–3323
radical modification, 3317
sample preparation, 3317
semifluorinated
x-ray, electron-induced modification of, 3317–3319
x-ray-induced modification, 3318–3319
surface analysis, 3317
vapor-phase metallization, 3317, 3323–3326
x-ray-induced modification, 3317
- Valine, 266
properties of, 3082
- Van der Waals force, 3805–3807
- Van der Waals interactions
carbon nanotubes, 589–591
with fullerene, 1473
- Van Hove singularities, carbon nanotubes, 576–580
- Vanadium, anion templated system, 55
- Vapor condensation methods, 1907–1908
- Vapor-grown carbon fibers, 484–486
- Vapor-phase metallization, self-assembled monolayer modification, vacuum conditions, 3317, 3323–3326
- Variant alpha subunit, properties of, 3082
- Vector with docking site for gene therapy, 256
- Vegetative bacteria, nanoparticle decontamination, 244
- Vertical cavity surface emitting lasers, 3122–3123
- Vertically aligned quantum dots, electronic coupling in, 3135–3143
coupled quantum dots, 3140–3143
electronic coupling in quantum dot columns, 3138–3140
quantum dots columns, 3135–3137
theory of quantum dot vertical alignment, 3137
- Vesicle morphology, tip compression scheme, 937
- Vesicles, ordered, at silicon-water interface, 2769–2777
- Vibrational spectroscopy, 1475–1476
- Virus detection, porous silicon microcavities, 344–345
- Visible-light-induced hydrogen generation, metal nanoparticle catalyst, 1877
- Vitronectin, 268
- VivaGel anti-HIV dendrimer, 256
- Vogtle's anion-templated rotaxane synthesis, 72
- Wacker oxidation, 2807–2809
- Warfare agent detection, biosensors for, 375–388
- Water
organofullerenes in, 2779–2789
quality monitoring, toxic agents used for, chemical structures, 379
surface tension, 1573
- Water-insoluble drugs, NanoCap micellar nanoparticle, 256
- Weapon decontamination, by nanoparticle, 241–245
- Wetting, surface nanostructure, self-assembled monolayers, 3331–3344
- Wide-angle x-ray scattering, 2377
- Wires, molecular, 2177–2195
conductance, measurement of, 2189–2191
electronics, molecular, 2177
optoelectronics, 2177–2178
organic molecular wires, 2178–2186
organometallic molecular wires, 2186–2188
- X-ray absorption spectroscopy, 170
catalyst nanostructures, 3953–3972
catalyst deactivation, 3964–3966, 3965–3966
catalyst preparation, 3956–3960
catalyst regeneration, cycles, 3966
future developments, 3966
heterogeneous catalysts, 3955–3956
structural characterization, 3960–3964
- X-ray crystal structure
chloride complex, 64
Gale's "anion-anion" assembled solid-state polymer, 77
- X-ray fluorescence, 1130–1131
- X-ray photoelectron spectroscopy, 284, 2034, 2333, 2551, 2553–2557, 2599, 2673
nanostructured composites, 2553–2557
nanotube sensors, 2673
- X-ray reflectometry, monolayer structure investigated by, 2520–2528

- Yttria-tetragonally stabilized zirconia,
3973–3979
aqueous chemistry, 3973–3974
synthesis methods, 3974–3975
wet processing of nanosized particles,
3975–3976
- Zatomic force microscopy, imaging artifacts,
143–153
electronic artifacts, 151
scanner artifacts, 150–151
- Zeolite, 227–230, 1149
amide clusters supported in, 230
nanocrystalline, 1137–1145
assembly, 1139–1140
environmental remediation, 1141–1142
hydrocarbons, partial oxidation reactions
of, 1140–1141
hydrothermal synthesis, 1137–1138
materials, 1140–1142
organic contaminants, photocatalytic
decomposition, 1142
self assembly, 1137–1140
synthesis, 1137–1140
templating methods, 1138–1139
- Zeolite lattice, hydrothermal extraction of
aluminum from, 636
- Zeolite membranes, 1157–1166
in environmental separation, 1159–1161
for energy-efficient alcohol/water
separations, 1160–1161
H₂ separation from gas mixtures,
1160
for membrane reactors, 1161–1163
with combined separation, catalytic
functions, 1162–1163
with separation functions, 1161–1162
preparation of, 1158–1159
types, 1157–1158
- Zeolite pores
alkali metal clusters in, 229–230
alkali metal oxides in, 227–229
- Zeolite/silica mass spectroscopy research, high-
resolution mass spectrometry,
heterogeneous catalytic reactions,
1384–1385
- Zeta potential, 1991, 2741
mineral nanoparticle, 1998
measurement, 1998–2000
- Zigzag nanotubes, cross-sectional models of,
530
- Zigzag single-walled carbon nanotubes, 3608
- Zintl salt metathesis, 718–719
- Zirconia, yttria-tetragonally stabilized,
3973–3979
aqueous chemistry, 3973–3974
synthesis methods, 3974–3975
wet processing of nanosized particles,
3975–3976